Composite Science and Technology

Part 1

Edited by
S.M. Sapuan, F. Mustapha, D.L. Majid, Z. Leman,
A.H.M. Ariff, M.K.A. Ariffin, M.Y.M. Zuhri,
M.R. Ishak and J.Sahari

TRANS TECH PUBLICATIONS

Composite Science and Technology

Editor:
S.M. Sapuan
F. Mustapha
D.L. Majid
Z. Leman
A.H.M. Ariff
M.K.A. Ariffin
M.Y.M. Zuhri
M.R. Ishak
J. Sahari

Composite Science and Technology

Selected, peer reviewed papers from the
Eight International Conference on Composite Science and Technology (ICCST8) 2011,
Kuala Lumpur, Malaysia, March 22-24, 2011

Edited by

S.M. Sapuan, F. Mustapha, D.L. Majid, Z. Leman, A.H.M. Ariff, M.K.A. Ariffin, M.Y.M. Zuhri, M.R. Ishak, J. Sahari



Copyright © 2011 Trans Tech Publications Ltd, Switzerland

All rights reserved. No part of the contents of this publication may be reproduced or transmitted in any form or by any means without the written permission of the publisher.

Trans Tech Publications Ltd
Laubisrutistr. 24
CH-8712 Stafa-Zurich
Switzerland
http://www.ttp.net

Volumes 471-472 of
Key Engineering Materials 2-vol.-set
ISSN 1013-9826
Full text available online at *http://www.scientific.net*

***Distributed** worldwide by*

Trans Tech Publications Ltd.
Laubisrutistr. 24
CH-8712 Stafa-Zurich
Switzerland

Fax: +41 (44) 922 10 33
e-mail: sales@ttp.net

and in the Americas by

Trans Tech Publications Inc.
PO Box 699, May Street
Enfield, NH 03748
USA

Phone: +1 (603) 632-7377
Fax: +1 (603) 632-5611
e-mail: sales-usa@ttp.net

Conference Joint Chairs:
Professor Mohd Sapuan Salit (UPM)
Dr Faizal Mustapha (UPM)

ICCST8 Organizing Committee
Dr Dayang Laila Abang Abd Majid (UPM) - Secretary
Dr Azmah Hanim Mohamed Ariff (UPM) - Co-secretary
Dr Zulkiflle Leman (UPM) - Treasury
Dr Edi Syams Zainudin (UPM)
Dr Mohd Khairol Anuar Mohd Ariffin (UPM)
Dr Azlan Ariffin (USM)
Dr Md Enamul Hoque (Nottingham, Malaysia)
Dr Khalina Abdan (UPM)
Dr Nur Ismarrubie Zahari (UPM)
Professor Shamsudin Sulaiman (UPM)
Dr Suraya Mohd Tahir (UPM)
Dr Faieza Abdul Aziz (UPM)
Dr Rizal Zahari (UPM)
Dr Suraya Abdul Rashid (UPM)
Dr Alyani Ismail (UPM)
Dr Shahruddin Mahzan (UTHM)
Mohd Zuhri Mohamed Yusoff (UPM)
Mohamad Ridzwan Ishak (UPM)
Sahari Japar (UPM)

International Advisory Board
S Adali (South Africa)
H El Kadi (UAE)
N. Qaddoumi (UAE)
A. Tamimi (UAE)
T. Ibrahim (UAE)
Peter Beaumont (UK)
Michele Meo (UK)
M Gadalla (UAE)
J Abdalla (UAE)
J N Reddy (USA)
A Seibi (UAE)
AMS Hamouda (Qatar)
Faiz Mohammad (India)
S. Hiziroglu (USA)
Hairul Abral (Indonesia)
M Shokrieh (Iran)
H. Hosseini-Toudeshky (Iran)
A Christoforou (Kuwait)
N Merah (Saudi Arabia)
M. Reza Eslami (Iran)
N Al-Huniti (Jordan)
T Pervez (Oman)

Editorial Board

Editors

S.M. Sapuan
F. Mustapha
D.L. Majid
Z. Leman
A.H.M. Ariff
M.K.A. Ariffin
M.Y.M. Zuhri
M.R. Ishak
J. Sahari

Editorial Panels

Edi Syams Zainudin
Riza Wirawan
Md Enamul Hoque
Khalina Abdan
Nur Ismarrubie Zahari
Shamsudin Sulaiman
Suraya Mohd Tahir
Faieza Abdul Aziz
Rizal Zahari
Suraya Abdul Rashid
Alyani Ismail

Editorial Assistants

Mohd Shukri Ibrahim
Mohd Fairuz Abdul Manab
Hanifawati Inai
Basher Ahmed Ahmed Ali
Aji Isuwa Suleiman
Dandi Bachtiar
Yousuf Ali Gumaan El-Shekeil
M. Sayuti
Mohd Firdaus Abdul Rahman
Mohd Firdaus Abdullah
Umar Abdul Hanan
Nurhaniza Mohamad

Preface

ICCST conference series was founded in 1996 and was initially held in Durban, South Africa. ICCST8 is held in Kuala Lumpur, Malaysia and is jointly organized by Department of Mechanical and Manufacturing Engineering, Department of Aerospace Engineering, Engineering Composite Research Group of Faculty of Engineering, Universiti Putra Malaysia (UPM) and supported by American University of Sharjah meant to boost composite enthusiasts locally and the world as a whole.

The ICCST8 organizers received over 320 abstracts of papers from all over the world. However, only 204 papers were accepted for the conference and published in Key Engineering Materials. All papers have undergone review process by at least two experts in composites.

The objective of this conference is to bring together composite scientists, engineers and technologists to exchange ideas, to discuss the latest development and to present their work to the international composite community. ICCST8 have managed to gather researchers and scientists not only from Malaysia but also from countries such as Turkey, Iran, Kuwait, Australia, UK, Qatar, UAE, Indonesia, India, France, Germany, Japan, Saudi Arabia, Thailand, Oman, Poland and Czech Republic. The response is very encouraging and shows a common ground of interest in composites.

In this conference, composites research topics presented include mechanics of composites, infrastructural composites, non destructive evaluation and characterization of composites, fracture and fatigue of composites, numerical and mathematical modelling, ceramic matrix composites, metal matrix composites, composite manufacturing, polymer composites, smart materials and structures, nano composites, bio composites and structural health monitoring.

In UPM, the work presented in this conference were mainly based on research performed by various groups of researchers funded by various funding agencies such Ministry of Science, Technology and Innovation (MOSTI), Ministry of Higher Education (MOHE), Ministry of Agriculture and Agro-Based Industry (MOA), Economic Planning Unit (EPU), UN Industrial Development Organisation (UNIDO) and UPM internal grants to whom the researchers are greatly indebted.

The editors would like to thank the authors for their contributions, to the reviewers for their expertise and valuable comments. The editors would also like to thank the organizing committee and international advisory board for their tremendous support. Deep gratitude is extended to the American University of Sharjah for their trust in UPM in organising the conference in particular to Associate Professor Dr Hany El Kadi.

The editors would also like to thank Tourism Malaysia for promoting the conference, the Faculty of Engineering, UPM for the financial assistance, and the Ministry of Higher Education Malaysia for their consent to organize this conference.

The Editors

Table of Contents

Sponsors, Committees and Preface

Composite Fracture: Getting to the Heart of the Matter
P.W.R. Beaumont 1

Recent Developments in PA6/PP Nanocomposites
H. Azman, M. Imran, M.U.B. Wahit and H. Balakrishnan 7

Fabrication and Characterization of Unidirectional Silk Fibre Composites
M. Ahmed, M.S. Islam, Q. Ahsan and M.M. Islam 20

Effect of Carbon Black and Fly Ash Fillers on Tensile Properties of Composites
R.S. Raja, K. Manisekar and V. Manikandan 26

Producing Particleboard Using of Mixture of Bagasse and Industrial Wood Particles
T. Tabarsa 31

Critical Speeds for Carbon/Epoxy Composite Rotors in Spacecraft Energy Storage Applications
V. Renuganth, F. Mustapha, D.L.A. Abdul Majid, R. Zahari and R. Kahle 37

Influence of Polyacrilonitrile (PAN) Concentration on the Mechanical and Physical Properties of Electrospun Fibres
S.S.A. Karim, A.B. Sulong, C.H. Azhari, N.M. Hwei and M.R. Yusof 43

Manufacture of Composite Panel from Sugarcane Bagasse
N.S. Shahidan and S. Muhammed 49

Assessment of Strength Properties of Biocomposite from Oil Palm Frond
F.M. Fauzi and S. Muhammed 55

Mechanical Properties of Composite Panels from Rice Husk
N.A. Abu Bakar and S. Muhammed 59

Manufacturing of Wood-Plastic Composite from Completely Recycled Materials
T. Tabarsa, H. Khanjanzadeh and H. Pirayesh 62

Rheology and Processing of Ni Based Nano-Composite Pastes for Electronic Assembly
R. Durairaja, L. Chiawea, K.C. Leong, W.M. Chu and L.M. Suan 67

Immediate and Long-Term Deflection of Carbon Fiber Reinforced Polymer (CFRP) Concrete Beams
E. Ahmed and H.R. Sobuz 73

Flexural Performance of RC Beams Strengthened with Different Reinforcement Ratios of CFRP Laminates
H.R. Sobuz and E. Ahmed 79

Evaluation of Physical and Mechanical Properties of Paulownia Wood Core and Fiberglass Surfaces Sandwich Panel
M. Sobhani, A. Khazaeian, T. Tabarsa and A. Shakeri 85

Optimum Condition of Manufacturing Wood-Based Composite from Mixture of Wood Particles/Walnut and Almond Shells
H. Pirayesh, A. Khazaeian, H. Khanjanzadeh and A. Bahrinejad 91

Microstructure Characterisation of Ag_2O_3-Bi_2O_3 Composite Cathodes for Intermediate Temperature Solid Oxide Fuel Cells (IT-SOFCs)
Dedikarni, A. Muchtar, N. Muhamad and W.R. Wan Daud 97

A Review of Non-Destructive Thermography Techniques Toward Structural Integrity of Bio-Composites
Z. Dashtizadeh, A. Ali and A. Khalina 103

Effects of Different Particles Sizes of Graphite on the Engineering Properties of Graphites/Polypropylene Composites on Injection Molding Aplication
Iswandi, J. Sahari and A.B. Sulong 109

Mechanical and Morphological Properties Evaluation of HDPE/Organoclay Nanocomposites with Various Percentages of NR Content
E.Z.E. Zawawi, A.H. Sahrim and R. Rashid 115

Nano-Alumina and Radiation Effect on the Mechanical Properties of High Density Polyethylene/Hydroxy Apatite Composite
N. Akmil, C.A. Luqman, M. Ahmad and D.K.M. Zaman 121

Influence of Crystallite Size on Consolidation of Carbon Nanotube Reinforced AA 4032 Composite Powders by Equal Channel Angular Pressing
M.S.S. Saravanan, K. Sivaprasad and S.P. Kumaresh Babu 127

Thermal Free Vibration Analysis of Temperature-Dependent Functionally Graded Plates Using Second Order Shear Deformation
A. Shahrjerdi, F. Mustapha, S.M. Sapuan, M. Bayat, D.L.A. Abdul Majid and R. Zahari 133

Optimal Sintering Procedure to Fabrication of Functionally Graded Hydroxyapatite-Titanium
A. Shahrjerdi, F. Mustapha, S.M. Sapuan, M. Bayat, D.L.A. Abdul Majid and R. Zahari 140

Processing and Characterization of Palm Fiber-Polypropylene Composites
R. Kahraman, S. Abbasi and B. Abu-Sharkh 145

Effects of Antioxidants Content on the Physical and Mechanical Properties of Wood Plastic Composites
M.H. Ab Ghani and A.H. Sahrim 151

Effect of Loading Concentration on the Electrical and Hardness Properties of MWCNT/Epoxy Nanocomposites
R.N. Royan, A.B. Sulong and J. Sahari 157

Effect of Wet Oxidation on the Dispersion and Electrical Properties of Multi-Walled Carbon Nanotubes/Epoxy Nanocomposites
R.N. Royan, A.B. Sulong, H. Suherman and J. Sahari 162

Tensile and Impact Properties of Sugarcane Bagasse/Poly(vinyl Chloride) Composites
R. Wirawan, S.M. Sapuan, K. Abdan and R. Yunus 167

Notch Effect on Discontinuous Fiber Reinforced Thermoplastic Composites
A.K. Haldar and S. Senthilvelan 173

Fabrication of Porous LSCF-SDC Carbonates Composite Cathode for Solid Oxide Fuel Cell (SOFC) Applications
R. Jarot, A. Muchtar, W.R. Wan Daud, N. Muhamad and E.H. Majlan 179

Developing Packaging by Using Smart Material which Helps to Realize Spoilage in Yoghurt
B. Eker and A.A. Eker 185

The Effect of Alkali Treatment Mechanical Properties of Kenaf Fiber Epoxy Composite
S.A. Mutasher, A. Poh, A.M. Than and J. Law 191

Effect of Organic Modification of Muscovite on the Polypropylene Layered Silicate Nanocomposite
M.F. Ahmad Rasyid, H.M. Akil and J.M. Sharif 197

Evaluation of Corrosion Properties of Electroless NiP/Nano-SiC Composite Coatings
A. Zarebidaki and S.R. Allahkaram 203

Thermal Properties and Thermal Degradation Kinetics of Polypropylene/ Organomodified Ni-Al Layered Double Hydroxide (LDH) Nanocomposites Prepared by Melt Intercalation Technique
K. Kakati, A. Prakash and G. Pugazhenthi 209

Analysis of Energy Absorption on Pultruded Composite Tube under Oblique Loading
A.B. Sulong, A.A. Ariffin, J. Sahari and H. Suherman 215

Fatigue Life Prediction of Composite Materials: Artificial Neural Networks vs. Polynomial Classifiers
H.A. El Kadi 221

Investigation on Improvement of Mechanical Properties of Kenaf / E-Glass Fiber Composites by Mercerization Process
A.M. Ya'acob, A. Abu Bakar, I. Hanafi and D.K.M. Zaman 227

Influence of Cutting Parameters on Surface Roughness for Wet and Dry Turning Process
M. Yusuf, K. Anuar, N. Ismail and S. Sulaiman 233

Development of Biocomposite Wall Cladding from Kenaf Fibre by Extrusion Molding Process
A. Khalina, E.S. Zainudin, A.R.M. Faizal, H. Jalaluddin, A.H. Umar and W.N.W.N. Syuhada 239

Characterisation and Properties of Sintered Recycled Glass Utilising CIP Method
N.R. Rosli, J.M. Juoi, A. Shaaban and N.F. Ayoob 245

Nanotechnology in Pulp and Paper Industries: A Review
S.D. Mohieldin, E.S. Zainudin, M.T. Paridah and Z.M. Ainun 251

Oscillatory and Creep Recovery Test on Nano-Composite Lead-Free Solder Pastes (Nickel and Platinum Powder)
R. Durairaja, K.C. Leong, L.C. Wea and W.M. Chu 257

Progressive Damage Analyses of Composite Laminates Exhibiting Free Edge Effects Using a New Micro-Meso Approach
H. Hosseini-Toudeshky, A. Farrokhabadi and B. Mohammadi 263

Fabrication and Characterisation of $La_{0.6}Sr_{0.4}Co_{0.2}Fe_{0.8}O_{3-\delta}$-SDC Composite Cathode
H.A. Rahman, A. Muchtar, N. Muhamad and H. Abdullah 268

$LiCF_3SO_3$ – CeO_2 Composite Electrolytes Prepared by Sol-Gel Technique: Structural and Conductivity Studies
N.A. Dzulkurnain and N.S. Mohamed 274

Shape Factors for Irregular Glass Reinforced Plastic Pipes – An Analytical and Numerical Approach
I.K. Ismail and A. Seibi 279

Field Layout of Glass Reinforced Epoxy Pipeline – A Practical Approach
A. Seibi, T. Pervez, X.L. Qu and A. Khalaf 285

Cotton-Epoxy Composites: Development and Mechanical Characterization
P.P. Gohil and A.A. Shaikh 291

Optimizing Processing Parameters and Fiber Size for Kenaf Fiber Reinforced Thermoplastic Polyurethane Composite
Y.A. El-Shekeil, S.M. Sapuan, E.S. Zainudin and A. Khalina 297

Effect of Hydroxyapatite Reinforced High Density Polyethylene Composites on Mechanical and Bioactivity Properties
M.R. Husin, M.U.B. Wahit, M.R. Abdul Kadir and W.A.W.A. Rahman 303

Microanalysis Techniques for the Investigation of Interphases Formed between Thermoset and Thermoplastic Polymers: Scanning Electron Microscopy and Energy Dispersive X-Ray Analysis
M.T. Heitzmann, M. Hou, M. Veidt, R. Paton and R. Rasch 309

Measurements of Interface Fracture Strength between Fiber-Reinforced Composite Laminates and Thin Surface Films Using the Blister Test
M.T. Heitzmann, M. Hou, M. Veidt and R. Paton 315

Influence of Surface Modifications on Interfacial Interaction of Zeolite Filled Polymer Composites
N. Zaharri, N. Othman and Z.A. Mohd Ishak 320

Studies on Development, Bioactivity and Corrosion Behaviour of Nanostructured Titania/Hydroxyapatite Composite Layer on Cp Ti
K. Venkateswarlu, N. Rameshbabu, A.C. Bose, V. Muthupandi and S. Subramanian 325

Optimal Design by Elitist-Genetic Algorithm for Maximum Fundamental Frequency of Fiber Metal Laminated Plates
H.G. Bargh and M.H. Sadr-Lahidjani 331

Fundamental Frequency Optimization of Laminated Cylindrical Panels by Elitist-Genetic Algorithm
M.H. Sadr-Lahidjani and H.G. Bargh 337

Finite Element Analysis of Fibre Reinforce Concrete Beam Subject to High Temperature by Using EURO-Code Models
Z.K. Awad and T.F. Yusaf 343

Responses of Aging Treatment to the Behavior of Aluminum Alloy with Addition of 0.02% Zirconium Element
M.S. Zakaria and A.B. Ismail 349

Poly(vinylidene Fluoride)/Microcrystalline Cellulose Nanocomposites with Enhanced Compatibility and Properties
X.G. Tang, M. Hou, J. Zou and R. Truss 355

Simultaneous Optimization for Multiple Responses on the Compression Moulding Parameters of Composite Graphite – Polypropylene Using Taguchi Method
M.Z. Selamat, J. Sahari, N. Muhamad and A. Muchtar 361

Modeling and Analysis of Elastoplastic Impacts on Supported Composites
M.A. Majeed, A.S. Yigit and A.P. Christoforou 367

PVDF-HFP-$NH_4CF_3SO_3$-SiO_2 Nanocomposite Polymer Electrolytes for Protonic Electrochemical Cell
N. Muda, S. Ibrahim, N. Kamarulzaman and N.S. Mohamed 373

Li_2CO_3 – Al_2O_3 Composite Solid Electrolytes Prepared by Sol Gel Method
M. Sulaiman, A.A. Rahman and N.S. Mohamed 379

Measurement on Strain Rate Sensitivity and Dynamic Mechanical Properties of Various Polymeric Materials
M.F. Omar, H.M. Akil and A.A. Zainal 385

Sandwich Composites of Glass Fibre Panel and Polyurethane/Coconut Coir Foam Core (GFRP - PUC)
M.A. Azmi, H.Z. Abdullah and M.I. Idris 391

The Study of Biodegradable Thermoplastics Sago Starch
A. Zuraida, H. Anuar and Y. Yusof 397

Cotton Reinforced Biopolymer Matrix Composite: Effect of Curing and Aging Conditions on its Mechanical Properties
A. Zuraida, Y. Yusof, H. Zahurin and M.Y. Fauziah 403

Comparison on Rheology Properties of Polypropylene and Polyethylene as Binder System with Stainless Steel 316L for Metal Injection Moding
M.F. Abdullah, A.B. Sulong, N. Muhamad, M.I.H. Chua Abdullah and N.H.N. Yahya 409

Optimizing the Curing Process of Epoxy-Clay Nanocomposites
M. Al-Qadhi, N. Merah and K. Mezghani 415

Effect of Mg Content on the Characteristics of Al/SiC Nanocomposite Powders Produced via *In Situ* Powder Metallurgy Method
M. Moazami-Goudarzi and F. Akhlaghi 420

A Semi-Energy Finite Strip Method for Post-Buckling Analysis of Relatively Thick Anti-Symmetric Cross-Ply Laminates
M. Hajikazemi, H.R. Ovesy and M.H. Sadr-Lahidjani 426

Large Deflection Behavior of Composite Laminated Plates under End-Shortening and Normal Pressure Loading Using a Semi-Energy Finite Strip Method
H.R. Ovesy, M.H. Sadr-Lahidjani, M. Hajikazemi and H. Assaee 432

Water Retention in Kenaf/Polypropylene Composites due to Repeated Immersion and Drying Conditions
W.H. Haniffah, A. Khalina and S.M. Sapuan 438

The Effect of Aging Temperature on Mechanical Properties of Banana Pseudostem Fiber Reinforced Polymer Composite
S.N.Z.M. Zain, Z.N. Ismarrubie and E.S. Zainudin 444

The Behavior of Construction Waste Concrete
S.I. Doh, C.H. Koid, G.Y. Ng, S.H. Teo and S. Adilen 449

Comparative Study of Physical Properties Based on Different Parts of Sugar Palm Fibre Reinforced Unsaturated Polyester Composites
J. Sahari, S.M. Sapuan, Z.N. Ismarrubie and M.Z.A. Rahman 455

Effect of Core Thicknesses on Impact Performance of Thermoplastic Honeycomb Core Sandwich Structure under Low-Velocity Impact Loading
N. Sawal and H.M. Akil 461

Boundary Condition Effects on the Parametric Stability of Moderately Thick Laminated Cylindrical Panels
J. Fazilati and H.R. Ovesy 466

The Effect of Silane Treatment on Tensile Properties and Morphology of Polypropylene/Recycled Acrylonitrile Butadiene Rubber/Rice Husk Powder Composites
S. Ragunathan, I. Hanafi and K. Hussin 472

The Effect of Silane Treatment on Processing Characteristic and Swelling Behavior of Polypropylene/Recycled Acrylonitrile Butadiene Rubber/Rice Husk Powder Composites
S. Ragunathan, I. Hanafi and K. Hussin 478

Parametric Study of Automotive Composite Bumper Beams Subjected to Frontal Impacts
J.M. Nursherida, B.B. Sahari and A.A. Nuraini 484

Effect of Sonication Time and Clay Loading on Nanoclay Dispersion and Thermal Property of Epoxy-Clay Nanocomposite
M.J. Adinoyi, N. Merah, Z.M. Gasem and N. Al-Aqeeli 490

Variation of Mechanical Properties of Epoxy-Clay Nanocomposite with Sonication Time and Clay Loading
M.J. Adinoyi, N. Merah, Z.M. Gasem and N. Al-Aqeeli 496

Investigation on Bending Strength and Stiffness of Sugar Palm Fibre from Different Parts Reinforced Unsaturated Polyester Composites
J. Sahari, S.M. Sapuan, Z.N. Ismarrubie and M.Z.A. Rahman 502

Properties of Kenaf Filled Unplasticized Polyvinyl Chloride Composites
M.F. Abdrahman and E.S. Zainudin 507

Rheological Behaviour of Polypropylene/Kenaf Fibre Composite: Effect of Fibre Size
A. Khalina, E.S. Zainuddin and I.S. Aji 513

Mechanical and Thermal Properties of Polyamide 6 Nanocomposite Toughened with Epoxidised Natural Rubber-25
N. Navid, U.W. Mat, H. Azman and M. Shaya 518

Comparative Study of Fiber Metal Laminates (FMLs) and Aluminum Skins for Polypropylene (PP) Honeycomb Core Sandwich Structure under Low Velocity Impact Loads
H.M. Akil and C.Y. Tan 524

Buckling and Post-Buckling Improvements of Laminated Composite Plates Using Finite Element Method
Z.A. Rasid, A. Ayob, R. Zahari, F. Mustapha, D.L. Majid and V. Renuganth 530

Thermal Buckling and Post-Buckling Improvements of Laminated Composite Plates Using Finite Element Method
Z.A. Rasid, A. Ayob, R. Zahari, F. Mustapha, D.L. Majid and V. Renuganth 536

Impedance Characteristics of Electrospun Nylon-6/TiO_2 Nanocomposite for Humidity Sensor
A. Hosseinmardi, M. Keyanpour-Rad and F.A. Hesari 542

A New Self Healing Method in Composite Laminates Using the Hollow Glass Fiber
M. Nademi, A. Mozaffari and A. Farrokhabadi 548

Viability of Synthetic Fibers to Replace Steel Wire Mesh in Composite Metal Decks Construction
S. Al Toubat, H. Ousman, S. Barakat and K.A. Rieder 552

Optimization of Injection Parameters Using 16µm Stainless Steel Powder (SS316L) at 63 Vol. %, 63.5 Vol. % and 64 Vol. % Powder Loading by Taguchi Method for Metal Injection Molding
M.I.H. Chua Abdullah, A.B. Sulong, N. Muhamad, M.F. Abdullah and C.H. Che Haron 558

Preliminary Review of Biocomposites Materials for Aircraft Radome Application
M.Y. Haris, D. Laila, E.S. Zainudin, F. Mustapha, R. Zahari and H. Zahurin 563

Fatigue Delamination Analysis of Composite Laminates with a Central Hole Using Interface Elements
H. Hosseini-Toudeshky, A. Jasemzadeh and B. Mohammadi 568

Mechanical and Physical Properties of Cement-Bonded Perticleboard Made from Tea Residues and Hardboards
H. Yel, A. Dönmez Çavdar and H. Kalaycioğlu 572

Responses of PFRP Cantilevered Channel Beams under Tip Point Loads
J. Thumrongvut and S. Seangatith 578

Effect of Nanoclay on the Mechanical and Thermal Properties of Rigid Polyurethane/Organoclay Nanocomposite Foams Blown with Cyclo and Normal Pentane Mixture
M. Valizadeh, M. Rezaei and A. Eyvazzadeh 584

Failure Modes of CFRP Flexural Strengthened Steel I-Beams
K. Narmashiri, M.Z. Jumaat and N.H. Ramli Sulong 590

Synthesis of MWCNT-Alumina Hybrid as Composite Reinforcement Using Nickel Catalyst
M.H. Abdul Kudus, H.M. Akil and M. Hasmaliza 596

Computer Simulation and Experimental Investigation of Solidification Casting Process
S. Suraya, S. Sulaiman, M.K.A. Arifin and M. Sayuti 601

Numerical Aspects of Delamination Modeling Using Interface Elements
H. Hosseini-Toudeshky, M. Jalalvand and M.H. Ghayour 606

A Review on the Performance of Adhesive Bonding in Polymer Composite Joints
S.N. Abdul Razak and A.R. Othman 610

Nonlinear Free and Forced Vibrations of Symmetric Laminated Panels
A. Shooshtari, S. Razavi, H.G. Bargh and M.H. Sadr-Lahidjani 616

The Partial Replacement of Halloysite Nanotubes (HNTs) and Precipitated Silica by Recycled Poly(ethylene Terephthalate) Powder on Cure Behavior, Tensile Properties and Morphology of Natural Rubber Composites
H. Nabil, I. Hanafi and A.R. Azura 622

The Influence of Recycled Poly(ethylene Terephthalate) Powder on Fatigue Life, Thermal Stability, and Morphology of Halloysite Nanotubes (HNTs) and Precipitated Silica Filled Natural Rubber Composites
H. Nabil, I. Hanafi and A.R. Azura 628

Analysis of MPV Dashboard Using SolidWorks and ABAQUS
M.K.A. Arifin, N.M.I.N. Hassan and M.F. Abdullah 634

Effect of Flame Retardants on Wood Plastic Composites-HDPE Based
M.R.Y. Hamid and A.H. Sahrim 640

Residual Strength and Failure Criterion of PP Thermoplastic Honeycomb Sandwich Subjected to Low Velocity Impact
A.F. Amir and A.R. Othman 646

Mechanical Properties of Carbon Fiber-Reinforced Polypropylene Composites
R. Yunus, N.H. Zahari, M.A.M. Salleh and N.A. Ibrahim 652

Free Vibration Analysis of Composite Sandwich Plate with Viscoelastic Core
S.S. Limouei, M. Sadighi and A. Ohadi 658

Mathematical Model for Axial Crushing of Hybrid Square Tubes
H. Akbarshahi, M. Sadighi, M. Shakeri and M. Mirzaei 664

Sintering of Fe-TiC Composite Prepared by Carbothermal Reduction of Hematite and Anatase
M. Salihin Hassin, P. Samayamutthirian and H. Zuhailawati 670

Optimizing Processing Parameters for Hybridized Kenaf/PALF Reinforced HDPE Composite
I.S. Aji, E.S. Zainuddin, A. Khalina and S.M. Sapuan 674

Effect of Fibre Size and Fibre Loading on Tensile Properties of Hybridized Kenaf/PALF Reinforced HDPE Composite
I.S. Aji, E.S. Zainuddin, A. Khalina and S.M. Sapuan 680

Tensile and Flexural Behavior of Hybrid Banana Pseudostem/Glass Fibre Reinforced Polyester Composites
I.N. Hanifawati, M.A. Azmah Hanim, S.M. Sapuan and E.S. Zainuddin 686

Retrofitting Pre-Cracked RC Beams Using CFRP and Epoxy Injections
R. Hawileh, A.K. Al-Tamimi, J.A. Abdalla and M.H. Wehbi 692

Flexural Performance of Strengthened RC Beams with CFRP Laminates Subjected to Cyclic Loading
R. Hawileh, J.A. Abdalla and A.K. Al-Tamimi 697

Experimental and Numerical Investigation of Mixed-Mode Fracture Properties of Woven Laminated Composite
M.H. Heydari and N. Choupani 703

Large Deflection Behavior of Relatively Thick Functionally Graded Plates under Pressure Loads Using Higher Order Shear Deformation Theory
M.H. Sadr-Lahidjani, M. Hajikazemi and M. Ramezani-Oliaee 709

A Novel Phenol – Based Composite Production: Features and Characterization
M. Ganji and T. Tabarsa 715

Mechanical Vibration Technique for Enhancing Mechanical Properties of Particulate Reinforced Aluminium Alloy Matrix Composite
M. Sayuti, S. Sulaiman, B.T.H.T. Baharudin, M.K.A. Arifin, S. Suraya and G. Esmaeilian 721

Effect of Quartz-Silicon Dioxide Particulate on Tensile Properties of Aluminium Alloy Cast Composites
M. Sayuti, S. Sulaiman, B.T.H.T. Baharudin, M.K.A. Arifin, T.R. Vijayaram and S. Suraya 727

Friction Forces between Sheet Molding Compound Charge and Mold Cavity Surface in Compression Molding
M.M. Shokrieh and R. Mosalmani 733

Free Vibration Analysis of Symmetrically Laminated Fully Clamped Skew Plates Using Extended Kantorovich Method
A. Fallah, M.H. Kargarnovin and M.M. Aghdam 739

Large Amplitude Thermo-Mechanical Vibration Analysis of Asymmetrically Laminated Composite Beams
A. Fallah, H.S. Alavijeh, A. Pasharavesh and M.M. Aghdam 745

Effect of Nanoclay on the Physical-Mechanical and Thermal Properties and Microstructure of Extruded Noncross-Linked LDPE Nanocomposite Foams
F. Zandi, M. Rezaei and A. Kasiri 751

Thermal Buckling Analysis of Moderately Thick Plates Using Functionally Graded Strips
M. Nassirnia, H.R. Ovesy and S.A.M. Ghannadpour 757

Polymer Based Filler Materials as Infill for GFRP Pile Connector
C.S. Sirimanna, M.M. Islam and T. Aravinthan 763

The Effect of Bentonite Clay on Green Compression Strength for Tailing Sands from Old Tin Mines in Perak State, Malaysia for Making Green Sand Casting Mould
A. Abdullah, S. Sulaiman, B.T.H.T. Baharudin, M.K.A. Arifin and T.R. Vijayaram 769

Effect of Electron Beam Irradiation (EB) on Gas Barrier Property of HDPE/EPDM Nanocomposites
N.A. Jamal, H. Anuar and S.B.A. Razak 775

Interfacial Shear Strength of Polylactic Acid-Kenaf Fibre Biocomposites
H. Anuar, A. Zuraida, B. Morlin and J.G. Kovács 781

Preparation and Thermal Properties of Cellulose/Layered Silicate Montmorillonite Nanocomposites Prepared via Ionic Liquids
M. Shaya, U.W. Mat, A.A. Yussuf and N. Navid 786

Investigation of Phase Transformation and Structure Evolution of Electrospun Copper Oxide Nanofibers during Thermal Annealing
D.J. Khadem, Z. Yaakob, S. Shahgaldi, W.R. Wan Daud and E.H. Majlan 792

Characterization of Tantalum Carbide Reinforced Copper Composite Developed Using Mechanical Alloying
E.M. Salleh and H. Zuhailawati 798

Effect of Milling Speed on Properties of Fe-NbC Composite Prepared by Mechanical Alloying
S.Z.M. Rasib and H. Zuhailawati 804

A Wavelet-Based Damage Detection Approach for Acousto-Ultrasonic *In Situ* Monitoring Systems
C.K. Liew and M. Veidt 809

The Influence of Mercerised Kenaf Fibres Reinforced Polylactic Acid Composites on Dynamic Mechanical Analysis
R.A. Talib, I.S.M.A. Tawakkal and A. Khalina 815

Investigation of Hardness of Short Abaca (*Musa Textile Nee*) Fibre-Reinforced High Impact Polystyrene (HIPS) Composites by Response Surface Methodology
E.H. Agung, S.M. Sapuan, M.M. Hamdan, D.K.M. Zaman and U. Mustofa 821

Influence of Processing Aids and Hydroxyapatite as Fillers on Flow Behaviour and Mechanical Properties of Ultra High Molecular Weight Polyethylene/High Density Polyethylene Composites
M. Ahmad, M.U.B. Wahit, M.R. Abdul Kadir and K.Z.M. Dahlan 827

Buckling Behavior of General Dome Ends under External Pressure, Using Finite Element Analysis
B. Abdi, H. Mozafari and A. Ayob 833

Feasibility of Manufacturing a Medium Density Fibreboard Made of 4-Year Old Rubber Tree RRIM 2020 Clone
H.A. Saffian, J. Harun, P.M. Tahir and A. Khalina 839

Curing Characteristics and Mechanical Properties of Rattan Filled Natural Rubber Compounds
K. Muniandy, I. Hanafi and N. Othman 845

The Effect of Chitosan Loading on the Properties of Chitosan Filled Epoxidized Natural Rubber Compounds
S.M. Shaari, I. Hanafi and N. Othman 851

Investigation on the Microwave Properties of Kenaf and Rice-Husk Fiber Reinforced Pla Composite Utilizing One-Port Coaxial Transmission Line Reflection Method
N.A. Zawawi, A. Ismail, A. Khalina and M.A. Mahdi 868

Influence of Mixed-Mode Ratio on Delamination Fracture Toughness and Energy Release Rate of Glass/Polyester Laminates
A. Khoramshahi and N. Choupani 874

Experimental and Numerical Investigation of the Mixed-Mode Delamination of PAN Based Carbon/Epoxy Composite Using Modified Arcan Fixture
M. Ziaee and N. Choupani 880

Effects of Thickness on Fracture Toughness of Carbon/Polyester Composite
M.H. Heydari and N. Choupani 886

Simulation of Cracks in Fiber Reinforced Composite Plate
P. Kumar and A. Kakyal 892

Effect of a Coupling Agent on Mechanical and Biological Properties of Polyetheretherketone/Hydroxyapatite Bioactive Composite for Prosthetic Medical Device
A.R. Rashidi, U.W. Mat and M.R. Abdullah 898

Impact Damage Detection in a Stiffened Composite Wing Panel Using Digital Shearography and Thermosonics
G. De Angelis, M. Meo, D.P. Almond, S.G. Pickering and U. Polimeno 904

Acoustic Emission Localization in a Composite Stiffened Panel Using a Time Reversal Algorithm
F. Ciampa and M. Meo 910

Multiscale Modeling of Hybrid Composite Structures
M. Růžička, J. Had, V. Kulíšek and O. Uher 916

Shell Mould Composite with Rice Husk
Z. Harun, N.H. Kamarudin, N.A. Badarulzaman and M.S. Wahab 922

Cotton Reinforced Biopolymer Matrix Composite: Effect of Ultraviolet (UV) on its Mechanical Properties
A. Zuraida, H. Anuar, H. Zahurin, D.L.A. Abdul Majid and M.Y. Fauziah 928

Characterisation and Properties of Sintered Glass-Ceramics Produced from Recycling Glass by Using Pressure-Less Method
N.F. Ayoob, J.M. Juoi, Z.M. Rosli and N.R. Rosli 933

Fiber Reinforced Composite Structure with Bolted Joint – A Review
K.J. Jadee and A.R. Othman 939

Development of Novel Polymer Composite Beam Using Ultrasonic Welding Process for Acetabular Cup Prosthesis
A. Goharian, A.R. Rashidi, M.R. Abdul Kadir, M.R. Abdullah and M.U.B. Wahit 945

Experimental Investigation and Finite Element Analysis of Dynamic Behavior and Damage of Glass/Epoxy Tubular Structures
M. Tarfaoui and P.B. Gning 951

Curing Characteristics, Fatigue Life and Morphological Properties of Natural Rubber Nanocomposites with Halloysite Nanotubes (HNTs)/Carbon Black (CB) Hybrid Filler
S.Z. Salleh, I. Hanafi and Z. Ahmad 957

Effects of Processing Temperature and Chemical Treatment on Tensile Strength of Kenaf Fiber - Reinforced Polypropylene Waste Composites
H. Judawisastra, F. Falencia and A.H.D. Abdullah 963

Damage Evolution in Structural Steel at Different Loading Conditions
R.M. Al-Himairee, F.H. Abed and A.K. Al-Tamimi 969

Modeling of Stiffness Reduction of Vibration Conveyor Springs Subjected to Ultra High Cyclic Loading under High Humidity
T. Yoshi, K. Okubo and T. Fujii 975

Lay-Up Design of Low Wind Speed Composite Turbine Blade
I.H. Nugroho, H. Judawisastra, M.G. Suada and M. Siswosuwarno 981

Effect of Stitching Density of Nonwoven Fiber Mat towards Mechanical Properties of Kenaf Reinforced Epoxy Composites Produced by Resin Transfer Moulding (RTM)
M.S. Salim, Z.A.M. Ishak and S. Abdul Hamid 987

Synthesis of TiO_2/Zno Core/Shell Type Nanocomposite via Sol-Gel Method
M.R. Golobostanfard, R. Ebrahimifard and H. Abdizadeh 993

Life Cycle Assessment of Particulate Recycled Low Density Polyethylene and Recycled Polypropylene Reinforced with Talc and Fiberglass
M. Al-Ma'adeed, G. Ozerkan, R. Kahraman, S. Rajendran and A. Hodzic 999

Differential Cubature Method for Static Solution of Laminated Shells of Revolution with Mixed Boundary Conditions
S.M. Mousavi 1005

Effects of Direct Current and Pulse Electrodeposition Parameters on the Properties of Nano Cobalt Coatings
S.R. Allahkaram, N. Towhid and M.S. Cheraghi 1010

Vibration of Nonlocal Euler Beams Using Chebyshev Polynomials
S.A.M. Ghannadpour and B. Mohammadi 1016

An Investigation on Relative Post-Buckling Stiffness Variations of Symmetrically Cross-Ply Laminates
S.A.M. Ghannadpour, H.R. Ovesy and M. Hajikazemi 1022

A Preliminary Study on Translational Kinetic Energy Absorption Using Coconut-Fiber (Coir) Sheets as a Potential Impact-Worthy Constituent in Advanced Aerospace Material
N.B. Affandi, A.S.M. Rafie, S. Basri, F.I. Romli, D.L.A. Abdul Majid and F. Mustapha 1028

Sugar Palm Fibre-Reinforced Unsaturated Polyester Composite Interface Characterisation by Pull-Out Test
Z. Leman, S.M. Sapuan and S. Suppiah 1034

Doping of Palladium in Silica Nanofibers via Electrospinning and Sol-Gel Synthesize as Hydrogen Storage Material
S. Shahgaldi, Z. Yaakob, D.J. Khadem, W.R. Wan Daud and E.H. Majlan 1040

Effect of Nickel Composition and Preparation Method for Production of Hydrogen via Glycerol Steam Reforming
H. Lukman, Z. Yaakob, I. Manal, W.R. Wan Daud and E.H. Majlan 1046

The Influence of Li on the Tensile Properties of Al-Mg_2Si Metal Matrix Composite
R. Khorshidi, M. Emamy and A.H. Raouf 1052

Effect of Fiber Loading on the Mechanical Properties of Kenaf Fiber Reinforced Thermoplastic Polyurethane Composite
Y.A. El-Shekeil, S.M. Sapuan, E.S. Zainudin and A. Khalina 1058

Flexural Mechanical Characteristic of Sawdust and Chipwood Filled Epoxy Composites
S. Hisham, A.A. Faieza, N. Ismail, S.M. Sapuan and M.S. Ibrahim 1064

Tensile Properties and Micromorphologies of Sawdust and Chipwood Filled Epoxy Composites
S. Hisham, A.A. Faieza, N. Ismail, S.M. Sapuan and M.S. Ibrahim 1070

A New Finite Fracture Mechanics Approach for Assessing the Strength of Bonded Lap Joints
P. Weißgraeber and W. Becker 1075

Metal Matrix Composites: Solidification Parameters of Aluminium-11.8% Silicon Alloy Reinforced with Titanium Carbide Particulates
N. Fatchurrohman, S. Sulaiman, M.K.A. Arifin, A.A. Faieza and B.T.H.T. Baharudin 1081

Parametric Study on Cohesive Element for Composite Fuselage Model
N.W. Sim, F. Mustapha, V. Renuganth, R. Zahari and D.L. Majid 1085

Manufacturing High Performance Wood Composite Panel from Paulownia
A. Rafighi and T. Tabarsa 1091

Kenaf Nanofiber/Polylactic Acid (PLA) Nanocomposite
A.S. Lasat, A. Khalina and N.A. Ibrahim 1095

Simulation of Thermoset Injection for Bulk Moulding Compounds (BMC)
M.K.A. Arifin, S. Sulaiman, B.T.H.T. Baharudin, T.S. Hong and S. Sreenivasan 1101

Flutter Analysis of a Hybrid Plate-Like Fiber-Reinforced Composite Wing
D.L.A. Abdul Majid, S. Basri, V. Renuganth and A.H. Attaran 1107

Selection of Polymeric Based Material Composite for Fibreglass Boat Components Using Expert System
A.M. Fairuz, S.M. Sapuan and E.S. Zainudin 1113

Tensile and Thermal Conductivity Properties of Epoxy Nanocomposites Thin Film by Spin Coating Technique
T.V. Voo, M. Mariatti and L.C. Sim 1118

A Structural Health Monitoring of a Pitch Catch Active Sensing of PZT Sensor on Normal, Damage and Repair Aircraft Spoiler
K.D. Mohd Aris, F. Mustapha, S.M. Sapuan and D.L.A. Abdul Majid 1124

Effect of Filler Loading and Coupling Agent on Tensile and Impact Properties of Polypropylene with Oil Palm Ash Composites
M.S. Ibrahim, A.A. Faieza, S.M. Sapuan and S.M. Tahir 1130

Multisphere Ceramic Composite Concept and its Numerical Study of the Ballistic Response
S. Stanislawek, A. Morka and T. Niezgoda 1136

A Composite Consisting of a Set of Hexagonal Ceramic Bars - The Numerical Study of the Ballistic Resistance
S. Stanislawek, A. Morka and T. Niezgoda 1142

Effects of Impregnation Time on Physical and Tensile Properties of Impregnated Sugar Palm (*Arenga pinnata*) Fibres
M.R. Ishak, Z. Leman, S.M. Sapuan, M.Z.A. Rahman and U.M.K. Anwar 1147

Effects of Impregnation Pressure on Physical and Tensile Properties of Impregnated Sugar Palm (*Arenga pinnata*) Fibres
M.R. Ishak, Z. Leman, S.M. Sapuan, M.Z.A. Rahman and U.M.K. Anwar 1153

Indentation Analysis of In-Plane Prestressed Composite Sandwich Plates: An Improved Contact Law
M. Hosseini, S.M.R. Khalili and K.M. Fard 1159

The Influence of Yttrium Rich Intermetallic Phases and Heat Treatment on the Microstructure, Hardness and Wear Properties of Al-15%Mg_2Si Composite
H.R. Jafari Nodooshan, M. Emamy, N. Nemati and A. Bahrami 1165

Microstructure and Tensile Properties of Al-15wt%Mg_2Si Composite after Hot Extrusion and Heat Treatment
A. Bahrami, A. Razaghian, M. Emamy, H.R. Jafari Nodooshan and G.S. Mousavi 1171

Vibration Analysis of Thick Arbitrarily Laminated Plates of Various Shapes and Edge Conditions
T. Pervez, F.K.S. Al-Jahwari and A. Seibi 1177

Influence of Iron Oxide Nano Particles on Electrospun Poly (Vinylidene Fluride)-Based Carbon Nanofibers on Hydrogen Storage
S. Shahgaldi, Z. Yaakob, N. Mat Jali, D.J. Khadem, W.R. Wan Daud and E.H. Majlan 1184

© (2011) Trans Tech Publications, Switzerland
doi:10.4028/www.scientific.net/KEM.471-472.1

Composite Fracture: Getting to the Heart of the Matter

Peter W. R. Beaumont

Cambridge University Engineering Department

Trumpington Street, Cambridge CB2 1PZ

UK

pwb1000@hermes.cam.ac.uk

Keywords: structural integrity; multiscale modelling; fracture; damage; composites

Abstract. The demands made on structural composite materials in modern design are increasingly stringent. Greater performance, lower costs, increased reliability and safety all require that the design engineer knows more and more of the material systems available. Bringing together new knowledge contained in constitutive models of continuum design and empirical information from a girth of experience is proving to be difficult because the number of service and process variables required for sophisticated, optimal design is becoming increasingly larger. Understanding Structural Integrity (SI) provides the key to the successful design, certification, and safety of large composite structures and engineering composite materials. This is because SI analysis treats simultaneously the design, the materials used, figures out how best components and parts are joined, and takes service duty into account. But predicting precisely where a crack will develop in a material under stress and exactly when in time catastrophic failure of the structure will occur remains an unsolved mystery.

Introduction

Traditionally, practical design methods followed time-consuming, expensive test programmes to establish damage tolerance certification of large composite structures. The consequences of changing laminate design or material system along the way would be disastrous. A heavy price is paid for making mistakes using this approach. Quite simply, the entire test matrix for material qualification has to be repeated. Furthermore, there are complications as the result of laminates being heterogeneous elastic bodies containing sites of stress singularity; and secondly, the mechanisms controlling damage initiation and propagation are non-linear. Anyway, the likelihood is those mechanisms simply would not be known.

Traditional empirical design formulations have not done well dealing with these challenges. That is because empirical "laws" do not have the power of prediction. Successful prediction of mechanical behaviour of material and design life of a structure requires detailed information of all possible failure mechanisms across the widest spectrum of size-scale under all sorts of operational conditions. An experimental programme that covers all eventualities would be immense and unaffordable. Not only would the findings be complicated to sort out because of the many different mechanisms of fracture and fatigue involved, the question of their interaction would have to be resolved. Eventually, the method of extended empiricism would just break down under such an unmanageable load of variables. Furthermore, the burden of testing to prove absolute safety of structure would be impossible to manage in practice.

Evolution of Mechanical Design

In the 20th century, modern mechanical design evolved with the development of the continuum theories of mechanics (mathematical and continuum models of elasticity and plasticity), diffusion and reaction rates. With the advent of computer power this resulted in finite element (FE) modelling, numerical analyses, and high-fidelity simulation. This leads to an optimisation to minimise cost or to maximise performance or safety. Thus, the modern designer shows dexterity in

the use of two boxes of tools: first, mathematics and continuum modelling, from which continuum theories and constitutive models have evolved, (a sort of "distilled empiricism"); and second, micro-mechanics modelling (or physical modelling) of the mechanisms of deformation and fracture. (Re-call: a constitutive model is a set of mathematical equations that describe the behaviour of a material element subjected to external influence: stress, temperature, etc).

Using these tools to determine constitutive equations relies on knowledge of the rules of materials behaviour. Tools from Box 1 (continuum mechanics) describe structural interactions at the component level of size; tools from Box 2 (micro-mechanics) use the constituent properties of the material on the microscopic scale where structure and spatial arrangement are the main variables of mathematical and physical models. The idea is that the response at one size level, which can be described by one (or more) parameters is passed to the next level up (or down). Combining information leads to the development of "Damage Mechanics"; constitutive equations based on physical models. The problem still remains, however, that constitutive equations of continuum design are based on experiment. This is where micro-mechanics helps by identifying those mechanisms responsible for cracking and an understanding derived from the theory of reaction rates, for example, to model them. Although micro-mechanical models cannot by themselves lead to precise constitutive laws, the result is a constitutive equation that contains the predictive power of physical modelling combined with the precision of ordinary curve fitting methods (called "model-informed empiricism").

Structural Integrity and Lengthscale

Various design methodologies exist, all dealing with critical issues of structure and all common to the overall design process of production, maintenance, and repair. Superimposed are two items – assessment by non-destructive inspection (NDI) and safety. Is safety compromised where the fatal flaw(s) in the structure is (are) smaller than the NDI detection limit? What initial flaw (damage) content is acceptable in the final structure as a result of the manufacturing process? Consequently, structures require though-life monitoring of damage growth by non-destructive means. But what is an appropriate inspection period? There are conflicting aims of designing a structure simultaneously for high efficiency and safety assurance throughout an economically viable lifetime and it comes down to the price of safety with an acceptable level of risk as decided by society's experts. Quite simply, how far from potential disaster are we prepared to go?

A key role in failure prediction, from empirical methods to high-fidelity simulations of damage evolution, is played by certain physical lengthscales in the damaging processes, which provide a rationale for making modelling decisions. A lengthscale arises because of the complexity of the nature of cracks for specific damaging mechanisms; de-lamination and splitting (shear) cracks, fibre rupture, fibre micro-buckling or kink formation, and diffuse micro-cracking or shear damage in the matrix. Corresponding physical models and mathematical theories describe these mechanisms on a micro-scale and crack growth in the large engineering structure. Boundaries on the lengthscale are delineated by a breakdown in the model and assumptions implicit to a particular size. Thus, we can define points on that scale by phenomena that are treated discretely from phenomena treated collectively. The two exceptions are the end points of the lengthscale. (Everything at the electronic level is treated discretely whereas everything at the macro size is treated collectively). Our confusion over how damage is interpreted along this lengthscale is causing difficulty as progress is made from one design stage to the next; from the size of architectural features of the laminate to that of the structural element, and from component and to the fully assembled large scale structure.

Understanding damage by experimentation and modelling across orders of magnitude of structural dimension, and linking analyses systematically to provide a total predictive design strategy is lacking with respect to absolute reliability and guaranteed safety. This is particularly critical regarding two design issues: (1) a structure capable of sustaining a potential damaging event *(damage resistance*) and (2) a structure's ability to perform satisfactorily and safely with damage present (*damage tolerance*) (Cox [1, 2]).

Even with the exponential growth of computational power, which has resulted in an abundance of numerical analytical models, there still exists fundamental barriers to overcome as progress is made by connecting one damage analysis to the next, from the time the smallest undetectable defect forms in the solid to the point where a visible crack is found in a full-scale engineering structure "down the road".

Lack of mastery in combining architectural design of the material at the micron (or less) size with the design of elements of the engineering structure metres in length, has led to the opening of a gap in our knowledge of composite failure. If we consider coming to terms with all sorts of material behavioural complexities at the (sub-) microscopic end of the scale, we might say that we have characterized the properties of the composite by reference to the fibre only. There has been no real consideration of the "make up" of the material or macroscopic geometry of the laminate or shape of part or component. Any notch, hole or cut-out is but a geometrical aberration. Conversely, at the size level of component design, we have tended to look at the overall geometric shape and thought of the material properties as being set (in a geometric sense) at global level.

Multi-scale Modelling: "Top-Down" versus "Bottom-Up" Methods

Multi-scale problems of structural failure that occur at the micro, meso, and the macro size of scale must be targeted by appropriate multi-scale modelling methods. Testing and analysis across a size spectrum reflect responses at all structural levels, which we call multi-scale modelling. The macroscopic response of a composite material system and component reflects responses at all levels beneath. The idea is that the response at one level is passed to the next level up (or down). Hierarchical and multi-scale modelling links top-down and bottom-up approaches. Almost always, behaviour at one level can be passed to the next level up (or down) as a simple mathematical function. Regrettably, distinct communities have pursued either "top-down" or "bottom up" methods of design only occasionally transferring information from one to the other.

The top-down (TD) method begins with a macroscopic engineering model, a procedure that depends only on knowledge of straightforward *macroscopically* measurable properties, like hardness or yield stress or ultimate tensile strength, which an engineer can handle. Bottom up (BU) methods on the other hand, seek to model (or simulate) failure by building upon events that initially take place at the atomistic (or microscopic) level, which in engineering terms are difficult to determine, let alone quantify. Whilst physical modelling as described by one (or more) parameters in a constitutive model, for example, can help rationalise those microscopic processes responsible for yield stress, toughness (notch sensitivity), fatigue, stress corrosion cracking etc, generally, these models are too imprecise for an exact engineering solution.

In fatigue, for example, life prediction based on a physical model only might give a prediction within a factor of 10. That is because the material parameters of the physical model are not known with any certainty and they are too difficult to determine or measure with any confidence. Knowledge of matrix crack density, for instance, would characterise the state of damage in a composite under fatigue but there is no straightforward way of quantifying it in a large structure. One way forward is to identify the broad rules governing material behaviour, and the rules governing the magnitudes of material properties, which are contained in the microscopic models, and use them as the basis of a "model-informed" empiricism. Even though the details of microstructure at the fibre architectural scale can be too complex to analyse, micro-mechanical models will obtain the effective properties at the micron scale to obtain, for example, the effective fibre weave properties. Then, a model or representative of a volume element is used to obtain the effective properties of the textile architecture at this size scale. Inserting these values into a structural model identifies the "hot spots". These hot spots are interrogated by reversing the process in order to determine whether the structure has to be re-designed or an alternative material system selected. Examples of challenges include dealing with large macroscopic gradients, non-periodic loads, including transient loads, non-periodic microstructure, mesh generation, and data management.

For coarse and fine microstructures the analyses involve discrete and homogenized modelling, respectively. What is not so clear is how to handle the "transitional microstructure", for which there is too much detail for discrete modelling, but too little repetition of representative behaviour to use homogenisation. One way is to use homogenisation, selective homogenisation, macro elements (finite elements that allow complex variation of properties within an element), and global to local interfacing techniques, including one technique based on modal analysis (Whitcomb [2]).

An aspect of multi-scale analysis often overlooked is the integration of different models. A common characteristic of many analytical studies is the need to construct and manipulate related models, related in the sense that they share some characteristics. In other words, there is a clear hierarchy in which many properties are "passed on" via inheritance. The hierarchical analysis environment can be used in parametric studies of structures or situations in which the constitutive behaviour is defined in a hierarchical sense (Whitcomb [1,2]).

Ideally, we require mathematical formulations that link TD and BU approaches in single design codes that represent fine-scale phenomena embedded in calculations representing larger-scale phenomena, tracing damage mechanisms through all size scales. Beware, however, of premature claims of success. In reality, is there a mechanism that has not been observed; is there a significant crack that has gone undetected?

Simulation and Virtual Testing

Simulation is a study of the dynamic response of a modelled system by subjecting the model to inputs, which simulate real events, ways in which complex structures evolve without the need to perform expensive time consuming experiments). Recent developments in multi-scale modelling strategies have lead to the virtual mechanical testing of composite structures right up to the point of failure. This route leads to a quantitative prediction that represents the actual performance of the material or component or full-size structure across a broad spectrum of size (or multi-scale) without the cost, time, accident risk, effort and repeatability, problems normally associated with real testing. In the virtual testing of realistic aerospace composite structures, for example, the validation of FE predictions has been mostly proven for simple coupon and benchmark test specimens. The difficulty is simulating the correct failure mechanisms of realistic structures: for example, post-buckled compression panels, impact-damaged shells, major joints or any component with geometrical discontinuities.

Commercial FE codes are powerful enough to capture the correct physics of the failure process. But having an FE code is just the beginning: the modeller has to create a FE model, which is capable of capturing the internal stress fields with the required accuracy. Assessing damage in sandwich structures under hard and soft impacts, for example, requires validated FE design tools together with structural impact test data in order to validate FE codes and airworthiness certification (Davies [1, 2]). But how much detail of failure mechanisms do we need to know in order that a successful physical model can be incorporated into a simulated virtual test that reproduces the outcome of a real structural situation? Creating physically sound damage simulations is difficult because damage initiation must first be predicted for parts containing no cracks.

Developments in non-linear elements in computational mechanics have led to damage simulations of sufficient fidelity in engineering design (Cox [1, 2]). A key feature is the incorporation into a finite element formulation, of elements that can explicitly represent displacement discontinuities associated with cracks – so-called "cohesive elements." These elements relate the displacement discontinuity across a crack to tractions that act across that crack. Examples include: fibrils in polymer craze zones, bridging fibres or ductile particles, fibre-matrix slippage following de-bonding (friction), and so on. Cohesive elements can be formulated that admit cracks crossing any surface within the finite element, so that the developing crack path in a damage simulation need not be specified *a priori*; it can simply follow any locus that the mechanics of the evolving failure process has determined.

However, a number of minor difficulties still exist before damage simulations of sufficient fidelity can replace qualification tests: (1) the implications of length scales associated with non-linear cohesive processes for correct mesh refinement; (2) the calibration of cohesive traction-displacement laws in order to confirm a physically-sound model of the particular crack wake mechanism; and (3) the problem of instability in numerical iteration of non-linear damage problems, which may have physical (not algorithmic) origins.

Those damage growth mechanisms that have been observed in laminates include: de-lamination and splitting (shear) cracks, which grow in various orientations and change in shape with time; fibre rupture; fibre micro-buckling or kink formation; global buckling of de-laminated plies; and diffuse micro-cracking or shear damage within individual plies. These mechanisms (with the exception of global buckling) can be represented by cohesive elements, by collapsing the non-linear processes onto surfaces, with the physics embedded in traction-displacement constitutive behaviour (rather than stress-strain behaviour).

Solving the problem of suitable mesh refinement might be achievable in terms of length scales associated with cohesive laws. Calibration of traction-displacement laws requires a successful physical model and appropriate set of experiments. This is not straightforward because different cohesive mechanisms often act simultaneously in a single crack, with their relative magnitudes depending on interaction effects with other cracks. Defining experiments is also challenged because traction laws must be deduced from experiments via inverse problem methods, which are vulnerable to numerical noise. Instability can be dealt with in one of two ways: (1) run the complete simulation as a dynamic model; or (2) invent algorithms that stabilize the model by controlling local displacements (Cox [1, 2]).

Modelling Structure that Evolves with Time

A structure under stress suffers damage with time: cracks form, which in turn increase the rate of damage formation. There is positive feedback. Ageing weakens the material; its structure changes and constitutive models (equations) describe this sort of behaviour, best derived using the *internal state variable* method. Briefly, the key ideas are based on the fact that constitutive models have two aspects: response equations and structural evolution equations. The response equation describes the relationship of (say) current modulus of the laminate, (a measure of the effect of damage), to the applied stress or stress range, load cycles, and to the current value of an internal state variable, D. The internal state variable is called *damage* because it describes a change in the state of a material, brought about by an applied stress or by load cycling. It (meaning D) uniquely defines the current level of damage in the material, for a given set of test variables. The internal state variable, D, evolves over time with the progressive nature of the damaging processes.

In fatigue, for example, we observe changes in the composite modulus (stiffness) with the accumulation of fatigue damage. The response equation describes this change of (damaged) modulus, to the stress magnitude, temperature, time (number of load cycles), and to the current value of the internal state variable D. But problems arise from a lack of detail of these microscopic parameters including number (or density) of fibre breaks, matrix crack density, etc, which can only be determined microscopically and this is not practical in real structures. Instead of characterizing a material property as a function of the independent variables, which experimentally is very time-consuming and expensive), fit data to a coupled set of differential equations, one for the modulus and one for D_1 (and D_2, D_3 etc) depending on the number of damaging mechanisms. Thus, where several mechanisms contribute simultaneously to the response, (e.g., where modulus degradation is the result of the coupling of de-lamination and matrix cracking), this time there are two internal state variables, D_1 and D_2, one for each mechanism. Consequently, the model suggests a constitutive equation having a completely different form than before.

Instead of trying to characterize the modulus E of the laminate as a function of the complete set of independent variables (although it is possible), seek to fit data to a coupled set of differential equations, one for the (damaged) modulus and two (or more), depending on the number of damaging mechanisms, for damage propagation, namely D_1', D_2', etc. D_1 describes the damage due

to one mechanism and D_2 describes a different damaging mechanism that, when combined with the first, eventually lead to composite failure. Consequently, E', D_1' and D_2' are their *rates of change* with time (or numbers of load cycles). There are now three independent variables whereas before there were eight. These equations can be integrated to track out the change of modulus with the accumulation of damage, and ultimately used to predict fracture of a component or the design life in fatigue. Thus, the modulus-time (cycles) response is found by integrating the equations as a coupled set, starting with $E = E_o$ (the undamaged modulus) and $D = 0$ (no damage). Step through time (cycles), calculating the increments, and the current values of E and D, and using these to calculate their change in the next step. We now have an equation that can be adopted as the constitutive equation for fatigue.

The State Variable Approach leads to the idea of a Mechanism Map or Damage Diagram, a versatile method of presenting both results of the model and experimental data (Beaumont [3]). The conceptual map displays the response (loss of stiffness or strength), identifies the mechanisms, and shows the extent of the damage for a given loading history. However, the model points to something else, and it is of the greatest value; it suggests the proper form that the constitutive equation should take. This physical model-informed empiricism has led to the development of a new branch of mechanics called *damage mechanics*.

NDE of Bonded Joints and Structural Integrity

The inability to discriminate non-destructively between a good bond and a "kissing" bond (intimate contact between adhesive and substrate but with no adhesion), is the key roadblock to the advancement of bonded structures. The inability to find these flaws has limited adhesive bonding to secondary (lightly) loaded structures and will continue to do so until non-destructive evaluation (NDE) is able to ensure that bonded joints remain bonded throughout the lifetime of large structures. There are many published claims of success but follow-up experiments did not yield validate claims. Most studies were based upon two assumptions: (1) a fundamental relationship exists between strength and stiffness, and (2) ultrasonic velocity depends on modulus, which is correlated with strength. Attempts have been made to correlate ultrasonic data with strength based on measurements of attenuation, velocity, spectral measurements of attenuation and velocity but no robust correlations have been found. Stress distribution within the joint simply was not considered. The thought was that if bond strength could not be predicted, then predict quality!

Acknowledgements

This paper draws upon the published work of others. I would like to acknowledge the work of Drs Brian Cox, Alastair Johnson, and Robert Crane; and Professors Mike Ashby, John Whitcomb, Josef Jančář, R Pyrz, J Sinke, Ramesh Taljera, Scott Case, and Glyn Davies.

References

[1] *Advances in Multi-Scale Modelling of Composite Material Systems and Components.* Special issue of the Journal of Materials Science, Volume 41, Number 20, October 2006 (ISSN 0022-2461). Invited Editor: Peter W R Beaumont.

[2] *Stretching the Endurance Boundary of Composite Materials: Pushing the Performance Limit of Composite Structures.* Special issue of the Journal of Materials Science, Volume 43, Issue 20, October 2008 (ISSN 0022-2461). Invited Editor: Peter W R Beaumont.

[3] *Multi-scale Modelling of Composite Material Systems* Edited by C Soutis and PWR Beaumont. CRC/Woodhead Publishing Limited (2005).

© (2011) Trans Tech Publications, Switzerland
doi:10.4028/www.scientific.net/KEM.471-472.7

Recent Developments in PA6/PP Nanocomposites

Azman Hassan[1,a], Muhammad Imran[1,b], Mat Uzir Wahit[1,c], Harintharavimal Balakrishnan[1,d]

[1]Department of Polymer Engineering, Faculty of Chemical Engineering, Universiti Teknologi Malaysia (UTM), Johor, Malaysia

[a]azmanh@fkkksa.utm.my, [b]imran@cheme.utm.my, [c]mat.uzir@cheme.utm.my, [d]harin_bala@yahoo.com

Keywords: Polyamide 6/Polypropylene blend, Nanocomposite, Organoclay, Rubber-toughened

Abstract. An overview of the recent developments in PA6/PP blend nanocomposites is presented in this paper with an emphasis on their mechanical, thermal and morphological properties. The role of organoclay as a reinforcing agent and polyethylene octene (POE) as an elastomer are discussed in detail. The organoclay increases the strength and stiffness while the POE elastomer increases the impact toughness of the nanocomposites. The effects of various parameters such as PA6/PP blend ratio, organoclay loading and the concentration of elastomer on the nanocomposites properties are also examined. The exfoliated state of organoclay platelets along with the fine particle size and uniform dispersion of POE demonstrate the nanocomposite with improved properties. These materials are attracting considerable interest in polymer research community because they exhibit substantial improvement in properties at low filler contents.

Introduction

Polymer nanocmposites are materials in which nanoscopic inorganic particles (at least one dimension of 10-100 Å) are dispersed in an organic polymer matrix in order to improve the performance properties of the resulting polymer composite. The polymer matrix may be single or multicomponent. Polymer nanocomposites are drawing considerable interest due to the development of the processing techniques and a broad scope of their usage in various practical applications. They possess substantially improved mechanical, thermal, and barrier properties as compared to their bulk counterpart.

Polymer nanocomposites, especially polymer clay nanocmposites that consist of layered silicates, have received significant attention due to their dramatic improvement in material properties by addition of just a small amount of clay into the polymer matrix. These composites have demonstrated a significant potential to become the basis for development of the next generation of enhanced performance polymer compounds [1]. Interest in nanoparticle-based polymer composites has expanded significantly since the late 1980s when the patent of Okada et al. [2] for in situ polymerization of a Nylon 6/clay nanocomposite was issued. As demonstrated by several researchers, a relatively small loading of properly dispersed (well-exfoliated) organoclay provides a substantial improvement in mechanical, thermal, flame resistance, and abrasion resistance properties [3,4]. Since there are many studies on the single polymer matrix nanocomposite, so the objective of this article is to highlight the development of polymer blend nanacomposites.

There has been growing interest in the development of polymer blends based on polyamide 6 (PA6) and polypropylene (PP) [5]. The reason of blending PA6 and PP is to bridge the property gap between the two polymers. The PP is widely employed because of its low cost, high barrier properties to moisture, and its ease of processing, but its high permeability to oxygen and many organic solvents limits its potential use. On the other hand, PA6 is a good barrier material for oxygen and organic compounds but it is relatively expensive, hygroscopic and thus a poor barrier for water. The blending of both could be advantageous but they are not miscible. The compatibilizer

such as maleic anhydride grafted PP (PPgMA) is generally added to get good mixing. However, the major drawback of PA6/PP blend is its poor impact strength at low temperatures [6].

The use of montmorillonite (MMT) clay as a reinforcing filler in polymer nanocomposites has attracted great interest. These composites often exhibit high strength and stiffness (both tensile and flexural) but at the expense of impact toughness. Thus blending of MMT filled nanocomposite with an elastomer (rubber) may lead towards improved impact strength and elongation at break of the resulting nanocomposite. The impact toughening of PA6/PP with various types of elastomers such as ethylene propylene rubber (EPR), ethylene propylene diene monomer rubber (EPDM) and styrene ethylene butadiene styrene rubber (SEBS) have been reported in the literature [7,8]. Another, relatively new elastomer, ethylene octene copolymer (POE) was used as a toughening agent to form rubber-toughened PA6/PP nanocomposite [9]. The POE is a novel polyolefin elastomer which was developed using metallocene catalyst by Dow Chemical Co. This elastomer offers a controlled level of chain branching along the polymer backbone. Compared with conventional elastomer (EPDM), POE exhibits faster mixing and better dispersion when blended with PP [10].

The organically modified MMT increases the strength and stiffness while the POE increases the impact toughness of the nanocomposites. The role of organoclay and POE rubber in order to get a relatively good balance among strength, stiffness and toughness of PA6/PP nanocomposites have been reviewed in this article. The effect of various parameters such as PA6/PP blend ratio, contents of organoclay and POE, and the types of elastomeric rubber on the mechanical, morphological and thermal properties of the PA6/PP nanocomposites have been studied by our group and will be discussed in detail in the following sections.

Effect of PA6/PP blend ratio

Mechanical properties. A series of PPgMA compatibilized PA6/PP blends of various (100/0, 70/30, 50/50, 30/70 and 0/100) compositions were prepared by melt compounding followed by injection molding [9]. The blends were reinforced with organoclay (4 wt%) and toughened by POE (10 wt%). The results have shown that the strength (tensile and flexural) and stiffness (E- and flexural modulus) of all the composites lie between neat PA6 and PP and declined monotonically as the weight fraction of PP increased. This happened because the strength and stiffness of PP are lower than PA6. On the contrary, the impact strength has increased with higher contents of PP. Tseng et al. [11] attributed this enhanced toughness to the PP disperse phase which has higher impact strength compared to PA6. Furthermore, the incorporation of PPgMA caused the formation of PA6 grafted PP (PA6gPP) copolymer which strengthened the interface between PA6 and PP phase. The reaction of graft copolymer formation was proposed by Duvall and co-workers [12] and is shown by the reaction scheme in Fig. 1. The grafter copolymer preferentially resides at the interface and improves the interfacial adhesion through the chemical linkage across the interface.

The tensile strength, E-modulus, flexural strength and flexural modulus of PA6/PP/organoclay/POE nanocomposites increased with the incorporation of 4 wt% organoclay. Fig. 2a shows the effect of clay and PA6/PP blend ratio on the tensile strength of the composites. Generally the enhancing effect of the organoclay on the strength and stiffness is due to the higher modulus of organoclay as compared to polymer [13]. These improvements are also related to the degree of exfoliation of layered silicates in the polymer matrix and high aspect ratio of platelet structure possibility because it increases the interaction between silicate layers and polymer matrix.

A notable difference in the level of strength and stiffness for PA6/PP neat blend and its nanocomposites has been observed upon increasing the PP contents [9]. The increase in tensile strength and E-modulus for the PA6/PP (70/30) nanocomposites was about 24 and 33%, respectively as compared to the neat PA6/PP (70/30) blend, whereas, for PA6/PP (30/70), the increase was about 9 and 5%, respectively. The remarkable increase with PA6 as the matrix (PP as disperse phase) is due to the better compatibility between polar PA6 and polar clay. On the other hand, the relatively less increase with PP as the matrix is due to the poor compatibility between non-polar PP and polar clay. The better compatibility resulted in exfoliated and homogenous dispersion

of silicate layers in the nanocomposite. Contrary to the observed increase in strength and stiffness by the addition of organoclay, the impact strength of the PA6/PP/organoclay nanocomposite is decreased compared to the neat PA6/PP blend as shown in Fig. 2b. In the case of PA6 and PA6/PP (70/30) blend, the Izod impact strength was reduced from 4.6 to 2.9 kJ/m^2 and 8.6 to 5.3 kJ/m^2, respectively. Wang et al. [14] have reported that the impact strength decreased from 115 J/m for neat PA6/PP to 17 J/m for PA6/PP filled with 5 wt% organoclay. This decrease with the addition of organoclay as a filler may be due to the hindrance offered by the silicates layers in macromolecule chain movement making the composite more brittle. However, this drawback can be compensated with the addition of a rubbery phase.

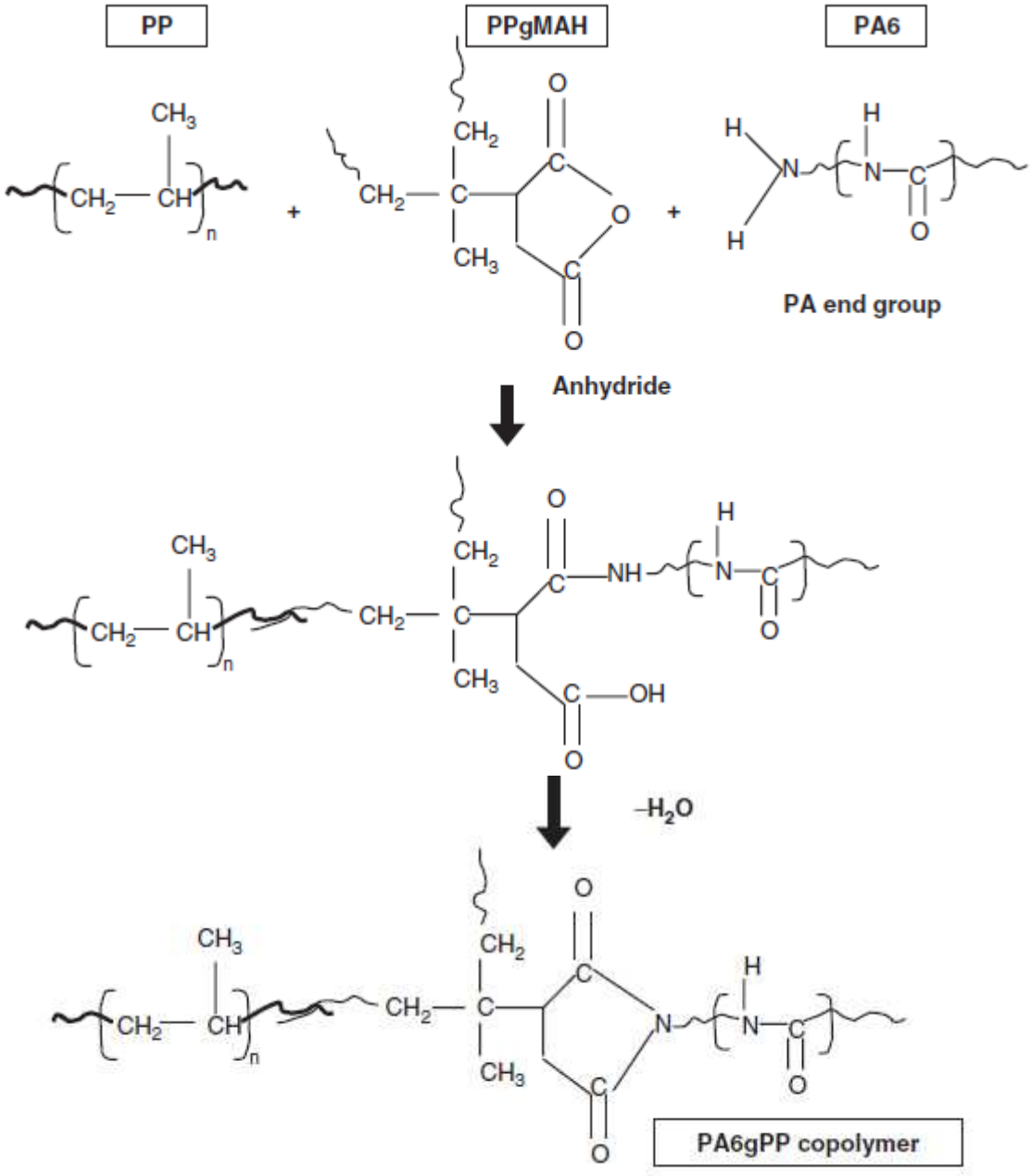


Fig. 1. The reaction scheme for PA6gPP copolymer formation [9].

The strength (Fig. 2) and stiffness of all the blends and composites dropped while the toughness (Izod impact strength) increased (Fig. 2b) by the incorporation of POE. The increase was more substantial with higher contents of PP. For PA6/PP (70/30)/POE blend, the impact strength improved about 26%, but for PA6/PP (30/70)/POE blend, it improved by about 40%. It was elucidated that the higher proportion of PP in the blend resulted in significantly enhanced impact strength which was due to the good compatibility between POE and PP. According to Yu et al. [15], POE exhibited faster mixing and better dispersion when blending with PP due to structure similarity. It is concluded that the incorporation of organoclay into polymer has increased the strength and stiffness and decreased the toughness while the incorporation of POE elastomer increased the toughness and decreased the strength and stiffness. The combination of both (organoclay reinforcing agent and POE elastomer) would produce a nanocomposite with good and balanced mechanical properties.

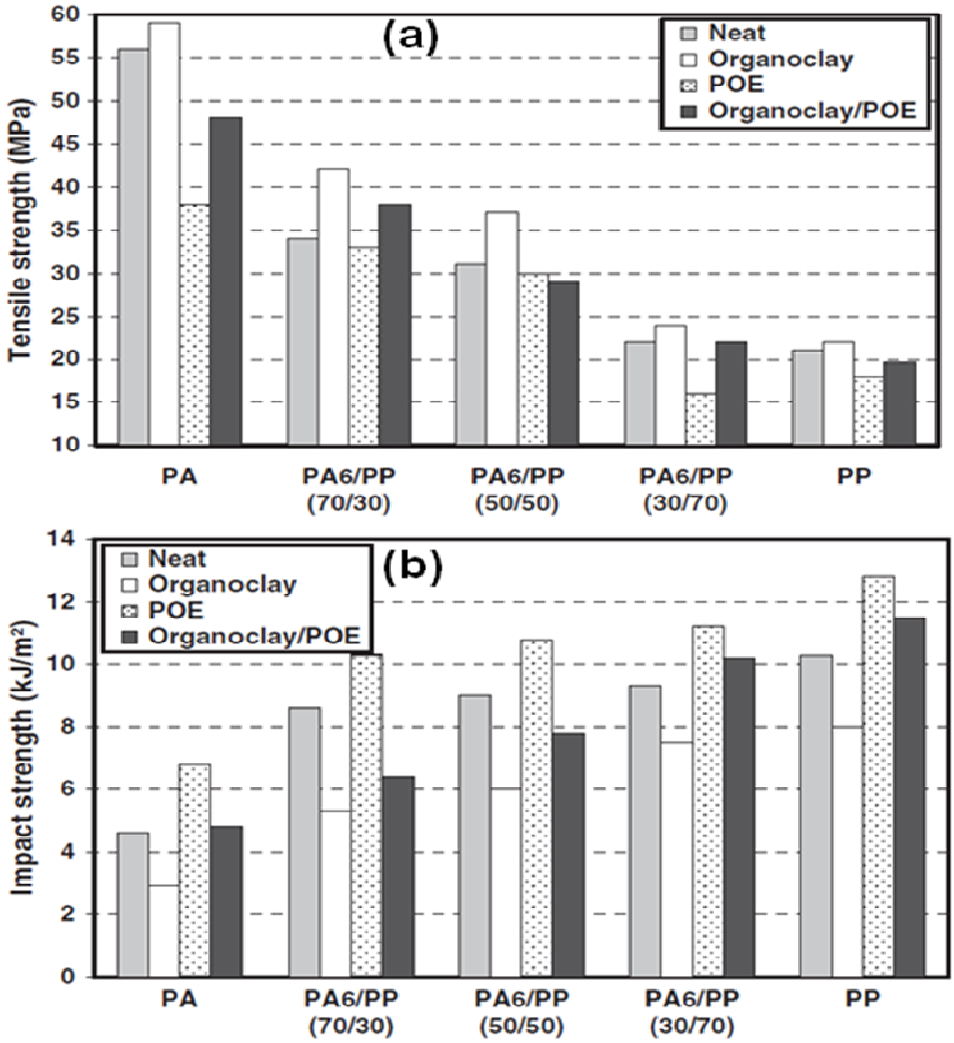


Fig. 2. Effect of PA6/PP blend ratio on the (a) tensile strength and (b) impact strength of the PA6/PP/organoclay/POE nanocomposites [9].

X-ray Diffraction. The XRD has been regarded as a tool for characterizing the microstructure of the nanocomposites. The XRD spectra for three different blend ratios of PA6/PP are shown in Fig. 3. It shows that for PA6/PP (30/70) and PA6/PP (50/50) nanocomposite systems, the (001) plane peak of the organoclay which originally appears at $2\Theta = 3.4^{o}$ were shifted to a low angle of $2\Theta = 2.7^{o}$ and $2\Theta = 2.4^{o}$, respectively. These decreased values of 2Θ indicate the increased interlayer

spacing of the MMT platelets from 2.59 nm (organoclay) to 3.30 nm (PA6/PP:30/70) and 3.62 nm (PA6/PP:50/50). It clearly demonstrates that the macromolecular chains have dispersed and intercalated into the galleries of organoclay. However, the clay is not fully exfoliated in case of PA6/PP (30/70) and PA6/PP (50/50) and the peaks in Fig. 3 show agglomeration of clay particles. This is because of the high content of PP phase which has poor compatibility with the polar clay. There was no diffraction peak in the case of PA6/PP (70/30) as shown in Fig. 3, which shows that the intercalate silicate layers are exfoliated and randomly dispersed in the PA6/PP matrix. This exfoliated state played a positive role in enhancing the mechanical properties of PA6/PP nanocomposites as compared to the neat PA6/PP blend.

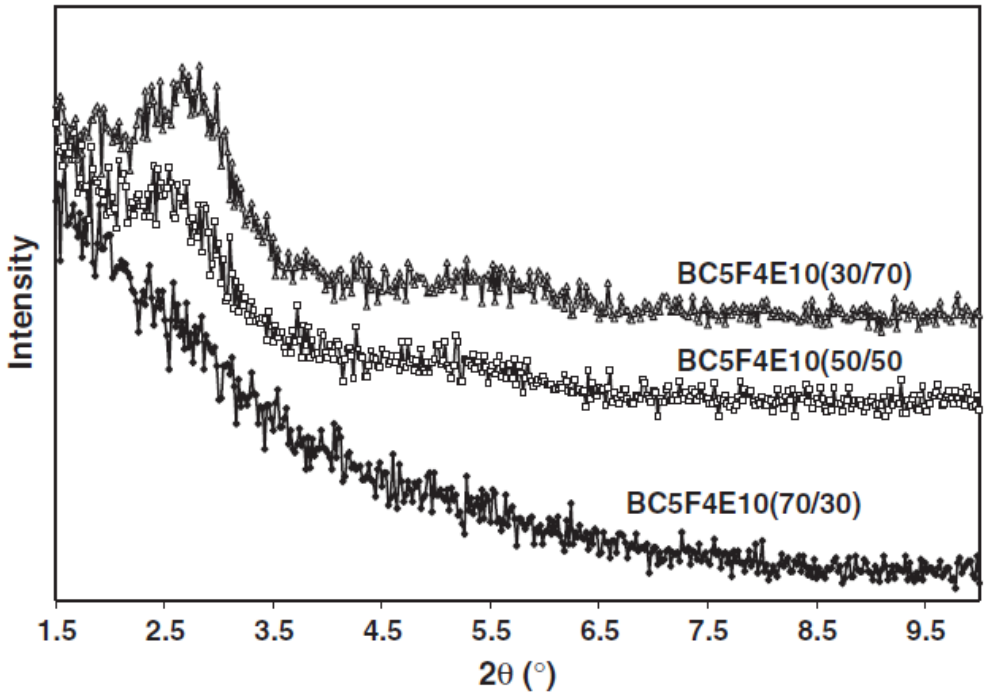


Fig. 3. XRD spectra of PA6/PP(BC5)/organoclay (F4)/POE (E10) with different PA6/PP blend ratios [9].

Morphological properties. Fig. 4 shows SEM images of the cryogenically fractured surface of heptane etched PA6/PP nanocomposites. The etched surfaces show voids which represent dissolved POE as the heptanes selectively dissolve the POE phase. Fig. 4 shows the morphology of the nanocomposites with PA6/PP: 100/0 (Fig. 4a) to PA6/PP: 0/100(Fig. 4e). The POE particle size is 7.55, 1.50, 1.32, 1.13 and 1.08 μm with PA6/PP/organoclay/POE (100/0), PA6/PP/organoclay/POE (70/30), PA6/PP/organoclay/POE (50/50), PA6/PP/organoclay/POE (30/70) and (e) PA6/PP/organoclay/POE (0/100), respectively. The particle size decreases with the increase in PP phase. The larger POE size shows low compatibility between PA6 and POE. The smooth edges of the holes (Fig. 4a) indicate a weak interfacial adhesion between the two phases. A similar observation was also reported in the literature on the study of PA6/POE blends [15]. As the ratio of PP increased, the size of the POE particles in the matrix decreased which is again attributed to the good compatibility between PP and POE as PP has become the major phase in the blends. The size of the POE particles with and without organoclay was also measured and it was found that the organoclay reduced the POE particle size. Khatua et al. [16] has proposed two reasons that might be attributed to the reduction of dispersed domain size, either the organoclay platelets change the rheological properties of the blends or the barrier effect prevents the coalescence of the dispersed phase. According to Lotti et al. [17], the particle size of the elastomer significantly effects the deformation and failure of the nanocomposite. The large particle size of POE was responsible for

the premature rupture of the samples, resulted in lowering the impact strength (Fig. 2b and 4a) while the smaller particle size favored shear yielding that resulted in increased impact strength. The blend ratio of PA6/PP: 70/30 would be considered as optimum in terms of balanced mechanical and morphological properties.

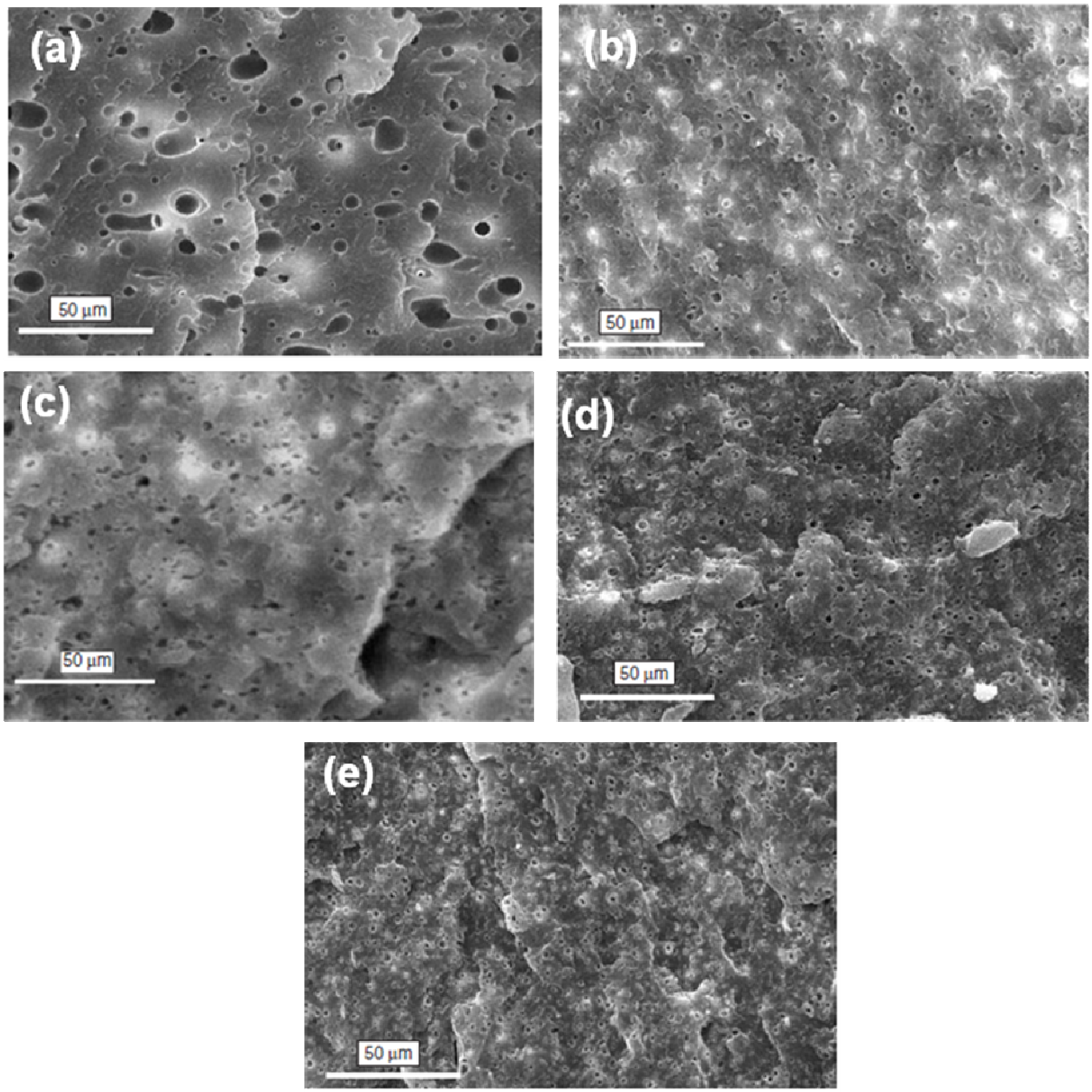


Fig. 4. SEM images of the nanocomposites with different PA6/PP blend ratios; (a) PA6/PP/organoclay/POE(100/0), (b) PA6/PP/organoclay/POE (70/30), (c) PA6/PP/organoclay/POE (50/50), (d) PA6/PP/organoclay/POE (30/70) and (e) PA6/PP/organoclay/POE (0/100) [9].

Effect of organoclay loading on the properties of PA6/PP nanocomposites

Mechanical Properties. The study on PA6/PP (70/30) blends containing 10 wt% of POE, 5 wt% of PPgMA and different loadings (2-6 wt%) of organoclay (MMT) was carried out using a twin screw extruder followed by injection molding [18]. Fig. 5 shows the mechanical properties of PA6/PP/organoclay/POE nanocomposites with different clay loading. The stiffness (E-modulus and

flexural modulus) increased by increasing clay loading. The results are consistent with the other studies [19,20]. According to Wang et al. [13], the reinforcement effect depends on four factors with respect to organoclay: rigidity, aspect ratio, the affinity with the polymer matrix, and the degree of exfoliation. Liu et al. [21] related the possibility of modulus improvement to the constraint of the polymer chains by their interaction with the clay surface. The strength (tensile and flexural) of the nanocomposites increased with the increase in clay contents but the tensile strength increased up to a certain (4 wt%) clay loading and then started to decrease. This increase in strength may be attributed to the following factors; good compatibility due to polar clay and polar PA6 phase [13], hydrogen bonding formation between amide group of PA6gPP copolymer and octadecylamine group of organoclay intercalant [6], the high aspect ratio of the clay which provide larger contact area with the polymer matrix, and the delamination or exfoliation of clay platelets. The decrease in tensile strength at high clay loading (6 wt%) may be explained with the filler-filler interaction resulting in agglomeration of clay platelets. This agglomeration reduces the contact surface area between clay and polymer matrix and also induces the local stress concentrations that leads to the brittle composite. The organoclay adversely affects the impact strength and elongation at break of the nanocomposites. This happened because of the inherent low toughness of the clay. The reduced toughness implies that the nanocomposites became more brittle by incorporating the clay as compared to PA6/PP/POE blends.

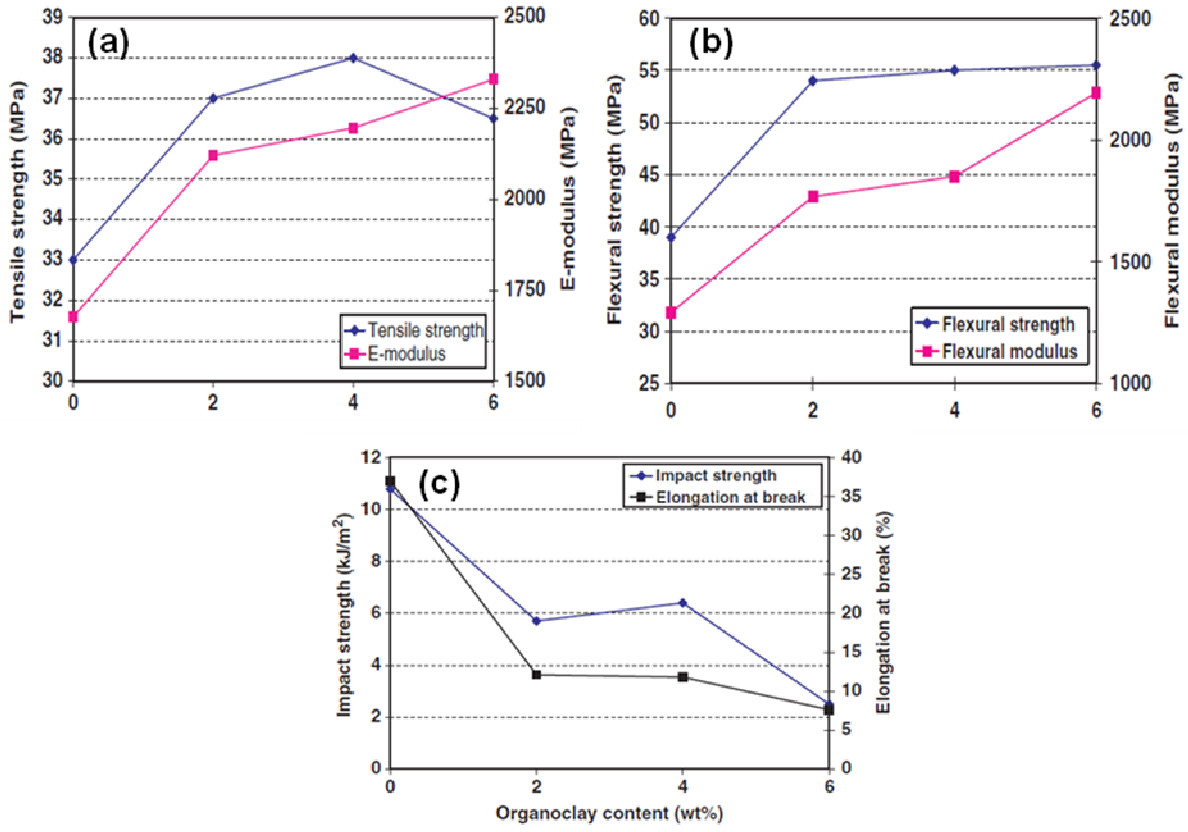


Fig. 5. Mechanical properties of PA6/PP/organoclay/POE nanocomposites with different clay loading; (a) tensile strength and E-modulus, (b) flexural strength and modulus and (c) impact strength and elongation at break [18].

Thermal properties. The thermal stability of the PA6/PP nanocomposites were examined using thermo gravimetric analysis (TGA) and differential scanning calorimeter (DSC) [18]. The results for 10 wt% degradation by TGA are shown in Table 1. The nanocomposites with 2 and 4 wt% organoclay have the higher decomposition temperature as compared to PA6/PP blend. However,

with 6 wt%, the decomposition temperature was same as that for the neat PA6/PP blend. It is well known that the improved thermal stability of the polymer/clay nanocomposites is mainly due to the formation of char which hinders the out-diffusion of the volatile decomposition products [22]. According to Ray and Okamoto [23], the significant increase in thermal stability may be due to the kinetic effects, with the platelets retarding the diffusion of oxygen into the polymer matrix [23]. Pramoda et al. [24] have suggested that only the exfoliated clay improve the thermal stability while the aggregated clay may adversely affect by increasing the diffusion of oxygen to the polymer matrix. The increased thermal stability with 2 and 4 wt% and the decreased thermal stability with 6 wt% clay demonstrate the exfoliated and aggregated state of clay, respectively.

Table 1. TGA data with different clay contents (BC5: PA6/PP, BC5/E: PA6/PP/POE, BC5/F2/E: PA6/PP/2 wt% clay/POE) [18].

Composition	Organoclay content (wt%)	TGA organoclay content	Temperature of composition (°C) at 10% weight loss
BC5	0	0	398.2
BC5/E	0	0	398.1
BC5/F2/E	2	1.9	410.1
BC5/F4/E	4	3.2	410.6
BC5/F6/E	6	4.6	398.7

The melting temperatures (T_m) and the degree of crystallinity (X_c) determined by DSC are shown in Table 2. The data shows that the addition of clay has a little effect on the T_m and X_c. Increasing the clay concentration resulted in slight reduction in the degree of crystallinity of the PP and PA6. According to Fornes and Paul [25], the presence of a higher concentration of dispersed organoclay would prevent large crystalline domain formation due to limited space and restrictions imposed on polymer chains by the large number of silicate platelets. Based on the results, the organoclay loading of 4 wt% in PA6/PP (70/30)/POE blend would be considered as optimum in terms of improved mechanical and thermal properties.

Table 2. DSC data of the PA6/PP/organoclay/POE nanocomposites [18].

	T_m (°C)		χ_c (%)	
Composition	PP	PA6	PP	PA6
BC5	165.633	222.6	32.8	31.6
BC5/E	164.533	221.2	31.1	28.8
BC5/F4	165.200	221.8	33.6	30.3
BC5/F2/E	164.533	221.4	35.4	31.0
BC5/F4/E	164.466	220.9	34.7	29.7
BC5/F6/E	164.166	221.6	31.2	29.0

Effect of an elastomer on the properties of PA6/PP nanocomposites

Effect of POE contents. The optimized PA6/PP (70/30) blend and organoclay (4 wt%) were compounded with PPgMA (5 wt%) and different proportions of POE elastomer (0-20 wt%) in a twin screw extruder followed by the injection molding [25]. The strength and stiffness of the POE

incorporated PA6/PP/organoclay nanocomposites decreased by increasing the contents of POE elastomer. This is generally found in various blends and has been attributed to the softening or diluting effect of the elastomer [26]. Contrary to the decreased strength and stiffness, the toughness (impact strength) of the nanocomposites increased by increasing the contents of POE. This enhancement in toughness can be explained by the PA6gPP copolymer formation that increase the interfacial adhesion between PA6 and PP, physical entanglement due to the structural similarities between PP and POE, and the hydrogen bonding formation between PA6gPP and the organoclay. These interactions (either physical or chemical) are shown by the reaction scheme in Fig. 6. It was also examined that the strength and stiffness sharply decreased when the POE contents were above 10 wt%.

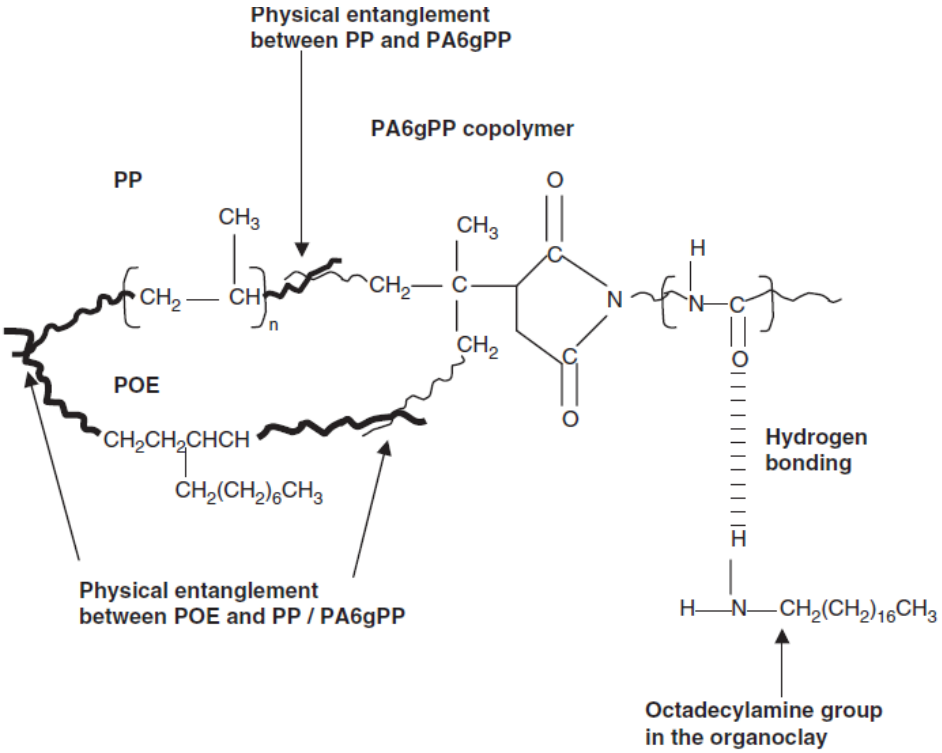


Fig. 6. Interactions among PA6gPP, POE and organoclay [25].

Morphology. The morphology of POE toughened PA6/PP/organoclay was different from that of POE toughened PA6/PP. It can be seen from Fig. 7 that the domain size of the POE in PA6/PP/organoclay is relatively small than the composite without organoclay (Fig. 7a). The POE particle size dropped from 4.98 μm (Fig. 7a) in the PA6/PP blends to 1.08 μm in PA6/PP/organoclay (Fig. 7c) blends of the same POE content (10 wt%). This confirms that incorporating organoclay makes the POE particles smaller and results in a finer dispersion of POE particles in the PA6/PP matrix. This is due to the incorporation of a substantial amount of organoclay could increase the PA6 viscosity and reduce the viscosity mismatch between PA6 and POE [27]. By increasing the POE, its particle size increased. The particle sizes of POE with 5, 10, 15 and 20 wt% POE are 0.91, 1.08, 1.50 and 2.38, respectively. Larger particle size shows agglomeration of POE which have detrimental effects on the strength and stiffness of the nanocomposites. Thus, 10 wt% of POE would be considered as optimum in terms of mechanical and morphological properties.

Effect of the type of elastomer. The effect of the type of elastomer on the PA6/PP/organoclay nanocomposites was studied in our group [28-31]. Four different types of elastomers were incorporated into the PA6/PP/organoclay blends as toughening agents; ethylene-octene elastomer (POE), ethylene-propylene rubber (EPR), maleated POE (POEgMA) and melated EPR (EPRgMA). It was observed that the rubber toughened nanocomposites using EPR and maleated EPR displayed a slightly higher tensile strength and E-modulus compared to the POE and maleated POE toughened nanocomposites. The higher tensile strength and modulus of EPR as compared to POE probably accounts for the higher values of the corresponding nanocomposites. Laura et al. [32] have found the same trend with SEBS and EPR in PA6/glass fibers composites. The SEBS elastomer has high

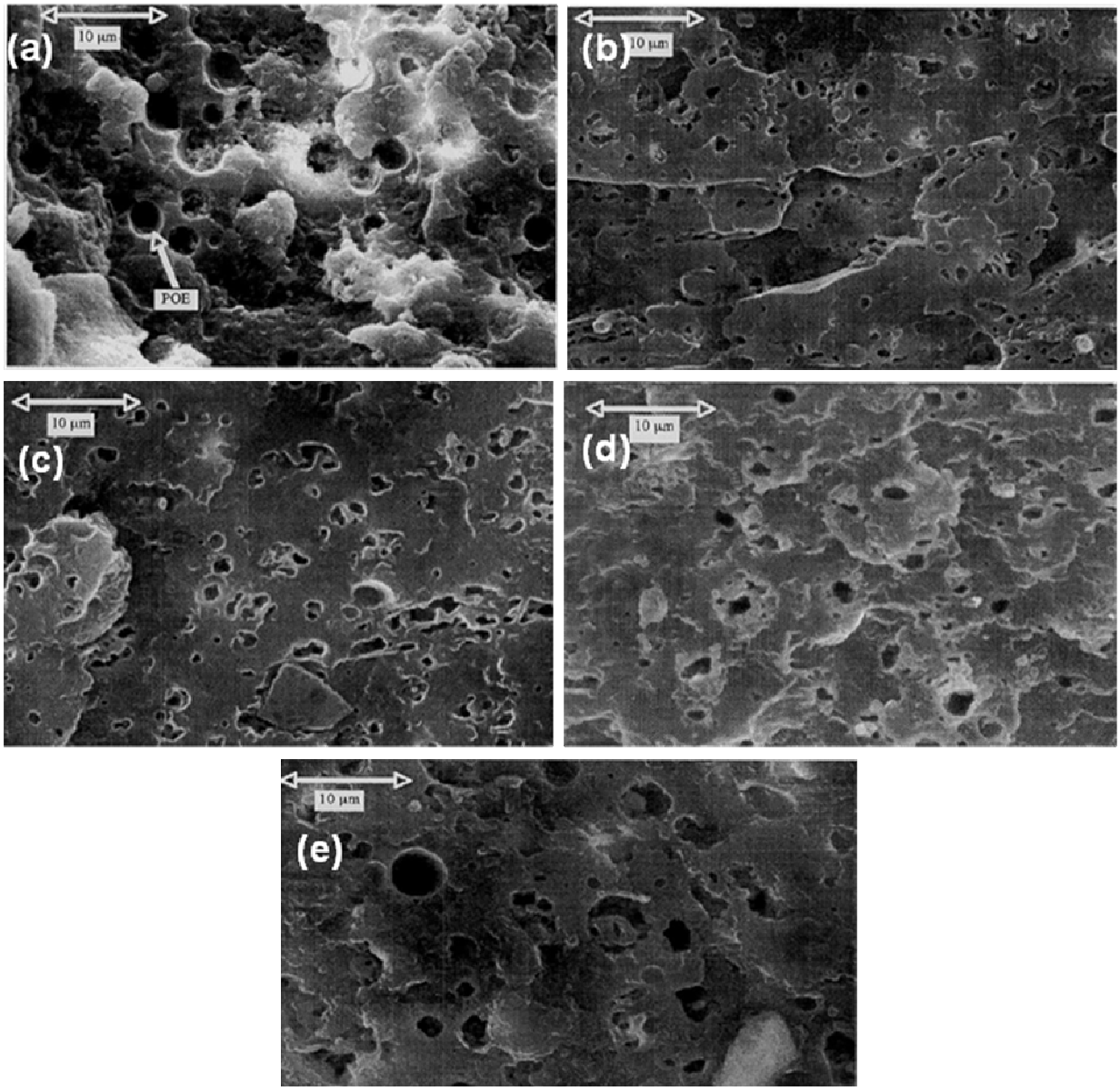


Fig. 7. SEM micrographs of (a) PA6/PP/POE (10 wt%), (b) PA6/PP/clay/POE (5 wt%), (c) PA6/PP/clay/POE (10 wt%), (d) PA6/PP/clay/POE (15 wt%) and (e) PA6/PP/clay/POE (20 wt%) [25].

tensile strength and modulus than EPR caused higher strength and stiffness of the PA6/SEBS/glass fiber composite. On the other hand, the impact strength and elongation at break of both POE and maleated POE toughened nanocomposites were higher than the corresponding EPR

nanocomposites. The smaller particle size and relatively better dispersion of POE and maleated POE may be responsible for the increased toughness.

The nanocomposites toughened with maleated rubber have shown lower strength and stiffness but higher toughness. Cimmino et al. [33] have reported a similar observation in their work on the mechanical properties of the PA6/maleated EPR and the PA6/EPR. Graft copolymer (EPRgMA)gPA6 formation has taken place at the interface of PA6 and the dispersed particles, which caused an increase in free volume. The higher free volume depicts easy chain movement which can absorb and dissipate the applied stress. By increasing the amount of elastomer (POE), the impact strength of the nanocomposite toughened with maleated POE has been increased significantly and shown in Fig. 8. An impact strength of 37 kJ/m2 which is about four times higher than the neat PA6/PP blend was recorded with POEgMA toughened nanocomposite. The functional group of POE is believed to react with terminal group of PA6 thus improving the distribution of the elastomer in the matrix.

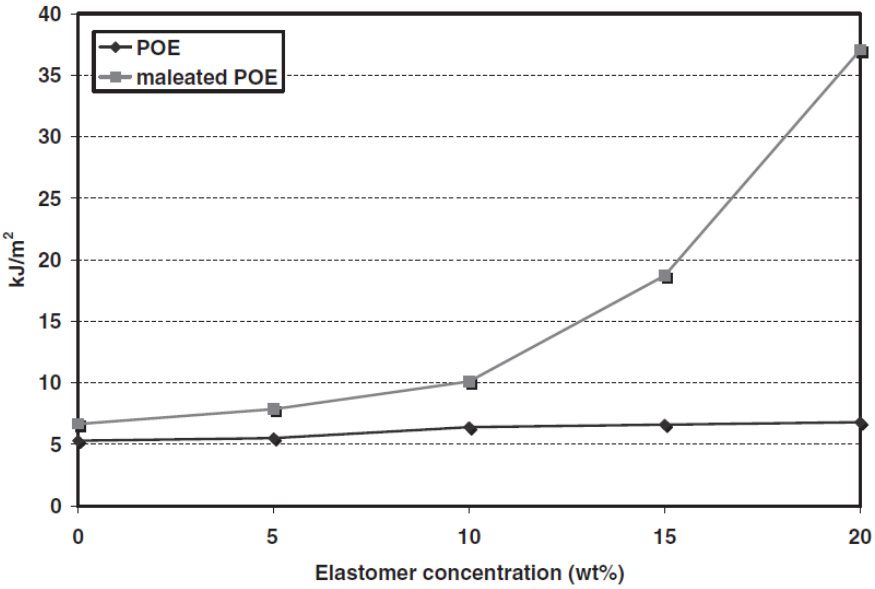


Fig. 8. The effect of elastomer on the impact strength of rubber toughened PA6/PP nanocomposites [28].

Morphology. The morphology of the maleated and un-maleated elastomer filled nanocomposites was analyzed by SEM [28-31]. The particle size of POE in PA6/PP/clay/POE, PA6/PP/clay/mPOE, PA6/PP/clay/EPR and PA6/PP/clay/mEPR is 1.59, 0.96, 1.39 and 0.98 μm, respectively. The smaller size with maleated elastomer improved the dispersion and hence the toughness of the PA9/PP/clay/mPOE nanocomposite.

Effect of mixing sequence on the properties of PA6/PP nanocomposites

Mechanical properties. Due to multiple components in the blend, the mixing sequence of those components is very important. Four different mixing protocols were tried (by keeping the composition of components fixed) and reported [34]; (1) direct melt intercalation single extrusion process (SD), (2) two times direct melt intercalation (S2x), (3) two step melt intercalation i.e. mixing of PA6/organoclay preblend with PP/PPgMA/POE preblend (S2sa), (4) two step melt intercalation i.e. mixing of PA6/PP/PPgMA/organoclay preblend with POE (S2sb). The effect of mixing protocols on the mechanical and morphological properties has been investigated [34]. No significant effect has been observed on tensile and flexural properties but the relatively high impact strength has been examined with S2sa mixing sequence. This high impact strength may be attributed

to the uniform dispersion of organoclay and elastomer in PA6/PP matrix. By S2sa process, the organoclay is able to react with the PA6 matrix before any rubber is incorporated. The strong polar interaction between PA6 and organoclay would keep the clay in PA6 rather migrating to the dispersed POE and PP phases. Dasari et al. [35] reported that the best microstructure with improved properties can be obtained with fully exfoliated organoclay in PA6 matrix rather than in other dispersed phases.

Morphology. The morphology of the nanocomposites was analyzed by SEM [34]. The particle size of POE with SD, S2x, S2sa and S2sb is 1.32, 1.41, 1.02 and 1.26, respectively. The smaller particle size with S2sa showed relatively better and uniform dispersion of POE in the nanocomposite resulted in high impact strength. Among the four mixing protocols, S2sa process had given better results.

Conclusions

The research work on PA6/PP/organoclay/POE nanocomposite done in our group has been mainly reviewed in this article. The effect of PA6/PP blend ratio, loading of organoclay, and the amount and type of elastomer on the mechanical, thermal and morphological properties of the nanocomposite have been investigated. The addition of organoclay (exfoliated) has led to the enhancement of strength and stiffness but at the expense of toughness. The addition of POE elastomer increased the toughness and decreased the strength and stiffness of the nanocomposite. The combined effect of organoclay and POE on the composite's properties are examined by the optimum proportion of each component i.e. PA6/PP:70/30, organoclay: 4 wt% and POE elastomer: 10 wt%. The incorporation of organoclay does not influence the melting temperature and crystallinity of PA6 or PP phase, however, some improvement in the thermal stability of the nanocomposite has been observed. The SEM morphology exhibits that the smaller POE particle size and uniform dispersion favor the nanocomposite with better mechanical properties.

References

[1] R.K. Gupta, E. Kennel and K.J. Kim, in: Polymer Nanocomposites Handbook, chapter 6, CRC Press, Taylor & Francis Group (2010).

[2] A. Okada, Y. Fukushima, M. Kawasumi, S. Inagaki, A. Usuki, S. Sugiyama, T. Kurauchi and O. Kamigaito: U.S. Patent 4,739,007. (1988).

[3] Z. Wang and T.J. Pinnavaia: Chem. Mater., Vol. 10 (1998), p. 3769.

[4] K.J. Yao, M. Song, D. J. Hourston and D. Z. Luo: Polymer Vol. 43 (2002), p. 1017.

[5] J. Piglowski, I. Gancarz, M. Wlazlak and H.W. Kammer: Polymer Vol. 41 (2000), p. 6813.

[6] W.S. Chow, Z.A. Ishak, J.K. Kocsis, A.A. Apostolov and U.S. Ishiaku: Polymer Vol. 44 (2003), p. 7427.

[7] S.V. Nair, L.A. Goettler and B.A. Lysek: Polym. Eng. Sci. Vol. 42 (2002), p. 1872.

[8] J.Z. Liang and R.K.Y. Li: J. Appl. Polym. Sci. Vol. 77 (2000), p. 409.

[9] M.U. Wahit, A. Hassan, A.R. Rahmat, J.W. Lim and Z.A. Mohd Ishak: Plastics and Composites Vol. 25 (2006), p. 933.

[10] D. Silva, A.L.N. Rocha, M.C.G. Coutinho, F.M.B. Bretas and C. Scuracchio: J. Appl. Polym. Sci. Vol. 75 (2000), p. 692.

[11] C.R. Tseng, J.Y. Wu, H.Y. Lee and F.C. Chang: Polymer Vol. 42 (2001), p. 10063.

[12] J. Duvall, C. Sellitti, C. Myers, A. Hiltner and E. Baer: J. Appl. Polym. Sci. Vol. 52 (1994), p. 195.

[13] H. Wang, C. Zeng, M. Elkovitch and M.L. Lee: Polym. Eng. Sci. Vol 41 (2001), p.2036.

[14] K.H. Wang, M.H. Choi, M.K. Chong, S.C. Yeong and J.C. In: Polymer Vol. 42 (2001), p. 9819.

[15] Z.Z. Yu, M. Lei, Y.C. Ou and G.H. Hu: J. Polym. Sci: Part B: Polymer Physics Vol. 37 (1999), p. 2664.

[16] B.B. Khatua, D.J. Lee, H.Y. Kim and J.K. Kim: Macromolecules Vol. 37 (2004), p. 2454.

[17] R.M. Holsti, J.V. Seppala, O.T. Ikkala and I.T. Reima: Polym. Eng. Sci. Vol. 34 (1997), p. 395.

[18] M.U. Wahit, A. Hassan, Z.A. Mohd Ishak, A.R. Rahmat and A. Abu Bakar: J. Thermoplast. Comp. Mat. Vol. 19 (2006), p. 545.

[19] J.W. Cho and D.R. Paul: Polymer Vol. 42 (2001), p. 1083.

[20] P. Reichert, B. Hoffmann, T. Bock, R. Thomann, R. Mulhaupt and C. Friedrich: Macromol. Rapid Comm. Vol. 22 (2001), p. 519.

[21] T.X. Liu, Z.H. Liu, K.X. Ma, L. Shen, K.Y. Zeng and C.B. He: Compo. Sci. Tech. Vol. 63 (2003), p. 331.

[22] T. Liu, K.P. Lim, W.C. Tjiu, K.P. Pramoda and Z.K. Chen: Polymer Vol. 44 (2003), p. 3529.

[23] S.S. Ray and M. Okamoto: Prog. Polym. Sci. Vol. 28 (2003), p. 1539.

[24] K.P. Pramoda, T. Liu, Z. Liu, C. He and H.J. Sue: Polym. Deg. Stab. Vol. 82 (2003), p. 47.

[25] M.U. Wahit, A. Hassan, Z.A. Mohd Ishak and A. Abu Bakar: Polymers & polymer compo. Vol. 13 (2005), p. 795.

[26] Q.F. Li, D.G. Kim, D.Z. Wu, K. Lu and R.G. Jin: Polym. Eng. Sci. Vol. 41 (2001), p. 2155.

[27] Z.Z. Yu, Y.C. Ke, Y.C. Ou, and G.H. Hu: J. Appl. Polym. Sci. Vol. 76 (1999), p. 1285.

[28] M.U. Wahit, A. Hassan, Z.A. Mohd Ishak, A.R. Rahmat and N. Othman: Polymer J. Vol. 38 (2006), p. 767.

[29] A. Hassan, N. Othman, M.U. Wahit, L.J. Wei, A.R. Rahmat, Z.A. Mohd Ishak: Macromol. Symp. Vol. 239 (2006), p. 182.

[30] M.U. Wahit, A. Hassan, Z.A. Mohd Ishak and T. Czigany: *eXPRESS Polymer Letters* Vol. 3 (2009), p. 309.

[31] N. Othman, A. Hassan, A.R. Rahmat and M.U. Wahit: Int. J. Polym. Mater. Vol. 56 (2007), p. 893.

[32] D.M. Laura, H. Keskkula, J.W. Barlow and D.R. Paul: Polymer Vol. 44 (2003), p. 3347.

[33] S. Cimmino, F. Coppola, L. D. Orazio, R. Greco, G. Maglio and M. Malinconoco: Polymer Vol. 27 (1986), p. 1874.

[34] M.U. Wahit, A. Hassan, A.R. Rahmat and Z.A. Mohd Ishak: J. Elasto. Plast. Vol. 38 (2006), p. 231.

[35] A. Dasari, Z.Z. Yu and Y.W. Mai: Polymer Vol. 46 (2004), p. 5968.

© (2011) Trans Tech Publications, Switzerland
doi:10.4028/www.scientific.net/KEM.471-472.20

Fabrication and Characterization of Unidirectional Silk Fibre Composites

Mansur Ahmed[1, a], Md Saiful Islam[1], Qumrul Ahsan[1] and Md Mainul Islam[2, b]

[1] Department of Materials and Metallurgical Engineering, Bangladesh University of Engineering and Technology (BUET), Dhaka 1000, Bangladesh

[2] Centre of Excellence in Engineered Fibre Composites, University of Southern Queensland, Toowoomba, Queensland 4350, Australia

[a] mansurbuet04@gmail.com, [b] mainul.islam@usq.edu.au

Keywords: Silk Fibre, Unidirectional, Composites, Fabrication, Characterization, MAPP, PP.

Abstract. Natural fibres offer a number of benefits as reinforcement for synthetic polymers since they have high specific strength and stiffness, high impact strength, biodegradability etc. The aim of this study is to fabricate and determine the performance of unidirectional silk fibre reinforced polymer composites. In the present initial study, alkali treated silk fibres were incorporated as reinforcing agent, while a mixture of 20% maleic anhydride grafted polypropylene (MAPP) and commercial grade polypropylene (PP) was used as matrix element. The unidirectional composites were fabricated by using hot compression machine under specific pressure, temperature and varying fibre loading. Tensile, flexural, impact and hardness tests were carried out by varying silk fibre volume fraction. Composites containing 45% fibre volume fraction had higher tensile and flexural strength, Young's modulus and flexural modulus compared to other fabricated composites including those with untreated silk fibres. SEM micrographs were taken to examine composite fracture surface and interfacial adhesion between silk fibre and the matrix. These micrographs suggested less fibre pull out and better interfacial bonding for 40% fibre reinforced composites.

Introduction

Natural fibre reinforced polymer composites have gained their popularity in the composite research because of versatility and diversified nature of their applications [1]. This is due to a range of potential advantages of natural fibres, especially with regard to their environmental performance. Natural fibres are renewable resources and even when their composite wastes are incinerated, they do not cause net emission of carbon dioxide to the environment. They are inherently biodegradable, which may be beneficial [2-4]. Among all the natural reinforcing fibrous materials, silk appears to be a promising fibre due to its high toughness and aspect ratio in comparison with other natural reinforcements [5, 6]. Moreover, the mechanical properties of silk fibres consist of a combination of high strength, extensibility, and compressibility. On the other hand, maleic anhydride grafted polypropylene (MAPP) and commercial grade polypropylene (PP) are commonly used matrices for fibre-reinforced composites due to their good interfacial bonding properties [7, 8].

Major aims of this work are to fabricate the unidirectional silk fibre reinforced polymer (MAPP and commercial grade PP) matrix composites by varying fibre volume fraction and to determine their mechanical properties such as tensile strength, flexural strength, impact strength and hardness.

Materials and Methodology

Collection of silk fibre and polypropylene resin. Silk fibres were supplied by Sapura Silk Industries, Rajshahi, Bangladesh. Commercial grade polypropylene resin was bought from a local chemical manufacturer and distributor. Maleic anhydride grafted polypropylene (MAPP) was bought from Belgium.

Fabrication of composites. Four types of composites were manufactured. Unidirectional silk fibre composites were made using polypropylene (PP) and maleic anhydrate grafted polypropylene

(MAPP) matrix. By varying fibre volume fraction (30%, 35%, 40%, 45%), 2 mm thick composites were manufactured. Steps for manufacture are given below:

a) At first, alkali treated silk fibre was weighted according to the required volume fraction needed. The required amount of weight of silk fibre was weighted.
b) Sufficient amount of commercial polypropylene was taken on a beaker and weighted and 20% MAPP was added with it. To prevent voids, water bubbles, poor fibre matrix adhesion the fibre and polypropylene were dried in an oven at about 100ºC for 3-4 hours.
c) Mould surface was cleaned very carefully and Teflon sheet was placed over the mould surface properly for the easy removal of the product.
d) A layer of polypropylene granule with MAPP was placed in a female mould and 2 mm thick die was placed surrounding the granule.
e) Then one layer of continuous fibres was aligned parallel to each other onto PP granule using glue at the edges of fibre (see Fig. 1) and another layer of fibres was placed over prior layer. And so on to produce as required fibre volume fraction.
f) Finally, another layer of mixture of PP and MAPP was placed onto silk fibre layer.
g) The female mould with aligned fibre with PP was covered by a male mould with Teflon sheet.
h) Plates were placed in hot pressing machine, 185°C temperature and 85 kN pressure was applied simultaneously for about 15 min and then cooled slowly using water-cooling system.
i) At last the specimen was carefully discharged from the mould.



(a) PP-MAPP layer (b) Fibre alignment (c) PP-MAPP layer on fibre

Fig. 1. Unidirectional silk fibre reinforced composite fabrication process.

Results and Discussion

Tensile Testing. Stress-strain curves of unidirectional fibre-reinforced composites under longitudinal loading are represented in Fig. 2. It is seen from this Fig. that ultimate tensile strength (UTS), modulus and percentage elongation are maximum for fibre volume fraction at highest end (45%), because the load applied to the fibre direction. Longitudinal strength is dominated by fibre strength. The stress-strain mode that operates for a specific composite will depend on fibre and matrix properties, and the nature and strength of the fibre-matrix interfacial bond. Fig. 3 represents the comparison between theoretical and experimental strength and modulus; the experimental values are lower than theoretical values. This may be due to the poor fibre-matrix interface for presence of some voids and misalignment of continuous unidirectional fibres. Fig. 4 shows that longitudinal strain increases with fibre volume fraction.

Stress-strain curves of unidirectional fibre-reinforced composites under transverse loading are shown in Fig. 5. With the increase of fibre volume fractions, UTS, modulus and strain increases. A variety of factors will have a significant influence on the transverse strength; these factors include properties of the fibre and matrix, the fibre-matrix bond strength, and the presence of voids. Transverse UTS, modulus and strain is lower than longitudinal UTS, modulus and strain (Fig. 6). Longitudinal strength depends upon the fibre strength and interfacial bonding between fibre and matrix. On the other hand, transverse strength depends upon the fibre-matrix interfacial strength.

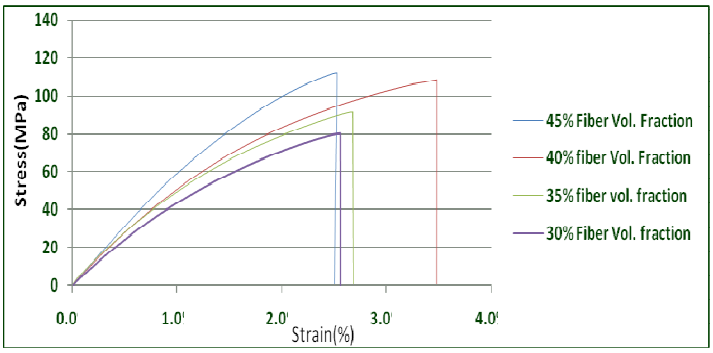
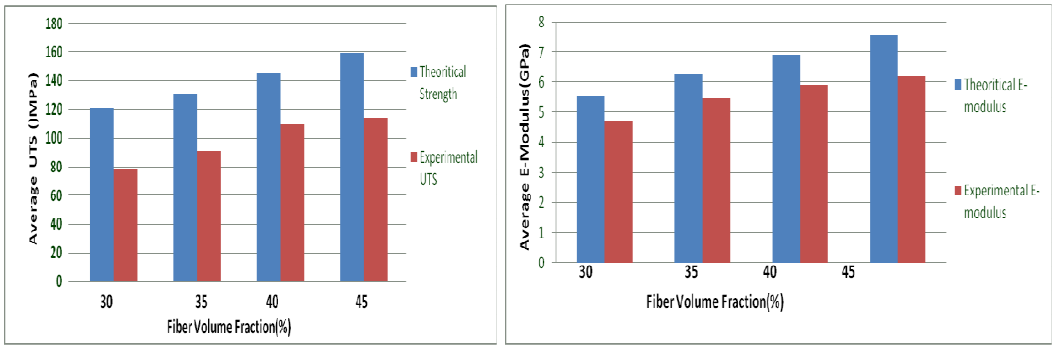


Fig. 2. Stress-Strain curve for composites under longitudinal loading.



(a) UTS (b) Young's modulus

Fig. 3. Comparison between theoretical and experimental longitudinal strength and modulus.

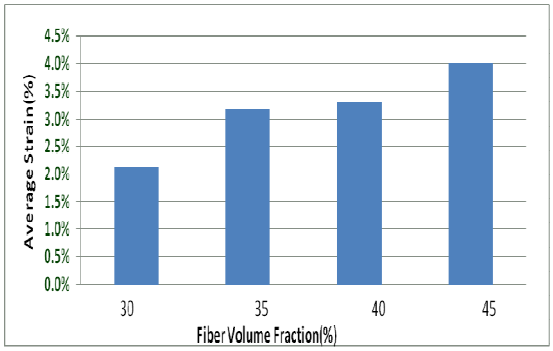


Fig. 4. Comparison of longitudinal average strain.

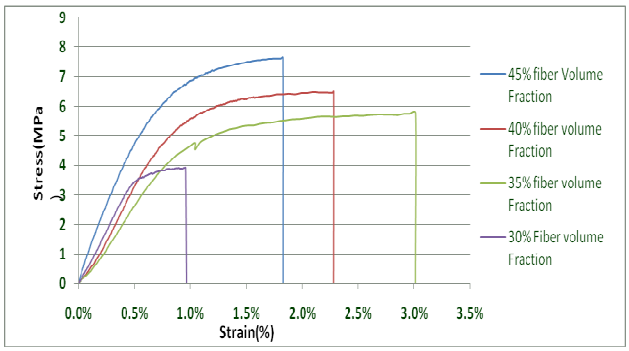
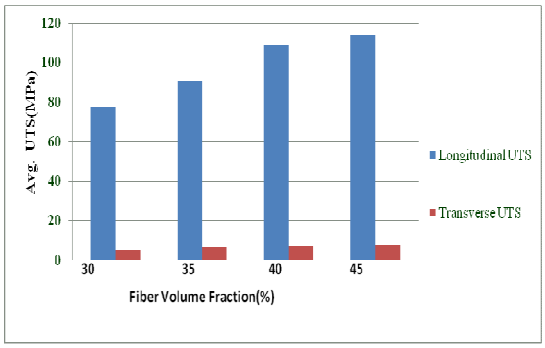
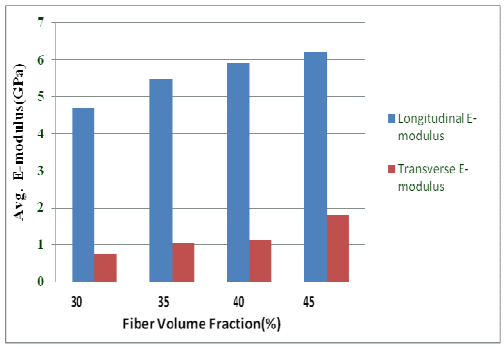


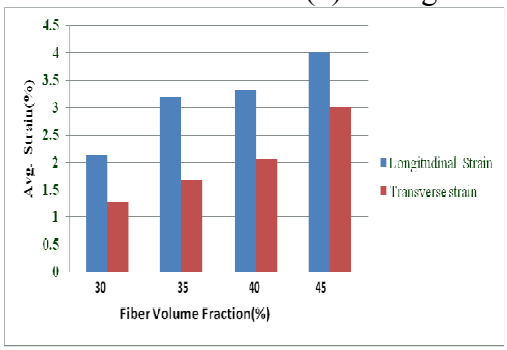
Fig. 5. Stress-strain curve for composites under transverse loading.



(a) UTS



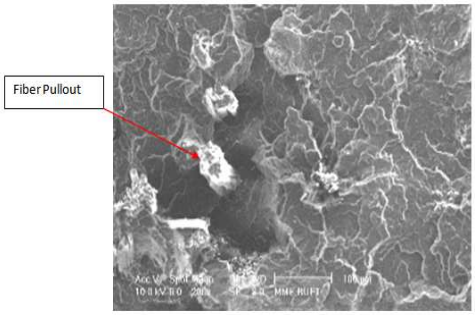
(b) Young's modulus



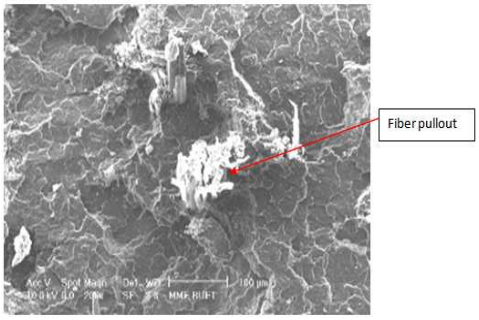
(c) Strain

Fig. 6. Comparison between longitudinal and transverse loading results.

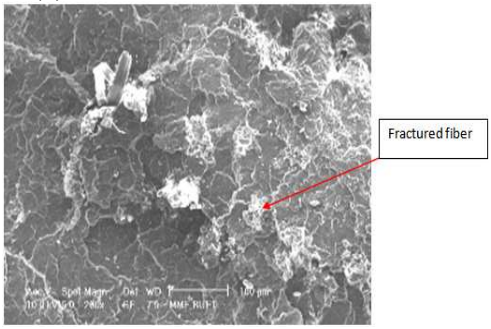
Microscopic Observations of Tensile Specimens. The fracture surfaces of the tensile test specimens were used to examine by scanning electron microscope (SEM). To study the surface morphology of the prepared composites SEM photographs were taken for 30%, 35%, 40%, 45% fibre volume fraction, as shown in Fig. 7. SEM of fracture surface of composite indicates that fibre pullout occurs. This is due to lack of interfacial adhesion between silk and PP-MAPP matrix. Due to intermolecular hydrogen bond formation between silk fibres and hydrophobic nature of the matrix, hydrophilic silk fibres tend to agglomerate into bundles (Fig. 7(d)), and become unevenly distributed throughout the matrix. It is seen that for 40% fibre volume fraction composite, less fibre pullout happens, better interfacial adhesion between silk and the matrix occurs (Fig. 7(c)).



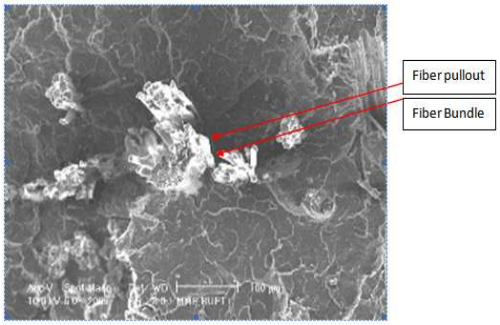
(a) 30% fiber volume fraction



(b) 35% fiber volume fraction



(c) 40% fiber volume fraction



(d) 45% fiber volume fraction

Fig. 7 SEM of fracture surface of silk fibre composites with various fibre fractions (200X)

Flexural Testing. Stress-strain curves achieved from flexure test for four volume fractions are shown in Fig. 8. It is observed from the Fig. that the values of flexural strength, modulus, and strain increase with the increase of fibre loading, as shown in Fig. 9 by a comparison. In addition to other factors such as voids, fibre orientation, longitudinal strength of the composites mainly depends upon the fibre strength and interfacial bonding between fibre and matrix and transverse strength depends upon the fibre-matrix interfacial strength.

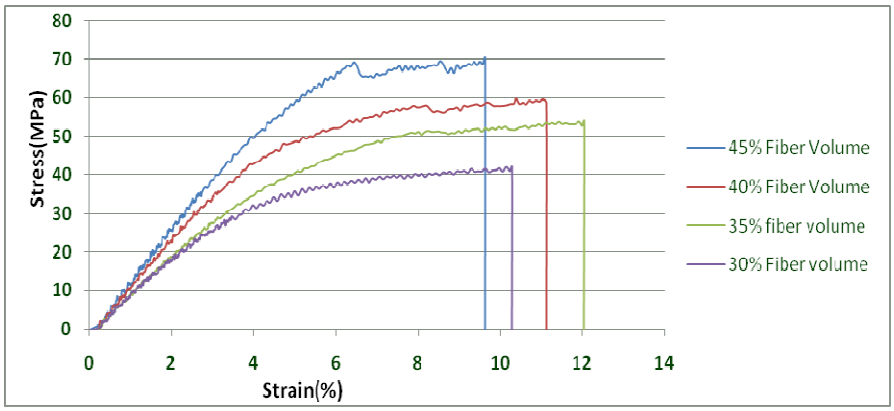
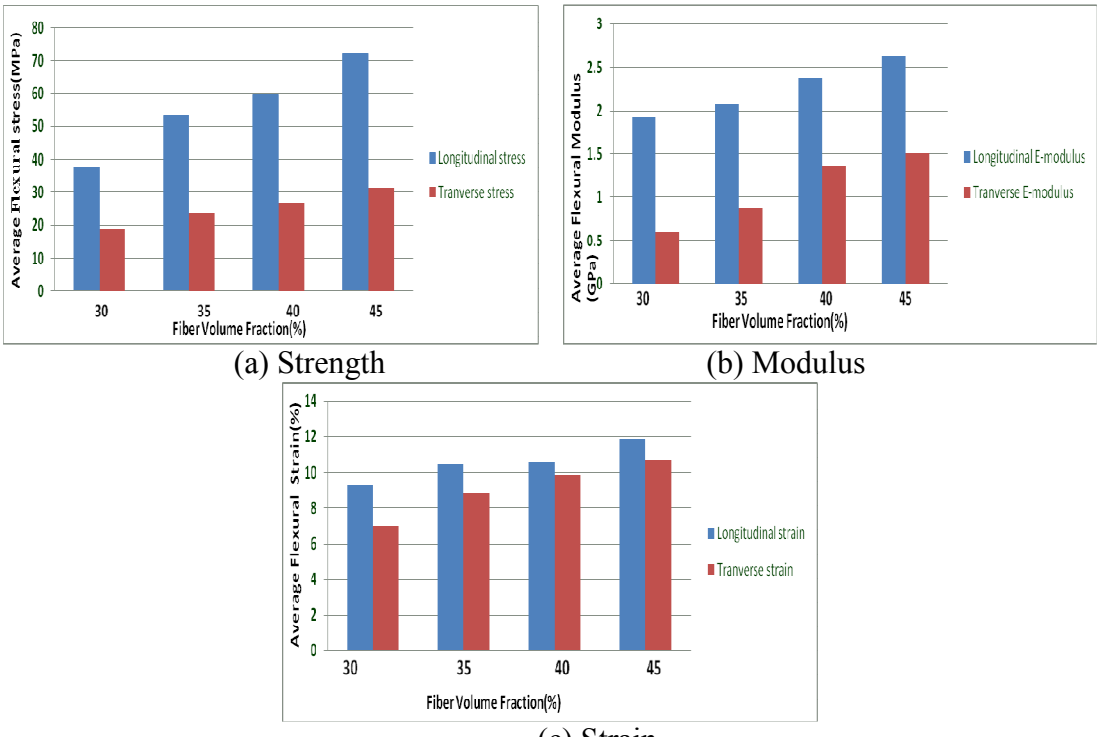


Fig. 8. Stress-strain curves for composites under longitudinal flexural loading.



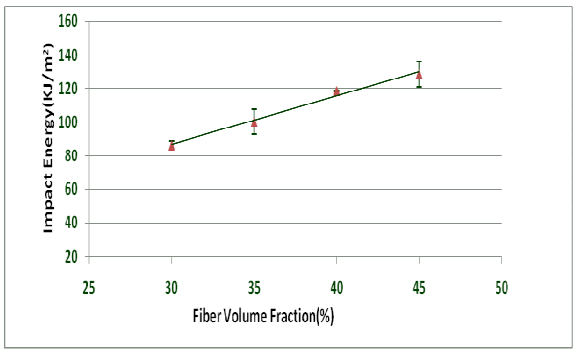
(a) Strength (b) Modulus

(c) Strain

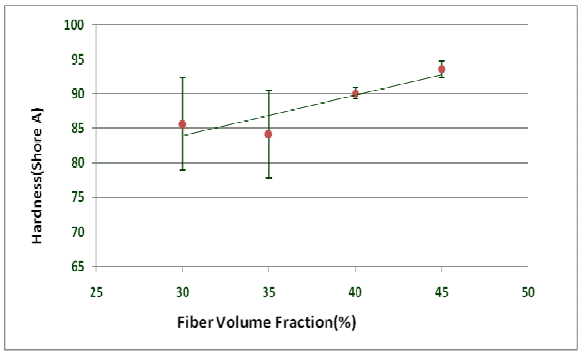
Fig. 9. Comparison between longitudinal and transverse flexural test results.

Impact testing. It is apparent from the test result presented in Fig. 10(a) that the impact strength increases with the fibre loading. There is no much variation in impact strength noticed among the composites with same fibre volume fraction.

Hardness testing. It can be noticed from the hardness test results presented in Fig. 10(b) that the hardness increases with the fibre loading. Hardness tests showed not very profound variation among all the composites.



(a)



(b)

Fig. 10 Variation of impact strength and hardness with fibre volume fractions of composites.

Summary

Variation of the properties by varying fibre volume fraction in the unidirectional silk fibre composites was observed. From the test results, it can be concluded based on the experimental range that composite containing 45% volume percentage shows higher strength than other lower fibre volume fraction composites. It was expected that with the increase of fibre volume fraction, strength of the composites will increase. As fibre contains inherent defects, strength of single fibres is not constant and poor adhesion between fibre and matrix, strength is less than theoretical strength. Hardness measurement shows not much variation in varying fibre volume fractions. Impact energy was greater in higher volume fraction composites as compared to lower volume fraction ones. Finally, it can be said that silk fibres should be incorporated highly aligned manner and parallel to each other to get substantial mechanical properties. Fibre volume fraction may be increased keeping in mind that these fibres are not entangled, defect free and do not impair proper wetting with the matrix phase. Further investigation is needed in addition to this initial study for better understanding of the behaviour of these composites.

References

[1] D. Gay, S.V. Hoa and S.W. Tsai: *Composite Material: Design and Applications* (CRC Press 2003), p. 17-25.

[2] I. Verpoest, A.W. Van Vuure, N. El Asmar and J. Vanderbeke, U.S. Patent Application Number: 20100040816 A1 (2010).

[3] A.C.N. Singleton, C.A. Baillie, P.W.R. Beaumont and T. Peijs: Composites – Part B, Vol. 34 (2003), p. 519-526

[4] E.M.F. Aquino, L.P.S. Sarmento and W. Oliveira: Journal of Reinforced Plastics and Composite, Vol. 26 (2007), p. 219-233.

[5] H.Y. Cheung, K.T. Lau, M. P. Ho and A. Mosallam: Journal of Composite Materials, Vol. 43 (2009), p. 2521-2531.

[6] A.U. Ude, A.K. Ariffin, K. Sopian, A. Arifin and C.H. Azhari: International Journal of Engineering Science and Technology, Vol. 2 (2010), p. 128-140.

[7] A. Karmarkar, S.S. Chauhan, J.M. Modak and M. Chanda: Composites – Part A, Vol. 38 (2007), p. 227-233.

[8] P. Wambua, J. Ivensand and I. Verpost: Composite Science and Technology, Vol. 63 (2003), p. 1259-1264.

© (2011) Trans Tech Publications, Switzerland
doi:10.4028/www.scientific.net/KEM.471-472.26

Effect of Carbon Black and Fly Ash Fillers on Tensile Properties of Composites

R.Satheesh Raja[1,a], K.Manisekar[2,b],V.Manikandan[3,c]

[1]Department of Mechanical Engineering, PET Engineering College, Vallioor-627117, India

[2]Centre for Manufacturing Sciences, National Engineering College, Kovilpatti-628503, India

[3]Department of Mechanical Engineering, SVCET, Puliangudi-627855, India

[a]nanosatheesh@gmail.com

Keywords: FRP, carbon black, Fly ash, filler, polyester

Abstract. Fibre reinforced polymer composites play an incredible role in almost all spheres of day to day life and the field of carbon composites is one of the prime research area in recent decade. Polymers are mostly reinforced with fibre or fillers to obtain better mechanical properties. The properties of the polymer composites can be improved largely by varying the type of filler/fibre materials and its volume percentage. Composites properties depend on the size, shape and other physical properties of the reinforcements. A relative easy way to improve the mechanical properties of a polymer is the addition of filler materials. In all particulate filled systems, the adhesion between the matrix and filler plays a significant role in determining the key properties such as strength and toughness. The mechanical properties of composites are also influenced by the filler's nature, size and distribution profile, aspect ratio, volume fraction, the intrinsic adhesion between the surfaces of filler and polymer. In this paper, the effect of filler material on mechanical properties of E-Glass fibre reinforced polymer has been studied out by varying filler materials. For these study three different types of specimens were prepared, viz FRP without filler material, the FRP with 10 volume percentages of carbon black and the FRP with 10 volume percentage of Fly ash as filler material. The polyester composites were fabricated by hand-layup method. Mechanical properties of the specimens are analyzed using computerized Universal Testing Machine as per ASTM D 638 standards. The resulting behavioral patterns of the FRP with filler material are listed and compared to those of the FRP without filler material. Mechanical properties such as ultimate tensile strength, percentage of elongation, yield strength, Poisson's ratio and percentage reduction in area were found out.

Introduction

Worldwide research is underway to develop newer composites with varied combinations of fibres and fillers so as to make them useable under different operational conditions. The properties of polymers are modified using fillers and fibres to suit the high strength/high modulus requirements. An advance in the polymer industry has been the use of fibre and particulate fillers as reinforcements in polymer matrix. Particulate fillers are of considerable interest, not only from an economic viewpoint, but as modifiers especially the physical properties of the polymer. It is well documented in the literature that majority fillers have a positive influence on mechanical properties [1].

The process of coal combustion results in fly ash. The problem with fly ash lies in the fact that not only does its disposal require large quantities of land, water, and energy, its fine particles, but also if not managed well, by virtue of their weightlessness, can become airborne. Currently, 90 million tones of fly ash is being generated annually in India, with 65 000 acres of land being occupied by ash ponds. Such a huge quantity poses challenging problems, in the form of land usage, health hazards, and environmental dangers. Both in disposal, as well as in utilization, utmost care has to be taken, to safeguard the interest of human life, wild life, and environment [1].The shape,

size, volume fraction, and specific surface area of such added particles in polymer have been found to affect mechanical properties of the composites greatly [2]. Fly ash contains fine mainly silica and alumina with minor amount of calcium and magnesium oxides [3]. Fly ash forms at temperature in the range of 920-1200 ºC and is collected as precipitator ash (solid particles) and cenospheres (hollow microspheres) that float on collection ponds [4].Cenosphere has a low density of about 0.6 g / cm3, and can be used for the synthesis of ultra-light composites materials, whereas precipitator fly ash has a density in the range of 2.0-2.5 g / cm3. It can improve various properties of selected matrix materials, including stiffness, strength, and wear resistance by its inclusion in small volume [5-7].

Tensile strength and modulus of the composites filled with carbon black and carbon fibre increase with increasing each of filler contents but impact strength and elongation at break are found to be reduced. Composites with more than 30% volume carbon black are very brittle and difficult to mix, using carbon fibre as a substitute for part of carbon black in carbon black-filled composites can decrease volume resistivity by a synergistic effect along with an improvement in mechanical properties of the composite [8].

Material

Polyester resin is used as matrix material and E-glass fibre as reinforced material. Filler materials used in this research were fly ash and carbon black. The fly ash was brought from National Thermal Power Station situated at Tuticorin in Tamilnadu, India. Carbon black is available commercially in chemical market at Paris in Chennai, India.

Experimental Procedure

Tensile samples of polymer composites (ASTM D 638) were prepared by using hand lay up method. Moulding box with the required size of 200 mm x 200 mm x 20mm was prepared and the moulding box surfaces were applied with wax polish which act as a release agent. Required amount of the polyester resin was mixed with cobalt napthanate which acts as an oxidizer. Measured amount fly ash or carbon black powder was added with the resin and stirred well. Methyl ethyl ketone peroxide was used as catalyst. The fibre mat was placed on the molding board and the prepared resin mixture was applied over the fibre mat, the trapped air bubbles were removed by rollers to avoid void formation. Then additional fibre mat was placed and above steps were continued till the required thickness was attained.

Tensile testes measure the force required to break a specimen and the extent to which the specimen stretches or elongates to that breaking point. Tensile tests produce a stress-displacement diagram and load-displacement diagram, which was used to determine tensile modulus. The data is often used to specify a material, to design parts to withstand application force and as a quality control check of materials.ASTM D 638 specimens are placed in the grips of the universal testing machine at a specified grip separation and pulled until failed at test speed of 50mm/min for measuring strength and elongation. Three specimens were tested in each case.

Result and discussion

Table1. gives the mechanical properties of fibre reinforced plastic with fly ash and carbon black fillers. A specimen A is prepared in the combination of polymer resin and fibre only. Specimens B and C were prepared by addition of 10% volume of fly ash and carbon black as filler in the FRP. These molded specimens were prepared as per ASTM D 638 and tested in computerized universal testing machine in 50 mm/min at room temperature.

Table 1. Mechanical Properties of FRP with fillers

Specimen	Combinations	% Volume	Weight [g]	Ultimate Tensile Strength, [MPa]	Yield Strength, [MPa]	Young's Modulus,[MPa]	% Elongation
A	Polyester resin E-glass fibre	65 35	430 240	115	75	34	4
B	Polyester resin E-glass fibre fly ash	65 25 10	430 170 70	50	35	14	2
C	Polyester resin E-glass fibre carbon black	65 25 10	430 170 70	52	36	15	3

Fig. 1. illustrates the graph of ultimate tensile strength (UTS) in MPa versus specimens of various combinations. It can be seen that the specimen A yielded 115 MPa, specimen B yielded 50 MPa for 10vol% increment of fly ash and specimen C yielded 52 MPa for 10vol% increment of carbon black. The ultimate tensile strength of specimen C is higher than that of specimen B. This is due to the proper bonding strength between the fine grained carbon black and FRP.

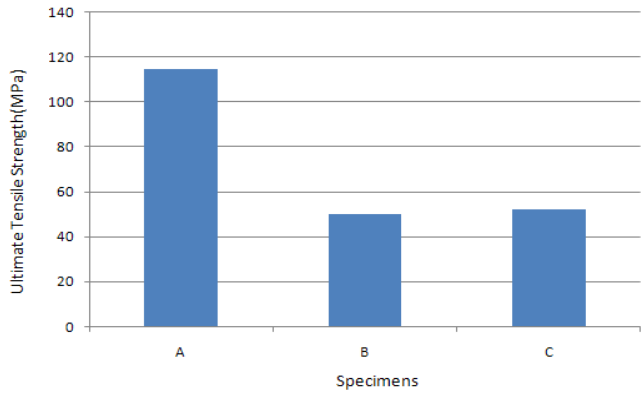


Fig. 1. Ultimate tensile strength for specimens

Fig. 2. illustrates the graph of yield strength in MPa versus different specimens. For 0 vol% of filler material, specimen A yielded 75 MPa. For the addition of 10 vol% of fly ash and carbon black filler material in the FRP, specimen B yielded 35 MPa and specimen C yielded 36 MPa. It shows that addition of 10 vol% of filler material increases the brittleness of the material.

Fig. 3. illustrates the measure of stiffness of the various specimen combinations.It is observed that the stiffness of the specimen A is higher the specimen B and specimen C due to the addition of 10vol% of fly ash and carbon black fillers. When compare with the specimen B and specimen C, stiffness of carbon black as filler in specimen is higher than the fly ash as filler material.

Fig. 4. illustrates the plots of % elongation versus specimens of various combinations. It is usually employed to measure ductility of the specimens. It can be seen that the specimen A elongates 4%, B elongates 2% due to the addition of 10 vol% of fly ash and C elongates 3% for the addition of 10 vol% of carbon black. For the increment of 10 vol% of fillers reduce the elongation 2% in specimen B and 1% in specimen C.

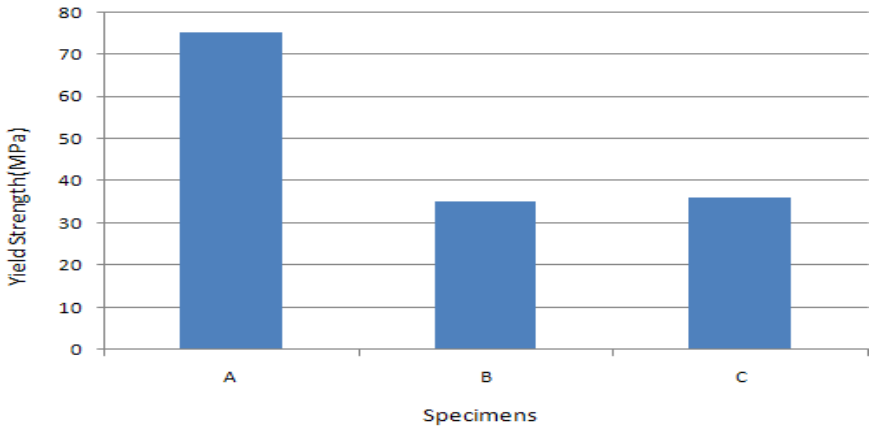


Fig. 2. Yield strength for specimens

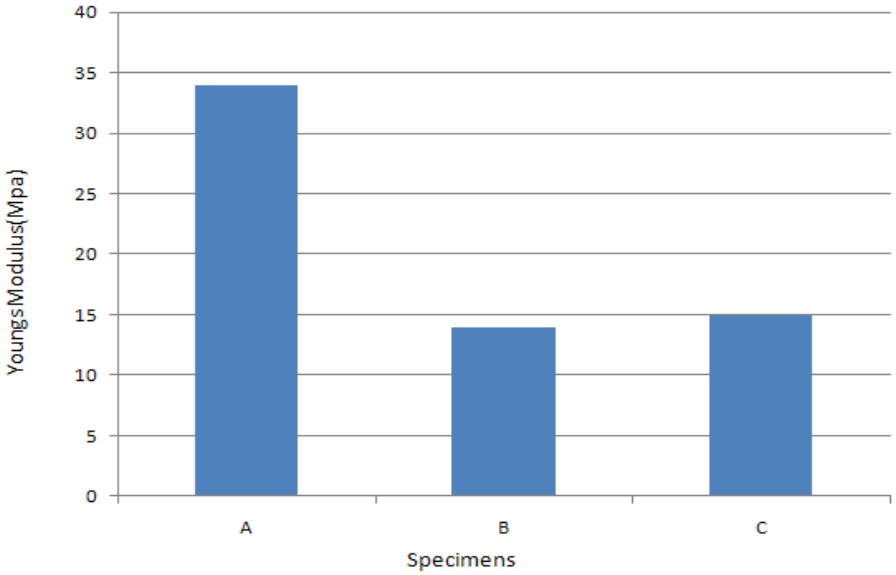


Fig. 3. Young's modulus for specimens

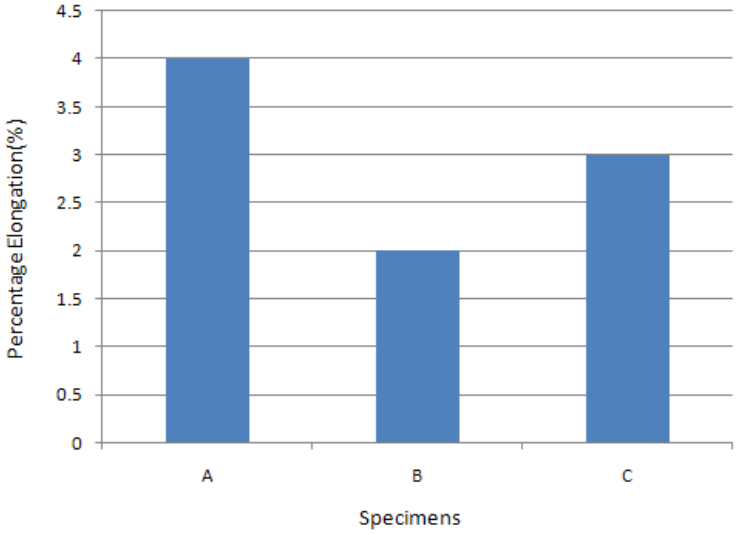


Fig. 4. Percentage elongation for specimens

Summary

Research is carried out on the impact of the addition of filler material in the fibre reinforced polymer composites. 10% volume of the filler materials, fly ash and carbon black are added to the FRP and tested. On analysis of the results, it is inferred that the FRP with carbon black possesses better tensile properties than the FPR with fly ash. On the other hand, it is also observed that the tensile properties of FRP with filler material are not satisfactory as compared to the FRP without filler material. The research work can be extended in future by changing the volume percentage and by reducing the grain size of the filler materials.

References

[1] Utility Bonanza from dust "Flyash" Published in Parisara Envis Newsletter by Department of forests, ecology & environment, government of Karnataka, Vol2 No 6, January 2007.

[2] I.Yamamoto, T. Higashihara and T. Kobayashi, Int. J. JSME, 46 (2) (2003) 145–153.

[3] K. Prabhakaran, K. G. K. Warrier, P. K. Rohatgi, Ceram. Int. 27, 749 (2001).

[4] S. Nonavinakere, B. E. Reed, Proc. 10-th Intern. Ash Use Symp., Vol. 1, EPRI TR-101774, 1993, p. 120.

[5] P. K. Rohatgi, R. Q. Guo, H. Iksan, E. J. Borchelt, R. Asthana, Mater. Sci. Eng. A244, 22-30 (1998).

[6] T. Matsunaga, J. K. Kim, S. Hardcastle, P. K. Rohatgi, Mater. Sci. Eng. A325, 333 (2002).

[7] P. K. Rohatgi, J. Met. 46, 55-59 (1994).

[8] Ali Farshidfar, Vahid Haddadi Asl, and Hossein Nazokdast, "Electrical and Mechanical Properties Of Conducive Carbon Black/ Polyolefin Composites Mixed With Carbon Fibre", Composites 2006 Convention and Trade Show American Composites Manufacturers Association October 18-20, 2006 St. Louis, MO USA

[9] ASTM C618-99 Standard specification for coal flyash and raw or calcined natural pozzolan for use as a mineral admixture in concrete.

[10] ASTM D638-10 Standard test method for tensile properties of rigid plastics.

© (2011) Trans Tech Publications, Switzerland
doi:10.4028/www.scientific.net/KEM.471-472.31

Producing Particleboard Using Of Mixture of Bagasse and Industrial Wood Particles

T.Tabarsa

Faculty of Forestry and Wood Technology, Gorgan University of Agricultural Sciences and Natural Resources, Beheshti st. Gorgan, Iran.

t.tabarsa@yahoo.com

Keywords: wood particle, bagasse, single layer particleboard, three layer particleboard, physical properties, mechanical properties, surface quality, slenderness

Abstract. In this study feasibility of using of mixture of bagasse and industrial wood particles for producing single and three layer particleboard . The aim of this study was to consider bagasse as partially substitute particleboard industry raw material. Variables were type of board at two levels (single and three layer), percentage of added bagasse to industrial particles at 4 levels (20%,30%, 40% and 50%) , and press temp. at two levels (165OC and 180 OC). In producing three layer particleboard wood and bagasse particles were separated and placed in different layers so that bagasse particles were located in the face layers and wood particles were placed in the core of board. But in one layer particleboard bagasse and wood particles were used in the form of mixture. Effect of variables on physical and mechanical properties of particleboard were determined. Results showed that in three layer particleboard physical and mechanical properties were better than single layer particleboard. Increasing press temperature caused improvement in particleboard properties in most cases due to intermeshing and increasing softening wood and bagasse particles. The optimum treatment in this study was found to be adding 50% bagasse and press temperature of 180 OC.

Introduction

Regarding raw material demand for particleboard industry and reduction of wood supply from natural forest due to environmental concerns utilization of alternative lngno-cellulosic materials such as bagasse is unavoidable. Compared with other ligno-cellulosic material such as wheat straw, reed and sunflower stem, bagasse is the most suitable material for manufacturing particleboard. This contains 53.4% cellulose, 18% lignin, 1.6% extractives and 0.08 % ash. Its fiber length is 1.5 mm which is suitable for making particleboard [1, 8 and 9]. Only 16% of bagasse is used in wood industry from this 2.4% is consumed for making particleboard [2]. Particleboard made from bagasse meets properties of particleboard manufactured from wood particles. Regarding low density and log fiber of bagasse, it can modify properties of particleboard made from heavy species such as eucalyptus when only particles are mixed whit their particles [3]. On the other hand, bagasse improves surface roughness of particleboard which is very important in finishing particleboard [3] . The aim of this study was to investigate on effect of bagasse on properties of particleboard manufactured from mixture of baggase and wood particles.

Materials and Methods

Bagasse was provided from a local sugar mill located in Shoshtar, South of Iran. Bagasse was dried to 4%. Industrial particles were provided from local company. Urea formaldehyde resin and ammonium chloride were provided by a local adhesive company. Amount of bagasse added to industrial particles at three levels (20%, 30, and 50%), press temperature at two levels (165°C and 180°C) and panel type at two levels (one layer and three layers). In total forty eight panels were manufactured. In manufacturing three- layer panels, bagasse was used as surface layers. Mechanical

properties of panels such as modulus of rupture (MOR), modulus of elasticity (MOE) and internal bond (IB) were evaluated following DIN 68793 and thickness swelling (TS) was evaluated based on ASTM 1037. Data was analyzed using ANOVA by SPSS software.

Results and discussion

Observations of experiments are shown in Table 1. and results of analysis of variances are shown in Table 2.

Table 1. Treatments and observations

Treatment	panel	Bagasse %	Press Temp. ^{O}C	Density	MOR MPa	MOE MPa	IB MPa	TS %
1	One layer	20	165	0.65	11.60	1549	0.54	12.7
2	One layer	20	180	0.66	10.00	1420	0.81	11.9
3	One layer	30	165	0.65	12.90	1269	0.51	14.8
4	One layer	30	180	0.65	11.30	1353	0.75	13.7
5	One layer	40	165	0.64	13.50	1193	0.42	15.9
6	One layer	40	180	0.64	13.00	1248	0.61	15.1
7	One layer	50	165	0.64	14.10	1020	0.39	17.5
8	One layer	50	180	0.65	14.00	1086	0.57	15.5
9	Three layer	20	165	0.63	9.00	1130	0.31	21.2
10	Three layer	20	180	0.63	10.00	1380	0.39	18.1
11	Three layer	30	165	0.64	11.00	1319	0.47	18.1
12	Three layer	30	180	0.65	13.00	1679	0.57	15.9
13	Three layer	40	165	0.66	14.00	1919	0.51	16.1
14	Three layer	40	180	0.67	15.00	2103	0.63	15.2
15	Three layer	50	165	0.67	16.00	1966	0.65	14.3
16	Three layer	50	180	0.69	12.96	2550	0.77	12.8
control	Three layer	-		0.65		1458	0.45	12.4

Table 2. Results of analysis of variance (ANOVA)

variables	TS	IB	MOE	MOR
Panel type 1	**	**	**	**
Bagasse 2	ns	**	**	**
Press temp. 3	**	**	**	*
1 X 2	**	**	**	**
1 X 3	ns	**	**	**
2 X 3	ns	**	ns	ns
1 X 2 X 3	ns	**	ns	ns

** = 99% confidence, *= 95% confidence , ns = not significant

Based on Table 2. effect of panel type on MOR is significant with 99 % confidence. This effect is shown in Fig. 1.

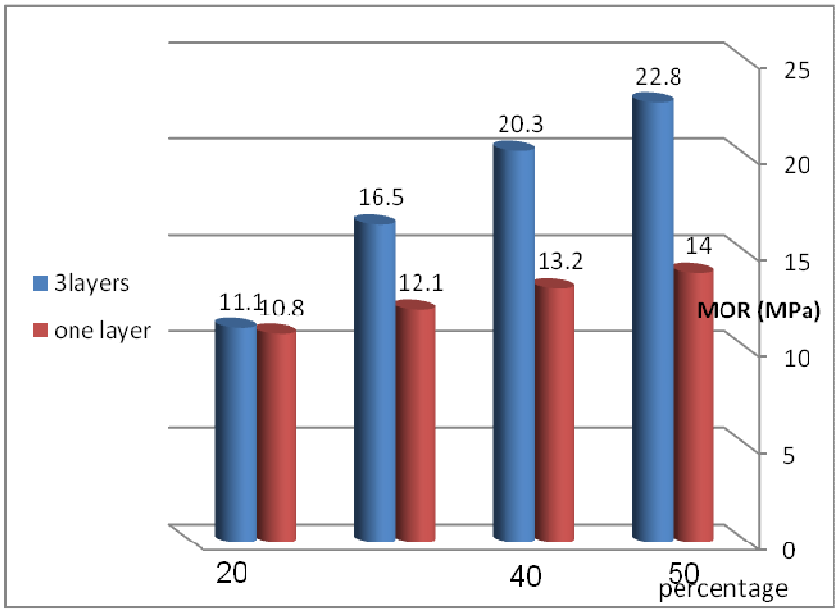


Fig. 1. Interaction effect of bagasse and panel type on MOR

As seen all panels made of 80% wood particles and 20% bagasse showed higher MOR. It is also obvious that by increasing amount of bagasse in the mixture, MOR increases which indicates that bagasse has strong effect on MOR of panel due to its slenderness ratio. Hiziroglu et al. 2005 [5] also mentioned that layering of particleboard increases its mechanical properties. Effect of bagasse on MOR of panels is shown in Fig. 2. As seen by increasing bagasse from 20% up to 50% MOR is increased. When bagasse was added to industrial particles, MOR of panels increased except when only 20% bagasse was added. This effect is attributed to high slenderness ratio of baggase particles. Alfonso and Herryman (1990) [2] also mentioned this effect. Effect of bagasse on panel IB is shown in Fig. 3. As seen in this figure IB of panels increase when bagasse is increased in the mixture.

The same effect was observed for modulus of elasticity. Interaction effects of panel type and bagasse on panel IB are shown in fig. 3. As seen by increasing of bagasse added to the mixture of panels IB increased and IB of all panels made of mixture of bagasse and industrial wood particles is higher than that of control. Interaction effects of panel type and bagasse are shown in Fig. 4. The

highest IB (0.71 MPa) is seen in three layer panels in 50 % bagasse and after that the IB of one layer panel (0.61 MPa) in which only 20% bagasse is used.

These two results are seemed to be contradictory but they are actually not because internal bond is a characteristics which indicate strength of bond between particles specially in the core of panels. In one layer panels in which amount of bagasse is low the negative effect of slenderness on IB is weak so panels presented high IB but when the amount of bagasse increases in one layer panel this negative effect dominates and causes reduction of IB. In three layer panels in which industrial wood particle placed in the core the presence of baggase in the faces has slight effect on internal bond so that even using 50% bagasse in the faces of panels has no effect on IB this is the reason that three layer panels with 50% bagasse present the highest IB. The effect of bagasse on thickness swelling is not significant fig. 5 but interaction effects have significant effect on thickness swelling fig. 6. Usually when light material such as bagasse and other agricultural residuals are used in manufacturing wood composites [7], thickness swelling of products is higher compared with products made of wood [6]. It can be seen that three layer panels generally present higher thickness swelling than one layer panel. This indicates that when non-wood material is used on the surface of composites where the most moist exposure takes place panels are not stable because of non wood material like bagasse is lighter and its structure is less compact compared with wood.

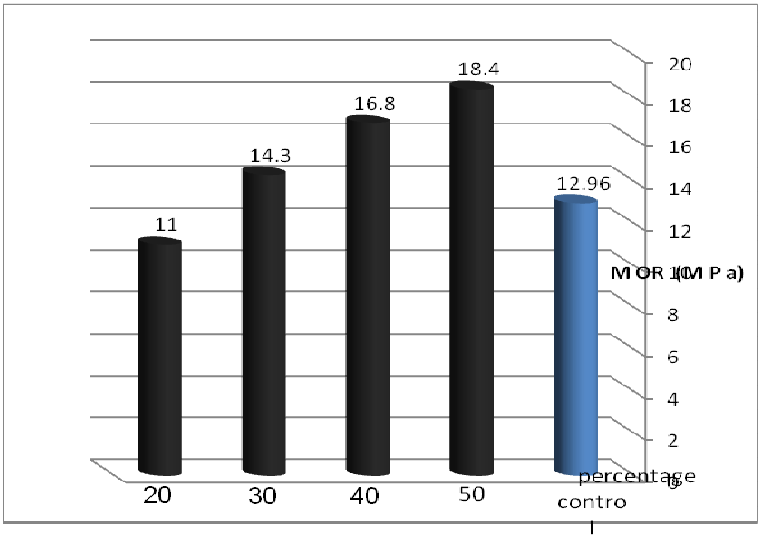


Fig. 2. Effect of Bagasse on MOR

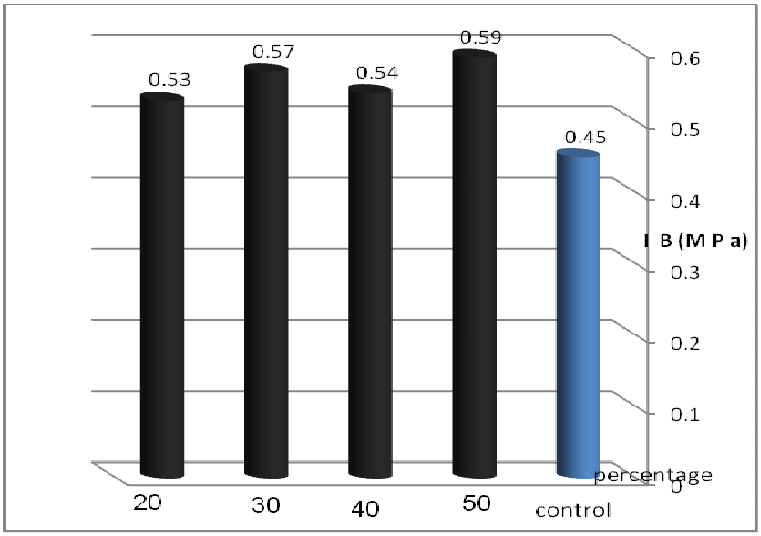


Fig. 3. Effect of bagasse on IB

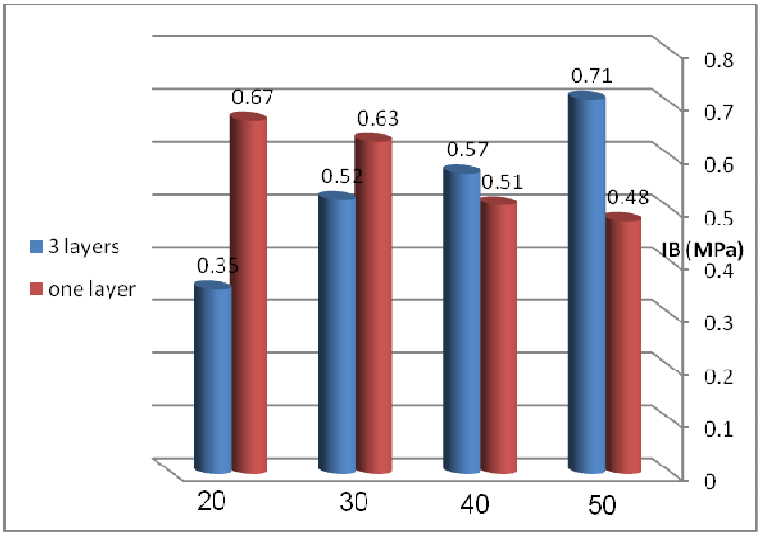


Fig. 4. Interaction effect of bagasse and panel type on IB

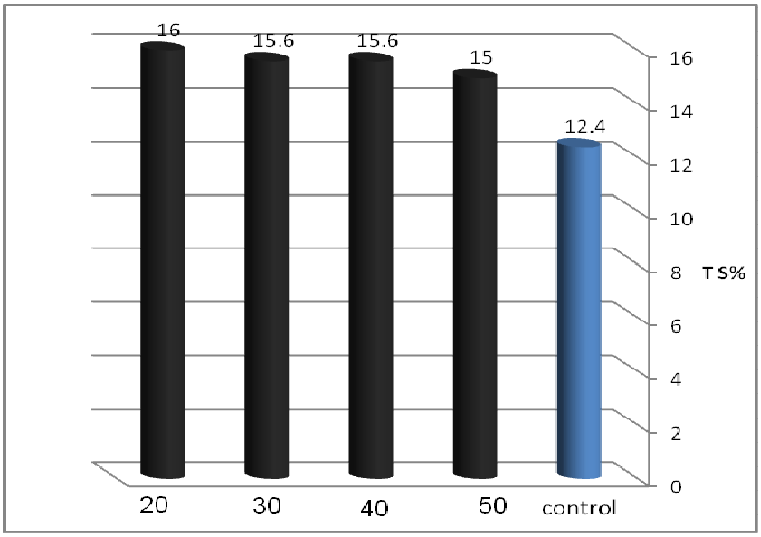


Fig. 5. Effect of bagasse on TS

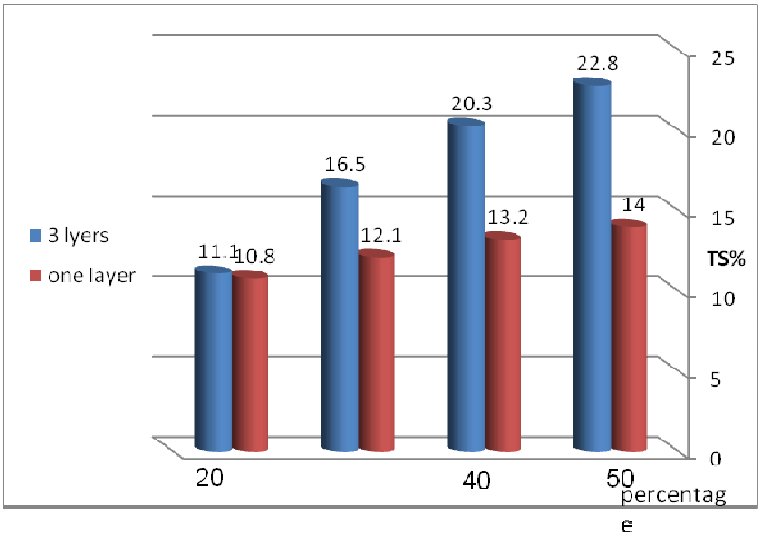


Fig. 6. Interaction effect of bagasse and panel type on TS

Summary

Results of this study indicate that bagasse a non wood ligno cellulosic material would be a good potential for wood substitution. This material not only saved natural forest but also improved most of applied properties of manufactured panels. Since bagasse produced light and slender particles it is very promising material to improve mechanical properties and even surface roughness of particleboard

References

[1] Atchison, J. E. 1987. *Rapid growth in the use of bagasse as a raw material for reconstitute panel board.* Pullman, Washington, PP, 154-163

[2] Alfonso, O. and Herryman, O. 1990. International aspects of the industrial utilization of bagasse . Institute Cubano (ICIDCA): 24(23): 33-24

[3] Payedar, J. 1998. Investigation on qualitative properties of particleboard made from Eucalyptus and bagasse. MSc thesis . Tehran University.

[4] Kehr, E. and Scholzel, E. 1962. Holz technologie 3(3):225-232

[5] Hiziroglu, S. and Holcomb, R. 2005. J. building and environment 40:710-723.

[6] Azizi, K. and Tabarsa, T. 2006. Proceedings of the 8th pacific rim bio-composites symposium.

[7] Tasooji M, T. Tabarsa, A. Khazaeian and R. P. Wool. 2010. Acrylated epoxidized soya oil as an alternative to Urea – formaldehyde in making wheat straw particleboard. Journal of adhesion science and technology 24:1717-1727.

[8] Dahmardeh Ghalehno M, M. Madhoushi, T. Tabrasa and M. Nazerian. 2010. European. J. of Wood product published on line 27 april 2010.

[9] Jahanshahei, S. Producing particleboard from wheat straw using tannin based PF.2009. MSc thesis. Faculty of forestry and wood tech. Gorgan University of Agricultural Sciences and Natural Resources.

© (2011) Trans Tech Publications, Switzerland
doi:10.4028/www.scientific.net/KEM.471-472.37

Critical Speeds for Carbon/Epoxy Composite Rotors in Spacecraft Energy Storage Applications

Renuganth Varatharajoo[1, a], Faizal Mustapha[1], Dayang Laila Abang Abdul Majid[1], Rizal Zahari[1], Ralph Kahle[2]

[1]Department of Aerospace Engineering, Faculty of Engineering, 43400 Selangor, Malaysia.

[2]German Space Agency, GSOC, 82234 Oberpfaffenhofen, Germany.

[a]renu99@gmx.de

Keywords: spacecraft flywheel, multi layer rotor, energy storage, finite element analysis

Abstract. A numerical investigation to optimize the carbon/epoxy multi layer composite rotor is performed for the spacecraft energy storage application. A high-speed double and triple layer rotor design is proposed and different composite materials are tested to achieve the most suitable recipe. First, analytical rotor evaluation was performed in order to establish a reliable numerical composite rotor model. Subsequently, finite element analysis is employed in order to optimize the double and triple layer composite rotors. Then, the modal analysis was carried out to determine the rotor natural frequencies. The rotor stress distributions and the rotor mode shapes show that a safe operational regime below 46, 000 rotations per minute is achievable.

Introduction

Flywheel technology is a promising technology for replacing the conventional battery as an energy storage device for spacecraft [1]. One of the key elements in flywheel energy storage system is the rotor inertia, which highly dependent on the rotor shape and material. The energy density is proportional to the ratio between maximum stress and density σ/ρ. The ratio also depends on the material selection. The maximum stress and the density (σ/ρ) of composite materials are significantly higher than any metals.

This paper provides a reasonable recipe for designing a space rated composite rotor. All the proposed composite materials in this work are commercially available [2]. The stress analysis and modal analyses are engaged to investigate the flywheel rotor design. One of the notable researches on the flywheel rotor optimization is performed by Kirk et al.; however, they have only focused on the stress distribution in multi layer rotors [3]. In fact, most recent researches performed for multi layer rotors are also dedicated to stress analysis [4, 5, 6, 7]. Instead, this current investigation was carried out for the stress distribution study incorporating the rotor dynamics (modal analysis) subjected to high rotational speeds.

Three high speed rotor configurations are investigated herein, i.e., single layer, double layer and triple layer rotors. First, the analytical and numerical stress analyses were conducted for a single layer rotor after considering the necessary properties, e.g., composite materials, rotor dimensions and rotor speeds. The single layer rotor analysis is also to establish a reliable rotor numerical model. Then, the finite element analysis (FEA) using ANSYSTM as well is employed for double and triple layer rotors' numerical stress analyses. The numerical solutions are discussed from the stress distribution point of view. Thereafter, the rotor dynamics is investigated to distinguish the natural dynamic behavior of rotors during high speed operations.

Spacecraft Flywheel

The stress equations for orthotropic rotors, describing the radial displacement ur, radial stress σ_r and tangential stress σ_t as functions of the radius are as described below [5]

$$u_r = C_1 r^k + C_2 r^{-k} - \frac{\rho\omega^2\left(1-\upsilon_{r\theta}\upsilon_{\theta r}\right)}{9E_r - E_\theta} r^3 \tag{1}$$

$$\sigma_r = \frac{E_r\left(k+\upsilon_{\theta r}\right)}{1-\upsilon_{r\theta}\upsilon_{\theta r}} C_1 r^{k-1} + \frac{E_r\left(-k+\upsilon_{\theta r}\right)}{1-\upsilon_{r\theta}\upsilon_{\theta r}} C_2 r^{-k-1} - \frac{\rho\omega^2\left(3+\upsilon_{\theta r}\right)E_r}{9E_r - E_\theta} r^2 \tag{2}$$

$$\sigma_\theta = \frac{E_\theta\left(1+k\upsilon_{r\theta}\right)}{1-\upsilon_{r\theta}\upsilon_{\theta r}} C_1 r^{k-1} + \frac{E_\theta\left(1-k\upsilon_{r\theta}\right)}{1-\upsilon_{r\theta}\upsilon_{\theta r}} C_2 r^{-k-1} - \frac{\rho\omega^2\left(1+3\upsilon_{r\theta}\right)E_\theta}{9E_r - E_\theta} r^2 \tag{3}$$

whereby k is a material constant, k=$\left(\frac{E_\theta}{E_r}\right)^{0.5}$ and the Poisson's ratio for the transverse direction is $v_{r\theta} = v_{\theta r}\frac{E_r}{E_\theta}$. The two constants C1 and C2 can be determined after setting the rotor boundary conditions. The outer radius is a free surface where no loads are applied; thus, σ_r at r =R0 is null. This would be the first boundary condition for the rotor. On the other hand, the innermost rotor has to support the metallic return rings that belongs to the magnetic bearings and motor/generator magnet slots [1]. These return rings are assumed to be segmented; and therefore, no hoop stresses are permitted to exist in the material. The rings are segmented to achieve higher flywheel rotational speeds [4]. If the return rings are continuous, the performance of the flywheel would be limited since metals are vulnerable to a high stress concentration at high speeds. The segmented rings introduce pressure to the inner rotor wall during high rotational speeds, resulting radial stresses. The second boundary condition is written as:

$$\sigma_r\left(r = R_i\right) = -p_i = -\rho_{return} t_{return} R_i \omega^2 \tag{4}$$

where t_{return} is the mean return ring radial thickness and ρ_{return} is the density of return ring material (cobalt ferrite with $\rho \approx 8150 kg/m^3$). Then, C1 and C2 are estimated as given below:

$$C_1 = \rho\omega^2 \frac{\left(1-\upsilon_{r\theta}\upsilon_{\theta r}\right)\left(3+\upsilon_{\theta r}\right)}{\left(9E_r - E_\theta\right)\left(\upsilon_{\theta r}+k\right)} R_o^{3-k} - \frac{\upsilon_{\theta r}-k}{\upsilon_{\theta r}+k} C_2 R_o^{-2k} \tag{5}$$

$$C_2 = \frac{1-\upsilon_{r\theta}\upsilon_{\theta r}}{\upsilon_{\theta r}-k}\left[\rho\omega^2 \frac{3+\upsilon_{\theta r}}{9E_r - E_\theta} R_i^k R_o^k \frac{R_i^3 R_o^k - R_i^k R_o^3}{R_o^{2k} - R_i^{2k}} + \frac{p_i}{E_r}\frac{R_o^{2k} R_i^{k+1}}{R_i^{2k} - R_o^{2k}}\right] \tag{6}$$

The constants depend on the rotational speed ω of the rotor. By using Eq. (1) and Eq. (2), the rotor stress distributions are calculated as a function of radius for certain operating speeds. These stresses are estimated for the usable material strength. The usable material strengths are derived from their ultimate strengths that are derated for space applications. The derated factor used for the longitudinal tensile strength is 0.65, and the derated factor of transverse tensile and compressive strength is 0.53 as given in Table 1.

Table 1. Safety factors for IM6 Carbon/Epoxy

Parameter	Longitudinal direction	Transverse direction	
Stress	Tensile	Tensile	Compressive
Maximum strength бmax [MPa]	3500	56	150
Vacuum fatigue coefficient	0.8	0.65	
Reciprocal safety coefficient	0.9	0.9	
Over speed factor	0.9	0.9	
Total product factor *f*	0.65	0.53	
Usable strength *f* бmax [MPa]	2275	30	80

The reference radial thickness for the rotor analysis is based on the magnetic bearing's return rings. The return rings that are attached to the rotor have typically a mean radial thickness of less than 3 mm; thus, the minimum rotor radial thickness should be higher than this mean thickness [1]. Eqs. (1-6) can be used for a single layer rotor analytical evaluation and can serve as a reference for the numerical rotor modeling through finite element analysis (FEA). Numerical modeling is preferred for multi layer rotors due to the complexity of their analytical solutions. Therefore, first the stress analysis is analytically and numerically carried out to establish a reasonable numerical rotor model for a single layer carbon/epoxy rotor with radii of Ri =0.07 m and Ro = 0.1 m (thickness of 3 mm) and height of 0.0183 m [1]. Figures 1 and 2 show the analytical stress distributions along the transverse and tangential directions, respectively.

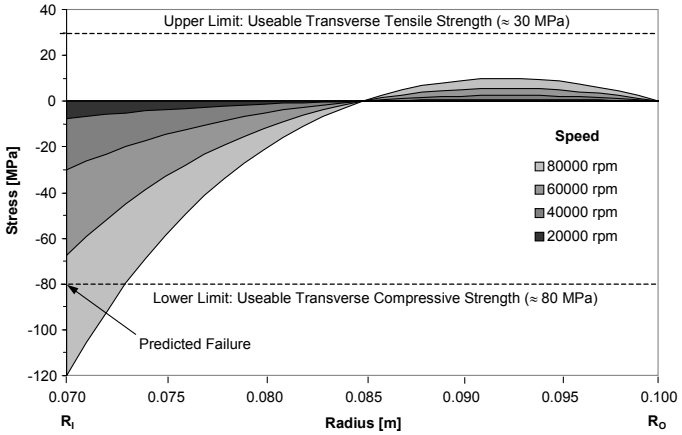


Fig. 1. Transverse (radial) stress distributions.

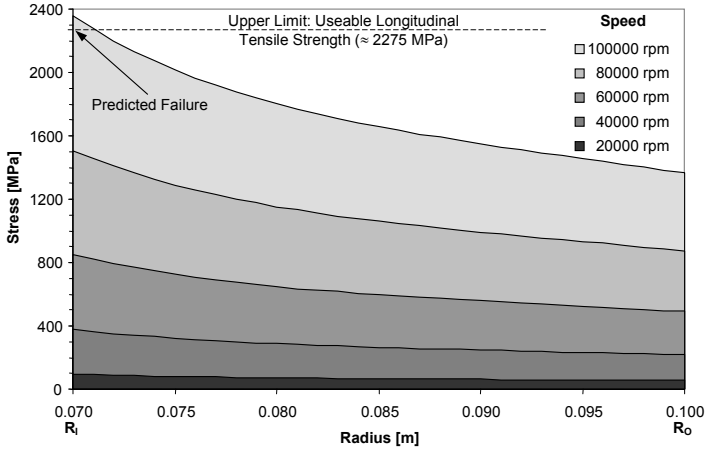


Fig. 2. Tangential (longitudinal) stress distributions.

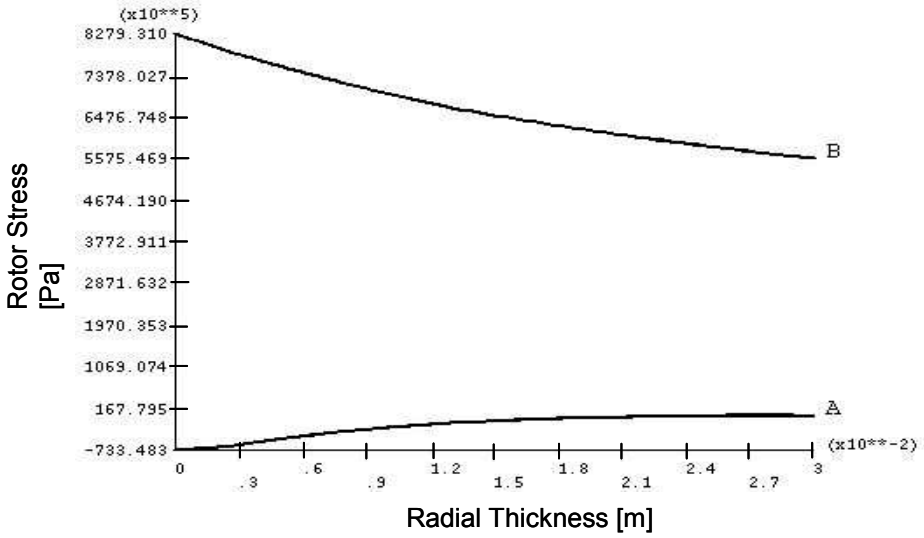
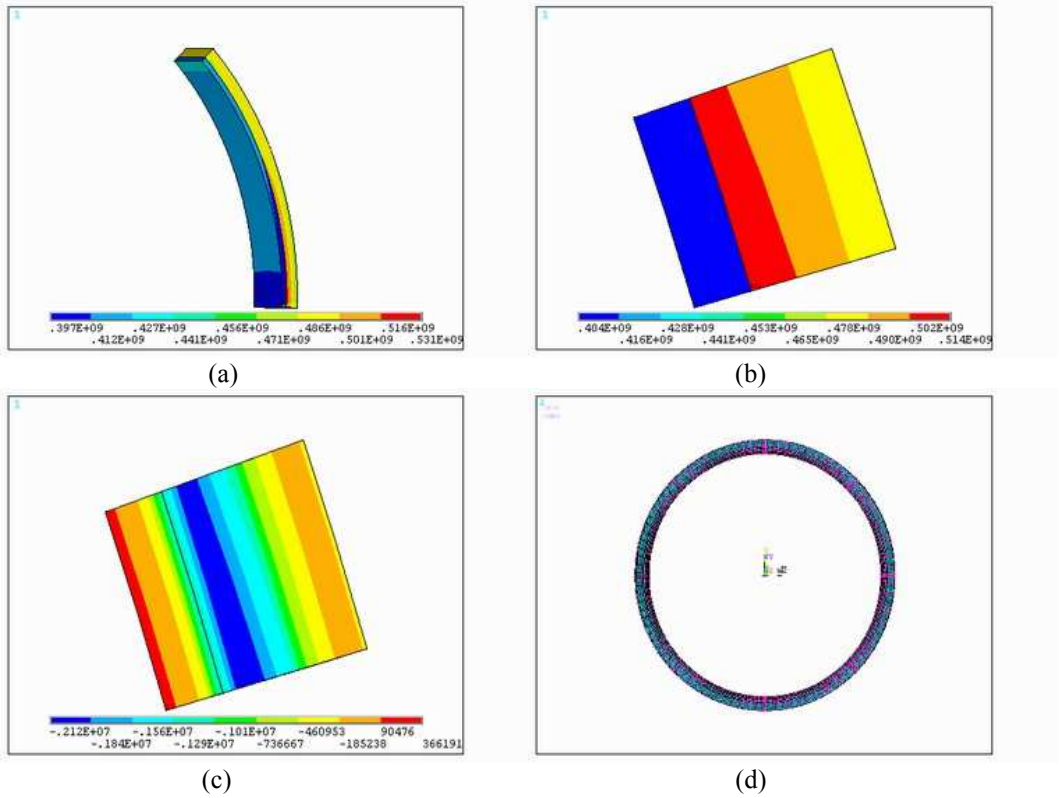


Fig. 3. Transverse (A) and tangential (B) stress distributions at 60 000 rpm.

Multi Layer Rotors

Double Layer Carbon/Epoxy Composite Rotor. The double layer 3D model is generated and analyzed by ANSYS^{TM} with the optimized radius of R_i =0.1106 m and R_o = 0.1174 m, and a rotor height h of 0.0183 m. The selected rotor dimension is suitable for small satellites (< 100 kg) [1]. The operating rotational speed for the model is 50,000 rpm. The 3D model in fig. 4 (a) displays the longitudinal/tangential rotor stress distribution MR50/LTM25 carbon/epoxy composite in the inner layer and T300/934 carbon/epoxy composite in the outer layer. A closer look at the 2D display in fig. 4 (b) shows the maximum longitudinal tensile stress of about 509 MPa appears in second layer of T300/934 carbon/epoxy composite. However, this value is well below the usable longitudinal tensile strength of this material, which is 1313.35 MPa. Having 1313 MPa of the usable longitudinal tensile strength, the inner layer also can sustain the maximum longitudinal tensile stress is 404 MPa. Figure 4 (c) shows the stress distribution for the transverse/radial direction. The peak transverse tensile stress of about 0.23 MPa occurs in the inner layer, and this value is lower compared to 10.87 MPa of the usable transverse tensile stress. The maximum transverse compressive strength occurs in the outer layer, which is 2.12 MPa. Besides that, 1.29 MPa maximum transverse compressive stresses occur in the inner layer. Both of the values are much lower compared to the usable transverse compressive stress that is 89.04 MPa and 76.85 MPa in the outer and inner layer, respectively. In this particular composite rotor, the maximum longitudinal tensile strength at the outer layer (509 MPa) is higher than the inner layer (404 MPa). For further enhancement, the triple layer design is proposed in order to have a better strength in the outer layer as the longitudinal tensile strength at the outer layer is obviously more critical. On the other hand, the modal analysis for this double layer rotor shows that the first natural frequency appears at 762.764 Hz or 45,766 rpm in fig. 4 (d), which is much lower than the rotor's operational frequency at 50,000 rpm. The second natural frequency is also at a lower frequency around 771.67 Hz than the operational frequency itself. It would be catastrophic for the space missions if the natural frequency is close the operational frequency.

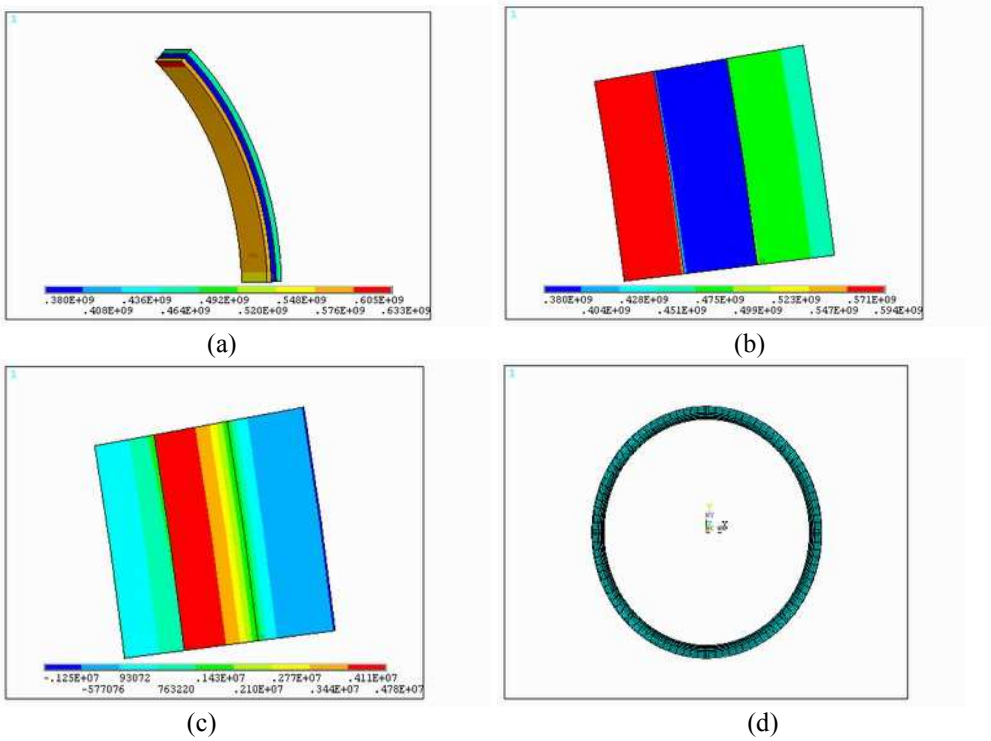


(a) (b)

(c) (d)

Fig. 4 Double layer carbon/epoxy composite rotor.

Triple Layer Carbon/Epoxy Composite Rotor. The triple layer composite rotor with the optimized radius of R_i = 0.1106 m and R_o = 0.1174 m, and a rotor height h of 0.0183 m consists of AS4/3501-6 carbon/epoxy composite in the innermost layer, MR50/LTM25 carbon/epoxy composite in the middle layer and T300/934 carbon/epoxy composite in the outer layer. The operational speed of 50,000 rpm is proposed for the triple layer rotor. Figure 5 (a) shows the 3D model of triple layer composite rotor.



(a) (b)

(c) (d)

Fig. 5. Triple layer carbon/epoxy composite rotor

Figure 5 (b) shows the maximum longitudinal tensile stress occurs in the innermost layer at 580 MPa that is below the usable longitudinal tensile stress of 1482 MPa in this particular layer. About 386 MPa and 483 MPa longitudinal tensile stresses occur in the middle layer and outer layer in which the usable values for these layers are 1313 MPa and 1313.35 MPa, respectively. The result fulfills the condition in which the longitudinal tensile stress is more critical at the outer layer of the rotor. This combination of composites also can sustain the transverse tensile and compressive strengths as shown in fig. 5 (c). For the triple layer composite material, the modal analysis shows that the first natural frequency appears at 774.69 Hz or 46,481 rpm in fig. 5 (d), which is much lower than the rotor operation frequency at 50,000 rpm. The second natural frequency is also at a lower frequency around 788.32 Hz than the operational frequency.

Summary

The thinner double layer carbon/epoxy composite rotor can be operated at a given rotor speed compared to a single layer rotor. The maximum longitudinal tensile strength at the outer layer (509 MPa) is higher than the inner layer (404 MPa) for the double layer rotor design. As the longitudinal tensile strength at the outer layer is more critical, the triple layer carbon/epoxy composite rotor would be preferred because the longitudinal tensile strength at the outer layer is lower (483 MPa). The triple layer carbon/epoxy composite rotor can be operated at higher speeds up to 46, 000 rpm, whereas the double layer rotor's operation is only up to 45, 000 rpm. In fact, their natural frequencies limit their operations at a higher speed. However, the operational speed gained in the triple layer rotor design contributes to a higher energy storage capability for the spacecraft energy storage. Future works will be focused on the rotor parametric study to enable its fiber laying process towards an experimental multi layer composite rotor model.

References

[1] R. Varatharajoo, R. Kahle, A Review of Conventional and Synergistic Systems for Small Satellites, Aircraft Engineering and Aerospace Technology, Vol. 77 (2005), pp. 131-141.

[2] Composite Material Mechanical Properties, http://composite.about.com, 2009.

[3] J. A. Kirk, J.R Schmidt, G. E. Sullivan, L. P. Hromada, An Open Core Rotor Design Methodology, Aerospace and Electronics Conference, NAECON, Dayton, USA, 1997, pp. 594-600.

[4] M. Krack, M. Secanell, P. Mertiny, Cost Optimization of Hybrid Composite Flywheel Rotors for Energy Storage, Structural Multidisciplinary Optimization, Vol. 41 (2010), pp. 779-795.

[5] K. H. Sung, K. Dong-Jin, S. Tae-Hyun, Optimum Design of Multi-ring Composite Flywheel Rotor Using a Modified Generalized Plane Strain Assumption, International Journal of Mechanical Sciences, Vol. 43 (4) (2001), pp. 993-1007.

[6] Y. Gowayed, F. Abel-Hady, G. T. Flowers, J. J. Trudell, Optimal Design of Multi-direction Composite Flywheel Rotors, Polymer Composites, Vol. 23 (3) (2004), pp. 433-441.

[7] S. K. Ha, J. H. Kim, Y. H. Han, Design of a Hybrid Composite Flywheel Multi-rim Rotor System Using Geometric Scaling Factors, Journal of Composite Material, Vol. 42 (8) (2008), pp. 771-786.

© (2011) Trans Tech Publications, Switzerland
doi:10.4028/www.scientific.net/KEM.471-472.43

Influence of Polyacrilonitrile (PAN) Concentration on the Mechanical and Physical Properties of Electrospun Fibres

Siti Saniah Ab. Karim[1, a], Abu Bakar Sulong[1,b], Che Husna Azhari[1,c], Ng Min Hwei[2,d] and Mohd Reusmaazran Yusof[3,e]

[1]Department of Mechanical & Material Engineering, Universiti Kebangsaan Malaysia 43600 UKM Bangi, Selangor.

[2]Tissue Engineering Centre, Universiti Kebangsaan Malaysia Medical Center, 56000 Cheras, Kuala Lumpur

[3]Material Technology Group, Malaysia Nuclear Agency, 43000 Kajang, Selangor

[a]saniah@vlsi.eng.ukm.my, [b]abubakar@eng.ukm.my, [c]mek@vlsi.eng.ukm.my, [d]angelaster@gmail.com, [e]reusmaazran@nuclearmalaysia.gov.my

Keywords: Electrospinning, Nano Fibres, Mechanical Properties, Polymer Concentration, Physical Properties.

Abstract. Electrospinning is direct process to produce polymer fibre with high specific surface area ratio. Apart from polymer fibre producing; electrospinning also can produce a continuous nano size of polymer fibre, which the benefit of this process is the fibre can be produced straight away with lower cost than conventional melt spinning process. Recently, successful attempts have been made to produce polymer fibre by adjusting the parameters of electrospinning such as the collector distance, needle size, polymer concentration voltage applied. From this study, the electrospun fibre was distributed randomly on collector plate surface. The diameter of the fibre produced increase as the polymer concentration was increased. The fibre distribution does not affected by the differ polymer concentrations electrospun, but there were polymer beads formed at the low polymer concentration in solvents. The fiber elongation value is the highest by polymer fiber of 9 wt % while the highest strength is by polymer fiber of 7 wt %. The polymer fibre with low concentration consequently showed the brittle characteristic.

Introduction

Anthony [1] reported, the most basic equipments required for demonstration of simple electrospinning in laboratory are viscous polymer solution, an electrode that is in contact with polymer solution, high-voltage DC generator connected to the electrode, and a grounded or oppositely charged collector to collect the nano fibre. Substantively, electrospinning phase consists of six phases which then made the existing of the polymer fibre. The sequences of the phases are droplet generation, Taylor's cone formation, jet launch, elongation of straight segment, instability region and eventually solidification of jet into nano fibre [2].

In more detail view, polymer solution was put in the syringe and escaped out in droplet through the needle (as in this research, needle will act as the electrode) [3]. As the power source supplied to the solution through the needle, the solution that experienced the electrical field would then emitted out droplet in the cone-like shape and next a narrow jet liquid was ejected from its point [4]. This phenomenon is called as the Taylor's cone formation which the main cause is the high surface tension [5]. The charge build up that supplied to the solution emanate out the jet and as for Demir et al. [6], reported that as many as six jets come out from single droplet and the average number of jets increasing linearly with the electric field (kV/cm).

The increasing in jet length was caused by the changing in electric field, reported by Bunyan et al. [7]. For instability region, high speed imaging studied by Reneker et al. [9], come into conclusion that the larger loops closer to the collector showed higher order bending instability

where jet being loops formed right and left handed coils. At the last phase, Anthony [1] had agreed that solvent volatility is the key to control fibre diameter as evaporation took places.

As for previous researches done, Reneker et al. [9] reported that as the viscosity of the polymer solution increased, the fewer beads formed as if the more solution changed into fibres. Lin and Wang [10] however reported that the less beads formed when the low viscosity or the low polymer concentration are spun. The objectives of this study are to investigate the relationship between the mechanical and physical properties of the electrospun polymer with its concentration and to know whether differ concentration does affect the fibre distribution.

Experiment

The polymer used in this study was Polyacrilonitrile (PAN) with the molecular weight was 150,000, which is purchased from Sigma Aldrich (M) Sdn Bhd located in Selangor, Malaysia. Dimethyl formamide (DMF) was chosen as solvent which is compatible with PAN. A chamber was fabricated to keep the process ran in the room temperature and humidity. The syringe needle chosen was 0.9 mm of internal diameter. The voltage source was set to be constant at 15 kV. When the voltage was supplied to the syringe needle, due to gravity effect and contrast charge between two electrode, polymer solution will the sprayed to the collector. Figure 1 shown schematic of electrospinning set-up.

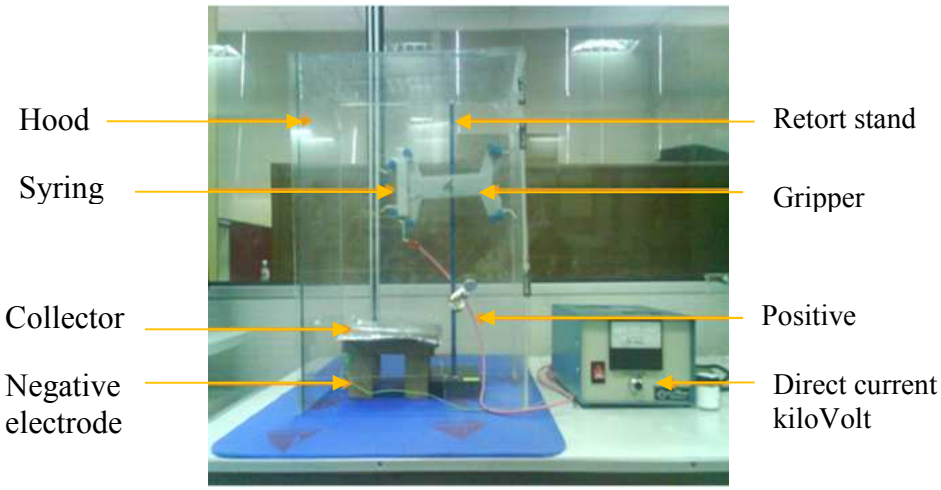


Fig. 1. Electrospinning set-up

The polymer fibres with micrometer in thickness were collected by the copper plate located 10 cm beneath of the syringe. These processes were repeated to polymer concentration of 5wt%, 6 wt%, 7 wt% , 8 wt%, 9 wt% and 10 wt% of solution weight. Three samples of each weight percent were tested through micro tensile tester (Instron Universal Tester 4381L) with 5N load cell to study mechanical properties of the electrospun PAN fibre. The tests were conducted at 2 mm/min cross head speed, with the data reading rate is a reading per 2 seconds. The PAN fibres structure and distribution were examined included its diameter of the fibre using Scanning Electron Microscope (Carl Zeis EVO MA10-SEM). The diameter measurements were done at approximately 100 fibres on each concentration. The main objective was to study the fibres orientation distribution at different solution concentration on the collector through elestrospinning.

Results and Discussion

Polymer Structure and Distribution. The study on the structure and distribtion of the polymer fibres were conducted on the 5 wt%, 7 wt% and 9 wt% of PAN in the DMF. Figure 2 shows random distribution of fibre at 1000 times magnification. Overall, the distribution of the fibre were in randomly orientation as shown in Figure 2.

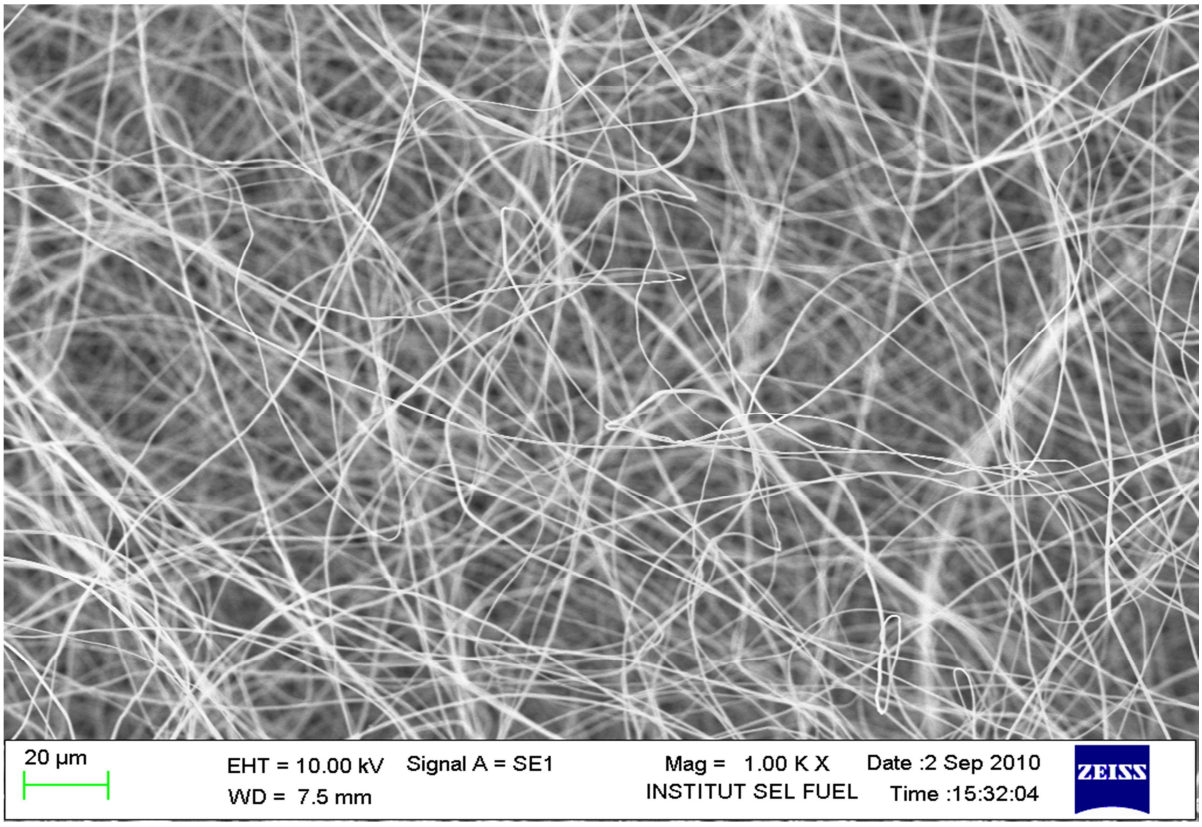


Fig. 2. SEM image of random orientation distribution of fibre with magnification of 1000 times.

Diameter of fibres and beads formation. Figure 3 (a), (b), and (c) show the effects of polymer concentration on the fibres and bead formation. More beads formed at 5 wt% PAN concentration, lesser beads formed at 7 wt% PAN and no bead formed at 9 wt% of PAN. Based on Figures 3, diameter of fibres were around 70~160 nm at 5 wt % polymer concentration. For fibres of 7 wt% of polymer concentration, the fibre diameter were around 220~430 nm. For fibres of 9 wt % of polymer concentration, the fibre diameter were around 320~860 nm. From this analysis, it is concluded that increasing the polymer concentration will increase the fibre diameter. Increasing the concentration will decrease the beads formation as well.

Mechanical properties of electrospun fibre. Figure 4 shows the highest stress, was measured by the PAN fibres of 7 wt% which value was 0.9 MPa. While, the lowest stress was measured by PAN fibres at 5 wt% with stress value of 0.2 MPa. Then, for the highest strain value, the fibres was PAN at 9 wt% with the value of 114 % of elongation. The lowest elongation was measured by PAN fibre concentration of 5 wt% with the strain value of 15% of elongation. The polymer fibre with low concentration, which were 5 wt%, 6 wt%, 7 wt% and 8 wt% consequently showed the brittle chracteristic.

Figure 5 (a) and (b) show variation of fibre elongation and ultimate tensile stress of fibres, respectively. From Figure 5 (a), the fibre elongation value is the best for polymer fibre of 9 wt %. It showed the highest elongation value which means that it was hard to fracture it while applied high load. In the other hand, Figure 5 (b) shows the ultimate stress of the polymer fibr with different concentration. The highest ultimate strength of PAN polymer fibre able to stand was 0.95 MPa, at the PAN polymer concentration of 7 wt %. This was also stated as the ultimate stress, which after this point, the stress reduced because the cross sectional area of the polymer sample decrease.

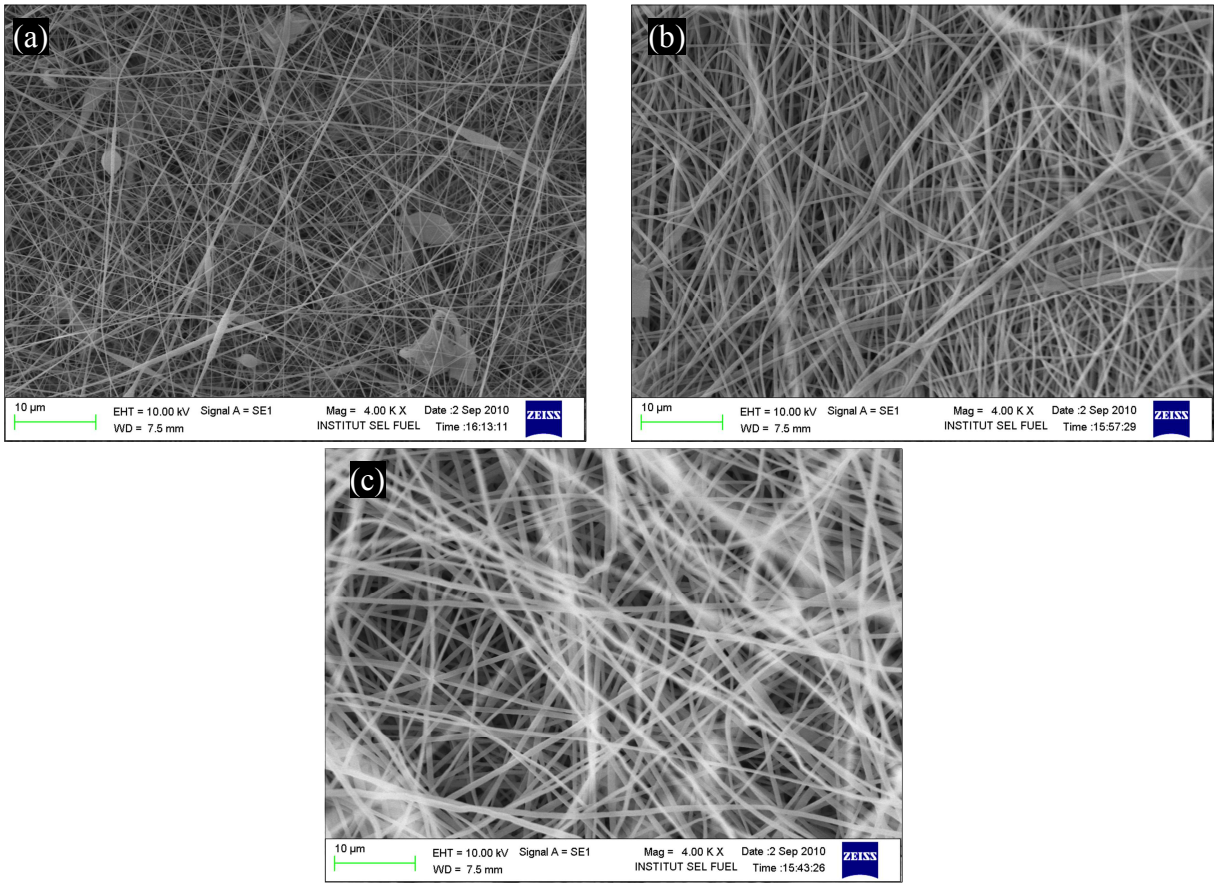


Fig. 3. SEM images of effects of (a) 5 wt%, (b) 7 wt% and (c) 9 wt% of PAN concentration on the fibres

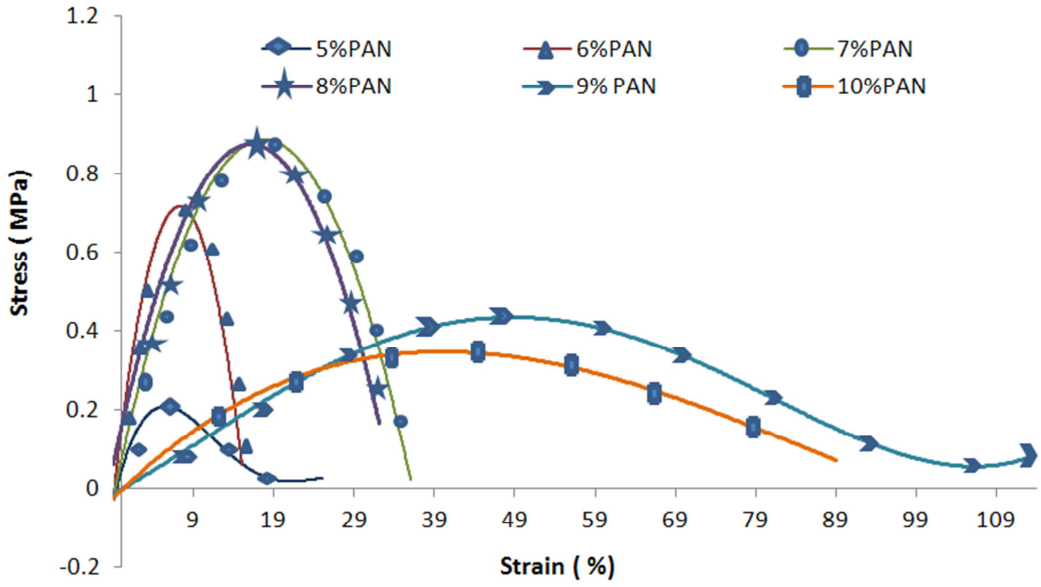


Fig. 4. Graph of stress vs. strain of different concentration of PAN

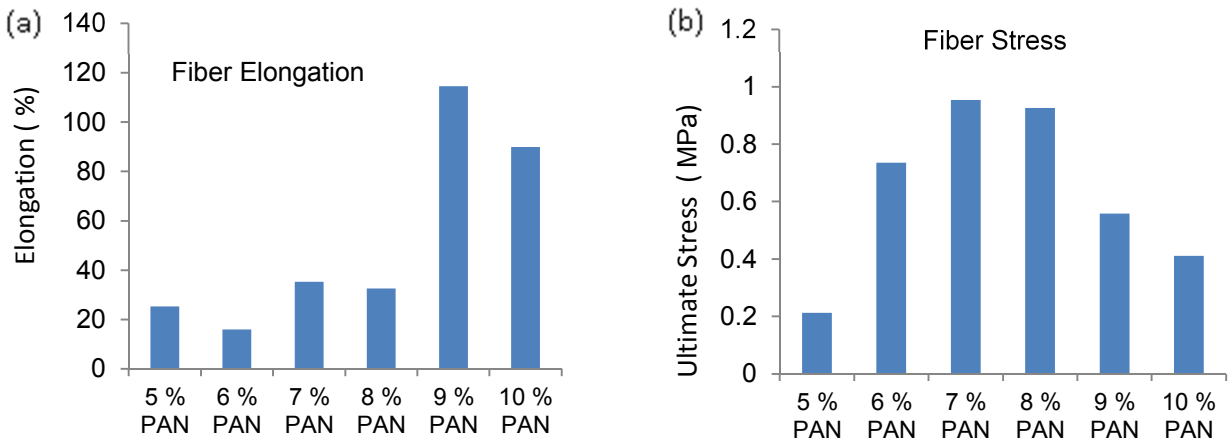


Fig. 5. Variation of (a) fibre elongation, and (b) ultimate tensile stress of fibres

Failure Mechanism of Electrospun Polymer Fibre. Figure 6 (a) and (b) show failure mechanism of fibres at 5 wt% and 9 wt%, respectively. The brittle characteristic can clearly be seen on Figure 6 (a) which shows the brittleness that occur on 5 wt% polymer concentration fibre. The similar behavior were observed of the others lower polymer concentration fibre. The ductility on the fibre sample were clearly seen of the higher concentrations of polymer used. Figure 6 (b) shows the necking on higher polymer concentration. Necking occured right away after the ultimate stress occured, because the cross sectional area began to decrease in a localized region of the sample, instead of decrease all over its entire length. This phenomenon was caused by the slip planes formed within the material, and the actual strains produced were caused by shear stress, and necking tends to form as the samples elongates further. It can concluded that at the higher the polymer concentration, the higher stress and ductility of the fibre produced.

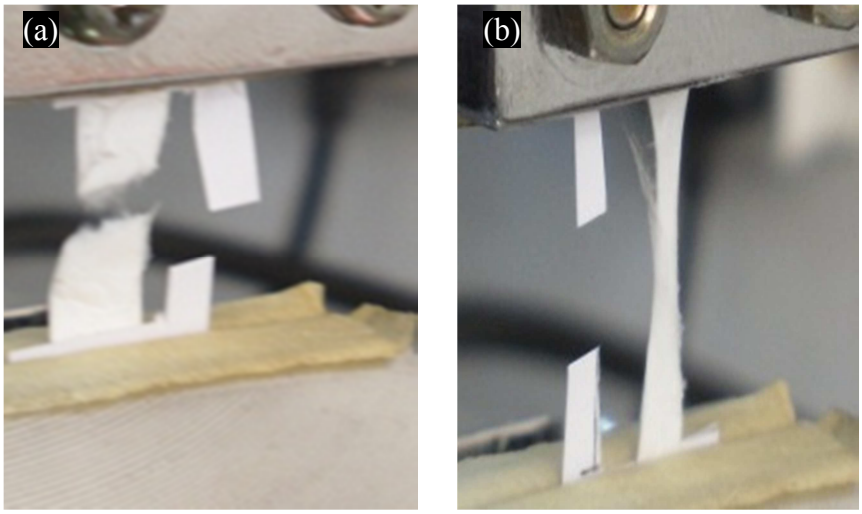


Fig. 6. Failure mechanism that occured on the sample while drawing the sample apart at (a) 5 wt% PAN, and (b) 9 wt% PAN.

Summary

The electrospun fibre was distributed randomly throughout the collector plate surface. The diameter of the fibre produced also increase as increasing polymer concentration in solvent. The fibre distribution does not affected by the various polymer concentrations used, but there were beads formed as decreasing the polymer concentration. The changes in polymer concentration for electrospinning process do affect the mechanical properties of fibre produced. The best polymer produced through electrospinning with the fixed parameter was at the higher weight percentage of PAN in the DMF solution because the mechanical properties of the electrospun polymer increased. The main usage that is very important to get the fibre with the good mechanical and physical properties are for the filtration process. The application is extremely necessary especially to the medical equipment such as haemodialysis filter and even necessary in industrial field, which is to filter the nano sized powder. For the future research topic, it is the best to get the continuous alligned nano sized biocompatible fibre for medical usage.

Acknowledgements

The authors would like to thank FRGS UKM-KK-02-FRG-0124 for sponsoring this work and also to Mr. Ruesmazran from Malaysia Nuclear Agency, Bangi, Selangor, Malaysia for his assistance and permission to use the micro tensile tester.

References

[1] Anthony, L. A, : *Science and Technology of Polymer Nanofibers*. John Wiley & Sons, New Jersey (2008), p. 9.

[2] Hou, H.Q, Reneker, D. H, : Advanced Material. Vol.16 (2004), p. 69.

[3] Ioannis, S. K, : Journal of Materials Processing Technology. Vol. 167 (2005), p. 283.

[4] Hibbeler, R.C, Fan S.C, : Mechanics of Material. Prentice Hall (2005), p. 3.

[5] Travis, J. S, Horst, A. R, : Biomaterials. Vol. 29 (2008), p. 1989.

[6] Demir, M. M, Yilgor, I, Erman, B, : Polymer. Vol. 43 (2002), p. 3303.

[7] Bunyan, N. N, Chen, J, Farboodmanesh, S, : *Polymeric Nanofibers.* Oxford University Press, USA. Vol. 918 (2006), p. 106.

[8] Ramakrishna, S., Fujihara, K, Wee, E. T, Teik C. L, Zu, W. M, : World Scientific (2005), p. 3.

[9] Reneker, D. H, Yarin, A. L, Fong, H, Koombhongse, H, : Journal of Applied Physiscs. Vol. 87 (2000), p. 4531.

[10] Lin, T, Wang, X., G, : *Nanofibers and Nanotechnology of Textiles.* Cambridge, England (2007), p. 90–110.

© (2011) Trans Tech Publications, Switzerland
doi:10.4028/www.scientific.net/KEM.471-472.49

Manufacture of Composite Panel from Sugarcane Bagasse

Nor Suhaina Shahidan[1, a] and Suhaimi Muhammed[2, b]

[1] Faculty of Applied Sciences, Universiti Teknologi MARA Pahang, 26400 Bandar Jengka, Pahang, Malaysia

[2] Faculty of Applied Sciences, Universiti Teknologi MARA Pahang, 26400 Bandar Jengka, Pahang, Malaysia

[a]suhainashahidan@yahoo.com, [b]dsuhaimi@pahang.uitm.edu.my

Keywords: Sugarcane Bagasse, Properties, Particleboard, Resin Content, Board Density, Wax

Abstract. Agricultural waste such as sugarcane bagasse is abundant in Malaysia and at present is mainly used as combustible material for energy supply in the sugar factory. This study was conducted to investigate the possibility of manufacturing composite panel from sugarcane bagasse at three density levels (450, 550, 650 kg/m^3), two resin content (10 and 12%) and with or without wax (1%) addition. The panel produced were tested for mechanical properties (modulus of elasticity and modulus of rupture) and physical properties (water absorption and thickness swelling) conforming to the British standard (BS EN 310 and BS EN 317). The results revealed that board with density 650kg/m^3 gave superior strength compared to those of 450kg/m^3 and 550kg/m^3 densities. The addition of 1% wax helped to improve the water absorption and thickness swelling of the composite panel. Thus, it can be concluded that composite panel can successfully be produced from sugarcane bagasse as the main source of raw materials.

Introduction

Sugarcane or Saccharum is one of the most natural fibers that produce with a worldwide annual production of 1170 million metric tons in 2005 [1]. Bagasse consists of approximately 46% cellulose, 24.5% hemicellulose, 19.95% lignin, 3.5% fat and waxes, 2.4% ash, 2.0% silica and other elements [2]. Bagasse is the solid lignocellulosic residue left after extraction of juice from the sugar cane stalk. Bagasse is used as combustible materials for energy supply in sugarcane factories as in thermal power station, in pulp and paper industries and for fiber board materials.

Usually manufacturing composites such as furniture, particleboard and others using wood because of their good properties but, nowadays using wood had some problems. Wood is hard to get and the price is high. This is because the plants take time to grown and need large space to plant them. Using wood, their production cost is also high.

Wood almost used, so the producers of products in wood-based industries need to find out the suppliers from other countries. When, this situation happen, producers need to spend a lot of money to import wood from other country for their production. This availability of sugarcane bagasse is abundant and easy to obtain. According to FAO statistics, 2006, found that sugarcane bagasse still a lot of amount waste with a worldwide annual production of 1170 million metric tones in 2005. In Malaysia production of bagasse was quite large in year 2005 which is 260,800 tonnes (Energy Statistics Database / United Nations Statistics Division).

Abundant of sugarcane bagasse in Malaysia happen because the usage of sugarcane fiber is not familiar to be commercialize especially in composite material. By increasing of the sugarcane dregs residues, it will bring both environmental and surrounding problems to mankind. Others, by using non wood fibers can provide balancing between supply and demand [3].

The aim of this research project is to study the mechanical properties (MOR and MOE) and physical properties (water absorption and thickness swelling) of the bagasse panel at three density levels (450, 550, 650 kgm-3), two resin content types (10% and 12%) and with or without wax (1%) addition.

Materials and Methods

The sugarcane bagasse milled by using hammer mill to get into small particles. The particles were screened to separated fiber from the parenchyma. The fibers in 2 mm are used and oven dried about 3% moisture content. Urea Formaldehyde from Malayan Adhesive and Chemicals (MAC) at Shah Alam, Malaysia are used as binder and wax with 60% solid content obtained from local wood particleboard manufacturer.

The densities for the particleboard were 450 kgm-3, 550 kgm-3 and 650 kgm-3. The board conducted by using different resin (10% and 12%) and wax content (0% and 1%) to measure their effected properties of panel. The panel dimension 34 cm x 34 cm x 0.6 cm. The wax and resin were sprayed by compressed air and blended with bagasse using adhesive mixer. The blended particles manually formed by hand forming and hot pressed under 165oC with pressure (1800 psi) for 12 min. Table 1 shown bagasse panel parameters:

Table 1. Parameters for the manufacture of bagasse panel

Density (kgm^{-3})	Resin Content (%)	Wax (%)
450	10	0
450	10	1
450	12	0
450	12	1
550	10	0
550	10	1
550	12	0
550	12	1
650	10	0
650	10	1
650	12	0
650	12	1

Data for each test were analyzed using analyze of variance (ANOVA) to determine significant difference between factors and variables.

Results and Discussion

Panel with density 650 kgm-3 gave superior properties than 450 kgm-3 and 550 kgm-3 board. Board produces with minimum resin content 10%, were able to meet minimum strength than 12% resin content. Board having 12% resin content and 650 kgm-3 density were observed to possess the highest value of MOR (10.69MPa) and MOE (1634.11MPa). Introduction of wax helped to improve the water absorption of bagasse panel. Board 650 kgm-3 with 1% of wax gave better WA and TS compared to same board density without wax. The properties of bagasse panel are shown in Table 2.

Table 2. Mechanical and physical properties of bagasse panel

RC (%)	Wax (%)	Density (kgm^{-3})	MOR (MPa)	MOE (MPa)	WA (%)	TS (%)
10	0	450	4.20	582.10	70.28	23.88
10	0	550	6.56	1185.42	56.69	28.53
10	0	650	10.11	1569.42	43.25	27.49
10	1	450	3.27	467.16	57.43	21.98
10	1	550	7.30	1120.08	41.02	24.47
10	1	650	9.95	1564.98	30.47	23.48
12	0	450	4.02	566.74	65.91	24.61
12	0	550	8.54	1187.16	39.73	24.55
12	0	650	10.69	1634.11	36.11	30.22
12	1	450	3.73	564.60	54.07	24.07
12	1	550	6.91	1115.59	36.07	24.40
12	1	650	9.55	1614.04	29.25	26.15

Note: RC- Resin Content, MOR-Modulus of Rupture, MOE-Modulus of Elasticity, WA-Water Absorption, TS- Thickness Swelling,

Statistical Significance. Table 3 shows the ANOVA of resin content (RC), wax (W) and board density (DEN) on the particleboard properties. It shows that resin content has no significant effect on MOE, MOR and WA but has significant effect on TS. For wax, effect on MOE, MOR and TS were not significant while the effect on WA was significant. Board density exhibits high significant effect for MOE, MOR and WA but no significant effect for TS. The interaction of RC*W, RC*DEN, W*DEN and RC*W*RC were found to be not significant.

Table 3. Summaries of the analysis of variance (ANOVA) on the effect of resin content, wax content and board density on the mechanical and physical properties of bagasse panel.

Source	df	MOE	MOR	WA	TS
RC	1	0.85ns	0.75ns	4.40*	1.06ns
W	1	2.87ns	1.56ns	12.64*	0.29ns
DEN	2	147.45**	267.95**	29.12**	2.00ns
RC * W	1	1.69ns	0.17ns	1.21ns	1.31ns
RC * DEN	2	0.86ns	0.22ns	0.64ns	0.19ns
W * DEN	2	0.04ns	0.22ns	0.1ns	0.76ns
RC * W * RC	2	2.21ns	0.31ns	0.29ns	0.88ns

Note: **F- values are highly significant at $p<0.01$, *F-values are significant at $p<0.05$and ns – not significant, W-Wax content and DEN- board density

Effect of Board Density. Figure 1 shows the effect of board density on MOE. Board density with 650 kgm^{-3} give superior properties with 1595.64MPa compared to other two board density, 450 kgm^{-3} (545.15MPa) and 550 kgm^{-3} (1152.06MPa). Higher density of board gave high compaction to board thus increase the strength properties. Increase board's density effected increasing the MOE and MOR. According to [4], high density board had lower porosity compared to lower density board caused the particles and adhesives interact each other more easily to form

stronger crosslink In figure 2, MOR increase by increasing the board density (450 kgm^{-3}, 3.81MPa; 550 kgm^{-3}, 7.33MPa and 650 kgm^{-3}, 10.08MPa) while WA were decrease (450 kgm^{-3}, 61.92%; 550 kgm^{-3}, 43.38% and 650 kgm^{-3}, 36.02%). However, increase in board density caused poor TS [5].

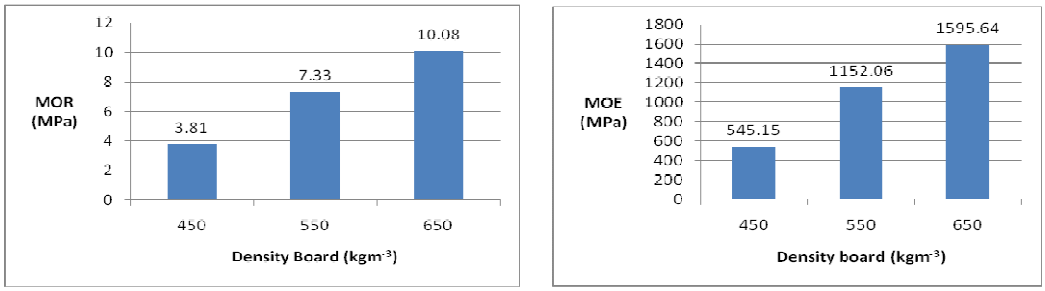


Fig. 1. Effect of board density on mechanical properties (MOR and MOE)

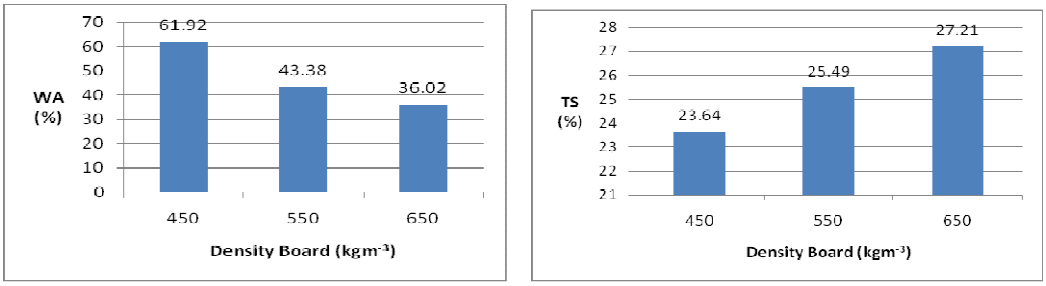


Fig. 2. Effect of board density on dimensional stability (WA and TS)

Effect of Resin Content. In general, increment of resin content decrease the WA and TS [6]. Figure 3 shows resin content effect on the MOE means increase the resin content 10% to 12%, the values of MOE increase 1081.53MPa to 1113.71MPa respectively. Figure 4 shows MOR increase while WA decreases with increasing the resin content. Resin content high caused more bonding sites and make board with high MOE and MOR.

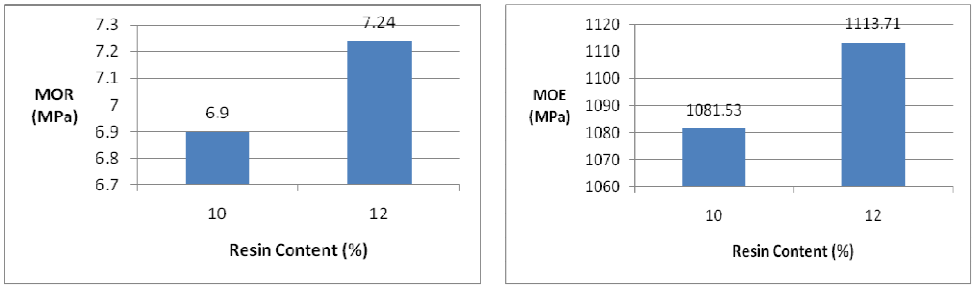


Fig. 3. Effect of resin content on mechanical properties (MOR and MOE)

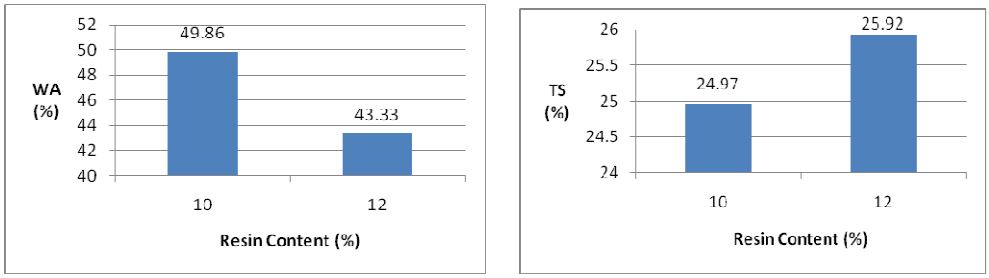


Fig. 4: Effect of resin content on dimensional stability (WA and TS)

Effect of Wax. Three different methods can be used to improve the water resistance and reduce the thickness swelling. First method is by adding wax during the manufacturing board, second method by reducing the density of particleboard [7] and third is used acetylation of particles [8, 9]. Addition 1% of wax is effectively and no negative influence to the strength properties. Wax sizing used in moderate levels showed positive influence on long term water absorption and thickness swelling. However, addition large amount of wax caused decreasing in MOE and MOR. Figure 6 shows effect of wax on MOE. By added 1% of wax, it can decrease the WA and TS. Although small changes in WA and TS but it help to improve the water from absorb too much inside the board. By adding 1% of wax, WA and TS decrease from 52% to 42.22% and 26.55% to 24.34% respectively.

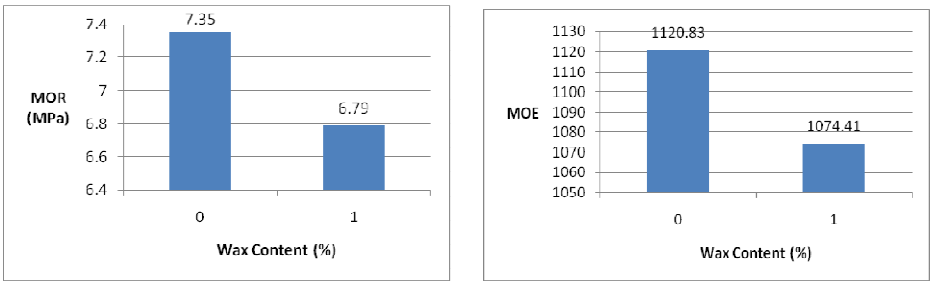


Fig. 5. Effect of wax on mechanical properties (MOR and MOE)

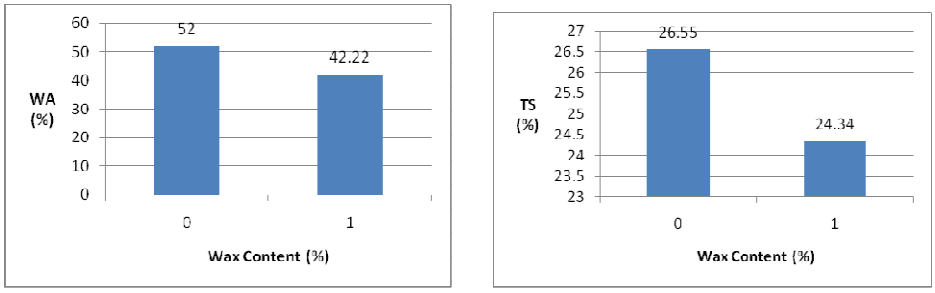


Fig. 6. Effect of wax on dimensional stability (WA and TS)

Summary

The bagasse panel with density 650 kgm^{-3} gave superior strength for MOR (10.69MPa) and MOE (1634.11MPa). Panel with wax provided less water absorption and thickness swelling because of wax's properties which are helped to improve water from absorb easily into panel. The WA and TS decrease from 52% to 42.22% and 26.55% to 24.34% respectively. Resin content (12%) is gave high mechanical properties compared to 10% of resin content, strength values of MOE were 1081.53MPa and 1113.71MPa while the MOR were 7.24% and 6.9% respectively.

References

[1] FAO Statistics: *Major Food and Agricultural Commodities and Producers* (2006), (consulted January 25)

[2] R.G. Anding, in: *The microbial generation of methane from alkali treated bagasse*. (Master thesis from Louisiana State University, United States 1978).

[3] G. Nemli and Kalaycioglu: submitted to Journal of Industrial Crops and Products 24,177-180. (2006)

[4] Y. Zheng, Z. Pan, R. Zhang, B.M. Jenkins and S. Blunk: submitted to Journal of Bioresource Technology 98, 1304-1310. (2007)

[5] K.C. Au and R.O. Gertjejansen: submitted to Journal of Forest Products 39 (4), 47-50. (1989)

[6] Z. Pan, Y. Zheng, R. Zhang and B.M. Jenkins: submitted to Journal of Industrial Crops and Products 26, 185-194. (2007)

[7] E.Y.A. Okino, D.E. Teixeira, M.R.D. Souza, M.A.E. Santana, and M.E.D. Sousa: *Properties of oriented strandboard made of wood species from Brazilian planted forests* .Part 1. 80 mm-long strands of pinus taeda L. Holz Roh Werkst 60, 36-39. (2004)

[8] K.D. Wishered and B. Wilson: submitted to Journal of Production 29 (2), 35-40. (1979)

[9] A.D. Hofstrand, A.A. Moslemi and J.F.Garcia: submitted to Journal of Production 25 (3), 48-53. (1984)

© (2011) Trans Tech Publications, Switzerland
doi:10.4028/www.scientific.net/KEM.471-472.55

Assessment of Strength Properties of Biocomposite from Oil Palm Frond

Faizah Muhamad Fauzi[1,a], Suhaimi Muhammed[2,a]

[1]Faculty of Applied Sciences, UiTM Pahang, 26400 Bandar Jengka, Pahang Darul Makmur, MALAYSIA

[2]Faculty of Applied Sciences, UiTM Pahang, 26400 Bandar Jengka, Pahang Darul Makmur, MALAYSIA

[a]faizahfauzi1603@gmail.com, [b]dsuhaimi@pahang.uitm.edu.my

Keywords: Agriculture residues, biocomposite, oil palm frond, strength properties.

Abstract. Shortage of solid wood supply as the main raw material for the wood-based industries is cute problem faced by the world wide wood industry. Agricultural residues especially from oil palm plantation are abundantly and is therefore hoped to solve the above problem. In this context, this study would like to venture into the utilization of oil palm frond (OPF) as the potential agricultural residues for the manufacture of biocomposite panel. Raw material (OPF) mixed with the binder urea formaldehyde at three resin levels (8%, 10%, and 12%) to produce board of two density levels (550 kg/m^3 and 650 kg/m^3). The boards produced were tested for the mechanical strength (MOE & MOR) in accordance with the European Standard (EN 310). The results showed that the MOE values increased as the resin content increased for both board densities. The values are 1755.54 MPa to 2147.44 MPa for 550 kg/m^3 and 2351.81 MPa to 2810.34 MPa for 650 kg/m^3. Respectively, similar trend of increment was exhibited for the MOR values 12.18 MPa to 14.98 MPa for 550 kg/m^3 and 16.62 MPa to 19.90 MPa for 650 kg/m^3. In conclusion, the utilization of oil palm frond for the production of strong biocomposite material stands a great potential.

Introduction

Particleboard is wood based composite that manufactured by pressing small wood particles at certain pressure with adhesive as the binding agent. It has been used all over the world in furniture, floor, wall, ceiling, partition, and cabinets [6]. Increase in world population has brought to the increase of particleboard utilization. Jamaludin et al. [4], had claimed that Malaysia which is presently uses rubberwood as main raw material in producing particleboard still cannot meet the industry demand. In consequence, had induced the industries involve for searching other sources as an alternative in manufacturing the composite panels like agriculture based residues. In Malaysia, the most abundant agriculture residues that very related are contributed from oil palm plantation.

Oil palm (Elaeis quineensis Jacq.) is one of the Aracaceae or palm families. The mature trees are single-stemmed, and may grow up to 20 m tall. The leaves are pinnate, and reach between 3 and 5 m long [7]. According to Abdul Khalil et al. [1], oil palm tree generally has life span of about 25 years. During pruning and replanting activities, the wastes like oil palm frond (OPF) are generated in a very large amount. Therefore, the utilization of the OPF as relative raw material hoped can stand bright prospect in manufacturing the composite panels. This paper focuses on the bending properties of single-layered bonded urea formaldehyde biocomposite board produced from Elaeis quineensis Jacq. The effects of board density and resin content on the board properties were discussed.

Materials and Methods

The raw material, oil palm frond (Elaeis quineensis Jacq.) was taken from Universiti Teknologi MARA`s (UiTM) oil palm plantation in Jengka Campus, Malaysia. The leaves were stripped off and went through chipping process. The chips produced were flaked in a Pallman ring-knife flaker to reduce the chips to particles shape and pre-dried. The OPF particles were screening to remove the over and under size particles.

The single-layer boards with 12 mm at size of 350 x 350 mm were produced at two different levels of density (550 kg/m3 and 650 kg/m3) at three level of resin content (8%, 10%, and 12%). Determined amount of particles then sprayed with resin mix contain of Urea Formaldehyde at solid content of 64.6-65.7%, hardener and water. The sprayed particles were then manually laid in the wooden mould and pre-pressed within 30 seconds at 3.5 kg/cm3 to reduce the mat thickness thus easier to handle. The consolidated mat then pressed at 165ºC within 9 minutes at 3 level press-cycles as shown in Table 1.

Table 1. Hot pressing time and pressure applied

Level	1	2	3
Time (min)	6	2	1
Pressure (psi)	1800	1200	800

A total of three boards were produced for each density at each of resin levels. The boards produced then tested to determine the modulus of elasticity (MOE) and modulus of rupture (MOR) according to European Standard (EN 310). Samples then trimmed and cut then left for conditioning as required by the standard at 65 ± 5% of relative humidity and at 20 ± 2 ºC of temperature. The sizes of the test samples for each density are shown in the following table.

Table 2. Test sample sizes

Property	Sample sizes (mm)	No. of Test Pieces
MOE and MOR	320 x 50	9

Statistical analysis was employed in determining the significance of data that had been collected. The statistical analysis was done by using the Statistical Package for Social Sciences (SPSS) software. The results of mechanical properties, resin contents and board density on the properties boards produced were evaluated by analysis of variance (ANOVA) where the significance interaction was analyzed.

Results and Discussion

All the strength properties of the boards produced are shown in Table 3. The results showed that the strength of boards was increased as the resin content increased. The board with 550 kg/m3 at 8% of resin content had gave the lowest value by 1755.54 MPa of MOE values, while board with 12% resin content at 650 kg/m3 had indicated to posses the highest value of MOE by 2810.34 MPa. The values of MOR also had shown the same trend as MOE values where the 550 kg/m3 with 12.18 MPa at 8% of resin content as the lowest and 650 kg/m3 with 19.90 MPa at 12% of resin content as

the highest one. These trends had been shown in many studies done by Mohamad et al. [5]; Jamaludin et al. [3] and Chew et al. [2].

Increase of the board properties by resin content were because of more bonding occurred within the particles surface. According to Mohamad et al. [5], by increase the resin content increased the MOE values as a consequence of better bonding among the particles. The positive relation between board properties and board density had been mentioned by Vital et al. [8] in their paper. Furthermore, improved in board properties also can be directly influenced by the board density due to high compaction ratio as pointed out by Jamaludin et al. [4]. The same results where increase in strength properties by density had been revealed in the study done by Jamaludin et al. [3] on the properties of particleboard made of Gigantochloa scortechinii.

Table 3. Mechanical properties of OPF panels at different board densities and resin levels

Board density	Resin content	Bending	
(kg/m^3)	(%)	MOE (MPa)	MOR (MPa)
550	8	1755.54	12.18
550	10	1924.24	13.51
550	12	2147.44	14.98
650	8	2351.81	16.62
650	10	2661.13	18.98
650	12	2810.34	19.90

Notes: MOE - Modulus of Elasticity, MOR - Modulus of Rupture

The ANOVA on the effect of DEN and RC on the board properties are shown on the Table 4. The density shows highly significant effect on all of the board properties for both MOE and MOR while, the resin content shows significant effect on the board properties. However, the interaction between DEN*RC shows non significant effect on the board properties.

Table 4. Summary of the analysis of variance (ANOVA) on the effect of density and resin content on the mechanical properties of OPF biocomposite board

SOV	df	MOE	MOR
DEN	1	117.93**	41.77**
RC	2	7.02*	6.30*
DEN*RC	2	0.16ns	0.27ns

Notes:**-values are significant at $p<0.01$, *-values are significant at $p<0.05$, and ns-not significant DEN-density, RC-resin content, df- degree of freedom, MOE-Modulus of Elasticity,
MOR- Modulus of Rupture, SOV-source of variance

Summary

The outcomes of the study are as follow: These single layer biocomposite boards which based on the different of density and resin content were found to be highly significant and significant effect on the strength properties of panels. Density was found to give more effect rather than resin content on the boards' properties. The panels made at density of 550 kg/m3 with 10% of resin content (1924.24 MPa), were able to meet the minimum strength requirement required by the standard. While, boards with the density of 650 kg/m3 at 12% of resin content (2810.34 MPa), resulted the highest value of the study. With further future invasion, other parameters are hopefully could improve the boards` properties. From this study, it seems that OPF can be applied as new lignocellulosic raw materials in manufacturing biocomposite boards such particleboard.

References

[1] H.P.S. Abdul Khalil, M.R. Nurul Fazita, A.H. Bhat, M. Jawaid and N.A. Nik Fuad : submitted to *Journal Materials and Design* (2009).

[2] L.T. Chew, S. Rahim, and K. Jamaludin: submitted to *Journal of Tropical Forest Science* Vol. 4, Issue 3 (1991), p. 249-256.

[3] K. Jamaludin, H. A. Abd. Jalil, H. Jalaludin, A. Zaidon, M. Abd. Latif and M. Y. Mohd Nor: submitted to *Pertanika Journal Tropical Agriculture Science* Vol. 24, Issues 2, (2001) pp. 151-157.

[4] K. Jamaludin, M. Zalifah, A. Nurrohana, N.A.T. Siti, S. Nor, and A.R. Nor. *Paper presented at the XXI Conference in Seoul, South Korea,* (2010).

[5] J. S. Mohamad, S. Rahim, M. P. Koh, B. Saimin, P. Nordin and S. Jalali, in: "Towards Meeting Global Challenges". (2004), pp: 77-82

[6] H. Kalaycioglu and G. Nemli, (2006): submitted to *Journal Industrial Crops and Products* Vol.24 (2006), pp. 177–180.

[7] S. Sumathi, S.P.Chai and A.R. Mohamed: submitted to *Journal Renewable and Sustainable Energy Reviews* Vol.12 (2008), pp. 2404–2421.

[8] B.R. Vital, W.F. Lehmann and R.S Boone: submitted to *Forest Products Journal Vol.* 24 Issues 12 (1974), pp. 37-45.

© (2011) Trans Tech Publications, Switzerland
doi:10.4028/www.scientific.net/KEM.471-472.59

Mechanical Properties of Composite Panels from Rice Husk

Nur Afidah Abu Bakar[1,a], Suhaimi Muhammed[2,b]

[1]Department of Woods Industries, Faculty of Applied Sciences, MARA Universiti of Technology, Jengka Campus, 26400 Jengka, Pahang, Malaysia

[a]nurafidahabubakar@gmail.com, [b]dsuhaimi@pahang.uitm.edu.my

Keywords: composite panel, mechanical properties, panel density, resin content, rice husk, urea formaldehyde

Abstract. The study involving utilization of agricultural residue is gaining attention. This is an attempt to investigate the possibility of producing composite panels from rice husk (RH), an abundant source of agricultural residues. Composite panels were produced by mixing 1mm of rice husk with a commercial binder called urea formaldehyde at different density levels namely 650kg/m^3, 700kg/m^3 and 750kg/m^3. Two types of resin content (10% and 12%) were used. Mechanical strength tests were performed on the panels conforming to British Standard (BS EN 310). Results obtained indicated that the modulus of elasticity (MOE) increased up to 1753.98MPa at 750kg/m^3 density level with 12% resin content. Similarly, modulus of rupture (MOR) increased up to 8.08MPa with increase in panel density and amount of resin content. Thus, the potential of producing reasonably good composite panels from rice husk for specific end usage is very promising.

Introduction

In recent years, industrial development has induced the increasing levels of environmental pollution and also lack of resources. Realizing on this situation, researchers have attracted toward efficient utilization of agricultural waste as an effort to maximize usage of residues. In the wood industry, agro-waste such rice husk, sugarcane, oil palm coir and corn stalk as a load bearing constituents has been studied few decades ago. By utilizing these agro-wastes for making some useful products, they can be name as new resources.

During milling process, rice husk will separate from rice grain as a waste. Over 40% of world population is depending on rice as primary food [1]. During harvest season in 2007, Malaysia contributes 2.2 million tones of global paddy production [2]. Therefore, RH is one of agricultural residue which easily available in huge amounts and also the most potential to be utilize as some beneficial product. Furthermore, the cost of producing RH reconstituted panel is quiet low than to wood composite. Compared to wood chips, panel from RH also having high aesthetic value.

In this study, we investigated the influence of resin content and density level on bending strength of rice husk reconstituted panel. Result of this study will help in further investigating on producing high quality if RH reconstituted panel, simultaneously maximize the usage of this residue.

Materials and Methods

The main feedstocks in making reconstituted panels were rice husk (RH) and urea formaldehyde (UF) resin. Rice husk with variety number of Malaysian Research (MR211) was obtained from Bernas Kuala Selangor while UF resin was supplied by Malayan Adhesive and Chemical Sdn Bhd at Shah Alam, Selangor.

Rice husk reconstituted panels with dimensions of 34cmx34cmx1.2cm were manufactured at target density of 650kg/m3, 700kg/m3 and 750kg/m3 and resin contents of 10% and 12%. Preparation of panels is started by mixing RH with UF resin. Liquid UF resin and 10% NH4Cl solution (hardener) were supplied to RH particles by spraying through spray nozzles in rotating mechanical mixer. The mixture is spread evenly on aluminum plate as a mat. Mat then experienced pre-press before transferred to hot hydraulic press at start pressure of 2000MPa and temperature

170ºC for 6 minutes. The final stage was cut and trimmed all panels according to British Standard (BS EN). The number of panels was 3 pieces per each trial.

Mechanical Testing. Three point bending test was conducted according to British Standard (BS EN 310) with a Instron Universal Testing Machine to determine the value of modulus of elasticity (MOE) and modulus of rupture (MOR). The test was performed at crosshead speeds of 10 mm/min. Each value obtained represented the average of five samples.

Results and Discussion

Bending strength of rice husk panel at different density level and resin content displayed in Table 1. MOE result of panel with density 750kg/m3 is 1753.98MPa which nearly meet the British Standard of BS EN 310. On the other hand, the results of MOR of all panels were far from the minimum requirement with 8.08MPa as the highest value.

Table 1. Bending strength properties of rice husk panel

Resin [%]	Board Density [kg/m^{3}]	MOE [Mpa]	MOR [Mpa]
10	650	1200.08	5.05
12		1392.7	6.86
10	700	1485.69	6.3
12		1512.08	6.86
10	750	1695.66	7.9
12		1753.98	8.08

Note; MOE-Modulus of Elasticity,
MOR-Modulus of Rupture

According to Moslemi [3], density level is one of the important factors contributed to effect of panel strength. Panel with highest density (750kg/m3) leads to better performance in both MOE and MOR strength (Table 1). This result is in agreement with other researchers [4,6]. Statistical (Table 2) and correlation (Table 3) analysis presented that there is high significance difference between MOE and MOR value with density level. Increase in surface area contact directly could increase the gap filling, as consequence improves the compaction ratio and can absolutely explain the density level-resin content relationship.

Similar trend goes to different resin content which showed panels at 12% of resin content having highest reading on both MOE and MOR compared to 10% resin content. Therefore, resin content showed significant effect on panel strength (Table 2). The correlation analysis (Table 3) indicates that both MOE and MOR increased insignificantly with resin content. Few studies also observed the similar influence of resin content on panel strength conducted by others [6,4,3]. Improve in strength properties with resin content increment could be explain by existing more surface area, which imply to more bonding site available.

Table 2. Summary of the analysis of variance on the panel properties

SOV	Df	MOE	MOR
Density (D)	1	74.41**	58.34**
Resin Content (RC)	1	8.97*	6.77*
D × RC	2	1.16ns	3.05ns

Note; SOV-source of variance, ns-not significance,
* significance at $P < 0.05$, ** significance at $P < 0.01$

Table 3. Summaries of the Duncan multiple range t-tests on the effect of resin content and density

Variables	MOE	MOR
Density	0.90**	0.87**
Resin content	0.22ns	0.21ns

Summary

In this study, density level and resin content proved to have strong relationship with panel strength. Increment these two variable will directly increase panel strength. However, there is no significance different observed from the statistical analysis (Table 2) between density level and resin content. Highest MOE value of panel is 1753.98MPa which nearly meet the requirement standard of BS EN 310. This demonstrated that rice husk panel had a great potential to be a beneficial product. On the other hand, all MOR values failed to meet the minimum standard. Enhancement in panel strength could be done by further revealed on treated RH or usage of other resin as an alternative.

References

[1] FAO, In: Rice market monitor, vol x, Issue 3, (Food and Agriculture Organization for the UN, http://www.fao.org/giews/english/countryupdates/0607e/02.asp,18th Jan, 2008.

[2] H. Pathak, A. Singh, A. Bhatia, and N. Jain, Paddy and Water Environment 4, (2006), pp: 111-117.

[3] A. Moslemi, 1974. Particleboard Vol.1: Materials, 241 pp. Southern Illinios University, USA

[4] F.W. Chen, K. Jamaludin and L.T. Chew. 1991. Particleboard from bamboo, FRIM Reports No. 56. Pp. 35-44. Forest Research Institute Malaysia, Kepong

[5] L.T. Chew, S. Rahim, and K. Jamaludin, J. Trop. Forest Science 4(3), (1992), pp: 249-256

[6] K. Jamaludin, A. Abdul Jalil, H. Jalaludin, A. Zaidon, M. Abd Latif and M.Y. Mohd Nor, 2001.

[7] Properties of Particleboard Manufactured from Commonly Utilized Malaysian Bamboo (Gigantichloa scortechinii). Pertanika J.Trop. Agric. Sci. 24(2): 151-157

© (2011) Trans Tech Publications, Switzerland
doi:10.4028/www.scientific.net/KEM.471-472.62

Manufacturing of Wood-Plastic Composite from Completely Recycled Materials

Taghi.Tabarsa[1,a], Hossein Khanjanzadeh[2,b] and Hamidreza Pirayesh[3,c]

[1] Department of Wood and Paper Science and Technologies, Gorgan University of Agricultural Sciences and Natural Resources, Iran

[2,3] Department of Wood and Paper Science and Technologies, Gorgan University of Agricultural Sciences and Natural Resources, Iran

t.tabarsa@yahoo.com[a], Khanjanzade@gmail.com[b], h_pirayesh30@yahoo.com[c]

Keywords: Wood-plastic, Recycled, Textile, Batch method, Coupling agent, Thickness swelling

Abstract. In this study, wastes of wood cutting mills (wood flour) as well as wastes of textile industry (granules of polypropylene) were used in manufacturing wood-plastic composites. Hence, wood flour with weight percent of 30, 35 and 40 was mixed with corresponding amount of polypropylene and coupling agent, polypropylene grafted maleic anhydride in amount of 6 percent was used in whole compounds. Production was done by batch method and with employment of hot press and after preparation and cutting of specimens physical and mechanical properties of them was studied. The results showed that with increase of wood flour up to 35 percent, MOR, MOE, water absorption and thickness swelling increases but further than it mechanical and physical properties decreases. Besides, increase of wood flour up to 40 percent increased the hardness of the specimens.

Introduction

Wood plastic composites (WPCs) are defined as composite materials containing wood (in various forms) and thermoplastic materials. These materials are a relatively new family of composite materials, in which a natural fiber and/or filler (such as wood flour/fiber, kenaf fiber, hemp, sisal, etc.) is mixed with a thermoplastic such as polyethylene (PE), polypropylene (PP), poly (vinyl chloride) (PVC), etc. Compared with the traditional synthetic fillers, natural fibers present lower density, less abrasiveness, lower cost and they are renewable and biodegradable. WPCs are becoming more and more commonplace by the development of new production techniques and processing equipment. Around 100 companies involved in WPC manufacturing have been identified worldwide [1]. In WPC manufacturing, virgin plastics such as high and low density polyethylene (HDPE and LDPE), PP, and PVC are commonly used. As for virgin plastics, any recycled plastic that melts and can be processed below the degradation temperature of wood (lignocellulosic fillers) (200°C) is usually suitable for manufacturing WPCs. Plastic wastes are one of the major components of global municipal solid waste and present a promising raw material source for WPCs (thanks to their large amount of daily generation and low cost). The utilization of recycled plastic for the manufacture of WPCs has been studied by a number of authors [2–4] Applications of such materials include floor parquets, flower vases, waste paper baskets, park benches, picnic tables, and plastic lumbers. Properties of some waste plastics are similar to those made from virgin materials. For instance, only slight changes in mechanical properties of recycled polyethylene have been reported [4]. The use of plastic and wood wastes seems inevitable and the present opportunities are promising [5], [6] Use of the word “waste” projects a vision of material with no value or useful purpose. However, technology is evolving that holds promise for using waste or recycled wood and plastics to make an array of high-performance products that are, in themselves, potentially recyclable. Preliminary research at the USDA Forest Service, Forest Products Laboratory (FPL), indicates that recycled plastics such as polyethylene, polypropylene, or polyethylene terephthalate can be combined with wood fiber waste to make useful reinforced

thermoplastic composites. Advantages associated with these composite products include lighter weight and improved acoustic, impact, and heat reformability properties—all at a cost less than that of comparable products made from plastics alone. In addition, previous research has shown that composite products can possibly be reclaimed and recycled for the production of second-generation composites.

The overall goal of this paper is to illustrate the potential that currently exists for manufacturing thermoform able composites from waste materials such as waste wood and plastics

Methods and Materials

Poplar- wood flour (particle size of 40– 60 mesh) was supplied from Kousar Co. (Golestan, Iran). Recycled PP, with the trade name Polinar SF060, was obtained from Polinar Petrochemical Company, Tabriz, Iran. Its melt flow index was 8.5–9.5 g/10 min and density of 0.91 g/cm3. The coupling agent, maleated polypropylene (MAPP) was obtained from Kimiya Javid Company with a melt index of 64g/10 min and 2.0 wt% maleic anhydride.

Composite Processing. The amount of wood flour was varied from 30, 35 and 40 wt % and MAPP was fixed at 6% on the basis of the total weight of PP (table1). The blends were compounded in a twin screw extruder (Borna Pars Mehr, Iran). The barrel temperatures of the extruder were controlled at 165, 170, 175, and 180°C for zones 1, 2, 3, and 4, respectively, whereas the temperature of the die was held at 185°C. The screw speed was 60 rpm. The extruded strand was passed through a water bath and pelletized. The resulting granules were subsequently placed in hot press at 175°C for 10 min. then cooled to room temperature under pressure. The pressure for heating was controlled at 35 bar.

Table1-treatments

treatment	Wood flour (%)	Recycled polypropylene (%)	MAPP (%)
1	30	64	6
2	35	59	6
3	40	54	6

Preparation of the Specimens. The resulting granules removed from the twin screw extruder were then pressed into sheets of 10mm nominal thickness and 20×30 cm^2 nominal dimensions using a laboratory hydraulic hot press at 175 °C. Specimens for mechanical testing were cut out of these sheets.

Mechanical Tests. The mechanical properties of the Wood flour/plastic composites were assessed through flexural and Hardness properties. These properties of Wood flour/waste plastic composites were determined according to ASTM D7031, using an Instron testing machine. All tests were done at room temperature (25°C) and constant relative humidity (65%) and three replicates for each test were performed. The specimens were conditioned at constant room temperature and relative humidity prior to testing.

Fig. 1 and 2 the flexural MOE and MOR of Wood flour/recycled plastic composites, respectively. It can be observed that the MOE and MOR of composites containing 35% Wood flour are higher than those containing 30 and 40% wood flour. When the wood flour content increased up to 35%, MOE and MOR significantly increased, while in switching from 35% to 40% there was slight decreases of MOE and MOR of PP composites.

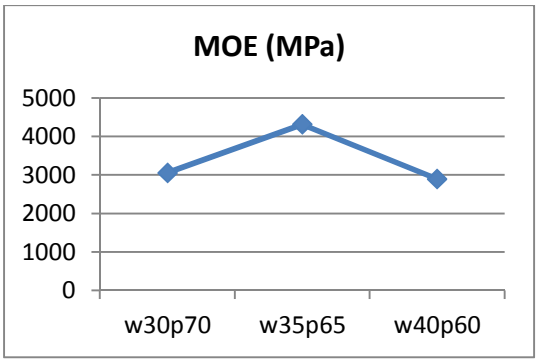


Fig. 1: MOE of Wood flour/ recycled polypropylene composites.

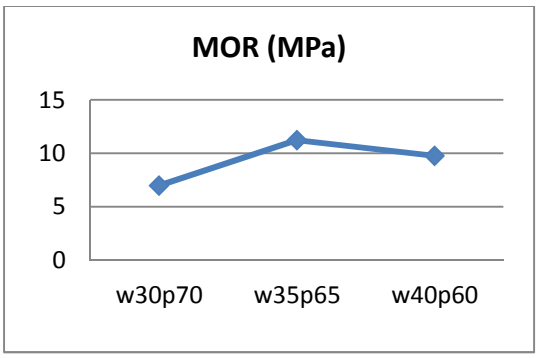


Fig. 2: MOR of Wood flour/ recycled polypropylene composites.

Hardness of wood flour/ recycled polypropylene composites is shown in Fig. 3. Increase of wood flour up to 40 percent increased the hardness of the specimen.

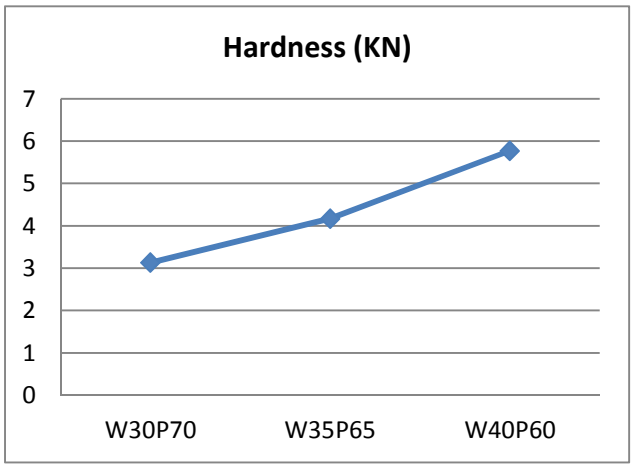


Fig. 3: Hardness of Wood flour/recycled polypropylene composites.

Physical Tests. The water absorption test was carried out according to ASTM D 570. The samples were immersed in distilled water at 23 ± 1°C for 2 and 24h intervals. Before testing, the weight and thickness of each sample were measured. Samples were removed at certain periods of 2 and 24h, wiped with tissue paper to remove the excess water on the surface, and immediately weighed and measured. WA was calculated according to the following Eq. 1:

$$WA(\%) = \frac{(m_t - m_0)}{m_0} \times 100 \quad (1)$$

One of the important properties that we evaluated for the WPCs was WA because it can limit their application. The fact that cellulosic fibers easily absorb water is actually one of the reasons for fiber surface treatments. The treated fibers may absorb less moisture and, thus, favor adhesion with the polymer matrix and also present better performance in humid environments.

Fig. 4 shows the percentages of the water uptake for the Wood flour/recycled polypropylene composites at different periods of immersion (2 and 24h), which varied depending on the wood flour content. The WA of the 60% polypropylene, however, was very low (~ 0.5%) because of its hydrophobic nature. In general, polymers absorb very little moisture; when polymers do slightly absorb moisture, this indicates that moisture is being absorbed by the cellulosic material in the composite.

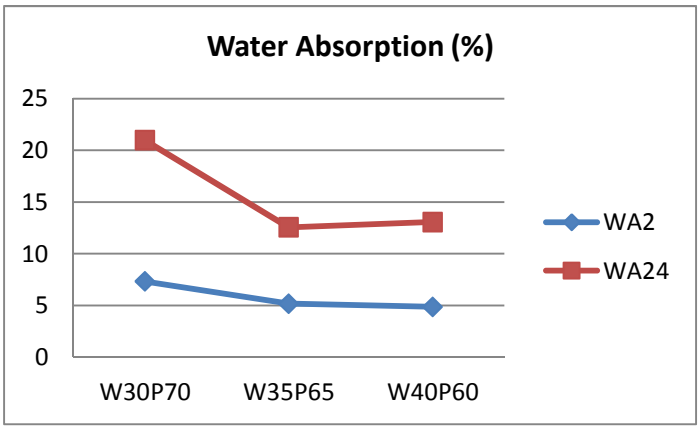


Fig. 4: Water absorption after 2 and 24 hours

Summary

Mechanical and physical properties of WPCs manufactured from Wood flour and recycled plastic (PP) were studied in this research. The following conclusions can be drawn from the results and discussions presented above:

- With increase of wood flour up to 35 percent mechanical and physical properties, increases but further than it decreases MOR, MOE, and physical properties.
- Generally the mechanical properties of specimens containing recycled plastics were statistically comparable with and even to somehow better than those of composites made from virgin plastics. This was considered as a possibility to expand the use of recycled plastics in the manufacture of WPCs.(Kazemi et al,2005)
- When polymers do absorb moisture slightly, this indicates that moisture is being absorbed by the cellulosic material existed in matrix of the composite.

References

[1] Clemons, C. Forest Prod J 1992, 52, 10.

[2] Avila, A. F.; Duaret, M. V. Polym Degrad Stab 2003, 80, 373.

[3] Chow P.; Bajwa D. S.; Lu, W.; Youngquist, J. A.; Stark N. M.; LiQ.; Cook C. G. in *Proceedings of the 1st Annual American Kenaf Society Meeting*, San Antonio, TX, 1998; p 38.

[4] Jayaraman, K.; Bhattacharyya, D. Resour Conservat Recycl 2004, 41, 307.

[5] Youngquist, J. A.; Myers, G. E.; Harten T. M. *in: Emerging Technologies for Materials and Chemicals from Biomass*; American Chemical Society: Washington, DC, 1992. ACS Symposium Series, 476, Chapter 4. *Proceedings of the ACS Symposium, August 26–31, 1990.*

[6] Wegner, T. H.; Youngquist, J. A.; Rowell, R.M. *in: Materials Interactions Relevant to Recycling of Wood-Based Materials,* Rowell, R. M., Laufenberg, T. L., Rowell, J. K., *Eds.; Materials Research Society:* Pittsburg, PA, 1992*; Vol.* 266*, p* 3.

[7] Kazemi Najafi S., Hamidinia E., Tajvidi M**.** *Mechanical Properties of Composites from Sawdust and Recycled Plastics*, Journal of Applied Polymer Science, Vol. 100, 3641–3645 (2006).

© (2011) Trans Tech Publications, Switzerland
doi:10.4028/www.scientific.net/KEM.471-472.67

Rheology and Processing of Ni based Nano-Composite Pastes for Electronic Assembly

R. Durairaja, L. Chiawea, Kau Chee Leong, Wong Mee Chu and Liang Meng Suan

Department of Mechanical and Material Engineering, Universiti Tunku Abdul Rahman (UTAR), Jalan Genting Kelang, Setapak, 53300 kuala Lumpur, Malaysia

arajkumar@utar.edu.my

Keywords: Rheology, Lead-Free, Solder Paste, Nano-material and Nano-composite

Abstract. Lead-free solder paste printing process accounts for majority of the assembly defects in the electronic manufacturing industry. In the stencil printing process, the solder paste must be able to withstand low and high shear rates, which results in continuous structural breakdown and build-up. The study investigates the effect of nickel additional to the thixotropic behaviour of lead-free Sn/Ag/Cu solder pastes using the structural kinetic model. A hysteresis loop test and constant shear test is utilized to investigate the thixotropic behaviour of the pastes using parallel plate rheometry in temperature 30 ^{o}C. In this study, the shear rates were increased from 0.01 s^{-1} to 10s^{-1} and the second curve was a result of decreasing shear rate from 10s^{-1} to 0.01s^{-1}. For the constant shear test, the samples were subjected to two constant shear rates of 0.1s^{-1} and 1s^{-1}. The constant shear rate test was designed to study the structural breakdown and build-up of the paste materials. From this investigation, hysteresis loop test was shown to be an effective test method to differentiate the extent of structural recovery in the solder pastes. The results of the structural parameter values obtained from the kinetic model showed a good correlation to the breakdown and build-up of the paste structure.

Introduction

Due to the toxicity of lead in electronic products, legislation has been proposed to reduce the use of and even ban lead from electronics. The two main directives are the European Union (EU) legislation 'Waste from Electronics and Electrical Equipment' (WEEE) and 'Restriction of the use of hazardous substances in the electrical and electronic equipment' (ROHS) directive that will ban the use of lead in new electronic products. A lead free solder (Pb-free solders) has been considered as the most promising alternatives of lead-based solder. These lead-free solders are mostly based on Sn-containing binary and ternary alloys. Among them, Sn–Ag system is one of the earliest commercially available lead-free solders and has been recommended for general-purpose use as substitutes for Sn–Pb eutectic solder. To obtain better solder alloys exhibiting refined microstructure, many researchers have concentrated on the addition of other elements into Sn-alloys solder [1-2]. The most attractive progress was achieved by adding minor rare earth elements into the Sn– alloys and thus leading to improve the microstructure stability of those solders. For the rare earth elements are surface active and almost insoluble in many metals, such as Ni, Sn, Ag, Bi, etc., they tend to be enriched at grain boundaries and/or phase boundaries for their relative large atomic radius and thus improve the microstructure stability of the solder.

Solder pastes can be classified into dense suspension and homogeneous mixture [3]. As a dense suspension, consisting of about 50% solid and 50% liquid (by volume), the paste can be described in terms of such attributes as volume fraction, particle size distribution and metal content. As a homogeneous and kinetically stable mixture [4], a solder paste can be described in terms of such properties as, surface tension, normal forces, viscosity, and density. The constituents and the composition of a given solder paste can have a direct impact on the performance of the sub-processes in the surface mount assembly process – starting from the paste printing process through to the reflow soldering, to the cleaning, inspection and testing. Solder pastes consist of three main constituents [5], namely: (1) solder alloy particles which form the base for the metallic bond, (2) the flux system which helps to promote the formation of the metallic bond by providing a good wetting

condition and for cleaning the surfaces, and (3) the vehicle carrier system which facilitates the binding together of the solder powder particles and the flux system together, and for providing the desired rheological properties for processing and depositing the paste onto the printed circuit board (PCB).

Solder pastes are non-Newtonian fluids which exhibits thixotropic behavior. The thixotropic is the characteristic of a suspension when it behaves as solids under very small applied stresses but under greater stresses become liquids. When the stresses are removed the suspension settles back into its original consistency. This property is particularly associated with certain colloids which form gels when left to stand but which become sols when stirred or shaken, due to a redistribution of the solid phase, as shown in Fig. 1. Characterizing the degree of thixotropy in pastes such as solder pastes and isotropic conductive adhesives is an important step in understanding the rheological behavior of the material. The thixotropy effect is a result of aggregation of suspended particles and the aggregation in the system is caused by the attractive forces such as van der Waals and repulsive forces due to steric and electrostatic effect on the particles. The repulsive force prevents the particles from approaching close to one another, and as a result, the particles are held together by weak physical bonds. When no force is exerted on the suspension, the particle aggregation can form a spatial network which creates an internal structure. When the suspension is sheared, these weak forces are broken, causing the network to break down into smaller aggregates. These aggregates can be broken down further into smaller flocs.

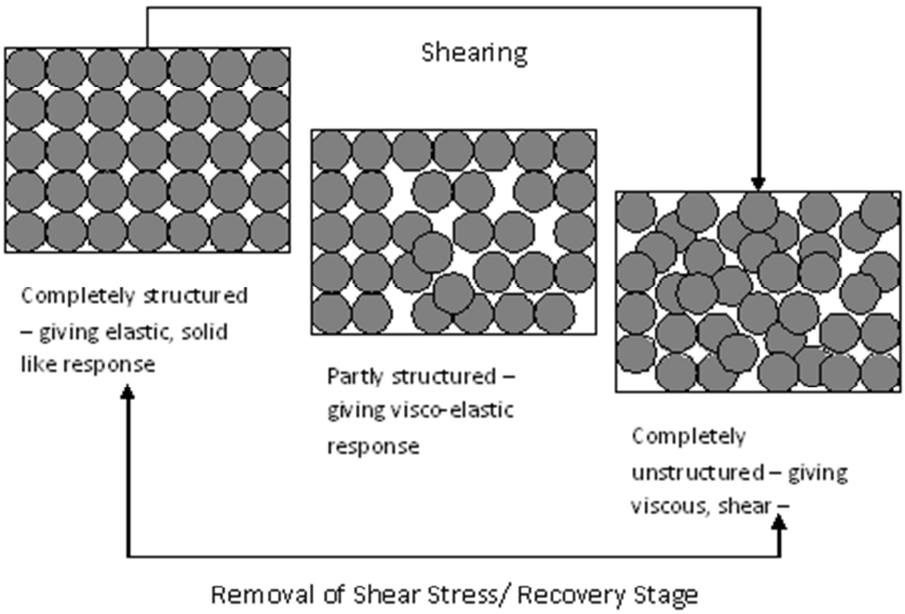


Fig. 1. Breakdown of thixotropic structure

On the other hand, in less concentrated suspensions the Brownian motion and inflow collision can cause the formation of aggregates. Shearing or inflow collision can cause the particle to attach to other parts of the microstructure which will increase the size of the aggregates. Besides shearing/inflow collision, Brownian motion can also cause an increase to the number of aggregates in the system. Brownian motion is the random thermal agitation of atoms and molecules, which cause them to move to a favorable position where they can, given the necessary attractive force, attach themselves to other parts of the microstructure [6]. After a period of time, at a given shear rate, a dynamic equilibrium is reached between the growth and destruction of aggregate.

Thixotropic materials can also exhibit shear thinning behavior. When a thixotropic material is subject to increasing shear rates, the viscosity drops but when the shear rate is removed, the material

structure recovers resulting in the hysteresis loop, shown in fig. 2. It should be noted that the rebuilding of the structure is not instantaneous upon the removal of stress. The area between the hysteresis loop is used as a measure of the 'amount' of thixtropy or the area enclosed within the loop can be used as an indication of energy required to break down the material structure.

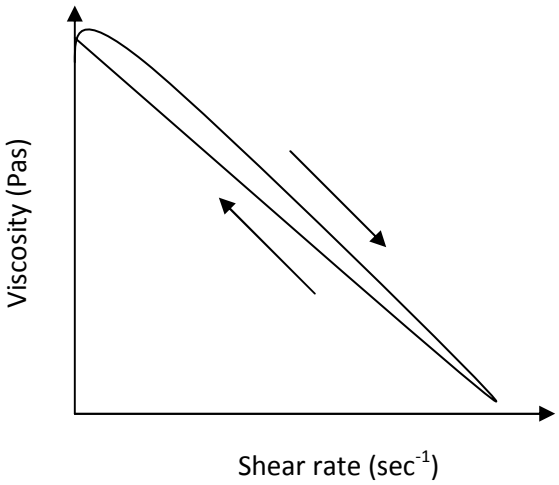


Fig. 2. Hysterisis loop obtained when shear rate is increased and decreased

In this research, a composite solder using nickel particle reinforcement, prepared by mechanically dispersing Ni particles into eutectic Sn/Ag/Cu solder paste, has been developed and has shown improved mechanical properties over the Sn/Ag/Cu. The study investigates the effect of nickel additional to the thixotropic behavior of lead-free Sn/Ag/Cu solder pastes using the structural kinetic model. It has also been reported that nickel particle may affect the mechanical properties over the lead-free solder paste. So the effects of Ni nano-particles addition on breakdown and build-up in Sn/Ag/Cu Lead-free solder paste was studied in this paper in order to observe the thixotropic behavior of the Lead-free solder.

Materials and Methods

Apparatus. A controlled stress rheometer (Model: Physica MCR 301) with a parallel plate geometry with a diameter of 25 mm and gap of 1.0 mm was used as a measuring device. Prior to loading a sample onto the rheometer, the solder pastes were hand mixed with a plastic spatula for about 1 to 2 min and left about half an hour after the stiring. A sample was loaded on the bottom plate and the top plate was then lowered to the desired gap height of 1.0 mm by squeezing the extra paste out from between the plates. The excess paste at the plate edges was neatly trimmed with a plastic spatula. Then the sample was allowed to rest for about 1 min before starting the test. Identical loading procedures were followed in all the tests. All tests were conducted at 30^0C with the temperature being controlled by a Peltier-Plate system.

Material and Sample Preparations. The solder pastes used for this investigation are shown in Table 1. The nickel powder content is the only variable parameter. The nickel powder particles size distribution is 20-25 μm. Samples P1, P2, P3, P4 and P5 were stored in the fridge at 4^0C, while the room temperature (which could not be controlled) was monitored to average 24^0C and 35% humidity. Before each rheological measurement the samples were taken out and left about 8 hours to reach room temperature.

Table 1. Constituent of lead free solder pastes investigated

Paste samples	Particle size distribution (μm)	Particle shape	Flux Medium	Solder alloys/materials	Nickel powder
P1	20-45	Spherical	Rosin Mildly Activated (RMA)	96.5% Tin/3% silver/0.5% copper	0%
P2	20-45	Spherical	RMA	96.5% Tin/3% silver/0.5% copper	2%
P3	20-45	Spherical	RMA	96.5% Tin/3% silver/0.5% copper	4%
P4	20-45	Spherical	RMA	96.5% Tin/3% silver/0.5% copper	6%
P5	20-45	Spherical	RMA	96.5% Tin/3% silver/0.5% copper	8%

Experimental test method

Hysteresis Loop Test. The thixotropic behaviour can be studied through the hysteresis loop test, also known as the thixotropic loop. In the hysteresis loop test, the shear rate is ramped up to a maximum shear rate, γ_m and then reversed back to the first (original) shear rate. In this study, the shear rates were increased from $0.01s^{-1}$ to $10s^{-1}$ (step-up) and the second curve was a result of decreasing shear rate $10s^{-1}$ to $0.01s^{-1}$ (step-down).

Constant Shear Rate Test. The constant shear rate test is used to investigate the paste sample's dependency on time. For a given constant shear rate, the viscosity of the paste sample decreases over time, ultimately reaching a steady value. In this study the sample is subjected to two different shear rates; $0.1\ s^{-1}$ and the tests was carried out for a period of 120 seconds.

Results and Discussion

Hysteresis Loop. The evolution of viscosity as a function of shear rate resulting from the hysteresis loop tests has been analyzed. The viscosity of the samples decreased with increasing shear rates indicating a shear thinning behavior. The sample pastes exhibit thixotropic behavior as the presence of a hysteresis area between the step-up curve ($0.01s^{-1}$ to $10s^{-1}$) and step down curve ($10s^{-1}$ to $0.01s^{-1}$). The region between the up curve and down curve in hysteresis curve is an indication of the thixotropic behaviour of the sample pastes. At 30 ^{0}C (Fig. 3), based on the area between the step-up and step-down curve, sample P5 showed the largest structural breakdown followed by sample P4. Samples P1, P2 and P3 seemed to show a very good recovery after gradual drop in the shear rate

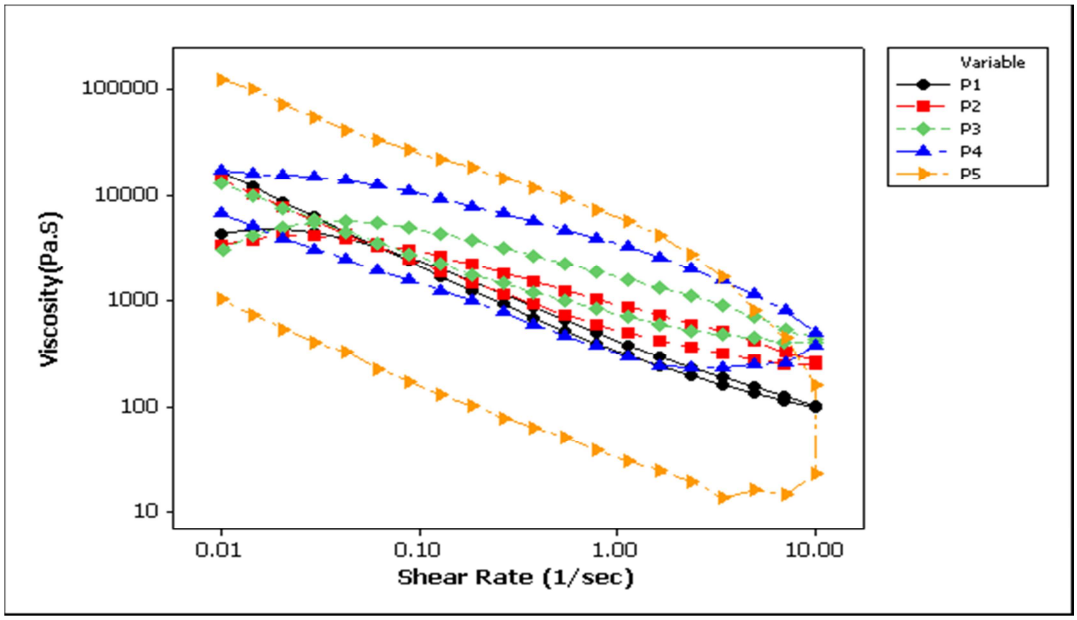


Fig. 3. Thixotropic flow curve at 30^0C

Constant Shear. In the constant shear rate experiment, the samples were sheared at $0.1s^{-1}$ and the temperature was maintained at 30^oC (shown in Fig. 4), the viscosity of samples P1, P2, P3 and P4 grows rapidly for the first 20 second, which shows the elastic behavior of the paste samples. In addition, the increase could also be due to the presence of the strong flocculation within the suspension. After this period, the viscosity increases and stabilizes. However, the viscosity of the sample P5 dropped significantly, which could be attributed to high concentration of nickel powder. Addition of nickel powder has resulted in the paste P5 losing its fluidity. As the shear rate increased to 1 s^{-1}(shown in Fig. 5), the viscosity of samples P4 and P5 dropped drastically, and the viscosity of the samples P1, P2 and P3 reach to a steady state. The result showed that the most the nickel content, the worst the structure stability. Both these samples P4 and P5, behaves like a solid material with a definite yield point. As a result, the sample P4 and P5 have a less stable structure compared to samples P1, P2 and P3.

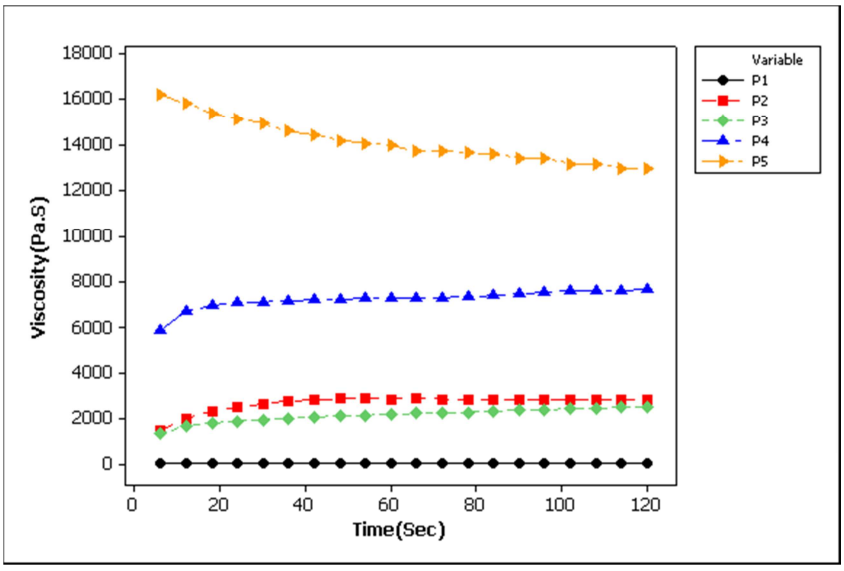


Fig. 4. Constant shear flow curve with 0.1 s^{-1} at 30^0C

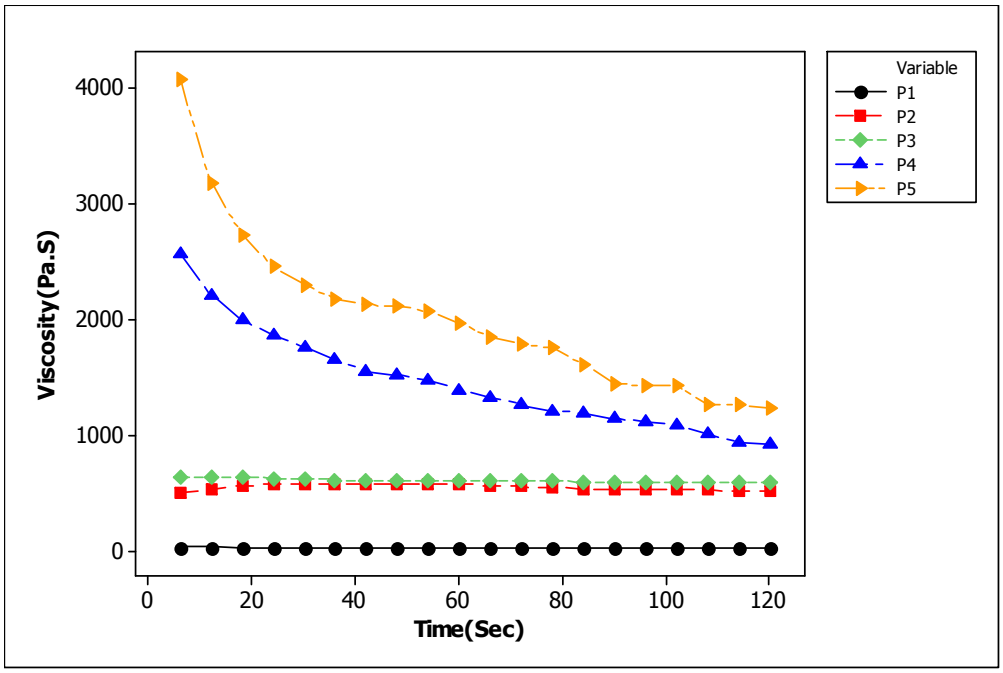


Fig. 5. Constant shear flow curve with 1 s^{-1} at 30^0C

Summary

The thixotropic behavior of nickel additional of lead-free Sn/Ag/Cu solder pastes is investigated in this study. The different nickel content samples were subjected to the hysteresis loop test and the constant shear test in order to observe the structural breakdown and build-up in the solder paste samples. In the hysteresis loop test, the larger the area between the step-up and step-down curves showed that to have a poor structural recovery rate. In the constant shear test, the less stable sample will have a drastically drop in viscosity when it is applied a shear. The result shown that, the samples P4 and P5 which consist of 6% and 8% nickel powder respectively have a bad recovery rate and worst structural stability.

References

[1] R. Durairaj and Lam Wai Man, Journal of Science and Technology in the Tropics (2009)

[2] Fangjuan Qi, Li Sun, Zhezhe Hou, Jianqiang Wang and Cha Qin, Electronic Packaging Technology & High Density Packaging 1-3 (2008).

[3] Hwang J.S. *Solder paste in electronics packaging.* Van Nostrand Reinhold, New York (1989).

[4] Currie M.A "Characterisation of solder pastes used in the reflow soldering of surface mount assembly," Ph.D. Thesis, University of Salford (1997).

[5] Barnes H.A. Journal Non-Newtonian Fluid Mechanic 70: 1-33 (1997).

[6] Cheng D.H. and Evans F. British Journal of Applied Physics 16: 1599-1617 (1965).

© (2011) Trans Tech Publications, Switzerland
doi:10.4028/www.scientific.net/KEM.471-472.73

Immediate and Long-Term Deflection of Carbon Fiber Reinforced Polymer (CFRP) Concrete Beams

Ehsan Ahmed[a] and Habibur Rahman Sobuz[b]

Department of Civil Engineering, Universiti Malaysia Sarawak, 94300, Kota Samarahan, Sarawak, Malaysia

[a]aehsan@feng.unimas.my, [b]habibkuet@yahoo.com

Keywords: Beams, CFRP, Sustained loading, Deflection, Structural performance, FRP ratio.

Abstract. This study presents the results of immediate and long-term deflections of reinforced concrete beams strengthened with carbon fiber reinforced polymer (CFRP) laminates under sustained loading The test parameters were sustained load and different degrees of strengthening scheme for both cracked and un-cracked sections of beams. The applied sustained load was 56% and 38% of the ultimate static capacities of the un-strengthened beams for cracked and un-cracked section respectively. The long term deflections of CFRP strengthened beams at six month were on average 1.42 times the immediate deflections for un-cracked beams and 1.45 times the immediate deflections for cracked beams. The experimental results indicate that the long-term deflection of cracked beam shows significantly higher value compared to that of un-cracked beams. A comparison of time dependent deformation between analytical and experimental results shows closer agreement for the un-cracked beam sections. More conservative theoretical estimation is observed in the case of cracked beam section in spite the inclusion of tension stiffening effect. Finally, factors affecting the long-term deflection of strengthened beams are discussed to get better understanding on the long term behaviour of strengthened beams.

Introduction

Traditionally, strengthening of reinforced concrete structures has been accomplished through external bonding steel plates to the tension face of the members by epoxy adhesive. At the early stage, bonding of steel plates has been recognized as an effective and convenient method to improve the loading capacities of the structural members. This technique has been used widely for both bridges and buildings [1-2], but the method often suffers the following disadvantages (i) difficulty in manipulating the plates at the construction site (ii) proper formation of joints, due to the limited delivery length of the plates (iii) deterioration of the bond at the steel-concrete interfaces due to corrosion of the steel. The basic concepts in the use of FRPs for strengthening of concrete structures are covered in a review article [3]. Studies [4-5] have shown that fiber reinforced polymer (FRP) composites in strengthening of RC members, in the form of sheets, have emerged as a viable, cost-effective, minimally disruptive technique for improving structural performance.

A number of studies have been conducted on the immediate deflection of reinforced concrete (RC) beams externally bonded with different types of FRP system [6-7]. Some researches [8-10] have also been carried out on the time-dependent behaviour of FRP strengthened reinforced concrete beams and it has received a considerable attention. Presently, along with ACI (American Concrete Institute) approach [1], some analytical methods [12-13] are available to compute the long-term deflections in RC members. In this study, experimental investigation on immediate and long-term deflections of reinforced concrete beams strengthened with different ratios of CFRP laminates are carried out to provide necessary experimental data. The experimental data is compared with the existing analytical solution. Finally, some critical issues related to the long-term serviceability performances of such structures are discussed.

Description of Experimental Investigation

Test program. Table 1. shows the test program that was initiated to investigate the effect of CFRP laminates on the long-term performance of RC beams for cracked and un-cracked section and to verify the accuracy of the analytical methods. A total of six beams having different level of strengthening scheme and subjected to different sustained loads to ensure cracked and un-cracked section were tested in the laboratory. Two beams (designated as CBC and CBU) were not bonded with CFRP laminates, two beams (FBC-1L and FBC-3L) for cracked section and the rest two beams (FBU-1L and FBU-3L) for un-cracked section were bonded with 1 and 3-layers of CFRP laminates. The FRP ratio, ρ_{FRP}, is the area of FRP composite laminate divided by the gross concrete area. Different CFRP configurations were chosen such as to facilitate comparison among these beams with the same sustained loads. The flexural capacities of different layered CFRP-bonded beams have been investigated from the laboratory test.

Table 1. Test program

Section type and sustained load	Beam designation	FRP ratio, ρ_{FRP} (%)	Service load	Type of strengthening
Cracked (22.56 kN)	CBC	0	0.56 P_0	Un-strengthened (control) beam
	FBC-1L	0.4	0.36 P_1	One layer of CFRP sheets strengthened beam
	FBC-3L	1.2	0.30 P_3	Triple layers of CFRP sheets strengthened beam
Un-cracked (15.31kN)	CBU	0	0.38 P_0	Un-strengthened (control) beam
	FBU-1L	0.4	0.25 P_1	One layer of CFRP sheets strengthened beam
	FBU-3L	1.2	0.21 P_3	Triple layers of CFRP sheets strengthened beam

Flexural capacity of Un-strengthened (Control) beam, P_0 = 40.3kN
Flexural capacity of 1-layer CFRP strengthened concrete beam, P_1 = 62.0kN
Flexural capacity of 3-layer CFRP strengthened concrete beam, P_3 = 74.4kN

Material Properties. The concrete mix proportion was set at 1:1.65:2.45:0.45 by weight of ordinary Portland cement, locally available natural sand, and crushed granite aggregate of 10mm nominal size and water. The concrete has a compressive strength of 36.0MPa, modulus of elasticity of 28.6GPa, and a modulus of rupture of 3.7MPa. High yield deformed steel reinforcement bars of 6mm and 10mm (T6 and T10) were used as compression and tension reinforcement for the beam specimens and plain round mild steel bar of 6 mm diameter (R6) is used as transverse shear reinforcement. Steel reinforcing bars average modulus of elasticity was 195GPa, 186GPa and 200GPa and yield strength was 482MPa, 470MPa and 215MPa for T10, T6 and R6 bars respectively. Unidirectional CFRP laminates of 1.2mm thickness per layer was used for the strengthening purposes of the beams and are cut from the Sika Carbodur S1012/160 [15] rolled laminate. The CFRP composite laminate was tested in the laboratory to get the tensile strength, yield strength, modulus of elasticity and the percentage of ultimate elongation until the failure. The other properties of the carbon fiber and epoxy adhesive as supplied by the manufacturer are also shown in Table 2.

Table 2. CFRP laminates and epoxy adhesive properties

Materials	Property	Values
CFRP laminate	Yield strength (MPa)	1315
	Modulus of Elasticity (GPa)	165
	Elongation at ultimate (%)	2.15
	Tensile strength (MPa)	1685
	Density (g/cm^3)	1600
Epoxy adhesive	Modulus of Elasticity (GPa)	3
	Elongation at ultimate (%)	2.6
	Tensile strength (MPa)	55

From the experimental investigation, the ultimate creep coefficient and ultimate shrinkage strain were established in the laboratory for conventional concrete as 1.3 and 352 $\times 10^{-6}$ respectively. Similarly, the creep coefficient of the FRP composite laminate also needs to investigate. The study conducted by Plevris and Triantafillou [15] showed that the carbon fibers laminates are practically creep free. Based on the outcome of that study, the creep coefficient of CFRP laminates is considered as zero for the long-term analysis of the section.

Specimen Fabrication. The specimen configuration is shown in Figure 1. All the beam specimens are 150 × 200 mm in cross section and 1900 mm in span length on a simply supported span. They were reinforced longitudinally with two T10 bars (10mm in diameter) as tensile reinforcement and two T6 bars (6mm in diameter) as compressive reinforcement. R6 stirrups were placed at a constant spacing of 125 mm throughout the entire length of the beams so as to prevent the beams from failing in shear. The tensile reinforcements were placed at a depth of 168 mm while the compressive reinforcement depth was 30 mm**.** The control beam was designed to fail in flexure following the British code of practice [16]. Figures 2(a) and 2(b) shows the schematic diagram of single and triple layer strengthening scheme of reinforced concrete beams.

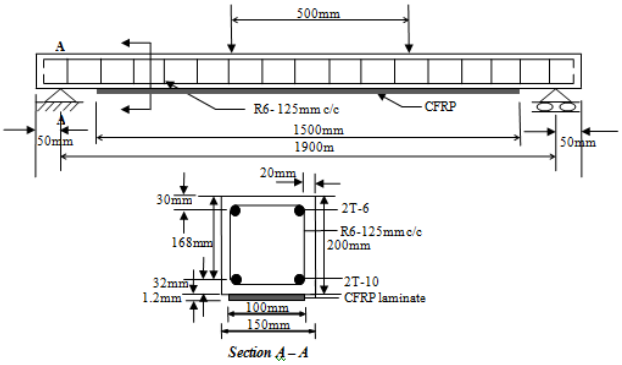


Fig. 1 Longitudinal and cross-section details of the test beams

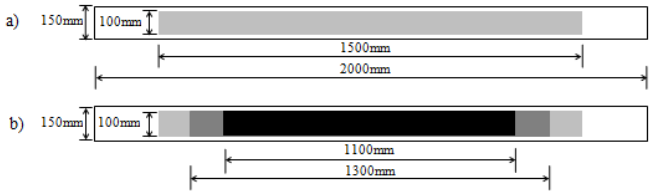


Fig. 2 Strengthening schemes of RC beams: CFRP laminates of (a) single, and (b) triple layers

Surface Treatment and Strengthening Phase. In the fabrication of beams, it is needed to prepare the substrate before composites sheets is bonded to the tensile face of the concrete. The surfaces were prepared as suggested by the manufacture instruction for proper bonding of the CFRP laminates into the concrete. Prior to the bonding of the CFRP laminates to the beams, the concrete substrate was mechanically abraded by using a grinding wheel, creating somewhat a rough surface to remove laitance, grease, and loosely adhering particle. The composites laminates were bonded to the tension face (bottom) of the concrete beams using a two-part cold curing epoxy resin Sikadur-30 (Part-A and Part-B) mixed at a proportion of 1:3 and then cured at room temperature. It was ensured

that the surface was kept free from any contaminant, air entrapment and unevenness areas and was smooth. The CFRP laminates were cleaned properly using sika colma cleaner. Sikadur-30 adhesive was applied on cleaned and prepared substrate components and then, the CFRP laminates were placed onto the prepared concrete surface. The composites laminates was attached starting at one end and applying enough pressure by rubber roller to press out any excess epoxy from the sides of the laminates. All the excess epoxy was removed from the sides of the laminates. To ensure a proper bonding, a minimum of 3 days curing of the externally applied adhesive is maintained for all the specimens.

Test Set-up and Procedure. The beams were set up over the simply supports with a clear span 1900mm to investigate the long-term performance of multi-layered CFRP strengthened cracked and un-cracked beams subjected to distributed sustained loads. During the testing, the deflections of all beams were measured at mid span and quarter span of the beams using digital dial gauges. Also, two dial gauges were placed at mid-span at 20mm from the front and back sides of the beam, to check for any unintentional rotation of the beams due to loading. The average of the two dial gauge readings was taken as the mid-span deflection. The quarter span dial gauges were used to check the symmetrical nature of the loaded beams. Readings were taken at regular interval starting 1, 3, 5, 7, 10, 14, 21 days, weekly up to 3 months and every 15 days thereafter for up to 6 months for the experimental beams. In long-term deflection test, the service load levels as mentioned in Table 1 that corresponds to the cracked and un-cracked sections are simulated.

Analytical Prediction of Deflections. Effective modulus approach based on the recommendation of ACI committee [11] was used to compute the immediate and long-term deflections of CFRP strengthened reinforced concrete beams. The immediate deflections were calculated based on the applied sustained loads by including the beam self-weight. ACI recommended creep and shrinkage model are adopted in this study in evaluating time dependent deformation. Unidirectional CFRP is considered to behave as linear elastic materials and it was assumed that CFRP laminates used in this study is creep free [15]. Similar approach was used by previous researchers [13] in predicting the time-dependent deflection un-strengthened and strengthened RC beams and a good correlation with the experimental results were observed in these studies.

Results and Discussion

Immediate and Long-Term Deflections. The measured immediate and long-term deflections under sustained loads at the end of six months for un-cracked and cracked beams are summarized in Table 3. It is observed that the immediate deflections for CFRP strengthened beams (FBU-1L, FBU-3L, FBC-1L and FBC-3L) are significantly lower than the un-strengthened (control) beams. The long term deflection after the six month period was on average 41% and 46 % higher to that of immediate deflection for CFRP strengthened beams while the long term deflection of control beam 64% and 65% higher to that of immediate deflection for the un-cracked and cracked section respectively. From the experimental investigation, it is identified that the long-term deflections of the CFRP strengthened beams were reduced 28% and 46% for un-cracked and cracked beams respectively as compared to the control beams. It is also seen that the higher the CFRP ratio, the smaller the long-term deflection due to sustained loads.

Table 3. Deflections of FRP-bonded RC beams

Beam	FRP ratio, ρ_{frp} (%)	Immediate deflection (mm)	Long-term deflection (mm)	Total deflection (mm)	Long-term/ immediate deflection
CBU	0	0.42	0.27	0.69	0.642
FBU-1L	0.4	0.38	0.17	0.55	0.447
FBU-3L	1.2	0.33	0.12	0.45	0.363
CBC	0	1.38	0.9	2.28	0.652
FBC-1L	0.4	0.99	0.45	1.44	0.454
FBC-3L	1.2	0.68	0.32	1.00	o.470

Comparison of Experimental Results with Analytical Predictions. Test results were collected up to 180 days after the sustained loading as mentioned in Table 1 were imposed on the six experimental beams. Fig. 3 to Fig. 5 show the experimental and predicted mid span long-term deflection versus time under sustained loading for beams with different FRP ratios. In the case of un-cracked beams CBU, FBU-1L and FBU-3L, the analytical predicted results based on effective modulus method agree well with the experimental results. Due to the unequal reinforcement at top and bottom faces, along with the creep, the shrinkage deformation will also occur in these beams. In general, the analytical results give conservative estimations for the long term deformation of the test beams. In case of cracked beams CB, FBC-1L and FBC-3L (refer to Fig. 6 to Fig. 8), it was observed that experimental deflection is slightly lower than the theoretical predicted deflection. In general, the long-term deflection of the beams using EMM approach again gives conservative estimate of the experimental results. For the cracked beam section, beside the creep coefficient and ultimate shrinkage strain, another factor which can influence the theoretical result is the tension stiffening, noting that concrete has the ability to carry tensile stress between cracks in the tension zone due to the bond between the steel and concrete. The tension stiffening model used in this study was that similar to that mentioned in ACI report [11]

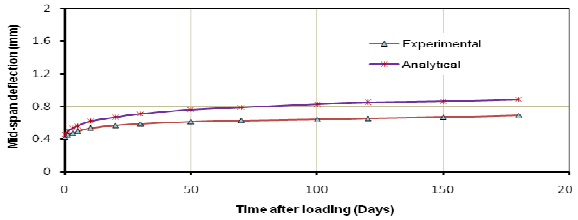


Fig. 3. Long-term deflection of un-strengthened (CBU)

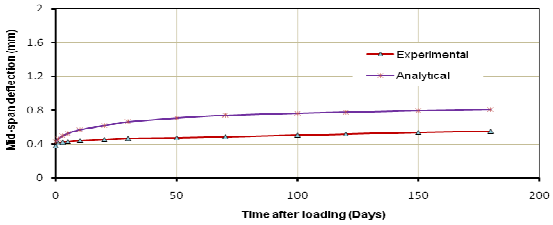


Fig. 4. Long-term deflection of one layer CFRP strengthened beams (FBU-1L)

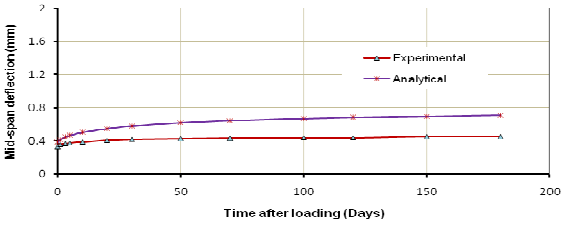


Fig. 5. Long-term deflection of three layers CFRP strengthened beams (FBU-3L)

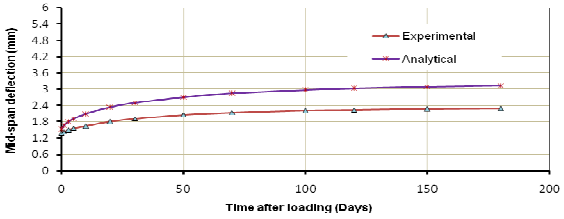


Fig.6. Long-term deflection of un-strengthened (CBC)

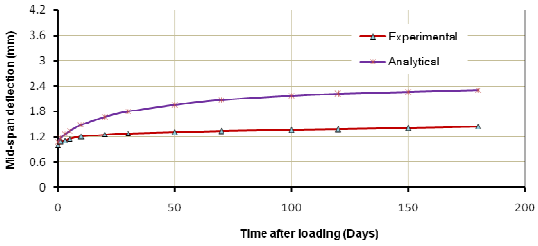


Fig.7. Long-term deflection of one layer CFRP strengthened beams (FBC-1L)

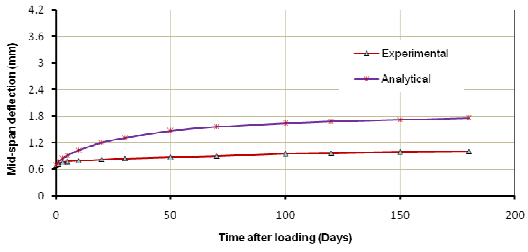


Fig. 8. Long-term deflection of three layers CFRP strengthened beams (FBC-3L)

Summary

From the experimental investigation, it is seen that the long-term deflections after six month period were about 1.64 times the immediate deflections for the control un-cracked beams and 1.65 times the immediate deflections for the control cracked beams; whereas, it was on average 1.42 and 1.45 times for the strengthened un-cracked and cracked beams respectively. This indicates attachment of FRP sheet not only reduces the instantaneous deflection but it is also effective in controlling the long-term deflection. Under the same sustained load, the larger the CFRP reinforcement ratio, the smaller is the long-term deflection. The experimental results are in good agreement with the theoretical predictions and in all cases the theoretical predictions are giving conservative estimate of the experimental results for the test beams.

Acknowledgement

This research work reported in this paper has been funded by the Ministry of Higher education, Malaysia and University Malaysia Sarawak under the project FRGS/02(09)/682/2008(15).

References

[1] D. A. Van Gemert: Proc., ICP/RILEM/IBK Int. Symp. On Plastics in mat. and Struc. Engineering., Prague, 1982, 519-526.

[2] R.N. Swamy, R. Jones and J.W. Bloxham: Structural Engineering, Part A, 65 (2), 1987, 59-68.

[3] T. C. Triantafillou: *Prog. Struct. Eng. Mater.,*1, 126–134, 1998.

[4] K. Saadatmanesh, M.R. Ehsani: Journal of Structural Engineering, pp.3434-3455, 1991.

[5] U. Meir, H. Kaiser:, Advanced Composite Materials, 1991, pp. 224-232.

[6] Allen Ross, David M. Jerome, Joseph W. Tedesco and Mary L. Hughe: ACI Structural Journal, Vol. 96, No.2, 1999, pp. 212–220.

[7] M. T. Ei-Mihilmy and J. W. Tedesco: ACI structural journal, Vol.97, No.5, 2000, pp.679-680.

[8] G. Al Chami, M. The´riault, K.W. Neale: Construction and Building Materials, Vol. 23, 2009, pp.1640–1652.

[9] M.K. Saha and K.H.Tan: Journal of Comp. for Const., Vol. 10, No. 6, 2006, pp.474-482.

[10] M. Arockiasamya, S. Chidambarama, A. Amera, M. Shahawy: Composites: Part B, 31, 2000, 577-592.

[11] ACI Committee 435R-95. American Concrete Institute, Redford Station, Detroit, Michigan, 2003.

[12] A. Ghali, R. Favre and M. Elbadry: *Concrete structures: Stress and Deformation*, 3rd edition, Spon press, 2002, London and New York.

[13] Gilbert R.I. Shrinkage, Electronic Journal of Structural Engineering, vol.1, 2001, pp. 15-37.

[14] Product data sheet Edition 0308/2 Sika carbudur plates. Sika Kimia Sdn. Bhd., 2008, Malaysia.

[15] N. Plevris, And T. C. Triantafillou: Journal of Structural Engineering, Vol. 120, No. 3, 1984, pp.1016-1045.

[16] BS 8110-1: Structural Use of Concrete- Part 1: Code of practice for design and Construction, London: 1997, British Standards Institute.

© (2011) Trans Tech Publications, Switzerland
doi:10.4028/www.scientific.net/KEM.471-472.79

Flexural Performance of RC Beams Strengthened with Different Reinforcement Ratios of CFRP Laminates

Habibur Rahman Sobuz[a] and Ehsan Ahmed[b]

Department of Civil Engineering, Universiti Malaysia Sarawak 94300, Kota Samarahan, Sarawak, Malaysia

[a]habibkuet@yahoo.com, [b]aehsan@feng.unimas.my

Keywords: Strengthened Beam, Flexural strength, CFRP laminates, Cracking load, De-bonding.

Abstract. In this paper, experimental study is carried out to evaluate the flexural performance of reinforced concrete beams strengthened with different ratios of carbon fibre reinforced polymer (CFRP) laminates. Four rectangular reinforced concrete beams strengthened with different reinforcement ratios of CFRP laminates are tested to failure under transverse bending on a simply supported span of 1.9 m. The increase of ultimate strength provided by the bonded carbon fiber is assessed and failure mode is identified. The results indicated that the flexural capacity of beam was significantly improved as the layers of laminates increased. It is concluded that the attachment of CFRP laminates has substantial influence on the performance of CFRP strengthened beams. However, de-bonding of CFRP laminates from the concrete surface is still a concern for the case of multi-layer strengthening of beam. Based on the observed results, recommendations are made to prevent the premature de-bonding failure of strengthened beams.

Introduction

Researches and field application [1-2] of reinforced concrete beams bonded with steel plates have been conducted in the past. Even though this technique has been recognized to be an effective in increasing flexural capacity and enhancing flexural stiffness thereby reducing deflection as well as controlling cracking it is difficult to implement and in practice it requires complicated manipulation. In the past two decades FRPs, which were originally developed for the aerospace and defense industries, have shown great potential for use in civil engineering structures [3]. Recently, one popular strengthening method has been developed, consists of using FRPs material as external bonded reinforcement strips [4]. In practice, FRP can be incorporated into concrete structures in different forms, like embedded bars, meshes, gratings and external plates [5]. Among them, external use of FRPs sheet appears to be the most convenient, fast, cost-effective and promising way of rehabilitation and strengthening over the steel plates [6].

In this paper, the effect of the number of CFRP layers on the flexural performance of strengthened beams is investigated. The effectiveness of using CFRP laminates to improve the stiffness and the structural capacity of RC beams is also discussed based on the experimental study. The failure modes and crack patterns are noted to get better understanding on the performance of beams strengthened with multi-layer CFRP laminates.

Methodology

Experimental Program. Table 1. shows the experimental program that was initiated to investigate the effect of CFRP laminates on the flexural performance of RC beams. A total of four beams having different level of strengthening scheme were fabricated in the laboratory. First beam (designated as CB) was not bonded with CFRP laminates and considered as control beam, the rest three beams namely, FB-1L, FB-2L and FB-3L were bonded with different layers of CFRP laminates (1, 2 and 3–layers respectively).

Table 1. Experimental Program

Beam designation	FRP ratio, ρ_{FRP} (%)	Type of strengthening
CB	0	Un-strengthened (control) beam
FB-1L	0.4	One layer of CFRP sheets strengthened beam
FB-2L	0.8	Two layers of CFRP sheets strengthened beam
FB-3L	1.2	Three layers of CFRP sheets strengthened beam

Specimen Details. The specimen configuration is shown in Fig. 1. All the beam specimens are 150 × 200 mm in cross section and 1900 mm in span length on a simply supported span. They were reinforced longitudinally with two T10 bars (10mm in diameter) as tensile reinforcement and two T6 bars (6mm in diameter) as compressive reinforcement. R6 stirrups were placed at a constant spacing of 125 mm throughout the entire length of the beams so as to prevent the beams from failing in shear. The tensile reinforcements were placed at a depth of 168 mm while the compressive reinforcement depth was 30 mm**.** The control beam was designed to fail in flexure following the British code of practice [7].

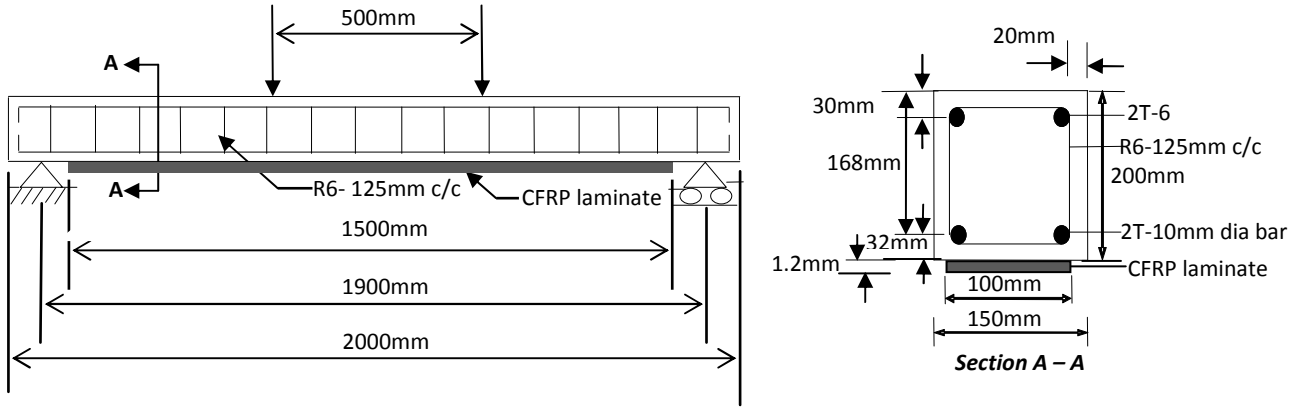


Fig.1 Longitudinal and Cross section detail of the experimental beams

Material Properties. The concrete mix proportion was set at 1:1.65:2.45:0.45 by weight of ordinary Portland cement, locally available natural sand, and crushed granite aggregate of 10mm nominal size and water. The concrete has a compressive strength of 36.0MPa, modulus of elasticity of 28.6GPa, and a modulus of rupture of 3.7MPa. High yield deformed steel reinforcement bars of 6mm and 10mm (T6 and T10) were used as compression and tension reinforcement for the beam specimens and plain round mild steel bar of 6 mm diameter (R6) is used as transverse shear reinforcement. The average modulus of elasticity of steel reinforcing bars was 195GPa, 186GPa and 200GPa and yield strength was 482MPa, 470MPa and 215MPa for T10, T6 and R6 bars respectively. Unidirectional CFRP laminates of 1.2mm thickness per layer was used for the strengthening purposes of the beams and are cut from the Sika Carbodur S1012/160 [8] rolled laminate. The CFRP composite laminate was tested in the laboratory to get the tensile strength, yield strength, modulus of elasticity and the percentage of ultimate elongation until the failure. The other properties of the carbon fibers and epoxy adhesive as supplied by the manufacturer are shown in Table 2.

Table 2. CFRP laminates and epoxy adhesive properties

Materials	Property	Values
CFRP laminate	Sheet form	Uni-directional roving
	Yield strength (MPa)	1315
	Modulus of Elasticity (GPa)	165
	Elongation at ultimate (%)	2.15
	Tensile strength (MPa)	1685
	Density (g/cm^3)	1600
Epoxy adhesive	Modulus of Elasticity (GPa)	3
	Elongation at ultimate (%)	2.6
	Tensile strength (MPa)	55

Strengthening System. The surfaces were prepared as suggested by the manufacture instruction for proper bonding of the CFRP laminates into the concrete. Prior to the bonding of the CFRP laminates to the beams, the concrete substrate was mechanically abraded by using a grinding wheel, creating somewhat a rough surface to remove laitance, grease, loosely adhering particle and other dirt. The composites laminates were bonded to the tension face (bottom) of the concrete beams using a two-part cold curing epoxy resin Sikadur-30 (Part-A and Part-B) mixed at a proportion of 1:3 and then cured at room temperature. The CFRP laminates were cleaned properly using sika colma cleaner. Sikadur-30 adhesive was applied on cleaned and prepared substrate components and then, the CFRP laminates were placed onto the prepared concrete surface. The composites laminates was attached starting at one end and applying enough pressure by rubber roller to press out any excess epoxy from the sides of the laminates. All the excess epoxy was removed from the sides of the laminates. To ensure a proper bonding, a minimum of 3 days curing of the externally applied adhesive is maintained for all the specimens. Fig. 2 shows the schematic diagram of single, double and triple layer strengthening scheme of reinforced concrete beams.

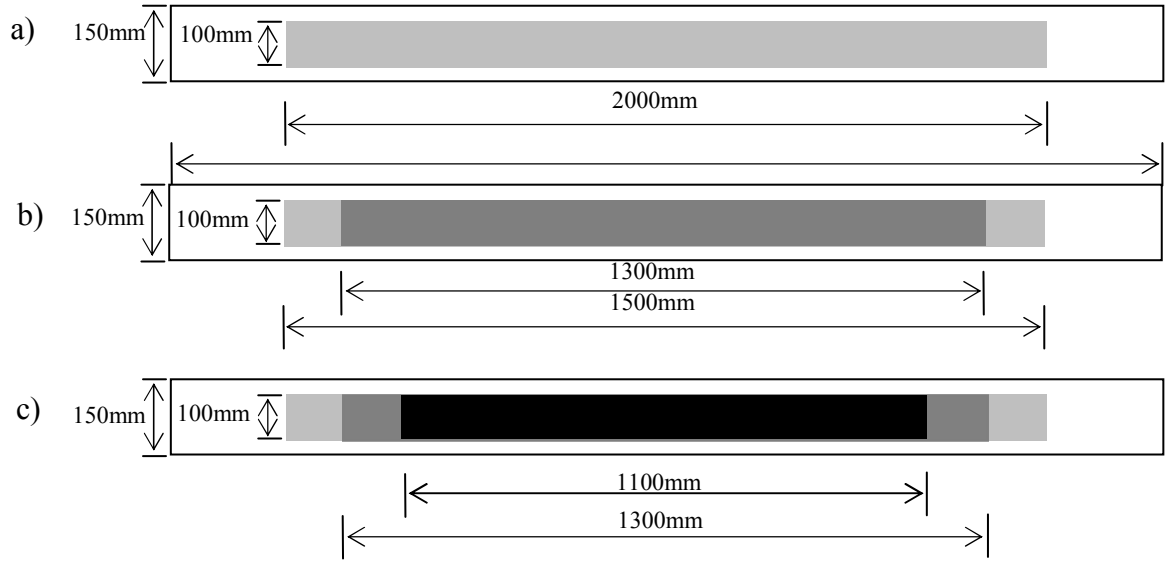


Fig. 2 Strengthening schemes of RC beams: CFRP laminates of (a) single, (b) double and (c) triple layers

Test Setup and Procedure. In the test, the load is applied monotonically and the bending test set-up is a four-point one. All the beams were tested over a simple span of 1900mm and instrumented for the measurement of quarter and mid-span deflections. Linear displacement transducers were used to measure the deflection of the beams. Portable electronic data logger was used to record the reading of deflections. Loads were applied by two hydraulic jacks, which are attached to the pressure gauge. After a regular increase of loading, the loading values and the corresponding deflections were recorded. The load and the corresponding deflection taken from the test were then

used to investigate the behavior of beams. The quarter span transducers were used mainly to check the symmetrical nature of the loaded beams. Cracks were visually detected using a magnifying glass and its propagation was traced and the corresponding loads were recorded on the surface of the beam.

Results and Discussion

Load-deflection Relationship. The load-deflection behavior of control beam and beam strengthened with different layers of CFRP laminates are shown in Fig.4. It is observed from Fig. 3, initially all the strengthened beams behave like the control beam with the internal steel reinforcing bars carrying the majority of the tensile force in the section. When the internal steel yields, the additional tensile force is carried by the FRP system and an increase of the load capacity of the member is obtained. Eventually, the FRP strengthened beams fail. The failure modes which are observed on the CFRP strengthened beams are different from that of the classical reinforced concrete control beam. CFRP reinforced beams behaves in a linear elastic fashion nearly up-to the failure. This brittle mode of failure is considered as a drawback for this way of reinforcement. The use of second and third layer of CFRP plates can lead to significant increase in the ultimate load and stiffness of the beam. During the test, no de-lamination is observed between the superimposed CFRP plates in the case of multi-layered strengthened beams.

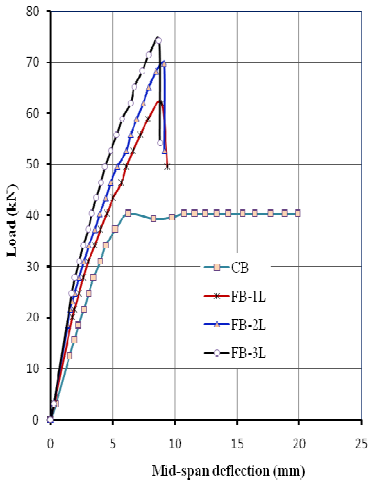


Fig. 3 Load-deflection response of control beam and multi-layer CFRP strengthened beams

Ductility Characteristics. When applied to RC members, the term ductility implies the ability to sustain significant inelastic deformation prior to collapse. In this study, the displacement ductility was investigated. The displacement ductility index (displacement at failure divided by displacement at yield) can give an estimation of the lack of ductility of these beams. Table 3 shows the displacement ductility of the tested RC beams using different CFRP laminates configurations. It was also observed that un-strengthened beam showed more displacement or ductility as compared to that of different CFRP configurations concrete beam. The maximum deflection prior to the final failure of the CFRP strengthened beams was found about 12.8mm and it indicate that the strengthened beams are less ductile compared to the un-strengthened beams. The lower value of ductility index for the CFRP strengthened beams (FB-1L, FB-2L and FB-3L) indicate the lacking of ductility of such strengthened beams.

First Cracking and Ultimate Loads. Table 3 shows the experimental results of control and strengthened beams in terms of the first cracking load and ultimate load. It also includes the theoretical prediction of first cracking loads and ultimate loading capacity of the test beams. Theoretical predictions of the first cracking load is calculated from the equivalent transformed

section analysis of the beam cross-section and ultimate load carrying capacity is predicted using equivalent stress block of the cracked cross section in accordance to the provision mentioned in British Standard [7].

Table 3. Experimental and Theoretical results

Beam designation	Experimental load (kN)		Theoretical load (kN)		$\frac{P_{ult(The.)}}{P_{ult(exp)}}$	Crack spacing(mm)	*Ductility Index*	Failure mode
	P_{cr}	P_{ut}	P_{cr}	P_{ult}				
CB	12.4	40.3	11.3	31.5	0.78	105	3.81	Concrete
FB-1L	15.5	62.0	12.3	82.6	1.33	126	1.65	De-bonding
FB-2L	18.6	69.75	13.4	98.8	1.41	138	1.48	De-bonding
FB-3L	21.7	74.4	14.4	106.8	1.43	149	1.29	De-bonding

Table 3 also tabulates the failure modes of the test beams. It was observed from the test result that the control beam failed by yielding of tensile steel reinforcement followed by crushing of the concrete directly under four-point bending test. When loaded in the laboratory, the control beam (CB) developed flexural tensile cracks in the constant bending region at load of 12.4kN. At load around 37.2kN, the tensile reinforcing steel yielded. Finally, the beam failed in flexure due to the crushing of extreme compression zone concrete at load 40.3kN.

In general, different level of CFRP strengthened reinforced concrete beams (FB-1L, FB-2L and FB-3L) showed significant increases in flexural stiffness and ultimate capacity as compared to that of control beam. From the experimental investigation, it is identified that the percentage increase of cracking load of 1, 2 and 3-layers CFRP strengthened beams are 25%, 50% and 75% respectively whereas the percentage increase of ultimate load are 54%, 73% and 85% respectively as compared to the control beam. The increase in first crack load of strengthened beams can be attributed to the increase of stiffness due to the laminates restraining effects. Thus, it is concluded that the laminate thickness significantly influence the structural performance of the strengthened beams. A comparison between experimental and theoretical result shows that the theoretical calculation give conservative estimation of the first cracking load but underestimate the ultimate capacity of the strengthened beams. In general, the experimental results are in close agreement with the theoretical predictions.

Failures Modes and Crack Patterns. The failure modes which are observed on the CFRP strengthened beams are different from those of the classical control beam. The failure modes of the experimental beams have been tabulated in Table 3. During the testing, the un-strengthened (control) beam exhibited widely spaced and greater number of cracks compared to the strengthened beams (refer to Table 3). The cracks have appeared on the surface of the strengthened beams at relatively closer spacing. This behavior shows the enhanced concrete confinement due to the influence of the CFRP laminates. Also the composite action has resulted in shifting of failure mode from flexural failure (steel yielding) in case of control beam to peeling of CFRP laminates for the strengthened beams. It was observed from the experimental investigation that all beams strengthened with CFRP laminates have failed in the same manner. The crack patterns and modes of failure of control beam, typical CFRP strengthened beams are shown in Figs. 4 (a) and 4 (b) respectively.



(a) **(b)**

Fig. 4 Mode of failure (a) Control beam (b) typical CFRP laminate strengthened beam

The peeling of CFRP laminates starts from the end of the beam in the region of high shear stress. Research shows that the de-bonding of FRP sheets can be prevented by introducing edge transverse strips at the location of critical shear stress. Hence, to get the full benefit of the strengthening effect, it is suggested to use U or W shaped edge CFRP strips to prevent the premature failure of de-bonding.

Summary

The result of the experimental study indicates that externally bonded CFRP laminates can be used effectively to strengthen the reinforced concrete beams. Regarding the effect of number of layers, an increase in stiffness and flexural strength is achieved with the increase of CFRP layers. It seems that the beam behaves as if the plate was thicker and no inter-layer de-lamination is observed in any cases. Nevertheless, the possible brittle failure of the strengthened beams still needs to be considered. Failure mode of beam strengthened with CFRP sheets was by de-bonding of the strips and concrete crushing in compression zone. To get the full benefit of strengthening effect, it is suggested to prevent the de-bonding failure by using edge strips. In general, the experimental results are in very good agreement with the theoretical predictions. A closer agreement for the ultimate load can be achieved provided the premature de-bonding of CFRP laminates can be prevented.

Acknowledgements

This research work reported in this paper has been funded by the Ministry of Higher education, Malaysia and University Malaysia Sarawak under the project FRGS/02(09)/682/2008(15).

References

[1] R.N. Swamy, R. Jones, and J.W. Bloxham, Structural Engineering, Part A, 65 (2), 1987, 59-68.
[2] L'Hermite RL, J. Bresson: Rilem, Int Symp Synth Resine Build Construct. 1967. p. 175–203.
[3] M. Arduini, A. Nanni, ACI Struct J, 1997; 94(5): 493–501.
[4] LC Hollaway, MB. Leeming, *Strengthening of reinforced concrete structures using externally-bonded frp composites in structural and civil engineering.* Woodhead Publishing limited; 1999.
[5] J. L. Clarke: *Alternative Materials for the reinforcement and Prestressing of Concrete*, Chapman & Hall Inc., Chapter 7, 1993, 151-171.
[6] K. Saadatmanesh, M.R. Ehsani, Journal of Structural Engineering, 1991, pp.3434-3455.
[7] BS 8110-1: Structural Use of Concrete- Part 1: Code of practice for design and Construction, 1997, British Standard.
[8] Product data sheet Edition 0308/2 Sika carbudur plates. Sika Kimia Sdn. Bhd., 2008, Malaysia.

© (2011) Trans Tech Publications, Switzerland
doi:10.4028/www.scientific.net/KEM.471-472.85

Evaluation of Physical and Mechanical Properties of Paulownia Wood Core and Fiberglass Surfaces Sandwich Panel

Maryam Sobhani[a], Abolghasem Khazaeian[b],Taghi Tabarsa[c], Alireza Shakeri[d]

Forestry And Wood Tech, Gorgan University Of Agricultural Sciences And Natural Sources, Beheshti St.Gorgan, Iran

[a]sobhani.m666@gmail.com, [b]khazaeian@gmail.com, [c]t.tabarsa@yahoo.com, [d]shakeri@gau.ac.ir

Keywords: Sandwich panels, Paulownia, multilayer Fiberglass, Physical and mechanical properties

Abstract. The purpose of this study was to determine some physical and mechanical properties of sandwich panels manufactured from the core of Paulownia wood and surfaces of multilayer of fiberglass and resins. Paulownia was selected among Hardwoods because of its s low density (0.26 g/cm3) and high strength/weight ratio. Eight treatments were used for experiments: Two kinds of fiberglass (needle and combination of the needle and curtain type), two various resins (polyester and epoxy) and two core thicknesses (9mm and 19mm). Physical properties including density, resistance to water absorption, Dimensional stability, and Mechanical Properties such as internal bonding, compressive and bending strength of panels were measured following ASTM Standard. The results indicated that panels with 19 mm thick core had lower density (0.5g/ cm3) compared to the 9mm thick panels (0.7g/cm3). Bigger volume of wood in the core of panels with higher thickness was the main reason of this result. The experimental results showed that thickness of wood was effective on the modulus of rupture, modulus of elasticity, and compressive strength, significantly. Epoxy resin presented higher internal bond compared to the polyester resin. The two kind of fiberglass (needle one and the combination of needle and curtain type) didn't have noticeable differences on mechanical properties. It also was found that Paulownia is a promising species for manufacturing sandwich panel.

Introduction

Sandwich panels offer great potential for the development of optimized structures with high stiffness and strength-to-weight ratio [1]. These panels are a combination of outer skins bonded with structural adhesives to a solid core, a foam core, or honeycomb core material.

This structure is a combination of thin, high strength facing on each side of a much thicker, light weight core material. Sandwich technology is gradually making the advantages of composites available for an ever wider range of applications [2].The performance characteristics of composite panels are greatly superior to those made from traditional materials, such as plywood or metal.

Composite sandwich panels are widely used in various industries, because they exhibit extremely high stiffness-to-mass ratios. The primary advantages of composite panels compared to conventional materials. Those are significantly lighter panels, vastly stronger panels, and fatter panels when manufactured and when in use, economically superior, capacity for medium to very large volume production runs [3]. Sandwich constructions has broad applications in diverse industries where lightweight, stiff panel construction is required, from boat hulls to aircraft structures, from truck sidewalls to building panels, from space platforms to bridge decks [4].

On the other hand the high specific strength and stiffness of reinforced polymer-matrix composite materials have made them attractive for use in sandwich constructions [5] and their environmental durability and corrosion resistance offer superior serviceability in many applications compared to traditional materials [6]. This product is fiberglass-reinforced Polymer facings laminated onto a Paulownia wood core. End-grain Paulownia core blocks is sandwiched between and adhered to facing skins.

There was some reason for selecting Paulownia wood in core. Paulownia low density (0.26g/cm3) was of main factors that we decided to use it. Physical and mechanical properties of Paulownia wood estimated before selection for using in sandwich panel core. End grain Paulownia is an ultra-light wood product with one of the highest strength to weight ratios for a core material [7].

It was supported that the vibration properties of this wood satisfy the necessary conditions (low loss tangent and high acoustic converting efficiency).This wood is a good thermal insulator and it has excellent heat/cool insulation properties [8]. In addition to these properties, Paulownia wood is suitable for weight critical applications. End grain Paulownia configuration has the ability to handle dynamic loads with high resistance to fatigue. However all of these properties make it suitable for aircraft, ship and building structures.

Material and Fabricating Method

Eight sandwich configurations are fabricated in Gorgan University of agricultural sciences and natural sources. The sandwich panels were manufactured using hand lay up method producing fiberglass laminate and resin transfer process was by hairbrush [9]. Fiberglass with epoxy/polyester resins used as face sheets over a Paulownia blocks core. Paulownia blocks used in the core had a cross section of 25*50 mm2 and 9 and 19 mm thicknesses .Wood blocks were conditioned at 23˚c and 50% relative humidity for a few days. Five layers of fiberglass with resin for covered every surface and the two kind of fiberglass (needle one and the combination of needle and curtain type) were used. Catalysts were added to resins. After preparing of resins, they applied to fiberglass layers by hairbrush. The glued layers were placed on core layer one by one. A small roller was used for flattening and removing of extra resins and air from fiberglass multilayer. When sandwich was assembled a weight block placed over that and left for one day. During this epoxy or polyester binder was cured and sandwich panels was produced.



Fig. 1. some stages of sandwich panel production (right to left)

Three variables were used for manufacturing sandwich panels: Two kinds of resins (epoxy and polyester), two kinds of fiberglass (needle one and the combination of needle and curtain type) and two core thickness (9mm and 19 mm). The experimental of design is shown in table 1.

Tests were determined using 5 specimens from each panel. Data for each test were statistically analyzed. Analyze of variance (ANOVA) was used to test for significant difference between factors and levels. When the ANOVA indicated a significant difference among factors and levels, a multiple comparison of the means was done employing tukey test to identify which groups were significantly different from other group. All data of measuring mechanical properties are presented in table 2.

Table 1. The experimental design

Panel type	resin	fiberglass	thickness
A	epoxy	curtain and needle	19(mm)
B	epoxy	needle	19(mm)
C	polyester	curtain and needle	19(mm)
D	polyester	needle	19(mm)
E	epoxy	curtain and needle	9(mm)
F	epoxy	needle	9(mm)
G	polyester	curtain and needle	9(mm)
H	polyester	needle	9(mm)

Evaluating Sandwich Panel Properties

Water Absorption. The present study evaluated the effect of water immersion on Paulownia wood as core material and fabricated panels. Those were subjected to water immersion to determine the relative resistance to property change. Samples were studied for dimensional change, weight gain after immersion .The results of immersed specimens were compared with dry specimens to determine the effect of immersion. Samples dimensions were 25*50 mm^2 for 19 and 9 mm thicknesses. Dimensional stability following water absorption test investigated. The water absorption performed according to ASTM 272_01.

Edgewise Compression Test. This test method covers the determination of flat structural sandwich construction compressive properties in a direction parallel to sandwich facing plane. The edgewise compressive strength of sandwich construction specimens provides a basis for judging the load carrying capacity of the construction in terms of developed facing stresses as compared to the facing yield stress [10]. The shorter edges of the specimens are sanded to ensure uniform load transfer and to avoid local yielding of the faces .Tests results are shown in table2. Samples dimensions were 19* 50*100 mm^3 or 9*50* 60 mm^3. The edgewise compression is performed according to ASTM C364–99.

Single-point-load Bending Test. Flexure tests on produced sandwich panels conducted to determine the sandwich modulus of rupture (MOR) and modulus of elasticity (MOE). Bending strength was determined in accordance with ASTM C393_00, as shown in fig. 2 and 3. Samples dimensions were 19*60*290 mm^3 and 9*30*170 mm^3 .The results summarized in table2.

Flatwise Tensile Test. This test method covers the determination of the flatwise tension strength between core and facings of an assembled sandwich panel. Samples dimensions were 25*25 mm^2 for19 and 9 mm thicknesses. Table 2 summarized the core/face bonding strength test properties. Tensile strength was determined in accordance with test method C297_ 94.

Results and Discussion

Bending Test. The experimental results showed that the thickness parameter was effective on the MOR, MOE, significantly.

Amount of shear in panels containing thicker wood blocks in the core was higher. This may be related to higher shear that occurs in solid wood part of panel in higher thickness. In accordance with this reason that thinner panels (9mm thick) presented higher MOR and MOE compared to thicker panels (19mm thick). Interaction effect resin and thickness also was found in MOE that is shown in fig.6. (1: polyester and
2: epoxy)

Although higher thicknesses (19mm) had negative influence on MOR and MOE ،this influence on panels that were produced with polyester resin was further .This may be due to higher brittle property in polyester resin that indicated increasing MOE and MOR further. Analyzed results are shown in fig. 2 and 3.

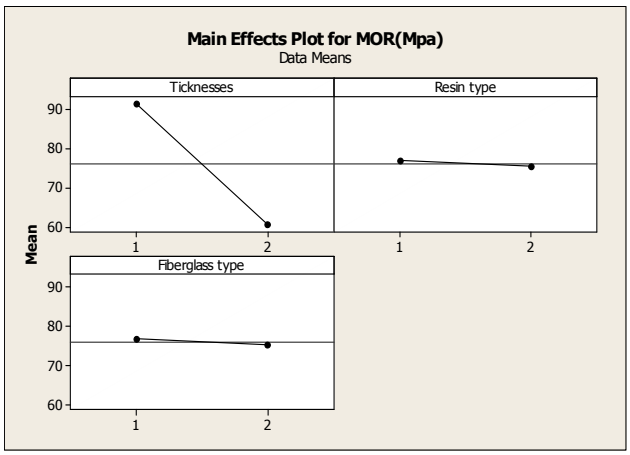


Fig. 2. Effect of different treatments On bending strength

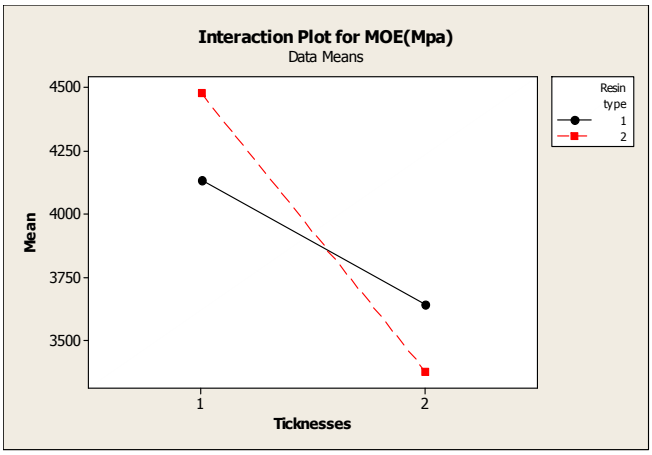


Fig. 3. Interaction effect between the resin and thickness on bending strength

Compressive Test. Positive influence of the core wood lower thickness on compression test´s samples is shown in fig..5 (1: 9mm thickness and 2: 19 mm thickness). It indicates that 9 mm thicknesses samples had higher compressive strength compared to 19mm thicknesses samples. Using of epoxy resin also showed higher compressive strengths in comparison to polyester resin. . This can be due to higher strength of epoxy resin after solidification in comparison to polyester resin .There wasn't significant influence between panels with facings produced with two type fiberglass (needle one and the combination of needle and curtain type). Effect of different treatments on compressive strength is shown in fig. 4.

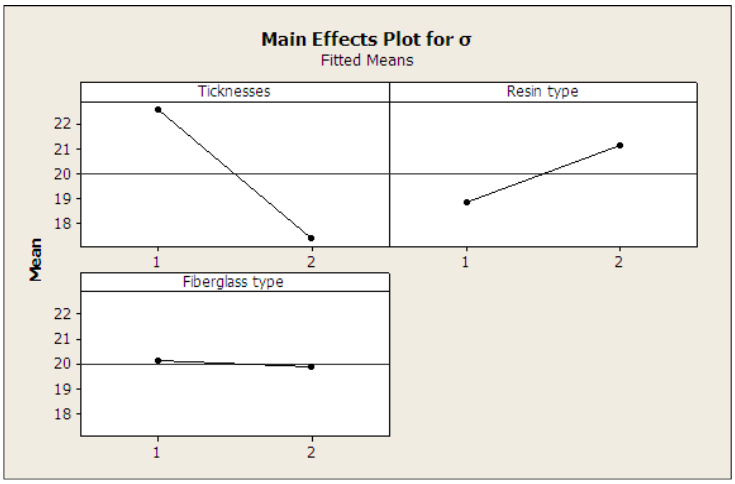


Fig. 4. Effect of experimental factors on sandwich panel, compressive strength

Bonding Test. Using of epoxy resin instead of polyester resin improved the tensile strength, significantly. Investigation of deboned propagation in composite sandwich panels with epoxy resin containing lower face/core delamination at the panel has been conducted. This can be due to higher adhesion property of epoxy resin in comparison with polyester resin. Thicknesses and fiberglass type influents on bonding strengths there weren't significantly. Effect of different treatments on bonding strength is shown in fig. 5.

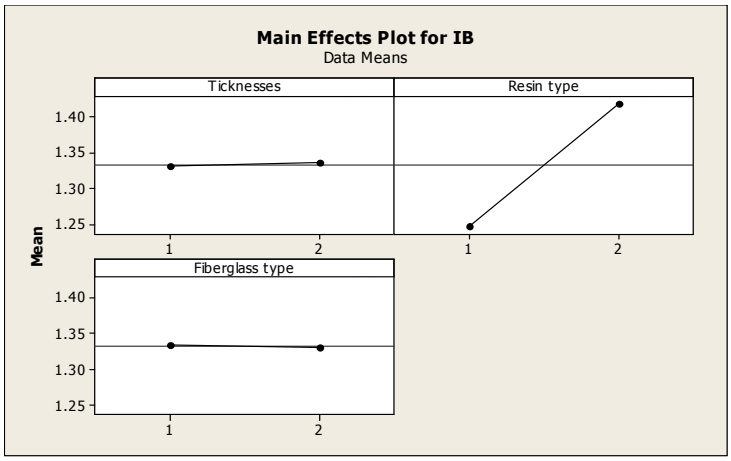


Fig. 5. Effect of different treatments on Sandwich panel, flatwise tensile strength

Water Absorption. The Paulownia wood samples showed average density value 0.26 g/cm^3. The Paulownia wood in water gained increase in density (around 20 %). This wood showed high percentage of weight gain (around41%). Reason for the water absorption of Paulownia wood is the more hydrophilic nature of its constitudes (such as cellulose fibers and hemi cellulose).This constituents attract more and more water which significantly weakness the interface between the constituents thereby reducing the durability. But results in panels indicated there is a few effect of water immersion on density. (around 6.9%). This property should be due to closing of wood vessels by facings that reduces influence of the water absorption.

Volume Stability. The effect of water immersion swelling characteristics (volume change) in Paulownia wood is high. The Paulownia wood expanded to about 22 % during the test time (24 hours). But a little volume change in sandwich panel's samples observed during 24 hours immersion time (4%).That's reason is referred to prevision section.

Table 2. Test mechanical results

Panel type	MOR[MPa]	MOE[MPa]	δ [MPa]	Bonding Strength [MPa]	Density [g/cm^3]
A	61.44	3399.93	18.99	13.91	0.5
B	57.32	3353.81	18.21	13.72	0.5
C	61.78	3542.48	16.20	11.95	0.5
D	62.1	3737.57	15.92	12	0.5
E	93.04	4637.77	22.66	15	0.7
F	91.04	4312.56	24.41	13.62	0.7
G	86.39	4065.46	21.65	12.34	0.7
H	96.86	4196.73	21.17	11.95	0.7
I	41.1	390.41	21.9	---	0.26
J	23	3200	15.5	---	0.15

I: Paulownia wood[11]
J:balsa wood [11]

Summary

1. Panel core thickness negatively effected the mechanical properties of panels. In addition to higher mechanical properties, smaller wood material is used which is economic.
2. Based on the initial findings of this study, it can be stated that Paulownia wood as and light and stiff raw material has various advantages for sandwich manufacturing.
3. The results of this study showed that Paulownia wood blocks used as core in manufacturing sandwich panels improved properties of the product. Therefore it has potential as a raw material for using in sandwich panel core and it was possible to produce valuable, strong sandwich panels.
4. In this study paulownia wood was used instead of balsa wood that is employed widespread all over the word that the results were satisfactory and it was revealed that function of paulownia wood is better than balsa one.
5. The increase in wood material consumption due to the increasing world population requires optimum utilization of the natural recourses. Paulownia wood in addition to good strength properties (table2) [11] is a fast-growing tree (5-6 years old) .It can be suggested for using in sandwich panel industries. On the other hand it has cost-reducing advantage.

References

[1] Joachim L. Grenestedt , *Analyses and preliminary tests of a balsa sandwich core with improved shear*, Lehigh University, Bethlehem ,USA(2003)

[2] J.R. Vinson, *The behavior of sandwich structures of isotropic and composite materials,* Technomic, Lancaster (1999)

[3] K. Chawla, *Composite Materials Science and Engineering*, Springer verlog, (1987)

[4] Brian D Flinn , *Fundamentals of composite sandwich panels*,University of Washington ,(2009)

[5] H.G. *Analysis and design of structural sandwich panels*, Pergammon press, Oxford, (1994)

[6] Espert, A., Vilaplana, F. and Karlsson, S. Composites: Part A. 35(11): 1267–1276,(2004)

[7] Shi, Q.S. and Gardner, D.J. Composites, Part A, 37: 1276–1285, 2006. 72(4): 429-437, (2006)

[8] Wood based panels and furniture industries, Beijing (China); (1981)

[9] FRP Technology, Fiber Reinforced Resin Systems, Applied Science Ltd., London, (1980)

[10] Francis Aviles, Experimental Study and debonded Sandwich Panels under Compressive loading Florida Atlantic university, USA (2006)

[11] A.Khazaeian and T.Tabarsa , Journal of Agricultural sciences and Natural Resources.Vol 16, No.3(pages 1-12), (2009)

© (2011) Trans Tech Publications, Switzerland
doi:10.4028/www.scientific.net/KEM.471-472.91

Optimum Condition of Manufacturing Wood-Based Composite from Mixture of Wood Particles/ Walnut and Almond Shells

Hamidreza pirayesh[1,a], Abolghasem khazaeian[2,b], Hossein khanjanzadeh[3, c], Arian Bahrinejad[4,d]

[1, 3,4] Department of wood and paper science and technologies, Gorgan University of Agricultural Sciences and Natural Resources, Iran

[2] Wood and Paper Technologies, Gorgan University of Agricultural Sciences and Natural Resources, Iran

[a] H_pirayesh30@yahoo.com,[b] Khazaeian@gmail.com, [c]H_khanjanzadeh@yahoo.com, [d]Bahrinejad_aryan@yahoo.com

Keywords: Wood-based composite, Walnut/almond shells, Mechanical and physical properties, Press condition

Abstract. The aim of this study was to manufacture wood based particleboard by using wood particles and agricultural residues of walnut and almond shells that have no economical value other than being used merely as low grade fuel and fodder and evaluating of its performance. This study was done at two stages; first determination of optimum press condition of producing boards from mixture of wood particles and walnut/almond shells and second stage was evaluation of the effect of different ratios of walnut/almond shells (10 and 30%) and the shell mesh size ($\leq$ 0.7 and $\geq$ 2 mm) on their mechanical (modulus of rupture and modulus of elasticity and internal bonding) and physical (thickness swelling and water absorption) properties. The result of first stage of the study showed that of press pressure of 2.5 and 5 MPa, press temperature of 150 and 180 °C and press time of 5 and 10 minutes, optimum press condition of producing boards from mixture of wood particles and walnut/almond shells are press pressure of 2.5 MPa, press temperature of 180 °C and press time of 5 minutes. The result of second stage of the study showed no meaningful difference between mechanical and physical properties of composite boards containing 10 percent of walnut and almond shell with reference one (board A). Besides, the range of used almond and walnut mesh size had no meaningful differences.

Introduction

Particleboard is a wood based composite panel manufactured by compressing small wood particles while simultaneously bonding them with an adhesive. It is a versatile engineered material within the group of nonstructural wood composite panels. It is used in furniture, desk and counter tops, cabinets, floor, wall, ceiling panels, and office dividers (Wang and Sun, 2002).The past 50 years have seen the successful developments within the particleboard industry. Much of this success can be attributed to the decided economic advantage of low cost wood raw material and inexpensive with binders (Hofstrand et al., 1984).Many political, economic, social, geographic and environmental factors determine the availability and end use of natural, renewable resources throughout the world. Due to environmental movement, landfill regulations, recycling trends, green movement, the available supply of wood is becoming scarce in the developed countries. The developing countries have already poor resources of wood for particleboard manufacturing. As a

result, non-wood fibers and material play a major role in providing the balance between supply and demand. It would seem that with suitable treatment almost any agricultural residue might be used as a suitable raw material for particleboard. Youngquist et al. cites research reports worldwide on the use of non-wood plants for the forest industry. All boards are not suitable for all applications; especially boards destined for the furniture industry. Researches have been carried out on a wide variety of crops from many different regions of the world. Among the raw materials are cereal straws (Mosesson, 1980), rice husks (Vasisth and Chandramouli, 1975), groundnut shells (Jain et al., 1967), bamboo (Rowell and Norimoto, 1988), waste of tea leaves (Ors and Kalaycioglu, 1991), bagasse (Turreda, 1983), cotton, hemp and jute stalks (Kollmann, 1966), cotton stalks (G¨uler et al., 2002), pomace (G¨ur¨u, 2001), kiwi pruning (Nemli et al., 2003), flax shiv (Papadopoulos and Hague, 2003), vine pruning (Ntalos and Grigoriou,2002), coir pith (Wiswanathan and Gothandapani, 1999), and almond shell (G¨ur¨u et al., 2005).

Walnuts are the fruit of the Juglans regia, (also J. nigra for the black walnut). Walnuts (genus Juglans) are plants in the family Juglandaceae. 21 species of it in the genus range across the north temperate Old World from southeast Europe east to Japan, and more widely in the New World from southeast Canada west to California and south to Argentina.

World almond production has been estimated to be about 334.000 tons (average from 1992 to 1996) of shelled product. The main producing country is the United States, which accounts for 68% of the world production. The other producing countries are Spain (16%), Italy (4%), Greece (3.7%), Iran (1.8%), Tunisia (1.8%), Morocco (1.7%), Portugal (1.1%), followed by Turkey and others countries with a lower production. Hazelnut shell as one agricultural residue has been utilized in the forest industry as shell powder in plywood production. Studies with various shell powder ratios indicated that 10–12% shell addition in the adhesive material had no negative effect on the mechanical properties of the plywood (C¸ olakoglu and Ors, 1992).The observed problems with industrial usage of agricultural residues in the forest industry are the high cost of collecting, transporting, and storing the residue material. Some of these problems could be overcome by building local, small-scale mills close to the rural areas (Copur et al., 2007).

Table1: The experimental design.

Board type*	Raw material (by weight)		Shell size (mm)
	Wood (%)	Walnut/ Almond Shells (50:50, %)	
A	100	0	-
B	0	100	<0.7
C	0	100	>2
D	90	10	<0.7
E	90	10	>2
F	70	30	<0.7
G	70	30	>2

* The density of all boards was 0.70g/cm$^{3.}$

The aim of this study was to determine the performance of particleboard made from mixture of wood particle and almond/walnut shells. Evaluated properties were modulus of rupture (MOR), internal bonding strength (IB), thickness swelling (TS) and water absorption (WA) after 2 and 24 hours water immersion. Water absorption and thickness swelling was measured after 2 and 24 hours immersion of samples into distill water at room temperature.

Materials and Method.

The almond and walnut shells were provided from a province in northern east of Iran. They were chipped using a hacker chipper before the chips were reduced into smaller particles using a knife ring flaker. Particles were dried to 3 percent moisture content. Dried particles were classified into two size categories, namely fine and coarse. A screening machine through meshes with 0.71 and 2.36mm apertures was used for this process. The wood particles size varied from 0.8 to 3 mm Based on oven dry particle weight, 10% Urea formaldehyde (UF) resin was used. Ammonium chloride solution was used as a hardener for the production of the panels. No wax or any other hydrophobic substances were applied for the panel manufacture. The properties of the UF adhesive are given below (Table 2):

Table 2: Some characteristics of the UF adhesive

Solid content (%)	60 ± 1
Density (at 20 °C)	1.26–1.28 g/cm^3
Viscosity (at 20 °C)	200–400 cps
pH (at 20 °C)	7.5–8.5
Free formaldehyde (%)	Max. 0.20

Density of boards (0.7gr/ cm^3), type of resin (UF), amount of resin (10%), amount of hardener (1%) was kept constant. A total of 21 panels with lengths of 42cm, widths of 42 cm, and thickness of 1.6 cm were made for the experiments. As a hardener 1% of ammonium chloride (solid content 33%) solution based on oven dry fiber was added in all the board production. The materials were mixed for 3 min to accomplish a homogenized resin distribution. The particleboards prepared were pressed then the produced particleboards were conditioned at 20 ± 1 °C and 65±5 relative humidity to the moisture content of about 12%. Panels were prepared at the thickness of 10 mm. Edges of the boards were trimmed to the final dimension of 40 × 40 × 1.6 cm. Test samples were prepared based on DIN6873 standard and conditioned for about three weeks at 65% relative humidity and at a temperature of 20 ◦C prior to tests. Modulus of elasticity (MOE), modulus of rupture (MOR), internal bond strength (IB), thickness swelling (TS) and water absorption (WA) after 2 and 24 hours water immersion was determined. The experimental design of this study is illustrated in Table 1. Data for each test were statistically analyzed. Analyze of variance (ANOVA) was used to test for significant difference between factors and levels.

Results and Discussion

Table 3 displays the results of both mechanical and physical tests. The average modulus of rupture ranged from 12.68 to 16.87 MPa. The minimum requirements of the modulus of rupture are 11.5 and 13 MPa for general purpose, and interior fitments (including furniture), respectively (EN 312-2, 1996; EN 312-3, 1996).While the E and D type panels satisfied the EN 312-2 requirement for general purposes, the other types had the required level of the modulus of rupture for furniture manufacturing. Increasing walnut/almond shells ratio from 10 to 30 percent, meaningfully decreased the MOR ($p \leq 0.05$) and thickness swelling ($p \leq 0.01$) after 2 and 24 hours water immersion. These can be attributed to non-fiber and relatively hydrophobic nature of walnut/almond shells in comparison to wood. Increasing shell mesh size from ≤ 0.7 to ≥ 2 mm,

resulted in significance decrease of thickness swelling after 24 hours water immersion. This can be due to less surface area in the last case.

The internal bond strength of the samples containing 10 percent walnut/almond shells satisfied EN 312-2 and EN 312-3 requirements for general purpose and furniture manufacturing according to which modulus of rupture and internal bonding for particleboards that are intended for general purpose is 12.5 and 0.28 MPa respectively. However, panels containing 30 percent walnut/almond shells had significantly lower Modulus of elasticity, internal bond strength and modulus of rupture than 10 percent ones. Thickness swelling of the panels containing 10 percent walnut/almond shells was lower than reference one ranging from 10.6% to 14.3% for 2 h water immersion. Similar panels made from tobacco, sunflower stalks, waste tealeaves, and kiwi pruning had 21.27%, 29.39%, 17.47%, and 15.63%, respectively, which are much higher than the produced Particleboards. All boards containing 30 percent walnut/almond shells regardless of shell mesh size had better physical properties performance than other boards.

Summary

1. The result indicated that increasing press pressure and press time adversely affect the properties of the boards.

2. Mesh size of walnut and almond shells had no meaningful differences on mechanical and physical properties of the boards except for thickness swelling after 24 hours that with increase of almond and walnut shells size this quantity decrease significantly.

3. The results of this study showed that it was possible to produce particleboards utilizing walnut/almond shells at lower percentages as a mixture with the wood particles.

4. The ratio of wood particles to walnut/almond shells, press time, and press pressure negatively affected the physical and mechanical properties of the panels while the increasing of press temperature improved the modulus of elasticity, modulus of rupture and internal bond strength.

5. It was revealed that both physical and mechanical properties of the panels containing 10 percent walnut/almond shells regardless of shell mesh size was better than those produced from neat wood particles.6. Based on the initial findings of this study, it can be stated that walnut/almond shells has potential as a cheap raw material for particleboard manufacturing.

Table 3: Experimental data

Board	MOR (MPa)	MOE (MPa)	IB (MPa)	Thickness Swelling after2 hour's water immersion (%)	Thickness Swelling after 24 hours water immersion (%)	Water Absorption after 2 hours water immersion (%)	Water Absorption after 24 hours water immersion (%)
A	11.77(0.16)	1750 (0.29)	5.3(0.27)	15.4(012)	19(0.21)	84(0.21)	95(0.21)
B	5(0.25)	860(0.24)	3.9(0.23)	6(0.17)	7.2(0.24)	39(0.19)	48(0.14)
C	5.7(0.24)	935(0.21)	4(0.17)	5.7(0.16)	6.6(0.21)	35(0.16)	44(0.13)
D	12.9(0.30)	1873 (0.22)	6.95(0.26)	14.3(0.25)	18(0.11)	69.6(0.23)	80(0.21)
E	12.7(0.24)	1920 (0.11)	6.21(0.11)	13(0.27)	17.33(0.19)	66(0.17)	77.3(0.14)
F	7(0.27)	1125 (0.17)	6.44(0.17)	11.33(0.28)	13.66(0.18)	67.6(0.24)	74(0.16)
G	7.8(0.24)	1197 (0.14)	6.54(0.28)	10.6(0.23)	12.33(0.23)	75(0.15)	80(0.17)

Note: Values in parenthesis are standard deviations

Reference

[1] Wang, D., Sun, X.S., 2002. *Low density particleboard from wheat straw and corn pith.* Ind. Crops Products 15, 47–50.

[2] Hofstrand, A.D., Moslemi, A.A., Garcia, J.F., 1984. *Curing characteristics of wood particles from nine Northern Rocky Mountains species mixed with Portland cement*. Forest Products J. 34 (7), 57–61.

[3] Mosesson, J.G., 1980. *The processing and use of waste straw as a constructional material*. Conserv. Recycling 3, 389–412.

[4] Vasisth, R.C., Chandramouli, P., 1975. *New panel boards from rice husks*. FAO background paper, FO/WCWBP/75.

[5] Jain, N.C., Gupta, R.C., Jain D.K., 1967. *Particleboard from groundnut shells*. Proceedings of 11th Silviculture Conference India.

[6] Rowell, R.M., Norimoto, M., 1988. *Dimensional stability of bamboo particleboards made from acetylated particles.* Mokuzai Gakkaishi 34 (7), 627–629.

[7] Ors, Y., Kalaycioglu, H., 1991. *Using of waste tea leaves on the particleboard industry*. Turkish J. Agric. Forestry 15, 968–974.

[8] Turreda, L.D., 1983. *Bagasse, wood and wood-bagasse particleboards bonded with urea formaldehyde and polyvinyl acetate/isocynate adhesives*. USDA Technol. J. 8 (3), 66–78.

[9] Kollmann, F., 1966. Holzspanwerkstoffe, holzpanplatten und holzspanformlange Rohstoffe, Herstellung, Plankosten qualitatskotrolle usw. Berlin, Heidelberg, New York.

[10] G¨uler, C., Ozen, R., Kalaycıo˘glu, H., 2002. *Utilization of cotton stalks as a possible raw material for the particleboard*. In: Proceedings of the 56th Appita Annual Conference. Rotorua, New Zealand,

[11] G¨ur¨u, M., 2001. Uc¸ucu k¨ul ve pirinadan yapı malzemeleri ¨uretimi. Politeknik Dergisi 4, 35–38.

[12] Nemli, G., Kırcı, H., Serdar, B., Ay, N., 2003. *Suitability of kiwi pruning for particleboard manufacturing*. Ind. Crops Products 17, 39–46.

[13] Papadopoulos, A.N., Hague, J.R.B., 2003. *The potential for using flax as a lignocellulosic rawmaterial for particleboard*. Ind. Crops Products, 17, 143–147.

[14] Ntalos, G.A., Grigoriou, A.H., 2002. *Characterization and utilization of vine pruning as a wood substitute for particleboard production*.Ind. Crops Products 16, 59–68.

[15] Wiswanathan, R., Gothandapani, L., 1999. *Optimum process variables for the production of coir pith particleboard*. J. Agric. Eng. Res., 74, 331–337.

[16] G¨ur¨u, M., Tekeli, S., Bilici, ˙I. *Manufacturing of urea formaldehyde based composite particleboard from almond shell.* Materials and Design, Available online at www.sciencedirect.com, in press.

17] Kalaycıoglu, H., 1992. *Use of agricultural residues in particleboard manufacture*. International Forest Products Congress. Unpublished Report, vol 1, Trabzon, Turkey.

[18] Copur, Y., Guler, C., Akgul, M., Tascıoglu, C., 2007. Some chemical properties of hazelnut husk and its suitability for particleboard production. Build. Environ. 42, 2568–2572.

© (2011) Trans Tech Publications, Switzerland
doi:10.4028/www.scientific.net/KEM.471-472.97

Microstructure Characterisation of Ag_2O_3-Bi_2O_3 Composite Cathodes for Intermediate Temperature Solid Oxide Fuel Cells (IT-SOFCs)

Dedikarni[1,2,a], Andanastuti Muchtar[1,2,b], Norhamidi Muhamad[1,2,c] and Wan Ramli Wan Daud[1,3,d]

[1]Fuel Cell Institute, Universiti Kebangsaan Malaysia, 43600 Bangi, Selangor, Malaysia

[2]Department of Mechanical and Materials Engineering, Faculty of Engineering and Built Environment, Universiti Kebangsaan Malaysia, 43600 Bangi, Selangor, Malaysia

[3]Department of Chemical and Process Engineering Department, Faculty of Engineering and Built Environment, Universiti Kebangsaan Malaysia, 43600 Bangi, Selangor, Malaysia

[a]dedikarn@eng.ukm.my, [b]muchtar@eng.ukm.my, [c]hamidi@eng.ukm.my, [d]wramli@vlsi.eng.ukm.my

Keywords: Bismuth oxide; slurry painting method; porous composite cathode

Abstract. Porous Ag-Bi_2O_3 composite cathodes on stainless steel (SS) substrate, an excellent mixed-ionic conductor that can be used as cathode material for the intermediate temperature solid oxide fuel cell (IT-SOFC) has been developed using the slurry painting method. Characterisation of the composite cathode includes the thermal analysis, morphology, and porosity of the porous cathode. Thermal analysis of the dried slurry was conducted in order to determine the heating schedule for eliminating the organic components using thermogravimetry analysis (TGA) and differential scanning calorimetry (DSC). The TGA and DSC analyses confirmed the organic vehicle was fully decomposed below 418°C and the formation of composite cathode oxide phase took place beyond 600°C. The microstructure of the thermally treated cathode was analysed using SEM and XRD. The SEM results showed that the grain size of the cathode increased with the increase of temperature during thermal treatment and the X-ray diffraction (XRD) analyses confirmed the presence of δ-Bi_2O_3 phase on the cathode. Porosity was obtained using the Archimedes method. The Ag_2O_3-Bi_2O_3 cathode on stainless steel substrates was found to have a porosity of 53%, 51%, 39% and 28% upon 1, 2, 3, and 4 coatings, respectively, as well as thermal treatment at 800°C for 1 hour.

Introduction

Solid oxide fuel cells (SOFCs) are electrochemical devices that convert the chemical energy of a fuel into electrical energy in a clean, cheap and efficient way [1]. The efficiency of energy conversion and durability of performance of the SOFCs mainly depend on the electrocatalytic activity of the cathode and its thermo-chemical compatibility with the oxide ion conducting solid electrolyte. Recent research has focused on a new material which is an electrocatalyst for the oxygen reduction reaction in the intermediate temperature range (600-800°C) [2,3]. Porous Ag-Bi_2O_3 composite cathodes has potential to be an alternative cathode instead of the conventional Au-Bi_2O_3. The composite of Ag_2O_3-Bi_2O_3 acting as cathodes for solid oxide fuel cells (SOFCs) therefore has properties such as high electrical conductivity, high catalytic activity for oxygen reduction and compatibility with other cell components [4]. The Ag_2O_3-Bi_2O_3 composite cathodes exhibit low resistance to oxygen reduction due to a combination of high catalytic activity for oxygen reduction of both phases, as well as the high ionic conductivity of the δ-Bi_2O_3 phase [5]. Bismuth oxides (Bi_2O_3) have attracted the attention of many researchers and have been the focus of study for applications in various fields. In particular, Bi_2O_3 has been extensively studied in recent years

because of its potential applications in solid oxide fuel cells and oxygen sensors [6,7]. However, Bi_2O_3 is associated with difficult stability of the material that still remains to be solved.

Microstructural features of cathode play an important role in the electrochemical performance of the SOFCs. Oxygen conduction in the cathode is strongly dependent on porosity and grain size [8]. For example, the LSCF perovskite cathode was found to yield the optimum porosity of 30% after sintering at 900°C and thus enabling the oxygen reduction to occur easily [9,10].

This paper presents the results from research work on the fabrication and characterisation of Ag_2O_3-Bi_2O_3 cathode on stainless steel (SS) substrates by the slurry painting method. The microstructure and porosity which were affected by the thermal treatment of the Ag_2O_3-Bi_2O_3 composite cathode and deposition of Bi_2O_3 were characterised using methods such as XRD, field emission scanning electron microscope (FESEM) and thermogravimetry (TG).

Experimental Procedure

Preparation of Slurry. To make the composite, a mixture of silver oxide and Bismuth oxide (Ag_2O_3-Bi_2O_3) was prepared by mixing silver (I) oxide (99.99 wt%, Sigma Aldrich Sdn. Bhd) and Bismuth (III) oxide (99.9 wt%, Sigma Aldrich Sdn. Bhd) at a weight ratio of 60:40. The composite was then mixed with organic vehicles (a-terpineol as the solvent, di-n-butyl phthalate as the plasticizer and polyvinylbuteral as a binder at a volume ratio of 3:1:2). To make the slurry, the compounds (Ag_2O_3-Bi_2O_3 and the organic vehicles) were mixed with ethanol at volume ratio of 1:1.
Coating, Heat Treatment and Characterisation. The composite film was prepared by slurry painting method on SS substrates at room temperature. The composite cathode material was coated up to four times on the SS substrates (25mm diameter) and tested by Archimedes method until the desired porosity has been achieved (20%-30%). The composite cathodes were then thermally treated at 400°C, 500°C, 600°C, 700°C and 800°C for 1 hour.

The mass loss and temperatures associated with phase transformation were determined by thermogravimetry (Jupiter 449F3). A Zeiss EVO MA10 emission scanning electron microscope (SEM) was used to examine the morphology of the composite cathode. The phase identification of the SS substrates and Ag-Bi_2O_3 composite cathodes was carried out using X-Ray Diffraction (Siemen D-500) with Cu-Kα radiation.

Result and discussion

Figure 1(a) show the DSC curves of the dried organic vehicles that underwent endothermic dehydration in the temperature range of 23°C-70°C, which is supported by a corresponding mass loss in TG curve. An endothermic high peak in the 340°C and 530°C range as shown in Fig. 1a, corresponds to the transition of the Bi_2O_3 phase. Sammes et al. [11] had earlier reported the transition of the bismuth oxide (α-Bi_2O_3) to monoclinic phase occurring at approximately 400°C. An endothermic peak at 530°C, corresponds to the transformation of α-Bi_2O_3 into β-Bi_2O_3. This result is in agreement with the XRD measurements as depicted in Fig. 2. Above 700°C, the transformation becomes more stable, therefore the changes of the structural morphology are quite similar until 800°C (Fig. 1a). This transition is a consequence of the continuous and gradual loss of the residual δ-Bi_2O_3 phase [11,12]. Similar results of phase transformations and calculated values of mass losses forming the three characteristic mass loss stages were obtained from thermogravimetry of Ag_2O_3-Bi_2O_3 cathode in a previous work by Sammes et al. [11].

The TG curve of the terpineol, D-n-Phthalate and and PVB (organic vehicles) on stainless steel (SS) substrates is shown in figure 1 (b). There are three regions of mass losses: that below 180°C, 180°C-279°C and 279°C-418°C. The mass loss of 75% is caused by the evaporation of the physically absorbed organic vehicle from the slurry. In the first region, the mass loss is caused by the decomposition reactions of terpineol. In the second region, the mass loss is caused by the 180°C-279°C range which proves the decomposition of D-n-Phthalate. In the third region, the mass loss is caused by the decomposition reactions of PVB, which is supported by a corresponding

weight loss in the TG curve. This is in accordance with data from the literature [12] which showed that the mass loss in the vehicle organic is higher than the mass loss in Ag_2O_3-Bi_2O_3 due to the smaller melting point and higher surface area available for vehicle organic adsorption.

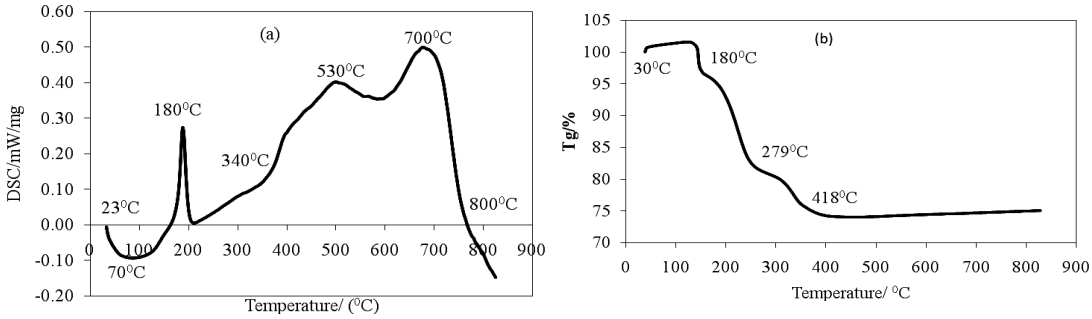


Fig. 1 (a) DSC curve and, (b) TG curve of the organic vehicles on stainless steel (SS) substrates.

Fig. 2 shows the XRD patterns of the stainless steel (SS) substrates as well as the Ag_2O_3-Bi_2O_3 composite cathode on the SS substrates after thermal treatment at various temperatures: (a) 400°C, (b) 500°C, (c) 600°C, (d) 700°C and (e) 800°C, respectively. The SS substrates were tested as reference. The Ag_2O_3-Bi_2O_3 composite cathode was found to display behaviour of typical Bi_2O_3 containing α-Bi_2O_3 and δ-Bi_2O_3 phases.

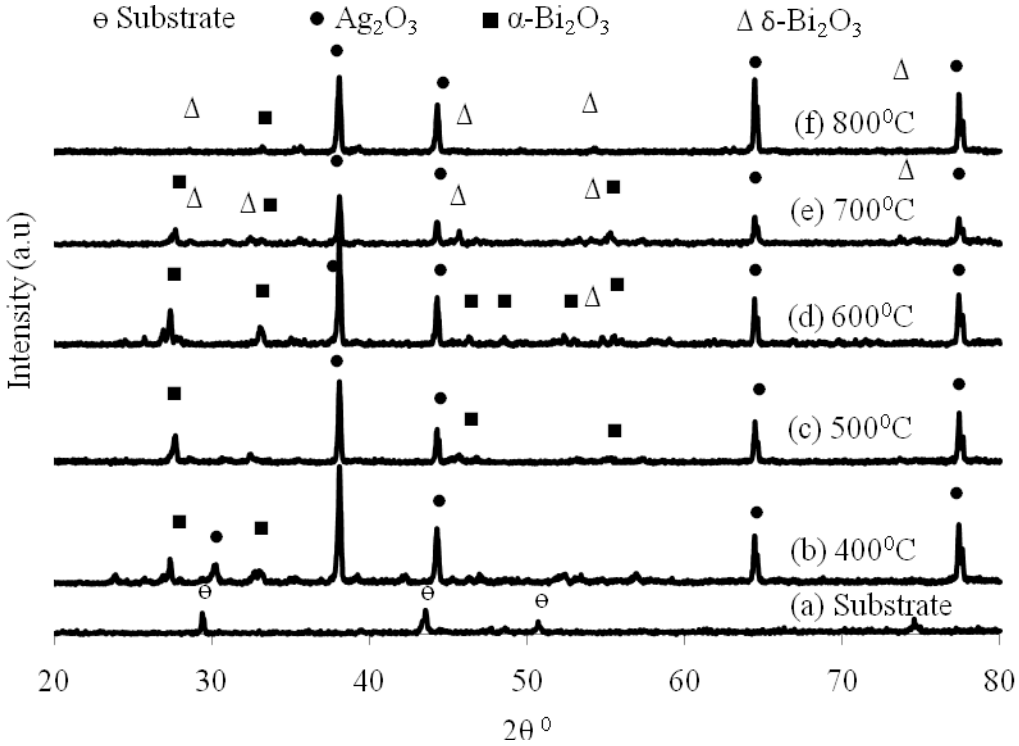


Fig. 2 XRD patterns of the stainless steel (SS) substrates and Ag_2O_3-Bi_2O_3 composite cathode on the stainless steel substrates with different thermal treatment temperatures: (a) 400°C, (b) 500°C, (c) 600°C, (d) 700°C and (e) 800°C.

Peaks corresponding to the Ag_2O_3-Bi_2O_3 (notably, those peaks at 27°, 38°, 44°, 64°, and 78° labelled ●, ■ and Δ, respectively) become apparent beginning at 400°C. Peaks at 27° and 55° become sharper after thermal treatment at 700°C (labelled Δ). These correspond to the phase transition from the monoclinic α-Bi_2O_3 phase to the high temperature cubic δ-Bi_2O_3 phase as earlier detected in Fig 2(e) and (f). The same observation was made by Sammes et al. [12] at approximately 700°C. New peaks at 33°, 38° and 65° are identified as δ-Bi_2O_3 which appears at a thermal

treatment temperature of 800°C (labelled ●). According to Helfen et al. [13] and Sammes et al. [12] the δ-Bi_2O_3 phase was found to be stable up to its melting point of approximately 825°C. Upon inspection of the XRD patterns of the Bi_2O_3 thin films on the Ag_2O_3-Bi_2O_3 composite cathode in Fig. 2, it can be observed that increasing the temperature of thermal treatment from 400°C to 800°C increases the sharpness of the peaks which meant an increase in the crystallinity of δ-Bi_2O_3 in the samples.

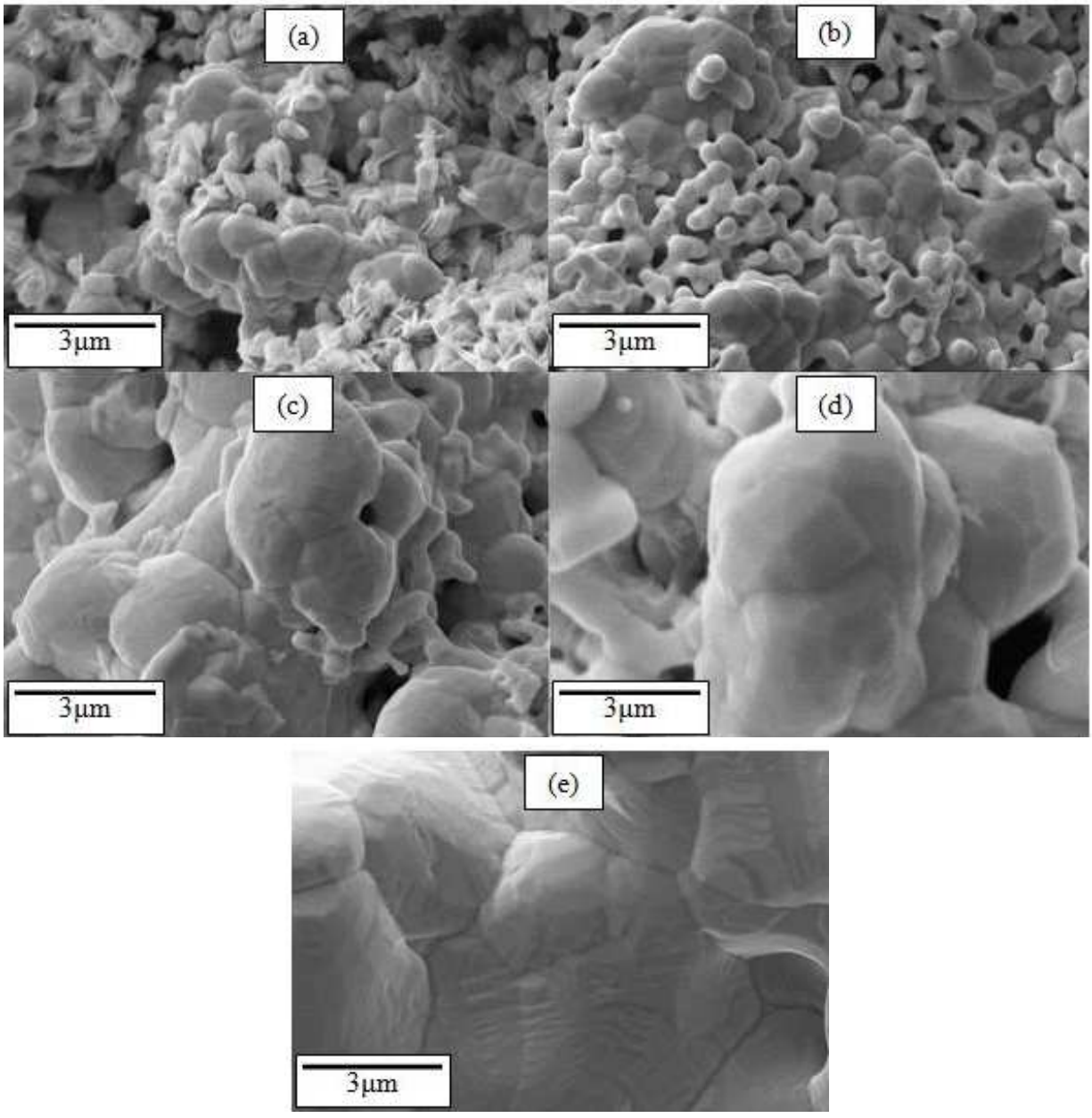


Fig. 3 SEM images of Ag_2O_3-Bi_2O_3 cathode film on porous SS substrates prepared by slurry painting method after four coatings and thermal treatment at different temperatures: (a) 400°C, (b) 500°C, (c) 600°C, (d) 700°C and (e) 800°C.

Scanning electron micrographs of the Ag_2O_3-Bi_2O_3 cathode on the porous SS substrates are shown in Fig.3. The average grain size of the Ag_2O_3-Bi_2O_3 composite cathode film is shown to increase after heat treatments at temperatures of between 400°C to 800°C. The average grain size increases as the porosity decreased. The results in Fig. 3 indicate that the growth of most of the small grains are retarded by the neighbouring large grains upon increase in the heat treatment temperature, leading to the larger average grain size. Fig. 3(e) shows the morphology of the oxidised

Ag_2O_3-Bi_2O_3 cathode at the highest temperature for thermal treatment (800°C). The average grain size of Ag_2O_3-Bi_2O_3 cathode after thermal treatment at 800°C is the largest as compared to that of other lower treatment temperatures (400°C-700°C) as depicted in Fig. 3(a-d). As the temperature for treatment (800°C) was lower than the melting point of Bi_2O_3 (825°C), the results in Fig. 3(a–d) imply that grain growth occurred during the heat treatment [14]. This is in agreement with the differential scanning calorimetry (DSC) results where apparent mass loss and heat absorption of the Ag_2O_3-Bi_2O_3 are started from temperature of 340°C (Fig 1a).

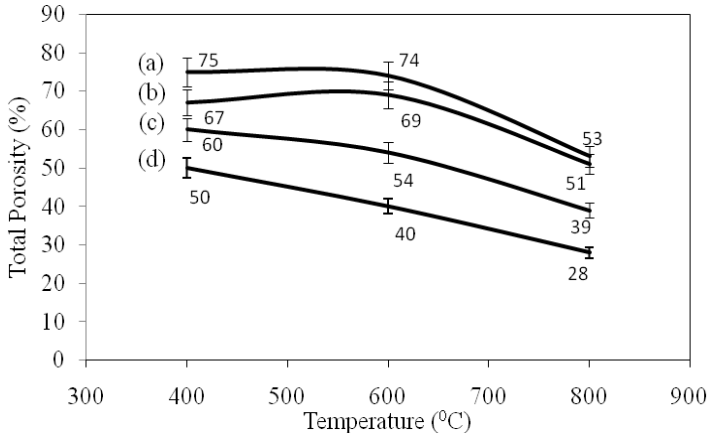


Fig. 4 The porosity measurements of the Ag_2O_3-Bi_2O_3 films which have been coated on the SS substrates in (a) 1, (b) 2, (c) 3 and (d) 4 repetitions of the coating process.

Slurry painting method is a not only a very cost effective method to produce these porous Ag_2O_3-Bi_2O_3 composite cathodes, it also a very scalable and simple process. In the present work, the effects of number of coating times and procedure of heat treatment on the porosity of the composite have been studied. Fig. 4 shows the porosity measurements of the Ag_2O_3-Bi_2O_3 films which have been coated on the SS substrates in 1, 2, 3 and 4 repetitions of the coating process. The results showed that the Ag_2O_3-Bi_2O_3 cathode have a porosity of 47, 42, 38 and 28 % after 1, 2, 3, and 4 repetitions of the coating process, respectively, and, after thermal treatment at 800°C for 1 hour. Deseure et al. [8] suggested that controlling the cathode porosity at 20-30% can improve the oxygen reduction process. Hence, the four repetitions of the coating process is the best process parameter since it gives 28 % of porosity.

Summary

Porous Ag_2O_3-Bi_2O_3 composite cathodes have been successfully produced by slurry painting on stainless steel substrates. Thermogravimetry analysis showed that the organic vehicle was fully decomposed below 418°C. XRD revealed the phase transition from the monoclinic α-Bi_2O_3 phase to high temperature cubic δ-Bi_2O_3 phase. It was found that the thermal treatment greatly affected the morphologies of the samples due to the increase of grain size upon increase of the temperature for thermal treatment. The lowest porosity achieved (28%) was for the Ag_2O_3-Bi_2O_3 composite cathodes which were heat treated at 800°C for 1 hour. The slurry painting method was thus found to be potentially suitable for the manufacture of these porous Ag_2O_3-Bi_2O_3 composite cathodes.

Acknowledgment

The authors would like to acknowledge Universiti Kebangsaan Malaysia and the Malaysian Government for research sponsorship under UKM-GUP-TK-08-17-324, UKM-OUP-TK-17-78/2008 and UKM-OUP-TK-16-75/2009.

References

[1] A. Jaiswal and E.D. Wachsman: Ionics Vol. 11 **(**2005), p. 161-170.

[2] J. Raharjo, A. Muchtar, W.R.W. Daud, N. Muhamad and E.H. Majlan : Key Engineering Material Vols. 447-448 (2010), p.666-670.

[3] H.A. Rahman, A. Muchtar, N. Muhamad, H. Abdullah : Advanced Materials Research Vols. 139-141 (2010), p.145-148.

[4] G.Y. Laurent, S. Wang, Tusseau-Nenez and Y. Leprince-Wang: Solid State Ionics. 178 (2008), p. 1735-1739.

[5] M. Camaratta & E.D. Wachsman: Solid State Ionics Vol. 178 (2007), p. 1242-1247.

[6] C.H. Chaur, Y.W. Teng and Z. F. Kuan: Materials Research Bulletin Vol. 41 (2006), p.110-118.

[7] E.W. Bohannan, C. Christopher, Jaynes, M.G. Shumsky, J.K. Barton and J.A. Switzer: Solid State Ionics Vol. 31 (2000), p. 97-107.

[8] J. Deseure, Y. Bultel, L. Dessemond and E. Siebert: Electrochimica Acta Vol. 50 (2005), p. 2037-2046.

[9] A. Muchtar, N.A. Hamid, N. Muhamad and W.R.W. Daud: Advanced Materials Research Vol. 38 (2010), p. 141-144.

[10] N.A. Hamid, A. Muchtar, W.R.W. Daud and N. Muhamad: Sains Malaysiana Vol. 38 (2009), p. 857-861.

[11] N.M. Sammes, G.A. Tompsett, H. Nafe and F. Aldinger: Journal of the European Ceramic Society Vol. 19 (1999), p. 1801-1826.

[12] M. Djosic, V. Miskovic-Stankovic and V. V. Srijac: Journal of the Serbian Chemical Society Vol. 72 (2007), p. 275- 287.

[13] A. Helfen, S. Merkourakis, G. Wang, M.G. Walls and E. Roy: Solid State Ionics.176 (2005), p. 629-633.

[14] G. Li, Z. Sun, H. Zhao, C. Chen and R. Ren: Ceramics International Vol. 33 (2007), p. 1503-1507.

© (2011) Trans Tech Publications, Switzerland
doi:10.4028/www.scientific.net/KEM.471-472.103

A Review of Non-Destructive Thermography Techniques Toward Structural Integrity of Bio-composites

Zahra Dashtizadeh[1,a], Aidy Ali[1,b], A.Khalina[2,c]

[1]Department of Mechanical and Manufacturing Engineering, UPM, Serdang, Malaysia.

[2]Department of Biology and Agriculture Engineering, UPM, Serdang, Malaysia.

[a]zdashtizadeh@gmail.com, [b]aidy@eng.upm.edu.my, [c]khalina@eng.upm.edu.my

Keywords: Quality control, Non-destructive testing, Composite materials, Thermal imaging, Infrared camera

Abstract. It is well known those two popular methods of testing; destructive testing based on fracture mechanics and non-destructive testing (NDT) which does not make any damage in the specimen. NDT was first used for military purpose but nowadays it is used widely in many fields such as composite materials, medical purposes, fire safety, laser welding, food safety and quality and characterization of materials. The aim of this paper is to review the recent advancement of thermography non-destructive methods especially in testing a quality of bio-composites materials. The review reveals the advantages and disadvantages of pursuing any of the available methods in NDT on bio composite materials.

Introduction

The structural integrity of materials, components and structures has to be assessed for quality control, safety regulations and product specifications. Numerous testing techniques have been developed for maintenance and condition monitoring. These techniques can be categorised into two main classes: destructive testing, based on fracture mechanics, and non-destructive testing which leaves the inspected component undamaged. The most commonly used NDT methods in industry include visual inspection, liquid penetrant inspection, magnetic particle inspection, eddy current testing, alternating current potential drop, alternating current field measurement, ultrasonic testing , radiography and thermography. The principal objective of a non-destructive examination (NDE) is to provide the inspector with quantitative as well as qualitative information. This is achieved by detecting, locating and sizing any detected flaws. Several types of defect exist, for example cracks, voids, corrosion, inclusions, delamination, impact damage and holes [1].

Infrared Thermography. Infrared thermography is the mapping of isotherms over the surface of a component using heat-sensitive devices. An infrared camera scans the surface of a component and records any changes in temperature. The presence of a defect appears as a cold or hot spot and can be rapidly located. Very often, the component inspected has to be pre-heated before inspection. Thermography is a non-contact method which provides rapid visual qualitative information about the structural integrity of a material. It is used for condition monitoring of composite materials and concrete and to check alignment of parts[1]. In numerically modelling the thermographic process associated with an infrared (IR) technique we can afford inspectors the ability to predict subsurface defect information associated with a specific material configuration[2]. Infrared thermography (IRT) provides colorful images (Fig.1) of specimens where local changes in surface temperature indicate subsurface defects. Although thermography provides colorful images, it provides a clear linkage between the true size of a defect and its thermographic image[3].

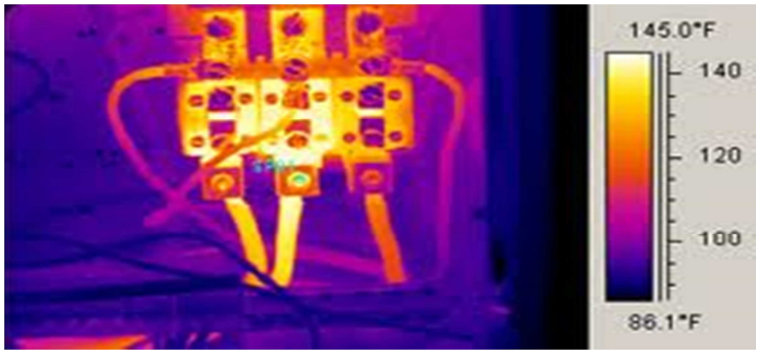


Fig.1. An example of infrared image

Pulsed transient thermography and lock-in thermography are the most commonly used thermographic NDT&E techniques. The two techniques are distinctly different but are used for very similar component/structure inspection applications [4]. Pulsed phase thermography (PPT) approach was introduced for non-destructive evaluation (NDE) in infrared thermography (IRT) applications a few years ago as an interesting signal processing technique. This approach combines somehow the pulsed acquisition procedure of the pulsed thermography (PT) with the phase/frequency concept of "lockin thermography (LT)" or modulated thermography (MT) for which specimens are submitted to a periodical excitation[5].

Thermography Fundamentals. Any object emits by radiation energy according to its surface temperature. Human eyes are struck by such energy only when the object is warm enough and emits in the visible band (0.4–0.8 μm). For low temperature values falling in the infrared region, thermography provides us with *artificial eyes* and gives us a chance to see invisible radiation. An infrared (IR) system basically includes a camera, equipped with a series of changeable optics, and a computer. The core of the camera is the infrared detector, which absorbs the IR energy emitted by the object (whose surface temperature is to be measured) and converts it into electrical voltage or current[6]. However, the energy really detected (by the infrared detector) depends on the emissivity coefficient of the surface under measurement and on the environment since a fraction may be either added as reflected from the surroundings either absorbed by the atmosphere between the object and the camera. To take into account these factors, calibration of the system by simulating real operating conditions has to be performed. The calibration function:

$$W = \varepsilon \frac{A}{e^{B/T - C}} \tag{1}$$

relays the real amount of detected energy flux W to the emissivity coefficient ε and to the surface temperature T of the object through the calibration constants A, B and C which take into account spurious quantities of energy from, or to, the environment[6]. After heating a surface, attenuated and dispersive waves are found inside the material close to the surface region. These waves are called ''thermal waves'' and were first investigated by the French mathematician J. Fourier and the Swedish physicist A.J. _A. Angstrom. Interestingly, these waves can be generated and detected remotely as in IRT[6]. For a semi-infinite specimen (planar specimen) onto which a uniform source deposits periodically heat with a modulation of angular frequency ω, the mathematical study is reduced to a one dimensional problem and the equation describing the resulting temperature T as function of depth z and time t due to this stimulation is expressed as:

$$T(xz,t) = T_0 e^{-z/\mu} \cos\left(\frac{2\pi z}{\lambda} - \omega t\right) \quad , T(xz,t) = T_0 e^{-z/\mu} \cos\left(\omega t - \frac{2\pi z}{\lambda}\right) \tag{2}$$

where μ is the thermal diffusion length expressed by:

$$\mu = \sqrt{2k/\omega\rho c} = \sqrt{2\alpha/\omega} \tag{3}$$

with thermal conductivity *k,* density ρ, specific heat *C*, modulation frequency ω in rad/s ($\omega = 2\pi f$ with *f* the frequency in Hertz), thermal diffusivity α and thermal wavelength λ defined as $\lambda = 2\pi\mu$ [7].

As for the propagation speed of these waves, it is obtained from previous equations as [5]:

$$\nu = \lambda\frac{\omega}{2\pi} = \sqrt{2\omega\alpha} \qquad 4$$

As it is seen in Eq. (3), μ is inversely proportional to ω. This indicates that high modulation frequencies limit the analysis to a close to the surface region while low frequency thermal waves propagate deeper but slowly (Eq. (4)) [5].

Pulsed Thermography. Pulsed thermography or pulsed transient thermography (PT) (Fig. 2) is an established thermal imaging technique that is used for NDE. It is based on thermal heat transfer that occurs during the cooling or heating of the item subjected to pulse heating[8]. In PT the specimen is pulsed heated and the following temperature decay is then recorded. Common heating sources are lamps, flashes, heat gun, etc[5]. The duration of the pulse is variable from ms to s depending to the thickness of material to be probed and its thermal properties[3]. PT was employed for the detection of disbands in bonded composite repair patches, although previous studies have demonstrated the capability of this technique to detect delaminated and disbanded areas in repair patches, such studies have focused on simulated flaws rather than real ones. However, PT has some limitations. One of the observed limitations in PT inspection of bonded patch repairs is sensivity of the technique to edge effects due to the tapered patch geometry. Another observed limitation of the PT is due to the variation in thermal properties inherent to adhesive bonded repairs caused by changes in adhesive or patch thickness [8].

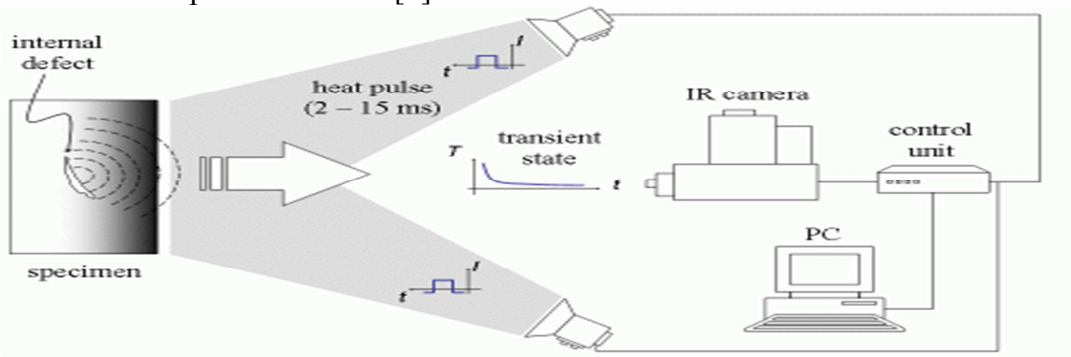


Fig. 2. Pulsed transient thermography, Gros, X. E. (1996). "Non-destructive Testing Techniques". *NDT Data Fusion. Oxford, Butterworth-Heinemann*: 43-81

Lockin Thermography. Since most NDT applications rely on a temperature difference between defective and healthy parts, artifacts (local non-uniform emissivity of the surface, air turbulence, environmental reflections, etc.) can lead to misinterpretation of the results. Also, materials with high thermal conductivity (diffusivity) are subject to too rapid propagation that results in poor image contrast. IRT detection capacity has been progressively improved using a lock-in technique (Fig. 3.The idea behind lock-in IRT is that temperature modulation induced at the surface of the inspected component from the outside propagates as a harmonic thermal wave. As this wave undergoes reflections at the boundaries just like any other wave, the surface phase is modified by thermal waves coming back from the inside of the material. The modified thermal waves are captured by the infrared camera, and the resulting changes in the thermal image can be analyzed to separate actual signals from by-signals. Lock-in IRT allows better defect inspection than common IRT and it is less sensitive to environmental conditions[3].

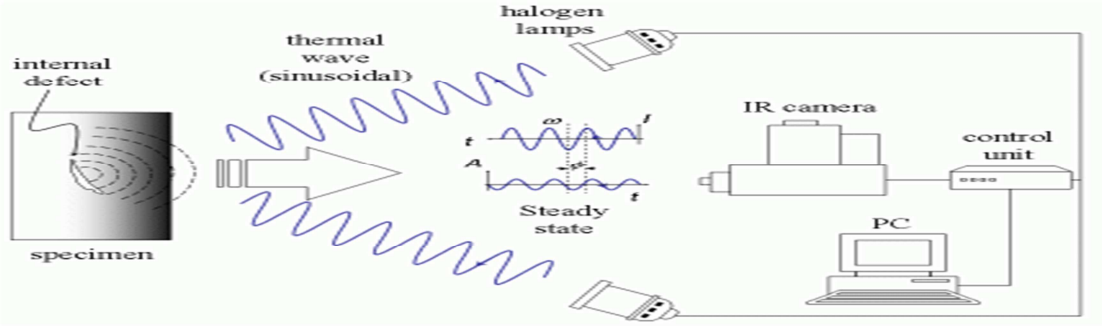


Fig. 3. Lockin thermography, Gros, X. E. (1996). "Non-destructive Testing Techniques". *ND Data Fusion. Oxford, Butterworth-Heinemann*: 43-81.

Modulated photothermal thermography or lock-in thermography – has been set-up for plasma facing components examination. No mechanical contact, no physical coupling nor cooling is required for this technique. Furthermore, the phase-shift is not dependent on optical properties of the sample or on the heat flux deposition pattern, usual difficulties in thermography[9].

Pulsed Phase Thermography (PPT). Mathematically, a pulse can be decomposed into a multitude of individual sinusoidal components. In that respect, when a specimen is pulse heated, thermal waves of various amplitudes and frequencies are launched into the specimen, in a transient mode as discussed before. Going back and forth between temporal and frequency domains is possible with mathematical tools such as the well-known Fourier transform. . Fig.4 shows an example of correspondence between these domains. In fact for PT, thermal waves of different frequencies are launched in the specimen simultaneously in the transient regime while in LT, one thermal wave of single frequency is tested in stationary regime. The possibility to link both techniques was then found interesting and this was called *pulsed phase thermography* processing(Fig.5) [5]

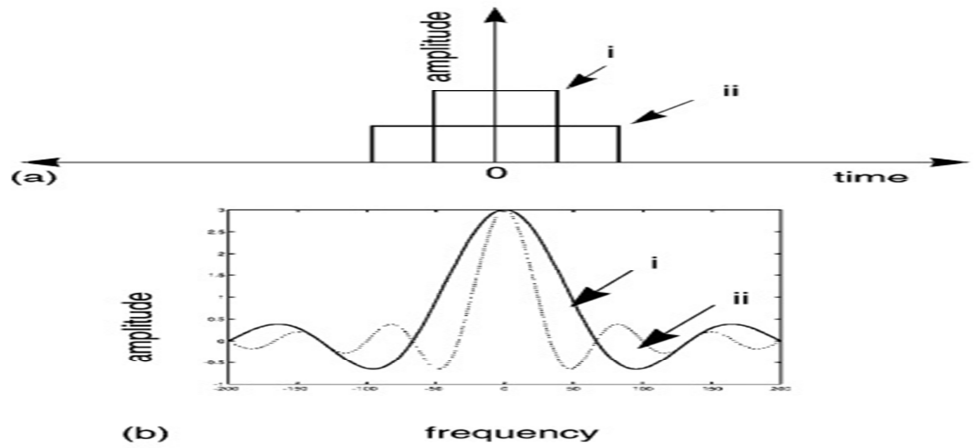


Fig. 4 Time frequency duality (a) two temporal pulses of (i) 15 and (ii) 30ms duration; (b)corresponding frequency spectra, Maldague, X. Galmiche, F. Ziadi, A. (2002). "Advances in pulsed phase thermography." *Infrared Physics & Technology* 43(3-5): 175-181

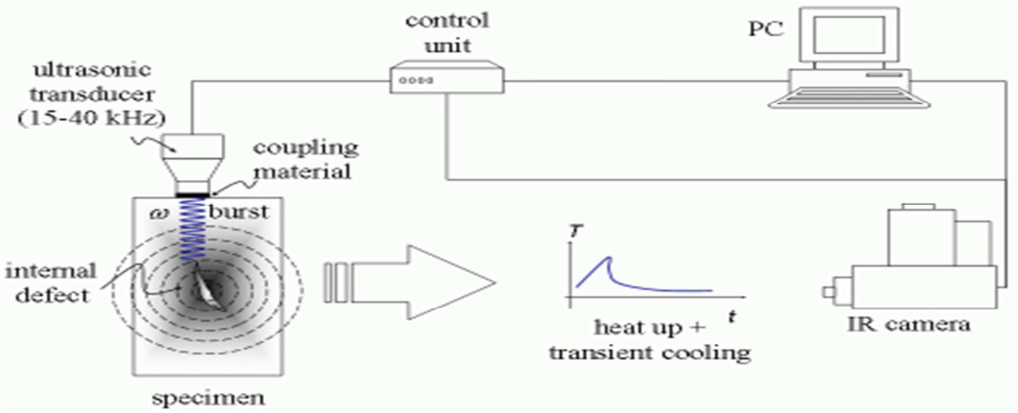


Fig. 5. Pulsed phase thermography, Maldague, X. Galmiche, F. Ziadi, A. (2002). "Advances in pulsed phase thermography." *Infrared Physics & Technology* 43(3-5): 175-181.

Extraction of the various frequencies in PPT is performed with the discrete one-dimensional Fourier transform on each pixel(x, y) of the thermogram sequence:

$$\sum_{k=0}^{N-1} T(k) e^{2\pi i k n / N} = Re_n + iIm_n \quad (5)$$

Where *i* is the imaginary number, Re and Im are respectively the real and imaginary parts of the transform and subscript *n* designates the frequency increment. First, the time evolution of each pixel(x, y) in the field of view is extracted as a vector $T(k)$ of *n* values. Next, Eq. (5) is applied to compute the real Re_n and imaginary Im_n parts. Amplitude A_n and phase ϕ are finally computed with:

$$A_n = \sqrt{(Re_n^2 + Im_n^2)} \quad \text{And} \quad \phi_n = a\tan\left(\frac{Im_n}{Re_n}\right) \quad (6)$$

The fact PPT sorts available information coherently in term of frequencies brings interesting features with respect to the more traditional contrast approach used in PT[5].

Application of Infrared Thermography. There is a wide range of applications for infrared thermography, such as Characterization of materials and Defect characterization [6], Analysis of fatigue damage processes in welded joints [10] and etc. Another application is in composites or more specifically in bio-composites. Cellulosic fiber reinforced polymeric composites are finding applications in many fields ranging from construction industry to automotive industry. Bio-composites or cellulosic fibers have natural base. The use of such materials in composites has increased due to their relative cheapness, their ability to recycle and for the fact that they can compete well in terms of strength per weight of material [11].

There are so many defects caused during manufacturing process or after that, which can affect the reliability of the bio-composites applications. Therefore NDT is a suitable method to detect the defects.

Infrared Thermography in Bio-Composites.. The use of biofibers reinforced composites has extended to almost all fields, such as Soybean oil in dielectric [11], Plastic/wood fiber composites in molded panel components [11, 12] and etc. Since infrared thermography is able to determine the surface defects and in some cases sub-surface defects, it can be used widely for determination of any kind of defects such as cracks, voids, bubbles, etc. in bio-composites. Post-impact damage characterization of hybrid configurations of jute/glass polyester laminates using acoustic emission and IR thermography determine that the combined use of two NDT techniques, acoustic emission and pulse thermography, offered means for a sounder comparison of the performance of two different configurations of E-glass/jute hybrid laminates in terms of falling weight impact resistance [13].

Summary

Infrared thermography as a NDT technique which was more specifically studied, has an application in defect detection of bio-composites, therefore some advantages and disadvantages of bio-composites with the applications of them was discussed. Still infrared thermography application in bio-composites needs more study. Since thermography is a surface method for detecting any inhomogeneities in the sample, the thickness of the sample has an important role.

References

[1] *Gros, X. E.. Non-destructive Testing Techniques. NDT Data Fusion.* Oxford, Butterworth-Heinemann, (1996) 43-81.

[2] Krishnapillai, M. Jones, R. Marshall, I. H. Bannister, M. Rajic, N. Composite Structures 75(1-4), (2006), 241-249.

[3] Choi, Manyong. Kang, Kisoo. Park, Jeonghak. Kim, Wontae. Kim, Koungsuk. *NDT & E* International 41(2), (2008), 119-124.

[4] Pickering, Simon. Almond, Darryl NDT & E International 41(7), (2008), 501-509.

[5] Maldague, X. Galmiche, F. Ziadi, A. Infrared Physics & Technology 43(3-5), (2002), 175-181,

[6] Meola, Carosena. Carlomagno, Giovanni M. Giorleo, Luca Journal of Materials Processing Technology 155-156, (2004), 1132-1137.

[7] Pickering, Simon. Almond, Darryl NDT & E International 41(7), (2008), 501-509.

[8] Genest, M. Martinez, M. Mrad, N. Renaud, G. Fahr, A. Composite Structures 88(1), (2009), 112-120.

[9] Escourbiac, F. Constans, S. Courtois, X. Durocher, A. Journal of Nuclear Materials 367-370(Part 2), (2007), 1492-1496.

[10] Ummenhofer, Thomas. Medgenberg, Justus. International Journal of Fatigue 31(1), (2009), 130-137.

[11] John, Maya Jacob.Thomas, Sabu Carbohydrate Polymers 71(3), (2008), 343-364.

[12] Li.Q, Matuana. L. M. Journal of Applied Polymer Science 88: (2003). 278–286.

[13] Igor M. De Rosa, Carlo Santulli, Fabrizio Sarasini, Marco Valente, Composites Science and Technology 69 (2009) 1142–1150.

© (2011) Trans Tech Publications, Switzerland
doi:10.4028/www.scientific.net/KEM.471-472.109

Effects of Different Particles Sizes of Graphite on the Engineering Properties of Graphites/Polypropylene Composites On Injection Molding Aplication

Iswandi [1,2,a], Jaafar Sahari [1,2,b] and Abu Bakar Sulong [1,2,c]

[1]Fuel Cell Institute, Universiti Kebangsaan Malaysia, 43600 Bangi,Selangor, Malaysia.

[2]Mechanical and Materials Engineering Departement Universiti Kebangsaan Malaysia, 43600 Bangi, Selangor, Malaysia.

[a]iswanfc@yahoo.com, [b]jaafar@.eng.ukm.my, [c]abubakar@eng.ukm.my

Keywords: particle size, rheology properties, mechanical, electrical properties

Abstract. The injection molding of polymer composite is one of the promising and practical methods in the manufacturing of bipolar plates in mass production. Graphite filler with higher loading concentration is mainly used for this purpose. The particle size and composition (wt. %) of graphite filler material influences on the mechanical properties and electrical conductivity of composite materials. The main challenge is the reduction of flow ability during injection of high load filler material. Flow ability of feedstock material is an important factor in the process of injection molding. This paper presents a development of the rheology approach on the effect of particle size in material flow ability occurs in the injection molding process. Polypropylene (PP) as polymer matrix and graphite as conductive filler mixed together with different size to form feedstock material. Graphite purchase from local Asbury Graphite Mills, Inc, grade 3243 with particle size in average after sieve of ≤40, ≤100, and ≤150 μm. Proportions of polymer matrix and graphite at (PP / G) 25 / 75 wt. %. Mixing of graphite in PP matrix is done using an internal mixer (Thermo Haake) at 50 rpm, temperature at 200 ^{o}C. Rheology behaviors of graphite composite were measured using a capillary rheometer type Shimadzu CFT-500D, with a diameter 1 mm and length 10 mm. The fracture surface morphology was examined using scanning electron microscopy (SEM). The electrical conductivity of composite materials was measured by the four point probe. The hardness property measurement of conductive material composite was performed using a Dynamic ultra micro hardness tester using a Vickers typed diamond indenter. The results indicate that the level of viscosity and shear rate on all eligible mixed particle size capable of injectable. The properties of composite materials is the highest in three mix particle size (40/100/150 μm) for the electrical conductivity of 9.13 S.cm^{-1} and hardness at 34.3 HV. Viscosity of 56 Pa.s at a temperature of 200 ^{o}C and shear rates generated in 3231 s^{-1}. The highest electrical conductivity for a single particle size is 49.2 S.cm^{-1} at 150 μm and hardness of Vickers to 47.2 HV at 100 um. The highest electrical conductivity and hardness due to the packing density and reinforcement different particle size.

Introduction

Bipolar plate one of the main components in the order of PEMFC with a total of up to 80% of weight and also a component of multi-function [1,2]. Bipolar plates are usually made of graphite / polymer composites [3], or composites such as metal plates with based on carbon. Bipolar plates made of carbon composite polymer is light in weight and lack of gas permeability, and can reduce manufacturing costs by mass production process [4]. The various methods are used in the manufacture of bipolar plates either by injection molding. Many investigations identified that injection molding is a promising process in cost reductions in graphite composites. However, at high filler content to increase the electrical conductivity, injection molding process is not easy to produce of bipolar plates [5]. High content of filler to give effect to the flow ability relating to feedstock and morphology viscosity materials such as shape and size of filler particles.The

performance of the bipolar plate manufacturing process is related to the graphite particle size and dispersion. This connection to note the decrease in electrical conductivity bipolar plates with the decrease in particle size and particle dispersion area [6]. Optimization of filler with different particle size variations can increase of the mechanical properties and electrical conductivity composite materials. The use of two different particle sizes produces of higher flexural strength and electrical conductivity than the composite containing large (> 90 μm). [7]. The particle size and particle size distribution is important in the process of injection molding [9]. This study focus on the effects of variations of particle size and flow ability with rheology approach is to determine the properties of bipolar plate polymer composite. Material properties such as electrical conductivity and hardness are investigated. The use of graphite in polymer composites is considered a suitable material for bipolar plate production. Graphite is a suitable material to increase the electrical conductivity properties of composite materials [8]. Advantages such as the simple composite containing graphite in the manufacture of bipolar plates by compression molding or injection molding [3].

Experiments

Materials. Materials used in the following is PP Impact Copolymer SM 240 injection molding grade with features such as the melting point of 160-170 ºC, MFR 10 (g/10 min), density of 0.9 (g / cm). PP has the advantage of a balance between the stiffness of the impact resistance. PP was purchased from the Polypropylene Malaysia Sdn. Bhd. Meanwhile Table 1 is shows the main materials properties. The filler material used in the present work are natural graphite by Asbury Graphite Mills, Inc, The images of powder used in this study are shown with scanning electron microscope (SEM) in Fig. 1 variation of particle size graphite, (a) G as produced (original), (b) G (40 μm) powders, (c) G (100 μm) powders, and (d) G (150 μm) powders. Characteristics of graphite used in this study are listed in Table 1 reported by supplier.

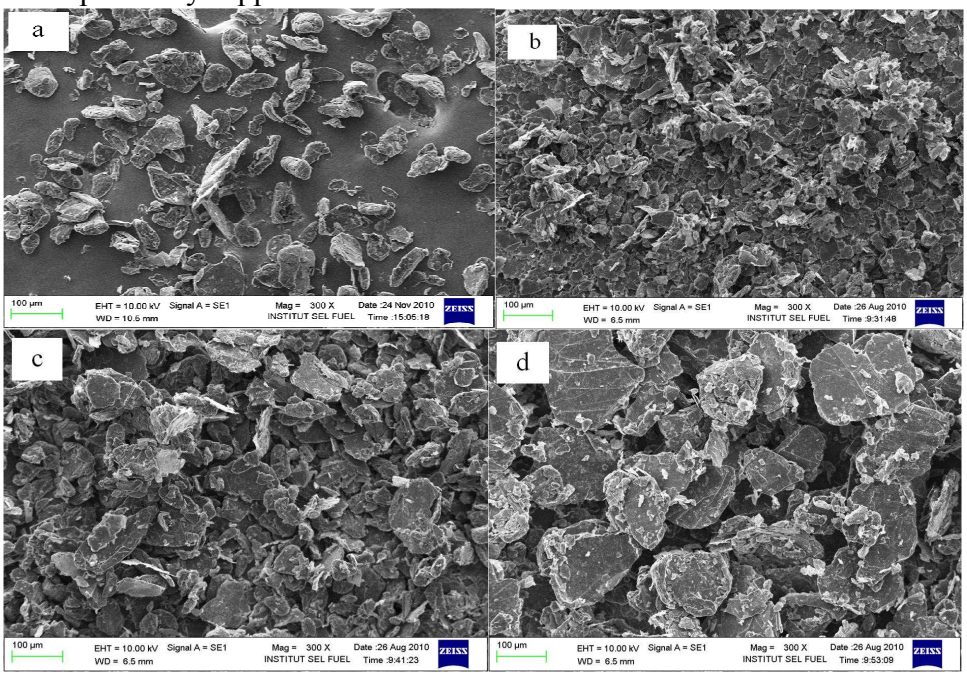


Fig. 1. Scanning Electron Micrographs of variation particle size after mesh to show graphite 3243; a) graphite as produced, b) (40μm), c) (100μm), dan (150μm).

Table 1. Material properties of graphite

Material	Grafit (G)
Gred	3243
Density	1.74 g/cm3
Thermal stability	3500-4000 °C
Size	≤60µm
Resistivity	0.036 Ωcm

The distribution of the particle size were determined by Mastersizer (Malvern MS2000) through measurement of sedimentation of the particle in water and their result had been summarized in Table 2. The graphite powders after sieved have narrower particle size distribution.

Table 2. Particle size distributions of graphite powders

Size (um)	Particle size (microns) at Volume percentage (%)		
	10	50	90
<40	16.8	34.6	64.4
40-100	31.8	65.3	120.8
100-150	26.1	73.5	158.4

Samples Preparation. The variation particle size and composition of samples will be selected as show in Table 3. Determining the composition of the sample are based on the results of investigations on the effects of carbon-based filler content on the flow ability of feedstock. The investigation showed that the content is in accordance with the parameters of the machine is 25 wt. % % PP and 75 wt. % % G.

Melt blending of PP/G composites was conducted by a internal mixer ThermoHaake Rheomix Polylab set at a barrel temperature of 200 ^{o}C,and the rotor speed was 50 rpm. The mixing time of all composites was fixed at 15 min. The samples obtained by melt compounding were crush and pulverized into granules in order to improve process ability of the samples for next forming process. The samples for electrical conductivity and hardness testing done were fabricated the preparation of samples through compression molding.

Table 3. The composition of variation particle size composite by weight percentage

Combination		PP (wt. %)	G (wt. %)			
Particle size (µm)	No		40	100	150	40,100,150,212
	1	25	75			
	2	25	0	75		
	3	25			75	
40/100	4	25	37.5	37.5	0	
40/150	5	25	37.5	0	37.5	
100/150	6	25	0	37.5	37.5	
40/100/150	7	25	25	25	25	
Original	8	25	0	0	0	75

Original: graphite as produced: combination of several sizes of 40, 100, 150, and maximum size 212 (µm).

The flow behavior of graphite polymer composite can be obtained by rheology data. Rheology properties on study with several of temperature (180 ^{o}C, 190 ^{o}C, 200 ^{o}C) and combination particle size. The viscosity and shear rate measured using Capillary Rheometer type Shimadzu CFT-500D. Hardness was measured using Dynamic Ultra Micro Hardness Test, DUH-W2019 SHIMADZU and with Vickers typed diamond indenter. The load 100 N and depth of indenture 10 micrometer.
The load times also can be varying 1 second up to few mints.

Conductivity measurements of the sample in the plane direction were measured by Jandel Multi Height Four Point Probe combined with RM3 Test unit. Microstructure surface and fracture of composite of the sample were investigated by SEM Zeis EVO MA10.

Results and Discussion

Rheology Properties. Fig. 2(a). Shows the result of viscosity againt shear rate at different temperatures and different particle size of graphite. The graph clearly indicated that as the viscosity was decreasing and by measuring the shear rate relatively to increase. The lowest viscosity is obtained at 28.12 (Pa.s) with the largest shear rate 5302.6 on particle size for a single variation (150 μm). The rheological behavior is not only influenced by the particle size but also particle size ratio [10] and particle size distribution. Increased particle size gives a significant influence on the viscosity reduction. The low viscosity at 150 μm particle size showed an ability to inject the feedstock. Decrease in viscosity is due to particle size distribution 150 has a size that is not uniform. It also can increase the shear rate. The uniform size distribution will increase viscosity and shear rate. Table.2 shows the distribution of particle size at 10 vol. %, 50 vol. %, and 90 vol. %,, which provide information on particle size are not uniform.

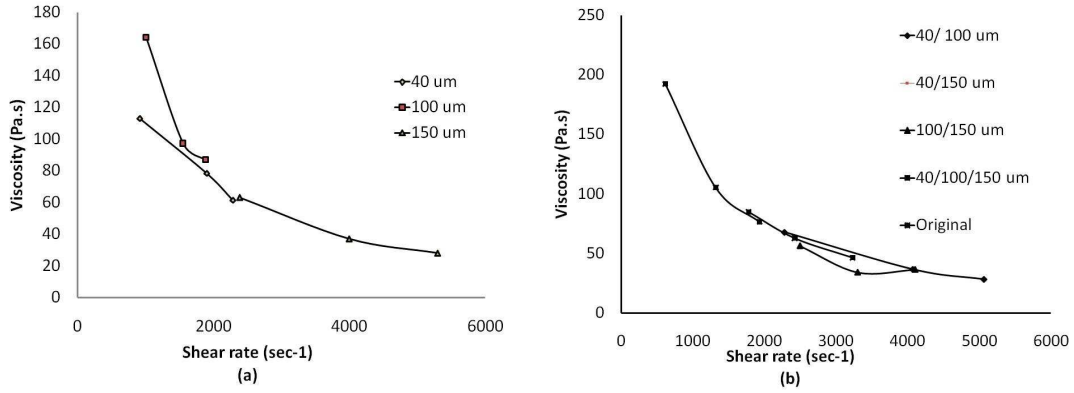


Fig. 2. The viscosity versus shear rate. (a) single particle size distribution. (b) two and three combination.

Fig. 2(b). show variation of composition on two and three of graphite particle size show are suitable material for different composition of graphite on the injection molding. This graph also shows the lowest viscosity at 28.49 (Pa.s) and shear rates of 5068 (s^{-1}) to variations in particle (40/100). Value of viscosity and shear rate on two variations of the mixture (40/100) is approximately equal to one mixture (150). The test results show that the merger of two particle sizes to provide additional particle size variations on each percentage volume of particles. Mixing of the two particle sizes generally yields low viscosity between 28 (Pa.s) - 36 (Pa.s). The significant increase in viscosity can be seen in three or more mixed particle sizes such as 40 / 100 / 150 and the original graphite.

Electrical Conductivity. The electrical conductivity of various particle size show in Fig. 3(a) and 3(b). The highest of electrical conductivity at single particle size obtained at 150 um particle sizes. The increase was due to the variation of particle size for each vol. % as at 10, 50 and 90 (vol.%). Where differences in particle size can increase the accumulation of particles so that the percolation of interconnected particles that can affect the increase in electrical conductivity (Fig. 3(a)). Fig. 3 (b) indicates that the electrical conductivity a mixture of two particle sizes (7-11 $S.cm^{-1}$) and three particle sizes (13.88 $S.cm^{-1}$) are lower compared with a mixture of single-size particles (49.2 $S.cm^{-1}$) . Electrical highest conductivity obtained on a mixture of three particle sizes (40/100/150 μm). Increased variations in the mixture to reduce particle size electrical conductivity significantly. Besides the binding ability of pp polymer in particle size variations on each of the

increasing influences of percolation and particle ability to connect with each other in a decrease in electrical conductivity.

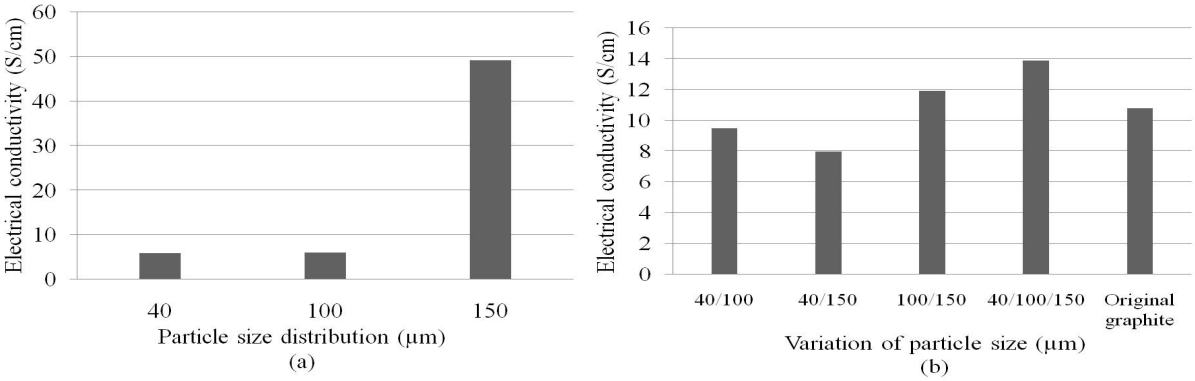


Fig. 3. Electrical conductivity: (a) single particle size, (b) combination particle size.

Composite Hardness. The highest value hardness of surface is correlation with the increase of packing density which is can also related to the electrical conductivity. Fig.4 (a) shows the sample hardness against particle size distribution change. According to this diagram, the highest hardness is obtain with at the particle size distribution 100 μm.

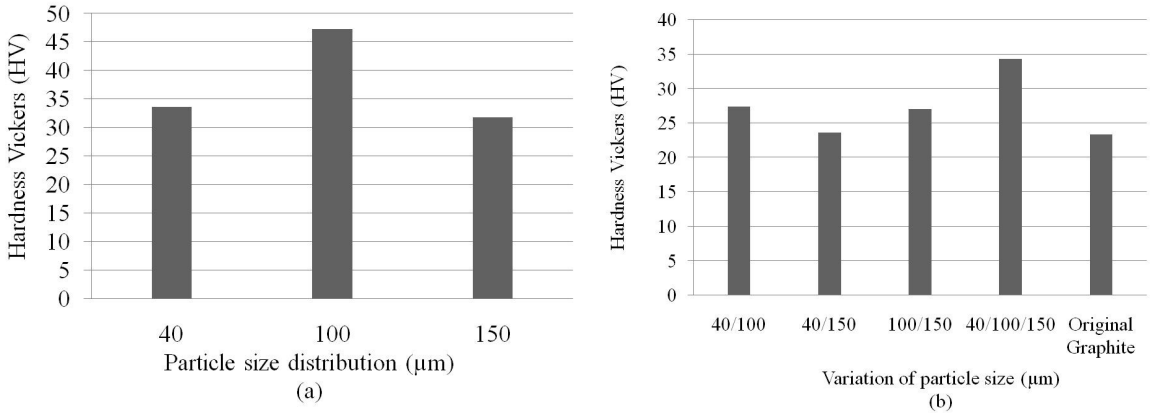


Fig. 4. (a) Hardness Vickers of single particle size graphite. (b). Hardness Vickers of combination particle size graphite

Mixing two and three particle sizes obtained the highest composite hardness of the mix 40/100/150 (μm) is shown in Figure 4 (b). The phenomenon of hardness vickers has the highest similarity with the increase of electrical conductivity variations 40/100/150 (um).

Scanning Electron Microscopy (SEM). Analysis of scattering and the effect of particle size on surface is carried out by SEM. Image of the surface is identical to the fracture surface indicates that the disperse of particles flak occurred evenly shaped with different sizes. The merger between the particle size distribution, 40 μm, 100 μm and 150 μm to form a solid bond with the PP shown in the figure with a white circle (Fig. 5(a)). This condition can increase the electrical conductivity, due to good dispersion represented in Fig. 5(a) and Fig. 5(b). The highest electrical conductivity and hardness of the composite materials is due to the packing density and distribution of particles size. Besides that, in the figure 5(a) it shows that the flak-shaped particles used in this study also have an influence on material properties and electrical conductivity. Flak-shaped particles tend to be arranged the layers and obtain the value of electrical conductivity higher than the spherical shape of particles [11].

Distribution of three particle size complements each other to form a solid bond between the graphite and the PP are highlighted with a white circle. The ability of PP polymer as a binder in the graphite evenly binding shown by the arrow on the surface of the microstructure and fracture surfaces.

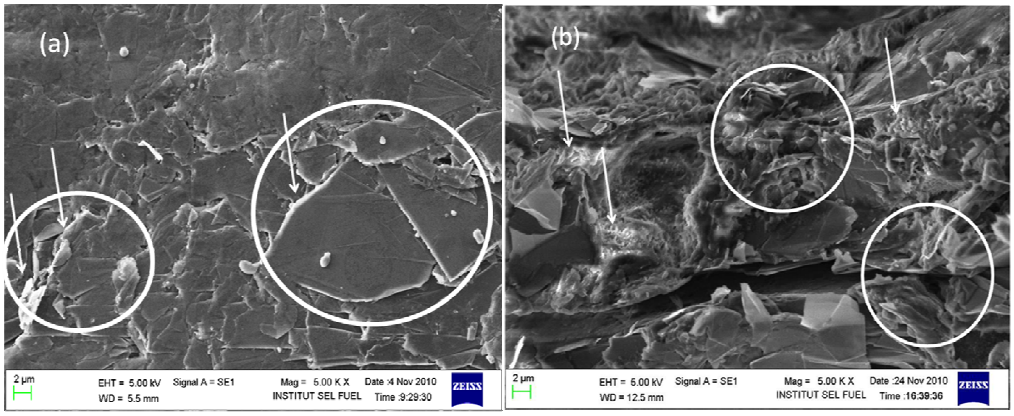


Fig. 5. SEM of particle size (40/100/150 μm); (a) on the surface, (b) on the fracture.

Summary

The variation of particle size distribution differences impact on the flow ability and composite materials properties. Mixing the two, three and more particle size graphite shows the properties of flow ability based on viscosity and shear rate. Results of rheological studies on the viscosity and shear rate showed that variations in the graphite mixing single and multi-composition of the particle size is suitable for injection molding process. The highest of electrical conductivity and hardness is obtained a mixture of three particle sizes (40/100/150 m) compared with other mixes.
The test results show that the incorporation of three types of particle size to form a packing density as a reinforcement mechanism which is one factor to improve the properties of materials at different particle sizes.

Acknowledgement

The authors gratefully acknowledge the financial support given for this work by the Malaysian Ministry of Science, Technology and Environment (MOSTE) 03-01-02-SF0453, and University Kebangsaan Malaysia UKM-GUP-TK-17-063: for supporting this work.

References

[1] F. Heinzel, O. Mahlendorf, Niemzig , and C. Kreuz: J. Power Sources Vol. 131 (2004), p. 35–40
[2] A. Hermanna, T. Chaudhuria, P. Spagnolb,. J. Hydrogen Energy., Vol. 30, (2005), p. 1297 - 1302
[3] J. H Lee, Y. K. Jang, C. E. Hong, N. H. Kim, L. Peng, H.K. Lee, J. Power Sources., Vol. 193 (2009), p. 523–529
[4] F.Mighri, M.A. Huneault, M.F. Champagne, J. Eng. Sci. Vol. 44 (2004), p. 9
[5] A. M¨uller, P. Kauranen, A. von Ganski, B. Hell: J. Power Sources., Vol. 154 (2006), p. 467–471
[6] Z. Jie , Z. Yan-wen, and H Jun, J. Zhejiang University SCIENCE., Vol. 6A(10) (2005), p.1080-1083
[7] S. Chunhui, P. Mu, Y. Runzhang, J. Hydrogen Energy., Vol. 33 (2008), p. 1035
[8] R Dweiri, and J. Sahari,. J. Power Sources., Vol.17 (2007), p.424–432
[9] I. Agote, A. Odriozola, M. Gutierrez , A. Santamarı, J. Quintanilla, P. Coupelle, J. Soares,. J.European Ceramic Society Vol. 21 (2001), p.2843–2853.
[10] S.M. Olhero, J.M.F. Ferreira, J. Powder Technology., Vol. 139 (2004),p. 69– 75.
[11] J. Zhang, Y. Zou, J. He, J. Zhejiang University SCIENCE., Vol. 6A(10) (2005), p. 1080-1083.

© (2011) Trans Tech Publications, Switzerland
doi:10.4028/www.scientific.net/KEM.471-472.115

Mechanical and Morphological Properties Evaluation of HDPE/Organoclay Nanocomposites with Various Percentages of NR content

Engku Zaharah Engku Zawawi[1,2,a], Sahrim Hj Ahmad[1,b], Rozaidi Rashid[1,c]

[1]School of Applied Physics, Faculty of Science and Technology, Universiti Kebangsaan Malaysia, Bangi, Selangor, Malaysia.

[2]Faculty of Applied Sciences, Universiti Tenologi MARA, Shah Alam, Selangor, Malaysia.

[a]engkuzaharah@yahoo.com.sg, [b]sahrim@ukm.my, [c]rozaidi@ukm.my

Keywords: Thermoplastic Natural Rubber, Organoclay, Nanocomposites, Blend

Abstract. Nanocomposites prepared from blend of high density polyethylene (HDPE), natural rubber (NR) and organoclay were melt compounded using an internal mixer. The phase morphology and mechanical properties of this thermoplastic natural rubber nanocomposites samples were examined. The transmission electron microscope (TEM) and wide angle X-ray scattering (WAXS) was used to determine the exfoliation of organoclay in this blend. The tensile and Izod impact test were used to evaluate the mechanical properties of HDPE/organoclay nanocomposites with and without the presence of NR. The Izod impact results shows an improvement more than 300% with addition of 10% NR content in the matrix. The X-ray diffraction results indicated intercalation of blend into the silicate interlayer of nano-filler I.44P and partially exfoliation of silicate layer into the blend. The SEM morphology revealed that there was some part of uneven dispersion of organoclay in the blend.

Introduction

Thermoplastic natural rubber (TPNR) is known as a blend of natural rubber and polyolefin. Its properties are between that of rubber and thermoplastic. The used of NR is an advantage since it can reduce cost of materials besides it can be processed using conventional thermoplastic machinery. Blending two or more immiscible polymers can be an effective way to obtain a polymeric system with useful combination of properties. However, blending of rubber and plastic will produce a thermoplastic elastomer (TPE) with inferior in their technical properties because of the presence of a weak rubbery phase and interface dispersed in a continuous plastic matrix. This limitation can be overcome by reinforcement of the rubber phase and the interface with the plastic matrix by fillers or the addition of crosslinks in the rubbery phase [1]. Studies on the microstructure-property correlation in dynamically vulcanized nanocomposites TPEs based on polypropylene/EPDM by Naderi et al. [2] found that the dimensions of the interface and strength of the interaction significantly influence the tensile strength properties of nanocomposites. Therefore it is beneficial to add nanoclay into the TPNR since it may enhance the physical, mechanical and thermal properties of this polymer even with very low loading of nanoclay.

Recently, polymer nanocomposites reinforced with low volume content of layered silicates have received considerable attention due to their unique physical and mechanical properties over their pristine polymers such as enhancement of tensile strength, stiffness, gas barrier resistance and thermal stability properties [3-4]. The unique properties of polymer nanocomposites are achieved by dispersing nanometer scaled layered silicates having large surface area and aspect ratio in polymer matrices [5]. Polyethylene (PE) is the most widely used polyolefin polymer, because of combination of many useful properties, light weight, low cost, good processability etc. However PE is a non-polar polymer, therefore it is difficult to prepare PE/clay nanocomposites. One of the effective ways to fabricate PE/clay nanocomposites is by melt intercalation. In the melt intercalation

process, the clay layers are directly dispersed in the molten polymers using the melt processing techniques. Normally good intercalation will increase the modulus and strength but decrease the toughness of the nanocomposites [6-7]. Study of impact toughness is fundamentally important because of semi-crystalline polymers such as polyethylene is ductile at low strain rates but at high strain rates such in Izod impact test it characterized by a brittle behaviour [8]. The aim of this study is to investigate the effect of 3 wt. % organoclay (Nanomer I.44P) in the blend of HDPE/NR (TPNR) at different NR content on the mechanical properties and correlation with the their morphological properties of a composites prepared by melt blending process.

Experimental

Materials. The HDPE material was provided by Polyethylene Malaysia Sdn. Bhd. The organic modified montmorillonite, Nanomer I.44P (Nanocor) was obtained commercially from Sigma-Aldrich. This nanoclay was chosen according to its known suitability for polyolefin matrices. Natural rubber (NR), Standard Malaysia Rubber, SMR L was purchased from Guthrie (M) Bhd.

Preparation of HDPE/NR/MMT nanocomposites. HDPE pallet and Org-MMT was melt-mixed in the Haaker Rheomix (Model 600). Mixing was performed with roller rotor for 12 min at a temperature of at 160°C and speed of 60 rpm. The HDPE/NR/org-MMT blends were also blended under the same compounding conditions. HDPE and NR were blended first for 4 minutes and was then mixed with Org-MMT. The blends were press moulded to get plaques of 1.5 and 4 mm thickness. The content of NR was set as 0, 10, 20 and 30 wt. %. The amount of organic modified montmorillonite, Org-MMT was kept constant (3 wt. %). All materials were dried at 80°C for 16 hours prior to blending.

Mechanical Testing. The compression plaques were subsequently cut into standard dum-bell shaped specimens (ASTM D638) for the tensile behaviour test and the impact samples with a V-sharp notch for Izod impact testing. Tensile tests were carried out with the Testometric tester at a crosshead speed of 50 mm/min. The values of Young's modulus and tensile strength were determined. At least five specimens of each composition were used for the mechanical measurements and the average values reported. Izod impact tests were performed using a Ray-Ran Universal impact tester at room temperature. The values reported here represent the average of ten specimens.

X-Ray Diffraction. XRD measurements were performed with a Bruker D8 Advance diffractometer. The data was recorded in the reflection mode in the range of 2 theta from 2.0-10°.

Transmission Electron Microscopy. Transmission electron microscope (TEM) analysis was performed on ultra-thin film sample of nanocomposites, prepared by ultracryo-microtome with a diamond knife at -100°C. The structure was observed using a Philips TEM model CM12 microscope.

Scanning Electron Microscope. The fracture surfaces of the gold-coated tensile test specimens were examined with a LEO 1450VP scanning electron microscope (SEM) at an acceleration voltage of 5 kV to evaluate the possible differences in fracture behaviour and to analyse clay dispersion.

Results and Discussion

Mechanical Properties. Fig. 1 shows the tensile properties of the nanocomposites at different NR contents. Addition of 3 wt. % organically modified nanoclays (Nanomer I.44P) showed an increase in the Young's modulus up to 35% and slight increase in tensile strength (2.8%) as compare to the neat HDPE. This increment in modulus and tensile strength is attributed to the reinforcing characteristics of nanoclay with high aspect ratio [5]. On the other hand, as was expected, the incorporation of NR in the composites tended to reduce the modulus and tensile strength significantly with increasing the NR content. This reduction in modulus of the HDPE/NR blend nanocomposites as compare with the nanocomposites without NR is attributed to the fact that NR have lower modulus as compare to HDPE.

The decrease in tensile strength is also attributed to the detrimental effect of nanomer agglomerate due to nonuniform dispersion of clay nanolayers in the polymer matrix. This was also confirmed by XRD and SEM results. The addition of NR contributed to the increased melt viscosity of the blend thus decreased in clay dispersion. It is known that a homogeneous dispersion of clay nanolayers in a polymer matrix will provides maximum reinforcement via load transfer and deflection of cracks resulting from an applied load [9]. The mechanical properties of nanocomposites are directly related to the homogeneous clay dispersion and exfoliation or intercalation in the polymer matrix. More homogeneous clay dispersion would result in higher modulus but at the expense of deformation and toughness such as elongation at breaks and impact resistance. It is, therefore, important to achieve an appropriate compound reinforcement by homogeneous stress and failure distribution resulting from the application of a load. It was reported [10] that interactions between the intercalated or exfoliated nanoclays with the polymer matrix showed relatively large interfacial areas that led to the improvement in mechanical properties.

From Fig.2 it can be seen the results of notched impact strength generally increase with an increase of the amount of NR. The impact strength of the HDPE decreased to 280% by incorporation of 3 wt.% of Org-MMT. The impact strength decreases because of strong polymer/clay network resulting more brittle failure behaviour [7]. The decrease in impact strength might also due to the effect of org-MMT agglomeration and nonuniform dispersion of clay nanolayers in the polymer matrix [11]. Most likely these large organoclay particles act as stress concentrators that lead to easy crack propagation, thus promote the failure with low energy absorption.

The addition of 10% NR in HDPE shows an improvement more than 300% of impact resistance in the HDPE nanocomposites. The decreases in Young's modulus and tensile strength but increases the Izod impact strength, mean that, there is a decrease of stiffness and an increase of toughness cause by incorporation of this elastomeric material. Therefore NR is effective for improving impact strength for binary nanocomposites of HDPE.

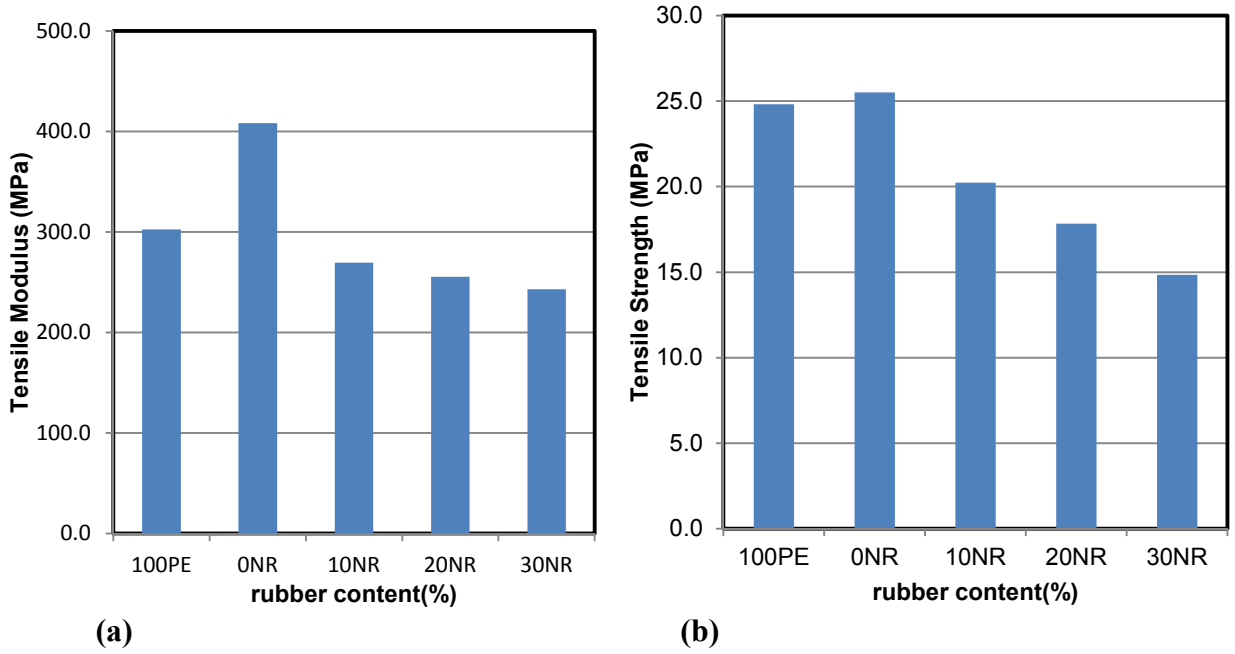


Fig. 1. Influence of the NR content on the (a) tensile modulus and (b) tensile strength of HDPE/NR/org-MMT samples.

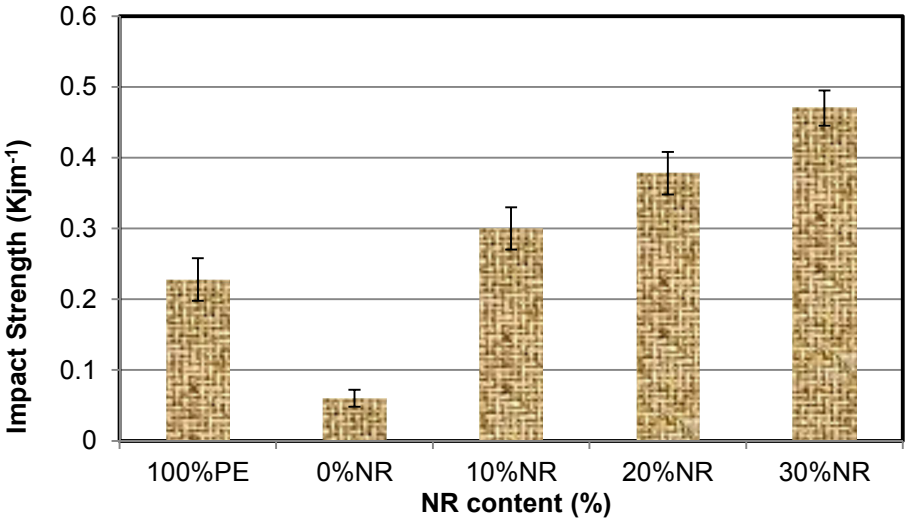


Fig. 2. The effects of NR content on Izod impact strength of HDPE/NR/Org-MMT sample.

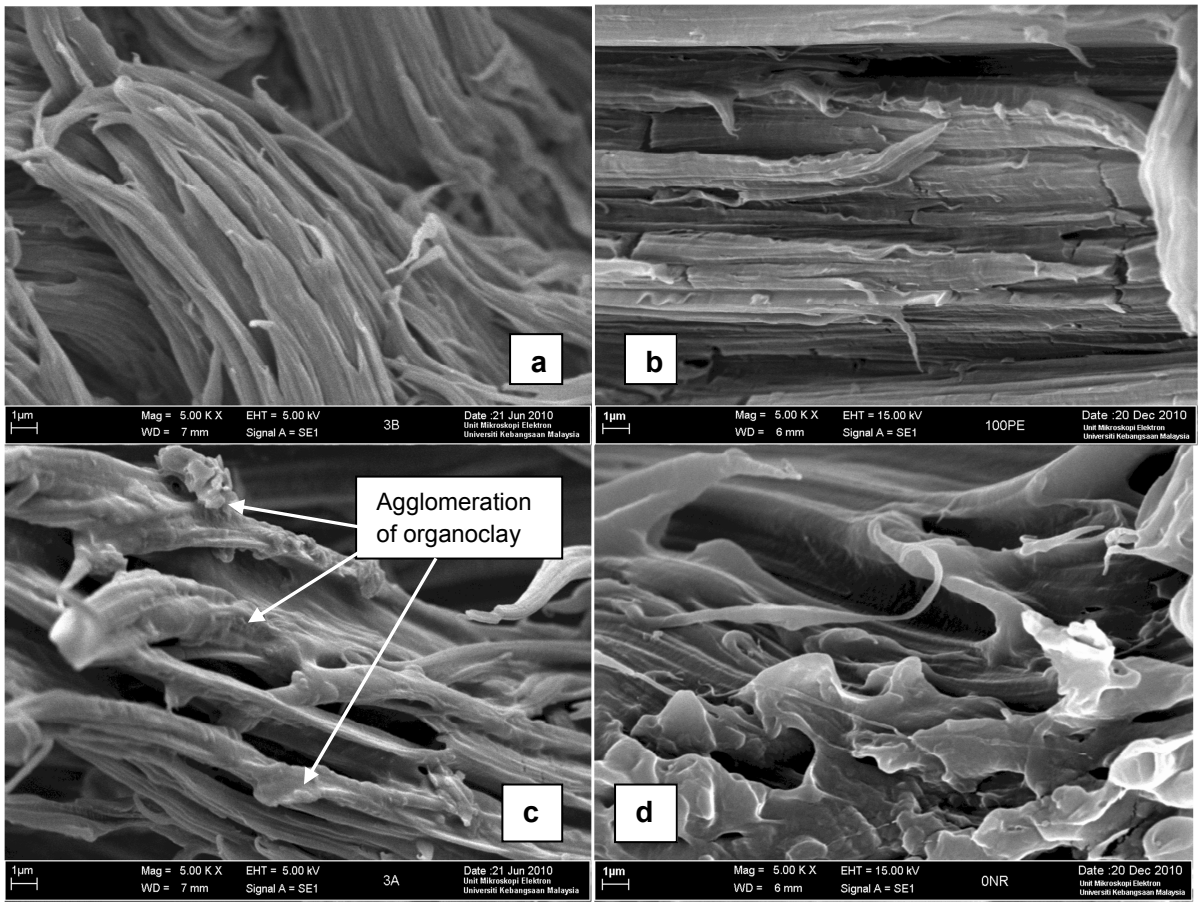


Fig. 3. SEM micrograph of fracture surface: HDPE/30% NR (a), 100% HDPE (b), and nanocomposites of 30% NR (c) and 0%NR (d) with 3% Org-MMT after tensile test.

Morphological Properties. SEM micrographs of HDPE/30% NR, 100% HDPE and their nanocomposites of 3% Org-MMT after tensile test are shown in Fig. 3. The TPNR matrix with 30% NR showed that ductile failure occurred during the tensile test since blend specimens had regions with large plastic deformation which resulting in extensive fibrillation of the matrix. Fig 3(c) shows incorporation of 3% Org-MMT into the blend does not suppress the fibrillation of the matrix. It also shows final fracture sample is initiated by some interior imperfection of the structure such as a large

filler particle or agglomerate in the specimen encounter by the propagating neck. This could be explanation for the reduction in the tensile strength. HDPE/NR does not have any polar group in their backbones, therefore it is difficult for its molecular chains to enter the gallery of Org-MMT thus contribute to low homogeneous dispersion.

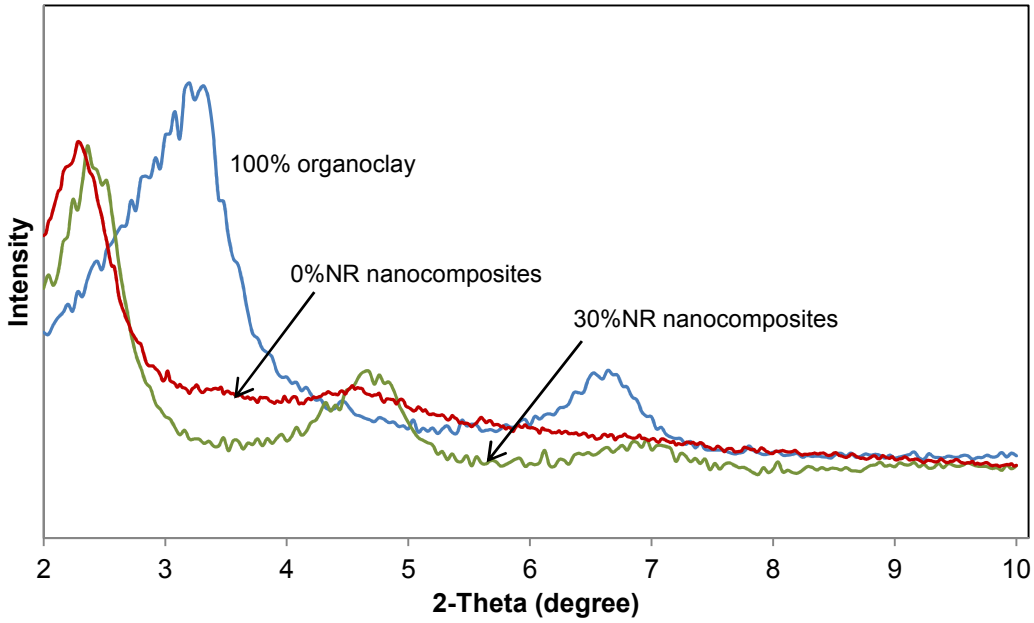


Fig. 4. Typical XRD patterns of Org-MMT, HDPE/0%NR and HDPE/30%NR nanocomposites.

The typical XRD diffraction peak of MMT I.44P is presented in Fig. 4 along with the diffraction spectra of the 0 wt.% and 20 wt.% NR nanocomposites. The d-spacing of nanomer I.44P calculated from Bragg's law was found to be 26 Å. The peak for nanocomposites each displayed the shifted to lower angles. The peaks located at the smaller angle corresponded to a larger distance separating in the clay particles, which is 38 Å for the 0% and 20% NR samples. The increased in distance between clay platelets indicates the exfoliation of clay has been formed in the composites. The second peaks shows there are some of intercalated of the blend matrices in between the Org-MMT platelets during melt processing of the nanocomposites or might due to stacked clays. Other researcher reported this may due to the degradation of some alkyl chains during processing [12]. Moreover, the addition of NR did not affect the diffraction peak since NR is an amorphous.

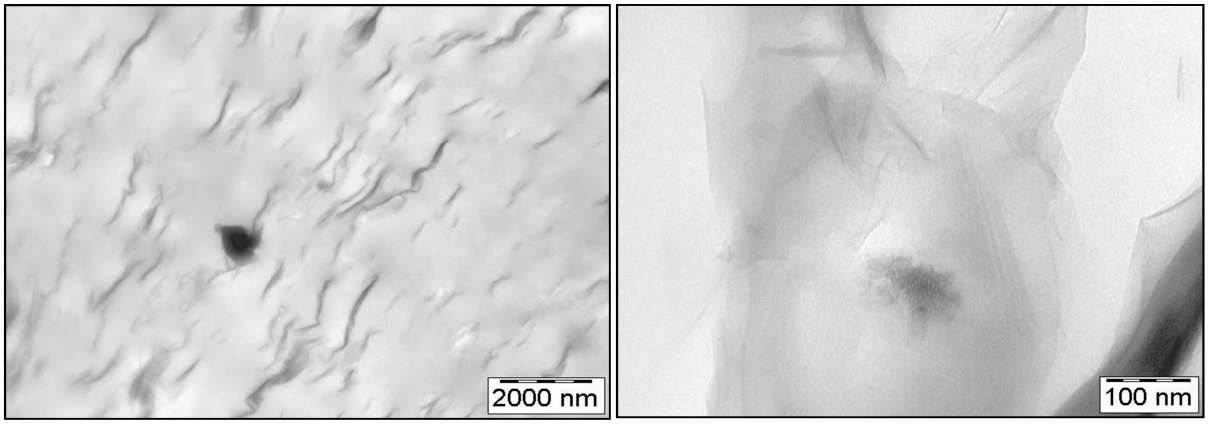


Fig. 5. TEM micrograph of nanocomposites HDPE/NR:70/30 with 3 wt% clay.

The TEM analysis was used in order to study the intercalation or exfoliation of the nanocomposites obtained. Fig. 5 shows the images for the nanocomposites HDPE/NR:70/30 with 3 wt% clay, it appears a slightly clay intercalated is observed, with formation of noticeable number of

clay aggregates or tactoids. This indicates that certain degree of exfoliation-intercalation is achieved which agrees with the XRD results, where the diffraction peak for this compound moved toward smaller angles.

Summary

The impact strength of HDPE/org-MMT nanocomposites were improved by adding the NR, but decreased in the modulus and tensile strength. The morphological results show this melt blending method was able to produce TPNR nanocomposites with relatively good tensile strength. The layered Org-MMT was intercalated or partially exfoliated within matrix in the HDPE/NR (TPNR) blend as shown in XRD.

Acknowledgements

The authors would like to thank; Mr Shamsul Bahri Ab Razak (Rubber Research Institute of Malaysia) for his efforts with TEM sample preparation, HDPE materials were kindly supplied by Polyethylene Malaysia Sdn. Bhd. and UiTM Malaysia for the scholarship.

References

[1] L.A. Goettler, K.Y. Lee and H. Thakkar: Polymer Vol. 47 (2007), p. 47
[2] G. Naderi, P.G. Lafleur and C. Dubois: Polymer Engineering and Science Vol. 47 (2007), p. 291
[3] T.G. Gopakumar, J.A. Lee, M. Kontopodo and J.S. Prent: Polymer Vol.43 (2002), p. 5483
[4] F-C. Chiu, S.M. Lai, J.W. Chen and P.H. Chu: Journal of Polymer Science Part B Polymer Physics Vol. 42 (2004), p. 4139
[5] C.G. Martins, N.M. Larocca, D.R. Paul and L.A. Pessan: Polymer Vol. 50 (2009), p. 1743
[6] M.Z. Rong, M.Q. Zeng, X.Y. Zheng, R. Walter and K. Friedrich: Polymer Vol. 42 (2001), p. 167
[7] S.J. Nikkhah, A. Ramazani, H. Baniasadi and F. Tavakolzadeh: Material and Design Vol. 30 (2009) p. 2309
[8] C. Deshmane, Q. Yuan, R.S. Perkins and R.D.K. Misra: Materials Science and Engineering A Vol.458 (2007), p. 150
[9] S.C. Tjong: Material Science and Engineering Vol. 53 (2006), p. 73
[10] H.R. Dennis, D.L. Hunter, D. Chang, S. Kim, J.L. white, J.W. Cho and D.R. Paul: Polymer Vol.42 (2001), p. 9513
[11] S.K. Samal, S.K. Nayak and S. Mohanty: Thermplastic Composites Materials Vol. 21 (2008), p. 243
[12] M. Modesti, A. Lorenzetti, D. Bon and S. Besco: Polymer Degradation and Stability Vol. 91 (2006), p. 672

© (2011) Trans Tech Publications, Switzerland
doi:10.4028/www.scientific.net/KEM.471-472.121

Nano-Alumina and Radiation Effect on the Mechanical Properties of High Density Polyethylene/Hydroxy Apatite Composite

N. Akmil [1, a], C. A. Luqman [2,b], M. Ahmad[3, c], K. Zaman[4, d]

[1]Institute of Tropical and Forest Product (INTROP),
Universiti Putra Malaysia 43400 UPM Serdang, Selangor, Malaysia.

[2]Department of Chemical Engineering,
Universiti Putra Malaysia, 43400 UPM Serdang, Selangor, Malaysia.

[3]Department of Chemical,
Universiti Putra Malaysia, 43400 UPM Serdang, Selangor, Malaysia.

[4]Malaysian Nuclear Agency, Bangi 43000 Kajang Malaysia

[a]akmil.mustaffa@gmail.com, [b]chuah@eng.upm.edu.my, [c]mansorahmad@science.upm.edu.my,
[d]khairul@nuclearmalaysia.gov.my

Keywords: nano alumina; polyethylene; hydroxyl apatite; mechanical properties; radiation

Abstract. The effect of nano-alumina and radiation on the mechanical properties of high density polyethylene hydroxyl apatite composite was investigated. The study showed that nano alumina as filler in the composite enhanced the strength of the polymer matrix and hence improved the mechanical properties of the composite. The study also showed that the mechanical properties of the composite depended on doses of nano alumina used and radiation dose of gamma ray. The maximum radiation dose used in this experiment 100 KGy is the best dose for the composite that enhances the tensile strength, impact, modulus and flexural strength. The interface behavior and strengthening mechanisms are discussed.

Introduction

Now days, a large number of research group are focused on developing of new materials for biomedical application. In the recent years, polymers are always being considered as on of the best choices due to low cost, easy handling, good compatibility, and versatile application. In previous works with HDPE as biomaterial, it was proved the low toxicity of this material by degradation in low molecular weight fragments, even reporting monomers [1]. Working with high density polyethylene (HDPE) mixed with inorganic compound like hydroxyl apatite is expected to provide data about the polymer properties. Kane et al. [2] determined the effect of HA reinforcement morphology on the mechanical properties of HA/HDPE composites under cyclic loading conditions. He concluded a fatigue testing protocol was developed and used to measure the effect of HA reinforcement morphology on the fatigue behavior of HA reinforced HDPE.

In this sense, Smolko et al. [3] studied on crosslinked hydroxyapatite-polyethylene composite as a bone-analogue material. Specimens were irradiated with g-rays up to 300 kGy. The most noticeable variation for the high-dose range is observed for the tensile strength of HA–MDPE composite, which increased slowly to reach at almost the same value as the pure MDPE matrix. In another context, the incorporation of HA resulted in an increase of the Young's Modulus and tensile strength at break for HDPE but in a decrease in tensile strength at yield and elongation. According to Wang, tensile testing results revealed that the strength and modulus of HA/chitin composite decreased with an increase in the amount of particulate HA in the composite. SEM examination of

fracture surfaces showed that HA particles were separated from the chitin matrix completely after tensile tests [4].

While Bodhak et al. [5] put their effort to study to enhance physical properties of HDPE in terms of elastic modulus and hardness, various ceramic fillers, like alumina (Al_2O_3) and hydroxyapatite (HA) are added. An important result is that the combined addition of 20 vol% HA and 20 vol% Al_2O_3 to HDPE leads to improved mechanical and wear resistance properties. From Crosby et al. [6] the presence of nanoparticles in a polymer netwoek can influence the polymer matrix in a similar manner to linear polymer matrices.

Based on what was mentioned above, the main objective of this work is modifying HDPE to be biocomposite reinforced nano-alumina filler that being modified with 3-(Trimethoxysily) propyl methacrylate (MPS) as a coupling agent. In the same way, gamma irradiation is used to promote crosslinking in order to enhance mechanical properties.

Methodology

Materials and preparation of Alumina. The nano-alumina used in this study was prepared by a sol-gel method using aluminium nitrate (ALN), aluminium peroxide (ALP) and sodium dodecyl benzene sulfonate (SDBS). ALN was stirred with 100 ml distilled water. Then ALP was added into ALN solution and stirred for 48 hours. After 48 hours, SDBS added into solution, and stir for 1 hour, then heater was turned on to 60°C until it became gel form solution. The gel solution was put in the oven at 80-85°C until solid formed and was heated up in furnace at 1200°C for 1 hour. Lastly, solid was grinded with mortar and pestle then sieved with sieve to have an average size. The nano-alumina was characterized by using election microscope (TEM) and x-ray diffraction (XRD).

The bi-functional coupling agent, (3-methacryloxypropyl) trimethoxysilane (MPS) and tetrahydrofuran (THF) used in this study was purchase from Sigma–Aldrich Chemical Company. A high-density polyethylene (HDPE) with a MFI of 4.88 g/min and Mw of 77456 g/mol supplied by Polyethylene Malaysia Sdn. Bhd was used in the preparation of the composites. The composite were irradiated using a 3 MeV electron beam accelerator NHV EPS-3000 at a required dosage.

Composite Preparation. Before nano-alumina can be used as filler in the polymer matrix, MPS was used to functionalize the nanoparticles due to its bi-functional nature: hydrolysable group (–$Si(OCH_3)_3$) and unsaturated carbon–carbon double bond. The amount of MPS used in this study is 4 wt% to the amount of the matrix. The treatment nano-alumina with the MPS were subjected to consisted of the following: nano-alumina was added into a mixture of MPS and THF then was ultrasonically (Branson 1510) stirred for one hour and precipitated by sedimentation at room temperature. The precipitated nano-alumina were rinsed with THF to remove the excessive MPS and dried completely in a vacuum oven at room temperature to remove the solvent.

As part for this study, the sample have been prepared through blending process by using HAAKE Rheomix 600 at conditions previously optimized of 150°C, 50 rpm and 10 min. The nano-alumina (treated with MPS) was mixed with HDPE at different loading as 1 to 5 % to the amount of the matrix. 10 % of HA was added into the intertal mixer during compounding process.

Irradiation. The molded sheets were irradiated using a 3 MeV electron beam accelerator NHV EPS-3000 at a required dosage. The acceleration energy, beam current, and dose rate were 2 MeV, 2 mA and 20 KGy per pass, respectively. The dosage used in this experiment is 20,40,60,80, and 100 KGy.

Mechanical Testing. Tensile strength, Young's modulus and elongation at break of the HDPE and its composites were obtained using a Universal Testing Machine following ASTM D-638. The gauge length of the specimens was 10 mm and the crosshead speed was 5 mm/min. For flexural strength and modulus (ASTM D-790), the speed test was 10 mm/min and the span length was 40 mm. Impact strength was the Izod type as ASTM D-256. For each test, at least 10 specimens were used in order examine the average values of the mechanical properties.

Results and Discussion

Fig. 1 shows the TEM photo of the synthesized nano-alumina. TEM has been used to measure the particle size of metal oxides before disperse into polymer resins. Besides that, in TEM images conformation of the agglomeration of the nanoparticles also can be investigate. From previous study, nano α-alumina was formed as a solid and spherical particle. Consequently, the TEM photo showed the spherical shape of the nano-alumina. In average, the size of the particle was around 20 nm to 40 nm. In other embodiment, Fig. 2 shows the diffraction spectrum of the synthesized nano alumina. There are peaks (012, 104, 110, 113, 024, 116, 122, 214, 300, and 119) corresponding to dominating sharp α-Al_2O_3 peaks.

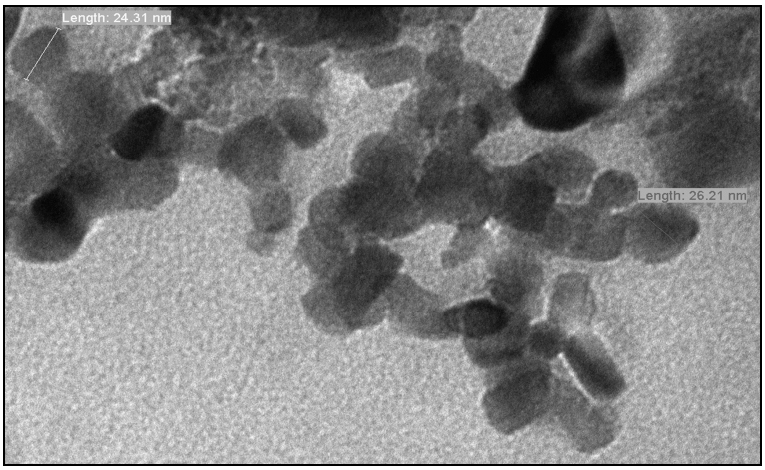


Fig. 1. TEM photo of the synthesized nano-alumina.

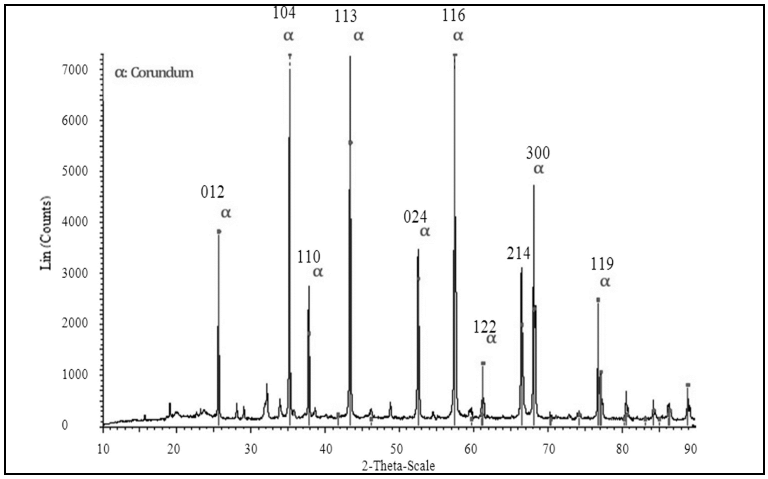


Fig. 2. Diffraction spectrum of the synthesized nano alumina.

The effect of the amount nano alumina treated MPS coupling agent on the mechanical properties of the HDPE/nano alumina (treated MPS) composite can be examined by varying the nano alumina (treated MPS) loading as follows: 1, 2, 3, 4 and 5 % with respect to the weight of matrix. When the amount of nano-alumina (treated MPS) is extended, the tensile strength of the composite is increased (Fig. 3). However, when the amount extended to 5 %, the strength dropped to 31.6 MPa but still higher than virgin HDPE strength (29.9 MPa). It is well know that the tensile strength of a particulate composite is usually reduced with filler content following a power law in the case of a poor filler/matrix bonding [7].

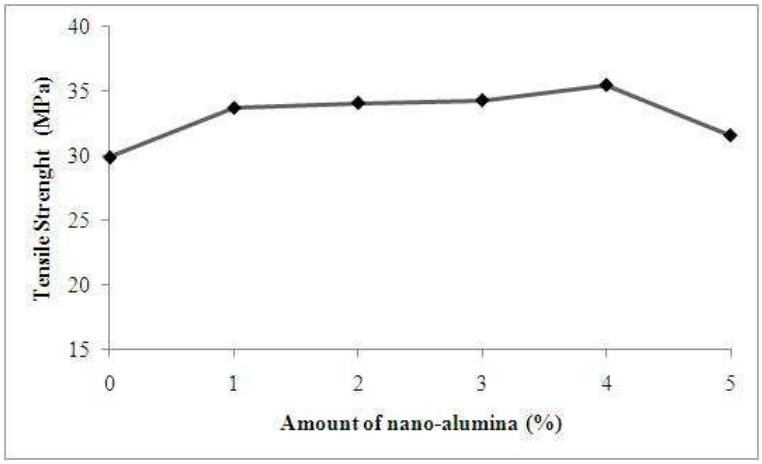


Fig.3: Tensile strength of HDPE/nano alumina treated MPS coupling agent

Fig. 4 shows the mechanical strength parameter value obtained from tensile test for different adsorbed doses. From the graph, it clearly can be seen that at dose 20 KGy, the tensile strength was decreased, but it gradually greater than before as the absorbed dose increased. The best result show at 100KGy, the composite has strength up to 27.05 MPa. This behavior may be due to crosslinking process on the polymer matrix that creates rigid regions at act as filler which absorbed most the applied load [8]. For Young's modulus of the composites irradiated at various doses, it shows the greatest Young's modulus appear at dose 100 KGy. Because of the composite shows greater stiffness that the non-irradiated composite, it causes a decline in % elongation at break [9]. Elongation at break (Fig. 5) showed a enormous decrease by increasing the filler content and decreased with radiation dose which was attributed to crosslinking of amorphous region [8].

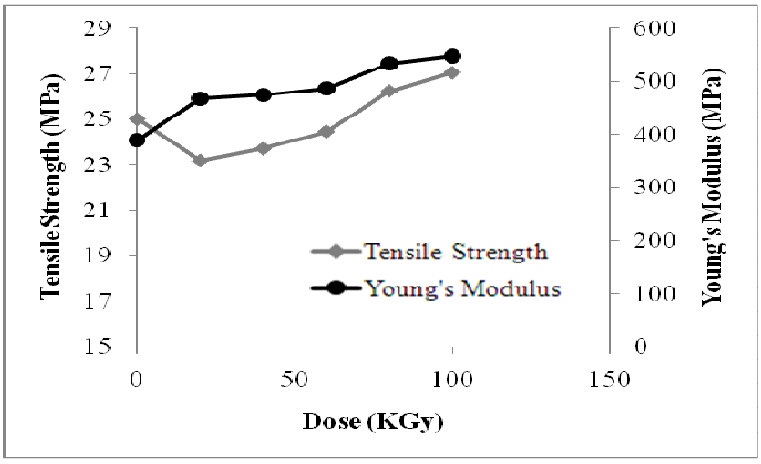


Fig. 4. Tensile strength and Young's Modulus of irradiated HDPE/HA/nano alumina (treated MPS) as a function of dose.

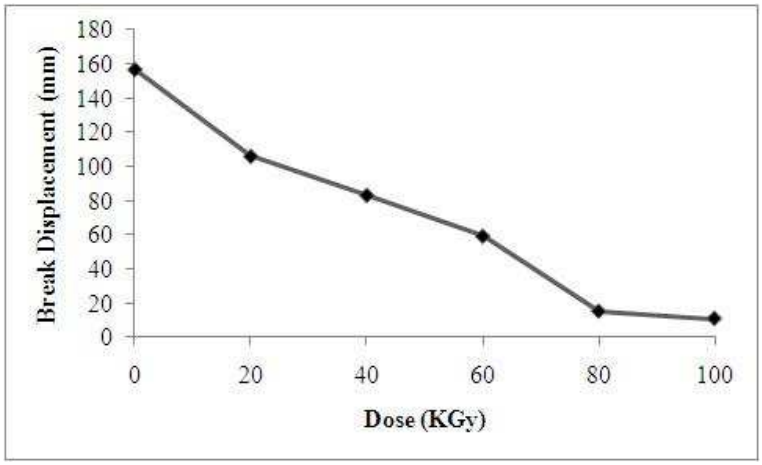


Fig. 5. Elongation at break of irradiated HDPE/HA/nano alumina (treated MPS) as a function of dose.

Flexural test is widely accepted test in the plastic industry, because it portrays well bending load cases, which often reflect realistic. In this study, flexural strength of irradiated HDPE/HA/nano alumina (treated MPS) can be clearly seen that flexural strength of the composite are enlarged in increasing irradiation dosage (Fig. 6). The maximum yield strength was at 100 KGy with 26.32 MPa compare to non-irradiated sample, the yield strength only at 24.97 MPa. The flexural strength was enhanced due to improvement of the interfacial boundary by the interaction between chains in composite as the predominance of crosslinking over the composite. Also for the impact test on notced composite specimens were carried out. The test was performed to study the effect of irradiation dosage on the impact properties of crosslinked and noncrosslinked composite. From fig. 7, it can be seen that the impact strength of the composite increased enormously when the amount of irradiation dose is increased. Especially at dose 100KGy, the impact strength improved about 49.69% from non-irradiated composite (0KGy). The enhancement in the composite impact strength was attributed to crosslinking of amorphous region. It helps absorbing impact energy from the reinforcement to the matrix; as a result, higher impact strength can be obtained [9].

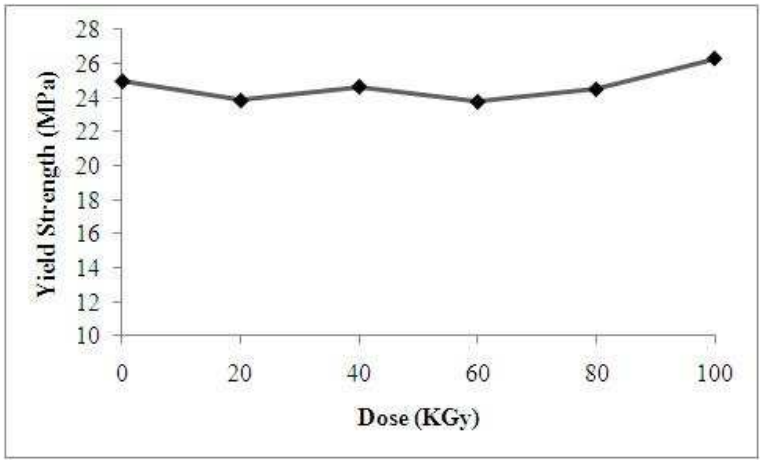


Fig. 6. Flexural strength of irradiated HDPE/HA/nano alumina (treated MPS) as a function of dose.

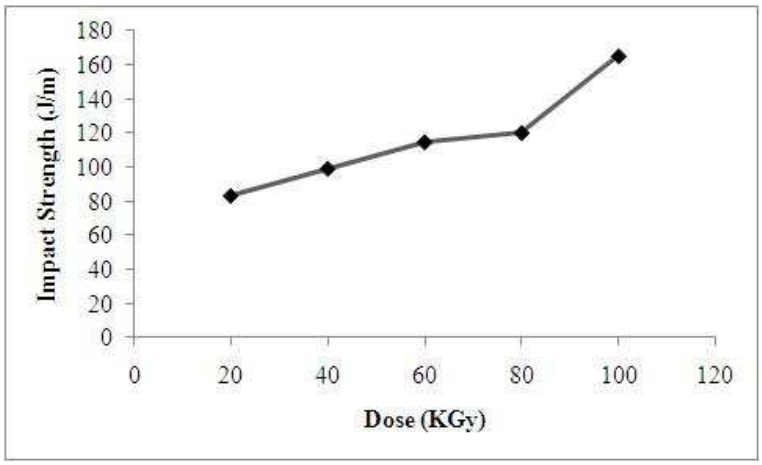


Fig. 7. Impact strength irradiated HDPE/HA/nano alumina (treated MPS) as a function of dose.

Summary

The experimental results presented in this research show that the addition of nano alumina treated with silane coupling agent in the HDPE/HA composite was improved the tensile strength of the composite. At the final stage, gamma ray irradiation was completely showed the greater enhancement to the mechanical properties of the composite due to the impact, tensile and flexural results. However, the crosslinking effect the elongation at break of the composite.

References

[1] G.E. Zaikov, K.Z. Gumargalieva, A.Y. Polishchuk, A.A. Adamyan, and T.I. Vinokurova. Polymer Plastic Technology Engineering. Vol. 38 (4) (1999), p. 621.

[2] Robert J. Kane, Gabriel L. Converse, and Ryan K. Roeder. Journal of the Mechanical Behavior of Biomedical Material. Vol. 1 (2008), p. 261-268.

[3] E. Smolko, G. Romero. Radiation Physics and Chemistry. Vol. 76 (2007), p. 1414-1418.

[4] Min Wang, Materials Research Society. Vol. 724 (2002), p. 1-11

[5] Subhadip Bodhak, Shekhar Nath and Bikramjit Basu. Journal of Biomaterials Applications. Vol. 0 (2008), P. 1-27.

[6] Alfred J. Crosby and Jong-Young Lee Polymer Reviews. Vol. 47(2007), p. 217-229

[7] Sirirat Wacharawichanant, Supakanok Thongyai, Tanakorn Siripattanasak, and Tunya Tipsri. Iranian Polymer Journal. Vol. 18 (8) (2009), p. 607-616.

[8] L.Catan˜o, C. Albano, A. Karam, N. Domı´nguez, Y. Sa´nchez, and J. Gonza´lez. Nuclear Instruments and Methods in Physics Research B. Vol. 236 (2005), p. 348-353.

[9] Jutarat Prachayawarakorn and Kanita Anggulalat. Songklanakarin J. Sci. Technol. Vol. 25(5) (2003), p. 595-606.

© (2011) Trans Tech Publications, Switzerland
doi:10.4028/www.scientific.net/KEM.471-472.127

Influence of Crystallite Size on Consolidation of Carbon Nanotube Reinforced AA 4032 Composite Powders by Equal Channel Angular Pressing

M.S.Senthil Saravanan[a], K.Sivaprasad[b], S.P.Kumaresh Babu[c]

Department of Metallurgical and Materials Engineering, National Institute of Technology, Tiruchirapalli-620015, Tamil Nadu, India

[a]senthilsaravanan@hotmail.com, [b]ksp@nitt.edu, [c]babu@nitt.edu

Keywords: Carbon nanotubes, ECAP, Nanocrystalline materials, Powder consolidation, Transmission electron microscopy, Scanning electron microscopy, Hardness

Abstract. Equal channel angular pressing (ECAP) is the one of the promising methods of severe plastic deformation to obtain bulk ultrafine grain structures. However, ECAP can also be used for powder consolidation. In the present study, fully dense bulk AA 4032 alloy was consolidated from nanocrystalline and microcrystalline powders. These materials were processed by ECAP until four passes at ambient temperature. It is observed that hardness and densification increased significantly with increase in number of ECAP passes. Transmission electron microscopic and scanning electron microscopic examinations evidenced that crystallite size of the nanopowders are unaltered, however a significant crystallite size reduction from around 50 μm down to submicron size is observed. Moreover, higher densification is achieved in microcrystalline powders than nano powders, whereas higher hardness in the case of nanopowders compared to microcrystalline powders.

Introduction

Powder metallurgy (PM) is a traditional technique to produce the near-net shape products. The inherent porosity of the PM processed components does affect the performance of the component. Thus, achieving a fully dense material is an important aspect in the powder processing methods. The consolidation of nano powders is generally difficult due to the accumulated strain associated with nanocrystalline powders especially produced through ball milling processing. Many studies have been reported to develop dense powder metallurgy components such as hot isostatic pressing (HIP), hot powder extrusion, hot pressing [2-4] apart from regular cold pressing followed by sintering. Recently, it has been shown that equal channel angular pressing (ECAP) is an effective method to consolidate the powders. Generally, ECAP process is used for grain refinement of materials by extruding metallic materials through specially designed channel dies without a substantial change in geometries [1]. Although a number of studies have been carried out with ECAP of many wrought metals and alloys, only limited research on ECAP powder consolidation is reported [5, 6] and no studies have been reported so far on ECAP consolidation of nanocrystalline powders.

Materials and Methods

Materials. Elemental powders of AA 4032 were taken as matrix material for the present study. The chemical composition of AA 4032 is shown in Table 1.

Table 1: Chemical composition of AA 4032 alloy

Composition	Silicon	Copper	Nickel	Magnesium	Aluminum
Wt %	11.5	1.0	1.0	1.0	Bal

Multi-walled carbon nanotubes (MWNTs), synthesized by electric arc discharge method, are used as reinforcement in the present investigation. The TEM picture of the MWNTs is shown in Fig 1, which reveals the multi wall nature.

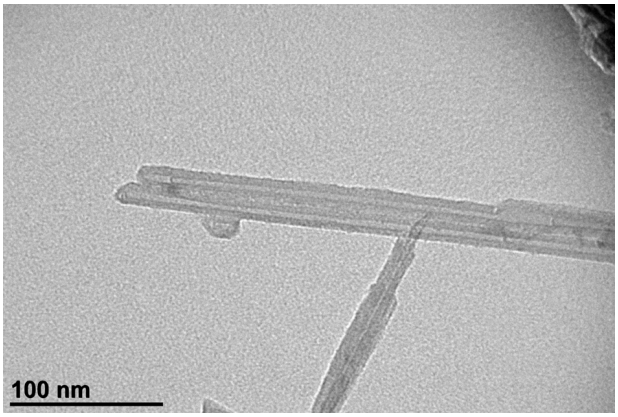


Fig. 1. TEM micrograph of MWNTs

Methods. For producing micro crystalline composite, elemental powders of AA 4032 were mixed using pot mill for 3 hours and subsequently mixed with 2 wt % of MWNTs using shear mixer. The mixed powders were canned in to a commercial pure aluminum can of Φ12mm OD, Φ10 mm ID and height of 60mm for the ECAP. After ECAP, the consolidated micro crystalline samples were sintered at 600°C in argon atmosphere for 90 minutes.

For the nanocrystalline AA 4032, the powders were ball milled for 30h using Fritsch P5 high energy ball mill in tungsten carbide milling media with a ball to powder of 10:1. The final crystallite size of ball milled powders is calculated as 17 nm using modified Williamson Hall analysis technique [7]. The MWNTs were added during last hour of milling so as to prevent the structural damage of nanotubes and to get uniform distribution in the matrix. The nanocrystalline powders were canned in commercially aluminum can as in the case of microcrystalline composites.

The aluminum can containing powder mixture was consolidated by ECAP at room temperature. In the ECAP, a sample is pressed through a die having two channels as shown in Fig. 2, having equal cross section with an intersect angles ψ of 20°, φ of 90°.

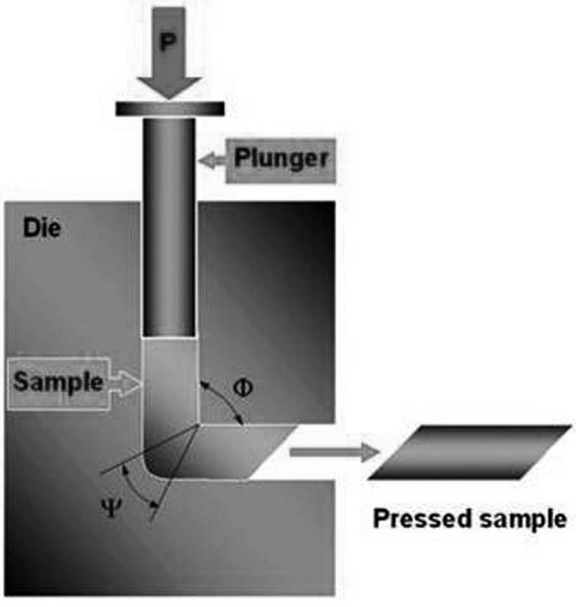


Fig. 2. A schematic diagram of ECAP

ECAP process was conducted up to 4 passes at room temperature following route B_A. The ECAP experiments were performed at room temperature with a cross head speed of 1mm/sec

without any a back pressure applied during ECAP. A complete lubrication of the ECAP set up was used by MoS_2 lubricant. The total strain developed during ECAP is calculated by [8].

$$\varepsilon_N = \frac{N\left[2\cot\left(\frac{\varphi+\psi}{2}\right)+\psi\cos ec\left(\frac{\varphi+\psi}{2}\right)\right]}{\sqrt{3}} \quad (1)$$

The consolidated nanocrystalline samples were cut into small pieces and sintered at 480°C in argon atmosphere for 90 min. The density of the consolidated samples was measured using Archimedes principle and the hardness was measured using Vickers hardness tester (Model No. BV-120) with a load of 5kg. The phase analysis of the consolidated samples was done using X-ray diffraction technique and the microstructural analysis using scanning electron microscope (SEM; Hitachi 3000s) and transmission electron microscope (TEM; Philips CM20).

Results and Discussion

The XRD pattern of both micro and nanocrystalline composites is shown in Fig. 3. The XRD pattern in Fig. 3(a) shows presence of Si peaks even after sintering. A small amount of carbon peak was observed in the composites which corresponding to CNTs. Meanwhile, no other elemental peaks were observed in the Fig.3 (b). It shows that during ball milling all the elemental powders were dissolved into the matrix forming a solid solution. The crystallite size was measured after 4 passes of ECAP and there is significant decrease in crystallite size in microcrystalline composites during the ECAP. The initial powders are around 50μm however, the ECAP followed by sintering resulted in a crystallite size of 600 nm. Hence, it is proved that ultra fine grain structured alloys and composites can be developed using ECAP consolidation of micro crystalline powders. However, there is reverse effect in the case of nanocrystalline powders. The initial crystallite size of ball milled powders is 17 nm and the crystallite size after consolidation through ECAP followed by sintering is 90 nm. The reason may be attributed to dynamic recovery and recrystallization during ECAP as well as during sintering. Large quantity of accumulated strains developed during ball milling were relieved and resulted in the grain grow up to 90 nm.

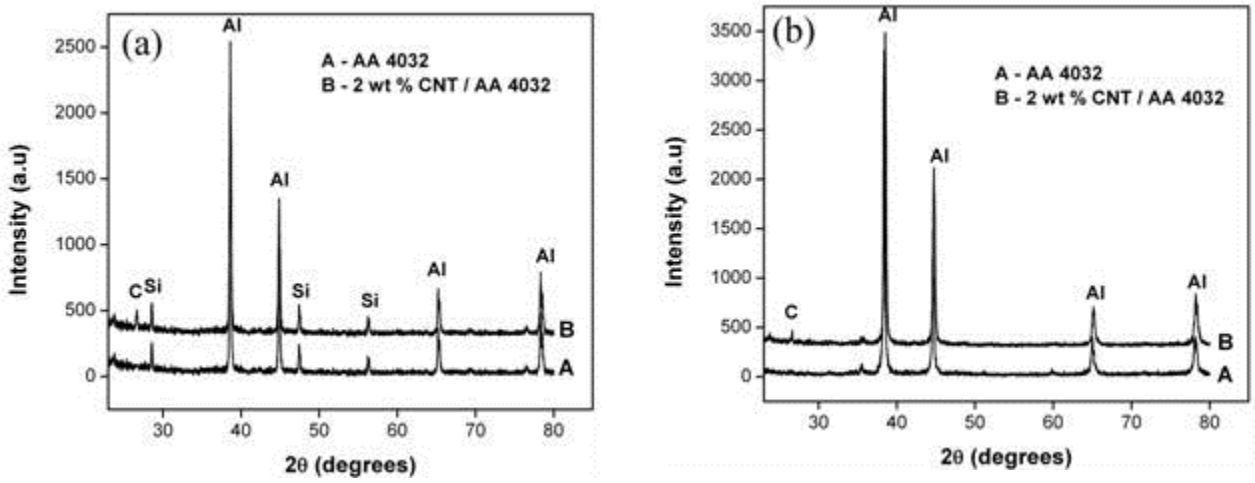


Fig.3. XRD pattern after 4 passes of ECAP; (a) Microcrystalline composites, (b) Nanocrystalline composites

Fig. 4 shows the SEM picture of the microcrystalline and nanocrystalline composites after consolidation. It is observed that the micro crystalline composites exhibit good densification compared to nanocrystalline composites due to large amount of strains in ball milled powders.

During ECAP, agglomerates of CNTs and the voids were reduced as large amount of strain is being applied on the sample as per the Eq. (1). The homogeneous distribution of CNTs was achieved in micro crystalline composites after ECAP passes. The densification was achieved by hydrostatic pressure acting on the powders and shear deformation during ECAP.

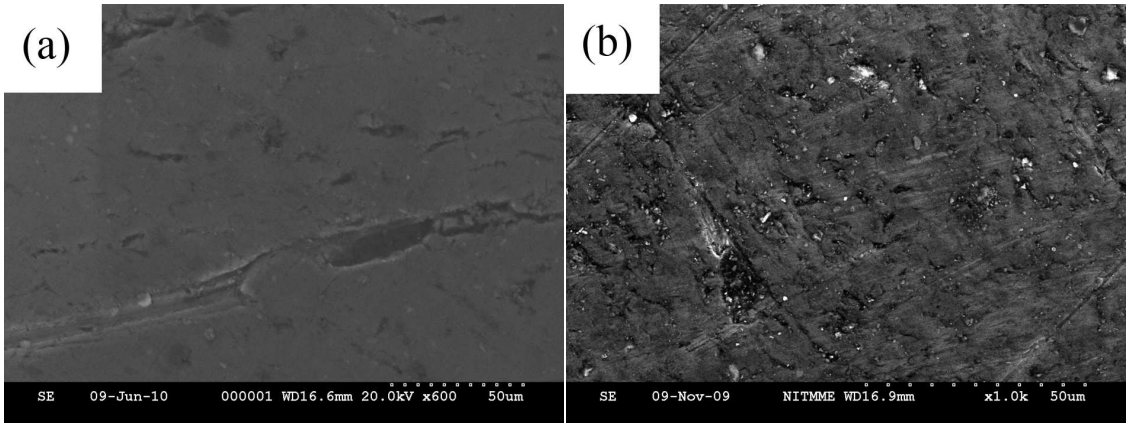


Fig.4. SEM micrograph of ECAP samples; (a) microcrystalline composite, (b) Nano crystalline composite

The TEM micrographs of microcrystalline and nanocrystalline composites are shown in Fig. 5. The microstructure of base alloy having large grains consisting of sub grain network in them, which is shown in Fig. 5(a). Similar kind of observations was made by Brochu et al [9]. It was reported that more grain refinement was achieved in microcrystalline Al-Mg alloy due to unstrained nature and better plastic deformation properties of aluminum. An interesting bimodal microstructure feature was observed in the microcrystalline composites after ECAP consolidation. It resulted in a microstructure with small fraction of coarse grains along with large amount of ultra fine grains (300-600 nm).

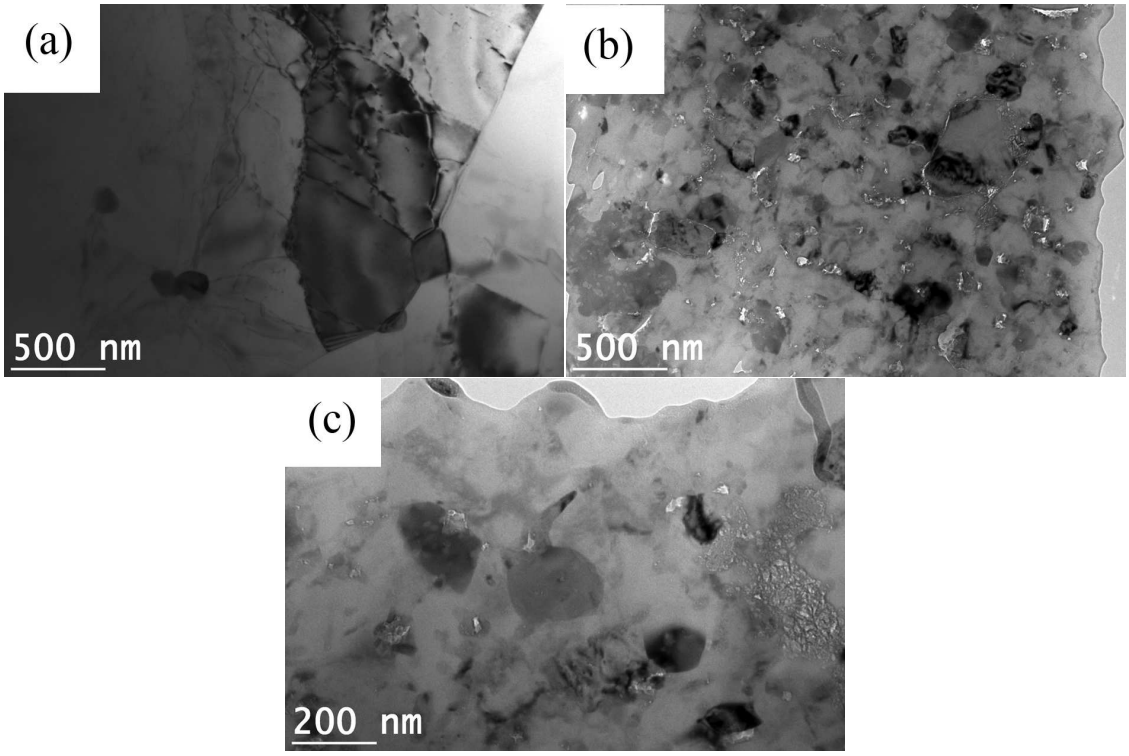


Fig. 5. TEM micrograph of ECAP samples; (a) micro crystalline sample; (b) nanocrystalline base alloy; (c) nanocrystalline composite reinforced with CNT.

Mechanical milling followed by ECAP was reported to be effective in developing bulk nanostructured materials [10]. It is also seen that through ECAP complete consolidation of nanoparticles with full density is acheived which is not possible by conventional compaction followed by sintering. In present work ECAP results in further structural refinement and more uniform distribution of CNTs in the matrix which is shown in Fig. 5 (b & c). It is shown that MWNTs were uniformly distributed in the aluminum matrix along less grain growth. CNTs are surrounded with the grain which retard the growth during sintering, thus the strength of the composites were improved. TEM investigations proved that excellent bonding between the particles can be achieved during ECAP. High shear exposes fresh and clean surface in each pass which could result in good densification of the composites [11].

The relative density and hardness of the micro and nanocrystalline consolidated samples are shown in Fig. 6. The microcrystalline composites show more densification than nanocrystalline composites. Reduced relative density of the nano powders is attributed to large amount strain accumulated during the ball milling. The increase in the hardness is due to combined effect of matrix strengthening, densification along with dispersion strengthening of MWNTs. The results show that ECAP induces a spatial homogenization of the powder particles [5]. ECAP provides a sufficient amount of strain necessary to deform the particles and filling pores with strong interfacial bonding in between the particles.

The high strength obtained by ECAP consolidation of nanocrystalline AA 4032 may be attributed to the Orowan mechanism where the nano sized particles and uniform distribution of reinforcement [12]. The uniform distribution of CNTs in the matrix retards the recrystallization and grain growth leads to high hardness.

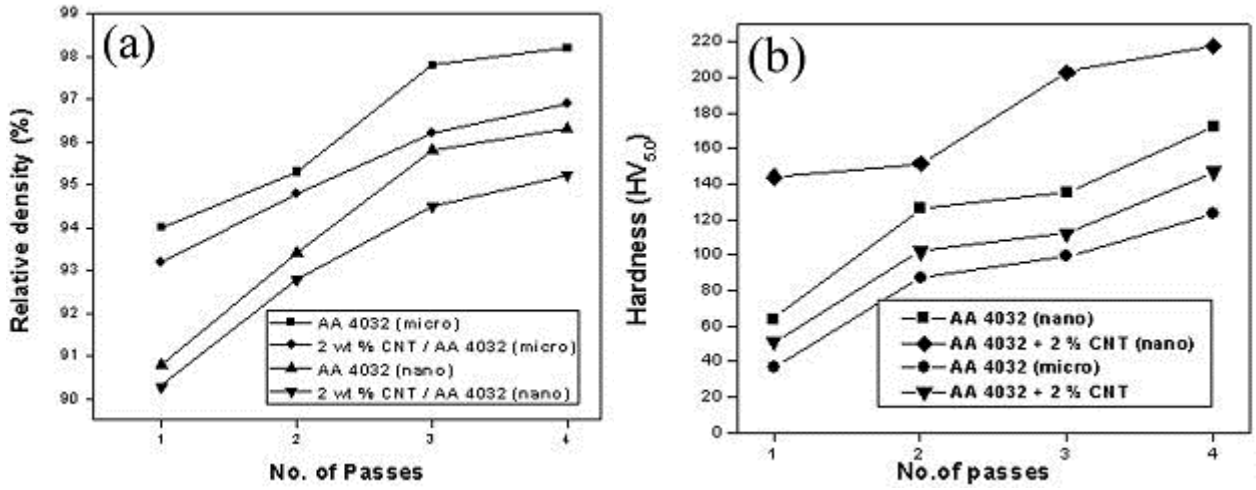


Fig. 6. Relative density and hardness of micro and nanocrystalline composites

Summary

Bulk CNT-AA 4032 from both microcrystalline and nanocrystalline powder mixtures were processed through ECAP at room temperature. It was found that nanocrystalline powder compacts exhibited better hardness than the microcrystalline. During ECAP, the packing of the powder particles is observed to be denser, however nanocrystalline powders compactability is less due to high strains in the powders than in microcrystalline powders. Even though the compaction is less dense, nanocrystalline powder compacts exhibited superior properties. Hence it is proposed that the ECAP processing of powders is suitable method to achieve powders with good density and improved mechanical properties especially in the case of nanocrystalline powders.

References

[1] R.Z. Valiev and T.G.Langdon: Rev. Adv. Mater. Sci. 13 (2006), p.15.

[2] B.Q. Han, Z. Lee, S.R. Nutt, E.J. Lavernia and F.A. Mohamed: Metal Mater.Trans. A 34 (2003), p.613.

[3] G. Liang, Q. Meng, Z. Li and E. Wang: Nanostruct. Mater. 5 (1995), p.673.

[4] J.H. Choi, K.I. Moon, J.K. Kim, Y.M. Oh, J.H. Suh and S.J. Kim: J. Alloys Compd. 315 (2001), p.178.

[5] P. Quang, Y.G. Jeong, S.C. Yoon, S.H. Hong, H.S. Kim: J. Mater. Proc. Tech. 187-188 (2007), p. 318.

[6] K. Matsuki, T. Aida, T. Takeuchi, J. Kusui, K. Yokoe: Acta Mater. 48 (2008), p.2625.

[7] M.S. Senthil Saravanan, K. Sivaprasad, P. Susila and S.P. Kumaresh Babu: Physica B 406 (2011), p.165.

[8] Y. Iwahashi, J.Wang, Z. Horita, M. Nemoto and T.G Langdon: Scripta Mater. 35 (1996), p.143.

[9] M.Brochu, T. Zimmerly, L. Ajdelsztajin, E.J. Lavernia and G. Kim: Mater. Sci. Engg. A 466 (2007), p. 84.

[10] S.Goussous, W. Xu and K. Xia: J. Phys: Conference Series. 240 (2010), p.12106.

[11] K. Xia and X. Wu: Scripta Mater. 53 (2005), p. 1225.

[12] R. George, K.T. Kashyap, R. Rahul and S. Yamdagni: Scripta Mater. 53 (2005), p.1159.

© (2011) Trans Tech Publications, Switzerland
doi:10.4028/www.scientific.net/KEM.471-472.133

Thermal Free Vibration Analysis of Temperature-dependent Functionally Graded Plates Using Second Order Shear Deformation

Ali Shahrjerdi[1, 2, a], F. Mustapha [3,b] , S.M. Sapuan[1, c], M. Bayat[4, d], D.L.A. Majid [3,e] and R.Zahari[3,f]

[1]Department of Mechanical and manufacturing Engineering, Universiti Putra Malaysia, 43400, Selangor, Malaysia

[2]Department of Mechanical Engineering, University of Malayer, Iran

[3]Department of Aerospace Engineering, Universiti Putra Malaysia, 43400, Selangor, Malaysia

[4]Department of Civil Engineering, Aalborg University, 9000 Aalborg, DK

[a]ailshahrjerdi2000@yahoo.com, [b]faizal@eng.upm.edu.my, [c]sapuan@eng.upm.edu.my, [d]meb@civil.aau.dk

Keywords: Functionally graded plate; Second order Shear deformation; Free vibration; Temperature dependent

Abstract. This research has been conducted to approach second-order shear deformation theory (SSDT) to analysis vibration characteristics of Functionally Graded Plates (FGP's). Material properties in FGP's were assumed to be temperature dependent and graded along the thickness using a simple power law distribution in term of the volume fractions of the constituents. FGP was subjected to a linear and nonlinear temperature rise. The energy method was chosen to derive the equilibrium equations. The solution was based on the Fourier series that satisfy the simply supported boundary condition (Navier's method). Numerical results indicated the effect of material composition, plate geometry, and temperature fields on the vibration characteristics and mode shapes. The results revealed that, the temperature field and volume fraction distribution had significant effect on the vibration of FGPs. It was observed the second order theory was very close to the other shear deformation theorem as reported in the literature.

Introduction

Functionally Graded Materials (FGMs) were initially designed for thermal barrier materials in aerospace structural applications and fusion reactors. Compared to pure material plate, FG plates of similar size give much lower weight and greater heat resistant. FGMs consist of a ceramic and a metal at which the volume fraction of the two materials is varied, according to a power-law distribution. This advantage of FGM was conducted for the thermal protection. It is seen from the literature that, considerable amount of works have been reported on the vibration characteristics of isotropic plates and composite laminates are exhaustive. However, the investigations of linear and nonlinear dynamic behaviors of shear deformable FG plates under thermo-mechanical environment are limited in number and are discussed briefly here.

FEM method and first order shear deformation theory employed by Praveen and Reddy [1], for nonlinear transient thermo-elastic responses of FG plates. However, they assumed that FG plates were temperature independent. Shukla and Huang [2] presented nonlinear static and dynamic responses of the FG rectangular plate using first order shear deformation theory (FSDT). However, they did not consider the temperature dependent and thermal conditions. Zhao et al. [3] employed a element-free kp-Ritz method to analyze the free vibration of temperature dependent FG plates based on the first order shear deformation plate theory. Ferreira and Batra [4] provided a global collocation method for Natural frequencies of FG plates by a mesh-less method with first order shear deformation theory (FSDT).

There are also several studies of FG plates employing three-dimensional exact solutions and other shear deformation theory such as the third order-shear deformation theory. To determine the effects of Non-linear, Huang et al. [5] compared vibration and dynamic response of the temperature dependent FG plates in thermal environment and based on the higher-order shear deformation theory. Uniform and varied temperature field in the thickness direction were examined in their study. Matsunaga [6] conducted the thermal buckling of FG plates according to a 2D higher order shear deformation theory. However, he was not considered the change of material properties due to temperature distribution in analysis.
Some studies apply second-order shear deformation theory (SSDT) such as Khdeir and Reddy [7], that studied free vibration of laminated composite plates using SSDT. A general formulation for FG circular and annular plates presented by Saidi and Sahraee [8], using Second order shear deformation theory and developed the bending solution that accounts for deflections and various boundary conditions. Shahrjerdi et Al. [9] presented free vibration analysis of quadrangle FG plate by using Navier's method based on second order shear deformation theory. Also, they [10] used second order shear deformation theory for stress analysis of FG solar plates subjected to in-plane and out-plane mechanical loads.

The temperature independent and temperature dependent materials in a constant temperature field and the temperature varies through the thickness direction if a heat flows from one surface to the other surface by applying first, third and higher order shear deformation theories considered for some researches. To the authors' knowledge, a few works has been done in the area of dynamic stability of FGM plate by using SSDT. In this paper, the analytical solution is provided for the vibration characteristics of FGP under temperature field and applying second order shear deformation theory (SSDT). The temperature is assumed to be constant in the plane of the plate. The variation of temperature is assumed to occur in the thickness direction only. The FGP is assumed to be simply supported with temperature-dependent and independent material properties to the power law distribution in terms of the volume fractions of the constituents and subjected to uniform, linear, nonlinear temperature rise. The frequency equation is obtained using Navier's method based on the second-order shear deformation plate theory.

Material and Method

Temperature dependent material properties. A FG rectangular plate at the thickness h, width, a, and length, b is considered as shown in Figure 1. The material in top surface ($x_3 = h/2$) and in bottom surface ($x_3 = -h/2$) is Full-Ceramic and Full-Metal respectively, and between these two pure materials, power law distribution of material is applied. According to this model, the position and temperature dependent material properties of FGP can be expressed as [11] :

$$\begin{aligned} E &= E\left(x_3,T\right) = (E_c(T) - E_m(T))\left(x_3/h + 1/2\right)^P + E_m(T) \\ \rho &= \rho\left(x_3,T\right) = (\rho_c(T) - \rho_m(T))\left(x_3/h + 1/2\right)^P + \rho_m(T) \\ \alpha &= \alpha\left(x_3,T\right) = (\alpha_c(T) - \alpha_m(T))\left(x_3/h + 1/2\right)^P + \alpha_m(T) \\ \nu &= \nu\left(x_3,T\right) = (\nu_c(T) - \nu_m(T))\left(x_3/h + 1/2\right)^P + \nu_m(T) \end{aligned} \quad (1)$$

Where E, ρ, α and ν denote the modulus of elasticity, density, thermal expansion coefficient and Poisson ratio of FGP, where subscripts m and c refer to the pure metal and pure ceramic plate respectively. FGP's Material properties can be expressed as a nonlinear function of temperature, see reference [12], as

$$P\left(T\right) = P_0(P_{-1}T^{-1} + 1 + P_1T + P_2T^2 + P_3T^3) \quad (2)$$

in which P denotes a generic material property and $T = T_0 + \Delta T(x_3)$ indicates the environmental temperature; $T_0 = 300(K)$ is room temperature; P_{-1}, P_0, P_1, P_2 and P_3 are the coefficients of temperature dependent material properties and unique to the constituent materials, also $\Delta T(x_3)$ is temperature rise only through the thickness direction, whereas, thermal conductivity k is temperature independent. Temperature-dependent typical values for some FGP material components such as silicon nitride and stainless steel are tabulated in Table 1 (from Ref. [11]).

Elastic equations.

Second order displacement field:

The displacement field based on second order shear deformation theory (SSDT) can be represented by [7]

$$u_1 = u + x_3\phi_1 + x_3^2\phi_2, \quad u_2 = v + x_3\psi_1 + x_3^2\psi_2, \quad u_3 = w \tag{3}$$

where (u_1, u_2, u_3) denote the displacement components in the (x_1, x_2, x_3) directions respectively; (u, v, w) define the displacements of a point on the mid plane $(x_1, x_2, 0)$; $(\phi_1, \phi_2, \psi_1, \psi_2)$ are the rotations of a transverse normal about the x_2, x_1. All of displacement components $(u, v, w, \phi_1, \phi_2, \psi_1, \psi_2)$ are functions of position (x_1, x_2) and time t.

Stress-Strain relations

The stress-strain relation of plates is [7; 10]

$$\begin{Bmatrix} \sigma_{11} \\ \sigma_{22} \\ \sigma_{23} \\ \sigma_{13} \\ \sigma_{12} \end{Bmatrix} = \begin{Bmatrix} q_{11} & q_{12} & 0 & 0 & 0 \\ q_{12} & q_{22} & 0 & 0 & 0 \\ 0 & 0 & q_{44} & 0 & 0 \\ 0 & 0 & 0 & q_{55} & 0 \\ 0 & 0 & 0 & 0 & q_{66} \end{Bmatrix} \begin{Bmatrix} \varepsilon_{11} \\ \varepsilon_{22} \\ \varepsilon_{23} \\ \varepsilon_{13} \\ \varepsilon_{12} \end{Bmatrix} \tag{4}$$

where q_{ij} are functions of position and temperature as follows

$$q_{11} = q_{22} = \frac{E(x_3, T)}{1 - \nu^2(x_3, T)} \quad q_{12} = \nu(x_3, T) q_{11} \quad q_{44} = q_{55} = q_{66} = \frac{E(x_3, T)}{2(1 + \nu(x_3, T))} \tag{5}$$

Thermal Conditions. For FGP, the temperature variation are assumed occurs in the thickness direction only and one-dimensional temperature field is considered to be constant in the plane of the plate. Following this, linear and non-linear temperature conditions have been applied.

Linear Temperature. Assuming the temperature T_b and T_t are imposed at the bottom and top of the plate, the temperature field under linear temperature rise along the thickness can be obtained as

$$T(x_3) = T_0 + T_b + \Delta T\left(\frac{x_3}{h} + \frac{1}{2}\right) \tag{6}$$

where $\Delta T = T_t - T_b$ is the temperature gradient of top and bottom surfaces.

Nonlinear Temperature. By imposing boundary condition of $T = T_0 + T_t$ at $x_3 = \frac{h}{2}$ and $T = T_0 + T_b$ at $x_3 = -\frac{h}{2}$ and solving steady-state heat transfer equation (7), the temperature distribution along the thickness can be obtained

$$\frac{-d}{dx_3}[k(x_3)\frac{dT}{dx}]=0 \tag{7}$$

$$T(x_3)=T_0+T_b-(T_t-T_b)(\frac{\int_{-h/2}^{x_3}\frac{1}{k(x_3)}dx_3}{\int_{-h/2}^{h/2}\frac{1}{k(x_3)}dx_3}) \tag{8}$$

where the thermal conductivity $k(x_3)$ is assumed to be independent to the temperature.

Equations of motion. The Hamilton's principle for an elastic body can be represented, if K, U and V are the kinetic, strain and potential energies of the body, respectively

$$\int_{t_1}^{t_2}\left(\delta K-\delta(U+V)\right)dt=0 \tag{9}$$

the inertias are also defined by

$$I_i=\int_{\frac{-h}{2}}^{\frac{h}{2}}\rho_0\left(x_3\right)^i dx_3 \qquad \left(i=0,1,2,...,6\right) \tag{10}$$

Applying equation (9) and (3) by considering SSDT leads to complete form of the equilibrium equations:

$$\frac{\partial N_{11}}{\partial x_1}+\frac{\partial N_{12}}{\partial x_2}+A_{11}^T\frac{\partial^2 u}{\partial x_1^2}+B_{11}^T\frac{\partial^2\phi_1}{\partial x_1^2}+D_{11}^T\frac{\partial^2\phi_2}{\partial x_1^2}+A_{22}^T\frac{\partial^2 u}{\partial x_2^2}+B_{22}^T\frac{\partial^2\phi_1}{\partial x_2^2}+D_{22}^T\frac{\partial^2\phi_2}{\partial x_2^2}=I_0\ddot{u}+I_2\ddot{\phi}_2+I_1\ddot{\phi}_1 \tag{11a}$$

$$\frac{\partial N_{22}}{\partial x_2}+\frac{\partial N_{12}}{\partial x_1}+A_{11}^T\frac{\partial^2 v}{\partial x_1^2}+B_{11}^T\frac{\partial^2\psi_1}{\partial x_1^2}+D_{11}^T\frac{\partial^2\psi_2}{\partial x_1^2}+A_{22}^T\frac{\partial^2 v}{\partial x_2^2}+B_{22}^T\frac{\partial^2\psi_1}{\partial x_2^2}+D_{22}^T\frac{\partial^2\psi_2}{\partial x_2^2}=I_0\ddot{v}+I_2\ddot{\psi}_2+I_1\ddot{\psi}_1 \tag{11b}$$

$$\frac{\partial Q_{13}}{\partial x_1}+\frac{\partial Q_{23}}{\partial x_2}-A_{11}^T\frac{\partial^2 w}{\partial x_1^2}-A_{22}^T\frac{\partial^2 w}{\partial x_2^2}=I_0\ddot{w} \tag{11c}$$

$$\frac{\partial M_{11}}{\partial x_1}+\frac{\partial M_{12}}{\partial x_2}-Q_{13}-B_{11}^T\frac{\partial^2 u}{\partial x_1^2}-D_{11}^T\frac{\partial^2\phi_1}{\partial x_1^2}-E_{11}^T\frac{\partial^2\phi_2}{\partial x_1^2}-B_{22}^T\frac{\partial^2 u}{\partial x_2^2}-D_{22}^T\frac{\partial^2\phi_1}{\partial x_2^2}-E_{22}^T\frac{\partial^2\phi_2}{\partial x_2^2}=I_2\ddot{\phi}_1+I_1\ddot{u}+I_3\ddot{\phi}_2 \tag{11d}$$

$$\frac{\partial L_{11}}{\partial x_1}+\frac{\partial L_{12}}{\partial x_2}-2R_{13}-D_{11}^T\frac{\partial^2 u}{\partial x_1^2}-E_{11}^T\frac{\partial^2\phi_1}{\partial x_1^2}-F_{11}^T\frac{\partial^2\phi_2}{\partial x_1^2}-D_{22}^T\frac{\partial^2 u}{\partial x_2^2}-E_{22}^T\frac{\partial^2\phi_1}{\partial x_2^2}-F_{22}^T\frac{\partial^2\phi_2}{\partial x_2^2}=I_2\ddot{u}+I_4\ddot{\phi}_2+I_3\ddot{\phi}_1 \tag{11e}$$

$$\frac{\partial M_{22}}{\partial x_2}+\frac{\partial M_{12}}{\partial x_1}-Q_{23}-B_{11}^T\frac{\partial^2 v}{\partial x_1^2}-D_{11}^T\frac{\partial^2\psi_1}{\partial x_1^2}-E_{11}^T\frac{\partial^2\psi_2}{\partial x_1^2}-B_{22}^T\frac{\partial^2 v}{\partial x_2^2}-D_{22}^T\frac{\partial^2\psi_1}{\partial x_2^2}-E_{22}^T\frac{\partial^2\psi_2}{\partial x_2^2}=I_2\ddot{\psi}_1+I_1\ddot{v}+I_3\ddot{\psi}_2 \tag{11f}$$

$$\frac{\partial L_{22}}{\partial x_2}+\frac{\partial L_{12}}{\partial x_1}-2R_{23}-D_{11}^T\frac{\partial^2 v}{\partial x_1^2}-E_{11}^T\frac{\partial^2\psi_1}{\partial x_1^2}-F_{11}^T\frac{\partial^2\psi_2}{\partial x_1^2}-D_{22}^T\frac{\partial^2 v}{\partial x_2^2}-E_{22}^T\frac{\partial^2\psi_1}{\partial x_2^2}-F_{22}^T\frac{\partial^2\psi_2}{\partial x_2^2}=I_2\ddot{v}+I_4\ddot{\psi}_2+I_3\ddot{\psi}_1 \tag{11g}$$

where N, M, L, Q and R are the stress resultants, $A_{ij}, B_{ij}, D_{ij}, E_{ij}$ *and* F_{ij} are plate stiffness and $A_{ii}^T, B_{ii}^T, D_{ii}^T, E_{ii}^T$ *and* F_{ii}^T are the plate temperature stiffness.

Method of solution. The boundary conditions are considered simply supported. Based on Navier's method with simply supported boundary condition the displacement fields are expressed as

$$u,\phi_1,\phi_2=\sum_{n=1}^{\infty}\sum_{m=1}^{\infty}[u_{mn}(t),\phi_{1mn}(t),\phi_{2mn}(t)]\cos\alpha x_1\sin\beta x_2 \quad ,u_{mn}(t),\phi_{1mn}(t),\phi_{2mn}(t)=(U,\Phi_1,\Phi_2)e^{-i\omega t}$$

$$\nu,\psi_1,\psi_2 = \sum_{n=1}^{\infty}\sum_{m=1}^{\infty}[\nu_{mn}(t),\psi_{1mn}(t),\psi_{2mn}(t)]\sin\alpha x_1\cos\beta x_2 \quad ,\nu_{mn}(t),\psi_{1mn}(t),\psi_{2mn}(t) = (V,\Psi_1,\Psi_2)e^{-i\omega t}$$

$$w = \sum_{n=1}^{\infty}\sum_{m=1}^{\infty} w_{mn}(t)\sin\alpha x_1\sin\beta x_2 \quad ,w_{mn}(t) = We^{-i\omega t} \tag{12}$$

where ω is natural frequency and

$$\alpha = \frac{m\pi}{a} \quad ,\beta = \frac{n\pi}{b}$$

Substituting the displacement fields (12) into equations of motion (11), the following frequency equation is obtained

$$[C]\begin{Bmatrix} U \\ V \\ W \\ \Phi_1 \\ \Phi_2 \\ \psi_1 \\ \psi_2 \end{Bmatrix} - \omega^2[M]\begin{Bmatrix} U \\ V \\ W \\ \Phi_1 \\ \Phi_2 \\ \psi_1 \\ \psi_2 \end{Bmatrix} = \begin{Bmatrix} 0 \\ 0 \\ 0 \\ 0 \\ 0 \\ 0 \\ 0 \end{Bmatrix} \tag{13}$$

where [C] and [M] are defined stiffness and mass matrix. By solving eigen-value problem the FGP's natural frequency and its corresponding mode shape can be derived.

Results

The results for temperature dependent FGP that obtain by applying SSDT in this study are compared with the results obtained by using higher order shear deformation theory in Ref. [5]. The close agreements between the present results and those of the referenced solutions are shown in Table 1.

Table 1: Non-dimensional natural frequency ($\bar{\omega} = \omega h\sqrt{\frac{\rho_m}{E_m}}$) of a simply supported square (Ti/Zro2) FG Plate, thickness-to-side is: $h/a = 0.2$

Mode (1,1) Natural frequency of FGP (ZrO2 and Ti-6Al-4V)		$T_b = 300k$ $T_t = 300k$	$T_b = 300k$ $T_t = 400k$ *Temperature dependent*	$T_b = 300k$ $T_t = 400k$ *Temperature independent*
ZrO2	Present	8.333	7.614	7.892
	Ref.[5]	8.273	7.868	8.122
p=0.5	Present	7.156	6.651	6.844
	Ref.[5]	7.139	6.876	7.154
p=1	Present	6.700	6.281	6.446
	Ref.[5]	6.657	6.437	6.592
p=2	Present	6.333	5.992	6.132
	Ref.[5]	6.286	6.101	6.238
Ti-6Al-4V	Present	5.439	5.103	5.333
	Ref.[5]	5.400	5.322	5.389

Figures 2-3 show the first four frequencies versus linear and nonlinear temperature fields in simply supported FGP. As expected, the decrease of Young's modulus with rising temperatures leads to the

frequencies decreasing with increasing temperature. The decreasing slope of frequencies in higher modes is greater than those in smaller modes. It can be explained in that the decreasing slope frequency in linear thermal loads is almost the same in Non-linear thermal load.

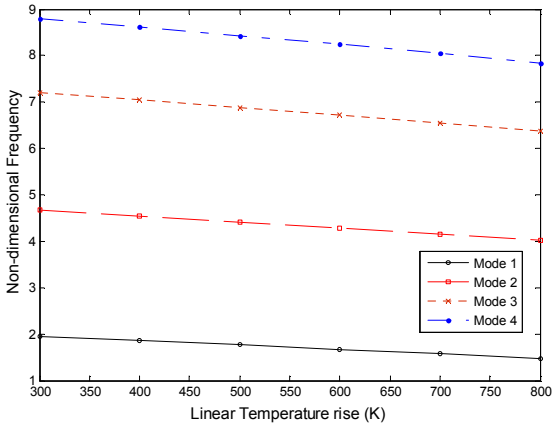


Fig2: First four Non-dimensional frequency parameters versus linear temperature field for simply supported (ZrO2/Ti-6Al-4V) FGP when *a/ h=10* and a=0.2, *p=1*.

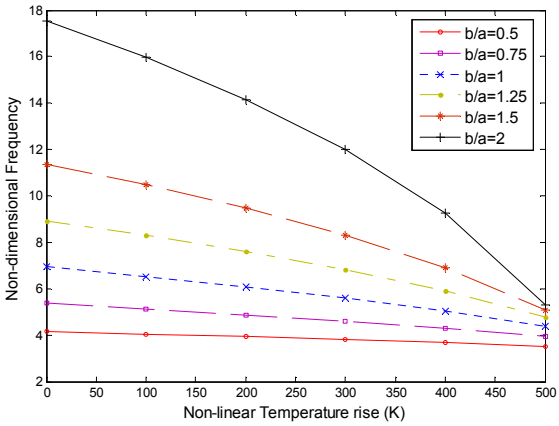


Fig3: First four Non-dimensional frequency parameters versus Non-linear temperature field for simply supported (ZrO2/Ti-6Al-4V) FGP when *a/ h=10* and a=0.2, *p=1*.

Summary

Temperature-dependent free vibration of functionally graded plates subjected to linear and nonlinear temperature fields are investigated by using an analytical approach (Navier's Method) for simply supported boundary condition. The formulations are based on the second-order shear deformation theory (SSDT) to account for transverse shear effects through the thickness. Material properties of FGPs are assumed to be temperature-dependent and vary along the thickness by a power-law distribution in terms of the volume fractions of constituents. The results are validated by comparing them with the published results and they are in a good agreement. Free vibration is at the maximum for pure ceramic, minimum for pure metal, and degrades gradually as the volume fraction index (p) increases and decreases as temperature change (T) increases in types of temperature fields. It is noted that the frequencies of FGPs with higher grading index are more sensitive to the temperature rise than those for other grading index.

Acknowledgment

The authors would like to thank to Universiti Putra Malaysia for providing the research grant (FRGS 07-10-07-398SFR 5523398) for this research work.

References

[1] G. Praveen, and J. Reddy, Nonlinear transient thermoelastic analysis of functionally graded ceramic-metal plates. International Journal of Solids and Structures 35 (1998) 4457-4476.

[2] K. Shukla, Nonlinear static and dynamic analysis of functionally graded plates Int. J. of Appl. Mech. and Eng. 11 (2006) 679-698.

[3] X. Zhao, Y. Lee, and K. Liew, Free vibration analysis of functionally graded plates using the element-free kp-Ritz method. Journal of Sound and Vibration 319 (2009) 918-939.

[4] A. Ferreira, R. Batra, C. Roque, L. Qian, and R. Jorge, Natural frequencies of functionally graded plates by a meshless method. Composite Structures 75 (2006) 593-600.

[5] X. Huang, and H. Shen, Nonlinear vibration and dynamic response of functionally graded plates in thermal environments. International Journal of Solids and Structures 41 (2004) 2403-2427.

[6] H. Matsunaga, Thermal buckling of functionally graded plates according to a 2D higher-order deformation theory. Composite Structures 90 (2009) 76-86.

[7] A. Khdeir, and J. Reddy, Free vibrations of laminated composite plates using second-order shear deformation theory. Computers & Structures 71 (1999) 617-626.

[8] A.R. Saidi, and S. Sahraee, Axisymmetric solutions of functionally graded circular and annular plates using second-order shear deformation plate theory, Proceedings of 8th Biennial ASME Conference on Engineering Systems Design and Analysis, ESDA2006, 2006.

[9] A. Shahrjerdi, M. Bayat, F. Mustapha, S.M. Sapuan, F. Mustapha, and R. Zahari, Free Vibration Analysis of Functionally Graded Quadrangle Plates Using Second Order Shear Deformation Theory. Australian Journal of Basic and Applied Sciences 3 (2009).

[10] A. shahrjerdi, M. Bayat, F. Mustapha, S.M. sapuan, and R. Zahari, Second Order Shear Deformation Theory to Analyze Stress Distribution for Solar Functionally Graded Plates. Mech. Based Des. Struct. Mach.

In press (2010).

[11] Y. Kim, Temperature dependent vibration analysis of functionally graded rectangular plates. Journal of Sound and Vibration 284 (2005) 531-549.

[12] J. Yang, and H. Shen, Vibration characteristics and transient response of shear-deformable functionally graded plates in thermal environments. Journal of Sound and Vibration 255 (2002) 579-602.

© (2011) Trans Tech Publications, Switzerland
doi:10.4028/www.scientific.net/KEM.471-472.140

Optimal Sintering Procedure to Fabrication of Functionally Graded Hydroxyapatite-Titanium

Ali Shahrjerdi[1, 2, a], F. Mustapha [3,b], S.M. Sapuan[1, c], M. Bayat[4, d], D.L.A. Majid [3,e] and R.Zahari[3,f]

[1]Department of Mechanical and manufacturing Engineering, Universiti Putra Malaysia, 43400, Selangor, Malaysia

[2]Department of Mechanical Engineering, University of Malayer, Iran

[3]Department of Aerospace Engineering, Universiti Putra Malaysia, 43400, Selangor, Malaysia

[4]Department of Civil Engineering, Aalborg University, 9000 Aalborg, DK

[a]ailshahrjerdi2000@yahoo.com, [b]faizal@eng.upm.edu.my, [c]sapuan@eng.upm.edu.my, [d]meb@civil.aau.dk

Keywords: Hydroxyapatite-Titanium, FGM, Sintering, Pressure-less method

Abstract. Functionally graded metal-ceramic composite was fabricated by pressure-less sintering. The pure metallic component (Ti) and the pure ceramic component (HA) were located at the ends of a cylindrical specimen. Titanium and-Hydroxyapatite were utilized as a metallic and ceramic layer. The target sample thickness was 6 mm with radius cylindrical 20 mm. The sample was made from the cylindrical type of carbon die consisting of 5 layers. The composition of layers were 100%Titanium; 75 % Titanium +25% HA; 50% Titanium +50% HA; 25% Titanium+75% HA, and 100% Hydroxyapatite. The optimum thermal load mapping was obtained experimentally. The properties of all FGM products were characterized by shrinkage, optical-microscope, energy dispersive spectrometry (EDX) scanning electron microscope (SEM). The grade of the FGM material was proven by comparing amount of shrinkage after sintering. Result from optical micrograph, SEM and EDX indicated that the HA-Ti FGM could be produced successfully by using the optimal sintering procedure that was highlighted in this paper.

Introduction

Functionally graded materials (FGMs) usually are composed of a ceramic and a metal at which the volume fraction of the two materials is varied. Functionally graded materials (FGMs) are those, in which the volume fraction of the two or more materials is varied, according to a power-law distribution as a function of position along certain dimension (s) of the structure [1].

Bio-medical applications are new field to FGMs as an implant and artificial parts of body [2]. Human body is supported by 206 bones and each of them directly or indirectly affects our brain and other organs. Efforts of researchers are established to find a new material that can work as replacement for bones. Several different physical and chemical methods depending on type of materials and facilities are used to fabricate FGMs [3]. A best-fit single method to fabricate of FGM is difficult to define due to each method has its own advantages and drawbacks. HA and Ti are two important materials that have been investigated in some studies as FG materials [4; 5] . Due to their advantages in biomedical, mechanical and biocompatibility properties of FG produced, some studies have been reported [6]. The effect of Ti additions through the composition, microstructure, thermal stability and the bonding strength of HA/Ti coating using hydrothermal–electrochemical technique was investigated by Xiao et al. [7]. Fabrication of HA/Ti as a FG dental implant using CIP and sintering method was experimented by Watari et al. [8] to ensure both mechanical and biocompatible properties. Chenglin et al. [4] developed a FG biomaterial in a HA/Ti system by an optimized powder metallurgical method. They successfully investigated micro-structural analysis and mechanical tests of the produced FGMs. Chu et al. [5] examined the fabrication of FG

biomaterial HA/Ti by a hot-pressing technique, they [9] also developed and fabricated FG biomaterial HA/Ti by adopting of the best mixing of their biocompatibility and mechanical properties. Some porosity reduction and sintering models using pressure-less sintering method was investigated by Pines and Bruck [10; 11]. The present work focuses on pressure-less sintering method for fabrication of HA/Ti functionally graded materials. The thermal map is optimized experimentally and the some physical effects of powders are discussed. Microstructure and properties of FG samples are evaluated and the gradation of HA/Ti FG cylinder is proven by some examinations.

Material and Method

HA (SIGMA-ALDRICH, USA) and Ti (SIGMA-ALDRICH, USA) powders are used here as a ceramic and metallic for the fabrication of FG plate. HA is a biomechanical and cohesive material having close melting point to Ti. The combination can be an excellent replacement component as a hard tissue in human body. The maximum difference in the melting points for components in cold pressing method should be small. It is noted that in order to have a good quality of FG structure, it needs at least five layers. The best composition (in %weight) of layers have been selected as 100% pure Titanium; 75% Titanium+25% HA; 50% Titanium+50% HA; 25% Titanium+75% HP; 100% pure HA. The details of the material can be observed in Figure.1. The powders should be blended separately for at least 1 hour and together for 5 hours to ensure the maximum dispersion of particles and can reach to the optimal physical properties. It is noted that the ball milling process the powders need to dried in an oven at 110°C for approximately 12 hours. This procedure is necessary in order to have a dry mixture without any moisture. During cold pressing procedure, the green compact is created using cylindrical type of carbon die with a diameter of 20 mm. It consists of 5 layers with the same thickness for all of the layers except the top and the bottom layers. In the fabrication process, the compositions are compacted at 10 (Ton) using uni-axial hydraulic press to make a green compact. The last step in the fabrication process, green compacts are sintered inside the tube furnace under flowing mixed argon as to prevent oxidation. The heating map depends on the melting points of the powders.The heating map is obtained by trial-and-error approach, as to have appropriate product and optimimal sintering map (see Fig.2). The temperature is increased from 30°C to 1200°C during 8 hours. The adhering of each layer to others is directly related to the maximum selected temperature during sintering. Beside the thermal specification as mention above; another two parameters, position and direction of the green compact inside the furnace are important. The best position for the green compact is at the middle of furnace. It is recommended that, the heavier component should be at the upper surface.

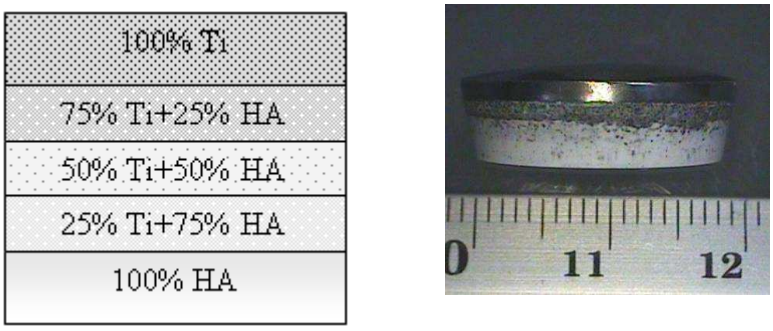


Fig. 1: composition (in %weight) of functionally graded HA/Ti layers

Result and Discussion

The gradation of the FG HA-Ti is proven by using shrinkage measurement. Linear shrinkage is one of the parameter needed evaluating the quality of the gradation of the component in the FG samples, the process can be calculated by accurately measuring of the green compact and then comparing with the size of the sample after sintering as shown in Figure 3. It is clear that, the linear variations of Ti to volumetric HA by scanning electron-microscope (SEM) for thickness and also for each layer individually (Figs.4). Figure 5 record the chemical component from full Ti and 75% HA by EDX examination. The percentage of Calcium that indicates the HA is decreased from Fig. 5a gradually in to full percentage of Ti in Fig.5b

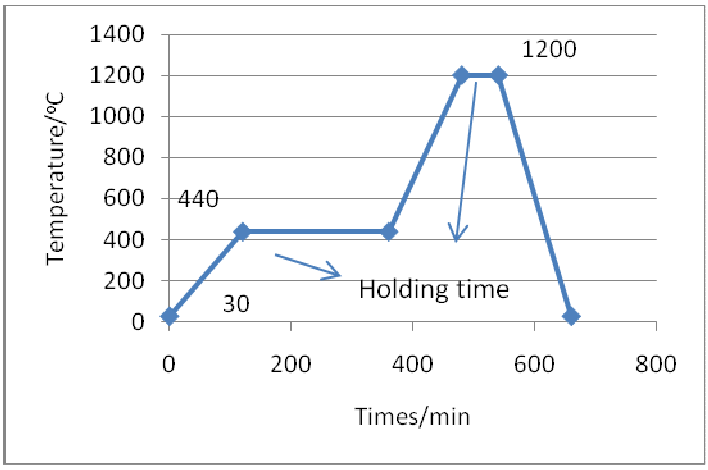


Fig.2: Optimal sintering map

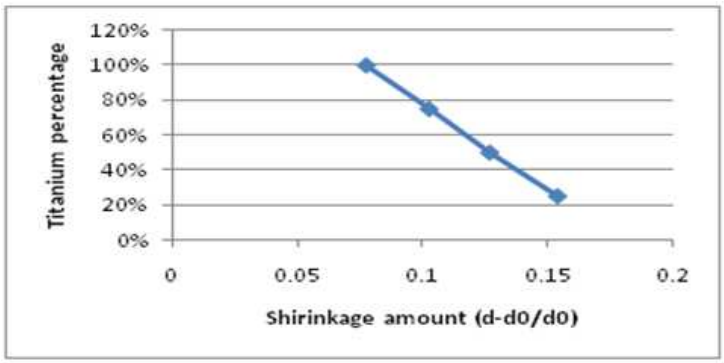


Fig.3: Titanium percentage against shrinkage amount

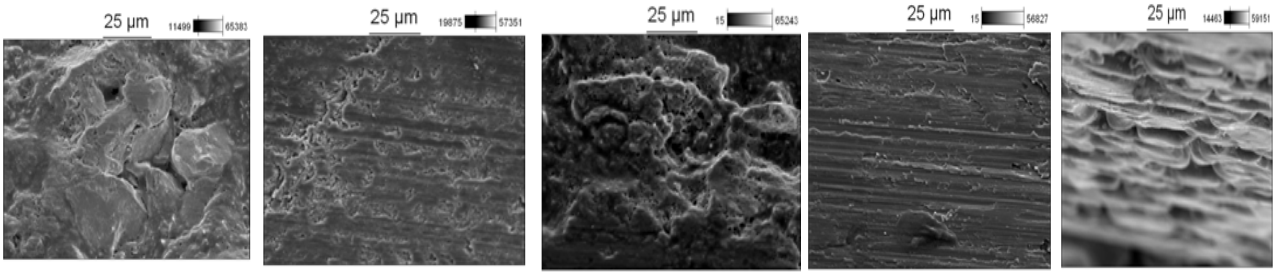


Fig.4: Digital SEM image of HA/Ti
SEM image of layers in experiments (Accelerating Voltage: 15.0 kV Magnification: 1000)

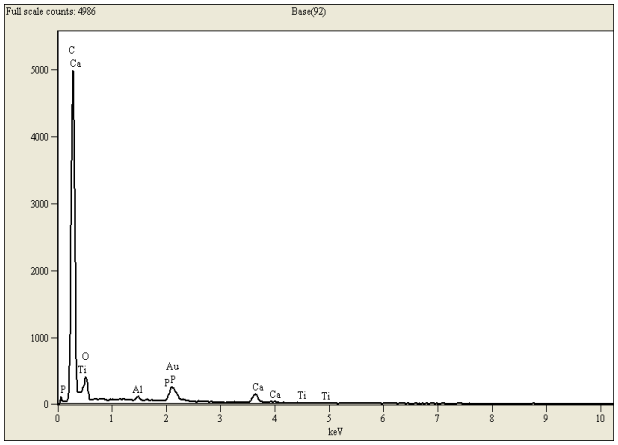


Fig. 5(a)

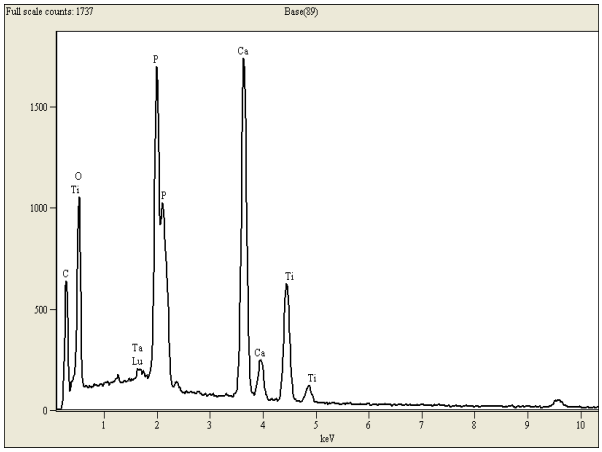


Fig 5(b)

Fig.5(a) and Fig. 5(b): EDX examination for full Ti and 75% HA+25% Ti

Summary

An optimum heat sintering map with Pressure-less powder metallurgy procedure is presented to fabricate the HA/Ti functionally graded (FG) cylinder. The gradation of components are considered from metallic (Ti) end to its ceramic (HA) end. Optimum sintering map has been derived experimentally. To validate the shrinkage study, SEM and EDX examination are employed. The structure and composition analysis of the FG cylindrical produced with different layers conforms the functionality of the design. The linear shrinkage obtained is an appropriate witness of validation.

Acknowledgment

The authors would like to thank to Universiti Putra Malaysia for providing the research grant (FRGS 07-10-07-398SFR 5523398) for this research work.

References

[1] S. Suresh, and A. Mortensen, Fundamentals of functionally graded materials: processing and thermomechanical behaviour of graded metals and metal-ceramic composites, IOM Communications Ltd, 1998.

[2] F. Watari, A. Yokoyama, M. Omori, T. Hirai, H. Kondo, M. Uo, and T. Kawasaki, Biocompatibility of materials and development to functionally graded implant for bio-medical application. Composites Science and Technology 64 (2004) 893-908.

[3] M. Schwartz, Encyclopedia of Smart Materials: smart materials, Wiley-Interscience, 2002.

[4] C. Chenglin, Z. Jingchuan, Y. Zhongda, and W. Shidong, Hydroxyapatite-Ti functionally graded biomaterial fabricated by powder metallurgy. Materials Science and Engineering: A 271 (1999) 95-100.

[5] C. Chu, J. Zhu, Z. Yin, and P. Lin, Structure optimization and properties of hydroxyapatite-Ti symmetrical functionally graded biomaterial. Materials Science and Engineering A 316 (2001) 205-210.

[6] H. Kondo, A. Yokoyama, M. Omori, A. Ohkubo, T. Hirai, F. Watari, M. Uo, and T. Kawasaki, Fabrication of titanium nitride/apatite functionally graded implants by spark plasma sintering. Mater Trans 45 (2004) 3156-3162.

[7] X. Xiao, R. Liu, and Y. Zheng, Hydoxyapatite/titanium composite coating prepared by hydrothermal-electrochemical technique. Materials Letters 59 (2005) 1660-1664.

[8] F. Watari, A. Yokoyama, F. Saso, M. Uo, and T. Kawasaki, Fabrication and properties of functionally graded dental implant. Composites Part B: Engineering 28 (1997) 5-11.

[9] C. Chu, J. Zhu, Z. Yin, and P. Lin, Optimal design and fabrication of hydroxyapatite-Ti asymmetrical functionally graded biomaterial. Materials Science and Engineering A 348 (2003) 244-250.

[10] M. Pines, and H. Bruck, Pressureless sintering of particle-reinforced metal-ceramic composites for functionally graded materials: Part I. Porosity reduction models. Acta materialia 54 (2006) 1457-1465.

[11] M. Pines, and H. Bruck, Pressureless sintering of particle-reinforced metal# 8211ceramic composites for functionally graded materials: Part II. Sintering model. Acta materialia 54 (2006) 1467-1474.

© (2011) Trans Tech Publications, Switzerland
doi:10.4028/www.scientific.net/KEM.471-472.145

Processing and Characterization of Palm Fiber-Polypropylene Composites

Ramazan Kahraman[1,a], Sarfraz Abbasi[2,b] and Basel Abu-Sharkh[2,c]

[1]Department of Chemical Engineering, Qatar University, P.O. Box 2713, Doha, Qatar.

[2]Department of Chemical Engineering, King Fahd University of Petroleum & Minerals, Dhahran 31261, Saudi Arabia.

[a] ramazank@qu.edu.qa , [b] shabbasi@kfupm.edu.sa , [c] sharkh@kfupm.edu.sa

Keywords: Cellulose, Palm, Polypropylene, Composites, Processing.

Abstract: Composites of palm fiber and polypropylene were compounded using a mixing device at various temperatures, mixing times, and mixing intensities. Two mixing options were utilized. Either the mixing device was mounted with a mixer or a single screw extruder. The composites were subsequently injection molded into standard tensile specimens for mechanical characterization. Tests were performed to determine the effects of processing parameters such as the mixing and molding temperatures, mixing speed, and mixing time on the mechanical performance of the palm-polypropylene composite. The optimum processing conditions for the mixer were determined to be: Mixing Speed = 50 rpm, Mixing Time = 8 min, and Processing Temperature = 200°C. Optimum extruder conditions, on the other hand, were determined as 40 rpm extruder screw speed and processing temperatures of Zone 1=195°C, Zone 2=200°C, Zone 3=205°C, and Nozzle 210°C. Use of the extruder resulted in higher composite strength with much shorter processing time. Further studies are also being conducted to include coupling agents in the processing to improve the interfacial adhesion between the palm fibers and the polypropylene matrix.

Introduction

Natural fibers are now increasingly used for the reinforcement of plastics along with traditional fibers. In the production of natural fiber reinforced plastic parts by injection molding, the mechanical properties of the material can be specifically improved [1]. It has been reported that, in the building community, there is a growing demand for high-performance, low-maintenance, and low-cost building components [2]. To meet this demand, natural fiber-thermoplastic composites are being used to produce such products as decking, window and door elements, panels, roofing, and siding. There has also been a rapid growth in the extrusion business with the use of wood-filled compounds for buildings and construction. The better provision for longevity, appearance, life-cycle cost and value makes wood-plastics composites popular in use in the markets. The extruder composites can eliminate sizing and calibration. This is because the stiff extrudate can hold its shape much better than unfilled plastics. Engineered wood materials, i.e. wood-plastic composites are also being investigated for waterfront construction applications primarily because of their superior durability characteristics compared to wood [3].

There are many applications of wood fiber/plastic composite in everyday life. Wood fiber/polypropylene composite are used in cars behind the vinyl carpeting on the doors, consoles and seat backs. Many window and door manufacturers are looking at wood fiber/ plastic composites as an alternative to solid wood in clad components [4].

Recent research is directed towards using inexpensive and scrap materials as reinforcing materials in thermoplastics. Rozman et al. [5] have used coconut fibers in the formation of thermoplastic composites. Scrap shipping containers are used as source for wood filled plastic

composites [6]. Jute has also been reported in usage for the manufacture of thermoplastic composites [7]. Oil palm empty fruit bunch has also been used as a reinforcing material for polypropylene composite [8].

The processing temperature of the cellulosic fibers in thermoplastics is limited due to the potential fiber degradation at higher temperatures. This limits their application with plastics of low melting temperatures. However, it has been reported that no deterioration of properties was observed when processing temperatures are maintained below 200°C [6]. Fiber composites can withstand higher stresses than either of their individual constituents because the fibers and matrix interact and redistribute the stresses. The ability of these two constituents to exchange stresses depends critically on the effectiveness of the coupling or bonding between them [9].

It was the objective of this study to investigate the feasibility in terms of mechanical properties for utilizing wood fibers obtained from waste palm tree branches in reinforcing polypropylene. Palm trees are abundant in Saudi Arabia and polypropylene is locally produced by Saudi Basic Industries Corporation (SABIC). If shown to be feasible, the utilization of waste palm tree branches in reinforcing thermoplastics will be an economical and useful service to the environment and society.

Experimental

Materials. Polypropylene used in the study was supplied by SABIC. The brand name for it is LADENE PP570P. It is a homopolymer for producing rigid injection molded articles. It is particularly suited for molding house ware items.

Branches obtained from palm trees were cut into pieces about 15 cm long. Thereafter they were dried in the sun for a few days so that most moisture is removed. The pieces of branches were then granulated to a small size using a Granulator. The fibers were then size separated by using sieving machine. Two different size distributions of fibers (called large and small fibers) were used for study. The fiber size distributions were characterized using a digital vernier caliper. The lengths of the fibers were determined to be 4.77 ± 1.75 mm and 2.96 ± 1.19 mm for large and small fibers, respectively. They both had aspect ratio of about 11.

The fibers obtained were then cleaned to remove the organic compounds by using ethanol and toluene in the ratio of (1:2) (V/V). The mixture of these two chemicals was prepared in a large container. The fibers were then added to the mixture and kept in it for about two days. The fibers were then washed with water and put in an oven at 80°C to remove the moisture.

Composite Processing. Mixing of composite components was done by a Mixing Device (Brabender Measuring Head, Model S-650, No:G126). This equipment can either be mounted with a mixer or a single screw extruder. Both mixer and extruder were used. In both cases the fibers and the resin were first hand mixed in a bowl and then transferred to the mixer and the extruder. The conditions of mixing was varied in such a way to determine the optimum conditions that will produce samples with maximum dispersion of fibers, good mechanical properties, good color and smell. Details are given in the results section. The mixed composite thus obtained from the extruder had a lumpy shape. It was granulated and transferred into a molding machine (Engel Electronics Model ES 80/25 ST Pressure 160 bar, T = 200°C) to obtain tensile specimens of ASTM test standard No. D 638.

Material Characterization. The samples were mechanically characterized using an Instron 5560 Mechanical Testing Machine according to the ASTM test standard D 638-94b, Type 4. The tests were conducted at constant strain rate of 2 mm/min.

Results and Discussions

Initially the mixing process was performed using the mixer mounted on the mixing device. Tests were performed to determine the effects of processing parameters such as the mixing and molding temperatures, mixing speed, mixing time and fiber content on the mechanical performance of the palm-polypropylene composite.

Optimum mixing and molding temperature was determined to be about 200°C. If the composite was molded at temperatures above 200ºC, it was observed that the palm fibers in the composite burned. At temperatures below 200ºC, on the other hand, there was difficulty in melting polypropylene completely.

Fig. 1 shows the effect of mixing speed on the mechanical properties of palm-polypropylene composite. The highest strength of the composite was obtained at 50 rpm. Adequate wetting of the fiber with the polypropylene matrix may not be achieved when the mixing speed is below 50 rpm and the fibers are damaged at mixing speeds above 50 rpm. The other processing conditions were: Mixing Time: 8 minutes, Mixing Temperature: 200ºC, and Molding Temperature: 200ºC.

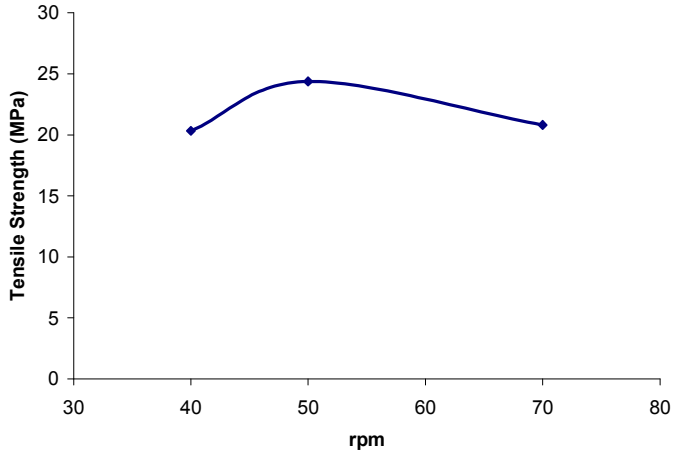


Fig. 1. Tensile strength of polypropylene with 30 wt% palm fiber versus mixing speed with a mixing time of 8 min at 200°C.

The effect of mixing time on tensile strength of the palm-polypropylene composite is presented in Fig. 2. It can be seen that composite strength drops at mixing times above 10 min which can probably be attributed to the fact that the mixing at 200ºC for too long causes the wood fibers to burn (the composite produced visually seemed burned as it was blackened). Mixing time could not be lowered below 8 min since it was taking about 7 min to melt the polypropylene matrix. The other processing conditions were: Fiber Content: 30 wt%, Mixing Speed: 50 rpm, Mixing Temperature: 200ºC, and Molding Temperature: 200ºC.

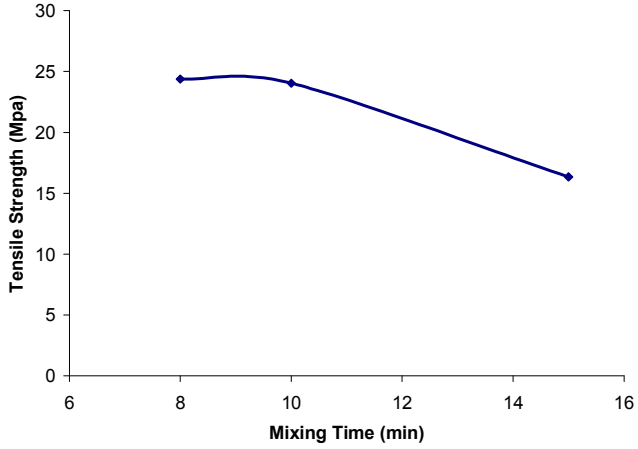


Fig. 2. Tensile strength of polypropylene with 30 wt% palm fiber versus mixing time with a mixing speed of 50 rpm at 200°C.

As a second option, an extruder was mounted on the mixing device, and similar tests were performed to see how the properties shall be affected by changing the mixing system.

The extruder had three zones and a nozzle. The temperature in the three zones and nozzle was: Zone 1 = 195°C, Zone 2 = 200°C, Zone 3 = 205°C, and Nozzle Temperature = 210°C. When the composite samples were extruded above 210ºC, as expected the palm fibers in the composite burned. On the other hand, any temperature less than 210ºC in the nozzle meant a subsequent drop in temperature in previous zone creating difficulties in melting polypropylene matrix. Moreover, higher stresses on the extruder screw at lower processing temperatures resulted in the breakage of the safety lock of the extruder.

Fig. 3 shows the effect of extruder screw speed on composite strength for 30 wt% fiber content. The other processing conditions were as just mentioned above. The slight increase in tensile strength with increase in mixing speed was not significant. The highest mixing speed possible was 40 rpm because higher speeds caused the safety lock on the mixing device to break. Hence 40 rpm was chosen as the processing speed for the extruder.

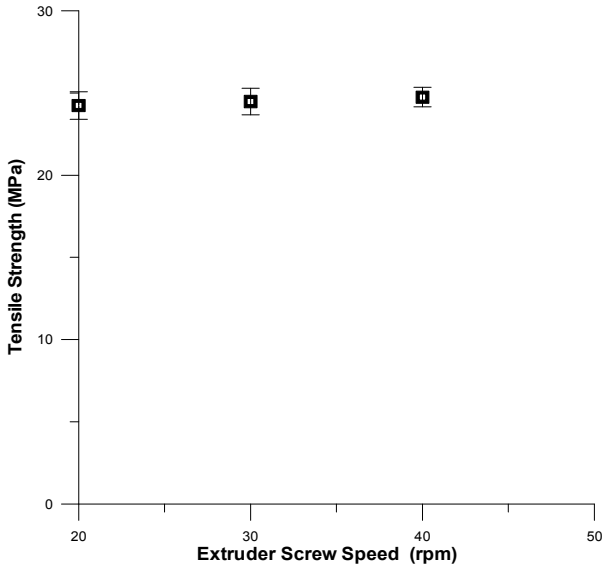


Fig. 3. Tensile strength of palm-polypropylene composite with 30 wt% fiber versus extruder screw speed at processing temperatures of Zone 1=195°C, Zone 2=200°C, Zone 3=205°C, and Nozzle=210°C.

Higher composite strength was achieved when the extruder was used (even though the difference was not so significant). This might be attributed to the fact that the fibers spend less time at a higher temperature in an extruder (2 min) than in the mixer (8 min). Moreover, cleaning of the mixer was quite troublesome. Therefore, use of the extruder was preferred for further studies.

Fig. 4 shows the effect of fiber size and content on the tensile modulus of palm-polypropylene composite. As seen the increase in fiber content increases the composite modulus for both small and large fiber which is an indication for the existence of adhesion to some extent between polypropylene and much stiffer palm fiber.

Fig. 5 shows the effect of fiber size and content on tensile strength of palm fiber-polypropylene composite. As the fiber content is increased the tensile strength decreases. This might be attributed to the poor adhesion between the fiber and polypropylene. This result does not contradict the improvement in composite stiffness with fiber addition shown in Fig. 4. The modulus is related to the stiffness of the material at small deformations (before fracture) and it is obtained from the slope of the straight portion of the stress-strain curve. Existence of adhesion (even weak) between fibers and the matrix would then improve composite modulus. However, composite tensile strength is a result of material fracture at the weakest point of the material, which might occur below the matrix strength if the adhesion between the fibers and the matrix fails at a lower stress.

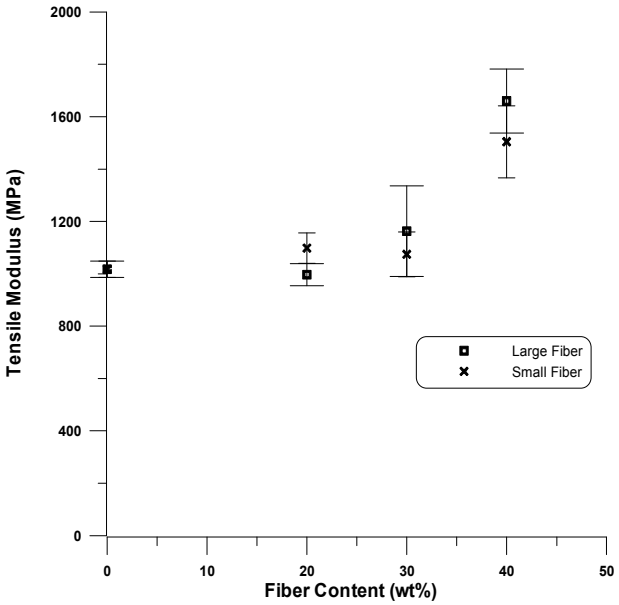


Fig. 4. Tensile modulus versus fiber content for polypropylene reinforced with small and large palm fiber.

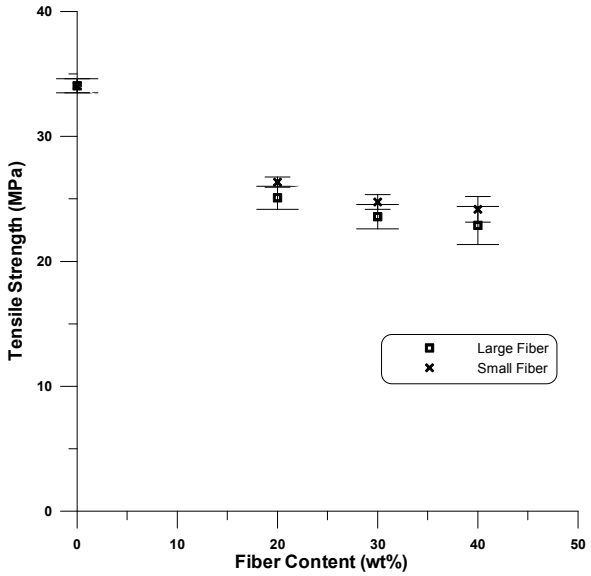


Fig. 5. Tensile strength versus fiber content for polypropylene reinforced with small and large palm fiber.

As also shown in Fig. 4 and 5, the difference in the results obtained with small or large fibers was not significant considering also the scatter in data. But still the composite strength with small fiber was observed to be consistently higher than that with large fibers while the same effect was not observed in the case of composite modulus. This was probably because of better mixing and more uniform distribution of small fibers in the polypropylene matrix as compared to large fibers. Accumulation or non uniform orientation of fibers at some parts of the composite can result in fracture at these weak points giving lower strength in the case of larger fibers. Non uniformities in fiber distribution here and there (if not so extensive) would not effect the composite modulus at the same extent since the modulus is the bulk material property before fracture.

The present work was extended to include utilization of a coupling agent such as maleated polypropylene to improve the interfacial adhesion between the palm fibers and the polypropylene matrix. Maleated (maleic-anhydride-modified) polypropylene has been particularly successful as a coupling agent in cellulose-polypropylene composites improving mechanical properties as a

consequence of enhanced interfacial adhesion [10-14]. It has been reported that [11] cellulose fibers treated with the copolymer turned totally hydrophobic due to the concentration of a considerable amount of copolymer on the fiber surfaces. The copolymer was bonded to the fibers by ester linkages and hydrogen bonds accounting for the adhesion in the system.

Summary

Optimum processing conditions for the mixer were determined to be: Mixing Speed = 50 rpm, Mixing Time = 8 min, and Processing Temperature = 200°C. On the other hand, optimum extruder conditions were 40 rpm extruder screw speed and processing temperatures of Zone 1=195°C, Zone 2=200°C, Zone 3=205°C, and Nozzle 210°C. Use of the extruder resulted in higher composite strength with much shorter processing time. As the fiber content increased the composite modulus also increased which is an indication for the existence of adhesion to some degree between polypropylene and much stiffer palm fiber. Composite tensile strength, on the other hand, decreased with fiber addition indicating an unsatisfactory interfacial adhesion between the cellulosic palm fibers and the polypropylene matrix, which might be improved by utilizing a compatibilizing agent.

Acknowledgments

This project has been funded by King Abdulaziz City for Science and Technology under Project # ARP 18-14. The authors also gratefully acknowledge the assistance of Qatar University and King Fahd University of Petroleum & Minerals in the performance of this work.

References

[1] A. Marek and H. Widdecke: Kunststoffe Plast Europe 91:1 (2001) 25-27.

[2] R. H. Falk, D. J. Vos, S. M. Cramer and B. W. English: Forest Products J. 51:1 (2001) 55-61.

[3] L. J. Malvar, D. E. Pendleton and R. Tichy: SAMPE J. 37:4 (2001) 70-75.

[4] J. A. Younguist: Forest Products J. 45:10 (1995) 25-30.

[5] H. D. Rozman, K. W. Tan, R. N. Kumar, A. Abubakar, H. Ismail and Z. A. M. Ishak: European Poly. J. 36 (2000) 1483-1494.

[6] N. M. Stark: Forest Products J. 49:10 (1999) 39-46.

[7] K. R. Harikumar, K. Joseph and S. Thomas: J. Reinforced Plast. and Compos. 18:4 (1999) 346-372.

[8] H. D. Rozman, G. S. Tay, R. N. Kumar, A. Abusamah, H. Ismail and Z. A. M. Ishak: European Poly. J. 37 (2001) 1283-1291.

[9] D. Quillin, M. Yin, J. A. Koutsky and D. F. Caulfield: J. Appl. Polym. Sci. 52 (1994) 605-615.

[10] J. M. Felix and P. Gatenholm: J. Appl. Polym. Sci. 50 (1993) 699-708.

[11] J. M. Felix, P. Gatenholm and H. P. Schreiber: Polym. Compos. 14:6 (1993) 449-457.

[12] M. M. Sain, B. V. Kokta and C. Imbert: Polym. Plast. Technol. Eng. 33:1 (1994) 89-104.

[13] A. R. Sanadi, D. F. Caulfield, R. E. Jacobson and R. M. Rowell: Ind. Eng. Chem. Res. 34 (1995) 1889-1896.

[14] R. Gauthier, C. Joly, A. C. Coupas, H. Gauthier and M. Escoubes: Poly. Compos. 19:3 (1998) 287.

© (2011) Trans Tech Publications, Switzerland
doi:10.4028/www.scientific.net/KEM.471-472.151

Effects of Antioxidants Content on the Physical and Mechanical Properties of Wood Plastic Composites

Mohd Hafizuddin Ab Ghani[1,a] and Sahrim Ahmad[1,b]

[1,2]Material Science Programme, School of Applied Physics

Faculty of Science and Technology, The National University of Malaysia

43600 Bangi, Malaysia.

[a]mr_merce7@yahoo.com, [b]sahrim@ukm.my

Keywords: Antioxidants, wood plastic composites, recycled HDPE

Abstract. We investigated the effects of amount of antioxidants variability on selected mechanical and physical properties of wood plastic composites. Recycled high density polyethylene (rHDPE) and natural fibers were compounded into pellets by compounder, then the pellets were extruded using co-rotating twin-screw extruder and test specimens were prepared by hot and cold press process. From the study, samples with 0.5 wt% of antioxidants produce the highest strength and elasticity of composites. The effect of antioxidants presence on water uptake is minimal.

Introduction

Wood Plastic Composites (WPC) is a biocomposites (biodegradable composites) group. Biocomposites are invented in response to recent significant changes in the patterns of materials research and development. It is now recognized that materials are often the limiting factor in bringing a new technical concept to fruition and that biocomposites are often the materials of choice in these demanding applications. A significant portion of the biocomposites material such as wood plastic composites ongoing in the world is directly or indirectly related to the solution of complex interdisciplinary problems whose successful resolution is necessary for achievement of broad system objectives.

Ecological concerns have resulted in a renewed interest in natural, renewable resources-based and compostable materials, and therefore issues such as materials elimination and environmental sustainability are becoming problems. According to L Avérous – 2006, biodegradable polymers can be considered as ‘‘solution to the matters’’ environmentally safe alternatives for the development of new biodegradable composites known as biocomposites [1].

In order to improve mechanical properties and to obtain the characteristics demanded usage of composites material products, nowadays various reinforcing fillers and binders are being prepared combined with various matrix polymers such as high density polypropylene (HDPE). The natural fillers are especially being sought after since the production of composites using natural substances as reinforcing fillers is not only inexpensive but also could minimize environmental pollution caused by the characteristic biodegradability so that these composites could play an important role in resolving environmental problems in the coming future [2].

Several studies were conducted to evaluate the performance of WPCs, most of them are focused on improving the compatibility between hydrophobic (non-polar) thermoplastics and hydrophilic (polar) wood flours. A few researches were conducted to study the thermal and morphological properties of WPCs [3,4]. Lu et al. [5] in their review of coupling and treatments classified the maleic anhydride grafted polyolefin as the most suitable chemicals for polyolefins.

According to A.A Klyosov – 2007, typically WPC are porous. The pores are formed by steam and by volatile organic compounds (VOC) during extrusion process. Presence of oxygen that flows into pores in WPC which is directly related to the decrease of density (specific gravity) of materials will attacks “from inside”, particularly at elevated temperatures. The attacks will cause oxidative degradation of WPC. This degradation is the most common reason for a premature mechanical failure in WPC. Oxidative degradation as a result of thermooxidation and photooxidation leads to

crumbling, surface becomes loose, powdery and weak. In order to prevent oxidative degradation, WPC commonly contain added antioxidants, typically in amounts between 0.05 and 0.15% by weight, and 0.2-0.5% for stabilization of regrinds. It significantly extends the lifetime of WPC compared to unprotected ones [6].

Methodology

Four variable percentages of antioxidants were investigated in this study: 0.0, 0.1, 0.3, and 0.5 wt%. The formulation of samples is shown in Table 1. The antioxidants were mixed between IRGANOX 1010 and IRGAFOS 168 as a ratio 1:1 (Ciba). The matrix is recycled high density polyethylene (rHDPE). The fillers are mixed between rice husk and saw dust (RePlas Sdn. Bhd.). Sawdust is essentially the same thing as wood flour except it is not ground but formed as a by-product of wood sawing. The rice husk can act as reinforcing fillers at certain optimum level of loading [7].

Table 1 Formulation of samples

Antioxidants [%]	HDPE [%]	Additive [%]	Fillers [%]	
			Rice Husk	Saw Dust
0.0	30	7.9	45	17.1
0.1	30	7.9	45	17.0
0.3	30	7.9	45	16.8
0.5	30	7.9	45	16.6

Samples were produced in two-stage processes. In the first stage, the materials were mixed in a high intensity mixer for 20 minutes to produce homogeneous blend. Then this homogeneous mixture was compounded in a laboratory scale co-rotating twin-screw extruder (Thermo Prism TSE 16PC) for better homogenization of the composite. Gravimetric feeding had been used to control materials fed into the extruder. The gravimetric feeding is preferred because of adequate feeding regardless of material shape or bulk density, improved product quality control, and material savings can be realized [8]. Barrel temperatures of the four zones were set as 165°C, 170°C, 175°C and 175°C from feeding to die zones. Screw speed was 80 rpm to reduce the fibres breaking. The extrudates were collected, cooled by left it at room temperature and granulated into pallets.

In the second stage, WPC test specimens were produced using hot and cold press processes (LP50, LABTECH Engineering Company LTD). Before that, WPC pellets were ground using grinder to make it fine to suit with the mold. The fine pellets were then put in the mold size 14 mm x 14 mm x 3 mm. The temperatures of the hot press were set 140°C for upper platen and lower platen respectively. The period of preheating, venting and full pressing were set 3, 2, 9 minutes respectively. The cold press was set 5 minutes to cool the specimens. The pressure used to press the specimens was set at 1000 psi for both hot and cold press. After finishing the molding processes, the specimens had been dried in oven for 24 hours with temperature 70°C in order to remove any moisture and stable the specimens. The specimens were then cut according to ASTM specifications for tensile (ASTM D 638-03), flexural (ASTM D 790-03), impact (ASTM D 256-05) and water absorption (ASTM D 570-98) testing. Water absorption was determined by the weight gain relative to the dry weight of the samples. The moisture content of a sample was computed as follows:

$$Mt = \frac{Wt - Wo}{Wo} \text{ x } 100\% \quad (1)$$

Where W_0 and W_t denote the dry weight of the sample and the weight at any specific time t, respectively. The morphology of the fractured surface of sample was observed under the JEOL JSM 6400 Scanning Electron Microscope (SEM), Philip Model XL30 ESEM. The summary of the methodology is shown below.

Flow Chart

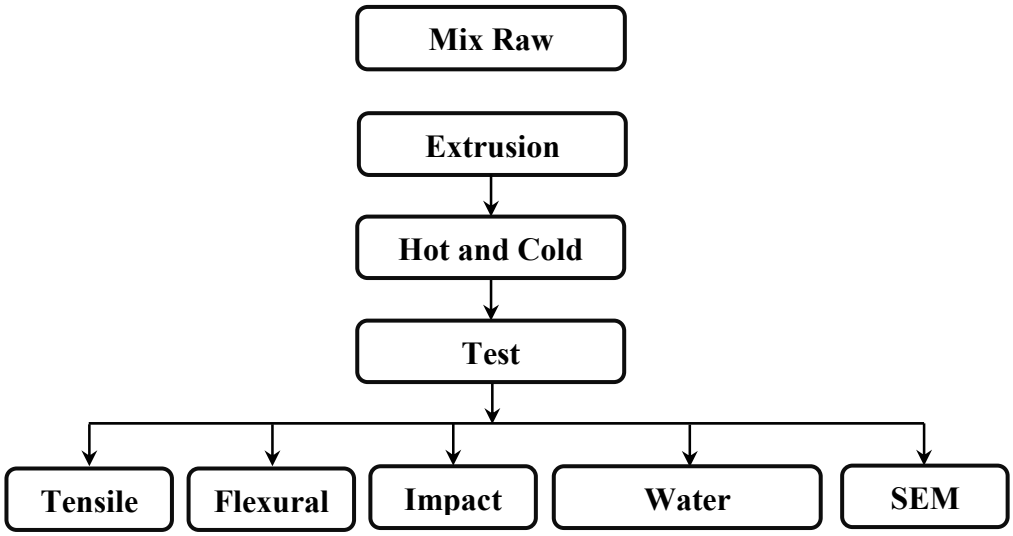
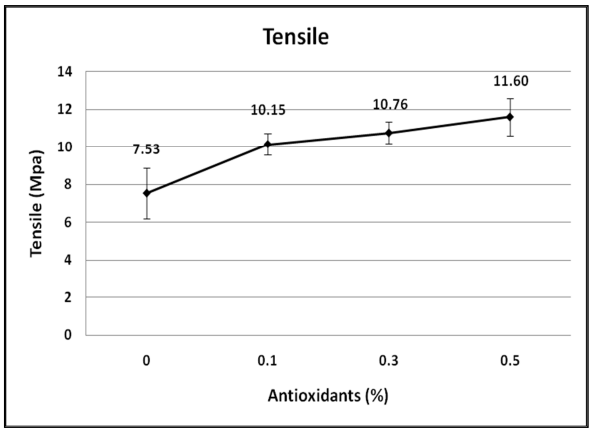


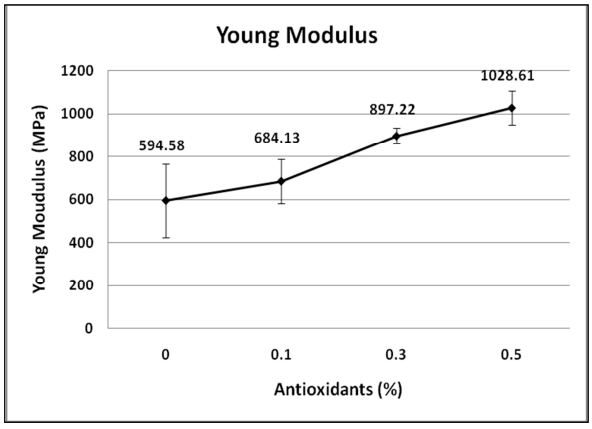
Fig.1 Flow chart of the methodology

Results and Discussion

From the testing, compositions with 0.5% antioxidants gave the most better results compared to other samples as shown:



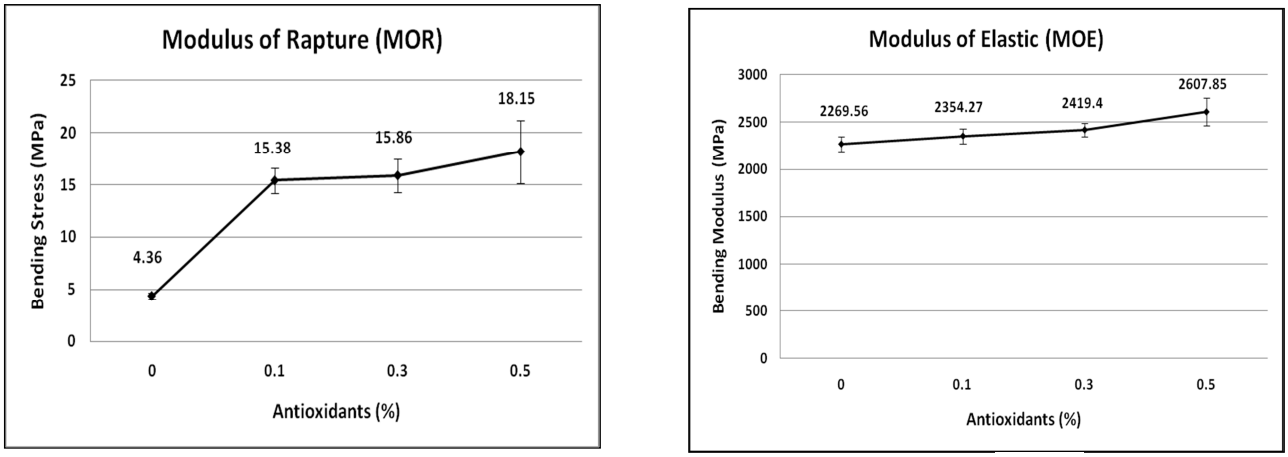
(a)



(b)

Fig. 2 (a) Graph tensile (b) Graph Young Modulus

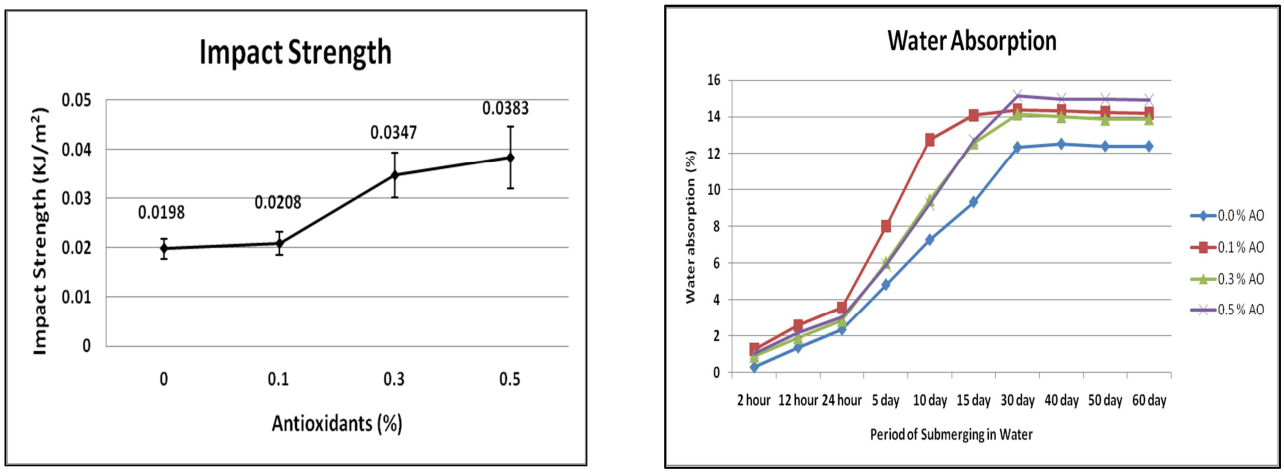
Fig. 2a and 2b depict graph of tensile and Young Modulus respectively. From the results, tensile test gave 11.6 MPa for sample that contain 0.5% of antioxidants. This is the highest value compared to other samples. The same sample also gives the best value of Young Modulus which is 1028.6 MPa. This result is mainly explained by high adhesion between the particles of rHDPE and fibers. Sample with 0.5% of antioxidants gave highest result probably due to decreasing fiber (saw dust) content in the matrix.



(a) (b)

Fig. 3 (a) Graph modulus of rapture (MOR) (b) Graph modulus of elastic (MOE)

Fig. 3a and 3b show graph modulus of rapture (MOR) and graph modulus of elastic (MOE) from flexural test. This test shows the increases value from 0.0% to 0.5% of antioxidants contents. The modulus of rapture (MOR) gives 18.15 MPa while Modulus of elasticity (MOE) gives 2607.85 MPa for 0.5% of antioxidants. Composite of 0.0 wt% antioxidants gave the lowest value for both MOR and MOE. The trend depicts increasing amount of antioxidants increases the value of MOR and MOE. The addition of rice husk and saw dust in the composites increased the stiffness and brittleness, however, reduced the elongation at break [9]. The result shows, addition of antioxidants from 0 – 0.5 wt% increases the flexural strength and stiffness of the composites significantly.



(a) (b)

Fig. 4 (a) Graph impact strength (b) Graph water absorption of distilled water

Fig. 4a shows graph of impact strength versus percentage of antioxidants. Samples 0.5 wt% of antioxidants provided significantly higher Izod impact strength compared to other samples which is 0.038 KJ/m^2. The lowest value of impact test was sample without addition of antioxidants, 0.02 KJ/m^2. Fig. 4b shows graph of water absorption of distilled water. Water absorption test for 0.5% antioxidants gave value 14.93% of water up take after two month immersion in distilled water. According to A.A Klyosov [6], water absorption for wood-plastic composite (WPC), typically are 0.7-2 % after 24 h, 1-5 % after a week, and up to 18-22 % after several months. This result could be explained by wood chemical composition itself; this is because wood fiber contains high hydrophilic content (cellulose and hemicelluloses). Besides that, poor adhesion between fiber particles and the polymer matrix generates void spaces around the fiber particles. These lead to higher water uptake in WPC.

Table 2 Water absorption rate

	Water absorption [%]			
Period of submerging in water [days]	0.0	0.1	0.3	0.5
1	2.33	3.55	2.84	3.02
15	9.30	14.09	12.56	12.72
30	12.32	14.38	14.15	15.17
60	12.38	14.21	13.88	14.93

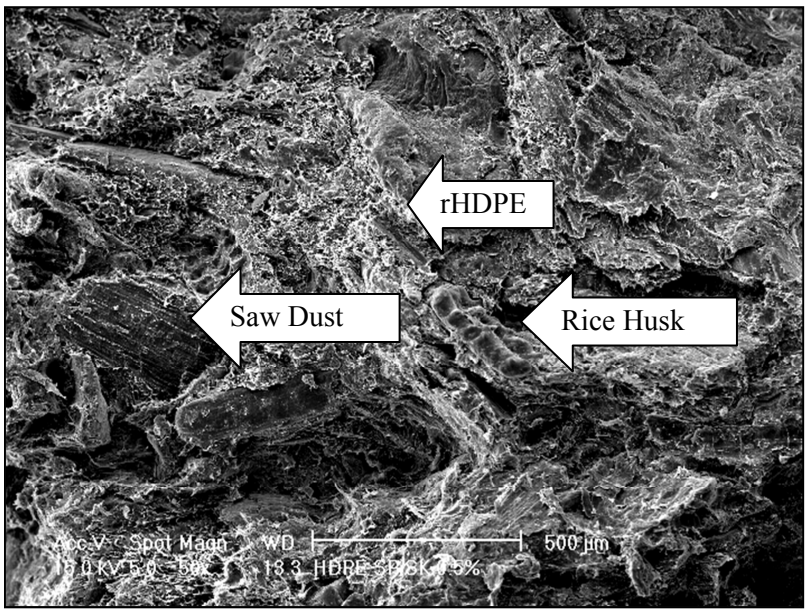


Fig. 5 SEM image (50x) of fractured surface of sample with 0.5% antioxidants content

Fig. 5 shows the SEM image of fracture surface of the sample with 0.5% antioxidants content. In this image, no clear chinks can be seen between fibers and rHDPE matrix, its indicating the good interface bonding between them. However, a gap is seen running through the saw dust, this could be a sign of stress-transfer from the weaker matrix to the stronger saw dust. The surface shows a very limited amount of ripped matrix which is mean that the WPC is more brittle.

Summary

Adding agro-based fibers to recycled high density polyethylene produced composites that are lower in cost and improve some properties as compared to composites containing no fiber. The addition of antioxidants to these composites gives additional benefits. These antioxidants are highly effective, low-volatile and hydrolysis resistant for coating resins. They protect the resin polymer against oxidation during resin synthesis, processing (thermal curing and overbaking) and the designed life-time of the final coating. They also provide excellent protection against change of physical properties caused by excessive heat exposure. The best amount of antioxidants that give highest strength and elasticity of wood plastic composites was clearly proven from this study which is 0.5 wt%.

References

[1] L. Avérous and F.L. Digabel: Carbohydrate Polymers Vol.66 (2006), p. 480-493.

[2] H-S. Yang: Role of Rice Husk Flour As Reinforcing Filler For Thermoplastic Polymer Bio-composites. Thesis for The Degree of Doctor of Philosophy, Department of Forest Products, Seoul National University, Seoul (2004).

[3] F. Mengeloglu and A. Kabakci: Int. J. Mol. Sci. Vol.9 (2008), p. 107-119.

[4] J.Z. Lu, Q. Wu and I.I. Negulescu: Wood and Fiber Sci. Vol.36 (4) (2004). p. 500-510.

[5] J.Z. Lu, Q. Wu and Jr.H.S. McNabb: Wood and Fiber Sci. Vol.32 (1) (2000), p. 88-104.

[6] A.A. Klyosov: Wood Plastic Composites. New York: John Wiley & Sons (2007).

[7] H. Azman and K. Sivaneswaran: The Effect Rice Husk Ash Fillers on Processability of ABS Impact Modified PVC-U, Thesis for The Degree of Doctor of Philosophy, Department of Polymer Engineering University of Technology Malaysia, Skudai (2006).

[8] D.J. Gardner and D. Murdock: Extrusion of Wood Plastic Composites, University of Maine, Orono (2010).

[9] K.B. Adhikary, S. Pang and M.P. Staiger: Composites: Part B Vol.39 (2008), p. 807-815.

© (2011) Trans Tech Publications, Switzerland
doi:10.4028/www.scientific.net/KEM.471-472.157

Effect of Loading Concentration on the Electrical and Hardness Properties of MWCNT/Epoxy Nanocomposites

R. Nishata Royan [1,2a], Abu Bakar Sulong[1,2b], Jaafar Sahari[1,2c]

[1] Fuel Cell Institute, Universiti Kebangsaan Malaysia, 43600 Bangi, Malaysia

[2] Department of Mechanical and Materials Engineering, Universiti Kebangsaan Malaysia, 43600 Bangi, Malaysia

[a]ry_nish@yahoo.com , [b]abubakar@eng.ukm.my, [c]jaafar@eng.ukm.my

Keywords: carbon nanotube, thermoset based nanocomposites, hardness, electrical conductivity

Abstract. Carbon nanotubes have excellent mechanical and electrical properties, and are also a good reinforcement material for composites than conventional materials. The matrix used in this study was epoxy and reinforcement filler in multi-walled carbon nanotubes (MWCNTs). The different MWCNTs loading concentrations (0 ~ 10 wt. %) were added into the epoxy resin. The dispersion of MWCNTs in epoxy resin was conducted using high speed mixer through mechanical shearing mechanism. The mixture of epoxy/MWNTs suspension was poured into the mold and compression molding was conducted for fabrication of MWCNTs/epoxy nanocomposites. The electrical conductivity of nanocomposite by variation of CNTs concentration was measured by the four point probe. Dispersion state of CNTs in epoxy matrix was observed on fractured surface by scanning electron microscopic. Hardness of the composite was tested using the *Dinamic Ultra Micro Hardness* machine. Non conductive epoxy polymer becomes conductor as addition of CNTs.. Electrical conductivity of nanocomposite plates increased with increasing CNTs concentration. Agglomerations of CNTs were observed on fractured surfaces. This phenomenon due to CNTs which used in this study was at as produced state where no modification is being done on it. Long and entanglement of individual CNTs easily lead to agglomerations. Van de Wall's force interactions between CNTs also contribute to the agglomerations of CNTs. Hardness of the composite increases with the CNTs loading concentrations until it reaches a maximum peak at the composition of 5wt% of CNTs but the hardness decreases rapidly with loading greater than 5wt% of CNTs.

Introduction

CNTs were first discovered by Iijima [1], and it was multi-walled carbon nanotube (MWCNT). The CNTs as mentioned before exist in two main types. SWCNTs consist of a single sheet of graphite rolled to form a cylinder with diameter in the order of 1 nm with length of up to few centimeters. MWCNTs consist of an array of a cylinder formed concentrically, are separated by 0.35 nm, can have diameter from 2 ~ 100 nm and length of tens of microns. Experimental and theoretical results have shown that the elastic modulus of CNT is greater than 1 TPa (that of a diamond is 1.2 TPa), and the strength is 10 ~ 100 times higher than the strongest steel at the same weight fraction [2]. Single walled carbon nanotubes (SWCNTs) consisting of a single graphite plane (so-called graphene) rolled up into a cylinder behave as either a metal or a semiconductor depending on their wrapping angle of graphene sheet and its diameter, while MWCNTs are reported to be always electrically conductive and to have an electrical conductivity approximately 1.85×10^3 S/cm [1,3,4,5]. In recent years, the demand for highly conductive polymer composites (CPCs) for the use of bipolar plates (BPs) in Proton Exchange Membrane Fuel Cells (PEMFC) is growing. Therefore, a fundamental knowledge on the CPCs and their mechanism of conduction as well as a review on the basic concepts and the design requirements for PEM fuel cell components is

necessary in this research. CNTs polymeric composites are aimed at the exploitation of the high electrical conductivity of CNTs coupled to high mechanical properties, thermal properties and others unique properties [2, 7]. Due to the low filler loading fractions required, the mechanical properties and the surface finish of the composite matrix can be maintained. In contrast, conventional surface coating such as Indium Tin Oxide (ITO) coating offer a high electrical conductivity but very high production cost and low quality of surface finish. Therefore, alternate approach using CNTs as conductive fillers in polymeric matrix promises a unique combination of low cost production, ease processing with high electrical conductivity. Indeed, these materials are increasingly used in the electronics sector, as well as for automotive and aerospace applications, where an electrical conductivity exceeding 10^{-8} S/cm is required for dissipation of electrostatic charges. The objective of this research is to study the effect of loading concentrations of CNTs on the electrical conductivity. Also the surface fracture is being observed in the study.

Experimental

The epoxy resin used in this research is bisphenol-A which was purchased from US Composites. A lower viscosity (6 poise) of epoxy matrix is selected for better wetting conditions with reinforcement fillers. The reinforcement filler used in this study is MWCNTs which is NC 7000 type purchased from Nanocyl, Belgium. The weight fraction of the CNTs ranged from 0 to 10 wt% to determine the effect on the electrical conductivity of the composite. Agglomerates of CNTs, called nanotropes, are difficult to separate and infiltrate with the matrix. For polymer matrix nanocomposites, high power dispersion methods, such as ultrasound and high-speed shearing, are the simplest and most convenient to improve the dispersion of nanosized fillers in a polymer matrix [8]. In this study, the CNTs were mixed into epoxy matrix using a high speed mechanical mixer, IKA-WERK. The dispersed MWCNTs in epoxy suspension was poured into a mold and cured under pressure with the hot press to minimize existing voids in epoxy nanocomposites. Finally, the bulk MWCNTs epoxy nanocomposites were machined to specimen with dimension of 13 mm (width) x 25 mm (length) x 2 mm (thickness) for the electrical conductivity measurement. The measured surfaces area of the specimen was polished with sand paper to reduce contact resistance and the electrical conductivity for in-plane direction was measured using four point probe.

Results and Discussion

Electrical Conductivity. The variation of electrical conductivity of epoxy nanocomposites as function of MWCNTs types and loading concentration in weight percentage (wt%) are plotted in Fig. 1. Non-conductor material of pure epoxy polymer become conductive as incorporated CNTs. At low loading concentration, MWCNTs gave a high electrical conductivity. The electrical conductivity of epoxy nanocomposites are increased with increasing of CNTs loading concentration. This similar result was reported by Allaoui et al. [9] and Sulong et al. [10]

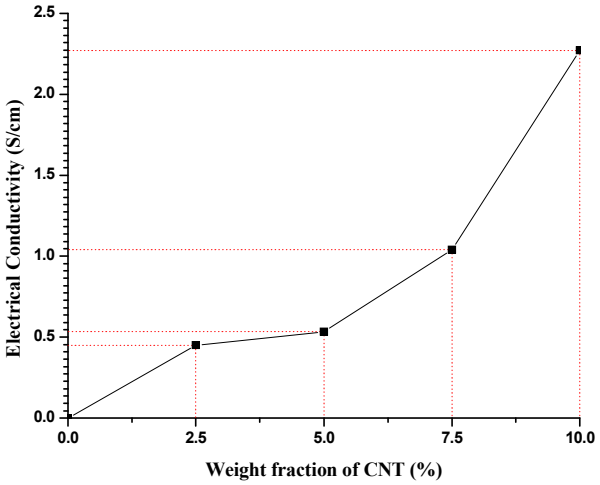


Fig. 1. Effect of CNT weight fraction on electrical conductivity of epoxy nano-composite

Fracture Surface. Fractured surface SEM images of the nanocomposite sample are given in Fig. 2. Significant CNTs agglomeration can be observed on both types of CNTs, which may play role as electrical conductive pathway in polymer matrix. The fracture surface structure is also observed under different magnification under *Scanning Electron Microscope* (SEM) as shown in Fig. 3. Increasing viscosity of the epoxy by addition of CNTs will contribute less energy transfer during mechanical mixing which will affect the dispersion of the CNTs into the polymer matrix.

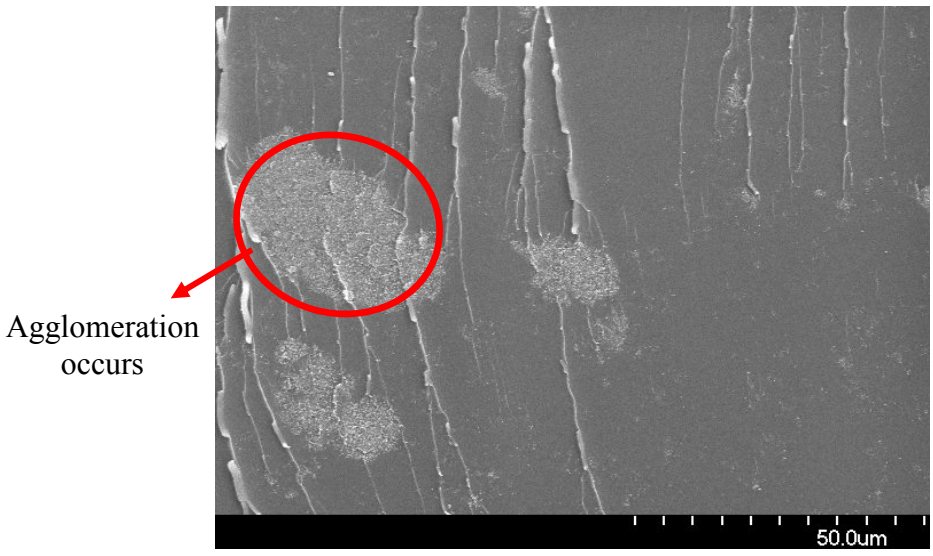


Fig. 2. SEM Fracture Surface of CNT composite

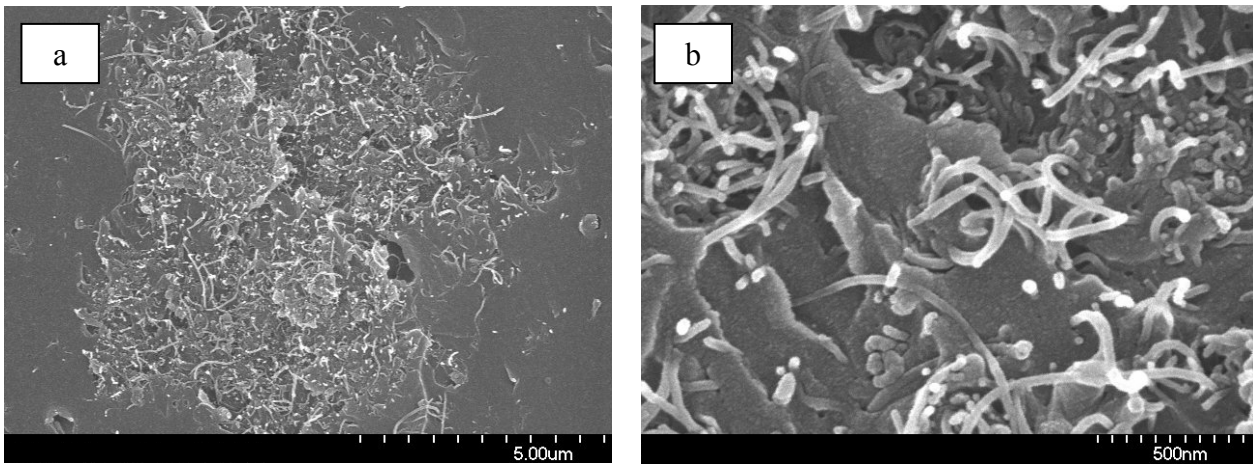


Fig. 3. (a) Fracture Surface with 5µm SEM magnification (b) Fracture Surface with 500nm SEM magnification

Hardness. Hardness of the composite was tested using the *Dinamic Ultra Micro Hardness* machine. The variation of hardness of epoxy nanocomposites as function of MWCNTs types and loading concentration in weight percentage (wt%) are plotted in Fig. 4. It shows that the hardness of the composite increases with the CNTs loading concentrations until it reaches a maximum peak at the composition of 5wt% of CNTs. However, the hardness decreases rapidly with loading greater than 5wt% of CNTs. This phenomenon takes place due to the improper mixing and surface, which is brittle and has many voids. Also the non-homogeneity of CNTs may reduce the effects on their mechanical properties. [9]

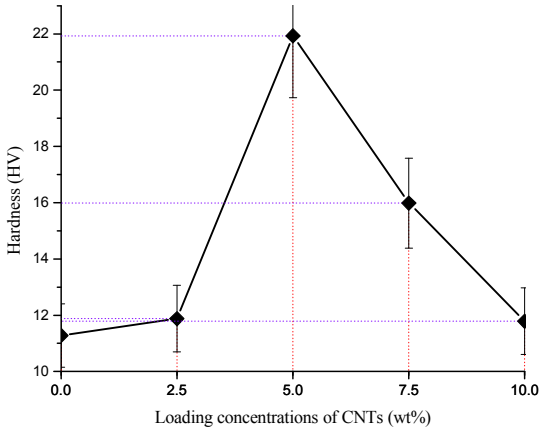


Fig. 4. Hardness behavior of epoxy nanocomposites

Summary

This study's result indicated that the addition of carbon nanotube will make a non-conductive material become a conductive material. The non-conductive material discussed here is the epoxy resin. Besides that, the electrical conductivity of epoxy resin increases with the weight percentages of CNTs. Agglomeration will affect the electrical conductive pathway in polymer matrix. The hardness of the composite obtained increases until a maximum value and then decreases rapidly due to the improper mixing, agglomerations of CNTs and also the non-homogeneity of CNTs. Influences of mixing method of CNTs on the electrical conductivity behavior are further investigated. Also, further study on the best interfacial bonding between the nano material, graphite and the polymer matrix will be done on the nanocomposite in this study using wet and dry oxidation.

Acknowledgement

The authors would like to thank the Fuel Cell Institute and also the Department of Mechanical and Materials Engineering, Faculty of Engineering & Built Environment, Universiti Kebangsaan Malaysia. This work is fully supported by grant No. UKM-AP-TK-05-2009.

References

[1] S. Iijima: Nature Vol. 354 (1991), p. 56

[2] Delmotte, J.P., A., Rubio. : Carbon ,Vol. 40 (2002), pp. 1729

[3] Thostenson, E.T., Z.,F., Ren, and T.W., Chou : Composite Science and Technology Vol. 61 (2001), p. 1899

[4] M. Paradise, T. Goswami: Material & Design Vol. 28 (2007): p. 1477

[5] Popov, V.N. :Mater Sci Eng R Vol. 43 (2004), pp. 61

[6] J.N. Coleman, U., Khan, W.J., Balu, Y.K., Gun'ko. Carbon (2006) p. 1624

[7] S. Saito: Science, Vol. 278 (1997), pp. 77

[8] Y.X.Zhou, P.X.Wu. Improvement in electrical, thermal and mechanical properties of epoxy by filling carbon nanotube" Polymer Letters Vol.2 (2008) p. 40

[9] A. Allaoui, S. Bai, HM Cheng, JB. Bai: Compos Sci Techn. Vol. 62 (2002):p. 1993

[10] A.B Sulong, M. Nurhamidi, S. Jaafar, R Ramli, M.D. Baba, J. Park: European Journal of Composite Material. Vol. 21 (2009):p. 13

© (2011) Trans Tech Publications, Switzerland
doi:10.4028/www.scientific.net/KEM.471-472.162

Effect of wet oxidation on the dispersion and electrical properties of Multi-walled Carbon Nanotubes /Epoxy Nanocomposites

R. Nishata Royan [1, 2a], Abu Bakar Sulong[1,2b], Hendra Suherman[1, c] and Jaafar Sahari[1, 2d]

[1] Fuel Cell Institute, Universiti Kebangsaan Malaysia, 43600 Bangi, Malaysia

[2] Dept. of Mechanical and Materials Engineering, Universiti Kebangsaan Malaysia, 43600 Bangi, Malaysia

[a]ry_nish@yahoo.com , [b]abubakar@eng.ukm.my, [c]henmeubh@yahoo.com, [d]jaafar@eng.ukm.my

Keywords: Carbon nanotubes, functionalization, dispersion, electrical properties, nanocomposites

Abstract. Carbon nanotubes (CNTs) have excellent mechanical and electrical properties than conventional materials (carbon black and glass fibers), and are promising candidates as reinforcement material for composites. Formation of electrical conductive with effective dispersion of filler remains a main challenge in the polymer matrix and fillers in order to achieve a good electrical conductivity. Therefore, one of the solutions is to functionalize through wet oxidation of the CNTs besides adding surfactants or assisted liquids. Functionalization of CNTs involves the generation of chemical moieties on their surface that can improve the solubility and processibility. Any functionalization that is undertaken must preferably not influence other key properties such as strength and electrical conductivity of the nano-composite. The matrix used in this study was epoxy and reinforcement filler was multi-walled carbon nanotubes (MWCNTs). MWCNTs were treated with sulfuric acid and nitric acid at 3:1 (v/v) ratio. The present of functional groups on CNTS were investigated using Fourier Transform Infrared (FT-IR). Different weight percentages of MWCNTs (functionalized and as produced) / epoxy composite were prepared. The electrical conductivity of functionalized MWCNTs nanocomposites and as produced MWCNTs nanocomposites were measured by the four point probe. Dispersion state of CNTs in epoxy matrix was observed on fractured surface by scanning electron microscopic. Functionalized CNTs gave better dispersion stability in solvents than non-functionalized CNTs. As expected, non- functionalized CNTs (as produced MWCNTs) are not dispersed at all in all the solvents. However, functionalized CNTs composites give low electrical conductivity. Defects from acid treatment are assumed will damage the original chirality of as produced CNTs and give unbalance polarization on the CNTs, which are the reasons for no formation of conductive pathway networks of acid treated CNTs under electric field.

Introduction

Since the discovery of carbon nanotubes (CNTs), they have been widely used in many different applications such as nano-fillers in composite materials, biological and chemical sensors, nano-electric devices, and field emitters [1]. Compared to the use of composites filled with carbon black or carbon fiber as conductive reinforcements, polymeric composite with MWCNTs can form the conductive path at a relatively very low content, owing to their high aspect ratio of 100–1000 and high specific surface areas. Therefore, their use in various applications, such as antistatic film, electromagnetic shielding materials etc., has long been anticipated [2]. Despite the range of potential applications, their use often remains problematic due to agglomeration caused by strong inter-tube van der Waals forces, and their high surface energy due to the strong curvature of the thin nanotubes [3]. Besides, effective dispersion remains a problem and one solution is to functionalize the nanotubes. CNTs have an intrinsic nature of extreme resistance to wetting which makes them difficult to disperse and dissolve in water and organic solvents [4]. Functionalization of CNTs

involves the generation of chemical moieties on their surface that can improve the solubility and processibility, which allows a combination with other types of materials, particularly with polymer matrix. For instance, functionalization can be undertaken in a range of ways: defect-group functionalization, covalent sidewall functionalization, non covalent exohedral functionalization with surfactants, non-covalent exohedral functionalization with polymers, and endohedral functionalization [5]. The main objective in this study is to investigate the effect of wet oxidation treatment on the dispersion and electrical properties of multi-walled carbon nanotubes/epoxy nanocomposites.

Experimental

The epoxy resin used in this research is bisphenol-A based epoxy resin (635), with viscosity 6 Poise was obtained from US Composites. A lower viscosity of epoxy matrix is selected for better wetting conditions with reinforcement fillers. The reinforcement filler used in this study is multi-walled carbon nanotubes (MWCNTs) NC 7000 type was purchased from Nanocyl, Belgium. The diameter is 9.5 nm, and length is 1.5 μm, with purity ≥90%, reported by manufacturer. The epoxy resin is a bisphenol-A based epoxy resin (635), with viscosity 6 Poise was obtained from US Composites. The experimental is done in two stages. First the wet oxidation functionalization of MWCNTs is being prepared followed by the fabrication of epoxy/MWCNTs nanocomposite. MWCNTs were treated with sulfuric acid and nitric acid at 3:1 (v/v) ratio to produce high concentration acid solution. The MWCNT were suspended in a dilute solution and refluxed under a given set of oxidation conditions. The oxidized MWNT were filtered and washed with distilled water subsequently until pH7. Then the functionalized MWCNTs were dried in oven at 40°C for 24 hours. For the fabrication of epoxy/MWCNTs nanocomposite plate, the epoxy and curing agent were mixed at ratio 3:1 in wt.%. The mixture was mixed using a high speed mechanical mixer (RW 20-KIKA-WERK) at 1200 rpm for 40 s. MWCNTs with different loading concentrations were added into epoxy and curing agent mixture, then the suspension was mixed again at 800 rpm for 3 min. The composites mixture was poured into a steel mould for compression molding at 130 °C for 1.5 hours. The present of functional groups on CNTs were investigated using Fourier Transform Infrared (FT-IR). The electrical conductivity of the nanocomposites were measured using a Jandel Multi Height Four-Point Probe combined with a RM3 Test Unit and fracture surface morphology was examined using scanning electron microscopy (FESEM, Model Supra 55/55VP).

Results and Discussion

FTIR Analysis. The FT-IR spectra of as produced MWCNTs and after oxidation treatment are presented in Fig. 1 and Fig. 2. Absorbance peaks at 1110, 1380, 1460, 1750, 2950 and 3200 ~ 3750 cm^{-1} corresponding to C-O-C, C-O, C=C, C=O, and O-H bonds in carboxylic functional groups (COOH) are observed after wet oxidation treatment. No significant peaks are observed at as produced MWCNTs. The broad shoulder peaks at 3200 ~ 3750 cm^{-1} are assigned to O-H stretches of terminal carboxyl groups. The peaks at 1210, 1380 and 1750 cm^{-1} correspond to C-O-C (aromatic acid esters), C-O (carboxylic acid dimers) and carboxylic C=O (quinone groups) [6]. It was suggested that absorption at 1460 cm^{-1} is from the C=C drawing mode of double bonds in CNTs backbone near the functionalized carbon atoms [7].

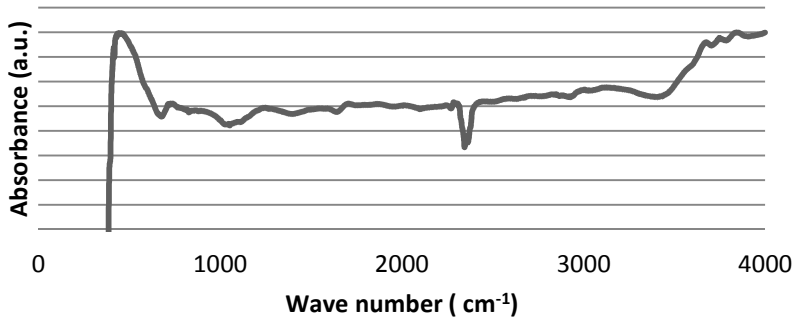


Fig. 1: FT-IR spectra of As-produced MWCNTs

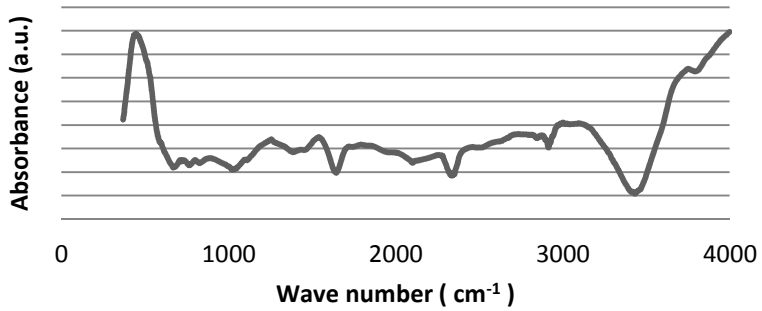


Fig. 2: FT-IR spectra of wet oxidation treated MWCNTs

Dispersion Stability of MWCNTs. The dispersion stability of MWCNTs in different solvents: (a) dimethylformamide (DMF); (b) acetone; and (c) methanol for: (i) as produced and (ii) acid treated MWCNTs before and after 48 hours are given in Fig. 3. Dispersion stability of acid treated MWCNTs remains stable until 48 hours in all three solvents. As expected, non- functionalized MWCNTs (As-produced MWCNTs) are not dispersed at all in all three solvents. Also for As-produced MWCNTs, precipitation occurred and the MWCNTs have been sediment to the bottom of the bottle after 48 hours.

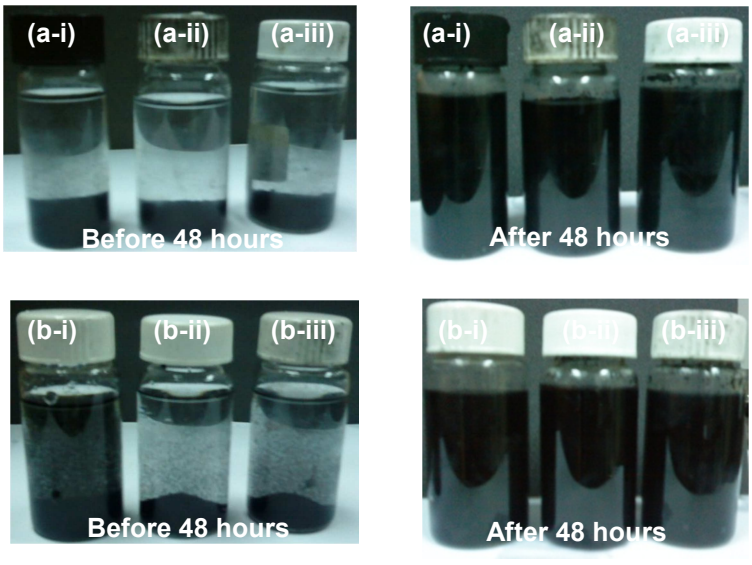


Fig. 3: Dispersion stability of: (a) as produced; (b) oxidised MWCNTs in solvents: (i) dimethylformamide (DMF); (ii) acetone; and (iii) methanol after 48 hours.

The reactive functional groups introduced into the MWCNTs would be expected to decrease the van der Waals attraction among the MWCNTs and improve the interfacial bonding between the MWCNT and the epoxy resin, and thus a better dispersion of the individual MWCNT in solutions could be expected. This has been reported that the active groups formed by the oxidation of the surfaces of the MWCNTs can dramatically increase the stability of their aqueous solubility [9].

The physical of the MWCNTs are shown in Fig. 4. It is observed under same magnification under *SEM*. The as-received MWNT were aggregated in tangles due to the van der Waals forces between the MWNT. The chemically treated MWNT, however, were dispersed well owing to the functional groups and negative charges formed at the external walls and end tips [2].

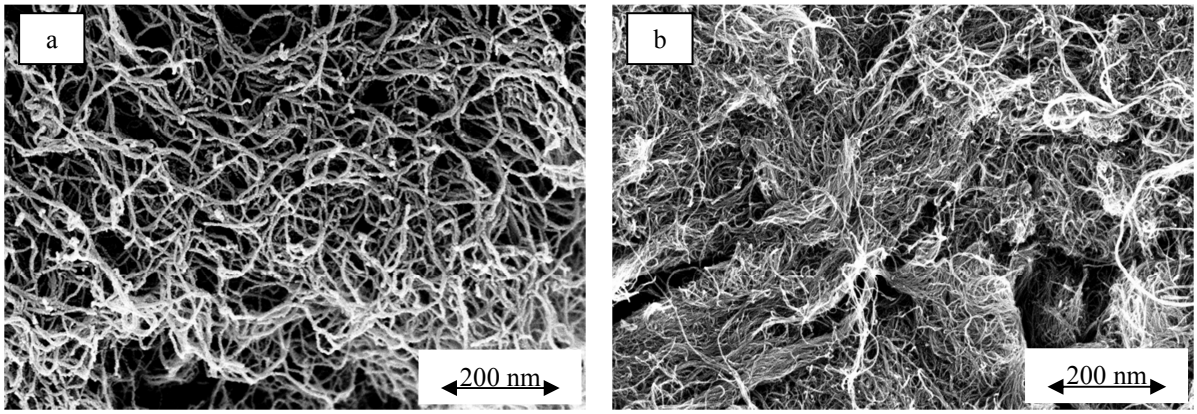


Fig. 4: SEM Images of MWCNTs (a) As-Produced; (b) Oxidised MWCNTs

iii) Electrical conductivity

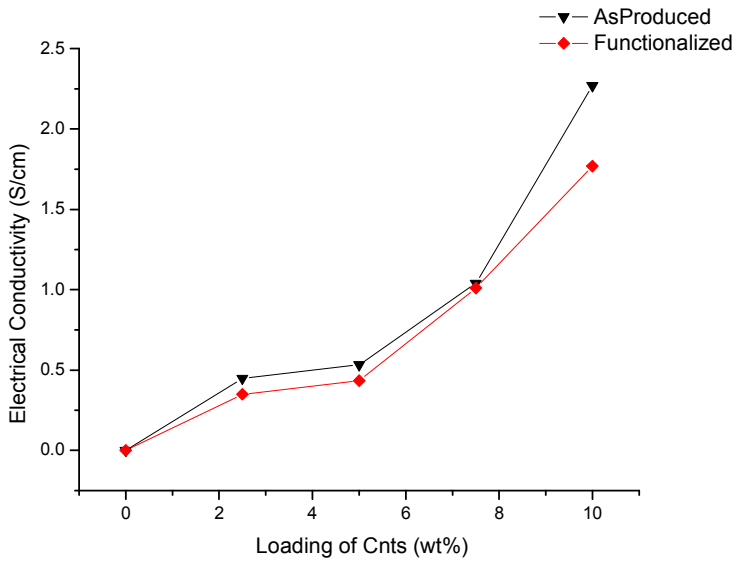


Fig. 5: Electrical conductivity behavior of As-produced and wet oxidation treated MWCNTs

The variation of electrical conductivity of epoxy nanocomposites of As-produced MWCNTs and wet oxidation treated MWCNTs against loading concentration in weight percentage (wt%) are plotted in Fig. 5. From the curve, the electrical conductivity of epoxy nanocomposites are increased with increasing of CNTs loading concentration. In our previous study reported that chemical functionalized MWCNTs improve the dispersion quality and strengthen of interfacial bonding strength with polymer matrix [10, 11]. In this study, chemical functionalized MWCNTs in epoxy matrix decrease the electrical conductivity of epoxy nanocomposite. This is due to the treatment of

strong acids during wet oxidation which cause the structural damage to the wall of MWCNTs and hence reduces the overall electrical conductivity of MWCNTs [12].

Summary

In summary, chemical functionalization can promote good dispersion in the polymer/CNT composites and will play a dominant role in future development and applications of these nanocomposites. However, wet oxidation cause defects on the structure of the MWCNTs surface which will degrade its electrical properties. Further works should be done to improve the dispersion and distribution of nano materials in polymer matrix by focusing on its interfacial bonding and its effect on electrical conductivity.

Acknowledgement

The authors would like to thank the Fuel Cell Institute and also the Department of Mechanical and Materials Engineering, Faculty of Engineering & Built Environment, Universiti Kebangsaan Malaysia. This work is fully supported by grant No. UKM-AP-TK-05-2009.

References

[1] S. Iijima: Nature Vol. 354 (1991) p. 56

[2] Y.J. Kim, T.S. Shin, H.D. Choi, J.H. Kwon, Y.C. Chung, H.G. Yoon: Carbon Vol. 43 (2005) p. 23

[3] M. Zhang, L.Su, L. Mao: Carbon Vol. 44 (2006) p. 276

[4] S.H. Tan. Purification and functionalization of carbon nanotubes and their application polymer composites. PhD Dissertation, Sejong University, 2007.

[5] A. Hirsh: Ang Chem Int Ed Vol. 41 (2002) p. 1853

[6] J. Chen, A.M. Rao, S. Lyuksyutov, M.E. Itkis, M.A. Hamon, H. Hu, R.W.Cohn, P.C. Eklund, D.T. Colbert, R.E. Smalley, R.C. Haddon: J Phys Chem B Vol. 105 (2001) p. 2525

[7] M.L. Sham, J.K. Kim: Carbon Vol. 44 (2006) p. 768

[8] G. Socrates. Infrared characteristic group frequencies, John Wiley & Sons, New York, 1980.

[9] M.S.P. Shaffer, X. Fan, A.H. Windle: Carbon Vol. 36 (1998) p. 1603

[10] A.B. Sulong, , J.H., Park, N.S., Lee, and J.C., Goak: Journal of Composite Material. Vol. 40 (2006) p. 1947

[11] A.B. Sulong, J.H. Park: Advanced Materials Research, Vol. 26 (2007) p. 285

[12] H. L. Cher., C. Raoul, R. S. Clarke, G. M. Milena, G. M. Janis, S.C. Hawkins, P. H. Chi, G.P. Simon: Journal of Nanoparticals Res Vol. 10 (2008) p. 77

© (2011) Trans Tech Publications, Switzerland
doi:10.4028/www.scientific.net/KEM.471-472.167

Tensile And Impact Properties of Sugarcane Bagasse/Poly (Vinyl Chloride) Composites

Riza Wirawan[1,a], S.M. Sapuan[1], Khalina Abdan[2], Robiah Yunus[3]

[1]Department of Mechanical and Manufacturing Engineering, Faculty of Engineering, Universiti Putra Malaysia, 43400 Serdang, Selangor, Malaysia

[2]Department of Chemical and Environmental Engineering, Faculty of Engineering, Universiti Putra Malaysia, 43400 Serdang, Selangor, Malaysia

[3]Department of Biological and Agricultural Engineering, Faculty of Engineering, Universiti Putra Malaysia, 43400 Serdang, Selangor, Malaysia

riza.wirawan@gmail.com

Keywords: Natural fibre composites,thermoplastics, bagasse, mechanical properties

Abstract. Sugarcane bagasse is divided into two main components, pith and rind, with "pith" representing the inner part of the sugarcane bagasse and "rind" as the outer part. In this study, the tensile and impact properties of untreated pith/ poly(vinyl chloride) composites were compared to that of untreated rind composites using the same matrix with variation of fibre content. It was observed that the tensile strength and modulus of rind/PVC composites are higher than the unfilled PVC at composite fibre contents of 30% and 40%. Additionally, the rind composites exhibited superior strength and stiffness in comparison with the pith composites.

Introduction

Sugarcane bagasse (SB) is a residue of the sugarcane milling process. During this milling process, the sugarcane stalk is crushed to extract sucrose, and the process produces a large volume (32%) of bagasse. In Malaysia, over a million tonnes of sugarcane were produced in 2002, and hence, bagasse is easily obtained as a waste product [1]. As a result, utilisation of SB may contribute to environmental and economic development.

Poly(vinyl chloride) is one of the most well-known polymers and is commonly abbreviated as PVC. As one of the cheapest thermoplastics, PVC is used in a broad range of applications and its use has grown rapidly. This material is easy to fabricate, long lasting, exhibits good mechanical and chemical properties, and can be used in wide range of corrosive fluid environments. Furthermore, the properties of PVC can be adjusted by the addition of plasticiser and other additives for production of a rigid or flexible product [2, 3]

Meanwhile, stalk of the sugarcane plant includes an outer rind and inner pith. The rind is made up of a hard fibrous substance surrounding a central core of pith, which is softer due to a spongy structured component. Studies of SB/PVC composites have been reported by other researchers [4]. However, studies focusing on the use of pith and rind components , especially in thermoplastic matrix, have not been widely reported. The only study of the use of pith and rind components in polymer composites used a thermoset, instead of thermoplastic, as the matrix [1].

In this study, the tensile properties of SB pith and rind were evaluated as well as the tensile properties of pith and rind PVC composites with variation of the bagasse content. The effects of bagasse content and stalk components (pith/rind) on the tensile properties of the composites were examined.

Materials and Methods

The matrix used in this study was unplasticised PVC compound IR045A supplied by Polymer Resources Sdn. Bhd., Klang, Selangor, Malaysia. This compound consists of medium molecular weight PVC, processing aids, lubricant, and certain additives. The studied SB (*Saccharum*

officinarum) is a residue of the sugarcane milling process gathered from sugarcane juice makers in Malaysia. For the purpose of single fibre tensile testing, single fibres of pith and rind were extracted manually. For the purpose of composite production, fibres were extracted and cut using a knife-ring flaker. The fibres were sieved and 40 mesh sizes of fibre were used in this study.

Preparation of Composites. A thermal mixing process was carried out using a Haake Polydrive R600 internal mixer at a temperature of 170°C and rotor speed of 50 rpm. PVC pellets were fed into the chamber and mixed for five minutes, followed by feeding of the SB. The total mixing time was 15 minutes. In this study, 10%, 20%, 30%, and 40% weight fractions of pith and rind fibre were prepared.

After the thermal mixing process, hot pressing was carried out at a temperature of 170°C for 12.5 minutes, and the mixture was then cooled under pressure to room temperature. The final products were in the form of plates with dimensions 15 cm x 15 cm x 1 mm and 15 cm x 15 cm x 3 mm. The former was used for tensile testing, whilst the latter was used for impact testing.

Single fibre tensile testing. The single fibre tensile test specimens were prepared based on the ASTM D3379 procedure for single fibre tensile testing. The specimen was then tensile tested with a 5 kN load-cell equipped Instron 3365. The gauge length was 50 mm with a cross-head speed of 2 mm/min. A total of 30 specimens were tested for each component.

Tensile testing. Specimens for tensile testing were cut using a dog-bone dumbbell as per ASTM D638. The specimen was then tensile tested using the Instron 3365 machine with a crosshead-speed of 2 mm/min. Tensile strength and tensile modulus were calculated and recorded, and averages of five specimens were reported.

Impact testing. Hot pressed products with 3 mm thickness were cut using a band saw machine to form a rectangular shape with dimensions 5.5 cm x 12 cm x 3 mm. A notching cutter was used to prepare a v-notched impact specimen conforming to ASTM 256. Izod impact testing was then executed using a TMI Monitor/Impact tester with a maximum pendulum capacity of 1 Joule.

Results and Discussion

Single fibre tensile testing. The tensile strength of SB was confirmed to be very non-uniform. In this experiment, single fibre tensile testing results show that the tensile strength of pith and rind varied from 13 MPa to 76 MPa and 58 MPa to 430 MPa, respectively. The Weibull distribution was used to describe and analyse the strength of the fibres. From the two-parameter Weibull model, the cumulative failure probability is given by Eq. 1 [5]:

$$F(\sigma) = 1 - \exp\left[-\left(\frac{\sigma}{\sigma_0}\right)^m\right], \sigma > 0 \quad (1)$$

where σ is the tensile stress, σ_0 is the Weibull scale parameter or the characteristic stress value, and m is a Weibull parameter that measures the variability of the fibre strength. A larger value of m means smaller scatter in strength value.

The cumulative failure probability, P_i, under a particular strength was approximated by Eq. 2 [5]:

$$P_i = \frac{n - 0{,}5}{N} \quad (2)$$

where n is the number of fibres that failed at or below a certain value of stress and N is the total number of fibres measured.

A plot of ln [-ln(1-P)] versus ln (σ) can be drawn for calculating the Weibull parameters, σ and m, where

$$\ln(-\ln(1-P)) = m\ln\sigma - m\ln\sigma_o \ , \sigma > 0 \quad (3)$$

Fig. 1 shows an example of the plot for the tensile strength of rind. Using Fig. 1 and equation (3), we obtain the value of the Weibull parameters, m = 2.6028 and σ_0 = 187 MPa. The same procedure

was carried out to calculate the Weibull parameters for the tensile strength of pith, and Table 1 shows the Weibull parameters for both pith and rind properties. It can be seen that the tensile strength and Young's modulus of rind are superior to those of pith. The strain at breaking of rind is lower than that of pith, but the difference is not significant.

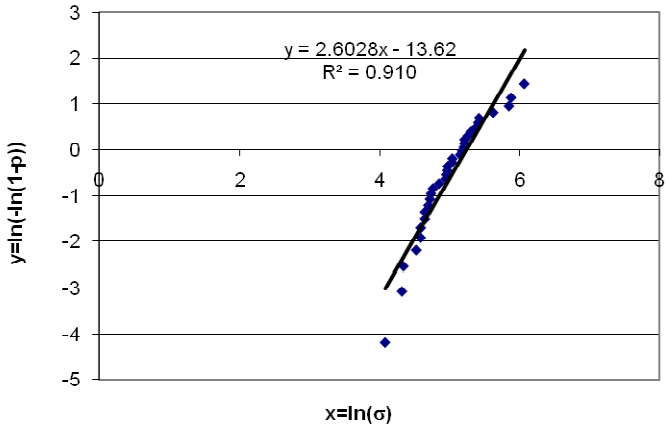


Fig. 1: Weibull distribution of rind fibres

Table 1: Tensile properties of SB fibres

	Weibull Parameter	
	Value	Variability
Tensile Strength (Mpa)		
Pith	52.35	2.56
Rind	187.32	2.60
Young's Modulus (Mpa)		
Pith	2147.42	4.16
Rind	10174.49	2.68
Maximum Strain (%)		
Pith	3.80	2.79
Rind	3.28	4.12

Tensile testing of composites. Fig. 2 shows that the tensile strengths of both pith/PVC and rind/PVC composites at low fibre content (10%) were lower than that of neat PVC. However, the tensile strength of rind/PVC composites was observed to increase with increased fibre content. The tensile strengths of 30% and 40% rind/PVC composites were higher than that of neat PVC. In addition, the observation of decreased tensile strength of pith/PVC composites continued up to a fibre content of 30%, but the tensile strength of 40% pith/PVC composite was higher than that of 30%. However, this value is still significantly lower when compared to that of neat PVC. Despite the fact that the tensile strength of pith/PVC composites was higher than that of rind/PVC composites at 10% fibre content, the tensile strength of rind/PVC composites were superior at higher fibre content. This is due to the higher tensile strength of rind fibre compared to that of pith fibre.

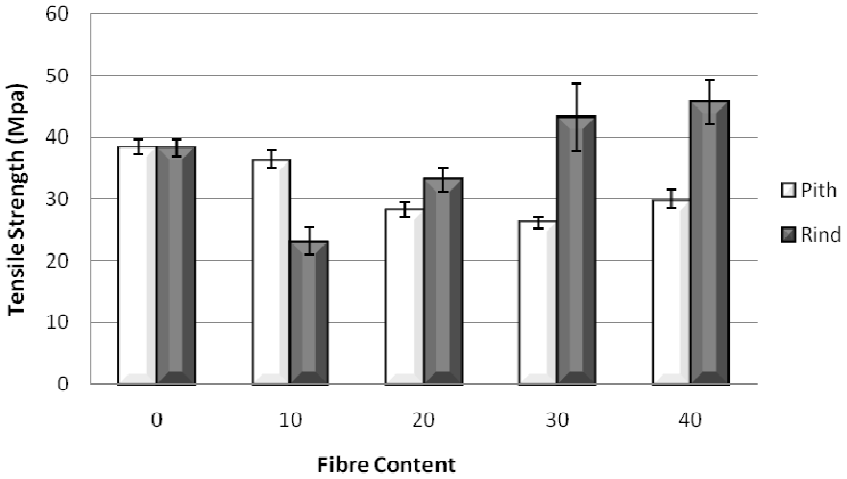
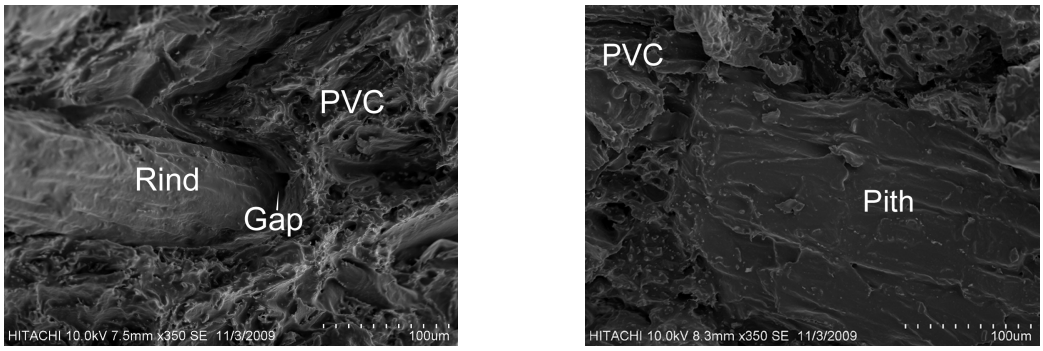


Fig. 2: Tensile strength of pith/PVC and rind/PVC composites

The low of tensile strength of rind/PVC at low fibre content (10%) can be explained by the fact that there is a big gap between pulled out fibre and PVC in the composites as shown in Fig. 3(a), which is not found at the pith/PVC composites due to better fibre-matrix interaction (Fig. 3(b)). This gap indicates low interfacial interaction between fibre and the matrix and is suspected as the origin of rupture or crack initiation [6]. On the other hand, a fibre may also act as crack inhibitor [7]. When a load is applied to the composite, a crack can be arrested by the fibre and prevent rupture from occurring. Hence, a higher load is needed to break up the composite at the increase of fibre content. Higher fibre content means higher density of crack inhibitors, and as a result, the tensile strength of the composite is increased.



(a) (b)

Fig. 3: SEM micrograph of fracture surface of the tensile-tested (a) rind/PVC and (b) pith/PVC composites.

At low fibre content, the effect of crack initiation was more dominant as compared to the effect of crack inhibition. As a result, the tensile strength of the composite was decreased. However, at high fibre content, the effect of crack inhibition was more dominant and a higher tensile strength of the composites was observed.

Another explanation is that the decrease of tensile strength, especially at low fibre content, may be caused by the reduction in area that participates in transfer of the loading stresses, called the effective cross-sectional area. If there is perfect adhesion between fibre and matrix, all of the loading stresses would be transferred to the fibre and no reduction of effective cross-sectional area would result. In the case of no adhesion, the interface layer between fibre and matrix are not able to transfer the stress [8]. In the actual case, there are variable qualities of adhesion between matrix and fibre, which range from poor (almost no adhesion) to excellent (almost perfect adhesion). This variable quality of adhesion affects the efficiency of stress transfer. Better quality of adhesion results in higher efficiency of stress transfer.

The effect of fibre content on the tensile modulus of the composites is presented in Fig. 4. It seems that there is a similar trend observable between the tensile modulus and tensile strength, especially for pith/PVC composites. The effect of crack initiation and crack inhibition, however, is not adequate to explain the trend of tensile modulus. This is because tensile modulus is calculated as ratio of strength and strain at the elastic region, whilst the phenomena of rupture occurs beyond the elastic region of the tress-strain curve. The trend was mostly affected by the efficiency of stress transfer. There was adequate quality of adhesion bonding between the PVC and bagasse fibres to increase the tensile modulus when the fibre content was increased. However, the reduction of effective cross-section results in a lower tensile modulus as compared to that of neat PVC, especially at low fibre content.

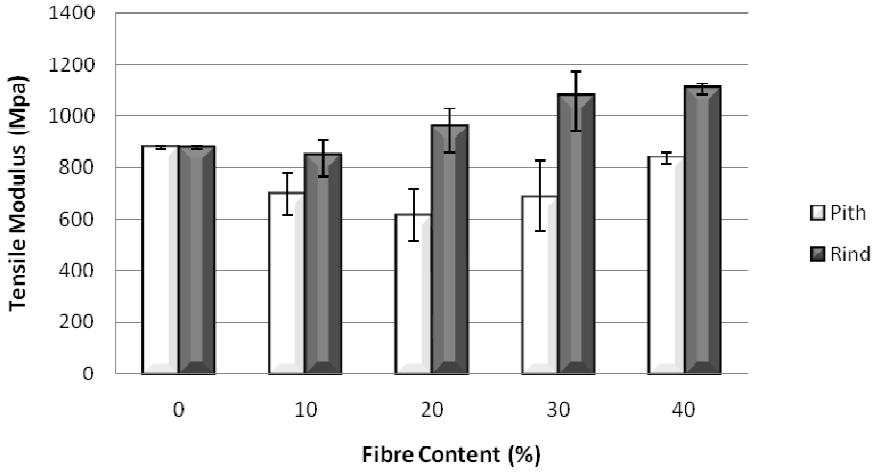


Fig. 4: Tensile modulus of pith/PVC and rind/PVC composites

Impact testing of composites. Fig. 5 clearly shows that the impact strengths of both pith/PVC and rind/PVC composites are lower than that of neat PVC. This is not surprising, since both pith and rind are less ductile as compared to PVC. Like other mechanical properties, the impact strength of composites is highly affected by the fibre. The maximum tensile strain of PVC may reach more than 50%, whilst that of pith and rind are below 5%, as presented in Table 1. This low ductility results in low energy required to break the fibre. Because the tensile strain of pith fibre is higher than that of rind fibre, the impact strengths of pith/PVC materials are higher than that of rind/PVC composites.

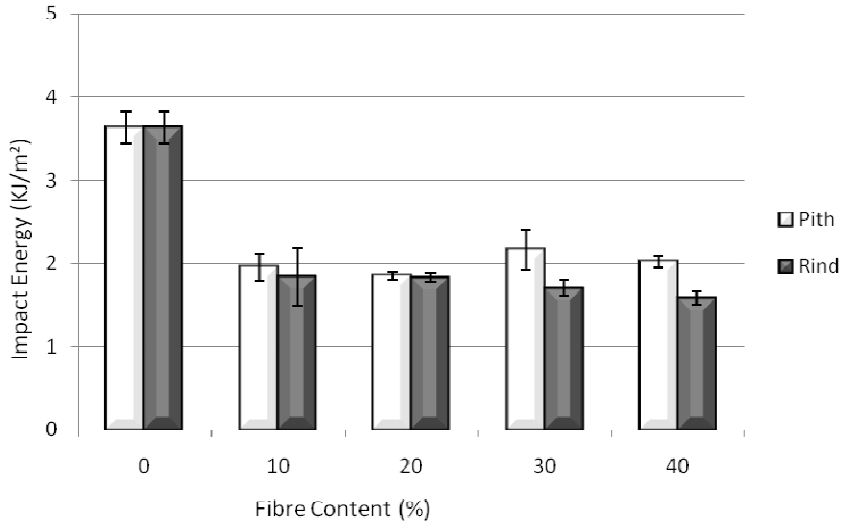


Fig. 5: Impact energy of pith/PVC and rind/PVC composites

Summary

The fibre content and fibre source (pith/rind) of SB affects tensile and impact properties significantly. In general, the incorporation of low content pith and rind fibre decreases the tensile strength and modulus of PVC. However, the tensile strength and modulus increase with the fibre content. Rind/PVC composites exhibited superior strength and stiffness as compared to pith/PVC composites. At fibre contents of 30% and 40%, the tensile strength and modulus of rind/PVC composites are higher than the matrix material. In contrast, the impact strengths of both pith/PVC and rind/PVC were lower than that of PVC.

Acknowledgements

The authors wish to thank Universiti Putra Malaysia for financial support of this study and fellowship funding for the main author through the Research University Grant Scheme (RUGS; Project no: 05/01/07/0190RU) and Graduate Research Fellowship (GRF).

References

[1] S. C. Lee, M. Mariatti: Mater. Lett. Vol. 62 (2008), p. 2253.

[2] D. Willoughby: *Plastic Piping Handbook* (McGraw-Hill, New York 2002).

[3] L. Nass: *Encyclopedia of PVC* (Marcel Dekker, New York 1985).

[4] Y.-T. Zheng, D.-R. Cao, D.-S. Wang, J.-J. Chen: Compos Part A Vol. 38 (2007), p. 20

[5] Y. Li, C. Hu, Y. Yu: Compos. Part A Vol. 39 (2008), p. 570-578.

[6] E. S. Zainudin, S. M. Sapuan, K. Abdan, M. T. M. Mohamad: Polym. Plast. Technol. Eng. Vol. 48 (2009), p. 97.

[7] R. T. Bocchieri, R. A. Schapery, M. R. Gorman: J. Compos. Mater. Vol. 37 (2003), p. 421.

[8] N. Wang, X. Zhang, X. Ma, J. Fang: Poly. Degrad. Stab. Vol. 93 (2008), p. 1044.

© (2011) Trans Tech Publications, Switzerland
doi:10.4028/www.scientific.net/KEM.471-472.173

Notch Effect on Discontinuous Fiber Reinforced Thermoplastic Composites

Amit Kumar Haldar[1,a] and S. Senthilvelan[1,b]

[1]Department of Mechanical Engineering, Indian Institute of Technology Guwahati

Guwahati 781039, India

[a]amithaldar86@rediffmail.com, [b]ssvelan@iitg.ernet.in

Keywords: Thermoplastic composite, Damage Tolerance, Fatigue, Failure

Abstract. Increasing utilization of thermoplastic composites in the structural application necessitates understanding of damage tolerance characteristics. In this work, unreinforced, 20 % short, 20 % long glass fiber reinforced polypropylene were injection molded and considered. Test specimens with different notch sizes were tested under static as well as fatigue loading conditions. Under static load condition, short fiber reinforced and unreinforced test material exhibited notch strengthening effect; whereas long fiber reinforced material exhibited notch weakening effect. Failure morphology under fatigue condition exhibited the influence of notch size and length of reinforced fibers over performance. Significant difference between notched and unnotched specimens is observed at low cycle fatigue and very less difference in performance is observed at high cycle fatigue condition.

Introduction

In recent years, discontinuous thermoplastic composites are being used in structural application due to its mass production capability and reasonable mechanical properties. Goel *et al.* [1] evaluated the fatigue performance of long glass fiber reinforced polypropylene. Material hysteretic loss and temperature rise were also investigated however notch effect was not considered. Ferreira *et al.* [2] evaluated the damage tolerant fatigue performance of woven glass fiber reinforced polypropylene. Effect of loading conditions and notch sizes were investigated; however effect of reinforced fiber lengths were not considered. Mariatti *et al.* [3] investigated the effect of notch size and location on the performance of woven thermoplastic composites; however this study was limited to static condition. Cowley and Beaumont [4] investigated the damage tolerant performance of thermoset and thermoplastic laminates and understood the effect of stress and temperature. Carlsson *et al.* [5] confirmed high notch sensitivity in graphite polyetherketone composite than that of graphite epoxy composite and highlighted the importance of stress relieving mechanism in reducing the notch sensitivity. Pinnell [6] observed higher open and filled hole tensile strength in thermoplastic than thermost composite and reported a greater stress relief at the hole edge in thermoplastic material. Author [7] molded leaf spring with thermoplastic composite and reported the joint fatigue performance, wherein ductile composite exhibited superior performance at low cycle fatigue condition and brittle material superior performance at high cycle fatigue condition. Static and dynamic performances of the composite pinned joints are exceedingly influenced by the joint geometry, environment and testing conditions [8-10]. Though sufficient work has been done to understand the effect of reinforcement and notch effect on the polymeric composite independently, no work reported the combined effect of notch and reinforced fiber length on thermoplastic materials and hence present work attempted the same.

Materials and Methodology

Unreinforced polypropylene (UFPP), 20 wt % short glass fiber reinforced polypropylene (SFPP) and 20 wt % long glass fiber reinforced polypropylene (LFPP) were injection molded into tensile specimens as per the ASTM D 638. The retention of fiber length in long and short glass fiber reinforced materials was 1.25 and 0.44 mm (weight average) and reported elsewhere [5]. Universal servo hydraulic testing facility (Instron 8801) was used for performance evaluation under static and fatigue conditions. Static tests were conducted with the displacement rate of 1 mm/min. Hole of 2, 4 and 6 mm diameter were made at the specimen centre to understand the effect of notch sensitivity. Fatigue tests were performed at 1 Hz frequency under tension-tension mode with 0.1 stress ratio.

Results and Discussions

Fig. 1 shows the load-deflection plot of test material with and without notch. For all the test materials, the failure load decreases due to the presence of notch with the reduction in extension. From this graph, it is confirmed that ductility of UFPP>> SFPP >> LFPP. To quantify notch sensitivity factor, following relation was used.

$$Q = \frac{K-1}{K_t-1} \tag{1}$$

where K_t is the theoretical/elastic stress concentration factors based on the width to diameter ratio, K is the strength reduction factor and it is given by the ratio of strength of unnotched specimen to the strength of notched specimen.

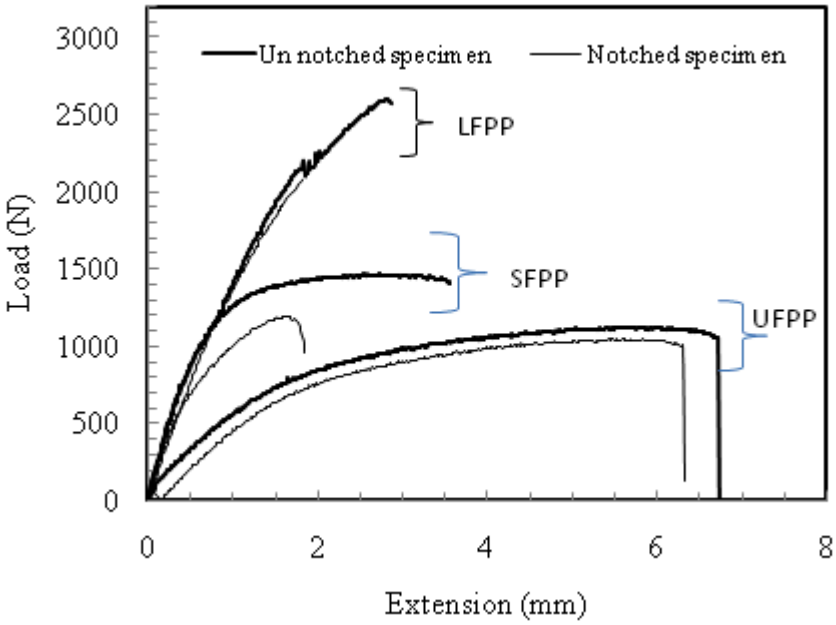


Fig. 1 Load-deflection plot of test material with 2 mm notch diameter

The fracture strength of notched and unnotched specimens of LFPP, SFPP and UFPP are illustrated in Fig. 2. It is to be noted, strength of notched specimen was estimated with the net area (by subtracting notch area from the original area). As the notch size of LFPP increases, the strength found to decreases, whereas strength found to increase in the SFPP and UFPP. With the computed strength reduction factor, the notch sensitivity of LFPP, SFPP and UFPP were obtained and plotted as shown in Fig. 3. It is confirmed that the presence of long reinforced fibers in LFPP make the material to be more notch sensitive. SFPP and UFPP showed a notch strengthening effect which is observed from the negative value of notch sensitivity factor. Notch strengthening effect implies the material ability to undergo localized yielding near the hole prior to failure [11]. Author [7]

evaluated joint performance of composite leaf spring under fatigue performance, wherein leaf spring made of SFPP and UFFP exhibited superior performance than that of leaf spring made of LFPP under low cycle fatigue condition.

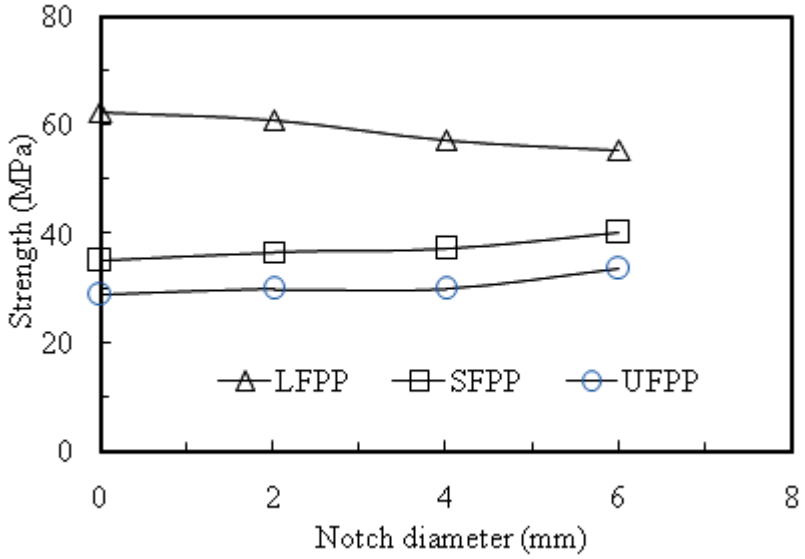


Fig. 2 Fracture strength of test materials

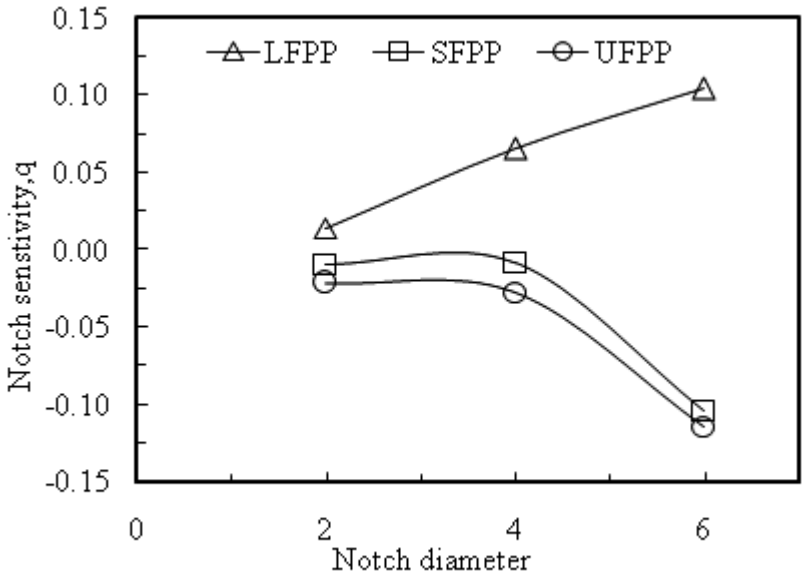


Fig. 3 Test material notch sensitivity

Fig. 4 shows the fatigue performance of notched test materials. At least three trails were conducted and mean was used for plot and the deviations were found to be within 8 %. Long fiber reinforced polypropylene material exhibited superior fatigue performance than that of short fiber reinforced and unreinforced polypropylene. Reinforced materials (LFPP and SFPP) exhibited substantial notch size effect at high stress level, 40 and 43.3 MPa; whereas notch effect was found to be less in the unreinforced material. The reason for the significant notch size effect on reinforced material performance at high stress level is explained as follows. When the material with small notch size (2 mm) is subjected to fatigue load, reinforced fibers carry significant amount of load resulted in more fiber bent as shown in Fig 5a. However, material with 4 mm notch size exhibited poor performance. Owing to the insufficient length, reinforced fibers do not carry major load

resulted in less fiber bent as shown in Fig 5b. Unreinforced material at high stress level exhibited less effect of notch size over fatigue performance due to the absence of reinforced fibers. SFPP and UFPP exhibited very less or no effect of notch size at low stress level, 26.66 MPa; whereas LFPP exhibited significant performance difference due to the notch size. This behavior is due to the notch sensitivity of test materials (Fig. 3); LFPP exhibited notch weakening effect and SFPP and UFPP material exhibited notch strengthening effect. Authors [12] conducted dynamic mechanical analysis on chosen material and found that storage modulus increases when the reinforced fiber length increases. Notch sensitivity of the composite is dependent on matrix and fiber material [6]. Guynn and Bradley [13] investigated composite materials and reported that the ductile matrix exhibited better ability to dissipate stress concentration near the notch than that of brittle material. Ferreira *et al.* [2] investigated the fatigue performance of glass fiber reinforced polypropylene specimens with central and offset holes having different diameters where significant difference between notched and unnotched specimens was observed at low cycle fatigue and very less difference in performance was observed at high cycle condition, similar to the present case.

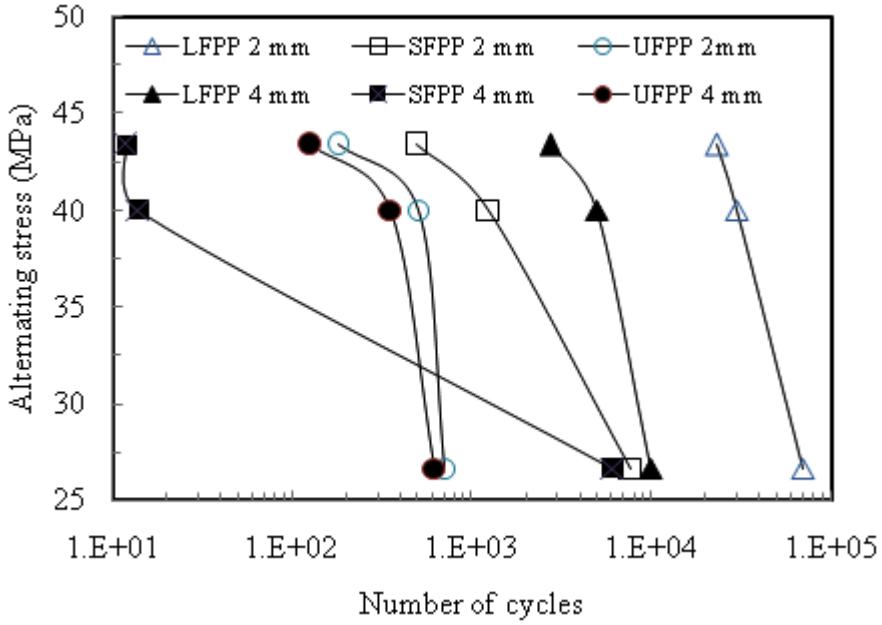
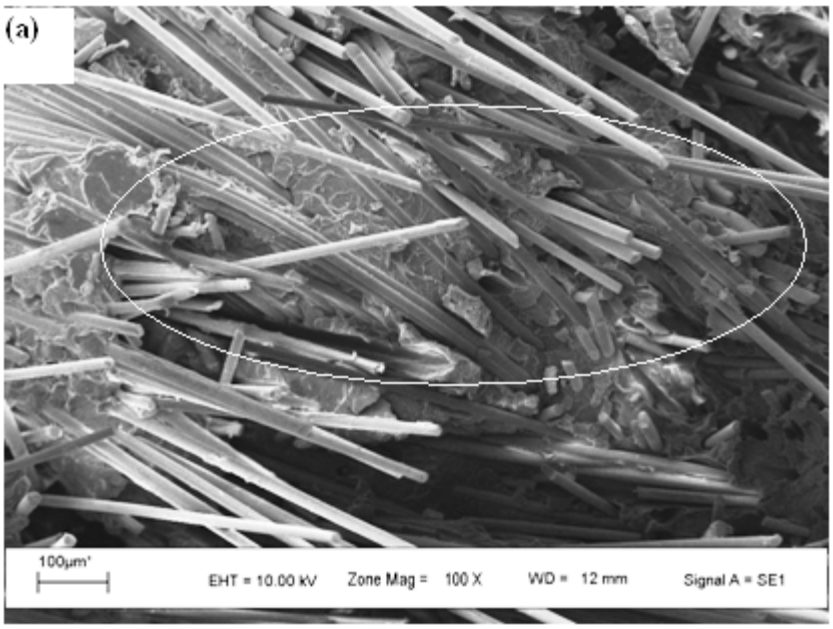


Fig. 4 Fatigue performance of notched test materials



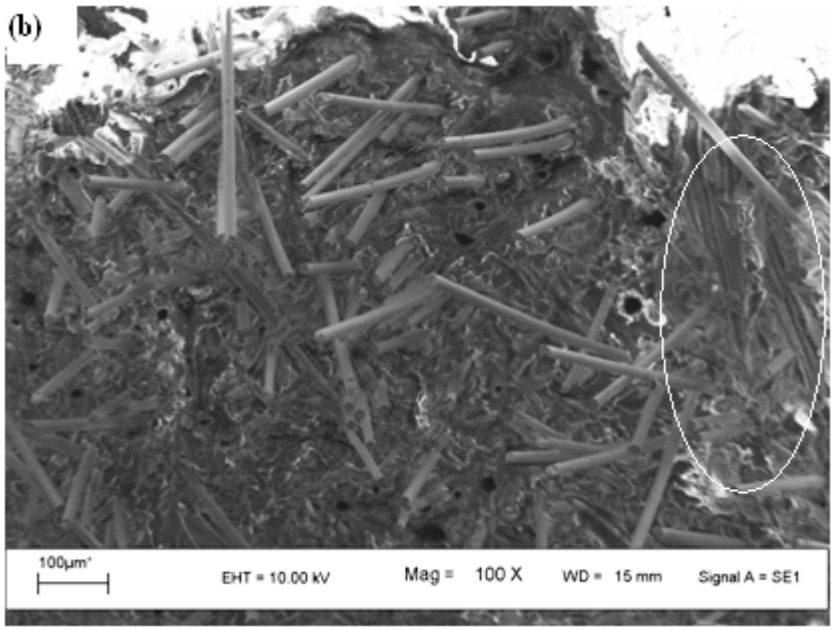
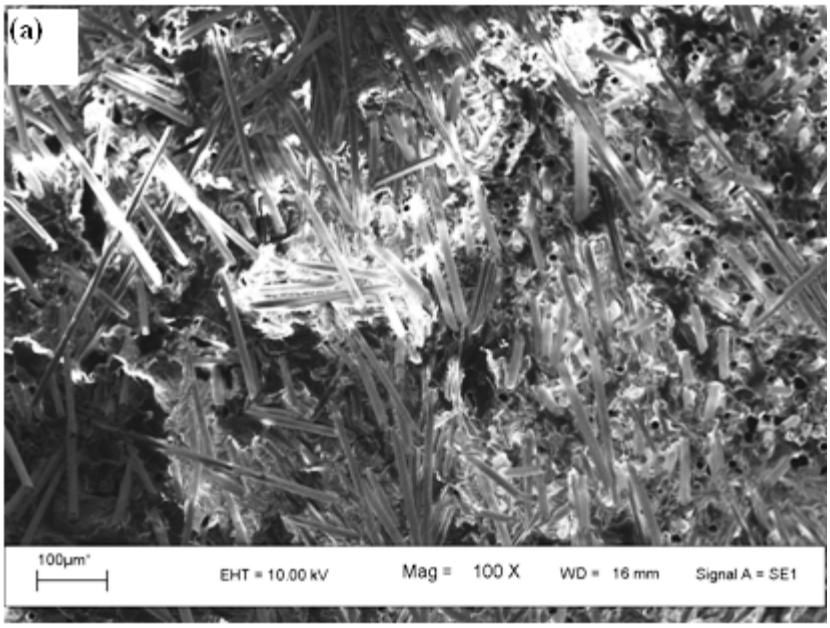


Fig. 5 Fracture surface of long fiber reinforced specimen subjected to 43.3 MPa (a) 2 mm notch diameter and (b) 4 mm notch diameter

Fractured specimens were observed under scanning electron microscope near the notch. When the notch size was small and reinforced fibers were long, bent reinforced fibers were observed near the notch (Fig. 5). However this feature was not observed when the test material was reinforced with relatively small length fibers and the notch diameter was sufficiently large (Fig. 6). Failure morphology was found to be influenced by the material as well as notch diameter. Due to the inadequate length of reinforced fibers; SFPP exhibited fiber pullout as major failure whereas LFPP exhibited very less fiber pull out. In the case of LFPP, when the notch diameter was 2 mm, most of the fibers near the notch, bent as marked in Fig. 5a; however when the notch specimen was 4 mm, only few fibers bent as marked in Fig.5b. In the case of SFPP, no fiber bending was observed since the reinforced fiber lengths were sufficiently smaller than that of notch diameter (Fig. 6). Fiber bend in the failure morphology indicated the role of reinforced fibers in the load bearing ability.



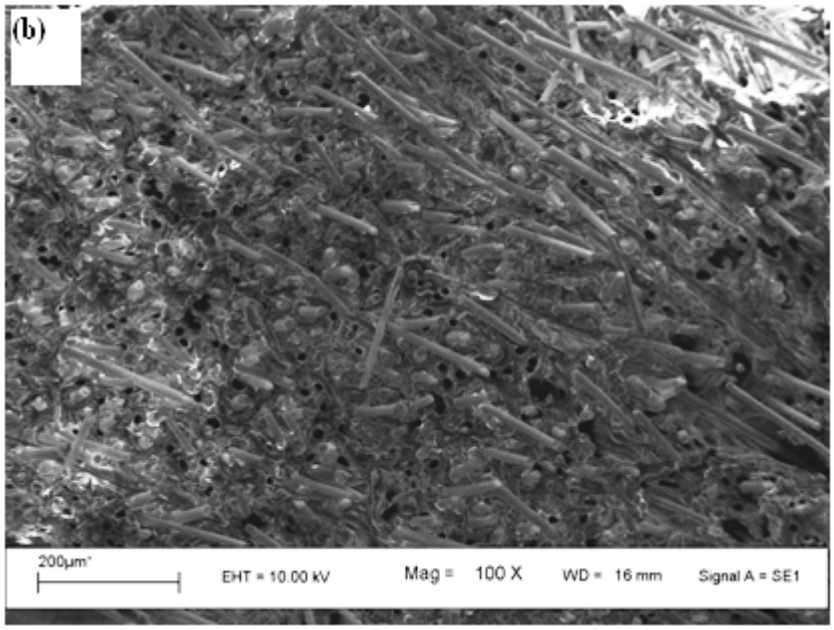


Fig. 6 Fractured surface of short fiber reinforced specimen subjected to 43.3 MPa (a) 2 mm notch diameter and (b) 4 mm notch diameter

Summary

Fracture strength of discontinuous fiber reinforced thermoplastic material with different notch size confirmed notch strengthening effect in ductile material and notch weakening effect in brittle material. This behavior is due to the fact that ductile material exhibited better ability to dissipate stress concentration near the notch than that of brittle material. Effect of different notch size under cyclic load confirmed the superior performance of reinforced material and specimens with small notch size. Failure morphology confirmed the role of reinforced length and notch size in the composite load bearing capability.

References

[1] Goel, K.K. Chawla, U.K. Vaidya, N. Chawla and M. Koopman: Materials Characterization, Vol. 60 (2009), p. 537
[2] J.A.M. Ferreira, J.D.M Costa and M.O.W Richardson: Composites Science and Technology, Vol. 57 (1997), p.1243
[3] M. Mariatti, M. Nasir and H. Ismail: Polymer Testing, Vol. 20 (2001), p. 179
[4] K.D Cowley and P.W.R Beaumont: Composite Science and Technology, Vol.57 (1997), P.1211
[5] L.A.Carlsson, C.G. Aronsson and J. Backlund: Journal of Material Science, Vol. 24 (1989), p. 1670
[6] M.F. Pinnell: Composite Science and Technology, Vol. 56 (1996), p. 1405
[7] C.Subramanian and S. Senthilvelan: Materials and Design, Vol. 31 (2010), p. 3733
[8] J.H. Stockdale and F.L Matthews: Composites, Vol.7 (1976) , p. 34
[9] A, Aktas, H. Imrek and Y. Cunedioglu: Composite Structures, Vol. 89 (2009), p.459
[10] T.S. Lim, B.C. Kim and D.G. Lee: Composite Structures, Vol. 72 (2006), p. 58
[11] H. Fouad: Materials and Design, Vol. 31 (2009), P.1117
[12] C. Subramanian and S. Senthilvelan: Proceedings of the Institutions of Mechanical Engineers Part L Journal of Materials: Design and Application, Vol. 223 (2009), p. 131
[13] E.G. Guynn and W.L. Bradley: Journal of Reinforced Plastics and Composites, Vol.8 (1989), p. 133

© (2011) Trans Tech Publications, Switzerland
doi:10.4028/www.scientific.net/KEM.471-472.179

Fabrication of Porous LSCF-SDC Carbonates Composite Cathode for Solid Oxide Fuel Cell (SOFC) Applications

JAROT Raharjo[1,3,4,a], ANDANASTUTI Muchtar[1,2,b], WAN RAMLI Wan Daud[1,3,c], NORHAMIDI Muhamad[1,2,d] and EDY HERIANTO Majlan[1,e]

[1]Fuel Cell Institute, Universiti Kebangsaan Malaysia, Malaysia

[2]Department of Mechanical and Materials Engineering, Universiti Kebangsaan Malaysia, Malaysia

[3]Department of Chemical and Process Engineering, Universiti Kebangsaan Malaysia, Malaysia

[4]Agency for the Assessment and Application of Technology, Jakarta, Indonesia

[a] jarot@vlsi.eng.ukm.my, [b] muchtar@eng.ukm.my, [c] wramli@vlsi.eng.ukm.my, [d]hamidi@eng.ukm.my, [e] edy@vlsi.eng.ukm.my

Keywords: Cathode, $La_{0.6}Sr_{0.4}Co_{0.2}Fe_{0.8}O_3$ (LSCF), SDC-$(Li/Na)_2CO_3$, pressureless sintering, microstructures, thermal expansion coefficient (CTE), porosity

Abstract. Composite cathodes made of perovskite $La_{0.6}Sr_{0.4}Co_{0.2}Fe_{0.8}O_3$ (LSCF) and SDC carbonates (SDC-$(Li/Na)_2CO_3$) were investigated in relation to their structure, morphology, thermal expansion coefficient and porosity. As a first step, the LSCF powder was prepared by sol-gel technique. This was followed by the preparation of the LSCF-SDC carbonates composite cathode by mixing the LSCF with SDC-$(Li/Na)_2CO_3$ electrolyte via solid state reaction in various compositions, i.e. 30, 40 and 50 wt.%, namely 70LSCF-30SDC7030, 60LSCF-40SDC7030 and 50LSCF-50SDC7030, respectively. The powder mixtures were then calcined at 680°C. The resultant powder was fine with surface area of about 3.39-7.42 m^2/g and particle size of 0.56-0.66μm. The powder consists of two distinct phases, i.e. LSCF and SDC-$(Li/Na)_2CO_3$ as confirmed with x-ray diffraction. The microstructures were observed under scanning electron microscopy (SEM). Increasing the amount of the SDC-$(Li/Na)_2CO_3$ electrolyte in the composite cathode was found to bring the thermal expansion of the cathode closer to that of the electrolyte. The cathode pellets were later compacted at different pressures (27, 32 and 37 MPa) and sintered at 600°C. The optimum porosity (20.99-24.98%) was achieved for samples with SDC-$(Li/Na)_2CO_3$ content of 30-50% sintered at 600°C and cold pressed at 37 MPa.

Introduction

Solid oxide fuel cells (SOFCs) are electrochemical devices that operate at high temperatures between 800-1000°C. The high operation temperatures can create problems such as difficulties on construction, material and process selection, thermal expansion mismatch, lower durability and fewer opportunities to mass product. In the last decade, research in SOFCs has focused on reducing their operational temperatures. Lower operational temperatures have been found to improve two large problems in the use of SOFCs, namely their life expectancy and reliability. However, decreasing the operational temperature of SOFCs leads to a performance loss of the cells. For this reason, research in this field has mostly focused on developing highly ionic conducting electrolyte with compatible high performance electrodes, both cathode and anode at lower temperatures.

Recently, low temperature SOFCs (LT-SOFCs) have been developed with operational temperatures between 400-600°C [1,2]. LT-SOFCs are based on unique dual-conducting electrolytes. These electrolytes are composites of conventional intermediate temperature solid oxide fuel cell (IT-SOFC) oxygen ion (gadolinium or samarium) conducting doped cerium with proton conducting carbonates. High performance LT-SOFCs of 300-1100mW/cm^2 have been achieved at

400-600°C [2]. However, the development of these composite electrolyte materials and their applications in LT-SOFCs is still being investigated.

The excellent performance of the SOFCs is not only because of the highly ionic conducting ceria-carbonate composite electrolytes, but also due to the highly electrocatalytic electrodes, especially the cathode. Thus the development of the compatible cathode is necessary to improve the performance of the SOFCs. Currently, only few works have reported research on the cathode material suitability for this system [3,4,5]. The requirements for cathode materials used in SOFC include good electrochemical activity, high electronic conductivity, proper porosity and thermal expansion compatibility with other components of the cell. Perovskite oxides have interesting properties, such as ionic conductivity, superconductivity, magnetorresistance and ferroelectricity. The perovskite oxide $La_2NiO_{4+\delta}$ and BSCF have been found to be suitable for use in this system and possessed good catalytic activity as reported by several researchers [4,5]. In addition, $La_{1-x}Sr_xCo_{1-y}Fe_yO_3$ (LSCF) has been found to be one of the most promising cathode materials for intermediate temperature SOFCs (IT-SOFCs) (600-800°C) with better compatibility to SDC electrolytes [6,7,8]. Therefore, the aim of this work is to develop the perovskite LSCF cathode material and its corresponding fabrication technique for the LT-SOFC system.

In this work, a mixture of LSCF and electrolyte SDC-$(Li/Na)_2CO_3$ in various compositions i.e. 70:30, 60:40 and 50:50 wt% were used as cathode material. The common method used to create single cells for use in LT-SOFC systems is using a single press with the uniaxial hot press. The uniaxial hot pressing technique is an expensive process which is unsuitable for the mass production of the cells. Pressureless sintering, on the other hand, is a process that is inexpensive, better suited for mass production and allows for the production of thin layers. In this paper, the fabrication of composite cathode pellets by pressureless sintering is reported. The following discussion is based on the experimental results.

Experimental Procedure

Synthesis and Characterisation of the Powder. The composite cathode was made of a mixture of $La_{0.6}Sr_{0.4}Co_{0.2}Fe_{0.8}O_3$ (LSCF) and electrolyte powder SDC-$(0.67Li/0.33Na)_2CO_3$. As a first step, the perovskite oxide $La_{1-x}Sr_xCo_{0.2}Fe_{0.8}$ (LSCF) with x=0.4 was prepared by sol-gel technique [9]. Stoichiometric amounts of $La(NO_3)_3.6H_2O$ (99.8wt%, Sigma Aldrich Sdn.Bhd.), $Sr(NO_3)_2.6H_2O$ (99.8wt%, Sigma Aldrich Sdn.Bhd.), $Co(NO_3)_2.6H_2O$ (99.8wt%, Sigma Aldrich Sdn.Bhd.) and $Fe(NO_3)_2.9H_2O$ (99.8wt%, Sigma Aldrich Sdn.Bhd.) were mixed and dissolved in ethanol. The precursor solution was refluxed at 80°C to produce the LSCF solution. The solution was then concentrated to 1/3 of the original volume using an evaporator to form a gel. The gel was later dried in an oven at 120°C overnight to remove the solution after which the dried gel was ground and sintered in air at 900°C for 4 hours to produce LSCF powder.

The composite electrolyte made of samarium doped cerium (SDC, $Ce_{0.8}Sm_{0.2}O_{1.9}$) and binary carbonates $(0.67Li/0.33Na)_2CO_3$ were prepared in two steps as detailed in a previous paper [10]. The electrolyte powder was mixed with 30 wt% carbonates content and this is called SDC7030.

Finally, the composite cathode was prepared by mixing LSCF and SDC7030 via solid state method at three different compositions, i.e. 70:30, 60:40 and 50:50 wt% and these are called 70LSCF-30SDC7030, 60LSCF-40SDC7030 and 50LSCF-50SDC7030, respectively. The powders were mixed and reduced in size in a ball mill for 16 hours. The mixture was next heat treated in a furnace at 680°C for 1 hour.

X-ray diffraction (XRD) patterns of the composite cathode powders were recorded at room temperature using an x-ray diffractometer (Shimadzu XRD-6000) with Cu Kα radiation (λ=1.5418A^0), 40kV and 40mA, with 2θ varying from 10° to 80°. A Zeiss EVO MA10 scanning electron microscope (SEM) was used to examine the morphology of the pellets of composite cathodes with magnification up to 30Kx. Surface area analysis was conducted on the composite

powders using a BET surface area analyser (Altamira Instruments AMI-200). The particle size distribution of the powder was measured using a laser particle sizer (Fritsch Analysette 22).

Thermal Expansion Analysis. It is important to study the thermal expansion properties of all components of SOFC when discussing their compatibility. In this work, thermal expansion analysis was conducted on the cathode using a dilatometer (Netzsch DIL402C). The samples for the coefficient thermal expansion (CTE) measurements were fabricated in cylinder form by standard pressureless sintering (~6mm x ~10mm).

Compaction, Sintering and Porosity Observation. The composite cathode material was manufactured in 20mm diameter pellets for porosity measurements (~1.0mm thick). The pellets were fabricated and later sintered by standard atmosphere pressureless sintering. The pressureless sintering technique involved the uni-axial pressing of the cathode powder in a stainless steel die with pressing pressures of 27, 32 and 37MPa. The pellets were thereafter sintered to the temperature 600°C for 1 hour in air. Porosity measurements of the cathode pellets were conducted by the Archimedes method. With this method, isopropanol was used instead of water, as the carbonates are slightly soluble in water.

Results and Discussion

Characterisation of The Powders. Fig. 1 shows the XRD patterns of LSCF-SDC7030 composite cathode with varying electrolyte contents of 30, 40 and 50 wt%, namely 70LSCF-30SDC7030, 60LSCF-40SDC7030 and 50LSCF-50SDC7030, respectively. The data indicate that the calcined powder consists of LSCF and SDC carbonates (SDC7030) existing as two distinct phases as confirmed from the x-ray diffraction pattern. The patterns for LSCF and SDC7030 are indexed in the cubic phase. These results are in agreement with reports from other authors [6,9,10]. The SDC carbonates phase diffraction peaks turn stronger and sharper along with increasing electrolyte content. The introduction of the carbonates in the electrolyte composite did not change the SDC phase structure [10]. The SDC was used to enhance the mixed (ionic and electronic) conductivity and increase activity in the electrodes. On the other hand, ceria salt composites possess both ion-oxide (ceria phase) and proton (from the interfacial regions between the two phases and also from carbonate phase) conductivity [11]. Therefore, introduction of the SDC-carbonate in the composite cathode can enhance the conductivity, compatibility of the cathode and improve performance of the LT-SOFCs.

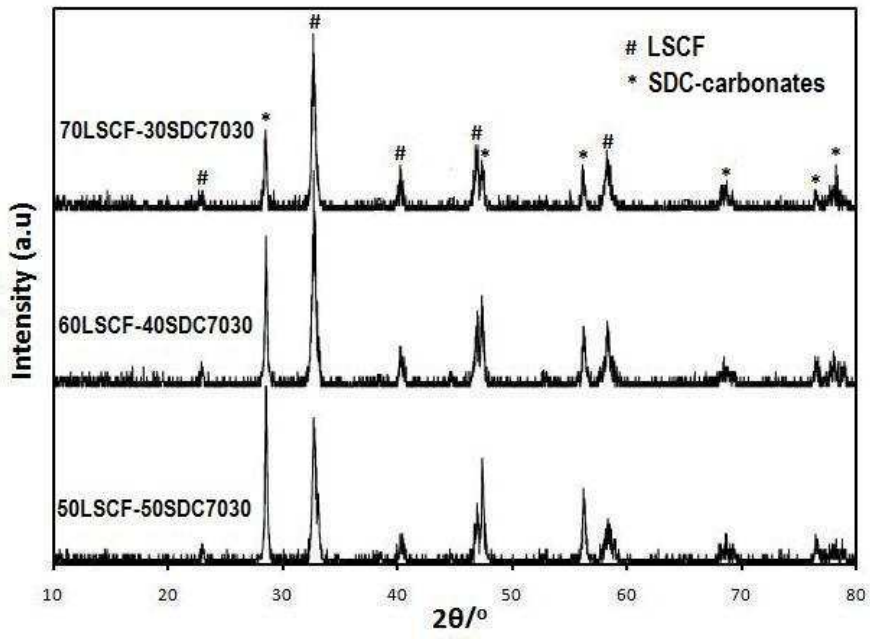


Figure 1. XRD patterns of LSCF-SDC7030 composite cathodes with varying electrolyte contents: 30%wt (70LSCF-30SDC7030), 40%wt (60LSCF-40SDC7030) and 50%wt (50LSCF-50SDC7030)

The crystallite sizes calculated from the XRD line broadening with Scherrer equation are listed in Table 1. The crystallite size of LSCF was found to have an average size of 41.55, 49.79 and 47.97nm while the size of SDC7030 were 80.90, 102.21 and 97.8 nm for the samples of 70LSCF-30SDC7030, 60LSCF-40SDC7030 and 50LSCF-SDC7030, respectively. It was thus concluded that the SDC7030 crystallite size is always a little bigger than LSCF for all electrolyte contents.

The specific surface area was measured using a BET surface area analyser. The samples were tested at approximately -180°C in liquid nitrogen during the analysis. Software analysis confirmed the results as 4.04, 3.39 and 7.42m^2/g, for samples 70LSCF-30SDC7030, 60LSCF-40SDC7030 and 50LSCF-SDC7030, respectively. This shows that the surface area of the composite did not change drastically with the electrolyte content in the composite. These results were close to the surface area of pure LSCF around 7.64m^2/g and comercial LSCF around 5-7m^2/g, which will be good for SOFC applications [7]. However, the greater the particle size, the smaller the surface area. In this case, ball miling proses and calcine temperature more effected to the surface area results rather than carbonate content.

Table 1. Particulate properties of the composite cathode LSCF-SDC7030 powders

Samples	Surface area (m^2/g)	Average particle size (μm)	Cyrstallite size (nm)	
			LSCF	SDC7030
50LSCF-50SDC7030	7.42	0.560	47.97	97.8
60LSCF-40SDC7030	3.39	0.655	49.79	102.21
70LSCF-30SDC7030	4.04	0.624	41.55	80.90

The particle size was measured using a laser particle sizer (Fritsch Analysette 22). The measurement method was through laser diffraction in a convergent laser beam. Table 1. shows the average particle size of the composite cathode powders with varying electrolytes contents. Software analysis confirmed the results of the distribution of particles for 70LSCF-30SDC7030 (0.216-0.859μm), 60LSCF-40SDC7030 (0.208-0.979μm) and 50LSCF-SDC7030 (0.194-0.772μm), with average particle size as 0.624, 0.655 and 0.560 μm for 70LSCF-30SDC7030, 60LSCF-40SDC7030 and 50LSCF-SDC7030, respectively. The data indicates that the average particle size of the cathode did not change drastically with the electrolyte content in the cathode composite. This corresponds well to the results of the BET measurement that a greater particle size results in a smaller surface area.

Thermal Expansion Analysis. One of the concerns with SOFCs is the mechanical stability of the cells during thermal cycles. The compatibility between the thermal expansions of the electrolyte and cathode should be examined. Table 2. shows the coefficient thermal expansion (CTE) results measured using standard dilatometry (Netzsch DIL402C) at 100-500°C. The SDC7030 composite electrolyte was tested as reference.

Table 2. Coefficient of thermal expansion of the cathodes and electrolyte

Samples	CTE (x10^{-6} K^{-1}) (100-500°C)
70LSCF-30SDC7030	2.27
60LSCF-40SDC7030	1.18
50LSCF-50SDC7030	0.88
SDC7030 (electrolyte)	0.78

The result in Table 2 shows that the CTE of the composite cathode materials was very sensitive to the amount of electrolyte in the composite cathode. The addition of electrolyte can reduce the CTE. Increasing the amount of electrolyte in the composite cathode was found to bring the CTE of the cathode closer to that of the electrolyte. The 50LSCF-50SDC7030 composite cathode (0.88x10^{-6} K^{-1}) was more compatible with the SDC7030 composite electrolyte (0.78x10^{-6} K^{-1}). While there is

no defined benchmark in literature for acceptable CTE between cathode and electrolyte, a smaller difference in CTE will decrease the interfacial thermal stress failure.

Porosity Analysis and Microstructure of The Composite Cathode Pellets. Pressureless sintering is a very cost-effective form of sintering to produce the LT-SOFC cathode pellets. Pressureless sintering uses standard pressing equipments and furnaces making it a very scalable and easily automated process. The three parameters that are optimised to improve the porosity of the cathode are composition, sintering temperature and pressing pressure. In the present work, the effects of the electrolyte content and packing pressure on the porosity of the composite cathode have been studied. Sintering of the pellets was conducted at 600°C after pressing under different pressures of 27, 32 and 37MPa. The results of the porosity study are depicted in figure 2.

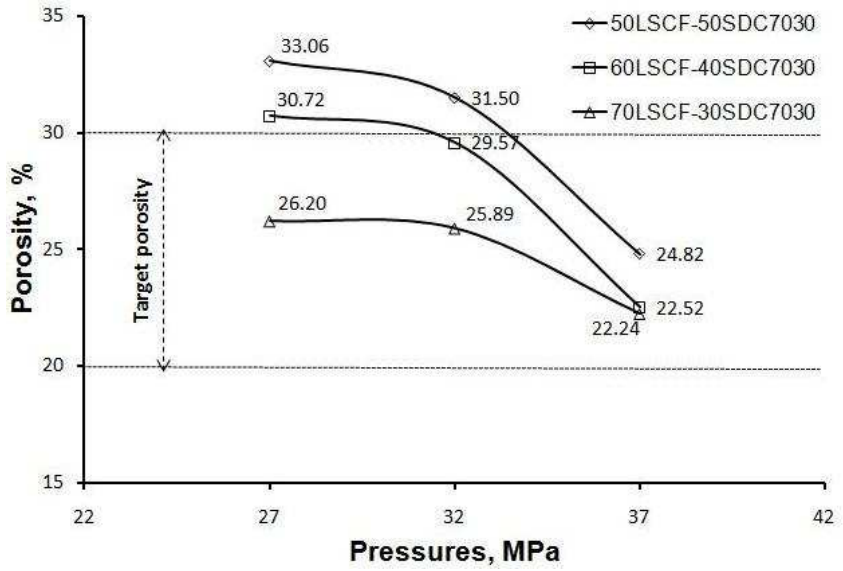


Figure 2. Porosity of cathode pellets after different cold press loadings (27, 32 and 37MPa), followed by sintering at 600°C.

The target porosity of 20-30% is indicated by the dashed line in figure 2. The data in fig. 2 shows that the porosity tends to increase with increasing electrolyte content regardless of the packing pressure. It is also shown in fig. 2 that the porosity of the pellets decreased upon the increase in pressing pressure. The composite cathodes 70LSCF-30SDC7030, 60LSCF-40SDC7030 and 50LSCF-SDC7030 were found to yield the optimum porosity of 22.24-24.82% upon pressing at 37MPa and a sintering temperature of 600^{0}C. From a previous study on the fabrication of electrolytes [10], it was shown that the carbonate content affected the densification of the final pellets. In the present work, the densification of the carbonate content did not seem to be influenced much by the carbonate content. On the other hand, the pressing pressure proved to be more influential than the carbonate content in the fabrication of the cathode.

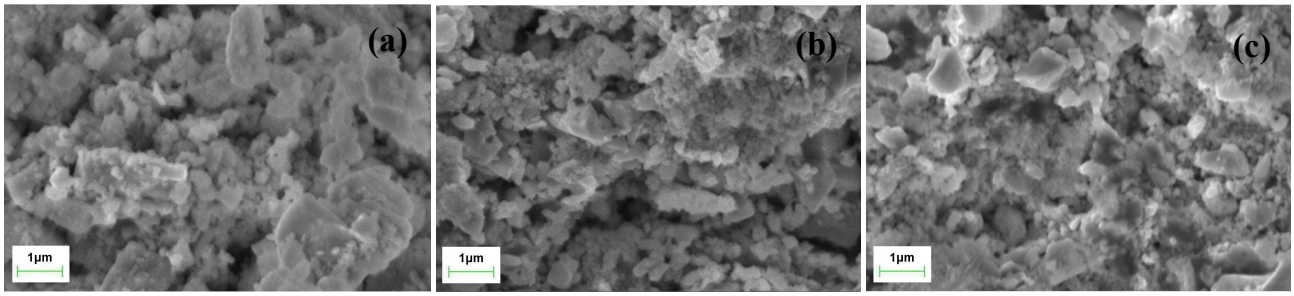


Figure 3. SEM of fracture surfaces of the composite cathode pellets: 50LSCF-SDC7030 at different pressing pressures i.e. 27MPa (a), 32MPa (b) and 37MPa (c), followed by sintering at 600°C.

Fig. 3 shows the SEM micrographs of fracture surfaces of the composite cathode pellets 50LSCF-50SDC7030 at different pressing pressures, i.e. 27MPa (a), 32MPa (b) and 37MPa (c), followed by sintering at 600°C. Electrodes (cathode) meant for use in LT-SOFCs must be porous (20-30%). Enough porosity is needed to supply oxygen gas into the cathode side. Fig. 3 shows that the dark areas in the micrographs correspond to the pores in the samples; the gray and white areas are the LSCF and SDC carbonates phases, respectively. From the SEM images , it is shown that the greater the pressing pressure, the porosity tends to decrease with pore sizes between approximately 97-183nm. These results correspond to the porosity measurements in fig. 2.

Summary

This paper presents results from our work on the fabrication of the porous composite cathode LSCF-SDC7030 with various electrolyte contents of 30, 40 and 50 wt%. A solid state reaction method was used to prepare LSCF-SDC7030 powders. The powders calcined at 680°C were fine with surface area of 3.39-7.42 m^2/g and an average distribution particle size of 0.56-0.66μm. The greater the particle size, the smaller the surface area. It has been shown that the powders consist of LSCF and SDC7030 as two distinct phases. Increasing the amount of electrolyte in the composite cathode brings the thermal expansion of the cathode closer to that of the electrolyte. The optimum porosity (20.99-24.98%) was achieved for samples with SDC-$(Li/Na)_2CO_3$ content of 30-50% sintered at 600°C and cold pressed at 37 MPa. The pore sizes of the pellets are about 97-183nm. The pressureless sintering method was thus found to be potentially suitable for the manufacture of these composite anodes.

Acknowledgement

The authors would like to acknowledge Universiti Kebangsaan Malaysia (UKM) and the Malaysian Government for research sponsorship under UKM-OUP-TK-16-75/2010 and UKM-GUP-TK-08-17-324.

References

[1] A. Boden, J. Di, C. Lagergren, G. Linbergh and C.Y. Wang : Journal of Power Sources Vol. 172 (2007), p. 520-529.
[2] J. Huang, Z. Mao, Z. Liu and C. Wang : Journal of Power Sources V.175 (2008), p.238-243.
[3] X. Sun, S. Li, J. Sun, X. Liu and B. Zhu : International Journal Electrochemical Science Vol. 2 (2007), p. 462-468.
[4] M.D. Mat, X. Liu, Z. Zhu and B. Zhu : International Journal of Hydrogen Energy Vol. 32 (2007), p.796-801.
[5] H. Jianbing, R. Gao. Z. Mao and J. Feng : International Journal of Hydrogen Energy Vol.35 (7) (2008), p.2657-2662.
[6] M. Ghouse, Y. Al-Yousef, A. Al-Musa, M.F. Al-Otaibi : International Journal of Hydrogen Energy 35 (17) (2010), p. 9411-9419.
[7] Muchtar, N.A. Hamid, N. Muhamad, W.R.W. Daud : Advanced Materials Research Vols.139-141 (2010), p.141-144.
[8] H.A. Rahman, A. Muchtar, N. Muhamad, H. Abdullah : Advanced Materials Research Vols. 139-141 (2010), p.145-148.
[9] N.A. Hamid, A. Muchtar, W.R.W. Daud, N. Muhamad : Sains Malaysiana Vol.38 (6) (2009), p.857-861. A.
[10] J. Raharjo, A. Muchtar, W.R.W. Daud, N. Muhamad and E.H. Majlan : Key Engineering Material Vol. 447-448 (2010), p.666-670.
[11] B. Zhu, X.R. Liu, P. Zhou, X.T. Yang, Z.G. Zhu and W. Zhu: Electrochemical Communication Vol. 3 (2001), pp.566.

© (2011) Trans Tech Publications, Switzerland
doi:10.4028/www.scientific.net/KEM.471-472.185

Developing Packaging By Using Smart Material Which Helps to Realize Spoilage In Yoghurt

Bülent Eker [1,a] Ayşegül Akdogan Eker [2,b]

[1] Namık Kemal University, Biosystems Engineering Department, Tekırdag-TURKEY
[2] Yıldız Technical University, Mechanical Engineering Department, Istanbul-TURKEY
[a] beker@nku.edu.tr [b] akdogan@yildiz.edu.tr

Keywords: Smart, material, polypropilen, kaoline, pack, yoghurt

Abstract The important effect of yoghurt on people's health caused increasing of many technological works and researches not only in our country but also all over the world.The environment in which yoghurt kept, may cause many sort of germs and contamination paths by the effects of some factors which are fairly similar to its own structure. These factors change the shelf-life of yoghurt and finally cause spoilage in yoghurt. In this context, it is known that the scientific works in this area which are aiming to minimize this spoilage effect, focus on the yogurt structure and packaging of yoghurt. The aim of this paper is to improve a smart polymer material which interacts with serum and changes color of the package by considering serum occurring within the shelf-life of yoghurt. PP based material will be used with the biological agencies like “kaoline” and “talc” and implemented mainly or superficial, the color change will be arised if the serum's PH increases. In practice, everyone can see the color changes with the window which will be placed on the label and the window will include the cautions according to the color levels.

Introduction

The rapid development of yoghurt depending on its important on human health has triggered technological studies not only in our country, but all over the world. As well known, health conditions must be fulfilled from production to consumption of yoghurt. The reason of this is that the microbial contaminations due to various effects and the factors within its structure. Today,these kinds of effects, affected the shelf life of yoghurt and causes it to spoil. In line of this consideration, the studies aiming to minimize or remove these effects concentrate on yoghurt structure and its packaging. Food engineers emphasize that healthy yoghurt can only be produced by fermentation of milk in natural conditions without additives. However it is known that the shelves of these yoghurts are short. Especially under conditions until usage, the increase of serum amount due to decomposition of proteins cause increase in pH level. It is a fact that, preservatives are used in order to delay this creation but they are not suggested due to health risks.

In the studies we made on local and foreign literatures, we observed that, serum and accordingly pH change should be monitored in yoghurt and that there are serious R&D studies made on intelligent packaging sensing the changes in food within. Changes on packaging material are considered as well as using pH and heat indicators.

On the other hand, the rapidly rising expectations on packaging sector can be summarized as improved barrier properties, heat consistency, high resistance against outer factors, being light, cheap and resistant, being visually attractive, etc. Also, the traceability of the product before it is consumed is important in means of health. Packaging waste should also be minimized in order to prevent environmental pollution. Accordingly [4], the importance of biodegradable packages increases day by day. The usage of recycled package will also be inevitable in the future. The development of intelligent packages by usage of nano-technological materials and technologies will also bring solution to all necessary issues [3]. Total active and intelligent packaging market will grow 13% and become totally 1.1 billion USD in 2011. Active packages will grow 7% and reach 975 million USD volume in 2011. European community defined the active and intelligent packages in the “80/590/EEC” directive issued on 27.10.2004. Accordingly, active package, changes the

conditions within the package actively to elongate the lifetime of the food, to preserve it and decrease its sensitivity against various factors. Intelligent package monitors the conditions in the package and condition of the product to follow up and provide information about the quality changes from production to consumption of the product. [5,7]

Pre-studies. First of all, in this study, the serum formation and pH increase from production to consumption stages of yoghurt are taken as a basis. This change is made by placing a transparent observation window on the label by changing the color of the intelligent material by usage of a special chemical structure to be used on yoghurt packaging material so that the consumer will be informed. In order to realize this purpose, it is important to analyze the yoghurt formation and consumption stages very well. If we look from this point of view, this project should be considered in two main topics ;

a.The food size,
b.The package size

The chemical composition of yoghurt varies according to the milk and applied technological process. The composition of yoghurt increases or decreases proportionately to milk, depending on the starter culture and the fermentation process. The coagulum of yoghurt is defined as an acid – casein jelly stimulated by heat. Accordingly, heat application and acidity development during incubation play important role in formation of yoghurt coagulum. With the effect of these two applications, some changes on milk proteins and some interactions between proteins occur.

The type, magnitude and stability of these interactions are effective on determining the physical properties of yoghurt coagulum. Shortly the physical structure of yoghurt is like a network formed by coagulating proteins. All this formation requires process content in the production of yoghurt. The changes in process conditions cause changes in yoghurt. The most obvious example of this is formation of serum. This formation proceeds during packaging and consumption and as a result of decomposing proteins, a liquid forms at the top of yoghurt which is named as serum. This liquid causes yoghurt to become sour in a short time.

Decreasing this serum formation is possible by examining all process from production to consumption. During our examinations, we observed that it is possible to decrease serum formation by checking all process stages in production. However, decreasing serum formation after packaging can only be made by changing the property of packaging material.

All our examinations show that the serum forming on yoghurt depends on chemical composition of yoghurt as well as packaging material, storage and transportation conditions and environmental factors. It is also another fact that this serum increases the PH of yoghurt. Up to a certain level, this does not have a negative effect on spoiling of yoghurt and emotional requests of consumers. Because of this fact, producer companies mention the expiry date on the packages. However, it was observed that yoghurt may spoil before expiry date under inconvenient conditions. In big markets, yoghurt prices are decreased as a promotion when their expiry dates are close. However cheating applications regarding yoghurt which is one of the main consumable food products are ethically and legally inacceptable.

It was observed in pre-studies that yoghurts which spoil before expiry date due to inconvenient cooling conditions are still being presented to consumers.

Solution Studies. The rapid developments in packaging sector are observed with care. Packaging solutions which decreases the human failure to zero and provides food presentation with full reliability are being designed in many countries. Active and intelligent packages draw attention in the basis of these studies. The high environmental effect values of polymers is another study subject.

In our literature study, few studies are observed about intelligent packages made of polymers, more over there are no studies regarding yoghurt packaging among these. Development of an intelligent yoghurt pack will persuade the consumers to classify the good and bad products in the market and demand will concentrate on healthy yoghurt. Therefore in a survey study made in 3 big supermarket groups, it was understood that markets sometimes cheat consumers about healthy yoghurt purchase and even the expiry dates are not reflecting the reality. When their opinions about an intelligent yoghurt pack that can sense the spoiling of yoghurt were asked, they said it would be a revolution and it will prevent the markets or producers from cheating the consumer and also it will remove the anxiety about the condition of the yoghurt in the fridge at home.

Two paths were followed in this study. One of these is determining the ratio of kaoline (clay) and masterbatch (material added to change color) additives to main material PP. The reason for kaoline usage is its prevalent usage in food and health tools, especially ceramics and its white color, its plastic structure, its relation to a soft clay group, possibility to decrease its grain size down to 2 micrometers, its density of 2,62 g/cm^3 and its hardness of 1,5-2. It's ideal composition is 46.5% SiO_2 ,39.5% Al_2O_3 and 14% H_2O. However instead of aluminium it includes small amounts of iron (Fe), sulphure (S) and potassium (K).

These properties show us that it can easily form a chemical bond with polypropylene. Also it was considered that the iron content in kaoline can be removed by the microorganisms in yoghurt which may lead to a color change. The weak acidic environment obtained by serum formation (pH > 2-3) does not dissolve the oxidized form of iron (Fe^{+3}) while it can dissolve the reduced form of iron. (Fe^{+2}) As a result the reduction of iron in kaoline occurs under control together with the organic acids and other metabolic products in the serum [1,2]. Accordingly, development of current yoghurt packs and PP based materials has been initiated in labs with the help of food, chemistry and material science. Test samples regarding this subject have been prepared and water soaking experiments (Fig.1).



Fig 1 Figures of samples obtained by various PP-Masterbach and kaoline mixtures prepared for tension tests and water soaking experiments of samples

The second method is to design a special slot on the pack in order to place a pH indicator. A kaoline plate was placed on the yoghurt contacting surface of the slot selectively. After these studies aiming target were finished, the formation of intelligent yoghurt packaging in real size was initiated. The yoghurt test pack was produced by computer based fast prototype technology. Later, the test mould was placed into the extruder after the harmony studies were made and later the intelligent material (mixture composed of PP, masterbatch and additives) were poured from the feeder and test containers were produced. The containers were filled with yoghurt by the support of yoghurt producer companies and serum formation was monitored from the special window on the container. The risk of low serum formation (or not serum formation at all) was minimized by forcing the environmental conditions [6].

Results and discussion

In intelligent yoghurt pack development studies, kaoline was added to main P material starting from 1% to 8%. Masterbatch for color change was used in 0.5% ratio. Water soaking experiment was made to the samples first. Water absorption increased with increasing kaoline ratio in the material. The increase is linear. This is an expected result. PH changes of the yoghurt was determined in the formed material compositions as shown in Fig.2.

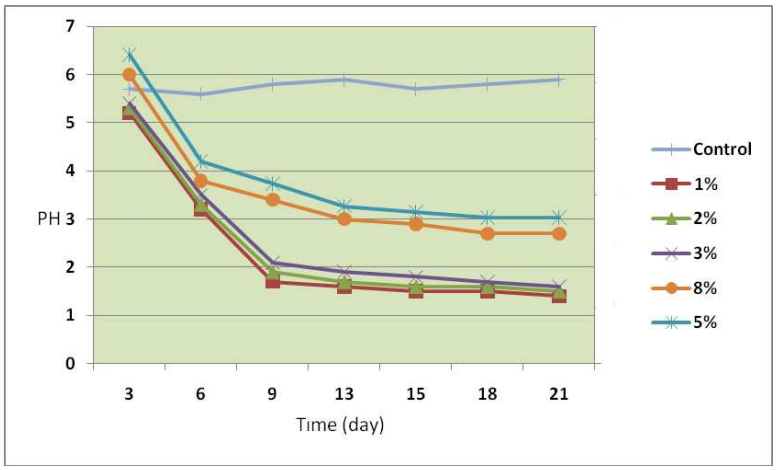


Fig. 2 PH changes of the yoghurt

It was observed that the drop of PH in the environment was rapid in first 12 days and ended in 18 days. This shows that the decomposition of proteins in yoghurt occurs rapidly in the first 12 days and nearly ends in day 18. The decomposition of Fe_2O_3 in kaoline to serum media is not affected only by the microorganisms in yoghurt but by the organic acids (oxalite and citric acid) released by them during the decomposition of proteins (Fig.3),(Fig. 4).

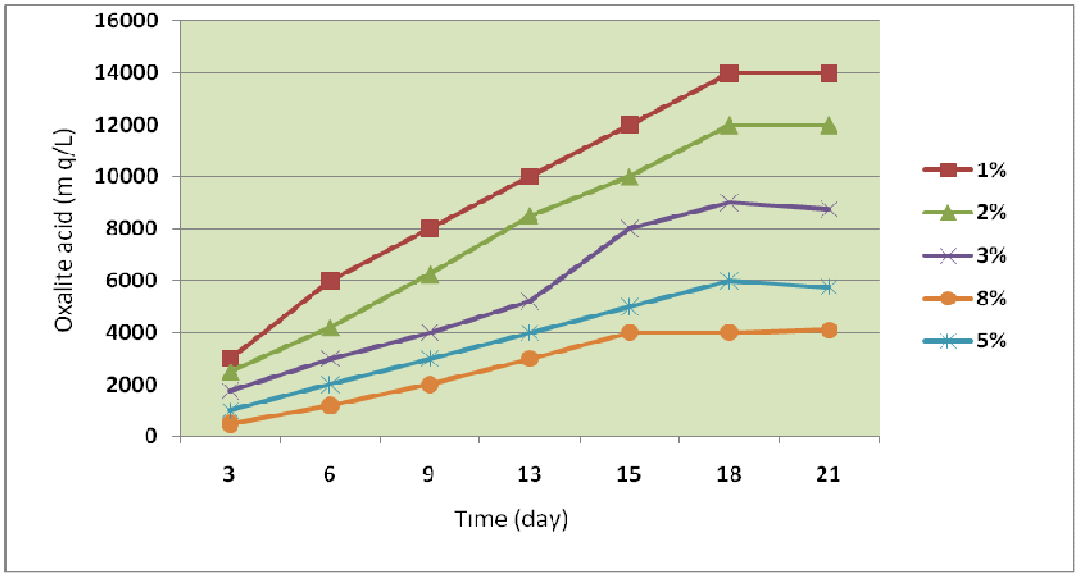


Fig.3 Oxalite acid changes of the yoghurt

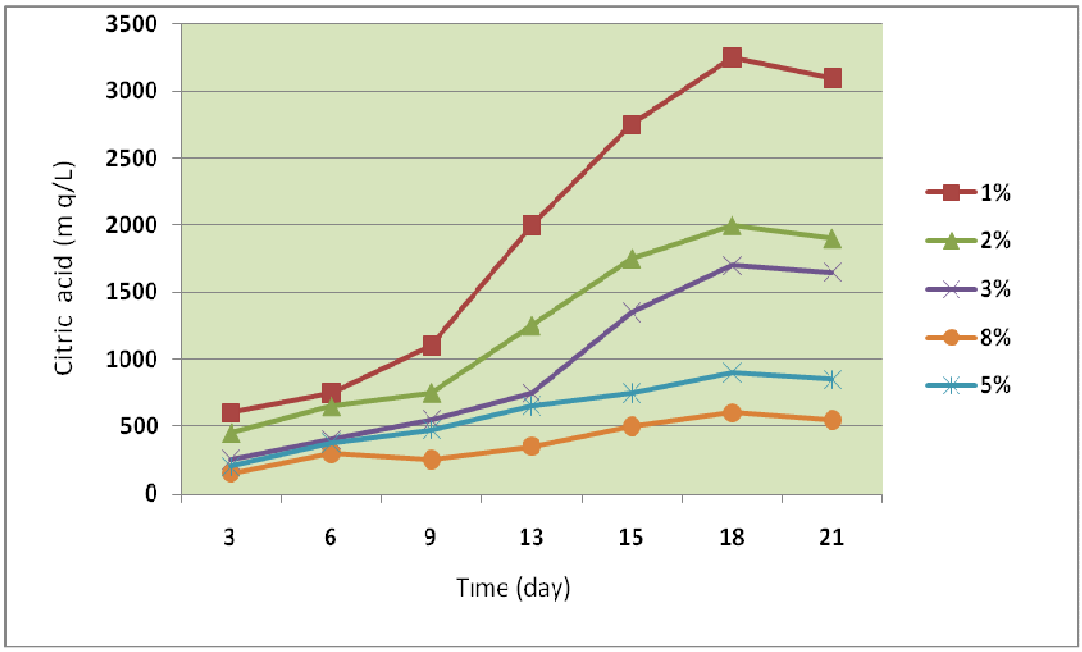


Fig.4 Citric acid changes of the yoghurt

In the formed materials without kaoline, it was observed that the white color ratio of 47.2% increased to 90.60% by addition of 8% kaoline. It showed us that our effort for changing the color is in correct path. When the effect of color changing masterbatch is added the color change on the pack became obvious.

Summary

As in all studies, it was shown one more time that there is no subject where material science is not taken into consideration. Parallel to technological developments, there is a trend for usage of intelligent materials in material science. This trend results in incredible studies not only on metallic materials but also on polymer materials. Looking at the technical results, interchangeability feature of the polymer color were revealed. However, it is important that the development of more advanced studies will be recommended. The concrete results of the study can be listed below.

1. The consumer will be informed about the condition of yoghurt (which is very important for human nutrition) in the pack until the final usage. Therefore, healthy yoghurt consumption will be achieved.
2. It will prevent the consumer to be cheated during the purchase stage.
3. Using this kind of package will increase the market share of the yoghurt producer in this competition environment and the consumer satisfaction will be achieved.
4. The intelligent packaging initiated by yoghurt pack will accelerate similar developments in dairy products sector.
5. It will put our country forefront in the world's yoghurt market and become a reference in forming a standard for this type of yoghurt packs.
6. It will provide monitoring for all stages of yoghurt consumption (starting from production) Yoghurts facing inconvenient environment and transportation conditions will not be able to enter the market no matter what their expiry date is.
7. It is a study which conveys the technology of today to the future.
8. This is a type of study which includes innovation on international basis.

References

[1] Eygi, M.S.in: The Investigation on Kaoline Which is The Use of Converted and Suitable Physical Characteristic for Ceramic Raw Material, Istanbul Technical University, Institute of Science and Technology, (2005) İstanbul.

[2] Uz, V,in: The Effect of Some Inorganic ,Organic and Biological Base Material Addition on Ceramic Characteristics. Osmangazi University, Institute of Science and Technology (2004), Eskisehir.

[3] Marsh and Bugushu,in: Food Packaging Roles, Materials and Environmental Issues, Journal of Food Science, (2007) Vol 72.

[4] Fomin, V.A.in: Biodegradable Polymers, Their Present State and Future Prospects. Progress In Rubber and Plastics Technology.(2001) 17(3): 186-204.

[5] Leaversuch, R.in: Biodegradable Polyesters; Packaging Goes Green. Plastics Technology.(2002)48(9): 66-73.

[6] Mukhopadhyay, P.in: Emerging Trends in Plastic technology. Plastics Engineering.(2002) 58(9):28-35.Mulder, K.F.

[7] Callister, W.D. in:Materials Science and Engineering: An Introduction. New York, N.Y.(1999) John Wiley and Sons.

© (2011) Trans Tech Publications, Switzerland
doi:10.4028/www.scientific.net/KEM.471-472.191

The Effect of Alkali Treatment Mechanical Properties of Kenaf Fiber Epoxy Composite

Saad A. Mutasher[a], Adrian Poh[b], Aaron Mark Than[c], Justin Law[d]

School of Engineering and Sciences Swinburne University of Technology (Sarawak Campus)Jalan Simpang Tiga, 93350, Kuching, Sarawak, Malaysia
[a]smutasher@swinburne.edu.my, [a]adrian_poh@hotmail.com, [c]aaron_than@hotmail.com, [d]justinlawyangching@gmail.com

Keywords: natural fiber, kenaf fiber, alkali treatment, mechanical properties, epoxy

Abstract. Increasing worldwide environmental awareness is an encouraging scientific research into the development of cheaper, more environmentally friendly and sustainable construction and packaging materials. Kenaf fibre is a natural fibre which is growing in popularity due environmental issues and its properties as filler. Epoxy is a versatile thermosetting polymer which has a low curing temperature and used in making carbon fibre and glass composites. In this paper the properties of kenaf bast fibre epoxy reinforced composite have been investigated. The effects of alkali surface treatment of the fiber on the composite properties are also investigated. A hand layup method was use to fabricate the test specimens. Generally, all the treated fibre composites performed better than the untreated fibre with an improvement approximately 5% to 10%. Epoxy has the highest tensile strength and flexural strength among all specimens. The 24wt% treated kenaf fibre composites has the highest tensile strength, 27.72MPa and flexural strength, 56.91MPa. The kenaf fiber weight fraction of 40% gave the highest impact strength. The impact strength of the 40wt% kenaf fiber increased 14.3% after alkali treatment.

Introduction

The conventional and traditional fibre reinforced composites are composed of carbon and glass fibres, which are incorporated into unsaturated polyester or epoxy resin. These composites show high mechanical and thermal properties but they are not environmentally friendly because they have to be incinerated after being disposed. The increasing interest in introducing degradable, renewable, and inexpensive reinforcement materials which have been environment friendly has stimulated the use of hard cellulose fibres. The low cost, less weight and abundant availability make the natural fibres an attractive alternative. Kenaf was chosen for the study because it is now a fiber crop grown commercially in the world. In tropical countries, like Malaysia, fibrous plants are available in abundance and at least some of them are agricultural crops and Malaysia government had allocated a lot of money for kenaf research under the Malaysian plans. Kenaf, *Hibiscus cannabinus,* is a 4,000 year old crop with roots in ancient Africa [1,2]. The stalk of the plant consists of two types of fibres. The outer, coarser, fibre is called the bast fibre and the inner, finer, fibre is called the core fibre.

There are many studies have been done around the world to prove that kenaf can be used to produce kenaf-based composites with acceptable physical and mechanical properties. The effect of the fibre compression on the composites made from kenaf and bamboo fibres and biodegradable resin were investigated by Shibata, et al [3]. The flexural modulus in composites was predicted by Cox model, which incorporates the effect of the fibre compression. The flexural modulus increased

with increasing the fibre content. Clemons and Sanadi [4] study the effects of fibre content, coupling agent and the temperature on the impact performance of kenaf fibre reinforced polypropylene (PP) composite. They concluded that at room temperature, kenaf greatly reduced energy to maximum load (EML) in reversed notch tests but had little effect in notched tests. Kenaf was used with unsaturated polyester to form composites [5]. They observed that the polyester composites gave the most superior bonding and adhesion and have a higher storage modulus. The tensile properties of kenaf bast fibres bundle (KBFB) and kenaf bast fibre-reinforced epoxy strands was evaluated through extensive experiments and micromechanics-based modelling [6]. The increasing in tensile modulus is 5% after high temperature conditioning when the moisture of KBFB is reduced to zero. This observation is consistent with the idea that the modulus of the natural fibre is inversely proportional to its moisture content observed in woods. The loss of moisture during high temperature treatment induces brittleness in the KBFBs, which is clearly demonstrated by the reduction in strength and failure strength. The effect of soil burial in the degradation of tensile properties of composites made from long kenaf fibre unsaturated polyester was studied by Rashdi et al. [7]. They observed that when the composite is exposed to moisture, the hydrophilic kenaf fibre swells, as results for fibre swelling, micro cracking of the brittle thermosetting resin occurs. In this paper the mechanical properties of kenaf bast fibre composite were investigated. A mould was design and fabricated to prepare the composite specimens with different weight fractions of fibre. In addition the effect of alkali treatment on the properties of the composite are also investigated.

Materials and Methods

Fibre preparation The long kenaf fibres supplied by Kenaf Natural Fiber Industries (KFI) is first soaked in hot water mixed with detergent for about an hour and then rinsed to wash away the dirt and other impurities. The washed fibres are then sun dried. The untreated Kenaf fibres are baked in an oven of temperature of 100°C for 4 hours. After that, the fibres are cut by hand using scissors. A sample of 100 chopped fibre were taken at random and the length of the fibers were measured with digital vernier calliper. The average fibre lengths is 2.78 mm and the distribution of the fiber length lies in the 2.0-2.99 mm section as shown in Fig. 1.

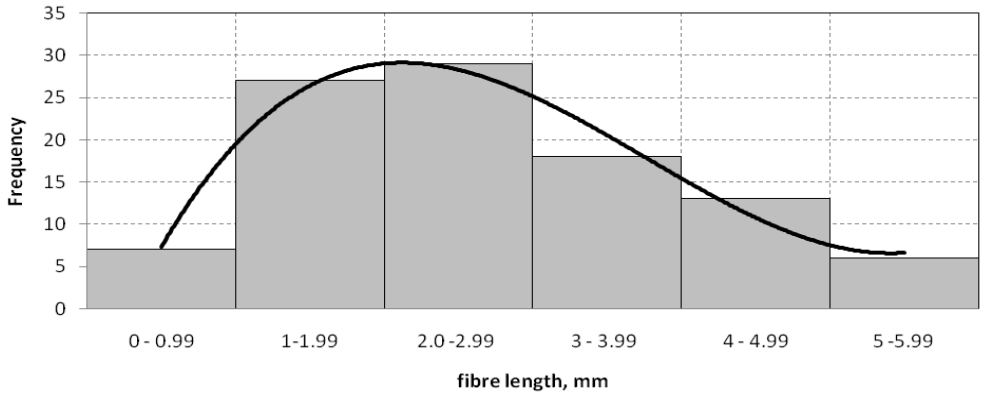


Fig. 1 Fibre length distribution

The chopped Kenaf fibres are soaked into 6% concentration of NaOH solution in a water bath in a constant temperature of 25±2°C for approximately 48 hours. Then the fibres are rinsed until the alkali is washed away before the drying. The treated fibres are then sun dried for 24 hours and baked in the oven at temperature of 110°C for 5 hours.

Specimen Fabrication. A hand layup process was used for fabrication process. Specimens from 0% to 40%, with increments of 10%, weight percentage of fibres are fabricated. The mould is cleaned and waxed properly to ensure that the specimen can be taken out smoothly after fabrication. The base of the mould is glued to the middle plate to ensure that there are no leakages later during the pressing time before the epoxy is fully cure on. The epoxy resin is mixed with the hardener with a ratio of 41. The kenaf fibre is then mixed into the epoxy mixture. The composite mixture is then poured in the mold cavities. The mixture is gently pressed using the fingers to make sure the cavity of the mould is properly filled. After the mould is filled, the top plate is put in place and the mixture is left to relax for about 45 min without putting weight on top of the mould or screwing the top plate tightly. The top plate is then screwed tightly in place. The composite is left to cure for about 24 hours at 25±2°C, then open the mold and take our the specimens..

Results and Discussions

Fiber weight fraction corrections. During fabrication, when the cover plate was put in place and screwed in, the mould actually forced some of the epoxy resin out which in turn affected the fiber weight fraction of the specimens. The procedure was modified where the fiber and resin mixture was allowed to rest in the mould for around an hour before the cover plate was put on to reduce the resin forced out. Table 1 shows the corrected fiber weight fraction of the specimens. Due to the closeness of the corrected weight fraction of 24.5% and 24.2%, the two weight fractions are merged and an average is taken for all the data points involved and renamed to 24%. Table1 is the updated list of weight fractions used in the paper.

Table 1 Corrected weight fractions

Weight fraction (%)	Corrected weight fraction (%)
10	24.5
20	24.2
30	30
40	40

Tensile Properties The stress-strain curves for treated and untreated fiber are shown in Figures 2 and 3. It is very clear that the behaviour of the material is similar to typical brittle material as the curve is close to linear till the breaking point with no deformations on the specimens. The composite generally breaks before the maximum elongation of the epoxy. This shows that the composites are more brittle compared to epoxy. The untreated 30%wt composite has the steepest stress strain curve slope at tensile stress of 18.36MPa and strain of 2.1%. For the treated 24%wt composite, the tensile stress are much higher than the untreated of the same weight percentage with the tensile stress of 26.03MPa and strain 3.32%.

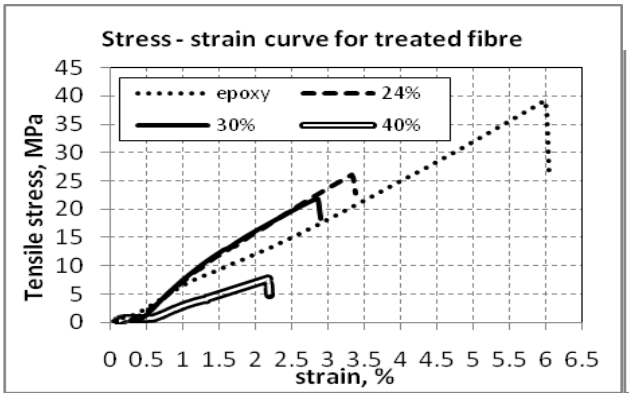


Figure 2: Stress-strain curves of treated fibre composites

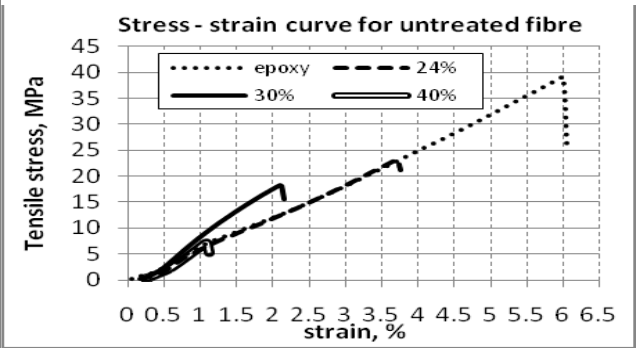


Figure 3: Stress-strain curves of untreated fibre composites

Tensile Strength. Average values of the tensile strength of three specimens are taken in this test with respect to each wt% of fibre. The tensile strength of the composite decreased as the weight percentage of fibres increased. When compared, all the treated fibre composites performed better than the untreated fibre composites as shown in Fig. 4. The tensile strength for the treated 24% wt of fibre is 27.72MPa while the untreated fibre of the same wt% is 26.46MPa. The improvement over the untreated fibres is approximately 5%. The alkali treatment removed the lignin and hemicelluloses from the fibre surface which made the fibre surface area rougher and bigger. The fibre surface increase resulted in a larger area of contact between the fibre and the matrix.

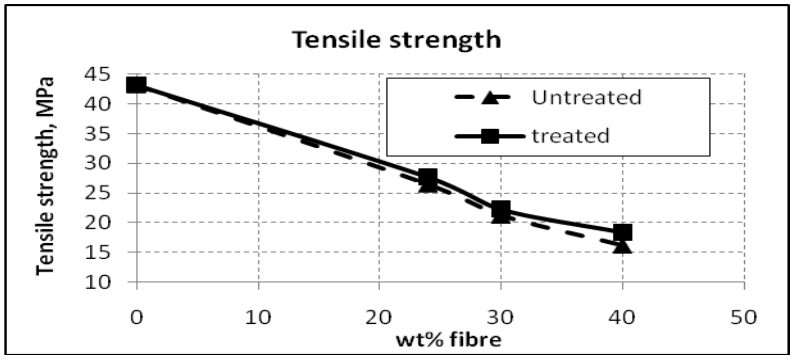


Fig. 4 Tensile strength of treated and untreated kenaf fibre composites

The matrix of the 40wt% treated fibres were not enough to cover the whole specimen, forming voids at places, making the surface rough and ductile as most of the fibres are exposed which shows that there is a high fibre-to-fibre interaction. In general, specimens failing very close to or at the grip and had lower strength as they fail earlier. Failure at the middle indicates uniform loading along the entire length of the specimen. The wide range of properties is attributed to the large variation of the natural fibre and distribution of the constituents, including inconsistencies in the diameter and length of a single kenaf fibre.

Tensile Modulus. The tensile moduli of the composites are generally higher than epoxy except for 40wt% composites as shown in Fig. 5. The composites are stronger when compared to the reference specimen as it is able to withstand higher loads before it breaks which shows that the composites are stiffer. The reinforced materials are able to withstand higher loading as the stresses are transferred to the fibres. This will eventually slow crack propagation of the materials. The improvement over untreated composites is approximately 5% to 10%. The tensile modulus of the untreated 30%wt is 3584.3MPa while the tensile modulus for the 24%wt of treated fibre is 3756.83MPa. Generally, the best mechanical properties in a composite depend mainly on fibre orientation where short fibre reinforced composites will always perform poorly compared to their unidirectional counterparts, but the adhesion between the fibre and the matrix is also important. This is especially true for short fibre reinforced composites. The fibres are loaded through the matrix and for good performance, the load must be transferred effectively to the fibre, and a strong bond between the fibre and the matrix is required.

Flexural Properties. Flexural strength depends very much on fibre alignment and the location of resin-rich areas. This is the reason why the 40wt% fibre composite did poorly as there were voids in the specimens where there is little resin. Epoxy had the highest flexural strength followed by the treated fibre composites and then the untreated fibre composite as shown in Fig. 6. The treated fibre composites generally did better than the untreated fibre composites which indicate that the increasing of the interfacial area of contact is beneficial to the flexural strength too. The 24%wt of treated fibre flexural strength is 56.91MPa while the untreated fibre of the same weight percentage is 53.49MPa. There is about a 6% improvement after the surface treatment is done.

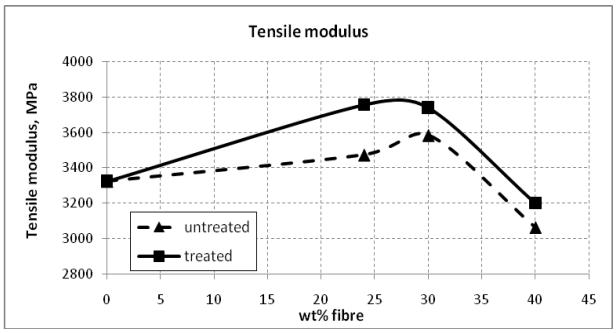


Fig. 5 Tensile modulus of treated and untreated kenaf fibre composites

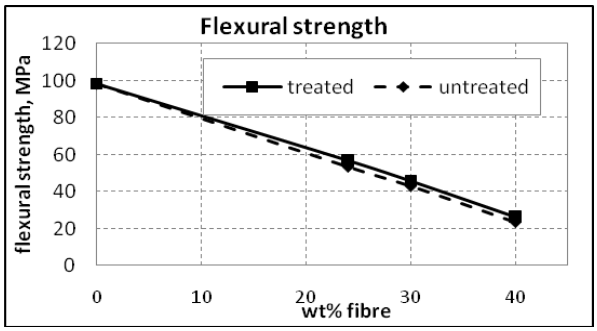


Fig. 6 Flexural strength of treated and untreated kenaf fibre composites

Impact strength. Fig. 7 shows the results of impact test. It can be seen that the impact strength increases as the weight fraction of kenaf fibre increased in the specimens. At low weight fractions, the impact strength is actually lower than that of the pure epoxy specimens. According to Bonnia et al. [8], at lower weight fractions, the short fibres ends act as additional stress concentration zones, and at higher weight fractions, the stress distribution is more even and this outweighs the effects of the flaws introduced by the fibre ends. There is 14.25% improvement in impact strength after fibre treatment for 40wt% of kenaf fibre in addition there is a 66.8% improvement impact strength for the 40wt% treated kenaf fibre specimens compared to the epoxy specimen.

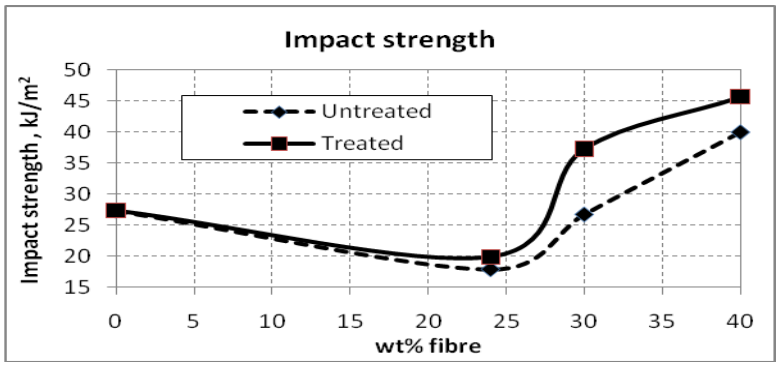


Fig. 7 Impact strength of treated and untreated kenaf fibre composites

Morphology. SEM micrographs of the fracture surface of the treated kenaf fiber composites can be seen in Fig. 8. Failure of the matrix resulted from brittle fracture, evident from the smooth planes on the fracture surface. There are some voids present in the composite and this is seen in Fig. 8 a and b. Fig. 8 c, shows a close-up of a one fiber breakage in the tensile specimen. It is very clear that the alkali treatment had increased the adhesion of the epoxy matrix to the kenaf fibers. In addition the strong bond between kenaf and epoxy is indicated by the short fibers stick out from the matrix. Moreover, the intensity of the bond interface can be seen in terms of the gaps between fiber and surrounding matrix in the SEM micrographs. Narrow gap leads to strong interface as shown in Fig. 8 a. The sudden failure of the tensile specimen is causing the fiber to split; resulting in fine fibrils being exposed as shown in Fig. 8 b.

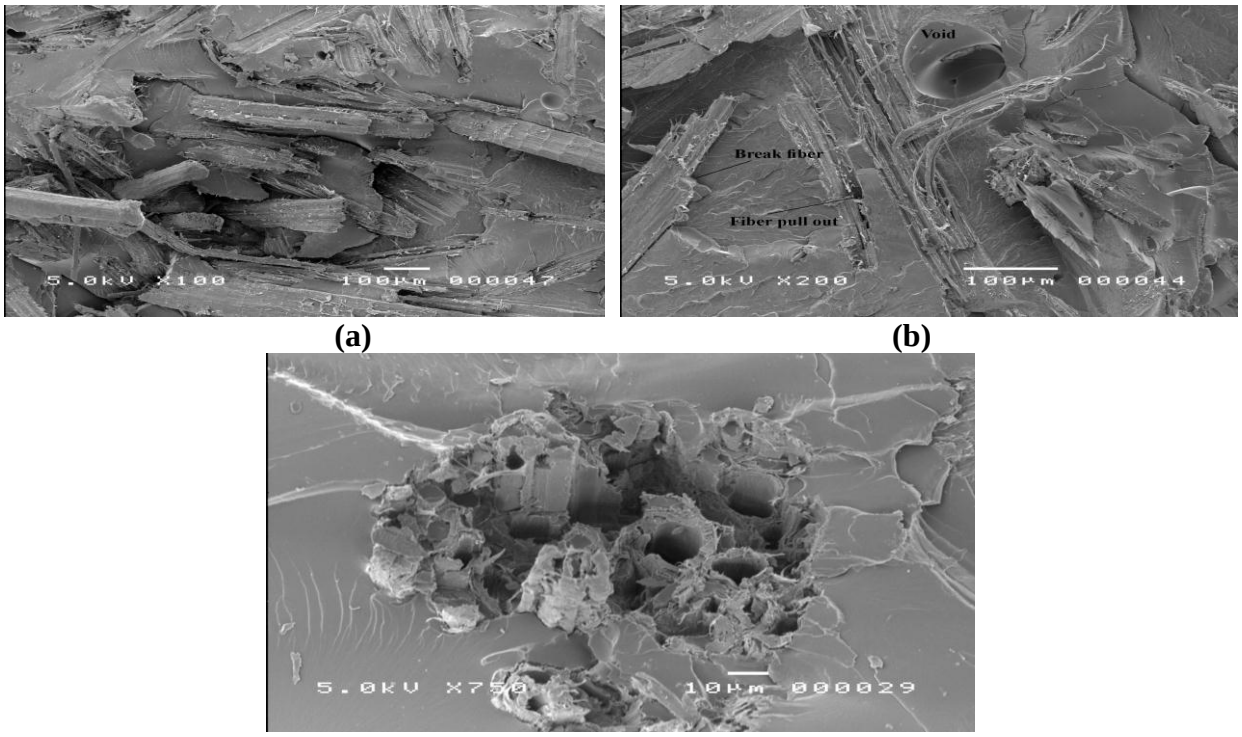


Fig. 8 SEM micrographs

Summary

The kenaf fibre reinforced composites were generally more brittle than epoxy. The specimens had an improvement in tensile modulus compared to epoxy for specimens with up to 30wt% fibre. Based on the findings, it can be concluded that by using the alkaline surface treatment, there is an improvement to up to 10% for the tensile modulus, 5% increase in tensile strength and 6% increase in flexural strength. The 24wt% treated kenaf fibre composites has the highest tensile strength, 27.72MPa and flexural strength, 56.91MPa. Forty % kenaf fiber gave lower tensile and bending strength while the impact strength is the highest. The impact strength of the 40wt% specimens increased 14.3% after Alkali treatment. The microscopic investigation of the brittle-fractured composite specimens revealed enhanced bonding between the matrix and the fibers after alkali treatment.

References

[1] Information on http//www.kenaf-fibre.com/en/cenni-storici.asp
[2] E. A. Osman, , A. Vakhguelt, I. Sbarski, S. A. Mutasher, (2010) proceedings of 7th
[3] International Materials Technology Conference and Exhibition, 13th -16th June 2010, Kuching, Sarawak, Malaysia.
[4] S. Shibata , I. Fukumoto, Y. Cao Polymer Composite, Vol 27,2, (2006), p 170.
[5] G. Clemons, A. R. Sanadi Journal of Reinforced Plastics And Composites, Vol 26,15, (2007), p.1587.
[6] S. H. Aziz, M. P. Ansell, S. J. Clarke, and S. R. Panteny Composites Science and Technology Vol 65, (2005), p. 525.
[7] Y. Xue, Y. Du, S. Elder, K. Wang, J. Zhang Composites Part B, Vol 40, (2009), p.189.
[8] A.A.A. Rashdi, S.M. Sapuan, M.M.H.M. Ahmad, and A. Khalina Journal of Food, Agriculture & Environment Vol.7, (3&4) (2009).
[9] N. N. Bonnia, S. H. Ahmad, I. Zainol, A.A. Mamun, M. D. H. Beg, A. K. Bledzki, eXPRESS Polymer Letters Vol.4, No.2 , (2010), p. 55.

© (2011) Trans Tech Publications, Switzerland
doi:10.4028/www.scientific.net/KEM.471-472.197

Effect of organic modification of muscovite on the Polypropylene layered silicate nanocomposite

Mohd Fadli Ahmad Rasyid[1, a], Hazizan Md Akil[1,b], Jamaliah Mohd Sharif[2,c].

[1]School of Material and Mineral Resouces Engineering, Universiti Sains Malaysia,

14300 Seberang Perai Selatan, Pulau Pinang, Malaysia

[2]Malaysian Nuclear Agency (Nuclear Malaysia)

Bangi, 43000 Kajang, Selangor, Malaysia

fadliahmadrasyid@gmail.com[a], hazizan@eng.usm.my[b], jamaliah@nuclearmalaysia.gov.my[c]

Keywords: polypropylene layered silicate nanocomposite, muscovite, melt compounding, exfoliation

Abstract. Polypropylene- layered silicate nanocomposite based on muscovite was prepared via melt compounding. Muscovite was organomodified with cetyltrimethylammoniumbromide (CTAB) by using different filler loading. The effects of muscovite content on mechanical and morphology properties were evaluated. Analysis of test data showed that the mechanical properties increased with an increase in filler loading up to a threshold of 3 wt%; thereafter the material properties were degraded. The enhancement of properties attributed to the formation of intercalated and exfoliation nanocomposite structure at these loadings of clay. At higher filler loading, degradation in mechanical properties maybe attributed to the formation of agglomerated clay tactoids.

Introduction

Polymer layered silicate nanocomposites (PLSNs) received a lot of attention over the last decade as a new kind of material which exhibit outstanding properties when compared either to the neat polymers or to conventional micro and macro-composite materials. It has been successfully introduced into thermoplastic and thermosetting resin such as polypropylene (PP) [1], polyethylene (PE) [2] and polyurethanes (PU) [3-4]. This is driven by the possibility of exceptional mechanical property enhancements that are synergistically derived from the organic and inorganic components at low filler levels [5]. In fact, it has been reported polymer layered silicate structures have higher elastic modulus, barrier properties, flame retardation behaviour, high temperature durability and thermal stabilities [6- 7]. The key to this enhancement depends upon spatial distribution, arrangement of intercalating polymer chains and interfacial interaction between the silicate layers and the polymer [8-9].

Generally, layered silicate minerals are divided into three major groups: (a) the kaolinite group, (b) the semctite group and (c) the illite or the mica-clay group. Among the three major groups, mica (especially muscovite), has attracted much less attention. Muscovite is a clay mineral of special interest because of its well-defined crystal structure, molecularly smooth surface, outstanding corona resistance, high aspect ratio and available in large amounts with relatively low cost [10]. The chemical formula of muscovite is $KSi_3Al_3O_{10}$ $(OH)_2$, with a very high layer charge density close to 1.0 equivalent per $O_{10}(OH)_2$. Muscovite belongs to monoclinic structure with the space group (C2/c), with the cell parameter a = 5.18A˚, b = 8.99A˚, c = 20.07A˚, and β = 95.751 [11].

In present investigation melt compounding technique has been adopted to synthesize PP-layered silicate nanocomposites using cetyltrimethylammoniumbromide (CTAB) as alkyl ammonium to treat Muscovite to produce organoclay (O-Muscovite). The aim of this work is to report and explain the effect of organic modification of muscovite to the properties of PP layered silicate nanocomposite.

Experimental Procedures

Materials- Polypropylene (PP, Profax PDC1274) used in this study was supplied by Titan Petchem (M) Sdn. Bhd. A complimentary sample of mica was supplied by Bidor Mineral (M) Sdn. Bhd. In ion exchange treatment for mica particles, CTAB was used as received as onium salt (Sigma-Aldrich).

The $LiNO_3$ treatment of muscovite/ Modification of Li+ -Muscovite by Lithium Nitrate

The mixture of 10 g Muscovite powder and 170 g $LiNO_3$ powder was mechanically mixed. After complete mixing, the mixture was heated in a furnace at 300°C for 12 h. The resulting product was washed several times with deionized water and filtered, and then dried at 110°C vacuum oven. The $LiNO_3$ treatment was repeated for seven times. The product is named Li-muscovite.

Modification of $CTAB^+$ Li^- Muscovite by cetyltrimethylammonium bromide.

The preparation of surfactant muscovite was undertaken by hydrothermal reaction method. First, 3.0 CTAB was dissolved in 50mL of deionized water, and then 0.5 g of Li-muscovite was mixed with the CTAB solution. To ensure the extent of ion exchange, excessive amount of CTAB has been used. For the hydrothermal reaction, the mixtures was placed in a hydrothermal reactor (100 mL) of Teflonlined stainless-steel autoclave and then heated at 170°C for 12 h. After the reactions, all the surfactant-muscovite (organoclay) products were filtered and then washed three times with ethanol, dried in a vacuum oven at room temperature.

Preparation of composite

The PP and organoclay were dried under vacuum at 90°C for 24 h. Melt compounding was carried out using an internal mixer Thermo Haake Polydrive R600 fitted with cam blades at 180°C with rotor speed of 60 rpm and for the prior of 8 min. Processing condition involved melting the PP in the preheated mixing chamber of the Thermo Haake for 4 min with rotation. Well-dried treated or treated muscovite was carefully fed into mixing chamber within 30 seconds. The mixing process of muscovite and PP was continued until 8 minutes. After that, the rotors were stopped and the compounding specimens were discharged from the mixing instrument.

Characterization. Fourier Transmission Infra Red (FTIR) - The FTIR measurements were conducted on a Perkin Elmer Paragon 1000 Fourier transform spectrometer at room temperature (25°C). In all cases, 64 scans at resolution of 2 cm^{-1} were used to record the spectra.

X-Ray Diffraction (XRD)- Wide Angle X-Ray Diffraction (Bruker AXS) measurement was used to determine basal spacing of the treated muscovite. Analysis was performed on both treated and untreated muscovite particles. The 2θ angles were varied between 1 and 20° to measure the basal spacing (d_{001}) of the modified muscovite. The scanning angle (2θ) was varied between 1 and 20°.

Flexural properties- Flexural tests under three-point bend configuration were performed according to ASTM D790. The machine was run under displacement control mode at a controlled crosshead speed of 5 mm/min and all tests were performed at room temperature. All specimens were cut from the panel using band saw. Five replicate specimens from four different compositions were prepared for static flexural tests.

Results and Discussion

Fourier Transmission Infra Red (FTIR). Infrared spectroscopy has been deeply related to the studies of structural features, such as chain conformation, chain packing, and even specific conformational sequence. Adsorption of CTAB on muscovite was examined by recording the FTIR spectra in the range 4,000– 400 cm-1. Fig.1a showed the FTIR spectra of CTAB and CTAB-capped muscovite particles, it is to be noted that the symmetric and asymmetric $–CH_2$ stretching vibrations of pure CTAB lie at 2,914 and 2,846 cm^{-1} and remained almost same in the presence of muscovite particles. The peaks at 1,550 cm^{-1} for pure CTAB are attributed to –C–H scissoring vibrations of $–N–CH_3$ moiety [12], which are shifted to 1,595 cm^{-1} in the presence of muscovite particles. The peak at 1,252 and 1,209 cm-1 is assigned to –C–N stretching is remained same. As for the peak at 1487 cm^{-1} in Fig. 1a is assigned to the asymmetric bending mode of the head $[(CH_3)_3N^+–]$ methyl group, which is sensitive to the extent of disorder and the packing of the headgroup [7]. For the treated muscovite, the asymmetric bending modes of CH_3 are almost the same as crystalline CTAB in both wavenumber and line width, indicating that the headgroups of CTA^+ in the samples are anchored to the aluminosilicate layers with highly ordered distribution. This is consistent with the high charge density and homogeneous charge distribution of muscovite.

From the FTIR analysis, the arrangement of the intercalated CTA+ in the interlayer of aluminosilicate could be speculated. The headgroups [(CH3)3N+–] of CTA+ are anchored to the surface of aluminosilicate layers uniformly. Therefore, from FTIR results, it is clear that the interaction occurred between CTAB and muscovite.

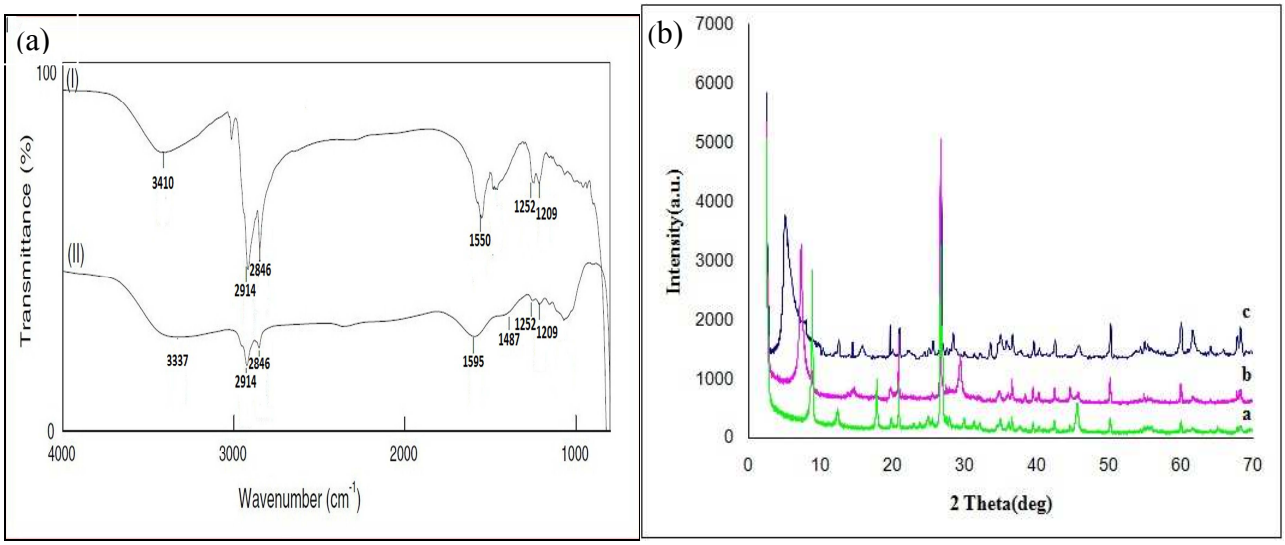


Fig. 1: **(a)** FTIR spectra of (I) CTAB; (II) CTAB-capped Muscovite particles, **(b)** XRD diffractograms of (1) muscovite, (2) LiNO3 treated muscovite and (3) CTAB treated muscovite particle

X-Ray Diffraction (XRD). It is expected that the basal spacing of silicate layer in muscovite will increase as a result of ion exchange treatment between Li-muscovite and CTAB. One way of determining the basal spacing is by using XRD where spacing could be calculated using Bragg Law. In general, muscovite is not easily treated using ion exchange method as compared to montmorillonite. Muscovite has stronger electrostatic force to hold aluminosilicate layers and the interlayer cation (K^+) together. Therefore, $LiNO_3$ treatment was done to replace the interlayer cations in muscovite with Li+ by melting LiNO3 [13]. In the $LiNO_3$ treatments, the spacing of (001) plane d (001) of muscovite was enlarged, providing the possibility for the intercalation of organic. During ion exchange treatment, a long alkyl chain (CTAB) was expected to replace the potassium ion and result in the expansion of the silicate layer and it will ease the penetration of the polymer

molecules in between of these layers. This characteristic will offers a good distribution of fillers particle and agglomeration effect could be avoided or reduced. This homogenizations effect will influence the behavior of the composites itself by mean of mechanical and thermal properties. The increase in basal spacing can be seen in the position of the peak in the X-Ray diffractogram result as shown in Fig. 1b. From the X-ray diffractogram, the basal spacing was calculated based on Braggs Law.

From Fig. 1b, basal spacing changes from 9.4 Å to 12.1Å indicating an increase in basal after the $LiNO_3$treatment has been carried out. For the second stage treatment by using CTAB, the basal spacing has enlarged about 5.2 Å from as 12.1 Å to 17.3 Å. This makes the total enlargement of the intergallery spacing up to 7.9 Å. Because the inorganic cations in the interlayer are replaced by CTA+, and the ion exchange has influenced the interlayer spacing dramatically [14]. From this XRD analysis it showed the interaction had occurred between muscovite particle and CTAB as shown in the FTIR analysis.

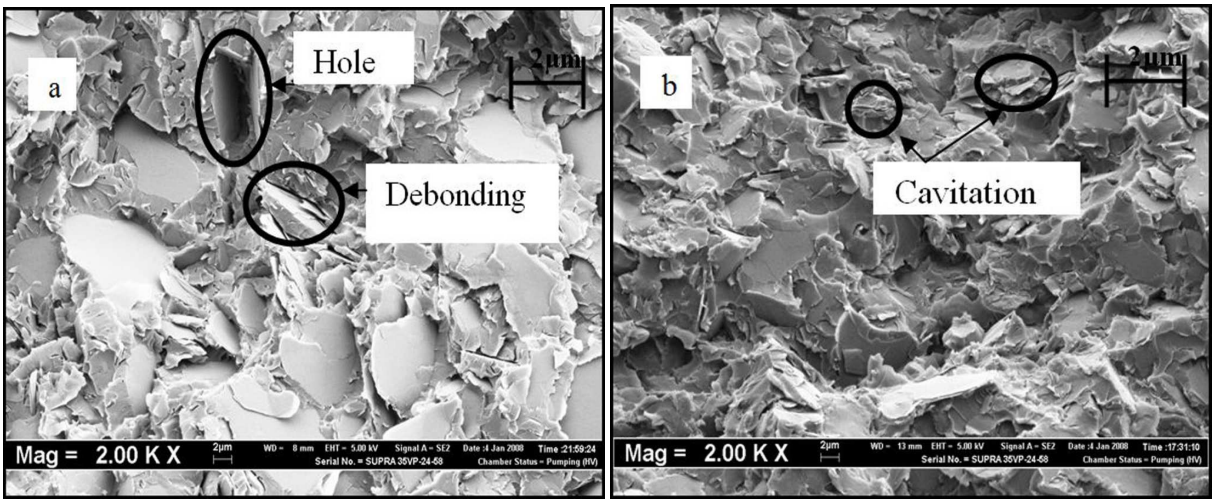


Fig. 2: Comparison of SEM micrographs of a) untreated muscovite and b) treated muscovite at 3wt% of muscovite loading.

Mechanical Properties of Polypropylene Layered Silicate Nanocomposite (PLSN). Fig. 3 shows the variation of mechanical properties of the nanocomposites as a function of organically modified muscovite is represented in Fig. 3. Addition organically modified clays content (O-Muscovite) in composite structure showed an increase in the mechanical properties with an optimum results with 3wt%, wherein flexural strength increased to the tune of 18% (UM), 28% (TM) and flexural modulus increased by 46% (UM), 45% (TM), respectively as compared to virgin matrix. The increase in flexural strength and modulus is attributed to the high stiffness of nanolayers due to the silicate layers interacts intensively with the chains of PP and organic modification improved interfacial adhesion between the treated muscovite and PP resin matrix as showed in Fig. 2. In light of the above discussion, it propose that the presence of the organoclay must have a positive effect on the mechanical properties of PP/organoclay nanocomposites [15].

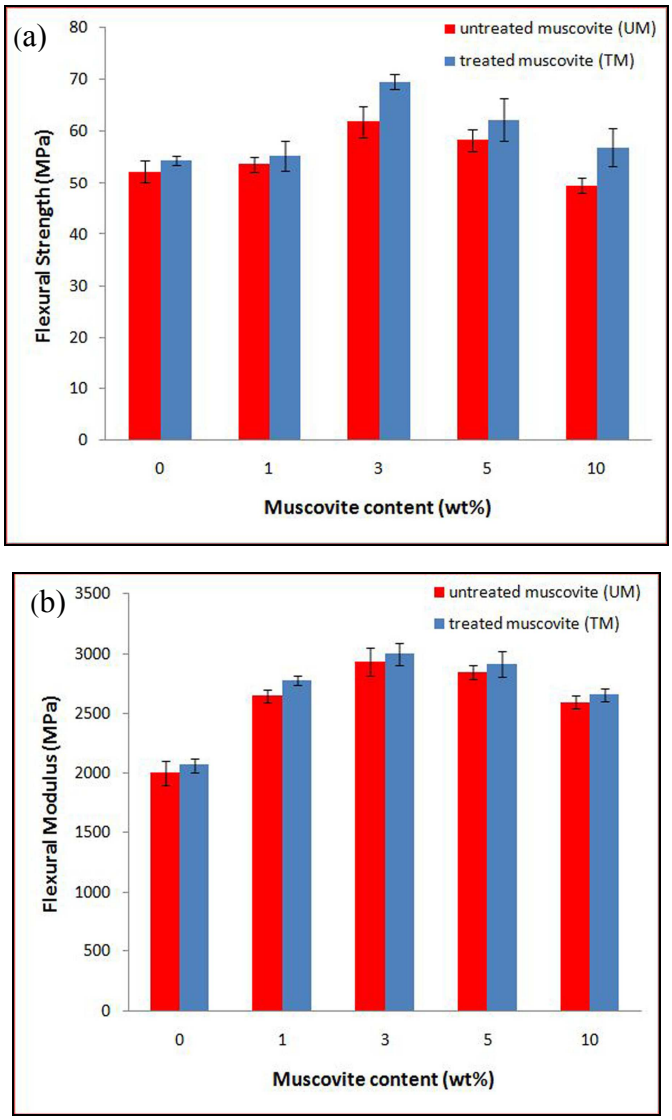


Fig. 3: (a) Variations of flexural strength for treated and untreated muscovite filled polypropylene composites, (b) Variation of flexural modulus for treated and untreated muscovite filled polypropylene composites

Summary

Organic modification of Muscovite was successfully prepared by alkylammonium ions. PP chains intercalated into organoclay to form an exfoliation structure. The XRD patterns and SEM images showed that the organic modification of clay can improved the interface between the muscovite particles and the flexural strength and modulus of PP/organoclay nanocomposites was obviously better than neat PP.

References

[1]Kurokawa Y, Yasuda H and Oya A: J Mater Sci Lett. Vol. 15 (1996), p. 1481-1483

[2]Rong, J., Jing, Z., Li, H. and Sheng: Macromol Rapid Commun. Vol 22 (2001), p.329–34

[3]Yao, K., Song, M., Hourston, D. and Luo, D: Polymer. Vol 43 (2002), p.1017–1020

[4]Xu, R., Manias, E., Snyder, A. and Runt: J Biomed Mater Res. Vol 64A (2003); 64A, p. 114–119

[5]Tjong SC: Mat Sci Eng R. Vol 53 (2006), p. 73–197

[6]Zanetti, M., Lomakin, S. and Camino, G: Macromolecular Materials and Engineering, Vol. 279 (2000), p. 1-9

[7]D. Paul and L. Robeson: Polymer, Vol. 49 (2008), p. 3187-3204

[8]LeBaron, P., Wang, Z. and Pinnavaia: Appl. Clay Sci. Vol 15(1999), p.11–29

[9]Ray, S.S. and Okamoto: Prog. Polym. Sci. Vol 28 (2003), p.1539–1641

[10]G. Brown and G. Brindley: Journal of Petrology

[11]J.J. Liang and F.C. Hawthorne: Can. Mineral. Vol 34 (1996), p. 115–122

[12]Sui, Z., Chen, X., Wang, L., Chai, Y., Yang, C. and Zhao, J: Chemistry Letter. Vol. 34 (2005), p.100-101

[13]Zhao, L., Wang, X., Wu, N. and Xie, Y: Colloid Polym. Sci. Vol 283 (2005), p.699–702

[14]Yu, X., Zhao, L., Gao, X., Zhang, X. and Wu, N: Journal of Solid State Chemistry. Vol. 179 (2006), p. 1525-1535

[15]G. Mingliang and J. Demin: Journal of Reinforced Plastics and Composites. Vol. 28, p. 5

© (2011) Trans Tech Publications, Switzerland
doi:10.4028/www.scientific.net/KEM.471-472.203

Evaluation of corrosion properties of electroless NiP/Nano- SiC composite coatings

Arman Zarebidaki[a], Saeed Reza Allahkaram[b]

School of Metallurgy and Materials Engineering, University College of Engineering, University of Tehran, Tehran, Iran, P.O.Box: 11155-4563, Tel/fax: +982161114108.

[a]arman.zare@gmail.com, [b]akaram@ut.ac.ir

Keywords: Ni-P coating; Nano-SiC; Corrosion.

Abstract. Ni-P/nano- SiC composite coatings were deposited in different concentrations of SiC nano-particles in the bath. The hardness and corrosion resistance of the composite coatings with different content of SiC nano-particles were measured. Moreover, the structure of the composite coatings was investigated by means of X-ray diffraction (XRD), while their morphologies and elemental composition were analyzed using scanning electron microscope (SEM) equipped with energy dispersive spectrometer (EDS). Results showed that co-deposited SiC nano-particles contributed to increase the hardness but corrosion resistance of electroless Ni-P coatings decreased due to agglomeration of nano-particles and increasing porosity of coatings.

Introduction

Electroless deposition has certain advantages over electrodeposited coatings. Complex-shaped substrates and isolated areas can be protected from various environments by using electroless coatings, and their surface properties can be enhanced to meet specific application requirements. Some of these characteristics include uniformity of the deposit, corrosion resistance, solderability, shielding, hardness, and wear resistance [1]. Moreover, it is known that the incorporation of particles into the Ni-P matrix provides enhanced surface properties, depending on the particle nature [2]. Hard particle-containing coatings (Ni-P/X, X=SiC, WC, Al_2O_3, Si_3N_4, etc.) have been developed when the main requirement for a composite coating was wear resistance [3, 4, 5]. Among these coatings, the Ni-P/ SiC composite coating has been proved to be the most cost-effective and best-performing combination [6]. The final properties of Ni-P-SiC coatings depend on the phosphorus content of the Ni-P matrix which determines the structure of coatings, and on the characteristics of embedded particles such as type, shape and size [7- 9].

There are few researches about influence of SiC particles on the corrosion resistance of the Ni-P/SiC composite coating. Study results of different researchers about the influence of nano-particles on the corrosion resistance of the composite coatings were different, even contradictory in many cases [9]. In general, the corrosion resistance of electroless Ni-P composite coatings is believed to be less than that of electroless Ni-P alloy coatings [2, 7]. The co-deposited second phase particles present in the electroless nickel matrix are thought to reduce passivity and corrosion resistance. Hence for applications requiring good corrosion resistance, a duplex coating, consisting of an initial electroless Ni-P coating followed by an electroless Ni-P composite coating, is recommended in place of electroless Ni-P composite coatings [2, 7, 10]. Further study on corrosion resistance of nano-composite coating is of great theoretical and practical value, and this paper focuses on the effect of nano-SiC particles on the corrosion resistance of the Ni-P coating. The aim of this study is to investigate the effect of nano-SiC particles incorporated in the coating on the corrosion properties of Ni-P-SiC nano-composites. The effects of bath particle concentration on the corrosion and mechanical properties of the Ni-P/nano- SiC composite coatings were investigated.

Experimental

The Ni-P and Ni-P/nano-SiC composite coatings were applied on API-5L X65 steel substrates (30×25×15 mm) while the sample was vertically positioned in a 250 ml bath . The substrate surface

was carefully polished with grade #400 SiC emery paper and after ultrasonic cleaning in acetone subjected to the following pre-treatment procedure:

1. Alkaline cleaning in a solution containing 20 g/l sodium hydroxide (NaOH), 5 g/l sodium silicate (Na_2SiO_3), 25 g/l sodium carbonate (Na_2CO_3), 25 g/l sodium phosphate (Na_3PO_4) at 70ºC for 8 min.
2. Cleaning in 10 Vol. % H_2SO_4 at room temperature for 30 s.
3. Cleaning in 5 Vol. % H_2SO_4 at RT for 30 s.
4. Electro cleaning in a solution containing 75 g/l sodium hydroxide (NaOH), 25 g/l sodium sulfate (Na_2SO_4), 75 g/l sodium carbonate (Na_2CO_3), at room temperature for 20 min. The current density applied was 10mA/cm^2 according to ASTM G1.

Between each step the specimen was rinsed by immersion in distilled water at room temperature.

An electroless nickel bath with sodium hypophosphite as reducing agent was used to obtain the coatings. Deposition was performed in two steps, first an interlayer of Ni-P coating with a thickness of 9±2 μm deposited on the substrate by immersing substrate in the 200 ml commercial electroless nickel bath. Temperature varied between 88 and 93˚C and the pH of the bath was 4.6 during the coating process. Bath was agitated using a magnetic stirrer with 300 rpm during coating process. This bath provided Ni-P deposits with a high phosphorous content, 9-10% P. Various Ni-P/nano-SiC composite coatings were also prepared with different SiC concentration (1-10g/l). To obtain Ni-P/nano- SiC composite coatings, proper amount of β-SiC nano-particles (average size 40 nm) was added to 50 ml bath and agitated by an ultrasonic probe (28 KHz frequency and 400 Watt power) with magnetic stirring for 1 hour. After deposition of Ni-P interlayer, SiC contained bath was added to the main bath and coating continued for 2 hours in the presence of SiC nano- particles without using surfactant. nano-particle concentrations in the main bath were changed between 1-10 Wt.%. Magnetic stirring was continued during the coatings deposition. Bath condition for deposition of composite coating was the same as depositing interlayer. For comparison purposes, pure Ni-P coating was also prepared under the same conditions.

The structures of the applied Ni-P and Ni-P/nano-SiC composite coatings were analyzed by X-ray diffraction (XRD) technique. X-ray diffraction phase analysis was performed by a PHILIPS X' Pert Pro. diffractometer, using Co K_a radiation. The morphologies of applied Ni-P and Ni-P/nano-SiC composite coatings were examined using CamScan MV 2300 Oxford scanning electron microscope (SEM). Phosphorus content and particle concentration in the Ni-P surface across the coating thickness were determined via energy dispersive spectrum (EDS). The hardness of coatings was measured using using Vickers diamond indenter (AMSLER D-6700) at a load of 150 g for a loading time of 20 sec. The average of five repeated measurements has been carried out. The corrosion resistance of the coatings in 3.5 wt. % sodium chloride solution was assessed by potentiodynamic polarization. The corrosion tests were conducted using an EG&G Potentiostat/Galvanostat Model 273A. A standard three-electrode configuration consisting of the sample as the working electrode, an Ag/AgCl as a reference electrode and a platinum counter electrode was used to evaluate the polarization behaviours. Potentiodynamic polarization test was carried out by sweeping the potential at a scan rate of 1mVs^{-1} in the range of ±400 vs. open circuit potential (OCP).

Results and discussion

Different Ni-P/nano- SiC composite coatings were prepared with various SiC concentrations (1-10 g/l) in the bath. A reference specimen (Ni-P coating) was prepared without SiC addition. Table 1 shows that the phosphorous content of the coatings was between 7-9 wt. % and a marginal variation in phosphorous content could be seen due to the co-deposition of nano-SiC particles in Ni-P matrix. Thus, with these coatings, differences in the corrosion behavior were unlikely to be attributable to differences in the P content of the coatings. Table 1 shows the level of incorporation obtained for nano-SiC particles in a Ni-P matrix achieved at a fixed stirring speed with different concentrations

of particles in the bath. As it can be seen concentration of the dispersed particles in the electroless nickel bath played a major role in influencing the incorporation level. Incorporation of SiC particles in electroless Ni-P matrix was found to increase with increasing their concentrations in the bath up to 4 g/l, beyond which there seemed to be saturation in spite of a continuous increase in concentrations up to 10 g/l. The observed increase in incorporation level up to a critical concentration could be ascribed to the increased flux of particles adjacent to the electrode surface. However, beyond this critical concentration, there is a possibility of grouping or agglomeration of these second phase particles due to a decrease in the mean distance between them resulting in settlement of the particles, causing either saturation or a slight decrease in the level of incorporation. Micro-hardness of electroless Ni-P and Ni-P/nano-SiC composite coatings are given in Table 1. In general, Ni-P/nano-SiC composite coatings had higher microhardness than Ni-P coatings up to 7 g/l concentration of SiC in the bath. It could be postulated that SiC nano-particles co-deposited in the Ni-P coating could act as a barrier to retard the plastic deformation of Ni-P matrix and hence increase its microhardness. Therefore, SiC nano-particles as a second phase was capable of reinforcing the Ni-P matrix which impeded fast propagation of dislocations in ductile Ni-P matrix. Maximum micro-hardness was achieved at a concentration of 4g/l SiC, because of more uniform distribution of particles in the coating.

Table1: Composition and hardness of various Coatings deposited at various concentrations of nano-SiC particles in the bath

coating (Concentration of nano-SiC in bath)	Ni (Wt. %)	P (Wt. %)	Si (Wt. %)	SiC (Wt. %)	Hardness (HV_{150})
Ni-P	91.79	8.21	-	-	608±4
Ni-P-SiC (1 g/l)	91.89	8.11	2.45	1.72	798±7
Ni-P-SiC (4 g/l)	91.35	8.65	3.50	2.45	932±20
Ni-P-SiC (7 g/l)	92.86	7.14	2.33	1.63	695±8
Ni-P-SiC (10 g/l)	91.5	8.49	2.30	1.62	421±5

Structure of Ni-P/nano-SiC composite coatings. The diffraction patterns of as-deposited Ni-P and Ni-P/nano- SiC composite coatings are shown in Fig. 1. It can be seen that the diffraction pattern of the Ni-P/nano- SiC composite coating has the same characteristics as compared to the Ni-P coating. The existence of nanometer-sized SiC particles did not change the structure of the matrix, and all coatings showed a broad peak around 52°. Measurements carried out according to Debye-Sherrer equation, revealed that the coatings had nanocrystalline structure. The grain size of the coatings was about 39 nm. Similar results for Ni-P coating were also obtained by Elsner and Revez [11]. According to these results, any changes in coatings properties could not be attributed to the structure of composite coating because they had similar crystalline structure.

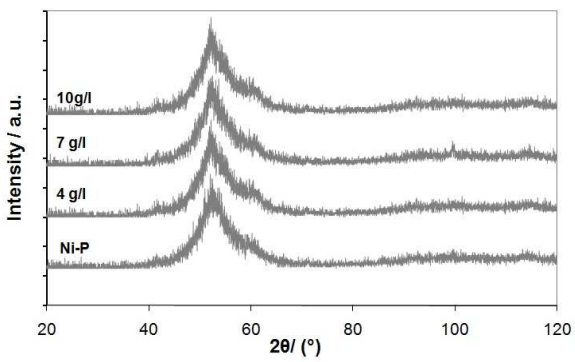


Fig. 1. XRD patterns of electroless coatings prepared with various concentrations of SiC particles: (a) without SiC; (b) 1g/l; (c) 4g/l; (d) 7g/l; (e) 10g/l.

SEM analyses of Ni-P/nano-SiC composite coatings. The distribution of SiC nano-particles through the thickness of the deposit, together with SEM micrographs of the cross-section of the electroless composite coatings are shown in the Fig. 2. It is seen that SiC nano-particles had been embedded in the Ni-P matrix via co-deposition. As it can be seen, SiC particles distributed uniformly throughout the thickness of the coating with various degrees of agglomerations. It could also be noticed that by increasing the concentration of SiC particles from 1g/l to 4g/l in the bath, the concentration as well as uniformity of distribution of SiC nano-particles in coating were also increased. This could be due to striking agglomerated particles in the bath that could detach agglomerated particles. At higher concentration of SiC (> 4g/l), collision probability between SiC nano-particles increased so that the sedimentation of large agglomerated particles decreased the quantity of particles in the coating, while the size of agglomerated particles embedded in the coating was also increased.

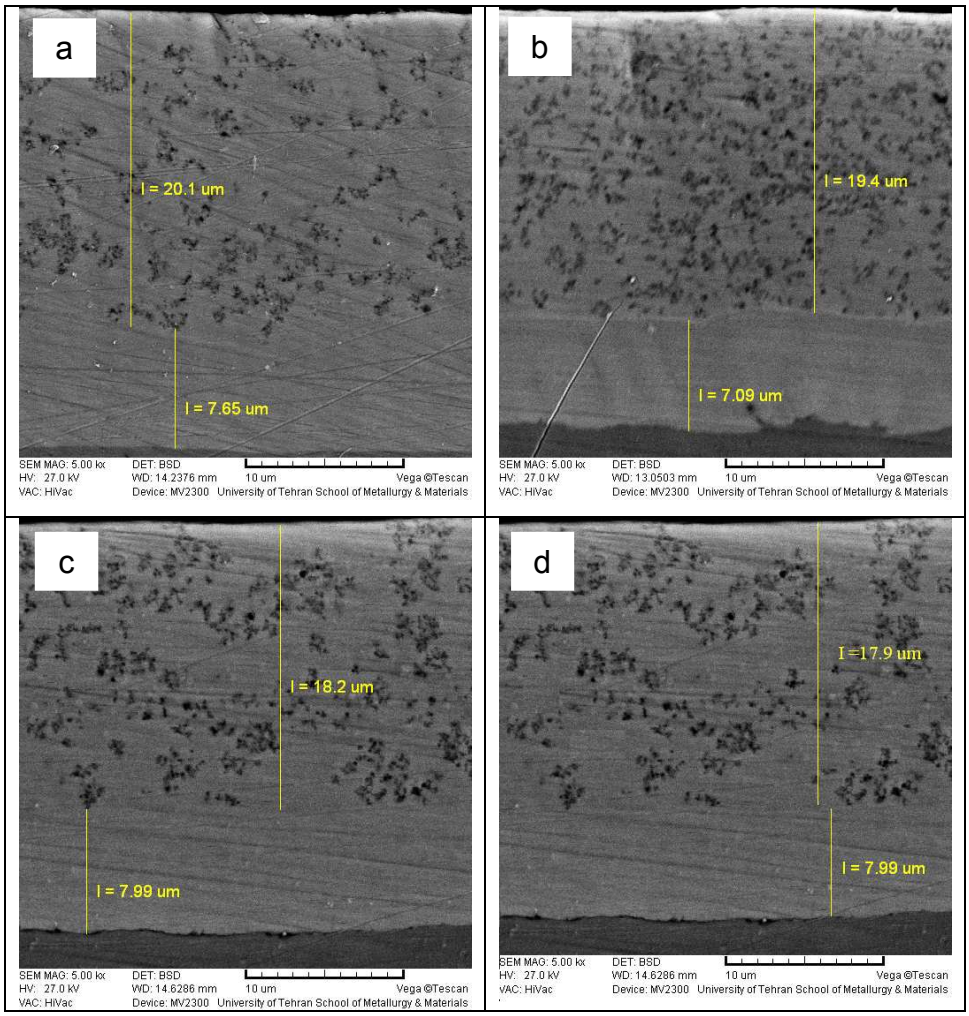


Fig. 2. SEM morphologies of the cross section of electroless coatings prepared with various concentrations of SiC particles: (a) without SiC; (b) 1g/l; (c) 4g/l; (d) 7g/l; (e) 10g/l.

Electrochemical corrosion performance of Ni-P/nano-SiC composite coating. Potentiodynamic polarization curves of Ni-P and Ni-P/nano-SiC composite coatings with different SiC contents, measured in 3.5wt. % NaCl solution, are presented in Fig. 3. As it can be seen typical passivation behaviour could not be clearly observed in the coatings. In general, the corrosion resistance of any alloy depends on its ability to form a surface protective film. Considering the fact that the pH of 3.5wt. % NaCl solution used was around 6.0, the most possible cathodic reaction would be the reduction of the dissolved oxygen (Eq. 1) [12].

$$O_2 + 2H_2O + 4e^- \longrightarrow 4OH^- \quad (1)$$

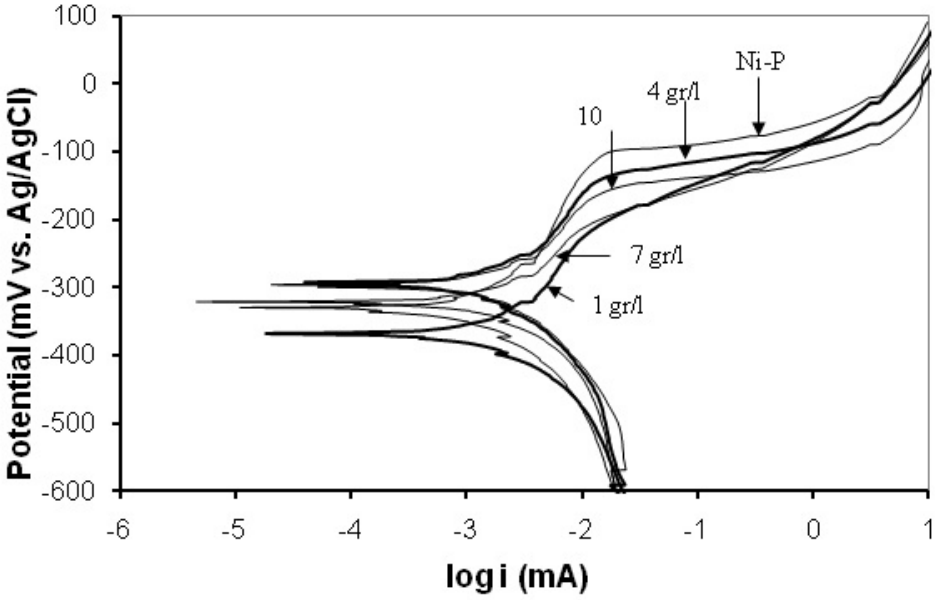


Fig. 3. Potentiodynamic polarization curves of electroless coatings prepared with various concentrations of SiC particles

Hence, in non-deaerated condition, the reduction of the dissolved oxygen could give rise to an increase in pH closer to the coated surface. This led to the formation of insoluble corrosion products $Ni(OH)_2$ covering the coating surface. Moreover, the preferential dissolution of nickel led to the enrichment of phosphorus on the surface layer [13,14]. This enriched phosphorous reacted with water to form a layer of adsorbed hypophosphite anions (H_2PO^{-2}). This layer in turn could block the supply of water to the electrode surface; thereby preventing the hydration of nickel. Corrosion characteristics of electroless Ni-P and Ni-P/nano-SiC composite coating are given in Table 2.

Table2: Electrochemical data obtained from potentiodynamic polarization curves of electroless Coatings prepared with various concentrations of SiC nano-particles.

coating (Concentration of nano-SiC in bath)	E (mV vs. Ag/AgCl)	i_{corr} (μA)
Ni-P	-337	116
Ni-P-SiC (1 g/l)	-375	822
Ni-P-SiC (4 g/l)	-295	890
Ni-P-SiC (7 g/l)	-328	961
Ni-P-SiC (10 g/l)	-290	1039

Among different coatings, nano-composite coatings have lower corrosion resistance compared to monolithic coating. This can be attributed to an effective metallic area available for the corrosive medium to attack as a result of agglomeration of nano-particles (Fig. 2), so electrolyte can permeate through the agglomerated nano-particles toward the coating. This can affect the effective metallic area prone to corrosive media in case of Ni-P/nano-SiC composite coatings. Malfatti [9] observed that the presence of SiC particles in electrodeposited Ni-P coating could reduce corrosion resistance of coatings due to an increase of phase interfaces (between particles and matrix alloy). On the other hand, when the particles are co-deposited, it is believed that the formation of passive layer might be disturbed and this could be the reason for slight decrease in corrosion resistance for composite coatings. Corrosion resistance of composite coatings depends on the distribution of nano-particles

in the coatings and their size, so decreasing in corrosion resistance with increasing of concentration of particles from 1g/l to 10 g/l can be due to the embedding larger size agglomerated particle and also more incorporation of particles in the coating.

Summary

1. SiC nano-particles have been successfully co-deposited with Ni-P matrix to generate Ni-P/nano-SiC composite coatings in the absence of any surfactants.
2. SiC nano-particles are capable of improving the mechanical properties of electroless Ni-P coating, leading to greatly increased micro-hardness.
3. XRD results obtained for both coatings revealed that application of particles did not influence the structure.
4. Corrosion behavior of coatings showed that the presence of nano particles decrease the corrosion resistance of Ni-P coating due to the agglomeration of nano particles.

References

[1]. D. Baudrand, B. Durkin: Met. Finish. (1998), p. 20

[2]. J.N. Balaraju, T.S.N. Sankara Narayanan and S.K. Seshadri: J. Appl. Electrochem. Vol. 33 (2003), p. 807

[3]. C.J. Lin, K.C. Chen and J.L. He: Wear Vol.261 (2006), p. 1390

[4]. Y.T. Wu, L. Lei, B. Shen and W.B. Hu: Surf. Coat. Technol. Vol.201 (2006), p. 441

[5]. A. Grosjean, M. Rezrazi, J. Takadoum and P. Berçot: Surf. Coat. Technol. Vol.137 (2001), p. 92

[6]. M.R. Kalantary, K.A. Holbrook and P.B.Wells: Trans. Inst. Met. Finish. Vol. 71 (1993), p. 55

[7]. Y.S. Huang, X.T. Zeng, X.F. Hu and F.M. Liu: Electrochim. Acta Vol.49 (2004), p. 4313

[8]. J.N. Balarajua, B. Kalavati and K.S. Rajama: Surf. Coat. Technol. Vol.200 (2006), p. 3933.

[9]. C.F. Malfatti, J. Zoppas Ferreira, C.B. Santos, B.V. Souza, E.P. Fallavena, S. Vaillant and J-P. Bonino: Corros. Sci. Vol. 47 (2005), p. 567

[10]. X.H. Chen, C.S. Chen, H.N. Xiao, F.Q. Cheng, G. Zhang and G.J. Yi: Surf. Coat. Technol. Vol.191 (2005), p. 351

[11] B. Elsener, M. Crobu, M.A Scorciapino and A. Rossi: J. Appl. Electrochem. Vol.38 (2008), p. 1053

[12] M.G. Fontana and N.D. Greene: Corrosion Engineering (McGraw-Hill Book Co., New York. 1967).

[13] J.L. Carbajal and R.E. White: J. Electrochem. Soc. Vol. 135 (1988), p. 2952

[14] R.B. Diegle, N.R. Sorensen and C.R. Clayton: J. Electrochem. Soc. Vol.135 (1988), p. 1085

© (2011) Trans Tech Publications, Switzerland
doi:10.4028/www.scientific.net/KEM.471-472.209

Thermal Properties and Thermal Degradation Kinetics of Polypropylene/ Organomodified Ni-Al Layered Double Hydroxide (LDH) Nanocomposites Prepared by Melt Intercalation Technique

Kaberi Kakati, Aditya Prakash, G. Pugazhenthi*

Department of Chemical Engineering, Indian Institute of Technology Guwahati,

Guwahati - 781039, India.

pugal@iitg.ernet.in

Keywords: LDH, PP, nanocomposite, thermal stability

Abstract. The objective of this work is to investigate the influence of LDH loading on the thermal stability and thermal degradation kinetics of the PP/Ni-Al LDH nanocomposites using thermogravimetric analysis (TGA) and to compare the results with that of the neat PP. For this, Ni-Al LDH was first prepared by co-precipitation method at constant pH using their nitrate salts and subsequently organically modified using sodium dodecyl sulphate (SDS) by regeneration method. A series of novel PP/Ni-Al LDH nanocomposites was then prepared with various amounts of LDH by melt intercalation method. The XRD results confirm the formation of exfoliated PP/LDH nanocomposites. PP/LDH nanocomposites exhibit enhanced thermal stability relative to the neat PP due to the presence of barrier effect of LDH lamellar layers and the thermal stability of the nanocomposites also increases with increase in the LDH loading. When 10% weight loss is selected as a point of comparison, the decomposition temperature of PP/LDH (5 wt %) nanocomposite is 15 ^{o}C higher than that of neat PP. The thermal degradation activation energy of the nanocomposites is determined via Coats-Redfern method and compared with that of neat PP. The improvement of thermal stability of PP nanocomposites is also confirmed by increasing the activation energies (E_a) and the integral procedural decomposition temperature (IPDT) compared with neat PP. Criado method is finally used to determine the degradation reaction mechanism of various samples.

Introduction

Polymer/clay nanocomposites exhibit remarkable improvement in mechanical properties, gas barrier properties, ionic conductivity, thermal stability and fire retardancy when compared to virgin polymer or conventional micro or macro-composites [1]. In general, these enhanced properties are realized only when clay particles are well dispersed in the polymer matrix. Two types of nanocomposite structures (intercalated/exfoliated) can be obtained when the nanoclays are dispersed in a polymer matrix. The exfoliated polymer nanocomposites attract much more interest because they have nanoscaled dispersion of clay layers in polymer matrix and thus give some better properties than micro composites and intercalated nanocomposites [2]. Several techniques are used for dispersing clay at nanoscopic scale, including the addition of clay during polymerization (in situ method), or to a solvent swollen polymer (solution blending), or to a polymer melt (melt blending method) [1]. Among these, melt blending of the polymer with organoclay is the most promising and economical method for industrial applications. Various organically modified nanoparticles have been incorporated within the PP matrix via melt blending to enhance mechanical and thermal performance [3-7]. Most of these research works have been focused on the cationic montmorillonites (MMT), while the polymer/LDH nanocomposites have much less studied because of the strong interlayer electrostatic interactions, small gallery space, and hydrophilic property of LDH. Recently, the study on the fabrication and properties of LDH nanocomposites with polyimide [8], poly(ethylene terephthalate) (PET) [9], poly(methyl methacrylate) [10], polystyrene [11] and LDPE [12, 13] has been reported. However, the majority of the above nanocomposites have been

prepared by either solution blending or in-situ polymerization technique. Wang et al. [14, 15] systematically investigated the thermal oxidative degradation behaviour of PET and its blend with montmorillonite nanocomposite. Recently, we have also reported the thermal degradation kinetics of PS/organoclay nanocomposites prepared via solvent blending method [16]. To our best knowledge, the development of PP nanocomposite using Ni-Al LDH as nanofiller has not been reported before. In view of this, the aim of the present investigation is to study the effect of organomodified Ni-Al LDH loading on the thermal properties and thermal degradation kinetics of PP/LDH nanocomposites prepared via direct melt intercalation using synthesized PP-g-MA as a compatibilizer.

Experimental

Preparation of organically modified Layered Double Hydroxide (OLDH). The detailed procedure for preparation of Ni-Al LDH was reported in our previous work [11]. An aqueous solution containing $Ni(NO_3)_2.6H_2O$, $Al(NO_3)_3.9H_2O$ and $NaNO_3$ was prepared by taking the mole ratio of the nitrate salts as 2:1:2, respectively. To this, an aqueous solution of NaOH (0.2M) was added drop wise with vigorous stirring until the pH reached 10. After aging the resulting slurry at room temperature for 16 h, it was filtered, washed with water and dried at 80 ^oC. For modification of LDH, the calcined LDH (2.5 g) was dispersed into a 120 ml of aqueous solution containing 2.5 g of SDS and the dispersion was refluxed at 80 ^oC for 12 h to yield the organically modified LDH. Finally, the modified LDH powders were filtered and dried.

Preparation of PP/LDH Nanocomposites. To prepare PP nanocomposites, a compatibilizing agent, maleic anhydride grafted PP (PP-g-MA) was first synthesized according to the reported method [17]. Nanocomposites containing 2 and 5 wt% LDH were prepared via melt intercalation technique in a single screw extruder (Make: Neoplast Engineering Pvt. Ltd., Ahmedabad, India; Model: SSE = 25; L/D=25). The ratio between the inorganic filler and PP-g-MA was maintained as 2:1 for all the samples. PP (REPOL H029SG supplied by Reliance Industries Limited, India), PP-g-MA and LDH were fed through the main hopper and the molten material was quenched in water. Then, the extrudate was cut into pellets and dried. Hereafter, they are referred as PP/LDH2 and PP/LDH5 for the PP nanocomposites containing 2 wt% and 5 wt% LDH content, respectively.

Characterization. X-ray diffraction (XRD) profile of organically modified LDH and PP nanocomposites was recorded under air at room temperature using AXS D8 ADVANCE Fully Automatic Powder X-Ray Diffractometer (Bruker) equipped with a Cu Kα radiation (1.5418 Å) and Ni filter. The patterns were acquired for 2θ range of 2° to 50° with a 0.05^o s^{-1} scan speed. Thermogravimetric (TG) analysis of the neat PP and PP nanocomposites was performed under nitrogen atmosphere on a TGA/SDTA851e/LF/1100 model (Mettler Toledo) instrument using a heating rate of 10 ^oC/min.

Result and Discussion

XRD analysis. XRD is an effective tool to characterize the types of the layered structure, that is, intercalated and/or exfoliated polymer/LDH nanocomposites because the peaks changed with the gallery height of the layered host crystals. In the case of intercalated nanocomposite, a XRD peak is seen at larger d-spacing than in the pristine clay whereas in case of exfoliated structure, no peak is seen. The XRD pattern of neat PP, organically modified LDH (OLDH) and PP/LDH nanocomposites in the 2θ range of 2-50° is shown in Fig. 1. The d-spacing value of the pristine Ni-Al LDH is calculated as 0.77 nm from 2θ value of 11.4^o by using Bragg's equation, $d = \lambda/2\sin\theta$, where λ is the X-ray wavelength (1.5418 Å). As expected, the position of the basal reflection (003) of the SDS modified LDH is shifted to higher d-value, which confirms the intercalation of SDS molecules into the clay galleries. The main diffraction peak of OLDH is obtained at 2θ value of 6.43^o and the corresponding d_{003} value is 1.37 nm. It seems that the basal spacing between interlayer

is increased due to the intercalation of anionic alkyl surfactant. However, the XRD patterns of PP/LDH nanocomposites do not exhibit any peak corresponding to LDH, which confirms that the organically modified LDH is exfoliated in the PP matrix.

Thermogravimetric analysis. TGA is used to characterize the degradation and thermal stability of the polymer. The dispersion of clay is known to improve the thermal stability of polymers. Fig. 2 represents the TGA curves for PP, PP/LDH2, and PP/LDH5 nanocomposites. The parameters that are important from TGA curves are the onset of degradation, which is usually taken as the temperature at which 10 % degradation occurs, $T_{10\%}$, and the midpoint temperature of degradation, $T_{50\%}$. From the TGA curves, it is clear that thermal stability of the PP/LDH nanocomposites for both 2% and 5% (by weight) loading is increased, which is confirmed by shifting of the TGA curve of

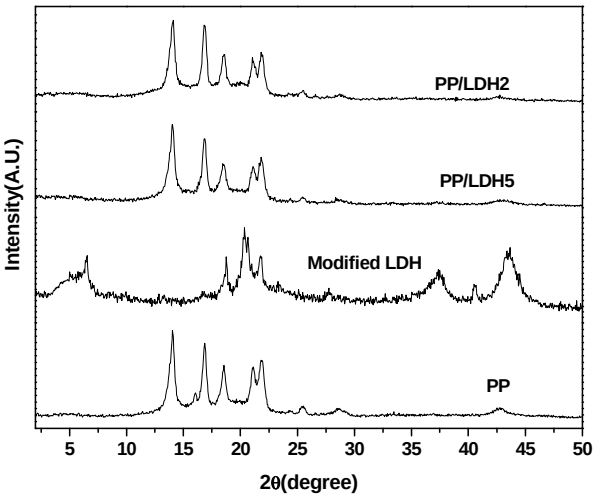


Fig.1. XRD patterns of neat PP, modified LDH and PP/LDH nanocomposites

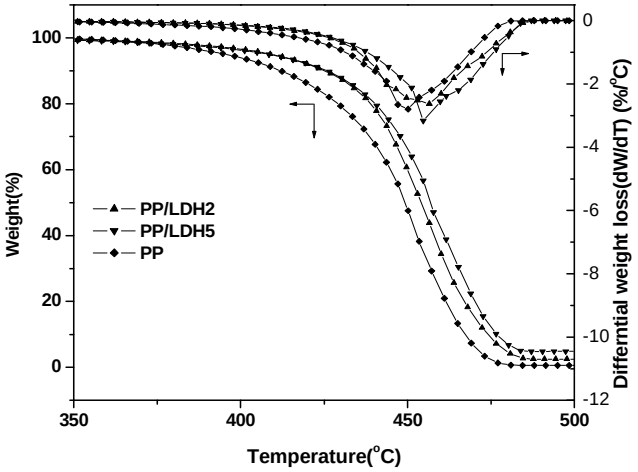


Fig.2. TGA and DTG curve of neat PP and PP nanocomposites between 350-500 ^{o}C

PP/LDH nanocomposites towards right of the TGA curve of the neat PP. When 10% weight loss is selected as a point of comparison, the decomposition temperature of neat PP, PP/LDH2 and PP /LDH5 nanocomposite is found to be 411, 424.5, and 426.3 ^{o}C, respectively. The results demonstrate that the degradation of the nanocomposites took place at higher temperatures than that of neat PP (13.5-15.3 ^{o}C higher than that of neat PP) in the presence of LDH. This behavior could be explained by the presence of barrier effect of LDH lamellar layers, which limited the emission of the produced degradation gases and transmission of heat therefore, resulted in the improvement in thermal stability of the nanocomposite material. The increase in the onset temperature signifies delayed degradation of PP/LDH nanocomposites. These results are in good agreement with the recently reported results by Zanetti et al. [18] on the thermal degradation of PP/layered silicate nanocomposites. The data of differential calculus of the TGA curves are also shown in Fig. 2. The peak indicates the maximum degradation temperature (T_{max}). The T_{max} value for neat PP, PP/LDH2 and PP/LDH5 is found to be 450 ^{o}C, 456 ^{o}C and 455 ^{o}C, respectively. This confirms further that the incorporation of LDH into PP matrix enhances the thermal stability of the nanocomposites.

Kinetics analysis using Coats-Redfern method. Coats-Redfern method (expressions are given in Equation 1) can deal with the main degradation region of TGA curve of material and only requires the TGA data at just one heating rate to calculate the related reaction order n, reaction activation energy E_a and pre-exponential factor A [19].

n=1 $$\ln\left(-\frac{\ln(1-\alpha)}{T^2}\right)=\ln\left[\frac{AR}{\beta E_a}\left(1-\frac{2RT}{E_a}\right)\right]-\frac{E_a}{RT} \quad (1a)$$

n≠1 $$\ln\left(\frac{1-(1-\alpha)^{1-n}}{T^2(1-n)}\right)=\ln\left[\frac{AR}{\beta E_a}\left(1-\frac{2RT}{E_a}\right)\right]-\frac{E_a}{RT} \quad (1b)$$

Where α is the conversion degree or fractional weight loss, T is the temperature, R is the gas constant, and β is the heating rate in TG analysis. In this work, the TG data of PP nanocomposite samples with heating rate of 10 ^{o}C/min were processed to evaluate the kinetic parameters. Firstly, we supposed that a certain thermal degradation reaction has a specified reaction order n and then substituted the supposed n value into Eq. (1). The plot of the left part of Eq. (1) against -1/T was fitted to calculate the correlation coefficient R. Above procedure was repeated till the best R value was obtained. The calculated reaction order at the best R value is just our required one. Subsequently, the apparent activation energy and the pre-exponential factor can be calculated from the slope and intercept of the fitted straight line, respectively. The estimated activation energy for neat PP, PP/LDH2 and PP/LDH5 sample is 195, 243, and 291 ^{o}C, respectively while reaction order is found to be 0.5, 0.9 and 0.7, respectively for PP, PP/LDH2 and PP/LDH5 nanocomposites. It clearly indicates that the E_a of PP/LDH nanocomposites is 48-96 kJ/mol higher than that of neat PP.

Determination of the reaction mechanism of thermal degradation using Criado method. Criado et al. [20] proposed a method which can accurately determine the reaction mechanism in the solid reaction process using the activation energy value. The following expressions are involved to estimate the reaction mechanism of the thermal degradation process.

$$Z(\alpha)=\frac{d\alpha}{dT}\frac{E_a}{R}\exp(x)\frac{e^{-x}}{x}\quad\frac{x^3+18x^2+86x+96}{x^4+20x^3+120x^2+240x+120} \quad (2)$$

$$Z(\alpha)=\frac{\beta}{A}g(\alpha)\frac{d\alpha}{dT}\exp(x) \quad (3)$$

where, $x = E_a/RT$. As far as the polymer is concerned, its degradation process, generally, obeys the sigmoidal or deceleration functions. For the different solid reaction mechanism, *g(α)* has different expressions [16, 20]. Eq. (3) is used to plot the master (theoretical) Z(α)-α curve of the different reaction mechanisms reported in reference 16, and eq. (2) is used to plot the experimental Z(α)-α curve according to the TG data. The comparison of the Z(α)-α master curve with the experimental Z(α)-α curve can easily and accurately predict the reaction mechanism of the thermal degradation reaction. Fig. 3(a-c) shows the Z(α)-α master and experimental curves of the neat PP, PP/LDH2 and PP/LDH5 nanocomposites. As can be seen, the experimental curve of the neat PP is closer to the master curve of Z(F1) except at the higher values of α where the deviation increases, indicating that the thermal degradation of neat PP is similar to F_1 reaction mechanism (random nucleation having one nucleus on individual particle, i.e. the identical probability of nucleation occurring at each active site) with rate-controlling step of the nucleation process in the initial phase of degradation but at higher conversion the experimental curve is close to A_4 mechanism which represent a type of nucleation and growth mechanism [16, 20]. In the case of PP/LDH2 nanocomposite, the experimental curve nearly overlaps with the master curve of Z(F1) at the whole range of α, indicating that the thermal degradation of PP/LDH2 is similar to F_1 reaction mechanism. For the PP/LDH5 nanocomposites, the experimental curve matches with Z(F1) for α<0.5 however at higher values of α, it is shifted towards the A_2 (nucleation and growth). The possible cause could be the shift of mechanism of thermal degradation at higher temperatures.

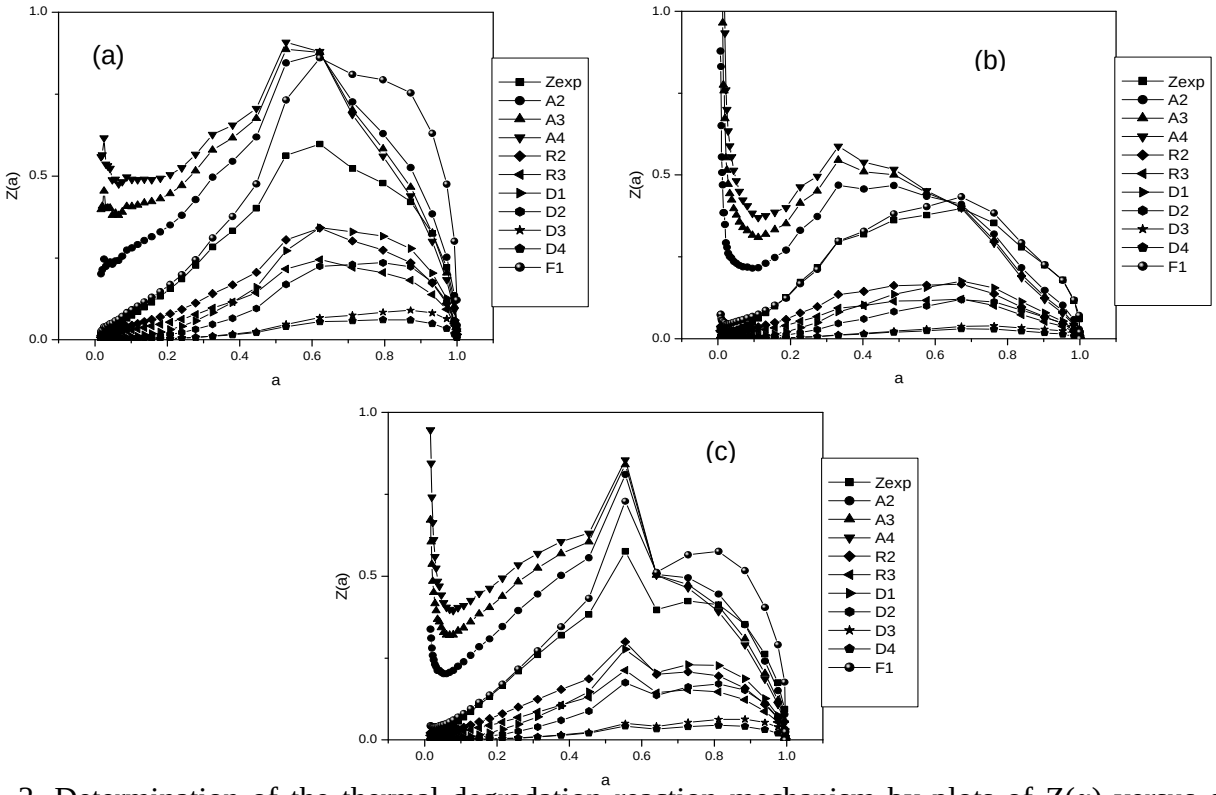


Fig. 3. Determination of the thermal degradation reaction mechanism by plots of Z(α) versus α using Criado model for (a) neat PP, (b) PP/LDH2 and (c) PP/LDH5 nanocomposite samples

Integral procedure decomposition temperature (IPDT). IPDT is a thermal stability factor of the nanocomposites, which is correlated to the volatile parts of the polymeric materials [16]. IPDT is determined on the basis of the overall shape of the TGA curve, so it can estimate the overall inherent thermal stability for the decomposition proceeded in a single or several consecutive steps. The IPDT value for neat PP, PP/LDH2 and PP/LDH5 is found to be 297.3, 361.4, and 373 ^{o}C, respectively. It clearly indicates that PP/LDH nanocomposites are relatively more thermally stable than the neat PP.

Summary

The influence of organomodified LDH on the thermal properties and thermal degradation kinetics of the PP/Ni-Al LDH nanocomposites has been successfully demonstrated. The XRD results authenticate the formation of exfoliated structure for all the PP nanocomposites. The TGA profiles of PP/LDH nanocomposites show a significantly enhanced thermal stability compared with neat PP. Thermal decomposition temperature for PP/LDH nanocomposite at 10 % weight loss is 15 ^{o}C higher than that of neat PP. The higher IPDT and activation energy value for PP nanocomposites also confirm the increase in the thermal stability of the nanocomposites. The reaction mechanism of thermal degradation of the neat PP and respective nanocomposites is successfully predicted using Criado method. The thermal degradation of the neat PP is similar to F1 reaction mechanism (random nucleation having one nucleus on individual particle) with rate-controlling step of the nucleation process in the initial phase of degradation but at higher conversion, the degradation gradually transits towards A_4 mechanism (nucleation and growth mechanism). For the PP/LDH2 nanocomposite, the involved system follows F_1 reaction mechanism for the whole range of conversion whereas PP/LDH5 nanocomposite, at the initial stage, the involved system has F_1 reaction mechanism and at higher conversion, the involved system, however, gradually transits towards A_2 mechanism (nucleation and growth mechanism).

References

[1] S.S. Ray and M. Okamoto: Prog. Polym. Sci. Vol. 28 (2003), p. 1539

[2] F. Leroux and J.P. Besse: Chem. Mater. Vol. 13 (2001), p. 3507

[3] J. Li, M.T. Ton-That, W. Leelapornpisit and L.A. Utracki: Poly. Engg. Sci. Vol. 47 (2007), p. 1447

[4] E. Deenadayalan, S. Vidhate and A. Lele: Polym. Int. Vol. 55 (2006), p. 1270

[5] G. Mani, Q. Fan, S.C. Ugbolue and Y. Yang: J. Appl. Polym. Sci. Vol. 97 (2005), p. 218

[6] H. Qin, S. Zhang, C. Zhao, M. Feng, M. Yang, Z. Shu and S. Yang: Polym. Degrad. Stab. Vol. 85 (2004), p. 807

[7] P. Svoboda, C. Zeng, H. Wang, L.J. Lee and D.L. Tomasko: J. Appl. Polym. Sci. Vol. 85 (2002), p. 1562

[8] H.B. Hsueh and C.Y. Chen: Polym. Vol. 44 (2003), p. 1151

[9] W.D. Lee, S.S. Im, H.M. Lim and K.J. Kim: Polym. Vol. 47 (2006), p. 1364

[10] B. Li, Y. Hu, J. Liu, Z. Chen and W. Fan: Colloid Polym. Sci. Vol. 281 (2003), p. 998

[11] B. Sahu and G. Pugazhenthi: J. Appl. Polym. Sci. in press (2010)

[12] F.R. Costa, M. Abdel-Goad, U. Wagenknecht and G. Heinrich: Polym. Vol. 46 (2005), p. 4447

[13] D.U. Long-Chao and Q.U. Bao-Jun: Chinese J. Chem. Vol. 24 (2006), p. 1342

[14] B. Wu, Y.Z. Wang, X.L. Wang, K.K. Yang, Y.D. Jin and H. Zhao: Polym. Degrad. Stab. Vol. 76 (2002), p. 401

[15] D.Y. Wang, Y.Z. Wang, J.S. Wang, D.Q. Chen, Q. Zhou and B. Yang: Polym. Degrad. Stab. Vol. 87 (2005), p. 171

[16] S.V. Krishna and G. Pugazhenthi: J. Appl. Polym. Sci., in press (2010)

[17] S.K. Chattopadhay, R.K. Khandal, R. Uppaluri and A.K. Ghoshal: J. Appl. Polym. Sci. Vol. 113 (2009), p. 3750

[18] M. Zanetti, G. Camino, P. Reichert and R. Mulhaupt: Macromol. Rapid Comm. Vol. 22 (2001), p. 176

[19] A.W. Coats and J.P. Redfern: Nature. Vol. 201 (1964), p. 68

[20] J.M. Criado, J. Malek and A. Ortega; Thermochim. Acta.Vol. 147 (1989), p. 377

© (2011) Trans Tech Publications, Switzerland
doi:10.4028/www.scientific.net/KEM.471-472.215

Analysis Of Energy Absorption On Pultruded Composite Tube Under Oblique Loading

Abu Bakar Sulong [1,2,a], Abdullah Atiq Ariffin[1,b], Jaafar Sahari[2,c], and Hendra Suherman,[1,3,d]

[2] Department of Mechanical and Materials Engineering, Faculty of Engineering and Built Environment, Universiti Kebangsaan Malaysia, 43600 Bangi, Malaysia

[2]Cell Fuel Institute, Universiti Kebangsaan Malaysia, 43600 Bangi, Malaysia

[3]Department of Mechanical Engineering, Universitas Bung Hatta, 25133 Padang, Indonesia

[a]abubakar@eng.ukm.my, [b]atiq@yahoo.com, [c]jaafar@eng.ukm.my, [d]henmeubh@yahoo.com

Keywords: Energy absorption; Pultruded composite tube; Oblique loading

Abstract. The capability of structures to absorb as much amount energy, particularly in automotive structures to reduce the damages due to impact energy during collision attract attention of many reserachers. During the actual collision, the crash box is not only experienced axially crash, but also in oblique crash. In this study, an experiment was carried out to study the crashworthiness parameters and behaviour of pultruded fibre E-glass/polyester pultruded composite tubes under oblique loading. Quasi-static loadings were applied axially and oblique on the pultruded composite to investigate the response of force-displacement during progressive collapses. The pultruded wall thickness of 6 mm tubes were used and four oblique angles of 0˚, 5˚, 10˚ and 15˚ were selected to study their effect on crushing behaviours and collapse modes using compression moulding. All specimens were chamfer 45˚ on top end for purpose to work as a collapse trigger mechanism. The results showed that the energy absorption of the structures increasing with decrease of the loading angle.

Introduction

Over the past few decades, composite materials have been adopted in a wide range of applications including many in the construction and automotive industries. Fibre Reinforced Polymer (FRP) composite profiles have become widely used in structural engineering applications. For structures subjected to impact loading, crashworthiness is highly desirable and depends on the energy absorption mechanisms of the system. The efficiency is measured in term of the crushing performance as a function of the specific energy absorption capability that is higher in composites than in metallic structures. Much of the working assessing the energy absorbing capability of composite materials and structures under compressive loading has been to a greater extent restricted to axisymmetric tubes. Therefore, while it is now well known how to design composite material tubes to develop a stable or controlled crushing response under sustained axial loading, it is not known how to design a composite material tube for stable load carrying capacity under oblique loading. Energy absorbers are often used in vehicles to protect passenger and the structure itself during impact. The absorption of energy is controlled by plastic work in crash box which is directly given from the area under the force-displacement curve. When the crash boxes are fully deformed, the deformations are transferred to the front rail and subsequently to the rest of the vehicle's structure. This may lead to both bending and axial loading of other structural parts. Analytical studies of both pure bending [1] and axial crushing of square columns by Al-Emran [2] have been completed over many years.

Most of the research on the energy absorption of metals has concentrated on thin wall cylinders of simple cross section and fairly well understood [3,4]. Previous investigations have indicated that the energy absorption mechanisms in composite materials are more complex than those observed in

conventional materials; include matrix cracking and fibre breakage [4]. In addition to the material properties, in the event of a collision, the dissipated energy also depends on geometry factors. Trigger mechanisms can be used to control collapse, thus increasing the dissipated energy. In this case, the trigger is a stress concentrator, which is located at a specific location within the structure, to cause failure in a progressive crushing mode. Quasi-static crush tests are carried out at a constant speed, and therefore, are simple and easy to control. Hence, they have been used by many researchers to study energy absorption properties of composite components. Melo et al. [5] stated by selecting appropriate crushing speeds, quasi-static tests may provide important information regarding the failure mechanisms and energy absorption capability of composite structures in crushing conditions.

Very limited studies were carried out on the effect of processing conditions on the energy absorption of pultruded composite and there are no comprehensive quasi-static analysis for pultruded composites on oblique loading has been found in literature but many can be on metallic materials. Only one paper reported on quasi-static loading applied axially on pultruded composite to investigate the response of force-displacement during progressive collapses. Reyes et al [3] has studied square aluminum columns in alloy AA6060 subjected to quasi-static oblique loading and investigated experimentally for three different load angles. The square columns were clamped at one end and oblique load conditions were realized by applying a force with different angles to the centerline of the column. Others studies on oblique loading reported by Al-Emran [4] and Reyes [6] on energy absorption for foam-filled extrusion under quasi-static oblique loading. The objectives of this study is to investigate the performance of energy absorption of pultruded composite tubes with square cross-section at thickness 6 mm under oblique loading in compression.

Experiment

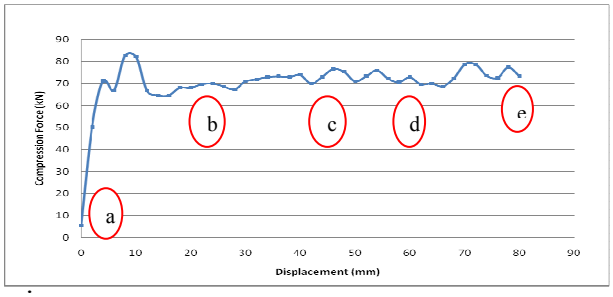
Composite tube with square cross-section was fabricated using E-glass fibres reinforced polyester resin with 55% by volume of glass mat and polyester. The pultruded tubes were manufactured at Intralink Techno Sdn. Bhd. located at Selangor, Malaysia. This process was carried out by drawing fibre mats through a resin bath to wet the fibre, and then through a heated die to form the desired final shape. Finally, the profile passed through a tunnel oven to accelerate curing, and the composite was cut to desired length. For this study, 8 specimens were used. The length (L), width (W) and breadth (B) of the test specimens were fixed at 120 mm (L), 75 mm (W), 75 mm (B), and 6 mm wall thickness. All test specimens were chamfered on top end with angle 45˚ each as a triggering mechanism [4]. Energy absorption is usually subjected for both axial force and moment in an oblique crash. In order to make oblique condition in this experiment, jigs with different angle of 5˚, 10˚, and 15˚were fabricated. The accuracy of jig angles was ensured using Universal Bevel Protractor. The quasi-static compression tests were carried out using a GOTECH 100 kN universal testing machine based on ASTM D365, in quasi-static compression mode. All tests were conducted under a displacement-controlled mode with cross-head speed of 5.0 mm/min. The load angles were $\theta_1 = 0^\circ$, $\theta_2 = 5^\circ$, $\theta_3 = 10^\circ$, and $\theta_4 = 15^\circ$. Compression test for each oblique angle was repeated three times, and an average data was reported. Peak force and mean crush load were the response parameters of compression test. A reasonable displacement to compare mean crush force was chosen as d_{max} = 80 mm. Every 20 mm displacement of crosshead, mode of crushing pultruded samples was recorded. All tests were conducted under a displacement-controlled mode with cross-head speed of 5.0 mm/min. This test was interrupted after the maximum load was reached. Then, the same tests will be carried out at oblique angle of 5˚, 10˚ and 15˚, respectively.

Results and Discussion

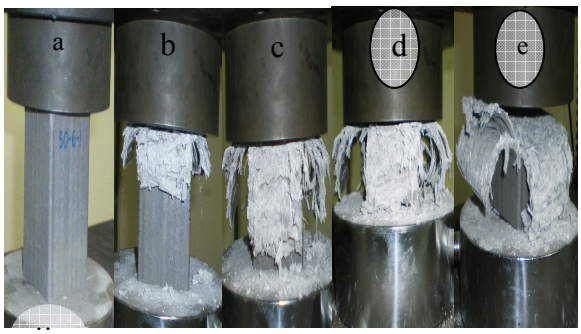
The maximum and average compression load are given in Table 1. The load-displacement curves and failure behaviour for specimens at $\theta = 0^{\circ}$, 5°, 10° and 15° are shown in Figure 1-4. It is clear from Figures 1-4 that the load did not oscillate while load angle was increased up to 15^{0}, rather it increases steadily up to a certain deflection, before decreasing continuously for the remaining of the crush cycle. The observed phenomenon can be explained in terms of the deformation profiles of the tubes, which are shown in Figure 1(ii), 2(ii), 3(ii) and 4(ii). The deformed profiles are shown up until 80 mm of displacement. All pultruded tubes had been compressed and fail through progressive collapse.

Table 1. Maximum and mean compression loads of pultruded tubes

Test No.	θ (^{o})	h(mm)	Response parameters		Mass (g)
			F_{max} (kN)	F_{mean} (kN)	
S0-6-1	0	6	82.87±3.75	72.33±2.13	334.6±1.75
S5-6-2	5	6	79.9±2.153	70.72±3.11	332.3±1.23
S10-6-3	10	6	83.52±5.61	72.02±4.13	333.0±2.12
S15-6-4	15	6	67.64±3.25	57.94±3.23	334.2±1.95

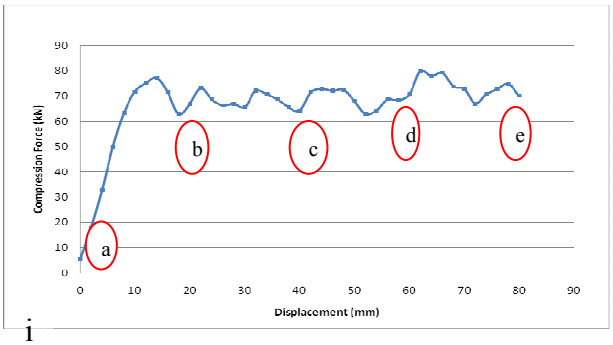


i

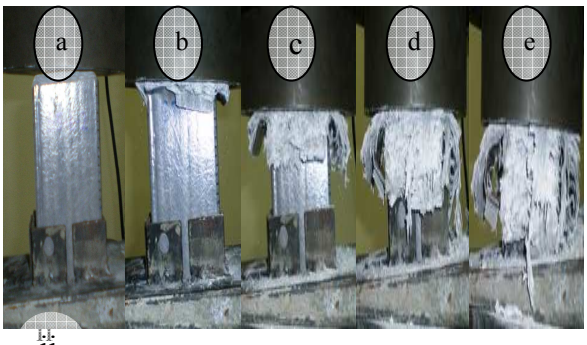


ii

Figure 1. (i) Load-displacement curve, and (ii) Failure behaviour of specimen S0-6-1

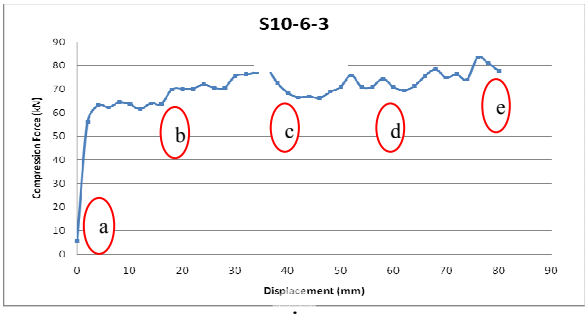


i

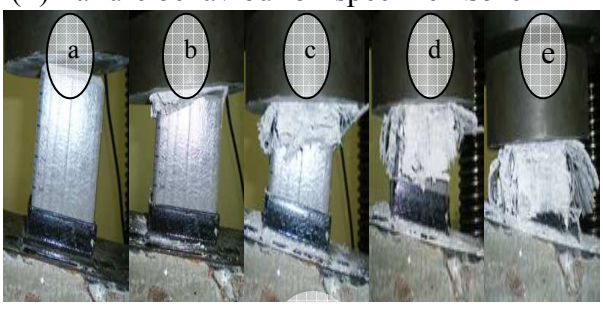


ii

Figure 2. (i) Load-displacement curve, and (ii) Failure behaviour of specimen S5-6-2

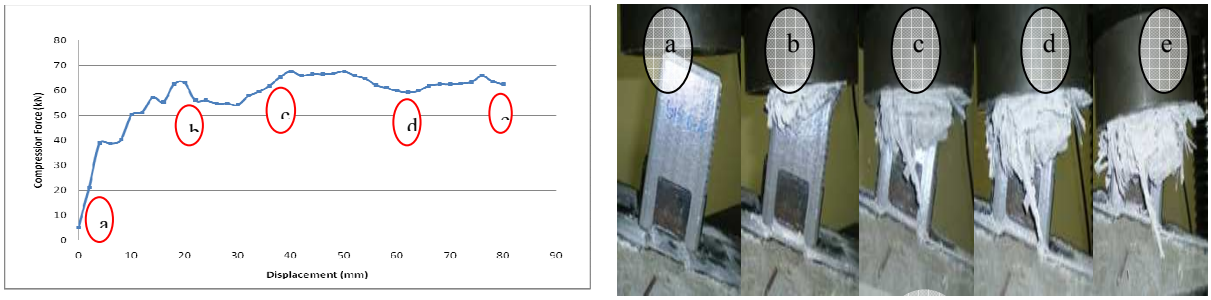


i



ii

Figure 3. (i) Load-displacement curve, and (ii) Failure behaviour of specimen S10-6-3



i ii

Figure 4. (i) Load-displacement curve, and (ii) Failure behaviour of specimen S15-6-4

Two different modes of failure were observed in during compressive mode. Mode I is brittle tube collapse observed by the progressive end-crushing of axial and oblique compressed tube. The formation of two continuous fronts per tube size which spread outward and inward. Splitting of the square tube was at its corners due to high absorption of crash energy [7,8]. This collapse mode was corresponding to the 'splaying' or 'lamina bending' type of stable brittle fracture. Specimen from Figure 1-4 show this characteristic, which is similar to mode I characteristic. The progressive end crushing of the pultruded tube was initiated with crack formation at the corners of the square tube due to local stress concentration, at the end of linear elastic loading phase, when the applied load attain a peak value , F_{max}.. Similar observation was reported by Mamalis et al. [8] where they concluded that F_{max} depend on geometric, orientation and material characteristic of tested specimen. Only specimen S15-6-4 shown mode no II of local buckling collapse that can be observed by crack formation at the tube corners, and it is followed by an immediate drop of the compressive load and its propagation parallel to the tube axis. Then, pultruded tube was split into two continuous front that spread outwards and inwards of the tube due to compressive load.

Figure 5 shows overlay compression force-displacement for wall thickness of 6 mm. The average load fluctuations is almost constant after initial loading until final crushed deformation. Another important characteristic of these curves are the shape of the force-displacement curve where as the crushing begins, load quickly rises to a peak value and then drops off significantly and stays relatively constant. Large force reduction occurred during the collapse and it showed that energy absorption has decreased. For crashworthiness applications, the initial peak load should not be much greater than the mean crush force because large peak force required initiating crushing and the goal in energy management is to absorb all the energies without imparting large forces to the people and transporter. This observation supports the hypothesis from previous study reported by Al-Emran and Hafizun [2]. Based on results in Figure 5, higher peak load is sustained for the tubes crushed with smaller angles and there is a large amount of scatter of data especially at post crushing region. The curve also exhibited an initial peak load followed by a large drop and then rise up to somewhat steady state. In the initial state of crushing, crack load increases and the front sides move outward and inward. Cracking process is observed along the tube as the compressive load increased.

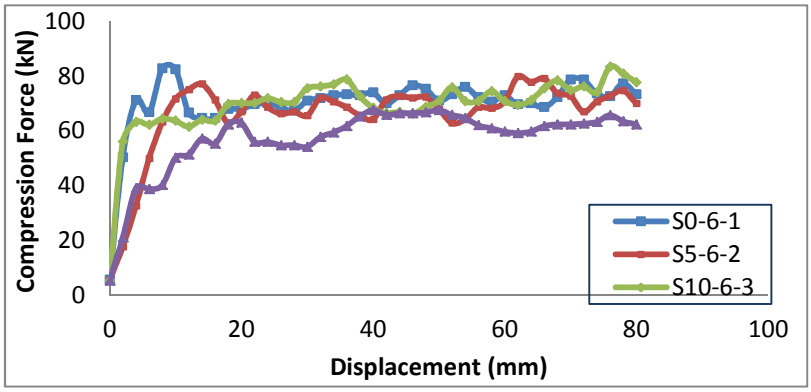


Figure 5. Overlay of compression force-displacement curves at oblique angles of 0°, 5°,10° and 15°

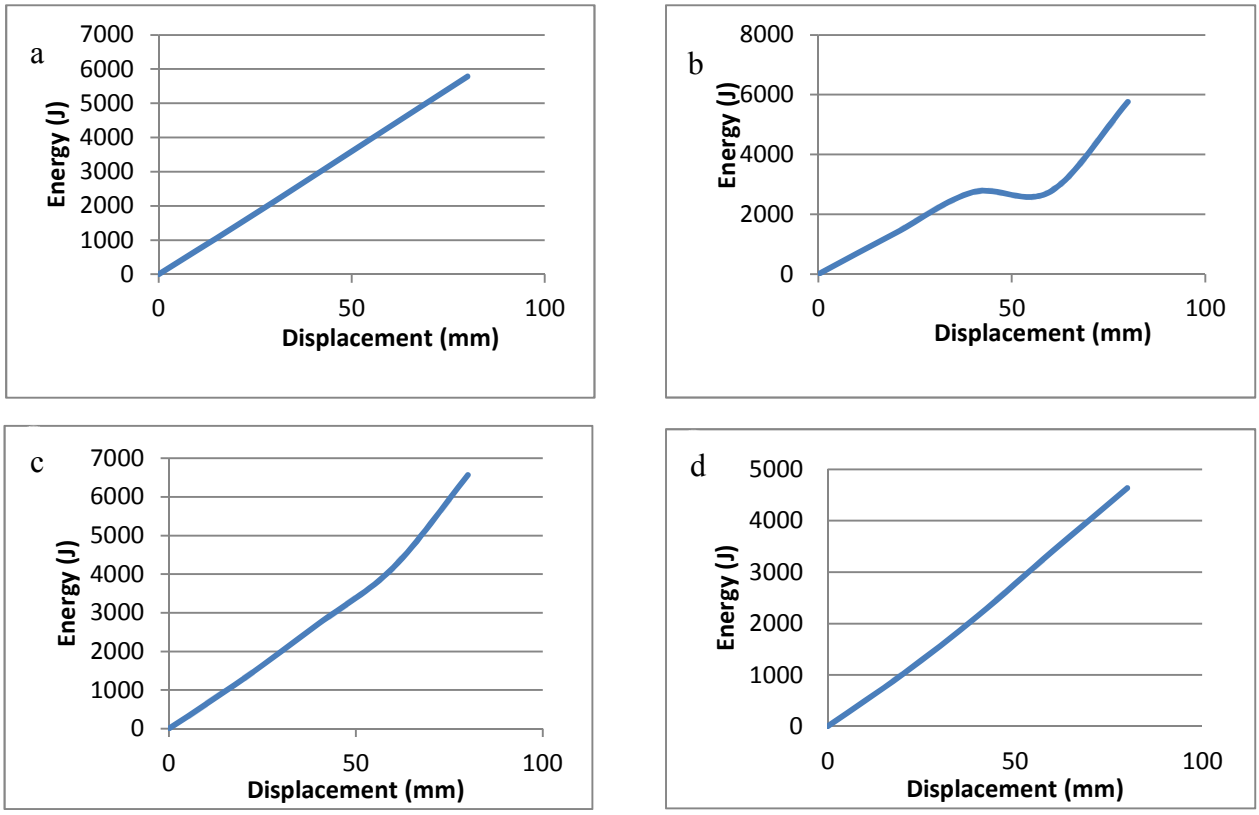


Figure 6. Variation of energy absorption against displacement, (a) S0-6-1, (b) S5-6-2, (c) S10-6-3 and (d) S15-6-4.

The load-displacement for the tube with 15˚ load angle shows initial peak load is smaller than other angle loaded tubes. The composites are easily crushed and the wall tubes are slided out and collapsed. The failure mechanisms of the tube at the front end tips are shear compression failure which has lowered the initial peak load. After that, unstable crack propagation occurred along the tube. From this result, it is shown large reduction of peak force which induced lower energy absorption performance. This observation supports hypothesis make by Reyes et al [6].

Variation of energy absorptions against displacement under oblique loading angle are given in Figure 6. Energy absorption performances were determined by taking the average mean force multiplied by crushed deformation distance. Lower energy absorption performance is clearly observed for pultruded tube with 15˚ load angle.

Summary

The quasi-static experiment on the crashworthiness behaviours of pultruded E-glass/polyester composites tube has been carried out under axial and oblique compressive loading. Square cross section tubes with thickness of 6 mm were used as specimen at 0°, 5°, 10°, 15° loading angle. The results highlight the performance and behaviour of pultruded tube for impact energy absorbers such as in crashworthiness applications. Brittle collapse and local buckling collapse mode are observed during compression test. It was found that the peak load and mean crush load were decreased when oblique angles increased. It also found that initial force for tube with 15˚ load angle is the lowest, which also give the lowest absorption energy. The results from this study can be used as reference in design composite structure under oblique loading. Effects of different thicknesses of tubes and oblique loading angle more than 15° will study in the future.

Acknowledgements

The authors gratefully acknowledge the technical support from Department of Mechanical and Materials Engineering, and Department of Civil and Structure Engineering, Universiti Kebangsaan Malaysia.

References

[1] Mertens. K.O: Master's thesis, University of Wisconsin, (2003).

[2] Al-Emran. I, Afizun. A. Mech. J. Vol. 24 (2007), p. 15

[3] Reyes. A, Langseth. M, & Hopperstad. O.S: Int. J. Mech. Sci. Vol. 44 (2002), p. 1965

[4] Al-Emran. I: Int. J. Eng. & Tech. Vol.5 (2008)p.11

[5] Melo. J.D.D, Silva. A.L.S, & Villena. J.E.N: Comp. Struct. Vol.82 (2008), p. 622

[6] Reyes. A, Hopperstad. O.S, & Langset. M: Int. J. Solids and Struct. Vol. 41 (2004), p. 1645

[7] Mamalis. A.G, Manolakos. D.E, Demosthenous. G.A, & Ioannidis. M.B: Thin-Walled Struct. Vol. 28 (1997), p. 279

[8] Mamalis. A.G, Manolakos. D.E, Demosthenous. G.A, Ioannidis. M.B, & Papapostolou. D.P, : Comp.Struct. Vol. 69 (2005), p. 407

© (2011) Trans Tech Publications, Switzerland
doi:10.4028/www.scientific.net/KEM.471-472.221

Fatigue Life Prediction of Composite Materials: Artificial Neural Networks vs. Polynomial Classifiers

Hany A. El Kadi

American University of Sharjah, College of Engineering, P.O. Box 26666, Sharjah,

United Arab Emirates

hkadi@aus.edu

Keywords: Composite materials, Fatigue, Artificial neural networks, Polynomial classifiers

Abstract. Artificial neural networks (ANN) and polynomial classifiers (PC) have been successfully used to predict the fatigue failure of fiber reinforced composite materials. This includes predicting the behavior of the same material subjected to different loading conditions as well as predicting the fatigue behavior of different materials. In this work, the fatigue life prediction obtained using both methods will be compared. The effect of the various parameters influencing the prediction will be presented and the advantages and disadvantages of each of the methods will be discussed.

Introduction

Artificial Neural Networks (ANN) are one of the artificial intelligence concepts that have proved to be useful for various engineering applications. Due to their massively parallel structure, ANN can deal with many multivariable non-linear modeling for which an accurate analytical solution is very difficult to obtain [1-3]. The ability to learn by example is one of the key aspects of ANN. Hence, the use of ANN in predicting a wide range of composite materials properties has been investigated by several researchers. A review by El Kadi [4] and another by Zhang and Friedrich [5] looked at the various applications of ANN to polymeric composites. Most of the reported work shows that the use of ANN can lead to predictions as accurate as, if not better, than those obtained by the conventional methods.

Lee et al. [6] and Al-Assaf and El Kadi [7] used ANN to predict the fatigue life of the same composite material used in the training process of the ANN under different loading conditions. They used experimental data of a single material with different fiber orientation angles subjected to various stress ratios. While the input and output parameters to the network varied in both studies, the results obtained showed that predictions obtained using ANN compared well with experimental data. In a later work, El Kadi and Al-Assaf [8] used different neural networks architectures to predict fatigue life. Their results showed that the choice of network structure can greatly influence the accuracy of the predictions obtained.

One of the anticipated benefits of the successful application of ANNs would be that it could be possible to predict the cyclic behavior of a material for which no fatigue data is available by using the known characteristics of other composites. Lee et al. [6] trained an ANN using fatigue data from four different material systems to predict the cyclic behavior of an additional material not used in the training. The results obtained appeared unsatisfactory as the average root mean square error (RMSE) obtained was of the order 100% - 170%. El Kadi [4] suggested that better predictions might be achieved if a larger number of representative materials was used in the testing and appropriate material properties were used in both the training and the testing stages. El Kadi and Al-Assaf [9], in a preliminary study, trained a modular neural network to predict the number of cycles to failure for different composite materials under a constant stress ratio. They used five materials to train the ANN and one additional material for testing. The input parameters were comprised of monotonic and cyclic properties. The RMSE was found to be 36.2% well below the value obtained by Lee et al. [6].

In a recent study, Al-Assadi et al. [10] used ANN to predict the fatigue life for composite materials other that those used for training. Seven different materials were used in training the network for the purpose of predicting the fatigue behavior of an eighth material. All materials used were subjected to a cyclic loading with a constant stress ratio of 0.1. The effect of the ANN architecture, the type of training algorithm as well as the number of neurons per hidden layer was addressed. Although no singular ANN architecture/training method combination was shown to consistently produce the best predictions for all materials, the results showed that ANN can accurately predict the fatigue life of a composite not used in the training of the network. Depending on the material and the network architecture used, the typical RMSE obtained varied between 8.8% and 16.3%.

For all previously mentioned studies, it can be shown that the use of ANN depends on several parameters that are crucial to the type of results obtained. The appropriate ANN architecture to use in a certain application, the number of hidden layers and the number of neurons in each hidden layer are issues that can greatly affect the accuracy of the prediction. Unfortunately, there is no direct method to specify these factors as they need to be determined on trial-and-error basis. In addition, since ANN uses an iterative process, the results obtained greatly depend on the initial values these networks use for the solution weights; this means that running the program several times might give different predictions. The conventional way to overcome this drawback is to perform numerous runs and report the average results of the predictions obtained.

For the above-mentioned reasons, the search for a method requiring less a priori decisions while leading to repeatable results with less computational requirements was sought. Al-Assaf and El Kadi [11] used fatigue experimental data obtained for unidirectional glass/epoxy with various fiber orientation angles and stress ratios to test the suitability of using polynomial classifiers (PC) for fatigue life prediction. The use of first and second order classifiers was investigated but the best predictions were obtained when using a first order classifier was supplemented by the addition of higher order terms [11].

In a more recent study, El Kadi et al. [12] used PC to predict the fatigue life in other composite materials not used in training. Different composite materials with a variety of fiber orientation angles were considered. Similar to the results obtained for a single material under various loading conditions, the use of polynomial classifiers led to adequate fatigue life prediction for materials not used in the testing when higher order terms were added to the first order classifier.

Factors Affecting the Fatigue Life Prediction using ANN. The fatigue life prediction obtained using ANN was shown to be dependent on a number of factors such as ANN architecture, number of hidden layers and number of neurons in hidden layers as well as the type of training function used [13]. El Kadi and Al-Assaf [7,8] used different neural networks structures to predict fatigue life of unidirectional glass/epoxy composites: feedforward neural networks, modular neural networks, radial basis function networks, self organizing features maps and principal component analysis. The effect of varying the number of hidden layers and neurons per hidden layer was also tested. Throughout their analysis, feedforward back-propagation training algorithm was used. They concluded that modular neural network with five sub-networks gave the best results as a NMSE of 5.7% was obtained.

In a later work, Al-Assadi et al. [10] have used a variety of training functions (resilient back-propagation, gradient descent, gradient descent with momentum, variable learning rate, and variable learning rate with momentum) to train a series of neural network architectures (cascade – forward neural networks, Elman networks, layer recurrent network).The best predictions were obtained using the resilient back-propagation training function. Using this training function, they observed that no matter what ANN architecture used, the best predictions were obtained using one hidden layer with 16-20 hidden neurons. Although no specific architecture consistently led to the best predictions, they showed that the type of ANN structure used does affect the prediction obtained.

In a subsequent study where the effect of the stress ratio on the fatigue life prediction was investigated, Al-Assadi et al. [14] experimented with a variety of training algorithms (back-propagation algorithm, Levenberg-Marquardt, BFGS quasi-Newton, resilient back propagation, scaled conjugate gradient, conjugate gradient with Powell/Beale restarts and Polak-Ribiére conjugate gradient). Once again they used cascade-forward neural networks, Elman neural networks and layer recurrent neural networks structures to predict the fatigue failure. As was the case in [1], resilient back propagation was found to consistently produce the best fatigue life prediction irrespective of the type of material or the type of network architecture used. With the use of a single hidden layer, a number of hidden neurons ranging between 6 and 12 yielded the best fatigue life predictions. Although acceptable predictions were obtained using feedforward and cascade-forward neural networks, more accurate results were obtained using other ANN architectures at the expense of a much longer training time.

As shown from the above-mentioned references, ANN can be used to accurately predict the fatigue life of composites once several parameters are adequately specified.

Factors Affecting the Fatigue Life Prediction using PC. Polynomial Classifiers (PC) were proposed and adopted in recent years for classification, regression, and recognition with remarkable properties and generalization ability. To the author's knowledge, the open literature only shows very few works where these classifiers were used to predict the fatigue life in composite materials [11,12]. Experimental data obtained for unidirectional Glass/Epoxy with various fiber orientation angles and stress ratios was used to test the suitability of using PC in predicting the fatigue life of composites. The use of first and second order classifiers was investigated but the best predictions were obtained when using a first order classifier supplemented by the addition of higher order terms [11]. When compared to predictions obtained using ANN, the PC were shown to provide adequate modeling between the input parameters and the number of cycles to failure. In addition, since the PC method is a direct method (not iterative), it leads to the same result no matter how many times is the analysis performed. Therefore there is no need to average the results of numerous runs as is the case for ANN.

In a recent study El Kadi et al. [12] used a first, second and higher order PC to predict the fatigue life of composites not used in the training. As was the case in [11], the addition of several higher order terms to the first order polynomial classifier was attempted. A selection of combination of higher order terms were used to predict the fatigue life. Eighteen cases were investigated to determine the combination of higher order terms resulting in the lowest RMSE. The RMSE obtained was found to vary significantly between the different materials depending on the higher order terms added to the PC. It is interesting to see however that the term combinations that produced the lowest RMSE were almost similar for the four materials considered [12].This might indicate the strong influence of some specific parameter combinations on the fatigue life irrespective of the type of material considered.

Although the values obtained for the RMSE are acceptable given the typical scatter expected in fatigue data, some of the results did not show a very good correlation between predicted and experimental fatigue life; i.e. in some cases, the slope of the log σ_{max} – log N_f curve did not match that of the experimental data. The addition of other higher order terms not included in the study might result in an adjustment in the log σ_{max} – log N_f relation slope and could therefore lead to a better fatigue life prediction. In the study [12], higher order terms were manually selected as certain terms were added / removed and the impact on RMSE was recorded. The combinations of terms were adjusted based on the change in RMSE values. A better method is needed to find the combination giving the best predictions; a technique such as the one used in [15] may accomplish this purpose. Work is underway to compare the results obtained using the group method of data handling (GMDH) to the published results.

Comparison between the Two Approaches. The results presented show that each of the two approaches has its own advantages and disadvantages when it comes to predicting the fatigue life of composites. While the variation in the type of neural network architecture, training algorithm and number of hidden neurons allows for more flexibility in the results, the fact that the criteria is an iterative one and the fact that parameters must be determined a priori make the use of ANN challenging. It should be noted however that a better fatigue life prediction compared to PC could be obtained should the proper parameters be selected.

Alternatively, using the PC is much simpler and needs less a priori decisions. Once the order of the classifier used is determined, the algorithm can be used to obtain the prediction needed. Since the experimental data will need to adhere to a polynomial relationship, this approach is rather rigid and only the addition of certain higher order terms to a first (or second) order polynomial can lead to acceptable predictions. Without specifying the correct higher order terms to use, the results obtained by this algorithm are not as accurate as those obtained using ANN.

Fig. 1 and 2 show a comparison between the predictions obtained using both methods for Scotchply 1003 glass/epoxy and AS/3501-5A graphite/epoxy, respectively. In both cases, higher order terms were added to the first order classifier to improve the solution. Details about the additional terms used and their effect can be obtained from [12]. The ANN used in Fig. 1 is a feedforward neural network with one hidden layers containing 20 neurons. In Fig. 2, a layer recurrent neural network with one hidden layers containing 16 neurons was used. Both networks were trained using the resilient back-propagation technique. Details about predictions obtained when these parameters are varied can be found in [10]. A comparison of the RMSE values obtained using both methods shows that the results obtained are comparable. One could notice that the current PC used in both cases does not accurately predict the behavior of the laminate with small fiber orientation angles. For these cases, ANN leads to better predictions. As mentioned earlier, the PC predictions might improve should alternate higher order terms be used. For both cases, the reported results obtained using ANN are the averages of three runs while those obtained using the classifiers were a result of a single run.

Summary

Both ANN and PC can be used to successfully predict the fatigue failure of composite materials. Using ANN, a number of parameters such as the type of network architecture and training function must be initially chosen. In addition, since the algorithm is an iterative one, to obtain reliable predictions, the procedure must be run a number of times and the overage used. On the other hand, PC can lead to a simpler and more direct approach to predict the failure of composites. Only the order of the classifier needs to be determined a priori. The results obtained might not be as accurate as those obtained using ANN unless particular higher order terms are added to a first or second order classifier.

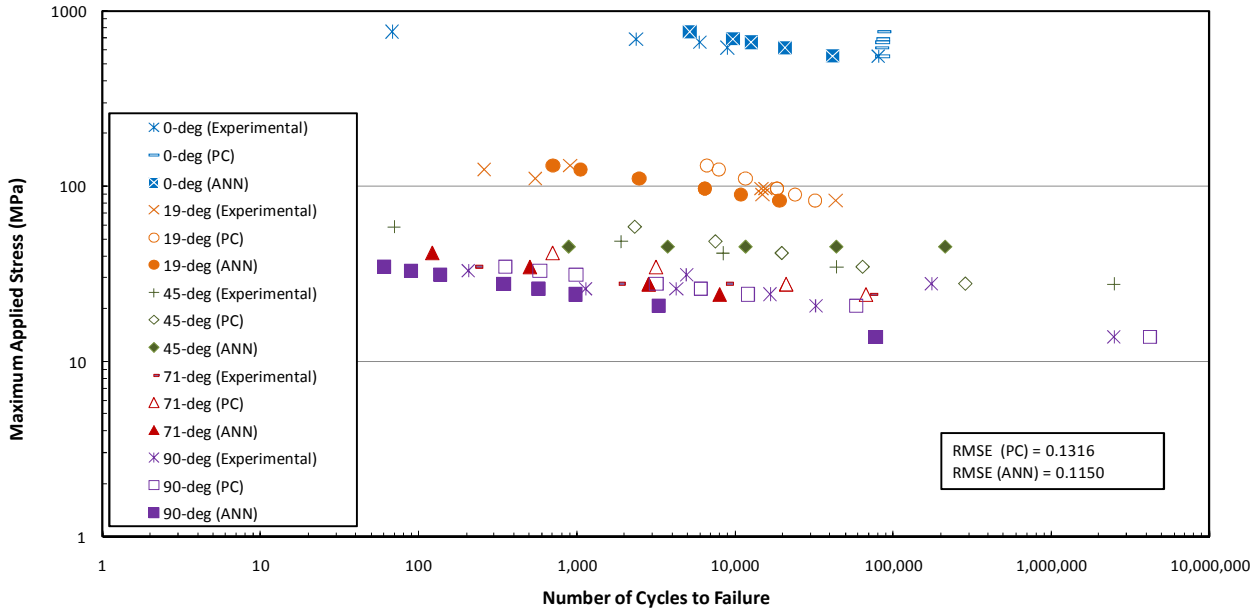


Fig. 1: Comparison of fatigue life prediction of Scotchply 1003 Glass/Epoxy using ANN and PC

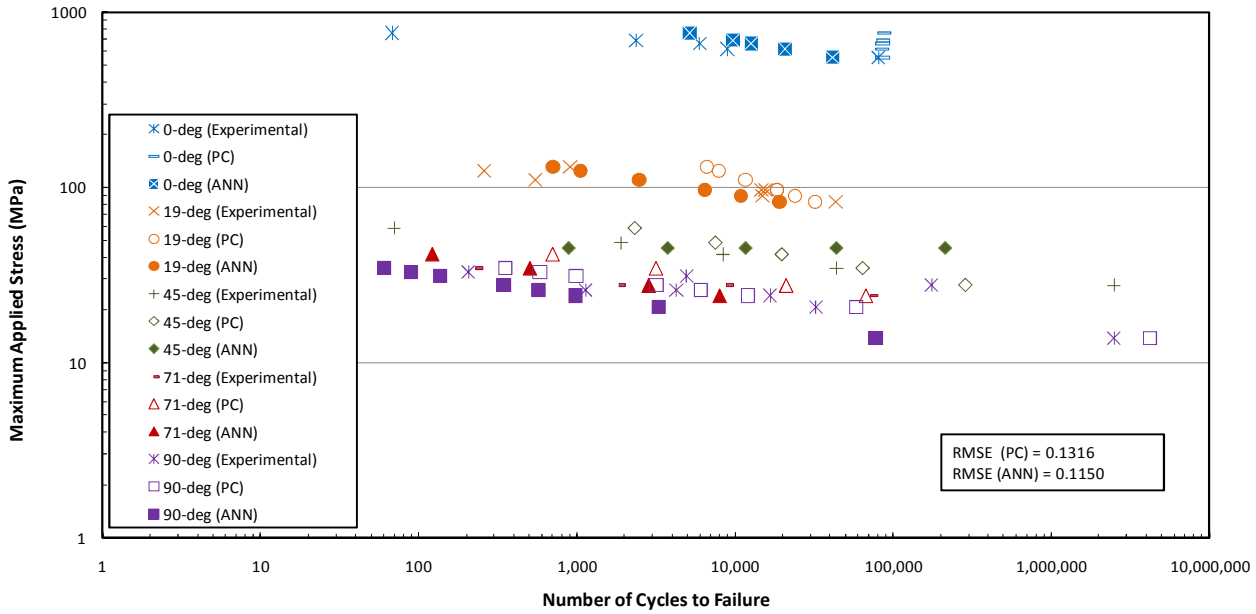


Fig. 2: Comparison of fatigue life prediction of AS/3501-5A Graphite/Epoxy using ANN and PC

References

[1] R.J. Schalkoff: *Artificial neural networks* (McGraw-Hill, 1997)

[2] S. Haykin: *Neural Networks – A comprehensive foundation* (Prentice Hall. 2nd ed., 1999)

[3] D. Skapura: *Building neural networks* (ACM Press, Addison-Wesley 1996)

[4] H. El Kadi: Compos. Struct. Vol. 73 (2006); p. 1

[5] Z. Zhang and K. Friedrich: Compos. Sci. Tech. Vol. 63 (2003); p. 2029

[6] J.A. Lee, D.P. Almond and B. Harris: Compos. A Vol. 30 (1999); p. 1159

[7] Y. Al-Assaf and H. El Kadi: Compos. Struct. Vol. 53 (2001); p.65

[8] H. El Kadi and Y. Al-Assaf: Compos. Struct. Vol. 55 (2002); p. 239

[9] H. El Kadi and Y. Al-Assaf: 16th Int. Conf. on Compos. Mater., Japan, July 8-13, 2007

[10] M. Al-Assadi, H. El Kadi and I.M. Deiab: App Compos Mater Vol. 17 (2010); p. 1

[11] Y. Al-Assaf and H. El Kadi: Compos. Struct. Vol. 77 (2007); p. 561

[12] H. El Kadi, I.M. Deiab and M. Al-Assadi: ASME J. of Eng. Mater. Techn. (2010), accepted for publication

[13] M. Al-Assadi: MS thesis. American University of Sharjah, 2009

[14] M. Al-Assadi, H. El Kadi and I.M. Deiab: App Compos Mater; (2010), in press

[15] Y. Abu-Kheil: MS thesis, American University of Sharjah, 2009

© (2011) Trans Tech Publications, Switzerland
doi:10.4028/www.scientific.net/KEM.471-472.227

Investigation on Improvement of Mechanical Properties of Kenaf / E-Glass Fiber Composites by Mercerization Process

Abdul Malek Ya'acob[1], Azhar Abu Bakar[2], Hanafi Ismail and [3]Khairul Zaman Dahlan

[1]Aerospace Department; University Kuala Lumpur-MIAT, Malaysia

[2]Material & Mineral Resources Engineering Department; University Sains Malaysia

[3]Malaysia Nuclear Agency, Malaysia

[1]abdulmalek@miat.unikl.edu.my, [2] azhar@eng.usm.my, [2]hanafi@eng.usm.my, khairul@nuclearmalaysia.gov.my

Keywords: Kenaf fiber, E-glass fiber (E-GF), weight ratio, fiber reinforce composites, sodium hydroxide (NaOH)

Abstract: A hybrid composites mechanical properties consisting of un-treated and treated bast Kenaf fiber and E- glass fiber was investigated by varying the fiber glass weight ratio and using interplay fabrication method. A further comparison was made with corresponding properties of 100% wt E-glass fiber composites sample. The expected results were to have better composites performance in terms of toughness and impact strength as a comparison between the E- glass fiber reinforced composites and Kenaf fiber reinforced composites alone. All samples are prepared using typical samples preparation techniques. Result shows that the incorporation of E – glass fiber resulted in brittle failure and a higher amount of E-Glass fiber with low percentage of Kenaf fiber resulted in high strength, low ductile and low toughness behavior.

Introduction

As general information, natural fibers are classified into three categories which are; [1]

1. Fruit fibers – Fibers that are extracted from the fruits of the plant.
2. Bast fibers – Fibers that are found in the stems of the plant.
3. Fibers extracted from the leaves.

There are several factors that affected the properties of natural fiber products such as fibers growing environment, environment temperature, percentages of humidity and the nature of the soil or the composition of the soil. All factors listed above generally effect the growth and height of the plant and eventually the final strength. [1] This report presents the comparison results between treated and un-treated bast Kenaf / E - glass fiber hybrid reinforced composites with various ratio of fibers reinforcement. As a basis for study, the Kenaf / E - glass fiber composite are fabricated using a un-treated Kenaf fiber. The second stage of fabrication involved with a treated Kenaf / E - glass fiber composite. The treatment uses sodium hydroxide to modify the surface of the natural fibers. In this study there is no modification was done to the surface of the glass fiber or the matrix system.

Experimental

Materials. Kenaf fiber in bast form was obtained from Malaysian Agricultural Research and Development Institute (MARDI), Malaysia thru Malaysian Nuclear Agency. Glass fiber use is a fabric type non-prepreg glass fiber (120-38 STD E-Glass). In this work the resins used were Alpha Epoxy resins (Part A and B)

Method. Fiber treatment – alkali [2-3] -the Kenaf fibers are soak in 6.0% sodium hydroxide for 4 hours at room temperature, washed with distilled water and dried at room temperature for 48 hours and oven dried at less than 50°C for 6 hours. Raw Kenaf are washed with distilled water and dried at room temperature for 48 hours. Hybrid samples of Kenaf and E-glass fiber produced for this study utilize the bidirectional orientation concept where one fibre layers runs in the weft direction and the second fibre layers runs in the warp direction. Hybrids are most commonly found in 0°/90° coding woven fabrics or also known as multi-axial fabrics. The main concern to produce bidirectional samples are to have better mechanical properties as there are more orientations of fiber per number of layers of fabric resulted in better stress distribution. Bast Kenaf fiber were chosen randomly, clean and cut with reference to the length of the mold of 30 cm x 30 cm. The matrix ratio used in this study is 2:1, where Epoxy resin and hardener are mixed well to achieve proper mixing by using air pressure mixing tool. Wet lay up method is used to fabricate the samples by laying down each fiber in sequence and with Kenaf core. To provide compression pressure to the composites preparations, an air pressure vacuum fixed at approximately 21 ± 3 Hg pressure was used by means of vacuum bagging method.

Characterization. Tensile testing is as per ASTM D 3039 and D 5083. Tensile test were carried out using Llyold 30 kN machine. A gauge length of 50 mm with cross head speed of 0.02 inch/min was employed. The average width and the specimen length were 25.4 mm and 172 mm respectively. The determination of flexural properties is accordance with ASTM D 790-98 and 92 for standard test methods for flexural properties of un-reinforced and reinforced plastics and electrical insulating materials using Instron 3–point bending system. The flexural test uses support span-to-depth ratio of 16:1 and the length of span of 100.0 mm with regards to an average of 6.0 mm sample thickness. The specimen's end prior to testing is 20 mm. Test specimen used was measured at 12.7 mm x 127 mm for width and length respectively. The crosshead speed is set at 2.6 mm/min. Impact properties were determined under specific conditions of humidity of 50% at temperature of 73°F. The width of all specimens was set at 12.7 mm and the length were standardize at 127.0 mm. The breaking energy for all specimens was estimated using 11.0 Joule pendulum. DSC measurement for this study uses the METTLER TOLEDO DSC STAR System whereby the temperature is set at room temperature (RT) to 200°C at a heating rate of 10°C / min. Samples are weight at approximately 5.00 miligram per crucible. The fibers were then examined in an SEM microscope type FEI Quanta 400 and observation was done at room temperature using high vacuum for 500 times resolution.

Results and discussion

Tensile strength. Tensile strength results in Fig. 1 shows a fluctuation pattern for the un-treated samples. Base on results received in this study, all fluctuation characteristics for un-treated samples are mainly due to the incompatibility of the fiber region. With regards to the tensile testing, the 2 phase region can be observed during the testing whereby it is clearly indicates that the E- glass fiber layers (skin) were peel off easily from the Kenaf layers. Another justification can be made due to results on the 100% wt Kenaf for un-treated Kenaf fiber as it shows the lowest tensile strength as an indication for incompatibility of Kenaf – epoxy interphase region. It is known that any un-treated Kenaf fiber are incompatible with either epoxy or glass fiber.

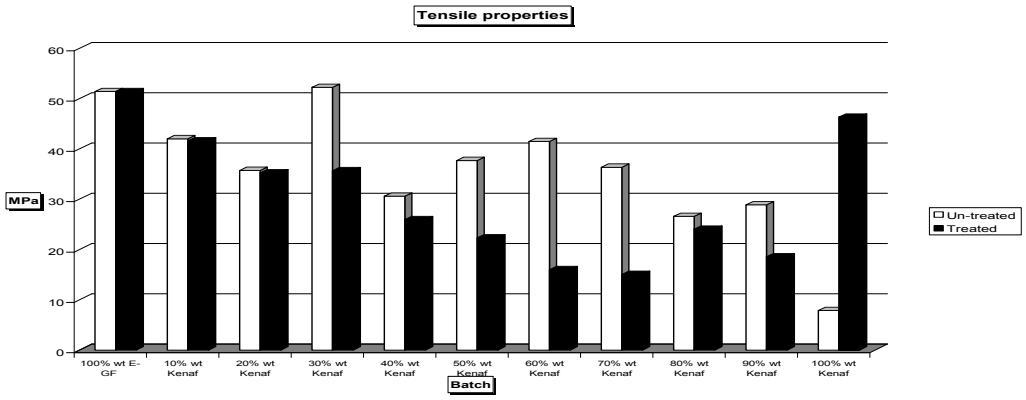


Fig. 1: Tensile strength comparison

Flexural strength. Fig. 2 shows the overall flexural strength for both treated and un-treated samples. Treated samples shows a consistency in bending characteristics at low percentage by weight Kenaf fiber up to 90% wt Kenaf. However the trend shows that by reducing the percentage by weight of the Kenaf fiber, the toughness of the samples also increases. As such it can be concluded for the bending characteristics the E – glass fiber also plays an important factor in increasing the toughness of the samples even at low percentage by weight. The un-treated samples shows inconsistent trend of flexural properties. It is observed that the highest flexural strength results are given by the un-treated samples hence showing that the increase in bending properties are mainly given by the Kenaf fiber characteristics rather than the E-glass fiber (brittle failure).

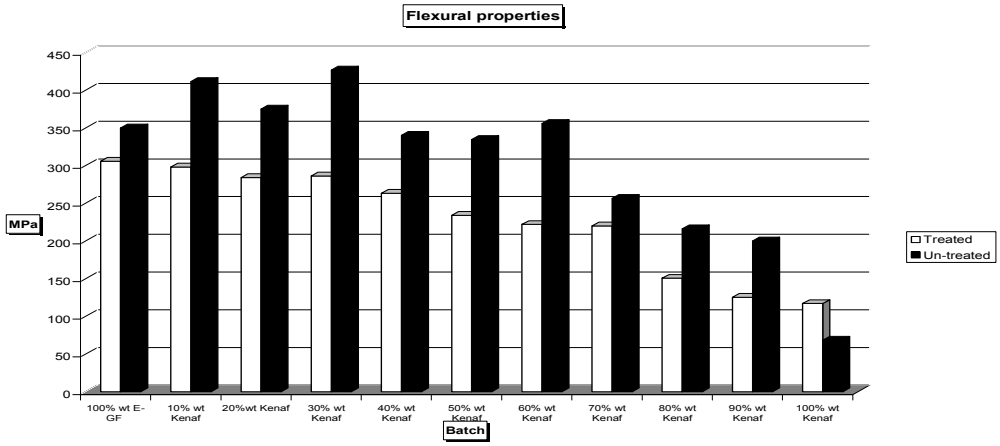


Fig. 2: Overall flexural strength results

Impact strength. Observation on the resilience value is shown in Fig. 3. Un-treated Kenaf fiber samples shows a higher impact value thus indicates a very tough samples. The improvement of the impact value for un-treated samples can be justify by the increase thickness of the samples itself. Increasing thickness means, difficulties in breaking the samples. It is suggested in this study that the tough characteristic for un-treated samples are mainly contributed by the raw Kenaf fiber rather than the E-glass fiber (brittle characteristics). Results in Fig. 3 also shows that at 20% wt and 10% wt Kenaf provide consistency even at lower percentage by weight Kenaf fiber.

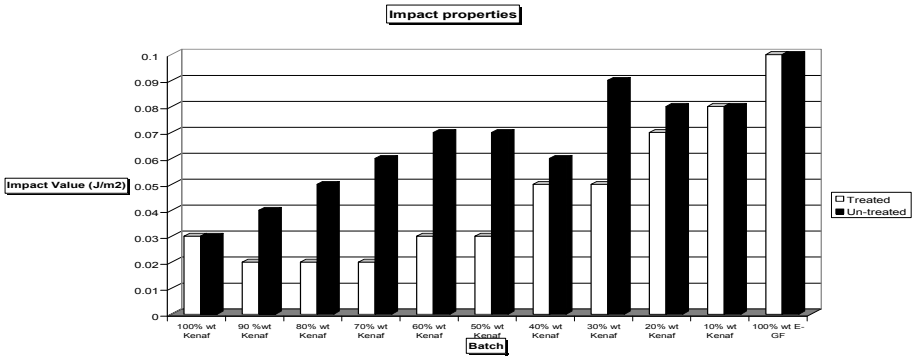


Fig. 3: Impact value comparison – Treated and untreated specimens

Differential Scanning Calorimetry (DSC). The measurement of transition glass, Tg is an indicator for evaluating the extent of crosslinking, blend composition, degradation and ageing of polymer [4]. Fig. 4 shows the Tg comparison between treated and un-treated samples. Results shows that samples for 10% wt, 20% wt, 30% wt Kenaf fiber and 100% wt Epoxy shows a similar trend of curing stages and degradation. However higher percentage by weight of Kenaf fiber resulted in inconsistent degree of curing.

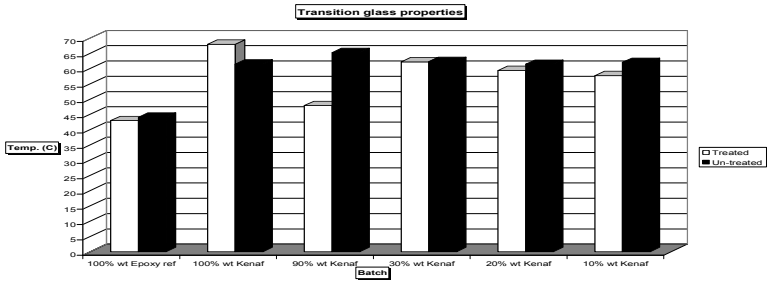
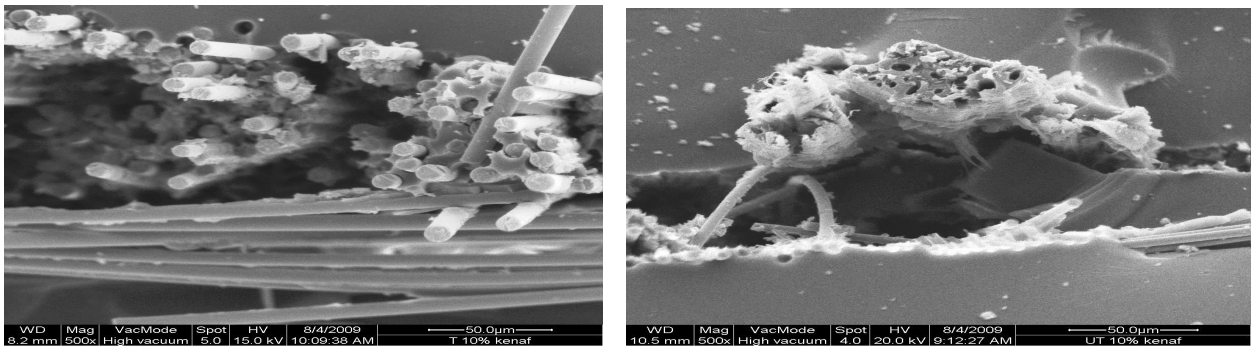


Figure 4: Tg comparison for Kenaf / E- GF samples

Fiber-matrix interaction. The results for SEM micrograph observations are shown for several treated and un-treated samples. Fig. 5 (a) for 10% wt treated NaOH Kenaf composites showing flat resin surfaces and fiber bundles fiber breakage, fully resin encapsulated kenaf fiber and minimum fiber pull out. Fig. 5 (b) showing high porosity; the presence of fiber aggregation and surface impurities; cellulose porous structure (lumen) due to non-treated fibers and high voids areas resulted in low fiber-matrix adhesion

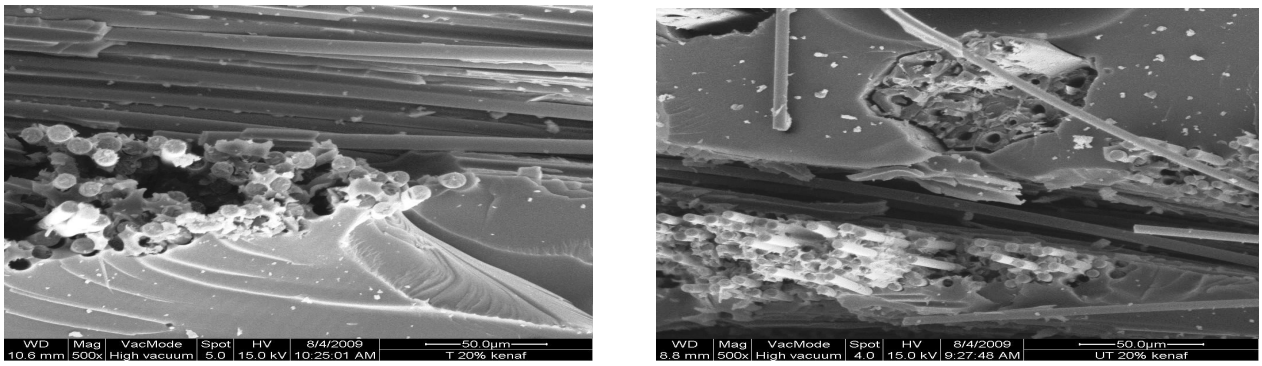


(a) 500 x (b) 500 x

Fig. 5: Fractured surface for 10% wt Kenaf (a) treated and (b) un-treated NaOH composites

Fig. 6 (a) for 20% wt treated NaOH Kenaf composites showing the presence of visible cavities (voids). Micrograph also showing surface porosity, surface impurities, fiber breakage and river pattern (resin rich region). Fig. 6 (b) showing visible cellulose porous structure (lumen) as prove of

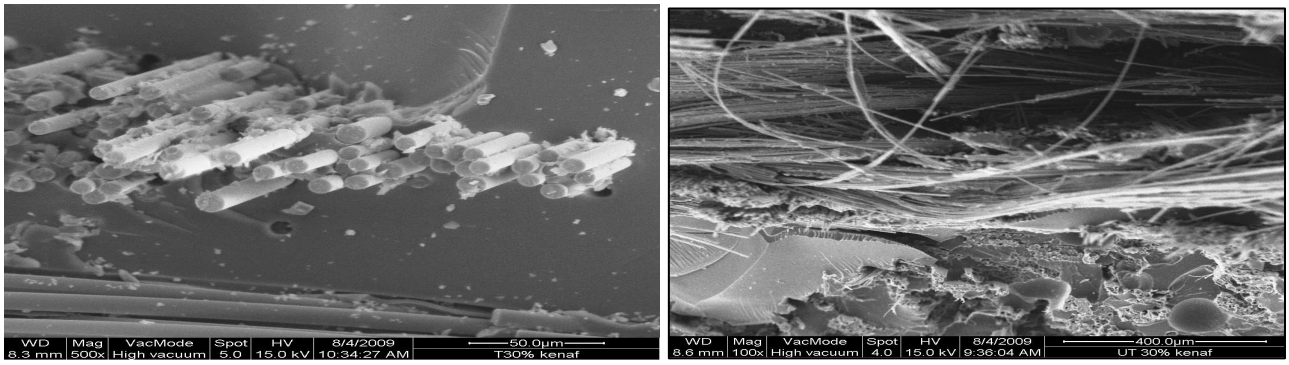
non-treated fibers; high surface impurities; poor fiber-matrix adhesion hence poor interfacial bonding and cellulose fiber aggregation hence fiber bundles.



(a) 500 x (b) 500X

Fig. 6: Fractured surface for 20% wt Kenaf (a) treated and (b) un-treated NaOH composites

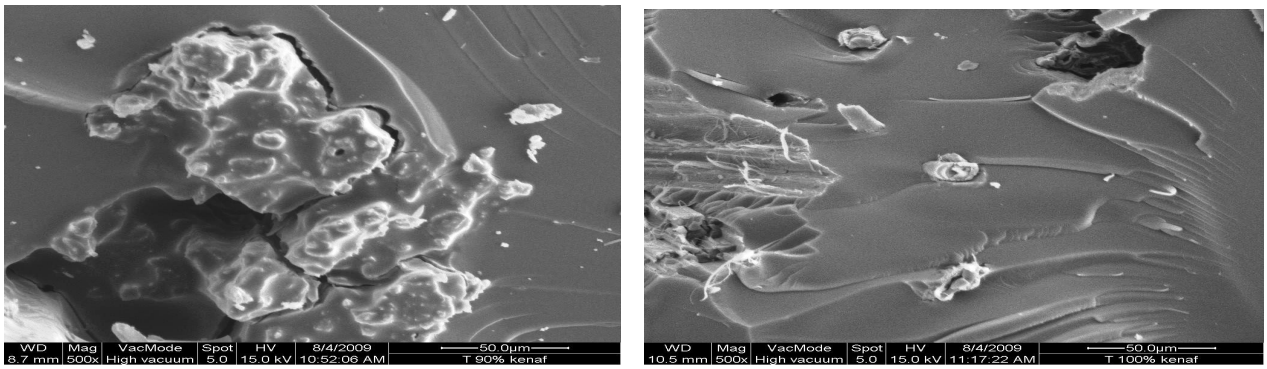
Fig. 7 (a) for 30% wt treated NaOH Kenaf composites shows even matrix surface that resulted from proper curing stages. Several observations can be identified for this samples which shows fiber bundles; good resin encapsulation thus showing good resin-fiber adhesion; well entrapped Kenaf fibers and fiber pull in certain areas as a result of poor adhesion and minimum fiber pull out. Fig. 7 (b) showing phase separation between the E-glass fiber and Kenaf fiber thus showing an indication of poor fiber-matrix adhesion; high porosity and inhomogenity at fractured surface areas.



(a) 500 x (b) 500x

Fig. 7: Fractured surface for 30% wt Kenaf (a) treated and (b) un-treated NaOH composites

Fig. 8 showing SEM observations for 90% wt treated Kenaf composites. Micrograph shows fiber aggregation bundles; poor interfacial fiber-matrix bonding; several Kenaf fiber full encapsulated or well trapped by the matrix by the resins thus showing good fiber-matrix adhesion in several fractured surface areas, minimum fiber pull out and an existing river pattern (resin rich areas).



500 x 50x

Fig. 8: Fractured surface for 90% wt Kenaf treated NaOH composites

Fig. 9: Fractured surface for 100% wt kenaf treated NaOH composite

Fig. 9 for 100% treated Kenaf / E-GF composites showing high porosity and voids. In this micrograph it also shows river pattern (resin rich areas) and even matrix surfaces showing stages of curing, obvious resin-rich areas; very compatible and homogeneous surfaces hence resulted in better fiber-matrix adhesion and minimum fiber pull out.

Summary

Observation on impact value shows a more consistent pattern for treated Kenaf fiber composites samples thus suggested a more control mechanical properties. It is suggested that the Kenaf / E-glass fiber hybrid samples are more suitable for impact and bending (flexural) application due to the tough characteristics that is shown in this study. This study shows that the treated Kenaf / E-glass fiber hybrids provide consistency in mechanical performance. Unfortunately un-treated Kenaf / E – glass fiber hybrids shows a inconsistency in all mechanical results hence difficulties in observing the characteristics and advantages of the un-treated systems. Both treated and un-treated samples have a higher thickness for every samples thus it is difficult to control the thickness even by using a vacuum fixed air pressure at 21 ± 3 Hg pressure by means of vacuum bagging. Base on the SEM micrograph it shows that the treatment increases the fiber matrix bonding mechanism resulting in stronger bonding at the fiber-matrix interface. Thus the application of sodium hydroxide treatment agent cleans the fiber surfaces from impurities. The treated samples shows better fiber-matrix interfacial properties and well embedded fiber inside the matrix and fiber aggregation or fiber bundles is also observed for treated Kenaf samples. In this study distinctive river pattern or resin rich region is observed for treated samples in certain areas hence resulted in failure at the region during testing.

Acknowledgements - The authors would like to thank Universiti Kuala Lumpur for financial support in the form of short term research grant (Vote number: STR06040).

References

[1] Amar K. Mohanty, Majnustri Misra, Lawrence T Drzal; (2005); CRC Press;

[2] V.Vilay; M.Mariatti; R.Mat Taib; Mitsugu Todo; Composites Science and Technology; 68; (2008); 631-638

[3] Jochen Gassan; Andrzej K. Bledzki; Composites Science and Technology; 59; (1999); 1303-1309

[4] Dipa Ray; B.K. Sarkar; S. Das; A.K.Rana; Composites Science and Technology; (62); (2002); 911 – 917

© (2011) Trans Tech Publications, Switzerland
doi:10.4028/www.scientific.net/KEM.471-472.233

Influence of Cutting Parameters on Surface Roughness for Wet and Dry Turning Process

Muhammad Yusuf[a], Khairol Anuar[b], Napsiah Ismail[c] and Shamsuddin Sulaiman[d]

Department of Mechanical and Manufacturing Engineering

Universiti Putra Malaysia 43400 Serdang, Selangor D.E. Malaysia

[a]m_yusoef@yahoo.com, [b]khairol@eng.upm.edu.my, [c]napsiah@eng.upm.edu.my, [d]suddin@eng.upm.edu.my

Keywords: turning, surface roughness, parameters process, design of experiment

Abstract. This paper presents a study of the quality of a surface roughness model for mild steel with coated carbide cutting tool on turning process. The experiments were carried out under wet and dry cutting conditions. The model is developed based on cutting speed, feed and depth of cut as the parameters of cutting process. This research applies the fractional factorial design of experiment approach to studied the influence of cutting parameters on surface roughness. The measured results were collected and analyzed using commercial software package called Minitab. Analysis of variances is used to examine the influence of turning factors and factor interactions on surface roughness. The result indicated that, there are inherent differences in surface roughness between wet and dry cutting process with the same parameters process model. Analysis of variance was found that feed parameter is the most significant cutting parameter, which influences the surface roughness. The most significant interactions were found between cutting speed and feed parameters for dry turning process. Therefore is a significant effect of using combination of the fluid for cooling the cutting operation.

Introduction

Turning is the primary operation in most of the production processes in the industry. The starting material is generally a workpiece generated by other processes such as casting, forging, extrusion, or drawing.

In turning operation, the quality of surface roughness is an important requirement for many turned workpieces. Thus, the evaluation of machine tool and the choice of optimized cutting parameters becomes very important to control the required surface quality. The quality of machined component refers to studies have been reported recently, the final surface roughness obtained during turning operation may be considered as the sum of two independent effects [2,4]:

- ideal surface roughness, the result of the tool geometry and the feed rate, and
- natural surface roughness, the result of the irregularities in the cutting operation.

The factors contributing to natural surface roughness is the productivity of machine tools and mechanical parts. The occurrence of chatter or vibrations and inaccuracies parts movements of the machine tool can be affect on the surface quality.

Although many factors affect the surface conditions of a machined component, optimize of cutting condition is extremely important task to determine surface quality of manufactured parts. Hence, surface roughness constitutes one of the most critical constraints for the selection of machine tools and cutting parameters in process planning. Majority of machining operations require the cooling and lubricating action of cutting fluids. But, due to ecological and human health problems, manufacturing industry are now being forced to implement strategies to reduce the amount of cutting fluids used in their production line. New approaches for elimination of cutting fluids application in machining processes have been examined and dry machining was presented as the solution.

Surface roughness as affected by the cutting conditions has been investigated by engineers and researchers for many years on different of materials and methods [3, 5, 8, 9, 12]. In this study, analyze the effects of cutting parameters (cutting speed, feed rate and depth of cut) on surface roughness (*Ra*) of mild steel using coated carbide tool. The experiment conducted under wet and dry cutting conditions. The aim of this research is focus on the analysis of optimum cutting conditions to get lowest surface roughness. The other factors can be affected on surface roughness such as vibrations of machine and tool chatter ignored for analysis.

Experiment Setup

The material used for experiment is mild steel of hardness 180 HB. The workpiece received in the form of 38 mm diameter long bar and cut to 150 mm length, it is machined under dry and wet cutting condition. The machine used for turning operation is Harrison conventional lathe machine**,** maximum spindle speed achievable on this machine is 2200 rpm and spindle power 5.5 KW. The Taegutec TNMG 160408 MT TT5100 cutting tool insert coated carbide was used in the experimental with Mitsubishi tool holder MTJNR. The surface roughness was measured using Mahr Surftes. Design of experiment methodology used to determine the effects of cutting parameters on surface roughness in the turning. The factors and factorial levels are summarized in Table 1.

Experiment Result and Discussion

The present experiment results for assessment of surface roughness which was influenced by cutting speed, feed rate, and depth of cut parameters with dry and wet cutting condition according to 2^3 full factorial design as given in Table 2. Based on the results, the surface roughness in wet and dry turning was obtained in the range of 1.04 μm to 3.36 μm and 1.91 μm to 2.65 μm. The minimum values are the good quality of surface roughness, it has obtained during wet and dry turning process with the parameters model (v = 88 mm/min, f = 0.05 mm/rev, a_p = 0.25 mm) and (v = 129 mm/min, f = 0.05 mm/rev, a_p = 0.5 mm). The comparison of the percentage difference in surface roughness between wet and dry process are illustrated in Fig. 1. The highest difference (45.8 %) occurred on the test no. 2 and lowest (9.5 %) on the test no. 7.

Table 1. Factors and factor levels

Level	Factors		
	Cutting speed v (m/min)	Feed f (mm/rev)	Depth of cut a_p (mm)
Low (-1)	88	0.05	0.25
High (+1)	129	0.09	0.5

Table 2. Detail of experiment and results of wet and dry turning

Cutting parameters				Surface roughness (wet) R_a (μm)			Surface roughness (dry) R_a (μm)		
Test No.	v	f	a_p	Observed Response		Average Response	Observed Response		Average Response
1	−1	−1	−1	1.10	1.14	1.12	1.90	1.92	1.91
2	−1	−1	+1	1.02	1.06	1.04	1.87	1.97	1.92
3	−1	+1	−1	2.95	3.10	3.03	2.40	2.63	2.52
4	−1	+1	+1	3.22	3.50	3.36	2.43	2.58	2.51
5	+1	+1	+1	2.77	3.16	2.97	2.53	2.77	2.65
6	+1	+1	−1	2.35	3.77	3.06	2.58	2.67	2.63
7	+1	−1	−1	1.22	2.02	1.62	1.68	1.90	1.79
8	+1	−1	+1	1.18	1.34	1.26	1.44	1.78	1.61

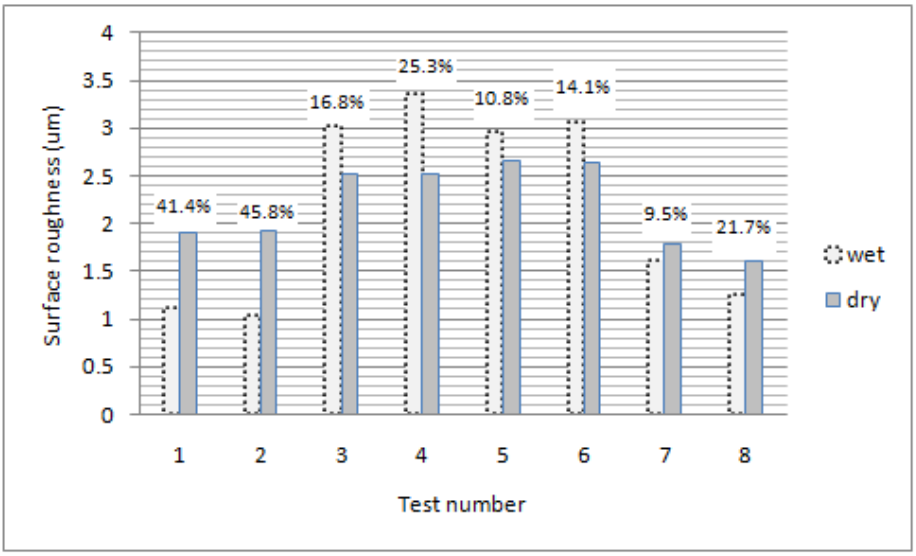


Fig. 1. The differences plots of surface roughness

Furthermore, the results were analyzed in the form of analysis of variance (ANOVA) in Minitab software. Its purpose is to determine which factors and factor interactions are statistically significant in affecting the surface roughness. Based on a 95% confidence interval, cutting speed, feed and depth of cut parameters have a statistically significant influence on surface roughness, since their *p*-values are smaller than 5%. Table 3 shows ANOVA for surface roughness in wet and dry turning processes. From the calculations can be inferred that feed has more influence on surface roughness in wet and dry turning processes, because their *p*-value are smaller than 0.05. In addition, the following two-factor the interactions of *v-f* parameters (cutting speed, feed) in dry turning process produce a statistically significant influence on the surface roughness, because *p*-values is also smaller than 0.05.

Further analysis can be conducted with the aid of the main effects and interaction plots. Fig. 2 gives the main effect plot of cutting speed on surface roughness in wet and dry turning. The surface roughness in wet turning appears to increase with increase of cutting speed, while it decreased with increase of cutting speed in dry turning. The surface roughness is tended increase with increase of feed in wet and dry turning are shown in Fig. 3. Fig. 4 gives the main effect plot of depth of cut on surface roughness, the surface roughness in wet and dry turning has a tendency to reduce with increase of depth of cut.

Table 3. Analysis of variance for surface roughness

Source	Wet					Dry				
	DF	SS	MS	F	P	DF	SS	MS	F	P
v	1	0.0324	0.0324	0.20	0.667	1	0.00766	0.00766	0.40	0.541
f	1	13.5792	13.5792	82.87	0.000	1	2.34856	2.34856	124.04	0.000
a_p	1	0.0100	0.0100	0.06	0.810	1	0.00601	0.00601	0.32	0.587
v * f	1	0.2916	0.2916	1.78	0.215	1	0.11731	0.11731	6.20	0.034
v * a_p	1	0.1260	0.1260	0.77	0.403	1	0.00601	0.00601	0.32	0.587
f * a_p	1	0.1156	0.1156	0.71	0.423	1	0.00856	0.00856	0.45	0.518
Error	9	1.4747	0.1639			9	0.17041	0.01893		
Total	15	15.6296				15	2.66449			

In order to determine the interaction effects of cutting process parameters on R_a, the three-dimensional surface plots were generated considering two parameters at a time. These interaction effects are depicted in Fig. 5, 6 and 7. From these figures, it is observed that the interaction effects

of cutting parameters on R_a in both turning processes wet and dry are almost similar. It can be observed from Fig. 5 and 6 that, the surface roughness sharply increases with the increase of feed parameters. On the other hand, the surface roughness slightly increases with increase of depth of cut with constant cutting speed. The minimal surface roughness results with combination of low feed rate and high depth of cut, as depicted in Fig. 7.

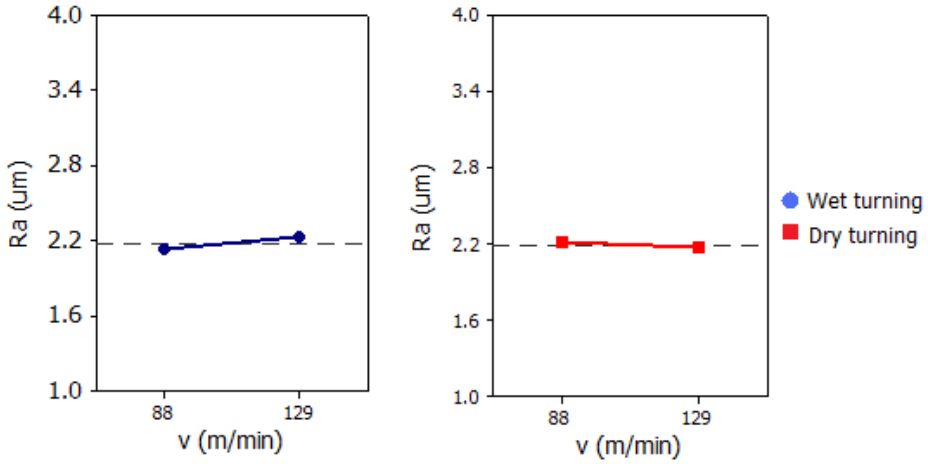


Fig. 2. The main effect plots of cutting speed on surface roughness

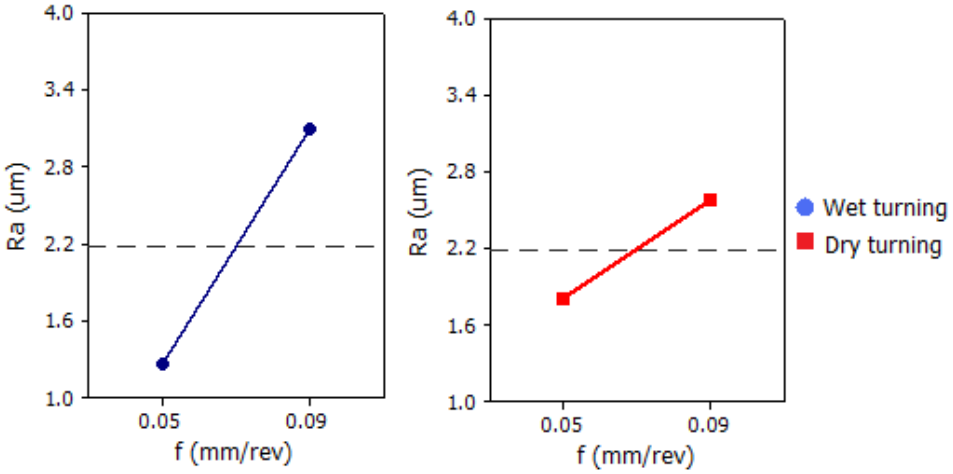


Fig. 3. The main effect plots of feed on surface roughness

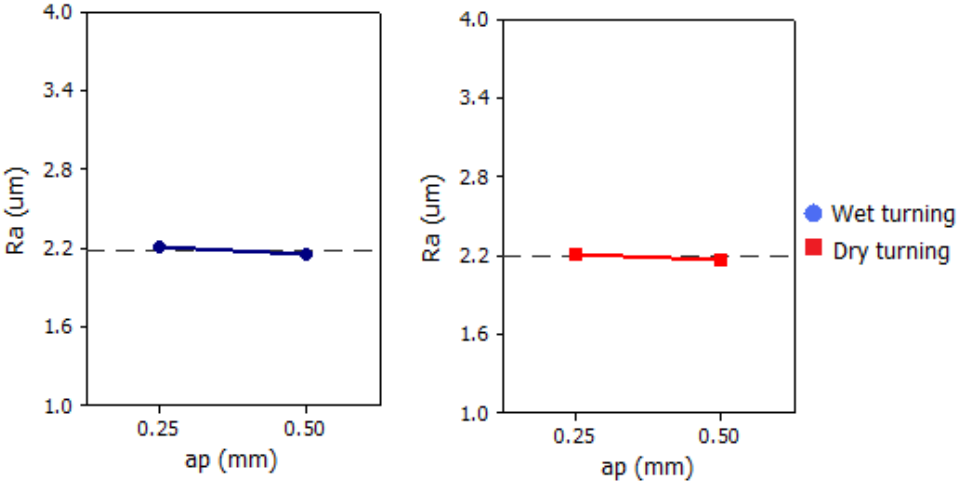


Fig. 4. The main effect plots of depth of cut on surface roughness

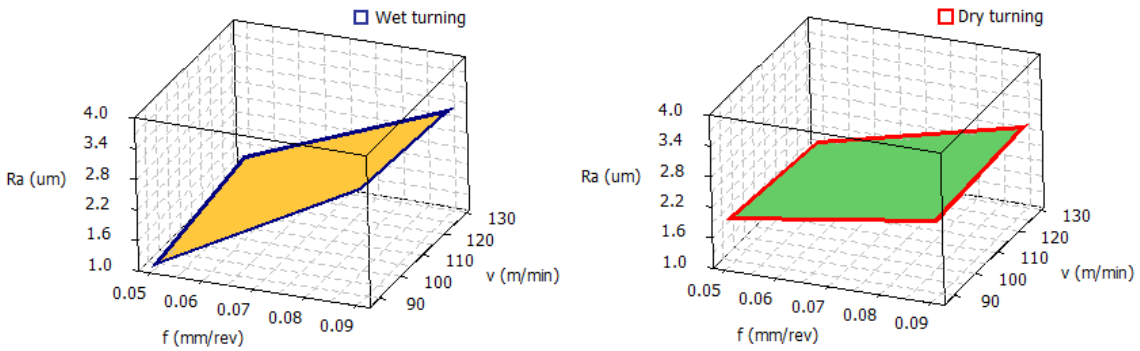


Fig. 5. Interaction effect of cutting speed and feed on surface roughness

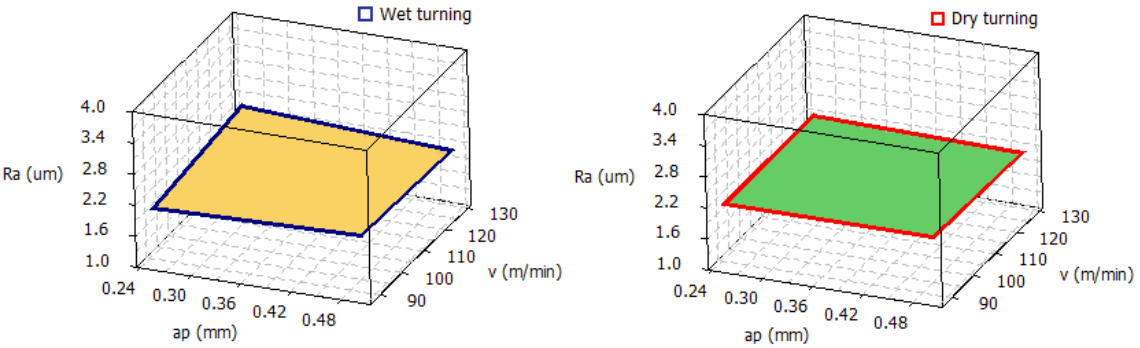


Fig. 6. Interaction effect of cutting speed and depth of cut on surface roughness

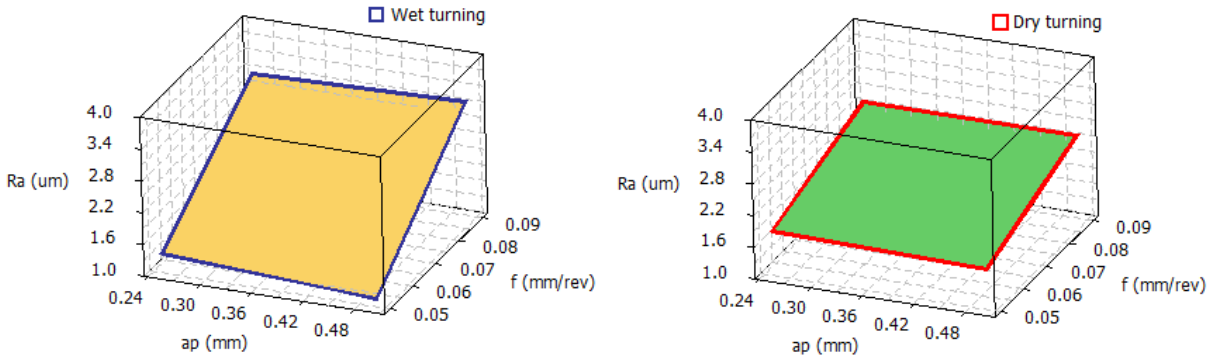


Fig. 7. Interaction effect of feed and depth of cut on surface roughness

Summary

In this paper, the influence of cutting process parameters on surface roughness for mild steel with coated carbide cutting tool during wet and dry turning process have been measured. Based on the results, it was found that cutting process parameters (cutting speed, feed and depth of cut) has influences on surface roughness in wet and dry cutting condition. The following conclusion can be drawn:

- The minimum values of surface roughness are the good quality, it obtained during wet and dry turning process with the parameters model (v = 88 mm/min, f = 0.05 mm/rev, a_p = 0.25 mm) and (v = 129 mm/min, f = 0.05 mm/rev, a_p = 0.5 mm).
- There are inherent differences in surface roughness between wet and dry cutting process with the same parameters of process, the highest difference (45.8%) occurred on the test no. 2 and lowest (9.5 %) on the test no. 7.

- From the ANOVA, it was found that feed parameter is the most significant cutting parameter, which influences the surface roughness. Most significant interactions were found between cutting speed and feed parameters for dry turning process.

Further research will investigate the quality of surface roughness in wet and dry turning based on the above models with different materials.

Acknowledgements

The authors thank Mr. Tajul Ariffin, Mr. Ahmad Shaifudin, Mr. Mohd Saiful Azuar and Mr. Muhammad Wildan Ilyas from the Department of Mechanical and Manufacturing Engineering, Universiti Putra Malaysia Universiti Putra Malaysia for their assistance.

References

[1] M. Anthony Xavior and M. Adithan: Journal of Materials Processing Technology Vol. 209 (2009), p. 900 – 909.

[2] G. Boothroyd and W. A. Knight, in: *Fundamentals of machining and machine tools*. 2nd Edition, Marcel Dekker, New York (1989).

[3] C.H. Che-Haron and A. Jawaid: Journal of Materials Processing Technology Vol. 166 (2005), p. 188–192.

[4] A. S. David and S. A. John, in: *Metal cutting theory and practice*. Taylor & Francis Group (2006).

[5] D.A. Fadare, W.F. Sales, E.O. Ezugwu, J. Bonney and A.O. Oni: Journal of Applied Scienes Research Vol. 5(7) (2009, p. 757-764.

[6] B. Fnides, M. A. Yallese, T. Mabrouki and J. F. Rigal: ISSN 1392 - 1207. Mechanika Vol. 3 (2009), p. 68 – 73.

[7] D. I. Lalwani, N. K. Mehta, and P. K. Jain: Journal of Materials Processing Technology Vol. 206 (2009), p. 167–179.

[8] J. Paulo Davim, V. N. Gaitonde and S. R. Karnik: Journal Of Materials Processing Technology Vol. 205 (2008), p. 16 – 23.

[9] Raviraj Shetty, R. Pai, V. Kamath and S. S. Rao: ARPN Journal of Engineering and Applied Sciences Vol. 3 (2008), p. 59 - 67.

[10] Yusuf Sahin and A. Riza Motorcu: Materials and Design Vol. 26 (2005), p. 321 – 326.

[11] S. Thamizhmanii, S. Saparudin and S. Hasan: Jounal of Achievements in Materials and Manufacturing Engineering Vol. 20 (2007), p. 503 - 506.

[12] Tugrul Ozel, Tsu-Kong Hsu and Erol Zeren: Int J Adv Manuf Technol Vol. 25 (2005), p. 262–269

[13] R. H. Myers and D. C. Montgomery, in: *Response Surface Methodology*. 2nd edition, John Wiley & Sons, 2002.

© (2011) Trans Tech Publications, Switzerland
doi:10.4028/www.scientific.net/KEM.471-472.239

Development of Biocomposite Wall Cladding from Kenaf Fibre by Extrusion Molding Process

K. Abdan[1,a], E.S. Zainudin[1,b], A.R. Mohd. Faizal[2,c], H. Jalaluddin[1], A.H. Umar[1,d] and W.N.W.N Syuhada[1,e]

[1]Institute of Tropical Forestry and Forest Product, Universiti Putra Malaysia, Selangor, Malaysia

[2]Radiation Processing Technology Division, Malaysian Nuclear Agency, Selangor, Malaysia

[a]khalina@eng.upm.edu.my, [b]edisyam@gmail.com, [c]faizal@nuclearmalaysia.gov.my, [d]umarhanan@yahoo.com, [e]nodiya_swada@yahoo.com

Keyword: Extrusion Molding, Kenaf-Plastic Composite, Polypropylene, Mechanical Properties, Kenaf

Abstract. Nowadays, natural fibre-thermoplastics composites (NFPC) are replacing the conventional wood and timber due to its lower cost, avoid deforestation, higher strength-to-weight ratio and resistant to termites. These composites can be utilized for non-structural components of a building system such as decking, wall cladding, floor tiles and window frame. A natural fiber/plastic composite was produced by extrusion molding process to create a wall cladding profile. The raw materials used for the composites are 40% kenaf fibre and 60% polypropylene (PP). These materials were compounded through a twin-screw extruder and then cut into pellets. The moisture content found in the kenaf/PP composites (KPC) pellets was 2.89%. Therefore, the pellets required to be oven dried every time right before entering the hopper of the extruder. The temperature along the barrel was set to 180°C and the die head temperature is set to 165°C. At the end of the extrusion molding process, pressurized air was used for cooling the profile. Then, samples of the wall cladding were taken back to the laboratory for product quality assurance. Measurements of the samples show that the product experiences 3% of shrinkage in term of width and 1% of shrinkage in term of thickness. Water absorption test indicates an increase of 13.6% of weight after 24 hours immersion of water. Impact strength test was also conducted on the wall cladding samples and the mean result was 2.55 kJ/m². Tensile test on the extruded KPC product indicates a low tensile strength at 4.51 MPa and tensile modulus of 205.01 MPa. The sample also proven to be light weight as the density of the material was found to be 0.618g/cm³.

Introduction

Natural fibres such as jute, kenaf, pineapple leaf, oil palm empty fruit bunch, sugar palm, sisal, rice husk, sugarcane bagasse and other ligno-cellulosic fibres have been used as fillers or reinforcement in plastic composites. The advantages of this type of fibres are it is abundance, easy to obtain, low cost, part of plants that are not use and thrown away, not abrasive hence avoid damaging machines and molds during fabrication process, prevent deforestation by reducing the dependency on wood, sustainable and can be replant [1,3]. Studies on fibres derive from agricultural sources are advancing to make use of lingo-cellulosic fibres in replacing synthetic fibres as reinforcing fillers.

Kenaf is a member of hibiscus family which is a biodegradable and environmentally friendly crop. It has been found to be important source of fiber for composites and other industrial application. Kenaf have excellent properties for reinforcing plastic composites as it has low density, no abrasion during processing, high filling levels, high specific mechanical properties and biodegradability. Kenaf, as compared to other non-wood fiber, is found to be comparatively higher in tensile strength [2], cheaper, sustainable as well as environmentally friendly.

Extrusion molding can be applicable in KPC processing, specifically for products that have continuous body such as beam, wall cladding and flooring. The single screw extruder is a common extrusion system for producing plastics or plastics composites profiles. The raw material will be fed

into the hopper at one end of the barrel and the product will go out through an orifice (die head) at the other end of the barrel (refer with: Fig. 1). The purpose of this research is to determine the feasibility of producing a biocomposite wall cladding from kenaf fibres and polypropylene.



Figure 1: The KPC wall cladding outgoing the die head orifice.

Methodology

Material Preparation. Kenaf stems were collected from Lembaga Tembakau Negara planted in Terengganu, Malaysia. The variety name called V36. The polypropylene (PP) pallet was purchased from Polypropinas Sdn Bhd (Malaysia). Kenaf stem was cut into chips size between 3 cm to 5 cm length. In this study about 100 kg of kenaf chip was pulverized into powder form and screened to obtain 150μm fibre size.

KPC Pellets Preparation. PP pellets were mixed thoroughly with 3% maleic anhydride grafted polypropylene (MaPP) pellets by using a rotating mixer that runs for 30 minutes. In producing the KPC pellets, a twin screw extruder which has a main feeder and one additional side feeder was used. The PP/MaPP pellets were placed into the main feeder at the end of the extruder barrel, while the kenaf fibres were placed into the side feeder. The speed of the feeders was calibrated to achieve 40 wt% of kenaf and 60 wt% of polymer. Finally, the pelletizer cuts the compounded KPC into pellets (refer with: Fig. 2 and 3). The KPC pellets were then examined to detect the level of moisture content.

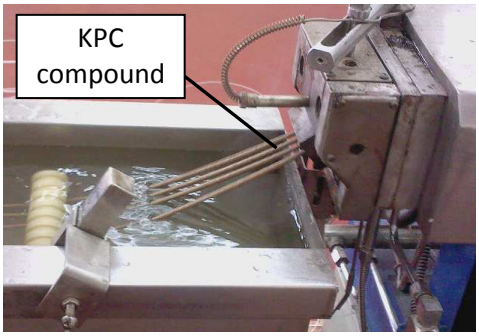


Figure 2: The extruded KPC compounds cooled by water bath.

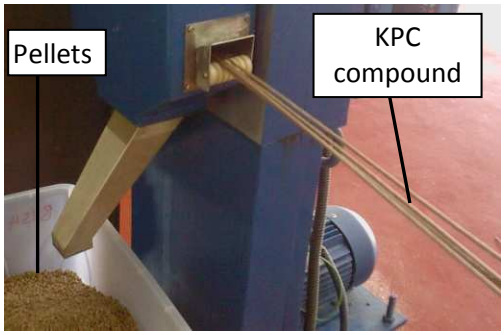


Figure 3: Pelletizer cuts the KPC compounds into pellets.

Extrusion Molding Process of Wall Cladding. A single screw extruder was used to produce the kenaf biocomposite wall cladding. Prior to the process, KPC pallets were oven dried for 24 hours at 60ºC to reduce moisture in the material. Extra additive such as zinc stearate pellets (0.5% by weight) was added together with KPC pellets for lubrication during processing by reducing adhesion of the plastic melt to the metal surface. The die head for wall cladding profile was installed on the extruder. Heating in the extruder barrel consists of three temperature zone. While, the die head temperature is controlled by one heater. The temperature in the extruder barrel must be set within the range of the melting point of polypropylene (171ºC) but lower than the degradation

point of kenaf fibres (210ºC). After four trials running the extruder for KPC wall cladding, the optimum temperature setting across the extruder is as shown in table 1:

Table 1: Temperature setting for extrusion process of wall cladding

	Zone 1	Zone 2	Zone 3	Die head
Set Temperature	180ºC	180ºC	180ºC	166ºC

Determining Physical and Mechanical Properties. The wall cladding profiles were taken back to laboratory for physical and mechanical testing (refer with: Fig. 4). Dimensions of the sample were recorded and compare with the original design (thickness: 6mm x width: 80mm) to identify any shrinkage. Water absorption experiment (according ASTM D570) was conducted to analyze the water uptake after 24 hours immersion. The density of the extruded KPC wall cladding was also measured. The mechanical properties of the product were also tested by determining impact strength (according ASTM D256) and tensile strength and tensile modulus (according ASTM D638-type I).



(a) (b)

Figure 4: (a) KPC wall cladding and (b) Tensile specimen following ASTM D638-type (i)

Result and Discussion

Moisture Content of KPC pallets. The KPC pellets were weighted before and after oven dry (105ºC for 24 hours). The weight difference shows that the pellets have moisture content (MC) of 2.89%. Generally materials derive from natural fibres which is hydrophilic will absorb water easily from atmosphere, typically from humid climate such as Malaysia. The MC is considered high for extrusion process, because moisture will cause the product to have crimple texture on product surface as proven by earlier trials. Beside that other researchers [4] found that the percentage of moisture uptake increased as the fibre volume fraction increased due to the high cellulose content. Since the fibre loading used in this study was 42% (approximately 50% volume fraction) the MC result was expected. Therefore, to overcome this condition the pellets were required to be oven dried at temperature of 60 ºC for 24 hours to obtain less than 0.5% MC prior entering the extruder

KPC Profile Shrinkage. The design of the wall cladding has the width of 80mm and thickness of 6mm. After the KPC wall cladding extruded and cool down, measurements shows that samples tend to shrink to an average thickness of 5.94mm and average width of 77.6mm with shrinkage percentage of 0.01% for thickness and 0.3% for width. Possible explanation for this situation is due to thermal expansion. Thermoplastic composite materials are generally shaped at elevated temperature and then cooled. Since in most cases the thermal expansion coefficients of polymers are much greater than reinforcement fibres this cooling process results in compressive radial stress

σ_r at the interphase [5]. Therefore, designers should consider the tolerance in width and thickness and width around ± 0.01 to 0.3mm of KPC material before designing a mold.

Density of KPC Profile. The extruded KPC wall cladding has an average density of 0.618g/cm³. The samples have lower density than liquid water and tend to float. Therefore, a weight must place upon the samples to keep it immerse during water absorption test. The porosity can clearly be observed by SEM micrograph at the fractured area of the KPC wall cladding (refer with: Fig.5). Porosity causes the product to become lightweight but loses it mechanical strength. Compare to injection molding, extrusion process does not have a closed mold, therefore no pressure exist to compact the KPC material. Other than that, the surface of the product is rough due to friction against the die head orifice during extrusion process (refer with: Fig.6).

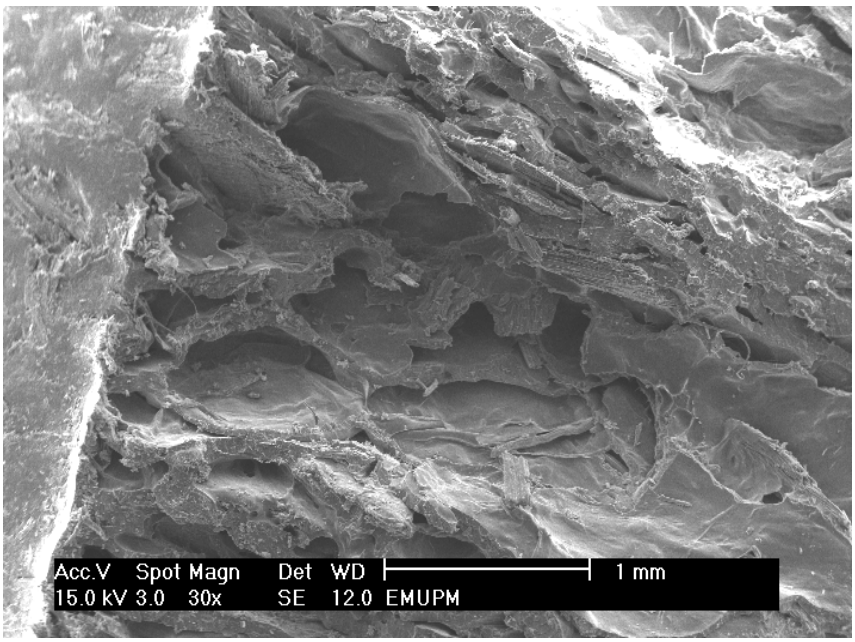


Figure 5: SEM micrograph at the fractured area of the KPC wall cladding

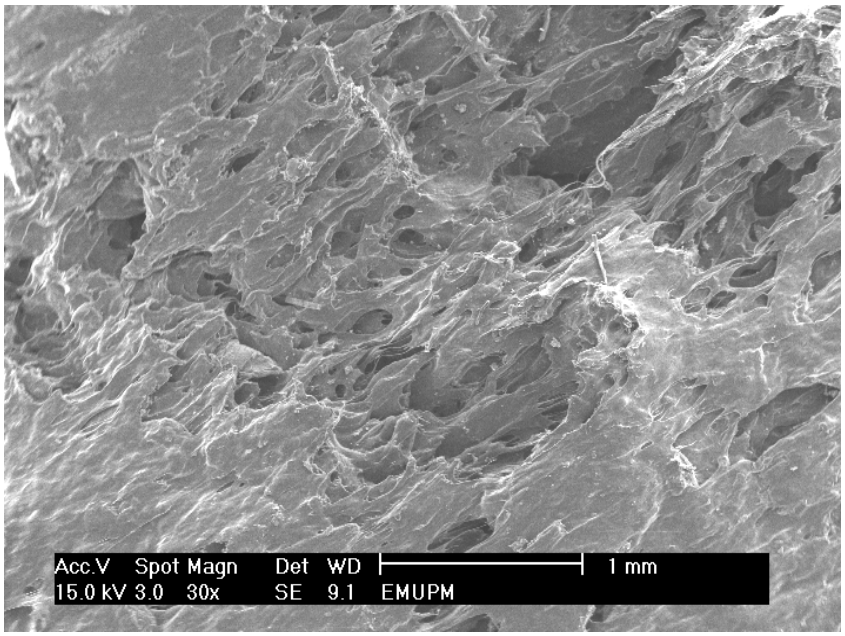


Figure 6: SEM micrograph at the surface of the KPC wall cladding

Water Absorption Test. Water absorption test indicates an increament of 13.6% of weight after 24 hours immersion in distilled water. The porosity of the material discussed earlier is the reason for the high water uptake. Other than that, natural fibres such as kenaf are hydrophilic which prone to absorb water. In addition all polymer composites absorb moisture in humid atmosphere and when they are immersed in water. The effect of moisture absorption leads to the degradation of fibre-matrix interface region which thus creates poor stress transfer efficiencies resulting in a reduction of mechanical properties [6,7]. Meanwhile, among the main concerns for the use of natural fibre reinforced composite materials are their susceptibility to moisture absorption and the effects on the physical and mechanical properties [8].

Mechanical Properties. Impact strength test was conducted on the wall cladding samples and the mean result was 2.55 kJ/m². Other than that, tensile strength test on the extruded KPC product indicates a low tensile strength at 4.51 MPa and tensile modulus of 205.01 MPa. Previous studies using the similar KPC formulation but by compression molding shows a higher tensile stress (22.95 MPa) and higher tensile modulus which is 320 MPa (refer with: Table 2) [9]. Due to extrusion process, the KPC become less dense and lost its mechanical properties. It might also contribute to the porosity behavior and high MC of the KPC as mentioned earlier.

Table 2: Effect of processing method to mechanical properties of KPC

Processing Method	Tensile Strength [MPa]	Tensile Modulus [MPa]	Impact Strength [kJ/m²]
Compression Molding	22.95	320	-
Extrusion Molding	4.51	205	2.55

Future Work

The fabrication of this KPC wall cladding is still in progress. There are biocomposite manufacturers that successfully achieve in producing a high quality NFPC product by extrusion process, thus it is possible to improve the physical and mechanical strength of the wall cladding and its aesthetic appearance. Upgrades of the extruder such as adding a motorized puller at the end of the conveyer to pull the wall cladding at constant speed may help to increase the tension of extruded profile and consequently increase the tensile strength. Moreover it is suggested to add conditional roller in order to avoid the profile in uneven shape like crumple. By installing a bakelite plate divider in between of die head heater will permit to isolate heat zone and controlling the processing temperature. All this countermeasure will be implement in the near future.

Summary

Overall, the development of kenaf/polypropylene composite for wall cladding application requires reassessment and improvement. The mechanical strength of the product is considered low compare to compression molding method. Flaws such as high porosity, bending extrudate profile and high surface roughness need to be eliminated. Improvements of KPC wall cladding will be made according the proposed future work mention above.

Acknowledgements

The author would like to thankful the Institute of Tropical Forestry and Forest Products (INTROP) grant EPUP01-01 for the sponsorship of this project. The author also likes to wish highly appreciation to Biocomposite Technology Laboratory technical staff. His assistance is much valuable in the successful of this study.

References

[1] A.K. Mohanty, M. Misra, T.D. Lawrence: *Natural Fibers, Biopolymers and Biocomposites* (CRC Press, Boca Raton, Florida 2005).

[2] R.M. Rowell and H.P. Stout, in: *Jute and Kenaf in Handbook of Fiber Chemistry*, CRC/ Taylor & Francis, Boca Raton (2007).

[3] A.K. Bledzki and J**.** Gassan, in: Prog. Polym. Sci. Vol. 24 (2) (1999).

[4] H.N. Dhakal, Z.Y. Zhang and M.O.W: *Effect of water absorption on the mechanical properties of hemp fibre reinforced unsaturated polyester composites.* Richardson Composites Science and Technology Volume 67, Issues 7-8, Pages 1674-1683 (2007).

[5] J.L. Thomason: *Why are natural fibres failing to deliver on composite performance?* In: 17th International Conference on Composite Materials, ICCM17, 27-31 July, Edinburgh, UK (2009).

[6] Abdalla A. Ab. Rashdi, Mohd Sapuan Salit, Khalina Abdan and Megat Mohamad Hamdan Megat: *Water absorption Behaviour of Kenaf Reinforced Unsaturated Polyester Composites and Its Influence on Their Mechanical Properties.* Pertanika J. Sci. & Technol. 18 (2): 433 – 440 (2010).

[7] G.C. Yang, H.M. Zeng, L.J., Jian, N.B. and Z. Wb: *Relation of modification and tensile properties of sisal fibre.* Acta Scientiarum Naturalium Universitatis Sunyatseni*, 35*, 53-57 (1996).

[8] M.M. Thwe and L. Kin: *Effects of environmental ageing on the mechanical properties of bamboo-glass fibre reinforced polymer matrix hybrid composites*. *Composites Part A*, *33*, 43-52 (2002).

[9] A. Ahmad Shamizan, A. Khalina, H. Jalaluddin, M.Z. Hasniza, W.H. Wan Mohamad Haniffah, M.Y. Yusri and M.G. Shuriati, in: *Tensile properties of Kenaf fiber reinforced polypropylene composite prepared by twin screw extruder*. Book chapter, Research in Natural Fiber Composite UPM Press (2009).

© (2011) Trans Tech Publications, Switzerland
doi:10.4028/www.scientific.net/KEM.471-472.245

Characterisation and Properties of Sintered Recycled Glass utilising CIP Method

N. R. Rosli[1,a], J. M. Juoi[1,b], A. Shaaban[1,c] and N. F. Ayoob[1,d]

[1]Department of Materials Engineering, Faculty of Manufacturing Engineering,

Universiti Teknikal Malaysia Melaka, Malaysia

[a]rifhan.rosli@gmail.com, , [b]jariah@utem.edu.my, [c]azizahs@utem.edu.my

[d]nurfarizan_ayoob@yahoo.com

Keywords: Sintering, Recycled Glass, Glass ceramic, Cold Isostatic Pressing (CIP)

Abstract. Recycling glass is chosen as an alternative raw material in upgrading ceramic into glass ceramic. The main objectives are to determine the effect of sintering temperature and the recycled glass to ball clay weight ratio on glass ceramic produced from recycled glass. The recycled glass powders are prepared by crushing and grinding waste glass bottles to a particles size distribution below than 75 μm. The raw materials (recycled glass powder and ball clay) are characterised by Differential Thermal Analysis (DTA) and its composition is determine by X-Ray Fluorescence (XRF). The recycled glass powder are then mixed with the ball clay according to the ratio of SLSG to ball clay of 95:5 wt.%, 90:10 wt.% and 85:15 wt.%. Green samples of glass ceramic are then fabricated using Cold Isostatic Pressing (CIP) with constant pressure at 40 MPa. Sintering process is conducted at three different temperatures at 750°C, 850°C and 950°C with 1 h holding time. The sintered glass ceramic were then characterised using X-Ray Diffraction (XRD) and Scanning Electron Microscopy (SEM) analyses. Results of physical analyses and microhardness testing conducted according to ASTM C 373 and ASTM C 1327 showed that better properties is achieved at batch composition compromised of 85:15 wt.% ratio of recycling glass to ball clay and sintered at 850 °C. SEM micrographs showed that samples produced from this optimum batch composition provide more homogeneous and dense surface. Furthermore, XRD analysis indicates that crystalline phases evolved during sintering contributes to the final strength of the glass ceramic. These encourage further development on the glass ceramic samples which intended for structural applications.

Introduction

Recycled glass such as soda-lime-silica (SLS) glass is well-known glasses for recycling purpose [1,2]. These urban wastes are buried in special landfill, which is unconstructive and unsatisfactory solution for environment [3,4]. Therefore, it is alternative way by upgrading the use of SLS waste glass in the heavy clay industry might be a potential solution to the problem and make them reasonably safe for the environment [5].

Glass ceramic made by recycling industrial wastes is a well-known technology where many researchers have paid much interest in producing glass, glass ceramic and sintered materials from these solid wastes [6]. Measurement of particle size distributions is a key for characterising a raw material powder in order to achieve the optimum batch composition and the ease of forming is afforded by high speed pressing processes [4,7].

Glass ceramic have significant advantages over standard glass ceramic product which the physical and mechanical testing towards the properties of glass ceramic samples was relatively better in performances [8]. In order to have good performances in properties, it is important to consider the rates viscous flow sintering and crystallisation processes. Differential thermal analysis

(DTA) is widely used in investigated the crystallisation behaviour of glass ceramic [2-4,6,10-14]. Appropriate parameters of batch composition and rates of sintering process is important to ensuring the densification and crystallisation take place simultaneously at the same temperature and desired properties, microstructures and phases can be identified. The aim of this research is to study the effect of sintering temperature to SLS glass and ball clay by characterise and investigate the properties of glass ceramic produced.

Experimental

Chemical composition and thermal analysis. The basic raw materials used in this study were SLS glass obtained from recycled transparent bottles of kitchen waste such as ketchup bottles, sauce bottles, beverage bottles and others unused transparent bottles. Ball clay is used as filler are purchased from Maju Saintifik Sdn. Bhd. The chemical compositions of the raw materials are shown in Table 1. SLS glasses were crushed and milled with an alumina ball in milling machine for 24 hours. Both SLS glass and ball clay was then sieved to get particle size distributions below than 75 μm. The thermal behaviour was studied by TG-DTA measurements in room temperature to 1200 °C at heating rate of 10 °C min^{-1}.

Table 1
Typical chemical composition, in wt.%, of SLS glass and ball clay

Oxides	SLS Glass [wt.%]	Ball Clay [wt.%]
SiO_2	72.60	62.40
CaO	19.30	0.23
TiO_2	0.17	2.22
Fe_2O_3	0.28	1.42
Al_2O_3	2.20	23.0
SO_3	0.31	0.07
Na_2O	2.70	0.04
MgO	1.06	0.24
K_2O	0.33	0.56
P_2O_5	0.07	0.15
MnO	0.01	0.06
L.O.I	0.96	9.69

Batch preparation and sintering. The mixtures of SLS glass and ball clay were prepared between ratio of 95-85 wt.% SLS glass to 5-15 wt.% ball clay, as shown in Table 2. All samples batches were compacted into 10 mm diameter pellet shape by uniaxial pressing at 40 MPa. The green body was then compressed in cold isostatic pressing (CIP) with the same pressure. Sintering was carried out at 750°C, 850°C and 950°C in a laboratory electric furnace with soaking time of 1 hour and heating rate 2 °C min^{-1}.

Table 2
The ratio of SLS glass and ball clay

SLS glass [wt.%]	Ball clay [wt.%]
95	5
90	10
85	15

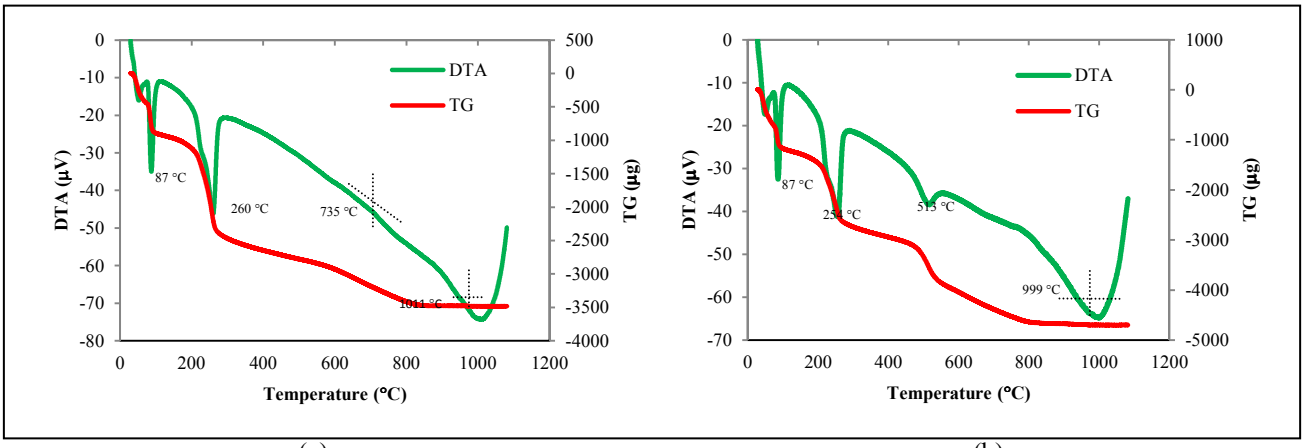
Physical analysis and mechanical test. The porosity, bulk density and water absorption of sintered samples was measured as described in the ASTM C 373. The preparation of the polished samples involved by grounding the pellet surface on 1200 grid SiC papers, then the samples were polished with alumina paste to achieve a mirror-smooth surface. Vickers microhardness measurements were done on the sintered glass-ceramic samples. The microhardness tester used in this study was Vickers Microhardness HM-200 Series with a load of 0.5 kgf.

Microstructural characterisations and phases analysis

The microstructure of the sintered samples were characterised by scanning electron microscope (SEM) EVO 50 (Carl Zeiss SMT, UK), the glass ceramic samples were Au-coated. The crystalline phases of the sintered samples were identified by X-ray diffraction analysis using PANalytical X'PERT PRO MPD Model PW 3060/60 operating at 40 kV and 30 mA with Cu kα radiation. The detector was scanned over a range of 2θ angles from 10° t0 90°, at step size size of 0.02°.

Results and discussions

Thermal analysis of raw materials. The TG-DTA curve for SLS glass and ball clay is presented in Fig. 1. Fig. 1 (a), the endothermic peaks appearing at 87 °C and 260 °C, whereas, in Fig. 1 (b) the endothermic peaks occurring at 87 °C and 254 °C which attributed to minerals dehydration of both materials. The glass transition point of SLS glass was found to be around 735 °C. In Fig. 1(b), another endothermic reaction at 513 °C corresponds to kaolinite inversion. At higher temperatures, an endothermic reaction indicating the melting point occurring at 1011 °C for SLS glass and 999 °C for ball clay. The results from TG-DTA analysis is used as a reference in determining the sintering temperature of the batch composition that is at a range of 750 °C to 950 °C.



(a) (b)

Fig. 1. DTA-TG curves recorded for (a) SLS waste glass and (b) ball clay.

Physical and mechanical properties of sintered glass ceramic. Figure 2 demonstrates value for the density, porosity, water absorption and microhardness of sintered glass ceramic samples at different batch compositions and sintering temperatures. Generally, the physical properties of porosity and water absorption had increased with the increasing of clay content in batch composition and sintering temperature meanwhile the bulk density had decreased with the increasing of clay content in batch composition but had increased with the increasing of sintering temperature. Both porosity and water absorption values is correlated to each other and decreased with the increase in the crystallisation degree in all sintered samples [6]. The trends of microhardness for all temperatures had increased with the increasing of clay content in batch composition and sintering temperature. The microhardness value is related with the microstructure that presences in glass ceramic produced. The mechanical behaviour is attributable to both the balance of crystal phases and microstructure and the addition of clay also considerable has an effect which gives improvement in microhardness value [11]. The crystallisation degree is also an important factor determining hardness and other properties of sintered glass ceramic samples. The factor regulating to physical and mechanical properties are crystalline phases, crystallisation degree and fine grained size [6]. Both mechanical and physical properties also influence by the sintering temperature of sintered glass ceramic which all the sintering temperature range are sufficient in mechanical strength and physical properties for practical usage [9]. The density, porosity and water absorption at 850 °C and 950 °C gives almost similar value but the hardness value at 850 °C was higher than those two. These results indicate that the optimum batch composition is achieved at

85:15 wt.% ratio of recycling glass to ball clay and the appropriate temperature for this study is at 850°C because had the best result (higher density measurement, lower percentage of porosity and water absorption, higher hardness value) of physical and mechanical properties.

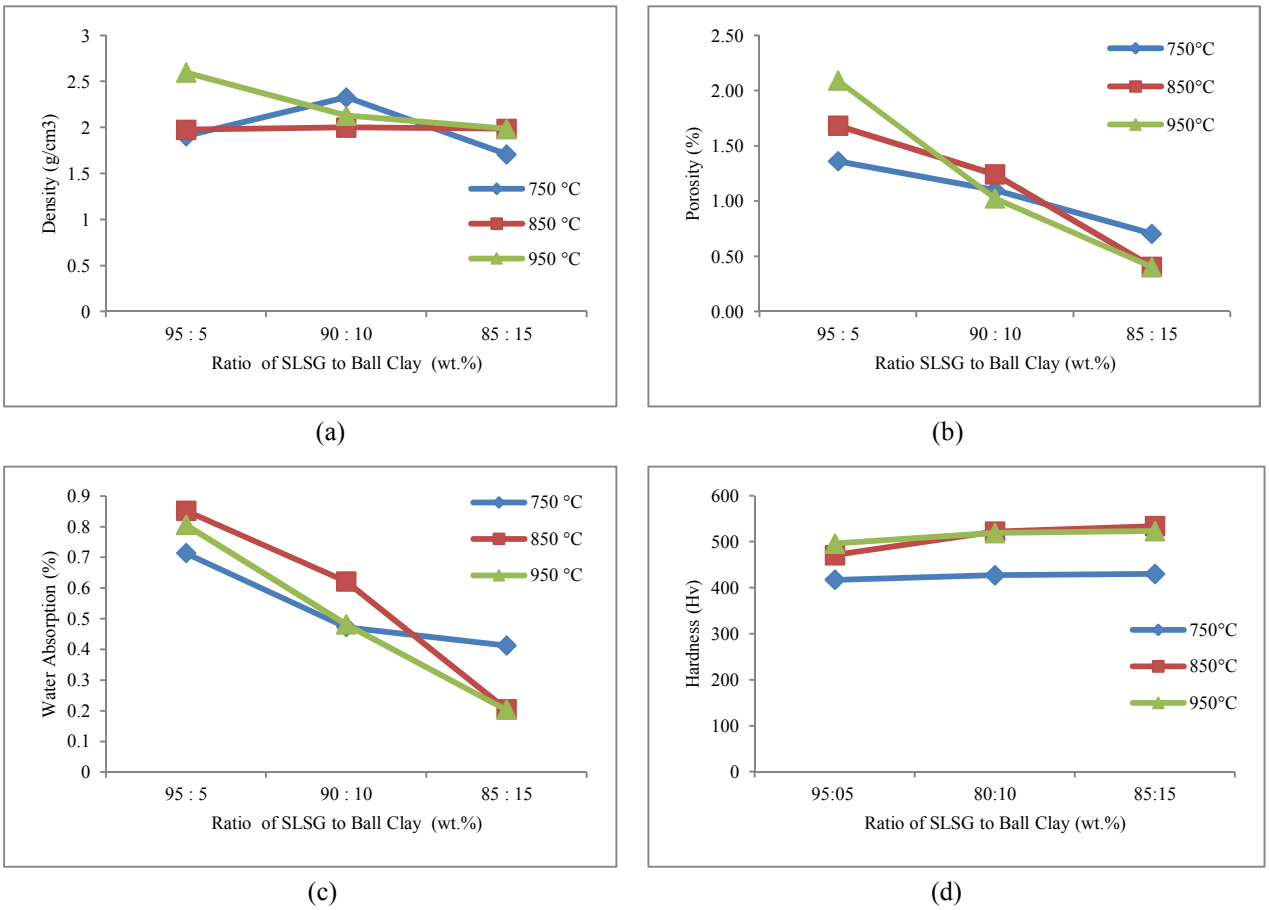


Fig. 2. Result of physical analysis and mechanical testing; (a) density measurement, (b) percentage of porosity, (c) percentage of water absorption and (d) microhardness towards glass ceramic produced at different batch compositions and sintering temperatures.

Microstructural observation by Scanning Electron Microscope (SEM). The SEM micrograph of optimized samples (sintered at 850 °C with 85:15 wt.% ratio of recycling glass to ball clay) are shown in Fig. 3. Based on the micrograph, the surface of the sintered glass ceramic are compact and homogenous with the presence of small group of pores (around 0.3 μm). Generally, the formation of closed pores decreased at higher sintering temperature due to the precipitation of crystalline phases, most probably nepheline, formed between glass and ceramic matrix [4]. The compact and homogenous of sintered glass ceramic observed is correlated with CIP technique that produced better uniformity of green body before sintering process.

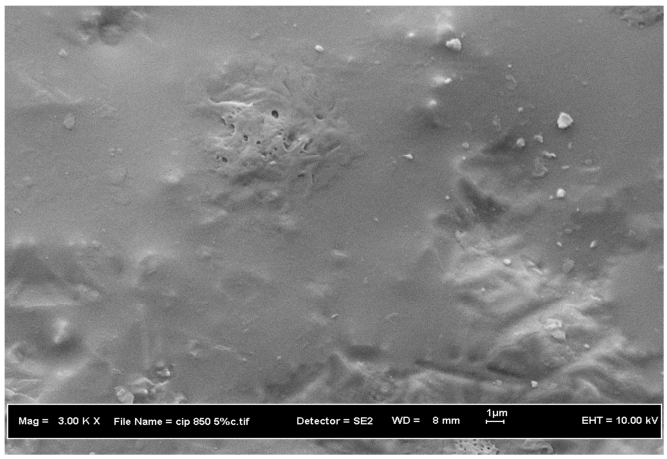
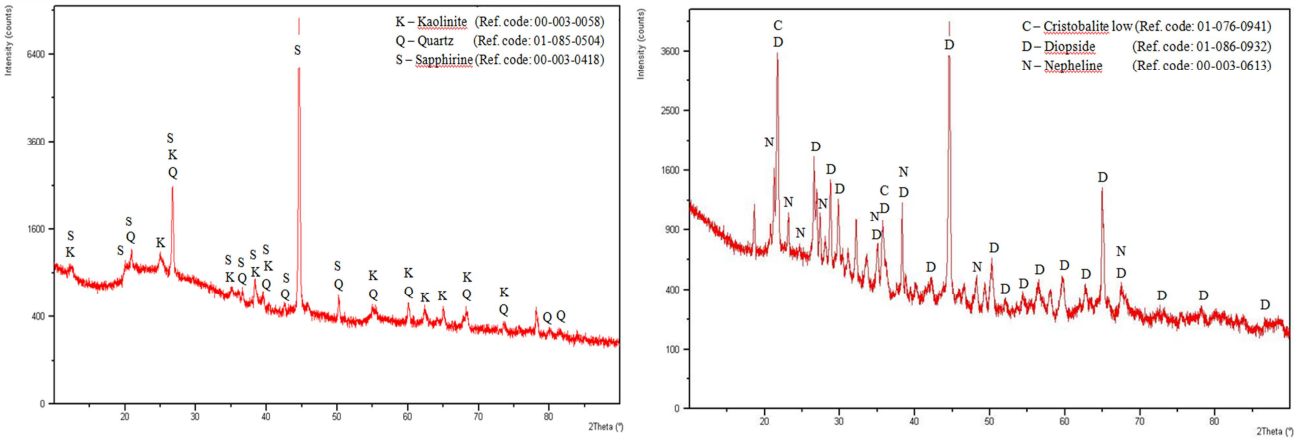


Fig. 3. SEM micrograph of glass ceramic sintered at 850 °C with 85:15 wt.% ratio of recycling glass to ball clay.

Phase analysis by X-ray Diffraction (XRD). The result of XRD measurement of optimized samples (sintered at 850 °C with 85:15 wt.% ratio of recycling glass to ball clay) are shown in Fig. 4. The crystalline phases present in the batch composition (before sintering) corresponding to sapphirine [$(Mg,Al)_8(Al,Si)_6O_{20}$], kaolinite [$Al_2Si_2O_5(OH)_4$] and quartz [SiO_2] as shown in Fig. 4(a). The higher peak at 2θ = 45° is corresponding to sapphirine and followed at 2θ = 27° is corresponding to sapphirine + kaolinite + quartz crystals. For the sintered glass ceramic, the identified phases were cristobalite low [SiO_2], diopside [$Ca(MgAl)Si_2Al_2O_6$] and nepheline [$Na_2OAl_2O_32SiO_2$] as shown in Fig. 2(b). The higher peaks observed at 2θ = 45° is corresponding to the presence of diopside and at 2θ = 22° is corresponding to the presence of cristobalite low + diopside crystal.

As clearly shown in Fig. 4, there are more crystalline peaks for sintered glass ceramic compared to the batch composition. The higher peak at 2θ = 45° corresponds to sapphirine for the batch composition was change to diopside when the glass ceramic is sintered. Many of peaks are corresponding to quartz in the batch composition and this lead to the existence of cristobalite low in the sintered glass ceramic. A diopside phase present as the main crystalline phase in sintered glass ceramic produced from industrial wastes when sintered at around 900 °C [6]. Nepheline phase were also determined during sintering of SLS glass and clay as similar system in agreement with finding of other researchers work [4].



(a) (b)

Fig. 4. XRD pattern of a) the batch composition (before sintering) at 85:15 wt.% ratio of recycling glass to ball clay; b) the sintered glass ceramic at 850 °C with 85:15 wt.% ratio of recycling glass to ball clay.

Summary

This study has clearly indicated that integrates glass ceramic can be produced from the mixture of SLS waste glass and ball clay by sintering method. Sintering process increased the number of crystalline phases present in the sintered glass ceramic bodies. The formation of cristobalite low, diopside and nepheline is contributed in achieving compact and homogenous glass ceramic. Mechanical and physical properties depended on the batch composition of SLS glass and ball clay, particle size distributions, forming method and sintering temperatures. It was observed that, in all glass ceramic samples, sample at 850 °C with 85:15 wt.% ratio of recycling glass to ball clay has the optimized properties in all sintered glass ceramic samples that suitable for industrial use in construction and tiling applications and CIP method is considered as profitable method in producing glass ceramic for future technology.

Acknowledgement

The authors would like to thank the financial support from the Ministry of Science, Technology and Innovation, Malaysia through FRGS Grant FRGS/2010/FKP/SG02/1 – F0082.

References

[1] F. Matteucci, M. Dondi and G. Guarini: submitted to Journal of Ceramic International Vol. 28, 873-880 (2002).

[2] L. Vorrada, T. Panyachai, K. Kaewsimork and C. Siritai: submitted to Journal of Waste Management Vol. 29, 2717-2721 (2009).

[3] L. Barbieri, I. Lancellotti, T. Manfredini, I. Queralt, J. M. Rincon and M. Romero: submitted to Journal of Fuel 78, 271-276 (1999).

[4] Y. Pontikes, L. Esposito, A. Tucci and G. N. Angelopoulos: submitted to Journal of European Ceramic Society Vol. 27, 1657-1663 (2007).

[5] P. Turgut and E. S. Yahlizade: submitted to International Journal of Environmental Science and Engineering Vol. 1, 202-207 (2009).

[6] M. Erol, S. Kucukbayrak and A. Ersoy-Mericboyu: submitted to Journal of Ceramic International Vol. 35, 2609-2617 (2009).

[7] D. W. Richerson, in: *Modern ceramic engineering properties, processing and use in design*, Third Edition. U.S.: Taylor & Francis Group (2006).

[8] M. Tanaka, S. Suzuki, T. Imai and T. Kaneko: submitted to Journal of the Ceramic Society of Japan Vol. 113, 573-578 (2005).

[9] C. Y. Park, S. D. Yoon and Y. H. Yun*:* submitted to Journal of Ceramic Processing Research Vol. 8, No. 6, 435-439 (2007).

[10] E. Bernardo, E. Bonomo and A. Dattoli: submitted to Journal of Ceramic International Vol. 36, 1675-1680 (2010).

[11] E. Bernardo : submitted to Journal of Non-crystalline Solids Vol. 354, 3486-3490 (2008).

[12] E. Bernardo: submitted to Journal of Ceramic International Vol. 33, 27-33 (2005).

[13] I. Rozenstrauha, D. Bajare, R. Cimdins and L. Berzina: submitted to Journal of Ceramic International Vol. 32, 115-119 (2006).

[14] M. Erol, S. Kucukbayrak, A. Ersoy-Mericboyu and M. L. Ovecoglu: submitted to Journal of European Ceramic Society Vol. 21, 2835-2841 (2001).

© (2011) Trans Tech Publications, Switzerland
doi:10.4028/www.scientific.net/KEM.471-472.251

Nanotechnology in Pulp and Paper Industries: A Review

S.D Mohieldin[1,2], E.S Zainudin[1,a], M.T Paridah[1] and Z.M Ainun[1]

[1]Laboratory of Biocomposite Technology, Institute of Tropical Forestry and Forest Products, Universiti Putra Malaysia
[2]The National Center for Research (NCR), Sudan
[a]edisyam@gmail.com

Keywords: Nanotechnology, Wood Industry, Pulp, Paper, Nanofibres

Abstract. Cellulose and lignocellulose have great potential as nanomaterials because they are abundant, renewable, have a nanofibrillar structure, can be made multifunctional and self-assemble into well-defined architectures. New methods for liberating these materials, including nanodimensional cellulose fibrils, macromolecules and nanominerals will be needed in order to use the techniques developed for other nanomaterials as platforms for creating new wood-based materials and products. Research findings showed promising results in application of nanotechnology at different aspects of papermaking. Electrospinning; chemical treatment followed by mechanical techniques; or mechanical isolation methods were applied by different research groups to prepare cellulose nanofibres.

Introduction

Nanotechnology is an emerging area of science and technology that will revolutionize materials use in the 21st century. The relatively crude and unsophisticated technologies on which we currently depend will be replaced with highly efficient and environmentally friendly nanotechnologies [1]. The discovery of novel materials, processes, and phenomena at the nanoscale and the development of new experimental and theoretical techniques for research provide fresh opportunities for the development of innovative nanosystems and nanostructured materials [2]. Nanotechnology has found an immediate spot on agendas of policy makers and industry leaders [3]. The nanotechnology is important because of: 1) Less space, faster, less material, and less energy; 2) novel properties and phenomena; 3) most efficient length scale for manufacturing; and intersection of living/non-living [4]. A diverse array of ultra-small-scale materials, including metal oxides, ceramics and polymeric materials, and wide-ranging processing methods including techniques that employ 'self-assembly' on a molecular scale, are either in use today or are being groomed for commercial-scale use. Other examples, in various stages of development, focused on pollution prevention and treatment [5]. Malaysia has started its own microtechnology and nanotechnology development since the early millennium year of 2000 and arise until this day. Nanotechnology R&D started by government in 2001 and categorized as a Strategic Research (SR) program under IRPA in the Eight Malaysia Plan (8MP). Malaysian government has taken a serious concern over the development of nanotechnology in the country. The third Industrial Master Plan (2005-2020) recognizes nanotechnology as the new emerging field [6]. The National Nanotechnology Initiatives was launched in 2006. Malaysia participated in different forums about nanotechnology [7].

Nanotechnology and the Forest Industry

Significant progress has been made in understanding the mechanical properties of bulk wood, isolated fibres, and cellulosic fribrils; however, much remains to be understood about characteristics of intact cell walls, interactions between cell wall layers, and properties of and interactions among the nanoscale domains (cellulose, hemicellulose, and lignin) that provide the basis for properties we observe in the system as a whole [8]. For the forest (lignocellulosic) products industrial sector,

nanotechnology will be used to tap the enormous undeveloped potential that tree's possess. The vision for nanotechnology in the forest products is to sustainably meet the needs of present and future generations for wood-based materials and products by applying nanotechnology science and engineering to efficiently and effectively capture the entire range of values that wood-based lignocellulosic materials are capable of providing [9]. Some possible application areas of nanotechnology in papermaking includes: New materials; wet-end chemistry; Nanofiltration in closure of water circulation; coating; calender rolls; sensors; microscopy; and nanoscale assemblers [10]. Among the many possibilities suggested to date for new woodfibre-based products incorporating nanomaterials are moisture-resistant cell-phone components, advanced membranes and filters, improved loudspeaker cones, and additives for paints, coatings, and adhesives [11]. Collaboration among industry, academia, and society must occur to overcome the challenges associated with the future of nanotechnology in various sectors of application. Moreover, because nanotechnology draws several fields, different sectors must contribute information and techniques to further development of nanotechnology [12].

Preparation and Characterization of Cellulose Nanofibres

Fibre-fibre and fibre-additive interactions are main factors for physical paper properties. Control and manipulation of these interactions are the focus of many research strategies. In particular nanotechnology-modified fibre compounds and products are promising materials for improved paper products [13]. Cellulose fibres on the nanoscale are prepared in four different ways: (1) bacterial cellulose nanofibres, (2) cellulose nanofibres by electrospinning, (3) microfibrillated cellulose plant cell fibres and (4) nanorods or cellulose whiskers. However, Table (1) summarise the different methods of nanofibres preparation and charachterization. Structure and properties of nanocellulose that are important include: morphology, crystalline structure, surface properties, chemical and physical properties, and properties in liquid suspension [14]. The investigations include the effect of the different pretreatments on chemical composition and structure of isolated nanofibers beside thier dimensions and properties [15].

Table 1 Nanofibres preparation and characterization.[14]

Preparation Electrospinning. Chemical Treatment followed by Mechanical techniques.		
	Chemical treatment Chemical Pulping and Bleaching. Sodium Hydroxide and acid hydrolysis. Acetylation of plant fibres. Solvent extraction followed by other chemical treatments. Enzymatic degradation.	**Mechanical Techniques** Refining/grinding/beating/blending/cryo-crushing followed by high pressure homogenization
Characterization	**Structure** Chemical Analysis. X-Ray Diffraction. Fourier Transform Infrared Spectroscopy.	**Morphology and Dimensions** Optical Microscopy. Transmission Electron Microscopy. Atomic Force Microscopy. Scanning Electron Microscopy.

Nanofibres in the papermaking industry

Cellulose and lignocellulose have great potential as nanomaterials because they are abundant, renewable, have a nanofibrillar structure, can be made multifunctional, and self-assemble into well-defined architectures [9]. Cellulosic nanofibres present a very high surface area which makes the adhesion properties the most important parameter to control for nanocomposite applications [14]. The contact angle measurements showed that the surface characteristics of nanofibres were changed from hydrophilic to more hydrophobic when acetylated. The microscopy study showed that the acetylation caused a swelling of the kenaf fibre cell wall and that the diameters of isolated nanofibres were between 5 and 50 nm. The papermaking industry can benefit a lot from nanotechnology. This versatile technolohy can also be used in the area of fillers for papermaking wet end applications [16].

Improved Properties and New Paper Grades

The next evolutionary steps of paper in the form of cellulose nanofiber paper were shown in many published articles. Ioelovich [17] reviewed that recent developments have shown the possibility to increase paper strength with additive of nanocellulose particles or nanofibrillated cellulose to paper composition. The potential of cellulose nanofibrils as a strength reinforcing agent was also demonstrated by Ahola [18]. The nanofibrils are used with a cationic polyelectrolyte, poly(amideamine) epichlorohydrin (PAE), to enhance paper strength. It is concluded that the paper strength experiments and fundamental interaction studies showed that the use of nanofibrils as a strength reinforcing agent together with PAE leads to superior improvements in strength properties. Nogi [19] reported the inception of a new kind of paper made of cellulose nanofibres, as opposed to micrometer-sized cellulose pulp fibres of ordinary paper. Nanopapers of different porosities and from nanofibrils of different molar mass are prepared. The high toughness of highly porous nanopaper is related to the nanofibrillar network structure and high mechanical nanofibril performance [20]. The superiority of nanopaper is likely to be caused by higher fibril strength, more favorable interfibril adhesion characteristics, and much smaller and more homogeneously distributed defects (voids) [20]. More stable mass production of the nanofibres can be realized because fibrillation methods are applicable to any natural fibre resource containing lignin such as flax, sugarcane bagasse, and wheat straw [21], beside woody lignocelluosic materials. With these potential the nanofibre paper could play the same role as or an even greater role than conventional paper in information storage and transfer for perhaps another millennium to come [19].

Nanotechnology and Papermaking Process

The papermaking application of employing nanoparticle systems has evolved to become more of a “properties” management system during papermaking, and beyond the mill at converting operations and printers. Nano-technology developments in areas of fibre science, minerals and other additives will give papermakers the means to put order and structure into the designs of a sheet [22]. Both lumen loading and *in situ* synthesis methods have been used in preparing magnetic papers. Papers obtained via lumen loading process possess higher magnetic properties compare to *in situ* synthesis method. This is due to its finite (nm) size of particles synthesized by using chemical coprecipitation method, which shows super paramagnetic behavior. Finite size particles are tended to aggregate and attach strongly between each other in order to minimize their surface energy and resulting the low detachment rate during the washing and papermaking process [23]. The magnetic particles deposited on the surface of the fibres had detrimental effects on the paper strength [24]. Agarwal [25] have demonstrated successful scale integration from nano to micro and macroscale (nanocoating–microfibres–macropaper) in developing new paper material. The layer-by-layer (LbL)

self-assembly technique was also applied to deposit organized multilayers of TiO_2 or SiO_2 nanoparticles of 30-80 nm diameter, and 50-nm diameter halloysite clay nanotubes on softwood fibres [26]. Recently, Fahmy and Mobarak [27] have shown that the nanoadditive sucrose can overcome the ultimate fate of deterioration in strength of paper, due to addition of inorganic fillers such as kaolin. Incorporating the nanoporous structure of cellulose fibers with sucrose, which leads to incorporation beating of the fibers, increases the strength of the produced paper nanocomposites.

Nanofibres in Composite Reinforcement

Cellulose micro/nanofibril (CMNF) as a reinforcing material for composites is becoming more and more attractive to researchers in composite science because of its potential lightweight and high strength [28]. Nakagaito and Yano [29] stated that a completely new kind of high-strength composite was manufactured using microfibrillated cellulose derived from kraft pulp. Iwamoto [30] reported that the nanofibres exhibit great potential as reinforcement material for optically transparent composites. Graham [31] explored the theoretical and practical benefits of using nanofibres in composite filter media and have been concluded that, nanofibres can provide an improvement in filter efficiency without a substantial increase in filter pressure drop. They have proven to enhance the life of filters in pulse-clean cartridge applications for dust collection, and increase the efficiency of air filters for personnel cabins of mining vehicles. Bhatnagar and Sain [32] prepared a polymer/nanofibres matrix where the nanofibres reinforcement content was 10% in 90% PVA. They observed that even 10% nanofibres provide a remarkable reinforcing potential. Peresin [33], obtained very smooth nonwoven mats with homogeneous nanofibers, of PVA reinforced with cellulose nanocrystals by the electrospinning technique. These fiber nanocomposites had shown enhanced thermomechanical properties. According to Zimmermann [34], the strength of the composites reinforced with the nanofibres is equivalent to that of mild steel or magnesium alloy. Due to the light weight of the microfibrillated cellulose, substantial reduction in automobile weight can be achieved when they replace that alloys. However, the use of biopolymers has been limited because of their usually poor mechanical and barrier properties, which may be improved by adding reinforcing compounds (fillers), forming composites [35]. Nanoparticles have proportionally larger surface area than their microscale counterparts, which favors the filler-matrix interactions and the performance of the resulting material. Besides nanoreinforcements, nanoparticles can have other functions when added to a polymer, such as antimicrobial activity, enzyme immobilization and biosensing. Nanocomposite edible films were developed by adding cellulose nanofibers (CNF) in different concentrations as nanoreinforcement to mango puree based edible films and chitosan films [36].

Summary

Cellulose and lignocellulosic materials have great potential as nanomaterials because they are abundant, renewable, have a nanofibrillar structure, can be made multifunctional and self-assemble into well-defined architectures. Different aspects of papermaking process can benefit from nanotechnology application either utilizing nanofibres and/or other nanomaterials (fillers, sizing and coating minerals) to improve the quality of the produced paper or producing new types of paper. Cellulose nanofibres could be generated successfully from different fibrous raw materials through chemical and mechanical treatments. Cellulose nanofibres has shown great potentiality as reinforcing materials in composites and especially in reinforcing biopolymers to produce biodegradable films favoring the environmental issues. Sufficient attention and plans of action was given to research and development activities in nanotechnology in Malaysia.

References

[1] Wegner, T. H. and Jones, E. P: A Fundamental Review of the Relationships between Nanotechnology and Lignocellulosic Biomass, The Nanoscience and Technology of Renewable Biomaterials Edited by Lucian A. Lucia and Orlando J. Rojas. Blackwell Publishing Ltd. (2009) p. 1-41.

[2] B. Bhushan: Introduction to Nanotechnology. In: Springer Handbook of Nanotechnology. 3rd Edition. Bharat Bhushan (Ed.) Springer-Verlag Berlin Heidelberg, (2010) p.1961

[3] J. Schulte: Introduction: Movement in Nanotechnology. In: Nanotechnology: Global Strategies, Industry Trends and Applications Edited by J. Schulte. John Wiley & Sons (2005). p. 1-4.

[4] S. Kamel: eXPRESS Polymer Letters, Vol. 1(9) (2007) p. 546-575.

[5] Theodore, L. and Kunz, R. G. (2005). Nanotechnology: Environmental Implications and Solutions. John Wiley & Sons, Inc. 378pp.

[6] Hashim, U., Nadia, E. and Salleh, S. (2009). Int. J. nanoelectronics and Materias 2(1): 119-134.

[7] Abdul Halim, R. R. (2010). Country Presentations: Malaysia. In: Innovation in Nanotechnology: Proceedings and Papers Presented at the Consultative Workshop on Promoting Innovation in Nanotechnology and Fostering Industrial Application. 93-98.

[8] Moon, R. J., Frihart, C. R. and Wegner, T. (2006). Forest Products Journal, 55(5): 4-10.

[9] Wegner, T. H. and Jones, E. P. (2006). Cellulose (2006) 13:115 –118.

[10] Puurunen K. and Vasara, P. (2007). Journal of Cleaner Production 15: 1287-1294.

[11] Ananymous (2005). Nanotechnology for the Forest Products Industry-Vision and Technology Roadmap. TAPPI Press, 2005. 84p.

[12] McCrank, J. (2009). Nanotechnology Applications in the Forest Sector. Her Majestry the Queen in Right of Canada. 14pp.

[13] Arndt, T. and Zelm, R. (2008). Das Papier, T110: 59-63

[14] Gardner, D. J., Oporto, G. S., Mills R. and Samir, A. S. A. (2008). Journal of Adhesion Science and Technology, 22: 545–567.

[15] Hassan, M. L., Mathew, A. P., Hassan, E. A. and Oksman, K. (2010). Wood and Fiber Science, 42(3): 362-376.

[16] Shen, J., Song, Z., Qian, X., Yang, F. and Kong, F. (2010). Bioresources, 5(3): 1328-1331.

[17] Ioelovich, M. (2008). BioResources, 3(4): 1403-1418.

[18] Ahola, Susanna (2008). Properties and Interfacial Behaviour of Cellulose Nanofibrils. Doctoral Thesis, Helsinki University of Technology.

[19] Nogi, M., Iwamoto, S., Nakagaito, A. N. and Yano, H. (2009). Adv. Mater., 20: 1-4.

[20] Henriksson, M., Berglund, L. A. Isaksson, P., Lindström, T and Nishino, T. (2008). Biomacromolecules, 9: 1579-1585.

[21] Abe, K. Iwamoto, S. and Yano, K (2007). Biomacromolecules, 8: 3276-3278.

[22] Innova, M. K. (2004). Pulp and Paper Canada, III 105(1): 18-21.

[23] Chia, C. H., Zakaria, S., Ahamd, S., Abdullah M. and Mohd. Jani, S. (2006). American Journal of Applied Sciences 3 (3): 1750-1754.

[24] Chia, C. H., Zakaria, S., Nguyen, K. L. and Abdullah, M. (2008). Industrial Crops and Products, 28: 333-339.

[25] Agarwal, M, Lvov Y. and Varahramyan, K. (2006). Nanotechnology, 17: 5319–5325.

[26] Lu, Z., Eadula, S., Zheng, Z., Xu, K., Grozdits, G. and Lvov, Y. (2007). Colloids and Surfaces A: Physicochemical and Engineering Aspects, (292) 1: 56-62.

[27] Fahmy, T. Y. A. and Mobarak (2009). Carbohydrate Polymers, 77: 316-319.

[28] Wang, S., Cheng, Q., Rials, T. G. and Lee, S. (2006). Cellulose Microfibril/Nanofibril and Its Nanocompsites. Proceedings of the 8th Pacific Rim Bio-Based Composites Symposium: 20-23 November, 2006, Kepong, Kuala Lumpur, Malaysia, Forest Research Institute Malaysia: 301-308.

[29] Nakagaito, A. N. and Yano, H. (2005). Appl. Phys. A 80: 155–159.

[30] Iwamoto, S., Nakagaito, A. N., Yano, H. and Nogi, M. (2005). Applied Physics A: Materials Science and Processing. 81(6): 1109-1112.

[31] Graham, K., Ouyang, M., Raether, T., Grafe, T., McDonald, B. and Knauf, P. (2002). Polymeric Nanofibres in Air Filtration Applications. Presented at the Fifteenth Annual Technical Conference & Expo of the American Filtration & Separations Society, Galveston, Texas, April 9-12.

[32] Bhatnagar, A. and Sain, M. (2005). Journal of Reinforced Plastics and Composites; 24; 1259-1268.

[33] Peresin, M. S., Habibi, Y., Zoppe, J. O., Pawlak, J. J. and Rojas, O. J. (2010). Biomacromolecules, 11, 674-681.

[34] Zimmermann, T., Pohler, E., and Geiger, T. (2004). Advanced Engineering Materials, 6(9): 754-761.

[35] Azeredo, H. M. C. (2009). Food Research International, 42:1240-1253

[36] Azeredo, H. M. C., Mattoso, L. H. C., Avena-Bustillos, R. J., Filho, G. C., Munford, M. L., Delilahwood and Mchugh T. H. (2010). Journal of Food Science, 75(1): 1-7.

© (2011) Trans Tech Publications, Switzerland
doi:10.4028/www.scientific.net/KEM.471-472.257

Oscillatory and Creep Recovery Test on Nano-Composite Lead-Free Solder Pastes (Nickel and Platinum Powder)

[a]R. Durairaj, [b]Kau Chee Leong, [c]Lim Chia Wea and Wong Mee Chu

Department of Mechanical and Material Engineering, Universiti Tunku Abdul Rahman (UTAR)

Jalan Genting Kelang, Setapak 53300 kuala Lumpur, Malaysia

[a]rajkumar@utar.edu.my, [b]kau1437@gmail.com, [c]chiawea@gmail.com

Keyword: Rheology; lead-free solder pastes; creep recovery and oscillatory test.

Abstract. This study investigates the relationship of rheological properties of nanoparticles added to lead-free solders paste. For lead-free solder paste, a large number of combinations can be made from different elements. Every ingredient plays a role of the paste and the rheological properties. The effect of filler concentration was studied in this present investigation. Creep recovery, stress is applied on samples for a period of time and later release in order for it to recovery itself. In the other words, creep recovery involves a tensile specimen under constant load maintained at a constant temperature. Oscillatory tests were carried out to study the visco-elastic behaviour and paste stability. The visco-elastic behaviour of the paste lies between solid and liquid characteristic of the paste, which could be used to study the flow behaviour of paste during stencil printing process. From this study, it was found that the solid characteristic, G' is higher than liquid characteristic, G" for all the samples. In addition, the results from the study showed that the 0.06 volume fraction sample system with a large yield point which G'= G" has a higher cohesiveness and hence resulting in poor withdrawal of the paste during stencil printing process. The phase angle, δ was used to correlate the quality of the dense suspensions to the formulation of solder paste materials. Lower value of phase angle for 0.06 volume fraction sample system may indicating that the paste is very tacky compare to the other samples. As the demand for lead-free pastes increases rheological measurements can assist with the formulation of new pastes.

Introduction

The electronic industry has gained a rapid growth in various sectors such as the computer, telecommunications and automotive during the past decade. As the current product miniaturisation trend is set to continue for hand-held consumer product, and consumers demand for portability, flexibility and better performance of the final product. As a result, this imposes tight requirements in term of size reduction, performance increase, higher reliability and lower cost. The assembly of these devices requires the printing of very small paste deposits consistently from pad to pad, and from board to board.

Recent developments, such as the introduction of closed print heads, ultra-fine pitch printing, high-speed printing, zero-defect printing and lead-free solder paste, will require a better understanding of the behaviour of solder paste [1]. The behaviour of the product should be studied throughout the steps between the manufacture of the solder paste, transport and storage, temperature-sensitivity during printing, the printing performance itself at defined speed, adhesion strength of components and issues such as tackiness. The printing process by itself is defined by many parameters such as equipment, setting, materials and environment. The printing of solder paste through a very small stencil apertures required for ultra-fine pitch and flip chip applications is known to result in increased stencil clogging and incomplete transfer of paste to the printed circuit boards. At these very narrow aperture sizes, achieving consistent solder paste deposits from board to board becomes very difficult and the solder paste withdraws because for smaller paste volumes the surface tension effects become dominant over viscous flow [2]. Solder paste rheology is

therefore considered to be one of the most important parameters which affect the paste printing process, the reflow soldering performance, and hence the resulting solder joint quality and reliability [3,4]. Evidently, the printing properties of solder paste need to be verified in order to assure that this key player in the process provides a consistent and reliable performance at all times. Monitoring rheological properties of solder paste such as viscosity and visco-elasticity are of paramount importance when setting goals for increasing yields [5].

Rheology is defined as the study of flow and deformation of materials. The Knowledge about the rheological behavior about the paste material will definitely help to optimize the electronic assembly process and decrease the rate of assembly defects. For the lead-free solder pastes, there can be a large number of combinations from the combination of elements: Sn, Ag, Bi, Cu, In, Sb, Zn in binary, tenary, or multi-component system [6]. For a typical composition for flex/flux system, it lies in the range 5-20 ingredients [7]. Every ingredient plays a role in the final performance of the paste. The rheological behavior of solder paste can greatly according to the ingredients [8]. This study investigates the affects of the rheological behavior of the addition of other elements in to solder pastes, as they may greatly influence the printing quality and the post printing behaviour. The objective of this study was to analyse and compare the rhelogy data of three solder pastes which are added different metal content.

Experimental

Material and sample preparations. The solder pastes used for this investigation are shown in Table 1. The nickel and platinum powder content is the only variable parameter which mixed with different weight percentage to the solder paste. The particles size distribution is 20-45(μm) and the particles are in a spherical form. Those samples P1, P2 and P3 were stored in the fridge at 4^0C, while the room temperature (which could not be controlled) was monitored to average 24^0C . Before each rheological measurement the samples were taken out and left about 4 hours to reach room temperature.

Table 1: Constituent of lead free solder pastes investigated

Paste samples	Particle size distribution (μm)	Particle shape	Flux Medium	Solder alloys/materials	Platinum powder	Nickel powder
P1	20-45	Spherical	Rosin Mildly Activated (RMA)	96.5% Tin/3% silver/0.5% copper	0.2wt%	1.8wt%
P2	20-45	Spherical	RMA	96.5% Tin/3% silver/0.5% copper	0.4wt%	3.6wt%
P3	20-45	Spherical	RMA	96.5% Tin/3% silver/0.5% copper	0.6wt%	5.4wt%

Apparatus. A controlled stress rheometer (Model: Physica MCR 301) with a parallel plate geometry with a diameter of 25 mm and gap of 1.0 mm was used as a measuring device. Prior to loading a sample onto the rheometer, the solder pastes were hand mixed with a plastic spatula for about 1 to 2 min and left about half an hour after the stirring. A sample was loaded on the bottom plate and the top plate was then lowered to the desired gap height of 1.0 mm by squeezing the extra paste out from between the plates. The excess paste at the plate edges was neatly trimmed with a plastic spatula. Then the sample was allowed to rest for about 1 min before starting the test. Identical loading procedures were followed in all the tests. All tests were conducted at 25^0C with the temperature being controlled by a Peltier-Plate system.

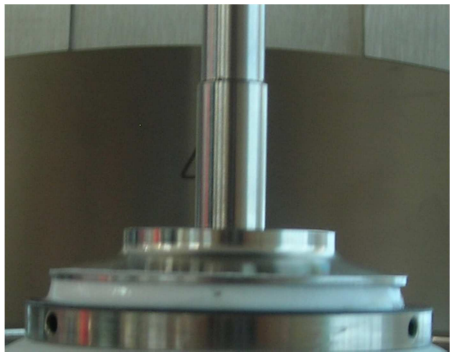


Fig. 1 Parallel plate measurement geometry

Oscillatory stress sweep test. In the oscillatory stress sweep experiment, a stress sweep which is below 100Pa is applied to all the pastes samples. It provides useful information about sample pastes microstructure, and it allows to determinate the linear visco-elastic region for the samples. A large stress applied may result in the paste sample to move outward from the measuring plate causing a small gap to form between the top plate and the sample; it may affect the results and inconsistency in the data, so the maximum stress is controlled.

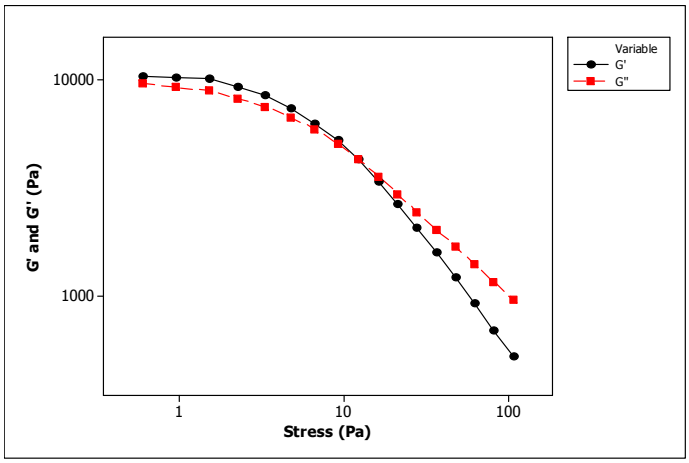
Creep-recovery test. The creep-recovery test can be used for the study of the slump behaviour in the pastes material. It can be related to the aperture filling and emptying process. In this test, the shear stress is applied instantaneously to the sample and maintained constant, the resulting stain is recorded. After a pre-set time (120 seconds), the stress is removed and the stain induced in the sample is recorded (120 seconds). The applied stress is 5 Pa, which is recommended perform all the tests in the linear visco-elastic region (LVR).

Results and Discussion

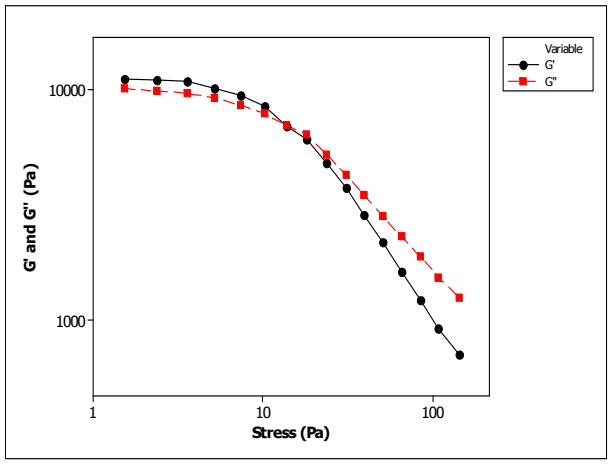
Oscillatory stress sweep test results. The values of G' and G'' in linear visco-elastic region (LVR), ratio of G''/G', crossover stress G'=G'', phase angle δ and linear visco-elastic region (LVR) are mapped in table 2. The linear visco-elastic region (LVR) is identified. As shown in figure 2 (c), P3 has showed the largest linear visco-elastic region (LVR) among all sample pastes with a shear stress value 8Pa. This mean that sample P3 has the higher structural resistance towards applied forces when compared to other pastes, it is because P3 has the highest nanoparticles content, in which may lead to have a strong physical bonds such as Van Der Waals and repulsive forces due to steric and electrostatic effect on the particles. The linear visco-elastic region (LVR) was quite difficult to identify due to it is very short range and also because the instability in G' value. All the sample pastes essentially showed a dominant solid like behaviour, which is G' being greater than G'' (G' > G'') within LVR. P3 shows the highest values of G' and G'', and P1 is the lowest values of G' and G'', in which P3 has the highest metal content compare to other pastes sample. The ratio of G''/G' given a notice of the strength of interaction within the internal structure. A low G''/G' value shows that the material has a dominant elastic (solid like) behaviour. As expected, P1 shows the highest G''/G' value of 0.93, followed by P2 and P1. That means the P3 has a very strong interaction within the internal structure due to it high concentration of nanoparticles. The crossover stress G'=G'' represent the change of elastic (solid like) behaviour to the viscous (liquid like) behaviour. Once the applied shear stress is beyond this point, the sample paste is experienced a dominant viscous (liquid like) behaviour. Again, P3 shows a highest value of G'=G''. The lower the stress at G'=G'', the more liquid like the material is [10]. As shown in figure 2 (a), P1 shows a lowest value of G'=G'' which is 12 Pa. The phase angle could provide a quick way of assessing the transition from solid to liquid like behaviour of the paste material, for example, a low phase angle may indicate the paste very tacky. A high phase angle may indicate that the paste is more liquid like and it tends to slump easily.

Table 2: Summary of oscillatory stress sweep results

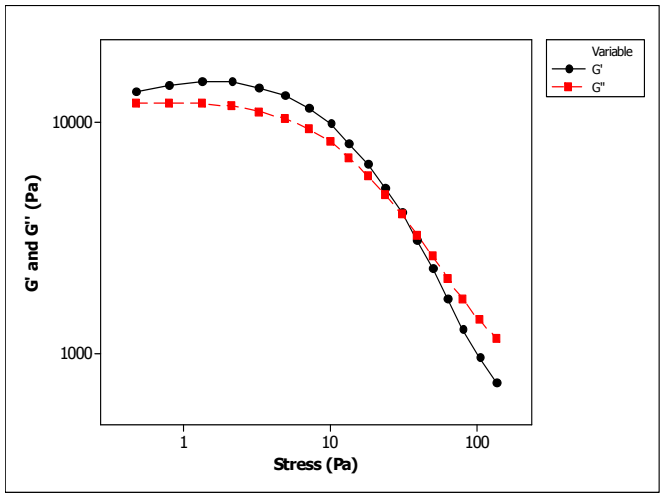
Samples	G'(Pa)	G''(Pa)	G''/G'	G'=G''(Pa)	δ (deg)	Linear visco-elastic region
P1	10400	9660	0.93	12	41.2-61.4	Up to 5Pa
P2	11200	10200	0.91	14	40.1-59.1	Up to 5 Pa
P3	13600	12000	0.88	30	38.1-57.2	Up to 8 Pa



(a) P1



(b) P2



(c) P3

Fig. 2 Oscillatory stress sweeps for (a) P1, (b) P2 and (c) P3

Creep-recovery test. From Fig. 3, P1 showed the highest J_C of 4.33 x 10^{-3} Pa^{-1} and J_R of 3.08 x 10^{-3} Pa^{-1}, followed by P2 with a J_C of 3.43 x 10^{-3} Pa^{-1} and J_R of 2.56 x10^{-3} Pa^{-1}, and P3 with a J_C 2.11 x 10^{-3} Pa^{-1} and J_R of 1.51 x 10^{-3} Pa^{-1}. The high creep compliance J_C value shows that the simple paste could be easily deformed and the extent of the deformation will depend on the strength of the microstructure. P3 has a highest metal content, in which may lead to have a lowest J_C and J_R due to the particle-particle interactions resulting in a higher degree of fillers agglomeration. The recovery compliance J_R as shown, it is always lower than creep compliance J_C, which means the sample paste did not recover back to its original structure after the removal of the applied stress. The recovery rate can be used to study the slump characteristic of the sample pastes; it can be calculated by using the ratio $(J_C-J_R)/J_C$. P1 has the highest recovery rate of 29% followed by P3 at 28.3% and P2 at 26%. The Bao et al. (1998) found that solder paste with lower compliance and high recovery rate are preferred to minimise print defect. As the results shown, P3 has the characteristic which is higher recovery rate and lower compliance (J_C and J_R). From figure 4, it shown that sample paste P3 has a stronger microstructure which may indicate that the strain is smaller when applied a same shear rate compare to the other samples.

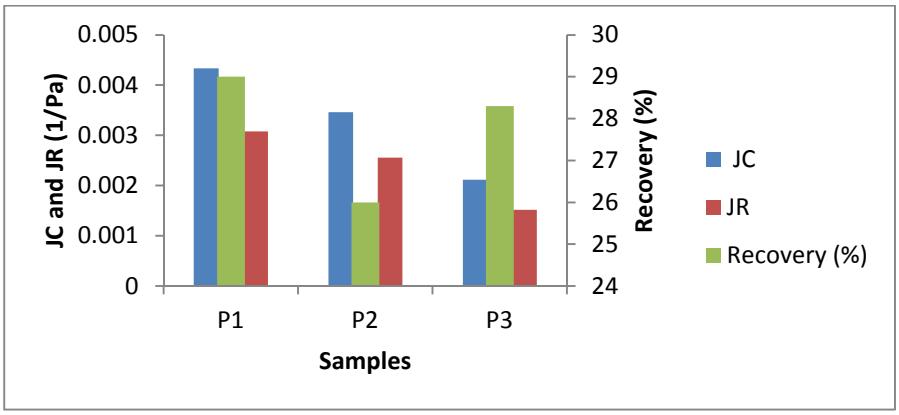


Fig. 3 J_C, J_R and recovery ratio for sample pastes P1, P2 and P3.

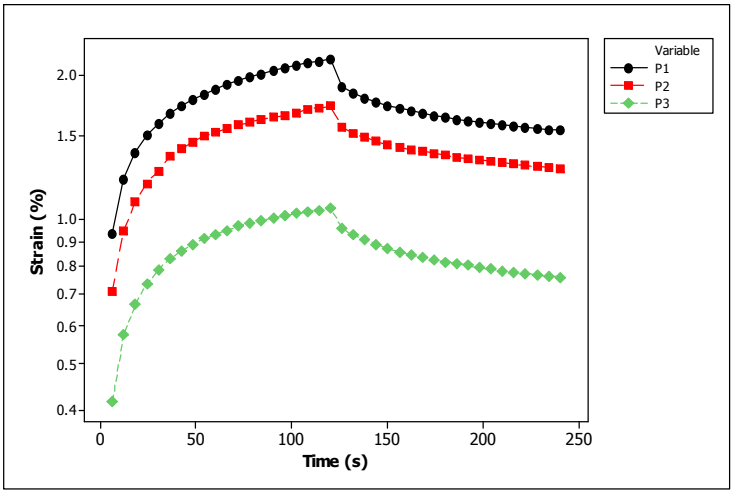


Fig. 4 Creep recovery test results for P1, P2 and P3

Summary

In this study, the visco-elastic properties of the solder pastes had been presented. The three sample pastes are added with different volume fraction of nanoparticles and investigated the effect of the rheological properties. The samples were carried out two different tests, which are Oscillatory stress sweep and creep-recovery test. In the Oscillatory stress sweep test, P3 shows to have a highest G' =

G'' value and the lowest G''/G' value among all the samples. Which mean, the higher the metal filler added, the tackier the paste is, and it has the dominant solid like behaviour. For the creep-recovery test, P3 has the characteristic which is higher recovery rate and lower compliance (J_C and J_R), which may expected to minimise the print defect. As the results shown, P3 has the highest content of nanoparticles, and has good microstructure stability. The concentrated nanoparticles are held together by physical bonds. When no force is exerted on the suspension, the particle aggregation can form a spatial network which creates an internal structure.

References

[1] Wong C.P. and Yi Li, *Journal of Materials Science and Engineering*, 51, 1-35 (2006).

[2] Haslehurst L. and Ekere N.N., *Journal of Electronics Manufacturing*, 6/4, 307 (1996).

[3] Barnes H.A., Hutton J.F., Walters K., *Elsevier Science Publishers*, New York (1989).

[4] Durairaj, R., Mallik, S., Seman, A., Marks, A., and Ekere, N.N., *Journal of Materials and Processing Technology*, 209, 3923 (2009).

[5] Dosten B. and Gerard M., "Fundamentals of solder paste technology", *BizEsp Limited*, Global SMT and Packaging, UK (2006).

[6] Hwang, J. S., Solder Paste in Electronics Packaging, Van Nostrand Reinhold (New York, 1989), pp. 31 69.

[7] Nimmo, K, "Alloy Selecions", In: Lead-free Soldring in Electronics Science, technology and environmental impact, Marcel Dekker, Inc. (New York 2004), pp 49 - 90.

[8] Anderson, R. *et ai, Journal of Rheology* (1995), pp. 12 18.

[9] Durairaj, R., Mallik, S., Seman, A., Marks, A., and Ekere, N.N., *Journal of Materials and Design, 30, 3812* (2009).

[10] Bao, X., Lee, N.C., Raj, R.B., Rangen, K.P. and Maria, A. (1998) Journal of Soldering and Surface Mount Technology, 10/2, pp. 26-35.

© (2011) Trans Tech Publications, Switzerland
doi:10.4028/www.scientific.net/KEM.471-472.263

Progressive Damage Analyses of Composite Laminates Exhibiting Free Edge Effects Using a New Micro-Meso Approach

Hossein Hosseini-Toudeshky[1, a], Amin Farrokhabadi[2,b] and Bijan Mohammadi[3,c]

[1, 2] Department of Aerospace Engineering, Amirkabir University of Technology, 424 Hafez Ave., Tehran, Iran

[3] School of Mechanical Engineering, Iran University of Sci. and Tec., Narmak, Tehran, Iran

[a] Hosseini@ aut.ac.ir, [b]amin-farrokh@ aut.ac.ir, [c] Bijan_Mohammadi@ iust.ac.ir

Keywords. micro-meso, edge-effects, angle-ply, progressive damage, composite.

Abstract. In this paper, the developed new micro-meso method by the authors is used for the edge-effects analyses of various angle-ply laminates such as $[10/-10]_{2s}$ and $[30/-30]_{2s}$. It is shown that the obtained stress-strain behaviors of laminates are in well agreement with the available experimental results. The stress variations through the laminate thickness and near the free edges are also computed and compared with the available CDM results.

Introduction

Due to the mismatching of elastic properties between layers with different orientations in the cross-section of laminated composites, these materials are considerably sensitive to edge effects. Edge effects lead to transverse cracking and induced delamination formation when the applied loading is even lower than the failure strength predicted by the classical lamination theory [1]. Experimental observations show that initiation and propagation of the edge delamination are due to the correlation between the transverse crack density and free-edge effects. Several approaches have been proposed for edge effects analysis including the finite difference, higher-order plate theory, boundary layer theory, and approximate elasticity solutions to finite elements method [2].

Recently, the authors of this paper developed a new method [3] to relate the physically based micromechanics approach with the meso-scale CDM considering the matrix cracking and induced delamination. In this method, a single lamina under general normal and shear stresses on all sides is considered which is prone for damage growth including matrix crack and delamination. The stress and displacements fields are extracted at a unit cell in the ply level with a specific crack density [4] and delamination length [5]. For this purpose, a generalized plane strain condition is considered for orthotropic composite lamina including matrix cracking and delamination. After crack formation in the single lamina, it assumed that the stress components of σ_{yy} and σ_{yx} have linear form in the x-direction (fiber direction) and independent of the z direction as [4];

$$\sigma_{yy} = \sigma_{yy}^{0}(1+\phi(y)), \qquad \sigma_{xy} = \sigma_{xy}^{0}(1+\psi(y)) \tag{1}$$

Where, $\phi(y)$ and $\psi(y)$ are perturbation stresses and should be determined. Using the equilibrium equations, other stress distribution will be defined. Combining these equations with three equations of constitutive laws and strain-displacement relations, the displacement fields are defined as function of perturbation stresses and their depravities. Having the stress and displacement equations for the damaged lamina, and combining with the remaining constitutive equations, the following homogeneous simultaneous differential equations are obtained:

$$F_i\phi'''(y) + G_i\phi''(y) + H_i\phi(y) = 0$$
$$S_i\psi''(y) + K_i\psi(y) = 0 \quad (2)$$

By solving these differential equations and imposing appropriate boundary conditions, the $\phi(y)$ and $\psi(y)$ functions will be defined [5]. Based on the obtained stress field, the energy release rates for further matrix cracking and its induced delamination are calculated. By increasing the crack density or delamination length and calculating the stress and strain fields of each unit cell in micro scale, the strain energy release rate of the recent unit cells are calculated to find the possibility of damage growth [5]. Using this new approach, the major disadvantage of meso modeling which is the requirement of specific tests for various lay-ups to obtain the non-associated flow rule parameters in damaged condition can be improved. In the present study, this approach is used for consideration of edge-effects in progressive damage analyses and final failure load calculation of various angle-ply laminates such as $[10/-10]_{2s}$ and $[30/-30]_{2s}$ under monotonic loading.

Nonlinear finite element code. The proposed micro-meso approach has been implemented in an available home CDM finite element code [6]. In this code, 8 nodes full layer-wise elements are used. For modeling of the nonlinear response due to damage initiation and growth, the developed micromechanics approach by the present authors is used. This procedure is employed in an extended subroutine for developing a proposed damage flow rule and numerical integration of constitutive relations. In this subroutine, having the boundary conditions and using the developed micromechanics approach, the stress and strain fields of the cracked unit cell and the strain energy release rate can be obtained. The obtained strain energy release rate is compared with finite fracture toughness of lamina, G_c, to recognize the evolution of transverse matrix crack density and/or delamination length at each element. Details of this nonlinear FE code were presented in [4]. Fig.1 depicts the procedure of the explained progressive damage analysis in this code.

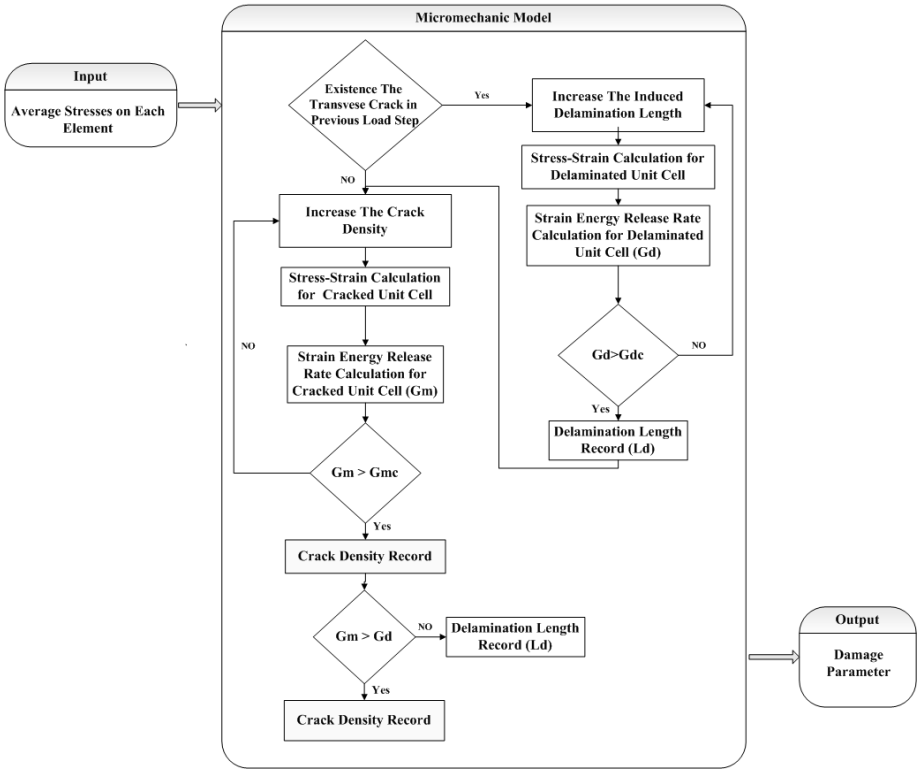


Fig. 1. Flow chart of the progressive damage analysis in developed nonlinear finite element code

Results and Discussions

In this section, two typical $[10/-10]_{2s}$ and $[30/-30]_{2s}$ angle ply laminate made of graphite/epoxy T300/5208 composite including free edge effects are analyzed. In these laminates, 3D state of stress is existed in the vicinity of the free edges. The geometry and boundary conditions for this angle-ply laminate is similar to Fig. 2. A non-uniform mesh along the lateral direction with a very fine distribution near the edges (19 elements) and discretization through the laminate thickness (20 divisions) are generated permitting the free edge effects to be resolved along the lateral edge and through the thickness respectively (Fig. 2). The elastic constants for the considered T300/5208 material are E_{11} = 137.11 GPa, $E_{22} = E_{33}$ = 9.58 GPa, $\nu_{12} = \nu_{13} = \nu_{23}$ =0.28, and $G_{12} = G_{13} = G_{23}$ =4.48 GPa [6]. The finite fracture toughness of lamina is also G_c=400J/m^2 [4]. The resulting stress–strain behaviors for $[10/-10]_{2s}$ and $[30/-30]_{2s}$ angle ply laminates are shown in Fig. 3. This figure shows a good agreement between the results of the present study and experiments [7] up to the final failure load. However the existed differences between the present study and CDM in [6] could be due to the ignorance of closure effects in [6].

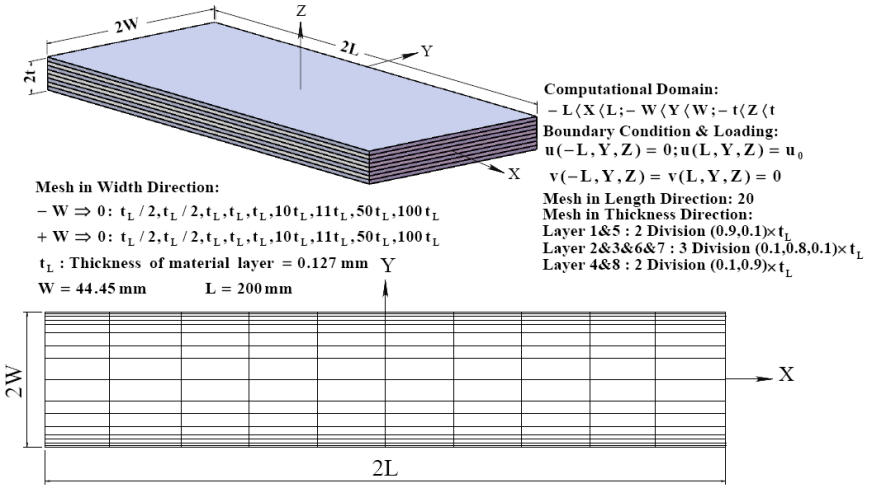


Fig. 2. Geometry, loading, boundary conditions, FEM mesh and discretization of a typical symmetric 8-layer laminate.

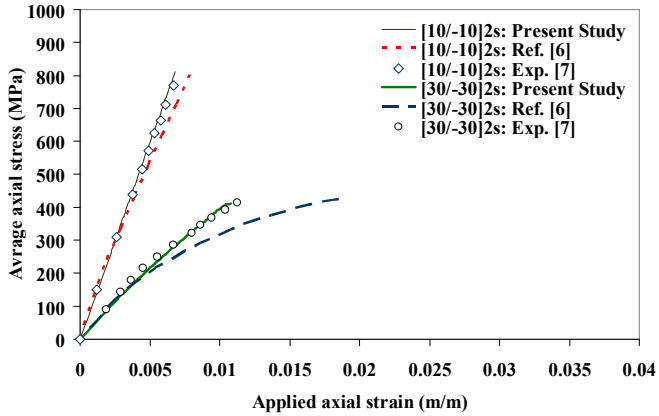


Fig. 3. Comparison of axial stress versus strain behaviors predicted by present study, Ref. [6] and experimental study [7] for $[10/-10]_{2s}$ and $[30/-30]_{2s}$ lay-ups

Fig. 4. also shows a good agreement between the obtained through the thickness stresses of σ_{XX} and τ_{XZ} from the present study with those obtained from [6] for both elastic-damage analysis and elastic analysis (undamaged) for the lay-up of $[10/-10]_{2s}$ near the free edges at the applied experimental failure stress (770 MPa). The minor differences between the obtained results of two

studies in elastic analysis could be due to the differences in selection of number of divisions through the thickness and number of elements. Fig. 5 shows a good agreement between the obtained through the thickness stresses of σ_{XX} and τ_{XZ} from the present study with those obtained from [6] for both elastic-damage analysis and elastic analysis (undamaged) for the lay-up of $[30/-30]_{2s}$ near the free edges at the applied experimental failure stress (410 MPa). In these analyses it was assumed that the induced delamination fracture toughness, G_{dc}, is equal to the transverse crack fracture toughness, G_{mc}. It is also worth to mention that the new micro-meso approach uses the finite fracture toughness, G_c, of lamina only to predict the progressive damage of laminate. This material property of lamina, G_c, can be obtained from standard tests. However, the CDM approach usually needs several damage surface and hardening material constants.

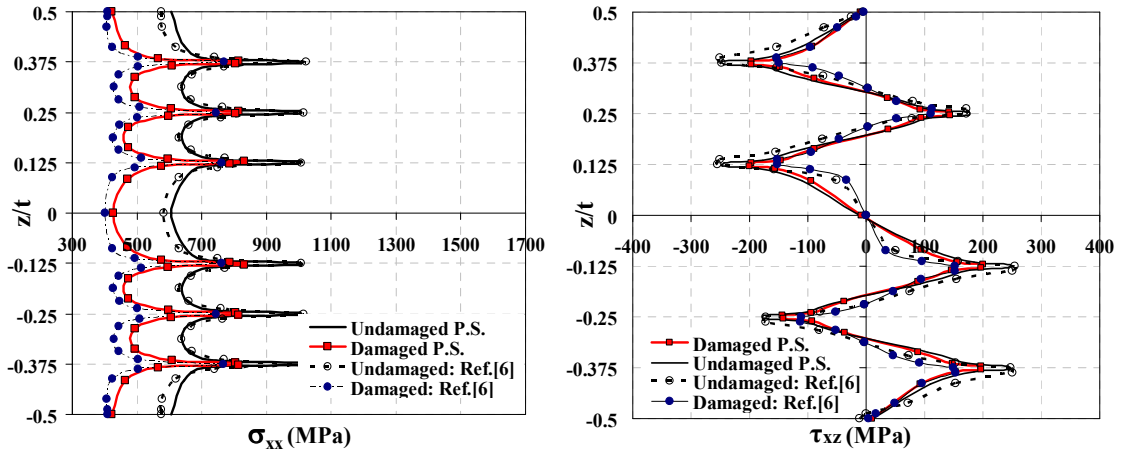


Fig. 4. Comparison of the stress variations through the laminate thickness near the free edges for $[10/-10]_{2s}$ lay-up obtained from the present study and [6]

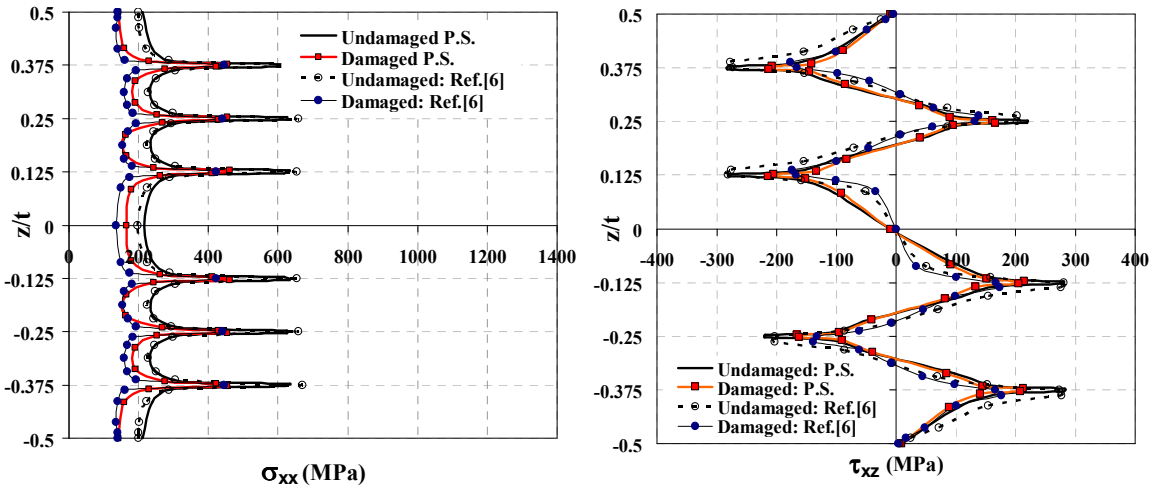


Fig. 5. Comparison of the stress variations through the laminate thickness near the free edges for $[30/-30]_{2s}$ lay-up obtained from the present study and [6]

Summary

In this paper, it was shown that the recently developed micro-meso approach by the authors for progressive damage analyses can be used for the edge-effects analyses of angle-ply laminates. The obtained stress-strain behaviors of laminate were in well agreement with the experimental results. The calculated stress variations through the laminate thickness near the free edges were also in good agreement with the available CDM results. The major advantage of the proposed micro-meso approach is using the well known finite fracture toughness of lamina only to obtain the damage flow rule.

References

[1] V.T. Nguyen and J.F. Caron, Comput. Struc., Vol. 84 (2006), p. 1538.

[2] T. Kant and K. Swaminathan, Compos. Struct., Vol. 49 (2000), p. 65.

[3] H. Hosseini-Toudeshky, A. Farrokhabadi and B. Mohhamadi, Proc. Eng., Vol. 1 (2009); p. 109.

[4] A. Farrokhabadi., H. Hosseini-Toudeshky and B.Mohamadi, Fat. Frac. Eng., Vol.33 (2010), p. 420.

[5] A. Farrokhabadi., H. Hosseini-Toudeshky and B.Mohhamadi, Com. Struct., Vol. 93 (2011), p. 443.

[6] B. Mohamadi, H. Hosseini-Toudeshki and M.H. Sadr, Fat. Frac. Eng., Vol.31 (2008), p. 549.

[7] C.T. Herakovich. *Mechanics of Fibrous Composites*. (John Wiley, New York 1998).

© (2011) Trans Tech Publications, Switzerland
doi:10.4028/www.scientific.net/KEM.471-472.268

Fabrication and Characterisation of $La_{0.6}Sr_{0.4}Co_{0.2}Fe_{0.8}O_{3-\delta}$-SDC Composite Cathode

Hamimah Abd.Rahman[1,2,3,a], Andanastuti Muchtar[1,2,b], Norhamidi Muhamad[1,2,c] and Huda Abdullah[2,d]

[1]Fuel Cell Institute, Universiti Kebangsaan Malaysia, 43600 UKM Bangi, Selangor, Malaysia

[2]Faculty of Engineering and Built Environment, Universiti Kebangsaan Malaysia, 43600 UKM Bangi, Selangor, Malaysia

[3]Faculty of Mechanical and Manufacturing Engineering, Universiti Tun Hussein Onn Malaysia, 86400 Parit Raja, Batu Pahat, Johor, Malaysia

[a]hamimah@uthm.edu.my, [b]muchtar@eng.ukm.my, [c]hamidi@eng.ukm.my, [d]huda@eng.ukm.my

Keywords: composite cathode, LSCF6428, SDC, SDC carbonate

Abstract. Composite cathode is a promising material to be used as electrodes in fuel cells. The fabricated composite cathode materials in this study are comprised of a mixture of submicron $La_{0.6}Sr_{0.4}Co_{0.2}Fe_{0.8}O_{3-\delta}$ (LSCF6428) powders with two types of nanoscale ionically conducting ceramic electrolyte materials, samarium-doped ceria (SDC) and SDC-carbonate (SDCc). 30 – 50 wt% of electrolyte materials are added to the LSCF6428 cathode via the solid state method. The composite powders were ball-milled in ethanol and calcined at the temperature range of 800°C to 900°C for 2 hours in air. The composite cathode powders are characterised in terms of morphology and crystal structure. It is found that after calcining, the LSCF and the electrolyte materials retained their original structures as there was no chemical reaction between the two components. In addition, the LSCF-SDC composite cathode powders were found to exhibit a narrower distribution in size compared to the LSCF-SDC carbonate powders.

Introduction

Recently, most research in solid oxide fuel cells (SOFCs) are devoted to the development of intermediate to low temperature (500-700°C) SOFCs. Lowering the operating temperature of SOFCs is necessary to reduce the degradation of the electrodes and electrolytes and to improve the material compatibility. However, the reduction of the operating temperature of the SOFCs also increases the electrolyte resistance and inefficiency of the electrode materials. Two current practices that have been found to be potentially able to solve the above problems are (1) reducing the thickness of the electrolyte which will reduce the electrolyte resistance and (2) designing a high performance electrode with a low polarisation resistance such as using a composite cathode. The latter practice appears as a promising way to attain better performance of SOFCs at lower operation temperatures [1,2,3].

The replacement of conventional cathode materials, lanthanum strontium manganite (LSM) with mixed ionic-electronic conducting ceramic electrode materials such as lanthanum strontium cobalt ferrite (LSCF) was the first approach that has been done to obtain a higher performance of cathodes. The second approach involves the addition of electrolyte with the cathode materials which are then called composite cathodes. Composite technology allows the creation of electrodes with higher effective surface area to increase the efficiency of the exchange reactions, and, consequently, to decrease the electrode over potentials [4].

Recently, lanthanum strontium cobalt ferrite (LSCF) has been considered to be one of the most highly potential cathode materials for intermediate to low temperature SOFCs. Since perovskite LSCF is a mixed oxygen ionic and electronic conducting material, it offers excellent over potential

and electrical conductivity at lower temperatures [5,6,7]. The combination of LSCF with ionic conducting materials especially with ceria-based electrolytes result in extending the electrochemical activation area due to the higher ionic conductivity of these electrolytes compared to perovskite. The performance of the LSCF composite cathode is significantly dependent on the sintering temperature, microstructure and composition [8,9,10,11]. Therefore, the influences of those parameters need to be closely monitored for the new developed composite cathode materials.

In the present study, the LSCF-based composite cathodes were made from commercial LSCF6428 and SDC electrolyte powders. Meanwhile, the in-house developed SDC-carbonate powders were employed to produce LSCF-SDCc composite powders. The relationship between calcining temperature, composition and properties of the composite cathode were investigated.

Methodology

The preparation of the SDC carbonate (SDCc) powder was conducted via solid state method. The 80wt% of SDC nanopowder (Sigma Aldrich Sdn. Bhd. Selangor, Malaysia) was mixed with 20wt% carbonates (67 mol% Li_2CO_3: 33 mol% Na_2CO_3) [12]. The mixture was heat treated at 680°C for 1 hour.

The LSCF-SDC composite cathode powders were prepared from a mixture of commercial lanthanum strontium cobalt ferrite (LSCF6428, $La_{0.6}Sr_{0.4}Co_{0.2}Fe_{0.8}O_{3-\delta}$) powder of particle size 0.3-0.6 μm and nanopowder samarium-doped cerium oxide (SDC, $Sm_{0.15}Ce_{0.85}O_{1.95}$) from Sigma Aldrich Sdn.Bhd.. Meanwhile, the LSCF-SDC carbonate (LSCF-SDCc) composite employed the combination of the in-house developed SDCc (20 wt% Na/Li carbonate in SDC) powder with the commercial LSCF6428 powder. Both the LSCF composite powders were ball-milled in ethanol for 2 hours followed by overnight drying in an oven at 60°C. The dried composite cathode powders were ground in an agate mortar and then calcined at a temperature range of 800-900°C for 2 hours in air. The LSCF-SDC and LSCF-SDCc composite powders had compositions varying from 50 to 70 wt% LSCF6428, and henceforth named as LSCF-SDC55 (or LSCF-SDCc55) to LSCF-SDC73 (or LSCF-SDCc73) respectively. Table 1 shows the composition of the composite cathode powders and the calcination temperature investigated.

Table 1. Composition of the composite cathode powders and calcination temperatures

Composite powder	LSCF6428 (wt%)	SDC (wt%)	SDCc (wt%)	Calcination temperature (°C)
LSCF-SDC55	50	50	-	Each of the composite powders were calcined at 800, 850 and 900°C
LSCF-SDC64	60	40	-	
LSCF-SDC73	70	30	-	
LSCF-SDCc55	50	-	50	
LSCF-SDCc64	60	-	40	
LSCF-SDCc73	70	-	30	

The powder preparation process was followed by its characterisation. The confirmation of phase and structure of the prepared composite powders were made using X-ray diffraction (XRD) (Bruker D8 Advanced diffractometer) at Cu Kα radiation, λ = 0.15406nm. The selected 2θ range was from 20° to 80° scanning at a step of 0.02°. The particle size of the composite powders was determined by using a laser particle analyser (Zetasizer Nanoseries ZS, Malvern). Surface area analysis was conducted on the composite powders using BET surface area analyzer (Altamira Instruments AMI-200). Additionally, a Zeiss Supra 55VP Field Emission Scanning Electron Microscope (FESEM) was employed to analyse the morphology of the calcined composite powders.

Results and Discussion

Fig. 1 shows the X-ray spectra of the pure LSCF6428 and the electrolyte SDC. The commercial powder LSCF6428 and SDC has the phase of rhombohedral pervoskite and cubic respectively [13,14]. The XRD patterns of the composite cathodes LSFC-SDC55 calcined at different temperature are also illustrated in the same figure. The resultant LSCF-SDC55 composite powders were able to maintain their own structures after calcination and no major second phases were observed. Furthermore, the XRD outcomes of the LSCF-SDCc (LSCF-SDCcarbonate) composite powders which can be referred to in Fig. 2 show good agreement with the analysis of the results for the LSCF-SDC composite powders. The molten carbonate in SDCc electrolyte powder exist as an amorphous phase and does not influence the phase of the pure SDC [12,15]. This demonstrated that there was no chemical reaction between the two components as no major second phases was observed [14].

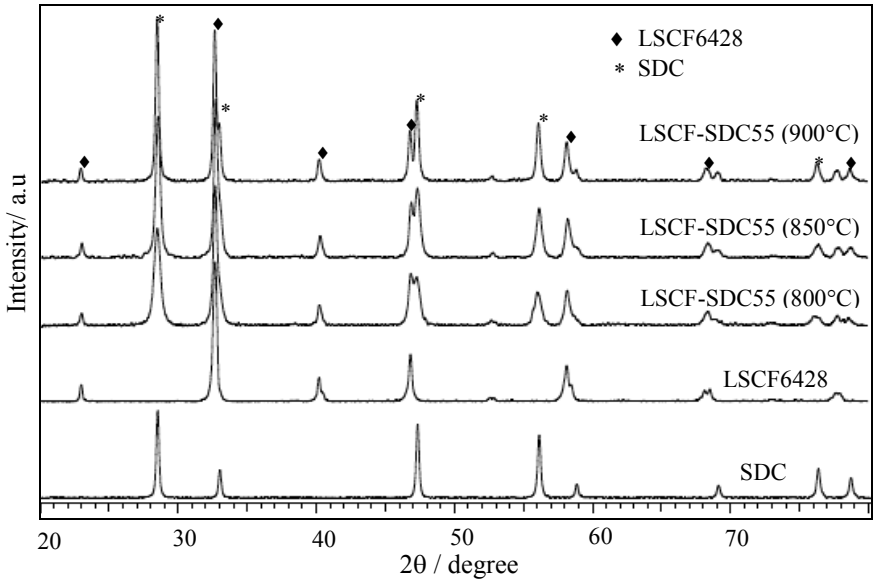


Fig 1. XRD patterns of the SDC, LSCF6428 powders and the calcined (800, 850 and 900°C) LSCF-SDC55 composite cathodes

The other LSCF-SDC and LSCF-SDCc composite powders with different compositions and calcination temperatures also depicted similar outlines as the LSCF-SDC55 composite powders. This can be seen in Fig. 3 which illustrates the X-ray pattern of various LSCF composite powders calcined at 900°C. It may be concluded therefore, that it is possible to get high performance cathode since each component in the composite cathode was able to maintain its own function such as enhancing the cathode reactions and reducing the polarisation between the electrode and the electrolyte.

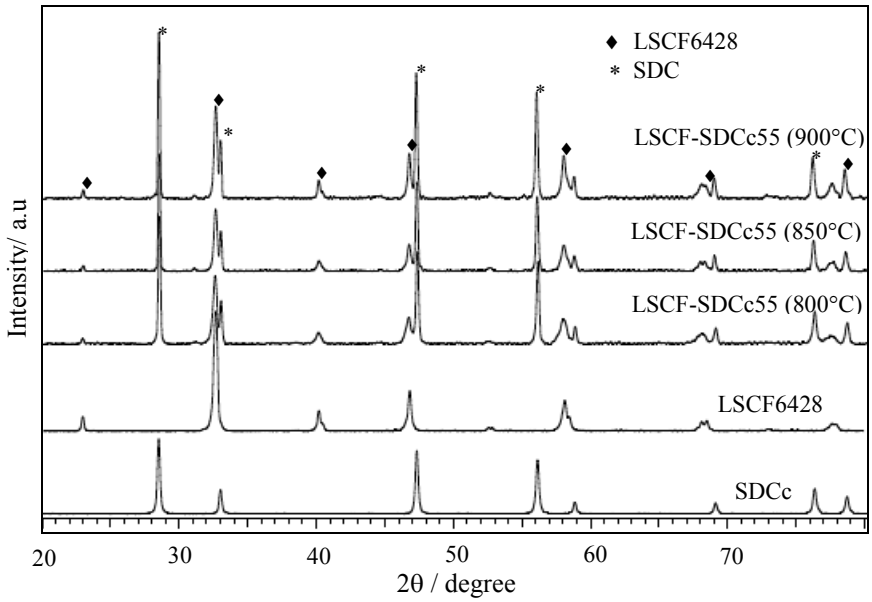


Fig 2. XRD patterns of the SDCc, LSCF6428 powders and the calcined (800, 850 and 900°C) LSCF-SDCc55 composite cathodes

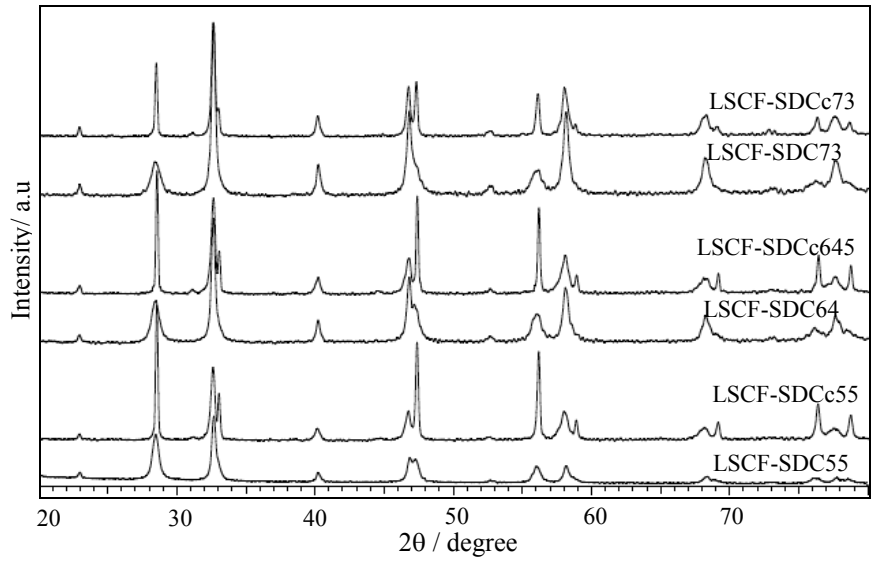


Fig 3. XRD patterns of the LSCF composite cathode powders calcined at 800°C

The particle size of the composite cathode powders was determined using laser Doppler velocimetry and phase analysis light scattering. The increment of particle size of the both types of the composite powders was observed upon the increment of the calcination temperature. This phenomena is due to the growth of the particles, as similarly reported by Seabaugh & Swartz [4]. The LSCF-SDC composite powders that were calcined between 800-900°C exhibited particles in the size range of 0.4-0.5 μm with surface area between 6-13 m^2/g. The surface area of the particles offers a guide in choosing the appropriate method for fabrication of the cathode. In the present work, the obtained surface areas of the prepared composite cathodes are suitable for screen printing process. In addition, the calcination temperatures, the starting sizes and surface areas of the composite cathode particles have been identified to give an influence to the electrode performance [4]. A wider distribution in particle size was obtained for the LSCF-SDCc composite powders at 0.4-1.0 μm with bigger surface area (3-1 m^2/g). With reference to Jarot et al. [12] and Bodén et al. [16], the increment in the particle size of the LSCF-SDCc composite powders compared to the LSCF-SDC composite was mostly due to the coating of the $(Li/Na)_2CO_3$ amorphous phase over the electrolyte and electrode particles.

Fig. 4(a)-(d) show the microstructure of the composite cathode powders calcined at 850°C for 2 hrs. In agreement with the particle size analysis and as can be seen in the SEM micrographs, the LSCF-SDCc composite cathode powders were found to have larger particle sizes compared to the LSCF-SDC powders. The morphology of the composite cathode powders supported the argument that molten carbonate from the SDCc electrolyte surrounded the LSCF-SDCc composite cathode particles and contributed to the increase in particle size.

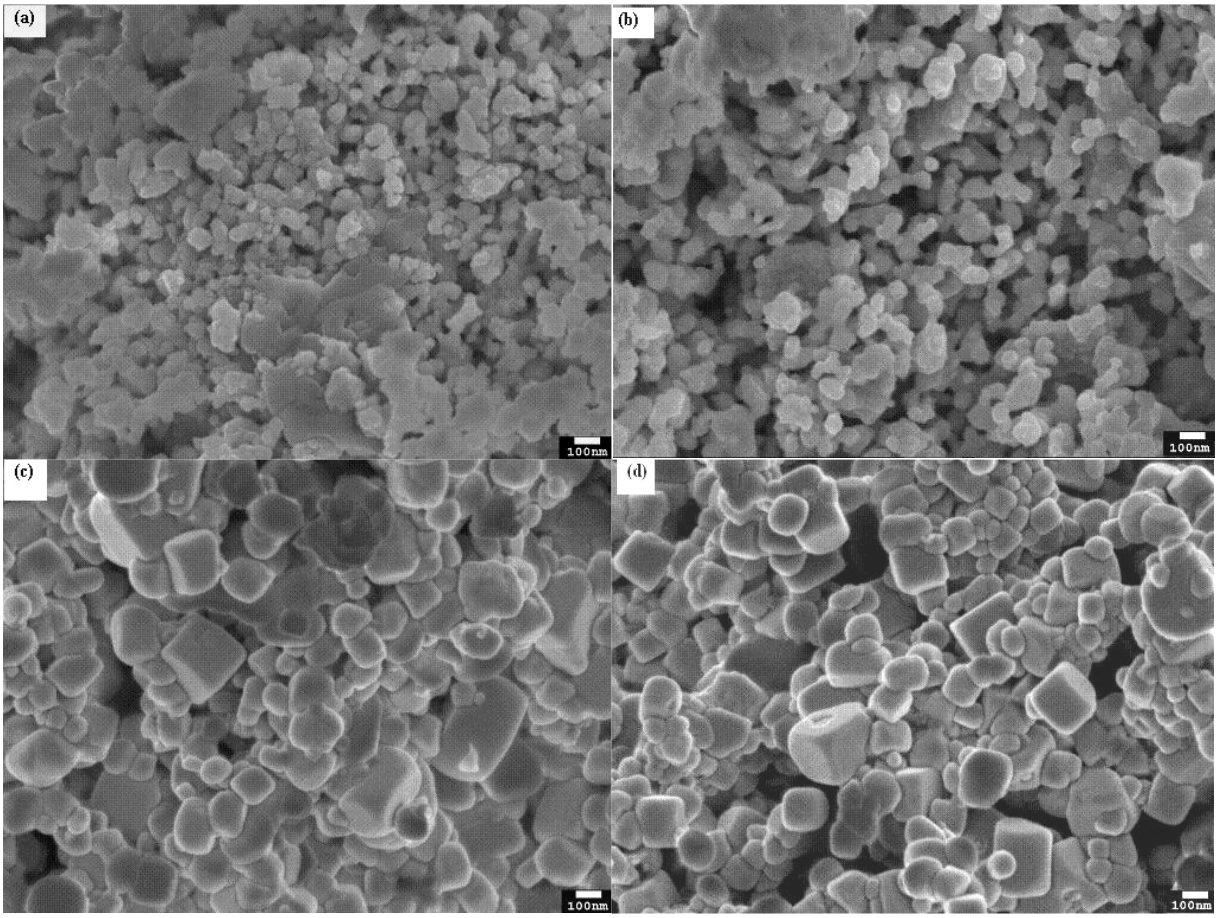


Fig 4. The SEM micrographs of the LSCF-SDC composite powders (a) LSCF-SDC64, (b) LSCF-SDC73 and LSCF-SDC carbonate composite powders (c) LSCF-SDCc64, (d) LSCF-SDCc73 calcined at 850°C

Summary

The mixing of electrode powder with a nanoscale electrolyte has been accomplished by a simple milling technique for the preparation of the LSCF6428 composite cathode powders. The obtained composite powders were calcined at different temperature and characterised in order to study their properties as cathode material for the SOFCs. The addition of 30-50 wt% of electrolyte powders into the LSCF6428 followed by calcining at temperature between 800-900°C showed good compatibility as no secondary phases or chemical reaction were produced. The findings in this work can be a preliminary indication for these composite powders to be used as cathode component of SOFCs. Further investigation is expected to explore on other characteristics such as thermal properties, electrochemical properties and electrical conductivity of these composite cathodes.

Acknowledgements

The authors gratefully acknowledge Universiti Kebangsaan Malaysia (UKM) and the Malaysian Government for research sponsorship under UKM-AP-TK-05-2009.

References

[1] J.W. Fergus: Hydrogen Economy (2007), p. 56.

[2] Y. Leng, S.H. Chan and Q. Liu: International Journal of Hydrogen Energy Vol. 33 (2008), p. 3808.

[3] S.C.C. Steven: Catalysis Vol. 18 (2005), p. 186.

[4] M.M. Seabaugh and S.L. Swartz, U.S. Patent 7,595,127 B2. (2009).

[5] D. Beckel, A. Dubach, A.R. Studart and L.J. Gauckler: Journal of Electroceramics Vol. 16 (2006), p. 221.

[6] C. Fu, K. Sun, N. Zhang, X. Chen and D. Zhou: Electrochimica Acta Vol. 52 (2007), p. 4589.

[7] NoorAshrina A. Hamid, Andanastuti Muchtar, Wan Ramli Wan Daud and Norhamidi Muhamad: Sains Malaysiana Vol. 38 (2009).

[8] Andanastuti Muchtar, Noorashrina A. Hamid, Norhamidi Muhamad and W.R.W. Daud: Advanced Materials Research Vol. 139-141 (2010), p. 141.

[9] Hamimah Abd.Rahman, Andanastuti Muchtar, Norhamidi Muhamad and Huda Abdullah: Advanced Materials Research Vol. 139-141 (2010), p. 145.

[10] S. Lee, H.S. Song, S.H. Hyun, J. Kim and J. Moon: Journal of Power Sources Vol. 195 (2010), p. 118.

[11] E.P. Murray, M.J. Sever and S.A. Barnett: Solid State Ionics Vol. 148 (2002), p. 27.

[12] Jarot Roharjo, Andanastuti Muchtar, Wan Ramli Wan Daud, Norhamidi Muhamad and E.H. Majlan: Key Engineering Materials Vol. 447-448 (2010), p. 666.

[13] L.-W. Tai, M.M. Nasrallah, H.U. Anderson, D.M. Sparlin and S.R. Sehlin: Solid State Ionics Vol. 76 (1995), p. 273.

[14] J. Zhang, Y. Ji, H. Gao, T. He and J. Liu: Journal of Alloy and Compounds Vol. 395 (2005), p. 322.

[15] B. Zhu: Journal of Power Sources Vol. 114 (2003), p. 1.

[16] A. Bod´en, J. Di, C. Lagergren, G.o. Lindbergh and C.Y. Wang: Journal of Power Sources Vol. 172 (2007), p. 520.

© (2011) Trans Tech Publications, Switzerland
doi:10.4028/www.scientific.net/KEM.471-472.274

$LiCF_3SO_3$ – CeO_2 composite electrolytes prepared by sol-gel technique: structural and conductivity studies

N.A. Dzulkurnain [1,a] and N.S. Mohamed [2,b]

[1] Institute of Graduate Studies, University Malaya, 50603, Kuala Lumpur, Malaysia

[2] Centre of Foundation Studies, University Malaya, 50603, Kuala Lumpur, Malaysia

[a]akmaliah@siswa.um.edu.my, [b]nsabirin@um.edu.my

Keywords: sol-gel, sintered, conductivity, space charge layer, defect.

Abstract. (100-*x*) $LiCF_3SO_3$ + (*x*) CeO_2 composite electrolytes were prepared using sol-gel technique followed by sintering at 300 °C for four hours. Structural property and conductivity of the prepared composite electrolytes were studied using X-ray Diffraction (XRD), Scanning Electron Microscopy (SEM), Energy Dispersive X-Ray (EDX) analysis and Impedance Spectroscopy. The XRD spectra show only crystalline peaks of CeO_2 indicating that $LiCF_3SO_3$ exists in the form of amorphous phase. This is confirmed by SEM and EDX analyses. The highest ionic conductivity at room temperature is found to be in the order of 10^{-3} S cm^{-1} for the composite of 70 mol % $LiCF_3SO_3$ - 30 mol % CeO_2. The conductivity of the composite electrolytes is observed to increase gradually with temperature.

Introduction

Composite solid electrolytes are ion-conducting materials which are suitable for practical applications as their electrical and mechanical properties can be easily controlled by variation of concentration of their host and dispersoid [1]. Composite electrolytes also exhibit high ionic conductivity and good mechanical properties and are promising materials for applications in many electrochemical devices such as solid-state batteries, fuel cells, supercapacitors, electrochromic displays, etc. [2]. Most composite electrolytes reported in the literature [3,4,5] were prepared by solid state reaction technique and they showed high ionic conductivity at high temperatures. For this study, sol-gel technique was used. This technique was chosen since it offers many advantages over conventional composite preparation methods [6]. Generally, in this technique, samples are synthesized at low temperatures, which is not only simplifies the procedure but allows thermally labile compounds to be entrapped in the sol-gel matrix. Furthermore, the final products are pure and homogeneous, and can be shaped into various forms [7]. In an earlier study, the authors have prepared $LiCF_3SO_3$ – CeO_2 composite electrolyte system using this method. The highest conductivity at room temperature achieved was 3.21×10^{-4} S cm^{-1} [8]. In this study, the same composite system was prepared using the same technique but sintered for a longer time. Structural property and conductivity of the composite are presented in this paper.

Experimental

Sample preparation. For sample preparation, lithium triflate ($LiCF_3SO_3$) (Sigma Aldrich) was dissolved in 40 ml of ethanol. After complete dissolution, cerium oxide (CeO_2) (Sigma Aldrich) was added into the solution. Samples were prepared using equation

$$(100\text{-}x)\ \mathrm{L} + (x)\ \mathrm{MO} \tag{1}$$

where L is $LiCF_3SO_3$, MO is CeO_2 and $0 \leq x \leq 90$ mol percentage. After stirring for 10 minutes, citric acid was added to the solution and then refluxed at 80 °C. The gel formed after around 30 minutes of stirring was heated until it became powder. The powder was then sintered at 120 °C for 24 hours.

Sample characterization. Structural properties of the composite samples were studied using D8 Advance X-ray Diffractometer-Bruker. Impedance and cross-section surface morphology analyses of the composite electrolyte pallets were done using Solartron 1260 impedance analyzer and FEI Quanta 200 respectively.

Result and Discussion

Structural property. Fig. 1 shows the XRD spectra of selected samples of solid composite electrolytes. There is no peak due to $LiCF_3SO_3$ related compounds appear even in the XRD spectra of the samples with high content of $LiCF_3SO_3$. This implies that $LiCF_3SO_3$ exists in an amorphous phase. These XRD spectra only show CeO_2 peaks. The intensities of CeO_2 peaks are observed to vary with CeO_2 content.

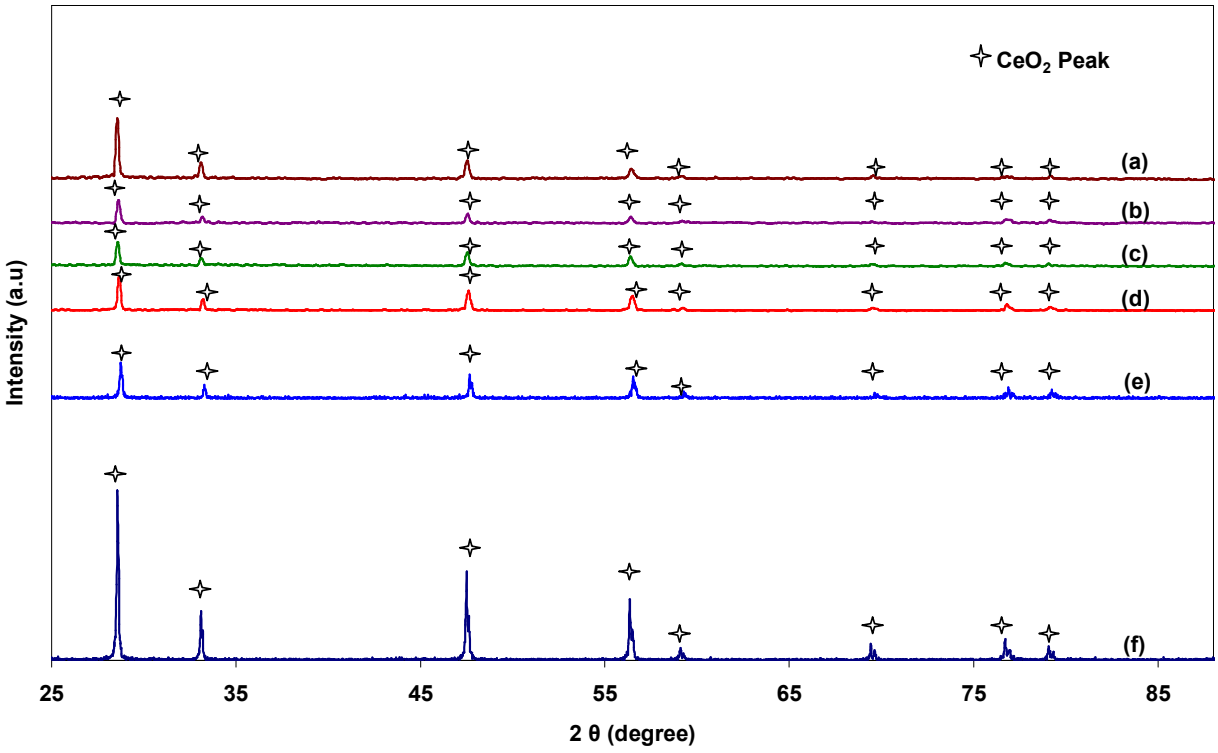


Fig. 1: XRD spectra of (100-x) $LiCF_3SO_3$ + (x) CeO_2 composite electrolytes containing (a) 10, (b) 20, (c) 30, (d) 40, (e) 60 and (f) 90 mol % of CeO_2.

Fig. 2 illustrates SEM micrograph and EDX spectrum of the composite sample with x = 30 mol % CeO_2. The EDX analysis indicates that the darker region in the SEM micrograph is a triflate rich region and thus confirming that $LiCF_3SO_3$ exists in amorphous phase. Fig. 2 also shows the presence of CeO_2 particles which are quite well distributed in the amorphous region of the sample.

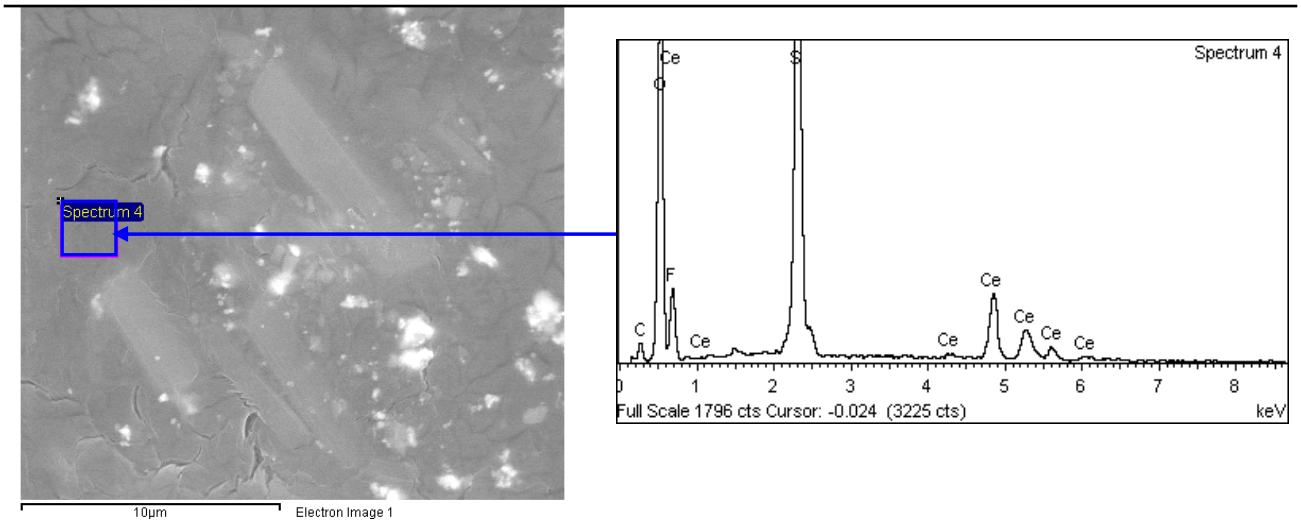


Fig. 2: SEM micrograph and EDX spectra of 60 mol % $LiCF_3SO_3$ + 40 mol % CeO_2 composite electrolyte.

Conductivity behaviour. Fig. 3 illustrates the variation of ionic conductivity with CeO_2 content. The conductivity can be divided into two regions. In region 1, the conductivity increases with increase in CeO_2 content up to a maximum conductivity at 30 mol % CeO_2. With further increase in CeO_2 content, conductivity decreases but increases again to reach another maximum value at CeO_2 content of 60 mol % before decreasing at higher content of CeO_2 (Region 2).

The variation of conductivity with CeO_2 content observed in Fig. 3 may be explained as follows: When CeO_2 wass added to the lithium triflate, surface charge layer formed at the host – dispersoid interface provided conducting pathways for free ions [9,10,11]. The increase in CeO_2 content led to a formation of greater number of conducting pathways giving rise to a conductivity enhamcement. However, when the CeO_2 content was further increased to 40 mol %, the conductivity decreases slightly because of the blocking some of the existing conducting pathways due to agglomerations of CeO_2 dispersoid that reduced the host – dispersoid interface [12]. Further increase in concentration of cerium oxide caused the highly conducting pathways to be interconnected as the dispersoid particles got close enough to each other [13]. Beyond the second conductivity threshold, the conducting pathways became disrupted due to larger agglomerations of excess CeO_2 which blocked the conducting pathways leading to a conductivity decrease. The highest room temperature conductivity achieved in this study is 5.48×10^{-3} S cm^{-1}. This value is an order of magnitude higher compared to the system sintered for shorter time (2 hours) reported earlier [8]. This higher conductivity may be due to enhanced interface interactions between the host and the dispersoid that leads to a formation of greater number of free ions and defects (vacancies).

The Arrhenius plots of (100-x) $LiCF_3SO_3$ + (x) CeO_2 composite electrolytes are depicted in Fig. 4. The conductivity is observed to increase with temperature due an increase in number of free lithium ions at the surface charge layer and number of defects [14,15]. Fig. 4 also reveals that the composite electrolytes show a gradual increase in conductivity with temperature which is a favorable characteristic for an electrolyte.

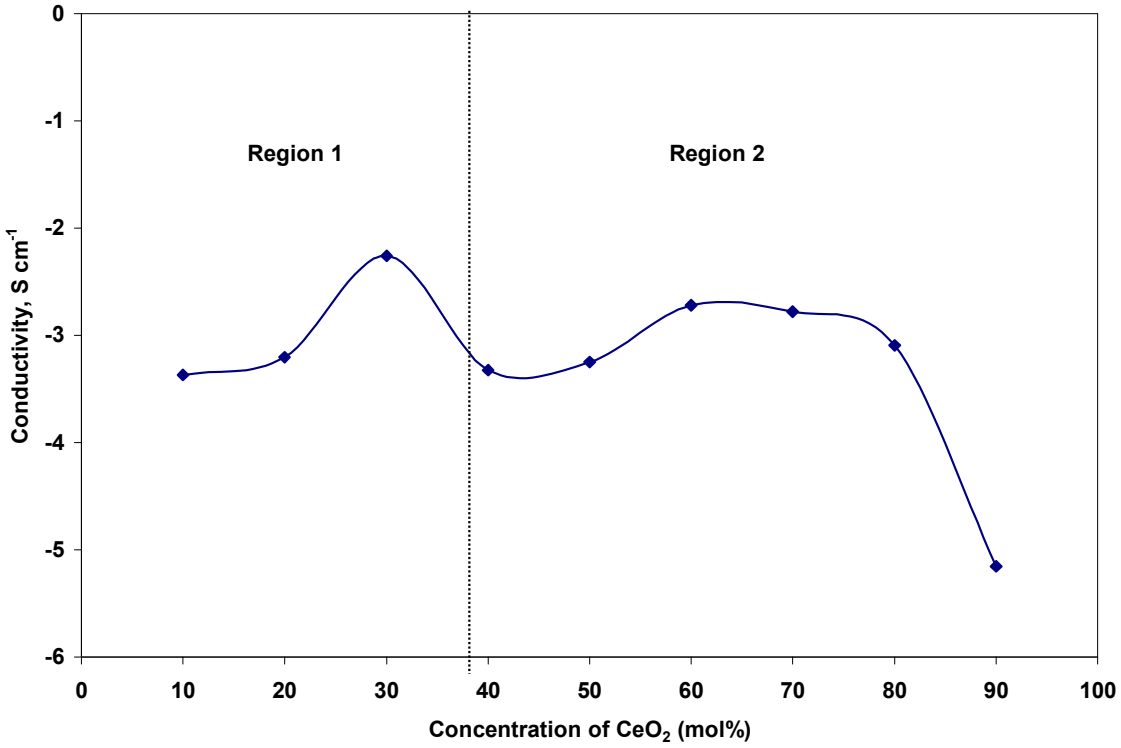


Fig. 3: Conductivity versus CeO_2 content.

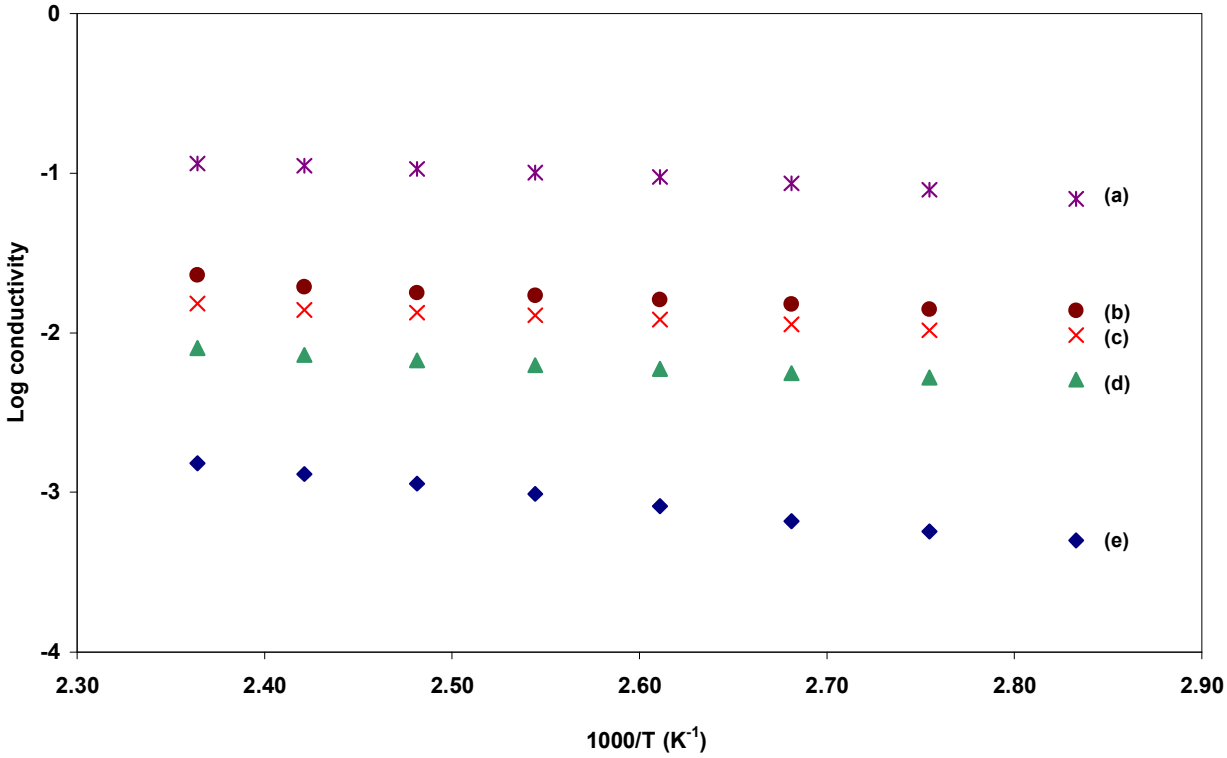


Fig. 4: Arrhenius plots of $LiCF_3SO_3$ - CeO_2 composite electrolyte with (a) 30, (b) 10, (c) 40, (d) 60 and (e) 80 mol % of CeO_2.

Summary

In this study, $LiCF_3SO_3$ - CeO_2 composite electrolyte system have been successfully obtained via sol-gel method. Its conductivity varies with the composition of CeO_2. The composite of 70 mol % $LiCF_3SO_3$ + 30 mol % CeO_2 exhibits the highest conductivity in the order of magnitude 10^{-3} S cm^{-1}. The composite system obtained in this study also shows favorable characteristic of temperature dependence of conductivity.

References

[1] M.V.M. Rao, S.N. Reddy and A.S. Chary: Physica B Vol. 362 (2005), p. 193,

[2] C.J. Leo, G.V. Subba Rao and B V.R. Chowdari: Solid State Ionics Vol. 148 (2002), p. 159,

[3] A.S. Ulihin, N.F. Uvarov, Y.G. Mateyshina, L.I. Brezhneva, A.A. Matvienko: Solid State Ionics Vol. 177 (2006), p. 2787,

[4] G.V. Lavrova, V.G. Ponomareva, N.F. Uvarov: Solid State Ionics Vol. 136-137 (2000), p. 1285,

[5] N.F. Uvarov, E.F. Hairetdinov, I.V. Skobelev: Solid State Ionics Vol. 86-88 (1996), p. 577,

[6] R.C. Agrawal and R.K. Gupta, J. Materials Science 34 (1999), p. 1131,

[7] K.S. Alber, J.A. Cox and P.J. Kulesza: Electroanalysis Vol. 9 (1997), p. 97.

[8] N.A. Dzulkurnain and N.S. Mohamed: Advanced Materials Research Vol. 129-131 (2010), p. 506.

[9] A.R. West, Solid State Chemistry and Its Applications, John Wiley and Sons, New York, 1984.

[10] N.F. Uvarov, P. Vaněk, M. Savinov, V. Železný, V. Studnička, J. Petzelt: Solid State Ionics 127 (2000), p. 253.

[11] W. Dieterich, O. Durr, P. Pendzig, A. Bunde and A. Nitzan: Physics A Vol. 266 (1999), p. 229.

[12] M.M.E. Jacob, S. Rajendran, R. Gangadharan, M.S. Michael and S.R.S. Prabaharan: Solid State Ionics Vol. 86-88 (1996), p. 595.

[13] A. Bunde: Solid State Ionics Vol. 75 (1995), p.147.

[14] F. Groce, L. Persi, B. Scrosati, F. Serraino-Fiory, E. Plishta and M.A. Hendrickson: Electrochim. Acta Vol.46 (2001), p. 2457.

[15] A. Mei, X.L. Wang, Y.C. Feng, S.J. Zhao, G.J. Li, H.X. Geng, Y.H. Lin and C.W. Nan: Solid State Ionics Vol. 179 (2008), p. 2255.

© (2011) Trans Tech Publications, Switzerland
doi:10.4028/www.scientific.net/KEM.471-472.279

Shape Factors for Irregular Glass Reinforced Plastic Pipes – An Analytical and Numerical Approach

IKRAM K. Ismail[1] and ABDENNOUR C. Seibi[2]

[1]Ecole Polytechnique de Tunis, Computational Mechanics Department,
P.O.BOX 743, LA Marsa, TUNISIA
[2]Petroleum Institute, Mechanical Engineering Department,
P.O. Box 2533, Abu Dhabi, UAE
aseibi@pi.ac.ae

Keywords: Glass Reinforced Plastics, irregular composite pipes, shape factor, finite element modeling, analytical solution.

Abstract. This paper presents the development of a mathematical model based on curved beam theory of composite pipes with irregular shapes under diametral loading. The analytical solution was validated through finite element models of the same pipe shapes under similar loading conditions. Four shapes (circular, elliptical, rectangular, and egg shaped pipes) were considered in this study. The analytical and finite element results were used to estimate the shape factor defined by the ratio of the maximum tangential stress of an irregular shape over the maximum tangential stress for a circular pipe. Comparison of the load-deflection curves for the four different shapes revealed that the egg pipe is the stiffest among the rest of the pipes while the square shape is the most flexible one. The analytical solution and finite element results were used to determine the shape factor for the four pipe shapes taking into account the circular pipe as the base shape. Both results were in good agreement and can be used as design guidelines for the irregular shapes without resorting to the conduct of any further testing.

Introduction

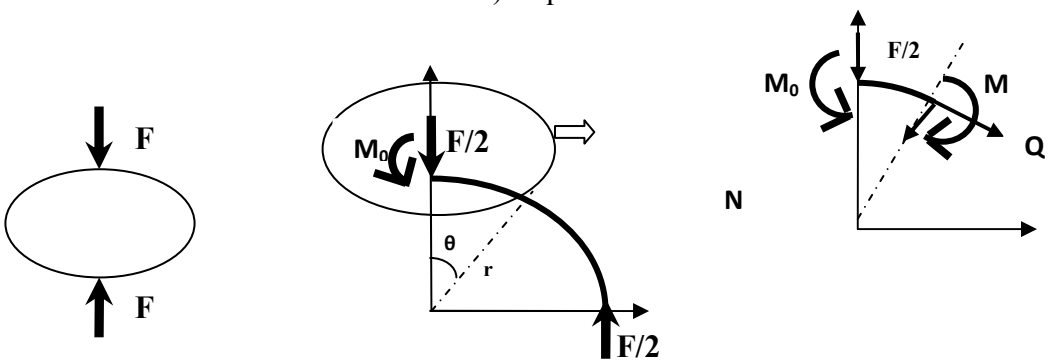
Glass reinforced plastic (GRP) materials have been receiving a widespread use in recent years and represent a practical alternative to metals especially in corrosive environments. The use of GRP materials ranges from simple civil structures such as decks, tanks, pipes, to more advanced applications. Recently, GRP pipes with irregular shapes have been used to rehabilitate aging sewerage and draining systems requiring special design criteria and tools for fabrication. Manufacturers of GRP pipes receive occasional requests from their clients to fabricate pipes with irregular shapes. To ensure their customers about the structural stability of the irregular pipe shapes, manufacturers tend to conduct an extensive experimental study to prove the viability of the specified shape for the intended application. This exercise is time consuming and costly. This necessitates the need for the development of a technique or a methodology that can accurately predict the structural behavior of any specific pipe shape using experimental data for circular pipes which can be easily obtained from the available literature or experimentally [1 – 4]. Characterization of the mechanical properties of cylindrically orthotropic thin composite sheets has been developed by Sinha et al. [5]. An analytical approach of an elementary elliptical ring under plane stress has been developed by Yves Gourinat et al. [6], Romano et al. [7], and recently by Kalfat Ismail et al. [8]. The present paper, therefore, presents a methodology of obtaining the shape factor for various shapes taking into account circular pipes as the basis of the study.

Theoretical Background

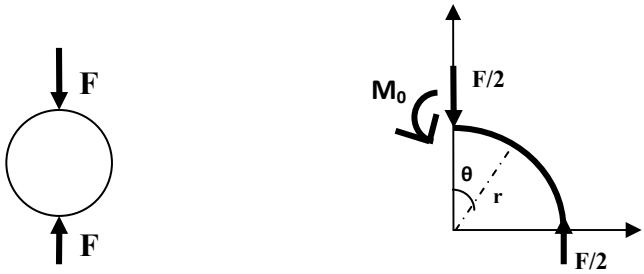
The present section discusses the development of a mathematical model for four different Glass Reinforced Epoxy pipe shapes under diametral compressive loads. Fig. 1 shows the four shapes under study with appropriate geometric configurations. Because of symmetry and depending on the pipe geometry, either one quarter or half of the pipe is considered (see Fig.1) from which the load deflection curves as well as the variation of tangential stress along the inner and outer layers of the pipe were obtained.



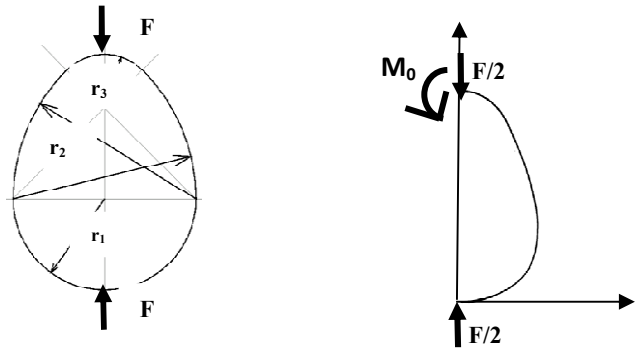
a) square



b) ellipse



c) circular



d) egg

Fig. Pipe Shapes Under Study

Mathematical Model. The tangential strain and stress at an infinitesimal element of any pipe shape are defined by [9]:

$$\varepsilon(\theta) = \varepsilon^{0}(\theta) + (r - r_0)\kappa(\theta)$$
$$\sigma(\theta) = E * \varepsilon^{0}(\theta) + E * (r - r_0)\kappa(\theta) \quad (1)$$
$$where \quad E = t * \sum_{i=1}^{n} Q_k * t_k$$

The curvature of the pipe, κ, is defined by $\frac{M(\theta)}{EI}$ and $\varepsilon^{0}_{\theta\theta} = \frac{N}{ES}$ is the tangential strain of the neutral axis located at $r = r_0$. The terms *S, M(θ),* and *N,* denote respectively the section modulus, bending moment, and normal force which is defined by

$$N = \begin{cases} 0 & for\ horizontal\ section\ of\ square\ shape \\ -\frac{F}{2}\frac{r_0}{r}\sin\theta & for\ any\ curved\ section \\ -\frac{F}{2} & for\ vertical\ section\ of\ square\ shape \end{cases} \quad (2)$$

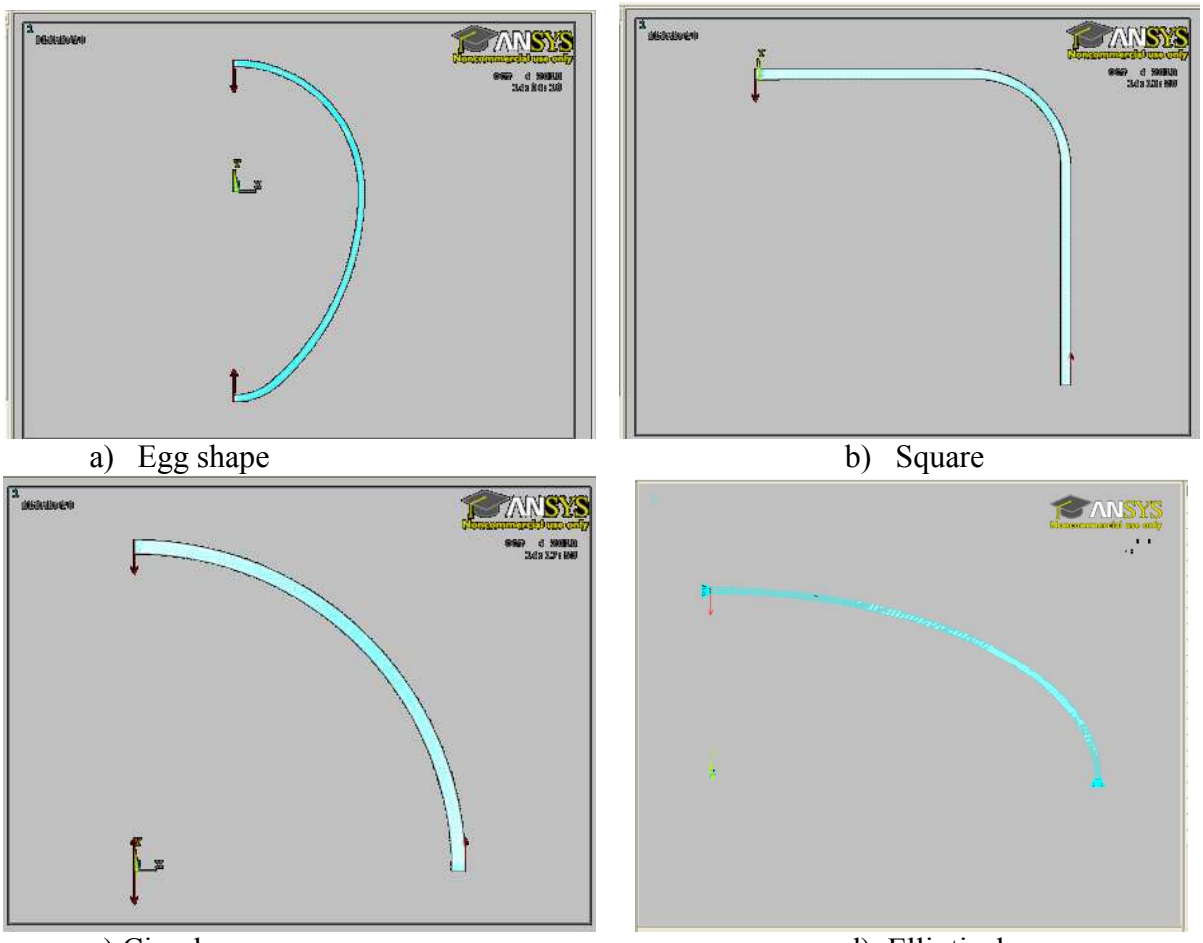
The term $r_0 = r - \frac{t}{2}$ denotes the distance of the neutral axis from one edge of the laminate where t is the laminate thickness. The elastic properties are defined in terms of elastic modulus E and laminate stiffness, Q_k. Details of the developed mathematical model can be found in [9].

Table 1 Equation for the radii of curvatures for different pipe shapes

Shape	Equation used in the analytical model
circular	r = constant
elliptic	$r = \frac{ab}{\sqrt{(a^2 \sin\theta^2 + b^2 \cos\theta^2)}}$
egg	$r = \begin{cases} r_c & for \quad \theta \in \left[\frac{-\pi}{2}; \frac{\pi}{2}\right] \\ 2r_c & for \quad \theta \in \left[\frac{-\pi}{2}; \frac{7\pi}{4}\right] \\ 2r_c - (\sqrt{2}\, r_c) & for \quad \theta \in \left[\frac{7\pi}{4}; \frac{9\pi}{4}\right] \end{cases}$
square	$r = \begin{cases} \frac{y_c}{cos(\theta)} & for \quad \theta \in \left[0, \frac{\pi}{6}\right] \\ r^* & for \quad \theta \in \left[\frac{\pi}{6}, \frac{2\pi}{6}\right] \\ \frac{x_c}{cos(\theta)} & for \quad \theta \in \left[\frac{\pi}{3}; \frac{\pi}{2}\right] \end{cases}$

Finite Element Modeling. This section aims at developing finite element models using ANSYS of the four pipe shapes to validate the developed mathematical model. Fig. 2 shows the finite element models for the four pipe shapes. All pipes consist of three layers made of two outer GRP layers and a core layer made of sand-epoxy mixture. The elastic properties of the individual layers were determined experimentally and used in the finite element models. The elastic modulus of the inner, core, and outer layers are 2.67, 1.45, and 3.22 GPa, respectively with an average Poisson's ratio of 0.303 for all layers. Due to symmetry, either one quarter or half of the pipe depending on the pipe

shape was modeled. Symmetry boundary conditions were applied along the planes of symmetry implying that all nodes lying along the x and y directions are respectively constrained from moving vertically and horizontally. The pipe dimensions were varied according to intended results except that the pipe height and pipe width of 300 mm were kept the same for all pipes. A plane stress with thickness element (Plane 82) was used to model the composite pipes. In order to mimic the parallel plate test method, the bottom nodes were fixed from moving in all directions; whereas, the top node was assigned the same downward vertical force of 40 kN.



a) Egg shape b) Square

c) Circular d) Elliptical

Fig. 2 Finite element models used in the study

Results and Discussions

An analytical solution and finite element analysis of the four pipe shapes (circle, ellipse, square, and egg) were conducted. Load deflection curves and tangential stress at the inner and outer layers of the pipes were determined. Fig. 3 shows the load deflection curves behave linearly for all pipe shapes. In addition, it can be seen that for the same applied force, the vertical deflection is minimum for the egg shape and highest for the square pipe. This indicates that the stiffest and most flexible are respectively the egg and square shapes. Moreover, it can be observed that the ellipse and circular shapes have the same response because i) the applied load and corresponding deflection were at $\theta = 0$, and ii) all pipes have the same height; thereby, aspect ratio for the ellipse has no effect on force deflection for both circular and elliptic shapes. Fig. 4 shows the tangential stress for the outer and inner layers of all pipes at $\theta = 0$. It can be observed that the outer and inner layers exhibit opposite responses due the nature of point load. Moreover, the stress is highest at the egg shape. Finite element results were also used to validate the developed mathematical model. Figure 5 shows the deformed shapes of the four pipes under the same vertical load. A comparison between the developed mathematical model and finite element results revealed a good agreement where the percent error ranges from 2 to 8%. This confirms the accuracy of the developed model. It can be observed that the percent error is smaller for regular pipe shapes (circular and elliptic).

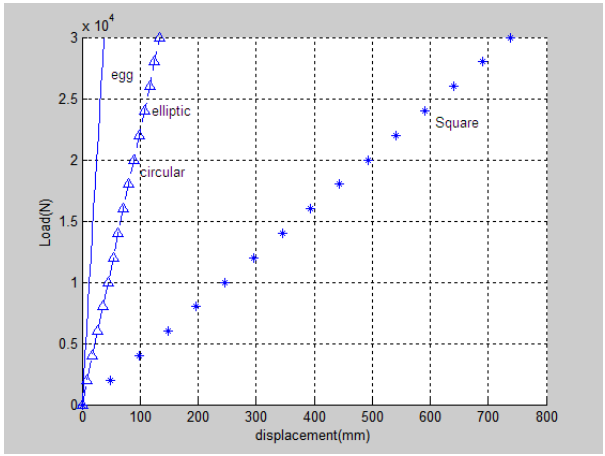
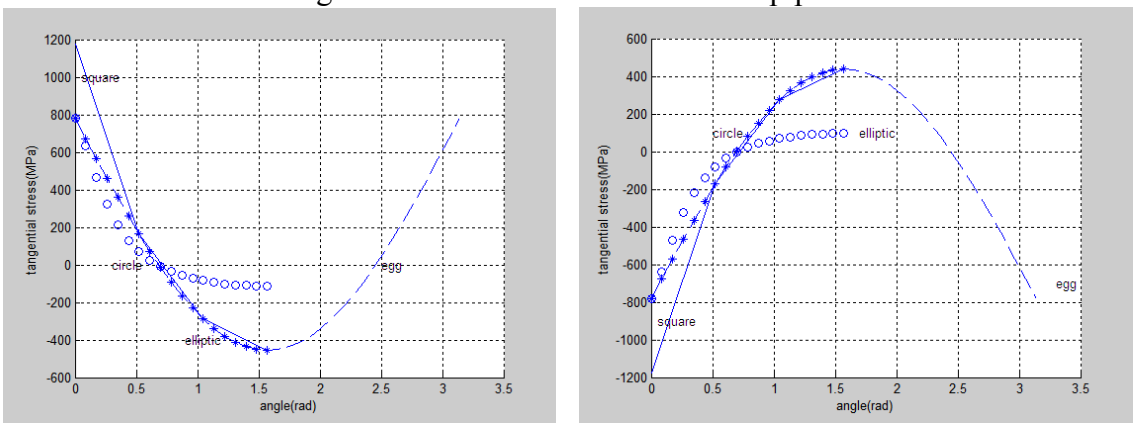
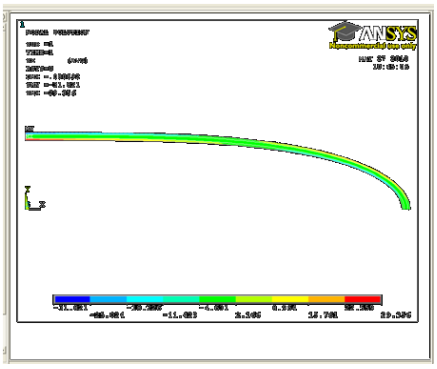


Fig. 3 Load-deflection curves for all pipes.

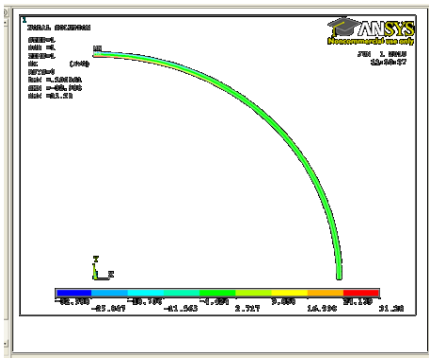


a) outer layer b) inner layer

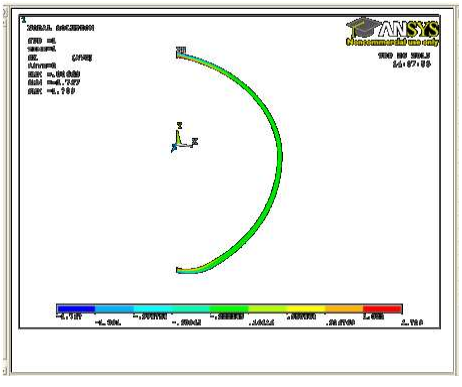
Fig. 4 Tangential stress for all pipes (t = 8 mm, h = 400 mm, w = 300 mm, F = 40 kN).



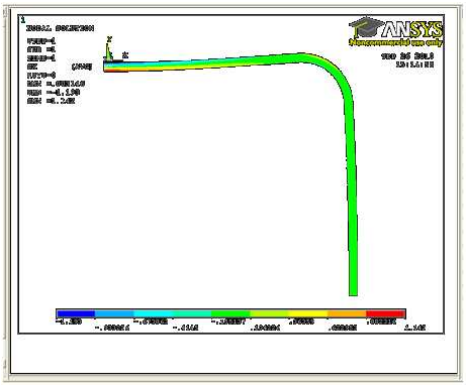
a) Elliptical shape



b) Circular shape



c) Egg shape



d) Square shape

Fig. 5 Deformed shapes of the four pipes

Table 1 Tangential stress σ_θ at $\theta = 0$ at inner layer (MPa) deg. for applied vertical force of 40 kN.

Shape	FEM	Analytical	Error (%)
Circle	830	890	4
Egg	1700	1600	5
Square	1140	1170	2
Ellipse	470	430	8

Shape Factor. The whole objective of this paper is to estimate the shape factor for irregular pipe shapes as compared with the regular circular pipes. The shape factor, defined as the ratio of maximum tangential stress of irregular shape to the maximum tangential stress of the circular pipe, is given by:

$$K = \frac{\sigma_{max|\,irregular}}{\sigma_{max|\,circular}} \qquad (3)$$

Table 2 summarizes the values of the shape factor for the four pipe shapes by comparing the analytical and finite element results. It can be seen that the egg has the highest shape factor since it represents the stiffest structure among the pipes considered in this study. These values can be used as design criteria for the irregular pipe shapes by taking into account the circular pipe as the base case.

Table 2 Shape factor for the different pipe shapes

Shape	Analytical	FEM	Error (%)
Circular	1	1	0
Egg	2	2.04	2
Elliptical	0.51	0.56	8
square	1.3	1.37	5

Summary

An analytical solution and finite element modeling of four GRP pipes with various shapes were developed. The developed models were used to determine the shape factor for irregular pipes to be used as design factors before fabrication of any irregular pipe shape. The obtained shape factors can save manufacturers a lot of time and cost. It was found that developed analytical model is in good agreement with finite element results.

References

[1] J.W. Hutchinson: Journal of Applied Mechanics, Vol. 35, (1968), pp.66 – 72.

[2] P.K. Sinha and B.L. Dhoopar: Composite Structures No. 5 (1986), pp. 51-59.

[3] B.L. Dhoopar and P.K. Sinha: Fibre Science and Technology No. 19 (1983), pp. 195-213.

[4] B.L. Dhoopar and P.K. Sinha: Fibre Science and Technology No. 13 (1980) pp. 269-280.

[5] R.M. Guedes: Elsevier (2009), pp. 188-194.

[6] Y. Gourinat, and V. Belloeil: J. Materials and Design, Vol. 27 (2005), pp. 1055 - 1064.

[7] W.J. Womack, B.G. Santoni and C.M. Puttiltz: Journal of Biomechanics No. 41 (2008), pp. 194-199.

[8] F. Romano and D. Ranlet; Journal of the Franklin Institute, Vol., 277, No.5, May 1964.

[9] I. Kalfat Ismail, A. C. Seibi and M. Neifar: Int. Conference on Applied Mechanics, Manufacturing, Materials, Muscat, Dec. 12- 15, 2010.

© (2011) Trans Tech Publications, Switzerland
doi:10.4028/www.scientific.net/KEM.471-472.285

Field Layout of Glass Reinforced Epoxy Pipeline – A Practical Approach

ABDENNOUR C. Seibi[1,a], TASNEEM Pervez[2,b], XIAOLIANG Qu[1,c], ADEL Khalaf[3,d]

[1]The Petroleum Institute, Mechanical Engineering Program
P.O. Box 2533, Abu Dhabi, UAE
[2]Sultan Qaboos University, P.O. Box 33, Al-Khod 123, Oman
[3]ADMA-Opco,
[a]aseibi@pi.ac.ae, [b]Tasneem@squ.edu.om, [c]xliang@pi.ac.ae, [d]amkhalaf@adma.ae

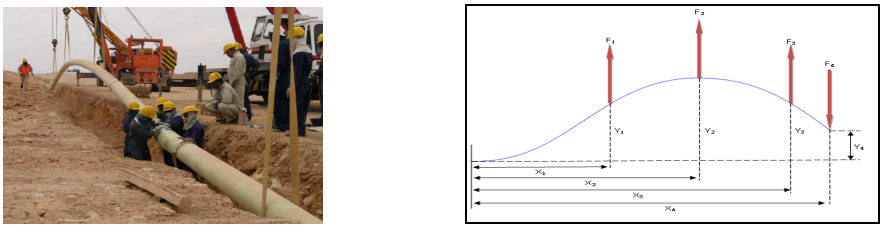
Abstract. This paper presents a practical approach dealing with the development of safe working envelops for field operators to avoid any potential GRE pipe failure during installation. Finite element modeling was used to model the pipeline. Two different element types available in ANSYS library (Beam and Shell elements) were used in the analysis. Various pipe sizes subjected to typical loading conditions similar to field layout conditions were considered. The finite element models were used to estimate pipe deflection, the internal normal and shear forces as well as bending moments for each pipe section along its length from which the induced stresses were determined. The maximum tensile stress was calculated and compared to the failure strength of GRE for various lifting scenarios. A sensitivity analysis on the various parameters affecting the structural integrity of the pipeline was also performed. It was found that the beam element over predicts the threshold lifting height as compared to the shell element results. In most cases, the estimated threshold value for the lifting height causing potential pipe failure for all pipe sizes is 2 and 1.2 m for beam and shell elements, respectively. Moreover, the results showed that the minimum threshold height increases for smaller pipe sizes.

Introduction

Most of the contractors handling pipeline layouts in the field are used to steel pipes; thereby, proper installation procedures related to pipe connection and ground layout for burial are well set. With the advent of technology, cost effective and corrosion resistant materials have been manufactured to replace steel pipes operating in harsh environments such as the one in the Gulf region. Recently, Glass Reinforced Epoxy (GRE) pipes have received a widespread use in the oil and gas industry for flow lines and water cooling systems. However, most of the workers dealing with GRE pipeline layouts are unskilled and do not know up to what extent pipe bending should be exerted to connect pipe sections for field layout. Thereby, a simple yet comprehensive procedure/guideline must be established to avoid any potential failure. The next decade will see onshore fluid transportation moving into ever increasing in volumetric flow rates and production. However, this in turn necessitate methods for laying pipelines of varying diameters in safe operations and without any failure that may result in loss of time, money, and performance. Many attempts have been made to understand the mechanics of composite pipes during offshore layout process and installation [1]. The sixties saw the development of the stinger-lay barge pipeline construction method, the articulated stinger, and the advent and general acceptance of the use of constant tensioning devices [2]. This development led to the use of shorter and more manageable stingers and opened the door for the possibility of deepwater pipelines. Dixon and Rutledge [2] and Powers and Finn [3] have recognized the limitations of the so-called catenary and beam-column procedures. Practical methods of how to handle pipeline layout onshore are not available. The lack of guidelines related to onshore pipeline installation inspired the authors to carry out a study that relates GRE pipeline lifting heights to the induced stress state during installation.

Problem Description

The structural integrity of GRE pipelines during field layout consists of predicting the pipe deflection and induced stresses. Fig. 1 illustrates the actual pipeline field layout and the corresponding mathematical model. Fig. 1a shows the lifting mechanism of the pipeline and the tie-in procedure during the installation process while Fig. 1b is a representation of the corresponding mathematical model.



a) GRP field layout b) Mathematical model of GRP pipe layout

Fig. 1 GRP pipeline field layout and its corresponding mathematical representation

The figure shows that the left end of the pipe is lying on the ground-level, while the other pipe sections are lifted to a certain height for tie-in purposes. The free end is usually lifted to approximately 1-m above ground-level to allow the worker to tie-in another piece of pipe and lay them on the ground. This process gets repeated several times till complete pipeline installation. During the lifting process, the external forces F_1, F_2 and F_3 represent the lifting forces provided by the cables of the crane while F_4 represents a force caused by the workers (Fig. 1). The locations of the forces F_1, F_2, F_3, and F_4 are represented by X_1, X_2, X_3 and X_4, respectively. Their corresponding lifting heights are denoted by Y_1, Y_2, Y_3 and Y_4. The heights depend on the depth of the trench, the pipe size and length as well as the connection mechanism of mating pipes. Therefore, the problem under study can be modeled as a continuous beam or shell with various pipe sizes subjected to varying transverse loads and uniform dead weights of the pipes. Field layout showed that the ratio of the maximum lifting height to its corresponding length from the fixed end (Y_2/X_2) is relatively high; thereby, resulting in large angular changes. To model such a problem, large deformation theory described by the following expression has been used:

$$\frac{M}{EI} = \frac{\frac{d^2y}{dx^2}}{\left[1 + \left(\frac{dy}{dx}\right)^2\right]^{\frac{3}{2}}} \qquad (1)$$

Consequently, the problem of predicting the deflection at any point along the pipeline during the layout operation is non-linear. Therefore, solution to the problem was performed numerically using ANSYS. Finite element models of various pipe sizes were built to study the structural integrity of Glass Reinforced Epoxy (GRE) pipes subjected to a combination of lifting heights. A sensitivity analysis on the various heights was performed to determine threshold heights for safe pipe layouts. The main objective of this paper is to develop operating envelops for failure prevention of GRE pipes. This was accomplished by identifying threshold heights above which pipe failure may take place.

Finite Element Modeling. Finite element models of the problem illustrated in Fig. 1 were built to study the structural integrity of GRE pipelines during field layout. Various pipe sizes were used in the models to estimate the induced stresses caused by the lifting mechanisms. The GRE pipeline was modeled using beam and shell elements where the nodes located at the right end were constrained from moving in all directions; whereas, the nodes at the far left end were given a downward displacement of 1 m (Fig. 2). The nodes at the points of application of the concentrated forces were given variable vertical displacements that reflect field conditions from which reaction loads were obtained. Moreover, since the problem is nonlinear, the nonlinear geometric option in ANSYS was activated. The finite element models require the elastic modulus of 11.9 GPa and Poisson's ratio of 0.4 of GRE pipe material.

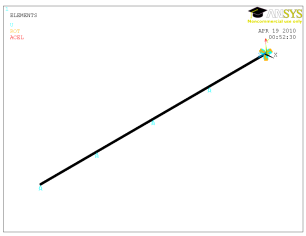


Fig. 2. Finite element model of the GRE pipe

Loading Procedure. At the beginning of the finite element modeling, the pipe was laid on the ground with zero displacement. The pipe was then constrained from moving in all directions at the far left node to mimic field conditions. Variable vertical displacements at three locations (X_1, X_2, X_3) as described in Fig. 1 were imposed at the corresponding nodes; while a 1 m vertical displacement was taken at X_4 for all cases. A combination of displacements at the three locations was varied until potential failure is reached. The reaction loads and maximum tensile stress applied along the pipeline were obtained for different heights.

Parameters Used in the FE Model. The finite element analysis was conducted for various field layout scenarios. Various pipe sizes (Table 1) and lifting heights were used in the finite element models to study the structural integrity of the pipeline under study. Table 2 summarizes the field parameters used in the analysis. It is worth noting that the distances X_1 to X_4 represent the locations of the crane cables used for lifting the pipeline relative to the left end of the pipeline which is lying on the ground; while, Y_1 to Y_4 were given various values to reflect the lifting heights of the pipeline during the installation process. Moreover, the heights were limited to certain values representative of field layout procedure. For instance, for cases 1 and 2, the difference in heights between locations 1 and 2 and 2 and 3 were kept the same in order to satisfy the symmetry condition and simplify the manipulation of the results adopted in practice. However, preliminary finite element results indicated that the symmetry condition for cases 3, 4 and 5 is not practical since the resulting reaction forces at locations 2 and 3 were negative. This is not representative of field conditions as the cables tend to lift the pipes; thereby, these forces must have upward directions instead of downward as predicted by finite element results. Therefore, only height values that produce upward forces in the cables were considered in this study.

Table 1 GRE pipes used in the FE analysis

Case	"ID" (m)	thickness (m)	Weight (N/m)
1	0.0271	0.0030	5.8800
2	0.0530	0.0031	10.7800
3	0.1052	0.0041	27.4400
4	0.1590	0.0041	40.1800
5	0.2088	0.0046	58.8000

Table 2 Parameters used in the FE analysis

Y2	Y2-Y1 (m)	Y2-Y3 (m)	Y2-Y4 (m)	Max normal stress
Case 1				
Y2=1	0.75	0	0	20.9
Y2=2	0.75	0.75	1	20.5
Y2=3	0.75	0.75	2	27.4
Y2=4	0.75	0.75	3	44.1
Y2=5	0.75	0.75	4	74.4
Y2=5.5	0.75	0.75	4.5	93.5
Case 2				
Y2=1	0.5	0	0	15.8
Y2=2	0.5	0.5	1	41.3
Y2=3	0.5	0.5	2	86
Y2=4	0.5	0.5	3	138
Case 3				
Y2=1	0.75	0	0	45.3
Y2=2	0.75	0.3	1	79.8
Y2=2.5	0.75	0.3	1.5	126
Y2=3	0.75	0.3	2	175
Case 4				
Y2=1	0.61	0	0	54.9
Y2=1.5	0.85	0	0.5	66.8
Y2=2	0.9	0	1	123
Y2=2.5	1	0	1.5	199
Case 5				
Y2=1	0.43	0	0	148

Results and Discussion

The finite element results of five cases were used to determine the threshold heights that might initiate pipe failure using beam and shell elements. The reaction forces and maximum stresses for different field conditions can be obtained. Focus was made on the stress level at the pipeline for various lifting heights. Fig. 3 shows a typical deformed shape of the pipeline for case 1 where the deformed shape resembles the actual field case. Moreover, plots showing relationships between the pipeline heights (Y_2) and stress levels for all cases were included.

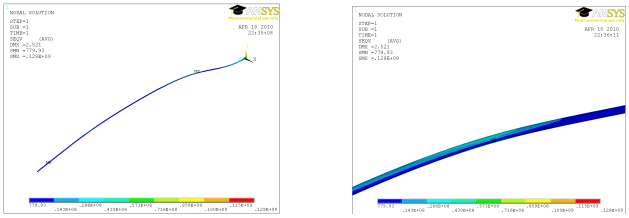
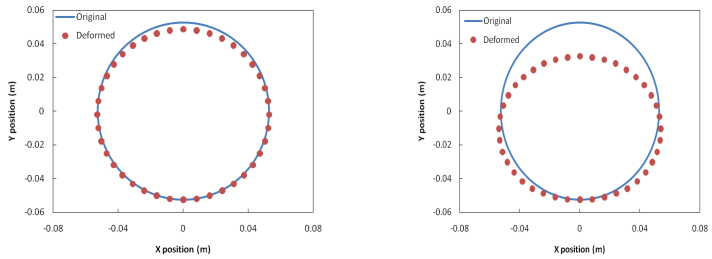


Fig. 3 Deflected shape of the pipeline.

Fig. 4 shows a typical pipe cross section using shell element where pipe ovality is obviously seen. This ovality may contribute in raising the stress level in the pipeline. Figure 4a shows the full scale of the deformed and undeformed pipe shapes for case 3; while Fig. 4b shows the same results scaled up by a factor of ten for better visualization. Table 3 summarizes the maximum stress acting

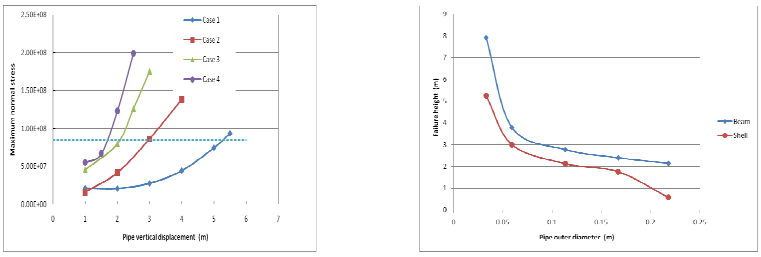
at the nodes where vertical displacements were applied for the five cases using beam and shell elements. It can be seen that the stress increases as the pipe is lifted more. This is expected since the higher the pipeline deflection the higher the required cable forces to lift the pipe. Therefore, failure may take place at these locations depending on how high is the pipeline. It is observed that for almost all the cases analyzed, the critical point within the system where the maximum normal stresses occur is at X=0 (fixed end). This is due to the high bending moment as a result of an increase in height and pipe size. In addition, it is depicted that as Y_2 becomes higher, the maximum normal stress increases. This is due to the fact that the reaction forces increase with increasing lifting heights (deflections). Fig. 5 shows the variation of maximum stress with respect to pipe lifting height as well as the failure heights for different pipe outer diameters analyzed in this study. Fig. 5a shows that the stress level exceeds the failure stress for all cases at various pipe lifting heights depending on the case under study; while Fig. 5b shows the lifting height that causes pipe failure. It can be observed that the beam element overestimates the stress level and cannot be used for such applications. These results can be used as guidelines for field operators to avoid any unexpected pipe failure during field layout. Due to limited space, the reaction forces are not included in this paper. It is worth mentioning that it was observed that the height at Y_3, for cases 4 and 5, sometimes exceeds the height of Y_2 that has been set as a constraint in ANSYS. This may be attributed to the large pipe stiffness (pipes are very thick and heavy relative to the other cases). However, for practical purposes, the pipelines must deflect downward after location 2 as observed in the field.



a) Full scale b) 10 x full scale

Fig. 4 Deformed pipe showing ovality where maximum stress takes place at 7.5m from the fixed end and it is lifted vertically by 1.75m

It is clearly shown from Fig. 4 that as the pipe diameter increases the safety factor decreases. For the first two cases, the failure heights are about 3.75 and 5 m, which are very high and unpractical. These heights are not practical when installing the pipeline indicating that failure in small size pipes will not occur. However, the other three cases exhibit potential pipe failure at heights lower than 2.5 m, which can be reached in practice. Therefore, these heights should be taken as the threshold values in order to avoid any unexpected pipe failure.



a) Maximum stress b) failure heights

Fig. 5 Maximum stress and failure heights (Y_2) for various GRE pipe lifting heights and outer diameters

Summary
Nonlinear finite element modeling of GRE field layout was conducted. It was observed that the applied stresses increase with increasing pipe size and height. The study also showed that the normal stress associated with the system at certain heights exceeds the failure strength of GRE pipes; thereby, failure can take place at these threshold lifting heights. The location where the maximum stresses occur, for all the cases analyzed, were identified and can be used as guidelines for field operators. It was found that beam elements overestimate the threshold failure heights as compared to shell elements. The obtained results can be used as guidelines for field operators to prevent any pipe pre-cracking.

References

[1] J. R. Wilkins, J. R. McDermott: Offshore Technology Conference, SPE 3139.

[2] D. A. Dixon, and Rutledge, D.R.: Trans. ASME, Petroleum Division, Paper 67-Pet-6

[3] J. T. Powers, and L. D., Finn: Offshore Technology Conference, Paper OTC 071

[4] S. B. Kochekseraii, M. Robinson: J. of Strain Analysis for Engineering Design, 2000, Vol. 39, 2, pp: 137 – 146.

[5] A.G. Gibson and J.L. Cantrill, S.J. Groves: Offshore Technology Conference, OTC 14063.

© (2011) Trans Tech Publications, Switzerland
doi:10.4028/www.scientific.net/KEM.471-472.291

Cotton-Epoxy Composites: Development and Mechanical Characterization

Piyush P. Gohil[1, a] and A.A. Shaikh[2, b]

[1]Department of Mechanical Engineering, CIT-Changa,
Charotar University of Science and Technology, Changa-388421 (Gujarat-India)

[2]Mechanical Engineering Department, SVNIT-Surat,

College Campus, Ichhchhanath, Surat -395007 (Gujarat-India)

[a]piyushgohil.me@ecchanga.ac.in, [b]aas@med.svnit.ac.in

Keywords: Cotton fibers; Unidirectional Composites; Testing, Experimental study.

Abstract. Composites are becoming essential part of today's material because they offer advantages such as low weight, corrosion resistance, high fatigue strength; faster assembly etc. composites are generating curiosity and interest all over the worlds. The attempts can be found in literature for composite materials high strength fiber and also natural fiber like jute, flax and sisal natural fibers provides data but there is need of experimental data availability for unidirectional natural fiber composite with seldom natural fiber like cotton, palm leaf etc., it can provide a feasible range of alternative materials to suitable conventional material. It was decided to carry out the systematic experimental study for the effect of volume fraction of reinforcement on longitudinal strength as well as Modulus of Elasticity (MOE) using developed mould-punch set up and testing aids. The testing is carried out as per ASTM D3039/3039M-08. The comparative assessment of obtained experimental results with literature is also carried out, which forms an important constituent of present work. It is also observed through SEM images and theoretical investigations that interface/interphase plays and important role in natural fiber composite.

Introduction

Composite material is a material composed of two or more distinct phases (matrix phase and dispersed phase) and having bulk properties significantly different from those of any of the constituents.[1,2]. Fig. 1 shows the classification of composites.

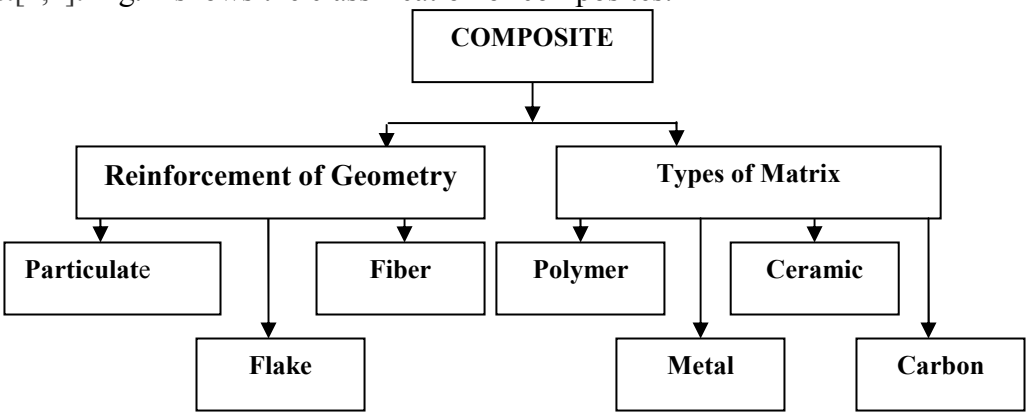


Fig. 1 Classification of Composites [2]

In past various studies have been carried out using natural fiber composites [3]. Natural fibers are based on renewable materials and depending upon the source can be subdivided mainly into two major groups: plant fibers (based on agricultural resources) and animal fibers (based on resources derived from animals). The group of plant fibers can be subdivided into several classes: straw, seed, bast, leaf and wood fibers. The attempts made for jute and other repeatedly used natural fiber, of

course provides data but there is paucity for experimental data for other seldom natural fiber like cotton, banana, pineapple leaf, and other. Hence there is a need to carry out systematic experimental research in this area. During the 1970s and 1980s natural fibers were partially replaced by petrochemical polymers because of their optimized properties and their faster manufacturing processes. In the mid 80s it was thought that the use of natural fiber reinforced composites could offer an interesting alternative to these plastics due to their technical, economic and ecological advantages and social benefits [4]. According to Karus et al. [5] in 2003 approximately 45,000 tons of domestic cotton fibers were used in the German automotive industry for interior applications, which results in 79,000 tons of composite parts and about 8 kg of cotton-fiber composites in a German car. Reclaimed cotton is mainly used as low cost fiber in composites used as interior parts for automotive devices. Since the late 1980s publications [6-12] can be found dealing with finding the limits and advantages of using cotton as an adequate reinforcement fiber.

The objective of the present study is to make the people aware with the opportunity of cotton-epoxy composite to replace some of the available conventional fiber composite.

Materials and Methods

Selection of Materials. Lot of work has been done for high strength fibers and data base for experimental value for high strength fiber composite is available. Looking to the inadequate data availability for cotton fiber composites the area need to be focused with in depth study. Therefore, it is decided to procure cotton fiber from local market. Looking to the relative merits and qualities of epoxy resin and ease of availability in nearby market vicinity epoxy has been selected. It is purchased from GIDC Odhav, Ahmedabad (Gujarat) INDIA.

Property Measurement. It is decided to test density, strength and Modulus of Elasticity (MOE) for cotton fiber and epoxy resin.

Density. The use of Archimedes law is recommended by Morton [13] for density measurement. So, here it is decided to carry out the density measurement of procured cotton fiber and epoxy resin. In this method, the sample of fiber/ casted resin is selected and its mass is measured on digital weight balance with a resolution of 0.001 gm. The volume of this fixed mass of fiber/Casted resin is measured using standard displacement technique. In this technique weighted fiber/Casted resin is immerged in 100 ml measuring cylinder filled with water. The displaced volume is measured with micro pipette having L.C. of 0.02 ml. Total 25 samples of cotton fiber/casted resin were used for this test. The final experimental values for density observed by measurement for constituents and by performing the descriptive statistics study are depicted in Table 1.

Table 1 Density of Constituents (experimental value)

Sr. No.	Constituent	Density (g/cm^3)
1	Cotton fiber	1.48 ± 0.083
2	Epoxy Resin	1.25 ± 0.020

Strength and Modulus of Elasticity (MOE). The testing of cotton fiber and epoxy resin was carried out. The measurement for the strength of casted neat epoxy resin was carried out as per ASTM D 638-90 [14]. The casted specimens of epoxy resin were made in specially prepared wooden mould with same proportions of initiator and accelerator. The specimen plate was cured for 24 hrs within the mould only. After curing the specimen were cut down as per dimension requirement of ASTM D 638-90 [14] using combination of diamond saw cutter and CO2 laser engraving machine. The dimensional detail of casted specimen dimension is given in Fig. 2.

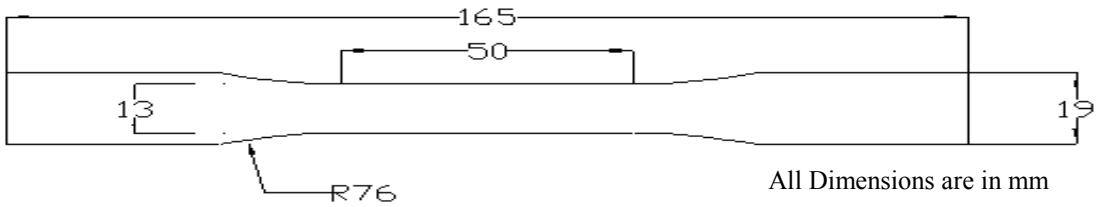


Fig. 2 Dimensional detail of casted specimen as per ASTM 638-90

The strength was measured using computerized tensometer (Make: Kudale Instruments L.C. of 1 kg,) and cross sectional area is measured based on geometrical measurement using digital vernier (Make: Mitutoyo, having L.C. of 0.01 mm). Table 2 shows the strength and Modulus of Elasticity (MOE) experimental value for procured materials.

Table 2 Strength and Modulus of Elasticity (MOE) (experimental value)

Sr. No.	Constituent	Strength (MPa)	Modulus of Elasticity (GPa)
1	Cotton fiber	200	8.20
2	Epoxy Resin	30.50	2.85

Composite Specimen Development. It is possible to have multiple specimens i.e. 7 specimens for longitudinal case for testing from the prepared composite plate and the average value are to use for depicting the final answer. Fig 3 shows the mould and punch set up used for the preparation of composite plate. Table 3 shows the measured fiber volume fraction of all four plates of different fiber volume fraction.

Table 3 Fiber volume fraction

Plate No.	Fiber Volume Fraction
1	0.1234
2	0.1961
3	0.2418
4	0.3268

ASTM allows using the mild steel tab for specimens, which is easier to handle and fix with flat specimens therefore; it is decided to adopt the ASTM D3039/3039M-08 [15] standard for the geometrical dimension. As per the dimensions of the prepared composite plates it is possible to have 7 specimens of same fiber volume fraction. Fig. 4 shows the photographs of developed specimens of cotton-epoxy composite for mechanical characterization.

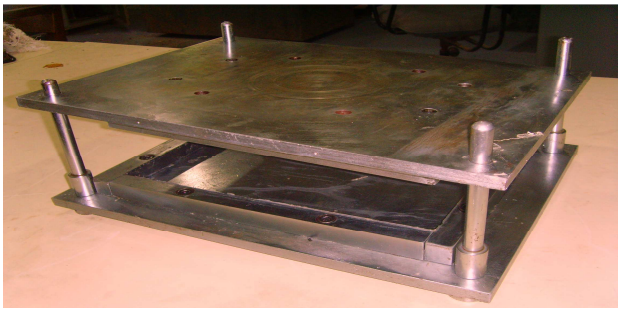


Fig. 3 Developed mould and punch setup



Fig. 4 Developed cotton-epoxy specimens

Mechanical Characterization- The uniaxial tensile test is the most widespread and the most studied mechanical test for composites. The characteristic obtained from uniaxial tensile tests are used both for material characterization and for estimations of load-carrying capacity. All the specimens were prepared and made ready for the tensile testing. It is decided to evaluate the composite strength and modulus of elasticity in longitudinal direction for the prepared cotton-epoxy composite. The computerized Tensometer (Make: Kudale Instruments L.C. of 1 kg) was used for

tensile testing. The load and displacement readings are observed through inbuilt software with available facilities of storing data as tabulated readings and graphs. The inbuilt software is based on windows XP.

Comparative Assessment -Varieties of predictive models in the literature available are either derived theoretically based on parametric constraints or semi empirically based on experimental studies. Whitney [16] described that the static equilibrium requires the total resultant force on the element must be equal to the sum of forces acting on the fiber and matrix. Combining the static equilibrium condition leads to formation of rule of mixture as shown in Eq. 1.

$$E_c = E_f v_f + E_m v_m \tag{1}$$

Puck [16] also proposes the model as shown in Eq. 2 which is based on the concept of approximation considering the properties of longitudinal equation.

$$E_c = E_m(3.92 v_f + 0.89) \tag{2}$$

Madson [17] has modified the rule of mixture and proposed two porosity components i.e. a processed governed component and structurally governed component. A modified rule of mixture supplemented with these two parameters of composite porosity content was given as Eq. 3.

$$E_c = \left(v_f E_f + \left(1 - v_f\right) * E_m\right) * \left(1 - V_p^2\right) \tag{3}$$

$$V_p = V_{p(\text{Processing})} + V_{p(\text{Structural Mechanism})}$$

$$V_{p(\text{Processing})} = 0.06 * W_f \qquad V_{p(\text{Structural Mechanism})} = 0.32 * W_f - 0.20, \text{ if } W_f > 0.625 \text{ else zero.}$$

Gohil and Shaikh [18, 19] have proposed the model based on concentric cylinder RVE and power law property variation of interphase region.

$$E_{CL} = \left(E_f v_{f1}\right) + \left(\frac{1}{t_i} \int_{r_{f1}}^{r_i} E_f \left(\frac{r}{r_{f1}} \right)^{\left(\frac{\ln\left(E_m / E_f\right)}{\ln\left(r_i / r_{f1}\right)} \right)} dr * v_i \right) + \left(E_m v_m\right) \tag{4}$$

All the above models were assessed and compared with the present experimental results and minimum bias average errors are determined. The results obtained are discussed in next section.

Results and Discussion

The salient features of results obtained from the mechanical characterization and comparative assessment of cotton-epoxy composites are presented and discussed here.

The experimental results on effect of reinforcement fraction on longitudinally placed cotton fiber on composite strength and composite Modulus of Elasticity (MOE) with epoxy combination are discussed here. All the specimens were subjected to longitudinal tensile testing. Fig. 5 and Fig. 6 show the variation in composite strength composite modulus of elasticity as a function of v_f for longitudinally placed cotton fiber with epoxy resin.

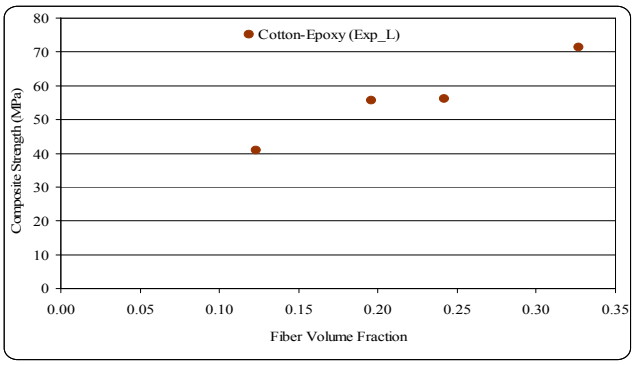


Fig. 5 Effect of volume fraction of cotton fiber with epoxy resin on longitudinal composite strength

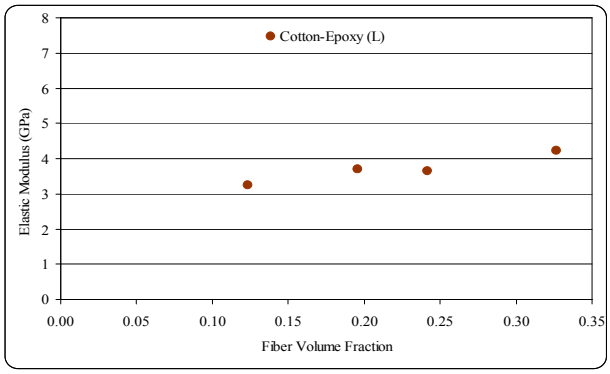


Fig.6 Comparative assessment of literature and proposed model for cotton-epoxy composite result

The experiment indicates that, as the fiber volume fraction increases the strength as well as longitudinal Modulus of Elasticity (MOE) increases linearly. This is inline with the rule of mixture which predicts the linear increase in composite strength with increase in volume fraction of fibres holds true for longitudinally placed fiber composite.

An attempt is made for comparative assessment available models in literature and proposed model for longitudinal Modulus of Elasticity with present experimental results. The deviations in terms of minimum average bias error obtained by available model are depicted in Table 4.

Fig. 7 shows SEM image of the tensile fracture of cotton fiber composites carried out through Scanning Electron Microscope (Model: Hitachi S-3400N), it can be seen that fibers are detached from the resin surface due to poor interfacial bonding. Thus interface/interphase characteristics plays very important role in natural fiber composites.

Table 4 Average bias error (%) of available models in literature and proposed model

Fiber volume fraction	ROM (Rule of Mixture)	Madson	Puck	Proposed Model
0.1234	8.4444	8.4364	20.9539	8.1241
0.1961	5.2176	5.1985	27.5602	4.5219
0.2418	13.7716	13.7408	43.8196	12.6799
0.3268	8.7830	8.7309	46.3749	7.0708
Average Bias Error (%)	9.0541	9.0267	34.6772	**8.0992**

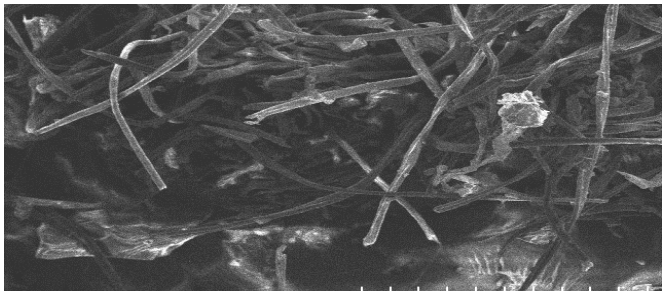


Fig. 7 SEM images of failed specimen surface

Summary

Based on Development and mechanical characterization of cotton-epoxy composite following conclusions are pinched. Longitudinal strength and Modulus of Elasticity (MOE) increases as the fiber volume fraction increases this shows that cotton-epoxy composite can be used. Thus, the use of cotton-epoxy composites can be employed to various applications based on the property needed for a product. Currently, about 40,000 composite products are in use for an array of applications in diverse sectors of the industry all over the world. While China and India started making use of composites almost simultaneously about 30 years ago, the progress made by china is rather

astounding with an annual consumption level of about 2,00,000 MT, as compared to about 30,000 MT in India, which needs awareness for composite product and their merits. Multiple commercial applications for composites and potential for export have not been tapped even in a limited way in the country. Interphase plays an important role in composites. The author's proposed models is giving good agreement compared to models available in literature as these models are derived without much emphasis on interphase phenomenon.

References

[1] A K. Kaw: *Mechanics of Composites Materials* (CRC Press Boca Raton, New York 1997).

[2] V. K. Lindroos and M. J. Talvitie: *Recent Advances in Metal Matrix Composite* (Helsinki University of technology, Laboratory of Physical Metallurgy and Materials Science, Finland1995).

[3] S.M. Sapuan and M.A. Malique: Materials and Design Vol. 26 (2005), p. 65

[4] H. Harig and J. Mussig:, *New materials for Innovative products and Social Relavance Trends* (Harig, Langenbach CJ (ed), Bd. 3. Springer Verlag, Berlin, Germany 1999).

[5] M. Karus, S. Ortmann and D. Vogt: Kunststoffe Plast Europe Vol. 95/7 (2005) p. 51

[6] D.H. Muller, A. Krobjilowski and J. Musig: *National Cotton Council of America (ed) Fourth international Nonwovens Symposium during the Beltwide Cotton Conferences* (Anaheim, CA, USA 2001-01-12–2001-01-13, National Cotton Council of America, Memphis, TN 2001).

[7] L. Jiang and G. Hinrichsen: Die Angewandte Makromolekulare Chemie Vol. 268 (1999) p. 13

[8] L. Jiang and G. Hinrichsen: Die Angewandte Makromolekulare Chemie Vol. 268 (1999) p. 18

[9] A. Stanojlovic-Davidovic, A. Bergeret, J.C. Benezet, L. Ferry and A. Crespy: *Royal Institute of Technology (ed) Eco Comp 2005*, (3rd international Conference on Eco-Composites, Stockholm, Sweden 2005).

[10] J.A. Foulk, W.Yo. Chao, D.E. Akin, R.B. Dodd and P.A. Layton: Journal of Polymers and the Environment Vol. 14 (2006) p. 15

[11] M. R. Piggot: *Load Bearing Fiber Composites* (Pergamon Press, Oxford 1980).

[12] G. Lubin: Hand Book of Composites (Van Nostrand Reinhold, New York 1982).

[13] W.E. Morton and J.W.S. Hearle: *Physical Properties of Textile Fibers* (The Textile Institute Heinemann, London 1980).

[14] ASTM D 638-90: *Standard Test Method for Tensile Properties of Plastic* (ASTM Standards and Literature References for Composite Material, 2nd Ed., American Society for Testing and Materials, Philadelphia PA. 1990).

[15] ASTM-D3039-D3039M-08, *Standard Test Method for Tensile Properties of Polymer Matrix Composite Materials*, (West Conshohocken PA 2008).

[16] J.M. Whitney: Journal of Composite Material Vol. 1 (1967) p. 180

[17] Bo. Madson and H. Lilholt: Composite Science and Technology Vol. 63 (2003) p. 1265

[18] P.P. Gohil and A.A. Shaikh: Vol. 29/4 Journal of Reinforced Plastics and Comp. (2010) p. 685

[19] P.P. Gohil and A.A. Shaikh: An International Journal Vol 1/3 (2010) p. 223

© (2011) Trans Tech Publications, Switzerland
doi:10.4028/www.scientific.net/KEM.471-472.297

Optimizing Processing Parameters and Fiber Size for Kenaf Fiber Reinforced Thermoplastic Polyurethane Composite

Y. A. El-Shekeil[1, a], S.M. Sapuan[1, b], E.S. Zainudin[2, c], Khalina Abdan[3, d]

[1] Department of Mechanical and Manufacturing Engineering, Universiti Putra Malaysia, 43400 UPM, Serdang, Selangor, Malaysia
[2] Laboratory of Bio-Composite Technology, Institute of Tropical Forestry and Forest Products, Universiti Putra Malaysia, 43400 UPM, Serdang, Selangor, Malaysia
[3] Department of Biological and Agricultural Engineering, Universiti Putra Malaysia, 43400 UPM, Serdang, Selangor, Malaysia

[a]y_shekeil@yahoo.com, [b]sapuan@eng.upm.edu.my, [c]edisyam@eng.upm.edu.my, [d]khalina@eng.upm.edu.my

Keywords: Natural fiber composites, thermoplastic polyurethane, kenaf fibers

Abstract. In this study, composite of Themoplastic polyurethane (TPU) reinforced with short fiber (*Hibiscus Cannabinus*) kenaf (KF) were prepared via melt blending method using Haake Polydrive R600 internal mixer. Effect of various processing temperatures, times and speeds on tensile strength was studied, together with effect of various fiber sizes on tensile, flexural properties and impact strength. Optimum blending parameters were 190°C, 11 min, and 40 rpm for temperature, time and speed, respectively. Using the optimum processing parameters TPU-KF composites with different fiber sizes were prepared. Composite sheets were prepared by hot press machine at 190 °C for 10 min. Five samples were cut from the composite sheet. Mean value was taken for each composite according to ASTM standards. Tensile and flexural strength were best for fibers between 125-300 micron. Impact strength showed an increasing trend with increasing fiber size.

Introduction

Natural fiber reinforced polymers are gaining more and more awareness due to benefits such as less abrasiveness to equipment, renewability, biodegradability and reduction in weight and cost. Incompatibility is amongst the difficulties that face natural fiber polymer composites. The reason behind incompatibility is that most polymers used in this field are hydrophobic; however natural fibres are hydrophilic. This causes lack of adhesion and wettability, hence coupling agents and binders in the interface are used to help make better adhesion. In this paper the advantage of polyurethane is its hydrophilicity (i. e. it is polar in nature).

Main components of polyurethane are polyols and isocyanates. The active isocyanate group can react with most materials that have active hydrogen groups [1]. In the case of natural fiber composites it will react with the hydroxyl group available in the cellulose. Isocyanate has been used as coupling agent for this reason [2-4]. As stated by Özgür and Oksman: "When polyurethane is used as a matrix, it is believed that no adhesion problem would occur and dispersion would be much better" [5].

Polyurethane thermoset has been compound with different natural fibers [6-11], however thermoplastic polyurethane (TPU) reinforced natural fiber composites have not yet been a focus of any scholars. Knowing the advantages of thermoplastics (e. g. reformability, less processing time and energy, better toughness, and recyclability) makes this study viable. TPU's most important properties are excellent abrasion resistance, good mechanical properties with rubber-like elasticity and tear resistance.

Optimizing processing parameters (i. e. temperature, time and speed) is an essential step in developing new composites. Processing at higher temperature might lead to thermal degradation, while processing at lower temperature results in non-homogeneous distribution of fibers due to high viscosity of the matrix [12]. Matrix and fibers need a certain mixing time to exhibit good mechanical properties. Shorter processing time results in inhomogeneous distribution of fibers during compounding, while longer processing time leads to thermal degradation of matrix and

breakage of polymer chain, due to shear stress and temperature [12,13]. Processing speed can also affect the compound properties. High speed will result in fiber breakage, and low speed is inadequate to mix the compounds well.

Fiber size and aspect ratio play major roles in fiber polymer composites, whereas, various fiber size results in significant affects on properties of the composites. It is stated by Pickering et. al. "below a critical aspect ratio the fiber will behave as a filler rather than reinforcement" [14]. On the other hand, larger fiber size will cause agglomerated and entangled fibers that will result in poor dispersion of fibers in the matrix. Several studies have been focusing on the effect of fiber size on properties of composites [15-17].

Kenaf (*Hibiscus cannabinus L., Malvaceae*) has a short growing period, high biomass output and good mechanical properties. It reaches 3-4 meters in 4-5 months. It can yield two to three harvests a year in tropical climates [18, 19]. It can produce 5-10 tons of dry fiber per acre. Two types of fibers can be extracted from this plant; bast fiber which is the outer layer, and core fiber which is the inner layer. Morphological and chemical analysis by Ashori et. al. [20] indicated that bast and core fibers were significantly different. Bast fiber represents nearly 1/3 of the plant and core represents 2/3.

Kenaf is planted commercially in China, Myanmar, India, Bangladesh and Thailand. Malaysia has paid more attention towards planting kenaf. Since 2000 more than RM48 million has been spent by Malaysian government for the research of kenaf plantation and utilization [21]. Objective of this study is to optimize processing parameters and fiber size of short kenaf fiber reinforced thermoplastic polyurethane composite.

Materials

Polyester based TPU was obtained from Bayer Co. (Malaysia) Sdn Bhd, Petaling Jaya, Selangor, Malaysia. Specific Gravity of TPU is 1.21. Tensile strength is 48 MPa. Melting temperature is 210 °C. Hardness is 55 D. Kenaf V36 bast fiber was supplied from KEFI (Malaysia) Sdn Bhd, Setiu, Terengganu, Malaysia.

Method

Preparation of Fiber. Bast fiber was extracted by mechanical decrotication. Pulverized fiber was sieved using an auto shaker sieve into three different sizes (<125, 125-300, and 300-425μm) using mesh 40-50, 50-120 and 120 and below.

Preparation of Composite. TPU-KF composite was compounded using Haake Polydrive R600 internal mixer. Matrix was charged into the mixer until torque was stabilized and then fiber was added. A 30% fiber loading was fixed throughout the study. Samples were prepared at different processing parameters, such as temperature, speed, and time.

The sample was hot pressed using Vechno Vation 40 ton compression moulding for 10 min at 190 °C. Prior to full-press, the sample was pre-heated for 7 min at 190 °C. The sheet was then placed between two plates of a cold press to cool at 25 °C for 5 min.

Characterization of Composite. Tensile properties were measured using Instron 3365 machine, according to ASTM D 638. Specimens were prepared by cutting them into dumbbell shapes using a hydraulic cutter machine. Five specimens were tested with crosshead speed of 5 mm/min.

Three point bending flexural test was conducted using Instron 3365 machine, according to ASTM D 790. Specimens were cut using a band saw machine with dimensions of 130 x 13 x 3 mm. Five specimens were tested with a crosshead-speed of 2 mm/min.

Notched impact strength was measured by 43-02-01 Monitor Impact Tester according to ASTM D 256. Dimensions of samples were 63 x 13 x 3 mm. At least five samples were tested. Impact strength (kJ/m^2) was calculated by dividing the recorded absorbed impact energy by cross-section area of the samples.

Results and Discussion

(1) Processing Parameters Optimization

The Effect of Processing Temperature on Tensile Strength of TPU-KF composite. Fig. 1 shows effect of processing temperature on tensile properties of TPU-KF composite. Melting temperature of TPU is 210 °C. One of the common drawbacks of natural fiber composites is the limited processing temperature [22]; therefore, more than 200 °C will be critical and thermal degradation will affect the composite. Temperature less than 180 °C will not be enough to soften the material; which might result in difficulty of mixing the materials. Actually 170 °C has been tried, and the outcome was inhomogeneous mixing (i. e. some pellets not even softened). Thus, three different temperatures were examined; 180, 190 and 200 °C. The rotor speed and time were fixed at 50 rpm and 15 min, respectively. From Fig. 1 it was found that the optimum processing temperature is 190 °C at 19.1 MPa. It can be seen from Fig. 1 that at low temperature the strength was low. This is attributed to higher viscosity of the matrix that causes non-homogeneous distribution of fibers during processing. At higher temperature thermal degradation might have affected the strength.

Effect of Processing Time on Tensile Strength of TPU-KF Composite. Fig. 2 shows the effect of processing time on tensile properties of TPU-KF composite. As aforementioned in the method matrix was charged into the mixer until torque was stabilized and then fiber was added into the mixer. After adding the fiber, torque was also observed. It is stated by Migneault et. al. that torque simulates real-life processing conditions. Measuring the torque allows characterizing the rheological changes of the mixed materials [23]. At a time less than 11 min the torque does not stabilize; which indicates that homogeneous mixing did not take place yet. Three different times were examined; 11, 13 and 15 min. The temperature and rotor speed were fixed at 190°C and 50 rpm, respectively. Processing temperature 190 °C is optimized in the previous step. From Fig. 2 it was found that the optimum processing time is 11 min at 23.6 MPa. It can be seen from Fig. 2 that increasing the time is decreasing the strength of material. This is most likely because of thermal degradation of matrix and breakage of polymer chain, due to shear stress and temperature [12,13].

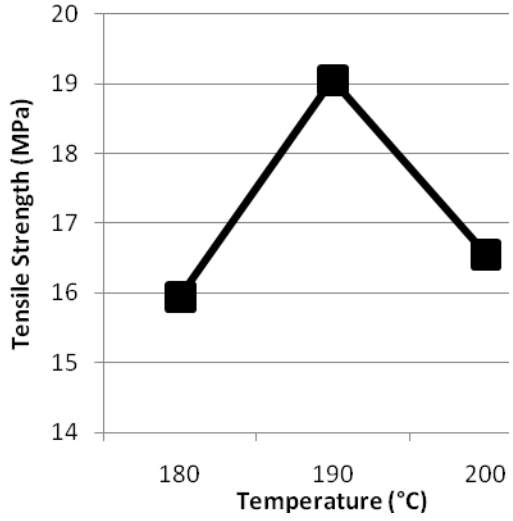


Fig. 1. Effect of processing temperature on tensile properties of TPU-KF composite.

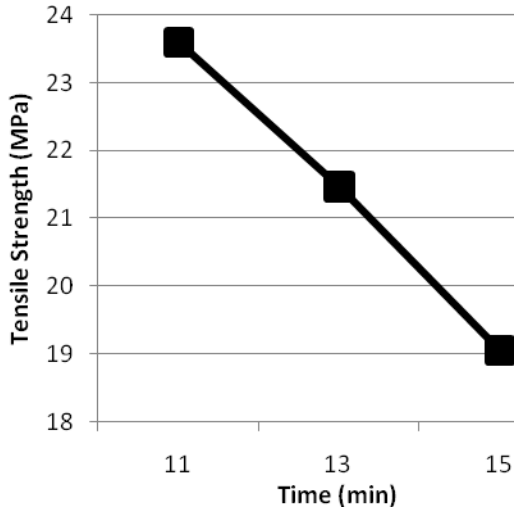


Fig 2. Effect of processing time on tensile properties of TPU-KF composite.

Effect of Processing Speed on Tensile Strength of TPU-KF Composite. Fig. 3 shows the effect of rotating speed on tensile properties of TPU-KF composite. Three different speeds were examined; 30, 40 and 50 rpm. Temperature and time were fixed at 190 °C and 11 min, respectively, as optimized in the previous steps. From Fig. 3 it was found that the optimum processing speed is 40 rpm at 33.4 MPa. It can be seen from Fig. 3 that increasing the speed reduced the strength. This

is due to the friction and breakage of the fibers. On the other hand, at lower speeds the materials are not mixed well (i. e. not homogeneous).

(2) Fiber Size Optimization

Effect of fiber size on Tensile Strength of TPU-KF Composite. Fig. 4 shows the effect of fiber size on tensile strength of TPU-KF composite. Three different sizes were examined mesh 40-50, 50-120 and 120 and below. Temperature, time and speed were fixed at 190 °C, 11 min and 40 rpm, respectively. From Fig. 4 it is noticed that fibers between 125-300 μm gave the best tensile strength. This means a better interfacial bonding and wettability. It can be seen from Fig. 4 that fiber size less than 125 μm resulted in lower strength. The reason behind this is probably because smaller size fiber which possessed larger surface area left more surfaces unreacted with the matrix. Thus, more stress points were created, resulting in reduced tensile strength [8]. For fibers between 300-425 μm, they showed lower strength because of poorer dispersion and agglomeration. Similar trend has been found by sobhy et. al. [16] when studied three different fiber size (i. e. <125 μm, 125-250 μm and 250-500 μm) of wheat husk fibers reinforced rubber composites.

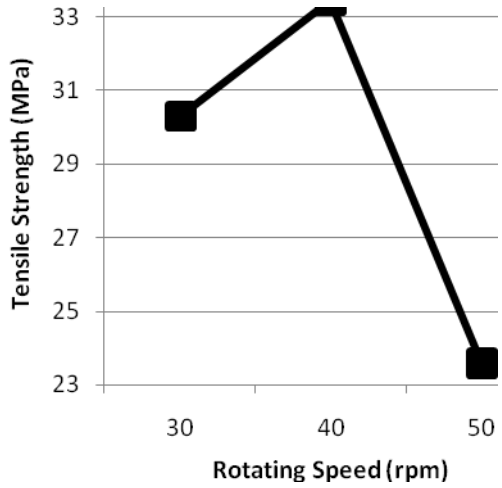


Fig. 3. Effect of processing speed on tensile strength of TPU-KF composite.

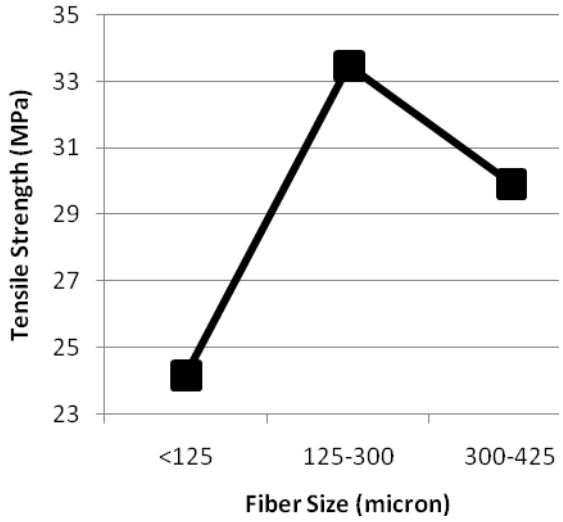


Fig. 4. Effect of fiber size on tensile strength of TPU-KF composite.

Effect of fiber size on Flexural Strength of TPU-KF Composite. Fig. 5 shows the effect of fiber size on flexural strength of TPU-KF composite. From Fig. 5 it is noticed that fibers between size 125-300 μm gave the best flexural strength. It can be seen from Fig. 5 that fiber size lower than 125 μm and fibers between 300-425 μm resulted in lower flexural strength. Flexural strength showed the same trend of tensile strength.

Effect of fiber size on Impact Strength of TPU-KF Composite. Fig. 6 shows the effect of fiber size on impact strength of TPU-KF composite. It can be seen that increasing fiber size resulted in an increasing trend of the impact strength. Fibers between 300-425 μm resulted in only 7 % increment in impact strength. This means that larger fiber size contributed more to absorption of energy.

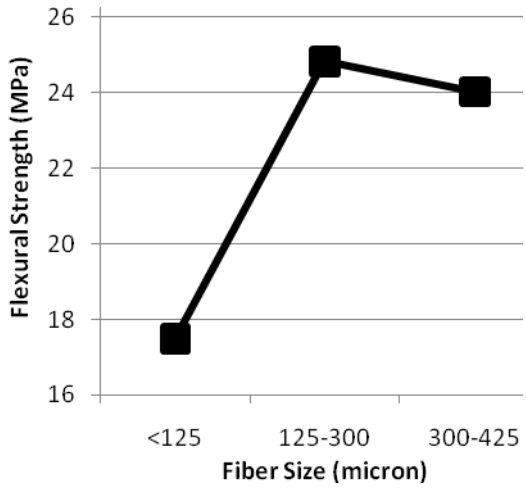


Fig. 5. Effect of fiber size on tensile properties of TPU-KF composite.

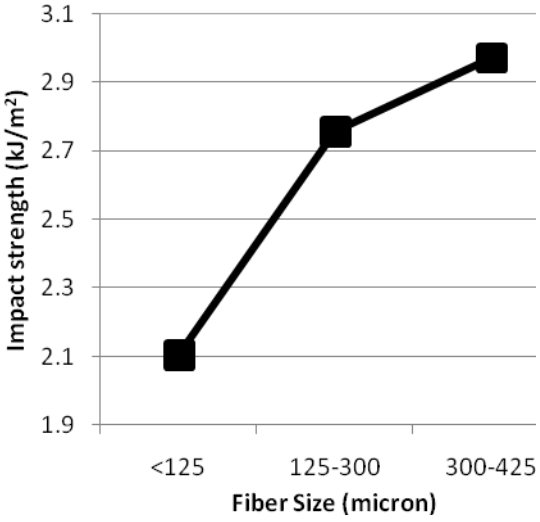


Fig. 6. Effect of fiber size on impact strength of TPU-KF composite.

Summary

TPU-KF composite was developed successfully. It can be concluded that varying processing parameters resulted in significant differences in tensile strength. It resulted in increment from the minimum value of around 16 MPa -for 180 °C, 15 min and 50 rpm; to a maximum strength of 33.5 MPa – for 190 °C, 11 min and 40 rpm. Fiber size between 120-50 mesh resulted in the optimum value among the three sizes examined. This fiber size showed best tensile and flexural strength, due to a better interfacial bonding and better wettability. A larger fiber size showed only a slight increment of impact strength of about 7%.

Acknowledgments

Fundamental Research Grant Scheme (FRGS), Ministry of Higher Education Malaysia grant number (01-10-10-924FR) is acknowledged for support of this study. The authors wish to thank Bayer Co. (Malaysia) Sdn Bhd, Petaling Jaya, Selangor, Malaysia for the TPU supply and information. Authors are also thankful to Mr. Riza Wirawan for many fruitful discussions during the progress of this work.

References

[1] Gao, Z. H., Gu, J. Y., Wang, X. M., Li, Z. G., & Bai, X. D. Pigment and Resin Technology, 34(5), (2005), p. 282.
[2] Girones, J., Pimenta, M. T. B., Vilaseca, F., de Carvalho, A. J. F., Mutje, P., & Curvelo, A. A. S. Carbohydr. Polym, 68(3), (2007), pp. 537–543.
[3] Lee, S. H., & Wang, S. Composites Part A, 37(1), (2006), pp. 80–91.
[4] Rozman, H. D., Tan, K. W., Kumar, R. N., & Abubakar, A. J. Appl. Polym. Sci., 81(6), (2001), pp. 1333–1340.
[5] Özgür Seydibeyoglu, M., & Oksman, K. (2008). Compos. Sci. Technol. 68(3-4), pp. 908–914.
[6] Rozman, H. D., Ahmadhilmi, K. R., & Abubakar, A. Polym. Test., 23(5), (2004), pp. 559–565.
[7] Rozman, H. D., Yeo, Y. S., Tay, G. S., & Abubakar, A. Polym Test, 22(6), (2003), pp. 617–623.
[8] Rozman, H. D., Tay, G. S., Abubakar, A., & Kumar, R. N. Eur. Polym. J. 37(9), (2001), pp. 1759–1765.
[9] Rozman, H. D., & Tay, G. S. J. Appl. Polym. Sci. (2008). 110(6).
[10] Mat Amin, K. A., & Haji Badri, K. J. Appl. Polym. Sci. (2007), 105(5).
[11] Bledzki, A. K., Zhang, W., & Chate, A. Compos. Sci. Technol. 61(16), (2001), pp. 2405–2411.

[12] Anuar, H., Wan Busu, W., Ahmad, S., & Rasid, R. J. Compos. Mater. 42(11), (2008), pp. 1075-1087.
[13] Kutty, S. K., & Nando, G. B. J. Appl. Polym. Sci. 43(10), (1991), pp. 1913–1923.
[14] Pickering,, K., & Kim Louise Pickering, M. *Properties and Performance of Natural Fibre Composites.* (CRC Press 2008).
[15] Geethamma, V. G., Joseph, R., & Thomas, S. J. Appl. Polym. Sci. 55(4), (1995), pp. 583-594.
[16] Sobhy, M. S., & Tammam, M. T. (2010). Int J. Polym. Sci. Article ID 528173, 8 pages.
[17] Takagi, H., & Ichihara, Y. JSME Int J., Ser. A. 47(4), (2004), pp. 551–555.
[18] H. Hutchinson. Mech. Engr. 128(7), 2006, pp. 26-33.
[19] Holbery, J., & Houston, D. (2006). JOM, 58(11), pp. 80–86.
[20] Ashori, A., Harun, J., Raverty, W., & Yusoff, M. Polym. Plast. Technol. Eng. *45*, (2006). pp. 131-134.
[21] Jalaluddin Harun. Presented at the International Conference on Prospects of Jute & Kenaf as Natural Fibres, (2009, February 8), Dhaka, Bangladesh.
[22] Rowell, R. M., Sanadi, A. R., Caulfield, D. F., & Jacobson, R. E. Sao Paulo, USP & UNESP, (1997), pp. 23–51.
[23] Migneault, S., Koubaa, A., Erchiqui, F., Chaala, A., Englund, K., Krause, C., & Wolcott, M. J. Appl. Polym. Sci. *110*(2), (2008), pp. 1085–1092.

© (2011) Trans Tech Publications, Switzerland
doi:10.4028/www.scientific.net/KEM.471-472.303

Effect of Hydroxyapatite Reinforced High Density Polyethylene Composites on Mechanical and Bioactivity Properties

Muhamad Rasyidi Husin[1,a], Mat Uzir Wahit[1,b], Mohammed Rafiq Abdul Kadir[2,c], Wan Aizan Wan Abd. Rahman[1,d]

[1]Faculty of Chemical Engineering, Universiti Teknologi Malaysia, 81310 Skudai, Johor, Malaysia,

[2]Faculty of Biomedical & Health Science Engineering, Universiti Teknologi Malaysia, 81310 Skudai, Johor, Malaysia

[a]hmrasyidi@gmail.com, [b]mat.uzir@cheme.utm.my, [c]rafiq@biomedical.utm.my, [d]w.aizan@cheme.utm.my

Keywords: High density polyethylene, hydroxyapatite, composites, mechanical properties, bioactivity properties.

Abstract: The biomaterial composites consisting of a polymer with a matrix addition of particulate bioactive phase that analogous to the bone microstructure had been extensively studied as a substitute for human's hard and soft tissues. In this work, HA reinforced HDPE composite (HDPE/HA) was made, with HA contents being up to 50 phr using single screw extruder nanomixer for the compounding process, and later followed by the injection moulding. These characteristics of the HDPE/HA composites were examined using various techniques including differential scanning calorimetry (DSC), scanning electron microscopy (SEM), tensile testing. Mechanical and thermal properties of the composite are differed when the amount of HA incorporated into the composite were varied. It is shown that HA particles were well dispersed and homogeneously distributed within the HDPE matrix. The elastic modulus and tensile strength were increased when the HA volume percentage increased from 10 phr to 50 phr with corresponding decreases in elongation at break. However no significant influence on thermal stability was found with increasing HA loadings. The enhancement of bioactivity has been proved while incorporation of HA into HDPE composite. SEM-EDX image showed the bulk formation of apatite layers on the composite surface with 30 wt% HA after 7 days immersed in simulated body fluid (SBF) solution. These results suggest the great potential of the composites for a range of temporary application in which bone bonding ability is a desired property.

Introduction

The choice of polymer composite as bone replacement material largely depends on the mechanical properties of the polymer and the ability to bond with bone or to induce bone ingrowths. Bonfield and coworkers were pioneered the development of Hydroxyapatite (HA) reinforced high density polyethylene (HDPE) composite as a bone substitute since early 1980s [1]. The inclusion of HA filler particles to form composites has been shown to enhance mechanical properties and exhibits excellent bioactivity properties [2]. In addition, HA ceramics do not exhibit any cytotoxic effects. In terms of processing, HA particles was successfully dispersed in HDPE matrix processed by twin screw extruder [1]. However, there was no reports on the inclusion of HA processed using single screw extruder nanomixer. There is a considerable interest in order to evaluate the bioactivity properties in simulated body fluid [3,4] to determine the effectiveness of the composite in bone formation. Thus, in this study the aimed is to produce HDPE/HA composite with combination of excellent mechanical and bioactivity properties produced by single screw extruder nanomixer.

Experimental

Materials. The synthetic hydroxyapatite ($Ca_{10}(PO)_6(OH)_2$) used was (grade 21223 Fluka, Sigma Aldrich, Malaysia.), was supplied in a powder form. The specific surface area of the powder (according to the Brunnauer- Emmett-Teller method) was found to be 33.05 m^2/g, and the particle size is 7.51 μm. HDPE (Etilinas HD5403AA) was supplied by Polyethylene Malaysia Sdn Bhd with density of 0.954g/cm^3 and melt flow rate (MFR) of 0.25g/10min.

Compounding and Sample Preparation. The granules of HDPE were grind into powder prior mixing with HA, in order to get uniform composition all through the batch size. These uniformly mixed polyethylene batches were then melt-blended in a single screw extruder nanomixer with a screw speed of 50 rpm with HA weight ranging from 10 to 50 phr as shown in Table 1.

Table 1: Blends composition of HDPE/HA

Designation	(Composition) phr	
	HDPE	HA
HDPE/10HA	100	10
HDPE/20HA	100	20
HDPE/30HA	100	30
HDPE/40HA	100	40
HDPE/50HA	100	50

The temperature profile of the extruder was set as 180, 190, 190 and 200 ^oC at the fed zone, metering zone and die, respectively. The material was extruded in the form of strands trough a two holes die into distilled water bath at room temperature to prevent oxidation of the polymer and subsequently, pelletized. Then the pelletized composites particles were dried at 80^oC for 2 hours in a vacuum chamber. The resin pellets were then injection moulding by using multiple-specimen mould into ASTM standard for tensile, flexural and izod impact test. The machine is a JSW model NIOOB II injection moulding machine with the barrel temperature of 180 - 240^oC.

Tensile Test. The injection moulded tensile specimens (standard ASTM D638 specimens: dumbbell specimens were 9.75 mm x 3.3 mm x 112 mm (width x thickness x length)) were used to evaluate main mechanical properties of the composite. Tensile tests were conducted on a Lloyd testing machine at a crosshead speed of 5 mm/min. At least five specimens were used for each composition of the composite.

Impact Test. The Izod impact tests will be carried out on notched specimens using Toyoseiki impact tester according to ASTM D256. In all cases, fives specimen were tested for each composite and the average values will be reported.

Simulated Body Fluid. In vitro test was carried out following the Kokubo method [5]. The SBF was prepared by dissolving reagent NaCl, $NaHCO_3$, KCl, $K_2HPO_4.3H_2O$, $MgCl_2.6H_2O$, $CaCl_2.2H_2O$ and Na_2SO_4 into distilled water and buffered with Tris (hydroxyl-methyl-amino-methane, $NH_2C(CH_2OH)_3$) and hydrochloric acid (HCl) to pH 7.4 at 37 ^0C. The solution of SBF containing ion concentrations was nearly the same with those in human blood plasma [5]. Each specimens was immersed in 200 ml of SBF and the solution was placed in an incubator for 1 to 7 days at temperature of 37 ^0C.

Result and Discussion

Impact property. The impact strength data presented in Figure 1 shows a significant reduction in impact strength after the initial loading of 10 phr HA and remain stable with increasing HA content. The low compatibility between HA and HDPE matrix disrupts the continuity of the matrix and restricted the capability of the matrix to dissipate impact energy applied. Therefore, lowering the energy absorbed and reduced the impact strength values.

Tensile Test. The tensile strength, elastic modulus and elongation at break of the composite are shown in Figure 2, 3 and 4 respectively. It can be observed that the tensile strength and elastic modulus increased gradually with the expense of elongation at break as the HA content increased from 10 to 50 phr. Incorporation of 50 phr HA results in 32% increment in tensile strength while the elastic modulus increases almost 78% of HDPE/HA composite as compared to HDPE. The results were consistent with previous study reported by Wang et al, [6] who found that tensile strength and elastic modulus increased with increasing HA loadings. Addition of HA to this polymer enhances rigidity and brittleness of these polymers matrix composites, thus enhances modulus of the composites. The elongation at break was found decreased by 86% with addition of 10 phr HA and maintained up to 50 phr HA. The increment in tensile strength is believed due to the uniform HA dispersion in polyethylene matrix. SEM results as shown in Figure 5 supports the result obtained. It is clearly observed that HA particles are well dispersed and embedded in the HDPE matrix. According to Wang *et al.*[7] filler dispersion and the wetting ability of the matrix to filler particles is greatly influenced the strength of the composite.

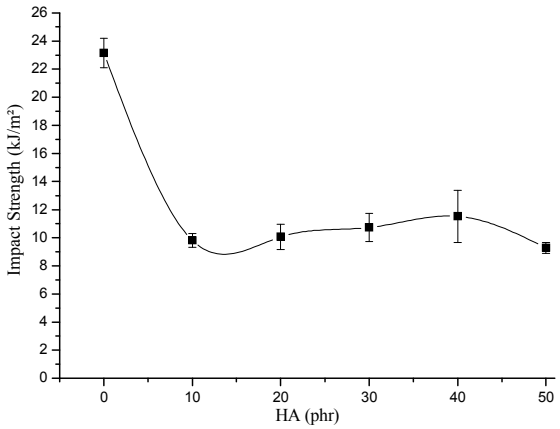


Figure 1: Impact strength of HDPE/HA composites.

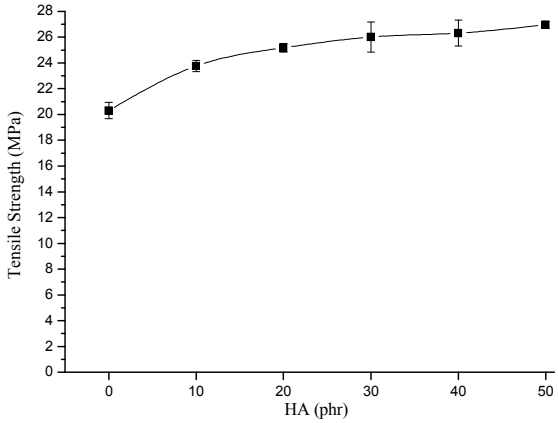


Figure 2: Tensile strength of HDPE/HA composites.

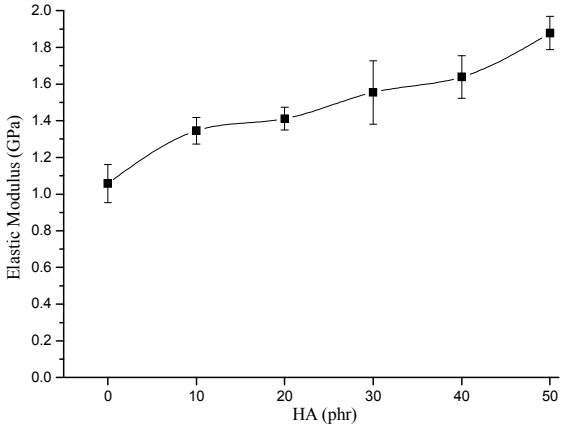


Figure 3: Elastic Modulus of HDPE/HA composites.

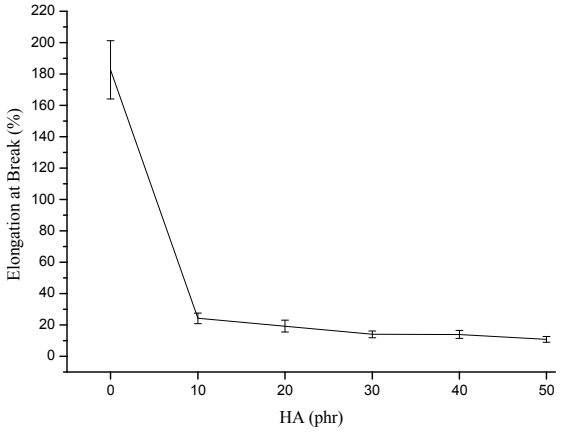


Figure 4: Elongation at breaks of HDPE/HA composites.

Scanning electron microscopy. SEM micrograph of impact fracture surfaces are shown in figure 5, it can be seen that the HA particles were well dispersed, with a homogeneous distribution in the polymer matrix.

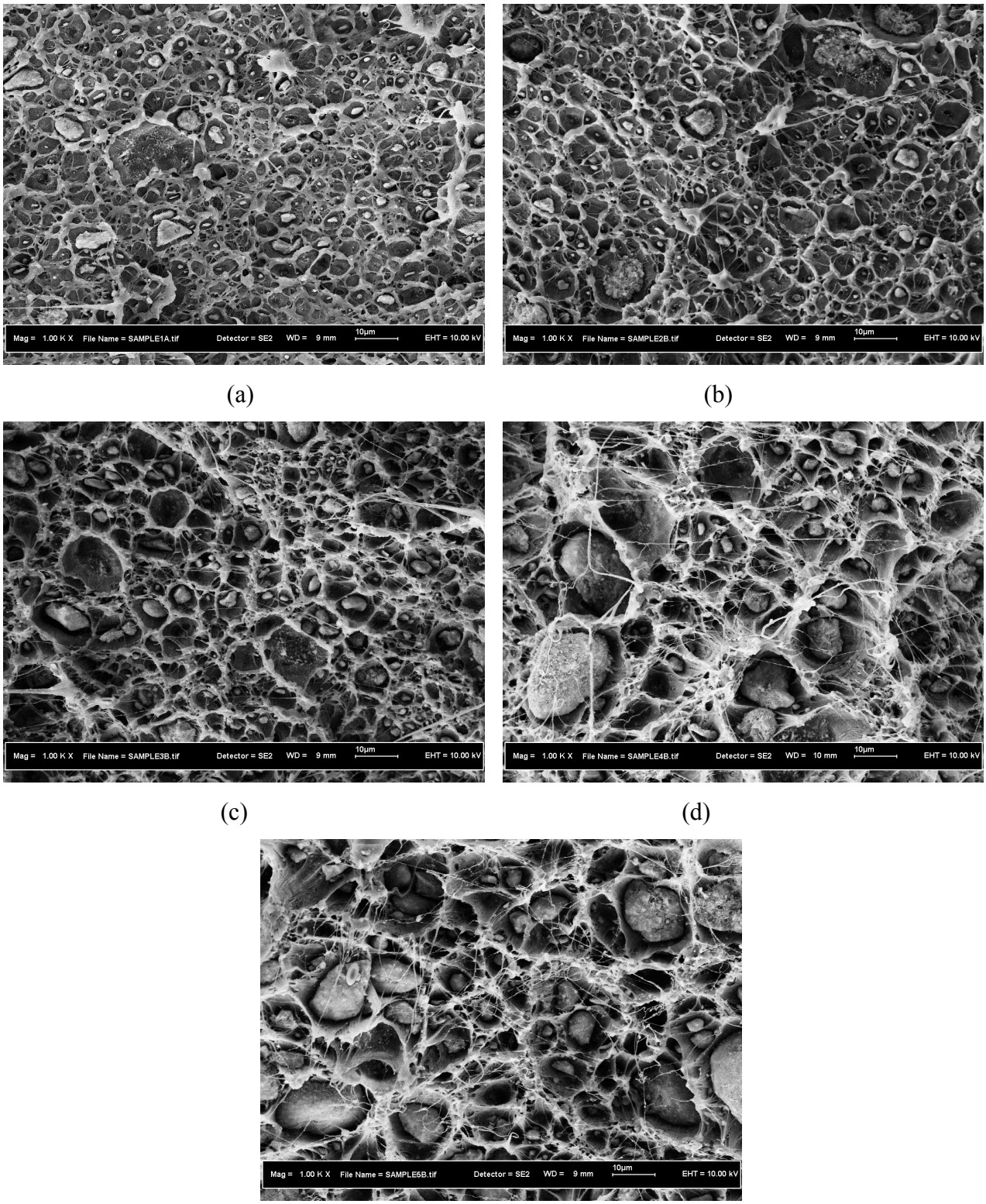


Figure 5: SEM micrographs showing on the fracture surface of (a) HDPE/10HA (b) HDPE/20HA (c) HDPE/30HA (d) HDPE/40HA (e) HDPE/50HA composites, HA particles embedded in the polymer matrix can be seen.

Bioactivity test. The result of bioactivity tests agreed with those obtained in SEM observations. A Ca-P formation was formed on the surface of the HDPE/HA composites after the immersion in the SBF for 7 days. The formations of apatite (Ca-P) layer as shown in Figure 6 confirm that the composite exhibits an in-vitro bioactivity behaviour. The bulk formation of apatite layer was result from the ion exchange occurs during immersion. Formation of apatite layer was unclear seen for composite soaked in 3 days. However, it is interesting to observe that the apatite layers growth rapidly within 7 days of SBF immersions. The apatite layers cover the surface of the composites and grew in size, indication of excellent bioactivity properties of HA. This was in aggrement with findings reported by others researchers [8]. From the results, it is suggested that the HDPE/HA composite with effective bioactive properties was successfully developed.

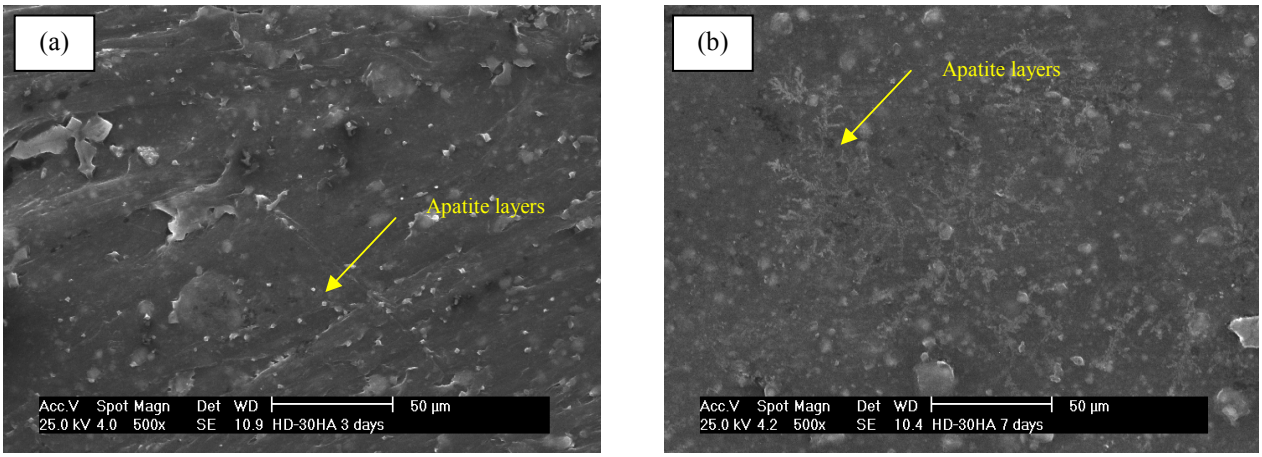


Figure 6: SEM micrographs showing of the CA-P layer on the surface of HDPE/30HA composite after 3 days (a) and 7 days (b) immersion in the SBF.

Summary

The effect of HA contents on the mechanical properties of HDPE/HA composites was investigated. Tensile test results showed an increase in elastic modulus and tensile strength with increasing HA contents for HDPE/HA composites. In contrast, the impact strength and elongation at break of the composite decreased drastically with increasing HA contents from 10 to 50 phr HA. The highest tensile strength and elastic modulus was observed in HDPE/HA composites with 50 phr HA loadings. It can be concluded that the composites with homogeneous distribution of HA particle in HDPE matrix with a combination of high elastic modulus and tensile strength was successfully developed by using single screw extruder nanomixer. In vitro study was conducted to investigate the biological response of HDPE/HA in SBF. It is also emerged from this study that HA particle loadings guarantee the growth of apatite layer as well as needed by the fracture part of bone during healing progression.

References

[1] W. Bonfiled, Grynpas, M. D., Tully, A. E., Bowman, J., and J. Abraham, (1981) "Hydroxyapatite reinforced polyethylene--a mechanically compatible implant material for bone replacement." *Biomaterials.* 2, 185.

[2] L. Fang, P. Gao, and Y. Leng, (2006)."Processing and Mechanical Properties of HA/UHMWPE Nanocomposites." Biomaterials. 27.3701-3707.

[3] M.H. Fathi, V. Mortazavi, S.I.R. Esfahani, (2008) "Bioactivity evaluation of synthetic nanocrystalline hydroxyapatite." *Dental Research Jurnal* 5, 2.

[4] W. Zhao, J. Chang, J. Wang, W. Zhai, and Z. Wang, (2007) "In vitro bioactivity of novel tricalcium silicate ceramics" *Journal of Materials Science: Materials in Medicine* Vol. 18, 5, 917-923,

[5] T. Kokubo, H. Kushitani, S. Kitsugi and T. Yammamuro, (1990). "Solutions able to reproduce in vivo surface structure changes in bioactive glass-ceramic A-W." *J Biomed Mater Res* 24, 721-34.

[6] M. Wang, D. Porter and W. Bonfield (1994) Processing characterisation and evaluation of hydroxyapatite reinforced polyethylene composites, *Br. Ceram.Trans.* 3, pp. 91–95.

[7] A. Wang, A. Essner, V.K. Polineni, C. Stark and J.H. Dumbleton (1998). "Lubrication and Wear of Ultra-High Molecular Weight Polyethylene In Total Joint Replacements". Tribology International, Vol. 31, Nos 1-3.Page 17-33.

[8] Y.W. Gu, K.A. Khor and P. Cheang (2003). "In vitro studies of plasma-sprayed hydroxyapatite/Ti-6Al-4V composite coatings in simulated body fluid (SBF)". *Biomaterials* 24, 1603-1611.

© (2011) Trans Tech Publications, Switzerland
doi:10.4028/www.scientific.net/KEM.471-472.309

Microanalysis techniques for the investigation of interphases formed between thermoset and thermoplastic polymers: Scanning electron microscopy and energy dispersive x-ray analysis

Michael T. Heitzmann[1,a], Meng Hou[1,b],Martin Veidt[1,c], Rowan Paton[2,d] and Ron Rasch[3,e]

[1]School of Mechanical and Mining Engineering, The University of Queensland, Brisbane, Australia

[2]Cooperative Research Centre for Advanced Composite Structures, 506 Lorimer Street, Melbourne, Australia

[3]Centre for Microscopy and Microanalysis, The University of Queensland, Brisbane, Australia

[a]m.heitzmann@uq.edu.au, [b]m.hou@uq.edu.au, [c]m.veidt@uq.edu.au, [d]r.paton@crc-acs.com.au, [e]r.rasch"uq.edu.au

Keywords: Micro analysis, SEM, EDX, semi interpenetrating networks

Abstract. Prepreg resin systems are typically of complex composition and require very specific manufacturing conditions. These characteristics restrict the use of some commonly used micro analysis techniques. This paper investigates the use of low acceleration voltage scanning electron microscopy and energy dispersive x-ray analysis for the characterization of diffused polymer interfaces. It is shown that, by operating at the dynamic charge balance, high resolution secondary electron images of polymer interfaces can be obtained and that conductive coating is not required. In addition, the effect of acceleration voltage on the interaction volume in EDX analysis is discussed using Monte Carlo simulation. X-ray intensity measurements in combination with afore mentioned Monte Carlo simulation is used to define practically obtainable spatial resolution limits. It is shown that by reducing the acceleration voltage below 5kV spatial resolution higher the 500nm can be obtained.

Introduction

Previous research has shown that certain thermoset resin, or parts thereof, can diffuse into thermoplastic polymers when co-cured in immediate contact [1-3]. These graded interfaces drastically improve the adhesion between the two polymers [4-6]. The study of the diffusion of epoxy based resin into thermoplastic polymers has received considerable attention over the last two decades due to the commercial significance of this resin system. Most previous research used relatively simple resin formulations, consisting of a maximum of three parts taking part in the curing reaction. With applications, making use of the enhanced adhesion trough interphase formation, pushing into commercial applications the attention will inevitably shift to the study of commercial resin formulations and in particular to prepreg resin systems. In contrast to resins selected from a scientific point of view, commercial prepreg resin systems commonly exhibit complex formulations consisting of multiple curatives, tougheners and various thermoplastic additives in often unknown quantities.

A series of different micro analysis techniques have previously been employed to study these interdiffusion phenomena, e.g. scanning electron microscopy (SEM) [7], electron micro probe analysis (EMP)[8], transition electron micron spectroscopy (TEM) [9], vibrational spectroscopy [10-12] and ion-beam analysis[13-15]. All these methods have their own advantages and disadvantages and best results are often obtained using multiple methods. When investigating interdiffusion mechanisms between commercial prepreg resin systems and comitial available thermoplastic polymer films, under industrial production manufacturing conditions, constrains in relation to sample preparation and experimental setup arise making some of the above methods cumbersome or impossible to employ. SEM and energy-dispersive X-ray analysis (EDX) are amongst the most commonly available micro analysis tools and have distinct advantages when it

comes to ease of use and sample preparation. Nevertheless, these techniques are sparingly used for the investigation of interphase phenomena. Sample decomposition and limited resolution due to a large interaction volume, in the case for EDX, explain some of the reservations.

The first section of this paper describes the use of ultra low voltage SEM and low acceleration voltage EDX as tools for the investigation of thermoplastic/thermoset interdiffusion interfaces. Dynamic charge balancing is used to obtain high resolution secondary electron (SE) images on uncoated samples. One of the major concerns when applying EDX for the characterization of interfaces is the influence of the interaction volume. In section two Monte Carlo simulation and EDX measurements on Epoxy/PSU interfaces are used to elaborate the influence of acceleration voltage, coating procedure, selection of a trace element on the accuracy and the resolution limit of this method.

Low voltage SEM.

Conducting SEM on polymer samples under conventional high acceleration voltage conditions, i.e. >10kV, can lead to sample decomposition, as shown in Fig. 1., inevitably distorting fine surface details. At high voltages, coating the sample with a conductive coating, e.g. platinum (Pt), carbon (C) or gold (Au), is necessary to avoid positive charging of nonconductive samples. Low acceleration voltage can help to avoid thermal damage to the polymer, however when using coated samples most of the electrons are absorbed in the coating layer and most information is collected from this area. Fig. 2. shows the energy distribution and the backscatter intensity as a function of depth for a 10nm platinum coating on a PSU polymer. It can be seen that only low energy electrons reach the actual sample surface and that no backscatter information can be obtained from the sample area.

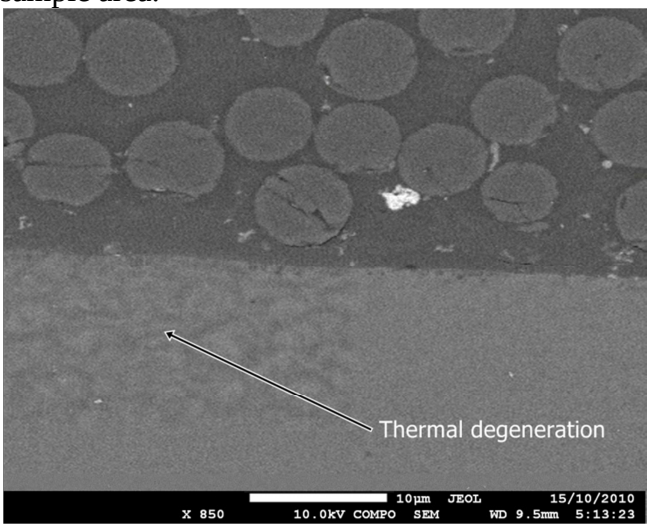


Fig.1: Sample degeneration due to high energy acceleration voltage

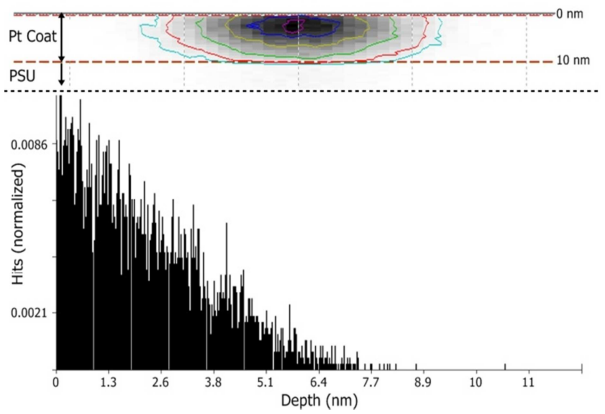


Fig.2: Interaction volume in 10nm Pt-coat (top) and backscatter electron density in dependence of depth at 1.5 kV

One way to avoid coating of samples is to make use of the charge balance. The charge balance is given by Kirchoff's law

$$I_B = (\eta + \delta)I_B + I_{SC} + \frac{dQ}{dt} \quad (1)$$

where δ, η are the backscatter electron (BSE) and secondary electron (SE) yields respectively, and Q is the charge deposited in the specimen after some time. For a non conductive sample $I_{SC} = 0$ and if we require the sample to stay charge neutral, then also $dQ/dt = 0$. With these assumptions we can derive a simple expression for the dynamic charge balance [16].

$$(\eta + \delta) = 1 \quad (2)$$

For the case that $(\eta+\delta)>1$ positive charging of the sample occurs and for $(\eta+\delta)<1$ the sample will charge negative. Most materials have two energies where the dynamic charge balance is obtained; these are typically referred to as E_1 and E_2. For most materials E_1 is at energies not suitable for SEM operation and also does not present a stable operating condition [16]. As shown by D. Joy [16] the E_2 points for most polymers are between 1-2 kV. When looking at polymer interfaces the two polymers are likely to have different E_2 points, however by operating the SEM just below the E_2 point of the material with the lower E_2 cross over charge free images can be obtained in most cases. This can be explained with an automatic compensation mechanism as negative charge locally increases the landing energy which moves the dynamic balance closer to E_2. Using this technique it is possible to obtain high resolution images of polymer-polymer interface regions with limited amount of sample preparation. Fig. 3 shows phase separation occurring on the interface between a fluoropolymer and a prepreg expoxy system. A JEOL 7001 FESEM system was used for this analysis.

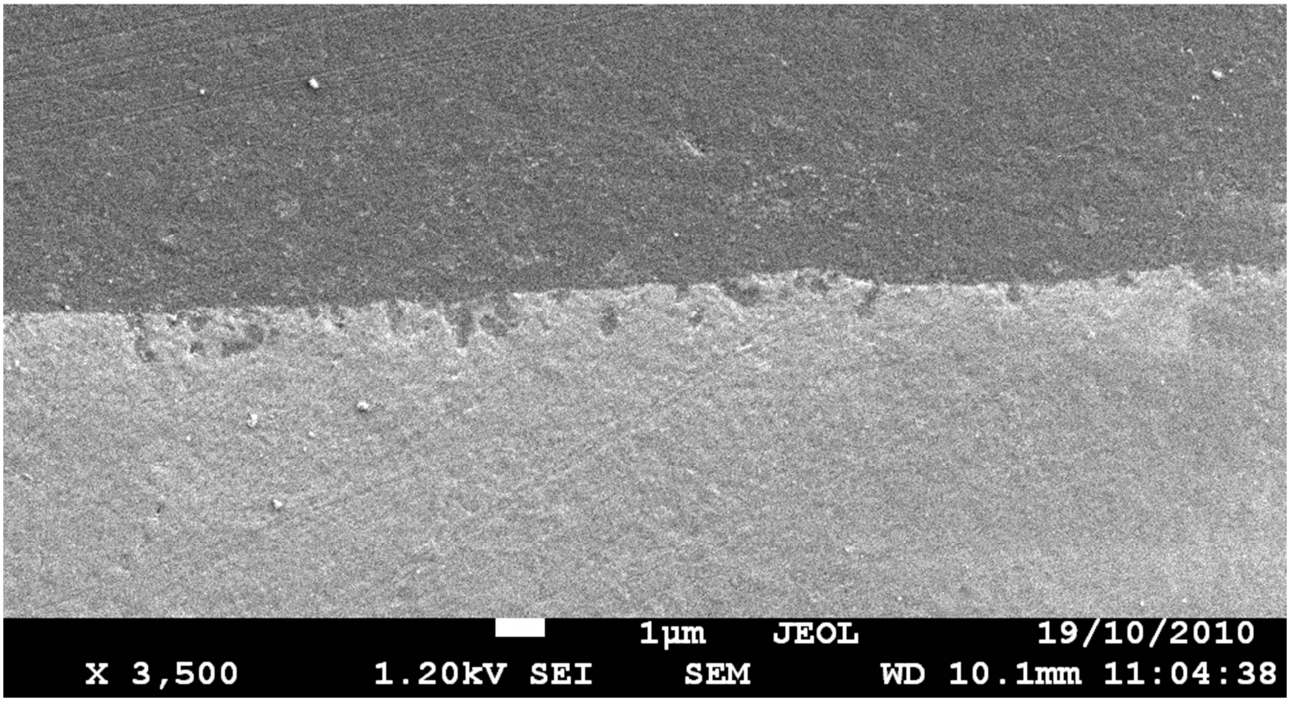


Fig. 3: Secondary electrone image of a fluoropolymer and epoxy interface showing phase separation in the interface region.

One limitation of this method is that the compositional contrast obtained in SE mode depends on the density of the polymers and the atomic number of their elements. In some cases no contrast can be obtained between two dissimilar polymers due to their similar densities and compositions. New through the lens systems (TTL) provide additional features which enable the collection of low energy backscatter which typically cannot be resolved with conventional backscatter detectors. Work is in progress to investigate the suitability of these novel systems.

Low voltage energy dispersive X-ray analysis

Energy dispersive X-ray analysis is a well known tool for compositional micro analysis. It is also well known that the interaction volume from which the X-rays are collected limits the maximum obtainable spatial resolution. In this research Monte Carlo simulation in combination with EDX measurements are used to investigate some of the important aspects and limitations of interface characterization using EDX. CASINO v.2.4 was used for the Monte Carlo simulation. A detailed description of the capabilities of this software can be found in [17]. For the present study two simplified material models for polysulfone (PSU) and TGMDA/MPDA Epoxy were used. Composition details are shown in Table 1.

Table 1: Composition details of materials used in Monte Carlo simulation

PSU			**Epoxy (TGMDA/MPDA)**		
Density	1.24 g/cm^3		Density	1.22 g/cm^3	
Element	**Z**	**Atomic Fraction**	**Element**	**Z**	**Atomic Fraction**
C	6	0.7105	C	6	0.3899
O	8	0.1053	H	1	0.5084
S	16	0.0263	N	7	0.0338
H	1	0.1579	O	8	0.0677

Using these two materials an EDX analysis across a non-diffused interface of the two materials was simulated to determine the effect of the interaction volume on the accuracy of this method in relation to the acceleration voltage. The acceleration voltage has the main influence on the interaction volume, however the beam diameter has also a influence on the interaction volume. This parameter mainly depends on SEM/EDX machine design and operating conditions and was set to 100nm for this analysis based on SEM spatial resolution measurements. Fig. 4 shows the normalized Kα X-ray intensity for nitrogen and sulfur. In practice nitrogen renders less suitable as a trace element as its Kα peak (0.392kV) is in close proximity to the carbon Kα peak (0.277), which makes separation of the two peeks difficult. However, in this case these two trace elements are particularly suitable as they occur in one material only and also highlight the effect of atomic number on the interaction volume. One can see that for acceleration voltages above 10kV, where EDX typically is conducted, the spatial resolution is lower than 1.5µm for the nitrogen trace and 1µm for the sulfur trace. However, when the acceleration voltage is reduced below 5kV the resolution is increased to 0.5 µm for nitrogen and 0.25 µm for the sulfur element respectively. Lowering the acceleration voltage has direct implication on the rate at which electrons are collected for analysis. To study this effect X-ray spectra were collected on PSU at different acceleration voltages.

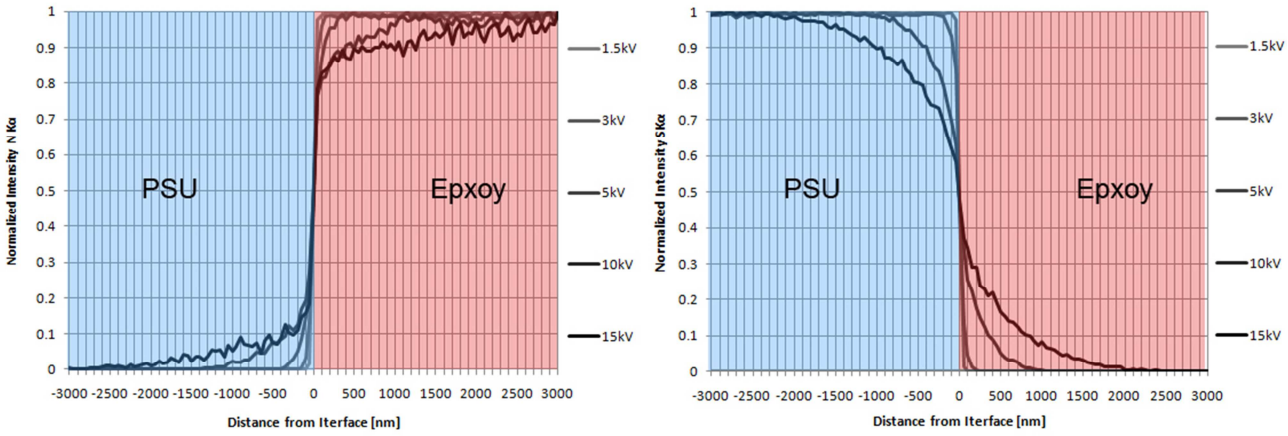
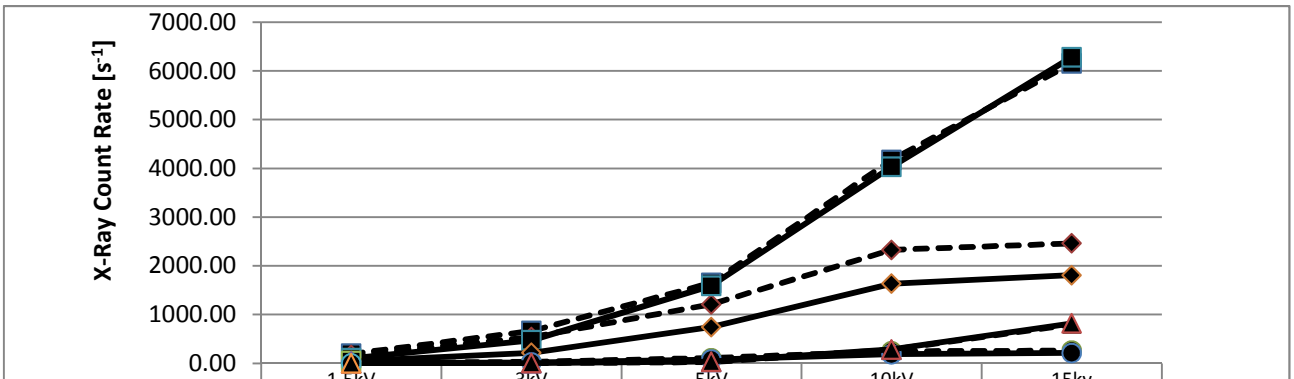


Fig. 4: Normalized N Kα and S Kα X-ray intensity across a non diffused PSU/Epoxy interface obtained from monte Carlo simulation for accaleration voltages between 1.5 and 15k

A JSM 6460LA with JEOL Mini-Cup EDX detector was used and all spectra were collected in spot mode for 60sec live time. The individual element X-ray count was calculated by the sum of counts for all bins 50eV above and below the peak. In order to study the effect of the conductive coating the analysis was conducted for carbon coated and PT coated samples. Coating thickness was approximately 10nm for both materials. As explained in the previous section coating free SEM/EDX must be conducted at acceleration voltages below E2, typically below 2kV. This energy is too low to excite X-ray with atomic numbers larger than 14. Fig. 5 shows a summary of the EDX results. One can see that there is very little difference in the recorded intensities for carbon and platinum coated samples. As a consequence of this platinum coating is regarded as the more favorable means of coating due to the lower electric resistance and the ability to be coated in thinner layers. The results also highlight that by lowering the acceleration voltage from 10 kV to 5kV the overall X-ray count rate is reduced by a factor of 2.5. This is also approximately the factor by which

the C Kα X-ray count is reduced. For higher atomic number elements the difference is more severe, for example the S Kα count is reduced by a factor of 8. Reduction to 3kV acceleration voltage yields 8 times lower C Kα X-ray count rate and more than 50 times lower S Kα count rate. Consequently this means that the acquisition time has to be adjusted in accordance to these factors. In many situations increasing the acquisition time by a factor of 8 is deemed acceptable. This leads to the conclusion that EDX analysis can be conducted at 5kV acceleration voltage for most polymers and at acceleration voltages as low as 3kV for polymers when only elements from the second row in the periodic table are used as a trace element. Under these operation constraints a spatial resolution higher than 500nm can be obtained which allows resolving small interphases as they are expected in combination with commercial prepreg resin systems.



	1.5kV	3kV	5kV	10kV	15kv
C-Coat (Total)	194.22	662.43	1650.70	4173.48	6152.95
C-Coat (C)	169.65	535.53	1209.88	2327.58	2462.25
C-Coat (O)	3.02	28.85	106.40	248.70	261.57
C-Coat (S)	0.00	1.15	24.15	277.97	799.60
PT-Coat (Total)	102.92	470.68	1591.78	4032.52	6281.53
PT-Coat (C)	45.18	216.65	742.92	1634.73	1806.72
PT-Coat (O)	5.97	19.83	78.90	186.83	212.18
PT-Coat (S)	0.00	4.85	35.62	284.53	819.73
No-Coat (Total)	49.07				
No-Coat (C)	40.67				
No-Coat (O)	1.23				
No-Coat (S)	0.00				

Fig. 5: X-Ray count rates obtained from EDX spot analysis

Summary

The research presented in this paper has shown that SEM/EDX can be valuable tools for the characterization of polymer interphases. SEM at low acceleration voltage and uncoated samples, by operating at the dynamic charge balance, can yield high resolution SE images of poymer interfaces exceeding 50nm resolution. A limitation of this technique is the missing compositional contrast when density and/or atomic number difference is not sufficient. Monte Carlo simulation and EDX spot analysis was used to demonstrate that low acceleration voltage EDX is an alternative to other micro analysis techniques for interphase characterization. By conducting EDX at acceleration voltages below 5kV a spatial resolution higher then 500nm can be obtained making this method competitive with other methods. As a consequence of the low acceleration voltage longer acquisition times are however required. Based on the conducted research one can conclude that the maximum practical obtainable resolution for light atoms is approximately 250nm. Additional research is required to investigate the suitability of new through the lens systems for SEM imaging of polymer interfaces and EDX analysis needs to be conducted to verify the results obtained from Monte Carlo simulation.

References

[1] Munz M, Sturm H, Stark W. Polymer. 2005;46(21):9097-9112.

[2] Munz M, Sturm H, Schulz E, Hinrichsen G. Composites Part A: Applied Science and Manufacturing. 1998;29(9-10):1251-1259.

[3] Rajagopalan G, Immordino KM, Gillespie Jr JW, McKnight SH. Polymer. 2000;41(7):2591-2602.

[4] McKnight SH, Don RC, Scott M, Braem A, Gillespie JW. Experimental investigation of diffusion enhanced adhesive bonding for thermoplastic composites. Conference Proceedings, Society of Plastics Engineers, Annual Technical Meeting. 1995.

[5] Rajagopalan G, Immordino KM, McKnight SH, Gillespie J.W, Jr. Proceedings of the 11th Technical Conference of the American Society for Composites. 1996:539.

[6] Immordino KM. Characterization of the Polysulfone/epoxy Interphase for Bonding Thermoplastic Composites. 1996.

[7] Gilmore PT, Falabella R, Laurence RL. Polymer/polymer diffusion. 2. effect of temperature and molecular weight on macromolecular diffusion in blends of poly(vinyl chloride) and poly(ε-caprolactone). Macromolecules. 1980;13(4):880-883.

[8] Oyama HT, Solberg TN, Wightman JP. Polymer. 1999;40(11):3001-3011.

[9] Spontak RJ, Williams MC, Agard DA. Interphase composition profile in SB/SBS block copolymers, measured with electron microscopy, and microstructural implications. Macromolecules. 1988;21(5):1377-1387.

[10] Jabbari E, Peppas NA. Journal of Materials Science. 1994;29(15):3969-3978.

[11] Eklind H, Hjertberg T. Determination of interdiffusion in thin polymer films using FTIR reflection absorption spectroscopy. Macromolecules. 1993;26(22):5844-5851.

[12] Hong PP, Boerio FJ, Clarson SJ, Smith SD. An investigation of the interdiffusion of polystyrene and deuterated polystyrene using surface-enhanced Raman scattering. Macromolecules. 1991;24(17):4770-4776.

[13] Tead SF, Kramer EJ, Russell TP, Volksen W. Interdiffusion at polyimide interfaces. Polymer. 1992;33(16):3382-3387.

[14] Kramer EJ, Green P, Palmstrøm CJ. 1984;25(4):473-480.

[15] Kramer EJ. Ion-beam analysis of polymer surfaces and interfaces. MRS Bulletin.

1996;21(1):37-42.

[16] Joy D. Charging Control. ACMM19, Sydney2006.

[17] Drouin D, Couture AR, Joly D, Tastet X, Aimez V, Gauvin R. CASINO V2.42—A Fast and Easy-to-use Modeling Tool for Scanning Electron Microscopy and Microanalysis Users. Scanning. 2007;29(3):92-101.

© (2011) Trans Tech Publications, Switzerland
doi:10.4028/www.scientific.net/KEM.471-472.315

Measurements of interface fracture strength between fiber-reinforced composite laminates and thin surface films using the blister test

Michael T. Heitzmann[1,a], Meng Hou[1,b],Martin Veidt[1,c] and Rowan Paton[2,d]

[1]School of Mechanical and Mining Engineering, The University of Queensland, Brisbane, Australia

[2]Cooperative Research Centre for Advanced Composite Structures, 506 Lorimer Street, Melbourne, Australia

[a]m.heitzmann@uq.edu.au, [b]m.hou@uq.edu.au, [c]m.veidt@uq.edu.au, [d]r.paton@crc-acs.com.au,

Keywords: Blister test, energy release rate, fracture toughness, fracture mechanics

Abstract. The blister test is a promising test method to determine the interface fracture toughness of thin films adhering to rigid fibre reinforced plastics. In this paper nonlinear finite element analysis is used to determine a suitable layout for both the shaft loaded and the pressurised blister test. On the example of a PET film adhering to a quasi-isotropic fibre reinforced plastic, it is shown that energy release rates in a range of 0-1500N/m can be obtained for a 0.5mm thick film if test parameters are carefully selected. The two main causes for deviations of the analytic solution from the FEA results is attributed to infringement of the membrane limit condition and plastic deformation in the film.

Introduction

Thin films or coatings are increasingly used across a variety of composite manufacturing processes and products. These films are used as protective films and coatings; tie layers; decorative finishes; and functional surfaces of various types. Strong adhesion to the substrate is often one of the main performance criteria and hence quantitative assessment of the interface bond strength is highly desired. However, deriving an accurate and physically meaningful value that characterizes the bond strength is often difficult.

The shaft-loaded blister test (SLBT) and the pressurized blister test (PRBT) are promising alternative to better known adhesion tests like the double-cantilever beam (DCB) test or the lap-shear test. When used for testing the bond strength of thin films or coatings on fibre reinforced plastics, sample preparation is often straight forward and less cumbersome than for other adhesion tests.

The blister test was initially proposed by Dannenberg [1] in the form of the pressurised blister test, where a pressurised fluid is used to form the blister. Based on Dannenberg's proposition, Malyshev and Salganik [2] derived the shaft-loaded blister test by using the loaded shaft as the crack driving force. Figure 1 shows a schematic of the two tests variants. When deriving analytical solutions, some fundamental assumptions have to be made, which significantly influence the application range of the test and its accuracy. The most important assumption is that of plate vs. membrane theory. Pure plate behaviour assumes that the bending moment created at the crack interface is the only cause for crack propagation [3, 4]. In contrast to pure bending, pure stretching assumes that the flexure rigidity is zero and hence stretching is the crack driving force [5].

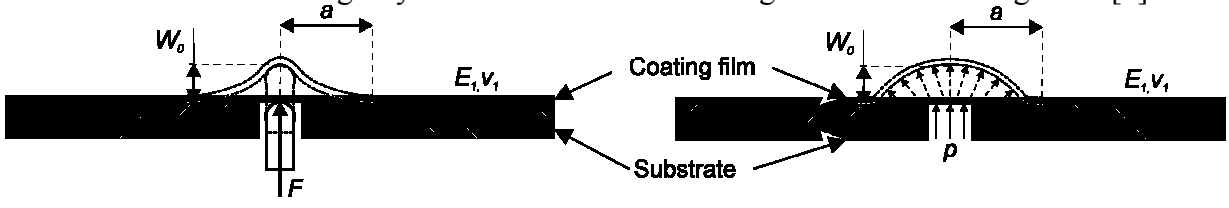


Fig. 1: Schematic representation of the SLBT (left) and the PRBT (right)

In reality both bending and stretching is present, which is the reason for numerous contributions describing the transition from bending to stretching. These solutions are based on the Karman equations which are adapted to circular plates. Jensen [6], Thouless and Jensen [7] and Wan [8] have all studied the transition from stretching to bending. Thouless [9], Margaretis et al. [10], Wan and Mai [5] have made propositions on how to include plastic deformations in the presence of pure membrane behaviour.

Despite a large volume of previous work devoted to the blister test few practical applications can be found. This is especially surprising as the shaft loaded blister test has a series of advantages over other adhesion tests. Major advantages are non-catastrophic crack propagation, representative loading condition and limited influence of sample preparation on test. When desiring to test the adhesion of thin films to fibre reinforced plastics, sample preparation is often straight forward and does not require alterations of the manufacturing conditions. A possible explanation for the few practical applications of this test is the high degree of nonlinearities occurring in the blister test. As a consequence of this, analytic solutions are not straight forward and simplifications have to be made to bring them to a closed form solution. Due to these simplifications the blister test analytic solutions are only applicable to a small parameter range and it is often difficult to choose suitable test parameters which are compatible with a chosen analytic solution.

This paper uses nonlinear finite element analysis (FEA) to model the behaviour of both the shaft loaded and the pressurized blister test. Based on FEA the accuracy of the analytical solutions can be studied and conclusions can be drawn for a suitable test parameter range and obtainable energy release rates. In Section 2 the nonlinear FEA is introduced and it is explained how the three forms of nonlinearities, namely contact, large displacement and elastic-plastic material behaviour were modelled. In this paper the FEA results are compared with the analytic solution provided by Jensen [11] . In Section 3 the analytic solution is introduced. Results and discussion of the comparison between FEA and analytic solutions are found in Section 4. Based on the results advantages and disadvantages of the two test configurations are discussed and a suitable test range is defined.

Finite element method

The commercial FEA package ANSYS Mechanical APDL 12.0 was chosen for this analysis. To minimise computational effort, PLANE183 elements in axisymmetric configuration were used. Element sizes are shown in Fig. 2. The contact area between the ball point and the film, for the SLBT, was modelled with TARGE169 and CONTA172 contact elements using Coulomb's friction law to allow for restricted slip between the film and the ball point. The nonlinear material behaviour was approximated by a bilinear isotropic hardening model for von Mises plasticity (TB,BISO). The crack tip singularity was modelled using crack tip concentration KSCON and the energy release rate was calculated using J-Integral evaluation in the solution step (CINT). The behaviour of the FE model was validated with experimental results using a constrained blister test setup for Polyethylene terephthalate (PET) film PP2410 provided by 3M. Fig. 3, shows the shaft displacement/load curve of the experimental results and the results from the FEA for different plastic module Ep. Good fit of the analytical and FE results is obtained for a plastic module Ep=200MPa. The subsequent analysis is based on the material properties shown in Table 1.

Table 1: Material properties of film and substrate used in the analysis

Material	Type	Poisson's ratio	Elastic modulus, MPa	Plastic modulus, MPa
Film	PET PP2410	0.4	4500	200
Substrate	Quasi-isotropic FRP	0.25	60000	-

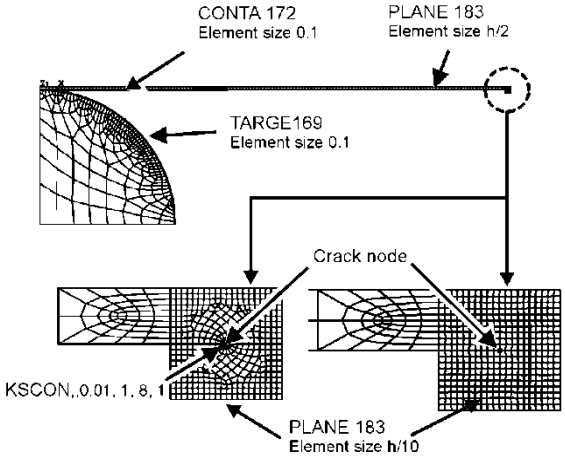


Fig. 1: Element type, size and crack singularity meshing used in the FEA

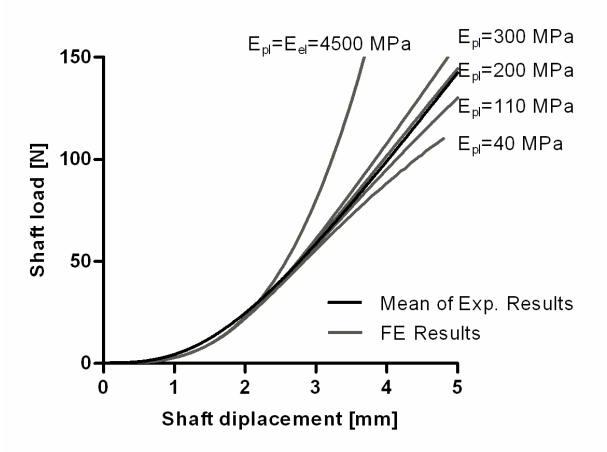


Fig. 3: Load/displacement curve obtained from experimental tests and FEA using a constrained blister with a crack start radius of 15mm

Analytic solution

For this research the analytic solution proposed by Jensen [11] is used. This analytic solution makes use of the well established bi-material fracture mechanics and is mostly based on work of Suo and Hutchinson [12]. The closed form solutions introduced below are only valid for the membrane limit (film thickness, $h \to 0$). This limit is identical with the large deboned limit (crack radius,$a \to \infty$) and high pressure limit (shaft load or pressure, $F \; or \; p \to \infty$)[11]. Parameters are defined as shown in Fig. 1. The energy release rate of the PRBT is calculated using Equation 1 and the energy release rate for the SLBT is given by Equation 2. The parameter γ varies with the Poisson's ratio, $\nu_1$and is not the same for the PRBT and the SLBT. Values for both cases are found in [11]. For this case where $\nu_1 = 0.4$, $\gamma_{PRBT} = 0.35$ and $\gamma_{SLBT} = 0.55$.

$$G = \left(\frac{p^4 a^4}{E_1 h}\right)^{\frac{1}{3}} \left(\frac{1}{8\gamma_{PRBT}} + \frac{\gamma_{PRBT}^2 (1-\nu_1^2)}{2}\right) \tag{1}$$

$$G = \left(\frac{F^4}{E_1 h \, a^4 \, \pi^4}\right)^{\frac{1}{3}} \left(\frac{1}{8\gamma_{PRBT}} + \frac{\gamma_{SLBT}^2 (1-\nu_1^2)}{2}\right) \tag{2}$$

Results and Discussion

In this paper the energy release rate obtained from J-integral evaluation in the FEA and the energy release rate calculated from the analytic solutions are compared to establish a reliable test range for both the SLBT and the PRBT. The results provided have been obtained for the parameters shown in Table 1 and Table 2. The chosen crack start radii, a=7.5mm, 15mm and 22.5mm, cover the range of previous experimental setups [13-15]. A film thickness of 0.5 mm was selected as results have shown that for this film thickness, energy release rates in the excess of 1500 N/m can be obtained. This covers the typical encountered energy release rates in FRPs. By increasing or decreasing the film thickness the test range can be extended to higher, respectively lower values.

Table 2: Material properties of film and substrate used in the analysis

SLBT			PRBT		
Parameter	**Value**	**Unit**	**Parameter**	**Value**	**Unit**
Film thickness, h	0.5	mm	Film thickness, h	0.5	mm
Crack radius, a,	7.5, 15, 22.4	mm	Crack radius, a,	7.5, 15, 22.4	mm
Displacement stepping	0.05	mm/step	Pressure stepping	0.01	MPa/step
Displacement range	0-5	mm	Displacement range	0-1	mm

When comparing the results obtained for the two tests (see Fig. 4 and Fig. 5) one can see that the PRBT provides more accurate results over a larger range then the SLBT. There is one exception however, for a small crack start diameter the analytically calculated energy release rate does not match the energy release rate calculated in the FEA. This mismatch can be explained trough the fact that the membrane limit is not satisfied for this case. Further investigation has shown that once the pressure is increased, also in this case, accurate results are obtained. Surprisingly the results for the SLBT show far less sensitivity towards infringement of the membrane limit. The divergence for higher load is due to the circumstance that the analytic solution does not consider elastic-plastic material behaviour and hence assumes too rigid blister behaviour once plastic yielding occurs. At the shaft contact local plastic yielding occurs much earlier than under the well distributed hydrostatic pressure load case. This fact also explains why the divergence between analytic and FEA solution increases quicker for the SLBT.

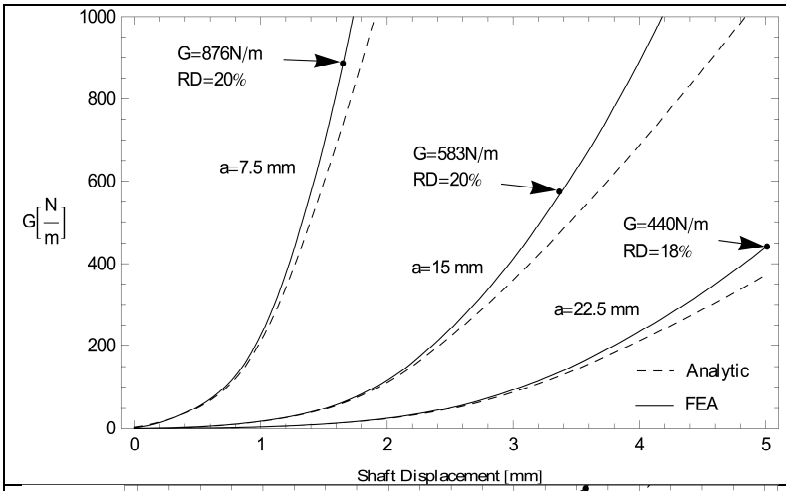


Fig. 4: Energy release rate vs. Shaft displacement for the analytical and numerical solutions of the SLBT for the three crack start radii

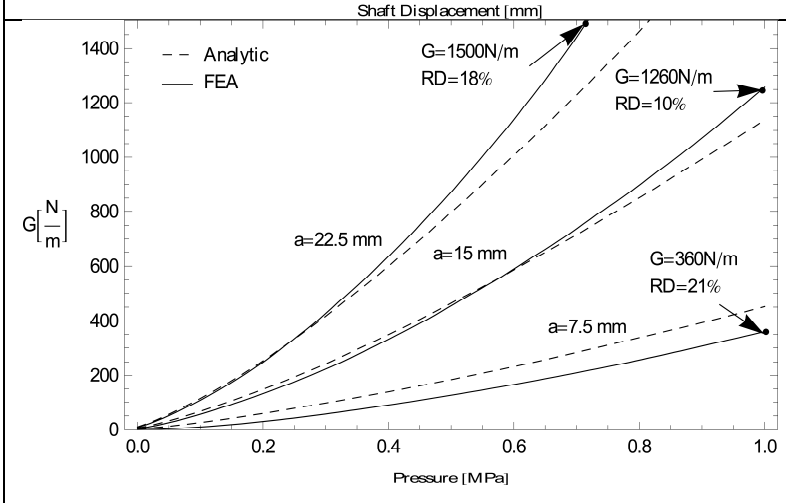


Fig. 5: Energy release rate vs. pressure for the analytical and numerical solutions of the PRBT for the three crack start radii

Summary

The comparison of the energy release calculated from FEA J-integral evaluation and the analytic solution for the membrane limit of both SLBT and PRBT, have revealed that both test configurations show good correlation (relative error <20%) between analytic and numeric solution. With the PRBT, higher energy release rates can be obtained using the same film thickness and without sacrificing accuracy. However care must be taken for small crack start radii and small pressures as in this case, the membrane limit condition is not satisfied. The SLBT has shown to be less sensitive to this condition but, due to local plastic yielding, the maximum energy release rate obtainable is significantly lower than for the PRBT. Based on these result one can conclude that the PRBT is the more favourable of the two test configurations. However, when considering experimental setup requirements for these tests, it becomes clear that the SLBT offsets these disadvantages with a much simpler experimental setup. For the testing of thin films on rigid FRPs both tests are equally suitable and high energy release rates can be obtained with relatively thin film thicknesses. Due to the nonlinear nature of the blister test, care must be taken when choosing the test configuration. It has been shown that the presented FEA analysis is a useful tool to select the right test parameters which greatly improve the reliability of both blister test variants.

References

[1] Dannenberg HJ.. *Journal of Applied Polymer Science*. 1961;5:134-134.
[2] Malyshev BM, Salganik RL.. *International Journal of Fracture Mechanics* 1965;1(2):114-128.
[3] Timoshenko SP, Wioinowsky-Krieger S. Theory of Plates and Shells. 2 ed: McGraw-Hill Book Company; 1959.
[4] Malyshev BM, Salganik RL. International Journal of Fracture Mechanics. 1965;1(2):114-128.
[5] Wan K-T, Mai Y. International Journal of Fractures. 1995;74(2):181-197.
[6] Jensen HM. The blister test for interfacial toughness measurement. Engineering Fracture Mechanics 1991;40(475-486).
[7] Thouless MD, Jensen MH.. Journal of Adhesion Science and Technology. 1994;8(6):579-586.
[8] Wan K-T.. Journal of Adhesion. 1999;70(2):209-219.
[9] Thouless MD.. IBM Journal of Research and Developement. 1994;38:367-377.
[10] Margaritis G, Sikorski SA, McGarry FJ. Journal of Adhesion Science and Tech..8:273-287.
[11] Jensen HM. The blister test for interface toughness measurement. Engineering Fracture Mechanics. 1991;40(3):475-486.
[12] Suo Z, Hutchinson JW. International Journal of Fracture. 1990;43(1-18).
[13] Zhao MH, Zheng WL, Fan CY. International Journal of Solids and Structures. 2010;47(18-19):2525-2532.
[14] O'Brien EP, Ward TC, Guo S, Dillard A. The Journal of Adhesion. 2003;79(1):69-97.
[15] Wan KT. Journal of Adhesion. 1999;70(3-4):209-219.

© (2011) Trans Tech Publications, Switzerland
doi:10.4028/www.scientific.net/KEM.471-472.320

Influence of surface modifications on interfacial interaction of zeolite filled polymer composites

N. Zaharri, N. Othman[a], Z.A.Mohd Ishak

School of Materials & Mineral Resources Engineering, Universiti Sains Malaysia, Engineering Campus, 14300 Nibong Tebal, Penang, Malaysia

[a]srnadras@eng.usm.my

Keywords: Zeolite, polymer composites, interfacial adhesion, Pukanszky model

Abstract. Interfacial interaction in zeolite filled polymer composites was investigated in this study. Two types of polymer which are polypropylene (PP) and ethylene vinyl acetate (EVA) were used as matrix in the preparation of the composites. Moreover, different modifications of zeolite filled polymer composites such as zeolite surface treatment with vinyl silane and alkylammonium and also chemical crosslinking were done to improve the interfacial adhesion between zeolite and polymer matrix. The zeolite filled polymer composites were homogenized using Thermo Haake Polydrive internal mixer and then compression molded into sheets according to standard test specimen. Uniaxial tensile test was performed in order to evaluate the mechanical behavior of the composites. The obtained experimental data for ultimate stress was correlated with Pukanszky theoretical model. The experimental results for all systems of zeolite filled polymer composites showed a good fit to the Pukanszky model. Interfacial interaction for each system of zeolite filled polymer composites was theoretically evaluated by determining the parameter B through this model. The value of parameter B for all zeolite filled polymer composite systems differs significantly from one another thus suggesting the applicability of this Pukanszky model in characterizing the filler-matrix interfacial adhesion.

Introduction

In achieving particulate filled composites with excellent mechanical properties, the primary goal is to enhance the interfacial interactions between the constituents [1, 2]. Furthermore, interfacial debonding is the major factor contributing to the first step of failure in polymer composites [3]. In order to overcome this problem, the surface of filler or polymer matrix is often modified via a wide variety of coupling agents, surfactant or even crosslinking agents [4-6]. As a result, the mechanical properties of the modified composites are significantly improved owing to the enhanced interactions at the polymer/filler interfaces. However, the type of surface modification method ought to be properly selected for a particular composite in yielding an efficient polymer-filler system. Due to this, theoretical model is often applied to quantitatively analyze the filler-matrix interfacial properties hence comparing the effectiveness of surface modifiers for instances coupling agent or compatibilizer used in the polymer composites. Although many theoretical models are found in the literature [7-8], only Pukanszky equation is presented here as it showed good agreement with our experimental data. Pukanszky model, Eq. 1 was proposed for the quantitative description of the composition dependence of the tensile yield stress of particulate filled polymers [3]. However, ultimate stress is considered instead of yield stress in our case since the composites systems do not exhibit a yield point.

$$\sigma_y = \sigma_{yo} \quad [(1-\Phi_f)/(1+2.5\,\Phi_f)] \quad \exp(B\,\sigma_y\,\Phi_f) \qquad (1)$$

where σ_y, σ_{yo}, Φ_f and $B\,\sigma_y$ is ultimate stress of the composite, ultimate stress of the polymer matrix, volume fraction of the filler and parameter characterizing interaction, respectively. The

parameter B σ_y can be determined by plotting the graph of ln [reduced ultimate stress], ln σ_{yred} as presented in Eq. 2 versus filler composition, Φ_f. The slope of the straight line gives the value of parameter B σ_y.

$$\ln \sigma_{yred} = \ln \sigma_y \, [(1+2.5 \, \Phi_f)/(1-\Phi_f)] \quad (2)$$

A wide variety of surface modification types have been studied in polymer composites [9, 10]. However, not much work has been done and very hard to find in the literature related to the effect of the modifications together with the quantitative study using Pukanszky theoretical model specifically on natural zeolite with mordenite type filled polymer composite especially EVA. Therefore, the purpose of this study is to investigate the dependence of tensile properties of PP and EVA filled with natural zeolite composites on the various types of surface modification used. Also, the effectiveness of each surface modification is quantitatively characterized using Pukanszky theoretical model hence proving the applicability of the model equation in predicting the mechanism of polymer-filler interaction.

Materials and experimental

Materials. Polypropylene (PP) homopolymer and ethylene vinyl acetate (EVA) containing 15% vinyl acetate were used as matrix in this study. The natural filler used was mordenite type of zeolite mineral species. The chemical formula is (Ca, Mg_2,K_2) $Al_2Si_{10}O_{24}$ $7H_2O$ with orthorhombic crystal system.

Experimental method. Altogether five composites were investigated and their compositions are compiled in Table 1. All of the five composites were homogenized by using an internal mixer Thermo Haake Polydrive with Rheomix, R600/610 model. The processing conditions were set at 180^0C and 130^0C for PP composites and EVA composites respectively with 7 min of mixing time and 50 rpm of rotor speed. After compounding, the composites were compression molded into 1mm of sample thickness. The samples were preheated for 8 minutes at 180^0C for PP composites meanwhile 130^0C for EVA composites followed by compression for 2 minutes. Finally, the samples were cold press for 4 minutes. The moulded tensile test sheet was cut into five dumbbell-shaped samples using Wallace die cutter. Thickness of each dumbbell-shaped sample was measured. The tensile properties were determined using electromechanical Instron machine, 3366 model according to ASTM D 638 with a crosshead speed of 50mm/min.

Table 1 The composition of the composites studied in this study

Polymer	Producer	Filler	Surface modification
PP	Titanpro PM655	Zeolite	-
PP	Titanpro PM655	Zeolite	Zeolite surface treatment with vinyl silane
EVA	Cosmothene Eva H2020	Zeolite	-
EVA	Cosmothene Eva H2020	Zeolite	Crosslinking of EVA using dicumyl peroxide (DCP)
EVA	Cosmothene Eva H2020	Zeolite	Cation-exchange method with octadecylamine

Results and discussion

Fig. 1 illustrates the dependence of tensile strength of PP and EVA composites on zeolite content and on the type of surface modification used. It can be clearly seen from the figure that different types of surface modification yield different effect on the tensile properties of the composites. The tensile strength of PP/zeolite composites is significantly increased in the presence of vinyl silane coupling agent especially at 10% zeolite loading. Meanwhile for EVA composites systems, the application of cation-exchange method exhibits greater effect on the tensile strength of EVA/zeolite composites compared to that of peroxide crosslinking. This is believed due to each surface modification results in different mechanism of interaction between zeolite and polymer matrix [3, 11].

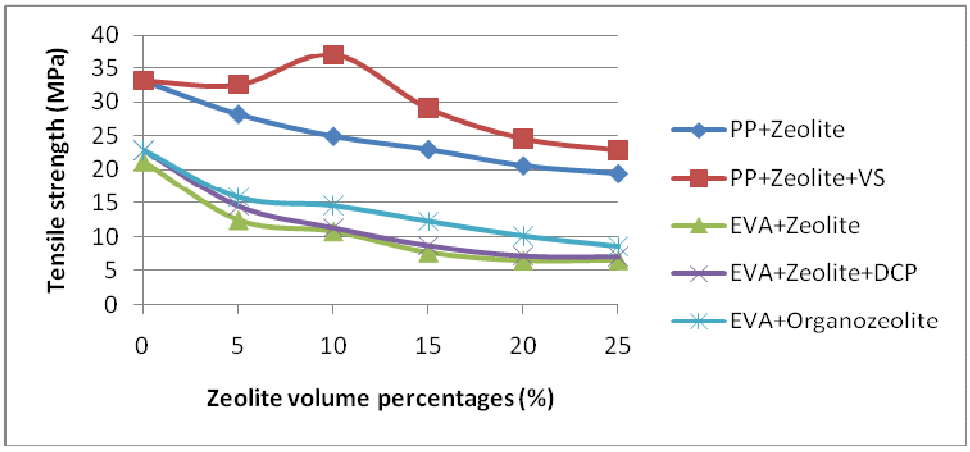


Fig. 1 Effect of zeolite content and surface modifications on tensile strength of the composites studied.

Fig. 2 indicates the comparison between experimental and theoretical data using Pukanszky model for ultimate tensile stress of all composites studied. As can be seen, a good correlation between experimental and theoretical data is obtained for all composites systems where the relative differences between measured and computed values of the composites ultimate stress (as presented in Table 2) being less than 4% . This suggests the validity of this Pukanszky model in predicting the ultimate tensile stress of composites thus explaining the effect of filler-matrix interfacial interactions. Furthermore, the strength of the interaction can be quantitatively characterized by determining parameter B through this theoretical model. As mentioned earlier, parameter B can be determined by plotting Eq. 2 versus filler composition, Φ_f as illustrated in Fig. 3. As Fig. 3 shows, slopes of the lines which represent the parameter B differ significantly from each other indicating changes in interaction between zeolite and PP or EVA matrix in the application of surface modification. By referring to Table 2, all composites exhibit a positive value of parameter B except for EVA/zeolite and EVA/zeolite/DCP composites. Although these composites show negative values of parameter B, which could be an indication of weak zeolite-EVA adhesion, the DCP crosslinked composites exhibit higher B value compared to that of uncrosslinked composites. This proves enhanced interaction between zeolite and EVA matrix in the presence of DCP crosslinking agent. However, the application of cation-exchange method on the EVA composites results in positive value of parameter B indicating that this cation-exchange method using octadecylamine has better effect in improving the zeolite-EVA strength of interaction compared with the DCP crosslinking method. Meanwhile in PP composites, the treatment of zeolite surface with vinyl silane results in higher B values suggesting that the silane groups may have some effect on the interfacial strength. This is expected since the incorporation of vinyl silane causes the formation of covalent bonds between PP matrix and the vinyl silane coupling agent adhered to the surface of zeolite hence

increasing the zeolite-PP adhesion. This quantitative characterization regardless of polymer matrix [PP or EVA] and various types of surface modification proves the universality of Pukanszky model in investigating the interfacial interactions of polymer composites.

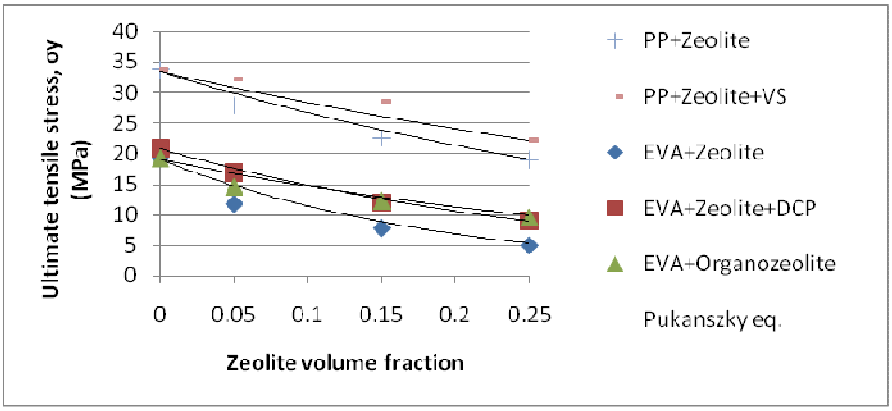


Fig. 2 Effect of zeolite content and surface modifications on the experimental and theoretical ultimate tensile stress of the composites studied. Lines represent the fit of the data with Pukanszky model.

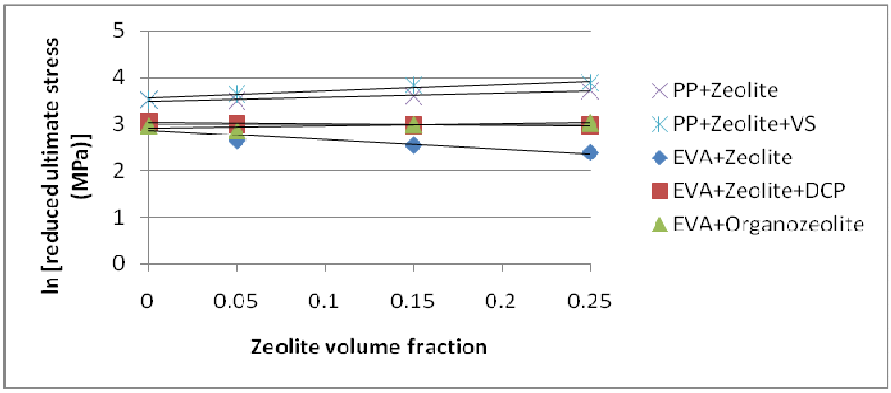


Fig. 3 Reduced ultimate tensile stress of the PP and EVA composites plotted in the linearized form of Pukanszky equation.

Table 2 Types of composite systems and parameters (σ, B) of the composites ultimate stress calculated from Pukanszky equation

Polymer composites type	σ [N mm^{-2}]	B	Δ [%]
PP+Zeolite	19.20	0.844	0.79
PP+Zeolite+Vinyl silane	22.38	1.458	0.16
EVA+Zeolite	5.35	-2.025	3.38
EVA+Zeolite+DCP	9.05	-0.259	0.28
EVA+Organo-zeolite	9.99	0.473	2.26

Summary

The surface modification of composites can significantly influence the filler-matrix interfacial strength hence mechanical properties of particulate filled polymer composites. The good correlation between theoretical and experimental data of both PP and EVA composites with various types of surface modification proves the universality of Pukanszky model. Also, this suggests the validity of the theoretical model in predicting the filler-matrix interfacial adhesion.

References

[1] J. L. Kardos, in: *Molecular Characterization of Composite Interfaces,* edited by H. Ishida and G. Kumar Plenum, NY (1985), in press.
[2] F. R. Eirich: J. Appl. Polym. Sci., Appl. Polym. Syrup Vol. 39 (1984) p. 93
[3] B. Pukanszky, F. Todos: J. Mater. Sci. Lett. Vol. 8 (1989) p. 1040
[4] V. P. Juskey and C. E. Chaffey: Canadian J. Chem. Eng. Vol. 60 (1982) p. 334
[5] M. S. Boaira and C. E. Chaffey: Polym. Eng. Sci. Vol.17 (1977) p. 715
[6] A. Garton, S. W. Kim and D. M. Wiles: J. Polym. Sci., Polym. Lett. Ed. Vol. 20 (1982) p. 273
[7] H. Wu, C. Liu, Y. Yang, J. Chen and Y. Chen: Polym. Composites. Vol. 31 (2010) p. 1938
[8] L. Cauvin, D. Kondo, M. Brieu and N. Bhatnagar: Polym. Testing. Vol. 29 (2010) p. 245
[9] Z. Xu, W. Kong, M. Zhou and M. Peng: J. Polym. Sci. Vol. 28 (2010) p. 615
[10] M. S. Huda**,** L. T. Drzal**,** and M. Misra: Composites Sci. Tech. Vol. 68 (2008) p. 424
[11] N. Othman and N.D. Zaharrri: J. Reinf. Plast. Composites. Vol. 29 (2009) p. 14

© (2011) Trans Tech Publications, Switzerland
doi:10.4028/www.scientific.net/KEM.471-472.325

Studies on Development, Bioactivity and Corrosion Behaviour of Nanostructured Titania/Hydroxyapatite Composite Layer on Cp Ti

K. Venkateswarlu[1,a], N. Rameshbabu[1,b], A. Chandra Bose[2,c], V.Muthupandi[1,d] and S. Subramanian[3,e]

[1]Department of Metallurgical and Materials Engineering, National Institute of Technology, Tiruchirappalli 620 015, Tamilnadu, India

[2]Department of Physics, National Institute of Technology, Tiruchirappalli 620 015, Tamilnadu, India

[3]Department of Materials Engineering, Indian Institute of Science, Bangalore 560 012, Karnataka, India

[a]kotharu.venkat@gmail.com, [b]rameshrohith@gmail.com, [c]acbose@nitt.edu, [d]vmuthu@nitt.edu, [e]ssmani@materials.iisc.ernet.in

Keywords: Cp Ti; hydroxyapatite; composite; bioactivity; corrosion

Abstract. Nanostructured titania/hydroxyapatite (HA) composite layer was developed on commercially pure titanium (Cp Ti) implant material by plasma electrolytic processing (PEP) technique in order to improve its bioactivity and corrosion resistance under physiological conditions. The phases present in the developed composite layer were studied by X-ray diffraction (XRD) technique. The surface morphology and thickness of the composite layers were observed by scanning electron microscopy (SEM). The corrosion characteristics of the developed layer were studied by potentiodynamic polarization scan under simulated body fluid (7.4 pH Hanks solution) and simulated osteoclast (4.5 pH) conditions. The *in-vitro* bioactivity of the composite layers was studied by using Kokubu's simulated body fluid (SBF) solution. The X-ray diffractograms reveal the presence of anatase TiO_2 and HA phases in the developed layer. The SEM results confirm the pore-free morphology of the implant material surface and the thickness of the developed composite layer was observed to be 110 ± 5 μm for 12 min of PEP. The potentiodynamic polarization study shows an improved corrosion resistance and the *in-vitro* bioactivity test results indicate enhanced apatite forming ability of PEP treated Cp Ti surfaces compared to that of the untreated Cp Ti, under simulated body fluid conditions.

Introduction

Titanium and its alloys are proven to be very suitable materials for load bearing bioimplant applications. Unfortunately, titanium exhibits poor bioactivity as compared to the bioactive materials such as HA and bioactive glass. This drawback can be addressed by coating the metallic implants with bioactive materials to improve its bioactivity. Titanium oxide (TiO_2) coatings on titanium alloys have demonstrated promising *in-vivo* corrosion resistance behaviour, acting as a chemical barrier against the release of metal ions from the implants [1]. However, the chemical bond with the living bone in the body is not very strong with TiO_2 [2]. Therefore a composite coating of TiO_2-HA on titanium can be envisaged to possess a very good combination of corrosion resistance and bioactivity.

Many techniques have been investigated as methods of depositing HA onto metallic surfaces. Among these techniques, plasma spraying is the most popular method for coating implants with HA, but it is difficult to apply uniform coatings on implants with complex geometries. Furthermore, thermal decomposition and transformation of HA can occur due to poor temperature control during

deposition and the adhesion to the metallic substrate is not sufficiently high. The purity of the HA film can also be a critical aspect with regard to increasing the *in-vivo* chemical and mechanical durability of HA coatings over the lifetime of bioimplant [3,4].

Interest in electrophoretic deposition for biomedical applications arises for a variety of reasons including the possibility to deposit stoichiometric, high purity materials onto complex shaped components. However, high temperatures during post-treatment (e.g. firing) for increasing adhesion of such coatings may degrade their properties and those of the substrate. In previous research on electrophoretic deposition of HA, various organic liquids (rather than water) were used as the suspension media, since deposition in water is often accompanied by significant gas evolution which interrupts the transfer of suspended particles to the treated components [5,6,7]. In the present work an aqueous electrolyte system containing suspended HA nanoparticles and dissolved tri-sodium orthophosphate (TSOP) is employed to develop a TiO_2-HA composite layer by PEP. The PEP technique employed here, utilizes the combination of plasma electrolytic oxidation (PEO) and electrophoretic deposition in a single electrolyte system containing both the oxidizing agents and suspended HA nanoparticles to develop a TiO_2-HA composite layer on Cp Ti. The highlight of this paper is the development of a TiO_2-HA composite layer on Cp Ti in a single step by PEP technique.

Materials and Methods

Development of TiO_2-HA Composite Coating. Analytical grade calcium hydroxide [$Ca(OH)_2$, E. Merck, Germany], diammonium hydrogen phosphate [DAP, $(NH_4)_2HPO_4$, E. Merck, Germany] were used for the preparation of hydroxyapatite (HA) nanoparticles by microwave processing. The microwave method of synthesizing nanocrystalline HA is reported elsewhere [8].

The HA aqueous suspension was prepared by adding 5 g of HA powder and 5 ml of ethylene glycol simultaneously to 1 L of distilled water taken in a conical flask. The addition of HA powder and ethylene glycol to distilled water was done in several number of steps and the added contents in the distilled water were hand shaken well at the end of each step to allow the reaction required to charge HA effectively. Triethanolamine was used to adjust the pH value of the solution to around 11. The aqueous HA suspension was also stirred using an ultrasonic agitator for 45 min to obtain dispersion stability and then finally 5 g of TSOP was added to the prepared HA suspension solution. This aqueous HA suspended TSOP solution was used as electrolyte for developing TiO_2-HA composite layer by PEP technique.

The Cp Ti test coupons with dimensions 25x15x1.5 mm were abraded down up to 1000 grit emery paper and then ultrasonically cleaned in alcohol, acetone and distilled water for 5 min successively before use. Prior to PEP treatment acid activation was performed for 30 s in a diluted mixture of nitric acid and hydrofluoric acid to remove the natural titanium oxide layer and surface contaminants.

For the PEP treatment, the specimens were immersed in the electrolyte system as anode and with increasing the DC potential up to 400 V, giving a current density of 50–200 mA/cm^2 at the work piece and raising the bath temperature from ambient to around 75 °C during treatment for 12 min. After the PEP treatment, the specimens were cleaned with distilled water and are dried at room temperature.

XRD and SEM Characterization of Coating. The phase composition of the coatings was analyzed by Rigaku X-ray diffractometer (UltimaIII, Rigaku, Japan) using Cu Kα radiation at 40 kV and 30 mA with a scan speed of 1°/min and a step size of 0.05°. The surface morphology of the developed coating was observed using a scanning electron microscope (S3000H, Hitachi, Japan). To measure the thickness of the coating, the cross section of the test sample was well polished and cleaned ultrasonically in ethanol and acetone and then subjected to SEM analysis.

Corrosion Testing under Simulated Body Fluid (SBF) Environments. Corrosion testing was carried out at two different pH conditions, one at 4.5 pH simulated osteoclast resorption and another at 7.4 pH Hank's simulated body fluid solution (SBF). The 4.5 pH condition is responsible for physiological conditions of osteoclast bone resorption [9]. The 4.5 pH test solution was obtained by adding appropriate amount of nitric acid to distilled water. The 7.4 pH Hanks physiological solution

for corrosion testing was prepared according to ASTM standard F2129−06. Potentiodynamic polarization curves were obtained for both conditions using ACM Gill AC corrosion testing unit to evaluate the corrosion behaviour of Cp Ti before and after PEP treatment. A three electrode cell, with sample as working electrode, saturated calomel electrode (SCE) as reference electrode and platinum foil as counter electrode, was employed in this test. During the anodic polarization scan, sample with an exposed area of 0.5 cm^2 was kept in contact with the solution and then polarized from cathodic to anodic region at a scan rate of 60 mV/min in the range -500 mV to 3000 mV with reference to SCE. From the polarization curve, the corrosion current density (I_{corr}) was determined by Tafel extrapolation method using the ACM software provided with the equipment.

Bioactivity Test. The bioactivity of the fabricated coating was tested by soaking in Kokubo's SBF solution prepared as suggested [10]. The SBF with ion concentrations nearly equal to the human body plasma was prepared by dissolving reagent grade chemicals: NaCl, $NaHCO_3$, KCl, $K_2HPO_4.3H_2O$, $MgCl_2.6H_2O$, $CaCl_2$ and Na_2SO_4 in double distilled water, and buffered at 37 $^{\circ}$ C and pH value 7.4 with $(CH_2OH)_3CNH_3$ and HCl. The SBF solution was refreshed every 24 h. After 10 days of incubation period, the samples were taken out of SBF, rinsed with distilled water, and then dried in a oven at 60 $^{\circ}$ C for 12 h.

Results and Discussion

The XRD patterns of the as prepared HA powder (used to prepare HA suspension solution) and the coating developed on Cp Ti by using PEP are shown in Fig. 1(a) and Fig. 1(b) respectively. The two XRD patterns show the characteristic diffraction peaks which can be indexed as hexagonal HA (JCPDS No: 09-432). In addition to HA diffraction peaks, Fig. 1(b) exhibits the characteristic diffraction peaks of both anatase (at $2\theta \approx 22.5^{\circ}$, 25.3°, JCPDS No: 21-1272) and rutile (at $2\theta \approx 27.7^{\circ}$, JCPDS No: 84-1286) TiO_2. Thus Fig. 1(b) confirms the presence of both TiO_2 and HA phases in the coating. The average crystallite size of the as prepared HA powder calculated from Scherrer formula was 40 nm. The diffraction peaks of the HA coating were observed to be a bit sharper compared to that of as prepared HA powder. This is due to the improved crystallinity of HA coating attributable to the higher temperature generated in PEP discharge channels under the applied high anodic potential.

The SEM micrographs of the surface of the Cp Ti treated for 4 min and 12 min are shown in Fig. 2(a) and (b) respectively. It is evident that the sample treated for 4 min contains uniformly distributed dark circular spots which are discharge channels open to the surface of the coating. The size of these pores or discharge channels was observed to be 3 to 6 μm. Figure 2(b) shows the TiO_2-HA coating on the substrate. It can be inferred from Fig. 2 (a) that the formation of TiO_2 takes place initially under low anodic potentials. The coating developed for 12 min was relatively free of pores due to the TiO_2-HA composite layer formation in comparison to the formation of only TiO_2 after 4 min.

Mechanism of TiO_2-HA Composite Coating Formation. During the initial stages of PEP processing, when the potential is applied, the OH^- ions in the electrolyte tend to move to the anodic surface (Cp Ti) and take part in the following reaction to form an oxide layer.

$$Ti^{4+} + 2OH^- + 2H_2O \rightarrow TiO_2 + 2H_3O^+ + 4e^- \quad (1)$$

When the oxide layer grows in thickness higher voltages need to be applied to reach the dielectric breakdown of the grown oxide layer and thereby allowing further anodic reaction to take place.

During the processing, under the high applied anodic potential, both OH^- and charged HA particles [$Ca_{10}(PO_4)_6(O^-)_2$] will migrate to the anodic surface and take part simultaneously in respective oxidation reaction and electrophoretic deposition to form both TiO_2 and HA concurrently thereby forming a TiO_2-HA composite layer. As the PEP processing time increases the tendency of electrophoretic deposition seems to be dominant than plasma electrolytic oxidation. Due to this, more $Ca_{10}(PO_4)_6(O^-)_2$ will migrate to the anodic surface and will be sintered by the plasma arc discharges. The characteristic pores of PEO observed after 4 min of processing [Fig. 2(a)] and the pore-free morphology observed after 12 min [Fig. 2(b)] suggest that the TiO_2 formation seems to be

a dominant activity during the initial stages of processing, whereas HA deposition becomes dominant at the later stages of processing.

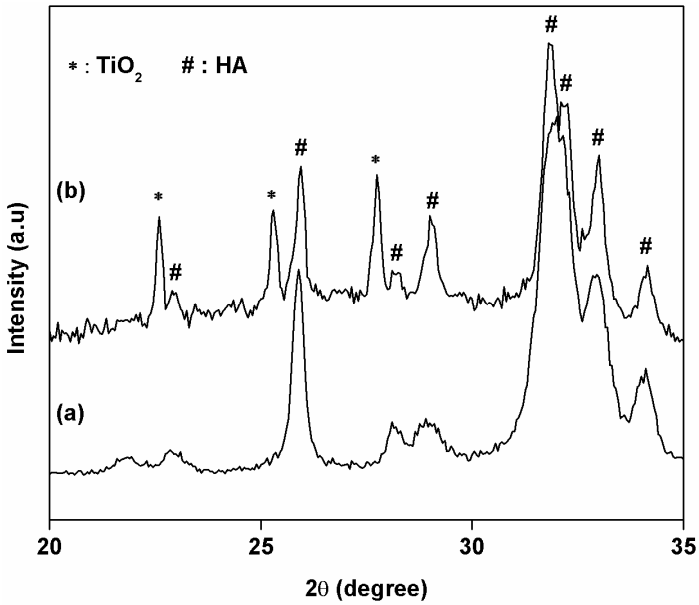


Fig. 1 XRD pattern (a) of as prepared HA powder and (b) of HA-TiO_2 composite coating.

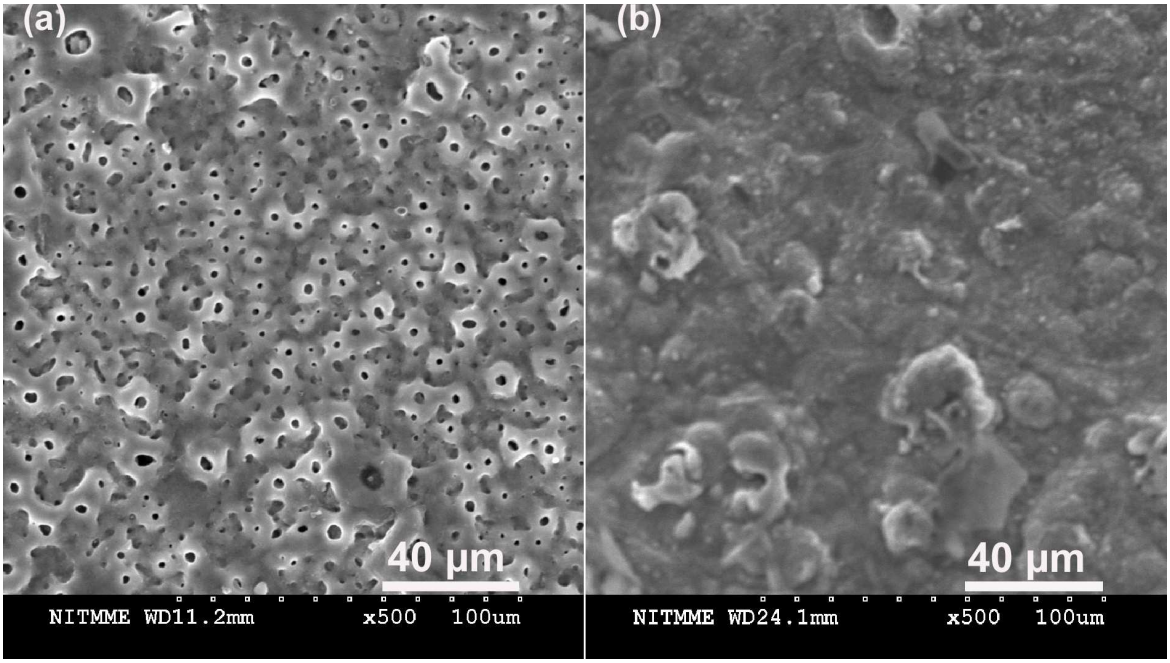


Fig. 2 SEM micrographs of PEP treated Cp Ti (a) for 4 min and (b) for 12 min.

The cross sectional morphology of the coating developed for 12 min is shown in Fig. 3. The coating seems to be more uniform and adherent with a thickness of 110 ± 5 µm. The substrate, substrate-coating interface, HA-TiO_2 composite layer could be seen clearly. The presence of TiO_2-HA composite layer is evidenced by the XRD result shown in Fig. 1. The presence of an inner HA-TiO_2 composite layer and a top HA layer in the coating developed by subsequent techniques of micro discharge oxidation (MDO) and electrophoretic deposition was reported by X. Nie et al. [7]. From the surface morphology of the PEP treated Cp Ti immersed in Kokubo's SBF solution for 10 days, it was observed that the surface of the treated specimen was almost fully covered by a newly formed HA layer indicating its improved bioactivity.

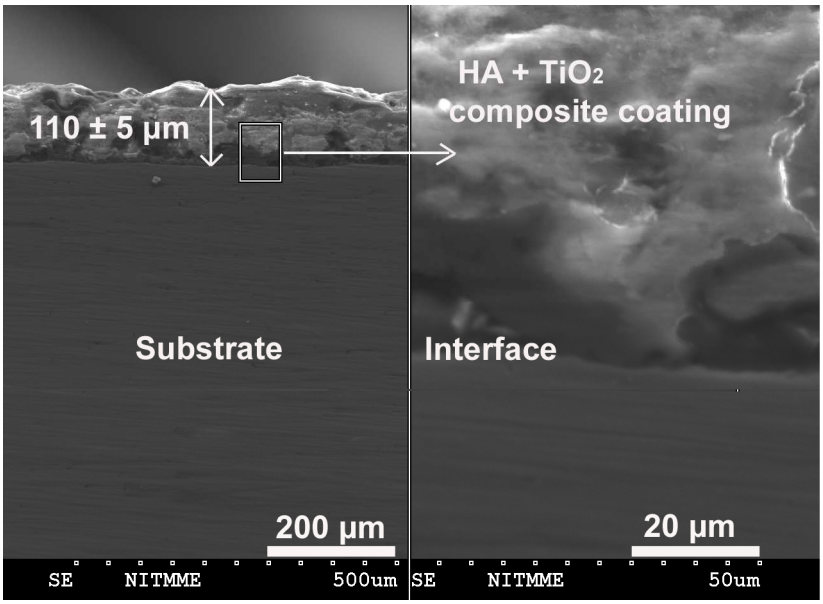


Fig. 3 SEM cross sectional micrograph of PEP treated Cp Ti for 12 min

The cyclic potentiodynamic polarization curves for untreated and PEP treated Cp Ti specimens in 4.5 pH corrosion medium are shown in Fig. 4. The polarization curve shows that both treated and untreated specimens remain passive up to 3000 mV. The corrosion parameters extracted from these curves were shown in Table 1.

Table 1 The corrosion parameter values determined for untreated and PEP treated Cp Ti

Corrosion parameter	4.5 pH corrosion medium		7.4 pH corrosion medium	
	Cp Ti	PEP treated	Cp Ti	PEP treated
Rest potential (mV)	-100	-284.35	-153.52	-110.44
I_{corr} (mA/cm^2)	5.766E-03	3.818E-06	8.009E-03	1.007E-04
LPR (ohm.cm^2)	22636	6832400	3257	25884
Corrosion rate (mm/year)	2.002E-02	6.636E-05	1.392E-01	7.51E-03

It could be seen that the corrosion current density and corrosion rate of treated specimen is nearly three orders of magnitude lesser than that of untreated specimen under simulated osteoclast resorption condition of 4.5 pH. The improved corrosion resistance was also evidenced by the higher linear polarization resistance (LPR) of treated specimen than that of untreated sample. Similarly, the corrosion resistance of the treated specimen was improved in 7.4 pH Hank's solution medium. However, the corrosion resistance of both treated and untreated specimens in 7.4 pH medium was lesser than the more severe 4.5 pH medium. This might be due to the presence of highly corrosive Cl^- ions in 7.4 pH Hank's SBF medium. This result can further be supported by the fact that corrosion is associated with the penetration of chloride ion and water into the coating, transport of ions through the coating, and the subsequent electrochemical reactions at the interface of barrier coating and substrate [11]. Thus in contradiction to the pH of the medium, the PEP treated specimens show relatively better corrosion resistance in 4.5 pH medium compared to that in 7.4 pH medium. However, the significant improvement in the corrosion resistance of the treated specimens in both 4.5 and 7.4 pH conditions is due to the fact that the TiO_2-HA layer acts as a barrier to the transport of electrons and ions between the substrate and the electrolyte, thus reducing the electrochemical reaction rate. The improved corrosion resistance of the coated Cp Ti is ascribed to the combined effect of the semi-insulating TiO_2-HA phases in the composite coating.

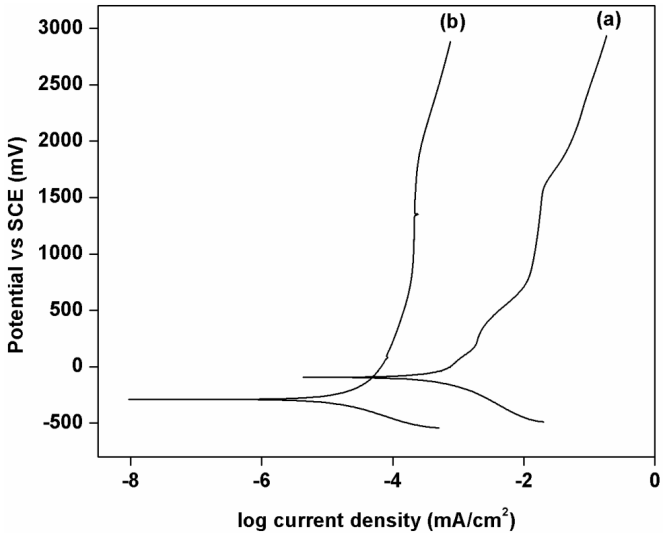


Fig. 4 Cyclic potentiodynamic polarization curves of (a) untreated and (b) PEP treated Cp Ti for 12 min in 4.5 pH corrosion medium.

Summary

TiO_2-HA nano composite layer is developed on Cp Ti in a single step by combining the PEO and electrophoretic deposition in a PEP technique. The composite coating with thickness of 110±5 μm is developed in 12 min of processing time. The potentiodynamic polarization study shows an improved corrosion of PEP treated Cp Ti surfaces compared to that of the untreated Cp Ti, under the both 7.4 pH and 4.5 pH simulated physiological conditions.

Acknowledgements

The authors would like to acknowledge the grant from the Department of Biotechnology, New Delhi (BT/PR-11731/MED/32/99/2008, dated 19-08-2009) and the collaborative research project sanctioned by UGC-Networking Resource Centre for Materials, Department of Materials Engineering, Indian Institute of Science, Bangalore.

References

[1] H. Kurzweg, R.B. Heimann, T. Troczynski and M. L. Wayman: Biomaterials Vol. 19 (1998), p. 1507
[2] P. Li, K.D. Groot and T. Kokubo: J. Sol–Gel Sci. Technol. Vol. 7 (1998), p. 27
[3] M. Ogiso: J. Long-term Effects of Medical Implants Vol. 8 (1998), p. 193
[4] R.B. Heimann, T.A. Vu and M.L. Wayman: Eur. J. Mineral. Vol. 9 (1997), p. 597
[5] I. Zhitomirsky and L. Galor: J. Mater. Sci.: Mat. in Med. Vol. 8 (1997), p. 213
[6] P. Sarkar and P. Nicholson: J. Am. Ceram. Soc. Vol. 79 (1996), p. 1987
[7] X. Nie , A. Leyland and A. Matthews: Surf. Coat. Technol. Vol. 125 (2000), p. 407
[8] N. Rameshbabu, K.P. Rao and T.S.S. Kumar: J. Mater. Sci. Vol. 40 (2005), p. 6319
[9] D. Tadic, F. Peters and M. Epple: Biomaterials Vol. 23 (2002), p. 2553
[10] T. Kokubo and H, Takadama: Biomaterials Vol. 27 (2006), p. 2907
[11] C.T. Kwok, P.K. Wong, F.T. Cheng and H.C. Man: Appl. Surf. Sci. Vol. 255 (2009), p. 6736

© (2011) Trans Tech Publications, Switzerland
doi:10.4028/www.scientific.net/KEM.471-472.331

Optimal Design by Elitist-Genetic Algorithm for Maximum Fundamental Frequency of Fiber Metal Laminated Plates

Hadi Ghashochi Bargh[1, a], Mohammad Homayoun Sadr[2,b]

[1,2]Aerospace Engineering Department, Centre of Excellence in Computational Aerospace Engineering, Amirkabir University of Technology, Hafez Avenue, Tehran, Iran

[a] h_bargi2003@yahoo.com, [b] Sadr@aut.ac.ir

Keywords: Elitist-Genetic algorithm, Fiber metal laminated plate, Optimization, Finite strip

Abstract. In this paper, fundamental frequency optimization of fiber metal laminated plates is studied using the combination of Elitist-Genetic algorithm (*E-GA*) and finite strip method (*FSM*). The design variables are the number of layers, the fiber orientation angles of inner composite layers, edge conditions and plate length/width ratios. The classical laminated plate theory (*CLPT*) is used to calculate the natural frequencies and the fitness function is computed with a semi-analytical finite strip method which has been developed on the basis of full energy methods. To check the validity, the obtained results are also compared with some other stacking sequences.

Introduction

Fiber metal laminate (*FML*) composites are laminates composed of alternating layers of reinforced polymeric composites and aluminum alloys in a way that aluminum alloy sheets are outer layers protecting the inner composite layers. *FMLs* main attribute is the improved fatigue resistance. Because of the outer aluminum alloy layers, *FMLs* have improved resistance to impacts and environmental conditions. The use of aluminum alloy layers improves specific stiffness and strength, and also results in weight savings in the design of tension-dominated stresses in structural components. These hybrid materials are divided into three groups according to the type of fiber used in polymeric composite layers, as follows: reinforced with aramid fibers (*ARALL*); glass fibers (*GLARE*) and carbon fibers (*CARALL*) [1-2]. They have been introduced as structural composite materials for advanced aerospace applications such as for the Airbus *A380* aircraft fuselage, aircraft lower wing skin and internal parts of the airplanes [3]. A fiber metal laminated plate is shown schematically in Fig. 1.

In the present paper, fundamental frequency optimization of *FMLs* is investigated using the *E-GA* with 15 different combinations of edge conditions. In order to reduce the calculation time, the elitist strategy is used in Genetic algorithm. The optimal layer sequences are found using the *E-GA* and *FSM* without yielding a local optimum for all cases.

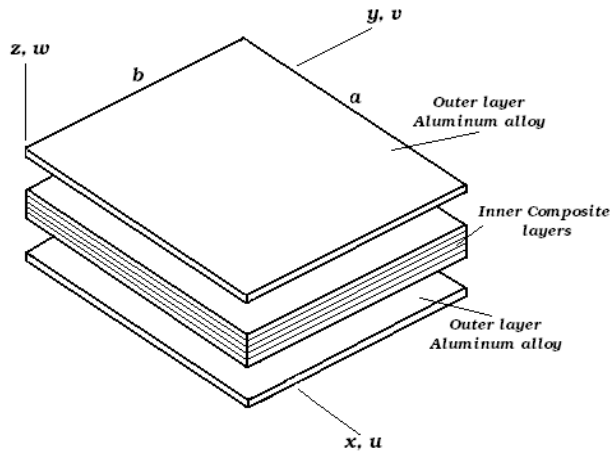


Fig. 1 A fiber metal laminated plate.

Problem Description

Based on the *CLPT*, the constitutive equations for a plate can be expressed as follows by performing appropriate analytical integration through the uniform thickness:

$$\begin{Bmatrix} N_x \\ N_y \\ N_{xy} \\ M_x \\ M_y \\ M_{xy} \end{Bmatrix} = \int_{-h/2}^{h/2} \begin{Bmatrix} \bar{\sigma}_x \\ \bar{\sigma}_y \\ \bar{\tau}_{xy} \\ z\bar{\sigma}_x \\ z\bar{\sigma}_y \\ z\bar{\tau}_{xy} \end{Bmatrix} .dz = \begin{bmatrix} A_{ij} & B_{ij} \\ B_{ij} & D_{ij} \end{bmatrix} \times \begin{Bmatrix} \varepsilon \\ \psi \end{Bmatrix}; \qquad \varepsilon = \begin{Bmatrix} u_{,x} \\ v_{,y} \\ u_{,y} + v_{,x} \end{Bmatrix}, \psi = \begin{Bmatrix} -w_{,xx} \\ -w_{,yy} \\ -2w_{,xy} \end{Bmatrix} \tag{1a}$$

where N_x, N_y and N_{xy} are the membrane direct and shearing stress resultants per unit length, M_x, M_y and M_{xy} are the bending and twisting stress couples per unit length and ψ, ε are the curvature vector and mid-plane strains. Moreover, the plate stiffness coefficients are defined as:

$$(A_{ij}, B_{ij}, D_{ij}) = \sum_{k=1}^{n} \int_{zk-1}^{zk} (\bar{Q}_{ij})_k (1, z, z^2) dz, \quad i, j = 1,\ 2,\ 6 \tag{1b}$$

where $\bar{Q}_{ij}$ are plane-stress stiffness coefficients.

Due to symmetry of lay-up the coupling between in-plane and out-of-plane force and deformations will not appear (*i.e.,* $B_{ij} = 0$).

The strain energy per unit volume is $1/2\,\bar{\sigma}^T\bar{\varepsilon}$.Using Eq. (1) and integrating through the thickness of the structure with respect to z gives an expression for the strain energy of a finite strip, which can be put into the following form:

$$U_s = \frac{1}{2}\iint \{\varepsilon^T.[A].\varepsilon + \psi^T.[D].\psi\} dxdy = \frac{1}{2}\{d\}^T.[k].\{d\} \tag{2}$$

The general expression for the strip kinetic energy is:

$$T_s = \frac{1}{2}\rho h \iint \{\dot{u}^2 + \dot{v}^2 + \dot{w}^2\} dxdy = \frac{1}{2}\{\dot{d}\}^T.[m].\{\dot{d}\} \tag{3}$$

where [*k*] is the strip stiffness matrix and [*m*] is the strip mass matrix and $\{d\}$ is a column matrix which contains the strip's degrees of freedom and ρ is a mean mass per unit area of the plate.

For the whole structure, the total strain energy and kinetic energy are obtained by summations of the corresponding energy components of all strips.

The structural equation of motions can be obtained by applying the Lagrange equations as:

$$[M].\{\ddot{\bar{d}}\} + [K].\{\bar{d}\} = \{0\} \tag{4}$$

The solution of this eigenvalue problem is:

$$\det([K] - \omega^2[M]) = \{0\} \tag{5}$$

where ω are natural frequencies. Natural frequency is normalized as a frequency parameter:

$$\Omega = \omega a^2 (\frac{\rho}{D_0})^{1/2} \quad , \quad D_0 = {E_2 h^3}/{12(1 - \nu_{12}\nu_{21})} \tag{6}$$

The optimal design problem can be stated as follows:

$$Find \quad \theta = (\theta_1, \theta_2, ..., \theta_j) \quad \Rightarrow \quad Maximize \quad \Omega = \Omega(\theta_1, \theta_2, ..., \theta_j) \quad Subject\ to \quad -90^0 \le \theta_n \le 90^0 \tag{7}$$

where j is half of the inner composite layers number. The optimal stacking sequences and ply angles are searched with the Elitist-Genetic algorithm.

The assumed in-plane displacement and out-of-plane displacement in the full-energy semi-analytical method are [4-5]:

$$u = \sum_{i=1}^{ru} ((1-\eta)u_{1i} + \eta u_{2i})\cos(i\zeta x)$$

$$v = \sum_{i=1}^{rv} ((1-\eta)v_{1i} + \eta v_{2i})\sin(i\zeta x)$$

$$w = \sum_{i=1}^{rw} ((1-3\eta^2+2\eta^3)w_{1i} + b_s(\eta - 2\eta^2 + \eta^3)\theta_{1i} + (3\eta^2 - 2\eta^3)w_{2i} + b_s(\eta^3 - \eta^2)\theta_{2i})W_i(x); \quad W_i(x) = \begin{cases} \sin(i\zeta x) & end\ simply\ \text{sup}\ ported \\ \sin(\zeta x).\sin(i\zeta x) & end\ clamped \end{cases} \tag{8}$$

where u_{1i}, u_{2i}, v_{1i} and v_{2i} are the undetermined in-plane nodal displacement parameters and $w_{1i}, w_{2i}, \theta_{1i}$ and θ_{2i} are the undetermined out-of-plane nodal displacement parameters along the edges of the strip and $\eta = y/b_s$ and $\zeta = \pi/a$.

Elitist-Genetic Algorithm

In this work Genetic algorithm with elitist selection based on cloning the best individuals in the generation is used in the optimization process. An individual in the present *E-GA* is an array of j chromosomes. Each ply angle is represented by a chromosome and each chromosome is introduced by 8 genes. In the optimization process, the individuals with better fitness are kept and automatically reinserted in the next generation, right before the next selection process take place [6-8]. The number of exchanged individuals (migration rate) and the scheme of migration determine how much genetic diversity can occur in the populations and the exchange of information between the populations. Schematic diagram of *E-GA* is shown in Fig. 2.

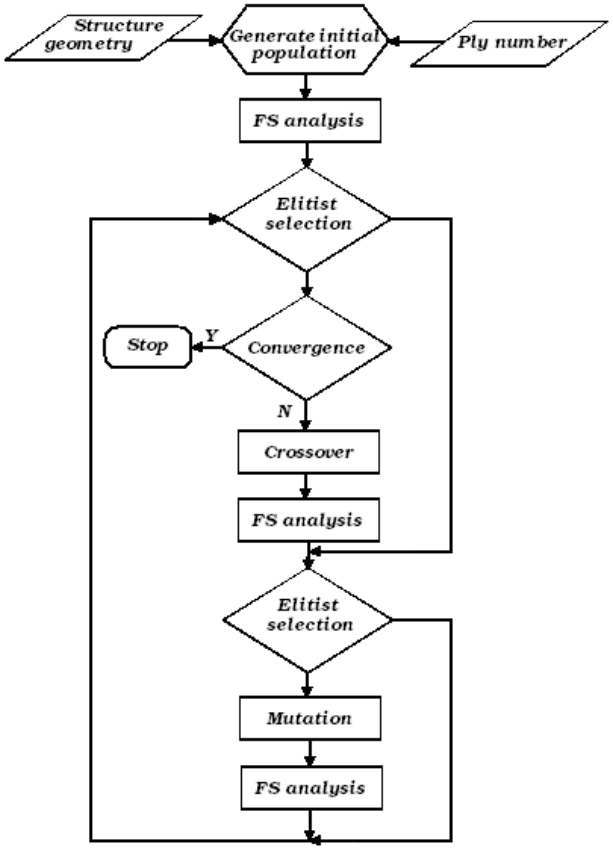


Fig. 2 Schematic diagram of Elitist-Genetic algorithm.

In the algorithm, the crossover operation mixes the chromosomes of the parents by swapping a portion of the data structure, and is repeated with diffrent parents to create a sufficient number of candidate solutions in the next generation population. This created offspring is randomly mutated by flipping bits in the chromosome data structure based on a fixed very small probability of mutation on the order of 0.01 or less.

Numerical Results

The optimization results of the fiber metal laminated plates (*h/a=0.01*) are given for *AS/3501* graphite/epoxy material [9] (inner composite layers) and aluminum alloy *2024-T3* [1](outer aluminum layers). The material properties are given as below:
Composite layers: $E_1=138$ GPa, $E_2=8.96$ GPa, $G_{12}=7.1$ GPa, $\upsilon_{12}=0.3$
Aluminum layers: $E=72.4$ GPa, $\upsilon=0.33$

Each of the lamina is assumed to be same thickness.

Fig. 3 compares the present optimal solutions $[Al/\theta_1/\ \theta_2/\ \theta_3]_{S,opt}$ of the 8-layerd fiber metal laminated square (*a/b=1*) and rectangular (*a/b=2*) plates with those of the square and rectangular *FMLs* with other stacking sequences. As inferred from the results, the good efficiency of the *E-GA* search strategy and its ability to provide high-quality solutions is confirmed for diffrent aspect ratios, and all the present optimal solutions yield higher natural frequencies than those of the square and rectangular plates with the other stacking sequences.

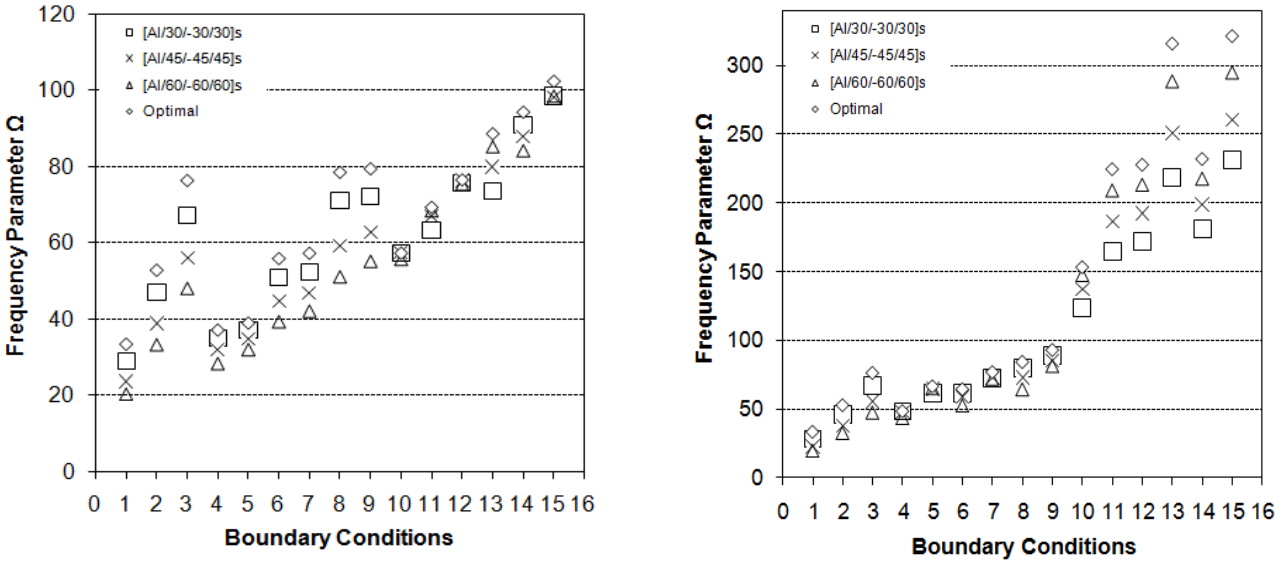


Fig. 3.Comparison of the optimum frequency Ω_{opt} and frequencies of symmetric eight-layered rectangular fiber metal plates for various ply angles: (a) a/b=1; (b) a/b=2. (1) SFSF, (2) SFCF, (3) CFCF, (4) SSSF, (5) SCSF, (6) SSCF, (7) SCCF, (8) CSCF, (9) CCCF, (10) SSSS, (11) SSSC, (12) SSCC, (13) SCSC, (14) CCCS, (15) CCCC.

Table 1 represents optimum solutions obtained by *E-GA* for the fiber metal laminated plates for 15 different edge conditions, the plate length/width ratios (*a/b= 1,2,4*), and the layer number (*n= 8,14*). The fiber angle of each ply in the inner composite layers is changed with a step of $\Delta\theta = 1^0$ between $(-90^o \le \theta_j \le 90^o)$. As inferred from the results, the natural frequencies of the fiber metal laminated plates are increased with increasing *a/b* ratios. The optimal fiber orientations also vary from 0° to 90° or 0° to -90° with increase in the *a/b* ratios and are associated with a smooth transitional region for the case of simply supported plates, such as *SSSF*. For the case of clamped plates, the optimal fiber orientations change from 0° to 90° or 0° to -90° in a sudden manner which occurred at the *a/b* ratio of unity, such as *CCCS*.

Table 1 also represents converged optimum solutions for the various combinations of free (*F*), simply supported (*S*) and clamped (*C*) edge conditions. As seen, the edge conditions play an important role on the natural frequency parameter of the *FMLs*. As the number of the clamped plate edges is increased an evident increase in the natural frequency parameters is observed, such as $\Omega = 76.333$ for the edge condition *CFCF* whereas the $\Omega = 102.413$ for the edge condition *CCCC* in *a/b=1*. This can be explained that the clamped edges provide less degrees of freedom and it is effective to stiffen the plates.

Table 1 also shows the effect of number of layers on the optimum design for various plate edge conditions and *a/b* ratios. As seen, the maximum natural frequency and the optimum fiber orientations are not influenced substantially and approach a limiting value with an increasing layer number.

Table 1 – Optimum solutions for symmetric fiber metal laminated plates

Layer number:		8		14	
BCs	a/b	$[Al/\theta_1/\theta_2/\theta_3]_{S,opt}$	Ω_{opt}	$[Al/\theta_1/\theta_2/\theta_3/\theta_4/\theta_5/\theta_6]_{S,opt}$	Ω_{opt}
SFSF	1	$[Al/0/0/0]_S$	33.318	$[Al/0/0/0/0/0/0]_S$	35.348
	2	$[Al/0/0/0]_S$	33.070	$[Al/0/0/0/0/1/0]_S$	35.160
	4	$[Al/0/0/1]_S$	32.785	$[Al/0/0/0/0/1/2]_S$	35.219
SFCF	1	$[Al/0/0/-1]_S$	52.790	$[Al/0/0/0/0/0/0]_S$	56.704
	2	$[Al/0/0/-1]_S$	52.524	$[Al/0/0/0/0/0/0]_S$	56.550
	4	$[Al/0/0/0]_S$	52.394	$[Al/0/0/0/0/0/0]_S$	56.403
CFCF	1	$[Al/0/0/-2]_S$	76.333	$[Al/0/0/0/0/0/1]_S$	80.699
	2	$[Al/0/0/8]_S$	76.085	$[Al/0/0/0/0/0/3]_S$	80.522
	4	$[Al/0/0/1]_S$	75.079	$[Al/0/0/0/0/0/0]_S$	80.954
SSSF	1	$[Al/0/0/0]_S$	37.036	$[Al/0/0/0/0/0/0]_S$	38.079
	2	$[Al/36/36/-40]_S$	48.202	$[Al/37/37/-37/-37/-38/37]_S$	48.554
	4	$[Al/43/-43/-44]_S$	84.119	$[Al/-43/-43/43/44/43/42]_S$	86.022
SCSF	1	$[Al/0/0/-2]_S$	38.874	$[Al/0/0/0/0/0/-1]_S$	39.410
	2	$[Al/57/-58/65]_S$	66.304	$[Al/58/59/59/57/65/-68]_S$	65.549
	4	$[Al/-87/-90/90]_S$	207.627	$[Al/90/90/-90/-89/-89/88]_S$	214.598
SSCF	1	$[Al/-4/-4/-5]_S$	55.818	$[Al/-4/-3/-3/-4/-4/-9]_S$	59.054
	2	$[Al/-19/-19/-15]_S$	64.195	$[Al/-19/-19/17/18/-16/17]_S$	65.422
	4	$[Al/-39/-37/-40]_S$	95.453	$[Al/-40/-39/-39/38/-38/-39]_S$	97.118
SCCF	1	$[Al/-5/-5/-5]_S$	57.216	$[Al/-5/-5/-5/-4/-6/-9]_S$	60.128
	2	$[Al/-31/-31/-23]_S$	76.633	$[Al/-32/-31/-31/32/-30/-28]_S$	75.671
	4	$[Al/-87/-90/-79]_S$	210.723	$[Al/90/-87/90/-90/90/90]_S$	217.337
CSCF	1	$[Al/0/0/3]_S$	78.465	$[Al/0/0/0/0/0/1]_S$	82.248
	2	$[Al/0/0/-2]_S$	84.098	$[Al/0/0/0/0/0/2]_S$	86.705
	4	$[Al/-36/-36/-31]_S$	105.801	$[Al/-36/-36/-36/-37/-38/-36]_S$	104.197
CCCF	1	$[Al/0/0/0]_S$	79.422	$[Al/0/0/0/0/0/0]_S$	83.169
	2	$[Al/0/0/0]_S$	92.850	$[Al/0/0/0/0/0/0]_S$	93.055
	4	$[Al/89/-90/-90]_S$	215.866	$[Al/90/-90/88/-90/89/90]_S$	220.333
SSSS	1	$[Al/-45/-44/49]_S$	57.241	$[Al/-45/-45/46/-45/-44/45]_S$	56.544
	2	$[Al/-87/-90/-90]_S$	153.168	$[Al/90/-90/90/-90/90/90]_S$	155.639
	4	$[Al/-87/-90/-90]_S$	557.552	$[Al/90/-90/90/89/-90/89]_S$	582.761
SSSC	1	$[Al/60/62/-64]_S$	69.289	$[Al/60/60/60/59/58/63]_S$	69.438
	2	$[Al/87/-90/90]_S$	224.662	$[Al/90/89/-87/90/89/90]_S$	232.533
	4	$[Al/-89/90/-90]_S$	856.570	$[Al/-90/90/88/-90/90/-88]_S$	900.130

Table 1 (continued)

Layer number:		8		14	
BCs	a/b	$[Al/\theta_1/\theta_2/\theta_3]_{S,opt}$	Ω_{opt}	$[Al/\theta_1/\theta_2/\theta_3/\theta_4/\theta_5/\theta_6]_{S,opt}$	Ω_{opt}
SSCC	1	$[Al/-40/-40/-41]_S$	76.490	$[Al/-39/-40/-40/-40/43/48]_S$	76.596
	2	$[Al/-87/90/-86]_S$	227.888	$[Al/90/87/90/-90/87/90]_S$	235.097
	4	$[Al/88/-90/-90]_S$	858.202	$[Al/-90/-88/90/90/-90/89]_S$	901.572
SCSC	1	$[Al/87/-86/-87]_S$	88.623	$[Al/90/-90/87/-89/-87/-90]_S$	89.473
	2	$[Al/87/-90/90]_S$	316.235	$[Al/90/90/90/-90/89/90]_S$	330.426
	4	$[Al/90/90/-90]_S$	1233.547	$[Al/90/90/90/90/-90/-87]_S$	1299.458
CCCS	1	$[Al/0/0/2]_S$	94.283	$[Al/0/0/0/0/0/-3]_S$	93.805
	2	$[Al/88/-90/-90]_S$	232.130	$[Al/90/-90/87/-90/90/90]_S$	238.008
	4	$[Al/-87/-90/-90]_S$	860.060	$[Al/90/90/90/90/-90/-90]_S$	902.831
CCCC	1	$[Al/1/0/-6]_S$	102.413	$[Al/0/0/0/0/1/8]_S$	99.666
	2	$[Al/-89/90/90]_S$	321.712	$[Al/90/-90/-90/89/90/88]_S$	334.393
	4	$[Al/-90/90/-90]_S$	1236.077	$[Al/90/-90/88/88/90/-90]_S$	1301.412

Summary

In this work, fundamental frequency optimization of symmetrically fiber metal laminated plates was studied using the combination of *E-GA* and *FSM* for various plate edge conditions, *a/b* ratios and layer number. As seen from the results, the combination of *E-GA* and *FSM* were successful in the determination of the fundamental frequency and optimal layered sequences in comparison with the other layered sequences without yielding a local optimum for all edge conditions. In addition, the maximum fundamental frequency and the optimum fiber orientations are substantially influenced for edge conditions and *a/b* ratios.

References

[1] A. Shooshtari and S. Razavi: Compos Struct. Forum Vol. 92. p. 2663-75 (2010).

[2] E.C. Botelho, A.N. Campos, E. Barros, L.C. Pardini, M.C. Rezende: Compos: Part B. Forum Vol. 37. p. 255-63 (2006).

[3] E.C. Botelho, L.C. Almeida, M.C. Rezende: Int J Eng Sci. Forum Vol. 45. p. 163-72 (2007).

[4] H. Assaee: *Post-local buckling analysis of composite thin-walled sections using semi-finite strip method*, PhD Thesis, Amirkabir University of Technology, Iran (2008).

[5] H. Assaee and H.R. Ovesy: Int J Numer Meth Engng. Forum Vol. 70. p. 1303-23 (2007).

[6] M.H. Sadr, H. Ghashochi Bargh: *Fundamental frequency optimization of angle-ply laminated plates using Elitist-Genetic algorithm and finite strip method*. In: Proceedings of the ASME 2010, 10th biennial conference on engineering systems design and analysis, ESDA2010, Istanbul, Turkey (2010).

[7] H. Ghashochi Bargh: *Layer optimization for maximum fundamental frequency of thin laminated composite plates*, Msc Thesis, Amirkabir University of Technology, Iran (2010).

[8] M.R. Ahmadian: *A general Strategy for the optimal design of laminated composites by the polar-Genetic Method*, PhD Thesis, Versailles Saint Quentin University, France (2007).

[9] J.R. Vinson, R.L. Sierakowski: *The behavior of structures composed of composite materials*, Dordrecht: Martinus Nijhoff (1986).

© (2011) Trans Tech Publications, Switzerland
doi:10.4028/www.scientific.net/KEM.471-472.337

Fundamental Frequency Optimization of Laminated Cylindrical Panels by Elitist-Genetic Algorithm

Mohammad Homayoun Sadr[1, a], Hadi Ghashochi Bargh[2,b]

[1,2]Aerospace Engineering Department, Centre of Excellence in Computational Aerospace Engineering, Amirkabir University of Technology, Hafez Avenue, Tehran, Iran

[a] Sadr@aut.ac.ir, [b] h_bargi2003@yahoo.com

Keywords: Elitist-Genetic algorithm, Cylindrical panels, Optimization, Finite strip

Abstract. In this paper, fundamental frequency optimization of symmetrically laminated cylindrical panels is investigated by the Elitist-Genetic algorithm (*E-GA*). The number of layers, the fiber orientation angles, edge conditions, length/width (*a/b*) and length/R (*a/R*) ratios are considered as design variables. The classical *shallow* shell theory (Donnell's formulation) is applied to calculate the natural frequencies of laminated cylindrical curved panels. To improve the speed of the optimization process, the elitist strategy is used in the Genetic algorithm and the fitness function is computed with a semi-analytical finite strip method (*FSM*). A program based on Maple is used for this purpose. To check the validity, the obtained results are also compared with some other stacking sequences.

Introduction

Thin shells and cylindrical panels which are made of layered composites are widely used in many activities of aerospace, mechanical, civil and marine engineering structures. A cylindrically curved panel can be regarded as a shallow shell that has small curvature (*i.e.,* large curvature radius) in one direction [1]. Fig.1 shows a cylindrical curved panel structure that is discretized by finite strips. In aerospace applications, vibration can be a problem when the excitation frequency coincides with the resonance frequency, which is essential to maximize the fundamental frequency in laminated cylindrical panels.

In the current paper, fundamental frequency optimization of symmetrically laminated cylindrical panels is studied. The combination of *E-GA* and *FSM* are used for this purpose. In order to reduce the calculation time, the elitist strategy is used in Genetic algorithm and the fitness function is computed with a semi-analytical finite strip model developed originally on the basis of full energy method. For this purpose, a program based on Maple is used for the optimization of shells. Finally, the effects of number of layers, boundary conditions, length-to- width and length-to-radius ratio on the optimum results are investigated and the results are compared.

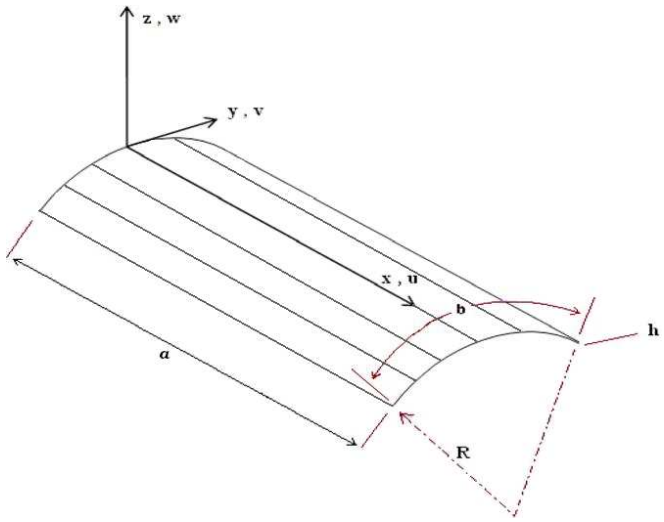


Fig. 1 Cylindrical curved panel structure discretized by finite strips.

Formulation

In the classical *shallow* shell theory, the constitutive equations for a cylindrical curved panel can be expressed as follows by performing appropriate analytical integration through the uniform thickness:

$$\begin{Bmatrix} N_x \\ N_y \\ N_{xy} \\ M_x \\ M_y \\ M_{xy} \end{Bmatrix} = \int_{-h/2}^{h/2} \begin{Bmatrix} \bar{\sigma}_x \\ \bar{\sigma}_y \\ \bar{\tau}_{xy} \\ z\bar{\sigma}_x \\ z\bar{\sigma}_y \\ z\bar{\tau}_{xy} \end{Bmatrix} dz = \begin{bmatrix} A_{ij} & B_{ij} \\ B_{ij} & D_{ij} \end{bmatrix} \times \begin{Bmatrix} \varepsilon \\ \psi \end{Bmatrix}; \qquad \varepsilon = \begin{Bmatrix} u_{,x} \\ v_{,y} + \dfrac{w}{R} \\ u_{,y} + v_{,x} \end{Bmatrix}, \psi = \begin{Bmatrix} -w_{,xx} \\ -w_{,yy} \\ -2w_{,xy} \end{Bmatrix} \tag{1a}$$

where N_x, N_y and N_{xy} are the membrane direct and shearing stress resultants per unit length, M_x, M_y and M_{xy} are the bending and twisting stress couples per unit length and ψ, ε are the curvature vector and mid-plane strains. Moreover, the shell stiffness coefficients are defined as:

$$(A_{ij}, B_{ij}, D_{ij}) = \sum_{k=1}^{n} \int_{zk-1}^{zk} (\bar{Q}_{ij})_k (1, z, z^2) dz, \quad i, j = 1,\ 2,\ 6 \tag{1b}$$

where $\bar{Q}_{ij}$ are plane-stress stiffness coefficients.

Bacause of the symmetry conditionabout the mid surface of the subject laminates, the in-plane and out-of-plane coupling stiffness coefficients are zero (*i.e.,* $B_{ij} = 0$).

The strain energy per unit volume is $\frac{1}{2}\bar{\sigma}^T\bar{\varepsilon}$.Using Eq. (1) and integrating through the thickness of the structure with respect to z gives an expression for the strain energy of a finite strip, which can be put into the following form:

$$U_s = \frac{1}{2}\iint \{\varepsilon^T.[A].\varepsilon + \psi^T.[D].\psi\} dxdy = \frac{1}{2}\{d\}^T.[k].\{d\} \tag{2}$$

The general expression for the kinetic energy of the panel due to translational motion is:

$$T_s = \frac{1}{2}\rho h \iint \{\dot{u}^2 + \dot{v}^2 + \dot{w}^2\} dxdy = \frac{1}{2}\{\dot{d}\}^T.[m].\{\dot{d}\} \tag{3}$$

where [k] is the strip stiffness matrix and [m] is the strip mass matrix and {d} is a column matrix which contains the strip's degrees of freedom and ρ is the average mass density of the panel per unit area of the mid-surface.

For the whole structure, the total strain energy and kinetic energy are obtained by summations of the corresponding energy components of all strips.

The structural equation of motions can be obtained by applying the Lagrange equations as:

$$[M].\{\ddot{\bar{d}}\} + [K].\{\bar{d}\} = \{0\} \tag{4}$$

The solution of this eigenvalue problem is:

$$\det([K] - \omega^2[M]) = \{0\} \tag{5}$$

where ω are natural frequencies. Natural frequency is normalized as a frequency parameter:

$$\Omega = \omega a^2 \left(\frac{\rho}{D_0}\right)^{1/2} \quad , \quad D_0 = E_2 h^3 / 12(1 - \nu_{12}\nu_{21}) \tag{6}$$

The optimal design problem can be stated as follows:

$$\begin{aligned} &Find \quad \theta = (\theta_1, \theta_2, ..., \theta_j) \\ &Maximize \quad \Omega = \Omega(\theta_1, \theta_2, ..., \theta_j) \\ &Subject \ \ to \quad -90^0 \le \theta_n \le 90^0 \end{aligned} \tag{7}$$

where j is half of the layer number. The optimal stacking sequences and ply angles are searched with the Elitist-Genetic algorithm.

The assumed in-plane displacement and out-of-plane displacement in the full-energy semi-analytical method are [2-3]:

$$\begin{aligned} u &= \sum_{i=1}^{ru} ((1-\eta)u_{1i} + \eta u_{2i}) \cos(i\zeta x) \\ v &= \sum_{i=1}^{rv} ((1-\eta)v_{1i} + \eta v_{2i}) \sin(i\zeta x) \\ w &= \sum_{i=1}^{rw} ((1-3\eta^2+2\eta^3)w_{1i} + b_s(\eta - 2\eta^2 + \eta^3)\theta_{1i} \\ &\quad + (3\eta^2 - 2\eta^3)w_{2i} + b_s(\eta^3 - \eta^2)\theta_{2i})W_i(x) \end{aligned} ; \qquad W_i(x) = \begin{cases} \sin(i\zeta x) & end\ simply\ \text{sup}\ ported \\ \sin(\zeta x).\sin(i\zeta x) & end\ clamped \end{cases} \tag{8}$$

where u_{1i}, u_{2i}, v_{1i} and v_{2i} are the undetermined in-plane nodal displacement parameters and $w_{1i}, w_{2i}, \theta_{1i}$ and θ_{2i} are the undetermined out-of-plane nodal displacement parameters along the edges of the strip and $\eta = y/b_s$ and $\zeta = \pi/a$.

Elitist-Genetic Algorithm

In this study Genetic algorithm is used as the optimization method and to improve the quality of the solution, the elitist strategy is used in the algorithm. An individual in the present Elitist-Genetic is an array of j_{chrom} chromosomes, each chromosome being an array of 8 genes (see Fig. 2). Basically, each design variable is coded in the form of a chromosome and likened to the chromosome position within the individual and gene position within the chromosome. The fittest individuals in the generation survive and are automatically reinserted in the next generation, right before the next selection process takes place. A parameter is defined to determine the amount of migration of individuals from one population to another (immigrants). Thus, given a process comprised of a number of populations, the same number of individuals will always be transferred from a population as the number it will receive from another population. A selection procedure based on the fitness function of the individuals picks individuals for migration and replaces individuals in a population with immigrants. In the present program, the worst individuals will be replaced by the best immigrants (elites) from the other population. Fig. 3 shows this migration paths implemented in the Elitist-Genetic algorithm. For each population, a pool of potential immigrants is constructed from the other populations. In fact, there is a strategy of exile either[3-4].

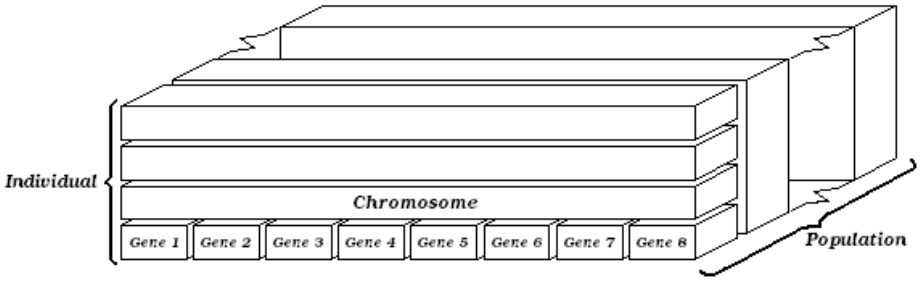


Fig. 2. Structure of a population in Elitist-Genetic algorithm.

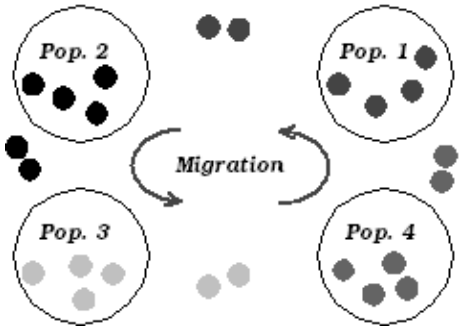


Fig. 3. Ring migration in Elitist-Genetic algorithm.

Numerical Results

The optimization results of the symmetrically laminated cylindrical panels (*h/a=0.01*) are given for *AS/3501* graphite/epoxy material [5]. The material properties are given as below:
$E_1=138$ *GPa*, $E_2=8.96$ *GPa*, $G_{12}=7.1$ *GPa*, $\upsilon_{12}=0.3$

Each of the lamina is assumed to be same thickness.

The panel degree of curvature is taken as *a/R=0* (plate), 0.2 and 0.5 in the results. A rise of the center is only 3 percent of the radius R for a shell of *a/R=0.5*, and this can be regarded as geometry within the shallow shell theory [1].

The effects of ply angles on the optimum design are shown for symmetric 8-layerd cylindrical laminated panels (*a/R*=0) in Fig. 4 with two aspect ratios. As inferred from the results, the good efficiency of the *E-GA* search strategy and its ability to provide high-quality solutions is confirmed for diffrent aspect ratios. It is also clear from those that the structural design engineer who is unaware of the effects of fibre orientations on frequency response could choose a stacking sequence which is far from the optimum.

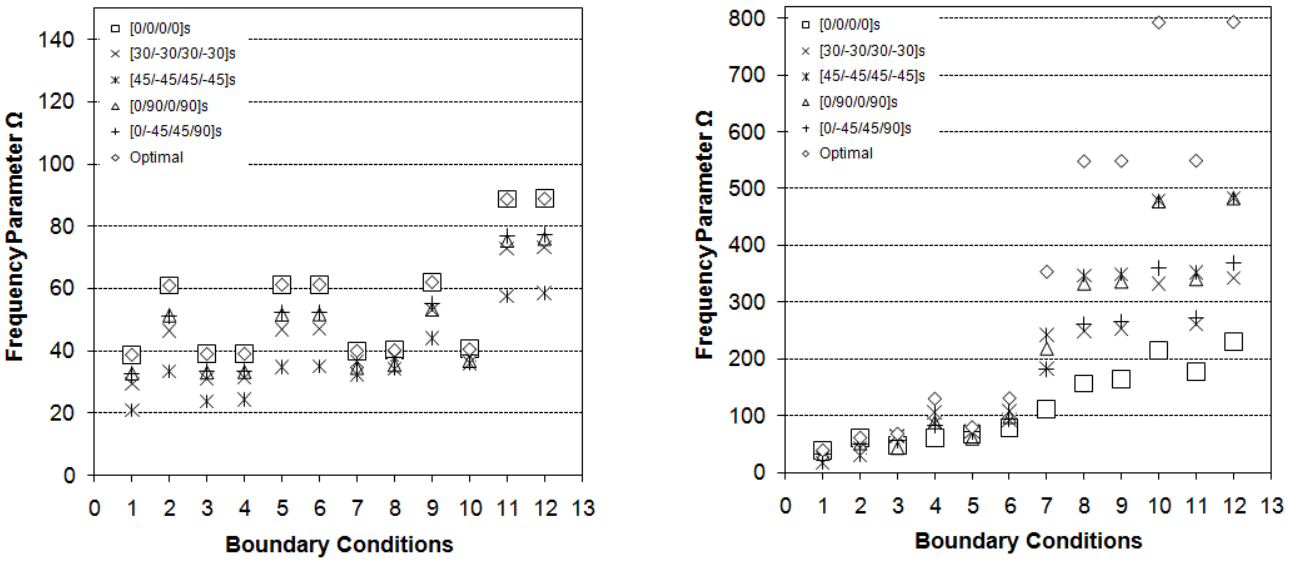


Fig. 4. Comparison of the optimum frequency Ω_{opt} and frequencies of symmetric eight-layered cylindrical panels for a/R=0 and various ply angles: (a) a/b=0.5; (b) a/b=3. (1) SFSF, (2) SFCF, (3) SSSF, (4) SCSF, (5) SSCF, (6) SCCF, (7) SSSS, (8) SSSC, (9) SSCC, (10) SCSC, (11) CCCS, (12) CCCC.

Table 1 and 2 represent the optimal layer sequences and maximum fundamental frequency of the symmetrical composite panels for 96 cases. As seen, with increase in the *a/b* ratios, the fundamental frequency increases for a symmetric cylindrical laminated panel except *SFSF* and *SFCF* edge

conditions. The optimal frequency of the symmetrical composite panels also increase, with increase in the *a/R* ratios.

Table 1 and 2 also show the effect of number of layers on the optimum design for various edge conditions. As seen, the maximum natural frequencies are not influenced substantially and approaches a limiting value with increasing layer number.

In this study, the different combinations of free (*F*), simply supported (*S*) and clamped (*C*) edge conditions are also considered. It can be noticed from the results that, the maximal natural frequency occurs at the *CCCC* edge condition, whereas the minimal natural frequency occurs at *SFSF* edge condition. This can be explained that the clamped edges provide less degrees of freedom and it is effective to stiffen the shells.

Table 1 – Optimum solutions for symmetric laminated cylindrical panels (a/R=0.2)

Layer number:		4		8	
BCs	a/b	$[\theta_1/\theta_2]_{S,opt}$	Ω_{opt}	$[\theta_1/\theta_2/\theta_3/\theta_4]_{S,opt}$	Ω_{opt}
SFSF	1	$[-28/-22]_S$	51.834	$[-32/-43/21/-1]_S$	52.147
	2	$[0/13]_S$	42.199	$[0/0/0/-33]_S$	42.576
SFCF	1	$[-3/30]_S$	69.054	$[-8/8/29/-60]_S$	69.373
	2	$[0/0]_S$	64.899	$[0/0/1/-36]_S$	65.220
SSSF	1	$[43/10]_S$	53.156	$[35/34/7/-73]_S$	53.818
	2	$[39/16]_S$	56.220	$[-37/35/46/2]_S$	56.547
SCSF	1	$[-26/57]_S$	53.169	$[36/-31/-21/87]_S$	54.161
	2	$[57/-24]_S$	66.782	$[56/56/-53/0]_S$	67.351
SSCF	1	$[6/39]_S$	71.739	$[14/12/-39/75]_S$	72.636
	2	$[5/40]_S$	72.786	$[14/16/-36/72]_S$	74.315
SCCF	1	$[7/48]_S$	71.654	$[27/-21/-75/86]_S$	72.900
	2	$[25/-68]_S$	76.599	$[29/-53/24/81]_S$	78.472
SSSS	1	$[-87/61]_S$	172.453	$[90/86/68/58]_S$	172.193
	2	$[87/-87]_S$	291.509	$[90/-87/79/-90]_S$	290.219
SSSC	1	$[-87/68]_S$	203.540	$[90/85/-85/-58]_S$	204.129
	2	$[-87/87]_S$	338.323	$[90/-87/-87/-87]_S$	338.567
SSCC	1	$[87/-70]_S$	203.491	$[88/-86/86/-58]_S$	204.429
	2	$[-87/-87]_S$	338.909	$[90/90/90/90]_S$	339.658
SCSC	1	$[-87/-87]_S$	237.692	$[90/-87/-87/89]_S$	237.925
	2	$[87/89]_S$	418.923	$[-90/85/-90/-88]_S$	419.023
CCCS	1	$[87/-74]_S$	205.028	$[90/87/84/-68]_S$	206.232
	2	$[-87/-89]_S$	339.507	$[-90/-89/-90/-90]_S$	339.770
CCCC	1	$[87/-88]_S$	238.972	$[90/-87/-87/90]_S$	239.330
	2	$[87/-87]_S$	419.954	$[-90/-87/90/87]_S$	420.455

Table 2 – Optimum solutions for symmetric laminated cylindrical panels (a/R=0.5)

		4		8	
BCs	a/b	$[\theta_1/\theta_2]_{S,opt}$	Ω_{opt}	$[\theta_1/\theta_2/\theta_3/\theta_4]_{S,opt}$	Ω_{opt}
SFSF	1	$[38/-1]_S$	68.317	$[-38/37/-11/-2]_S$	68.338
	2	$[0/24]_S$	58.308	$[0/0/10/-36]_S$	57.986
SFCF	1	$[4/81]_S$	82.661	$[-8/27/-43/86]_S$	86.695
	2	$[-2/-87]_S$	79.168	$[-3/-1/30/-82]_S$	81.305

Table 2 (continued)

Layer number:		4		8	
BCs	a/b	$[\theta_1/\theta_2]_{S,opt}$	Ω_{opt}	$[\theta_1/\theta_2/\theta_3/\theta_4]_{S,opt}$	Ω_{opt}
SSSF	1	$[-48/8]_S$	74.161	$[48/-47/15/0]_S$	74.261
	2	$[-48/-8]_S$	80.513	$[-48/-50/-15/0]_S$	80.493
SCSF	1	$[48/-5]_S$	74.374	$[48/-49/-15/2]_S$	74.384
	2	$[54/-10]_S$	82.398	$[54/56/22/0]_S$	82.574
SSCF	1	$[24/-86]_S$	90.388	$[26/-48/20/84]_S$	87.301
	2	$[28/-85]_S$	94.826	$[29/-48/12/79]_S$	98.174
SCCF	1	$[23/-85]_S$	90.588	$[27/-21/-75/86]_S$	85.345
	2	$[28/-85]_S$	95.985	$[33/-55/9/79]_S$	98.966
SSSS	1	$[-70/-61]_S$	242.946	$[73/65/-64/60]_S$	243.180
	2	$[88/-89]_S$	623.184	$[90/-85/87/-89]_S$	623.223
SSSC	1	$[67/-48]_S$	262.352	$[77/59/50/46]_S$	263.535
	2	$[88/-87]_S$	623.376	$[-90/-87/-90/87]_S$	624.123
SSCC	1	$[69/-51]_S$	256.356	$[79/-62/-53/47]_S$	267.281
	2	$[-87/-88]_S$	623.949	$[-90/-87/-79/-89]_S$	620.755
SCSC	1	$[87/48]_S$	285.936	$[90/73/-51/45]_S$	286.747
	2	$[-87/-87]_S$	660.457	$[90/-86/-79/-90]_S$	657.038
CCCS	1	$[-69/-53]_S$	233.495	$[-77/61/-56/51]_S$	268.070
	2	$[87/-87]_S$	624.337	$[-90/-87/-90/-90]_S$	625.474
CCCC	1	$[-87/54]_S$	281.923	$[89/87/-55/51]_S$	291.013
	2	$[87/87]_S$	661.346	$[90/-85/-82/-90]_S$	657.579

Summary

In this study, the optimum lay-ups for the maximum fundamental frequencies of laminated curved panels with diffrent edge conditions were determined by the combination of the analysis method and the optimization procedure. As seen from the results, the maximum fundamental frequencies were substantially influenced for edge conditions, *a/R* and *a/b* ratios. As seen, the maximum fundamental frequencies are not substantially influenced and approach a limiting value with an increasing layer number.

References

[1] Y. Narita and P. Robinson: Int J Mech Sci. Forum Vol. 48. p. 1516-24 (2006).

[2] H. Assaee and H.R. Ovesy: Int J Numer Meth Engng. Forum Vol. 70. p. 1303-23 (2007).

[3] M.H. Sadr, H. Ghashochi Bargh: *Fundamental frequency optimization of angle-ply laminated plates using Elitist-Genetic algorithm and finite strip method*, In: Proceedings of the ASME 2010 10th biennial conference on engineering systems design and analysis, ESDA2010, Istanbul, Turkey, 12-14 July 2010.

[4] H. Ghashochi Bargh: *Layer optimization for maximum fundamental frequency of thin laminated composite plates*, Msc Thesis, Amirkabir University of Technology, Iran (2010).

[5] J.R. Vinson, R.L. Sierakowski: *The behavior of structures composed of composite materials*, Dordrecht: Martinus Nijhoff (1986).

© (2011) Trans Tech Publications, Switzerland
doi:10.4028/www.scientific.net/KEM.471-472.343

Finite Element Analysis of Fibre Reinforce Concrete Beam Subject to High Temperature by Using EURO-Code Models

Ziad K Awad[1,a] and Talal F. Yusaf[2,b]

[1,2] Faculty of Engineering and Surveying, University of Southern Queensland
Qld 4350, Australia

[a]awad@usq.edu.au, [b]yusaft@usq.edu.au

Keywords: Finite element, Concrete, Glass fibre composite, Fire, Temperature, Analysis.

Abstract. Glass fibre composite reinforcement bars have been used in the reinforced concrete structures as a powerful solution of the steel corrosion problem. This research work aims to use a 3D finite element method and EURO – code models to simulate a concrete beam reinforced with fibre composite bars under the effects of high temperature. The behaviour of the structure is very complex due to load combination and different material response. The applied load was an external mechanical load and a thermal load. The material response was considered as thermal expansion, cracking, crushing, yielding and changing of material properties with the temperature increase. The FE element was modified to allow temperature distribution and material properties changing to throw thickness of the concrete beam. In addition, the geometrical non – linearity is considered in the analysis due to the large deflection of the structure. The prediction results were compared with the available experimental results, and it gives a well correspond.

Introduction

Fibre reinforced polymer (FRP) composite material has been attracted by many industrial sectors due to its robust characteristics such as high strength and high stiffness to weight ratio. Fibre composite materials have become an important target for the solution of degradation problems in conventional structural materials such as steel, wood and concrete [1]. Fire accident to the structure is more popular in our life; therefore, many studies have been done in the last three decades to find two strategies caused by fire or temperature rising. Some of these studies were concerned to find the behaviour of material properties, and it is proportion to the temperature variation, but other researches concerned with studying the behaviour of structure when the temperature rising through all or some of structur's parts. Therefore, many formulas have been found to represent the structure materials behaviour under specific external load and rising temperature. Ferrier et al. [2] studied the effect of the temperature on the adhesive layer in a concrete structure strengthening with external FRP composite layers. A conclusion was made that the temperature rising effect on the creep of the FRP composite and the FRP composite should not carry more than 30-40% of its ultimate strength. In addition, many research studies have done to find the stress-strain behaviour of different concrete strength material under different temperature conditions, for example (Adnerburg-Themerandersson model, Schineider model, Diederiches model and Khouryand Terro model) [3-5]. Nechnech et al. [6] introduced an elasto – plastic damage model of reinforce concrete structure under high temperature. This model used a coupling procedure between temperature effect and mechanical external load effect and included the effect of material creep as well. This approach was divided into two important parts mechanical damage effect and non – mechanical damage effect. Abbasi and Hogg [7] proposed a semi-empirical model of properties and thermal distribution prediction through fibre reinforced concrete beam. Abbasi and Hogg [8] tested a fibre reinforced concrete beam under elevated temperature. It was found that the fibre reinforced concrete beam could stay up to 2 hours. Euro – Code 2 gives a model for the behaviour of concrete under the effect of high temperature. A reduction factor was recommended for concrete strength according to its temperature [3].

The objective of this paper is to develop a non-linear 3D finite element (FE) model to simulate the behaviour of fibre reinforce concrete structure subject to fire until failure. The complex features of concrete and glass fibre reinforce polymer (GFRP) bars in fire condition are considered, such as crushing, cracking and expansion. In addition, changing of the mechanical properties of the materials is considered as a consequence of temperature rising. All temperature effects on the geometry, stiffness of the structure, the internal forces, are included in the model.

Numerical Solution Procedure

In the present study the solution procedure depends on the total strain at any time (t) is calculated as:

$$\varepsilon^{T} = \varepsilon^{m} + \varepsilon^{nm} \tag{1}$$

where, ε^{m} is a mechanical strain due to external load. $\boldsymbol{\varepsilon}^{nm}$ is a non-mechanical strain due to temperature effect at time (t). ε^{T} is total strain at time (t).

The non-mechanical strain load vector (ΔQ_n^{nm}) at time step (t_n) could be calculated from the non – mechanical strain ($\Delta\varepsilon_n^{nm}$) as an equivalent nodal forces [9]:

$$\Delta Q^{nm} = \int_v B^T . D . \Delta\varepsilon_n^{nm} . dv \tag{2}$$

where, B geometry matrix. D material matrix.
The calculated nodal forces should be added to the residual forces:

$$\Delta R_n = \Delta Q_n^{nm} + \Delta R_{n-1}^{u} \tag{3}$$

where, ΔR_n is the total residual forces and ΔR_{n-1}^{u} is the unbalance forces of (n-1) increment.
At time step t_n all joint displacement are U, total strain ε_n and total non mechanical strain:

$$\varepsilon_n^{nm} = \varepsilon_{n-1}^{nm} + \Delta\varepsilon_n^{nm} \tag{4}$$

The total mechanical strain in structure at time step (t_n):

$$\varepsilon^{m}{}_n = \varepsilon^{T} - \varepsilon_n^{nm} \tag{5}$$

Thermal Properties

By the nature any material might have a thermal expansion as a consequence of temperature rising and this will affect the initial volume of the material. Concrete material has a thermal strain coefficient expressed by linear function of temperature [10]:

$$\alpha_c = (0.008 * T + 6) * 10^{-6} \tag{6}$$

where, T is a temperature C^0.

A specific heat and thermal conductivity of concrete are assumed equal to 1000 J/kg K and 2 W/mK respectively [11]. The thermal strain coefficient of GFRP is assumed constant and equal to:

$$\alpha_g = 1 * 10^{-5} \tag{7}$$

The specific heat and thermal conductivity is assumed equal to 500 J/kg K and 0.22 W/mK respectively [12].

Concrete Constitutive Model

Barzegar – Jamshidi proposed envelop for concrete in biaxial stress as a function of temperature as shown in Fig. 1. Whereas, the compressive strength (f_c) and tensile strength (f_t) of concrete regard as functions of temperature. The failure surface of a biaxial strength envelope is divided into

four regions. The stress in these regions depends on the principle stresses ratio. Compression stresses is negative and tensile stresses is positive [6]. Euro-code proposes full models to represent the concrete behaviour at high temperature [3, 13]. The elastic modulus of the concrete as a function of the temperature is shown in Fig. 2. The concrete material loses 50% of its elastic modulus at 200 C^o. The compressive strength is changing with temperature, and it is described in Fig. 3. Constant compression strength is maintained below 200 C^0. The reduction happens in strength as a consequence of temperature rising. The tensile strength of concrete is assumed to be change with temperature as shown in Fig. 4. Whereas, no change in tensile strength when the temperature is less than 100 C^0.

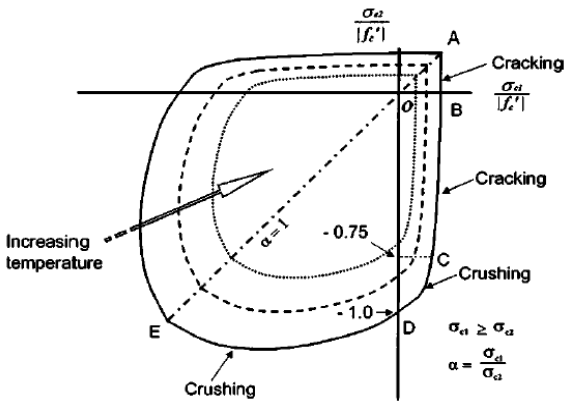


Fig. 1. Biaxial envelop of concrete

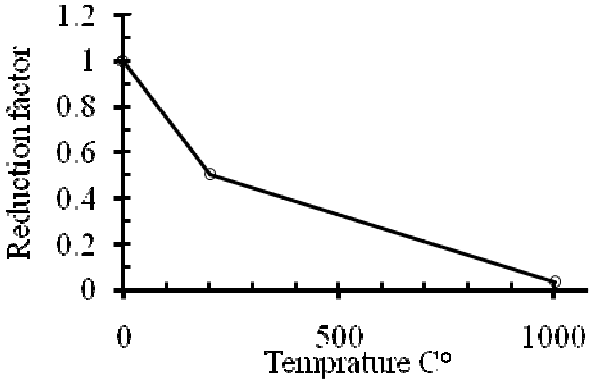


Fig. 2. Concrete elastic modulus

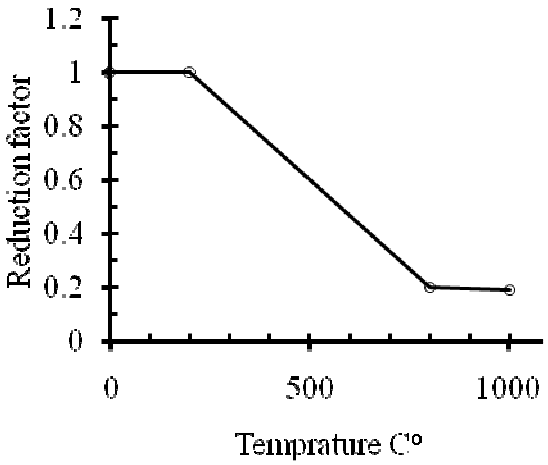


Fig.3. Concrete compressive strength

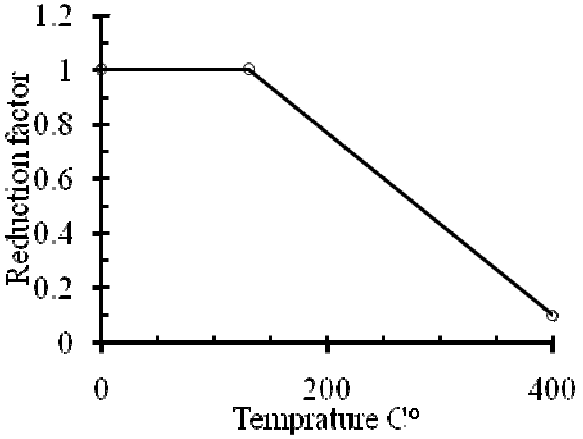


Fig. 4. Concrete tensile strength

Uni-axial GFRP Model

In this study, the main GFRP bars are modelled as 3D single bar reinforcement. The GFRP stirrups are modelled as embedded region with axial stiffness only. A perfect bond between GFRP and concrete is assumed in the model. The GFRP behaviour is assumed constant when it is temperature less than 100 C^0 for GFRP elastic modulus and tensile strength [14]. GFRP materials will loss the strength when the temperature exceeds 600 C^0 as shown in Fig. 5 and Fig. 6.

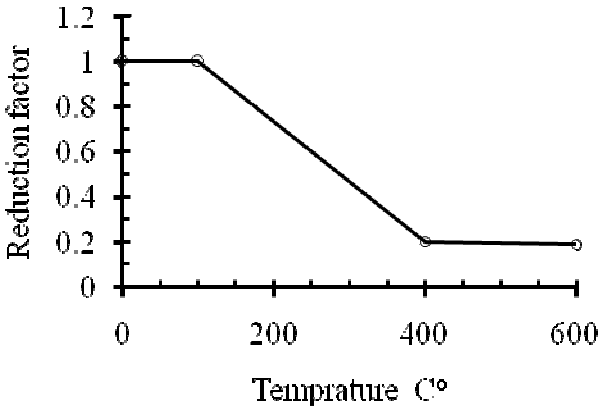


Fig. 5. GFRP tensile strength [13]

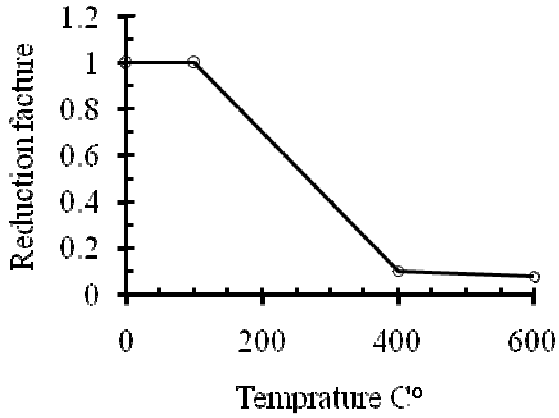
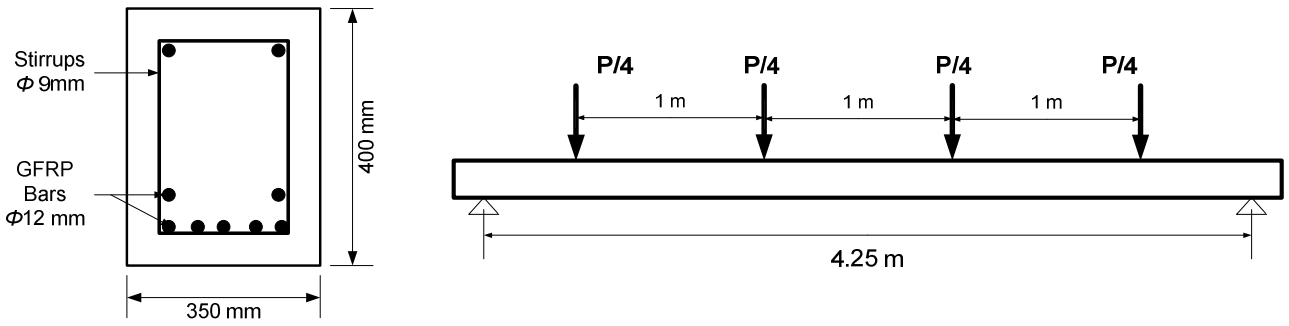


Fig. 6. GFRP elastic modulus [13]

Numerical Fire Test Simulation

A full fire test of fibre reinforced concrete beam was done by Abbasi and Hogg [8]. The test was done according to the BS 476. The beam was simply supported with a rectangular cross section 350 mm x 400 mm with total length 4.4 m as shown in Fig. 7 and the reinforcements concrete cover was 75 mm. The external applied load was 40 kN as shown in Fig. 7. The materials mechanical properties are shown in Table 1. The concrete compressive strength is 42 MPa. The GFRP tensile strength for bars and stirrups are 760 MPa and 690 MPa respectively. The GFRP elastic modulus was 40.8 GPa. The 3D FE model was developed to simulate a half beam due to symmetry. The external load was applied on the top edge of the beam. The simulation of fire action was done by applying a heat flex on the left, right and bottom edges of the beam. The BS 476 furnace temperature was used as amplitude for the temperature simulation with time. The 3D FE geometry is shown in Fig. 8. The non-linear geometry was used in the analysis because of the large deformation. The analysis was divided into two stages stage one is the mechanical external load and stage two is the fire action. The concrete failure is shown in Fig. 9. Stress distribution in concrete and reinforcement are described in Fig. 10-11. The deflection with the time is explained in Fig. 12 and it shows a good agreement with experimental results. In addition, cross section temperature distribution is explained in Fig. 12. The heat transfer was used in the model to allow the temperature to go inside the beam from external edges. In the FE analysis the concrete starts cracking at time 4 min. The first yield of the bottom GFRP reinforcement is noticed at time equal to 126 min.



a- Cross section b- Beam load details

Fig. 7. Beam details

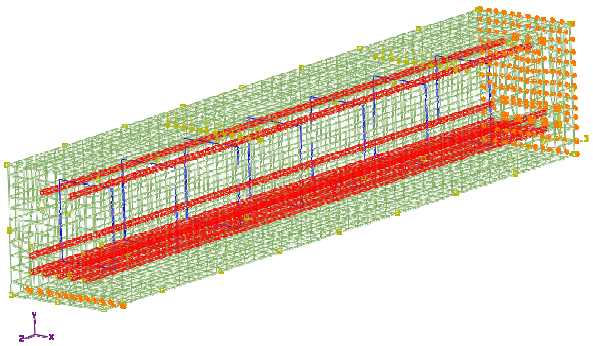


Fig. 8. 3D FE geometry

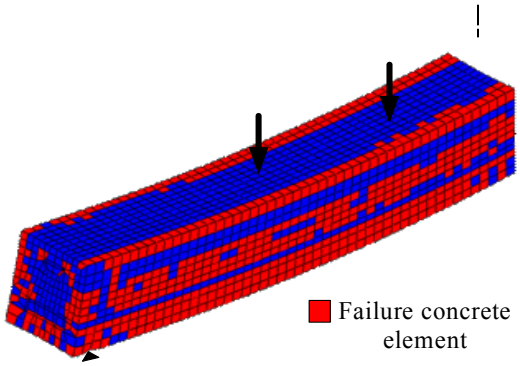


Fig. 9. Failure of beam

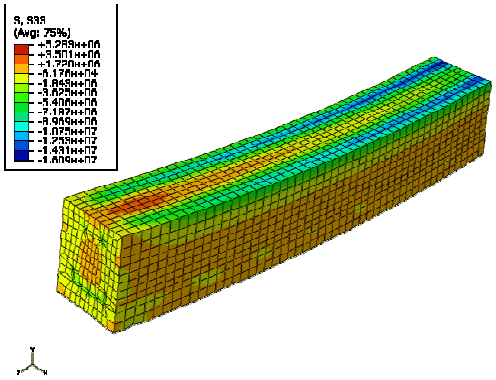


Fig. 10. Stress_33 in concrete at time 100 min

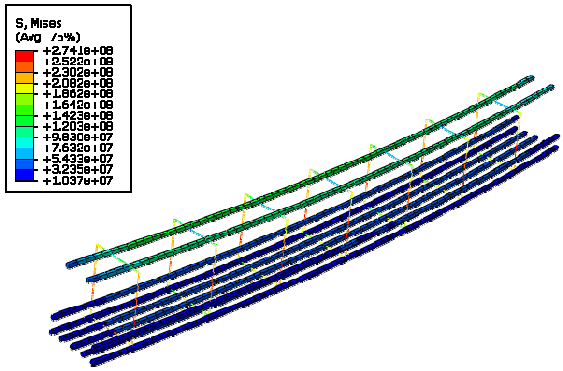


Fig. 11. Stress Von-Mises in reinforcement at time 100 min

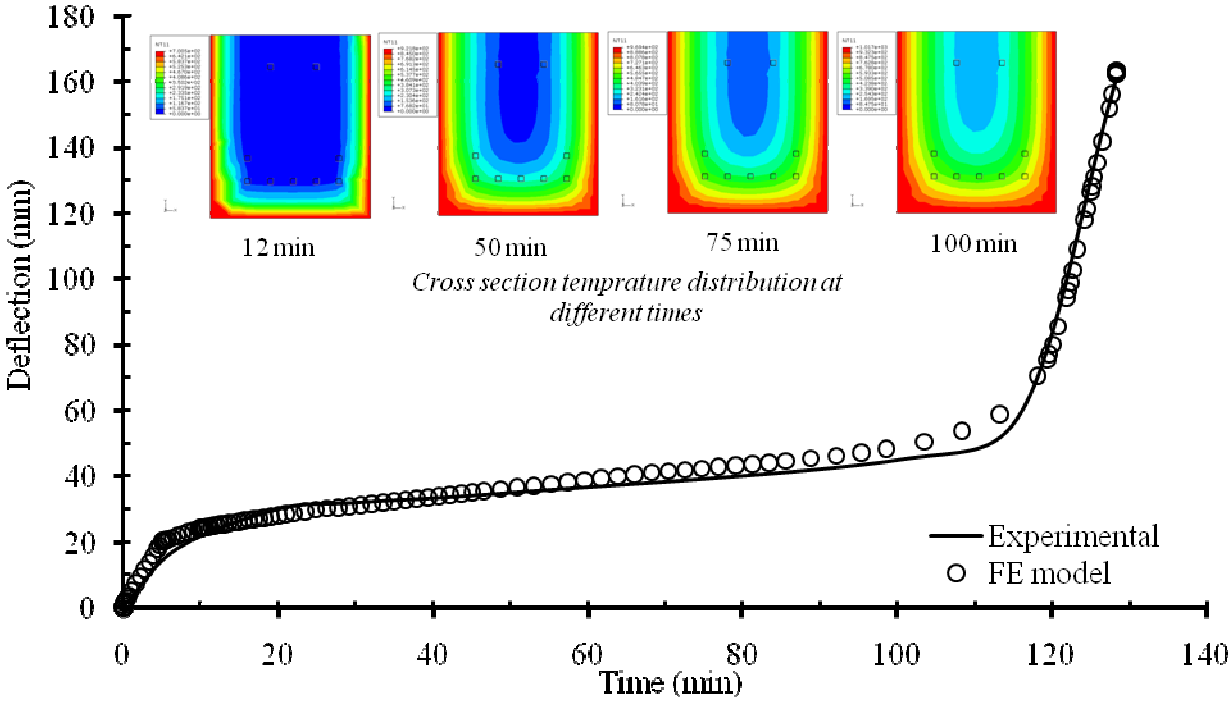


Fig. 12. Time deflection curve

Summary

The research was focused on the FE simulation of fibre reinforced concrete structure under fire condition. Euro-code models behave very well in the simulation of fibre reinforced concrete structures. Using 3D element to simulate the bar reinforcement works fine with the heat transfer. Furthermore, applied fire effect after applying the external load to the structure is an acceptable procedure. The calculated deflection matches the experimental behaviour. Although the GFRP bars lose its strength after 600 C^o, the fibre reinforced beam could stay for 2 hrs. The concrete cover plays an important role in the protection of GFRP bars from fire. Finally, the creep and shrinkage strain might be considered in the future studies

References

[1] Z.K. Awad, T. Aravinthan, Y. Zhuge, in: CICE 2010 - The 5th International Conference on FRP Composites in Civil Engineering, Beijing, China, 2010.

[2] E. Ferrier, G. Lagarde, P. Hamelin, Composites Science and Technology, 61 (2001) 425-431.

[3] E. Eurocode, Ref. No. prEN 1992-1, 1 (2002).

[4] S. Bratina, B. Cas, M. Saje, I. Planinc, International Journal of Solids and Structures, 42 (2005) 5715-5733.

[5] L. Li, J. Purkiss, Fire Safety Journal, 40 (2005) 669-686.

[6] W. Nechnech, F. Meftah, J. Reynouard, Engineering Structures, 24 (2002) 597-611.

[7] A. Abbasi, P. Hogg, Composites Part B: Engineering, 36 (2005) 384-393.

[8] A. Abbasi, P. Hogg, Composites Part A: Applied Science and Manufacturing, 37 (2006) 1142-1150.

[9] A. Mari, B.S.E.L. University of California, Nonlinear geometric, material and time dependent analysis of three dimensional reinforced and prestressed concrete frames, Dept. of Civil Engineering, University of California, 1984.

[10] X. Zha, Journal of Constructional Steel Research, 59 (2003) 769-779.

[11] R. Demirboga, I. Türkmen, M. Burhan Karako Building and Environment, 42 (2007) 349-354.

[12] A. Mekjian, FRP International, 2 (2005).

[13] Z. Huang, I. Burgess, R. Plank, Journal of Structural Engineering, 129 (2003) 1093-1102.

[14] L. Bisby, M. Green, V. Kodur, Progress in Structural Engineering and Materials, 7 (2005) 136-149.

© (2011) Trans Tech Publications, Switzerland
doi:10.4028/www.scientific.net/KEM.471-472.349

Responses of Aging Treatment to The Behavior of Aluminum Alloy With Addition of 0.02% Zirconium Element

Mohd Syukry Zakaria[1,a], Ahmad Badri Ismail[2,b]

[1, 2]School of Material and Mineral Resources Engineering, Universiti Sains Malaysia, Malaysia

[a]syukryz@gmail.com, [b]ahmad.badri@gmail.com

Keywords: Aluminum alloy, Artificial aging, Natural aging, Hardness, Zirconium

Abstract. Response of aging treatment on aluminum alloy towards its hardness has been investigated. Alloy used on this research was develop base on a US patent 4121951 that is use to produce aluminum cable with excellent strength and conductivity [1]. Solutioninzing treatment was carried out to the alloy at 520 °C for 2 hours. Alloy then were artificial aged at 180 °C, 200 °C and 220 °C for various periods up to 10 hours. Natural aging also has been carried out for 2 weeks right after solution quenching. By referring to the results, hardness increase as the aging time increase until it reaches the maximum peak and then decreases as the result of overaging. Hardness of artificial aged alloy then was compared with 99.99% pure aluminum, as-cast and naturally aged alloy. Alloy aged at 180 °C for 2 hours give the highest value of hardness which is 34.26 Hv followed by naturally aged alloy and pure aluminum with 30.92 Hv and 15.2 Hv. The effect of different time of artificial aging gives significant change in hardness in order to improve the strength of aluminum alloy. Minor addition of zirconium during the aluminum processing will probably cause by the precipitation of Zr particles towards the aluminum matrix [2], thus increase the strength even these particulate cannot be detected by XRD. These particles will retard the grain movement and also stable upon heating due the low solubility of zirconium in aluminum matrix.

Introduction

Nowadays, the age-hardenable of aluminum alloys has been widely used in industry such as automotive, architectural and structural application [3]. The attractive properties that contribute to its widespread use are their high strength-to-weight ratio compare with steel, resistance to corrosion by many chemicals and atmospheric condition, high thermal and electrical conductivity nearly as well as copper, nontoxicity, reflectivity for decorative purposes, appearance, and ease of formability and of machinability [4-5]. This research was focusing on application of aluminum alloy as an electrical conductor since it's has been introduce early 1960s due to facts that aluminum wire has the advantage of better resistivity/weight than copper, as well as being cheaper.

Aluminum alloy usually strengthened through precipitation hardening that involves two different heat treatments which is solution heat treatment and then followed by artificial or natural aging. During solution heat treatment (normally above 500 °C) all solute atoms are dissolving to form a supersaturated solid solution [6]. Single phase then will be retained by application of quenching either in cold water or, when distortion control is critical, in air or hot water to maintain supersaturation [7]. Precipitates will form through the aluminum matrix after solution heat treatment by aging either at room temperature (natural aging) or above it (artificial aging). The mechanical properties of the alloy will change with time, as they are affected by the type, size and distribution of the precipitates that can be formed [8].

To improve the hardness and wear resistance of the alloys at higher temperatures, a microstructure containing a thermally stable and coarsening resistant dispersoid is required [9]. According to theory, a particle will be resistant to coarsening if the energy of its interface with the matrix is low, and if the diffusivity and solubility of its rate-controlling element are small. Among the transition metals, Zr has the smallest diffusion flux in aluminum, and its addition to aluminum base alloys results in the formation of Al_3Zr phase. Addition small amount of Zr to wrought aluminum alloy also done to improve workability an formability by refining the microstructure [10],

and to impede recrystallization during heat treatment due to the obstacle action of the coherent particle [11-12].

Experimental Procedure

The aluminum alloy used in this research has been prepared by melting the requisite of pure metals in melting box furnace. Pure metals of 99.99%Al, 99.98Fe, 98.5%Si, 99%Mg, 99.5%B, and 99.9% Cu, and 99.8% Zr were used to prepare the aluminum alloy. All the pure metals then were charged into an alumina crucible, which was place in the melting box furnace. Temperature has been raised up to 800 °C and then soaked for 2 hours and stirred to obtain the melt homogeneity. The melt was then poured in a cylindrical steel mould to produce cast ingot of 16 mm in diameter and 150 mm in length. After solidification and cooling, the ingot was removed from the mould. Table 1 shows chemical composition of the as-cast alloys determined by X-ray fluorescence (XRF). That alloys then were solution-treated at temperature of 520 °C for various periods of time up to 4 hours and quenched in water at room temperature. Artificial ageing was carried out for selected solution-treated samples at temperature ranging from 180 °C to 220 °C for various periods of time up to 10 hour prior to oven cooling. For natural ageing, samples have been kept for two weeks right after solution quenching. X-ray diffraction (XRD) was carried out on selected samples for different experimental conditions.

Samples used for the hardness test were cut into size 10 mm in thickness. The hardness of the pure aluminum, as-cast and heat-treated specimens was performed by using Vickers hardness equipment, with a load of 0.5 kgf and 10 sec dwell time. Each reading was an average of at least five separate measurements taken from the sample surface.

Table 1. Chemical composition (wt %) of the as-cast alloy determined by X-ray fluorescence.

Element	Al	Si	Fe	Cu	Zn	Zr	Mg
Weight percentage (wt %)	98	0.1	0.89	0.26	0.016	0.022	0.53

Results and Discussions

Fig. 1 shows the variation of hardness value with aging time in the temperature range 180 °C to 220 °C. After solution treatment at 520 °C which was followed by water quenching, the aluminum alloy give hardness value of 26.5 Hv. It can be seen that all aluminum alloy curves in each condition give an obvious age-hardening behavior as many researchers have reported [3, 7-9, 11-12]. In the early stage of aging, those alloys give significant increase in hardness until it reaches at 2 hours. During this stage, fine and profuse GP zones homogeneously distribute in the matrix thus lead to significant increase of hardness. At intermediate stage of aging, after a little decrease the hardness increases again and reach second peak at 6 hours for alloy aged at 180 ° while 8 hours and 10 hours for 200 °C and 220 °C respectively. During intermediate stage, metastable phases will formed and kept semi-coherence with the aluminum matrix thus will give a little strengthening effect to the alloy. The decreasing of hardness between initial stage and intermediate stage can be presumed by the dissolution of GP zones. These GP zones remarkably dissolve before metastable phase formation then will decrease the number of GP zones presence, while metastable precipitates have not grown up and the size of them are too small to resist the movement of dislocation, so that age hardening effect of alloy must be low at this stage. At the final stage of aging, the hardness of the alloys decreases as a result of over-aging except for alloy aged at 220 °C [13].

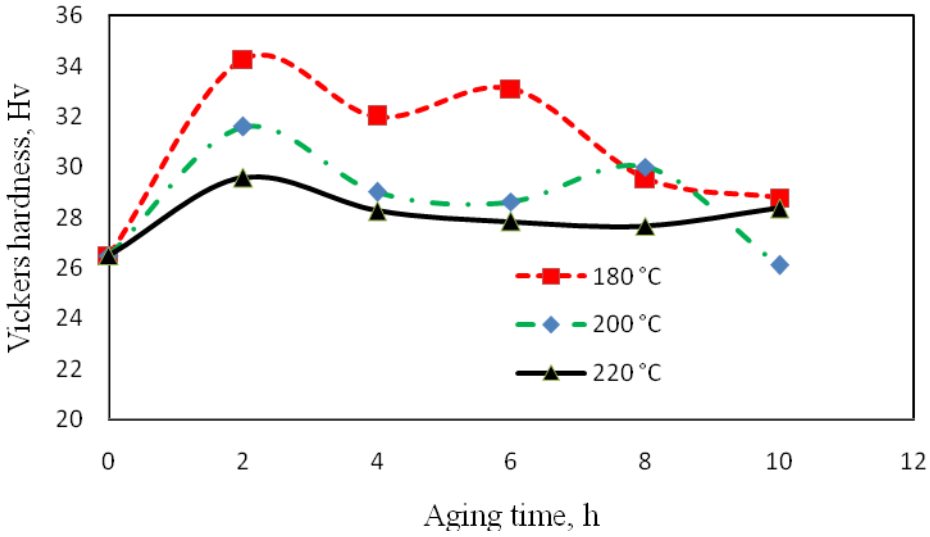


Fig. 1 The variation of hardness measurement of aluminum alloy with various temperature of artificial age hardening.

During this experiment, aluminum alloy also been naturally aged in order to compare with the artificially aged harden alloy. The variation of hardness of alloy can be represented by referring to Fig. 2. Hardness increase at initial stage until it reaches the maximum at 7 days of aging. Natural aging give hardness value of 30.92 Hv when it reach maximum peak. A summary of hardness data for 99.99% pure aluminum and aged aluminum alloy data are given in Table 2.

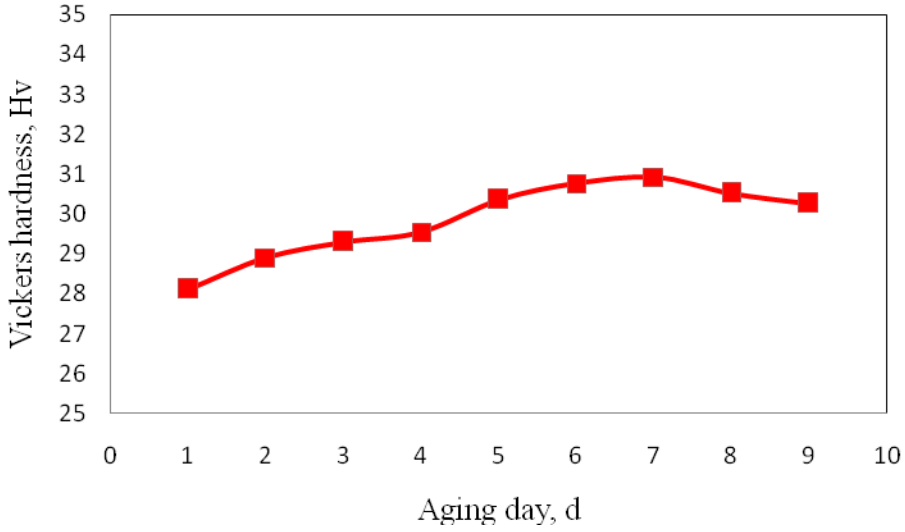


Fig. 2 The variation of hardness measurement of aluminum alloy

Table 2 Summary of hardness value for every condition of 99.99% pure aluminum and aluminum alloy

Condition		Peak hardness (Hv)
99.99 % pure aluminum		15.2
Aluminum alloy	Naturally aged	30.92
	Artificially aged at 180 °C	34.26
	Artificially aged at 200 °C	31.6
	Artificially aged at 220 °C	29.58

The XRD analysis was employed in order to identify the type of the precipitated phases. Fig. 3 shows the XRD pattern of the selected alloy natural and artificially aged. Based on Fig. 3, there are only aluminum peak present in the pattern although there are other addition elements detected by XRF. All the expected phases such as Al_3Zr, Mg_2Si, and Al_2Cu are visible due to small amount addition of alloying element. Recent study by Mahmudi et. al use 0.15 wt% of Zr as addition to A319 aluminum in order to precipitates the Al_3Zr particles towards the aluminum matrix. Mahmudi et. al also reported that, the XRD pattern of Al_3Zr is overlap with aluminum matrix due to their fcc lattices with close parameter, so that it is not logical to consider these phase as Al_3Zr in A319 aluminum. Therefore Mahmudi et. al use a bulk extraction technique to dissolve the aluminum matrix and then give the deposited of Al_3Zr which occurrence of the main at $2\theta = 39°$ [2]. By referring to the research made by Mahmudi et. al, there is at least 0.15 wt% of zirconium needed in order to form the Al_3Zr particle towards the aluminum matrix.

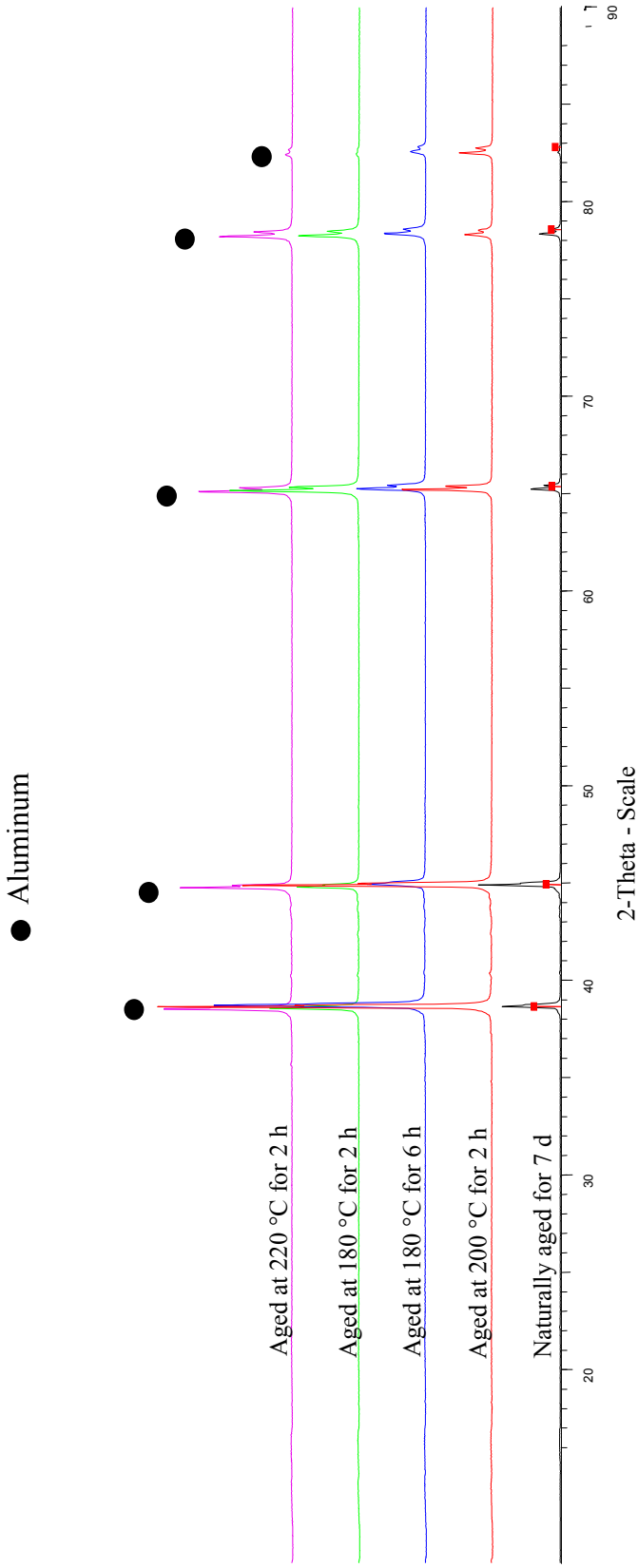


Fig. 3 X-Ray diffraction pattern of aluminum alloy aged at different time and temperature.

Summary

1. Aluminum alloy produced during this research give highest hardness when alloy were artificially aged at 180 °C compare with 200°C, 220 °C and naturally aged alloy.
2. Aluminum alloy artificially aged for 2 hours give the highest hardness among of the other aging time.
3. Weight percentage of zirconium element should be increased in order to precipitate Al_3Zr towards aluminum matrix [2], so that the hardness/strength will significantly increase.

References

[1] Paul Emile Fortin, F.H., *Alminum Alloy Electrical Conductor and Method Therefore*, U.S. Patent, Editor. 1976, Alcan Research and Developement: Kingston, Canada. p. 1-7.

[2] Mahmudi, R., P. Sepehrband, and H.M. Ghasemi, Materials Letters, 2006. **60**(21-22): p. 2606-2610.

[3] Zuo, X. and Y. Jing, Journal of Materials Processing Technology, 2009. **209**(1): p. 360-366.

[4] Altenpohl, D.G., in *Aluminum: Technology, Applications, and Environment* S.K.D. J. Gilbert Kaufman, Editor. 1999, The Aluminum Association and The Minerals, Metals & Materials Society: Washington. p. 3.

[5] Serope Kalpakjian, S.R.S., *Aluminum and Aluminum Alloys*, in *Manufacturing Engineering and Technology*. 2006, Jurong Singapore, Pearson Prentice Hall. p. 170.

[6] William D. Callister, J., *Precipitation Hardening*, in *Material Science and Engineering An Introduction*. 2003, John Willey & Sons, Inc. p. 370-373.

[7] Bates, C., Journal of Heat Treating, 1987. **5**(1): p. 27-40.

[8] Cavazos, J.L. and R. Colás, Materials Characterization, 2001. **47**(3-4): p. 175-179.

[9] Chen, Y.C., M.E. Fine, and J.R. Weertman, Acta Metallurgica et Materialia, 1990. **38**(5): p. 771-780.

[10] Srinivasan, D. and K. Chattopadhyay, Materials Science and Engineering: A, 2001. **304-306**: p. 534-539.

[11] Nes, E., Acta Metallurgica, 1972. **20**(4): p. 499-506.

[12] Waheed, A. and G. Lorimer, Journal of Materials Science Letters, 1997. **16**(20): p. 1643-1646.

[13] Li, R.X., et al., Materials Letters, 2004. **58**(15): p. 2096-2101.

© (2011) Trans Tech Publications, Switzerland
doi:10.4028/www.scientific.net/KEM.471-472.355

Poly(vinylidene fluoride)/Microcrystalline Cellulose Nanocomposites with Enhanced Compatibility and Properties

Xue-Gang Tang[1], Meng Hou[1,a], Jin Zou[1], Rowan Truss[2]

[1]School of Mechanical & Mining Engineering, The University of Queensland, Brisbane, QLD 4072, Australia

[2]Schools of Chemical Engineering, The University of Queensland, Brisbane, QLD 4072, Australia

[a]m.hou@uq.edu.au

Keywords: Microcrystalline Cellulose; Poly(vinylidene fluoride); Nanocomposites;

Abstract. Poly(vinylidene fluoride)/Microcrystalline cellulose (MCC) nanocomposites were prepared by ultrasonic treatment and magnetic stir. Poly(vinylidene fluoride)-graft-maleic anhydride (PVDF-g-MAH) was added to promote matrix–filler compatibility. Transmission electron microscopy (TEM) results showed that the diameter of the MCC was decreased to several tens nanometers by the treatment of ultrasonic and magnetic stir. The results of differential scanning calorimetry (DSC) showed that the peak crystallisation temperatures (T_c) and the crystallisation enthalpy ΔH_c increased with the addition of MCC, and the melting enthalpy ΔH_m increased. With the addition of the compatibilizer (PVDF-g-MAH), peak crystallisation temperatures increased further, while without further increase of the ΔH_c. Attenuated total reflectance Fourier transform infrared spectroscopy (ATR-FTIR) showed that the addition of MCC induced β-phase PVDF, and the addition of PVDF-g-MAH can induce more β-phase PVDF. Mechanical properties of the nanocomposites were evaluated and the results showed that the addition of MCC did not increase the Young's modulus, while the tensile strength and elongation at break decreased.

Introduction

The idea of using rigid fillers as a reinforcing agent is nothing new: straw has been used to reinforce mud bricks since about 4000 BC [1]. Recently, much interest has focused on the development of polymer nanocomposites based on highly anisotropic nanofillers. Polymers reinforced with cellulose nanofibers are interesting because of the high aspect ratio and potentially excellent mechanical properties of cellulose nanofibers (modulus of ca. 150 GPa and tensile strength of ca. 10 GPa) [2]. Poly(vinylidene fluoride) (PVDF) is a semi-crystalline polymer with a variety of interesting properties, which has been widely studied because of its potential as piezoelectric and pyroelectric materials. These properties, combined with high elasticity and processing ability, provide a variety of technological applications for this polymer [3]. Our previous research showed that PVDF has high potential in the thermoset composite welding (TCW). The world-class international patented technology showed great potential for cost saving in the joining and repairing of composite materials and represents the "Next-Generation" assembly technology for aerospace composite structures [4]. However, the poor creep resistance has hampered the application in TCW.

In this research, cellulose fibers were used to reinforce the PVDF. PVDF is hydrophobic, leading to compatibility issues when mix with polar surfaces, such as cellulose used here. The problem can be resolved by incorporating functionalised PVDF, such as PVDF-g-MAH. The structural similarity of PVDF and PVDF-g-MAH permits the occurrence of segmental co-crystallisation that is desirable for cohesive coupling, while the carboxylic anhydride groups can provide covalent bonding to the surface of cellulosic fibres [5].

Experimental Section

Materials. PVDF (Kynar 741, powder) and maleic anhydride grafted PVDF (PVDF-g-MAH, Kynar ADX-161) named from here on as ADX were kindly supplied by Arkema (Australia, New Zealand). Analytical grade N-methyl-2-pyrrolidone (NMP) purchased from Aldrich was used as solvent. Microcrystalline cellulose (MCC) powder with average particle size of 20 micro was purchased from Sigma-Aldrich.

The preparation of PVDF/MCC composites. The procedures for the fabrication of nanocomposites were as follows: 1) MCC were dispersed in solvent NMP with strong magnetic stirring and ultrasonic treatment (60 kHz, 1.5 h). At the same time, the polymer, PVDF, was dissolved in NMP to form PVDF solution (the ratio of PVDF and solvent was 1:5 by weight); 2) The MCC dispersion and the PVDF solution were mixed together again with strong magnetic stirring and ultrasonic treatment; 3) The mixed solution was poured onto a glass plate, and then compressed with another glass plate; 4) the glass plates were placed into deionized water (the antisolvent to NMP), which caused the film to solidify in several minutes. The wet films were then dried in a vacuum oven for 72h at 80 °C (to avoid the remnant of the solvent). For samples with the addition of ADX, an NMP solution of ADX (the ratio of ADX and solvent was 1:10 by weight) was firstly added into MCC liquid with magnetic stirring and ultrasonic treatment for 3h, and then PVDF-NMP liquid was added. The prepared nanocomposites films were compression molded at the temperature of 190 °C to make sheets for mechanical test and other characterizations. As summarized in Table 1, various blend formulations were prepared and analyzed.

Table 1 Samples codification

Sample	Composition
PVDF	PVDF (100% wt.)
PM_2	PVDF (100%wt) +MCC (2%wt.)
PM_5	PVDF (100%wt) + MCC (5%wt.)
PM_5A_2	PVDF (98%wt) + ADX (2%wt) + MCC (5%wt.)
PM_5A_5	PVDF (95%wt) + ADX (5%wt) + MCC (5%wt.)
PM_5A_{10}	PVDF (90%wt) + ADX (10%wt) + MCC (5%wt.)

Characterisation. Transmission electron microscopy (TEM) images of the prepared nanocomposites were obtained using a JEOL 1010A high-resolution transmission electron microscope operated at 100 kV. A Reichert-Jung Ultracut-E microtome was utilized to cut thin sections out of nanocomposites sheets with thickness of 50–70 nm for TEM characterisation.

DSC tests were conducted by means of a DSC 2910 (TA Instruments, New Castle, DE, USA). In the tests, samples of about 5 mg were heated to 190 °C at a rate of 10 °C /min under a nitrogen atmosphere and held at 190 °C for 5 min to eliminate the thermal history. Afterward, the samples were cooled to 20 °C at a rate of 20 °C /min, held about 3 min at 20 °C, and then heated again to 190 °C at a heating rate of 10 °C /min. The temperature and heat flow scales were calibrated using the melting of high-purity indium and zinc samples before testing. ATR FT-IR spectrum was obtained using a Nicolet 6700 ART spectrometer with an average of 200 scans in the range 400-2000 cm^{-1} in order to obtain the crystal structural for the nanocomposites.

The mechanical properties of all materials were measured by an Instron 5584 universal testing machine with a 100N load cell at a crosshead velocity of 5 mm/min until failure. Dumbbells were punched out of the nanocomposites sheets according to ATSM D-638 (type V). At least five samples were measured for each batch. Creep tests were conducted at the stress level of 20MPa. The samples were loaded for 2 h according to ASTM D 2990-01.

Results and discussion

Morphological Characterization. Cellulose fibres are bundles of microfibrils (elementary fibrils) where the cellulose molecules are stabilized laterally by hydrogen bond between hydroxyl groups. The microfibrils consist of monocrystalline cellulose domains linked by amorphous

domains. Normally special treatment, like chemical or ultra sonification treatments is needed to obtain nano-scale dispersed cellulose fiber [6].

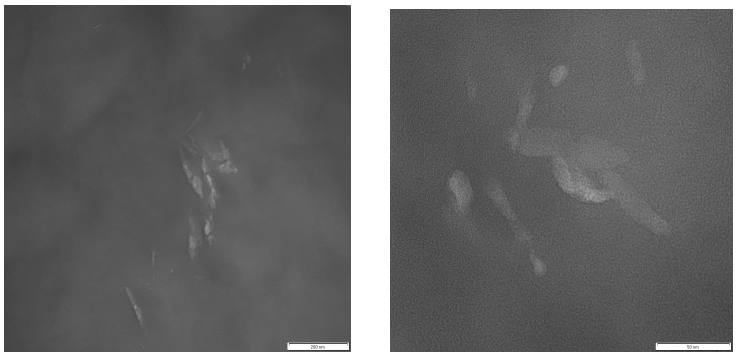


Fig. 1. TEM image of PM_5 (Nanocomposites with 5%wt MCC)

In order to assess the diameter and dispersion of the MCC, the thin sections of the nanocomposites were examined by TEM. To obtain a true representation of the microstructure, at least ten positions were investigated for each film, and representative images were taken. Figure 1 shows the typical TEM images of the nanocomposites with 5%wt MCC. Figure 1(left) shows the low magnitude image with a lot of fibers dispersed separately in the matrix. There were some bundles, but they were very loose, and matrix intercalated into them. Detail image can be found in Figure 1 (right), which shows that the diameter of the nano-fiber was around 10 nm. It can be concluded that the PVDF/MCC nanocomposites were fabricated here by the treatment of ultrasonic and strong magnetic stirring in the solvent of NMP.

Crystal structures. Some research results show that the nanofillers, like Multi-Wall Carbon Nanotubes (MWCNTs), layered silicate, can act as nucleating agents during the crystallization process of semi-crystalline polymers. As a result, the rate of crystallization of the polymer increases, and in most cases the melting temperature also increase [7, 8]. The melting and crystallisation curves of PVDF and various nanocomposites are shown in Figure 2 and 3, respectively. DSC results of the pure PVDF and its nanocomposites are summarized in Table 2. It can be seen from Figure 3, pure PVDF exhibited a crystallisation exotherm, with peak crystallisation temperatures (T_c) at 134.74°C. After the addition of MCC (5%wt), the peak crystallisation temperatures (T_c) shit to 137.27°C. At the same time, the crystallisation enthalpy ΔH_c increased from 35.82 to 46.13(J/g). For the melting behaviour, it's observed that the melting enthalpy ΔH_m increased, however, the melting temperature (T_m) decreased. All of those information shows that the addition of MCC can induce more crystal, while the perfection of the crystal decrease. With the addition of the compatibilizer (PVDF-g-MAH), peak crystallisation temperatures (T_c) increased further, while without further increase of the ΔH_c. At the same time, for the melting behavior, there was a decrease of the ΔH_m and a small variation of the melting temperature (T_m).

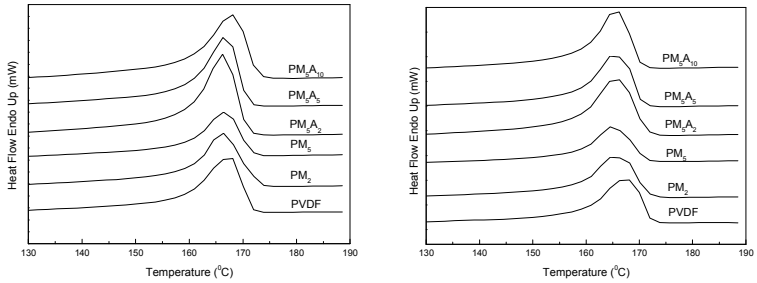


Fig. 2. Non-isothermal DSC scans of PVDF and its nanocomposites. Left is the first heating round, and right is the second heating round

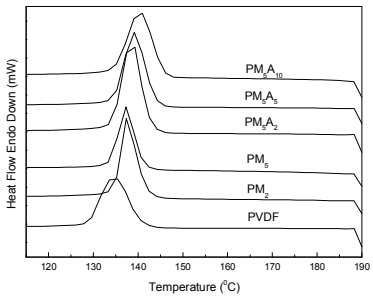


Fig. 3. Crystallization DSC curves for PVDF and its nanocomposites

Table 2 DSC parameters of PVDF and its nanocomposites

Sample	ΔH_m [J/g]		T_m [°C]		ΔH_c [J/g]	T_c [°C]
	1st Heating	2nd Heating	1st Heating	2nd Heating		
PVDF	25.06	23.79	167.47	167.79	35.82	134.74
PM_2	31.42	33.19	166.18	165.18	44.68	137.90
PM_5	29.73	36.20	166.69	164.85	46.13	137.27
PM_5A_2	30.90	34.04	166.37	165.91	45.24	138.47
PM_5A_5	32.38	33.71	166.77	166.94	40.48	139.02
PM_5A_{10}	27.77	29.20	168.26	165.55	43.85	140.31

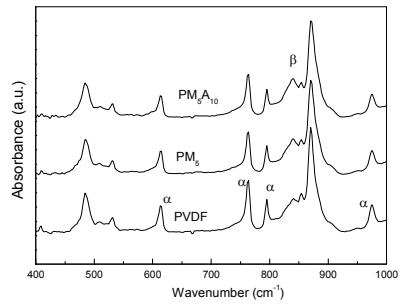


Fig. 4. ART-FTIR spectra of PVDF and its nanocomposites.

To verify the crystal structures of the nanocomposites, ATR-FTIR was conducted, and the result is shown in Figure 4. The formation of β phase was confirmed by the absorption peaks in FTIR spectra. The α-phase PVDF bands at 974, 795,764 and 614 cm^{-1} can be clearly observed in pure PVDF as well as in all nanocomposites. β-phase PVDF bands are observed at 840cm^{-1} in the nanocomposites, indicating a change in the crystalline morphology [9]. A lot of research showed that the addition of the nano-fillers will induce the β-phase PVDF [8, 10-12]. It's observed that there was a very tiny peak of β-phase for pure PVDF, but the α-phase is the dominated phase. With the addition of the MCC and PVDF-g-MAH, the β-phase increased. This may relate with the high surface energy of the nano-scale MCC, and the improvement of the interfacial interaction, which may affect the polymer conformation during crystallization, and finally affect the crystal structures.

Mechanical properties. There are four main requirements for effective reinforcement. These are a large aspect ratio, good dispersion, alignment, and interfacial stress transfer [13-15]. Dispersion is a fundamental issue. Uniformly dispersed CNTs coated with polymer is imperative to achieve efficient load transfer to the nanotube network, which results in a more uniform stress distribution and minimizes the presence of stress-concentration centres. Probably the most important requirement for a nanotubes reinforced composite is that external stresses applied to the composite as a whole are efficiently transferred to the nanotubes, allowing them to take a disproportionate share of the load [1]. Here PVDF-g-MAH was added to promote matrix–filler compatibility.

Tensile and creep tests were carried out in order to determine the mechanical properties of PVDF and its nanocomposites. Typical stress–strain curves at 5 mm/min for PVDF and its nanocomposites are shown in Figure 5, and the mechanical properties calculated from the stress-strain curves are shown in Table 3. The results showed that Young's modulus didn't change, while the tensile strength and elongation at break decreased with the addition of MCC. The reason for this is due to the poor interaction between the MCC and PVDF. It's well-known that PVDF is a non-polar polymer, which is hydrophobic. Hence the compatibility between the PVDF and MCC would be poor. Even though the diameter of the MCC was decreased to nano-scale, there was no improvement in mechanical properties. However, with the addition of ADX, the Young's modulus increased from 2.05 to 2.53 GPa (about 23.4%) and tensile strength from 46 to 51MPa. This is because the ADX (PVDF-g-MAH) has functional groups, which can form special interaction with the MCC, and then improve the interfacial interaction [5].

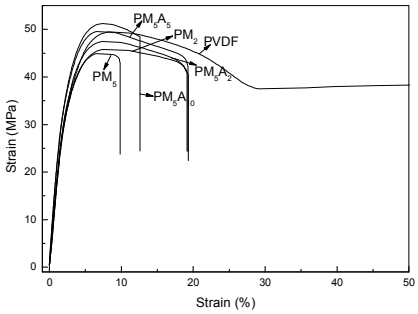


Fig. 5. Typical stress-strain curves of PVDF and its nanocomposites

Table 3. Mechanical Properties from Tensile Testing for PVDF and its Nanocomposites

Sample	Young's modulus [GPa]	Tensile strength [MPa]	Elongation at break [%]
PVDF	1.97(0.04)	49.3 (0.5)	254.3(121.2)
PM_2	1.95(0.13)	48(0.5)	27.0(8.5)
PM_5	2.05(0.16)	46.0(0.4)	16.4(5.6)
PM_5A_2	2.11(0.16)	47.0(0.4)	20.0(2.4)
PM_5A_5	2.44(0.12)	50(1.0)	14.0(2.7)
PM_5A_{10}	2.53(0.06)	51(0.8)	16(5.0)

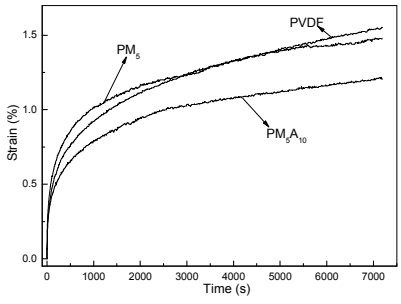


Fig. 6. Tensile creep strain vs. test duration-curves of PVDF and its nanocomposites under 20MPa

Typical creep strain curves are shown in Figure 6. Normally, several regions can be found in the creep curve of PVDF with the application of load. The first one is the instantaneous increase in strain because of the elastic response of PVDF, and then followed by a viscoelastic response, where time dependent molecular rearrangement occurred. After longer time, for the end of the load application period, viscous flow of the polymer occurred [16]. Here, it's observed that the addition

of the MCC increased the strain at the first stage, which means the MCC has side effect on the instantaneous strain. The reason is due to the poor interaction between MCC and PVDF, and the stress is very hard to transfer from PVDF to MCC. At the same time, the interface here now works like a drawback, so the increase of the creep strain was observed.

Summary

Poly(vinylidene fluoride)/Microcrystalline cellulose (MCC) nanocomposites were fabricated successfully by ultrasonic treatment and magnetic stir. DSC results showed that the peak crystallisation temperatures (T_c) and the ΔH_c increased with the addition of MCC. For the melting behaviour, ΔH_m increased, while melting temperature decreased. With the addition of the compatibilizer (PVDF-g-MAH), peak crystallisation temperatures increased further, while no further increase of the ΔH_c. ATR-FTIR results showed that the addition of MCC induced β-phase PVDF, and the addition of PVDF-g-MAH can induce more β-phase PVDF. Tensile test showed that even diameter of the MCC was decreased to nano-scale, no improvement of the mechanical properties was achieved because of the poor interface between PVDF and MCC.

Acknowledgements

Mr. Tang gratefully acknowledge the support from IPRS (Endeavour International Postgraduate Research Scholarship, Australia), UQRS (University of Queensland Research Scholarship).

References

[1] J.N. Coleman, U. Khan, W.J. Blau and Y.K. Gun'ko: Carbon 44 (2006), 1624.

[2] E.H. Qua, P.R. Hornsby, H.S.S. Sharma, G. Lyons and R.D. McCall: J. Appl. Polym. Sci. 113 (2009), 2238.

[3] L. Priya and J.P. Jog: J. Polym. Sci. Pol. Phys. 40 (2002), 1682.

[4] M. Hou, A. Beehag and Q. Yuan: Welding Techniques For Polymer Or Polymer Composite Components, in, Advanced, Composite Structures (AU), 2004.

[5] S. Spoljaric, A. Genovese and R.A. Shanks: Compos. Part A-Appl. 40 (2009), 791.

[6] K. Oksman, A.P. Mathew, D. Bondeson and I. Kvien: Compos. Sci. Technol. 66 (2006), 2776.

[7] S.S. Yu, W.T. Zheng, W.X. Yu, Y.J. Zhang, Q. Jiang and Z.D. Zhao: Macromolecules, 42 (2009), 8870.

[8] J. Buckley, P. Cebe, D. Cherdack, J. Crawford, B.S. Ince, M. Jenkins, J.J. Pan, M. Reveley, N. Washington and N. Wolchover: Polymer 47 (2006), 2411.

[9] T.U. Patro, M.V. Mhalgi, D.V. Khakhar and A. Misra: Polymer 49 (2008), 3486.

[10] L. Priya and J.P. Jog: J. Appl. Polym. Sci. 89 (2003), 2036.

[11] P.H. Nam, P. Maiti, M. Okamoto, T. Kotaka, N. Hasegawa and A. Usuki,: Polymer 42 (2001), 9633.

[12] N. Levi, R. Czerw, S.Y. Xing, P. Iyer and D.L. Carroll: Nano Letters 4 (2004), 1267.

[13] J.N. Coleman, U. Khan and Y.K. Gun'ko: Adv. Mater. 18 (2006), 689.

[14] W.J. Ma, L.Q. Liu, Z. Zhang, R. Yang, G. Liu, T.H. Zhang, X.F. An, X.S. Yi, Y. Ren, Z.Q. Niu, J.Z. Li, H.B. Dong, W.Y. Zhou, P.M. Ajayan and S.S. Xie: Nano Lett. 9 (2009), 2855.

[15] X.L. Xie, Y.W. Mai and X.P. Zhou: Mat. Sci. and Eng. R 49 (2005), 89.

[16] A. Genovese and R.A. Shanks:Macromol. Mater. Eng. 292 (2007), 184.

© (2011) Trans Tech Publications, Switzerland
doi:10.4028/www.scientific.net/KEM.471-472.361

Simultaneous Optimization for Multiple Responses on the Compression Moulding Parameters of Composite Graphite – Polypropylene Using Taguchi Method

Mohd Zulkefli Selamat[1,a], Jaafar Sahari[2,b], Norhamidi Muhamad[3,c] and Andanastuti Muchtar[2,c]

[1]Faculty of Mechanical Engineering, Universiti Teknikal Malaysia Melaka,

Karung Berkunci 1200, Hang Tuahjaya, 75450 Melaka, Malaysia

[2]Fuel Cell Institute, Universiti Kebangsaan Malaysia, 43600 Bangi, Selangor, Malaysia

[3]Department of Mechanical and Materials Engineering,

Faculty of Engineering and Built Environment,

Universiti Kebangsaan Malaysia, 43600 Bangi, Selangor, Malaysia

[a]zulkeflis@utem.edu.my, [b]jaafar@eng.ukm.my, [c]hamidi@eng.ukm.my and [c]muchtar@eng.ukm.my

Keywords: Graphite; Conducting Polymer Composite (CPC); Taguchi Method; Analysis of variance (ANOVA); Flexural strength; Electrical Conductivity.

Abstract. This research concerns the effect of compression molding parameters on conducting polymer composite (CPC) properties such as electrical conductivity and flexural strength. In the present work on CPC, focus is given to graphite (G) as filler and polypropylene (PP) was use as the binder. The Taguchi's L_9 orthogonal array has been used as design of experiment (DOE) while the electrical conductivity and flexural strength were assumed to be quality characteristic (responses). The electrical conductivity was measured using four point probes and flexural strength was measured using three point tests according to ASTM D638. Classical analysis of variance (ANOVA) was used to investigate the significant of each compression molding parameters and finally propose the optimum compression molding parameters. But for several responses, the optimum condition for one response is not very likely to the optimum condition for other response.

Introduction

A brief history on the development of CPC from 1930 to 2001 has been reported by Thongruang [1]. The areas of application of CPC include electromagnetic interference (EMI) shielding, electrostatic dissipation (ESD) [2], temperature, pressure and gas sensors [3], passive components (e.g. capacitors) in integrated circuit devices [4] and fuel cell bipolar plates [5]. One of materials attracting the researchers in CPC is polymer-graphite composites. The main materials as a filler in CPC is G powder. G powder can be grouped either naturally or synthetically, which has significant effects on the electrical and thermal conductivity of filled polymers. It is frequently used especially for improvement of electrical conductivity, antistatic properties as well as thermal conductivity of plastics [6-8]. Another material in CPC is the binder. In this research the polymeric material used is PP as the binder to improve the brittleness of graphite. Based on finding of single filler conductive composite [9-12], Middelman [11] stated that single filled of CPC have relatively low electrical conductivity most of that in ranges of 1~33 S/cm.

Taguchi method is called the full factorial design and it takes into account a large number of experiments, which can be costly and time consuming. Taguchi [13] proposed a design of experiment (DOE) method, which minimizes the number of experiment to a practical level for optimization process. Taguchi's parameter design has proved to be an effective approach producing high quality products at a relatively low cost [14]. The main objectives of the Taguchi method for parameters design are to establish the optimal combination of design parameters and reduce variations in the product quality by rendering the parameters design robust to effects of noise.

The Taguchi method employs a generic signal-to-noise (S/N) ratio to quantify the present variation. Depending on the particular types of characteristics involved, different S/N ratios may be applicable, including "lower is better" (LB), "nominal is best" (NB) or "higher is better" (HB). The S/N ratio for the HB characteristics related to the present study is given by equation (1)

$$\frac{S}{N} = -10\log\left|\frac{1}{n}\sum_{i=1}^{n}\frac{1}{y_i^2}\right| \quad (1)$$

Where n is the number of simulation repetition under the same design parameter condition, y_i indicates the measured results and subscript i indicates the number of simulation design parameters arranged in the orthogonal array (OA) table.

DOE in Taguchi was used in this study to optimize the compression molding parameters and the experimental results are then transformed into a signal-to-noise (S/N) ratio. ANOVA also can be used to determine the contribution of each factor which influences the properties of the product. With the S/N ratio and ANOVA analysis, the optimal combination of the process parameters can be predicted. Finally, a confirmation experiment is conducted to verify the optimal process parameters obtain from the parameter design.

In many experimental situations in practice more than one response will be measured for the difference combination of values which a set of design variable may take. When it involved several responses, the optimum condition for one response is not very likely equal to the optimum condition for the response [15]. In this paper, authors will discuss how to fine the overall optimum condition for several responses when parameter designs using orthogonal arrays was employed, through simultaneous optimization using ANOVA is the best method for the optimization of multiple characteristics problem.

Materials and Methods

Materials. The materials used to produce CPC samples in the present work are natural G produced by Asbury Graphite Mills, Inc and PP was purchased from the Polypropylene Malaysia Sdn. Bhd. Meanwhile Table 1 is shows the main materials properties.

Preparation of CPC. Nine samples of CPC based on the composition of G:PP with weight percentage of 80:20 will be selected. The process sequence for obtaining the CPC samples are; the G:PP was mixed used melt compounded with PP in a Rheomix mixer Haake-Polylab TM with roller type rotors. The samples obtained by melt compounding were crush and pulverized into granules in order to improve homogeneity of the samples for next forming process. A 200 Ton high precision hydraulic compression molding machine was used to prepare the samples. The granules were poured into steel mould with dimension of 140 mm x 60 mm. Before begin the formation process the main factors needed to be selected and set in the machine. After formation process finished the mold was cooled by air until reach the temperature of 120 ^{0}C. After that the mould was placed in a water bath for 5 min to be cooled and the sample was then released from the mould.

Table 1. Material properties of G and PP

Material	Graphite	Polypropylene
Grade	3243	Titan (600)
Density	1.74 g/cm^3	0.91-0.92 g/cm^3
Thermal stability	3500-4000 ºC	180-220 ºC
Size	≤30μm	1~2 mm
Shape	Flake	Granular
Resistivity	0.036 Ωcm	1(1014Ωm)

DOE. The Taguchi method uses a special of orthogonal arrays to study all the designed factors with a minimum of experiment. Orthogonally means that factors can be evaluated independently of one another, the effect of one factor does not interfere with the estimation of the influence of other factors [13]. Four factors which are (formation temperature (A), compression loads (B), preheating times (C) and compressing times (D)) with three levels were selected as shown in Table 2.

Table 2. The compression molding factors for three levels Taguchi design of CPC

Factors	Variables	Level 1	Level 2	Level 3
		1	2	3
A	Formation temperaturs (^{0}C)	175	180	185
B	Loads (kN)	550	750	950
C	Praheating times (Minute)	15	20	25
D	Pressing times (Minute)	5	10	15

Electrical Properties Test. Conductivity measurements of the sample in the plane direction were measured by Jandel Multi Height Four Point Probe combined with RM3 Test Unit. Each sample was measured three times at three different places.

Flexural Test. The flexural tests were test by used Universal Testing Machine (UTM) Model Instron 5567. The method of three point test was conducted according to ASTM D790-03. The test sample has a dimension of length 100 mm, width 13 mm and thickness 3 mm. Each experiment number was repeated with 3 specimens of 50 mm spend length.

Results and Discussion

Electrical Conductivity. All samples has been measured the electrical conductivity and the results as shown in Table 3. After that the results were analyzed used ANOVA and the results as shown in Table 5. From the ANOVA result was shown in Table 5, the effects of compression molding factors on the electrical conductivity were determined. The results show the formation temperatures (A) and pressing times (D) gives the effects on the electrical conductivity at the 99.5% and 95% significant level respectively. Meanwhile the loads (B) and preheating times (C), the F value did not exceed 90% of significant level but both factors still gives 1.03% and 1.59% contribution to the experiment. Based on ANOVA, the main effects of the experiment were calculated. According to the optimum condition of "higher is better" HB, the levels of the factors that contribute to the highest average values are preferred. From the response graphs (not not in this paper), the highest electrical conductivity could be attained at the combination setting of optimum condition are (Formation temperatures) A2, (Loads) B2, (Preheating times) C2 and (Pressing times) D1. The confirmation experiment has been done based on optimum condition from ANOVA analyzed and the results as shown in Table 5.

Table 3 Results of electrical conductivity and SN ratios for G/PP (80/20) composite

Experiment Number	Replication, Electrical Conductivity (S/cm)			Average	SN
	E1	E2	E3		
1	16.60	14.76	14.44	15.27	23.63
2	14.61	18.21	16.98	16.60	24.29
3	15.23	13.96	10.60	13.26	22.14
4	14.53	13.37	15.51	14.47	23.16
5	17.21	15.05	16.01	16.09	24.09
6	17.33	16.64	15.42	16.46	24.30
7	10.09	9.17	10.43	9.90	19.87
8	10.34	10.05	10.74	10.38	20.31
9	13.73	10.65	10.71	11.70	21.18
			Average	13.80	
			Maximum	16.60	
			Minimum	9.90	

Table 4. ANOVA for electrical conductivity for G/PP (80/20) composite

Factors	Degrees of freedom, f_o	Sum squared, S_n	Variance, V_n	Variance ratio, F_n	Critical F value	Percent of Contribution, P_n
A	2	134.46	67.23	34.92	$F_{0.005,2,18}$= 7.2148	65.96
B	2	5.90	2.95	1.53		1.03
C	2	7.00	3.5	1.82		1.59
D	2	16.00	8.0	4.16	$F_{0.05,2,18}$= 3.5546	6.14
Error	18	34.66	1.93			25.28
Total	26	198.02				100

Table 5. Optimum setting of electrical conductivity

Optimum Condition A2, B2, C2 and D1 Temperatures, 180 ^{0}C; Loads, 750 kN; Preheating times, 20 minute and Pressing times 5 minute				
Confirmation Experiment				
Replication	1	2	3	Average
S/cm	16.10	15.32	15.26	15.56

Flexural Strength. The same set of samples were used and each sample has been measured the flexural strength and the results as shown in Table 6. After that the results were analyzed used ANOVA and the results as shown in Table 7. From the ANOVA results as shown in Table 7, the effects of compression molding factors on the flexural strength were determined. The results shown the temperatures (A) and pressing times (D) given the effects on the flexural strength at 99.5% significant level. Meanwhile the loads (B) and preheating times (C), gives the effects on the flexural strength at 95% and 90% significant level respectively. Based on ANOVA, the main effects of the experiment were calculated. According to the optimum condition of HB, the levels of the factors that contribute to the highest average values are preferred. From the response graphs (not shown in this paper), the highest flexural strength could be attained at the combination setting of optimum conditions are (Formation temperatures) A3, (Loads) B2, (Preheating times) C2 and (Compression times) D3. The confirmation experiment has been done based on optimum condition from ANOVA analyzed and the results as shown in Table 8.

Table 6. Results of flexural strength and SN ratios for G/PP (80/20) composite

Experiment Number	Replication, Flexural strength (MPa)				
	F1	F2	F3	Average	SN
1	18.53	18.29	18.05	18.29	25.24
2	22.75	21.41	20.54	21.57	26.65
3	20.79	20.83	19.73	20.45	26.21
4	24.70	24.75	26.29	25.25	28.03
5	24.10	22.88	20.72	22.56	27.02
6	20.25	19.48	19.86	19.86	25.96
7	26.19	25.19	26.36	25.91	28.27
8	25.70	26.09	27.17	26.32	28.40
9	24.18	25.63	18.44	22.75	26.87
			Average	22.55	
			Maximum	26.32	
			Minimum	18.29	

Table 7. ANOVA for flexural strength for G/PP (80/20) composite

Factors	Degrees of freedom f_o	Sum squared S_n	Variance V_n	Variance ratio F_n	Critical F value	Percent of Contribution P_n
A	2	107.71	53.86	23.09	$F_{0.005,2,18}$= 7.2148	44.26
B	2	32.145	16.07	6.89	$F_{0.01,2,18}$= 6.0129	11.81
C	2	15.40	7.70	3.30	$F_{0.1,2,18}$= 2.6239	4.61
D	2	35.56	17.78	7.62	$F_{0.005,2,18}$= 7.2148	13.27
Error	18	41.98	2.33			26.05
Total	26	232.80				100

Simultaneous Optimization. The results of confirmation experiment for optimum condition of each response was summarized and shown in Table 9. The optimum condition for each response is not very likely equal to the optimum condition for the other response. Meanwhile the results of electrical conductivity and flexural strength show that, if the electrical conductivity high the flexural strength is low and it also invert if the flexural strength high the electrical conductivity is low. So that by used simultaneous optimization and overall analysis based on both properties, a set of factors which is considering both properties can be determined. A set of factors through

simultaneous was selected based on high value of SN ratios or the most significant factors. The set of optimum factors for both responses is A2, B2, C2 and D3. The results of conformation experiment of electrical conductivity and flexural strength as shows in Table 10. Table 11 shows the optimization result of each response and simultaneous for both responses. Through simultaneous optimization or overall optimization by considering both responses the conflicts between these two responses can be solved. The value of electrical conductivity and flexural strength allies within the range of each response.

Table 8 Optimum factors and the result of confirmation experiment for flexural strength

Optimum Condition				
A3, B2, C2 and D3				
Formation temperatures, 185 ^{0}C; Compression loads, 750 kN; Preheating times, 20 minute and Compression times 15 minute				
		Confirmation Experiment		
Replication	1	2	3	Average
MPa	27.61	27.20	25.17	26.66

Table 9.Optimization results for each response of electrical conductivity and flexural strength G/PP (80/20) composite

Optimization	Electrical conductivity (A2, B2, C2 and D1)	Flexural strength (A3, B2, C2 and D3)
Electrical conductivity (S/cm)	15.56	10.56
Flexural strength (MPa)	19.53	26.66

Table 10 The results of confirmation experiment for both responses composite G/PP (80/20).

Optimum Factors				
A2, B2, C2 and D3				
Formation temperatures (A2); 180 ^{0}C, Load (B2); 750 kN, Preheating times (C2); 20 minute and Compression times (D3); 15 minute				
	Confirmation experiment			
Replication	1	2	3	Average
Electrical conductivity (S/cm)	16.64	16.75	16.43	16.61
Flexural strength (MPa)	20.03	19.01	20.42	19.82

Table 11 The results of overall optimization for electrical conductivity and flexural strength of G/PP (80/20) composite.

Optimization	Electrical conductivity (S/cm) (A2, B2, C2 and D1)	Flexural strength (MPa) (A3, B2, C2 and D3)
Electrical conductivity	15.56	10.56
Flexural strength	19.53	26.66
Simultaneous	A2, B2, C2 and D3	
	16.61	19.82

Summary

Based on the result by using the Taguchi method, the electrical conductivity and flexural strength were optimized. An ANOVA was used to accommodate the 3^4 experiment. The result shows that for electrical conductivity the temperatures (A) and pressing times (D) 99.5% and 90% significant level respectively. This contributed the major affected significantly. Meanwhile for flexural strength the result shows that all factors affect accordingly. The temperatures (A) and pressing times (D) 99.5% significant level, loads (B) and preheating times 95% and 90% significant level respectively.

Acknowledgment

The authors would like to thank the Malaysia Ministry of Higher Education, Malaysia and Ministry of Science, Technology and Innovation for sponsoring this work under IRPA 02-02-0002 PR0023/11-07.

References

[1] Thongruang, W., 2001. Properties of Polymer Blends Filled with Mixtures of Conductive Filler, North Carolina University, United States, Raleigh. PhD Thesis.

[2] Strumpler R, Glatz-Reichenbach J., 1999. *J Electroceram* 4: pp. 320-346

[3] Martin JE, Anderson RA, Odinek J, Adolf D, Williamson J., 2003 *Phys Rev. B* 67: 094207.

[4] Raj PM, Balaraman D, Abothu IR, Yoon C, Kang NK, Tummala R. 2007. *IEEE Trans Compon Packag Technol* 30: pp 569-578.

[5] Dweiri R, Sahari J. 2007. J Power Source 171: pp 424-432

[6] Acosta, J.L., Ojeda, M. C. & Rio C. D., 2006. *Polymer Bulletin* (57): pp. 199-206.

[7] Ezquerra, T.A., Connor, M.T., Roy, S. & Kulescza, M., 2001. *Compos. Sci. Tech*. 61: pp. 903

[8] Zou, J.F., Yu, Z.Z., Pan, Y.X., Fang, X.P. & Ou, Y.C..2002. *Journal of Polymer Science: Part B: Polymer Physics* 40: 954-963.

[9] Wu, M. & Shaw, L.L. 2004. *Journal of Power Sources* 136: 37-44.

[10] Hermann, A. Chaudhuri, T. & Spagnol, P. 2005. *Int J. Hydrogen Energy*. 30(12): pp. 1297-1302

[11] Middelman, E., Kout, W., Vogelaar, B., Lenssen, J. & de Waal, E. 2003. *Journal Power Sources*. 118: pp. 44-46

[12] Dweiri, R., & Sahari, J., 2008. *Composites Science and Technology* (68) :pp. 1679–1687

[13] Roy, R.K., 1990, A Primer On The Taguchi Method, Society of manufacturing Engineers, USA

[14] P.J. Ross,1988, Taguchi Techniques for Quality Engineering, McGraw Hill International Edition, USA.

[15] Park,S.H, Robust Design and Analysis for Quality Engineering, Chapman & Hall, London 1996.

© (2011) Trans Tech Publications, Switzerland
doi:10.4028/www.scientific.net/KEM.471-472.367

Modeling and Analysis of Elastoplastic Impacts on Supported Composites

Majed A. Majeed[1, a], Ahmet S. Yigit[1,b] and Andreas P. Christoforou[1,c]

[1]Department of Mechanical Engineering, Kuwait University

P.O. Box 5969, Safat 13060 Kuwait

[a]m.majeed@ku.edu.kw, [b]ahmet.yigit@ku.edu.kw, [c]andreas.christoforou@ku.edu.kw

Keywords: Impact, elastoplastic contact, composites, damage.

Abstract. This paper presents an elastoplastic impact model for a spherical object impacting a supported composite layer or a half-space. The model utilizes a contact law that has been developed based on elastic-plastic and fully plastic indentation theories. For an impact event, the model parameters can easily be obtained analytically, computationally using Finite Elements (FE), and from experiments, by assuming transversely isotropic material behavior. Simulations are compared to those from a nonlinear FE model developed in ABAQUS, and to limited experimental data, with excellent results.

Introduction

Impact damage in composite structures is still a major problem that prevents their full utilization in commercial and other applications [1]. A proper impact damage assessment requires a thorough understanding of the impact dynamics that includes phenomena such as contact and structural damage, and wave propagation. In general these phenomena occur simultaneously and interact with each other. However, in many practical situations, these effects can be isolated and studied separately [2]. If the impactor mass is relatively small, and/or the structure is relatively stiff, then the impact event is said to be wave controlled and local contact dominates the impact response. On the other hand, if the impactor mass is relatively large and the structure is relatively flexible, then structural deformations dominate the response [3,4]. In both cases, accurate knowledge of impact force is very important for damage assessment, which requires an adequate contact law.

The purpose of this paper is to present a general impact model for the elastoplastic impact of a spherical indenter and a supported composite layer or a half-space. A static contact law that is based on elastic-plastic indentation theory is developed and used. The results are compared to those from a nonlinear Finite Element Model developed in ABAQUS, and to available experimental data with excellent results. The effects of various parameters, such as composite thickness, damage properties, impactor mass and velocity on the impact response are also investigated.

Impact Model

In the case of impact between a spherical object having an initial velocity of v_0, and an elastoplastic half-space or a thin layer supported by a rigid substrate, the motion of the impactor is described by,

$$m\ddot{\alpha} = -F \tag{1}$$

where m is the mass of the impactor, α is the indentation or the total displacement of the impactor, and F is the impact force to be obtained from a contact law given in general as,

$$F = \begin{cases} f(\alpha) & if \quad F > 0 \\ 0 & if \quad F \le 0 \end{cases} \tag{2}$$

with initial conditions, $\alpha(0) = 0$ and $\dot{\alpha}(0) = v_0$.

Hertz Contact Law. In cases where impacts are elastic in nature, i.e. no plastic deformation or damage, the classical Hertz contact theory [5] may be used to obtain the impact force. The relationship between the contact force and local deformation for an elastic spherical indenter and an elastic isotropic half-space is given as,

$$F = K_h \alpha^{3/2} \tag{3}$$

where K_h is the Hertzian contact stiffness given as,

$$K_h = \frac{4}{3}\sqrt{R}E^* \tag{4}$$

R is the radius of the indenter, and E^* is the effective contact modulus given as,

$$\frac{1}{E^*} = \frac{1-\nu_1^2}{E_1} + \frac{1-\nu_2^2}{E_2} \tag{5}$$

where ν_i and E_i are the Poisson's Ratios and Elastic Moduli of the two contacting bodies, respectively. Using the Hertzian elastic contact law alone at very low impact speeds is a very good approximation [6]. At higher speeds, there is energy loss due to local damage and plastic deformation [6,7]. Therefore, in composites, the Hertzian contact law has been used as part of more complicated contact laws that include damage effects due to plastic or permanent deformation [8,9].

In the following, a general elastoplastic contact law for a transversely isotropic composite half-space, or for a rigidly supported thin composite layer in contact with a spherical indenter is given.

Elastoplastic Contact Law. Experimental evidence suggests that during impact between metallic bodies, even at very low impact velocities, there is plastic deformation [5-7]. A similar behavior was observed in the case of composite laminates [8-11], with "yielding" denoting a combination of different failure modes such as matrix, delamination and fiber damage.

In order to account for permanent deformations, an elastoplastic contact law can be used to obtain the impact force. The contact law consists of three phases as given below:

Phase I: Elastic loading

$$F = K^* \alpha^n \qquad 0 \le \alpha \le \alpha_p \tag{6}$$

Phase II: Elastic-plastic loading

$$F = K_p(\alpha - \alpha_p) + K^* \alpha_p^n \qquad \alpha_p \le \alpha \le \alpha_m \tag{7}$$

Phase III: Elastic unloading

$$F = F_m \left(\frac{\alpha - \alpha_f}{\alpha_m - \alpha_f} \right)^n \tag{8}$$

where the superscript $n = 1.5$ for the half-space (i.e. Hertzian contact) [5-9], and $n = 2$ for the thin supported layer [11]. Assuming transversely isotropic material behavior, the contact stiffness during

elastic loading, K^*, is given respectively for the half-space and the rigidly supported thin layer with thickness *h* as,

$$K^* = K_h \quad , \; K^* = \frac{\pi E^* R}{h} \tag{9}$$

The effective contact modulus, *E**, between the sphere and the transversely isotropic target is given as,

$$\frac{1}{E^*} = \frac{1-\nu_s^2}{E_s} + \frac{1-\nu_{xz}\nu_{zx}}{E_z^*} \tag{10}$$

The transverse modulus and Poisson's Ratios for the transversely isotropic material are calculated by considering an equivalent quasi-isotropic layup as follows [12],

$$\frac{1-\nu_{xz}\nu_{zx}}{E_z^*} = \frac{1}{E_{TI}}, \quad E_{TI} = \frac{2}{c_1 c_3} \quad , \quad \frac{\nu_{xz}}{E_x} = \frac{\nu_{zx}}{E_z^*} \tag{11}$$

$$c_1 = \sqrt{\frac{E_x / E_z - \nu_{xz}^2}{1-\nu_{xy}^2}}, \quad c_2 = \frac{E_x / 2G_{xz} - \nu_{xz}(1+\nu_{xy})}{1-\nu_{xy}^2} \quad , \quad c_3 = \frac{1-\nu_{xy}}{G_{xy}}\sqrt{\frac{c_1 + c_2}{2}} \tag{12}$$

The transition from elastic to elastic-plastic loading occurs at α_p, where fully plastic conditions are assumed. At this force level the slope of the loading curve is linear and is given as [5],

$$K_p = 2\pi R p_0 \tag{13}$$

where p_0 is the mean pressure, which is constant within the contact region at fully plastic conditions. For metals this occurs when $p_0 = 2.8 S_y$, where S_y is the yield strength of the target material [5-7]. Note that at fully plastic conditions the indentation and contact radius, *a*, are related by $\alpha = a^2/2R$. As it is well known initial yielding occurs well before and below the surface at $p_0 = 1.1 S_y$. By ignoring the transition from initial yield to fully plastic conditions, the slope given by Eq. 13 is matched with the slope of the elastic loading curve given by Eq. 6, at an intermediate load level, i.e. at $p_0 = kS_y$ where *k* is a constant between 1.1 and 2.8. After some algebra the indentation at this transition is obtained as,

$$\alpha_p = \left(\frac{2\pi R k S_y}{n K^*} \right)^{1/(n-1)} \tag{14}$$

For the cases of a half-space and a thin supported laminate, respectively, the above equation yields the following expressions of this indentation,

$$\alpha_p = \frac{\pi^2 k^2 S_y^2 R}{E^{*2}} \quad , \quad \alpha_p = \frac{k S_y h}{E^*} \tag{15}$$

After maximum indentation α_m and force F_m level is reached, the unloading is elastic as prescribed by Eq. 8. At the end of impact, the force is zero and the permanent deformation α_f is given as [7],

$$\alpha_f = \alpha_m \left[1 - \frac{\alpha_y}{\alpha_m} \left(\frac{2\alpha_m}{\alpha_y} - 1 \right)^{1/2} \right] \tag{16}$$

where α_y is the indentation where initial yielding or damage occurs and is given respectively for the half-space and thin supported laminate as,

$$\alpha_y = \frac{0.68\pi^2 S_y^2 R}{E^{*2}} \ , \ \alpha_y = \frac{1.1 S_y h}{E^*} \tag{17}$$

The expressions in Eq. 17 are obtained by matching the force at yield given by Eq. 6 with the mean pressure distribution at yield, i.e., $F_y = K^* \alpha_y^n = p_0(\pi R \alpha_y)$, with $p_0 = 1.1 S_y$. Note that before initial yield conditions the indentation and contact radius are related by $\alpha = a^2/R$.

Simulation Results and Discussion

The elastoplastic contact law presented in the previous section was used to simulate the response of a rigidly supported thin laminate of thickness h = 2.4 mm in contact with a steel spherical indenter of radius R = 7.94 mm. Table 1 shows the lamina properties as well the resulting quasi-isotropic laminate properties, which resemble transverse isotropy. Equations 10-12 yield: E_{TI} = 9.987 GPa, E_z^* = 9.875 GPa, ν_{zx} = 0.042, and effective contact modulus E^* = 9.573 GPa. Figure 1 shows the force-indentation response for quasi-static loading. As it can be seen the prediction of the contact law is in reasonable agreement with the experimental data [10].

Also shown in Fig. 1 are the simulation results of a contact model using ABAQUS/Standard. In the model the thin layer was modeled using bilinear 4-node axisymmetric stress elements (CAX4R) with reduced integration. For convenience and to reduce the computational complexity of the model, the sphere was modeled by using a rigid surface, and the thin layer material as a homogeneous isotropic material with an equivalent isotropic contact modulus, i.e. $E^* = E/(1-\nu^2)$, with E = 9.465 GPa and ν = 0.106. The equivalent isotropic 'yield' strength of the composite laminate was taken as S_y = 310 MPa. Poe [13] showed that using isotropic elastic-plastic properties can yield very informative results for the stress distributions and the various failure mechanisms, from matrix failure to fiber failure being the lower and upper bounds of damage thresholds. Non-visible damage initiation was reported to occur at an average contact pressure of p_0 = 1.1 S_y and visible or substantial damage above p_0 = 2.2 S_y.

In order to simulate a half-space type of response the experiments presented by Sutherland and Soares [14] were used. Quasi-static indentation tests were carried out on woven E-glass/polyester laminates using various hemispherical indenters. It was reported that the initial contact response was Hertzian in nature. At higher loads the response became linear as damage became significant. The slope of the linear response was found to increase linearly with the indenter radius. This behavior was attributed to the complex damage behavior and mainly to delamination. In the absence of laminate material properties the effective contact properties were deduced from the data for the 20 mm diameter (R = 10 mm) indenter results since there were the only force-indentation traces that had been reported. From the data the following were obtained: K_h = 12.05 kN/mm$^{1.5}$, K_p = 16.7 kN/mm, α_p = 1.1 mm, F_p = 14 kN, α_m = 2.7 mm, F_m = 43 kN, a_f = 1.5 mm. By using these values and the contact law equations the rest of the effective transversely isotropic contact properties were obtained as E^* = 2.85 GPa, α_y = 0.2813 mm, S_y = 185 MPa. As in the case of the thin layer, the

material properties used in the FE simulations were obtained for an equivalent isotropic layer with, $E = 2.82$ GPa and $\nu = 0.1$. As it can be seen in Fig. 2 both analytical and ABAQUS simulations are in excellent agreement with the experimental data. This is not surprising since the model parameters were obtained using the experimental data. However, this should not undermine the fact that a simple elastoplastic contact law captures the essential physics of a very complex event.

The effects of laminate thickness on the contact response have also been demonstrated by the simulations presented earlier. As it can be seen the responses using FE are in reasonable agreement with the analytical contact simulations for the asymptotic cases of the thin layer and half-space. All simulations have thus far been quasi-static. Since low-velocity impact conditions are considered here, dynamic simulations will be identical to quasi-static simulations. From the model, the effects of damage ('yield'), impactor velocity, and mass on the impact response can easily be identified. Lower yield properties will reduce the impact force and increase the permanent indentation and contact time. The impact force will increase with increasing impactor mass and velocity, causing more damage and permanent deformations. Figure 3 shows an example of a dynamic simulation with mass $m = 1$ kg and impact velocity $v_0 = 10$ m/s. The half-space case presented above was used in the dynamic simulations, and the FE results were obtained using ABAQUS/Explicit.

Table 1. Material properties used in the simulations

Composite lamina (IM7/55A carbon/epoxy)	*Resulting quasi-isotropic laminate properties*
$E_{11} = 169$ GPa	$E_x = E_y = 62.94$ GPa
$E_{22} = E_{33} = 6.72$ GPa	$E_z = 6.72$ GPa
$G_{12} = G_{13} = 5.26$ GPa, $G_{23} = 2.58$ GPa	$G_{xz} = G_{yz} = 5.26$ GPa, $G_{xy} = 24.21$ GPa
$\nu_{12} = \nu_{13} = 0.266$, $\nu_{23} = 0.3$	$\nu_{xz} = \nu_{yz} = 0.266$, $\nu_{xy} = 0.3$
$\rho = 1580$ kg/m^3	
Steel (impactor)	
$E = 210$ GPa, $\nu = 0.3$, $\rho = 7960$ kg/m^3	

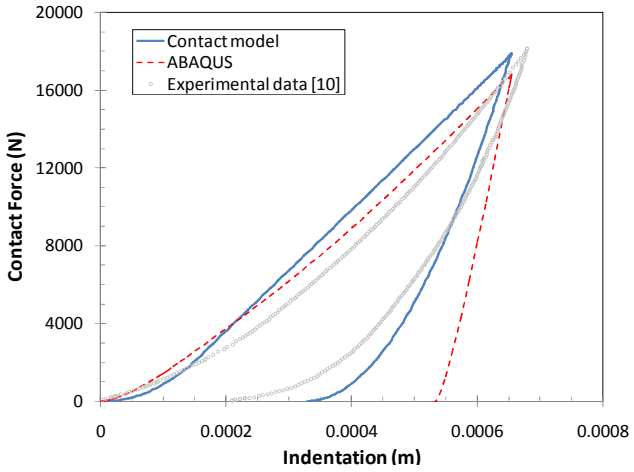


Fig. 1. Force-indentation response of a sphere contacting a rigidly supported thin laminate

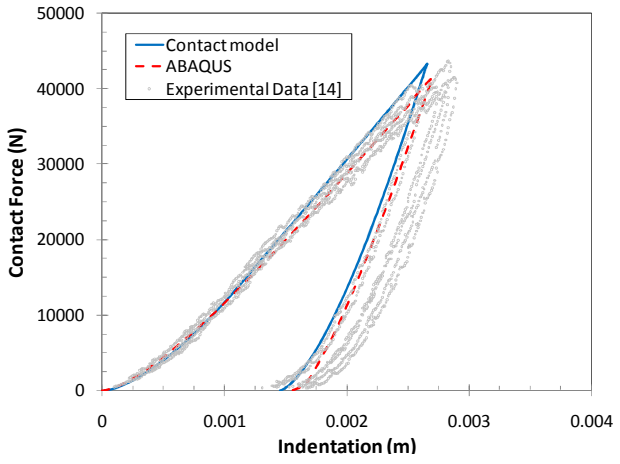


Fig. 2. Force-indentation response of a sphere contacting a composite half-space

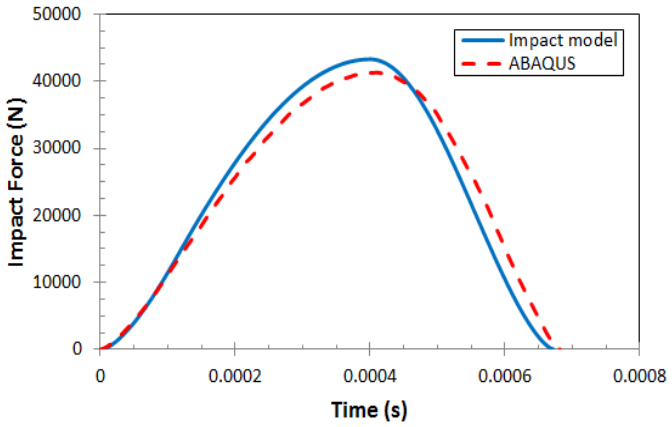


Fig. 3. Impact response of a sphere impacting a composite half-space

Summary

A static contact law that is based on elastic-plastic indentation theory has been developed and used to investigate the response of supported laminates. The simulation results have been compared to those from a nonlinear Finite Element Model developed in ABAQUS, and available experimental data with excellent agreement. It has been shown that by using equivalent isotropic properties, reasonable good predictions could be achieved for an otherwise very complex and difficult contact damage problem. Decreasing the target thickness of the rigidly supported laminate increases the force and plastic deformation for a given impact energy. On the other hand, as expected, impact force and damage increase by increasing impact energy.

Acknowledgment

This work was supported by Kuwait University Research Grant No. [EM-03/07].

References

[1] R. Karakuzu, E. Erbil and M. Aktas: Compos. Part B Vol. 41 (2010) p. 388

[2] A.P. Christoforou and A.S. Yigit: Compos. Struct. Vol. 91 (2009) p. 358

[3] R. Ollson: Compos. Struct. Vol. 59 (2003) p. 341

[4] A.S. Yigit and A.P. Christoforou: Compos. Struct. Vol. 81 (2007) p. 568

[5] W. Goldsmith: *Impact*, Edward Arnold, London (1960)

[6] K.L. Johnson: *Contact Mechanics*, Cambridge University Press, Cambridge (1985)

[7] W.J. Stronge: *Impact Mechanics*, Cambridge University Press, Cambridge (2000)

[8] T.M. Tan and C.T. Sun: J. Appl. Mech. Vol. 52 (1985) p. 6

[9] A.S. Yigit and A.P. Christoforou: Compos. Eng. Vol. 4(11) (1994) p. 1143

[10] S.R. Swanson and H.G. Rezaee: Compos. Sci. Technol. Vol. 38 (1990) p. 43

[11] A.P. Christoforou: Compos. Struct. Vol. 26 (1993) p. 77

[12] S.R. Swanson: Compos. Part A Vol. 36 (2005) p. 1421

[13] C.C. Poe Jr.: J. Reinf. Plastics Compos. Vol. 10 (1991) p. 293

[14] L.S. Sutherland and C. Guedes Soares: Compos. Struct. Vol. 70 (2005) p. 287

© (2011) Trans Tech Publications, Switzerland
doi:10.4028/www.scientific.net/KEM.471-472.373

PVDF-HFP-$NH_4CF_3SO_3$-SiO_2 Nanocomposite Polymer Electrolytes for Protonic Electrochemical Cell

N. Muda[1, a], S. Ibrahim[2, b], N. Kamarulzaman[3, c] and N.S. Mohamed[4,d]

[1]Institute of Postgraduate Studies, University of Malaya, 50603 Kuala Lumpur, Malaysia

[2,4]Centre for Foundation Studies in Science,

University of Malaya, 50603 Kuala Lumpur, Malaysia

[3]Institute of Science, University Technology MARA, 40450 Shah Alam, Selangor, Malaysia

[a]fizamuda@yahoo.com.my, [b]salmiah01@um.edu.my, [c]norlyk@salam.uitm.edu.my
[d]nsabirin@um.edu.my

Keywords: Composite, Protonic electrochemical cell

Abstract. This paper describes the preparation and characterization of proton conducting nanocomposite polymer electrolytes based a polyvinylidene fluoride-co-hexapropylene (PVDF-HFP) for protonic electrochemical cells. The electrolytes were characterized by Differential Scanning Calorimetry (DSC) and Impedance Spectroscopy (IS). It is observed that the crystallinity of the PVDF-HFP-$NH_4CF_3SO_3$ system slightly increase upon addition of SiO_2 nanofiller. The PVDF-HFP-$NH_4CF_3SO_3$-SiO_2 electrolytes reveals the existence of two conductivity maxima at 1 and 4 wt% of SiO_2 concentration attributed to two percolation thresholds in the nanocomposite polymer electrolyte. The optimum value of conductivity of 1.07×10^{-3} S cm^{-1} is achieved for the nanocomposite polymer electrolyte film with 1 wt% SiO_2. Protonic electrochemical cells was fabricated with a configuration Zn + $ZnSO_4.7H_2O$ + PTFE (anode) | PVDF-HFP:$NH_4CF_3SO_3$+SiO_2 (electrolyte) | MnO_2 + PTFE (cathode). The maximum open circuit voltage (OCV) is ~1.50 V and discharge characteristics of the cell were studied at different loads of resistances.

Introduction

In recent years, proton conducting polymer electrolytes have received considerable attention as electrolyte materials for various electrochemical devices such as fuel cells, sensors, supercapacitors, electrochromic displays and smart windows [1,2]. This type of polymer electrolytes can be obtained by complexing strong inorganic acids such as H_3PO_3, H_2SO_4 and HCl, with electro-donor polymers. Many of these complexes show good protonic conductivity [3,4]. However, the polymer electrolytes containing inorganic acids have been found to suffer from chemical degradation and mechanical stability making them unsuitable for practical applications [2]. As alternatives, ammonium salts which are good proton donors have been employed. It has been reported that polymer electrolytes containing ammonium salts exhibited conductivity comparable to those containing inorganic acids. In the present study, proton conducting nanocomposite polymer electrolytes of PVDF-HFP doped with $NH_4CF_3SO_3$was added with SiO_2 nanofiller in order to improve its conductivity. The characteristics of the proton conducting nanocomposite polymer electrolytes have been investigated. The electrolyte with the highest conductivity was used for fabrication of all-solid-state protonic electrochemical cells. In order to investigate the performance of the cells, they were discharged under different loads.

Experimental

Preparation of electrochemical cell. The proton conducting nanocomposite polymer electrolytes were prepared by solution casting technique. The PVFD-HFP (Mw~400000, from Aldrich), ammonium trifluoromethane sulfonate ($NH_4CF_3SO_3$) (99%, from Aldrich) and silicon dioxide (SiO_2) (15 nm) were used as received. PVDF-HFP and $NH_4CF_3SO_3$ in the weight ratio of 60:40

were dissolved in a dimethylformamide (DMF). After a homogenous solution was formed, SiO_2 of desired amount was added to this solution. The polymer electrolyte solution was then cast into Petri dishes. This solution was allowed to evaporate at room temperature to form films. The highest conducting nanocomposite polymer electrolyte was used for the fabrication solid state of electrochemical cells with the following configuration: Zn + $ZnSO_4.7H_2O$ + PTFE | PVDF-HFP: $NH_4CF_3SO_3$+SiO_2 | MnO_2 + PTFE. The cathode was prepared at using simple physical grinding method by mixing manganese dioxide (MnO_2) (TOSOH Corporation) and carbon (of mass ratio 4:1) polytetrafluoroethylene (PTFE) (Aldrich, USA) binding agent and pressing the mixtures under a pressure 1.4 x 10^3 kg m^{-2} to form pellets of thickness 0.4 mm. The same method was used to prepare the anode but for the anode a mixture of zinc powder (Zn) (SHOWA Chemical co.ltd, Japan) and zinc sulphate ($ZnSO_4.7H_2O$) (of mass ratio 4:1) (R & M chemical, U.K) were used.

Characterization of electrochemical cell. Ionic conductivity of polymer electrolytes was evaluated using HIOKI 3532-50 LCR HiTester impedance analyzer in the frequency range 45 Hz to 5 MHz. Differential Scanning Calorimetry (DSC) of the samples was performed using Mettler Toledo DSC instrument (DSC822e with Gas Control TS0800GC1). The open circuit voltage (OCV) and cell potential measurements were carried out with the help of True RMS Multimeter. The cells were discharged under different loads of 1.5 kΩ, 10 kΩ and 100 kΩ. Their voltage and current were recorded as a function of time.

Results and Discussion

DSC analysis. The DSC curves of PVDF-HFP-$NH_4CF_3SO_3$-SiO_2 electrolytes are depicted in Fig. 1. The T_m of PVDF-HFP-$NH_4CF_3SO_3$-SiO_2 electrolyte films slightly differ from that of unfilled PVDF-HFP-$NH_4CF_3SO_3$. The degree of crystallinity (X_c) of the electrolytes are listed in Table 1. The X_c of the polymer electrolytes was calculated using the equation below:

$$X_c = \frac{\Delta H_m}{\Delta H^o_m} \times 100\% \quad (1)$$

where ΔH_m is the enthalpy of fusion of the polymer electrolyte sample and ΔH^o_m is the heat of fusion for 100 % crystalline PVDF which is assumed to be 104.7 J g^{-1} [5,6]. Enthalpy of fusion, ΔH_m can be obtained from area of the baseline connecting two points at which the instant value of its derivative curve becomes zero near T_m. The X_c for PVDF-HFP- $NH_4CF_3SO_3$-SiO_2 is observed to increase with increase in SiO_2 content. A similar observation has been reported by Choi et. al, [7] who reported that, the formation of crystalline phase is possible if the ceramic filler particles act as nucleation centers of the crystalline polymer phase.

Table 1 Relative degree of crystallinity for PVDF-HFP-$NH_4CF_3SO_3$-SiO_2 electrolyte films

Sample (wt% of SiO_2)	ΔH_{m1} (± 0.01)	ΔH_{m2} (± 0.01)	X_c (%)
0	5.38	2.46	7.84
1	6.98	1.69	8.67
2	4.83	4.04	8.87
3	5.44	4.39	9.83
4	6.12	4.37	10.49
5	7.80	3.90	11.70

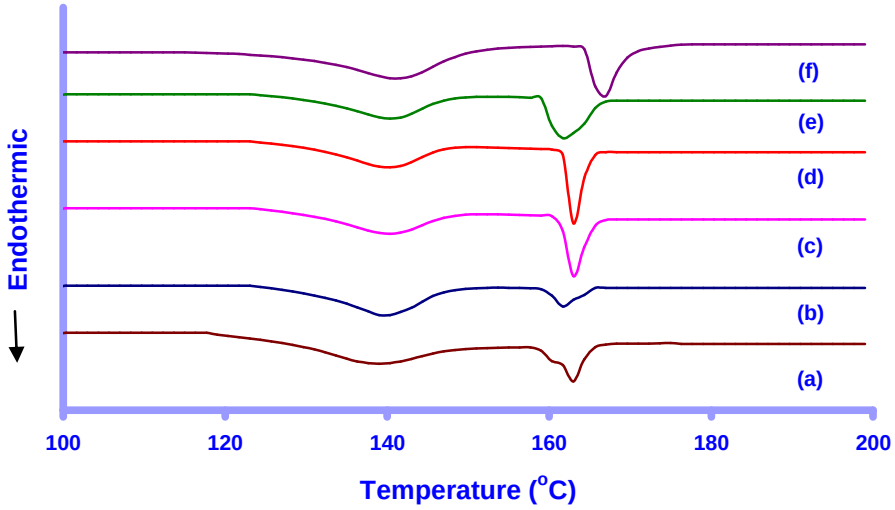


Fig. 1 DSC curves of PVDF-HFP- $NH_4CF_3SO_3$ with (a) 0 wt%, (b) 1 wt%, (c) 2 wt%, (d) 3 wt%, (e) 4 wt% and (f) 5 wt% SiO_2

Conductivity Study. The ionic conductivity study of PVDF-HFP based proton conducting nanocomposite polymer electrolytes have been carried out as a function of concentration of filler via impedance spectroscopy using stainless steel electrodes. The relationship between the concentration of SiO_2 and ionic conductivity of polymer electrolyte is shown in Fig. 2. The higher value of conductivity of nanocomposite polymer electrolytes studied could not be related to the increase in amorphocity but may be due to the existence of additional sites for migrating ionic species through transient bonding with O/OH groups on the filler surface as suggested by previous workers [8]. The electrolyte exhibits two conductivity maxima at 1 wt% and 4 wt% SiO_2. The conductivity increases at low inorganic filler loading of 1 wt% SiO_2 which may be due to the formation of surface charge layer at the polymer interface which provides a conducting pathway for mobile ions [9]. However, when the SiO_2 nanofiller content is further increased to 3 wt%, the conductivity tends to decrease slightly but then increases again as the filler content is increased to 4 wt%. The decrease in conductivity as filler content increases to 3 wt% is ascribed to the blocking of some of the existing conducting pathways and the possible agglomeration of the excess SiO_2 nanofiller that reduces the polymer filler interface and hence reduces the conducting pathways. As the filler content increases to 4 wt%, conducting pathways are again created but for the conduction of triflate anions. Further addition of SiO_2 nanofiller leads to a decrease in conductivity results in the blocking and termination of the formation of conducting pathways. Dissanayake et. al, [10] reported that at higher filler concentration, the grains get close to each other that the blocking effect imposed by the more abundant alumina grains could make the long polymer chains more immobilize leading to the decrease in conductivity.

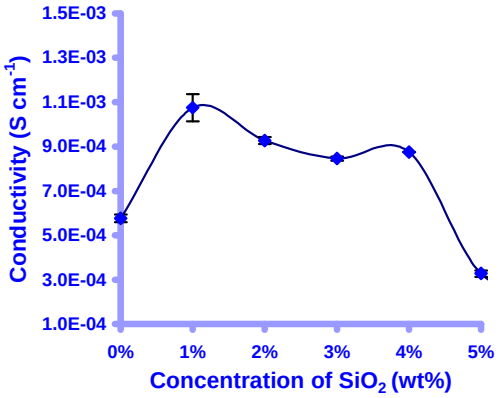


Fig. 2 The concentration of SiO_2 dependence conductivity

Battery Characteristics. Fig. 3(a) shows the open circuit voltage during 24 hours storage time of the cell. It can be seen that the initial voltage of the three cells is 1.50 V. Within 1 hour, the OCV of Cell A stabilizes to ~1.20 V. The voltage remains constant at this value for a period of 23 hours. Meanwhile, Fig. 3(b) shows that the initial voltage of Cell B decreases after 1 hour to a value of ~1.20 V and remains constant at this voltage for a period of 23 hours. Cell C discharged itself from initial voltage ~1.50 V to ~1.29 V within 1 hour and subsequently remains nearly constant at the value ~1.25 V for 23 hours. From this study, it can be concluded that the cells are stable in open circuit condition.

In order to study discharge performance, Cell A, Cell B and Cell C were discharged at the loads of 1.5 kΩ, 10 kΩ and 100 kΩ respectively. From Fig. 4(a), it can be observed that the discharge voltage of Cell A exhibits a rapid decrease. The voltage drops from an initial voltage of ~1.39 to ~0.85 V within 1 hour and decreases to ~0.15 V in 7 hours. The initial drop is attributed to the cell polarization [11]. The voltage subsequently remains nearly constant at this value for up to 7 hours after which it drops further. The same trend is seen for the current drawn from the cell, Fig. 4(a). For higher load resistances, the voltage drop is not as fast as that for the load of 1.5 kΩ. The time duration of stable performance (plateau region) of the cell is found to increase with increase in load resistance. The voltage for cell B shows a plateau region for 14 hours after initial drop of voltage from ~1.50 V to ~0.95 V, Fig. 4(b). For this cell, a plateau region in the current-time plot is observed but the plateau current is lower than that for Cell A (Fig. 4(b)). For Cell C (Fig. 4(c)), the voltage slowly decreases from ~1.50 V to ~0.99 V in 20 hours. A plateau region is observed extended well over 90 hours. Similarly, the current versus time plot shows that the current remains constant for 90 hours at 0.99 μA. Table 2 lists some important electrochemical cell parameters evaluated from discharge profile of Cell A, Cell B and Cell C. The cell applied with 100 kΩ gives the highest current density 0.91 mA h and open circuit voltage ~1.50 V compared with literature.

Table 2 Some important parameters for Cell A, Cell B and Cell C

Parameters	**Cell A**	**Cell B**	**Cell C**
Cell weight (± 0.0001 g)	0.9541	0.9576	0.9289
Cell thickness (± 0.001 mm)	1.386	1.390	1.323
Cell area (± 0.1 cm)	3.0	3.0	3.0
Open circuit voltage (± 0.01 V)	1.50	1.50	1.50
Load (k Ω)	1.5	10	100
Plateau time (Hour)	7	14	90
Plateau voltage (± 0.01 V)	0.13	0.79	0.99
Discharge capacity (mA h) (calculated for plateau region)	0.61	0.84	0.91

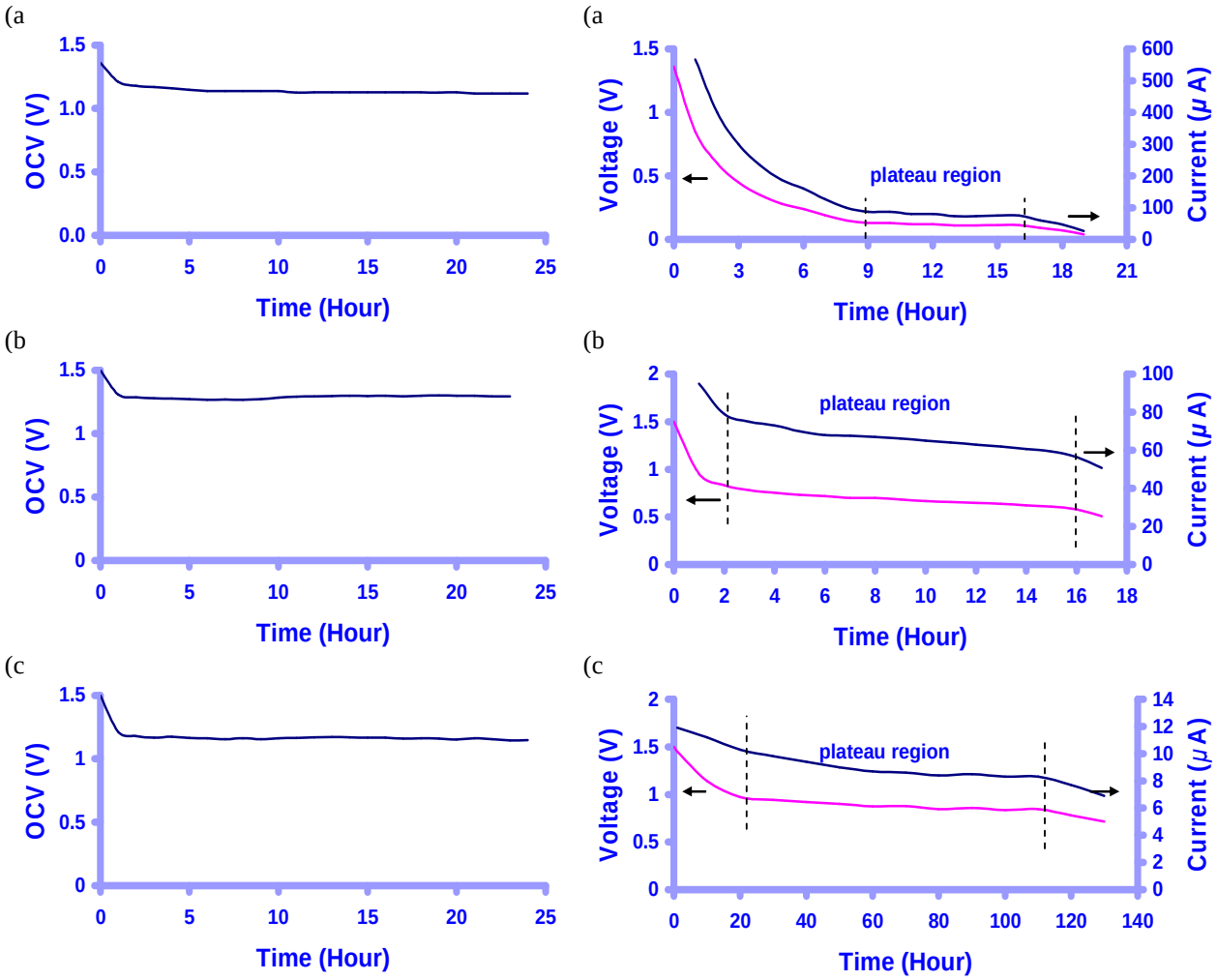


Fig. 3 OCV versus time for (a) Cell A, (b) Cell B and (c) Cell C

Fig. 4 Discharge voltage and current versus time for (a) Cell A, (b) Cell B and (c) Cell C

Summary

Proton conducting nanocomposite polymer electrolytes based on polyvinylidene fluoride-co-hexapropylene (PVDF-HFP), ammonium triflate ($NH_4CF_3SO_3$) and silicon dioxide (SiO_2) have been obtained by solution casting technique. The dispersal of SiO_2 nanofiller into PVDF-HFP-$NH_4CF_3SO_3$ electrolyte resulted in an optimum conductivity enhancement of one order of magnitude. The discharge characteristics of the cells fabricated using the highest conducting electrolyte has been studied for different loads. The protonic cell based on PVDF-HFP-$NH_4CF_3SO_3$-SiO_2 nanocomposite polymer electrolyte performed fairly well when discharged at low current drain or with high load resistance. This means that the cell is suitable for low current drain application.

References

[1] A. M. M. Ali, N. S. Mohamed, and A. K. Akof: Journal of Power Sources Vol. 74 (1998), p. 135-141.

[2] S. Chandra, S. S. Sekhon, R. Srivastava, and N. Arora: Solid State Ionics Vol. 154-155 (2002), p. 609-619.

[3] M. A. Navarra, S. Panero, and B. Scrosati: Journal Solid State Electrochemica Vol. 8 (2004), p. 804-808.

[4] G. G. Kumar, P. Kim, K. S. Nahm, and R. N. Elizabeth: Journal of Membrane Science Vol. 303 (2007), p. 126-131.

[5] K. W. Kim, N. G. Park, K. S. Ryu, and S. H. Chang: Electrochimica Acta Vol. 51 (2006), p. 5636-5644.

[6] V. Aravindan, and P. Vickraman: European Polymer Journal Vol. 43 (2007), p. 5121-5127.

[7] B. K. Choi, Y. W. Kim, and K. H. Shin: Journal of Power Sources Vol. 68 (1997), p. 357-360.

[8] H. M. J. C. Pitawala, M. A. K. L. Dissanayake, and V. A. Seneviratne: Solid State Ionics Vol. 178 (2007), p. 885-888.

[9] L. Fan, C. W. Nan, and S. Zhao: Solid State Ionics Vol. 164 (2003), p. 81-86.

[10] M. A. K. L. Dissanayake, P. A. R. D. Jayathilaka, and R. S. P. Bokalawele: Electrochimica Acta Vol. 50 (2005), p. 5602-5605.

[11] S. M. Bansod, S. S. Bhoga, K. Singh, and R. U. Tiwari: Vol. 13 (2007), p. 329-332.

© (2011) Trans Tech Publications, Switzerland
doi:10.4028/www.scientific.net/KEM.471-472.379

Li_2CO_3 – Al_2O_3 Composite Solid Electrolytes Prepared By Sol Gel Method

Mazdida Sulaiman[1,a], A.A. Rahman[1,b] and N.S. Mohamed[1,c]

[1]Centre for Foundation Studies in Science,

University of Malaya, 50603 Kuala Lumpur, Malaysia

[a]mazdidas@um.edu.my, [b]azilahar@um.edu.my,[c]nsabirin@um.edu.my

Keywords: Composite, sol gel, conductivity

Abstract. Composite solid electrolytes in the system $(1-x)Li_2CO_3$-xAl_2O_3, where x = 0.1–0.7 were prepared by sol gel method using lithium carbonate and aluminum oxide precursors in ethanol. The gels obtained due to the addition of citric acid were calcined at 80 and 100 ^oC. Their structural, thermodynamic and electrical properties were investigated by X-ray diffraction (XRD), Field emission scanning electron microscopy (FESEM), differential scanning calorimetry (DSC), Fourier transform infrared spectroscopy (FTIR) and impedance spectroscopy. The results indicated that interface phases of crystalline and amorphous exist in this composite system of $(1-x)Li_2CO_3$-xAl_2O_3. The presence of the interface phases are due to the chemical and physical interactions between both crystalline Li_2CO_3 and Al_2O_3. The Arrhenius plot of the composite system showed non-linear curves and reached maximum values of $\sim 10^{-4}$ - 10^{-5} S cm^{-1} at 150 -180 °C. Based on the results of this study, it can be concluded that the sol gel method used in the preparation of the composite system, has an important role to crystal morphology changes that results in high ionic conductivity.

Introduction

Various techniques, involving low and high temperatures have been employed in the preparation of composite materials of solid electrolytes. They are hand milling, ball milling, solid-state reaction, precipitation, hydrothermal technique, quenching, and others. Different preparative techniques result in different properties of composite materials such as structural, thermal and electrical properties.

However, higher ionic conductivity for composites can be expected when smaller insulator particles with larger surface area are dispersed into a host. In this composite system, it is important that insulating particles are well dispersed in the host so that both phases are interconnected three-dimensionally. Porous materials are also attractive because they usually have large surface area to give large interfaces between insulators and ionic conductors [1]. These porous materials, which are also homogeneous can be prepared by a sol-gel process [2,3,4]. The homogeneity of the porous materials may result in enhanced conductivity.

The purpose of this study is to prepare composite solid electrolytes at low temperature with high ionic conductivity and is also to investigate the mechanism of the ionic conductivity. The conductivity enhancement of composites is caused by the presence of great number of surfaces and interfaces [5]. The structure of the interfaces phase may be epitaxial, crystalline or amorphous.

In this work, we synthesized composite solid electrolytes by a sol gel technique with ethanol as the solvent of the solution. We also studied the compositional and temperature dependence of their ionic conductivity.

Experimental

Powders of composition x = 0.1–0.7 (mol %) were prepared by a sol gel method. Li_2CO_3 (high purity grade) and Al_2O_3 (high purity grade) powders were used as starting materials. First, lithium

carbonate and alumina, with desired mol percentages were dissolved in ethanol. The solution was left to cool down to room temperature. Next, citric acid was added to the initial solution and then stirred at 60 ^{o}C for 20 minutes. This is followed by refluxing at 80 ^{o}C on a hot plate with continuous stirring for 2 hours. The mixture was further slowly heated at 80 ^{o}C for overnight until a white gel was obtained. In the final step of the sol gel process, the wet gel was fully dried at 100 ^{o}C in an oven for 16 - 48 hours, depending on its composition. The powder obtained was then ground in an agate mortar until fine powders were obtained. Afterwards, the resulting powder was redissolved in ethanol, dried at 100 ^{o}C and reground. Structural characterization was performed on D8 Advanced X-ray Diffractometer-Bruker with Cu Kα radiation (at room temperature), Field Emission Scanning Electron micrograps were taken using FEI Quanta 200 and Perkin Elmer (RX1 Spectrometer) was used for taking FTIR data. The thermal properties of the samples were measured by using a METTLER TOLEDO DSC 822 with continuous heating at a rate of 10 ^{o}C/min. For conductivity studies, pellets were compacted by pressing the powder in a press die at a pressure of 6-8 tones/cm^2. Conductivities were measured using a SOLATRON 1260 impedance analyzer from room temperature to 180 ^{o}C over a frequency range of 10^{-1}–10^{7} Hz.

Results and Discussion

FESEM. FESEM micrographs of the composite samples with x = 0.3 and x = 0.5 are shown in Fig. 1. Fig. 1(a) shows the presence of both crystalline and amorphous Li_2CO_3 in the sample with x = 0.3. It is also observed that crystalline Al_2O_3 is embedded between the crystalline and amorphous Li_2CO_3. The presence of some voids in the sample indicates poor contact between its grains.

Fig. 1(b) depicts the presence of only amorphous phase Li_2CO_3, without the appearance of its crystalline phase in the sample with x = 0.5. The formation of the amorphous Li_2CO_3 is due to chemical and physical interactions of crystalline Li_2CO_3 and Al_2O_3 [6-9]. The figure also reveals improved contact between Li_2CO_3 and Al_2O_3 as no voids are present in the sample.

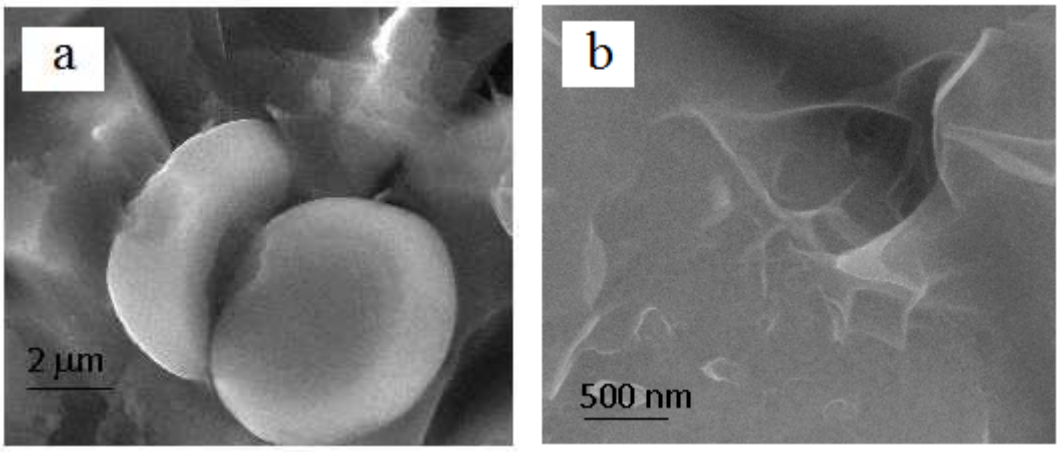


Fig. 1 FESEM images of samples with (a) x = 0.3 and (b) x = 0.5

XRD. Fig. 2(a) presents the XRD spectra of (1-x)Li_2CO_3-xAl_2O_3 composites. The peaks of pure Li_2CO_3 (x = 0.0) is indexed as a monoclinic structure (a = 8.35900Å, b = 4.97670Å, c = 6.19400 Å and β=114.72^{o}). The peaks at 2θ = 21.3^{o}, 23.1^{o}, 28.9^{o}, 30° - 40° and 48.5^{o} in the spectra of composite samples with $x \leq 0.3$, are attributed to Li_2CO_3. However, the intensities of the Li_2CO_3 peaks are observed to decrease when x increases. For x = 0.2, additional reflections at 2θ around 19°, 23° 26°and 38° appeared. These reflections are attributed to crystalline Li_5AlO_4. This means that at this point of composition, a new crystalline phase of Li_5AlO_4 is formed. This crystalline phase is not present in other composite samples. Some peaks of Li_2CO_3 are found absent when x = 0.4 - 0.5. The peaks missing are those at 2θ ≈25° and also between 38° and 50°. This change

indicates the formation of an amorphous phase and is supported by the broadening of remaining Li_2CO_3 peaks. In the amorphous state, the anionic sublattice of CO_3^{2-} is orientationally disordered and thus helps to facilitate ionic conduction [6]. On the other hand, Table 1 shows slight changes in lattice parameters of Li_2CO_3. The changes of lattice parameters presented in the table shows that monoclinic structure of Li_2CO_3 has slightly distorted. This distortion weakens the ionic bond of Li_2CO_3 and may lead to easier formation of free Li^+ ions [10]. For composites with $x > 0.5$, no peaks of crystalline Li_2CO_3 are present. In this case, the ionic salt is totally transformed into the amorphous state as seen in FESEM micrograph.

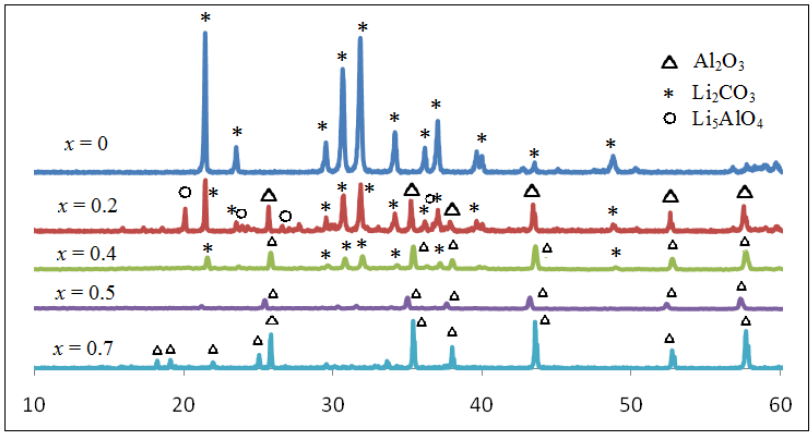


Fig. 2 X-ray powder diffractograms of (1-x) Li_2CO_3-xAl_2O_3 composites

Table 1 Monoclinic lattice parameters of Li_2CO_3 in the system (1-x) Li_2CO_3 - xAl_2O_3

Sample	a / Å	b / Å	c / Å	β	Bravais Lattices
$x = 0.0$	8.35900	4.97670	6.19400	114.72^0	Base Centred
$x = 0.4$	8.35930	4.97250	6.19750	114.83^0	Base Centred
$x = 0.5$	8.30000	5.00000	6.21000	114.50^0	Base Centred

DSC. Results of calorimetric studies of the (1-x)Li_2CO_3-xAl_2O_3 composite samples are displayed in Fig. 3. At $x > 0.2$, two endothermic arrests are observed. The little broad endothermic peak at 60 – 80 °C observed in DSC curves of the samples with = 0.4 and x = 0.7 is attributed to glass transition temperature of amorphous phase formed in the samples. The formation of amorphous is revealed by the FESESM micrographs shown in Fig. 1. Second endothermic peaks are seen in the temperature range 130 - 200 °C. These peaks may be attributed to some chemical reactions between the composite components. The decomposition of residual ethanol occurred after 200 °C [11,12]. For sample with x = 0.2, incomplete crystallization is observed near 110 °C, followed by a decomposition.

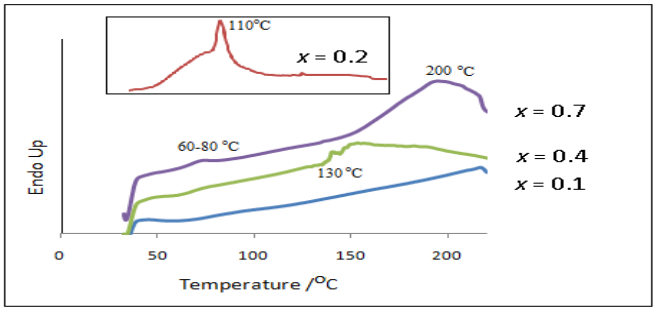


Fig. 3 DSC for (1-x) Li_2CO_3-xAl_2O_3 composites

FTIR. To further examine the characteristic of the composite sample with x = 0.2, FTIR spectrum was recorded in the wavenumber range 4000-450 cm^{-1} (Fig. 4). The absorption bands in the range 900-450 cm^{-1} are due to Al-O stretching vibrations [13]. This confirms the formation of Li_5AlO_4 as indicated by the XRD results discussed earlier.

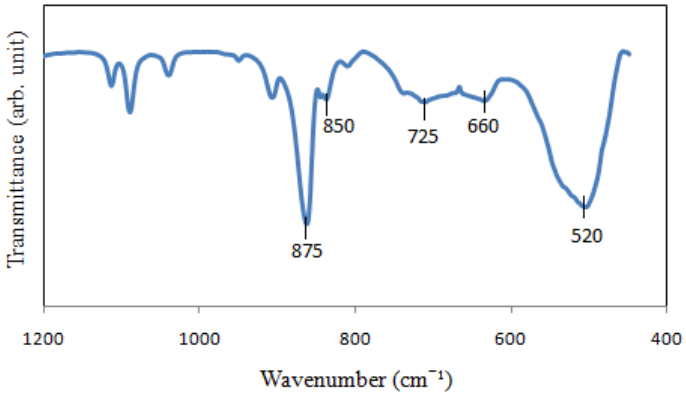


Fig. 4 FTIR spectrum of composite sample with x = 0.2

Electrical Conductivity. As shown in Fig. 5, the conductivity goes through two maxima, which takes place for composites with x = 0.2 and 0.6. In the first region (x = 0.1 - 0.3), it is observed that the conductivity increases from x = 0.1 to x = 0.2 and decreases at x = 0.3. The high conductivity of the sample x = 0.2 is due to the formation of a new crystalline phase of Li_5AlO_4 which is a highly conducting crystalline phase [14]. In the second region (x = 0.4 - 0.7), the conductivity increases from x = 0.4 to x = 0.6 followed by a slight decrease at x = 0.7. The increase in conductivity is attributable to an increase in amorphicity in the sample and number of free Li^+ ions due to increased interactions between Li_2CO_3 and Al_2O_3 as mentioned earlier. However, the conductivity decreases at x = 0.7. This may be due to agglomeration of Al_2O_3 as indicated by the increase in intensity of the Al_2O_3 peaks in the sample's XRD spectrum presented in Fig. 2.

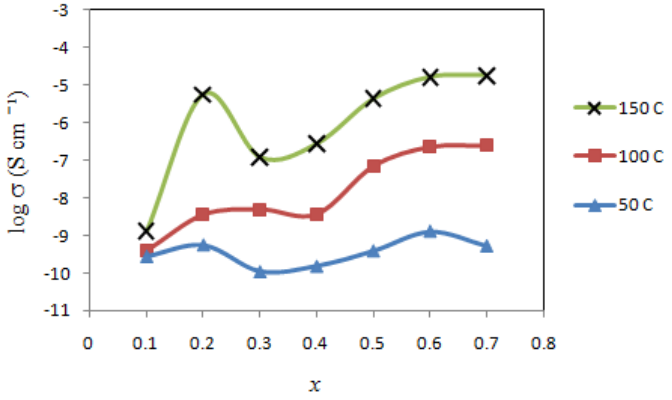


Fig.5 Conductivity of (1-x) Li_2CO_3-xAl_2O_3 composites as a function of x

Temperature dependence of the ionic conductivity for (1-x)Li_2CO_3-xAl_2O_3 composites are shown in Fig. 6. The conductivity values of the composites are in the order of 10^{-9} S cm^{-1} at 50°C. In general, for all composites (except for that with x = 0.1), the conductivity increases with temperature. Arrhenius curves are non-linear which is characteristic of highly amorphous ionic conductor near the glass transition temperature which is determined to be around 60 °C for the studied composite system [15].

For the composite sample with $x = 0.1$, it is observed that the conductivities are about constant from 50 to 110 °C. This is due to minimum interactions between crystalline Li_2CO_3 and Al_2O_3 as shown by its DSC spectrum. The conductivity increases with a little slope beyond 110 °C which may be due to greater interactions between the components.

A significant conductivity increase occurred at $x = 0.2$ at a temperature of 110 °C. This sharp conductivity increase may be connected to the formation of a new phase of Li_5AlO_4 as indicated by its XRD spectra. The high conductivity at this temperature is possibly due to better crystallinity of Li_5AlO_4 at higher temperature [16]. However, the conductivity drops beyond 150 °C is due to its incomplete crystallization and decomposition.

The highest conductivity achieved in this system is 1.05×10^{-4} S cm^{-1} at 150 °C for $x = 0.2$ and 7.46×10^{-5} S cm^{-1} at 180 °C occurs for $x = 0.6$. The values are higher compared to those reported by Agrawal [17] for the system Li_2CO_3-Al_2O_3 measured at 300 °C.

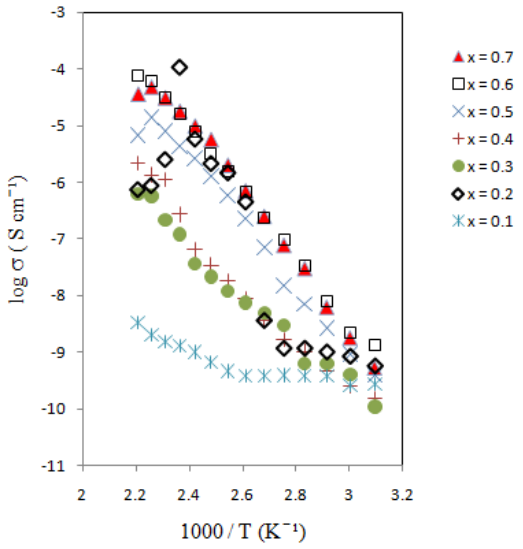


Fig. 6 Temperature dependence of conductivity of $(1-x)Li_2CO_3$-xAl_2O_3 composites

Summary

In this study, $(1-x)Li_2CO_3$-xAl_2O_3 composite solid electrolytes were prepared by sol gel method. The present results show that interface phases of crystalline and amorphous exist in this composite system of $(1-x)Li_2CO_3$-xAl_2O_3. These interface phases contribute to the enhancement in conductivity of the Li_2CO_3 salt in the samples. The highest conductivity values of 1.05×10^{-4} S cm^{-1} (150 °C) and 7.46×10^{-5} S cm^{-1} (180 °C) occurs for $x = 0.2$ and $x = 0.6$, respectively. Considering these results, it can be concluded that the synthesis route of sol gel has an important role to crystal morphology changes that leads to an increase in composite conductivity value. More work preparative parameters is in progress in order to obtain composite electrolytes with higher ionic conductivity values at lower temperatures.

References

[1] H. Yamada, I. Moriguchi and T. Kudo: Solid State Ionics Vol. 176 (2000), p. 945

[2] K.S. Alber and J.A. Cox: Mikrochim. Acta 127 (1997), p. 131

[3] P. Muralidharan, I. Prakash, M. Venkateswarlu and N. Satyanarayana in: NSTI-Nanotech, www.nsti.org, ISBN 0-9728422-9-2 Vol. 3 (2004).

[4] L.J. Fu, H. Liu, C. Li, Y.P. Wu, E. Rahm, R. Holze and H.Q. Wu: Materials Science Vol. 50 (2005), p. 881

[5] N.F. Uvarov and P. Vanek: Journal of Materials Synthesis and Processing Vol. 8 (2000), p. 319

[6] N.F. Uvarov et al.: Solid State Ionics Vol. 90 (1996), p. 201

[7] G.V. Lavrova, V.G. Ponomareva and N.F. Uvarov: Solid State Ionics Vol. 136-137 (2000), p. 1285

[8] N.F. Uvarov, P. Vanek, M. Savinov, V. Zelezny, J. Studnicka and J. Petzelt: Solid State Ionics Vol.127 (2000), p. 253

[9] K. Tadanaga, K. Imai, M. Tatsumisago and T. Minami: Journal of Electrochem. Soc. Vol. 147 (2000), p. 4061

[10] V.K. Deshpande and K. Singh: Solid State Ionics Vol. 6 (1982), p. 151

[11] F. Oksuzomer, S.N. Koc, I. Boz and M.A. Gurkaynak: Materials Research Bulletin Vol. 39 (2004), p. 715

[12] S.W. Kwon and S.B. Park: Journal of Nuclear Materials Vol. 246 (1997), p. 131

[13] M. Chatterjee and M.K. Naskar: Journal of Materials Science Letters Vol. 22 (2003), p. 1747

[14] R.M. Biefield and R.T. Johnson: Journals of Solid State Chemistry Vol. 19 (1979) p. 393

[15] N.F. Uvarov, E.F. Hairetdinov and I.V. Skobelev.: Solid State ionics Vol. 86-88 (1996), p. 577

[16] S. Hashimoto et. al.: Material Research Bulletin Vol. 44, Issue 1 (2009), p. 70

[17] R.C. Agrawal and R.K. Gupta: Journal of Material Science Vol. 34 (1999), p.1131

© (2011) Trans Tech Publications, Switzerland
doi:10.4028/www.scientific.net/KEM.471-472.385

Measurement on Strain Rate Sensitivity and Dynamic Mechanical Properties of Various Polymeric Materials

Mohd Firdaus Omar[1,2], Hazizan Md Akil[1a], Zainal Arifin Ahmad[1]

[1]School of Materials and Mineral Resources Engineering, Universiti Sains Malaysia,

14300 Seberang Perai Selatan, Pulau Pinang, Malaysia.

[2]School of Materials Engineering, Universiti Malaysia Perlis,

02600, Jejawi, Kangar, Perlis, Malaysia.

[a]hazizan@eng.usm.my

Keywords: Mechanical properties, Stress/strain curves, split Hopkinson pressure bar apparatus

Abstract. Strain rate sensitivity and dynamic mechanical properties of polymeric materials are affected to a certain extent especially by the rate of loading. However, there is limited number of works reported on that particular issue. Therefore, the paper presents on static and dynamic mechanical properties of various polymeric materials across strain rate from 10^{-2} to 10^{-3} s^{-1}. The specimen were tested using universal testing machine (UTM) for static loading and a conventional split Hopkinson pressure bar (SHPB) apparatus for dynamic loading. From the results, the compression modulus and compressive strength of all tested specimen increased significantly with increasing strain rates. In addition, positive increment in terms of strain rate sensitivity was recorded for all tested polymers over a wide range of strain rate investigated. Meanwhile, the thermal activation volume has decreased as increasing strain rate. Of the three polymers, polypropylene shows the highest strain rate sensitivity at static region. On the other hand, at dynamic region, polycarbonate shows the highest strain rate sensitivity than that of polypropylene and polyethylene.

Introduction

Dynamic mechanical properties of polymeric materials under high loading rates have received an extraordinary attention for past few decades [1-3]. This particular phenomenon is related with the natural ability of the polymeric materials which can provide a good balance between impact resistance and production cost and weight [4]. Recently, polymeric materials have been used in various engineering applications, such as automotive and structural components, which may be subjected to dynamic loading. Hence it is very crucial to investigate the performance of the polymeric material under high strain rates condition in order to avoid any unexpected failure during services. High strain-rate behaviour of various polymeric materials has been reported by several researchers [5-7]. However, the difficulty to perform high strain rate testing still remains as a major challenge in dynamic characterisation of polymeric materials. Therefore, in the present paper, an experiment technique based on the compression split Hopkinson pressure bar technique was introduced to perform high rate compression testing of various polymeric materials. Meanwhile, universal testing machine was used to perform low strain rate testing. Three common polymeric materials have been used in this study which is polyethylene (PE), polypropylene (PP) and polycarbonate (PC). For comparison purpose, stiffness and strength properties of all tested polymers were characterised under both static and dynamic loading conditions. In addition, the strain rate sensitivity of flow stresses and thermal activation volume of various polymers were also determined over a wide range of strain rate investigated.

Experimental Details

Materials and Sample Preparation. Three common polymeric materials which are Polyethylene (PE), Polypropylene (PP) and Polycarbonate (PC) were chosen for static and dynamic compression testing at room temperature. PE (HI-2081) and PP (PX-617) were supplied by Titan Chemicals Corp. Bhd. Meanwhile, PC (PC-088) was obtained from Polymer Technology and Services, LLC. Cylindrical specimens were fabricated by the hot compression technique. The specimen pellets were compression moulded in an electrically heated hydraulic press, using the button mould, into sizes of 12 mm diameter and 27 mm thickness, for both static and dynamic testing, respectively.

Static Compression Test. A slenderness ratio (l/d) of compression specimen was reported to give significant influence to the frictional effects during static testing, where ASTM Designation E9-89 was highly recommended for the slenderness ratio of polymeric materials, as well as metallic materials [8-9]. Therefore, the specimen length was cut, based on ASTM Designation E9-89, where the l/d (d =12mm) of the specimen, was approximately 1.5. In this study, the specimens were tested under constant crosshead speeds of 10.8 mm/min and 108 mm/min, corresponding to the strain rates of 0.01×10^{-3} s^{-1} and 0.1×10^{-3} s^{-1}, respectively, using an Axial-Torsion Universal Testing Machine. In order to reduce the frictional constraint during the test, a thin film of lubricant was applied at both of the specimen's interfaces.Five measurements were taken for each loading rates to quantify the average behaviour of each specimen.

Dynamic Compression Test. In SHPB testing, the specimen geometry is one of the vital requirements which need to be considered. Thus, the issue of specimen geometry, especially thickness, was actively debated by the previous researchers [10-12]. However, the majority of experts agreed that the thickness effect was not due to wave propagation effects in the specimen, but more on the radial inertia and friction considerations [8, 13-14]. Therefore, the tests reliability is highly related to the slenderness ratio of the specimen, rather than the specimen's thickness. In this experiment, the slenderness ratio used was based on previous studies, which was 0.5 [8-9, 11]. Therefore, the specimen length was created, so that the l/d (d =12 mm) value was equal to 0.5. Similar to the static test, five measurements were performed for each loading rates in order to determine the average dynamic behaviour of all specimens.

Result and Discussion

Strength and Stiffness Properties. Stiffness and strength properties are the best statistical indicator to evaluate the performance of the materials. Therefore, the compression modulus and ultimate compressive strength (UCS) were carried out and demonstrated in Fig. 1 and Fig. 2, respectively. From the graphs in Fig. 1 and Fig. 2, it is clearly shows that the compression modulus as well as compressive strength was significantly increased with increasing strain rates. The increment in compression modulus was closely related with the secondary molecular processes where an increasing strain rates decreases the mobility of polymer chains, thus make the polymeric material stiffen [9]. On the other hand, the enhancement of the compressive strength was attributed by the shifting of the molecular relaxation for polymeric materials during impact, as previously reported by [15-16]. Accumulated heat during high strain rates loading has slightly altered the shifting of the glass transition for polymeric materials where at low strain rate (static), the polymeric materials is near rubbery-like regime, whereas at high rates, it has transformed to fully leathery regime, where intermolecular interaction in the amorphous region begin to pose significant resistant to deformation. Therefore, all polymeric materials become stronger as increasing strain rates (from static to dynamic loading). Quantitatively, PC has recorded highest compression modulus and ultimate compressive strength values than that of PP and PE over a wide range of strain rate investigated.

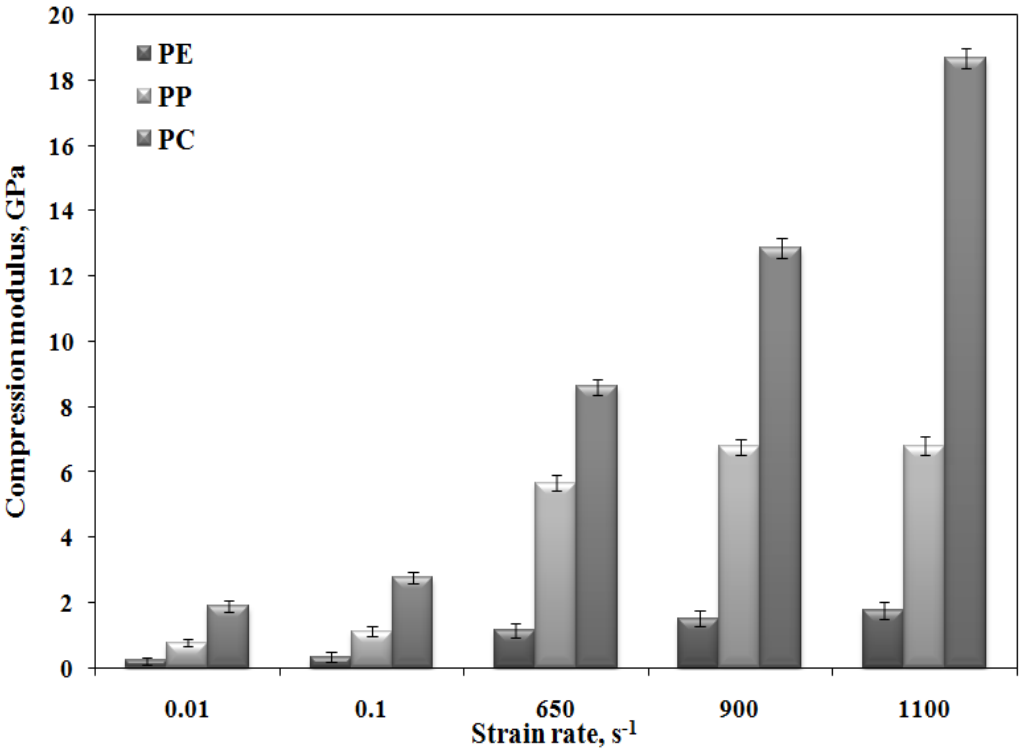


Fig. 1 The compression modulus of various polymers under low and high strain rate loadings.

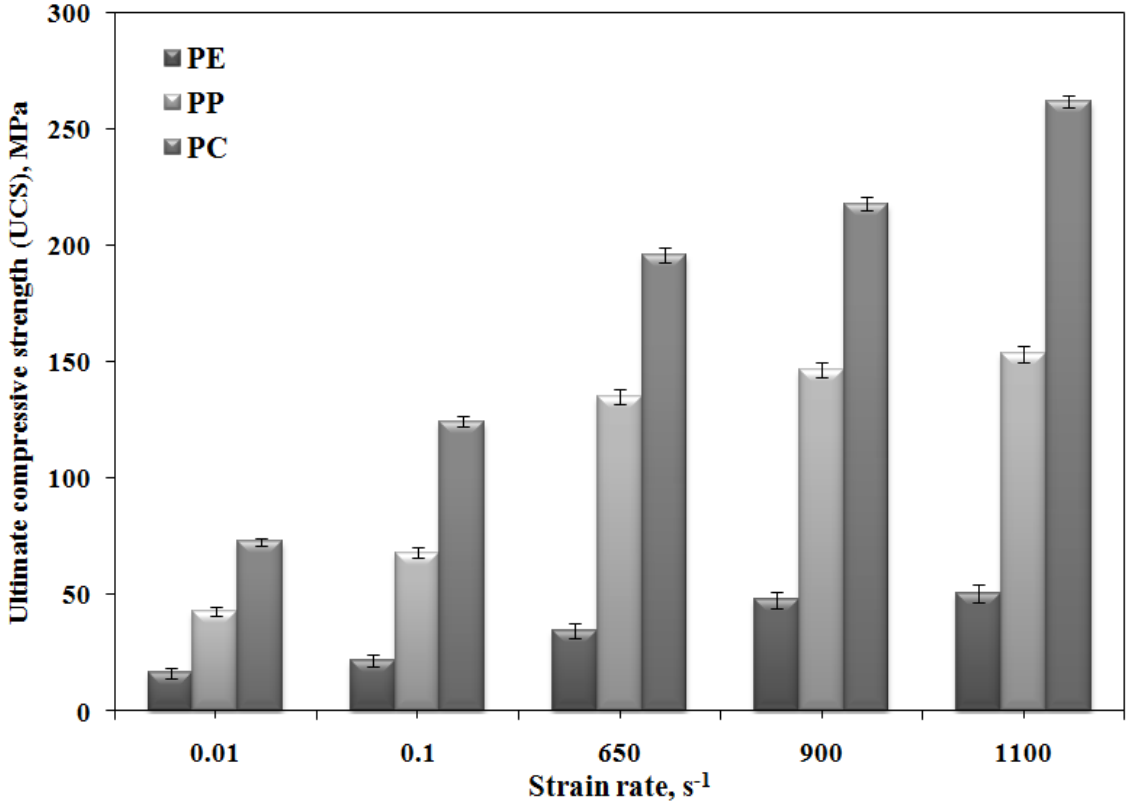


Fig. 2 The compressive strength of various polymers under low and high strain rate loadings

Strain Rate Sensitivity and Thermal Activation Volume. Each material reacts differently under various loading condition. The magnitude of the changed can be directly measured using several methods. For example, the sensitivity of flow stresses can be measured by using strain rate sensitivity parameter. However, strain rate sensitivity is always presented in terms of stress-strain

curves, which show the effect of strain rates on the proportion of materials, such as Young's modulus, strength, flow stress etc. In real world, it is always useful if the strain rate sensitivity can be carried out in terms of values in order to easily compare the materials. Therefore, in this study the strain rate sensitivity of the polymeric material was based on the definition of strain rate sensitivity, which can be expressed as follows [15]:

$$\beta = \frac{\sigma_2 - \sigma_1}{\ln(\dot{\varepsilon}_2 / \dot{\varepsilon}_1)} \quad \left| \begin{array}{l} \dot{\varepsilon}_2 > \dot{\varepsilon}_1 \\ \varepsilon = 0.025 \end{array} \right. \tag{1}$$

Where σ_1 and σ_2 is the flow stress at the fixed strain (in this case, the strain used is 0.025) under different strain rates. Alternatively, there is a way to relate the strain rate sensitivity with thermal activation volume of the material as previously reported by [17].Therefore, the derivation of the thermal activation volume, taking into account the strain rate sensitivity, can be expressed as follows [15, 17]:

$$V^* = kT \left[\frac{\ln(\frac{\dot{\varepsilon}_2}{\dot{\varepsilon}_1})}{\sigma_2 - \sigma_1} \right] = \frac{kT}{\beta} \tag{2}$$

Where k is the Boltzmann Constant and T is the absolute temperature. All calculated strain rate sensitivities and thermal activation volumes of each sample, have been grouped in Table 3.

From Table 1, the strain rate sensitivity of all polymeric specimens increased as the range of strain rate increased. In addition, PP has recorded highest level of strain rate sensitivity in static and quasi-static region (static to dynamic) as compared to PE and PC. However, at dynamic region of strain rate investigated, PC displays highest strain rate sensitivity than that of PP and PE. On the other hand, the thermal activation volume of each specimen was decreased significantly with an increasing strain rate. Overall, PE has recorded the highest amount of thermal activation volume for all tested loading rates as compared to others. Theoretically, in polymeric material, thermal activation volume corresponding to the localized motions of segment or possibly side group of polymer chains[18]. Hence, at high strain rate where the mobility of the molecular chain was restricted, it will indirectly contribute to the higher thermal activation volume. Meanwhile, at low strain rate, the entanglement of the polymer chains has increase thus, decrease the thermal activation volume.

Table 1 The strain sensitivities and thermal activation volume of various polymeric materials under different region of strain rates

Polymers	Range of strain rates (s^{-1})	Classification	$\beta = \frac{\sigma_2 - \sigma_1}{\ln(\dot{\varepsilon}_2 / \dot{\varepsilon}_1)}$ (MPa)	$V^* = kT\left[\frac{\ln(\frac{\dot{\varepsilon}_2}{\dot{\varepsilon}_1})}{\sigma_2 - \sigma_1}\right] = \frac{kT}{\beta}$
			$\dot{\varepsilon}_2 > \dot{\varepsilon}_1$ $\varepsilon = 0.025$	$\dot{\varepsilon}_2 > \dot{\varepsilon}_1$ $\varepsilon = 0.025$
PE	0.01 to 0.1	Static	0.621	6.069×10^{-27}
	0.1 to 650	Static to dynamic	1.653	2.280×10^{-27}
	650 to 1100	Dynamic	4.087	9.222×10^{-28}
PP	0.01 to 0.1	Static	3.105	1.214×10^{-27}
	0.1 to 650	Static to dynamic	7.647	4.929×10^{-28}
	650 to 1100	Dynamic	48.869	7.713×10^{-29}
PC	0.01 to 0.1	Static	1.889	1.995×10^{-27}
	0.1 to 650	Static to dynamic	7.180	5.249×10^{-28}
	650 to 1100	Dynamic	119.846	3.145×10^{-29}

Summary

Static and dynamic testing on the three different polymeric materials have been successfully performed at different levels of strain rate up to nearly 1100 s^{-1} using the conventional universal testing machine and the Split Hopkinson Pressure Bar apparatus, respectively. From the results, the following conclusion can be drawn:

- The mechanical properties of all tested polymeric show great dependency on the strain rate applied. The compression modulus and compressive strength of all tested specimens were proportionally increased as the strain rate increased.
- The strain rate sensitivity and the thermal activation volume of the PE, PP and PC were successfully measured. The strain rate sensitivity of all polymeric specimens was significantly increased with increasing strain rate, whereas the thermal activation values show contradictory trend.

Acknowledgements

The authors would like to acknowledge the Universiti Sains Malaysia (USM) (Grant no: 1001/PBAHAN/ 8043057 & 811070) and the Universiti Malaysia Perlis (UNIMAP) for sponsoring and giving financial assistance during this research work. Omar M.F. wants to thank to Prof. Takashi Yokoyama from the Okayama University of Science, Department of Mechanical Engineering, for his valuable suggestions, during several discussions, regarding this research effort.

References

[1] Li, Z. and J. Lambros: Int J. Solid Structure Vol. 38 (2001) p. 3549.

[2] Chen, W., F. Lu, and M. Cheng: Polym. Test.Vol. 21 (2002) p. 113.

[3] Ouellet, S., D. Cronin, and M. Worswick: Polym. Test. Vol. 25 (2006) p. 731.

[4] Fu, S. and Y. Wang: Polym. Test.Vol. 28 (2009) p. 724.

[5] Rietsch, F. and B. Bouette : Eur Polymer J Vol. 26 (1990) p. 1071.

[6] Sato, Y., et al.: Int. J. Impact Eng. Vol. 35 (2008) p. 1778.

[7] Xiao, X.: Polym. Test. Vol. 27 (2008) p. 164.
[8] Nakai, K. and T. Yokoyama : J Solid Mech Mater Eng. Vol. 2(2008) p. 557.
[9] Omar, M., et al.: J Mater Design Vol. 31(2010) p.4209.
[10] Guo, Y. and Y. Li : Mat Sci Eng A Vol.458 (2007) p. 330.
[11] Davies, E. and S. Hunter, J Mech Phys Solids. Vol.11(1963) p.155.
[12] Dioh, N., P. Leevers, and J. Williams: Polym. Vol.34(1993) p.4230.
[13] Zhao, H.: Polym. Vol.39(1998) p.1103.
[14] Woldesenbet, E. and J. Vinson: AIAA J Vol.37 (1999) p.1102.
[15] Omar, M., H. Akil, and Z. Ahmad: Mat Sci Eng A doi:10.1016/j.msea.2010.10.071
[16] Deschanel, S., et al.: Polym. Vol. 50 (2009) p. 227.
[17] Chiou, S., W. Cheng, and W. Lee : Mater Sci Eng A. Vol 392(2005) p.156.
[18] White, J.: J mater Sci. Vol.16(1981) p.3249.

© (2011) Trans Tech Publications, Switzerland
doi:10.4028/www.scientific.net/KEM.471-472.391

Sandwich Composites of Glass Fibre Panel and Polyurethane/Coconut Coir Foam Core (GFRP - PUC)

M. A. Azmi[a] H. Z. Abdullah[b] and, M. I. Idris[c]

Department of Material and Design Engineering, Universiti Tun Hussein Onn Malaysia,

86400 Parit Raja, Batu Pahat, Johor, Malaysia.

[a]azham@uthm.edu.my, [b]hasan@uthm.edu.my, [c]izwana@uthm.edu.my

Keywords: Coconut Coir, Polyurethane Foam, Polyurethane Moulding, One Shot Process

Abstract. In this work, sandwich composite properties were investigated by addition of coconut coir (CC). Fibres in the polyurethane foam cores ranges from 0 to 20 wt.%. Glass fibre reinforced epoxy panels were used as a skin and polyurethane foam as a core, these materials adhesively bonded to keep the whole structure attached with each other. Sandwich composite skins and core-skin bonding were attained via adhesive bonding technique. While polyurethane foam reinforced by coconut coir fibres were manufactured by using one shot process and polyurethane moulding method. Sandwich composite panels with different coir fibres compositions were subjected to the density test, weight per area test and flexural testing in order to investigate their physical and mechanical properties. From the experimental results and analysis, it was found that the sandwich composites with 10 wt.% of coir fibres offer higher mechanical properties.

Introduction

Agricultural products appear to be new and inexpensive materials with a great acceptable in both commercial and environmental areas. One of the agricultural sources which can be potentially used as reinforcement in the polymer matrix composite is coconut coir fibre. This is due to the natural fibres such as coconut fibre exhibit high tensile strength, high toughness, low density, and recyclable [1,3]. Moreover, coconut coir is easy to mill to be short fibre or particles [2]. Particles and fibres act as a reinforcement to sustain the applied load and avoid the material from sudden failure.

Sandwich panels have two outer face sheets and core in the middle. The combination of these parts offer sandwich panels a relatively high strength and stiffness at low densities. Face sheets can be made of composite laminate panels, aluminium alloys, titanium steel or plywood. Core is the constituent that requires low density materials such as polymer foams, balsa wood, synthetic rubbers or inorganic cements [5,6]. Commonly sandwich composites were used in aerospace, automotive, sporting goods, marine, construction and civil structures.

In this research, a new hybrid sandwich structure has been developed by adding the coir fibre with a low density into the polyurethane foam core in order to increase the properties of polyurethane foam as the density and weight decreased. This sandwich composites use fibreglass reinforced epoxy as a skin material.

Experimental

Panel Preparation. There are several stages in the construction of the sandwich composites panel of glass fibre and polyurethane/coconut coir foam core (GFRP - PUC):

(i) Coconut coir treatment: The coconut coir fibres were crushed using granulator machine with the fibre length ranging from 2-3mm. Later it has been treated by using alkaline treatment method. The treatment begins when the coir fibres treated with 5 wt.% Natrium Hydroxide (NaOH) and 95 wt.% water. The treatment with NaOH solutions were required to remove impurities from coconut fibre, such as hemi cellulose, lignin and aromatic acids, which could be reduced the adhesion between fibre and matrix. The duration for this treatment was 24

hours at room temperature. Lastly, the coir fibres were cleaned and dried up in oven for 12 hours at 80° [7].

(ii) Polyurethane foam: Three types of polyurethane foam cores were fabricated which are polyurethane foam with 0 wt.% coir fibre, 10 wt.% coir fibre and 20 wt.% coir fibre. The polyurethane foam was produced by mixing the polyol and isocynates by using one shot process. When the mixing of polyol and isocynate were prepared, coir fibres will be added and stirred to ensure the coir fibre was uniformly distributed. Lastly, these mixed components were poured into the mould and cured at a room temperature.

(iii) Skin preparation: Skins were prepared by using hand layup technique with woven glass fibre mat and Dow® epoxy matrix with ratio of 2:1. Skin panels consist of three plies of fibre glass woven mat with panel dimension of 350mm x 350 mm. These panels were then cured for 12 hours at room temperature.

(iv) Sandwich composite construction: Glass fibre skins were ground with 120 grid abrasive paper to provide rough surface with polyurethane foam core. Moreover Araldite® epoxy paste was placed and cured for three hours at room temperatures to ensure excellent bonding between them. Fig. 1 shows the sandwich composites with two skins placed at the outer surface and foam core located between them**.** Fig 2 and 3 show the polyurethane foam core and sandwich panels at 0 wt.% coir fibres.

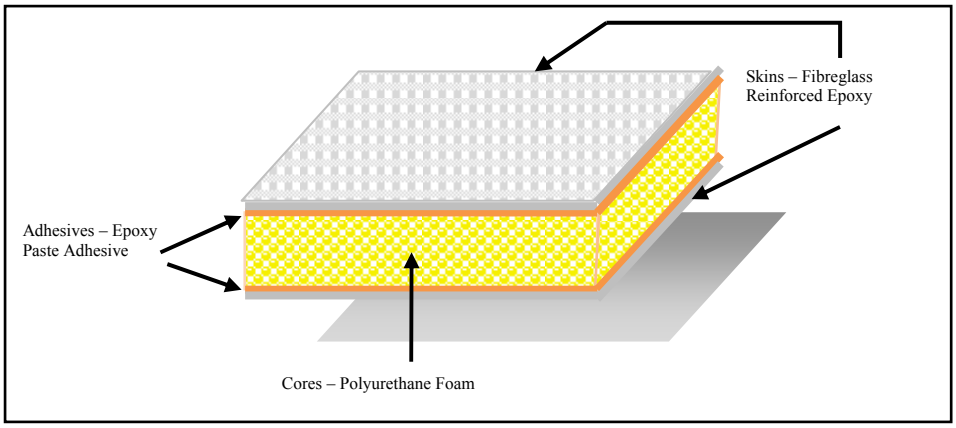


Fig. 1 Sandwich composites panel of glass fibre and polyurethane/coconut coir foam core (GFRP - PUC).



Fig. 2 Polyurethane foam core at 0 wt.% coir fibres

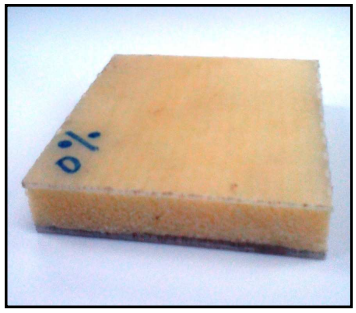


Fig. 3. Sandwich Panel at 0 wt.% coir fibres

Test Method

Density Test. The objective of this test is to determine the density of core materials. The density test was conducted under ASTM C 271. The samples dimensions were 300x300x18 mm^3. In this test, panels were tested to determine the effect of coir fibre to the panels' density. The density was measured as the mass of the panel divided by its volume [8].

Weight per Area Test. This test method covers the determination ratio of weight per area for each of specimens. This test measures the lightest structure among the samples which have the similar dimension but with different weight properties. All specimen sizes are 300x300x18mm^3. In this test the sample weighted and divided by its area.

Flexural Test. The flexural test conducted by using three point bending test (ASTM C 393). The objectives of this test are to determine the flexural strength and stiffness properties of sandwich composites panels. For this test, the specimen dimensions were 350x75x18 mm^3 and the test velocity was 2mm/min [9].

Result and Discussion

Lightweight Properties. It can be clearly seen that the density of the sandwich panel decreased as the percentage of coir fibre in polyurethane foam increases (Fig. 4). The density of sandwich panel reduced as 2.66% and 3.3% when the coir fibre was added 10 wt.% and 20 wt.% in the polyurethane foam cores, respectively. This is mainly due to the plant fibres properties that have low density as compared to synthetic fibres [10].

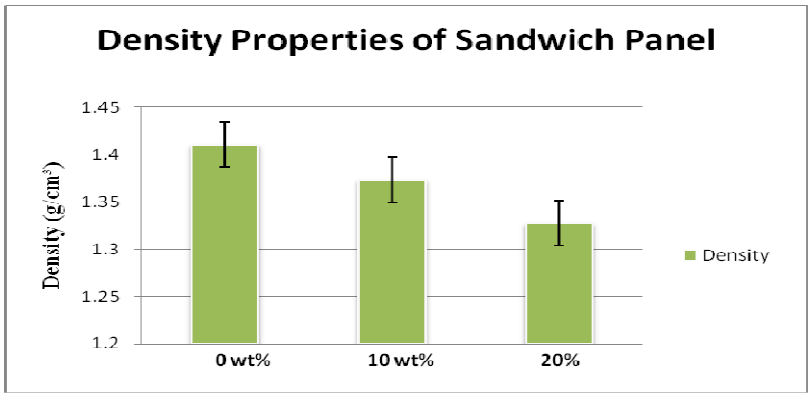


Fig. 4 Density of sandwich panel with different percentage of coir fibres

As well as in the weight per area result, it was also found that the weight of sandwich panel decreased by the addition of coir fibre in the polyurethane foam cores. It is means that the higher percentages of coir fibre in the polyurethane foam cores resulted in a lower weight of sandwich panels. Fig.5 shows that the weight per area result of sandwich panel with 0 wt.%, 10 wt.%, 20 wt.% coir fibre in the polyurethane foam cores. The average weight per area of sandwich panels

with 0 wt.% fibres was 0.098 g/cm^2. While for the average weight per area test result for sandwich panels with 10 wt.% fibres was 0.096 g/cm^2. For 20 wt.% fibres sandwich panels, the average value of weight per area was 0.093 g/cm^2.

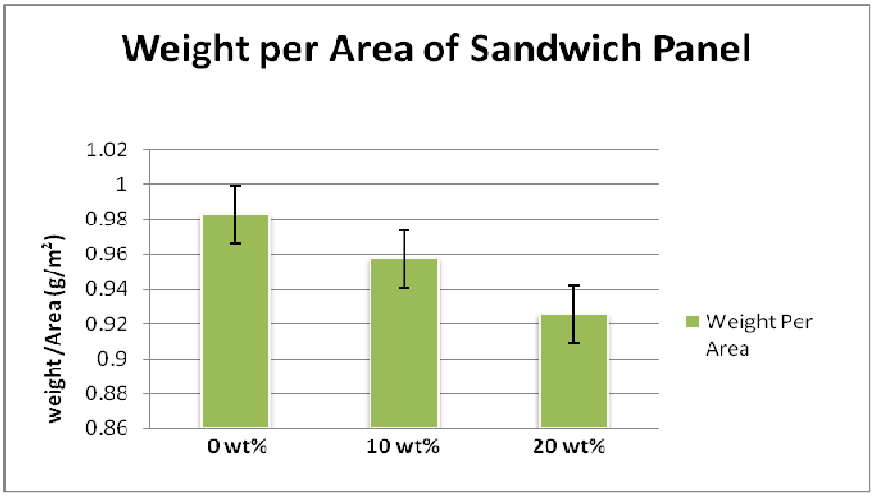


Fig. 5 Weight per area of sandwich panel with different percentage of coir fibre

Flexural Properties. The result of maximum load was obtained from the three point bending test on the polyurethane foam cores is shown in the Fig. 6. The maximum load of polyurethane foam cores consisted of 0 wt.% coir fibres exhibits highest maximum load of 100.86 N as compared to the others. This result demonstrates that the contribution of coir fibre content is not significant since it is not able to increase the properties of the polyurethane foam.

On the other hand, the maximum load of the sandwich panels consists of 10 wt.% coir fibre offer a better result with the maximum load of 518.28N (Fig. 6). However, the addition of 20 wt.% coir fibre decreased the sandwich panel properties when the maximum load was recorded at 375.47 N. This is due to the maximum contribution of fibre in polyurethane foam core. In previous study, it was observed that the optimum coir fibre in the composites were 25 wt.%. They revealed that the properties were decreased if the fibre amount exceed 25 wt.% due to the weaker interface and poor wetting, then led to interface crack [11].

The comparison for the maximum load between polyurethane foam cores and sandwich panels is also shown in the Fig. 6. It was found that the maximum load for sandwich panel is higher than the maximum load for polyurethane foam core. It is obviously shows that the coir fibres at 10 wt.% offer a higher properties to sandwich panels because it provides a sufficient fibre-matrix adhesion in order to resists deformations and shear perpendicular to the face plane [11, 1]. In addition, the construction of sandwich panel with the fibreglass skins also led to the higher strength since skin acts as the main component to sustain most of the in-plane loading and any transverse bending stress [1].

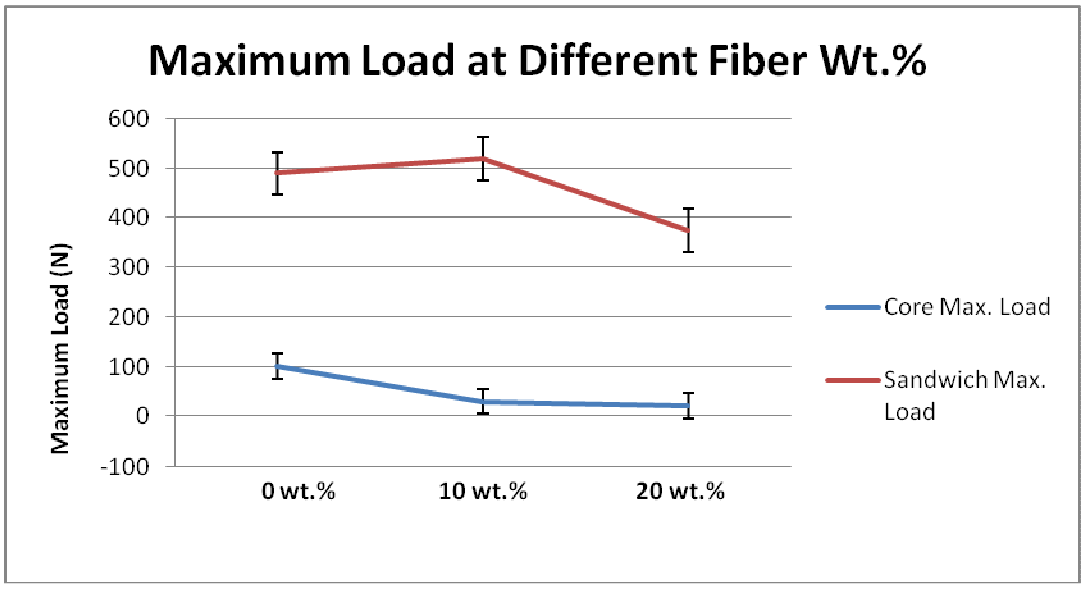


Fig. 6. Comparison of the results from maximum load of polyurethane foam core and sandwich panel with different coir fibre percentage

Fig. 7 shows the comparison of maximum strength between polyurethane foam cores and sandwich panels. The maximum strength was 2.72MPa for polyurethane foam cores without addition of coir fibres and the polyurethane foam cores with 20 wt.% coir fibre gives the lowest maximum strength of 0.56MPa. While for the sandwich panels, the highest maximum strength was 6.57MPa when added with 10 wt.% coir fibres and the lowest maximum strength is 4.90MPa when the sandwich panel consisted of 20 wt.% core fibres. The similar reason is also applicable as previous when the higher strength obtained from 10 wt.% of coir .

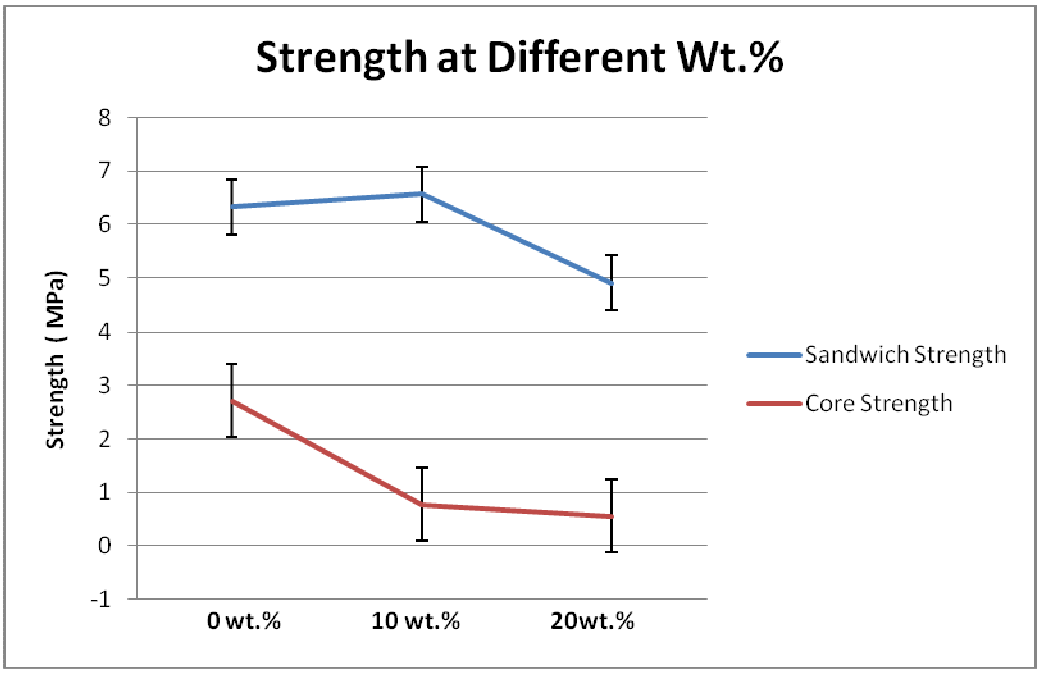


Fig. 7. Comparison of the results from maximum strength of foam core and sandwich panel with different coir fibre percentage

Summary

From the physical tests, it was found that the addition of the coir fibre produced lighter polyurethane foam cores and sandwich panels. Then, the maximum load and strength results reveal that the sandwich panels with 10 wt.% coir fibre offer the highest performance as compared to the others.

References

[1] P.K Mallick (1993). "*Fibre Reinforced Composite (Material, Manufacturing And Design)*". London:Taylor & Francis Group.

[2] D. Ray, and J. Rout. (2005). *Thermoset Biocomposites*. In A. K. Mohanty, M. Misra, and L. T. Drzal. (2005). *Natural fibres, Biopolymers, and Biocomposites*. Florida:CRC Press. pp. 315

[3] A. Bismark, S. Mishra, and T. Lampke, In A. K. Mohanty, M. Misra, and L. T. Drzal. (2005). *Natural fibres, Biopolymers, and Biocomposites*. Florida:CRC Press. pp. 90-92

[4] S.K. Mazumdar. (2001). *Composites Manufacturing*, 1st Ed. Florida : CRC press.

[5] A.G. Mamalis, K. N. Spentzas, N. G. Patelelis, D. E. Monolakus, and MB Lonnidis. Composites Structures. 83(2008), pp. 335-340.

[6] W. D. Callister Jr. (2003). *Material Science and Engineering An Introduction*. 6th Ed. New York:
John Wiley & Sons.

[7] P. J. Herrera and A. Valadez-González. In A. K. Mohanty, M. Misra, and L. T. Drzal. (2005). *Natural fibres, Biopolymers, and Biocomposites*. Florida:CRC Press. Pp. 187; 196-197.

[8] American Society for Testing and Materials (2002). *Standard Test Method for Density of Sandwich*
Core Materials. Philadelphia:ASTM C 271.

[9] American Society for Testing and Materials (2002). *Standard Test Method for Core Shear Properties of Sandwich Constructions by Beam Flexure*. Philadelphia:ASTM C393.

[10] A. K. Bledzki, W. Zhang and A. Chate, Composites Science and Technology. 61(2001), pp. 2405-2411.

[11] D. Ray and Jogeswari Rout. *Thermoset Biocomposites*. In A. K. Mohanty, M. Misra, and L. T.
Drzal. (2005). *Natural fibres, Biopolymers, and Biocomposites*. Florida:CRC Press. Pp. 315-317.

© (2011) Trans Tech Publications, Switzerland
doi:10.4028/www.scientific.net/KEM.471-472.397

The Study of Biodegradable Thermoplastics Sago Starch

Zuraida Ahmad[a] , Hazleen Anuar and Yusliza Yusof

Kulliyyah of Engineering,

International Islamic University Malaysia,

P.O. Box 10, 50728, Kuala Lumpur, Malaysia

[a]zuraidaa@iium.edu.my

Keywords: Sago starch, Biodegradable, Thermoplastic Starch (TPS)

Abstract. The motivation of this work is to lessen the dependence on non-degradable plastic packaging which can lead to waste disposal problems. In this paper, the alternative biodegradable material developed by using local available sago starch in the present of biodegradable glycerol as plasticizer, as well as a set of composition added with citric acid as co-plasticizer is reported. Starch was added with 15-30 w/w% of glycerol to prepare workable bioplastics. The samples were characterized by Thermal Gravimetric Analysis (TGA), Fourier Transform Infrared (FTIR) and tested for mechanical properties. The results reveale that, the tensile strength of the bioplastic is increasing with the increasing of glycerol until the optimum amount of 30 w/w%. The similar trend is also observed upon the addition of the citric acid. The decrease of the strength after the optimum point, however is obvious in the specimens with the addition of citric acid which is about 50% lower than the specimen without citric acid.

Introduction

It is undeniable, although conventional plastic is good, but it still has some limitations. As a fact, many researchers emphasized that plastic waste leads to environmental problems. According to Santos [1], conventional plastic offer bad consequences for the environment due to common polyolefins which have very poor degradation rate. This fact is supported by Fischer [2], who claimed that high cost is needed to store the non-degradable plastic while burning it will produce carbon dioxide (CO_2) which leads to green house effect. For the stated reasons, it can be concluded that the usage of conventional thermoplastic make the environmental problem become crucial [1-2].

Thermoplastic starch has been introduced as an attempt to overcome these drawbacks. Thermoplastic starch (TPS) is a homogenous thermoplastic substance made from native starch. After undergoes several processes, thermoplastic starch may transform from semi-crystalline into amorphous polymeric material. It should be noted that, thermoplastic starch is practical to be used due to it has starch content more than 70% and with the use of specific plasticizing solvents, materials with good properties and biodegradability can be produced.

Sago starch is a true wonder of nature and known as the most important raw material due to its low cost, availability as a renewable resource, biodegradable and the harmless degradation products [3]. Sago starch can be processed into thermoplastic starch under the action of temperature and shearing action. Plasticizer need to be used while processing, because of the low decomposition temperature of the granular starch [4].

This work is undertaken to explore the potential of sago starch as natural sources for the production of biodegradable thermoplastic. The objectives of this study are to optimize the process condition in order to produce high performance materials and to study the effect of co-plasticizer on the mechanical and thermal properties of the thermoplastic starch. Further, tensile fracture specimen was viewed under scanning electron microscope for morphological analysis.

Experimental Method

Materials. Sago starch powder (25% amylose) was purchased from Hup Seng Heng Sdn Bhd, Malaysia, glycerol (95% purity) with density of about 1.261 g/cm³ and citric acid were supplied by Merck.

Fabrication Process. In this experiment there were two compositions prepared. First is a mixture of starch and glycerol. Secondly, a blend of starch powder, glycerol and citric acid. Basically, the starch was plasticized with glycerol (95% purity) while citric acid was used as a co-plasticizer. Material ratios were stated specifically in the Table 1 and Table 2 below and glycerol-mono-stearate was added as a lubricant.

Table 1 Thermoplastic starch with different glycerol's content.

Sample	Glycerol (w/w%)
G1	15
G2	20
G3	30
G4	40

Table 2 TPS with the addition of citric acid

Sample	Glycerol (w/w%)	Citric Acid (w/w%)
C1	30	10
C2	30	20
C3	30	30
C4	30	40

Thermoplastic starch (TPS) was produced in a three distinct steps. The materials were weighted by using digital lab weight scales and mixed using stirrer. The obtained mixture was stored for 24 hrs in an air tight polyethylene bags at room temperature before processed with a twin screw extruder Thermo HAAKE Rheomix 600 which is used for melt blending purposes at a temperature 130°C, 100 rpm. Then, the extrudate was granulated and stored under controlled conditions for 48 hours. Finally, the granulates were injection molded according to the parameter in Table 3:

Table 3 Injection moulding parameters

Injection Pressure	Injection rate	Holding pressure	Temperature Z1	Temperature Z2	Temperature Z3	Temperature Z4	Temperature Z5
1400 bar	50 cm^3/s	600 bar	110°C	115°C	120°C	125°C	150°C

Results and Discussion

Tensile Strength. The effect of adding glycerol on the tensile strength of TPS is shown in the Fig. 1. It should be noted that**,** TPS with less than 20w/w% glycerol content had low tensile strength and was not considered for further studies. Increasing the concentration up to 30w/w% resulted in a maximum tensile strength value and also provides flexible product. The tensile strength decreased as the increased of glycerol up to 40%. Thus, 30% glycerol provided the maximum tensile strength and was used for subsequent studies. A primary concern, at low concentrations of glycerol (<15w/w %), is that, there is not enough plasticising effect and the starch molecules become brittle (Ma, 2009). At concentrations above 30w/w%, the plasticising effect is too pronounced and makes the starch molecules move easily. Thus, in this project the optimum amount of glycerol to be added is 30w/w% due to it leads to high strength (23.060 MPa).

Furthermore, addition of citric acid to the mixture improved the tensile strength. Concentration of citric acid less than 20w/w% however, provide relatively low improvement while concentration at 30w/w% gives high molecular weight of the starch and provides better interactions between molecules and result in better tensile strength compared to mixing starch with glycerol alone. As consequences, 30w/w% addition of citric acid into TPS gave an optimum value of tensile strength which is 24.766 MPa.

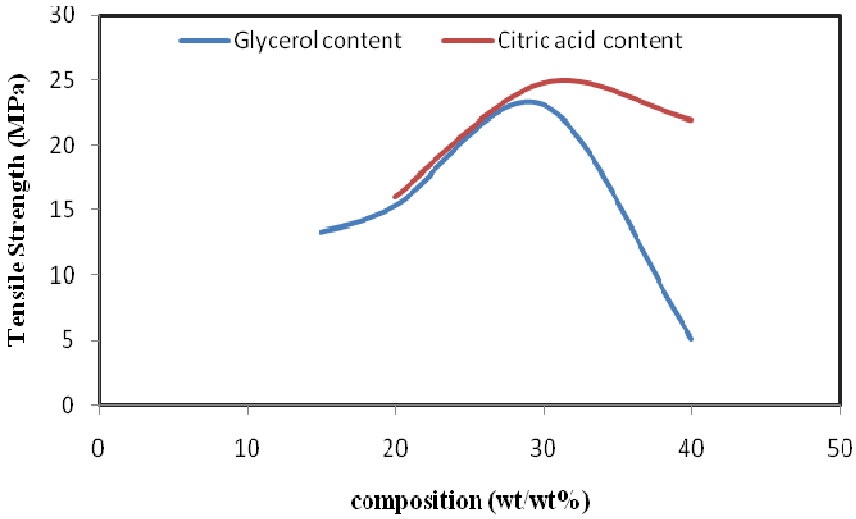


Fig. 1 Tensile strength vs. % Composition

Fourier Transform Infrared Spectroscopy (FTIR) Analysis. The analysis of Fourier Transform Infrared Spectroscopy (FTIR) spectra of the blends enabled the hydrogen bond interaction to be identified. According to Yang (2006), lower wave number results in stronger interaction of hydrogen bond. Fig. 2 shows that the characteristic peaks 1080 cm^{-1} and 1157 cm^{-1} indicate the C-O bond stretching of C-O-H group [6]. The peak 1080 cm^{-1} was shifted to 1078 cm^{-1} and from 1150 cm^{-1} to 1148 cm^{-1} which means the OH group of starch took part in the hydrogen bond formation. Another two peaks at 999 cm^{-1} and 1020 cm^{-1} are attributed to C-O bond stretching of C-O-C group [6]. The peaks were shifted from 998 cm^{-1} to 995 cm^{-1} and 1018 cm^{-1} to 1016 cm^{-1} respectively. In sum, the FTIR test for composition 1 is clearly showed that glycerol could form a more stable hydrogen bond.

In addition, Fig. 3 illustrates the FTIR result for the effect of acid citric content (composition 2). The change of the peaks position from 1709 cm^{-1} in pure citric acid to 1729 cm^{-2} in thermoplastic starch (TPS) illustrates that the ester bond existed. Peak at 1729 cm^{-1} reflect the increase of ester bonds. The peak's height increased as the citric acid content increased. It is noted that, the citric acid is more capable in disrupting inter and intra molecular hydrogen bonds.

Scanning Electron Microscopy (SEM). Stable hydrogen bond was formed between plasticizer and starch by the analysis of FTIR spectra. The morphology of sago starch granules and the extruded TPS were shown in Figs 4. Fig. 4(a) illustrates that the sago starch has an amorphous homogeneous matrix surrounds with predominant granular domains. TPS plasticized by 20% of glycerol result in a less coarse granules compared to native sago starch. This occurred due to starch granule has fused into homogeneous phase as revealed in Fig. 4(b) which led to some empty space in the TPS. Furthermore, plasticized TPS with glycerol had a clear and smooth surface as seen in Fig. 4(c) for the compositions of 30w/w%, and vice versa for 40w/w% plasticization. It should be noted that, as plasticizer content increases, melt viscosity decreases which made the plasticization of starch difficult, due to the reduction in shear during processing [6]. As a conclusion, glycerol with 30w/w% concentration is the most preferable composition to be used in the further studies.

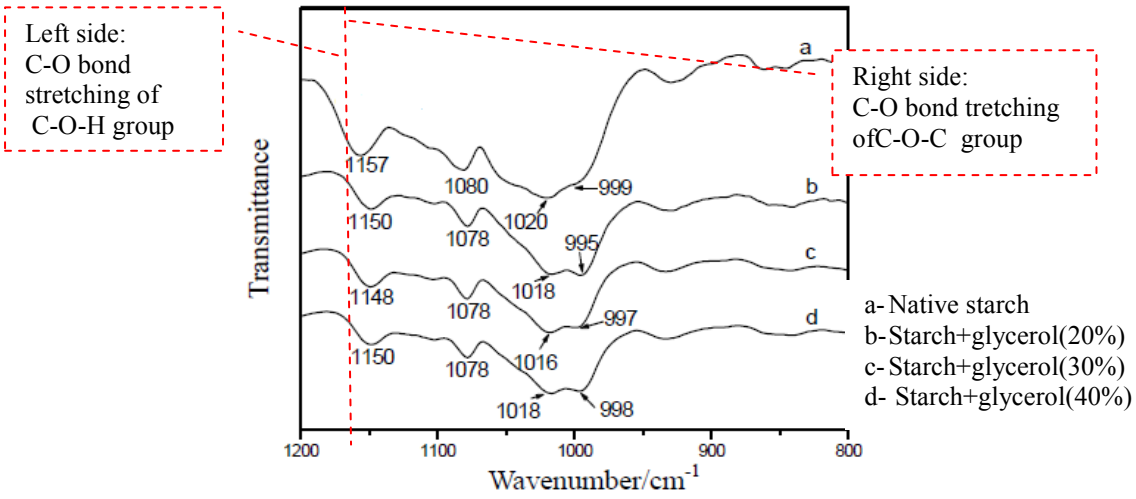


Fig. 2 FTIR shows the effect of glycerol content on TPS

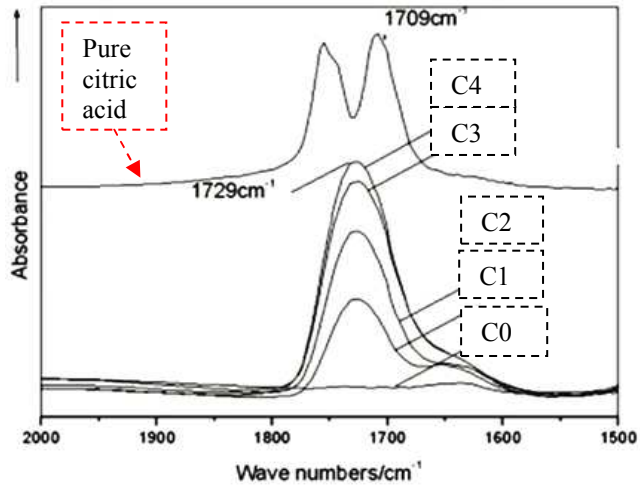
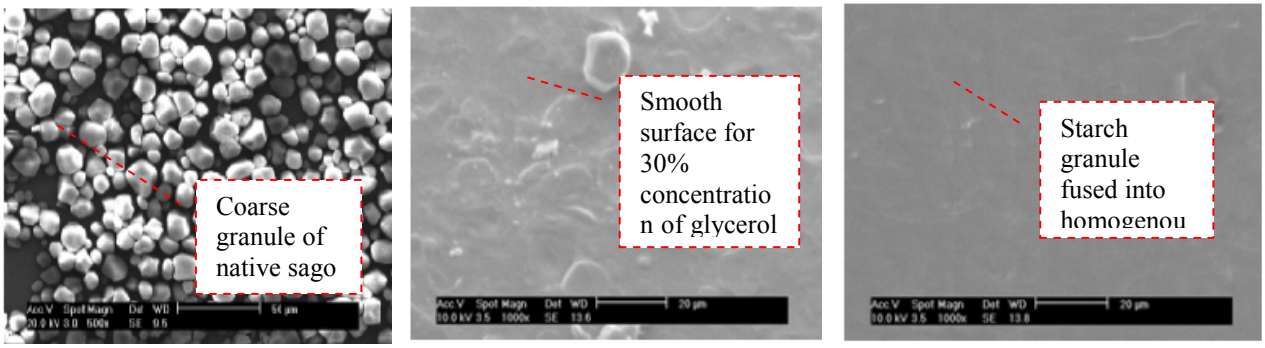


Fig. 3 FTIR shows the effect of acid citric content on TPS



(a) (b) (c)

Fig. 4 (a) SEM micrograph of sago starch (b) SEM micrograph of 20w/w% Glycerol (c) SEM micrograph of 30w/w% Glycerol

Thermo Gravimetric Analysis (TGA). Generally, TGA is a testing that is performed in order to determine the changes in weight with temperature. Fig. 5 show the thermogravimetric curves of TPS with and without addition of citric acid. It is noted that, the weight loss below 100°C was

mainly caused by water evaporation, while above 100°C are referring to evaporation of water and other plasticizers and thermal decomposition of the starch. Therefore, the differences in the onset temperatures of starch thermal decomposition and weight loss at onset temperature were mainly due to the type and content of the plasticizers [6]. There is only one weight loss step on the TG curve of TPS without citric acid, but two steps on the curves of TPS with citric acid. Specifically, the first weight loss step that started from 150 °C may be due to the heat decomposition of the residual citric acid in TPS with citric acid.

The second step was mainly caused by the thermal decomposition of the starch chains [6]. The onset temperatures of the second weight loss steps are strongly related to the interactions between plasticizers and the starch. TPS with citric acid had higher onset temperature and lower mass loss than TPS without citric acid. This indicated that the presence of citric acid is significant in increased the binding of plasticizers to starch. In other words, the bonding between the citric acid and starch is stronger than that between glycerol and starch.

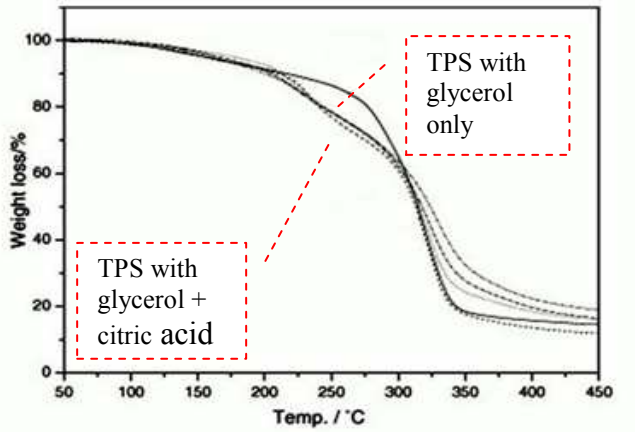


Fig. 5 TGA for TPS with and without citric acid

Summary

- Fourier Transform Infrared Spectroscopy (FTIR) analysis showed that glycerol could form a stable hydrogen bond while the addition of citric acid could disrupt inter and intra molecular hydrogen bond effectively.
- Scanning Electron Microscopy (SEM) proved that thermoplastic starch (TPS) plasticized with 30% glycerol result in fined granule compared to native starch had a clear and smooth surface.
- Optimum tensile strength for composition 1 (starch+glycerol) was 23.060 MPa while for composition 2 (starch+glycerol+citric acid) was 24.766 MPa.
- Thermo Gravimetric (TGA) analysis showed that the residual weight percentage of composition 2 increased with citric acid content.

References

[1] D.S. Santos, M. A.G. Bardi, L.D.B. Machado, D.B.D. Dias, G.A. Leonardo, K. Kodama, Journal of thermal analysis and calorimetry 97 (2) (2009), 565-570.

[2] S. Fischer, J. D. Vlieger, T. Kock, L. Batenburg and H. Fischer, *"Green" nano-composite materials-new possibilities for bioplastics.* Netherlands: Materials Research Society (2001).

[3] C. Corradini, Carvalho, A.J.F., Antonio A., Jose A.M., & Luiz H.C. (2007). Materials Research 10 (3) (2007), 227-231.

[4] P. Tomasik, P. Wang and J. Jane, Starch/Stärke 47(1995), p. 96.

[5] Jin Hui YANG, Jiu Gao YU, Xiao Fei MA, Chinese Chemical Letters 17 (1), (2006), 133-136.

[6] Xiaofei Ma, Peter R. Chang, Jiugao Yu[a] and Mark Stumborg, Carbohydrate Polymers 75 (1), (2009), 1-8.

© (2011) Trans Tech Publications, Switzerland
doi:10.4028/www.scientific.net/KEM.471-472.403

Cotton Reinforced Biopolymer Matrix Composite: Effect of Curing and Aging Conditions on its Mechanical Properties

Zuraida Ahmad[1,a], Yusliza Yusof[1], Zahurin Halim[1] and Fauziah Md. Yusof[2]

[1]Department of Manufacturing and Materials Engineering, Kulliyyah of Engineering, International Islamic University Malaysia, PO Box 10, 50728 Kuala Lumpur, Malaysia

[2]Faculty of Mechanical Engineering, Universiti Teknologi MARA, Malaysia

[a]zuraidaa@iium.edu.my

Keywords: composites; lay-up; curing, aging; moisture content; morphology

Abstract. The attention in natural fiber reinforced biopolymer composite materials has been rapidly growing both in terms of industrial applications and basic research. This study investigated on the effect of aging time on mechanical properties and morphological structure of thermoset protein-based composites from egg albumen reinforced by natural cotton fibres. The cotton/albumen composites (CAC) were fabricated by hands lay-up technique with 10 w/w % of fiber content. The samples were cured and aged at room temperature for different aging time from 7 to 32 days. The cotton fibres have contributed in a significant improvement in mechanical strength and toughness of the composites. Tensile strength of the composites achieved the optimum strength of 9 MPa after 21 days of aging time and constant till 32 days. As the aging time increased, impact strength of the composites also improved to some value of 20 kJ/m^2. Thereby after 21 days observation, the composites show an equilibrium moisture content of 6-9 wt%, and the strength remains stable at room condition with 50-60% relative humidity (RH). Morphology studied using SEM justify that the moisture content after aging time influenced mechanical properties of the composites.

Introduction

At present, several researchers have focused on introducing biopolymer resources from food proteins as the main encapsulating materials. In fact, the protein network plays an important role to provide mechanical properties of the encapsulating matrix. The strength of a protein network could be manipulated during the attractive and repulsive forces among polymer molecules, polymer network and surrounding solvent [1]. A wide variety of proteins have been produced at huge scale for instance, wheat gluten, soy and pea proteins from vegetables resources; egg albumen, fish myofibrillars and wool keratin proteins from animal resources [2].

Egg white proteins (albumen) is highly functional food protein that is frequently used in food matrix applications due to its ability to form gel networks, increase solution viscosity, and stabilize emulsions and foams. Egg albumen consists mainly of 10-15% numerous proteins dissolved in water, which contains 95.5% of protein on dried weight basis [3]. However, for non-food applications protein denaturation turn out to be a further variable for the design of new materials. Protein denaturation takes place when the protein changes from the biologically active and loses its native state, which involves the disruption of both secondary and tertiary structures. Denaturation may occur because of changes of several external parameters, such as increasing temperature, pressure, denaturant concentration and changing the pH, salts, acids, alkalis, alcohols, or denaturing agents like urea [3-4].

In fiber-reinforced composites, the fibers serve as reinforcement by giving strength and stiffness to the structure while the plastic matrix provides the adhesive to hold the fibers in place so that the desired structure components can be obtained. Advantages of natural fiber over synthetic fibers or man-made fibers such as glass are low cost, low density, competitive specific mechanical properties, carbon dioxide sequestration, renewable resources, sustainability, recyclability and biodegradability [4]. Cotton can be categorized as a natural cellulose fiber that is a highly crystalline high-molecular weight biomaterial. The fibers were used as early as 1908 in the

fabrication of large quantities of sheets, where paper or cotton was used to reinforce sheet made of phenol or melamin-formaldehyde resins [5]. The cotton waste also has been used as reinforcing fibers due to its cost-effective, and biodegradability. Cotton fibers consist of mainly cellulose that enhances stress transfer due to their effectively high aspect ratio (2000). The low value of waste cotton fibers also has a high potential in the manufacturing of nonwoven composite materials, especially in the insulation market of automobile industries.

The focus of the present work is to develop protein-based thermoset composites from egg albumen reinforced by cotton fibres. The mechanical performance and morphological properties of the composites will be reported as the effect of different curing and aging time interval.

Materials and methods

Materials. The material investigated was albumen protein that obtained from hens' egg white. The albumen has protein content of 10% - 15% dispersed in water. The fibres were purchased from Able Enterprise (M) Sdn Bhd, Malaysia, in the form of cotton wool that mainly consists of *natural* cellulose.

Composites Preparation. Albumen matrix was prepared by separating egg white from the yolk, blood or chalazae (the stringy tissue). The albumen solution was beated for 5 minutes into froth and left to settle overnight at room temperature. Once the albumen was settled and turn into homogeneous solution, it was ready to be used as the natural binder. The CAC were fabricated at fiber content of 10 w/w % by using hands lay-up technique. The samples were cured different curing time interval of 7 days, 14 days, 28 days and 32 days before they were subjected for their mechanical tests and moisture content.

Mechanical Testing. The final products of composites were cut in accordance to the American Society for Testing Materials (ASTM) standards for the mechanical testing of polymer composite materials. The tensile tests were conducted in accordance to ASTM D3039 by using Materials Testing Machine. Impact tests were carried out using an Advanced Pendulum Impact Dynosco (model API-230-0). The test results were typically the average of the five specimens of each test.

Results and Discussion

Tensile Properties. In this work, the CAC was cured (hardened) within up-to 32 days of drying and aging period at normal room condition of 25°C and 60% RH. The samples were analyzed for their mechanical properties and equilibrium moisture content at different curing time interval of 7 days, 14 days, 28 days and 32 days. The results show that tensile strength of the CAC after 7 days is very low of only 6 MPa as shown in Fig. 1. After 14 days and upwards the composite strength however, did not experienced a significant change since the means values were not significantly different. The strength however increased by 27% after 14 days. The tensile properties achieved the optimum strength of 9 MPa after 21 days of curing time and remain almost constant till 32 days. For the purpose of comparison; 100 ml of pristine albumen would take almost a week to cure at the similar conditions. On the same graph, the tensile modulus is increasing in similar trend when the curing days increased. Fig. 2 illustrates the composites have a strength-elongation characteristics with the same trends as seen in Fig. 1, when the curing time were increased. The high elongation characteristic of raw cotton fiber increased the elongation at break of the composites from 7 to 21 days approximately by 70% increment, and yet further curing time the value of elongation at break remained in constant. This is attributed to the complete curing process to harden the CAC.

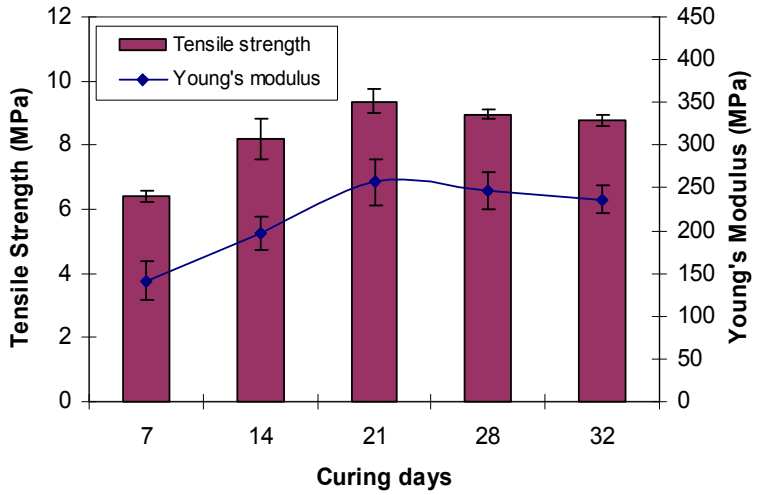


Fig. 1 The effect of curing time on tensile strength and Young's modulus of the CAC.

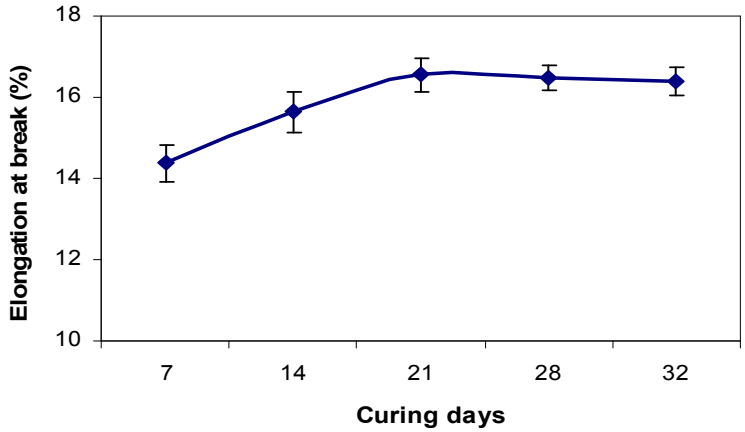


Fig. 2 Elongation at break of the CAC for different curing time.

Upon drying process of the CAC, the hydroxyl groups (-OH) in the secondary and tertiary protein structure of albumen could provide sites for hydrogen bonding to the surface of cotton fiber, which contains many hydroxyl groups in their chemical structure. In high moisture content, the CAC shows poor mechanical properties because the water molecules acts like a separating agent in the fiber-matrix interface. It is believed that the presence of noncrystalline cellulose (amorphous cellulose), lignin, hemicellulose and the surface of crystalline cellulose influenced the amount of moisture content that is absorbed from the environment. The main reason for moisture absorption of natural fibers however, is attributed to the hemicellulose content. Due to the hydroxyl and oxygen-containing groups, moisture is attracted to the natural fiber and formed hydrogen bonds. Thus, natural fiber can absorb and desorbs moisture from the atmosphere and equilibrate with the surrounding environment. The CAC was assumed cured at room temperature of 50-60% relative humidity (RH) when the properties of the composites did not change significantly and achieved equilibrium moisture content (MC) of 6-10 wt%. This is attributed to the moisture content of cotton fiber in their hydrophilic nature.

In recent study [6] mentioned that the cross-linked protein might exhibit bulk properties and adhesive strengths comparable with those reported for the fibrin sealants, a standard adhesive in the blood coagulation cascade. For biomedical applications, gelation, a denatured form of collagen in connective tissue protein, can be cross-linked within a few minutes in the presence of microbial transglutaminase as the cross-linking catalyst. In this case, without protein cross-linking catalyst, the curing period for CAC consumed longer duration to cure at room temperature. The protein cross-linking has probably occurred due to self-assisted intermolecular disulfide bond that confirmed in a previous study [7]. It was mentioned in other studies, that the disulfide cross-links are created between the functional groups (carboxyl group and amino group) in the polypeptide side

chains during drying of albumen [8]. This explanation would satisfy the hardening of albumen that making it less soluble.

Impact Properties. The Charpy impact test was used to determine the impact strength and energy of the samples at fracture. In this context, it also provides the measure of the toughness for the composite materials. As the tensile strength and modulus of the CAC increased with curing time, the same trend was observed for impact properties.

The curing process was maintained at room temperatures to ensure good strength and stiffness of the cotton fiber. This effort is underway to derive new low-temperature, bio-based thermosetting materials where the combination and shaping options of the biocomposites are most favorable without a significant deformation, as most natural fibers are inhibited by the high curing temperature in excess of 150°C [8]. In addition, high temperature drying is not necessary for albumen composite at temperature above 80°C, since it caused reduction in rheological behavior of albumen and it would become hard and brittle. Upon drying even the protein matrix lost its strength and toughness and became stiff and brittle over time. However with the reinforcement of cotton fiber, the impact properties of CAC had improved to the some value of 20.0 kJ/m^2 after they have been cured and aged for 21 days as in Fig. 4. The curing process undertaken at common room temperatures condition was favorable to maintain all elasticity of cotton fiber that was responsible for the improvement in impact resistance of the CAC. Nevertheless, if the cotton fibers are dried out at temperature above 25°C, it becomes hard and brittle. It appears that hardening of albumen component did not significantly influence the impact resistance of the composite. This result was also reflected by the similar trend elongation at break. It seems that impact strength and elongation at break are always directly correlated.

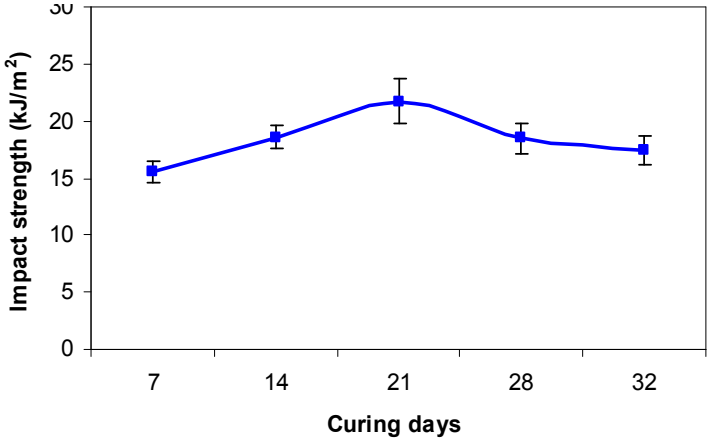
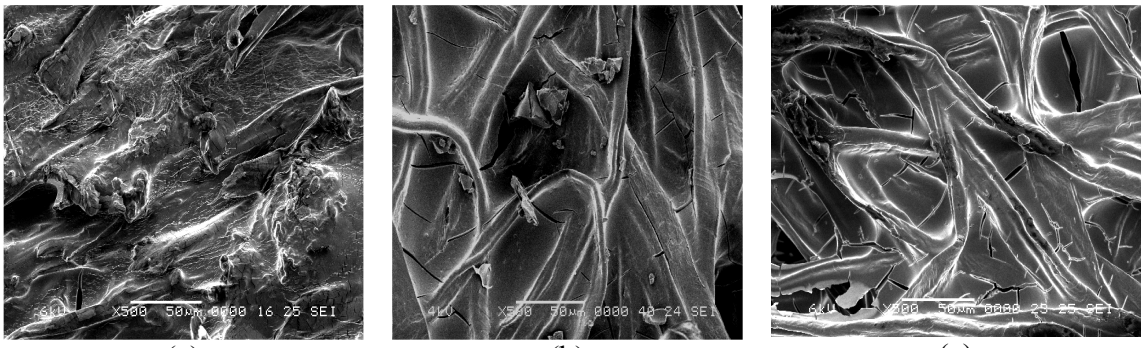


Fig. 3 The effect of curing time at the room temperature on impact strength of the CAC.

Scanning Electron Micrograph (SEM). SEM images were taken for the composite samples that were cured and aged at room temperature for 7, 14 and 21 days (Fig. 4.5). The SEM images revealed that microstructure of the CAC after 7 days of curing has high moisture content and appeared to be more heterogeneous than that of the CAC after 21 days. At high moisture content of 17 wt%, there were pores formed in the composite since the water is lost during drying of the sample preparation for the SEM. The lower in mechanical properties of the CAC at high moisture content can be attributed to a decrease in protein stability of the matrix in the presence of water. This is due to the ability of the water molecules to plasticize the protein and therefore increased the segmental mobility of the protein chain, as mentioned in previous research.



(a) (b) (c)

Fig. 4 SEM showing effect of curing at room temperature 25°C and 60% RH on the microstructure of CAC (a) after 7 days with MC of 17 wt%, (b) after 14 days with 11 wt%, and (c) after 21 days with MC of 7 wt%.

The moisture content of 11 wt%, observed after 14 days of curing days. Drying is always slow at the end of the process because movement of water through a solid is generally slow since the solid has compacted due to water loss and make the structure less open. The drying process always induced molecular distortion and further mechanically denatures the protein polymers causing the distortions permanent. Thereby the protein molecules would become densely packed and seemed more transparent and glassy. It is believed that covalent cross-links also exist in the mechanically denatured albumen upon drying, while the hydrogen bonds dominated the solid composites. As the samples were further cured and aged till 21 days showed low moisture content of 7 wt%. This is attributed to the moisture content of most typical cotton fibers due to their surface geometry and chemical contents that always initiates air bubble growth. To some extent air always present in the fibers.

Summary

Incorporation of cotton fibres played an important role to optimize the mechanical and morphological properties of albumen as protein-based thermoset composites. The results obtained showed an improvement in mechanical properties when curing time of the CAC increased from 7 to 21 days, the tensile strength also increased significantly by 33%, and impact strength increased by 27%. Nevertheless, no significant change in the mechanical strength after 21 days, because of the composite was assumed fully cured at room temperature. At this state, the CAC achieved an equilibrium moisture content of 6-9 wt%, and the strength remained constant at room condition with 50-60% RH.

References

[1] S. Wongsasulak, T. Yoovidhya, S. Bhumiratana, P. Hongsprabhas, D.J.McClements, and J. Weiss. Food Research International, 39, (2006) p. 277.

[2] A. Jerez, P. Partal, I.Martinez, C. Gallegos, and A. Guerrero. Food Engineering, 82, (2007), p. 608.

[3] S. Wongsasulak, T. Yoovidhya, S. Bhumiratana, P. Hongsprabhas, Food Research International. 40(2) (2007), p. 249.

[4] A.K. Mohanty, M. Misra, L.T Drzal. *Natural Fibers, Biopolymers, and Biocomposites*. Taylor & Francis Group (2005).

[5] S.A.R. Hashmi, Dwivedi, and U.K, Navin, C. Wear, 262, (2007), 1426.

[6] J.M. Raquez, M. Deleglise, M.F. Lacrampe, and P. Krawczak, Progress in Polymer Science, 35, (2010), 487.

[7] A. Schmitz, M. Klein, I. Gestmann, and V. Herzog. Methods in Enzymology, Vol.348, (2002), 306.

[8] Y.P. Ham, H.S. In, H.K Jung, and S.K. Woo. International Journal of Pharmaceutics, 175, (1998), p. 231.

© (2011) Trans Tech Publications, Switzerland
doi:10.4028/www.scientific.net/KEM.471-472.409

Comparison on Rheology Properties of Polypropylene and Polyethylene as Binder System with Stainless Steel 316L for Metal Injection Moding

Mohd Fazuri Abdullah[1,a], Abu Bakar Sulong[1,b], Norhamidi Muhamad[1,c], Muhammad Ilman Hakimi Chua Abdullah[1,d], Nor Hamdan Nor Yahya[2,e]

[1]Department of Mechanical and Material Engineering, Faculty of Engineering and Built Environment, Universiti Kebangsaan Malaysia, 43600 Bangi, Malaysia

[2]Department of Orthopedic, Universiti Kebangsaan Malaysia Medical Centre, 56000 Cheras, Kuala Lumpur

[a]faxury@yahoo.com, [b]abubakar@eng.ukm.my, [c]hamidi@eng.ukm.my, [d]kimi_ilmn@yahoo.com, [e]nhny@hotmail.com

Keyword: Rheology properties, binder separation, metal injection molding

Abstract. The comparison of binder system between PP/ palm stearin and PE/ palm stearin both mixed with palm stearin were studied based on the rheological properties to (MIM) process. The microstructure of distribution and dispersion studied using scanning electron microscope (SEM) to observe the pattern of the attached binder with stainless steel powder. The types of binder system used were palm stearin with Polypropylene (PP) and Polyethylene (PE). The powder loading for stainless steel 316L with average size of 20μm used was determined at 66 vol %. The palm stearin was the main significant factor for both viscosity and sensitivity of the feedstock behavior. Less content of palm stearin reduce the viscosity of the feedstock in the range of 100-10000 Pa.s and less influence on changing towards temperature and pressure. As the percentage of addition of palm stearin increase, the feedstock becomes less viscous with high sensitivity. PP and PE feedstock shows dilatant and pseudoplastic flow behavior respectively. PE homogenously coated each of stainless during morphology observation. Meanwhile poor distribution of PP can be observed from SEM observation at 1000x magnification.

Introduction

Metal injection molding (MIM) comprises of several processing stage which are mixing, injection molding, debinding and sintering respectively [1]. Palm stearin which was studied earlier [2] was found to be a suitable binder and feedstock was successfully prepared. Palm Stearin is a potential binder system that can be used since it is very cheap material, can be recycled and highly available in Malaysia [3]. One of the most noticeable characteristics of oil and fats is their ability to form a lubricating film. However, fatty oils have a special advantage; they are able to cling to metal surface in the form of very thin films [4]. It is believed that Palm Stearin has possibility as a binder component since it is consists of fatty acid which is used as a surface active agent for many binder used [5]. So the fatty oils are able to replace the stearic acid as a surfactant. In MIM process, mold filling depends on the viscous flow which requires specific rheological characteristic [6]. It is known that a feedstock viscosity with low sensitivity to both temperature and shear thinning behavior is desired [7]. Some of the feedstock showed pseudoplastic behavior of flow behavior index, $n<1$ with their viscosity displayed a strong dependence on the shear rate. Feedstock of lower powder loading displayed the best rheological behavior [8] was studied. The reason of using palm stearin as a binder system is due to the contents of palm stearin itself that can be an advantage during debinding process [9].

Experiment

Water atomized 316L stainless steel powder of average size 20μm purchased from Epson Atmix Corporation, Japan was used as the metal powder. There are three types of binder system with

different composition were used. The weight eprcentage (wt%) of binder system for palm stearin with both PP and PE are shown in Table 1. The feedstock was mixed using Brabender mixer with roller blade type at different temperature depending on the melting point of the binder. The melting point of PP and PE are 170°C and 120 °C respectively. Feedstock PP / palm stearin and PE / palm stearin was prepared at temperature of 180°C and 140°C. The feedstock was studied in terms of viscosity and shear rate by using Shimadzu CFT-500D rheometer with die capillary of 1mm at the various temperature based on the melting point of PP and PE.

Table 1 Content of binder

Label	Composition, wt%		
	Palm Stearin	PP	PE
Binder A	60	-	40
Binder B	70	-	30
Binder C	70	30	-

The viscosity versus shear rate graph was plotted. Based on Power Law equation (Eq. 1), the slope (n-1) was calculated from the graph to determine the flow behavior index, n for each feedstock formulations:

$$\eta = K\gamma^{n-1} \quad (1)$$

where η is the viscosity while K is the constant. Arrhenius's equation is applied to determine the activation energy, E for the samples:

$$\eta = \eta_o exp(E/RT) \quad (2)$$

where η_o is the viscosity at reference temperature, R is the gas constant and T is the temperature in Kelvin unit. According to Eq. (2), a group of plots of ln η vs. 1/T at a certain shear rate can be obtained. The graphs tend to fit into straight lines. The slopes of the graph indicate the temperature dependence of viscosity, or the activation energy, E. Large values of E shows a high sensitivity of viscosity to temperature.

Results and Discussion

Fig. 1 until 3 demonstrate the apparent viscosity of the binder A, binder B and binder C respectively at variable temperature. A different distribution of flow behavior was shown for each temperature for different types of composition in the binder systems. Dilatant flow behavior was observed for all feedstock containing PP with both viscosity and shear rate increased. Meanwhile, pseudoplastic flow behavior was obtained for feedstock containing PE with the viscosity decreased while the shear rate increased. The viscosity of the feedstock becomes lower as the content of palm stearin in the feedstock increases. By using PP as the binder, the feedstock's flow was unstable and its sensitivity to both temperature and pressure is higher. Massive drastic distribution of data was plotted with difference of 5°C with the flow type still unchanged which is dilatant flow. Meanwhile, smooth flow distribution of data for pseudoplastic behavior was plotted for feedstock mixed with PE.

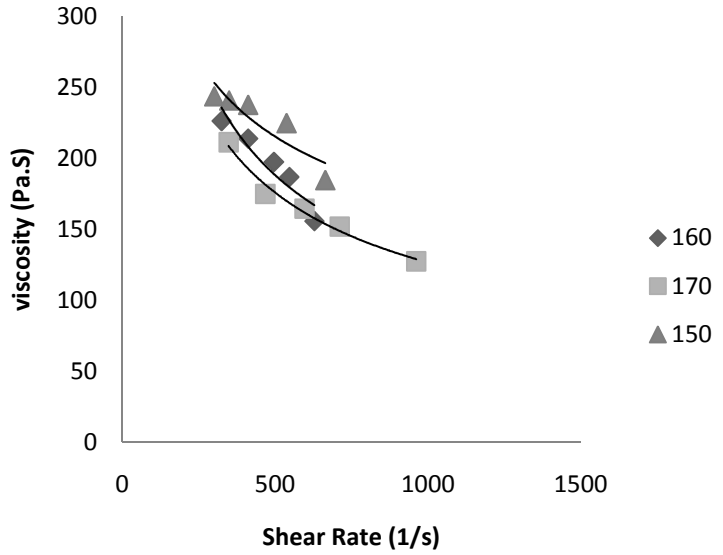


Fig. 1 Viscosity and shear rate of the SS316L feedstock binder A

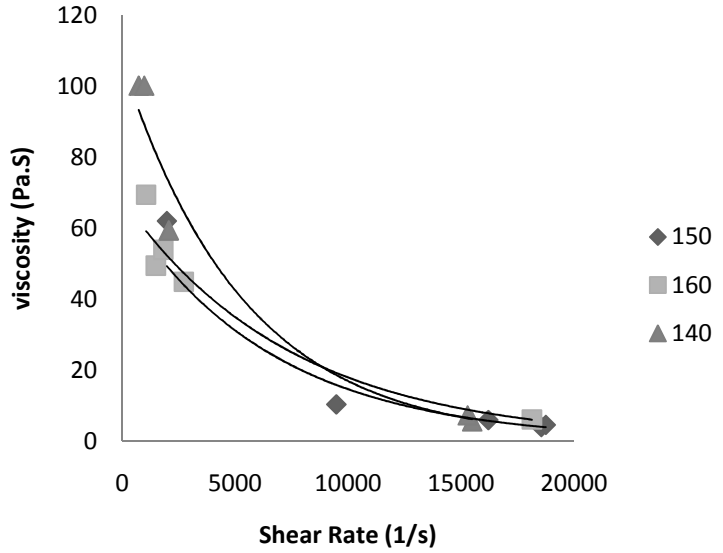


Fig. 2 Viscosity and shear rate of the SS316L feedstock binder B

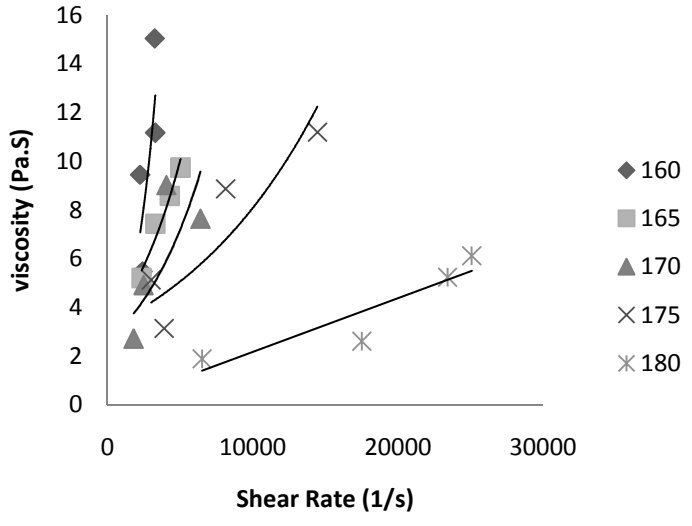


Fig. 3 Viscosity and shear rate of the SS316L feedstock binder C

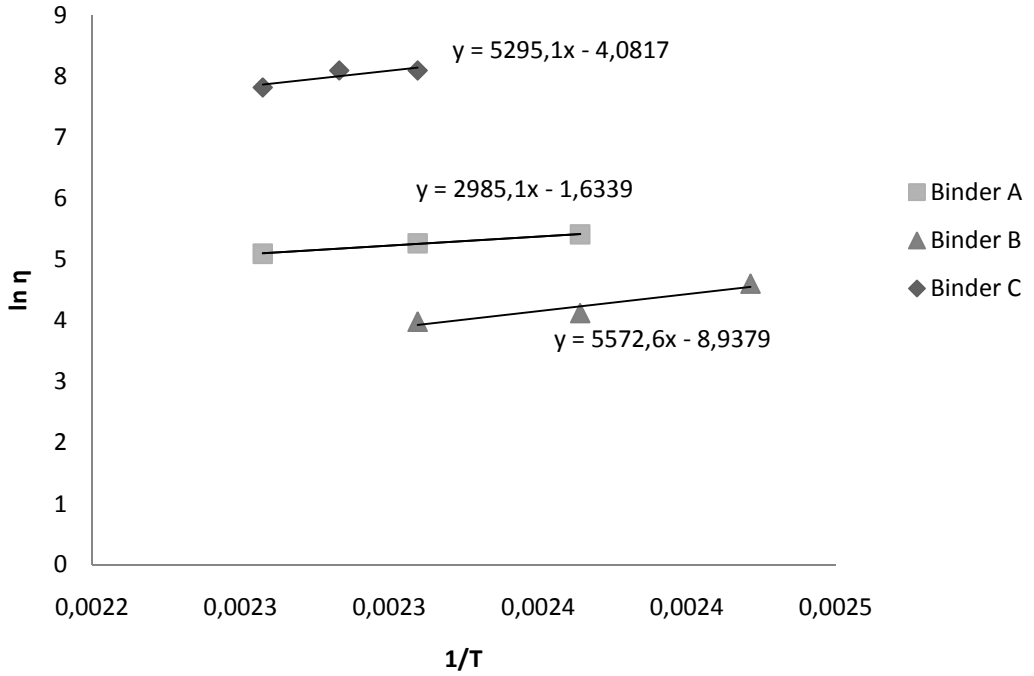
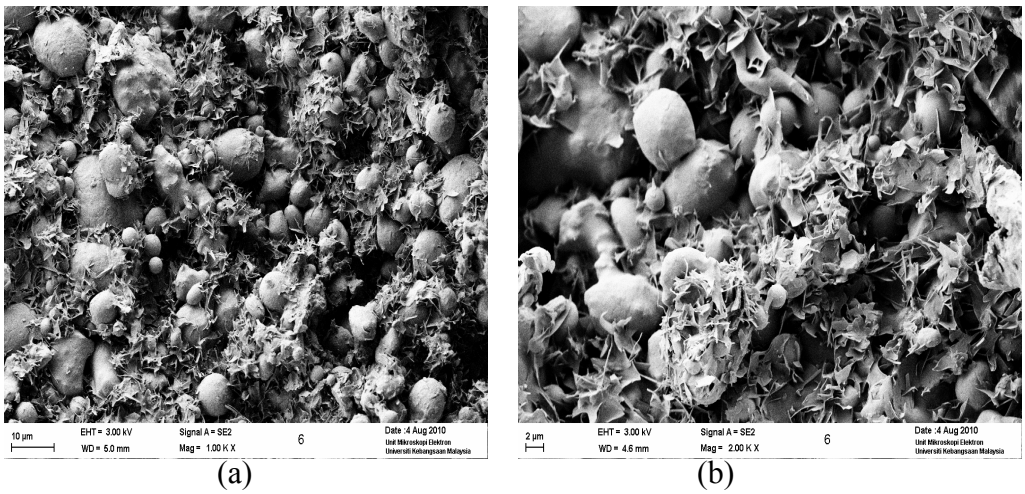


Fig. 4 Graph ln η vs 1/T

Fig. 4 shows graph of ln η against 1/T which is the graph's gradient of each binder systems can be input into Eq. 2 to find the activation energy to as a indicator for the temperature dependence of viscosity. The activation energy calculated for binder A, B and C were 24.82kJ/mol, 46.33kJ/mol and 44.02kJ/mol respectively. Binder A was the smallest activation energy followed by binder C and binder B. Small difference of activation energy for both binder B and C can be explain by percentage of palm stearin used is the same for B and C.

Morphology studies were carried out by SEM to study the distribution and dispersion for powder binder. Fig. 5 shows the feedstock containing palm stearin with polypropylene at 1000x and 2000x magnification. The surface of the binder with SS316L powder was not good because much porosity is observed. The powder-binder separation phenomenon was detected at Fig. 5 (b) with more powder distribution observed at the upper region compared to the lower region.

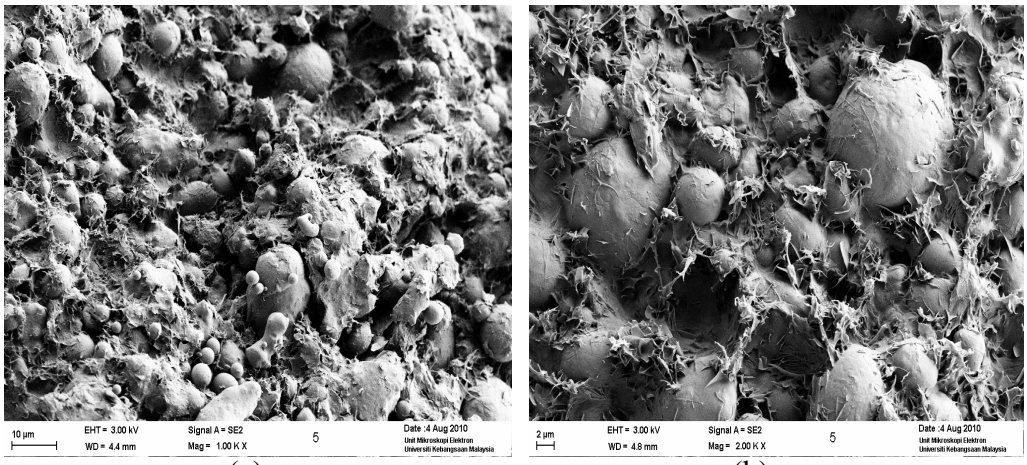


(a) (b)

Fig. 5 Feedstock of the stainless steel with palm stearin / polypropylene (a) 1000 magnification (b) 2000 magnification

Fig. 6 (a) and (b) shows feedstock of palm stearin with polyethylene at 1000x and 2000x magnification. The contact surface powder with binder was good because the particle were coated

by binder. There was no powder-binder separation phenomenon occurred in this feedstock because of the good contact surface between binder and powder. Good surface contact between binders with powder will make sure metal particle will hold tightly and prevent cracked or damage in the further processes.



(a) (b)

Fig. 6 Feedstock of the stainless steel with palm stearin / polyethylene (a) 1000 magnification (b) 2000 magnification

Summary

Dilatant flow behavior was shown for PP / palm stearin feedstock by great changes of viscosity at every temperature. In contrast, significant smooth pseudoplastic flow was observed for PE / palm stearin feedstock at all temperature. Feedstocks with PE shows better rheological properties with maintain low viscosity at increment temperature and load. The viscosity of the feedstock highly depending on the composition of palm stearin in the feedstock. As palm stearin increases, viscosity of feedstock decreases. The suitable composition of palm stearin should be 60 wt % in order to obtain viscosity in the range of 100 to 10000 Pa.s. Meanwhile, palm stearin also closely related with the feedstock's sensitivity to temperature and pressure. Higher sensitivity of feedstock resulted from increasing the content of palm stearin. The oil and fats content in palm stearin which form lubricant film will decrease viscosity and increase the feedstock sensitivity. Weak distribution of PP coating the particles of SS316L was observed while smooth and homogenously distributed of PE covering SS316L particles using SEM was viewed and studied.

References

[1] R.M. German and A. Bose: *Injection Molding of Metals and Ceramics*. MPIF. New Jersey. (1997).

[2] Iriany, N Muhamad, J. Sahari and A.K. Arifin: J. Inst. of Mat. Malaysia, Vol. 2, (2001) p.71.

[3] N.H.M Nor, N. Muhamad, S. Ahmad, M.H.I. Ibrahim, M.R.Harun, K.R. Jamaludin: Key Engineering Materials Vol. 443 (2010) p. 69.

[4] F. Ismail, M.A. Omar, I. Subuki, N. Abdullah, E.A.G.E. Ali, and N. Hassan: Reg. Conf. On Eng. Math., Mech., Manu., & Arch (EM3ARC), (2007), p. 85.

[5] I.Sabuki: *Injection moulding of 316L stainless steel powder using Palm Stearin based binder system,* Doctoral dissertation, Universiti Kebangsaan Malaysia. (2010).

[6] S.Y.M Amin, N. Muhamad, K.R. Jamaludin: submitted to Journal of *World Engineering Congress 2007,* Penang, Malaysia, 5 – 9 August. (2007).

[7] M. Khakbiz, A. Simchi, R. Bagheri: J. Mat. Sci. and Eng. Vol. 407 (2005) p. 105.

[8] K.R. Jamaludin, N. Muhamad, M.N. Ab. Rahman, Murtadhahadi, S.Y.M. Amin, S. Ahmad, M.H.I. Ibrahim, and N.H.M Nor: Advanced Materials Research Vols. 83-86 (2010) p. 945.

[9] R. Ibrahim, M.A. Omar, G.C. Wei, and M. Mohamad: J. Solid State Sci. and Tech. Vol. 15 (2007), p. 197.

© (2011) Trans Tech Publications, Switzerland
doi:10.4028/www.scientific.net/KEM.471-472.415

Optimizing the Curing Process of Epoxy-Clay Nanocomposites

M. Al-Qadhi[1,a], N. Merah[1,b] and K. Mezghani[1,c]

[1]Department of Mechanical Engineering,

P.O. Box 457, Dhahran 31261, Saudi Arabia

[a]alqadhi@kfupm.edu.sa, [b]nesar@kfupm.edu.sa, [c]mezghani@kfupm.edu.sa,

Keywords: DSC, Glass transition temperature, Curing Temperature, Curing time, Nanocomposite

Abstract. Epoxy resin is one of the most applied thermoset polymers as a matrix for Glass Fiber Reinforced Pipes (GFRP). Curing process of epoxy resin is important for the integrity of the GFRP. The present work has been conducted to determine the proper pre-curing and post-curing temperatures and duration to develop epoxy-clay nanocomposite. During this study a differential scanning calorimeter (DSC) was used to determine the glass transition temperature and hence the degree of curing. Several samples of epoxy were prepared at different pre-curing and post-curing temperatures and durations. Pre-curing temperatures ranging from 80 to 150ºC and post-curing temperatures ranging from 150 to 200ºC were studied. The results show that the optimum pre-curing and post-curing temperatures are 100 and 170ºC, respectively. Regarding the effect of curing duration, several specimens were prepared at the same pre-curing and post-curing temperatures with different curing durations of 1, 2, and 3 hours. It was observed that beyond one hour curing, the changes in the T_g and the degree of crosslinking were negligible. Using these optimum conditions samples of epoxy-clay nanocomposites were prepared using ultrasonication. The results showed that the addition of nonoclay to epoxy resulted in a reduction of the T_g.

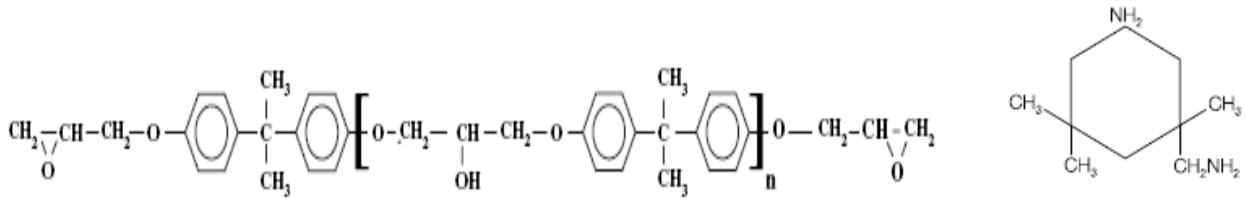
Introduction

Epoxy resins are very convenient polymer materials because of their good mechanical, thermal, and electrical properties. Many kinds of epoxy resins are known, including bisphenol-A, bisphenol-F, aliphatic cyclic, and phenol novolac types. It is well known that physical properties and mechanical strength during the working life of epoxy are greatly affected by the structure of the whole system. This depends mainly on the curing conditions and selected type of epoxy and hardener. During the thermal curing of epoxy, the sample changes from a low-molecular weight liquid mixture to a highly crosslinked network. The molecular mobility in the system decreases as the curing reaction proceeds. Curing process of a resin system is the most controlling step during the fabrication of thermosetting matrix composites including nanocomposites. Epoxy resins are one of the thermosets polymer that exhibiting an attractive combination of stiffness, strength, high heat distortion temperature, creep resistance, thermal and environmental stability. Addition of organically modified montmorillonite (MMT) nanoclay to the epoxy matrix can greatly improve the properties of epoxy resins [1-3]. The results showed that the presence of organic silicate decreases the curing temperature [4]. Recently, the epoxy-clay nanocomposites have attracted considerable attention because this kind of materials has layered structure and offer many new and greatly improved properties over pristine polymer.

Depending on the type of epoxy and hardener used, different pre-cuing and post-curing temperatures and duration have been used to cure the epoxy. Previous studies showed that the curing temperatures can range from 80 to 200°C and the duration of curing from 1 to 10 hours [5-9]. In this study, the effect of pre-cuing and post-curing temperatures and durations on the degree of crosslinking for the Araldite GY 6010 epoxy with IPDA hardener has been studied. The effect of nanoclay addition on the glass transition temperature, and hence the degree of curing, of the epoxy was investigated using differential scanning calorimeter (DSC).

Experimental

Materials. The epoxy used in this study is the diglycidyl ether of bisphenol A (DGEBA), Araldite GY 6010, supplied by JANA, KSA. The material properties were provided by the same company. These properties include the average weight per epoxide, 186 g/eq, viscosity at 25 ^{o}C, 11 Pa.s, and density, 1.16 g/cm^3. The curing agent used is isophoronediamine (IPDA), product of HUNTSMAN. The average viscosity and density at 25 ^{o}C of this hardener, as indicated on the supplied package, are 15 mPa.s and 0.92 g/cm^3, respectively. The chemical structure of the epoxy and curing agent are shown in Figure 1. Organically modified clay, Nanomer I.30 E, from Nanocor, is used as the filler material. This montmorillonite nanoclay, that belongs to the smectite clays, has been modified with primary octadecyl ammonium ion.



DGEBA IPDA

Fig. 1 The chemical structure of the DGEBA epoxy and IPDA curing agent

Sample Preparation of Pure Epoxy. A quantity of 14.4 g of the hardener was added to 60 g of the epoxy and completely mixed. The mixture was then degassed in a vacuum oven for 30 min to eliminate air bubbles that generated during mixing. After that the bubble free mixture was poured into an aluminum mold and pre-cured and post-cured at the required temperatures and duration. To study the effect of the curing temperature and duration more than 30 samples have been prepared at different pre-curing and post-curing temperatures and durations. The pre-curing temperatures ranged form 80 to 150 ^{o}C while the post-curing temperatures were in the range of 150-200 ^{o}C. Few samples have also been cured at intermediate temperatures. To investigate the effect of curing duration, several samples were synthesized at the same pre-curing and post-curing temperatures but for different curing durations of 1, 2, and 3 hours.

Sample Preparation of Epoxy-Clay Nanocomposites. The preparation of epoxy-clay nanocomposites started with manually mixing of 2 wt% nanoclays into the epoxy for 10 min to ensure good distribution of the clay particles in the epoxy. Ultrasonication was then used to disperse the nanoclay layers into epoxy resin. During the sonication the temperature of the mixture was controlled to be in the range of 60 to 70 ^{o}C. After that the mixture was degassed using a vacuum oven for 1 hour. The hardener was then added to the mixture and completely mixed. After that, the mixture was degassed again under vacuum for 30 minutes and then poured into an aluminum mold. Finally, the mixture was pre-cured and post-cured at the required temperatures and durations.

DSC Measurements. The differential scanning calorimeter (DSC) was used to determine the glass transition temperature (T_g), which is considered as an indicator of the degree of curing and crosslinking. Samples weighing 5 to 10 mg were prepared and placed in the DSC pan and heated from 25 to 200°C at a constant heating rate of 10 ^{o}C/min. Flow of nitrogen gas of 100 ml/min was used to provide inert environment and minimize the oxidation of the sample.

Results and Discussion

The effect of pre-curing temperature on the glass transition temperature (T_g) and hence on the degree of curing, was investigated. Fig. 2 shows four DSC curves for samples that have been pre-cured for 2 hours at different temperatures without any post-curing. These results illustrate that all pre-cured samples display a clear sudden drop of heat flow followed by an exothermic hump due to additional crosslinking of the samples during the DSC test. This exothermic hump and the additional crosslinking indicate that the samples were not adequately cured during the pre-curing process. It is observed that the size of the hump has decreased while the T_g has increased with

increasing the pre-curing temperature. This means that there is an improvement in the degree of crosslinking with increasing the pre-curing temperature. The T_g increases from 98 ^oC for the sample pre-cured at 80 ^oC to 156 ^oC for the sample pre-cured at 150 ^oC. However, this clear effect of pre-curing temperature has diminished when post-curing at elevated temperature is used. For example, Fig. 3 illustrates two samples that have been pre-cured at different temperatures of 100 and 120 ^oC while post-cured at the same temperature of 180 ^oC for the same duration of 3 hours. The analysis shows that both samples have approximately similar degree of curing with slight improvement in T_g for the sample that has been pre-cured at 100 ^oC. Similarly, when comparing the T_g of four samples that have been pre-cured at different temperatures of 80, 100, 120, and 150 ^oC, and then post-cured at the same temperature of 170 ^oC, it has been observed that the sample that pre-cured at 100 ^oC produced the highest T_g. As a consequence, the optimum pre-curing temperature is considered to be the 100 ^oC.

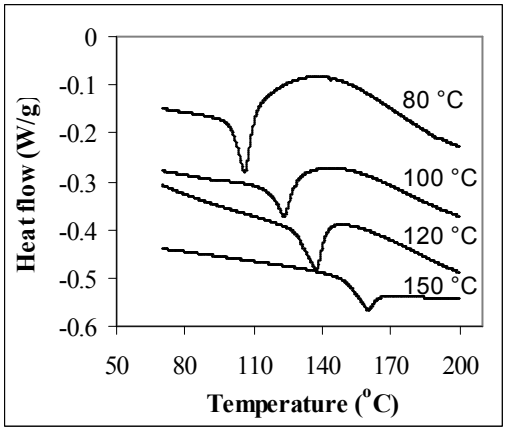


Fig. 2 DSC curves for four samples pre-cured for 2 hours at the indicated temperatures.

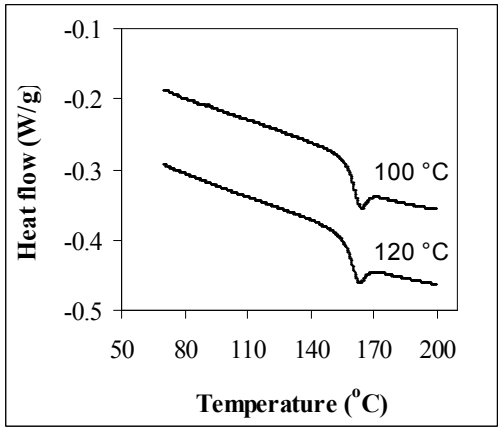


Fig. 3 DSC curves for two samples post-cured at 180 ^oC and pre-curing at the indicated temperature.

Study of the effect of intermediate curing temperature has also been conducted. Two samples have been pre-cured at 100 ^oC. One of these samples was then post-cured at 180 ^oC while the other was cured at an intermediate temperature of 140 ^oC and then post-cured at 180^oC. The curing duration at each temperature was 3 hours. The results showed that the glass transition temperatures were almost the same for both samples; around 161 ^oC. This outcome indicates that the intermediate curing temperature has negligible effect on the curing of epoxy samples.

The effect of curing time on the degree of curing has been studied. Several samples were prepared at the same pre-curing and post-curing temperatures with different durations. Fig. 4 illustrates the effect of curing time for two samples that have been pre-cured at 100 ^oC and post-cured at 180 ^oC for two different durations; one has been pre-cured and post-cured for one hour each while the second has been pre-cured and post-cured for three hours each. As shown in the figure both samples have almost the same T_g values of 161 ^oC. Also, similar results have been observed for other samples. Therefore one hour duration for each pre-curing and post-curing temperatures is considered to be sufficient for producing good samples.

To determine the optimum post-curing temperature several samples that have been pre-cured at 100 ^oC were post-cured at different temperatures as shown in Fig. 5. All samples have been pre-cured and post-cured for one hour at each curing temperature. The effect of post-curing temperature on the T_g is shown in Fig. 6. It is clear that, T_g values has increased with increasing the post-curing temperature up to 170 ^oC, and then stabilized at higher temperatures. In addition, color change from white to brown has been observed for samples prepared at post-curing temperatures above 175 ^oC. For example, samples prepared at post-cured temperature of 200 ^oC developed a golden brown color. This change in color is an indication of degradation that started when the post-curing

temperature exceeded 175 ^{o}C. Therefore, 170 ^{o}C is considered to be the optimum post-curing temperature.

The optimum conditions for curing neat epoxy, were utilized for epoxy-clay nanocomposites to determine the effect of adding nanoclay on T_g. For this purpose and based on the above results three samples were prepared using 2 wt% of nanoclay. The first sample has been pre-cured and post-cured using the optimum conditions of pre-curing at 100 ^{o}C and post-curing at 170 ^{o}C for one hour each. The other two samples have also pre-cured at 100 ^{o}C for one hour but with different post-curing temperatures; one has been post-cured at 160 ^{o}C and the other at 180 ^{o}C for one hour each. Fig. 7 shows the DSC curves for the three epoxy-clay nanocomposites samples. The results show that the degree of curing has been improved when the post-curing temperature increased from 160 to 170 ^{o}C, the T_g increased from 154 to 158 ^{o}C. Whereas no improvement in the degree of curing when the post-curing temperature increased to 180 ^{o}C, T_g is 158 ^{o}C. Therefore the optimum curing condition for the epoxy-clay nanocomposites is similar to that of the neat epoxy.

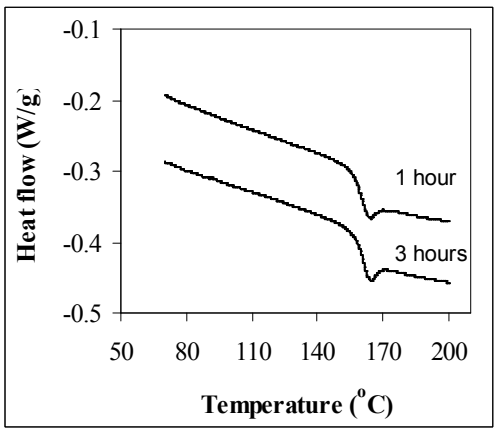


Fig. 4 DSC curves shows the effect of curing time for two samples pre-cured at 100 ^{o}C and post-cured at 180 ^{o}C.

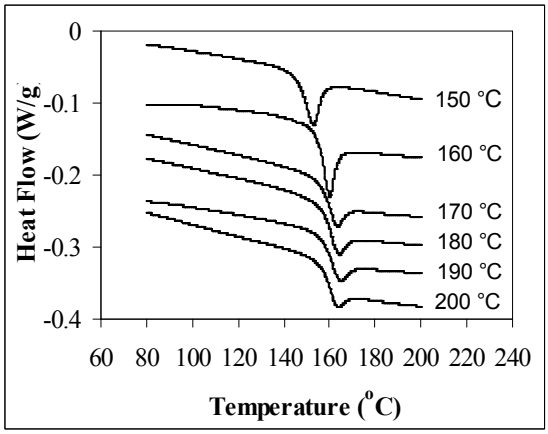


Fig. 5 DSC curves for samples pre-cured at 100 ^{o}C while post-cured at the indicated temperature.

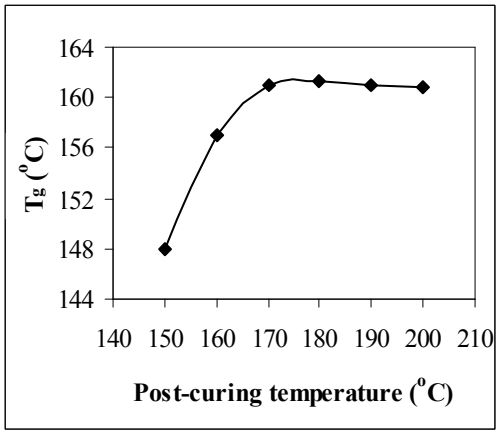


Fig. 6 Variation of T_g with post-curing temperature for the samples pre-cured at 100 ^{o}C for one hour.

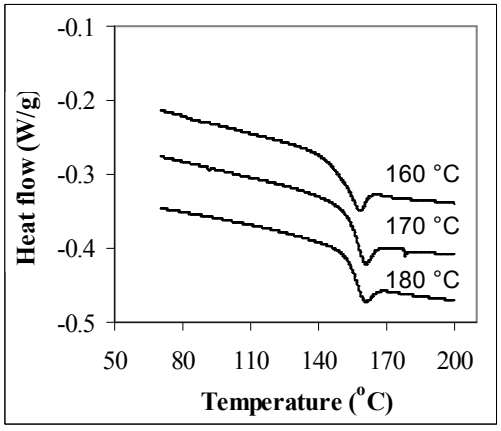


Fig. 7 DSC curves for the epoxy-clay nanocomposites pre-cured at 100 ^{o}C and post-cured at the indicated temperature.

The addition of nanoclay led to a decrease in the glass transition temperature by about 3 ^{o}C. The reduction in the T_g as a result of nanoclay addition was also reported in other studies [3,10]. This reduction in the T_g can be attributed to the lower cross-linking density in the galleries between the silicate layers and to the negative effect of clay as a barrier that decreases the cross linking density.

It should be mentioned that other studies showed improvement in T_g with the addition of nanocaly [1,9], while others found that the addition of nanoclay to the epoxy matrix has almost no effect on the T_g [11]. Xidas and Triantafyllidis [1] showed that the increase or decrease of T_g were based on the type of nanoclays used to synthesize the epoxy-clay nanocomposites.

Summary

In this study the effect of pre-curing and post-curing temperatures and durations have been investigated for Araldite GY 6010 epoxy cured with IPDA hardener. Several samples were pre-cured and post-cured at different temperatures for different cuing times to find the optimum curing conditions. Differential scanning calorimeter (DSC) was used to determine the glass transition temperature (T_g) and hence the degree of crosslinking. The results showed that the optimum pre-curing temperature was 100 ^oC for one hour and the optimum post-curing temperature was 170 ^oC for one hour. The study showed that the degree of curing is more sensitive to the curing temperature than the curing time, especially when the curing time exceeds one hour. The investigation showed also that no improvement in the degree of curing for samples that were additionally cured at intermediate temperatures. It was found that the optimum curing conditions for the epoxy-clay nanocomposites is similar to that for the neat epoxy. The addition of modified organoclay has led to a decrease in the glass transition temperature by about 3 ^oC.

Acknowledgement

The authors greatly acknowledge the support of King Fahd University of Petroleum and Minerals and NSTIP program (project number 08-ADV6804) for this work.

References

[1] Panagiotis I. Xidas, Kostas S. Triantafyllidis: European Polymer Journal Vol. 46 (2010), p. 404.

[2] Sorina-Alexandra Garea, Horia Iovu, Ancuta Bulearca: Polymer Testing Vol. 27 (2008), p.100.

[3] B. Akbari and R. Bagheri: European Polymer Journal Vol. 43 (2007), p. 782.

[4] Dian Liu, Zixing Shi, Masashi Matsunaga, Jie Yin: Polymer Vol. 47 (2006), p. 2918.

[5] T. D. Ngo, M. T. Ton-That, S. V. Hoa, K. C. Cole: Composites Science and Technology Vol. 6 (2009), p. 1831.

[6] S. C. Zunjarrao, R. Sriraman, R. P. Singh: J Mater Sci. Vol. 41 (2006), p. 2219.

[7] Weiping Liu, Suong V. Hoa, Martin Pugh: Composites Science and Technology Vol. 65 (2005), p. 2364.

[8] Ke Wang, Ling Chen, Jingshen Wu, Mei Ling Toh, Chaobin He, Albert F. Yee: Macromolecules Vol. 38 (2005), p. 788.

[9] S. Zainuddin, M.V. Hosur, Y. Zhou, Alfred T. Narteh, Ashok Kumar, S. Jeelani: MaterialsScience and Engineering A Vol. 527 (2010), p. 7920.

[10] X. Kornmann, M. Rees, Y. Thomann, A. Necola, M. Barbezat, R. Thomann: Composites Science and Technology 65 (2005), p. 2259.

[11] Emrah Bozkurt, Elcin Kaya, Metin Tanoglu: Composites Science and Technology Vol. 67 (2007), p. 3394.

© (2011) Trans Tech Publications, Switzerland
doi:10.4028/www.scientific.net/KEM.471-472.420

Effect of Mg Content on the Characteristics of Al/SiC Nanocomposite Powders Produced via in situ Powder Metallurgy Method

Mohammad Moazami-Goudarzi[1, a], Farshad Akhlaghi[2,b]

[1]School of Metallurgy and Materials Engineering, College of Engineering,
University of Tehran, P.O.Box:11155-4563, Tehran, Iran

[2]School of Metallurgy and Materials Engineering, College of Engineering,
University of Tehran, P.O.Box:11155-4563, Tehran, Iran

[a]mohmoazami@ut.ac.ir, [b]fakhlagh@ut.ac.ir

Keywords: In-situ powder metallurgy (IPM), fluidity, Al/SiC nanocomposite powders.

Abstract. In the present study the effect of Mg addition on the characteristics of Al/SiC nanocomposite powder particles produced via a relatively new method called in situ powder metallurgy (IPM) is investigated. Commercially pure Al and Al-Mg alloy melts containing different amounts of Mg were used as the matrix alloy. Nano-sized SiC particles with the average size of 60 nm were used as the reinforcing material. The effect of Mg content on the fluidity of the melt as an influencing factor affecting both the process yield and wettability of SiC with molten metal was investigated. The size distribution of produced powders was characterized using a laser particle size analyzer. Scanning electron microscopy was utilized to investigate the possibility of embedding of SiC nanoparticles within the metallic matrix. Results of microhardness measurements together with SEM micrographs and EDS analysis showed that nano-sized SiC particles could be embedded in the relatively coarse Al-Mg powders containing at least 1 wt.% Mg.

Introduction

In particulate metallic nanocomposites, nano-sized ceramic particles are embedded within a metallic matrix. A wide range of nano-sized ceramic particles including SiC, $Al_2O_3$and B_4C have been incorporated into various metallic powders such as Al, Mg and Cu to be used for production of metal matrix nanocomposites (MMNCs) [1,2]. It has been reported that the tensile strength of these composites is improved as compared with their monolithic alloy counterparts [3,4]. They also exhibit higher strength than metal matrix composites containing similar volume percentage of micron-sized reinforcing particulates [5]. In addition, an improvement in ductility of pure metals due to the addition of nanometric reinforcing particles has also been reported [6]. It must be noted that for achieving such improved properties, it is necessary to obtain a uniform distribution of nanoparticles in the matrix alloy. However, in conventional composite processing methods used for nanocomposites, agglomeration and clustering are inevitable. Many researchers have attempted to solve this problem by modifying different processing routes such as powder metallurgy [4], mechanical alloying [7,8], casting [9-11] and in situ methods [12,13].

In situ powder metallurgy (IPM) method is a relatively new process which was originally developed for fabrication of aluminum/graphite particulate composites [14]. Later, it was demonstrated that the IPM method could be successfully employed for processing a wide range of composites with different matrix alloys containing various reinforcing particles [15-18]. However, in those studies, micron-sized ceramic particles were used as reinforcing materials. Recently, the present authors have attempted to use the IPM method for processing of Al-SiC nanocomposites by using coarse micron sized SiC particles as the disintegrating medium and nano-sized SiC particles as the reinforcing phase [19]. The micron-sized ceramic particles were then sieved out and the remaining mixture of aluminum and nano-sized SiC particles were ready to be used as a feedstock for processing of Al-SiC nanocomposite by conventional powder metallurgy methods. However, the

key factor for obtaining improved mechanical properties for these composites is the proper embedding of nano-sized SiC particles within the Al powders. It is clear that for proper incorporation of ceramic particles in the metallic alloys, these particles must be wetted by the molten alloy. It has been widely reported that addition of Mg to aluminum improves its wettability with most of the ceramic particles [20]. Another factor that may be influential in embedding of nano-sized SiC particles within the matrix alloy is the size of produced molten droplets generated in the IPM process. It has been reported that the fluidity of the molten metal affects the size of the generated droplets when solid particles are used as the disintegrating medium [21]. It is expected that addition of Mg to aluminum melts affects both the size distribution of droplets generated in IPM method (via its effect on melt fluidity) and the wettability of SiC particles by the molten metal. The aim of present study is to investigate the effect of Mg addition to aluminum melt on embedding the nano-sized SiC particles into the Al powder particles generated by IPM method.

Materials and Experimental Procedures

Al-x wt. %Mg (where x=0, 1, 2.5 or 5) alloys were used as the base materials. The fluidity of these alloys as an influencing factor for powder production process in IPM technique was quantified by vacuum suction method. The fluidity tests were performed on the melts with 100 °C superheat for CP Al and Al-Mg alloys which were identical to those melt temperatures used in the IPM process. The fluidity length was measured in terms of the distance that the molten metal could flow in the suction tube under a vacuum of 400 mmHg before solidification. The inner diameter of suction tube was 7 mm.

In order to produce powders via IPM method, the required amount of aluminum (CP Al or Al-Mg alloy) melted in a crucible using an electrical resistance-heating laboratory furnace. Then a specific quantity of pre-heated SiC particles with a size range of 250-600 μm was added to the melt in an amount of 2 times the weight of aluminum charge. In some experiments, 2.5 wt.% of micron-sized SiC particles was replaced by nano-sized SiC powders (average size of 60 nm). The slurry was subsequently stirred via a spiral graphite impeller (d=36 mm) at 1400 rpm using an electrical motor for 6 min while its temperature was kept constant at 100 °C superheat. After completion of stirring, the charge was evacuated in a steel container and the alloy was allowed to solidify at ambient temperature and atmosphere. The powder mixture was screened through a 250 μm sieve to separate coarse SiC particles from the mixture of solidified aluminum particles and nano-sized SiC powders. The mass median diameter (D_{50}) of the resultant powder mixture was determined by a Cilas 1064 laser particle size analyzer (LPSA). The microhardness of produced powders in three different size ranges of 90-106, 125-150 and 180-250 μm was measured by a Wolpert D-6700 Vickers microhardness tester. The average value of the microhardness of 20 different powders in each powder sample was considered. The cross section of the produced composite particles was studied by a CamScan MV2300 scanning electron Microscope (SEM).

Results and Discussion

Figure 1 show the variation of the measured fluidity of Al melts at 100 °C superheat as a function of their Mg content. It can be seen that the fluidity of Al melts reduces with the increase of Mg content. However, the increased Mg content from 0 (in CP Al) to 1 wt. % reduced the fluidity by 20 %, whereas further increase of Mg had less pronounced effect on fluidity. The reduced fluidity length with increased Mg content is attributable to widening of the alloy freezing range which in turn changes the solidification pattern from planar to mushy mode as reported by many researchers [22,23].

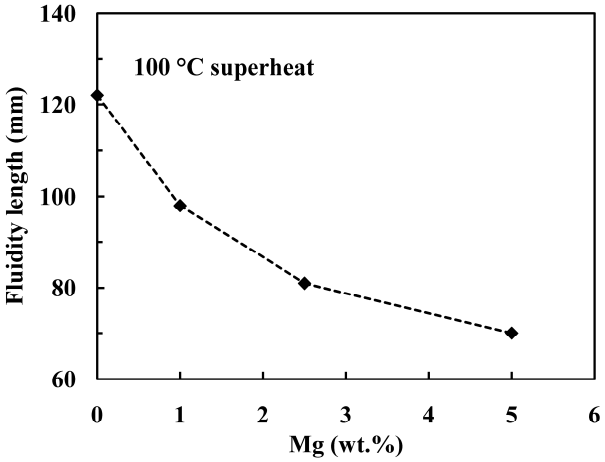


Fig. 1 Variation of fluidity length of Al melts with their Mg content.

The values of mass median diameter (D_{50}) and the yield of sub-250 μm sized powders produced by addition of both micron and nano-sized SiC powders during IPM process are tabulated in Table 1. The yield of each run was calculated by dividing the weight of the Al powders passed through the 250 μm sieve by the weight of the charged aluminum. An increase in the Mg content of the melt resulted in a reduction in D_{50} and increased process yield indicating that finer powders were produced. By considering the effect of Mg content of the melt on the fluidity length (Fig. 1), it can be concluded that the higher fluidity of the melt resulted in generation of coarser particles. These results are consistent with the previous report on the effect of fluidity of Al melts with different Si contents on the resultant Al powders generated by a process based on solid assisted melt disintegration [21]. Detailed description of generation of powder particles by solid assisted melt disintegration can be found elsewhere [21,24].

Table 1 The values of mass median diameter (D_{50}) and the yield of different powder samples

Base alloy	D_{50}	Yield
CP Al	79	0.73
Al-1 wt.% Mg	67	0.90
Al-2.5 wt.% Mg	56	0.91
Al-5 wt.% Mg	52	0.93

In the previous research [19], the present authors showed that CP Al powders could be successfully produced by using micron-sized SiC particles as a disintegrating medium. Furthermore, it was shown that the addition of SiC nanoparticles to the IPM process improved melt disintegration and consequently resulted in the increased yield of the process. However, the added nano-sized particles were not wetted by CP Al melt and after sieving out the coarse SiC particles, a mixture of metallic CP Al powders and free SiC nanoparticles was obtained.

The cross section view of coarse (180-250 μm) Al-Mg alloy powders generated in the present study by using both micron and nano-sized SiC particles is shown in Fig. 2. As confirmed by EDS analysis (Fig. 3), these are Al-Mg alloy powders containing individual or agglomerated nano-sized SiC particles. As it is shown in Fig. 4, Neither CP Al powder nor fine Al-Mg powders (under 106 micron) included nano-sized SiC powders. In fact, embedding of SiC nanoparticles were only detected in the coarse Al powders containing at least 1 wt.% Mg.

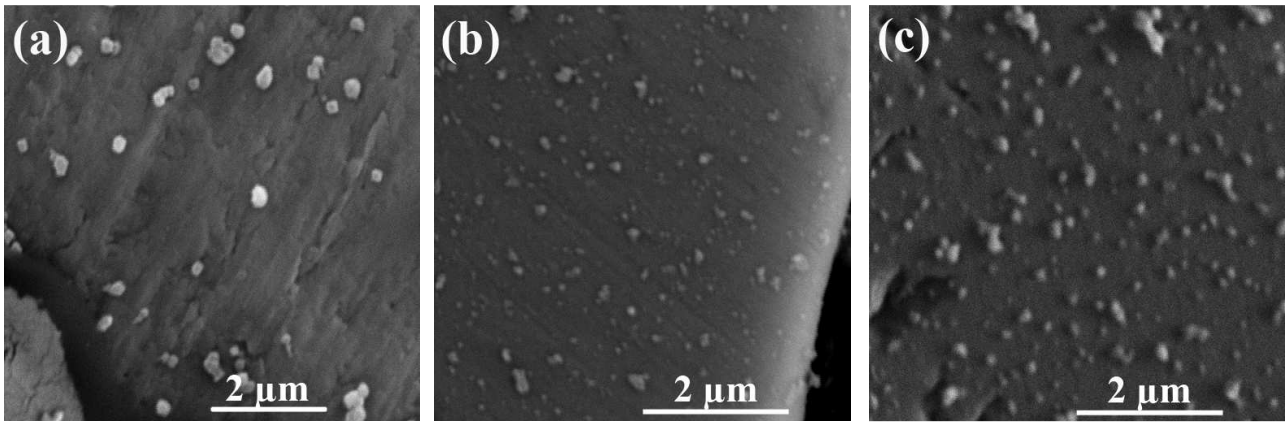


Fig. 2 SEM image of cross-section of produced powder samples: (a) Al-1Mg, (b) Al-2.5Mg and (c) Al-5Mg containing 5 wt.% SiC nanoparticles.

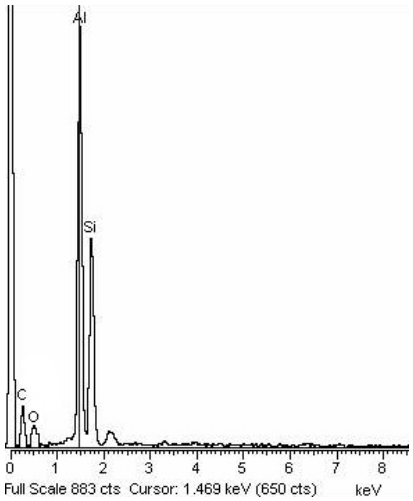


Fig. 3 EDS analysis from cross section of Al-1Mg powders within the size range of 180-250 µm.

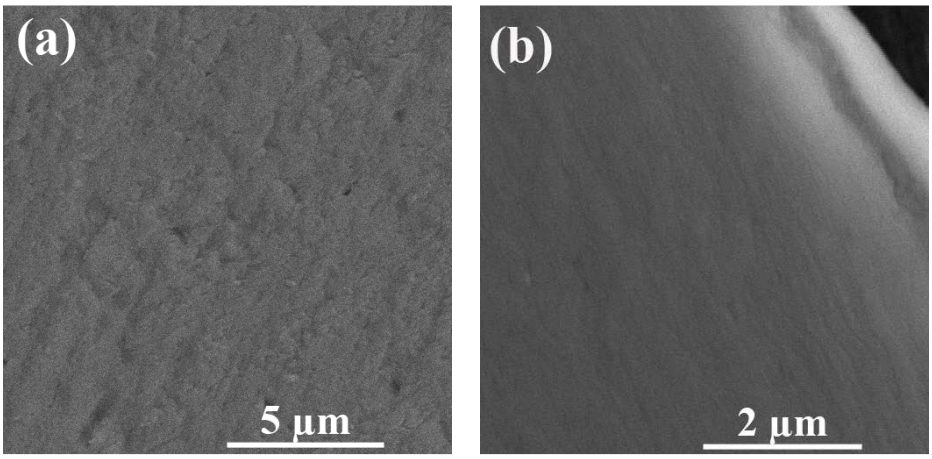


Fig. 4 SEM image of cross-section of coarse CP Al (a) and fine Al-5Mg (b) powders produced by using both micron and nano-sized SiC particles for melt disintegration via IPM method.

Figure 5 shows the microhardness values of produced Al-Mg powders in three different size ranges of 90-106, 125-150 and 180-250 µm. The nomenclature used for powder samples is based on the matrix alloy and the size of SiC powders used for melt disintegration during IPM process. For example, Al-1Mg[SiC(m+n)] indicates that Al-1wt.% Mg was used as the base material and the IPM process was carried out using both micron (m) and nano-sized (n) SiC particles. As illustrated

in Fig. 5, the microhardness of powder samples generated by using micron-sized SiC particles [SiC(m)] increased with increased Mg content of the alloy without any considerable effect of the powder size. As mentioned before, these powder samples are free of nano-sized SiC particles and these observations can be attributed to the hardening effect of intermetallic particles. It means that the effect of powder particle size on the microstructure (i.e. grain size) of these particles was negligible. These results are consistent with the literature [25]. However, when SiC nanoparticles were involved in the process, the mean hardness value of produced powders significantly increased with the powder size. These results confirm that nano-sized SiC particles are embedded in the Al-Mg alloy matrix of coarse (180-250 μm) and middle sized (125- 150 μm) powders regardless of their Mg content. However, SEM studies revealed that the fine particles (smaller than 106 μm) did not contain any reinforcing SiC particles resulting in identical hardness values for Al-xMg[SiC(m+n)] samples as compared with their Al-xMg[SiC(m)] counterparts, regardless of their Mg content.

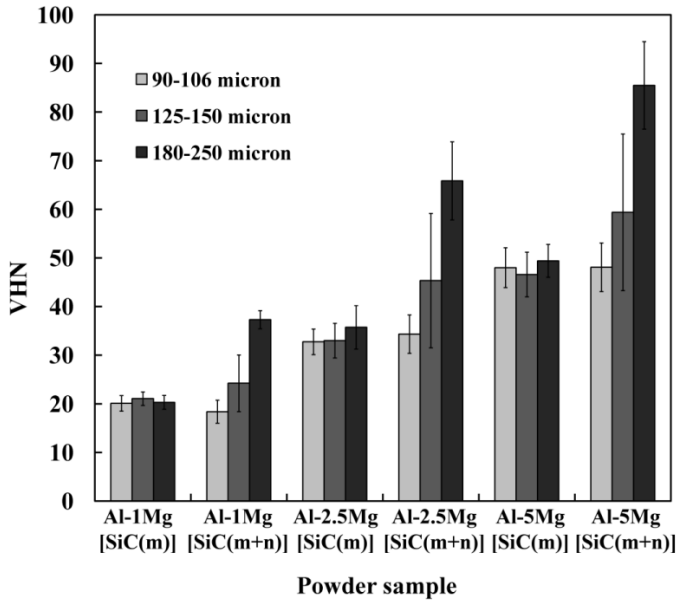


Fig. 5 Hardness values of Al-Mg powders in three different size ranges.

An important common feature to all the middle sized (125- 150 μm) Al-xMg[SiC(m+n)] powders is the wider scatter obtained in the hardness values as compared with that of finer (106-125 μm) and coarser (180- 250 μm) powders. This reveals that some of the middle sized powders are free of nano-sized SiC particles. This aspect was confirmed by SEM studies. In fact, in the initial stage of melt disintegration in the IPM process, some fine droplets are formed. As a result of rigorous turbulence created by mechanical agitation, these small droplets may solidify before they wet SiC nanoparticles. However, larger droplets would have sufficient time to be incorporated by nano-sized SiC particles before solidification. That is why solidified large droplets may contain more SiC nanoparticles.

The results of present study confirms that while nano-sized SiC particles have not been wetted by CP Al, addition of a reactive element such as Mg to the melt will improve the wettability so that nano-sized SiC particles are embedded in the metallic matrix. In addition, the as-received micron-sized SiC particles have not been wetted even by different Al-xMg (where x=1, 2.5 and 5 wt.%) melts and acted as a powerful disintegrating medium. It seems that these micrometric SiC particles induce an abrasive force to the nano-sized SiC agglomerates and contribute to introduction and reasonably uniform distribution of them in the Al-Mg powders, as shown in Fig. 2.

Summary

1. Addition Mg to CP Al up to 5 wt.% decreases fluidity length of the melt which contributes to production of finer powders via IPM method.
2. Addition of at least 1 wt.% Mg to CP Al is necessary for embedding of SiC nanoparticles within produced powders.
3. SiC nanoparticles could only be embedded in the coarse (180-250 μm) and some of the middle sized (125- 150 μm) Al-Mg alloy powders produced via IPM method.

References

[1] P.M. Ajayan, L.S. Schadler and P.V. Braun: *Nanocomposite Science and Technology* (Wiley-Vch, Germany 2003).

[2] M.Khakbiz and F. Akhlaghi: J. Alloys Compd. Vol. 479 (2009), p. 334.

[3] Y. Yang, J. Lan and X. Li: Mater. Sci. Eng. A Vol. 380 (2004), p. 378.

[4] Y.C. Kang and S.L.I. Chan: Mater. Chem. Phys. Vol. 85 (2004), p. 438.

[5] Z.Y. Ma, S.C. Tjong and Y.L. Li: Compos. Sci. Technol. Vol. 59 (1999), p. 263.

[6] S.F. Hassan, M. Gupta: Metall. Mater. Trans. A Vol. 36A (2005), p. 2253.

[7] M. Sherif El-Eskandarany: J. Alloys Compd. Vol. 279 (1998), p. 263.

[8] F. Tang, M. Hagiwara and J.M. Schoenung: Mater. Sci. Eng. A Vol. 407 (2005), p. 306.

[9] X. Li, Y. Yang and X. Cheng: *J. Mater. Sci.* Vol. 39 (2004), p. 3211.

[10] A. Ansary Yar, M. Montazerian, H. Abdizadeh and H. R. Baharvandi, J. Alloys Compd. Vol. 484 (2009), p. 400.

[11] A. Mazaheri, H. Abdizadeh and H. R. Baharvandi: Mater. Sci. Eng. A Vol. 518 (2009), p. 61.

[12] H. Arami and A. Simchi: Mater. Sci. Eng. A Vol. 464 (2007), p. 225.

[13] D. Roy, S. Ghosh, A. Basumallick and B. Basu: J. Alloys Compd. Vol. 436 (2007) p. 107.

[14] F. Akhlaghi and S.A. Pelaseyyed: Mater. Sci. Eng. A Vol. 385 (2004), p.258.

[15] F. Akhlaghi and A. Zare-Bidaki: Wear Vol. 266 (2009), p.37.

[16] S. Mahdavi and F. Akhlaghi: J. Mater. Sci., in press.

[17] F. Akhlaghi and S. Pournaderi, in: Proc. of 7th Int. Con. on Composite Science and Technology (ICCST/7), paper ID: 20958, Sharjah, UAE (2009).

[18] F. Akhlagh and S. Mahdavi, in: Proc. of the int. Conf. on Advances in Materials and Processing Technologies (AMPT'09), paper ID: 328, Kuala Lumpur, Malaysia (2009).

[19] F. Akhlaghi and M. Moazami-Goudarzi, in: Proc. of Int. Conf. on Nanotechnology: Fundamentals and Applications (ICNFA2010), paper ID: 417, Ottawa, Canada (2010).

[20] J. Hashim, L. Looney and M.S.J. Hashmi: J. Mater. Process. Tech. Vol. 92-93 (1999), p. 1.

[21] F. Akhlaghi and P. Delshad-Khatibi: Powder Metall., in press.

[22] K.R. Ravi, R.M. Pillai, K.R. Amaranathan, B.C. Pai and M. Chakraborty: J. Alloys Compd. Vol. 456 (2008), p. 201.

[23] P. Beeley: *Foundry Technology* (Butterworth-Heinemann, UK 2001).

[24] F. Akhlaghi and H. Esfandiari: Mater. Sci. Technol. Vol. 23 (2007), p. 646.

[25] F. Akhlaghi and H. Esfandiari: Mater. Sci. Eng. A Vol. 452–453 (2007), p. 70.

© (2011) Trans Tech Publications, Switzerland
doi:10.4028/www.scientific.net/KEM.471-472.426

A Semi- Energy Finite Strip Method for Post-Buckling Analysis of Relatively Thick Anti-Symmetric Cross-Ply Laminates

Mohammad Hajikazemi[1, a], Hamid Reza Ovesy[1,b] and Mohammad Homayoun Sadr[1,c]

[1]Aerospace Engineering Department and Centre of Excellence in Computational Aerospace Engineering, Amirkabir University of Technology, Tehran, Iran

[a]hajikazemi@aut.ac.ir, [b]ovesy@aut.ac.ir, [c]sadr@aut.ac.ir

Keywords: Semi-energy approach; finite strip method; post buckling analysis; Anti-symmetric laminates; von Karman's compatibility equation; ANSYS package.

Abstract. In the current paper, a new semi-energy finite strip method is developed based on the concept of first order shear deformation theory (FSDT) in order to attempt the post-buckling solution for relatively thick composite plates subjected to uniform end-shortening. The main advantage of the semi-energy finite strip method (FSM) is that it is based on the closed form solution of von Karman's compatibility equation in order to derive the analytical shape functions for the in-plane displacements fields. The developed finite strip method is applied to analyze the post buckling behavior of a relatively thick anti-symmetric cross-ply composite plate with clamped out-of-plane boundary conditions at its loaded ends. The results are discussed in detail and compared with those obtained from finite element method (FEM) of analysis. The study of the results has provided confidence in the validity and capability of the developed finite strip in handling post-buckling problem of relatively thick laminated plates.

Introduction

Early works concerned with the use of FSM in predicting the geometrically non-linear response of single rectangular plates and prismatic plate structures are those of Graves-Smith and Sridharan [1] and Hancock [2]. The semi-energy method, as referred to by Rhodes and Harvey [3], was first used by Marguerre [4], and has since been used by various researchers. In the previously developed version of the semi-energy finite strip approach [5,6], which was suitable for the post-buckling analysis of thin composite plate structures, the out-of-plane displacement field of the finite strip is the only displacement which is postulated by a deflected form due to the application of classic laminated plate theory (CLPT).

In the current paper, a new semi-energy FSM is developed based on the concept of first order shear deformation theory (FSDT) in order to attempt the post buckling solution for thin and relatively thick composite plates subjected to uniform end-shortening. In addition to the out-of-plane displacement field of the finite strip, the rotations with respect to x and y axes are also postulated by two deflected forms. The postulated deflected forms (i.e. w, φ_x, φ_y) are substituted into von Karman's compatibility equation which is solved exactly to obtain the corresponding forms of the mid-plane stresses and displacements. The solution of von Ka´rma´n's compatibility equation and the postulated deflected forms are then used to evaluate the potential energy of the respective finite strip. Finally, by invoking the Principle of Minimum Potential Energy, the unknown deflection coefficients existing are determined and thus the problem is solved. The post buckling behaviour of relatively thick Anti-symmetric cross-ply composite plates is analyzed. In order to investigate the effects of through-the- thickness shear stresses on the post buckling behaviour of laminated plates, a previously developed finite strip method based on the concept of classic laminated plate theory (CLPT) [5] is also employed. Moreover, in order to validate the FSM results, they are compared with those obtained from finite element method (FEM) of analysis.

Semi Energy Finite Strip Formulation using FSDT

The semi-energy theory has been developed for the finite strip shown in Fig.1. This finite strip is assumed to be made of orthotropic layers constructing a balanced laminate. The strip is clamped out-of-plane at both ends (i.e. at end $x = 0$ and L), and is subjected to a uniform end shortening $\bar{u}$ at end $x = L$ only. It may be noted that $u, v, w, \varphi_x \,\&\, \varphi_y$ correspond to the mid-plane displacements and rotations. The boundary conditions at loaded ends of the finite strip are summarized as follows:

$$w = \varphi_x = N_{xy} = 0 \quad at \quad x = 0 \,\&\, L \qquad and \quad u = \begin{cases} 0 & at \quad x = 0 \\ -\bar{u} & at \quad x = L \end{cases} \tag{1}$$

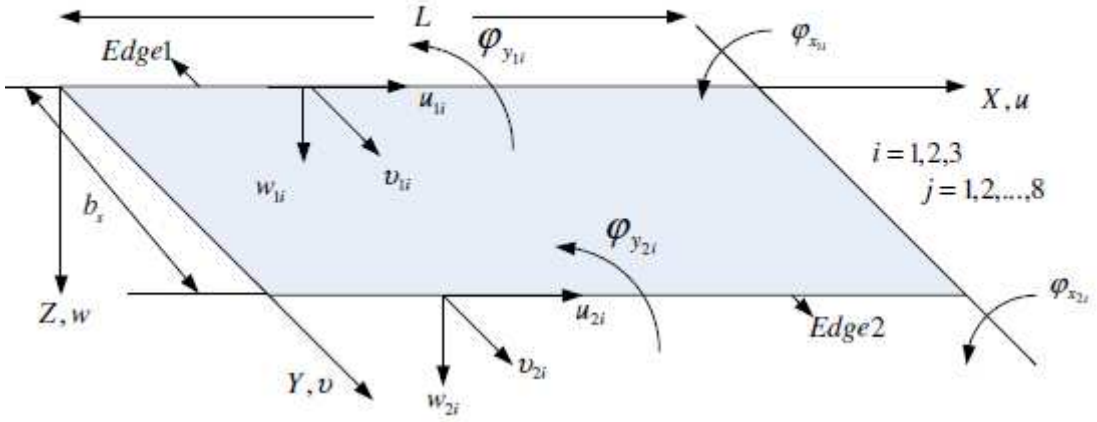


Fig 1 A Finite Strip Subjected to a Prescribed Uniform End-Shortening.

The Von Karman's compatibility equation for large deflections of anti-symmetric cross-ply balanced laminated plates as given in Reference [5] is modified as Eq.2, in which the FSDT assumptions are incorporated.

$$\Im(F) = A_{22}^* \frac{\partial^4 F}{\partial x^4} + (2A_{12}^* + A_{33}^*)\frac{\partial^4 F}{\partial x^2 \partial y^2} + A_{11}^* \frac{\partial^4 F}{\partial y^4} = \left(\frac{\partial^2 w}{\partial x \partial y}\right)^2 - \left(\frac{\partial^2 w}{\partial x^2}\right)\left(\frac{\partial^2 w}{\partial y^2}\right) - B_{21}^*\left(\frac{\partial^3 \varphi_x}{\partial x^3}\right)$$
$$- B_{12}^*\left(\frac{\partial^3 \varphi_y}{\partial y^3}\right) + (B_{33}^* - B_{22}^*)\left(\frac{\partial^3 \varphi_y}{\partial x^2 \partial y}\right) + (B_{33}^* - B_{11}^*)\left(\frac{\partial^3 \varphi_x}{\partial y^2 \partial x}\right), \quad A^* = A^{-1} \;\&\; B^* = -A^{-1}B \tag{2}$$

Where A is the in-plane stiffness and B is the in-plane out-of-plane coupling stiffness matrix. Also function F (i.e. $F = F(x, y)$) is the so-called Airy stress function. The following functions are found to be suitable to represent the out-of-plane displacement and rotations fields.

$$w = \sum_{n=1}^{3} f_n \sin(\zeta x)\sin(n\zeta x), \quad \varphi_x = \sum_{n=1}^{3} g_n \sin(\zeta x)\cos(n\zeta x), \quad \varphi_y = \sum_{n=1}^{3} s_n \sin(\zeta x)\sin(n\zeta x)$$
$$f_n(y) = (1 - \frac{19}{3}\eta + \frac{32}{3}\eta^2 - \frac{16}{3}\eta^3)w_{1n} + (8\eta - \frac{56}{3}\eta^2 + \frac{32}{3}\eta^3)w_{1\frac{1}{4}n} +$$
$$(-\frac{8}{3}\eta + \frac{40}{3}\eta^2 - \frac{32}{3}\eta^3)w_{1\frac{3}{4}n} + (\eta - \frac{16}{3}\eta^2 + \frac{16}{3}\eta^3)w_{2n} \tag{3}$$
$$g_n(y) = (1 + 2\eta^2 - 3\eta)\varphi_{x_{1n}} + (-4\eta^2 + 4\eta)\varphi_{x_{1\frac{1}{2}n}} + (2\eta^2 - \eta)\varphi_{x_{2n}}$$
$$s_n(y) = (1 + 2\eta^2 - 3\eta)\varphi_{y_{1n}} + (-4\eta^2 + 4\eta)\varphi_{y_{1\frac{1}{2}n}} + (2\eta^2 - \eta)\varphi_{y_{2n}}, \qquad \eta = \frac{y}{b_s}, \zeta = \frac{\pi}{L}$$

The displacement fields are then substituted into Eq.2, in order to find the corresponding in-plane displacement functions. In this process, the stress function F may be considered as follows:

$$F(x,y)=\sum_{k=0}^{8}F_k(y)\cos(k\zeta x) \tag{4}$$

Substituting F from Eq.4, and w,φ_x,φ_y from Eq.3, in Eq.2, a set of forth-order ordinary differential equations will be achieved as Eq.5.

$$\left\{A_{11}^{*}F_k''''-(k\zeta)^2(2A_{12}^{*}+A_{33}^{*})F_k''+(k\zeta)^4A_{22}^{*}F_k=\zeta^2\Psi_k(f_i,g_i,s_i),\quad k=0,1,2,...,8\ \ and\ \ i=1,2,3\right. \tag{5}$$

It should be mentioned that $\Psi_0,\Psi_1,\Psi_2,...,\Psi_8$ are known functions and can be derived analytically. The first equation can be solved easily, but the solutions for the remaining eight equations are composed of two parts, namely the particular integral and the complementary function solutions. The particular integral solutions depend on the functions $f_n(y),g_n(y),s_n(y)$ (where $n=1,2,3$) only, thus it can be conveniently evaluated. But, for the complementary function solutions three cases may appear in accordance with the sign of Delta of forth-order characteristic equation of differential equations [7]. For cross ply laminated plates which are considered in this paper Delta is positive, thus the following solutions can be considered for the mentioned stress function:

$$\begin{aligned}&\mathrm{F_k}(y)=C_{k1}\cosh(My)+C_{k2}\sinh(My)+C_{k3}\cosh(Ny)+C_{k4}\sinh(Ny)+\Phi_k(y)\\&where\\&M=\sqrt{\frac{2A_{12}^{*}+A_{33}^{*}+\sqrt{\Delta}}{2\mathrm{A}_{11}^{*}}}(k\zeta)\ \ and\ \ N=\sqrt{\frac{2A_{12}^{*}+A_{33}^{*}-\sqrt{\Delta}}{2\mathrm{A}_{11}^{*}}}(k\zeta)\ \ k=1,2...6\end{aligned} \tag{6}$$

In the above equations the functions $\Phi_k(y)$ (i.e. $k=1,2,...,8$) are the particular integral solutions. The 32 coefficients $C_{k1}\to C_{k4}$ $(i.e.\ k=1,2,...,8)$ are unknown at present, but it is assumed that these coefficients are known. By taking this assumption into account and imposing the appropriate boundary conditions from Eq.1, and solving the stress-strain constitutive equations, the in-plane displacements will be derived analytically as follows:

$$u=-\frac{\bar{u}}{L}x+\sum_{k=1}^{8}f_{uk}(y)\sin(k\zeta x) \tag{7a}$$

$$\begin{aligned}\upsilon=&-(\frac{A_{21}^{*}}{A_{11}^{*}})\frac{\bar{u}}{L}y+\sum_{k=0}^{8}f_{\upsilon k}(y)\cos(k\zeta x)-(f_{\upsilon 1}(y)+f_{\upsilon 2}(y)+f_{\upsilon 3}(y)\\&+f_{\upsilon 4}(y)+f_{\upsilon 5}(y)+f_{\upsilon 6}(y)+f_{\upsilon 7}(y)+f_{\upsilon 8}(y))\big|_{y=0}+\upsilon\big|_{x=y=0}\end{aligned} \tag{7b}$$

$$\begin{aligned}&f_{uk}=f_{uk}(F_k(y),f_i(y),g_i(y),s_i(y))\quad ,\quad f_{\upsilon k}=f_{\upsilon k}(F_k(y),f_i(y),g_i(y),s_i(y))\\&f_{\upsilon 0}=f_{\upsilon 0}(F_k(y),f_i(y),g_i(y),s_i(y))\ ,\ f_{\upsilon 0}\big|_{y=0}=0\qquad k=1,2,...,8\qquad and\quad i=1,2,3\end{aligned} \tag{7c}$$

The amplitude of second term on the right hand side of Eq.7a evaluated at $y=0$ and $y=b_s$ (i.e. $f_{uk}(y)\big|_{y=0}$ and $f_{uk}(y)\big|_{y=b_s}, k=1,2,...,8$) represents the local DOF u_{1k} and u_{2k}, respectively. The second term on the right hand side of Eq.7b (i.e. $f_{\upsilon 0}(y)$) describes the transverse in-plane movement of lines parallel to x-axis across a strip. The next eight terms describe the in-plane waviness of the lines which lie parallel to x-axis. The amplitude of these terms evaluated at $y=0$

and $y = b_s$ (i.e. $f_{\upsilon k}(y)\big|_{y=0}$ *and* $f_{\upsilon k}(y)\big|_{y=b_s}, k = 1,2,...,8$) represent the local DOF υ_{1k} and υ_{2k}, respectively. By defining the DOF, as outlined above, the compatibility conditions will be ensured on the adjacent edges of two strips. It is noted that in the above equations (i.e. Eq.7a and 7b), functions $F_k(y)$ ($k = 1,2,...,8$) are not yet fully known, due to the coefficients $C_{k1} \to C_{k4}$ (*i.e.* $k = 1,2,...,8$) being unknown. These coefficients are obtained by treating them as unknown, and solving for them while all other parameters, including all DOF are assumed to be known. In this process, the following set of equations should be solved analytically.

$$f_{u_k}(y)\big|_{y=0} = u_{1k}, \quad f_{u_k}(y)\big|_{y=b_s} = u_{2k}, \quad f_{\upsilon_k}(y)\big|_{y=0} = \upsilon_{1k}, \quad f_{\upsilon_k}(y)\big|_{y=b_s} = \upsilon_{2k} \qquad k = 1,2,..8 \tag{8}$$

With 32 set of equations presented in Eq.8, the 32 coefficients $C_{k1} \to C_{k4}$ (*i.e.* $k = 1,2,...,8$) are explicitly evaluated in the terms of DOF and other strip constants. Having derived the in-plane displacement functions (i.e. u and υ), the mid-plane strain and curvatures with respect to von-Kármán's assumptions can be derived as follows:

$$\begin{aligned} \{\varepsilon\}^T &= \left\{ \frac{\partial u}{\partial x} + \frac{1}{2}\left(\frac{\partial w}{\partial x}\right)^2, \frac{\partial \upsilon}{\partial y} + \frac{1}{2}\left(\frac{\partial w}{\partial y}\right)^2, \frac{\partial u}{\partial y} + \frac{\partial \upsilon}{\partial x} + \frac{\partial w}{\partial x}\frac{\partial w}{\partial y} \right\} \\ \Psi^T &= \left\{ \frac{\partial \varphi_x}{\partial x}, \frac{\partial \varphi_y}{\partial y}, \frac{\partial \varphi_x}{\partial y} + \frac{\partial \varphi_y}{\partial x} \right\}, \; \lambda^T = \left\{ \varphi_x + \frac{\partial w}{\partial x}, \varphi_y + \frac{\partial w}{\partial y} \right\} \end{aligned} \tag{9}$$

The strain energy for the finite strip is presented as follow:

$$V_s = \frac{1}{2}\iint (\{\varepsilon\}^T [A]\{\varepsilon\} + 2\,\varepsilon^T [B]\Psi + \{\Psi\}^T [D]\{\Psi\} + (SCF)(\{\lambda\}^T [E]\{\lambda\}))dxdy \tag{10}$$

Where D is out-of-plane stiffness matrix, E is shear stiffness matrix and SCF is the shear correction factor. By invoking the principle of minimum potential energy the strip equilibrium equations, and subsequently the global equilibrium equations are obtained for the whole structure. The latter set of equations is then solved using the Newton-Raphson (N-R) iterative procedure. The in-plane stresses at any point on the strip are known by following relations:

$$N_x = \sigma_{xx} \cdot t = \frac{\partial^2 F}{\partial y^2}, \quad N_y = \sigma_{yy} \cdot t = \frac{\partial^2 F}{\partial x^2}, \quad N_{xy} = \sigma_{xy} \cdot t = -\frac{\partial^2 F}{\partial x \partial y} \tag{11}$$

Where N_x, N_y are the in-plane axial forces per width, N_{xy} is the shear forces per width, $\sigma_{xx}, \sigma_{yy}, \sigma_{xy}$ are the corresponding average stresses, and *t* is the thickness of finite strip.

A previously developed finite strip method based on the concept of CLPT is also employed. The mentioned analysis is carried out in the same manner as that already described in reference [5].

Numerical Results and Discussion

Square plate with loaded ends clamped out-of-plane, and with the unloaded edges simply supported out-of-plane and free to move in plane are considered. The length to thickness ratios are $L/t = 100$ or $L/t = 40$, and the plates are assumed to be manufactured from high strength carbon–epoxy pre-impregnated plies with the material properties as follows:

$$E_1 = 140\ \text{GPa} \qquad E_2 = 10\ \text{GPa} \qquad \nu_{12} = \nu_{23} = 0.3 \qquad G_{12} = 5\ \text{GPa} \tag{12}$$

The lay-up configuration in laminates is assumed to be anti-symmetric cross-ply $[0/90]_2$. The results are presented in terms of dimensionless deflection and longitudinal load as follows:

$$P^* = 10PL/(E_2 t^3) \qquad U^* = 1000\bar{u}/L \qquad W^* = w_{center}/t \tag{13}$$

where P is total mean force acting on the plate. In addition to semi-energy finite strip analyses, a finite element study is also performed in this paper. The FEM analysis has been carried out using general purpose ANSYS software. The three dimensional shell element (SHELL99) of the ANSYS library has been used [7]. The convergence study has revealed that a total number of eight finite strips (corresponding to 309 and 192 DOFs in the case of FSDT and CLPT analysis respectively) and a mesh arrangement composed of 400 square elements with the uniform size (corresponding to 10086 DOFs), for the FEM analyses will produce converged post-buckling solutions for the laminated plates assumed in this paper.

The variation of load factor P^* with dimensionless end-shortening U^* and with dimensionless central deflection W^*, for the plates with $L/t = 100$ and $L/t = 40$ are depicted in Fig. 2 and Fig. 3, respectively.

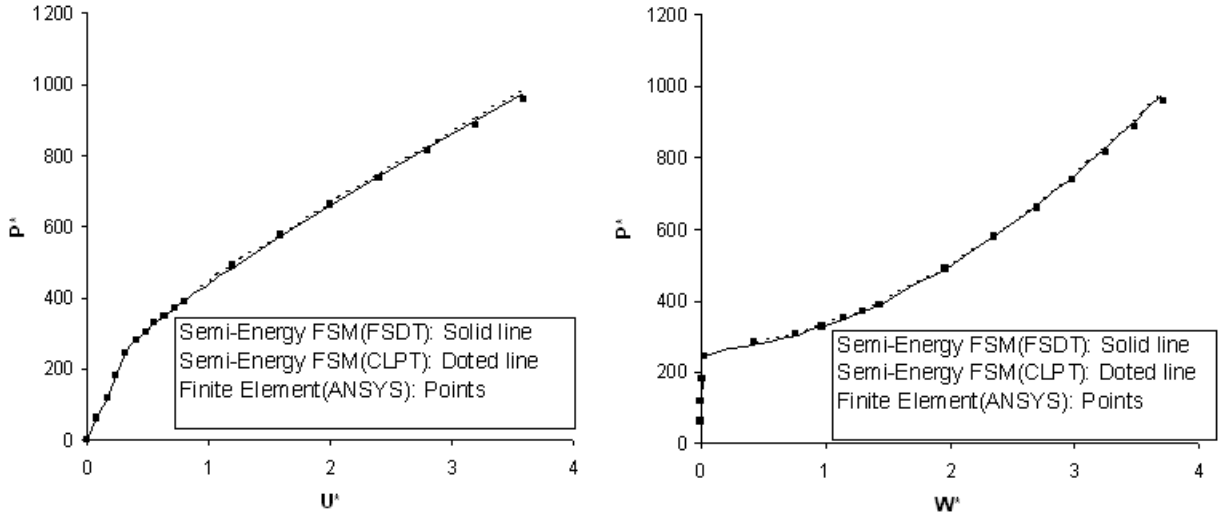


Fig 2. Variation of non-dimensional longitudinal load versus end-shortening and versus central deflection for Anti-symmetric cross-ply square plates with (L/t=100)

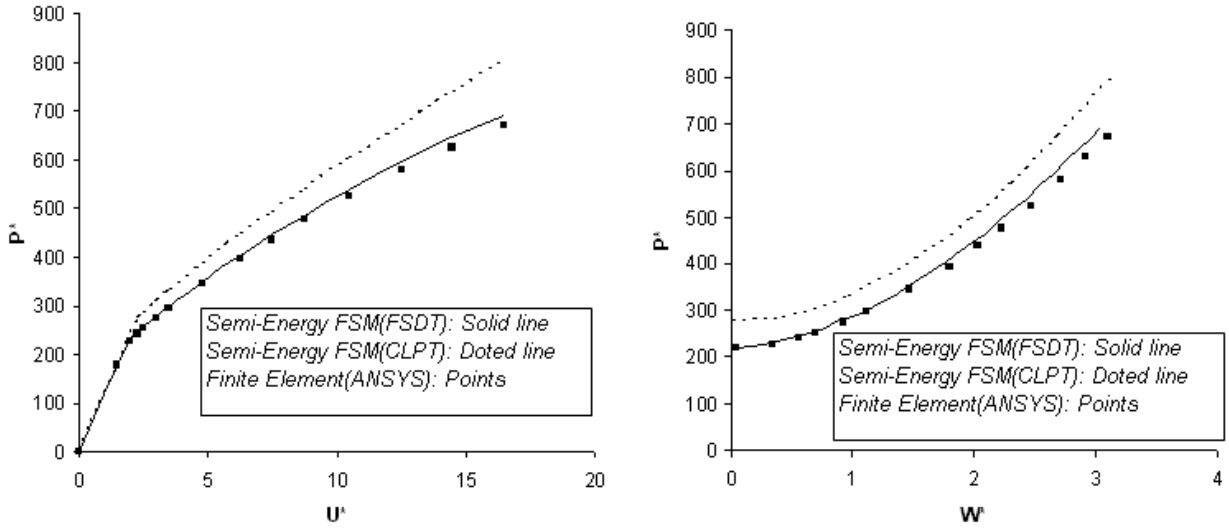


Fig 3. Variation of non-dimensional longitudinal load versus end-shortening and versus central deflection for Anti-symmetric cross-ply square plates with (L/t=40)

It is seen in Fig.2 that the three sets of results compare very closely and hence that the present approaches for the post buckling behaviors of thin laminated plates under uniform end shortening are verified**.** It is noted that due to the high length to thickness ratio of plate, the effects of through-the-thickness shear stresses on the post-buckling behavior of the plate have appeared to be insignificant. It may be observed from Fig. 2 and Fig. 3 the anti-symmetric cross ply plate with clamped boundary conditions has remained flat up to the buckling load and hence, a bifurcation point has occurred [5]. It is clearly seen in Fig. 3 that the results obtained from FSDT theory and FEM analysis are very close. Thus, the present FSDT approach for the post buckling analysis of relatively thick laminates is more suitable than the CLPT approach. In other words, for the more accurate post-buckling analysis of relatively thick plates, the effects of transverse shear strain energy should be taken into account. Also, for a given level of accuracy in the results, the developed semi energy FSM approaches require markedly lower number of degrees of freedom (corresponding to 309 and 192 DOFs in the case of FSDT and CLPT analysis respectively) compared to that needed by the more conventional versions FEM (corresponding to 10086 DOFs).

Summary

A novel semi-energy FSM based on the concept of first order shear deformation theory (FSDT) for the post buckling analysis of thin and relatively thick composite plates under uniform end-shortening is developed. It has been revealed that the formulation of the semi-energy FSM based on FSDT is generally more accurate than that of the previously developed semi energy FSM based on CLPT [5] for the post-buckling analysis of relatively thick laminated plates with clamped boundary condition at loaded ends. Besides, it is worth mentioning that, for a given level of accuracy in the results, the developed semi-energy approaches are more computationally efficient than the conventional energy based schemes.

References

[1] S. Sridharan, T.R. Graves-Smith, J. Eng. Mech. Div., ASCE, 1981, Vol.107, pp. 869–88.

[2] G.J. Hancock, J. Struct. Div., ASCE, 1981, Vol.107, pp. 455–71.

[3] J. Rhodesand, J.M. Harvey, J. of Eng. Mech. Div. ASCE, 1977, 103, 461-478.

[4] K. Marguerre, NACA Technical Memorandum, 1937, 833.

[5] H. Assaee, H.R. Ovesy, Semi-Energy Finite Strip Post-Buckling Analysis of Anti-Symmetric Cross-Ply Laminated plates Concerning the Effects of Mechanical Coupling, fifth international conference on thin-walled structures, Brisbane, Australia 2008.

[6] H.R. Ovesy, H. Assaee, M. Hajikazemi, "An investigation on post buckling behaviour of functionally graded plate using a semi energy finite strip approach", proceeding of the IJSSD Symposium on Progress in Structural Stability and Dynamics, Hong Kong, (16-19 Dec. 2009).

[7] H.R. Ovesy, M. Hajikazemi, H. Assaee, "A semi energy finite strip method for post buckling analysis of relatively thick laminates", Proceeding of the 10th International Conference on Computational Structures Technology (CST 2010),Valencia , (14-17 Sep. 2010).

© (2011) Trans Tech Publications, Switzerland
doi:10.4028/www.scientific.net/KEM.471-472.432

Large Deflection Behavior of Composite Laminated Plates under End-Shortening and Normal Pressure Loading Using a Semi-Energy Finite Strip Method

Hamid Reza Ovesy[1, a], Mohammad Homayoun Sadr[1, b], Mohammad Hajikazemi[1, c] and Hassan Assaee[2, d]

[1]Aerospace Engineering Department and Centre of Excellence in Computational Aerospace Engineering, Amirkabir University of Technology, Tehran, Iran

[2]Mechanical and Aerospace Engineering Department, Shiraz University of Technology, Shiraz, Iran

[a]Ovesy@aut.ac.ir, [b]Sadr@aut.ac.ir, [c]Hajikazemi@aut.ac.ir, [d]Assaee@sutech.ac.ir

Keywords: Semi-energy approach; finite strip method; Large Deflection Behavior; Anti-Symmetric angle ply laminate; von Ka´rma´n's compatibility equation, ANSYS

Abstract. In this paper, the application of previously the semi energy finite strip method (FSM) for the non-linear post-buckling analysis of rectangular anti-symmetric laminates is extended to include the effects of normal pressure loading in addition to the progressive end-shortening. One of the main advantages of the semi-energy FSM is that it is based on the closed form solution of von Kármán's compatibility equation. The developed finite strip method is applied to analyze the large deflection behavior of anti-symmetric angle ply composite laminated plates with simply supported boundary conditions at its loaded ends. To validate the results, they are compared with those obtained from finite element method (FEM) of analysis.

Introduction

The investigation of the effects of out-of-plane pressure loading is of utmost interest in the design and analyses of aero structures. The non-linear large deflection behavior of a plate can be analyzed by solving the von-Kármán non-linear equations. Unfortunately, the von-Kármán equations are coupled and forth-order and thus no rigorous solutions are available. This has prepared the ground for the development of the approximate methods such as finite element method, finite strip method (FSM), etc.

Early works concerned with the use of FSM in predicting the geometrically non-linear response of single rectangular plates and prismatic plate structures are those of Graves-Smith and Sridharan [1] and Hancock [2]. The semi-energy method, as referred to by Rhodes and Harvey [3], was first used by Marguerre [4], and has since been used by various researchers.

In the current paper, the application of the previously developed semi energy [5] for the analysis of the non-linear behavior of rectangular anti-symmetric laminates is extended to include the effects of normal pressure loading in addition to the progressive end-shortening. The out-of-plane displacement field of the finite strip is the only displacement which is postulated by a deflected form. The postulated deflected form is substituted into von-Kármán's compatibility equation, which is solved exactly to obtain the corresponding forms of the mid-plane stresses and displacements. The solution of von-Kármán's compatibility equation and the postulated out-of-plane deflected form are then used to evaluate the potential energy of structure. Finally, by invoking the principle of minimum potential energy, the unknown deflection coefficients existing in the postulated deflected form are determined. The method is applied to analyze the large deflection behavior of anti-symmetric angle ply composite laminates with simply supported boundary conditions at its loaded ends. In order to validate the results, they are compared with those obtained from finite element method (FEM) of analysis.

Semi Energy Finite Strip Formulation

The semi-energy theory has been developed for the finite strip shown in Fig.1. This finite strip is assumed to be made of orthotropic layers constructing a balanced laminate. The finite strip is simply supported out-of-plane at both ends (i.e. at ends $x = 0 \& L$), and is subjected to a uniform end shortening $\bar{u}$ at end $x = L$ only. It may be noted that u, υ and w correspond to mid-plane displacements. The degrees of freedom (DOF), called nodal displacement parameters, are depicted in Fig.1 for a finite strip. The aforementioned boundary conditions are summarized as:

$$w = \mathrm{M}_x = \mathrm{N}_{xy} = 0 \qquad \text{at} \qquad x = 0 \,\&\, \mathrm{L} \quad \textit{and} \quad u = \begin{cases} 0 & \text{at} \quad x = 0 \\ -\bar{u} & \text{at} \quad x = \mathrm{L} \end{cases} \tag{1}$$

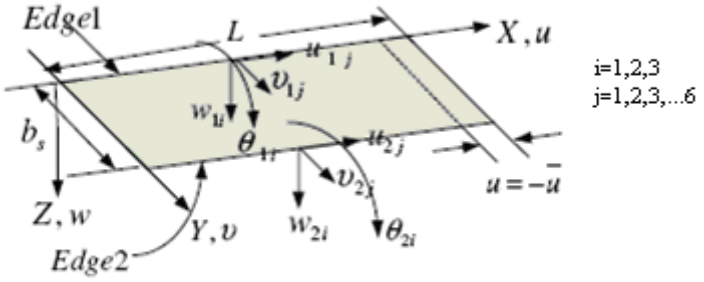


Figure 1: A Finite Strip Subjected to a Prescribed Uniform End-Shortening.

The plates are assumed to be sufficiently thin so that the application of the Classical Laminated Plate Theory (CLPT) in the theoretical analysis is valid. The von-Kármán compatibility equation for large deflections of Anti-symmetric angle ply laminated plates is given as Eq.2 [5].

$$\begin{aligned} \Im(F) &= A_{22}^* \frac{\partial^4 F}{\partial x^4} + (2A_{12}^* + A_{33}^*) \frac{\partial^4 F}{\partial x^2 \partial y^2} + A_{11}^* \frac{\partial^4 F}{\partial y^4} = \left(\frac{\partial^2 w}{\partial x \partial y}\right)^2 - \left(\frac{\partial^2 w}{\partial x^2}\right)\left(\frac{\partial^2 w}{\partial y^2}\right) \\ &+ (2B_{23}^* - B_{31}^*)\left(\frac{\partial^4 w}{\partial x^3 \partial y}\right) + (2B_{13}^* - B_{32}^*)\left(\frac{\partial^4 w}{\partial y^3 \partial x}\right) \quad \textit{where} \quad A^* = A^{-1} \quad \textit{and} \quad B^* = -A^{-1}B \end{aligned} \tag{2}$$

Where A is the in-plane stiffness and B is the in-plane out-of-plane coupling stiffness matrix. Also function F (i.e. $F = F(x, y)$) is the so-called Airy stress function. The following function found to be suitable to represent the out-of-plane displacement field for the developed semi-energy finite strip.

$$\begin{aligned} w &= f_{w1}(y)\sin(\zeta x) + f_{w2}(y)\sin(2\zeta x) + f_{w3}\sin(3\zeta x) \\ f_{wi} &= (1 - 3\eta^2 + 2\eta^3)w_{1i} + b_s(\eta - 2\eta^2 + \eta^3)\theta_{1i} + (3\eta^2 - 2\eta^3)w_{2i} + b_s(\eta^3 - \eta^2)\theta_{2i} \\ \zeta &= \frac{\pi}{L}, \quad \eta = \frac{y}{b_s}, \quad i = 1,2,3 \end{aligned} \tag{3}$$

The out-of-plane displacement w is then substituted in the von Kármán's compatibility equation in order to find the corresponding in-plane displacement functions. In this process, the stress function F may be considered as follows:

$$F(x, y) = \sum_{k=0}^{6} F_k(y)\cos(k\zeta x) \tag{4}$$

Substituting F from Eq.4 and w from Eq.3 in Eq.2, the following equation is achieved.

$$\left\{A_{11}^{*}F_k^{''''}-(k\zeta)^2\left(2A_{12}^{*}+A_{33}^{*}\right)F_k^{''}+(k\zeta)^4A_{22}^{*}F_k=\zeta^2\Psi_k\left(f_{w1},f_{w2},f_{w3}\right)\right. \quad where\ \mathrm{k}=0,1,2,...,6 \qquad (5)$$

It should be mentioned that $\Psi_0,\Psi_1,\Psi_2,...,\Psi_6$ are known functions and can be derived analytically. The first equation can be solved easily, but the solutions for the remaining six equations are composed of two parts, namely the particular integral and the complementary function solutions. The particular integral solution depends on the functions $f_{wi}\,(i=1,2,3)$ only, thus it can be conveniently evaluated. But, for the complementary function solutions three cases may appear in accordance with the sign of Delta of forth-order characteristic equation of differential equations, which is given as:

$$\Delta=\left(2A_{12}^{*}+A_{33}^{*}\right)^2-4A_{11}^{*}A_{22}^{*} \qquad (6)$$

For angle-ply laminated plates which are considered in this paper Delta is negative, thus the following solutions can be considered for the mentioned stress function:

$$\begin{aligned}&if\quad \Delta<0\quad then\\&F_k(y)=(C_{k1}\cos(Qy)+C_{k2}\sin(Qy))\sinh(Py)+(C_{k3}\cos(Qy)+C_{k4}\sin(Qy))\cosh(Py)+\phi_k(f_{wi}(y))\\&where\\&P=\sqrt{2\sqrt{\frac{A_{22}^{*}}{A_{11}^{*}}}+\frac{2A_{12}^{*}+A_{33}^{*}}{A_{22}^{*}}}\left(\frac{k\zeta}{2}\right)\quad and\quad Q=\sqrt{2\sqrt{\frac{A_{22}^{*}}{A_{11}^{*}}}-\frac{2A_{12}^{*}+A_{33}^{*}}{A_{22}^{*}}}\left(\frac{k\zeta}{2}\right)\qquad k=1,2,...,6\end{aligned} \qquad (7)$$

In the above equations the functions $\phi_k(f_{wi}(y))$ (i.e. $k=1,2,...,6$) are the particular integral solutions. The 24 coefficients $C_{k1}\rightarrow C_{k4}$ ($i.e.\ k=1,2,...,6$) are unknown at present, but it is assumed that these coefficients are known. By taking this assumption into account and imposing the appropriate boundary conditions from Eq.1 and solving the stress-strain constitutive equations, the in-plane displacements will be derived analytically as follows:

$$\begin{aligned}&u=-\frac{\bar{u}}{L}x+\sum_{k=1}^{6}f_{uk}(y)\sin(k\zeta x)\\&where\\&f_{uk}=f_{uk}(F_k(y),f_{w1}(y),f_{w2}(y),f_{w3}(y))\quad k=1,2,..6\end{aligned} \qquad (8a)$$

$$\begin{aligned}&\upsilon=-\left(\frac{A_{21}^{*}}{A_{11}^{*}}\right)\frac{\bar{u}}{L}y+\sum_{k=0}^{6}f_{\upsilon k}(y)\cos(k\zeta x)-(f_{\upsilon1}(y)+f_{\upsilon2}(y)+f_{\upsilon3}(y)\\&+f_{\upsilon4}(y)+f_{\upsilon5}(y)+f_{\upsilon6}(y))\big|_{y=0}+\upsilon\big|_{x=y=0}\\&f_{\upsilon k}=f_{\upsilon k}(F_k(y),f_{w1}(y),f_{w2}(y),f_{w3}(y))\\&f_{\upsilon0}=f_{\upsilon0}(f_{w1}(y),f_{w2}(y),f_{w3}(y))\ ,\ f_{\upsilon0}\big|_{y=0}=0\qquad\qquad k=1,2,..6\end{aligned} \qquad (8b)$$

The amplitude of second term on the right hand side of Eq.8a evaluated at $y=0$ and $y=b_s$ (i.e. $f_{uk}(y)\big|_{y=0}\ and\ f_{uk}(y)\big|_{y=b_s}, k=1,2,...,6$) represents the local DOF u_{1k} and u_{2k}, respectively. The second term on the right hand side of Eq.8b (i.e. $f_{\upsilon0}(y)$) describes the transverse in-plane movement of lines parallel to x-axis across a strip. The next six terms describe the in-plane waviness of the lines which lie parallel to x-axis. The amplitude of these terms evaluated at $y=0$

and $y = b_s$ (i.e. $f_{\upsilon k}(y)\big|_{y=0}$ *and* $f_{\upsilon k}(y)\big|_{y=b_s}, k = 1,2,...,6$) represent the local DOF υ_{1k} and υ_{2k}, respectively. By defining the DOF, as outlined above, the compatibility conditions will be ensured on the adjacent edges of two strips. It is noted that in the above equations (i.e. Eq.8a and 8b), functions $F_k(y)$ ($k = 1,2,...,6$) are not yet fully known, due to the coefficients $C_{k1} \to C_{k4}$ $(i.e.\ k = 1,2,...,6)$ being unknown. These coefficients are obtained by treating them as unknown, and solving for them while all other parameters, including all DOF (i.e. $u_{1k}, \upsilon_{1k}, w_{1i}, \theta_{1i}, u_{2k}, \upsilon_{2k}, w_{2i}, \theta_{2i}$ ($i = 1, 2, 3$, $k = 1,2,...,6$)), are assumed to be known. In this process, the following set of equations should be solved analytically.

$$f_{uk}\big|_{y=0} = u_{1k},\ \ f_{\upsilon k}\big|_{y=0} = \upsilon_{1k},\ \ \ f_{uk}\big|_{y=b_s} = u_{2k},\ \textit{and}\ f_{\upsilon k}\big|_{y=b_s} = \upsilon_{2k}.\ \ \ k = 1,2,...,6 \tag{9}$$

With 24 set of equations presented in Eq.9, the 24 coefficients $C_{k1} \to C_{k4}$ $(i.e.\ k = 1,2,...,6)$ are explicitly evaluated in the terms of DOF and other strip constants.

Having derived the in-plane displacement functions (i.e. u and υ), the mid-plane strain and curvatures with respect to von-Kármán's assumptions can be derived as follows:

$$\{\varepsilon\}^T = \left\{ \frac{\partial u}{\partial x} + \frac{1}{2}\left(\frac{\partial w}{\partial x}\right)^2, \frac{\partial \upsilon}{\partial y} + \frac{1}{2}\left(\frac{\partial w}{\partial y}\right)^2, \frac{\partial u}{\partial y} + \frac{\partial \upsilon}{\partial x} + \frac{\partial w}{\partial x}\frac{\partial w}{\partial y} \right\},\ \Psi^T = \left\{ -\frac{\partial^2 w}{\partial x^2}, -\frac{\partial^2 w}{\partial y^2}, -2\frac{\partial^2 w}{\partial x \partial y} \right\} \tag{10}$$

The strain energy for the finite strip in terms of mid-plane strains and curvatures is presented as follow:

$$V_s = \frac{1}{2}\iint (\{\varepsilon\}^T [A]\{\varepsilon\} + \{\Psi\}^T [D]\{\Psi\} + 2\{\varepsilon\}^T [B]\{\Psi\}) dxdy \tag{11}$$

The uniformly distributed pressure load of intensity p_w acts in the z-direction over the whole strip surface and is of fixed intensity in any particular application, whilst the end-shortening is applied progressively. For any finite strip the change in potential energy of the normal pressure loading during the deformation process is:

$$V_{sp} = -\int_0^{b_s}\int_0^{L} w.p_w\, dxdy \tag{12}$$

The total energy of any strip becomes:

$$U_s = V_{sp} + V_s \tag{13}$$

By invoking the principle of minimum potential energy the strip equilibrium equations, and subsequently the global equilibrium equations are obtained for the whole structure. The latter set of equations is then solved using the Newton-Raphson (N-R) iterative procedure. Once the global equilibrium equations are solved and the nodal degrees of freedom are found for a particular prescribed end shortening, the in-plane stresses at any point on the strip are known by following relations:

$$N_x = \sigma_{xx} \cdot t = \frac{\partial^2 F}{\partial y^2},\ \ N_y = \sigma_{yy} \cdot t = \frac{\partial^2 F}{\partial x^2},\ \ N_{xy} = \sigma_{xy} \cdot t = -\frac{\partial^2 F}{\partial x \partial y},\ \ N_{av} = \frac{\int_0^{L}\int_0^{b_s} N_x dxdy}{L} \tag{14}$$

Where N_x, N_y are the in-plane axial forces per width, N_{xy} is the shear forces per width, $\sigma_{xx}, \sigma_{yy}, \sigma_{xy}$ are the corresponding average stresses, t is the thickness of finite strip and N_{av} is total force acting on a finite strip.

Numerical Results and Discussion

It is noted that the plates are assumed to be simply supported on all edges as far as the out-of-plane deflection is concerned, and a pressure load factor is defined as $Q = (36.09 \times p_w \times L^4)/(E_2 \times t^4)$. The Anti-symmetric angle-ply laminated$[-45/45]_2$ square plates, which are constructed of plies with equal thickness, and with the material properties of $E_1 / E_2 = 40$, $G_{12} / E_2 = 0.5$ and $\nu_{12} = \nu_{23} = 0.3$ are studied. The length to thickness ratio is $L/t = 150$. The unloaded edges are free to expand laterally in their plane. A fixed normal pressure load is applied corresponding to values of a pressure load factor Q of 0, 10000, and 50,000 in turn, in conjunction with a progressive end-shortening $\bar{u}$. In presenting the results a load factor $F^* = -LN_{av} / E_2 t^3$, a dimensionless end-shortening $U^* = 1000 \times \bar{u} / L$ and a dimensionless central deflection $W^* = w_c / t$ are defined. In addition to semi-energy finite strip analyses, a finite element study is also performed in this paper. The FEM analysis has been carried out using general purpose ANSYS software. The three dimensional shell element (SHELL99) of the ANSYS library has been used. The convergence study has revealed that a total number of eight finite strips (corresponding to 156 DOFs) and a mesh arrangement composed of 400 square elements with the uniform size (corresponding to 10086 DOFs), for the FEM analyses will produce converged post-buckling solutions for the laminated plates assumed in this paper. The variation of load factor F^* with dimensionless end-shortening U^*, and the variation of load factor F^* with dimensionless central deflection W^* are depicted in Figs. 2 and 3 respectively.

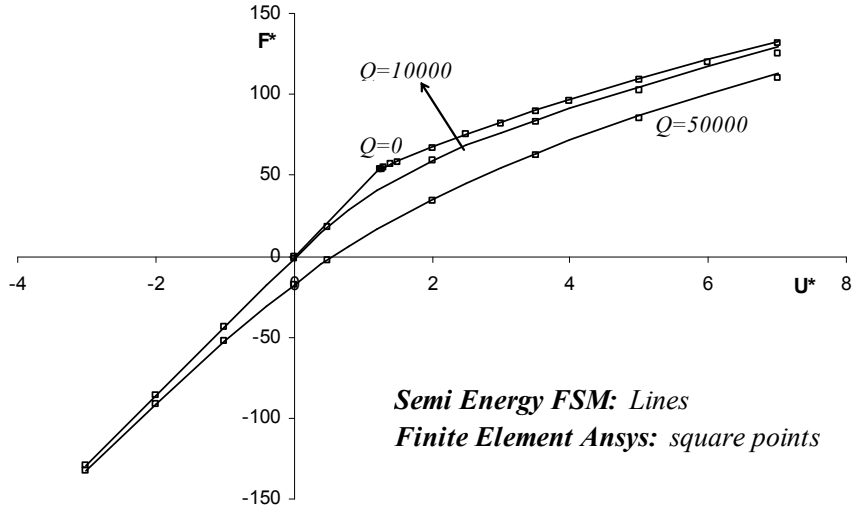


Fig. 2 Variation of non-dimensional longitudinal load versus end-shortening for Anti-symmetric angle-ply square plates with (L/t=150)

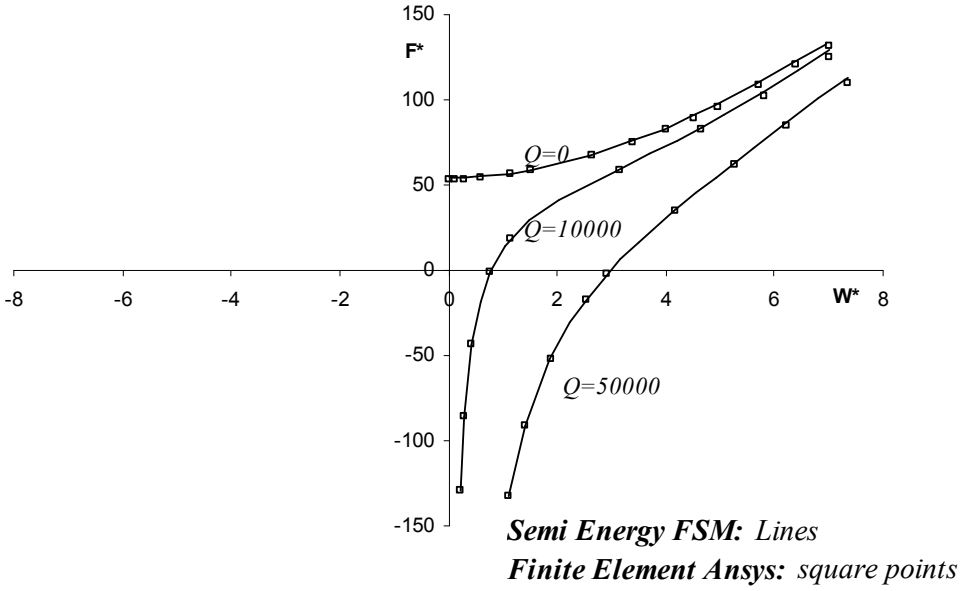


Fig. 3 Variation of non-dimensional longitudinal load versus dimensionless central deflection for Anti-symmetric angle-ply square plates with (L/t=150)

It is clearly seen that the two sets of results demonstrate very good agreement and hence that the present approach for problems involving the end-shortening behavior of anti-symmetric plates carrying a fixed normal pressure loading is verified. Moreover, from the computational economy point of view, the semi-energy FSM has incorporated very lower number of degrees of freedom (i.e. 156DOFs) compared to those of FEM (10086DOFs), thus the computational advantage of the developed semi-energy FSM is revealed.

Summary

The application of the semi energy method is extended to the analysis of the non-linear behavior of rectangular anti-symmetric laminates subjected to progressive end-shortening as well as normal pressure loading. The study of results has revealed that the post buckling response of the laminates is significantly influenced by the application of the normal pressure loading and has provided confidence in the validity and capability of the developed finite strip in handling post-buckling problem of anti-symmetric laminated plates under end shortening and normal pressure loading. It is noted that for a given level of accuracy in the results, the developed semi-energy FSM is more computationally efficient than the conventional energy based schemes.

References

[1] S. Sridharan, T.R. Graves-Smith , J. Eng. Mech. Div., ASCE, Vol.107 (1981)p. 869.

[2] G.J. Hancock , J. Struct. Div., ASCE, Vol.107 (1981), p. 455.

[3] J. Rhodes, J.M. Harvey, J. of Eng. Mech. Div. ASCE, Vol. 103 (1977), p. 461.

[4] K. Marguerre, NACA Technical Memorandum, (1937), p. 833.

[5] H.R. Ovesy, H. Assaee, Composite Structures 2009 Vol. 89 (2009), p. 120.

© (2011) Trans Tech Publications, Switzerland
doi:10.4028/www.scientific.net/KEM.471-472.438

Water Retention in Kenaf/Polypropylene Composites Due to Repeated Immersion and Drying Conditions

W.H. Haniffah [1, a]; A. Khalina [1, 2, b] and S.M. Sapuan [3, c]

[1] Laboratory of Biocomposite Technology, Institute of Tropical Forestry and Forest Products (INTROP), Universiti Putra Malaysia, 43400 UPM Serdang, Selangor Malaysia.
[2] Department of Biological and Agricultural Engineering, Universiti Putra Malaysia, 43400 UPM Serdang Selangor Malaysia
[3] Department of Mechanical and Manufacturing Engineering, Universiti Putra Malaysia, 43400 UPM Serdang Selangor Malaysia

[a]wmh76wh@yahoo.com, [b]khalina@eng.upm.edu.my, [c]sapuan@eng.upm.edu.my

Keywords: repeated water immersion, absorption, retention, kenaf/PP composite, kenaf

Abstract. Lignocelluloses based natural fibers composites are very prone to water absorption due to OH functional group within cellulose and hemicelluloses of natural fibers. In this work, the water retention in the kenaf/polypropylene (kenaf /PP) composite due to repeated immersion and drying are studied. The composites (40%, 50%, 60% and 70% fiber loading) are immersed in the water and then dried in room condition (24°C and 48 % humidity) for 4 cycles (1 cycle is 10 days of immersion and drying). The parameters are 8\2 (imply 8 days immersion\ 2 days drying), 6\4, 4\6 and 2\8 per cycle. Continuous immersion (100% immersion) is used as a reference of water absorption behavior of the composite. The results for 70% fiber loading under minimum drying days of 8\2, shows that the water retention reduced to 36% from the water absorbed and further drying only reduced to 31%. When the experiment are repeated for several cycles, 70% fiber loading composites shows a decreasing pattern in water retention at the second cycle whereas 40% fiber loading composite showing an increasing pattern. Duration of immersion\drying does play an important role in the amount of water retention in the composite. The water retention of the composites either show an increasing or decreasing pattern depending on kenaf fiber loading and repetition of the immersion\drying for several cycles.

Introduction

It is commonly known that outdoor application will expose the products to inconsistent weather elements such as water, UV light, wind and temperature [1]. Most of the application of natural fiber composite is limited to indoor application whereby it is not directly exposed to water. Water absorption has been one of the weakness of natural fiber composite, it reduce the mechanical properties and also physical properties of the composites [2,3,4,5,6,7]. The condition of the outdoor application does not only involve with water absorption, it is also involve with repeated absorption and desorption process due repetition of rain and sunshine on the material.

It was reported by Costa et al [2] that the increase of immersion time corresponds to water content, reduce stress at rupture and elastic modulus of the composites. Meanwhile Panthapulakkala et al [3] results showed that when wet samples are re-dried (60°C for 5 days in an air oven), the tensile strength and modulus is decreased more lower compare with original samples but still higher than wet samples. Roger et al [8] has conclude that under cyclic humidity and cyclic water soaking conditions of aspen fiber/polypropylene composites , the composites showed a small but steady increase in moisture sorption with each humidity cycle and wetting cycle.

Espert et al [7] were mentioned regarding 3 mechanisms of moisture penetration into composites materials. The main mechanism stated that it was by diffusion of water molecules into the micro gaps between polymer chains. The second mechanism is capillary mechanism and transport by micro cracks. The capillary mechanism involves movement of water molecules into the interface between fibers and matrix. This mechanism is particularly important in composites with weak interfacial adhesion and during debonding between fiber and matrix. On the other hand, flow and

storage of water inside the cracks, pores or small channels in the composite structure are classified as third mechanism, transport by micro cracks.

Wang et al [9] used percolation theory to get better understanding on moisture absorption mechanism of in natural fiber reinforced composites. The results concluded that at high fiber loading, fibers are highly connected, and the diffusion process is found to be dominant mechanism; while at low fiber loading close to and below the percolation threshold (may below 50% fiber loading), the formation of a continuous network is the key and hence percolation is the dominant mechanism.

Eligon et al [10] have mentioned that in wood, adsorption and desorption of moisture under constant temperature exhibit hysteresis. When subjected to higher relative humidity and the return back to early humidity, the path of moisture content does not follow the same path. The moisture on returned path is higher than the original moisture content i.e. the woods retained the moisture. Kenaf and any lignocelluloses material are similar to wood in term of its constituent, so it also exhibit hysteresis. Thus it is expected that kenaf is one of main reason why water retention occur in composite.

Hysteresis also happened in porous material, the simplest term to explain the hysteresis phenomena are using pore blocking concept in ink-bottle model. Hysteresis is expected to occur if the only access for large pore of ink-bottle is through the narrower neck of ink-bottle. The wide body of inkbottle pore is filled at vapor pressure which corresponds to delayed condensation in the ink bottle. The ink-bottle remains filled until the narrow neck empties first at lower vapor pressure. In much complex network model; factors like the size of the neck, connectivity of the network and the condition of neighboring pores determine the vapor pressure at which the pore body start drying. The pores network empties when the relative pressure is below the characteristic percolation threshold which associated with the onset of continuous cluster of pores open in the surface.[11,12]

Material and Methodology

Kenaf used in study are harvested from Terengganu and processed at Institute of Tropical Forestry and Forest Products (INTROP) into kenaf fibre size ≤500 μm. The polypropylene (PP) used is TitanPro Grade PD6331 with melt flow index of 14 gram/minute at 230°C manufactured by Titan Petchem (M) Sdn. Bhd., Malaysia. Kenaf and PP are compounded using Micromac twin srew extruder model MCT-30 (Micromagna Engineering Sdn. Bhd., Malaysia). Kenaf and PP are compounded into pallet using 40%, 50%, 60% and 70% of fibre loading for next injection moulding process into flexural shape specimens.

25 flexural specimens of each fibre loading are selected for this study. There are 4 immersion\drying parameter for this experiment whereby 5 specimens used in each immersion\drying parameter. The specimen are pre-dried in the oven for 24 hours at 105°C and weighing using AND balance model GR200 with accuracy of 1mg.

The immersion\drying process involve in this experiment are: 10\0, 8\2, 6\4, 4\6 and 2\8. and 10\0 is actually continuous immersion. The first number dedicated to days of immersion and the second number dedicate to days of drying. On 50 days of immersion it indicates by number 50\0. Similarly for 2, 4, 6 and 8 days of continuos immersion will be indicate by number 2\0, 4\0, 6\0 and 8\0 respectively.

For continuous immersion, after immersed in distilled water, the specimen will remove from water,wipe and immediate weigh. Meanwhile immersion\drying treaments data is collected after completed a cycle or every 10 days. The specimens directly undergone room drying process without wipe at 24°C and 48 % humidity. There are 2 water retention formula used, water retention based on original weight which refer to formula (1) and water retention base on water absorbed which refer formula (2).

$$Water\ Retention, W_R\ [\%] = \frac{W_t[g] - W_o[g]}{W_o[g]} \times 100\% \quad (1)$$

$$Water\ Retention\ based\ on\ Water\ Absorbed\ [\%] = \left(1 - \frac{W_A[\%] - W_R[\%]}{W_A[\%]}\right) \times 100\% \quad (2)$$

Where W_t is weight at time t, W_o is weight before immersion, W_A is percentage of water absorbed, W_R is percentage of water retention after immersion\drying process; W_A-W_R /W_A is actually ratio of water loss over water absorbed.

The immersion\dryings are repeated for 4 cycles. After completed the cycle, specimen from 4\6 undergo continuous immersion for 4 days, its note by 4\0 cycle 5. Rate of absorption are calculated using formula

$$\text{Rate of Water Absorption, } \left[\%\ day^{-1}\right] = \frac{W_t[\%] - W_{(t-1)}[\%]}{1\ day} \quad (3)$$

Results and Discussion

Continuous Immersion. From the Figure 1 it can be seen that composite with 40% fibre loading shows almost linear water absorption increment but still remained below than 10% until day 50. Meanwhile the 50% and 60% fibre loading, the water absorption are consistent until day 20 and level off at 12-13% while 70% fibre loading level off on day 10 at 15%. In a system where hydrophilic cellulosic material are well encapsulated within the hydrophobic PP, the only way the water can penetrate into the composite is through the gap between PP molecular chains. A well disperse and low fibre loading composites are encapsulated by thicker PP thus the rate of water absorption is very low due to low water penetration between gaps of PP molecular chain. In this situation, water penetration by the means of capillary and micro crack mechanism is minimal as mention by Espert at el [7]. High fibre loading composites form a network of hydrophilic fibre, thus a higher fibre loading gives better interconnected fibre and bigger 'neck' for the water to penetrate deeper into the composite. This is the possible reasons why 40% fibre loading absorption rate is lower compare to the rest of the fibre loadings as shown in Fig.1.

Effect of Drying 70 % fibre loading is expected to have more fibres on the surface as compared to other fibre loading. Therefore during the drying process, 70% fibre loading lost most of the water and only retain about 36-28% after 2 days of drying. This loss is due to well connected network of fibres with most of them connected to the surface where water vapour evaporates into environment. Meanwhile for 40% fibre loading, majority of fibres are expected to be fully encapsulated by PP which contribute to discontinuation of network between fibres; thus, the dominant mechanism of water movement is through micro cracks and gaps between polymer molecular chains. These conditions contribute to high water retention which can be explained by ink-bottle concept; smaller 'neck' and discontinued network to the open surface block water in pores from drying.

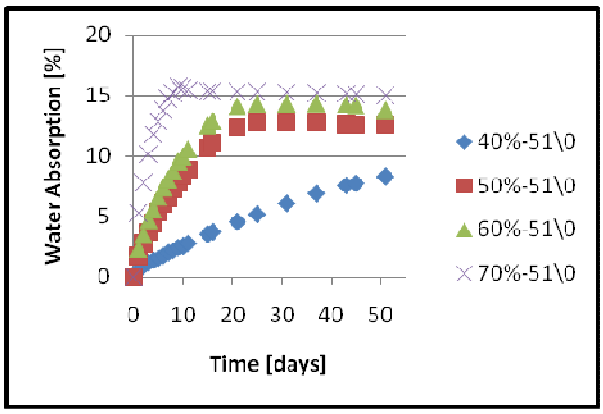


Fig. 1 Water Absorption in Continuous Immersion

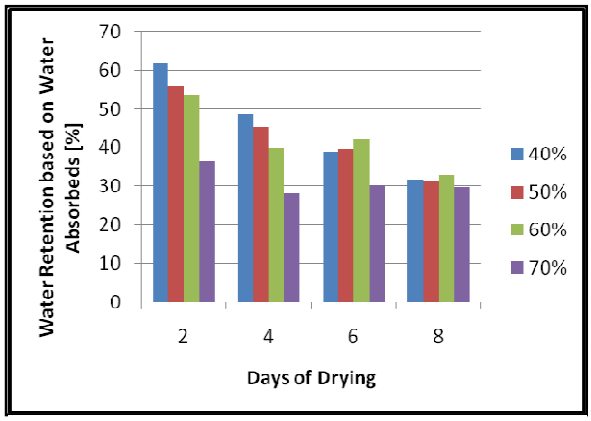


Fig.2 Water Retention Based on Water Absorbed

Repeated Immersion\Drying Effect on Absorption Rate. When the immersion and drying are repeated until the 5th cycle, first day immersion of the 5th cycle absorbed more water than first day immersion of the 1st cycle (positive value shown by the graph in Fig 3). This indicates the passage of fiber network become wider thus allowing water to re-penetrate the composite faster.

Mazuki [6] had mentioned about white material suspected to be extracts of kenaf ooze out from the composite after long immersion and Yu[13] observed that a microbial retting has reduce most of the constituent of kenaf. The missing kenaf constituents, either due to by the means dissolve of soluble extract or microbial retting process, contribute to larger porosity or gaps between fibre and PP within the composite.

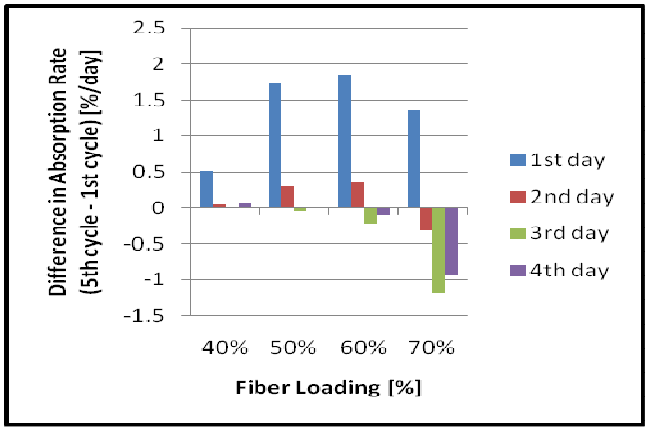


Fig.3 Difference of Absorption Rate Between 5th Cycle and 1st Cycle.

Fig. 3 also suggests that majority material loss occur dominantly on the surface and become lesser as it was extended deep into the composite. After the rapid first day absorption rate, the difference of absorption rate between 5th cycle and 1st cycle rate for 40% fibre loading tend to be zero (indicate same absorbing rate) while for 70% fibre loading become negative (indicate slow absorption rate as composite nearly attained saturation point).

Fig 4 shows that influence of missing constituent can be detected in weight difference, after drying over night in oven at105°C, before and after the experiment.

As a result of larger passage and increase in pores, water retention based on absorbed value decrease significantly into negative value which means loss due to drying is more than 100% i.e. the composites could not retained as much water as it absorbed it absorbed, as shown in Fig 5.

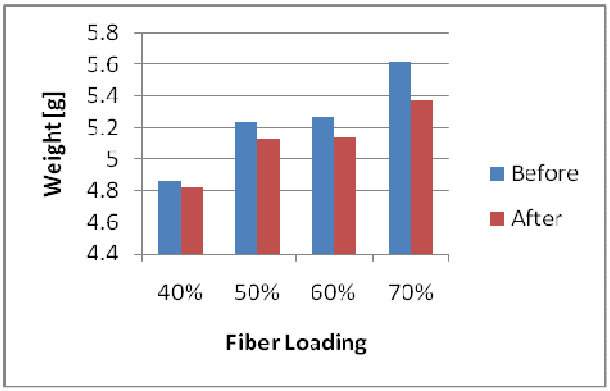


Fig.4. Weight difference before experiment and after 4\6 treatment.

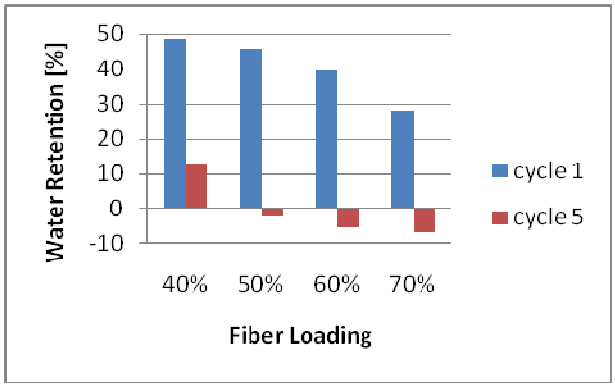


Fig. 5 Difference of water retention based on absorbed water, of 4\6 treatment

Effect of Fibre Loading on Immersion\Drying Repetition. The final results of repeated immersion\drying are shown in fig 6 below. It was found that the data do not exceed the value of water absorbed in the first immersion except 40% fibre loading. 70% fibre loading shows a decreasing pattern in all immersion\drying, while 60% loading shows a decreasing pattern in high immersion (Fig. 6 C &D). 40% fibre loading shows an increasing pattern in all immersion\drying repetition.

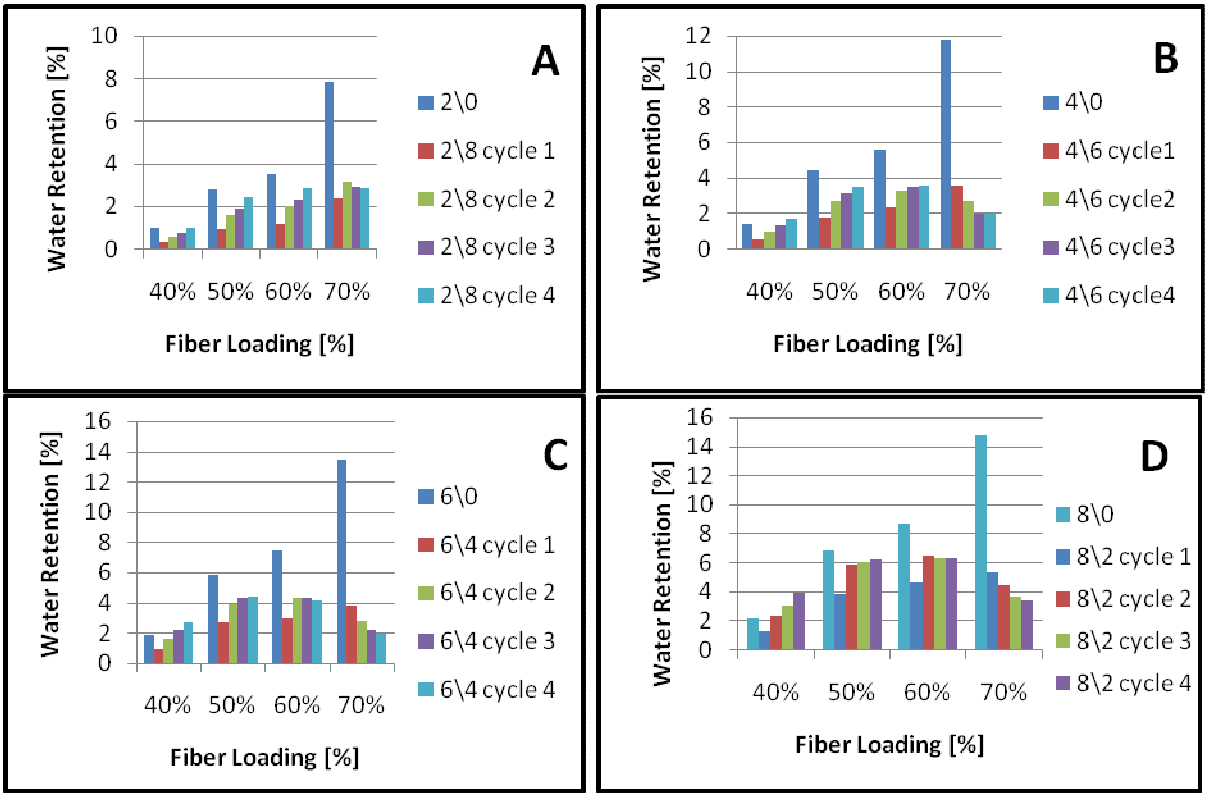


Fig 6. Water retention of repeated immersion\drying at various cycles (A) 2\8, (B) 4/6, (C) 6/4 and (D)8/2

Summary
Duration of immersion and drying does affect the amount of water retention in the composite. Longer immersion and shorter drying exhibit the greatest amount of water retention. Drying process has reduced more water retention in high fibre loading composite. Fibre loading contributes significant effect on water retention. In low fibre loading the water retention increase exceed the water absorbed in the first cycle of immersion. The pattern increase and decrease of repeated immersion depends on number of repetition, duration of immersion and drying, and fibre loading too.

References

[1] R. M. Rowell, in : Science and Technology of Polymers and Advanced Materials, edited by P. N. Prasad et al., Plenum Press, New York, 1998
[2] F. Costa and J.R.M. D'Almeida: Polymer-Plastics Technology and Engineering Vol. 35 (1999), p. 1081
[3] S. Panthapulakkal and M. Sain: Journal of Composite Materials, Vol. 41 (2007), p. 1871
[4] A.A.A. Rashdi, S.M. Sapuan, M.M.H.M. Ahmad and A. Khalina: International Journal of Mechanical and Materials Engineering (IJMME), Vol. 5 (2010), p. 11.
[5] N. Nosbi, H.M. Akil , Z.A.M. Ishak, A.A.Bakar: Materials and Design Vol.31 (2010), p. 4960
[6] A.A.M. Mazuki, H.M. Akil, S. Safiee, Z.A.M. Ishak and A.A. Bakar: Composites: Part B Vol. 42 (2011), p.71
[7] A. Espert, F. Vilaplana, S. Karlsson: Composites: Part A Vol 35 (2004), p 1267
[8] R.M. Rowell, S.E. Lange and R.E. Jacobson: in Proceeding of 7th Pacific Rim Bio-Based Composites Symposium 2004, Nanjing, China, edited by X. Zhou, Science and Technique Literature Press (2004), p. 216
[9] W. Wang, M. Sain, P.A. Cooper: Composites Science and Technology Vol 66 (2006), p 379
[10] A.M.Eligon, A. Achong, R. Saunders: Journal Of Materials Science Vol. 27 (1992), p 3442
[11] A.V. Neimark, K.S.W. Sing, M. Thommes in: Handbook of Heterogeneous Catalysis, 2nd Ed. Edited by G. Ertl, Wiley-VCH Verlag GmbH & Co. KGaA, Weinheim (2008)
[12] B. Libby and P. A. Monson: Langmuir Vol. 20 (2004), p. 4289
[13] Hongqin Yu, Chongwen Yu: Enzyme and Microbial Technology Vol. 40 (2007), p.1806

© (2011) Trans Tech Publications, Switzerland
doi:10.4028/www.scientific.net/KEM.471-472.444

The Effect of Aging Temperature on Mechanical Properties of Banana Pseudostem Fiber Reinforced Polymer Composite

Siti Nur Zafirah M. Zain[1,], Z.N. Ismarrubie[1,a] and E.S. Zainudin[2,b]

[1]Department of Mechanical and Manufacturing Engineering, Faculty of Enginnering Universiti Putra Malaysia, Serdang 43400 Selangor, Malaysia.

[2]Laboratory of Biocomposite Technology, Institute of Tropical Forestry and Forest Products (INTROP), Universiti Putra Malaysia, Serdang 43400 Selangor, Malaysia.

[a]rubie@eng.upm.edu.my, [b]edisyam@eng.upm.edu.my

Keywords: High density polyethylene, Banana pseudostem fiber reinforced polymer composite, Mechanical properties.

Abstract. Polymer composites using natural fibers as the reinforcing agents have found their use in many applications. The initial development of polymer composite based on high density polyethylene (HDPE) with banana pseudostem fiber was studied based on the effect of non-aging and aging treatments. Tensile, flexural and impact tests were performed to investigate the mechanical properties of banana pseudostem fiber reinforced composite. Flexural and impact test results show that the specimen strength improved after aging treatment was applied. However, the tensile test results gave a reverse effect on the strength of the composite after aging. The specimen became more brittle when the composite was exposed to the aging temperature.

Introduction

There is a growing attention in the use of natural fiber acquired from the plants and trees. Natural fiber composites have become a popular new material because of their high strength and stiffness, natural availability and environmental friendliness [1,2]. Furthermore, the natural fibers are also recyclable, renewable and have a very low raw material cost [3]. As a tropical country, Malaysia has plentiful resources of natural fibers and one of the well promising ones is the banana fiber *(Musa acuminata)*. In fact, banana fiber has good mechanical properties such as tensile strength, flexure strength and impact stress compared with material based on plastic such as polypropylene and acrylonitrile butadiene styrene (ABS). Banana fiber can be used as a composite to replace partial industrial components. They also can be used to encourage market place product development as well as to evaluate and compare their potential in the polymer industry. The major component of most plant fibers is cellulose (α-cellulose) [4]. This raw material from biological resources can reduce the cost of production, environmentally friendly and biological degradable [5]. For the matrix, high density polyethylene (HDPE) was chosen because of its chemical and thermal stability as well as its structural similarity to the hydrophobic components of banana fiber [6]. Aging or degradation induces detrimental changes in mechanical properties and temporary or permanent transformation in matrix-fiber interfaces [7]. The glass transformation process and the associated structural changes that occur in the non-equilibrium glassy state was rather general and it was not associated with specific details of chemical structure [8]. This study focused on how to determine the effect of both aging and non-aging temperature on the mechanical properties of banana fiber reinforced composites.

Experimental Procedures

Materials Preparation. In this study, banana pseudostem fiber was used as a raw material. They were mixed with HDPE. Both of these items must be cleaned and dry, in order to avoid the presence

of any substances which can affect the specimen. The mixing of these raw materials based on ratio 2:3, where 40% of fiber and 60% of HDPE resin.

Preparation of Preliminary Testing. The percentage of banana fiber used in the composite is 40% and short fiber are randomly inside the mold. An accelerated aged composite is obtained by applying the standard material age acceleration under ASTM F1980. The parameters involved in this experiment are as follows:

Time of real time aging in a natural environment :	70 days
Ambient temperature :	25 °C
Accelerated aging temperature :	70 °C
Accelerated aging factor :	2.0

Accelerated aging rate and accelerated aging time duration can be determined by using Eqs. 1 and 2.

$$AAR = Q_{10}\frac{AAT - AT}{10} \tag{1}$$

$$AATD = \frac{DRTA}{AAR} \tag{2}$$

where, AAR : accelerated aging rate,
AAT : accelerated aging temperature,
AT : ambient temperature,
Q_{10} : accelerated aging factor,
$AATD$: accelerated aging time duration,
$DRTA$: desired real time aging.

By substituting the parameter values into the equations, we found that the accelerated aging time of 74 hours and 10 minutes was equivalent with an aging of tens weeks of natural environment.

Fabrication of Composites. Combination between HDPE resin and banana fiber in this study case was 60% for HDPE resin and 40% for banana fiber. From the sample weight result, the weight of HDPE resin and banana fiber was 27.24 g and 18.16 g, respectively. The temperature, time and RPM rotor was set in screen machine. Samples were prepared in a thermo Haake internal mixer before they were produced into sheets using a compression molding machine. HDPE resin was put inside the mixer chamber for 7 minutes, then followed by banana fiber. After the mixing process completed, the composite was pulled out and chilled under the room temperature. The hot press process was done after the mixing process by hot press. Then the composite was placed on the transparent paper and then lay it on iron mould where the size was 150 mm × 150 mm.

Preparation of test specimen. The fully-cured composite was cut using electrical saw into desired dimension. All the specimens were cut into 30 pieces according to the standard which is ASTM D638 for tensile test, ASTM D790 for flexural test and ASTM D256 for impact test. The 30 pieces of specimen were divided into two divisions which one for aging and another for non-aging temperature. Five specimens were prepared for each tensile, flexural and impact tests for each type of specimens; non-aging and aging treatments. A notch for impact test standard was introduced by using a special notch driller with dimension of 65 mm × 10 mm. The specimen for aging temperature was heated in an oven for 74 hours 10 minute at 70° C. Then, the specimens were left at room temperature to avoid sudden cooling.

Results and Discussion

Fig. 1 gives the plot for tensile stress of non-aging and aging banana fiber reinforced polymer composite. It is understood that the non-aging specimen have higher stress than aging specimen, but value of strain of the aging specimen has higher strain than non-aging specimen. The tensile test results show that tensile strength of non-aging is in a range of 9-15 MPa and the mean is 12.187 MPa. The strength of aging specimen decreased by 11.94% compared to non-aging specimen. However, even with aging, the strength is still relatively higher in comparison with a pure HDPE. For example, from the mechanical properties of typical implant materials and tissues data, the tensile strength range of a HDPE cartilage without aging is 7-10 MPa. Meanwhile, the strength of banana composite prior to non-aging and subsequent to aging is 12.188 MPa and 10.733 MPa, respectively. Table 1 shows the summary of test result for aged and non-aged of banana fiber reinforced polymer composite. The values were taken from the average of five specimens. The interfacial adhesion between the fibers and the matrix also make the strength weak because the composite produced bubbles during the sample preparation step [9].

The plot of flexural stress between non-aging and aging banana fiber reinforced polymer composite is shown in Fig. 2. It is rational to suggest that oxygen content in aging specimen reduce so it make the strength higher from non-aging specimen. The oxygen space between fiber and matrix become smaller, so the interface bonding between fiber and matrix become stronger. This happen because the oxygen content in the specimen was increased, so it make the flexural strength lower. Overall from this result, the oxygen content of the environment is a principal factor affecting the strength reduction [9].

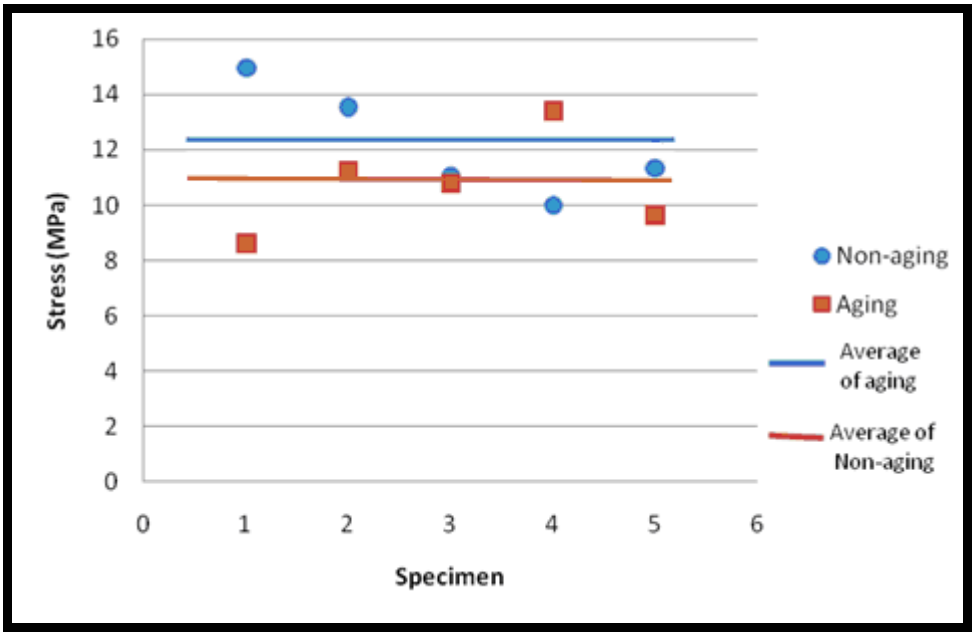


Fig. 1 Plot for tensile stress between non-aging and aging banana fiber reinforced polymer composites.

Table 1 The tensile test result for non-aging and aging banana fiber reinforced polymer composite.

Sample Type		Non-Aging	Aging
Tensile strain at break		4.05049	6.884232
Tensile stress at break	[MPa]	12.18781	10.73336
Modulus of Elasticity	[MPa]	300.9	155.91

The results of the flexural test for both accelerated non-aging and aging banana fiber reinforced polymer composite are summarized in Table 2. We can see that after the banana composite was treated with temperature (aging), the strength of the specimen increased drastically by 64.24% from the value of the non-aging specimen. The properties of the resin also make the strength lower because HDPE have the higher elastic modulus (strong viscoelastic).

The impact test result for non-aging and aging banana fiber reinforced polymer composite are given in Table 3. It is understood that the aging specimen have a higher average of break energy and higher standard deviation than non-aging specimen. The fracture of the aging banana fiber is higher than non-aging banana composite. It is found that the effects of aging process are improving the interfacial bonding between the fiber and matrix. The aging process removes oxygen from the composite during the heating process in oven which makes the strength of the specimen increase. The composite can be weak or not strong when the oxygen content in the fiber is higher [10].

Table 2 The flexural test result for non-aging and aging banana fiber reinforced polymer composite.

Sample Type		Non-Aging	Aging
Tensile strain at break		22.02852	5.039459
Tensile stress at break	[MPa]	26.30911	43.21009
Modulus of Elasticity	[MPa]	119.432	857.435

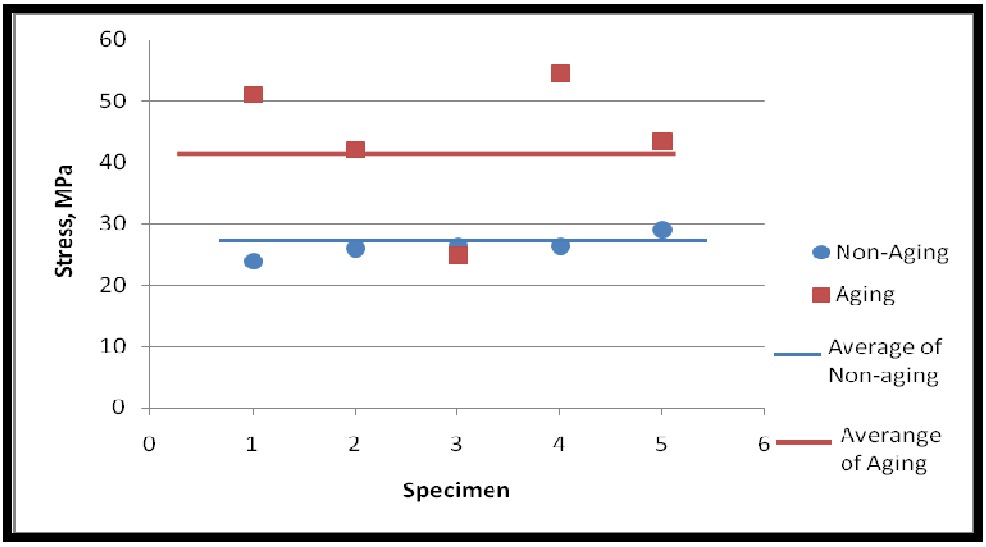


Fig. 2 Plot of flexural stress between non-aging and aging banana fiber reinforced polymer composite.

Table 3 The impact test result for non-aging and aging banana fiber reinforced polymer composite.

Sample Type		Non-Aging	Aging
Average brake energy	[J/m]	13.430	16.397
Standard deviation	[J/m]	1.304	3.741
Percentage of complete break	[%]	100	100
Percentage of complete non-break	[%]	0	0

Summary

An aging banana fiber reinforced polymer composite was successfully produced using a compression process and applying standard (ASTM) accelerated material aging. Tensile, flexural and impact tests were performed on non-aging and aging BPFRC in order to compare the mechanical properties. The tensile test result shows decreased tensile strength by 11.94% for the aging composites compared to that of the non-aging composites, but with aging the strength is still relatively higher in comparison with a pure HDPE. For flexural test, after the banana composite was treated with temperature (aging), the strength of the specimen increased by 64.24% from the value of the non-aging specimen. For impact test, it is understood that the aging specimen have a higher average of break energy and higher standard deviation than non-aging specimen. The fracture of the aging banana fiber is higher than non-aging banana composite.

References

[1] Sapuan SM, Leenie A, Harimi M, Beng YK (2006), Mater Des., Vol. 27, p. 689.

[2] Mukhopadhyay S, Srikanta S (2008). 2008; Vol. 93, p. 2048.

[3] Justiz-Smith NG, Junior Virgo G, Buchanan VE. Mater Charact" Vol. 59, p. 1273.

[4] Caroline Baillie (2004). "Green Composites, Polymer Composites and Environment." CRC Press, p. 67.

[5] Amar K Mohanty, Manjusri Misra, Lawrance T.Drzal (2005). "Natural Fiber Biopolymer and Biocomposites." Tylor & Francis, p. 5.

[6] Charles A Harper (2006). "Handbook of Plastic Technologies." Mc Graw-Hill, p. 34.

[7] Glenn Petrie, Eastman Chemical, "http://www.plastemart.com/upload/Literature/Accelerated-ageing-tests-to-meet-performance-needs-of-plastic-medical-devices.asp", assessed on November 3, 2009.

[8] John M.Hutchinson, (1995), Prog. Polym. Sci, Vol. 20, p. 703.

[9] Hoi-yan Cheung, Mei-po Ho, Kin-tak Lau (2009), Composites: Part B 40, p. 655.

[10] H.Parvatareddy, J.Z Wang, D.A Dillard, T.C Ward (1995), Composites Science and Technology, p. 399.

© (2011) Trans Tech Publications, Switzerland
doi:10.4028/www.scientific.net/KEM.471-472.449

The Behavior of Construction Waste Concrete

DOH Shu Ing[1, a], KOID C. H.[1], NG G. Y.[1], TEO S.H.[1] and ADILEN Suil[2]

[1]Universiti Tunku Abdul Rahman, Faculty of Engineering and Green Technology,
31900 Kampar, Perak, Malaysia

[2]Politeknik Ungku Omar, Department of Civil Engineering, Jalan Raja Musa Mahadi,
31400 Ipoh, Perak, Malaysia

[a]dohsi@utar.edu.my

Keywords: Construction waste, compressive strength, flexural strength, waste management.

Abstract. Due to urbanisation and rapid development in Malaysia, the waste generated from the construction has increased tremendously. Such waste accumulation has been a major issue not only in Malaysia but also worldwide. In line with this, recycling construction as coarse aggregate can be introduced to solve two environmental aspects namely waste disposal crisis while protecting from depleted natural resources. In this study, three types of construction waste namely floor tiles, clay bricks and crushed concrete aggregate were used to replace coarse aggregate in concrete production. The effect of coarse aggregate replacement on the workability, compressive strength, and flexural strength Grade 30 concrete were investigated and discussed. The concrete specimens that made of crushed floor tiles, crushed bricks, and crushed concrete aggregate were termed as tile concrete (TC), brick concrete (BC) and crushed aggregate concrete (CAC). The result for all specimens has shown good workability with slump ranging from 51-85 mm. BC showed optimum brick replacement of 17% with the 28-day compressive strength of 36 N/mm^2. TC and CAC on the other hand showed optimum result at 20% and 16% replacement with 28-day compressive strength of 31.43 N/mm^2 and 31.25 N/mm^2 respectively. It can be concluded that optimum result for BC, TC and CAC have achieve concrete G30. The flexural strength of BC, TC and CAC ranges from 3.03-4.49 N/mm^2, 3.62-4.60 N/mm^2, and 4.05-5.43 N/mm^2.

Introduction

Construction waste has caused much environmental problem worldwide [1, 2]. The rapid development in Malaysia, the waste from construction industries has increased tremendously. Begum et al. (2006) suggested that construction waste contributed approximately 28% of the total waste in Central and Southern Malaysia [3]. The investigation conducted by Lau et al. (2008) concluded that concrete contributed the highest percentages among concrete waste of 64.7%, followed by mortar (20.8%), bricks (13.4%) and others (1.1%) [4]. The current construction industries basically manage their waste by dumping them into landfill which bring environmental problem which give negative implication to current and future generations [2, 5, 6].

The annual worldwide concrete usage has reached about 10 billion tons has caused depletion of non-renewable natural stones used in concrete production [7]. Pappu et al. (2007) on the hand suggested that the continuous exploitation of material from the existing natural resources will damage the environment [8]. Furthermore, the over quarrying due to construction has caused insufficient high and marginal quality aggregate [9, 10]. In order to reduce the environmental problem, the potential of recycling construction to replace coarse aggregate can be investigated [2]. In Europe, construction waste are used for road base and sub-base material while in Japan construction waste has been recycled to substitute natural aggregate particularly for non structural applications [11,12]. Therefore, investigation aimed to achieve concrete grade G30 which is suitable for structural applications using crushed tiles, brick and concrete as replacement of coarse aggregate besides reducing the environmental problems caused by construction waste.

Materials. The raw materials used in this study were all locally available. They include the ordinary Portland cement (OPC) as binder, river sand as fine aggregate, crushed granite, crushed brick, crushed tile and crushed concrete as coarse aggregate, and superplasticiser Type F (ASTM C494).

Preparation of coarse aggregate from construction waste. The construction waste namely bricks and tiles were sourced from building demolition and renovation projects sites in Kampar while the concrete waste were obtained from concrete testing laboratory in Ipoh, Perak. Construction waste such as bricks, tiles and concrete comes in many form and shape. Before construction wastes are suitable to be used, it was be broken down into suitable size for concrete production. Knapton (1999) suggested that aggregate size less than 20 mm to be used for concrete production [13]. With this size, it would help to reduce drying shrinkage which in turn means less curling, fewer cracks and more stable joints, improve aggregate interlocking at cracks and induced joint and also reduce cement consumption to achieve the same concrete strength [14]. All crushed construction waste were sieved using KENCO sieving machine to obtain suitable aggregate size which range from 5-20 mm. Nawy (2008) suggested that crushed aggregate should be clean and free from impurities such as silt and dirt [15]. Table 1 shows the physical properties of coarse aggregate.

Table 1 Physical Properties of Coarse Aggregate

Properties	Crushed Granite	Crushed Brick	Crushed Tile	Crushed Concrete
Maximum size (mm)	20	20	20	20
Bulk density (kg/m^3)	1451	1068	1145	1371
Moisture content, as received, (%)\	0.60	2.32	3.73	0.65
Water absorption, 24 hr (%)	2.04	11.52	6.41	3.11
Fineness modulus	3.78	2.73	3.46	2.61

Table 2:Mix Design of Concrete

Properties	Cement	Sand	Granite	Brick	Tile	Concrete	w/c ratio	Remark
G1 (control)	1	2	2.0	0	0.0	0.0	0.39	No replacement
BC_{10}	1	2	1.8	0.2	0.0	0.0	0.39	10% brick replacement
BC_{20}	1	2	1.6	0.4	0.0	0.0	0.39	20% brick replacement
BC_{30}	1	2	1.4	0.6	0.0	0.0	0.39	30% brick replacement
BC_{40}	1	2	1.2	0.8	0.0	0.0	0.39	40% brick replacement
TC_{20}	1	2	1.6	0.0	0.4	0.0	0.39	20% tile replacement
TC_{40}	1	2	1.2	0.0	0.8	0.0	0.39	40% tile replacement
TC_{60}	1	2	0.8	0.0	1.2	0.0	0.39	60% tile replacement
TC_{80}	1	2	0.4	0.0	1.6	0.0	0.39	80% tile replacement
TC_{100}	1	2	0.0	0.0	2.0	0.0	0.39	100% tile replacement
CAC_{25}	1	2	1.5	0.0	0.0	0.5	0.39	25% concrete replacement
CAC_{50}	1	2	1.0	0.0	0.0	1.0	0.39	50% concrete replacement
CAC_{75}	1	2	0.5	0.0	0.0	1.5	0.39	75% concrete replacement
CAC_{100}	1	2	0.0	0.0	0.0	2.0	0.39	100% concrete replacement

The bulk densities of crushed aggregate were in the range of 1068 to 1451 kg/m^3 which fall within normal weight aggregate. Crushed bricks have relatively high water absorption of 11.52% as compared to crushed granite, 2.04%, crushed concrete, 3.11% and crushed tile, 6.41%. Due to high water absorption, crushed bricks were used in saturated surface dry (SSD) condition for all the mixes.

Mixing and Compaction. The mix designs of concrete were shown in Table 2. Mixing of concrete was carried out conforming to BS 1881: Part 125 (Clause 6.2 for SSD aggregates) [16]. A small rotary drum of 40kg capacity was used. Compaction for concrete was done according to BS 8110: Part 108 [17]. When casting 100 mm cubes and prism 100 x 100 x 500 mm specimens, vibrating table was utilized as external vibrator. Immediately after casting, all specimens were covered with plastic sheet for 24±2 hours prior to demoulding. The specimens then were water cured for 3, 7 and 28 days testing. The concrete mixes were designed to achieve concrete grade G30.

Results and Discussion

Workability. The slump test was carried out as per BS 1881: Part 102 [18] for all concrete mix. The slump test results for all concrete mixes are tabulated in Table 3. It is observed that the slump for all concrete mixes ranges from 51-85mm which complied with ASTM C143 of 75±25 mm [19].

Compressive strength. The compressive strength of hardened concrete was conducted according to BS 1881: Part 116 [20]. Result at the age of 3, 7, 28 days were tabulated in Table 3. Figure 1 shows the relationship between compressive strength with curing time for BC of different percentages of brick replacement. In general, the compressive strength of B_{10}, B_{20}, B_{30} and B_{40} exceeded 25 N/mm^2 which is suitable for structural application. From the observation, the replacement of brick up to 20% has shown highest compressive strength for BC for 3, 7 and 28 days. B_{10} and B_{20} have shown 10% improvement of compressive strength as compared to the control specimen. Similar result was shown in the investigation conducted by Bektas et al. [21].

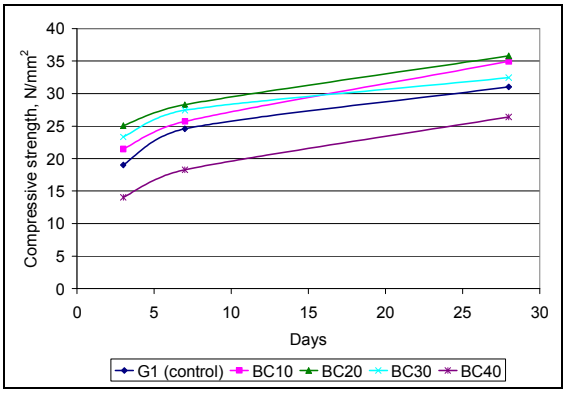


Fig. 1 Compressive strength-curing time of BC

Fig. 2 shows the relationship between compressive strength with curing time for TC of different percentages of tile replacement. Similar to BC, the compressive strength for all crushed tile concrete exceeded 25 N/mm^2 and is suitable for structural application. There is no significant different in 28 days compressive strength of T_{20}, T_{40}, T_{60}, T_{80} and T_{100} ranges from +1.3% to -12.80% compared to control concrete of 31.02 N/mm^2. Therefore, crushed tile can be used effectively to replace granite in concrete production.

Fig. 3 shows the relationship between compressive strength and curing time for CAC of different percentage of crushed concrete aggregate replacement. Generally, the CAC showed negative compressive strength result as compared to control concrete. The 28 days compressive strength reduces as the percentage of replacement with crushed concrete aggregate increases from 30.88 N/mm^2 to 23.32 N/mm^2. The reduction in compressive strength is due to the portion of coarse aggregate which is smaller than 2 mm [7, 22]. From the investigation, only C_{25}, C_{50} and C_{75} were suitable to be used for structural application.

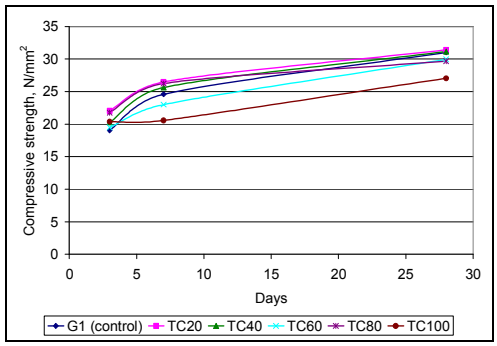


Fig. 2 Compressive strength-curing time of TC

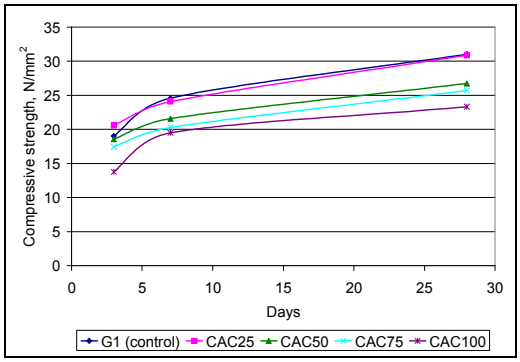


Fig. 3 Compressive strength-curing time of CAC

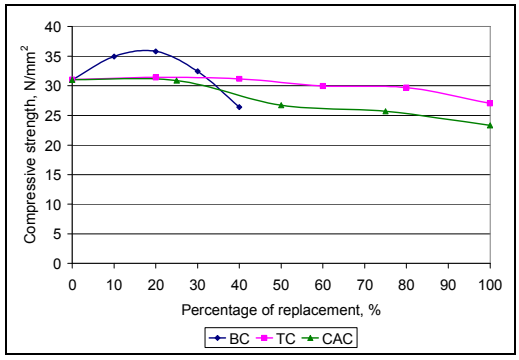


Fig. 4 Compressive strength versus replacement percentages of different aggregate types

Fig. 4 shows the relationship between compressive strength with replacement percentages of different types of aggregate. From the graph it is observed that BC in general showed higher compressive strength as compared to TC and CAC. Such observation occurred due to lower fines in brick concrete as crushed bricks were soaked and wash prior to casting. Besides that, the porous characteristic of crushed brick at approximately 20% gives good absorbing qualities. The amount of fines increases the percentage of replacement increases for recycled aggregate concrete. The occurrence of high fines increases the surface area of coarse aggregate thus requires higher content of cement to bind it together.

Table 3 Physical and Mechanical Properties of Aggregate Replacement Concrete

Properties	Slump (mm)	Compressive Strength (1) (N/mm^2)	Flexural Strength (2) (N/mm^2)	(1)/(2)
G1 (control)	56	31.02	4.54	14.64
B_{10}	85	34.96	3.03	8.67
B_{20}	71	35.81	3.23	9.02
B_{30}	65	32.44	3.57	11.00
B_{40}	64	26.41	4.49	17.00
T_{20}	52	31.43	4.60	14.64
T_{40}	57	31.17	4.40	14.12
T_{60}	60	29.96	4.17	13.92
T_{80}	52	29.69	3.84	12.93
T_{100}	52	27.05	3.62	13.38
C_{25}	58	30.88	5.43	17.58
C_{50}	55	26.73	5.05	18.89
C_{75}	53	25.69	4.28	16.66
C_{100}	51	23.32	4.04	17.32

BC showed optimum brick replacement of 17% with the 28-day compressive strength of 36 N/mm^2. TC and CAC on the other hand showed optimum result at 20% and 16% replacement with 28-day compressive strength of 31.43 N/mm^2 and 31.25 N/mm^2 respectively. It can be concluded that construction waste can be used as coarse aggregate provided with appropriate percentage of replacement.

Flexural strength

The flexural strength of hardened concrete was tested according to ASTM C 78-02 [23]. Result at the age of 3, 7, 28 days were tabulated in Table 3. From table 3, it is observed that the flexural strength of concrete increases as the days of curing increases. In general CAC showed the highest flexural strength followed by TC and BC.

The 28 day flexural strength of BC which range from 3.03-4.49 N/mm^2 is lower than control of 4.54 N/mm^2. The flexural strength of BC increases as the percentage of brick replacement increases from 10-40%. Brick are generally porous and have good energy absorbing qualities. The 28 days flexural strength of TC and CAC reduces as the percentage of replacement increases. From the observation the flexural strength of T_{20} (4.60 N/mm^2), C_{25} (5.43 N/mm^2) and C_{50} (5.05 N/mm^2) is higher than the control concrete. Since, the shape, and surface texture of aggregate considerably influence the flexural strength, the addition of crushed tile (up to 20%) and crushed concrete aggregate (up to 50%) as partial replacement gives positive in flexural strength compared to the control concrete [24, 25]. Too high concentration of hard and brittle aggregate in concrete production will reduce the flexural strength.

Summary

From the investigation, the following conclusion were drawn

i. The slump of the mix was in the range of 51-85 mm, which is the range of a workable concrete and is suitable for structural normal weight concrete.

ii. The BC (B_{10}, B_{20}, B_{30}, B_{40}), TC (T_{20}, T_{40}, T_{60}, T_{80}, T_{100}) and CAC (C_{25}, C_{50}, C_{75}) has achieved the compressive strength of more than 25 N/mm^2 which is suitable for structural application. The optimum compressive strength for BC was 36 N/mm^2 at 17% replacement, TC 31.43 N/mm^2 at 20% and CAC 31.25 N/mm^2 at 16%.

iii. The flexural strength of BC was in the range of 3.03-4.49 N/mm^2 as it increases from 10-40%. The flexural strength of TC reduces from 4.60 to 3.62 N/mm^2 as it reduces from 20

to 100%. Similar with TC, the flexural of CAC reduces from 5.43 to 4.04 N/mm^2 as the percentage of replacement increases from 25 to 100%.

References

[1] T. Esin and N. Cosgun: Building and Environment 42 (2007), p. 1667.

[2] V.W.Y. Tam and C.M. Tam: Building and Environment 41 (2006), p. 1649.

[3] R.A. Begum, C. Siwar, J.J. Pereira and A.H. Jaafar: Journal Resources, Conservation and Recycling Vol. 48 (2006), p. 86.

[4] H.H. Lau, A. Whyte and P.L. Law: International of Journal Resources, Vol. 2 (2008), p. 261.

[5] L.Y. Yie and M. Noor Zalina: Malaysian Journal of Science, Vol. 25 (2006), p. 1.

[6] J.P. Couto and A.M. Couto: Unpublished MSc dissertation, University of Minho. (2002)

[7] C. Meyer: Cement and Concrete Composites, Vol. 31 (2009), p. 601.

[8] A. Pappu, M. Saxena, and S.R. Asolekar: Building and Environment, Vol. 42 (2007), p. 2311.

[9] M.A. Mannan and C. Ganapathy: Construction Building and Material, Vol. 16 (2002), p. 29.

[10] M.A. Mannan, J. Alexander, C. Ganapathy, and D.C.L. Teo: Construction Building and Material, Vol. 41 (2006), p. 1239.

[11] T. Hansen, E. K. Lauritzen: American Concrete Institute, (2004), p. 35.

[12] Y. Kasai: American Concrete Institute, (2004), p. 11.

[13] J. Knapton, in: *Single Pour Industrial Floor Slab*, Thomas Telford Publishing (1999)

[14] G. Garber, in: *Design and Construction of Concrete Floor*, Oxford Butterworth-Heinemann (2006).

[15] E.G. Nawy: Concrete Construction Engineering Handbook, Florida: CRC Press (2008)

[16] BS 1881: Part 125: *Method for Mixing and Sampling Fresh Concrete Samples in the Laboratory*, London: British Standard Institution.

[17] BS 8110: Part 108: *Method for Mixing and Sampling Fresh Concrete Samples in the Laboratory*, London: British Standard Institution

[18] BS 1881: Part 102: *Method for Determination of Slump*, London: British Standard Institution

[19] ASTM C143: *Standard test method for slump of hydraulic-cement*, Annual Book of ASTM Standards

[20] BS 1881: Part 106: *Method for Determination of Compressive Strength*, London: British Standard Institution

[21] F. Bektas, K. Wang, H. Ceylan: Construction Building Material, Vol. 22 (2008), p. 1288-1298

[22] T.C. Hansen: RILEM Report No. 6. London (1992)

[23] ASTM C78-02: *Standard test method for flexural strength of concrete (using simple beam with third point loading)*, Annual Book of ASTM Standards

[24] A.M. Neville: Properties of Concrete, Malaysia: Longman (1999)

[25] A. Mark, M. Sidney: Aggregates in Concrete, New York: Taylor and Francis (2005)

© (2011) Trans Tech Publications, Switzerland
doi:10.4028/www.scientific.net/KEM.471-472.455

Comparative Study of Physical Properties Based on Different Parts of Sugar Palm Fibre Reinforced Unsaturated Polyester Composites

J. Sahari[1, 2a], S.M. Sapuan[1, 2b], Z. N. Ismarrubie[2c] and M.Z.A.Rahman[3d]

[1] Laboratory of Advanced Materials and Nanotechnology, Institute of Advanced Technology,
[2] Department of Mechanical and Manufacturing Engineering,
[3] Department of Chemistry, Faculty of Science,
Universiti Putra Malaysia, 43400 Serdang, Selangor, Malaysia

[a]Kandhalawi_86@yahoo.com, [b]sapuan@eng.upm.edu.my, [c]rubie@eng.upm.edu.my,
[d]mzaki1212@putra.upm.edu

Keywords: physical properties, water absorption, thickness swelling

Abstract. This research was conducted to evaluate the potential of sugar palm residue as a raw material to produce the new green composites. The physical properties of sugar palm fibre reinforced unsaturated polyester composites from different part which are sugar palm frond (SPF/PE), sugar palm bunch (SPB/PE), sugar palm trunk (SPT/PE) and black sugar palm fibre (*ijuk*/PE) were studied. Samples were submerged in distilled water for 24 hours. The water absorption and thickness swelling were investigated in order to determine the dimensional stability of the composites. It is found that SPF/PE showed the higher value of water absorption and thickness swelling which are 1.57%, and 1.56% followed by SPB/PE (1.35%, 1.11%), *ijuk*/PE (0.65%, 0.76%) and SPT/PE (0.39%, 0.50%). Generally, this investigation is valuable for researchers in order to evaluate the potential and some possible application of sugar palm residues as a new natural composites product.

Introduction

Natural Fibre are now become the new alternatives material that can replace glass fibres either alone or combined with another material to produce green composite materials. One of the most important natural fibres that become popular among the researches is sugar palm fibre that is obtained from sugar palm tree. Traditionally, the fibre was used in various applications such as broom, rope, paintbrush and roof. Over the years, these materials have a potential to apply as a biocomposites. Mostly all the investigation that have been done previously on sugar palm fibre composites were using epoxy as the matrix but there is still lack of research has been carried out using unsaturated polyester as the matrix. It have been reported that unsaturated polyester matrix is the most widely used matrix system and now becoming the important material in industries which dominating the market. These are due to its good properties in mechanical, electrical and chemical [1]. Beside that, the combination of fibre from different part of sugar palm plants which are sugar palm frond (SPF), sugar palm bunch (SPB), sugar palm trunk (SPT) and black sugar palm fibre locally known as *ijuk* with unsaturated polyester can give the new potential material that can apply in various application. Natural fiber reinforced polymer composites nowadays are used in widely field such as for outdoor furniture, fishing gear, automobile and marine craft. Almost all of these composites material are exposed to ultraviolet (UV), moisture from rain, snow and humidity and hence, issues of weathering, moisture uptake, creep, and decay resistances are important properties to study in order to determine the change in properties as a function of environmental stresses. These researchs are focused only to the water absorption behavior and its thickness swelling of sugar palm fibres reinforced unsaturated polyester composites. Genarally, all natural fibre reinforced polymer composites absorb moisture in humid atmosphere and when they are immersed in water due to the existing of celluloses, hemicelluloses and lignin in the fibres which have the hydrophilic behaviour. It has been reported that the main concerns for the use of natural fibre reinforced

composite materials are their susceptibility to moisture absorption which gives high effects to its physical and mechanical properties. Therefore, it is important to investigate the drawback of natural fibres and this problem should be considered when applying as reinforcement in the composite materials [2].

Materials and Method

Preparation of sugar palm fibres. The sugar palm fibre from different part of sugar palm tree was collected at Jempol, Negeri Sembilan. All of these fibres were extracted, cut into chips, grind until reduce to 75-150 μm and dried. All of these fibres seperated into plastic samples and labelled as SPF for sugar palm frond, SPT for sugar palm trunk, SPB for sugar palm bunch and *ijuk* for black sugar palm fibre.

Fabrication of Composites. The composite plates were fabricated using compression moulding technique. First of all, the fibres were dried in an oven at 80 ºc for 24 hours. The fibre and unsaturated polyester were mixed by using glass rod for 5 minutes. The liquid composite were poured in an open mould made by galvanic iron plates. The composite were pressed by using cold press machine and left to cure in room temperature for 24 hours. Different parts of sugar palm fibre reinforced unsaturated polyester composites which are SPT, SPF, SPB and *ijuk* with 30% volume fraction were prepared and labelled as SPT/PE, SPB/PE, SPF/PE and *ijuk*/PE.

Water absorption and thickness swelling test. The water absorption and thickness swelling were conducted based on method conducted by other research group [3]. All of the specimens with a dimension of 50 mm × 25 mm × 3 mm marked as SPT/PE, SPB/PE, SPF/PE and *ijuk*/PE were immersed in distilled water for 24 hours. 10 specimens of each type of composites were tested and the results averaged. Water absorption and thickness swelling were calculated using the following equations [4]:

$$\text{Water absorption (\%)} = \frac{W2-W1}{W1} \times 100 \quad (1.1)$$

where,
$W1$ = weight before soaking (g)
$W2$ = weight after soaking (g)

$$\text{Thickness swelling (\%)} = \frac{d2-d1}{d1} \times 100 \quad (1.2)$$

where,
$d1$= initial thickness (mm)
$d2$ = final thickness (mm)

Result and Discussion

Fig. 1 and 2 below shows the water absorption and thickness swelling values of sugar palm fibres from different parts of sugar palm tree reinforced unsaturated polyester composites. The water absorption test of the samples was calculated based on weight of the specimens before and after immersion in water for 24 h. While the thickness swelling test was measure by using digital vernier calipers with a precision of 0.01 mm. Based on the figures below, it found that SPF/PE gives high value of water absorption and thickness swelling which are are 1.57%, and 1.56% followed by SPB/PE (1.35%, 1.11%), *ijuk*/PE (0.65%, 0.76%) and SPT/PE (0.39%, 0.50%).

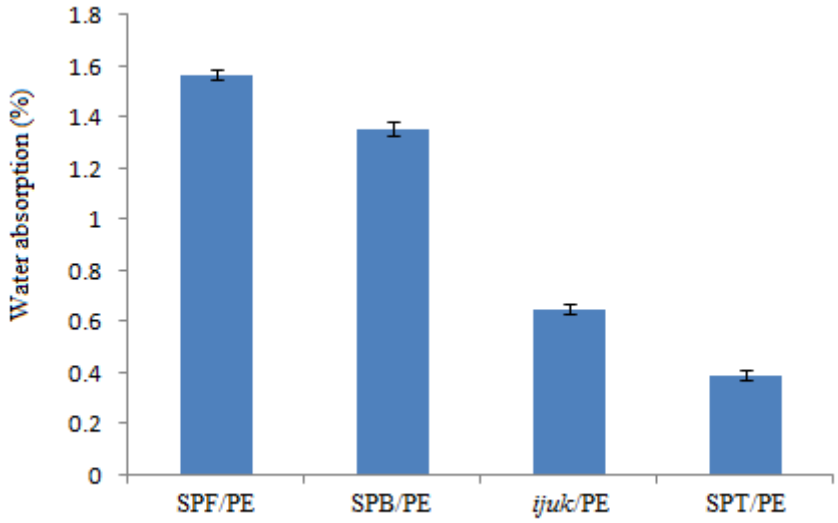


Fig. 1: Water absorption of sugar palm fibre from different parts reinforced unsaturated polyester composites

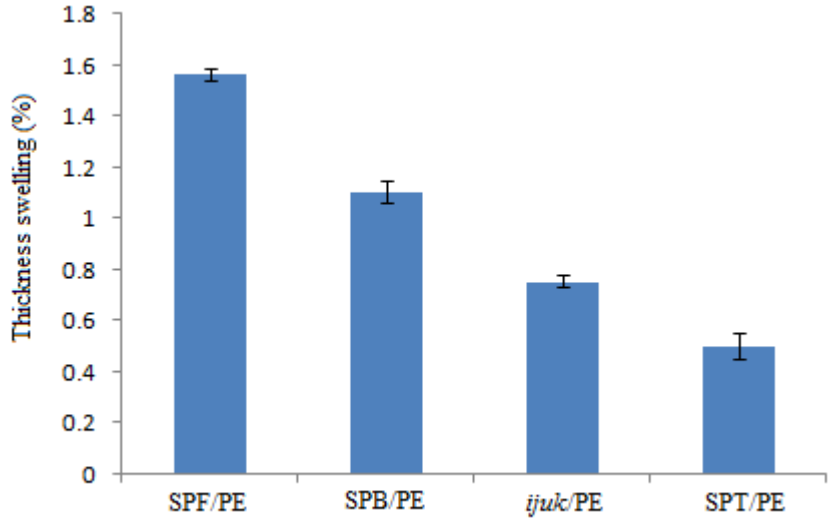


Fig. 2: Thickness swelling of sugar palm fibre from different parts reinforced unsaturated polyester composites

Actually, the value of water absorption and thickness swelling was caused by the hydrophilic in nature of the fibres and not by the hydrophobic behaviour of the unsaturated polyester. All lignocellulosic material mostly composed of celluloses, hemicelluloses and lignin which have hydrophilic natural polymeric material. All of these contents play an important role in water absorption behaviour. This substance possessing many –OH groups, which is able to combine with water molecules. Therefore, when a composite containing lignocellulosic material is applied in moist areas, the composite will absorbs water [5]. These results also prove the previous finding for the single fibre that there are relationships between the holocelluloses content and water absorption behaviour. Our previous research shows that sugar palm frond (SPF) has the highest holocelluloses content which is 81.22% gave the highest water absorption which is 132.80% followed by sugar palm bunch (SPB), *ijuk* and sugar palm trunk (SPT) as shown in Table 1 [6]. If compared to the other natural fibre reinforced polymer composites show in Table 2, its found that water absorption of SPF/PE and SPB/PE have a little bit same with kenaf/PP, acacia/PP and banana/PP which are in

range 1.30-1.70%. Meanwhile, for *ijuk*/PE and SPT/PE, the water absorption is very low compare to the other natural fibre composites which are below 0.70%.

Table 1: Celluloses content and water absorption of single fibres [6]

Fibres	Holocelluloses (%)	Water absorption (%)
SPF	81.22	132.80 (25.79)
SPB	71.78	123.71 (14.13)
ijuk	65.62	103.80 (23.82)
SPT	61.10	61.38 (11.05)

( ) refers to standard deviation

Table 2: Water absorption and thickness swelling of some natural fibre-composites

Composites	Water absorption (%)	Thickness swelling (%)	References
kenaf/PP	1.30	0.97	[4]
acacia/PP	1.58	2.21	[4]
banana/PP	1.64	3.29	[4]
EFB/PP	2.07	4.18	[4]

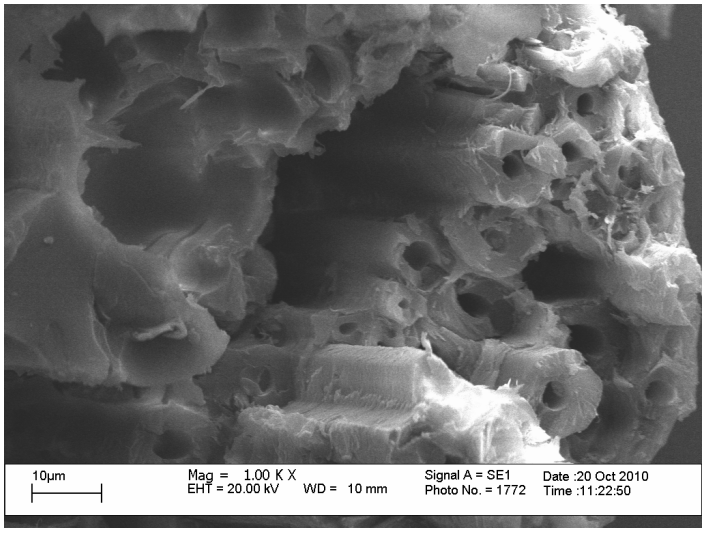


Fig. 3a: The SEM micrograph of SPF/PE composites at 1000X magnification

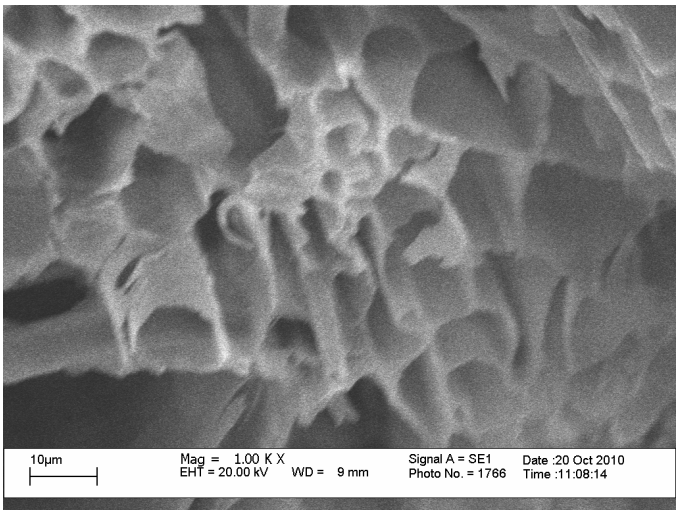


Fig. 3b: The SEM micrograph of SPB/PE composites at 1000X magnification

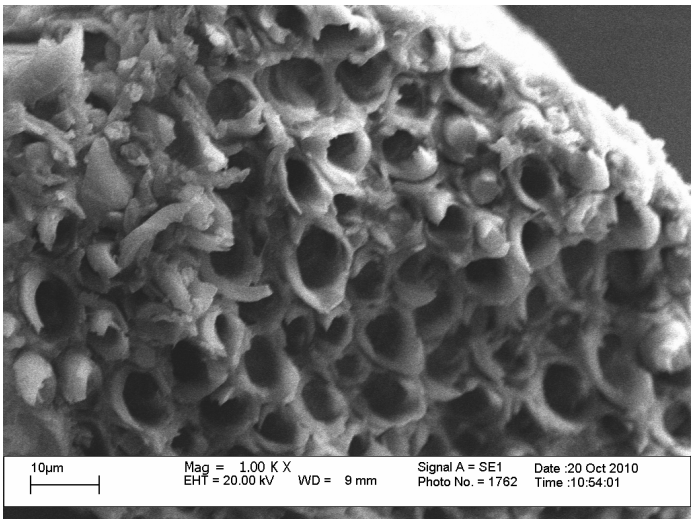


Fig. 3c: The SEM micrograph of *ijuk*/PE composites at 1000X magnification

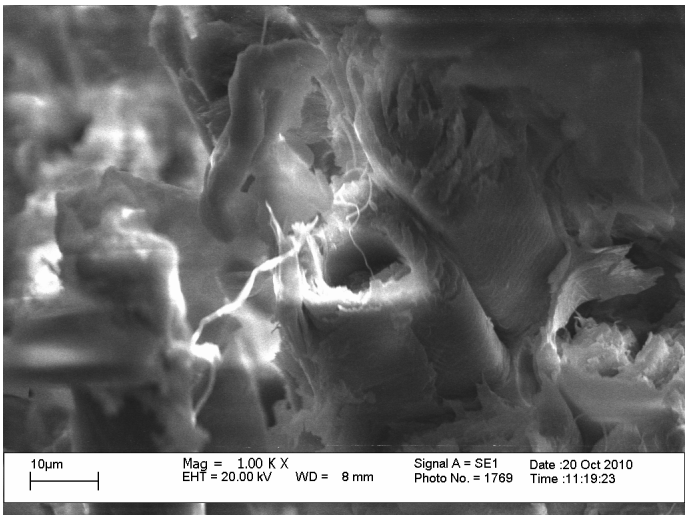


Fig. 3d: The SEM micrograph of SPT/PE composites at 1000X magnification

Summary
From this investigation, the physical properties of fibre from different part of sugar palm tree reinforced unsaturated polyester which are SPF/PE, SPB/PE, SPT/PE and *ijuk*/PE have been evaluated. From the results, it is found that SPF/PE showed the higher value of water absorption and thickness swelling which are 1.57%, and 1.56% followed by SPB/PE (1.35%, 1.11%), *ijuk*/PE(0.65%, 0.76%) and SPT/PE (0.39%, 0.50%). Generally, there are no slightly difference in physical properties of sugar palm fibre from different parts of sugar palm tree reinforced unsaturated polyester composites compared to the other established natural fibre composites.

Acknowledgement
The authors wish to thank to Ministry of Agriculture and Agro Based Industry Malaysia for funding the research grant (Project No.: 03-01-04-SF0246). Special thanks also to the staff of Department of Mechanical and Manufacturing Engineering, Universiti Putra Malaysia and Institute of Tropical Forestry and Forest Products (INTROP), Universiti Putra Malaysia for their support during the research were conducted.

References
[1] D. Ray and J. Rout, in: Natural fibers, biopolymers, and biocomposites, edited by Mohanty et al. in Thermoset biocomposites pp. 291-345. CRC Press, Boca Raton (2005).
[2] M.M. Thwe and L.Kin: Comp. App. Sc. Manu. Vol. 33 (2002), p. 43-52.
[3] K. Myrtha, O. Holia and S. Anung: J. Bio. Sc. Vol. 7 (2007) , p.393-396.
[4] U.M.K. Anwar, M.T. Paridah, H. Hamdan, S.M. Sapuan and E.S. Bakar: Ind. crops prod. Vol. 29 (2009), p. 214–219.
[5] H.S. Yang, H.J. Kim, H.J. Park, B. J. Lee and T.S. Hwang: Comp. Struc. Vol. 72 (2006), p. 429–437.
[6] J. Sahari, S.M Sapuan, Z. N. Ismarrubie, M.Z.A.Rahman: Tensile and chemical properties of different morphological parts of sugar palm fibres: submitted to International Journal of Physical Sciences (2010).

© (2011) Trans Tech Publications, Switzerland
doi:10.4028/www.scientific.net/KEM.471-472.461

Effect of Core Thicknesses on Impact Performance of Thermoplastic Honeycomb Core Sandwich Structure Under Low-Velocity Impact Loading

Nurashikin Sawal[1,a], Hazizan Md. Akil[2,b]

School of Materials and Mineral Resources Engineering, Engineering Campus, Universiti Sains Malaysia, 14300 Nibong Tebal, Penang, Malaysia

[a]nurashikinsawal@gmail.com, [b]hazizan@eng.usm.my

Keywords: Sandwich panels, low-velocity impact, honeycomb, damage

Abstract. Low-velocity impact test on sandwich panels composed of aluminum face sheets and thermoplastic honeycomb cores have been performed to characterize the impact performance as a function of core thickness and drop heights. Impact parameters like maximum impact force, impact energy and impact damage area were evaluated and compared. Consequent damages were inspected visually on the impact surface as well as the rear surface. The experimental results found that panels with thicker core exhibited higher impact force than thinner core counterparts, allowing the panel to absorbed more energy. Higher degree of impact damage can be observed at elevated drop heights as most of the damage took the form of local core crushing, face sheet buckling and debonding between the face sheet and core,. Resulting damage area were different according to the core thickness as thicker core prone to absorbed more energy that lead to more damage propagation.

Introduction

Nowadays sandwich structures are widely applied in various applications such as aerospace, marine, civil and mechanical industries due to their excellent stiffness-to-weight ratio, energy absorption, thermal and acoustic insulation [1]. Generally, sandwich structure is consists of three different elements; the core, adhesives and face sheet. There are many wide varieties of core materials currently in use includes honeycomb, foam, balsa and corrugated cores are the most widely used [2]. Impact response and damage characteristics are strongly dependent on the core and face sheet materials and their thickness [3]. Each element plays a major role in providing strength and resistance towards damage. The core was placed between the face sheets in order to transmit shear between them which will provide shear rigidity to the structure. The face sheets withstand almost all the applied in-plane loads and flat wise bending moments which eventually offer bending rigidity to the system. However, one of the major concerns in the use of monolithic and sandwich material is their behavior under low-velocity impact loading [4]. The conception that sandwich structures are susceptible to localized damage is one of the main reasons for this [5]. Localized impact damage can be induced from tool drops, runway debris, and hail storms which can cause a drastic strength reduction of the structure. Low-velocity impact damage on sandwich structure is considered to be potentially dangerous since the impact damage might not be visible as the surface appeared to be undamaged. Even though the high potential of sandwich structures is well acknowledged [6-8], their ability to resists localized impact damage which could lead to reduction in its load-bearing properties has not yet been established. Various studies have been conducted to investigate the behavior of sandwich structure under low-velocity impact loading [9-11]. Unfortunately, only one has actually studied the use of thermoplastic honeycomb core on the sandwich structure under low-velocity impact loading [12]. Then again, only a few studies focused on the effect of core thickness on the impact response of the structure [1, 13]. However, none of the studies above have been actually focused on the effect of core thickness on low-velocity impact response of sandwich structure. Currently, most of the scientific studies only showed the simulation of the impact phenomena and impact behavior of the studied material under different loading conditions. By varying the thickness of the core, the potential to achieve interesting properties and

desired performance is nearly possible. The aim of this study is to investigate the effect of core thicknesses on the impact performance of sandwich structure made from thermoplastic honeycomb core for it can be used to improve the impact performance and resistance towards impact damage.

Experimental Procedure

Material Properties. The thermoplastic honeycomb core examined in this study, PP8T40F core were supplied in the form of large flat panels by Qingdao Polycore Technology Co. Ltd. PP8T40F indicates that the core is made from polypropylene (PP), with 8 mm cell size diameter and both sides of the core are laminated with 40g/m^2 non-woven polyester tissue. Three core thicknesses were investigated in this study (20, 30 and 40 mm). The face sheet used in the sandwich structure was 1.0 mm thick aluminum 1100 consists of 99.6% pure aluminum, with excellent welding characteristics and good corrosion resistance. Adhesive consists of epoxy resin with hardener were used to combine both elements; the core and face sheets together and the sandwich structure was ready for testing after 8 hours. Properties of the core and face sheet material can be referred to Table 1.

Table 1. Properties of sandwich structure component material

Properties	Core Material	Face sheets Material
Density (kg/m^3)	80	2710
Elastic Modulus (GPa)	1.02	70
Yield Strength (MPa)	-	105
Shear Strength (MPa)	0.53	69
Compressive Strength (MPa)	2.05	-

Specimen Construction. In this experiment, the given dimension for the samples is according to ASTM C365 standard. A hand lay-up method was used to fabricate the sandwich panels. The panels were cured at room temperature and normal pressure was applied to the components in order for the adhesive to uniformly distribute on the surface of the core-face sheet interface.

Test Method. Impact tests were conducted using a 2.1 kg instrumented drop-weight impact tower with a 12.5 mm diameter hemispherical nose indenter. The specimens were tested at different drop heights release from 0.2 m up to 1 m. By varying the drop height, the impact energies can be determined. The impact force was measured using Kistler 9333A piezo-electric load cell located just above the indenter. The variation of time was recorded by the dedicated computer respectively. During the test, the specimens were simply supported on two 12.5 mm diameter stainless steel cylinders positioned on movable angle supports. Tests on sandwich panels was based on 20 mm thick core with 35 mm wide samples supported over 156 mm span calculated according to ASTM C365. Each reading was an average of at least three separate measurements taken during the impact test.

Results and Discussion

To investigate the effect of core thickness on the impact performance of sandwich structure, low-velocity impact tests has been carried out and average data was collected for each sample, which included maximum impact force, energy, and impact damage area. One sample was sectioned at the impact location and observed under optical microscope to determined and calculate the impact damage area. Fig. 1, 2 and 3 shows maximum impact force versus impact energy and impact damage area following impact tests on 3 different panels with thickness varied between 22 mm and 42 mm. From the figure, it is clear that the maximum impact force continues to increase with core thickness since thicker core was able to absorb large amount of energy which resulting in damage initiation across the core [8]. For more understanding about the system, Eq. 1 describes the relationship between impact energy and drop heights

$$E = mgh \quad (1)$$

Where E is the impact energy, g is the gravitational force, and h is the drop heights. From the system studied, increase in drop height results in increase of impact energy. Referring to Eq. 1, as the height increases, the energy increases also since it is directly proportional. Hence, higher amount of impact energy absorbs results in more impact force. Increase in energy absorption is also portrayed in the sample. Thinner core exhibits localized damage but for thicker core the damage is uniformly distributed. The observation also shows that the thinner core suffers from bending as it results in more bending force occurred at the face sheet compared to shear loads on the core which transforms it into permanent deflection at the rear surface of the panel. In addition, due to lower bending stiffness, thinner core was expected to experience some bending or deflections as it cannot withstand higher shear load than thicker core. Compared to thinner core counterparts, higher degree of core crushing can be seen in the sample of thicker core as most of the shear loads were uniformly distributed throughout the core thickness. In addition, after the impact event, most of the panels are suffering from core crushing, face sheet buckling, and debonding between the face sheet and core. Visual inspection shows that the panels encounter a series of energy-absorbing condition which divides the loads. The damage occurred explained the condition of the structure under impact that causes the panel to reduce its structural integrity and load bearing properties. From the figure, it can be observed that as the impact energy increased, a continuous increased in impact damage area is also noticed. It is obvious that the 20 mm core panel has; however, has the lowest impact force and damage area. These may be caused by the core thickness: the thinner core has lower rigidity in compression and more deflection due to impact loading and consequently, the lowest impact load and damage area. In the case of thinner core, the face sheet will play a major role when the structure is subjected to low-velocity impact. This is because the face sheet needs to withstand as much bending load as they can due to lower stiffness of the thin core. In other words, panels with thinner core are likely to deflect due to lower stiffness [7]. For thicker core counterparts, most of the energy was absorbed by the core which endures the shear load and transforms it into permanent damage. As a result, it increased the contact duration between the impactor and the top face sheet. Since the contact duration increased with core thickness, the damage area constantly increased which at the end reduced the structural capacity of greatly damage panels. Furthermore, both top and bottom face sheets were deforms in elastic way because they do not absorb, but accumulate the energy towards the core [13]. Additionally energy-absorbing capacities of sandwich structures are closely linked to the core crushing. From the observation, it can conclude that the thicker core experienced most of the core crushing compared to the thinner core.

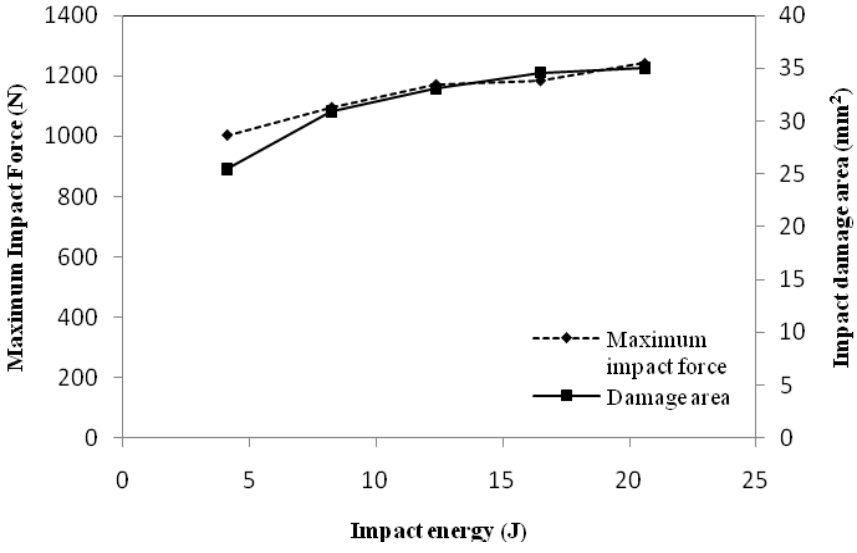


Fig.1 Effect of impact energy (drop heights) on the maximum impact force and impact damage area for core thickness = 20mm.

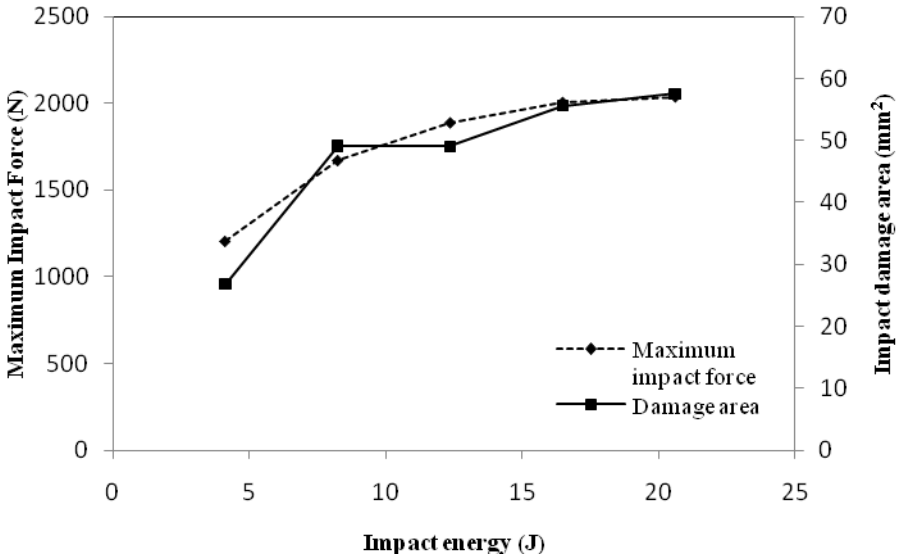


Fig.2 Effect of impact energy (drop heights) on the maximum impact force and impact damage area for core thickness = 30mm.

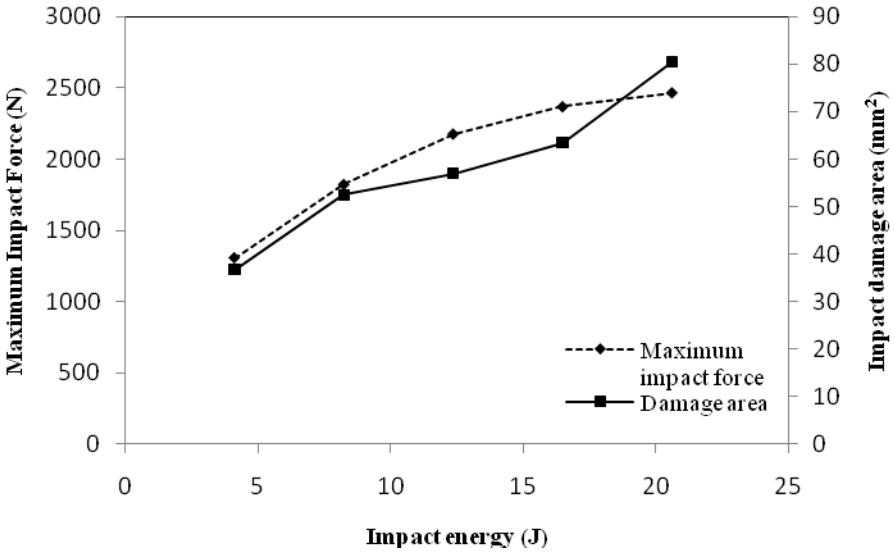


Fig.3 Effect of impact energy (drop heights) on the maximum impact force and impact damage area for core thickness = 40mm.

Summary

The effect of core thicknesses of thermoplastic honeycomb core sandwich structure was investigated to determine their behavior under low-velocity impact loading. It was proved that thicker core can absorbed more energy compared to thinner core counterparts and hence, causes more damage to initiate in the core. In addition, the damage behavior of the panels can be explained by determine the damage area of the panels. As the thickness of the core increased, the damage area is also continuously increased as more shear load were distribute across the sandwich structure, allowing the panel to absorbed more energy. Larger damage area in thicker core proves that more energy was absorbed and suffers less permanent damage compared to thinner core.

References

[1] J. Leijten, H.E.N. Bersee, O.K. Bergsma, A. Beukers: Composites: Part A Vol.40 (2009), p.164.

[2] M.V. Hosur, M. Abdullah, S. Jeelani: Composite Structures Vol.65 (2004), p. 103.

[3] S. Tien-Wei, P. Yu-Hao: Composite Structures Vol. 64 (2004), p.189.

[4] M. Aktas, C. Atas, B.M. Icten, R. Karakuzu: Composite Structures Vol. 87 (2009), p. 307.

[5] M. A. Hazizan and W.J. Cantwell: Composites: Part B Vol. 33 (2002), p.193.

[6] J.P. Dear, H. Lee, S.A. Brown: International Journal of Impact Engineering Vol. 32 (2005), p.130.

[7] J.H. Park, S.K. Ha, K.W. Kang, C.W. Kim, H.S. Kim: Journal of Materials Processing Technology Vol. 201(2008), p. 425.

[8] A.R. Othman, D.C. Barton: Composite Structures Vol. 85 (2008), p.126.

[9] M. Meo, R. Vignjevic, G. Marengo: International Journal of Mechanical Sciences. Vol. 47 (2005), p. 1301.

[10] C.C. Foo, L.K. Seah, G.B. Chai: Composite Structures Vol. 85 (2008), p. 20.

[11] M.A. Hazizan, W.J. Cantwell: Composites: Part B Vol. 34 (2003), p. 679.

[12] P. Griškevičius, D. Zeleniakienė, V. Leišis, M. Ostrowski: Materials Science Vol. 16 (2010), p. 2.

[13] F.J. Yang, W.J. Cantwell: Impact Damage Initiation in Composite Materials. Composites Science and Technology Vol.70 (2010), p. 336.

© (2011) Trans Tech Publications, Switzerland
doi:10.4028/www.scientific.net/KEM.471-472.466

Boundary Condition Effects on the Parametric Stability of Moderately Thick Laminated Cylindrical Panels

Jamshid Fazilati[1,a] and Hamid-Reza Ovesy[1,b]

[1]Aerospace Engineering Department and the Center of Excellence in Computational Aerospace Engineering, Amirkabir University of Technology, Hafez Ave., Tehran, Iran

[a]jfazilati@aut.ac.ir, [b]ovesy@aut.ac.ir

Keywords: Higher order theory, composite structures, dynamic instability, cylindrical shell, finite strip method.

Abstract. A Reddy type, third order shear deformation theory of shells is applied to the development of two versions of finite strip method (FSM), namely semi-analytical and spline methods, to predict the parametric stability and instability regions in the case of cylindrical moderately thick composite laminated panels. The structures are assumed to be under harmonic in-plane loads in the context of the so-called parametric loading. The linear strain terms are expressed in terms of the Koiter-Sanders theory of shallow shells. In order to demonstrate the capabilities of the developed methods in predicting parametric behavior of the subject structures, some representative results are obtained and compared with those in the literature wherever available.

Introduction

Good strength-to-weight and stiffness-to-weight ratio as well as design versatility have made composite laminates very popular engineering structures. In sizing shell structures, the stability becomes a critical design criterion. In static conditions, the stability is characterized by the buckling phenomenon while in the dynamic loading cases, according to the nature of the load, different kinds of stability can be observed. One type of dynamic instability problem called “parametric instability” corresponds to the stability conditions under in-surface harmonic excitation. This loading condition consists of a constant mean excitation and a harmonically varying part. There are instability situations in relation with three main loading parameters e.g. its mean value, harmonic part amplitude and excitation frequency.

Bolotin [1] has pioneered the study of the dynamic stability of isotropic cylindrical shells under axial parametric excitation. In this approach, the governing equations are converted into a set of Mathieu equations where an approximation of the complete Fourier series type is made to solve the equation. Ng *et al.* [2] have studied the dynamic stability of simply-supported isotropic cylindrical panels under combined static and periodic axial forces based on Donnell's shallow shell theory and a FSDT formulation. Sahu and Datta [3] have summarized the studies on the parametric instability of conservative models of plates and shells up until the year 2005. More recently, the authors of the current paper have developed a semi-analytical finite strip (S-a FS) formulation as well as a B-spline finite strip formulation on the basis of classical shells assumptions and subsequently investigated the parametric instability of layered composite thin-walled structures [4,5]. The authors have also developed FSM based on the Reddy’s higher order shells theory to investigate the parametric instability of moderately thick laminated and FGM structures [6,7].

Two versions of FSM, namely the semi-analytical FSM and B-spline FSM, are developed based on a Reddy type higher order shell theory and used to investigate the effects of boundary conditions on the regions of parametric instability. Whilst both versions of FSM are formulated based on the full energy concepts, the two methods have differences in the displacement field approximations. Based on the energy minimization concepts, the governing equations of the problem are derived in

the form of a system of Mathieu-Hill type differential equations. The first order Bolotin's approximation is then utilized to extract the instability margins of the structure.

Theoretical Development

In this section, the fundamental elements of the theory of the developed finite strip methods are briefly represented. The single curved cylindrical model geometry is assumed to be made up of a series of longitudinal strips. Fig. 1 depicts a typical curved and layered finite strip with radius R, length L, width b_s and thickness t. The strip is subjected to a uniform harmonically time varying in-surface loading with the frequency ω. It is presumed that the loading consists of a static (constant) and a harmonically time-varying dynamic component with amplitudes N^S and N^D, respectively. The load component coefficients can also be expressed with regard to the critical static buckling load of the structure, N_{cr}. (a^S, a^D are static and dynamic load coefficients) Thus:

$$N_i = N^S + N^D \cos(\omega t) \quad \leftrightarrow \quad N_i = a^S N_{cr} + a^D N_{cr} \cos(\omega t) \quad , \quad \{i \equiv x, y\} \tag{1}$$

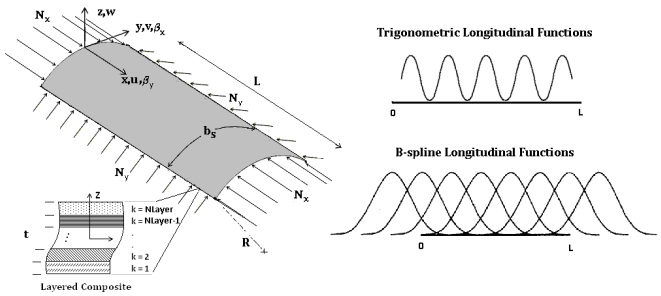


Fig. 1: Geometry, loading configuration and longitudinal estimation functions for a typical strip.

Displacement Functions in the Higher Order Theory. In order to include the effects of through the thickness transverse shear strains as parabolic variation functions of the thickness dimension, the assumptions that imply the stress-free conditions at the two free surfaces is applied. So, the displacement field functions can be expressed as [6],

$$\begin{cases} u(x,y,z,t) = u^o + \beta_x \left(z + \dfrac{-4}{3t^2} z^3 \right) + \dfrac{\partial w^o}{\partial x} \left(\dfrac{-4}{3t^2} z^3 \right) \\ v(x,y,z,t) = v^o \left(1 - \dfrac{C_0}{R} z^2 - 8 \dfrac{C_1}{R} z^3 \right) + \beta_y \left(-z - 2C_0 z^2 + C_1 (8 - \dfrac{t^2}{R^2}) z^3 \right) + \dfrac{\partial w^o}{\partial y} \left(C_0 z^2 - 8 C_1 z^3 \right) \\ w(x,y,z,t) = w^o \qquad\qquad C_0 = \dfrac{4}{R(-24 + t^2/R^2)}, C_1 = \dfrac{4}{t^2(-24 + t^2/R^2)} \end{cases} \tag{2}$$

where u,v,w are the displacement parameters at an arbitrary point whilst u^0,v^0,w^0 are related to displacements of the corresponding coordinates on the middle surface. There are five unknown functions in the right-hand side of the approximation equations (i.e. $u^0,v^0,w^0,\beta_x, \beta_y$) that are to be defined.

The Strain-Displacement Relationships. The Koiter-Sanders theory of shells for cylindrical geometry is assumed to formulate the strain-displacement (compatibility) relationships. The linear strains are expressed as,

$$\begin{cases} \varepsilon_x = u_{,x} \\ \varepsilon_y = v_{,y} + w/R \\ \gamma_{xy} = u_{,y} + v_{,x} \end{cases} \qquad \begin{cases} \gamma_{yz} = v_{,z} + w_{,y} - v/R \\ \gamma_{xz} = u_{,z} + w_{,x} \end{cases} \tag{3}$$

Substituting the displacement functions (Eq. 2) into strain Eq. 3 leads to the strain field as [6],

$$\begin{cases} \varepsilon_x = \varepsilon_x^{(0)} + z.\varepsilon_x^{(1)} + z^2.\varepsilon_x^{(2)} + z^3.\varepsilon_x^{(3)} \\ \varepsilon_y = \varepsilon_y^{(0)} + z.\varepsilon_y^{(1)} + z^2.\varepsilon_y^{(2)} + z^3.\varepsilon_y^{(3)} \\ \gamma_{xy} = \gamma_{xy}^{(0)} + z.\gamma_{xy}^{(1)} + z^2.\gamma_{xy}^{(2)} + z^3.\gamma_{xy}^{(3)} \end{cases} \quad \begin{cases} \gamma_{yz} = \gamma_{yz}^{(0)} + z.\gamma_{yz}^{(1)} + z^2.\gamma_{yz}^{(2)} + z^3.\gamma_{yz}^{(3)} \\ \gamma_{xz} = \gamma_{xz}^{(0)} + z.\gamma_{xz}^{(1)} + z^2.\gamma_{xz}^{(2)} + z^3.\gamma_{xz}^{(3)} \end{cases} \tag{4}$$

With the terms defined in reference [6].

The Constitutive Equations. A laminated strip is considered to be made from some plies of unidirectional fibrous composite materials. Integrating the plies mechanical effects through the thickness direction gives the load-strain relationships as:

$$\begin{Bmatrix} \{N\} \\ \{M\} \\ \{O\} \\ \{P\} \end{Bmatrix} = \begin{bmatrix} [A] & [B] & [D] & [E] \\ [B] & [D] & [E] & [F] \\ [D] & [E] & [F] & [I] \\ [E] & [F] & [I] & [H] \end{bmatrix} \begin{Bmatrix} \{\varepsilon^{(0)}\} \\ \{\varepsilon^{(1)}\} \\ \{\varepsilon^{(2)}\} \\ \{\varepsilon^{(3)}\} \end{Bmatrix}, \begin{Bmatrix} \{Q\} \\ \{R\} \\ \{T\} \\ \{U\} \end{Bmatrix} = \begin{bmatrix} [A^S] & [B^S] & [D^S] & [E^S] \\ [B^S] & [D^S] & [E^S] & [F^S] \\ [D^S] & [E^S] & [F^S] & [I^S] \\ [E^S] & [F^S] & [I^S] & [H^S] \end{bmatrix} \begin{Bmatrix} \{\gamma^{(0)}\} \\ \{\gamma^{(1)}\} \\ \{\gamma^{(2)}\} \\ \{\gamma^{(3)}\} \end{Bmatrix} \tag{5}$$

where *N,M,O,P,Q,R,T,U* are the force resultants and A,B,D,E,F,H,I are the equivalent stiffness matrices.

Problem Formulation. Solution of the instability problems is sought through the principle of virtual work. The total energy of a strip (Π) is defined as summation of kinetic (T), pre-stress (U_g) and strain ($U_{elastic}$) energy component effects:

$$\Pi = U_{elastic} - U_g - T \tag{6}$$

Where

$$\begin{aligned} T &= \frac{1}{2}\rho t \iint_L \left(\dot{u}^{o\,2} + \dot{v}^{o\,2} + \dot{w}^{o\,2} + \frac{t^2}{12}\left(\dot{\beta}_x^{\,2} + \dot{\beta}_y^{\,2}\right)\right) dx\,dy \\ U_g &= \frac{t}{2}\iint_L \begin{pmatrix} N_x \left[u^{o\,2}_{,x} + v^{o\,2}_{,x} + w^{o\,2}_{,x} + t^2\left(\beta^{\,2}_{x,x} + \beta^{\,2}_{y,x}\right)/12 \right] \\ + N_y \left[u^{o\,2}_{,y} + (v^{o}_{,y} + w^{o}/R)^2 + (w^{o}_{,y} - v^{o}/R)^2 + t^2\left(\beta^{\,2}_{x,y} + \beta^{\,2}_{y,y}\right)/12 \right] \end{pmatrix} dx\,dy \\ U_{elastic} &= \frac{1}{2}\iint \left(\left\langle N\ M\ O\ P \right\rangle . \left\langle \varepsilon^{(0)}\ \varepsilon^{(1)}\ \varepsilon^{(2)}\ \varepsilon^{(3)} \right\rangle^T + \left\langle Q\ R\ T\ U \right\rangle . \left\langle \gamma^{(0)}\ \gamma^{(1)}\ \gamma^{(2)}\ \gamma^{(3)} \right\rangle^T \right) dx\,dy \end{aligned} \tag{7}$$

Where ρ is the uniform material mass density, '.' represents the differentiation with respect to time and ',' defines a non-time differentiation operator. Substituting the energy terms in Eq. 6, applying the principle of virtual work, factorizing with respect to degrees of freedom vectors and building matrices, assembling the strip matrices and implementing the necessary boundary conditions, a system of Mathieu type differential equations is obtained as follows:

$$M\ddot{\delta} + (K_{elastic} - a^S K_g^S - a^D \cos\omega t\ K_g^D)\,\delta = 0 \tag{8}$$

Where M, $K_{elastic}$, K_g^S and K_g^D are square global structural matrices corresponding to mass, strain energy, static and dynamic applied in-plane stress energies, respectively. By applying Bolotin's first order approximation [1] corresponding to the periodic solution with period $2T$, where $T=2\pi/\omega$, a problem of known eigen-system of equations appears (Eq. 9),

$$\begin{pmatrix} K_{elastic} - a^S K_g^S + 0.5\,a^D K_g^D & 0 \\ 0 & K_{elastic} - a^S K_g^S - 0.5\,a^D K_g^D \end{pmatrix} - \frac{1}{4}\omega^2 \begin{pmatrix} M & 0 \\ 0 & M \end{pmatrix} = 0 \tag{9}$$

By utilizing the QZ method to solve the eigen-value problems, the boundaries of the instability region for the structure are obtained for given pairs of a^S, a^D.

Mid-Surface Displacement Field. The unknown displacement functions, designated in the right-hand sides of Eq. 2, are introduced as the multiplication of the longitudinal and transverse

displacement functions in which the degrees of freedom are varying with respect to time. In case of semi-analytical version of FSM, the trigonometric functions (*cos* for u^0, β_x / *sin* for others) are assumed as the longitudinal approximation functions while a series of Bezier-spline of third order are utilized in the same direction for the spline version. The transverse approximation functions are polynomials of various types and orders. The undetermined displacement coefficients are related to transverse terms in semi-analytical version but are coefficients of longitudinal terms in the spline version. Representing the in-plane displacement and also rotations across a strip, the linear Lagrange polynomials are used in transverse direction, whilst in representing *w* the cubic Hermitian polynomial is utilized to support C^1-type continuity.

The boundary conditions at the two curved ends are restricted to the type of simply supported for semi-analytical version (due to the assumed longitudinal trigonometric functions.). But the spline version is versatile and has no limitations. The side unloaded edges in both approaches can accommodate any kind of boundary conditions, namely simply supported, built-in or free.

Applications and Results

As a validation attempt, some simply-supported curved panels made from isotropic material are considered. The geometry and material data are,

$$\begin{cases} E = 70.0\,GPa,\ v = 0.3,\ \rho = 2700\,kgm^{-3} \\ R = 100m,\ R / L = 10\ ,L / t = 10\ ,\ b / L = 0.5\ ;1.;1.5\ ;2. \end{cases} \tag{10}$$

The dimension-less fundamental natural frequency ($p = L\omega\sqrt{\rho(1-\upsilon^2)/E}$) as well as first buckling dimension-less load ($\lambda = 100\,\sigma_{cr} / E$) is calculated and presented in Table 1. The comparison of the natural frequency results with the corresponding results from the literature shows the good accuracy of the calculations. The results show that the S-a FSM gives smaller differences with the 3D results. Furthermore, it is seen that the greater the *b/L* ratio, the larger the difference will be.

Table 1: comparison of free vibration frequencies and buckling loads for isotropic curved panel.

	Ref [8]	Ref [9]	Ref [10]	S-a FSM HSDT (present)		Spline FSM HSDT (present) (q=6)	
b/L	Free Vib. 3D elasticity	Free Vib. FSDT	Free Vib. HSDT DQ	Free Vib. 20 strips	Buckling 20 strips	Free Vib. 20 strips	Buckling 20 strips
0.5	1.31742	1.336	1.31597	1.31732	11.3761	1.31732	11.3773
1	0.55049	0.5563	0.55136	0.55714	3.4561	0.55771	3.4632
1.5	0.39987	0.4044	0.40266	0.41049	1.8761	0.41116	1.8824
2	0.34612	0.3505	0.35019	0.35925	1.4370	0.35980	1.4416

Cross-ply laminated square curved cylindrical panels are considered. Two material property sets are also assumed. These materials are used for the case of free vibration and static buckling analysis, respectively. The material properties are given in Table 2 and the geometry specifications are as:

$$R / L = 5\ ;6\ ;20\ ,\ L = b\ ,L / t = 10\ ,\ t = 0.01\ m \tag{11}$$

Table 2: orthotropic material property sets. [11]

	E_1 (Pa)	E_1 / E_2	G_{12} / E_2	G_{23} / E_2	ν_{12}	$\rho\ (kgm^{-3})$
Set 1:	140 e9	25	0.5	0.2	0.25	4000
Set 2:	140 e9	40	0.6	0.5	0.25	4000

Two lay-ups (0/90/0) and (0/90) are assumed. The two straight sides of the model are simply-supported. The curved ends are either simply supported or clamped. In all boundaries the slip motion are also restrained. Tables 3 and 4, respectively, represent the dimension-less fundamental natural frequencies ($p = \omega L^2\sqrt{\rho / E_2 t^2}$) as well as buckling loads ($\lambda = \sigma_{y\,cr} L^2 / E_2 t^2$) for the structure

under different boundary condition sets. In the buckling analysis, it is assumed that the panels are under uniform and unidirectional in-surface circumferential stresses (N_y). A generally good comparison can be seen among the results. The 20-strip spline models with 6 knots are found to deliver the converged results.

Table 3: dimension-less principle natural frequency of cross-ply panel for various boundary conditions. (End-Side-End-Side; S: Simply supported, C: Clamped, F: Free)

R/L	S-S-S-S				C-S-S-S			C-S-F-S	
(Lay-up)	[11]	[12]	S-a	Spline	[11]	[12]	Spline	[11]	Spline
5 *(0/90)*	9.024	8.95	8.883	8.883	10.871	10.701	10.972	6.600	6.387
5 *(0/90/0)*	11.846	11.763	12.636	12.636	13.866	13.671	15.551	6.123	6.240
20 *(0/90)*	8.973	8.835	8.868	8.868	10.822	10.61	10.959	6.594	6.403
20 *(0/90/0)*	11.793	11.702	12.595	12.594	13.825	13.624	15.524	6.089	6.208

Table 4: dimension-less critical buckling loads of cross-ply laminated panel for various boundary conditions.

R/L	S-S-S-S			C-S-S-S		C-S-C-S		S-S-F-S		C-S-F-S	
(Lay-up)	[11]	S-a	Spline	[11]	Spline	[11]	Spline	[11]	Spline	[11]	Spline
6 *(0/90)*	11.789	11.570	11.570	17.434	17.389	21.486	20.890	5.443	5.356	6.343	6.244
5 *(0/90/0)*	12.483	12.345	12.344	14.582	14.765	17.032	16.701	2.448	2.427	5.575	5.660
20 *(0/90)*	11.576	11.356	11.356	17.161	17.078	21.467	20.785	5.442	5.335	6.277	6.165
20 *(0/90/0)*	12.470	12.313	12.312	14.569	14.728	17.029	16.684	2.448	2.418	5.503	5.553

Orthotropic layered square curved panels are assumed and the principle region of instability is investigated. Two symmetric lay-ups, e.g. (90/0/90) and (0/90/0), are considered. The slip motion in clamped boundaries is restrained. A typical ply material properties and the geometry are assumed as,

$$\begin{cases} E_1 = 140\ GPa,\ E_1 / E_2 = 40,\ G_{12} / E_2 = 0.5\ ,\ v = 0.25,\ \rho = 4000\ kgm^{-3} \\ R / L = 4\ ,L = b, L / t = 10 \end{cases} \tag{12}$$

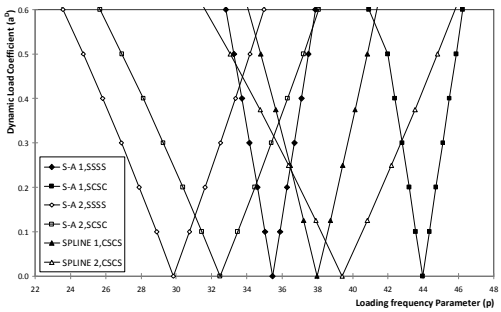


Fig. 2: instability regions for different boundary conditions (N_y=0, a^s=0.2),(1: (90/0/90), 2: (0/90/0))

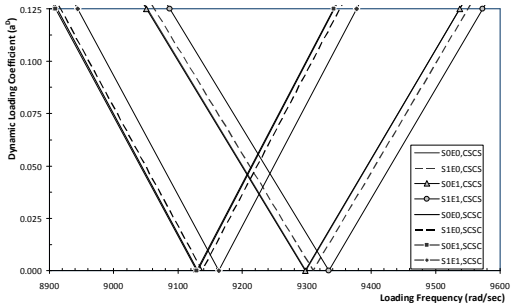


Fig. 3: Instability regions for different tangential constraints (N_y=0, a^s=0.2),(S: sides, E: ends; 0: free , 1: kept)

Fig. 2 depicts the principle instability region of the panels with different lay-ups and boundary sets ($p = L^2\omega\sqrt{\rho / E_2 t^2}$). It is shown that by keeping the unloaded sides from rotation the panel becomes stiffer. Furthermore, it is seen that in the case of simply-supported loaded ends, by including more 90 degree-oriented layers in the lay-up configuration, the panel resistance against axial harmonic loading becomes more pronounced. In other words, the lay-up (90/0/90) leaves a stiffer panel. On the contrary, in the case of clamped loaded ends, it is seen that the lay-up (0/90/0) has resulted in a stiffer panel.

The angle-ply square cylindrical panel is considered with the lay-up $(45/-45)_s$. The material properties are as the second set in Table 2 and the geometry specifications are,

$$R / L = 4.0\ ,\ L / t = 5.0\ ,\ L = b\ ,\ t = 0.1\ m \tag{13}$$

Four cases are considered to investigate the effects of the tangential movement constraints at the boundaries of the panel. These cases are notified by the format SxEx where S stands for the Side and E is an abbreviation for the End constraints condition for the tangential movement term. The x item declares whether the corresponding boundary is free or kept (0 or 1, respectively). Fig. 3 depicts the principle instability regions calculated for these models using spline FSM (20 strips;q=6). It is to be noted that due to the nature of its presumed functions, the s-a FSM cannot sense the effect of tangential constraints at the ends. A comparison between the results shows that for the lay-up under investigation, the stabilizing effect of tangential constraints on two straight sides is little more than that at the end constraints.

Summary

A S-a as well as a spline full-energy FSM has been formulated for the analysis of the parametric instability behavior of moderately thick composite laminated cylindrical shell panels. The analysis has been conducted in the context of third order shear deformation theory of shells with the assumptions of free traction surfaces. Using the virtual work concepts, the governing equations in the form of Mathieu differential equation are derived where the instability regions have been determined using the Bolotin's first order approximation. The validation and various applications of the developed approaches have been presented to investigate the effects of boundary constraints on the parametric instability behavior of cylindrical shell panels. The effectiveness of the tangential constraints in case of assumed lay-ups are shown.

References

[1] V.V. Bolotin, *The dynamic stability of elastic systems,* Moscow: GITTL 1956, English Translation: San Francisco, Holden-Day, 1964.

[2] T.Y. Ng, K.Y. Lam, J.N. Reddy: Int. J. Solids and Structures 36 (1999) 3483-96.

[3] S.K. Sahu, P.K. Datta: Applied Mech. Review 60 (2007) 65-75.

[4] J. Fazilati, H.R. Ovesy: 1st Int. Conf. Composites: Characterization, Fabrication, and Application (CCFA-1), Kish Island, Iran (2008).

[5] J. Fazilati, H.R. Ovesy: Composite Structures 92 (2010) 2060–65.

[6] J. Fazilati, H.R. Ovesy, IJSSD Symposium on progress in Structural Stability and Dynamics, Hong Kong, China (2009).

[7] H.R. Ovesy, J. Fazilati, 10th Int. Conf. Computational Structures Technology (CST2010), Valencia, Spain (2010).

[8] Y.C Chern, C.C. Chao, J. Sound Vibration 230 (2000) 1009–30.

[9] Y. Kobayashi, A.W. Leissa, Int. J. Non-Linear Mechanics 30 (1995) 57–66.

[10] J. Yang, H.S. ShenJ. Sound and Vibration 261 (2003) 871–93.

[11] A.K. Khdeir, J.N. Reddy: Comput Struct., 34(6) (1990) 817–26.

[12] J.S. MOITA, C.M. MOTA SOARES, C.A. MOTA SOARES: COMPUT. STRUCTURE, 73 (1999) 407–23.

© (2011) Trans Tech Publications, Switzerland
doi:10.4028/www.scientific.net/KEM.471-472.472

The Effect of Silane Treatment on Tensile Properties and Morphology of Polypropylene/Recycled Acrylonitrile Butadiene Rubber/Rice Husk Powder Composites

S. Ragunathan[1, a], H. Ismail[1, b] and K. Hussin[2,c]

[1]School of Material and Mineral Resources,Engineering Campus, Seri Ampangan,

Universiti Sains Malaysia,14300 Nibong Tebal, Pulau Pinang, Malaysia

[2]School of Environmental Engineering, Kompleks Pengajian Jejawi 3,Universiti Malaysia

Perlis,02600 Arau, Perlis,Malaysia

[a]raguna@unimap.edu.my, [b]hanafi@eng.usm.my, [c]kamarudin@unimap.edu.my

Keywords: Polypropylene; Recycled acrylonitrile butadiene rubber; Silane; Compatibilization; Rice husk powder; Tensile properties; Morphology

Abstract. The effect of silane treatment on tensile properties and morphology of recycled acrylonitrile butadiene rubber(NBRr)/polypropylene(PP)/rice husk powder(RHP) composites has been studied. Polypropylene/recycled acrylonitrile butadiene rubber/rice husk powder (PP/NBRr/RHP) composite were prepared by melt mixing technique at 180º C for 9 minutes and 50rpm rotor speed using an internal mixer. Five different composites compositions (70/30/0, 7030/5, 70/30/10, 70/30/15 and 70/30/30), with silane treated RHP(treated) and without silane treatment(untreated) was studied. The specimens were analyzed by different techniques i.e. tensile test and scanning electron microscopy (SEM). The result obtained showed lower tensile properties with increasing amount of NBRr content. Lower tensile strength and tensile modulus was exhibited with increasing NBRr content. However higher tensile strength, greater tensile modulus and lower elongation at break in PP/NBRr/RHP was exhibited for silane treated RHP composites compare with untreated RHP. PP/NBRr/RHP composite was found to become more brittle with strong attachment between PP/NBR matrix and RHP filler with silane treatment. Good adhesion between silane treated RHP filler and PP/NBRr matrix was confirmed by the morphological studies.

Introduction

The use of natural fibers as reinforcements or fillers in polymer composite systems has gained more attentions in recent years. Considerable amount of studies have been carried out on the utilisation of natural fillers such as sago, sisal, short silk fibre, oil palm empty fruit bunch, rice husk ash, jute fibre, rubber wood powder, jute, hemp, sisal, cotton stalk, kenaf, sugarcane banana fibers and cellulose fibres as reinforcement materials. Compared with traditional reinforcement materials such as inorganic fiber, natural fibers such as rice husk have the advantages of low density, low cost, harmless, abundant, renewable less abrasiveness, high toughness, comparable specific strength and easily biodegradable. Advantages of natural fibers over man-made fibers make natural fibers the potential replacement for traditional reinforcement materials such as glass fiber in composite material systems. Its capacity as filler or additives in plastic materials is not well define. The reason is because these composites are found to be incompatible or immiscible due to poor physical and chemical interaction between the phases. The incompatibility may be due to the fact that the polyolefin is non-polar and hydrophobic, whereas lignocelluloses material is polar, due to the hydroxyl groups in the cellulose.

In order to solve this problem, studies have been performed on surface modification for the purpose of making the polyolefin chains more hydrophilic [1]. Chemical treatment on fibers surface and usage of coupling agent are excellent methods to improve compatibility between hydrophobic

matrixs and hydrophilic fillers [3-4]. Many investigations have been carried out by numerous researchers [4-6]. Coupling agents based on alkoxysilanes are frequently employed for cellulosic fibers. Hydrolysis of the alcoxyl groups with subsequent reaction with hydroxyl groups from cellulose can provide chemical bonding with the fibers [7]. Bledzki et al. [8] modified jute fiber with alkali, silane and maleated polypropylene (MAPP), and found that surface modification enhanced the mechanical properties of jute fiber reinforced polypropylene composites. Ismail et al. [9] utilized silane coupling agent on white rice ash-polypropylene/natural rubber composites, and found that silane coupling agent have improved the mechanical properties of the composite. Liu et al. [10] modified jute fiber with alkali and silane, and found that chemical treatments on the surface of jute fiber have improved the mechanical properties of jute fiber reinforced poly(butylenes succinate) bio-composites. However, so far no work has been reported on PP/NBRr/RHP composites and its effect with the APS coupling agent.The aim of this study is to evaluate the effect γ-aminopropyltrimethoxysilane (APS) coupling agent on the PP/NBRr/RHP composites. Mechanical properties and morphological studies of PP/NBRr/RHP composites were investigated.

Experimental

Table 1: Materials specification and description

Material	Description	Source
Polypropylene(PP)	Code: 331 MFI: 14g/10 min at 230° C Density: 0.9g/cm^3	Titan Pro Polymers (M) Sdn. Bhd. Johor, Malaysia
Recycled Acrylonitrile Butadiene Rubber (NBRr)	Content:33% of Acrylonitrile Density: 1.015g/cm^3	Juara One Resources Sdn. Bhd. Penang, Malaysia
Rice Husk Powder(RHP)	Cellulose :35% Hemicellulose: 25% Lignin :20% Ash :17% Density:1.4702g/cm^3 Size: 300-500μm	Thye Heng Chan Enterprise Sdn. Bhd
Silane Coupling Agent	γ-aminopropyltrimethoxysilane (APS)	Alfa Aesar (M) Sdn Bhd

The materials used for the preparation of PP/NBRr/RHP composites are shown in Table1. The rice husk powder were ground in a table type pulverizing machine (Rong Tsong Precision Technology Co. Product Id: RT-34) with speed of 2850 rpm, sieved at 300-500μm in particle size and dried at 110ºC for 24 hours in a vacuum oven to produce rice husk powder of homogeneous fractions.

The treatment reaction was carried out in a mixture of water/ethanol (40/60 volume). 3g of γ-aminopropyltrimethoxysilane was first introduced into 1000 ml of the mixture water/ethanol and was allowed to stand for 1 hour. The pH of the solution was maintained at 4 with the addition of acetic acid. Then, 10 g of rice husk powder was added into the solutions and the solutions were continuously stirred for 1.5 hours. The filler was filtered and was dried in the air and then in the vacuum oven at 80°C for 24 hours.

Polypropylene (PP) was mixed with recycled acrylonitrile butadiene rubber (NBRr) and rice husk powder (RHP) at various loading (0, 10, 15, 20, 30) phr. Rice husk powder was dried at 110ºC for 24 hours in a vacuum oven prior to mixing. A constant PP and NBRr was used at 70phr and 30phr respectively. Table 2 shows the formulation of PP/NBRr/RHP composites.

Table 2: Formulation for PP/NBRr/RHP composites

Composite Materials	PP/NBRr /RHP composites (phr)								
	S1	S2	S3	S4	S5	S6	S7	S8	S9
PP	70	70	70	70	70	70	70	70	70
NBRr	30	30	30	30	30	30	30	30	30
Pure RHP	–	5	10	15	30	–	–	–	–
γ-APS Treated RHP	–	–	–	–	–	5	10	15	30

The composites were prepared by melt mixing using a Haake Rheomix Polydrive R 600/610 mixer at 180^0C with the rotor speed of 50 rpm. PP was charged into the mixing chamber and melted for 4 min before NBRr was added. At 6 min the RHP was added and the mixing was continued for another 3 min for a total mixing time of 9 min. PP granules and NBRr powder were dried for 24 h at 80°C under vacuum prior to melt mixing in an internal mixer. The compounded samples were compression-moulded in a Go-Tech compression moulding machine a. A seven min of preheating at 180ºC, 2 min of compression at 1000psi and another 2 min of cooling for sample fabrication. Moulded samples were cut into 1 mm thickness dumbbell with a Wallace die cutter S6/1/6.A.

Tensile tests were carried out according to ASTM D638 using the Instron tensile machine model no 3366. Dumbell tensile specimens with 1 mm thickness were utilized for tensile test. Young's modulus, tensile strength and elongation at break were measured at a cross head speed of 5mm/min and tests were performed at room temperature (25± 3°C). Five specimens were used for each test and the average data with corresponding standard deviation were reported.

The failure mode of the fractured tensile specimens was examined using Field Emmission Scanning Electron Microscope (FESEM ZEISS SUPRA36VP-24-58). SEM micrographs were taken at various magnifications for fracture and other observations. Prior to the SEM observations the fractured ends of the specimens were mounted on aluminium stubs and were sputter coated with a thin layer of gold to avoid electrical charging during examinations.

Results and Discussion

Tensile Properties

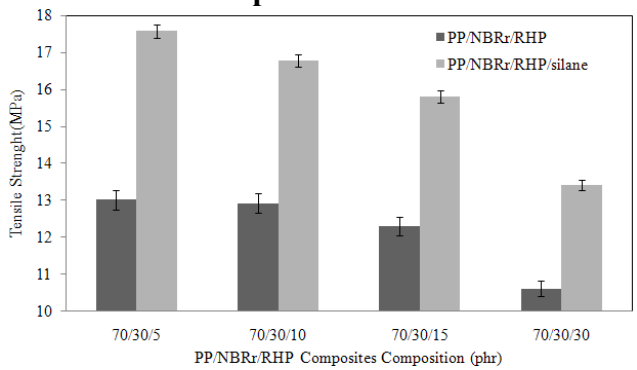


Fig. 1. Tensile strength versus filler loading of PP/NBRr/RHP composites

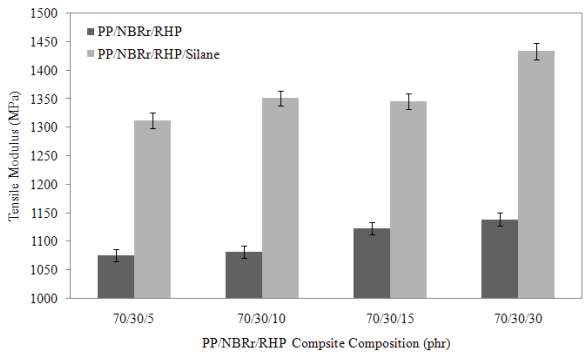


Fig. 2. Tensile modulus versus filler loading of PP/NBRr/RHP composites.

Fig. 1 shows plot of tensile strength versus filler loading of PP/NBRr/RHP composites. Both treated and untreated filler exhibited reduction in tensile properties for PP/NBRr/RHP composites at higher filler loading. This is resulted to weak interaction between filler and matrix. Similar finds are reported by Gassan et al. [8] in their studied on polypropylene and modified jute fibre. However, for composites with silane treated filler it can be seen that, tensile strength is much higher then the untreated fillers. This is due to the addition of coupling agent which enhances the filler-matrix interactions. The evidence of better interactions between matrix and filler can be seen from SEM

micrographs shown later in Fig. 5. Improved interaction between PP/NBRr matrix and silane treated RHP was also supported by the increase tend of tensile modulus as shown in Fig. 2.

Fig. 2 shows plot of tensile modulus versus filler loading of PP/NBRr/RHP composites. Tensile modulus increases with the increase of filler loading. This observation indicates that the incorporation of RHP filler into the matrix improves the stiffness of the composites. The addition of RHP filler into the PP/NBRr matrix reduces the chains' mobility, consequently producing more rigid composites. At a similar filler loading, tensile modulus for composites with silane treated filler exhibited higher tensile modulus compared to composites with untreated filler. According to Bledzki et al. [7] an increase of 50% tensile modulus was reported in natural vegetable fiber due to improved interactions between matrix and filler with the presence of silane coupling agent. This finds is in also in agreement with Liu et al.[10] whereby higher rigidity of biocomposites is exhibited in surface modified jute fibers with silane coupling agent. The elongation at break (E_b) supports this finding as shown in Fig.3.

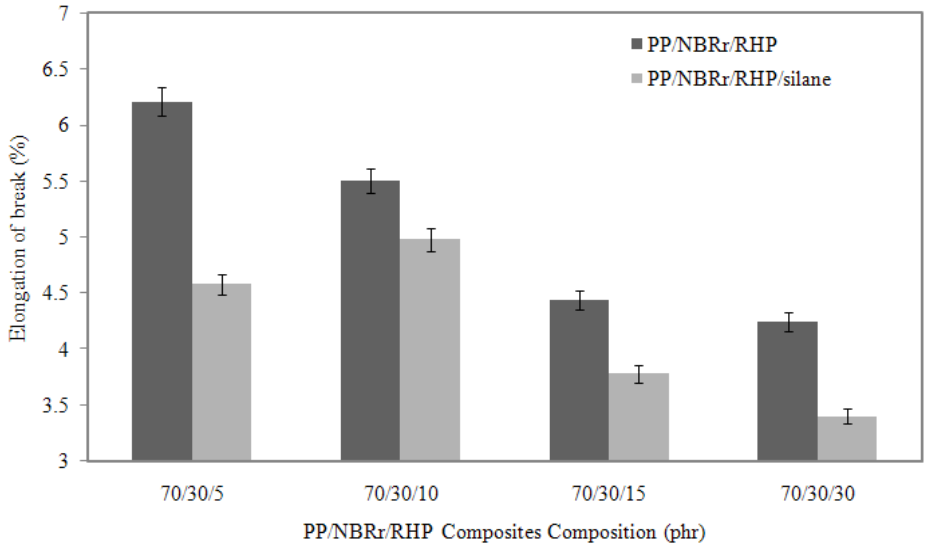
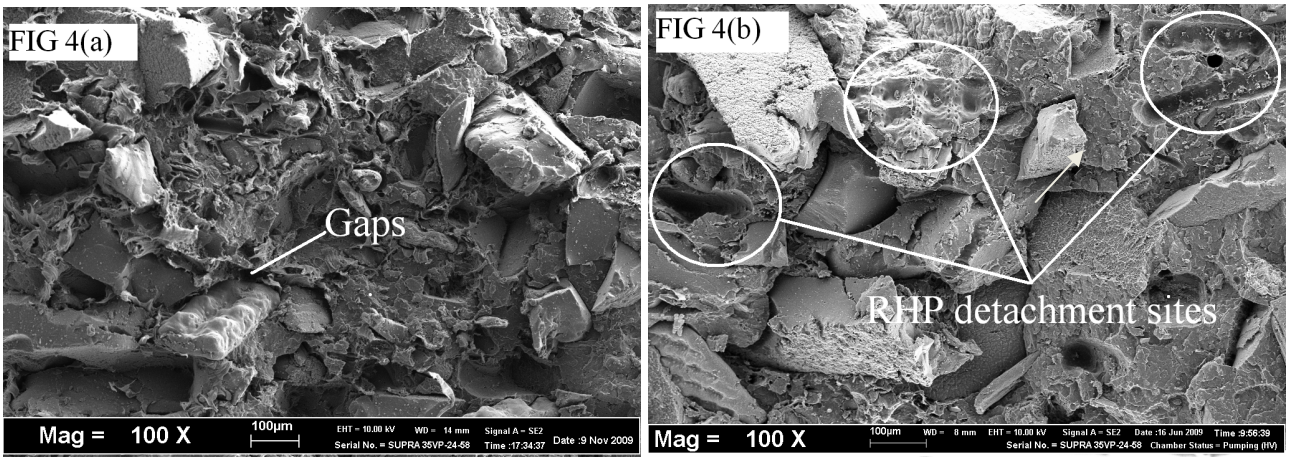


Fig. 3 Elongation at break versus fiber loading of PP/NBRr/RHP composites

Fig. 3 shows plot for elongation at break versus fiber loading of PP/NBRr/RHP composites. Elongation at break decreased with the increasing of fiber loading. This is due to the increasing of stiffness and brittleness of the composites. At similar filler loading, the elongation at break for PP/NBRr/RHP composites with silane treated filler is much lower than the composites with untreated filler. This findings further confirms the presence of silane coupling agent enhance the matrix and filler interactions in PP/NBRr/RHP composities. Hong et al. [12] reported that silane treatment of natural fiber yielded a stronger interfacial adhesion resulting in low elongation at break at in composites. This phenomenon can be observed from SEM micrographs study of fractured surface in as shown in Fig. 4 and Fig.5.

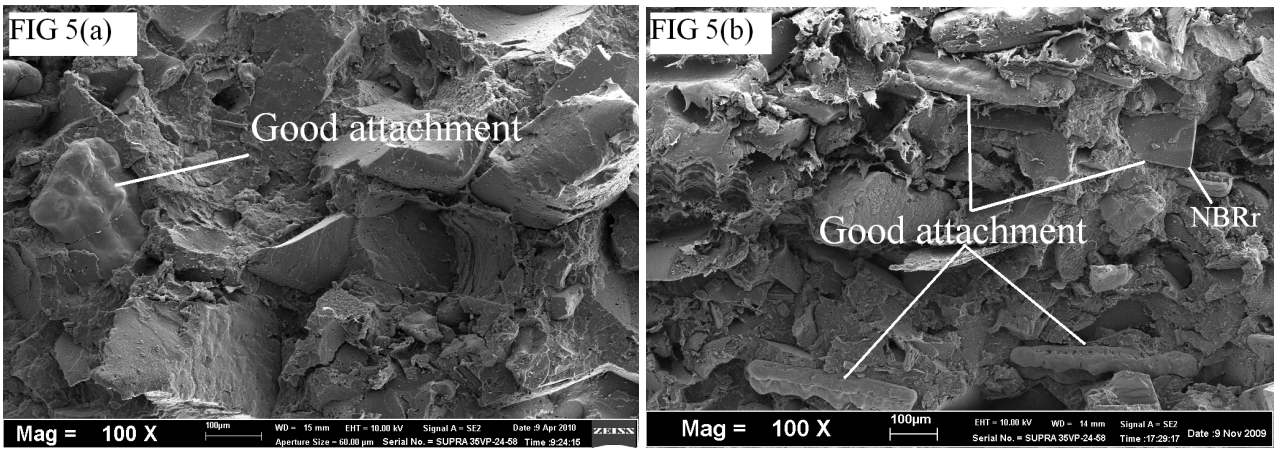
SEM Micrographs Study



4a)70/30/10 4b)70/30/30

Fig. 4. SEM micrograps of PP/NBRr/RHP composite without silane

Fig. 4 shows SEM micrographs of fractured surface of PP/NBRr/RHP composites with 10 and 30 phr RHP loading. The SEM micrographs shows that poor adhesion of RHP to the PP/NBRr matrix is the main factor for the reduction of the tensile strength with an increasing of filler loading in the composites. The incorporation of RHP filler into the PP/NBRr matrix increase the rigidity of the material thus reduces the ductility of the composites[11,13]. Figure 4(a) some noticeable gaps between the filler and matrix which is the evident of poor adhesion between the filler and matrix. Figure 4(b) shows that the RHP fillers were pulled out from the matrix which marked with circles exhibited more detachment of RHP filler from the matrix. This is due to the poor dispersion and poor wettability of the filler by the PP/NBRr matrix. In contrast, as similar filler loading, treated filler exhibit good adhesion between the filler and matrix as shown in Fig.5.



5a)70/30/10_Silane 5b)70/30/30_Silane

Fig. 5. SEM micrograps of PP/NBRr/RHP composite with silane treatment

Fig. 5 shows SEM micrographs of fractured surface of PP/NBRr/RHP composites with silane treated filler at 10 phr and 30 phr filler loadings. It can be seen that, in Figure 5(a) & 5(b), good attachment between the filler and matrix. The adhesion between filler and matrix were enhanced with the usage of γ-aminopropyltrimethoxysilane as a coupling agent. This explains why higher mechanical properties for PP/NBRr/RHP/Silane treated composites were exhibited.

Summary

The following conclusion can be drawed from this work:-

1. Tensile strength and Young modulus of both silane treated and untreated RHP composites decreased with the increasing amount of NBRr matrix.
2. Higher tensile strength, greater tensile modulus and lower elongation at break in PP/NBRr/RHP proof that the composite become more brittle with strong attachment between PP/NBR matrix and RHP filler.
3. Good adhesion between RHP filler and PP/NBRr matrix was found with filler treated with γ-aminopropyltrimethoxysilane for PP/NBRr/RHP composites. The morphological studies confirm good attachment of silane treated RHP filler with PP/NBRr matrix.

References

[1] M.J. John, B. Francis, K.T. Varughese, S.Thomas: Comp. Part A: Appl. Sci. and Manuf. Vol. 39(2008), p. 352

[2] H. Ismail, L. Mega: Poly. Plastic Tech. Eng. Vol.40(2001), p. 463

[3] S.A. Paul, A. Boudenne, L. Ibos, Y. Candau, K. Joseph, S. Thomas: Composites Part A: App. Sci. and Manuf. Vol.39(2008), p.1582

[4] H. Ismail, M.R. Edyham, B. Wirjosentono: Polymer Testing, Vol.21(2002),p. 139

[5] M. Kazayawoko, J.J. Balatinecz, L.M. Matuana:J.Mater. Sci. Vol.34(1999), p. 6189

[6] Q. Li, L.M. Matuana: J. App. Poly. Sci., Vol. 88 (2003), p. 278

[7] A.K. Bledzki, S. Reihmane, J. Gassan: J. App. Poly. Sci.,Vol.59 (1996), p. 1329

[8] J. Gassan, I. Mildner, A.K. Bledzki: Comp. Interfaces Vol.8 (2001), p. 443

[9] H. Ismail, L. Mega, H.P.S. Abdul Khalil: Poly. International Vol.50 (2001), p. 606

[10] L. Liu, J. Yu, L. Cheng, W. Qu: Comp. Part A: App. Sci. and Manuf. Vol.40 (2009), p. 669

[11] H. Ismail, S. Ragunathan, K. Hussin: Poly. Plastic Tech. Eng. Accepted-2010

[12] C.K Hong, I. Hwang, N. Kim, D.H. Park, B.S. Hwang, C. Nah: J. Indust. and Eng. Chem. Vol. 14(2008), p. 71

[13] H. Ismail, S.Ragunathan, K. Hussin: J. Vinyl and Additive 2010-Accepted

© (2011) Trans Tech Publications, Switzerland
doi:10.4028/www.scientific.net/KEM.471-472.478

The Effect of Silane Treatment on Processing Characteristic and Swelling Behavior of Polypropylene/Recycled Acrylonitrile Butadiene Rubber/Rice Husk Powder Composites

S. Ragunathan[1, a], H. Ismail[1, b] and K. Hussin[2,c]

[1]School of Material and Mineral Resources,Engineering Campus, Seri Ampangan,Universiti Sains Malaysia,14300 Nibong Tebal, Pulau Pinang, Malaysia

[2]School of Environmental Engineering, Kompleks Pengajian Jejawi 3,Universiti Malaysia Perlis,02600 Arau, Perlis,Malaysia

[a]raguna@unimap.edu.my, [b]hanafi@eng.usm.my, [c]kamarudin@unimap.edu.my

Keywords: Polypropylene; Recycled acrylonitrile butadiene rubber;Silane; Compatibilization; Rice husk powder; Tensile properties; Morphology

Abstract. The effect of silane treatment on processing characteristic and swelling behavior of recycled acrylonitrile butadiene rubber (NBRr)/polypropylene (PP)/rice husk powder (RHP) composites has been studied. Polypropylene/recycled acrylonitrile butadiene rubber/rice husk powder (PP/NBRr/RHP) composite were prepared by melt mixing technique at 180º C for 9 minutes and 50rpm rotor speed using an internal mixer. Five different composites compositions (70/30/0, 7030/5, 70/30/10, 70/30/15 and 70/30/30), with silane treated RHP (treated) and without silane treatment RHP (untreated) was studied. The specimens were analyzed for swelling behavior with ASTM oil No.3 and processing torque of composites was obtained during composite preparation. The results showed that swelling percentage for both composites increased with NBRr content. However the treated composites exhibited lower swelling characteristics. Processing torque of both composites also showed higher torque reading with increasing NBRr content. However the treated composite with silane exhibited much higher torque value for similar composition composites. Better interaction between RHP filler and PP/NBRr matrixs was obtained with treated composites.

Introduction

Advantages of natural fibers over man-made fibers make natural fibers the potential replacement for traditional reinforcement materials such as glass fiber in composite material systems. Its capacity as filler or additives in plastic materials is not well define. The reason is because these composites are found to be incompatible or immiscible due to poor physical and chemical interaction between the phases. The incompatibility may be due to the fact that the polyolefin is non-polar and hydrophobic, whereas lignocelluloses material is polar, due to the hydroxyl groups in the cellulose.

In order to solve this problem, studies have been performed on surface modification for the purpose of making the polyolefin chains more hydrophilic [1,2]. Chemical treatment on fibers surface and usage of coupling agent are excellent methods to improve compatibility between hydrophobic matrixs and hydrophilic fillers [3-4]. Many investigations have been carried out by numerous researchers [4-6]. Coupling agents based on alkoxysilanes are frequently employed for cellulosic fibers. Hydrolysis of the alcoxyl groups with subsequent reaction with hydroxyl groups from cellulose can provide chemical bonding with the fibers [7]. Bledzki et al. [8] modified jute fiber with alkali, silane and maleated polypropylene (MAPP), and found that surface modification enhanced the mechanical properties of jute fiber reinforced polypropylene composites. Ismail et al. [9] utilized silane coupling agent on white rice ash-polypropylene/natural rubber composites, and found that silane coupling agent have improved the mechanical properties of the composite. Liu et

al. [10] modified jute fiber with alkali and silane, and found that chemical treatments on the surface of jute fiber have improved the mechanical properties of jute fiber reinforced poly(butylenes succinate) bio-composites. However, so far no work has been reported on PP/NBRr/RHP composites and its effect with the APS coupling agent. The aim of this study is to evaluate the effect γ-aminopropyltrimethoxysilane (APS) coupling agent on the PP/NBRr/RHP composites. Processing stabilization torque, water absorption and swelling behavior of PP/NBRr/RHP composites were investigated.

Experimental

Material	Description	Source
Polypropylene(PP)	Code: 331 MFI: 14g/10 min at 230°C Density: 0.9g/cm^3	Titan Pro Polymers (M) Sdn. Bhd. Johor, Malaysia
Recycled Acrylonitrile Butadiene Rubber (NBRr)	Content:33% of Acrylonitrile Density: 1.015g/cm^3	Juara One Resources Sdn. Bhd. Penang, Malaysia
Rice Husk Powder(RHP)	Cellulose :35% Hemicellulose: 25% Lignin :20% Ash :17% Density:1.4702g/cm^3 Size: 300-500μm	Thye Heng Chan Enterprise Sdn. Bhd
Silane Coupling Agent	γ-aminopropyltrimethoxysilane (APS)	Alfa Aesar (M) Sdn Bhd

Table 1: Materials specification and description

The materials used for the preparation of PP/NBRr/RHP composites are shown in Table 1. The rice husk powder were ground in a table type pulverizing machine (Rong Tsong Precision Technology Co. Product Id: RT-34) with speed of 2850 rpm, sieved at 300-500μm in particle size and dried at 110ºC for 24 hours in a vacuum oven to produce rice husk powder of homogeneous fractions.

The treatment reaction was carried out in a mixture of water/ethanol (40/60 volume). 3g of γ-aminopropyltrimethoxysilane was first introduced into 1000 ml of the mixture water/ethanol and was allowed to stand for 1 hour. The pH of the solution was maintained at 4 with the addition of acetic acid. Then, 10 g of rice husk powder was added into the solutions and the solutions were continuously stirred for 1.5 hours. The filler was filtered and was dried in the air and then in the vacuum oven at 80°C for 24 hours.

Polypropylene (PP) was mixed with recycled acrylonitrile butadiene rubber (NBRr) and rice husk powder (RHP) at various loading (0, 10, 15, 20, 30) phr. Rice husk powder was dried at 110ºC for 24 hours in a vacuum oven prior to mixing. A constant PP and NBRr was used at 70phr and 30phr respectively. Table 2 shows the formulation of PP/NBRr/RHP composites.

The composites were prepared by melt mixing using a Haake Rheomix Polydrive R 600/610 mixer at 180^{0}C with the rotor speed of 50 rpm. PP was charged into the mixing chamber and melted for 4 min before NBRr was added. At 6 min the RHP was added and the mixing was continued for another 3 min for a total mixing time of 9 min. PP granules and NBRr powder were dried for 24 h at 80°C under vacuum prior to melt mixing in an internal mixer. The compounded samples were compression-moulded in a Go-Tech compression moulding machine. A seven (7) min of preheating at 180ºC, 2 min of compression at 1000psi and another 2 min of cooling for sample fabrication. Moulded samples were cut into dumbbell with a Wallace die cutter S6/1/6.A according to ASTM D638.

Table 2: Formulation for PP/NBRr/RHP composites

Composite Materials	PP/NBRr /RHP composites (phr)								
	S1	S2	S3	S4	S5	S6	S7	S8	S9
PP	70	70	70	70	70	70	70	70	70
NBRr	30	30	30	30	30	30	30	30	30
Pure RHP	–	5	10	15	30	–	–	–	–
γ-APS Treated RHP	–	–	–	–	–	5	10	15	30

The specimens were dried for 4 h in a vacuum oven at 100°C until a constant weight was attained prior to immersion in water in thermostated vessels at ambient temperature. Weight gains, after exposure, were recorded by removal of the specimen from the environment and by weighing them periodically on a Stanton balance with a precision of 1 mg. The moisture content at any time t, M_t as a result of moisture absorption, was calculated by using Eq. 1.

$$Mt\ (\%) = \frac{W_o - W_d}{W_o} \times 100\% \quad (1)$$

where W_d and W_o were, weight of dry material (i.e., the initial weight of the material prior to exposure to the environment) and weight of moist material. The percentage equilibrium moisture absorption, M_m, was calculated as an average value of several consecutive measurements that showed no appreciable additional absorption.

Determination of the swelling percentage in ASTM oil No. 3 was carried out in accordance with ASTM D471 test method. The test pieces of dimension 30 mm x 5mm x 1mm were weighed and immersed in ASTM oil No.3 at room temperature for 70 hours. As for toluene the test, samples were immersed for 48 hours at room temperature. The swelling percentage of the samples for both ASTM oil No.3 and toluene was calculated using Eq. 2.

$$\text{Swelling}\ (\%) = \frac{\text{swollen weight} - \text{original weight}}{\text{original weight}} \times 100 \quad (2)$$

Results and Discussion

Fig. 1 shows plot of stabilization torque at end of mixing 9 min for PP/NBRr/RHP composites. The stabilization torque can be a direct measurement for evaluating the viscosity and processability of molten polymer composite systems. An increase in the torque value means an increase in the viscosity of the molten polymer composite systems, whereas processability is decreased. It can be seen that stabilization torque increases gradually with the increase in filler loading. This is due to the presence of more rigid filler and interfacial interactions between filler and matrix, therefore reducing the polymer chains' mobility [2,12]. At a similar filler loading, the composites with silane treated filler shows higher stabilization torque as compared to the composites with untreated filler which indicates more force is needed for each compounding to be done. This is due to the presence of γ-aminopropyltrimethoxysilane which enhances interfacial interactions between filler and matrix and resulted in the increases of viscosity of the molten materials. We have reported a similar observation in our previous study on the PP/NBRr/RHP with PPMAH(Polypropylene Maleic Anyhdride) compatibilization [11] whereby higher stabilization torque resulted for composites with good interfacial interactions between RHP and PP/NBRr matrixs.

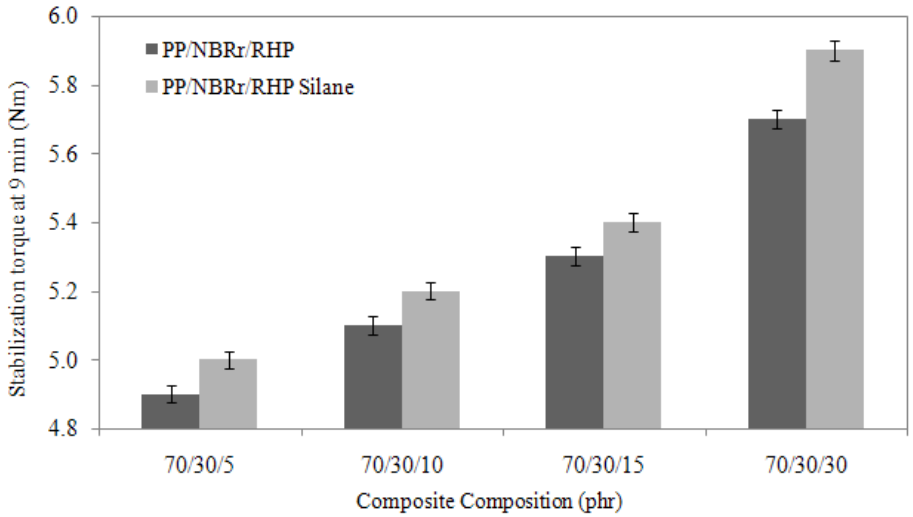


Fig 1: Stabilization torque at end of mixing 9 min for PP/NBRr/RHP composites

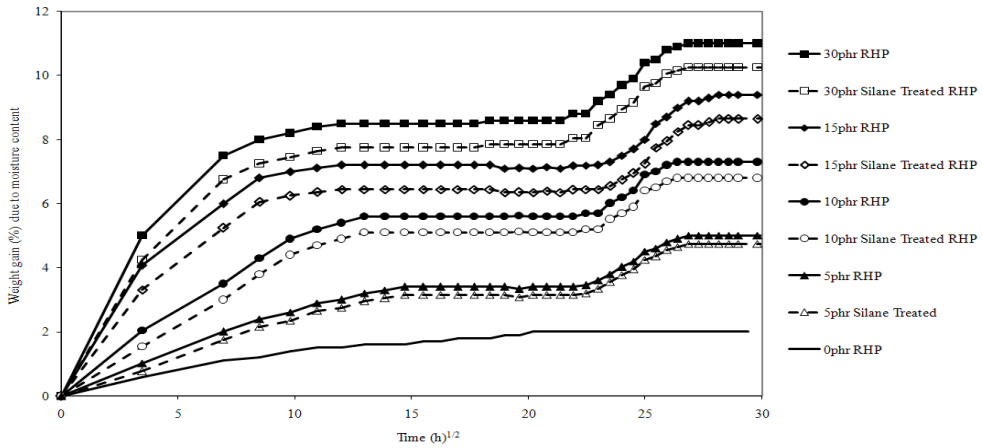


Fig 2. Water absorption of PP/NBRr/RHP composites with and without silane treatment

Fig. 2 shows plot of water absorption of PP/NBRr/RHP composites with and without silane treatment. Each data point represents the average of five specimens. Water uptake increased with immersion time and increasing filler loading as also reported by other researchers [7,9,14-15]. However in our previous research PP/NBRr/RHP were found to exhibit 2 stage absorption behavior [13]. The RHP in continues matrix absorb water much easier compared to the RHP particles encapsulated by NBRr. It can be seen in Figure 10 that filler content had a significant effect on water absorption properties of the composites. It indicates that, the higher the filler content, the higher the percentage of equilibrium water absorption [15]. This is due to the fact that, the increases of filler content in composite will increase the number of free OH groups of lignocellulosic fiber. Free OH groups come in contact with water through hydrogen bonding which results in water uptake and weight gain in the composites. At a similar filler loading, it can be seen that the composites with silane treated filler shows a lower water uptake compared to the composites with untreated filler. This result provides a clear indication that the RHP treatment with γ-aminopropyltrimethoxysilane enhances the filler-matrix interactions at the interface thus decrease the amount of equilibrium water uptake by the composites. Ismail et al.[16] reported similar findings whereby lower absorption in in PP/NR/RHP ash attributed to the ability of the chemical to form a protective layer at the interfacial zone to consequently prevent the direct diffusion of water molecules into silane treated composites.

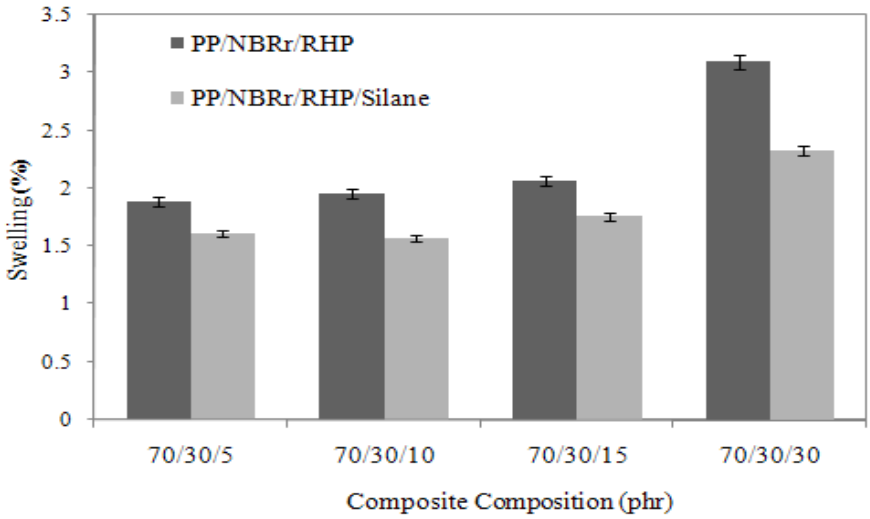


Fig 3. Swelling percentage of PP/NBRr/RHP composites with and without silane treatment

Fig. 3 shows plot of swelling percentage of PP/NBRr/RHP composites with and without Silane treatment in ASTM oil No. 3 for 70 hours. It was found that swelling percentage increased with increasing of RHP content in both silane treated and untreated PP/NBRr/RHP composites. This was due to the properties of natural fiber RHP which absorb oil on its surface[10]. However for the similar composites composition, the treated composites exhibited lower swelling percentage due to better interaction of RHP particles in the continuous PP/NBRr matrix which limit the penetration of oil into the treated composites matrix. This might due to the ability of silane coupling agent to form better interaction and a protective layer at the interfacial zone to consequently prevent the direct diffusion of water and oil molecules into the composites. We have reported similer observation on polypropylene-maleic-anhydride(PPMAH) compatibilization to PP/NBRr/RHP composites in our previous work [13].

Summary

The following conclusions can be made based on the results presented in this work.

1. The processing torque and tensile modulus and swelling in oil increases with increasing RHP filler loading in untreated composites. It is attributed to the brittle nature of RHP.
2. Silane treated composites exhibits higher processing stabilization torque, tensile modulus and lower elongation compared to untreated composites might due to strong interfacial bonding between RHP filler and PP/NBRr matrixs.
3. Silane treatment is effective in reducing water and oil absorption in PP/NBRr/RHP/ composites. This might due to the ability of silane coupling agent to form better interaction and a protective layer at the interfacial zone to consequently prevent the direct diffusion of water and oil molecules into the composites.

References

[1] M.J. John, B. Francis, K.T. Varughese, S.Thomas: Comp. Part A: Appl. Sci. and Manuf. Vol. 39(2008), p. 352
[2] H. Ismail, L. Mega: Poly. Plastic Tech. Eng. Vol.40(2001), p. 463
[3] S.A. Paul, A. Boudenne, L. Ibos, Y. Candau, K. Joseph, S. Thomas: Composites Part A: App. Sci. and Manuf. Vol.39(2008), p.1582
[4] H. Ismail, M.R. Edyham, B. Wirjosentono: Polymer Testing, Vol.21(2002),p. 139
[5] M. Kazayawoko, J.J. Balatinecz, L.M. Matuana:J.Mater. Sci. Vol.34(1999), p. 6189
[6] Q. Li, L.M. Matuana: J. App. Poly. Sci., Vol. 88 (2003), p. 278
[7] A.K. Bledzki, S. Reihmane, J. Gassan: J. App. Poly. Sci.,Vol.59 (1996), p. 1329

[8] J. Gassan, I. Mildner, A.K. Bledzki: Comp. Interfaces Vol.8 (2001), p. 443
[9] H. Ismail, L. Mega, H.P.S. Abdul Khalil: Poly. International Vol.50 (2001), p. 606
[10] L. Liu, J. Yu, L. Cheng, W. Qu: Comp. Part A: App. Sci. and Manuf. Vol.40 (2009), p. 669
[11] H. Ismail, S. Ragunathan, K. Hussin: Poly. Plastic Tech. Eng. Accepted-2010
[12] C.K Hong, I. Hwang, N. Kim, D.H. Park, B.S. Hwang, C. Nah: J. Indust. and Eng. Chem. Vol. 14(2008), p. 71
[13] H. Ismail, S.Ragunathan, K. Hussin: J. Vinyl and Additive 2010-Accepted.
[14] Z.A.M. Ishak, A. Ariffin, R. Senawi: Europ. Poly.J. Vol.37(2001), p.1647
[15] M. Razavi-Nouri, F. Jafarzadeh-Dogouri, A. Oromiehie, A.E. Langroudi: Iranian Poly. J. Vol. 15(2006), p.757

© (2011) Trans Tech Publications, Switzerland
doi:10.4028/www.scientific.net/KEM.471-472.484

Parametric Study of Automotive Composite Bumper Beams Subjected to Frontal Impacts

Mai Nursherida J. [1,a], B.B. Sahari[1,2,b], Nuraini A.A.[1,c]

[1] Department of Mechanical and Manufacturing, Universiti Putra Malaysia,
43400 UPM Serdang, Selangor, Malaysia

[2] Institut Teknologi Maju, ITMA, Universiti Putra Malaysia,
43400 UPM Serdang, Selangor, Malaysia

[a]erida295@yahoo.com, [b]barkawi@eng.upm.edu.my, [c]nuraini@eng.upm.edu.my

Keywords: Front bumper beam, internal energy, specific energy absorption, E-glass/epoxy composite, carbon/epoxy composite

Abstract. The parametric study of automotive composite bumper beam subjected to frontal impact is presented and discussed in this paper. The aim of this study is to analyze the effect of steel and composite material on energy absorption of automotive front bumper beam. The front bumper beams made of e-glass/epoxy composite and carbon epoxy composite are studied and characterized by impact modeling using LS-DYNA V971, according to United States New Car Assessment Program (US-NCAP) frontal impact velocity and based on European Enhanced Vehicle-safety Committee. The most important variable of this structure are- mass, material, and Specific Energy Absorption (SEA). The results are compared with bumper beam made of mild steel. Three types of materials are used in the present study which consists of mild steel as references material, Aluminum AA5182, E-glass/epoxy composite and carbon fiber/epoxy composite with three different fiber configurations. The beams were subjected to impact loading to determine the internal energy and SEA and to reduce mass of the conventional bumper beam. The in-plane failure behaviors of the composites were evaluated by using Tsai Wu failure criterion. The results for the composite materials are compared to that of the reference material to find the best material with highest SEA. LS-DYNA Finite Element Analysis software was used. The results showed that carbon fiber/epoxy composite bumper can reduce the bumper mass and has highest value of SEA followed by glass fiber/epoxy composite.

Introduction

Bumper beams are one of the key structures in passenger cars for which careful design and manufacturing should be considered in order to achieve good impact behavior [1, 2].

The bumper beam is the main structure for absorbing the energy of collisions. It has been known that a front crash in passenger cars is the most fatal accident among traffic mishaps [3]. Recently, in order to reduce the weight of cars and increase energy absorption capacity, most manufacturers of passenger vehicles use composite plastics bumpers. Bumper beams are usually made of steel, aluminum, plastic, or composite material [4-6].

The new cars safety assessment was performed using the Unites States New Car Assessment Program (US NCAP) criteria which is 100% frontal crash at 56 km/h into rigid barrier requirement [7]. Finite element model of the front bumper was created and the structural analysis was performed in accordance with NCAP requirements. Three main parameters were studied; namely material, shape and impact condition. By doing this, the effects of material on the impact specifications can be obtained. Suitable materials that can be used to replace mild steel can be determined. In addition, the suitable shape for easier manufacturing processes and reducing material volume with constant impact strength can be determined, and the effect of test conditions on the impact behavior can be assessed.

Steel and aluminum structures with specified thickness that did not fail during impact test showed clearly that they are not suitable as bumper beam structure due to increasing weight. They increased the weight of the structure by nearly 500% and 100% respectively, in comparison with the composite bumper [8]. In this paper, three different thicknesses of 1.6 mm, 1.8 mm and 2.0 mm were used for aluminum bumper. Apart from aluminum, E-glass/ epoxy composite and carbon/ epoxy composite are also studied in order to find best materials to achieve high impact characteristics and achieve minimum weight behavior.

The objectives of this study were to develop and propose a suitable bumper that satisfies following requirement:

1. Achieving reduced weight of front bumper beam by using lightweight material.
2. Achieving specific energy absorption similar to or better than the bumper beam that uses conventional – steel material.

To study the characteristics of composite materials, e-glass/epoxy and carbon/epoxy composite material properties were used to model the bumper. The e-glass/ epoxy bumper and carbon/epoxy bumper were simulated under the same test conditions as steel in three different fiber configurations; $[0^o/60^o]_S$, $[0^o/30^o/60^o]_S$, and $[0^o/30^o/60^o/90^o]_S$.

The Tsai-Wu Failure Criterion. Tsai-Wu theory is used as the failure criteria for the composites [9]. It state that failure occurs when

$$f_i\sigma_i + f_ij\sigma_i\sigma_j = 1 \qquad \text{where} \qquad i, j = 1,2,3,4,5,6 \tag{1}$$

For plane-stress condition Eq. 1 becomes (refer Eq 2 and Eq. 3):

$$f_1\sigma_1 + f_2\sigma_2 + f_6\tau_6 + f_{11}\sigma_1^2 + f_{22}\sigma_2^2 + f_{66}\tau_6^2 + 2f_{12}\sigma_1\sigma_2 + 2f_{16}\sigma_1\tau_6 + 2f_{26}\sigma_2\tau_6 = 1 \tag{2}$$

$$f_1\sigma_1 + f_2\sigma_2 + f_{11}\sigma_1^2 + f_{22}\sigma_2^2 + f_{66}\tau_6^2 + 2f_{12}\sigma_1\sigma_2 = 1 \tag{3}$$

Where σ are stresses and f are the related functions.

Finite element modeling. The CAD model of the bumper was first created using CATIA software and the data was imported and the surfaces were created and meshed using LS-DYNA V971 software. Since the average thickness of bumper was much smaller than the other dimensions, the best element for the mesh was the shell element.

For impact analysis, implicit and explicit elements can be considered. For the present work, a nonlinear explicit impact modeling elements were used. The bumper beam and bumper system is attached to rigid block that represent the mass of the car. The mesh for the bumper beam, bumper system and rigid box was developed using HyperMesh finite element pre-processor. Material type 24 (mat_piecewise_linear_plasticity) are used for simulation of metallic materials. Material type 20 (mat_rigid) are used for simulation of rigid box. Material type 54 and 55 (mat_enhanced_composite_damage) are used for simulation for the composite materials in this study. Fig. 1 shows the model of bumper beam, bumper system and the rigid wall. As shown, the rigid wall collides to the bumper beam in perpendicular direction. Table 1 shows the FEM characteristics of each component in the modeling. It was assumed that there is no friction between the rigid wall and bumper surfaces.

The rigid wall velocity was 56 km/h for frontal impact (representing condition of full frontal impact in Unites States New Car Assessment Program).

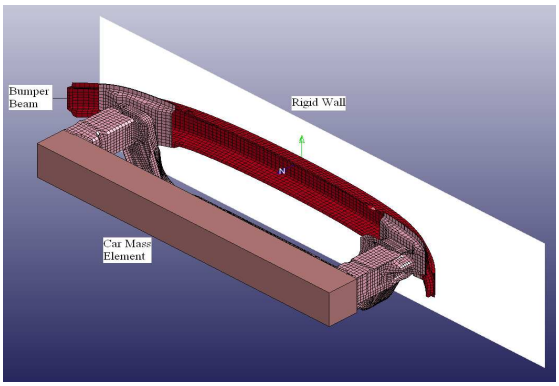


Fig. 1 - Isometric view of impact layout

To investigate the effect of the bumper beam material on the impact behavior, two parameters are studied here: modulus of elasticity and the yield strength. The effects of each parameter are presented as follows [8].

Table 1 FEM characteristics of the models.

No	Part of model	Material	FEM element	Element number	Thickness or weight
1	Bumper beam	St, Al, E-glass/ epoxy, carbon/ epoxy	Shell	2291	1.2 mm, 1.6 mm, 1.8 mm, 2.0 mm, 2.1 mm
2	Rigid Wall	-	Solid	-	160 kg

Results and discussion

Metallic bumper beams. Steel and aluminum were two conventional metals whose specifications assigned to the bumper in separate tests. The properties for steel and aluminum AA5182 are given in Table 2. Other characteristics of the model such as bumper system including brackets, reinforcement rigid wall, etc, remained constant for all the case studies. The rigid wall impacted perpendicular to the bumper beam at velocity of 56 km/h. Fig. 2(a) shows the internal energy of steel bumper. From Fig. 2(a), maximum internal energy of 3.87 kJ is obtained. Fig. 2(b) shows the energy balance for whole system. It can be seen that the total energy remains constant.

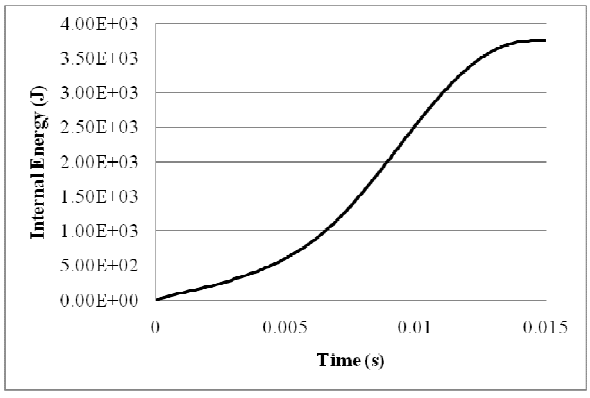


Fig. 2(a) - Internal energy of steel bumper

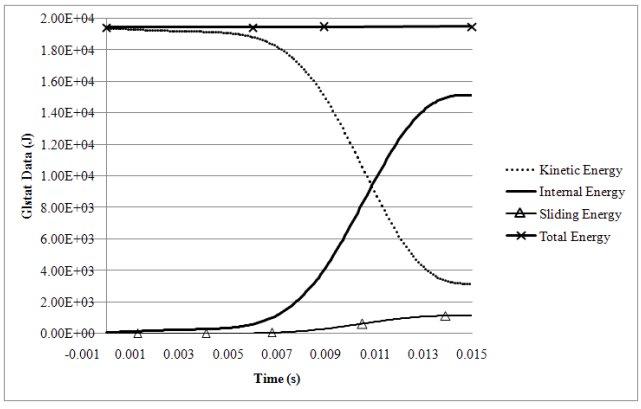


Fig. 2 (b) - Energy balance for whole system

The aluminum used for the bumper in this research is type AA5182. Three different thickness values are simulated for AA5182 and the result are compared with steel bumper. Simulation results for aluminum bumper are shown in Fig. 3. From Fig. 3, it clearly shows that AA5182 with thickness 2.0 mm has the highest value for internal energy of 4.269 kJ followed by 1.8 mm thickness with 3.835 kJ and 1.6 mm thickness with 3.337 kJ.

Table 2 Material properties of steel and aluminum AA5182.

Material	E (GPa)	υ	S_y (MPa)	ρ (kg/m^3)
Steel	260	0.3	168	7850
AA5182	69.6	0.33	134.84	2650

Composite bumper beams

The e-glass/epoxy bumper and carbon/epoxy bumper used in this research is a structure made from woven-fabric laminated composite with epoxy as a resin. A woven fabric is a fabric produced by the process of weaving in which the fabric is formed by interlacing the warp and fill strands[9]. In the present paper, the bumper beam being studied is made of e-glass/epoxy composite and carbon/epoxy composite with three different thickness values of 2.0 mm, 2.1 mm and 2.4 mm. The material properties for E-glass/epoxy composite and carbon/epoxy composite are given in Table 3. There are three different fiber configuration are simulated; $[0^o/60^o]_S$ for Glass A and Carbon A, $[0^o/30^o/60^o]_S$ for Glass B and Carbon B and $[0^o/30^o/60^o/90^o]_S$ for Glass C and Carbon C.

Table 3 Material properties of e-glass/epoxy composite and carbon/epoxy composite.

Material	E_{11} (GPa)	E_{22} (GPa)	E_{33} (GPa)	G_{12} (GPa)	G_{13} (GPa)	G_{23} (GPa)	υ_{12}	υ_{13}	υ_{23}	ρ (kg/m^3)
E-glass/epoxy	44.6	13.4	13.4	4.4	4.4	5.0	0.317	0.317	0.342	2040
Carbon/epoxy	150.7	13.3	13.3	4.9	4.9	4.8	0.287	0.287	0.390	1554

Table 4 Result Comparison

No	Bumper Beam Material	Fiber Configuration	Thickness of each layer(mm)	Total Thickness (mm)	Internal Energy (kJ)	Specific Energy Absorption (kJ/kg)	Mass (kg)	Mass reduction compared with steel (%)
1	Steel	Isotropic	N/A	1.2	3.76	1.405	2.676	0
2	AA5182	Isotropic	N/A	1.6	3.38	2.798	1.208	54.86
3	AA5182	Isotropic	N/A	1.8	3.84	2.826	1.359	49.22
4	AA5182	Isotropic	N/A	2.0	4.27	2.828	1.510	43.57
5	Glass A	$[0^o/60^o]_S$	0.5	2.0	4.01	3.481	1.152	56.95
6	Glass B	$[0^o/30^o/60^o]_S$	0.4	2.1	4.26	3.521	1.210	54.78
7	Glass C	$[0^o/30^o/60^o/90^o]_S$	0.3	2.4	4.88	3.531	1.382	48.36
8	Carbon A	$[0^o/60^o]_S$	0.5	2.0	4.95	5.638	0.878	67.19
9	Carbon B	$[0^o/30^o/60^o]_S$	0.4	2.1	5.03	5.461	0.921	65.58
10	Carbon C	$[0^o/30^o/60^o/90^o]_S$	0.3	2.4	5.68	5.394	1.053	60.65

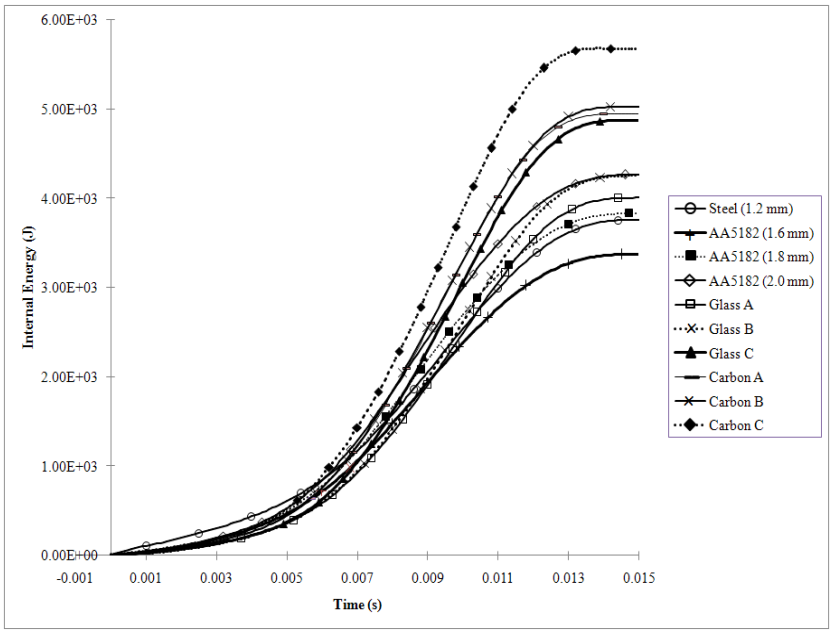


Fig. 3 - Internal Energy vs Time for result comparison

The internal energy for steel, aluminum AA5182, e-glass/epoxy and carbon/epoxy bumpers are shown in Fig. 3. It is observed that for composite bumpers, increasing beam thickness to 2.0 mm, 2.1 mm and 2.4 mm increases the Specific Energy Absorption (SEA) compared with conventional steel bumper beam. In carbon epoxy bumper (Carbon A) the maximum weight reduction is 67.2% compared with steel bumper mass as shown in Table 4. The result of the comparison in SEA for steel, aluminum and composite bumpers are shown in Fig. 4(a). The variation of maximum internal energy with mass is shown in Fig. 4(b). It can be seen that carbon fiber/epoxy composite gave the highest internal energy at low mass compared with e-glass/epoxy and aluminum AA5182.

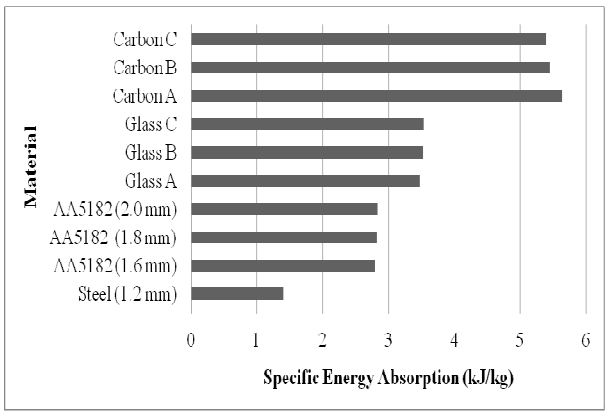


Fig. 4 (a) - Result comparison in SEA

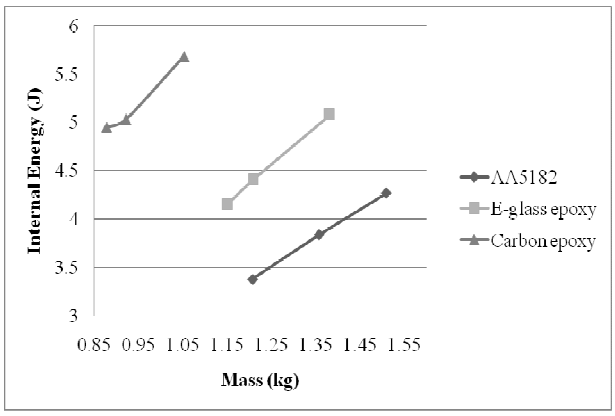


Fig. 4 (b) - Internal energy vs Mass

Summary

From the result presented, the following conclusion can be made:

1. Carbon/epoxy composite bumper reduced the bumper mass with 67.2% of weight reduction and has highest value of SEA with 5.638 kJ/kg followed by e- glass composite bumper with 3.531 kJ/kg of SEA.
2. Carbon/epoxy and e-glass epoxy bumpers were proposed to replace conventional steel bumper beam.

References

[1] S R Reid, G.Z., *Woodhead Publishing Limited,* 320 pages (2000)

[2] Hosseinzadeh, R., M.M. Shokrieh, and L.B. Lessard: Composite structures, Vol. 68 p. 419-427 (2005).

[3] Cheon, S.S., J.H. Choi, and D.G. Lee: Composite structures, Vol. 32 (1995), p. 491-499.

[4] Clausen, A.H., O.S. Hopperstad, and M. Langseth: Journal of Materials Processing Technology, (2000) Vol. 102, 1-3, p. 241-248.

[5] Kim, S.: Society of Automotive Engineers (1998).

[6] Fenton, J., *Handbook of vehicle design analysis*, Society of Automotive Engineers (1996).

[7] Paulius Griskevicius, A.Z., Transport - 2003, Vol XVII, No 2, 97-101 (2003).

[8] Marzbanrad, J., M. Alijanpour, and M.S. Kiasat, Thin-Walled Structures, Vol. 47, p. 902-911 (2009).

[9] Naik, N.K., Y. Chandra Sekher, and S. Meduri, Composites Science and Technology, Vol. 60, p. 731-744(2000).

© (2011) Trans Tech Publications, Switzerland
doi:10.4028/www.scientific.net/KEM.471-472.490

Effect of Sonication Time and Clay Loading 0n Nanoclay Dispersion and Thermal Property of Epoxy-Clay Nanocomposite

M. J. Adinoyi[1, a], N. Merah[1, b], Z. Gasem[1, c] and N. Al-Aqeeli[1, d]

[1]Department of Mechanical Engineering,

P.O. Box 8242, Dhahran 31261, Saudi Arabia

[a]jadinoyi@kfupm.edu.sa, [b]nesar@kfupm.edu.sa, [c]Zuhair@kfupm.edu.sa, [d]naqeeli@kfupm.edu.sa.

Keywords: Nanocomposite, sonication, d-spacing, XRD, DSC, EDS, SEM.

Abstract. The development of nanoclay-epoxy nanocomposite material requires a suitable blending process to be employed. Amongst blending techniques, sonication has been one of the promising means for polymer-clay nanocomposite fabrication. In this study, epoxy-clay nanocomposites with 2, 4 and 5% clay loadings were fabricated using different sonication periods ranging from 5 to 60 minutes. The effect of sonication time and clay loading on the nanocomposite structure was investigated using Differential Scanning Calorimetry (DSC), X-ray diffraction (XRD), Scanning Electron Micropscope (SEM) and Energy Dispersive Spectroscopy (EDS). Differential Scanning Calorimetry analysis indicated that while clay loading reduced the glass transition temperature (T_g), sonication time did not alter T_g significantly. Upon examining the structure of the resulting nanocomposites both exfoliation and intercalation structures were present, yet, neither structure was fully achieved; evident by the XRD patterns. Nonetheless, the predominant structures for most of the nanocomposites were intercalation. Intergallery spacing of the nanocomposites were enhanced with increased sonication time mainly at 2%wt loading; whereas further increase in nano-clay loading resulted in a reduction of the d-spacing. SEM analysis showed that clay agglomerates were present in the nanocomposites irrespective of the sonication time. However, the analysis revealed that dispersion of clay was better in the nanocomposite fabricated at higher sonication time. From the EDS analysis, the different sites in the nanocomposites' microstructure were identified which were then correlated with the observation made in the fractographic analysis.

Introduction

The mixing of clay with epoxy to synthesize nanocomposite has attracted vast attention due to the usually enhanced physical, mechanical and thermal properties of the resulting nanocomposite. The synthesis of any polymer-clay nanocomposite requires a suitable blending means such that the resulting microstructure produces a nanostructured material that is better in performance than its conventional counterparts. Towards this end, researchers have employed shear mixing and ultrasonication [1-10], high pressure mixing and direct mixing [11], centrifugal mixing [12], and three-roll mill [13] to mix epoxy with clay. The resulting microstructures as revealed by X-ray diffraction (XRD) and transmission electron microscopy (TEM) are usually linked to the processing techniques adopted [1, 4, 5, 10, 11, 13].

The use of X-ray in analyzing the structure of polymer-clay nanocomposite has almost become an integral part of polymeric nanocomposite research. Though, probing a small area when compared to the bulk of the material, the area coverage is much bigger than the TEM. Thus, XRD gives a better representation of the nanocomposite structure. The scanning electron microscopy (SEM) or the high resolution SEM (HRSEM) are other important tools in nanocomposite structural analysis. It provides micro-structural details of the nanocomposite usually from fractured surfaces useful for comparison purpose. The XRD, SEM or HRSEM and TEM have been used complementarily to analyze polymer nanocomposite synthesized from ultrasonication and other processing method [1, 4, 6, 8, 10, 13].

In this study epoxy/nanoclay composites with clay loadings of 2, 4 and 5%wt are developed using sonication. The effect of sonication time and clay loading on nanoclay dispersion and glass transition

temperature, T_g, of epoxy-clay nanocomposite are investigated using XRD, EDS, DSC and SEM.

Experimental procedure

Materials. The epoxy used in the present work is Araldite GY6010 CRS, based on bisphenol A and epichlorohydrin, manufactured locally by Jubail Chemical Industries Company (JANA), Saudi Arabia. The curing agent is Aradur 42^{TM}, a low viscosity, cycloaliphatic polyamine, manufactured by Huntsman Advanced Materials Americas, USA. The nanoclay is I.30E, an onium-ion modified clay, acquired from Nanocor Inc, USA.

Nanocomposite sytnthesis. Sixty grams of the epoxy was measured and poured into a beaker. The clay proportion (1.5, 3.1 and 3.9 g, respectively for 2, 4 and 5 wt%) was added and gently mixed together with a stirring rod. The hand-mixed epoxy-clay was placed under Sonic vc-33 high intensity ultrasonicator and sonicated for 5, 10, 30 or 60 minutes over a water bath with a temperature range of 60-70°C. Sonication was followed by degassing for 45 minutes under complete vacuum at room temperature in a vacuum oven. The curing agent, was then added to the epoxy-clay mixture at room temperature in the ratio of epoxy to hardener 100g: 24g and hand stirred for 7 minutes. The entire mixture was degassed again, and then poured into an aluminium mold for curing. The initial curing was at 120°C for 2 hours, followed by post curing at 150°C for 2 hours and 170°C for another 1.5 hours.

Characterizaion. Thin samples weighing between 6-10 mg were chipped from the neat epoxy and nanocomposites. They were placed in 40-µl aluminium crucibles and heated in Differential scanning calorimeter, DSC-822^e DSC from 25 to 200ºC in an argon gas inert environment flowing at 100 ml/min. The heating rate was 10ºC/min and cooling was by liquified nitrogen gas.

X-ray diffraction was conducted on nanoclay powder, cured pure epoxy and nanocomposites for all conditions on a Shimadzu WAXD equipment. Test pieces for the cured epoxy and nanocomposites were approximately 10 x 10 x 2.5 mm. Continuous scans were perfomed at a scan rate of 0.5^o/min, 0.02^o scan size and the Bragg's angle (2θ) range of 2-10°.

Microstructural examinations and energy dispersive spectroscopy (EDS**)** of the fractured surfaces of the tensile specimens were performed on a Joel 6460 Scanning Electron Microscopy (SEM).

Results and discussion.

Effect of sonication time and clay loading on nanocomposite d-spacing. A total of six tests per condition were performed on specimens cut out from different sections of the bulk materials. Fig. 1. is representative x-ray diffraction spectra of pure epoxy, as received powder clay and the nanocomposites. Table 1 shows the mean angular positions (extracted from the XRD database by matching angle (2θ) with peak position) and the average d-spacings calculated using Bragg's equation (refer Eq. 1).

$$d = \frac{\lambda}{2\sin(\theta)} \quad . \qquad (1)$$

Where d is the intergallery spacing, λ is the x-ray wavelength, and θ is the half Bragg's angle.

The value of the basal spacing obtained for the nanoclay in the present work is 21.1 Å which is comparable to what was reported by a number of researchers for similar clay compositions [5, 8, 9].

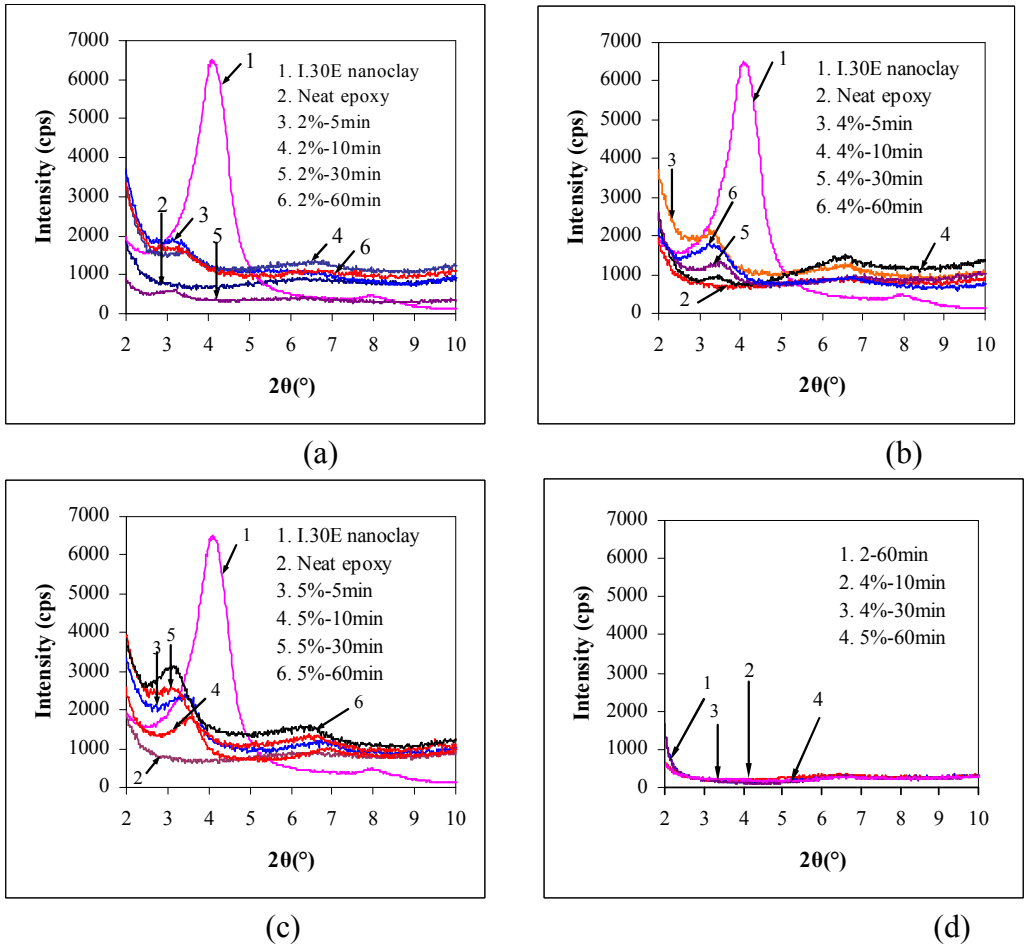


Fig. 1. XRD spectra of (a) nanoclay, neat epoxy and 2% nanocomposites, (b) nanoclay, neat epoxy and 4% nanocomposites, (c) nanoclay, neat epoxy and 5% nanocomposites, sonicated for 5, 10, 30 & 60 minutes with intercalated structure, and (d) 2, 4 & 5% nanocomposites with exfoliated structure

Table 1: Mean Bragg's angle (2θ) and d-spacings for the nanocomposites.

Clay loading (%)	2		4		5	
Sonication Time (min)	Mean 2θ(°)	Mean d-spacing(Å)	Mean 2θ(°)	Mean d-spacing(Å)	Mean 2θ(°)	Mean d-spacing(Å)
5	3.26±0.32	26.7±2.8	3.29±0.17	26.9±1.4	3.44±0.19	25.6±1.5
10	3.34±0.08	26.4±0.7	3.41±0.03	25.9±0.2	3.51±0.07	25.2±0.5
30	3.22±0.16	27.7±1.2	3.37±0.10	26.2±0.8	3.18±0.19	27.8±1.6
60	3.25±0.16	27.2±1.4	3.20±0.19	27.7±1.7	3.19±0.13	27.8±1.2

It is obvious that the peak (Fig. 1a-c) of the clay is prominent and sharp, indicating a highly ordered stack, but the pure epoxy shows no peak confirming its amorphous nature. Meanwhile, observable peaks are present in the nanocomposites. These peaks are however less than the nanoclay both in height and angular positions (2θ's). Lower angular positions in nanocomposites indicate higher d-spacings according to Bragg's law. This implies that epoxy polymer diffused between the clay layers causing finite increase in the intergallery spacing. The broad peaks with weak variance observed in the nanocomposites, as opposed to the sharp peak of the clay, is an indication of wide distributions of intergallery spacing within the nanocomposites. The results show that in general, the lower the clay

loading the lower is the peak. The clay loading in the 2% nanocomposite was less than that in the 4% and 5% nanocomposites, hence causing less diffraction of the X-ray beam. Therefore, higher peak intensity implies the presence of more orderly structure of clay layers from higher clay loading. Similar trend have been reported by Jinwei et al. and Man-Wai et al. [9, 14]. It is worth mentioning that the standard deviation in the former table represents intercalated site distribution.

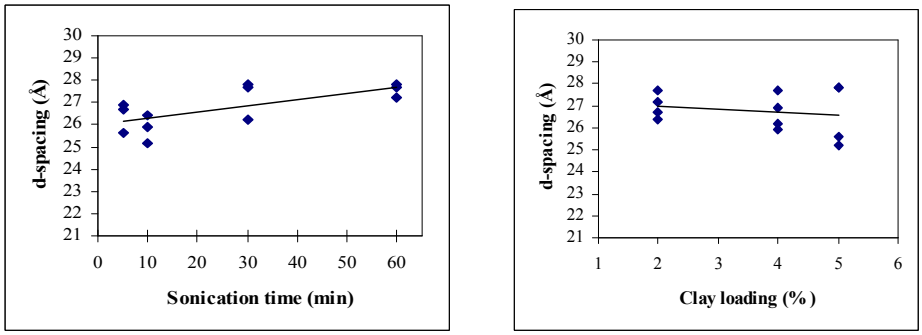
From both Fig. 1 and Table 1, intercalation is the predominant structure, but exfoliation or disorder intercalation was also observed occasionally as shown in fig. 1d. The X-ray diffractorgram in fig. 1d indicates that epoxy resins diffused into the interlayer spacing resulting in extensive separation of the nanoclay layers. The spectra are hardly distinguishable, all superimposing on one another, which contrasts with intercalation in which spectra show peaks with varied intensity relative to intercalation level. Hence, a mixture of intercalated and partially exfoliated/disorderly intercalated structure are present in some of the nanocomposites synthesized in the current study. A mixture of partial exfoliation and intercalation resulting from sonication process have been reported by Luo and Daniel [1]. Single delaminated layers representing exfoliation in a predominantly intercalated nanocomposites structures have also been reported [7].

The effect of sonication time and clay loading with d-spacing have been investigated. Fig. 2 shows the variation of intergallery spacing with sonication time and clay loading. The results show that while d-spacing increases with sonication time for all clay loadings, it decreases with increase in clay loading for all sonication time. The trend in both figures can be approximated by a linear relationship using Excel curve fitting. Eq. 2 expresses the correlation between d-spcing and sonication time and Eq. 3 gives the reltionship between d-spacing and clay loading.

$$d = 0.0277t + 26.032 \qquad \text{for } 5 \le t \le 60 \qquad (2)$$

$$d = 27.263 - 0.1375x \qquad \text{for } 2 \le x \le 5 \qquad (3)$$

Where d is in Angstron (Å), t in minute (min) and x in percentage (%).



(a) (b)

Figure 2: Variation of d-spacing with (a) sonication times, and (b) clay loadings

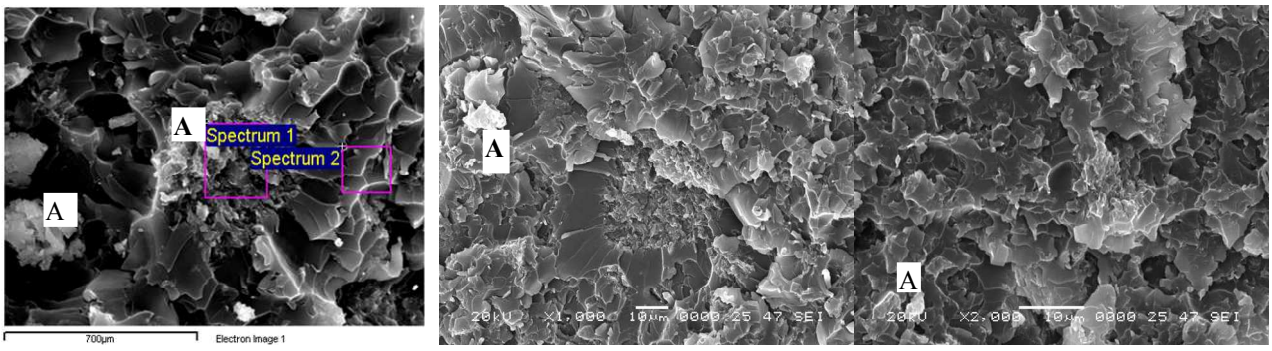
Effect of clay loading, sonication time and curing state on glass transition temperature, T_g. The glass transition temperatures, T_g, (Table 2) for the neat epoxy and 2% nanocomposites were found from the DSC scan using the midpoint construction method. The curing level achieved showed that the curing agent can only provide partial curing for this type of epoxy and its nanocomposites. To gain an insight into the T_g for a fully cured condition, and study the effect of curing condition on the T_g, a repeated DSC scan was done on a previouly-scanned sample. The heating effect of the first scan caused the sample to crosslink completely. From Table 2, the T_g obtained for the epoxy and nanocomposites from the repeated DSC scan are higher than those from the single scan. Yet, the T_g in both cases for the epoxy are close. Thus, the curing cycle adopted was good and can be regarded as the optimim. The 2%

nanocomposites have T_g lower than the neat epoxy at all sonication times. Therefore, the addition of clay reduced the T_g of the epoxy. It is noticed that there was a T_g difference of about 2°C between the single and repeated scan for the neat epoxy, but about 5 to 6ºC variation for the nanocomposite, except for the 2% nanocomposite mixed for 5 minute (2%-5min). Hence, low T_g for the nanocomposite resulted from clay loading, sonication time and curing level achieved from the hardner. Low T_g is linked to the crosslinking density due to the modifying agent in the silicate clay [8-10]. Also, there is slight decrease in T_g (Table 2) in the first scan as sonication time was increased. But for the repeated scan, change in sonication time did not produce any significant variation in the T_g of the nanocomposite. Therefore, variation in T_g is probably due to effect of the curing agent rather than the sonication time.

Table 2: Effect of curing condition, nanoclay addition and sonication time on the glass transition temperature, T_g, of neat epoxy and 2% nanocomposites.

	Glass Transition Temperature, T_g (ºC)			
	Neat epoxy	2%-5min	2%-10min	2%-30min
1st DSC scan	159.26±0.07	155.66±0.23	150.42±0.4	148.45±0.36
2nd DSC scan	161.54±0.38	155.25±0.02	154.87±1.07	154.39±0.07

Fractographic Analysis and Energy Dispersive Spectroscopy. Figure 3 represents SEM micrographs performed on 2% nanocomposites sonicated at different mixing times. It can be seen that nanocomposite with higher mixing time has a more uniformly blended microstructure. Sizes of clay agglomerates (indicated by letter A) are smaller in the nanocomposite sonicated for longer time which suggests that continuing sonication helped further break down of clay particles. Therefore, the distribution of clay particles in the epoxy material increased with sonication time. This is in agreement with the results reprted in Table 1 where nanocomposites with high sonication time possessed low standard deviation, signifying better distribution of intercalated sites. The microstructures of the nanocomposites present several features, which are mainly due to the different clay loading, the distribution of the clay in the epoxy matrix and the interaction of clay with the epoxy.



(a) (b) (c)

Fig. 3. SEM microraphs of 2% nanocomposite sonicated for (a) 5, (b)10, and (c) 60 minutes

Areas marked as spectrum were picked for EDS analysis (Fig. 3a). Table 3 shows the composition and distribution of elements in the 2% clay nanocomposites sonicated for 5 minutes. Oxygen and carbon are the major elements in the epoxy while silicon and oxygen are the main elements in the nanoclay. The rest of the elements are from the clay as well. The distribution of clay in the nanocomposites can also be inferred from these results. As an example, spectrum 1 (approximately 227 μm^2) contains a clay agglomeration site (Fig. 3a). This site is richer in clay elements than the region of spectrum 2 as shown in Table 3. The EDS analysis reveals that there is the presence of more clay agglomerates (21.38%) than in the the region of spectrum 2 that was probably more uniformly blended. This varied dispersion of clay particles correlates with the distribution of clay dispersion which was already determined from the XRD analysis.

Table 3: Element composition in the nanocomposite

Spectrum	Carbon (%)	Oxygen (%)	Magnesium (%)	Aluminium (%)	Silicon (%)	Chlorine (%)	Iron (%)	Total (%)
1	25.88	42.27	1.29	7.52	21.38	0.57	1.09	100
2	45.45	51.92	NA	NA	2.63	NA	NA	100

Summary
Investigation on the effect of clay loading and sonication time on nanocomposite intergallery spacing have been carried out in this study. The sonication process produced largely intercalated nanocomposites with few sites of exfoliation/disorder intercalation. It can be concluded that the nanocomposite interplanaer spacings decreased with increasing clay loadings, but increased with increasing sonication time. Dispersion levels were enhaced by longer sonication periods as was revealed by SEM images. The distribution of clay in the epoxy matrix varied from point to point as per EDS, confirming the result of the XRD. The T_g of the nanocomposites investigated were lower than that of the neat epoxy probably due to clay modifying agent, sonication time and the curing condition.

Acknowledgement
The authors greatly acknowledge the support of King Fahd University of Petroleum and Minerals, Dhahran, Saudi Arabia, for this work.

References

[1] J. J. Luo and I.M. Daniel: Comp. Sci. and Tech. Vol. 63 (2003), p. 1607–1616
[2] I. Isil, Y. Ulku and B. Goknur: Polymer Vol. 44 (2003), p. 6371–6377.
[3] K. Dean, J. Krstina, W. Tian and R. J. Varley: Macromolecular Material and Engineering Vol. 292 (2007), p. 415–427.
[4] S.C. Zunjarrao, R. Sriraman and R.P. Singh: Journal of Mater. Sci. Vol. 41 (2006), p. 2219–2228.
[5] L. Chun-ki, L. Kin-tak, C. Hoi-yan and L. Hang-yin. Materials Letters 59 (2005), p. 1369-1372.
[6] R. Velmurugan and T.P. Mohan: Journal of Material Science Vol. 39 (2004), p. 7333-7339.
[7] H. Farzana , C. Jihua and H. Mehdi: Mater. Sci. and Eng. Part A, 445–446 (2007), p. 467–476.
[8] W. Jinwei and Q. Shuchao: Materials letters Vol. 61 (2007), p. 4222-4224.
[9] W. Jinwei, K. Xianghua, C. Lei and H. Yedong: Journal of University of Science and Technolology Beijing Vol. 15 Number 3 (2008), p. 320.
[10] M. Hernandez, B. Sixou, J. Duchet and H. Sautereau: Polymer Vol. 48 (2007), p. 4075-4086.
[11] L. Weiping, V. H. Suong and P. Martin: Composites Sci. and Technol. Vol. 65 (2005), p. 307-316.
[12] S.S Saeed, A.K. Akbar and B. Domagoj: Composites, Part B, Vol. 38 (2007), p.102-107.
[13] Y. Asma, L. A. Jandro, and I. M. Daniel: Scripta Materialia Vol. 49 (2003), p. 81-86.
[14] H. Man-Wai, L. Chun-Ki , L. Kin-tak, H. L. Dickon and H. David: Composites Structure Vol. 75 (2006), p. 415-421.

© (2011) Trans Tech Publications, Switzerland
doi:10.4028/www.scientific.net/KEM.471-472.496

Variation of Mechanical Properties of Epoxy-Clay Nanocomposite with Sonication Time and Clay Loading

M. J. Adinoyi[1, a], N. Merah[1, b], Z. Gasem[1, c] and N. Aqeeli[1, d]

[1]Department of Mechanical Engineering, KFUPM,

P.O. Box 8242, Dhahran 31261, Saudi Arabia.

[a]jadinoyi@kfupm.edu.sa, [b]nesar@kfupm.edu.sa, [c]zuhair@kfupm.edu.sa, [d]naqeeli@kfupm.edu.sa.

Keywords: Nanocomposite, sonication, tensile properties, hardness.

Abstract. Epoxy-clay nanocomposites have recently gained considerable attention due to their interesting physical, thermal and mechanical properties. These properties, however, depend on a number of parameters such as the clay type, clay modifying agent, polymer matrix and the adopted mixing process. In the current work, epoxy-clay nanocomposites were prepared from Araldite GY6010 CRS and Nanomer I.30E nanoclay using different sonication (mixing) periods (5 to 60 minutes) and different concentrations of clay (2 to 5%wt). The effect of sonication time and clay loading on the tensile and hardness properties of the resulting nanocomposites were investigated. The results showed that the ultimate strength and fracture strain of the nanocomposites were below that of the neat epoxy, but the elastic modulus was generally enhanced by the addition of the nano-clay content. Increasing the sonication time enhanced the tensile strength on the expense of reducing the modulus of elasticity. Hardness of the nanocomposites did not show significant change with either the addition of clay or processing under different sonication times.

Introduction

Polymer-clay nanocomposites, especially epoxy-clay nanocomposite have gained considerable attention because of their improved mechanical, physical and thermal properties. These properties are however influenced by a number of parameters such as the clay type, clay modifying agent, clay loading, the polymer matrix and the mixing process employed. Generally, mechanical properties of nanocomposites are linked to, among other things, the mixing method and the parameters of mixing such as blending force, speed and time for mixing. Consequently, mechanical properties along with other properties have been investigated in relation with mixing method and the associated parameters. It was reported by Oh [1] that nanocomposite mixed for longer time in a mechanical stirrer had better mechanical properties. Lam et al. [2] assessed the micro-hardness of nanocomposites prepared under different sonication times and reported that 10 minutes of sonication was the optimum mixing time. Yasmin et al. [3] found that the low tensile strength recorded for the nanocomposite in their study was due to the processing (mixing) technique utilized. Dean et al [4] concluded that nanocomposite samples mixed by sonicator showed improvement in mechanical properties than those blended by shear mixer. However, Zunjarro et al [5] reported that the high speed shear mixer produced nanocomposites of better mechanical properties than the ultrasonicator.

From the aforementioned studies, the effect of processing parameters seems significant to nanocomposites' properties. In the present study, the variation of hardness and tensile properties, namely ultimate strength, modulus of elasticity and fracture strain are investigated with respect to sonication time and clay loading.

Experimental procedure

Materials. Nanomer I.30E, an onium-ion modified clay was acquired from Nanocor Inc, USA. Araldite GY6010 CRS, a diglycidyl ether of bisphenol A (DGEBA) based epoxy, produced locally by Jubail Chemical Industries Company (JANA), Saudi Arabia, and Aradur 42^{TM}, a low viscosity, cycloaliphatic polyamine hardener, from Huntsman Advanced Materials Americas, USA, were utilized for the present study.

Nanocomposite synthesis. Clay proportion of 1.5, 3.1 and 3.9 g were hand-mixed differently with sixty gram of the epoxy to formulate 2, 4 and 5 wt% nanocomposites, respectively. The hand-mixed epoxy-clay blend was placed under Sonic vc-33 high intensity ultrasonicator and sonicated for 5, 10, 30 or 60 minutes over a water bath maintained at a temperature of 60-70°C. Sonicator preset amplitude of 40% was used for all mixing. The sonicated mixture was degassed under total vacuum for 45 minutes in a vacuum oven at room temperature. The hardener was then added, 14.4 g to 60 g of the epoxy, at room temperature and stirred for 7 minutes until the mixture became homogeneous. The entire blend was degassed again and poured into an aluminium mold for curing. The curing cycle was 120°C for 2 hours, followed by 150°C for 2 hours and 170°C for 1.5 hours.

Mechanical properties test. Type MI tensile test specimen was used to conduct tensile test as per ASTM standard D638M-93 [6]. Silicon carbide abrasive paper of the grade 200 CW and 600 CW were used to smooth the edges of the specimens to remove any obvious flaws. Uniaxial tensile tests were conducted on Instron 5569 at a constant crosshead movement of 5±25% mm/min to measure the tensile stress, the modulus of elasticity and the strain at fracture. For repeatability, six specimens were tested for each condition of nanocomposites and the neat epoxy.

Hardness tests were conducted from a BUEHLER micro hardness tester equipped with a diamond shape indenter. Four flat pieces each in the shape of blocks of dimensions 20 x 20 x 4.5 mm were cut from different sections of both the unfilled epoxy and the nanocomposites samples. A load of 200 gf was used to indent each specimens for 10 second. Ten tests were conducted per condition to determine the mean hardness.

Results and discussion

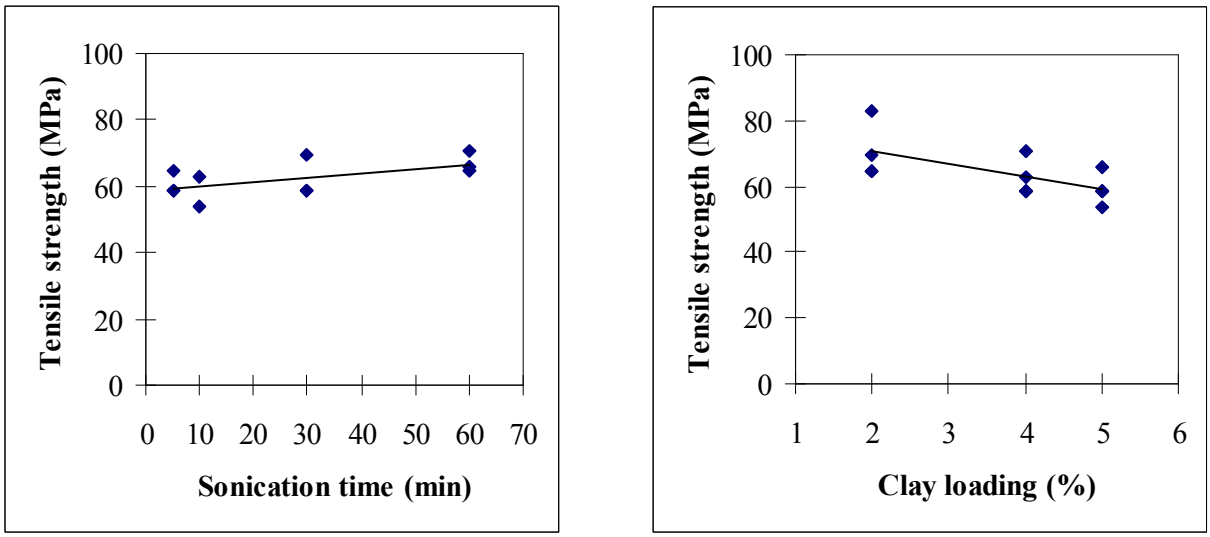
Effect of sonication time and clay loading on nanocomposites' tensile properties. The mean value of the tensile properties found for the nanocomposites and the epoxy are given in Table 1.

Table 1. Average tensile properties of neat epoxy and nanocomposites

Samples	Ultimate strength (MPa)	Modulus of elasticity (GPa)	Fracture strain (%)
Neat epoxy	80 ±0.9	2.3±0.18	6±0.54
2%-5min	64.7±5.1	2.25±0.07	4.6±0.59
2%-10min	82.9±1.2	2.96±0.08	4.5±0.12
2%-30min	69.7±1.5	2.41±0.02	4.5±0.17
2%-60min	64.9±1.1	2.5±0.05	3.9±0.11
4%-5min	58.8±2.7	2.3±0.17	3.5±0.60
4%-10min	63.±6.4	2.7±0.03	3.45±0.66
4%-30min	58.6±7.3	2.85±0.12	3.35±1.3
4%-60min	70.6±1.5	2.45±0.04	3.9±0.70
5%-5min	58.1±5.2	2.6±0.10	3.1±0.74
5%-10min	53.7±3.6	2.5±0.19	2.6±0.32
5%-30min	58.5±6.5	2.6±0.07	2.6±0.18
5%-60min	65.6±8.1	2.6±0.37	3.7±0.84

It can be observed from the result that the addition of clay to epoxy reduces its strength and strain at all sonication time and clay loadings. It is noticed however that the 2%-clay nanocomposites sonicated for 10 minutes (2%-10min) showed a marginal increase of 3.6 % in tensile strength. About 29% increase in the modulus of elasticity was also achieved for the nanocomposite at the same clay loading and sonication time. Moreover, it is noted that almost all the 2%-clay nanocomposites have higher tensile strength and fracture strain than their 4% and 5% counterparts sonicated for the same duration. This suggests that increasing the clay concentration will lower the tensile strength and fracture strain further. Generally, the modulus of elasticity of

nanocomposite is higher than that of neat epoxy. Similar results for tensile properties have been reported for epoxy-clay nanocomposites elsewhere [3, 7, 8,9].
From the data presented in Table 1, the overall trend of ultimate tensile strength with sonication times and clay loadings is shown in Fig. 1.



(i) (ii)

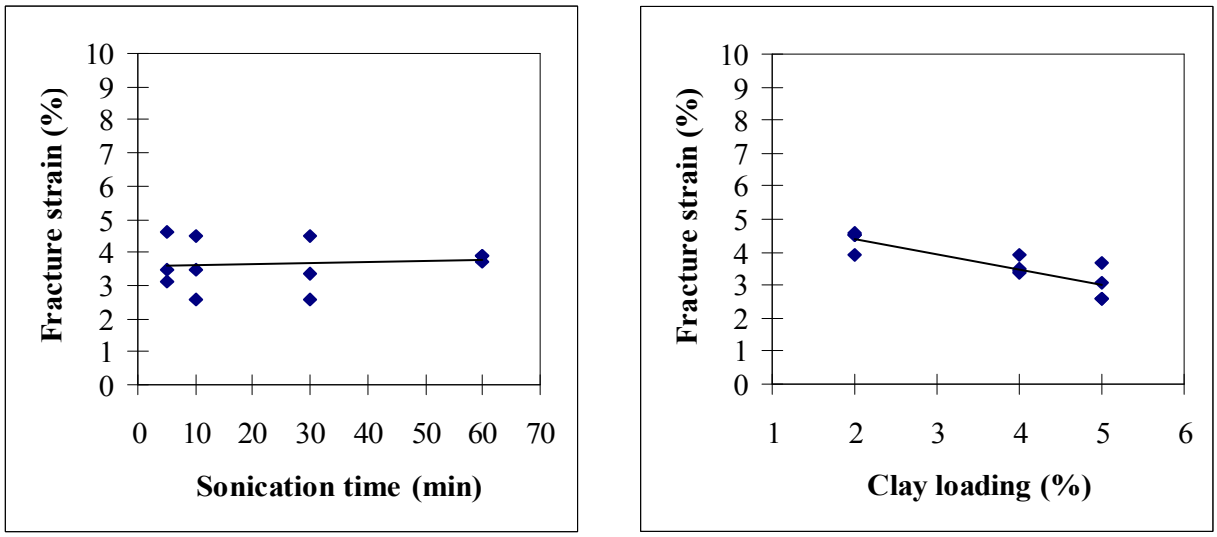
Fig 1. Trend of tensile strength with (i) sonication times for 2, 4 and 5% clay loadings (ii) clay loading at sonication times of 5, 10, 30 and 60 minutes

It can be seen that while tensile strength increased with sonication time, it decreased with clay loading. The increase in ultimate strength with increasing sonication time can be attributed to the increase in interplanar-spacings and clay distribution. The intergallery spacings of the nanocomposites increased as sonication time was increased [10]. The clay layer separation in nanocomposite is representative of its microstructures and performance. The trend in the relationship between sonication time and d-spacing can be reflected in other properties which are dependent on the microstructure, as it is observed here in the variation of the tensile strength with sonication time. Tensile strength decreases with clay loading might be due to clay agglomeration that create stress concentration areas from which cracks initiate resulting in premature failure. Void presence in nanocomposite also form weak site from which failure can start.

Fig. 2 depicts the relationship between the facture strain and sonication time on one hand, and the fracture strain and the clay loading on the other hand. While in Fig. 3, the variation of modulus of elasticity with both sonication times and clay loadings are shown. It is noted that fracture strain increases with increasing sonication time, but it decreases with increasing clay concentration. However, the modulus of elasticity decreases with sonication time yet increases with increase in the clay loading.

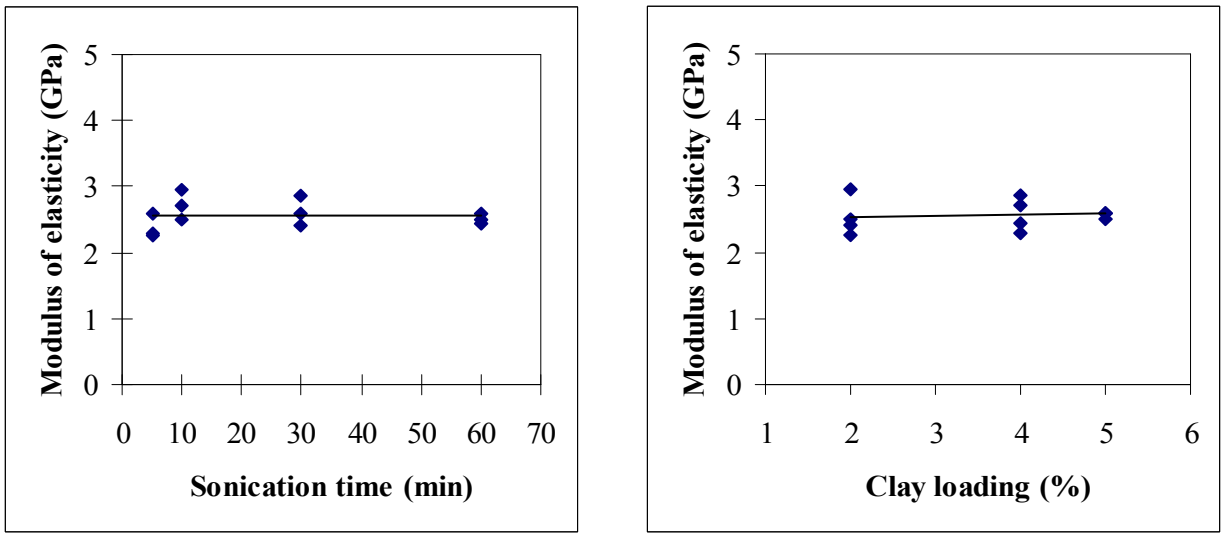
The drop in fracture strain can be attributed to the reduced mobility in the polymer chains as a result of clay particles attachment to them. Clay particles rigid attachment to the epoxy chains constrain their movement resulting in higher stiffness. Nanoclay has higher stiffness compared to the polymer matrix [8]. This would normally lead to higher modulus of nanocomposite. Thus, as clay loading was increased, the polymer chain become more restricted resulting in reduced fracture strain but with higher modulus of elasticity. Nonetheless, this is dependent on the amount of interaction between the clay and polymer.

It is noted that sonication time and clay loading show opposite trend with respect to tensile properties. The effect of clay loading on tensile properties is more vivid than the effect of sonication time at all conditions, as evident by the slopes of the trends.



(i) (ii)

Fig. 2: Trend of fracture strain with (i) sonication times for 1, 2, 4 and 5% clay loadings, (ii) clay loadings at sonication times of 5, 10, 30 and 60 minutes.



(i) (ii)

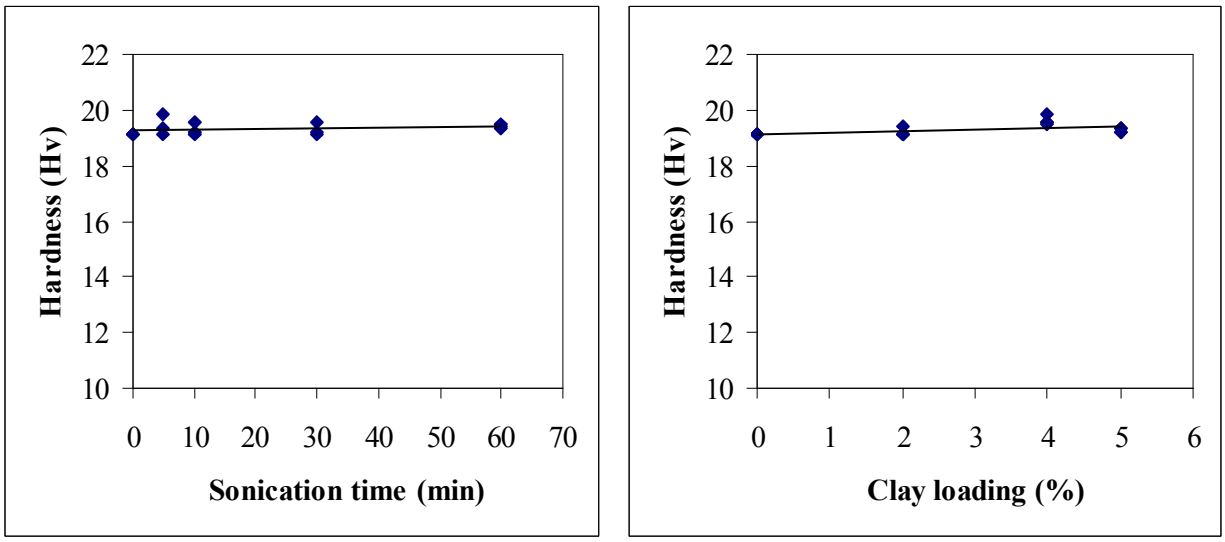
Fig.3: Trend of modulus of elasticity with (i) sonication times for 2, 4 and 5% clay loadings, (ii) clay loadings at sonication time of 5, 10, 30 and 60 minutes.

Effect of sonication time and clay loading on nanocomposites' hardness. The average values of ten indentations per synthesized samples are given in Table 2. The highest increase in hardness for the 2% nanocomposite is 1.2% at 60-minute of sonication time. Maximum improvement of 3.2% in hardness was obtained for the 4% nanocomposites at 5 minutes of sonication. Also, 1.1% increase in hardness was found for the 5% nanocomposites at 60 minutes of mixing. It is noted that the 4% clay loading showed the highest marginal increase in hardness at all sonication time. The increases are 3.22%, 1.66%, 1.89 and 1.5% at 5, 10, 30 and 60 minutes sonication time, respectively. While 2% nanocomposite hardness fluctuates with change in the sonication time, the 4% and 5% nanocomposites have their hardness values marginally higher than the neat epoxy at all sonication time. From the results in Table 2, the general trend of variation of hardness with sonication times and clay loadings is given in Fig. 4. In general, the result shows that there is no significant change in hardness with increasing sonication time at all clay contents. Although, the trends show an increase in the hardness with increase in both sonication time and clay loading, the increases are

marginal to make any significant difference in performance. The low level of increase may mean that an optimum clay loading have not been reached to make any significant impact on the epoxy or the clay and epoxy are not compatible with relation to hardness property.

Table 2: Average hardness of nanocomposites at diferent clay loadings and sonication times.

Sample	Average hardness, (Hv)	Standard deviation	%change
Neat epoxy	19.15	0.15	
2%-5min	19.11	0.14	-0.47
2%-10min	19.16	0.16	0.05
2%-30min	19.08	0.18	-0.62
2%-60min	19.4	0.21	1.23
4%-5min	19.82	0.35	3.22
4%-10min	19.52	0.11	1.66
4%-30min	19.56	0.16	1.89
4%-60min	19.49	0.08	1.52
5%-5min	19.30	0.08	0.81
5%-10min	19.22	0.08	0.38
5%-30min	19.18	0.29	0.14
5%-60min	19.36	0.09	1.09



(a) (b)

Fig. 4. Trend of hardness with (a) sonication times for 2, 4 and 5% clay loadings, and (b) clay loadings at sonication times of 5, 10, 30 and 60 minutes

Summary

The effect of different weight of clay additions to epoxy at variable mixing times has been studied. While sonication time increased the tensile strength, it marginally increased the fracture strain, but on the expense of reducing the modulus of elasticity. On the contrary, the clay loading increased the modulus of elasticity but decreased both the tensile strength and fracture strain. It can be concluded that the effect of sonication time on the nanocomposites' tensile properties is reversible to the effect due to clay loading. The increase in tensile strength is due to the homogeneity in clay distribution and clay intergallery space. The enhancement in modulus of elasticity can be attributed to the better interaction between clay and polymer chains. Hardness of epoxy changed with both sonication time and clay loading; but the changes are not that significant.

Acknowledgment

The authors would like to acknowledge the support provided by the Deanship of Scientific Research at King Fahd University of Petroleum & Minerals (KFUPM) and NSTP (Project No 08-ADV68-4).

References

[1] T.K. Oh: Effect of Shear Force on Microstructure and Mechanical Property of Epxy/Clay
[2] Nanocomposite, Master thesis, University of Florida (2004).

[3] C.K. Lam, K.T. Lau, H.Y. Cheung and H.Y. Ling: Materials Letters 59 (2005), p. 1369-1372.

[4] Yasmin, J.L. Abot and I. M. Daniel: Scripta Materialia Vol. 49 (2003), p. 81-86.

[5] K. Dean, J. Krstina, W. Tian and R. J. Varley: Macromolecular Material and Engineering. Vol.
[6] 292 (2007), p. 415–427.

[7] S.C. Zunjarrao, R. Sriraman and R.P. Singh: Journal of Mater. *Sci.* Vol. 41 (200), p. 2219–
[8] 2228.
[9] Annual Book of ASTM Standards, Designation: Plastic, D638M-93, vol.8 (1995).

[10] F. Hassan, J. Chen and M. Hojjati: Mater. Sci. and Eng. Part A, 445–446 (2007), p. 467–476.

[11] B. Qi., Q.X. Zhang, M. Bannister and Y.-W Mai: Composite Structures, Vol. 75 (2006), p.
[12] 514-519.

[13] K. Wang, L. Chen, J. Wu, M. L. Toh, C. He and A. F. Yee: Macromolecules, Vol. 38 (2005), p
[14] 788-800.

[15] M. J. Adinoyi, N. Merah, Z. Gasem and N. Aqeeli: Submitted to 8th International Conference
[16] on Composite Science and Technology (2010).

© (2011) Trans Tech Publications, Switzerland
doi:10.4028/www.scientific.net/KEM.471-472.502

Investigation on Bending Strength and Stiffness of Sugar Palm Fibre from Different Parts Reinforced Unsaturated Polyester Composites

J. Sahari[1, 2a], S.M. Sapuan[1, 2b], Z. N. Ismarrubie[2c], M.Z.A.Rahman[3d]

[1] Laboratory of Advanced Materials and Nanotechnology, Institute of Advanced Technology,
[2] Department of Mechanical and Manufacturing Engineering,
[3] Department of Chemistry, Faculty of Science,
Universiti Putra Malaysia, 43400 Serdang, Selangor, Malaysia
[a]Kandhalawi_86@yahoo.com, [b]sapuan@eng.upm.edu.my, [c]rubie@eng.upm.edu.my,
[d]mzaki1212@putra.upm.edu

Keywords: sugar palm tree, unsaturated polyester, bending strength, stiffness

Abstract. This investigation is done to select the best composite on bending strength and stiffness derived from different parts of sugar palm fibre reinforced unsaturated polyester composites. Sugar palm tree is one of the most popular natural fibres. The fibre was obtained from the sugar palm tree and mixed with unsaturated polyester (PE). All of the composites are labelled as SPF/PE for sugar palm frond composite, SPB/PE for sugar palm bunch composite, SPT/PE for sugar palm trunk composite and ijuk/PE for black sugar palm fibre composite. The bending strength and stiffness tests were done according to ASTM D 790-(2000). The higher value of bending strength and stiffness obtained by SPT/PE which is 41.906 MPa and 3.363 GPa respectively followed by SPF/PE (38.906 MPa and 3.001 GPa), SPB/PE (35.168 MPa and 2.749) and ijuk/PE (33.742 MPa and 2.424 GPa)

Introduction

Increasing awareness among the world population to protect our environment has promoted many researches in agriculture residues. This is due to the abundant sources of agriculture crop wastes that cause problem to handle them. Agriculture crop residues such as oil palm, pineapple leaf, banana, sugar palm and others produced in billion of tons around the world. So to overcome this entire problem, all of these residues can be used as reinforcement in polymer composites to produce a useful product for our daily applications. Sugar palm plants are considered as one of the most diverse multipurpose tree species in culture [1]. Almost all part of these plants is usefull for mankind such as its fruit, sugar, root, sago that obtained from inner part of the trunk and its fibres as well. Nowadays, researchers are more focused on production of bioethanol that can be derived from *neera* sugar. This phenomenon makes sugar palm plants produced large number of residue and the settlers facing problem to handle it. To overcome this problem, the combinations of these residues with polymer can produce a new green product that can fulfill the desire of manufacturers and costemers. This investigation is to utilize by-products from sugar palm tree. Its purpose is to convert all of these by-products into value-added product such as biocomposites. In order to completely drive the potential of sugar palm tree fibres for new applications, a comprehensive and detailed investigation of fundamental information such as chemical and mechanical properties are necessary [2]. So this research was done in order to gain a better understanding and knowledge about the bending strength and stiffness of new green composites from different morphological parts of sugar palm plant and their potential to use as reinforcement for polymer composites.

Materials and Method

Fabrication of Composites. The composite plates were fabricated using compression moulding technique with the dimension 300mm × 300mm × 3.2. The fibres were dried in an oven at 80 ºc for the duration of 24 hours. Different parts of sugar palm fibre reinforced unsaturated polyester composites which are SPT, SPF, SPB and *ijuk* with 30% volume fraction were prepared and labelled as SPT/PE, SPB/PE, SPF/PE and *ijuk*/PE. The fibre and unsaturated polyester were mixed by using glass rod and mixer with a constant frequency of 500 Hz for the duration of 5 minutes. The liquid composite were poured in an open mould made by galvanic iron plates. The composite were pressed by cold press machine and left to cure in room temperature for 24 hours. The specimens were cut from composite plates by using vertical saw.

Determination of Bending Strength and Stiffness. Bending strength and stiffness test were carried out using universal testing machine type Instron according ASTM D 790-(2000). The specimens were placed on two supports beam. The support span-to-depth (*L/d*) used was 16:1. The rate of crosshead motion for each specimen was calculated by using the equation (1), bending strength are calculated from the measured load using the equation (2) and stiffness are calculated by the equation (3).

$$R = ZL^2 / 6d \quad (1)$$

$$\sigma_{max} = 3PL/2bd^3 \quad (2)$$

$$E_H = L^3m/4bd^3 \quad (3)$$

σ_{max}= bending strength (MPa)
E_H = stiffness(MPa)
R = rate of crosshead motion, mm/mm
L = support span, mm
Z = rate of straining of the outer fibre, mm/mm/min; Z shall equal 0.01
P = load at yield (maximum load)
L = support span (mm)
b = width (mm)
d = thickness (mm)

Results and Discussion

Bending Strength Behaviour. The bending load-extension curve for sugar palm fibres reinforced unsaturated polyester composites presented in Fig. 1. From the fig., it is that the bending load increase linearly with extention up to fracture point. The curve reveal that all type of the composites broke immediately after first crack indicated its brittle behaviour. Similar finding obtained by Devi et al. [3] and Ishak [4] that the brittle behaviour also refers to pure unsaturated polyester. However, in their study, they found that more addition of fibers make the composite ductility become higher which is totally different to the present study. Their claimed that addition of fibres allows the composite to withstand the fracture under the bending stress. These results different to the current studies are due to different fibre sizes that are used for reinforcement. The longer the fibre size, the more ductile the materials are.

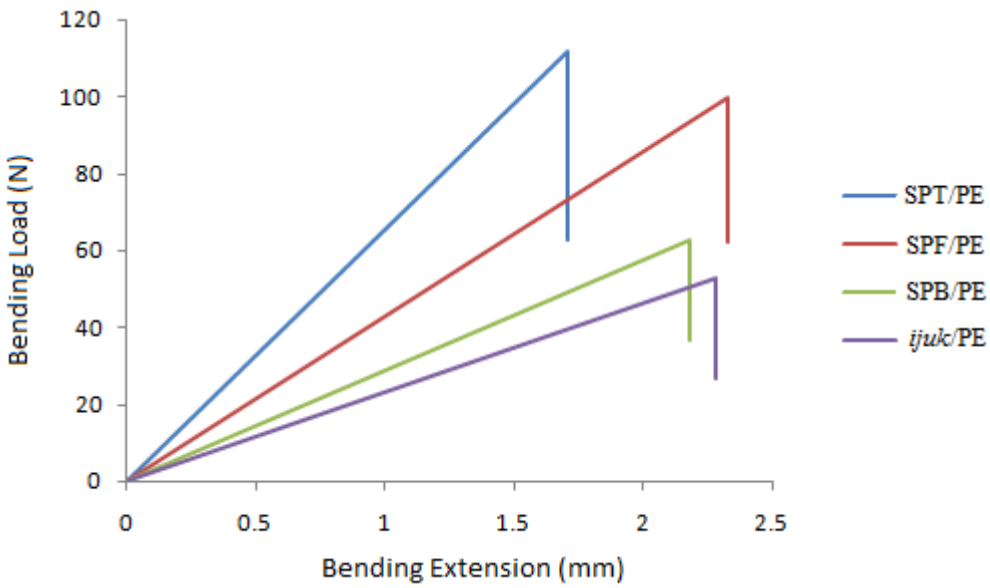


Fig. 1: Bending load-extension curve of sugar palm fibres reinforced unsaturated polyester composites

Bending Strength. Fig. 2 shows the bending strength of sugar palm fibres reinforced unsaturated polyester composites. Based on the fig, it is found that SPT/PE gave the higher bending strength which is 41.904 MPa followed by SPF/PE, SPB/PE and ijuk/PE which are 38.906 MPa, 35.168 MPa and 33.742 MPa respectively. However, it is seen that the bending strength for all types of sugar palm fibres reinforced unsaturated polyester composites are found to be less than than the neat unsaturated polyester obtained by Devi et al. [3] and Ishak [4]. Similar trend also reported by Sreekala et al. [5] that the bending strength of pure phenol formaldehyde higher than its glass/OPEFB hybrid reinforced phenol formaldehyde composites.

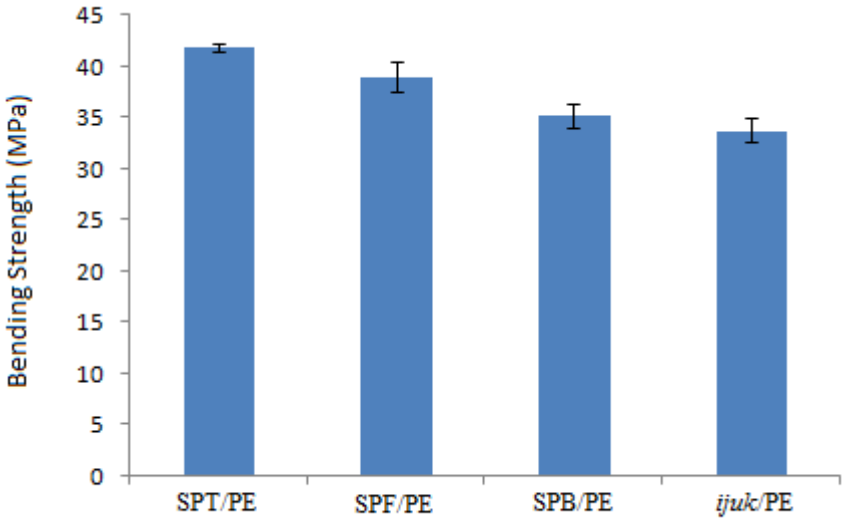


Fig. 2: Bending strength of sugar palm fibres reinforced unsaturated polyester composites

Bending Stiffness. The specific bending stiffness for sugar palm fibres reinforced unsaturated polyester composites shown in Fig. 3. The value of bending stiffness is to measure the ability of material to resist deforming in bendding failure. Based on the fig., it is found that SPT/PE shows the higher stiffness which is 3.363 GPa followed by SPF/PE, SPB/PE and ijuk/PE i.e. 3.001 GPa, 2.749 GPa and 2.424 respectively. If compared to the bending stiffness of pure unsaturated polyester, it is found that the value of all types of sugar palm fibres reinforced unsaturated polyester composites are more higher. That means that the addition of fibre into unsaturated polyester improve the flexural stiffnes of composites [3,4].

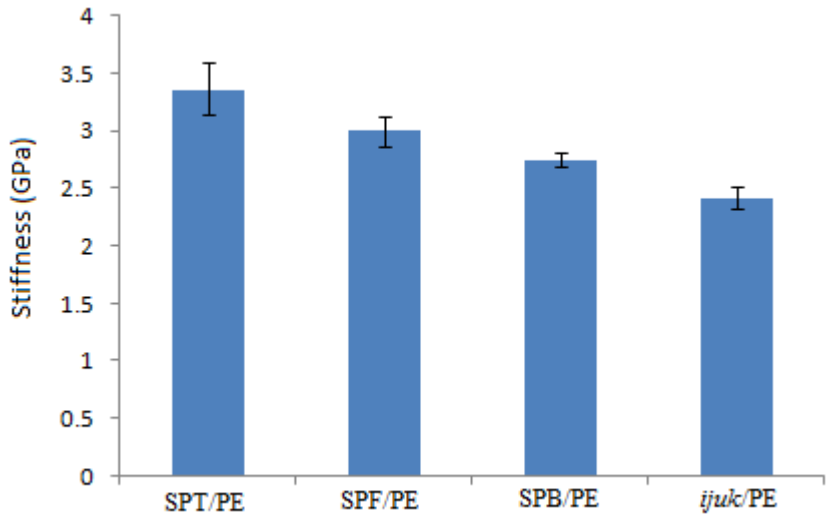


Fig. 3: Stiffness of sugar palm fibres reinforced unsaturated polyester composites

Summary

The result from this investigation showed that a new green composite with good bending strength and stiffness could be successfully developed from by-product of sugar palm fibres as a reinforcement material for the unsaturated polyester. Overall, sugar palm fibres from all parts of sugar palm tree reinforced unsaturated polyester composites exhibits superior mechanical properties same as the others established natural fibre reinforced polymer composites. The bending strength and stiffness tests were done according to ASTM D 790-(2000). The higher value of bending strength and stiffness obtained by SPT/PE which is 41.906 MPa and 3.363 GPa respectively followed by SPF/PE (38.906 MPa and 3.001 GPa), SPB/PE (35.168 MPa and 2.749) and ijuk/PE (33.742 MPa and 2.424 GPa)

Acknowledgement

The authors wish to thank to Ministry of Agriculture and Agro Based Industry Malaysia for funding the research grant (Project No.: 03-01-04-SF0246). Special thanks also to the staff of Department of Mechanical and Manufacturing Engineering, Universiti Putra Malaysia and Institute of Tropical Forestry and Forest Products (INTROP), Universiti Putra Malaysia for their support during the research were conducted.

References

[1] J.P Mogea : Revisi Marga Arenga (Palmae) (Ringkasan). Disertai ilmu Matematika dan Pengetahuan Alam, Universiti Indonesia, Fak. Pascasarjana, (1991).
[2] H.P.S Abdul Khalil, M. Siti Alwani, R. Rizuan, H. Kamarudin, A.Khairul : Chemical composition, morphological characteristics, and cell wall structure of Malaysia oil palm fibres. Poly Plast Technol Eng (2008), 47: 237-280.
[3] L. Uma Devi, S.S Bhagawan, S.Thomas: Mechanical properties of pineapple leaf fiber-reinforced polyester composites. App Poly Sci (1997) 64: 1739- 1748.
[4] Ishak MR. Mechanical properties of treated and untreated woven sugar palm fibre-reinforced unsaturated polyester composites. MS Thesis, Universiti Putra Malaysia, Selangor, Malaysia.(2009).
[5] M.S. Sreekala, J.George, M.G. Kumaran, S.Thomas : The mechanical performance of hybrid phenol-formaldehyde-based composites reinforced with glass and oil palm fibres. Comp Sc. Technol.(2002), 62:339-353.

© (2011) Trans Tech Publications, Switzerland
doi:10.4028/www.scientific.net/KEM.471-472.507

Properties of Kenaf Filled Unplasticized Polyvinyl Chloride Composites

Mohd Firdaus Abdrahman[1, a] and E. S. Zainudin[1, 2, b]

[1]Department of Mechanical and Manufacturing Engineering,

Universiti Putra Malaysia, 43400 UPM Serdang, Selangor, Malaysia

[2]Institute of Tropical Forestry and Forest Products (INTROP),

Universiti Putra Malaysia, 43400 UPM Serdang, Selangor, Malaysia

[a]farha156@gmail.com, [b]edisyam@eng.upm.edu.my

Keywords: Kenaf, PVC, PMPPIC, lignocellulosic fiber, coupling agent, FTIR

Abstract. Combination of lignocellulosic fiber with thermoplastic is leading to the new areas of research in plastic composite field. Due to the problem of petroleum shortages and encouragement for reducing the dependence on fossil fuel products, thus increased the people interest in maximizing the utilize of renewable materials like kenaf fiber. By adding optimum natural fiber to thermoplastics could provide some cost reduction to the world of plastic industry as well as to dominance the agro-based industry. With a view to identifying the effect of fiber content and effect of coupling agent in kenaf fiber reinforced unplasticized poly (vinyl chloride) (UPVC) composite on the mechanical properties, the fiber and matrix mixture were mixed with poly [methylene poly (phenyl isocyanate)] (PMPPIC) using thermal mixing process followed by compression molding technique for the composite preparation that required for tensile characteristic (ASTM D638). The fiber loading were 10%, 20%, 30%, and 40% in weight. Since the kenaf fiber and UPVC are chemically different, the compatibility and dispersability of kenaf fiber in UPVC can be improved by lowering the surface energy of the fiber to make it less polar, consequently more similar to the plastic matrix. Generally, PMPPIC act as a bonding agent that facilitates the optimum stress transfer at the interface between fiber and matrix which gives an optimal mechanical performance of kenaf fiber reinforced UPVC composites. Meanwhile, the addition of 30% fiber contents with PMPPIC was successful to enhance the tensile properties and the efficiency of PMPPIC was verified using Fourier Transform Infra-Red (FTIR) spectroscopy.

Introduction

In several decades ago, the use of fiber-reinforced polymeric materials is attracting interest for a wide range of industries furthermore have substituted the monolithic materials. These composite materials (notably aramid, carbon and glass fiber reinforced plastics) now dominate the construction, marine, automotive and aerospace industries.

However recently, natural fiber composites (biocomposite) have attracted the attention of scientists and engineers, especially when it demonstrates competitive performance to glass fibers in various composite applications. The rationale behind this interest is that the advantages of natural fibers (e.g. sisal, jute, hemp, and kenaf) over synthetic or man-made fibers which including lower cost, lower density, less abrasiveness to equipment, acceptable specific strength properties, ease of separation, renewable nature and biodegradability. An increased market demand for biocomposite ecoproduct is due to increasing environmental awareness, concern for environmental sustainability, and the continuously rising high crude oil prices. Due to initiation of the new environmental regulation and encouragement of independent to fossil fuel, green composites made entirely from renewable agricultural resources could offer a unique alternative for these matters.

The widely used acronym for unplasticized poly (vinyl) chloride is UPVC. It is one of the most worldwide used thermoplastics in terms of volume produce due to its blending versatility (ability to be modified through the introduction of various additives) and cost effective thermoplastic. It plays

an important role in the plastic industry especially in all building supply and hardware stores for household plumbing. Cost reduction is achieved when fillers are incorporated into the UPVC matrix.

Based on previous finding, there is no study has been reported the use of Kenaf fiber in the UPVC matrix. There are some studies on Kenaf fibers with other polymer composites as well as UPVC with other natural fiber composite were carried out. The challenge in the materials development of engineering thermoplastics composite is to get an excellent combination of properties and manufacturing process at a moderate cost. Since mechanical properties are concerned, the main target is to focus on stiffness, strength and toughness.

Therefore, in this research where Kenaf is used as filler and PMPPIC as coupling agent (Fig. 1) in this composite to get a good combination of mechanical properties and manufacturing process, several factors that influence and affect the properties of the composites need to be considered. Thus the optimum formulation of the composite will be investigated. By determining the properties of Kenaf filled UPVC composite, the applications of the composite can be firmed and engineers would be able to develop new product or improved it by replacing some of the conventional materials using this new materials.

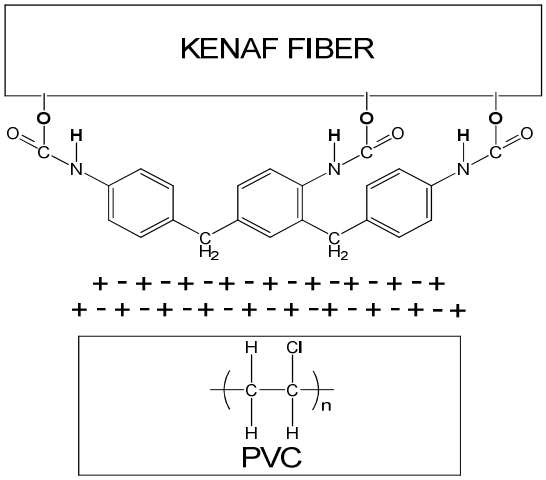


Fig. 1: The –N=C=O fuctional group of isocyanate react with –OH group of kenaf fiber. The non-polar benzene ring of PMPPIC linked by Van der Waal's bonding with the PVC [1,2,3].

Experimental

Materials. The matrix used in this study was unplasticized poly (vinyl) chloride (UPVC) IR045A (Fig. 2) supplied by Polymer Resources Sdn. Bhd., Kelang, Selangor, Malaysia. This injection grade rigid PVC was designed for general articles and fitting applications.

The kenaf fiber used in this study was Kenaf V36 bast fiber, which been planted in BRIS soil land type at Wakaf Gelam Farm. The kenaf fiber was pulverized followed by sieving to obtain 30 mesh size of fibers.

The poly [methylene poly (phenyl isocyanate)] (PMPPIC) (Fig. 3) were used as coupling agent in this study were supplied by Poly Science Inc., U.S.A.

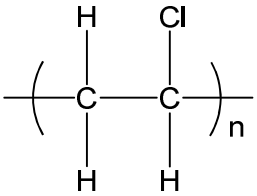


Fig. 2: PVC

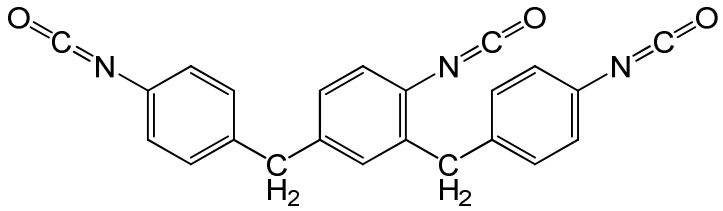


Fig. 3: PMPPIC

Preparation of composites. Melt blending process was carried out using the Haake Polydrive R600 mixer at temperature of 170°C and rotor speed 50rpm as follows. When the desired temperature was reached, UPVC compounds was charged into the mixing chamber and mixed for 5 minutes, followed by feeding of the kenaf fiber and the mixing was continued for another 15 minutes. The kenaf fiber content were 10%, 20%, 30%, 40%, of the total weight of composite. The blending process for the incorporation of PMPPIC, the dosage used was 2% by weight of polymer were mixed with UPVC before kenaf fiber is charged.

The blends from the Haake Polydrive R600 mixer were then compression molded into 150mmX150mmX 1mm sheet with the pressing temperature and time were set to 170°C, 5 minutes preheated press, 5 times venting cycle, and 5 minutes full press. Finally the sheet was immediately cooled under pressure of two plates of cold press at 25°C for 5minutes.

Tensile testing. The tensile characteristic was carried out on a tensile testing dumbbell-shaped sample according to ASTM D 638 with an Instron 3365 machine with crosshead-speed was set at 10 mm/min, and the test was carried out at room temperature (25 ± 2°C). The tensile strength and modulus were recorded and the averages of 5 specimens were reported.

Fourier Transform Infra-Red (FTIR). The infrared spectra for this study were obtained using a Fourier transform infra red (FTIR) spectrometer Perkin–Elmer Spectrum 2000 instrument with the diamond attenuated total reflectance (ATR) techniques and recorded in the range of 4000 – 280cm^{-1}.

Results and Discussion

Fig. 4 shows that 30% fiber content of kenaf/UPVC with PMPPIC coupling agent have the highest tensile strength which is 51.47MPa. In addition, tensile strength of kenaf/UPVC composites with PMPPIC coupling agent were higher compared to kenaf/UPVC composites without PMPPIC coupling agent at the same fiber content. The graph also shows the effect of fiber content on tensile strength of kenaf/UPVC composites. It shows the tensile strength clearly increased as the fiber content increased and the optimum fiber content of kenaf/UPVC composites to produce maximum tensile strength was achieved at fiber content of 30%.

The enhancement in tensile strength of 30% fiber content of kenaf filled UPVC composites with PMPPIC coupling agent indicates that the PMPPIC had reacted with the hydroxyl group of kenaf fiber effectively and result in improvement of the interfacial adhesion. [1] Besides, mechanical interlocking mechanism could be responsible for the adhesion thus made the kenaf fibre perform as an agent of reinforcement in UPVC matrix. [4, 5, 6]

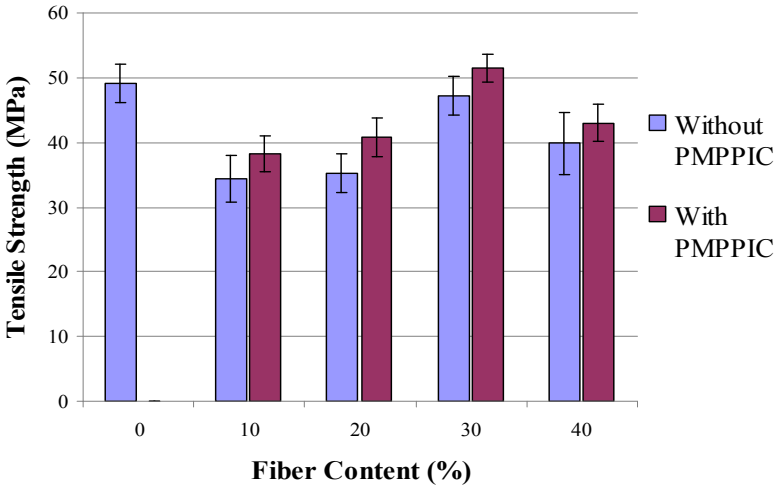


Fig. 4: Tensile strength of Kenaf/UPVC composites

As shown in Fig. 5, the tensile modulus of composites increased gradually with increasing kenaf fiber compared to unfilled UPVC. With similar trend shows on tensile strength, the highest tensile modulus which is 1770MPa was achieved at 30% fiber content of kenaf/UPVC composite with PMPPIC coupling agent. Thus, the improvement upon addition of kenaf fiber has verified that reinforcing natural fiber was able to enhance the stiffness of the composites. [4]

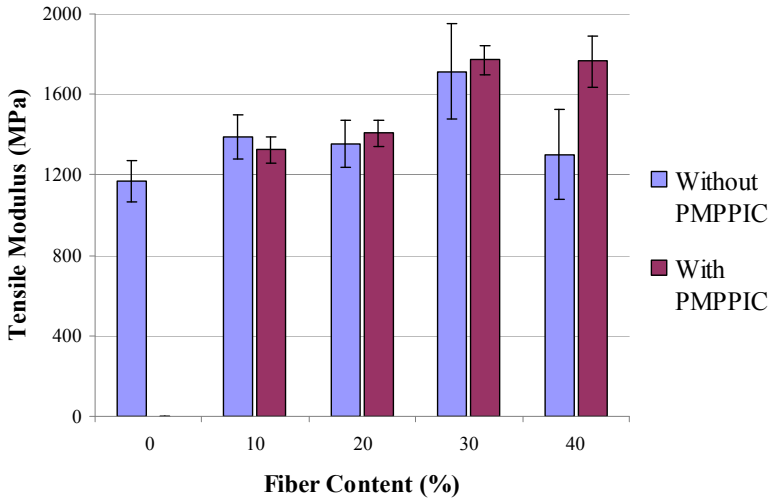


Fig. 5: Tensile strength of Kenaf/UPVC composites.

The spectrum of UPVC, kenaf fiber, and 30% fiber content of kenaf/UPVC composites with and without PMPPIC are illustrated in figure 6. Band assignments for UPVC and kenaf fiber according to the literature are listed in Table 1 and Table 2.

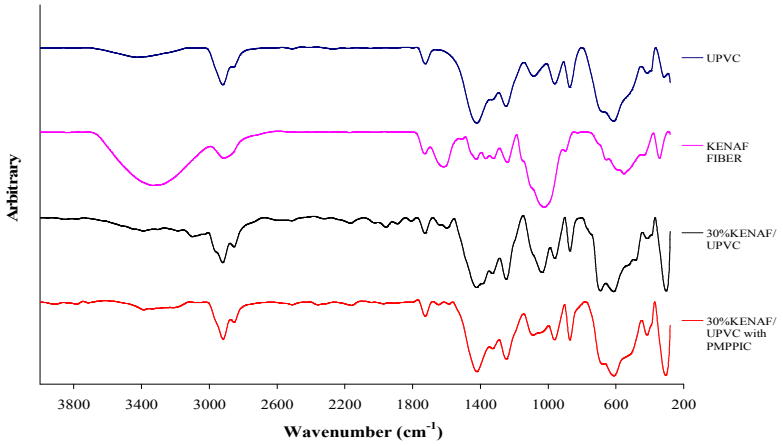


Fig 6: FTIR spectra of UPVC (IR045A), kenaf bast fiber (V36), and kenaf/UPVC composite.

Table 1: Assignments of infra-red bands of UPVC (IR045A)

Band Position [cm-^{1}]	Functional group
2920	C-H stretching from CH-Cl or CH_2
1725	Additive in UPVC product [7]
1423	CH_2 bending
1249	C-H stretching from CH-Cl
615	C-Cl stretching

Table 2: Assignments of infra-red bands of kenaf bast fiber (V36)

Band Position [cm-^{1}]	Functional group
3400-3200	O-H stretching
2917	C-H stretching in methyl and methylene
1729	C=O stretching in carbonyl
1619	C=C alkene
1425	CH_2 bending
1368	CH_3 bending
1242	C-O phenolic
1025	C-O alcohol (primary and secondary) and aliphatic ethers

As seen in figure 6, the FTIR spectra for 30% kenaf/UPVC composite shows lower intensity of O-H stretching frequencies at range 3400-3200 cm-^{1}. Furthermore, the intensity of O-H stretching for composite with PMPPIC coupling agent was almost absent is due to reaction of OH groups in the kenaf fiber with the PMPPIC.

Summary

This study investigated the effect of kenaf fiber and PMPPIC coupling agent on the tensile characteristic of UPVC. Among all of the composites, incorporation of 30% kenaf fiber content and addition of PMPPIC coupling agent played an important role in enhancing the tensile strength and tensile modulus of UPVC composite. Thus, both elements demonstrated the improvement in interfacial adhesion and stiffness of the composites and were confirmed by FTIR analysis.

Acknowledgments

The authors wish to thank Universiti Putra Malaysia for financial and facilities support to conduct this research.

References

[1] B.V Kokta, D. Maldas, C. Daneault, and P. Beland: Polymer-Plastic Technology and Engineering Vol.29 (1) (1990), p. 87-118.

[2] D. Maldas, B.V. Kokta, and C. Daneault: Journal of Vinyl Technology Vol.11 (2) (1989), p. 90-99.

[3] R.G. Raj, B.V. Kokta, D. Maldas, and C. Daneault: Polymer Composites Vol.9 (6) (1988), p. 404–411.

[4] J. E. Crespo, L. Sa ´ Nchez, F. Parres and J. Lo´ Pez: Journal of Termoplastic Composite Materials Vol.22 (2009), p. 259-272.

[5] Y.-T. Zheng, D.-R. Cao, D.-S. Wang, J.-J.Chen: Composites: Part A: Applied Science and Manufacturing Vol.38 (2007), p. 20–25.

[6] B.-H. Lee, H.-J. Kim, and W.-R. Yu1: Fibers and Polymers Vol.10 (1) (2009), p. 83-90.

[7] R. Bodîrlău, C.A. Teacă, and I. Spiridon: BioResources Vol.4 (4) (2009), p. 1285-1304.

© (2011) Trans Tech Publications, Switzerland
doi:10.4028/www.scientific.net/KEM.471-472.513

Rheological Behaviour of Polypropylene/Kenaf Fibre Composite: Effect of Fibre Size

A.Khalina[1,2,a], E.S.Zainuddin[2,b] and I. S. Aji[3,c]

[1]Department of Biological and Agricultural Engineering,

Universiti Putra Malaysia, 43400 UPM Serdang, Selangor, Malaysia

[2]Laboratory of Biocomposite Technology, Institute of Tropical Forestry and Forest Products (INTROP),

Universiti Putra Malaysia, 43400 UPM Serdang, Selangor, Malaysia

[3]Department of Mechanical & Manufacturing Engineering,

Universiti Putra Malaysia, 43400 UPM Serdang, Selangor, Malaysia

[a]khalina@eng.upm.edu.my, [b]edisyam@gmail.com, [c]suleimanaji@yahoo.com

Keywords: Rheology, composites, apparent viscosity, apparent shear stress, kenaf

Abstract. In evaluating thermoplastics for their effective performance during processing, rheology properties are very useful. Similarly, in designing processing apparatus, knowledge of rheological behavior of composite melt is critical. In this study, melt flow and viscosity behavior of polypropylene/kenaf fibre composite was investigated using a single-screw extruder. Subsequently, flow behavior of the compounded formulation were evaluated by comparing the melt flow index, flow curve and viscosity curve of the PP and that of the composites at 190°C processing temperature and varying the fibre size. There appears to be a positive linear increase of the apparent shear stress with increase in the apparent shear rate and, as expected, viscosity values for the composite samples are much higher than the PP especially at larger fibre size. The additional of kenaf fibre in composite reduces the MFI value basically because of the hindrances in the plastic flow of the polymer. In addition the increase in viscosity with increase in fibre loading might contributed to the high specific area of the fibre in the matrix thereby increasing the shear stress in the composite. Moreover loading of polymer system with fibre tends to disturb or disorganize the normal free movement of the polymer and certainly hindered the mobility chain segments in flow.

Introduction

Fibres have been found useful for many years as reinforcement of material with the support of combining matrices. Natural plant fibres has been found very useful for many decades because of its superb properties; i.e. ease of processing, ability to fully degrade after usage, lower cost, low density, good specific properties, and reduced wear and tear in processing. Their advantages and usage as composite have been reported in form of reviews and research by many scholars [1-5]. In evaluating thermoplastics for their effective performance during processing, rheology properties are very useful. In addition, in designing processing apparatus, knowledge of rheological behavior of composite melt is critical. It is worthy of note that capillary and oscillatory measurements have been reported supply good rheological data for composites. A lot of research on the rheological behavior of fibre-reinforced thermoplastics has already been reported [6-9]. Compatibilizers have been used in natural plant fibre composites to enhance properties especially where polypropylene is used as the matrix; Maleated polypropylene (MAPP), is a good example of such compatibilizers that have proven to improve mechanical properties of composites [10,11]. In this study, attempt is

made to analyze the rheological behavior of kenaf fibre reinforced polypropylene (KF/PP) with respect to varying fibre size using capillary method. The KF/PP was prepared using a twin-screw extruder.

Experimental

Polypropylene copolymer grade Pro-Fax SM638 with melt index of 3g/10min (ASTM D1238) supplied by Titan PP Polymer Malaysia was used as the matrix. Kenaf fibre was obtained from National Kenaf and Tobacco Board (NKTB) Kelantan, Malaysia. Varying kenaf fibre sizes where compounded with PP in a twin screw extruder to prepare the composite pallets. The fibre sizes used in the experiment were 250µm, 450 µm and 850 µm and the fibre content was fixed at 42%wt. Compounding method was carried out using twin screw extruder machine in Laboratory of Biocomposite Technology, UPM. The processing parameters and material conditions were prepared as [15]. MFI test and rheological studies were carried out using capillary method [12]. However, in this study the temperature was maintained at 190°C.

Results and discussion

In the result of flow curve (Shear stress vs Shear rate), there seems to be positive linear increase of the apparent shear stress with increase in the apparent shear rate and, as expected, values for the various sample is much higher than the PP. This is because as the quantity of fibre content increases, flow resistance increase and caused a further rise in pressure. Sample 250µm and 450µm seem to be closely related in value starting at 0.9 s^{-1} share rate. The 850µm fibre size show an increase of apparent shear stress along the apparent shear rate and it much higher as compare that others fibre loading.

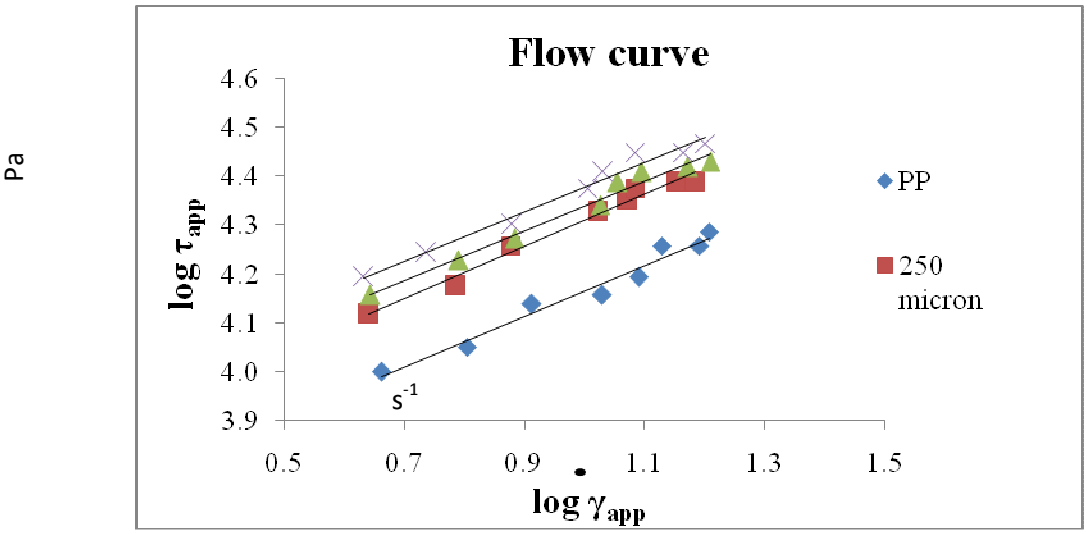


Fig. 1. Flow curve of KF/PP composite as compared to PP

The relationship between apparent shear stress and share rate also holds here as evident from the graph. There is generally no significant difference in the results obtain in 250µm and 450µm fibre size even though it close to 100% increase on the fibre size especially at 42%wt loading. This means that there is still a better distribution of kenaf fibre in the matrix at that stage. In any case, higher percentage of fibre in the composite is responsible for the rise in the processing pressure mainly because of the greater filler to filler interaction as compared to filler to matrix interaction. [12] reported that, construction of a flow curve is necessary in determining the processing properties of polymer melts under certain extrusion conditions. Even though the power law relation

may not be able to predict the experimental observation of a Newtonian plateau at very low and very high shear rates, it can be use in a non-Newtonian fluids in many engineering applications to show that shear stress is very much dependent on shear rate.

Fig 2. shows the relationship between apparent melt viscosity (η_{app}) with respect to that of apparent share rate (γ_{app}) at the test temperature of 190°C. Viscosity curves of Kenaf/PP composites showed a pseudoplastic behavior. The melt viscosity of composite is governed by the fibre orientations that control the wall slip and the fibre-matrix interaction. Distributions of fibre in the composite do also control the viscosity. A better distribution of fibre has been reported to reduce the viscosity of the composite too.

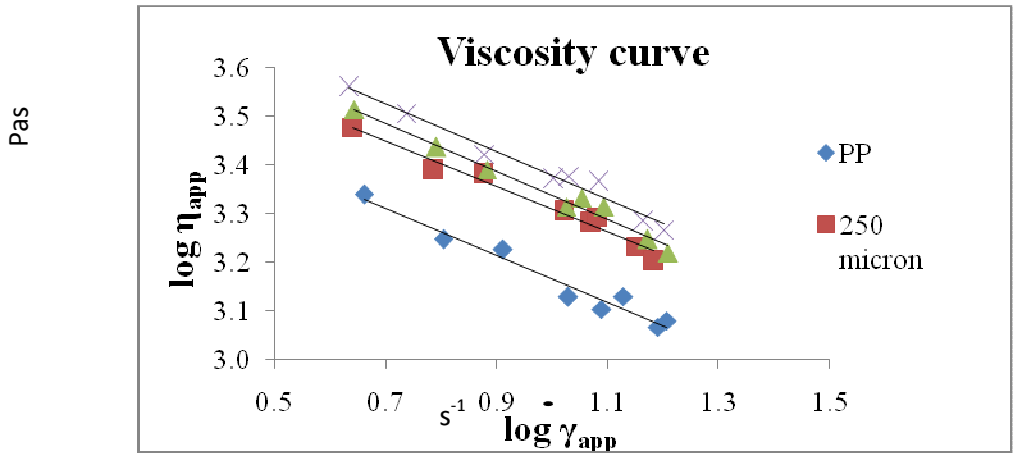


Fig. 2. Log of apparent viscosity to share rate

The result clearly shows a sharp decrease in shear viscosity with increase in the shear rate. In one of the publication, [14] reported that normally, shearing does not cause chain scission but rather a reversible process of disentanglement. The sharp decrease in apparent viscosity could also be because of shear thinning behavior of kenaf. There is far greater fibre-to-fibre interaction especially at the wall, which can raise the pressure. Evidence of agglomeration has also begun to show as a little linearity deviation is observed. Agglomeration can itself raise the composite viscosity and shear rates because more fibre are intertwined and thus prevent free flow of matrix through the composite. [12] Similarly reported that the effective collisions among particle at high shear forces could lead to their dense packing by virtue of their closeness. Obviously, the fibre to fibre interaction is more dominant compare to fibre to matrix interaction, as a result, the polymer chain mobility are significantly affected. In a situation where test temperature is fixed, extrusion rate increases with the increase of shear stress at the channel wall, allowing corresponding increase in the converging flow [13].

Composite Kenaf/PP consisting of 250, 450 and 850 micron fibres also follow same trend, which means the difference in their fibre sizes show a small difference in result. At 42%wt fibre content, there is greater freedom of the fibre to align especially since the nature of kenaf fibre allows it to align with itself. It is clear from the result that in the case of longer fibres, the chance of orientation is high and this leads to increase in wall-slip. The fibre-matrix interaction can most likely be lower in this case; lower viscosity can quite rightly be less when the fibre is also less in the composite. It is generally observed that as the fibre length increase, the chance for fibre orientation also increases and fibre-matrix interaction unfortunately decreases. This answered for the low value of viscosity in the case of 250 and 450micron fibre composites. That notwithstanding, the distribution of the fibre will be maximum in the lowest length fibre, i.e. 250micron fibre composite which of cause reduces the viscosity.

Melt density results is illustrated in Fig. 3; the melt density of composite measured at 190 decree C temperature is obviously lower compared with the PP melt density. Normally the melt density

seems to decrease with increasing temperature and it was also observed that, all fibre sized used decreased gradually with increasing fibre size. This might have been contributed by addition of natural fiber which resulted in changes of glass transition temperature, Tg. In addition, the density reduction was influenced by density of kenaf fibre which is lower than that of PP material.

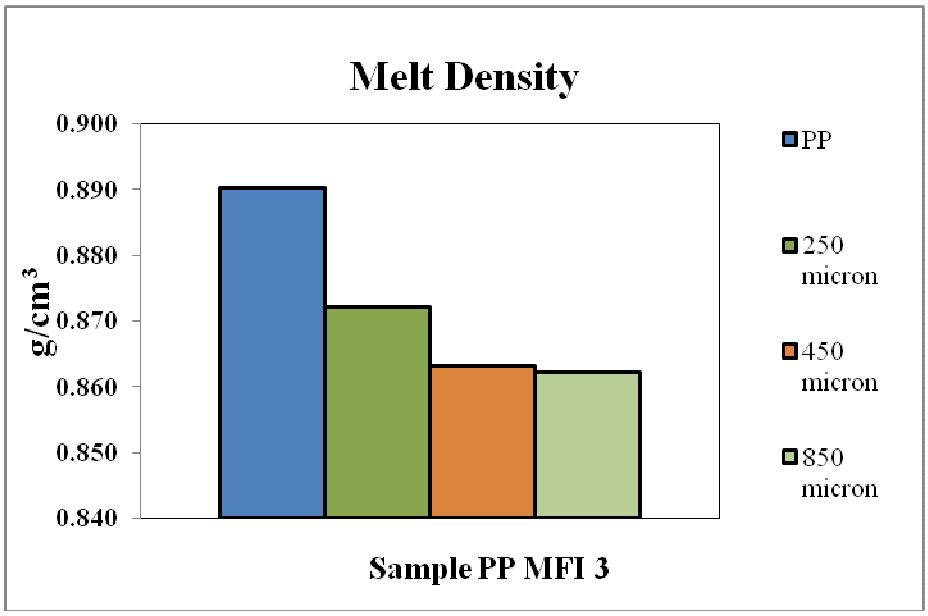


Fig. 3 Melt density of PP and KF/PP composite

Summary

Generally speaking, results grouped together on the bases of similar fibre size showed a remarkable closeness in the pressure experienced, linearity relationship of the apparent share stress and share rate where values are mostly seen to almost overlap each other with trend showing increase in viscosity with increase in fibre size. The increase in viscosity with increase in fibre loading contributed to the high specific area of the fibre in the matrix thereby increasing the shear stress in the composite. However, at low shear rate, increase in viscosity is observed especially at lower fibre size. Loading of a polymer system with fibre tends to disturb or disorganize the normal free movement of the polymer and will certainly hinder the mobility chain segments in flow. In conclusion, kenaf fibre loading reduces the Melt density value mainly because of the hindrances in the plastic flow of the polymer.

References

1. Aji IS, Sapuan SM, Zainudin ES, Abdan K., International Journal of Mechanical and Materials Engineering (IJMME). 2009;4(3):239–248.
2. Wollerdorfer M, Bader H. Industrial Crops and Products. 1998;8(2):105–112.
3. Oksman K, Skrifvars M, Selin JF., Composites Science and Technology. 2003;63(9):1317–1324.
4. George J, Sreekala MS, Thomas S., Polymer Engineering & Science. 2001;41(9).
5. Mohanty AK, Misra M, Hinrichsen G. Biofibres, Macromolecular Materials and Engineering. 2000;276(1).
6. Alvarez VA, Terenzi A, Kenny JM, Vazquez A. Polymer engineering and science. 2004;44(10):1907–1914.
7. Nair KCM, Kumar RP, Thomas S, Schit SC, Ramamurthy K., Composites Part A: Applied Science and Manufacturing. 2000;31(11):1231–1240.
8. Thomas S, Nair KCM, Kumar RP, Schit SC, Ramamurthy K., Composites Part A: Applied Science and Manufacturing(UK). 2000;31(11):1231–1240.

9. Crowson RJ, Folkes MJ, Bright PF., Polymer Engineering and Science. 1980;20(14):925–933.
10. Harun J, Abdan K, Zaman K., Molecular Crystals and Liquid Crystals. 2008;484(1):134–142.
11. Felix JM, Gatenholm P., Journal of Applied Polymer Science. 1991;42(3):609–620.
12. Rahim NA, Ariff ZM, Ariffin A, Jikan SS., Journal of Applied Polymer Science. (pages 73–83) 16Volume 119, Issue 1
13. Liang JZ. Polymer Testing., 2008;27(8):936–940.
14. 0623.PDF [Internet]. [cited 2010 Oct 7];Available from: http://www.sperecycling.org/GPEC/ANTEC2001/papers/0623.PDF
15 Khalina A, Shamizan A & Jalaluddin H., Chapter in book Biocomposite, Derivatives and economics ; Paridah Tahir, Luqman Chuah Abdullah & Norfaryanti Kamaruddin Year : 2009 No. of Pages :178 Pustaka Prinsip Sdn Bhd National ISBN : 978-983-053-562-3

© (2011) Trans Tech Publications, Switzerland
doi:10.4028/www.scientific.net/KEM.471-472.518

Mechanical and Thermal Properties of Polyamide 6 Nanocomposite Toughened with Epoxidised Natural Rubber-25

NAVID Nematzadeh [a], MAT Uzir Wahit [b], AZMAN Hassan [c] and SHAYA Mahmoudian [d]

Enhanced Polymer Research Group, Department of Polymer Engineering,

Faculty of Chemical Engineering, Universiti Teknologi Malaysia, Johor, Malaysia

[a]nnavid2@live.utm.my, [b]mat.uzir@fkkksa.utm.my,

[c]azman.h@gmail.com, [d]shaya_mahmoodian@yahoo.com

Keywords: PA6, Epoxidised Natural Rubber, Toughening, Nanocomposite.

Abstract. Polyamide (PA6) is an engineering plastic with wide range of applications and the development in the field of montmorillonite (MMT) filled polymer nanocomposites has resulted in the development of PA6/MMT nanocomposites. However, MMT filled PA6 nanocomposites are notch sensitive and brittle at low temperatures, which posed as a major setback for many of its applications. The main objective of this study is to enhance the toughness of PA6/MMT (100/4) nanocomposites with epoxidised natural rubber-25 (ENR25). The ENR-25 content in the composites ranged from 15 to 30 wt%. The PA6/ENR/MMT nanocomposites were extruded and injection molded into tensile and impact test samples. The addition of ENR25 into PA6/MMT nanocomposites improved the impact strength of the nanocomposites while tensile modulus and tensile strength decreased with increasing ENR25 content. The thermal properties of PA6/ENR/MMT nanocomposites were also investigated via thermal gravimetric analysis (TGA). Both T10% and derivative thermal analysis (DTA) determined the lower thermal stability of PA6/MMT nanocomposites after addition of ENR.

Introduction

One class of polymer nanocomposites uses a filler material that is based on aluminum silicate clays, the most common representative of which is montmorillonite [1]. Numerous studies have shown that only a few percent of layered silicate can bring about a wide array of property enhancement, e.g. improved stiffness and strength [2-5], increased solvent and UV resistance ,[6-7], greater dimensional stability [3-6], superior flame retardancy [8-9], properties of the nanocomposite will differ remarkably. Polymer nanocomposites can be differentiated from conventionally polymer composite by size of the filler [10-12]. The reason can be justified to the incorporation of thin (<1 nm) silicate-lamellae that exhibit both high surface area (up to 103 m2 g-1) and large aspect ratios (often P100) which, when combined with their high tensile modulus (>100 GPa), produce efficient reinforcement of a polymer-matrix [11, 13-14].

Polyamide 6 /organoclay nanocomposites as the first successfully commercialized polymer/clay nanocomposites have been widely studied. It is well established that PA 6 is a notch-sensitive plastic. It is sensitive to crack propagation and becomes embrittled at low temperature. Furthermore, by addition of organoclay its brittleness becomes more severe. Toughening of polymers that are ductile but notch-sensitive is obviously among the most significant advances in the development of new polymeric materials [15-17].

Recently, many researchers have investigated the polymer/clay nanocomposites toughened with thermoplastic elastomer. A variety of thermoplastics and elastomers have been used to achieve a balance between stiffness/strength versus toughness/ductility [15, 17-20].

The objective of this study is to develop PA6/MMT nanocomposite by using MMT nanoclay. Furthermore, the loss in ductility due to addition of nanoclay will be improved by addition of ENR25 as a toughening agent to finally achieve toughened nanocomposites of PA6/ENR/MMT. The effects of both MMT and ENR addition and variation of ENR concentration on mechanical properties was investigated.

Materials. Polyamide 6 (PA6) was obtained from Toray Plastics Japan (product name Amilan CM1017-K) with Melt Mass Flow Rate (MFR) at 230°C and 2.16 kg load of 35g/10 min and density of 1.14 g/cm³. Epoxidized natural rubber, ENR-25 with 25 mol% epoxidation (grade EPOXYPRENE 25) and specific gravity 0.97, used in this study was used as received from the Malaysian Rubber Board, Malaysia. Montmorillonite (MMT) obtained from Nanocor Inc. Arlington Heights IL, USA (Nanomer 1.30TC) organically modified with octadecylamine with mean dry particle size of 16-22 μm.

Nanocomposite preparation. PA6 pellets were dried at 82°C for 24 hours prior to compounding. The PA6/ENR blend and nanocomposites were compounded by simultaneous addition of all components to Brabender Plasticoder P 2000 counter-rotation twin screw extruder. PA6 and ENR blends were prepared by weight while MMT was added as parts per hundred (phr) in the blends. The barrel temperature profile adopted during compounding of all formulations was 190°C at feed section, increasing to 240°C at the die head. The screw rotation speed was fixed at 60 rpm. The extruded materials were injection molded into standard tensile, flexural and Izod impact specimens by using a JSW (Muraron, Japan) Model NIOOB II injection-moulding machine with a barrel temperature of 200-240°C. After injection specimens were sealed and kept in desiccator for a minimum of 24 hours under ambient conditions prior to mechanical testing.

Characterization. Tensile test was carried out according to ASTM D 638 using an Instron (Bucks, UK) 5567 under ambient conditions with crosshead speeds of 50 mm min^{-1}. Izod impact tests were carried out on notched impact specimens according to ASTM D 256, by using a Toyoseiki (Tokyo, Japan) impact testing machine under ambient conditions. Five specimens of each formulation were tested and the average values reported.

Thermogravimetric analysis (TGA) tests were carried out on a Perkin Elmer-TGA7 instrument at a heating rate of 10 ˚C/min with temperature range from 30 to 650 ˚C both under nitrogen and air atmospheres. Approximately 10 mg of samples was tested with the flow rate of 50 ml/min.

Results and discussion

Mechanical Properties.

The Effect of Organoclay Inclusion on PA6. As it is shown in Fig. 1 the stiffness of the neat PA6 was raised by incorporation of 4wt% of nanoclays. Same observations were detected in terms of tensile strength (Fig. 2). Similarly, enhancement of stiffness and strength was reported [10, 21].

According to Liu [22], the stiffness of the silicate layers also contributes to the presence of immobilized or partially immobilized polymer phase. In this respect, improvement of tensile modulus in PA6/clay hybrids was justified to the constrained region where the polymer chains have a restricted mobility. On the other hand, incorporation of nanoclay has the drawback of impairing ductile properties. According to Shishan [21], there are two main reasons for this influence. One important reason is that a significant volume fraction of the polymer, which can dissipate stress through the shear yielding or crazing mechanism, is replaced by the filler, which generally cannot deform and dissipate the stress easily. However, this is particularly true at high filler concentration. The second reason is that certain filler, such as polymeric filler that are miscible in the polymer

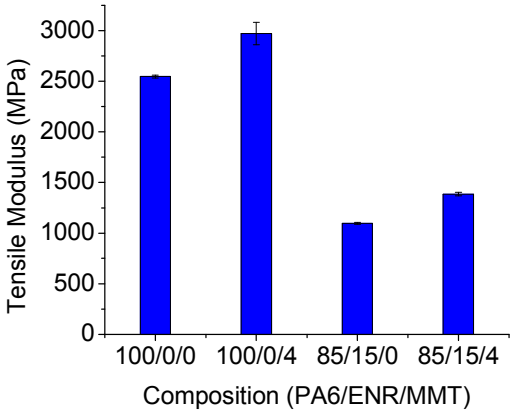


Fig. 1. The effect of nanoclay and ENR on tensile modulus of PA6 and PA6/ENR blend

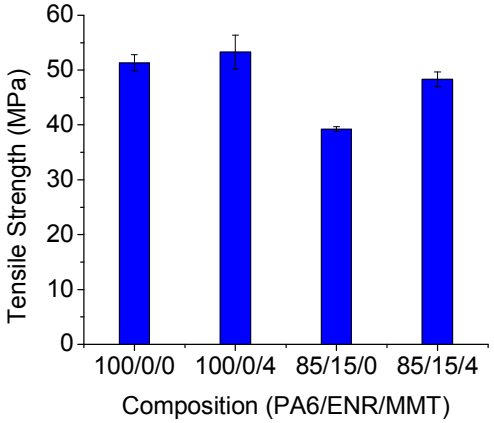


Fig. 2. The effect of nanoclay and ENR on tensile strength of PA6 and PA6/ENR blend

matrix, may hinder the local chain motions of the polymer molecules that enable them to shear yield, which can sharply decrease the impact resistance of the materials.[23]. However, this drawback is believed can be overcome by the incorporation of rubber phase.

The Effect of ENR inclusion on PA6 and PA6/MMT. The effects of ENR inclusion on mechanical properties of PA6 and PA6/MMT blend are depicted in Fig. 1 and 2.The strength and stiffness diminished by incorporation of ENR. This observation is usually referred as diluting or softening effect of second component which is reported frequently [16, 20].

The effect of ENR on Izod impact strength and Elongation at break of PA6 and PA6/MMT blend is shown in Fig. 3 and 4 respectively. Both parameters rose remarkably by ENR incorporation. Similar pattern was reported by Tanrattanakul [16] in the case of PA6 and ENR 50 where impact strength elevated 4-10 folds.

For polymer based micrometric and nanometric composites debonding of reinforcement is an important mechanism in promoting fracture toughness of polymer-matrix based composites as it allows plastic stretching of polymer ligaments between the debonded particles. Elastomers like POE-g-MA can support the debonding mechanism because in situ formation of PA66-Co-POE-g-MA copolymer improves the interfacial adhesion between elastomer particles and matrix. So POE-g- MA is expected to be an ideal elastomer to toughen PA66/PA6 blend [19]. In the same way, ENR reacts as a debonding agent which enhances plastic stretching of matrix particles.

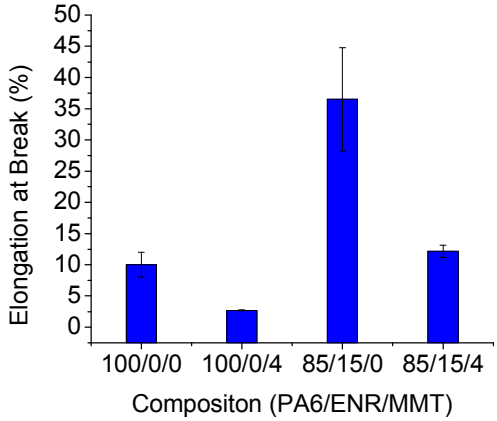


Fig. 3. The effect of nanoclay and ENR on impact strength of PA6 and PA6/ENR blend

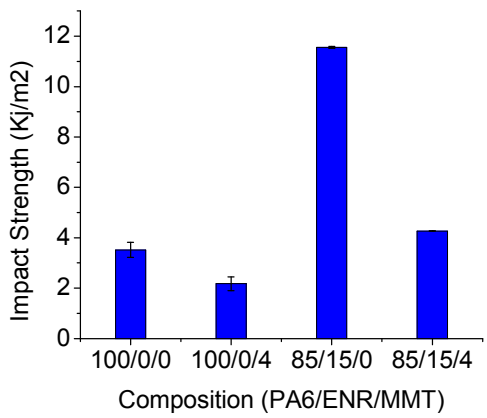


Fig. 4. The effect of nanoclay and ENR on elongation atbreak of PA6 and PA6/ENR blend

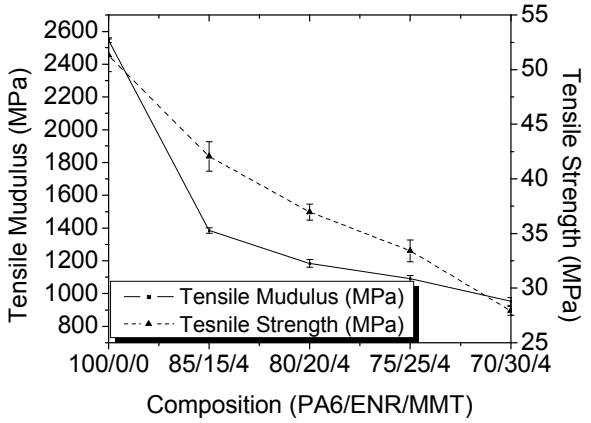


Fig. 5. The effect of organoclay and elastomer on tensile modulus and tensile strength of virgin PA6

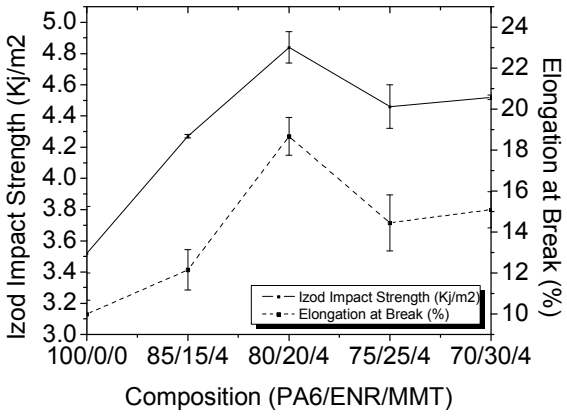


Fig. 6. The effect of organoclay and elastomer on impact strength and elongation at break of PA6

The Effect of ENR/Organoclay inclusion on PA6. A proper solution to gain a balance of stiffness, strength and toughness is by combination of both elastomer and organoclay. The results from simultaneous incorporation of organoclay and elastomer are illustrated in Fig. 5 and 6. The results revealed that stiffness and strength of nanocomposites dropped and this drop became more prominent by higher elastomer loading. In contrast, impact strength of nanocomposites successfully intensified, though the intensification was not steady as it rose up from about 3.52 (KJ/m^2) in neat PA6 to 4.27 (KJ/m^2) in the first batch then it peaks at 4.84 (KJ/m^2) and finally goes down.

Optimum Formulation. In order to evaluate the most appropriate combination of properties, multiplication between the impact strength and stiffness has been done as shown in Fig. 7. From Figure 7, when the effect of elastomer on impact strength and stiffness is considered, the optimum formulation is the formulation with 20 wt% ENR. Therefore, the second (80/20/4) is suggested to be the optimum formulation in this study.

Considering the Fig. 7, while impact strength increased noticeably from nanocomposite with 15% ENR to nanocomposite with 20% ENR, the drop in stiffness is negligent.

Thermal analysis

Thermogravimetric analysis (TGA). Fig. 8a and 8b show the TGA and corresponding derivative TGA (DTGA) curves of PA6 and PA6/ENR and their nanocomposites with varying ENR content, respectively. It can be seen that all the samples displayed single-step degradation process. The initial thermal stabilities are characterized by the temperatures at 10 wt% weight losses occurred, referred to as $T_{10\%}$ and maximum decomposition (T_d) temperature attained from DTGA curves are summarized in Table 1. The $T_{10\%}$ of neat PA6 was registered at 385 °C and a higher $T_{10\%}$ value was observed with addition of 4 phr MMT (395 °C). It is noteworthy to highlight that the T_d of PA6/ENR also increased with addition of 4 phr MMT in PA6/ENR/MMT nanocomposites.

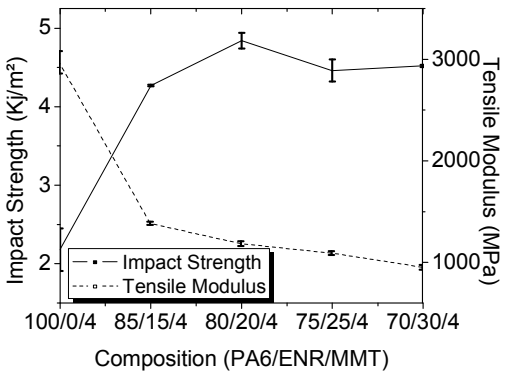


Fig. 7. Multiplication between impact strength and tensile modulus as a function of ENR content

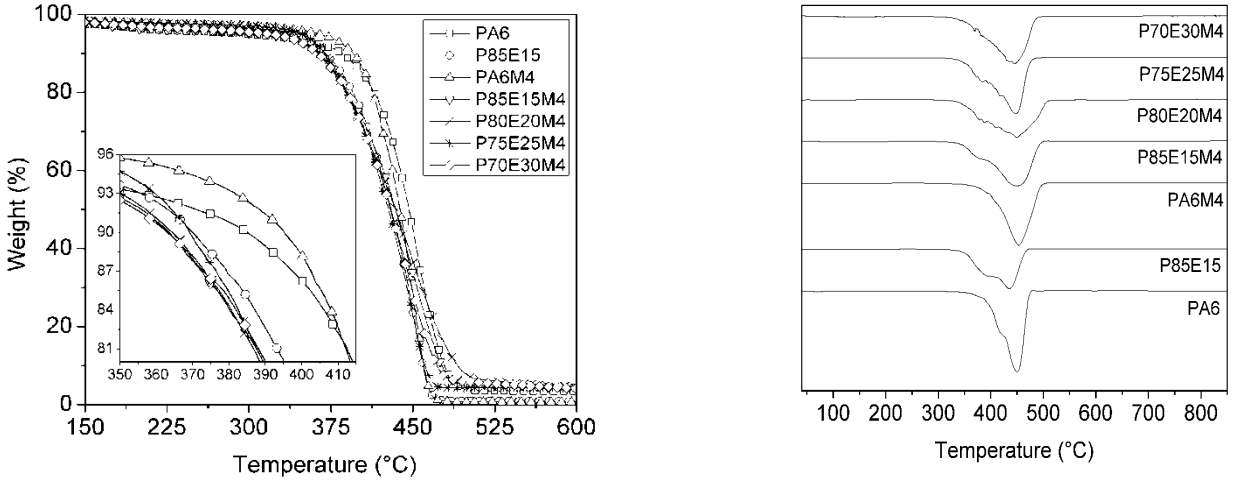


Fig. 8: (a) TGA curves of PA6, PA6/ENR and their nanocomposites. The insert shows the zoomed portion of the curves at 90 wt% as a function of temperature (b) Derivative TGA curves of PA6, PA6/ENR and their nanocomposites

The enhancement in thermal stability could be attributed to the well dispersed MMT platelets which hindered diffusion of volatile decomposition products within nanocomposites [20, 24].

However, according to Table 1, the $T_{10\%}$ of PA6 and PA6/MMT decreased with the blending of ENR. The magnified decomposition curves at 90% weight with temperature range of 350 to 420 °C in Fig. 8 shows that PA6/ENR and all PA6/ENR/MMT nanocomposites decomposed earlier than PA6 and PA6/MMT nanocomposites. This may be due to the lower T_d of ENR at ~405 °C [25] as the blending of a second phase which has a relatively lower T_d will lower the thermal stability of the respective blend and composite. Fig. 8 and Table 1 depicted the decrement of T_d values for PA6 and PA6/MMT nanocomposites with the blending of ENR. Nevertheless, the finding contradicts with previous studies by Kusmono et al. [24] and Chiu et al. [20] who reported enhancements in $T_{10\%}$ and T_d temperatures with the blending of rubber phase. We believe that the graft esterification reaction between PA6 and ENR played a positive role solitarily in the enhancement of mechanical and morphological properties but not in thermal stability. The lower T_d of ENR in comparison to PA6 has resulted in the early degradation of PA6 in PA6/ENR and PA6/ENR/MMT nanocomposites thus, it can be deduced that the presence of ENR reduced the overall thermal stability of PA6 and PA6/MMT nanocomposites.

Table 1: TGA results of PA6 and PA6/ENR nanocomposites

Designation	$T_{10\%}$	T_{decomp}	Char residue (600°C)
PA6	385	445	0.7
PA6M4	395	452	3.4
P85E15	374	438	0.9
P85E15M4	363	447	4.6
P80E20M4	364	450	4.5
P75E25M4	369	446	4.4
P70E30M4	363	443	4.3

Summary

The mechanical properties of nanocomposite systems were found to be highly dependent on the ratio of rubber incorporated in the matrix. For any PA6, PA6/MMT and PA6/ENR/MMT systems, the tensile strength and elastic modulus increased by either incorporation or elevation of elastomer content. On the other hand, toughness decreased by incorporation or elevation of elastomer content. An optimum concentration of PA6/ENR/MMT was achieved at 20 wt% ENR at which a balance between stiffness, strength and toughness was reached. The thermal stability of PA6 and PA6/MMT deteriorated with the addition of ENR and resulted in lower $T_{10\%}$ and T_d values.

References

[1] P. D. Fasulo, *et al.:* Polym. Eng. Sci. Vol. 44 (2004), p. 1036-1045

[2] M. Kato, *et al.*: J. .Appl. Polym. Sci. Vol. 66 (2007), p. 1781-1785

[3] L. Liu, *et al.*: J. Appl. Polym. Sci. Vol. 71 (1999), p. 1133-1138

[4] T. Lan and T. J. Pinnavaia: Chem. Mater. Vol. 6 (1994), p. 2216-2219

[5] Z. Wang and T. J. Pinnavaia: Chem. Mater. Vol. 10 (1998), p. 3769-3771

[6] Y. Kojima, *et al,:* J. Mater. Res. Vol. 8 (1993), p. 1185-1189

[7] J. C. Huang, *et al.*: Polymer Vol. 42 (2001), p. 873-877

[8] J. W. Gilman. Appl. Clay Sci. Vol. 15 (1999), p. 31-49

[9] R. A. Vaia, *et al.*: Appl. Clay Sci. Vol. 15 (1999), p. 67-92

[10] D. F. Eckel, *et al.*: J. Appl. Polym. Sci. Vol. 93 (2004), p. 1110-1117

[11] T. D. Fornes, *et al.* Polymer Vol. 43 (2002), p. 5915-5933

[12] T. D. Fornes, *et al.*: Polymer Vol. 42 (2001), p. 9929-9940

[13] A. N. Wilkinson, *et al.*: Compos. Sci. Technol. Vol. 67 (2007), p. 3360-3368

[14] T. D. Fornes and D. R. Paul: Polymer Vol. 44 (2003), p. 4993-5013

[15] L. Zhang, *et al.*: Polym. Eng. Sci. Vol. 49 (2009), p. 209-216

[16] V. Tanrattanakul, *et al.*: Polym. Test. Vol. 27 (2008), p. 794-800

[17] I. González, *et al.*: Compos. Sci. Technol. Vol. 66 (2006), p. 1833-1843

[18] Y. C. Ahn and D. R. Paul: Polymer Vol. 47 (2006), p. 2830-2838

[19] J. Chen, *et al.*: J. Appl. Polym. Sci. Vol. 115 (2010), p. 588-598

[20] F. C. Chiu, *et al.*: Polymer Vol. 46 (2005), p. 11600-11609

[21] W. Shishan, *et al.*: Polym. Eng. Sci. Vol. 44 (2004), p. 2070-2074

[22] T. X. Liu, *et al.*: Compos. Sci. Technol. Vol. 63 (2003), p. 331-337

[23] K. T. Gam, *et al.*: Polym. Eng. Sci. Vol. 43 (2003), p. 1635-1645

[24] Kusmono, *et al.*: Eur. Polym. J. Vol. 44 (2008), p. 1023-1039

[25] M. Zurina, *et al.*: Polym. Test. Vol. 27(2008), p. 480-490

© (2011) Trans Tech Publications, Switzerland
doi:10.4028/www.scientific.net/KEM.471-472.524

Comparative Study of Fiber Metal Laminates (FMLs) and Aluminum Skins for Polypropylene (PP) Honeycomb Core Sandwich Structure under Low Velocity Impact Loads.

Hazizan Md. Akil[a] and C.Y. Tan[b]

School of Materials and Mineral Resources Engineering,

Universiti Sains Malaysia,

14300 Nibong Tebal, Penang, Malaysia

[a]hazizan@eng.usm.my, [b]tcy09_min057@student.usm.my

Keywords: low-velocity impact, polypropylene honeycomb, fiber metal laminate, sandwich structure

Abstract. In this study, the impact responses of sandwich structure with both FML and aluminum skins were compared. The force-time histories from the low-velocity drop weight impact tester were recorded under various impact energies. Energy absorbed from the two types of sandwich structures under various impact energies were also calculated by measuring its initial velocity before impact from a series of recorded high speed camera pictures and force-time histories. Based on results obtained, pure aluminum skins with PP honeycomb core that being impacted by lower impact energies shows higher absorbed energies as compared to FML skins. However with higher impact energies the FML skins shows improvement over the aluminum with higher energy absorption capacity. Damages created were also being characterized under optical microscope for further investigation.

Introduction

A typical sandwich structure may consist of two thin but stiff skins bonded to a thick, lightweight core. Each component by itself is relatively weak and flexible, but putting together, they produce a sandwich structure that is stiff, strong and lightweight. The basic concept of a sandwich panel is that the facings carry the bending loads and the honeycomb core carries the shear loads [1].

Sandwich structures are gaining popularity being used as an alternative material to achieve the same structural performance as conventional materials with less weight. In terms of today's transportation industry, weight saving plays an important part in lowering cost in fuel consumption. Other application also includes aerospace and marine industries. Previous studies on low-velocity impact response of sandwich structures used either Nomex or aluminum honeycomb cores [2-4]. While both of these two cores have their own advantages and disadvantages, thermoplastic such as polypropylene offers much benefits as it can be processed easily by thermoforming and can be recycled. Nomex cores do give higher mechanical properties compared to aluminum and polypropylene, however its higher price made it not quite suitable for consumers or low end products which desperately needed weight reduction while maintaining excellent strength and low cost. Besides cost effective, polypropylene honeycomb do offer excellent strength to weight ratio, corrosion resistant, high energy absorption and moisture resistant making it a perfect substitute for component that requires structural rigidity yet cheap compared to aluminum and nomex cores [5].

Thermoplastics composite sandwich panels are now being considered as an alternative material in automotive applications such as cargo load floors, engine shields, trunk panels, backrests, aerodynamic skid plates, spare wheel pans, and front and rear bumpers [6]. In this study, polypropylene cores with both aluminum and FMLs skins of the same thickness were used.

Materials. The polypropylene honeycomb sheet's (PP8T40F) cell size and density are 8 mm and 80 kg/m^2, respectively. The sheet is supplied with both sides laminated with non-woven polyester tissue in 40g/m^2. This allows better bonding of the honeycomb to different panels. The thickness of the core materials is 20mm. The facesheets used consist of aluminum sheet (1100) and fiber metal laminates.

Fiber metal laminates used in this study were based on an aluminum (1100) and a glass-fiber-reinforced thermoplastic prepreg (Atenply GFPP45 from Jonam Composites, UK).

The fiber metal laminates were produced using a frame mould by stacking the prepreg, the interlayer material and the aluminum plies with dimensions of 200 x 140mm. The stack was loaded into a hot press at 180 ^{o}C and soaked for 10mins. After that it is compressed under a pressure of 0.4 MPa for 20mins before cooling slowly to room temperature. These laminates were then bonded to the top and bottom of the honeycomb core with similar sizes using an Araldite Rapid Resin with an Araldite Rapid Hardener. The fabricated sandwich structure was placed under weights for 1 day to ensure curing of the adhesive. Fig.1 shows the schematic diagram of sandwich structure configuration.

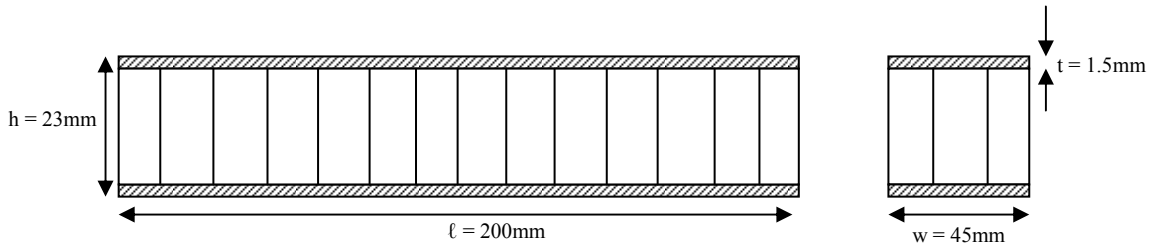


Fig. 1: Schematic diagram of sandwich structure configuration.

Experimental

Impact test were conducted using an instrumented drop weight impact machine. Here, a 2kg carriage with a 25 mm diameter hemi-spherical indenter was released from heights of up to 1.0m. Impact energy levels up to 20J were achieved by varying the drop height. The specimens were supported on two 12mm diameter steel cylinders positioned on movable right angle supports. The impact force history during the test was measured using a piezo-electric load cell located just above the impactor tip. The signals from the load cell were then recorded and stored by computer using data acquisition software. The schematic of the setup is shown in Fig. 2.

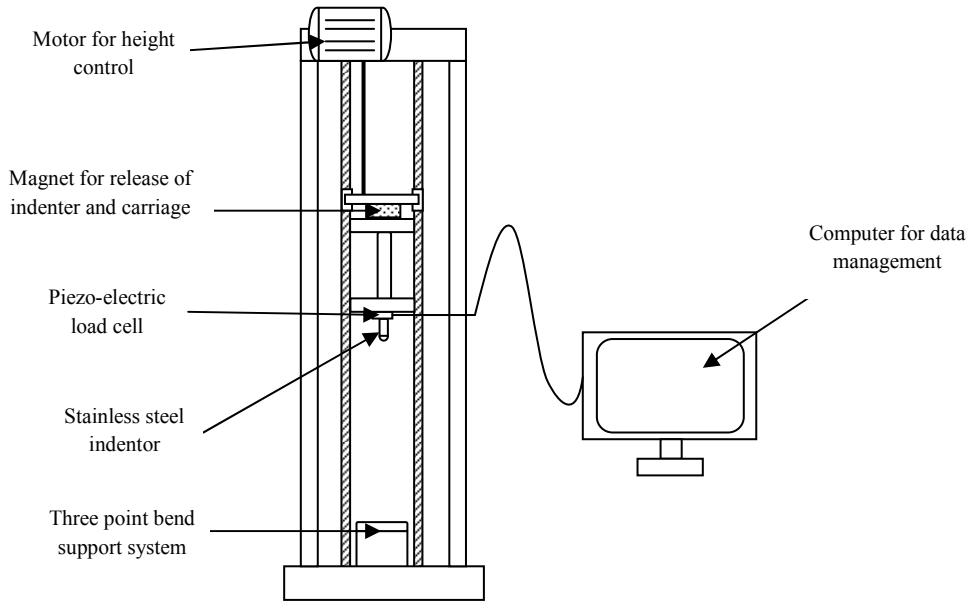


Fig. 2: Schematics of the drop weight impact tester.

Results and Discussion

The low velocity impact on both aluminum and FML skins on polypropylene honeycomb sandwich structure were compared using force-time histories obtain from the impact tester. It should be noted that the data acquisition system for this drop weight impact tester can only measure the forve vs time directly. However, a series of high speed camera pictures had been used to measure the initial velocity of the impactor. The remaining parameters, such as absorbed energy, velocity of impactor and deflection are calculated using equations of motion.

Energy calculations

Impact energy is the kinetic energy of the impactor at the instant it strikes the specimen. This impact energy can be controlled by varying the mass of the impactor or the height which it is dropped. Thus the potential energy of the impactor before release is an upper bound for the kinetic energy of the impact. Energy loses during acceleration, friction and air resistance on the impactor can be accounted by measuring the velocity of the impactor just before impact, $V_{impactor}(0)$. Impact energy is then calculated by the kinetic energy prior to impact (refer with Eq. 1)

$$\text{Impact energy} = \frac{m_{impactor}}{2} V_{impactor}(0)^2 \tag{1}$$

The absorbed energy is then calculated by the kinetic energy loss of the impactor, in which the impactor velocity, $V_{impactor}(t)$, is integrated for the contact force, F(t), by Newton's second law, which is (refer with Eq. 2),

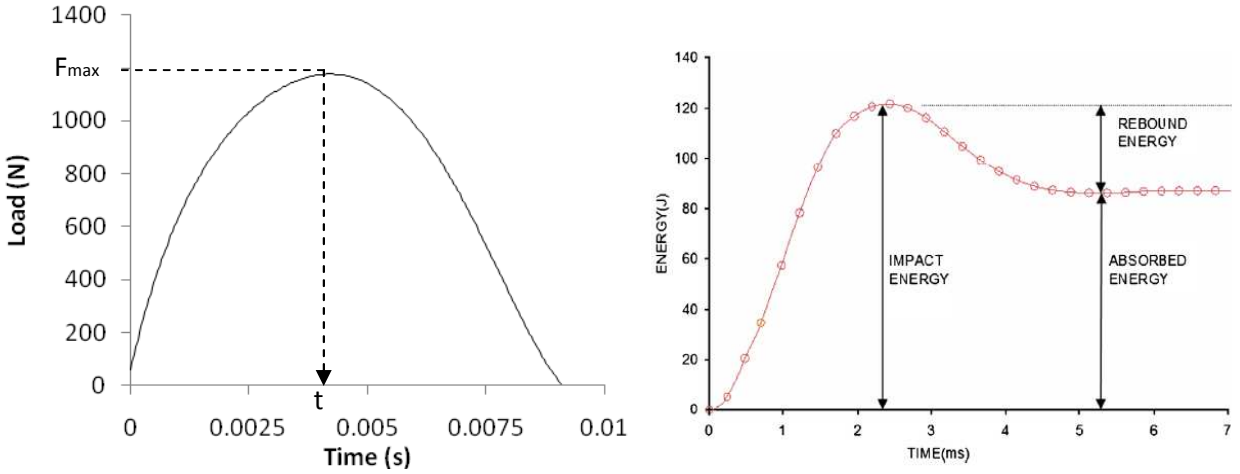
$$V_{impactor}(t) = V_{impactor}(0) - \frac{1}{m_{impactor}} \int_0^t F(t)dt \tag{2}$$

The kinetic loss of the impactor, or energy E(t) is then (refer with Eq. 3)

$$E(t) = \frac{m_{impactor}}{2} (V_{impactor}(0)^2 - V_{impactor}(t)^2) \tag{3}$$

Thus, absorbed energy is a calculated not directly measuared quantity. Its accuracy will depend on measured velocity $V_{impactor}(0)$, the measured mass $m_{impactor}$, and the neglected frictional losses during the impact event [7]. In this study, the impact energy ranges from 4-20J.

Fig. 3(a) shows a typical force-time history data which shows a linear increase with a decreasing slope. After the maximum point was reached, F_{max}, the force decreased following almost a linear and non-oscillating curve and eventually become zero. This kind of curves shows none or little damage to the structure. The impact force time histories of aluminum and FML specimen showed quite similar shapes under impact energy of 4.12J, Fig. 4a and c. The entire impact event took about 8-9 ms and the maximum force occurred around 4ms. At impact energy of 12.36J, the force-time histories for aluminum skins show the similar trend with higher maximum force. On the other hand, for similar impact energies on FML skins, the force-time histories exhibited a different pattern. The load increased linearly with a decreasing slope until maximum load point was reached as it was seen in lower impact energy until a sudden drop around 1700 N was observed. Noticed that a sudden load drop occurred at 5ms was right after the maximum forced was reached around 4 ms. For impact energies up to 20.60J, both aluminum and FML skins the load shows a sudden drop right after the maximum force was recorded. The drops in the force time histories happened very early. Maximum force values were lower or similar with what recorded for impact energy at 12.36J.



(a) (b)

Fig. 3 (a): Typical force-time histories for a drop-weight impact test. (b) A typical energy curve for drop weight impact test when rebound of the impactor occurs.

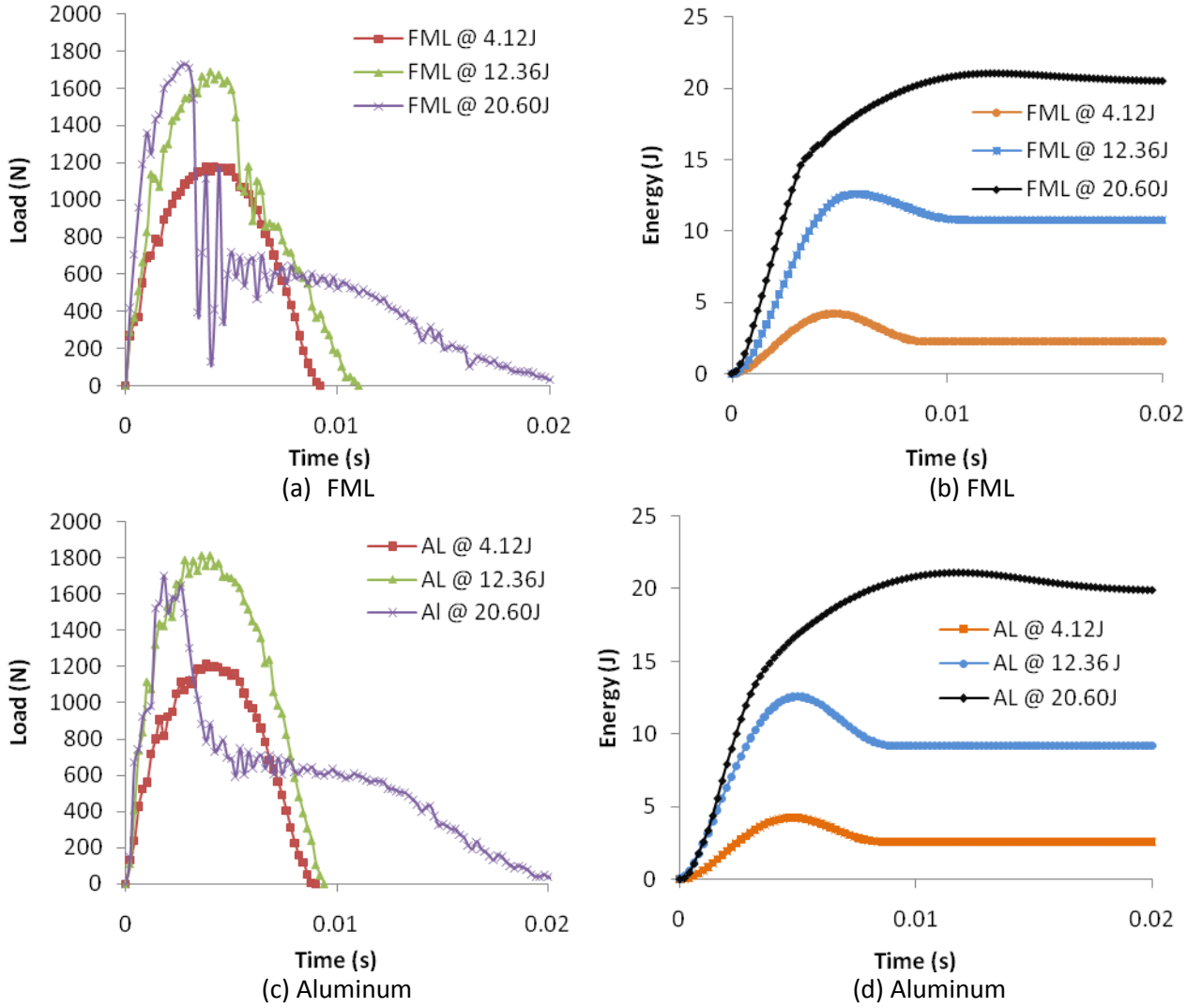


Fig. 4: Force-time histories and energy-time histories of drop-weight impact test onto composites.

After the force-time histories of the drop impact test and optical pictures of the impacted composites were evaluated, we can conclude that impact test, which created global bending, core crushing and delamination on skin laminates, exhibited sudden load drops at their force-time histories; whereas the force-time histories of the test which produce no or very little global bending and core crushing, did not show any significant drop. According to E.sevkat *et al* [8], the force generated due to contact of impactor-composite was linear at the beginning, because the impactor was just pushing the specimen down and no damage had been formed yet. As soon as the damage appeared in the composite, the force time-histories will show oscillations. The damage could be in the form of delamination, surface cracks or front surface indentation. In our sample, the oscillations of the load is not significant enough to conclude any damage generated yet, but somehow with higher impact energies the force-times histories of the test with both aluminum and FML skin does show a point where there is sudden load drop and continue to rise again to reach maximum force.

The maximum force increased with increasing impact energy during the testing for FML skin. However for aluminum skin, the maximum force dropped when the specimen was subjected to impact energy at 20.60J compared to 12.36J.

If a composite structure absorbs little energy, the impactor will bounce back. This is said when no rebound occurs, most of the energy of impactor is absorbed by the composite. Figure 3(a) shows a typical energy curve for a drop-weight impact test where rebound of the impactor occurs. The absorbed energy is shown as the energy which has not returned to zero after the impact. In this study, most of the energy-time histories, as shown in figure 4(b) and (d), are similar to the one depicted in Fig. 3(b). Based on previous studies, when the impactor penetrates the sample, no rebound would occur therefore the energy curve will show initial rising of the energy level to reach a plateau indicating the absorbed energy is equal to the impact energy. At impact energy of 4.12J the aluminum skin showed a slight higher amount of absorbed energy compared to FML skin. However at 12.36J the FML had an edge over aluminum skin mainly due to the fact that delamination started to occur at the FML layers. At 20.60J, the energy curves shows only slight amount of rebound energy. This indicates that most of the energy had been absorb by both skin types through global bending of the composite structure. The energy absorption of the composite increased with increasing impact energy.

Summary

- Under impact energy below or at 4.12J, aluminum skins show comparable impact loads and energy absorption to FML skins.
- At higher impact energy of 12.36J, aluminum skins had a slight edge over FML skins with FML showing signs of delamination.
- At impact energy of 20.60J, FML shows better energy absorption compared to aluminum skins and less global bending on specimen structure.

Acknowledgements

This study has been carried out by the financial assistance from Universiti Sains Malaysia Fellowship and the Research University Postgraduate Research Grant Scheme **(**USM-RU-PRGS - Grant No.: 1001/PBAHAN/8043039).

References

[1] J. Kindinger, in: Lightweight Structural Cores-ASM Handbook, edited by: D.B. Miracle and S.L. Donaldson, Volume 21: Composites*,* ASM International Handbook Committee (2001).
[2] M. Meo, R. Vignjevic and G. Marengo: Mech. Sci. Vol.47 (2005), p.1301.
[3] M.A. Hazizan and W.J. Cantwell: Comp. Part B: Engineering. Vol.34 (2003), p.679.
[4] C.C. Foo, L.K. Seah and G.B. Chai: Comp. Struc. Vol.85 (2008), p.20.
[5] Information on http://www.hexacor.com/

[6] Information on http://composite.about.com/library/PR/2001/blventure1.htm
[7] E.J. Herup and Anthony Palazotto: Comp. Sci. Tech. Vol.57 (1997), p.1581.
[8] E. Sevkat, B. Liaw, F. Delale and B.B. Raju: Comp. Part A: Applied Science and Manufacturing. Vol.40 (2009), p.1090.

© (2011) Trans Tech Publications, Switzerland
doi:10.4028/www.scientific.net/KEM.471-472.530

Buckling and Post-Buckling Improvements of Laminated Composite Plates using Finite Element Method

Zainudin A. Rasid[1,a] , Amran Ayob [2,b], Rizal Zahari [3,c], F. Mustapha [3,d], D.L. Majid [3,e], Renuganth Varatharajoo[3,f]

[1] Department of Mechanical Engineering, Universiti Teknologi Malaysia, Kuala Lumpur, Malaysia

[2] Faculty of Mechanical Engineering, Universiti Teknologi Malaysia, Skudai, Johor, Malaysia

[3] Department of Aerospace Engineering, Universiti Putra Malaysia, 43400 UPM Serdang, Selangor Malaysia

[a]zainudin@ic.utm.my, [b]amran@fkm.utm.my, [c]rizal@eng.upm.edu.my

Keywords: Shape memory alloy, laminated composite plates, non-linear finite element model, buckling and post-buckling

Abstract. The improvements of buckling and post-buckling behaviours of laminated composite plates were done by changing the composite related parameters such as the level of anisotropy, thickness to width ratio and boundary condition. In recent years, shape memory alloy has been used to achieve such improvements. A study is conducted on the buckling and post-buckling improvements of composite plates due to the combined effects of composite and shape memory alloy related parameters. Shape memory alloy wires are embedded within laminated composite plates and the amount of recovery stress induced by the shape memory wires is predicted using the Brinson's model. A geometric non-linear finite element method is used to model the buckling and post-buckling behaviours of shape memory alloy composite plates and source codes are developed to solve the model. It is found that significant improvements in buckling and post-buckling behaviours of composite plates can be attained by combining the effect of shape memory alloy and composite related parameters.

Introduction

Fibre reinforced composite (FRC) meets the weight saving requirement in many design applications. However when compressive mechanical loads are subjected to thin composite plates in these applications, the problems of buckling and post-buckling of composites become significance. It is important to study not only the critical load of a composite plate but also the large geometrically nonlinear deflection that occurs following the occurrence of this buckling in order to maximize the usage of the composite plates. The improvements of these buckling behaviours were made by varying composite related parameters such as the level of anisotropy, thickness to weight ratio and the aspect ratio. In recent years however shape memory alloy (SMA) with its inherent property of inducing a huge amount of recovery stress has been used to improve buckling and post-buckling behaviours of composite structures. The SMA's behaviour of inducing stress is called the shape memory effect (SME) behaviour. Several constitutive models have been proposed to predict the thermomechanical response of the SMA such as the model of Tanaka [1], Liang and Rogers [2] and Brinson. In this research, the Brinson's model is used since it is valid at any temperatures, unlike the previous two models. The material parameters for the Brinson's model that are used in this research are experimental values taken from Zak et al [4].

Ro and Baz [5] conducted experimental and numerical studies on the buckling characteristic of flexible fiberglass composite beams. Loughlan and co-workers [6-7] showed that the embedded activated pre-strained SMA wires can enhance postbuckling behaviour of laminated composite

plate. For the $[0_2/90_2]_s$ stacking sequence, the out-of plane deflection was found to reduce up to 40.1% upon SMA activation. In his recent study, Zak et al [8] conducted parametric study to see the effect of the orientation and location of SMA wires, the orientation and relative volume fraction of reinforcing fibres, the thickness to length and length to width ratios and boundary conditions on the free vibration and critical load of SMA composite plates. The effect of non-uniformly distributed SMA fibers along transverse direction on the linear buckling of laminated plate was studied by Kuo et al [9] using FEM. They found that when the fibers are concentrated in the centre of the plate, the buckling load of the plate will be improved considerably. The literature review shows that studies on the postbuckling behaviours of SMA composites due to mechanical loading were mainly done by Loughlan and his co-workers. As more research is needed to enhance the understanding of the subject, these studies are continued here numerically where FEM model are developed and solved using the source codes developed in-house. The study starts with the study on linear buckling to enhance the understanding on the subject. The analysis on the effects of varying composite related parameters and the SMA parameters are then conducted.

Mathematical Model

The formulation developed here is based on the strength of material approach such as suggested by Rogers et al [10]. The SMA is treated as perfectly bonded wires within the matrix. As such the rule of mixture can be used to determine the effective properties of the SMA composite. The von Karman's is included in the strain formulation that is based on the first order shear deformation theory (FSDT) of laminated composite plates.

Constitutive Relationship. The constitutive relationship in terms of stress resultants are

$$\begin{Bmatrix} N \\ M \end{Bmatrix} = \begin{bmatrix} A & B \\ B & D \end{bmatrix} \left(\begin{Bmatrix} \varepsilon_l \\ \kappa \end{Bmatrix} + \begin{Bmatrix} \varepsilon_{nl} \\ 0 \end{Bmatrix} \right) \qquad T < A_s \qquad (1a)$$

$$= \begin{bmatrix} A & B \\ B & D \end{bmatrix} \left(\begin{Bmatrix} \varepsilon_l \\ \kappa \end{Bmatrix} + \begin{Bmatrix} \varepsilon_{nl} \\ 0 \end{Bmatrix} \right) + \begin{Bmatrix} N^r \\ M^r \end{Bmatrix} \qquad T \geq A_s \qquad (1b)$$

where

$$([A],[B],[D]) = \sum_{k=1}^{n} \int [\bar{Q}]_k (1, z, z^2)\, dz \qquad (2)$$

$$(\{N^r\},\{M^r\}) = \sum_{k=1}^{n} \int V_a \{\sigma^r\}(1, z)\, dz \qquad (3)$$

$\{N\}$ and $\{M\}$ are the force and moment resultant vectors respectively while $[A]$, $[B]$ and $[D]$ are the laminate stiffness matrices. $\{N^r\}$ and $\{M^r\}$ are the resultant force and moment vectors due to the recovery stress, respectively.

The FEM governing equation. The FEM governing equation for the non-linear deflection of SMA composite plates under compressive loading is such as

$$\left([K_L] + [K_s] + [K_r] + [K_G] + \frac{1}{2}[N1] + \frac{1}{3}[N2]\right)\{q\} = \{P_e\} - \{P_r\} \qquad (4)$$

where $\{q\}$ are the nodal displacement vector. $[K_L]$ and $[K_s]$ are the linear membrane and shear stiffness matrices, respectively. $[K_r]$ and $[K_G]$ are the recovery stress matrix and the geometric stiffness matrix respectively. $[N1]$ and $[N2]$ are the first order and the second order non-linear stiffness matrix respectively. $\{P_e\}$ and$\{P_r\}$ are the external load and the recovery force vectors.

Equation (4) is a nonlinear equation that can be related to buckling problem in two ways. Firstly, it can be reduced to the standard classical buckling equation in the following form.

$$([K_L] + [K_s] + [K_r] + \lambda[K_G])\{q\} = 0 \qquad (5)$$

where λ is the eigen value or the critical load. Secondly, equation (4) can be solved using the Newton Raphson's method.

Results and Discussion

Dimensions. Similar dimensions, orientations and properties were previously used for linear buckling analysis in [8]. The plate is 500 mm x 500 mm. The lamination scheme is $[0/(\theta/-\theta]_n/0]$ where n is an integer to be specified. SMA layers are the outer most layers correspond to the 0^0 angle of orientation while θ is the orientation angle of the graphite fibres. SMA layers is the mixed of nitinol and epoxy (N-E) while graphite-epoxy (G-E) are the other layers. The volume fraction of nitinol in a N-E layer is to be specified while the volume fraction of the graphite in a G-E layer is 0.5. The thickness of each layer depends on the ratio of side to thickness that is to be specified. Both of the loaded sides of the plates have simply supported (SS) boundary conditions while the boundary conditions correspond to the non-loading sides of the plates can be both SS, both clamped (CC) or one simply supported and one clamped (SC). The properties for graphite and epoxy are given in Table 2.

Table 2. Properties of graphite fibers and epoxy [8]

	Young's Modulus , E (GPa)	Shear Modulus,G (GPa)	Poisson's Ratio (ν)
Graphite	275.6	114.83	0.2
Epoxy	3.43	1.27	0.35

Validation. To get the appropriate mesh size for the buckling analysis, a test was conducted on 3 configurations of SMA composite plates. This test, at the same time can validate the FEM model developed. The SMA wires were simply embedded but not activated for this test.

Table 3. Element selection for SMA composite plates

	$[0/(45/-45)_2/0]$	$[0/(45/-45)_4/0]$	$[0/(45/-45)_6/0]$
CLT[1]	235.75	264.43	269.88
FSDT[1]	233.8	261.98	267.33
3x3	236.49	270.06	264.70
4x4	234.07	262.29	267.45
5x5	233.78	261.99	267.34
6x6	233.72	261.92	267.27
7x7	233.70	261.88	267.25
8x8	233.69	261.88	267.24

[1]Reddy [10]

Comparing the results to the analytical results of the classical lamination theory (CLT) and FSDT of composite plates [10], Table 3 shows quick convergence that occurs in this finite element analysis for all three SMA composites. In this study, the decision was to use the 6x6 mesh.

The effect of the angle of orientation. This study is to see the effect of the angle of orientation of the SMA wires with respect to the loading direction on the critical loads. The angle of orientation of the SMA composite plates is $[\alpha/(45/-45)_5/\alpha]$ where α is the angle of orientation for the nitinol wires that is to be varied. Fig. 1 shows plots of critical load, P_{cr} against α for cases of composite plates without SMA, with non-activated SMA and with activated SMA.

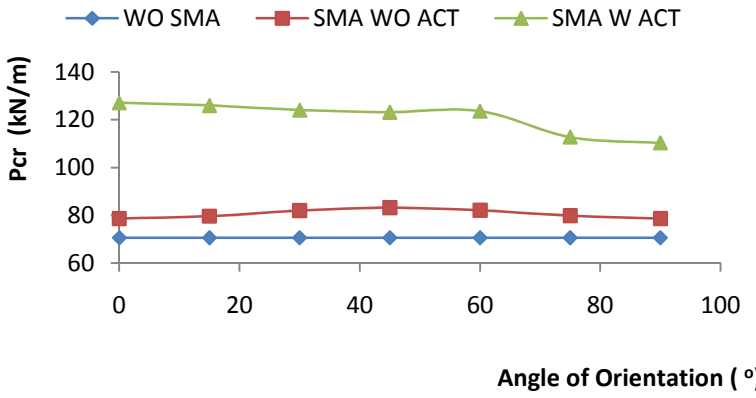


Fig. 1: The effect of the angle of orientation of the SMA on the critical loads

It is clear that with the activation of SMA wires, the P_{cr} increases significantly and the values of P_{cr} can be seen to decrease with the increase of the angle of orientation of the SMA, α. The effect of SMA can be measured through a quantity called the relative critical load (RCL) [8] which is the ratio between the critical load of the composite plate with SMA and the critical load of the plate without SMA. Fig. 2 shows that the highest RCL is 1.8 correspond to $\alpha = 0^0$ while the RCL for plate with non-activated SMA occurs at $\alpha = 45^0$.

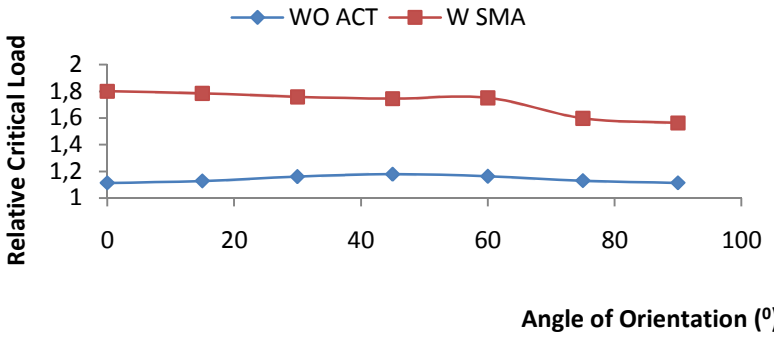


Fig. 2: The effect of the angle of orientation of the SMA on the RCL

The effect of the side to thickness ratio. Fig. 3 shows the graphs of the RCL against the angles of orientations of the SMA for several values of the side to thickness ratio, a/t. It can be seen that the relative effect of the SMA on the critical loads of the composite plates is greater for thin plates. Again, the RCL is seen to decrease as the angles of orientations of the SMA wires are increased.

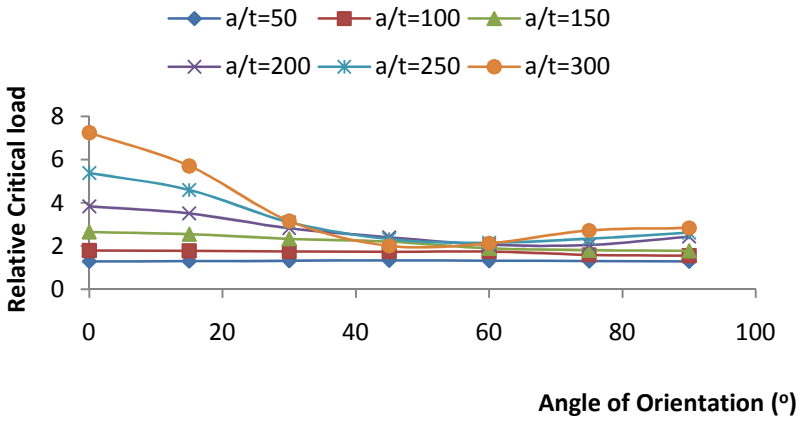


Fig. 3: The effect of the side to thickness ratio on the RCL

The effect of the boundary conditions. The effect of the boundary conditions (BC) on the critical loads of composite plates is studied for composites with angle of orientation of $[0/(45/-45)_n/0]$ where n varies from 1 to 7. In all cases, boundary conditions corresponding to loading sides are simply supported while BC for the other two sides varies between simply supported (SSSS) on both sides, one side simply supported and the other side clamped (SSSC) and both sides simply supported (SSCC). Fig. 4 shows that the critical loads are greater for the SSSC boundary conditions. Furthermore the critical loads can be seen to increase as the number of layers is increased. However, the relative effect of the SMA is greater for the SSSS boundary condition such as shown in Fig. 5. Fig. 5 also shows that the greatest RCL correspond to the SSSS boundary condition. The RCL also decreases as the number of layers is increased.

The effect of the SMA volume fractions. The effect of the volume fraction of the SMA on the postbuckling of the SMA composite plates is studied. The configuration of $[0/(45/-45)_3/0]$ is used in this study while the volume fraction of the SMA is varied from 10% to 50%. Fig. 6 shows the plots of the ratio of P_{cr}/P against the maximum lateral deflection of the plates for several values of SMA's volume fractions.

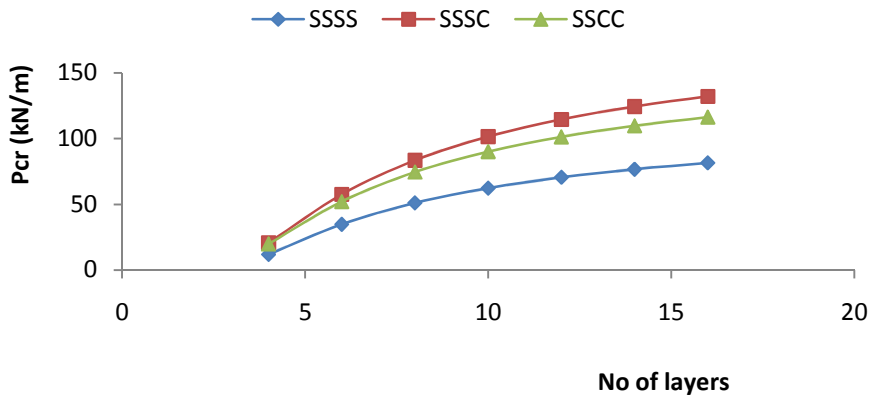


Fig. 4: The effect of the boundary condition on the critical loads

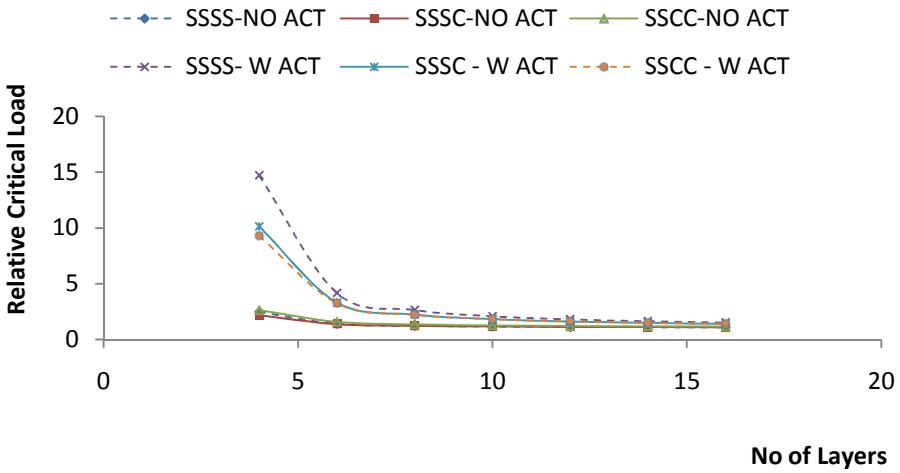


Fig. 5: The effect of the boundary conditions on the RCL

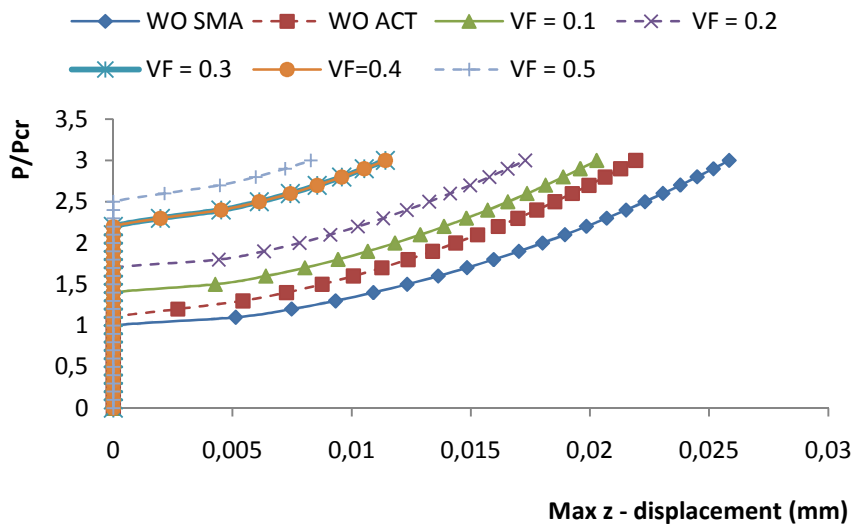


Fig. 6: The effect of the volume fraction of the SMA on the post buckling of composite plates

It can be seen that the bifurcation occurs at $P_{cr}/P = 1$ for the plate without SMA. Furthermore it is clear that as the volume fraction of the SMA is increased, the P_{cr} is increased too.

Summary

Studies on the effects of SMA on the buckling and postbuckling behaviours of laminated composite plates were conducted. From the linear analysis, it can be concluded that the orientation of SMA wires in the N-E layer that gives the highest improvement of buckling behavior is at at $\alpha = 0^0$. The effect of the SMA is also greater for the thin composite plates. The boundary condition of SSSS shows the highest improvement due to the SMA even though the boundary condition of SSSC gives the highest critical loads. Furthermore SMA provides a stable postbuckling path while increasing the postbuckling strength of the composite plates.

References

[1] K. Tanaka: Journal of Applied Mechanic Vol. 112 (1990), pp. 158-163.

[2] C. Liang and C.A. Rogers: Journal Intelligent Material and System Structure Vol. 1 (1990), pp. 207-1234.

[3] L.C. Brinson: Journal of Material and Devices Vol. 1(1990), pp 729-743.

[4] A. Zak, M.P. Cartmell, W.M. Ostachowicz and M. Wiercigroch: Smart Materials and Structures, Vol. 12 (2003), pp. 338– 346.

[5] J. Ro and A. Baz: Composites Engineering Vol. 5(1) (1995), pp. 77-90.

[6] S.P. Thompson J. Loughlan: Composite Structures Vol. 38 (1997), pp. 667-678.

[7] S.P. Thompson J. Loughlan: Thin walled structures. Vol. 36 (2000), pp. 231– 263.

[8] A. Zak, M.P. Cartmell and W. Ostachowicz: Journal of Applied Mechanics Vol. 470 (2003), pp. 313– 327.

[9] S.Y. Kuo, L.C. Shiau and K.H. Chen: Composite Structures Vol. 90(2)(2009), pp.188-195.

[10] C.A. Rogers, C. Liang and J. Jia: Computer and Structures Vol. 38(5-6) (2003), pp. 569-580.

[11] J.N. Reddy: *Mechanics of Composite Plates and Shells: Theory and Analysis* (CRC Press, New York 2002)

© (2011) Trans Tech Publications, Switzerland
doi:10.4028/www.scientific.net/KEM.471-472.536

Thermal Buckling and Post-Buckling Improvements of Laminated Composite Plates using Finite Element Method

Zainudin A. Rasid[1,a] , Amran Ayob [3,b], Rizal Zahari [2,c], F. Mustapha [3,c], D.L. Majid [3,c] and Renuganth Varatharajoo[4,c]

[1] Department of Mechanical Engineering, Universiti Teknologi Malaysia, Kuala Lumpur, Malaysia

[2] Faculty of Mechanical Engineering, Universiti Teknologi Malaysia, Skudai, Johor, Malaysia

[3] Department of Aerospace Engineering, Universiti Putra Malaysia, 43400 UPM Serdang, Selangor Malaysia

[a]zainudin@ic.utm.my, [b]amran@fkm.utm.my, [c]rizal@eng.upm.edu.my

Keywords: Shape memory alloy, laminated composite plates, non-linear finite element model, thermal buckling and thermal post-buckling

Abstract. Thermal buckling and thermal post-buckling behaviours of laminated composite plates are improved by embedding shape memory alloy wires within laminates of composite plates. The procedure is to use the recovery stress that is induced when the reverse transformation of the shape memory alloy from martensite to austenite phases is constrained. For aerospace applications where the source of the shape memory alloy heating is the high temperature environment itself, a study is conducted to see the effect of shape memory alloy in improving the thermal buckling and post-buckling of composite plates. Due to the temperature dependent nature of the composite matrix and the shape memory alloy, the finite element formulation developed here is in the incremental form. Solving this non-linear model using the developed in-house source code, critical loads are determined and the post-buckling paths of the shape memory alloy composite plates are traced. This study shows that by embedding the shape memory alloy within composite plates, the thermal buckling and post-buckling behaviours of composite plates can be improved substantially.

Introduction

The problems of thermal buckling and post-buckling of composites is important in aerospace industry since many aerospace structural components that are thin and curvy are subjected to thermal compressive loading. These buckling behaviours can be improved by using a smart material called the shape memory alloy (SMA). The shape memory effect behaviour of the SMA induces stress that can increase the strain energy of the composite plate and in turn improve its buckling behaviours. Thermal buckling of laminated composite plates was studied using the finite element method by researchers such as Chang [1] and Chen et al [2]. They showed that for symmetric angle-ply composite plates, the maximum critical load occurred at the angle of orientation, $\theta = 45^0$ while these critical loads vary symmetrically about $\theta = 45^0$. The thermal post-buckling path of laminated composite plates can be determined either by conducting the geometric nonlinear analysis or by solving a sequence of linear eigen-value problems [3]. Singha et al [4] considered the temperature dependent properties and the linearly varying temperature rise through the thickness of the plates while studying thermal post-buckling composite plates. Kumar and Singh [5] used the layerwise theory of composite plates to study the effect of varying several composite parameters such as the side-thickness ratio, fibre orientation, aspect ratio, stacking sequence and boundary condition on the thermal buckling of the SMA composite plate. It was found that the critical temperatures were enhanced by the addition of the SMA. The studies on the effect of SMA on the post-buckling behaviour of laminated composites were conducted by Tawfik et al [6] and Park [7]. The effects of

SMA parameters such as the initial strain of the SMA and the volume fraction of the embedded SMA were studied. It was proven that SMA fibres can significantly improve the post-buckling behaviour of laminated composites.

In this study, the work of Park [7] is extended to different types of composite lamination schemes. The geometric nonlinear finite element model is developed to represent the thermal post-buckling behaviour of composite plates. The source of activation for the SMA is the heat from the environment. As such the incremental formulation is used to cater the temperature dependent properties of the composites [7] and SMA. This study uses the experimental values of recovery stress and Young's modulus that are taken from Cross et al [8]. The study is conducted on the anti-symmetric angle-ply composite plates. The effects of several composite related and SMA related parameters on the thermal buckling and post-buckling of composite plates are studied.

Finite Element Formulation

The incremental formulation developed here considers the effects of the recovery stress, temperature, thermal degradation properties of matrix and the initial stress and strain. Furthermore, the effective properties of the SMA composite are determined using the rule of mixture.

Strains. Using the Mindlin's first order shear deformation theory [9] while including the von Karman's strain terms, the incremental strain can be expressed as

$$\{\Delta\varepsilon\} = \begin{Bmatrix} \Delta\varepsilon_x \\ \Delta\varepsilon_x \\ \Delta\gamma_{xy} \end{Bmatrix} = \begin{Bmatrix} \dfrac{\partial \Delta u}{\partial x} \\ \dfrac{\partial \Delta \mathrm{v}}{\partial y} \\ \dfrac{\partial \Delta u}{\partial y} + \dfrac{\partial \Delta \mathrm{v}}{\partial x} \end{Bmatrix} + \frac{1}{2}\begin{Bmatrix} \left(\dfrac{\partial \Delta \mathrm{w}}{\partial x}\right)^2 \\ \left(\dfrac{\partial \Delta \mathrm{w}}{\partial y}\right)^2 \\ 2\left(\dfrac{\partial \Delta \mathrm{w}}{\partial x}\right)\left(\dfrac{\partial \Delta \mathrm{w}}{\partial y}\right) \end{Bmatrix} + \begin{Bmatrix} \left(\dfrac{\partial \Delta \mathrm{w}}{\partial x}\right)\left(\dfrac{\partial w_0}{\partial x}\right) \\ \left(\dfrac{\partial \Delta \mathrm{w}}{\partial y}\right)\left(\dfrac{\partial w_0}{\partial y}\right) \\ \left(\dfrac{\partial \Delta \mathrm{w}}{\partial x}\right)\left(\dfrac{\partial w_0}{\partial y}\right) + \left(\dfrac{\partial \Delta \mathrm{w}}{\partial y}\right)\left(\dfrac{\partial w_0}{\partial x}\right) \end{Bmatrix} + z\begin{Bmatrix} \dfrac{\partial \Delta\theta_x}{\partial x} \\ \dfrac{\partial \Delta\theta_y}{\partial y} \\ \dfrac{\partial \Delta\theta_x}{\partial y} + \dfrac{\partial \Delta\theta_y}{\partial x} \end{Bmatrix} \quad (1)$$

or

$$\{\Delta\varepsilon\} = \{\Delta\varepsilon_p\} + z\{\Delta\kappa\}$$

$$= \{\Delta\varepsilon_m\} + \{\Delta\varepsilon_{nl}\} + \{\Delta\varepsilon_o\} + z\{\Delta\kappa\} \quad (2)$$

where $\{\Delta\varepsilon_m\}$, $\{\Delta\varepsilon_{nl}\}$, $\{\Delta\varepsilon_o\}$ and $\{\Delta\kappa\}$ are the incremental in-plane linear strain vector, the incremental in-plane nonlinear strain vector, the incremental in-plane vector due to the initial deflection and the incremental curvature strain vector, respectively. Δu, $\Delta \mathrm{v}$ and $\Delta \mathrm{w}$ are the incremental displacements in the x, y and z directions respectively. w_0, $\Delta\theta_x$ and $\Delta\theta_y$ are the total initial deflection, incremental rotation in the xz-plane and the incremental rotation in the yz-plane respectively.

Finite element implementation. Eight noded isoparametric quadrilateral elements with each node carries 5 degrees of freedom are used in this study. FEM governing equation for the thermal post-buckling of SMA composite plates is

$$\left([K_L] + [K_s] - [K_{\Delta T}] + [K_{\Delta r}] + [K_0] + [K_{w0}] + \frac{1}{2}[N1] + \frac{1}{2}[N1_{w0}] + \frac{1}{3}[N2]\right)\{\Delta q\} = \{P_{\Delta T}\} -$$

$$\{P_{\Delta r}\} - \{P_0\} - \{P_{w0\Delta T}\} - \{P_{w0\Delta r}\} - \{P_{0w0}\} \quad (3)$$

where $\{\Delta q\}$ is the incremental nodal displacement vectors. $[K_L]$ and $[K_s]$ are the linear membrane and shear stiffness matrices, respectively. $[K_{\Delta T}]$ and $[K_{\Delta r}]$ are the incremental temperature and recovery stress matrices respectively. $[K_0]$ and $[K_{w0}]$ are the initial stiffness matrix and the initial stiffness matrix due to initial deflection respectively. $[N1]$, $[N1_{w0}]$ and $[N2]$ are the first order non-linear stiffness matrix, first order non-linear stiffness matrix due to initial deflection and the second order non-linear stiffness matrix respectively. $\{P_{\Delta T}\}$ and $\{P_{\Delta r}\}$ are the incremental temperature and recovery force vectors respectively. $\{P_{w0\Delta T}\}$, $\{P_{w0\Delta r}\}$ and $\{P_{0w0}\}$ are the vectors of forces due to the coupling of initial deflection and temperature increment, initial deflection and recovery stress increment and initial deflection and initial load respectively. Equation (3) is a nonlinear equation that can be solved using the Newton Raphson's method.

Dimensions and properties. In this study the effects of SMA on buckling behaviours are studied on anti-symmetric angle-ply composite plates such as shown in Fig. 1.

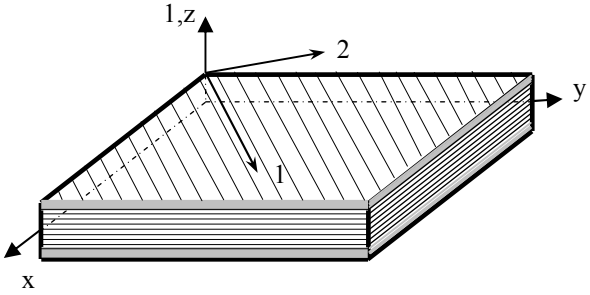


Fig. 1: SMA composite plate (▭ : GE layer, ▭ :N-GE layer]

The angle of orientation of the composite is $[\alpha/\text{-}\alpha]_n$ where n = 3 in most cases. Nitinol wires are embedded at the outer most layers of the lamination so that the SMA layers consist of nitinol and matrix graphite-epoxy (N-GE) while other layers are merely matrix graphite-epoxy (GE) layers. The plate is 100 mm length and 100 mm width while the side to thickness ratio, $\frac{a}{t} = 200$. The volume fraction (VF) of nitinol in a N-GE layer is specified case by case. The immovable edge (HH) and the simply supported (SS) boundary conditions are used in this study. The properties for the graphite-epoxy and SMA are given below. Notice that the properties for graphite-epoxy are temperature dependent where $dT = T - T_{ref}$ and $T_{ref} = 24^0C$.

Matrix (GE) property :

$E_1 = 40\text{E}9(1 - 3.53(10^{-4})dT)\text{Pa}, \text{E}_2 = 1\text{E}9(1 - 4.27(10^{-4})dT)\text{Pa}, \upsilon_{12} = 0.22,$
$\text{G}_{12} = 0.6\text{E}9(1 - 6.06(10^{-4})dT)\text{Pa}, \text{G}_{13} = \text{G}_{12}, \text{G}_{13} = 0.5\text{E}9(1 - 6.06(10^{-4})dT)\text{Pa},$
$\alpha_1(1/\,^0\text{C}) = -0.07(10^{-6})(1 - 1.25(10^{-3})dT),\ \alpha_2(1/\,^0\text{C}) = 30.1(10^{-6}))(1 + 0.41(10^{-3})dT)$

SMA property :

$$\upsilon = 0.33, \alpha\left(\frac{1}{^0\text{C})}\right) = 10.26(10^{-6})$$

Results and Discussion

Element Selection and Validation. An element selection test was conducted on SMA composite plates to determine the appropriate mesh size for the buckling analysis, besides providing the validation to the model developed. Table 1 shows three configurations of composite plates without SMA that are used for the element selection test: $[45/45]_2$, $[45/\text{-}45]_s$ and $[45/\text{-}45/0/90]_s$. The critical thermal buckling loads (ΔT_{cr}) are represented in the non-dimensional form of $\lambda = \alpha_2 \Delta T_{cr}(\frac{a}{t})^2$. It shows that the results from the current analysis are in good agreement with the referenced results. It was decided that the 6x6 configuration will be used in this study.

Table 1: The non-dimensional critical loads of composite plates without SMA

Configurations	$\lambda = \alpha_2 T_{cr} (\frac{a}{t})^2$					
	Ref.	4x4	5x5	6x6	7x7	8x8
$(45/-45)_s$	**[10]** 9.2398	10.162	9.574	9.427	9.341	9.292
$(45/-45)_2$	**[10]** 11.5031	11.573	11.535	11.533	11.529	11.527
$(0/45/-45/90)_s$	**[7]** 20.085	21.073	20.716	20.603	20.561	20.543

A post-buckling analysis of laminated composite plate was conducted for the configuration of $[45/-45]_2$. Fig. 2 shows that the results of the present analysis agree excellently to the results of Singh et al [3].

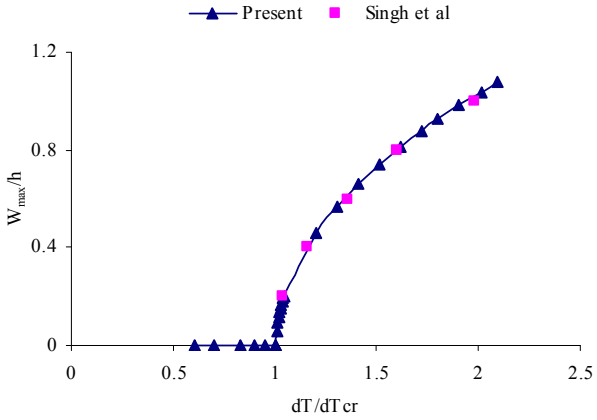


Fig. 2: The thermal post-buckling of anti-symmetric angle-ply composite plate

The effect of the angle of orientation. The effect of the angle of orientation of the SMA wires on the critical temperature of SMA composite plates is studied here. The lamination scheme of the SMA composite plates is $[\alpha/-\alpha]_3$ where α varies from 0^0 to 90^0. The volume fraction of the SMA in each SMA layer is 10%. Fig. 3 shows plots of critical temperature, ΔT_{cr} against angle of orientation for cases of composite plates without SMA and with activated SMA.

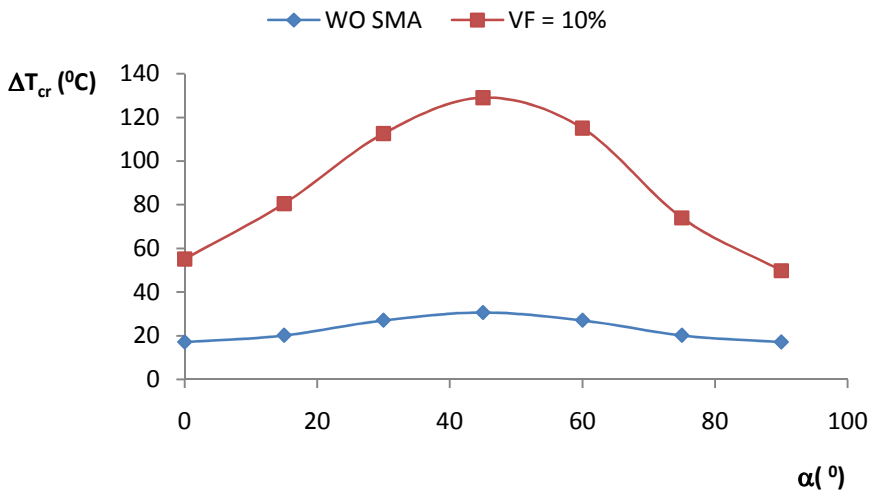


Fig. 3: The effect of the angle of orientation of the SMA on the critical loads

It is clear that SMA can increase the critical temperature, ΔT_{cr} significantly. Obviously, the critical temperature is maximum at $\alpha = 45^0$.

The effect of the boundary conditions. The effect of the boundary conditions on buckling behaviours of SMA composite plates is studied. The angle of orientation of composites is $[45/-45]_3$. The volume fraction of SMA within the SMA layers is 5%. Two types of BC are used i.e the HH and the SS boundary conditions. The plots of the ratio of the maximum deflection over thickness, w_{max}/t against temperature, T in Fig. 4 show that the critical loads are greater for the case of SS boundary condition. Furthermore the amount of shifts of the post-buckling paths created by the addition of the SMA in both cases is almost the same.

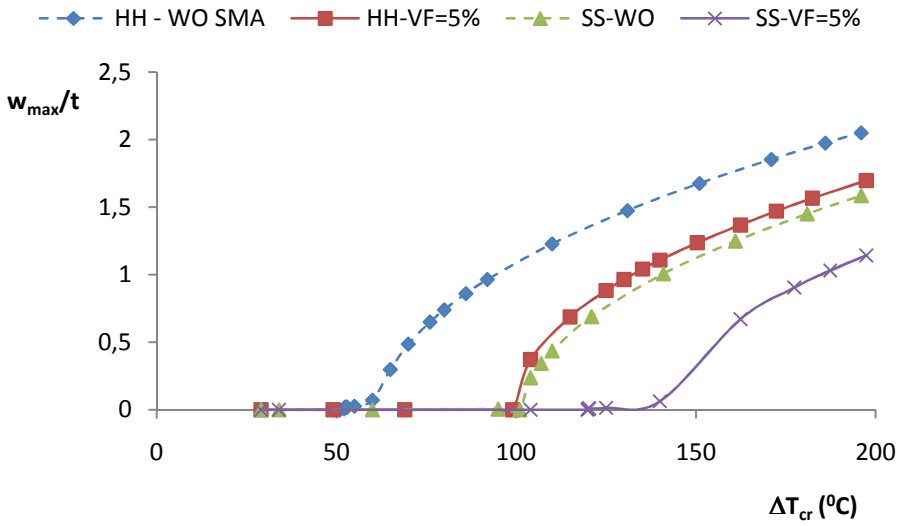


Fig. 4: The effect of the boundary conditions on the post-buckling SMA composite plates

The effect of the SMA volume fraction. The effect of the volume fraction of the SMA on the post-buckling of the SMA composite plates is studied. The configuration of $[45/-45]_3$ is used in this study while the volume fraction of the SMA is varied from 3% to 10%. Fig. 5 shows the plots of the w_{max}/t against T of the composite plates for several values of SMA's volume fractions.

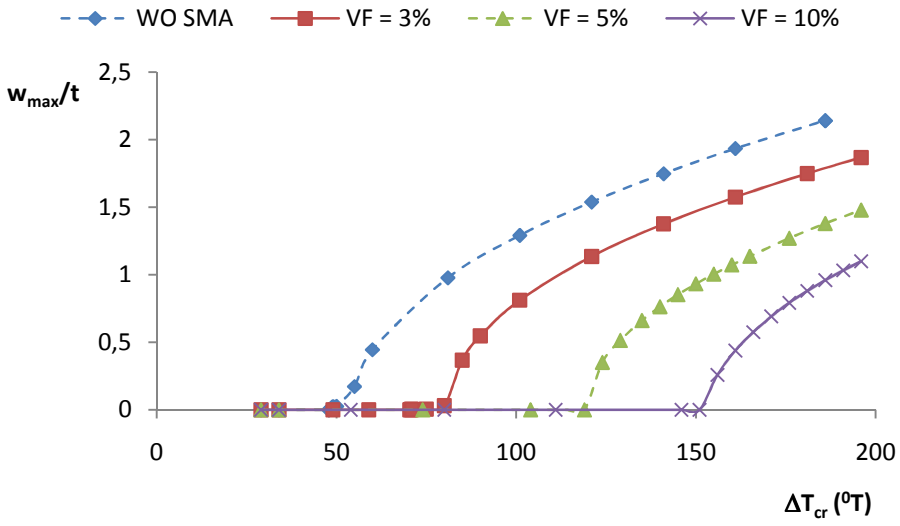


Fig. 5: The effect of the volume fraction of the SMA on the post buckling of composite plates

It can be seen that the post-buckling remain stable with the additions of SMA up to 10% in the SMA layers. The increase of volume fraction of SMA has greatly shifted the critical temperature and the post-buckling path to the right.

The effect of the initial strain. The amount of initial strain (IS) of the SMA wires before they are activated determines the amount of recovery stress induced. The effect of the initial strain on the post-buckling behaviour is studied. Fig. 6 shows the significant amount of shifts of the critical temperatures and the post-buckling paths when the initial strain is increased.

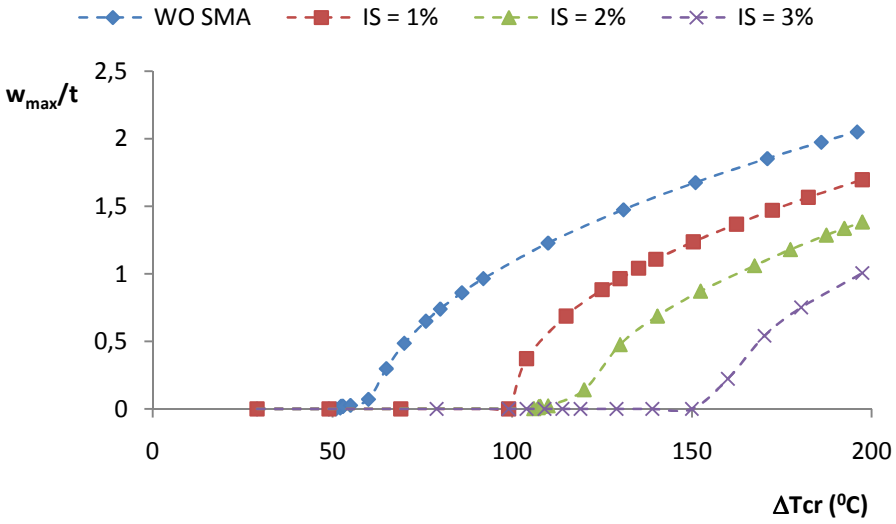


Fig. 6: The effect of the initial strain of the SMA on the post-buckling of composite plates

Summary

Studies on the effects of SMA on the thermal buckling and post-buckling behaviours of laminated composite plates were conducted. It was shown that SMA can make significant increase in the critical temperatures and also significant stable shift of the post-buckling path to the right. In the study on the effect of the angle of orientation of SMA wires on the critical temperatures, it was shown that that the highest improvement of critical temperature occurs at $\alpha = 45^0$. The simply supported boundary condition gives the higher post-buckling path as compared to the hinged boundary condition. Furthermore the increase of volume fraction of the SMA of up to 10% and the increase of initial strain of the SMA of up to 3% can significantly shift the post-buckling paths to the right.

References

[1] J. S. Chang: Computer and structures Vol. 37 (1990) pp. 925– 946

[2] W. J. Chen, P. D. Lin and L.W. Chen: Computer and structures Vol. 41 (1991) pp. 637– 645

[3] G. Singh, G.V. Rao and N. G. R. Iyengar: AIAA Journals Vol. 59(1993) pp. 1336– 1338

[4] M. K. Singha, L. S. Ramachandra and J. N. Bandyopadhyay : Composite Structures Vol. 54 (2001) pp. 453-458

[5] S. K. Kumar and B. N. Singh: Journal of Aerospace Engineering Vol. 22 (2009) pp. 342-353.

[6] M. Tawfik, J .J. Ro and C. Mei: Smart Material Structure Vol. 11 (2002) pp. 297-307.

[7] J. S. Park : Composite Part B: Engineering Vol. 36 (2005) pp. 627-636

[8] W. B. Cross, A. H. Kariotis and F. J. Stimler, NASA CR – 1433. (1970)

[9] J.N. Reddy: *Mechanics of Composite Plates and Shells: Theory and Analysis* (CRC Press, New York 2002)

[10] V.S. Thankam, G. Singh, G.V. Rao, and A. K. Rath : Composite Structures Vol. 59 (2003) pp. 351– 359

© (2011) Trans Tech Publications, Switzerland
doi:10.4028/www.scientific.net/KEM.471-472.542

Impedance Characteristics of Electrospun Nylon-6/TiO_2 Nanocomposite for Humidity Sensor

Alireza Hosseinmardi[1, a], M. Keyanpour-Rad[1, b] and F. Alikhani Hesari[1, c]

[1]Department of Nano Technology and Advance Materials,

Materials and Energy Research Center (MERC), P.O. Box 14155-4777, Tehran, Iran

[a]arhm1364@gmail.com, [b]m_kianpourrad@yahoo.com,[c]hessarifa@gmail.com

Keywords: Nanocomposite, Humidity sensor, Interdigital electrode, Nanofibers, Electrospinning.

Abstract. Resistive relative humidity (RH) sensors were fabricated by nano composites of nylon-6 and titanium dioxide nanopowders. The results indicated that these sensors can be fabricated as a reliable, low cost and fast response instruments. Different percentages of nylon-6 and TiO2 were studied and average diameters of the resultant nanofibers were found the 80 to 120 nm. The nano composite of nylon-6/TiO_2 nanofibers was electrospun on the interdigital gold electrode on the glass substrate. It was found that the impedance of the mat ranged from 10^7 Ω to 10^2 Ω while the relative humidity was increased from 11% RH and 97.3% at room temperature. Transition electron microscopy (TEM) and scanning electron microscopy (SEM) were used to study the morphology of the nano composite.

Introduction

The electrospinning technique is a comparatively simple, low cost and multi applicable process for making continues sub-micron to nano scale polymeric fibers in the nonwoven mat form. Therefore, the resulting electrospun fibers take advantage of large surface area to volume and also high porosity [1-3]. In this process, a high voltage is applied to a slowly ejected polymer solution moving in a strong electric field, and when the electrical force is higher than the surface tension of the solution, a charged jet of fluid reaches its critical point and the polymeric fibers are erupted toward the collector. During electrospinning process the jets lose their solvent and become thin and nano metric in size [4-6].

Relative humidity sensors have many applications in meteorology like measuring relative air humidity, forecasting the weather and also applied in food, drug, electronic and agricultural industries. Consequently, design and fabrication of reliable and cost-effective humidity sensor have attracted considerable attention, especially in recent year [7-9]. Fabrication of humidity sensors by polymers, ceramics or composite membrane is very common and the unique characteristics of these kinds of sensors characterized by two distinct properties, namely changing electrical resistance of the polymeric membrane or capacity with respect to humidity increase [10, 11]. Recently the attention has been paid to the advantages of resistive kind of polymeric humidity sensors such as simple and low cost fabrication, fast response, reliability [12, 13].

Nylon-6, $[-NH(CH_2)_5CO-]_x$ is one of the popular synthetic polymers in industry which possess excellent mechanical and aberration properties and also takes advantage of good chemical resistivity, simple and cheap method of production. It can absorb up to 2.4% water which makes this polymer an excellent candidate for fabricating humidity sensors [14, 15]. Polymeric resistance humidity sensors are usually fabricated from polymer electrolytes or a polymer-salt complex. Nylon-6 is considered as an electrolyte polymer which its electrical resistance decreases by absorbing water molecules [15, 16].

Among metal oxides, titanium dioxide (TiO_2) has found many applications in dye solar cells, photo catalysts, gas sensors, optical filters and also is used as an antibacterial agent [17-21]. Extensive researches have been done for investigating the relations of morphology and crystallite

types of TiO_2 and its humidity sensing properties. Different morphologies of TiO_2, such as thin and thick films, nanopowder and electrospun nano fibers have been used for fabricating humidity sensors. It has been reported that TiO_2 nanofibers containing anatase and rutile phases show better humidity sensing properties [22-24].

In this paper, we report, for the first time, an attempt to prepare humidity sensor with nanocomposite of electrospun nylon-6/TiO_2 nanopowder as the membrane. The variation of electrical impedance with respect to relative humidity was also investigated.

Experimental procedure

TiO_2 nanopowder with average diameter of 21 nm (Degussa P25) was completely dispersed with the aid of ultrasonic probe (Sartorius stedim, LABSONIC® P) in 90% formic acid (BDH chemical Ltd). Nylon-6 pellets (99.5% purity, Asia Int'l Enterprise) were added to the solution and stirred at ambient temperature for 3 hours. A stable solution resulted which was poured into a 50 ml syringe with steel needle (inner diameter of 0.495 mm (21G) and length of 0.5 inch). The solution was electrospun with a constant feed rate (by syringe pump, top-3500) of 0.2 ml/h at the positive voltage of 20 KV (Glassman High Voltage Inc). The distance from needle to collector were fixed at 15 cm. Different percentages of nylon-6 and TiO_2 nanopowder were used in the experiments which are listed in table 1.

Table 1: List the weight percentage of nylon-6 and TiO2 nanopowder.

Samples	Nylon-6 wt%	TiO_2 nanopowder wt%
Ny 15/Ti 0	100% (Nylon-6 15 Wt %)	0
Ny 15/Ti 2	98% (Nylon-6 15 Wt %)	2
Ny 15/Ti 5	95% (Nylon-6 15 Wt %)	5
Ny 20/Ti 5	95% (Nylon-6 20 Wt %)	5

Ceramics that used as substrates have good thermal and chemical stability so they can be applied as reliable substrates for humidity sensors [25]. Therefore in this work pure gold was coated on the glass substrate. The six pairs of Interdigitated electrodes (5 mm × 7.5 mm with electrodes width and distance: 0.195mm) were fabricated by laser (YAG-50). Fig. 1a shows the image of interdigital electrode on the ordinary glass substrate. Complex impedance was measured by Auto lab and the the voltage applied in our studies was alternative current (ac) 1 V, and the frequency varied from 100 Hz to 1 MHz. The RH laboratory atmosphere was set at 25 % RH and 25˚C using a conventional fan. The fix humidity chambers have been prepared using a super saturated salt solution. LiCl, $MgCl_2.6H_2O$, $Mg(NO_3)_2.6H_2O$, NaCl, KCl, and K_2SO_4 which made 11%, 32.5%, 54%, 75%, 84.3% and 97.3% RH, respectively. It took 7 hours for the sensors in the chambers to be sure that the humidity reached the equilibrium value [26].

The morphology of the spun fibers was investigated by Scanning Electron Microscope (SEM, Philips XL30), Transmission Electron Microscopy (TEM, Philips CM200) and Optical Microscopy (OM, Olympus DP72). The phases and crystalline structure of the samples were studied with X-ray Diffraction (XRD, unisantis-XMD300). Average diameter of nanofibers was measured from 100 taken randomly of the nanofibers, using SEM image with magnification of 10Kx with help of ImageJ software.

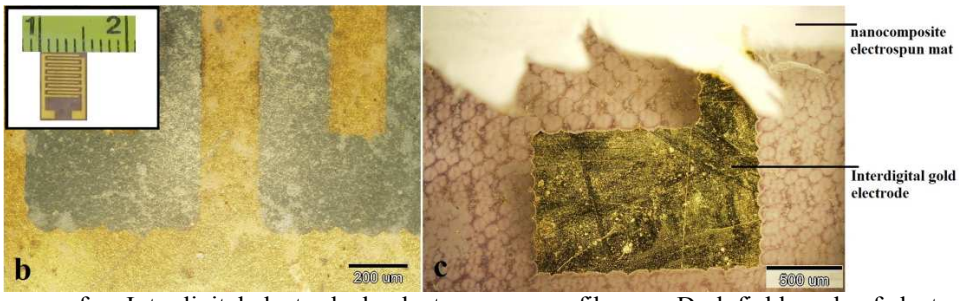


Fig. 1: a.OM image of: a. Interdigital electorde, b. electrospun nano fibers, c. Dark field mode of electrode and mat interface

Results and Discussion

Interdigital electrode was fixed on the aluminum collector and nano composite fibers directly were electrospun on it as is shown in Fig. 1b. Fig. 1c shows OM image of the interface between electrode and electrospun mat by dark field mode.

Fig. 2 presents the SEM images and histogram plots of nano fiber diameter distribution of the samples. The mean diameter of samples Ny15/Ti0, Ny15/Ti2, Ny15/Ti5 and Ny20/Ti5 were calculated to be 108, 112, 80 and 119 nm, respectively.

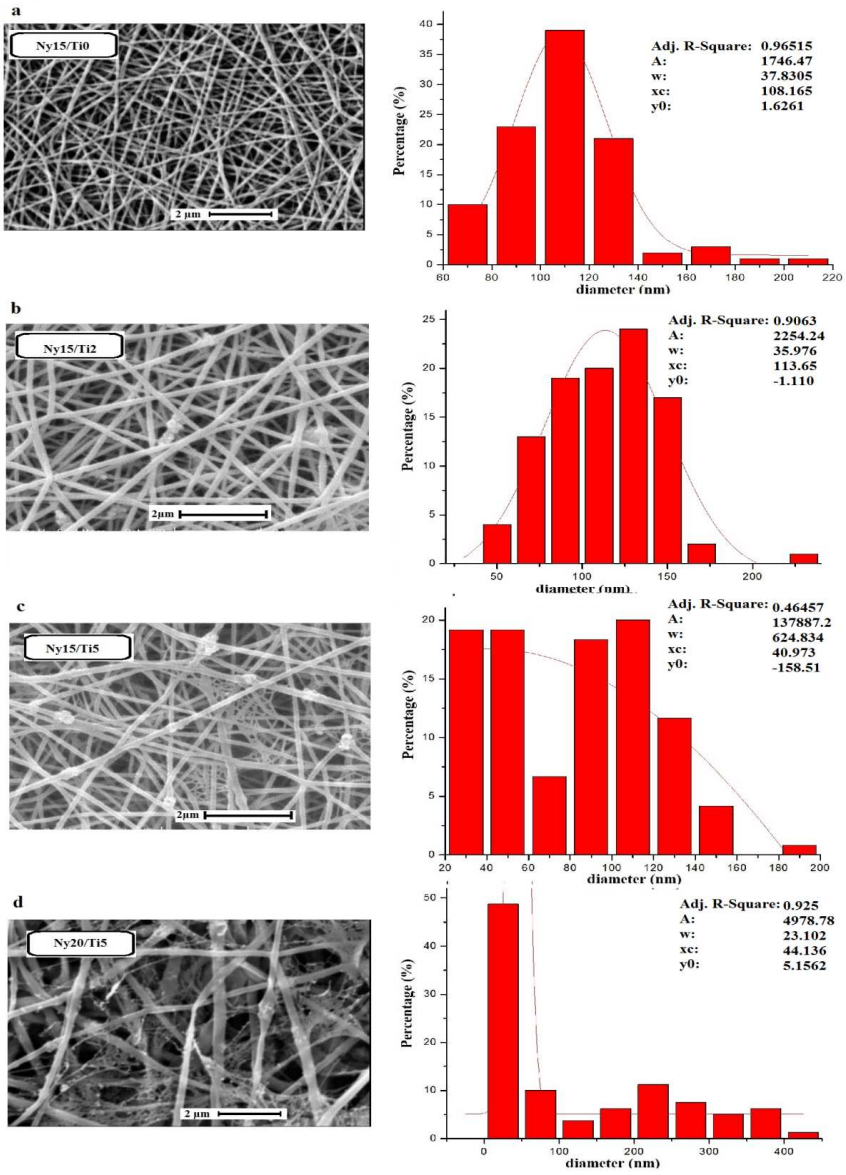


Fig. 2: SEM images, the histogram diagram of samples and Gaussian model for fitting the histograms of samples a. Ny15/Ti0, b. Ny15/Ti2, c. Ny15/Ti5 and d. Ny20/Ti5

The Gaussian model was fitted on histograms plots and it was found that adjusted square root (R-Square) were more than 90% in sample Ny15/Ti0, Ny15/Ti2 and Ny20/Ti5. The R-square of sample Ny15/Ti5 was deviated from Gaussian distribution model by 46% which show the sizes of fibers are not uniform in this sample. SEM images show smooth and beadles nano fibers in all samples. Nanopowder agglomeration can be observed by increasing the weight percentage of the nanopowder. The spider-net nano fiber structure was observed by increasing polymer concentration and weight percentage of nanopowder. The spider-net nano fibers are thinner fiber than smooth nanofibers [16, 27]. In viscous samples (Ny15/Ti5 and Ny20/Ti5) at Fig. 3c and d, spider-net nano fiber structure is obvious.

Fig. 3 shows TEM images of spider-net nanofibers structure in sample Ny20/Ti5. The diameter of spider-net nano fibers are about 4 to 12 nm which are distributed among the smooth and larger nanofibers. The main reason for forming spider-net nano fiber in viscous solution is instability of polymer jet at high voltage (20KV), free ions in solutions and hydrogen bonding [28].

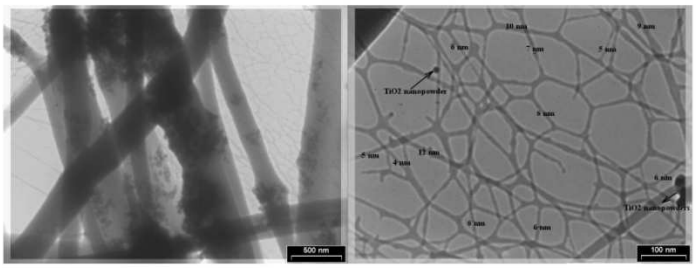


Fig. 3: TEM images of sample Ny5/Ti5 with different magnifications

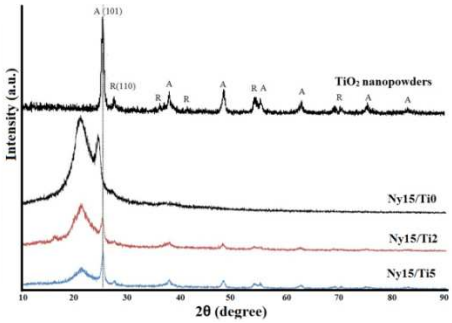


Fig. 4: XRD patterns of samples

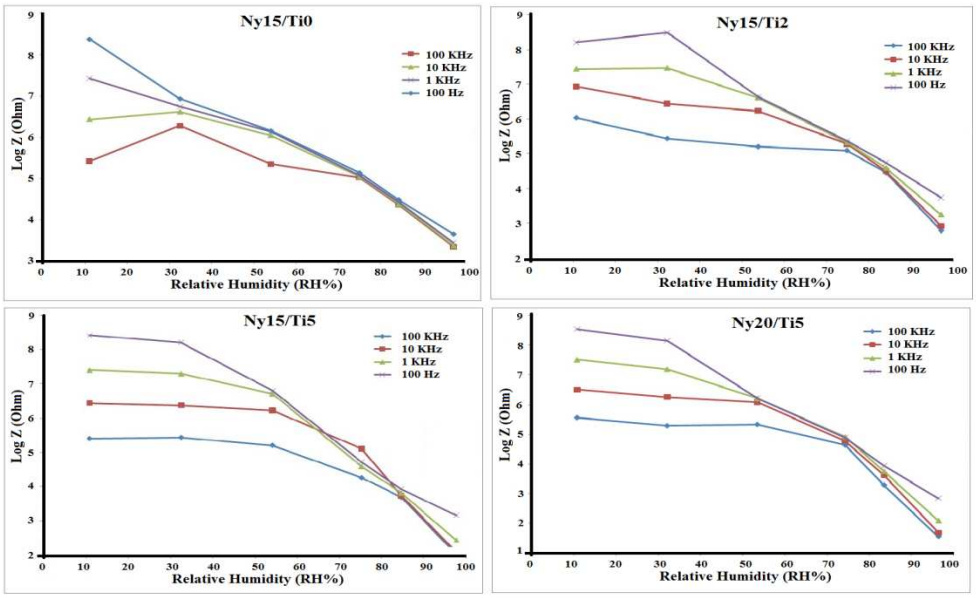


Fig. 5: Impedance verse relative humidity for samples at various frequencies.

Fig. 4 illustrated the XRD patterns of TiO_2 nano powders and samples. As it is clear the TiO_2 nanopowder consists of anatase and rutile structures as compare with JCPDS card No. 71-1167 and No. 78-1508. XRD pattern of Ny15/Ti0 can be well indexed to JCPDS card No.50-2235. The TiO_2 peaks appear in sample Ny15/Ti2 containing 2 wt% of titanium dioxide in XRD pattern of Fig. 4. The intensity of TiO_2 peaks raise when the weight percentage of nanopowder increases to 5 wt% in sample Ny15/Ti5.

Fig. 5 shows the dependences of logarithm of impedance (log Z) on relative humidity (%RH) at different frequencies of samples. It is observed that the impedance decreases by increasing of %RH.

Since the absorbed water cannot be polarized at high frequencies, the log Z turned flat [29]. At low RH, the frequency influence on the impedance was larger than at high RH.

Fig. 6 compares the log Z of samples at 1 KHz frequency in different levels of humidity. It is found that the electrical resistance decreased by increasing the humidity level. The log Z varies from around 7.5 to 2 when humidity changes from 11 %RH to 97.3 %RH as it is shown in Fig. 6. The impedance of the mate is same for all samples in low range of relative humidity (11 %RH). The effect of TiO_2 nanopowder addition in humidity sensing was evident at high level of RH. The log Z of samples Ny15/Ti0, Ny15/Ti2 and Ny15/Ny5 in 97.3 %RH is 3.45, 3.25 and 2.42 respectively. Increasing the weight percentage of TiO_2 nanopowder raises the humidity sensor sensitivity. The pristine nylon-6 nanofibers (Ny15/Ti0) showed the best linearity (y=-0.0446x+8.1806; R^2=0.9632), while Ny20/Ti5 had the best sensitivity among all samples. Log Z of sample Ny20/Ti5 in 97.3 %RH at 1 KHz is 2.08. The sensing improvement can be explained by existence of spider-net nano fibers with fiber diameter less than 10 nm, which increase the free surface area.

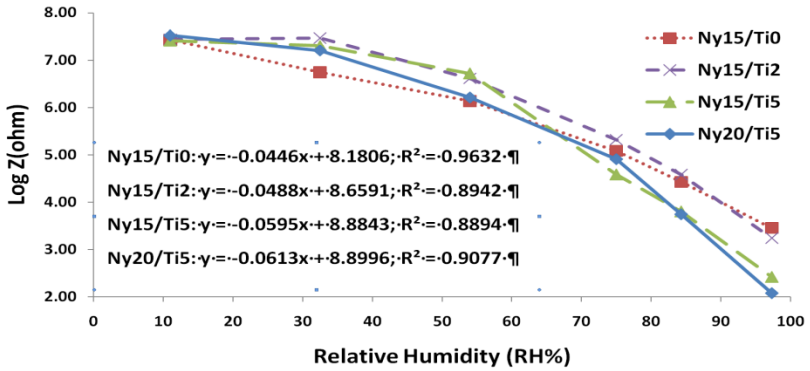


Fig. 6: Impedance verse relative humidity for samples Ny15/Ti0, Ny15/Ti2, Ny15/Ti5, Ny20/Ti5

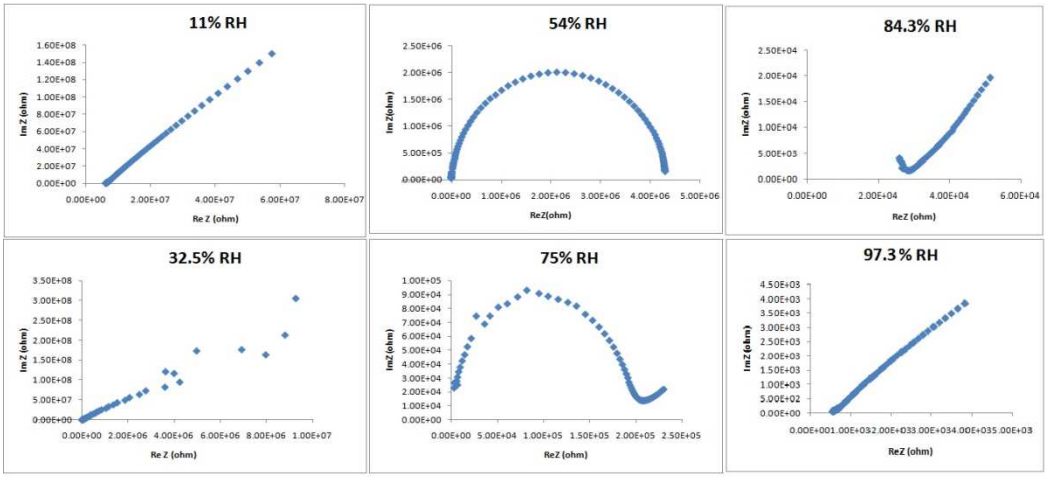


Fig. 7: Complex impedance plots of the Ny15/Ti2 at different relative humidity percentage.

The analysis of complex impedance plots was used to study the sensing behavior of humidity sensor. Fig. 7 shows the Complex impedance plots of the Ny15/Ti2 at different relative humidity and the frequency was changed from 100Hz to 1MHz. At low humidity level (11%, 32.5%, and 54%), a semi circle due to the electrospun mat impedance is observed. This semicircles show 'non-Debye' behavior. At high level of humidity a longer line and smaller semi circles are absorbed which presents 'Warburg impedance'[22].

As relative humidity increases water molecules diffuse to the nylon-6 network and ionisable into proton (H^+) and hydroxyl ions (OH^-); consequently absorbed water molecules act as a source of protons ('ion transport' or 'proton effect') and increased the electrical conductivity of mat [30]. Otherwise water vapor molecules can make hydrogen bonding with C-H, C=O, N-H and N: in nylon-6 structures. H-bonding between polymer chains through water molecules have also been

suggested to contribute to the conductivity increase [31]. The relative humidity sensitivity of the ceramics is related to the water adsorption mechanism on the oxide surface. At low RH, conduction is due to proton tripping between hydroxyl ions on the first layer of chemical absorbed water; while at high RH protons hop between physical absorbed molecules [23].

Summary

In conclusions, nano composite of nylon-6/TiO_2 nanofibers have been synthesized by electrospinning method and it is successfully used as a membrane on the interdigital electrode for humidity sensor. The logarithm of impedance changes from 7.5 to 2. By increasing nylon-6 concentration and TiO_2 spider-net nano fibers have been produced with range of 4-12 nm. Addition of titanium dioxide caused increases the sensitivity of compare with pristine nylon-6 nanofibers. Ionic transport (proton effect) and hydrogen bonding are two suggested mechanisms which are increased the conductivity by rising of humidity. Therefore, this nanocomposite is a low cost and promising high-performance humidity sensor candidate

References

[1] N. Bhardwaj and S. C. Kundu: Biotechnology Advances Vol. 28 (2010), p. 325
[2] F. Jian, N. HaiTao, et al.: Chinese Science Bulletin Vol. 53 (2008), p. 2265
[3] D. H. Reneker and A. L. Yarin: Polymer Vol. 49 (2008), p. 2387
[4] D. Aussawasathien, J. Dong, et al.: Synthetic metals Vol. 154 (2005), p. 325
[5] J.-H. He, Y. Wu, et al.: Polymer Vol. 46 (2005), p. 12637
[6] S. Ramakrishna and K. Fujihara: *An Introduction to Electrospinning and Nanofibers* (World Scientific Publishing Co. Pte. Ltd., Singapore 2005).
[7] J. Steele, M.Taschuk, et al.: Sensors and Actuators B Vol. 140 (2009), p. 610
[8] B. C. Yadav, R. C. Yadav, et al.: Sensors and Actuators B Vol. 148 (2010), p. 413
[9] S. Si, S. Li, et al.: Chemical Physics Letters Vol. 493 (2010), p. 288
[10] P.-G. Su and L.-N. Huang: Sensors and Actuators B Vol. 123 (2007), p. 501
[11] E. Zampetti, S. Pantalei, et al.: Sensors and Actuators B: Chemical Vol. 143 (2009), p. 302
[12] B. Adhikari and S. Majumdar: Progress Polymer Science Vol. 29 (2004), p. 699
[13] M. Packirisamy, I. Stiharu, et al.: Sensor Review Vol. 25 (2005), p. 271
[14] J. E. MARK: *Polymer data handbook* (Oxford University Press, Inc., England 1999).
[15] B. Yang, B. .Aksak, et al.: Sensors and Actuators B Vol. 114 (2006), p. 254
[16] H. R. Pant, M. P. Bajgai, et al.: Materials Letters Vol. 64 (2010), p. 2087
[17] Q. Cheng, C. Li, et al.: Applied Surface Science Vol. 252 (2006), p. 4154
[18] B. Karunagaran, P. Uthirakumar, et al.: Materials Characterization Vol. 58 (2007), p. 680
[19] M. Y. Song, D. K. Kim, et al.: Synthetic Metals Vol. 155 (2005), p. 635
[20] C. J. Tavares, S. M. Marques, et al.: Thin Solid Films Vol. 517 (2008), p. 1161
[21] S. J. Doh, C. Kim, et al.: Journal of Hazardous Materials Vol. 154 (2008), p. 118
[22] H. Zhang, Z. Li, et al.: Talanta Vol. 79 (2009), p. 953
[23] K. P. Biju and M. K. Jain: Thin Solid Films Vol. 516 (2008), p. 2175
[24] P. G. Su and C. P. Wang: Sensors and Actuators B Vol. 129 (2008), p. 538
[25] Y. Miyoshi, K. M. a, et al.: Sensors and Actuators B: Chemical Vol. 142 (2009), p. 28
[26] T. Lu and C. Chen: Measurement Vol. 40 (2007), p. 591
[27] N. A. M. Barakat, M. A. Kanjwal, et al.: Polymer Vol. 50 (2009), p. 4389
[28] R. Nirmala, K. T. Nam, et al.: Applied Surface Science Vol. 256 (2010), p. 6318
[29] Q. Qi, Y. Feng, et al.: Sensors and Actuators B Vol. 139 (2009), p. 611
[30] G. Casalbore-Miceli, M. J. Yang, et al.: Solid State Ionics Vol. 131 (2000), p. 311
[31] F. Zeng, X. X. Liu, et al.: Sensors and Actuators B Vol. 143 (2010), p. 530

© (2011) Trans Tech Publications, Switzerland
doi:10.4028/www.scientific.net/KEM.471-472.548

A New Self Healing Method in Composite Laminates Using the Hollow Glass Fiber

Majid Nademi[1,a], Ali Mozaffari[2,b] and Amin Farrokhabadi[3,c]

[1]Department of Aerospace Engineering, KN Toosi University of Tech., Tehran, Iran

[2] Department of Aerospace Engineering, KN Toosi University of Tech., Tehran, Iran

[3] Department of Aerospace Engineering, Amirkabir University of Tech., Tehran, Iran

[a]majid_nademi@yahoo.com, [b]mozaffari@kntu.ac.ir, [c]amin-farrokh@aut.ac.ir

Keywords: Self-healing, Strength reduction, Healing efficiency, Hollow fiber

Abstract. The purpose of the present study is to obtain the least strength reduction and uttermost healing efficiency in a typical [(90/0)/(90/0)$_{Hollow}$/90/(0/90) $_{Hollow}$/90/(0/90) $_{Hollow}$/(0/90)] self-healing laminate. It has been done using a hollow glass fiber (HGF) with a given diameter and an individual method to distribute the HGF in the host laminate. The results of three-point bend flexural strength testing indicated that for the investigated distribution, the inclusion of HGF imparts little reduction in undamaged strength (4%) which is due to the non-integrity of self-healing laminate related to the host laminate. After healing it was found that the laminate had a residual strength of 97% compared to the undamaged control and 100% compared to an undamaged self healing laminate.

Introduction

Composite materials have wide applications due to their favorable properties such as strength and stiffness combined with lightness. These materials are susceptible to damage induced by mechanical, chemical, thermal, UV radiation, or a combination of these factors. The intra-ply matrix crack and inter-ply delamination are two major damage modes which couldn't be detect easily in laminated composites. Traditional repair methods are not effective for healing invisible microcracks within the structure during its service life. In this method, once the damage has been detected in a polymer composite, a temporary structural repair is used. These repair schemes changes from simplistic external patches to complex intrusive tapered or stepped scarf repairs with the aim of restoring some or all of the material's stiffness and strength. The concept of self-healing polymeric materials was proposed in the 1980s as a means of healing invisible microcracks for increasing the working life and safety of the polymeric components [1]. A self-healing material responds to the damage by applying an automatic repair mechanism. This mechanism acts without any interference of outside agent to restore the mechanical integrity of the material, whether that involves bridging a crack or sealing a hole. The most common approaches for autonomic self-healing of thermoset-based materials involve two approaches: 1- Storage of self-healing agents within a brittle vessel before the addition of the vessels into the polymeric matrix [2-4] and 2- A microencapsulated healing agent is embedded in a structural composite matrix containing a catalyst capable of polymerizing the liquid healing agent [1].

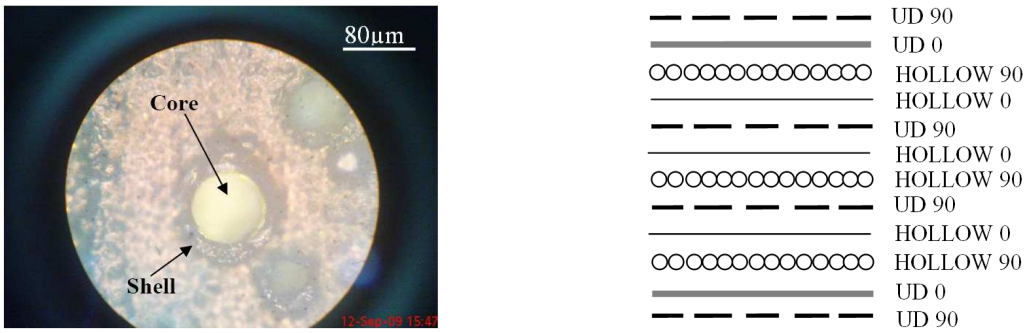
In the present study, using the second approach of self-healing, effects of hollow fiber diameters and their distributions in host laminate on stiffness/strength reduction and healing efficiency will be examined for a hand-made specimen.

Definition of present experiment approach. The E-glass unidirectional fiber (UD) with EPIKOTE828 epoxy resin is selected as the host laminate. The hand-made HGF for the self-healing laminate has the outer diameter of 80±7μm and a hollowness fraction (ratio of internal to external area) of 50% (Fig. 1-a). This HGF is manufactured by a specific method (extension of the heated

micro-tubes on a special machine) in the laboratory. The storage healing resin in hollow fiber is EPOLAM5015/5016 epoxy.

Two stacking sequence composites laminate is selected for investigation of healing in specimens. A $[90/0/90]_s$ E-glass UD/EPIKOTE828 epoxy resin without HGF is manufactured using a hand lay-up process for control laminate (nominal thickness of 4.5 mm). the volume fraction of fiber is %53.

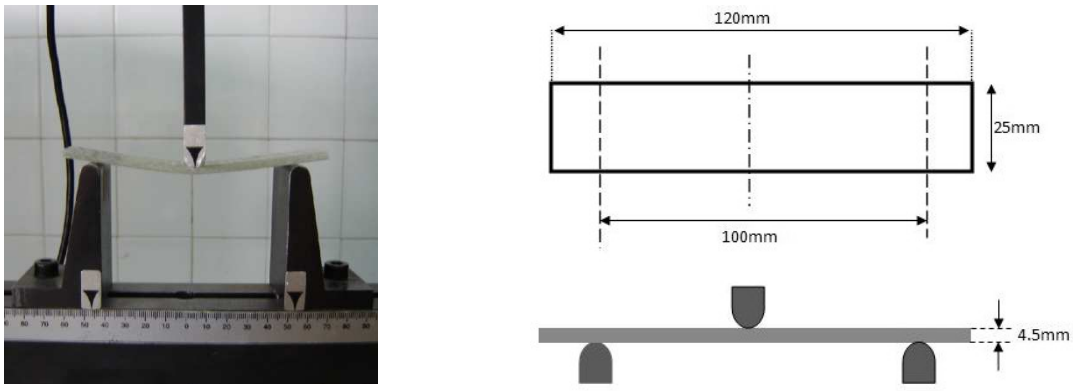
For the self-healing laminate specimens, some of the HGF is filled with healing agent (EPOLAM5015/5016) and distributed at the spacing of 300 μm in 0 directions and another HGF filled with hardener and distributed at the spacing of 700 μm in 90 directions. The HGF spacing in 0 and 90 directions is according to the proportion of resin/hardener (100/36) for healing agent. These [0/90] HGF laminate is located directly at the interface of 0 and 90 layers to produce the self healing laminate as shown in Fig. 1-b. The HGF volume fraction related to E-glass is 1.5 % in the host laminate. The stacking sequence of the mentioned laminate is $[(90/0)/(90/0)_{Hollow}/90/(0/90)_{Hollow}/90/(0/90)_{Hollow}/(0/90)]$ (Fig1-b).



(a) **(b)**

Fig.1: (a) Optical microscopy image of hollow glass fiber section, (b).The stacking sequence of the self-healing laminate

To characterize the strength of control laminate and self healing laminate, before and after damage, the three-point bend flexural strength test (ASTM D790M) with the rate of 3.2 mm/min is done (Fig. 2a). The specimen dimension for three-point bend test is shown in Fig. 2b. For each type of laminates, 10 specimens are tested.



(a) (b)

Fig. 2 (a).Experimental set-up for three-point bend, (b) dimension of test specimen

In order to specify the indentation load for damage formation in test specimens, the load–displacement curve of self-healing specimen is used as shown in Fig. 3. In this graph, during the indentation process, two load reduction points are occurred at approximately 1000 and 1250 N denoted by A and B symbols respectively. These load reduction points correspond to damage progress through the thickness of the laminate in the form of matrix cracking, delamination and hollow fiber fracture occurring at the ply interfaces. Under the load control, a peak load of 1250N is applied to initiate matrix shear cracks and delamination within the laminate. After the indentation,

the self-healing laminate specimen is permitted to heal according to its curing prescription (16 hours in $50°C$). In order to obtain similar conditions for control and self-healing laminates, control laminate is exposed in the same condition of self-healing laminate.

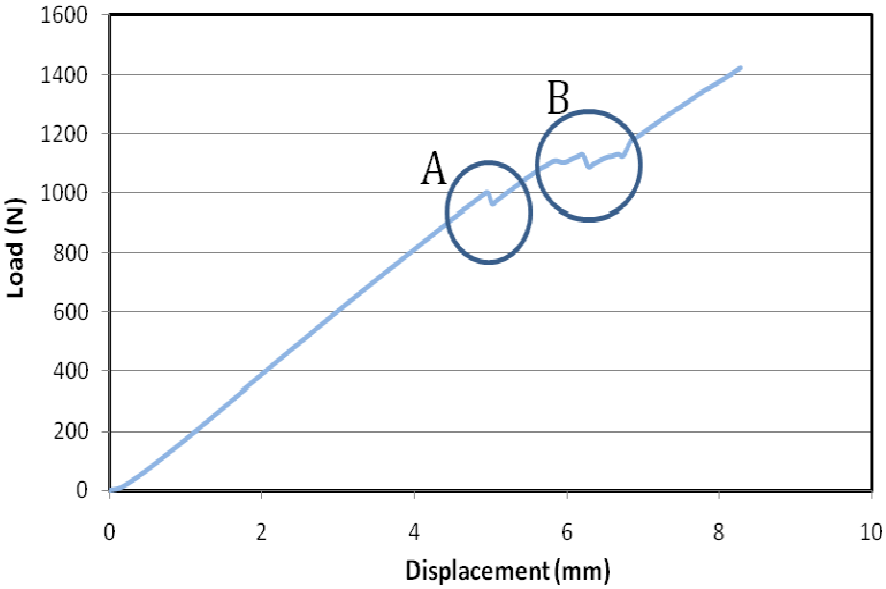


Fig. 3: The load- displacement curve of mentioned self-healing laminate

Results and Discussion

The result of three-point bend tests is obtained in Fig. 4 and Table1 for undamaged, damaged and healed specimens. The performance comparison is done between the HGF laminate and the control laminate without HGF. The obtained results show that the inclusion of HGF is caused to little strength reduction related to undamaged strength (4%) which is due to the non-integrity of self-healing laminate related to the host laminate. After healing operation, it was found that the laminate had a residual strength of 97% compared to the undamaged control and 100% compared to an undamaged self healing laminate.

The obtained results by previous works [2-4] show that in a self-healing laminate, by reduction the HGF volume fraction in host laminate, the self-healing efficiency reduces but the flexural strength of laminate is increased. This can be attributed to three effects [3]:

1. Distortion of the reinforcing fiber architecture.
2. Generation of resin rich regions.
3. Displacement of reinforcing fibers with non-structural HGF.

To improve the mentioned defects, in present study, the HGF-spacing increased to descend the HGF volume fraction and to lessen effects of mentioned above. The larger hollow fiber diameter also gives a significant volume for healing agent storage. Using a hollow glass fiber with a larger diameter of 80 μm and better HGF-spacing of 300-700 μm, it is shown that the mechanical properties of damaged laminate is improved related to previous works.

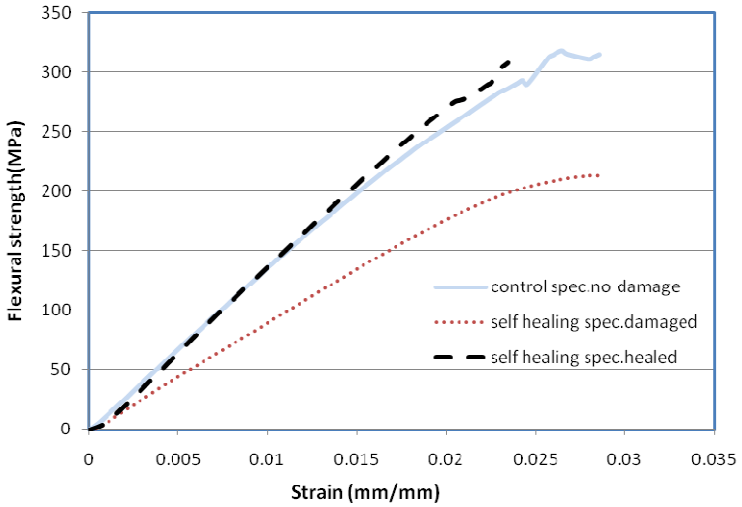


Fig. 4: Flexural strength- strain curves under 3-point bend for undamaged control laminate, damaged, and healed self-healing laminate

Table1. Summary of three- point bend flexural testing and healing efficacy for E-glass unidirectional composite laminate

Specimen Type	Flexural Strength (MPa)	Residual Strength (%) (compared to control laminate)	Residual Strength (%) (compared to self-healing laminate)
Control laminate – no damage	318	100	------
Self healing laminate – no damage	304	96	100
Control laminate – damaged (1250N peak load)	200	63	-------
Self healing laminate – damaged, no repair	214	68	71
Self healing laminate – damaged, healed 16 h at 50˚C	308	97	101

Summary

In this paper by using a hollow glass fiber (HGF) with a lager diameter in a self-healing laminate, the strength reduction and healing efficiency of laminate was measured. The results of three-point bend flexural strength testing indicated that for the distribution investigated, the inclusion of HGF imparts little reduction in undamaged strength (4%) attributable to the reduced disruption to the host laminate. After healing it was found that a laminate had a residual strength of 97% compared to the undamaged control and 100% compared to an undamaged self healing laminate.

References

[1]. White SR, Sottos NR, Geubelle PH, Moore JS, Kessler MR, Sriram SR: Nature, Vol.409 (2001), p.794.

[2]. Pang JWC, Bond IP: Compos Sci Technol, Vol. 65(2005), p.1791.

[3]. Williams G.: Appl Sci Manuf, Vol.38(2007), p.1525.

[4]. Trask RS, Bond IP.: Smart Mater Struct, Vol. 15(2006), p.704.

© (2011) Trans Tech Publications, Switzerland
doi:10.4028/www.scientific.net/KEM.471-472.552

Viability of Synthetic Fibers to Replace Steel Wire Mesh in Composite Metal Decks Construction

Salah Al Toubat[1,a], Hussein Ousman[2], Samer Barakat[3]
and Klaus-Alexander Rieder[4]

[1]Department of Civil and Environmental Engineering, University of Sharjah-UAE

[2]Department of Civil and Environmental Engineering, University of Sharjah-UAE

[3]Department of Civil and Environmental Engineering, University of Sharjah-UAE

[4] Grace Construction Products, Luegde, Germany

[a]saltoubat@sharjah.ac.ae

Keywords: Fiber reinforcement; composite decking; diaphragm behavior

Abstract. Composite metal decking has become one of the prevalent forms of Fast Track Construction for multi-story steel buildings. The in-plane stiffness of composite metal decks however is of considerable importance as they typically act as a diaphragm in lateral-load- resisting systems and thus attract a large in-plane shear. The diaphragm action or the in-plane shear capacity of composite metal decks remained a concern for structural engineers and designers.
The present work aims to investigate the in-plane shear behavior of fiber reinforced composite metal decks and compare it to that reinforced with welded wire mesh. A comprehensive experimental program involving testing large scale slabs was conducted. Steel decking of trapezoidal profile with a sheet thickness of 0.9 mm was used to construct the composite slabs. Conventional WWF mesh reinforcement and synthetic macro fibers at different reinforcing rates were considered in the test program. The slabs were tested under monotonically increasing in-plane shear force until failure. Load-deflection responses were plotted and cracking pattern and sequence were recorded. The test results show that fibers provide comparable deck behavior as that with steel mesh. Both imparted similar ultimate in-plane shear capacity and enhanced the ductility and the post peak behavior of the composite metal decks relative to the control slab. The results demonstrate the viability of synthetic macro fibers to replace the steel mesh in this type of composite flooring systems.

Introduction

The use of elevated composite metal deck slabs in steel framed buildings has become nowadays a prevalent construction practice [1,2]. Composite metal decks typically consist of a cold formed corrugated steel sheet, a WWF mesh and a concrete topping. The corrugated steel sheet serves as a permanent formwork for the young concrete and as the principal slab reinforcement once the concrete has hardened. The WWF mesh is used as secondary reinforcement to control rather than prevent concrete cracks associated with restrained shrinkage and temperature changes in the concrete [1]. However, there are several concerns with the use of WWF mainly with regard to the time and labor effort consuming placement of the mesh, the costs associated with shipping and storage and the crane time required to lift the mesh. Furthermore, WWF reduces the concrete depth available to accommodate ducts and electricity supply, while the sharp ends pose safety hazards. Fibers added to the concrete during the mixing phase would efficiently substitute the WWF in controlling shrinkage and temperature cracks. However, as the WWF has been a standard practice for secondary reinforcement in composite decks for long time, there is little data supporting the effects of fibers on the strength of the composite metal deck.

When used as floor systems in steel-framed buildings, composite decks act as diaphragms to resist lateral load such as those due to wind loads and seismic events and to transfer in-plane shear forces to adjacent lateral load resisting elements [3-6]. Though it is well established that fibers could replace the WWF in controlling temperature and shrinkage cracks, their effect on the diaphragm action and hence their contribution to the in-plane shear strength of composite metal decks requires further investigations. This raises the question whether fibers could substitute the mesh or not in this application. The present study aims to address theses concerns through an experimental program in which the in-plane shear performance of fiber reinforced composite metal decks will be compared to that of composite metal decks reinforced with conventional WWF mesh.

Objectives and Scope

The objective of this study is to investigate the influence of synthetic fibers compared to the regular WWF mesh on the in-plane shear capacity of composite metal decks. To achieve this, an experimental program which involves construction and testing of large-scale composite deck specimens was designed. A total of four large scale slabs (1800 mm x 1800 mm x 125 mm) were cast on trapezoidal profile of 0.9 mm sheet thickness. The secondary reinforcement systems used were Synthetic macro fibers (Strux 90/40) at two different dosage rates (5.3 kg/m^3 and 3.0 kg/m^3); and a atypically used WWF mesh (A142).

Materials and Method

The experimental program consists of testing large-scale cantilever composite metal deck diaphragms. A test rig was designed exclusively for this purpose [7] and is shown in Figure 1. It consists of a slab support and a reaction frame to which a 500 KN actuator is attached. The slab support is made up of a reaction beam that provides the fixed end condition of the cantilever diaphragm and rollers that support the free end of the diaphragm and allow for free in-plane movement.



Fig. 1, Test Set up

Material Properties. Material properties details of the material used in this study.

- *WWF mesh*: A typical size of WWF mesh (A142) commonly used in the construction industry is adopted in this experiment. The mesh has an equivalent cross sectional area of 142 mm^2 /m.
- *Synthetic Macro Fiber*: The synthetic macro fiber used in this project is commercialized under the brand name of Strux 90/40 and is mainly made of polypropylene and polyethylene and it has

geometry and mechanical properties that enhance dispersibility in the concrete mix. It is rectangular in shape with nominal length of 40 mm; an average width of 1.4mm; an average thickness of 0.105 mm and an aspect ration of 90. The fiber has tensile strength of 620 MPa and a modulus of elasticity o f 9.500 GPa. The fiber was added at two dosage rates of 5.3 kg/m^3 and 3 kg/m^3.

- *Steel Decking*: A trapezoidal profile of 60 mm depth and 300 mm rib spacing was used in this project. The profile has a sheet thickness of 0.9 mm and is manufactured from material meeting the specifications of BS EN 10147 – S350 GD + Z275-N-A-C and has yield strength of 350 MPa.
- *Concrete Mix Design*: A typical concrete mix with a targeted compressive strength of 40 MPa was used. The mix proportions are shown in Table 1. The maximum aggregate size used was 20 mm. The coarse aggregate used had a specific gravity of 3.1. The fine aggregate used was crushed stone with a specific gravity of 2.5. The concrete mixes were supplied from the mix plant in batches, for each concrete batch, cube samples were prepared and tested according to BS 1881-101 and BS 1881-116, [8,9] respectively.

Table 1, Mix Design

Material (kg/m^3)	Mix 1	Mix 2	Mix 3	Mix 4
Cement OPC	380	380	380	380
20 mm Aggregate	630	630	630	630
10 mm Aggregate	440	440	440	440
Fine Aggregate	880	880	880	880
Free water, L	190	196	200	200
Super plasticizer, L	0.50	0.50	1.50	1.50
Water Cement Ratio	0.50	0.52	0.53	0.53
Synthetic fibers	-	-	3.0	5.3
Average Cube Compressive Strength, MPa	46.9	46.77	41.9	45.8

Testing. Four large-scale composite metal deck slabs were designed, instrumented and tested in displacement control mode under monotonic in-plane shear force in a cantilever diaphragm configuration. The main experimental parameters in the test series were the type and amount of the secondary reinforcement. The secondary reinforcement systems used were: Synthetic macro fibers (Strux 90/40) at two dosage rates of 5.3 kg/m^3 and 3 kg/m^3; and the typical WWF mesh size of A142. All the slabs were 1800 mm x 1800 mm x 125 mm and were constructed with trapezoidal metal deck with sheet thickness of 0.9 mm. The slabs were tested with the corrugations of the metal deck spanning perpendicular to the main beam to represent the so called “strong direction”.

A total of 12 Linear Voltage Displacement Transducers (LVDTs) were used to record the in-plane deflection of the slab. Four LVDTs connected to the 500 kN hydraulic actuator were placed at the four corners of the slab. Eight other LVDTs were mounted at equal spacing along the slab edges and center line and connected to a data acquisition system. The slabs were tested under cantilever diaphragm configuration using displacement controlled system with a rate of 0.02 mm/sec.

Results and Discussions

The load deflection curves for all the slabs are presented in Figure 2. The response of all the slabs to the applied was almost linear until a load value of 180 kN. An exception to this was the slab reinforced with 5.3 kg/m^3 of synthetic fibers which exhibited a linear response to the applied load until a load of 240 kN, then a nonlinear response was observed afterwards until the peak load of 270 kN was reached. The response in the post-peak phase was marked by a smooth and gradual

decrease in the load carrying capacity followed by a steady response towards the end of the test.

The control slab had the lowest ultimate load (190 kN) in the set and its behavior in the post-peak phase was marked by faster degradation of stiffness. This was quite expected since no internal reinforcement was used in this specimen. The slab reinforced with 3.0 kg/m^3 of synthetic macro fibers and the one with A142 mesh exhibited similar behavior with ultimate loads of 208 kN and 207 kN, respectively and a quite similar behavior in the post-peak phase.

These results reveal the effectiveness of fibers in resisting in-plane shear and their ability as viable secondary reinforcement in elevated composite metal deck slabs.

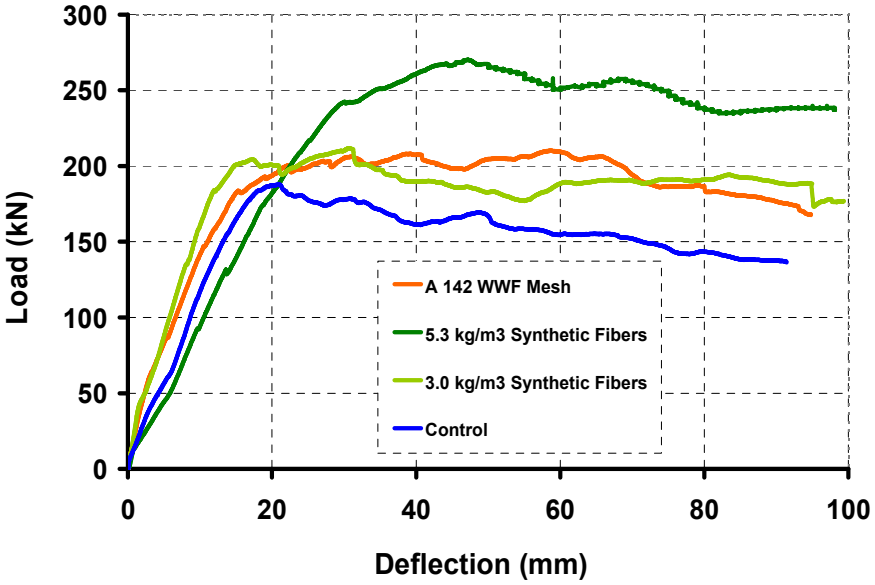


Fig.2. Load Deflection Response

Influence of Secondary Reinforcement on Diaphragm Ultimate Capacity. As presented in the previous sections, the load-deflection curves for control specimens reveal that the load carrying capacity degraded rapidly after the peak load, compared to the slabs reinforced with synthetic fibers or WWF mesh. This reflects the improvement in ductility imparted by fibers and mesh reinforcement as mentioned earlier. In addition to the improvement in ductility, the ultimate capacity of the metal deck slabs was also improved significantly. Table 2 presents the percentage increase in ultimate capacity of the diaphragms reinforced with fibers or mesh relative to the un-reinforced diaphragm (Control).

Table 2, Increase in Ultimate Capacity Compared to the Un-reinforced Slab

Test	Label	Designation	Ultimate Load	Increase in Ultimate Load (%)
1	C	Control Slab	190	-
2	M_{142}	Slab with A142 mesh	207	9
3	$SN_{3.0}$	Slab with 3 kg/m^3 synthetic fibers	211	11
4	$SN_{5.3}$	Slab with 5.3 kg/m^3 synthetic fibers	270	42

Cracking and Failure Mode. Test observations and results showed that all the tested slabs failed trough developing diagonal tension cracks. Moreover, all the slabs exhibited cracks at the fixed end with the slabs reinforced with synthetic macro fibers exhibiting greater crack density than the control slabs and the slabs reinforced with WWF. The greater crack density was associated with narrower individual cracks. It was noticed that the diagonal tension cracks developed in the slab

reinforced with A 142 mesh occurred after the peak load while in fibrous slabs it occurred prior to, and after the peak load. This contributed to delay the failure load and provide higher ductility and to impart a gradual degradation of load carrying capacity. Figures 3 shows the cracking pattern of the slab reinforced with A142 mesh and the slab reinforced with 5.3 kg/m^3 of synthetic fibers. Unlike the control slab and the slab reinforced with A 142 WWF mesh which exhibited large crack opening at the fixed end, the slabs with 5.3 kg/m^3 and 3.0 kg/m^3 of synthetic fibers exhibited multiple narrow cracks at the fixed end.

The occurrence of multiple cracking in fibrous slabs and consequently the improved ultimate load and the ductility imparted by fibers can be attributed to many characteristic features of fibers such as the confinement they provide to the shear connectors. In fact, upon the application of force the diaphragm, the load is transferred from the reaction beam to the composite deck through the shear connectors. The use of fibers provides a dense and stiff concrete confinement around the shear connectors which allows for an effective transfer of load form the shear connectors to the reaction beam.



Fig 3, Cracking Pattern:
Slab with A142 Steel Mesh (Left), and Slab with Synthetic Fiber (Right)

Summary

The test results revealed that the type and quantity of the secondary reinforcement is a primary factor affecting the diaphragm capacity and behavior of composite metal decks. The result showed that the slabs reinforced with synthetic macro fibers, and the slab reinforced with A142 steel mesh, all exhibited multiple shear diagonal cracking prior to failure. The multiple diagonal cracking contributed to the improved ductility and post-peak behavior of these slabs compared to the control slab which failed in a less ductile manner with a single and wide diagonal crack. The addition of fibers and steel mesh also increased the ultimate shear capacity of the slab relative to the control. The use of A142 mesh increased the ultimate capacity over the control slab by 9%, whereas the addition of synthetic macro fibers (Strux 90/40) at dosage rates of 3.0 kg/m^3 and 5.3 kg/m^3 increased the ultimate shear capacity by 11% and 42%, respectively. These results show that the synthetic macro fibers at the added dosages can provide metal deck slabs with in-plane shear capacity comparable to that obtained using the conventional WWF mesh and hence can be seen as a viable alternative in diaphragm applications of metal decking.

Acknowledgements

The authors would like to thank to Emirates Stones Company Ltd, Sharjah who supported this project during the construction stage. Special thanks are due to Eng. Jawdat Al Bargawi, the General Manager and Eng. Mohammed Ali, the Operation Manager for their helpful cooperation. In addition, the authors want to express their gratitude to Grace Middle East, Dubai-UAE for

providing the fibers (Strux 90/40), and to Richard Lee Steel Decking, UK for supplying the steel decking.

References

[1] ASCE (1985), "*Specifications for the design and construction of composite slabs*." New York, N.Y

[2] Davies JM & Fisher J (1979). "*The Diaphragm Action of Composite Slabs*." Proc. Institution of Civil Engineers, London, England, 67 (Part2), 891–906.

[3] Easterling, W. S. and Porter, ML.(1994). "*Steel - Deck - Reinforced Concrete Diaphragms-I*." Journal of Structural Engineering ASCE, Vol. 120, No. 2, February,1994, p560-576.

[4] Easterling, W. S. and Porter, ML.(1988). "*Behavior, Analysis and Design of Steel - Deck - Reinforced Concrete Diaphragms*." Final Report, Iowa State University, Engineering Research Institute - Ames-88305 Project 1636.

[5] Easterling, W.S. and Young, C. Y. (1992). "*Strength of Composite Slabs.*" Journal of Structural Engineering, ASCE, 118(9), pp. 2370-2389

[6] Easterling, W. S. (1987). "*Analysis and design of steel deck reinforced concrete diaphragms*." PhD dissertation, Iowa State University, Ames, Iowa.

[7] Hussein Ousman "Diaphragm Behavior of Fiber Reinforced Concrete Composite Decks," Master Thesis, University of Sharjah, UAE, pp 187.

[8] BS 1881-101,1983 "*Standard Test Method for Sampling Fresh Concrete on Site*"

[9] BS 1881-101,1983 "*Standard Test Method for Method for the Determination of Compressive Strength of Concrete Cubes*"

© (2011) Trans Tech Publications, Switzerland
doi:10.4028/www.scientific.net/KEM.471-472.558

Optimization of Injection Parameters Using 16μm Stainless Steel Powder (SS316L) at 63 vol. %, 63.5 vol. % and 64 vol. % Powder Loading by Taguchi Method for Metal Injection Molding

Muhammad Ilman Hakimi Chua[1, a], Abu Bakar Sulong [1,b],

Norhamidi Muhamad [1,c] , Mohd Fazuri Abdullah [1,d] and

Che Hassan Che Haron[1,e]

[1] Department of Mechanical and Material Engineering,

Faculty of Engineering and Built Environment,

Universiti Kebangsaan Malaysia, 43600 Bangi, Malaysia

[a]kimi_ilmn@yahoo.com, [b]abubakar@eng.ukm.my, [c]hamidi@eng.ukm.my,

[d]faxury@yahoo.com, [e]chase@eng.ukm.my

Keywords: Metal Injection Molding (MIM), Taguchi Method, green compact mechanical strength

Abstract. In this paper, injection molding parameters are optimized using the L_{18} Taguchi orthogonal array for mechanical strength and surface quality of the green part. The feedstock used consists of stainless steel powder (SS316L) with the powder loading of 63 vol. %, 63.5 vol. % & 64 vol. %. The binder compositions used are polyethelene glycol (PEG-73 wt.%), polymethyl methacrilate (PMMA-25 wt.%) and stearic acid (4 wt.%). Mould temperature, injection temperature, injection pressure, injection time, holding time and powder loading ware selected as signal factors using Taghuci's method based on literature, where these parameters were significant in MIM. Results showed that the optimum parameters are: mold temperature at 65^0C, injection temperature at145^0C, injection pressure at 650 bar, injection flow rate at 20 m^3/s, holding time at 5 s and powder loading of 64 vol.%. Analysis of Variance (ANOVA) result shown that mold temperature is the most influence in order to produce good green part's surface quality while powder loading give the best result for green part's strength.

Introduction

Metal injection molding (MIM) is a near net shape molding process for fabrication complex and intrinsic metal component that combines theology in injection molding and powder metallurgy [1]. The Taguchi method is use to optimize the injection molding parameters by considering the physical quality and the mechanical strength of the green compact which more statically method compare to trial an error method. The chosen injection molding parameters were mold temperature, injection temperature, injection pressure and packing time. Mold temperature and the packing time is the most influences parameter to the physical quality of green compact reported by Jamaludin et al. [2]. Similar conclusion reported by Tatt [4] that the mold temperature is the most influences parameter for the criteria of physical quality, density and mechanical strength of the green compact.

Methodology

SS316L water-atomized powders with the pycnometer density of 7.93g/cm^3 were mixed with 73 wt.% of polyethylene glycol (PEG 4000), 25 wt.% of polymethyl methacrylate (PMMA) and 2 wt.% of stearic acid as a surfactant using the sigma blade mixer to three powders loading as mention earlier. Acetone was added into the feedstock with the ratio 4ml of acetone with every

gram of PMMA to improve the mixing properties of the feedstock since by adding up acetone, it will reduce the viscosity.

Rheology analysis of the feedstocks were carried out using the Shimadzu CFT-500D to study the rhelogy properties of the feedstock is suitable for determination of injectability. Green compact were injected by Battenfeld BA 250 CDC injection molding machine in form of ASTM standard tensile bar shape. The mechanical strength of green compacts was measured by INSTRON Universal Tester 5567 through three point bending test.

Result and Discussion

Figure 1 shows the relation of viscosity again shear rates. All powder loading, 63 vol. %, 63.5 vol. % and 64 vol. % showed pseudoplastic behavior with the flow index, n lesser than 1 are determined in Table 1. The measured viscosity and the shear rate value are also in the acceptance range of 10 Pa.s - 1000 Pa.s and 10^2 s^{-1} - 10^5 s^{-1}. The respectively range of the value indicates the fluidability of the feedstock in injection molding process which need to determined first before proceed to injection molding process. The most preferred rheology properties are given by 64 vol. % powder loading which giving the highest value for flow index, *n* which is showed in Table 1. The higher fluidability index value, the more stable feedstock react to the temperature change which can reduce the green part's distortion and cracking [4].

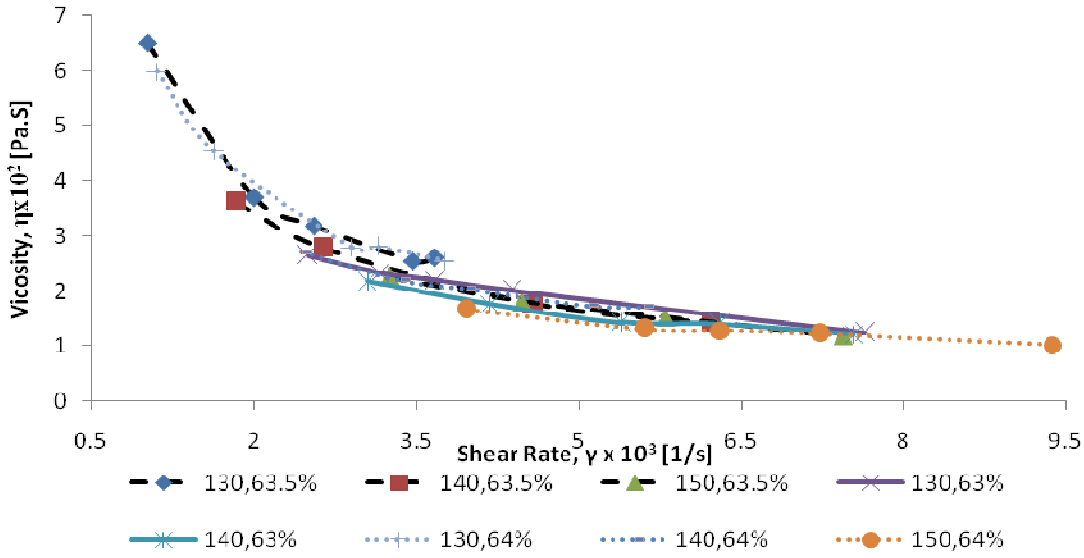


Fig. 1: Viscosity against shear rate at different temperature

Table 1 Flow index at various temperatures

Powder Loading (vol.%)	Temperature (^{0}C)	Flow index, *n*
63	130	0.33
	140	0.37
63.5	130	0.27
	140	0.23
	150	0.24
64	130	0.28
	140	0.44
	150	0.46

Fig. 2 and Fig. 3 show the optimized injection molding. The physical quality and green compact strength are defined as the evaluate factor. The optimized injection molding parameter for physical quality are at mold temperature at 65^0C, injection temperature 145^0C, injection pressure 700 bar, holding time of 5s and powder loading of 64 vol. % which shown in Fig 2. Mold temperature give significant effects to the physical quality compare to other parameters since the mold temperature kept the surface constantly heat to stably the green compact structure.

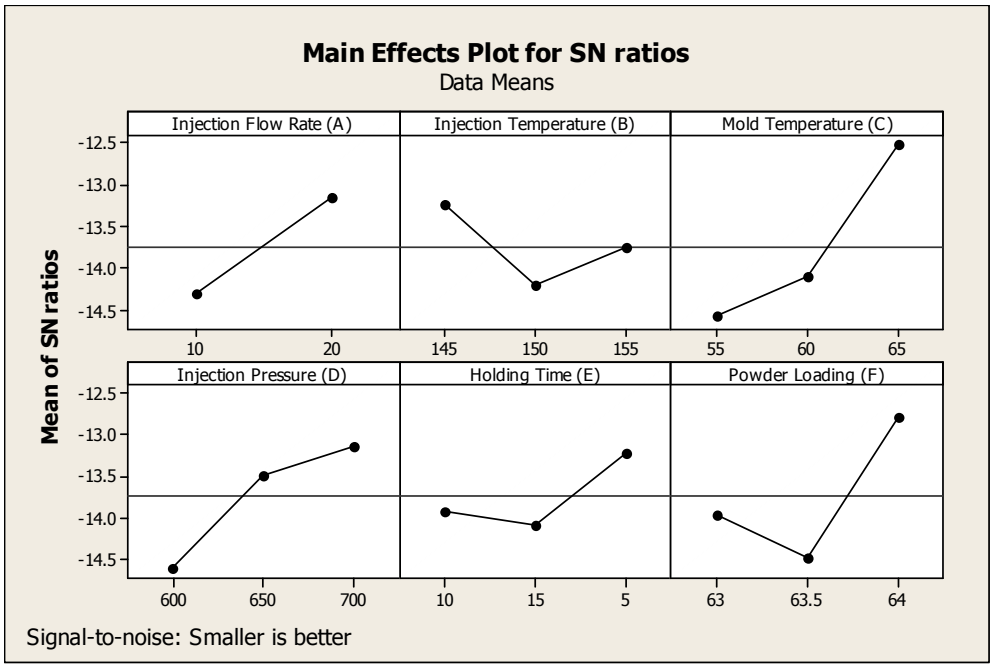


Fig. 2: S/N ratios for physical quality against of injection molding parameters

The optimized injection parameter for green component mechanical strength are mold temperature at 60^0C, injection flow rate 20 m^3/s, injection temperature 145^0C, injection pressure 650 bar and holding time of 15 s as shown in Fig 3. Powder loading give significant effect on the green strength evaluation but the more powder added didn't show that the more strengthen the green part produce. In this stage the bonding between the metal powder still didn't occur yet so the bonding only between the polymers which act as backbone for green compact.

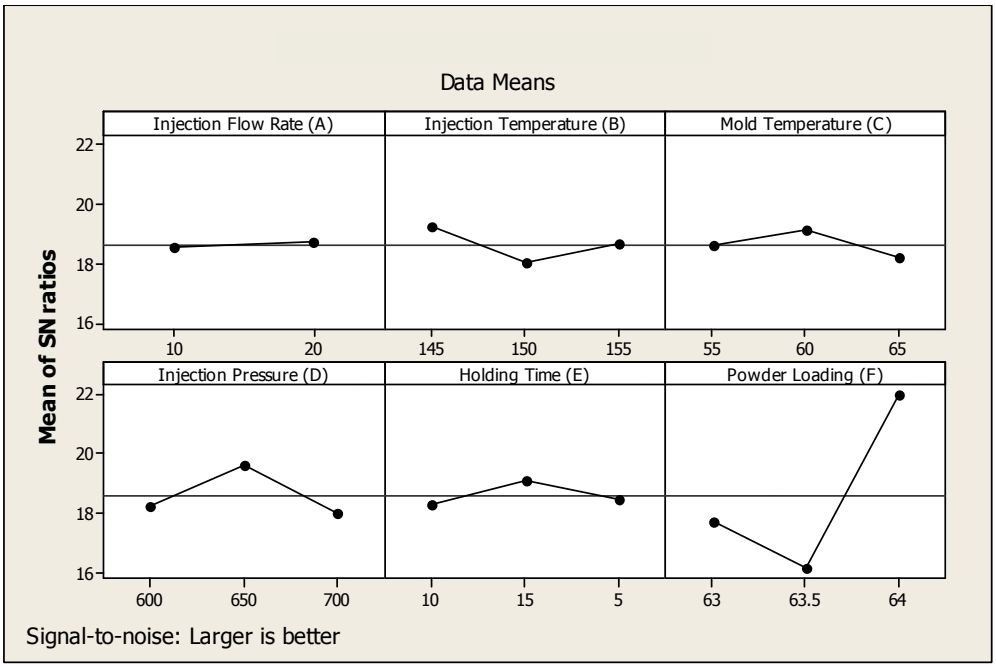


Fig. 3: S/N ratios of mechanical strength against injection molding parameters

Table 2 Optimum injection parameter and contribution percentage of the factor

Factor	Optimum parameter	Contribution percentage, %	
		Physical quality	Strength
Injection Flow Rate (A)	$20m^3/s$	7.8	0.05
Injection Temperature (B)	145^0C	4.59	1.42
Mold Temperature (C)	65^0C	16.41	2.76
Injection Pressure (D)	650bar	12.65	5.4
Holding Time (E)	5s	4.02	0.92
Powder Loading (F)	64 vol.%	11.64	81.33
Error		42.89	8.12

Analysis of variance (ANOVA) is applied to determine the most significant contribution factor. Mold temperature is the most influence parameter for green compact physical quality based on Table 2. Powder loading shown to be the most influence parameter on the mechanical strength.

Summary

It was concluded that all the three different feedstock powder loadings were shown pseudoplastic flow behavior thus suitable for MIM process. The Taguchi method successfully optimized the injection parameters with minimum repetition of experiment needed compared to try and error method since on 18 set of experiments required while try and error more than that. Based on the results, mold temperature is the most significant factor to obtain the best physical quality for the green part. Powder loading is the major factor for the green part's strength evaluation criteria. The combination of the optimum parameter of both criteria are injection flow rate 20 m^3/s, mold

temperature 65^0C, injection temperature 145^0C, injection pressure 650 bar, powder loading 64 vol.% and holding time 5 s.

Acknowledgements
This work supported by UKM-GUP-NBT-08-26-092. Authors would like acknowledge fellowship supported from Ministry of Science, Technology & Innovation, Malaysia (MOSTI).

References

[1] Z.Y. Liu, N.H. Loh, S.B. Tor & K.A. Khor: Materials characterization. Vol. 49 (2003), p. 313-320

[2] K. R. Jamaludin, N. Muhamad, M.N.Ab. Rahman, S. Ahmad, M.H.I. Ibrahim & Nor H.M.Nor: J.Sci. Vol.36 No. (2009) p. 349-358

[3] T .K.Tatt. Optimization Parameters of Injection Process by using Taghuci Method for Metal Injection Molding (MIM) M.Sc Thesis, Universiti Kebangsaan Malaysia, Malaysia, 2009.

[4] M. Khakbiz, a. Simchi and R. Bagheri: *Powder Metallurgy*, Vol.48 No.2 (2005) p. 144-150.

© (2011) Trans Tech Publications, Switzerland
doi:10.4028/www.scientific.net/KEM.471-472.563

Preliminary Review of Biocomposites Materials for Aircraft Radome Application

M.Y.Haris[1,a], D.Laila[1,b], E.S.Zainudin[2,c], F.Mustapha[2,d], R. Zahari[2,e] and Z. Halim[3,f]

[1]Department of Aerospace Engineering, Universiti Putra Malaysia,
43400 UPM Serdang, Selangor, Malaysia
[2]Department of Mechanical and Manufacturing Engineering, Universiti Putra Malaysia,
43400 UPM Serdang, Selangor, Malaysia
[3]Department of Manufacturing and Materials Engineering,
International Islamic University Malaysia, Selangor, Malaysia

[a]mohdyusoff2010@gmail.com, [b]dlaila@eng.upm.edu.my, [c]edisyam@eng.upm.edu.my,
[d]faizal@eng.upm.edu.my, [e]rizal@eng.upm.edu.my, [f]zahureen@iium.edu.my

Keywords: Biocomposites, Radome, Kenaf

Abstract. An aircraft radome usually refer to radar transparent, dome-shape structures which protects radar antennas on aircraft from aerodynamic loading, weather as well as impacts from bird strikes. Materials that are used for small aircraft radome usually have low dielectric constant and high toughness. Current composite material using high strength fibers such as glass fiber, carbon and aramid are commonly used in aerospace structures. However, the need for biodegradable materials has prompted the usage of natural fibers. Natural fibers have comparable mechanical properties such as low weight, low cost, renewable and biodegradable. In this preliminary work, comprehensive reviews of biocomposites materials are discussed in term of their properties for the purpose of evaluation for aircraft radome application. The present review will cover five local natural fibers namely bamboo, banana, kenaf, oil palm and pineapple leaf fiber.

Introduction

A radome usually refer to radar transparent, dome-shape structures which protects radar antennas on aircraft from aerodynamic loading, weather as well as impacts from bird strikes. The history of radome largely follows the introduction of microwave antenna, particularly for those exposed to wind or aerodynamic force. Since 1940, they have become larger as antennas have increased in size, and more complex design, due to demand for higher performance and to the tighter tolerance demanded by the use of shorter length. Materials that are used for light aircraft radome usually have low dielectric constant and high toughness composites [1].



Fig. 1: several types of aircraft radome

During the past decades, natural fibers have attracted the interest of material scientists, researchers and industries because of their specific advantages as compared to synthetic fibers. Advantages of natural fibers are low density, low cost, renewable and biodegradable. In recent years, research on application of natural fibers as fiber reinforcement for composites are widely conducted ranging from local fibers [2-18] as well as flax [19-21], jute [22,23] and hemp [24,25]. However, in the present paper, the material selection process for aircraft radome application will

consider 5 types of local natural fibers ie banana fiber, bamboo fiber, kenaf fiber, oil palm empty fruit bunch (OPEFB) and pineapple leaf fiber(PALF) as reinforcement for biocomposite. There are many factors influencing the properties of a composite material whereby they are dictated by intrinsic properties of both fiber and matrix. The mechanical properties obtained depend largely on the fiber architecture as well as the fiber-matrix interface. The fiber architecture encompasses the fiber geometry, orientation, packing arrangement and fiber volume faction [26]. For biocomposites fabrication, the most important factor is the adhesion of fiber to the resin material, moisture absorption. Therefore, the various chemical treatments available will also be reviewed.

Dielectric. Dielectric property is a part of consideration in selecting material for radome. The choice of dielectric material will be constrained by requirement for structural strength, low weight and rain erosion resistance [27]. The dielectric constants for natural fibers range from 2.8 to 3.2 [28]. Glass fiber type E and resin epoxy or polyester is commonly used for radome applications. The dielectric constant for E-glass woven with epoxy and polyester ranges from 4.03 to 4.43.

Biocomposite Material. Composites are termed as biocomposite materials when one of its phases either matrix (polymer) or reinforcement comes from natural source [32]. The origin of natural fiber comes from plant's seed, leaf, bast, fruit and stalk. The basic component of natural fiber is cellulose, hemicellulose and lignin. The hemicellulose, lignin and pectin collectively function as matrix and adhesive, helping to hold together the cellulosic framework structure of the natural composite fiber. Table 1 showed the origin and chemical composition of selected fibers. A comparison of the mechanical properties of the natural fibers with glass fibers are listed in Table 2. Data on mechanical characterization conducted by various researchers [2-19] on these 5 local fibers with various resins namely polypropylene (PP), polyethylene (PE), high density polyethylene (HDPE), polylactic acid (PLA), polyvinly chloride (PVC), phenol formaldehyde (PF), polyester and epoxy was collected and compiled into table 3.

From table 3, the following general conclusions are drawn for biocomposites. Increase in fiber length and to improve the strength and stiffness since higher aspect ratio (length/transverse dimension) will give greater reinforcing efficiency. Likewise, aligning the packing arrangement (unidirectional versus random) improves the properties, which also lead to an increase in fiber volume fraction (fiber content) and hence better performance. In terms of resin types, thermoplastic or thermoset polymers are commonly used.. Heating temperature, curing temperature and curing time is important in selecting type of resin because fibers cannot withstand high temperature. According to S.Ochi, tensile strength of kenaf fibers decreases at 200°C [5]. The density of resin will also influence the impact strength. Comparison of the properties of the five local fibers and glass hybrid showed that by introducing glass fiber into biocomposite has increased the overall mechanical properties of biocomposite. Kenaf has shown good overall performance and is deemed suitable for further analysis.

Table 1: The origin and chemical composition of natural fibers

Fiber	Origin	Cellulose %	Hemicellulose %	Lignin %	Pectin %	Microfibrillar Angle (deg)
Bamboo [31]	Stalk	60.8	-	32.2	-	2-10
Banana [30]	Leaf	43.46	38.54	9	-	-
Kenaf [33]	Bast	31-57	21.5-23	15-19	-	-
OPEFB [15]	Fruit	48	22	25	-	-
PALF[29]	Leaf	70-82	-	5-12	-	8-14

Table 2: Mechanical properties of natural fibers and synthetic fibers

Fiber	Density (g/cm^3)	Tensile Strength (MPa)	Tensile Modulus(GPa)	Elongation at Failure (%)
Bamboo [35]	0.94	503	35.9	1.4
Banana [3]	0.712	500	12.0	5.9
Kenaf [8]	1.55	930	53	1.6
OPEFB [18]	0.7-1.55	0.1-0.4	1-9	8-10

PALF [13]	1.526	170	6.21	3
E-glass [33]	2.5	2000-3500	70	2.5-3.0
S-glass [33]	2.5	4570	86	2.8

Table 3: Mechanical properties of biocomposites

Fiber	Matrix	Fiber Length (mm)	Fiber Content (%)	Tensile Strength(MPa)	Young's modulus(GPa)	Impact Strength	Packing Arrangement
Bamboo [9,11]	Epoxy	-	-	87.0	6.74	15.6kJ/m^2	unidirectional
	Polyester	-	-	74.0	4.20	18.1kJ/m^2	
	PP	0.25-0.5	20	20.5	2.08	-	
	HDPE	6.0	10	18.58	0.33	71.2kJ/m^2	random orientation
			20	22.03	0.76	69.6kJ/m^2	
			30	25.47	2.67	57.4kJ/m^2	
			40	21.21	2.75	51.2kJ/m^2	
Banana [3,4]	PP	6.0	10	37.50	0.64	38.5 J/m	random orientation
			20	41.00	0.81	42.0 J/m	
			30	45.25	0.98	46.0 J/m	
			40	39.00	1.05	41.0 J/m	
	PLA	2 - 5	10	27.12	2.72	21.1 J/m	random orientation
			20	30.00	2.90	19.0 J/m	
			30	35.00	3.03	19.7 J/m	
			40	32.00	3.12	19.3 J/m	
Kenaf [2,7]	PP		40	28.6	6.8	14 kJ/m^2	random orientation
	PP	0.3-0.5	5	21.2	0.42	3.4 kJ/m^2	random orientation
			10	21.4	0.45	4.4 kJ/m^2	
			15	22.1	0.52	4.4 kJ/m^2	
			20	21.4	0.53	4.8 kJ/m^2	
	PLA	500	30	130.5	14.4	-	unidirectional
			50	210.9	19.8	-	
			70	223.3	22.8	-	
	PF	8-12	19	35.66	-	8.2 kJ/m^2	random orientation
			28	45.60	-	7.9 kJ/m^2	
			36	49.60	-	8.8 kJ/m^2	
			43	74.82	-	9.7 kJ/m^2	
			52	56.0	-	9.5 kJ/m^2	
			62	52.80	-	12.0kJ/m^2	
OPEFB [14-16]	PP	0.5	40	11.65	1.58	-	random orientation
			50	10.13	1.93	-	
			60	9.52	1.99	-	
	Polyester		45	35.1	3.29	16.7kJ/m^2	random orientation
	PVC	75 μm	20	41.38	1.38		
PALF [12,13]	PP	4.0	5	24.96	0.65	32.3 J/m	random orientation
			10	26.95	0.69	35.3 J/m	
			15	29.92	0.69	41.5 J/m	
	Polyester	5	30	15.6	0.81	-	random orientation
		10		35.0	1.87	24.4kJ/m^2	
		20		39.2	1.99	19.9kJ/m^2	
		30		52.9	2.29	24.2kJ/m^2	
		40		38.4	1.97	22.0kJ/m^2	
(continued)							
Bamboo/ Glass [9]	PP	0.25-0.5	20(15/05)	21.0	2.44	-	random orientation
Banana/ Glass [3]	PP	6.0	30(25/05)	44.50	1.07	51.0 J/m	random orientation
			30(20/10)	49.00	1.15	54.5 J/m	
			30(15/15)	57.00	1.35	58.0 J/m	
			30(10/20)	53.0	1.21	52.0 J/m	
			30(05/25)	51.0	1.13	47.0 J/m	
Kenaf/	Epoxy	-	-	153	7.5	26.0 J/m	unidirectional

Glass [17]							
OPEFB/ Glass [18]	Polyester	OPEFB 50-500 μm Glass 2-25 μm	35(10/90)	77.4	5.5	16.7kJ/m^2	random orientation
			35(30/70)	61.2	4.9	15.8kJ/m^2	
			35(50/50)	57.6	3.9	14.7kJ/m^2	
			35(70/30)	50.4	3.8	13.7kJ/m^2	

Chemical Treatment. The main disadvantages of natural fibers in composites are the poor adhesion between fiber and matrix and the relative high moisture absorption. Therefore, chemical treatments are considered in modifying the fiber surface properties [33]. The chemical treatments of fiber aimed at improving the adhesion between the fiber surface and the polymer resin resulting in increase fiber strength and lower water absorption. The chemical treatment can be chemical modification to the fiber prior to composite fabrication or introduction of compatibility agents to the polymer/fiber mix during the processing [26]. Table 4 was tabulated to show types of treatment available and their effects on the mechanical properties. The table indicated that by using sodium hydroxide (NaOH), the tensile strength and tensile modulus increased except for PALF. Banana and OPEFB show positive effect when maleic andydride and silane are introduced. However, tensile modulus for bamboo decrease with maleic andydride and tensile strength for PALF reduce with silane as a coupling agent.

Table 4: Effect of chemical treatment on biocomposite

Fiber	matrix	Treatment	Fiber Content Reinforcement Effect		Remark
			Tensile Strength	Tensile Modulus	
Banana [4]	PLA	NaOH	+	+	5 % NaOH
		Maleic Andydride	+	+	1 wt %
		Glycerol Triacetate Ester	+	+	5 wt %
Bamboo [9,11]	PP	Maleic Andydride	+	-	
	Epoxy	NaOH	+	+	5% NaOH for 30 min
Kenaf [32]	Polyester	NaOH	+	+	6 % NaOH for 12 hours
		NaOH	+	+	9 % NaOH for 12 hours
OPEFB [13,14]	PP	NaOH	+	+	10 %
		NaOH	+	+	20 %
	Polyester	Acetic Anhydride	+	+	
		Silane	+	+	
		Titanate	-	+	
PALF [13]	Polyester	NaOH	+	-	2 %
		Silane	-	+	
		Glacial Acetic Acid	-	-	

+ represents improvement of property value; - represents reduction of property value

From the compilation data, a hybrid kenaf-glass fibers with epoxy and NaOH as a chemical treatment can be the potential material for radome application in this preliminary review. Standard mould size 15 inches to 20 inches usually for generic radome. Manufacturing method is hand lay-up and vacuum bag with laminate kenaf and glass fiber. Tensile test, bending test and quasi static test will be conducted to investigate the mechanical and impact properties.

Summary

This review focused on the mechanical properties of five type natural fibers as part of selection process for radome application. Initial review that has been presented is in favor in potential kenaf fiber for radome application. Kenaf fiber has shown comparable stiffness to glass and low dielectric constant, therefore, it is suitable for radome application. Combination of glass fiber with kenaf as a hybrid composite will help to improve the mechanical properties and rain erosion resistance. Further extensive review in term of other factors such as microstructure characteristic will conducted.

Acknowledgement
This research was supported by Fundamental Research Grant Scheme (FRGS/2/2010/TK/UPM/03/2).

References

[1] W.M.Cady, in: *Radar Scanners and Radome*, Vincent Press, ISBN-10: 1443727172
[2] P.Wambua, J.Ivens, I.Verpoest: Compos Sci Technol 63 (2003) 1259-1264
[3] S.K.Nayak, S.Mohanty, S.K.Samal: Polym Compos(2010) 1247-1257
[4] S.K.Majhi, S.K.Nayak, S.Mohanty, L.Unnikrishnan.: Int J Plast Technol (2010)
[5] S.Ochi: Mech mater 40 (2008) 446-452
[6] H.Anuar, S.Ahmad, R.Rasid.:J. Solid St. Sci. and Technol. Letters, vol 12, No 1 & 2 (2005) 1-5
[7] Sultan Ozturk: J Compos Mater, Vol. 44, No. 19/2010
[8] Bismarck A., Mishra S., and Lampke T., in: *Natural Fibres, Biopolymers, and Biocomposites*, ed. A.K., Mohanty, M., Misra, and L. T., Drzal, Boca Raton: CRC Press. (2005) pp. 37-108.
[9] M.M.Thwe, K.Liao: Compos Sci Technol 63 (2003) 375-387
[10] S. Mohanty, S.K.Nayak: J Reinforced Plast Compos Vol. 29, No 14/2010
[11] P.Kushwaha, R.Kumar: J Reinforced Plast Compos, Vol. 28, No. 23/2009
[12] R.M.N. Aib, S.M. Sapuan, M.M.H.M. Ahmad, M.T. Paridah, H.M.D.K. Zaman:Materials and Design 27 (2006) 391-396
[13] L.U.Devi, S.S.Bhagawan, S.Thomas: J Appl Polym Sci 64 (1997) 1739-1748
[14] G.S.Tay, J.M.Zaim, H.D.Rozman: J Appl Polym Sci, vol. 116, 1867-1872(2010
[15] C.A.S.Hill, H.P.S.A.Khalil: J Appl Polym Sci, vol. 78, 1685-1697 (2000)
[16] A.A.Bakar, T.B.Keat, A.Hassan: J Appl Polym Sci, vol. 115, 91-98(2010)
[17] M.M.Davoodi, S.M.Sapuan, D.Ahmad, A.Ali, A.Khalina, M.Jonoobi: Materials and Design 31 (2010) 4927-4932
[18] H.P.S.A. Khalil, S. Hanida, C.W. Kang, N.A.N. Fuaad: J Reinforced Plast Compos, Vol. 26, No.2/2007
[19] K.Oksman, M. krifvars, J.F.Selin: Compos Sci Technol 63 (2003) 1317-1324
[20] B.Bax, J.Mussig: Compos Sci Technol 68 (2008) 1601-1607
[21] Q.Liu, M.Hughes: Compos: Part A 39 (2008) 1644-1652
[22] C.K.Hong, I.Hwang, N.Kim, D.H.Park, B.S.Hwang, C.Nah: Journal of Industrial and Engineering Chemistry 14 (2008) 71-76
[23] D.Plackett, T.L.Anderson, W.B.Pedersen, L.Nielsen: Compos Sci Technol 63 (2003) 1287-1296
[24] A.Bourmaud, C.Baley: Polymer Degradation and stability 92 (2007) 1034-1045
[25] T.Yuanjian, D.H.Isaac: Compos Sci Technol 67 (2007) 3300-3307
[26] P.A.Fowler, J.M.Hughes, R.M.Elias: Journal of the Science of Food and Agriculture 86:1781-1789 (2006)
[27] G.A.E.Crone, A.W.Rudge, G.N.Taylor: IEE Proc, Vol. 128, Pt. F, No. 7 1981
[28] N.Sgriccia, M.C.Hawley: Compos Sci Technol 67 (2007) 1986-1991
[29] S.Mishra, A.K.Mohanty, L.T.Drzal, M.Misrra, G.Hinrichsen: Macromolecular Materials and Engineering 289 (2004) 955-974
[30] N.Venkateshwaran, A.Elayaperumal: J Reinforced Plast Compos, Vol. 29, No. 15/2010
[31] K.Okubo, T.Fujii, Y.Yamamoto: Compos: Part A 35 (2004) 377-383
[32] A.Hassan, A.A.Salema, F.N.Ani, A.A.Bakar: Polym Compos 2010
[33] X.Li, L.G.Tabil, S.Panigrahi: Journal Polymer Environment (2007) 15:25-33
[34] M.Yuhazri, Y.Phongsakorn, H.Sinhombing: IJBAS-IJENS Vol: 10 No: 63
[35] M.M.Rao, K. and K.M Rao: Journal of Composite Structures 77 (2007) 288-295
[36] A.W.Rudge, K. Milne, A.D. Olver, P.Knight., *The Handbook of Antenna Design, Vol. 2*, Institution Of Engineering And Technology, ISBN-10: 0906048877

© (2011) Trans Tech Publications, Switzerland
doi:10.4028/www.scientific.net/KEM.471-472.568

Fatigue Delamination Analysis of Composite Laminates with a Central Hole using Interface Elements

H. Hosseini-Toudeshky[1, a], A. Jasemzadeh[1, b], B. Mohammadi[2, c]

[1] Department of Aerospace Engineering, Amirkabir University of Technology, 424 Hafez Ave., Tehran, Iran
[2] School of Mechanical Engineering, Iran University of Science and Technology, Tehran, Iran

[a]Hosseini@aut.ac.ir, [b]jasemzadeh@aut.ac.ir, [c]Bijan_Mohammadi@iust.ac.ir

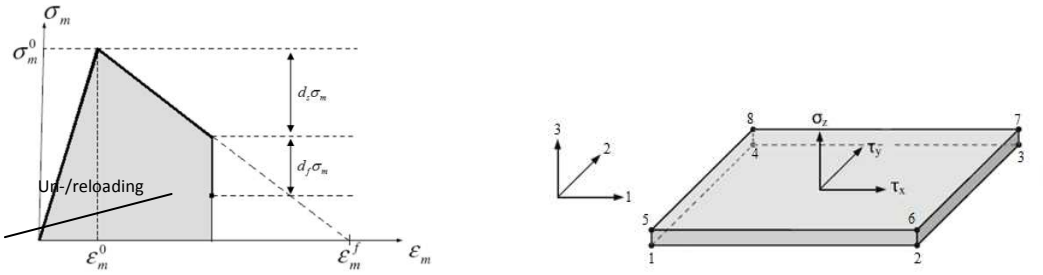
Keywords: Cyclic loading; Delamination; Cohesive element; Composite laminate;

Abstract. In this paper a solid like interface element along with a fatigue constitutive law is used to study the damage behaviour of holed composite laminates under cyclic loading. For this purpose a user element routine and a material routine was developed include the interface element and to handle the formulation of progressive fatigue damages. The developed procedure is used to predict delamination initiation and growth in mixed-mode condition for a typical composite laminate. The obtained results for damage and stresses are compared with the available results in the literature.

Introduction

The stress gradient occurs in the geometric discontinuities like holes and could promote delamination, and result in a loss of structural integrity. Delamination reduces the strength of a laminate structure and consequently, it must be taken into account in the failure analyses of composite structures. The interface element concept is able to link the fracture mechanics and damage mechanics, as a technique that altering the crack growth rate to the degradation material in each Gauss integration point. Turon et al. [1], developed a damage model based on the cohesive element concept for the analyses of fatigue delamination propagation of DCB and ENF specimens under quasi-static and high cycle loadings. Harper and Hallet [2] performed a new formulation for predicting of fatigue damage growth by relating the damage accumulation law of cohesive interface elements to the Paris type crack growth law. Beghini et al. [3] used an Ultrasonic (US) scanning apparatus system and reported evolution of damage during fatigue testing in carboresin composite plates containing a central hole. Hosseini-Toudeshky et al. [4] used interface elements with cohesive constitutive law, to predict the failure load of various laminates under monotonic loading in which delamination is the dominant failure mode of them. In this paper, three dimensional finite element method with a thin layer solid like interface element are employed for the analysis of mixed mode delamination growth in a composite laminate with a central hole under cyclic loading. For this purpose, the interface element formulation and required material constitutive law were implemented to the ANSYS code, as a User Programmable Features.

Constitutive Law. The formulation of the interface element is like an isoparametric hexahedral solid element but carries only interlaminar stresses. In the simulation of each model, an initial static loading followed by a cyclic loading is considered. A bilinear softening constitutive law based on the developed formulations by Wagner and Balzani [5] is used to model the initial static loading. In the followed fatigue load modeling, a damage mechanic approach which is linked to the fracture mechanic method [1] is used. The interface element formulation and material constitutive law were implemented to the ANSYS code, as a User Programmable Features (UPF). Figures 1(a) and 1(b) show a bilinear stress-strain constitutive law containing both fatigue and static parts of degradation in material strength and the geometry and interlaminar stresses of interface element respectively.



(a) (b)

Fig. 1: (a) Bilinear constitutive law. (b) Geometry and stresses of solid like interface element

Fatigue Analysis Procedure. Fatigue process should be computed in two steps as shown in Fig. 2. The first step is static loading which the applied load is increased from zero to the maximum load in 5 seconds, and the second step is cyclic loading which the load amplitude remains constant and fatigue process starts at fatigue zone. For this purpose, two UPF routines are developed to add the solid like interface element formulation and fatigue degradation process to the element and material ANSYS's library.

One of the essential parts in fatigue damage analysis is the distinction of the fatigue damaged region. It is assumed that fatigue damage or increase of damage parameters leading to delamination growth occur in this area only. Different methods have been proposed to calculate a fatigue zone length, like analytical formulation for cohesive zone presented in [7], but they have difficulties in mixed-mode delaminations. In this article the concept of cohesive zone is used to calculate the fatigue region size which can be used in each fracture mode and mixed-mode conditions. This region can be defined as an area close to the crack-front in the considered cohesive zone in which interface elements have exceeded their linear-elastic stress and experience irreversible deformation. In the damage analysis process, cohesive zone initiates from the crack-front until the element location in which the stress is equal to the maximum stress in the constitutive model. [8]. It is worth to note that the cohesive zone is updated in un-/reloading process according to the obtained new stress field that is showed in Fig. 2.

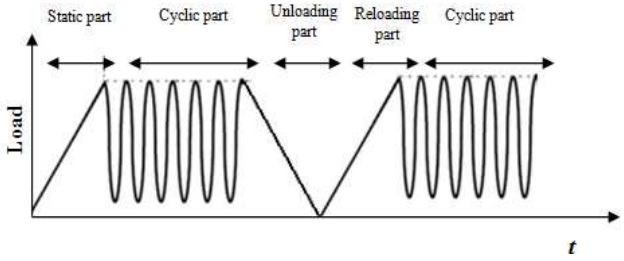


Fig. 2: Schematic of static, fatigue, unloading and reloading

Analyses of Holed Specimen. Fig. 3(a) shows the geometry and Fig. 3(b) shows the mesh of the holed specimen made of AS-4/3501-6 graphite/epoxy and high strength carbon fiber (T300) material with mechanical properties listed in Table 1. A quasi-isotropic laminates of $[45/90/-45//0]_S$ with ply thickness of 0.125 mm containing hole with the diameter of 3.175 mm is considered. Primary elastic analyze prove that the most critical stresses exist between layers -45° and 0°, then the cohesive elements are used just in this region.

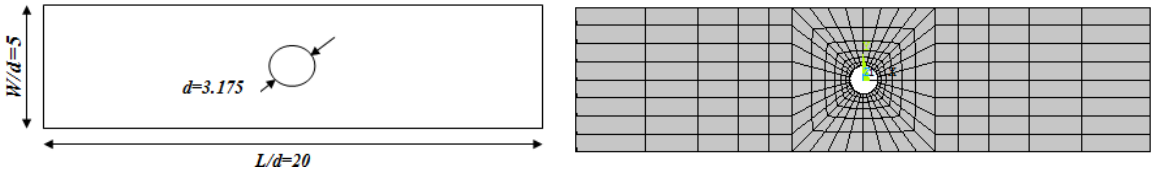
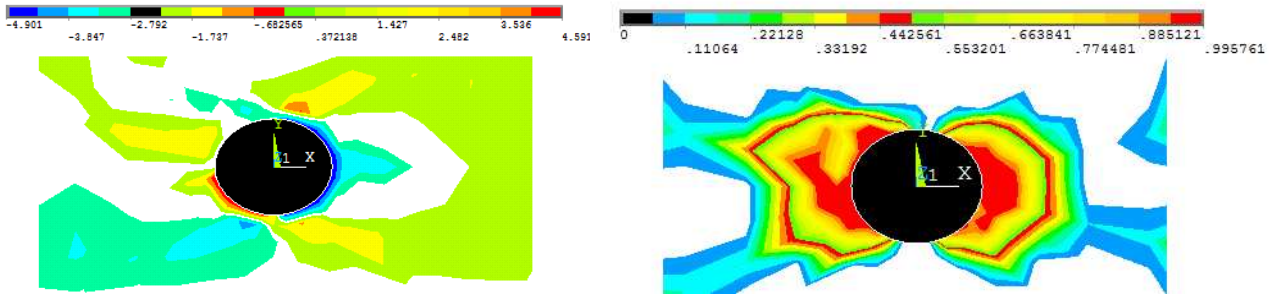


Fig. 3: (a) Schematic Specimen geometry (b) Typical FEM mesh of the model.

Table 1: Material properties of adhesive and layers [4] and Propagation coefficients for fatigue delamination [6].

E_{11}(MPa)	$E_{22}=E_{33}$ (MPa)	$G_{12}=G_{13}$(MPa)	G_{23}(MPa)	$\upsilon_{12}=\upsilon_{13}$	υ_{23}	G_{Ic}(N/mm)
161000	11380	5170	3920	0.32	0.45	0.26
G_{IIc} (N/mm)	$\sigma_{I,\max}$ (MPa)	$\sigma_{II,\max}$ (MPa)	K_I (N/mm)	K_{II}(N/mm)	G_{Ith}	G_{IIth}
1.002	2.5	5	10^3	10^3	0.06	0.1
C_I (mm/cycle)	C_{II} (mm/cycle)	C_m (mm/cycle)	m_I	m_{II}	m_m	η
2.21e-3	1.22e-1	6.09e5	5.09	4.38	5.48	2.73

Fig. 4(a) shows the stress field around the hole. There is a good agreement between the results in this figure and those presented in [4] for the same geometry under monotonic loading. Fig. 4(b) shows the distribution of damage at the interface layer around the hole in the first step before fatigue. It defines the first point witch damage parameter start to be growth.



(a) (b)

Fig 4: (a) Stress contour around the hole. (b) Damage at interface layer around the hole.

The stress contour of the interface layer after the total delamination during the fatigue test is shown in Fig. 5. This stress distribution was obtained after 300000 cycles under 0.3 mm displacement. The stresses are mostly close to zero value showing the delaminated area. More results and discussion are prevented due to the space limitation.

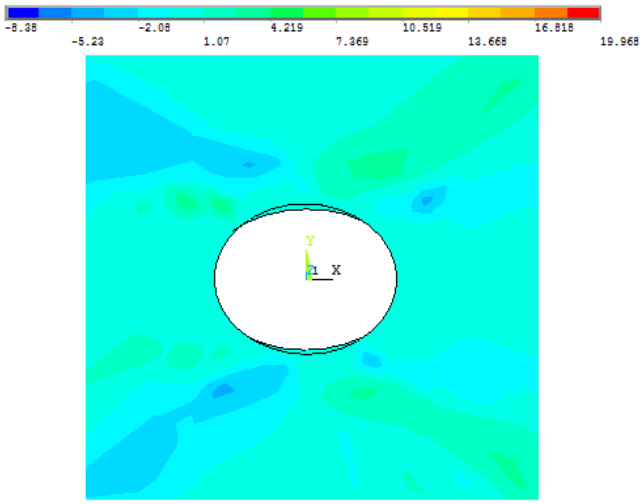


Fig. 5: Stress contour around the hole in cyclic part

Summary

In this paper, the required formulation of a solid like interface element and a fatigue constitutive law were implemented to two UPF routine in ANSYS. The developed procedure was used for the analyses of delamination growth in a holed composite laminate under fatigue loading. It was shown that this procedure can be used for fatigue delamination growth analyses of laminates with cutouts.

References

[1] A. Turon, J. Costa, P.P. Camanho, and C.G. Davila: Composites Part A: applied science and manufacturing Vol. 38, (2007), p. 2270–82.

[2] P.W. Harper and S.R. Hallett: Int. J. Fatigue Vol. 32, (2010), p. 1774–1787

[3] M. Beghini, L. Bertini and E. Vitale: Composite Structures, Vol. 17, (1991), p. 257-274

[4] H. Hosseini-Toudeshky, M. Jalalvand, B. Mohammadi: Procedia Engineering Vol. 1,(2009), p.39–42

[5] W. Wagner, C. Balzani: Eng. Fract. Mech. Vol. 75, (2008), p.2597–2615.

[6] N. Blanco, E.K. Gamstedt, L.E. Asp, J. Costa: Int. J. Of Solids and Structures Vol. 41, (2004), p.4219–35.

[7] A. Turon, J. Costa, P.P. Camanho, P. Maimi:Mechanical response of composites Vol. 10, (2008), p. 77–97.

[8] P.W. Harper, S.R. Hallett: Eng. Fract. Mech. Vol. 75, (2008), p.4774–92.

© (2011) Trans Tech Publications, Switzerland
doi:10.4028/www.scientific.net/KEM.471-472.572

Mechanical and Physical Properties of Cement-bonded Perticleboard Made from Tea Residues and Hardboards

Hüsnü YEL[1,a], Ayfer DÖNMEZ ÇAVDAR[2,b] and Hülya KALAYCIOĞLU[2,c]

[1]Artvin Çoruh University, Dept. of Forest Industrial Engineering, Artvin, TURKEY

[2]Karadeniz Technical University, Dept. of Forest Industrial Engineering, Trabzon, TURKEY

[a]yel33@hotmail.com, [b]donmez103@hotmail.com, [c]khulya@ktu.edu.tr

Keywords: Tea residues, hardboards, cement bonded particleboard, physical and mechanical properties

Abstract. The residues of tea factory and waste hardboards are generally incinerated without utilizing their heat performances. The first objective of this study was to manufacture cement bonded particleboard using residues of tea factory (Camellia sinenses L.) and waste hardboards. The second objective was to evaluate modulus of rupture (MOR), modulus of elasticity (MOE), internal bonding strength (IB), water absorption (WA) and thickness swelling (TS) properties of the boards produced. The boards were produced at two density levels of 800 and 1200 kg/m^3 and at five lignocellulosic mixture ratios of poplar chips/hardboards/tea residues (1/0/0; 1/1/0; 1/0/1; 0/1/0; 0/0/1, based on weigth). All the boards were produced at lignocellulosic material/cement ratio of 1:2.75 on a weight to weight basis. As cement curing accelerators, $Al_2(SO_4)_3$ and Na_2SiO_3 were used at ratios of 1.5% and 3.5%, based on cement weight, respectively. The MOR values ranged from 0.8 to 10.99 MPa and MOE values ranged from 254 to 2979 MPa. The mean values of WA and TS after 24 h of water soaking of the cemen bonded particleboards ranged from 28% to 43.5% and 1.3% to 8.08%, respectively.

Introduction

The increased demands of raw materials in wood based panel manufacturing have led to a research of utilization potentials of substitute lignocellulosic biomass. Unfortunately, not all the countries in the world engage in recycling of waste materials, especially hardboards and tea residues. Large parts of this quantity of tea residues and hardboards generated in developing countries are normally burnt off in the factory or dumped in landfills, while the remaining part is used as fuel. These methods of disposal are certainly wastage of a primary resource. Burning of these hardboard and tea residues in the open air is likely to cause environmental pollution as carbon dioxide (CO_2) and carbon-monoxide (CO) would be released into the atmosphere as a result of insufficient oxygen in the heap of the tea residues. In addition, the biodegradation of lignocellulosic wastes in landfills, emits methane, a green house gas which has 72 times heating effect relative to that of CO_2 [1]. The release of these gases into the atmosphere changes the climate, thereby resulting in global warming, which is now one of the greatest threats to our world. Based on this fact, there is the need to find uses for both waste hardboard and tea residues generated in the world, especially in developing countries. Apart from the fact that the use of these wastes will serve as an environmental management system, it will also contribute positively to the economic growth of the countries.

For these reasons, we aimed to utilize waste hardboards and tea residues in manufacturing cement bonded particleboard. For this purpose, one-layer cement bonded particleboards were produced by mixing both waste hardboards and tea residues with poplar chips and the boards produced were subjected to mechanical (modulus of elasticity, modulus of rupture and internal bonding strength) and physical (water absorption and thickness swelling) tests in accordance with the related standards.

Materials and method

The tea residues (Camellia sinenses L.) used was collected from a tea producing factory in Trabzon, Turkey. Waste hardboards and poplar chips (Popules euroamericana cv.) used in this study were collected from KTU campus in Trabzon, Turkey. Portland cement, PC 42,5 type, used as binder was purchased from Aşkale cement factory in Trabzon, while aluminium sulphate [$Al_2(SO_4)_3$] and sodium silicate (Na_2SiO_3) was added as an accelerator for cement curing. The waste hardboards were severed into small pieces by means of a laboratory–scale wood flaker. The tea residues and poplar chips after chipped by hammer mill were sieved with 1.5-mm and 3-mm screens to remove the dust and oversize particles. The chips on 1.5-mm sieve and passed 3-mm sieve were used for the production of the boards.

The wood/cement ratio for all the board was 1/2.75, a weight to weight basis. Aluminium sulphate and sodium silicate were used at ratios of 1.5% and 3.5% based on cement weight, respectively. The quantity of distilled water added to the particle–cement mixture was computed using the formula developed by Simatumpang (1979) [2] and applied by other researchers as well (Johns et al. 1985; Moslemi and Pfiser 1987; Fuwape 1995; Sudin et al., 1995) [3, 4, 5, 6]. Therefore, the volume of water required was determined as follows Eq. 1:

$$\text{Water (I)} = 0.35C+(0.30-MC)W \quad (1)$$

where C is the cement weight (kg), MC is the particle MC (oven-dry basis) and W is the oven-dry particle weight (kg). The experimental boards were produced at two different density of 800 kg/m^3 and 1200 kg/m^3 and at five different mixtures of poplar chips/wastehardboards/tea residues (1/0/0; 1/1/0; 1/0/1; 0/1/0; 0/0/1, based on weigth). The cement bonded particleboards (CBPBs) produced were of one layer with the sizes of 400 mm (length) by 400 mm (width) by 10 mm (thickness). The boards were conditioned at a temperature of 20°C and a relative humidity of 65% for 1 week prior to the test. Values for internal bond strength (IB), flexural modulus of rupture (MOR), flexural modulus of elasticity, thickness swelling (TS) and water absorption (WA) after 2 h and 24 h water immersion were then determined according to procedures defined in the American Standard ASTM D1037 [7] and in the European Union standards EN 310, EN 317 and EN 319 [8, 9, 10].

Results and discussion

Means, standard deviation and Duncan's multiple comparison of water absorption (WA) and thickness swelling (TS) of the cement-bonded boards soaked in water for 2 and 24 hours were shown in Table 1. LPT (low density poplar and tea residues), LTH (low density tea and hardboard), HTH (high density tea and hardboard), LH (low density hardboard), LT (low density tea residues) and HT (high density tea residues)-coded board groups did not form sufficiently because the tea residues impeded the curing of cement. Therefore, TS, WA, MOR, MOE and IB values of these boards could not be measured and were shown as “untested (UT)” in the tables. The board groups with LPH sample code, which were made from a mixture of poplar chips (50%) and hardboard wastes (50%) and at a density of 800 kg/m^3, showed the highest water absorption for both 2 and 24 hours soaking. These values were mainly due to the high porosity and high cellulose-contained waste hardboards. The lowest values of water absorption for both 2 and 24 hours were obtained from the HP (high density poplar) boards. This was why portland cement had good compatibility with poplar wood and the HP-coded boards had a tighter and a more compact structure (lower porosity) due to high density. The difference between water absorption values of LPH and HPT-coded boards after 2-hours water soaking was not statistically significant.

Table 1. Means, standart deviation and Duncan's multiple comparison for thickness swelling (TS) and water absorption (WA) of the cement-bonded boards after 2 and 24 hours water-soaking

Board groups	Sample code	Density (Kg/m^3)	Thickness Swelling (%)		Water Absorption (%)	
			2 h	24 h	2 h	24 h
Control (Poplar 100%)	LP	800	0,9 (0,15) A	1,3 (0,14) A	34,3 (0,09) A	38,4 (0,11) A
	HP	1200	1,7 (0,13) B	2,07 (0,13) B	22,7 (0,12) B	28,0 (0,13) B
Poplar +Hardboard wastes (50%+50%)	LPH	800	2,5 (0,17) C	3,04 (0,12) C	36,7 (0,09) C	43,5 (0,10) C
	HPH	1200	5,0 (0,19) D	5,9 (0,19) D	30,8 (0,10) D	34,2 (0,10) D
Poplar + Tea residues (50%+50%)	LPT	800	UT	UT	UT	UT
	HPT	1200	6,7 (0,16) E	8,08 (0,16) E	36,6 (0,09) C	40,0 (0,10) E
Tea residues + Hardboard wastes (50%+50%)	LTH	800	UT	UT	UT	UT
	HTH	1200	UT	UT	UT	UT
Hardboard wastes (100%)	LH	800	UT	UT	UT	UT
	HH	1200	6,3 (0,17) E	7,7 (0,17) E	32,4 (0,10) E	35,4 (0,11) F
Tea residues (100%)	LT	800	UT	UT	UT	UT
	HT	1200	UT	UT	UT	UT

Numbers in parenthesis are standard deviation.
Means within a column followed by the same capital letter are not significantly different at 5% level of significance
Untested (UT) means TS and WA values of the boards could not be obtained due to insufficient curing of the boards

As shown from Table 1, the highest and lowest values of thickness swelling after both 2 and 24 hours water soaking were obtained from HPT-coded boards and LP-coded boards, respectively. The difference between thickness swelling values of HPT- and HH-coded boards after both 2 and 24 hours water soaking was not statistically significant. TS values of the boards with 800 kg/m^3 showed lower than that of the boards with 1200 kg/m^3, while WA values of the boards with 800 kg/m^3 showed higher than that of the boards with 1200 kg/m^3. Fuwape et al. [11] reported the mean values of WA and TS after 24 h of water soaking of the cement bonded boards produced from sawdust and wastepaper ranged from 18.18% to 40.49% and 3.55% to 12.13%, respectively. The average values of WA obtained in this study were found higher than those reported by Fuwape et al, but the TS values were found lower than those reported by Fuwape et al. In addition, both TS and WA values in this study were generally found higher than those of bamboo and fiber cement composites reported by Sudin and Swamy [12].

Fig. 1 shows mean values of water absorption and thickness swelling of the board groups soaked in water for 2 and 24 hours. As observed in Figure 1, water absorption values of the LP and LPH-coded boards were higher than those of the other board groups, while their thickness swelling values were lower than those of the other board groups. This is why the LPH and LP boards contain less lignoselulosic materials than the other groups due to their low densities. The HPT boards had high values in both TS and WA because the tea residues impeded the curing of portland cement more than poplar chips and hardboard wastes.

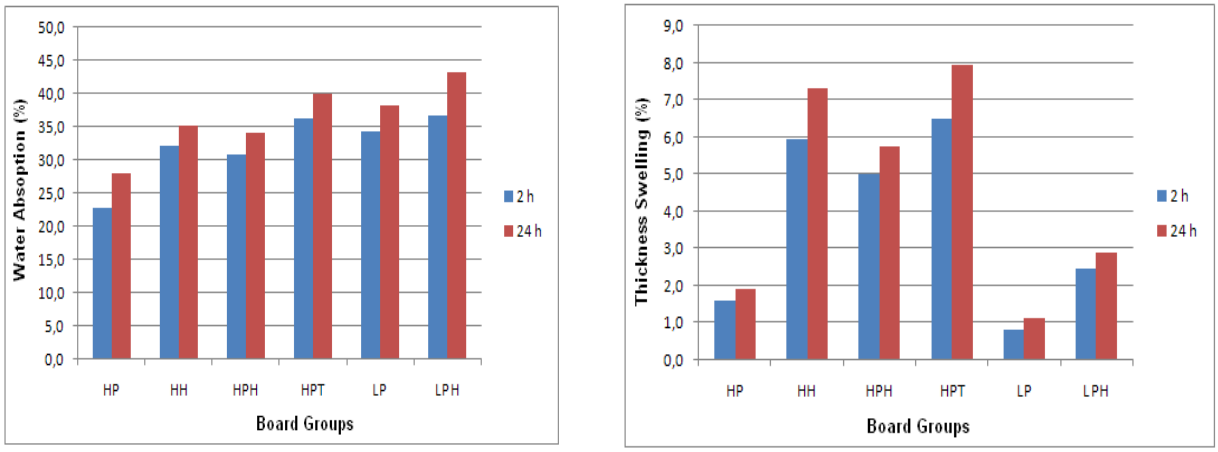


Fig. 1. Mean values of water absorption and thickness swelling of the board groups soaked in water for 2 and 24 hours.

Mechanical properties. Means, standard deviation and Duncan's multiple comparison of modulus of rupture (MOR), modulus of elasticity (MOE) and internal bonding strength (IB) of the cement-bonded boards were presented in Table 2. The HP-coded board groups, which were made from poplar chips (100%) and at a density of 1200 kg/m3, showed the highest values in all the mechanical properties (MOR, MOE and IB).

The lowest values for MOR, MOE and IB, were obtained from the HPT-coded boards. This is why tea residues impede curing of portland cement. This implies that mixtures with poplar chips by 50%, the use of tea residues is not suitable for the production of the cement bonded boards as well as using 100% of tea residues. The boards at a density of 1200kg/m^3 generally had higher mechanical properties than the boards at a density of 800 kg/m^3. The highest values among the boards produced with the lignocellulosic mixtures were obtained from the HPH-coded boards consisting of poplar chips (50%) +hardboard wastes (50%). In addition, HPH-coded boards showed higher mechanical properties (except IB strength) than the LP-coded boards. There is statistically no difference between the MOR values of the LP- and HPH-coded boards. In addition, there is statistically no difference between the MOR values of the HPT-and LPH-coded boards. As observed, the differences between the IB values of LPH and HPT- coded boards, and HPH- and HH- coded boards are not statistically significant.

Papadopoulos [13] carried out hydration tests on eight Greek wood species to determine their inhibitory index and reported that the mixture with the highest compatibility (low inhibition) was that of poplar and cement with an inhibition index of 7.44. Sudin and Swamy [12] reported the best mechanical and physical properties were obtained from the bamboo-cement bonded boards with chemical additive mixture of [$Al_2(SO_4)_3$] and (Na_2SiO_3). Nevertheless, the LPH, HPH, LPT and HPT-coded boards produced from the mixtures of poplar chips+hardboard wastes and poplar chips+ tea residues showed lower mechanical properties than expected. It was shown that the LP, HP, HPH and HH-coded board groups had higher mechanical properties than the cement bonded boards produced from eucalyptus by Semple and Evans [14].

Table 2. Means, standard deviation and Duncan's multiple comparison of modulus of rupture, modulus of elasticity and internal bonding strength of the cement bonded particleboards

Board groups	Sample code	Density (Kg/m^3)	MOR	MOE	IB
			MPa		
Control (Poplar 100%)	LP	800	3,45 (0,18) A	1199 (1,95) A	0,26 (0,02) A
	HP	1200	10,99 (0,10) B	2979 (1,24) B	0,58 (0,02) B
Poplar +Hardboard wastes (50%+50%)	LPH	800	1,04 (0,23) C	348 (3,94) C	0,03 (0,02) C
	HPH	1200	3,79 (0,17) A	1270 (1,95) D	0,1 (0,01) D
Poplar + Tea residues (50%+50%)	LPT	800	UT	UT	UT
	HPT	1200	0,80 (0,23) C	254 (4,26) E	0,02 (0,01) C
Tea residues + Hardboard wastes (50%+50%)	LTH	800	UT	UT	UT
	HTH	1200	UT	UT	UT
Hardboard wastes (100%)	LH	800	UT	UT	UT
	HH	1200	1,95 (0,19) D	416 (3,95) F	0,13 (0,02) D
Tea residues (100%)	LT	800	UT	UT	UT
	HT	1200	UT	UT	UT

MOR: Modules of rupture, MOE: Modules of elasticity,IB: Internal bonding strength,Numbers in parenthesis are standard deviation.Means within a column followed by the same capital letter are not significantly different at 5% level of significance. Untested (UT) means TS and WA values of the boards could not be obtained due to insufficient curing of the boards

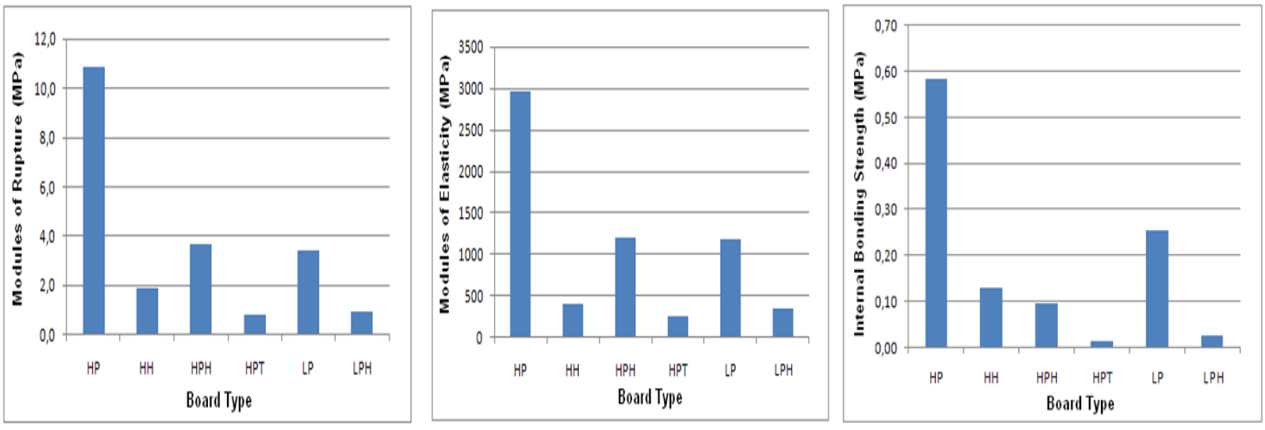


Fig. 2. Mean values of modules of rupture, modeles of elasticity and internal bonding strength of the cement bonded particleboards

Fig. 2 shows mean values of modulus of rupture, modulus of elasticity and internal bonding strength of the cement bonded particleboards. As shown from Figure 2, MOE and MOR values of the boards showed similar column charts. However, IB strength values of the boards showed a different chart from MOR and MOE values. MOR and MOE values of the HH-coded boards were lower than those of the HPH-coded boards, while IB value of the HH-coded boards was higher than that of the HPH-coded boards, Fig. 2.

Summary

Tea residues negatively affected both mechanical and physical properties of the cement bonded boards. Even the boards produced by mixing tea residues with poplar chips (HPT) could not give the expected results. The boards containing waste hardboards had higher values of thickness swelling and water absorption due to high cellulose content of the hardboards. Therefore, it can be recommended that these boards are used for indoor applications. The water absorption values of the LP and LPH- coded boards were higher than those of the other board groups, while their thickness swelling values were lower than those of the other board groups because the LPH and LP boards contain less lignoselulosic materials than the other groups due to their low densities. However, the mechanical properties of these boards sharply decreased, based on their densities.The boards containing waste hardboards and LP boards can be used for insulation purposes in the parts of the buldings where it is not exposed to direct loads.

References

[1] J. Leliveld and P.J. Crutzen: Nature, 41, 355-339, (1992).

[2] M.H. Simatumpang: Holz Roh-Werkst 37, 273–382, (1979).

[3] W.E. Johns, R.M. Rammon, and J. Youngquist: Proceedings of the 19th Washington State Symposium on Particleboard, 363-377, (1985).

[4] A.A. Moslemi and S.C. Pfister: wood fiber science 19, 165-175, (1987).

[5] J.A. Fuwape: 2nd International Conference, Moscow, 45, (1995).

[6] R. Sudin, K. Shaari and S. Selamat: Journal of Tropical Forest Products 1, 71-77, (1995).

[7] ASTM D1037: Standard Test Method for Evaluating Properties of Wood-Base Fiber and Particle Panel Materials, ASTM, USA, (2006).

[8] EN 310: Wood Based Panels-Determination of Modulus Elasticity Bending and Bending Strength, European Committee for Standardization, Brussels, Belgium, (1993).

[9] EN 317: Particleboard and Fiberboards Determination of Swelling in Thickness After Immersion, European Standardization Committee, Brussels, (1993).

[10] EN 319: Particleboards and Fiberboards, Determination of Tensile Strength Perpendicular to the Plane of The Board, European Committee for Standardization, Brussells, Beligum, (1993).

[11] J.A. Fuwape, J.S. Fabiyi and E.O. Osuntuyi: Waste Management 27, 1611-1616, (2007).

[12] R. Sudin and N. Swamy: Journal of Material Science, 41, 6917–6924, (2006).

[13] A.N. Papadopoulos: Holz Roh Werkst, 65, 245-246, (2006).

[14] K.E. Semple and P.D. Evans: Wood-cement composites—Suitability of Western Australian mallee eucalypt, blue gum and melaleucas, Joint Venture Agroforestry Program, 2004.

© (2011) Trans Tech Publications, Switzerland
doi:10.4028/www.scientific.net/KEM.471-472.578

Responses of PFRPCantilevered Channel Beams Under Tip Point Loads

Jaksada Thumrongvut[a] and Sittichai Seangatith[b]

School of Civil Engineering, Suranaree University of Technology,

Nakhon Ratchasima, Thailand.

[a] jaksada@g.sut.ac.th, [b] sitichai@g.sut.ac.th

Keywords: Pultruded fiber reinforced plastic, Lateral-torsional buckling, Channel profile, Cantilever beam

Abstract. In this paper, the experimental results on the structural behaviors of the pultruded fiber reinforced plastic (PFRP) cantilevered channel beams under tip point load are presented. The dimensions of the beam specimens are $76\times22\times6$, $102\times29\times6$ and $152\times43\times10$ mm. The span-to-depth ratios of the specimens are in the range of 10 to 46. A total of 36 specimens were tested to investigate the effect of unbraced length of the beam on the behavior of lateral-torsional buckling and buckling load. Then, the obtained buckling loads were compared to the critical buckling loads calculated by using the modified classical beam theory. From the tests, it was found that the beams have linear elastic responses up to 90-95% of their buckling loads. The mode of failure of the specimens is in the form of lateral-torsional buckling. The modified Timoshenko and Gere's equation unsatisfactorily predicts the critical buckling loads of the beams. Finally, by using a curve fitting, a modification factor was proposed, and the obtained test results and those calculated by the proposed modified equation are in good agreement.

Introduction

Fiber reinforced plastic (FRP) composite materials have been used over the past few decades in a varieties of structures [1]. Structures made of the FRP composites have been shown to provide efficient and economical applications in new structural construction, and in the rehabilitation and strengthening of deficient structures. They have many desirable characteristics over the conventional civil engineering materials such as high corrosion resistance, high strength-to-weight ratio, magnetic transparency, excellent fatigue resistance, high energy absorption, tailoring of the material to specific applications and ease of installation [2]. However, since they are typically orthotropic materials, their analysis and design are much more complex. Among various types of manufacturing processes, the pultrusion process appears to offer the highest productivity-to-cost ratio. The FRP manufactured by this process is called pultruded fiber reinforced plastic (PFRP). Generally, they have the standard PFRP structural profiles similar to the structural steel, including wide-flange sections, I-sections, angles, channels and etc. However, due to relatively low stiffness of the material and thin-walled sectional geometry, the strength is not usually the governing design parameter of the PFRP structural profiles. Mostly, their design is governed by the serviceability parameters such as large deflection or buckling instability, depending on the geometry of the cross-section, the material properties, and the loading conditions [3]. In addition, the critical obstacles to their widespread applications in construction are the lack of simplified and reliable design criteria.

Several researches have been carried out on the experimental and theoretical evaluations of the lateral-torsional buckling of the PFRP structural beams. However, most of these studies have emphasized on the lateral-torsional behavior of the PFRP beams having doubly symmetric cross-sections such as wide-flange, I, and box profiles [4]. Only few research works on the mono-symmetric channel profiles were carried-out [5]. In recent years, the applications of the channel profile have been increased considerably in a variety of the secondary structures such as purlins,

trusses, and bracing members because they can be easily fabricated and erected. Also, in order to create further confidence in the application of the profile, it is necessary to enhance knowledge of its structural performance, particularly the global behaviors and the global instability. This paper is intended to satisfy a portion of that need. Therefore, the objectives of this paper are to present the experimental results on the lateral-torsional buckling behaviors of the PFRP cantilevered channel beams subjected to tip vertical end load passing through the shear center of the section, and to compare the obtained critical buckling loads with those calculated by using the modified Timoshenko's classical beam theory (CBT) in order to check the adequacy of the equation.

Test Specimens and Test Set-up

The PFRP channel beams used in this study were made of E-glass fiber-reinforced and polyester resin and manufactured by a pultrusion process. They have three nominal sizes of $76\times22\times6$, $102\times29\times6$ and $152\times43\times10$ mm. A total of 36 specimens with span-to-depth ratios (L/d) ranging from 10 to 46 were tested. Two tests were performed on each specimen number. Details of the test profiles are presented in Table 1. The specimen numbers were denominated in the form of "C*d*-L_b". For example, the specimen number C152-2.0 is the PFRP channel beams, having the depth *d* of 152 mm and the unbraced length L_b of 2.0 m, respectively.

Table 1. Geometric properties of the pultruded FRP channel specimens

Specimens number	$(d\times b\times t)$ (mm × mm × mm)	L_b (m)	L/d	I_y (mm^4)	J (mm^4)	C_w (mm^6)	Number
C76-1.0	$76\times22\times6$	1.00	13.2	21812	8208	2.660×10^7	2
C76-1.5	$76\times22\times6$	1.50	19.7	21812	8208	2.660×10^7	2
C76-2.0	$76\times22\times6$	2.00	26.3	21812	8208	2.660×10^7	2
C76-2.5	$76\times22\times6$	2.50	32.9	21812	8208	2.660×10^7	2
C76-3.0	$76\times22\times6$	3.00	39.5	21812	8208	2.660×10^7	2
C76-3.5	$76\times22\times6$	3.50	46.1	21812	8208	2.660×10^7	2
C102-1.5	$102\times29\times6$	1.50	14.7	53996	11088	1.161×10^8	2
C102-2.0	$102\times29\times6$	2.00	19.6	53996	11088	1.161×10^8	2
C102-2.5	$102\times29\times6$	2.50	24.5	53996	11088	1.161×10^8	2
C102-3.0	$102\times29\times6$	3.00	29.4	53996	11088	1.161×10^8	2
C102-3.5	$102\times29\times6$	3.50	34.3	53996	11088	1.161×10^8	2
C102-4.0	$102\times29\times6$	4.00	39.2	53996	11088	1.161×10^8	2
C152-1.5	$152\times43\times10$	2.00	9.9	285281	76000	1.379×10^9	2
C152-2.0	$152\times43\times10$	2.00	10.5	285281	76000	1.379×10^9	2
C152-2.5	$152\times43\times10$	2.50	11.8	285281	76000	1.379×10^9	2
C152-3.0	$152\times43\times10$	3.00	13.2	285281	76000	1.379×10^9	2
C152-3.5	$152\times43\times10$	3.50	16.4	285281	76000	1.379×10^9	2
C152-4.0	$152\times43\times10$	4.00	19.7	285281	76000	1.379×10^9	2

To correlate the analytical results with the obtained test results, the values of the longitudinal modulus (E_L) and the in-plane shear modulus (G_{LT}) were determined from the tension test in accordance with ASTM D3039 and the in-plane shear coupon test in accordance with ASTM D5379, respectively. This shear coupon test is in the form of V-notched beam test with the pure shear under a four-point asymmetric bending configuration. From the coupon tests, it was found that the average values of E_L and G_{LT} were 35.20 GPa and 2.18 GPa, respectively.

The typical test set-up in the form of cantilevered beam is shown in Fig. 1. The fixed end was set-up by using wood clamp. At the free end, a part of steel angle with notched groove was firmly

installed so that the tip concentrated vertical load can be applied directly through the shear center of the cross-section in order to provide the flexural and transverse shear stress to the beams. The loads were applied by successive adding of steel plates on a loading platform. The incremental loads were added until reaching the failure of the beams. After each load increment, the vertical end displacement was measured with linear variable differential transducers (LVDTs) and was automatically recorded by a MW100 YOKOGAWA data acquisition unit.

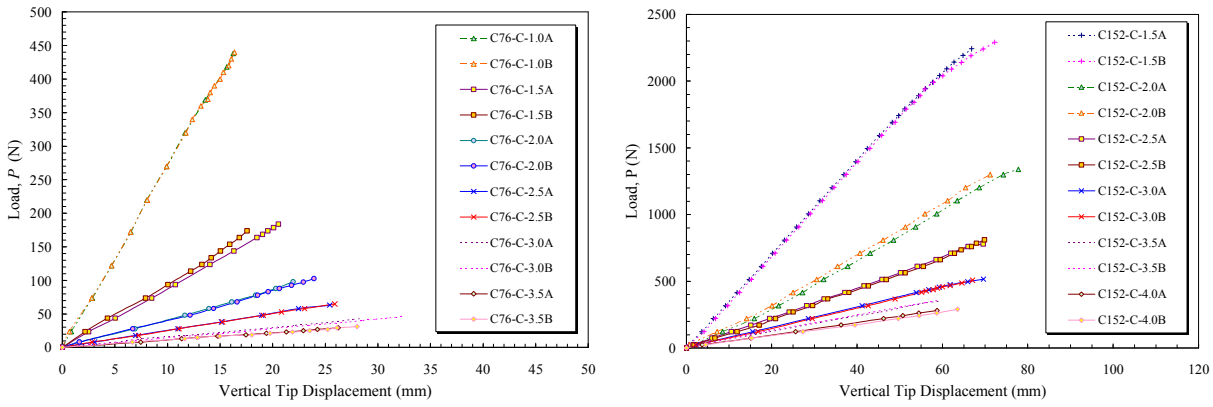


Fig. 1 Typical test set-up used in this study.

Experimental Results and Discussions

Specimen Behaviors and Modes of Failure. Fig. 2 shows the plots of the load versus the vertical tip displacement of the PFRP cantilevered channel beam specimens. It can be seen that the specimens have a linear elastic response up to 90-95% of the obtained buckling load. After that, the responses are gradually becoming nonlinear, leading to the lateral-torsional buckling failure in the form of twisting and large lateral displacement occurred simultaneously. Also, it is noticed that the buckling loads are very susceptible to the large span-to-depth ratio. With the increasing unbraced length (L_b), the failure mode is more outstanding and no external material damage was observed. Fig. 3(a)-3(c) show the failure modes of the specimens with the nominal sizes of $76\times22\times6$, $102\times29\times6$ and $152\times43\times10$ mm, respectively.

Critical Buckling Load and Comparison with Classical Beam Theory. The averaged critical buckling load for each pair of the specimens is considered as the experimental critical buckling load $(P_{cr,\mathrm{EXP}})$. Table 2 shows the experimentally obtained critical buckling load $(P_{cr,\mathrm{EXP}})$. It can be seen that the critical load increases as the unbraced length decreases. Thus, the degree of lateral-torsional buckling depends on the unbraced length of the beam specimens.



(a) $76\times22\times6$ mm (b) $152\times43\times10$ mm

Fig. 2 Typical loads versus vertical tip displacement curves



(a) (b) (c)

Fig. 3 Typical modes of failure (a) 76×22×6 mm, (b) 102×29×6 and (c) 152×43×10 mm of pultruded FRP cantilever channel beams with ratio L/d = 13.2, 14.7 and 19.7, respectively.

Based on classical beam theory (CBT), Timoshenko and Gere [6] have proposed an approximate equation used to predict the elastic buckling load of an isotropic cantilevered beam subjected to vertical point load acting through the shear center of the free end cross-section in the form of:

$$P_{cr} = \gamma \frac{\sqrt{EI_y GJ}}{L_b^2} \tag{1}$$

in which γ is a dimensionless factor depending on the ratio $L_b^2 C/C_1$, E is the modulus of elasticity, I_y is the moment of inertia of the cross-sectional area about minor axis, G is the shear modulus of elasticity and J is the torsional constant or polar moment of inertia, the values of γ can be determined by using the equation:

$$\gamma = \frac{4.013}{\left(1 - \sqrt{\frac{C_1}{L_b^2 C}}\right)^2} \tag{2}$$

where $C = GJ$ is the torsional rigidity, $C_1 = EC_w$ is the warping rigidity and C_w is the warping constant.

Since the PFRP material is usually considered as orthotropic homogeneous material, characterized by using two independent elastic constants: the longitudinal modulus of elasticity (E_L) and in-plane shear modulus (G_{LT}). Therefore, it is proposed that Eq. 1 and Eq. 2 should be modified by using the PFRP material properties. Then, Eq. 1 and Eq. 2 can be rewritten as:

$$P_{cr,\mathrm{CBT}} = \frac{4.013}{\left(1 - \sqrt{\frac{C_1}{L_b^2 C}}\right)^2} \frac{\sqrt{E_L I_y G_{LT} J}}{L_b^2} \tag{3}$$

Table 2. Experimental critical buckling load and comparison with modified CBT

Specimens number	L_b (m)	L/d	Experimental			Analytical		
			Test A $P_{cr,A}$ (N)	Test B $P_{cr,B}$ (N)	Average $P_{cr,\mathrm{EXP}}$ (N)	CBT $P_{cr,\mathrm{CBT}}$ (N)	$\frac{P_{cr,\mathrm{EXP}}}{P_{cr,\mathrm{CBT}}}$	$\frac{P_{cr,\mathrm{EXP}}}{\alpha P_{cr,\mathrm{CBT}}}$
C76-1.0	1.00	13.2	438	440	439	791	0.56	1.08
C76-1.5	1.50	19.7	184	174	179	291	0.61	1.02
C76-2.0	2.00	26.3	98	103	100	150	0.67	1.03
C76-2.5	2.50	32.9	63	65	64	91	0.70	1.04
C76-3.0	3.00	39.5	43	46	45	61	0.73	1.05
C76-3.5	3.50	46.1	29	31	30	44	0.68	0.97
C102-1.5	1.50	14.7	418	388	403	726	0.56	1.02
C102-2.0	2.00	19.6	204	199	201	341	0.59	0.98
C102-2.5	2.50	24.5	129	124	126	197	0.64	1.00
C102-3.0	3.00	29.4	78	83	80	128	0.63	0.95
C102-3.5	3.50	34.3	62	63	62	90	0.69	1.02
C102-4.0	4.00	39.2	48	42	45	67	0.67	0.97
C152-1.5	1.50	9.9	2241	2290	2265	5632	0.40	0.95
C152-2.0	2.00	13.2	1339	1299	1319	2433	0.54	1.05
C152-2.5	2.50	16.4	780	810	795	1349	0.59	1.04
C152-3.0	3.00	19.7	516	508	512	856	0.60	0.99
C152-3.5	3.50	23.0	350	360	355	591	0.60	0.96
C152-4.0	4.00	26.3	282	292	287	433	0.66	1.02

Table 2 presents the obtained critical buckling load compared with those predicted ($P_{cr,\mathrm{CBT}}$) by Eq. 3. The $P_{cr,\mathrm{EXP}}/P_{cr,\mathrm{CBT}}$ ratios are also presented to show the correlation between the experimental results and the predicted results. Based on the analytical results, the $P_{cr,\mathrm{EXP}}/P_{cr,\mathrm{CBT}}$ ratios are in the range of 0.56 to 0.73 for the $76\times22\times6$ mm specimens. Similarly, for the specimens with $102\times29\times6$ and $152\times43\times10$ mm, the $P_{cr,\mathrm{EXP}}/P_{cr,\mathrm{CBT}}$ ratios are in the range of 0.56 to 0.69 and 0.40 to 0.66, respectively. It should be noted that the $P_{cr,\mathrm{EXP}}/P_{cr,\mathrm{CBT}}$ ratios increase as the unbraced length decrease.

Fig. 4 shows the plots between the test results with the predicted results from the modified Timoshenko and Gere's equation in order to verify the adequacy of the equation. It is clear that the trend of the obtained test results goes along the modified equation pretty well. However, due to initial crookedness, shear effects and material property variations; the modified Timoshenko and Gere's equation overestimates the obtained buckling load by approximately 26-60%, depending on the span-to-depth ratio (L/d). Therefore, a further modification on the proposed equation is needed.

To study the relationship between $P_{cr,\mathrm{EXP}}/P_{cr,\mathrm{CBT}}$ and L/d ratios, the values of $P_{cr,\mathrm{EXP}}/P_{cr,\mathrm{CBT}}$ ratios were numerically calculated and plotted for L/d ratios in the range of 10 to 46, as shown in Fig. 5. The results were analyzed statistically to obtain the 95% confidence limit by using nonlinear regression with the inverse first order function. By using a curve fitting, the modification factor is proposed in the form of Eq. 4, and Eq. 3 can be rewritten in the form of Eq. 5.

$$\alpha = 0.78 - \frac{3.50}{(L/d)} \tag{4}$$

$$P_{cr,\mathrm{proposed}} = \alpha P_{cr,\mathrm{CBT}} \tag{5}$$

Based on the analytical results in Table 2, the $P_{cr,\mathrm{EXP}}/\alpha P_{cr,\mathrm{CBT}}$ ratios are also presented to show the correlation between the test results and the predicted results. The average $P_{cr,\mathrm{EXP}}/\alpha P_{cr,\mathrm{CBT}}$ value is

1.01 with coefficient of variation (COV) equal to 0.04. Most of the $P_{cr,\mathrm{EXP}} / \alpha P_{cr,\mathrm{CBT}}$ ratios show the values close to 1.0; this indicates that the predicted buckling loads are relatively in good agreement with the test results.

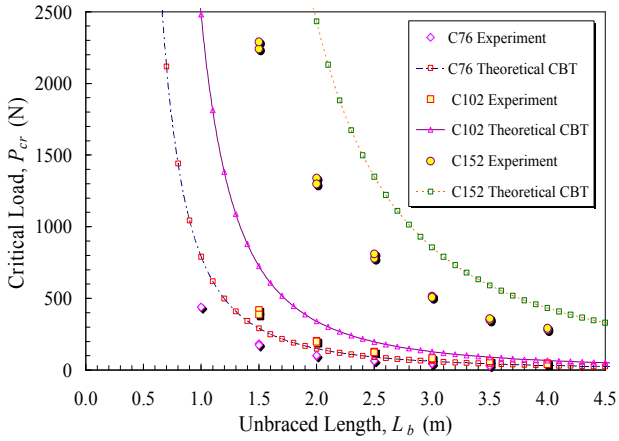


Fig. 4 Critical load versus unbraced length relationship of the PFRP cantilever beams

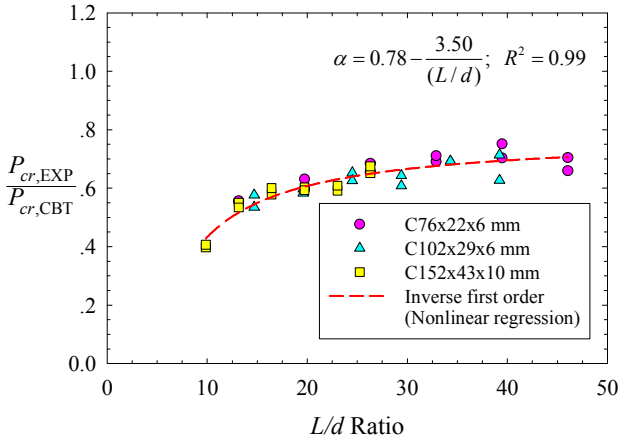


Fig. 5 Normalized critical buckling load

Summary

In this paper, the experimental results on the structural behaviors of the PFRP cantilevered channel beams are described. Based upon the results, the following conclusions can be drawn:

1. The responses of the PFRP channel beams subjected to the tip point load through the shear center of the cross-section are linear elastic up to 90-95% of the lateral-torsional buckling load. Subsequently, the responses are gradually becoming nonlinear, leading to the buckling failure of the beam specimens. All of the specimens were failed in the form of twisting and large lateral displacement occurred simultaneously in the form of the lateral-torsional buckling mode of failure. Based on the test results, the critical buckling load increases as the span-to-depth ratios of beam decreases.
2. By comparing the obtained critical buckling load with those predicted by the modified Timoshenko and Gere's equation, it was found that the equation overestimate the test results in the range of 26-60%, depending on the span-to-depth ratios. By using a curve fitting, a modification factor was proposed. Finally, the obtained test results are in good agreement with those calculated by the proposed equation.

Acknowledgments

The authors gratefully acknowledge all the supports of Suranaree University of Technology for this study, which is a part of the research project "The Development of Design Equation for Pultruded-Fiber Reinforced Plastic Having C-Section under Compression and Flexure".

References

[1] T.P. Vo and J. Lee: Engineering Structures Vol. 30 (2008), p. 1958
[2] R.J. Brooks and G.J. Turvey: Composite Structures Vol. 32(1-4) (1995), p. 203
[3] N.I. Kim, D.K. Shin and M.Y. Kim: Engineering Structures Vol. 29 (2007), p. 1739
[4] P.Z. Qiao, G.P. Zou and J.F. Davalos: Composite Structures Vol. 60 (2003), p. 205
[5] L.Y. Shan and P.Z. Qiao: Composite Structures Vol. 68(2) (2005), p. 211
[6] S.P. Timoshenko and J.M. Gere: *Theory of Elastic Stability.* (McGraw-Hill, New York 1961).

© (2011) Trans Tech Publications, Switzerland
doi:10.4028/www.scientific.net/KEM.471-472.584

Effect of Nanoclay on the Mechanical and Thermal Properties of Rigid Polyurethane/Organoclay Nanocomposite Foams Blown with Cyclo and Normal Pentane Mixture

M. Valizadeh[a], M. Rezaei[b], A. Eyvazzadeh[c]

Institute of Polymeric Materials, Polymer Engineering Department,
Sahand University of Technology, Tabriz, Iran

[a]mvalizadeh63@gmail.com, [b]rezaei@sut.ac.ir, [c]alirezaeyvazzadeh@gmail.com

Keywords: Nanocomposite, Polyurethane Foam, Organoclay, Thermal Conductivity, Microstructure

Abstract. Polyurethane (PU)/Clay nanocomposite rigid foams were synthesized with modified layered silicate clay (organoclays, Cloisite 30B). PU foams were prepared by a batch reaction injection molding process. Organoclay was dispersed first in the isocyanate component using an ultrasonic homogenizer and then mixed with polyol and physical blowing agent mixture to produce nanocomposite PU foams. To study the reaction possibility between cloisite 30B and isocyanate as well as the effect of sonication on the reaction, Fourier transfer infrared (FTIR) analysis was conducted. The dispersion of organoclay in the rigid PU/clay nanocomposite foams was analyzed by wide angle X-ray diffraction (XRD). The microstructure of the foams was studied by an optical microscope and image analysis software. It was concluded that with increasing of nanoclay content the cell size is decreased and the cell size distribution is narrowed. The mechanical properties of pure and nanocomposite foams were examined by compression test. The data obtained from the compressive stress-strain curves reveals that the strength and modulus of polyurethane foam increase by addition of organoclay up to 1wt% and then decrease. Thermal conductivity coefficient (k-factor) of rigid PU nanocomposite and neat foams was measured by a simple transient method. The thermal conductivity results demonstrated that the polyurethane foam k-factor continuously decrease by addition of organoclay. It can be attributed to the reduced cell size as well as narrow cell size distribution in of nanocomposite foams.

Introduction

Rigid polyurethane foams (PUFs) are widely used in many application such as insulation, cushioning, packing and structural materials [1]. Conventional blowing agents used in production of PUFs such as monofluoro-trichloro-methane (R11) and difluoro-dichloro-methane (R12) have recently been regulated in many countries from the environmental considerations. Recently many studies have been done to use of low thermal conductive and diffusion coefficient environmentally acceptable blowing agents like pentane to replace chlorinated fluorocarbons (CFC), which were phased out due to their tendency to deplete atmospheric ozone. But replacement of such blowing agents has negative effect on thermal insulation properties of PUFs due to their high thermal conductivity coefficient. Furthermore PUFs have some deficiencies, such as low thermal stability and low mechanical strength. To overcome these problems, a great deal of efforts has been devoted to develop polyurethane (PU)/montmorillonite (MMT) clay nanocomposite foams in recent years [2, 3]. Nanoclays generally possess higher mechanical and thermal properties to the polymer matrix. In PUFs/clay nanocomposites, clay has been reported to act as heterogeneous nucleating agent where is led to PUFs with uniform cell structure and small cell size [4, 5]. The best performance is commonly observed for exfoliated nanocomposites. However this is very difficult to attain by simple mixing methods. Therefore, many researchers have been interested in the application of

ultrasound technique for synthesis of polymer/clay nanocomposite foams to overcome the limitations of existing methods [6-8]. High-intensity ultrasonic waves may be useful in this context as they generate some important nonlinear effects in the liquids namely transient cavitation and acoustic streaming [8, 9].

Montmorillonite (MMT), a kind of clay, consists of two external silica tetrahedral sheets and a central octahedral sheet of alumina. This clay structure plays important roles in improving mechanical, thermal, and diffuse-barrier properties of polymer layered silicate nanocomposites. Lately different kind of organo-modified MMT (organoclay) have been used for development of PU/clay nanocomposites [10, 11]. Some promising results have been obtained with Cloisite 30B (which is MMT organo-modified by an alkyl ammonium cation bearing two primary hydroxyl functional groups) indicated that improved thermal and mechanical properties of PU nanocomposite foams. However few researches on low density rigid nanocomposite PUF have been reported. It was observed that the mechanical properties of nanocomposite PUFs can be increased or decreased in presence of organoclay which depend on molecular weight of polyol, oraganoclay modifier, preparation method and so on. However, most researchers have deduced that the cell size of PUF decreases and thermal insulation properties improve by addition of low content of organoclay[11].

In this study, we synthesized rigid PU/clay nanocomposite foams using an environmental friendly blowing agent. This investigation reports an extensive study on the effect of nanoclay (Cloisite 30B) at different contents (1 and 3wt%) on the thermal and mechanical properties as well as microstructure of rigid PUFs.

Experimental

The materials used for preparation of rigid PUFs and their formulation (by weight %) are presented in Table 1. Methane diphenyl diisocyanate (MDI, Desmodur 44V20L) and polyether polyol, (Uronole 210R) were obtained from Bayer Co., Germany. Cyclo pentane and normal pentane as physical blowing agents were prepared from Merk Co., Germany and mixed by weight ratio 60/40 respectively. Modified organoclay Cloisite 30B (C30B), prepared from Southern clay Co., USA.

The foams's mold density were kept constant (30-32kg/m^3), at different formulations. The weight ratio of MDI to polyol mixture was kept at 1.42 in these formulations.

The reaction between –NCO groups of MDI and –OH groups of organoclay was studied by FTIR spectroscopy (UNICAM Matson 1000) at the frequency ranges between 400 to 4000 cm^{-1}. The morphology of the nanocomposites was characterized by X-ray diffraction (XRD, Siemens model D5000). The mechanical properties of rigid PU foam was examined by compression test using a Zwick/Roell (model TI-FR010) tensile/compression machine at room temperature and strain rate 5 mm/min. The microstructure of the foams was studied by an optical microscope (Bel, Italy) and Bel View image analysis software. The thermal conductivity coefficient of samples was determined by a simple transient method thermal conductometer.

Table 1: Materials used to produce rigid PUFs

Materials [%wt]	PU_naet	PU_C30B [1wt%]	PU_C30B [3wt%]
Polyol 501	38.78	38.57	38.15
Isocyanate 301	55.13	54.83	54.24
Cyclo / Normal pentane (60/40)	6.08	6.05	5.98
Cloisite 30B	0	0.55	1.63

Results and Discussion

In order to investigate the reaction possibility between the organoclay and MDI the FTIR spectra of MDI and MDI/ organoclay (3%wt) mixture were recorded and compared in Fig 1. Furthermore in order to analyze the effect of sonication, the FTIR spectra of MDI mixture before sonication process, is shown in Fig 1. Comparison of these spectra shows that the area under the characteristic peak of isocyanate group in 2274 cm^{-1} in MDI/organoclay mixtures was diminished while the intensity of the characteristic peak of carbonyl groups in (1720 cm^{-1}) was increased. The ratios of isocyanate and carbonyl peaks height to the aromatic peak height at 1607 cm^{-1}were calculated and presented in Table 2.

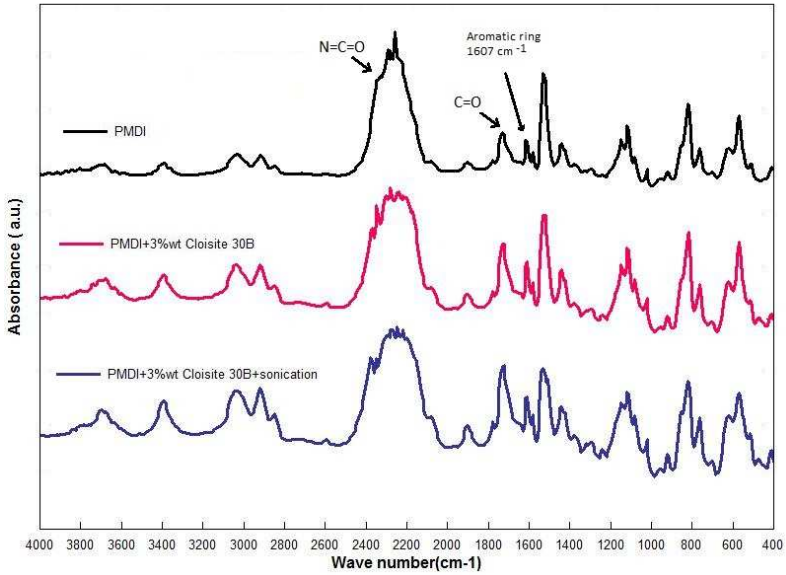


Fig 1. FTIR spectra of MDI and MDI/Cloisite 30B (3 wt%) mixture before and after sonication.

Table 2. Ratios of isocyanate and carbonyl peaks height (H_{2274},H_{1720}) to the aromatic peak height(H_{1607}) for MDI and MDI/ Cloisite 30B (3 wt%) mixture before and after sonication.

Peak ratio	Isocyanate	Isocyanate+3 wt% Cloisite 30B Before sonication	Isocyanate+3 wt% Cloisite 30B After sonication
H_{2274}/H_{1607}	6.12	3.31	1.75
H_{1720}/H_{1607}	1.2	2.2	3.16

These results show that the isocyanate peak ratio is decreased by addition of Cloisite 30 B while the carbonyl peak ratio is increased. These results confirm the reaction between –OH groups of organoclay and –NCO group of MDI and urethane bond formation between them. Furthermore the results show that the sonication process increases the chemical reactivity between the isocyanate and Cloisite 30B.

The XRD patterns of nanocomposite foams are presented in Fig 2. The peak at 2θ=4.2˚ in the organoclay correspond to d-spacing of 1.85 nm. In nanocomposites foams with 1 and 3 wt% Cloisite 30B such peak isn't observed within the scan range. Disappearing of the Cloisite 30B peak in nanocomposite foams may be attributed to the delaminating or exfoliation of nanoclay layers in polyurethane matrix.

Fig. 3 shows typical compressive stress-strain curves for pure and nanocomposite PUFs with 1 and 3 wt% organoclay in the foam rise direction. It can be observed that addition of 1 wt% organoclay to PUF increases the modulus from 2.22 to 2.63 MPa. Furthermore increasing of

organoclay from 1 to 3 wt% decreases modulus from 2.22 to 1.85 Mpa in nanocompoite PUFs. This can be attributed to the inhibitory effects of organoclay fillers on hydrogen bonding formation between polyurethane chains and deficiency in the reaction stoichiometry.

Fig. 4 illustrates cell size normal distribution of neat and nanocomposite PUFs. It can be observed that with increasing nanoclay content the cell size decreases and the cell size distribution is narrowed (Tables 3). This can be attributed to the fact that nanoclay can potentially serve as a bubble nucleating agent to create more and, therefore, smaller bubbles in nanocomposite foams.

In general, the thermal conductivity of PUF depends on the foam density, cell size, cell orientation, ratio of close to open cell content as well as on the thermal conductivity of the filling materials [1]. The effect of the organoclay content on the thermal conductivity of PUF/ clay nanocomposites is shown in Fig. 5. Regarding to the foams cell structure, it is shown that PUFs with a small cell structure shows lower thermal conductivity, because with reducing the cell size, the radiation contribution on the foam thermal conductivity is decreased.

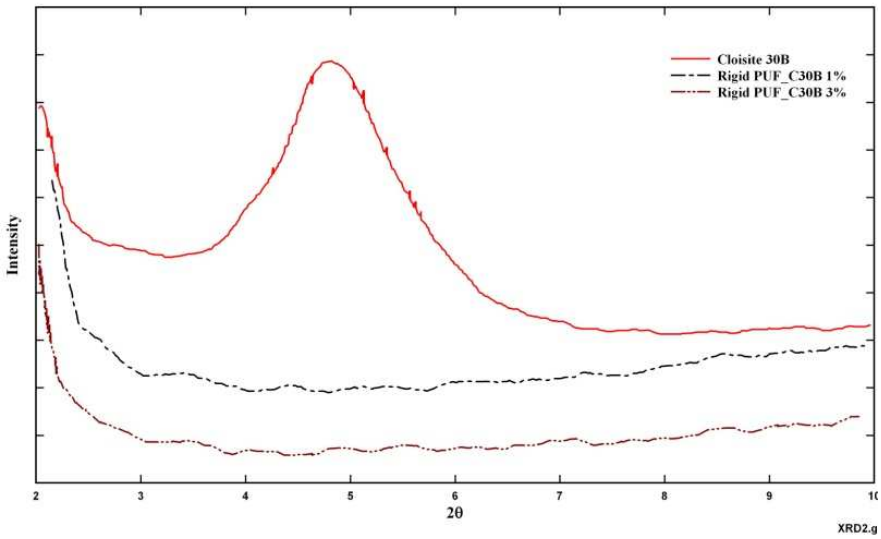


Fig 2. XRD patterns of Cloisite 30B, rigid nanocomposite PUFs with 1 and 3 wt% Cloisite 30B.

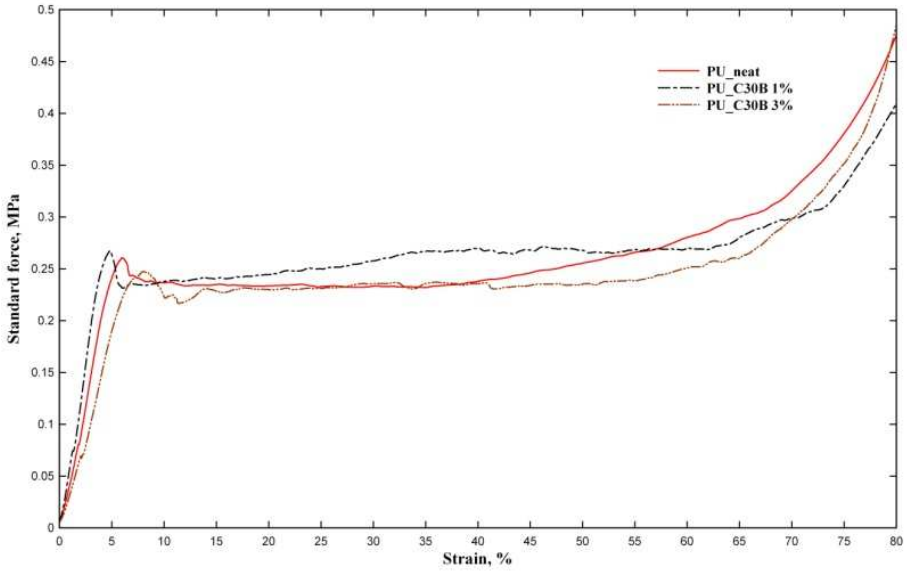


Fig 3. Compressive stress-strain of rigid neat and nanocomposite PUFs in the rise direction.

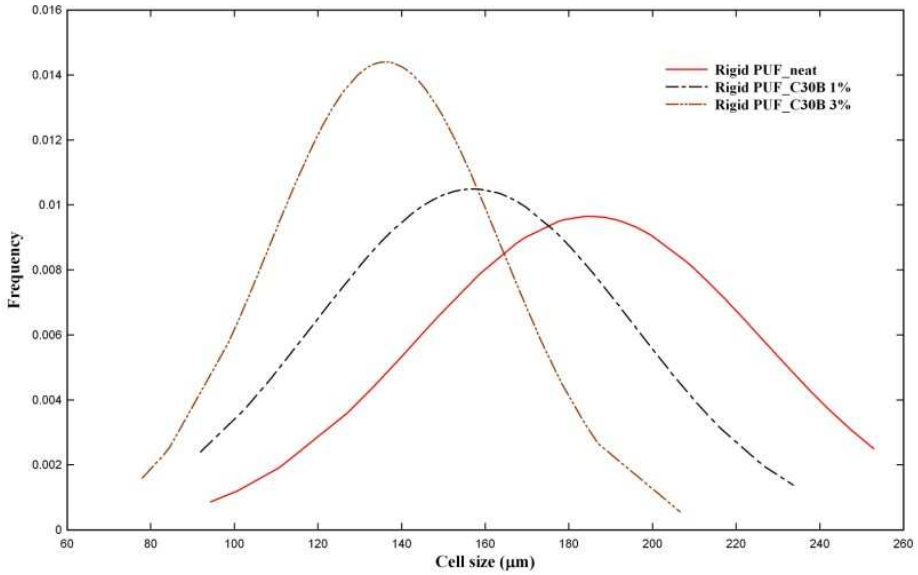


Fig 4. Cell size distribution of rigid neat and nanocomposite PUFs in the rise direction.

Table 3. Mean cell size of neat and nanocomposites PUFs

Foam	PU_neat	PU_C30B 1wt%	PU_C30B 3wt%
Mean cell size [μm]	184.97	157.32	136.05

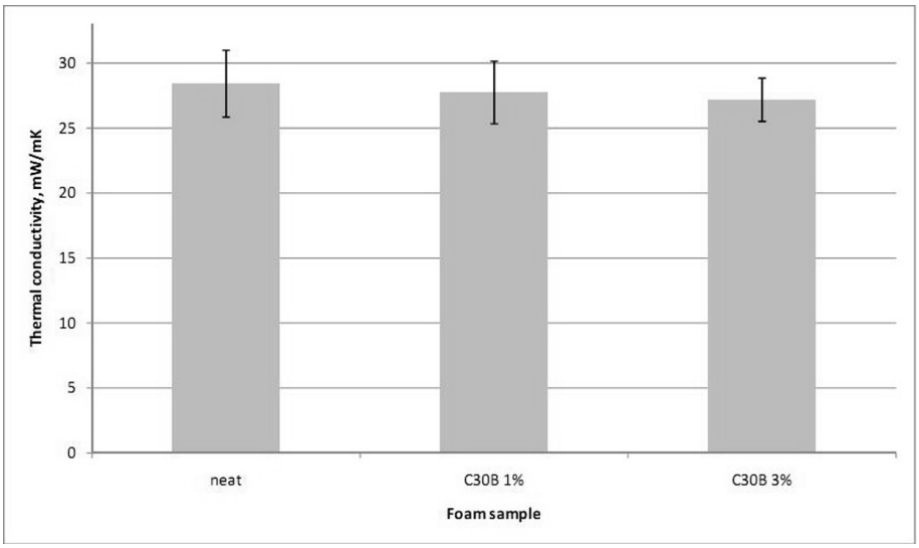


Fig 5. Effect of organoclay content on the thermal conductivity of PUFs.

Summary

It was found that the organoclay was effectively intercalated/ exfoliated to produce rigid PUFs /clay nanocomposite. With addition of Cloisite 30B, –OH groups of clay react with –NCO groups of isocyanate to form polyurethane linkage. XRD Patterns indicated that layers of the nanoclay are delaminated or exfoliated in nanocomposite foams. Incorporating of the Cloisite 30B nanoclay into the PU matrix decreased cell size and narrowed cell distribution which led to the reduced thermal conductivity coefficient in PUF/clay nanocomposites foams. Furthermore addition of 1 wt% Cloisite 30B leads to the improved mechanical properties.

References

[1] M. Thirumal, D. Khastgir, N. K. Singha, B. S. Manjunath and Y. P. Naik: Macro. Sci. Part A, Vol. 46 (2009), p. 704
[2] X. Coa, L. J. Lee, T. Widya and C. Macosko: Polym. Vol. 46 (2004), p. 775
[3] M. M. Alavi Nikje, Z. Mazhari Tehrani: Polym. Eng. Sci. Vol. 50 (2009), p. 468
[4] M. C. Saha, Md. E. Kabir and S. Jeelani: Mater. Sci. Eng. 479 (2008), p. 213
[5] S. H. Kim, M. C. Lee, H. D. Kim, H. C. Park, H. M. Jeong, K. S. Yoon and B. K. Kim: Appl. Polym. Sci. Vol. 117 (2010), p. 1992
[6] T. Widya, C. W. Macosko: Macro. Sci. Part B, Vol. 44 (2005), p. 897
[7] W. J. Seo, Y. T. Sung, S. B. Kim, Y. B. Lee, K. H. Choe, S. H. Choe, J. Y. Sung and W. N. Kim: Appl. Polym. Sci. Vol. 102 (2006), p. 3764
[8] Md. E. Kabir, M. C. Saha, S. Jeelani: Mater. Sci. Eng. Vol. 459 (2007), p. 111
[9] P. Mondal, D. V. Khakhar: Appl. Polym. Sci. Vol. 103 (2007), p. 2802
[10] Z. Xu, X. Tang, A. Gu and Z. Fang: App. Polym. Sci. Vol. 106 (2007), p. 439
[11] S. Solaski, S. Benali, M. Rochery, E. Devaux, M. Alexandre, F. Monteverde and P. Dubois: Appl. Polym. Sci. Vol. 95 (2005), p. 238

© (2011) Trans Tech Publications, Switzerland
doi:10.4028/www.scientific.net/KEM.471-472.590

Failure Modes of CFRP Flexural Strengthened Steel I-Beams

KAMBIZ Narmashiri[1, a], MOHD Zamin Jumaat[2, b] and N.H. Ramli Sulong[2, c]

[1]Civil Engineering Department, Faculty of Engineering, Islamic Azad University, Zahedan Branch, Zahedan, Iran

[2]Civil Engineering Department, Faculty of Engineering, University of Malaya, Kuala Lumpur, Malaysia

[a] narmashiri@siswa.um.edu.my, [b] zamin@um.edu.my, [c] hafizah_ramli@um.edu.my

Keywords: Carbon Fiber Reinforced Polymer (CFRP); Failure modes; I-beam; Steel; Strengthening

Abstract. This paper presents the experimental and numerical studies on the flexural strengthened steel I-beams by using Carbon Fiber Reinforced Polymer (CFRP) strips. Nowadays, strengthening existing steel structures by using CFRP has been widely interested. One of the common usages of CFRP to strengthen steel beams is the flexural upgrading. In this case, CFRP strips are pasted on the tensile flange to improve flexural behaviors. The problems that are frequently reported for CFRP strengthened steel beams are the debonding, delaminating (peeling), and splitting. Identification these failure modes are essential to provide an appropriate level of safety for strengthened steel beams. To investigate the CFRP failure modes, four strengthened steel I-beams were chosen. The CFRP plates with different thicknesses in single and double (splice) layers were used. Both experimental test (four-points bending test) and numerical simulation (full 3D simulation with ANSYS) were employed. The incremental loading was applied until failure while deformations in the critical regions were recorded. The results reveal that for the CFRP flexural strengthened steel beams the following failure modes occurred: (a) debonding at the CFRP plate tips, (b) debonding below point loads, (c) delaminating at the ends of CFRP plate, and (d) splitting below point loads. The sequence of failure modes depended on the specifications of CFRP plate. Some recommendations are provided to overcome/retard these failures.

Introduction

Recently, the application of CFRP for the purpose of strengthening steel structures has increased significantly because of its high tensile strength, low weight, and high resistance against corrosion. For flexural strengthening of I-beams, the CFRP strips are installed on the tensile flange. CFRP has high tensile strength and can improve the flexural behavior of beams.

One of the most important criteria for the CFRP strengthened steel structures is the bonding between CFRP, adhesive, and steel surfaces.

Hollaway and Cadei [1] reviewed the problems encountered in the bonding onto metallic structures and discussed how these problems might be overcome. Buyukozturk et al. [2] reviewed the achievements in the strengthening of both reinforced concrete and steel members. The failure modes of FRP strengthened steel members that were observed by these authors are:

a) Buckling of top flange in compression
b) Buckling of web in shear
c) FRP rupture
d) FRP debonding

The progressive debonding failure of the FRP retrofitted beam can be simulated by incorporating the proposed bond failure model into its finite element analysis [3]. Schnerch et al. [4] indicated that the bond behavior of FRP strengthened steel structures was different than concrete structures. In addition, high bond stresses occurred for steel structures because of the amount of strengthening requirements. The surface preparation methods were investigated to determine the bond stresses and their application for design. Al-Emrani et al. [5] studied the behavior of composite steel-CFRP

members experimentally and using FE-analysis. They found that the bonding behavior of CFRP strengthened steel beams before and after yielding are different. Besides, they showed that before yielding, the ends of CFRP reinforcement are more critical, but after yielding, high stress also occurred at the mid-span (below the point load). Also, they reported that four failure modes have been identified for flexural strengthened steel-concrete beams:

a) Mid-rupture.
b) End-debonding
c) Below load-debonding
d) End-peeling

Lenwari et al. [6] found that the steel beams had two types of failure mode, depending on the length of the plate:

a) Plate debonding in beams with short plates
b) Plate rupture at mid-span in beams with long plates.

Schnerch et al. [7] investigated the strengthening of steel structures and bridges by using FRP materials. They indicated that the bond behavior of FRP to steel structures was completely different from concrete structures. The test results indicated that for steel structures and bridges very high bond stresses occurred. Al-Emrani and Kliger [8] developed a new type of test specimen to examine the effect of various material parameters on the behavior and strength of bonded steel-CFRP elements. Finite element analysis of the tested elements was also employed to examine the type and magnitude of interfacial stresses in the bond line of these elements. Lenwari et al. [9] presented the debonding behavior of partial-length, adhesively bonded CFRP plates that were applied for strengthening steel beams. The bonded CFRP plates have the propensity to debond under loadings because of the high stress at the plate tip. The steel/adhesive corner was the region where the debonding began. Haghani et al. [10] investigated the possible techniques to reduce the magnitude of the interfacial stresses along the bond line. The methods include changing the geometric and mechanical properties of the strengthening components and modifying the distribution of interfacial stresses along the bond line. Benachour et al. [11] developed a closed-form rigorous solution for interfacial stress in simply supported beams strengthened with bonded prestressed FRP plates and subjected to a uniformly distributed load, arbitrarily positioned single point load, or two symmetric point loads using linear elastic theory and including the variation in FRP plate fiber orientation. The results show that high concentration of both shear and normal stresses at the ends of the laminate exist, which might result in premature failure of the strengthened specimens at these locations.

In this research, the below objectives were researched:

a) Investigation on the CFRP failure modes used in strengthening steel I-beams.
b) Study on the effects of applying different thicknesses and modulus of elasticity on the CFRP failure modes.

To study the CFRP failure modes of the flexural strengthened steel I-beams, both experimental test and numerical simulation were employed.

Materials and Methods

In this paper, four steel I-beams are chosen, tested, and numerically modeled in the four-points bending test and the finite elements modeling methods while deformations are measured by using Linear Variable Deformation Transducers (LVDT) to failure.

Specimens. Figs. 1and 2 show the specifications and dimensions of the steel beams and the CFRP strips. Also, the specifications of the chosen steel I-beams are tabulated in Table 1. Specimen F1 was not strengthened and used as the non-strengthened control beam. Beam F2 and F3 were strengthened by using the CFRP type CF1 and CF2 with the same length (1500 mm) and thicknesses of 1.2 and 1.4 mm, respectively. Specimen F4 was strengthened by using the CFRP type CF2 with 1500 mm in length and 1.4 mm in thickness. Also, an additional CFRP layer type CF1 with 1000 mm in length and 1.2 mm in thickness was installed at the mid-span.

Steel. The Mild steel is selected for the beams [12, 13, 14, 15].

CFRP. The unidirectional CFRP materials (LaMaCo™ Build Seal® Strip 514-1CF and LaMaCo™ Build Seal® Strip 514-2CF) are chosen to strengthen steel beams [12, 13, 14, 15].

Adhesive. The adhesive Sikadur® -30 is used to bond the CFRP strips on the steel beams [12, 13, 14, 15].

Preparation of the Specimens. Before starting the tests, the specimens must be prepared carefully. This includes surface preparation, cutting and cleaning CFRP strips, mixing adhesive, applying adhesive on the CFRP and steel surface, and installing CFRP [12, 13, 14, 15].

Test Setup. The four-points bending test [12, 13, 14, 15] is used to test the specimens. Fig. 1 indicates the test setup for the beams.

Numerical Simulation. To model the specimens, the full 3D simulation using ANSYS software was performed. The steel I-sections, steel stiffeners, CFRP plates, and adhesive were simulated by using the 3D solid triangle elements (Ten-Nodes 187.) The interface of common surfaces was defined between the steel I-beam, adhesive, and CFRP plates. Debonding and peeling occurred when the plastic strains exceeds the ultimate strain. Non-linear static analysis was carried out to achieve debonding and peeling. In this case, the load was applied incrementally until the plastic strain in the first element reached the ultimate strain. The linear and nonlinear properties of materials were defined. The CFRP plate material properties were defined as linear and orthotropic because CFRP materials have linear properties and they were unidirectional. The steel beams were defined as nonlinear properties. For meshing, combination of the auto meshing and map meshing were used. In the critical region, the elements were meshed smaller than the other regions. Since the 3D simulation and non-linear analysis have the best accuracy to the experimental method [12], these methods are used to simulation of the specimens.

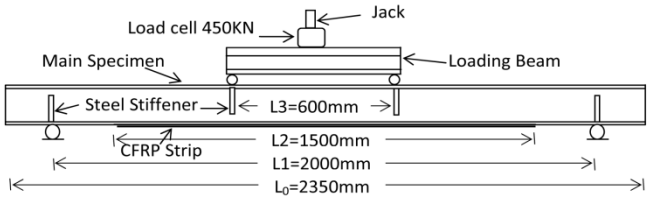


Fig. 1. Specifications and dimensions of steel I-beam

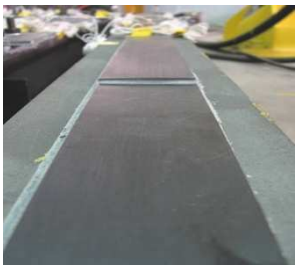


Fig. 3. Application of splice CFRP layer at the mid-span

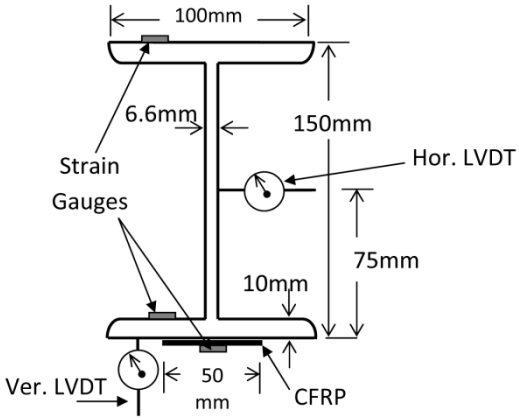


Fig. 2. Dimensions of steel I-beams and locations of CFRP strips

Table 1. Specifications of the beams

No	Beam ID	Specifications of CFRP reinforcements					
		Main Layer			Splice Layer		
		CFRP type	CFRP length (mm)	CFRP thick. (mm)	CFRP type	CFRP length (mm)	CFRP thick. (mm)
1	F1	N/A	N/A	N/A	N/A	N/A	N/A
2	F2	CF1	1500	1.2	N/A	N/A	N/A
3	F3	CF1	1500	1.4	N/A	N/A	N/A
4	F4	CF2	1500	1.4	CF1	1000	1.2

Results and Discussions

CFRP Failure Modes. The sequences of CFRP failure modes for different specimens are tabulated in Table 2. For the strengthened control beam (F2), the below failure modes were observed, consecutively:

a) Splitting below point loads (Fig. 4.a)
b) Debonding below point loads (Fig. 4.b)
c) Delaminating at the CFRP tips (Fig. 4.c)
d) Debonding at the CFRP tips (Fig. 4.d)

One major problem of strengthened steel beams is the presence of high interfacial stresses near the end of the composite laminate which might govern the failure of the strengthening schedule [16]. Also, end-debonding was occurred because of high stress and strain intensity on adhesive at the CFRP tips [17, 18].

Al-Emrani et al. [5] showed that before yielding, the ends of CFRP reinforcement were more critical, but after yielding, the high stress also occurred at the mid-span (below the point load) that caused below the point loads debonding [5]. These procedures also were seen in the present research.

Another CFRP failure mode that was observed during the present tests is end-delamination/ peeling. An important feature of the reinforced beam is the significant stress intensity at the tip of CFRP plate because there is a discontinuity by the abrupt termination of the strip [19].
The other CFRP failure that was observed in this study is the CFRP splitting below point load. It began from below point loads and developed to the whole length of the strip.

The reason for this failure mode (splitting below point load) was due to the effects of combination of the overall lateral-torsional-buckling (Fig. 5.a) and local buckling and stress intensity below the point loads (Fig. 5.b). Since the lateral deformation was not prevented in this study the beams deformed in both vertical and horizontal directions. CFRP strips have high axial and low transverse strength because the fibers of CFRP plates are located in the longitudinal direction, so they could not carry the lateral deformation resulted in splitting.

Table 2. Sequences of the CFRP failure modes

No	Beam ID	Sequences of CFRP failure modes*
1	F1	N/A
2	F2	BSM-BDM-EPM-EDM
3	F3	BDM-EPM-EDM
4	F4	EDS-EPM-EDM-BDM

*BDM: Below load-debonding of main layer, EDS: End-debonding of splice layer, EDM: End-debonding of main layer, BSM: Below load-splitting of main layer, EPM: End-peeling of main layer

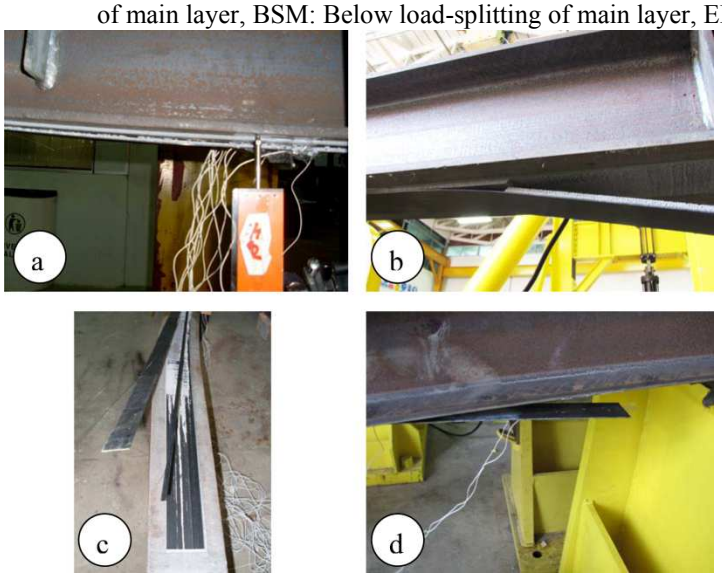


Fig. 4. CFRP failure modes (a) below load-splitting, (b) below load-debonding, and (c) end- delaminating, (d) end-debonding

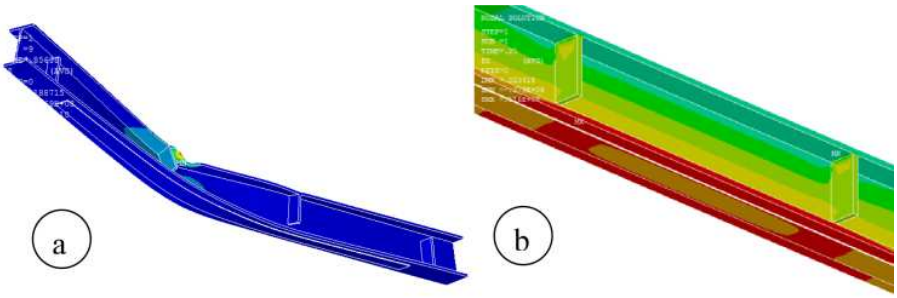


Fig. 5. Finite element results (a) effect of lateral buckling on deformation of bottom flange and (b) stress intensity below point loads

For the specimen F3 that was strengthened by using thicker CFRP plate (1.4mm), the below failure modes were observed:

a) Below load-debonding
b) End-peeling
c) End-debonding

The below load-splitting problem was not seen for thicker CFRP plates. It seems that one of the most appropriate approaches to increase the strength of beam against the below load-splitting is the increase in the thickness of CFRP plate.

For non-restrained (laterally) steel beams, the below load splitting is one of the most critical (primary) failures which can retard by using thicker CFRP plates. Applying thicker CFRP for whole length of plate is not economic, so using thicker plate only below point loads and mid-span (additional layer) may improve the CFRP failure modes. For the specimens with splice layer (F4), the below failure modes were observed:

a) End-debonding of splice layer
b) End-peeling of main layer
c) End-debonding of main layer
d) Below the load-debonding of main layer

Applying splice CFRP layer increased the bonding of layers at the mid-span, but the end-debonding occurred for the splice layer. By increasing the load, the end of main layer debonded suddenly (no end-peeling was seen). This means applying splice layer caused premature end-debonding of the main layer because of high strain intensity on the adhesive at the end of main plate. It shows that application of splice layer requires usage of longer main layer [20].

Summary

This study has shown that the CFRP flexural strengthened steel I-beams suffer some problems such as below load-splitting, below load-debonding, end-delaminating, and end-peeling. The primary (critical) failure mode for non-restrained (laterally) steel beams was the below load-splitting which caused premature failure. To overcome (retard) this failure mode, it is suggested:

a) Increasing the thickness of CFRP layer
b) Applying additional CFRP layer at the mid-span and below point loads

Since splitting occurred below point load, application of thicker CFRP plate for whole length of plate was not economic. Covering the mid-span and below point loads by using an additional CFRP layer overcame the splitting problem. High stress intensity occurred at the tips of main layer due to applying splice plate, so applying longer main layer is recommended.

Acknowledgement

This study was financially supported by the University of Malaya. The authors would like to record their appreciations for the support.

References

[1] L. C Hollaway, L. Zhang, N. K. Photiou, J. G. Teng and S. S. Zhang: Adv. Struct. Eng. Vol. 9 (2006), p. 791

[2] O. Buyukozturk, O. Gunes and E. Karaca: Const. Build. Mater. Vol. 18 (2004), p. 9

[3] S. P. Chiew, S. T. Lie, C. K. Lee and Y. Yu. In: Fourth International Conference on Advances in Steel Structures, Shanghai (2005).

[4] D. Schnerch, K. Stanford, E. Sumner and S. Rizkalla. In: International Symposium on Bond Behaviour of FRP in Structures (BBFS 2005) (2005).

[5] M. Al-Emrani, D. Linghoff and R, Kliger. In: International Symposium on Bond Behaviour of FRP in Structures (BBFS 2005) (2005).

[6] A. Lenwari, T. Thepchatri and P. Albrecht: J. Compos. for Const. Vol. 9 (2005), p. 296

[7] D. Schnerch, M. Dawood, S. Rizkalla, E. Sumner and K. Stanford: Adv. Struct. Eng. Vol. 9 (2006), p. 805

[8] M. Al-Emrani and R. Kliger: Adv. Struct. Eng. Vol. 9 (2006), p. 819

[9] A. Lenwari, T. Thepchatri and P. Albrecht: J. Compos. for Const. Vol. 10 (2006), p.69

[10] R. Haghani, M. Al-Emrani and R. Kliger. In: Asia-Pacific Conference on FRP in Structures (APFIS 2007), HongKong, China (2007).

[11] A. Benachour, S. Benyoucefa, A. Tounsi and E. A. A. Bedia: Engn. Struct. Vol 30. (2008), p. 3305

[12] K. Narmashiri and M.Z. Jumaat: Simul. Model. Pract. Theory Vol. 19 (2011), p. 564

[13] K. Narmashiri, M.Z. Jumaat and N.H. Ramli Sulong: Int. J. Phys. Sci. Vol. 5 (2010), p. 1360

[14] K. Narmashiri, M.Z. Jumaat and N.H. Ramli Sulong: Sci. Res. Essays, Vol. 5 (2010), p. 2155

[15] K. Narmashiri, M.Z. Jumaat and N.H. Ramli Sulong: Adv. Mater. Res., Vols. 163-167 (2011), p. 3838

[16] R. Haghani, M. Al-Emrani and R. Kliger: Const. Build. Mater. Vol. 23 (2009), p. 1413

[17] J. Deng, M.M.K. Lee and S.S.J. Moy: Compos. Struct. Vol. 65 (2004), p. 205

[18] J. Deng and M.M.K. Lee: Compos. Struct. Vol. 78 (2007), p. 232

[19] J. Deng and M.M.K. Lee: Compos. Struct. Vol.78 (2007), p. 222

[20] S. Rizkalla and M. Dawood. In: Developments in Composites: Advanced, Infrastructural, Natural and Nano-compsoites, Sydney, Australia (2006).

© (2011) Trans Tech Publications, Switzerland
doi:10.4028/www.scientific.net/KEM.471-472.596

Synthesis of MWCNT-Alumina Hybrid as Composite Reinforcement using Nickel Catalyst

Muhammad Helmi Abdul Kudus, Hazizan Md Akil[a], Hasmaliza Mohamad

School of Materials and Mineral Resources Engineering, Engineering Campus,
Universiti Sains Malaysia,14300 Nibong Tebal, Pulau Pinang, Malaysia
[a]hazizan@eng.usm.my

Keywords: MWCNT-alumina; hybrid compound; catalyst; calcinations; reduction

Abstract. This work focuses on synthesis of MWCNT-alumina hybrid compound via methane decomposition process using nickel catalyst. The catalysts prepared through in situ process by using nickel salt and aluminium powder which then calcined at 900°C followed by methane decomposition process to grow MWCNT on alumina surface. The Scanning Electron Microscopy (SEM) and High Resolution Transmission Electron Microscopy (HRTEM) images confirmed the formation of MWCNT with homogenous dispersion on alumina particles.

Introduction

Nowadays, polymer matrix composites system moves on using hybrid particles as conductive and reinforcement materials [1-5]. Hybrid particles contain more than one entities of material, combined together and share the advantages to improve the composites reinforcement system. There are many hybrid particles have been studied including multiwalled carbon nanotube – alumina (MWCNT-alumina) hybrid particles. Recently, MWCNT-alumina hybrid particles attracted many researchers because of it process ability easiness and high service performance as polymer composites reinforcement instead of using MWCNT or alumina alone. Beside of the MWCNT high performance, there were the reports that the MWCNT is difficult to handle in term of distribution in polymer matrix and need to undergo purification and treatment. By combining MWCNT and alumina in hybrid form, the purification and treatment of MWCNT can be avoided [6, 7, 8]. There are several ways of preparing MWCNT-alumina hybrid such as mechanical blending, magnetic stirring and sonication mixing of MWCNT and alumina together using mechanical approach, and some of researchers used to prepare the hybrid particles using chemical approach such as methane decomposition [7-11]. By using the methane decomposition method, the produced MWCNT-alumina has better interaction of MWCNT and alumina particles compared to blended MWCNT-alumina. In methane decomposition process, there are many parameters that affect the properties of MWCNT-alumina hybrid particles such as type of catalyst, calcination and reduction temperature, calcination and reduction time, gas flow rates, methane decomposition temperature, and duration of methane decomposition [10-11]. In this study, a simple chemical approach of synthesizing MWCNT-alumina being investigated using nickel catalyst. Effect of the catalyst calcination and reduction process which correlated to the yield of MWCNT growth also investigated and the possible explanations on the effect are discussed.

Experimental

Catalyst Preparation. The catalyst was prepared by precipitating aluminium powder (0.38 mol) with $Ni(NO_3)_2.6H_2O$ (0.01 mol) in 1 litre of distilled water. NaOH (0.02 mol) was dissolved in distilled water (50 ml) and added into previous mixture with constant stirring. The precipitated

catalyst then aged at room temperature for 24 hours without stirring. After 24 hours the green paste was washed, filtered and followed by drying at 110°C for 2 hours. Consequently, the catalyst was calcined at 900°C for 10 hours. Finally the catalyst divided into two. Some underwent the reduction process under hydrogen gas at 400°C for 2 hours. Another half underwent no reduction process.

Growth of MWCNTs. The growth of MWCNT on alumina surface was conducted in custom-made chemical vapour decomposition (CVD) setup with horizontal tube furnace with precise gas flow controller. The catalyst then reacted in CH_4/N_2gas mixture at 800°C for 30 minutes to grow MWCNT in the tube furnace with a significant flow rates ratio of CH_4 to N_2 of 1:7. **Fig. 1** shows a schematic diagram of custom-made horizontal furnace used in this study.

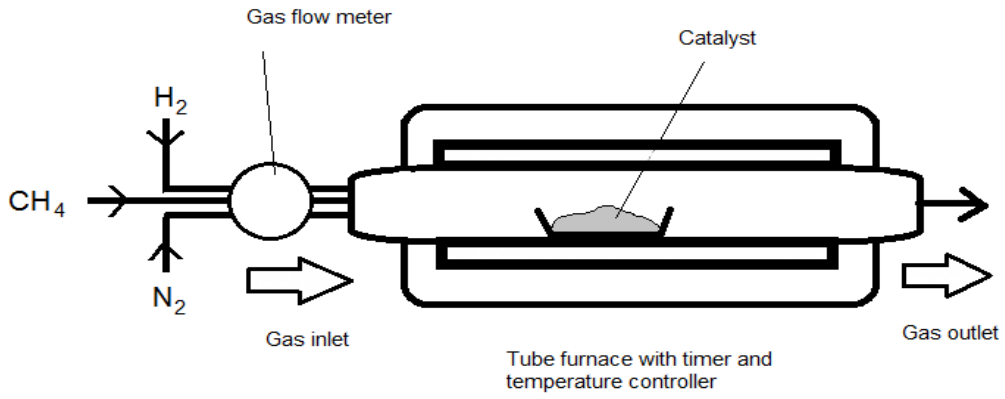


Fig. 1: Schematic diagram of custom-made horizontal furnace

Characterizations of MWCNT-Alumina Compound. The yields were analysed using X-Ray Diffraction (XRD) method. Intensity was measured by step scanning in the 2θ range of 10°-80°. The morphology of MWCNT-alumina was analysed using Leo Supra-35VP Field Emission Scanning Electron Microscope (FESEM) and high Resolution Transmission Electron Microscope (HRTEM - Model Philip TECNAI 20 (200kV)). The compositions of carbon (C) and alumina (Al_2O_3) were analysed using Energy Dispersive X-ray spectroscopy (EDX).

Results and Discussion

The produced MWCNT-alumina hybrid appears to be entangled wire-like structures and attached onthe surface of micro-sized alumina particle as shown on HRTEM image in Fig.2a and 2b. There are some particles found to be either capped on each nanotube end or being encapsulated by carbon-tube which believed to be nickel particles. The outer diameter of grown MWCNTs is about the same as nickel particle size as shown in Fig.2c. The hollow structure and multi-layered wall which is demonstrated in Fig. 2c also confirms that the produced CNT is MWCNT. The MWCNT morphology contains about ~10-40 graphene sheets which formed hollow-tube structure by the catalytic activities of the nickel particles.

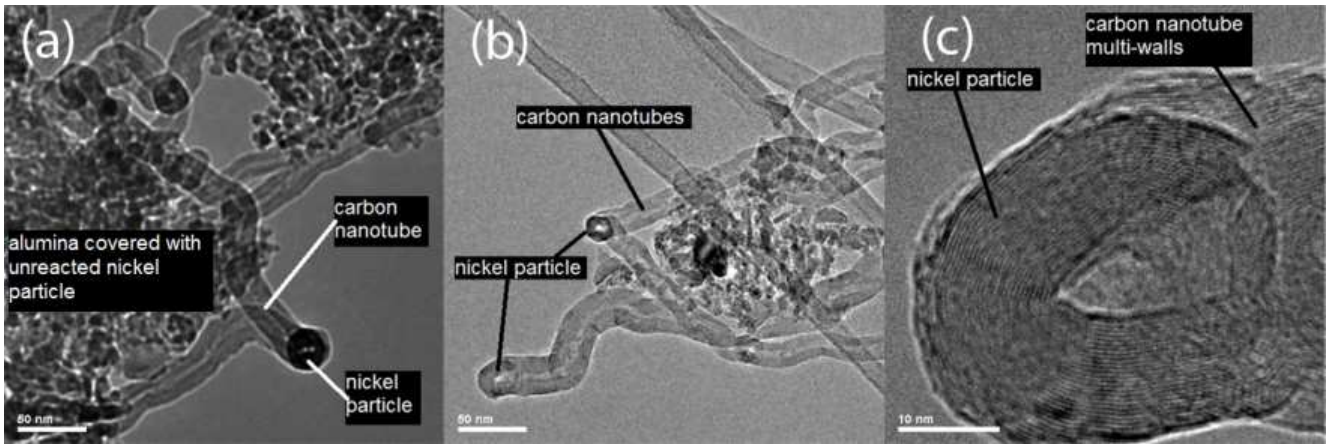


Fig. 2: HRTEM images of synthesized MWCNT-alumina hybrid [13]

Random morphology and catalytic activities of nickel catalyst are believed to be the factor of variation in MWCNT layers for each single MWCNT. The synthesized nickel particles had irregular shapes before synthesizing MWCNTs, but the particles that plunged at the end of the MWCNT tips had consistent shape. Fig. 2a also shows unreacted nickel particles sizes which cover the alumina surface had smaller size than nickel particle at the end tips of MWCNT. This observation seems to be parallel to Li et al. [12].

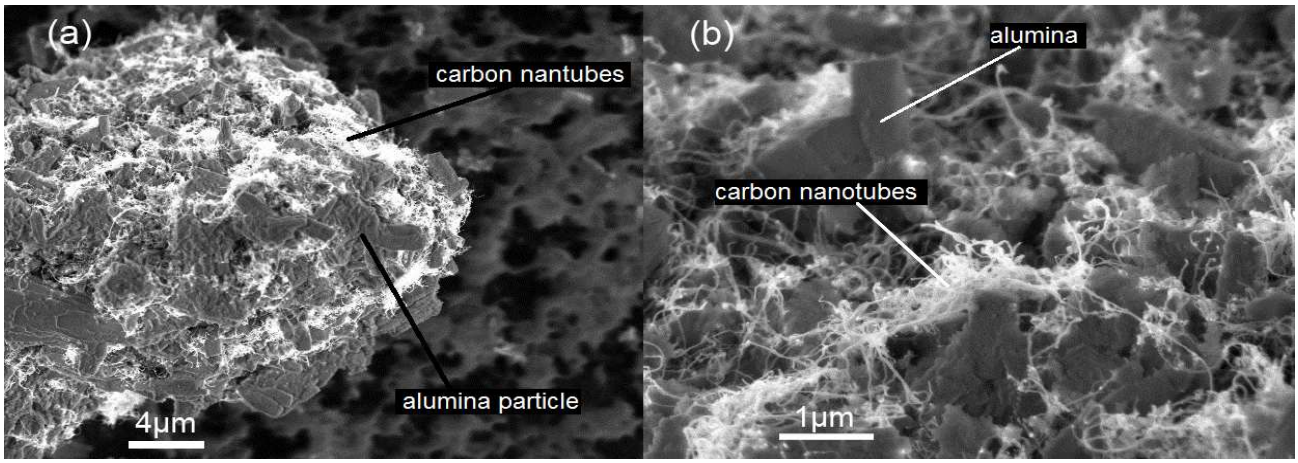


Fig. 3: SEM images of synthesized MWCNT-alumina hybrid [13]

The SEM images in Fig. 3a and 3b show the distribution of MWCNT on alumina surface. This homogenous distribution of MWCNT on alumina surface is necessary to optimize the effect of MWCNT-alumina hybrid properties as reinforcement in polymer matrix composites. The ability of alumina to disperse homogenously in polymer matrix serves as vehicle for MWCNT. With the presence of alumina, it is expected that MWCNT can be dispersed more homogenous in polymer matrix even by using conventional processing method [8], where the homogeneity is the main obstacle when using MWCNT as a single reinforcement for polymer composites. During reaction in methane gas, the sizes of nickel catalyst particles remain unchanged and suitable interaction provide higher catalytic activities to grow MWCNT [9].

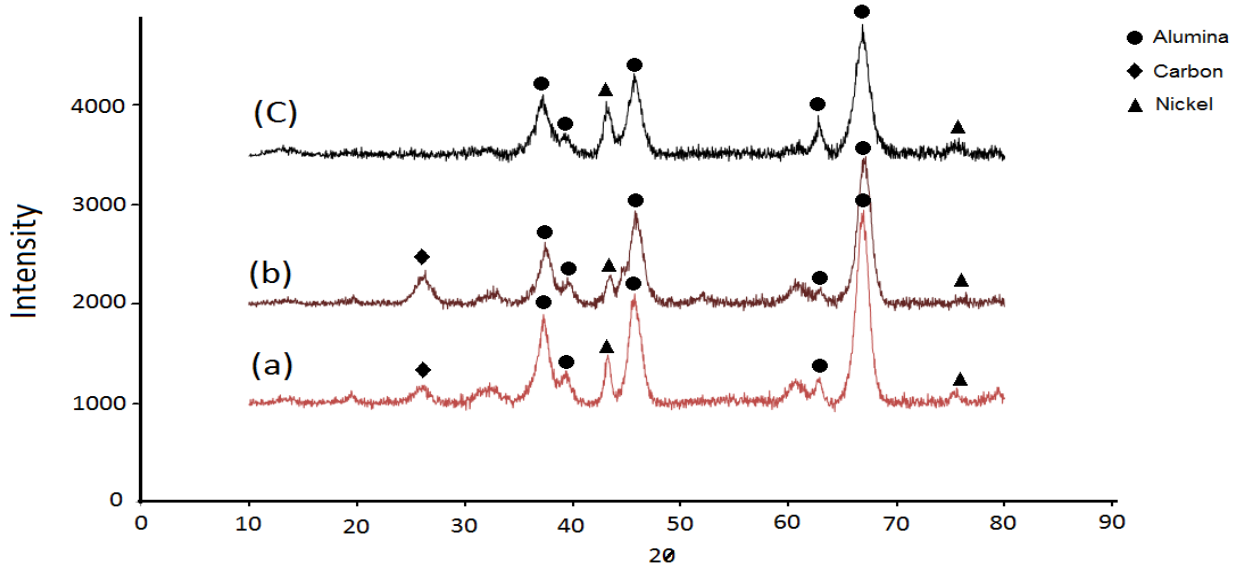


Fig. 4: XRD pattern of synthesized MWCNT-alumina using (a) catalyst with calcination and reduction, (b) catalyst without reduction, and (c) catalyst without calcination and reduction

Fig. 4a-c show the XRD analysis pattern of after growth particles which (a) growth using catalyst with calcination and reduction process, (b) growth without reduction process and (c) growth without calcination and reduction process. From each XRD analysis pattern, the catalyst that underwent calcination and reduction process successfully grew the MWCNT on alumina surfaces similar as reported elsewhere [7, 8, 12]. Interestingly, the MWCNT also grew successfully on alumina surface by using the catalyst which underwent calcination but avoided reduction process, which is presented by pattern (b). It is believed that during methane decomposition process, the produced H_2 gas from catalytic decomposition used to reduce the catalyst at suitable temperature before the temperature reached at MWCNT growth temperature. The reaction of carbon forming by the catalytic decomposition of methane is as follows Eq. 1.

$$CH_4 \rightarrow 2H_2 + C \quad (1)$$

The catalyst without performing calcination and reduction process did not show the carbon presence as shown in pattern (c).

Summary

The methods and parameters used in the synthesizing of MWCNT-alumina hybrid are suitable for catalytic activities of the Ni-alumina catalyst during methane decomposition process.This method shows that the CNTs were homogenously distributed on alumina surface to optimize the performance of CNT-alumina hybrid system. The XRD pattern shows that calcination of the catalyst is very important to synthesize MWCNT-alumina hybrid while the reduction process can be avoided to save the time, energy and material cost.

Acknowledgement

The authors would like to gratefully acknowledge Universiti Sains Malaysia for all the assistance that has resulted in this article.

References

[1] A.B.D Nandiyanto, Y. Kaihatsu, F. Iskandar and K. Okuyama: Materials Letters, Volume 63, Issue 21, 31 August 2009, Pages 1847-1850

[2] X. Wang, Z. Zhao, J. Qu, Z. Wang and J. Qiu: Journal of Physics and Chemistry of Solids 71 (2010) 673–676

[3] R. George, K.T. Kashyap, R. Rahul, S. Yamdagni: ScriptaMaterialia 53 (2005) 1159–1163

[4] Z. Fan, J. Chen, M. Wang, K. Cui, H. Zhou and Y. Kuang; Diamond & Related Materials 15 (2006) 1478 – 1483

[5] Geoffrey M. S., S. R. Shin, G. G. Wallace, P. G. Whitten, S. I. Kim and S. J. Kim: Sensors and Actuators B 115 (2006) 678–684

[6] L. Kumari, T. Zhang, G.H. Du, W.Z. Li, Q.W. Wang: Ceramics International 35 (2009) 1775–1781

[7] C.N. He, F. Tian, S.J. Liu: Journal of Alloys and Compounds 478 (2009) 816-819

[8] C.N. He and F. Tian: Scripta Materialia 61 (2009) 285-288

[9] S. P. Chai, S. H. S. Zein, A. R. Mohamed: Carbon 45 (2007) 1535-1541

[10] I. Chen, S. Y. Lin and D. W. Shiu: Ind. Eng. Chem Res. 1988, 27, 926-929

[11] I. Chen and D. W. Shiu: Ind. Eng. Chem Res. 1988, 27, 926-929

[12] Z. Li, J.Chen, X. Zhang, Y. Li and K. K. Fung: Carbon 40 (2002) 409-415

[13] M. H. A. Kudus, H. M. Akil , H. Mohamad, L. E. Loon: Journal of Alloys and Compounds; Article in Press (2011)

© (2011) Trans Tech Publications, Switzerland
doi:10.4028/www.scientific.net/KEM.471-472.601

Computer Simulation and Experimental Investigation of Solidification Casting Process

Suraya. S[a], Sulaiman. S[b], Ariffin. M.K.A[c] and Sayuti.M[d]

Department of Mechanical and Manufacturing Engineering,

Universiti Putra Malaysia, 43400 Serdang, Selangor, Malaysia

[a]sue_bahira@yahoo.com, [b]suddin@eng.upm.edu.my,

[c]khairol@eng.upm.edu.my, [d]tgk_sayuti@yahoo.co.uk

Keywords: Casting process, Computer simulation, Filling and Solidification

Abstract. Computer simulation is widely used and conventional in manufacturing as a way to improve the manufactured goods quality as at same time plummeting invention costs, development time and scrap. In this study, three-dimensional model have been developed to simulate the filling and the solidification pattern in an aluminum casting with "AnyCasting" software. Using this software, solidification of aluminium 11.8% Si alloy in sand and metal mould was simulated and the results were compared with the experimental results. The solidification time and temperature was experimentally determined from thermocouple located at diverse distances. A data logger is used in experiment to gain the temperature division contour during the process of solidification of the aluminium 11.8% Si alloy. Experiments were set up to legalize the simulation results and it is confirm that the results from the two mould methods be in good agreement and the solidification of cast aluminium alloy using copper mould was much faster compared to the one cast sand mould. From this work it is concluded that simulation using AnyCasting software can be use to initially calculate. The simulation shows result that matches with the experimental data qualitatively and therefore the validation procedure is successful.

Introduction

Casting simulation is a new technology that has adopted in industry as a way to reduce scrap, reduce lead times, cut costs, use less energy, has a better final design and to improve the parts design and manufacturing processes. Trial-and-error methods of the past to design casting processes are finding it more and more difficult to compete. This approach is expensive and inflexible because many variable affect the solidification of the metal inside the mold [1, 2]. Using simulation, the behavior of the molten aluminium during the filling, heat transfer and solidification of different casting methods can be studied [3-5].

Casting simulation has the ability to analyze various physical phenomena occurring during casting process. From previous research, the simulation of metal casting about fluid flow, heat transfer and solidification has been treated extensively [1, 5]. It allow researchers to observe and quantify what is not usually visible or measurable during real casting process. Simulation produces a tremendous amount of data that characterize the transient flow behaviour (e.g., velocity, temperature), as well as the final quality of the casting (e.g., porosity, grain structure). It takes good understanding of the actual casting process, and experience in numerical simulation, for a designer to be able to relate one to the other and derive useful conclusions from the results [4].

In this study, the AnyCasting software will be used for investigates the behavior of the molten metal during the melt filling and solidification in casting process. This software is a 3D solidification and fluid flow package used in the die casting industry to model the molten metal flow and solidification in dies. It employs the finite difference method to solve the heat and mass transfer on a rectangular grid. It is a useful tool for simulating molten metal flow in a permanent mould since it can provide useful information about the filling pattern. It also produces reasonable accurate data on casting related features such as premature solidification, air entrapment, velocity distribution, runner and gate effectiveness.

Methodology

The research activity are divided into two parts. The first part explains about the experimental works and the second part explains about simulation works.

Part 1: Material Preparation for Experimental. The aluminium-11.8% silicon alloy or LM6 was used as a matrix in this research. This alloy conforms to British Standard 1490 LM6. LM6 alloy is a eutectic alloy that have lowest melting point that can be seen from Al-Si phase diagram. The mechanical, thermal and electrical properties and the chemical composition of LM6 are shown in Table 1 and 2. In this research, sand and permanent metallic mold was used. The thermocouple was insert at specific measured points for temperature measurement. The process starts when LM6 ingots were cut into small pieces and the process continue by melts the ingots in an coreless induction furnace. The ingots is left to melt until it reaches 750°C. After that, the composite slurry are poured into the sand and permanent metallic mold as shown in Fig. 1 by gravity, and then allowed to solidify. Then the casting is broken out of the mold to complete the process. The casting used in this research is a cylinder shaped. The temperature of the molten metal must maintain while transferring to the mold to ensure the quality of the cast product.

Table 1: Properties of LM6 (wt%) [6]

Physical Properties	**Values**
Density (g/cc)	2.66
Mechanical Properties	**Values**
Tensile strength, Ultimate (MPa)	290
Tensile strength, Yield (MPa)	131
Elongation %; break (%)	3.5
Poissons ratio	0.33
Fatigue strength (MPa)	130
Machinability	30
Shear strength (MPa)	170
Hardness (BHN)	50
Modulus of elasticity (N/sq.mm)	71000
Thermal Properties	**Values**
CTE, linear 20°C (µm/m-^{o}C)	20.4
CTE, linear 250°C (µm/m-^{o}C)	22.4
Heat of fusion (J/g)	389
Thermal conductivity (W/m-K)	155
Melting point (^{o}C)	574
Solidus, (^{o}C)	574
Liquidus (^{o}C)	582
Electrical Properties	**Values**
Electrical resistivity (Ohm-cm)	0.0000044

Table 2: Chemical composition of LM6 (wt%) [7]

Aluminium (Al)	Silicon (Si)	Copper (Cu)	Manganese (Mn)	Tin (Sn)	Iron (Fe)	Nickel (Ni)	Zinc (Zn)	Magnesium (Mg)
88.0%	11.0%	1.0%	0.3%	0.15%	1.3%	0.5%	0.5%	0.1%

Part 2: Simulation. In this research, AnyCasting software was used to predict the filling and solidification characteristics of the LM6 cylinder cast. This software are divided into 3 step. First, the 3-D models of the mold and cast was developed and save as in stereolithography (STL) format and imported to software. The diameter of the cylinder cast is 40mm and the height is 170mm as shown in Fig. 2. The simulation starts with the generation of FDM mesh after reading the CAD data. The FDM mesh is done to devide the geometry into cells or control volumes. In this simulation, about 2,000,000 elements were created for 3-D models. Next, the simulation parameter and specific materials for the mold and casting was set up. In this simulation the mold material is assigned as silica sand and copper and the casting material is aluminium 11.8% silicon alloy. Table 3 shows the assumption parameter were considered in this simulation. Next step was set up the condition of analysis for operating at anySOLVER. Lastly, the filling and solidification results can be viewed in 3-D graphic at anyPOST.

Table 3: The parameter input for simulation

Parameters (LM6)			
Density	2660 kgm^{-3}	Liquidus temperature	582°C
Specific heat	963 $Jkg^{-1}K^{-1}$	Coefficient of thermal expansion	1.824e-008K^{-1}
Thermal conductivity	155$Wm^{-1}K^{-1}$	Latent heat	389000Jkg^{-1}
Solidus temperature	574°C	Volumetrix change of solidification	3.8%

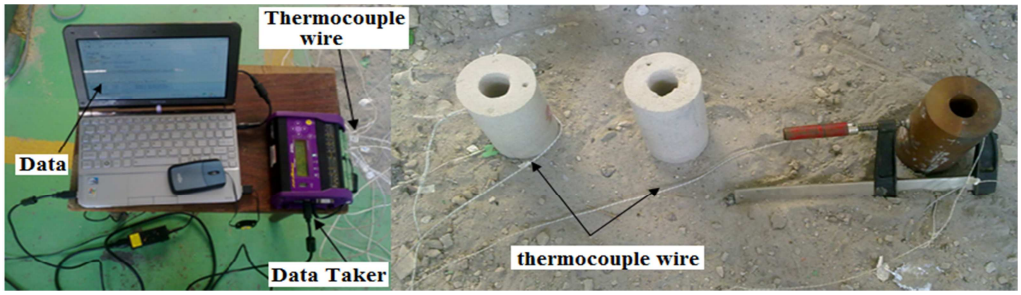


Fig. 1: The mould is connected to datataker data logger using thermocouple wires

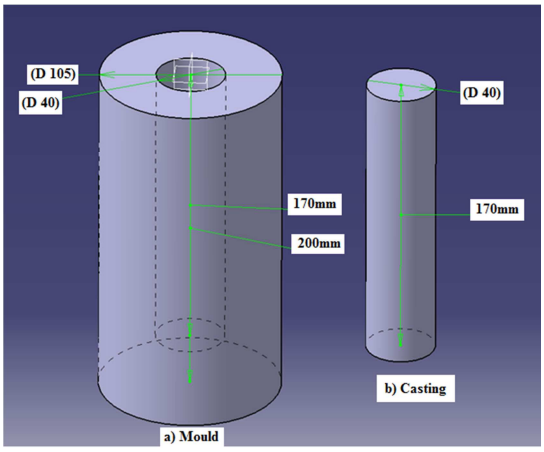


Fig. 2: CAD drawing of mould and casting

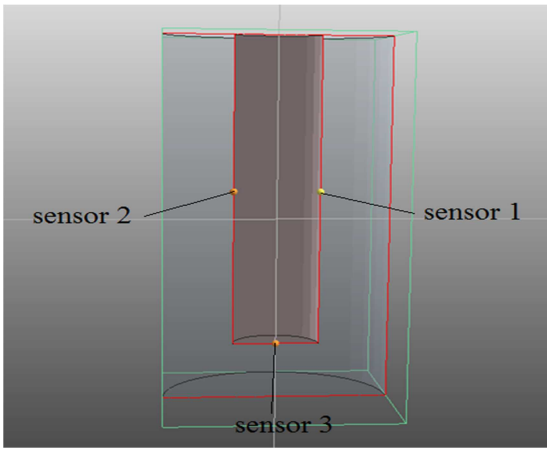


Fig. 3: The location of sensor

Results and Discussion

The visualization of mold filling is shown in Fig. 4 and 5. The duration time for molten metal fill in the mould is about 11.1934 second for sand casting and 11.1937 second for permanent metallic mold. By simulation, the temperatures versus time helps to visualize the temperature contours and the distribution inside the solidifying composites. The verified model based on the experimental observations. The simulations were run by applying the input parameter data as shown in Table 1 and Table 3. From Table 1, the liquidus temperature of LM6 is 574°C and for solidus temperature

is 582°C. Fig. 6 shows the solidification process begins near the liquidus temperature at 549.37 °C and ends near the solidus temperature of 520°C.

Fig. 6 to Fig. 8 shows the simulated temperature curve from the simulation of present study and Fig. 7 and 9 shows the cooling curves of the solidification of LM6 from the experimental. The shape of both simulation and experimental are very similar to each other. From the graph, the solidification for the casting using permanent metallic mold (copper) is shorter than using sand casting. Higher thermal conductivity of the copper mold causes faster solidification compare the solidification of sand mold. The molten metal that poured into the copper mold has higher cooling rate than those poured into the sand mold. The thermal conductivity of copper is 401$Wm^{-1}K^{-1}$ and sand is 0.733$Wm^{-1}K^{-1}$.

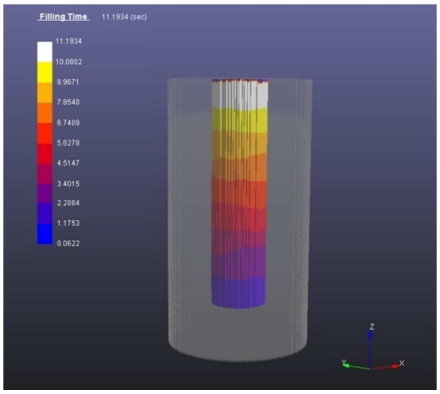


Fig. 4: The filling time (sand casting)

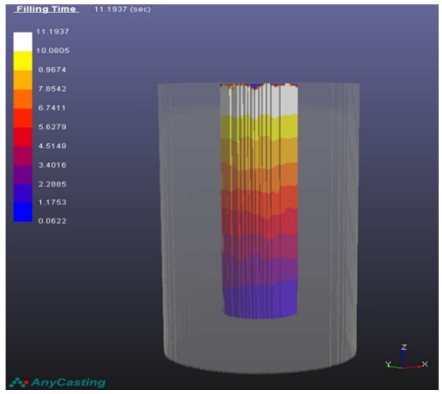


Fig. 5: The filling time (permanent metallic mold)

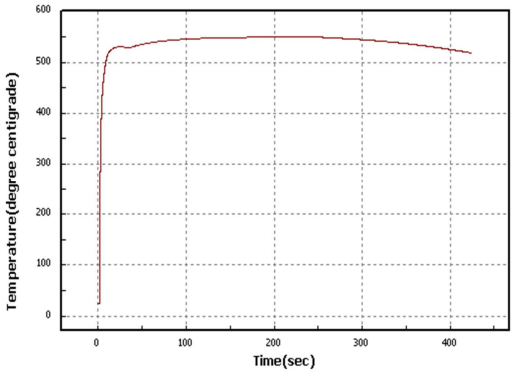


Fig. 6: Temperature curve from LM6 simulation for sand casting methods

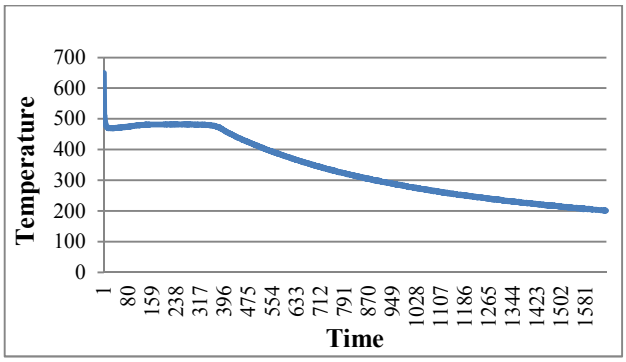


Fig. 7: The cooling curves using sand casting method

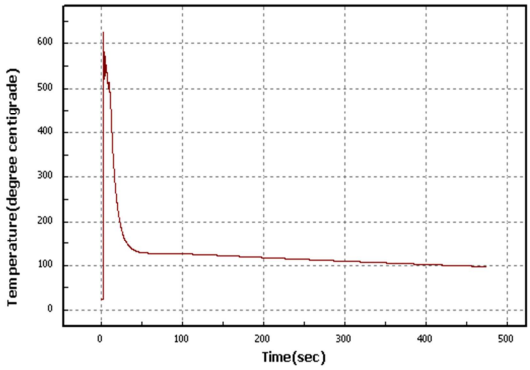


Fig. 8: Temperature curve from LM6 simulation for sand casting methods

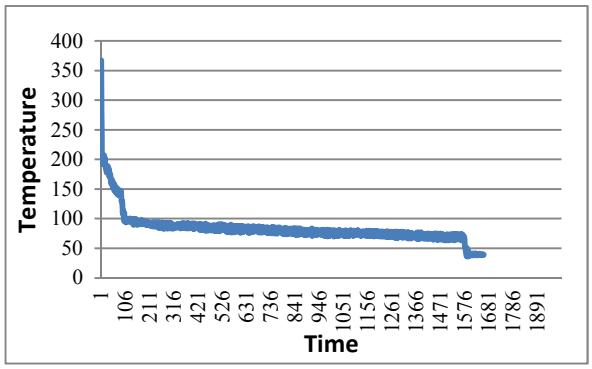


Fig. 9: The cooling curves using permanent metallic methods

Summary
A 3-D model has been developed for the simulation of casting solidification using sand and permanent metallic mold. The effects of the mold on the solidification time have been investigated using this model. Solidification and cooling rate using permanent metallic mould are higher than sand mold and the value of thermal conductivityis influence the results. The solidification and the cooling rate of simulation is very similar to the experimental results.

Acknowledgement

The authors of this paper express their deep gratitude and sincere thanks to the staff and laboratory technicians of the Departments of Mechanical and Manufacturing, Universiti Putra Malaysia for their help with the experiments.

References

[1] C. K. Jung, J. H. Jang and K. S. Han: Metallurgical and Materials Transactions A vol.39A (2008), p.2736-2748.

[2] S. Abis, S: Metallurgical Transactions B vol.17B (1986), p.209-216.

[3] C. E. Esparza, P. Martha, Guerrero-Mata, Z. Roger and Rios-Mercado: Optimal design of gating systems by gradient search methods. (2005)

[4] A. Kermanpur, M. Eskandari, H. Purmohamad, M. A. Soltani and R. Shateri: Materials Processing Technology vol.206 (2008), p.62-68.

[5] T. R. Vijayaram, S. Sulaiman, A. M. S. Hamouda and M. H. M. Ahmad: Materials Processing Technology vol.178 (2006), p.29-33.

[6] T. R. Vijayaram: Properties of Metal Matrix Composite of Aluminium-11.8% Silicon Reinforced with Different Particulates. Doctor of Philosophy, University Putra Malaysia. (2006)

[7] A. L. K. Hooi: Thermal Analysis of Two and Three-Gate Sand Casting Mould. Master of Science, University Putra Malaysia. (2001)

© (2011) Trans Tech Publications, Switzerland
doi:10.4028/www.scientific.net/KEM.471-472.606

Numerical Aspects of Delamination Modeling Using Interface Elements

Hossein Hosseini-Toudeshky[1,a], Meisam Jalalvand[1,b] and
Mohammad Hossein Ghayour[1,c]

[1]No. 424, Hafez Ave, Tehran, Iran

[a]hosseini@aut.ac.ir, [b]jalalvand@aut.ac.ir, [c]mh_ghayoor@aut.ac.ir

Keywords: Delamination, Interface Element, Spurious Stress Oscillation, Dominant Process Zone

Abstract. In spite of a vast background on cohesive constitutive law and its use for various analyses such as delamination in composite laminates, some numerical aspects of that have been less explored and reported in the literature. The aim of this paper is to study the phenomenon of spurious stress oscillation and also dominant process zone (where damage has its most significant evolution) in delamination modeling. For this purpose, distribution of normal stress and damage parameter of different DCB specimen are analyzed. Distribution of stress around the process zone indicates spurious oscillation just ahead of the delamination tip where damage parameter is zero and no effect of this phenomenon is seen on results of applied load versus opening displacement. Additionally, it is shown that larger values of penalty stiffness lead in smaller length of dominant process zone and very large values of penalty stiffness pushes the distribution of damage parameter to become step-like function. Authors believe that this effect is in fact the main reason of un-converged solution of models with too large penalty values.

Introduction

Delamination is one of the most critical and common types of failure modes in laminated composites which occur due to the low interlaminar strength. Dealing methods with delamination problem may be generally divided into three categories of; i) stress-based criteria determining the crack initiation, ii) fracture mechanics dealing with crack propagation, and iii) the approach of cohesive zone and interface element which is capable to model both crack initiation and propagation. The growing ability of available computational tools along with the inherent attractive features of interface elements convinced many researchers to use this technique for delamination analysis and today, it can be found in some commercial FEM packages. In spite of many advantages of this approach, some difficulties such as artificial elastic compliance of the interface prior to onset of delamination [1], spurious stress oscillation ahead of delamination front [2] because of the presence of a high stiffness value have been addressed in the literature. In this paper the effect of spurious stress oscillations with both elastic and elastic-damage cohesive law is investigated. Then, examining the variation of damage parameter around the process zone, a discussion about dominant process zone and the reason of un-convergence results with large values of penalty stiffness will be presented.

Cohesive Constitutive Law. The applied cohesive constitutive model in this paper is inspired from [3], however some necessary changes have been made in the formulation. It was tried to decrease the complexity of the model while preserving its generality. Only one internal damage variable, d, is employed and the elastic-damage constitutive model with no permanent displacement discontinuity is considered. Therefore the stress components can be defined by Eq. 1. The proposed quadratic failure criterion for delamination initiation in classical methods is used for determining of damage surface, Eq. 2.

$$\sigma_i = (1-d)K_i\delta_i \quad (i = 1,2 \text{ for shear and } i = 3 \text{ for normal direction}) \tag{1}$$

$$\lambda = 1 - d = \sqrt{\left(\frac{\sigma_1}{\sigma_1^0}\right)^2 + \left(\frac{\sigma_2}{\sigma_2^0}\right)^2 + \left(\frac{\sigma_3}{\sigma_3^0}\right)^2} \quad (2)$$

where and σ_i^0 $(i = 1,2$ are stress and strength components in the cohesive zone respectively. determines the damage surface and it is associated with damage parameter and decreases with damage growth. A mixed-mode crack propagation criterion was also used to control crack growth in complex loadings. More details are not mentioned due to brevity.

Spurious Stress Oscillation. Spurious stress oscillation usually occurs when a large gradient of stress distribution exists on the plane of interface elements. It is called spurious because it is observed only in numerical simulation and does not exist in reality. One of the most important parameters that affect stress oscillation is the value of penalty stiffness [4]. Fig. 1 shows the obtained stress distributions a head of delamination tip for a DCB specimen containing linear elastic interface elements with different values of penalty stiffness the opening displacement of 3.0 mm. The geometry and material characteristics of the specimen are [5]: L=150 mm, a_0=31.75 mm and t=3.05 mm, E_{11}=138 GPa, E_{22}=8.96 Gpa, G_{12}=7.1 GPa, υ_{12}=0.3, $\sigma_3^0 = 51$MPa, $\sigma_1^0 = 9$MPa, G_{IC}=0.222 N/mm, the angle of all layers is 0° and the size of interface elements are 0.5 mm.

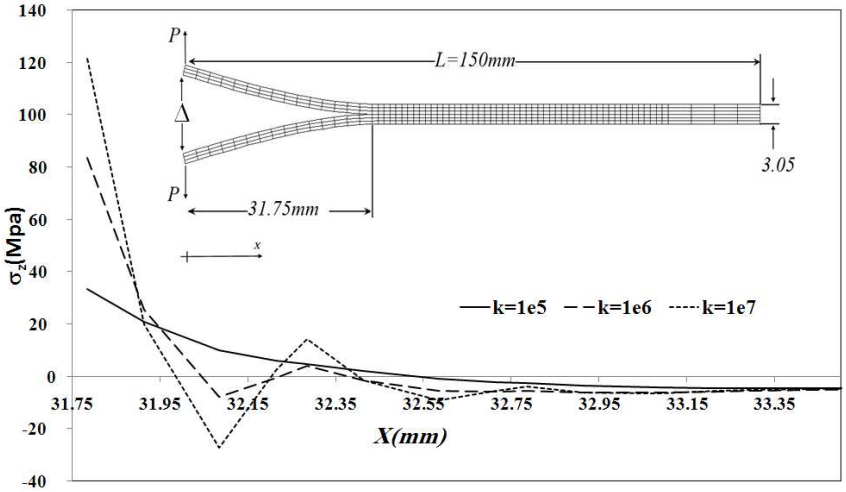


Fig. 1: Stress distributions a head of delamination tip for DCB specimen with linear elastic interface elements

This figure shows that for the smallest penalty value of k=10^5 N/mm^2 no oscillation is observed but when it is increased to 10^6 N/mm^2, the stresses are oscillating. Such oscillation becomes more significant by increasing the penalty value to k=10^7 N/mm^2.

The nonlinear elastic-damage analyses were also performed for DCB specimens with the same geometry, mesh and material with damageable cohesive constitutive law to study this phenomenon in crack propagation and in-elastic condition. Fig. 2 shows the distributions of normal stress, , and damage parameter, *d,* for various penalty values around the process zone. Considering the damage parameter in this figure, three different regions can be distinguished. Region I is the place where the value of damage parameter is equal to one showing the full delaminated area and no load carrying material exists (σ_3 =). The obtained results for various penalty values are completely coincident in this region. Region II is in fact the process zone where damage is evolving (*0<d<1*) and the obtained stress distributions for different penalty values are approximately the same. The non-zero stresses in this region are not oscillating. In region III, no damage occurred (*d=0*) and obvious distinction between various stress distributions for three different penalty values can be observed. Similar to the results of linear elastic solution shown in Fig. 1, the larger values of penalty stiffness leaded to more critical spurious oscillation of stresses.

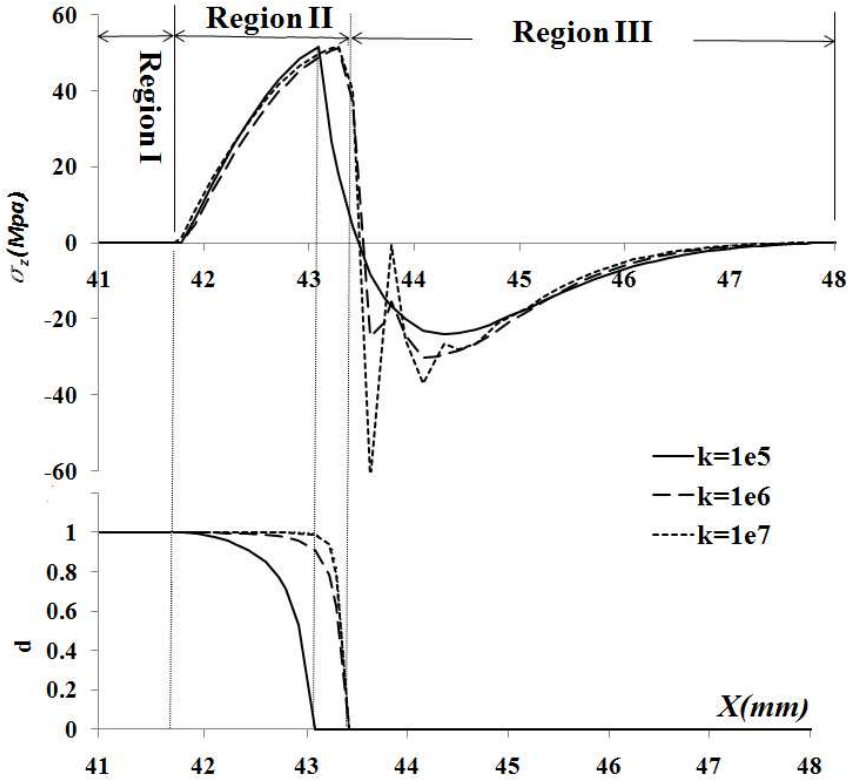


Fig. 2: Stress and damage parameter distributions around the process zone for DCB specimen with elastic-damage interface elements

Fig. 3 compares the obtained variations of applied load, P, versus opening displacement, for different penalty stiffness values with those from other numerical and experimental investigations [4]. It indicates that the penalty value does not have considerable effect on the load-displacement results. This can be also interpreted that in spite of significant differences and oscillations of the stress distributions in region III, there are not considerable variations on the obtained load-displacement results for various penalty values. In another word, this curve is completely associated with energy release rate which is a function of the stress of present and past process zone (zone I and II) and while the stress in these two region are the same, the P- curves of different models becomes similar. It is worth to mention that positive values of normal stress were also seen for k=3*10^7 N/mm^2 ahead of crack tip in region III where the normal stress supposed to be compressive. Such a matter is completely in contradiction with the nature of the problem. The obtained results are not showed here to prevent crowding of the results.

Dominant Process Zone Length. A deeper assessment of distribution of damage parameter *d* along cohesive zone (Fig. 2) shows that as the penalty values are increased, the gradient of damage variation around the beginning of region III becomes larger. This means that in large values of penalty stiffness, the distribution of damage becomes approximately like a step function. Examining a part of the process zone in which 0<*d*<0.95 ( ) can show this behavior. For k=10^5 N/mm^2 =0.86 mm, for k=10^6 N/mm^2 =0.50 mm and k=10^7 N/mm^2 =0.21 mm. It is clear that as the value of penalty stiffness is increased, is decreased. Such a conclusion could also be validated with formulation of elastic-damage cohesive law. Eq. **Error! Reference source not found.** can be rearranged to find damage parameter, *d*, as follows.

$$d = 1 - \frac{\sigma_3}{K_3 \delta_3} \tag{3}$$

Eq. 3 indicates that in two similar models with different penalty stiffness, if stress and opening at a certain point of process zone are the same (see curve of in Fig. 2 and Fig. 4), the

model with larger penalty value has larger damage parameter *d*. Therefore, more points of such model get the damage parameter of 1<d<0.95 and then in the model with larger values of penalty stiffness becomes smaller.

It worth to mention that none of the authors efforts for solving the same problem and same mesh size with $k=5*10^7$ N/mm^2 and larger values resulted in convergence. With this penalty value, in a certain sub-step, all of the iterations reached a constant non-ignorable unbalanced force. Authors believe that such a problem is indeed due to very small dominant process zone length where $0<d<0.95$ and too high damage gradient at the beginning of region III for this value of penalty. In fact, increasing the value of penalty values pushes the damage distribution to a singular step function.

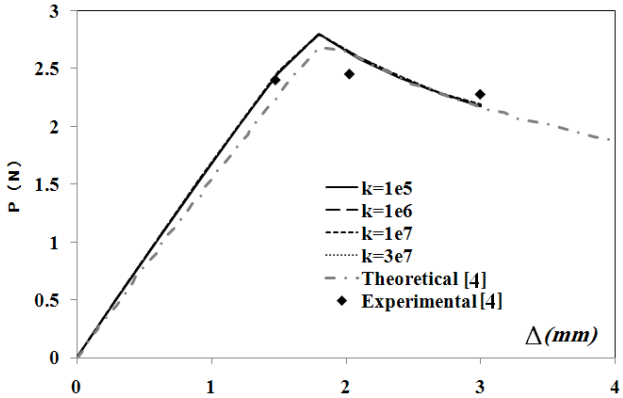


Fig. 3: Applied load versus opening displacement of a DCB specimen

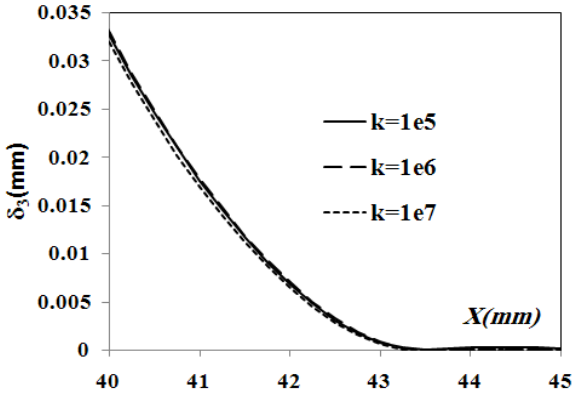


Fig. 4: Distribution of opening displacement around process zone

Summary

In this paper, the phenomenon of spurious stress oscillation was examined in both elastic and damageable models of a DCB specimen. It was shown that large values of penalty stiffness can cause spurious stress oscillation in elastic models and un-damaged part of elastic-damage models. The stress in process zone was approximately equal for all of the penalty values and no oscillation was found in this part of curve. In spite of such a great difference ahead of crack tip (where $d=0$), the P- curve of all models was coincident because the stress distribution in process zone affect this curve. Although the distribution of stress in process zone was approximately similar, the distribution of damage parameter in this zone was shown to be completely different. In larger penalty values, damage distribution curve looks more like a step function. To compare this parameter, concept of dominant process zone length was defined as the points in which $0<d<0.95$. It was indicated that larger values of penalty stiffness leaded to smaller values of . The un-convergence in large values of penalty stiffness was associated to .

References

[1] R. de Borst: Engineering Fracture Mechanics Vol. 70 (2003), p. 1743

[2] J.G. Rots: PhD thesis Civil Eng. Dep. Delft University of Technology (1988)

[3] C.G. Davila, P.P. Camanho and M.F. de Moura: 42nd AIAA/ASME/ASCEIAHS/ASC Structures, Structural Dynamics and Materials Conference. 2001: Seattle, Washington. Paper AIAA-01-1486.

[4] J.C.J. Schellekens and R. de Borst, Int. J. for Numerical Meth. in Eng. Vol. 36 (1993), p. 43

[5] C. Balzani and W. Wagner: Engineering Fracture Mechanics Vol 75 (2008), p. 2597

© (2011) Trans Tech Publications, Switzerland
doi:10.4028/www.scientific.net/KEM.471-472.610

A Review on the Performance of Adhesive Bonding in Polymer Composite Joints

S.N. ABDUL RAZAK[1,a], A.R. OTHMAN[*2,b]

[1] School of Aerospace Engineering, Engineering Campus, Universiti Sains Malaysia, 14300 Nibong Tebal, Pulau Pinang, Malaysia

[2] School of Mechanical Engineering, Engineering Campus, Universiti Sains Malaysia, 14300 Nibong Tebal, Pulau Pinang, Malaysia

[a] siti.noorseri@gmail.com, [b] merahim@eng.usm.my

Keywords: Adhesive joint, sandwich structure, strain energy release rate, virtual crack closure technique.

Abstract. Past and on-going research works on adhesive bonding in composite and sandwich were reviewed. Discussion was emphasized on critical failure mechanisms (e.g. mechanism of peel fracture) to enhance the performance of the bonding. This paper also focused on the application of good adhesive bonding in the application of sandwich structures. Debonding between skin and core is one of the failure mechanisms that should be given more attention in fabrication of sandwich structures. Incorporating fillet in composite bonding is one of the alternative ways to reduce the stress concentration at the edges of overlap length and to produce high peel strength for bonding. Basic understanding of the designs, theories and manufacturing of adhesive bonding were also presented. Several important parameters in the design such as the strain energy release rate (SERR) and formation of fillet also discussed. The analysis of SERR using virtual crack closure technique (VCCT) has also been highlighted to achieve high strength of adhesive bonding, providing the key element for optimization of the delamination resistance in maximizing energy absorption during fracture. Significant challenges or limitations in improving and optimizing the design were also highlighted.

Introduction

Most of the applications of composite in aircraft structures involved joining together either composite parts or composite and metal parts because it is virtually impossible to create a structure in a single piece due to the high cost involved or simply for geometrical applications [1]. But, the joint has been considered as the region of weaknesses, in which approximately 70% of the structural failures were found to initiate from joints [1-2]. The joining of composite structures can be achieved through the use of bolted, riveted or adhesive bonded joints but the latter provide much more efficient load transfer capability and increasingly used in structural applications which is justified by its well-known advantages over mechanically fastening joints [3-4]. Sandwich is a three-layer structure, consisting of a top and bottom facesheet or skin and a core at the middle which are glued together [5]. The honeycomb materials have been extensively used as energy absorbers to resist external loads due to their high energy absorption capacity [6]. Michael Schlotter [7] was proposed the important criteria that should be considered in selecting the core materials because the requirements for core material differ in every application.

Debonding of the facesheet from the core is a serious problem in sandwich construction where the structural integrity of any sandwich especially, the interlaminar shear and flatwise tensile strengths depends on the quality of the adhesive bond between skin and core. Further understanding on the effect of several processing parameters, the quality of the skin-core bond was studied [8-9]. Besides that, Ural et al [10] has studied the dependence of cell geometry, cell size, cell wall thickness, face sheet material and face sheet thickness on the physical/mechanical properties of honeycomb sandwich structures. Based on Okada and Kortschot [11], resistance of such structures

to delamination or peel has been measured extensively, but details of the fracture mechanism have not been quantified and well understood. In addition, peel strength is an important quality control parameter, since the replacement or repair process of honeycomb sandwich structure is costly and is likely to be a long-term problem if its root cause is not well identified [12].

Stress concentrations have a large influence in determining the failure strength of the joint either in composite laminates or sandwich structures. Since the failure will occur at the region with higher stress distribution [2], thus, it is necessary to analyse the distribution to compensate or minimize the effects of stress concentration in adhesive bonding. Papanicolaou et al [13] has developed a simple new analytical approach to study stress distribution along the length of skin-core interface in specimens under tension. The work proved to be useful for designing purposes and quality control of the sandwich structures manufacturing. According to Scott et al [14], current development indicated that no analysis has been published with regards to details of load transfer characteristics of the adhesive joint, as a function of both adhesive and geometric parameters of the facesheet and core components.

Many researchers studied on the important of fillet between skin-core bonding and at the edges of overlap region in lap joint [9,11-12,15-19]. Although the fillet is the effective way to reduce the stress concentration, but in lap joint between composite laminates is also depends on the thermal stress distribution at the joint. Previous work [16] has shown that if the thermal stress was not significant, tensile strength of the adhesive remained high, and the internal taper and fillet would increase the joint strength. Otherwise, the use of internal taper and fillet would not give any improvement. Nevertheless, the formation of fillet remains the primary goal of the manufacturing process for honeycomb sandwich panels since the structural strength relies on the formation of a fillet of adhesive at the interface between cell wall and skin [8]. However, void in the resin fillet should be prevented because it can be one of the crack initiation in the skin-core bondline [9,11]. This study provides the first step for the understanding of bonding mechanisms between honeycomb core and skin and will be useful for subsequent optimization of the adhesive weight and process [20].

This paper presented a review on the adhesively bonded joint in composite materials and sandwich structures by considering the improvement on fabrication techniques that provide maximum bond strength and longevity particularly for aircraft structure. Detailed of failure mechanism and their roles in influencing the performance of adhesive bonding were also highlighted. The fundamental of strain energy release rate was also comprehensively presented in this paper, where it provides the key for optimization of the delamination resistance in maximizing the bonding between skin-core in sandwich construction.

Failure Mechanism

There are many reasons why adhesive bonds fail. This section reviews some of the universal factors related to adhesive failures and the several types of failure occurred in adhesive bonding. Taib et al [21] has described several classes of failure modes which were identified from the series of ASTM D5573 tests, which are essential for further analysis; adhesive failure, cohesive failure, thin-layer cohesive failure, fiber-tear failure (FTF), light fiber-tear failure (LFTF), stock-break failure and mixed failure.

In adhesive composite joint, delamination in adherend is one of the critical failure modes [22-23]. Kim et al [22] presented the relationship between bonding method and strength of adhesive that influenced the modes of failure in adhesive bonding. Figure 1 below shows that the typical failure process of the secondary bonded specimens that were tested by them.

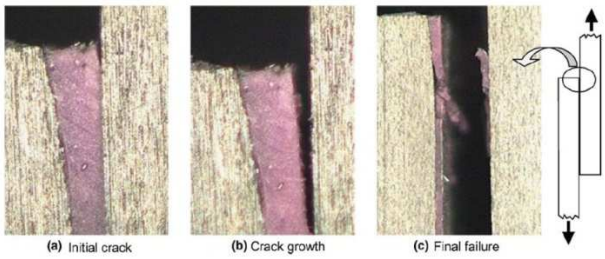


Fig. 1. Typical failure process of the secondary bonded specimens [22].

Similar to delamination of adhesive lap joints for composite laminates, Sanjib et al [5] presented that sandwich structure also showed this kind of defect and very common defect is a facesheet/core debonding or delamination. Delamination in sandwich structures along the interface between the facesheet and core or along the adherend/adhesive interface in adhesively bonded joint is one of the most common failure modes [24]. Unfortunately, the defect or failure cannot be seen from outside of the sandwich structure and because of this reason, Thomas et al [25], was proposed a rapid inspection procedure for detection of composite skin delamination from a honeycomb core with ultrasonic guided waves and showed a superior sensitivity which explained in terms of the displacement field variation as frequency is swept.

The methods to improve the peel resistance and dealing with the quality problems can be discovered by understanding the failure mechanism of sandwich panels and the role of resin fillet. In Ryo et al study [11], the 'stick-slip' crack growth behaviour was observed during the peel test. It was explained that 'stick' occurred when the crack is temporarily arrested at cell wall during peeled off. Crack could not propagate further as the energy required to peel the face sheet is absorbed by the fillet and used to deform them. Bubbles on fillet surfaces (formed during curing due to vapor release) could act as crack initiation sites and eventually developing the fillet fractures. Subsequently, crack runs across the interface between core and face sheet and once the crack reaches the next rows of cell walls, crack is arrested again and process is repeated which is known as 'slip'.

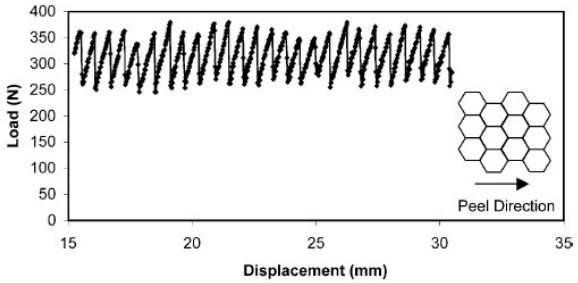


Fig. 2. Load-displacement curve in ribbon direction [11].

Crack propagation between the skin and the honeycomb core is found unstable because of the presence of multiple interfaces (core) serves as a source for failure initiation and growth [26]. The 'saw-tooth' pattern on the force-displacement graph as shown in Figure 2, also observed during the climbing drum peel test, is attributed to skin-core delamination of sandwich structures with a honeycomb core, when performed in the ribbon direction [8,11]. Besides that, high levels of porosity in prepreg laminate also indicated different crack propagation because of permitting water ingression where can results in increasing weight and possibility of skin delamination [15]. Conversely, Cantwell et al [27] has concluded that the adhesion between honeycomb and composite skin was good if the crack had not propagated at the skin-core interface but instead at several tenths of a millimetre away from it within the honeycomb core.

The weaknesses of the bonding properties between skin-core interface could be the result of the manufacturing imperfection and service loading such as inadvertent introduction of foreign matter

or improper gluing at the interface, wave slamming and underwater explosions [5,24,28-29]. Accurate knowledge of mechanical behaviour of sandwich panels, such as critical buckling loads, mode shapes and debonding behaviour is essential for reliable and lightweight structural design. The great majority of the debonded sandwich panels failed due to local buckling of the debonded facesheet followed by rapid propagation of the debond that perpendicular to the direction of load application. If such structure was loaded in compression, the facesheet over the debonded region may buckle allowing propagation of the debond and possible structural collapse. Hence, there was a need for systematic study to understand how the core and face sheet properties affect the compression behaviour of a debonded sandwich structure. Deflectometers, strain gages, and the shadow moiré technique were recommended to be used to monitor and examine the local buckling [20,28-30].

Nonetheless, delamination and debonding is a very fundamental problem for both composite and sandwich materials. Failure of the interface between the load-bearing skin material and the low density core may result in a total loss of structural integrity, almost certainly leading to complete structural failure of the part [31].

Bonding Performance

There are lots of challenges involved in adhesive bonding that can affect the mechanical properties of the joint which are currently unresolved and to some extent, require reconsideration and improvement for development in aircraft structures. Most of the results from previous studies either from experimental or numerical/theoretical studies showed that the bonded joint fracture was always the result of crack propagation initiated from the location of high stress concentration at the edges of the overlap region [1-4,21]. There are several ways to overcome this problem, in which the stress concentration at the end of overlap could be reduced significantly by introducing a fillet so that it can carry a portion of shear strain in transferring the longitudinal load [18]. Fillet carries appreciable amounts of shear strain and helps to reduce shear and normal stress concentrations at the end of the overlap as well as to prevent the crack initiation at the corner of the adhesive layer [18-19,21-22].

It is similar as in the sandwich structures, where the resin fillets also influence the delamination resistance of these materials in a significant way. To develop a strong adhesive performance in sandwich structure, adhesive must rigidly attach the skin to the core material in order for loads to be transmitted from one skin to the other. Fillet or menisci was developed at the junction between the honeycomb cell wall and skin as shown in Figure 4, playing an important role in determining the fracture toughness and peel fracture due to the absorption of energy and hence, the load transfer between skin and cell walls [8-9,11]. Fillet formation needs to be given more attention because to a achieve a good attachment to an open cell core such as honeycomb, the adhesive should flow sufficiently to form a fillet without running away from the skin to core joint. Unfortunately, from study was done by Chongxin et al [9], the cure cycle process will affect the formation of fillet where the outflow of resin influence by the different applications of pressure. They were found that, fillet area and resin content between top and bottom skin are different because more resin can be squeezed out when the pressure was applied at low viscosity of resin. It is results in dropping of the squeezed resin of the top skin directly on the bottom skin or flow down along with the core wall because of the gravitational attraction. To some extent, it was found that fillet size influenced the peel strength. Higher peel strength and higher debonding energy was associated with relatively large, regular-shaped adhesive fillets between the honeycomb cell walls and skin [8]. It was different as more resin was used, the more voids were developed within the fillet in which they acted as crack initiation points that weakened the bonding performance [11]. On the other hand, ramp rate was also prone to void growth. Higher ramp rate would give higher inner pressure that indicates an increase in the temperature within the core where the void would be developed [9].

Brian et al [15] have discussed not only on the fillet size, but also the effect of quantity of the resin fillet. They have prepared a sandwich with a commercial self-adhesive prepreg and a home-made model prepreg with less solvent content. It has been shown that the solvent leads to porosity formation and then to a decrease in debonding energy. It is essential to recognize that the peel strength and peak tensile stress could be varied by the resin distribution (impregnation) within the prepreg. By placing most of the resin on the surface of the model prepreg, better fillets were formed between the honeycomb core and the prepreg skin. A low level of impregnation resulted in the best bonding to the honeycomb core, while still producing essentially void-free parts.

Strain Energy Release Rate (SERR)

SERR is the total energy dissipation during fracture per unit of newly created fracture surface area. Virtual Crack Closure Technique (VCCT) has started to attract attention from industries as it is believed to have great potential in composites applications. Experimentally, the SERR was usually determined using the Double Cantilever Beam (DCB) test, and the Climbing Drum Peel Test provides an alternative to DCB testing [10-11,26]. Wang et al [24] developed an analytical expression for the SERR which provides enhanced accuracy with consideration of the effect of shear deformation. In addition, Sanjib et al [5] assessed the SERR by means of Irwin's crack closure growth integral using finite element analysis (FEA) that has been verified with an energy balance approach. They proposed that in calculating the SERR due to debonding and subsequent crack growth under in-plane loading, it was considered completely sufficient just to study the behaviour of a representative unit cell as the smallest structural portion that represents the whole sandwich structure (core and top/bottom face skin together). On other work, Yuan et al [9] has suggested that the total energy dissipated was divided by the resulting fracture surface.

Alternatively, Kenneth et al [30] have studied about the modified crack closure technique to determine the SERR. It has been revealed from the parametric studies that the face sheet thickness and stiffness possessed the largest effect on SERR values. Almost uniformly, 60% proportion of the strain energy in adhesive was found higher for panels with thicker face sheet [14]. The cross-ply adherends would provide greater strain energy release rate than in the unidirectional adherends [23].

Summary

Overviews on the main parameters that influence the performance of the adhesively bonded joint in polymer composite materials especially in aircraft structure were presented. The paper exclusively highlighted from the basic to the advanced knowledge in bonding composite lap joint and between skin-core in sandwich structures. Each joining application must be considered with regard to its specific processing and performance requirements. There are times when adhesives may be the worst possible option for joining two adherends, and on the contrary, adhesives may be the best or an alternative way for the composite joint.

The formation of fillet were comprehensively discussed, where the resin fillet formed between skin and cell wall played an important role to enhance the strength of bonding on the skin-core interface. Failure mechanism and energy release rate were also presented; the major parameters that should be given more attention to create an improvement for skin-core bonding in sandwich structure and composite laminates lap joint in order to allow the structure to sustain high loads over a long service life.

Therefore, it is essential to investigate the alternative means of bonding that could reduce cost and weight consumption, but offer high mechanical performance as these are becoming increasingly important in design criteria of aircraft structures. Failure mechanism such as delamination in the composite laminates should be avoided since it could contribute to more complicated and problematic circumstances in the establishment of composite inspection and repair procedures.

References

[1] A. F. avila, P. O. Bueno; Compos Struct, 64 (2004), p. 531.

[2] S. C. Her; Compos Struct, 47 (1999), p. 673.

[3] A. G. Magalhaes, et al; Int J Adhes Adhes, 25 (2005), p. 313.

[4] F. Mortensen, O.T. Thomsen; Compos Sci Technol, 62 (2002), p. 1011.

[5] S. Goswami and W. Becker; Compos Struct, 54 (2001), p. 515-521.

[6] M. K. Khan; Proc. IMechE, Part G: J. Aerosp Eng, 220 (2006), p. 375.

[7] M. Schlotter; June 2002. http://people.bath.ac.uk/enpms/study/docs/sandwcore_mat.pdf

[8] S. M. Grove, E. Popham and M. E. Miles; Composites Part A, 37 (2006), p. 804.

[9] C. Yuan, M. Li, Z. Zhang and Y. Gu; Appl Compos Mater, 15 (2008), p. 47.

[10] A. Ural, A. T. Zehnder and A. R. Ingraffea; Eng Fract Mech, 70 (2003), p. 93.

[11] R. Okada and M. T. Kortschot; Compos Sci Technol, 62 (2002), p. 1811.

[12] T. C. Radtke, A. Charon and R. Vodicka; DSTO-TN-0263. DSTO Aeronautical and Martitime Research Lab., Melbourne, Australia, May 2000.

[13] G. C. Papanicolaou, D. J. Bakos and T. V. Kosmidou; Composites Part A, 38 (2007), p. 1099.

[14] W. S. Burton and A. K. Noor; Finite Elem Anal Des, 26 (1997), p. 213.

[15] B. S. Hayes, J. C. Seferis and R. R. Edwards; Polym Compos, 19 (1998), p. 54.

[16] L. F. M. da Silva and R. D. Adams; Int J Adhes Adhes, 27 (2007), p. 227-235.

[17] G. Belingardi, L. Goglio and A. Tarditi; Int J Adhes Adhes, 22 (2002), p. 273-282.

[18] M.Y. Tsai, J. Morton; Compos Struct, 32 (1995), p. 123.

[19] J. Deng and M. M. K. Lee; Composites Part B, 39 (2008), p. 731-739.

[20] J. Rion, Y. Leterrier and J. E. Manson; Composites Part A, 39 (2008), p. 1547.

[21] A.A. Taib, et al; Int J Adhes Adhes, 26 (2006), p. 226.

[22] K.S. Kim, J.S. Yoo, Y.M. Yi, C.G. Kim; Compos Struct, 72 (2006), p. 477.

[23] M. Qin, Y. A. Dzenis; Composites Part B, 34 (2003), p. 167-173.

[24] J. Wang and C. Zhang; Int J Solid Struct, 46 (2009), p. 4409.

[25] T. R. Hay, L. Wei, J. L. Rose and T. Hayashi; J Compos Mater, 37 (2003), p. 929.

[26] T. S. Gates, et al; Compos Sci Technol, 66 (2006), p. 2423.

[27] W. J. Cantwell and P. Davies; J Mater Sci Lett, 13 (1994), p. 203.

[28] J. L. Avery III and B. V. Sankar; J Compos Mater, 34 (2000), p. 1176.

[29] F. Aviles and L. A. Carlsson; J Sandwich Struct Mater, 8 (2006), p. 7.

[30] K. M. Liechti and B. Marton; Exp Mech, 42 (2002), p. 206.

[31] W. J. Cantwell and P. Davies; Appl Compos Mater, 3 (1996), p. 407.

© (2011) Trans Tech Publications, Switzerland
doi:10.4028/www.scientific.net/KEM.471-472.616

Nonlinear Free and Forced Vibrations of Symmetric Laminated Panels

Alireza Shooshtari[1,a], Soheil Razavi[1,b], Hadi Ghashochi Bargh[2,c]

and Mohammad Homayoun Sadr[2,d]

[1]Mechanical Engineering Department, Bu-Ali Sina University, 65175-4161 Hamedan, Iran

[2]Aerospace Engineering Department, Centre of Excellence in Computational Aerospace Engineering, Amirkabir University of Technology, Hafez Avenue, Tehran, Iran

[a]shooshta@basu.ac.ir, [b]soheilrazavi140@gmail.com, [c]h_bargi2003@yahoo.com, [d]Sadr@aut.ac.ir

Keywords: Laminated panel, Galerkin method, Perturbation method, Nonlinear vibration

Abstract. In this paper, free and forced vibrations of symmetric laminated composite plates are studied analytically by using a perturbation method where the analytical results for transverse displacement are compared with the numerical results. The external force is taken to be harmonic in time and having uniform amplitude.

Introduction

Laminated composite structures, due to their high specific strength and stiffness, have been increasingly applied in many engineering fields such as aerospace, marine vehicles and nuclear engineering [1]. To use them efficiently, it is necessary to develop appropriate models capable of accurately predicting their structural and dynamical behavior [2]. A. Shooshtari et al investigated the nonlinear free vibration of laminated and fiber metal laminate rectangular plates with immovable simply supported boundary conditions by using multiple scales method [3].

In this paper, a perturbation method is used to solve the obtained nonlinear ordinary differential equation of motion in reference [3] for the free and forced vibration. The panels are simply supported with various combinations of in-plane boundary conditions. The effects of plate properties and plate geometry on the nonlinear vibration are investigated.

The Solution for the Equation of Motion. The boundary conditions considered here are:

Immovable (SS1) $w = w_{,xx} = \psi_{,xy} = u_0 = 0$ at $x = 0, a$; $w = w_{,yy} = \psi_{,xy} = v_0 = 0$ at $y = 0, b$
Partially movable (SS2) $w = w_{,xx} = \psi_{,xy} = 0$ at $x = 0, a$; $w = w_{,yy} = \psi_{,xy} = 0$ at $y = 0, b$

$$\int_0^a (\psi_{,xx})_{y=0,b}\, dy = 0, \quad \int_0^b (\psi_{,yy})_{x=0,a}\, dx = 0.$$

The equation of motion in time domain, which is presented in reference [3], is used here:

$$f_{,\tau\tau} + \omega^2 f + \alpha_1^2 f^3 + \beta_1^2 f_{,\tau\tau} f^2 + \gamma_1^2 f_{,\tau}^2 f = Q \cos\left(\Omega \frac{a^2}{\sqrt{\Lambda}} \tau\right), \tag{1}$$

where for the free vibration, the right hand side of Eq. 1 is equated to zero and for the external force having uniform amplitude (i.e., $q = q_0 \cos \Omega t$), it is obtained that $Q = \frac{a^4 [I_2 \Omega^2 K (A_{44} + A_{55}) - K^2 A_{44} A_{55}] q_0}{Z_1 \Lambda}$.

To solve Eq. 1 by using a perturbation method, a small dimensionless parameter (ε) is defined and used in Eq. 1 so that it is changed to the following equation:

$$f_{,\tau\tau} + \omega^2 f = \varepsilon\left(Q \cos(\Omega \bar{\Lambda} \tau) - \alpha^2 f^3 - \beta^2 f_{,\tau\tau} f^2 - \gamma^2 f_{,\tau}^2 f\right), \tag{2}$$

where $\bar{\Lambda} = \frac{a^2}{\sqrt{\pi}}$, $Q = \frac{a^6[I_2\Omega^2 K(A_{44}+A_{55})-K^2 A_{44}A_{55}]q_0}{E_1 A h^2}$, $\alpha^2 = \alpha_1^2 \times \left(\frac{a}{h}\right)^2$, $\beta^2 = \beta_1^2 \times \left(\frac{a}{h}\right)^2$, and $\gamma^2 = \gamma_1^2 \times \left(\frac{a}{h}\right)^2$. ω and Ω are dimensionless frequency and excitation frequency, respectively. The coefficients of Eqs. 1 and 2 are functions of plate properties and are computed for each plate by using MATLAB® software.

For using the method of multiple scales, the detuning parameter is defined by $\Omega = \omega_L + \varepsilon\sigma$, where ω_L is the circular natural frequency. So, equating the like powers of ε, according to the procedure explained by Nayfeh [4], leads to:

$$D_0^2 f_0 + \omega^2 f_0 = 0, \tag{3}$$

$$D_0^2 f_1 + \omega^2 f_1 = -2D_0 D_1 f_0 - 2\mu D_0 f_0 - \alpha^2 f_0^3 - \beta^2 f_0^2 (D_0^2 f_0) - \gamma^2 f_0 (D_0 f_0)^2 + Q\cos[\omega T_0 + \bar{\Lambda}\sigma T_1]. \tag{4}$$

The solution for Eq. 3 can be written in the following form:

$$f_0 = A_2(T_1)\exp(i\omega T_0) + cc. \tag{5}$$

The solvability condition of Eq. 4, which is obtained by substitution of Eq. 5 into Eq. 4, is:

$$\left[-2i\omega A_2' - 3A_2^2 \bar{A}_2 \alpha^2 + \omega^2 A_2^2 \bar{A}_2 \beta^2 + \tfrac{1}{2}Q\exp(i\bar{\Lambda}\sigma T_1)\right] = 0, \tag{6}$$

where by defining A_2 in the form of $\frac{1}{2}r\exp(is)$ and substituting it into Eq. 6, the first approximation of f is obtained in the following form:

$$f = r\cos(\omega\tau + s) + O(\varepsilon), \tag{7}$$

where amplitude (r) and phase (s) are obtained by:

$$r' = -\mu r + \frac{Q}{2\omega}\sin(\bar{\Lambda}\sigma T_1 - s),$$

$$rs' = \left(\frac{3}{8\omega}\alpha^2 - \frac{1}{8}\omega\beta^2\right)r^3 - \frac{Q}{2\omega}\cos(\bar{\Lambda}\sigma T_1 - s). \tag{8}$$

For an autonomous system, the substitution of $\eta = (\bar{\Lambda}\sigma T_1 - s)$ is used in Eq. 8. So, in the steady-state motion, where $r' = \eta' = 0$, the frequency response equation is obtained in the following form:

$$\left[\frac{1}{8}\left(\frac{3}{\omega_L}\alpha^2 - \omega_L\beta^2\right)r^2 - \sigma\right]^2 = \frac{(Q/2)^2}{4\omega_L^2 r^2}, \tag{9}$$

where the nonlinear frequency ratio in the free vibration is obtained by substituting $Q = 0$ in Eq. 9:

$$\frac{\hat{\omega}}{\omega_L} = \left[1 + \frac{q_4}{4\omega_L^2}\left(\frac{h}{a}\right)^2 p_0^2 + \frac{1}{8\omega_L^2}\left(\frac{h}{a}\right)^4\left(\frac{q_2^2}{8\omega_L^2} + \frac{q_2}{2} + \frac{q_3}{8} + q_4\right)p_0^4\right]^{1/2}, \tag{10}$$

where $\hat{\omega}$ are is the nonlinear free frequency. p_0 and r are dimensionless amplitudes of vibration in free and forced vibration, respectively and other parameters are:

$$q_1 = 3\alpha^2 - \beta^2\omega^2, \quad q_2 = \frac{1}{8\omega^2}q_1(\alpha^2 - 3\beta^2\omega^2), \quad q_3 = \frac{-1}{\omega^2}q_1^2, \quad q_4 = -\beta^2 q_1. \tag{11}$$

Numerical Examples. The variation of nonlinear frequency ratio with non-dimensional maximum amplitude (p_0) is evaluated for simply supported thin (a/h = 100) square plates and the results are shown in Table 1 along with the published results. It is observed that the present results for the nonlinear frequency of isotropic plates are in close agreement with the available solutions. In Table

1, $\nu = 0.3$ and $G = E/(2(1+\nu))$ are used for the isotropic plate. It is seen that the degree of hardening nonlinearity (i.e., increase of frequency with amplitude) is more for immovable (SS1) plate compared with the partially movable (SS2) plate.

Table 1. Comparison of the nonlinear frequency ratio of isotropic square plates.

p_0	Boundary condition			
	SS1		SS2	
	M. K. Singha [5]	Present study	M. K. Singha [5]	Present study
0.2	1.01967	1.01960	1.00516	1.00511
0.4	1.07669	1.07661	1.02049	1.02031
0.6	1.16597	1.16656	1.04559	1.04525
0.8	1.28131	1.28406	1.07959	1.07936

The back-bone curves of an isotropic plate and a three-layered [90°/0°/90°] plate are studied and shown in Fig. 1. In the isotropic plate $\nu = 0.3$ and $G = E/(2(1+\nu))$, and the properties of the composite plate are: $G_{12} = G_{13} = 0.6E_2$, $G_{23} = 0.5E_2$, $\nu_{12} = 0.25$.

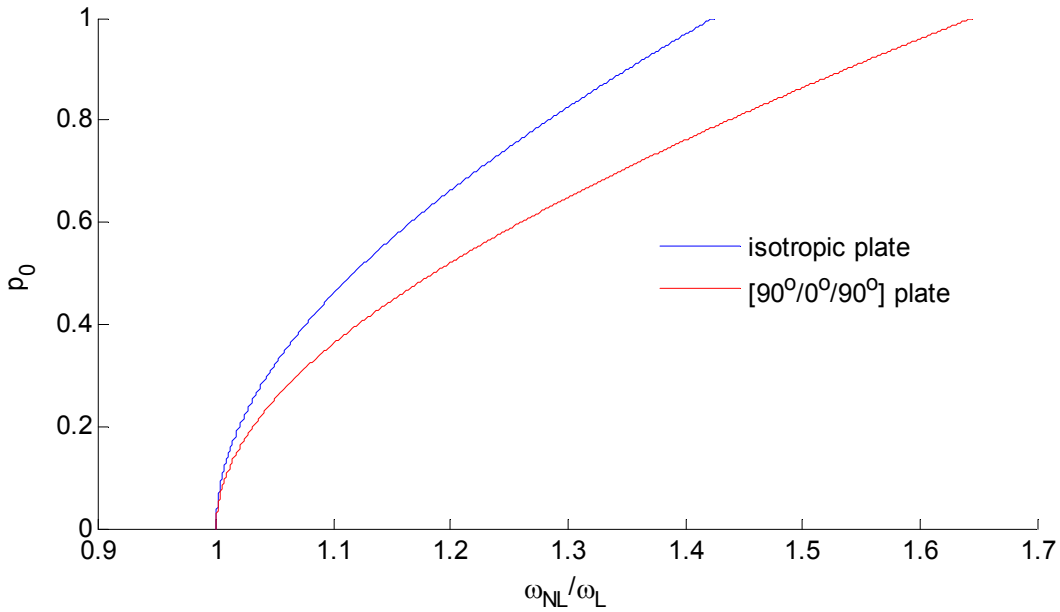


Fig. 1. Comparison of the back-bone curves for two types of square plates.

Frequency response curves of a five-layered [90°/0°/90°/0°/90°] glass reinforced (GFRC) square plate for boundary conditions of (SS1) and (SS2) are investigated and shown in Fig. 2, where the length and the total thickness of the plate are taken to be 100 mm and 1 mm, respectively. In Fig. 2 q_0 is taken as 10 MPa.

It is seen from Fig. 1 that the increase of frequency with amplitude is more for the cross-ply square plates compared to the isotropic square plates. Fig. 2 shows that the nonlinear terms in immovable case (SS1) are bigger than that of the partially immovable case (SS2) because the curve of (SS1) has smaller slope.

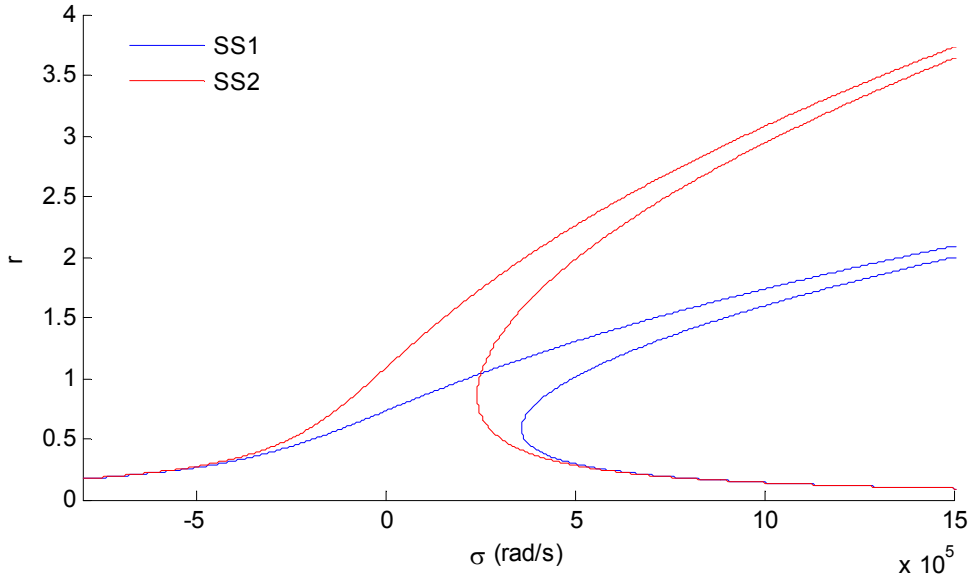


Fig. 2. Frequency response curve of a five-layered cross-ply laminated plate for different in-plane boundary conditions.

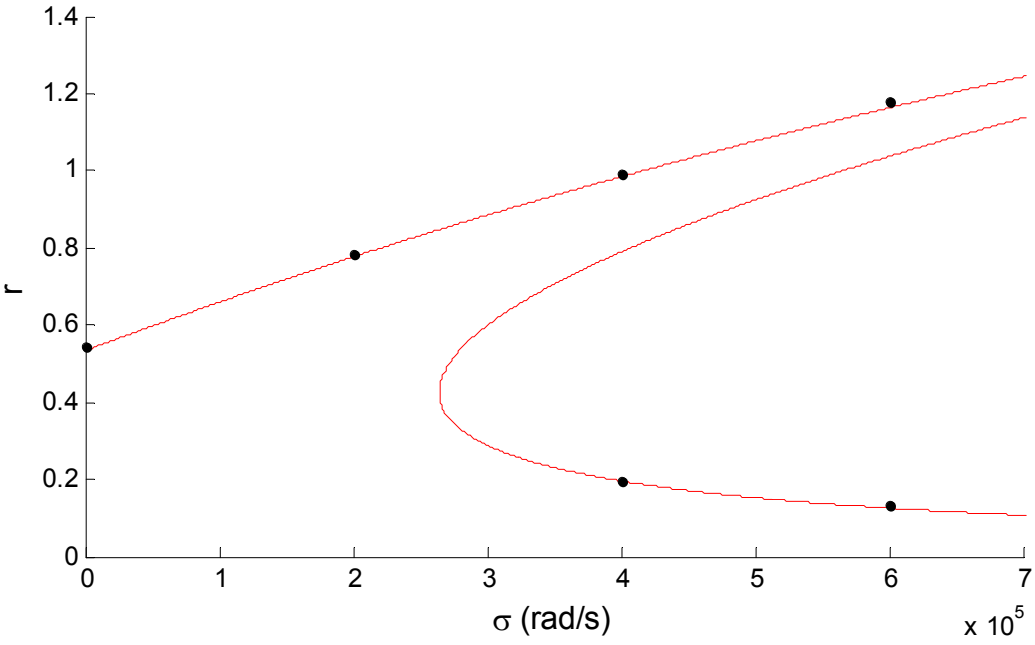


Fig. 3. Comparison of numerical and analytical solution of nonlinear ode of motion for immovable boundary condition; • numerical, ——— analytical.

Eq. 1 is solved numerically for a square aluminum alloy plate (a = 100 mm, h = 1mm), on the immovable simply supported boundary condition, by using the Rung-Kutta method and compared with the analytical solution. The result is shown in Fig. 3. It is observed that there is a good agreement between the numerical and the analytical solution of Eq. 1. In Fig. 3 q_0 is taken to be 10 MPa.

The variation of amplitude of motion with excitation amplitude (amplitudes curve) is investigated and shown for a five-layered [90°/0°/90°/0°/90°] GFRC square plate (a = 100 mm, h = 1 mm) in Fig. 4. It is seen that the multi-valued region in partially movable (SS2) case is bigger and

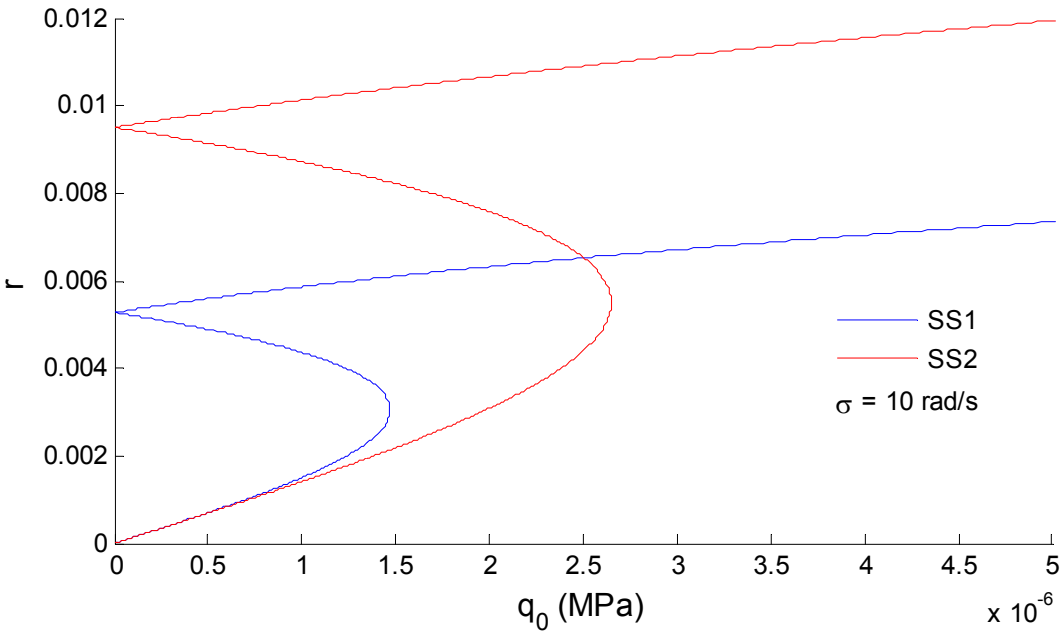


Fig. 4. The variation of amplitude of motion with excitation amplitude (amplitudes curve) of a five-layered GFRC square plate

the dimensionless amplitude (r) increases with higher rate after the jump phenomenon, when compared with the results of immovable (SS1) case.

The effect of aspect ratio (a/b) on the nonlinear vibration of a rectangular plate is studied and shown in Fig. 5 for a five-layered [90°/0°/90°/0°/90°] GFRC plate on (SS1) boundary condition. It is noticed that for smaller aspect ratios, the amplitude of motion is bigger for specific excitation amplitude.

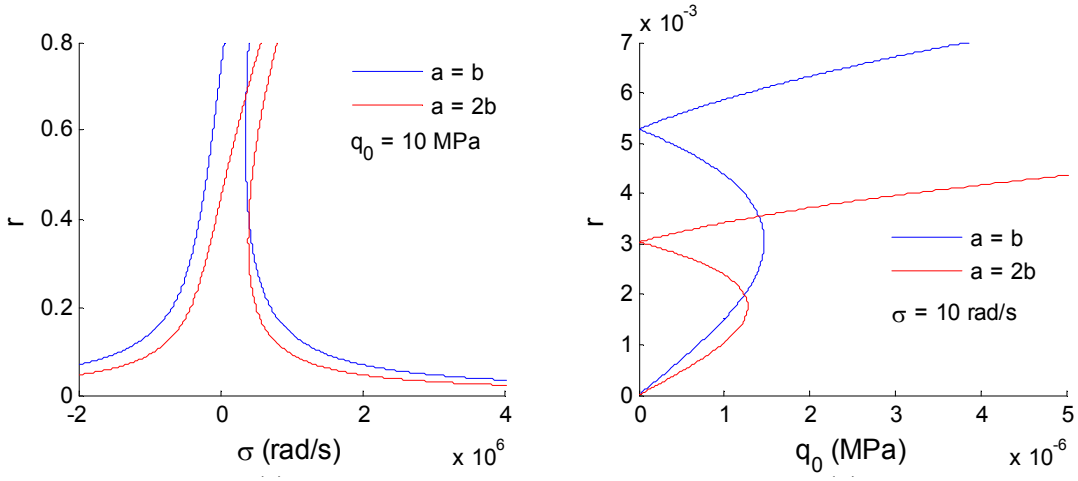


Fig. 5. Effects of aspect ratio on the (a) frequency response curve, (b) amplitudes curve.

The effects of some of lamination parameters on the nonlinear vibration of a rectangular plate are also investigated and the results are shown in Fig. 6 for a laminated GFRC square plate on (SS1) boundary condition. It is seen that the number of layers and layup have very small effect on the nonlinear behavior of laminated panels. This claim can be proved by Eq. 12, too, in which the frequency response equation of each laminated plate is obtained by using Eq. 9 and the properties of

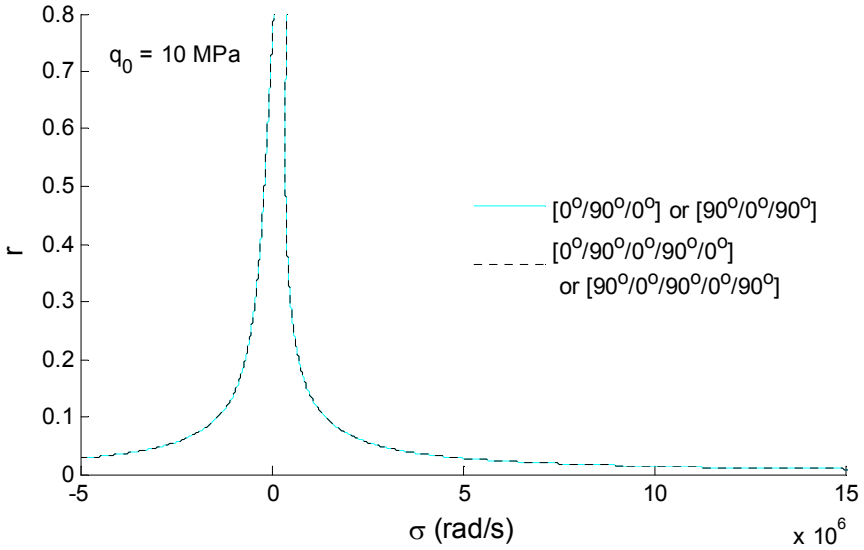


Fig. 6. Frequency response curves of two square GFRC plates with different number of layers and layup.

studied plates.

$$\sigma = 359266.829r^2 \pm 13812.172(q_0/r) \quad \text{for} \quad [0^\circ/90^\circ/0^\circ],$$
$$\sigma = 359289.571r^2 \pm 13811.493(q_0/r) \quad \text{for} \quad [0^\circ/90^\circ/0^\circ/90^\circ/0^\circ],$$
$$\sigma = 359291.189r^2 \pm 13811.387(q_0/r) \quad \text{for} \quad [0^\circ/90^\circ/90^\circ/90^\circ/0^\circ]. \qquad (12)$$

Summary

Nonlinear free and forced vibration of symmetric rectangular plates considering two forms of simply supported boundary conditions is studied analytically and the effects of several parameters on the nonlinear behavior of these plates is investigated. The results are compared with the published results and the numerical solution and good agreement is found.

References

[1] Ömer Civalek: Finite Elements in Analysis and Design. Forum Vol. 44. p. 725-731 (2008).
[2] Wu Zhen, Chen Wanji: Journal of Sound and Vibration. Forum Vol. 298. p. 333-349 (2006).
[3] A. Shooshtari, S. Razavi: Composite Structures. Forum Vol. 92. p. 2663-2675 (2010).
[4] A.H. Nayfeh, TMook Dean: *Nonlinear Oscillation*. (John Wiley & Sons, Inc 1995).
[5] M.K. Singha, Rupesh Daripa: Journal of Sound and Vibration. Forum Vol. 328. p. 541-554 (2009).

© (2011) Trans Tech Publications, Switzerland
doi:10.4028/www.scientific.net/KEM.471-472.622

The Partial Replacement of Halloysite Nanotubes (HNTs) and Precipitated Silica by Recycled Poly(ethylene terephthalate) Powder on Cure Behavior, Tensile Properties and Morphology of Natural Rubber Composites

H. Nabil[1,a], H. Ismail[1,b] and A.R. Azura[1,c]

[1]Department of Polymer Engineering, School of Materials and Mineral Resources Engineering, Universiti Sains Malaysia, Engineering Campus, 14300 Nibong Tebal, Penang, Malaysia

[a]nabil_ty@hotmail.com, [b]hanafi@eng.usm.my, [c]azura@eng.usm.my

Keywords: Recycled polyethylene terephthalate, Natural Rubber, Halloysite nanotubes, Silica

Abstract. In this article, halloysite nanotubes (HNTs) and precipitated silica were replaced by recycled polyethylene terephthalate powder (R-PET) in natural rubber composites. Five different compositions of NR/HNTs/R-PET and NR/Silica/R-PET composites [i.e. 100/20/0, 100/15/5, 100/10/10, 100/5/15, and 100/0/20 parts per hundred rubber (phr)] were prepared on a two-roll-mill. Comparison of the curing behavior, tensile properties, and morphological characteristics of natural rubber composites was studied. The results indicated that the replacement of HNTs and silica by R-PET decreased the tensile strength, tensile modulus, and elongation at break of composites, but NR/Silica/R-PET composites showed the lower trend than that NR/HNTs/R-PET did. The negative effect of these properties could be explained by the decrement of crosslink density, R-PET is unable to be transferred the stress due to the weal rubber-fillers interactions, and the reducing of ductility of rubber matrix. The curing results revealed that, with replacement of HNTs and Silica by R-PET, the scorch time (ts_2) and cure time (tc_{90}) were decreased. Scanning electron microscopy investigation of tensile fracture surfaces confirmed that co-incorporation of NR/HNTs/R-PET would improve the dispersion of R-PET and enhanced the interactions between fillers and NR matrix rather than NR/Silica/R-PET composites.

Introduction

Filler is one of the major additives used in natural rubber compound and has marked effect and influence on rubber materials filler functions to modify the physical and to some extent the chemical properties of vulcanizates. Particulate fillers are added to rubbers either to extend and cheapen the rubber compound, or to add desirable qualities to the final compound and enhance theproducts' service qualities [1,2]. Precipitated silica is the important reinforcing fillers for non-black applications. However, for some applications where cost and processability are of greatest concern, the use of semi-reinforcing fillers as well as other fillers from renewable resources and wasted materials [3-6] is highly recommended. Recently, halloysite nanotubes or HNTs have been incorporated as reinforcing filler in many polymer matrix and elastomer [7-11]. HNTs are a kind of naturally occurring aluminosilicate ($Al_2Si_2O_5(OH)_4 \cdot H_2O$ 1:1) with a predominantly hollow nanotubular structure in the submicron length and chemically similar to kaolin [12]. As for most natural materials, the size of halloysite paticles varies within 1-15 μm of length and 10-150 nm of inner diameter, depending on the deposits [13-15].

Polyethylene terephthalate or PET, plays a major role in our daily activities due to its transparency, thermal stability, chemical resistance and excellent resistance to oxygen and carbon dioxide [16]. PET has become a material of choice for bottling beverages, such as mineral water and carbonated soft drinks. Unfortunately, these same useful of PET can make a huge pollution problem. Since it is very highly resistance to atmospheric and biological agents, PET bottles become noxious materials of concern in relatively recent environmental protection issues [17]. As a consequence of this, to eliminate or reduce waste PET from the environment and to reduce costs of some manufacturing products, a relatively new area of interest is the use of recycle polyethylene terephthalate (R-PET) bottling powder as filler for natural rubber. Since over the years, utilization of R-PET has been done in many studies, i.e., polymer concrete [18], blending with virgin PET and

commercial plastics [19,20], and use of R-PET as a matrix in filled composites [21,22], but no attempts have been made so far the used of R-PET bottles as filler in natural rubber compound.

Therefore, the purpose of this work is to study the potential and the reinforcing effect of hybrid composites as well as to eliminate or reduce waste PET from the environment with partially replacing halloysite nanotubes, and precipitated silica by R-PET powder in natural rubber composites. Curing characteristics, swelling study, tensile properties, and morphology were conducted on the natural rubber composites.

Experimental

Materials. Table 1 shows the compounding formulation used in this study. Natural rubber and L grade SMR were supplied by Rubber Research Institute of Malaysia (RRIM). The recycled polyethylene terephthalate (R-PET) flakes were supplied by Toray Plastic (Malaysia) Sdn. Bhd. Precipitated silica, Ultrasil VN3 was obtained from Degussa Ltd. Halloysite nanotubes (HNTs), ultrafine grade was supplied by Imerys Tableware Asia Limited, New Zealand, with brightness of 98.9% as measured by a Minolta CR300 using D65 light source. The elemental composition is as follow (wt%); SiO_2, 49.5; Al_2O_3, 35.5; Fe_2O_3, 0.29; TiO_2, 0.09 [23]. Other compounding ingredients such as zinc oxide, stearic acid, *N*-cyclohexyl-2-benzothiazole-sulphenamide (CBS), *N*-isopropyl-*N'*-phenyl-*p*-phenylenediamine (IPPD) and sulphur were purchased from Bayer (M) Ltd. and used as received.

Table 1.Formulation used in NR/N550/R-PET, NR/HNTs/R-PET and NR/Silica/R-PET composites.

Ingredients (phr:phr)	NR/HNTs/R-PET	NR/Silica/R-PET
SMR L	100	100
Stearic acid	1.5	1.5
ZnO	1.5	1.5
CBS	1.9	1.9
IPPD	2.0	2.0
Sulphur	1.6	1.6
HNTs/R-PET	20:0 15:5 10:10 5:15 0:20	-
Silica/R-PET	-	20:0 15:5 10:10 5:15 0:20

R-PET Particle Preparation. The R-PET flakes were ground into powder using a Table Type Pulverizing Machine from Rong Song Precision Technology Co.Ltd. The powder was then sieved with an Endicott's sieve to get particles around 125-212 μm in size. The R-PET powder was dried in a vacuum oven at 80°C for 24 hours to expel moisture. Dried R-PET powder was used in rubber compounding without further treatment.

Mixing and Vulcanization Procedures. The compounding of SMR L with HNTs, Silica, R-PET and other additives such as zinc oxide, stearic acid, CBS, IPPD and sulphur were prepared at ambient temperature using on a laboratory-sized (160 mm × 320 mm) two-roll-mill, model XK-160. The cure characteristics were carried out using a Monsanto Moving Die Rheometer (MDR 2000) according to ASTM D 2240-93. Samples of the respective compounds were tested at the vulcanization temperature (150°C). The compounds were subsequently compression moulded using a stainless steel mould at 150°C with a force of 10 MPa using a laboratory hot-press based on the respective curing times.

Measurements of Rubber-Filler Interaction. Cure test pieces of dimension 30 mm × 5 mm × 2 mm were swollen in toluene until equilibrium, which took 72 hours at room temperature. The samples were taken out from the liquid, the toluene removed from the samples' surface and the weight was determined. The samples were then dried in an oven at 60°C until a constant weight was obtained. The Lorenz and Parks equation was used to study the rubber-filler interaction [24]:

$$\frac{Q_f}{Q_g} = ae^{-z} + b \qquad \text{(Eq. 1)}$$

Where Q is defined as grams of solvent per gram of rubber hydrocarbon, as follows:

$$Q = \frac{\text{Swollen weight - Dried weight}}{\text{Original weight} \times \frac{100}{\text{Formula weight}}} \quad \text{(Eq. 2)}$$

The subscripts f and g in the equation refer to filled and gum composites, respectively. z is the ratio by weight of filler to rubber hydrocarbon in the composites, while a and b are constants. The higher the Q_f/Q_g values, the lower the rubber-filler interaction.

Measurements of Tensile Properties. Dumbbell-shaped samples were cut from the moulded sheets according to ASTM D 412. Tensile tests were performed at a cross-head speed of 500 mm/min. Tensile tests were carried out with a universal tensile machine Instron 3366 to determine the tensile properties in terms of tensile strength, stress at 300% elongation (M300) and elongation at break.

SEM Micro-Fracture Surfaces. Tensile fracture surfaces analysis was carried out using a scanning electron microscope (SEM), model Zeiss Supra-35VP, to obtain information regarding filler dispersion and to detect the possible presence of micro-defects. The fractured pieces were coated with a layer of gold palladium to eliminate electrostatic charge build-up during examination.

Results and Discussion

Cure Characteristics. The curing characteristics of NR/HNTs/R-PET and NR/Silica/R-PET composites are revealed in Table 2. The scorch time (ts_2) and cure time (tc_{90}) of NR/HNTs/R-PET and NR/Silica/R-PET obviously decreased with the increasing R-PET loading ratio. The decrement of ts_2 and tc_{90} of HNTs and silica composites when these two fillers were replaced by R-PET is attributed to the low tendency of HNTs and silica to interact with accelerators which led to increase the number of active sulfurating agents and hence increase in ts_2 and tc_{90} of these two composites. It was also found that the ts_2 and tc_{90} of NR/HNTs/R-PET were shorter than NR/Silica/R-PET composites. It is well accepted that HNTs has higher surface area and low porosity than silica [11], which absorbs certain rubber ingredients less than the silica does, the number of sulfurating agents was increased and subsequently the ts_2 and tc_{90} of the composites decreased.

Table 2. Curing characteristics of NR/HNTs/R-PET and NR/Silica/R-PET composites.

Composition	**NR/HNTs/R-PET**					**NR/Silica/R-PET**				
Fraction (phr:phr)	**20:0**	**15:5**	**10:10**	**5:15**	**0:20**	**20:0**	**15:5**	**10:10**	**5:15**	**0:20**
ts_2 (min)	4.81	4.27	3.95	3.50	3.21	5.28	5.10	4.80	4.22	3.21
tc_{90} (min)	6.12	6.01	5.55	5.01	4.65	8.02	7.59	7.02	6.52	4.65
H_H (d.Nm)	9.00	8.82	8.78	8.60	8.50	8.84	8.70	8.64	8.56	8.50
$\Delta S=M_H-M_L$ (d.Nm)	8.92	8.71	8.63	8.58	8.39	8.63	8.49	8.46	8.41	8.39

A maximum torque (M_H) and torque differences (M_H-M_L) were found to decrease with increasing the R-PET loading. The deterioration of M_H and M_H-M_L of the composites is due to the presence of R-PET which has a lower restriction to molecular motion of the macromolecule and may be attributed to the sparse crosslinking [25,26]. Among these two hybrid composites, the degree of torque values of NR/HNTs/R-PET rather than NR/Silica/R-PET. This observation could be due to the HNTs in NR/HNTs/R-PET composite having a smaller particle size and higher surface activity as well as higher structure compared to silica in the NR/Silica/R-PET composites, which may have improved the rubber-filler interactions between the rubber matrix and HNTs. Wolff and Wang [27] reported that the maximum torque (M_H) depends on the crosslink density and

chain entanglement, results in the natural rubber molecular chains being more easily trapped and occluded in the voids of the HNTs aggregates, thus forming more occluded rubber. Increasing occluded rubber increased the effective concentration of the HNTs aggregates in the rubber and the fluidity of the gross rubber increased during the mixing processing as well.

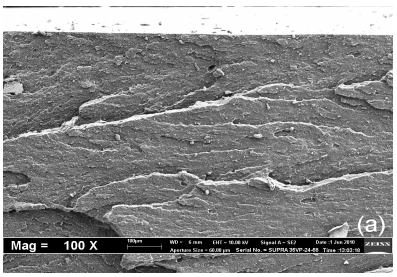
Tensile Properties. The effect of the replacement of HNTs and silica by R-PET on the 300% elongation (M300), tensile strength and elongation at break are shown in Table 3. It is clearly seen that with replacing HNTs and silica by R-PET reduced the M300 of natural rubber composites. Due to processing the R-PET without melting, it was not dispersed to form new surfaces and bound rubber was less than with the HNTs and silica particles. A decrease in bound rubber content allowed the content of freely mobile molecular chains to increase, which resulted in decreasing tensile modulus [28]. Furthermore, the tensile modulus correlates with the crosslink density, which will be discussed later. The tensile strength (T.S.) of the composites was found to decrease with increasing R-PET loading. As discussed earlier, the bigger particles and lower structure of R-PET resulted in more agglomeration and less dispersion of R-PET than HNTs and silica to the natural rubber composites. Thus, stress was unable to be transferred by the rubber matrix because the rubber-filler interactions are weak. It can also be seen that the tensile strength of NR/HNTs/R-PET composite was higher than NR/Silica/R-PET composites respectively. HNTs has a unique structure, which leads to form zig-zag structure and forms as three dimensions orientations inside the composites [11], the enhancement of efficiency of HNTs occurred when compared to the NR/Silica/R-PET composite (as seen from the tensile strength), the lower tensile strength of NR/Silica/R-PET may be due to high silica-silica interactions. This phenomenon is in agreement with our previous work using carbon black and recycled newspaper hybrid filler [6].

The elongation at break (E.B.) of NR/HNTs/R-PET and NR/Silica/R-PET composites exhibited the decreasing trend with increasing of R-PET loading ratio. The increasing in R-PET loading resulted in the reduction of the ability to resist crack propagation and consequently decrease in the elongation before catastrophic fracture [29]. It is also evident from Table 3 that NR/HNTs/R-PET composites possessed slightly higher elongation at break compared to the corresponding NR/Silica/R-PET composite. For NR/HNTs/R-PET composites, as reported by Yang et al. [10] and Ismail et al [11]. the factors influencing the higher elongation at break includes good dispersion of HNTs, inter-tubular interaction, between HNTs and rubber matrix as well as the homogenous dispersion of HNTs inside rubber matrix are responsible to improve the stiffness and ductility of the composites in comparison to NR/Silica/R-PET composites.

Table 3. Tensile properties of NR/HNTs/R-PET and NR/Silica/R-PET composites.

Composition	**NR/HNTs/R-PET**					**NR/Silica/R-PET**				
Fraction (phr:phr)	**20:0**	**15:5**	**10:10**	**5:15**	**0:20**	**20:0**	**15:5**	**10:10**	**5:15**	**0:20**
M300 (MPa)	3.06	2.88	2.60	2.28	2.20	2.55	2.50	2.33	2.26	2.20
T.S. (MPa)	23.70	20.10	16.99	15.44	14.40	20.26	16.20	15.15	14.54	14.40
E.B. (%)	962.70	883.57	870.26	849.56	766.66	863.32	825.00	817.50	793.30	766.66

SEM Observation of Tensile Fracture Surfaces. SEM micrographs of tensile fracture surfaces of NR/N550/R-PET, NR/HNTs/R-PET, and NR/Silica/R-PET composites are shown in Fig. 1, 2, and 3 respectively. The micro-fracture surface at 20 phr of HNTs, and silica, is shown in Fig. 1. Comparing Fig. 1(a) and 1(b) revealed how roughness and tortuous path of the fracture surfaces decreased when HNTs was used as compared to silica, which indicating that failure occurred in a more difficult manner and resulted in a high tensile strength. Fig. 2 (a-b) presents the tensile fracture surfaces of NR/HNTs/R-PET and NR/Silica/R-PET composites at 10:10 (phr:phr) loading ratio. It exhibited less uniform together with many detachment of R-PET, indicating a lower tensile strength than the NR composites with high HNTs and silica loading (Fig. 1). Furthermore, Fig. 3 exhibited many R-PET agglomerates and filler pull out, which leads to many holes and therefore resulted in a lowest tensile strength.



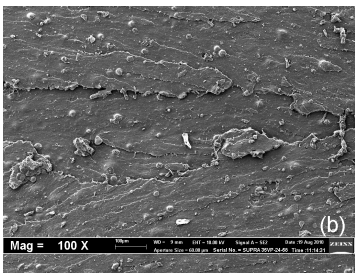
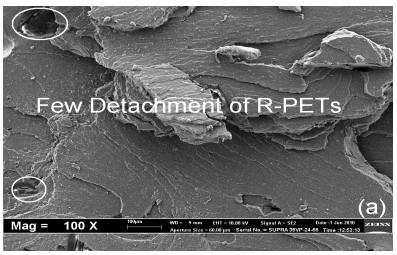


Fig. 1. SEM micrograph of tensile fracture surface of hybrid natural rubber composites (phr/phr): (a) HNTs/R-PET; 20/0, and (b) Silica/R-PET; 20/0 (magnification 100x)



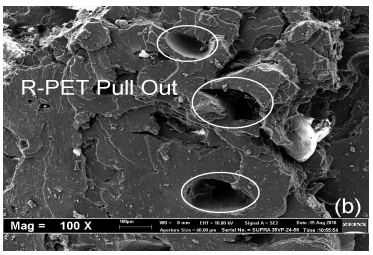


Fig. 2. SEM micrograph of tensile fracture surface of hybrid natural rubber composites (phr/phr): (a) HNTs/R-PET; 10/10, and (b) Silica/R-PET; 10/10 (magnification 100x)

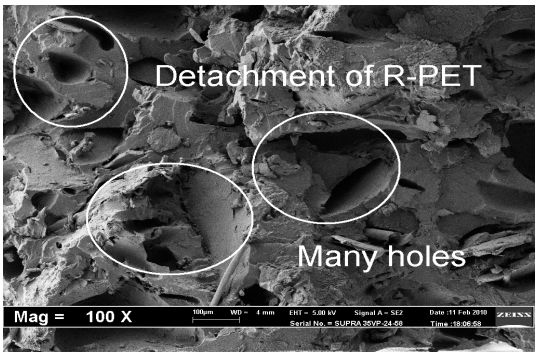


Fig. 3. SEM micrograph of tensile fracture surface of 20 phr R-PET filled natural rubber composites. (magnification 100x)

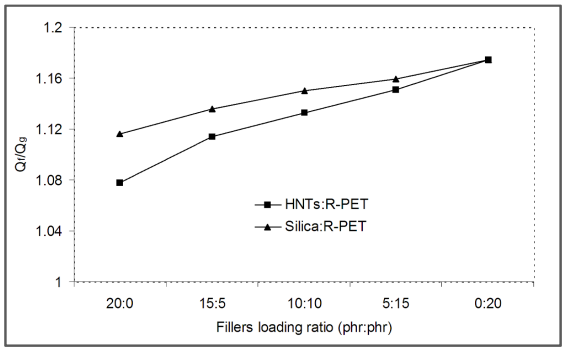


Fig. 4. Comparison of Qf/Qg values of NR/HNTs:R-PET and NR/Silica/R-PET composites.

Rubber-Fillers Interaction. Fig. 4 shows the rubber-filler interaction, Q_f/Q_g values of NR/HNTs/R-PET and NR/Silica/R-PET composites. It can be seen that the Q_f/Q_g values of the composites increased with increasing R-PET loading. The result correlated to the previous work, which indicated that the smaller the particles size of the filler, the better the rubber-filler interactions [30]. This finding may be due to the R-PET hinders the interactions between rubber matrix and reinforcing fillers, the free volume between the rubber matrix molecules therefore increases, leading to more penetration of toluene into the natural rubber composites with the addition of R-PET. It is revealed that the rubber-fillers interaction of NR/HNTs/R-PET composite was higher than NR/Silica/R-PET composites. The higher interactions observed in NR/HNTs/R-PET in comparison to NR/Silica/R-PET composites might be due NR/HNTs/R-PET composite has strong physical interactions between HNTs and elastomers on the surface and inner walls of HNTs as well as the edge-to-edge and face-to-edge interactions between HNTs each other, which leads to form zig-zag structure. This observation might be also due to the inter-tubular diffusion of NR inside the HNTs is higher compared to the occluded rubber of silica that takes place in NR/Silica/R-PET composite.

Summary

When reinforcing fillers, such as HNTs, and precipitated silica were replaced by R-PET in NR composite, R-PET causes a decreased in scorch time and cure time in NR/HNTs/R-PET and NR/Silica/R-PET composites. The maximum torque, torque differences, tensile strength, and tensile modulus (M300) decreased with the replacement of HNTs and silica with R-PET in NR composites. SEM investigation of tensile fracture surfaces confirmed that co-incorporation of HNTs/R-PET would improve the dispersion of R-PET and enhanced the interactions between fillers and NR matrix than Silica/R-PET hybrid fillers.

References

[1] P. Sae-oui, C. Sirisinha and P. Thaptong: J. Mater. Cycles. Waste. Manag. Vol. 11 (2009), p. 168
[2] A.H. Charles in: Handbook of Plastics Technologies: The Complete Guide to Properties and Performance. Edition: 2, illustrated Published by McGraw-Hill Professional, New York, USA (2006)
[3] H. Ismail, H.D. Rozman, R.M. Jaffri and Z.A. Mohd Ishak: Euro. Polym. J. Vol. 33 (1997), p. 1627-1632
[4] H. Ismail and F.S. Haw: J. Appl. Polym. Sci. Vol. 110 (2008), p. 2867-2876
[5] F.E. Okieimen and J.E. Imanah: J. Appl. Polym. Sci. Vol. 100 (2006), p. 2562
[6] H. Ismail, O. Hakimah and J. Mariatti: J. Vinyl. Addi. Technol. Vol. 14 (2008), p. 142-143
[7] M. Liu, B. Guo, M. Du, X. Cai and D. Jia:.Nanotechnol. Vol. 18(45) (2007),(art. No. 455703)
[8] N. Ning, Q. Yin, F. Luo, Q. Zhang, R. Du and Q. Fu: Polym. Vol. 48 (2007), p. 7374
[9] M. Liu, B. Guo, M. Du and D. Jia: Appl. Phys. A. Vol. 88 (2007), p. 391
[10] B.X. Yang, J.H. Shi, K.P. Pramoda and S. Hong Goh: Nanotechnol. Vol. 18(12) (2007), (art. No 12606)
[11] H. Ismail, P. Pasbakhsh, M.N. Ahmad Fauzi and A. Abu Bakar: Polym. Test. Vol. 27 (2008), p. 841-850
[12] S. Rooj, A. Das, V. Thakur, R.N. Mahaling, A.K. Bhowick and G. Heinrich: Matt. Design. Vol. 31(2010), p. 2151-2156
[13] S.R. Levis and P.B. Deasy: Intern. J. Pharm. Vol. 243 (2002), p. 125
[14] P. Pooria, H. Ismail, M.N. Ahmad Fauzi and A. Abu Bakar: J. App. Polym. Sci. Vol. 113 (2009), p. 3910–3919
[15] E. Joussein, S. Petit, G.J. Churchman, B.K.G. Theng, D. Righi and B. Delvaux: Clay Miner. Vol. 40 (2005), p. 383-426
[16] T.R. Curlee, Plastic Wastes: Management, Control, Recycling and Disposal, Environmental Protection Agency, USA (1991).
[17] D.S. Achilias and G.P. Karayannidis: Macromol. Mater. Eng. Vol. 292 (2007), p. 128-146
[18] D.J. Moon, Y.J. Kimc, M. Lachemi and Y.W. Choi: Construc. Build. Mater. Vol. 23 (2009), p. 2830
[19] G. Burilloa, P. Herrera-Francob, M. Vazquez and E. Ademc: Radia. Phys. Chem. Vol. 63 (2002), p. 242
[20] Y. Zhang, W. Guo, H. Zhang and C. Wu: Polym. Degrad. Stab. Vol. 94 (2009), p. 1136
[21] A. Pegoretti, J. Kolarikb, C. Peroni and C. Migliaresi: Polym. Vol. 45 (2004), p. 2752
[22] A. Pegoretti, and A. Penati: Polym. Vol. 45 (2004), p. 7996
[23] Technical Report of Imerys Tableware Asia Limited, Available from http://www.imerys-ceramics.com/Upload/Fichiers/Halloysite_table1.pdf
[24] O. Lorenz and C.R. Parks: J. Polym. Sci. Vol. 50 (1961), p. 299-312
[25] H.M. da Costa, L.L.Y. Visconte, R.C.R. Nunes and C.R.G. Furtado: J. Appl. Polym. Sci. Vol. 87 (2003), p. 1405-1413
[26] H. Ismail, N. Rosnah and H.D. Rozman: Polym. Vol. 38 (1997), p. 4059–4064
[27] S. Wolff and M-J. Wang: Rubb. Chem. Technol. Vol. 62 (1992), p. 329-342
[28] L. Qiuying, M. Yulu, W. Chifei and Q. Shengying: J. Macromol. Sci. Part B: Phys. Vol. 47 (2008), p. 838-843
[29] H. Ismail, H.B. Hong, C.Y. Ping and H.P.S. Abdul Khalil: J. Thermoplastic Comp. Mater. Vol. 16 (2003), 121-137
[30] H. Ismail, H.D. Rozman, R.M. Jaffri and Z.A. Mohd Ishak: Euro. Polym. J. Vol. 33 (1997), p. 1627-1632

© (2011) Trans Tech Publications, Switzerland
doi:10.4028/www.scientific.net/KEM.471-472.628

The Influence of Recycled Poly(ethylene terephthalate) Powder on Fatigue Life, Thermal Stability, and Morphology of Halloysite Nanotubes (HNTs) and Precipitated Silica Filled Natural Rubber Composites

H. Nabil[a], H. Ismail[b] and A.R. Azura[c]
Department of Polymer Engineering, School of Materials and Mineral Resources Engineering, Universiti Sains Malaysia, Engineering Campus, 14300 Nibong Tebal, Penang, Malaysia
[a]nabil_ty@hotmail.com, [b]hanafi@eng.usm.my, [c]azura@eng.usm.my

Keywords: recycled polyethylene terephthalate, natural rubber, halloysite nanotubes, silica, fatigue life

Abstract. In this paper, the influence of recycled polyethylene terephthalate powder (R-PET) on fatigue life, thermal properties and micro-fracture surfaces of halloysite nanotubes (HNTs) and silica filled natural rubber composites have been studied. The total amount of hybrid filler in each formulation was kept constant at 20 parts per hundred rubber (phr). The final properties of HNTs/R-PET and Silica/R-PET compounds are considered separately and comparatively. Results indicated that the fatigue life of the natural rubber composites decreased with the replacement of these two fillers by R-PET powder. This observation might be due to the R-PET itself, which reduces the interfacial adhesion and wettability between rubber matrix and fillers. By replacing of HNTs and silica with R-PET powder, the thermal degradation of natural rubber composites was shifted to a lower temperature and the char residues was decreased, in which HNTs/R-PET composites expressed the higher temperature and char residues than silica/R-PET composites. This findings may be due to the HNTs/R-PET has less volatile matter than silica/R-PET that might enhance the degradation temperature of the natural rubber composites. SEM micrographs also exhibited weak interfacial adhesion when these two fillers were replaced with R-PET powder in NR composites.

Introduction

Natural rubber technology has been developing rapidly [1]. Filler becomes the most important additive and second largest following the base polymer in rubber compounding. They are incorporated into rubber compound for improving processability and physico-mechanical properties. Precipitated silica is the most important reinforcing fillers for non-black applications. However, for some applications where cost and processability are of greatest concern, the use of non or semi-reinforcing fillers such as clay, talc, and calcium carbonate ($CaCO_3$) is highly recommended. Recently, halloysite nanotubes or HNTs have been incorporated as reinforcing filler in many polymer matrix and elastomer [2,3]. HNTs are a kind of naturally occurring aluminosilicate ($Al_2Si_2O_5(OH)_4 \cdot H_2O$ 1:1) with a predominantly hollow nanotubular structure in the submicron length and chemically similar to kaolin [4]. HNTs are an economically viable material that can be mined from the consequent deposit as a raw mineral. The size of halloysite paticles varies within 1-15 µm of length and 10-150 nm of inner diameter, depending on the deposits [5-6]. Due to legislative pressures to recycle and reduce scrap in the environment, the disposal of plastic waste products is of significant concern. Landfill disposal and transportation costs are expected to increase. The recycling of thermoplastic materials seems to be widely carried out, whereas there are some limitations in terms of the possible selection of a material to achieve a particular purpose in the recycling of thermoplastic materials [7].

Currently, poly(ethylene terephthalate) or PET plays a major role in our daily activities due to its transparency, thermal stability, chemical resistance and excellent resistance to oxygen and carbon dioxide [8]. PET has become a material of choice for bottling beverages. Unfortunately, these same useful of PET can make a huge pollution problem. Since it is very highly resistance to atmospheric and biological agents, PET bottles become noxious materials of concern in relatively recent environmental protection issues. As a consequence of this, to eliminate or reduce waste PET from the environment and to reduce costs of some manufacturing products, a relatively new area of

interest is the use of recycle polyethylene terephthalate (R-PET) bottling powder as filler for natural rubber. Since over the years, utilization of R-PET has been done in many studies, i.e., polymer concrete [9], blending with virgin PET and commercial plastics [10,11], and use of R-PET as a matrix in filled composites [12,13], but there is no research related to the used of R-PET bottles as filler in natural rubber compound reported by researcher yet.

Therefore, the purpose of this work is to study the effect of the partial replacement of HNTs and precipitated silica by R-PET powder on the fatigue life, thermal stability and morphology natural rubber compounds, whereby the R-PET was ground into powder form to be more easily get into natural rubber matrix. The use of mixed fillers has been recognized for many years [14-16].

Experimental

Materials. Table 1 shows the compounding formulation used in this study. Natural rubber and L grade SMR were supplied by Rubber Research Institute of Malaysia (RRIM). The recycled polyethylene terephthalate (R-PET) flakes were supplied by Toray Plastic (Malaysia) Sdn. Bhd. Precipitated silica, Ultrasil VN3 was obtained from Degussa Ltd. Halloysite nanotubes (HNTs), ultrafine grade was supplied by Imerys Tableware Asia Limited, New Zealand, with brightness of 98.9% as measured by a Minolta CR300 using D65 light source. The elemental composition is as follow (wt%); SiO_2, 49.5; Al_2O_3, 35.5; Fe_2O_3, 0.29; TiO_2, 0.09 [17]. Other compounding ingredients such as zinc oxide, stearic acid, *N*-cyclohexyl-2-benzothiazole-sulphenamide (CBS), *N*-isopropyl-*N'*-phenyl-*p*-phenylenediamine (IPPD) and sulphur were purchased from Bayer (M) Ltd. and used as received.

Table 1. Formulations of NR/HNTs/R-PET and NR/Silica/R-PET composites.

Ingredients (phr:phr)	NR/HNTs/R-PET	NR/Silica/R-PET
SMR L	100	100
Stearic acid	1.5	1.5
ZnO	1.5	1.5
CBS	1.9	1.9
IPPD	2.0	2.0
Sulphur	1.6	1.6
HNTs/R-PET	20:0 15:5 10:10 5:15 0:20	-
Silica/R-PET	-	20:0 15:5 10:10 5:15 0:20

R-PET Particle Preparation. The R-PET flakes were ground into powder using a Table Type Pulverizing Machine from Rong Song Precision Technology Co.Ltd. The powder was then sieved with an Endicott's sieve to get particles around 125-212 μm in size. The R-PET powder was dried in a vacuum oven at 80°C for 24 hours to expel moisture. Dried R-PET powder was used in rubber compounding without further treatment.

Mixing and Vulcanization Procedures. The compounding of SMR L with HNTs, Silica, R-PET and other additives such as zinc oxide, stearic acid, CBS, IPPD and sulphur were prepared on a laboratory-sized (160 mm × 320 mm) two-roll-mill, model XK-160. The cure characteristics were carried out using a Monsanto Moving Die Rheometer (MDR 2000) according to ASTM D 2240-93. Samples of the respective compounds were tested at the vulcanization temperature (150°C). The compounds were subsequently compression moulded using a stainless steel mould at 150°C with a force of 10 MPa using a laboratory hot-press based on the respective curing times.

Fatigue Life Test. The various rubber compounds were compressed at 150°C in accordance with their respective t_{90} values, into rectangular sheets (22.9 cm × 7.6 cm × 0.15 cm) with beaded edges. Individual dumbbell samples were cut at right angles using a BS type E dumbbell cutter. Fatigue tests were then carried out using a Monsanto fatigue to failure tester (FTFT). The samples were

subjected to repeated cyclic strain at 100 cpm. The extension ratio used was 1.61. Six specimens were used for each formulation. The numbers of cycles were recorded automatically. The fatigue life in kilocycles for each sample was calculated as the JIS (Japanese Industrial Standard) average, which was obtained from the four highest values, recorded using this formula:

$$\text{JIS average} = 0.5A + 0.3B + 0.1(C+D) \quad \text{(Eq. 1)}$$

where A is the highest value followed by B, C and D

Measurements of Rubber-Filler Interaction. Cure test pieces of dimension 30 mm × 5 mm × 2 mm were swollen in toluene until equilibrium, which took 72 hours at room temperature. The samples were taken out from the liquid, the toluene removed from the samples' surface and the weight was determined. The samples were then dried in an oven at 60°C until a constant weight was obtained. The Lorenz and Parks equation was used to study the rubber-filler interaction [18]:

$$\frac{Q_f}{Q_g} = ae^{-z} + b \quad \text{(Eq. 2)}$$

Where Q is defined as grams of solvent per gram of rubber hydrocarbon, as follows:

$$Q = \frac{\text{Swollen weight - Dried weight}}{\text{Original weight} \times \dfrac{100}{\text{Formula weight}}} \quad \text{(Eq. 3)}$$

The subscripts f and g in the equation refer to filled and gum composites, respectively. z is the ratio by weight of filler to rubber hydrocarbon in the composites, while a and b are constants. The higher the Q_f/Q_g values, the lower the rubber-filler interaction.

Thermo Gravimetric Analysis. TGA analysis was observed using a Perklin-Elmer Pyris 6 TGA analyser with temperature range from 30°C to 600°C at heating rate of 20°C/min under nitrogen atmosphere at flow rate of 10 ml/min.

SEM Micro-Fracture Surfaces. Fatigue to failure fracture surfaces analysis was carried out using a scanning electron microscope (SEM), model Zeiss Supra-35VP, to obtain information regarding filler dispersion and to detect the possible presence of micro-defects. The fractured pieces were coated with a layer of gold palladium to eliminate electrostatic charge build-up during examination.

Results and Discussion

Fatigue Life. Fig. 1 shows the influence of R-PET on the fatigue life of HNTs and silica filled natural rubber composites. It can be seen that the replacement of HNTs and silica by R-PET reduced the fatigue life of NR composites. This finding might be due to the lower interfacial adhesion or the poor rubber-fillers interactions, which can increase heat build-up during cyclic loading or repeated cyclic deformation, thus increasing the chain scission and deteriorating the fatigue life. Furthermore, the decrement in fatigue life may be due to the decrease in effectiveness of the stress transferred from the rubber matrix to the filler, which increases the progression of damage. Ismail and Haw [19] reported that the decreasing in fatigue life might be due to worse dispersion of the fillers where were unable to improve the filler dispersion near the rubber matrix leading to increase the formation of stress concentration points and therefore decrease the fatigue life. It was also found that at similar loading ratio of hybrid composites. The fatigue life of NR/HNTs/R-PET was higher than NR/Silica/R-PET composites. It could be explained from the higher interfacial adhesion and the physical interactions between rubber and HNTs, which due to the edge-to-edge and face-to-edge interactions between HNTs could help to reduce of heat buildup during cyclic loading or repeated cyclic deformation, thus reduce the chain scission and consequently enhance the fatigue life.

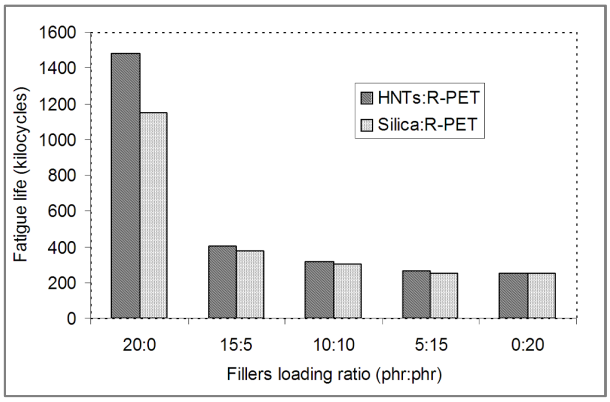


Fig. 1. Fatigue life of NR/HNTs/R-PET and NR/Silica/R-PET composites.

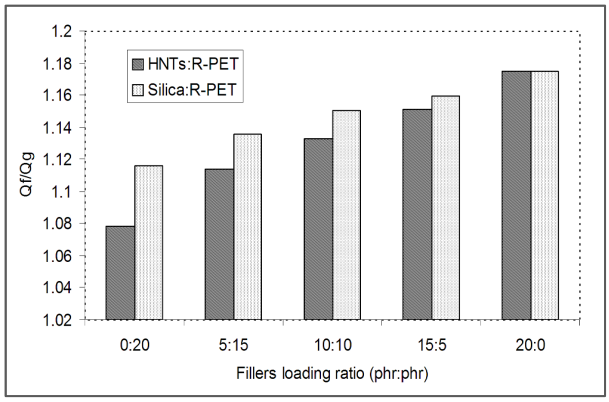


Fig. 2. Q_f/Q_g values of NR/HNTs/R-PET and NR/Silica/R-PET composites.

Rubber-Filler Interaction. Fig. 2 shows the rubber-filler interaction, Q_f/Q_g values of NR/HNTs/R-PET and NR/Silica/R-PET hybrid composites. The Q_f/Q_g shows the rubber filler interactions of the composites. The higher values, the lower the rubber-filler interaction is. It can be seen that the Q_f/Q_g values of the composites increased with increasing R-PET loading ratio. It can be concluded that with the replacement of HNTs and Silica by R-PET, the rubber-fillers interactions of the composites were reduced, and the rubber-fillers interaction of NR/HNTs/R-PET composite was higher than NR/Silica/R-PET composites respectively. The higher interactions observed in NR/HNTs/R-PET in comparison to NR/Silica/R-PET composites might be due NR/HNTs/R-PET composite has strong physical interactions between HNTs and elastomers as well as the edge-to-edge and face-to-edge interactions between HNTs each other, which leads to form zig-zag structure and. One probable is that the inter-tubular diffusion of NR inside the HNTs is higher compared to the occluded rubber of silica that takes place in NR/Silica/R-PET composite [20].

Scanning Electron Microscopy. SEM micrographs of fatigue fracture surfaces of NR/HNTs/R-PET and NR/Silica/R-PET composites are shown in Fig. 3, 4, and 5. The enhancement of the



Fig. 3:SEMmicrographs showing fatigue to failure fracture surfaces of NR/HNTs/R-PET (a) and NR/Silica/R-PET (b) composites at the loading ratio of 20:0 (phr:phr) (magnification 100X).

micro-fracture surface is obvious at 20 phr of HNTs, and Silica, as seen in Figure 3. Comparing Fig. 3(a) and 3(b) revealed how roughness and tortuous path of the fracture surfaces decreased respectively, indicating that failure occurred in a more difficult manner and result in a high fatigue life. Fig. 4 (a-b) also presented the fatigue fracture surfaces of NR/HNTs/R-PET, and NR/Silica/R-PET composites at 10:10 (phr:phr) loading ratio. It exhibited a less uniform together with few detachment of R-PET and a less smooth surface, indicating a lower fatigue than the composites with high HNTs, and silica loading. Furthermore, Fig. 5 revealed that the more agglomeration and detachments of R-PET from NR matrix occurred, which leads to many holes and therefore resulted in a lowest fatigue life [21]



Fig. 4:SEMmicrographs showing fatigue to failure fracture surfaces of NR/HNTs/R-PET (a) and NR/Silica/R-PET (b) composites at the loading ratio of 10:10 (phr:phr) (magnification 100X).

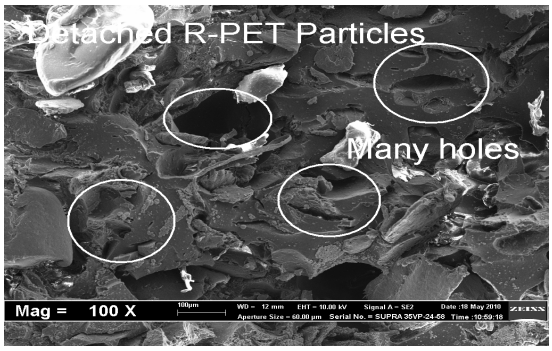


Fig. 5: SEM micrographs showing fatigue to failure fracture surfaces of at 20 phr R-PET filled natural rubber compound. (magnification 100X).

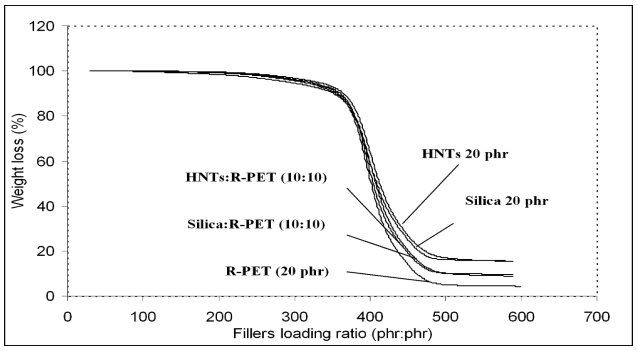


Fig. 6: TGA curves of NR/HNTs/R-PET and NR/Silica/R-PET composites.

Thermal Properties. The thermal decomposition behaviour of NR/HNTs/R-PET and NR/Silica/R-PET composites is shown in Fig. 6. Because there is only one type of rubber matrix used in the compounds, the curves are displayed in a single step degradation process for all samples. The weight losses are measured as a function of temperature. The first mass loss of all samples started at around 250°C because the absorbed water disappeared, and was completed at 400°C due to the thermal decomposition of rubber matrix. The second mass loss at approximately 400°C–580°C is associated with the thermal decomposition of carbonaceous residues from the rubber [22]. Table 2 shows the temperature at 5% weight loss and 50% weight loss of NR/HNTs/R-PET and NR/Silica/R-PET composites. The temperature at 5% weight loss indicates the initial thermal stability, whereas the temperature at 50% weight loss shows the half degradation rate of the rubber compounds. It can be seen that, once the rubber matrix was replaced with a small amount of R-PET particles, the temperature at 5% and 50% weight loss decreased gradually. Maximum weight loss also increased with higher R-PET loading. It is clearly seen that with higher loading of R-PET resulted in overall deterioration of thermal stability. The degradation temperature can be related to the volatile material in the fillers. The co-incorporation of Silica/R-PET, which has more volatile matter, might decay the degradation temperature of the natural rubber composites [23, 24].

Table 2. The thermal stability parameter of NR/HNTs/R-PET and NR/Silica/R-PET composites.

Loading ratio (phr:phr)	$T_{-5\%}$ (^{o}C)		$T_{-50\%}$ (^{o}C)		Maximum weight loss (%)	
	HNTs:R-PET	Silica:R-PET	HNTs:R-PET	Silica:R-PET	HNTs:R-PET	Silica:R-PET
20 : 0	330.97	320.37	412.48	409.52	84.47	84.64
15 : 5	324.37	317.25	408.25	408.50	87.29	87.45
10 : 10	322.03	315.45	403.25	406.31	91.15	92.42
0 : 20	313.29	313.29	401.09	401.09	95.67	95.67

Summary
R-PET caused a decrease in fatigue life, which might be due to the poor rubber-fillers interactions. By replacing of HNTs and silica with R-PET powder represented that the thermal degradation of natural rubber composites was shifted to a lower temperature and the char residue decreased. SEM micrographs of fatigue fracture surfaces exhibited more agglomeration and achieved more detachment which shows weak interfacial adhesion when both two fillers were replaced by R-PET in NR composites.

References

[1] P. Sae-oui, C. Sirisinha and P. Thaptong: J. Mater. Cycle. Waste. Managet. Vol. 11 (2009), p.166–171**.**

[2] M. Liu, B. Guo, M. Du, X. Cai and D. Jia: Nanotechnol. Vo. 18 (2007), (art. No. 455703)

[3] N. Ning, Q. Yin, F. Luo, Q. Zhang, R. Du and Q. Fu: Polym. Vol. 48 (2007), p. 7374

[4] M. Liu, B. Guo, M. Du and D. Jia: Appl. Phys. A. Vol. 88 (2007), p.391

[5] B.X. Yang, J.H. Shi, K.P. Pramoda and S. Hong Goh: Nanotechnol. Vol. 18 (2007), (art. No 12606)

[6] H. Ismail, P. Pasbakhsh, M.N. Ahmad Fauzi and A. Abu Bakar: Polym. Test. Vol. 27 (2008), p. 841-850

[7] N. Sombatsompop: Polymer-Plastic. Technol. Engineer. Vol. 37 (1998), p. 1-18.

[8] M. Ahmad: J. Elasto. Plast. Vol. 40 (2008), p. 179-188

[9] D.J. Moon, Y.J. Kimc, M. Lachemi and Y.W. Choi: Construc. Build. Mater. Vol. 23 (2009), p. 2829–2835

[10] G. Burilloa, P. Herrera-Francob, M. Vazquez and E. Ademc: Radia. Phys. Chem. Vol. 63 (2002), p. 241–244

[11] Y. Zhang, W. Guo, H. Zhang and C. Wu: Polym. Degrad. Stab. Vol. 94 (2009), p. 1135–1141

[12] A. Pegoretti, J. Kolarikb, C. Peroni and C. Migliaresi: Polym. Vol. 45 (2004), p. 2751–2759

[13] A. Pegoretti and A. Penati: Polym. Vol. 45 (2004), p. 7995–8004

[14] H.M. da Costa, L.L.Y. Visconte, R.C.R. Nunes and C.R.G. Furtado: J. Appl. Polym. Sci. Vol. 87 (2003), p. 1405-1413

[15] J. Maya, T. Sabu K.T. Varughese: Compos. Sci. Technol. Vol. 64 (2004), p. 955-965

[16] N. Nugay B. Erman: J. Appl. Polym. Sci. **79 (2001)**, p.366-371

[17] Technical Report of Imerys Tableware Asia Limited, Available from http://www.imerys-ceramics.com/Upload/Fichiers/Halloysite_table1.pdf

[18] O. Lorenz and C.R. Parks: J. Polym. Sci. Vol. 50 (1961), p. 299-312

[19] H. Ismail and F.S. Haw: J. Appl. Polym. Sci. Vol. 110 (2008), p. 2867-2876

[20] H. Ismail, H.D. Rozman, R.M. Jaffri and Z.A. Mohd Ishak: Euro. Polym. J. Vol. 33 (1997), p. 1627-1632

[21] H. Ismail, R. Nordin and A.M. Noor: Polym. Test. **21** (2002), p. 568-569

[22] C. Benjawan, P. Pattaraporn and P. Sirilux: J. Sol-Gel. Sci. Technol. Vol. 52 (2009), 223.

[23] A. Laachachi, M. Cochez, M. Ferriol J.M. Lopez-Cuesta and E. Leroy: Mater. Letter. Vol. 59 (2005), p. 36-39

[24] L.G. Hanu, G.P. Simon and Y.B. Cheng: *Polym. Degrad. Stab*. Vol. 91 (2006), p. 1373-1379

© (2011) Trans Tech Publications, Switzerland
doi:10.4028/www.scientific.net/KEM.471-472.634

Analysis of MPV Dashboard Using SolidWorks and ABAQUS

Mohd Khairol Anuar Mohd Ariffin[1,a], Nik Mohd Idham Nik Hassan[2,b] and Mohd Firdaus Abdullah[2,c].

[1]Laboratory of Biocomposite Technology, Institute of Tropical Forestry and Forest Products, Universiti Putra Malaysia

[2]Department of Mechanical and Manufacturing Engineering, Universiti Putra Malaysia Serdang, 43400, Serdang, Selangor, Malaysia
[a]khairol@eng.upm.edu.my

Keywords: Impact analysis, simulation, ABAQUS

Abstract. The study is intended to measure the reliability of MPV dashboard to endure interior impact by using finite element analysis (FEA) method. A model which represents MPV dashboard was made using Solidworks and the impact simulation was done using ABAQUS. Current material being used for dashboard is ABS-GF40 and this material was proven to be reliable to withstand interior impact through the simulation that has been done in this study. Besides, this study also serve the purpose to reduce manufacturing cost using alternative materials with no less reliability compared to ABS-GF40. Similar simulation routines were applied for ABS copolymer, PP copolymer, and PVC copolymer. The simulation results showed that ABS-CF40 performance is similar to ABS-GF40, whereas the PP-CF10, PP-GF10, and PVC-GF30 exhibit almost identical behavior under impact loading. Cost assessment was carried out for all materials to assist in selecting alternative material for replacement of ABS-GF40. Hence, it was found that PP-GF10 can be used as an alternative material with cost reduction up to RM33.17 on each dashboard.

Introduction

The cockpit module of automobiles usually consists of an instrument panel (IP), a steering column system, a HVAC system. To satisfy its design goals which are the quality requirements specified by manufacturer and to meet safety regulations such as Federal Motor Vehicle Safety Standard No. 201 (FMVSS 201)

Most of the analytical tools used for cockpit module safety and comfort analyses are based on Finite Element Methods (FEM), which have become increasingly robust and powerful over the years due to the advance in computing power [1].

The purpose for this analysis is to measure crashworthiness of automobile dashboard against interior impact which is commonly caused by passenger during frontal crash. To achieve it, an interior impact simulation was created using finite element software which is ABAQUS FEA software was used. With these, reduction of manufacturing cost by mean of finding an alternative material to substitute current material is possible.

At the initial development phase, predictions of safety-related performance of the cockpit module have a higher priority than other items and are mostly accomplished by numerical simulations before making prototypes [2].

Methodology

This chapter describes the methods used in carrying out this project which involves only simulation works. The head form, dashboard, and cross cowl structure assembly are shown in Figure 4. This simulation is developed to determine the impact energy resulted from the collision of

head form and dashboard. From the energy plot, analysis of crashworthiness can be done in order to determine whether the current design can withstand interior impact. The graphical presentation of workflow is shown in Figure 1. Difficulty in this choice resides in being able to combine robustness, accuracy and stability of the algorithm. Implicit algorithms require iterative solutions for each time increment (time step), contrarily to explicit ones. But for stability reasons, explicit methods use smaller time steps than implicit ones [3].

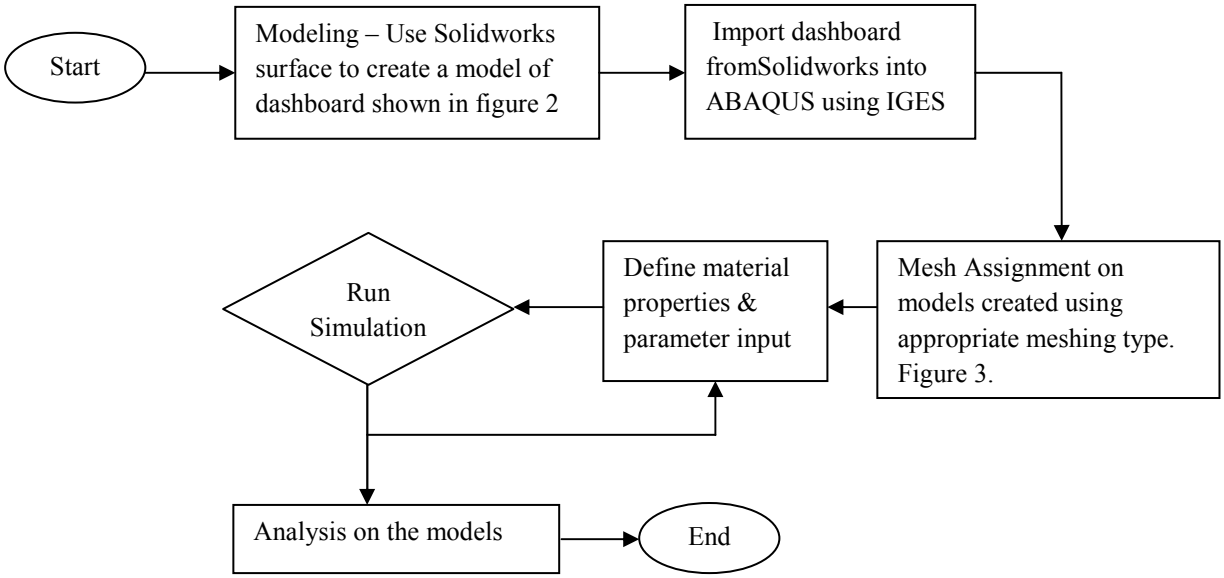


Fig. 1: Flowchart for work methodology

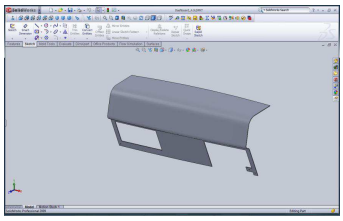


Fig. 2: Surface modeling using SolidWorks.

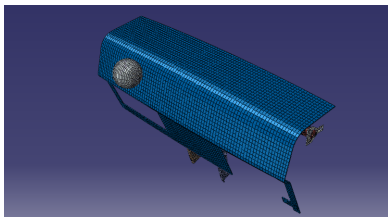


Fig. 3: Mesh assignment using ABAQUS/CAE.

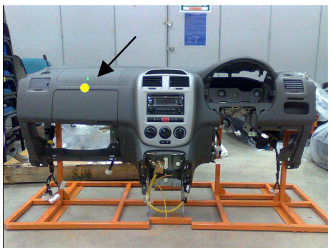


Fig. 4: Location of head form impact marked as yellow spot.

Results

The input variable is material which is thermoset polymer or engineering polymer. The materials being assessed were Polyvinyl Chloride (PVC) copolymer, Polypropylene (PP) copolymers, and Acrylonitrile Butadiene Styrene (ABS) copolymers.The result outputs from the simulation are kinetic energy (ALLKE), strain energy (ALLSE), internal energy (ALLIE), and total energy (ETOTAL). In Figure 5(b), ALLKE decreases quadraticaly after the indenter contacted with dashboard surface. Minimum kinetic energy reduction for each material is shown in Table 1. This result can be related to rigidity properties of material. ABS-CF10 has higher Young's modulus value compared to ABS-GF10 which makes it stiffer and thus the kinetic energy from the impact can be highly reduced.

Table 1: Minimum kinetic energy for PP and PVC copolymer.

Material	Kinetic energy at t=0.036 s (J)
PP-CF10	4.729
PP-GF10	4.707
PVC-GF30	3.717

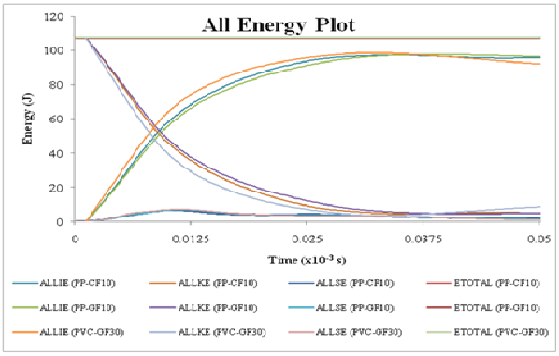


Fig. 5(a)

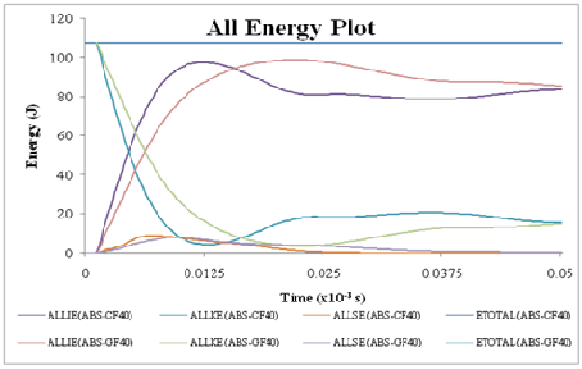


Fig. 5(b)

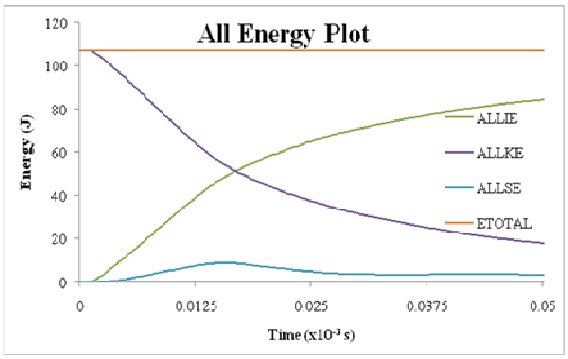


Fig. 5(c)

Fig. 5(a), 5(b), & 5(c): All energy plots for all materials.

The other result from the graph plot to be discussed is ALLSE. Strain energy is the energy expanded from the impact of head form in deforming the dashboard. ABS-CF10 has higher strain energy and the energy dissipation is faster compared to ABS-GF10. Fig. 5(c) shows all energy plots for PP-PTFE where it can be seen that the material exhibit large difference in material behavior compared to other PP copolymers. PP-PTFE is not suitable since it shows a long impulse time during impact which also indicates that the material is too ductile. This behavior restricting the use of PP-PTFE with current design of MPV dashboard. Due to its soft behavior, large deformation occurred on the dashboard which is caused by impact of head form. The dashboard displacements due to impact of head form are shown in Fig. 6 and the visualizations of impact of simulation are shown in Fig. 7 that shows dashboard deformation. It was found that all material pass the requirement of non failure under impact loading.

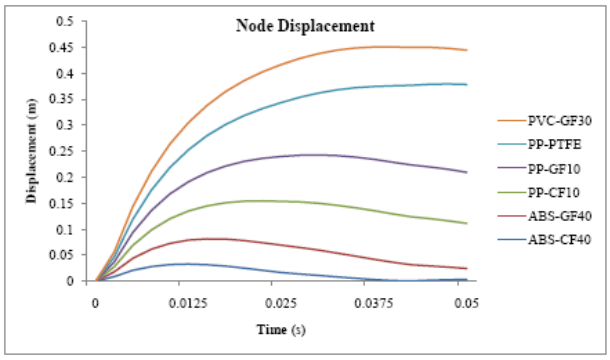


Fig. 6: Maximum node displacement on dashboard due to head form impact.

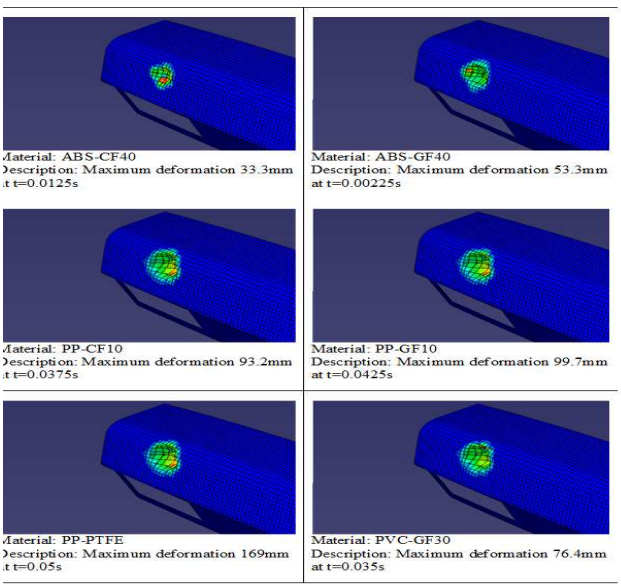


Fig. 7 Maximum dashboard deformation.

Mass for all materials type can be obtained from ABAQUS/CAE. The value of mass is verified using Equation (1) which is the density-volume relationship. Mass for all different type of materials selection is shown in Table 2. Hence, the raw material cost can be calculated using Equation (2) and from the raw material price in Table 2. From the energy plot, PP-GF10 is the most favorable choice based on the raw material price and material behavior under impact which is no less inferior to ABS plastics. Switching to PP-GF10 as alternative material can reduce cost up to minimum of RM 33.17 for every single dashboard produced.

$$M = \rho \times V \quad \text{(Eq. 1)}$$

Where; M = mass, ρ = density, V = volume

$$Price = Cost\ rate\ \frac{(RM)}{(kg)} \times M(kg) \quad \text{(Eq. 2)}$$

Table 2:Raw material price of each polymer material to produce dashboard.

Material	Volume, V (m^3)	Density, ρ (kg/m^3)	Mass, M (kg)	Raw plastic price (RM/kg)	Price (RM)
ABS-CF40	0.00415	1305	5.42	18.30	99.19
ABS-GF40	0.00415	1427.5	5.93	15.41	91.38
PP-CF10	0.00415	950	3.94	14.77	58.19
PP-GF10	0.00415	1180	4.90	11.88	58.21
PP-PTFE	0.00415	2250	9.34	9.22	86.11
PVC-GF30	0.00415	1580	6.56	14.70	96.43

Discussion

The impact was simulated at 50 millisecond interval for all type of materials. Since impact occurs in a very short interval, dashboard must be able to absorb most of the impact energy and the dashboard itself must not fail. Polymeric material which exhibits a low yield stress, with a high Young's modulus and a large plastic strain to failure (highly ductile) should be considered for replacement [4]. ABS is the most stiff based on the high elastic modulus value and it was proven from the energy plot with a very short response time. Despite its short response time, this behavior for ABS may inflict internal damage to the passenger.

Material behavior during the impact simulation for PP-CF10, PP-GF10, and PVC-GF30 are quite similar. PP-PTFE exhibit different material behavior compared to other PP polymers. PP-PTFE is not suitable since it shows a long impulse time during impact. From the results, PP-GF10 is the most favorable choice based on the raw material price and material behavior under impact which is no less inferior to ABS plastics. Switching to PP-GF10 as alternative material can reduce cost up to minimum of RM 33.17 for every single dashboard produced.

Summary

Modeling and impact simulation on automobile MPV dashboard was successfully developed using SolidWorks and ABAQUS software. The time for developing a prototype can be greatly reduced from months to only few weeks through the FEA simulation method. From the results, it was proven that the current design is reliable to withstand interior impact according to standard regulations stated in the literature review section.

In this paper, the author also uses this software as a key solver to reduce manufacturing cost of dashboard. It was found from the results that Polypropylene copolymer can be the replacement material for reinforced ABS which is currently being used to manufacture MPV dashboard. PP-GF10 was chosen as replacement material as it complies with the safety regulation and the material is cheaper than ABS-GF40. Validation of FEA results need to be carried out using experimental method. Results from numerical and experimental methods are evaluated using percentage difference as preliminary step [4]. Several testing procedures need to be carried out (for both numerical and experimental and the procedure with the lowest percentage difference will be selected as the preferred testing procedure. Geometry optimization can be implemented as one of the solutions to impact crashworthiness improvement without material replacement. However, it will lead to higher degree of workload since manufacturing consideration will be the main concern.

References

[1] J.Z. Lin & S.M. Pitrof: *Analytical Design of Cockpit Modules for Safety and Comfort* (SAE Technical Paper Series, 2004-01-1481)

[2] T. Gholami, J. Lescheticky, & R. Paßmann, A. Theobald, W. Jansohn, S. Niedermeyer, EDAG, M. Schrank, & B. Engelmann: *Finite Element Analysis of Head Impact According to Extended FMVSS 201* (ABAQUS Users' Conference, Newport, Rhode Island, 2002, page 1-11).

[3] L. Noels, L. Stainier, J. –P. Phontot: *Combined Implicit/Explicit Algorithms for Crashworthiness Analysis* (International Journal of Impact Engineering, vol. 30, 2004, page 1161–1177).

[4] A. William, P. Saverio, Z. Nader & G. Robert: *An Experimental and Finite Element Investigation Into The Energy Absorption Characteristic of A Steering Wheel Armature In An Impact (* International Journal of Impact Engineering, vol. 27, 2002, page 197–212).

© (2011) Trans Tech Publications, Switzerland
doi:10.4028/www.scientific.net/KEM.471-472.640

Effect of Flame Retardants on Wood Plastic Composites-HDPE Based

Mohd Rashid Yusof Hamid[1] and Sahrim Ahmad[2]

[1]School of Applied Physics, Faculty of Science and Technology,

Universiti Kebangsaan Malaysia, 43600 UKM Bangi, Selangor, Malaysia

[2]Faculty of Science and Technology, Universiti Kebangsaan Malaysia,

43600 UKM Bangi, Selangor, Malaysia

[1]shidberry@gmail.com, [2]sahrim@ukm.my

Keywords: wood plastic composites; natural fiber; low cost; flammability.

Abstract. Recently, research on natural fiber reinforced polymer composites has gained importance due to the abundant sources of fibers that can be obtained at very low cost. In this study, wood plastic composite (WPC) materials is made by mixing (compounding) high density polyethylene (HDPE) and (ligno) cellulose fiber, i.e. rice husk reinforced with sawdust have been manufactured using a high volume process using counter rotating twin screw extruder. Different fire retardant agents have been employed in order to improve fire behavior in this study. The flammability and thermal stability of WPC-HDPE based in different compositions have been carried out by fire test method according to ASTM D635-06 and evaluated by thermo gravimetric analysis respectively. The properties of flexural strength and impact strength were also included.

Introduction

Wood plastic composites (WPC) are widely used in USA and Europe country. They are basically produced by mixing wood flour and plastics, a similar process to produce 100% plastic-based products. Some of the major advantages of WPC include their resistance against biological deterioration for outdoor applications where untreated timber products are not suitable. The sustainability of this technology becomes more attractive when the low cost and high availability of fine particles of wood waste is considered. Due to all the advantages they offer, it is necessary to improve their physical and mechanical properties as well as appearance of such products to have a strong market share in wood composite panel industry [1].

Nowadays, by-products which traditionally cost money for proper disposal become a beneficial resource in term of profitable and environmentally recycling conscious [2, 3]. Rice husk is one of the by-products from rice harvesting and hence has been produced in huge quantities every year. Most of them are just been burned or disposed of in the landfill due to limited alternative application. This ligno cellulose-containing natural composite exhibits many potential advantages, e.g. renewable source, low cost, biodegradability, etc. Moreover the high silica content in rice husk may play certain synergistic roles in the flammability of the resulted composites [4]. WPCs can also be fabricated using recycled wood fibers, such as from sawdust (wood flour), providing an additional usage for recycled wood fibers and thus further reducing waste in landfills. In previous studies, the addition of sawdust to a polymer increases the stiffness and strength of the resulting material especially at low fibre content [5,6,7]. However, few studies have been made of rice husk and sawdust as reinforcing fibre to enhance processing. In this case, suitable coupling agents are required to promote interfacial adhesion between the matrix and the fibre.

Fire resistant is another important criterion as safety issues always demand fire resistant materials especially for building and consumer product applications. In order to improve the fire retardancy in polymers, different types of fire retardant additives have been used. Chemical flame-retardants (such as halogen- and phosphorus-based compounds) have proved to be effective in suppressing the flame behavior of synthetic polymers, but the expense of the negative environmental impact and health concern will cause more problems in future [4]. Various studies

were developed regarding fire performance of composites reinforced by natural fibres. However, few studies have been carried out on this aspect in WPCs [5,8].

Different pieces of compounding equipment can be employed to make WPCs although the use of a twin screw extruder is standard in the industry and very popular among manufacturer. It is due to the results in composites having a high modulus and a low rate of water absorption [9]. Inspired by prior studies, calcium carbonate, sodium metasilicate and zinc borate were used as fire retardants agents. The aim of this study is to examine the effects of flame retardants on WPCs and also to develop a fire-resistant wood plastic composite that will maintain its level of mechanical performance and maintain economically competitive. The other properties include thermal stability, flexural strength, and impact strength also been discussed in this study.

Experimental

Materials. The polyethylene used was HDPE. It has a bulk density of 0.960 g/cc and a melt flow rate (190/5) of 23 g/10 min. Rice husk fillers with particle size of 60 meshes. Before the processing, the rice husk was dried in an air-circulating oven at 80ºC for about 12 h. The sawdust had cubic structure (non fibrous) and length of 300–500 lm. Moisture content of the fibers was not determined. Fibers were not chemically treated prior to processing.

Three percent of coupling agent was added to the formulation together with five percent of additives to enhance processing.

The fire retardants used were calcium carbonate, zinc borate and sodium metasilicate. No halogen containing fire retardant was selected in order to use environmentally friendly fire retardants. All the composites contained 25% of fire retardants except for the control batch sample.

Processing. Firstly, the HDPE, rice husk and sawdust were dried at 80°C for 12 h. Then the components were compounded by extrusion in order to obtain a good compatibility level between the phases, together with a homogeneous fibre distribution. The extrusion process was carried out in a counter-rotating twin screw extruder at a screw speed of 50 rpm and temperature profile of 170–175°C in the barrel and 180°C in the nozzle. The parameters of the hot press and cold press process were as follows:

- Temperature profile: i. upper = 140°C
  ii. lower = 140°C

- Injection pressure: 1500psi/10.34MPa.

Characterization. Thermogravimetric analysis (TGA) was carried out on a SDTA 851 (Mettler Toledo) system. Samples of about 4–6 mg in weight were used for each measurement. The samples were heated from 30ºC to 600ºC, under an air flow rate of 40 mL/min.

Testing and Experiments. Tests were conducted according to the standards proposed in ASTM D635-06 ‘‘Standard Test Method for Rate of Burning and/or Extent and Time of Burning of Plastics in a Horizontal Position”. At least five specimens were tested in all tests. The data given is the arithmetic mean of the test values.

Flexural tests were performed according to ASTM D 790-03 ‘‘Standard Test Methods for Flexural Properties of Unreinforced and Reinforced Plastics and Electrical Insulating Materials” (at 2.8 mm/min with 130 x 12.7 x 6.4mm), impact tests were carried out according to ASTM D 256-05 ‘‘Standard Test Methods for Determining the Izod Pendulum Impact Resistance of Plastics” (at 89 to 160mm/min with 12.7mm x 12.7mm x 6.35mm). Test conditions were selected from the values recommended in ASTM standards.

Table 1. Compositions of WPC-HDPE based prepared in this study.

Batch sample code	RH (wt. %)	Sawdust (wt. %)	HDPE (wt. %)	Flame retardants (wt. %)		
				CC	ZB	NM
A	45.6	16.5	29.5	0	0	0
B	30	10	26.6	20	4	1
C	30	10	26.6	15	7	3
D	30	10	26.6	10	10	5
E	30	10	26.6	5	13	7

* Batch A is set as control with no flame retardant agent.
RH= rice husk; CC = calcium carbonate; ZB = zinc borate; NM = sodium metasilicate.

Results and Discussion

Flexural Properties. Table 2 shows the result from flexural strength according to ASTM D790 with comparison from all batches of WPCs.

Table 2. Result of flexural modulus and flexural strength with comparison from all WPCs batches.

Batch sample code (Average of 6 samples each)	MOE (MPa)	MOR (MPa)
A	2006.74	16.39
B	2518.42	14.09
C	2329.83	11.09
D	2369.30	17.64
E	2373.43	15.42

As usual in WPCs, the addition of wood fibres increased the flexural modulus and flexural strength of the composites in this test. Fibres promote a major stiffness in the composite. The addition of wood fibres improved such behavior and the composite maintained its integrity during the whole experiment [5].

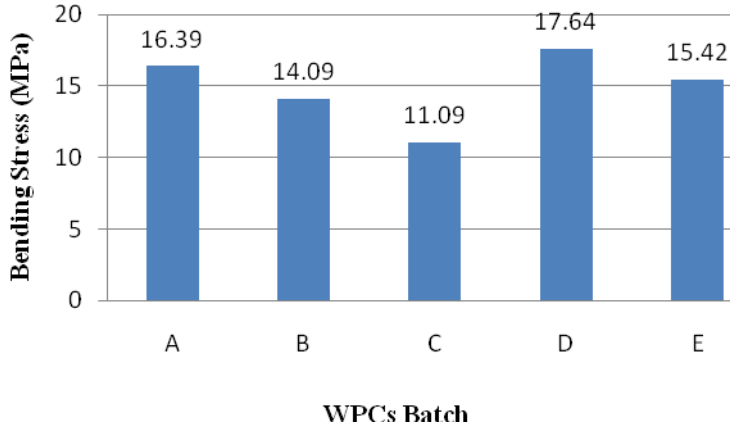


Fig. 1. Bending stress (MOE) for WPC-HDPE based with different flame retardants composition.

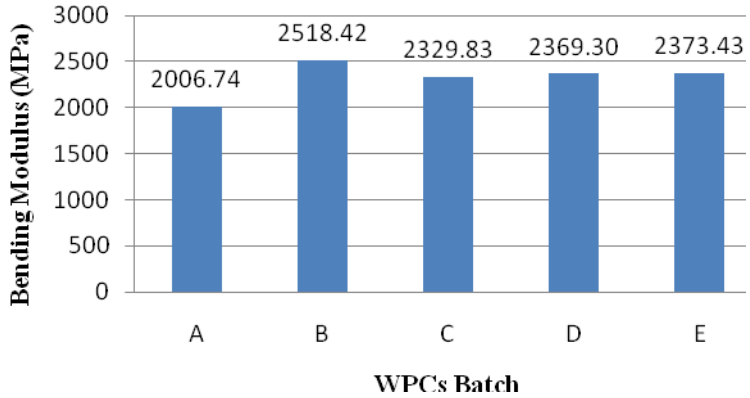


Fig. 2. Bending modulus (MOR) for WPC-HDPE based with different flame retardants composition.

Impact Test Result. Table 3 shows the result of impact resistance as per ASTM D256.

Table 3. Result of impact resistance with comparison from all WPCs batches.

Batch sample code (Average of 6 samples each)	Impact strength (KJ/m^2)
A	0.02517
B	0.03217
C	0.03333
D	0.03400
E	0.03683

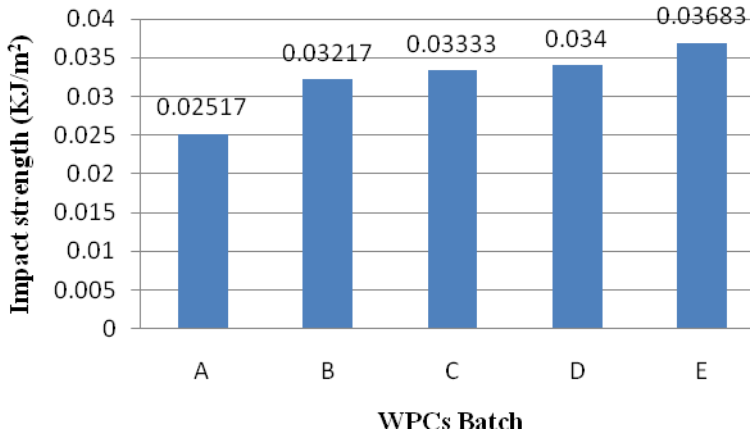


Fig. 3. Impact strength for WPC-HDPE based with different flame retardants composition.

The interaction between neighboring fibers appears to hinder matrix flow, resulting in embrittlement of the matrix. This behavior can lower the impact strength of the composites. The reduction of impact energy during crack formation and failure has been noted before. However, the impact strength decreased as wood fiber content increased. This is due to the increase in stiffness which simultaneously reduced the impact strength as filler loading increased [6].

TGA Result. The thermo-oxidative degradation of rice husk reinforced sawdust-filled HDPE was studied using thermo gravimetric analysis (TGA) under atmospheric air flow condition. From the TG curves (Fig. 4), it can be seen that three degradation curves were obtained which are from rice husk, saw dust and HDPE.

Based from the observation, the control batch samples had the lowest temperature curve among the other batches. Batch E is the highest and followed slightly by batch C, batch B and batch D.

This reflects the improved thermal stability of HDPE matrix due to the incorporation of fire retardants agents. From the peaks it can be explained that as the samples were heated close to 300ºC the sawdust components first to begin decomposed due to its low thermal stability compared with rice husk and HDPE. Rice husk start to decompose after the temperature increases to 350ºC and finally HDPE components slowly decomposed until the temperature is raised to 500ºC [4].

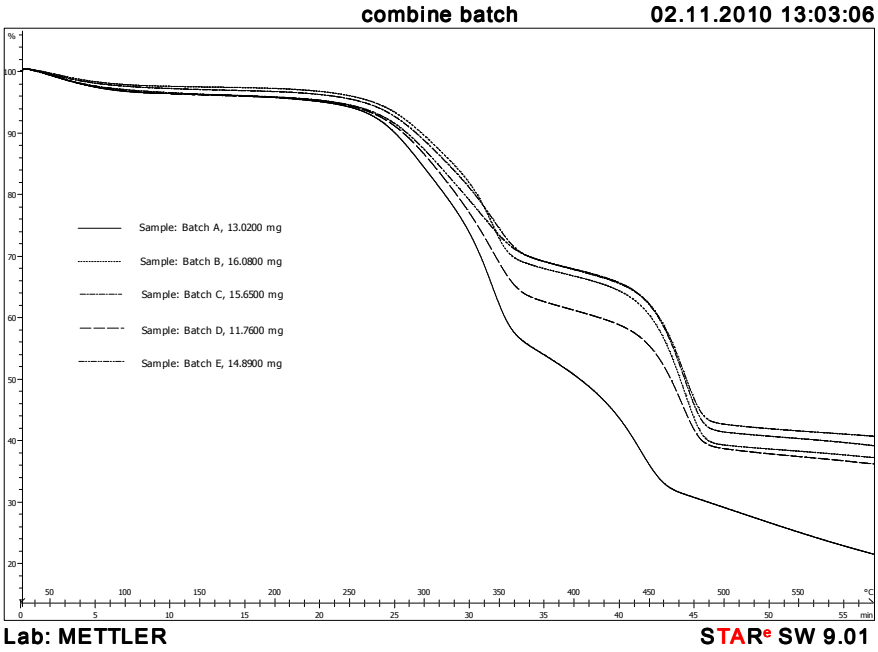


Fig. 4. Comparison of TGA curves for WPC-HDPE based with different flame retardants composition.

Fire Test as per ASTM D 635-06. Fire test method covers a small-scale laboratory screening procedure for comparing the relative linear rate of burning or extent and time of burning, or both, of plastics in the form of bars, molded or cut from sheets, plates, or panels, and tested in the horizontal position. The test conditioning room was conditioned at 27ºC and 50% relative humidity. All specimens are 125 mm long by 13 mm wide, and provided in 5.0 mm thickness. Five specimens were been tested out [8].

Table 4. Result of fire test according to ASTM D 635-06 with comparison from all WPCs batches.

Batch sample code (Average of 5 samples each)	Average time for flame to stop	Average time for smoke to stop
A	2min 9s	1min 33s
B	-	1min 33s
C	1min 45s	39s
D	1min 48s	26s
E	2min 22s	38s

Flame front did not pass the 25mm reference mark for all the batch specimens. The flame was applied for 30s and the time to burn for each specimen was determined. Batch B showed better flame retardancy among others as it only had visible glow without flame before taking time for smoke to stop.

Summary
It can be concluded that the best composition of WPCs in term of better flame retardancy is batch B but the flexural and impact strength must be slightly improved. It can be concluded that the mechanism for the improved flame retardancy was due to the thermal shielding and diffusion barrier effects yielded by the effective silica layer formed during the combustion process together with the addition of flame retardant agents. The addition of flame retardants not only improved the fire resistant aspect but also the durability performance of wood plastic composite.

References

[1] A. Wechslera, S. Hiziroglub: Building and Environment Vol. 42 (2007), p. 2637

[2] J. Giancasproa, C. Papakonstantinou, P. Balaguru: Composites Science and Technology Composites Science and Technology Vol. 68 (2008), p. 1895

[3] K.B. Adhikary, S. Pang, M.P. Staiger: Composites Part B Vol. 39 (2008), p. 807

[4] Q. Zhao, B. Zhang, H. Quan, C.M.Y Richard, K.K.Y Richard, K.Y.L Robert:

Composites Science and Technology Vol. 69 (2009), p. 2675

[5] M. García, J. Hidalgo, I. Garmendia, J. García-Jaca: Composites Part A Vol. 40 (2009), p. 1772

[6] Y. Cui, S. Lee, B. Noruziaan, M. Cheung, J. Tao: Composites: Part A Vol. 39 (2008), p. 655

[7] H. Bouafif, A. Koubaa, P. Perré, A. Cloutier: Composites Part A Vol. 40 (2009), p. 1975

[8] A. A. Klysov, in: Wood-plastic composites. Published by John Wiley & Sons, Inc. Hoboken, New Jersey (2007).

[9] Y. Shu-Kai, R.K. Gupta: Composites Part A Vol. 39 (2008), p. 1694

© (2011) Trans Tech Publications, Switzerland
doi:10.4028/www.scientific.net/KEM.471-472.646

Residual Strength and Failure Criterion of PP Thermoplastic Honeycomb Sandwich Subjected to Low Velocity Impact

A. Freeda Amir[1,a] and A. R. Othman[1,b]

[1] School of Mechanical Engineering, Universiti Sains Malaysia,
14300 Nibong Tebal, Malaysia

[a]freedamir_5626@yahoo.co.uk, [b]merahim@eng.usm.my

Keywords: Polypropylene thermoplastic honeycomb; Low velocity impact; Compression after impact; Failure analysis; Energy absorbed

Abstract: This paper presented the effect of constituent materials on impact damage and strength reduction of sandwich structure, composed of laminated woven E-glass facesheets and polypropylene thermoplastic honeycomb core. Effect of low-velocity impact was the main interest in a variety of layered configurations. Compression after impact (CAI) has been carried out to determine the residual strength of impacted sandwich structures. Three different thicknesses of core of 20, 40 and 60mm subjected to three different levels of impact energy of 15, 30 and 45J were investigated. Impact response of the panel was recorded and analyzed in terms of peak load, indentation, energy absorbed and time. A profile analysis using optical 3D surfaces profiler was carried out to attain the indentation depth and damage area of the samples. The tested samples were then sectioned into halves to capture the failure mode or damaged sequence of the polypropylene thermoplastic honeycomb core. The dominant failure modes of the core indicated that polypropylene thermoplastic honeycomb core is a high strength material which can absorb higher impact energy and retain a higher degree of structural integrity.

Introduction

Nowadays, sandwich structures are increasingly used in aerospace, offshore, marine industries, load bearing structures, railway vehicles and commercial structures which based on strong, stiff composite skins bonded to a low density core material since they possess a number of advantages over conventional materials. Among the benefits of sandwich construction is its capability to provide improved bending rigidity without significant increase in structural weight [1].

A number of studies have focused on low-velocity impact responses and failure behavior of composite laminates and sandwich structure. Hosur et al [2] fabricated sandwich panels with neat and nanophased foam core and layers of plain weave carbon fabric/SC-15 epoxy composite facesheets. From the impact response of the panels, it was found that nano-phased foam sustained higher loads and experienced lower damage areas as compared with the neat counterparts. This was supported by Bhuiyan et al [1], which nanophased system showed best performance where more energy was absorbed at low energy level, but less energy absorption at high impact energy. Aktas et al [3] considered energy profile diagrams and associated load-deflection curves on impact response of unidirectional glass/epoxy laminates. They found that for lower impact energies, the main damage mode was detected as delamination and matrix cracks. However, for the higher impact energies, fiber failures were dominant due to the brittle characteristics of glass fabrics. Significant delaminations were observed at the bottom layers, resulting from vertical displacement of the broken and unbroken fibers at point of impact rather than bending mismatching. Agreement was found between the analytical and FEA solutions studied by Lee and Tsotsis [4] on behavior of honeycomb core sandwich panels, where the distributed-load model to be effective for analyzing sandwich panel indentation. Similar analysis was also carried out by Ik Hyeon Choi [5] in which comparable agreement has also been established.

In brief, in order to determine the residual strength for impacted sandwich structures, compression after impact (CAI) is performed. Bruno et al [6] have studied a core crush criterion to

determine the residual strength of impacted sandwich structures made of Nomex honeycomb core. This model involves a linear elastic response of the skins that is a strong hypothetical especially for thick skins. In addition, Othman and Barton [7] have concluded that the thickness of the honeycomb core did not have any significant effect on the overall energy-absorbing capacity of the sandwich composite beams. For smaller core thicknesses, smaller bending rigidity was observed whereas for a larger core thickness, damage was more local due to the overall stiffness of the sandwich [8,9].

However, from the study above, impact behavior of sandwich structures is apparently still an open problem. Therefore in this paper, the interest will be on the sandwich structures damage/failure investigation. Sandwich beams were then subjected to low-velocity impact using an instrumented falling-weight impact tower with different energy levels of 15J, 30J and 45J. Subsequently, a series of compression after impact (CAI) tests have been conducted to examine the percentage of strength reduction following the impact. In addition, impact response of the panels was analyzed and impact damage of the core was also characterized through microscopic studies.

Experimental Materials and Method

Materials and Fabrication of Sandwich. The polypropylene thermoplastic cores used in the construction of honeycomb sandwich structures were supplied by the Qingdao Polycore Technoly Co.Ltd with the thicknesses of 20, 40 and 60mm. The sandwich beams studied here were fabricated at Universiti Sains Malaysia using a heated press machine, in which the composite skins were pre-cured before subsequently bonding to the honeycomb core. The skins were fabricated of seven layers of woven E-glass fiber laminates with orientation of $[(0,90)/(\pm 45)/\overline{(0,90)}]$. Two-part adhesives of Part A (resin) and B (hardener) were mixed with 2:1 ratio and the skin was post-cured at 80°C for 2 hours. The final skin thickness was obtained as 1.64mm.For the sandwich construction, liquid epoxy resin was used as the bonding mechanism and the sandwich was clamped using the hydraulic press to complete the curing process. The temperature of the process was 60°C, with the curing time of 10 minutes. The final thicknesses of the sandwich samples were approximately 23.28, 43.28 and 63.28 mm respectively with in-plane area of 210mm x 70mm.

Low Velocity Impact Test. The impact tests were performed on the sandwich beams with a three-point bending arrangement using an instrumented drop-weight impact testing rig. The set-up was equipped with data acquisition software of DEWESoft v6.0 in order to simultaneously record the impact force and penetration time. For each type of laminates, at least three samples were subjected to impact at 15, 30 and 45 J each. In addition, a high-speed video camera was employed to continuously record the real-time impact progression and deformation of the impact sandwich.

Compression After Impact (CAI). Compression tests were carried out in order to determine the residual strength of the post-impact sandwich honeycomb specimens. Test data of the compressive load and the displacement of compressive surface of the specimens were measured using a 30kN Instron universal testing machine. The specimen size chosen for the compression test is 5777mm^2 based on the ASTM C 365-03 with the crosshead speed at 1 mm/min. The compressive strength and modulus of the impact sandwich were determined to evaluate the reduction percentage of the properties.

Optical Surfaces Metrology. The failure analysis of the damage structure was analyzed using Infinite Focus Alicona machine and damage was also captured by using Nikon SLR D90 digital camera. With Alicona, a profile analysis was carried out to attain the indentation depth of the samples and damage area. Subsequently, the damage area was determined by the optical measurement and inspection.

Result and Discussion

Various parameters that included maximum load, total energy absorbed, damage area and indentation depth are highlighted in Table 1 for the sandwiches tested. From DEWEsof transient data, load and energy versus time were plotted using the parameters for different energy level and compared as shown in Fig. 1. Significant drop in load is a qualitative indication of severe damage which due to the penetration of the facesheet at the impact region which caused bottom skin failure

for smaller core thickness (i.e. 20mm). At 15J, these parameters were mainly dominated by the elastic response which is a function of the structural stiffness. Lower portion of the facesheet failed in tension allowing the impactor to penetrate through its thickness.

Table 1. Impact parameters for sandwich samples with PP honeycomb core impacted at 15, 30 and 45 (J) for core thicknesses of 20, 40 and 60 (mm).

Thickness (mm)	Impact Energy (J)	Max. Load (N)	Total Energy Absorbed (J)	Damage Area (cm^2)	Indentation depth (mm)
20	15	1989.45	14.96	1.5320	-5.2761
	30	1726.72	28.94	1.5475	-5.3181
	45	1788.99	40.97	1.5559	-2.2511
40	15	1597.64	10.84	1.4773	-4.6319
	30	1954.52	28.75	1.6559	-4.8169
	45	1673.57	28.67	2.1028	-5.7358
60	15	1746.46	13.89	1.5667	-3.8154
	30	2835.35	29.33	1.4694	-4.4013
	45	2704.74	44.77	1.6627	-5.7969

In case of higher impact energies, impact parameters were influenced by the state of damage rather than the elastic response of the samples. As the energy level was significant, there was considerable damage in the samples especially at the top skin. The amounts of energy were measured for the perforation of both the upper and lower skins. In addition, major core crushing involved and appeared at samples and penetration through the whole thickness of the core was observed. Following the failure, the load was found to increase again and was corresponded to crushing of the core together with lengthening of cracks in the upper skin. The energy absorbed was through the top skin indentation at the point of impact and core damage beneath the skin. Also, based on the high speed camera (Fig. 2), it was found that cushioning behavior was apparent during penetration of the impactor.

Moreover, polypropylene thermoplastic possesses the properties of elasticity, thus, the energy absorption capability for core with thicknesses of 40 and 60mm will be higher which is corresponded linearly with the total impact time. Different thicknesses of PP thermoplastic honeycomb panels lead to different compression resistance. Therefore, as the thickness of the core increased, compression resistance will be higher, which lead to more energy being absorbed and longer time taken for the whole sandwich panel to fail.

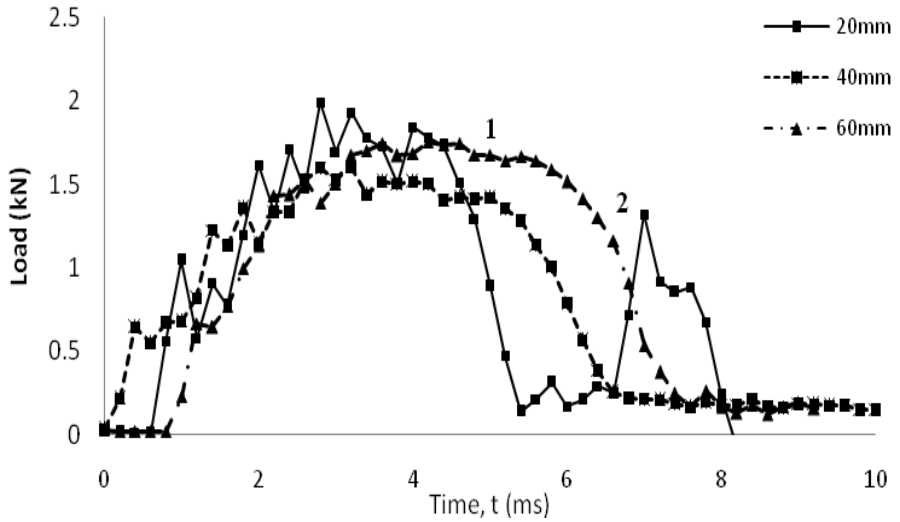


Fig.1. Load versus time plot for sandwich structures impacted at 15 (J); (Point 1: Top skin failure; Point 2: Penetration at impact region).

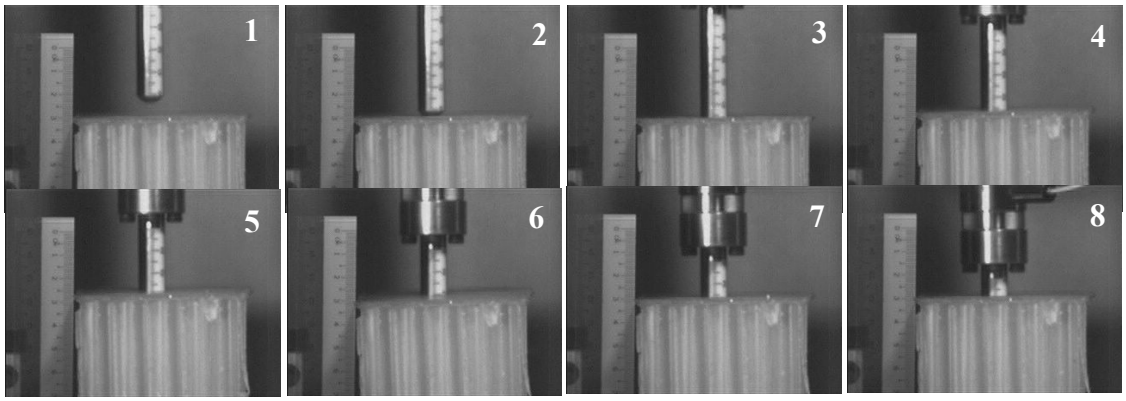


Fig. 2. Impact sequences obtained from the high speed video camera.

Fig. 3(a) clearly indicates the sequence of failure on the sandwich composites. Also, consideration of the presence of stress waves from the impact loading resulted not only in localized indentation and fracture of the top skin, but also notably skin delamination and lower skin-core debonding. Moreover, possible causes for the non-linear response may be due the existence of microdamages, such as fiber/matrix microcracking or skin delamination in the upper skin prior to the failure. Also, the curves of compressive load as a function of its displacement for three indented specimens with different depth of indentation are plotted in Fig. 3(b). The first peak of the curve indicated the ultimate compression strength of the specimen. For all of the specimens, the initial stiffness was identical and corresponded to the elastic behavior of the skins. Thus, it has been observed that at the beginning of compression, the dimension of damage area caused by impact did not have a significant influence to the compressive characteristic. As the compression load increased, an inflexion was observed following the peak load which was quantified as the residual strength of the indented structure. The residual strength has found to increase with the increase in core thickness. In addition, this residual strength was also depending on the depth of the maximum indentation.

Table 2 indicated the summary of the CAI test results on the sandwich comparison. In general, it was found that the ultimate compressive strength of the impacted specimens was varied between 3.79 to 6.54 MPa. On the other hand, the reduction in crush strength of the sandwich was observed up to 29.27% in comparison to the value quoted by manufacturer. Note that, the trend indicated inconsistency for those various test parameters, where decisive conclusion could not be established.

The exact indentation depth and area can be seen clearly given by the optical 3D surfaces profiles as shown in Fig. 5. Failure modes obtained from the observation such as local indentation, fiber delamination, core dimpling, crimping, wrinkling and buckling were highlighted. PP thermoplastic honeycomb core played an important role in progressively controlling the sequence in which failure mechanisms occurred and predominated.

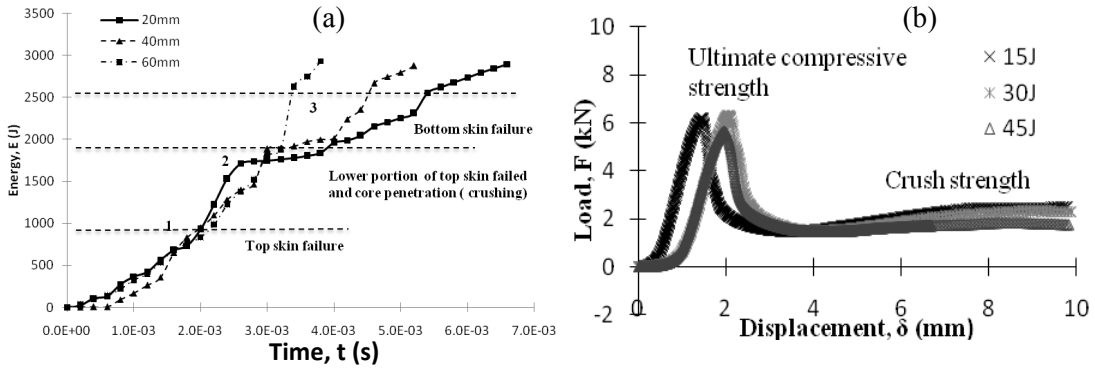


Fig.3. (a) Energy versus time plot for sandwich structure impacted at 30 (J), (b) Load versus displacement plot for core thickness 40 (mm).

Table 2. Summary of CAI tests for sandwich samples with PP honeycomb core sandwich.

Core Thickness (mm)	Impact Energy (J)	Ult. Compressive Strength (MPa)	Min Crush Strength (MPa)	Crush Strength (MPa)*	Strength Reduction (%)
20	15	6.11	1.66	2.05	19.02
	30	3.79	2.03		1.01
	45	6.54	1.56		23.90
40	15	6.21	1.48	2.05	27.81
	30	6.32	1.49		27.31
	45	5.64	1.47		28.29
60	15	6.23	1.72	2.05	16.10
	30	4.50	1.45		29.27
	45	6.22	1.72		16.09

* From manufacturer

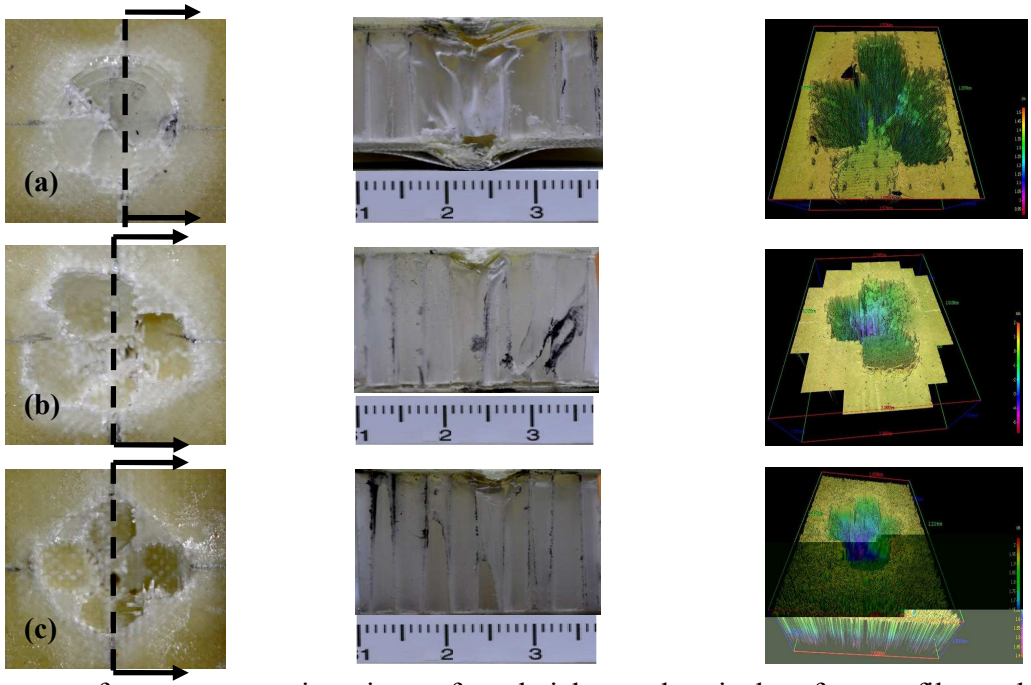


Fig. 5. Impact surfaces, cross section views of sandwiches and optical surface profilers subjected to impact of 45 [J] for thicknesses; (a) 20mm, (b) 40mm and (c) 60mm respectively.

Therefore, it was suggested that, although testing the samples with low-velocity impact test and CAI tests may indicate energy absorbing capability and essential failure mechanisms of the sandwich, it may offer a conclusive finding if more tests are performed, for example, flexural test, and quasi static test. Verification of the damage modes could be made which can develop a better performance of sandwich composite.

Summary
In this study, residual strength and failure analysis on composite laminated panels have been investigated. Generally, failure initiated from the indentation, followed by core crushing and bottom skin failure. Top skin should be greatly influenced the stability of the sandwich panels and failure mechanism. However, the importance of the top skin in controlling the structural behavior of the sandwich panels during impact was surprisingly reduced. Overall performance not only the properties of the skin and core need to take into account but also the adhesive bonding which displayed varies failure modes. It was found that the dominant impact damages were mainly delamination in the facesheets. As for the core material, thicker core sustained a higher load in the core crushing process before total failure. As a result, as the core thickness is increased, higher energy is absorbed before failure compared to thinner core. The dominant failure modes of the core indicated that polypropylene thermoplastic honeycomb core possess high strength and stiffness in which it can absorb higher impact energy and retain a higher degree of structural integrity.

Acknowledgement
Project supported by School of Aerospace Engineering, School of Mechanical Engineering and School of Material and Mineral Resources Engineering of Universiti Sains Malaysia under Grant short term (grant number 304/PBAHAN/60310001).

References

[1] Md.A Bhuiyan, M.V. Hosur, S.Jeelani: submitted to Composite: Part B (2009).

[2] M.V. Hosur, A.A. Mohammed, S. Zainuddin, S. Jeelani: Mater. Sci. and Engineering A Vol. 498 (2008), p.100-109.

[3] Mehmet Aktas, Cesim Atas, Bulent Murat Icten, Ramazan Karakuzu: Comp. Struc. Vol. 87 (2009) p. 307-313.

[4] Shaw M. Lee, Thomas K. Tsotsis. Comp. Sci. and Tech. Vol. 60 (2000) p. 1147-1159.

[5] Ik Hyeon Choi. Comp. Struc. Vol. 75 (2006) p. 582-586.

[6] Bruno Castanie, Yulfian Aminanda, Christophe Bouvet, Jean-Jacques Barrau. Comp. struc. Vol. 86 (2008) p. 243-250

[7] A.R Othman, D.C Barton. Comp. Struc. Vol. 85 (2008) p. 126-138.

[8] Ki-Weon Kang. Heung Seob Kim, Man Sig Kim, Jung-Kyu Kim. Mater. Sci. and Engineering A: Vol. 483-484 (2008) p. 333-335.

[9] Joris Leijten, Harald E.N. Bersee, Otto K. Bergsma, Adriaan Beukers. submitted to Composite: Part A (2008)

© (2011) Trans Tech Publications, Switzerland
doi:10.4028/www.scientific.net/KEM.471-472.652

Mechanical Properties of Carbon Fiber-Reinforced Polypropylene Composites

R.Yunus[1a], N. H. Zahari[1b], M. A. M. Salleh[1c], N. A. Ibrahim[2d]
[1] Department of Chemical and Environmental Engineering, Universiti Putra Malaysia, 43400 Serdang, Selangor, Malaysia
[2] Department of Chemistry, Universiti Putra Malaysia, 43400 Serdang, Selangor, Malaysia

[a]robiah@eng.upm.edu.my, [b]musjakindi@yahoo.com, [c]asalleh@eng.upm.edu.my, [d]norazowa@science.upm.edu.my

Keywords: Carbon Fiber, polypropylene, composite, MFI, mechanical properties.

Abstract. In this paper, the mechanical properties of carbon fiber polypropylene composites prepared under various process conditions were investigated. Two different types of polypropylene composites were produced by mixing and compressing the mixtures using hot press. The mixture was prepared by mixing polypropylene with chopped carbon fiber and carbon fiber percentage (wt%) was varied. Mechanical properties investigated were tensile test, impact test, bending test and density test. The Scanning Electron Microscopy (SEM) was employed to study the morphology of the composites. The highest tensile strength was obtained for polypropylene (MFI 60) composites reinforced with 10 wt% carbon fiber. The composite also exhibited the best tensile and flexural properties.

Introduction

Plastic offers auto engineers a variety of practical, costs-effective alternatives, as well as tremendous advantages over traditional automobile production materials. By using plastics, manufacturers have the possibility of adopting modular assembly practices, lowering production costs, improving energy management, achieving better dent resistance, and using advanced styling techniques for sleeker, aerodynamic exteriors. However, plastic outer cover does not promise good protection if it performs alone [1]. With current technology, many manufacturers are using composite instead of plastic alone to fabricate the automotive parts including the bumper. Fuel efficiency and emission gas regulations are the main causes for reducing the weight of passenger cars by using composite structures [2]. While glass fiber reinforced plastics (GFRP) are used in several vehicle components, the carbon fibers as reinforcing material are of relative low significance for the lightweight construction in motor vehicles [3]. The use of a short-carbon-fiber or discontinuous carbon fiber reinforced polypropylene (SCF/PP) composite has been investigated by Rezaei et.al [4] for car bonnet application. They found that the SCF/PP composite is a good option for replacing steel in car bonnet and can achieve the standards of car bonnet with remarkable lower weight and higher mechanical properties. However, this study focuses on the use of discontinuous carbon fiber reinforced polypropylene composite for the application of car bumper which requires different specifications.

Experimental Parts

Materials Description. The carbon fibers are a product of Composite Oracle^{TM} Ltd. The PAN carbon fibers are a high strength (HS) type (Torayca T700S 12K). For the matrix (or resin), two types of commercial polypropylene impact copolymer was used. The first was Titan Pro SM950 where the melt flow index is 60 g/10 min (PP MFI 60) and the other was Titan Pro EPC40R with 7 g/10 min of melt flow index (PP MFI 7). Both PP are manufactured in pellet forms by Titan Polymer (M) Sdn. Bhd.

Material Preparation. The processing condition involves melting the thermoplastics PP in the Thermo Haake PolyDrive with Rheomix R600/610 twin screw kneader at 170°C for PP MFI 60 and 185°C for PP MFI 7 while the rotor speed was maintained at 50 and 60 rpm respectively due to different melt flow index of PP. After 2 minutes of preheating, the fibers were added and the mixing

process was set for 13 minutes. The mixtures were then collected and ready for compression molding. The mixtures were molded using HSINCHU Hot Press Machine. The mold size is 15 x 15 cm while the thickness of every sample is 1mm and 3mm prepared for the mechanical testing. The samples were first preheated between two hot plates for 5 minutes and compressed for another 5 minutes under the pressure of 150 kg/cm^2 at 170°C (PP MFI 60) and 185°C (PP MFI 7). The sheets obtained were then cooled between two cold plates at room temperature for 5 minutes.

Tensile Test, Flexural Test, Notch Impact Test and SEM Observation. Tensile properties were determined using an Instron Universal Testing Machine 4302 with a load capacity of 1 kN. The specimens were prepared of 1mm thickness and cut into dumbell-shaped. The procedure follows the ASTM D638M-98 with crosshead-speed of 5 mm/min. Instron Universal Testing Machine 4302 with a load capacity of 5 kN were used to measure the flexural properties. The cross-speed was set at 3mm/minute with a span length of 60 mm. The specimens were cut into 3 mm thickness, 12 mm width and 124 mm length according to ASTM D790-98. Izod Impact testing was conducted by Izod/Charpy Impact Tester. The 3 mm samples thickness were cut into 12 mm width and 62 mm length. This is in accordance with ASTM D256-93. Notch was made by Notch Cutter for 2.55 mm. With 5 J stricker and span length of 70 mm the test were operated at 30°C.

Results and Discussion

Tensile properties. Figure 1 shows the effect of fiber loading on the tensile strengths of CFPP MFI 7 and CFPP MFI 60. The result indicates that the tensile strength of PP MFI 60 increases with addition of 5 wt% CF to 10 wt% CF and decreases at higher CF loadings. The maximum stress is obtained at 10 wt% CF loading at 48 MPa. According to Thomason and Vlug [5], tensile strength increases with fiber loading. When the CFPP composite is subjected to load, the CF acts as the load carrier where stress is being transferred from the PP matrix to the CF leading to an efficient and uniform stress distribution within the composites. At a low amount of CF loading, the CF is not able to transfer load to one another effectively and stress gets accumulated at certain location in the composites. This then leads to a lower tensile strength. This phenomenon was as similar as the behaviour of nano-particle composites where in accordance with Frogley et al., [6], at higher filler loadings, the proportion of the filler in the matrix is sufficient for maximum orientation and the filler is able to actively participate in stress transfer. It is discovered that the composite was able to absorb a maximum load at 10 wt% CF content but the effect was poor at higher content. When the filler loading increases, there will be a stage where the filler aggregate is not dispersed or not completely wetted by matrix [7].

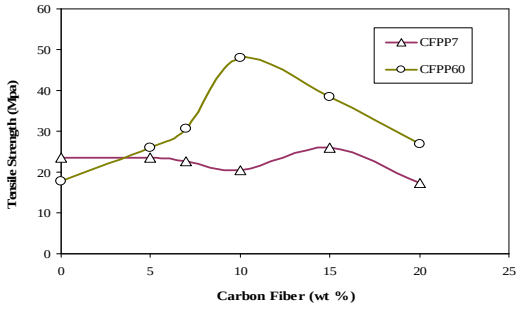


Figure 1-Tensile Strength (MPa) versus Carbon Fiber (wt %)

Thus, it will result in a weak fiber-matrix interaction while the interaction of fiber-fiber stronger [8]. It is interesting to note that, in the case of the CFPP MFI 7, the incorporation of the CF does not give a significant effect to the polymer strength. It has clearly shown that the tensile strength was reduced as the percentage of CF increased from 5 to 10 wt%. In fact, the highest strength is only at 15 wt% (26 MPa) and dropped at 20 wt% CF (17 MPa). The incorporation of the CF into the PP matrix reduced the ability of the composites to transfer applied stress. The existence of the entangled CF is also believed to reduce the tensile strength of the CF filled PP composites. This is

because the agglomeration of the CF can act as a stress concentration point and increase the ability of the composites to initiate cracks which cause the poor interfacial adhesion [9]. Figure 2 shows the modulus of CFPP MFI 60 and CFPP MFI 7 at various fiber loadings. The CFPP MFI 60 composites showed remarkable improvement in tensile modulus after CF addition from 5 to 20 wt% as compared to pure PP. This is due to the addition of CF into the PP matrix where the CF as the filler will act as a load carrier [1] in the composite thus the stiffness is increasing upon CF loading. However, the Young's modulus for PP MFI 7 was only improved when it was loaded with 5 to 15 wt% CF content. The addition of 20% of the CF to PP MFI 7 reduced the modulus compared to the composites. This may be attributed to the presence of too much CF which has caused agglomeration in the PP matrix. There is no interfacial bonding between the CF and PP. This is due to the behavior of PP MFI 7 matrix where the polymer has a high viscosity where restricts the incorporation of CF in between its molecule. In turn it reduced the elasticity of the composites. Many researchers have reported similar findings where at higher loading of the CF, the composites would not perform as well as composites lower loadings [10, 11].

Flexural Properties. The data for flexural strength in Figure 3 reveal a general trend of an increase in strength due to an increase in fibre concentration. It can be seen that, at 15 wt% of CFPP MFI 60, the composite has the highest flexural strength of 50 MPa. However, this is not a linear trend, and particularly at higher concentrations it appears that the flexural strength values may plateau out and even drop off. The flexural strength decreased at 20 wt% due to the occurrence of fiber-fiber interaction which is caused by a higher filler loading. This then makes the composite unable to absorb stress transfer due to poor interaction between the fiber and the matrix [12]. For structural applications, good interfacial adhesion between fibers and matrix is required in order to achieve high strength and good dimensional stability of composites [13]. However CFPP MFI 7 composites show less improvement compared to the plain PP. At 5 to 10 wt% CF loading, the flexural strength for this composite is increased and decreased gradually with further addition.

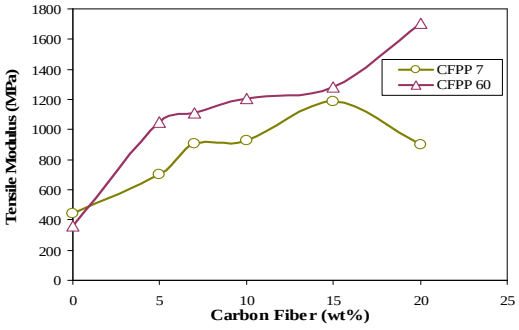


Figure 2: Tensile Modulus (MPa) for CFPP Carbon Fiber (wt%)

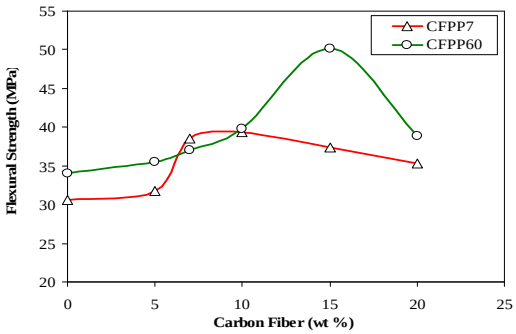


Figure 3: Flexural Strength (MPa) versus Carbon Fiber (wt%)

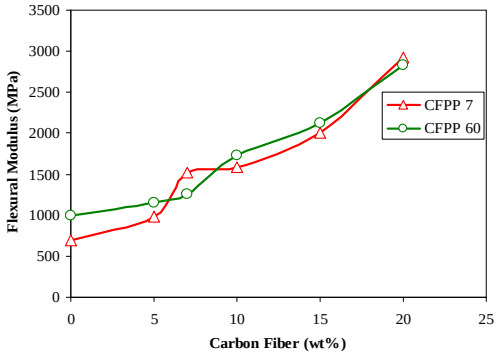


Figure 4: Flexural Modulus (MPa) versus Carbon Fiber (wt%)

The graph for the flexural modulus of CFPP MFI 60 and CFPP MFI 7 is shown in Figure 4. It shows that the flexural modulus increased significantly with the CF addition. This indicates that stiffness of CF is affecting the PP matrix thus increase the resistance of the composites upon compression force. In accordance with Ibrahim [14], good interfacial adhesion between CF and PP region is also increase the stiffness of the composite. Based on the graph, the increments are 41, 118, 129, 188 and 320% respectively for CFPP MFI 60 composites of 5% to 20% CF addition. Meanwhile the flexural modulus of CFPP MFI 7 composites increased to 982, 1519, 1519, 2003 and 2926 MPa respectively for CF loading between 5, to 20 wt %.

Impact Properties. The results from the notched Izod impact testing are summarized in Figure 5. The graph shows that the impact properties of the CFPP MFI 60 (CFPP60) which increased gradually with the increase of carbon fiber loading. The highest strength for this composite was 62 J/m which was at 15 wt% CF. The increase in the amount of filler content also increased the interfacial region. This thus improved the strength of the composite. However, for the CFPP MFI 7 (CFPP7) composite, the impact strength decrease with CF loading but started to increase at 7 wt% CF. The reduction in impact properties can be attributed to the immobilization of the macromolecular chains by the filler.

SEM Morphology. The images show the differences of polymer structure between PP MFI 60 and PP MFI 7 where the lower the MFI, the soft the polymer. The micrographs observation on CFPP MFI 60 (Figure 6) revealed that the matrix could be found have the fiber–matrix adhesion. It is probable that carbon fibers have been covered with a thin layer of the matrix as fibrils linking the fiber surface to the matrix. This suggests that the fibers have some interaction with the matrix, which led to better stress transfer between the matrix and the reinforcing fibers. However the CFPP MFI 7 in Figure 7 does not show any interfacial adhesion. Therefore these micrograph images are strengthening the differences between PP MFI 7 and PP MFI 60. PP MFI 7 is more ductile compared to PP MFI 60. Therefore more heat is required to degrade this polymer.

Summary

This study has revealed that CFPP MFI 60 at 10 wt% carbon fiber composite has a good performance in terms of specific properties in tensile strength, flexural strength and flexural modulus compared to the CFPP MFI 7 composites and the commercial plastic bumper fascia. However, the composite fails to comply with the impact properties where both CFPP composites exhibited lower specific impact strength.

Acknowledgment

The authors would like to thank UPM, SIRIM and MOSTI for providing the financial support.

References

[1] Mallick, P. K. (1993). *Fiber-Reinforced Composites, Material, Manufacturing and Design*, New York: Marcel Dekker, Inc.

[2] Hosseinzadeh, R., Shokrieh, M. M. and Lessard, L. B. (2005). *Composite Structures* 68: 419-427.

[3] Adam, H. (1997). *Material & Design*, 18:349-335.

[4] Rezaei, F., Yunus, R., Ibrahim, N.A., Mahdi, E. S., (2008). *Polymer-Plastics Technology and Engineering.* 47: 351-357.

[5] Thomason, J. L. and Vlug, M. A. (1995). *Composites*: *Part A Applied Science and Manufacturing*, 27:447-484.

[6] Frogley, M. D., Ravich, D., Wagner, H. D., (2003). *Composite Science and Technology*, 63:1647-1656.

[7] Hanafi, I., (2004). Komposit Polimer Diperkuat Pengisi dan Gentian Pendek Semulajadi, pp. 1-249. Pulau Pinang: Universiti Sains Malaysia

[8] Chen, J., Yang, S., Tao, Z., Hu, A., Gao, S. and Fan, L., (2006). *High Performance Polymer* 18: 265-282.

[9] Ramirez, C., Albano, C., Karam, A., Dominguez, N., Sanchez, Y. and Gonzalez, G. (2005). *Nuclear Instruments and Methods in Physics Research B, Beam Interactions with Materials and Atoms* 236: 531-535.

[10] Zaixia F., Zhangyu, Yanmo C. and Hairu L., (2006). *Journal of Thermoplastic Composite Materials* 19:113.

[11] Kumar, S., Rath T., Mahaling R.N., Reddy C.S., Das C.K., Pandey K.N., Srivastava R.B., and Yadaw S.B., (2007). *Materials Science and Engineering* 141: 61–70.

[12] Thomason, J. L. and Vlug, M. A. (1996). *Composites Part A Applied Science and Manufacturing*, 96: 1075-1084.

[13] Husic, S., Javni, J. and Petrovic, Z. S. (2005). *Composites Science and Technology* 65: 19-25.

[14] Ibrahim A., (2005). Modification of Oil Palm Empty Fruit Bunch Fibre by Graft Copolymerization and Application of Their Products in Composites, PhD. Thesis, Universiti Putra Malaysia.

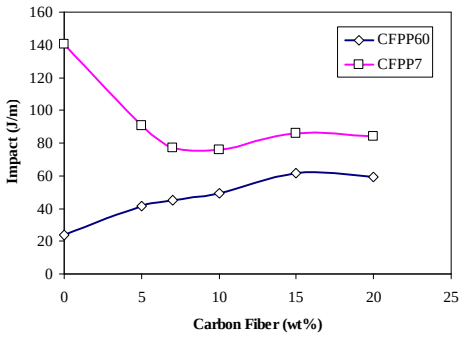


Figure 5: Impact Strength for Various CF Loading

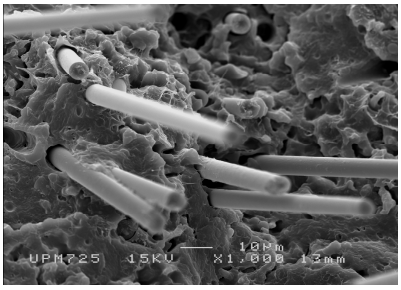


Figure 6: SEM micrograph of tensile fracture surface of 10 wt% CF reinforced PP MFI 60 composite

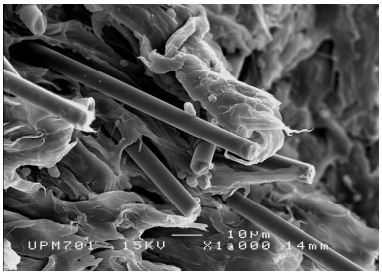


Figure 7: SEM micrograph of tensile fracture surface of 10 wt% CF reinforced PP MFI 7 composite

© (2011) Trans Tech Publications, Switzerland
doi:10.4028/www.scientific.net/KEM.471-472.658

Free Vibration Analysis of Composite Sandwich Plate with Viscoelastic Core

Soroush Sadeghnejad Limouei[1,a], Mojtaba Sadighi[2,b] and Abdolreza Ohadi[2,c]

[1]Department of Mechanical Engineering,

Amirkabir University of Technology, Hafez Ave., Tehran, Iran

[2]Department of Mechanical Engineering,

Amirkabir University of Technology, Hafez Ave., Tehran, Iran

[a]s.sadeghnejad@aut.ac.ir , [b]mojtaba@aut.ac.ir , [c]a_r_ohadi@aut.ac.ir

Keywords: composite sandwich plates, viscoelastic core, higher-order theory, natural frequency, 3D elastic.

Abstract. New Reddy-type elements based on Reddy's higher-order theory are used in the analysis of composite sandwich plates with viscoelastic core, which is achieved by considering independent transverse displacements on two faces and linear variations through depth of plate core. In addition, Young modulus, rotational inertia, and kinetic energy of core are considered and core is assumed as 3D elastic structure with the properties of an orthotropic viscoelastic material. To improve the Reddy's higher-order theory, a rectangular element with four nodes, which each node has seven degrees of freedom, is proposed. Hamilton's principle has been used to obtain the equations of motion. A finite element code for structural response analysis of the free vibration is developed. The obtained results are compared with existence researches. The influence of material properties, lamination schemes, and fiber angle on natural frequencies of composite plates are investigated.

Introduction

The use of sandwich structures in marine, transport, civil construction and aerospace applications, is growing rapidly because of the advantageous features such as high strength to weight ratio and low maintenance cost [1].

Of all the higher-order theories, the one proposed by Reddy [1] was the first to obtain the equilibrium equations in a consistent manner using the principle of virtual displacements. Free vibration analysis of composite sandwich plates by using Reddy's higher-order theory and investigating the influence of material property parameters and plate geometry variables on the natural frequencies, have been done by Meunier and Shenoi [2]. Numerous finite element models of the various theories have been put forward over the years due to necessity of designing structures with complicated geometry. Wang and Chen [3] applied discrete layer annular finite element to derive the equations of motion for the three-layered annular plate with an incompressible viscoelastic core layer and two polar orthotropic laminated face layers. They presented the effects of material properties and geometrical properties on the natural frequencies and modal loss factors of this system. Vibration and thermal buckling behaviour of sandwich beams with composite facings and viscoelastic core in comparison with sandwich plate, have been seen in Pradeep et al. researches [4]. They examined the effects of fiber angle, aspect ratio and the core thickness on the performance of the beam and plate elements. Arvin et al. applied higher order theory of sandwich beams to study free and force vibration of sandwich composite beams with viscoelastic core. They have examined the effects of impressive parameters including fiber angle, thickness of faces and core thickness on the loss factors and natural frequencies of the beam. Zhang and Chen [5] used ANSYS 7.0 to develop a 3-D finite element model for laminated composite beams with integral viscoelastic layers. They presented the comparisons of the effects of damping of fiber-reinforced

composite materials, ply angle of compliant layers, and location of viscoelastic layers on the loss factor and frequency of damped composite beams with previous studies.

Following the previous study of the present authors [6] on the sandwich beams, in this article, new Reddy-type elements based on Reddy's higher-order theory are used in the analysis of composite sandwich plates. Hamilton's principle has been used to obtain the equations of motion. A finite element code for structural response analysis of the free vibration is developed. The obtained results are compared with existence researches. By considering present results, a designer can provide necessary required natural frequencies for sandwich plate and even can be controlled frequency response of the sandwich plate.

Mathematical Formulation. For calculating natural frequency response of composite sandwich plate with viscoelastic core, Reddy's higher order element displacements field for faces are given in forms:

$$\begin{cases} u_i = u_{oi} + z\psi_{xi} - \frac{4z^3}{3h_s^2}\varphi_{xi} \\ v_i = v_{oi} + z\psi_{yi} - \frac{4z^3}{3h_s^2}\varphi_{yi} \\ w = 0 \end{cases} \qquad \text{i=1,3} \tag{1}$$

where, u_{0i} and v_{0i} are the mid plane longitudinal displacements, ψ_{xi} and ψ_{yi} are rotations, φ_{xi} and φ_{yi} are warping functions, u_i and v_i are general longitudinal displacement and w is the transverse displacement which are introduced for upper and lower faces. Assume that the core transverse and axial displacements are linearly dependent on coordinate z and by using no slip assumption between faces and core, Reddy's higher order element displacement fields for core are given in forms [6]:

$$\begin{gathered} w_2 = \frac{w_1 - w_3}{h_c}z + \frac{w_1 + w_3}{2} \\ u_2 = \frac{u_1 + u_2}{2} + \frac{h_c}{4}(\psi_{x1} - \psi_{x3}) - \frac{h_c^3}{12h^2}(\varphi_{x1} + \varphi_{x3}) + \left\{\frac{u_1 - u_3}{h_c} + \frac{1}{2}(\psi_{x1} + \psi_{x3}) + \frac{h_c^3}{6h^2}(\varphi_{x3} - \varphi_{x1})\right\}z \\ v_2 = \frac{v_1 + v_2}{2} + \frac{h_c}{4}(\psi_{y1} - \psi_{y3}) - \frac{h_c^3}{12h^2}(\varphi_{y1} + \varphi_{y3}) + \left\{\frac{v_1 - v_3}{h_c} + \frac{1}{2}(\psi_{y1} + \psi_{y3}) + \frac{h_c^3}{6h^2}(\varphi_{y3} - \varphi_{y1})\right\}z \end{gathered} \tag{2}$$

By considering the classical theory of the plate for face sheets, and regarding to the mentioned displacements, strain–displacement relations for faces and core can be calculated as equations (3) and (4).

$$\begin{Bmatrix} \varepsilon_{xi} \\ \varepsilon_{yi} \\ \varepsilon_{zi} \\ \gamma_{xyi} \\ \gamma_{xzi} \\ \gamma_{yzi} \end{Bmatrix} = \begin{Bmatrix} \frac{\partial u_{0i}}{\partial x} + z\frac{\partial \psi_{xi}}{\partial x} + z^3(-\frac{4}{3h_s^2}\frac{\partial \varphi_{xi}}{\partial x}) \\ \frac{\partial v_{0i}}{\partial y} + z\frac{\partial \psi_{yi}}{\partial y} + z^3(-\frac{4}{3h_s^2}\frac{\partial \varphi_{yi}}{\partial y}) \\ 0 \\ \frac{\partial u_{0i}}{\partial y} + \frac{\partial v_{0i}}{\partial x} + z(\frac{\partial \psi_{xi}}{\partial y} + \frac{\partial \psi_{yi}}{\partial x}) + z^3[-\frac{4}{3h_s^2}\left(\frac{\partial \varphi_{xi}}{\partial y} + \frac{\partial \varphi_{yi}}{\partial x}\right)] \\ \frac{\partial w_{0i}}{\partial x} + \psi_{xi} + z^2(-\frac{4}{h_s^2}\varphi_{xi}) \\ \frac{\partial w_{0i}}{\partial y} + \psi_{yi} + z^2(-\frac{4}{h_s^2}\varphi_{yi}) \end{Bmatrix} \qquad i = 1,3 \tag{3}$$

in which, $\varepsilon_{xi}, \varepsilon_{yi}, \varepsilon_{zi}, \gamma_{xyi}, \gamma_{xzi}, \gamma_{yzi}, \varepsilon_{x2}, \varepsilon_{y2}, \varepsilon_{z2}, \gamma_{xy2}, \gamma_{xz2}$ and γ_{yz2} are the faces sheet longitudinal, the faces sheet transverse, the faces sheet shear, core longitudinal, core transverse and core shear strains, respectively. To obtain the equations of motion by the Hamilton's principle, the strain and kinetic energy of sandwich layers are required. By ignoring the transverse normal stress, and also by using the constitutive relation for upper and lower composite face sheets, the strain energy of each layer can be written as equation (5) [6]. $\bar{Q}_{ij})_i$, are reduced stiffness constants of the sandwich.

$$\begin{Bmatrix} \varepsilon_{x2} \\ \varepsilon_{y2} \\ \varepsilon_{z2} \\ \gamma_{xy2} \\ \gamma_{xz2} \\ \gamma_{yz2} \end{Bmatrix} = \begin{Bmatrix} 0 \\ 0 \\ \dfrac{w_1 - w_3}{h_c} \\ 0 \\ \dfrac{u_1 - u_3}{h_c} + \dfrac{1}{2}(\psi_{x1} + \psi_{x3}) + \dfrac{h_c^3}{6h^2}(\varphi_{x3} - \varphi_{x1}) + \dfrac{w_{1,x} + w_{3,x}}{2} + \dfrac{w_{1,x} - w_{3,x}}{h_c} z \\ \dfrac{v_1 - v_3}{h_c} + \dfrac{1}{2}(\psi_{y1} + \psi_{y3}) + \dfrac{h_c^3}{6h^2}(\varphi_{y3} - \varphi_{y1}) + \dfrac{w_{1,y} + w_{3,y}}{2} + \dfrac{w_{1,y} - w_{3,y}}{h_c} z \end{Bmatrix} \tag{4}$$

$$V_i = \frac{1}{2} \int_{\frac{h_c}{2}}^{\frac{h_c}{2} \pm h_s} \int_0^b \int_0^a \Big\{ \bar{Q}_{11})_i (\varepsilon_{xi})^2 + \bar{Q}_{12})_i \varepsilon_{yi} \varepsilon_{xi} + \bar{Q}_{12})_i \varepsilon_{yi} \varepsilon_{xi} + \bar{Q}_{16})_i \varepsilon_{xi} \gamma_{xyi} + \bar{Q}_{16})_i \varepsilon_{xi} \gamma_{xyi} + \bar{Q}_{22})_i (\varepsilon_{yi})^2 + \bar{Q}_{26})_i \varepsilon_{yi} \gamma_{xyi} + \bar{Q}_{26})_i \varepsilon_{yi} \gamma_{xyi} + \bar{Q}_{66})_i (\gamma_{xyi})^2 \Big\} dx dy dz \quad i = 1,3 \tag{5}$$

The strain energy for each of face sheets is divided in two parts. The strain energy due to bending and the strain energy due to shear, which may be written as:

$$V_i = V_{bi} + V_{si} \qquad i = 1,3 \tag{6}$$

By substituting Eq. (3) for strain-displacement relation, Eq. (5) will lead to a large equation for each face sheets. By assuming the core as an orthotropic material without an angle, and by substituting the stress-strain relation in the strain energy equation, the result can be simplified as:

$$V_2 = \frac{1}{2} \int_{-\frac{h_c}{2}}^{\frac{h_c}{2}} \int_0^a \int_0^b \Big\{ \bar{Q}_{33} (\varepsilon_{z2})^2 + \bar{Q}_{55} (\gamma_{xz2})^2 + \bar{Q}_{44} (\gamma_{yz2})^2 \Big\} dx dy dz \tag{7}$$

in which $\bar{Q}_{ii}$ $i = 3,4,5$ will be introduced as:

$$\bar{Q}_{33} = Q_{33} = \frac{E_c^*}{1 - v_c^2} \quad , \quad \bar{Q}_{44} = Q_{44} = G_{cyz}^* \quad , \quad \bar{Q}_{55} = Q_{55} = G_{cxz}^* \tag{8}$$

E_c^* is the complex young modulus of elasticity, υ_c is the poisons ratio of the core and G_{cyz}^* and G_{cxz}^* are the complex shear modulus of elasticity. By using Eq. (4) for strain-displacement relation, Eq. (8) will lead to the core formulation of strain energy. By substituting displacement of layers into the kinetic energy of the plate [1], kinetic energy of plate is obtained as equation (9). By using the Hamilton's principle and Eqs. (5), (7) and (9), the equations of the motion can be obtained:

$$T = \frac{1}{2} \int \begin{Bmatrix} \rho_1 [\left(\dot{u}_{01} + z\dot{\psi}_{x1} - \frac{4z^3}{3h^2} \dot{\varphi}_{x1} \right)^2 + \left(\dot{v}_{01} + z\dot{\psi}_{y1} - \frac{4z^3}{3h^2} \dot{\varphi}_{y1} \right)^2 + (\dot{w}_{01})^2] \\ + \rho_2 [\left(\frac{\dot{u}_1 + \dot{u}_2}{2} + \frac{h_c}{4}(\dot{\psi}_{x1} - \dot{\psi}_{x3}) - \frac{h_c^3}{12h^2}(\dot{\varphi}_{x1} + \dot{\varphi}_{x3}) + \left\{ \frac{\dot{u}_1 - \dot{u}_3}{h_c} + \frac{1}{2}(\dot{\psi}_{x1} + \dot{\psi}_{x3}) + \frac{h_c^3}{6h^2}(\dot{\varphi}_{x3} - \dot{\varphi}_{x1}) \right\} z \right)^2 \\ \left(\frac{\dot{v}_1 + \dot{v}_2}{2} + \frac{h_c}{4}(\dot{\psi}_{y1} - \dot{\psi}_{y3}) - \frac{h_c^3}{12h^2}(\dot{\varphi}_{y1} + \dot{\varphi}_{y3}) + \left\{ \frac{\dot{v}_1 - \dot{v}_3}{h_c} + \frac{1}{2}(\dot{\psi}_{y1} + \dot{\psi}_{y3}) + \frac{h_c^3}{6h^2}(\dot{\varphi}_{y3} - \dot{\varphi}_{y1}) \right\} z \right)^2] \\ + \left(\frac{\dot{w}_1 - \dot{w}_3}{h_c} z + \frac{\dot{w}_1 + \dot{w}_3}{2} \right)^2 \\ + \rho_3 [\left(\dot{u}_{03} + z\dot{\psi}_{x3} - \frac{4z^3}{3h^2} \dot{\varphi}_{x3} \right)^2 + \left(\dot{v}_{03} + z\dot{\psi}_{y3} - \frac{4z^3}{3h^2} \dot{\varphi}_{y3} \right)^2 + (\dot{w}_{03})^2] \end{Bmatrix} dx dy dz \tag{9}$$

Finite Element Implementation.

The discretized element displacement vector consists of eight nodal displacement vectors as (10).

$$q = \{u_{i1} \quad v_{i1} \quad w_{i1} \quad \psi_{xi1} \quad \psi_{yi1} \quad \varphi_{xi1} \quad \varphi_{yi1} \quad u_{i3} \quad v_{i3} \quad \cdots \quad \varphi_{yi3} \quad u_{j1} \quad v_{j1} \quad \cdots \quad u_{j3} \ldots \quad u_{k1} \quad v_{k1} \quad \ldots \quad u_{k3} \quad v_{k3} \quad \ldots \quad u_{m1} \quad v_{m1} \quad \cdots \quad u_{m3} \quad \cdots\} \tag{10}$$

In equation (10) *i, j, k, m* represent the node number and 1 and 3 represent the upper and lower layers. A rectangular element with 56 degree of freedom has been used. By introducing 7 degrees of freedom for each node of rectangular element and because there are two node on each corner of the element for upper and lower layers, in each corner of the rectangular element, can be supposed to have 14 degrees of freedom. By using linear shape functions which is introduced in serendipity coordinate, the stiffness and mass matrices of the sandwich plate element will be obtained. By substituting the element displacements into the strain energy of different layers, the strain energy in terms of the nodal displacements will be derived as:

$$V_e = \frac{1}{2}\{q^e\}^T[K^e]\{q^e\} \tag{11}$$

By substituting the derivatives of the plate global parameters, which are defined as the shape functions and by using Eqs. (11), (5) and (7) the stiffness matrices may be obtained for the upper and lower face sheet and core layer, respectively. The stiffness matrix for one element is obtained by summation of the stiffness matrices of three layers as:

$$[K_e] = [K_1] + [K_2] + [K_3] \tag{12}$$

in which $[K_e]$,$[K_1]$,$[K_3]$ and $[K_2]$ are the stiffness matrices for the element, the upper and lower face sheets and core layer, respectively. It is necessary to mention that the stiffness matrices for upper and lower layers are consisting of two parts, the bending stiffness and the shearing stiffness. By substituting the element displacement into the kinetic energy of different layers, the kinetic energy in terms of the nodal displacements will be derived:

$$T_e = \frac{1}{2}\{\dot{q}^e\}^T[M^e]\{\dot{q}^e\} \tag{13}$$

Using Eqs. (9), (11), and (13), the mass matrix for one element will be obtained. By assembling stiffness and mass matrices of elements, the stiffness and mass matrices of structure are obtained. Then, based on the assembled matrices and the vector of the nodal degrees of freedom ({q}), the potential and kinetic energies of the sandwich structures can be obtained using Eqs. (11) and (13), respectively. By employing Lagrange equation, the general equation of motion of the composite sandwich structures with viscoelastic core is obtained:

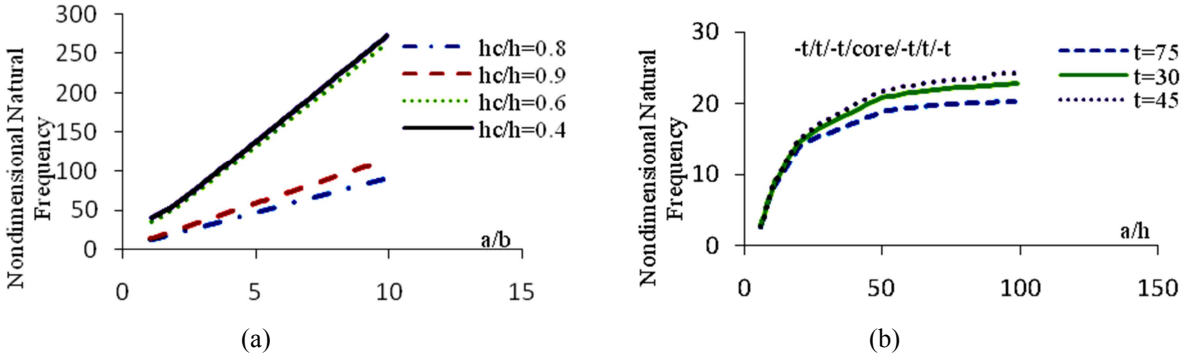
$$[M]\{\ddot{q}\} + [K]\{q\} = \{0\} \tag{14}$$

in which [K] and [M] are the stiffness and mass matrices, respectively.

Simulation and Results

The eigen-frequencies of the system are calculated from the stiffness and mass matrices ([K] and [M] in Eq. (14)). Since the core Young modulus and shear modulus are the complex value, these eigenvalues are complex. So, natural frequencies of the composite sandwich plate with viscoelastic core are presented in some cases.

Case 1- Effect of length to width ratio of the plates. Boundary conditions assumed to be *SSSS* for all edges, core has the properties of plate in [1] and, the ratio of core thickness to overall plate thickness is 0.88. Fig.1.a. shows that whenever core has the lower thickness value, non-dimensional natural frequency is higher. On the other hand, if the value of length to width ratio increases, natural frequency will show an increasing behavior.



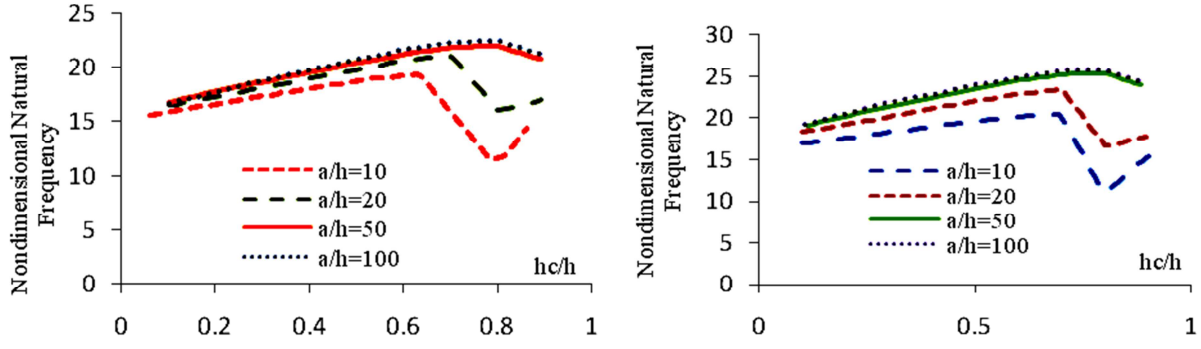
(a) (b)

Fig. 1 Non-dimensional natural frequencies. of composite sandwich plate with viscoelastic core, effects of (a) length to width ratio (b) fiber angle

Case 2- Effect of fiber angles of the face sheets. Boundary conditions assumed to be *SSSS* on all edges, core and the face sheets have the properties of plate in [1] and, the ratio of core thickness to plate thickness is 0.88. the hand-layup will assume to be $-\theta/\theta/-\theta/core/-\theta/\theta/-\theta$. Fig.1.b. shows that whenever the fiber angles reach to the value of $\theta = 45$, non-dimensional natural frequency will reach the maximum value, it is due to the maximum stiffness of face sheets in this angle. Again, by increasing the value of length to width ratio, non-dimensional natural frequency shows an increasing behavior, also by increasing the value of a/h this condition will happen.

Case 3-Layup configuration effect of the composite face sheets. Boundary conditions assumed to be *SSSS* for all edges, the layup configurations is assumed to be cross-ply and angle-ply with both soft and hard cores. The geometrical and mechanical properties of the core and the face sheets are represented in [1].

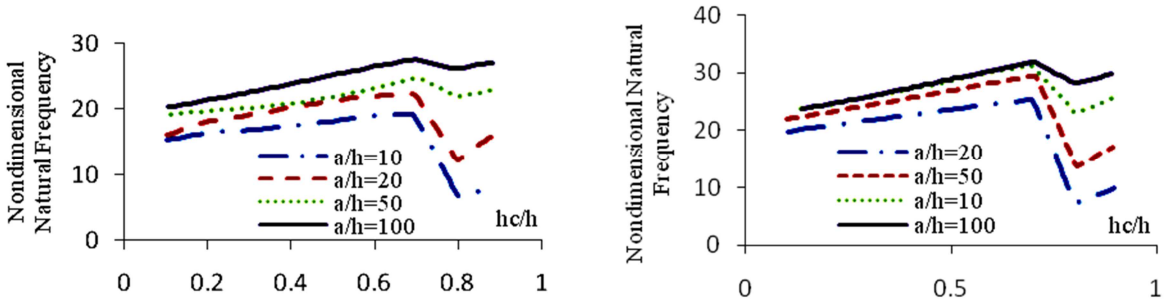
a.Layup configuration effect of face sheets in composite plates with hard core. In this case, core and overall plate thicknesses will be changed. Fig. 2.a. indicates that thicker plates have the higher value of non-dimensional natural frequencies. It reaches its maximum value in the ratio of core thickness to overall plate thickness equal to 0.8. On the other hand, in thin plates, by increasing the value of core thickness, non-dimensional natural frequency will increase. Fig. 2.b. shows that angle-ply face sheets have the higher value of natural frequencies in comparison to the case that the face sheets are cross-ply.



(a) (b)

Fig. 2 Non-dimensional natural frequencies. of composite sandwich plate with viscoelastic core, effects of (a) face sheets with cross-ply configuration (b) face sheets with angle-ply configuration.

b.Layup configuration effect of face sheets in composite plates with soft core. Fig.3 indicates that by increasing the core thickness value of thin plates, non-dimensional natural frequencies will increase but in thick plates in high value of the core thickness, the former results have a decreasing behavior. In this case, results from angle-ply configuration for soft core has the same behavior as the cross-ply with hard core, but the non-dimensional natural frequencies for this case in comparison to cross-ply configuration has increased.



(a) (b)

Fig. 3 Non-dimensional natural frequencies. of composite sandwich plate with viscoelastic core, effects of (a) face sheets with cross-ply configuration (b) face sheets with angle-ply configuration.

Summary

The present study follows a higher order theory of 'Reddy' for composite sandwich plate with viscoelastic core in two cases of thin and thick plate. By supposing the face sheets as a composite material, and by changing some parameter like angle of fibers and the type of layup configuration, the natural frequencies can be increased or decreased as the requested and favorable results. By comparing a sandwich plate with a viscoelastic core to the plate with an isotropic core, it is obvious that by choosing the viscoelastic core, natural frequency will be decreased. By increasing the thickness of the core and keeping, the overall thickness of plate as a constant parameter and by decreasing the thickness of face sheets and keeping the overall plate thickness as a constant parameter, in special case of h_c/h plate can have less values of natural frequencies. By increasing the fibers angle of the face sheets, plate can have further lower values of natural frequencies.

References

[1] A.K. Nayak, S.S.J. Moy and R.A. Shenoi: Composites, Part B, Vol. 33, (2002), p. 505.

[2] M. Meunier, RA. Shenoia and Proc ImechE, Part C: J Mech Engng Sci, 213(7), (1999), p. 715.

[3] HJ. Wang and LW. Chen: Composite Structure, Vol. 58, (2002), p. 563.

[4] V. Pradeep and N. Ganesan: Composite Structure, Vol. 81, (2007), p. 600.

[5] SH. Zhang and HL. Chen: Composite Structures, Vol. 74, (2006), p. 63.

[6] H. Arvin, M. Sadighi and A.R. Ohadi: Composite structures, Vol. 92, (2010), p. 996.

© (2011) Trans Tech Publications, Switzerland
doi:10.4028/www.scientific.net/KEM.471-472.664

Mathematical Model for Axial Crushing of Hybrid Square Tubes

H.Akbarshahi[a], M.Sadighi[b], M.Shakeri[c] and M.Mirzaei[d]

Department of Mechanical Engineering,

Amirkabir University of Technology, Tehran, Iran

[a]hossein.a2198@aut.ac.ir, [b]mojtaba@aut.ac.ir, [c]shakeri@aut.ac.ir, [d]m_mirzaei@aut.ac.ir,

Keywords: mathematical model, crushing force, hybrid square tubes, energy absorption

Abstract. In this paper, to investigate energy absorption capability of hybrid (metal-composite) square tubes under axial loading, a new theory is proposed based on collapse mode of metal square tubes and considering off-axis strength of each layer of composite. An expression is derived for mean crushing load and folding wave length in terms of mechanical properties and geometrical dimensions of metal tube and composite prepregs wrapped around it. To validate the theoretical model, predicted values for mean crushing load are compared with experimental and numerical results that show reasonably good agreement.

Introduction

In the last decades, advances in technology have caused raising the speed of vehicles. So engineers have paid extra attentions to the problem of security of passengers and tried to build safer vehicles [1]. Whereas most parts of a vehicle's body are made of thin-walled structures, much amount of impact energy in an accident is sustained by these structures. So, there are many studies on the field of characterization of energy absorption capability of these structures especially circular and square tubes under axial, transverse and combined impact loads. Wierzbicki and Abramowicz [2] studied axial collapse of metal square tubes theoretically and presented a simple model to predict mean crushing load. Later, they developed previous model, considering extensional mode, and presented expressions for various multi-corner prismatic columns such as square and hexagonal tubes [3]. Meng et al. [4] used elastic buckling analysis of a simply supported plate and proposed a model to predict maximum collapse load of square tubes and applied plastic analysis after collapse. Hybrid tubes (Metal-composite tubes) are new shapes of tubular structures that because of their good absorbed energy/weight ratio are of interest in many applications. Although most of the studies on axial collapse of hybrid tubes are limited to the experimental and numerical ones, a few theoretical works have been presented too. Hanefi and Wierzbicki [5], Wang and Lu [6] reported simple models for circular hybrid tubes based on Alexander's model. They used equivalent yield strength for metal-composite section [7]. Shin et al. [8] analyzed axial and transverse collapse of square hybrid tubes theoretically and compared with experimental results. Bambach and Elchalakani [9] investigated square steel tubes reinforced by CFRP layers and predicted their behavior through collapse phenomenon.

It is noted that previous theory models can't predict the behavior of a tube wrapped with composite layers of different angles of orientation and consider layers of just one angle. On the other hand, the effects of number of layers and their stacking sequence are not observed.

El. Hage et al. [10], using numerical simulations, compared hybrid square tubes collapse with different tube wall thickness, number of layers and angles of orientation under quasi-static axial loading and suggested empirical equations for square tubes reinforced by two and four composite layers. Also, the effects of triggers, coefficient of friction and adhesion between the aluminum tube and composite layers were examined numerically and compared with experimental results [11].

In this paper, considering collapse mode of metal square tubes for hybrid tubes, and using Tsai-Hill criterion for calculating the off-axis strength of an orthotropic lamina a new model is extended and an expression is derived for mean crushing load and folding wave length of hybrid square tubes in terms of mechanical properties and geometrical dimensions of metal and composite materials

such as width and thickness of tube, number of composite layers and fiber orientation of each layer. To validate the presented model, results are compared with experimental and numerical values that show good agreement.

Analytical Model. Collapse mode of hybrid square tubes is assumed based on Wierzbicki's collapse model of bare metal square tubes [2], Fig. 1.

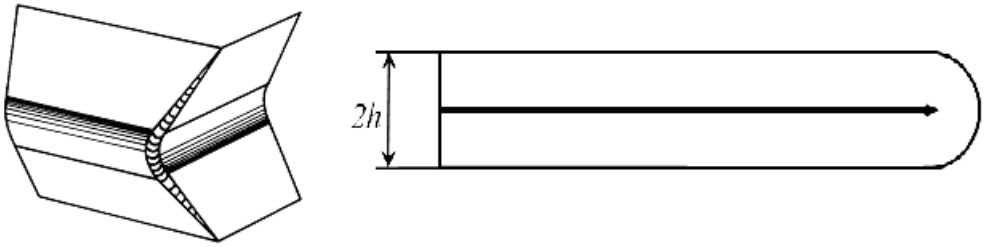


Fig. 1. Schematic crushing model of square tubes [2].

In this model, dissipated energies through a fold are as follows, respectively:

Dissipated energy in toroidal surfaces, dissipated energy in plastic hinges of the cylindrical surfaces and dissipated energy in plastic hinges of the conical sections:

$$E_1 = 16HbN_0I_1(\Psi_0) \tag{1}$$

$$E_2 = 8\pi M_0 c \tag{2}$$

$$E_3 = 16M_0\frac{H^2}{b}I_3(\Psi_0) \tag{3}$$

Where, M_0 and N_0 are fully plastic bending moment and membrane force respectively. H, b, c and t are half of folding wave length, small radius of toroidal shell, width and thickness of tube wall respectively. σ_0 is flow stress that is assumed as the average of yield and ultimate strength of tube material. In square tubes $\Psi_0 = \frac{\pi}{4}$ and I_1=0.5778, I_3=1.1478. External work and mean crushing load are:

$$W_{ext} = P_m \times 2H \tag{4}$$

$$P_m = \frac{4}{H}(2HbN_0I_1 + \pi M_0 c + 2M_0\frac{H^2}{b}I_3) \tag{5}$$

To investigate the effects of wrapping composite layers around metal square tubes in absorbing energy, presented method in [7] is used. In the present work, each composite layer is studied as a separate layer wrapped around the tube with angle θ_i to the axis of tube. Strength of each composite layer is calculated by Tsai-Hill criterion. According to this criterion, tensile and compressive off-axis strength of an orthotropic lamina is:

$$\sigma_{\theta\,\mathrm{T,C}} = \left[\frac{\cos^4\theta}{X_{T,C}^2} + \left(\frac{1}{S^2} - \frac{1}{X_{T,C}^2}\right)\sin^2\theta\cos^2\theta + \frac{\sin^4\theta}{Y_{T,C}^2}\right]^{\frac{-1}{2}} \tag{6}$$

Where X_T and X_C are respectively tensile and compressive strength in the fiber direction, Y_T and Y_C are tensile and compressive strength perpendicular to the fiber direction and S is inplane shear strength. Indices T and C correspond to tensile and compressive off-axis strengths respectively.

Calculating strength of each composite layer in the direction of tube axis, equivalent strength of hybrid square tube is derived.

Equivalent Strength of Hybrid Section. Fig. 2 shows a hybrid section of metal and composite layers with thickness of t_m and t_c respectively. Each composite unidirectional layer has an angle of θ_i $(1 \le i \le N)$ to the axis of tube and strength of σ_i in the direction of tube axis, that is computed using Eq. 6. Position of plastic neutral axis (x), is obtained from:

$$\sigma_{ym}(t_h - x) = \sigma_{ym}(x - t_c) + \sum_{i=1}^{N} \sigma_i t_i \tag{7}$$

$$x = \frac{t_h + t_c}{2} - \frac{1}{2\sigma_{ym}} \sum_{i=1}^{N} \sigma_i t_i \tag{8}$$

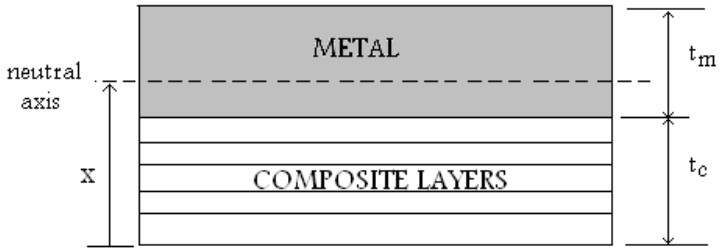


Fig 2. Section of hybrid square tube

Where t_i is thickness of ith composite layer and $t_c = \sum_{i=1}^{N} t_i$. x is measured form the end of composite layers and σ_{ym} is flow stress of metal material of the tube. Assuming that neutral axis is located in metal section, i.e. $x > t_c$, plastic bending moment is:

$$M_p = \sigma_{ym}(t_h - x)\frac{(t_h - x)}{2} + \sigma_{ym}(x - t_c)\frac{(x - t_c)}{2} + \sum_{i=1}^{N} \sigma_{iC} t_i r_i \tag{9}$$

Where, r_i is the distance of center of ith composite layer to the neutral axis:

$$r_i = x - t_c + \sum_{j=1}^{i-1} t_j \tag{10}$$

Substituting Eq. 8 and Eq. 10 in Eq. 9:

$$M_p = \frac{\sigma_{ym}}{2}\left\{2(\frac{t_m}{2})^2 + 2(\frac{1}{2\sigma_{ym}}\sum_{i=1}^{N}\sigma_{iC}t_i)^2\right\} + \sum_{i=1}^{N}\left[\sigma_{iC}t_i(\frac{t_m}{2} - \frac{1}{2\sigma_{ym}}\sum_{k=1}^{N}\sigma_{kC}t_k + \frac{t_i}{2} + \sum_{j=1}^{i-1}t_j)\right] \tag{11}$$

Assuming constant thickness for all composite layers and defining dimensionless ratios $t_r = \frac{t_c}{t_m}$ and $k_i = \frac{\sigma_{iC}}{\sigma_{ym}}$, we have:

$$M_p = \frac{\sigma_{ym} t_m^2}{4}\left\{1 + (\frac{t_r}{N}\sum_{i=1}^{N}k_i)^2 + \frac{t_r}{N}\sum_{i=1}^{N}\left[k_i(2 - 2\frac{t_r}{N}\sum_{j=1}^{n}k_j + \frac{4(i-\frac{1}{2})}{N}t_r)\right]\right\} \tag{12}$$

Then, for the equivalent strength of hybrid section:

$$M_p = \frac{\sigma_{eq} t_h^2}{4} \tag{13}$$

$$\sigma_{eq} = \frac{\sigma_{ym}}{(1+t_r^2)}\left\{1+(\frac{t_r}{N}\sum_{i=1}^{N}k_i)^2+\frac{t_r}{N}\sum_{i=1}^{N}\left[k_i(2-2\frac{t_r}{N}\sum_{j=1}^{n}k_j+\frac{4(i-\frac{1}{2})}{N}t_r)\right]\right\} \quad (14)$$

Which for particular case N=1, derived expression for σ_{eq} is same as [7]:

$$\sigma_{eq} = \frac{1+2kt_r+2kt_r^2-k^2t_r^2}{(1+t_r)^2}\sigma_{ym} \quad (15)$$

For fully plastic membrane force (N_0) supposed expression in [5] is used as follow:

$$N_0 = \sigma_{ym}t_m + \frac{1}{2}\sum_{i=1}^{N}\sigma_{iT}^{\phi}t_i \quad (16)$$

Where, σ_{iT}^{ϕ} denotes tensile strength of ith composite layer in hoop direction. It should be noted that because in collapse mode of square tubes, Fig. 2, adjacent sides behave opposite (i.e. when a side bends inward the other one bends outward and vice versa) and also because composite materials, dislike isotropic materials (e.g. metals), behave differently in tension and compression, so x and M_p should be calculated in both inward and outward cases and then average value of them considered as final value.

As mentioned above, derived expressions for x and M_p are based on the assumption that, neutral axis is located in metal section, if not it should be noticed that strength of composite layers is used correctly, i.e. in this situation some composite layers are in compression and the others in tension.

Mean Crushing Load

To obtain an equation for mean crushing load of hybrid square tube, we use expressions derived in previous section for M_p and N_p. Substituting these expressions in Eq. 6 as M_0 and N_0, leads to:

$$P_m = 8bN_pI_1 + 4\pi M_p\frac{c}{H} + 8M_p\frac{H}{b}I_3 \quad (17)$$

In the above equation, H and b are yet unknown. To obtain them we have:

$$\frac{\partial P_m}{\partial H} = 0 \ , \ \frac{\partial P_m}{\partial b} = 0 \quad (18)$$

Solving two above equations:

$$H = 1.55\sqrt[3]{\frac{M_pc^2}{N_p}} \ , \ b = 1.75\sqrt[3]{\frac{M_p^2c}{N_p^2}} \quad (19)$$

Then, substituting Eq. 19 in Eq. 17:

$$P_m = 24.33\sqrt[3]{M_p^2N_pc} \quad (20)$$

As it can be seen, having M_p and N_p, mean crushing load of a hybrid square tube is determined.

Comparison with Experimental and Numerical Results. In this section, to verify the presented model, predicted values for mean crushing load are compared with experimental and numerical results in [11], [10]. In these studies square aluminum tubes with thicknesses of 1.4, 1.6, 1.8 and 2 mm are wrapped with 2 and 4 layers of angle $\pm\theta$ designated as $1L\theta SHt_a$ and $2L\theta SHt_a$ respectively. θ shows angle of wrapped layers and t_a shows aluminum wall thickness. Table 1 compares predicted values by present model with experimental results [11] and Table 2 and Table 3 compare with numerical results [10].

Table 1. Experimental results versus theoretical results

Model	Experimental results [11] (KN)	present model (KN)	Error (%)
1L45SH1.6	16.85	20.04	17.61
2L45SH1.6	23.89	26.80	14.82

Table 2. Numerical results versus theoretical results – Two composite layers

Model	Numerical results [10] (KN)	present model (KN)	Error (%)
1L90SH1.8	24.37	28.68	17.69
1L75SH1.8	23.71	23.94	0.97
1L60SH1.8	21.86	22.59	3.34
1L45SH1.8	20.36	22.91	12.52
1L30SH1.8	20.07	25.03	24.71
1L90SH2	27.51	32.01	16.36
1L75SH2	27.05	27.00	-0.18
1L60SH2	26.11	25.59	-1.99
1L45SH2	23.98	25.94	8.17
1L30SH2	23.81	28.21	18.48

Table 3. Numerical results versus theoretical results – Four composite layers

Model	Numerical results [10] (KN)	present model (KN)	Error (%)
2L90SH1.4	23.17	29.90	29.05
2L75SH1.4	23.15	25.80	11.45
2L60SH1.4	21.95	23.53	7.20
2L45SH1.4	20.25	23.84	17.73
2L30SH1.4	20.94	24.85	18.67
2L90SH1.6	26.40	36.40	37.88
2L75SH1.6	26.03	28.78	10.56
2L60SH1.6	25.08	26.42	5.34
2L45SH1.6	23.34	26.80	14.82
2L30SH1.6	25.18	29.84	18.51
2L90SH1.8	30.50	39.90	30.82
2L75SH1.8	29.68	31.91	7.51
2L60SH1.8	28.30	29.48	4.17
2L45SH1.8	26.71	29.90	11.94
2L30SH1.8	28.00	33.21	18.61
2L90SH2	36.31	43.65	20.21
2L75SH2	34.75	35.20	1.29
2L60SH2	35.20	32.68	-7.16
2L45SH2	31.75	33.16	4.44
2L30SH2	33.11	36.71	10.87

Summary

A theory is presented to predict mean crushing load of hybrid square tubes based on Wierzbicki's model of collapse of metal square tubes [2]. Each composite layer is considered as a separate layer and it's strengths in the direction of tube axis and hoop directions are calculated using Tsai-Hill criterion. Obtaining equivalent strength of hybrid section of metal and composite layers using presented method in [7], an equation is derived for mean crushing load of hybrid square tubes. To validate the model, predicted values are compared with experimental and numerical results in literature that show reasonably good agreement. This model has an important advantage over previous models that predicts mean crushing load of a square tube reinforced by composite layers with different angles of orientation, also the effect of number of composite layers is observed.

References

[1] N. Aya and K. Takahashi, Energy Absorption Characteristics of Vehicle Body Structure, Transactions of the Society of Automotive Engineers of Japan, (1974), No. 7, May.

[2] T. Wierzbicki and W. Abramowicz: Asme Journal Of Applied Mechanics, (1983b), Vol. 50, pp. 727-739.

[3] W. Abramowicz and T. Wierzbicki: Journal of Applied Mechanics, (1989); 56:113–20.

[4] Q. Meng, S. T. S. AI-Hassani and P. D. Soden: Int. J. Mech. Sci., Special issue for Structural Crashworthiness Conf., (1983), Vol. 25: 747-773.

[5] E.H. Hanefi and T. Wierzbicki: Composites Part B (1996); 27B:387–94.

[6] X.A. Wang and G. Lu: Proc Inst Mech Eng 2002; 216:863–73.

[7] A.G. Mamalis, D.E. Manolakas, G.A: Int J Impact Eng 1991; 11(2):185–96.

[8] K.C. Shin, J.J. Lee, K.H. Kim, M.C. Song and J.S. Huh: Composite Struc (2002) ; 57:279–287.

[9] M.R. Bambach and M. Elchalakani: Thin Wall Struct (2007);45(2):159–70.

[10] H. El-Hage, P.K. Mallick and N. Zamani: Composite Structures (2006); 73:505–514.

[11] H. El-Hage, P.K. Mallick and N. Zamani: International Journal of Crashworthiness (2004) ;9: 6, 653 - 664.

[12] J.M. Babbage and P.K. Mallick. Axial crush resistance of aluminium composite hybrid tubes, Proceedings of 17th Annual Technical Conference of the American Society for Composites, Paper No. 070, 2002.

[13] J.M. Babbage, P.K. Mallick. Static axial crush performance of unfilled and foam-filled aluminum-composite hybrid tubes Composite Structures (2005); 70:177–184.

© (2011) Trans Tech Publications, Switzerland
doi:10.4028/www.scientific.net/KEM.471-472.670

Sintering of Fe-TiC Composite Prepared by Carbothermal Reduction of Hematite and Anatase

Mohd Salihin Hassin [1,a], Samayamutthirian Palaniandy[2,b] and Zuhailawati Hussain [3,c]

[1,2,3]School of Materials and Mineral Resources Engineering,

Engineering Campus, Universiti Sains Malaysia,

14300 Nibong Tebal, Penang, Malaysia

[a]salihin212@gmail.com, [b]samaya@eng.usm.my, [c]zuhaila@eng.usm.my

Keywords: Hematite; Fe-TiC composite; Carbothermal reduction; Sintering temperature

Abstract. In this study, the formation of Fe-TiC composite through carbothermal reduction of hematite and anatase was investigated with various sintering temperature. Mixture of hematite and anatase powders was milled with graphite for 20 hours in a high energy ball mill in argon atmosphere with composition of Fe-30%volTiC. The as-milled powder was analyzed with X-ray diffraction analysis and the result shows broadening of hematite peaks with disappearance of anatase and graphite peaks due to refinement of powder and diffusion of carbon. The as-milled powder was cold pressed under 200 MPa and sintered in argon atmosphere at various sintering temperature i.e, 1200°C, 1300°C and 1400°C. Higher sintering temperature facilitated reduction of hematite and anatase to produce Fe-TiC composite.

Introduction

Development of iron based composite considerably attracts many interests due interest due to an outstanding properties for wear resistance in chemical and process industries application [1,2]. Iron based composite commonly reinforced by ceramic materials such as Al_2O_3, ZrO_2, TiN_2, Si_3N_4 and TiC [1]. Among ceramics reinforcement, TiC has proved its suitability in Fe. TiC is extensively used in iron matrix because its extremely good properties such as good wettability, high hardness, low density and thermal stability since it is useful for manufacturing of cutting tool, grinding wheels and steel-coated press tools [1,3,4].

There are several routes for fabrication of iron based composites such as powder metallurgy, conventional melting and casting and carbothermal reduction route [1]. The carbothermal reduction of iron oxides by reductant materials performed by mechanical activation improved the rate of reduction because energy during mechanical milling provides a driving force for reaction to take place [5,6]. The energy transferred to activated powder during milling influences kinetic of chemical reactions between powder due to an increase in crystal defect such as dislocation density and structural distortion which are associated with the formation of amorphous structure [5]. For example, synthesis of Fe-TiC by reduction of ilminite (FeTiO3) with graphite successfully occurred at 1250°C after 50 h milling [6]. Without milling, phase of Fe and TiC cannot be observed by XRD analysis after 1250°C of heat treatment temperature [6]. Meanwhile, TiC is commercially produced by reduction of TiO_2 by carbon in a temperature range between 1700°C and 2100°C [7].

Besides the reduction of ilmenite (FeTiO3), the possible carbothermal reduction of hematite and anatase with graphite result in formation of Fe-TiC composite should occurs as summarized in Eq. 1:

$$Fe_2O_3 + TiO_2 + 6C \rightarrow 2Fe + TiC + 5\,CO \quad (1)$$

Thus, the aim of this study is to investigate the suitable heat treatment temperature of formation iron based composite reinforced titanium carbide by using iron oxide (Fe_2O_3), titanium dioxide (TiO_2) and graphite. The temperatures selected are in the range for solid state sintering.

Experimental Procedure

A mixture of hematite (Fe_2O_3), anatase (TiO_2) and graphite were mechanically milled together in argon atmosphere by using a high-energy Fritsch Pulverisette P-5 planetary mill for 20 hours milling time. The milling speed was set at 400 rpm. The weight ratio of ball to powder was 10:1. The activated milled powder which corresponds to Fe-30%TiC was analyzed with X-ray diffraction (XRD) analysis in order to identify phase presence in the as-milled powder. The milled powder was consolidated under 200 MPa of pressure by using cold pressing machine. The pellets was heat treated in tube furnace with argon flow in various temperature i.e 1200°C, 1300°C and 1400°C at heating rate of 10°C/min for 1 hour of soaking time and cooled in furnace to room temperature. X-Ray diffraction (XRD) analysis was done on the sintered pellets to investigate the formation of TiC in iron matrix after carbothermal reduction of oxide metals at high temperature.

Results and Discussion

Fig. 1 presents the XRD pattern of the as-milled powder after 20 hours milling time. The phase detected by XRD in the sample is only hematite (Fe_2O_3). The disappearance of TiO_2 and C phases in the as-milled powder most probably because of the formation of amorphous structure during mechanical milling since the powder particle undergo repeated flattening, cold welding and fracturing [8]. The absent peaks of C and TiO_2 also indicate that these phases are easily deformed and changed into an amorphous structure compared with the harder Fe_2O_3 phase after milling [4]. The mixture cannot be reduced to form Fe and TiC phases after milling because Fe_2O_3 and TiO_2 are very stable phases and formation of Fe-TiC composite needs a larger amount of energy that cannot be provided by milling process.

X-ray diffraction of sintered pellet of difference heat treatment temperature is shown in Fig. 2. The presence of Fe and TiC indicate the successful of carbothermal reduction of Fe_2O_3 and TiO_2 after sintering. The intensity of iron and titanium carbide peaks increased with increasing sintering temperature. At 1200°C of heat treatment, the intensity of Fe and TiC peaks is low compared with higher temperature. This situation occurred because of a significant effect in enhancement of reduction rate with increasing temperature. Increasing the carbothermal reduction temperature to 1400°C significantly enhanced the formation of TiC phases. Stronger intensity of Fe and TiC peaks are obviously seen after sintering at 1400°C.

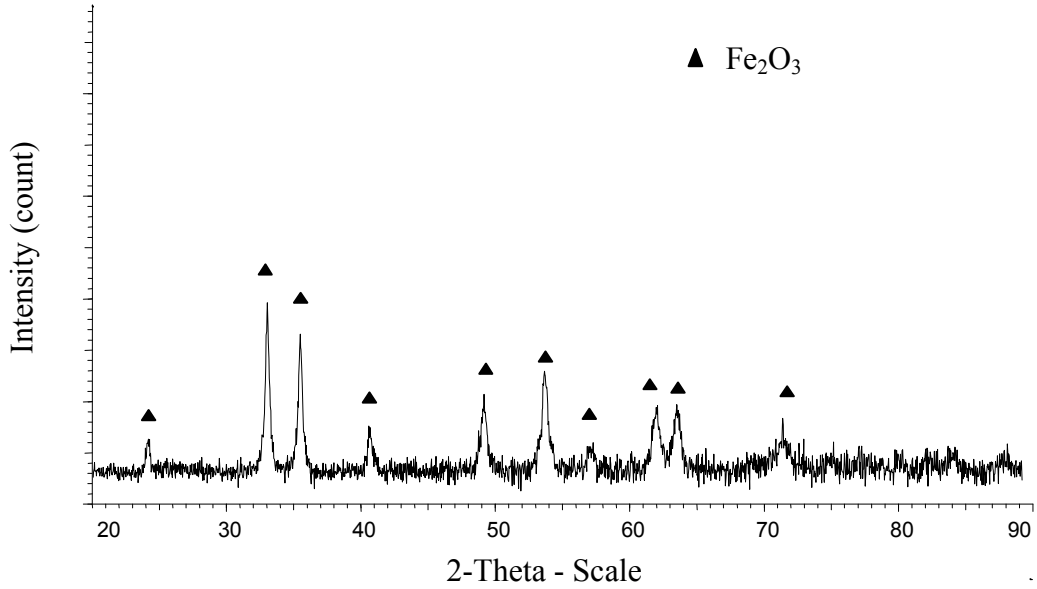


Fig. 1: XRD pattern of Fe_2O_3-TiO_2-C as-milled powder after 20 h milling

Mechanical milling of mixture plays the major effect of carbothermal reduction at lower temperature. The statement is well agree with Razavi and Rahimipour [6], who observed after 50 hours of mechanical milling, $FeTiO_3$ has been reduced by C to form Fe-TiC after sintering at 1250 °C compared with non-milled sintered pellet whereby the Fe-TiC was not observed at the same sintering temperature. Besides, mechanical milling also plays a function as a medium to overcome the solid-state diffusion limitation of the mixture by increasing the crystalline defect such as dislocation, small particle size, formation of amorphous phase and atom displacement which reduce the heat treatment temperature to form Fe-TiC composite [4,5].

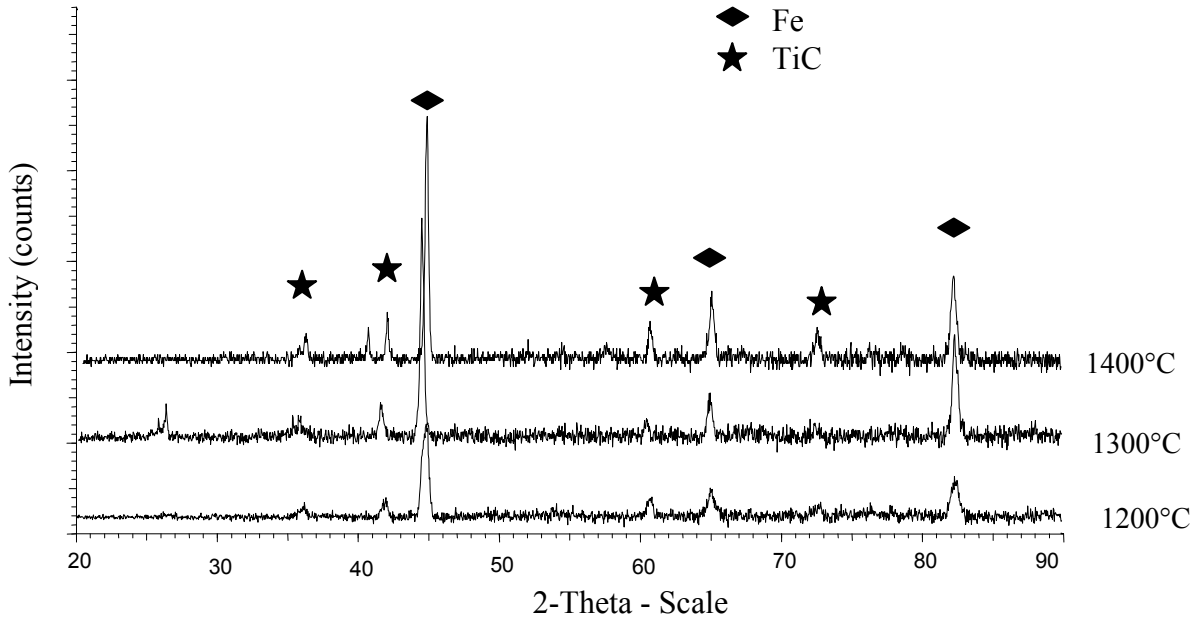


Fig. 2: XRD patterns of Fe-TiC composite formation at various heat treatment temperatures

Summary

In this study, the amorphous structure of hematite and anatase has been obtained after 20 hours of mechanical milling since TiO_2 and C phase not been. The carbothermal reduction of hematite and anatase was significantly affected by sintering temperature. The reduction rate increased with increasing sintering temperature. The formation of TiC-reinforced iron based composite of milled powder in argon flow was possible to take place at low temperature (1200°C) as shown in XRD pattern.

Acknowledgement

The authors are pleased to acknowledge the financial support for this research by Universiti Sains Malaysia (USM) Fellowship, RU-PGRS (8043042) research grant and FRGS (6071194) research grant.

References

[1] K. Das, T. Bandyopadhyay, and S. Das: J. Mater. Sci. 37, 3881 (2002).

[2] E. Pagounis, M. Talvitie, and V. K. Lindroos: Compos. Sci. Technol. 56, 1329 (1996).

[3] M. Razavi, M. R. Rahimipour, and R. Kaboli: J. Alloys Compd. 460, 694 (2008).

[4] N. Setoudeh, A. Saidi, and N. J. Welham: J. Alloys Compd. 395, 141 (2005).

[5] R. Tahmasebi, M. Shamanian, M. H. Abbasi, and M. Panjepour: J. Alloys Compd. 472, 334 (2009).

[6] M. Razavi, and M. R. Rahimipour: Ceram. Int. 35, 3529 (2009).

[7] M. Dewan, G. Zhang, and O. Ostrovski: Metall. Mater. Trans. B 40, 62 (2009).

[8] C. Suryanarayana: Prog. Mater. Sci. 46, 1 (2001).

© (2011) Trans Tech Publications, Switzerland
doi:10.4028/www.scientific.net/KEM.471-472.674

Optimizing Processing Parameters for Hybridized Kenaf/PALF Reinforced HDPE Composite

I. S. Aji [1,a], E.S. Zainudin [2,b], A. Khalina [3,c] and S. M. Sapuan [1,d]

[1] Department of Mechanical and Manufacturing Engineering, Universiti Putra Malaysia,43400 UPM Serdang, Selangor, Malaysia

[2] Laboratory of Biocomposite Technology, Institute of Tropical Forestry and Forest Products, Universiti Putra Malaysia, 43400 UPM Serdang, Selangor, Malaysia

[3] Department of Biological and Agricultural Engineering, Universiti Putra Malaysia, 43400 UPM Serdang, Selangor, Malaysia

[a]suleimanaji@yahoo.com [b]edisyam@gmail.com [c]khalina@eng.upm.edu.my [d]sapuan@eng.upm.edu.my

Keywords: Hybrid, processing, mixing, fibre, parameters, conditioned, reinforced

Abstract. This work is aimed at achieving optimum processing parameters for Kenaf/PALF/HDPE. Processing parameters like temperature, speed of rotor and duration of composite mixing in an internal mixer were examined. Oven conditioned and unconditioned specimen were prepared and tested. The best tensile strength and tensile modulus were obtained at an optimum processing parameters of 190°C, 40rpm, and 15min for temperature of processing, speed of rotor and duration of mixing respectively, while 190°C, 40rpm and 20min gave the best flexural strength and 190°C, 40rpm and 25min for flexural modulus. Conditioning of composite tends to reduce its tensile modulus while increasing its strength and flexural modulus. All samples were produced at only 10w%(mass) of fibre in the composite at 1:1 and less than 0.3mm fibre ratio and length respectively. Utilization of these parameters according to end requirement can help in achieving optimum mechanical properties on hybridized composites.

Introduction

Natural fibres have been blended with polymers in the production of composite with the aim of producing environmentally friendly products, i.e. products that are environmentally degradable; some of which are fully green in the sense that both the fibre and the polymer can fully degrade at the end of the product life [1-4], as was recently reviewed [5-9]. Availability of natural fibre, its market readiness and acceptance, market outlook and trends, product substitution, cost effectiveness and concern for the environment, are some of the general advantage enveloped in the use of this nature's provision. [10], reviewed kenaf blended with Polyolefin to ascertain the viability of different combinations on the formulation of composite and highlighted contributions done by scholars in this all-important area of research. [11] emphasized that, homogenization of the properties of the fibres, degree of elementarization and degumming, degree of polymerization and crystallization, good adhesion between fibre and matrix, moisture repellence and flame-retardation, are factors considered in using natural fibre; are partly influenced by different fibre separation process, even though fibre treatment process are more influential.

Two or more different fibres can be incorporated into a single matrix to obtain hybrid composites that can advantageously substitute positive properties on itself for ones that may be a disadvantage to it; the term hybrid effect in the sense of synergism has been used to describe this. However, this is only possible where careful and adequate selection of the combining fibres is done, i.e. combining fibres from leaf and that of stem, fibres with lower microfibrila angle which can help to achieve higher tensile strength in composite, fibres with higher aspect ratio, and comparable elongation at break to avoid sudden transfer of load unto one of the combining fibres and perhaps cause a catastrophic failure of the composite in operation. Recently more research is tending towards combining two different natural fibres in a single matrix to achieve this effect [12]. This challenge is geared towards replacing synthetic fibres in composites without sacrificing structural

and functional stability during usage. [13], explored the concept of "Engineered Natural Fibre" to obtain superior strength biocomposites. Here, fibres from stem and leaf are suitably blended to achieve optimum hybrid effect on the composite properties; combination of fibres from stem and leaf is expected to provide a stiffness-toughness balance in the resulting composites [14]. This work is focused on the optimization of processing parameters for hybridized Kenaf/PALF/HDPE Reinforced composite. Apart from the problem of selecting the type of compatible fibres and the level of their properties in formulating composite, temperature of processing, speed of rotor and duration of mixing during formulation are critical.

Table 1. Typical properties of kenaf and PALF

	Density [g/cm^3]	**Microfibrilla angle[^{o}]**	**Elongation at break[%]**	**Fibre Diameter [μm]**	**Cellulose [wt%]**	**Ten Str. [MPa]**	**E-Modulus [GPa]**
Kenaf	1.3	20	1.6	14-33	45-57	427	53
PALF	1.526	14	1.6	20-80	70-82	413-1627	34.5-82.5

Experimental

Pineapple leaf (*Ananas Comosus*) bought from Kraftangan Malaysia with source from Johor pineapple plantation, and Kenaf (*Hibiscus cannabinus*) Bast of variety V36, purchased from KEFI Malaysia Sdn. Bhd. were utilized in this research. These fibres were used as reinforcement for HDPE that was also purchased from KEFI Malaysia. The HDPE use has a melt mass flow rate of 190°C/2.16kg, tensile strength at 17μm blown film is 44.1MPa, tensile elongation of 700% and a melting point of 180-240°C. Kenaf bast and PALF at a ratio of 1:1 and fibre length of ≤0.3mm were carefully and thoroughly mixed together before mixing it with the matrix in a Thermo Haake internal mixer at a fibre to matrix ratio of 10:90 percent. The mixer was preheated and set at the various temperature requirements. The HDPE pellets were charged into the mixer at specified temperature and allowed to stabilize (melt) before introducing the fibres. Mixed composite was obtained from the internal mixer and pelletized to help in compression molding operation. Tensile and flexural specimen sheet were prepared in a compression-moulding machine. The Compression molding machine was set at 170°C; 5min preheat, 5min full press, 7 times venting process and 5min cooling. Thereafter, a Dog-bone specimen of (10 X 1.5 X 1)mm and rectangular specimen of (150 X 15 X 3)mm were cut using a pneumatic tensile sample cutter and a powered-saw respectively. Some of these specimens were put in an industrial oven for conditioning at 105°C for 18hrs. Table 2 shows the codes and its designated operating parameters utilized in the internal mixer. Each sample was given physical inspection to see its state and level of mixing which served as a preliminary guide. Test was carried out sequentially on each group of sample as outlined.

Table 2- Operating parameters utilized in the internal mixer

Code		A1	A2	A3	A4	B1	B2	B3	C1	C2	C3
Operating parameters	Temp (^{o}C)	170	160	180	190	180	180	180	190	190	190
	Speed (rpm)	20	20	20	20	30	30	30	40	40	40
	Time (min)	10	10	10	10	15	20	25	15	20	25

Tensile and flexural measurement of the hybrid composite samples was conducted using a 5kN Bluehill INSTRON universal testing machine according to ASTM D638 and ASTM D790 as test conditions for tensile and flexural testing respectively. 2mm/min crosshead speed was used for the tensile specimen while 10mm/min cross head speed and 100mm span length were utilized for the three point flexural test. Five samples were tested for each of the code and the mean values taken. Conditioned specimens were also tested to see if it would have any significant effect on the samples.

Result and Discussions

Static mechanical test was carried out to see the sample that will give better properties, which was then used to conduct the next set of experiment until an optimum result of the hybridized composite was obtained. Fig 19(a-d) shows the result obtained for the first set of test conducted i.e. code "A", with the number "2" signifying the conditioned samples.

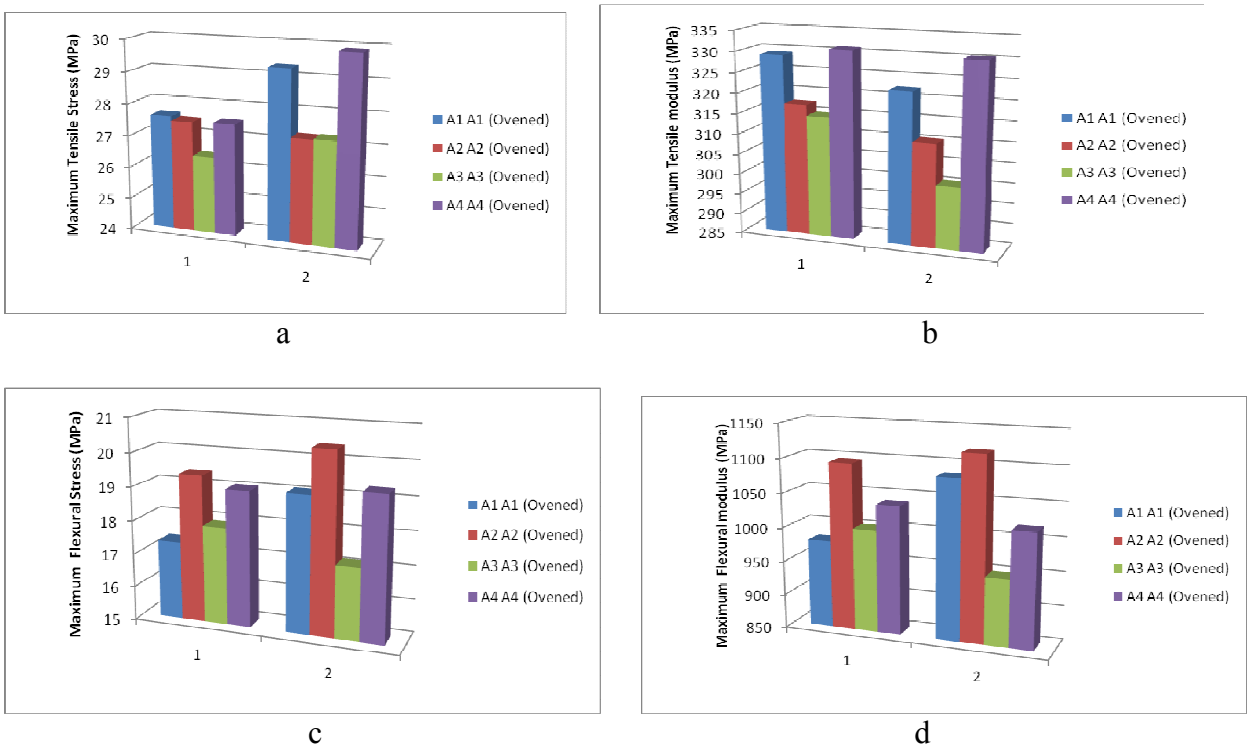


Fig. 1 Results of mechanical test conducted on sample code "A"

Even though the tensile test values obtained from A1 and A4 seems to be closely related, physical observation showed that A1 sample did not mix properly because free fibres could be seen and the matrix mostly does not show sign of full melting and flow in the composite. This means that the operating temperature may not be good enough to achieve free flow of the matrix through the composite in addition to proper interaction to obtain a good hybrid effect especially at higher fibre loading. To be sure it was not because the duration of mixing was not long enough to allow proper mixing, the same operating speed was used at 20% fibre content and increasing the duration of mixing to 25mins. The result showed poor outcome than what was obtained even at 10% fibre content with maximum tensile strength and tensile modulus as 22.77MPa and 346.28MPa at 170°C. The better result obtained earlier may be because of percentage of fibre content in the composite, which has shown to decrease at increased fibre loading. Conditions for A2 and A3 gave the lowest property with little impact of conditioning observed unlike A1 and A4 that showed significant improvement after conditioning. However, A3 and A4 operating temperatures were utilized in subsequent experiment because physical inspection showed greater potential if other operating conditions could be altered. It can also be seen that conditioning of the test sample generally improved the tensile and flexural strength result of the hybrid composite while the tensile modulus showed a decrease of 0.2 – 2%. Flexural results showed improvement after conditioning except A3 which showed lower value in both flexural stress and modulus. Sequel to observations made above, operating temperature of A3 and A4 were used in subsequent experiments since they showed better prospect in addition to higher melting temperature of the matrix in question. Fig.2(a-d) shows the test results obtained for the next set of test sample conducted, i.e. sample "B"

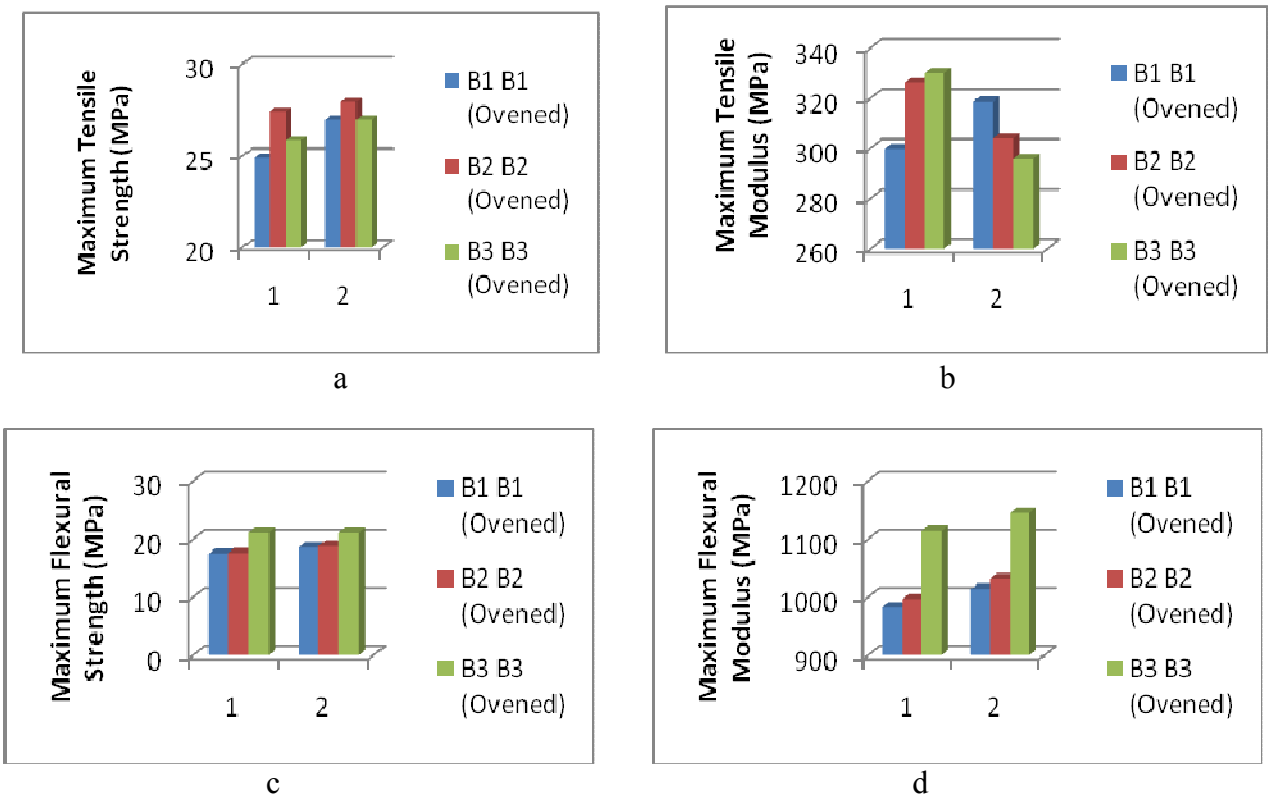


Fig 2 Results of mechanical test conducted on sample code "B"

In this section, a constant operating temperature and rotor speed of of 180°C and 30 rpm respectively was used in the mixer while varying the duration of composite mixing. This is to know if increasing the duration could offer better mechanical properties than the ones obtained in sample code "A". Careful increase of the rotor speed is necessary because at higher speed, there may be a possibility of fibre breakage, which could negatively affect the mechanical properties of the composite. Report has shown that the tensile strength, σ_c, of a one directional oriented short fibre composite tends to increase with fibre length and fibre matrix adhesion [15], according to the equation: $\sigma_c = (\varphi_f E_f + \varphi_m E_m)\epsilon_c - (\varphi_f E^2_f)/4\tau q$; where φ is the volume fraction, E the modulus, ϵ the composite strain, τ the interfacial shear stress, and q the aspect ratio.

While B2 (ovened) showed a better tensile strength in this group, B3 had a better flexural strength and modulus. It was similarly observed that tensile modulus decreased when the samples were conditioned in an oven just as in sample "A". However, all the result of the flexural modulus showed improvement unlike in the results obtained in "A" earlier. This could be due to a better interaction of the fibre and matrix because of the higher temperature used which help to increase the flow of the matrix through the fibres and the increase in the duration of mixing the composite. [16], reported that the adhesion efficiency between fibres and matrix in composite determines its strength properties which is dependent on the nature, shape and surface roughness of the reinforcing material. The best tensile test result for this group was observed in B2 having a mixing duration of twenty minutes while flexural properties of B3 yielded the best in this set. Increasing the duration of mixing showed positive improvement in both the flexural stress and flexural modulus of the composite with the tensile strength remaining relatively normal. Fig.3(a-d) shows the test results obtained for the next set of test sample conducted, i.e. sample "C"

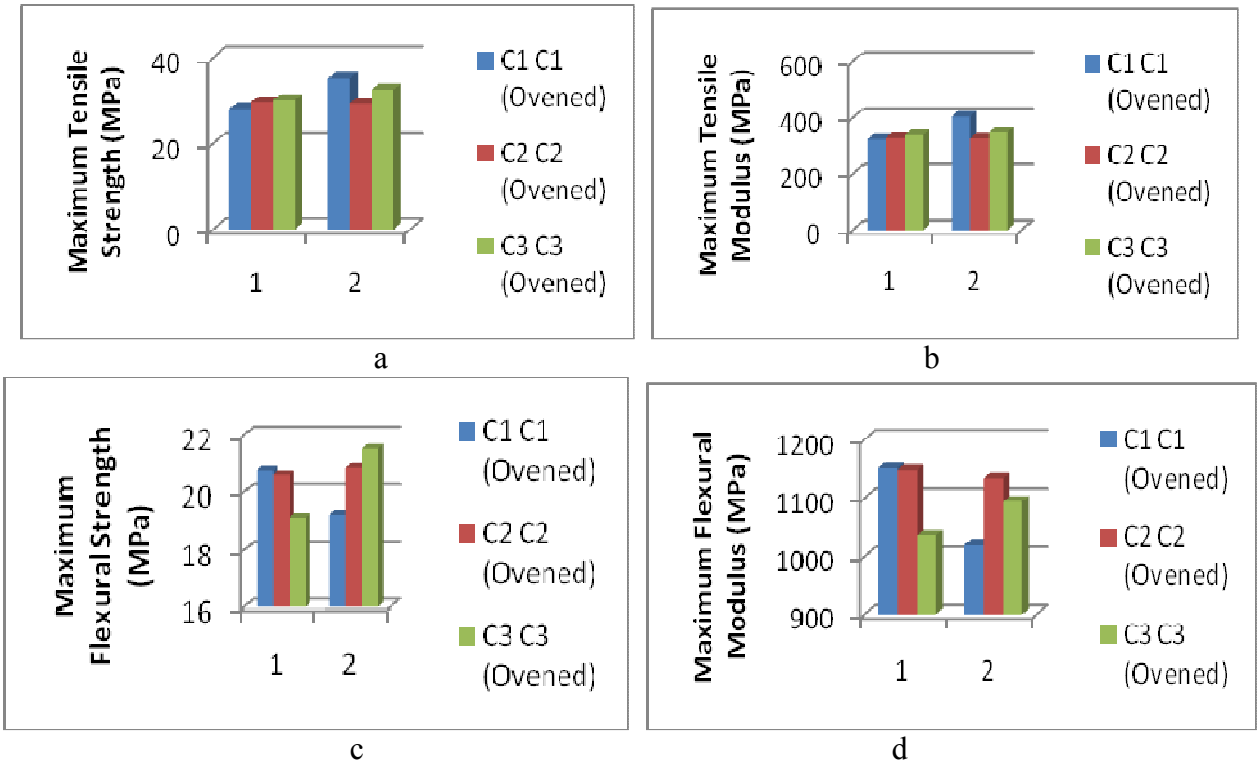


Fig 3. Results of mechanical test conducted on sample code "C"

It can be inferred from the result obtained in sample "C" that tensile properties has more significantly improved compared to test results obtained from sample A or B. The positive jump in the tensile properties of this composite could be because the matrix has melted and flowed freely through the fibre, which gave better interaction in the composite and made the stress transfer to the fibres even better. However, unlike previous results, the flexural modulus decreased when conditioned in an oven which could be because of the dispersion of fibres in the composite with much higher percentage of matrix than the fibres; this reduced the strength perpendicular to the fibre orientation. However, its flexural strength and tensile modulus showed some level of increase. This twist in the respective modulus is an interesting phenomenon in composite formulation and production. Result obtained from this group has shown good prospect in selecting processing parameters with C1 and C3 proving to be the better option. However, it should be noted that higher temperature can degrade fibre and drastically reduce the mechanical properties of composite. Kenaf fibres could begin to degrade above 210°C [17-20] while PALF can possibly degrade at even a lower temperature[21,22], therefore going beyond 190°C could harm the strength of the fibres used here and reduce its ability to receive and maintain stress during operation. Similarly, because of the possibility of rise in temperature inside the internal mixer with increase in the duration of mixing, going beyond 25 minutes could also affect the hybrid composite negatively. For these reasons, preprocessing conditions of C is taken as appropriate in this kind of composite depending on resulting end use of the product.

Summary

Optimization of processing parameters of hybrid composite from Kenaf/PALF/HDPE with conditioning was achieved by melt mixing and compression molding technique. The best tensile strength and modulus were obtained at an optimum processing parameters of 190°C, 40rpm, and 15min, while 190°C, 40rpm and 20min gave the best flexural strength and 190°C, 40rpm and 25min for flexural modulus. In conclusion, conditioning of composite has shown to improve mechanical properties. Utilization of these parameters according to end requirement can help in achieving optimum mechanical properties in hybridized composites.

References

[1] Information on http://repository.matdl.org/repository/eserv/matdl:761/n2007_CCMR_REU_cooley.pdf
[2] W. Liu, M. Misra, P. Askeland, L. T. Drzal, and A. K. Mohanty, Polymer, Vol. 46, No. 8, (2005), p. 2710–2721
[3] S. Nam and A. N. Netravali, Fibers and Polymers, Vol. 7, No. 4, (2006), p. 380–388.
[4] D. Plackett, T. L\ogstrup Andersen, W. Batsberg Pedersen, and L. Nielsen, Composites Science and Technology, Vol. 63, No. 9, (2003), p. 1287–1296.
[5] V. A. Fomin and V. V. Guzeev, Progress in rubber and plastics technology, Vol. 17, No. 3, (2001) p. 186–204.
[6] S. Mishra, A. K. Mohanty, L. T. Drzal, M. Misra, and G. Hinrichsen, Macromolecular Materials and Engineering, Vol. 289, No. 11, (2004), p. 955–974.
[7] A. K. Mohanty, M. Misra, and G. Hinrichsen, Macromolecular Materials and Engineering, Vol.276, 1, (2000).
[8] L. Pinchuk, Journal of biomaterials science. Polymer edition, Vol. 6, No. 3, (1994) p. 225.
[9] S. Sinha Ray and M. Bousmina, Progress in Materials Sci., Vol.50, No.8, (2005) p. 962-1079.
[10] I. S. Aji, S. M. Sapuan, E. S. Zainudin, and K. Abdan, International Journal of Mechanical and Materials Engineering (IJMME), Vol. 4, No. 3, (2009), p. 239–248.
[11] A. Bismarck et al., Polymer Composites, Vol.23, 5, (2002) p. 872–894.
[12] M. Thiruchitrambalam, A. Alavudeen, A. Athijayamani, N. Venkateshwaran, and A. E. Perumal, Materials Physics and Mechanics, Vol. 8, (2009), p. 165–173.
[13] A. K. Mohanty, M. Misra, and L. T. Drzal, Journal of Polymers and the Environment, Vol. 10, No. 1, (2002) p. 19–26.
[14] M. J. John, R. D. Anandjiwala, and S. Thomas, Natural Fibre Reinforced Polymer Composites: From Macro to Nanoscale, (2009).
[15] M. M. Thwe and K. Liao, Composites Science and Tech., Vol. 63, No. 3, (2003), p. 375–387.
[16] M. S. Sreekala, J. George, M. G. Kumaran, and S. Thomas, Composites Science and Technology, Vol. 62, No. 3, (2002) p. 339–353.
[17] K. Akita and M. Kase, Journal of Polymer Science Part A-1: Vol.5, No. 4, (1967), p. 833-848.
[18] S. Ochi, Mechanics of Materials, Vol. 40, No. 4, (2008), p. 446-452.
[19] S. H. Aziz and M. P. Ansell, Composites Science and Tech.,Vol. 64, No.9, (2004), p.1219-1230.
[20] A. R. Sanadi, D. F. Caulfield, R. E. Jacobson,and R. M. Rowell, Industrial & Engineering Chemistry Research, Vol.34, No.5, (1995), p.1889–1896.
[21] J. George, S. S. Bhagawan, N. Prabhakaran, and S. Thomas, Journal of Applied Polymer Science, Vol. 57, No. 7, (1995), p. 843–854,.
[22] J. George, S. S. Bhagawan, and S. Thomas, Journal of Thermal Analysis and Calorimetry, Vol. 47, No. 4, (1996), p. 1121–1140.

© (2011) Trans Tech Publications, Switzerland
doi:10.4028/www.scientific.net/KEM.471-472.680

Effect of Fibre Size and Fibre Loading on Tensile Properties of Hybridized Kenaf/PALF Reinforced HDPE Composite

I. S. Aji[1,a], E.S. Zainudin[2,b], A. Khalina[3,c] and S. M. Sapuan[1,d]

[1] Department of Mechanical and Manufacturing Engineering,
Universiti Putra Malaysia, 43400 UPM Serdang, Selangor, Malaysia

[2] Laboratory of Biocomposite Technology, Institute of Tropical Forestry and Forest Products,
Universiti Putra Malaysia, 43400 UPM Serdang, Selangor, Malaysia

[3] Department of Biological and Agricultural Engineering,
Universiti Putra Malaysia, 43400 UPM Serdang, Selangor, Malaysia

[a]suleimanaji@yahoo.com, [b]edisyam@gmail.com, [c]khalina@eng.upm.edu.my,
[d]sapuan@eng.upm.edu.my

Keywords: Hybridization, Tensile, Modulus, fibre, loading, length

Abstract. Hybridization, especially where only variant natural lignocelluloses are combined, is fast receiving encouraging attention because it offers range of properties that are quite difficult to obtain with a single kind of reinforcement. In this work, tensile strength and modulus of hybridized kenaf/PALF reinforced HDPE composite was examined. Pellets were produced form the mixture of the composite in an internal mixer at 190°C, 40rpm and 25minutes for processing temperature, speed and duration of mixing respectively. The composite sheets with thickness of 1mm produced from pellets were prepared using compression moulding. Then the tensile specimen were prepared and tested using an INSTRON bluehill universal testing machine according to ASTM D638 requirements. All samples were prepared at 1:1 kenaf:PALF ratio; ≤0.25mm and ≤0.5mm fibre length; fiber loading of 10 to 40% were utilized. Linear relationship of tensile modulus was observed with about 26% reduction in tensile strength at 10% fibre loading that subsequently reduced but with a reversal increase at 40% fibre loading. This was attributed to a better supportive load at that fibre content and a better interaction between fibre and matrix. Furthermore, the result also corroborates with the one obtained for the tensile modulus at same fibre loading. The best tensile strength and tensile modulus obtained was 32.43MPa;642.61MPa and 30.01MPa;636.73MPa for 0.25mm and 0.5mm fibre length respectively. Increase in fibre length did not show any significant improvement in tensile strength which may have been coursed by fibre attrition. It is possible to achieve improved mechanical properties if the fibres are given some kind of treatment.

Introduction

Ecological advantages of using natural fibres instead of man-made fibres as generally necessitated the paradigm shift in production and processing of reinforced composites. Scholars have been finding ways to replace or at least reduce the use of synthetic fibres for decades now. Hybridization, especially where only variant natural lignocelluloses are combined, is fast receiving encouraging search because it offers a range of properties that is quite difficult to obtain with a single kind of reinforcement. The type of matrix used, proper interaction of the matrix with the fibre(s) and the reinforcement is strongly linked to good mechanical performance that can be achieved in composites. Because of various use of composites in both structural and non structural application, combining two or more different fibres that can offer competitive advantage in service is very much desired. There has been a renewed interest in finding cost effective use of natural fibre-reinforced composite [1-3]. Work has been done by various scholars on the effect of fibre length and fibre loading on the mechanical performance of both wholly synthetic hybrid natural fibre composite and natural ones [4,5], most have shown some improvement in properties in

increase in the variables under consideration. Review recently conducted on polyolefin in combination with kenaf by us also showed this valuable information [6]. So natural fibres have already been accepted for their role in composites and can be competitively utilized for the development of environmentally friendly composite materials with desired physical properties[7]. It is important though to make use of strain compatible fibres in hybridization so that catastrophic failure can be avoided. Failure of one of the combining fibres will automatically transfer the whole load on the remaining unbroken fibre which obviously will not be able to hold; it is therefore worthy of note that the strength of a collection of fibres is governed by the fibre component having the smallest elongation at break because when it fails, the whole composite fails.

This work is targeted at determining the effect of fibre size and fibre loading on tensile properties of hybridized kenaf/PALF reinforced HDPE composite.

Experimental

Pineapple leaf (Ananas Comosus) bought from Kraftangan Malaysia with source from Johor pineapple plantation, and Kenaf (Hibiscus cannabinus) of variety V36, purchased from KEFI Malaysia Sdn. Bhd. were utilized in this research. These fibres were reinforced with High Density Polyethylene also purchased from KEFI Malaysia. The properties of HDPE used are shown in table 1.

Table 1. Properties of HDPE used

Density	**Melt Mass Flow rate**	**Ten. Str. (MPa)**	**Dart Drop Impact**	**Tensile Elongation**	**Forms**	**Melt Temp. ^{o}C**	**Sec. Mod (MPa)**
	190°C/2.16kg	TD:Break, 17µm, Blown film	17µm, Blown film	TD : Break 17 µm, Blown film			1% Sec, TD 17 µm, Blown film
0.95g/cm^{3}	0.10g/10 min	44.1	140g	700%	Pellets	180-240	1270

Fibres of Kenaf and PALF at a ratio of 1:1 and fibre length of ≤0.25mm and ≤0.5 were utilized for this experiment. Each of the sized fibre was carefully and thoroughly mixed together at the ratio of 10:90 to 40:60 fibre to matrix in a Thermo Haake internal mixer. The Thermo Haake Polydrive machine was preheated and set at 190°C and 40rpm processing speed. The HDPE in the form of pellets was introduced at the required temperature and allowed to stabilize (melt) before introducing the fibres. The total time used for mixing the hybrid composite was 25 minutes. The mixed composite was then obtained from the internal mixer and cut into pellet to help in compression molding operation. The pellets obtained were then measured according to the weight requirement for production of tensile and flexural specimen sheet before its introduction into a compression-molding machine for the production of square sheets of 150mm X 150mm X 1mm and 150mm X 150mm X 3mm for tensile and flexural specimen respectively. The Compression molding machine was set at 170°C; 7min preheat, 5min full press, 5 times venting process which was then followed by 5min cooling. Thereafter, a Dog-bone specimen of 10mm X 1.5mm X 1mm and rectangular specimen of 150mm X 15mm X 3mm were cut using a pneumatic tensile sample cutter and a powered-saw respectively.

Tensile and flexural measurement of the hybrid composite samples was conducted using a 5kN Bluehill INSTRON universal testing machine according to ASTM D638 and ASTM D790 as test conditions for tensile and flexural testing respectively. 2mm/min crosshead speed was used for the tensile specimen while 10mm/min cross head speed and 100mm span length were utilized for the three point flexural test. Five samples were tested for each of the code and the mean values taken.

Result and Discussions

Mechanical test was carried on the sample to see the effect of fibre size and fibre loading on the hybridized composite. It is worthy of note that in hybrid composite, its properties is basically dependent on the modulus and percentage elongation at break of the individual reinforcing fibres.

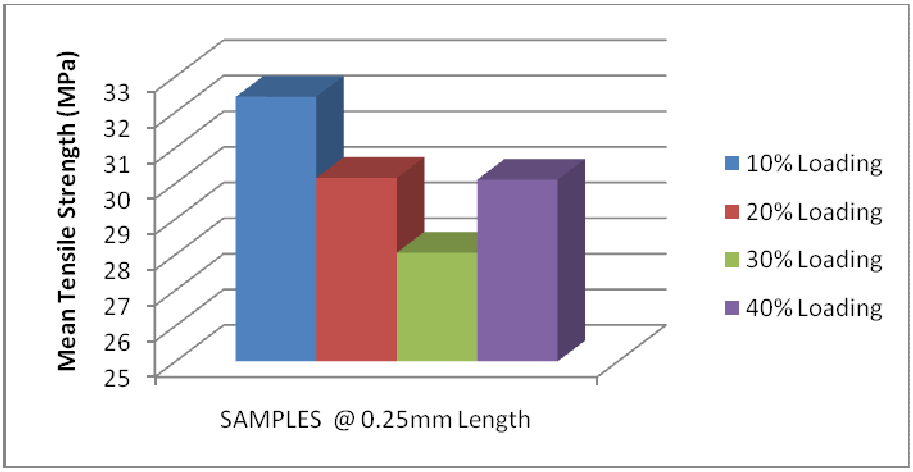


Fig 1 Tensile properties of samples at 0.25mm fibre length

Figure 1 describes the variation in tensile strength of the hybrid composite with increase in fibre loading. The tensile strength of the hybrid containing 10% fibre reduced by about 26% when compared to pure HDPE used in the experiment and this reduction continued up to 30% fibre loadingt before its eventual rise 40% fibre loading. This result is similar to what Arbelaiz et al obtained where they said that the tensile strength of un modified natural fibre composite tends to decrease with fibre loading[8]. Other authors also observed similar trend [9-11]. The effect of PALF on the hybrid began to show up at this loading, which could have been as a result of good interaction between the matrix and its reinforcing fibres. Similarly, it can also be said that supportive stress transfer is gradually beginning to show between the two fibres and their combining matrix. In the case of the composite tensile modulus, i.e. fig. 2, there seems to be a linear relationship; increase in fibre loading increased the modulus of the composite as in ROM. The result of the relationship seen in the tensile strength at 40% fibre content is also clearly reflected in the dramatic jump of the modulus from 30% to 40% fibre content of the hybrid.

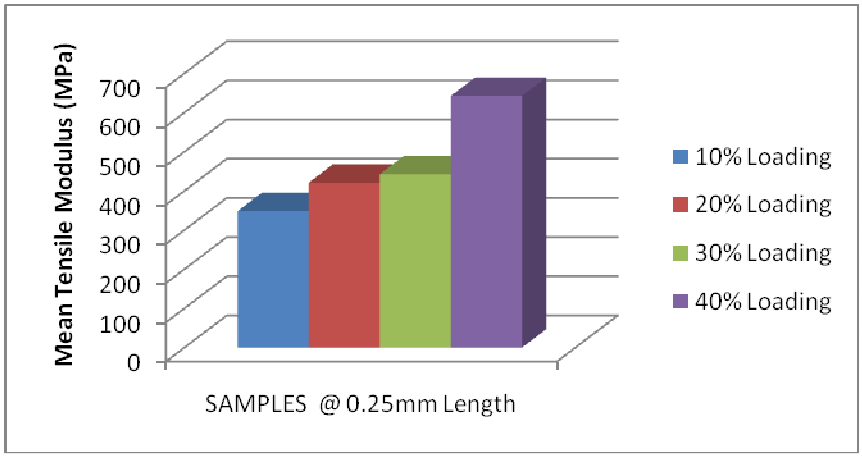


Fig. 2 Tensile Modulus of samples at 0.25mm length

Increasing the fibre length to 0.5mm did not yield significant difference with the previous as can be seen in fig.3. Generally, at 10% fibre content, the tensile strength is the same as that of the fibre size of 0.25mm. This may be because of fibre agglomeration, which may lead to decrease in adhesion efficiency between the fibre and the matrix. Usually, fibre aspect ratio is affected by mechanical processing which consequently affect the mechanical properties of the resulting composite [12]. [13,14] reported that processing composites in an internal mixer and injection machine can contribute to high fibre attrition owing to the very high shear stress acting on the viscous polymer[15] and fibres can be broken into smaller ones when the hydrodynamic forces acting exceeds the fibre strength[14]. The weak links and kink bands serve as natural and artificial flaws in natural fibre which be the most expected rupture points along the fibre length when it is mechanically stressed[13,16]. These issues and many more could have resulted in the reduction of the hybrid properties.

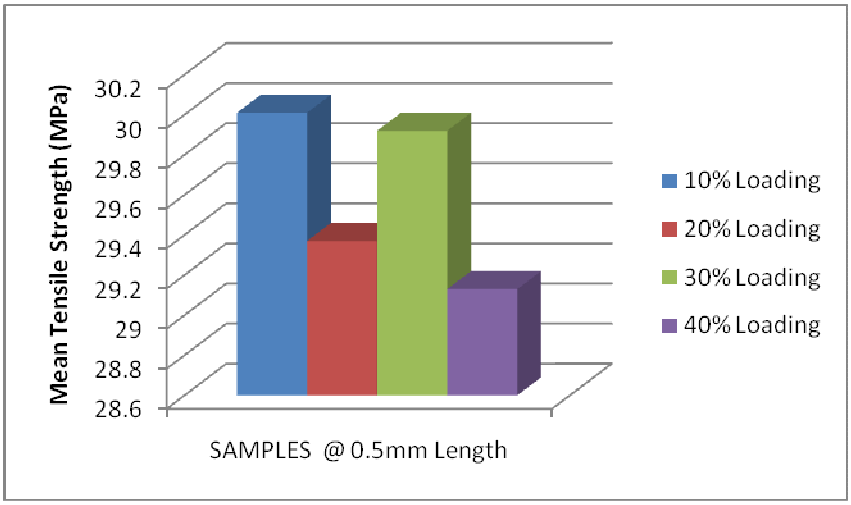


Fig. 3 Tensile Modulus of samples at 0.5mm length

Tensile modulus at 0.5mm fibre length showed some linear improvement from that of 0.25mm fibre length. At 40% fibre content however, the moduli obtained at the two varying fibre sizes are almost the same. This is clearly depicted in fig. 4; it similarly followed ROM.

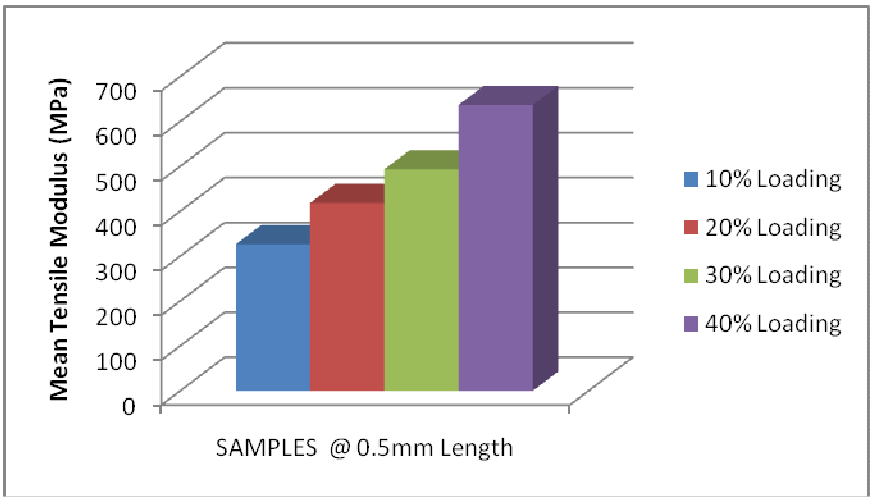


Fig. 4 Tensile Modulus of samples at 0.5mm length

Summary

Tensile strength and modulus of hybridized kenaf/PALF HDPE reinforced composite was studied considering the fibre size of 0.25mm and 0.5mm length under varying loading conditions. Linear relationship of their tensile modulus was observed with about 26% reduction in tensile strength at 10% fibre loading. This reduction continued up 30% fibre loading before its subsequent rise at 40% fibre content. This can be attributed to a better supportive load at that fibre content and a better interaction between fibre and matrix. This result corroborates with the one obtained for the tensile modulus at same fibre loading. Increase in fibre length did not show any serious improvement in tensile strength which may have been coursed by fibre attrition. It is possible to achieve improved mechanical properties if the fibres are given some kind of treatment.

Aknowledegment

The first author would like to thank Educational Trust Fund Nigeria for financial support during his study in UPM.

References

[1] M. Idicula, N. R. Neelakantan, Z. Oommen, K. Joseph, and S. Thomas, Journal of Applied Polymer Science, Vol. 96, No. 5, (2005), p. 1699–1709.

[2] K. L. Fung, X. S. Xing, R. K. Y. Li, S. C. Tjong, and Y. W. Mai, Composites Science and Technology, Vol. 63, No. 9, (2003), p. 1255–1258.

[3] M. Z. Rong, M. Q. Zhang, Y. Liu, G. C. Yang, and H. M. Zeng, Composites Science and Technology, Vol. 61, No. 10, (2001), p. 1437–1447.

[4] M. Miwa and N. Horiba, Journal of materials science, Vol. 29, No. 4, (1994), p. 973–977.

[5] M. S. Sreekala, J. George, M. G. Kumaran, and S. Thomas, Composites science and technology, Vol. 62, No. 3, (2002) p. 339–353.

[6] I. S. Aji, S. M. Sapuan, E. S. Zainudin, and K. Abdan, International Journal of Mechanical and Materials Engineering (IJMME), Vol. 4, No. 3, (2009) p. 239–248.

[7] A. K. Bledzki and J. Gassan, Progress in Polymer Science, Vol. 24, No. 2, (1999) p. 221–274.

[8] A. Arbelaiz, B. Fernández, A. Valea, and I. Mondragon, Carbohydrate Polymers, Vol. 64, No. 2, (2006), p. 224–232.

[9] A. R. Sanadi, D. F. Caulfield, R. E. Jacobson, and R. M. Rowell, Industrial & Engineering Chemistry Research, Vol. 34, No. 5, (1995), p. 1889–1896.

[10] J. M. Felix and P. Gatenholm, Journal of Applied Polymer Science, Vol. 42, No. 3, (1991) p. 609–620.

[11] H. D. Rozman, G. B. Peng, and Z. A. Ishak, Journal of Applied Polymer Science, Vol. 70, No. 13, (1998), p. 2647–2655.

[12] A. M. Rezadoust and M. Esfandeh, Polymers & polymer composites, Vol. 9, No. 6, (2001), p. 403–407.

[13] A. C. Karmaker and J. A. Youngquist, Journal of Applied Polymer Science, Vol. 62, No. 8, (1996), p. 1147–1151.

[14] R. Ali, S. Iannace, and L. Nicolais, Journal of Applied Polymer Science, Vol. 88, No. 7, (2003) p. 1637–1642.

[15] M. Baiardo, E. Zini, and M. Scandola, Composites Part A: Applied Science and Manufacturing, Vol. 35, No. 6, (2004), p. 703–710.

[16] A. Arbelaiz, G. Cantero, B. Fernández, I. Mondragon, P. Ganán, and J. M. Kenny, Polymer composites, Vol. 26, No. 3, (2005), p. 324–332.

© (2011) Trans Tech Publications, Switzerland
doi:10.4028/www.scientific.net/KEM.471-472.686

Tensile and Flexural Behavior of Hybrid Banana Pseudostem/Glass Fibre Reinforced Polyester Composites

I.N Hanifawati[1,a], M.A Azmah Hanim[1,b], S.M Sapuan[1,c] and E.S Zainudin[2,d]

[1] Department of Mechanical and Manufacturing Engineering,
Universiti Putra Malaysia, 43400 UPM Serdang, Selangor, Malaysia
[2] Laboratory of Biocomposite Technology, Institute of Tropical Forestry and Forest Products,
Universiti Putra Malaysia, 43400 UPM Serdang, Selangor, Malaysia

[a]wati@btu.upm.edu.my, [b]azmah@eng.upm.edu.my, [c]sapuan@eng.upm.edu.my,
[d]edisyam@gmail.com

Keywords: hybridization, mechanical properties, banana fibre, glass fibre, unsaturated polyester

Abstract. Natural fibre-based thermoset composites are generally lower in strength performance compared to synthetic thermoset composites. Hybridization with some amount of synthetic fibre enhanced the mechanical properties of the composites. This study focused on the performance of mechanical properties of hybrid banana/glass fibre reinforced polyester composites. Hybrid composites with different volume ratios of banana to glass fibre were prepared. The reinforcing effect of both fibres in polyester is also evaluated in various fibre loadings. Results showed that both flexural and tensile properties have been improved with the increasing level of overall fibre content loading. Tensile and flexural strength shows great enhancement by the introduction of a slight amount of glass fibre to the banana fibre polyester matrix.

Introduction

In recent years there has been a growing interest in the use of lignocellulosic or natural fibre in composites application among all over the world. Compared to synthetic fibre, lignocellulosic fibre have lower densities, available in abundance, biodegradable, renewable and are carbon dioxide (CO_2) neutral [15]. However, a direct substitution of synthetic fibre by lignocellulosic fibre is not easily achieved. Lignocellulosic-based composites suffer from low strength, low modulus, limited thermal stability and poor moisture resistance compared to synthetic fibre composites. The hydrophilic nature of lignocellulosic fibre also leads to low compatibility with hydrophobic polymer matrices and poor adhesion between fibres and matrices.

Hybridization of lignocellulosic fibre with moisture-resistant and corrosion-resistant synthetic fibers is one technique to enhance the strength and stiffness as well as moisture resistance of the resulting hybrid fiber composites. Currently, plenty of research materials are being generated on the potential of natural fibre and glass fibre as reinforcement in composites. Velmurugan et al., [7] studied the properties of palmyra/glass fibre hybrid composite at 55 wt% and found the improvement of stiffness, strength properties as well as moisture resistant behavior of the composites. It is obvious that synthetic fibre have superior properties than the natural fibre but only small amount of synthetic fibre added will improved mechanical and barrier properties of composites. Al Emran et al. [1] studied the effect of fibre hybridization on the mechanical behavior under tensile and impact test. The result shows that the incorporation of the coir and glass fibres induced an increase in Young's modulus, tensile strength and impact strength but resulted slightly decreasing in elongation of break. . The hybridization of silk fabric and glass fibre was investigated by Padma Priya et al. [8]. It was observed that the mechanical properties increase with the increase in the weight fraction of the reinforcement.

Banana fiber obtained from the stem of banana tree, which is left unutilized after the removal of the fruit and its leaves. Banana fiber was the chosen material, due to it abundance and relative cheapness. According to Sapuan et al. [10], the result obtained from the study showed that mechanical behavior of woven banana fibre reinforced epoxy composites under different test are very stable. Therefore, this result gave a good opportunity to investigate more in detail about the use of this natural fibre as an effective reinforcement to form agro-hybrid composites. To study the influence of hybridizations, both banana pseudostem and glass fibre are used to reinforce the polyester composites. Different fibre loadings are introduced. Tensile and flexural test was employed to evaluate mechanical properties of banana/glass hybrid polyester composites such as tensile strength, tensile modulus, elongation at break, flexural strength and flexural modulus.

Experimental

Materials. Banana (*Musaceae*) fibres were obtained from Baala Bharat Agri Industries, Andhra Pradesh, India. The glass fibre (GF) with an average fibre length of 30 mm was obtained from Berjaya Bintang Timur Sdn. Bhd. Cheras, Kuala Lumpur. Unsaturated polyester acted as matrix while methyl ethyl ketone peroxide (MEKP) as hardener, both supplied by Berjaya Bintang Timur Sdn. Bhd. Cheras, Kuala Lumpur. The mixing ratio used was 99:1.

Methods. The composites with fibre loading 10, 20, 30 and 40% of volume fraction were fabricated using hand lay-up method followed by compression moulding. Banana fibres were cut into optimum length of about 30-40mm [7,12]. Hybrid banana and glass fibre in the ratio of 100/0, 75/25, 50/50, 25/75 and 0/100 were evenly arranged in the mould and covered with the matrix. The composite was compressed at a constant pressure (10kg/cm^2) at room temperature to eliminate the bubbles in the composites and cured for 24 h. The test specimens were cut as per ASTM D5083 [3] and flexural test specimens were cut as ASTM D790 [4] specifications. The tests were measured by employing a universal testing machine (UTM), INSTRON model 5566. The cross head speed for tensile and flexural tests were maintained at 5 mm/min. In each case five samples were tested and the average values were reported.

Results and Discussion

Tensile Properties. Fig. 1 and 2 shows the variation of tensile properties of banana/glass fibre hybrid composites. The effect on tensile properties of hybrid composites containing 10, 20, 30 and 40% of volume fraction were studied. The figure clearly indicates that tensile strength and Young's modulus of the composites increase linearly on increasing the total fibre loading in the composites. These results are in agreement with the observation of various studies [1,6,7,9] where both tensile and flexural modulus were improved with the increasing level of overall fibre loading.

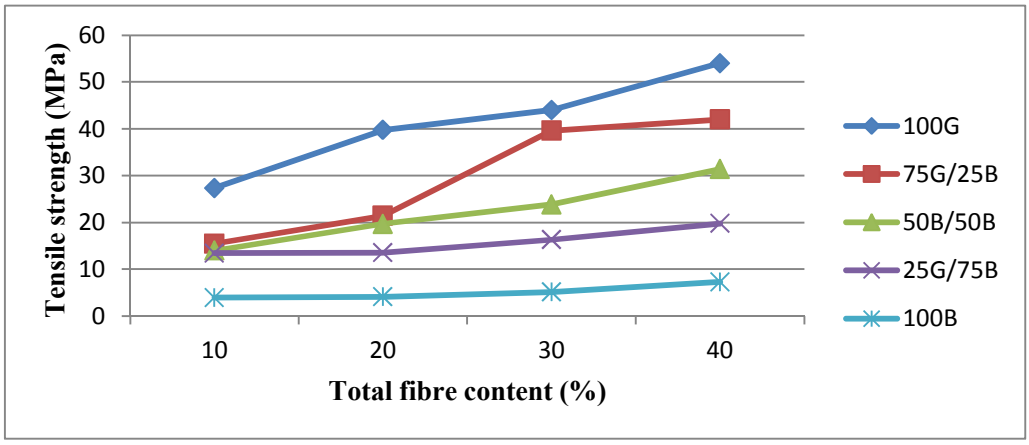


Fig. 1 Tensile strength of banana/glass hybrid composites at different fibre loading.

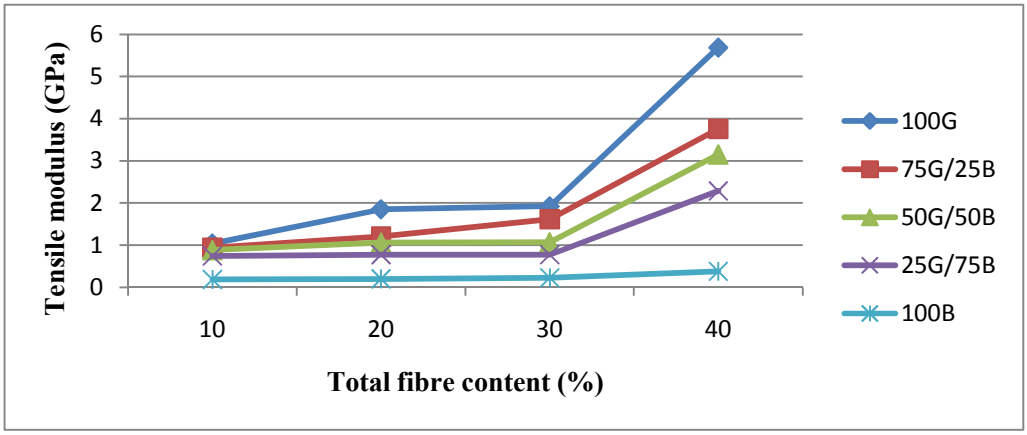


Fig. 2 Tensile modulus of banana/glass hybrid composites at different fibre loading.

The figure clearly shows that the composites having 40% fibre loading shows the highest tensile strength. As the fibre volume ratio is increased, load is distributed to more fibre, which is well bonded with polyester matrix resulting in better tensile strength. At a low stage of fibre content, the amount of fibre is not enough to restrain the matrix and the fibres are unable to contribute to the effective stress transfer between the fiber and the matrix. Poor fibre alignment at low stage of fibre loading results larger free space for fibre movement thereby reducing the effective stress transfer from fibre to matrix. Other than that, in glass/polyester composites, the tensile strength is found to be much higher than banana/polyester composites. It was due to the inherent property of glass fibre.

The result shows a common phenomena as shown by conventional lignocellulosic-thermoset composites [7,9,14], where the tensile strength and modulus increases as the glass fibre is increased. Composites with 100% glass fibre (0% banana fibre) as reinforcement agent, display significantly higher strength than the composites with 100% banana (0% glass fibre). It can be seen that the strength is reduced as the amount of banana fibre is increased. As the relative volume fraction of banana is increased, the incompatibility in the interfacial region between the banana and polyester matrix is also increased. This is due to hydrophilic nature of natural fibre and the hydrophobic polyester matrix. The hydrophilic properties may somehow affect the mechanical and physical properties of the composites. Banana fibre is a lignocellulosic fibre with a highly hydrophilic and this may lead to poor bonding quality between fibre and matrix. This results in low tensile properties at the higher volume fraction of banana fibre.

Instead of hydrophilic, lignocellulosic fibres generally show nonuniform size and lower length-to-diameter ratio than synthetic fibres. According to Rozman et al[9], nonuniform cross-section and lower fiber aspect ratio may contribute to failure in stress transfer and finally, lower tensile strength.

Incorporation of 100% volume ratio of glass fibre in hybrid composites gave the highest value of tensile properties among all the hybrid composites. According to Velmurugan et al. [14] the strength of the hybrid composites depend on the type of the fibre, fibre length, fibre orientation and the bonding between fibre and matrix. In this case, the increase in strength of the hybrid composite is mainly due to the high tensile strength of glass fibre (2500-3500 MPa) compared to low strength of banana fibre (54-754 MPa). The incorporation of 25% glass fibre into banana/polyester composites at 40% fibre loading increased its strength value by 19.81MPa by about 200% than banana/polyester composites. When both fibre content (banana and glass) is about 50% each, the increment is about 330%.

The addition of relatively small amount of glass fibre to the banana fibre polyester matrix enhanced the tensile properties of the resulting hybrid composites. In a hybrid composite, the properties of a hybrid composite are mainly dependent on the modulus and percentage elongation at break of the individual reinforcing fibre [8]. Due to the presence of the higher modulus of the glass fibre (66-72GPa) than that of the banana fibre (7-20GPa), as the percentage of glass fibre in the composites increases, the modulus also increases.

The variation of elongation at break of hybrid composites is shown in Fig. 3. Theoretically, the addition of banana fibre increases the elongation at break value because of the higher elongation at break value of banana fibre (1-4%) compared to glass fibre (2.8%). However, the elongation at break of hybrid composites decrease with the increase of banana fibre even though banana fibre has higher elongation at break compare to glass fibre. This can be related to the low strength nature of banana fibre and interfacial incompatibility between the fibre and the matrix. The reduction of elongation becomes more severe when banana fibre is increased because banana fibre fails catastrophically even before reaching its actual extensible strain.

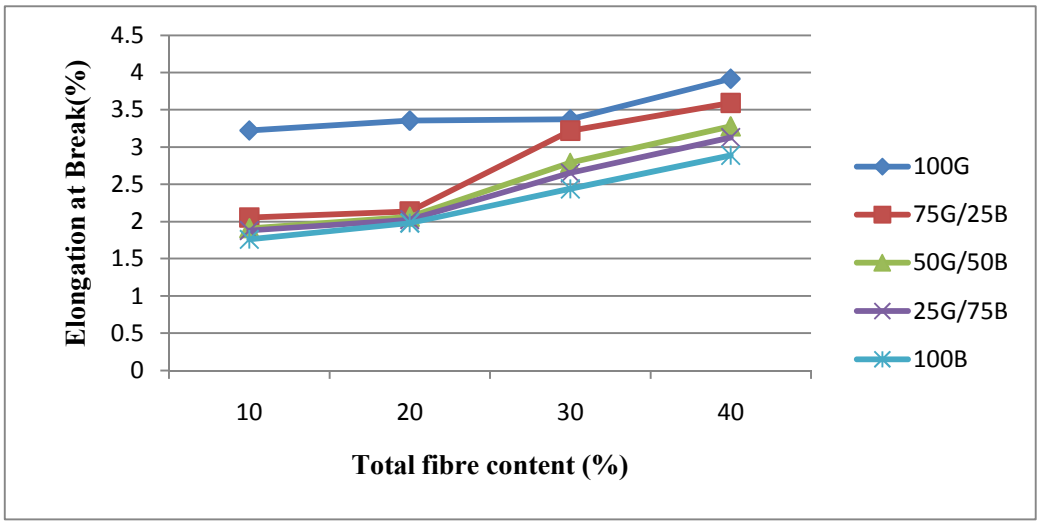


Fig. 3 Elongation at break of banana/glass hybrid composites at different fibre loading.

Flexural Properties. Fig. 4 and 5 shows the results of flexural strength and modulus of banana/glass fibre hybrid composites. Overall, it can be seen that flexural properties increase as the volume fraction of fibre increases in hybrid composites. From the graph, it is observed that 40 vol% of fibre has the highest value of the flexural strength while fibre with 10vol% of fibre has the lowest value of flexural strength. This is due to the fact that the composites are able to withstand more loads when the population of fibre in composites increased. Flexural modulus of hybrid composites tends to be increased as the total fibre content is increased. This trend is also similar to the tensile modulus of hybrid composites where by addition of fibre the value of flexural modulus is increased.

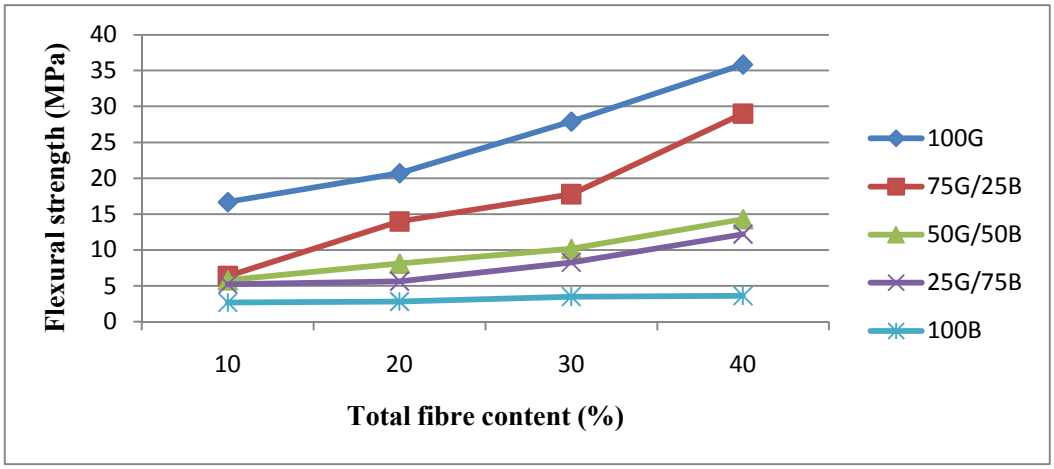


Fig. 4 Flexural strength of banana/glass hybrid composites at different fibre loading.

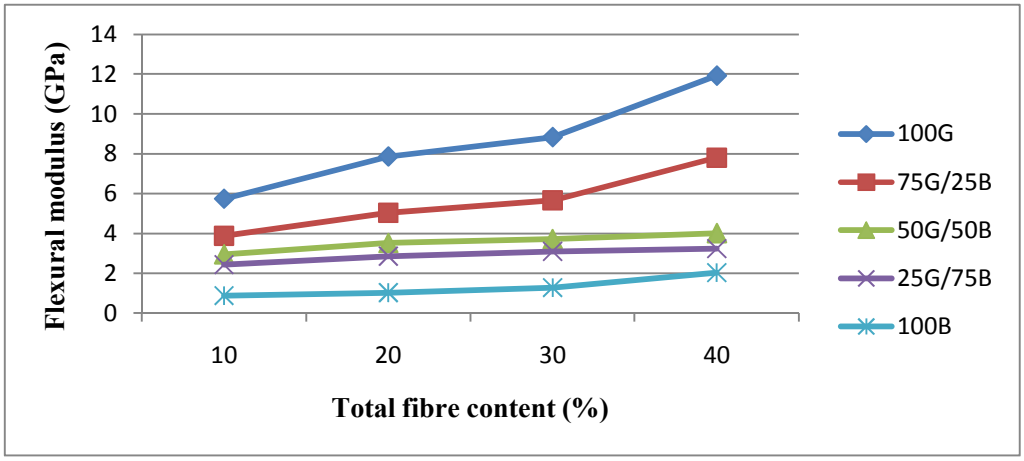


Fig. 5 Flexural modulus of banana/glass hybrid composites at different fibre loading.

With the addition of relatively small amount of glass fibre (25:75, glass:banana) , the flexural modulus of banana/glass hybrid polyester composites increases by about 150%. The enhancement in the strength of these composites is attributed to the higher modulus of glass fibre (66-72 GPa) than that of the banana fibre (7-20 GPa). It was also reported by Samal et al [11], addition of glass fiber in banana fiber reinforced polypropylene composites also helps to attain a uniform dispersion of banana fiber and avert fibre to fibre contact in the matrix.

As depicted in Fig. 4, it is observed that the flexural strength of hybrid composites had a similar trend as the tensile properties where the flexural strength linearly increases with the increase in glass fibre. In a three point flexure test, various mechanisms such as shear, tension and compression will take place concurrently. According to Sreekala et. al [12], the increase flexural strength of the hybrid composites as a result of the increased glass fibre content is mainly due to the increased resistance to shearing. The higher strength of glass fibre is mainly accounted for increase in flexural strength due to capability to bear the applied shear, tensile and compressive stress subjected on hybrid composites.

Summary

In this paper, the tensile and flexural properties of hybrid banana pseudostem/glass fibre reinforced polyester composites have been measured. Based on these results, it was found that tensile and flexural properties showed an increasing trend as the total fibre loading was increased. Composites showed the highest mechanical performance at 40vol % of total fibre loading. It was also found that mechanical properties of banana reinforced composites are improved by the incorporation of small amount of glass fibre in these composites, showing positive hybrid effect.

Acknowledgement

The authors thank to Mr. Tajul Ariffin and Mr. Muhammad Wildan Ilyas from the Department of Mechanical and Manufacturing Engineering, Universiti Putra Malaysia for their assistance.

References

[1] Al Emran Ismail, Nor Azila Zamani: International Conference on Environmental Research and Technology (ICERT), (2008).
[2] Al-Qureshi, H.A.: 2nd International Wood and Natural Fiber Composites Symposium, June 28-29 in Kassel/Germany, 321-328 (1999).
[3] ASTM D 5083. American Society for Testing Materials. (2002).
[4] ASTM D 790. American Society for Testing Materials. (2000).
[5] Herera-Franco PJ, Valadez-Gonzalez A.: Composites, Part A, 35: 339-345 (2004).
[6] John, K. and Venkata Naidu, S.: Journal of Reinforced Plastic and Composites, 23(12): 1253-1258 (2004).
[7] Joseph, S., Sreekala, M.S., Oommen, Z., Koshy, P. and Sabu, T.: Composites Science and Technology, 62, pp. 1857-1868 (2002).
[8] Padma Priya, S. and Rai, S.K.: Journal of Reinforced Plastic and Composites, 24(15): 1605-1610 (2005).
[9] Rozman H.D, Tay G.S and Kumar R.N.: Europian Polymer Journal 37: 1283-1291 (2000).
[10] Sapuan S. M, Leenie A., Harimi M. And Beng.Y.K.: Materials and Design, 27(8): 689-693.
[11] Samal, Sushanta K., Mohanty, Smita and Nayak, Sanjay K.: Polymer-Plastics Technology and Engineering, 48: 4, 397 – 414 (2009).
[12] Sreekala, M.S., Jayamol George, M.G Kumaran, Sabu Thomas: Composites Science and Technology, 62, pp. 339-353 (2002).
[13] Udaya C.Kiran, Ramachandra G.Reddy, B.M. Dabade and S. Rajesha: Journal of Reinforced Plastics and Composites, 26: 1043 (2007).
[14] Velmurugan, R. and Manikandan, V.: Composites, Part A: Applied Science and Manufacturing, 38: 2216-2226 (2007).
[15] Wamboa, P., Ivens, J. and Verpoest, I.: Composites Science and Technology, 63, pp. 1259-1264 (2003).

© (2011) Trans Tech Publications, Switzerland
doi:10.4028/www.scientific.net/KEM.471-472.692

Retrofitting Pre-cracked RC Beams Using CFRP and Epoxy Injections

R. Hawileh[1, a], A. Tamimi[1,b], J. A. Abdalla[1,c] and M. H. Wehbi[1,d]

[1]Department of Civil Engineering,

American University of Sharjah, Sharjah, UAE

[a]rhaweeleh@aus.edu, [b]atamimi@aus.edu, [c]jabdalla@aus.edu, [d]b00021158@aus.edu

Keywords: Reinforced Concrete, CFRP, Pre-crack, RC Beam, Epoxy Injection

Abstract. The applications of Carbon Fiber Reinforced Polymers (CFRP) in construction have been grown drastically in the last 20 years because of the wide range of advantages and benefits of using CFRP in buildings, bridges and other type of structures. Nowadays, it is used for retrofitting concrete, masonry, steel and timber structures to resist both static and dynamic loads. Since the cost of replacing an existing structure is far more expensive than using FRP materials to strengthen it, CFRP strengthening techniques seem to be cost effective and easy to implement. Numerous experimental and numerical studies have been conducted to investigate the flexural and shear performance of uncracked reinforced concrete (RC) members externally strengthened with CFRP laminates or strips. However, the most practical usage of CFRP is to retrofit sections that had already been cracked and in need of maintenance. The fact that there have been limited studies to investigate the behavior and performance of pre-cracked beams strengthened with CFRP systems necessitated new and further investigations. In this study, the flexural performance of cracked RC beams retrofitted with CFRP plates and epoxy injections are investigated. The results of the cracked beams are compared with two control beams, a virgin un-strengthened beam and an uncracked beam strengthened with a CFRP plate covering 90% of the beam's span. Load-midspan deflections for these beams were generated and compared. It is observed that the retrofitted cracked beams displayed more strength than the control beam. The results presented herein can aid designers in establishing a better understanding of the flexural performance of pre-cracked beams and how to economically retrofit such structural members.

Introduction

The use of different strengthening systems to retrofit aging structures such as bridges has been an active area of research during the last few decades. Several advanced materials has been used to accomplish this task. In spite of the emergence of many promising materials as the result of the numerous studies and investigations, the use of Fiber Reinforced Polymers (FRP) materials is still considered to be a the-state-of-the-art in this field by proving its dominance in increasing the strength and stiffness of existing structural members. The use of FRP materials has grown rapidly because of their well recognized advantageous, i.e., high strength to weight ratio, ease of installation as well as resistance to electro-chemical corrosion [1-2]. Aging structures are becoming a liability since they were designed based on older provisions and experience significant increase in loads. In addition, the exposure to aggressive environment, humidity, formation of cracks and carbonation of concrete are considered the main reasons for corrosion of internal steel reinforcement which may trigger a brittle failure that requires an immediate action [3-4]. Although many attempts have been made to study the behavior of uncracked RC members strengthened with FRP, however there is still a need for further experimental investigations to fully understand the behavior of cracked sections retrofitted with FRP and epoxy injections.

One of the few attempts to study the effect of FRP strengthening systems on precracked RC members was done by Buyukozturk & Hearing [5]. They investigated different types of failure modes, i.e., FRP delamination, in addition to generating different constitutive models. Different parameters were investigated such as shear strength, bonded laminate length and epoxy types. They concluded that retrofitting precracked beams with FRP increases the strength; however, the failure mode varies depending on the effect on the mentioned parameters.

Arduini and Nanni [6] studied the behavior of precracked RC beams Strengthened with CFRP laminates. They investigated some experimental variables that affect the strength provided by the CFRP. The variables investigated include CFRP material system, concrete surface preparation, cross sectional area, number and location of CFRP plates and external prestressing during the adhesion of the CFRP. They concluded that some variables have significant effect and others had a modest effect. They also simulated failure modes on different models.

This paper aims to provide further understanding of the behavior of retrofitted RC beams using CFRP plates and epoxy injections. A comparison between using externally bonded FRP materials and using epoxy injections on the behavior of precracked sections is presented. Different observations and conclusions will be also drawn.

Experimental Program

Three RC beams were tested under monotonic loading up to failure as a part of an extensive experimental study. The RC beams have a rectangular cross section of 180 mm in depth by and 110 mm in width and 1840 mm in length. The clear span length is 1700 mm and the beams were reinforced with two 10 mm diameter top and bottom flexural reinforcement bars. The shear reinforcements comprised of eight mm diameter stirrups spaced at 80 mm center to center. The steel rebars used to reinforce the concrete beams have an average modulus of elasticity and yield strength of 200 GPa and 460MPa, respectively. All the tested beams were casted from the same concrete mix and the tested average compressive strength is 52 MPa.

The RC beams were tested under four point monotonic loading up till failure. The loading setup is shown in Fig. 1. The first specimen (CB) is served as a virgin unstrengthened beam. The second specimen (B90P) was strengthened using a CFRP plate covering 90% of the beam's span while the third specimen (B90PC) was retrofitted via epoxy injections and then strengthened with a CFRP plate covering 90% of the beam’s span. The CFRP plate used was CFL210 manufactured by ConMix Company. The used CFRP plate has a thickness and width of 1.0 mm and 100 mm, respectively. On the other hand, the epoxy injection used is a low viscous epoxy (ReCon Live) and manufactured by ConMix Company and was injected along cracks for sealing purposes. The mechanical properties of the CFRP plates and epoxy injection used are given in Table 1. Table 2 shows details of each specimen as well as the strengthening technique used. The testing setup is shown in Fig. 1 and the specimens are loaded using an Instron Universal Testing Machine (UTM) that has a static capacity of 2200 kN.

The precracking strengthening technique was prepared by loading the (B90PC) specimen to 35 kN until flexural cracks of 0.03 mm width were developed A measuring telescope were used to monitor the clacks at the sides of the beams and the load was removed once the desired crack width were developed. After that, a 40 mm diameter hole was drilled at 45° angle to install the injection nozzles. Then, the cracks were sealed by using the (ReCon FCE) resin. After that, the epoxy injection (ReCon Live) is pumped into the cracks through the epoxy nozzles. Finally, prior to the specimen testing, the other side of the nozzle was removed. Figure 2 shows the installed epoxy nozzle at the beam's soffit.

Table 1 Mechanical Properties of the strengthening system used in the study

Material	Modulus of elasticity [GPa]	Ultimate Tensile strength [MPa]	Elongation at failure [%]
CFL210	215	>2500	0.45
ReCon Live	NA	25	NA
ReCon FCE	NA	20	NA

Table 2 Experimental program

Specimen	Designation
CB	Control Virgin beam
B90P	Virgin beam + 90% CFRP plate
B90PC	Cracked beam + epoxy injections + 90% CFRP plate



Fig. 1 Test setup



Fig. 2 Installed epoxy nozzle

Results and Discussion

Figure 3 draws the plot of the test results and a comparison between the tested beams in terms of the load-defection response. Upon comparing the (CB), (B90P) and (B90PC) specimens, it is observed that the use of epoxy injections increased the capacity of the RC beams more than the use of the conventional externally bonded CFRP plate. Figure 3 also shows that the increase of strength of the tested beams resulted in reduction of ductility. The (CB) failed at a load of 48 kN, while both (B90P) and (B90PC) specimens achieved an ultimate load prior to failure of 60.6 and 71.6kN, respectively. Table 3 draws a comparison of the tested beams in terms of the ultimate load, maximum mid-span deflection and deflection percentage difference.

The tested control RC beams (CB) failed in a flexural manner after the formation of flexural cracks upon yielding of steel reinforcement. On the other hand, both (B90P) and (B90PC) specimens achieved higher load capacities and failed by concrete cover separation.

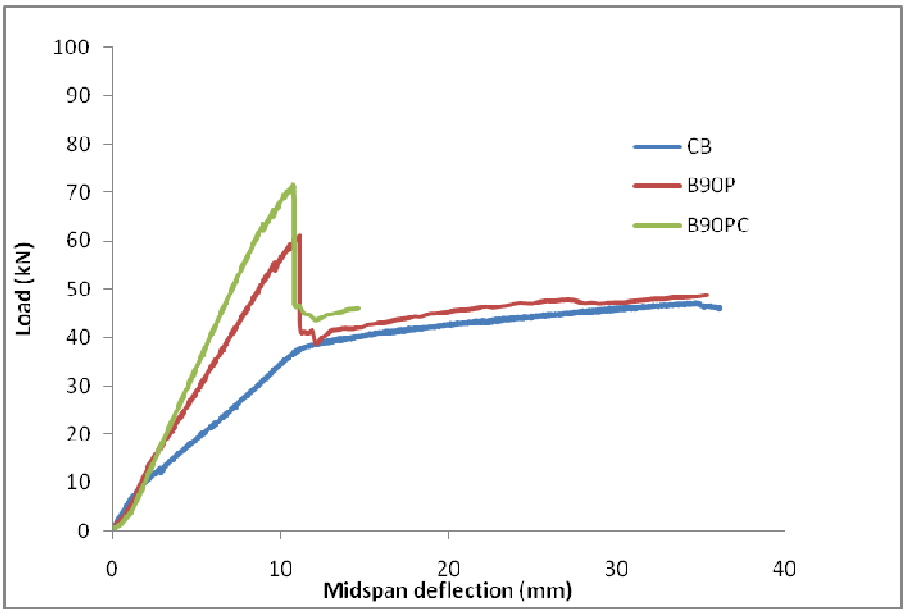


Fig. 3 Load response of the tested specimens

Table 3 Comparison between the tested specimens

Specimen	Ultimate load [kN]	Maximum deflection [mm]	% reduction in deflection at failure compared to CB
CB	48	39	-
B90P	60.6	36	-0.08
B90PC	71.6	12	-69.2

Summary

In this study, three RC concrete beams were tested. Different strengthening techniques were investigated and the specimens were loaded monotonically up to failure of the specimens under four point loading. Based on the tested data, both FRP external strengthening systems and epoxy injections can improve the state of RC beams and increase their strength and stiffness upgrade their capacities. The main findings of this study are:

1. The use of CFRP materials and epoxy injection as strengthening systems seems to significantly increase the strength of RC precracked members.
2. The use of CFRP plates and epoxy injections increases both the stiffness and strength on the expense of the ductility.
3. The ultimate achieved load capacity of the strengthened specimens (B90P) and (B90PC) was higher than that of (CB) specimen by 26.3%, and 49.2%, respectively.
4. The mid-span deflection of the strengthened specimens (B90P) and (B90PC) at failure was lower than that of (CB) specimen by 0.08%, and 69.2%, respectively.

Further studies are required on the behavior of precracked strengthened RC beams with CFRP laminates to further investigate and study the behavior and performance of such systems.

Acknowledgement
The authors acknowledged the technical support and materials provided by CONMIX Ltd. Sharjah, and the help provided by the following final year civil engineering students: Mr. Abdalla Haitham, Mr. Hussam Sardast, and Mr. Muhamed Bahaa. We also want to acknowledge the help of Eng. Arshi Faridi and Muhanad Naser for their help in conducting the tests.

References

[1] C. Zeris, J. Anastasakis and J. Kyriakidis: ACI J. Struct. Engrg.Vol. 106-1 (2009), p. 3.

[2] E. Nigro, M. Di Ludovico and A. Bilotta: ASCE J. Mat. in Civ. Engrg., (2010) in press.

[3] W. Qu, X. Zhang and H. Huang: J. Compos. for Constr. Vol. 13-5 (2009), p. 350.

[4] H. Böhni: *Corrosion in reinforced concrete structures*, Woodhead, Cambridge, U.K, 2005.

[5] O. Buyukozturk and B. Hearing: ASCE J. Compos. for Constr. Vol. 2-3 (1998), p. 3.

[6] M. Arduini and A. Nanni: ASCE J. Compos. for Constr. 1-2 (1997), p. 63.

[7] ACI Committee 440, *Externally Bonded FRP Systems for Strengthening Concrete Structures (ACI 440.2R-02)*, American Concrete Institute, Farmington Hills, MI (2002), 45 pp.

© (2011) Trans Tech Publications, Switzerland
doi:10.4028/www.scientific.net/KEM.471-472.697

Flexural Performance of Strengthened RC Beams with CFRP Laminates Subjected to Cyclic Loading

R. Hawileh[1, a], J. A. Abdalla[1,b] and A. Tamimi[1,c]

[1]Department of Civil Engineering,

American University of Sharjah, Sharjah, UAE

[a]rhaweeleh@aus.edu, [b]jabdalla@aus.edu, [c]atamimi@aus.edu

Keywords: Reinforced Concrete beam, CFRP, Flexural strength, Cyclic loading, external strengthening systems

Abstract. Seismic retrofitting of reinforced concrete (RC) beams by means of carbon fiber reinforced polymer (CFRP) composites is one of the state-of-the-art techniques that have been widely practiced lately. Such external strengthening schemes seem to enhance both stiffness and strength of RC beams when subjected to static and cyclic loading. Extensive research investigation has been carried out for beams subjected to monotonic static loading while limited research data is available for beams subjected to cyclic loadings. Therefore, this study is initiated and its aim is to present the results of full scale experimental testing of RC beams under four-point-bending loading and subjected to monotonic and cyclic loading histories up to failure of the specimens. An unstrengthened RC beam was tested monotonically to serve as a bench-mark. The remaining two externally strengthened RC beams with different anchorage schemes were tested under cyclic loading. The strengthening test matrix included beams bonded with a unidirectional CFRP plate that covers 90% of the beam's soffit length, with one or two unidirectional layers of CFRP wraps at anchorage locations along the beam's length. The anchorage locations were at the edges of the CFRP plate and at the middle of the beam's span. The results presented herein show an increase in the overall strength for the strengthened beams over the unstrengthened ones. The different failure modes and the resulting ductility of the tested specimens are also discussed. This study is considered to be the first part of an extensive program that aims to investigate the different parameters that govern the external strengthening techniques of RC beams when subjected to cyclic loading.

Introduction

Many innovative ideas and materials have been introduced in the last few years to aid engineers to design strong and ductile structures as well as retrofit aging ones. The use of the Fiber Reinforced Polymers (FRP) is considered to be one of the latest additions to the materials used in the strengthening and retrofitting of existing structural members. The need to strengthen aging structures rises from the fact that such elements were designed based on older methods and codes that their current states are considered deficient in today's measures [1-2]. Furthermore, the exposure to aggressive environment, humidity, formation of cracks and carbonation of concrete are considered as the main reasons for the corrosion of internal steel reinforcement. Such effects might trigger a brittle failure and as a consequence require an immediate action of repair and retrofitting [3-4].

The use of FRP materials seems to be one of the most efficient solutions to strengthen RC structural members. Their well known advantageous i.e. high strength to weight ratio as well as

resistance to electro-chemical corrosion favors their use within the civil engineering applications. There are many successful attempts on which FRP has been used as strengthening materials [5-6]. Limited research has been carried out on the performance of structural members strengthened with CFRP sheets or laminates when subjected to cyclic loading. Zeris et al. [1] conducted an experimental program that included eight two-span rectangular RC beams strengthened with CFRP and Glass FRP (GFRP) sheets and Near Surface Mounted (NSM) bars tested under monotonic and cyclic loadings. The authors compared different strengthening schemes based on over strength, ductility and deflection capabilities. They concluded that the use of FRP could increase both the overall strength and ductility of RC beams under monotonic and cyclic loadings. Different failure modes and comparison with the ACI 440 [7] code were also discussed.

On the other hand, Nigro et al. [2] conducted cyclic tests on CFRP plates and sheets externally bonded to RC prisms to study the bond behavior of CFRP materials under cyclic loading. The authors compared the effect of applying different cycles as well as percentages from the maximum peak load on the bond action. They concluded that the current codes of practice in strengthening structural members impose conservative limits and thus they recommended that further studies on strengthened structural elements are warranted to develop a better understanding of such systems when subjected to cyclic loading. The aim of this paper is to presents the results of RC beams strengthened with CFRP plates and anchored with CFRP sheets, and subjected to cyclic loading history.

Experimental Program

A total of three RC beams were tested as a first part of an extensive experimental research investigation on the performance of strengthened RC beams with CFRP plates when subjected to cyclic loading. The tested RC beams have a rectangular cross section of 240 mm in depth, 120 mm in width and 1840 mm in length. The clear span length of the tested specimens is 1690 mm. The beams were reinforced with two top and bottom 10mm diameter reinforcement bars. The shear reinforcements comprised of 8mm diameter Stirrups spaced at 80mm center to center. The steel reinforcement had an average elastic modulus and yield strength of 200 GPa and 460MPa, respectively. All the specimens were casted from the same concrete mix with a measured average cylinder compressive strength of 50 MPa.

The first beam (MC) is unstrengthened and was selected to serve as a control beam. The specimen (MC) was tested under monotonic loading up to failure. The other two RC specimens were strengthened with Sika® CarboDur® S1012 CFRP plates bonded to the soffit of the beams and anchored with SikaWrap®-300 C/60 CFRP sheets. The used CFRP plate has a thickness and width of 1 and 100mm, respectively. The CFRP sheets were unidirectional and have a thickness of 0.17mm. The mechanical properties of the CFRP plates, sheets and epoxy used in this study are provided in Table 1. The CFRP sheets were wrapped as a U-shape on three locations along the span of the RC beam, namely, at both edges and at midspan of the beam specimens. Table 2 shows details of each specimen as well as the strengthening technique used.

The beams were tested using the universal Instron testing machine (UTM) shown in Fig. 1 that has static and dynamic capacities of 2200 and 2000kN, respectively. Figure 2 shows the cyclic load history used in testing the strengthened specimens, CPW1-90 and CPW2-90. The specimens were loaded to the same peak level twice before proceeding to the higher load level and unloaded to 25 kN at the end of each cycle up to failure.

Table 1 Mechanical Properties of the strengthening system used in the study

Material	Modulus of elasticity [GPa]	Ultimate Tensile strength [MPa]	Elongation at failure [%]
Sika® CarboDur® S1012	160	3100	1.7
SikaWrap®-300 C/60	230	3900	1.5
Sikadur®-30 LP	10	Concrete Fracture	-
Sikadur®-330	4.5	30	0.9

Table 2 Experimental program

Specimen	Designation
MC	Monotonic Control
CPW1-90	Cyclic test with 1 layer of wrapping & plate 90%
CPW2-90	Cyclic test with 2 layers of wrapping & plate 90%

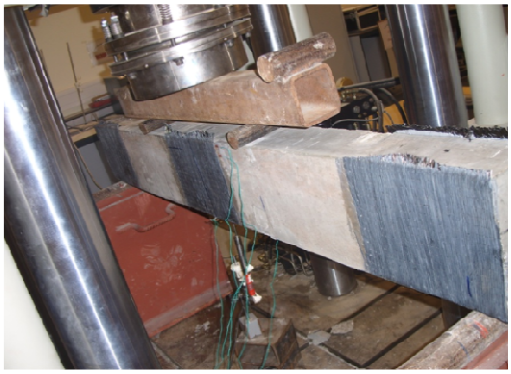


Fig. 1 Test Setup

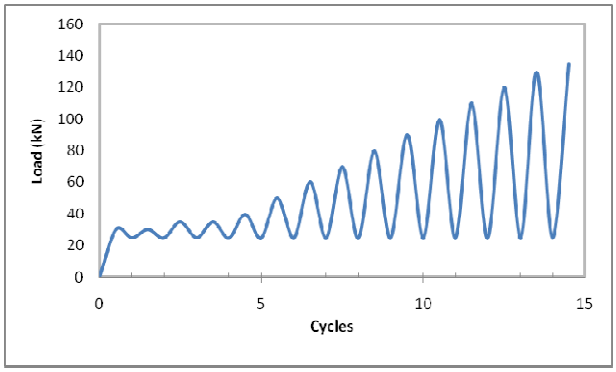


Fig. 2 Sample Cyclic loading History

Results and Discussion

Figure 3 shows the load-defection history of the control beam tested under monotonic loading in addition to the response envelopes of CPW1-90 and CPW2-90 tested under cyclic loading. The response envelopes curves were drown by connecting the peak points of the loading cycles. Upon comparing CPW1-90 and CPW2-90 with respect to the control beam, it is observed that the two strengthened RC beams showed significant improvement in strength and stiffness and drastic loss on ductility. Furthermore, Fig. 3 clearly shows that the use of two layers of CFRP sheets increased the stiffness and reduced the beam's ductility compared to both CPW1-90 and MC specimens, respectively.

Figure 4 shows the hysteresis load-deflection loops for the cyclic tested specimens. It is evident from Fig. 4 that both specimen (CPW1-90) and (CPW2-90) behaved in the same manner. The area under the hysteresis curve indicated the amount of energy dissipation of the specimens. It is clear from Fig. 4 that little energy is dissipated by the strengthened beam specimens indicating low ductility when subjected to cyclic loading. In addition, it seems that the increase number of CFRP sheet layers didn't contribute much to the strength nor to the ductility due to plate debonding prior to reaching the beams' full capacity.

Table 3 draws a comparison of the tested beams in terms of the ultimate load, maximum mid-span deflection, deflection percentage difference and failure modes. The MC specimen failed in a flexural manner at a load of 58kN after the formation of excessive flexural cracks upon yielding of the steel reinforcement. CPW1-90 specimen failed at a significantly higher load of 136kN by plate debonding followed by rupture of one of the CFRP sheets placed at the edge, while CPW2-90 specimen failed at a load of 130kN by plate debonding. The maximum mid-span deflection at failure of (CPW1-90) and (CPW2-90) was less than the (MC) specimen by 38.2 and 31.2%, respectively. Figure 5 shows the failure modes of specimens (CPW1-90) and (CPW2-90).

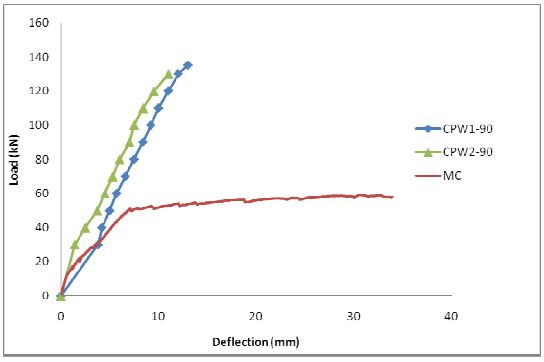
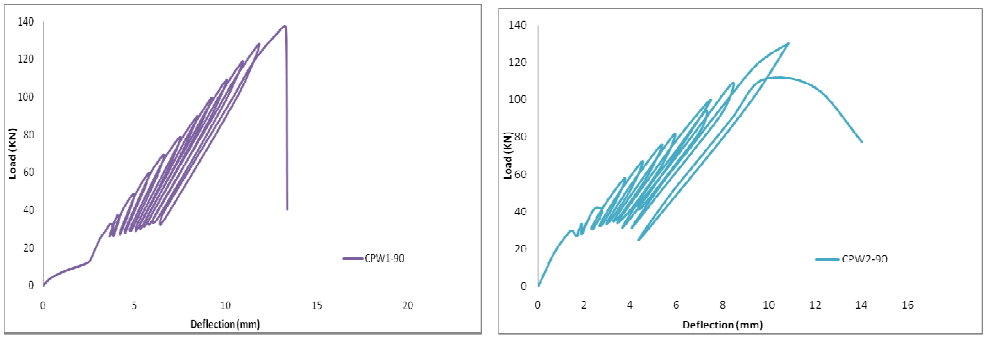


Fig. 3 Load history of the tested specimens



(a) CPW1-90 (b) CPW2-90

Fig. 4 Hysteresis loops of the strengthened beams

Table 3 Comparison between the tested specimens

Specimen	Ultimate load [kN]	Maximum deflection [mm]	% reduction in failure deflection compared to (MC)	Failure mode
MC	58	34	-	Flexural
CPW1-90	136	13	-38.2	Plate debonding followed by sheet rupture
CPW2-90	130	10.8	-31.8	Plate debonding



(a) CPW1-90 (b) CPW2-90

Fig. 5 Failure modes of the specimens tested under cyclic loading

Summary

In this study, three RC concrete beams were tested under four-point loading subjected to cyclic loading as a part of an extensive experimental research investigation program. Based on the tested data, it can be concluded that:

1. FRP external strengthening systems can improve the stiffness and overall strength of RC beams if designed properly.
2. The use of CFRP laminates as externally strengthening systems seems to significantly increase the strength on the expense of the ductility as observed from comparing the different tested specimens in this study.
3. The ultimate load capacity of the strengthened specimens CPW1-90 and CPW2-90 have increased by about 134.5 and 124.1%, respectively compared to that of the MC specimen.
4. The deflection at failure of the strengthened specimens CPW1-90 and CPW2-90 have decreased by about 38.2 and 31.2%, respectively compared to that of the MC specimen.

Further studies are warranted on the behavior and performance of strengthened RC beams with CFRP sheets when subjected to cyclic loading. It should be noted that the authors are currently conducting further experimental tests on beam specimens externally strengthened with CFRP

laminates using different schemes and configurations to investigate the performance of several strengthening parameters under cyclic loading.

Acknowledgement
The authors acknowledged the technical support and materials provided by Sika, UAE, and the help provided by the following civil engineering senior students: Mr. Ghanim Kashwani, Mr. Ali Sayed, Mr. Saber Abedi, Ms. Chaza Hoteit, Ahmed Ansari, Mr. Raed Abukuwaik, and Mr. Ramez Alqumssan. We also want to acknowledge the help of Eng. Arshi Faridi and Muhanad Naser for their help in conducting the tests.

References

[1] C. Zeris, J. Anastasakis and J. Kyriakidis: ACI J. Struct. Engrg.Vol. 106-1 (2009), p. 3.

[2] E. Nigro, M. Di Ludovico and A. Bilotta: ASCE J. Mat. in Civ. Engrg., in press (2010).

[3] W. Qu, X. Zhang and H. Huang: J. Compos. for Constr. Vol. 13-5 (2009), p. 350.

[4] H. Böhni: *Corrosion in reinforced concrete structures*, Woodhead, Cambridge, U.K (2005).

[5] M. So and T. Harmon: ACI J. Struct. Engrg.Vol. 105-2 (2008), p. 196.

[6] B, Li and H. Chua: ASCE J. Struct. Engrg. Vol. 135-10 (2009), p. 1177.

[7] ACI Committee 440, *Externally Bonded FRP Systems for Strengthening Concrete Structures (ACI 440.2R-02)*, American Concrete Institute, Farmington Hills, MI (2002), 45 pp.

© (2011) Trans Tech Publications, Switzerland
doi:10.4028/www.scientific.net/KEM.471-472.703

Experimental and Numerical Investigation of Mixed-mode Fracture Properties of Woven Laminated Composite

Mohammad Hossein Heydari[a], Naghdali Choupani[b]

Sahand University of Technology, Tabriz, Iran

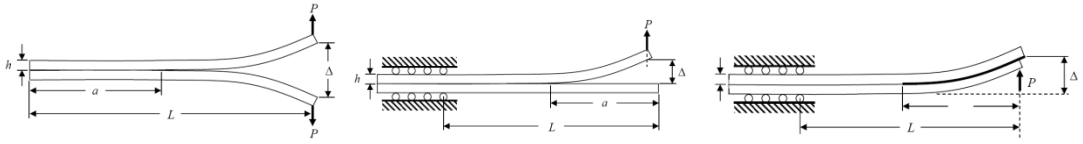
[a]Mhh.Mechanic@gmail.com , [b]Choupani@sut.ac.ir

Keywords: Fracture Mechanics, Arcan, Composite, Abaqus, Correction Factors

Abstract. Delamination is a major problem associated with composite materials that reduce the stiffness of structure used in aerospace, marine and automotive technology. Interlaminar fracture toughness, non dimensional stress intensity factors and delamination crack growth behavior were investigated for carbon fiber (CF)-polyester laminates. All tests were performed with modified version of *Arcan* specimen. By changing the loading angles in range of 0-90° mode-I, mode-II and all mixed mode fracture toughness data were obtained. Correction factors were obtained with finite element analysis using *Abaqus* software. By employing experimentally measured critical loads and the aid of the finite element method, mixed-mode *fracture toughness* for the composite under consideration determined. The fracture surfaces of the CF-P under different mixed-mode loading conditions were examined by optical and scanning electron microscopy (SEM) to gain insight into the failure responses.

Introduction

Carbon fiber composites, particularly those with polymeric matrices, have become the dominant advanced composite materials for aerospace, automobile and other applications due to their high strength, low density, and reasonable cost. The properties of the laminate depend very much on the properties of the lamina. The behavior of each lamina is, in turn, governed by its constituents, i.e. the properties of the fibres, the surrounding matrix, the interface and the relative amount of fibres and matrix in the lamina [1-3, 16]. Delamination represents the weakest failure mode in laminated composites, and is considered to be the most prevalent life-limiting crack growth mode in most composite structures. Delamination may be introduced during processing or subsequent service conditions. It may result from low-velocity impact or from discontinuities in structures, which induce a significant out-of-plane stress [4, 17]. For a given defect, crack propagation may be accomplished in opening-mode (mode-I), shearing mode (mode-II), and tearing-mode (mode-III). The most widely accepted specimen geometry for determining the mode-I strain energy release rate of adhesively bonded joints and composite materials, as shown in Fig 1.a, is the double cantilever beam (DCB). For study of mixed mode interlaminar fracture behavior of composite materials, the single leg bend (SLB) specimen has been used (Fig. 1.b). The end loaded split (ELS) specimen configuration (Fig. 1.c), mostly has been utilized for the mode-II interlaminar fracture testing of composite materials [5,6,18, 19].



(a) (b) (c)

Fig.1, Schematic of (a) double cantilever beam (DCB), (b) single leg bend (SLB) and (c) end loaded split (ELS) specimen configuration [5]

The main purpose of this paper is detecting the interlaminar fracture properties of woven Carbon-Polyester composite using modified version of Arcan specimen. By changing the loading angle from 0 to 90° mode-I, mode-II and all mixed mode fracture data were obtained. With Arcan

specimen both normal and shear fracture are determined. Arcan specimen for the first time in 1978 was presented for providing plane stress condition in fracture test of mode-I, mode-II and mixed mode conditions. The use of Arcan apparatus has been extended to the measurement of quasi-static energy release rate of cracked carbon/epoxy specimens as tested in modes I and II. In an in-depth study, Hung and Liechti were interested in the determination of shear moduli and the most suitable geometry of carbon fiber reinforced thermoplastic specimens submitted to Arcan tests [7, 8].

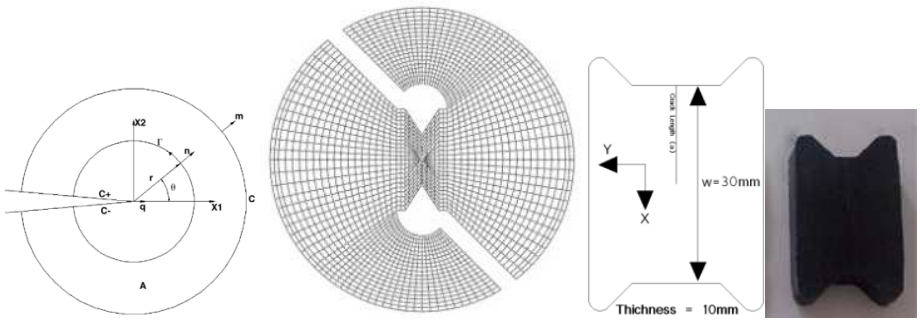
Finite Element Analysis. Finite element analysis results were obtained with ABAQUS software [9]. The stress intensity factors K_I, K_{II} and K_{III} play an important role in linear elastic fracture mechanics. They characterize the influence of the load or deformation on the magnitude of crack tip stress and strain fields and measure the propensity of crack propagation or the crack driving forces. Furthermore, the stress intensity can be related to the energy release rate (the J-integral) for a linear material through [9]:

$$J = \frac{1}{8\pi} K^T .B^{-1} .K \qquad (1)$$

Where $K= [K_I \quad K_{II} \quad K_{III}]^T$ and B is called the pre logarithmic energy factor matrix. In order to calculate stress intensity factors, interaction integral method is commonly used. In general, the J-integral for a given problem can be written as:

$$J = \frac{1}{8\pi} [K_I B_{11}^{-1} K_I + K_I B_{12}^{-1} K_{II} + K_I B_{13}^{-1} K_{III} + (\text{Terms not involving } K_I)] \qquad (2)$$

Where I, II, III correspond to 1, 2, 3when indicating the components of B. Fig. 2.a,b shows example of the mesh pattern of the specimen, which were performed with ABAQUS under a constant load of 1000 N. The entire specimen was modeled using eight node collapsed quadrilateral element and the mesh was refined around crack tip, so that the smallest element size found in the crack-tip elements was approximately 0.25mm.



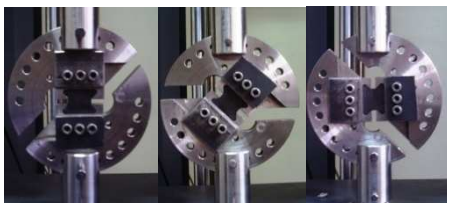
(a) (b) (c) (d)

Fig.2, (a) Contour integral around the crack tip (b) mesh pattern (c, d) schematic of the Specimen

To prepare the specimens by hand layup method, 130 layers of cross-ply carbon laminates each of 0.2 mm thickness and 350 mm length and 50 mm width was put together to form a block with dimension of 350*50*26 mm. To create a pre crack in specimens, before hot press step, a layer of Teflon with 0.1mm thickness and the dimensions of 25*350mm inserted between 65th and 66th layer, this layer had the dimensions of 25*350mm. To reduce the effect of involved errors, experiments in each angle was repeated 3 times and the average value was counted as final rapture load or critical load. Test specimens are demonstrated in Fig. 2.d.

While the Arcan apparatus was primarily suited for the biaxial testing of fiber-reinforced materials, recent developments have shown that the Arcan test can also be used with adhesives, isotropic and composite materials [10]. A simple and compact fracture mechanics specimen was

used for the determination of fracture toughness under mode-I, mode-II and mixed-mode loading conditions. The loading device is simply installed in the universal testing machine (Fig. 3).



(a) (b) (c)

Fig.3 Overview of loading device and test setup: (a) pure mode-I (b) mixed-mode (c) pure mode-II

An Overview of Mixed-Mode Fracture Mechanics. The purpose of fracture toughness testing is to determine the value of the critical stress intensity factor, or plane strain fracture toughness K_C. This material property is used to characterize the resistance to fracture in the design of structural members. ASTM standards E399 [11] and D5045 [12] give some guidance for plane strain mode-I fracture toughness K_{IC} for metals and plastics. The stress intensity factor K_C at the tip of the pre crack in a compact tension specimen is given by:

$$K_c = \frac{P_c\sqrt{\pi a}}{wt} f\left(\frac{a}{w}\right) \tag{3}$$

Where P_C is the fracture load, a is the crack length, w is the specimen width, t is the specimen thickness, and $f\ (a/w)$ is a geometrical factor. Linear elastic fracture mechanics and plane strain conditions are the primary requirements. Due to presence of weak planes between the layers of a composite laminate, interlaminar fracture are often subjected to a mixed-mode stress field. The stress intensity factors ahead of the crack tip for a modified version of Arcan specimen were calculated by using the following equations [11-15]:

$$K_{Ic} = \frac{P_c\sqrt{\pi a}}{wt} f_I\left(\frac{a}{w}\right), \qquad K_{IIc} = \frac{P_c\sqrt{\pi a}}{wt} f_{II}\left(\frac{a}{w}\right) \tag{4}$$

Where P_C is critical load at fracture, w is specimen length, t is specimen thickness and a is crack length. In turn K_I and K_{II} are obtained using geometrical factors $f_I\ (a/w)$ and $f_{II}\ (a/w)$, respectively, which are obtained through finite element analysis of Arcan test specimen.

Results and Discussion

Numerical Results. In order to assess stress intensity factors at fracture K_{Ic} and K_{IIc} using Eq.4, geometrical factors or non-dimensional stress intensity factors $f_I(a/w)$ and $f_{II}(a/w)$ for pure mode-I and pure mode-II and all mixed mode loadings were determined using ABAQUS software. To compare the non-dimensional stress intensity factors for different loading angles from fig.4, it can be seen that as mode-II loading contribution increases, the mode-I stress intensity factor decreases and the mode-II stress intensity factor increases. It is also seen that for loading angles $\alpha < 67°$ the mode-I fracture becomes dominant. For $\alpha > 67°$mode-II fracture becomes dominant.

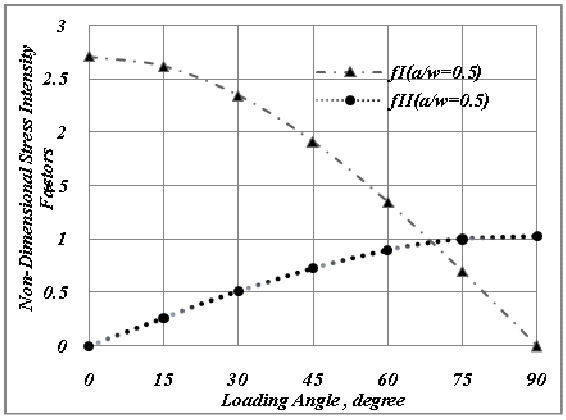


Fig.4. Non-dimensional stress intensity factor vs. loading angle of C-P for the crack length =15mm

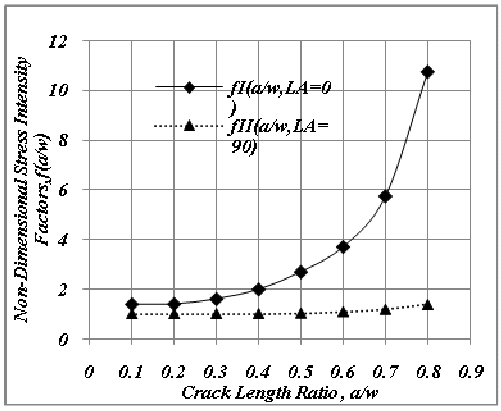


Fig.5. Non-dimensional stress intensity factor vs. crack length ratio of Carbon-Polyester composite

In order to assess geometrical factors or non-dimensional stress intensity factors $f_I(a/w)$ and $f_{II}(a/w)$ for C-P composite, the a/w ratio was varied between 0.1 and 0.8 and a fourth order polynomial was fitted through finite element analysis as (Fig. 5):

$$f_I\left(\frac{a}{w}\right)(\alpha = 0) = 173.65\left(\frac{a}{w}\right)^4 - 298.22\left(\frac{a}{w}\right)^3 + 182.17\left(\frac{a}{w}\right)^2 - 34.32\left(\frac{a}{w}\right) + 4.23 \quad (5)$$

$$f_{II}\left(\frac{a}{w}\right)(\alpha = 90°) = -16.25\left(\frac{a}{w}\right)^4 + 41.02\left(\frac{a}{w}\right)^3 - 38.45\left(\frac{a}{w}\right)^2 + 9.95\left(\frac{a}{w}\right) + 0.102 \quad (6)$$

Here a/w is the crack length ratio, where a is the rack length and w is the specimen width.

Experimental Results. Fracture tests were conducted by controlling the constant displacement rate of 0.5 mm/min and the maximum fracture loads and displacements were recorded. For each of the three specimens, mode-I, mode-II and five mixed-mode loading conditions were used as shown in Table 1. By applying the non dimensional stress intensity factor from fig.4 and critical loads to Eq.4, critical interlaminal fracture toughness (K_C) for C-P composite were obtained (Table 2). By increasing loading angle, α, from 0° to 90° K_{IC} decreases, that maximum value is 1.08(MPam^0.5) where α=0° Also by increasing loading angle, α, from 0° to 90° K_{IIC} increases that maximum value is 1.2(MPam^0.5) where α=90°. It is seen that for loading angles $\alpha \leq 60°$, the mode-I contribution is greater than that of mode-II and the opening-mode fracture becomes dominant. For loading angles $\alpha \geq 75°$ there is an opposite trend and the shearing mode fracture becomes dominant. From Table 2, it can be seen that the shearing mode (α=90°) interlaminar fracture toughness is larger than the opening mode (α=0°) interlaminar fracture toughness. This means that the interlaminar cracked specimen is tougher in shear loading conditions and weaker in tensile loading conditions.

Table 1 Critical mixed-mode interlaminar fracture loads P_c for C-P with crack length =15 mm

		Loading Angle(deg)						
	State	*0*	*15*	*30*	*45*	*60*	*75*	*90*
Critical	*1*	*520*	*540*	*600*	*635*	*850*	*1150*	*1680*
Load	*2*	*580*	*560*	*585*	*645*	*870*	*1070*	*1690*
(N)	*3*	*550*	*585*	*595*	*660*	*870*	*1090*	*1510*
Average		*550*	*561.7*	*593.3*	*646.7*	*865*	*1103.3*	*1626.7*

Table 2, Critical stress intensity factors (MPam$^{1/2}$) for C-P composite with crack length = 15 mm

		Loading Angles(deg)						
		0	*15*	*30*	*45*	*60*	*75*	*90*
Fracture Toughness	K_{Ic}	*1.08*	*1.06*	*1.00*	*0.89*	*0.84*	*0.56*	-----
	K_{IIc}	-------	*0.10*	*0.22*	*0.34*	*0.56*	*0.8*	*1.2*

Failure Surfaces of Mixed-Mode Interlaminar Fracture. The mode-I interlaminar fracture surfaces were examined using a scanning electron microscope (SEM) (Fig.6-a, b). Fig. 6-a shows the fractograph of the mode-I fracture of the initiation area taken just beyond the pre crack insert film of the woven carbon-polyester composite. Therefore, the fracture surfaces show the first increment of interlaminar crack growth which corresponds to the measured fracture toughness. The mode-I fracture surface is indicative of a brittle cleavage failure with relatively smooth and flat matrix fracture and shows debonding between fibre and matrix (Fig. 6-b), which would explain the low mode-I fracture toughness. Bundles of fiber which are in the direction of crack extension, also, were peeled out in the edge of warp fibers that confirm the opening-mode of loading (6-c).

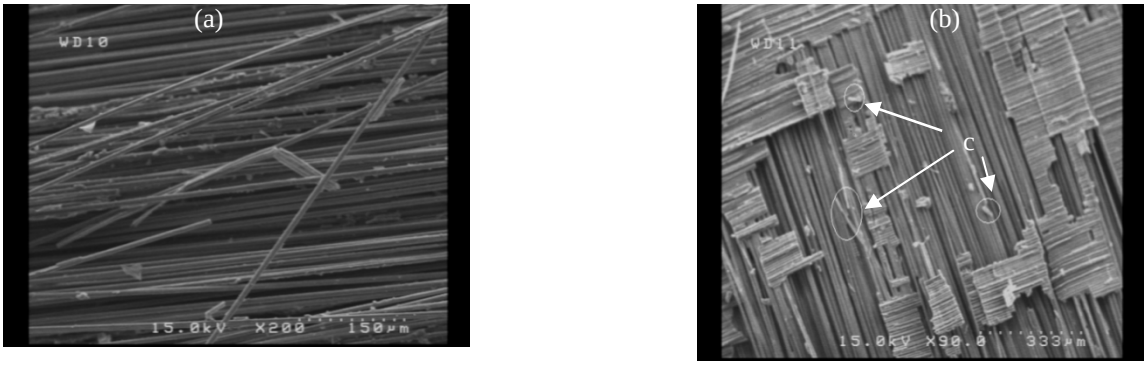


Fig.6, SEM micrograph of mode-I (α=0°) fracture surface (a) Initiation fracture surface, (b) propagation fracture surface

The observations of the mode-II fracture surfaces were carried out with scanning electron microscopy (SEM), are shown in Fig. 7-a and b. A scanning electron micrograph of the area at the rear of the crack tip of the fracture surface of the mode-II specimen is shown in Fig. 7-a. everywhere on the fracture surface of the specimens, broken fibres were observed, as the marks of fibre- matrix debonding and hackles accompanied by fragmentation of the matrix phase. Fig. 7-b shows the fractograph of a mode-II fracture at the propagation area. Its characteristic is numerous inclined hackles of the matrix fracture and troughs where fibres have been pulled away from the matrix indicating interfacial failure (7-c).



Fig.7, SEM micrograph of a mode-II (α=90°) fracture surface of C/PE composite: (a) initiation areas and (b) propagation areas.

Summary
In this study, interlaminar fracture toughness, non dimensional stress intensity factors and delamination crack growth behavior were investigated for carbon fiber (CF)-polyester laminates. All tests were performed with modified version of *Arcan* specimen. By changing the loading angles in range of 0-90°, mode-I, mode-II and all mixed mode fracture toughness data were obtained.

References

[1] Martin Knops: *Analysis of Failure in Fiber Polymer Laminates*. The theory of Alfred Puck, Springer (2008)

[2] Deborah D. L. Chung: *Carbon Fiber Composites* (Butterworth-Heinemann, 1994)

[3] M. J. Hinton, P. D. Soden, A. S. Kaddour: *Failure Criteria in Fibre Reinforced Polymer Composites*, Elsevier (2004)

[4] Jang-Kyo Kim, Yiu-Wing Mai: *Engineered Interfaces in Fiber Reinforced Composites*, Elsevier, (1998)

[5] David J. Pohlit II: *Dynamic Mixed-Mode Fracture of Bonded Composite Joints for Automotive Crashworthiness*, Master of Science in Engineering Mechanics (Blacksburg, Virginia, 2007)

[6] D. Cartie, P. Davies, M. Peleau, I.K. Partridge, Compos: Part B, 37, (2006)

[7] P.B. Gning, D. Delsart, J.M. Mortier , D. Coutellier, Compos: part B, (2010), PP: 308–316

[8] M. Nikbakht and N. Choupani, Int. J of Mech. Indus. and Aero. Eng (2008)

[9] Hibbit, Karlsson and Sorensen, HKS Inc, Pawtucket, *"ABAQUS User's Manual*, USA (2004)

[10] R. Hasanpour, N. Choupani, Int. J of Rock Mech & Mining Sci (2009), PP. 346–354

[11] ASTM E399. *Standard test method for plane strain fracture toughness and strain energy release rate of metalic materials*. In: Annual book of ASTM standards (1983)

[12] ASTM D5045. *Standard test method for plane strain fracture toughness and strain energy release rate of plastic materials*. In: Annual book of ASTM Standards (1995)

[13] Choupani N. Mater. Sci. Eng. A (2008), 478, PP. 229–42

[14] Noury PM, Shenoi RA, Sinclair I, Int. J Fract. (1998); 92:pp.131–51

[15] Gdoutos EE, *Problems of Mixed mode Crack Propagation*, Boston, USA: Kluwer (1984)

[16] Z. Wei, L.H. Yam, L. Cheng, Compos. Struc. 64 (2004), PP. 377–387

[17] Shun-Fa Hwang, Shu-Mei Huang, Compos Struc 68 (2005), PP. 157–165

[18] Ki-Young Kim, Lin Ye, Compos: Part A, 35 (2004), PP. 477–487

[19] C.T. Sun, C. Han, Compos: Part B, 35 (2004), PP. 647–655

© (2011) Trans Tech Publications, Switzerland
doi:10.4028/www.scientific.net/KEM.471-472.709

Large Deflection Behavior of Relatively Thick Functionally Graded Plates under Pressure Loads using Higher Order Shear Deformation Theory

Mohammad Homayoun. Sadr[1, a], Mohammad. Hajikazemi[1,b] and Mona. Ramezani-Oliaee [1,c]

[1]Aerospace Engineering Department and Centre of Excellence in Computational Aerospace Engineering, Amirkabir University of Technology, Tehran, Iran

[a]sadr@aut.ac.ir, [b]hajikazemi@aut.ac.ir, [c]Mona.ramezani@yahoo.com

Keywords: Functionally graded material; Large deflection; Power law; Higher order shear deformation theory; First order shear deformation theory, classical laminated plate theory

Abstract. Large deflection analysis of thin and relatively thick rectangular functionally graded plates is studied in this paper. It is assumed that the mechanical properties of the plate, graded through the thickness, are described by a simple power law distribution in terms of the volume fractions of constituents. The plate is assumed to be under lateral pressure load. The fundamental equations for rectangular plates of FGM are obtained using the classical laminated plate theory (CLPT), first order shear deformation theory (FSDT) and higher order shear deformation theory (HSDT) for large deflection and the solution is obtained by minimization of the total potential energy.

Introduction

FGMs are heterogeneous composite materials usually made from a mixture of metals and ceramics, By gradually varying the volume fraction of constituent materials, their material properties exhibit a smooth and continuous change from one surface to another, thus eliminating interface problems. With the increased use of these materials, it is important to understand the nonlinear behavior of functionally graded plates under pressure load. Many initial nonlinear studies of isotropic and composite laminated plates have been performed. However, investigations on relatively thick FGM plates under pressure loading are limited in number. Yang et al [1] studied the large defection and post-buckling responses of functionally graded rectangular plates under transverse and in-plane loads by using a semi-analytical approach. Ghannadpour et al [2] studied the large deflection behavior of perfectly thin functionally graded square plates. They used CLPT theory and in their analysis and the displacement functions were based on the single term solution.

In this study, a large deflection behavior of square plate made of functionally graded material is studied. The material properties of the functionally graded plates, except for the Poisson's ratio, are assumed to vary continuously through the thickness of the plate, according to the simple power law distribution. The plates are assumed to be simply supported along all edges and the Classical Plate Theory (CPT), First-order Shear Deformation Theory (FSDT) and higher order shear deformation theory (HSDT) are applied throughout this work. The solution is obtained by minimization of the total potential energy of the plate. The effects of material properties on the stress field through the thickness and central deflection of the plates are determined and discussed. The effect of thickness and boundary conditions on the accuracy of the results obtained by different plate theories are determined and discussed.

Theoretical Formulation

A FGM square plate of side A and thickness h, made from a mixture of ceramics and metals, as shown in Fig. 1, is considered. It is assumed that the composition is so varied that the top surface of the plate ($z=h/2$) is ceramic-rich, whereas the bottom surface ($z=-h/2$) is metal-rich. Thus, the material properties of the FGM plate ($\mathcal{P}$), such as the Young's modulus (E) and the shear modulus (G) are functions of depth (z).

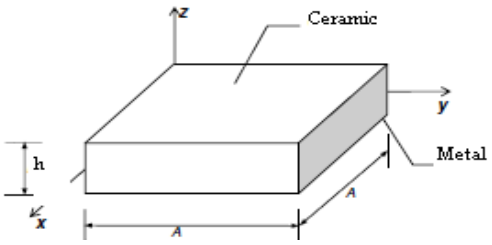


Fig.1. Typical FGM square plate.

In this study the simple power law is used [3]. The functional relationship between ϑ and z for ceramic and metal FGM plates is given by [4] as:

$$\vartheta(z) = \vartheta_{tb}\left(\frac{z}{h}+\frac{1}{2}\right)^{n} + \vartheta_b \tag{1}$$

where $\vartheta_{tb} = \vartheta_t - \vartheta_b$. $\vartheta(z)$ denotes a typical material property (E, G). ϑ_t and ϑ_b denote values of the variables at top and bottom surfaces of plates, respectively. It is evident that when $z=-h/2$, $\vartheta=\vartheta_b$ and when $z=h/2$, $\vartheta=\vartheta_t$.

In the following, the fundamental equations of the large deflection analysis of pressure-loaded functionally graded plates are briefly outlined. The plates are assumed to be simply supported along all edges and the CLPT, FSDT and HSDT are applied throughout this work. As a result of the HSDT assumption:

$$\begin{aligned}
&\overline{u}(x,y,z) = u(x,y) + z\varphi_x(x,y) - z^3 C_1(\varphi_x(x,y) + \frac{\partial w(x,y)}{\partial x})\\
&\overline{\upsilon}(x,y,z) = \upsilon(x,y) + z\varphi_y(x,y) - z^3 C_1(\varphi_y(x,y) + \frac{\partial w(x,y)}{\partial y})\\
&\overline{w}(x,y,z) = w(x,y) \qquad Where \quad C_1 = 4/3h^2
\end{aligned} \tag{2}$$

where $\overline{u},\overline{\upsilon}$ and $\overline{w}$ are components of displacement at a general point, whilst u,υ and w are similar components at the middle surfaces (z=0) and φ_x,φ_y are rotations respect to y,x axis respectively. Using Eq.2 the non-linear in-plane strains and through the thickness shear strains at a general point are:

$$\begin{aligned}
&\overline{\varepsilon} = \left\{\overline{\varepsilon}_x,\overline{\varepsilon}_y,\overline{\varepsilon}_{xy}\right\}^T = \varepsilon_0 + z\varepsilon_1 + z^3\varepsilon_3 \quad , \quad \overline{\gamma} = \left\{\overline{\gamma}_{yz},\overline{\gamma}_{xz}\right\}^T = \gamma_0 + z^2\gamma_2\\
&Where:\ \varepsilon_0{}^T = \left(\frac{\partial u}{\partial x}+\frac{1}{2}\left(\frac{\partial w}{\partial x}\right)^2, \frac{\partial \upsilon}{\partial y}+\frac{1}{2}\left(\frac{\partial w}{\partial y}\right)^2, \frac{\partial u}{\partial y}+\frac{\partial \upsilon}{\partial x}+\frac{\partial w}{\partial y}\frac{\partial w}{\partial x}\right)\\
&\varepsilon_1{}^T = \left(\frac{\partial \varphi_x}{\partial x}, \frac{\partial \varphi_y}{\partial y}, \frac{\partial \varphi_x}{\partial y}+\frac{\partial \varphi_y}{\partial x}\right),\ \varepsilon_3{}^T = -C_1\left(\frac{\partial \varphi_x}{\partial x}+\frac{\partial^2 w}{\partial x^2}, \frac{\partial \varphi_y}{\partial y}+\frac{\partial^2 w}{\partial y^2}, \frac{\partial \varphi_x}{\partial y}+\frac{\partial \varphi_y}{\partial x}+2\frac{\partial^2 w}{\partial x \partial y}\right)\\
&\gamma_0{}^T = \left(\varphi_y+\frac{\partial w}{\partial y}, \varphi_x+\frac{\partial w}{\partial x}\right), \qquad \gamma_2{}^T = -3C_1\left(\varphi_y+\frac{\partial w}{\partial y}, \varphi_x+\frac{\partial w}{\partial x}\right)
\end{aligned} \tag{3}$$

The stress-strain relationship at a general point for the plate becomes:

$$\begin{aligned}
&\left\{\bar{\sigma}_x, \bar{\sigma}_y, \bar{\tau}_{xy}\right\}^T = \left[Q_{ij}\right]\left\{\bar{\varepsilon}_x, \bar{\varepsilon}_y, \bar{\gamma}_{xy}\right\}^T, \qquad \text{where} \qquad i, j = 1,2,3 \\
&\left\{\bar{\tau}_{yz}, \bar{\tau}_{xz}\right\}^T = \left[Q_{ij}\right]\left\{\bar{\gamma}_{yz}, \bar{\gamma}_{xz}\right\}^T, \qquad \text{where} \qquad i, j = 4,5 \\
&Q_{11} = Q_{22} = \frac{E(z)}{1-v^2}; Q_{12} = Q_{21} = \frac{vE(z)}{1-v^2}; Q_{33} = Q_{55} = Q_{44} = \frac{E(z)}{2(1+v)}; Q_{13} = Q_{45} = Q_{23} = 0
\end{aligned} \tag{4}$$

The constitutive equations for a plate can be obtained by the use of Eqs.3 and 4 and appropriate integration through the uniform thickness.

$$\begin{aligned}
&\begin{Bmatrix}\{N\}\\ \{M\}\\ \{P\}\end{Bmatrix} = \begin{bmatrix}[A] & [B] & [E]\\ [B] & [D] & [F]\\ [E] & [F] & [H]\end{bmatrix}\begin{Bmatrix}\{\varepsilon_0\}\\ \{\varepsilon_1\}\\ \{\varepsilon_3\}\end{Bmatrix} \\
&\left(A_{ij}, B_{ij}, D_{ij}, E_{ij}, F_{ij}, H_{ij}\right) = \sum_{k=1}^{N}\int_{z_k}^{z_{k+1}} Q_{ij}\left(1, z, z^2, z^3, z^4, z^6\right)dz \quad (i, j = 1,2,3) \\
&\begin{Bmatrix}\{Q\}\\ \{R\}\end{Bmatrix} = \begin{bmatrix}[A_s] & [D_s]\\ [D_s] & [F_s]\end{bmatrix}\begin{Bmatrix}\{\gamma_0\}\\ \{\gamma_2\}\end{Bmatrix} \\
&\left(A_{ij_s}, D_{ij_s}, F_{ij_s}\right) = \sum_{k=1}^{N}\int_{z_k}^{z_{k+1}} Q_{ij}\left(1, z^2, z^4\right)dz, \quad (i, j = 4,5)
\end{aligned} \tag{5}$$

In the above equation, $\{N\},\{M\},\{P\},\{Q\},\{R\}$ are the stress resultants per unit length and $A, B, E, D, F, H, A_s, D_s, F_s$ are the plate stiffness matrices.

The strain energy per unit volume is $\frac{1}{2}\bar{\sigma}^T\bar{\varepsilon}^T + \frac{1}{2}\bar{\tau}^T\bar{\gamma}^T$. Using Equations (4) and (5) to form the strain energy, and integrating through the thickness with respect to z gives an expression for the strain energy of the plate which can be put into the form:

$$U_s = \frac{1}{2}\iint\left(\begin{aligned}&\varepsilon_0{}^T[A]\varepsilon_0 + 2\varepsilon_0{}^T[B]\varepsilon_1 + 2\varepsilon_0{}^T[E]\varepsilon_3 + \varepsilon_1{}^T[D]\varepsilon_1 + 2\varepsilon_1{}^T[F]\varepsilon_3 + \\ &\varepsilon_3{}^T[H]\varepsilon_3 + \gamma_0{}^T[A_s]\gamma_0 + 2\gamma_0{}^T[D_s]\gamma_2 + \gamma_2{}^T[F_s]\gamma_2\end{aligned}\right)dxdy \tag{6}$$

As previously indicated, the present concern is the evaluation of the response of plates under uniform pressure. Thus the external force exists in the current problem. As a result, the total potential energy is equal to the summation of strain energy and potential energy of uniform pressure, i.e.

$$V = U_s + V_P \tag{7}$$

where V_P is the potential energy of uniform pressure and is equal to :

$$V_P = \iint qwdxdy \tag{8}$$

Where q is the uniform pressure. Solution of the non-linear problem is sought through the application of the principle of Minimum Potential Energy. This, of course, requires the assumption of a displacement field to represent the variations of u, υ, w and φ_x, φ_y over the middle surfaces. It is assumed that all four edges of plates are simply supported with no in-plane displacements, i.e., they are prevented from moving in the x and y directions. These following displacement fields are same for both CLPT, FSDT [5], HSDT analyses.

$$u=\sum_{i=1}^{m}\sum_{j=1}^{m}u_{i,j}\sin\left(\frac{2i\pi x}{A}\right)\sin\left(\frac{(2j-1)y}{A}\right),\quad v=\sum_{i=1}^{m}\sum_{j=1}^{m}v_{i,j}\sin\left(\frac{2i\pi y}{A}\right)\sin\left(\frac{(2j-1)x}{A}\right)$$
$$w=\sum_{i=1}^{n}\sum_{j=1}^{n}w_{i,j}\sin\left(\frac{(2i-1)x}{A}\right)\sin\left(\frac{(2j-1)y}{A}\right) \tag{9}$$

And for φ_x,φ_y in FSDT, HSDT analysis:

$$\varphi_x=\sum_{i=1}^{n}\sum_{j=1}^{n}\varphi_{xi,j}\cos\left(\frac{(2i-1)\pi x}{A}\right)\sin\left(\frac{(2j-1)\pi y}{A}\right)$$
$$\varphi_y=\sum_{i=1}^{n}\sum_{j=1}^{n}\varphi_{yi,j}\cos\left(\frac{(2i-1)\pi y}{A}\right)\sin\left(\frac{(2j-1)\pi x}{A}\right) \tag{10}$$

where $u_{i,j},v_{i,j},w_{i,j}$ *and* $\varphi_{xi,j},\varphi_{yi,j}$ are undetermined displacement coefficients. The displacement functions could be in a variety of forms, but in the present work they are Harmonic functions. With the establishment of the plate displacement field, according to the above mentioned equations, the potential energy of a plate can ultimately be calculated in terms of $u_{i,j},v_{i,j},w_{i,j},\varphi_{xi,j},\varphi_{yi,j}$. The plate equilibrium equations are obtained by applying the principle of minimum potential energy. That is to say the partial differentiation of the plate potential energy with respect to $u_{i,j},v_{i,j},w_{i,j},\varphi_{xi,j},\varphi_{yi,j}$. In turn gives a set of non-linear equilibrium equations. The latter set of equations must be solved in term of undetermined displacement coefficients. After finding the undetermined displacement coefficients, it is possible to calculate the displacements u, υ ,w and φ_x,φ_y at any point in plate using Eqs. 9 and 10, to determine stress quantities through use of Eqs. 3 and 4.

Numerical Results and Discussion

As previously indicated, the analysis of FGM plate is conducted for type of ceramic and metal combination. The set of materials considered is alumina and aluminum. Young's modulus and Poisson's ratio were selected as being 70 GPa and 0.3 for aluminum, and 380 GPa and 0.3 for alumina, respectively. In all cases, the lower surface of the plate is assumed to be metal (aluminum) rich and the upper surface is assumed to be pure ceramic (alumina).

The analytic results are presented in terms of dimensionless deflection and stress. The dimensionless parameters used are as follows:

center deflection $W = w/h$

load parameter $Q = qA^4/(E_bh^4)$

axial stress $\sigma = \sigma_xA^2/(E_bh^4)$

thickness coordinate $Z = z/h$

where E_b is Young's modulus of metal (bottom surface) used in the functionally graded material, q is an uniformly distributed pressure load, A is a projected length of the plate in the xy plane, and h is a thickness of that plate. The analysis is performed on square plates with $A/h=20$ and $A/h=5$.

The number of terms needed for convergence is carefully examined. For generating the converged results, the essential number of terms in the displacement fields for u,v is 9 and for w,φ_x,φ_y is 16.

Figure 2 show the central deflection due to mechanically applied load Q for four simply supported square aluminum-alumina plates with $A/h=20$ using HSDT ,FSDT and CLPT assumptions. Under the same load, the pure aluminum plate has the largest central deflection. This is due to the fact that it has the lowest Young's modulus E_b. Even though the FGM plate (n=2)

contains a small volume fraction of alumina, it is much stiffer than the pure aluminum plate. This figure shows a negligible difference between three theories due to the high length to thickness ratio and the high level of in-plane restraints imposed at the edges, thus causing relatively small transverse deflections at the centre [5, 6]. In other words, the effects of transverse shear strain energy for relatively thin plates with high level of in-plane restraints imposed at the edges are negligible.

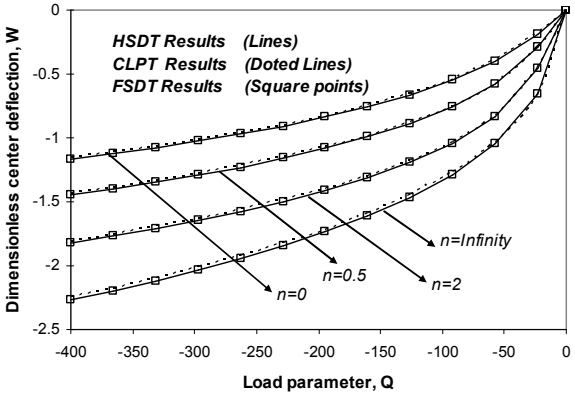


Fig.2. Dimensionless central deflection versus uniform pressure load for A/h=20.

Figures 3 and 4 show the variation of the dimensionless axial stress σ across the thickness Z at the center of the four plates investigated due to a load parameter Q=-400 for *A/h=20* and *A/h=5* respectively. The stress distribution in the aluminum and alumina plates is linear; whereas, for functionally graded material, the behavior is nonlinear and is governed by the variation of the properties in the thickness direction. The differences between results from three theories in Fig.4 are due to consideration of shear stress through the thickness in HSDT and FSDT and eliminate of that effect in CLPT.

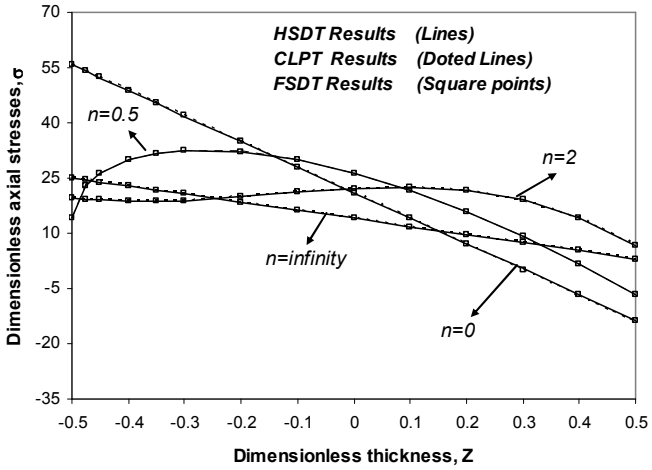


Fig.3. Dimensionless axial stress σ along the thickness Z at the center of the plate under load Q=-400 for A/h=20.

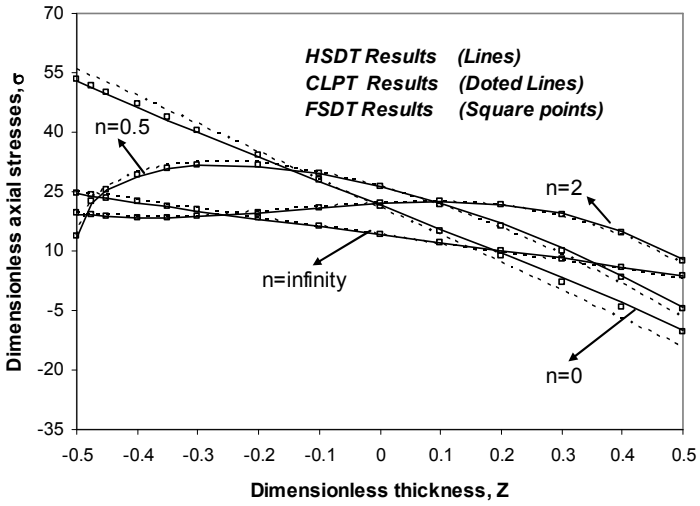


Fig.4. Dimensionless axial stress σ along the thickness Z at the center of the plate under load Q=-400 for A/h=5.

Summary

The large deflection of plates made of FGMs under pressure load is studied. The material properties of FGM plate are assumed to vary continuously through the thickness of the plate, and were graded according to a power law distribution of a volume fraction of the constituents. The solution is obtained by minimization of the total potential energy. Dimensionless deflection and stresses were computed for metal-ceramic combination of functionally graded plates with various lengths to thickness ratio. The effects of material properties on the stress field through the thickness are determined and discussed.

References

[1] J Yang, H.S. Shen, Non-linear analysis of functionally graded plates under transverse and in-plane loads. International Journal of Non-linear Mechanics 2003; 38: 467-482.

[2] S. A. M Ghannadpour, M. M Alinia. Large deflection behavior of functionally graded plate under pressure load. Composite structures 2006; 75, 1-4: 67-71.

[3] Markworth AJ, Ramesh KS, Parks Jr WP. Modeling studies applied to functionally graded materials. Journal of Material Science 1995; 30: 2183–93.

[4] Ma L.S, Wang T.J. Relationships between axisymmetric bending and buckling solutions of FGM circular plates based on third-order plate theory and classical plate theory. International Journal of Solids and Structures 2004; 41: 85-101.

[5] S. A. M Ghannadpour, M. Hajikazemi, H. R. Ovesy, "Large deflection behavior of functionally graded plates under pressure loads", proceeding of the First international conference on composites (CCFA-1),Kish island, IRAN , (15-18 Dec. 2008).

[6] J.N Reddy, Mechanics of laminated composite plates and shells theory and analysis, CRC press,2004.

© (2011) Trans Tech Publications, Switzerland
doi:10.4028/www.scientific.net/KEM.471-472.715

A Novel Phenol – Based Composite Production: Features and Characterization

Marzieh Ganji[1,a], Taghi Tabarsa[2,b]
[1] Department of Wood and Paper Science and Technology,
University of Agricultural Sciences and Natural Resources, Gorgan, Iran
[2] Department of Wood and Paper Science and Technology,
University of Agricultural Sciences and Natural Resources, Gorgan, Iran.
[a]m.ganji_87 @yahoo.com, [b]t.tabarsa@yahoo.com

Keywords: Paulownia, Tannin-phenol formaldehyde, Composite, Plywood, Mechanical properties

Abstract. The aim of this study is to investigate on manufacturing new tannin phenol-formaldehyde resin as adhesive in paulownia composite. For this purpose, renewable tannin was introduced in the classic adhesive formulation in order to supply a part of phenol–formaldehyde (PF). Variables were substituted tannin with phenol at two levels (0%, 10 % and 20%) and press temperature (150c° and 170c°). plywood panels were manufactured in laboratory. Mechanical (MOR and MOE and) and physical (TS and WA) properties of panels were evaluated according to ASTM standard. Data collected based on factorial design and using SPSS software were analyzed. The Results showed that substitution tannin with phenol had slight effect on mechanical properties but when press temperature increased mechanical properties were improved. Physical properties of plywood panels bonded with tannin–PF resins (20:80) were better than plywood panels PF made.

Introduction

Reduction of big diameter trees in natural forests caused plywood industry to reduce their capacities and some of them forced to stop production. Paulownia from plantations is a light species and very fast grown it would be considered as an alternative for trees from natural forest. On the other hand oil originated adhesive prices is rising up annually so that wood composite products manufactured using this high price adhesive cannot compete in market/3/. Recently tannin has attracted scientist because of its phenolic nature. Dalton (1950 and 1953) started basic research on tannin based adhesive then plamly (1959 and 1966) continued Dalton work and proved that Acasia bark contain material which can be used for manufacturing plywood/5/. Torkaman investigated on extractives of some hardwoods and concluded that extracts of this trees has components which can react with formaldehyde/7/. In this study feasibility of manufacturing plywood from paulownia using tannin based phenol formaldehyde resin was investigated.

Methods and material

Paulownia trees cut from a plantation located in forest of Gorgan university/ Iran. Logs were debarked and converted to layers in local plywood factory. Veneers were dried to 2% in a drier. Commercial resol-type liquid PF resin (P/F = 0.45, which is a plywood binder resin) was supplied by local company. A phenol formaldehyde resol with a solids content of 63% and a viscosity of about 450 cp was prepared using a 2.2:1 formaldehyde phenol ratio and 7.3% (w/w) of NaOH. The adhesives were prepared by copolymerization at room temperature of tannins in variable quantities with resols. Two levels of resin powder were used (10% and 20% based on oven dry weight of resin).

5 ply laboratory plywood panels of dimension 400mm×400mm×15mm were prepared from 3mm thickness Paulownia veneers of moisture content of 2% at a glue mix spread of 120 g/m2 single glue line. Glued layers were assembled and hot pressed under 15bar pressure for 10 minutes. Two press temperatures (150c° and 170c°) were used for hot pressing. Panels were kept in a conditioned room with a relative humidity of 65% and a temperature of 20 C° until they reached equilibrium moisture content. Bending strength and modulus of elasticity values of plywood panels were determined according to EN 310 (1993). Water absorption and thickness swelling (TS) after 2 and 24 h immersion of the samples were determined according to ASTM standards.

Results

The mean values of Physical and mechanical properties of plywood panels are given in Table 1 and 2. In table 1 effect of tannin on modulus of rupture(MOR), modulus of elasticity (MOE), water absorption (WA) were not significant but this effect on thickness swelling (TS) was significant with 95% confidence. The results of effect of press temperature on physical and mechanical properties of paulownia plywood are presented in table 2.

The results obtained for effect of press temperature on MOR and MOE is showed that no differences were noticeable between treatments, but its effect on thickness swelling and water absorption is significant. Interaction effects of press temperature and tannin on water absorption after two 2 and 24 hours immersion is shown in fig.1 and 2.

Table.1 Effect of tannin on physical and mechanical properties of plywood

Value of Tannin(%)	Water adsorption (%)		Thickness swelling (%)		Bending strength (MPa)		Modulus of elasticity (MPa)	
	2h	24h	2h	24h	Parallel-to-grain	Perpendicular-to-grain	Parallel-to-grain	Perpendicular-to-grain
0	27.3	48.82	5.2[b]	6.53[b]	55.13	35.2	10426.5	5364.91
10	27.84	49.74	5.18[b]	6.97[b]	51.44	30.09	9873.94	4673.63
20	26.54	48.29	3.36[a]	4.61[a]	55.83	31.29	9952.89	3928.88
Sig.	ns	ns	*	*	ns	ns	ns	ns

ns: non signification * :sig.95%

Table.2 Effect of Press temperature on physical and mechanical properties of plywood

Temperature C^{o}	Water adsorption (%)		Thickness swelling (%)		Bending strength (MPa)		Modulus of elasticity (MPa)	
	2h	24h	2h	24h	Parallel-to-grain	Perpendicular-to-grain	Parallel-to-grain	Perpendicular-to-grain
150	30.36	52.19	5.39	7.03	50.7	32.42	9475.59	4393.05
170	24.09	45.71	3.77	5.04	57.55	33.95	10693.06	4918.55
Sig.	ns	ns	*	*	ns	ns	ns	ns

ns: non signification * :sig.95%

Water absorption of control panels (0:100 T:P) is lower than all other panels. Addition tannin to PF, its reactivity with formaldehyde increases therefore stronger bond is formed which prevent water penetration inside the panel. When press temperature increased from 150C° to 170C° water absorption of panels decreased more which indicates that bond between layers became stronger. After 24 hours immersion samples the difference between control panels and experimental panels were remained however the difference between other panels removed.

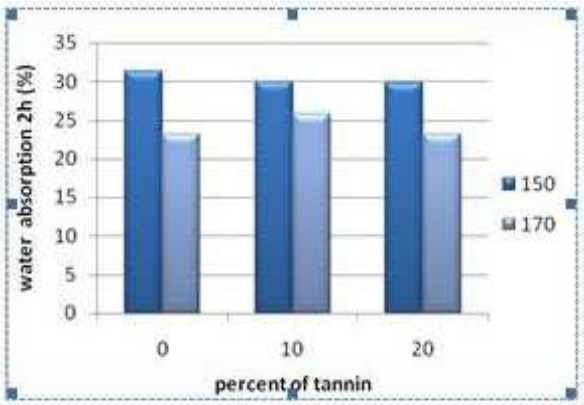


Fig.1. Interaction effects of press temperature and tannin on water absorption after 2h immersion

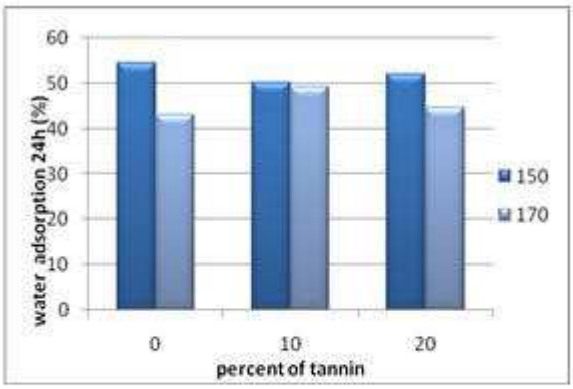


Fig.2. Interaction effects of press temperature and tannin on Water absorption after 24h immersion

Interaction effects of press temperature and tannin on thickness swelling after 2 and 24 hours immersion in fig.3 and fig.4. As seen, effect of tannin on thickness swelling is much outlined. Adding tannin to PF resin causes considerable reduction (40%) in thickness swelling of all experimental panels while thickness swelling of control panels and panels made using 10% tannin and pressed at 150 c° were high (around 6%).

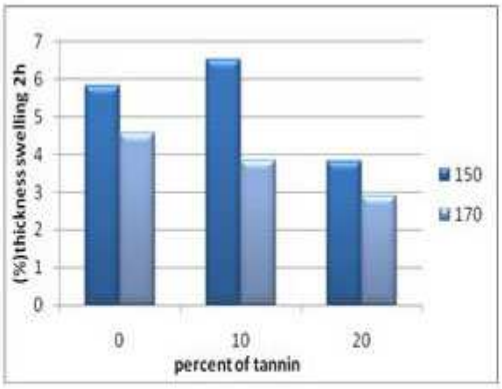


Fig.3. Interaction effects of press temperature and tannin on Thickness swelling after 2h immersion.

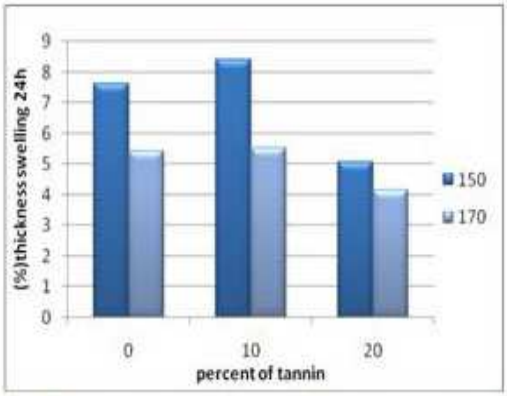


Fig.4. Interaction effects of press temperature and tannin on Thickness swelling after 24h immersion

Effect of tannin and press temperature on MOR of panels when loaded in parallel to grain direction is shown in fig.5. As seen, panels made of PF containing 20% tannin and pressed at 170C° showed the highest MOR which indicates that tannin has significant effect on MOR.

When panels were loaded in perpendicular to grain direction, control panels pressed at 170 c° had the highest MOR (fig.6). Effect of press temperature and tannin on MOE is shown in fig.7. As seen, panels pressed at 170 c° presented higher MOE than those pressed at 150 c° which indicate

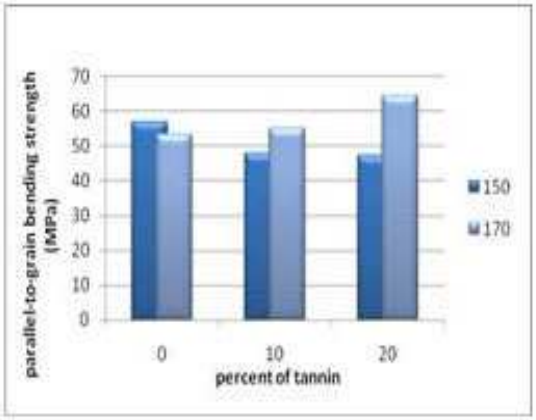


Fig.5. Interaction effects of press temperature and tannin on parallel to grain MOR

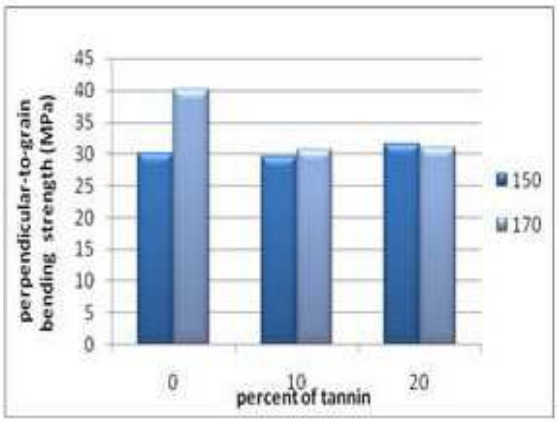


Fig.6. Interaction effects of press temperature and tannin on perpendicular to grain MOR.

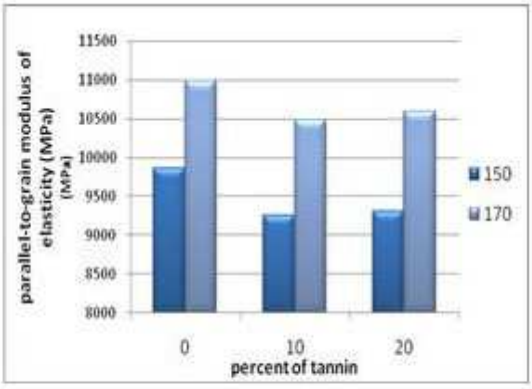


Fig.7. Interaction effects of press temperature and tannin on parallel to grain MOE

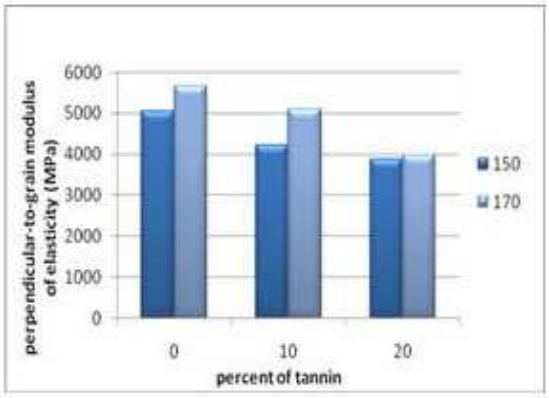


Fig.8. Interaction effects of press temperature and tannin on perpendicular to grain MOE

that effect of press temperature was stronger than effect of tannin. But when panels were loaded in perpendicular to the grain direction effect of tannin became more pronounced. However control panels and panels containing 10 percent tannin present high

Summary

Generally, it can be said that based on results of this study effect of tannin was more pronounced on thickness swelling or dimensional stability. On the other hand mechanical properties of paulownia plywood panels bonded with tannin based PF resin is promising. There is a relationship between increased addition of tannin and reduction in bond strength properties. However, it has been demonstrated that tannin could be used to replace 20% of the PF resins used to bond plywood panels, without adversely affecting bond properties. Panels manufactured using press temperature of 170c° and PF resin containing 20% tannin would meet standard requirements. Petrochemical PF could substitute in resols in industrial applications by addition of tannin extract.

References

[1] Annual Book Of ASTM Standards, West Conshohcken,AA.Vol04,10(2002)

[2] F. Faraji, Investigation On Feasibility Of Producing Moisture Resistant Plywood From Poplar, Research Report. Gorgan University Of Agricultural Sciences.(2005)

[3] S. Kazemi Najafi And K. Doosthosseini. Magazin Of Iran Natural Resources. Vol 23-31. (2000)

[4] L. Jamali Rad, , Doosthosseini, K; And S. A. Mirshokraei. Magazin Of Iran Natural Resources. Vol.60(3) (2007),P981-988.

[5] A. Moubarik, , A. Pizza, A. Allal, And B. Charrier. In: Indestrial Crops And Products,Vol. 30(2009) P.188-193.

[6] P.M. Stefani, C. Pena, R.A. Ruseckaite, J. C. Piter And I. Mondragon.In:Bioresource Technology, Vol.99 Issue13 (2008), p. 5977-5980.

[7] J. Torkaman, K. Doosthosseini, And A.J. Latibari. In: Magazin Of Iran Natural Resources, Vol.57 (2005), p.345-352.

© (2011) Trans Tech Publications, Switzerland
doi:10.4028/www.scientific.net/KEM.471-472.721

Mechanical Vibration Technique for Enhancing Mechanical Properties of Particulate Reinforced Aluminium Alloy Matrix Composite

Sayuti, M[a], Sulaiman, S[b], B.T.H.T. Baharudin[c], Arifin, M.K.A[d], Suraya, S[e] and Gholamreza Esmaeilian[f]

Department of Mechanical and Manufacturing Engineering,
Universiti Putra Malaysia, 43400 Serdang, Selangor, Malaysia

[a]tgk_sayuti@yahoo.co.uk, [b]suddin@eng.upm.edu.my, [c]tuah@eng.upm.edu.my,
[d]khairol@eng.upm.edu.my, [e]suraya@yahoo.com, [f]gre@eng.upm.edu.my

Keywords: Mechanical vibration, Impact properties, composite, metal matrix composite, LM6.

Abstract. The effects of subjecting solidifying particulate reinforced aluminium alloy matrix composite to various sources of vibration on the resulting casting quality, a mechanical vibration technique for inducing vibration resulting in enhanced mechanical properties, such as impact properties is devised. TiC particulate reinforced LM6 alloy matrix composites are fabricated by different particulate weight fraction of titanium dioxide and microstructure studies were conducted to determine the impact strength and density, respectively. Preliminary works show that the mechanical properties have been improved by using vibration mold during solidification compared to gravity castings without vibration.

Introduction

A number of literature surveys have been reported on the influence of mechanical, electromagnetic and ultrasonic vibration to metals. It is generally accepted that in certain circumstances different sources of vibration during processing of metals can enhance metallurgical and mechanical properties. Applying mechanical vibration during the solidification process it's a fairly simple technique that does not require complicated procedure or expensive setup. It can be applied for the current existing processes and does not require extensive modifications on the design of the equipments used. It requires less energy as compared to electromagnetic vibration and semisolid processes and less expensive. The low energy requirement made it the most environmentally-friendly process than any other grain refinement methods. There are three practicable methods of application of vibration; vibration of the whole of the mould, vibration of liquid, and electromagnetic induction [1-3].

Moreover, many researchers have found that mechanical vibrations of sonic, electromagnetic and ultrasonic character, when applied during solidification of metals and alloys, modify conventionally obtained macrostructures and microstructures, hence effecting its mechanical properties [4-10]. The well-documented beneficial effects of subjecting a solidifying ferrous or nonferrous melt to vibration shown in Table 1.

The objective of the present work is to study the effect of mechanical vibrations on mechanical properties of the Titanium Carbide (TiC) particulate reinforced aluminium-silicon alloy matrix composite.

Table 1. Researchers review using mould vibration to enhancing mechanical properties

Materials	Types Vibration	Influence of vibration
Aluminium LM6	Mechanical vibration [1]	Uniform distribution and refinement of primary Al Primary grains contact/connect each other forming Improvement in tensile strength with increasing amplitude of vibration
Al–18 wt%Si, Al–12% Si, A356 aluminum alloy Al-Si Alloy, Al 11.8%Si Alloy	Mechanical vibration [2-9]	Coarsening of eutectic Si, reduced of eutectic cell size, uniform distribution and refinement of primary Al, improve the density, hardness, UTS and % elongation. Decrease of porosity with increasing intensity of vibration Reduced eutectic cell size as well as primary dendrite size
Al alloy Mg composite Zn-SiC particulate	Ultrasonic [10-13]	Degassing, The refined effect enhances with the increase of vibration time, grain refinement
AZ91 alloy A356 alloy	Ultrasonic vibration [14-16]	Improve of compressive strength, ultimate compressive strength and fracture strain. Initial hydrogen concentration and reduction in porosity and shrinkage concentration in a spot achievement of uniform grains Reduced solidification time and eutectic temperature
Al-5Ti-1B	Ultrasonic [17- 19]	The narrower particle size spreads significantly improve the grain refining performance of the master alloy.
Al-Si alloy	Ultrasonic irradiation [20]	Improvement of mechanical properties Promotion of grain refinement Ductility enhancement Reduced solidification time and eutectic temperature
Al–Si alloys, Al-6%Si alloy, A356	Electromagnetic Stirring (EM) during continuous Casting [21,22]	Reduce of porosity, increase of UTS and modulus Modified eutectic only in EM mould
Al-Si Alloy Al alloy 7150 A356 Al alloy, Al-Zn-Mg-Cu-Zr ingot	Electromagnetic stirring [23-26]	Reduction in Si segregation in hypereutectic alloy Dendrite fragmentation Promotion Uniform distribution and refinement of primary Al Reduced solidification time and eutectic temperature Lest dendrite or net-global grains
Al–5Mg AZ80 Mg	Electromagnetic field [27]	Reduced diffusion layer thickness in front of the solidification front Increased concentration of alloying elements in solid solution Decreased volume of nonequilibrium eutectics Refinement of dendritic microstructure and fine distribution of nonequilibrium eutectic phases
Al–5Mg , Al–4.5Cu	Electromagnetic generator at 30 and 150 Hz, 0.05–5.52mm amplitude, 1–120 g peak acceleration [28]	Extensive grain refinement especially with high accelerations

Experimental Procedure

Material. The material used in this work was aluminium-11.8%silicon alloy. This matrix was chosen because of excellent combination of strength and damage tolerance at elevated temperatures. The reinforcement was Titanium carbide particles of size 44 microns (μm), were used as the dispersoid, respectively. Casting method was used for processing of the composite.

Fabrication of Composites. In this investigation, large ingots of aluminium-11.8%silicon alloy material weighing approximately 4 kgs were cut into small pieces for accommodating into the graphite crucible. The mechanical vibration of the mould was applied to the aluminium alloy matrix composite with and without vibration at a frequency 0 Hz and 10.2 Hz with 0.120mm amplitude. The titanium carbide particulate used as a second phase reinforcement in the alloy matrix was added on by different weights fraction 0.2, 0.6, 1 and 2% wt.

In this research work, the particulate were preheated to 200oC in a heat treatment muffle furnace for 2 hours and was then transferred immediately in the crucible containing liquid LM6 alloy for mixing by an impeller blade of the vortex stirring machine. Next, the composite liquid material was poured into the mould, which was attached on the system that provides the mechanical vibration with 10.2 Hz and 0.120 mm amplitude (Fig. 1a) and without vibration or normal position (Fig. 1b). Then, the casting was ejected from the mould after solidification and gating system was removed to get the specimens. In the final stage, the specimen was prepared to the accurate dimensions according to the standard. The actual specimens prepared for the impact tests are shown in Fig. 1c.

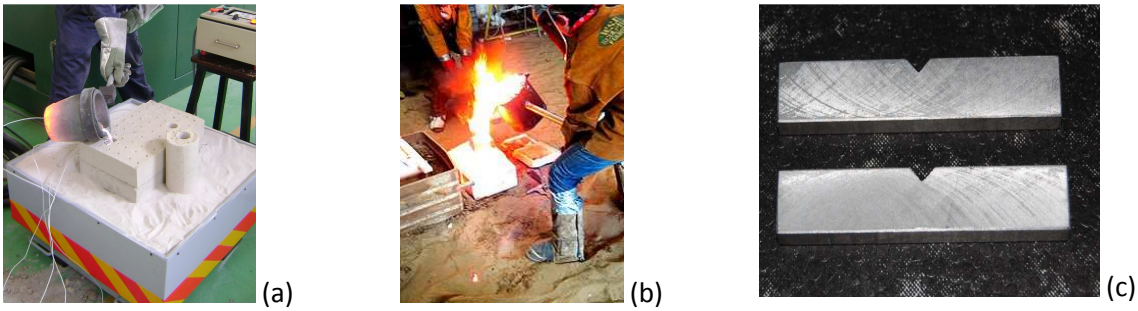


Fig. 1. (a) With vibration mould , (b) Normal Position, (c) Finished specimen for impact test.

Testing. The impact test was conducted in accordance with ASTM E 23-05 standards at room temperature using izod impact tester, Fig. 2 and Fig. 3 show the machines used to conduct the impact tests and A&D-GR 200 – Analytical Balance for density measurement, respectively.

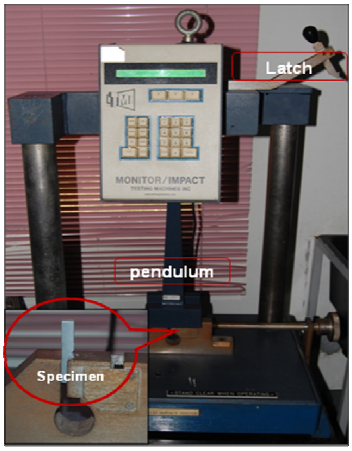


Fig. 2. Izod impact tester

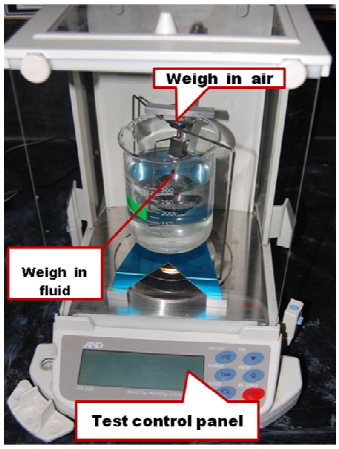


Fig. 3. Analytical balance

Experimental Results

The impact properties of particulate reinforced aluminum alloy matrix composite with and without vibration composite are given in Fig. 4. The mechanical properties of the composite with vibration are always better than that of correspondent without vibration. As shown in the figure, the impact energy value increases with increase in percent weight fraction of TiC and with using vibration during solidification. Mechanical vibration makes solidification microstructure of aluminium matrix composite fine and homogeneous and decrease the amount of defect such as shrinkage cavity and inclusions. The effect of vibration to help in the promotion of nucleation and thus reducing as-cat grain size, reducing hydrogen, reducing shrinkage porosities due to improved metal feeding, and producing a more homogenous composites structure [1,2,13]. These improved features lead to improve mechanical properties and lower susceptibility to cracking. Literature review on the effects of vibration on casting and reported an improvement of mechanical properties by as much as 40% [29]. It can be concluded that these effects play an important role on the improvement of impact energy. Fig. 5 offer the comparison of the mechanical vibration effect and weight fraction of the particles effect on the density. It is easy to draw a conclusion that, by mechanical vibration during solidification, the size of shrinkage cavity and inclusion are reduced and the amount of defects is also decreased. The densities of the samples are measured using A&D-GR 200 – Analytical Balance. It can be found that the density is higher in the sample with mechanical vibration mould than in without vibration mould. It is obvious that the amount of defect such as shrinkage cavity and inclusion is decreased and the compactness is enhanced due to applied mechanical vibration during the solidification process. The values of density in composites also increase with increasing weight fraction of the particles, because density of particles is higher than the Aluminium -11.8% Si Alloy (the density of LM6 is 2.65grs/c^3 and of TiC is 4.93grs/c^3) and hence the increase in wt.% of TiC will increase the density of the composite based on the role of mixtures [30].

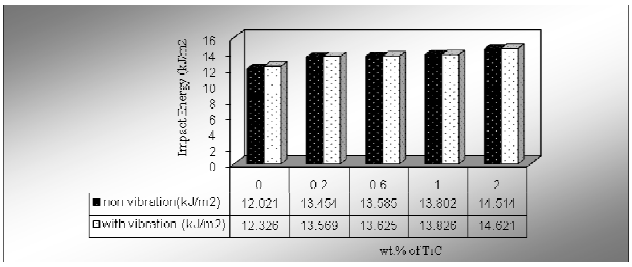


Fig. 4. Average of Impact energy vs wt.% of TiC

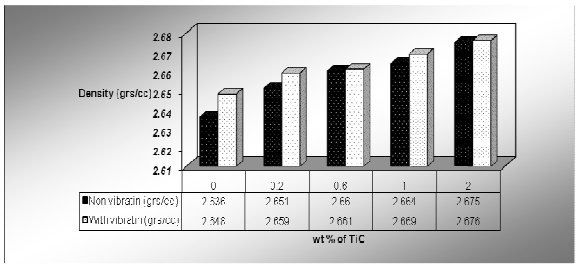


Fig. 5. Average of density energy vs wt.% of TiC

Summary

The optimum process was found in this study for production of TiC reinforced aluminium alloy matrix composite by casting technique using mechanical vibration during solidification. Density and impact energy of MMC were investigated. The following conditions have been drawn:

1. The impact energy increase with increasing in weight percentages of particles at room temperature.

2. It is possible to produce metal matrix composites having relatively better mechanical properties, by dispersing TiC in to molten aluminum alloy using mechanical vibration mould.

Acknowledgement

The authors would like to express their deep gratitude and sincere thanks to the Department of Mechanical and Manufacturing Engineering, Universiti Putra Malaysia for their help to complete this work.

References

[1] K. Kocatepe and C.F. Burdeff: Journal Materials Science 35 (2000) p. 3327–3335.

[2] G. Chirita., I. Stefanescu, D.Soares and F.S. Silva: Journal materials and Design, 30 (2009) p. 1575-1580.

[3] F. Taghavi, H. Saghafian, and Y.H.K. Kharrazi: Materials and Design 30 (2009) p. 115–121.

[4] Shusen Wu, Lizhi Xie, Junwen Zhao and H. Nakae: Scripta Materialia 58 (2008) p. 556–559.

[5] G. Chirita, I. Stefanescu, D. Soares and F.S. Silva: Materials & Design, Vol.30 (2009), p. 1575-1580.

[6] Numan Abu-Dheir, Marwan Khraisheh, Kozo Saito and Alan Male: Materials Science and Engineering A 393 (2005) p. 109–117.

[7] N.H.S. Swamy, M.A.Josepth, N.m.Nagarajan, M.K.Muralidhara and Sundaramurthy: Technical paper, Indian Foundry Journal, vol.54 (2008) p. 119-125.

[8] Chauwalid Limmaneevichitr, Songwid Pongananpanya and Julathep Kajornchaiyakul: Journal of Materials Design,vol. 30 (2009) p. 3925-3930.

[9] X.Jian, H.Xu, T.T.Meek and Q.Han: Material letters, 59 (2005) p. 190-193.

[10] R.M. Pillai, K.S. Biju Kumar and B.C. Pai: Journal of Materials Processing Technology 146 (2004) p. 338–348.

[11] Chen Ke, Li Zi-quan, Zhou Heng-zhi and Wang Wei: Trans nonferrous Met. Soc. China 18 (2008) p. 842-846.

[12] S. Maleksaeedi, M.H. Paydar, S. Saadat, and H. Ahmadi: Journal of the European Ceramic Society, Volume 28, Issue 16, December 2008, p. 3059-3064.

[13] Zhiwu Xu, Jiuchun Yan, Wei Chen and Shiqin Yang: Materials letters, 62 (2008) p. 2615-2618.

[14] Jianbo YU, Zhongming REN, Weili REN, Kang DENG and Yunbo ZHONG: Acta Metall. Sin.(Engl. Lett.)Vol.22(2009) p. 35-39.

[15] Xinbao Liu, Yoshiaki Osawa, Susumu Takamori, and Toshiji Mukai:Materials Science and Engineering A 487 (2008) p. 120–123.

[16] Hanbing Xu, Xiaogang Jian, Thomas T. Meek and Qingyou Han: Materials Letters 58 (2004) p. 3669–3673.

[17] Yanfeng Han, Ke Li, Jun Wang, Da Shu and Baode Sun: Materials Science and Engineering A 405 (2005) p. 306–312.

[18] Yanfeng Han, Ke Li, Jun Wang, Da Shu and Baode Sun: Materials Science and Engineering A 405 (2005) p. 306–312.

[19] Yanfeng Han, Da Shu, Jun Wang and Baode Sun: Materials Science and Engineering A 430 (2006) p. 326–331.

[20] ZHAO Jun-wen, WU Shu-sen, XIE Li-zhi, AN Ping and MAO You-wu: Trans nonferrous Met. Soc. China 18 (2008) p. 842-846.

[21] Ch. Vives: J.Materials Science and Engineering (1993) p. 169-172.

[22] Ch. Vives: JOM-e vol.50 (1998).

[23] W.D. Griffiths and D.G. McCartney: Materials Science and Engineering A216 (1996) p. 47-60.

[24] W.D. Griffiths and D.G. McCartney: Materials Science and Engineering A222 (1997) p. 140-148.

[25] Liu Zheng, Mao Weiimin and Zhao Zheng-duo: Transaction of Nonferrous Metals Society of China, 16 (2006) p. 71-76.

[26] Liu Zheng, Mao Weiimin and Zhao Zheng-duo: Acta Metallurgical Sinica vol.21 (2008) p. 57064.

[27] Shijie Guo, Qichi Le, Zhihao Zhao, Zhongjun Wang and Jianzhong Cui: Materials Science and Engineering A 404 (2005) p. 323–329.

[28] D.P. Shukla and P.C.Pandey: Metallurgical Transaction B, 11B (1980) p. 166-168.

[29] J. Campbell: Intenational Metals Reviews, 26 (1981) p. 71-108.

[30] M.K. Premkumar and M.G.Chu: Material Science and Engineering A202 (1995) p. 172-178.

© (2011) Trans Tech Publications, Switzerland
doi:10.4028/www.scientific.net/KEM.471-472.727

Effect of Quartz-Silicon Dioxide Particulate on Tensile Properties of Aluminium Alloy Cast Composites

Sayuti, M[1,a], Sulaiman, S[1,b], B.T.H.T. Baharudin[1,c], Arifin, M.K.A[1,d], Vijayaram, T.R[2,e] and Suraya, S[1,f]

[1]Department of Mechanical and Manufacturing Engineering,
Universiti Putra Malaysia, 43400 Serdang, Selangor, Malaysia;
[2]Faculty of Manufacturing Engineering,
Universiti Teknikal Malaysia Melaka, Durian Tunggal, 76109 Melaka, Malaysia

[a]tgk_sayuti@yahoo.co.uk, [b]suddin@eng.upm.edu.my, [c]tuah@eng.upm.edu.my,
[d]khairol@eng.upm.edu.my, [e]vijayaran@gmail.com, [f]suraya@yahoo.com

Keywords: cast composites, tensile properties, quartz-silicon dioxide strength, MMC, LM6.

Abstract. This paper describes an experimental investigation of the tensile properties of quartz-silicon dioxide particulate reinforced LM6 aluminium alloy composite. In this experimental, quartz-silicon dioxide particulate reinforced LM6 composite were fabricated by carbon dioxide sand moulding process with variation of the particulate content on percentage of weight. Tensile tests were conducted to determine tensile strength and modulus of elasticity followed by fracture surface analysis using scanning electron microscope to characterize the morphological aspects of the test samples after tensile testing. The results show that the tensile strength of the composites decreased with increasing of quartz particulate content. In addition, this research article is well featured by the particulate-matrix bonding and interface studies which have been conducted to understand the processed composite materials mechanical behaviour. It was well supported by the fractographs taken using the scanning electron microscope (SEM). The composition of SiO^2 particulate in composite was increased as shown in EDX Spectrum and Fractograph.

Introduction

The metal casting industry had established aggressive performance especially in the industrial castings because of a wide variety of metals and alloys were processed by casting and consequently there are increasing demand and need for new materials. This make the particulate of reinforced composites or discontinuously reinforced metal matrix composites, constitute 5 – 20 % of these new advanced materials [1,2]. The choice of the processing method depends on the property requirements, cost consideration and future applications prospects [3]. The advantage of processing composites by casting technology leads to near-net shape manufacturing which is a simple and cost-effective process [4,5]. Incorporation of hard second phase particles in the alloy matrices to produce a metal matrix composite (MMC) has been reported to be more beneficial and economical [6-9] due to its high specific strength and corrosion resistance properties. Metal matrix composites have an outstanding benefits due to the combined metallic and ceramic properties, thereby yielding improved physical and mechanical properties [10,11]. Among the various types of MMCs, particulate-reinforced composites are the most versatile and economical one [12]. In the past, various studies have been carried out on MMC. Carbides, such as SiC, TiC, TaC, WC and B4C are the most commonly used particulates to reinforce the metal or alloy matrix while the study of silicon dioxide, SiO_2 reinforcement in LM6 alloy is still rare. Very limited studies have been reported and the information available on the mechanical properties and fracture surface analysis are scarce. In this study quartz particulate reinforced LM6 alloy matrix composite specimens were fabricated and processed by casting method [13,14].

This paper focuses in studying the process of Aluminium LM6 alloy with SiO_2 as particulates by sand casting. The parameter of different percentage of SiO_2 particulate addition in the LM6 alloy matrix was examined to study the mechanical behaviour and fracture surface characteristic. Tensile testing and scanning electron microscopy was employed to evaluate the young's modulus, tensile strength and SEM was used to characterize the morphological features of the fracture surfaces of Silicon Dioxide (quartz) - particulate reinforced LM6 alloy composites after the tensile testing.

Methodology

Materials preparation. The materials used in this work were Aluminium LM6 alloy as the matrix and SiO_2 as reinforcement particulates with different weight percentages. The tensile test specimens were prepared according to ASTM standards B 557 M-94 [15]. Sodium silicate and CO_2 gas was used to produce CO_2 sand mould for processing composite casting. The aluminium alloy, LM6, was based on British standards that conform to BS 1490-1988 LM6.

Alloy of LM6 is actually an eutectic alloy having the lowest melting point that can be seen from the Al-Si phase diagram. The main composition of LM6 is about 85.95% of aluminium and 11.8% of silicon.

The SiO_2 particulate used as a second phase reinforcement in the alloy matrix was added on the molten LM6 by different weights fraction such as 5%, 10%, 15%, 20%, 25%, and 30%. The mesh size of Silicon Dioxide particulate is 230 and the average particle size equal to 65 microns (65μm).

Fabrication of composites. Only one type of pattern was used in this project and the procedure for making the pattern involves the preparation of drawing, selection of pattern material and surface finishing. Carbon dioxide moulding process was used to prepare the specimens as per the standard moulding procedure. Quartz-particulate reinforced MMCs were fabricated by casting technique. Six different weight fractions of SiO_2 particle in the range from 5%, 10%, 15%, 20%, 25%, and 30% are used. In this research work, the particulates were preheated to 200 ^{o}C in a heat treatment muffle furnace for 2 hours and it is transferred immediately in the crucible containing liquid LM6 alloy. The casting processing steps show are shown in Fig. 1.

Tensile testing. Tensile test was conducted to determine the mechanical properties of the processed SiO_2 particulate reinforced LM6 alloy composites. Test specimens were made in accordance to ASTM standard B557 M-94. A 250 KN servo hydraulic INSTRON 8500 UTM was used to conduct the tensile tests. The tensile testing of the samples was performed based on the following specifications and procedures according to the ASTM standards, the which one crosshead speed of 2.00 mm/minute, grip distance 50.000 mm, specimen distance 50.000 mm and temperature 24^0 C.

Scanning electron microscopy. The Scanning Electron Microscope (SEM) using LEO 1455 variable pressure microscope with Inca 300 Energy Dispersive X-ray (EDX) was used to investigate the morphological features. Results and data obtained from the tensile tested samples are correlated with the reported mechanical properties for each volume fraction of silicon dioxide percentage addition to the LM6 alloy matrix.

Density measurement. The density of a material is defined as its mass per unit volume. A&D-GR 200 – Analytical Balance was used to conduct the density measurement. The theoretical density of each set of composites was calculated using the rule of mixtures [16]. Each pellet was weighed in air (Wa), then suspended in Xylene and weighed again (W). The density of the pellet was calculated according to the formula :

$$\text{Density} = {Wa}/{(Wa - Ww)} \text{ x } density \;\; of \;\; Xylene \qquad (1)$$

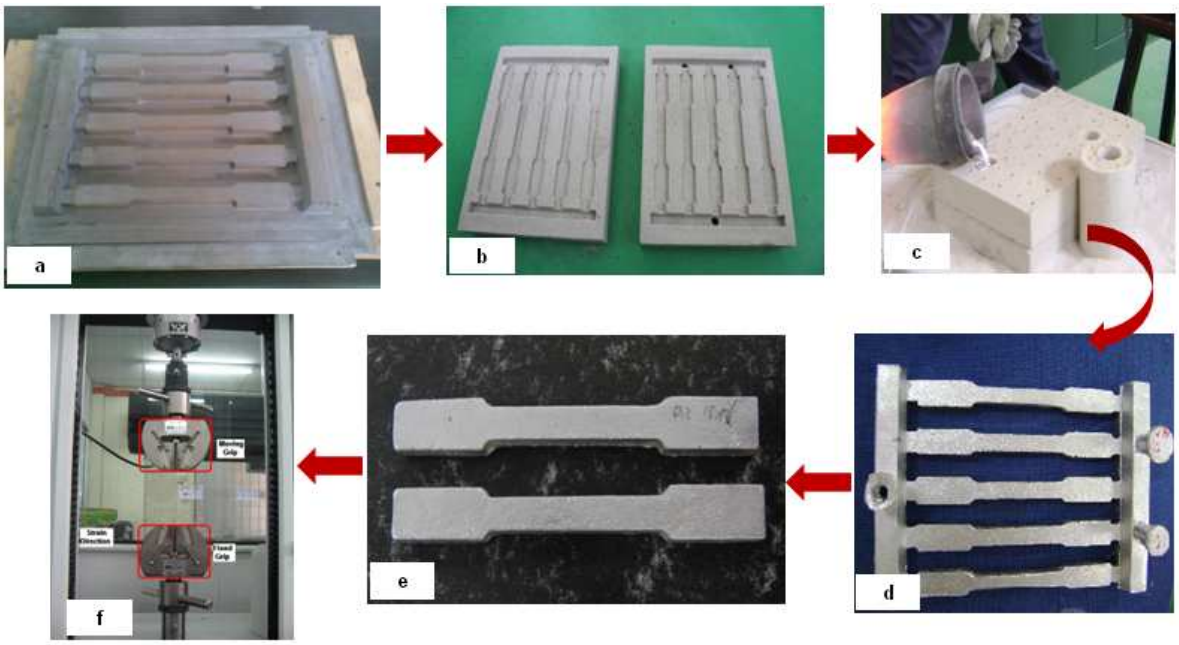


Fig. 1. The casting processing steps; (a) Pattern of mould (b) sand mould : drag and copper (c) melting and pouring in the sand mould (d) tensile specimens with gating system (e) tensile specimen after removing of gating systems (f) tensile testing.

Results and Discussion

Tensile test Properties. The average value of tensile strength (MPa) and Young's Modulus (MPa) versus weight fraction of SiO_2 is shown in the Fig. 2 and Fig. 3.

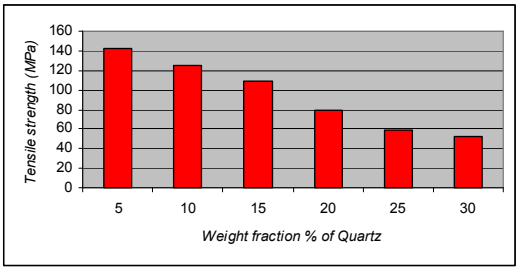


Fig.2. Tensile strength vs % weight fraction

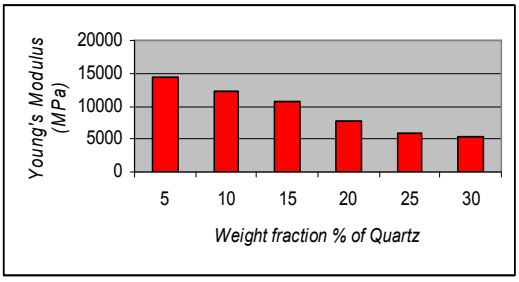


Fig.3.Young Modulus Vs % weight

The graph plotted between the average tensile strength and young modulus versus variation in weight fraction of quartz particulate addition to LM6 alloy indicates that both the properties decreases with increases addition of quartz particulate. The increase of closed pores content with increasing quartz particulate content would create more sites for crack initiation and hence lower down the load bearing capacity of the composite. The fluctuation maybe due to the non-uniform distribution of quartz particulates, due to experimental errors and or also depends on the cooling rate of the castings [14]. When particulates increase, particles are no longer isolated by the ductile aluminium alloy matrix, therefore cracks will be not arrested by ductile matrix and gap would propagate easily between the quartz particulates. This residual stress affects the material properties around it and the crack tips and the fracture toughness values would be altered.

Consequently, these residual stresses would probably contribute for the brittle nature of the composites. It should be noted that the compressive strength of the quartz particulate dominates and more than the tensile strength of the LM6 alloy matrix and so the tensile strength is decreasing with more addition of quartz particulate and this is well supported and evidenced from the literature citation [16, 17].

Density. Fig. 4 give the influence of quartz addition on density, respectively. The graph shows that as the quartz-silicon dioxide content was gradually increased, the density of the Aluminium composite decreased. Slight decrease was observed in the density because quartz-silicon dioxide has a slight lower density value than LM6 (the density of LM6 is 2.65grs/cc and of quartz is 2.23grs/cc) .

The investigation of aluminium composite is well documented. The percentage of the closed pores in the sintered composites increased with increasing quartz content. This can be attributed to silica being harder than aluminum and does not deform at all under the applied compaction load and the morphological features of quartz particles are significantly different from those of Aluminium and as a result, the interparticle friction effects are different. Therefore, the increase in the amount of closed pores with increasing quartz content would justify the observed decrease in density [16].

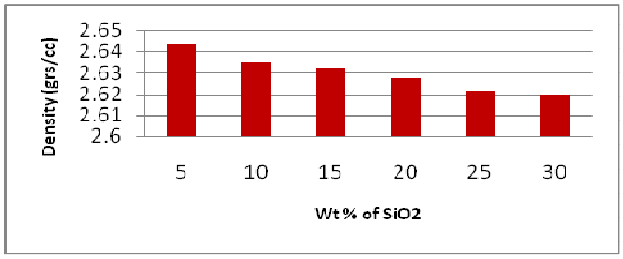


Fig. 4. Graph plotted on density versus weight fraction of S_iO_2

Scanning electron microscopy (SEM) and energy dispersive spectroscopy (EDS). Scanning Electron Microscopy and energy dispersive spectroscopy was employed to obtain some qualitative evidences on the particle distribution in the matrix and bonding quality between the particulate and the matrix. Besides, the fracture surface of the composite was analyzed by using SEM to show the detail of chemically reacted interfaces. Thus, in order to increase the potential application of MMCs, it is necessary to concentrate on the major aspects, like particle size of quartz and quartz distribution concentration.

The fracture surfaces or fractographs are shown in the Fig. 5-10 after tensile testing of the specimens having different weight fraction of quartz particulate. It was observed that the increase of SiO_2 content would create more sites for crack initiation and would lower the load bearing capacity of MMCs. In addition the number of contacts between quartz particles would increase and more particles are no longer isolated by the ductile aluminium alloy matrix. Therefore, cracks are not arrested by the ductile matrix and they would propagate easily between quartz particulates. Decreasing of SiO_2 content less than 30% in the matrix and with the particle size of 230 mesh could increase the tensile strength, hence cracking on the surface is not too dominant This phenomenon is shown in Fig. 5. The problem on interfacial bonding between the particulate quartz and the matrix during the solidification of composites can be ignored because the phenomena cracking occurs only in a small part of the surface. Meanwhile the surface crack is not distributed to all of the parts. In contrast, when the content of quartz was increased (30%), interfacial bonding concept is an important phenomenon because the surface cracking will be distributed on the surface of the parts. The other problem caused by the interaction between Aluminium alloy and quartz particle is not a significant one and it is removed while solidification during the pouring process and due to slip inter bonding/ inter granular movement which is illustrated with the aid of Fig. 6 [17].

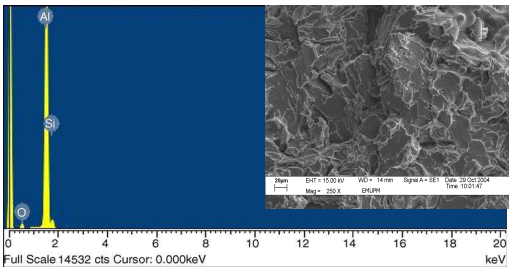


Fig. 5. EDX Spectrum and Fractograph of 5% quartz particulate reinforced in quartz -LM6 alloy matrix composite at 250X magnification by SEM after tensile testing.

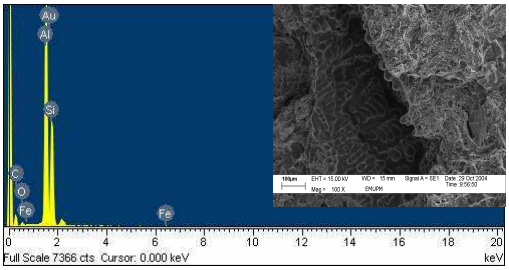


Fig. 6. EDX Spectrum and Fractograph of 10% quartz particulate reinforced in quartz -LM6 alloy matrix composite at 100X magnification by SEM after tensile testing.

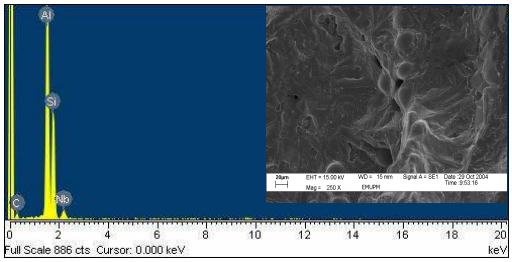


Fig. 7. EDX Spectrum and Fractograph of 15% quartz particulate reinforced in quartz -LM6 alloy matrix composite at 250X magnification by SEM after tensile testing.

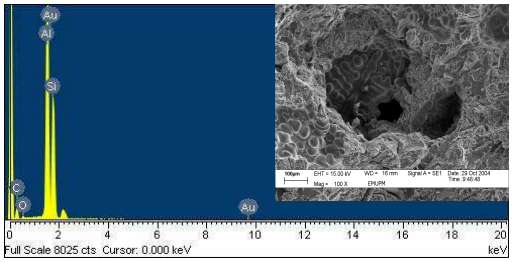


Fig. 8. EDX Spectrum and Fractograph of 20% quartz particulate reinforced in quartz -LM6 alloy matrix composite at 100X magnification by SEM after tensile testing

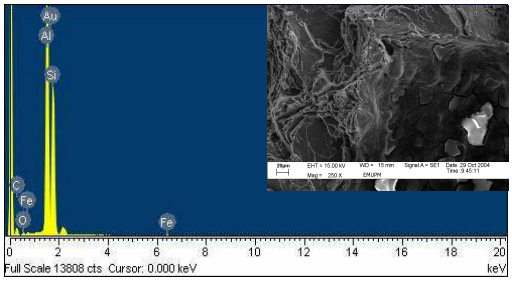


Fig. 9. EDX Spectrum and Fractograph of 25% quartz particulate reinforced in quartz -LM6 alloy matrix composite at 250X magnification by SEM after tensile testing

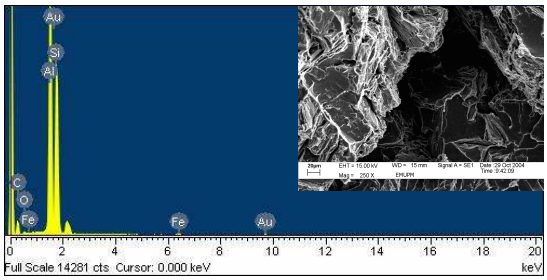


Fig. 10. EDX Spectrum and Fractograph of 30% quartz articulate reinforced in quartz -LM6 alloy matrix composite at 250X magnification by SEM after tensile testing

Summary

In this study, the compressive strength of the silicon dioxide particulate dominates and influences more effective than the tensile strength of the LM6 alloy matrix phase, hence the values of tensile strength and modulus of elasticity are decreased with the increased addition of silicon dioxide particulate from 5 to 30% by volume fraction basis. This fact from the experimental research is well supported and validated from the literature. The mechanical behaviour of the processed composite had a strong dependence on the volume fraction addition of the second phase reinforcement particulate on the alloy matrix. On the other hand, decreasing the silicon dioxide particulate content less than 30% along with the particle size constraint as 230 mesh-65 microns would increase the tensile strength and cracking on the surface might not be too dominant.

The density of these composites decreased slightly with increasing quartz content. Slight decrease was observed in the density because quartz-silicon dioxide has a slightly lower density value than LM6.

In future work, it is strongly recommended that tensile tests be performed by reinforcing the second phase quartz particulate addition to the LM6 alloy matrix limited up to 15%. In addition, compressive strengths testing of the processed composite samples can be done to highlight the benefits, advantages and applications of these composites. It is also worthwhile to conduct heat treatment studies of these processed composites and this will be taken for future research work.

Acknowledgements

The authors of this paper express their deep gratitude and sincere thanks to the staff and laboratory technicians of the Department of Mechanical and Manufacturing, Universiti Putra Malaysia for their help with the experiments.

References

[1] Daniel Gay, Suong V.Hoa, Stephen W.Tsai: CRC Press LLC, USA, (2003).

[2] A.J. Clegg: Ed.1st, Pergamon Press, New York, (1991).

[3] Chadwick, G: Fourth European Conference on Composite Materials. (1990).

[4] J. Hasyim, L Looney and M.S.J Hashmi: Journal of Materials Processing Technology (2002) 123 p. 251-257.

[5] J. Hasyim, L Looney and M.S.J Hashmi: Journal of Materials Processing Technology 123 p. (2002), 258-263,

[6] F.L Matthew and R.D. Rawlings. Composite Material; Engineering and Science, Woodhead Publishing, Cambridge, UK, 1999.

[7] P.K. Malick. Composite Engineering Handbook, CRC Press, New York, 1997.

[8] S. C. Sharma, K.H.W, Seah, B.M, Girish, and R.B.M Kamath: Journal of Materials & Design, 18 (1997) p. 149-153.

[9] P. Moldovan, G. Poperscu and M. Zsigmond: Journal of Advanced Materials, 35 (2002) p. 12-15.

[10] A.K. Kau, Mechanics of composite materials, Second edition, CRC Press Boca Raton, New York, USA, 1997.

[11] A.M.S. Hamouda and M.S.J. Hashrni: Journal of Materials Processing Technology 56 (1996) p.743-756.

[12] B. Cantor and M.J. Goringe, Metal and ceramic matrix composite, Institute of Physics Publishing Bristol and Phyladelphia, UK, 2004.

[13] E.N. Gregolin, H. Goldenstein and R.G. Santos: Journal of Material Processing Technology 157 (2004) p. 688-694.

[14] K.H.W Seah, Hemanth J and S.C. Sharma: International Journal of Material Science and Engineering 24 (2003) p. 87–93.

[15] American Society for Testing and Material. 1999. Annual Book of ASTM Standards, USA.

[16] H.L. Rizkalla and A. Abdulwahed: Journal of Materials Processing Technology, 56 (1996) p. 398-403.

[17] K.H.W. Seah, J. Hemanth, and S.C. Sharmac: Materials and Design 24 (2003) p. 87-93.

© (2011) Trans Tech Publications, Switzerland
doi:10.4028/www.scientific.net/KEM.471-472.733

Friction Forces between Sheet Molding Compound Charge and Mold Cavity Surface in Compression Molding

Mahmood M. Shokrieh[1,a], Reza Mosalmani[1,b]

[1]Composites Research Laboratory,

Center of Excellence in Experimental Solid Mechanics and Dynamics,

Mechanical Engineering Department, Iran University of Science and Technology,

Narmak, Tehran, 16846-13114, Iran,

[a]Shokrieh@iust.ac.ir, [b]Mosalmani@iust.ac.ir

Keywords: SMC; Compression Molding; Lubricating Layer; Temperature; Hydrodynamic Friction

Abstract. In this study, three relevant friction forces: constant friction force, hydrodynamic friction force and coulomb friction force are considered between sheet molding compound (SMC) charge and contact surface of the mold. The power law model is implemented to propose a model for prediction of hydrodynamic friction as the dominant friction of the SMC compression molding. The proposed model is simple and does not need any extra experimental parameters. Finally, a model has been developed to predict the molding pressure under non-isothermal conditions. The obtained results of the model are in a very good agreement with the experimental data.

Introduction

The SMC consists of thermosetting polyester resin, filler, and fiber reinforcement. SMC technology comprises two distinct manufacturing steps: compounding and molding. When the compound is ready for molding it is cut into pieces (charge layer). The pieces are then stacked in a specific arrangement (charge pattern) in the mold. The SMC blanks are smaller than the projected surface of the molded part. As shown is Fig. 1 SMC is processed into molded parts in heated steel molds operated by hydraulic presses. In this stage, SMC filled the mold and in the next stage, SMC is cured to prepare the molded part. The flow of SMC is achieved by the compression and thermal action of the mold [1].

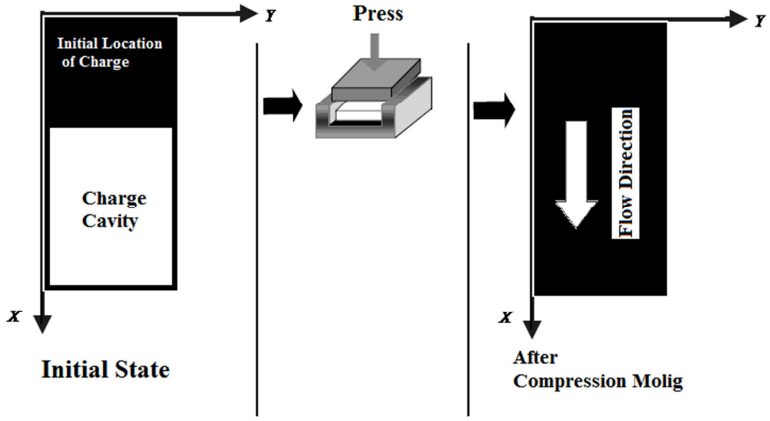


Fig. 1: Schematic diagram of SMC compression molding.

The present paper consists of three main parts. In the first part, hydrodynamic friction as dominant friction is characterized and methods to obtain its parameters are discussed. In the second part, temperature distribution in charge in the filling stage is studied and the results are used to predict the lubricating layer thickness and required molding pressure. In the third part, analytical solution for applied pressure is determined by using presented friction model and is compared with available experimental data.

Theoretical model

Basic Assumptions. The SMC is seen as a two-phase continuum medium. The filling stage duration is very short so that it is reasonable to neglect the curing stage of the polyester resin. SMC is assumed as an incompressible and purely viscous body that follows power-law model [2].

Kinematic Analysis. The flow field can be divided into two regions: the core, which occupies most of the flow domain and a thin lubricating layer (softened resin-rich surface as a result of heat conduction and its thickness is δ) [3]. If the continuity equation is used and incompressible flow and flow in one direction ($v_U = v_y = v_U = 0$) is assumed, the equations of velocity components can be determined for upper and lower lubricating layer and core region. In this research, the effect of thickness is neglected. Therefore, the velocity components are functions of lubricating layer thickness.

Heat Conduction in SMC. Referred to contributions were developed by Barone and Caulk [4], the temperature in the SMC charge, $T(z,t)$ at any instant time t in the filling stage can be found as:

$$\frac{T(z,t)-T_0}{T_M-T}=1+\sum_0^{\infty}\frac{4\,(-1)^{n+1}}{\pi(2n+1)}Exp[-\alpha(2n+1)^2\pi^2\frac{t}{h_0(h_0-Ut)}]\,Cos[(2n+1)\pi\frac{z-\frac{h}{2}}{h}] \qquad (1)$$

where T_0 is initial temperature of SMC charge, α is the transverse thermal diffusivity, and h_0 is the initial thickness of the charge. The mold surface temperature is set constant (T_M) and the mold closes at a constant speed (U).

Rheology of SMC. In this research, a continuum one-phase rheological model proposed by Dumont, *et al.* [5] has been modified to consider instantaneous thermal effects. The instant temperature of charge is used instead of its initial temperature because it is found that this process is non-isothermal.

Friction Response at the Mold Surface. Barone and Caulk [4] developed three alternatives to be considered for the friction response at the mold surface: constant friction, hydrodynamic friction (proportional to the relative velocity), and coulomb friction (proportional to the normal component of the stress vector). The simplest assumption is when the friction at the mold surface is constant in magnitude such that:

$$\tau_w = -k_0 \qquad (2)$$

where τ_w is the surface friction and k_0 is a constant. Using this response, Barone and Caulk [4] found that regardless of the thickness of the initial SMC charge, the velocity distribution would be the same. Therefore, two charges with identical shape but different thickness will have identical flow patterns for the same closing speed. They found that this result contradicts the observations found by Lee, et al. [8].

The hydrodynamic friction assumption motivated by the existence of a very thin resin-rich layer adjacent to the mold surface. This thin layer of fluid serves to lubricate the relative motion between the SMC and the mold. This mechanism is characterized by a linear velocity relation:

$$\tau_{wi} = -\frac{1}{2}\lambda v_i \tag{3}$$

where λ is the friction coefficient that depends on SMC paste viscosity and the thickness of the lubricating layer. This mechanism represents the shear stress at the boundary layers.

In the case of coulomb friction, the friction arises from direct fiber-to-metal contact without significant resin lubrication. The friction force is taken proportional to the normal stress vector at the mold surface such that:

$$\tau_w = -k_c \bar{p} \tag{4}$$

where k_c is a constant and $\bar{p}$ is the average pressure at the mold surface.

To evaluate the alternative assumptions for the fiction response, Barone and Caulk [4] examined the developing shape of an initially elliptical charge at various stages of deformation. Analytical solutions for the initially elliptical charge were obtained for both cases and compared with experimental results. The analytical solution for hydrodynamic and coulomb fiction is compared with the experimental results. By comparing these solutions with experimental results, they concluded that the hydrodynamic model for the friction response was the best of the three proposed alternatives.

Determination of Hydrodynamic Friction. It is shown that hydrodynamic friction is dominant friction in SMC compression molding [2, 3, 4]. By using the concept of lubricating layer, the hydrodynamic friction can be determined by:

$$\tilde{T}_x = \underline{\tilde{T}}^{-} = \frac{-k}{\delta}\left|\frac{U}{(h-\delta)}\right|^{m-1}\left(4+\frac{x^2}{\delta^2}\right)^{\frac{m-1}{2}}\left(\frac{U}{h-\delta}x\right) \tag{5}$$

Power law consistency index (k), power law index (m) and thickness of lubricating layer (δ) are hydrodynamic friction parameters. By determination these parameters, the hydrodynamic friction can be predicted. The introduced method in the literatures [2, 2] is assumed that the thickness of lubricating layer is very small and in comparison with the thickness of charge (h) is negligible. In addition, parameter λ as the friction coefficient is defined and determined by very noisy experimental data. In this paper, a new method to determine the parameters of hydrodynamic friction individually is proposed.

Total applied stress. Under above assumptions and by using the mass and momentum balance equations, the applied stress on SMC charge is $\sum_{zz}(x,h) = \sum_{zz}^{v} + P(x,h)$, where

$$P(x) = \frac{\dfrac{-2k}{\delta(h-2\delta)}\left(\dfrac{U}{h-\delta}\right)^m\left(4+\dfrac{x^2}{\delta^2}\right)^{\frac{m+1}{2}}\delta^2}{(1+m)}\left[\left(4+\frac{x^2}{\delta^2}\right)^{\frac{m+1}{2}}-\left(4+\left(\frac{h_0 l_0}{h\delta}\right)^2\right)^{\frac{m+1}{2}}\right] + \eta_{ps}^{0}\,(1+98\phi+980\phi^2)\left(2\frac{1+H}{1+2H}\right)^{-\frac{n+1}{2}}\frac{2}{1+2H}\left(\frac{2(1+H)}{(1+2H)D_0^2}\right)^{\frac{n-1}{2}}\left(\frac{U}{h-\delta}\right)^n \tag{6}$$

$$\sum_{zz}^{v} = \eta_{ps}^{0}\,(1+98\phi+980\phi^2)\left(2\frac{1+H}{1+2H}\right)^{-\frac{n+1}{2}}\frac{-2H}{1+2H}\left(\frac{2(1+H)}{(1+2H)D_0^2}\right)^{\frac{n-1}{2}}\left(\frac{U}{h-\delta}\right)^n \tag{7}$$

where ϕ is volume fraction of fiber and H is rheological function introduced in [5].As well as η_{ps}^{00} is the plane strain axial viscosity of the paste at D_0 and T_0 (arbitrary choice) and $T(z,t)$ is temperature of charge in the moment of *t* and height *z*.

Results and Discussion

Heat Effects on SMC. The temperature distribution vs. height in Fig. 2 shows that isothermal assumption for filling stage of SMC compression molding is not valid, especially in the normal compression molding velocities that are rather low. Therefore, thermal effects on the determination of compression pressure are considered.

Determination of (k). According to high temperature of mold surface and thermal property of thermoset resins, determination of Power law consistency index (k) is experimentally difficult [6]. Thermal behavior of thermoset compositions are coupled by cure process. As well as, Power law consistency index is proportional to the paste viscosity. Viscosity of thermoset composites is decreased by increasing of temperature and increased by increasing of curing process [7]. SMC viscosity is an Arrhenius-like function of temperature and for filling stage, curing effect on the viscosity could be neglected [2]. It is shown that viscosity of SMC in contact with hot mold surface decreases dramatically. These reduction causes the paste in this region behaves like lubricant [6-11].

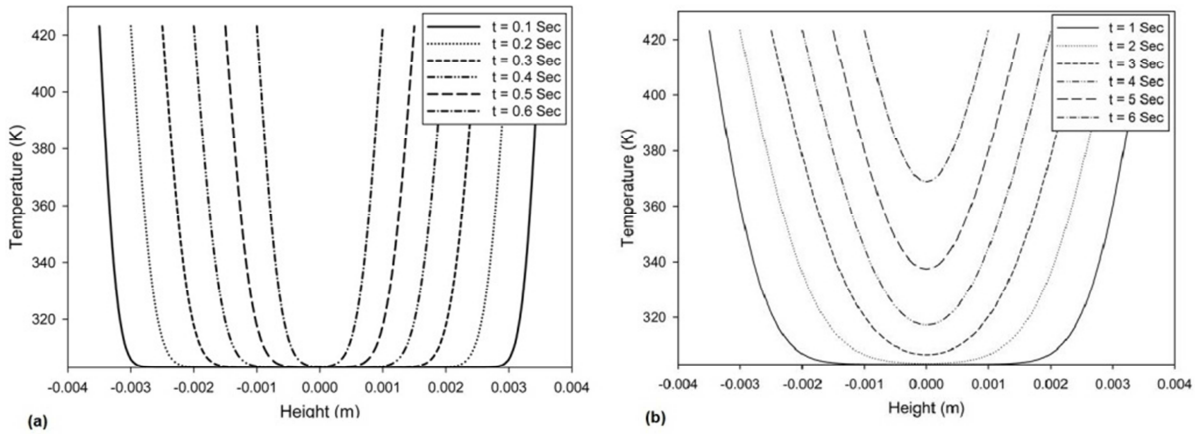


Fig. 2 Typical temperature distribution vs. height in different time steps *a)* u= 10 *mm/s* and *b)* u= 1 *mm/s*.

It is shown [10] that for high temperature less than the temperature of the mold surface, parameters of Arrhenius-like relation are changed. For simplify, it is assumed that the first Arrhenius-like relation is valid, but this relation is multiplied by a constant coefficient. By this assumption, one definite point is needed to determine the value of this coefficient. For the paste composition introduced in [2] and according to usual values of viscosity of the paste before applying thickener, this constant could be determined. Due to the low paste viscosity of SMC in high temperatures, as a rough but useful and simple assumption, it is assumed that viscosity of SMC in the mold surface temperature is equal to viscosity of SMC before adding the thickener. It is a reasonable assumption because of dramatic reduction of SMC viscosity near surface mold temperature. Moreover, this assumption is equal to assume heat conduction eliminate thickener effects in the paste of SMC. By using introduced Arrhenius-like relation and this point, it is possible to determine this constant coefficient.

Determination of (δ). The temperature has an important role in the formation of the lubricating layer. Further, heat conduction from the hot mold to the cold charge is a function of time. Therefore, thickness of lubricating layer (δ) is a time dependent variable. However, it is assumed that in a moment, δ is not a function of the location. In addition, it is assumed that the δ is an indirect function of U.

This thermal difference between upper and lower surface of lubricating layer is shown by ΔT_δ. Therefore, temperature of the upper surface of lubricating layer is equal to $T(\delta,t) = T_M - \Delta T_\delta$. In general, ΔT_δ is a function of time (t), mold-closing speed (U), initial temperature of charge (T_{Ch})

and temperature of mold surface (T_M). ΔT_δ function is not known and it could not be determined experimentally. As a first option, it is assumed that ΔT_δ is a constant function. By trial and error and comparing the final pressure calculated by the model and experimental data, it could be shown that in order to calculate the thickness of lubricating layer, about 1 ^oC thermal difference is needed between the top and the bottom of the lubricant layer ($\Delta T_\delta = 1\,^\circ\mathrm{C}$). For different initial temperature of charge and same mold surface temperature, analytical result of lubricating layer thickness (δ) as a function of filling time are shown in Fig. 3. The results are expected and are similar with Fig. 3.

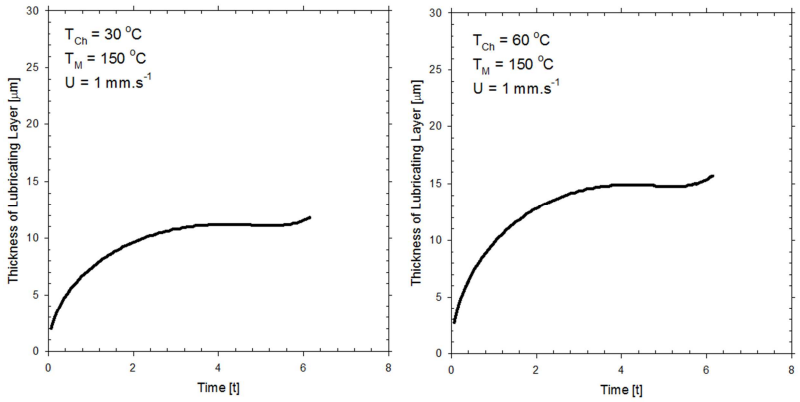


Fig. 3: Analytical diagram of lubricating layer thickness (δ) vs. time during filling stage, for temperature of mold surface ($T_M = 150\ ^oC$), closure speed of mold ($U = 1\,mm.s^{-1}$) and initial temperatures ($T_{ch} = 30\ ^oC$) and ($T_{ch} = 60\ ^oC$).

Comparison between the Model and Experiment. In this research, material properties of SMC paste and experimental configuration are similar to those introduced by Dumont, et al. [2]. SMC Samples were initially located at the left side of the mould (SL, sample-left). A Comparison between the results of the present model and the experimental data [2] for the same conditions is shown in Fig. 4.

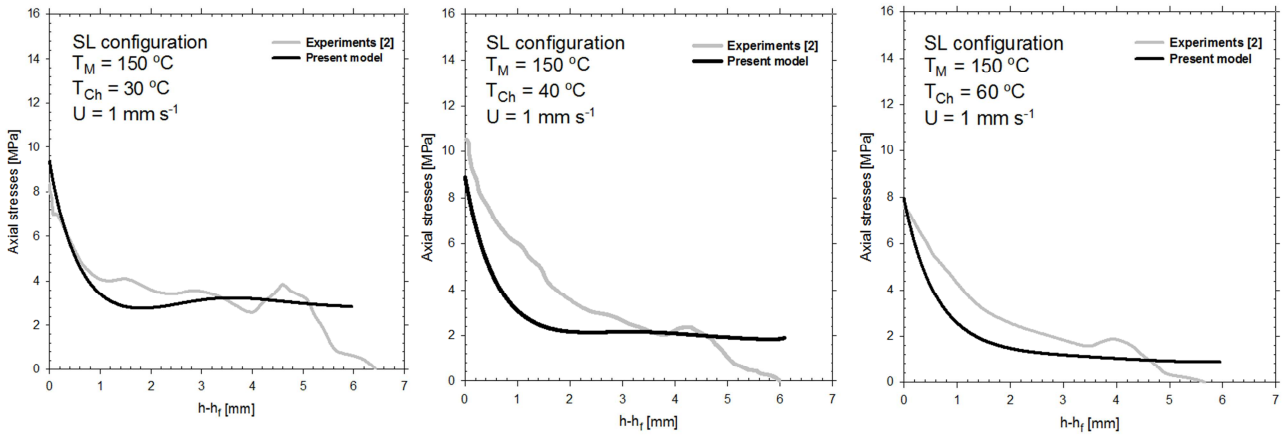


Fig. 4: Comparison between the prediction of the present model and the SL experiment with temperature of mold surface ($T_M = 150\ ^oC$), closing-speed of mold ($U = 0.001\,mm.s^{-1}$) and initial temperatures of charge ($T_{Ch} = 30\ ^oC$),($T_{Ch} = 40\ ^oC$) and ($T_{Ch} = 60\ ^oC$).

Summary

In this research, it is shown that isothermal assumption in the filling stage is not reasonable. Then the relationship between the applied stresses and heat conduction in SMC, during the filling phase is studied and a novel hydrodynamic friction model is proposed. By considering SMC as a viscous transversely isotropic material, the applied stress on the SMC charge is determined. The proposed method considers the variation of temperature in the charge during the filling stage and gives a better prediction of applied pressure. Also, the presented model is more general, needs less experimental data and its results in comparison with experimental results shows good agreement.

References

[1] ASM International Handbook Committee: ASM Handbook- Composites, Vol 21. (2001).

[2] Dumont P., Orge´As L., Favier D., Pizette P., Venet C.: Compos Part A 38, (2007), p. 353–368.

[3] Abrams L., Castro J.: Polym Compos 24, (2003),p. 291-303.

[4] Barone MR. And Caulk DA.: J Applmech 53(191), (1986), p. 361-370.

[5] Dumont P, Orge´As L, Le Corre S, Favier D.: Int J Plast 19(4), (2003), p. 625-46.

[6] Barone M. And Caulk D.: Polymeng And Sci 21 (17), (1981), p. 1139-48.

[7] Kia G. H.: Sheet Molding Compounds Science And Technology. Hanser, Munich (1993).

[8] Jackson W. C., Advani S. G. And Tucker C. L.: Compo Mat 20, (1986), p. 539-57.

[9] Silva-Neito R. J., Fisher B. C. And Birely A. W.: Polymeng And Sci 21, (1981), p. 499-506.

[10] Fan J. D.: Process Analysis Of Sheet Molding Compounds In Molds With Or Without Substructures, Doctoral Dissertation, Dep. Of Chemical Engineering, Univ Ohio State, (1988).

[11] Lee L. J., Marker L. F. And R. Griffith M.: Polym Compos 2(4), (1981), p. 209-18.

© (2011) Trans Tech Publications, Switzerland
doi:10.4028/www.scientific.net/KEM.471-472.739

Free Vibration Analysis of Symmetrically Laminated Fully Clamped Skew Plates Using Extended Kantorovich Method

Ali Fallah[1, a], Mohammad Hossein Kargarnovin[1, b] and Mohammad Mohammadi Aghdam[2, c]
[1]School of Mechanical Engineering, Sharif University of Technology, Iran
[2]Department of Mechanical engineering, Amirkabir University of Technology, Iran

[a]ali.fallah.66@gmail.com, [b]mhkargar@sharif.edu, [c]aghdam@aut.ac.ir

Keywords: Free vibration analysis; composite skew plate; Multi-term extended Kantorovich method.

Abstract. In this paper, free vibration analysis of thin symmetrically laminated skew plates with fully clamped edges is investigated. The governing differential equation for skew plate which is a fourth order partial differential equation (PDE) is obtained by transforming the differential equation in Cartesian coordinates into skew coordinates. Based on the multi-term extended Kantorovich method (MTEKM) an efficient and accurate approximate closed-form solution is presented for the governing PDE. Application of the MTEKM reduces the governing PDE to a dual set of ordinary differential equations. These sets of equations are then solved with infinite power series solution, in an iterative manner until convergence was achieved. Results of this study show the fast rate of convergence of the MTEKM. Usually two or three iterations are enough to obtain reasonably accurate results. The frequency parameters of laminated composite plates are obtained for different skew angles and lay-up configuration for different composites laminates skew plates. Comparisons have been made with the available results in the literature which show the accuracy and efficiency of the method.

Introduction

Skew plates are widely used in many engineering applications such as aircraft wings, marine industries, and as intersection elements in many bridges and highways. Composite structures are also used widely in aerospace and other industries because of their high strength-to-weight ratios. Therefore, it is necessary to study their dynamic behavior to have efficient and reliable design. Most studies related to the laminated plates are concerned with rectangular composite plates. However, skew laminated composite plates have received relatively less concern.

Furthermore, since the governing equation for the skew plates is more complicated than rectangular plates the exact solution for the skew plates is almost impossible. Therefore, application of different numerical techniques for the free vibration of the laminated skew plates seems to be mandatory. For instance, Leiw and Wang [1] employed pb-2 Rayleigh-Ritz method for free vibration analysis of isotropic and orthotropic skew plates. Krishnan and Deshpanda [2] employed the finite element method for the free vibration analysis of skew isotropic plates, single layer laminas and three-layered cross-ply laminates. Hosokawa et al. [3] investigated free vibration of fully clamped symmetrically laminated skew plate using the Green's function approach. Reddy and Palaninathan [4] presented the free vibration analysis of skew laminated composite plates with both simply supported and clamped edges based on finite element method. Anlas and Goker [5] studied free vibration of skew laminated composite plates with simply supported and clamped edges using orthogonal polynomials with Ritz method. Malekzadeh [6] employed differential quadrature method for large amplitude free vibration analysis of laminated composite skew thin plates. Ashour [7] investigated the free vibration of thin symmetrically skew laminated plate with fully clamped edges based on the finite strip transition matrix method.

On the other hands, numerical methods have their own limitations. Closed form solutions even if they are approximate solutions are more interesting due to various advantages such as ease of parametric studies and considering of physics of the problem. Among approximate analytical

methods for the solution of the PDEs one may refer to extended Kantorovich method (EKM). The EKM was introduced and developed by Kerr [8]. The method employs the novel idea of Kantorovich method and it is an efficient technique to obtain semi analytical solutions for PDEs. EKM is used for the solution of various types of 2D problems such as free vibration [9], buckling [10] and bending [11-13].

In all these studies [8-13], just one term in the expansion of the EKM solution is considered and it was proved that the single term formulation leads to a reasonable accuracy for rectangular plates. However, some researches [14-15] show that the one term assumption fails in more complex condition such as nonrectangular quadrilateral geometries. To overcome this shortage, MTEKM is used instead of the single term EKM. For instance, Yuan and Jin [14] studied the buckling analysis of isotropic rectangular plates based on MTEKM. Recently, Shufrin et al. [15], present a semi-analytical solution for the geometrically nonlinear analysis of trapezoidal plates based on MTEKM.

In this study, semi analytical solution is presented for the free vibration analysis of thin symmetrically laminated skew plates with fully clamped edges based on the MTEKM. The governing equation for skew plate is obtained by transforming the differential equation in Cartesian coordinates into skew coordinates. Application of the MTEKM reduces the governing PDE to dual set ordinary differential systems of equations. These systems of equations are then solved with infinite power series solution, in an iterative manner until convergence was achieved. Results prove the fast rate of convergence of the MTEKM. Usually two or three iterations are enough to obtain results with desired accuracy.

The frequency parameters for laminated composite plates are obtained for different skew angles and lay-up configuration for different composites laminates skew plates. The results are compared with the available results in the literature which showed the accuracy and efficiency of the method.

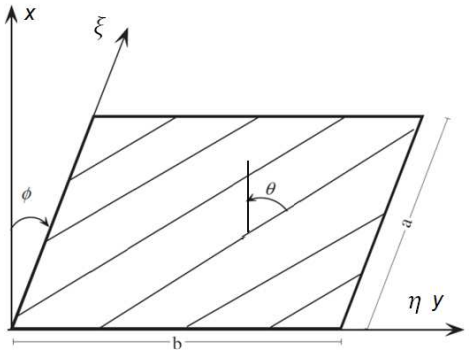


Fig.1. Schematic figure of skew plate

Governing equation. Consider the fully clamped laminated skew plate shown in Fig.1. The governing equation of free vibration of symmetrically laminated skew plate in rectangular coordinates *x*, *y* is given by [7]:

$$D_{11}\frac{\partial^4 w}{\partial x^4}+4D_{16}\frac{\partial^4 w}{\partial x^3\partial y}+2(D_{12}+2D_{66})\frac{\partial^4 w}{\partial x^2\partial y^2}+4D_{26}\frac{\partial^4 w}{\partial x\partial y^3}+D_{22}\frac{\partial^4 w}{\partial y^4}-\rho h\omega^2 w=0 \qquad (1)$$

where w, ρ and h are lateral deflection, mass density and height of the plate, respectively and other constants are defined as:

$$D_{ij}=\sum_{k=1}^{n_L}\frac{1}{3}\overline{Q}_{ij}\,(Z_k^3-Z_{k-1}^3) \qquad (2)$$

in which $\overline{Q}_{ij}$ is the plane stress transformed reduced stiffness coefficients of the lamina in the laminate coordinate system *xyz*, Z_k is the height of the *k*th layer and n_L is the number of laminas.

Using the skew coordinate system (ξ, η) as shown in Fig.1:

$$\xi = x\sec(\phi)\ ; \eta = y - x\tan(\phi) \tag{3}$$

where ϕ is skew angle, the governing equation in the skew coordinate system can be written as:

$$A_1\frac{\partial^4 w}{\partial \xi^4} + A_2\frac{\partial^4 w}{\partial \xi^3 \partial \eta} + A_3\frac{\partial^4 w}{\partial \xi^2 \partial \eta^2} + A_4\frac{\partial^4 w}{\partial \xi \partial \eta^3} + A_5\frac{\partial^4 w}{\partial \eta^4} - A_6 w = 0 \tag{4}$$

where $A_i$are defined in Appendix A. The plate is clamped along all the edges and corresponding boundary conditions are as:

$$\xi\ = 0\ or\ a\ ; w = \frac{\partial w}{\partial \xi} = 0\ \ ;\ \ \eta\ = 0\ or\ b\ ; w = \frac{\partial w}{\partial \eta} = 0 \tag{5}$$

Application of the MTEKM. According to MTEKM, displacement is considered as multiplication of N-term separable functions as:

$$w(x, y) = \sum_{i=1}^{N} F_i(\xi) G_i(\eta) \tag{6}$$

where $F_i(\xi)\ , G_i(\eta), i = 1,2, \cdots N$ are unknown functions of ξ and η to be determined and N is the number of terms in the series. Based on the general procedure of the Galerkin weighted residual method, Eq. 4 is multiplied by the appropriate weighting functions. Assuming $G_i(\eta)$ as prescribed functions, as initial guess, multiplying Eq. 4 by the prescribed functions and integrating over the entire length of the plate in the η direction leads to a system of ordinary differential equations in terms of $F_k(\xi)$ as:

$$\sum_{j=1}^{N}\left(\alpha_{1jk}\frac{d^4 F_j}{d\xi^4} + \alpha_{2jk}\frac{d^3 F_j}{d\xi^3} + \alpha_{3jk}\frac{d^2 F_j}{d\xi^2} + \alpha_{4jk}\frac{dF_j}{d\xi} + (\alpha_{5jk} - \alpha_{6jk})F_j\right) = 0\ ; k = 1,2, \cdots N \tag{7}$$

where α_{ijk} are defined in Appendix B. The boundary conditions in terms of the separable functions are:

$$\xi\ = 0\ or\ a\ ; F_k = \frac{dF_k}{d\xi} = 0\ ; k = 1,2, \cdots N \tag{8}$$

The ODE system Eq. 7 together with corresponding boundary conditions Eq. 8 is solved with infinite power series to obtain first estimate for functions $F_i(\xi)$. Now $F_i(\xi)$ are used as the weighing functions and multiplying them to Eq. 4 and integrating over ξ direction leads to another ODE system in terms of $G_k(\eta)$ as:

$$\sum_{j=1}^{N}\left(\beta_{1jk}\frac{d^4 G_j}{d\eta^4} + \beta_{2jk}\frac{d^3 G_j}{d\eta^3} + \beta_{3jk}\frac{d^2 G_j}{d\eta^2} + \beta_{4jk}\frac{dG_j}{d\eta} + (\beta_{5jk} - \beta_{6jk})G_j\right) = 0\ ; k = 1,2, \cdots N \tag{9}$$

where $\beta_{ijk}$are defined in the Appendix B. The boundary conditions in terms of the separable functions are:

$$\eta\ = 0\ or\ b\ ; G_k = \frac{dG_k}{d\eta} = 0\ ; k = 1,2, \cdots N \tag{10}$$

Here, again ODE system Eq. 9 and corresponding boundary conditions Eq. 10 is solved with infinite power series which is leads to the first estimate of functions $G_k(\eta)$. At this step, the first iteration is completed. Now the updated functions $G_k(\eta)$ can be used to determine α_{ijk} constants in Eq. 7 which solution of the equations provides new and updated functions of $F_k(\xi)$. This procedure is continued until convergence with desired accuracy is achieved.

Solution Procedure. In this study, infinite power series solution is employed for the solution of Eq. 7 and Eq. 9. Therefore, unknown functions $F_k(\xi)$ and $G_k(\eta)$ are consider as:

$$F_k(\xi) = \sum_{l=0}^{\infty} a_{lk}\xi^l \; ; \; k = 1,2,\cdots N \tag{11}$$

$$G_k(\eta) = \sum_{l=0}^{\infty} b_{lk}\eta^l \; ; \; k = 1,2,\cdots N \tag{12}$$

Substituting Eq. 11 and Eq. 12 into Eq. 7 and Eq. 9, respectively, leads to a recursive formula for the a_{lk}, b_{lk} as:

$$\sum_{j=1}^{N} a_{(l+4)k}\alpha_{1jk} = \left(\frac{-1}{(l+1)(l+2)(l+3)(l+4)}\right)\left(\sum_{j=1}^{N}\left((l+1)(l+2)(l+3)a_{(l+3)k}\alpha_{2jk} + (l+1)(l+2)a_{(l+2)k}\alpha_{3jk} + (l+1)a_{(l+1)k}\alpha_{4jk} + a_{(l+3)k}(\alpha_{5jk} - \alpha_{6jk})\right)\right); k = 1,2,\cdots N\,; l = 0,1,2\cdots \tag{13}$$

$$\sum_{j=1}^{N} b_{(l+4)k}\beta_{1jk} = \left(\frac{-1}{(l+1)(l+2)(l+3)(l+4)}\right)\left(\sum_{j=1}^{N}\left((l+1)(l+2)(l+3)b_{(l+3)k}\beta_{2jk} + (l+1)(l+2)b_{(l+2)k}\beta_{3jk} + (l+1)b_{(l+1)k}\beta_{4jk} + b_{(l+3)k}(\beta_{5jk} - \beta_{6jk})\right)\right); k = 1,2,\cdots N;\; ; l = 0,1,2\cdots \tag{14}$$

From Eq. 13 and Eq. 14, the a_{lk}, b_{lk} determined based on the first four terms in each series. The first four terms are determine after imposing boundary conditions in both ξ and η directions, for example by imposing boundary conditions related to ξ=*0* and a, a_{0k}, a_{1k}, a_{2k} and a_{3k} and natural frequencies are determined.

Results and discussion

In this section, accuracy of the presented MTEKM technique to obtain semi analytical solution for free vibration analysis of fully clamped thin symmetrically laminated skew plates is examined. At first, in order to study accuracy of the presented method, an isotropic fully clamped skew plate is considered. The material properties are E=200*(GPa)*, v=0.3, ρ=7800*(Kg/m^3)*.

In Table 1, the first three dimensionless natural frequencies of the skew plate for four different values of the skew angle ($\phi = 0°, 15°, 30°, 45°$) are presented. As mentioned before, single term EKM cannot be used for skew plates, then results of the two-term EKM together with results of the finite element method obtained by Reddy and Palaninathanare [4] also included in the table. From Table 1, it can be concluded that the predictions of two-term EKM show very good agreement with published data from Reddy and Palaninathanare [4]. Therefore, in next examples a two-term EKM is used to obtain natural frequencies of the skew plates.

One of the most important advantages of the EKM in comparison to other weighted residual methods is that the initial guess functions are arbitrary and they are not even required to satisfy boundary conditions and the method converges very rapidly to a final form, irrespective of the initial guess functions. As next example, the dimensionless fundamental natural frequency of an isotropic fully clamped skew plate is presented to investigate the effect of the initial guess function

on the results, see Table 2. It can be seen that, for small skew angles ($\phi < 30°$) after two and for large skew angles ($\phi > 30°$) after three iterations, the predictions are converged and independent from the initial guess functions.

The effects of the skew angle on the natural frequencies of the fully clamped symmetrically laminated skew plates are investigated and results are presented in Table 3 and Table 4. At first, a five-layer symmetrically laminated (-45 45 -45 45 -45) skew plate is considered. Material properties of each lamina are $\frac{E_{11}}{E_{22}} = 40$; $\frac{G_{12}}{E_{22}} = 0.6$; $v_{12} = 0.25$. The first six dimensionless natural frequencies of the fully clamped laminated skew plate are presented in Table 3. The results of B-spline Rayleigh-Ritz method obtained by Wang [1] and the results of Ritz method obtained by Anlas and Goker [5] are also included in the table. From Table 3 it can be seen that, the predictions of the MTEKM show a good agreement with results of the Wang [1] and Anlas and Goker [5], see Table 3.

Table 1. Natural frequency of isotropic fully clamped skew plate. ($\bar{\omega} = (\omega a^2/\pi^2)\sqrt{\rho h/D_{11}}$, $a = b = 1$)

Method	$\phi°$			
	0	15	30	45
EKM -1Term	3.6487	3.9665	4.7934	8.0281
EKM-2 Term	3.6484	3.8694	4.7016	6.9047
[4]	3.648	3.872	4.672	6.663

Table 4. Natural frequencies of (30 -30 30) clamped skew plate ($\bar{\omega} = (\omega a^2/(\pi^2 h))\sqrt{\rho/E_{22}}$,$a = b = 1$).

$\phi°$		$\bar{\omega}_1$	$\bar{\omega}_2$	$\bar{\omega}_3$
10	MTEKM	1.33	2.73	2.92
	[5]	1.32	2.55	2.80
20	MTEKM	1.42	2.57	3.10
	[5]	1.39	2.69	2.94
30	MTEKM	1.48	2.69	3.26
	[5]	1.55	2.89	3.41

Table 2. Arbitrariness of initial guess and convergence of MTEKM for fundamental natural frequency of isotropic fully clamped skew plate ($\bar{\omega} = (\omega a^2/\pi^2)\sqrt{\rho h/D_{11}}$, $a = b = 1$).

Initial guess	$\phi°$	Iteration				
		1st	2nd	3rd	4th	[5]
$G_1(\eta) = Sin\ (\eta/b)$ $G_2(\eta) = Sin\ (2\eta/b)$	0	2.3238	3.6484	3.6484	3.6484	3.648
	15	2.3876	3.8694	3.8694	3.8694	3.872
	30	2.9159	4.7018	4.7016	4.7016	4.672
	45	4.4762	6.9086	6.9047	6.9047	6.663
$G_1(\eta) = Cos\ (\pi\eta/b)$ $G_2(\eta) = Cos\ (2\pi\eta/b)$	0	2.9342	3.6484	3.6484	3.6484	3.648
	15	3.1383	3.8694	3.8694	3.8694	3.872
	30	3.9187	4.7016	4.7016	4.7016	4.672
	45	5.9964	6.9063	6.9047	6.9047	6.663

Table 3. First six dimensionless natural frequencies of (-45 45 -45 45 -45) fully clamped laminated skew plate ($\bar{\omega} = (\omega a^2/(\pi^2 h))\sqrt{\rho/E_{22}}$,$a = b = 1$).

$\phi°$		$\bar{\omega}_1$	$\bar{\omega}_2$	$\bar{\omega}_3$	$\bar{\omega}_4$	$\bar{\omega}_5$	$\bar{\omega}_6$
0	MTEKM	3.90	7.19	8.53	11.31	13.35	14.79
	[1]	3.90	7.15	8.46	11.21	13.32	14.74
	[5]	3.90	7.15	8.46	11.21	13.32	14.75
30	MTEKM	4.55	8.40	9.94	13.09	15.92	17.52
	[1]	4.54	8.38	9.88	12.85	15.69	17.49
	[5]	4.54	8.38	9.88	12.85	15.69	17.49
45	MTEKM	6.37	10.89	14.57	15.56	20.78	22.31
	[1]	6.31	10.82	14.50	15.47	21.06	22.08
	[5]	6.31	10.82	14.50	15.47	21.09	22.13

In Table 4, the first three dimensionless natural frequencies of a three-layer symmetrically laminated (30 -30 30) E-glass/Epoxy skew plate for different skew angles is presented. Material properties of E-glass/Epoxy are $E_{11} = 60.7\ GPa;\ E_{22} = 24.8\ GPa; G_{12} = 11.99 GPa; v_{12} = 0.23$. Results of the Anlas and Goker [5] are also included. Again, results show a good agreement with results of Ritz method [5]. From Table 3 and Table 4, it can be concluded that as the value of the skew angle increased dimensionless natural frequencies also increased.

Summary

Applicability of the MTEKM to obtain highly accurate approximate closed form solution for free vibration analysis of fully clamped thin symmetrically laminated skew plates is examined. The governing PDE for skew plate is obtained by transforming the differential equation in Cartesian coordinates into skew coordinates. Application of the MTEKM reduces the governing PDE to dual set ordinary differential system of equations. These systems of equations are solved with infinite power series solution, in an iterative manner. Results reveal the fast rate of convergence of the MTEKM. Usually two or three iterations are enough to obtain reasonably accurate results. Comparisons have been made with the available results in the literature which show the accuracy and efficiency of the method. The frequency parameters for laminated composite plates are presented for different skew angles and lay-up configuration for different composites laminates skew plates. Results show that as the value of the skew angle increased the natural frequencies increased.

References

[1] K.M. Liew and C.M. Wang: Comp. Struc. Vol. 49 (1993), p.941
[2] A. Krishnan and J.V. Deshpanda: J Sound Vibration Vol. 153 (1992), p.351
[3] K. Hosokawa, Y. Terada and T. Sakata: J Sound Vibration Vol. 189 (1996), p.525
[4] A.R.K. Reddy and R. Palaninathan: Comp. Struc. Vol. 70 (1999), p.415
[5] G. Anlas and G. Goker: J Sound Vibration Vol. 242 (2001), p.265
[6] P. Malekzadeh: J Thin Wall Struct. Vol. 45 (2007), p.237
[7] A.S. Ashour: J Sound Vibration Vol. 323 (2009), p. 444
[8] A.D. Kerr: Int. J Solids Struct. Vol. 5 (1969), p.559
[9] I. Shufrin and M. Eisenberger: J Sound Vibration Vol. 290 (2006), p. 465
[10] M.M. Aghdam and S.R. Falahatgar:Compos. Struct., vol. 62(2003), pp.279–83
[11] V. Ungbhakorn and P. Singhatanadgid: Comp. Struc. Vol. 73 (2006), p. 120
[12] M.M. Aghdam, M. Mohammadi, andV. Erfanian: J Thin Wall Struct. Vol. 45 (2007), p. 990
[13] F. Alijani, M.M. Aghdam, and M. Abuhamze: Eur. J.Mech. A-Solid, vol. 27(2008), p. 378
[14] S. Yuan and Y. Jin: Comp. Struc. Vol. 66 (1998), p. 861
[15] I. Shufrin, O. Rabinovitch and M. Eisenberger: Int. J Mech. Sci. Vol. 52 (2010), p. 1588

Appendix A

$A_1 = D_{11}\sec^4(\phi)\ ;\ A_2 = 4\sec^3(\phi)\,(D_{16} - D_{11}tan(\phi)); A_3 = 2\sec^2(\phi)\left((D_{12} + 2D_{66}) - 6D_{16}tan(\phi) + 3D_{11}\tan^2(\phi)\right)$

$A_4 = 4\sec(\phi)\,(D_{26} - (D_{12} + 2D_{66})tan(\phi) + 3D_{16}\tan^2(\phi) - D_{11}\tan^3(\phi))$

$A_5 = D_{22} - 4D_{26}tan(\phi) + 2(D_{12} + 2D_{66})\tan^2(\phi) - 4D_{16}\tan^3(\phi) + D_{11}\tan^4(\phi)\ ;\ A_6 = \rho h\omega^2$

Appendix B

$$\alpha_{1jk} = \int_0^b A_1 G_j(\eta) G_k(\eta)\, d\eta \quad ;\ \alpha_{2jk} = \int_0^b A_2\, G_j'(\eta) G_k(\eta)\, d\eta\ ;\ \alpha_{3jk} = \int_0^b A_3\, G_j''(\eta) G_k(\eta)\, d\eta\ ;$$

$$\alpha_{4jk} = \int_0^b A_4\, G_j'''(\eta) G_k(\eta)\, d\eta\ ; \alpha_{5jk} = \int_0^b A_5\, G_j^{(4)}(\eta) G_k(\eta)\, d\eta\ ; \alpha_{6jk} = \int_0^b \rho h\omega^2 G_j(\eta) G_k(\eta)\, d\eta;$$

$$\beta_{1jk} = \int_0^a A_5 F_j(\xi) F_k(\xi)\, d\xi \quad ;\ \beta_{2jk} = \int_0^a A_4\, F_j'(\xi) F_k(\xi)\, d\xi \quad ;\ \beta_{3jk} = \int_0^a A_3\, F_j''(\xi) F_k(\xi)\, d\xi;$$

$$\beta_{4jk} = \int_0^a A_2\, F_j'''(\xi) F_k(\xi)\, d\xi\ ;\ \beta_{5jk} = \int_0^a A_1\, F_j^{(4)}(\xi) F_k(\xi)\, d\xi\ ; \beta_{6jk} = \int_0^a \rho h\omega^2 F_j(\xi) F_k(\xi)\, d\xi;$$

© (2011) Trans Tech Publications, Switzerland
doi:10.4028/www.scientific.net/KEM.471-472.745

Large Amplitude Thermo-Mechanical Vibration Analysis of asymmetrically Laminated Composite Beams

Ali Fallah[1,a], Hamid Shahsavari Alavijeh[2,b], Abdoreza Pasharavesh[1,c] and Mohammad Mohammadi Aghdam[2,d]

[1]School of Mechanical Engineering, Sharif University of Technology, Iran
[2]Department of Mechanical engineering, Amirkabir University of Technology, Iran
[a]a_fallah@mech.sharif.edu [b]h.shahsavari@aut.ac.ir, [c]pasharavesh@mech.sharif.edu, [d]aghdam@aut.ac.ir

Keywords: Nonlinear analysis; asymmetrically Laminated Beams; Thermo-mechanical vibration;

Abstract. In this paper, simple analytical expression is presented for large amplitude thermo-mechanical free vibration analysis of asymmetrically laminated composite beams. Euler-Bernoulli assumptions together with Von Karman's strain-displacement relation are employed to derive the nonlinear governing partial differential equation (PDE) of motion. He's variational method is employed to obtain a simple and efficient approximate closed form solution of the nonlinear governing equation. Comparison between results of the present work and those available in literature shows the accuracy of presented technique. Some new results for the nonlinear natural frequencies of the laminated beams such as the effect of vibration amplitude, lay-up configuration and thermal loading are presented for future references.

Introduction

The vibrational properties of composite structures depend in a complex way upon the elastic properties of the components making up the composite structure. Multilayer composite beams are increasingly used in a wide variety of applications, such as tennis racket, civil and aerospace equipments and etc. Because of difference between the making temperatures and working temperature of composite structures, for more detailed analysis, temperature effects must be considered in the equations. For low temperature difference, to avoid thermal effects, is logical, but for high temperature difference, such as Aerospace Structures, the effects of temperature difference must be considered. Furthermore, the study of thermo-mechanical Vibration behavior at large amplitudes of multi layered composite beams is necessary. Hence, natural responses of these structures are essentially nonlinear and are described by nonlinear equations.

Due to difficulties in the analytical solution of nonlinear equations, application of different numerical techniques seems to be necessary. However, closed form solutions even if they are approximate solutions are more interesting due to various advantages such as ease of parametric studies and considering of physics of the problem. Among approximate analytical solutions for nonlinear problems one may refer to the He's variational method [1-3].

Most studies for nonlinear free vibration analysis of beams are concerned on isotropic and symmetrically laminated composite beams [4-8]. Due to the bending-stretching coupling in asymmetrically laminated beams their nonlinear vibrations analyses are different from that of isotropic and symmetrically composite beams. A few studies can be found in the literature for nonlinear analysis of asymmetrically laminated beams [9-10]. For instance, Patel et al. [9] investigated nonlinear free flexural vibrations and post-buckling of laminated orthotropic beams resting on a class of two parameter elastic foundation using a three-nodded shear flexible beam element. Free vibrations and post-buckling analysis of asymmetrically laminated composite beams on nonlinear elastic foundation have been developed by Baghani et al. [10]. However, with the best knowledge of the authors studies related to the thermo-mechanical nonlinear vibration of asymmetrically laminated beams are not found in the open literature.

In this paper, simple analytical expression is presented for large amplitude thermo-mechanical free vibration analysis of asymmetrically composite beams. Von Karman's strain-displacement relation with Euler-Bernoulli assumption is employed to derive the nonlinear

governing partial differential equation of motion. The governing PDE is reduced to an ordinary differential equation (ODE) using one parameter Galerkin method. He's variational method is employed to obtain a simple and efficient approximate closed form solution of the nonlinear governing ODE. Comparison between results of the present work and those available in literature shows the accuracy of presented technique. Some new results for the nonlinear natural frequencies of the laminated beams such as the effect of vibration amplitude, lay-up configuration and thermal loading are presented.

Problem formulation. Consider an asymmetrically laminated composite beam with length L, width b and height h in x, y and z direction, respectively as shown in Fig.1.

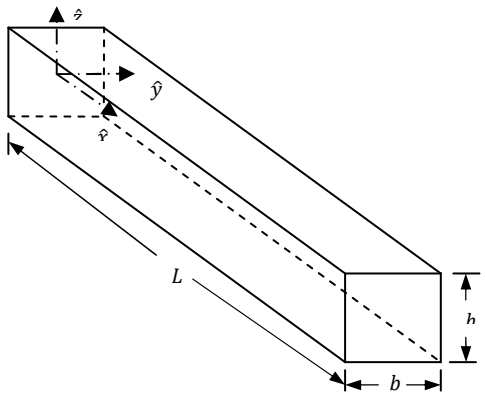


Fig .1. Geometry of composite beam and its coordinate system

When temperature effects are considered in the problem, resultant force and moment consist of thermal and mechanical components. Based on the classical lamination theory, mechanical force and moment resultants can be written as:

$$N_{M\hat{x}} = A_{11}\left(\frac{\partial \hat{u}}{\partial \hat{x}} + \frac{1}{2}\left(\frac{\partial \hat{w}}{\partial \hat{x}}\right)^2\right) + B_{11}\frac{\partial^2 \widehat{W}}{\partial \hat{x}^2} \tag{1}$$

$$M_{M\hat{x}} = B_{11}\left(\frac{\partial \hat{u}}{\partial \hat{x}} + \frac{1}{2}\left(\frac{\partial \hat{w}}{\partial \hat{x}}\right)^2\right) + D_{11}\frac{\partial^2 \widehat{W}}{\partial \hat{x}^2} \tag{2}$$

in which the stiffness coefficients A_{11}, B_{11} and D_{11} are defined as:

$$A_{11} = \sum_{k=1}^{N} \bar{Q}_{11}^k(\hat{z}_k - \hat{z}_{k-1}), B_{11} = \frac{1}{2}\sum_{k=1}^{N} \bar{Q}_{11}^k(\hat{z}_k^2 - \hat{z}_{k-1}^2), D_{11} = \frac{1}{3}\sum_{k=1}^{N} \bar{Q}_{11}^k(\hat{z}_k^3 - \hat{z}_{k-1}^3) \tag{3}$$

It is assumed that initial temperature is zero. Therefore, temperature difference is T instead of ΔT. In a cross-ply composite beam, the thermal axial load and thermal moment due to a constant temperature rise T can be written as:

$$N_{T\hat{x}} = \int_{\frac{-h}{2}}^{\frac{h}{2}} \bar{Q}_{11}.\alpha_{\hat{x}}.T.dz = \sum_{k=1}^{N} \bar{Q}_{11}^k.\alpha_{\hat{x}}^k.T.(z_k - z_{k-1}) \tag{4}$$

$$M_{T\hat{x}} = \int_{\frac{-h}{2}}^{\frac{h}{2}} \bar{Q}_{11}.\alpha_{\hat{x}}.T.z.dz = \frac{1}{2}\sum_{k=1}^{N} \bar{Q}_{11}^k.\alpha_{\hat{x}}^k.T.(z_k^2 - z_{k-1}^2) \tag{5}$$

where thermal coefficient $\alpha_{\hat{x}}$ is defined as:

$$\alpha_{\hat{x}} = \alpha_1 cos^2\theta + \alpha_2 sin^2\theta \tag{6}$$

in which, θ is the angle between the fiber direction and the longitudinal axis of the beam and α_1 and α_2 are the thermal expansion coefficients of the fibers along the longitudinal and transverse

directions, respectively. In terms of beam notations, the total induced axial force N and bending moment M are related to the stress resultants as follows:

$$N = bN_{\hat{x}} = b(N_{M\hat{x}} + N_{T\hat{x}}) = bA_{11}\left[\frac{\partial \hat{u}}{\partial \hat{x}} + \frac{1}{2}\left(\frac{\partial \hat{w}}{\partial \hat{x}}\right)^2\right] + bB_{11}\frac{\partial^2 \hat{W}}{\partial \hat{x}^2} + bN_{T\hat{x}} \tag{7}$$

$$M = bM_{\hat{x}} = b(M_{M\hat{x}} + M_{T\hat{x}}) = bB_{11}\left[\frac{\partial \hat{u}}{\partial \hat{x}} + \frac{1}{2}\left(\frac{\partial \hat{w}}{\partial \hat{x}}\right)^2\right] + bD_{11}\frac{\partial^2 \hat{W}}{\partial \hat{x}^2} + bM_{T\hat{x}} \tag{8}$$

The equilibrium equations by assuming thermo-mechanical loading can be written as:

$$m\frac{\partial^2 \hat{u}}{\partial \hat{t}^2} - \frac{\partial N}{\partial \hat{x}} = 0 \tag{9}$$

$$m\frac{\partial^2 \hat{w}}{\partial \hat{t}^2} + \frac{\partial^2 M}{\partial \hat{x}^2} - N\frac{\partial^2 \hat{w}}{\partial \hat{x}^2} = 0 \tag{10}$$

where m is mass per length. After some mathematical simplifications, the governing equation in terms of transverse displacement can be written as:

$$m\hat{w}_{,\hat{t}\hat{t}} + b\left(D_{11} - \frac{B_{11}^2}{A_{11}}\right)\hat{w}_{,\hat{x}\hat{x}\hat{x}\hat{x}} - b.\left[N_{T\hat{x}} + \frac{A_{11}}{2L}\int_0^L \hat{w}_{,\hat{x}}{}^2 d\bar{x} + \frac{B_{11}}{L}\left(\hat{w}_{,\hat{x}}(L,\hat{t}) - \hat{w}_{,\hat{x}}(0,\hat{t})\right)\right]\hat{w}_{,\hat{x}\hat{x}} = 0 \tag{11}$$

in which comma denotes derivative with respect to $\hat{x}$ or $\hat{t}$. The following dimensionless variables can be defined:

$$x = \frac{\hat{x}}{L} \;\; ; \; w = \frac{\hat{w}}{r} \; ; \quad t = \hat{t}\sqrt{b\left(D_{11} - \frac{B_{11}^2}{A_{11}}\right)/mL^4} \tag{12}$$

where $r = \sqrt{I/A}$ is the radius of gyration of the cross section. Using Eq. 11 and the dimensionless variables defined in Eq. 12, the dimensionless form of the governing equation becomes:

$$w_{,tt} + w_{,xxxx} - \left[N_{Tx} + \Lambda\int_0^1 w_{,x}^2\, dx + \Upsilon\left(w_{,x}(1,t) - w_{,x}(0,t)\right)\right]w_{,xx} = 0 \tag{13}$$

where:

$$N_{Tx} = \frac{N_{T\hat{x}}L^2}{b\left(D_{11} - \frac{B_{11}^2}{A_{11}}\right)} \; ; \quad \Lambda = \frac{A_{11}r^2}{2\left(D_{11} - \frac{B_{11}^2}{A_{11}}\right)} \; ; \; \Upsilon = \frac{B_{11}r}{\left(D_{11} - \frac{B_{11}^2}{A_{11}}\right)} \tag{14}$$

Assuming $w(x,t) = V(t)\phi(x)$ where $V(t)$ is an unknown time-dependent function and $\phi(x)$ is a trial function which satisfies the kinematic boundary conditions and presented in Table 1.

Table 1. Admissible trial functions for a beam with different boundary condition [11].

Boundary condition	$\phi(x)$
Simply supported (SS)	$\sin(\pi x)$
Clamped-Clamped (CC)	$(\cosh(qx) - \cos(qx)) - \frac{\cosh(q) - \cos(q)}{\sinh(q) - \sin(q)}(\sinh(qx) - \sin(qx));\; q = 4.7300$

Assuming prescribed functions for $\phi(x)$ together with the Galerkin technique, the equation of motion in terms of unknown function $V(t)$ can be obtained as:

$$\ddot{V}(t) + \left(\alpha_1 + \alpha_{N_{Tx}}\right)V(t) + \alpha_2 V(t)^2 + \alpha_3 V(t)^3 = 0 \tag{15}$$

where coefficients α_i are defined in Appendix. The center of the beam is subjected to the following initial conditions:

$$V(0) = a \quad , \quad \frac{dV(0)}{dt} = 0 \tag{16}$$

where *a* denotes the dimensionless maximum amplitude of oscillation.

Solution procedures. In order to simplify the analysis, Eq. 15 is rewritten as:

$$\ddot{V} + \beta_1 V + \beta_2 V^2 + \beta_3 V^3 = \ddot{V} + f(V) = 0 \tag{17}$$

where $\beta_1 = \alpha_1 + \alpha_{N_{Tx}}$, $\beta_2 = \alpha_2$ and $\beta_3 = \alpha_3$. Variational principle of Eq. 17 can be obtained using the semi-inverse method [1]:

$$J(V) = \int_0^{T/4} \left\{ -\frac{1}{2}\dot{V}^2 + \frac{\beta_1}{2}V^2 + \frac{\beta_2}{3}V^3 + \frac{\beta_3}{4}V^4 \right\} dt \tag{18}$$

where *T* is period of the nonlinear oscillation. The approximate solution considered as:

$$V(t) = a\, cos(\omega t) \tag{19}$$

where *a* and ω are the amplitude and nonlinear natural frequency of the oscillator, respectively. Substituting Eq. 19 into Eq. 18 together with transformation $\tau = \omega t$ results in:

$$J(a,\omega) = \frac{1}{\omega}\int_0^{\pi/2} \left\{ -\frac{1}{2}a^2\omega^2 sin^2(\tau) + \frac{1}{2}\beta_1 a^2 \cos^2(\tau) + \frac{1}{3}\beta_2 a^3 \cos^3(\tau) + \frac{1}{4}\beta_3 a^4 \cos^4(\tau) \right\} d\tau \tag{20}$$

The stationary condition with respect to *a* leads to:

$$\frac{\partial J}{\partial a} = \frac{1}{\omega}\int_0^{\pi/2} \left\{ -a\,\omega^2 sin^2(\tau) + \beta_1 a \cos^2(\tau) + \beta_2 a^2 \cos^3(\tau) + \beta_3 a^3 \cos^4(\tau) \right\} d\tau = 0 \tag{21}$$

The nonlinear natural frequency of the motion can be determined from Eq. 21 as:

$$\omega^2 = \frac{\int_0^{\frac{\pi}{2}} \{\beta_1 \cos^2(\tau) + \beta_2 a \cos^3(\tau) + \beta_3 a^2 \cos^4(\tau)\} d\tau}{\int_0^{\frac{\pi}{2}} \sin^2(\tau)\, d\tau} = \beta_1 + \frac{8}{3\pi}\beta_2 a + \frac{3}{4}\beta_3 a^2 \tag{22}$$

Therefore, the approximate solution can be easily determined as:

$$V(t) = a\, cos\left(\sqrt{\beta_1 + \frac{8}{3\pi}\beta_2 a + \frac{3}{4}\beta_3 a^2}\; t \right) \tag{23}$$

Result and discussion

At first, in order to examine the accuracy of the presented analytical solution, an isotropic beam is considered with both simply supported and clamped boundary conditions. In Table 2, the nonlinear to linear frequency ratio (ω_{NL}/ω_L) of the isotropic beam are presented. Included in the table are also results of other available studies in the literature. It can be concluded from the results that predictions of the presented solution shows very good agreement with published data.

The next example is a Graphite/Epoxy composite beam with the following material properties:

$E_{11} = 137(GPa); E_{22} = 9.96(GPa); G_{12} = 7.1(GPa);\ \nu_{12} = 0.3; \rho = 1200\frac{kg}{m^3}; \alpha_1 = -0.3 \times 1^{-6}/℃; \alpha_2 = 26.08 \times 1^{-6}/℃$

Nonlinear thermal vibration analysis of beams with various lay-up schemes and boundary conditions are investigated and results presented in this section.

As mentioned before, Eq. 18 contains a quadratic nonlinearity mainly due to the bending stretching coupling. However, for clamped-clamped beams either isotropic or composite the quadratic term vanishes and therefore, Eq. 18 reduces to a Duffing equation. In this case, the exact nonlinear frequency (ω_{ex}) can be determined as:

$$\omega_{ex} = 2\pi \left(4 \int_0^{\frac{\pi}{2}} \frac{1}{\sqrt{\beta_1 + \frac{1}{2}(1 + \sin^2(\tau))\beta_3 a^2}} d\tau \right)^{-1} \quad (24)$$

As another verification attempt, frequency ratio obtained by Eq. 22 for a fully clamped four layer laminated (0 90 0 90) beam with different temperature difference versus dimensionless amplitude is presented in Table 3. Results obtain from exact frequency ratio using Eq. 24 are also included in the table. Again, reasonably good agreement with exact solution for nonlinear analysis of laminated beams can be observed. Maximum discrepancy between results of this study and those of the exact solution Eq. 24 is about 0.3%.

Table 2. Comparison of frequency ratio (ω_{NL}/ω_L).

a	SS				CC			
	Present	[6]	[5]	[4]	Present	[6]	[5]	[4]
1	1.0897	1.0897	1.0897	1.0891	1.0552	1.0572	1.0628	1.0 21
2	1.3229	1.3228	1.3229	1.3177	1.2056	1.2125	1.2140	1.0856
3	1.6393	1.6393	1.6394	1.6256	1.4214	1.4344	1.3904	1.1831
4	1.9999	1.9999	--	--	1.6776	1.6171	1.5635	1.3064

Table 3. Frequency ratio (ω_{NL}/ω_L) of CC laminated composite beam (0 90 0 90).

a	T(℃)					
	0		50		100	
	Present	Exact	Present	Exact	Present	Exact
0.5	1.0085	1.0085	1.0086	1.0086	1.0087	1.0087
1.0	1.0336	1.0335	1.0340	1.0339	1.0344	1.0343
2.0	1.1285	1.1274	1.1300	1.1289	1.1314	1.1303
3.0	1.2710	1.2672	1.2739	1.2700	1.2768	1.2728

The effects of the temperature difference on the nonlinear natural frequency of laminated composite beams are studied and results are presented in Figs. 2-3. In these figures, the dimensionless frequency ratio (ω_{NL}/ω_L) versus dimensionless amplitude (a) for four different lay-up configuration is presented. It can be seen that all CC beams and SS beams [0 90 90 0] and [0 45 0 45] exhibit a typical hardening behavior, i.e. the nonlinear frequency ratio increases as the oscillation amplitude is increased. However, in the case of SS beam [90 0 90 0], frequency ratio decreased and then increased as oscillation amplitude is increased.

It can be concluded from Figs. 2-3 that as the values of the temperature difference increased the value of frequency ratio also increased.

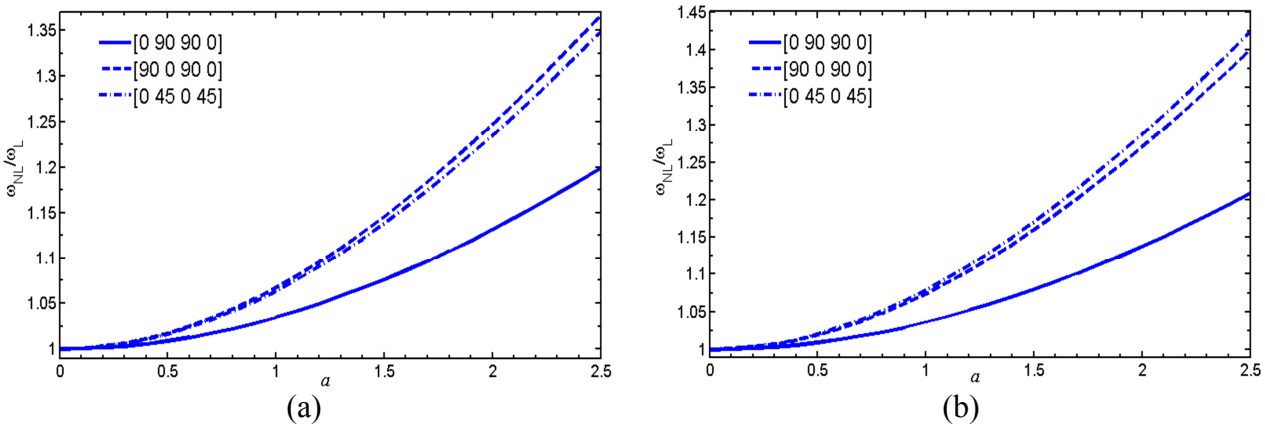


Fig. 2. Effect of the Temperature on frequency ratio of CC beam a) $T = 100$℃, b) $T = 300$℃

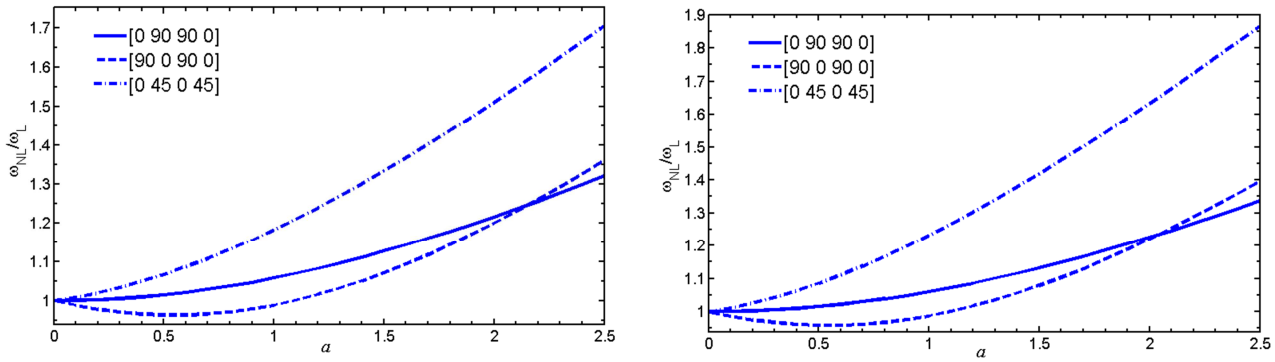


Fig. 3. Effect of the temperature on frequency ratio of SS beam, a) $T = 50℃$, b) $T = 100℃$.

Summary

In this paper, simple analytical expression is presented for large amplitude thermo-mechanical free vibration analysis of asymmetrically laminated composite beams. The presented expressions are convenient and efficient for the nonlinear analysis of the laminated beams. In spite of other analytical techniques such as perturbation methods, the obtained expression is valid for a wide range of vibration amplitudes. Von-Karman's assumption is used to model geometrical nonlinearity. Euler-Bernoulli assumption is employed to derive the nonlinear governing partial differential equation of motion. He's variational method is employed to obtain a simple and efficient approximate closed form solution of the nonlinear governing equation. Comparison between results of the present work and those available in literature shows the accuracy of presented technique. Some new results for the nonlinear natural frequencies of laminated beams such as the effect of vibration amplitude, lay-up configuration and temperature distribution are presented. Results show that as the values of the temperature difference and vibration amplitude increased the value of frequency ratio also increased.

Acknowledgment

Third author wishes to acknowledge fruitful supports of Elite National Foundation (Bonyade Melli Nokhbegan).

References

[1] J.H He: Chaos Solitons Fractals Vol. 34 (2007), p. 1430
[2] J.H He: Chaos Solitons FractalsVol. 19 (2004), p. 847
[3] J.F. Liu: Comput. Math. Appl. Vol. 58 (2009), p. 2423
[4] L. Azrar, R. Benamar and R.G. White: J Sound Vib Vol. 224 (1999), p. 183
[5] M.I. Qaisi: Appl. Acous. Vol. 40 (1993), p.141
[6] T. Pirbodaghi, M.T. Ahmadian and M. Fesanghary: Mech Res Commun Vol. 36 (2009), p. 143
[7] A.S. Emam and A.H. Nayfeh: Compos. Struct. Vol. 88 (2009), p. 636
[8] X. Song and K.M Wang :Thin-Walled Structures Vol. 47 (2009), p.304
[9] B.P. Patel, M. Ganapathi and M. Touratier: Compos. Struct. Vol. 46 (1999), p. 189
[10] M. Baghani, R.A. JafariTalookolaei and H. Salarieh: Appl. Math. Model. Vol. 35 (2011), p. 130
[11] S.S Rao: *Vibration of continuous systems,* Jhon Wiley & Sons Inc, New Jersy (2004).

Appendix

$$\alpha_1 = \frac{\int_0^1 \emptyset_{,xxxx}.\emptyset.dx}{\int_0^1 \emptyset^2.dx};\ \alpha_2 = \frac{-\Upsilon\left[\emptyset_{,x}(1) - \emptyset_{,x}(0)\right]\int_0^1 \emptyset_{,xx}.\emptyset.dx}{\int_0^1 \emptyset^2.dx}$$

$$\alpha_3 = \frac{-\Lambda\int_0^1 \emptyset_{,x}{}^2.dx\int_0^1 \emptyset_{,xx}.\emptyset.dx}{\int_0^1 \emptyset^2.dx};\ \alpha_{N_{Tx}} = \frac{-N_{Tx}\int_0^1 \emptyset_{,xx}.\emptyset.dx}{\int_0^1 \emptyset^2.dx}$$

© (2011) Trans Tech Publications, Switzerland
doi:10.4028/www.scientific.net/KEM.471-472.751

Effect of Nanoclay on the Physical-Mechanical and Thermal Properties and Microstructure of Extruded Noncross-linked LDPE Nanocomposite Foams

F. Zandi[a] , M. Rezaei[b] and A. Kasiri[c]

Institute of Polymeric Materials, Polymer Eng. Dept., Sahand University of Technology, Tabriz, Iran.
[a]Farhadzandi78@gmail.com , [b]Rezaei@sut.ac.ir, [c]alikasiri1983@gmail.com

Keywords: Nanocomposite, LDPE Foam, Microstructure, Thermal Conductivity, Flame Retardancy

Abstract. Novel noncross-linked low density polyethylene (LDPE) foams were produced by extrusion process. In this study the effects of Organophilic Montmorillonite (OMMT) nanoclay (DK1) on thermal conductivity, flame retardancy, morphological and mechanical properties of LDPE foams have been investigated. Nanoclay dispersion in LDPE foam structure was examined by X-ray diffraction (XRD), microstructure was observed by an optical microscope and analyzed by Bel View image analyzer, thermal conductivity was studied by a simple transient method, mechanical properties was investigated using a tensile-compression Zwick-Roell machine as well as the flame retardancy of the samples was examined by flammability test. The optimum nanoclay content was determined by comparison of the properties in nanocomposite and neat LDPE foams. Due to the presence of nanoclay in the foam and decreasing the cell nucleation energy around the nanoclay, the average cell size was decreased as well as the cell density and microstructure uniformity was increased. In XRD patterns of LDPE nanocomposite foams, OMMT (DK1) characteristic peak was not observed as evidence of nanoclay intercalation-exfoliation in the polymer matrix, which led to the production of foams with homogenous microstructure. Furthermore, this nanocomposites showed lower thermal conductivity compared to neat LDPE foam, which can be attributed to the cell size reduction as well as narrow cell size distribution in nanocomposite foams. Compression test results demonstrated that LDPE nanocomposite foams with proper clay contents have improved mechanical properties (Young's modulus, compressive strength). Furthermore due to the presence of DK1 nanoclay, LDPE foam showed a good char formation as an evidence of their flame retardancy.

Introduction

Extrusion has long been known as an effective and efficient process to produce polymeric foams by blending blowing agent into molten polymer to generate a homogenized high pressure solution for instantaneous free expansion at the extrusion exit [1,2]. Extrusion processes usually consists of four stages:(a) the dissolution of foaming agent into a polymer melt at elevated pressure; (b) the nucleation of bubbles in a supersaturated solution of foaming agent in a molten polymer; (c) the growth of bubbles in a molten polymer and (d) the stabilization of the cellular structure by lowering the temperature below the melting point or the glass transition temperature of polymer [3].

Considerable effort has been devoted to develop the foams with reduced cell sizes and narrower cell size distribution for many applications, such as packaging, textile, agriculture and construction, due to improved physical, mechanical, thermal and morphological properties [3-7]. It is known that talc (as an additive) content significantly affects the cell density of low density polyethylene (LDPE) foam. In terms of spontaneous nucleation theory, this situation is quite reasonable: the work of formation of a critical nucleus in cavities of talc particles is smaller than that in the balk of polymer matrix [1].

So much attention have recently conducted on the polymer-layered silicate nanocomposites as they offer new possibilities to provide superior properties compared to neat polymers and conventional filled composites [4]. OMMT nanoclay structure plays important roles in improving mechanical, thermal, and diffuse-barrier properties of polymer layered silicate nanocomposites. Diffuse-barrier properties can improve LDPE foam flame retardancy; furthermore a decrease in cell size leads to improvement of the thermal insulating properties. Most efforts related with this kind of experiments have been focused in the production of microcellular foams fabricated using a continuous process and studying the influence of the addition of nanoclays into the polymer matrix, both on foaming process and cellular structure [4,5]. The properties include high dimensional stability, high cell density, small cell size, narrow cell size distribution, homogenous microstructure, high mechanical properties and low flammability [3, 4]. Adding a small amount of nanoclay (Cloisite 20A) to PE foam showed that the burning rate for the PE foam nanocomposites was lower than that for the neat PE foams [6].

In this work we used various contents of Organophilic Montmorillonite OMMT (DK1) nanoclay in extrusion foaming process. This investigation reports an extensive study on the effect of DK1 at different properties of non-crosslinked LDPE nanocomposite foams.

Experimental

The material used for manufacturing of the uncrosslinked low density poly ethylene foams and their formulation (by 0.1, 0.3 and 0.6wt% DK1) are presented in Table 1.

LDPE (0020,density: 920 kg/m^3, MFI: 2.0 gr/10 min) prepared from Bandar Imam Petrochemical Co., talc (contain: SiO_2,MgO,CaO,Fe_2O_3,Al_2O_3) supplied from Azarbaijan Co., was used as nucleating agent, glycerol monostearat (GMS-Atmer129 with T_m: 69^{0}C, prepared from FACI, Italy), used as cell stabilizer. Iso butane and iso pentane mixture (weight ratio: 70/30) prepared from Tabriz petrochemical Co., was used as blowing agent. Modified organoclay (DK1) was supplied by Fenghong Clay Chemical Corp., China. The foams's mold densities were kept constant (22-25kg/m^3).

The materials used for manufacturing of the non-crosslinked low density polyethylene foams and their formulation (by 0.1 wt%, 0.3 wt% and 0.6 wt% DK1) are presented in Table [1].

Table1. Materials used to produce LDPE neat and nanocompoite foams

	Neat foam	Nanocomposite foam		
Materials [wt%]		**0.1wt% DK1**	**0.3wt% DK1**	**0.6 wt% DK1**
GMS	0.5	0.5	0.5	0.5
Talc	0.3	0.3	0.3	0.3
DK1	—	0.1	0.3	0.6

The samples were produced on single-screw extruder (Polycell Korea corporation, machine model: PKC 105 M/M), the morphology of nanocomposite was characterized by X-ray diffraction (XRD), (Siemenes model D5000) and the microstructure of the LDPE foams was studied by an optical microscope (Bel Italy) and Bel View image analysis software. The mechanical properties of LDPE foam and nanocomposite was examined by compression test using a Zwick/Roell (model TI-FR010) tensile–compression machine at room temperature with strain rate 5 mm/min and the sample size 50×50×50 mm^3 [DIN 53577]. The samples' thermal conductivity coefficient examined by using a simple transient needle probe method thermal conductmetry.

Finally to estimate the flammability of the foams, the amount of dripping during burning test and the burning rate of the samples using (FAR 25.853) was examined [9]. In this experiment the specimen was (368 ×76 × 10 mm^3) held vertically using a cramp and the flame of burner was applied at the lower end of the specimen for 12 seconds, then flame was removed (ASTM D 635–03) and burning rate (cm/min) and the amount of dripping were calculated.

Result and Discussion

The XRD patterns of nanocomposite foams are presented in Fig.1. The peak at 2Θ =3.48° for DK1 correspond to d-spacing of 2.02 nm. In nanocomposite foams with 0.1, 0.3 and o.6 Wt% DK1 no such peak is observed within the scan range as an evidence of intercalation or exfoliation of the nanoclay into the LDPE foam matrix.

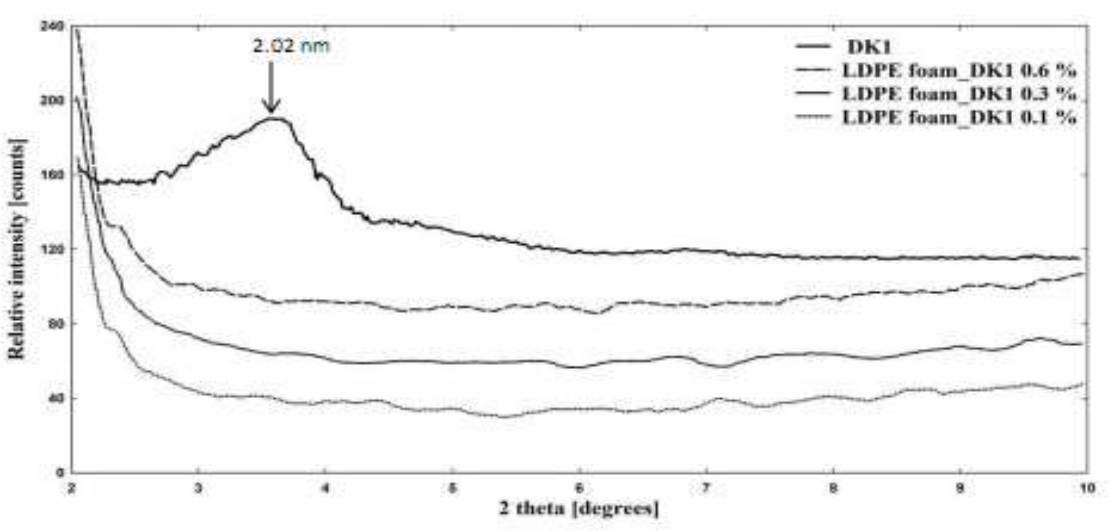


Fig.1 XRD patterns of DK1 and LDPE/DK1 nanocomposites.

The micrographs in Fig. 2 illustrate that the increase in clay content up to 0.3 wt%, results a more homogenous structure. After that, increasing the clay content up to 0.6%wt will have a negative effect on the nanocomposite foam microstructure, due to the cells coalescence.

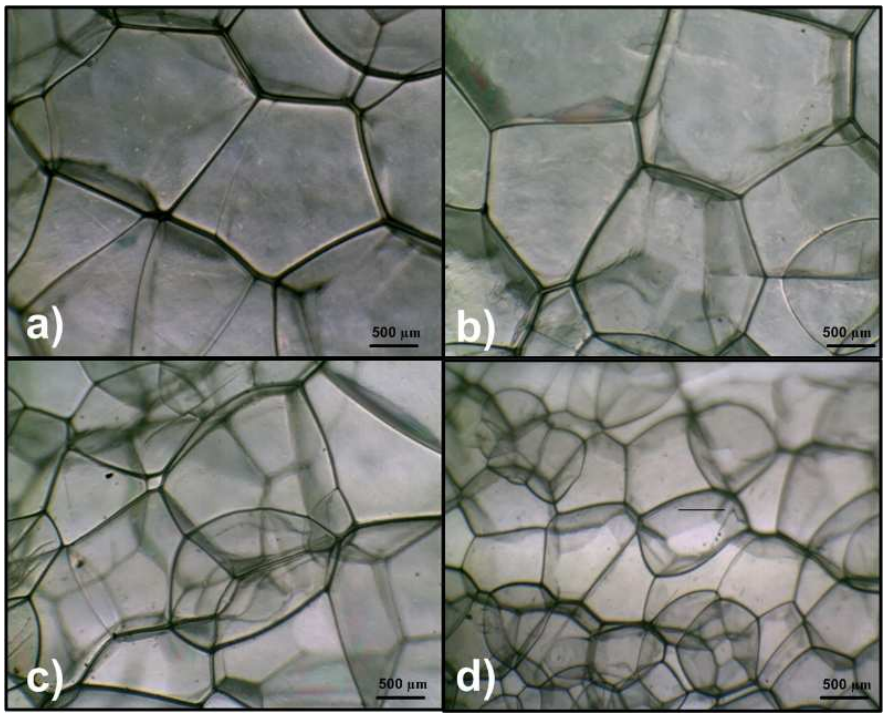


Fig. 2 Micrographs of foamed samples: a) neat LDPE, b) LDPE with 0.1%wt DK1, c) LDPE with 0.3 % wt DK1 and d) LDPE with 0.6 %wt DK1.

Nanoclay and talc, act as nucleating agents for the foaming process. Incorporating of the nanoclays into the LDPE matrix leads to a decrease in work of formation of the nucleus around the nanoclays. In fact, DK1 nanoclay as a nucleating agent can increase the number of cells per volume (cell density) of LDPE foam, and decrease the cell size. As it was demonstrated in Fig. 3 cell density has been raised from 4.1203×10^8 [cells/m^3] for neat foam to 8.0614×10^8 [cells/cm^3] for 0.6%wt clay content nanocomposite foam.

Fig. 4 indicates cell size normal distribution of LDPE neat and nanocomposite foams. Because of proper nanoclays dispersion in prefoamed materials matrix, it can be concluded that with increasing nanoclay content the cell size is decreased and the cell size distribution is homogeneously narrowed.

Fig. 5 demonstrates the effect of the modified DK1 (OMMT) content on the thermal conductivity of LDPE foam and its nanocomposites. Concerning the cell microstructure and the fact that "reduction in cell size leads to reduce the radiation contribution of thermal conductivity", it can be observed that LDPE nanocomposite foam with smaller cell size shows lower thermal conductivity compared to neat LDPE. It can be concluded that by adding nanoclay to LDPE foam, the thermal conductivity coefficient will be decreased and consequently its insulating properties will be increased.

Incorporating DK1 nanoclays to LDPE foam will affect the microstructure, and produce foams with homogeneous properties. This homogeneity, will improve the mechanical properties of the samples up to the nanoclay contents of 0.3 wt%. But further increase in nanoclay content, causes deficiencies in LDPE foam microstructure and the mechanical will be decreased. As it can be observed in Fig. 6 Young modulus, has been increased from 0.108 MPa for neat foam to 0.142 MPa for nanocomposite foam contain 0.3 wt% DK1, and finally has been reduced to 0.123 for the nanocomposite foam contain 0.6 wt% nanoclay. This behavior can be attributed to the nanoclays dispersion states in nanocomposite foams with different clay contents.

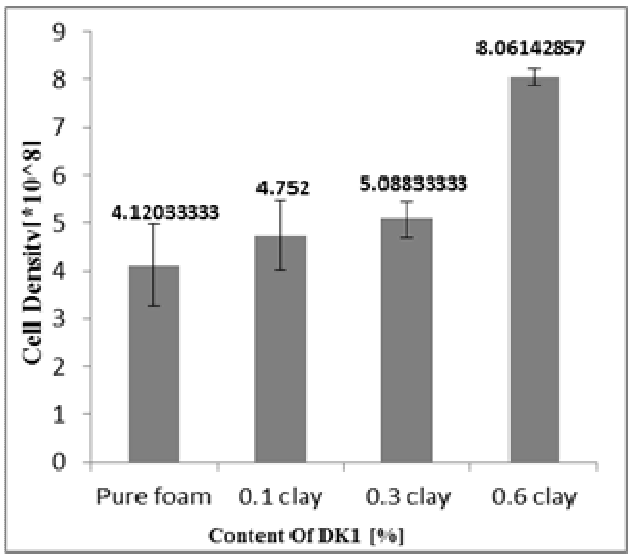


Fig. 3 Effect of clay content on the cell density of neat and nanocomposites foams.

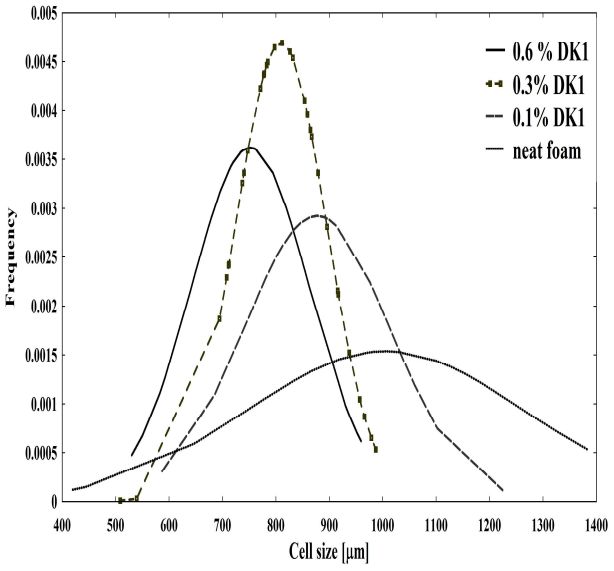


Fig. 4 Effect of clay content on the cell size distribution of neat and nanocomposite foams.

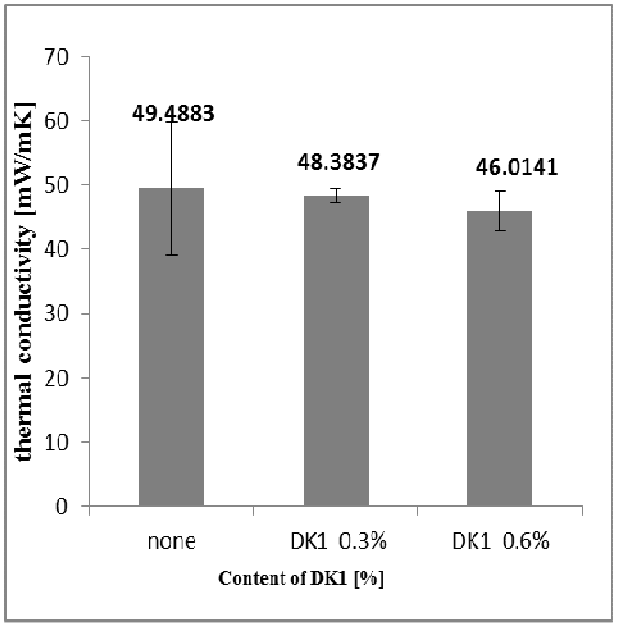


Fig.5 Effect of clay content on thermal conductivity coefficient of LDPE neat and nanocomposite foam.

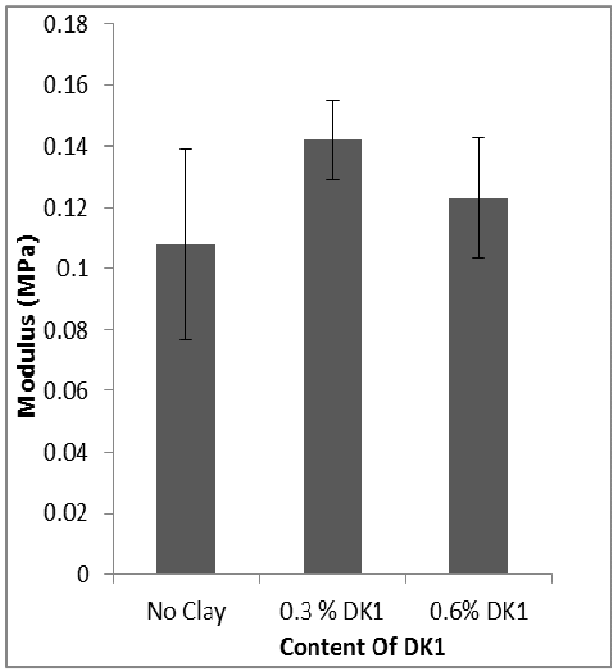


Fig.6 Effect of clay content on Young's modulus of LDPE neat and nanocomposite foams.

In this study, due to utilizing n-butane and n-pentane as blowing agent, flame retardancy is quite small. DK1 nanoclay can improve this behavior by presence in the LDPE foam walls. Incorporation of DK1 nanoclay has improved the LDPE foam flam retardancy, in other words, burn rate as well as dripping content have been decreased in nanocomposite foams compared to neat LDPE foam, as is illustrated in Fig. 7.

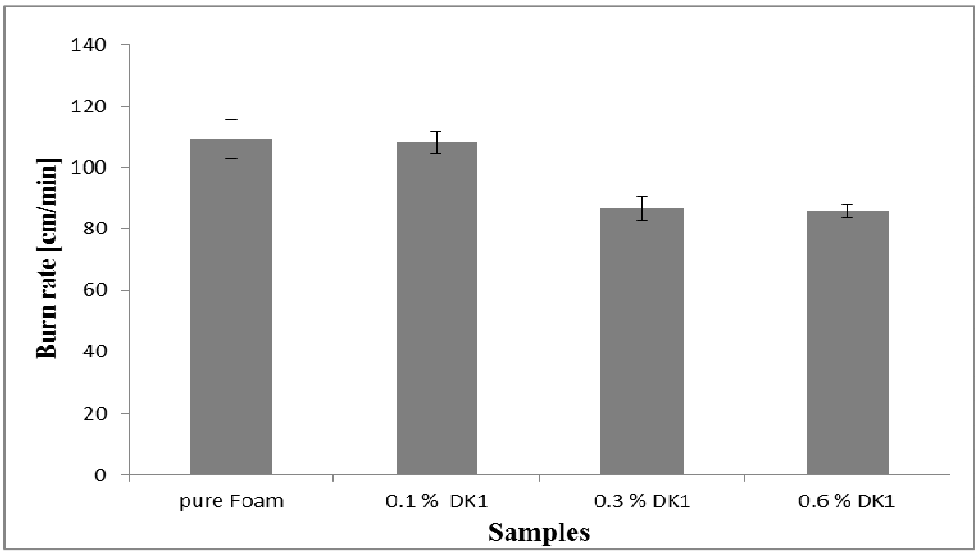


Fig.7 Burning rates of LDPE and nanocomposites foams.

Summary

In this study the X-ray diffraction (XRD) patterns has no DK1 (OMMT) characteristic peak, as an evidence of intercalation/exfoliation of the nanoclay in the polymer matrix. Due to the presence of nanoclay in the foam and decreasing the work of cell nucleation around the nanoclays, the cell density will be increased but the average cell diameter will be decreased. Achieving the proper dispersion of DK1 (OMMT) nanoclays in the foams, led to the production of foams with homogenous microstructure, and improved thermal and mechanical properties, as well as LDPE nanocomposites foams showed a good char formation as an evidence of flame retardancy. Finally the results of this study revealed that LDPE nanocomposite foams with 0.3 wt% DK1 nanoclay content showed the best physical and mechanical properties with narrow cell size distribution and homogenous microstructure.

References

[1] B. V. Kichatov and A. M. Korshunov: J. Theo. Found. Chem. Eng. Vol.30 (2005), P.643

[2] S.-T LEE and K.LEE: J. Add. Polym. Tech. Vol.19 (2000), P.87

[3] Gabriel O. Aloku, Xue-Feng Yuan; Chem. Eng. Sci. Vol.65, Issue 12 (2010), P.3749.

[4] J. I. Velasco, M. Antunes, O. Ayyad, C. Saiz-Arroyo, M. A. Rodriguez-Perez, F. Hidalgo,

J. A. de Saja. Polym. Vol.48, Issue 7 (2007), P.2098.

[5] C. H. Lee, K. J. Lee, H. G. Jeong, S. W. Kim: J. Add. Polym. Tech. Vol.19 (2000), P.97

[6] G. Guo, K. H. Wang, C. B. Park, Y. S. Kim, G. Li: J. App. Polym. Sci. Vol.104 (2007), P.1058

[7] J. H. Lee, K. H. Wang, C. B. Park, M. sain: J. App. Polymer. Sci. Vol.103 (2007), P.2129

[8] j. C. Costa, M. Oliveira, A. V.Machado, S. Lanceros-Mendez, G. Betelho: J. App. Polym.

Sci. Vol.112 (2009), P.1595

[9] Yoshizawa, Choji Kohara, Kuniaki Komal and Motoyoshi Hatada: J. App. Polym. Sci. Vol. 51 (1994), P.84

© (2011) Trans Tech Publications, Switzerland
doi:10.4028/www.scientific.net/KEM.471-472.757

Thermal Buckling Analysis of Moderately Thick Plates using Functionally Graded Strips

Mohammad Nassirnia[1,a], Hamid Reza Ovesy[1,b], Seyyed Amir Mahdi Ghannadpour[2,c]

[1] Aerospace Engineering Department and Centre of Excellence in Computational Aerospace Engineering, Amirkabir University of Technology, Tehran, Iran
[2] Aerospace Engineering Department, Faculty of New Technologies Engineering, Shahid Beheshti University, G.C., Tehran, Iran

[a]mnassirnia@aut.ac.ir, [b]ovesy@aut.ac.ir, [c]a_ghannadpour@sbu.ac.ir

Keywords: Thermal Buckling, Functionally Graded Material, Power law, First Order Shear Deformation Theory, Finite Strip Method

Abstract. In the current study, the critical buckling of functionally graded plates (FGPs) subjected to thermal loads is evaluated using the finite strip method based on the first order shear deformation theory (FSDT). The material properties of these plates are assumed to vary in the thickness direction of the plate according to the power law distribution in terms of volume fractions of the constituents. The plates' boundary conditions are assumed to be simply supported in all the edges or clamped in side edges and simply supported on the ends. The fundamental eigen-buckling equations for the plates are obtained by discretizing the plate into some strips, called functionally graded strip (FGS). The solution is obtained by the minimization of the total potential energy as well as solving the eigenvalue problem. The effects of material gradient index, aspect ratio and different thermal loadings (i.e. uniform temperature rise and nonlinear temperature change across the thickness) on the critical buckling temperature difference will be presented in some graphical forms.

Introduction

Functionally graded materials (FGMs) are those in which the volume fractions of two or more constituents are varied continuously as a function of position along certain dimension of the plate to achieve a required function. By gradually varying the volume fraction of constituent materials, their mechanical properties exhibit a smooth and continuous change from one surface to the other one. The ceramic constituent of the material provides the high-temperature resistance due to its low thermal conductivity. Thus FGMs have received considerable attention as one of advanced inhomogeneous composite materials in many engineering applications by eliminating interface problems and alleviating thermal stress concentrations. Javaheri and Eslami [1] studied the buckling analysis of functionally graded plates under in-plane compressive loading using classical plate theory (CPT). They [2] also used the thermal buckling of functionally graded plates based on the classical plate theory. They used energy method and reached at the closed-form solution. Lanhe [3] studied thermal buckling of moderately thick rectangular FGPs based on the first-order shear deformation theory and derived a closed-form solution for critical buckling temperature as well. Ghannadpour et al. [4] presented the thermal buckling of functionally graded plates by discretizing the plate into some strips, called functionally graded strip (FGS). This was the first time that the concept of FGS was introduced for the thermal buckling analysis. Their FGS was developed on the basis of the classical plate theory. In the current paper, the scope of the previously developed FGS is extended to the thermal buckling analysis of moderately thick plates by obtaining the corresponding eigen-buckling equations on the basis of the first order shear deformation theory (FSDT). Numerical results for some functionally graded plates subjected to thermal loadings are given in some dimensionless graphical forms as well as compared with the available data in the literature.

Theoretical Formulations

FGS Material Properties. FGMs are usually made from a mixture of metals and ceramics. The FGS considered here consists of alumina and aluminum as ceramic and metal phase, respectively. The strip length, width and thickness are A, b and h, respectively, as shown in Fig. 1.

The composition is assumed to be varied in such a way that the surface of the strip at $z = h/2$ is ceramic, whereas the surface at $z = -h/2$ is metal. Thus, it is assumed that the material properties of the FGS, such as the modulus of elasticity E and shear modulus G, are changed in the thickness direction z. The variations of the properties through the thickness are postulated by a function $\vartheta(z)$ and are introduced by power law variations of material properties distribution as

$$\vartheta(z) = \vartheta_{cm}\left(\frac{z}{h} + \frac{1}{2}\right)^n + \vartheta_m \tag{1}$$

where $\vartheta_{cm} = \vartheta_c - \vartheta_m$ and $\vartheta(z)$ denotes a typical material property (E, α, K). The subscripts m and c refers to metal and ceramic, respectively. It is evident that when $z = -h/2$, $\vartheta = \vartheta_m$ and when $z = h/2$, $\vartheta = \vartheta_c$. It is noted that in the above equation the term $(z/h + 1/2)^n$ is known as the volume fraction of the ceramic phase, and n (volume fraction index) indicates the material variation profile through the thickness direction, and is non-negative real number.

Buckling Analysis. In this section, the fundamental elements of the theory of the developed semi-analytical finite strip method are briefly outlined. It is noted that a single FGS (shown in Fig. 1) forms part of a rectangular functionally graded plates of length A (i.e. the same length as that of a strip) and width B (with $B \geq b$). Thus, a rectangular functionally graded plate can be modeled by assigning several functionally graded strips to it, while the strips are laid parallel to one another and to the edge of the plate. The discretization of a FGP subjected to the first loading case (i.e. uniform temperature rise (ΔT)) is shown schematically in Fig. 2.

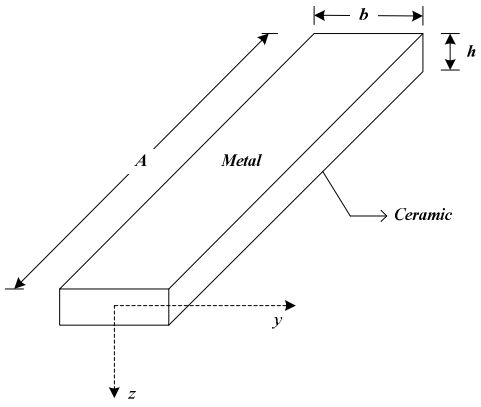


Fig. 1 A conventional FGS

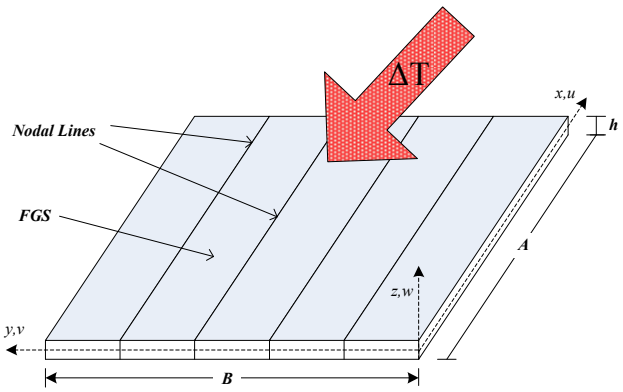


Fig. 2 A flat FGP Discretized to some FGS subjected to thermal loading

It is also noted that an initially flat FGS is assumed throughout the theoretical developments of this paper. Moreover, the functionally graded strips are assumed to be simply supported out of their plane at both ends (i.e. at $x = 0, A$). As a result of the FSDT assumption, the strains of the plate can be expressed as $\varepsilon = \varepsilon_l^0 + \varepsilon_{nl} + z\psi$ where

$$\{\varepsilon\}=\begin{Bmatrix}\varepsilon_{xx}\\ \varepsilon_{yy}\\ \gamma_{yz}\\ \gamma_{zx}\\ \gamma_{xy}\end{Bmatrix}\ \{\varepsilon_l^0\}=\begin{Bmatrix}\frac{\partial u_0}{\partial x}\\ \frac{\partial v_0}{\partial y}\\ \frac{\partial w_0}{\partial y}+\varphi_y\\ \frac{\partial w_0}{\partial x}+\varphi_x\\ \frac{\partial u_0}{\partial y}+\frac{\partial v_0}{\partial x}\end{Bmatrix}\ \{\varepsilon_{nl}\}=\begin{Bmatrix}\frac{1}{2}\left((\frac{\partial u}{\partial x})^2+(\frac{\partial v}{\partial x})^2+(\frac{\partial w}{\partial x})^2\right)\\ \frac{1}{2}\left((\frac{\partial u}{\partial y})^2+(\frac{\partial v}{\partial y})^2+(\frac{\partial w}{\partial y})^2\right)\\ 0\\ 0\\ \left(\frac{\partial u}{\partial x}.\frac{\partial u}{\partial y}+\frac{\partial v}{\partial x}.\frac{\partial v}{\partial y}+\frac{\partial w}{\partial x}.\frac{\partial w}{\partial y}\right)\end{Bmatrix}\ \{\psi\}=\begin{Bmatrix}\frac{\partial \varphi_x}{\partial x}\\ \frac{\partial \varphi_y}{\partial y}\\ 0\\ 0\\ \frac{\partial \varphi_x}{\partial y}+\frac{\partial \varphi_y}{\partial x}\end{Bmatrix} \quad (2)$$

where u, v, w and u_0, v_0, w_0 are the components of displacement in the x, y and z directions at general point and middle surface of the plate, respectively. Additionally, the quantities φ_x and φ_y are the rotations of initial plate normals about the y and x axes. On the assumption that the plate is in a state of plane stress and in the presence of a temperature change ΔT, the stress-strain relationship at a general point for the functionally graded strip becomes:

$$\sigma_x=\frac{E(z)}{1-\upsilon^2}[\varepsilon_x+\upsilon\varepsilon_y-\alpha\times\Delta T] \quad ; \quad \sigma_y=\frac{E(z)}{1-\upsilon^2}[\varepsilon_y+\upsilon\varepsilon_x-\alpha\times\Delta T]$$
$$\tau_{xy}=\frac{E(z)}{2(1+\upsilon)}\gamma_{xy} \quad ; \quad \tau_{xz}=\frac{E(z)}{2(1+\upsilon)}\gamma_{xz} \quad ; \quad \tau_{yz}=\frac{E(z)}{2(1+\upsilon)}\gamma_{yz} \quad (3)$$

where E, ν and α are elastic modulus, Poisson's ratio, and thermal expansion coefficient, respectively. The forces and moments per unit length of the plate in terms of the stress components express as

$$N_{ij}=\int_{-h/2}^{h/2}\sigma_{ij}\,dz \quad ; \quad M_{ij}=\int_{-h/2}^{h/2}\sigma_{ij}\,z\,dz \quad ; \quad \overline{Q}_{ij}=k_ik_j\int_{-h/2}^{h/2}\tau_{ij}\,dz \quad (4)$$

where k_ik_j is the shear correction coefficient of FGP which is assumed to be 1 in the current study in order to verify the calculated results. In the above equation, N_{ij} contains the membrane direct and shearing stress resultants, M_{ij} include the bending and twisting stress couples and $\overline{Q}_{ij}$ is transverse force resultants per unit length. The constitutive equations for a functionally graded strip can be obtained by the use of Eq. (2) and (3) and appropriate integration through the thickness.

$$\begin{Bmatrix}\{N\}\\ \{M\}\end{Bmatrix}=\begin{bmatrix}[E_1] & [E_2]\\ [E_2] & [E_3]\end{bmatrix}\begin{Bmatrix}\{\varepsilon^0\}\\ \{\psi\}\end{Bmatrix}-\begin{Bmatrix}\{N^T\}\\ \{M^T\}\end{Bmatrix} \quad (5)$$

where $\{N^T\}$ and $\{M^T\}$ are thermal force resultant and defined as

$$\{N^T\}=\int_{-h/2}^{h/2}Q_{ij}\alpha(z)\Delta T\,dz \quad ; \quad \{M^T\}=\int_{-h/2}^{h/2}Q_{ij}\alpha(z)\Delta T\,z\,dz \quad (6)$$

where ΔT is the temperature difference with respect to reference temperature(T_0). The strip stiffness coefficients are defined as

$$(E_{1_{ij}}, E_{2_{ij}}, E_{3_{ij}})=\int_{-h/2}^{h/2}Q_{ij}(1, z, z^2)\,dz; \qquad i, j=1,2,6 \quad (7)$$

where Q is the transformed reduced stiffness matrix. The strain energy component can be written as

$$U_s = \frac{1}{2}\iint \left\{ \varepsilon_l^{0\,\mathrm{T}}[E_1]\,\varepsilon_l + 2\,\varepsilon_l^{0\,\mathrm{T}}[E_2]\,\psi + \psi^{\mathrm{T}}[E_3]\,\psi \right\} \mathrm{d}x\,\mathrm{d}y. \tag{8}$$

The potential energy component, which accounts for the effect of initial stresses, can be written in terms of these stresses if these are known a priori; thus:

$$\begin{aligned} V_g = {} & \frac{1}{2}h \times \int_{-b/2}^{b/2}\int_{0}^{A} \{\sigma_x^0[(u_{0,x})^2 + (v_{0,x})^2 + (w_{0,x})^2] + \sigma_y^0\left[(u_{0,y})^2 + (v_{0,y})^2 + (w_{0,y})^2\right] \\ & + 2\,\tau_{xy}^0[(u_{0,x})(u_{0,y}) + (v_{0,x})(v_{0,y}) + (w_{0,x})(w_{0,y})]\}dxdy \\ & + \frac{h^3}{24} \times \int_{-b/2}^{b/2}\int_{0}^{A} \{\sigma_x^0\left[(\varphi_{x,x})^2 + (\varphi_{y,x})^2\right] + \sigma_y^0\left[(\varphi_{x,y})^2 + (\varphi_{x,y})^2\right] \\ & + 2\,\tau_{xy}^0\left[(\varphi_{x,x})(\varphi_{x,y}) + (\varphi_{y,x})(\varphi_{y,y})\right]\}dxdy \end{aligned} \tag{9}$$

where applied in-plane stresses σ_x^0, σ_y^0 and τ_{xy}^0 (arising from the pre-buckling analysis) act on the finite strip. In this paper, for both the loading cases, the pre-buckling stress vector, σ^0, which is linearly dependent on the temperature change distribution is presented as [2]

$$\left\{\sigma^0\right\} = \left\{\sigma_x^0 \quad \sigma_y^0 \quad \tau_{xy}^0 \quad \tau_{yz}^0 \quad \tau_{zx}^0\right\}^T = -\frac{E(z)\times\alpha(z)\times\Delta T(z)}{(1-\nu)}\left\{1 \quad 1 \quad 0 \quad 0 \quad 0\right\}^T \tag{10}$$

where in the case of uniform temperature rise, $\Delta T(z)$ is the temperature difference of final and initial temperature($\Delta T = T_f - T_i$) and in the case of nonlinear loading, $\Delta T(z) = T(z) - T_0$ where temperature distribution across the plate thickness, $T(z)$, can be obtained by solving the steady-state heat conduction equation and the following boundary conditions across the plate thickness as

$$\frac{d}{dz}\left[K(z)\frac{dT}{dz}\right] = 0. \qquad \begin{cases} T = T_c & at \quad z = h/2 \\ T = T_m & at \quad z = -h/2 \end{cases} \tag{11}$$

Solution of the eigenvalue problem is sought through the application of the principle of Minimum Potential Energy. This, of course, requires the assumption of a displacement field to represent the variations of u, υ and w over the middle surface. The buckling displacements pertaining to any individual functionally graded strip are described by the following functions:

$$\begin{aligned} & u_0 = \sum_{i=1}^{3} U_i(x) g_i^u(y) \quad ; \quad v_0 = \sum_{i=1}^{3} V_i(x) g_i^v(y) \quad ; \quad w_0 = \sum_{i=1}^{3} W_i(x) g_i^w(y) \\ & \varphi_x = \sum_{i=1}^{3} \varphi_{x_i}(x) g_i^{\varphi_x}(y) \quad ; \quad \varphi_y = \sum_{i=1}^{3} \varphi_{y_i}(x) g_i^{\varphi_y}(y) \end{aligned} \tag{12}$$

The $U_i(x), V_i(x), W_i(x), \varphi_{x_i}(x)$ and $\varphi_{y_i}(x)$ are longitudinal functions, taken here to be trigonometric functions ($\cos(i\pi x/A)$ for u and φ_x, $\sin(i\pi x/A)$ for v, w and φ_y), and the various $g_i(y)$ are crosswise polynomial interpolation functions which the linear form is selected for u and v and the second order Lagrange interpolation functions (with the middle node) are implemented for w, φ_x and φ_y.

One of the most important advantages of FSM (rather than other presented methods [3] in the thermal buckling analysis) is its capability to generalize the boundary conditions. For example, in the current study, the plate is assumed to be either simply supported on all the edges (SSSS) or simply supported on the $x = 0 \& A$ ends and clamped on the longitudinal edges (SCSC). The solution is obtained by the minimization of the total potential energy. The eigenvalue problem is solved by the QZ algorithm.

Results and Discussions

A ceramic-metal functionally graded plate which consists of aluminum and alumina is considered. Young's modulus, thermal expansion coefficient, and thermal conduction coefficient are selected as being $380\ GPa$, $7.4\times10^{-6}/^{\circ}C$ and $10.4\ W/m^{\circ}K$ for alumina and $70\ GPa$, $23\times10^{-6}/^{\circ}C$ and $204\ W/m^{\circ}K$ for aluminum, respectively. Poisson's ratio is chosen to be constant, 0.3, for both alumina and aluminum. The reference temperature assumed to be zero and the temperature of fully-metal surface (T_m) is assumed to be $5\ ^{\circ}C$. Furthermore, the side-to-thickness ratio B/h is considered to be 20. It is worth mentioning that the convergence studies with regard to the number of strips have revealed that 7 functionally graded strips are sufficient to obtain converged results.

SSSS FGM Plate. In this section, the calculated critical buckling temperature of some FGM plates under uniform temperature change and nonlinear temperature change across the thickness in comparison with the available data [3] are presented. Fig. 3 andFig. **4** show that the critical buckling temperature increases by increasing the plate aspect ratio A/B, while the same parameter decreases with the increase in power law index n.

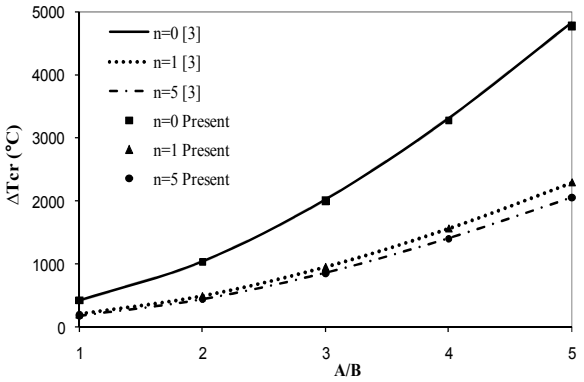


Fig. 3 Critical temperature differences of SSSS FGPs due to the uniform temperature rise with respect to n and A/B

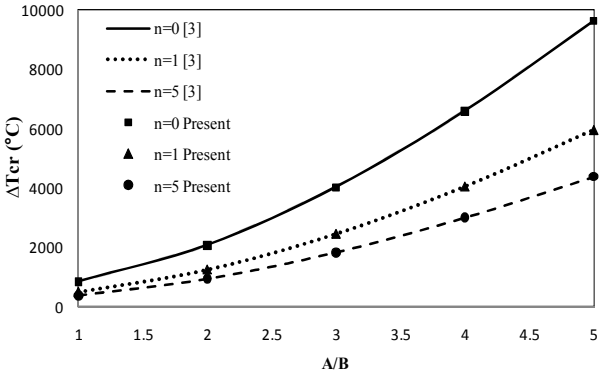


Fig. 4 Critical temperature differences of SSSS FGPs due to the nonlinear temperature distribution with respect to n and A/B

The close agreements between the present results and those of the referenced solutions as shown in Fig. 3 and Fig. 4 demonstrated the accuracy and effectiveness of the present method.

SCSC FGM Plate. As mentioned before, the two ends of the plate (i.e. at $x = 0, A$) are simply supported and since the finite strip method used in the present study has no limitation regarding boundary conditions in the longitudinal edges (i.e. at $y = 0, B$), the boundary conditions at these edges can be considered to be clamped.

The variation of the critical buckling temperature ΔT_{cr} versus the variation of the parameters A/B has been plotted for both the uniform and nonlinear temperature change in Fig. 5 andFig. 6.

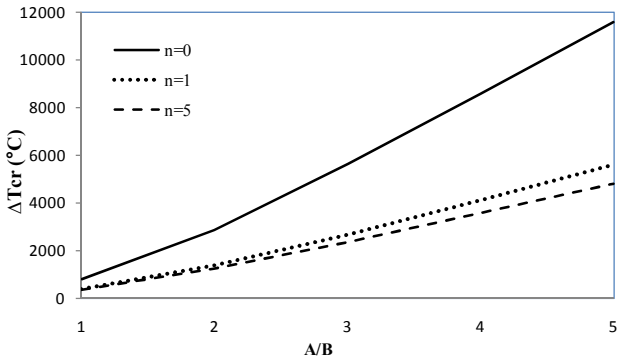


Fig. 5 Critical temperature differences of SCSC FGPs due to the uniform temperature rise versus n and A/B

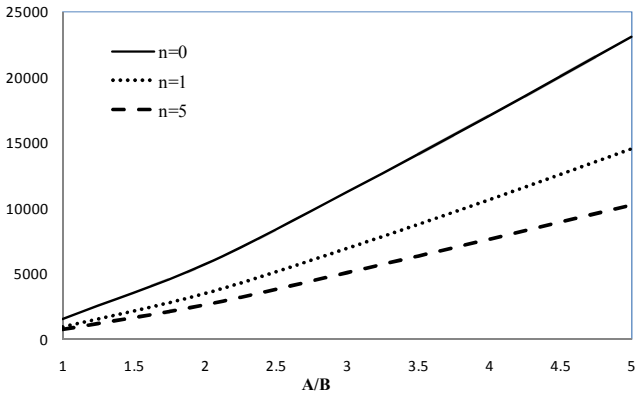


Fig. 6 Critical temperature differences of SCSC FGPs due to the nonlinear temperature distribution versus n and A/B

With the consideration of the above figures, it is obvious that the critical buckling temperature of SCSC FGM plates are higher than those of the corresponding SSSS FGM plates, since the boundary condition on longitudinal edges of SCSC plate are stiffer than those of SSSS plate.

Summary

The application of the FSM has been extended to the analysis of buckling behavior of FGPs subjected to the two types of thermal loadings, namely; uniform and nonlinear temperature change across the thickness. The formulations are based on the first-order shear deformation plate theory and with the assumption of power law composition for the material. It can be concluded from all the figures that the critical buckling temperature difference for functionally graded plates generally decreases with the increase in power law index while increases by increasing in the dimensionless parameter A/B. After comparing the present results with the closed-form ones for some cases available in the literature, thermal buckling behaviors of FGPs with SCSC boundary conditions have been investigated. It is shown that the critical buckling temperature differences of SCSC FGM plates are higher than those of the corresponding values for SSSS FGM plates.

References

[1] Javaheri R., Eslami MR.: *Buckling of functionally graded plates under in-plane compressive loading,* ZAMM J., Vol. 82 (2002), 4, pp. 277–83.

[2] Javaheri R., Eslami MR.: *Thermal buckling of functionally graded plates,* AIAA J. Vol. 40 (2002), 1, pp. 162–9.

[3] Lanhe W.: *Thermal Buckling of a Simply Supported Moderately Thick Rectangular FGM Plate,* Comp. Struct. J., Vol. 64 (2004), 2, pp. 211–218.

[4] Ghannadpour S. A. M., Ovesy H. R., Nassirnia M.: *Thermal Buckling Analysis of Functionally Graded Plates Using the Finite Strip Method*, The 10th International Conference on Computational Structures Technology, Spain (2010).

© (2011) Trans Tech Publications, Switzerland
doi:10.4028/www.scientific.net/KEM.471-472.763

Polymer Based Filler Materials as Infill for GFRP Pile Connector

Chamila Sampath Sirimanna [a], Md Mainul Islam [b] and Thiru Aravinthan [c]

Centre of Excellence in Engineered Fibre Composites, University of Southern Queensland, Toowoomba, Queensland 4350, Australia

[a] chamila.sirimanna@usq.edu.au, [b] mainul.islam@usq.edu.au, [c] thiru.aravinthan@usq.edu.au

Keywords: GFRP; Polymer; Compression; Shrinkage; Gel time; Plastic region.

Abstract. Recently glass fibre reinforced polymer (GFRP) tubular piles have been developed for civil engineering applications instead of conventional concrete piles. Considering their suitable applications, the new polymer based filling materials are being developed at the University of Southern Queensland as a part of work done for timber pile rehabilitation. This ongoing project aims to replace portion of the deteriorated timber pile by using GFRP piles. Due to good compressive strength, pumpability and workability, the new polymer base materials are to be filled in between GFRP pile and existing timber pile base. An ongoing research program has been initiated to improve fundamental understanding of these materials and to provide the knowledge required for their broad utilization.

In this development, sample trial mixes were considered based on several weight percentages of polymer resin, fly ash and sand. Material parameters such as compressive strength, stiffness, shrinkage and gel time were achieved from the experimental investigation. It has been found that most polymer based trial mixed fillers have high compressive strength and considerable plastic region with more than 10% strain. These results imply that the polymer based filling materials are suitable for both compression and tensile loading situations. However, the behaviour of fillers with GFRP pile connector under different loading conditions is yet to be fully understood.

Introduction

Timber piles are widely used to support buildings, bridges, trestles, wharves and a variety of other structures. Australia has a large number of timber bridges that require ongoing maintenance and rehabilitation. As an example, the approximate numbers of timber bridges around the states shown in Table 1:

Table 1: Population of timber bridges in Australia [1]

State	local council owned	state road authority owned	state rail authority owned
NSW	4000	150	700
QLD	3000	500	
WA	3000		
VIC	600	25	
TAS	100		

These figures indicate that there are a large number of timber bridges within the local government regions. The serviceability of these bridges is affected due to the age and the minimum level of maintenance of these bridges. Locally available wood piles provide a low cost foundation system. Untreated wood piles are subjected to deterioration from marine borers, crustaceans, fungi and other sources. For this reason many wood piles have been treated in the past with preservatives, like creosote or chromated copper arsenate (CCA) [2]. With time, preservatives will be leached from the wood, and thus deterioration will begin in treated wood piles similar to that of untreated wood piles.

When wood piles deteriorate, the conventional repair is to dismantle the pier, extract the deteriorated piles, drive new piles and rebuild the pier over the new piles. In addition, treated extracted piles may need special disposal. For some facilities, especially when road bridges sit on piers, extraction of all piles and driving of new piles can be difficult and costly. In these cases replace deteriorated part with new pile becomes a viable alternative. Replacements are possible since the portion of the pile below the mud line is normally fully intact. The major deterioration occurs in the portion of the pile in the inter-tidal zone and in the splash zone (above high tide).

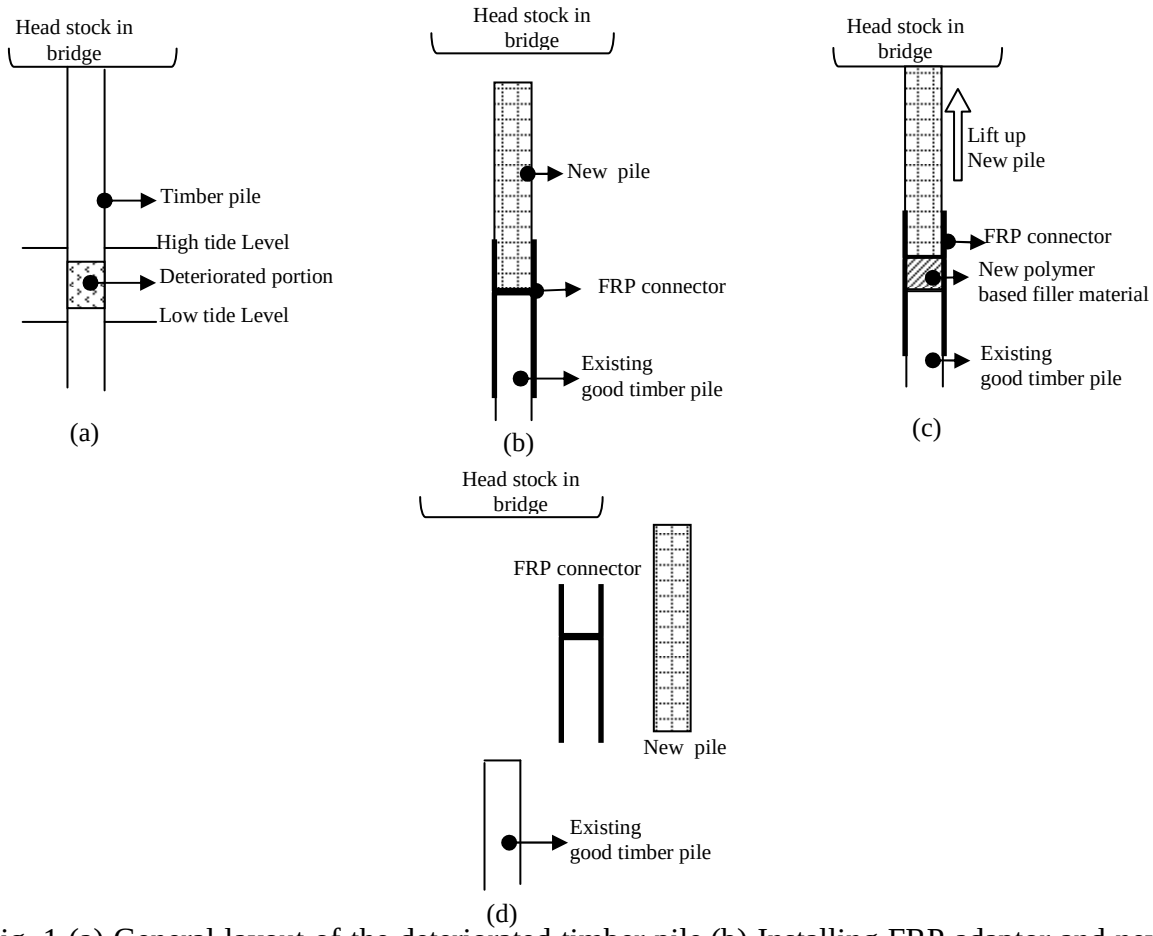


Fig. 1 (a) General layout of the deteriorated timber pile,(b) Installing FRP adaptor and new pile in to the remaining non deteriorated timber pile, (c) Filling new polymer base filler material in to the adaptor, (d) Major components use in pile rehabilitation.

The replacement system basically consists of new pile which was made out from any material like timber, FRP or concrete and GFRP tubular connector (Fig. 1(d)). The connector was used to join existing timber pile and new pile. To make easy constructability, first connector was inserted to existing timber stump (Fig. 1(b)).Then, new pile was inserted to the connector and both lifted up, until attach to the head stock. After that, void in between connector and existing timber pile was filled with new filler to transfer the vertical load from the connector to the original stump (Fig. 1(c)).

The objective of this paper is to develop polymer based filler materials for GFRP tubular connector. Here GFRP connector was acted as a confinement for the filler. As per the Figure 1(c) this filler material used for filled in between connector and existing timber pile. Here this filler must have good workability, less curing time, fair compressive capacity and reasonable pumpability qualities.

Polymers are being increasingly used in civil engineering applications as adhesives, modifiers, and matrix materials in concrete. As structural and repair materials, polymers, and their composites must be able to withstand high stresses under extreme service conditions. Polymer Concrete (PC) is a composite material formed by combining a mineral aggregate such as sand and gravel with a polymerizing monomer [3]. Polyester PC has good mechanical strength, relatively good adhesion to other materials, and good chemical and freeze thaw resistance. This filler material development, polyester was used as a resin. Therefore development of this new polymer base filler was important in this replacement technique and will be discussed in this paper.

Experimental Programme

Mix proportions and materials: In this filler development, sample trial mixes were considered based on several weight percentages of polyester resin, fly ash and sand given in Table 2. 40% to 60% (w/w) polyester resin content was used to achieve good pumpability and workability requirements. The following constituent materials were used in the production of the polymer base filler.

Polyester Resin - Medium reactivity, rigid orthophthalic polyester resin was used. Compared with other polyester families orthophthalic polyester have good chemical resistance and processibility [4].

Initiator - Methyl ethyl ketone peroxide (MEK) in dimethyl phthalate (DMP) was used as initiator. Chemical lattice structure and composition are given below.
Peroxide content: 30%, Balance: 63% DMP, 4% MEK + Water

Table 2 Mixing proportions

Sample Number	(Resin+Initiator)% -By total weight -(R)	Filler (%)		Initiator(%)- Weight % of resin
		Sand -(S)	Fly ash -(F)	
1000	50	25	25	2.5
1001	50	20	30	2.5
1002	50	30	20	2.5
1003	50	50	-	2.5
1004	60	40	-	2.5
1005	40	60	-	2.5
1006	56	-	44	2.5
1007	65	-	35	2.5
1008	45	-	55	2.5

Fly ash - Unprocessed Concrete grade fly ash with d50 of approximate 15µm obtained from Wagners in Queensland, Australia.

Sand - Fine dry sand with a bulk density of 1650kg/m3 and particle size smaller than 425µm.

Testing: Following tests were done to identify material properties.

Compression Testing - Compressive capacity and modulus behaviour was investigated using uniaxial compression method. Testing was done accordance to ASTM standard D 695 M-91 [5].

Flexural Testing - Flexural behaviour was assessed using three point bending test accordance with ISO standard 178:1993 [6].

Shrinkage Testing - A linear method was selected to assess the shrinkage in accordance with the ASTM standard D6289 – 98 [7].

Gel Time- Trial Mixes were prepared and record temperature with respect to time. Then determined interval of time required for a colloidal solution to become semisolid jelly or gel. This time is known as gel time and allow for mixing and pumping operations.

Experimental Results and Discussions

In this section, the material properties of the polymer base filler material as measured from the experiments are reported and discussed. In most cases the results are the average of three tests.

Physical properties: Table 3 shows the densities of the test mixes. It is seen that the densities are considerably low that of normal density Ordinary Portland Cement (OPC) mortars and concretes.

This test mixes was observed to shrink as it hardened. This phenomenon is similar to OPC concrete that shrink as it hardens. The measured volumetric shrinkages of the test mixes were between 5% and 8%, depending on the mix proportions. Comparing samples 1003-1005 and 1006-1007, it is obvious that higher polymer content gives maximum linear shrinkage. This shrinkage property is important in this filler as it may lead to cracking due to confinement in FRP connector.

In this filler development, all the samples were mixed with 2.5% (weigh % of resin) of initiator. All three categories of mixes (1000-1002, 1003-1005 and 1000-1007), gel time proportionate to the percentage of fine material used. For example (samples 1000 to 1002), when fly ash amount change from 20 to 30 percent, gel time increases from 60 to 80 minutes. Therefore amount of fine material directly affect to the test mixes gel time.

Table 3 Test results from compression test, shrinkage test and gel time test.

Sample Number	Gel time (Minutes)	Compressive Capacity (MPa)	Compression Elastic modulus (MPa)	Linear Shrinkage (%)	Volumetric Shrinkage (%)	Density (kg/m3)
1000(R-50%, S-25%, F-25%)	65	68	3869.23	0.98	8	1451.83
1001(R-50%, S-20%, F-30%)	80	67	3357.14	0.73	6	1410.00
1002(R-50%, S-30%, F-20%)	60	68	3300.00	0.78	7	1443.85
1003(R-50%, S-50%)	75	63	3304.35	0.74	7	1514.06
1004(R-60%, S-40%)	40	45	1642.00	1.2	5	1468.69
1005(R-40%, S-60%)	180	50	2866.67	0.36	5	1660.88
1006(R-56%, F-44%)	40	58	2800.00	0.56	7	1288.05
1007(R-65%, F-35%)	20	43	2058.82	0.70	7	
1008(R-45%, F-55%)	Difficult to mix – low percentage of resin					

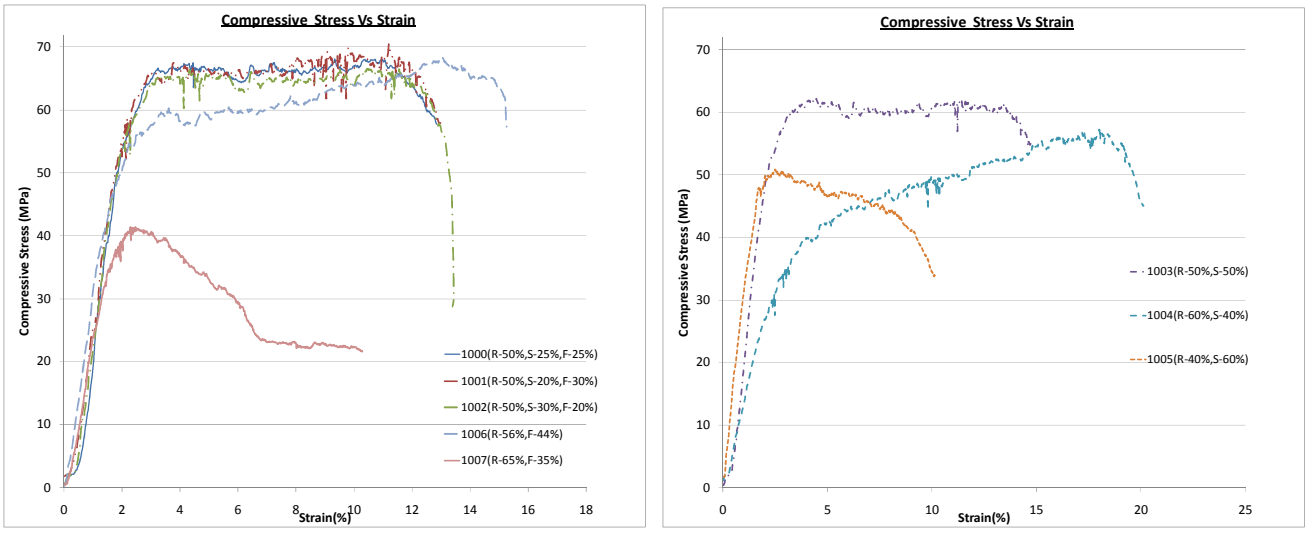


Fig. 2 Compressive stress Vs strain graphs for trial mixes

Compressive strength: All the samples were achieved high mean compressive strength more than 40MPa.In Figure 2 shows that sample numbers 1000, 1001 and 1002 has more than 60MPa compressive stress with considerable uniform plastic region with more than 10% strain. Also these

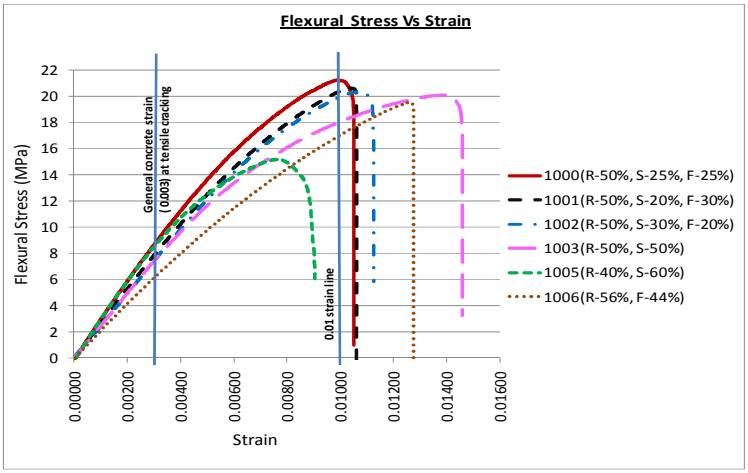


Table 4 Flexural modulus

Sample Number	Flexural modulus (MPa)
1000(R-50%, S-25%, F-25%)	2828.37
1001(R-50%, S-20%, F-30%)	2550.31
1002(R-50%, S-30%, F-20%)	2558.85
1003(R-50%, S-50%)	2343.05
1005(R-40%, S-60%)	2818.91
1006(R-56%, F-44%)	1902.70

Fig. 3 Flexural stress Vs strain graphs

trial mixes has comparatively higher compressive elastic modulus value more than 3000MPa. Here all samples used 50% resin by weight (resin: materials= 1:1).

But other samples have not uniform plastic regions except sample number 1003. This 1003 also used 50% resin by weight (resin: material= 1:1). Therefore comparing Figure 2 all the times nearly 50% resin (Resin: material =1:1 trial mixes) gives more uniform plastic region.

Flexural strength: Flexural test samples were selected based on compressive strength and compressive elastic modulus values. Here sample numbers 1004 and 1007 were not considered for flexural test because of low elastic modulus and low compressive strength. Table 4 and Figure 3 show flexural values and flexural stress vs. strain graph. According to Figure 3, all the samples except 1005 shows good flexural stresses with more than 0.01 strains at failure, which is 3.3 times, compare to reinforce concrete (0.003).

Finite Element Modeling for the Filler. For the understanding of the stress strain behavior of the new polymer filler in pile connector, STRAND 7 modeling was done. Initially, this deterioration pile replacement concept supposes to adopt in rural areas under class 4 road classifications in AS 5100.7-2004. Following loads per pile were considered

Dead Load (DL) = 120kN (Typical two lane bridge with timber superstructure)
Traffic Load (TL) = 160kN (Two A160 axle loading)
Debris load (DEB L) = 80kN (1.2m Debris mat with 1.97m/s mean velocity for ultimate limit state at the level of the superstructure)

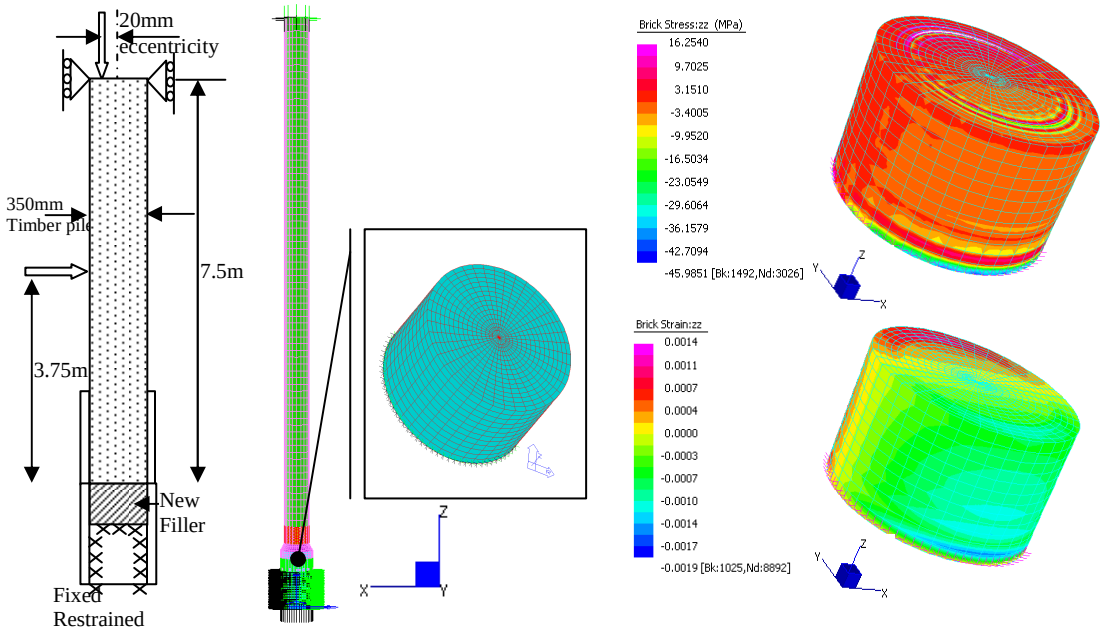


Fig. 4 (a) schematic diagram and FE model in STRAND 7, (b) Stress strain behavior of the filler in zz direction under critical load combination 2

Load combinations: As per the AS 5100.7-2004 following ultimate load combination were considered.

Load combination 1: 1.2DL+1.8 TL (1)
Load combination 2: 1.2DL + 1.8TL+ 1.65 DEB L (2)
Load combination 3: 1.2DL + 1.65DEB L (3)

For all vertical loading 20mm eccentricity and 7.5m long replacement new timber pile were considered to take maximum stress strain behavior in the filler (Figure 4 (a)). For the FE modeling, it was assume that bottom of the pile connector behave as fixed restrained and top of the timber pile as pinned support with rollers. 20-node hexahedral brick elements were used to create filler portion in FE modeling. The laminate layup for the connector is: (i) 8 layers 600/225 g/m^2 Biax/CSM glass (inner top); (ii) 8 layers 600/225 g/m^2 Biax/CSM glass (inner bottom); and (iii) 12 layers 600/225 g/m^2 Biax/CSM glass (outer). Biax fibres were aligned at 0 degrees to the cylinder axis.

After analyzing all three combinations, Load combination 2 was identified as critical. Table 5 shows stress and strain variation in brick elements in load combination 2. This connector and pile

Table 5 Brick stress in the filler after analyzing FE model.

	Brick Stress (MPa)			Corresponding Brick Strain		
	zz*	xx*	yy*	zz*	xx*	yy*
Maximum compression	45.9851	45.9832	45.9853	0.0019	0.0005	0.0014
Maximum Tension	16.2540	16.2518	16.2523	0.0014	0.0004	0.0011

*- zz, xx & yy – local coordinate system

model was acted as combination of three point bending test with end moment and axial force. Therefore result outputs came from STRAND7 can be compared with flexural test results. Referred to Table 5, strains were in three local axes less than 0.01 [All trial mixes exceed 0.01 strain as flexural failure except sample 1005(R-40%, S-60%)]. As per the Table 5 maximum compressive and tension in three local axes were less than 50MPa, 18MPa respectively. Therefore no compression or tensile failure occurred in trial mixes except 1005(R-40%, S-60%) under this loadings. Hence this preliminary study, sample 1001(R-50%, S-20%, F-30%) recommended as filler material based on less shrinkage and considerable gel time.

Summary

Based on experimental work of the tests presented in this paper, the following conclusions are drawn:

- More than 60MPa compressive strength can be achieve easily in the filler material development when polyester resin content vary from 40% to 60% (w/w) with fly ash and sand.
- Polyester base fillers having considerably low density compare to OPC concrete.
- The percentage of finer material used in the mixes directly affected to their gel time.
- Most polyester fillers having more than 10% compressive strain with plastic region. If polyester resin: Materials ratio 1:1, this plastic region becomes more uniform.
- Most of tested trial polyester fillers can be used in this connector, based on fine compressive and flexural stress, strain behavior compared to concrete and stress and strain output from FEA. But shrinkage and gel time play important role to select appropriate mix configuration. Hence this preliminary study, sample 1001(R-50%, S-20%, F-30%) recommended as filler material based on less volumetric shrinkage and considerable gel time.

References

[1] I. Scott and K. Wheeler: *Application of Fibre Reinforce Polymer Composite in Bridge Construction*, IPWEA NSW Division Annual Conference (2001).

[2] R. Lopez-Anido, A.P.Michael and T.C. Sandford: *Experimental characterization of FRP composite wood pile structural response by bending tests*, Marine Structures Vol. 16 (2003), p. 257- 274.

[3] C. Vipulanandan and E. Paul: *Characterization of Polyester Polymer and Polymer Concrete*, J. Mat. in Civ. Eng Vol. 5 (1993), p. 62- 82.

[4] C.D.Dudgeon: *Engineered Materials Handbook* (ASM International, Metals Park 2003).

[5] ASTM D 695, Standard Test Method for Compressive Proper-ties of Rigid Plastics. West Conshohocken: American Society for Testing and Materials.

[6] ISO 178:1993, Plastics Determination of Flexural Properties, Geneva, International Organisation for Standardisation.

[7] ASTM D 6289-98, Standard Test Method for Measuring Shrinkage from Mold Dimensions of Molded Thermosetting Plastics: American Society for Testing and Materials.

© (2011) Trans Tech Publications, Switzerland
doi:10.4028/www.scientific.net/KEM.471-472.769

The Effect of Bentonite Clay on Green Compression Strength for Tailing Sands from Old Tin Mines in Perak State, Malaysia for Making Green Sand Casting Mould.

A. Azhar[1,a], S. Shamsuddin[1,b], B.T.H.T. Baharudin[1,c], M.K.H. Ariffin[1,d], T.R.Vijayaram[2,e]

[1]Department of Mechanical and Manufacturing Engineering, Faculty of Engineering, Universiti Putra Malaysia, Selangor, Malaysia;
[2]Department of Manufacturing Process, Faculty of Manufacturing Engineering, Universiti Teknikal Malaysia Melaka, Melaka, Malaysia.

[a]azija656@yahoo.com, [b]suddin@eng.upm.edu.my, [c]tuah@eng.upm.edu.my, [d]khairol@eng.upm.edu.my, [e]vijayaram1@gmail.com

Keywords: Tailing Sand, Clay; Moisture; Green Compression Strength.

Abstract. Clay has an important role in making green sand casting mould beside water. Clay acts as binders, holding the sand grains together. Water is needed to activate the clay bond. Without the addition of water on clay, no strength would be achieved on sand mould, as the sand and clay would be just two dry materials. Bentonite clay was used in this study. Adequate clay content with suitable moisture in moulding sand is important for optimum strength and casting quality. Too little or too much clay will not give proper strength. Green compression strength is one of the mechanical properties to be considered for making green sand casting mould. The green compression strength of foundry sand is the maximum compressive strength that a mixture is capable of sustaining when prepared, rammed and tested according to standard procedure. For this study, test is conducted according to Foundry Sand Testing Equipment Operating Instructions from Ridsdale and Dietert. Result from this study indicates that tailing sand has potential for making green sand casting mould in term of green compression strength. Other factors that must be considered are permeability and shatter index.

Introduction

This study focuses in investigating the effect of clay on green compression strength of tailing sand from 4 identified ex-tin mines locations in Perak State for making green sand casting mould. The locations are Taiping, Tronoh, Batu Gajah and Tanjung Tualang.

Determination of the grain size distribution and average grain size of tailing sand from the same locations from previous study indicated that their size range from 66.4% - 94.55% and falls in 4 selected adjacent sieve (150, 212, 250 and 355 μm). The average grain sizes sand range from 217μm – 281 μm [1]. For this study, tailing sand taken as specimen sand for testing is from 4 selected adjacent sieves. The green compression strength is a study to determine the maximum compressive strength that a mixture (tailing sand, clay and water) is capable of sustaining when prepared, rammed and tested according to standard procedure. This is because sufficient strength of moulding sands is required during withdrawal of the pattern from the mould and during pouring processes where the mould must retain shape independently without distortion or collapse.

Clay has a significant role in improving the strength of greensand mould where it acts as binder agent mixes with water to bind the sand particles. The quantity of clay in the mould sand influences the green compression strength. From this study, the effect of increasing the amount of clay with addition of 3% and 5% of water, the green compression strength can be investigated. Clay maybe present in an amount of 2 to 50%. With suitable water content, it is the principal source of the strength and plasticity of the molding sand. If clay content is higher in the mould mixture, it will increase the strength but the permeability of the moulding sand will be decreased. This is because, as the clay content increased, more fine clay particles occupy the available spaces between the sand

grains, thereby lowering the permeability of the moulding of the mixture. The development of bond strength depends upon hydration of the clay, the green strength of a moulding mixture increases with water content up to an optimum value determined by the proportion of clay. Above this value, additional free water causes the green strength to diminish [2]. The clay adsorbs the water up to a limiting amount. Only that water rigidly held (adsorb) by the clay appears to be effective in developing strength. This is because of the increasing on thickness of the water films, so that the clay becomes less stiff and the sand grains are held further apart [3]. Additional water, however, can act as a lubricant, and makes the sand more plastic and more moldable, though the strength may be lowered [4]. If the amount of water is further increased, then the water films become so thick and the clay so soft, that it is unable to hold the grains apart and the sand grains become closer together with increase in permeability [3]. Incorrectly chosen amount of clay and water in the mould mixture can cause casting defects.

Fig. 1 shows the relationship between increasing of clay content with the presence of water on green compression strength for green sand casting mould.

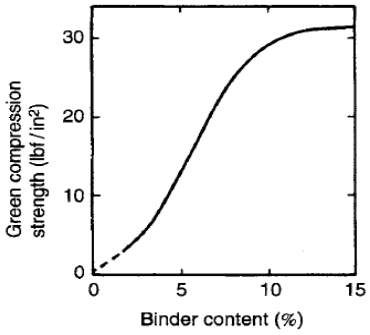


Fig. 1: Influence of binder content on strength of moulding sand (silica sand bonded with Wyoming bentonite [4].

Green sands may be considered as clay-saturated when it has high enough percentage of clay so that any further increase in clay content will not cause an increase in maximum green compressive strength of the aggregate [4] as shows in Fig. 2.

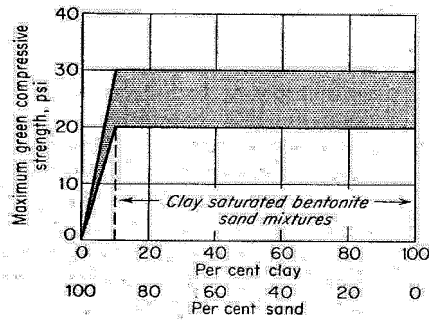


Fig. 2: Schematic diagram showing the approximate effect of bentonite clay on the maximum green compressive strength of clay-water mixtures.

Materials and Methods

Mixture was prepared by weighted out 1500 g of dry sand and mixed with 3% of water and milled for 5 minute. Clay was added to the mixture started with 2% by weight, which is appropriately 30 g. Then, the mixture was milled appropriately 3 minutes and then sample tested for moisture using moisture tester.

A test piece 50 mm x 50 mm d specimen was prepared for green compression test using Ridsdale-Dietert Metric Standard Rammer. The specimen test piece was prepared by weighing sufficient mixture to form a test piece within the permitted tolerance (ranged from 138g to150g depending on the sand/clay/water ratio)[5]. Then, the mixture was transferred to the Ridsdale-Dietert Metric Standard Rammer to form a test piece 50 mm x 50 mm d as shows in Figure 3. The specimen test piece was stripped using strip block and removed from the tube carefully as shows in Figure 4 and tested using Ridsdale-Dietert Universal Sand Strength Machine as shows in Figure 5. The green compression test was repeated three times and after the readings were obtained; 2% of clay was added until the amount of clay reached to 8%. 1% of clay was further added until the reading of the green compression strength reached consistency. The procedures were then repeated with mixture of 5% water.



Fig. 3: Ridsdale-Dietert metric standard rammer



Fig. 4: Strip block and specimen test piece



Fig. 5: Ridsdale-Dietert universal strength machine

Results

Tables 1-4 and Figures 6-9 show the data obtained from the testing.

Table 1: Green compression strength of Batu Gajah's tailing sand for 3% and 5% water mixture

Clay (%)	3% Moisture				Clay (%)	5% Moisture			
	*GC1	*GC2	*GC3	Average		*GC1	*GC2	*GC3	Average
2	12.0	14.0	14.0	13.3	2	12.0	13.0	12.0	12.3
4	27.0	27.0	25.5	26.5	4	29.0	30.5	30.0	29.8
6	45.0	43.5	45.0	44.5	6	45.5	45.0	45.0	45.2
8	72.0	72.0	70.0	71.3	8	60.0	59.5	62.0	60.5
9	83.0	84.0	81.0	82.7	10	78.0	80.0	79.0	79.0
10	84.0	85.0	83.5	84.2	11	93.0	95.5	89.0	92.5
11	86.0	79.0	79.0	81.3	13	135.0	135.0	130.0	133.3
					14	155.00	150.0	150.0	151.7
					15	155.0	155.0	150.0	153.3

GC - Green Compression Strength (kN/m^2)

Table 2: Green compression strength of Taiping's tailing sand for 3% and 5% water mixture

Clay (%)	3% Moisture				Clay (%)	5% Moisture			
	*GC1	*GC2	*GC3	Average		*GC1	*GC2	*GC3	Average
2	13.0	14.0	14.0	13.7	2	14.0	13.0	13.0	13.3
4	27.5	28.0	30.0	28.5	4	30.5	30.5	29.0	30.0
6	47.5	49.0	49.5	48.7	6	46.0	44.0	44.0	44.7
8	75.0	76.0	78.0	76.3	8	58.0	61.0	59.0	59.3
9	104.5	105.5	102.5	104.2	10	83.0	83.5	81.5	82.7
10	119.0	122.0	120.5	120.5	11	100.5	98.0	100.0	99.5
11	135.0	137.5	127.5	133.3	12	130.0	130.0	130.0	130.0
12	130.0	122.5	130.0	127.5	13	150.0	155.0	155.0	153.3
					15	200.0	200.0	195.0	198.3
					16	202.5	210.0	202.5	205.0

GC - Green Compression Strength (kN/m^2)

Table 3: Green compression strength of Tanjung Tualang's tailing sand for 3% and 5% water mixture

Clay (%)	3% Moisture				Clay (%)	5% Moisture			
	*GC1	*GC2	*GC3	Average		*GC1	*GC2	*GC3	Average
2	12.0	12.0	13.0	12.3	2	14.0	14.0	13.0	13.7
4	32.0	32.0	31.0	31.7	4	30.0	30.0	30.0	30.0
6	52.0	51.5	49.0	50.8	6	46.0	48.5	47.0	47.2
8	82.0	84.0	85.0	83.7	8	63.5	64.0	65.0	64.2
10	105.0	104.0	102.0	103.7	11	130.0	135.0	135.0	133.3
11	115.0	110.0	105.0	110.0	12	162.5	160.0	160.0	160.8
12	110.0	112.5	107.5	110.0	13	175.0	175.0	180.0	176.7
13	107.5	102.5	110.0	106.7	14	200.0	190.0	190.0	193.3
					15	195.0	200.0	200.0	198.3

GC - Green Compression Strength (kN/m^2)

Table 4: Green compression strength of Tronoh's tailing sand for 3% and 5% water mixture

Clay (%)	3% Moisture				Clay (%)	5% Moisture			
	*GC1	*GC2	*GC3	Average		*GC1	*GC2	*GC3	Average
2	11.0	11.0	10.5	10.8	2	9.0	9.0	10.0	9.3
4	25.5	25.0	25.5	25.3	4	23.0	24.0	24.0	23.7
6	42.0	43.0	40.5	41.8	6	39.5	40.0	39.0	39.5
8	71.0	67.0	69.0	69.0	8	55.0	56.0	58.0	56.3
9	86.5	86.0	84.5	85.7	10	81.0	81.0	83.0	81.7
10	110.0	105.0	110.0	108.3	11	99.0	99.0	99.0	99.0
11	115.0	110.0	110.0	111.7	12	124.0	125.0	124.0	124.3
					14	155.0	155.0	150.0	153.3
					15	157.5	160.0	157.5	158.3

GC - Green Compression Strength (kN/m^2)

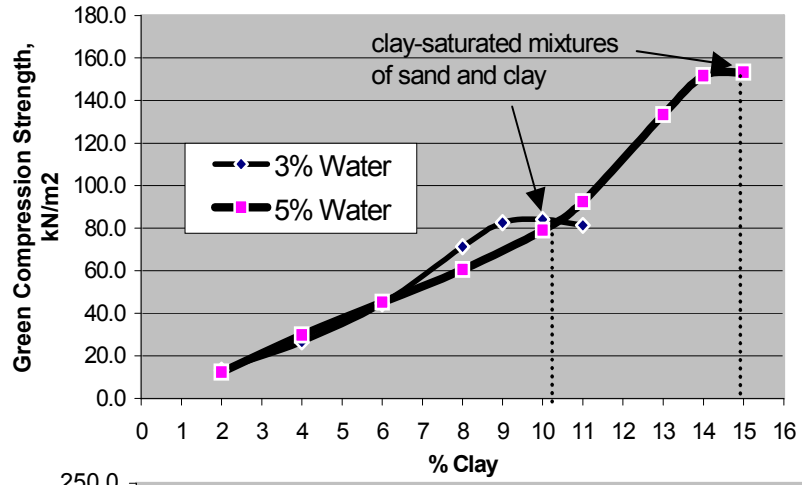


Fig. 6: Green compression strength for Batu Gajah's tailing sand with addition 3% and 5% of water and the approximate effect of bentonite clay on the maximum green compressive strength of clay-water mixtures.

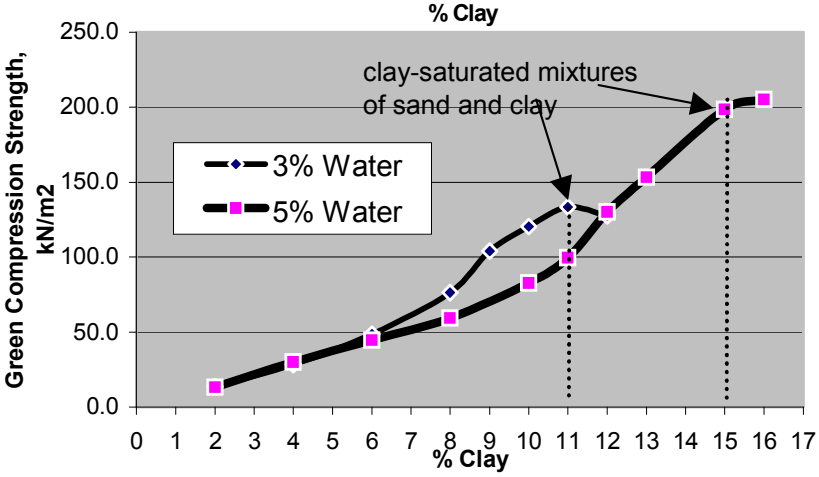


Fig. 7: Green compression strength for Taiping's tailing sand with addition 3% and 5% of water and the approximate effect of bentonite clay on the maximum green compressive strength of clay-water mixtures.

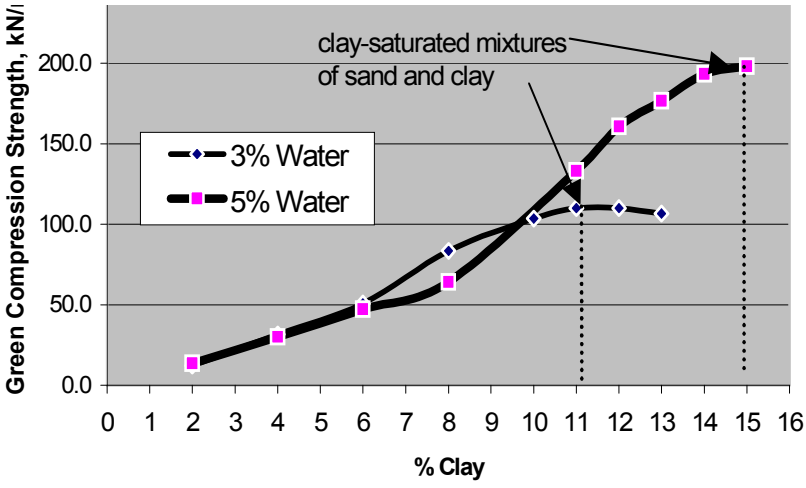


Fig. 8: Green compression strength for Tanjung Tualang's tailing sand with addition 3% and 5% of water and the approximate effect of bentonite clay on the maximum green compressive strength of clay-water mixtures.

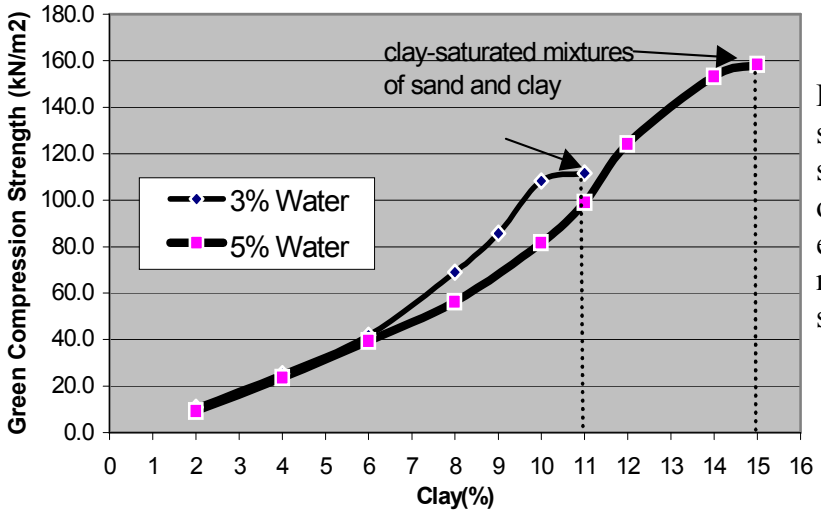


Fig. 9: Green compression strength for Tronoh's tailing sand with addition 3% and 5% of water and the approximate effect of bentonite clay on the maximum green compressive strength of clay-water mixtures.

Discussion

Table 1 - 4 show the results for green compression strength of tailing sand from the identified locations with addition of 3% and 5% water with increasing the amount of clay while Fig. 6 - 9 show the graphs for green compression strength versus percentage of clay. The tables and graphs indicate that green compression strength for all samples has increased incrementally with the increasing of percentage of clay in mixtures until it reaches the maximum point where any increasing the amount clay will not increase the strength. This point is called *clay-saturated mixtures of sand and clay*. For instance, tailing sand from Batu Gajah as shown in Figure 6; for mixture of 3% water, the green compression strength is increased from 13.3 kN/m^2 at 2% clay until 84.2 kN/m^2 at 10% clay but further addition of clay, will not increased the strength. On the other hand for mixture of 5% water, the strength is increased from 12.3 kN/m^2 at 2% clay until 155 kN/m^2 at 14-15% clay. The reason is because at that point, the mixture has high enough percentage of clay and the strength is only increased when the clay absorbs the water up to a limiting amount. At low clay content, the strength was also low, due to small amount of clay with high percentage of water, which was not sufficient to develop adequate strength. This is the point where the mixture is in wet condition and the water acts as lubricant. By increasing the amount of clay, the green compression strength is increased until it achieves the maximum strength. The increment of strength is because the mixture now has high content of clay and becomes dry, as the clay content increased more fine clay particles occupying the available spaces between the sand grains. If further increment of clay content continues, it will not increase the strength because the mixture becomes clay-saturated mixture. This scenario is similar for all tailing sand from other locations.

The Tables and Figures also show the comparison on green compression strength between mixture of 3% and 5% water when the amount of clay is increased for both mixtures. At low percentage of clay, mixture of 5% water has lower strength compared to mixture 3% water. The reason of this situation is because the mixture of 5% water has thicker water films compared to mixture of 3% water, making the clay to be too soft which is unable to hold the grains together. The strength for both mixtures is increased when the percentage of clay is increased. Mixture of 3% water is saturated earlier than mixture of 5% water, which is at approximately 11% clay. At this point, mixture of 5% water still has the water to be absorbed by the clay until it reaches 15% clay where it starts to saturate. The reason of this characteristic is because, mixture with high water content needs more clay in developing strength and this will result in the delay of its saturation stage.

Summary

The result indicates the effect of bentonite clay on green compression strength of tailing sand with water presence. The amount of clay should be controlled in getting the suitable green compression strength and furthermore some types of clay are expensive. The study shows that bentonite clay can be used for tailing sand as a binder to bind sand particles with presence of water where it gives strength to the sand for making green sand casting mould. Other important properties that should be considered are the permeability and shatter index. Consideration of these two properties is vital for moulding sand.

References

[1] A. Azhar & S. Shamsuddin: Preliminary Study On Tailing Sand From Ex-Tin Mine Sites In Peninsular Malaysia For Use As Foundry Sand: Grain Size Distribution And Average Grain Size. Proceedings of the Advances in Material and Processing Technologies Conference, Kuala Lumpur, Malaysia (2009).

[2] B. Peter: Foundry Technology, Second Edition, Elsevier Ltd. (2001)

[3] P.D. Webster: Fundamentals of Foundry Technology, Surrey, Portcullis Press, Redhill.(1980)

[4] R.W. Heine, C.R.Jr. Loper & P.C. Rosenthal: Principle of Metal Casting. New York: McGraw-Hill Book Company (1967), pp.86-89.

[5] Foundry Sand Testing Equipment Operating Instructions, Ridsdale & Co. Ltd., Newham, Hall, Newby, Middlesbrough, Cleveland, England.

© (2011) Trans Tech Publications, Switzerland
doi:10.4028/www.scientific.net/KEM.471-472.775

Effect of Electron Beam Irradiation (EB) on Gas Barrier Property of HDPE/EPDM Nanocomposites

N.A., Jamal[1, a], H., Anuar[1, b] and S.B. A., Razak[2, c]

[1]Department of Manufacturing and Materials Engineering, Faculty of Engineering, International Islamic University Malaysia, Kuala Lumpur, Malaysia

[2] Crop Improvement and protection Unit, Production Development Division, Rubber Research Institute Malaysia (RRIM), Sungai Buloh, Selangor, Malaysia

[a]ayuni_jamal@yahoo.com, [b]hazleen@iium.edu.my, [c]shamsul@lgm.gov.my

Keywords: OMMT, EB Irradiation, Doses Rate, Oxygen Transmission, Nanocomposite

Abstract. In this study, electron beam irradiated (EB) was applied as a crosslinker agent for both pristine high density polyethylene (HDPE) and HDPE/ ethylene propylene diene monomer (EPDM) nanocomposite systems. The doses rate for EB irradiated technique were varied between 50, 100, 150 and 200 kGy. The nanocomposites systems were first prepared via melt intercalation method with different organophilic montmorillonite (OMMT) loadings. It was found that, with 4 vol% organophilic montmorillonite (OMMT) loading, the barrier resistance of nanocomposite against oxygen transmission was significantly enhanced by EB irradiation dose rate of 100 kGy. The oxygen transmission for nanocomposite was reduced by 23.48%. The interplanar spacing, *d*-spacings of OMMT in nanocomposites were monitored using x-ray diffraction (XRD) and the extent of delamination was examined by transmission electron microscope (TEM). The wide angle of XRD patterns showed the increased interplanar spacing, *d* of clay layers, indicating enhanced compatibility between polymer matrix and OMMT with EB irradiation. TEM photomicrographs illustrated the mixed intercalated and partial exfoliated structures of the nanocomposites with the irradiation process.

Introduction

Different types of filler or reinforcement can be incorporated into polymer blending system but using silicate layered is more preferable compared to traditional fillers such as talc and mica which require less amount than the latter fillers. Because of this reason, clay silicate which requires less content to achieve similar or improved mechanical, thermal as well as barrier properties has been used in this research work [1, 2]. Small amounts of well dispersed natural clay can lead to environmental friendly and inexpensive plastic composites with improved specialized properties. However, immiscibility or incompatibility of most polymers is a serious obstacle to processing blends of polymer matrix and nano filler. A common approach to alleviate this problem involves the addition (or the in situ formation) of an interfacially active agent, or so called compatibilizer, to the blend [3].

High energy electron beam (EB) irradiation processing has been used for many years to modify the properties of formed polymer parts. The property enhancements achieved include increased operating temperature, improved mechanical properties, increased chemical and solvent resistance. Chain crosslinking and scission are the two reactions that occur during EB processing of polymers. Polymers typically undergo simultaneous scission and crosslinking, but in most cases with one or the other clearly predominating [4, 5]. Crosslinking is the intermolecular bond formation of polymer chain. The degree of crosslinking is proportional to the radiation dose [6]. Much works have been done on radiation crosslinking of uncrosslinked polymers and crosslinking of various rubbers and plastics by electron beam irradiation [6-8].

In contrast, scission is the opposite process of crosslinking in which the rupturing of carbon-carbon bond occurs. Scission reduces crosslinking efficiency and degrades the properties of

polymers (chemical resistance, mechanical and thermal properties). The current study was initiated to vary and highlight the interest of EB irradiation technique for HDPE/EPDM, where pristine composites and nanocomposites were prepared with different irradiation dose rates and organophilic montmorillonite (OMMT) loadings. The results obtained for the EB irradiated system were then compared with the control system to determine the optimum system.

Experimental Design

Materials. Homopolymer high density polyethylene (HDPE) (Melt index 3-6 g/10min, density 900 kg/cm^3) supplied by Cementhai Chemicals Group, Thailand and Ethylene Propylene Diene Monomer (EPDM) supplied by Centre West Sdn Bhd, Malaysia were used as the base polymer matrix. Commercially available organophilic montmorillonite (OMMT) surface modified with 15-35 wt% octadecylamine and 0.5 wt% aminopropyltriethoxysilane obtained from Sigma-Aldrich Group, Malaysia was used as reinforcing agent to prepare nanocomposites.

Compounding. Melt blending of HDPE (70 vol%), EPDM rubber (30 vol%) and OMMT content at 4 vol% was carried out in an internal mixer (Thermo Haake Rheomix 600P). Prior to mixing, the matrix polymer and the nanoclays were dehumidified in a dry oven at 110 ^{o}C for a period of 1 hr.

Specimen Preparation. Subsequently, the blended samples were compression molded as per ASTM-F-412 using a compression molding machine at a temperature range of 135–155 ^{o}C with 8 tone metric pressures for 14 min.

High Energy EB irradiation. The melt compounding samples were exposed under high energy EB irradiation at different dose rate of 50, 100, 150 and 200 kGy at room temperature by using 3 MeV electron beam accelerator. The acceleration energy, beam current and dose rate were set to 2 MeV, 2 mA and 50 kGy/pass respectively.

Characterization Techniques

Gas Barrier Test: Oxygen Transmission Rate (O_2TR). O_2TR of nanocomposites was analyzed in MOCON OX-TRAN 2/20 devices in accordance to the ASTM D3985 standard method. Specimens having circular shape with thickness of 1 mm and diameter of 130 mm were conditioned in a desiccator at room temperature for a minimum of 48 hours. The test conditions used to determine the O_2TR of nanocomposites were 23 °C and 0% relative humidity (RH) with nitrogen flow rate of 20 ml/min. The resulting permeability was recorded as cm^3/m^2/day.

X-Ray Diffraction (XRD) Analysis. X-ray diffractograms of OMMT and the nanocomposites were recorded using Shimadzu 6000 (Japan), X-ray crystallographic unit equipped with nickel filtered Cu Kα radiation source operated at 40 kV and 40 mA. The basal spacing or d_{001} reflection of the samples was calculated from Bragg's equation by monitoring the diffraction angle 2θ from 2 to 10°.

Morphological Examination

Transmission Electron Microscope (TEM). The morphology of the nanocomposites was observed using a JEOL JEM electron microscope with an accelerating voltage of 100 kV. Ultrathin specimens of 100 nm thickness were cut from the middle section of the compression molded bar using a Leica ultra microtome. The specimens were collected on a trough filled with water and placed on a 200 mesh grid.

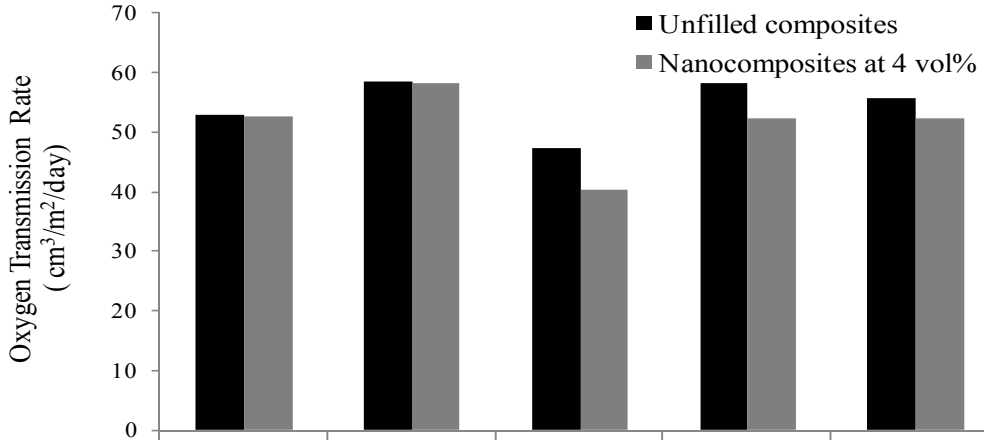
Results and Discussion

Gas Barrier Testing: Oxygen transmission rate (O_2TR). The resistance of pristine HDPE and HDPE/EPDM nanocomposite systems against the oxygen (O_2) permeation is measured by using the oxygen transmission rate technique (O_2TR). The effect of clay loading at 4 vol% as well crosslinking techniques on the oxygen (O_2) permeability is summarized in Table 1. As evident from Table 1, the O_2 permeability significantly decreased with clay loading whereas the introduction of crosslinking agents has further reduced the value of O_2 permeability. It should be noted that the lower the permeation value, the better the gas barrier resistance. For the control system without EB irradiated treatment, no enhancement in O_2 permeability was observed.

In the context of gas transportation, the nanocomposites is considered to consist of a permeable phase (polymer matrix) in which non permeable nano platelets are dispersed [9]. Nanoclay layers are believed can act as a trap to preserve the active oxygen foragers in the polymer while reducing the rate of oxygen transmission. Moreover, the degree of dispersion or delamination of the nano platelet in the polymer matrix will introduce a tortuous path for a diffusive penetration for gasses.

A little enhancement of 11.4% was obtained with EB irradiation at 100 kGy dose rate for unfilled composite, whereas an improvement of 32% was observed with the incorporation of 4 vol% OMMT loading. This indicates that the introduction of physical crosslinker significantly modified the gas barrier property of the system with the aids of OMMT filler. Upon irradiation, dense network is always desired as at this stage, crosslinking is more prominent than chain scission and thus resulted in improve gas barrier property. This is believed due to the increase of the free volume that facilitates the diffusion process as the easier pathways has been created for the O_2 transmission.

Table 1: Oxygen Transmission Rate (O_2TR) of unfilled composites and nanocomposites for control and EB irradiated systems



	Control	EB irradiated-50 kGy	EB irradiated-100 kGy	EB irradiated-150 kGy	EB irradiated-200 kGy
Unfilled composites	52.8	58.5	47.2	58.3	55.8
Nanocomposites at 4 vol%	52.6	58.3	40.4	52.5	52.4

X-Ray Diffraction Analysis (XRD). The changes in the interlayer distance of clay can generally be elucidated using XRD. The peak for control system (untreated) was blunted, indicating that most of the clay is still in the original stacking condition. The diffraction angle and interplanar spacing values are summarized in Table 2.

Nanocomposites with exposure to EB irradiation dose rate of 100 kGy revealed intercalated with partial exfoliated structure based on the absence of any basal reflections in the XRD patterns. This is evidenced by TEM images. It can be seen from Fig. 1 and Table 2, the diffraction peak was

significantly shifted towards lower angle and higher diffraction peak which were about 0.83º and 6.30Å. This suggested that the face to face interaction between the OMMT particles layers was decreased at the benefit of improving the surface interaction between OMMT particles and polymer matrix. Moreover, this might be implied that the interlayer distance between the OMMT particles have become shrinked due to the formation of crosslinking structure [10]. However, the shift in the diffraction peak to lower 2θ value may not necessary offer evidence for complete exfoliation, it may also indicate the mixed OMMT structure of intercalated and exfoliated structure, which has been confirmed by TEM examination.

Table 2: Interplanar spacing and diffraction angle values for control and EB irradiated systems

Systems	2Ɵ [°]	Interplanar spacing, d [Å]
Control/4 vol% OMMT	3.570	24.73
EB irradiated-100 kGy/4 vol% OMMT	2.845	31.03

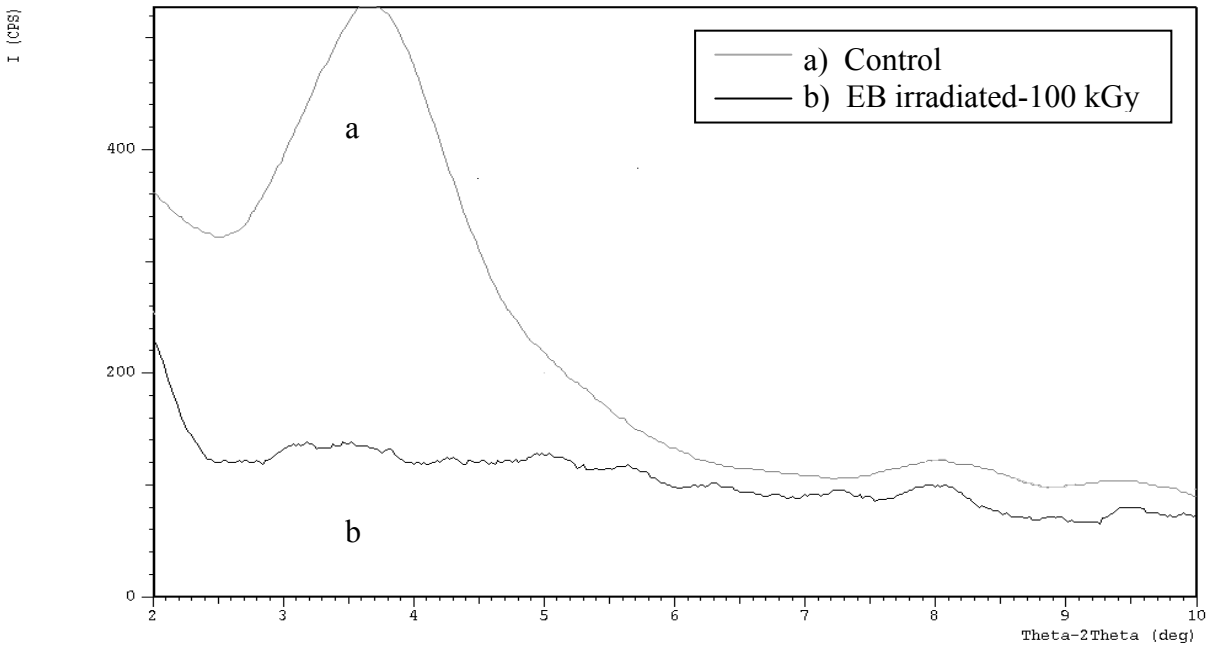


Fig. 1: XRD analysis for a) control and b) EB irradiated systems

Transmission Electron Microscope (TEM). The nanometer scale dispersion of the treated clays OMMT within the polymer matrix is further corroborated with TEM images as depicted in Fig. 2 and 3, respectively. The lighter region represents HDPE matrix, the dark region represents EPDM part whereas the dark lines corresponding to silicate layers (OMMT). Individual silicate layers along with two to three layer stacks were found to be intercalated in the polymer matrix for control system as evidenced in Fig. 2. In the case of control system, the non-uniform of OMMT agglomerates was easily detected. Moreover, it can be seen that the dispersion of the clay particles was poor and many large aggregates (in microns) were observed.

However, in the case of the EB irradiation dose rate of 100 kGy as shown in Fig. 3, partially exfoliated and fine dispersion of the clay layers within the polymer matrix were observed. Modification of clay with high energy EB irradiation lowered the electrostatic interactions between the clay layers enlarged their intra-gallery spacing thus facilitating exfoliation and efficient dispersion of the clay [11-13].

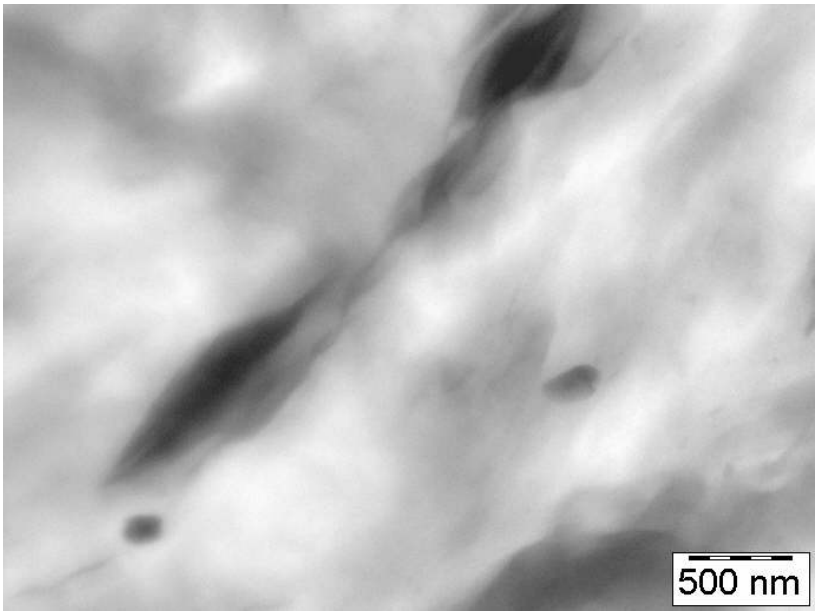


Fig. 2: TEM micrograph of control system (untreated)

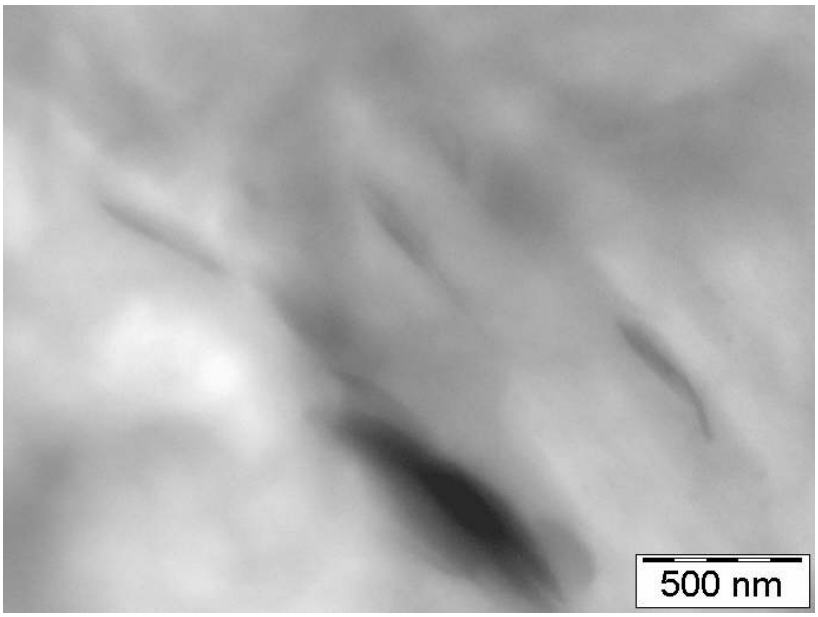


Fig. 3: TEM micrograph of EB irradiated system at dose rate of 100 kGy

Summary

The current study has found that the electron beam irradiation with different dose rates that varied between 50, 100, 150 and 200 kGy was found to decrease the values of oxygen O_2 permeation. These value were further decreased with the aids of OMMT particles which could suggest that more tortuous path has been created inside the nanocomposite system. This is evidenced from the homogenous dispersion of OMMT particles particularly by EB irradiation dose rate of 100 kGy as revealed by TEM micrograph.

Acknowledgement

The authors wish to express their gratitude to University of Malaysia, Perlis and International Islamic Malaysia University for the financial assistance and all the staffs in MRB, MINT, SIRIM and IIUM for their help in making this study success.

References

[1] H.R. Dennis, D. Chung, S. Kim, J.L. White and J.W. Cho: Polymer Vol 42(23) (2001), 9513-9522.

[2] D.F. Eckel, M.P. Balogh, P.D. Fasulo and W.R. Rodgers: Journal of Polymer Science Vol 93 (2004), p. 7 .

[3] H.F. Guo, S. Packirisamy, N.V. Gvozdic and D.J. Meier: Polymer Vol 38(4) (1997), p. 785-794.

[4] J. Sharif, K.Z. Mohd Dahlan and W.M.Z. Wan Yunus: Journal of Nuclear and Related Technologies. Vol 5(1) (2008), p. 65-80.

[5] M. Zenkiewicz and J. Dzwonkowski: Polymer Testing.Vol 26 (2007), p. 903 – 907.

[6] A. Bhattacharya: Prog. Polym. Sci. Vol 25 (2000), p. 371-401.

[7] I. Banik and A.K. Bhowmick: Rad. Phys. Chem. Vol 54 (2000), p. 135- 142.

[8] I. Banik, A.K. Bhowmick, V.K. Tikku, I.A.B. Majali and R.S. Despande: Radiation Phys. Chem Vol 51 (1998), p. 195-204.

[9] Information on http://www.findarticles.com.

[10] G. Choudalakis and A.D. Gotsis, A.D: European Polymer Journal Vol 45 (2009), p. 972-980

[11] H. Azizi, J. Morshedian, W. Barikani, M.H. Wagner: *Express Polymer Letters* Vol 4(4) (2010), p. 252–262, 2010.

[12] M. Bousmina, S.S. Ray and J. Bandyopadhyay: J. Ind. Eng. Chem Vol 13(4) (2007), p. 614-623.

[13] M.N. Bureau, F. Perrin-Sarazin, and M.T. Ton-That: Polymer Engineering and Science Vol 44 (2004), p. 1142-1151.

© (2011) Trans Tech Publications, Switzerland
doi:10.4028/www.scientific.net/KEM.471-472.781

Interfacial Shear Strength of Polylactic Acid-Kenaf Fibre Biocomposites

H. ANUAR[1, a], A. ZURAIDA[1, b], B. MORLIN[2, c], J. G. KOVÁCS[2, d]

[1]Department of Manufacturing and Materials Engineering, Kulliyyah of Engineering, International Islamic University Malaysia, Kuala Lumpur, Malaysia.
[2]Department of Polymer Engineering, Budapest University of Technology and Economics, Budapest, Műegyetem rkp. 3., H-1111, Hungary.
[a]hazleen@iium.edu.my, [b]zuraidaa@ium.edu.my, [c]morlint@pt.bme.hu, [d]jozsef@pt.bme.hu

Keywords: Polylactic acid; kenaf fibre; biocomposite; micromechanical; interfacial shear strength.

Abstract. This paper reported the interfacial shear strength (IFSS) between kenaf fibre (KF) and polylactic acid (PLA) matrix which was measured using microbond tests device. The value of IFSS obtained in PLA-KF is comparable to other polymer with natural fibre reinforcements. The properties of single kenaf fibre was determined from tensile tests and also described in this paper. From single kenaf fibre properties, various mechanical properties can be estimated for various applications.

Introduction

Mechanical performances of biocomposite materials are strongly depend on the properties of the reinforcement fibre and matrix. Excellent properties of each constituent can be transferred from one phase to another if the interface between fibre and matrix is good. Up to-date research on micromechanical and interfacial adhesion of natural fibre and biodegradable matrix are rarely studied until recently reported by Le Duigou and coworkers [1] on flax fibre and PLA matrix. They reported that interfacial region is very complex and can be performed at various scale levels including nanoscopic, microscopic and macroscopic.

Investigation on surface adhesion between single fibre and matrix can be divided into two groups, namely direct and indirect methods [2]. Examples of direct methods comprises of fragmentation [3], Broutman test [4], fibre push-out [5], fibre pull-out and microbond test [6-8]. Indirect methods consist of conventional mechanical testing and acoustic emission. There are various parameters that can be evaluated during characterization of the interface such as the effect of matrix chemistry, fibre surface treatments, and fibre diameter on the behavior of composite materials [7]. Day and Cauich Rodrigez [8] found that the position of the grips which support the microdroplet is important and affects the interfacial shear stress distribution. In addition, they also suggested using two droplets where one of these will be restrained while the other will be displaced.

The purpose of this paper is to investigate the applicability of microbond tests and to determine the surface adhesion of kenaf fibre and polylactic acid matrix by adopted test method developed by Morlin and Czigany [2]. Single kenaf fibre properties has been determined and also reported in this paper.

Experimental

Materials. Polylactic acid, PLA (3051D) used for the experiment was obtained from Nature Works Ltd. The kenaf bast fibre was supplied by Kenaf Natural Fibre Industries Sdn. Bhd. (Kelantan, Malaysia) in the form of long fibre and was harvested at 6 months aged.

Microbond Test. Microbond test is a method which is used to measure interfacial shear strength between fibre and matrix. Microbond tests were conducted using a microbond device and fixed onto the Zwick 005 tensile tester. The device contains of two steel blades that can be positioned with micrometers. The role of the steel blades is to support the droplet and hold them during the debonding process as shown in Fig. 1.

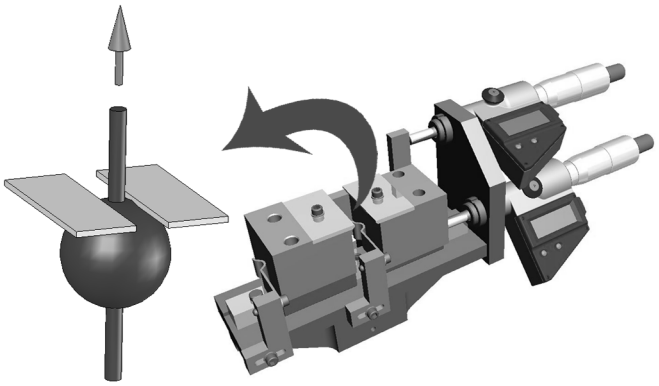


Fig. 1 Schematic diagram shows microdroplet test arrangement.

A microdroplet of PLA is placed onto the kenaf fibre, and then, the diameter of the microbond (D), length of the microbond (L_0) and diameter of kenaf fibres (d_f) were determined using optical microscope (Olympus BX51) attached to photo-camera (C-5060). Fig. 2 shows photomicrograph of kenaf fibre with PLA matrix droplet. Forty specimens were prepared for the microbond tests. Assuming shear stress is constant along the interface, the average values of interfacial shear strength were calculated by using Equation 1. From the microbond tests, the maximum force (F_{max}) was measured during the pull-out of the fibre.

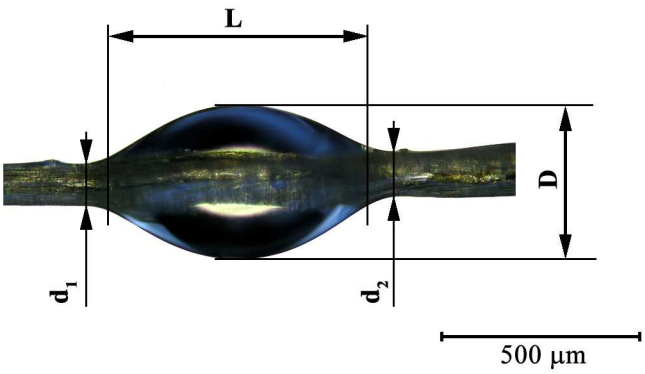


Fig. 2 Kenaf fibres with PLA matrix droplet.

$$\tau = \frac{F_{\max}}{d_f \cdot \Pi \cdot L_0} \tag{1}$$

Single Kenaf Fibre Test. Single fibre test was used to measure the strength and stiffness of the single fibre. This test was carried out using Zwick Z005 tensile tester with 20 N load cell and strain rate used was 0.5 mm/min. Initial length of kenaf fibre based on window frame was 25 mm as shown in Fig. 3. Thirty samples were prepared and tested.

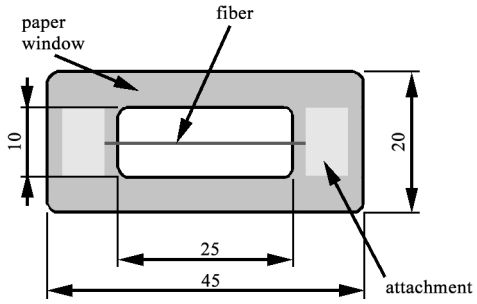


Fig. 3 Window frame used in the preparation for single fibre tests.

Results and Discussion

Microbond Tests. Microbond test was carried out to measure the interfacial adhesion between kenaf fibre and polylactic acid. Details of the diameter of kenaf fibre, dimension of microdroplet, and force needed for pulling-out fibre from the matrix are tabulated in Table 1. It is noted that the force recorded during microbond tests were varied in a wide range. The average interfacial shear strength is 5.41 ± 2.23 MPa. The data obtained is comparable to PP-flax, PP-hemp and PP-sisal as reported by [2]. Tensile strength of the PLA matrix is 63.3 MPa. Hence, interfacial adhesion normalized to the tensile strength of the matrix is 8.55%.

Force-displacement curve of single kenaf fibre and PLA matrix is shown in Fig. 4. Debonding has occurred at maximum force, F_{max}, followed by drastic failure which assign to breakage of the fibre. At the end of microbond tests, friction of fibre-matrix occurred due to uneven and bump surfaces of the kenaf fibre. Generally surface of kenaf fibres are naturally rough and the dimension were inconsistent. Peak in Fig. 4 was due to the debonding of the kenaf fibre and droplet. After kenaf fibre and PLA droplet has debonded, the droplet starts to move on the fibre.

Table 1 Interfacial shear strength according to Equation (1).

	Kenaf Fibre	Microdroplet		Force, F	Interfacial Shear
	Average Diameter, d_f (mm)	Diameter, D (mm)	Length, L (mm)	(N)	Strength, IFSS (MPa)
1	0.18	0.60	0.95	2.71	5.06
2	0.13	0.52	0.92	2.89	7.81
3	0.07	0.45	0.50	0.93	5.23
4	0.14	0.63	1.07	1.88	4.09
5	0.11	0.36	0.44	0.67	4.55
6	0.07	0.32	0.51	0.28	2.62
7	0.09	0.33	0.40	0.95	8.65
8	0.15	0.39	0.74	0.67	1.87
9	0.04	0.24	0.32	0.32	7.27
10	0.11	0.38	0.71	1.72	6.91
				Average	5.41
				Standard Deviation	2.23

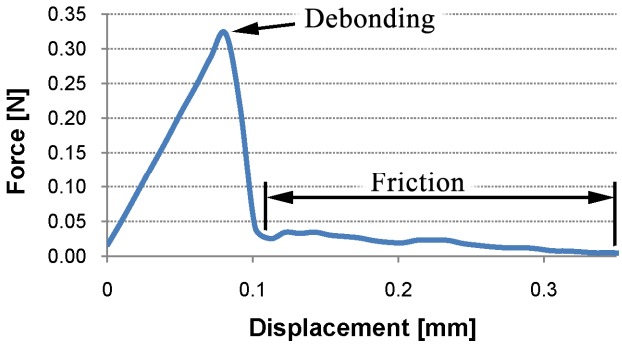


Fig. 4 Force-displacement curve obtained from microbond tests for single kenaf fibre.

Single Kenaf Fibre Test. Single kenaf fibre tests were carried out to characterize stress and elongation at break of kenaf fibre. Table 2 shows properties of single kenaf fibre. Typical force-displacement curve obtained from single kenaf fibre test is shown in Fig. 5. Properties of single kenaf fibre are very useful to predict theoretical values of tensile properties and compare to the true values obtained from experimental. Density of kenaf fibre measured is 1.13 g/cm^3 [9]. Hence specific tensile strength and modulus are 117.30 MPa/g/cm^3 and 9.89 GPa/g/cm^3, respectively.

Table 2 Properties of single kenaf fibre determined from single fibre test.

Force (N)	0.72 ± 0.32
Elongation at Break (mm)	0.39 ±0.13
Strain at Break (%)	1.56 ± 0.53
Tensile Strength (MPa)	132.55 ± 18.80
Tensile Modulus (GPa)	11.18 ± 2.44

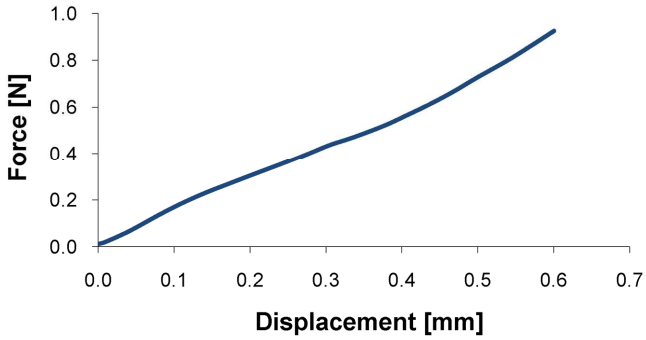


Fig. 5 Typical tensile curve obtained from single kenaf fibre tests.

Summary

The micromechanical properties of PLA-KF biocomposite was investigated using microbond tests. Interfacial shear strength of PLA-KF is 5.41 ± 2.23 MPa. From single fibre tests, tensile strength and tensile modulus of single kenaf fibre are 132.55 ± 18.80 MPa and 11.18 ± 2.44 GPa, respectively.

Acknowledgement

Hazleen Anuar wish to thanks Brain Gain Malaysia and International Islamic University Malaysia (through its Research Matching grant Scheme) for the financial support, and Department of Polymer Engineering, Budapest University of Technology and Economics, Hungary for the use of facilities and equipment in making this studies success.

References

[1] Antoine Le Duigou, Peter Davies, Christophe Baley. Compos. Sci. and Technol. Vol. 70 (2010), 231.

[2] B. Morlin, T. Czigány. Proceeding of the 8th Polymers for Advanced Technologies International Symposium Budapest, Hungary, (2005).

[3] M.J. Greenfield, A. Pedicini, L.S. Penn. Int. J. Adhesion & Adhesives Vol. 20 (2000), 403.

[4] Broutman LJ. Measurement of the fiber-polymer matrix interfacial strength. Interfaces in Composites; ASTM STP Vol. 452 (1969), 27.

[5] X.F. Zhou, H.D. Wagner, S.R. Nutt. Compos. Part A Vol. 32 (2001), 1543.

[6] S.J. Eichhorn, R.J. Young. Compos. Sci. and Technol. Vol. 64 (2004), 767.

[7] P. Zinck, H.D. Wagner, L. Salmon, J.F. Gerard. Polym. Vol. 42 (2001), 5401.

[8] R. J. Day & J. V. Cauich Rodrigez. Compos. Sci. Technol. 58 (1998) 907-914.

[9] Anuar, H., Ahmad, S.H., Rasid, R., Czigany, T., Romhany, G. and Surip, S.N. J. Compos. Mater. Vol. 41 (2007), 3035.

© (2011) Trans Tech Publications, Switzerland
doi:10.4028/www.scientific.net/KEM.471-472.786

Preparation and Thermal Properties of Cellulose/Layered Silicate Montmorillonite Nanocomposites Prepared via Ionic Liquids

Shaya Mahmoudian [a], Mat Uzir Wahit [b], A. A. Yussuf [c], and Navid Nematzadeh [d]

Enhanced Polymer Research Group, Department of Polymer Engineering, Faculty of Chemical Engineering, Universiti Teknologi Malaysia, Johor, Malaysia

[a]shaya_mahmoodian@yahoo.com, [b]mat.uzir@fkkksa.utm.my, [c]abdirahman@fkkksa.utm.my, [d]nnematzadeh@yahoo.com

Keywords: Cellulose, Montmorillonite, Ionic liquid, Nanocomposites

Abstract. Environmentally friendly nanocomposites comprising of cellulose and montmorillonite (MMT) were prepared via a green solvent, ionic liquid, 1-butyl-3-methylimidazolium chloride (BMIMCl) using solution casting method. The cellulose concentration and MMT content were varied according to predetermine formulation. The regenerated cellulose nanocomposites were characterized using X-ray diffraction (XRD). The thermal and thermal oxidative properties of regenerated cellulose nanocomposites were studied by thermogravimetric analysis (TGA). Mechanical properties of the nanocomposites films were investigated by tensile strength measurements. The intercalation and exfoliation of MMT in the cellulose matrix were confirmed by XRD results. TGA results showed an increment in degradation temperature and char yield for the nanocomposites. Multistep TGA graph was observed for degradation under air. The results indicated that the addition of MMT up to 6 wt% in regenerated cellulose matrix improved the tensile properties.

Introduction

Biodegradable polymers for renewable resources have achieved high interest in material science as alternative for petroleum based polymers. [1-2]. Cellulose which is the most abundant natural polymer on the earth has many attractive properties such as environmentally friendly, biocompatible, low cost, renewable and non-toxic. Cellulose can be used in unmodified form in clothing, furniture and medical products and it can be also extracted from its natural resource to produce cellulose derivatives and regenerated cellulose for manufacturing artificial fibers, films, food casing, membranes, sponge, coating and etc. However, only about 2% (around 200 million tons of the 40 billion tons) of cellulose renewed annually are used as raw material in manufacture of cellulose material and goods [3-4]. The major setback to the more extensive use of cellulose is the lack of suitable solvent for cellulose since this natural polymer is neither meltable nor soluble in water and common solvents. This is due to the strong hydrogen bonding between cellulose molecules. Therefore, the research and development of more effective cellulose processing methods is necessary to make full use of cellulose resources [5-6].

For more than one century, polluting viscose process was the main technique for cellulose regeneration and it is still applied for the production of regenerated cellulose fibers [7]. Recently, several cellulose solvents such as LiCl/N,N-dimethylacetamide (DMAc) [8], NaOH/urea aqueous solution [9], LiCl/1,3-dimethyl-2-imidazolidinone (DMI) [10], N-methylmorpholine-N-oxide (NMMO) [11-12] have been developed for cellulose processing. However these solvents have some drawbacks such as toxicity, volatility, side reactions and high cost [13].

Room temperature ionic liquids are group of new solvents which have many attractive properties such as thermal and chemical stability, non flammability, low melting point, low vapor pressure and ease of recycling [14-15]. Recently, it has been found that room temperature ionic liquids can be used to dissolve cellulose. Rogers and his coworkers [16-17] reported for the first

time that ionic liquid 1-butyl-3-methylimidazolium chloride (BMIMCl) has a good dissolving power for cellulose which opened up a new way of developing a class of cellulose solvent systems.

In recent years, polymer/layered silicate (PLS) nanocomposites have attracted great interest. These type of nanocomposites are important because of their nanoscale dispersion, as even with very low level of nanofiller incorporation (<5wt%). PLS nanocomposites exhibit remarkable improvement in material properties compare to polymer alone in the terms of thermal stability, gas barrier properties, tensile strength and biodegradability [18-20].

In this article, we report an environmentally friendly preparation of cellulose/montmorillonite (MMT) nanocomposites by incorporation of MMT into the microcrystalline cellulose (MCC) matrix using ionic liquids as solvent. The structure, thermal and mechanical properties of these regenerated cellulose nanocomposites are investigated.

Materials

Microcrystalline cellulose a commercial reagent from Sigma, average powder size 50 μm, Avicel type was used. 1-Butyl-3-methylimidazolium chloride (BMIMCl) was supplied by Sigma Aldrich. Montmorillonite (MMT) clays include, unmodified sodium montmorillonite (NaMMT) and Nanomer 1.30TC were obtained from Nanocore Inc. (Arlington Heights IL, USA.) Nanomer 1.30TC is organically modified with octadecyl amine with average dry particle size of 16–22 μm.

Nanocomposite Preparation.

Cellulose/MMT nanocomposites with MMT loadings of 2, 4, 6 and 8 wt% were prepared according to the following procedure; cellulose was dissolved in ionic liquid BMIMCl with magnetic stirring for 4 hours in 80˚C at the cellulose concentration of 8 wt.%. Meanwhile MMT nanoclays were dispersed in BMIMCl using sonicator (Model FB15053, Fisher Scientific Co., Germany) for 30 min and then stirring for 4 hours at 80˚C. Two solutions were mixed out and stirred for 24 hours to get a completely homogenous mixture. After degassing the solution in vacuum oven the solution was casted on a glass plate with thickness of about 0.5 mm and immersed immediately into a distilled water bath at room temperature for 24 hours. The obtained nanocomposite films were washed with running water and dried in vacuum oven

Characterization.

X-ray diffractometry (XRD) was performed using Siemens (Berlin, Germany) D5000 X-ray diffractometer with Cu-Ka radiation. The X-ray diffraction patterns were recorded with a step size of 0.05˚ and scanning speed of 0.02˚/min from 2θ = 2 to 80˚. The interlayer spacing (d-spacing) were calculated from the Bragg's equation (1).

$$\text{d-spacing} = \lambda/\sin\theta \qquad (1)$$

where θ is the diffraction angle giving the primary diffraction peak, and λ is the wavelength of X-ray radiation. In these experiments, λ = 0.15147 nm (Cu Kα) were used.

Thermogravimetric analysis (TGA) tests were carried out on a Perkin Elmer-TGA7 instrument at a heating rate of 10 ˚C/min with temperature range from 25 to 650 ˚C both under a nitrogen and an air atmosphere. Approximately 10 mg of samples was tested with the flow rate of 50 ml/min.

Tensile testing was performed on a LRX Tensile Testing Machin (Lloyd, USA) according to ASTM D638-03 type V with crosshead speed of 10 mm/min under ambient temperature; a gauge length of 25 mm was used.

Results and Discussion

X-ray Diffraction Studies. The XRD results of unmodified NaMMT, nanomer 1.30TC and cellulose/MMT nanocomposites are shown in Fig. 1. Diffraction angle values and calculated interlayer spacings are listed in Table 1. The diffraction pattern of NaMMT has shifted from 2θ of 6.7 (corresponding to d-spacing of 13.27Å) to 6.15 (d-spacing 14.52 Å), which is only a minor shift towards the small angle direction suggest that Na MMT layers were intercalated in the cellulose matrix [6, 21]. The d-spacing peak of MMT 1.30TC in cellulose matrix disappeared indicates as random dispersion and possible exfoliation of MMT plate in cellulose nanocomposite. These results indicate that modification of MMT can result on its better dispersion in cellulose matrix. Organic modification of MMT increases the interlayer spacing of MMT pellets which provide the possibility for polymer chains to diffuse between the layers during processing and it will consequently affect the properties of the nanocomposites [19].

Thermogravimetric Analysis. Thermal-degradation of regenerated cellulose and cellulose/MMT nanocomposites was studied by thermogravimetry analysis under nitrogen and air flow. The traces recorded at 10 °C/min for regenerated cellulose and cellulose nanocomposites are reported in Fig. 2. The decomposition temperature of the nanocomposites was higher than that of

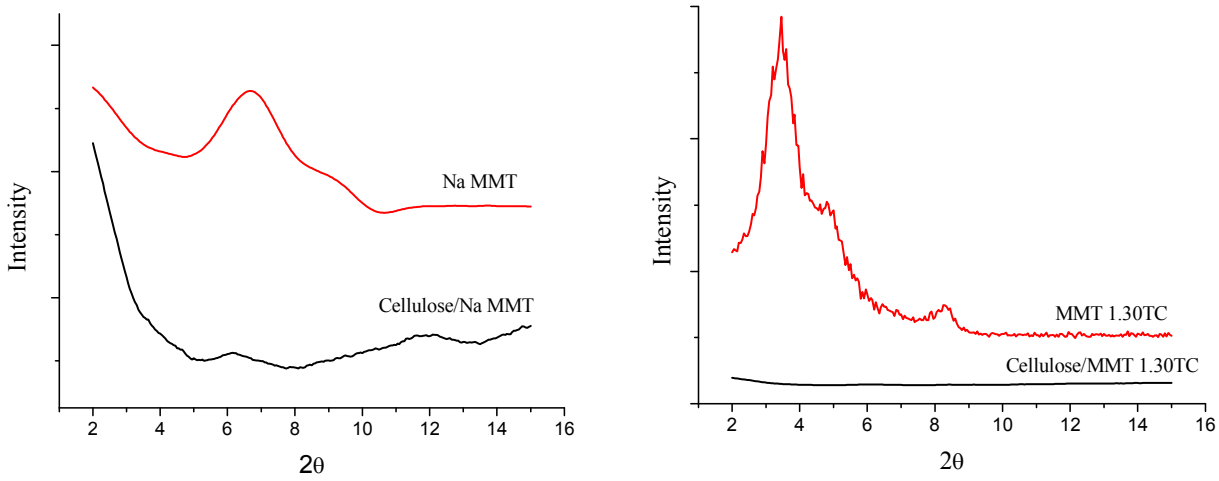


Fig. 1 X-ray diffraction pattern of MMT nanoclays and their corresponding cellulose nanocomposites: (a) cellulose/ NaMMT; (b) cellulose/MMT 1.30TC

Table 1 Interlayer spacing and 2θ values for NaMMT, MMT 1.30TC and their corresponding cellulose nanocomposites

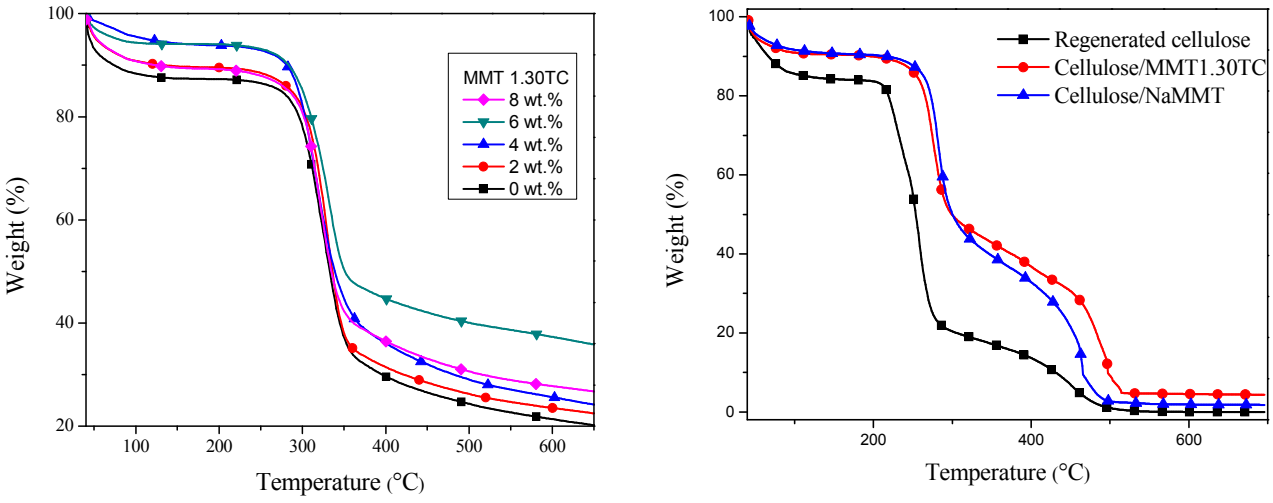
Sample	2θ (°)	d-spacing (Å)
NaMMT	6.7	13.27
Cellulose/NaMMT	6.15	14.52
MMT 1.30TC	3.45	25.16
Cellulose/MMT 1.30TC	–	∞

pure regenerated cellulose films, which indicates the involvement of good interaction between cellulose and MMT leading to improve the thermal stability of the nanocomposites. Fig. 2a exhibited the effect of clay content on thermal properties of regenerated cellulose/MMT 1.30TC nanocomposites. The thermal stability of the nanocomposites enhanced by increasing MMT loading up to 6 wt.% prior to decrease at 8 wt%. This is perhaps because of the formation of MMT agglomerates in the regenerated cellulose nanocomposite with 8 wt% MMT. It can also be seen that the residual weight of the films increased by MMT incorporation in cellulose and it increased with increasing the MMT content up to 6 wt%. For example, the char yield of pure regenerated cellulose films was about 38 wt% at 350 °C, whereas regenerated cellulose/MMT nanocomposites containing 4wt% and 6 wt% MMT had char yield of about 44 wt% and 49 wt% respectively. It is indicated that MMT remained in the nanocomposite in high temperatures.

According to Fig. 2b, TG curves show a double decomposition step in air atmosphere. That is due to the oxidation which is occurred during the first weight loss stage and it is believed that the presence of MMT also enhanced cellulose thermo-oxidative stability [22]. At second weight loss step which occurs at the range of 300-500°C, cellulose nanocomposites showed slower decomposition rate due to the increased stability.

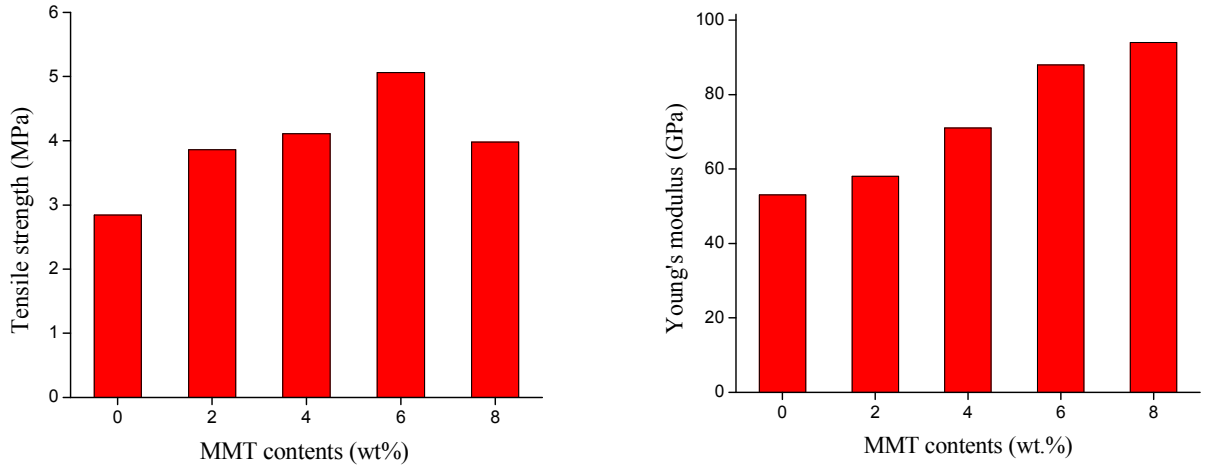
Tensile Properties. The influence of MMT content on tensile strength and young's modulus of the regenerated cellulose and nanocomposite films are shown in Fig. 3. The addition of MMT increased the tensile strength of the films. The tensile strength reached the maximum value for regenerated cellulose/MMT nanocomposite containing 6 wt.% MMT. As the MMT loading further increased, the tensile strength decreased due to the aggregation of MMT particles. Previous study by Wilkinson, et. al. [23] showed that incorporation of higher than 4 wt% of MMT in PA6/MMT nanocomposites also decreased the tensile properties, suggesting that defects or voids increase as the content of MMT increases.

The tensile modulus of regenerated cellulose nanocomposites is enhanced linearly with increasing the amount of MMT up to 8 wt%. The regenerated cellulose/MMT nanocomposites containing 4 wt% and 8 wt% MMT exhibited 18% and 41% increase in tensile modulus respectively. The enhancement of modulus with incorporation of MMT in to polymer is reported in many studies [23-24]. The results indicate that the addition of MMT up to 6 wt% in to regenerated cellulose matrix improved the tensile properties.



(a) (b)

Fig. 2 TGA thermograms of regenerated cellulose and its MMT nanocomposites (a) under nitrogen; (b) under air



(a) (b)

Fig. 3 Effect of clay content on mechanical properties of regenerated cellulose/MMT nanocomposites films, (a) tensile strength; (b) Young's modulus

Summary

In this study, cellulose based nanocomposites were obtained from regenerated cellulose and MMT using ionic liquid BMIMCl, as the solvent. XRD pattern exhibited that unmodified NaMMT were intercalated and modified MMT possibly exfoliated in the cellulose matrix indicates that modification of MMT can result on its better degree of dispersion. Significant improvement in thermal and thermal oxidative stability was observed by introduction of MMT in to cellulose matrix. Tensile strength exhibited increase at 2 to 6 wt% of MMT loading whereas modulus increased according to the MMT content up to 8 wt%.

Acknowledgements

The authors would like acknowledge the fundamental research grant scheme (FRGS) Vote No: 78690 by Universiti Teknologi Malaysia from Ministry of Science, Technology and Innovation (MOSTI).

References

[1] G. Scott: Polymer Degradation and Stability Vol 68 (2000), p. 1-7

[2] S. Sinha Ray and M. Bousmina: Prog. Mater. Sci. Vol 50 (2005), p. 962-1079

[3] F. Hermanutz, F. Meister, and E. Uerdingen: Chemical Fibers International Vol 56 (2006), p. 342-344

[4] R. L. Wu, X. L. Wang, F. Li, H. Z. Li, and Y. Z. Wang: Bioresour. Technol. Vol 100 (2008), p. 2569-2574

[5] S. Zhu, Y. Wu, Q. Chen, Z. Yu, C. Wang, S. Jin, Y. Ding, and G. Wu: Green Chem. Vol 8 (2006), p. 325-327

[6] J. Lee, Q. Sun, and Y. Deng: Journal of Biobased Materials and Bioenergy Vol 2 (2008), p. 162-168

[7] T. Heinze and T. Liebert: Prog. Polym. Sci. Vol 26 (2001), p. 1689-1762

[8] M. Terbojevich, A. Cosani, G. Conio, A. Ciferri, and E. Bianchi: Macromolecule Vol 18 (1985), p. 640-646

[9] L. Zhang, D. Ruan, and J. Zhou: Ind. Eng. Chem. Res. Vol 40 (2001), p. 5923-5928

[10] N. Tamai, D. Tatsumi, and T. Matsumoto: Biomacromolecules Vol 5 (2004), p. 422-432

[11] H. P. Fink, P. Weigel, H. J. Purz, and J. Ganster: Prog. Polym. Sci. Vol 26 (2001), p. 1473-1524

[12] T. Rosenau, A. Hofinger, A. Potthast, and P. Kosma: Polymer Vol 44 (2003), p. 6153-6158

[13] H. Zhang, J. Wu, J. Zhang, and J. He: Macromolecules Vol 38 (2005), p. 8272-8277

[14] H. Olivier-Bourbigou, L. Magna, and D. Morvan: Appl. Catal., A Vol 373 (2009), p. 1-56

[15] Y. Cao, J. Wu, J. Zhang, H. Li, Y. Zhang, and J. He: Chem. Eng. J. Vol 147 (2009), p. 13-21

[16] R. D. Rogers and K. R. Seddon: Science Vol 302 (2003), p. 792-793

[17] R. P. Swatloski, S. K. Spear, J. D. Holbrey, and R. D. Rogers: J. Am. Chem. Soc. Vol 124 (2002), p. 4974-4975

[18] S. Sinha Ray and M. Okamoto: Prog. Polym. Sci. Vol 28 (2003), p. 1539-1641

[19] M. Alexandre and P. Dubois: Mater. Sci. Eng., R Vol 28 (2000), p. 1-63

[20] F. Chivrac, E. Pollet, and L. Avérous: Mater. Sci. Eng., R Vol 67 (2009), p. 1-17

[21] H. C. Koh, J. S. Park, M. A. Jeong, H. Y. Hwang, Y. T. Hong, S. Y. Ha, and S. Y. Nam: Desalination Vol 233 (2008), p. 201-209

[22] P. Cerruti, V. Ambrogi, A. Postiglione, J. RychlyÌ , L. MatisovaÌ -RychlaÌ , and C. Carfagna: Biomacromolecules Vol 9 (2008), p. 3004-3013

[23] A. N. Wilkinson, Z. Man, J. L. Stanford, P. Matikainen, M. L. Clemens, G. C. Lees, and C. M. Liauw: Compos. Sci. Technol. Vol 67 (2007), p. 3360-3368

[24] H. Balakrishnan, A. Hassan, M. U. Wahit, A. A. Yussuf, and S. B. A. Razak: Materials & Design Vol 31 (2010), p. 3289-3298

© (2011) Trans Tech Publications, Switzerland
doi:10.4028/www.scientific.net/KEM.471-472.792

Investigation of phase transformation and structure evolution of electrospun copper oxide nanofibers during thermal annealing

[1] Dariush Jafar Khadem, [2] Zahira Yaakob, [3] Samaneh Shahgaldi,

[4] Wan Ramli Wan Daud, [5] Edy Herianto Majlan

Fuel Cell Institute, University Kebangsaan Malaysia, Malaysia

[1] D.Khadem@ukm.my, [2] zahira@eng.ukm.my, [3]Sami_shahgaldi@yahoo.com,
[4]wramli@vlsi.eng.ukm.my, [5]edy@vlsi.eng.ukm.my

Keywords: Copper oxide nanofibers, electrospinning, surface area

Abstract. One-dimensional nanostructures, like nanofibers, nanobelts, nanotubes, nanorods have been regarded as a new class of nanomaterials that have been attracted as the most promising building blocks for verity applications in the last few years. As one type of important structures with intensive research efforts have been devoted to the production and investigation of the metal oxides. Metal oxide nanofibers have different potential to play an essential role in a series of application such as optics, nanoelectronics, catalysts, sensors, storage, optoelectonics, and full cell. Copper oxide nanostructures is a promising semiconductor material with potential applications in photochemical, electrochemical, electrochromic especially in water splitting, catalysts, and fabrication of photovoltaic devices. In this paper electrospinning method via sol-gel was used to fabricate copper oxide nanofibers. Copper oxide nanofibers with different morphology were synthesized by different calcinations temperature. In this paper, effective parameters such as voltage, concentration of precursor and different calcinations temperature were characterized by thermal gravimetric analysis, scanning electron microscopy (SEM), Transmission electron microscopy, x-ray diffraction(XRD), Fourier transform infrared spectroscopy (FTIR) and Brunauer Emmett and Teller (BET) .

Introduction

One-dimensional nanostructures, like nanofibers, nanobelts, nanotubes, nanorods have been regarded as a new class of nanomaterials that have been attracted as the most promising building blocks for verity applications in the last few years. As one type of important structures with intensive research efforts have been devoted to the production and investigated of the metal oxides. Copper oxide nanostructures is a promising semiconductor material with potential applications in photochemical, electrochemical, electrochromic especially in water splitting, catalysts, and fabrication of photovoltaic devices [1-7]. There are two famous oxides form for copper: cuprous (Cu_2O) with cubic p-type and cupric oxide (CuO) with monoclinic p-type structures, respectively. In 1991, Li and et al reported an intermediate compound, Paramelaconite (Cu_4O_3) which is state between two previous oxides with tetragonal structure [8]. CuO is readily available, non toxic and one of the attractive semiconductor materials as a low cost and selective solar absorber with high solar absorbency and a low thermal emittance. The electrochromic characteristic of cuprous, cupric, and combination in silica thin film on Ito substrate by sol gel method was reported in reference [9]. The result shows that the cuprous thin films are suitable for light intensity modulation application in narrow wavelength (blue-green) region. The majority of researches in copper oxide are in the shape of thin film that deposited with sputtering, thermal oxidation, vacuum evaporation and sol gel [10-11]. Copper oxide nanofibers recently synthesized by chemical routs, thermal decomposition, vapour-solid oxidation, the main problem of the synthesize from Cu substrate is the problem of mismatching among the copper substrate and CuO layer that result poor electrical contact between nanofibers and substrate [12-15].Villa and et al [16] have been reported the optical and magnetic

properties of CuO nanowirs synthesized by thermal oxidation, but copper oxide nanofibers prepared by electrospinning has rarely been reported. It is well known that electrospinning represented a simple and cost effective method for fabrication of organic compounds nanofibers with both solid and hollow interiors. Electrospinning, a spinning method that invented 70 years ago, an electrical potential is applied between a droplet of polymer in the state of solution or melt held at the end of the nozzle of the spinneret and a grounded target. When the applied electric field overcomes the surface tension of the droplet, a charged jet of solution is ejected. Due to the bending instability, jet become longer and thinner until it collects on the collector. Fig. 1shows the schematic set up of electrospinning. In this paper, we investigated the effect of voltage and different concentration of copper precursor and also different calcinations temperature. Samples were characterized by thermal gravimetric analysis, scanning electron microscopy (SEM), Transmission electron microscopy, x-ray diffraction (XRD), Fourier transform infrared spectroscopy (FTIR) and Brunauer Emmett and Teller (BET).

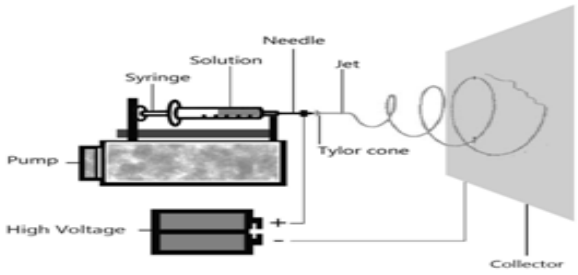


Fig. 1 Schematic diagram of electrospinning

Materials and methods

In this study, Copper nitrate trihydrate Cu $(NO_3)_2.3H_2O$ (99% purity), poly (vinyl butyral-co-vinyl alcohol-co-vinyl acetate) (PVB-CVA-CVAc; Mw= 80,000), N, N dimethylformamide (DMF) (99.8% purity), and ethanol (100% purity) were used as the starting chemicals without any purification.For the electrospinning of PVB \ copper nitrate composite nanofibers, a precursor gel solution was prepared as mentioned below. Different weight ratio electrospinning solutions were prepared by mixing 1.8gr of polymer (PVB-CVA-CVAc) as a carrier with 18ml ethanol with some drop of DMF under continuous stirring at 27 °C for 1h to obtain a well-dissolved solution in a baker. Cu $(NO_3)_2.3H_2O$ with the ration of 1, and 2 to polymer was mixed in anhydrous ethanol in another baker. Subsequently, the metal precursor/ ethanol solution was added slowly to the PVB/ethanol solution under stirring at room temperature. The final homogeneous viscous solution was immediately drawn into the hypodermic syringe. This syringe is utilized to force the PVB/metal solution to flow through a needle. The needle was attached to a high voltage supply (electrospinze high voltage) that is able to produce DC potentials up to 30 kv. The solution feeding rate was controlled at the rate of 0.1 ml/ h using a motor syringe pump (new era pump). Electrospun nanofibers were calcined at 300◦C, 400 ◦C, and 500◦C for 3 h. As electrospun nanofibers were characterized by thermal gravimetric analysis (TGA) in the temperature of 25-1000 °C, Fibers surface and morphology were exam by SEM, calcined sample in different temperature were investigated by X-Ray Diffractometer (xrd) by scanning over 2θ angles of 20-80°.

Results and Discussion

One- dimensional copper oxide nanofibers can be used in many fields according to introduction, in this work it was synthesized by the sol-gel via electrospinning method under a condition at a tip-to collector distance of 13 cm, and feeding rate of 0.1 ml/h. To investigate the effect of external electric field and ratio of polymer to $CuNO_3$ in the resulting nanofibers, different applied voltage

such as 10,16,22 ,25,28,30 kv and different ratio of polymer to $CuNO_3$ (1/1, 1/2) in order to achieve the lowest diameter were prepared . By preparing the ratio of 1/2 PVB/ Cu $(NO_3)_2$ sol-gel and applying the voltage 10,16, 22 kv drop by drop solution fell down from syringe, by increasing voltage spark generating prevent of forming fibers. By preparing the ratio of 1/1, PVB/ Cu $(NO_3)_2$ electrospun nanofibers were formed. Fig. 2(a, b) shows morphology of electrospun PVB fibers in 8% wt that obtained after trying different concentration of polymer to reach the bead free of surface. The as-spun polymer nanofibers are completely smooth due to the amorphous structure of polymers and also having the length up to several micrometers. PVB/Cu $(NO_3)_2$ with ratio 1/1 were electrospun with different voltage. At applied voltage below 22 kv a droplet of solution remains suspended at the end of the needle without being fibers or ejecting of jet and also upper than 29 kv spark generation . Fig. 2(c) depicts the PVB/Cu $(NO_3)_2$ electrospun nanofibers with 25 kv. Nanofibers are quite smooth and uniform due to the amorphous structure of PVB/Cu $(NO_3)_2$. By increasing the voltage to 28kv, the diameter of fibers not change a lot but decreasing about 30- 50 nm that was shown by Fig. 2(e). Humidity is the other effective parameters in preparation of nanofibers. In high humidity around 70% the fibers tend to attach together as shown in Fig. 1(d). Fig. 1(f) reveals the SEM micrographs of PVB/Cu $(NO_3)_2$ after calcinations at 400 °C for 3h. The surface of nanofibers becomes rough in this temperature. Fig. 1 (g, h) shows the nanofibers after 550 °C as it is clear, the shape of nanofibers completely change to the packed particles or crystalline. The diameter of nanofibers decreased by calcinations because the loss of polymer and thermal Oswald ripening during the calcinations process. The diameter of nanofibers after calcinations reaches to 100 to 400nm. Fig. 3 reveals the thermal decomposition behavior of Cu $(NO_3)_2$ / PVB fibers after spinning. The TG-DSC was applied on from room temperature to 1000 ° C to characterize electrospun PVB/ $Cu(NO_3)_2$. The weight loss was carried in three stages in TG curves until 580 °C. The first weight loss in the range until 200 °C accompanied by two opposite thermal event was observed probably due to the loss of the surface absorbed water or residual water and ethanol in the composite fibers. The second major weight loss, was observed from 200 °C and 382 °C in the DSC curve is due to the decomposition of the nitrate and side- chain of polymer. The last weight loss is belonging to decomposition of main chain of polymer and formation of copper oxide nanofibers. The TG/DSC shows that most of organic groups were disappeared after 580 °C. In order to investigate the structure and variety of phase, the PVB \ Cu $(NO_3)_2$ electrospun nanofibers and samples obtained after different calcinations temperature were revealed by XRD.

As Fig. 4(a) depicts the PVB/Cu $(NO_3)_2$ composit nanofibers with only a broad peak due to amorphous structure, this peak is the typical peak of polymers indicating amorphous structure of polymers. As it can be seen in Fig. 4(b), by calcinations of PVB/Cu $(NO_3)_2$ composite at 300 ◦C, all the polymer peaks disappear and two separate phases related to CuO and Cu_2O without any extra peak or impurity successfully grown. CuO with Monoclinic and Cu_2O with Cubic structure were well indexed by 04-007-1375, 04-007-9767 respectively. By increasing the temperature of calcinations at 400◦C well crystalline of CuO and Cu_2O with higher intensity were formed. Fig. 4(d) shows the formation of pure CuO nanofibers by calcinations at 500 ◦C. The formation of pure CuO nanofibers is proved by the FT-IR spectra in Fig. 5. It is clearly obvious from Fig 5(a, b) that PVB and PVB/Cu $(NO_3)_2$ have almost identical spectra. All the absorption peak at about 3500, 2955, 1424, 1379, and 1135 cm^{-1} are refer to the vibration of OH groups, C-H,C=O, C-H, and C-O respectively. All the organic peaks are vanished by increasing the temperature of calcinations and new absorption peaks appear at low wave number. Fig. 5(c) shows peaks around606, 503 and 430 cm^{-1} which are related to the CuO, and Cu_2O structure and by increasing calcinations temperature to 500 ◦C all peaks reveal CuO structure. The specific surface areas of the calcined nanofibers were characterized by N2 adsorption using a BET instrument. This measurement reveals that copper oxide nanofibers to compare the nanoparticles have higher surface area that shows one of the advantages of fibers. CuO nanofibers with 30.02 $m^2 g^{-1}$ surface area are more applicable for many fields.

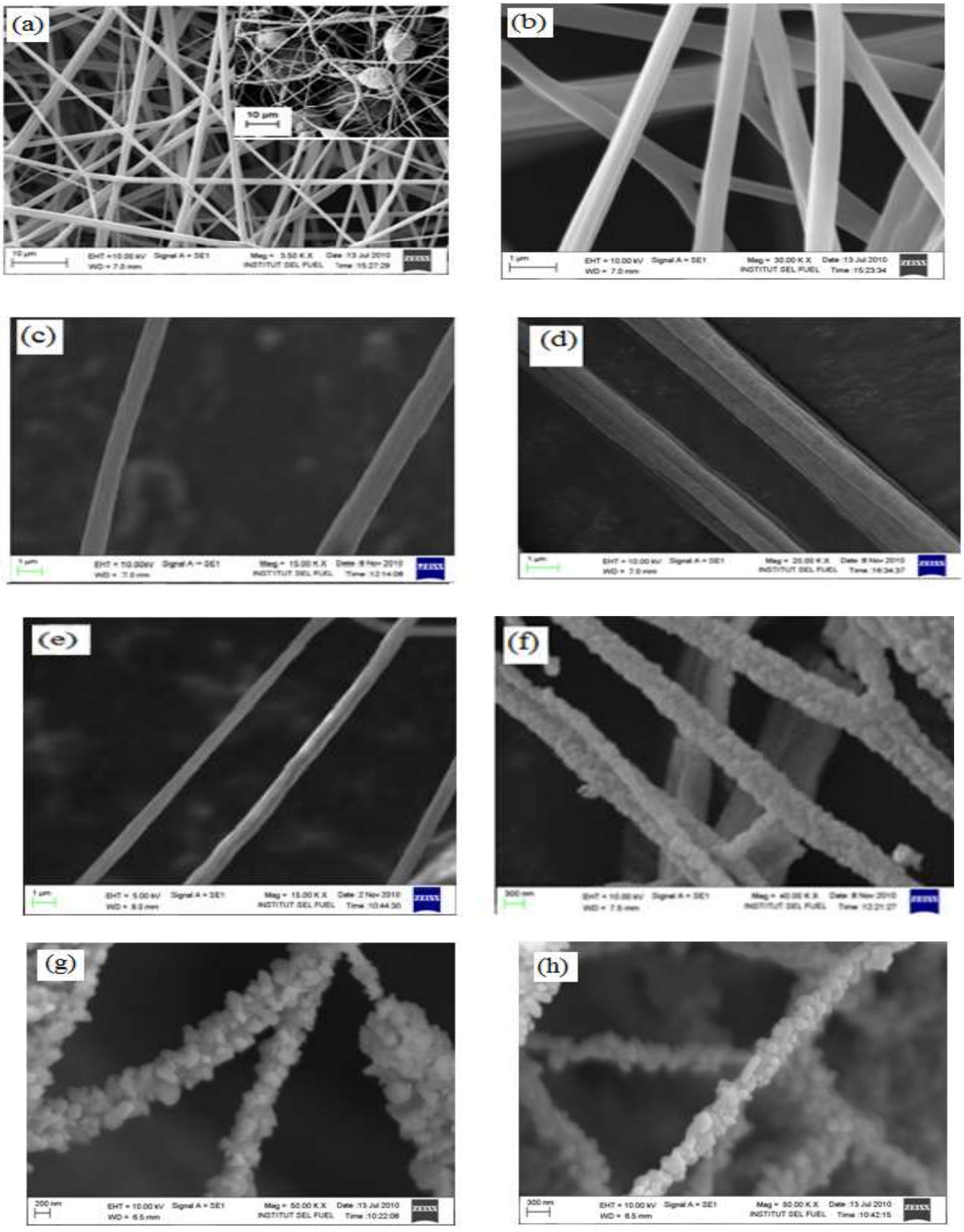


Fig. 2. SEM images of sample; (a, b) as spun PVB fibers; (d) spun BVP/Cu $(NO_3)_2$ 25V; (d) spun BVP/Cu $(NO_3)_2$ 28kV high humidity; (e) 28kV 30%humidity (f) calcined at 400°C;(g, h) 580 °C

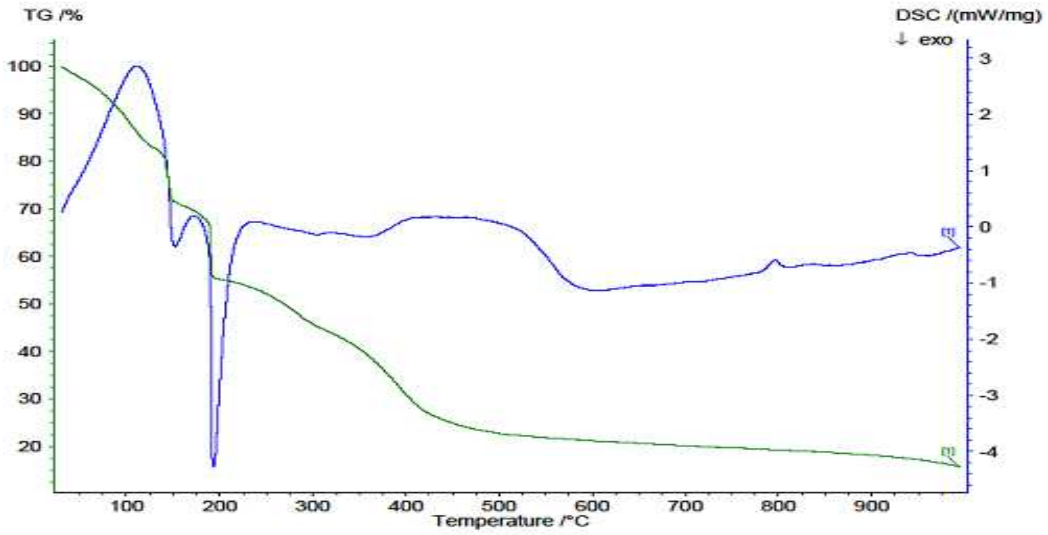


Fig. 3.TG-DTA curve of PVB/ $Cu(NO_3)_2$

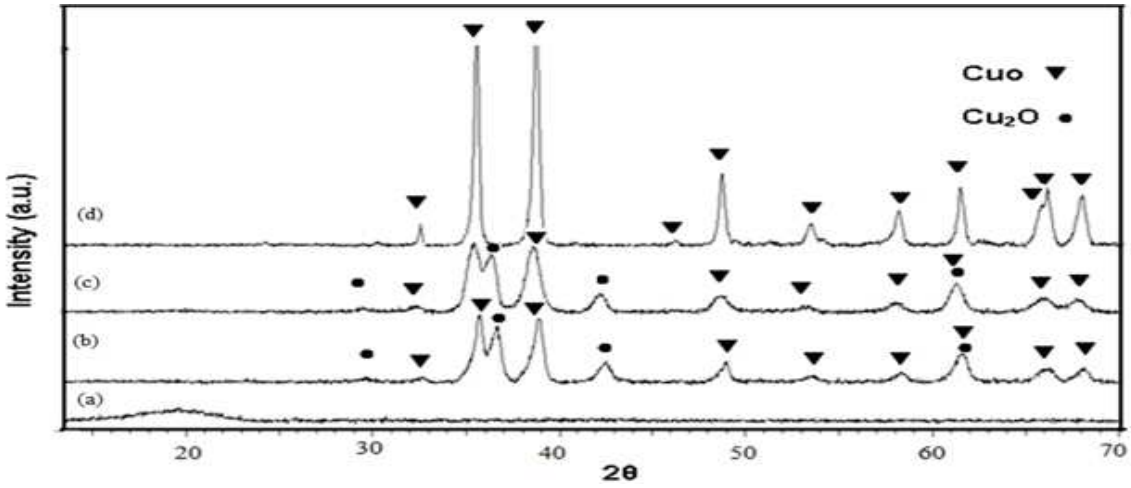


Fig. 4. X-ray diffraction pattern of (a)PVB+ $Cu(NO_3)_2$ composite (b)PVB+ $Cu(NO_3)_2$ calcined at 300°C (c)PVB+ $Cu(NO_3)_2$ calcined at 400 °C (d)PVB+ $Cu(NO_3)_2$ calcined at 500°C

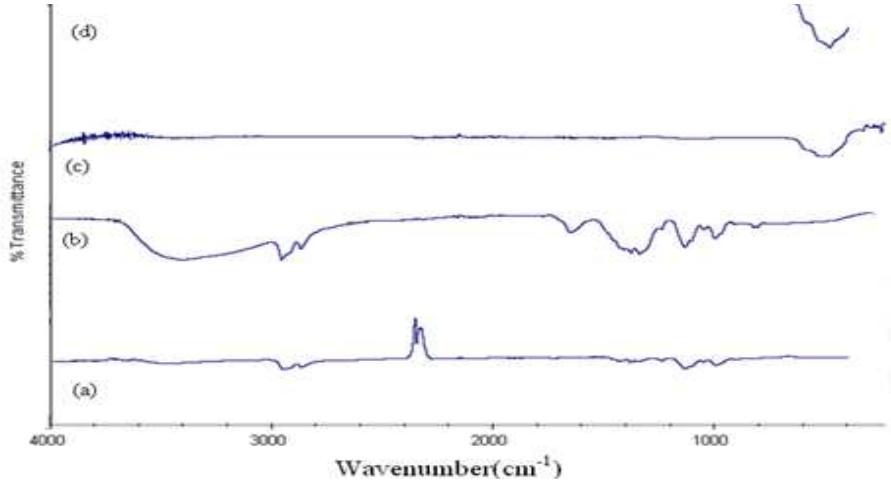


Fig. 5.FT-IR spectra of (a) PVB (b) as PVB\Cu $(NO_3)_2$ composite (c) PVB\Cu $(NO_3)_2$ composite after calcined at 400°C (d) calcined after 500 °C

Summary

The long length CuO and Cu_2O nanofibers with a good crystalinity were prepared by the sol-gel via electrospinning method. Pure copper oxide nanofibers with the diameter of 100-300 nm as confirmed by XRD and FT-IR were synthesized after calcinations of the PVB\ Cu $(NO_3)_2$ in air at 500 °C for 3h. In 300 °C and 400°C two phases structure related to CuO and Cu_2O were formed without any impurity or extra peaks. The composite morphology reveals the smooth surface due to the amorphous structure and after calcinations rough nanofibers with packed particles or crystallites were formed as revealed by SEM. The voltage and concentration have straight effect in preparation of copper nanofibers. In high humidity, the fibers desired to connect together with increasing the diameter. The optimized voltage by this investigation is 25kv. By increasing the amount of copper nitrate to polymer the drop of solution from the tip of needle were dropped and by applying high voltage the fibers could not produce. We believe the electrospun copper oxide nanofibers could have potential in many fields.

References

[1]. Wu DC, Du ZL, Gao XS, *Nanofibers*, Chemical Industry, Beijing, 2003

[2]. Xia YN, Yang PD, Sun YG, Wu YY, Mayers B, Gates B, Yin YD, Kim F, Yan YQ, *Adv Mater*, **15**, 353-389, 2003.

[3] M. Hara, T. Kondo, M. Komoda, S. Ikeda, K. Shinohara, A. Tanaka, J.N. Kondo, K. Domen, Chem. Commun. (Cambridge) 1998 (1998) 357.

[4] A.A. Ogwu, E. Bouquerel, O. Ademosu, S. Moh, E. Crossan, F. Placido, Acta Mater. 53(2005) 5151.

[5] G. Larsen, S. Noriega, Appl. Catal. A: Gen. 278 (2004) 73.

[6] K. Zhang, C. Rossi, C. Tenailleau, P. Alphonse, J.-Y. Chane-Ching, Nanotechnology 18 (2007) 275607.

[7] T. Ghodselahi, M.A. Vesaghi, A. Shafiekhani, A. Baghizadeh, M. Lameii, Appl. Surf.

Sci. 255 (2008) 2730.

[8] li ,et al 1991, journal Appl. Physics

[9] O. Akhavan, H. Tohidi, A.Z. Moshfegh, Journal Thin Solid Films , 2009,517-6700-6706.

[10] H. V. Spighker, D.Simon, F.Ooms, Journal Hydrogen energy, 33 , 2008, 6414-6419

[11] D.S.C.Halim, I.A.Talib, A.R.Daud, J,Solid state and technology, 16, 2008, 232-237

[12] Chengfa Li, Yidong Yin _, Haige Hou, Naiying Fan, Fulong Yuan, Yanmei Shi, Qingling Meng, Solid State Communications 150 (2010) 585_589.

[13] M.Villa, C.Divaz- Guerra, J.Piqueras. J.Appl physics, 43,2010, 135403-6

[14] C.Wang, G.Yuan, H.Niu, E. Yan. H.Zhao, Pigment and resin Technology, 38/1, 2009, 25-32.

[15] Glenn Guglietta, Timon Wanga, Ranjan Pati, J Solar Hydrogen and Nanotechnology. 7408 2009, 740807- 7.

[16] M.Villa, C.Divaz- Guerra, J.Piqueras. J.Appl physics. 43, 2010, 135403-6.

[17] C.A. Melendres and G.A. Bowmaker, *J. Electroanal. Chem.* 449 (1998), p. 215.

© (2011) Trans Tech Publications, Switzerland
doi:10.4028/www.scientific.net/KEM.471-472.798

Characterization of Tantalum Carbide Reinforced Copper Composite Developed Using Mechanical Alloying

Emee Marina Salleh[1,a] and Zuhailawati Hussain[2,b]

[1, 2]School of Materials and Mineral Resources Engineering,Engineering Campus,

Universiti Sains Malaysia, Penang, Malaysia

[a]emarina39@yahoo.com, [b]zuhaila@eng.usm.my

Keywords: Cu-TaC composite; Mechanical alloying; Consolidation pressure: TaC phase

Abstract. The effects of the consolidation pressure on the properties of novel Cu-15vol% TaC composite was investigated. The copper-based composite has been prepared using a high energy planetary mill via in-situ route. A mixture of copper, tantalum and graphite powder was mechanically alloyed for milling time of 8 hours at speed of 400 rpm. The as-milled powder was consolidated by cold pressing under various pressure (i.e. 100, 200, 300 and 400 MPa) at room temperature and sintered in argon atmosphere at 900 °C for an hour. TaC phase was formed in copper matrix after sintering process. An increase in consolidation pressure resulted in an increase in hardness, electrical conductivity and density of the composites. The changes of bulk properties of the in-situ Cu-TaC composite were correlated to the formation of TaC phase and a reduction of porosity which led to an increasing in densification.

Introduction

High electrical and thermal conductivity of copper (Cu) and low coefficient of thermal expansion and high hardness of tantalum carbide (TaC) constructs accessible properties for spot resistance welding electrodes, contact bars and electrical conductors [1]. The in-situ formation of tantalum carbide reinforced copper matrix composite can be achieved via mechanical alloying (MA) process.MA is one of the most promising techniques used to produce heat-resistant dispersion strengthened copper alloys. MA can also be successfully used to produce in-situ Cu-matrix composites reinforced with particles of materials such as borides, carbides, oxides and intermetallic compounds [2]. High energy mechanical milling (HEMM) with a subsequent heat treatment has been used in producing in-situ developed metal matrix composite. MA process greatly depends on a number of process parameters to achieve the desired product phase, microstructure and properties. The more complete the control and monitoring of the milling conditions, the better end-product might be attained [3]. However, in producing in-situ composite, the focus is not only emphasized on the MA processing variables alone. It also involves the controlled parameters of the subsequent processes which are consolidation (i.e. exerted pressure, type of pressing technique etc.) and heat treatment processes (i.e. sintering temperature, soaking time, sintering atmosphere etc.).

Generally, powder metallurgy (PM) is a useful route to the near net-shape fabrication of engineering components for a variety of applications. It allows consolidation without a melt-processing step, which can be advantageous for high-melting-point materials such as the refractory metals or ceramics. However, the densification of hard and soft powder mixtures is usually inhibited by the refractory phase [4]. Therefore, this present work aims to investigate the structural and properties of in-situ copper-tantalum carbide composite developed through mechanical alloying. Emphasis is also given on the consolidation behaviour of in-situ Cu-TaC composite by cold pressing techniques. The results were discussed according to phase formation, particles distribution and properties of the copper-based composite.

Experimental Procedure

Powder mixture of elemental copper (99.7 % pure, < 63 μm), tantalum powder (99.99 % pure, < 25 μm), and graphite powder (99.99 % pure, < 0.1 mm) with composition of Cu-Ta-C which correspond to Cu-15vol%TaC composite was mechanically alloyed under argon atmosphere in a high-energy Fritsch Pulveristte P-5 planetary mill. The rotation speed and stainless steel ball mill size used in this experiment were 400 rpm and 20 mm, respectively. Powder to ball weight ratio was kept constant at 1:10. 3% of n-heptane was added to the powder mixture before milling to prevent excessive cold welding of the powder. The Cu-Ta-C powder mixtures those has been milled for 8 hours milling duration were compacted into pellet under different exerted pressures of 100, 200, 300 and 400 MPa at room temperature. The compacted samples then were sintered at 900 ºC for an hour in argon flow. Density of the sintered composites was measured using immersion method according to Archimedes' principle. Vickers microhardness test was performed by applying an indentation load of 500 gf using diamond pyramid indenter for 10 seconds dwell time. Seven readings were taken from each sintered composites and the values were then averaged. Whilst electrical conductivity was conducted using a four point probe technique. Microstructure observation and energy dispersive X-ray (EDX) were carried out using a scanning electron microscope (SEM) while TaC formation in the in-situ composite was confirmed by X-ray diffraction (XRD) analysis.

Results and Discussion

XRD Analysis. The structural evolution of the sintered mixtures that has been compacted under various consolidation pressures can be seen from X-ray diffraction (XRD) spectra shown in Fig. 1 TaC phase is observed after heat treatment at 900 ºC for one hour soaking time. This result indicates that at 900 ºC, Ta reacted with graphite to form TaC and being precipitated in the Cu matrix. Basically, TaC compound can be synthesized directly from tantalum and graphite, according to the following chemical reaction:

$$\longrightarrow \qquad C + Ta \qquad TaC \qquad (1)$$

The present results signified that TaC phase was formed in-situ by mechanical alloying of tantalum and graphite powder with subsequent heat-treatment at a relatively low temperature could be explained by a decrease in activation energy resulted from mechanical milling [5]. From XRD diffraction, there were Cu and TaC phases existed in the composite powder that has been compacted under pressure between 100 to 400 MPa.

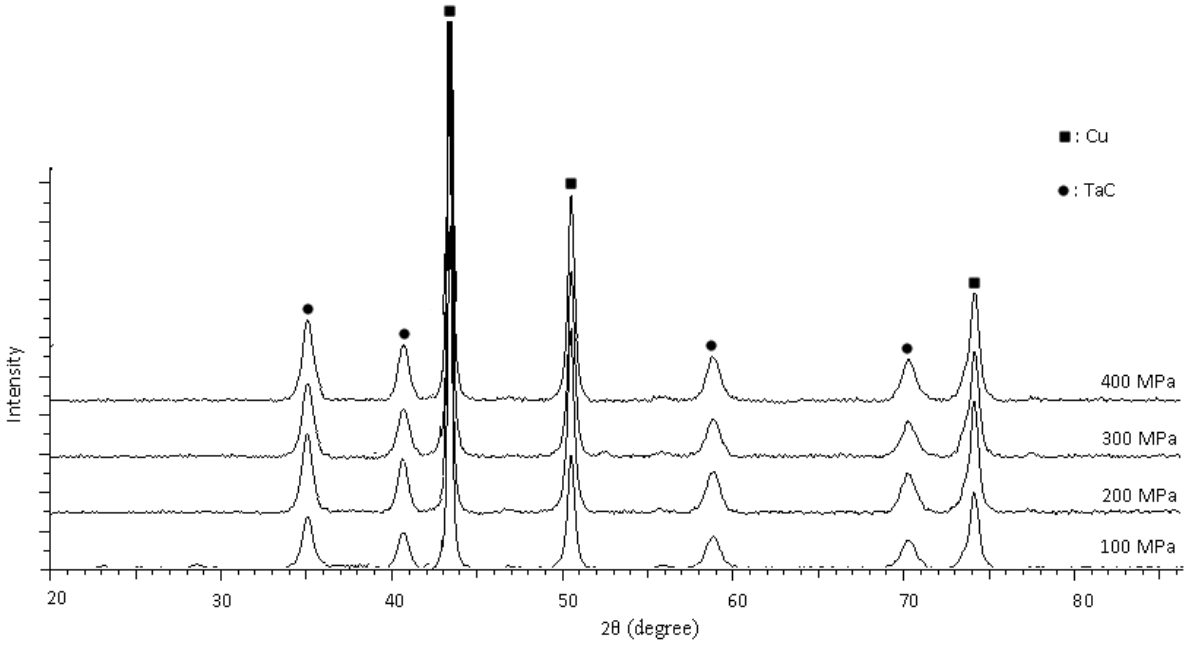
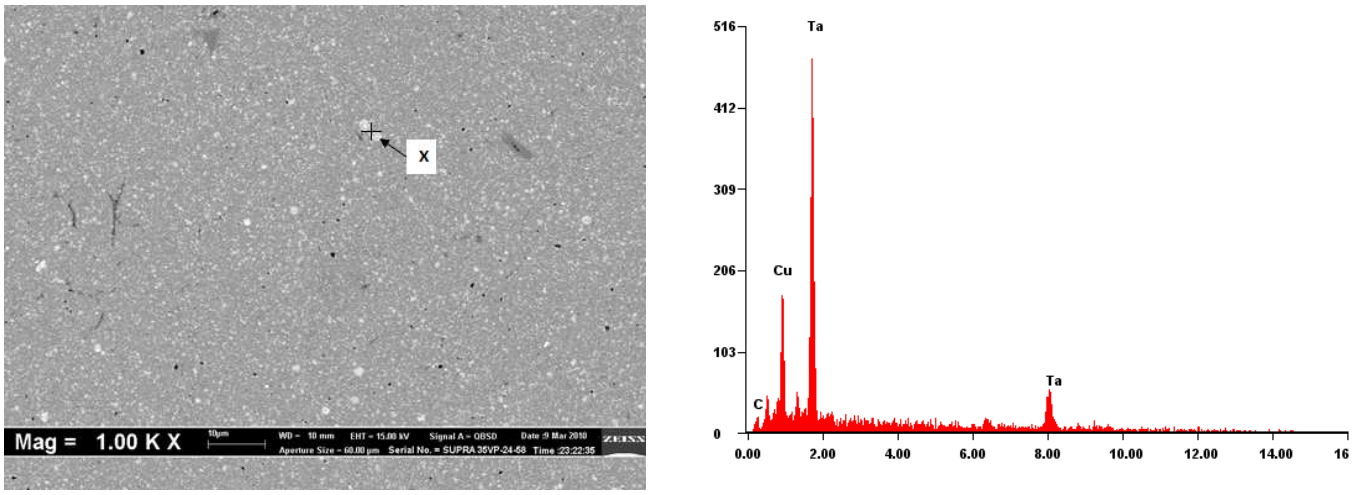


Fig. 1: XRD patterns of sintered Cu-TaC composites consolidated under various pressures

Microstructure Evolution. Fig. 2 shows the SEM micrograph and EDX analysis for Cu-Ta-C pellet that has been compacted under 400 MPa pressure and sintered at 900 ºC for an hour. EDX analysis indicates that besides of a trace of high copper percentage, fine white spot (labeled as X) consists of Ta and C. Based on EDX and XRD analysis, one can explain that the white spot is TaC particles which was finely distributed in copper matrix.



(a) (b)

Fig. 2: (a) SEM micrograph and (b) EDX spectrum of Cu-TaC composite compacted under 400 MPa

Density measurement. As the exerted consolidation pressure was increased, the density of the compacted Cu-TaC composites increased. According to Abdoli and Farnoush [6], with increasing applied pressure, the density of the powder mass increases or porosity decreases. Thus, the higher pressure would provide a higher densification effect. The determination of the densification behaviour of a powder is usually based on the measurement of the density of the sintered composite as a function of the compaction pressure. Fig. 3 shows the plotted graph for green density and sintered density as function of compaction pressure. An exertion of higher loads increased both green and sintered densities of the composites. Increasing pressure provides better packing which contributes to a reduction of porosity with the formation of new particle contacts. As reported by Tjong and Ma [7], the contact area between the grains increased and particles underwent extensive plastic deformation when the pressure increased. High pressure increased density which due to the contact enlargement leading to the formation of solid bridges through plastic deformation [8]. As the consolidation loads increased, the large pores were eliminated first and the particle contacts increased to further distribute load. As can be observed in the green density curve, the response of the as-milled composite powders shows the continuous increment of the densification from 5.427 g/cm^3 to 6.967 g/cm^3. While the sintered density increased from 5.999 g/cm^3 to 7.581 g/cm^3 when increasing compaction pressure from 100 MPa to 400 MPa.

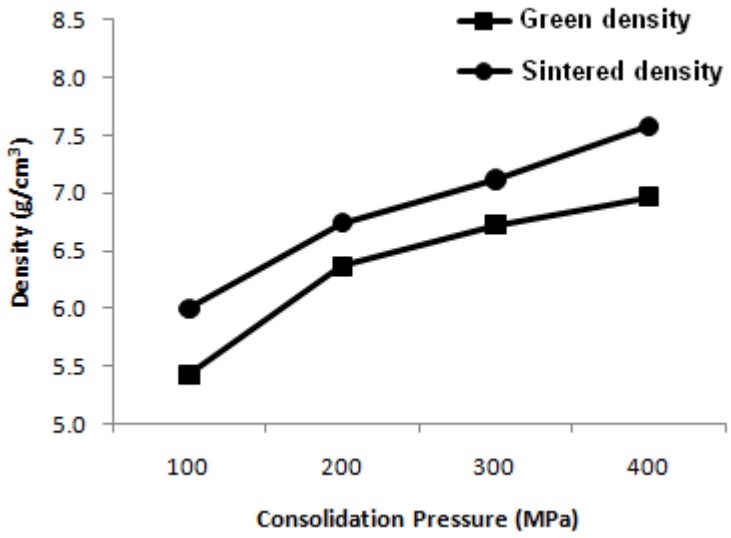


Fig. 3: Green and sintered densities of Cu-TaC composites compacted under various pressures

Microhardness of Cu-TaC composite. The microhardness values increased from 134.72 H_{mv} to 254.05 H_{mv} when increasing compaction pressure from 100 MPa to 400 MPa (Fig. 4). The increase in microhardness was the result of work hardening which took place due to severe plastic deformation during uniaxial consolidation. Microstructurally, base on SEM micrograph, the Ta and C particles were distributed and diffused homogeneously in Cu matrix. As consolidation pressure increased, the diffusivity of reinforcement phase of Ta-C particles to the Cu has also increased during sintering. As a result, besides of densification, formation of TaC was also enhanced as indicated by XRD patterns. Thus, it caused the formation of stronger bonding between those particles. In addition, an increment of particles diffusivity caused a reduction of pore formation. According to Hussain [9], the harmful effect of pores in composites is indicated by a proportional relationship between density and hardness. Pores lead to weakening of the material because the available stress bearing area is reduced and thereby lower the amount of stress that a material is able to withstand. Therefore in this present study, the combination of good diffusivity of the reinforcement particles into the matrix and less formation of pores, has slightly improved the hardness of the Cu-TaC composites.

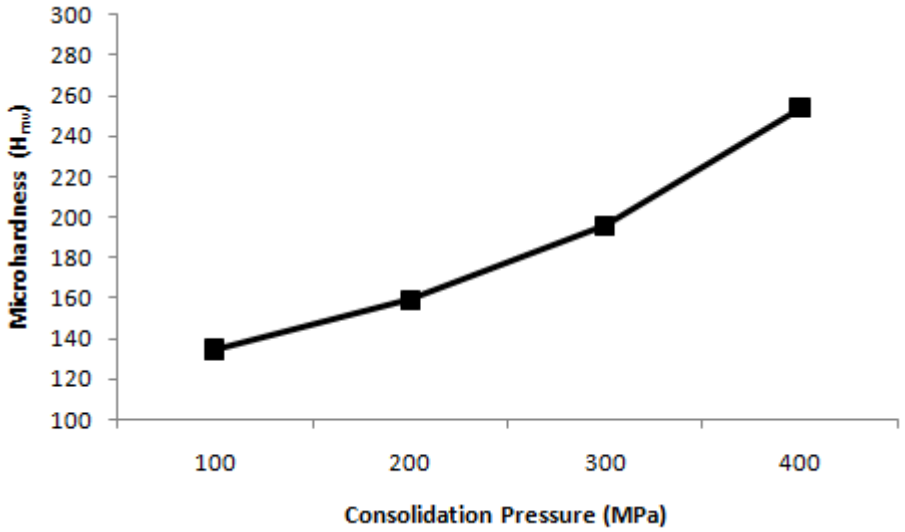


Fig. 4: Average value of microhardness of sintered Cu-TaC composites

Electrical Conductivity. The dependence of electrical conductivity on the consolidation pressure is plotted in Fig. 5. Namely, the electrical conductivity of the composite increased from 0.256 to 0.307 ($\Omega m^{-1}x10^7$). Electrical conductivity of the sintered composite is found to be a strong function of compaction pressure. As can be seen, the plotted electrical conductivity graph shows an ascending trend as a function of compaction pressure. This result is corresponding to an increase in composite density at higher compaction pressure. A reduction of pore formation at higher applied pressure contributed in increasing in electrical conductivity. This is because the less the pores the higher the electrical current flow might pass since pores acted as a non-conducting phase network within the conducting copper matrix [10]. Elimination of pores by increasing the compaction pressure gives function to enhance the electrical conductivity of copper composite.

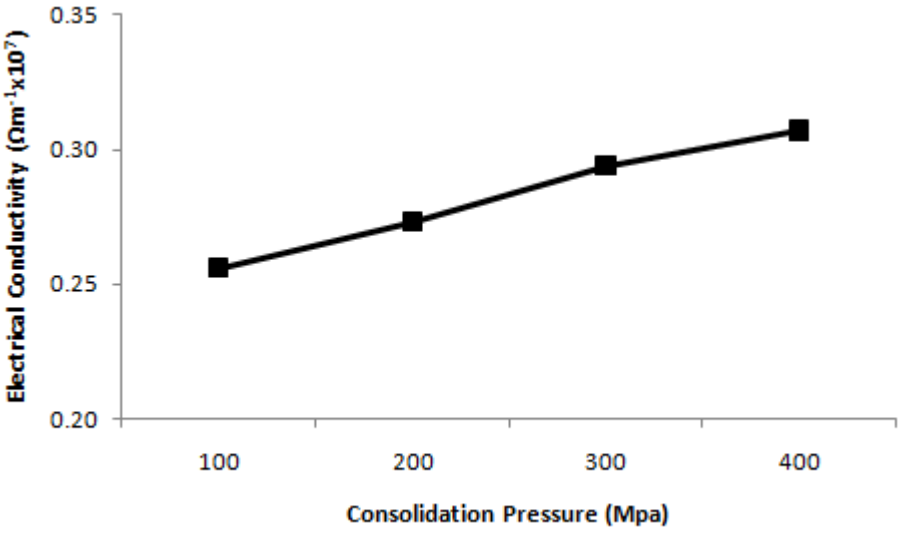


Fig. 5: Electrical conductivity of sintered Cu-TaC composites

Summary

In this paper, Cu-15vol%TaC composite has been prepared by in-situ method using mechanical milling of Cu-Ta-C powder mixture. The mechanically alloyed powders were uniaxially compacted under various pressures. The increase in consolidation pressure caused the enhancement of the bulk properties in term of density, microhardness and electrical conductivity. This is because an increment of pressure provided better powder packing and led to a decrease in porosity with the formation of new particle contacts. It was found that to produce Cu-TaC with high microhardness and electrical conductivity, the optimum consolidation pressure is 400 MPa, where the microhardness and electrical conductivity were 254.05 H_{mv} and 0.307 $\Omega m^{-1}x10^7$, respectively.

Acknowledgement
The authors are pleased to acknowledge the financial support for this research provided by Universiti Sains Malaysia (USM) Fellowship Scheme.

Reference

[1] D.W. Lee and B.K. Kim: Mater. Let. Vol. 58 (2004), p.378

[2] M.T. Marques, A.M. Ferraria, J.B. Correia, A.M. R.D. Botelho, R. Vilar: Mater. Chem. and Phys. Vol. 109 (2008), p.174

[3] M.S.E. Eskandarany: *Mechanical Alloying for Fabrication of Advanced Engineering Materials*, edited by William Andrew Publishing, Norwich, NY (2001).

[4] L.P. Martin, A.M. Hodge, and G.H. Campbell: Met. Mater. Trans. Vol. 40A (2009), p.2124

[5] H. Huang and P.G. McCormick:Alloys and Compds. Vol.256 (1997), p.258

[6] H. Abdoli, H. Farnoush: Mater. Sci and Eng. A. Vol.486, (2008), p.580

[7] S.C. Tjong and Z.Y. Ma: Mater. Sci. and Eng. 29 (2000) p. 49

[8] M.T. Marques, V. Livramento, J.B. Correia, A. Almeida and R. Vilar: Mater. Sci. Eng. A. Vol. 399 (2005), p.382

[9] Z. Hussain, T.L. Yong: Mater. Sci. and Eng. Vol. 505 (2009), p.27

[10] T. Venugopal, K.P. Rao and B.S. Murty: Acta Mater. Vol. 55 (2007), p.4439

© (2011) Trans Tech Publications, Switzerland
doi:10.4028/www.scientific.net/KEM.471-472.804

Effect of Milling Speed on properties of Fe-NbC Composite Prepared by Mechanical Alloying

Siti Zalifah Md Rasib[1,a] and Zuhailawati Hussain[1,b]

[1]School of Materials and Mineral Resources Engineering, Engineering Campus,

Universiti Sains Malaysia, 14300 Nibong Tebal, Penang, Malaysia

zalifahmdrasib@gmail.com[a],zuhaila@eng.usm.my[b]

Keywords: mechanical alloying, amorphous, milling speed, nbc phase

Abstract. Nowadays, mechanical alloy (MA) method has turned up as one of a new and applicable method for metal matrix composite fabrication due to some advantages such as the ability to form nanocrystalline structure with improved properties. In this work, different milling speed of MA process (100, 200, 300 and 400 rpm) was performed on Fe-17.21wt%Nb-2.23wt%C with milling duration of 10 hours. The mixture was pressed and sintered at 1300°C into a pellet form. Investigation by X-ray diffraction, measurement of hardness and density were carried out. High milling speed resulted on crystalline-to-amorphous transition of XRD peaks of Fe and NbC phases. Different level of MA at different speed also produced fine NbC particles and strain hardening which resulted in increase value of hardness. The presence of pores, particularly in the composite with high milling speed, decreased the density of Fe-NbC composite.

Introduction

MA method which has been introduced by John S. Benjamin and his colleagues in 1966 [1] is continuously investigated by other researchers with a purpose to gain advance understanding of MA behaviour's. MA method is preferred in this work due to several attributes such as its ability to produce metal matrix composite (MMC) [2]. Better final product of MMC can be achieved by controlling the variables and most of the variables controlled during processing/fabrication. Milling speed included as a factor during MA which is one of the process of MMC product.

High kinetic input and high impact on powder increase temperature inside the vial [3]. Heat produced at different level of milling speed influences crystallization of amorphous phase. Easy formation of amorphous as the milling speed is increased is due to the increase strain and defect concentration [1]. However, very high milling speed results in contamination due to the excessive heating and wear between balls inside the vial [3]. Effect of milling speed on the properties of NbC reinforced copper composite was discussed by Zuhailawati et al. [2]. However, there will be some different in the properties of mechanical alloyed of NbC reinforced iron composite since iron is simply to be amorphous as shown by previous work [4]. Therefore, further discussion on the effect of milling speed on properties of iron-based was investigated in this work.

Experimental Procedure

Mixture with composition of Fe-17.21wt%Nb-2.23wt%C was prepared from three types of raw materials, iron powder (99.5% pure, <90μm), niobium powder (99.8% pure, <19μm) and graphite powder (99.8% pure, <0.1 mm). The mixture was milled using Fritsch Pulverisette 5 planetary mill with different milling speed for 10 hours. 100, 200, 300 and 400 rpm of milling speeds were used to study the effect of milling speed on the obtained iron metal matrix composites by investigating their properties. Ball to powder weight ratio was kept at 10:1 and stainless steel milling balls with diameter 20mm were used. Then, the as-milled powder was measured by using Mastersizer

Malvern Instruments for particles size analysis and was characterized by X-ray diffraction (XRD) technique. The as-milled powder was compacted using a hand pressing machine in a cylindrical stainless steel die with diameter of 10mm in size with pressure of 600MPa. The pellet then was sintered at 1300°C under argon atmosphere and characterized by XRD to observe the formation of Fe and NbC phases. Hardness test was carried out using Future Tech Vickers Hardness Tester under a load of 500g with dwell time of 10 seconds while Archimedes' principle was used to measure the composite sintered density.

Results and Discussion

XRD Analysis. Fig. 1 shows the XRD pattern of the as-milled Fe-Nb-C mixture prepared by mechanical alloying with different milling speed. There are many peaks can be observed clearly at 100rpm compared to the others speed. The intensity of Fe at 44.673°, 65.023° and 82.335° markedly decreased and some disappeared as the speed was increased. Similar trend is observed for peaks of Nb which the intensity markedly decreases and started to disappear at 200rpm. When milling speed was increased, high kinetic energy with high energy impact was applied on the particles in the vial [5]. High energy impact resulted on transformation from crystalline phase of the mixture to the amorphous phase. Peak of graphite was not being observed at any speed probably because of amorphization of the graphite during MA [4].

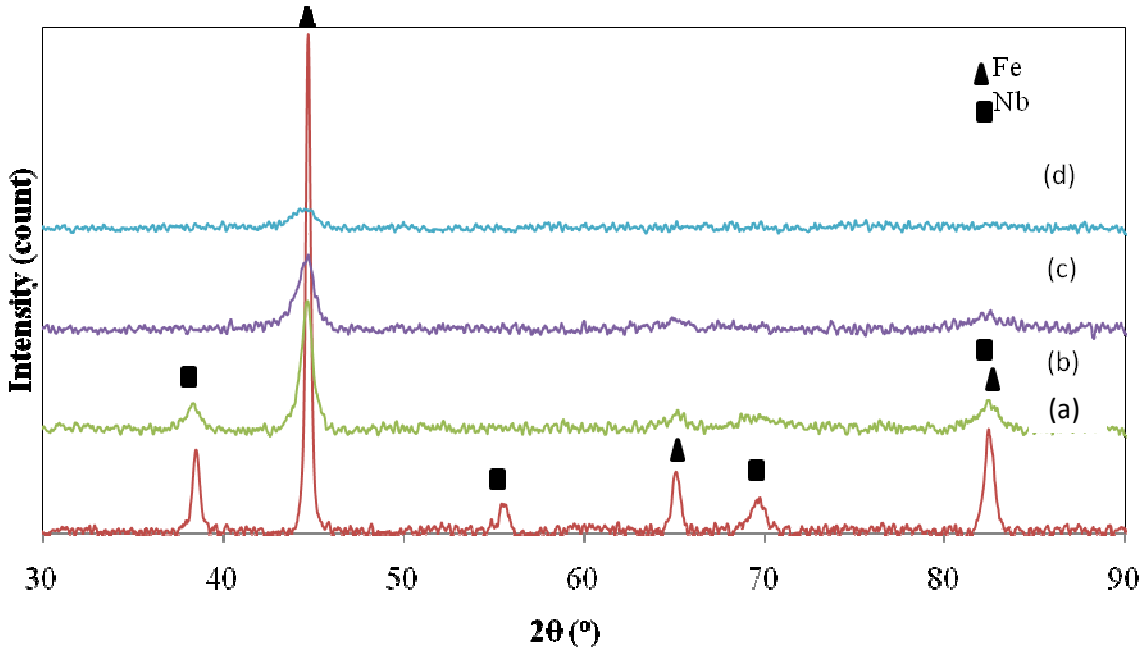


Fig. 1. XRD pattern of Fe-NbC powders as-milled with milling speeds of (a) 100, (b) 200, (c) 300, and (d) 400 rpm.

Fig. 2 shows the XRD pattern of sintered Fe-NbC composite for different milling speed. Result illustrate that crystalline Fe and NbC phase have been observed after sintering at 1300°C which is contrast to the as-milled result that mostly shows amorphous phase. This shows an unstable form of as-milled mixture of Fe-Nb-C which tends to transform to crystalline structure during sintering. High in intensity for peaks at 100rpm were clearly shown compared to the others speed and the intensity markedly decreased as the milling speed was increased. This observation suggests the formation of an amorphous of Fe-NbC that started to take place with increasing milling speed.

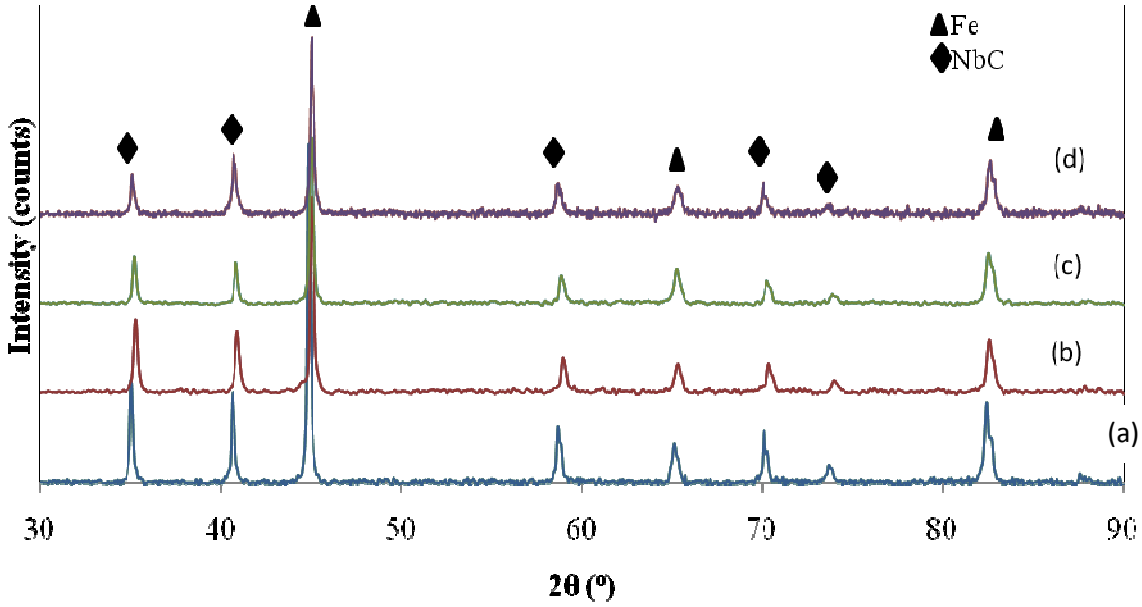


Fig. 2 XRD patterns of sintered Fe-NbC sintered at 1300°C with milling speeds of (a) 100, (b) 200, (c) 300, and (d) 400 rpm.

Composite Properties. Fig. 3 shows density of sintered Fe-NbC against milling speed which shows that the sintered density decreased with the increase in the milling speed. Accumulation of strain energy occurred and hardened the particles. Therefore, higher the milling speeds, harder the particles which made them difficult to be compacted [1, 6, 7]. As a result, more pores were formed during powder compaction. After the compacted body was sintered, there are pores that have not completely removed which contributed to a decrease in density of sintered Fe-NbC composite.

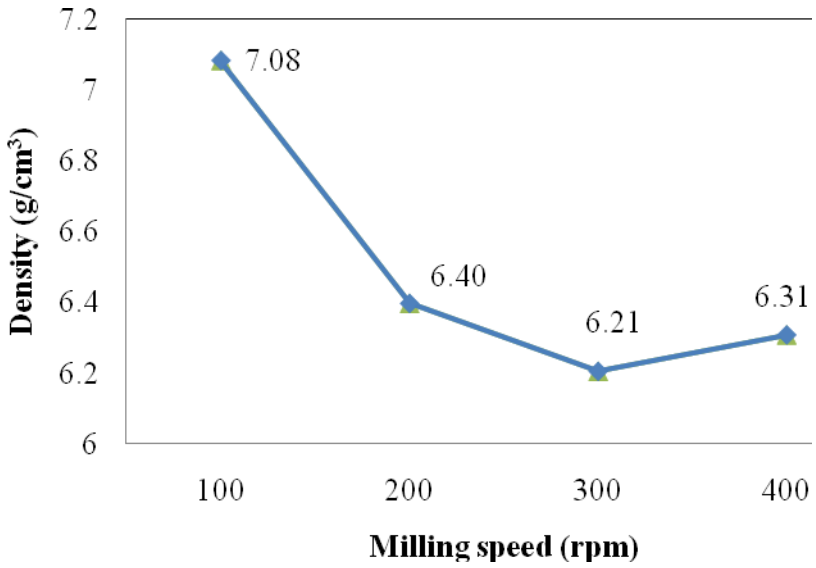


Fig. 3 Sintered density of Fe-Nb-C compact at different milling.

The density of sintered composite MAed at 400rpm was slightly increased. This is due to fracturing of the powder agglomeration due to impact with ball collision [1]. Compaction of fine powder reduced the porosity of the green compact body and consequently increases the density of composite after sintering [2]. Fig. 4 shows descend in particles size at 400rpm due to fracturing of agglomeration which is formed by cold welding during milling.

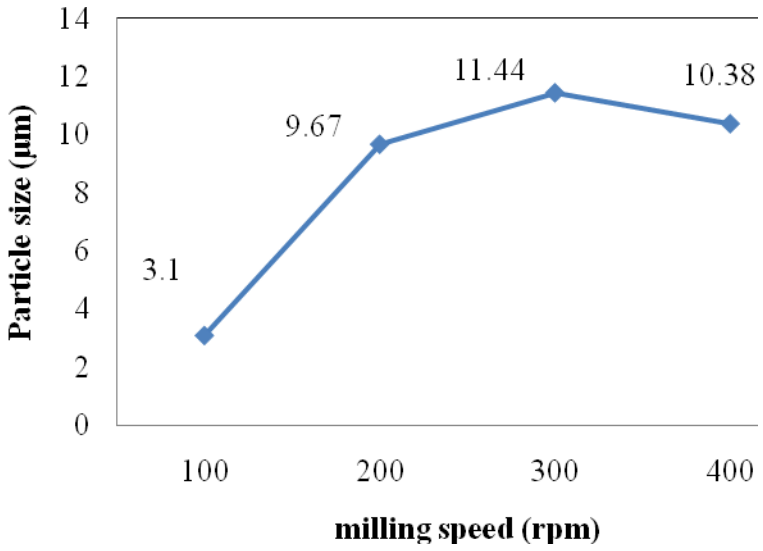


Fig. 4 Particle size of Fe-NbC mixture with different milling speeds.

Higher milling speed led to presence of strain hardened due to the powder collision. Strain hardening aids to increase the hardness of the powder after sintering as shown in the Fig. 5. Another explanation of increase hardness is by the distribution of refinement NbC particles into the iron matrix acting as an obstruction of dislocation [8].

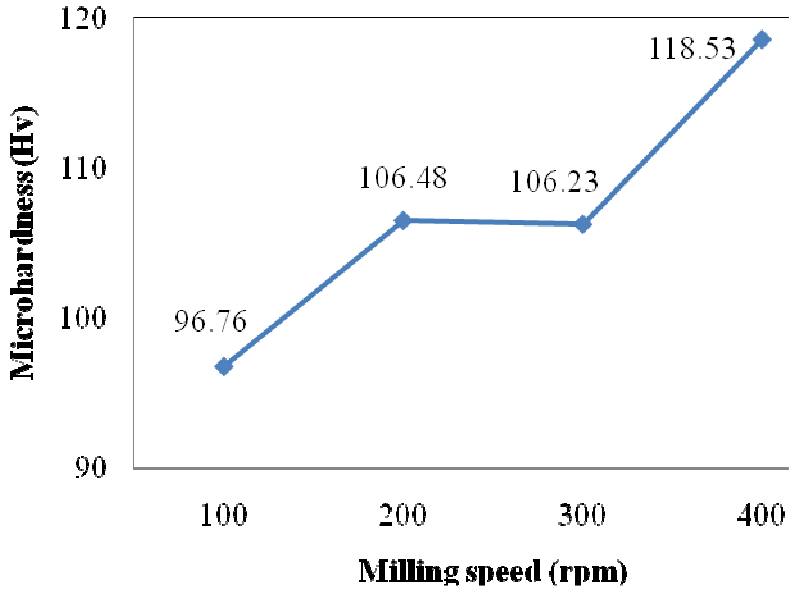


Fig. 5 Hardness properties of sintered Fe-NbC composite with different milling speeds.

Summary

The effect of milling speed on properties of mechanically alloyed prepared Fe-NbC composite has been studied. XRD result shows that the as-milled powder, either with low or high speed, does not formed NbC phase. At low milling speed, higher intensity of Fe and NbC phases were observed which transformed to unstable amorphous phase at higher milling speed. However, high intensity of Fe and NbC phases were shown after sintering at 1300°C for lower milling speed while the intensity decreased as the milling speed was increased. Composite prepared at high milling speed showed low sintered density due to the presence of pores. Consequently, composite hardness increases as the increase in milling speed due to the refinement of NbC reinforcement and strain hardening.

Acknowledgement

This research was supported by USM fellowship from Institute Postgraduate Studies, Universiti Sains Malaysia and also by and Research University Postgraduate Research Student Grant Scheme of Universiti Sains Malaysia (project number: 8033009).

References

[1] C. Suryanarayana, Chapter 4, Mechanical Alloying, Pergamon Materials Series Volume 2, Pergamon, 1999, pp. 49-85.

[2] H. Zuhailawati, H.M. Salihin, Y. Mahani: Journal of Alloys and Compounds 489(2010) 369-374.

[3] P.R. Soni, Mechanical Alloying: Fundamentals and Applications, Cambridge Int Science Publishing, 1999.

[4] T. Lou, B. Ding, X. Gu, G. Li, Z. Hu: Materials Letters 28(1996) 129-132.

[5] N.T. Rochman, S. Kuramoto, R. Fujimoto, H. Sueyoshi: Journal of Materials Processing Technology 138(2003) 41-46.

[6] H. Zuhailawati, S.B. Jamaludin: Journal of Materials Engineering and Performance 18(2009) 1258-1263.

[7] N. Parvin, R. Assadifard, P. Safarzadeh, S. Sheibani, P. Marashi: Materials Science and Engineering: A 492(2008) 134-140.

[8] S. Sivasankaran, K. Sivaprasad, R. Narayanasamy, V.K. Iyer: Journal of Alloys and Compounds 507 236-244.

© (2011) Trans Tech Publications, Switzerland
doi:10.4028/www.scientific.net/KEM.471-472.809

A Wavelet-Based Damage Detection Approach for Acousto-Ultrasonic In-Situ Monitoring Systems

Chin Kian LIEW[1, a] and Martin VEIDT[1, b]

[1]School of Mechanical and Mining Engineering, The University of Queensland, Brisbane, Queensland 4072, Australia

[a]c.liew@uq.edu.au, [b]m.veidt@uq.edu.au

Keywords: Structural health monitoring, guided wave ultrasonics, fibre-reinforced composites, damage detection, wavelet analysis.

Abstract. In this research, an advanced signal processing technique using wavelet analysis has been developed for a guided wave structural health monitoring system. The approach was applied for the detection of delamination in carbon fibre reinforced composites. A monolithic piezoceramic actuator was attached to a laminate plate for wave generation while laser vibrometry was used to facilitate the measurements of the wave response in a sensor network. This database of wave response was then processed using the continuous wavelet transform to obtain the positional frequency content. Transforms between damaged and undamaged states were compared to ascertain the presence of defects by evaluating the total energy of the time-frequency density function. Results show high damage detection indices depending on the location of the sensor and normalisation factor applied while there are positive indications that this methodology can be extended for damage characterisation.

Introduction

Guided waves have gained significant recognition as an effective inspection tool to monitor large areas in short periods of time, particularly for aerospace metal and composite structures [1]. This is possible because guided waves have wavelengths larger than at least one of the characteristic dimensions of the structure and thus energy is constrained within the structural boundaries, allowing wave propagation through large distances [2]. In comparison, bulk waves used in conventional ultrasonic testing is a slow process involving local point inspection through the thickness of the structure. Other benefits of guided waves are their low cost required in actuation and sensing using piezoelectric elements as well as high sensitivity and consistent response to material property changes resulting from the presence of defects [3].

Despite the advantages, application of guided waves poses a major challenge with respect to the interpretation of the complex transient wave response due in part to an infinite number of propagating frequency modes [4]. The situation can be worsened with the presence of noise, dispersion and mode conversion in the wave signals [5]. Dispersion causes phase shifts due to velocity variations in different frequency modes while mode conversion occurs as a result of interaction with defects, discontinuities and boundaries.

To analyse the complex guided waves response, the present research investigated the potential of wavelet analysis. Wavelet analysis has been shown in the past to be a promising signal processing tool in damage detection using structural waves [6]. Wavelets have been specifically applied in damage detection schemes for composites either as a direct diagnostic tool [7] or to extract sensitive parameters prior to damage identification using methods like pattern recognition [8]. The ability of wavelet transforms to present information in the time-frequency domain, remove high-frequency noise and sensitivity to local changes is useful in the analysis of guided waves [9].

In this paper, the continuous wavelet transform (CWT) was used to extract the positional frequency content of the wave response for baseline comparison of local wave properties at multiple levels of detail. The comparison was made by evaluating the conditional moment from the time-frequency density function [10]. This provided a quantitative measure to describe the change in the wavelet transform for defect detection. Previous application of this approach to laminate beams

fabricated with impact damages has demonstrated that the wavelet analysis yielded more sensitive defect detection parameters compared to amplitude and Fourier-based methods [11]. The present work is an extension of this previous study to laminate plates with delaminations.

Material and Method

Experimental Approach. For each quadrant of a composite plate, an equally distributed 7-sensor network labelled S1-S7 was used to monitor a spatial area with guided waves excited from a single bonded Pz27 piezoceramic actuator, as shown in Fig. 1. The piezoceramic element was excited with an 8-cycle 80 kHz sinusoidal Hanning windowed pulse via a SRS DS345 function generator with amplification. To facilitate wave response measurements, a Polytec OFV 303/OFV 3001 laser Doppler vibrometer system was used to acquire signals at the sensor locations in the monitoring network. Data was obtained at a sampling rate of 10 MHz, which was displayed on an oscilloscope and stored on a computer for processing.

The composite plate was manufactured from 9 plies of autoclave cured M18/1/43%/G939 woven carbon fibre epoxy prepreg in the $[45/0_2/45/0/45/0_2/45]$ orientation. Two 600 mm x 600 mm panels were made with an average thickness of 2.05 mm. Three quadrants on each panel were inserted with Teflon films prior to curing in order to simulate delamination damages. 10 mm and 20 mm delamination diameters at three different depths were considered i.e. between 2nd-3rd ply, between 4th-5th ply, and between 6th-7th ply, measured from the sensor surface. Each defect was located at the centre of the sensor network as a preliminary approach to investigate the potential of the wavelet-based monitoring system. The arrangement of the actuator-sensor network on the panel was such that there was minimum interference from boundary reflections, Fig. 1. The undamaged fourth quadrant in each panel was used to obtain baseline signals.

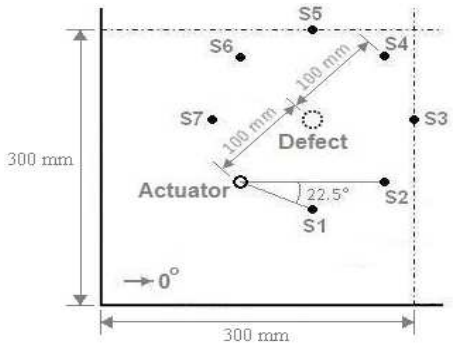


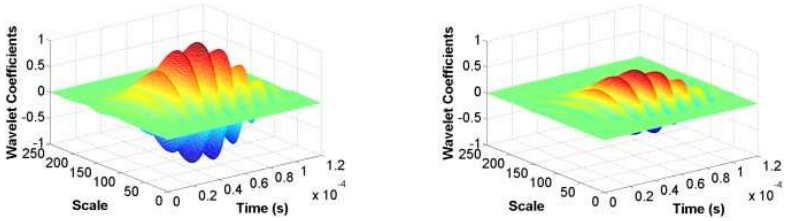
Fig. 1: Actuator-sensor network in a quadrant of a laminate specimen.

Wavelet Analysis Scheme. Signals measured in a quadrant were initially normalised by the maximum amplitude of the Hilbert transform of a reference signal measured close to the actuator to optimise the accuracy of the baseline comparison process. Prior measurements of the wave velocity in the laminate at different directions then allowed the extraction of the first travelling pulse based on the pulse arrival time for each sensor location. Wavelet coefficients, $C(\alpha, \beta)$, was obtained by employing the CWT to resolve the time-based normalised extracted pulse signal, $S(t)$, to the time-frequency domain according to

$$C(\alpha,\beta) = \int_{-\infty}^{+\infty} S(t) \frac{1}{\sqrt{\alpha}} \psi_{db8}\left(\frac{t-\beta}{\alpha}\right) dt \qquad (1)$$

where α and β are the wavelet scale and translation factors, respectively. The convolution process was performed using the 8th Daubechies wavelet, ψ_{db8}, due to its orthogonality and high regularity to locate local properties [9]. A sample plot of wavelet coefficients is shown in Fig. 2 for a sensor measurement in both a damaged region and its equivalent baseline. Cubic spline interpolation was then applied on the wavelet transforms across the actuator-sensor network to increase the resolution

of the results in the spatial area by ten times. A range between the 55th and 160th scales in each wavelet transform was considered for assessing the damage. This translated to a frequency band of 41.67 kHz – 121.21 kHz, which adequately covered the operating range of the excited wave pulse.



(a) (b)

Fig. 2: CWT coefficients for sensor S4 (a) at baseline, and (b) at damaged region with a delamination 20 mm in the 2nd-3rd ply from the measurement surface.

Conditional moments have been identified as sensitive parameters for structural damage identification [12] and hence were applied in the present study. The time-frequency conditional moment can be evaluated as follows

$$M^{i,j} = \int_{-\infty}^{+\infty} \int_{-\infty}^{+\infty} t^i f^j E(t,f)\, dt\, df \tag{3}$$

where i and j are orders of the moments in the time and frequency domains, respectively, while the time-frequency energy density function, $E(t, f) = |C(\alpha, \beta)|^2$, found from the wavelet power spectra. The zeroth-order moment ($i = j = 0$) has been reported to achieve peak sensitivity to damage when compared to higher order moments [10]. Taking this into consideration, the zeroth-order moment was applied as a basis to compare guided waves response measured from undamaged baseline and damaged cases, denoted by b and d, respectively. Subsequently, the comparison was made using the formulation

$$D = \frac{1}{N} \int_{-\infty}^{+\infty} \int_{-\infty}^{+\infty} \left| E^b(t,f) - E^d(t,f) \right| \, dt\, df \tag{4}$$

where D is the damage detection index developed and N is the normalisation factor. D was used to determine the level of change in the wavelet transform from baseline and thus served as a quantitative indicator for the presence of defect. Normalisation factors considered,

$$N^b = \int_{-\infty}^{+\infty} \int_{-\infty}^{+\infty} \left| E^b(t,f) \right| \, dt\, df \quad \text{and} \quad N^d = \int_{-\infty}^{+\infty} \int_{-\infty}^{+\infty} \left| E^d(t,f) \right| \, dt\, df \tag{5}$$

where some interesting differences were found between them in the damage sensitivity results, presented in the next section.

Defect Sensitivity. In Fig. 3 when there is no normalisation ($N = 1$), the damage detection index D is naturally large due to the summation of difference in moments between baseline and damaged cases in the wavelet power spectra. Some potential in damage size characterisation can be observed here as there are consistently larger D values for the 20 mm delamination compared to the 10 mm delamination although no trend can be observed with respect to defect depth. The largest relative differences occur within ±90° from the actuator, peaking at around 30° and 330° from the actuator, while above ±90°, indices are almost insignificant. This is an unexpected result as sensors closer to the actuator should display less sensitivity to the defect as the considered first leading pulse, due to a faster arrival time, would contain less scattered waves from the defect when compared to sensors

located further from the actuator. The consistency of the results in Fig. 3 for both delamination sizes at the different depths in two separate panel specimens dismisses the suggestion of an anomaly.

The difference in zeroth-order moments between baseline and a damaged case is governed by wave scattering due to the presence of defect and experimental variations. Large differences close to the actuator shown in Fig. 3 indicate that the latter has a major influence on the results. It needs to be appreciated that due to restrictions in delamination fabrication, baseline had to be measured from a separate location on the plate. This could cause discrepancies in the measured wave response due to variations in material properties, initial excitation, dispersion, mode conversion, attenuation and boundary reflections, which were difficult parameters to control in experiment. Consequently, uncertainties exist in the damage detection indices. The level of uncertainty is related to the measured wave response, either in the baseline or damaged case, and hence normalisation is important to extract useful information regarding the damage. To investigate the effect of the normalisation factor N on the damage detection index D, two cases are considered, namely, $N = N^b$ and $N = N^d$.

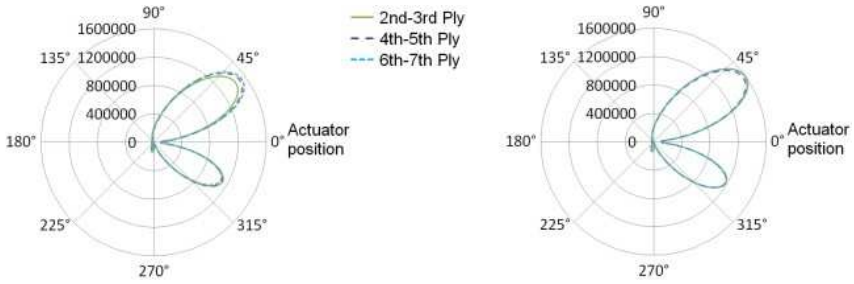


Fig. 3: Damage detection indices with $N = 1$. (a) 10 mm delamination. (b) 20 mm delamination.

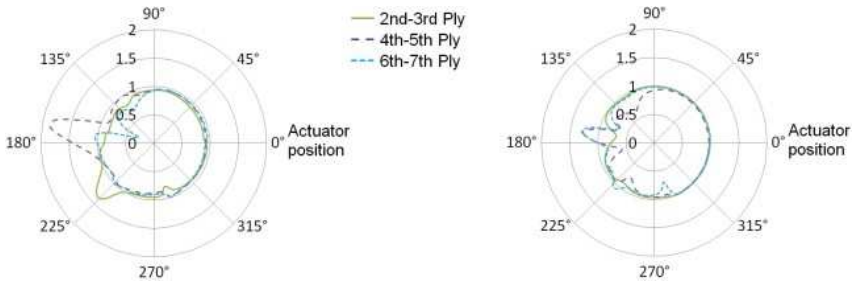


Fig. 4: Damage detection indices with $N = N^b$. (a) 10 mm delamination. (b) 20 mm delamination.

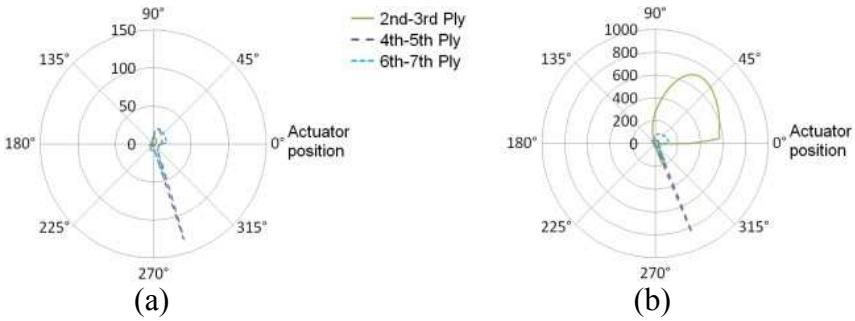


Fig. 5: Damage detection indices with $N = N^d$. (a) 10 mm delamination. (b) 20 mm delamination.

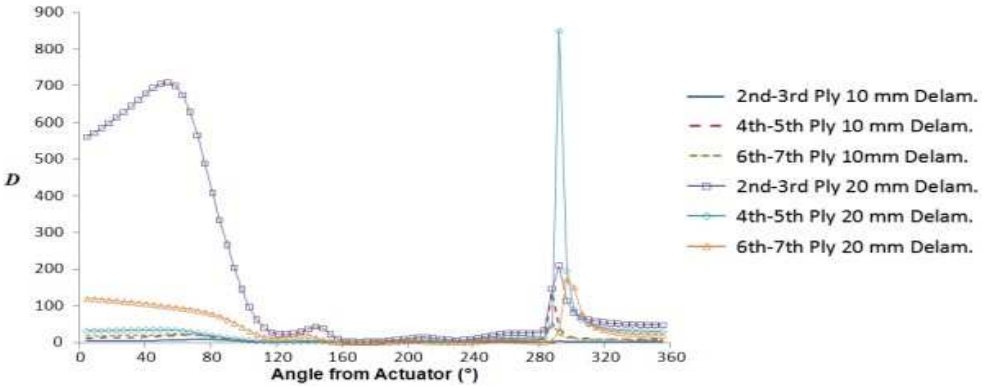


Fig. 6: Damage detection indices with $N = N^d$ in Cartesian space.

When normalised by the pulse response from the baseline signal as shown in Fig. 4, it is clear that the large magnitudes close to the actuator seen in Fig. 3 with no normalisation are no longer present. In comparison, D values for all damage cases are approximately unity at angles less than ±90° from the actuator, conjecturing the proportionality between response uncertainty and the normaliser. Above ±90° from the actuator, differences among damage cases start to emerge with peak changes occurring around the direct opposite angles to the actuator with the exception of the 10 mm delamination at the 2nd-3rd ply. This is an expected result as the proportion of wave scattered from the defect considered in the wavelet analysis scheme is largest around this angle due to the centrally located delamination. For damage characterisation, the change of the index D from unity can serve as an indication of the position of the defect. Accurate quantification however is not possible at this stage due to the presence of inherent uncertainties from experimental variations.

The index D displays a different behaviour when normalised by the pulse response from the damaged case, as shown in Fig. 5. There is no longer any obvious linear relationship between the uncertainty level and the pulse response which is expected as the normalisation is performed by varying responses from different damage cases. Sharp peaks can be observed from the actuator, indicating a region of moment difference which is very sensitive to the defect. The defect size can also be distinguished here by marked difference in peak amplitudes but there remains no strong correlation with the defect depth. The results are replotted on a Cartesian space in Fig. 6 for a better visualisation of the D magnitudes and peaks for different damage cases. In this plot, it is clear that the sharp peaks occur between 280°–300° from the actuator but varying in peak amplitudes for the different damage cases. These peaks can be used as strong indicators for the presence of damage with high probability of detection.

The exception here is the 10 mm delamination at the 2nd-3rd ply case where no peaks can be found in the results. This corresponds to the previous exception in Fig. 4(a), suggesting that there could be an anomaly in the original wave response for this particular damage case. Another possible anomaly is the unusual rise in D value within 90° from the actuator for the 20 mm delamination at the 2nd-3rd ply in Fig. 4. However, this behaviour seems to be consistent with the same damage size at the other two depths although the rises here are relatively much smaller in comparison. If not an anomaly, the rise in D magnitude from the mean can also serve as another indicator of the presence of defect. Further elaborate investigations are required to examine the scattered wave patterns from the damage and interference effects to confirm this as well as to fully explain the occurrence of the sharp peaks.

Conclusions

A wavelet analysis scheme based on conditional moments was investigated for a guided waves damage detection approach using a distributed actuator-sensor network on a composite plate panel. The zeroth-order moment in the time-frequency energy density function exhibited large differences in baseline comparison and thus can function as a sensitive parameter to detect the presence of damages in structures. However, uncertainties caused by experimental variations can be minimised

by normalising the results. It was found that the uncertainty level was linearly related to the baseline signal and approximated to unity when normalised by the baseline. This allowed the detection of the defect when fluctuations from unity were observed. When normalised by the response from the damaged case, sharp peaks of the damage detection indices provided a strong evidence for the presence of defect, which can function to improve the probability of detection and reduce false calls.

The results obtained also showed potential for quantitative damage evaluation. When normalised by the baseline, the largest changes from unity were consistently measured around the direct opposite angles to the actuator where wave scattering from the defect considered in the analysis was also largest for a centrally positioned delamination. These changes were thus related to the defect location and proximity to the sensors. Zeroth-order moment differences without normalisation and with normalisation by the response from the damaged case also provided some indications of defect size characterisation from the amplitudes of the damage detection indices.

This preliminary study established the feasibility of the signal processing approach developed from wavelets and conditional moments for delamination detection in composite panels. For more practical implementations including accurate damage identification, research into the interaction of guided waves on different defects is required to quantify the scattered waves and determine their influences on the wavelet power spectra. The ideal approach to perform these studies is to improve baseline comparison with minimum uncertainties by acquiring signals from the same measurement space in undamaged and later damaged conditions. This can be achieved by considering impact damages or stiffness changes due to reduced thickness or bonded masses. There are also opportunities to combine results from different sensor locations to improve robustness and reliability of the monitoring system as well as numerical simulation studies to assist in quantifying the potential of this wavelet-based damage evaluation approach.

References

[1] W.J. Staszewski, C. Boller and G.R. Tomlinson: *Health Monitoring of Aerospace Structures* (John Wiley & Sons Ltd., UK 2004).

[2] M. Staudenmann: *Structural Waves in Nondestructive Testing* (Institute of Mechanics, ETH Zurich 1995).

[3] A. Raghavan and C.E.S. Cesnik: The Shock and Vibration Digest Vol. 39 (2007), p. 91.

[4] J.L. Rose: *Ultrasonic Waves in Solid Media* (Cambridge University Press, UK 1999).

[5] K.F. Graff: *Wave Motion in Elastic Solids* (Dover Publication Inc., UK 1991).

[6] A.C. Okafor and A. Dutta: Smart Materials and Structures Vol. 9 (2000), p. 906.

[7] C.A. Paget, S. Grondel, K. Levin and C. Delebarre: Smart Materials and Structures Vol. 12 (2003), p. 393.

[8] C.U. Sung, J.H. Oh, C.G. Kim and C.S. Hong: Journal of Intelligent Material Systems and Structures Vol. 11 (2000), p. 180.

[9] I. Daubechies: *Ten Lectures on Wavelets* (CBMS, Vol. 61, SIAM, USA 2006).

[10] W.L. Bayissa and N. Haritos: Proceedings of the 1st International Conference on Structural Condition Assessment, Monitoring and Improvement (Perth, Australia 2005), p. 123.

[11] C.K. Liew and M. Veidt: Proceedings of the 13th Australian International Aerospace Congress (Melbourne, Australia 2009).

[12] P. Loughlin and F. Cakrak: Mech. Systems and Signal Processing Vol. 14 (2000) p. 511.

© (2011) Trans Tech Publications, Switzerland
doi:10.4028/www.scientific.net/KEM.471-472.815

The Influence of Mercerised Kenaf Fibres Reinforced Polylactic Acid Composites on Dynamic Mechanical Analysis

Rosnita A. Talib[1,a], Intan Syafinaz Mohamed Amin Tawakkal[1,b]

and Khalina Abdan[2,c]

[1] Department of Process and Food Engineering, Faculty of Engineering,

Universiti Putra Malaysia 43400 Serdang, Selangor D.E., Malaysia.

[2] Institute of Tropical Forestry and Forest Products (INTROP), Universiti Putra Malaysia

43400 Serdang, Selangor D.E., Malaysia.

[a]rosnita@eng.upm.edu.my, [b]intan85@eng.upm.edu.my, [c]khalina@eng.upm.edu.my

Keywords: DMA; cellulose; polylactic acid; ESEM; thermal stability

Abstract: The potential of using cellulose to reinforce the thermal stability of kenaf derived cellulose (KDC)/polylactic acid (PLA) composite was investigated in this study. The cellulose was derived from kenaf bast fibre which was chemically treated via chlorination and mercerisation processes. The composites with various loadings of cellulose (dry weight basis) ranging from 0% to 60% were produced by melt mixing and compression moulding. Dynamic mechanical properties namely storage modulus (E'), loss modulus (E") and tan δ of the KDC/PLA composites and the commercial PLA were analysed and compared as a function of temperature. ESEM micrographs demonstrated that the mercerisation of kenaf fibres have successfully removed the lignin and hemicellulose, thus producing cellulose which can be observed by its rougher surface and greater size reduction than the raw fibre. The DMA results demonstrated that the storage modulus of 60% KDC/PLA composite is twice higher than the commercial PLA and the rest of the composites within a high temperature range (above 80°C). The glass transition temperatures (T_g) generated from the loss modulus curves exhibit that the peak of the loss modulus was shifted to higher temperature as the percentage of the cellulose loading was increased. These results show a better thermal stability of the composites when incorporated with the cellulose.

Introduction

Nowadays, the utilisation of biodegradable polymers especially in packaging application has become popular due to its environmental benefits and the growing economic pressure to reduce the dependence on petroleum-based resources. These are among the deliberating issues for a successful packaging policies development [1].

Biodegradable polymers possess several advantages such as biodegradability, low gas emission and renewability of the raw material. In packaging application, these polymers offer comparable properties as traditional petroleum-based polymers such as polyethylene (PE), polypropylene (PP), polystyrene (PS) and polyethylene terephthalate (PET) [2]. Among the biodegradable polymers, PLA is one of the most widely used and has received much attention in composite's research and development area [3]. PLA is thermoplastic polyester which comprised of lactic acid monomers that was derived from renewable resource (i.e. corn, sugar beet and wheat). It is produced either via ring opening polymerisation of lactice or by polycondensation of lactic acid monomers [4]. PLA offers good packaging properties such as strength, clarity, glossy, safe and UV stability [2]. Nevertheless, the brittle characteristic of PLA limits the effort to diversity its application in some area. One of the ways to improve the brittleness and rigidity of the PLA is by adding natural fibres as reinforcement

[5-7]. The advantages of combining natural fibre with biodegradable polymer have been well known as environmental friendly and much low cost per volume.

In Malaysia, the government has replaced tobacco with kenaf (*Hibiscus cannabinus* L.) crop since its export is very demanding due to the versatility of the kenaf fibre [8]. For example, long kenaf fibre (bast) has a great potential to be reinforced with polymer due to its own high strength properties [9]. The chemical composition of the kenaf fibres consist of mainly cellulose, hemicelluloses and lignin whereby the amount of cellulose in the bast is more than the core [10]. However, the main drawback in combining these materials is their low compatibility due to the hydrophilic and hydrophobic characteristic of natural fibre and polymer respectively. Thus, modification of the natural fibres via chemical treatment was done in this study since it has been proven to increase the interfacial adhesion between the fibres and the matrix [6, 11-12]. Mercerisation is a chemical process of subjecting natural fibres to an interaction with a relatively strong base aqueous solution to produce sufficient swelling by removing waxy materials, lignin, hemicelluloses and impurities [13]. Cellulose which can be obtained from cotton or derived from natural fibres is widely used as a starting material for the production of regenerated fibres such as rayon, microcryatalline cellulose (MCC) and cellulose derivatives [14]. However, there is only few literature on pure cellulose reinforced with polymer [15].

To date, cellulose has successfully been derived from natural fibre, while the combination of cellulose/polymer composites has possessed good mechanical properties [16]. However, there is still lack of study on the dynamic mechanical properties of cellulose reinforced biodegradable polymer composites. Dynamic Mechanical Analysis (DMA) has become widely used thermal properties test in determining the viscoelastic characteristic of molten polymer system. Thus, the aim of this paper is to study the dynamic mechanical properties of KDC/PLA composites so as to obtain better material performance compared to commercial PLA.

Materials and Method

Materials. Commercial PLA 2002D resin was purchased from NatureWorks LLC, USA. Kenaf bast fibre was supplied by the Institute of Tropical Forestry and Forest Products (INTROP), Malaysia. Reagent grade sodium hydroxide (NaOH), acetic acid (CH_3COOH) and sodium chlorite ($NaClO_2$) of 80% purity were purchased from Fisher Chemicals Sdn. Bhd., Malaysia.

The Preparation of the KDC and Composites. The preparation of the KDC involves two steps. The first step was the production of holocellulose via chlorination or bleaching process. The second step involved the conversion of the holocellulose through mercerization process. The details of the procedure have been reported elsewhere [17]. Prior to the mixing, KDC was dried in an oven at 105°C for 12 hours to remove the moisture content. The dried KDC was ground into smaller size and passed through a 500μm sieve to obtain a uniform size. KDC/PLA composites with various percentages of KDC loadings (0-60%) were prepared at 170°C and 30 min via internal mixer. Meanwhile, the moulded composite sheet was produced at 160°C for 10 min via hot press machine.

ESEM and DMA. The characteristic of kenaf fibre and cellulose was observed and analyzed via Environmental Scanning Electron Microscope (ESEM) Philips XL30, Holland under acceleration of 20 kV. Each sample was coated with gold for 30 min to improve its surface conductivity. Dynamic mechanical analysis (DMA) measurement was carried out via TA Q800 Dynamic Analyzer, UK using dual cantilever mode. The samples were subjected to an oscillatory deformation with a frequency of 1 Hz and heated from room temperature 25°C-100°C under controlled scan rates of 5°C/min.

Results and Discussion

ESEM. The ESEM micrographs of kenaf fibre and cellulose are depicted in Figure 1. Generally, the major differences between kenaf fibres and cellulose micrographs are the diameter size of the fibres and the surface topography. The cellulose represents almost triple times smaller in diameter as compared to the kenaf fibre with approximately 71% reduction. This is attributed due to the fibre fibrillation prior to mercerisation whereby the fibre bundle was broken down into a smaller fibre and thus, increases the aspect ratio [18]. Besides, the kenaf fibre demonstrated smoother surface than the cellulose, and this was due to the presence of lignin and waxy substances. In general, lignin, pectin and waxy substances covering the surface of the natural fibre cell wall would be removed after an alkali treatment [19]. The rough surface topography of cellulose was probably attributed to the removal of the interfibrillar materials which comprised of hemicellulose and lignin [20-21]. This is in line with the finding which derived by FTIR as in our previous study [17]. In a (A) n, it could be observed tl (B) e microfibrils were almost (C) led on the surface of the cellulose and thus, contributed to the roughness matter.

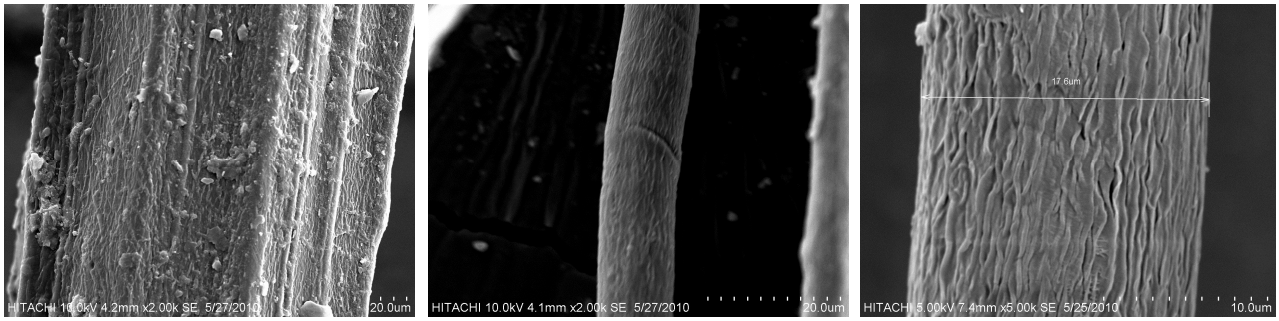


Fig. 1: The ESEM micrographs of the (A) kenaf fibre at 2000x magnification (B) cellulose at 2000x magnification (C) cellulose at 5000x magnification.

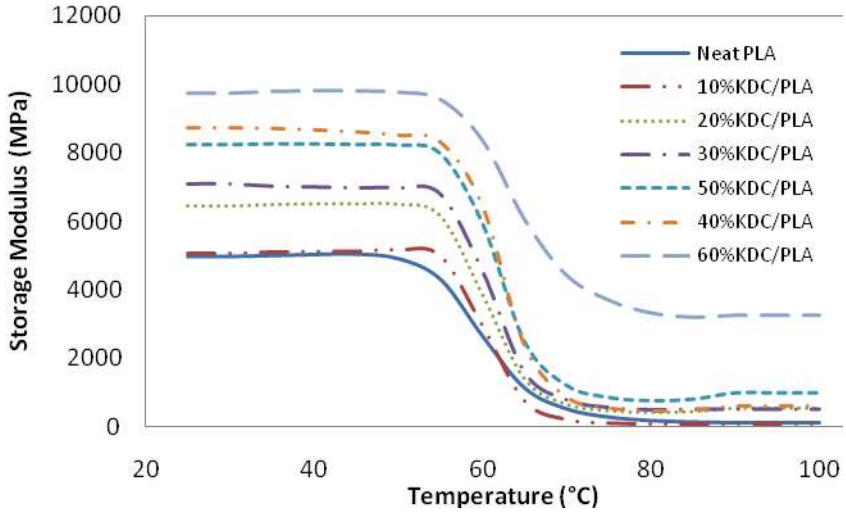
DMA. The temperature dependence of the storage modulus, loss modulus and tan δ of the neat PLA and KDC/PLA composites were presented in Fig 2. Fig 2A demonstrates that the presence of KDC increased the storage modulus of PLA. This might be due to the stiffness characteristic of the reinforcement that allows greater degree of stress transfer at the interface [7]. Further increase in the storage modulus was also observed with increasing KDC loading. From Fig. 2A, both the storage modulus of neat PLA and KDC/PLA composites were decreased with increasing temperature. A significant fall in the storage modulus was noticed at temperature of 50-70°C, which also corresponds to the glass transition region. The reduction in storage modulus as a function of temperature is related to the increased in the viscosity and polymer chain mobility or the softening effect of the matrix [22]. Interestingly, at higher temperature (above 80°C), the 60% KDC/PLA composite demonstrated the highest storage modulus. This is due to the restriction in chain mobility of the matrix with the composite remains stiffer and the matrix flow is restricted. According to Soom and co-workers [23], the thermal properties of the cellulose were reported to be resistant to heat than the holocellulose and native fibre. This is because the cellulose is thermally stable and thus, more heat energy is required to break down its crystalline structure and bonds. The presence of reinforcement and/or crystalline structure may also act as a physical crosslink, deacreasing mobility of amorphous regions and increasing the composite stiffness [24].

As seen in Fig. 2B, the α relaxation was observed and this relaxation is associated with the chain segment mobility in the crystalline phase. The effect of polymer chain mobility could be clearly explained based on the glass transition temperature, T_g that had been obtained from the peak of the loss modulus curves (Fig. 2B) [6]. The incorporation of the KDC into PLA matrix has enhanced the T_g value whereby the loss modulus peak was shifted to higher temperatures with increasing KDC. By incorporating filler into the matrix there will be some reduction in chain mobility and thus, higher T_g were obtained [7]. Besides, this is also attributed due to the segmental immobilisation of

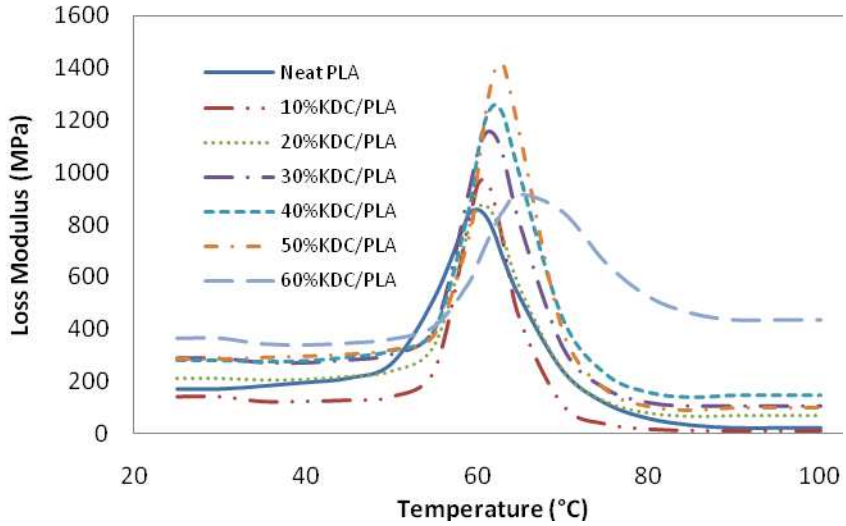
the matrix chain at the filler surface [24], whereby the rough surface topography of the cellulose might contribute to a good mechanical interlocking between the cellulose and PLA matrix. As seen in Fig 2B, it was found that the composites exhibit higher loss modulus at the transition region except for 60% KDC/PLA composite. This is probably due to the presence of a genuine interface as suggested by John and co-worker [25].

The ratio of the loss modulus to storage modulus is measured as the tan δ or damping properties. The variation of the tan δ as a function of temperature is represented in Fig. 2C. Tan δ is an indicator of how efficient a material loses energy to molecular rearrangements and internal friction [26]. The damping peak of composites above 50% KDC loading showed a decrease magnitude in comparison to neat PLA. Whereas, the tan δ increased sharply at low KDC loading. This might be attributed due to the restriction of the molecular movement of polymer chain at higher KDC loading. By adding more KDC, the molecular mobility of the matrix decreased and the mechanical loss is reduced. This is because less energy is required to overcome the frictional forces between the molecular chain. Besides, a good interface between the filler and matrix could bear greater stress and less energy disipation [26-27].

(A)



(B)



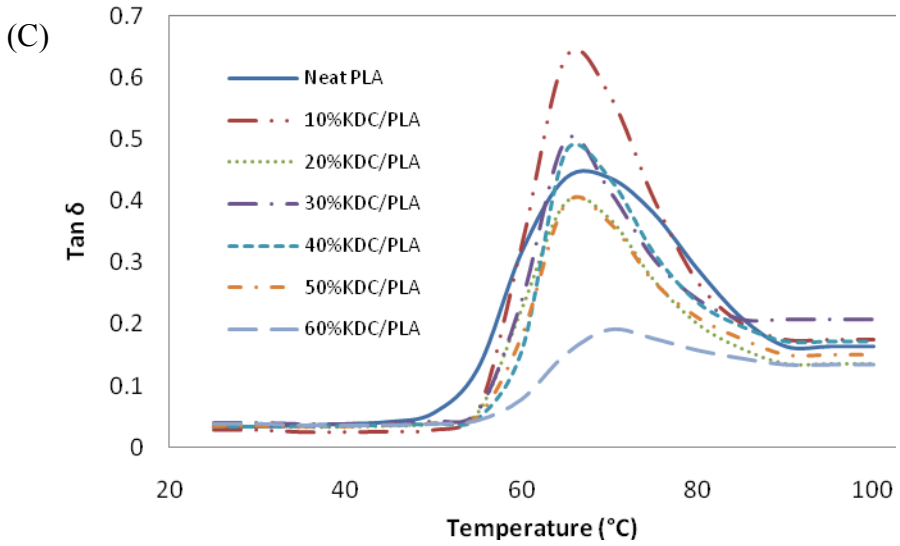


Fig. 2: Dynamic mechanical analysis of the KDC/PLA composites and neat PLA over a wide temperature range. (A) Storage modulus, (B) Loss modulus and (C) Tan delta.

Summary

In this paper, the significant morphological differences between kenaf fibre and cellulose were observed via ESEM. The cellulose has rougher surface and smaller diameter than the kenaf fibre. These differences are believed due to the removal of cementing materials namely lignin and hemicellulose. DMA results of the composites demonstrated higher storage modulus at higher KDC loading. Interestingly, the 60% KDC/PLA composite can withstand high temperatures and twice higher than the storage modulus of commercial PLA. Higher T_g value of the composites as compared to the neat PLA exhibited the effectiveness of the mercerised fibre as a reinforcing agent and consequently enhanced the thermal stability of the composites.

Acknowledgements

The authors acknowledge the financial support from Universiti Putra Malaysia, Malaysia under grant (grant no.: 91491) and would like to thank Institute of Tropical Forestry and Forest Products (INTROP), Malaysia for the supply of kenaf fibres.

References

[1] Information on: http://www.ids-publishing.com/publishing/europe/EUROPEN/Packaging_Industry_Trade_Organization/13_0/g_supplier.html

[2] R. Auras, B. Harte, and S. Selke: Macromolecular Bioscience Vol. 4 (2004), p. 835-864.

[3] P.R. Gruber: Industrial Ecology Vol. 7 (2003), p. 209-213.

[4] D.E. Henton, P. Gruber, J. Lunt and J. Randall, in: *Natural Fibers, Biopolymers and Biocomposites,* edited by A. K. Mohanty, M. Misra and L.T. Drzal CRC Press, London (2005), p. 528-568.

[5] K. Oksman, M. Skrifvars and J.F. Selin: Composites Science and Technology Vol. 63 (2003), p. 1317-1324.

[6] M.S. Huda, L.T. Drzal, A.K. Mohanty and M. Misra: Composites Science and Technology Vol. 68 (2008), p. 424-432.

[7] A.K. Bledzki, A. Jaszkiewicz and D. Scherzer: Composites Part A: Applied Science and Manufacturing Vol. 40 (2009), p. 404-412.

[8] Information on: http://www.introp.upm.edu.my/PDF/intropica1.pdf

[9] I.S. Aji, S.M. Sapuan, E.S Zainudin and K. Abdan: International Journal of Mechanical and Materials Engineering Vol. 4 (2009), p. 239-248.

[10] A. Ashori, J. Harun, W.D. Raverty and M.N.M. Yusoff: Polymer-Plastics Technology and Engineering Vol. 45 (2006), p. 131 - 134.

[11] T. Nishino, K. Hirao, M. Kotera, K. Nakamae and H. Inagaki: Composites Science and Technology Vol. 63 (2003), p. 1281-1286.

[12] N.A. Ibrahim, W.M.Z. Wan Yunus, M. Osman, K. Abdan and A. Hadithon: Reinforced Plastic and Composites Vol. 29 (2010), p. 1099-1111.

[13] K. Goda, M.S. Sreekala, A. Gomes, T. Kaji and J. Ohgi: Composites Part A: Applied Science and Manufacturing Vol. 37 (2006), p. 2213-2220.

[14] H. Sixta: *Handbook of Pulp* (Wiley-VCH Verlag GMBbH, & CoKGaA, Germany 2006).

[15] B. Tajeddin, R.A. Rahman and L. C. Abdullah: American-Eurasian Journal of Agriculture & Environment Sciences Vol. 5 (2009), p. 777-785.

[16] M. Khalid, C.T. Ratnam, T.G. Chuah, S. Ali and T.S.Y. Chong: Materials and Design Vol. 29 (2008), p. 173-178.

[17] I.S.M.A. Tawakkal, R.A. Talib, A. Khalina, N.L. Chin and M.N. Ibrahim: Asian Journal of Chemistry Vol. 22 (2010), p. 6652-6662.

[18] K. Joseph and S. Thomas: Polymer Vol. 37(1996), p. 5139-5149.

[19] L.Y. Mwaikambo and M.P. Ansell in: The Effect of Chemical Treatment on the Properties of Hemp, Sisal, Jute and Kapok Fibres for Composite Reinforcement, 2nd International Wood and Natural Fibre Composites Symposium, Kassel/Germany, June 28-29 (1999), p. 12-1-12-6.

[20] L. Liu, M.L. Fishman, K.B. Hicks and C.K. Liu: Agricultural and Food Chemistry Vol. 53 (2005), p. 9017-9022.

[21] N. Sgriccia, M.C. Hawley and M. Misra: 2008. Composites Part A: Applied Science and Manufacturing Vol. 39(2008), p. 1632-1637.

[22] M.S. Huda, L.T. Drzal, M. Misra and A.K. Mohanty: Applied Polymer Science Vol. 102(2008), p. 4856-4869.

[23] R.M. Soom, W.H. Wan Hassan, A.G. MD Top and K. Hassan: Oil Palm Research Vol. 18 (2006), p. 272-277.

[24] S. Mohanty, S.K. Verma and S.K. Nayak: Composites Science and Technology Vol. 66 (2006), p. 538-547.

[25] B. John, K.T. Varughese, Z. Oommen, P. Pötschke and S. Thomas: Applied Polymer Science Vol. 87 (2003), p. 2083-2099.

[26] L.E. Nielsen and R.F. Landel: *Mechanical Properties of Polymers and Composites* Marcel Dekker Inc., New York (1994).

[27] T. Yu, J. Ren, S. Li, H. Yuan and Y. Li: Composites Part A: Applied Science and Manufacturing 41(2010), p. 499-505.

© (2011) Trans Tech Publications, Switzerland
doi:10.4028/www.scientific.net/KEM.471-472.821

Investigation of Hardness of Short Abaca (*Musa textile Nee*) Fibre-Reinforced High Impact Polystyrene (HIPS) Composites by Response Surface Methodology

E.H. Agung[1,a], S.M. Sapuan[2,b], M.M. Hamdan[3,c], H.M.D.K. Zaman[4,d] and U. Mustofa[5,e]

[1,2]Department of Mechanical and Manufacturing Engineering, 43400 UPM Serdang, Selangor, Malaysia

[3]Faculty of Engineering, Universiti Pertahanan Nasional Malaysia, Kem Sungai Besi 57000, Kuala Lumpur, Malaysia

[4]Radiation Technology, Malaysia Nuclear Agency, Bangi, 43000 Kajang, Malaysia

[5]Faculty of Engineering, Universitas Malahayati, Kemiling, 35127 Bandar Lampung, Indonesia

[a]efriyo@yahoo.com, [b]sapuan@eng.upm.edu.my, [c]megat@upnm.edu.my, [d]khairul@NuclearMalaysia.gov.my, [e]alfha_usman@yahoo.com

Keywords: High impact polystyrene (HIPS), Abaca fibre, Maelic anhydride (MAH), Impact modifier, Response surface methodology.

Abstract. In this paper, the hardness property of abaca (*Musa textile Nee*) fibre reinforced high impact polystyrene (HIPS) composites with maelic anhydride (MAH) used as coupling agent and styrene butadiene styrene (SBS) copolymer rubber (Cyclo resin) used as impact modifier was investigated using response surface methodology.. The composites were initially fabricated using a rolling machine and finally using a hot press machine to obtain a desired thickness. These samples were then tested for Brinell hardness test. A statistical approach of response surface methodology was used to obtain the interaction between various compositions mentioned above for abaca fibre reinforced HIPS composites. The BHN (Brinell hardness number) was analyzed using response surface methodology (Box Behnken method).

Introduction

Abaca (*Musa textile Nee*) is the family of banana but not bearing fruits. Abaca (Manila hemp) is the most economically important member of the genus *Musa* plant, which from pseudo-stems; yield a strong and resilient fibre. Abaca fibre was widely used in the production of handicrafts, manufacture of marine ropes and in the fishing industry due to its resistance to humidity and salty water [1]. Generally cellulosic fibres were obtained from the pseudo-stems of banana plant (*Musa Sepientum*) and abaca plant (*Musa textile Nee*) in the form of bast fibre [2]. The fibers are coarse and very long (up to 15 feet). It is a strong, durable, and flexible fibre. This characteristic is generated for abaca fibre properties. In tropical countries, agricultural plants like banana plants are available in abundance. Banana fibre is a waste product of banana cultivation and can be obtained for handcraft and home industrial purposes. However, unlike ordinary banana, abaca is cultivated for the purpose of obtaining fibres. The improvement of mechanical properties of fibres can be achieved by treatment and coupling agents and in this study, impact modifier and coupling agent (maelic anhydride (MAH)) are used in composites and the statistical analysis of hardness property at various composite compositions were carried out.

Experimental

Materials. Abaca(*Musa textile Nee*) fibres are obtained from Ridaka Hand Craft, Pekalongan, Central Java, Indonesia. High impact polystyrene (HIPS) is obtained from Petrochemical (M) Sdn. Bhd, Malaysia. Maleic anhydride (MAH) is supplied by Sigma Aldrich Malaysia (M) Sdn. Bhd, Malaysia.

Sample Preparation. The abaca fibres were dried under the sun light between 27^0 - 30^0C for four days. The dry abaca fibres were cut into 2 – 3 mm by means of an electronic cutting machine. The matrix, high impact polystyrene (HIPS), maelic anhydried (MAH), cyclo resin and abaca fibres were measured based on the design of experiment and they are classified into three levels (high [+], intermediate [0], and low [-]). The processing of abaca fibre reinforced HIPS composites were accomplished using a rolling machine as shown in Figure 2. The working temperature of the rolling machine was kept approximately 200^0 C. The composites were produced in the rolling machine by manually dropping the matrix and fibre in the rolling machine at very slow rate. The speed of first cylinder roll was on 6.0 meter/minute and the second cylinder roll was on 10.8 meter/minute. The process was continued until all the materials were well mixed. Sheets of abaca fibre reinforced HIPS composites produced have the thickness of an average of 1 mm.



Fig. 2 The production of abaca fibre reinforced HIPS composites by rolling machine

The composite materials produced were then crushed and pressed to thicknesses of 3 mm using hot press machine. Standard specimens with load 17.5 kg were prepared for the determination of Brinell hardness number (BHN) properties.

The Brinell Hardness Number. The Brinell hardness number uses a desk top machine to press a 10mm diameter, hardened steel ball into the surface of the test specimen [3]. The load is applied for 10 to 15 seconds. The hardness is calculated by dividing the load by the area of the curved surface of the indention, (the area of a hemispherical surface is arrived at by multiplying the square of the diameter by 3.14159 and then dividing by 2). The BHN (Brinell hardness number) is calculated according to equation:

$$\text{BHN} = \frac{P}{(D-(D^2-d^2)^{\frac{1}{2}})\,\pi\, D/2} \quad (1)$$

Where

BHN: the Brinell hardness number
P : the imposed load in kg
D : the diameter of the spherical indenter in mm
d : diameter of the resulting indenter impression in mm

Two diameters of impression at right angles are measured, and the mean diameter is used as a basis for calculating the Brinell hardness number (BHN), which is done using the conversion table given in the standard.

Design of Experiments. Response surface methodology designs the sample into three levels [4]. This research uses the Box-Behnken design (BBD) to analyze the Brinell hardness number (BHN) of abaca fibre reinforced HIPS composites. The responses of three factors are to be determined and these three factors are designated as X_1 (abaca fibre), X_2 (maelic anhydride (MAH)) and X_3 (impact modifier (IM)), respectively as shown in Table 3. The BBD consists of a set of points lying at the midpoint of each edge and the replicated center point of the multidimensional cube [5]. All experiments were performed in triplicate and the average values of Brinell hardness test were taken as responses.

Table 3. Levels and code of variables for Box Behnken design

Variables	Symbol		Coded Levels		
	Uncoded	Coded	-1	0	+1
Abaca	X_1	x_1	30	40	50
MAH	X_2	x_2	1	2	3
IM	X_3	x_3	4	5	6

For predicting the optimal point, a second-order polynomial model was fitted to correlate relationship between independent variables and responses (Brinell hardness test), the equation is:

$$y = \beta_0 + \beta_1\chi_1 + \beta_2\chi_2 + \beta_3\chi_3 + \beta_{11}\chi_1^2 + \beta_{22}\chi_2^2 + \beta_{33}\chi_3^2 + \beta_{12}\chi_1\chi_2 + \beta_{13}\chi_1\chi_3 + \beta_{23}\chi_2\chi_3 + \varepsilon \quad (2)$$

where y is the predicted response; β_0 is model constant; x_1, x_2 and x_3 are independent variables; β_1, β_2, and β_3 are linear coefficients; β_{12}, β_{13} and β_{23} are cross-product coefficients; and β_{11}, β_{22} and β_{33} are the quadratic coefficients. The quality of fit of the polynomial model equation was expressed by the coefficient of determination R^2.

Brinell Hardness Number (BHN) of Abaca Fibre Reinforced High Impact Polystyrene (HIPS) Composites

Brinell hardness number (BHN) is the response that was measured at three levels and three factors in abaca fibre reinforced HIPS composites. A three-factor, three-coded level BBD was used to determine the response, i.e. the hardness property for different percentages of abaca fibres, maelic anhydride (MAH) and impact modifier (IM). Abaca fibres, MAH and IM were independent variables used in this study to predict the response (BHN). The experiments were carried out based on the design of experiment given in Table 4.

Table 4. The BBD matrix employed for three independent variables with observed values

Run	Factor 1 Abaca (A) Wt %	Factor 2 MAH (B) Wt %	Factor 3 IM (C) Wt %	Response BRINELL HARDNESS BHN (Kg/mm^2)
1	50	1	5	10.68
2	30	1	5	8.92
3	40	2	5	10.82
4	40	1	4	10.23
5	30	2	6	13.18
6	40	2	5	10.68
7	40	2	5	10.51
8	50	2	6	12.34
9	30	3	5	9.05
10	40	2	5	10.62
11	40	2	5	10.54
12	40	3	6	10.93
13	50	3	5	11.02
14	30	2	4	9.02
15	40	3	4	10.18
16	50	2	4	13.83
17	40	1	6	11.82

In order to ensure the adequacy of the model for abaca fibre reinforced HIPS composites, test for significance on individual model coefficients and test for lack-of-fit need to be performed. The ANOVA in Table 5 describes the response surface of quadratic model for Brinell hardness number (BHN) of abaca fibre reinforced HIPS composites.

Table 5. ANOVA table (partial sum of squares) for quadratic model (response: BHN)

Source	Sum of Squares	DF	Mean Square	F Value	p-value	
Model	28.65	9	3.18	67.42	<0.0001	*significant*
A	7.41	1	7.41	157.00	<0.0001	*significant*
B	0.03	1	0.03	0.58	0.4694	
C	3.14	1	3.14	66.46	<0.0001	*significant*
A^2	0.36	1	0.36	7.66	0.0278	
B^2	4.29	1	4.29	90.90	<0.0001	*significant*
C^2	5.72	1	5.72	121.16	<0.0001	*significant*
AB	0.01	1	0.01	0.23	0.6437	
AC	7.98	1	7.98	169.06	<0.0001	*significant*
BC	0.18	1	0.18	3.74	0.0945	
Residual	0.33	7	0.05			
Lack of Fit	0.27	3	0.09	5.88	0.06	*not significant*
Pure Error	0.06	4	0.02			
Cor Total	28.98	16				
				R-Squared		
Std. Dev.	0.22			Adj R-Squared	0.9886	
Mean	10.85			Pred R-Squared	0.9739	
				Adeq Precision	0.8480	
					29.9900	

The value of "p-value" in Table 5 for the model is less than 0.05, which indicate that the model is significant. The conditions of the interaction of the factors are as desired, indicating that the terms in the model has a significant effect on the response. For Brinell hardness number (BHN) of abaca fibre reinforced HIPS composites, the ratios of abaca fibre (A), impact modifier (C), square of abaca fibre (A^2), maleic anhydride (B^2), impact modifier (C^2), and also the abaca fibre to impact modifier (AC) are significant. The ANOVA analysis indicates a linear relationship between the main effects of abaca fibre wt% maleic anhydride wt%, and impact modifier wt%, and the quadratic relationships with factors of abaca fibre wt%, maelic anhydride wt%, and impact modifier wt% and interaction between the three factors. Independent variables and their levels for the Box-Behnken design used in this study are as shown in Table 3. Using the relationship in Table 3, the actual levels of variables for the experiment in the design matrix were calculated and experimental results obtained are given in Table 4. The final mathematical equations based on coded factors given in equations 3 is obtained after the analysis of variance (ANOVA) and they give the levels of weight percentages of abaca fibres, maelic anhydride (MAH) and impact modifier (IM) as determined by Design-expert software.For Brinell hardness test, model equation is:

$$y = 10.63 + 0.96X_1 - 0.059X_2 + 0.63X_3 + 0.29X_1^2 - 1.01X_2^2 + 1.17X_3^2 + 0.052X_1X_2 - 1.41X_1X_3 - 0.21X_2X_3 \quad (3)$$

This model has been used to predict the Brinell hardness test of abaca fibre reinforced HIPS composites within the limits of the experiment. Figure 3 shows the relationship between the actual (experiments) and predicted values of abaca fibre reinforced HIPS composites for Brinell hardness number (BHN) response.

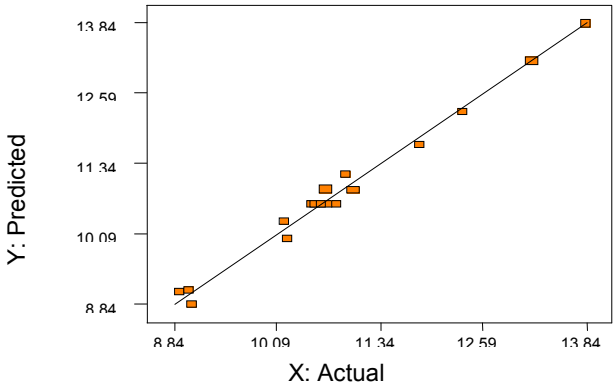


Fig. 3 Relation between experimental and predicted BHN (kg/mm^2)

It is seen in Figure 3 that the developed models are adequate because the residuals for the prediction of the response are minimum, since the residuals tend to be close to the diagonal line. The R^2 value for Brinell hardness test is 0.9886 and the value is close to 1, which is desirable. The predicted R^2 of Brinell hardness number of abaca fibre reinforced HIPS composites are in agreement with the adjusted R^2 (see Table 5). The adequate precision measures the signal (response) to noise (deviation) ratio. A noise ratio of precision greater than 4 is desirable. In this research the ratio is found to be > 29 (see Table 5) which indicates an adequate signal of the model to be significant for measuring the Brinell hardness number (BHN) of abaca fibre reinforced HIPS composite. The results are that the values of Brinell hardness number (BHN) are strongly affected by the variables selected in the study. The main effects of X_1 (abaca fibre) and X_2 (MAH), represent the average results of changing 1 (one) variable at a time from its low level to its high level. The interaction terms (X_1X_2, X_1X_3, X_2X_3) show how the Brinell hardness number (BHN) of abaca fibre reinforced HIPS composites change when 2 (two) variables simultaneously changed. The positive coefficients for all 3 (three) independent variables indicate a favorable effect on Brinell hardness number (BHN). The negative coefficients among 3 (three) independent variables indicate a partitioning on favorable effect on Brinell hardness number (BHN).

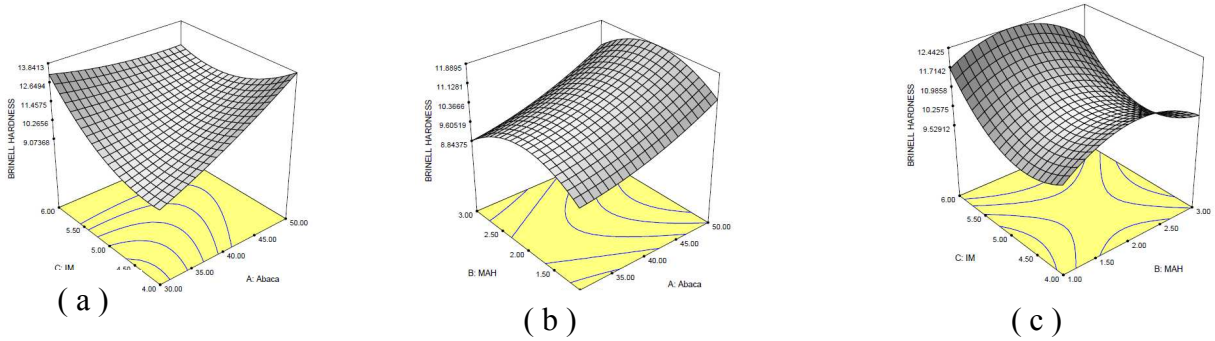
Table 6. Regression coefficients of approximate polynomials for BHN in experimental design

Regression Coefficients	Brinell hardness test (BHN)
Main Effects	
β_1	0.5576
β_2	4.8192
β_3	- 4.9588
Interaction Effects	
β_{12}	0.0053
β_{13}	- 0.1413
β_{23}	- 0.2100
R^2	0.9886
"p-value" < 0.05 indicate model terms are significant. R^2 : determination coefficient obtained by ANOVA	

Table 6 reviewed characteristic of Brinell hardness number (BHN) of HIPS reinforced with abaca fibres composites. The negative coefficients for the main effect (β_3) indicate that impact modifier represented unfavorable effect for abaca fiber reinforced HIPS composites within the range of the research plotted. In this study, the main effect of abaca fibre represented favorable results of Brinell hardness number (BHN). Among the 3 (three) independent variables of Brinell hardness number (BHN), the coefficient value for X_1 (β_1= 0.5576 and p-value < 0.05) indicates that this variable is significant in the prediction of abaca fibre reinforced HIPS composites. The negative coefficient value is for X_3(β_3= -4.9588 and p-value < 0.05), indicates that this variable is significant by partitioning in the prediction of abaca fibre reinforced HIPS composites. In this significant terms,

the negative value of interactions between abaca fibre and impact modifier (β_{13} = -0.1413 and p-value < 0.05) indicate an unfavorable effect. The relationship between dependent and independent variables of Brinell hardness number (BHN) was studied in experimental design shown in Table 6 and the effect of the response variables is demonstrated using model in equations 3. Through 3 D plots, the effects of variables with their interaction on abaca fibres reinforced HIPS composites at one fixed level of variable (medium level) are shown in Figures 4.

Figure 4a show that at any given abaca fibre wt%, the Brinell hardness number (BHN) of abaca fibre reinforced HIPS composites increasing with the increase of coupling agent (MAH). The curve for this condition is curvilinear. The yield of Brinell hardness number (BHN) response was affected by interaction between abaca fibre (β_1) and impact modifier (β_3). Figure 4b and 4c describe the graphs of Brinell hardness number (BHN) yields for 5 wt% of impact modifier and for 40 wt% abaca fibres. Based on the ANOVA analysis, the Brinell hardness number (BHN) was not influenced by contribution of increased abaca fibre and coupling agent (maleic anhydride (MAH)) significantly and also interaction between impact modifier and coupling agent (maleic anhydride (MAH).



(a) (b) (c)

Fig 4a,b,c Response surface 3D plots showing the effect of abaca fibre, MAH and impact modifier for BHN (kg/mm ^{2})

Summary

Based on the ANOVA analysis, the Brinell hardness number (BHN) was not influenced by contribution of increased abaca fibre and coupling agent **(**maleic anhydride (MAH)) significantly and also interaction between impact modifier and coupling agent **(**maleic anhydride (MAH). The ANOVA analysis also described that abaca fibre that represented by the coefficient X_1 (β_1= 0.5576 and p-value < 0.05) influence the composites significantly. The interaction between abaca fibre and impact modifier, represented by the negative coefficient X_{13} (β_{13} = -0.1413 and p-value < 0.05) was indicated unfavorable effect and partitioning influence in the abaca fibre reinforced HIPS composites. The addition of abaca fibres and impact modifier has less potency for Brinell hardness number (BHN) of the composites.

References

[1] Sharrock, S. Diversity in the genus *Musa*. The banana and its relatives. In: INIBAP. Networking Banana and Plantain. Annual Report 1997, Focus Paper III. International Network for the Improvement of Banana and Plantain, Montpellier, France. (1998), p:52-55

[2] Joseph S., Sreekala M. S., Oommen Z., Koshy P., Thomas S.: Composites Science and Technology, Vol. 62, (2002), p. 1857–1868

[3] ASTM (American Society for Testing and Materials) Composite Materials 2nd Edition, Philadelphia, PA, (1990), p.10 – 80.

[4] Ryan, Thomas P., Modern Experimental Design, Jhon Wiley & Sons, Inc., Hoboken, New Jersey, (2007)

[5] Anderson, M.J., Whitcomb, P.J., RSM Simplified – Optimizing Processes Using Response Surface Methods for Design of Experiments, Productivity, Inc., New York NY, (2005)

© (2011) Trans Tech Publications, Switzerland
doi:10.4028/www.scientific.net/KEM.471-472.827

Influence of Processing Aids and Hydroxyapatite As Fillers on Flow Behaviour and Mechanical Properties of Ultra High Molecular Weight Polyethylene/High Density Polyethylene Composites

Mazatusziha Ahmad[1a], Mat Uzir Wahit [1b,]Mohamed Rafiq Abdul Kadir[2c,] Khairul Zaman Mohd Dahlan[3d]

[1]Faculty of Chemical Engineering , Universiti Teknologi Malaysia, Skudai, Johor, Malaysia

[2]Faculty of Biomedical and Health Science, Universiti Teknologi Malaysia, Skudai, Johor, Malaysia

[3]Malaysia Nuclear Agency, Bangi, Kajang, Selangor, Malaysia

[a]mazatusziha@yahoo.com, [b]mat.uzir@cheme.utm.my, [c]rafiq@fkbsk.utm.my, [d]khairul@mint.gov.my

Keywords: High density polyethylene, ultra high molecular weight polyethylene, hydroxyapatite, mechanical, rheological behavior.

Abstract. In this study, blends of ultra high molecular weight polyethylene/high density polyethylene/polyethylene glycol (UHMWPE/HDPE/PEG) and the composites containing Hydroxyapatite (HA) as reinforcement filler were prepared via single screw extruder nanomixer followed by compression moulding. PEG (2phr) was used as processing aid and HA loadings were varied from 10 to 50 phr. HDPE and PEG were introduced to improve the extrudability of UHMWPE. Rheological behavior was studied via capillary rheometer while flexural and izod impact tests were conducted in order to investigate the mechanical properties of the blends and composites. Melt viscosity of the blends was found to decrease with increasing shear rate indicating a pseudoplastic behaviour. Incorporation of PEG shows a synergism effect on the reduction of blends viscosity. Blend of 40% UHMWPE/ 60% HDPE/ 2 phr PEG was chosen as the optimum blend composition with a balance properties in terms of the mechanical properties and processability. The incorporation of HA fillers from 10 to 50 phr into the blend resulted in the increase of flexural modulus and flexural strength with a slight decline of impact strength values. It can be concluded that the composites having adequate strength and modulus within the range of cancellous bone properties were succesfully developed to be used as biomedical implant devices.

Introduction

Ultra high molecular weight polyethylene (UHMWPE) is widely used in artificial hips and knees owing to its good wear resistance and biocompatibility [1]. However, a need still exist for implant material with improved biocompatibility, excellent combination of high strength and low modulus, high fatigue and wear resistance, high ductility and be without cytotoxity. Due to that, much attention has been paid towards the development of polymer composites with HA as bioactive material in bone tissue engineering [2,3]. The inclusion of HA filler particles to form composites has been shown to enhance mechanical properties and exhibits excellent bioactivity properties [3]. In terms of processing study, it has been a great challenge to ensure the HA are sufficiently dispersed in UHMWPE matrix due to the extremely high viscosity of UHMWPE which resulting in resistance to flow and causes difficulties in processing by common techniques. There is a considerable interest for several decades in improving processability of UHMWPE through blending with conventional polyolefin such as polypropylene (PP) [4], high density polyethylenes (HDPE) [5] and incorporating small quantities of processing aids [6]. It was reported that HA particles was effectively dispersed in UHMWPE with combination of HDPE as a matrix, with the production limits through internal mixer [7]. Meanwhile, a study by Fang et al., [3] reported using a new method to develop the HA/UHMWPE composite by combining solid state mixing, solution

gelation and melt compounding methods by twin screw extrusion. Up to the time of this report no detailed study has been reported on development of HA reinforced UHMWPE/HDPE/PEG blends processed using single screw extruder. PEG has been chosen due to its potential in medical and pharmaceutical area. PEG was reported to be biocompatible, which is usually used as a coating in the field of biomaterials [8]. PEG was proven to be effective in reducing the extrusion pressure and melt viscosity, and has been widely studied in view of its importance in processing [9]. Thus, the main target of this work is to reduce the viscosity of UHMWPE to a processable value, while retaining as much as possible its mechanical properties.

Experimental

Materials. The UHMWPE used was GUR 1020 (Ticona, United Kingdom), was supplied in a powder form. HDPE (Etilinas HD5403AA) was supplied by Polyethylenes, Malaysia with density of 0.954g/cm^3 and melt flow rate (MFR) of 0.25g/10min. PEG (*M*w=8000) and HA is a calcium phosphate ceramic ($Ca_{10}(PO)_6(OH)_2$), grade 21223 (Fluka) were supplied by Sigma Aldrich, Malaysia. The specific surface area of the powder (according to the Brunnauer- Emmett-Teller method) was found to be 33.05 m^2/g, and the particle size is 7.51 μm. The morphology of HA particles is shown in Fig. 1.

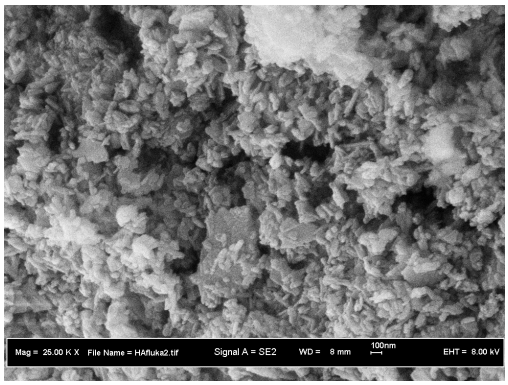


Fig. 1: Morphology of HA particles.

Sample Preparation. The granules of HDPE was grind into powder prior mixing with UHMWPE, and compounded in a single screw extruder nanomixer with a screw speed of 80rpm followed with compression-molded into samples at 210°C for 25 min (including 15 min of preheat) under 14MPa.The test specimen was cut followed the dimension specified in the ASTM. The blend and composite formulations are summarized in Table 1.

Rheological Experiment. Rheological measurements were carried out on a capillary rheometer (Gottfert Rheograph 2002) at temperature of 195°C. A round die with a length/diameter (L/D) ratio of 10 and 20 were used. The range of apparent shear rates is between 10–2000 s^{-1}. No Bagley correction was applied.

Flexural Test. Flexural test was carried out using the Llyod machine according to the ASTM D790 standard, three point bending system. A cross-head speed of 5mm/min was used.

Scanning Electron Microscopy (SEM). SEM characterization was performed using Philip XL 40 in order to examine the morphology of fracture surface of the specimens.

Table 1 : Composition of the UHMWPE/HDPE/PEG Blends and Composites

Designation	UHMWPE (wt%)	HDPE (wt%)	PEG (phr)	Designation	UHMWPE (wt%)	HDPE (wt%)	PEG (phr)	HA (phr)
U10H90G	10	90	2	UHGHA10	40	60	2	10
U20H80G	20	80	2	UHGHA20	40	60	2	20
U30H70G	30	70	2	UHGHA30	40	60	2	30
U40H60G	40	60	2	UHGHA40	40	60	2	40
U50H50G	50	50	2	UHGHA50	40	60	2	50
U60H40G	60	40	2					

Results and Discussion.

Viscosity Reduction of UHMWPE/HDPE/PEG Blends. The rheological behavior of UHMWPE/HDPE/PEG blends is shown in Fig. 1. The blends show a noteable difference in viscosity at low apparent shear rate, while at high apparent shear rate the blends viscosity is almost the same. The viscosity of all blend decreased with the increase of shear rate, indicating pseudoplastic behaviour. All blends exhibit the non-Newtonian and shear thinning behaviors. At low shear rate, blends with the lowest amount of UHMWPE shows the lowest viscosity, while at high shear rate, the overlapping trend of the viscosity were observed for all blend compositions. Overall, the viscosity of the blends appeared almost the same, without any significant reduction in viscosity with increasing HDPE concentration. The viscosity reduction is attributed to the alignment of PEG chains in neighbouring molecules of polyethylene blends due to the stronger interchain interactions, reduced the tendency for entanglement between different polymers to occurs and contribute to the chain alignment. PEG was succesfully align the polymer chain, thus increased the movement of polymer chain and therefore reduce the viscosity. According to Wu [10] it was concluded that specific interchain interactions responsible for molecular compatibility of dissimilar polymers, tend locally to align the chain segments for association and thus stiffen the chains. This result reflects that synergistics effects was obtained with combination of PEG together with HDPE. It can be concluded that PEG was succesfully act as internal lubrication due to the good lubrication characteristics and promotes the interphase slippage of the blend. The SEM results supports the evidence of the existance of PEG in the interior of extrudate samples as shown in Fig. 2. Overall, as the main target to produce composites with a good mechanical properties and processability, thus blend of 40% UHMWPE/ 60% HDPE/ 2 phr PEG is deduced as the optimum composition to be used to investigate the effect of HA on mechanical properties of UHMWPE/HDPE/PEG blends.

Flexural Strength. The effect of HDPE content on the flexural strength of UHMWPE/HDPE/PEG blends are shown in Fig. 3(a). In general, there was a considerable increased in flexural strength with increasing HDPE content from 40 to 60 wt% of both of the blends. The flexural strength was maintained up to 60wt% of HDPE, with further reduction in strength observed with increasing HDPE concentration. UHMWPE forms as a major phase at composition of 60wt% UHMWPE/40wt% HDPE thus the blends reverts to that of UHMWPE properties, resulting in a lower strength. The slight increment in tensile strength for UHMWPE/HDPE/PEG from 40 to 60 wt% HDPE is indication of a good interaction between HDPE and UHMWPE. Mohanty and Nando [11] reported that a good interaction between the blend components is one factor leads to a synergistic effect. The reduction in strength from 70 to 90 wt% HDPE is expected for blends with high fractions of HDPE. HDPE as the main matrix with shorter chains required lower tensile force to disentangle thus decreased the flexural strength. In addition, the very low viscosity of PEG forms dispersed particles as it is incompatible with UHMWPE/HDPE matrix creating a poor adhesion between the matrix and PEG which in turn lowering the ability of the polymer to sustain higher stress, thus dropped the strength values. SEM results as shown in Fig. 2 supports the results

obtained. The very low viscosity of PEG forms dispersed particles as it is incompatible with UHMWPE. A lot of holes resulted from the pulling out of the dispersed phase during the fracture.

The effect of HA content on the flexural strength of UHMWPE composites is shown in Fig. 4(b). The UHMWPE composites exhibit a marginally increase in flexural strength with inreasing HA loadings. The strength of the composites was slightly higher than the UHMWPE blends with increment about 18% . The gradual increase with increasing HA content indicates the homogenous distribution of HA in the polymer matrix which contribute to the improvement in mechanical bonding between fillers and polymer matrix. Thus, it is believed that the wetting ability of the matrix to the surface area of fillers was enhanced, entrapped the HA particles in the matrix and enable more stress to be transferred from the matrix to the fillers. This subsequently prevents filler debonding to fracture at lower strength. Filler with higher surface areas will contribute to more surface contact between the filler and matrix, thus increasing the mechanical properties of the composite [12]. In this work the specific surface area of HA is 33.05 m^2/g (from particle size distribution data) and the particle size is 7.51 μm, with its irregular shape (Fig. 3c) showing encouraging result and is favorable to improve surface contact between the filler and matrix, thereby increasing the strength of the composites. This was in agreement with study reported on HA filled polyethylene composites where the strengthening effects of HA is highly influenced by the filler dispersion in polyethylene matrix and the wetting ability of the matrix to filler particles [13]. Amount of surface contact between the polymer matrix and the filler can be determined by the specific surface area as it determines the interfacial interactions which significantly affects the mechanical properties of the composites.

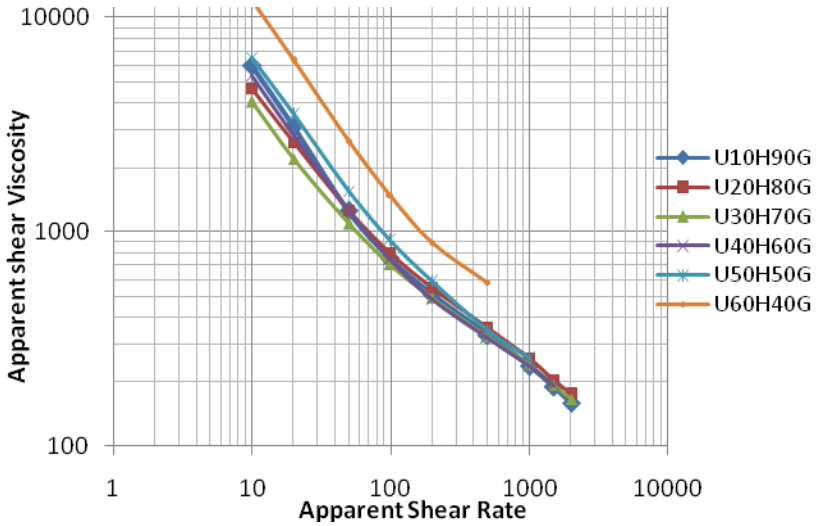


Fig. 1: Apparent flow curves of UHMWPE/HDPE/PEG blends at temperatures of 195°C.

Flexural Modulus. As shown in Fig. 4(a), the flexural modulus of UHMWPE/HDPE/PEG blends increased progressively as the HDPE content increased. This is an expected behavior that addition of HDPE enhances the stiffness of the blends. It is believed that combination of HDPE and PEG chains in the amorphous part thus have a high tendency to produce rigid amorphous phase. The system with rigid amorphous phase therefore results in increment of elastic modulus. This is reasonably since previous study by Xie and Li, [14] was also expected the role of PEG additives in the amorphous phase. The effect of HA loadings on flexural modulus of UHMWPE/HDPE/PEG composites is shown in Fig. 4(b). It was found that incorporation of HA results in a significant improvement in flexural modulus of UHMWPE composites with further increased with increasing HA fillers content. The results showed that the modulus of UHMWPE composites marginally

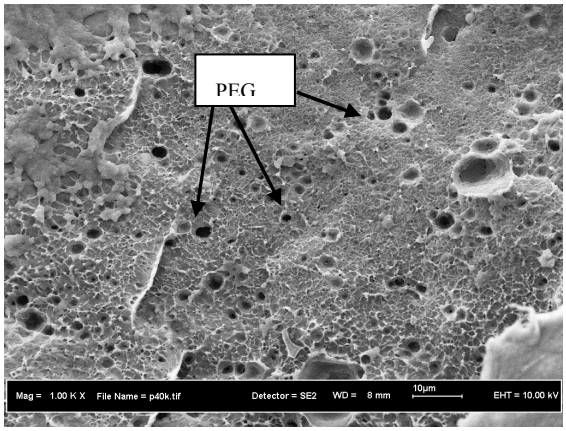


Fig. 2: Fractured surfaces of UHMWPE/HDPE (80/20) blend containing 2 phr PEG.

increased up to 30 phr HA, which is 23% higher than the blends. A sharp increased observed as the HA content increased from 30 to 50 phr with the increment of modulus about 92%. The modulus of the composites clearly reveals that HA was effectively reinforced the UHMWPE blends and demonstrates the stiffening effect of HA particles. The increment of modulus is expected, as it is well known that HA has higher modulus and rigidity than the polymer. The trend is consistent with previous studies who investigated on the effect of HA on PE composites [15].

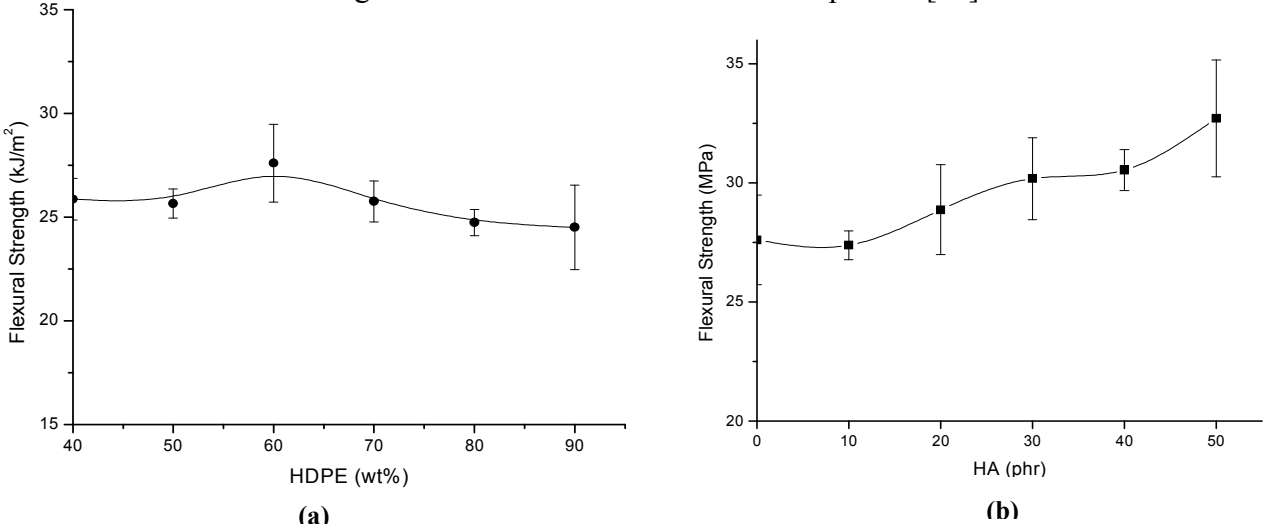


Fig. 3: Flexural strength of (a) UHMWPE/HDPE/PEG blends, (b) UHMWPE/HDPE/PEG/HA composites, and (c) The insert shows the morphology of HA particles with the irregular shape.

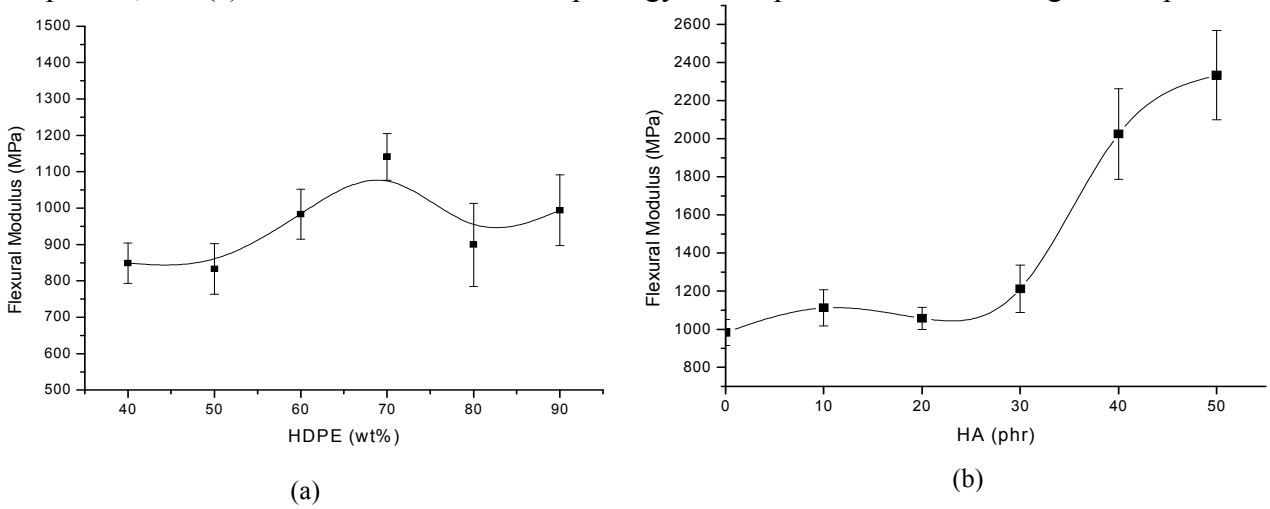


Fig. 4: Flexural Modulus of (a) UHMWPE/HDPE/PEG Blends and (b) UHMWPE/HDPE/PEG/HA Composites.

Summary.

The viscosity of UHMWPE/HDPE/PEG blends reduced significantly with incorporation of PEG. The incorporation of PEG in the amorphous regions, produce rigid amorphous phase which therefore results in increment of modulus. The impact strength reduces with incorporation of PEG by the retardation of stress distribution. Good interaction between the blend components is one factor leads to a synergistic effect and contribute to strength enhancement. Blend of 40% UHMWPE/ 60% HDPE/ 2 phr PEG showed the optimum properties in terms of the mechanical properties and processability. Incorporation of HA results in improvement of modulus and strength of the composites at the expense of impact strength with increasing filler concentration. The properties of the composites is comparable to the cancellous bone properties and suitable to be used in biomedical applications.

References

[1] Plumlee, K., Schwartz, C. J. Wear 267. (2009), p. 710–717.

[2] Abu Bakar, M. S., Cheang, P., and Khor, K. A. Composite Science and Technology, 63. (2003), p. 421-425.

[3] Fang, L., Gao, P., and Leng, Y. Biomaterials. 27. (2006), p. 3701-3707.

[4] Xie, M., Liu, X., and Li, H. Journal Of Applied Polymer Science. 100. (2006), p. 1282-1288.

[5] Boscoletto, A. B., Franco, R., Scapin, M., and Tavan, M. European Polymer Journal, Vol. 33, No.1. (1997), p. 97-105.

[6] Utsumi, M., Nagata, K., Suzuki, M., Mori, A., Sakuramoto, I., Torigoe, Y.,Kaneeda, T.,Moriya, H. Journal of Applied Polymer Science, Vol. 87. (2003), p. 1602-1609.

[7] Lim, K.L.K., Mohd Ishak, Z. A., Ishiaku, U.S., Fuad, A. M. Y., Yusof, A. H.,Czigany, T., Pukanszky, B., Ogunniyi,D.S. Journal of Applied Polymer Science, Vol. 97. (2005), p. 413-425.

[8] Alcantar, N. A., Aydil, E. S., and Israelachvili, J.N. Journal Biomed Mater Res. 51. (2000), p. 343- 351.

[9] Xie, M. and Li, H. Journal of Applied Polymer Science. Vol. 18. (2008), p. 3148-3153.

[10] Wu, S.. Polymer, Vol 28. (1987).

[11] Mohanty, S. and Nando, G. B. Encyclopedia Of Polymer Science & Technology. Polymer, 37. (1996), p. 5387.

[12] Leong, Y. W., Abu Bakar, M. B., Mohd Ishak, Z. A., Ariffin, A., Pukanszky, B. Journal of Applied Polymer Science, Vol. 91. (2004), p. 3315-3326.

[13] Wang, A., Essner, A.,Polineni, V. K., Stark, C., and Dumbleton, J.H. Tribology International, Vol. 31, Nos 1-3. (1998), p. 17-33.

[14] Xie, M. and Li, H. Journal of Applied Polymer Science. Vol. 18. (2008), p. 3148-3153.

[15] Bonfield, W., Grynpas, M.D. and Tully, A. E. Biomaterials, Vol. 2, (1981), p. 185-186.

© (2011) Trans Tech Publications, Switzerland
doi:10.4028/www.scientific.net/KEM.471-472.833

Buckling Behavior of General Dome Ends under External Pressure, using Finite Element Analysis

Behzad Abdi[a], Hamid Mozafari[b], Amran Ayob[c]

[a,b,c] Faculty of Mechanical Engineering, Universiti Teknologi Malaysia,
81310 UTM Skudai, Johor, Malaysia
[a] Behzad.abdi@gmail.com, [b] mozafari.h@gmail.com, [c] amran@fkm.utm.my

Keywords: General Domes; Buckling Pressure; External Pressure; Finite element analysis

Abstract. In this paper, the finite element analysis is used to investigate the effect of shape of dome ends on the buckling of pressure vessel heads under external pressure. The Finite Element Analysis (FEA) with the use of elastic buckling analysis was applied to predict the critical buckling pressure. The influence of geometrical parameters such as thickness, knuckle radius, and the ratio of minor axis to the major axis of dome ends, on the weight and the critical buckling pressure of hemispherical, ellipsoidal, and torispherical dome ends, was studied. The four-centered ellipse method was used to describe the geometry of the dome end.

Introduction

Buckling behavior of ellipsoidal and torispherical dome ends under external pressure has not attracted as much attention as hemispherical dome end over the last few decades, although these dome ends have been used widely in industries from airspace, land to sea-based.

One of the earliest experimental investigations into the buckling of shallow torispherical domes subjected to external pressure was that of [1], where the test result of experimental buckling pressure was reported on 24 externally-pressurized torispherical steel shells. Clamped torispherical shells under external pressure were studied by Blachut and Galletly [2]. The use of numerical methods on buckling of shells was carried out in [3, 4].

The study into the effect of axisymmetric imperfections of Legendre polynomial type on the buckling strength was carried out in [5] while in [6] the effect of local increased-radius imperfection was assessed.

The three commonly used dome geometries are hemispherical, ellipsoidal, and torispherical dome ends (Fig. 1). The four-centered ellipse method is quite useful in designing and constructing the dome structures, therefore, the four-centered ellipse method is used in this study to construct the three types of dome ends. The four-centered ellipse method only takes advantage of two parameters, i.e. the ratio (K) of the length of major axis to the length of minor axis and the length of the major axis (a) to define any dome end.

There are not many buckling test results for ellipsoidal dome ends under external pressure. In a recent review of the past work into buckling of ellipsoidal dome ends under external pressure, it has transpired that these studies had almost entirely concentrated on static elastic stability [7].

One of the aims of this paper is to study the effect of geometry of hemispherical, ellipsoidal, and torispherical dome ends on the critical external buckling pressure and weight. The study will be complemented by numerical comparison of buckling pressure of dome ends.

Geometric description of torispherical dome end

Consider an elastic dome end with constant thickness t under uniform external pressure. In this study the flange is not included and the dome is completely clamped at the edge.

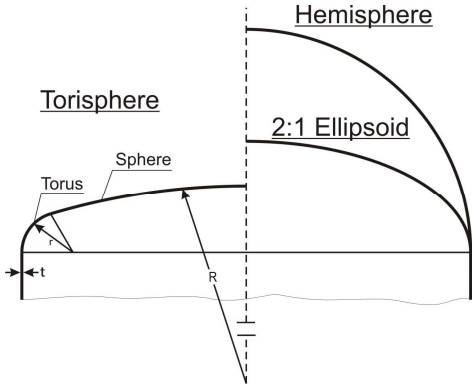


Fig. 1: Typical dome end profile

According to the four-centered ellipse method, the geometry of torispherical dome end can be generated. Given the ratio $K = b/a$, then the other parameters θ, ϕ, r, and R can be determined from the following equations:

$$\theta = \tan^{-1}\left(\frac{b}{a}\right) = \tan^{-1} K \quad , \quad \varphi = \frac{\pi}{2} - \theta \tag{1}$$

$$R = \frac{a}{2\sin\theta}\left[1 + \frac{1-\sin\theta}{\cos\theta}\right] , \qquad r = \frac{a}{2}\left[\frac{1+\sin\theta-\cos\theta}{\cos^2\theta}\right] \tag{2}$$

Subsequently, the total weight of torispherical dome end with constant thickness is [8]

$$W_T = 2\pi\gamma t\left[r\omega\left(\frac{\pi}{2} - \Phi\right) + r^2\cos\Phi + \left(1-\cos\Phi\right)R^2\right] \tag{3}$$

where

$$\omega = \frac{D}{2} - r = a - r \qquad , \qquad \Phi = \sin^{-1}\left(\frac{\omega}{R-r}\right) \tag{4}$$

γ is the specific gravity of the shell material.

By using the four-centered ellipse method to construct the torispherical dome end, the radius of spherical cap R and the radius of toroidal knuckle r have relations which can be expressed as function of ratio $K = b/a$ and the angle of spherical cap θ. Therefore, the effects of the ratio K and thickness t on the critical buckling pressure are studied in this paper.

Finite element analysis. The linear elastic buckling analysis of hemispherical, ellipsoidal, and torispherical dome ends under external pressure was carried out by using finite element analysis. Two hemispherical dome, 2 ellipsoidal dome, and 2 torispherical dome ends were considered and studied in this paper. Also, the effect of thickness at the onset of buckling was carried out in this study.

Model description. In this study, two models each of hemispherical dome end, ellipsoidal dome end and torispherical dome end are identified. All models have the same elastic modulus of $3.0\times10^7\,(psi)$ and the same Poisson's ratio of 0.3. The fixed major axis a for all Model 1 is $63.98\,in$ and $91.73\,in$ for Model 2. The range of the ratio $K = b/a$ is selected as $0.1 \le K \le 1$ and the range of the thickness t is $0.2 \le t \le 2$. The principal dimensions for two models of ellipsoidal dome end and two models of torispherical dome end with various K are listed in Table 1 and 2.

Table 1: Principal data of ellipsoidal dome end

Ratio		1:1	1.2:1	1.5:1	2:1	2.5:1	3:1	4:1	5:1	6:1	7:1
$K = b/a$		1	0.83	0.67	0.5	0.4	0.33	0.25	0.2	0.17	0.14
Minor axis, $b(in)$	Model 1	63.98	53.31	42.65	31.99	25.59	21.32	15.99	12.79	10.66	9.142
	Model 2	91.73	76.43	61.15	45.86	36.69	30.57	22.93	18.35	15.29	13.11

Table 2: Principal data of torispherical dome end

$K = \frac{b}{a}$	Toroidal knuckle radius, $r(in)$		Spherical cap radius, $R(in)$		Toroidal knuckle angle, θ		Spherical cap angle, φ	
	Model 1	Model 2	Model 1	Model 2	Model 1	Model 2	Model 1	Model 2
0.1	3.375	4.839	612.449	878.086	5.710	5.7106	84.289	84.289
0.2	7.171	10.281	296.842	425.591	11.309	11.310	78.690	78.691
0.3	11.490	16.474	194.161	278.374	16.699	16.699	73.300	73.301
0.4	16.436	23.565	144.452	207.106	21.801	21.801	68.198	68.198
0.5	22.104	31.692	115.741	165.941	26.565	26.565	63.434	63.435
0.6	28.584	40.981	97.3817	139.619	30.963	30.964	59.036	59.036
0.7	35.951	51.543	84.8282	121.621	34.992	34.992	55.008	55.008
0.8	44.270	63.472	75.8213	108.707	38.659	38.659	51.340	51.340
0.9	53.598	76.845	69.1175	99.096	41.987	41.987	48.013	48.013
0.1	-----	-----	63.98	91.73	-----	-----	-----	-----

Results And Discussion. For the hemispherical dome ends, the effect of thickness on the buckling pressure are studied and showed in Table 3. Also in the table the effect of thickness on the weight of hemispherical dome end are presented. If thickness is kept constant, the influence of ratio $K = b/a$ on the buckling pressure of ellipsoidal dome end is studied and the results are displayed in Table 4 and Fig 2.

Table 3: Buckling pressure and dome weight at some corresponding thickness of hemispherical dome ends

Thickness (in)	Weight (lbf)		Buckling Pressure (psi)	
	Model 1	Model 2	Model 1	Model 2
0.2	190.3268	391.232	359.12	183.9
0.4	380.6536	782.464	1439.56	704.01
0.6	570.9804	1173.696	3210.58	1574.55
0.8	761.3072	1564.928	5649.12	2785.29
1.0	951.634	1956.16	8825.65	4329.8
1.2	1141.961	2347.392	12873.5	6181.21
1.4	1332.288	2738.624	17552.05	8441.81
1.6	1522.614	3129.856	23170.89	11023.54
1.8	1712.941	3521.088	28910.36	13952.59
2.0	1903.268	3912.32	35736.8	17430.50

For ellipsoidal dome ends, the thickness effect of the dome on buckling pressure and weight are studied and showed in Fig 3. For torispherical dome end, the effect of dome shape on the buckling pressure and weight are studied and displayed in Table 5 and Fig 4. Also, for torispherical dome end with the ratio $K = 0.3$, the effect of thickness on the weight and buckling pressure of dome are studied and showed in Fig 5.

From Table 3 (hemispherical dome end), Fig 3 (ellipsoidal dome end) and Fig 5 (torispherical dome ends), it can be seen that the effect of thickness on the buckling pressure in domes that have small major axis are more. For other sizes of domes and for domes with big major axis the effect of thickness is small. The effect of shape of dome are more critical than thickness effect.

Table 4: Buckling pressure at some corresponding ratio of K - Ellipsoidal dome ends

Ratio	$K=(b/a)$	Weight (lbf)		Buckling Pressure (psi)	
		Model 1	Model 2	Model 1	Model 2
1:1	1	1199.06	3462.403	13926	13376
1.2:1	0.83	1068.31	3084.86	10309	9892.4
1.5:1	0.67	943.95	2725.777	6856.4	6576.0
2:1	0.5	828.62	2392.745	4010.2	3845.1
2.5:1	0.4	765.58	2210.712	2633.7	2524.9
3:1	0.33	726.93	2099.108	1866.0	1788.2
4:1	0.25	683.48	1973.639	1096.8	1049.4
5:1	0.2	660.54	1907.377	740.26	707.04
6:1	0.17	646.80	1867.707	545.35	519.95
7:1	0.14	637.87	1841.904	427.44	406.77

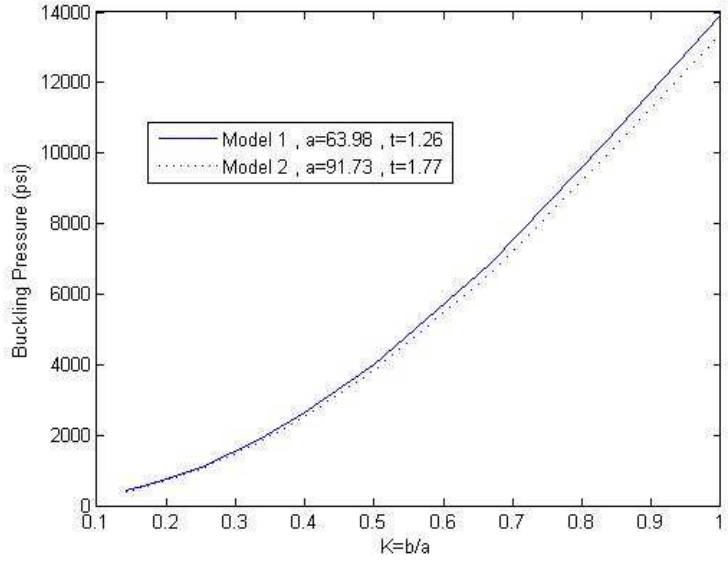


Fig. 2: The buckling pressure via the scope K of ellipsoidal dome end

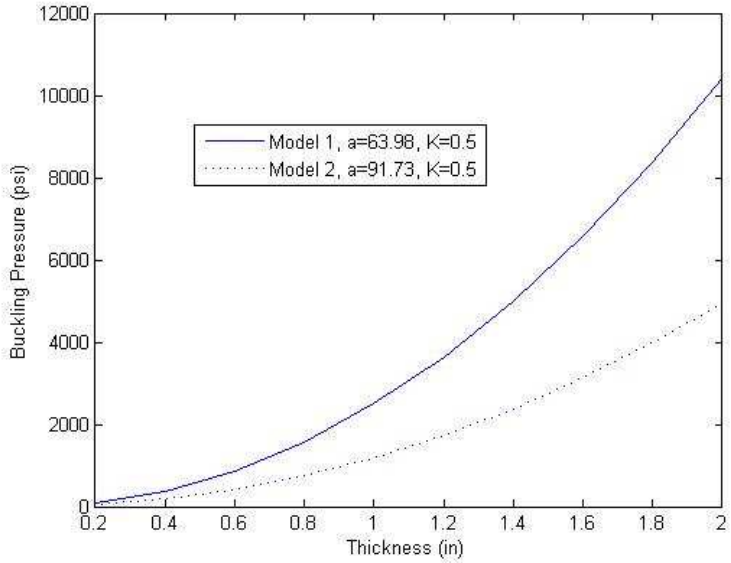


Fig. 3: Buckling pressure via thickness of ellipsoidal dome end

Table 4: Buckling pressure at some corresponding ratio of K - Torispherical dome ends

$K = (b/a)$	Weight (lbf)		Buckling Pressure (psi)	
	Model 1	Model 2	Model 1	Model 2
1	636.74	1838.6	211.52	200.36
0.83	679.88	1963.2	676.45	647.44
0.67	728.77	2104.3	1543.4	1482.5
0.5	783.09	2261.2	2809.8	2696.7
0.4	842.47	2432.7	4354.4	4179.4
0.33	906.45	2617.4	6162.1	5910.6
0.25	974.56	2814.1	8147.7	7851.2
0.2	1046.3	3021.3	10182	9774.1
0.17	1121.3	3237.8	12162	11677
0.14	1199.06	3462.403	13926	13376

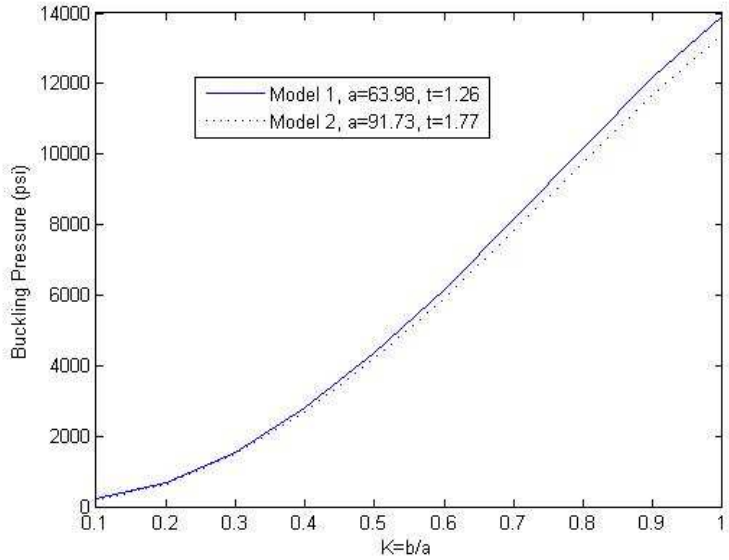


Fig. 4: The buckling pressure via the scope K of torispherical dome end

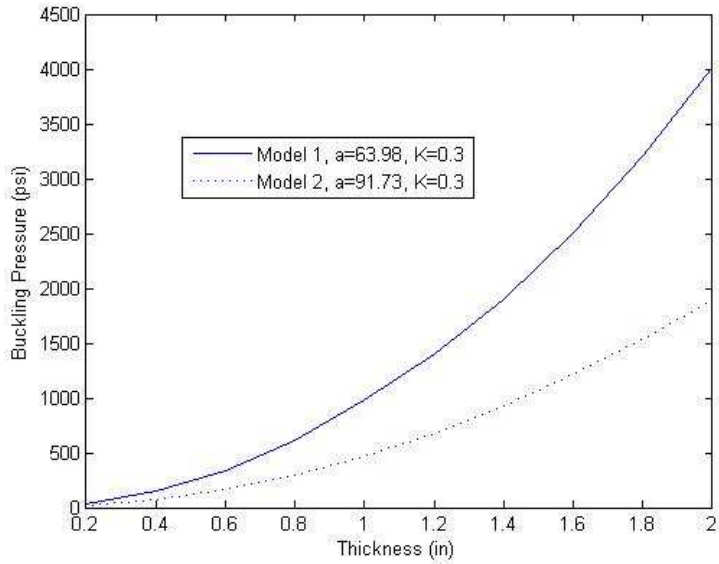


Fig. 5: The buckling pressure via thickness of ellipsoidal dome end

From Fig 2 (ellipsoidal dome end) and Fig 4 (torispherical dome end), it can be seen that buckling pressure and weight of these types of domes are very similar to each other. In the ASME code, for calculating the maximum working pressure of torispherical dome end, the ellipsoidal formulations are used and the results are very close to the maximum working pressure of torispherical dome ends.

From Figs 2 and 4, the maximum critical buckling pressure was found at $K = 1$ because at this value of *K*, the ellipsoidal and torispherical dome ends become hemispherical in shape. Therefore flat ellipsoidal and torispherical dome ends have small critical buckling pressure.

Summary

In this study, the four-centered ellipse method was adopted to describe the shape of ellipsoidal, hemispherical and torispherical dome ends. In this method only two variables are used to define the shape of domes. The finite element analysis was also used to verify the buckling behavior of general dome ends.

For further study, finite element analysis can be used to analysis the buckling behavior of general dome ends under internal pressure on under suddenly load and so on.

References

[1] G. D. Galletly, J. Kruzelecki, D. G. Moffat, and B. Warrington, *Buckling of shallow torispherical domes subjected to external pressure – a comparison of experiment, theory, and design codes*. The Journal of Strain Analysis for Engineering Design, Vol 22, No 3, pp 163-175, (1987)

[2] J. Blachut and G. D. Galletly, *Clamped torispherical shells under external pressure*. The Journal of Strain Analysis for Engineering Design, Vol 23, No 1, pp 9-24, (1988)

[3] D. Bushnell, *Computerized buckling analysis of shells in mechanics of elastic* stability (Edited by H. H. E. Leipholtz and A. E. Oravus). Martinus Nijhoff, Netherlands (1985)

[4] D. Bushnell, *BOSOR 5-Program for buckling of elastic-plastic complex shells of revolution including large deflections and creep*. Comput. Struct. 6, 221-239, (1976)

[5] G. D. Galletly, J. Blachut and J. Kruielecki, *Plastic buckling of externally pressurised dome ends'. Advances in Marine Structures* (Edited by C. S. Smith and J. D. Clarke), pp. 238-261 (1986).

[6] J. Blachut and G. 'D. Galletly, *Externally pressurized hemispheres and shallow torispheres*. Proc. ECCS Co11 on Stability of Plate and Shell Structures, Ghent (Edited by P. Dubas and D. Vandepitte), pp. 361-366, (1987).

[7] G.D. Galletly, J. Blachut, *Stability of complete circular and non-circular toroidal shells*. Proc IMechE: C,209:245±55, (1995)

[8] M. F. Yang, C. C. Liang, and C. H. Chen, *a rotational shape design of externally pressurized torispherical dome ends under buckling constraints*, Computers & Structures, vol. 43, No. 5, pp. 839-851, 1992

© (2011) Trans Tech Publications, Switzerland
doi:10.4028/www.scientific.net/KEM.471-472.839

Feasibility of Manufacturing a Medium Density Fibreboard Made of 4-Year Old Rubber Tree RRIM 2020 Clone

Harmaen Ahmad Saffian[1,a], Jalaluddin Harun[1,b], Paridah Md Tahir[1,c] and Khalina Abdan[2,e]

[1]Institute of Tropical Forestry and Forest Products (INTROP),

Universiti Putra Malaysia, 43400 UPM Serdang, Selangor, Malaysia.

[2]Department of Biological and Agricultural Engineering,

Universiti Putra Malaysia, 43400 UPM Serdang, Selangor, Malaysia.

[a]harmaen@putra.upm.edu.my, [b]jalaluddin@mtib.gov.my, [c]parida_introb@yahoo.com,

[c]khalina_eng@yahoo.com

Keywords: MDF boards, fibres;internal bending

Abstract. This research was conducted to study the feasibility of producing medium density fibreboard (MDF) from 4-year old rubberwood clone RRIM 2020. The 4-year old rubberwood is obtained from different planting densities, which is 500, 1000, 1500 and 2000 trees/ha and were processed to produce MDF. The MDF is analyzed in term of its mechanical properties (static bending and densities to comply with JIS A 5905-2006 Standard (Type 30, MOR > 30.0 MPa and MOE > 2500 MPa and Type 25, MOR > 25.0 - 30.0 MPa and MOE > 2000 - 2500 MPa). MDF made from 25 year trees clone, PB260 which come from the same clone was used as a control. The results showed that the PB260 and the 4-year old rubberwood clone with planting densities of 500 trees/ha satisfied the requirement of Type 30, and the remaining passed at Type 25. It shows that it is feasible to produce an MDF using the 4-year old rubberwood clone.

Introduction

The utilization of rubberwood in Malaysia, as replacement of hardwood in the wood industries has achieved a tremendous success. The achievement of this success was resulted from a series of research, development and promotion that has been conducted during few decades. At present rubberwood has become an essential raw material for economic growth in Malaysia particularly for wood industry. It was indicated by increasing demand from the wood industry especially in the wood panel product sector. Wood panel product sector activities are mainly involves the major products such as plywood, MDF and chipboard. The demand of the rubberwood in Malaysia is shown in Table 1. From the table it can be seen the Fig. of export wood based product in 2008 in Peninsular Malaysia.

Table 1. Export of Wood-Based Products: Peninsular Malaysia for 2007 and 2008

	Items	Volume (m^3)	FOB value (RM)
1	Mouldings	89,161	254,733,461
2	Plywood	148,688	219,808,044
3	Fibreboard (MDF)	554,133	574,654,493
4	Chipboard/particleboard	298,860	170,573,765

Source: Malaysian Timber Industry Board (2008)

In order to cope with the industrial demands, Malaysian Rubber Board (MRB) was introduced the new rubber trees clone, called RRIM 2000 series in the last few years. The rubber tree clones made by Malaysian Rubber Board (MRB) has revolutionize the wood based industries. The RRIM 2000 series is able to produce high volume of wood, and at the same time it can produce high latex yield. In another study [2] related to rubberwood clone created by the MRB shows that RRIM 900, RRIM 2000 and PB260 series can produce as much as 300% more timber than the current RRIM 600 series and are able to harvest in a short rotation of 12 to 15 years. The latest RRIM 2000 series clone has a capability to grow relatively better compared to the PB260 series and RRIM 600 series [2]. In the MRB's experimentation, these trees are planted at high planting density more than 1000 trees/ha with the purpose of generating as much wood material as possible. If this planting practice is favourable, the system can be introduced to the estate owners, and rubber trees can be harvested at early age and supplied to the wood industry.

A lot of studies have been conducted involving the mechanical properties of MDF. One of the examples was conducted [5] to determine the possibility to manufacture MDF using large plantation method of *Eucalyptus saligna* series from Brazil. The results showed that those series was complied with Euro MDF and ANSI-AHA standard. Another researchers [6, 7] focused on the feasibilities of radical formation in wood fibre surfaces by treating it with lactase, fenton reagent or gamma radiation. The result showed that an increment in internal bending (IB) found in the board with treated fibre with laccase or fenton reagent when defibration temperature increased. Other study using the statistical reliability tools to assess the improvement of MDF mechanical properties [8] concluded that the board density is one of the main key of improving the IB of the MDF.

For rubberwood RRIM 2020 clone, it has faster growth rate, good performance high timber volume, and has straight trunk. Furthermore, it is harvestable in a shorter rotation, thus it can be considered a potential wood supply to MDF manufacturer. Therefore, in this study, we attempt to create MDF made from the 4-year old rubberwood RRIM 2020 clone with planting densities of 500, 1000, 1500 and 2000 trees/ha as variables, while the 25 years old rubberwood PB260 as a fixed variable for control purpose. The purpose of this study is to evaluate either it is feasible to create an MDF that complies with the current standard using young rubberwood in order to compensate the current shortage of raw materials in MDF industries.

Materials and Methods

The planting location for this clone series of rubber tree is determined, at latitude N5^o and longitude E112^{o}E which has average of rain is about 4000 mm a year. It was planted in four different planting densities of 500, 1000, 1500 and 2000 trees/ha within the same plantation site. The average height of this rubberwood trees around 3-5 m and has circumference diameter of 45-60 cm. The density limitation for all specimen type was set at 700 kg/m^3. Three set of MDF were produced for each planting density. MDF produced from rubberwood PB260 clone fibres was used as a control. The experiment is tested according to JIS A 5905-2003 Standard. The processing of

rubberwood begins when logs were chipped as shown in Fig. 1. The wood chips were digested for 5 minutes and refined in a Sprout-Bauer refiner at a steam pressure of 8kg/m^2 to 9kg/m^2 and at a temperature of 170°C. The gap of the refiner plate was varied between 0.1-1.5 mm. In the process, the refined fibres will pass through the blow machine to reduce its moisture content, to achieve about 5% to 10%MC. The processed fibre is shown in Fig. 2.



Fig. 1. Rubberwood chips.



Fig. 2. Rubberwood fibres.

Next the dried fibres were screened using the Vibrator Fibre Screener to obtain two different sizes of 0.5-1.0 mm and 1.0-2.0 mm which were used to fabricate the MDF. Afterwards, the screened fibres were dried in an oven that was set at 70-90 ºC overnight in order to achieve the targeted moisture content of ≤5%. Next, the adhesive mixture was sprayed on the fibres in a rotary blender. The amount of fibre and the amount E1-grade urea formaldehyde resin for each board were calculated based on the oven dry weight of the fibre materials. The blending time between 5-10 minutes is sufficient to well mix the formulation. After blending, the formulation was poured into a 400x400 mm forming wooden box to produce a loose mat. Next the mat was pressed to obtain approximately 80-100 mm mat thickness prior to hot pressing. Afterwards, the mat was hot pressed into12 mm thick board at 170°C and 160 kgf/cm^2 for 6 minutes. 15 boards were made, and placed in a conditioned room at 20ºC and humidity of 65% for 7-10 days prior to testing. The board assessment was conducted to determine moisture content, board density and static bending in accordance with JIS A5905:2003 Standard and the data was analysed using ANOVA statistical method.

Results and Discussions

Density. The result shows that the density of MDF is in the range of 643 kg/m^3 to 673 kg/m^3, which is 30% lower than the targeted board density of 700 kg/m^3. Table 3 illustrates MDF density and moisture content from various planting density. The different of density is insignificant from one planting densities to another. However large discrepancies between the PB260 and the RRIM 2020 can be observed. The reason of the high relative density might attributed by the soft and young fibre that resides the 4-year old RRIM 2020 that more compaction after hot pressed as compares to older tree of PB260.

Table 3. Density of MDF made from rubberwood at different planting density.

Planting Density	Board density (kg/m^3)	MC (%)
PB260 (Control)	643^{b} (19.3)	6.5^{b} (0.76)
500 trees/ha	666^{b} (19.42)	7.1^{a} (0.41)
1000 trees/ha	655^{ba} (20.34)	6.7^{ba} (0.67)
1500 trees/ha	673^{a} (27.26)	6.8^{ba} (0.13)
2000 trees/ha	665^{a} (23.75)	6.7^{b} (0.18)

15 Replications

Moisture Content. Result on the moisture content found that the percentage varies from 6.5 to 7.1%. Referring to table 3, it is clear that the planting density of 500 trees/ha shows the highest percentage of moisture content, while the rest doesn't shows significant differences in moisture content.

Modulus of Rupture (MOR) and Modulus of Elasticity (MOE). MOR is used to determine the suitability of material for structural applications. The bending properties are dependent on the density of raw material, which in turn determines the compression ratio. Fig. 3 shows the MOR of MDF PB260 and RRIM 2020 clone at various planting density.

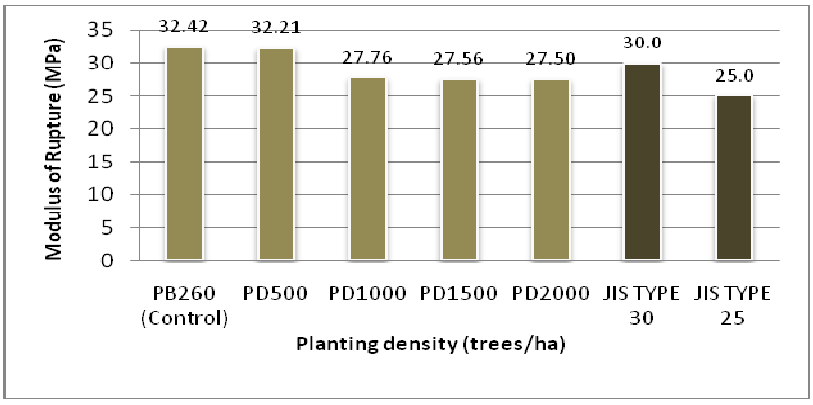


Fig. 3 Modulus of rupture for MDF rubberwood RRIM 2020 clone from different planting densities.

As shown in Fig. 3, the highest value of MOR is 32.42 MPa, from PB260 and RRIM 2020 with planting densities of 500 indicated 32.21MPa. These two MDFs passed the JIS A5905-2003 Standard Type 30. However the lowest MOR value observed was at 27.50 MPa and all MDF passed type 25 standard. According to the standard, these types of MDF are suitable for making furniture, such as writing table and building component such as door frame. Fig. 3 shows that MDF made from rubberwood PB260 and that from the planting density of 500 trees/ha gives the highest strength compared to others. In this study, the superior performance by the matured rubberwood is expected since it has longer fibre length, 1.3 mm compared to young rubberwood with planting densities of 500 trees/ha, which is 1.1 mm. Similar study was reported [10] where MDF made from 25-year old rubber tree with MOR value at 40.0 MPa compared to 4 year old tree which level at 38.0 MPa. Amongst the MDFs with different planting densities, there is a significant difference in the bending strength.

Similar results were obtained for MOE value which shown in Fig. 4. Such trend can be observed with rubberwood at different planting density. It is clear that PB260 board produced from mature tree wood obtained better MOE than other young wood. In this study, the mature and young wood from the different clone varied in strength and stiffness, whereby the young rubber trees possessed lower strength. Rubberwood from PB260 is stronger and stiffer thus provides the better performance of MDF. In mature woods, longer and thicker fibre provides better strength and stiffness of wood fibres. Unlike PB260, the young woods have shorter and thinner fibre especially at high planting density which contributed in lower strength and stiffness of MDF.

Moreover according to Fig. 4, the MDF made from PB260 (control) and planting density of 500 trees/ha give the highest mean value of MOE with 2282 and 2125 MPa respectively. Boards from planting density 1500 trees/ha give the lowest value of MOE with 1868MPa.

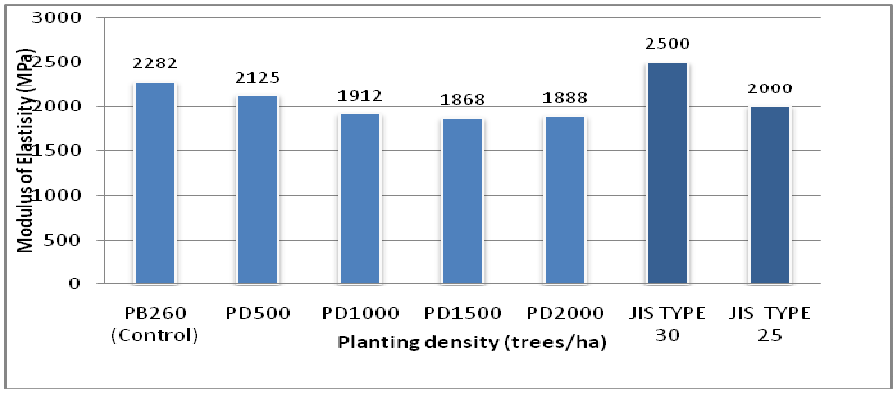


Fig. 4. Modulus of elasticity for MDF rubberwood RRIM 2020 clone from different planting densities.

It was found that at low planting density of 500 trees/ha shows high MOE result from thicker cell wall diameter and thinner fibre lumen [11]. The larger fibre size allows resin to penetrate at the large area of fibre which produce higher strength and stiffness of MDF. Apart from the fibre size, the specific gravity of wood, in most cases play major influence especially in term of board compaction, which eventually influence overall properties of the board produced. Furthermore wood from young trees (different planting density) may behave differently than mature woods (such as PB260) of the same species particularly on its strength and stiffness properties. In term of chemical constituents, young rubberwood from all planting density contains higher cellulose and hemicelluloses but lignin content is lower compared to 25-year old rubberwood. It was reported that presence of high amount of cellulose is responsible for the low strength and stiffness found in many young trees [12].

Summary.

MDF made from rubberwood obtained from different planting densities tree has significant differences in term of MC, Board Density, MOR and MOE in comparison with PB260. The most apparent differences were seen in MOR where those MDF produced from the wood obtained from the 500 tress/ha planting density were comparable to the PB260. MDF made from rubberwood of 500 trees/ha consistently give higher stiffness while the other properties such as MOR, MC, and Board density were less affected. Boards from PB260 and trees of 500 trees/ha planting density satisfied the requirement of MOR in JIS A5905-2006 Type 30 while MOE from PB260 (control) and 500 trees/ha only satisfied Type 25 of the same standard. In conclusion the 4-year old young rubberwood clone is suitable for the application of MDF and could be harvested in short duration for the purpose of application in fibreboard industries.

References

[1] Annual Report Malaysian Industry Timber Board [Internet]. Kuala Lumpur: Malaysian Timber Industry Board; c2008-2010. Annual Report Malaysian Industry Timber Board. [updated 2010 Sept 23; cited (2009) Jan 10]. Available from: http://www.mtib.gov.my/index.php?option=com_exile_stats&Itemid=65&lang=en

[2] Lembaga Getah Malaysia (LGM). LGM Planting Recommendations. Malaysia Rubber Board Monograph 7. (2003). 24p.

[3] Rahim S, Mohd Nor MY and Norralakam S. Utilisation of Oil Palm Residues for Various Composite Products. Proceedings of the Forestry and Forest Products Research; Kepong, Malaysia. (1993).

[4] Liew L.L. Properties of Medium Density Fibreboard from Oil Palm (*ElaeisguinensisJacq.)*fibres [dissertation]. University Putra Malaysia; (1996).

[5] Krzysik MK, Muehl JH, Youngquist JA and Franca FS. Medium Density Fiberboard Made from Eucalyptus Saligna, Forest Prod J. (2001);51(10):47-50.

[6] Widsten P, Laine JE and Tuominen S. Radical formation on laccase treatment of wood defibrated at high temperatures. Part 1. Studies with hardwood fibers. Nord Pulp Pap Res J (2002);17(2):139-146.

[7] Widsten P, Laine JE. and Tuominen S. Radical formation on laccase treatment of wood defibrated at high temperatures. Part 2. Studies with softwood fibers. Cell Chem Technol (2002);36:1-2.

[8] Young TM, Guess FM, Edwards DJ., and Pickrell TM. Exploring Graphically and Statistically the Reliability of Medium Density Fibreboard. International Journal of Reliability and Applications. (2003);4:157-170.

[9] Maloney TM. Modern Particleboard and Dry-Process Fibreboard Manufacturing. San Francisco; Miller Freeman: (1977).

[10] Wong ED, Razali AK and Siti NY, editors. Manufacture of MDF from 5-year old Heveabrasiliensis. Proceedings of the 5th Pasific Rim, Bio-Based Composites Symposium; Dec 10-13. Canberra, Australia.(2000)

[11] Harmaen A.S. Master Thesis, Utilisation of 4-year old Rubberwood (*Hevea Brasiliensis*) RRIM 2000 Clone and Oil Palm (*Elaeis guineensis Jacq*.)Empty Fruit Bunch in Medium Density Fibreboard Manufacture. Universiti Putra Malaysia. (2009).

[12] Haygreen JG and Bowyer JL. Forest Products and Wood Science. An Introduction. Third Edition. The IOWA State University press; (1996).

© (2011) Trans Tech Publications, Switzerland
doi:10.4028/www.scientific.net/KEM.471-472.845

Curing Characteristics and Mechanical Properties of Rattan Filled Natural Rubber Compounds

Komethi Muniandy [1, a], Hanafi Ismail [1, b], Nadras Othman [1, c]

[1]School of Materials and Mineral Resources Engineering, Universiti Sains Malaysia, Engineering Campus, Penang, Malaysia.

[a] kom_angel31@yahoo.com , [b] hanafi@eng.usm.my, [c] srnadras@eng.usm.my

Keywords: Rattan fiber, natural rubber, curing characteristics, tensile properties, rubber-filler interaction, scanning electron microscope

Abstract. Rattan for its potential as a new type of filler was investigated in natural rubber (NR) compounds. Natural rubber (NR) compounds were prepared by the incorporation of rattan at different loadings into a natural rubber matrix with a laboratory size two roll mill. The effect of rattan loading as filler on curing characteristics, tensile properties, morphological properties using scanning electron microscopy (SEM) and rubber–filler interaction of rattan filled natural rubber compound were studied in the filler loading range of 0 to 30 phr. The results indicate that the scorch time (t_{s2}) and cure time (t_{90}) shorten with increasing filler loading, whereas the maximum torque (M_H) showed an increasing trend. As the filler loading increases, the tensile strength and elongation at break decreases whilst tensile modulus; stress at 100 % elongation and stress at 300 % elongation increased. The rubber filler interactions of the rubber compound decreased with increasing filler loading. SEM studies indicate that the increasing rattan loading weakens the rubber-rattan interactions.

Introduction

Natural fibers and natural fiber-reinforced composites have attracted the attention of scientists and technologists due to the advantages of these fibers provide over commercial fillers. Natural fibers are naturally occurring composites consist of hollow cellulose fibrils held together by a lignin and hemicelluloses matrix [1]. Advantages of these fibers are abundantly available with low density, cheap, recyclability and biodegradability [2]. The biodegradability nature of plant fibers can contribute to a healthy ecosystem. Their low cost has favored the economic interest of industry [3]. Extensive works has been carried out to investigate the use of natural fibers such as bamboo, oil palm wood and fiber, coconut fiber, pineapple leaf fiber, rice husk and wood as filler in natural rubber compounds [4-10].

In this research study, rattan for its potential as new type filler in natural rubber compounds is studied. Rattans are abundant natural resource in Asia including Malaysia where they are extensively used for making furniture and baskets. Rattan is lightweight, strong and durable cane [11]. Thus, the waste rattans have spurred the interest to explore the possibility to be use as filler in rubber compounds. The cure characteristics, mechanical properties, rubber-filler interaction and surface morphology study of rattan filled natural rubber compounds are investigated.

Experimental

Materials and formulation. Table 1 shows the formulation, materials and their suppliers used in this study. Rattan wastes were collected and ground into size < 180 μm.

Table 1: Formulation of rattan filled NR compounds

Ingredients	Formulation [phr]	Supplier
Natural Rubber	100	Rubber Research Institute Malaysia
Rattan	0, 5, 10, 15, 30	Seng Huat Shop
Zinc Oxide	1.5	Bayer (M) Ltd
Stearic Acid	1.5	Bayer (M) Ltd
CBS[a]	1.9	Bayer (M) Ltd
BKF[b]	2.0	Bayer (M) Ltd
Sulphur	1.6	Bayer (M) Ltd

[a]CBS - N-cyclohexyl-2-benzolthyazolsulfenamide
[b]BKF - 2,2 methylene-bis-(4-methyl-6-tert-butylphenol)

Sample Preparation. Mixing was carried out in a laboratory model two roll mill according to method in ASTM D 3184-80. The cure characteristics of rubber compounds were studied using a Monsanto Rheometer, model MDR 2000 at 150°C. Cure time (t_{90}), scorch time (t_{s2}) and maximum torque (M_H) were obtained from the rheographs. The rubber compounds were molded into sheets with respective cure time, t_{90} at 150°C using Hot Press Machine.

Measurement of tensile properties. Dumbbell shaped samples were cut from vulcanized rubber sheets and tensile test were carried out according to ASTM D 412 at a constant rate of 500 mm/min by Instron Universal testing machine, model 1114.

Scanning Electron Microscopy (SEM). Examination of the tensile fracture surface was carried out using a scanning electron microscopy (SEM) Model Leica Cambridge S-360 (10 kV of operating volume). The fracture surfaces were sputter coated with gold to avoid electrostatic changing and poor image resolution.

Rubber-Filler interaction. The vulcanized sample (30 mm × 5 mm × 2mm) were accurately weighed and immersed in toluene and allowed to swell in closed bottle for 48 hours at room temperature (25°C). The sample was removed and the surface of swollen sample was quickly wiped and weighed. The sample was dried in an oven at 60°C for 15 minutes and weighed. Q, the weight of toluene uptake per gram of rubber hydrocarbon was determined according to the Eq. 1.

$$Q = \frac{\text{Swollen weight} - \text{Dried weight}}{\text{Original weight} \times 100/\text{Formula weight}} \quad [1]$$

The rubber-filler interaction was calculated using Lorenz and Park equation as Eq. 2:

$$\frac{Q_f}{Q_g} = ae^{-z} + b \quad [2]$$

The subscripts *f* and *g* in Eq. 2 refer to filled and gum vulcanizates, respectively. Z is the ratio by weight of filler to rubber hydrocarbon in the vulcanizate, while a and b are constants. The higher the Qf/Qg values, the lower will be the extent of interaction between filler and matrix.

Results and Discussion

Curing characteristics. The values of cure time (t_{90}), scorch time (t_{s2}) and maximum torque (MH) of rattan filled natural rubber (NR) compounds are presented in Fig.1 and Fig.2**.** The scorch time (t_{s2}) and cure time (t_{90}) shorten with increasing filler loading. Several researchers [4-5,8,12-13] also reported similar observation. As filler loading increases, the time for filler addition into rubber compounds also increases. As a consequence, the rubber compounds remains longer on the mill during mixing and leads to reduction of scorch and cure time. According to Ismail et al. [14]**,** the cure enhancement can be associated to filler related parameters such as particle size and surface area. In this study the cure enhancement might due to the lower surface area of irregular shaped fillers. Fig.2 illustrates that the maximum torque of NR compounds increases with filler loading. The mobility of the macromolecular chains of rubber is limited by the inclusion of the unstrained filler. Thus, the more restriction is imparted when the filler loading increased and consequently composite becomes harder and stiffer [12-16].

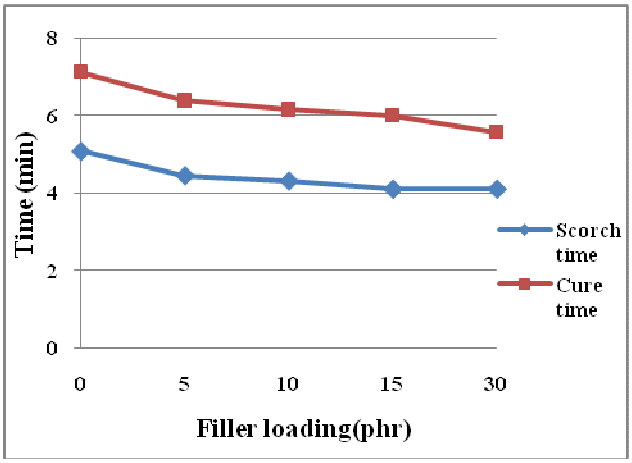


Fig. 1: Effect of rattan loading on scorch time (t_{s2}) and cure time (t_{90}) of rattan filled NR compounds

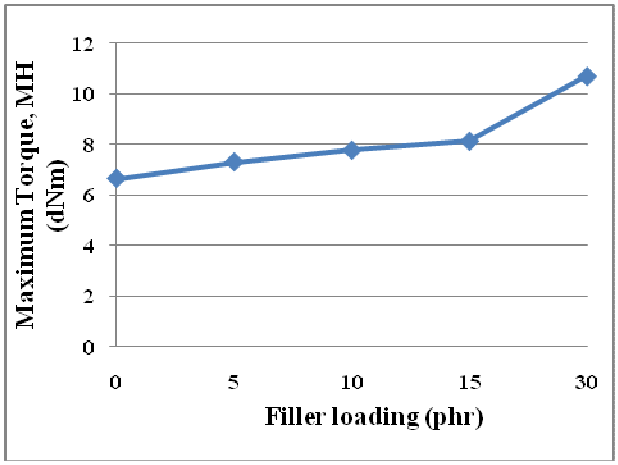


Fig. 2: Effect of rattan loading on maximum torque (MH) of rattan filled NR compounds

Tensile Properties. The effect of filler loading on tensile properties of rattan filled natural rubber compounds are shown in Fig.3- Fig.5. It is clearly seen from the Fig.3 that the tensile strength of control (without filler) is higher than the filled NR compounds. The tensile strength shows decreasing trend as increasing filler loading. This is due to various shape, size and length of filler and also the poor adhesion or incompatibility between polar fiber and non-polar rubber. This results to a weaker rubber-filler interaction, as a consequence the filler unable to support the uniform transmission of stresses from the rubber matrix [4,5,9,12,15].

Fig.4 & 5 present the elongation at break and tensile modulus, stress at 100 % elongation and stress at 300 % elongation of rattan filled compounds. Elongation at break decreases as increasing filler loading, whereas, the opposite trend is observed for the tensile modulus of rattan filled NR compounds. Da Costa et al. [10], Ismail et al. [4], Ichazo et al. [9] and Saramolee et al. [15] also obtained similar results in their work of other filled compounds. As filler loading increases, a higher restriction to movement of macromolecules or resistance to flow is experienced by the compounds. The elasticity of compound is reduced resulting in more stiff and rigid compounds. This leads to lower resistance to break. Thus, the elongation at break decreases and the modulus increase**s.**

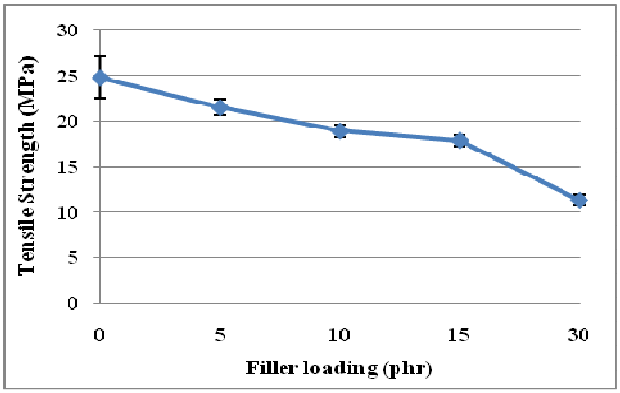


Fig. 3: Effect of filler loading on tensile strength of rattan filled NR compounds

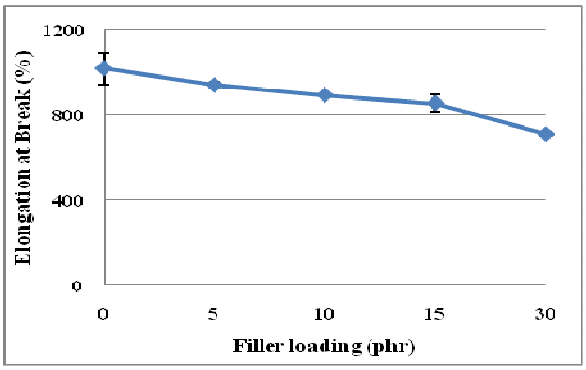


Fig. 4: Effect of filler loading on elongation at break of rattan filled NR compounds

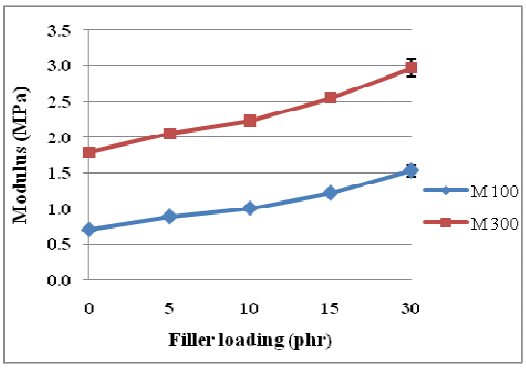


Fig. 5: Effect of filler loading on stress at 100 % elongation (M 100) and stress at 300 % elongation (M 300) of rattan filled NR compounds

Rubber-Filler Interaction

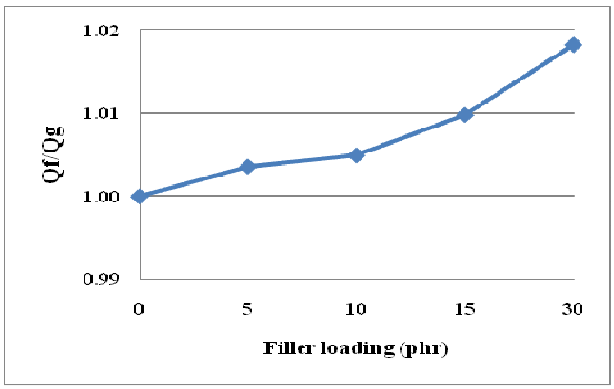
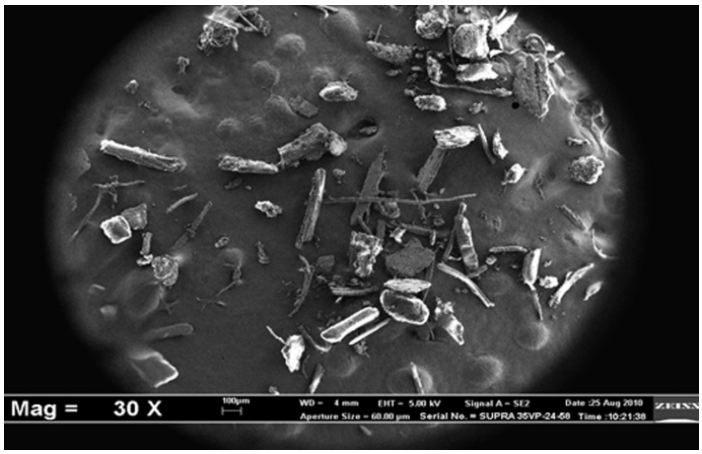


Fig. 6: Rubber-filler interaction of rattan filled NR compounds

The rubber-filler interactions, Q_f/Q_g of rattan filled NR compounds are illustrated as in Fig.6. It is known the higher the Q_f/Q_g value, the lower the extent of interaction between fiber and matrix. The different nature between rubber which is hydrophobic and rattan filler, hydrophilic makes rubber filler interactions become weaker, results in poor mechanical properties. This result supports our previous result of reduction in tensile strength and elongation at break as increasing filler loading.

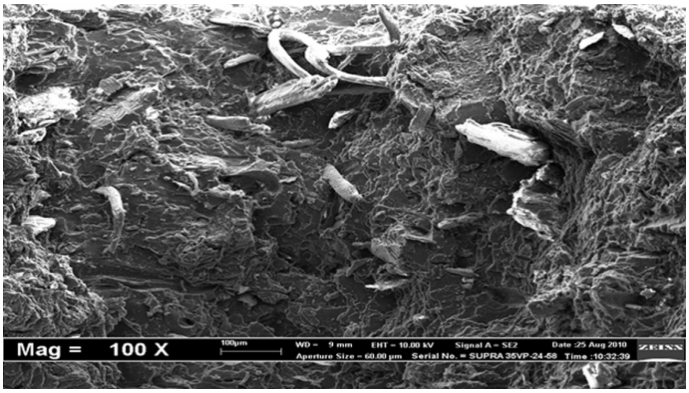
Scanning Electron Microscopy (SEM). The SEM micrographs of rattan fiber and tensile fracture surfaces of rattan filled NR compounds with 5, 10 and 30 phr rattan loading are shown in Fig.7. Fig.7 (a) proves that the rattan fiber is in various shape, size and length. It can be seen from Figs.7 (b), (c) and (d) that as the filler loading increases, the fracture surface becomes rougher. Besides, we can also observe several breakage of fibers and fiber pullouts or detachment of fiber from the rubber matrix. There are more holes resulted from the fiber pullouts. It is proven in Fig.7 (d) that the surface becomes rougher with many holes with increasing filler loading compared to other filled fracture surfaces. This phenomenal indicates that the poorly wetted irregular shaped fibers by rubber matrix results in poor rubber filler interaction and reduction in tensile properties. Similar result is obtained and explained by other researchers such as Saramolee et al. [15]. It is also well explained by the SEM micrograph.



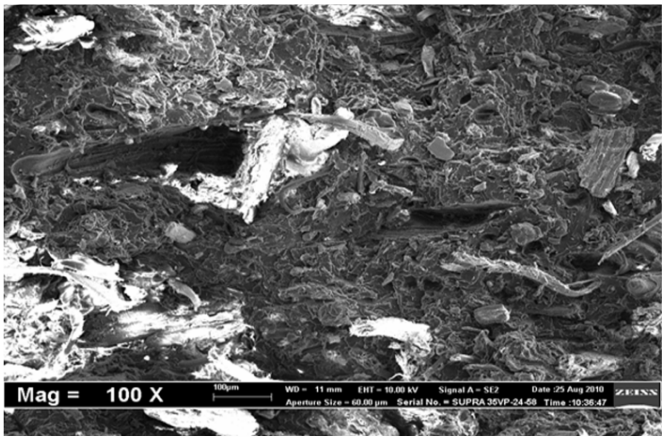
(a)



(b)



(c)



(d)

Fig. 7: Scanning electron microscopy of (a) raw rattan fiber and tensile fracture surfaces of rattan filled NR compounds at different rattan loadings (b) 5 phr; (c) 10 phr; (d) 30 phr at magnification×100.

Summary.
The incorporation of rattan filler has shortened the scorch and cure time but increased the maximum torque. As the filler loading increases the tensile modulus increases but reduction is observed for tensile strength and elongation at break. This reduction is due to the poor or weaker rubber filler interaction which also has supported by the SEM micrographs. Nevertheless, rattan still can be used as filler depending on the performance desired for a given application, for instance application that requires moderate tensile properties.

References

[1] M.J. John and R.D. Anandjiwala: Polym. Compos (2008), p. 187-207

[2] X. Li, L.G. Tabil and S. Panigrahi: J. Polym. Environ Vol. 15 (2007), p. 25-33

[3] S. Taj, M.A. Munawar and S. Khan: Proc. Pakistan Acad. Sci Vol. 44(2) (2007), p. 129-144

[4] H. Ismail, S. Shuhelmy and M. R. Edyham: Eur. Polym. J Vol. 38 (2002), p. 39-47

[5] H. Ismail, R.M. Jaffri and H.D. Rozman: J. Elast. Plast Vol. 35 (2003), p. 181-192

[6] H. Ismail, N. Rosnah and H.D. Rozman: Polym Vol. 38(16) (1997), p. 4059-4064

[7] P.A. Egwaikide, E.E. Akporhonor and F.E. Okieimen: Int. J. Phys. Sci Vol. 2 (2007), p. 39-46

[8] N. Lopattananon, K. Panawarangkul, K. Sahakaro and B. Ellis: J Appl. Polym. Sci Vol. 102 (2006), p. 1974-1984

[9] M.K. Ichazo, M. Hernandez, C. Albano and Gonzalez: J. Macromol. Symp Vol. 239 (2006), p. 192-200

[10] H.M. Da Costa, R.C.R. Nunes, L.L.Y. Visconte, and C.R.G. Furtado: Physical Properties and swelling of natural rubber compounds containing rice husk ash, Raw Materials and Applications (2001), 242-249

[11] A.N. Rao and V.R. Rao: Priority Species of Bamboo and Rattan, IPGRI-APO, Serdang, Malaysia, (1998)

[12] H. Ismail and F.S. Haw: J. Appl. Polym. Sci Vol. 110 (2008), p. 2867-2876

[13] H. Ismail: J. Elast. Plast Vol. 33 (2001), p. 34-46

[14] H. Ismail, H.D. Rozman, R.M. Jaffri and Z.A.M. Ishak: Eur. Polym. J Vol. 33(10) (1997), p. 1627-1632

© (2011) Trans Tech Publications, Switzerland
doi:10.4028/www.scientific.net/KEM.471-472.851

The Effect of Chitosan Loading on the Properties of Chitosan Filled Epoxidized Natural Rubber Compounds

S.M. Shaari, [a]H. Ismail and N. Othman
Division of Polymer Engineering, School of Materials & Mineral Resources Engineering, Engineering Campus, Universiti Sains Malaysia, 14300 Nibong Tebal, Penang, Malaysia
[a]hanafi@eng.usm.my

Keywords: chitosan, epoxidized natural rubber, curing characteristics, mechanical properties

Abstract. The study of chitosan loading onto epoxidized natural rubber compounds were prepared by incorporation of chitosan into epoxidised natural rubber matrix using a two-roll mill. The effects of chitosan loading on the curing characteristics, tensile properties and morphology of the compounds were investigated. Results indicated that slight changes in curing time (t_{90}), and scorch time (t_{S2}) of the compounds with the incorporation of chitosan. An increment is observed in the maximum torque, tensile modulus and durometer hardness of the compounds while tensile strength and elongation at break declines with chitosan loading.

Introduction

The name filler is given widely to almost all material which is added in sufficiently large quantities to reduce the amount of rubber needed. Reinforcing fillers are those fillers which increase the service life of the product by improving mechanical properties such as elongation, tensile strength, and resistance to tear, abrasion, and friction while, the other type fillers, namely inert fillers, do not impart these properties but help in processing, reduce cost and modify elongation, stiffness and hardness but not tensile strength, tear strength and abrasion resistance [1].

The concept of reinforcement for rubbers is complex to define, but may be considered as the enhancement of the modulus, failure properties (tensile and tear strength), and abrasion resistance of the vulcanizates [2]. Hence, the main goal for filler addition is to improve certain properties and cheapen the compound. It is also well known that the particle size, structure, and surface characteristics of the fillers are the main factors controlling the reinforcing ability, in particular, the particle size.

Reinforcing rubbers with commercial fillers have been a common practice in yielding properties for intended applications such as tires, gaskets, mountings and bearings. The vast demand of modern materials with superior properties has limited the exploration of natural fillers while expanding the usage of commercial fillers. The use of these commercial fillers have revolutionized in which nano-sized fillers are later being used.

The reinforcement of polymers using renewable resources is a new technique recently developed in corresponds to the emerging environmental awareness. The recent development has seen researchers incorporating these resources such as oil palms [3], rice husks [4-6], bamboo [7], kenaf [8] and chitin [9-11] into polymeric matrices. The properties of these new biomaterials have shown to be comparable with those commonly used commercial fillers. One of the advantages of these fillers apart from their degradable properties is that they are easily available at a low cost as compared to the commercial fillers.

Chitosan is a linear polymer of α (1→4)-linked 2-amino-2-deoxy-β-D-glucopyranose obtained from N-deacetylation of chitin, a common structural polymer found in exoskeletons [12]. The primary source of chitin and chitosan are from crustaceans such as crabs, shrimps and lobsters which are highly abundant biomass from the consumption and canning industries. Due to its physical and chemical properties, chitosans has received much attention as functional biopolymers and are being used in a wide range of applications ranging from biomedical engineering, pharmaceutical and cosmetic products to water treatment and plant protection [13]. Compared to

the effort made in those fields, there are limited works that has been reported on chitosan and rubber especially in natural rubber compounds. Attempts however have been made to blend chitosan with natural rubber latex [14-17]. In this study however, we are concentrating on implementing chitosan into natural rubber as a new type of filler. One of the most important requirements for chitosan to be successfully employed as fillers in natural rubber is ensuring a good interaction with the natural rubber at a reasonable loading. In this study, epoxidized natural rubber was used instead of natural rubber due to the presence of polar groups (epoxide) in its backbone. The effect of chitosan loading on the curing characteristics and mechanical properties were investigated.

Experimental

Materials. Epoxidized Natural rubber grade ENR with 25% mol epoxidization obtained from Rubber Research Institute Malaysia (RRIM) was used as the matrix. Chitosan powder, average particle size 90μm purchased from Euro Chemo Pharma Sdn. Bhd., Penang was used as filler. Other compounding ingredients were zinc oxide, stearic acid, sulphur, N-cyclohexyl-2-benzothiazole sulfonamide (CBS) and 6-tert-butyl-4 methyl-phenol (BKF).

Preparation of compounds. The compounds were prepared based on the formulations listed in Table 1. Mixing and compounding procedure of chitosan and ENR were carried out in accordance with ASTM D3184-80 using a laboratory size two-roll mill. The compounds produced were then kept in a closed container maintained at 23 ± 3°C for 24 hours before testing.

Table 1 Composition of the rubber compounds

Materials	Compounds (phr)*
ENR-25	100
Zinc oxide	5
Stearic acid	3
BKF	1
CBS	0.5
Sulphur	2.5
Chitosan	0, 10, 20, 30, 40

ENR-25, Epoxidized natural rubber
BKF, 6-tert-butyl-4 methyl-phenol;
CBS, N-cyclohexyl-2-benzothiazole sulfonamide
*parts per hundred rubber

Measurements. The measurements of curing characteristics of the compounds such as cure time (t_{90}), scorch time (t_{S2}), and maximum torque (M_H) were determined with Monsanto Moving Die Rheometer (MDR 2000) according to ASTM 2084 at 150°C. The compounds were then subsequently compression moulded at 150 °C, based on respective t_{90} values. The measurement of the tensile properties was performed using Instron Machine IX3366 at a crosshead speed of 500 mm/min according to ASTM D412.

Results and Discussion

Curing Characteristics. Fig. 1 & 2 show the effect of filler loading on the cure characteristics of chitosan-filled epoxidized natural rubber compounds determined through a Monsanto Rheometer. It can be observed from Fig. 1 that there is a decrease in the scorch time (t_{S2}) and the cure time (t_{90}) with the introduction of 10 phr chitosan. In most cases, cure enhancement are governed by the filler parameters such as surface area, surface reactivity, particle size, moisture content and metal oxides [18]. Therefore, the reduction of scorch (t_{S2}) and cure time (t_{90}) at this point shows an enhancement in cure rate obtained possibly due to the low surface area provided by the chitosan.

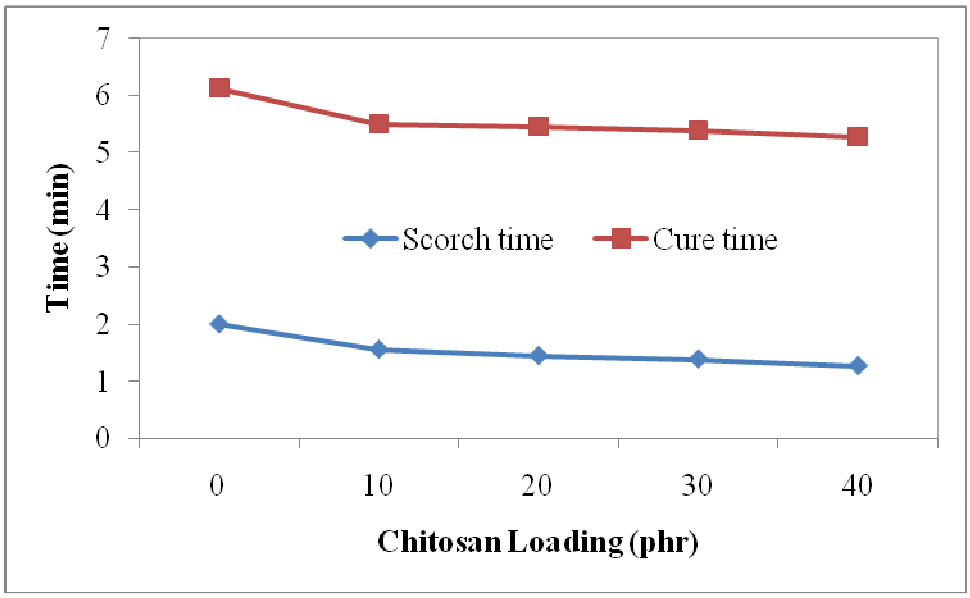


Fig. 1: Scorch time and cure time of chitosan-filled epoxidized natural rubber compound at different chitosan loadings

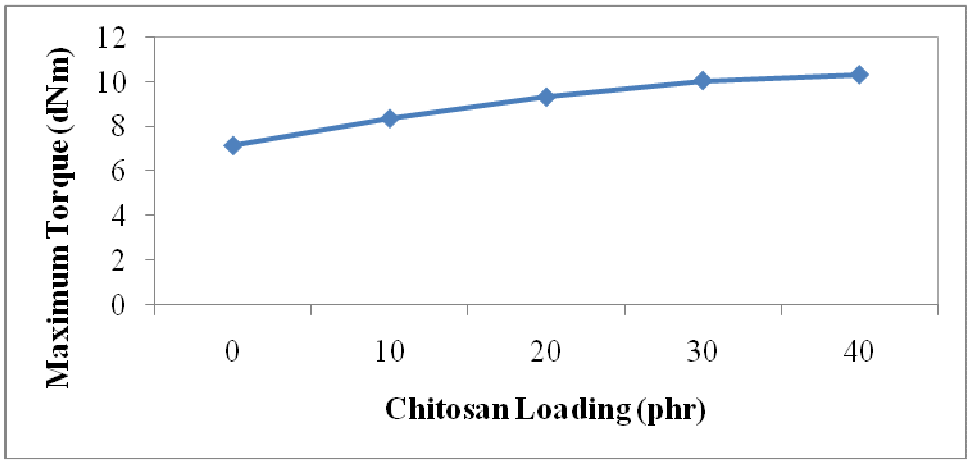


Fig. 2: Maximum torque of chitosan-filled epoxidized natural rubber compound at different chitosan loadings

The maximum torque (M_H) values exhibit an increasing trend as the chitosan loading is increased. The increment of maximum torque values is caused by the increased in stiffness and hardness of the compound due to the restriction of the mobility of the rubber chains as fillers are incorporated [18-20]. Therefore the increasing torque values indicate that the incorporation of chitosan increases the stiffness of the rubber compound. At higher filler loading, the mobility of the chains becomes more limited thus higher maximum torque values are exhibited.

Tensile Properties. Fig. 3 & 4 show the effect of chitosan loading on the tensile properties of chitosan-filled epoxidized natural rubber compounds. As observed in Fig. 3, the tensile strength of the chitosan-filled epoxidized natural rubber exhibited reduction of strength with increasing chitosan loading. The tensile properties of filled compounds generally depend on the size and geometrical factor of the filler. Irregular shaped fillers tend to decrease the strength of the

compounds due to the failure of the fillers to support the stress transferred from the matrix [21]. Whereas, large particle size fillers provide a smaller surface area of interaction hence gives rise to a weaker interaction between filler and rubber matrix [22]. In this study, the reduction of tensile properties may be attributed to the particle size of the chitosan due to the large particle size filler used. A similar observation has also been reported by Ismail et al. [18] when using oil palm wood flour as filler of different size. At higher filler loading, the tensile strength is greatly reduced as a result of poor interaction between the components.

The elongation at break (Eb) observed in Fig. 3 shows a gradual reduction of its values with chitosan loading. The reduction of elongation at break is mainly caused by the increasing brittleness in the composite as a result of the transaction from rubber to plastic nature with increasing chitosan loading [23]. Therefore, the reduction of elongation at break with increment of filler loading is a result of the stiffening of the compounds by the filler. At higher loading of chitosan, the elongation at break decrease further as a result of filler-filler interaction becoming more dominant in the compound [18].

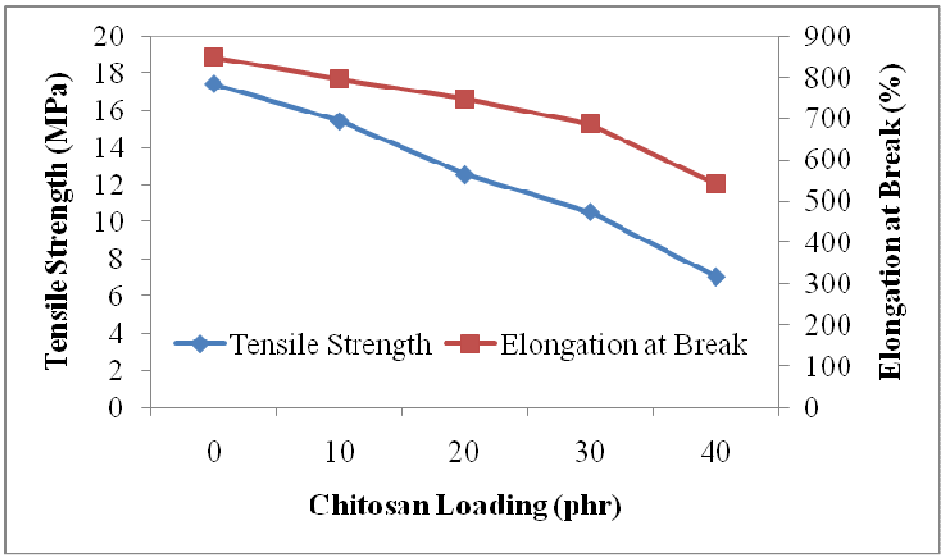


Fig. 3: Tensile strength and elongation at break of chitosan-filled epoxidized natural rubber compound at different chitosan loadings

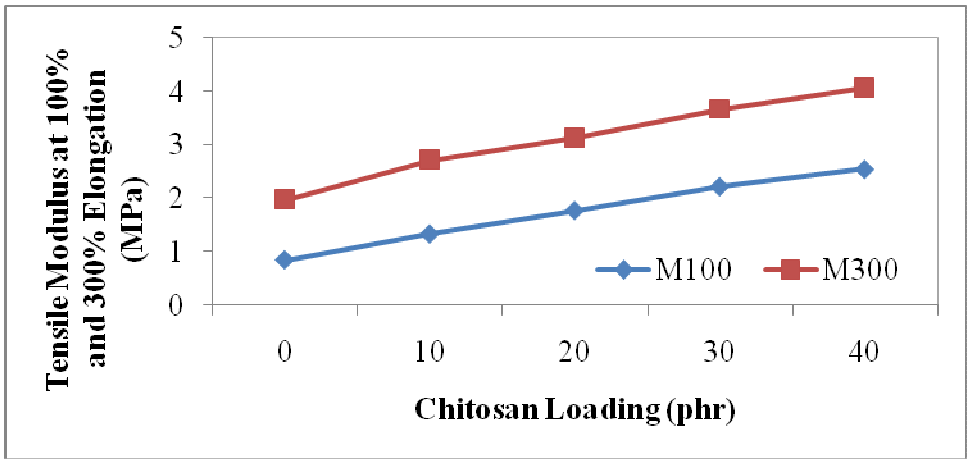


Fig. 4: Tensile modulus at 100% and 300% elongation of chitosan-filled epoxidized natural rubber compound at different chitosan loadings

Referring to Fig. 4, both tensile modulus at 100% and 300% elongation exhibited an increment with chitosan loading. The increased in tensile modulus is associated with stiffness of the compounds [19, 20] whereby the values has increased with filler loading. This indicates that the addition of chitosan into natural rubber compounds improves the stiffness of the compound by reducing the elasticity of the rubber chain and thus produces a more rigid and stiff material.

Summary.

From this study, the following conclusion can be drawn:

1. Reduction of scorch time (t_{S2}) and cure time (t_{90}) with the introduction of chitosan shows an enhancement in cure rate due to the low surface area provided by the chitosan filler.
2. Increment of maximum torque values were caused by the increased in stiffness of the composites due to the restriction of mobility of the rubber chains as chitosan are incorporated.
3. Low tensile strength exhibited by the compounds with chitosan is governed by particle size and geometry of the fillers. These factors play an important role in determining the tensile strength of the compounds.
4. Elongation at break decreases along with the increasing chitosan content is a sign of increment of brittleness of the compound with increasing chitosan loadings.
5. The tensile modulus at 100% and 300% elongations values increases with the filler loading due to the increment of stiffness with increasing chitosan loadings.

Acknowledgements

The authors acknowledge the research facilities and assistance provided by Universiti Sains Malaysia. Shazlin Mohamed Shaari wishes to acknowledge the financial support provided by Universiti Sains Malaysia under the USM Fellowship Scheme in pursuing her PhD study.

References

[1] G. P. Maurya, *Technology of Rubber Products*, Small Business Publication, Delhi, 1972.

[2] M. Arroyo, M. A. Lopez-Manchado, and B. Herrero: Polymer Vol. 44 (2003), p. 2447.

[3] H. Ismail and H. P. S. A. Khalil: Polym. Test. Vol. 20 (2001), p. 33.

[4] H. M. d. Costa, L. L. Y. Visconte, R. C. R. Nunes, and C. R. G. Furtado: J. Appl Polym Sci Vol. 87 (2003), p. 1194.

[5] H. M. d. Costa, L. L. Y. Visconte, R. C. R. Nunes, and C. R. G. Furtado: J. Appl Polym Sci Vol. 90 (2003), p. 1519.

[6] H. M. d. Costa, L. L. Y. Visconte, R. C. R. Nunes, and C. R. G. Furtado: J. Appl Polym Sci Vol. 87 (2003), p. 1405.

[7] H. Ismail, M. R. Edyham, and B. Wirjosentono: Polym Test Vol. 21 (2002), p. 139.

[8] H. Ismail, A. M. Norjulia, and Z. Ahmad: Polym-Plast Tech Eng Vol. 49 (2010), p. 938.

[9] K. G. Nair and A. Dufresne: Biomacromolecules Vol. 4 (2003), p. 657.

[10] K. G. Nair and A. Dufresne: Biomacromolecules, Vol. 4 (2003), p. 666.

[11] K. G. Nair, A. Dufresne, A. Gandini, and M. N. Belgacem: Biomacromolecules, Vol. 4 (2003), p. 1835.

[12] P. K. Dutta, J. Dutta, and V. S. Tripathi: J. Sci Ind Research Vol. 63 (2004), p. 20.

[13] M. N. V. Ravi-Kumar: React Funct Polym Vol. 46 (2000), p. 1.

[14] J. Johns and V. Rao: Int J Polym Anal Char Vol. 14 (2009), p. 508.

[15] J. Johns and V. Rao: Fibres and Polymers Vol. 10 (2009), p. 761.

[16] J. Johns and V. Rao: J Mat Sci Vol. 44 (2009), p. 4087.

[17] J. Johns and V. Rao: Int J Polym Anal Charac Vol. 13 (2008), p. 280.

[18] H. Ismail, H. D. Rozman, R. M. Jaffri, and Z. A. Mohd Ishak: Eur Polym J Vol. 33 (1997), p. 1627.

[19] X. Yuan, Y. Zhang, and X. Zhang: J Appl Polym Sci Vol. 71 (1999), p. 333.

[20] H. Ismail and S. M. Shaari: Polym Test Vol. 29 (2010), p. 872.

[21] H. Ismail and F. S. Haw: J Appl Polym Sci Vol. 110 (2008), p. 2867.

[22] B. T. Poh, H. Ismail, and K. S. Tan: Polym Test Vol. 21 (2002), p. 801.

[23] V. Rao and J. Johns: J Appl Polym Sci Vol. 107 (2008), p. 2217.

© (2011) Trans Tech Publications, Switzerland
doi:10.4028/www.scientific.net/KEM.471-472.868

Investigation On The Microwave Properties Of Kenaf And Rice-Husk Fiber Reinforced Pla Composite Utilizing One-Port Coaxial Transmission Line Reflection Method

Nor`aini Ahmad Zawawi[1], Alyani Ismail[2], Khalina Abdan[3] and Mohd Adzir Mahdi[4]

[1,2,4]Centre of Excellence for Wireless and Photonic Networks
Department of Computer and Communication Systems Engineering
Faculty of Engineering, Universiti Putra Malaysia, Selangor, Malaysia
[3] Laboratory of Biocomposite Technology, Institute of Tropical Forestry and Forest Products, Universiti Putra Malaysia, Selangor, Malaysia

[1]ai_nee3@yahoo.com; [2]alyani@eng.upm.edu.my; [3]khalina@eng.upm.edu.my; [4]mdadzir@eng.upm.edu.my

Abstract: The paper investigates the microwave properties of natural fiber reinforced biodegradable plastic composites in order to recognize their potential as alternatives to common printed circuit board (PCB) for electronic communication industries. Thus, the paper reports on measured dielectric properties for two new composites under study: Kenaf/Poly Lactic Acid (PLA) and rice husk/PLA and their results are compared. The sample is made from equal weight percentage loading (50%wt - 50%wt) of kenaf and PLA. Another sample has also equal weight percentage loading (50% wt - 50%wt) of rice husk and PLA. The complex dielectric permittivity ($\varepsilon = \varepsilon' - j\varepsilon''$) and loss tangent ($tan\ \delta$) of the two samples of natural fibers plastic composites have been studied in the frequency range of 500 MHz to 10 GHz. The dielectric permittivity is measured by scattering parameter (S-parameter) using a Vector Network Analyzer (VNA). The concentration dependence of permittivity and loss tangent is analyzed for each sample. It is observed that from 500 MHz to 3.32 GHz, real permittivity (ε') values are consistent throughout the wide frequency range, at approximately 3.3. However, the permittivity seems to decrease at higher frequencies starting from 3.35 GHz for both samples, down to 2.5 at 10 GHz. Measured results show that kenaf/PLA mixture has higher permittivity (ε') than the rice husk/PLA composite across the wide frequency range. Meanwhile, loss tangent ($tan\ \delta$) is low and remains similar for both types of fiber compositions.

Introduction

Natural fiber composites consist of natural plant such as leaf, wood, empty fruit bunch and others that comes from the plant itself. Related to the environmental issues, many researchers have found alternative ways to replace the existing and commonly used materials based on natural fiber. There are many advantages of using natural-based materials, for instance, they can be recycled, easy to find, cheap and environmental friendly. With the fast advancement of technologies, natural fiber applications can be seen as a new solution to the occurring environmental problems.

Due to increasing global awareness, researchers found that bio-composite materials can replace the non-degradability plastics. As a solution, biodegradable polymers like PLA, is having a good potential because of its good properties in mechanical strength, transparency, compostability and safety to use [1, 2]. Apart from being biodegradable, the fact that PLA originated from a renewable resource for example corn, potatoes, sugar beets and wheat, makes it recognized as a material with low environmental burden.

Among thousands of natural fibers, kenaf and rice husk have attract interest of researchers. Kenaf is an excellent source for cellulose fibers with less energy and chemical requirements than standard wood sources [3]. In addition, it grows up faster and can be planted in a wide range of weather, and has been actively cultivated [4]. There are many researches being reported on mechanical properties for kenaf/ PLA composites [5, 6].Mechanical properties of kenaf and PLA

composites [5] reported tensile strength of kenaf fibers did not decrease, after being heat-treated at 160°C for 60 minutes, and flexural strength ability increased linearly for fiber content up to 50%, whereby biodegradability of kenaf/PLA composites decreased by 38% after 4 weeks of compositing. Reported in [7], mechanical properties of kenaf/PLA composites were better than PLA on its own. Different to kenaf, rice is a main meal to some countries especially in Asia. In the process to get rice, rice husk was separated from paddy grain and normally the husk was burnt with no value for other uses. There has been research for rice husk/PLA composites by [6] in terms of its mechanical properties. Flexural strength of 85 MPa, flexural modulus of 4.0 GPa and impact strength of 30.0 Jm^{-1} has been reported for rice husk/PLA composites [6].

One of the environmental concerns is the increasing volume of electronic waste contributed by emerging electronic industries. The electronic wastes being dumped are commonly printed circuit boards (PCB) whereby the copper parts being the only valuable waste, and the substrate (commonly toxic substances) being dumped. Therefore, our aim in this study is to provide alternatives for electronic industries, from conventional and toxic PCB to environmental friendly substrates (green substrates). We demonstrate here for frequency-dependent substrates, especially for communication industries. For frequency dependent substrates, permittivity value of the material is important to be determined. This paper reports on a study involving the evaluation of complex dielectric permittivity, given by:

$$\varepsilon = \varepsilon' - j\varepsilon'' \quad (1)$$

and loss tangent

$$tan\ \delta = \varepsilon''/\varepsilon' \quad (2)$$

of two types of fiber reinforce composites namely kenaf/PLA and rice husk/PLA with 50% loading each in the frequency range of 500 MHz to 10 GHz.

Fiber preparation. In this experiment, PLA was chosen as filler while kenaf and rice husk were used as raw materials as a basis for the fibers. The whole stem kenaf (WSK) of variety V36 was obtained from Malaysian National Kenaf Tobacco Board (MNKTB). The kenaf stems were chipped before being flaked to reduce the size of fibers. The kenaf flakes were then screened into different particular sizes. In this study, the kenaf fibers were sieved using 250 μm sieve shaker. The fibers were dried up in the oven at 70°C for 24 hours until a constant weight was reached for further process. Meanwhile, rice husks were supplied by the Forest Research Institute of Malaysia (FRIM) in the form of fibers and used as received in the original form. The process did not involve chemical treatment of the fibers prior to processing.

Polymer. The Poly Lactic Acid (PLA) granules used for this experiment was supplied by Biomer (Biomer ® L9000, molecular weight M_w: 220 kDa; M_n: 101 kDa, density: 1.25 gcm^{-3}, MFI: 3-6 g/10 min).

Composite sample preparation. The composites were prepared using melt blending technique using Haake Internal Mixer at 50% fiber loadings meaning that the samples are being made of a composition in equal weight between the filler (PLA) and fibers. The melt blending was carried out at 170°C at 50 rpm of rotor speed. The required amount of PLA was preheated for 2 minutes and then mixed with required amount of kenaf or rice husk fiber for 8 minutes. After the process of melt blending, the composites were removed and cooled at room temperature. Scraped composites were weighted according to the volume of the mold (150 mm x 150 mm x 1 mm). The composite samples were preheated at 175°C without applying any pressure for 20 minutes to allow complete melting using hot platen press. The melted composite was then pressed for 5 minutes at 70 bar and then placed between two plates of a cold press platen to solidify and cool for 5 minutes at 25°C.The samples were cut into a ring shape with inner diameter of 3.05 mm and outer diameter of 6.97 mm. To calculate the permittivity of all the prepared samples, the scattering parameters (S-parameters) from the VNA were needed to be evaluated.

Experimental set-up. Fig. 1 depicts the experimental set-up involving a vector network analyzer (VNA), sample support for the one-port reflection measurement, and a personal computer as data logger. GPC7 coaxial transmission line from KEYCOM Company [10] is used as the sample holder, while the VNA was set to measure at the frequency range of 500 MHz to 10 GHz. The thickness of the sample has to be known precisely since it will affect the calculations of complex permittivity (ε). Fig. 2 shows a schematic representation of the KEYCOM sample placement at the coaxial holder.

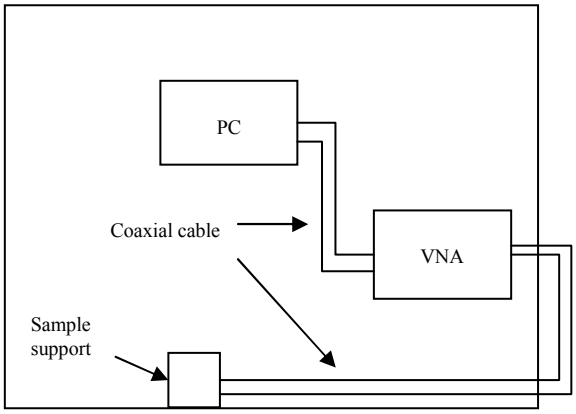


Fig. 1: Representation of measurement set up for permittivity measurement

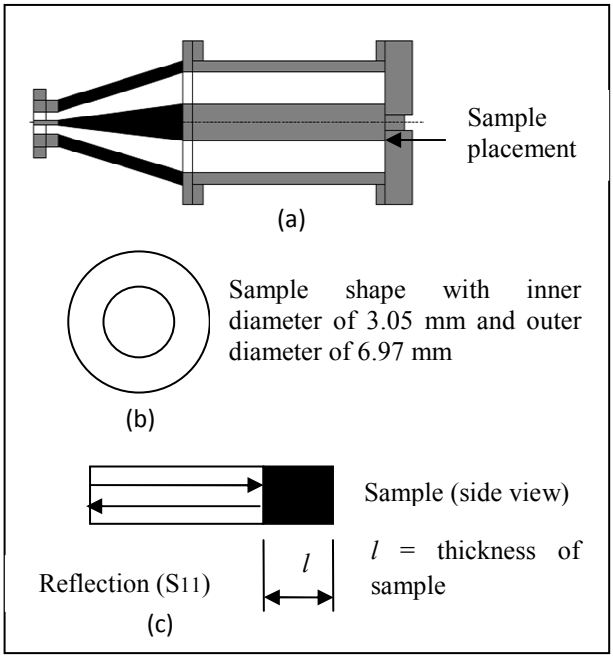


Fig. 2: Representation of the transmission/reflection line (a) coaxial sample holder (b) sample in ring shape (top view) (c) input/output inner conductor of side view

Results and discussion

The measured dielectric permittivity (ε' and ε'') and loss tangent ($tan\ \delta = \varepsilon''/\varepsilon'$) for kenaf/PLA and rice husk/PLA results are shown in Fig. 3.

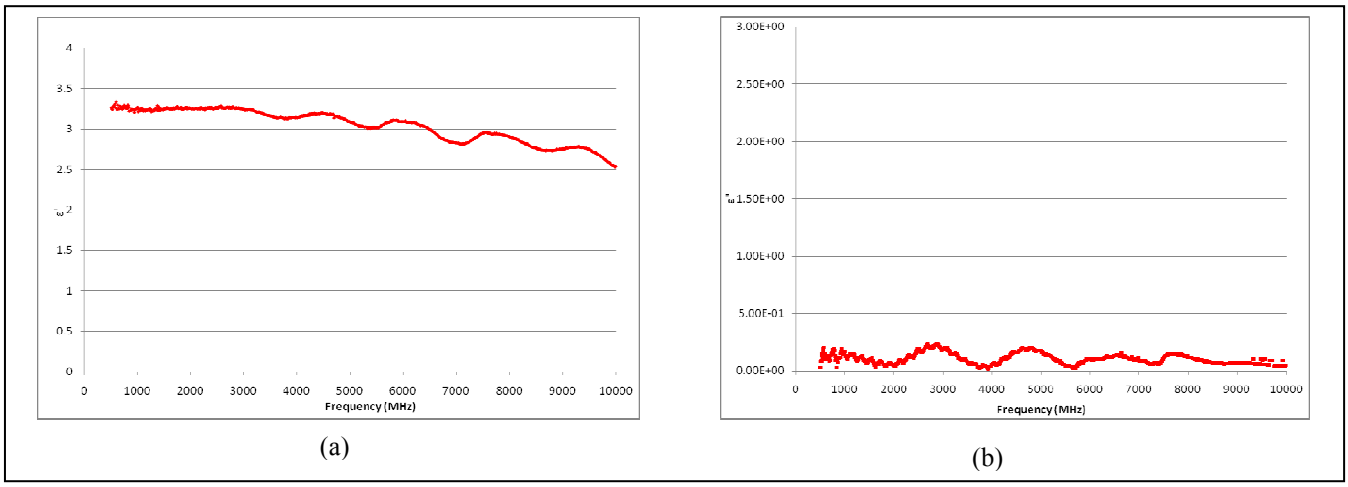


Fig. 3: (a) Real (ε') and (b) imaginary (ε'') of dielectric permittivity of kenaf/PLA (50% mass concentration of kenaf)

From 500 MHz to 3.35 GHz, ε' can be seen remaining constant at about 3.3. As it goes further to higher frequency, the permittivity value seems to decrease slowly. Results show that the permittivity value ranging from 3.3 down to 2.5 across the huge frequency range. The imaginary components, ε'' also consistently low values that is (0.0180 – 0.240) across the frequency range.

Fig. 4 shows real (ε') and imaginary part (ε'') of the permittivity for 50 % rice husk and 50% of PLA loading. As frequency increases, the real permittivity (ε') value seems to decrease slowly.

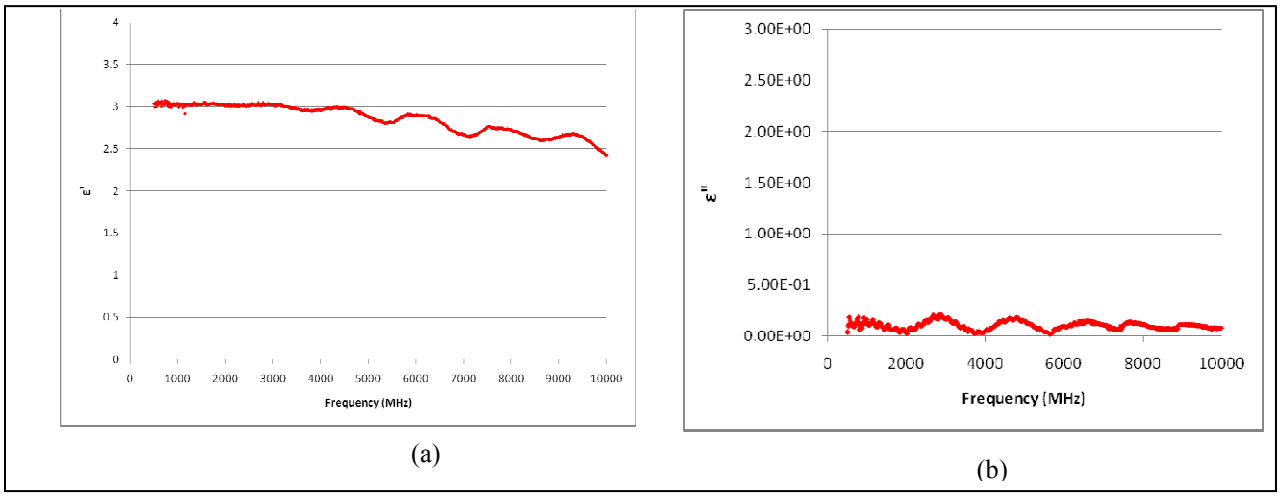


Fig. 4: (a) Real (ε') and (b) imaginary (ε'') of dielectric permittivity of rice husk/PLA (50% mass concentration of rice husk)

Value of real (ε') permittivity is almost at 3 from 500 MHz to 3.35 GHz. The value decreases until it reaches 2.42 at 10 GHz. Meanwhile, imaginary part values (ε'') are in the range of 0.0168 to 0.218. Loss tangent for each composition is shown in Fig. 5. Loss tangent is calculated from Equation (2). In general, there are not so much differences between the loss tangents for kenaf/PLA composition with rice husk/PLA composition. Both composites have low loss tangent not exceeding 0.1.

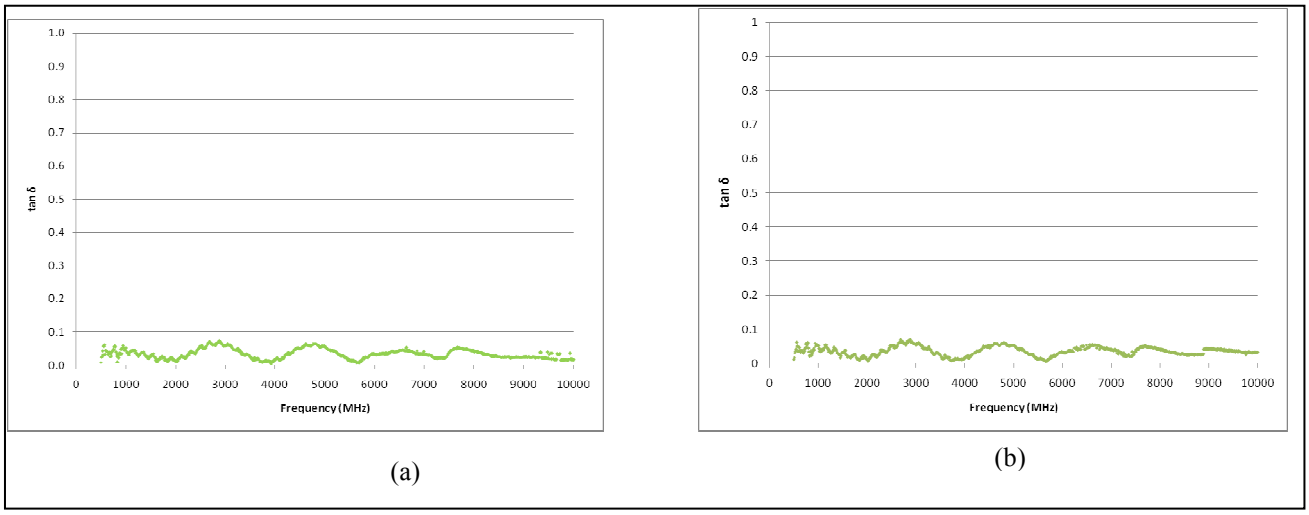


Fig. 5: Loss tangent (tan δ) of (a) kenaf/PLA and (b) rice husk/PLA of the composites

To get the best results, sample size should be accurately matched the size of the inner and outer conductor which is 3.05 mm and 6.97 mm for inner and outer diameter perfectly. Even a small air gap between the sample and the coaxial transmission line test fixture may cause great errors [8, 9].

The placement of sample should be smoothly at the end of short or open panel. It might also have an air gap if the sample is not placed correctly at the end of panel. Having state that, this paper provide excellent starting point data that have not been reported elsewhere before, for the circuit or device designers to effectively design any frequency-dependent components based on the permittivity values presented.

Summary

The results of this experiment involving the dielectric properties of kenaf/PLA compositions and rice husk/PLA compositions show the dependency of complex permittivity (ε' and ε'') parameters on the frequency, in the range of 500 MHz to 10 GHz. From observation, real permittivity (ε') parameter shows significant variation with frequency range. It is also observed that kenaf/PLA composition with the same weight content have higher permittivity (ε') value compared with rice husk/PLA composition. The results show that both kenaf/PLA composite and rice husk/PLA composite can be used for microwave applications due to its permittivity range and low loss tangent comparable to existing commercial substrates for example, epoxy-based dielectrics.

References

[1] M. Ajioka, K. Enomoto, K. Suzuki and A. Yamaguchi: submitted to Journal of Polymers and the Environment (1995)

[2] H. Balakrishnan, A. Hassan and M. Wahit: submitted to Journal of Elastomers and Plastics (2010)

[3] C.L Webber and R. Bishop.: International Conference on Management Issues and Challenges in the Third Millennium. IEMC '98 Proceedings (1998), p. 508

[4] F. Ardente, M. Beccali, M. Cellura, and M. Mistretta: submitted to Journal of ScienceDirect (2008)

[5] S. Ochi: submitted to Journal of ScienceDirect (2008)

[6] A. Yussuf, I. Massoumi and A. Hassan: submitted to Journal of Polymers and the Environment (2008)

[7] M. Huda, L. Drzal, A. Mohanty and M. Misra, submitted to Journal of ScienceDirect (2008)

[8] R. Huang Huang, D. Huang: submitted to Journal IEEE Transactions (2008)

[9] L. Liu, S. Matitsine, Y. Gan, L. Chen, L. Kon, and K. Rozanov:submitted to Journal of Applied Physics (2007)

[10] "S-Parameter Reflection Mode for type GPC7, KEYCOM Corporation, Japan"

© (2011) Trans Tech Publications, Switzerland
doi:10.4028/www.scientific.net/KEM.471-472.874

Influence of Mixed-mode Ratio on Delamination Fracture Toughness and Energy Release Rate of Glass/Polyester Laminates

Astiaj Khoramshahi[1,a], Naghdali Choupani[2,b]

[1] Mechanical Engineering Department, Sahand University of Technology,
P.O. Box 51335-1996, Tabriz, Iran

[2] Mechanical Engineering Department, Sahand University of Technology,
P.O. Box 51335-1996, Tabriz, Iran

[a]a_khorramshahi@sut.ac.ir, [b]Choupani@sut.ac.ir

Keywords: Glass fibers, Delamination, Fracture toughness

Abstract. Glass fiber reinforced materials are particularly attractive for transportation industries because of their high strength/mass ratio and their low cost compared to other materials. Therefore, the composite material system used in this study consists of polyester resin layers reinforced with E-glass fabrics. In this paper, the effect of mixed-mode loading on fracture parameters of glass reinforced polyester composite specimens is investigated both experimentally and numerically. Geometric factors were calculated for modified Arcan specimen using finite element analysis. The finite element results indicated that for loading angles close to pure mode-II loading, a high ratio of mode-II to mode-I fracture is dominant and there is an opposite trend for loading angles close to pure mode-I loading. According to experimentally measured fracture toughness for glass/polyester, the opening-mode and shearing mode interlaminar critical strain energy release rates, were found. Results indicated that the interlaminar cracked specimen is tougher in shear loading condition and weaker in tensile loading conditions.

Introduction

Fiber-reinforced polymeric composites have been studied as advanced materials for many applications such as automotive, aerospace and marine industries because of their potential for outstanding mechanical properties. The ability of these materials to be designed to suit a particular purpose makes them desirable for many usages [1, 2].

There are several fracture modes in fiber reinforced composite materials: fiber breakage, matrix cracking, fiber/matrix debonding, fiber pull-out, plugging, and interlaminar delamination, etc. [3]. Delamination, by definition, is the separation between two lamina in a laminated structure, and is usually evaluated or estimated as the type of fracture toughness that is the constant property of a material. Due to the strong anisotropy of composite structures, the fracture is usually not a result of pure mode-I or pure mode-II loading; hence, the delamination occurs in the mixed-mode loading conditions. For this reason, the study of the mixed-mode interlaminar fracture toughness is very important. The aim of this paper is to investigate the mode I, mixed mode I/II and mode II fracture toughness of glass fiber composite system. The ratios used for mixed mode testing were 16%, 33%, 50%, 66%, and 80% ratio of mode II.

In the present study, a test procedure developed by Arcan et al. [4] was employed. By varying loading angles of arcan specimen all above mentioned mixed modes, including pure mode I and mode II were created. The effect of loading position on geometric factors of Arcan specimen were investigated via two-dimensional finite element analysis. The obtained finite element results accompanied by experimentally measured critical loads in order to propose an interlaminar fracture toughness of glass reinforced polyester composite material under consideration.

Theoretical backgrounds

The strain energy release rates in plane-stress and plane-strain conditions for anisotropic materials can be calculated from the Eq. 1 as [5]:

$$G_I = K_I^2 \Big/ E_I$$
$$G_{II} = K_{II}^2 \Big/ E_{II} \quad (1)$$

where E_I and E_{II} are effective modules, and K_I and K_{II} are mode-I and mode-II stress intensity factors, respectively. It is assumed that the specimens are orthotropic linear elastic material. For plane strain conditions, effective modules E_I and E_{II} are mentioned in [5]. By incorporating the mixed-mode loading allowable in the Arcan fracture specimen, the stress intensity factors ahead of the crack tip for a modified version of an Arcan specimen are calculated through Eq. 2 [6], where P_c is the critical load at fracture, *w* is the specimen length, t is the specimen thickness, and *a* is the crack length of the specimen.

$$K_I = \frac{P_c\sqrt{\pi a}}{wt} f_1(a/w)$$
$$K_{II} = \frac{P_c\sqrt{\pi a}}{wt} f_2(a/w) \quad (2)$$

Experimental procedure

Laminates of E-glass fabrics were prepared by simple hand lay-up technique in a mold at laboratory temperature. All the laminates were made with total 12 plies of E-glass layers to obtain a desired specimen thickness. In order to make an appropriate bond between composite specimens and holders, a two component adhesive based on epoxy system was employed. Bonded specimens were pinned into the Arcan device in order to transmit, and to apply loads. The mixed mode loading for a modified version of Arcan specimen is shown in Fig. 1. Fracture tests were conducted by controlling the constant displacement rate of 0.5 mm/min, and the fracture loads and displacements were recorded. Tests were repeated three times for every loading angle. All the test samples were fractured suddenly from the crack tips, with negligible non-linear deformation showing the brittle fracture behavior of the tested composite material. Table 1, demonstrates the interlaminar fractured specimen data, during experiments.

Elastic constants of glass-polyester used in this investigation are summarized in Table 2. For glass-polyester composite, while the direction of the crack coincides with the fiber direction material, 1 is the direction parallel to the crack, and 2 and 3 are the directions normal to the crack path extension.

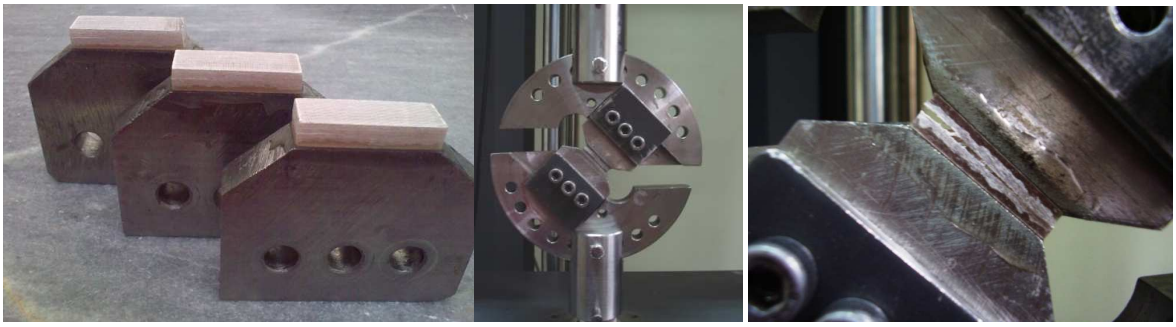


Fig. 1. Arcan loading fixture in mixed mode dalamination test

Table 1 Experimental data at failure for tested specimens

Loading angle	Number of tests	Average failure loads	Shear stress (Mpa)	Tensile stress (Mpa)
0	3	441	0	1.47
15	3	461	0.398294	1.486453
30	3	518	0.863889	1.496299
45	3	595	1.403214	1.403214
60	3	737	2.12946	1.229444
75	3	994	3.200434	0.857554
90	3	1378	4.594444	0

Table 2 Elastic properties of glass-polyester laminated composite

E_1	E_2	E_3	G_{12}	G_{13}	G_{23}	υ_{12}	υ_{13}	υ_{23}
18.8	11.3	7.7	4.2	2.4	2.4	0.27	0.29	0.31

E and *G* are in (GPa). Directions: 1 – parallel to crack, 2 – normal to crack, 3 – along thickness

Finite element analysis

The two-dimensional auxiliary fields are introduced and superposed on the actual fields. By judicious choice of the auxiliary fields, the interaction integral can be directly related to the stress intensity factors $\mathbf{K} = 4\pi\mathbf{B}\cdot\mathbf{J}_{\text{int}}$ where $\mathbf{J}_{\text{int}} = [J_{\text{int}}^{I}, J_{\text{int}}^{II}, J_{\text{int}}^{III}]^T$. Based on the definition of the J-integral, the interaction integrals $\mathbf{J}_{\text{int}}^{\alpha}$ can be expressed as:

$$J_{\text{int}}^{\alpha} = \lim_{\Gamma\to 0}\int_{\Gamma}\mathbf{n}\cdot\left(\sigma:\varepsilon_{aux}^{\alpha}\mathbf{I} - \boldsymbol{\sigma}\cdot\left(\frac{\partial\mathbf{u}}{\partial\mathbf{x}}\right)_{aux}^{\alpha} - \sigma_{aux}^{\alpha}\cdot\frac{\partial\mathbf{u}}{\partial\mathbf{x}}\right)\cdot\mathbf{q}\,d\Gamma \tag{3}$$

The subscript *aux* represents three auxiliary pure mode-I, mode-II, and mode-III crack-tip fields for α=I, II, III, respectively. Γ is an arbitrary contour from the top surface of a crack to the bottom surface of the same crack, n is the unit vector normal to Γ and pointing outwards, σ the stress tensor, u the displacement vector, q a unit vector in the crack advancement direction, and I is the unit 2nd order tensor. Detail explanations and formulations are given by Shin [7].

The commercial finite element code ABAQUS 6.9/Standard was used for simulation. The entire specimen was modeled by 8-node biquadratic plain strain quadrilateral, reduced integration elements (CPE8R), and the mesh was refined around crack tip, so that the smallest element size found in the crack-tip elements was approximately 0.25mm. Fig. 2 shows the contour for evaluation of J-integral, and mesh pattern of the specimen. A linear elastic finite element analysis was performed under a plain strain condition using $1/r^{0.5}$ stress field singularity. To obtain a $1/r^{0.5}$ singularity term of the crack tip stress field, the elements around the crack tip were focused on the crack tip and the mid side nodes were moved to a quarter point of each element side. As mentioned above, the method used to calculate the stress intensity factor is an interaction integral method, which in linear elastic fracture machanics, the J-integral coincides with total energy release rate.

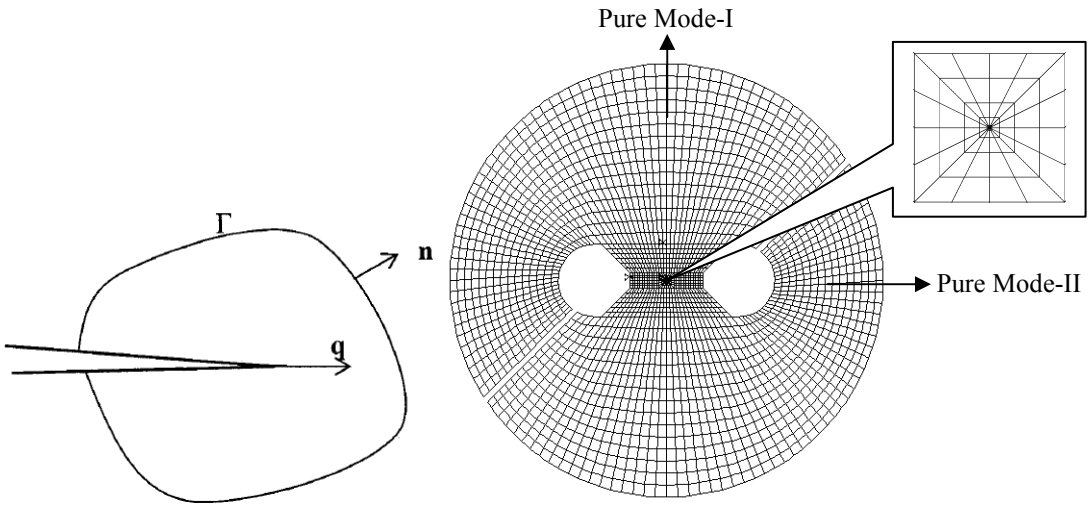


Fig. 2. Contour for evaluation of the *J*-integral and fixture mesh pattern for crack length a=15mm

Results and Discussion

Linear elastic analysis of stress field in cracked bodies is generally only confined to ideal brittle materials. But in most cases, however, there is some inelasticity in the form of plasticity, creep or phase change in vicinity of the crack tip. A study of the local stress fields for the three modes of loading showed that they have general applicability and are governed by the value of three stress intensity factors. In other words, the applied loading, the crack length and the geometrical configuration of the cracked bodies influence the strength of these fields only through the stress intensity factors. This means, the stress and deformation fields near the crack tip will be the same if the stress intensity factors are equal. In order to achieve this goal, geometric factors f (a/w) were calculated for modified Arcan specimen using finite element analysis. The variation of 2D non-dimensional geometric factors f_1(a/w) and f_2(a/w) for E-glass/polyester composite versus loading angle between 0°-90° by 15 interval is shown in Fig. 3.

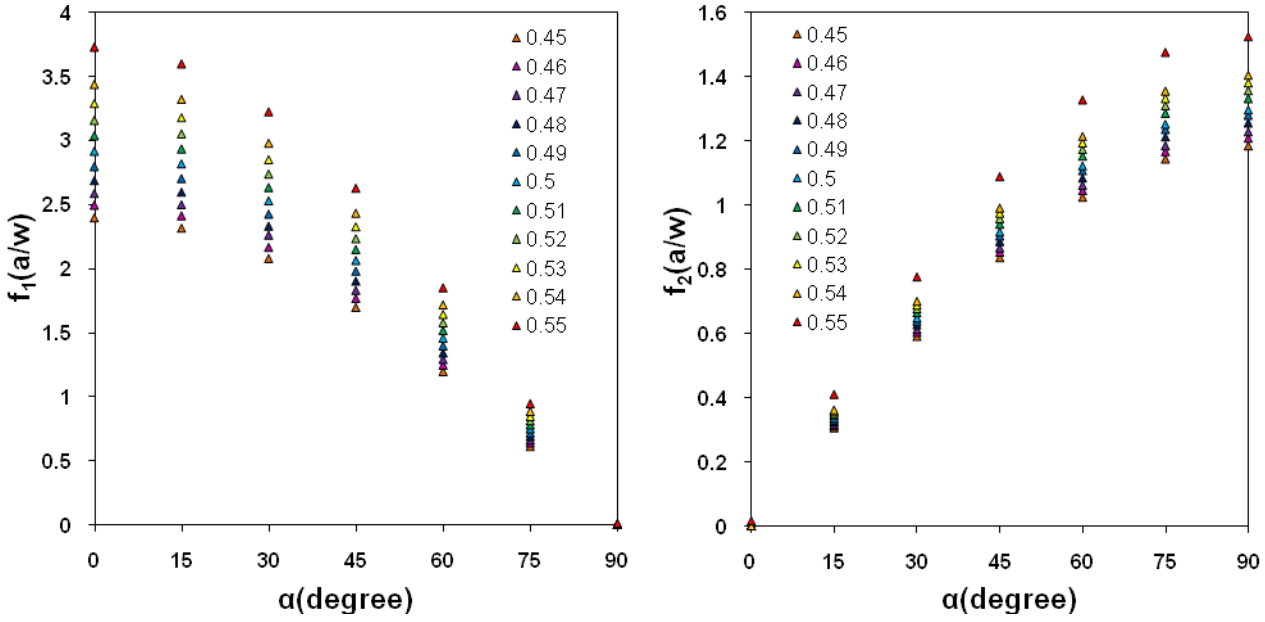


Fig. 3. Variation of mode-I and mode-II geometric factor vs. applied loading positions for crack tip field

According to experimentally measured critical fractured loads, the average values of mixed-mode interlaminar critical stress intensity factors (K_{Ic}, K_{IIc}) for the glass reinforced composite material obtained via Eq. 2, and are summarized in Table 3. It can be seen that the shearing mode interlaminate fracture toughness is larger than that of opening-mode. This means that the interlaminar cracked specimen is tougher in shear loading conditions and weaker in tensile loading conditions. The calculated critical interlaminar strain energy release rate values G_{IC} and G_{IIC} which have been obtained from Eq. 1 under various loading conditions are also summarized in Table 3. G_{IC} remains almost unchanged while G_{IIC} increases with an increase in mode-II loading contribution. The opening mode and shearing mode interlaminar critical strain energy release rates were found approximately 19.21 J/m^2 and 47.45 J/m^2, respectively.

Data points from fracture toughness experiments were used to construct a delamination resistance curve (R curve), which is the graph of fracture toughness (G) versus crack length (a). From the R-curve, two types of fracture toughness values can be calculated, the initiation (G_{init}) and propagation (G_{prop}) values. The initiation value is the fracture toughness value where the crack starts to initiate or propagate. This value can vary for each specimen as the value depends on the crack tip conditions [8, 9]. The R-curves for the 50% mixed mode tests are presented in Fig. 4. It can be seen that the G_{init} values increase until the crack length reaches the value 15 mm and then they become stable as the crack length proceeds until the final fracture steps. As with the tests results, G_T generally increased with the crack length until a stable value was reached at a crack length of about 15 mm. For calculating G_{prop}, only data points corresponding to crack lengths ranging above 15 mm have been employed.

Table 3, Fracture toughness of E-glass/polyester in terms of stress intensity facor $K(Mpa)$ and energy release rate $G(J/m^2)$, a=15mm

Loading angle	Number of tests	$K(Mpa)$		$G(J/m^2)$	
		$(K_I)_C$	$(K_{II})_C$	$(G_I)_c$	$(G_{II})_C$
0°	3	0.41	-	19.21	-
15°	3	0.39	0.11	18.8	3.12
30°	3	0.35	0.19	16.06	7.53
45°	3	0.32	0.26	14.25	15.6
60°	3	0.34	0.65	15.48	28.3
75°	3	0.27	0.78	13.12	31.32
90°	3	-	1.05	-	47.45

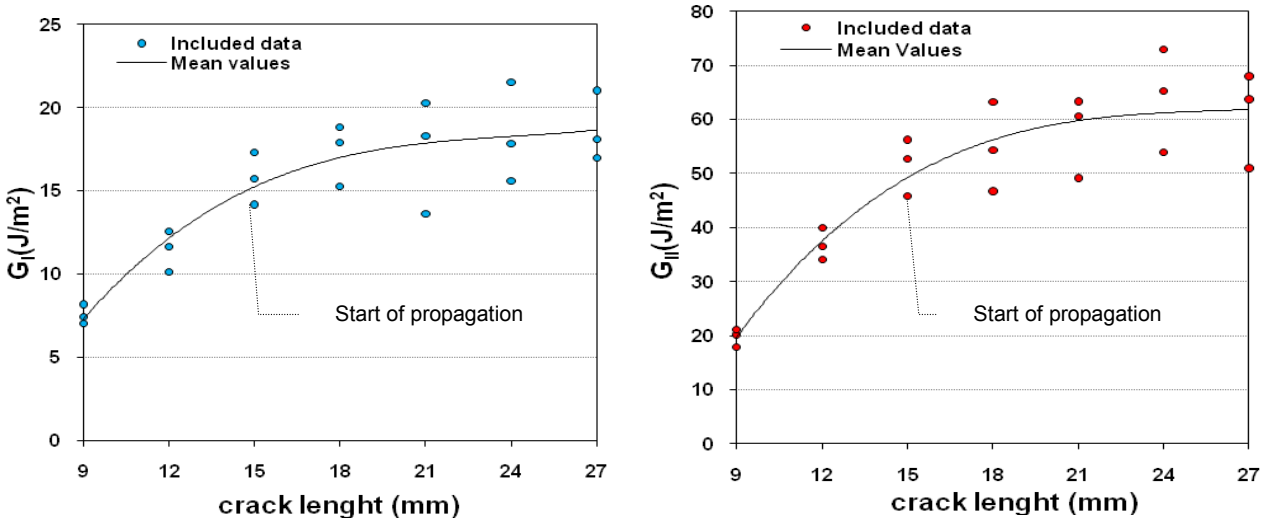


Fig. 4. R-curve for 50 % mixed mode ratio G_{II}/G_T

Summary

In this paper the effect of mixed-mode loading on fracture parameters of Glass reinforced polyester composite specimens was investigated both experimentally, and numerically. Geometric factors *f* (a/w) were calculated for modified Arcan specimen using finite element analysis. The finite element results indicated that for loading angles close to pure mode-II loading, a high ratio of mode-II to mode-I fracture is dominant and there is an opposite trend for loading angles close to pure mode-I loading. The results also revealed that f_1 play an important role in determining fracture behavior of the specimen for mode mixities lower than $\alpha=60^o$. In the same way, the dispersion of f_2 values in the distance between 45° till 90°, emphasized the important role of mode-II stress intensity factor in determination of interlaminar fracture toughness in this range. According to experimentally measured critical fracture loads for glass/polyester, the opening-mode and shearing mode interlaminar critical strain energy release rates, were found approximately 19.21 J/m^2 and 47.45 J/m^2, respectively, showing that the interlaminar cracked specimen is tougher in shear loading and weaker in tensile loading conditions. Finally, by using data points from fracture toughness experiments, delamination resistance curve for both pure mode I and pure modeII were generated, and the propagation values where the G value is stable with respect to crack length for both pure mode-I, and pure mode-II, were obtained.

Refrences

[1] S. Majumdar and D.Hunston, *Continuous Parallel Fiber composite fracture*, Encyclopedia of materials: science and technology, p. 1618-1629, (2001)

[2] Dharmawan, G. Simpson, I. Herszberg, S. John, *Mixed Mode fracture Toughness Tests of GFRP Composites*, International Journal of Composite Structures,75, p. 328–338, (2006)

[3] Kim BW, Nairn JA, *Observations of fiber fracture and interfacial debonding phenomena using the fragmentation test in single fiber composites*, Journal of Composite Materials, 36, pp. 1825–1858, (2002)

[4] Arcan M, Hashin Z, Voloshin A. *A method to produce uniform plane stress states with applications to fibre reinforced materials*, Experimental Mechanics, 18, pp.141–146, (1978)

[5] E.E.Gdoutos, *Fracture Mechanics*, An Introduction, second ed., Springer, Democritus University of Thrace, Xanthi, Greece, ISBN 1-4020-3153-X, (2005)

[6] Choupani N, *Experimental and numerical investigation of the mixed-mode delamination in Arcan laminated specimens*, Journal of Material Science and Engineering A, 478, p. 229–242, (2008)

[7] Shin CF,Moran B,Nakamura T, *Energy release rate along a three-dimensional crack front in a thermally stressed body*, International Journal of Fracture, 30, p. 79-102, (1986)

[8] Martin RH, *Delamination characterization of woven glass/polyester composites*, Journal of Composites Technology and Research, 19, p. 20–28, (1997)

[9] *Standard Test Method for Mode I Interlaminar Fracture Toughness of Unidirectional Fiber-Reinforced Polymer Matrix Composites*. USA ASTM Standard D5528-01, (2001)

© (2011) Trans Tech Publications, Switzerland
doi:10.4028/www.scientific.net/KEM.471-472.880

Experimental and Numerical Investigation of the Mixed-Mode Delamination of PAN Based Carbon/Epoxy Composite using Modified Arcan Fixture

M.Ziaee[1,a] and N.Choupani[2,b]

[1] Mechanical Engineering Department, Sahand University of Technology,Tabriz, Iran,

[2] Mechanical Engineering Department, Sahand University of Technology,Tabriz, Iran

[a]Mohsen_622@yahoo.com,[b]Choupani@sut.ac.ir

Keywords: Mixed Mode, Modified Arcan Specimen, Stress Intensity Factor, PAN Based Carbon/Epoxy Composite, Fracture Toughness

Abstract. The present research examines analytically and experimentally the mode-I and mode-II and mixed mode-Interlaminar fracture toughness of PAN based carbon/epoxy composite. A modified Arcan fixture, well-suited for the study of the behavior of used composite assemblies, was developed in order to focus on the analysis of the fracture behavior of the material. The edge effects are minimized by using an appropriate design of the substrates so that experimental results give reliable data. Also the mode-I and mode-II stress intensity factors were computed for different crack lengths and load orientation angles using finite element analysis. The numerical results show that the modified Arcan specimen is able to provide pure mode-I, pure mode-II and any mixed mode loading conditions. It is shown that the results obtained from the fracture tests are consistent very well with mixed mode fracture theories. Obtained results indicated that fracture toughness and stress intensity factor for sliding mode enhanced up when the loading angle increased. Mechanism of fracture and toughening were examined by using scanning electron microscopy.

Introduction

The widespread use of composites for structural designs implies having a better understanding of their fracture mechanical behavior. Many defects, resulting from the fabrication process or other natural fact such as corrosion, are often the cause of initial cracks in materials [1]. At the crack tip the stress field can be broken up into three components, called Mode-I, Mode-II and Mode-III, as shown in Fig. 1. Mode-I causes the crack to open orthogonal to the local fracture surface and results in tension or compressive stresses on surfaces. Mode-II causes the crack surfaces to slide relative to each other in the x_1 direction and results in shear stresses in the x_2 direction ahead of the crack. Mode-III causes the crack surface to slide relative to each other in the x_3 direction and results in shear stresses in the x_3 direction ahead of the crack [2].

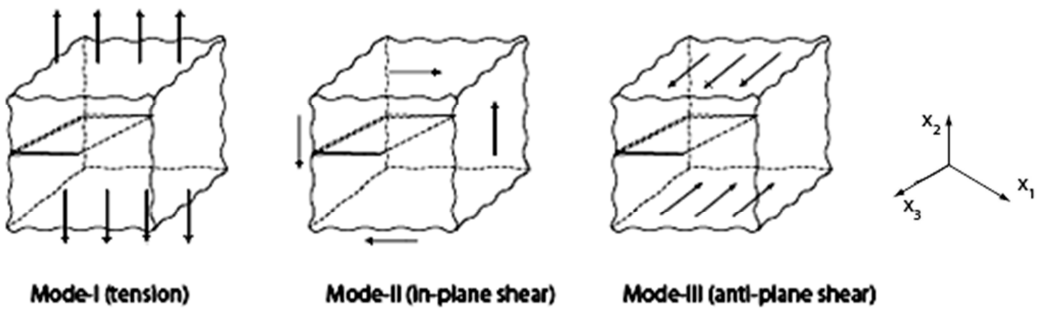


Fig. 1. Three pure mode loadings [2]

The stress intensity factors for a modified version of an Arcan specimen are functions of crack length ratio (a/w) and loading angle (α) and can be written as:

$$K_I = \frac{P_c\sqrt{\pi a}}{wt}\cos\alpha.\, f_I\left(\frac{a}{w}\right) \quad (1)$$

$$K_{II} = \frac{P_c\sqrt{\pi a}}{wt}\sin\alpha.\, f_{II}\left(\frac{a}{w}\right) \quad (2)$$

where P_c is the critical load at fracture, α is loading angle, w is the specimen length, t is the specimen thickness and a is the crack length. In turn K_I and K_{II} are obtained using geometrical factors $f_I(a/w)$ and$f_{II}(a/w)$, respectively, which are obtained through finite element analysis of an Arcan test specimen [3]. The strain energy release can be calculated from the following relationships:

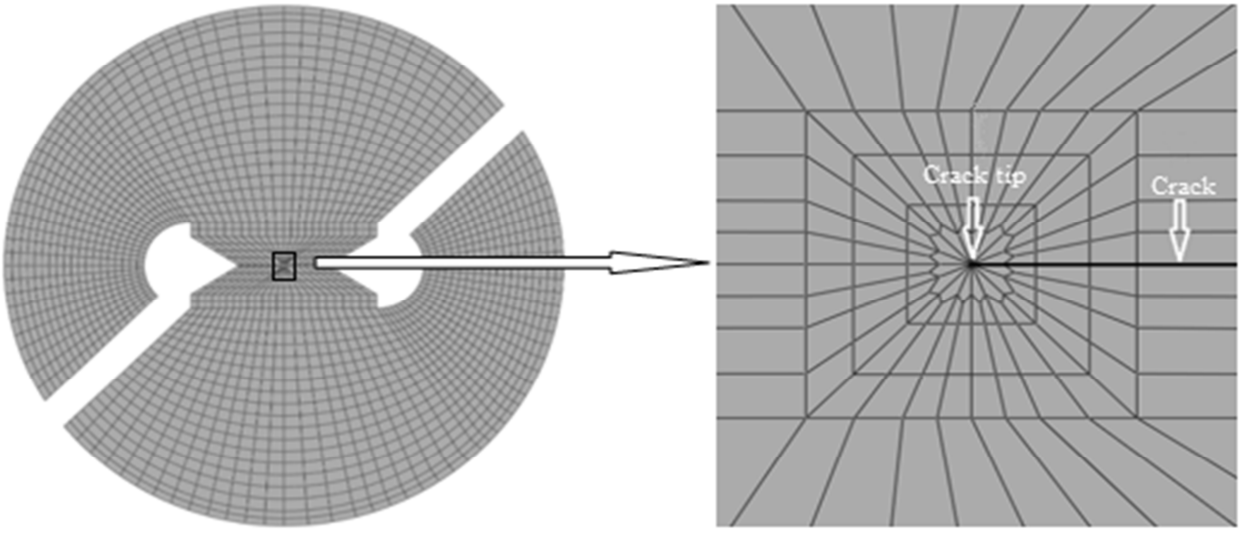
$$G_I = \frac{K_I^2}{\overline{E}_I} \quad (3)$$

$$G_{II} = \frac{K_{II}^2}{\overline{E}_{II}} \quad (4)$$

where $\overline{E}_I$ and $\overline{E}_{II}$ are effective module, and K_I and K_{II} are mode-I and mode-II stress intensity factors, respectively [4].

FE Analysis

Finite element modelling was conducted using ABAQUS/CAE 6.9. The fixture and specimen were modeled in two dimensions under plane strain conditions using an 8-node biquadratic plane strain quadrilateral, reduced integration. Meshing was carried out under structured-meshing conditions. An example of the mesh used is presented in Fig. 2(a). In the models, the following geometry and loading conditions were considered: w = 30 mm, t = 10 mm, P = 1000 N and loading angles from $0^{\circ}$to 90° with intervals of 15°.Also the crack length ratio a/w was varied from 0.1 to 0.8. A J-integral based method built in ABAQUS was used for obtaining the stress intensity factors directly from software [5]. Elastic constants of twill PAN based Carbon/Epoxy composite are listed in Table 1.



(a) (b)

Fig. 2.Representative meshing for finite element model for (a/w=0.5), showing: (a) entire fixture and specimen; (b) close-up of meshing at crack-tip

Table 1. Elastic properties of twill PAN based Carbon/Epoxy composite

Property	Elastic Constants
E_1[GPa]	133
E_2[GPa]	133
E_3[GPa]	8.2
G_{12}[GPa]	3
G_{13}[GPa]	4.2
G_{23}[GPa]	4.2
v_{12}	0.3
v_{13}	0.36
v_{23}	0.36

Figs. 3 and 4 show the values of $f_I(a/w)$ and $f_{II}(a/w)$ calculated from extensive finite element analyses performed for various crack lengths and loading orientations.

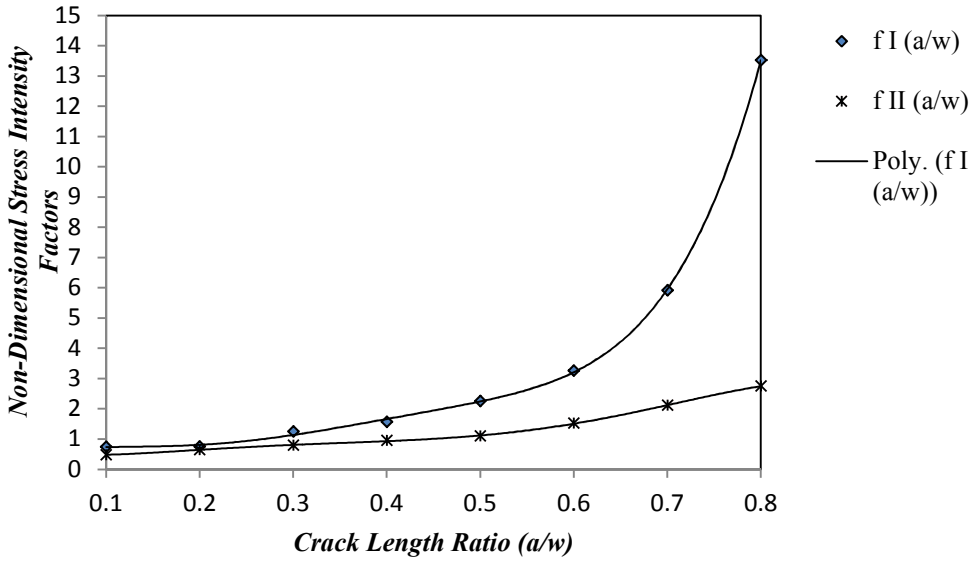


Fig. 3.Variation of mode-I and mode-II geometery factors for different values of a/w

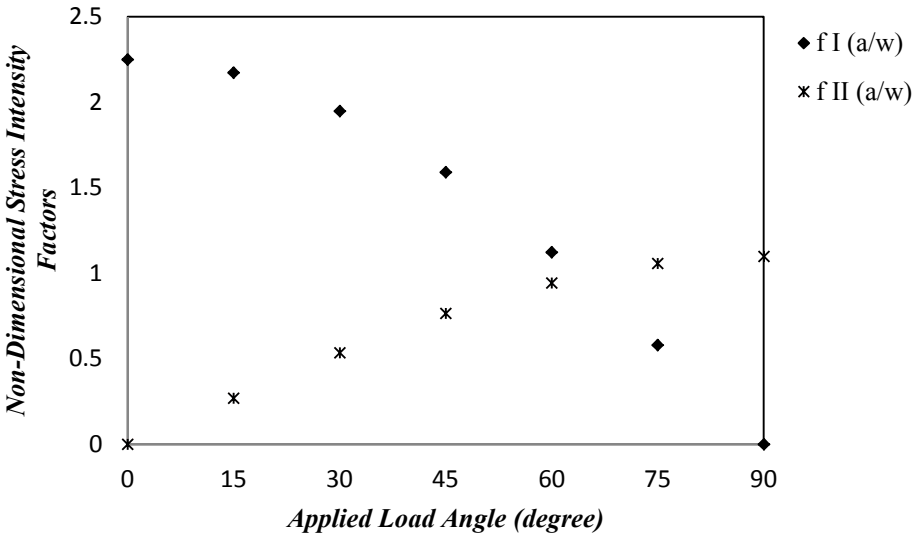


Fig. 4.Variation of mode-I and mode-II geometery factors vs. loading angles for a/w=0.5

For various crack length ratios a fourth order polynomial was fitted to the results.

$$f_I\left(\frac{a}{w}\right) = 321.4\left(\frac{a}{w}\right)^4 - 458.4\left(\frac{a}{w}\right)^3 + 231.3\left(\frac{a}{w}\right)^2 - 43.43\left(\frac{a}{w}\right) + 3.236, R^2 = 0.999 \quad (5)$$

$$f_{II}\left(\frac{a}{w}\right) = -17.47\left(\frac{a}{w}\right)^4 + 39.04\left(\frac{a}{w}\right)^3 - 24.39\left(\frac{a}{w}\right)^2 + 6.94\left(\frac{a}{w}\right) - 0.017, R^2 = 0.998 \quad (6)$$

The total strain energy release rate (G_T) decreases rapidly for loading angles close to pure mode-II loading with the reduction of opening-mode strain energy release rate. The results are shown in Fig. 5.

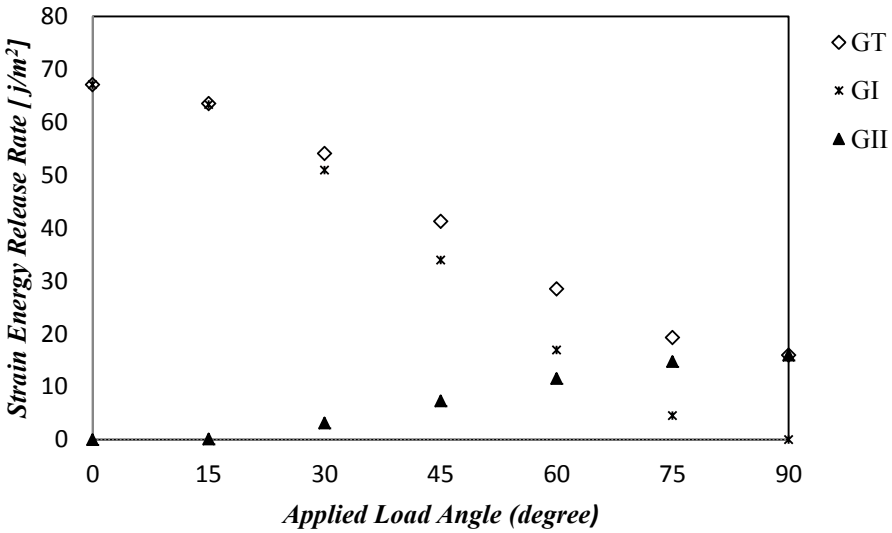
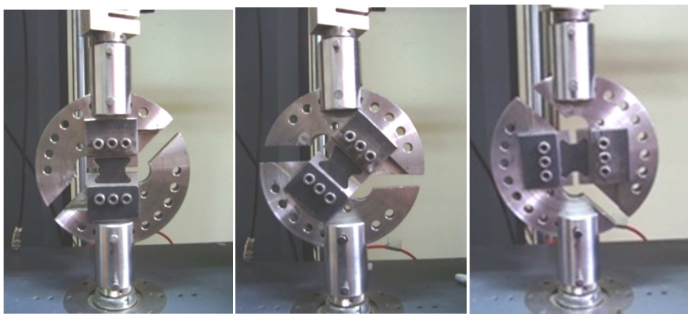


Fig. 5. Strain energy release rates G_I, G_{II}, $G_T = G_I + G_{II}$ vs. loading angle for twill PAN based Carbon/Epoxy composite for a/w=0.5

Experiments

In Figure 6, the loading device and modified version of Arcan specimen are shown. This specimen was used in order to study the mixed-mode Interlaminar fracture toughness of twill PAN Based Carbon/Epoxy composite material. The interlaminar fracture toughness was determined experimentally with the modified version of the Arcan specimen under different mixed-mode loading conditions.



(a) (b) (c)

Fig. 6. Overview of test rig and set up: (a) Mode-I test; (b) Mixed-mode test; (c) Mode-II test

The average values of mixed-mode-Interlaminar critical stress intensity factors for twill PAN based Carbon/Epoxy composite are summarized in Table 2.

Table 2. Average critical mixed-mode-Interlaminar fracture toughness for twill PAN based Carbon/Epoxy composite for a/w=0.5

Loading Angle	*0°*	*15°*	*30°*	*45°*	*60°*	*75°*	*90°*
K_{IC}[MPa.m$^{0.5}$]	2.583	2.572	2.51	2.472	2.41	2.379	---
K_{IIC}[MPa.m$^{0.5}$]	---	0.319	0.6899	1.1909	2.029	4.3366	5.876

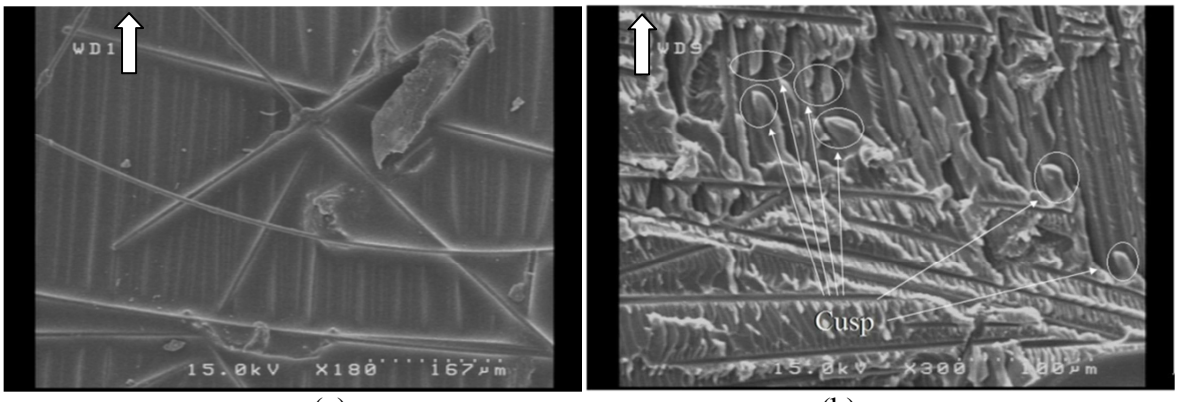
The calculated critical interlaminar strain energy release rate values G_{IC} and G_{IIC} using experimental data under various loading conditions are summarized in Table 3. G_{IC} decreases while G_{IIC} increases as the mode-II loading contribution increases.

Table 3. Average critical strain energy release rates G_C [J/m^2] for twill PAN based Carbon/Epoxy composite for a/w=0.5

Loading Angle	*0°*	*15°*	*30°*	*45°*	*60°*	*75°*	*90°*
G_{IC}[J/m^2]	171.167	169.62	161.54	156.68	148.9	145.2	---
G_{IIC}[J/m^2]	---	2.61	12.2	36.36	105.56	482.2	885.32
$G_{T,C}$[J/m^2]	171.167	172.23	181.74	193.05	254.49	627.407	885.32

Fracture Surfaces

Scanning electron microscopy was used to study the fracture surfaces. Mode-I fracture surfaces shown in Fig. 7(a), are generally smooth with few fiber fractures. The mode-II fracture surface is rough with failure in the matrix and fiber layer breaks. Existence of cusps shows the shear loading condition, also their direction shows the fracture extension direction approximately, which is shown in Fig. 7(b) [6].



(a) (b)

Fig. 7. SEM micrographs of fracture surfaces for twill PAN based Carbon/Epoxy composite under: (a) mode-I loading; (b) mode-II loading (The arrow indicates the direction of crack propagation)

Summary

In this study the mixed-mode-Interlaminar fracture behavior of twill PAN based Carbon/Epoxy composite specimens was investigated based on experimental and numerical analyses. A modified version of the Arcan specimen was employed to conduct a mixed-mode test using the special test loading device. The full range of mixed-mode loading conditions including pure mode-I and pure mode-II loading can be created and tested. It is a simple test procedure, clamping/unclamping the specimens is easy to achieve and only one type of specimen is required to generate all loading conditions. The finite element results indicate that for loading angles close to pure mode-II loading, a high ratio of mode-II to mode-I fracture is dominant and there is an opposite trend for loading angles close to pure mode-I loading. It confirms that by varying the loading angle of Arcan specimen pure mode-I, pure mode-II and a wide range of mixed-mode loading conditions can be created and tested. The interlaminar fracture toughness was determined experimentally with the modified version of the Arcan specimen under different mixed-mode loading conditions. The results indicated that the interlaminar cracked specimen is tougher in shear loading conditions and weaker in tensile condition loading. The SEM fracture surfaces observations showed that the mode-I fracture surface was indicative of a brittle cleavage failure with relatively smooth and flat matrix fracture and showed only little debonding between fibre and matrix. As the mode-II loading contribution was added, cusps appeared on the fracture surfaces and surfaces became rougher [7].

References

[1] R. Moutou Pitti, F. Dubois, C. Petit, N. Sauvat, O. Pop: Engineering Fracture Mechanics 75 (2008) 4450–4465.

[2] Alan T. Zehnder: *Lecture Notes on Fracture Mechanics*, Dept. of Theoretical and Applied Mechanics Cornell University, 2008.

[3] N.Choupani: *Mixed-mode cohesive fracture of adhesive joints: Experimental and numerical studies*, Engineering Fracture Mechanics 75 (2008) 4363–4382.

[4] N. Choupani and M. Nikbakht: Journal of Mechanical, Industrial and Aerospace Engineering 2:4 2008.

[5] Hibbit, Karlsson and Sorensen, HKS Inc, Pawtucket, *"ABAQUS User's Manual*, USA (2004)

[6] N. Choupani, M. Nikbakht, S.R. Hosseini: Materials Science and Engineering A 516 (2009) 162–168

[7] N. Choupani and M. Nikbakht: J Mater Sci (2009) 44:3428–3437

© (2011) Trans Tech Publications, Switzerland
doi:10.4028/www.scientific.net/KEM.471-472.886

Effects of Thickness on Fracture Toughness of Carbon/Polyester Composite

Mohammad Hossein Heydari[a], Naghdali Choupani[b]

Sahand University of Technology, Tabriz, Iran

[a]Mhh.Mechanic@gmail.com, [b]Choupani@sut.ac.ir

Keywords: Arcan, Composite, Fracture Toughness, Delamination

Abstract. The aim of this paper is to evaluate interlaminar fracture toughness and non dimensional stress intensity factors of woven Carbon-Polyester composite based on numerical and experimental methods. A modified version of Arcan specimen was employed to conduct a mixed-mode fracture test using a special loading device. By changing the loading angle, α, from 0° to 90°, mode-I, mode-II and all mixed-mode data were created. The finite element analysis was performed with Abaqus software. The interaction j-integral was used to separate the mixed mode stress intensity factors and energy release rate at the crack tip under different loading conditions and different thickness of specimens. The results of fracture toughness tests revealed that the interlaminar fracture of composite is strong under the shearing-mode loading but weaker to the opening- mode loading. It can be seen that by increasing the thickness of the composite specimen, non dimensional stress intensity factors for pure mode I (α=0°) and pure mode II (α=90°) loading conditions were decreased.

Introduction

Due to wide existing and potential applications, composite technology has been developed very intensively over recent decades, and there exist numerous publications that cover anisotropic elasticity, mechanics of composite materials, design, analysis, fabrication, and application of composite structures [1]. Composites are most often classified in terms of their matrix, and are designated as polymer matrix composites (PMCs), metal matrix composites (MMCs), or ceramic matrix composites (CMCs). Although these systems possess widely different mechanical properties, they experience similar damage accumulation processes [2, 3]. The manufacturing process, if not properly controlled, can introduce defects into the laminate. Typical defects are voids (small cavities in the resin), delaminations (on bonded areas between layers) or, unusually, longitudinal cracks (lack of bonding between fibre and matrix) [4]. Due to the lack of through-the-thickness reinforcement, structures made from laminated composite materials and adhesively bonded joints are highly susceptible to failure caused by interfacial crack initiation and growth. The delamination phenomenon in a laminated composite structure may reduce the structural stiffness and strength, redistribute the load in a way that the structural failure is delayed, or may lead to structural collapse. For a given interlaminar defect, crack propagation may be accomplished in opening-mode (mode-I), shearing-mode (mode-II), and tearing mode (mode-III) (Fig. 1) and their combinations.

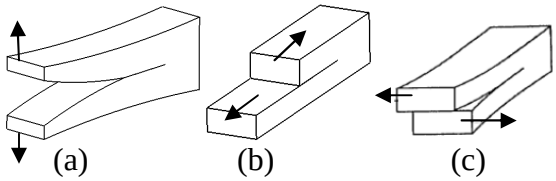


Fig.1, Modes of interlaminar crack propagation: (a) mode-I opening mode; (b) mode-II sliding or shear mode; (c) mode- III tearing mode.

This paper seeks to extend understanding the interlaminar fracture behavior of carbon-polyester composite under deferent thicknesses via numerical and experimental analysis. Characterizing the

influence of thickness on mechanical properties, stress intensity factor and strain energy release rate is an important topic that engineering are faced, because such parameters may vary through material thickness. Non dimensional stress intensity factor and strain energy release rate were determined through numerical analysis under different thicknesses and critical strain energy release rate was obtained via experimental analysis.

Theoretical Background

It is assumed that the specimens are made of an orthotropic linear elastic material with deformability defined by the generalized Hooke's law [5-9]:

$$\begin{pmatrix} \varepsilon_x \\ \varepsilon_y \\ \varepsilon_z \\ \gamma_{yz} \\ \gamma_{xz} \\ \gamma_{xy} \end{pmatrix} = \begin{pmatrix} a_{11} & a_{12} & a_{13} & a_{14} & a_{15} & a_{16} \\ a_{21} & a_{22} & a_{23} & a_{24} & a_{25} & a_{26} \\ a_{31} & a_{32} & a_{33} & a_{34} & a_{35} & a_{36} \\ a_{41} & a_{42} & a_{43} & a_{44} & a_{45} & a_{46} \\ a_{51} & a_{52} & a_{53} & a_{54} & a_{55} & a_{56} \\ a_{61} & a_{62} & a_{53} & a_{64} & a_{65} & a_{66} \end{pmatrix} \begin{pmatrix} \sigma_x \\ \sigma_y \\ \sigma_z \\ \sigma_{yz} \\ \sigma_{xz} \\ \sigma_{xy} \end{pmatrix} \tag{1}$$

Where the terms of the nonzero entries a_{ij} of the orthotropic compliance matrix are defined in terms of the following engineering elastic constants:

$$a_{11} = \frac{1}{E_x} \qquad a_{22} = \frac{1}{E_y} \qquad a_{33} = \frac{1}{E_z} \qquad a_{44} = \frac{1}{G_{yz}} \qquad a_{55} = \frac{1}{G_{xz}} \qquad a_{66} = \frac{1}{G_{xy}}$$

$$a_{12} = a_{12} = -\frac{\upsilon_{xy}}{E_x} = -\frac{\upsilon_{yx}}{E_y} \qquad a_{13} = a_{31} = -\frac{\upsilon_{xz}}{E_x} = -\frac{\upsilon_{zx}}{E_z} \qquad a_{23} = a_{32} = -\frac{\upsilon_{yz}}{E_y} = -\frac{\upsilon_{zy}}{E_z} \tag{2}$$

For a thin plate with its major dimension and principal material axes in the *xy*-plane, the relation between strain and stress is approximated by plane stress:

$$\sigma_z = \tau_{yz} = \tau_{xz} = 0 \tag{3}$$

If the stresses according to above equation are substituted into Eq. 1, it can be simplified to yield:

$$\begin{pmatrix} \varepsilon_x \\ \varepsilon_y \\ \varepsilon_{xy} \end{pmatrix} = \begin{pmatrix} a_{11} & a_{12} & a_{16} \\ a_{12} & a_{22} & a_{26} \\ a_{16} & a_{26} & a_{66} \end{pmatrix} \begin{pmatrix} \sigma_x \\ \sigma_y \\ \tau_{xy} \end{pmatrix} \tag{4}$$

Where $\sigma_x, \sigma_y, \tau_{xy}$ and $\varepsilon_x, \varepsilon_y, \gamma_{xy}$ are in-plane stresses and strains. For thick plates, conditions of plane strain are commonly assumed by taking:

$$\varepsilon_z, \gamma_{xz}, \gamma_{yz} = 0 \tag{5}$$

This assumption in combination with Hooke's generalized law leads to

$$\sigma_z = \frac{-(a_{13}\sigma_x + a_{23}\sigma_y + a_{36}\tau_{xy})}{a_{33}} \tag{6}$$

Consequently, σ_z is not an independent quantity and may be removed from Hooke's generalized law (together with τ_{yz} and τ_{xz}) to yield:

$$\begin{pmatrix} \varepsilon_x \\ \varepsilon_y \\ \varepsilon_{xy} \end{pmatrix} = \begin{pmatrix} b_{11} & b_{12} & b_{16} \\ b_{12} & b_{22} & b_{26} \\ b_{16} & b_{26} & b_{66} \end{pmatrix} \begin{pmatrix} \sigma_x \\ \sigma_y \\ \tau_{xy} \end{pmatrix} \tag{7}$$

Where the terms of the constants b_{ij} are defined in terms of the following nonzero entries a_{ij} of the orthotropic compliance matrix:

$$b_{ij} = a_{ij} - \frac{a_{i3}a_{j3}}{a_{33}} \ldots \text{ (i,j =1,2,4,5,6)} \tag{8}$$

For the case in which the *xy*-system coincides with the principal material axes:

$$a_{16} = a_{26} = a_{36} = a_{45} = 0, \qquad b_{16} = b_{26} = 0, b_{11} = \frac{a_{11}a_{33} - a^2_{13}}{a_{33}}, \qquad b_{12} = \frac{a_{12}a_{33} - a_{13}a_{23}}{a_{33}},$$
$$b_{22} = \frac{a_{22}a_{33} - a^2_{23}}{a_{33}}, \qquad b_{66} = \frac{a_{66}a_{33} - a^2_{36}}{a_{33}} \tag{9}$$

For many composites crack growth is self-similar because of delamination and this leads to partition *G* into mode-I and mode-II. The energy release rates for orthotropic material with the crack line parallel to the principal orthotropic direction which coincides with the fibre orientation can be calculated from the following relationships [5-6, 9-11]:

$$G_I = \frac{K^2_I}{E_I}, \quad G_{II} = \frac{K^2_{II}}{E_{II}} \tag{10}$$

Where E_I and E_{II} are effective moduli, and K_I and K_{II} are mode-I and mode-II stress intensity factors, respectively. If the crack plane coincides with the direction of minimum crack resistance in interlaminar problems, the direction of crack propagation is collinear with the original crack and the computed values of G_I, G_{II} and $J=G_T = G_I + G_{II}$ are physically meaningful. It is assumed that the specimens are orthotropic linear elastic material and effective moduli E_I and E_{II} are defined as:

$$E_1 = \sqrt{\frac{2}{a_{11}a_{22}}} \frac{1}{\sqrt{\sqrt{\frac{a_{22}}{a_{11}}} + \frac{2a_{12} + a_{66}}{2a_{11}}}}, \qquad E_{II} = \frac{\sqrt{2}}{a_{11}} \frac{1}{\sqrt{\sqrt{\frac{a_{22}}{a_{11}}} + \frac{2a_{12} + a_{66}}{2a_{11}}}} \quad \text{(Plane Stress)}$$

$$E_I = \sqrt{\frac{2}{b_{11}b_{22}}} \frac{1}{\sqrt{\sqrt{\frac{b_{22}}{b_{11}}} + \frac{2b_{12} + b_{66}}{2b_{11}}}}, \qquad E_{II} = \frac{\sqrt{2}}{b_{11}} \frac{1}{\sqrt{\sqrt{\frac{b_{22}}{b_{11}}} + \frac{2b_{12} + b_{66}}{2b_{11}}}} \quad \text{(Plane Strain)} \tag{11}$$

The purpose of fracture toughness testing is to determine the value of the critical stress intensity factor, or plane strain fracture toughness K_C. This material property is used to characterize the resistance to fracture in the design of structural members. ASTM standards E399 [12] and D5045 [13] give some guidance for plane strain mode-I fracture toughness K_{IC} for metals and plastics. The stress intensity factor K_C at the tip of the pre crack in a compact tension specimen is given by

$$K_c = \frac{P_c\sqrt{\pi a}}{wt} f\left(\frac{a}{w}\right) \tag{12}$$

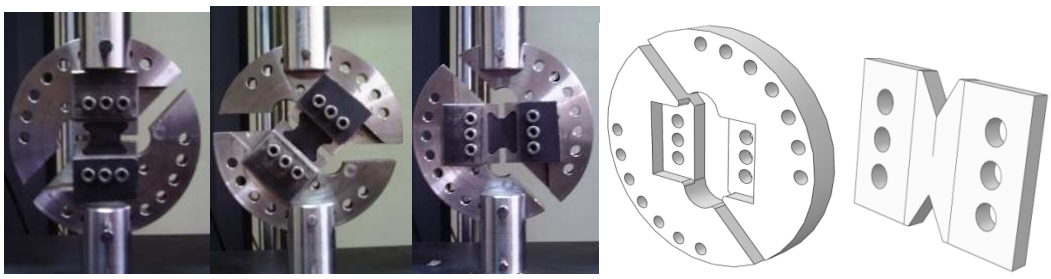
Where P_C is the fracture load, a is crack length, w is the specimen width, t is the specimen thickness, and f (a/w) is a geometrical factor. Linear elastic fracture mechanics and plan strain conditions are the primary requirements. Due to presence of weak planes between the layers of a composite laminate, interlaminar fracture are often subjected to a mixed-mode stress field. The stress intensity factors ahead of the crack tip for a modified version of Arcan specimen were calculated by using the following equations [5, 14-15]:

$$K_{Ic} = \frac{P_c\sqrt{\pi a}}{wt} f_I\left(\frac{a}{w}\right), \qquad K_{IIc} = \frac{P_c\sqrt{\pi a}}{wt} f_{II}\left(\frac{a}{w}\right) \tag{13}$$

Where P_C is the critical load at fracture, w is specimen length, t is specimen thickness and a is crack length. In turn K_I and K_{II} are obtained using geometrical factors f_I (a/w) and f_{II} (a/w), respectively, which are obtained through finite element analysis of Arcan test specimen [4].

Test Method and Set up

Experimental tests were carried out using modified version of Arcan specimen. With Arcan specimen, by changing the loading angle from 0° to 90°, mode-I, mode-II, and all mixed-mode loading data were obtained (Fig.2). Originally was used for testing of composite specimens by Arcan as reported in reference [4], and the fixture was modified by Amstutz and his co-workers as also reported in reference [4] for stable tearing tests. Fixture is made of high tensile steel with thickness of 20mm and be able to test a 10mm specimen. Loading was performed with a tensile loading device with the rate of 0.5mm per minute to reduce the dynamic effects until the final rapture. The loading device and modified version of Arcan specimen are shown in Fig.2.



(a) (b) (c) (d)

Fig.2, Overview of loading device and test setup: (a) pure mode-I test; (b) mixed-mode test; (c) pure mode-II test (d) Specimen modeled in Abaqus software

Results and Discussion

Numerical Results. In order to determine fracture toughness from Eq. 13 the correction factors of f_I (a/w) and f_{II} (a/w) must be calculated through finite element modeling of specimen. Arcan fixture and specimen were modeled in Abaqus software under constant load of 1000N. The relationship between non-dimensional stress intensity factors and loading angle is demonstrated in Fig. 3. It can be seen that for loading angles less than 67°, mode-I is dominant and after that mode-II is dominant and as the mode-II stress intensity factor increases, mode-I stress intensity factor decreases. Changes of strain energy release rate versus change of loading angle are demonstrated in Fig. 4. Increase of loading angle from 0 to 90° leads to a vast reduction of strain energy and this causes a great increase of fracture resistance of structure. Also, strain energy release rate measurements for the modified version of Arcan specimen under pure mode-I loading show the average strain energy release rate of G_I= 124 (J/m^2). For pure mode-II, the average strain energy

release rate for the specimen under consideration was found G_{II}= 20 (J/m^2). Figures 5 and 6 show changes of stress intensity factors and strain energy release rate versus different thicknesses. It can be seen that by increasing the thickness of specimen, stress intensity factor and strain energy release rate tends to decrease. It means that as the thickness of specimen increases, the fracture resistance decreases.

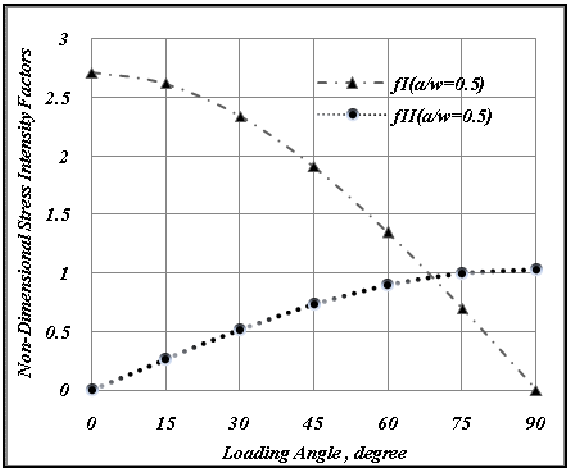


Fig.3, Non-dimensional stress intensity factor vs. loading angle of C-P for the crack length =15mm

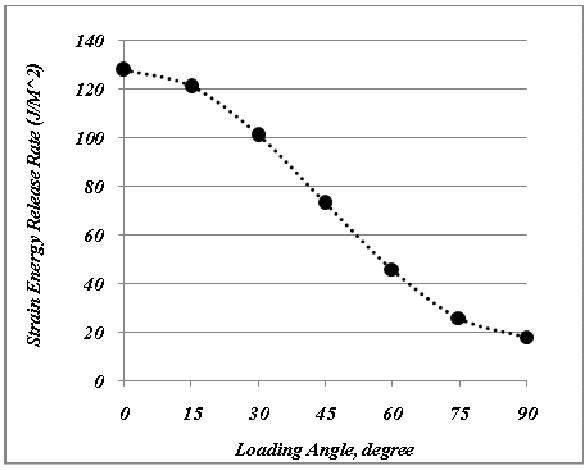


Fig.4, Strain energy versus loading angle of C-P for the crack length=15mm

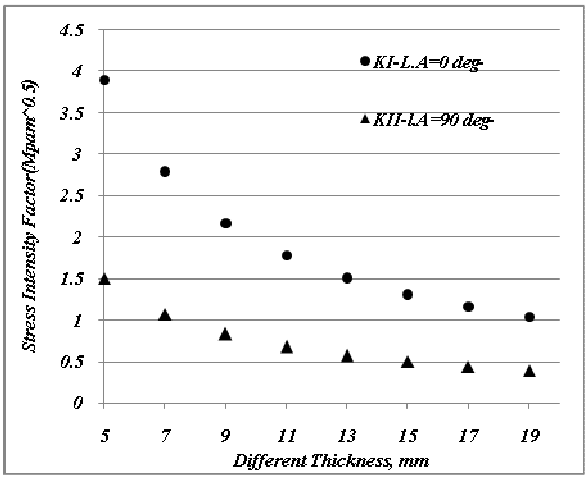


Fig.5, Stress intensity factor vs. different thickness of C-P for the crack length =15mm

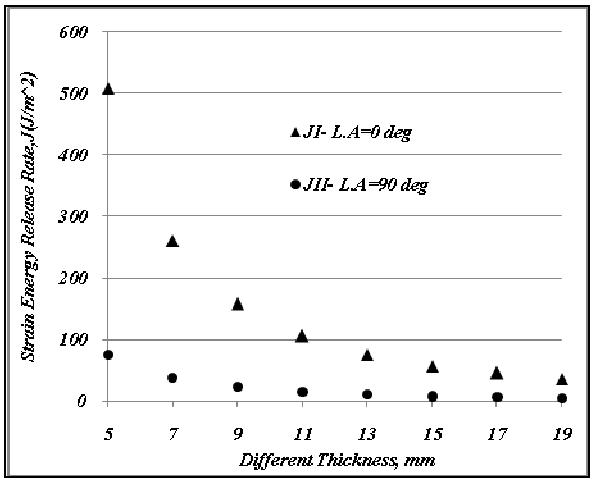


Fig.6, Strain energy vs. different thickness of C-P for the crack length=15mm

Experimental Results. After determining critical loads experimentally, and using the correction factors from Fig.3, the critical stress intensity factors can be calculated. By using critical stress intensity factors and using E_I, E_{II} from Eq.11, the critical strain energy release rate can be obtained as the Table 1.

Table1. Critical Strain Energy Release Rate (J/m^2)

α	0	15	30	45	60	75	90
G_I	39	37.2	33.2	26.5	23.4	10.4	---
G_{II}	------	0.34	1.62	4.1	10.5	21.4	48
G_T	39	37.54	34.82	30.6	34	31.8	48

The average values of mixed-mode critical strain energy release rate for the C-P composite under consideration are summarized in Table 1. G_{IC} decreases and G_{IIC} increases as the mode-II loading contribution, i.e. as α increases from 0° to 90°. It is seen that for loading angles α<60° the mode-I contribution is greater than that of mode-II and the opening-mode fracture becomes dominant. For loading angles α>75° there is an opposite trend and the shearing-mode fracture becomes dominant. Also, strain energy release rate measurements for the modified Arcan specimen under pure mode-I loading show the average strain energy release rate of G_I= 39 (J/m^2). For pure mode-II loading using modified Arcan specimen, the average strain energy release rate for the specimen under consideration was found G_{II}= 48 (J/m^2).

Summary
Interlaminar fracture toughness and non dimensional stress intensity factors of woven carbon-polyester composite based on numerical and experimental methods were evaluated. A modified version of Arcan specimen was employed to conduct a mixed-mode fracture test using a special loading device. By changing the loading angle, α, from 0° to 90°, mode-I, mode-II and all mixed-mode data were created.

References

[1] Valery V. Vasiliev, Evgeny V. Morozov: *Mechanics and Analysis of Composite Materials*, Elsevier (2001)

[2] M. Nikbakht, N. Choupani, Int. J of Mech, Indu and Aerospace Eng 2:4 (2008)

[3] Robert M. Jones: *Mechanics of Composite Materials*, Second edition, published by Taylor and Francis (1999)

[4] *Mechanical testing of advanced fibre composites*, Edited by J M Hodgkinson, CRC Press, Cambridge England

[5] Rohola Hasanpour, Naghdali Choupani, Int. J of Rock Mech & Mining Sci,PP: 346–354, (2009)

[6] J.W. Gillespie, L.A. Carlsson, *Delaware Composites Design Encyclopedia*, vol. 6, Technomic Publishing Co. Inc., PP: 113–119 (1990)

[7] G.C. Sih, E.P. Chen, *Cracks in Composite Materials: A Compilation of Stress Solutions for Composite Systems with Cracks*, The *Hague*, M. Nijhoff: Distributors for the U.S. and Canada/Kluwer Boston, Boston/Hingham, MA, USA, ISBN 9024725593 (1981)

[8] S.H. Ju, R.E. Rowlands, Int. J. Fract. 120.PP: 601–621 (2003)

[9] Y.A. Dzenis, *Durability and Intelligent Nondestructive Evaluation of Adhesive Composite Joints*, University of Nerbraska-Lincoln, Arlington, Report No, F49620-96-1-0458 (1996)

[10]G.C. Sih, in: G.C. Sih (Ed.), *Engineering Application of Fracture Mechanics*, Kluwer Academic Publishers, London, PP: 279–305, (1981)

[11] R.F. Gibson, *Principles of Composite Material Mechanics*, McGraw-Hill, New York (1994)

[12] ASTM E399, *Standard Test Method for Plane Strain Fracture Toughness and Strain Energy Release Rate of Metallic Materials*, Annual Book of ASTM Standards (1983)

[13] ASTM D5045, *Standard Test Method for Plane Strain Fracture Toughness and Strain Energy Release Rate of Plastic Materials*: Annual Book of ASTM Standards (1995)

[14] R.A. Jurf, R.B. Pipes, J. Compos. Mater. 16, PP:386–394 (1982)

[15] M. Arcan, Z. Hashin, A. Voloshin, Exp. Mech. 18. PP: 141–146 (1978)

© (2011) Trans Tech Publications, Switzerland
doi:10.4028/www.scientific.net/KEM.471-472.892

Simulation of Cracks in Fiber Reinforced Composite Plate

Pramod Kumar[1a], Ashish Kakyal [2]

[1] Department of Mechanical Engineering

Dr B R Ambedkar National Institute of Technology, Jalandhar, India

[2] Department of Mechanical Engineering

Dr B R Ambedkar National Institute of Technology, Jalandhar, India

[1a] kushwahapramod@nitj.ac.in

Keywords: Glass fiber composite; Strain energy release rate; Cracks; stress intensity factor

Abstract. Material flaws, pre-cracks and crack initiation due to cyclic loading often lead to undetected crack propagation in commercial structures like aircraft components, automotive parts and computer motherboard. Cyclic loading can make the crack grow large into any shape with an arbitrary orientation, depending on the structure geometry, boundary and loading conditions. Since crack propagation in many cases may lead to catastrophic failure with human and monetary loss as a result, it is important to enable crack growth prediction at all stages of development and during maintenance in order to prevent such scenarios. Micro mechanical approach is used for modelling the crack in composite materials. Crack propagation in a single edge crack plate is carried out by using FEM analysis. 2D model is analysed to determine the crack growth. The crack propagation rate, stress intensity factor and strain energy release rate are predicted by varying the crack length in fiber reinforced epoxy composite using NISA/ENDURE.

Introductions

Glass fiber reinforced composite materials have been widely applied in a variety of engineering and industrial fields over a past few decades requiring high strength and low weight. Transverse cracking in laminated composite materials plays an important role in the mechanical performance degradation of materials. Significant consequences of such cracks are the reduction in stiffness, strength, and life of the laminate. It is important to understand the cracking behaviour in a composite laminate in order to access the strength and useful life of the laminate used in structural components at the earlier possible stage. Many experimental investigations have been conducted and several models have been proposed to determine the change in modulus of composite materials subjected to cyclic loads. The mechanism of failure associated to transverse loads is commonly known as inter-fiber failure (also known as matrix failure). Under the particular case of tension loads, the mechanism of failure is characterized by the appearance of small debonds (interface cracks) at the fiber–matrix interface that grow along the interface.

The strain energy release rate increases with increase in crack length [1]. The crack growth rate increases with increase of stress intensity ratio[2]. Noh and Whitcomb [3] found that the opening of transverse matrix cracks and transverse crack-induced delamination can be directly related to reduction in effective moduli.

Davidson et al., [4] applied a non-classical, energy release rate based approach to predict delamination growth of different graphite reinforced laminated polymeric matrix composites, and results are obtained using classical, linear elastic fracture mechanics. Both methods predict delamination advance by comparing the strain energy release rate to its critical value or toughness.

Arguelles et al., [5] showed decrease in crack growth rate with increase in crack length. Kassapoglou [6] presented an approach to construct the stress (or load) verses cycles curve for composite structures under constant amplitude loading and derived expressions for the cycles to failure as a function of R ratio. The stress decreases with number of cycle and similar behaviour observed with energy release rate. Levay et al., [7] investigated the influence of testing conditions

on fracture mechanics characteristic and mechanical damping of a short glass fiber reinforced polyamide. Chandra et al., [8] represented the damage in glass fiber reinforced epoxy by considering gap/friction element in the fiber matrix interface. Variation of energy dissipated and loss factor due to sliding at the fiber matrix interface by using gap/friction element under transverse and transverse shear loading is considered. FEM analysis carried by them indicates the effect of damage on composite damping and showed that it is sensitive to gap orientation and type of loading.

Many authors assume that fatigue damage occurs during the loading stage of a fatigue cycle although the precise mechanics which lead to crack growth are not necessarily fully understood. On the other hand much literature is available on damage in fiber reinforced composite laminates. But knowledge of damage mechanisms at micromechanical level in composite materials is essential for the elaboration of physically based failure criteria to be applied in the design of composite structures. Fiber reinforced composite materials are usually designed to work mainly in the direction of the fibers (longitudinal direction) so that they are particularly prone to failure in the transverse direction. Although sufficient literature is available on crack or delamination prediction and propagation, the theoretical work on damping behaviour in delaminated composite structures is almost nonexistent.

Finite Element Modeling. FEM has the advantage over the analytical method in its adaptability to the analysis of crack growth in structures that are with complicated geometry or multiple irregular cracks, especially when subject to complex loading. This paper uses the NISA14 software package to evaluate the fracture mechanics parameters. A model of the edge cracked specimens is analysed. Due to the complexity and imprecision of the experimental measurement of stress, numerical analysis has been used as an alternative.

Modelling Of Single Edge Cracked Composite RVE. 2D RVE of composite with crack at its edge is subjected to tensile loading has been considered for the present FE analyses. It is assumed that there is no fiber crack. The crack is propagated in the matrix not in the fiber in a composite material. 2D static FEM model is analyzed for the prediction of Stress intensity factor, Strain energy release rate of glass fiber reinforced composite. 2D single edge cracked RVE is shown in Fig. 1

The model contains 8000 plane-stress eight noded quadrilateral elements with the mesh pattern shown in Fig. 1. The model is subjected to mode I loading condition with unit force at each node. The boundary conditions are the all displacements and reaction are zero at y = 0 as shown in Table 1. Nodal thickness is taken is 0.1 . The geometry, along with the relevant boundary conditions, is depicted in Fig. 1. For the better analysis extremely fine meshes surrounding the crack tip are taken. The eight-node quadrilateral elements, except the mid-side nodes on the two sides corresponding to the crack tip are moved to the quarter point location. The corresponding mesh can be increasingly finer until the solution has converged. Material properties chosen for a glass fiber reinforced epoxy composite given in Table 2[8].

The analysis has been carried out for the different crack length under the applied load. Strain energy release rate is calculated under two different loading conditions. The results are formulated in graphs with variation of strain energy release rate with respect to crack length. The crack propagation remains stable until the crack length reaches a critical value beyond which the growth becomes unstable leading to failure. Fatigue crack closure FEA modelling methodology presents some significant difficulties. The first one is that it is not feasible to reproduce cycle by cycle the actual phenomenon, which is composed of thousands of loading/unloading cycles, and this makes it necessary to resort to some approximations. These give different results depending on the method utilized.

The effect of crack length on damping is calculated. The existence of crack in structure is related to the decrease in its strength. The damping is calculated in terms of energy dissipated. The energy is dissipated during fracture per unit of newly created fracture surface area. This quantity is

central to fracture mechanics because the energy that must be supplied to a crack tip for it to grow energy must be balanced by the amount of an energy dissipated due to the formation of new surfaces and other dissipative processes such as plasticity. The loss can also be calculated by calculating the strain energy in the matrix. Presence of crack effects strain energy of the matrix. The damping is calculated in terms of loss factor. The loss factor of the material is given by

$$\eta = \frac{U_d}{2\pi U} \quad (1)$$

where U_d is density of energy dissipated per cycle of motion (energy per unit volume per cycle) and U is the maximum strain energy density during the cycle.

2D model is analyzed to determine the crack growth. The crack propagation rate, stress intensity factor and strain energy release rate variation with the crack length in fiber reinforced epoxy composite are predicted using NISA/ENDURE. 2D model is analysed to determine the crack growth in glass fiber reinforced epoxy composite under the force of 1N at each node. The model contains eighty nodes on the face where force of 80 N is applied. It is assumed that the crack is propagating in the matrix.

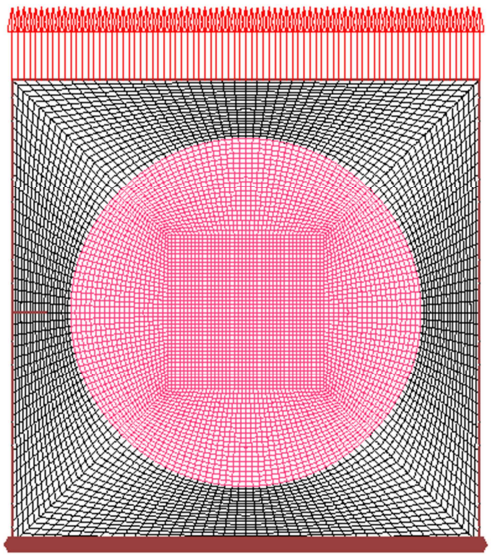


Figure 1 2D RVE of composite.

Table 1 Boundary conditions for RVE of composite.

Displacement and rotation constraints	Ux	Uy	Uz	Rx	Ry	Rz
At the nodes where y = 0	0	0	0	0	0	0

Results and Discussions

A full model is analysed by considering the plane stress case taking into consideration the crack tip singularity. The von misses stress contour of the single edge crack composite RVE is shown in Fig.1 with the V_f=0.4 where as the crack tip stress contour is given in Fig. 2. The stress at the crack tip predicted by finite element analysis is 170.5 units. However, deformation under the uniform force of 1N is shown in Fig. 3. The analysis is carried out for different crack length. The

value of stress is higher at the crack tip as predicted from the analysis. The strain energy release rate and stress intensity factor is predicted by virtual crack extension technique in FEM. Ten finite element models are constructed to accommodate ten different crack lengths to plot the results. 2D RVE of composite shows the excellent formulation of crack propagation in the form of strain energy release rate (SERR) for the different loading condition. Fig. 4 represents the SERR under the mode I loading condition. The crack propagation remains stable until the crack length reaches a critical value, beyond which the growth becomes unstable, leading to failure. The corresponding energy release rate is denoted as G_{cr}. The crack propagation in a composite material depends on the loading condition also. Fig. 4 shows the variation of strain energy release rate with respect to crack length. It shows that the strain energy rate increases with increase in the crack length. This variation is small for the lower applied load (0.5 N at each node), where as higher for higher load (1 N at each node). Further it can be seen that for the same crack length, for example for crack length of 0.45µm, corresponding energy release rate are $9.2\text{x}10^{-4}$ and $36.8\text{x}10^{-4}$ KJ/m^2 for the load 40 N and 80 N respectively. Increase in load will increase the SERR as shown in Fig. 4. Fig. 5 shows stress intensity factor with respect to crack length. The stress intensity factor is 3.18 MPa$\sqrt{}$mm when the crack length reaches 0.45µm. The variation of total strain energy is shown in Fig. 6. It shows the increasing behaviour with the crack length because the presence of crack increases the strain in the matrix hence the strain energy. The total strain energy of the model is equal to the summation of strain energy of all elements, and its value for each crack growth increment can be extracted from the output data base of NISA. Fig. 7 depicted the variation of loss factor with increase of crack length. Loss factor increases with increase of crack length.

Table 2 Basic properties of GFRE constituents

Properties	E-Glass fiber	Epoxy
E(GPa)	72.4	2.76
G(Gpa)	30.2	1.02
υ	0.2	0.35
Loss factor	0.0018	0.015

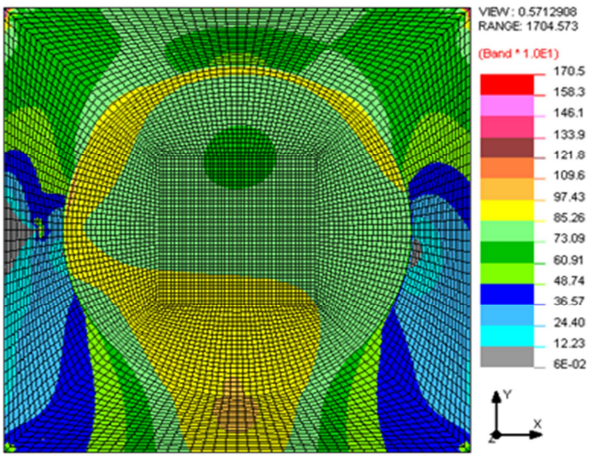


Fig. 2 Von misses stress contour of composite

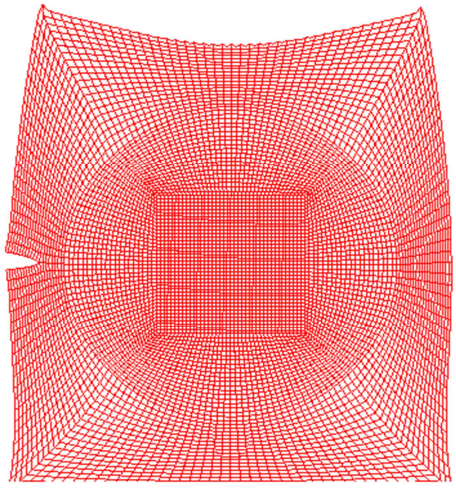


Fig. 3 Deformation of composite RVE.

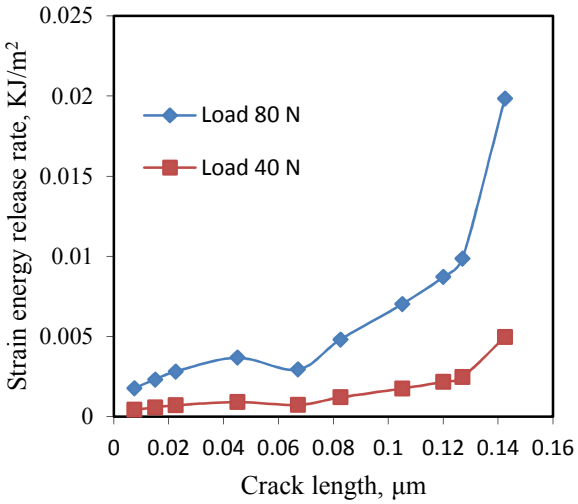


Fig. 4 Variation of strain energy release rate with crack length.

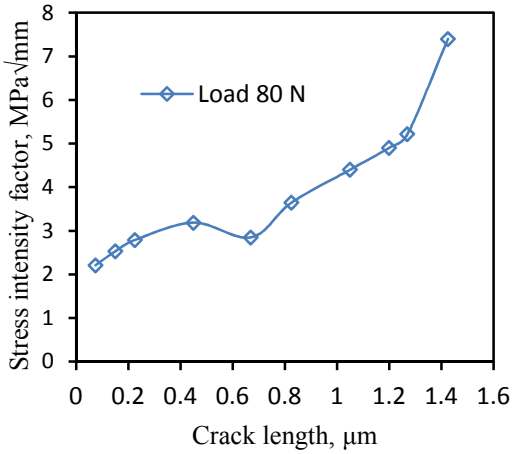


Fig. 5 Variation of stress intensity factor with crack length.

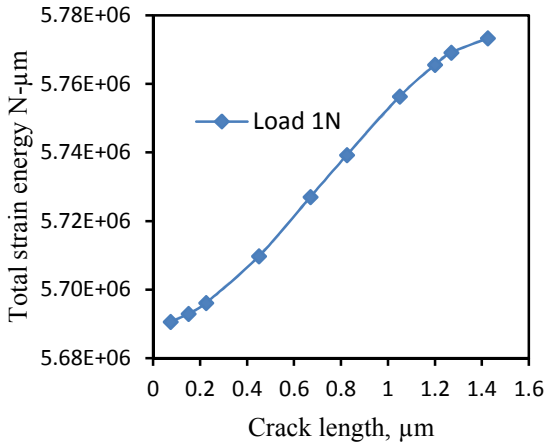


Fig. 6 Variation of total strain energy with crack length..

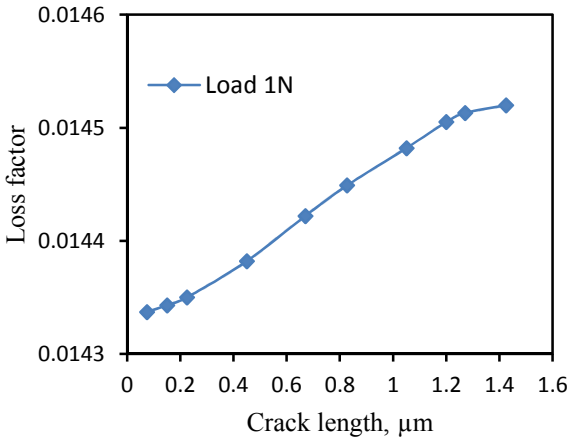


Fig. 7 Variation of loss factor with crack length

Summary

The Finite element analysis has been done to simulate crack propagation using NISA/ENDURE application. The stress intensity factor and the strain energy release rate are calculated under static analysis using the plane stress eight nodded quadrilateral element by varying the crack length and following conclusions are drawn:

(i) The strain energy release rate and stress intensity factor of the composite RVE increases with increase in crack length.
(ii) The Strain energy release rate depends on the loading condition. Higher the loading value higher is the release rate.
(iii) The total strain energy increases with the crack length.
(iv) The matrix crack affects the damping of the glass fiber epoxy composite. The damping of the GFRE increases with increase in crack length.

References

[1] S. Charoenphan, M. E. Pleshal and L. C. Bank: Simulation of Crack Growth in Composite Material Shell Structures, Int. J. Numer. Math. Eng, Vol. No. 60, (2004) p. 2399–2417.

[2] J. Andersons, M. Hojo and S. Ochiai: Empirical Model for Stress Ratio Effect on Fatigue Delamination Growth Rate in Composite Laminates, International Journal of Fatigue, Vol. No. 26, (2004), p. 597–604.

[3] J. Noh and J. Whitcomb: Effect of Delamination on Opening of Transverse Matrix Cracks, Journal of Composite Materials, Vol. No. 39. (2005), p. 543-558.

[4] B. D. Davidson, R. D. Bialaszewski and S. S. Sainath: A Non-Classical, Energy Release Rate Based Approach for Predicting Delamination Growth in Graphite Reinforced Laminated Polymeric Composites, Composites Science and Technology, Vol. No. 66, (2006), p. 1479–1496

[5] A. Arguelles, J. Vina, A. F. Canteli, M. A. Castrillo and J. Bonhomme: Interlaminar Crack Initiation and Growth Rate in a Carbon-Fibre Epoxy Composite under Mode-I Fatigue Loading, Composites Science and Technology, Vol. No. 68, (2008), p. 2325-2331.

[6] Kassapoglou: Fatigue Life Prediction of Composite Structures under Constant Amplitude Loading, Journal of Composite Materials, Vol. No. 41, (2007), p. 2737-2744.

[7] Levay, G. B. Lenkey, L. Toth and Z. Major: The Effect of Testing Condition on the Fracture Mechanics Characteristic of Short Glass Fiber Reinforced Polyamide, Journal of Materials Processing Technology, Vol. No. 133, (2003), p. 143-148.

[8] R. Chandra, S. P Singh and K. Gupta: A Study of Damping in Fiber-Reinforced Composites, Journal of Sound and Vibration, Vol. No. 262, (2003), p. 475-496.

© (2011) Trans Tech Publications, Switzerland
doi:10.4028/www.scientific.net/KEM.471-472.898

Effect of a Coupling Agent On Mechanical and Biological Properties of Polyetheretherketone/Hydroxyapatite Bioactive Composite for Prosthetic Medical Device

Ahmad Ramli Rashidi[1,a], Mat Uzir Wahit[1,b], Mohamed Ruslan Abdullah[2,c]

[1]Department of Polymer, Faculty of Chemical Engineering,

Universiti Teknologi Malaysia (UTM) Skudai, Johor, Malaysia

[2]Deparment of Applied Mechanic, Faculty of Mechanical Engineering,

Universiti Teknologi Malaysia (UTM) Skudai, Johor, Malaysia

[a]ar3_mrsm@yahoo.com, [b]mat.uzir@fkkksa.utm.my, [c]ruslan@fkm.utm.my

Keywords: Polyetheretherketone (PEEK), Hydroxyapatite (HA), (3-Aminopropyl)trimethoxysilanes, Nano-single screw extruder.

Abstract. For many years, research was focused on developing a medical part of human body from polymer as to replace metal. In this study, the aim is to produce a Polyetheretherketone/Hydroxyapatite (PEEK/HA) composite which posses balance mechanical properties and good spreading of bioactive ceramic, hydroxyapatite. The composite consist of 10-30 wt% HA were compounded via nano-single screw extruder and sample for testing were produced by injection molding. Each formulation of HA was treated with (3-Aminopropyl)trimethoxysilanes coupling agent to compare with untreated HA. The result showed that the slight increasing value of Elastic modulus, flexural strength, tensile strength while decreasing flexural modulus for 10 and 20 wt% HA compared to untreated composite. The enhance of bioactivity has been proven with the incorporation of HA into PEEK. SEM-EDX image showed the bulk formation of apatite layers on the composite surface with 30 wt% HA after 3 days immersed in SBF solution. Finally, these composite be capable of being one of the biomedical part seing as the mechanical properties were found to be within the properties of human cortical and cancellous bone.

Introduction

Medical practice today has been concerned about the existing of prosthetic device originally created from polymer. According to report by worldwide orthopedic market 2004-2005, the estimate global market for orthopedic device such as fracture repair, spinal implant and reconstructive devices is in the range of US$25-30 billion [1]. This was lead to stimulate research focuses on producing medical product especially from polymeric materials. Since metal has many disadvantage such as the presence of corrosions, fatigue failure of metal alloys, and release of metal ions such as Nickel or Chromium which may cause loosening of the implant, polymer are widely choose as to replace metal. One of the biocompatible polymer is polyetheretherketone (PEEK). The PEEK has excellent properties in term of highly chemical resistance, inert to all organic and inorganic liquid. Additionally, PEEK can retain to highly exposure of gamma radiation and its has an ability to maintain flexural and tensile properties at very high temperature (250 ^{0}C) or more [2,3,].

In view of the fact that PEEK is bioinert, hydroxyapatite (HA) were corporate into PEEK matric to enhance the bioactivity. HA is bioactive ceramic in which chemical nature is similar to the mineral component of hard tissue in human[4]. In load bearing application, HA is widely used because its bond to bone directly and promotes the new bone formation [5,6]. However, controlling the mixing between PEEK/HA phases is a critical challenge in the design of these composite. Homogeneously dispersed HA in the PEEK matrix play a key role, mainly in mechanical properties.

The interfacial strength between HA and PEEK is a very important factor because poor adhesion between two phases will result in early failure. In order to prepare bioactive composite containing HA particles within PEEK matrices, this problem must be undertake in such a way to produce great combination of composite.

Many studies have been carried out to evaluate the mechanical, thermal properties and morphology of PEEK/HA composite, however limited report were found regarding the PEEK/HA composite treated with silanes coupling agent and processing using nano-single screw extruder. Previous study of PEEK/HA composite does not using a coupling agent to improve interface adhesion. In this study a silanes coupling agent will be corporated into PEEK/HA composite. Therefore, this study goal is to evaluate the mechanical properties of silane-treated HA and the biological performance of this composite during in vitro testing.

Methodology

Materials. Polyetheretherketone (PEEK 450G, medium grade) with a density of 1.3 g/cm^3 in crystalline region and a melt viscosity of 0.46 kNs/m^2 obtained according to TM-VX-12 was purchased from Victrex Plc. United Kingdom. Hydroxyapatite (HA Fluka, 3.16 kg/cm^3) was purchased from Sigma Aldrich. The specific surface area of the powder, measured by N, absorption (according to the Brunnauer-Emmet-Teller method was found to be 33.05 m^2/g , and the particle size is 57.5 nm. Silane coupling agent, (3-Aminopropyl)trimethoxysilane (Fluka, density : 1.027 g/mL at 25 ^{0}C, boiling point : 91-92 ^{0}C) were obtained from Sigma Aldrich Malaysia.

Surface modification of Hydroxyapatite. The surface modification of HA was carried out as follows, firstly certain amount of ethanol and water was mixed up (volume ratio between ethanol and water was 1:9) for 10 mins followed by the addition of coupling agent (volume ratio between ethanol and coupling agent was 1:90) stirred for 15 mins. This ratio prior to 100 gram of Hydroxyapatite. Next, the solution was mixed with the powder of HA, under stirring at 300 rpm for 1 h. After that, the solution was filtered to get the modified powder. At last, the surface modified hydroxyapatite was dried for 2 h in an oven at 60 ^{0}C.

Composite manufacturing. Based on the formulation in Table 1, the sample was prepared through the series of processing which involve nano-single screw extruder (NANO TECHRUDER, 2010 machine). The temperature was set up from 350 ^{0}C – 390 ^{0}C and the constant screw speed of 30 rpm was used during compounding . All the compounded materials were bring to injection section.The tensile, flexural and impact specimens were produced on an injection molding machine with an injection temperature between 360 ^{0}C – 420 ^{0}C. Injection pressure was set to 140 MPa and its varies along with content of HA.

Table 1 : Blend formulation of PEEK with untreated HA and treated HA (SiHA)

Designation	PEEK content (wt%)	Untreated HA content (wt%)	Treated HA content (wt%)
10HA	90	10	-
20HA	80	20	-
30HA	70	30	-
10SiHA	90	-	10
20SiHA	80	-	20
30SiHA	70	-	30

Mechanical Testing. Tensile testing was carried out according to ASTM D638 in room temperature to evaluate the strength of sample as well as Elastic modulus. The izod impact measurement of the composite was conducted on IMPats 15 machine manufactured by ATS FAAR, Italy according to ASTM D256-88. Last but not least, flexural testing was conducted using Llyod machine with standard according to ASTM D790.

Simulated Body Fluid. In vitro test was carried out following the Kokubo method [7]. The SBF was prepared by dissolving reagent NaCl, $NaHCO_3$, KCl, $K_2HPO_4.3H_2O$, $MgCl_2.6H_2O$, $CaCl_2.2H_2O$ and Na_2SO_4 into distilled water and buffered with Tris (hydroxyl-methyl-amino-methane, $NH_2C(CH_2OH)_3$) and hydrochloric acid (HCl) to pH 7.4 at 37 ^{0}C. The solution of SBF containing ion similar to human blood plasma. Each specimens was immersed in 200 ml of SBF and the solution was placed in an incubator for 1 and 3 days at temperature of 37 ^{0}C.

Surface analysis. Morphological study of SBF specimen was analyzed by using PHILIPS XL 40 SEM-EDX microscope. In order to avoid charging during electron irradiation, the composite sample was covered with thin layer of platinum in BIO-RAD SEM coating system, using a covering time of 120 s at 2 mA.

Result & Discussion

Elastic modulus and tensile strength of PEEK composites with silane-treated HA (PEEK/SiHA) and untreated HA (PEEK/HA) are shown in Figure 1(a) and 1(b). In the case of PEEK/SiHA composite, Elastic modulus of 10wt% increased rapidly from 3.74 GPa to 3.98 GPa. Similarly, the tensile strength of PEEK/SiHA composites increased steeply from 77.5 MPA to 85.6 MPa with SiHA content of 10 wt%. These value were higher compared to untreated HA indicating that HA structure modified by silane working on interfacial adhesion between PEEK matrix and silane-treated HA. However, both tensile properties for 30wt% SiHA result in decreasing value of composite, indicating the limited effect of coupling agent as filler content increase. This was due to the plasticizing effect of silane coupling agent [8]. The major benefit of using silane coupling agent is improving ductility and fracture behaviour of composite at lower content of SiHA.

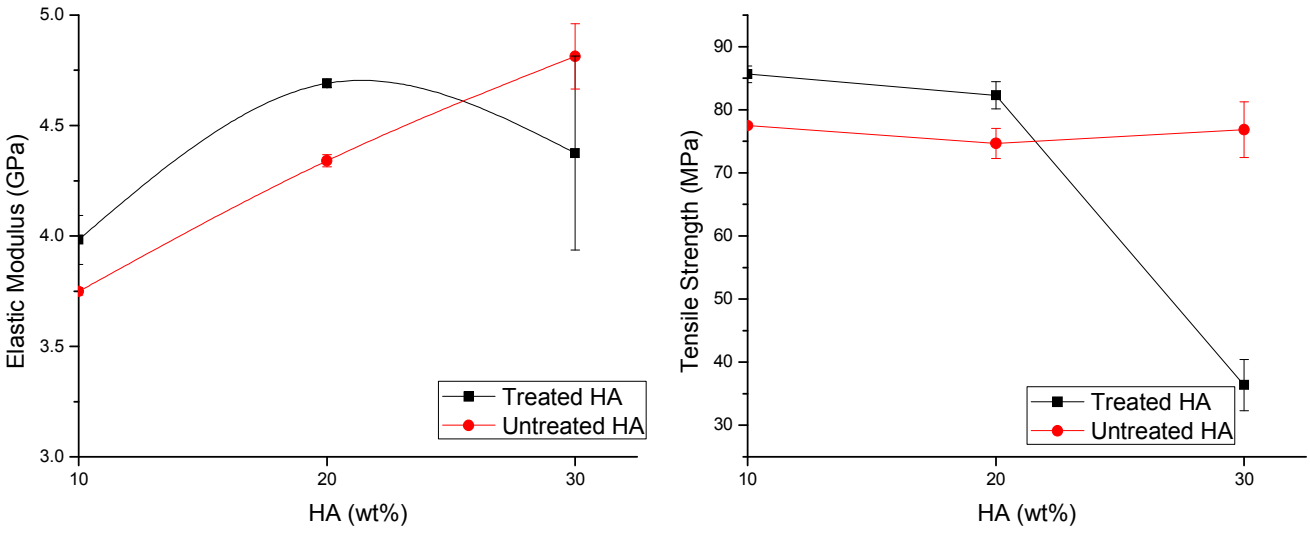


Figure 1 : Effect of silane coupling agent on (a) Elastic Modulus and (b) Tensile strength of PEEK/HA composite

Figure 2(a) and 2(b) show the flexural modulus and flexural strength of the PEEK composite containing silane-treated HA and untreated respectively. It can be seen that, all silane-treated HA showed the increase of flexural strength compared to untreated HA as SiHA content increased. The melioration of flexural strength due to enhance interfacial adhesion within PEEK matrix and silane-treated HA. Unfortunately, these HA surface treatment lower the flexural modulus of 10 and 20 wt% SiHA and the reason for that might be structural change in polymer. Grubbstrom et. al [9] in their research also reveal that the stiffness of the crosslinked composites was affected by the unintentional crosslinking, where the degree of crosslinking in the extrusion process seemed correspond to the decrease in modulus.

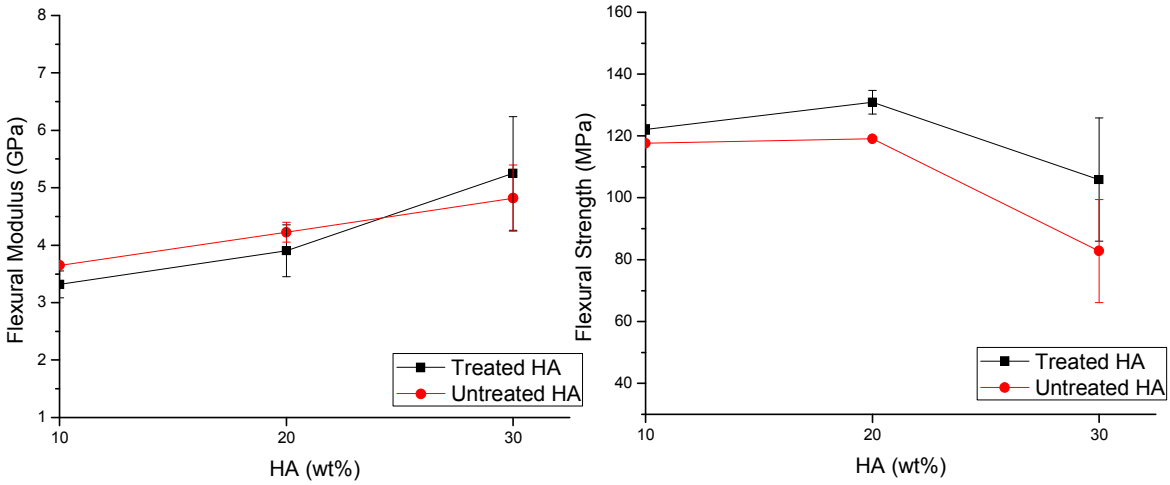


Figure 2 : Effect of silane coupling agent on (a) flexural modulus and (b) flexural strength of PEEK/HA composite

Morphological study on SBF sample is shown in Figure 3 after 3 day of immersion. It was observed that the bulk formation of apatite layer were result from the deposition of inorganic phase from SBF. Tree-like shape of apatite layers growth rapidly within 3 days prior to silane-treated hydroxyapatite contains in composite, demonstrating high in vitro bioactivity of the composite. As the time increases, these apatite layers was grew in size and formed a layer to completely cover the entire composite, as apparent from figure 5c. Thus, it is suggested that the bone-like apatite layer may promote the bone bonding with living tissue. Furthermore, EDX analysis of trees-like layer formed on the surface shows the presence of C, Ca, O, and P. It is believed that the carbon (C) demonstrate in the layer maybe the carbonate-containing apatite [10]. This was also in aggrement with findings reported by Bigi et.al [11] where EDX spectra recorded from HA-gelatin sponge indicates a Ca/P molar ratio in between 1.40 to 1.60.

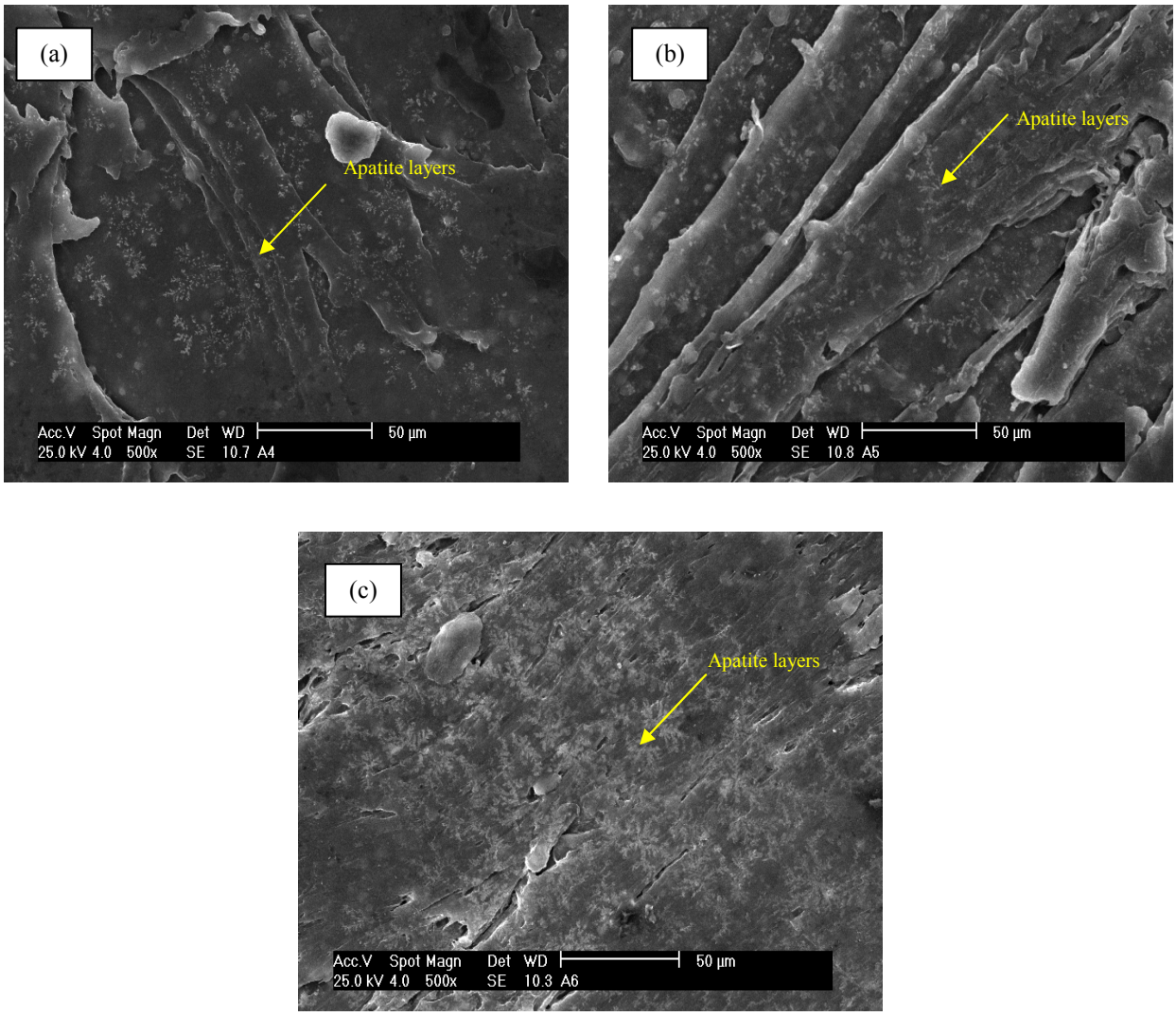


Figure 3 : SEM image of apatite layers growth on (a) 10, (b) 20, (c) 30 wt% SiHA/PEEK after 3 day of immersion in SBF

Summary

In summary, a low concentration of (3-Aminopropyl)trimethoxysilane was used as treatment medium to chemically change the structure of HA. Particularly, the result showed that the optimum Elastic modulus and tensile strength was observed from 20 wt% SiHA. Mechanically this composite offer the promises properties for prosthetic bone such as spine cage, boneplates and screws. In vitro study was conducted to investigate the biological response of PEEK/SiHA in SBF. It is also emerged from this study that HA particle loadings guarantee the growth of apatite layer as well as needed by the fracture part of bone during healing progression.

References

[1] Robert, M. S., Martin, S., and Silvana, F: Nanomedicine Volume 2 (2007), p. 861-874.

[2] Rae, P. J., Brown, E. N., and Orler, E. B: Polymer Volume 48 (2007), p. 598-615.

[3] Attwood, T. E., Dawson, P. C., Freeman, J. L., Hoy, L. R. J., Rose, J. B., and Staniland, P. A: Polymer Volume 22 (1981), p. 1096-103.

[4] Ayers, R. A., Wolford, L. M., Bateman, T. A., Ferguson, V. L., and Simske, S. J: Journal Biomed Res Volume 47 (1999), p. 54-9.

[5] Yu, S., Hariram, K. P., Kumar, R., Cheang, P., and Aik, K. K: Biomaterials Volume 26 (2005), p. 2343-2352.

[6] Chang, H., Bastari, K., Saraswati., and Philip, C: In "ICBME 2008" (C. T. Lim, ed.), Volume 23 (2009), p. 261-264.

[7] Kokubo, T., Kushitani, H., Kitsugi, S., and Yammamuro, T: Journal Biomed Mater Res Volume 24 (1990), p. 721-34.

[8] Deb, S., Wang, M., Tanner, K. E., and Bonfield, W: Journal of materials science : materials in medicine Volume 7 (1996), p. 191-193.

[9] Grubbstrom, G., Holmgren, A., and Oksman, K: Composite : Part A Volume 41(2010), p. 678-683.

[10] Gu, Y. W., Khor, K. A., and Cheang, P: Biomaterials Volume 24 (2003), p. 1603-1611.

[11] Bigi, A., Boanini, E., Panzavolta, S., Roveri, N., and Rubini, K: Journal of Biomedical Materials Research Volume 59 (2001), p. 709-715.

© (2011) Trans Tech Publications, Switzerland
doi:10.4028/www.scientific.net/KEM.471-472.904

Impact Damage Detection In A Stiffened Composite Wing Panel Using Digital Shearography And Thermosonics

G. De Angelis[1,a], M. Meo[2], D.P. Almond[2], S.G. Pickering[2], U. Polimeno[2]

[1]Chemistry Department, Flight Test Centre, Italian Air Force,

Aeroporto De Bernardi, Pomezia (Rome), Italy

[2]Department of Mechanical Engineering, UK Research Centre for NDE,

University of Bath, Bath BA27AY, UK

[a]giovanni.deangelis@aeronautica.difesa.it

Keywords: Thermosonics; BVID; Non Destructive Evaluation; Flaws assessment; Shearography.

Abstract. There has been a growing interest in the use of composites especially in structural application ranging from aerospace to automotive and marine sectors. However, their performances under impact loading represent one of the major concerns as impacts may occur during manufacture, normal operations and maintenance. This paper presents two novel NDT techniques, thermosonics and digital shearography (DISH) to detect and assess barely visible impact damage (BVID) produced on a stiffened composite wing panel by unknown low energy impacts. Thermosonics is based on synchronized infrared imaging and ultrasonic excitation. Despite the apparent simplicity of the experimental setup, thermosonics involves a number of factors, e.g. acoustic horn location, horn crack proximity, horn-sample coupling etc., that significantly tend to influence both the degree and the period of the excitation. Then, a numerical-experimental procedure for the assessment of the size and depth of delamination by digital shearography (DISH) is proposed. The flaw detection capabilities of DISH have been evaluated by measuring the dynamic response of the delaminated area to applied stresses. The shearographic methodology is based on the recognition of the (0 1) resonance mode per defect. A simplified model of thin circular plate, idealized above each impacted area, is used to calculate the natural frequency of vibrating delamination. The numerical difference between experimental resonance frequencies and those computationally obtained is minimized using an unconstrained optimization algorithm in order to calculate the delamination depth. The results showed that thermosonics is a quick and effective method to detect and localize BVID damage while the combined shearography and optimization methodology was able to size and localize delamination due to low velocity impacts.

Introduction

The durability of composite laminates based products can be affected by delaminating damage, which may develop to failures when structural components are under fatigue loading [1]. Traditional technique, such as Ultrasonic Testing (UT) have been used to provide the detection of delaminations especially in the aerospace sector. However, the need to inspect large areas and moreover the necessity to use a coupling agent between ultrasonic probes and the surface of the test objects has led the NDT community to develop alternative techniques. In particular, non contact methodologies and those based on the investigations of the non-linear elastic waves for damage localization have shown attractive expectations [2-7]. The NDT techniques include: Pulse Thermography (PT), Lock-in Thermography (LT), thermosonics as well known as Sonic Infrared (SIR) and digital shearography (DISH) [8-11]. In this work, we report the experimental optimization of both thermosonics and DISH by investigating a stiffened composite wing panel damaged by low velocity impacts. Thermosonics was experimentally optimized by taking into account different factors, such as the period of excitation, the frequency frame rate, the position of the horn tip on the inspected surface etc. DISH has given the possibility to perform vibration analysis to complement thermosonics results for the assessment of both size and depth of a few

delaminations recognized per each flawed site. In the literature, it is reported that fringe patterns recognized for overlapping debonds are visually similar to those obtained in the form of a single debond [12]. Therefore, the quantitative flaws assessment was ascertained by combining the experimental results with an optimization algorithm. As final target, a method computationally inexpensive and easily validated by numerical data and laboratory experiments was undertaken to predict the range of natural frequencies to be applied for detecting delaminations having either variable size or depth.

Materials And Methods

Materials. The specimen investigated is an important aircraft component as shown in figure 1, used as upper skin panel of wings as well as horizontal stabilizer, which results to be predominantly loaded by compression. The main issues of this aerospace structure are often correlated to the presence of delaminations produced by impact events.

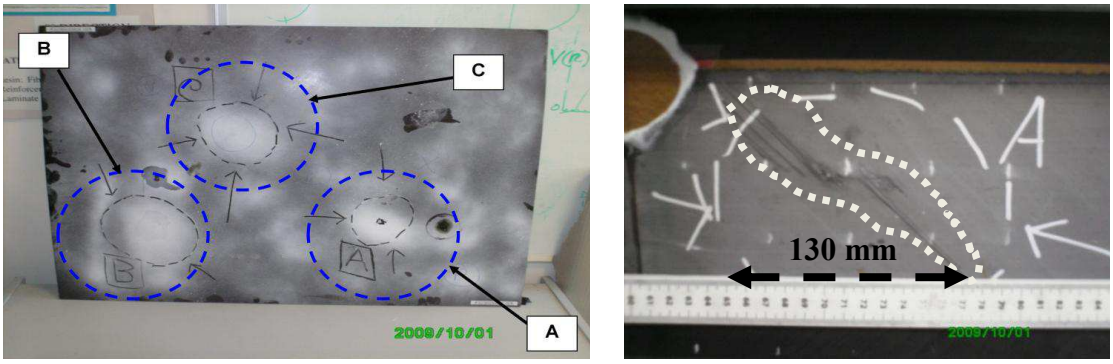


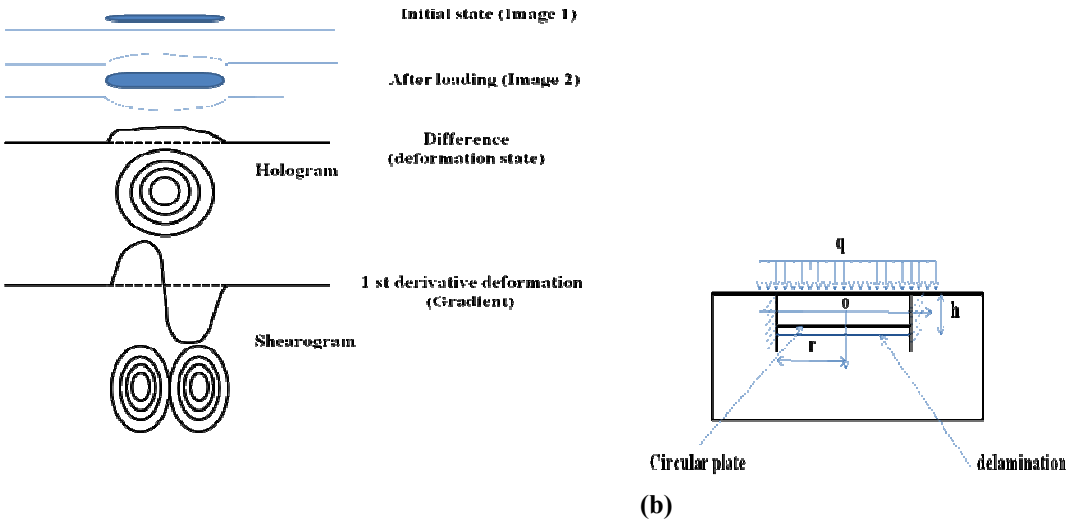
Fig. 1 Visual inspection of composite stiffened wing panel site A. **(a)** Front side, **(b)** back site.

From the visual control of the front surface in figure 1, no indentations resulted visible. For this reason, the stiffened panel was inspected on the back side and the main evidence was related to the recognition of debonding areas as shown in the figure 1 (b). The identification of these regions proved the possibility that a complicated pattern of developing delaminations could be arranged through the entire thickness of those parts of the investigated component.

Digital Shearography. Shearography involves the difference, figure 2 (a), of two speckle patterns, collected one before and another after the sample is stressed. This paper is focused at performing DISH by dynamic loading induced by a piezo-electrical actuator applied on the external surface of the test object. Standard shearography measurements were taken in order to evaluate the defect size. As a result, the depth of the delamination was the only unknown variable. The delamination behaviour was assumed to respond to the theory of elastic plates [13]. This simple model of circular plate is basically used to simulate the deflection out-of-plane of the flaws or the bending mode excited by DISH. This circular plate with radius (r) and thickness (h), figure 2 (b), was assumed fully clamped at its border, whose dimension (d) and thickness (h) are respectively identical to those of the perturbed fringe patterns recorded and to the depth (z) at which each delamination is placed [14].

For a free vibration, the governing law of motion is given by

$$D\nabla^2\nabla^2 w_0 + \kappa\omega_0 + I_0\frac{\partial^2\omega_0}{\partial t^2} - I_2\frac{\partial^2}{\partial t^2}(\nabla^2\omega_0) = 0 \qquad (1)$$



(a) **(b)**

Fig. 2 (a) Interpretation of measuring results. (b) Clamped circular plate under dynamic load (q).

where I_0 and I_2 are respectively the principal and rotatory inertia moment. For a circular plate clamped at its border, the natural frequency, related to the (0 1) mode of vibration, can be expressed by the following equation:

$$f_n = \frac{\kappa_n}{2\pi}\sqrt{\frac{Dg}{\omega r^4}} \qquad (2)$$

where ω is the uniform load per unit area including its own weight, r is the radius of the circular plate, k_n is a constant correlated to both resonance mode and nodal diameter [15]. The numerical difference between experimental (f_{exp}) and theoretical resonant frequencies, Equation 3, (f_n) was handled by an unconstrained optimization algorithm, written in Matlab language, and based on Levenberg-Marquard coupled with the line search method [16].

$$F_n = \left| f_{exp} - f_n\,(E_0, h_0) \right| \qquad (3)$$

This methodology of optimization involved an initial guess expressed for the unknown variables (E_0, h_0) in order to produce a sequence of improving approximations to the minimum point. In a previous work, the authors proved that the boundary conditions specified by the equivalent circular plate model are satisfied for a circular plate clamped and free at its border [17]. From this evidence, this work involves the extension of DISH methodology on Non Destructive Evaluation (NDE) of multiple delaminated parts having delaminations with different shapes. The corresponding data of density, Poisson's ratio and the initial guess for Young's modulus were taken from literature [18].

Thermosonics. Thermosonics is based on the effects generated on an investigated structure when it is under load conditions. The resulting vibrations, often called chaotic, cause the generation of complicated not reproducible spectra containing multiple harmonics and sub-harmonics of the driving frequency, all of which, varying in time and amplitude, contribute to the release of heat at the crack [19]. The main part of the system employed, figure 3, is an ultrasonic welding horn, pressed against the surface of the test object, and the small infrared camera for detecting the heat flux produced at flawed regions. Four feet were used to impose the appropriate pressure and therefore for optimizing the "right" level of excitation over the entire test object [20]. The "heating index" HI has been suggested as a measure of the total heating, Equation 4, released around a crack during the period of excitation. Where *t* is the time integration and *k* is a decay constant estimated from the temporal decay of heating when the excitation is switched off. The term EI stand for the "Energy Index", computed to weight the correct amount of energy delivered per each mode with its own frequency of vibration, f_n, to the reference frequency, f_0, (in our case the driving frequency (35 KHz) of the exciter.

$$HI\,(\tau) = \int_0^{\tau} e^{\kappa(t-\tau)} EI(t)dt \qquad (4)$$

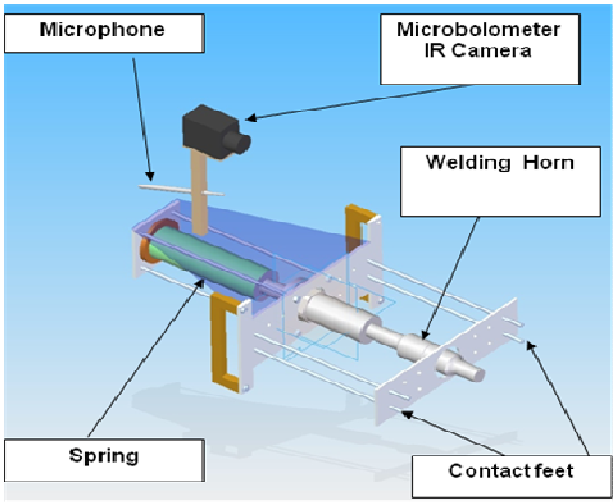


Fig. 3 Thermosonics compact system.

The solution was found by an experimental methodology by which the EI was monitored during the excitation phase of the test [20]. Formerly workers used to monitor the excited vibrations by using strain gages bonded at the parts under testing [21]. However, this experimental set–up could result unsatisfactory for full field inspection of the parts. Therefore, the structural response acquisition was provided by using a high frequency microphone to be recorded by using a high frequency sampling oscilloscope. In the end, the short-time Fourier transform algorithm was used to analyze the vibration spectra throughout the excitation phase and from these passages the heating indices were obtained in the way indicated above.

NDT Results And Discussion

Thermosonics. For this NDT inspection, the level of power in use was kept below 50 watts and the acoustic source was coupled with the test object by using a thin layer of teflon in order to avoid the melting damage. In the first step of this NDT investigation sixty (60) measurements were required in order to evaluate at seven (7) seconds the optimal period of excitation, and at the interval ranging from 9 to 10 mm the appropriate distance to compress the contact feet, figure 3, against the surface to be inspected. Under these conditions, a force around 55 N was applied over the investigated areas. Therefore, thermosonics inspections were carried out by recording 25 frames during the background acquisition and 175 frames (7 seconds) for the period of excitation. During this time, both the microbolometer and the microphone recorded respectively thermal images related to the excitation period and the vibration spectrum to be stored in the laptop. The (k) factor was evaluated by fitting the thermal decay, figure 4 (a), from the 200th frame. In this way, the peak value of the HI of around 2551 unit, figure 4 (b), was estimated sufficient to assess the adequacy of the ultrasound excitation for a reliable test on the site under investigation. The visibility of the final image was significantly improved by binarization and then by integrating all images collected during the excitation period. The theoretical thermal image, introduced at the attention of the NDT inspector, is shown in the

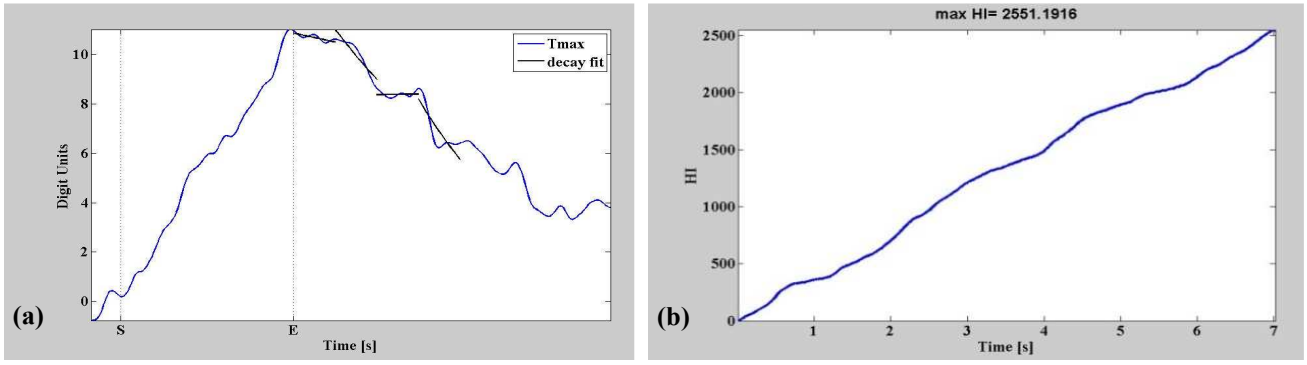


Fig. 4. Thermosonics investigation. **(a)** Thermal decay data fitting, **(b)** heating index (HI) assessment.

figure 5 (b). The optimized operative conditions, the period of excitation and the force applied on the investigated area, were also used to set this thermosonics device to test the other sites.

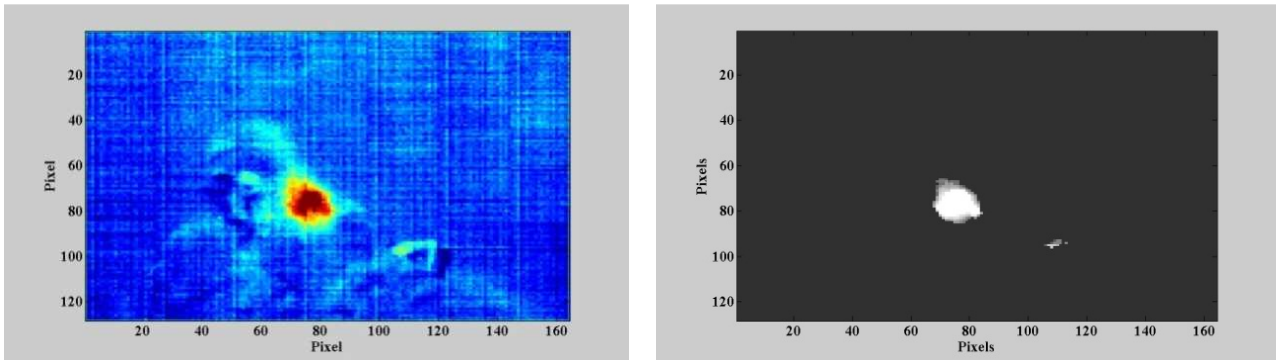


Fig. 5 Thermosonics inspection of site A. **(a)** Raw thermal image, **(b)** Thermal image after image processing.

Digital Shearography: Numerical Optimization. The BVID sites, recognized by visual inspection and thermosonics, were also investigated by DISH. In particular, a multiple sweep of frequencies was used to define the appropriate interval of natural frequencies to be applied to perform the single frequency approach. An example of shearogram, obtained through the inspection executed on the site A, is shown in the figure 6.

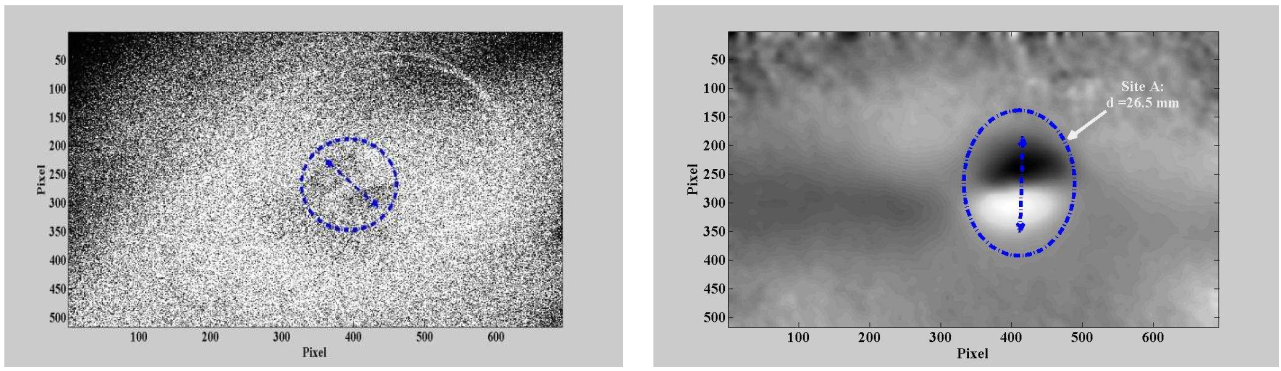


Fig. 5 (a) Raw and **(b)** demodulated phase map distribution on the site (A) along Y-shearing direction at 6.10 KHz.

The delamination size (d_{exp}) was experimentally approximated, table 1, by the measure of the width of the fringe derivative contours. On the other hand, the depth (z) of each defect was ascertained by using the thin plate model previously described in combination with an unconstrained optimization procedure assuming clamped and free mode conditions. The results, reported in table 1, show that a single delamination was assessed on the site A, whilst two overlapping delaminations were identified on the other two sites.

Table 1 DISH Inspection of the stiffened composite wing panel. Experimental sizes (d) and numerical depths (z).

Site	f_{exp} (KHz)	$Z_{Clamped}$	Z_{Free}	d_{exp} (mm)
A	6.10	0.45	0.50	26.5
B_1	5.89	0.70	0.80	32.5
B_2	7.33	1.10	1.20	36.4
C_1	4.47	1.10	1.20	48.6
C_2	5.53	0.61	0.70	31.6

Summary

In this work, thermosonics was used to investigate the BVID produced in a stiffened composite wing panel. The adequate HI of around 2551 units was identified after sixty (60) tests. This value resulted for the minimum threshold of heat flux released from the flawed regions recognized. After an impact, due to the presence of simultaneous failure modes, it is very difficult to evaluate the location as well as the size of a single delamination from the temperature mapping. The use of the shearographic technique has given the opportunity to detect single debonds placed throughout the multiple delaminated parts. In particular, the assumed relationship between the bending mode of the circular plate and the deflection out of plane of a delamination was used in combination with an unconstrained optimization algorithm to estimate the depth of the defect. In conclusion, thermosonics was evaluated as an intrinsically fast method of inspection by which providing a pass/fail test on the respective absence/presence of flawed regions. In contrast, DISH investigation were carried out for the depth profiling of the debonds recognized. The accuracy of DISH methodology will be proved by estimating the positions of artificial overlapping delaminations introduced throughout the thickness of a composite laminate.

References

[1] Abrate , Impact on Composite Structures. , Cambridge University Press, Cambridge (1998).
[2] Maldague, X.P.V.,"Theory and Practice of Infrared Technology for Non destructive Testing" Canada: John Wiley & Sons (2001).
[3] Zou, L., L. Tong and G.P. Steven: Journal of Sound and Vibration 230 (2) (2000), 357-378.
[4] Polimeno, U., Meo, M.: Composite Structures Vol. 91 (4) (2009) p. 398-402.
[5] Zumpano, G., Meo, M.: Computers & Structures Vol. 86 (3-5) (2008) p. 483-490.
[6] Meo, M., Polimeno, U., Zumpano, G.: Applied composite materials Vol.15 (3) (2008) p.115-126.
[7] Zumpano, G., Meo, M.: Intern. Journal Of Non-Linear Mechanics Vol.43 (3) (2008) p. 217-230.
[8] Meola, C. and G. M. Carlomagno. Measurement Science & Technology 15 R27 (2004).
[9] Avdelidis, N. P., D. P. Almond : Insight Vol. 48 (5) (2006) p. 286-289.
[10] Barden, T. J., D. P. Almond : Insight Vol. 48(2) (2006) p. 90-93.
[11] Chen, F. (1999). Machine Vision Systems for Inspection and Metrology Viii 3836: 52-70.
[12] Hung, Y.Y., Luo, W.D., Lin, L., Shang, H.M.: Composite Structures Vol. 50 (2000) p.353 – 362.
[13] Reddy, J.N.. "Theory and Analysis of ElasticP". Taylor & Francis. (2003)
[14] Hung, Y.Y., H.P. Ho. (2005). Materials Science and Engineering R 49 (61-87).
[15] Young W C and Budynas R C *Roark's Formulas for Stress and Strain* 7th edn (New York: McGraw-Hill) (2002).
[16] Nocedal, J. and Stephen J. Wright. "Numerical Optimization" Springer series in Operation Research (1999).
[17] G. De Angelis, M. Meo, D.P. Almond, S.G. Pickering, S.L. Angioni.' A new technique for the assessment of defect size and depth in composite structures using digital shearography and unconstrained optimization, Submitted to NDT & E International.
[18] Matweb material property data. Available from http://www.matweb.com/
[19] X. Y. Han, W. Li, Z. Zeng, L. D. Favro, and R. L. Thomas: Applied Physics Letters Vol. 81(17) (2002). p. 3188–3190.
[20] U. Polimeno and D.P. Almond: ICCST7 proceedings (2009).
[21] Morbidini, M., Thesis (PhD). Imperial College, London. (2007).

© (2011) Trans Tech Publications, Switzerland
doi:10.4028/www.scientific.net/KEM.471-472.910

Acoustic Emission Localization in a Composite Stiffened Panel using a Time Reversal Algorithm

Francesco Ciampa[1], Michele Meo[1,a]

[1]Department of Mechanical Engineering,

University of Bath, Bath, UK

[a]m.meo@bath.ac.uk

Keywords: stiffened panel, impact localization, wave propagation, time reversal

Abstract. This research work presents an *in-situ* imaging method for the localization of the impact point in complex anisotropic structures with diffuse field conditions, using only one passive transducer. The proposed technique is based on the time reversal approach applied to a number of waveforms stored into a database containing the experimental Green's function of the medium. The present method exploits the benefits of multiple scattering, mode conversion and boundaries reflections to achieve the focusing of the source with high resolution. The optimal re-focusing of the back propagated wave field at the impact point is accomplished through a "virtual" imaging process, which does not require any iterative algorithms and a priori knowledge of the mechanical properties of the structure. The robustness of the time reversal method is experimentally demonstrated on a stiffened composite panel and the source position can be retrieved with a high level of accuracy (error less than 3%). The simple configuration, minimal processing requirements and computational time (less than 1 sec) make this method a valid alternative to the conventional imaging structural health monitoring systems for the acoustic emission source localization.

Introduction

Traditionally, the determination of the impact location is an inverse problem achieved by optimization methods based on wave propagation approaches. These techniques are usually divide in two steps. First, the time of arrival (TOA) of the *ballistic waves* (direct waves from the source to the receiver) are recorded by a network of passive transducers. The waveforms are usually analyzed with advanced signal processing techniques and then resolution algorithms can be employed to obtain the impact coordinates. Even though most of these methods are able to find the impact source with satisfactory accuracy in isotropic [1, 2] and anisotropic [3, 4, 5] structures, a number of issues still need to be addressed. At first, they require a relatively large number of transducers, especially in composite materials, wherein the group velocity due to structural anisotropy is angular dependent. Then, only the coherent part of the wave field that arrives first to the sensors is used, regardless the contribution from the remaining part of the signal. Indeed, the dispersive nature of guided Lamb waves, as well as the presence in geometrically complex structures of multiple scattering, reflections from the boundaries and mode conversion (known from seismology as *coda*) can alter the resulting signal, leading to a wrong estimation of the TOA. That is, the wave field of complex structures (with stiffeners, rivets, holes and voids), excited over a finite bandwidth, becomes diffuse incoherent [6]. However, the acoustic emission (AE) propagation can be described in terms of signal processing as a linear system with different impulse responses. Lobkins and Weaver [7] showed that the structural impulse response (Green's function) could be retrieved from the cross-correlation of the elastic diffuse wave field at the sensors location. This concept was widely used in seismology and ultrasonic applications, and only recently it was examined through a time reversal (TR) process. Based on the principle of time-reversal invariance and spatial reciprocity of the acoustic wave equation in a lossless medium, in a TR experiment, the elastic waves diverging

from a point-like target can be focused back to the original source if the output measured by a set of transducers is time reversed and re-emitted back onto the excitation point [8]. Nevertheless, a perfect localization would require a totally covering array of sensors (closed cavity), which is impossible to obtain in practise. Hence, the closed cavity is replaced by a time reversal mirror (TRM) of finite bandwidth and aperture that limits the focusing quality. However, it was illustrated by Derode et al. [9] that the reverberations of a diffuse wave field in a complex medium enhance the focusing resolution of the re-emitted signal. Such a combination of TR and diffusive wave fields is known as Correlation of a Diffuse Field (CDF). From a physical point of view, this phenomenon [10] is due to the presence of scatterers within the medium that allows the *evanescent modes* (waves that decay exponentially with the distance to the source) to be converted in propagating modes. These waves, carrying the information of the impact source to the far field, where the TRM is located, can participate to the focusing process. The result of such operation creates a "virtual" enlargement of the transducers angular aperture (*kaleidoscopic effect*) of the TRM and thus the number of sensors can be drastically reduced. This paper reports a one-channel imaging method aimed to detect in real time the impact source in complex anisotropic structures with diffuse field conditions. The proposed technique, based on the time reversal approach, allows achieving the optimal focalization of the AE source (impact event) as it overcomes the drawbacks of most impact identification methods. In a first step, the impulsive responses of the medium were acquired and stored into a computer. Then, exploiting the benefits of multimodal conversion and scattering effects, a virtual focusing procedure was performed by using only one passive sensor placed on a generic point of the structure. The robustness of this approach is experimentally demonstrated on a dissipative stiffened carbon-fibre composite panel. The layout of the paper is as follow: in Section 2, the imaging method for the localization of the impact source is presented, section 3 reports the experimental set-up and Section 5 reports the results for two different impact points. Then, the conclusions are discussed.

One channel impact localization algorithm. The idea of using TR as an imaging method of the impact source was originally developed by Ing et al. [11] for the detection of a finger knock on a glass plate. Here, we combine the CDF method with the advantages of a TR process, already used in conventional pulse-echo [12] and imaging [13, 14] damage detection. The presented work represents a SHM technique based on the correlation of the signals representing the experimental Green's function of a reverberant field, measured by only one passive transducer, and its reversed in the time domain. Hence, in order to obtain the optimal re-focusing at the impact source in complex anisotropic structures, the transfer matrix of the structure H(ω) is first introduced, and then TR imaging techniques is analyzed.

The structural transfer matrix H. The TR process was split into two steps. In a first step, the surface structure ("focusing plane") was entirely divided in M = 50 x 15 "observation points" distributed along a grid at interval of 2 cm. At each point, the acoustic emission was generated by impact loads. (Fig. 1).

Due to linearity, the acoustic field measured by the transducer from the mth observation point is:

$$f(t) = \sum_{m=1}^{M} \mathbf{h}_m(t) \otimes \mathbf{e}_m(t) = \int_{-\infty}^{\infty} \sum_{m=1}^{M} \mathbf{h}_m(\tau)\mathbf{e}_m(t-\tau)d\tau \quad (1)$$

where the symbol "$\otimes$" represents a temporal convolution and $\mathbf{h}_m(t)$ ($1 \le m \le M$) is the linear propagator operator defining the Green's function measured by the sensor. This term includes all the propagation effects through the medium from the mth observation point to the receiver (included its acoustic-electric response). $\mathbf{e}_m(t)$ is the column vector of the input signal sent by the mth source on the focusing plane and *f(t)* is the output signal measured by the transducer at each instant in time. In the frequency domain, equation (1) is:

$$F(\omega) = \sum_{m=1}^{M} \mathbf{H}_m(\omega)\mathbf{E}_m(\omega) \quad (2)$$

which can be written in matrix form as:

$$\underbrace{F(\omega)}_{1\times1} = \underbrace{\mathbf{H}_m(\omega)}_{1\times M}\underbrace{\mathbf{E}_m(\omega)}_{M\times1} \tag{3}$$

where the matrix $\mathbf{H}_m(\omega)$ is the *transfer matrix* of the system (Fourier transform of the Green's function) and represents the amplitude of the *i*-th guided Lamb mode associated to the *i*-th eigenfrequency. For the spatial reciprocity condition, the transpose of $\mathbf{H}_m$ ($\mathbf{H}_m{}^T$) corresponds to the propagation between the transducer and the observation points (Fig. 2):

$$\mathbf{E}_m(\omega) = \mathbf{H}_m^T(\omega)F(\omega) \tag{4}$$

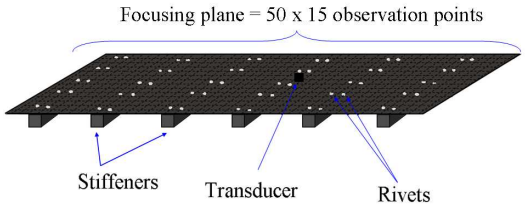


Fig. 1 Experimental set-up.

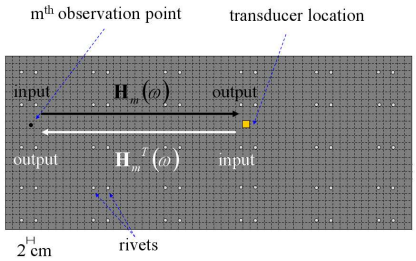


Fig. 2 Reciprocity condition of the transfer matrix H(ω).

Hence, the M signals representing a library of impulse responses $\mathbf{H}_m(\omega)$ of the structure were recorded by the transducer and stored into the computer memory.

Time reversal focusing approach. The second step consisted in recognition of the optimal refocusing procedure at the source location. The basic idea was to time reverse not only the Green's function associated to the AE source, but also to neighbouring points (observation points). Thereby, a new impact was applied in one of the points (of unknown location) of the focusing plane and its impulse response was measured by the sensor. TR behaves as a spatio-temporal matched filter that maximizes the ratio between the amplitude of the output signal (waveform acquired) and the square root of the input energy (impulse applied). Hence, assuming that the impact source in the second step is located at m_0, the input column vector $e_{m0}(t)$ from the mth observation point can be mathematically approximated to a temporal delta function δ(t) only when $m = m_0$. In the frequency domain, the emitted signal is $E_{m0}(\omega)=\{0,\ldots0,1,0,\ldots0\}$. According to (3), the wave field received by the transducer is:

$$F_{m0}(\omega) = \mathbf{H}_{m0}(\omega)\mathbf{E}_{m0}(\omega) \tag{5}$$

and the Time Reversal (TR) operation of the Green's function [$\mathbf{h}_{m0}(-t)$] in the time domain is equivalent to taking its complex conjugate in the Fourier domain. Hence, time reversing the spectrum of the transducer output, we have:

$$F_{m0}{}^*(\omega) = \mathbf{H}_{m0}^*(\omega)\mathbf{E}_{m0}^*(\omega) = \mathbf{H}_{m0}^*(\omega)\mathbf{E}_{m0}(\omega) \tag{6}$$

where the superscript '*'denotes complex conjugate and $\mathbf{E}_{m0}(\omega)$ is real. Combining equations (4) and (6), the back-propagated signal at the source is:

$$\mathbf{E}_{TR}(\omega) = \mathbf{H}_m{}^T(\omega)F_{m0}{}^*(\omega) = \mathbf{H}_m{}^T(\omega)\mathbf{H}_{m0}^*(\omega)\mathbf{E}_{m0}(\omega) \tag{7}$$

and $\mathbf{H}_m{}^T(\omega)\mathbf{H}_{m0}^*(\omega)$ is called the TR operator. Since equation (7) has a maximum at the focus point, the information associated to the AE source location can be extracted from a "virtual" TR experiment. Fig. 3 illustrates the procedure for obtaining the imaging focusing with a TR analysis.

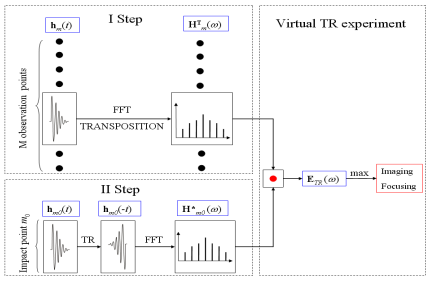


Fig. 3 Architecture of the time reversal imaging process.

Experimental set-up. The experiments were carried out on a riveted carbon-fibre stiffened composite panel (100cm x 30 cm x 3 mm) reinforced with six vertical stiffeners (7.9 mm of diameter) (Fig. 4). For the library of signal needed to implement the technique, the impacts were applied to 750 observation points spaced 2 cm apart using a hand-held modal hammer, manufactured by Meggit-Endveco. The experimental Green's function from each observation point was acquired using an acoustic emission sensor instrumented with an oscilloscope (Picoscope 4224) with a sampling rate of 25 MHz. The passive sensor employed was a surface bonded acoustic emission sensor with a central frequency of 300 kHz. The transducer output was connected to a pass-band filter with a frequency bandwidth between 200 and 400 kHz and a preamplifier. According to the d_{31}/d_{32} electromechanical coupling mechanism of the acoustic emission sensor, at the mentioned finite bandwidth, only the fundamental antisymmetric Lamb wave A_0 was measured. The time histories of the signal received by the sensor were stored on a computer and processed using a Matlab software code implemented by the authors. All the impacts were carried out manually (with different forces applied) in order to avoid damaging the structure. In addition, as it can be seen from Fig. 5, the signals were normalized in amplitude and averaged in the first step. Due to the long reverberation present in the waveform, the time window of the signals was chosen at 100 ms.

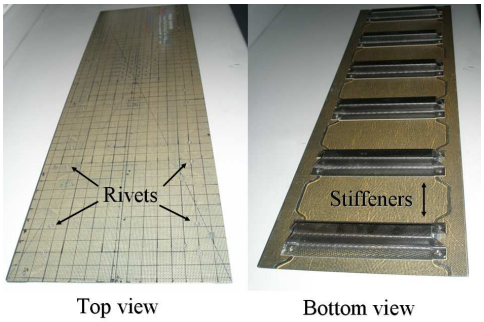


Fig. 4 Top and bottom view of the stiffened carbon-fibre composite panel used in the experiments.

Imaging localization results

The imaging results are illustrated in Fig. 6. The refocusing diffused wave field at the source location is represented by a 2-D map and the maximum of $\mathbf{E}_{TR}(\omega)$ [Eq. (7)] is deduced from the values nearest to 1 (characterized by a dark red colour) with a computational time lower than 1 sec. From the figures, it can be clearly seen that the TRA method provides an optimal focusing with reasonable accuracy and the maximum error in estimation of the source location was less than 3% (maximum percentage error given by the error function expressed in [5]) for all the case tested. In fact, as it can be observed from Fig. 6, a maximum value of the refocusing equal to 1 was found even in points close to the true impact source (see the points at x = 38 cm and y = 10 cm for case I1 and x = 80 cm and y = 28 cm for case I2). Such ambiguity might be due to the non-linear attenuation with the wave amplitude that induces distortions of the wave front propagating in the structure [15].

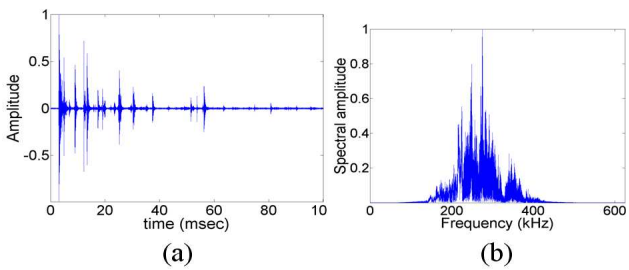


Fig. 5 (a) (b) Normalized time history (a) of one the focusing point and its frequency content (b).

Table 1

	X-coordinates [cm]	Y-coordinates[cm]
Sensor position (case I1)	60	16
Sensor position(case I2)	24	14
Impact I1	40	10
Impact I2	80	26

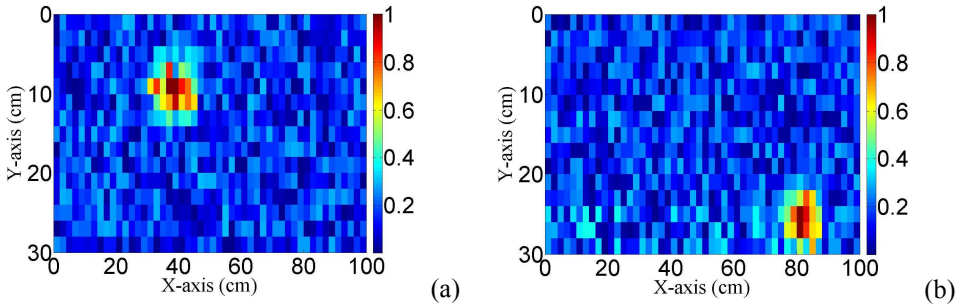


Fig. 6 (a) (b) 2D map of the optimal refocusing with a simulated TRA experiment for impact I1 (a) and I2 (b).

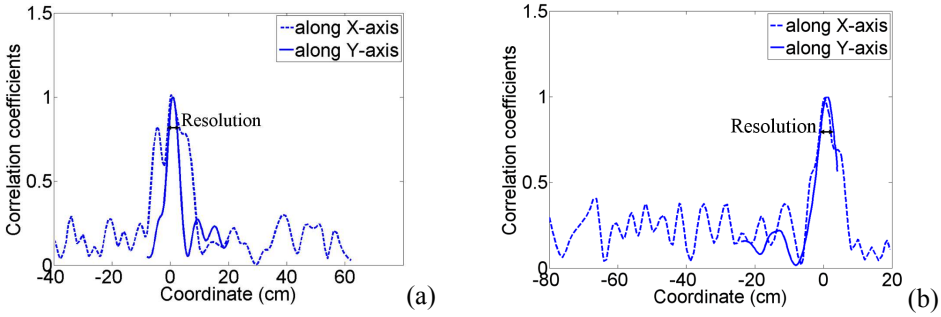


Fig. 7 (a) (b) Correlation coefficients pattern along the X and Y-axis - I1 (a) and impact I2 (b).

However, a combination of the physical principles of a correlation diffuse field (CFD) technique with the advantages of a time reversal process has shown to provide an optimal re-focusing at the impact location. In other words, the "benefits" of multiple scattering from rivets and modal conversion due to the presence of stiffeners (ultrasonic diffused wave field) allow achieving a high refocusing quality of the recompressed waves without the need to increase the number of sensors for improving the spatial resolution [16]. In fact, from Fig. 7, the correlation coefficients pattern along the X and Y-axis shows that a high resolution can be achieved even using only one passive transducer. Therefore, a very simple configuration is needed for the identification of the AE source, leading to an effective decrease of the number of sensors employed, resulting into costs savings and weight reduction. Nevertheless, during the experiments it was observed that a decrease of the number of observation points led to an increase of the maximum error in retrieving the impact location, with lower values of $max\ \mathbf{E}_{TR}(\omega)$ compared to the previous case (Fig. 8). In particular, assuming 200 observation points the location error was found nearly 10% for impact I1 (Fig. 8-a) and approximately 12% for impact I2 (Fig. 8-b). Unlike other techniques, this method presents the great advantage that it does not require any iterative algorithms as well as a priori knowledge of the mechanical properties, lay-up and anisotropic angular-group velocity pattern of the medium.

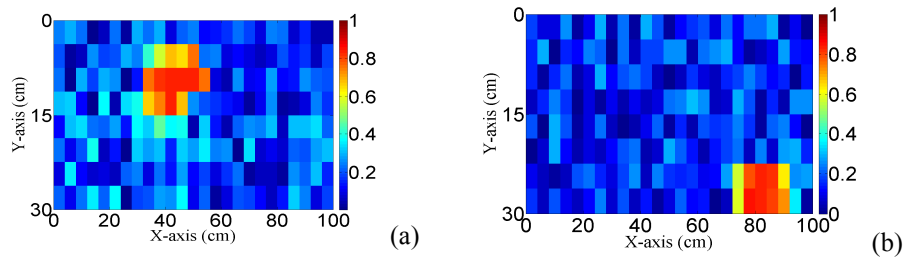


Fig. 8 (a) (b) 2D map of the optimal refocusing for impact I1 (a) and I2 (b) with 200 observation points.

Summary

In this paper, an *in situ* imaging method able to detect in real-time the impact source on a stiffened composite panel with diffuse field conditions is presented. This technique based on time reversal approach, is directly applied to the experimental impulse responses of the structure recorded by only one passive sensor and stored into a database. The proposed method allows achieving the optimal focalization of the acoustic emission source in the time and spatial domain as it overcomes the drawbacks of other ultrasonic techniques. Exploiting the benefits of a diffuse wave field, a high refocusing quality (spatial resolution), with only one sensor can be accomplished. The efficiency of this method is experimentally demonstrated showing high accuracy in detecting the impact source location (error < 3%).

References

[1] Ciampa F, Meo M.: Smart Mater. Struct. Vol. 19 (2010) p. 1-14.

[2] Tobias A.: Non-Destructive Testing, Vol. 9 (1976) p. 9-12.

[3] Meo M, Zumpano G, Pigott M, Marengo G: Compos. Struct. Vol. 71 (2005) p. 302-306.

[4] Ciampa F., Meo M: Composites: Part A (2010).

[5] Paget C A, Atherton K, O'Brien E.: Proc. of the 4th Int. Workshop on Structural Health Monitoring, Stanford, CA, (2003) p. 363-370.

[6] Weaver R. : J. Acoust. Soc. Am. Vol. 71 (6) (1982) p.1608–1609.

[7] Lobkis O.-I, Weaver R. : J. Acoust. Soc. Am. Vol. 110 (6) (2001) p.3011–17.

[8] Dorme C, Fink M.: J. Acoust. Soc. Am. Vol. 98 (2) (1995) p. 1155–1162

[9] Derode A, Larose E, Tanter M, de Rosny J, Tourin A, Campillo M, Fink M.: J. Acoust. Soc. Am. Vol. 113 (6) (2003) p.2973–2976.

[10] Fink M. : Journal of Physics: Conference Series, Vol. 124 (2008) p. 012004.

[11] Ing R.-K, Quieffin N, Catheline S, Fink M.: Appl. Phys. Lett. Vol. 87 (2005) p.204104.

[12] Zumpano G, Meo M: Int. J. Solids Struct. Vol. 44 (2007) p. 3666–3684.

[13] Barbieri E, Meo M: Int. J. Solids Struct. (2010).

[14] Wang C.–H, Rose J.–T, Chang F.–K.:. Smart Mater. Struct. Vol. 13 (2004) p. 415-423.

[15] Tanter M, Thomas J.-L, Fink M.: J. Acoust. Soc. Am. Vol. 103 (5) (1998) p. 2403–2410

[16] Ribay G, Catheline S, Clorennec D, Ing R K, Queffin N, Fink M: IEEE Trans. Ultrason. Ferroelectr. Freq. Control Vol. 54 (2) (2007) p. 378-85

© (2011) Trans Tech Publications, Switzerland
doi:10.4028/www.scientific.net/KEM.471-472.916

Multiscale Modeling of Hybrid Composite Structures

RŮŽIČKA Milan[1, a], HAD Jiří[1,b], KULÍŠEK Viktor[2,c] and UHER Ondřej[3,d]

[1]Faculty of Mechanical Engineering, Czech Technical University in Prague

Technická 4, 166 07 Praha 6, Czech Republic

[2]Research Centre of Manufacturing Technology, Czech Technical University in Prague

Horská 3, 128 03 Praha 2, Czech Republic

[3]CompoTech Plus s.r.o., Družstevní 159, 34 201Sušice, Czech Republic

[a]milan.ruzicka@fs.cvut.czl, [b] jiri.had@gmail.com,

[c]v.kulisek@rcmt.cvut.cz, [d]ondrej@compotech.com

Keywords: multiscale modeling, three-dimensional composite structure, pitch-based carbon fibre, hybrid composite structure.

Abstract. A novel type of hybrid composite structure has been developed, experimentally investigated and used for many practical applications. The main supporting elements of composite structures are formed by the stamping process of partially cured and axially-oriented carbon fibre rods. This system can fill relatively thick parts of cross sections of beams without risk of delamination. Typical macroscopic sub-cells are formed in the transversal cross section of the part due to this technology. An advantage of this final 3D composite structure is its high shear strength and stiffness in comparison with thick unidirectional composite parts. To absorb the dynamic energy and increase the damping, a rubber-cork layer can be inserted during production, before the final pressing and curing of the whole part. The final stiffness property of the whole 3D composite is obtained from multiscale modeling. It is based on an averaging process and a homogenization technique in FEA. A parametric study was carried out to determine the influence of the size, orientation and thickness of the cell border winding layer on the components of the global elastic material matrix. A comparison of a numerical analysis prediction with experimental results shows acceptable agreement of the elastic modules. A mezzo scale model can be applied for designing a real part on a macro scale.

Introduction

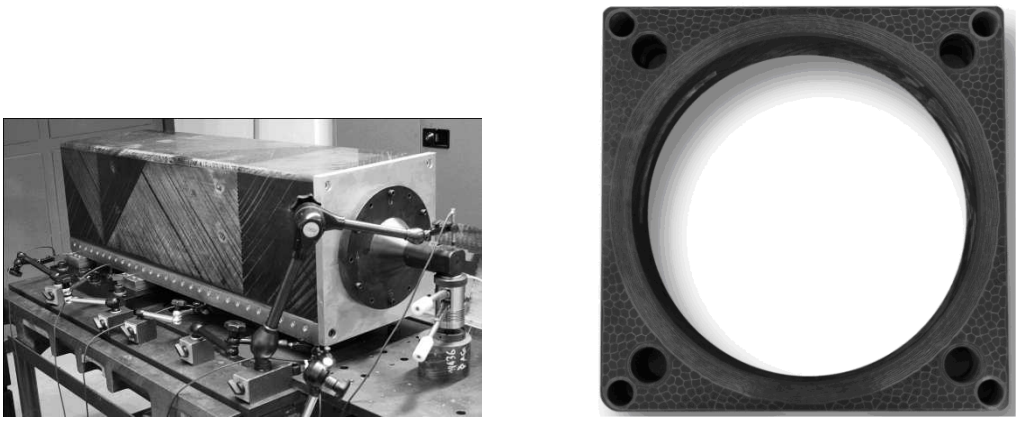
The design of a composite part with ultra-high stiffness leads to thick-walled reinforcing members characterized by fibres oriented in the direction of the maximal force-flow. However, the low shear static and fatigue strengths of these unidirectional thick structures often limit their application. This is due to the low strength of the composite matrix and the multiaxial stress state. Cracks arise at several points between the fibres (thick-walled pultruded composite flanges), or delaminations occur between the laminae (laminated composite plates).

An increase in shear strength is usually produced by various laminate techniques, such as stacking optimization of composite layers or the use of sandwich structures. This problem can also be solved technologically. Three dimensional, father (3D) braided fabric and 3D strengthening (transversal needling) can improve or partially eliminate delamination or matrix cracking. However, these techniques lead to a rapid decrease in stiffness in the dominant load direction. Filament fibre winding technology combined with stamping and wrapping was used to manufacture a hybrid three-dimensional fibre cell structure.

The goal of this study is to build and verify an FE-model for these complex hybrid composite structures. Because the materials, and thus the elastic properties and strengths, are different in different locations in the structure, multiscale modeling is used.

A hybrid 3D structure

A novel type of hybrid composite structure has been developed, experimentally investigated and used for many practical applications [1]. This technology was developed by CompoTech Ltd. in research cooperation with the Czech Technical University in Prague. The main application of these structures is for thick-walled or nearly solid beams with maximum bending strength (spars, wing flanges, etc.) or with high stiffness, e.g. machining centre spindle beams, etc., see Fig. 1.



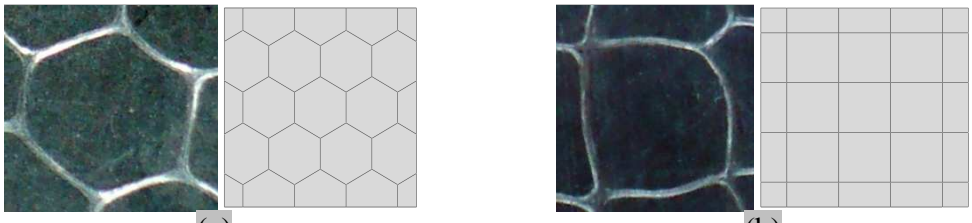
(a) (b)

Fig. 1. A composite spindle beam (a) and its cross-section (b), formed by central and corner tubes and an axially-oriented 3D sub-cell structure

A typical hybrid composite beam consists of the main supporting element (e.g. a wound composite tube beam). The stamping process of partially cured and axially-oriented carbon fibre rods is used to form the final composite structure. The square or rectangular cross section of this spindle beam is filled in all corners by a sub-cell structure, as is shown in Fig. 2. These sub-cells are formed on the basis of unidirectional composite fibre tows (usually containing high modulus C/E fibres), which are over-wound at given angles by a thin high-strength C/E layer. The wrap is created with thickness between 0.2 and 0.5 mm and fibre angle orientation from 0 to 89 degrees. An FEM parametric study is shown below to optimize the final configuration of the whole structural part.

Multiscale modeling of a 3D structure

Two main different configurations of the cells can be observed in the cross-section of the 3D structural part, which is hexagonal or rectangular. The idealized geometry of the representative volume elements (RVE) containing the periodic structure with both typical sub-cell shapes is shown in Fig. 2. On the real part, of course, many deviations of sub-cells from the ideal shape can be observed, due to the emerging technology as is depicted in Fig. 3.



(a) (b)

Fig. 2. Hexagonal (a) and rectangular shape (b) of sub-cells and periodic RVE models

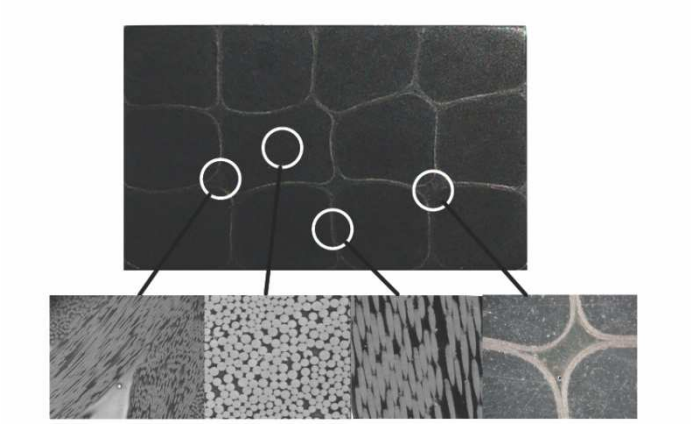
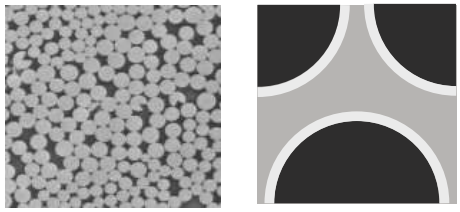


Fig. 3. Composite cell structure cross-section on mezzo and micro scales

Homogenization on a micro scale. The microstructure of a sub-cell contains tows of carbon fibres and matrix that fill the space between the individual fibres (see Fig. 4).



(a) (b)

Fig. 4. 3D Microstructure of a sub-cell (a) and an FEA model (b) with a fibre interface

Computational homogenization on this level can be conceived analytically or with the use of FEM. A lot of authors have published a number of different approaches [2], [3]. For an analytical calculation of the unidirectional transversely isotropic structure, law-of-mixture and empirical variations were applied

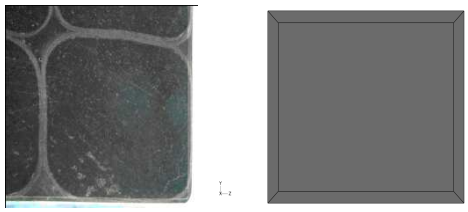
$$E_1 = V_f E_f + V_m E_m, \qquad \nu_{12} = \nu_{13} = V_f \nu_f + V_m \nu_m, \tag{1}$$

$$\frac{1}{E_2} = \frac{1}{E_3} = \frac{V_f}{E_f} + \frac{V_m}{E_m}, \qquad \frac{1}{G_{21}} = \frac{1}{G_{31}} = \frac{V_f}{G_f} + \frac{V_m}{G_m}. \tag{2}$$

The volume ratio of the fiber in the cores and winding is observed using image processing an electron microscope. This formula cannot affect the influence of the interface between fibre and matrix. A more concise estimate of the micro-scale stiffness is provided by FEM analysis with modeling of the fibre interface [4].

Homogenization on a mezzo scale. The representative periodic volume element (RVE) with hexagonal and with rectangular cell shape was modelled in the FE program, according to Fig. 3. The finite element model of a periodic unit cell (PUC) consists of a core and a wrap. It is assumed that the cell contains the homogenized elastic properties of uniaxial oriented fibres tows (high modulus PITCH type fibres). The packaging wrapped around the core can be wound with various angles and thicknesses. High strength PAN type fibres are usually used for this layer. The elastic properties of a PUC calculated on a micro scale level were considered. This assumption is in fact the main idea of the homogenization technique. An example of the square shape of the sub-cell and the FE model of a PUC is shown in Fig. 5. The whole FEA was performed in Abaqus Standard

software. The FE model contains 3D linear brick elements (C3D8). The material properties of the fibres and resin are given in Table 1. The core and winding fibre volume ratios were given for the calculations of the properties, as is shown in Table 2.



(a) (b)

Fig. 5. Square shape of a sub-cell (a) and the FE model of a PUC (b) with an fibre interface

Table 1. Material parameters of fibres and resin

Material	Fibres		Resin
Elastic moduli	PITCH HM Fibre (Mitsubishi) k63712 12k	PAN HS Fibre (Toray) T700 12k	Anhydride resins + 2% of nano particles (Amroy) Hybtonite + AA
E_L [GPa]	640	235	3
E_T [GPa]	5	15	3
G_{LT} [GPa]	20	50	1.1
ν_{LT} [-]	0.35	0.3	0.4
Thermal expansion α_L [-]	-13.8 e-07	-3.80E-07	8.1 e-05
Tensile strength R_{mL} [MPa]	2600	4900	79

Table 2. Volume ratio of the samples

Orientation of the winding	Total thickness of the winding	Volume ratio of the core	Volume ratio of the winding
88°	0.18mm	65%±2%	65%±3%
±45°	0.30mm	60%±2%	55%±4%

The aim of the FE mezzo-scale analysis was to obtain the matrix of homogenized elastic modules $\bar{\mathbf{C}}$ according to the relation of the tensor

$$\overline{\sigma_{ij}} = \overline{C_{ijkl}} \cdot \overline{\varepsilon_{kl}}\,, \tag{3}$$

where the macro stress and macro strain on a PUC can be solved by the following expressions

$$\overline{\sigma_{ij}} = \frac{1}{V} \int_V \sigma_{ij} \cdot dV\,, \tag{4}$$

$$\overline{\varepsilon_{kl}} = \frac{1}{V} \int_V \varepsilon_{kl} \cdot dV\,. \tag{5}$$

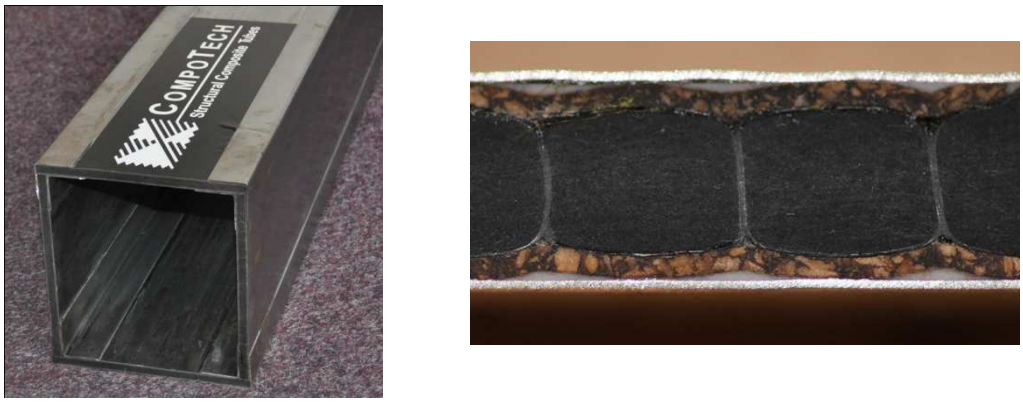
Homogenization has to be implemented by the boundary conditions [5]. Therefore periodic boundary conditions are assumed on RVE, and the displacement of the two opposite boundary surfaces can be expressed as

$$u_i^{j+}(x,y,z) - u_i^{j-}(x,y,z) = c_i^j\,, \quad i,j = (1,2,3)\,. \tag{6}$$

where j^+ means along the positive direction of the j-axis, and means along the negative direction of the j-axis. A "dummy" node is added to the model to define the displacement c_i^j. This node is not a

part of any element. Six of such nodes are added to the FEM model, and Eq. 6 is realized by the keyword *EQUATION.

Calculation on a macro scale. A matrix of homogenized elastic modules $\bar{\mathbf{C}}$ of PUC was applied to build the final stiffness matrix of the whole hybrid composite structure containing a 3D sub-cell technology [6]. For example, the spindle beams of the machining centre shown in Fig. 1 were designed and experimentally investigated. Another application is depicted in Fig. 6. This beam is composed of thin sandwiches consisting of metal coverings, cork layers and a high modulus sub-cell structure. FE calculations of such hybrid structures based on the multiscale homogenization described above give very satisfied results, and can be used for the construction design of machines. Experimental verification of the FE calculations of static stiffness showed differences up to 10 % in deflections by bending.



(a) (b)

Fig. 6. A thin-walled sandwich beam (a) and a detail of its wall (b) containing metal coverings, cork layers and high modulus sub-cell structure

Results

Two types of over-winding were considered numerically. An over-winding with one layer with orientation $+\phi$ is compared with an over-winding with two layers oriented at angle $\pm\phi$. It was shown that the cell border radius (in a small range) has a negligible influence on the static effective properties, and a simple FE model without the radii gives a sufficient estimation of the effective properties. A change in the orientation and thickness of the over-winding results in approximately the same behaviour of the longitudinal and transversal stiffness. The longitudinal stiffness is inversely proportional to the transversal stiffness, depending on the orientation and thickness of the cell over-winding, according to Fig 7. This is particularly true for a low ratio of the thickness of the wrap. The optimal wrap thickness value is between about 0.2 mm and 0.4 mm. Shear stiffness G_{yz} increases monotonically with orientation and thickness, while G_{xz} has a maximum for +/- 45° over-winding angle, see Fig. 8. This is very convenient for the possibility of increasing the bending stiffness, especially to eliminate the deflection due to the shear force loading.

Summary

Multiscale homogenization on a micro scale and on a mezzo scale and final FE analysis on the hybrid material composite structure leads to satisfactory design of complicated machine parts.
A sub-cell 3D composite structure can be used primarily in complex thick-walled composite structures, e.g. in aircraft spars, in pressure vessels, or in machine tool applications. It has also been applied successfully in a thin-walled sandwich beam. The purpose of the thin over-winding of the axial fibres is not only to stabilize the position of the fibres in thick profiles, but also to form the size and shape of the cells. The over-winding of the cell contributes to the high shear modulus and to very high stiffness properties of the whole structural part.

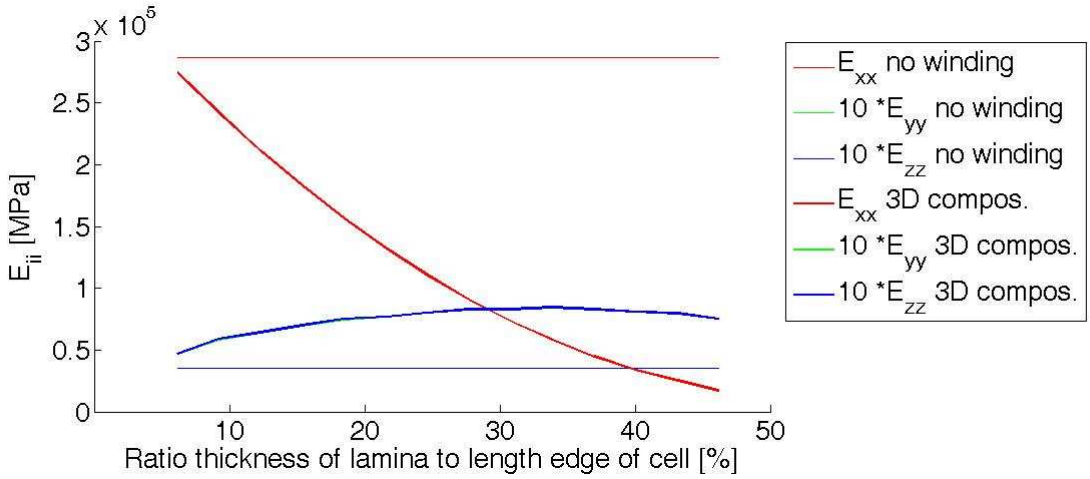


Fig. 7. Dependence of the orthotropic tensile components of the elastic material matrix on the thickness of the winding

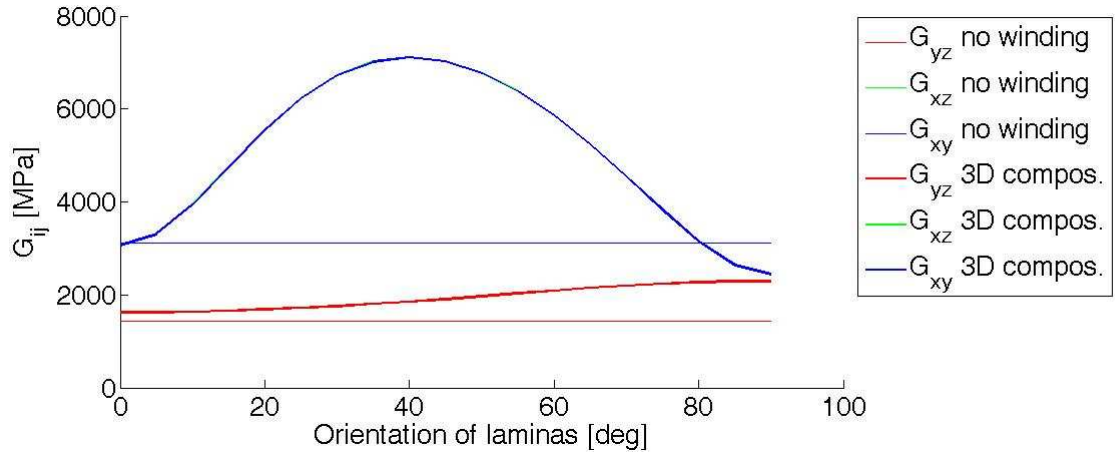


Fig. 8. Dependence of the orthotropic shear components of the elastic material matrix on the orientation of the winding

Acknowledgements

This work was supported by the Grant Agency of the Czech Republic, project number 101/08/0299.

References

[1] O. Uher, J. Smolík, and M. Růžička in: *Proceedings of the 17th International Conference on Composite Materials*. 27-31 July 2009, Edinburgh, UK.

[2] J. Zeman, M. Šejnoha: in: Journal of the Mechanicals and Physics of Solid 49, No. 1, (2001), p.69-90.

[3] V. Kouznetsova, M.G.D. Geers, W.A.M. Brekelmans in: Int. Journal for Numerical Methods in Engineering 54, No. 8, (2002), p. 1235-1260.

[4] G. Steven: Int. J. for Computer-Aided Engineering and Software, Vol. 34, No.4, (2006), p. 432.

[5] Barbero, E. J: *Finite Element Analysis of Composite Materials*. CRC Press, 2008.

[6] M. Růžička, V. Kulíšek, J. Had, O. Prejzek: Bulletin of Applied Mechanics, Vol 5, No 19 (2009), ISSN 1801-1217

© (2011) Trans Tech Publications, Switzerland
doi:10.4028/www.scientific.net/KEM.471-472.922

Shell Mould Composite With Rice Husk

Z. Harun[1, a], N. H. Kamarudin[1], N. A. Badarulzaman[1] and M.S.Wahab[1]

Faculty of Mechanical and Manufacturing Engineering,

Universiti Tun Hussein Onn Malaysia, Malaysia.

[a] zawati@uthm.edu.my

Keywords: reinforced ceramic shell mould, rice husk, cracking mechanism.

Abstract. For many years, precision investment casting foundries have periodically reported serious casting defects. One source is associated with the brittle ceramic shell mould which is very weak in tension and highly expose to the cracking mechanism. This situation not only lead to the appearance of defect in the end cast product but always attribute to the handling problem at the earlier stage in the investment casting industry. Due to this fact the strengthening mechanism of the brittle shell mold using reinforcement method was studied and investigated in this work. Rice husk was chosen as a reinforcement material as it contains silica element which can withstand high temperature of molten metal. Several testing procedures and characterization technique were carried out in order to measure the performance of the reinforced shell mould. Results show that the MOR value for the green reinforced shell mould is higher than the green body of non reinforced shell mould. Scanning electron microscope observations also show that the fiber alignment across the matrix structure increase the failure resistance and yet increase the strength of the shell mould green body. Furthermore, this reinforcement method using organic fiber leads to the pore enhancement and also leads to the new phase formation (zircon) in the fired reinforced body. Overall, this reinforcement method using rice husk increase the properties of the green and fired body of ceramic shell mould system.

Introduction

In investment casting the production of casting component involves the making of ceramic shell mould at the beginning stage using wax pattern. Basically, the making of shell mould involves the dipping of wax pattern into ceramic slurry for several times and follows by the consolidation of ceramic structure via drying and firing stages [1]. This consolidation ceramic structure increases the strength of the shell mould and allows the pouring process of hot molten metal into the mould. Typically most of the failure in casting component is due the failure of the brittle fired shell mould and the low strength of the green shell mould system. The defects can be originated in the firing stage due to the excessive shrinkage or low strength of the dried green body that highly exposed to the breaking failure. Therefore, The strength and integrity of the mould play an important role in ensuring that the end cast product has a proper dimension and is free from any defects and cracks .

In general production of investment casting ceramic shell mould is a crucial part of the whole process. The requirement for investment casting shell mould are; sufficient green strength for handling process and can withstand the dewaxing process, sufficient fired strength to withstand the weight of cast metal, high thermal shock resistance to avoid cracking mechanism during casting, sufficient mould porosity for the air cavity during pouring process etc [2]. These shell mould characteristics are especially critical for manufacturing high performance components, such as super alloy parts used in the air craft and power generation energy. Many conventional shell moulds do not exhibit sufficient strength at high casting temperatures. Therefore, the mould becomes susceptible to bulging and cracking when it filled with the molten metals that result in failure of the

mould [1]. The failure in producing the ceramic shell mould not only leads to the defect appearance in cast component but also increase the cost of raw material and the production time.

As reported recently, the advancement of the shell mould system involves the fiber reinforcement into the brittle ceramic shell mould [3, 4]. This reinforcement method increases the strength of the green shell mould and prevents an excessive change in dimension by holding together its particles via network alignment across the structure; this directly can reduce the possibility of the defects appearance the final cast body. Typically colloidal slurry produces ceramic shell mould with very low green strength which is prone to cracking especially during dewaxing and handling[5]. Furthermore, the ceramic structure theoretically is highly sensitive to any thermal changes and also inherited the brittle property [6,7] which are very critical especially during the handling part in the processing stage. Therefore, in the present work the strengthening mechanism of the shell mould system using reinforcement method with organic fibers was introduced. In fact in the last few years, several investigations have been carried out in order to improve casting quality by incorporating fiber either in the form of organic and synthetic [2, 8, 9] into the ceramic shell mould system. Most of these researches proved that these fibers enhance the strength of the green and fired body of the shell mould system [2].

In this research, rice husk which is an organic fiber was chosen as fiber reinforcement. The selection of organic fiber from the agro waste is one alternative in reducing abundant agro waste problem [10] and also reducing emission level that always associated to the shell mould casting industry. Typically burning rice husk also resulting to the formation of black ash containing silica that carries too many impurities [11]. Most of the rice husk ash contains 90-97% of silica and it has a great potential to be used as reinforcing filler in natural rubber products as its can increase the mechanical properties of products compared to the commercial silica [11]. In fact, the use of rice husk ash in concretes also showed that the positive effect on the compressive strength of concretes [12]. Prior to the mixing and reinforcement stage, in this work the rice husk fiber was treated using certain chemical solutions regarding to the previous work [13, 14]. Most of the lignin layer will be eliminated via this treatment and in fact this treatment also leads to the formation of rough surface. Previous work on the reinforced composite with treated natural fiber indicates that this procedure can improve the mechanical properties of the composite system.

Experimental

Chemical treatment of rice husk. The raw rice husk used in this work was collected from Kelantan. As mentioned before, the rice husk fiber is chosen as reinforcement in this work because it consists of silica element which is can withstand high melting temperature of molten metal and sintering temperature. Silica forms the main component (90–97%) of the ash with trace amounts of CaO, MgO, K_2O and Na_2O [15, 16]. When rice husk is burnt, the resulting black ash contains silica that carries too many impurities. It has been reported that purity of silica is highly affected from chemical treatment [17-20], than thermal treatment [21]. Therefore in this work, the rice husk was treated chemically to produce high purity of silica. Prior to use, the rice husk was ground and sieved to produce 6mm particle size. The rice husk was immersed chemically in 5% NaOH and 95% of water for 24 hours. Then, the rice husk was thoroughly washed by distilled water several times to remove the chemical. After that, it dried in the drying oven at 80°C for 12 hours.

Strength measurements. The strength of brittle ceramic property can be measured using Modulus of Rupture (MOR) testing procedure. Three point bending test was done according to ISO 178:93 (International Standards Organization) methods by a SHIMADZU Universal Testing Machine (Model AG-1). This testing procedure was carried out for several samples for each case. The samples were prepared upon a wax pattern with dimensions of 100mm length x25mm width x5mm thickness.

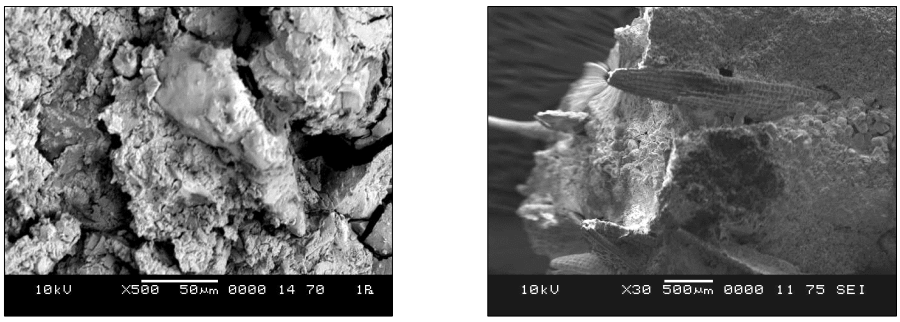
Microscopy. Scanning electron microscopy machine was used to view the fracture surface of the green body and microstructure of the fired body of ceramic shell mould. Micrographs of the samples were obtained by using a JEOL, JSM-638OLA of Scanning electron microscopy machine. Samples observed under the SEM were sputter coated with either gold or carbon to form a conducting layer to avoid electrical charge.

Results and discussion

Modulus of Rupture and fracture surface. The result of MOR values for the green shell moulds with four layers system are shown Table 1. In both cases five samples of the green shell mould were prepared and tested to get the range of MOR values. Green shell mould reinforced with rice husk fiber shows the higher MOR value compared shell mould without fiber as shown in Table 1 below. Further observation on the fracture surface using secondary electron image indicates that the higher mould value is due to the resistance in fracturing the ceramic structure especially in the embedded fiber zone. As shown in Fig 1 below the green fracture with fibers which appears to have been pulled from the ceramic network.

Table 1: MOR value of the green shell mould system with 4 layers

Shell mould system	MOR value(MPa)
Shell moulds without fiber	0.5-1.0
Shell moulds with rice husk fiber	1.2-1.5

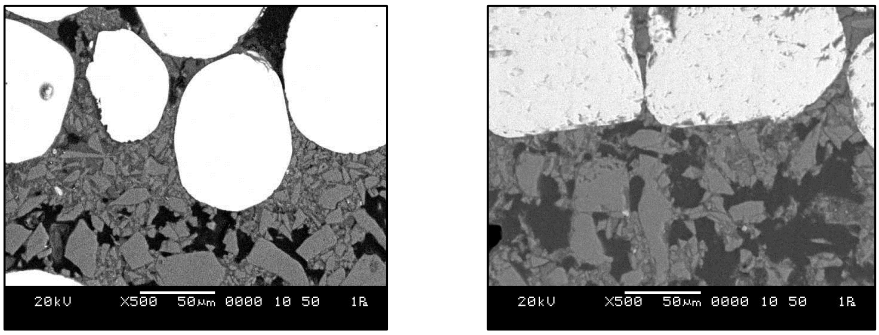


(a) (b)

Figure 1: (a) brittle fracture surface of green shell mould without rice husk fiber, (b) fracture surface of green shell mould with treated rice husk

This is as expected with a composite system in nature, where the energy required to remove fibers in this manner increases the strength required to break the sample [11, 12]. Furthermore the rough surface of fiber (treated rice husk) creates a strong bonding with the brittle ceramic matrix structure and increase the friction between fiber and matrix and increase the energy required of fiber to pull out and ultimately increase the strength. The strength of the shell mould green body before firing stage is very important in most of investment casting industry in order to avoid any crack in the shell mould at the early stage or to control the dimension changes in the later firing stage [5, 7].

Pore Structure



(a) (b)

Figure 2: Backscattered electron SEM image of cross sectional view of ceramic shell mould showing porosity left (a) ceramic shell mould without fiber; (b) ceramic shell mould with rice husk fiber

Fired microstructure of the shell mould with and without fiber were analyzed using SEM via back scattered SEM to determine the porosity distribution. As clearly shown in Fig 2 above the fired shell mould with rice has a bigger porosity compared to the nonreinforced shell mould. This is due to the fact that the rice husk fiber contains volatile material (80%) and treatment procedure only eliminates the lignin layer but not the others volatile materials. This volatile element will contributes to the increment of the pore structure in the fired shell mould body. Basically the firing and drying of the shell mould lead to the bigger pore formation due to the consolidation of ceramic particles via diffusion process between particles. In fact, the connected nature of this porosity enhances the porosity of the fired shell, providing a great deal of connected pathways through the ceramic and greatly increasing the permeability of the ceramic during casting. This is very import during the pouring and casting process so that the air leaves the cavity quickly and completely can prevent trapping and subsequent porosity during the displacement of liquid metal [4, 8,10].

X-ray diffraction. XRD analysis was carried out to identify any phase changes in the shell mould body after firing process. All XRD patterns of the fired shell mould as presented by (a) raw material of shell mould before firing stage, (b) fired shell mould without fiber (c) fired shell with nontreated rice husk, (d) fired shell with treated rice husk were compared and observed as can be seen in Fig. 3 below. As clearly shown in this figure there is an obvious different on the XRD patterns in the 2θ ranging from 50° to 60°, indicating that influence of fused silica originated from rice husk that lead to the new phase transformation of the shell mould reinforced with rice husk for both cases (treated and nontreated). Comparison and observation of the difference in peak appearance within this range are shown in Fig. 4 show that the appearance of new phase which is zircon ($ZrSiO_4$). Basically, burning of rice husk under uncontrolled condition below 1000°C produced fused silica in amorphous condition, as mentioned and proved by the previous works [22, 23]. This was shown and proved with the comparison of the XRD pattern in Fig. 4 where the shell mould without reinforcement only shows the peak of SiO_2 at angle 2θ=50.167˚ indicates the silica from the raw material of mulgrain flour. Most of this synthetic silica exists in the form of crystalline with a stable condition until up to 1700°C [23]. The appearance of this new zircon phase could benefited to the shell mould as its has a low thermal expansion coefficient and high resistance to the thermal shock [24] which can avoid cracking mechanism especially during the pouring of hot molten metal.

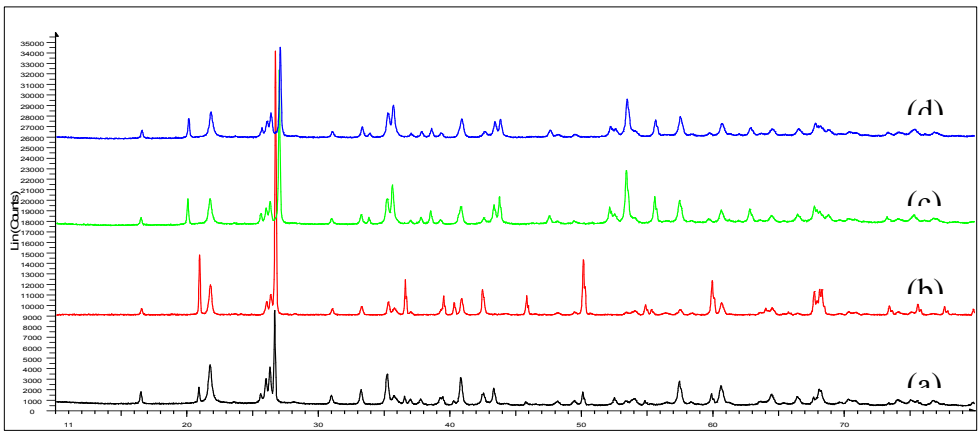
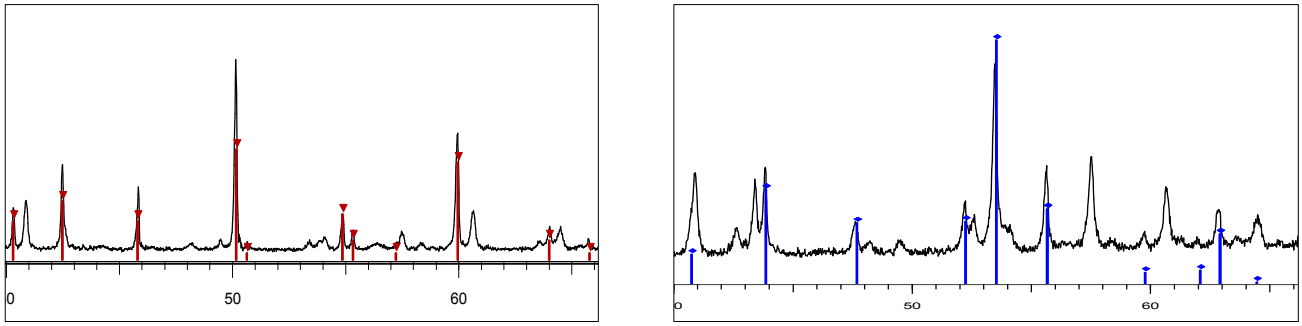


Figure 3: X-ray diffraction patterns for different shell mould composite systems.



(a) (b)

Figure 4: (a) Shell mould without fiber show the appearance of SiO_2 at peak θ=50.167˚, (b) Shell mould with treated shell mould show the appearance of $ZrSiO_4$ at peak θ=53.531˚.

Summary

The use of rice husk fibers increase the green strength of the shell mould by creating a strong network and the fracture resistance. The advantages of embedded of this organic fiber also lead to the enhancement of pore structure in the fired shell mould as it contains high volatile material. This structure can promote the permeation of air and avoid the trapped bubbles in the casting component. In fact the addition of rice husk lead to the new zircon phase formation which has a low thermal expansion and resistance to the thermal shock and this provide a great benefit for high temperature applications like investment casting.

References

[1] B.K. Chakrabarti: Material Science and Technology, Vol. 18(2002), p. 935-940.

[2] S,Jones : Journal of Materials Processing Technology, Vol.135 (2003), p. 258-265.

[3] D.W. A.Duffey, in: Proceedings of 25th BICTA Conference on Investment Casting, (2001)

[4] S. Jones: Journal Mater. Process. Technology, Vol 135 **(**2003), p. 258-265.

[5] S.Jones: *Improved Sol Based ceramic mould for the use in investment casting*. University Of Birmingham, Egbaston, UK, (1993)

[6] G.W. Scherer: Journal of American Ceramic Society, 73 (1990), p. 3-14.

[7] J.Manuel Guerra,in: *22nd EICF Conference*, (1992), Paris.

[8] C. Yuan, S.J.: Journal of the European Ceramic Society, Vol.23(2003), p. 399-407.

[9] C. Yuan, S. Blackburn: Journal of the European Ceramic Society, Vol 25 (2004), p.1081-1087.

[10] Z. Harun, N.S., M. N. Mohd Hatta, A. Khalil, A. M. Ahmad Zaidi: *Reinforced Shell Mould (with palm oil fiber).* ITEX, (2009)

[11] C. Saowaroj , P.P.Suooarat Eiumnoh: *Using Silica from Rice Husk as a Reinforcing Filler in Natural Rubber.*(2001)

[12] A. A. Ramezanianpour, M.M.K., G. Ahmadibeni: International Journal of Civil Engineering, Vol. 7,(2009).

[13] L.Y. Mwaikambo, A.M.: Chemie, Vol.272(1999), p.108-24.

[14] A.K, Mohanty, G.Hinrichsen: Composite Sci. Technol, Vol. 60(2000), p. 1115-24.

[15] E.Natarajan, A. Nordin, and A. N. Rao: Biomass Bioenergy, Vol. 14(1998), p. 533.

[16] A.Kaupp: *Gasification of Rice Hulls: Theory and Practice.* (1984).

[17] H. D. Banerjee, H. N. Acharya:. Materials Science and Engineering, Vol. 52(1982), p.173-179.

[18] P. Mishra, H. D. Banarjee: Journal of Materials Science, Vol. 20(1985), p. 4387-4391.

[19] A. A. M. Daifullah, N.S.A., S.A. El- Reefy: Chemical Engineering and Processing, Vol 43(2004), p.193-201.

[20] M. Patel, A.K., P. Prasanna: Journal of Materials Science, Vol. (22)1987, p.2457-2464.

[21] M.A.N. Ikram: Journal of Materials Science, Vol.23(1988), p. 2379-2381.

[22] S. H. Javed, S.N., N. Feroze, M. Zafar, M. Shafaq: Journal of Quality and Technology Management, Vol.6(2010), p. 81-90.

[23] D. Singh, R. Kumar, A. Kumar, K. N. Rai: Vol. 54 (2008), p.203-212

[24] P. Tartaj, C.J.S., J. S. Moya, J. Requena, M. Ocana, S. De Aza, F. Guitian: Journal of Materials Science, 31(1996), p.6089-6094.

© (2011) Trans Tech Publications, Switzerland
doi:10.4028/www.scientific.net/KEM.471-472.928

Cotton Reinforced Biopolymer Matrix Composite: Effect of Ultraviolet (UV) on Its Mechanical Properties

[1]ZURAIDA Ahmad[a], [1]HAZLEEN Anuar, [1]ZAHURIN Halim[b],
[2]DAYANG LAILA Abg. Abd. Majid, FAUZIAH Md Yusof

[1]Department of Manufacturing and Materials Engineering, Kulliyyah of Engineering, International Islamic University Malaysia, PO Box 10, 50728 Kuala Lumpur, Malaysia

[2]Department of Mechanical and Manufacturing Engineering, Universiti Putra Malaysia

[a]zuraidaa@iium.edu.my, [b]zahureen@iium.edu.my

Keywords: Composites; Cotton fiber; Albumen; UV; Water absorption

Abstract: Research on the production of composites from natural fibers has an enormous attention from researchers due to environmental awareness, which focusing to produce compostable bio-based composites and renewable raw materials that can be safely disposed after their use without polluting the environment. This paper reports the study on the effect of the ultraviolet (UV) to the cotton/albumen composites (CAC). The CAC were prepared by using hands lay-up technique with 10 w/w % of cotton content and cured at room temperature for 14 days. The cured samples were cut before exposing to UV light up to 20 days. The increase in tensile strength was observed up-to 10 days of exposure before it is decreasing to about 15% after 20 days of exposure to UV. The morphological study through SEM micrograph shows that fibers breakage and the biopolymer matrix loss is more with longer duration of UV exposure.

Introduction

Recently an increasing number of novel polymers is developed, with the aim of fulfilling new ecological requirements regarding the solution of the environmental problem caused by the disposal of large volumes of non-biodegradable materials. Therefore, biopolymers from agriculture sources are becoming focus of study by some researchers as a suitable alternative not only as biodegradable films, food packaging but also plastics stuff which required improved mechanical properties. Proteins, lipids and polysaccharides have been used as biopolymers sources for many years. It is well known that a wide variety of proteins are produced at huge scale for instance, wheat gluten soy and pea proteins from vegetables resources; egg proteins, fish myofibrillars and wool keratin proteins from animals resources [1]. An extra value added to the materials developed from this biopolymers, is their biodegradability properties. Protein-based biomaterials degradation rates have been proved to be among the rates of fast degrading polymers which completely degrading in 50 days when buried in farmland soils [2].

Cotton is a soft fiber, which is categorised as seed fiber because the fiber is collected from cotton's seedpod. The cotton fiber mainly consists of cellulose, a natural polymer. The cellulose is arranged in a direction to give the cotton fibers a high degree of strength, durability and absorbency. This natural fiber can stand at high temperature and dries easily. The cotton fiber however, when is dried out, it becomes hard and brittle and loses all elasticity at temperatures above 25°C. Extended exposure to light causes similar problem [3]. The optimal temperature range for mold development is from 25°C to 35°C. At temperature below 0°C, rotting of wet cotton stop and sometimes the damage cotton is stored at these temperatures to prevent further deterioration [4]. Cotton stalks fiber has been proposed by earlier researchers as building material due to its low density, good thermal and acoustic insulation, and high strength to weight ratio. Study shows that by suitably combining cotton and other cellulose fibers with appropriate biodegradable fiber in the right combination, a strong nonwoven fabric used for panel in construction industry can be produced [5].

The ultraviolet (UV) light spectrum consists of radiant energy between 280 and 400 nm. As the wavelengths within the spectrum get shorter, the radiant energy increases to the point that it can split the bonds of chemical substances and produces changes within the materials. This UV has a destructive effect on cellulose, and degrades it by increasing the rate of chemical reaction.

In this paper the biodegradability of the cotton/albumen composites (CAC) are reported and the focus are given to the study on the effect of ultraviolet (UV). Aspects investigated limited to the effect to the mechanical properties and the morphological study.

Experimental Method

Materials. The natural fibers of cotton (Gossypium hirsutum) with a density of 1.51 g/cm^3 were purchased from Able Enterprise (M) Sdn Bhd (Malaysia) that mainly consists of cellulose. In this work, the fibers were used without further chemical treatment. Fresh eggs were obtained from Farm Sdn Bhd (Malaysia). The egg white (albumen) was separated from the egg yolk and the chalazae were removed. Egg albumen had a protein content of 10% - 15%, which consisting of a mixture of different protein dispersed in water with the specific gravity (relative) density of 1.03.

Fabrication process. Prior to the composite production, the albumen matrix was denatured by beating process. The albumen solution was beated for 5 minutes into froth and left to settle overnight at room temperature. The remaining dirty froth was removed and the albumen was filtered through muslin to get a yellowish and homogeneous albumen solution with a pH value of 9.0. The CAC with 10 w/w% cotton loading was prepared by using the hands lay-up method. Dimension of the cotton fibers were 150 x 250 mm x 3 mm and arranged layer by layer with total of four layers, followed by applying the albumen at the cotton fiber interlayer and on its surface. The CAC samples were subjected to 100 kN pressure and allowed to dry at room temperature for 24 hours. This process was conducted in order to make sure the cotton is entirely wetted and the bonding between the fiber and albumen is good. The CAC samples were cured for another 14 days before they were tested for the effect of UV, temperatures and water absorption.

Testing Procedure

Ultraviolet testing. The UV test was conducted in accordance to ASTM G 53-99 which is a standard practice for operating light and water exposure apparatus (Florescent UV-Condensation Type) for exposure of non-metallic materials. The UV wavelength used is in the range of 295-370 nm and the CAC samples were exposed to this light within 200-480 hours (8 to 20 days). The intensity of the light is varying from 0.64 W/m^2/nm – 0.77 W/m^2/nm.

Tensile test. The tensile test was carried out by using Materials Testing Machine model LLOYD and conducted according to ASTM D 3039 where the dimension of the samples were cut into 250 x 25 x 3 mm.

Impact test. The notched Charpy method, utilising Advanced Pendulum Impact API DYNISCO model API-230-0 machine was used for measuring the impact strength and the test was conducted according to ASTM D256.

Morphological analysis. The Scanning Electron Microscopy (JEOL JSM 5600) was employed to analyse the morphology the CAC samples.

Results and Discussion

Physicals Properties. The physical changes of CAC specimens subjected to UV exposures after 10 and 20 days are shown in the Fig. 1(a) and (b) respectively. The CAC specimens are observed started to warp after 10 days and the warping is more rigorous after 20 days of exposure. This change is observed due to the evaporation of moisture in the CAC samples influence by the heat generated during the UV exposure. Since the rate of evaporation is different at different at the outer-layers towards the inner-layers of CAC, the shrinkage which contributed to bending phenomenon is

also different. Surface area which is having direct exposure to the UV shrinks more than the inner part. In addition, the heat from the light is measured above 30°C, enough to cause weight lost of the CAC samples and introducing the stress to the molecules arrangement and thus also exhibit the warping phenomena.



Fig. 1(a) CAC specimens after 10 days of UV exposure

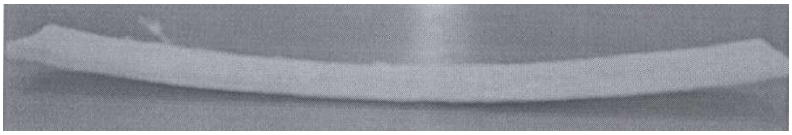


Fig. 1(b) CAC specimens after 20 days of UV exposure

The density and shrinkage measurement results are tabulated in the Table 1. It is obvious that the density of CAC is slightly decreased when exposed to a longer duration of exposure to UV due to moisture loss and the matrix cracking and erosion. The biopolymer matrix tends to degrade and loss which resulted in decreasing in density.

Table 1

UV Exposure (days)	Density (g/cm^3)	Shrinkage (%)
0	0.3892	0.995
5	0.3761	2.513
10	0.3691	6.085
15	0.3679	13.35
20	0.3215	14.33

It is shown that the percentage of shrinkage increasing tremendously up to 15 days and there is no significant difference in the percentage of shrinkage for CAC samples afterwards. Again, this shrinkage is due to moisture loss from the biopolymer matrix protein.

Tensile and impact strengths of CAC specimens. Figs. 2 and 3 show the relationship between duration of exposure to UV and tensile as well as impact strengths of the CAC specimens, respectively. From these figures, it can be seen that the tensile strengths is increasing with the increase duration of exposure to UV up-to 10 days of exposure, however the decrease in the tensile strength is observed when the duration of exposure is extended. The protein biopolymer matrix in the CAC loss their moisture content when subjected to UV heat which attributed to irreversible denaturation. As a result of denaturation, proteins suffer certain changes in their properties as solubility and crystallizability. These changes also involved the breakage of the hydrogen bond, the uncoiling of polypeptide chain and the exposure of the reactive group. Therefore, the protein structure began to unfold and the three networks formed and when dried, the molecules transform into a rigid body which increased the strength of CAC. This strength however, decreased with the extended of exposure to UV due to the putrefaction of protein and fiber.

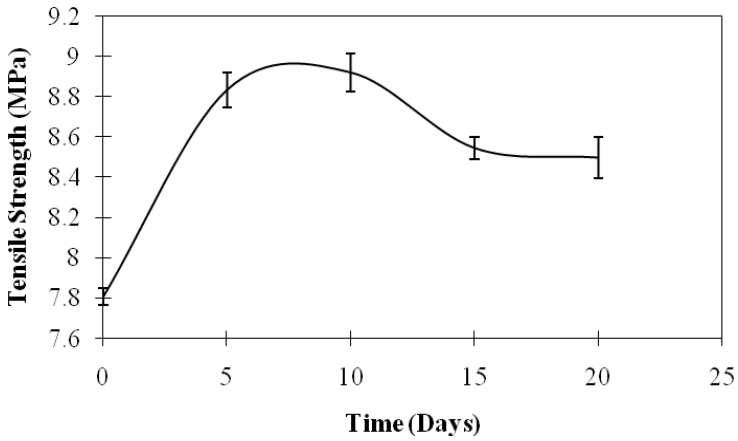


Fig. 2 The effect of UV exposure to the tensile strength

On the other hands, the impact strength is decreasing with the increasing duration of UV exposure. The major decreasing is observed between day 5 and 10 with the impact strength value of 12 kJ/m^2 and 8 kJ/m^2. The matrix inside the composite started to debase and damage when exposed to UV. Some of the matrixes cracked and loss due to the heat exerted from the UV light. This UV also again changed the protein networking in the biopolymer matrix which leads to the brittleness of this matrix lowered the energy absorbed during the impact test [6]. The impact strength difference is not significance in samples expose to the UV for 15 and 20 days as the strength is mainly depends on the cotton fibers, owing to diminishing of the biopolymer matrix in CAC samples.

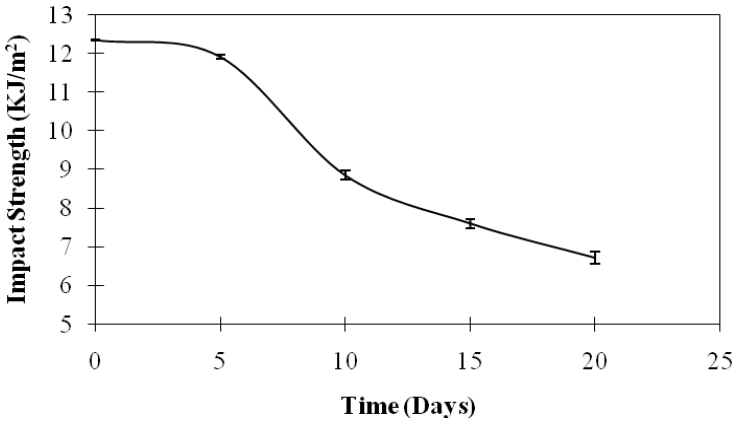
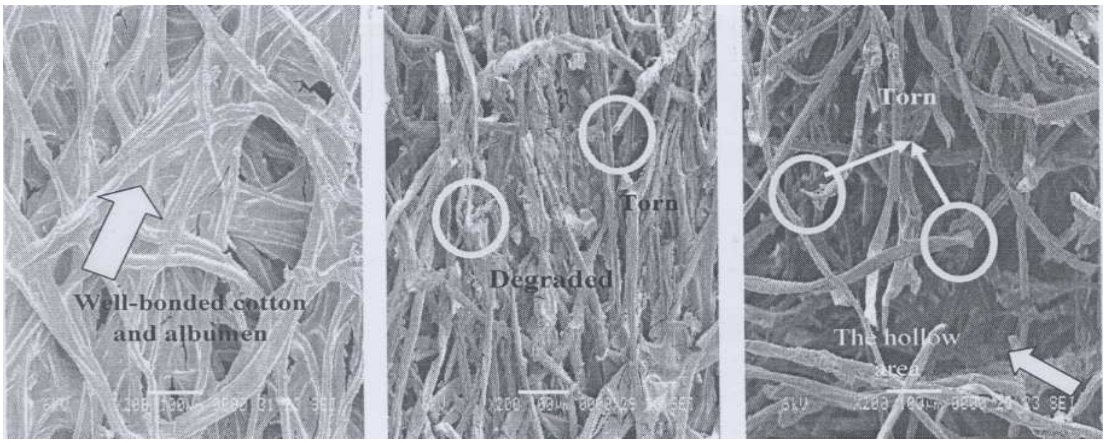


Fig. 3 The effect of UV exposure to the impact strength

Morphological Study. Figs. 4(a), (b) and (c) show the micrograph taken by SEM for the samples not exposed to UV (control samples) and samples exposed to UV for 10 and 20 days respectively. From the control CAC samples, the micrograph shows the biopolymer matrix rich area which attributed to higher strength due to the efficient load transfer from matrix to cotton fibres. The biopolymer matrix enveloped the cotton fiber.



(a) (b) (c)

Fig 4 SEM micrograph showing CAC samples (a) not exposed to UV (b) 10 days exposure to UV and (c) 20 days exposure to UV

Fig 4(b) shows the early stage of biopolymer degradation and some of the cotton fiber started to expose. The cotton fiber started to degrade, erode and delaminate. Extended exposure for 20 days lead to the total loss of matrix and the fibers was observed not enveloped by the biopolymer matrix anymore [7]. The fibers broke severely as shown in Fig 4(b) which contributed to the lower in strength of the CAC samples.

Summary

The cotton/albumen composite (CAC) were fabricated and subjected to the UV exposure for different durations of 0, 5, 10, 15 and 20 days. The density is observed to decrease, however the percentage of shrinkage is increased tremendously with the increase of the duration of UV exposure. Tensile strength is increased upto 10 days before decreasing when the exposure is extended to 20 days. Longer duration of UV exposure decreased the impact strength of CAC.

References

[1] A. Jerez, P. Partal, I. Martinez, C. Gallegos, and A. Guerro, *Egg white-based bioplastics developed by thermomechanical processing.* Journal of Food Engineering 82 (2007) 608-617

[2] S. Domenek, P. Feuilloley, J. Gratraud, M.H. Morel, and S. Guilbert, *Biodegradability of wheat gluten based bioplastics.* Chemosphere, 54 (2004) 551-559.

[3] M.J. John, S. Thomas, *Biofibers and Biocomposites*. Cabohydrate Polymers 71 (2008) 343-364.

[4] V. Tserki, P. Matzinos, C. Panayiotou, *Effect of Compatibilisation on the Performance of Biodegradable Composites Using Cotton Fiber Waste as Filler*. J. Appl. Polm. Sci. (2003). 88: 1835

[5] S.A.R. Hashmi, U.K. Dwivedi, N. Chand, *Friction and Sliding Wear Study of UHMWPE Modified Cotton Fibre Polyester Composites*. Tribology Letters. (2006) 21(2):79

[6] A. Schmitz, M. Klein, I. Gestmann, and V. Herzog. *Protein cross-linking by self-assisted intermolecular disulfide bond* formation. Methods in Enzymology, Vol.348, (2002), 306-313.

[7] Y.P. Ham, H.S. In, H.K Jung, and S.K. Woo. Preparation of Thermally Denaturated Albumin Gel and Its pH-Sensitive Swelling. *International Journal of Pharmaceutics*, 175, 231-236 (1998).

© (2011) Trans Tech Publications, Switzerland
doi:10.4028/www.scientific.net/KEM.471-472.933

Characterisation and Properties of Sintered Glass-Ceramics Produced from Recycling Glass by Using Pressure-less Method

N.F. Ayoob[1,a], J.M. Juoi[1,b] Z.M. Rosli[1,c] and N.R. Rosli[1,d]

[1]Department of Engineering Materials, Faculty of Manufacturing Engineering,

Universiti Teknikal Malaysia Melaka, Durian Tunggal, 76109 Melaka, Malaysia

[a]nurfarizan_ayoob@yahoo.com, [b]jariah@utem.edu.my, [c]zmr@utem.edu.my
[d]rifhan.rosli@gmail.com

Keywords: batch formulation, sintering optimization, pressure-less method and soda lime silica glass, mechanical properties and SEM.

Abstract. The aim of this research is to develop glass ceramic produced from recycling glass. Waste glass (e.g. container and bottles) of soda lime silica (SLS) glasses is utilised as main raw materials for the formulation of glass ceramic batch composition with the addition of ball clay. The ball clay was added in order to favour shaping. The recycled glass powder are then mixed with the ball clay according to the ratio of SLSG to ball clay of 95:5 wt.%, 90:10 wt.% and 85:15 wt.%. Differential Thermal Analyses (DTA) was carried out in order to determine the thermal characteristic glass powder prior to the batch formulation. The glass was then crushed, milled and sieved to < 75μm and mixed with the ball clay before it was pressed to a pellet by pressure-less method. This pressure-less route is conducted as an approach to a simple fabrication route of the glass-ceramic samples. The green samples are then sintered at different temperature. The dense and strong glass ceramic samples were obtaining at 850°C, with holding time of one hour and morphological characterized with X-Ray Diffraction (XRD) and Scanning Electron Microscopy (SEM) analyses. Results shown that glass ceramic samples produced at this optimized sintering profile had high density and microhardness value with low porosity and negligible water absorption. Overall results indicates that glass ceramic samples have good mechanical properties (e.g. microhardness exceeding 700H_v) and physical properties (e.g. water absorption, density, porosity making them attractive to the structural application. These results are also utilised as a comparison to a glass ceramic samples produced via Cold Isostatic Press (CIP) from the same batch composition formulation and sintering profiles for the purpose of optimizing the waste glass utilization.

Introduction

Nowadays, there is a great concern regarding to the large amount of waste that are generated by the industrial development. Waste such as toxic and hazardous inorganic wastes which need proper attention in handling, immobilization and disposal is one of the issue that receives a lot of attention and waste management is considered as a critical national issue. Among these wastes are solid wastes that can be breakdown into different type e.g. paper, household waste, steel, glass, plastic and others. Many researchers have paid much attention to produce glass, glass ceramic and sintered materials from industrial wastes such as container glass, coal fly ash, incinerator fly ash and steel fly ash in order to make them reasonably safe for the environment. For examples, glass ceramics, intended for building applications such as Russian Slagsitalls, developed as early as the 1960s, by employing several slags of ferrous and non-ferrous metallurgy, ashes and wastes from mining and chemical industries, constitute an undoubtedly well developed and widespread way to absorb glasses obtained from the treatment of several wastes [1]. In addition to the environmental advantage of immobilizing wastes into materials with a generally high chemical resistance like glass ceramic, a certain economic benefit may be found in entering the large market of construction materials. Moreover, glass ceramic obtained from industrial wastes have several desirable properties to fulfil many applications such as wall covering panels, floors and roofs in industrial and

public buildings, interior facing of containers for the chemical industry and as road surfacing. The feasibility of glass recycling into clay bodies was already proved in the case of wastes from car windshields, soda-lime float and container glasses [2].

Glass ceramic materials are generally produced by a traditional glass forming technique starting from the melted glass, followed by controlled nucleation and crystallization heat treatment processes. In recent years, glass ceramics were developed using the technique of sinter crystallization of glass powders. The advantages of this method are essentially that it does not require high investment and is suitable for the production of small quantities of articles of complicated shapes [3]. Because of that, it has been widely investigated by researchers and companies and employed in this research. Many valuable products (such as cellular glasses, glass-ceramics, glass, and glass-ceramic matrix composites) are manufactured by sintering fine glass powders, easily obtained by grinding glass pieces. In particular, fine glass powders are useful in the glass-ceramic processing: the processing of sintered glass-ceramics depends on the surface crystallization of glass ("sinter-crystallization'), which is largely favoured for small glass granules, so that catalysts in the glass formulation or long nucleation/crystals growth treatments are not needed.

The objective of this study was to characterise the sintered glass ceramic from recycling glass by using pressureless method. It is also to establish a better understanding of treating recycling glass to produce glass ceramic materials in application for tiles. The product were characterized by X-ray diffractometry (XRD) for crystal structure determination and scanning electron microscopy (SEM) for morphology observation. In addition, its density, porosity and water adsorption rate were also investigated.

Experimental Procedure

Batch glass preparation and sintering. The raw material used in this study was soda lime silica glasses obtained from household waste with the addition of ball clay. The glass and ball clay were then crushed, milled and sieved to <75μm. Differential Thermal Analyses (DTA) was carried out in order to determine the thermal characteristic glass powder prior to the batch formulation. The DTA allowed to identify the glass crystallisation temperature. This analysis constituted an important reference point for sintering processing temperature for achieving glass ceramics was coincident with the crystallisation temperature [4]. The recycled glass powder are then mixed with the ball clay according to the ratio of SLS glass to ball clay of 95:5 wt.%, 90:10 wt.% and 85:15 wt.% as shown in Table 1. The ball clay was added in order to favour shaping. The mixture pressed into a 10mm diameter pellet without any binders under a pressure of 3.5 tonnes by pressure-less method at room temperature. All pellets were sintered at 750°C, 850°C and 950°C with one hour soaking time and heating rate of 2°C /minute and natural cooling. Typical chemical composition of soda lime silica glass obtained from household waste and ball clay were given in Table 2.

Table 1. The batch composition of the prepared samples

SLS glass (wt.%)	Ball clay (wt.%)
95	5
90	10
85	15

Table 2. Typical chemical composition of soda lime silica glass and ball clay in terms of oxide contents [5,6]

Oxides	SLS glass (wt.%)	Ball clay (wt.%)
SiO_2	66.498	58.0
CaO	25.995	<0.1
Fe_2O_3	0.381	0.90
P_2O_5	0	-
ZnO	0.011	<0.1
NiO	0	-
Al_2O_3	2.12	27.0
SO_3	2.215	-
Na_2O	1.426	0.2
MgO	0.632	<0.1
TiO_2	0	1.5

Measurement of Density, Porosity and Water Adsorption. Density, porosity and water adsorption of the produced glass ceramic samples were measured according to the official standard EN ISO 10545-3 (water absorption, bulk density, porosity). At least ten fragments are analyzed for each samples.

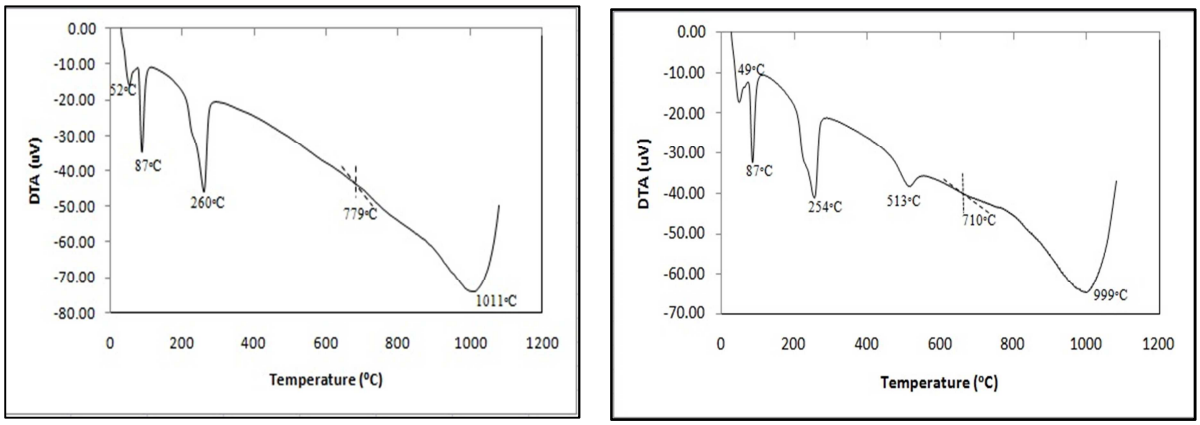
Microhardness. Vickers microhardness measurements were done on the produced glass ceramic samples. The microhardness tester used in this study was HM-200 Series Microhardness. Samples were ground and polished with diamond paste. A load of 0.5N was selected. In order to obtain reliable statistical data, at least 5 indentations were made on each sample.

Scanning electron microscopy (SEM) analysis. The microstructure observations were conducted using SEM EVO Carl Zeiss SMT with secondary electron mode operated at 20kV. Samples were ground flat by 1200 grit abrasive paper and polished with alumina paste to achieve a mirror-smooth surface. The samples were coated with gold prior to examination.

X-ray diffraction(XRD) analysis. XRD has been used in order to identify the crystalline phase occur in all produced samples. Samples were ground to fine powder form and analysed using Philips XRD model PW3050/60 operated at 40kV and 30mA utilizing Cu Kα radiation. The detector was scanned over a range 2θ of 10-90 ^{o} with 0.001 ^{o} in step sized. The data are then analyzed utility X'Pert HighScore software.

Results and Discussions

Differential thermal analysis. DTA investigation were carried out to determine the nucleation and crystallization temperatures used in producing a glass ceramic sample with optimum properties. Figure 1(a) shows the DTA of the SLS glass. It shows that the transition temperature T_g can be observed at about 779°C, a slight melting endothermic peak is shown at about 1011°C. The first and second endothermic peaks at around 52°C and 87°C are attributed to burning of contaminants(e.g. organic compounds) present in the glass powder, in spite of no weight loss being recorded on the TG curve. Around 290°C, some weight loss was observed as a result of the release of absorbed water. DTA experiment was also performed on ball clay. The observed DTA graph was given in Figure 1(b). It shows three endothermic peak at 254°C, 513°C and 999°C. The first endothermic peak is attributed to burning of organic compounds present in the ball clay and the second endothermic peak is release of absorbed water. The melting endothermic peak for ball clay was at about 999°C. Sintering process were performed with temperature range 750-950°C with holding time of 1 hour. This temperature is chosen based on the differential thermal analysis (DTA) results.



(a) Glass powder (b) Ball clay

Figure 1. DTA graph of soda lime silica glass powder and ball clay

Physical and mechanical properties of the sintered glass ceramic samples

Table 3. Summary of sintered glass ceramic properties

Ratio clay addition to glass powdered (wt. %)	Properties	Sintered glass ceramic in different temperatures		
		750°C	850°C	950°C
95:05	Hardness (H_v)	470	483	492
	Water Adsorption (wt. %)	0.125	0.249	0.306
	Porosity (%)	0.272	0.515	0.673
	Bulk Density (g/cm^3)	2.166	2.067	2.200
90:10	Hardness (H_v)	480	494	518
	Water Adsorption (wt. %)	0.977	0.113	0.203
	Porosity (%)	2.190	0.217	0.364
	Bulk Density (g/cm^3)	2.241	1.924	1.794
85:15	Hardness (H_v)	490	492	496
	Water Adsorption (wt. %)	0.732	0.727	0.131
	Porosity (%)	1.818	1.461	0.369
	Bulk Density (g/cm^3)	2.485	2.010	2.827

Table 3 gives values for the mirohardness, density, porosity and water adsorption of sintered glass ceramic samples in different temperature and clay addition. The general trend in microhardness found is that as sample become more crystalline, the average microhardness increases [7]. Based on the result, the microhardness trend is consistent with what can be expected based on crystallization. However, the changes in microhardness are not consistent with the addition of ball clay. This proves that sintering temperature and clay addition plays an important role in microhardness. The water adsorption values changed depending on the amount of porosity presence. This presence increase in the sintering temperature resulted in less water adsorption due to less porosity presence. Most of the sintered glass ceramic samples containing a large proportion of glass are rigid. Bulk density measurements showed that the bulk density of the sintered glass ceramic depends strongly on the composition of the mixture and the sintering temperature. In agreement with the hardness values, density values of the sintered glass ceramic samples increased with the increase in sintering temperature. The good performance in mechanical properties of this sintered glass ceramic sample is particularly significant since it exceed the values exhibited by the traditional ceramics, well known to be prepared at much higher temperatures higher than 1100°C [8].

Microstructural characterization of the produced glass ceramic samples. SEM micrographs of surface sample at 850°C with ratio of SLSG to ball clay of 90:10 wt.% is chosen as the best result and is shown in Figure 2. The microstructure highlights the texture of the sintered glass ceramics surface with needle like crystals growing from the surface towards the centre of the grains and appear residual porosity. The crystal length is shorter than the other samples and a semi-transparent appearance is obtained. The crystalline size and shapes changed with the holding time at crystallization temperature. The amount of pores decreased with the increasing in sintering temperature. This occurred since the number of the crystallites increased. On heating above glass transition temperature, the nuclei are surrounded by liquid and their growth would be three dimensional. This result to bulk crystallization [3]. Ball clay bonds the glass powders together and with the sintering process a denser product was obtained. The particle size of the glass powder is an important in sintering process. When the glass milled into 75µm, the surface area greatly increase.

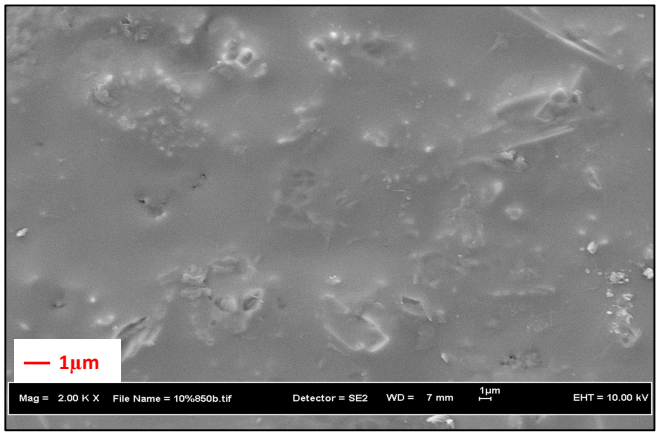


Figure 2. SEM micrograph of glass ceramic sample at 850°C with the ratio of SLSG to ball clay of 90:10 wt.%

X-ray diffractometry (XRD) pattern of batch mixture (before sinter) and glass ceramic produced by sintering at 850°C is shown in Figure 3. Analysis revealed that the mineral phases of glass ceramic powder with addition of 10wt.% of ball clay(before sinter) are Kaolinite($Al_2Si_2O_5(OH)_4$) (Ref. code:00-001-0527) and Flusston($SiO_2Al_2O_3NaOH$) (Ref. code:00-003-0413). In contrast XRD patterns of the sintered glass ceramic produced at 850°C with holding time of 1hour shows the main crystalline phase occurred after sintering process were Anorhite($CaAl_2Si_2O_8$) (Ref. code:00-041-1486), Sanidine($KNa(AlSi_3)O_8$) (Ref. code:00-019-1227) and Cristobalite(SiO_2) (Ref. code: 01-089-3434). Since the parent glass contains high alumina, it becomes harder for free Ca^{2+} to meet [SiO_4] during crystallization, thus Anorthite deposits from the parent glass[9].

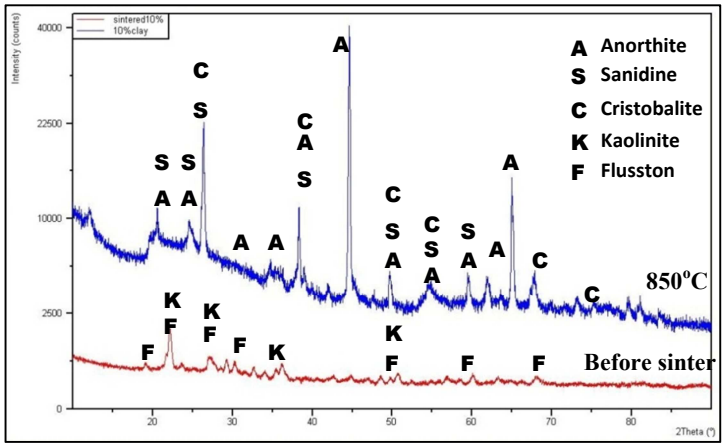


Figure 3. XRD patterns of glass ceramic sample at 850°C with the ratio of SLSG to ball clay of 90:10 wt.%

Summary

To utilize recycling glass waste and to resolve environmental problems, sintered glass ceramic have been prepared. The investigated recycling glass with addition of ball clay has good vitrification characteristics by using pressure-less method and sintering process. It is possible to producing glass ceramic products from recycling glasses. The properties of the sintered glass-ceramic samples depended on the glass composition, particle size, the addition of the binder and firing temperature. It has been proved that sintered glass ceramic samples with good microstructural, mechanical and physical properties were produced from soda lime silica glass with the addition of 10 wt.% of ball clay at 850°C. The results reported that the crystallization phase takes place at 850°C with formation of Anorhite ($CaAl_2Si_2O_8$), Sanidine($KNa(AlSi_3)O_8$) and Cristobalite(SiO_2). The material has a good potential for applications in of industrial buildings(e.g. floor tiling).

Acknowledgements

The authors are thankful to the financial support for this work from the Ministry of Higher Education of Malaysia through fundamental grant FRGS/2010/FKP/SG02/1-F0082.

References

[1] Bernardo, E., Castellan, Hreglich, S., (2007). "Sintered glass-ceramics from mixtures of wastes" *Ceramics International.* Vol. 33, pp. 27-33.

[2] Matteucci, F., Dondi, M., Guarini, G., (2002). "Effect of soda-lime glass on sintering and technological properties of porcelain stoneware tiles" *Ceramic International.* Vol. 28, pp. 873-880.

[3] Erol, M., Kucukbayrak, S., Ersoy-Mericboyu, A., (2009). "The influence of the binder on the properties of sintered glass-ceramics produced from industrial wastes" *Ceramic International.* Vol. 35, pp. 2609-2617.

[4] Bernardo, E., Doyle, J., Hampshire, S., (2008). "Sintered feldspar glass-ceramics and glass-ceramic matrix composites" *Ceramic International*. Vol. 34, pp. 2037-2042.

[5] Raimondo, M., Zanelli, C., Matteucci, F., Guarini, G., Dondi, M., Labrincha, J. A., (2007). "Effect of waste glass (TV/PC cathodic tube and screen) on technological properties and sintering behaviour of porcelain stoneware tiles" *Ceramic International*. Vol. 33, pp. 615-623.

[6] Syaharudin, Z., Zaidan, A. W., Norfarezah, E. H., Hilmi, M. M. Z., Thai, M. Y., (2010). "Production of glass-ceramic from sls glasses and wastewater sludge" *Solid State Science and Technology*. Vol. 18(1), pp. 7-14.

[7] Erol, M., Küçükbayrak, S., Ersoy, A. M., (2007). "Production of glass ceramics obtained from industrial wastes by means of controlled nucleation and crystallization" *Chemical Engineering Journal*. Vol. 132, pp. 335-343.

[8] Bernardo, E., Bonomo, E., Dattoli, A., (2010). "Optimisation of sintered glass-ceramics from an industrial waste glass" *Ceramic International*. Vol. 36, pp. 1675-1680.

[9] Peng, F., Liang, K. M., Hu, A. M., (2005). "Nano-crystal glass-ceramics obtained from high alumina coal fly ash" *Fuel*. Vol. 84, pp. 341-346.

© (2011) Trans Tech Publications, Switzerland
doi:10.4028/www.scientific.net/KEM.471-472.939

Fiber Reinforced Composite Structure with Bolted Joint – A Review

Khudhayer J. Jadee[1,a] and A.R. Othman[1, b]

[1]School of Mechanical Engineering, Universiti Sains Malaysia,

Engineering Campus, 14300 Nibong Tebal, Malaysia

[a]khudhayer1970@yahoo.com; [b]merahim@eng.usm.my

Keywords: Bolted joints, Fiber-reinforced composites, Failure mechanisms

Abstract. Fiber reinforced composite structures are widely used in the aerospace, aircraft, civil and automotive applications due to their high strength-to-weight and stiffness-to-weight ratios and these applications require joining composite either to composite or to metal. There are three main methods for joining composite structures namely, bonding, mechanically fastened or a combination of the two. Bolted joint are preferred in structures where the disassembly is required for the purpose of maintenance and repair. Due to the stress concentration around the holes, bolted joints often represents the weakest part in the structure, and therefore it is important to design them safely. A review on the study of bolted joints in fiber reinforced composite structure is presented. It was found that the behavior of bolted joints in composite structure is affected by many factors, such as geometry, joint material, clamping–load provided by the bolts, ply orientations, etc. Accordingly, various researches have been conducted on the analyses of stress distribution, failure prediction, and strength properties of bolted joint both experimentally and numerically. Accurate prediction of stresses in bolted joints is essential for reliable design of the whole structure; if it is not optimally designed, premature and unexpected failures may be occurred.

Introduction

The extensive use of fiber reinforced composites in aircraft, automotive, marine and construction industry owing to their high specific modulus and high specific strength make the materials becoming more popular. These applications require the joining of composite structures, and the design of joints represents one of the major challenges in the development of composite engineering. The failure and strength of composite joints are considerably different from many metallic joints due to their anisotropic and inheterogeneity of composites [1, 2].

There are three types of joints that are commonly used in composite structures, which are mechanically fastened joints, adhesively bonded joints and hybrid mechanically fastened/adhesively bonded joints [3]. Mechanically fastened joints using bolts, pins, screws and rivets are widely used to assemble composite parts and they are unavoidable in complex structures because of their low cost, simplicity in facilitation of disassembly for maintenance and repair [4], and free from surface treatment [5,6].

Despite of aforementioned advantages, mechanical joining of composite structures require holes to be drilled; these holes causes complicated stress concentration in the vicinity of the boundary of the holes, and thus significant reduction of load carrying capacity of the composite structure [7]. Nonetheless, it was found that the bolted joints are the most efficient form of all mechanical fastening [8].

Indeed, the present review work concentrates on the bolted joints in fiber reinforced composite, whereas pinned joints represent a particular case of bolted joint when there is no clamping force [9]. A comprehensive review of the studies concerning with bolted joints in fiber reinforced composite structures can be found in the present study.

Failure Characteristics of Bolted Composite Joints

The strength and failure of bolted composite joints are significantly influenced by damage accumulated inside the composites [10]. In general there are three main modes of failure in composite joints, named as net-tension, shear-out and bearing modes. Another mode that can be included is mixed or cleavage mode. Fig. (1) illustrates these modes schematically.

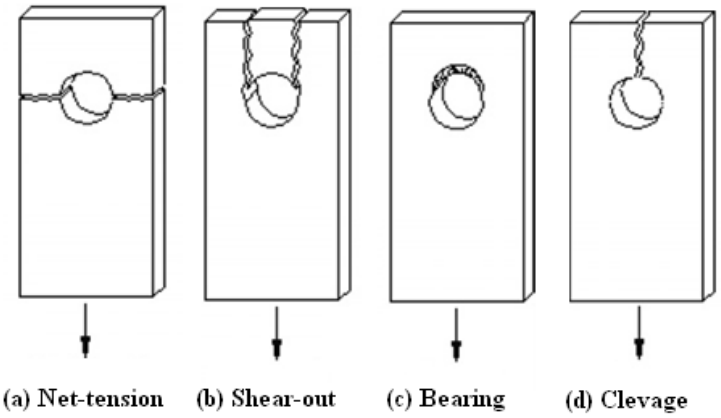


Fig. 1. Common failure modes in bolted composite plates [11].

Net-tension failure occurs in the area between hole and the side edge of the structure (Fig. 1-a), typically take place when the area of cross section of the sample is particularly small and results from excessive tensile stress [1]. While the shear-out failure can be found in the area along the shear-out plane on the hole boundary (Fig. 1-b), it occurs mainly when the distance between the hole edge and the edge of the laminate is small [12].

On the other hand, bearing failure (Fig. 1-c) is a compressive failure observed at the location close to the contact region at the hole edge caused by compressive stress acting on the hole boundary [12]. Bearing failure is desirable in bolted composite joints since it propagates gradually and provides forewarning prior to total failure [13].

It has been observed that the net-tension and shear-out failure modes are catastrophic and contribute in different ways to fracture [12]; both net-tension and shear-out failures can be avoided by improving the joint geometry [14]. However, it has shown that the bearing failure cannot be avoided by any geometrical modification [14].

Factors Affecting Joint Strength

Geometric Parameters. Several authors have investigated the effects of the geometric parameters towards the joint strength. Fig. 2 illustrates the typical pinned joint geometry. In recent study, Faruk et al [15] has performed an experimental study including the effect of two different geometrical parameters (i.e. W/D and E/D) on the bearing strength of single bolted glass reinforced epoxy laminated composite plates. It was found that the bearing strength has increased with the E/D and W/D ratios for different ply orientations. With Murat and Ramazan [16] investigating failure strength and failure mode of a pinned joint of carbon-epoxy composite plate in orbitrary orientation, the bearing strength has been found to reach higher values when the E/D and W/D ratios were increased. Similar study on the glass-epoxy laminated composite bolted joint has shown that the failure load and hence, the bearing strength has increased with E/D and W/D ratios [17].

Increasing W/D and E/D ratios beyond a certain values provides an insignificant effect on the ultimate load capacity; Buket et al [18] has determined these values as 2 and 3 for E/D and W/D, respectively for a pin-loaded woven glass fiber reinforced epoxy laminate. At this point, a transition in failure modes has been observed. On the other hand, Osman [19] showed that the failure mode of the woven fabric laminate with different densities was a bearing mode for specimens with $W/D > 2$ and $E/D > 2$, and maximum bearing strength at $W/D=4$ and $E/D=4$ for all densities.

In general, bearing strength increases with increasing both E/D and W/D ratios [5,18-22] and there is a certain value for these ratios to instigate bearing failures according to various parameters such as stacking sequence, laminate thickness, laminate material, etc.

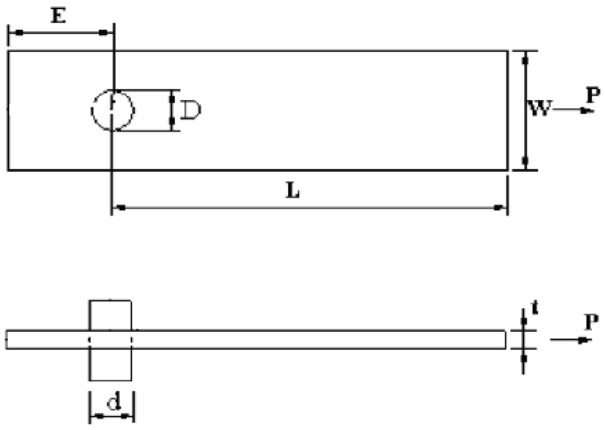


Fig. 2. Typical pinned-joint configuration

Effects of the laminate thickness of composite joints have been investigated by many authors. Dahsin et al [23] investigated a pinned joint with combination of various composite thicknesses and pin diameters, where the results showed that thick composites with small pins and thin composites with large pins possessed lower joint stiffness and strength than those having similar dimensions. Similarly, Li and Dahsin [24] have observed that the joint strengths of double-lap, single-pin joints in glass-epoxy composites have decreased with the increase in three-dimensional size.

Karakuza et al [25] has performed numerical and experimental work in order to investigate the effect of geometrical parameters on the failure load and failure modes in woven glass-venylester composite laminate with two serial pin-loaded holes. It was found that the failure load increased with the increasing ratio of the distance between the two series holes-to-hole diameter. However, this parameter is not as dominant as the E/D ratio in increasing the failure load. In a different study, the authors [26] have studied the composite plate with two parallel holes; it was found that the ratio of the distance between the two parallel holes-to-hole diameter was the determinative factor to obtain mixed mode (i.e. bearing + shear or bearing + net tension), while the ratio of the distance from upper or lower edge of the specimen to the holes center-to-hole diameter determine the type of mixed mode. Also, these two ratios were not as effective as E/D ratio in increasing the bearing strength. In addition, Nada et al [27] investigated numerically and experimentally three and four pin joints, in which they found that there was damage propagation between the holes at a certain value of the pitch-to-hole diameter ratio (i.e. ≤ 6), and beyond this value, no damage propagation has observed.

Preload Moment and Clamping Pressure. Preload moment provided clamping pressure to the bolt which results in lateral constraint of area under the washer; this significantly increases the joint strength. Increasing the value of preload moment could cause increase in load carrying capacity and hence, the bearing strength of the joint [11,15,17,28,29]. Maajid et al [30] tested the effect of bolt torque on the progressive failure of single-lap composite joint using the torques of 4.206N.m and 2.103N.m and compared with zero torque. An increase of approximately 7.2% and 3.4%, respectively in maximum failure load were observed. Furthermore, Claire et al [31] has compared the experimental results from specimens tested with a dowel pin, finger-tightened bolt and torque-tightened bolt. The effective pressure under washer was evaluated with sensor film. The increase in average maximum bearing stress was at least 105% when comparing the results of the tests done with the dowel pin to those of the tests with a tightened bolt and ≥56% to the results with a finger tightened bolt. Approximately similar results were confirmed by Servet et al [32] for wet and dry conditions.

It was found that the ultimate bearing strength increases with increasing clamping pressure until a certain values, where beyond this value, there is no increase in the ultimate bearing strength. Besides, it may cause delamination under the constraint area [33].

Stacking Sequence (Fiber Orientation). Bearing strength and failure modes are found to be influenced by ply orientation (fiber orientation angles with respect to the load direction). In one of many studies, Faruk et al [15] experimentally tested unidirectional GFRE bolted joint with different ply orientation $[30^o]_4$, $[45^o]_4$, $[60^o]_4$ and $[90^o]_4$, and it was found that $[30^o]_4$ laminate was the strongest, while $[90^o]_4$ was the weakest with damage observed as net-tension for all W/D and E/D ratios (matrix failure). Furthermore, the maximum bearing strength of arbitrary orientation (woven) was generally observed at 0° and 90° of orientation angles the while minimum one was at 45° [34]. Thus, it is necessary to design the layers in different direction with respect to load direction in order to avoid catastrophic failure to the composite laminates [35].

Likewise, stacking sequence of the laminate has also a great influence on the failure load, failure mode, stiffness and bearing strength of the bolted joints. A large number of studies have been carried out on this subject matter. It was found that shear-out failure mode occurred predominantly in laminate of 0° [16,36].

Park [37] has utilized an unusual acoustic emission (AE) technique to examine bolted joints in carbon-epoxy laminates, where a comparison between the two orthotropic laminates of $[0_6/90_6]_s$ and $[90_6/0_6]_s$ indicated that both configurations have the same ultimate bearing strength, but the latter has higher delamination bearing strength. This signified that 90° layer on the outermost surface was more advantageous than those of 0° layer. This validated the similar findings of Quinn and Matthews [38], in which they have suggested in placing the 90° layer at or next to the surface would increase the bearing strength.

Bolt-hole Clearance. The dimensional tolerance of the machined holes and fasteners can lead to large clearance in mechanically fastened joints [39]. Clearance between the hole and the pin strongly influences the stress distribution around the hole. Many investigators have studied the effects of the bolt-hole clearance on the structural behavior of composite joints using two dimensional (2-D) finite element analyses [40-43]. In the analysis, many effects such as clamp-up, secondary bending and through-thickness stress could not be accounted for [44], and also inadequate to represent the true strength properties as the analysis could not take into account the effect of delamination buckling [41].

To overcome those shortcomings, Carthy and Carthy [44] have developed 3-D FE models of single- and multi-bolts, and of single-shear joints, using bolts of 8mm diameter with clearance varied from a neat-fit to slightly larger than those found in aerospace primary structures. The specimens studied were made from graphite-epoxy, quasi-isotropic lay-ups $[45/0/-45/90]_{5s}$. Results showed that increasing the clearance could instigate the effect of stiffness reduction of the single-bolt joint due to decreasing contact area between bolts and holes as well as modifying the load distribution in multi-bolt joints. Similar findings have been verified with the experimental work [45], where a good agreement was observed. Experimentally, the out-of-tolerance clearance could have a significant effect on joint strength and even a small variation in clearance could cause substantial changes in the load distribution of multi-bolt joints [46].

Likewise, Lawlor et al [47] has carried out an experimental study on the effect of bolt-hole clearance in single-shear, single-bolt arrangement. Clearances were ranging from net-fit to 240 microns (i.e. larger than the allowed clearance in aircraft industry). The results indicated that if the clearance range is outside of those of the standard fitting used in aerospace industry (f7/H10), the parameter would contribute to a significant effect on joint stiffness and ultimate strain, but less effect on the strength.

In a different work, Tong [48] has performed an experimental investigation on the effect of non-uniform bolt-to-washer radial clearance under different clamping force, where two cases have been studied. The center of the washer was varied with respect to the direction of the applied load; one was in the same direction, whilst the other was in the opposite. The results indicated a lower initial failure load in the former, but no significant difference in the ultimate failure load was observed.

Summary
Numerous publications concerned with mechanical fastening of laminated composite structures using bolts (or pins) have been reviewed. It was apparently observed that the performance of bolted joints was affected by various parameters; these parameters may be related to the laminate coupon configuration, laminate materials or the joint types. The inclusion of these parameters in the joint design yields a big challenge for the engineers/designers. Bolted composite joint requires a huge task in modulating the different parameters that contribute to the mechanical properties of a comprehensive bolted joint design. In order to decisively establish the bearing strength and failure load of the bolted joint and the correlation with the aforementioned parameters, a thorough joint failure map may indeed required.

References

[1] H.S. Wang, C.L. Hung and F.K. Chang: J. of Composite Mat., 30 (1996), pp. 1248-1313.

[2] F. Pierron, F. Cerisier and M. Grediac: J. of Composite Mat., 34 (2000), pp. 1028-1054.

[3] B.G. Kiral: Materials and design 31 (2010), pp. 85-93.

[4] S.A. Goswami: J. of Reinforced Plastics and Composites, 24 (2005), pp. 161-171.

[5] J.H. Choi, C.S. Ban and J.H. Kweon: J. of Composite Mat., 42 (2008), pp. 1415-1429.

[6] C.O. Ryu, J.H. Choi and J.H. Kweon: J. of Composite Mat., 41 (2007), pp. 865-878.

[7] B. M. İcten, R. Karakuzu and E. Toygar: Compos. Struct., 73 (2006), pp. 443-450.

[8] T.A. Collings: Composites, Vol.8, no. 1 (1977), pp. 43-55.

[9] A.N. Kishore, S.K. Malhorta and N.S. Prasad: Mechanics of Advanced Materials and Structures, 17 (2010), pp. 204-214.

[10] C. Girard, M.L. Dano, A. Picard and G. Gendron: Mechanics of Advanced Materials and Structures, 10 (2003), pp. 23-42.

[11] S. Faruk, P. Murat, S. Onur and B. Semih: Materials and Design, 29 (2008), pp. 1159-1169.

[12] A. Valenza and V. Fiore: J. of Composite Mat., Vol. 41, No. 8 (2007), pp. 951-964.

[13] C. Cooper and G. J. Tuvey: Compos. Struct., 32 (1995), pp. 217-226.

[14] Y. Taner, S. Tamer: Mechanics and Design, 28 (2007), pp. 520-527.

[15] S. Faruk, S. Onur, O. Rest and S. Ramazan: Indian J. of Engineering and Materials Sciences, Vol. 17 (2010), pp. 39-48.

[16] B. Murat and K. Ramazan: Compos. Sci. and Technol, 62 (2002), pp. 1259-1271.

[17] S. Faruk, P. Murat, S. Onur and B. Semih: Int. J. of Damage Mechanics, Vol. 0 No. 00 (2009).

[18] O. Buket, A. Züleyah and K. Ramazan: Compos. Sci. and Technol., 61 (2010), pp. 1491-1497.

[19] A. Osman: Composite Structures, 90 (2009), pp. 43-52.

[20] B. Murat, B. Okutan and R. Karakuzu: J. of Composite Mat., Vol. 37, No. 15 (2003), pp. 1337-1350.

[21] A. Riccio and L. Marciano: J. of Composite Mat., Vol. 39, No. 23 (2005), pp. 2071-2090.

[22] G. Caprino, G. Giorleo, L. Nele and A. Squillance: Composites: Part A 33 (2002), pp. 779-785.

[23] L. Dahsin, B.R. Basavaraju and Y. Junling: J. of Composite Mat., Vol. 33 (1999), pp. 2-21.

[24] H. Li and L. Dahsin: J. of Composite Mat., Vol. 37 (2003), pp. 2003.

[25] R. Karakuzu, C. Riza , M. Aktaş and B. Murat: Compos. Struct., Vol. 82 (2008), pp. 225-234.

[26] R. Karakuzu, N. Taylak, B. Murat and M. Aktaş: Compos. Struct., Vol.85 (2008), pp. 1-9.

[27] A.K. Nada, S.K. Malhorta and N.S. Prasad: Compos. Struct., Vol. 91 (2009), pp. 266-277.

[28] J. H. Oh, Y.G. Kim and D.G. Lee: Compos. Struct., Vol. 38, No. 1-4 (1999), pp. 329-341.

[29] M. Pakdil: Indian J. of Engineering and Materials Sciences, Vol. 16, April (2009), pp. 79-85.

[30] C. Maajid, H.W. Chn, S.T. Rodney and O. Adrian: Mat. Sci. and Eng., 10 (2010), pp. 1-10.

[31] G. Claire, L.D. Marie, P. Andre and G. Guy: Mechanics of Advanced Materials and Structures, 10 (2003), pp. 1-21.

[32] K. Servet, S. Onur, O. Mustafa and B. Semih: Materials and Design, 31 (2010), pp. 4933-4942.

[33] R. Karakuzu, T. Gülem and B. Murat: Compos. Struct., 72 (2006), pp. 27-32.

[34] A. Aktas and R. Karakuzu: Mech. of Compos. Mat. and Struct., 6 (1999), pp. 347-361.

[35] C. Atas: Compos. Struct., 88 (2009), pp. 40-45.

[36] B. Okutan: Composites: Part B, 33 (2002), pp. 567-578.

[37] H.J. Park: Compos. Struct., 53 (2001), pp. 213-221.

[38] W.J. Quinn and F.L. Matthews: J. of Composite Mat., Vol.11 (1977), pp. 139-145.

[39] G. Kelly and S. Hallstrom: Composites: Part B, 35 (2004), pp. 331-343.

[40] A. J. DiNicola and S.L. Fantle: Composite Materials: Testing and Design, Vol. 11 (1999), ASTM STP 1206, pp. 220-237.

[41] D.F. Lanza, F. Cappello, G.L. Cloud: J. of Thermoplastic Composite Materials, Vol. 12 (1999), pp. 13-33.

[42] W.X Fan, and C.T. Qiu: Int. J. of Solid and Structures, Vol. 30, No. 21 (1993), pp. 3013-3033.

[43] R.A. Naik and J.H. Crew: AIAA J, 24 (1985), pp. 134-1353.

[44] M. A. McCarthy and C.T. McCarthy: J. of Plastics, Rubber and composites, The Institute of Materials, London, UK, Vol. 32, No. 2 (2002), pp. 1-11.

[45] W. F. Stanley, M. A. McCarthy and V. P. Lawlor: J. of Plastics, Rubber and composites, The Institute of Materials, London, UK, Vol. 31, No. 9 (2002), pp. 412-418.

[46] M.A. McCarthy, C.T. McCarthy and G.S. Padhi: Compos. Struct., Vol. 73 92006), pp. 78-87.

[47] V. P. Lawlor, M. A. McCarthy and W. F. Stanley: J. of Plastics, Rubber and composites, The Institute of Materials, London, UK, Vol. 31, No. 9 (2002), pp. 405-411.

[48] L. Tong: Composite: Part A, Vol. 31 (2000), pp. 609-615.

© (2011) Trans Tech Publications, Switzerland
doi:10.4028/www.scientific.net/KEM.471-472.945

Development of Novel Polymer Composite Beam using Ultrasonic Welding Process for Acetabular Cup Prosthesis

Amirhossein Goharian[1, a], Ahmad Ramli B. Rashidi[3], Mohd Rafiq bin kadir[1,c], Mohd Ruslan bin Abdullah[2,b], and Mat Uzir B. Wahit [3]

[1]Medical Implant Technology Group, Faculty of Health Science and Biomedical, University Technology Malaysia, Malaysia

[2]Faculty of Mechanical Engineering, University Technology Malaysia, Malaysia

[3]Depatment of Polymer Engineering, Faculty of Natural Resource and Chemical engineering, University Technology Malaysia, Malaysia

[a]amir.gouhar@gmail.com, [b]ruslan@fkm.utm.my, [c]rafiq@biomedical.utm.my

Keywords: Acetabular cup, carbon fiber reinforced polyetheretherketone, hydroxyapatite polyetheretherketone, ultrasonic welding, polymer composite

Abstract. The objective of this study was to prepare a basic contributed model in beam to examine this novel composition supposed to apply for acetabular cup. Injection molding process used to manufacture of the component whereas ultrasonic welding was utilized to joint two components. Molding and welding value parameters were carried out by trial and error process. Strength bonding of two components was evaluated by single cantilever beam (SCB) test. The Interfacial fracture energy attained by single cantilever beam (SCB) test was exceeded over 1800 J/m^2 after 70 mm crack propagation.

Introduction

Acetabular cup component is implanted in the patient's hip socket (Fig. 1 and Fig. 2) the acetabulum [1]. In this investigation a novel composition structure using for acetabular cup is developed. The material selection, material processing, and manufacturing process were determined for the beam specimen and the mechanical test results are carried out to evaluate the specimen in view of manufacturing strength. As this composition supposed to use in human body as part of hip prosthesis, some issues should be considered while material selection process. The acetabular cup seated on pelvis bone (acetabulum) should integrate biologically with pelvis bone and has a superior wear resistance in contact with femoral head.

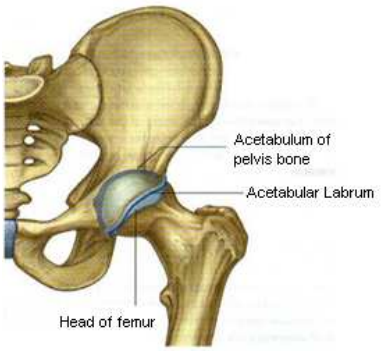


Fig. 1 Hip joint and internal structure [2]

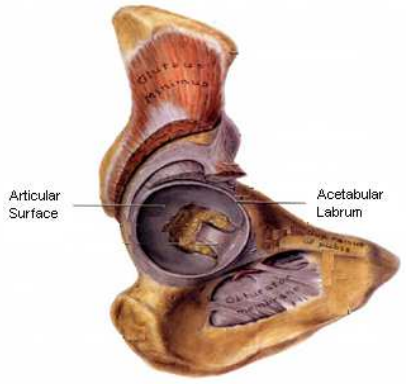


Fig. 2 Pelvis bone and acetabulum [2]

Conventional biomaterials have been used in most orthopedic implants, have elastic modulus higher (e.g. cobalt–chrome, titanium and alumina) or lower (e.g. most polymers) than that of the extracellular matrix of bone tissue. Reduced implant stiffness results in increased load transfer to

the peri-implant tissue, which leads to decreased bone resorption due to stress shielding and increased mechanical stimulus for new bone formation. On the other hand, the implant and biomaterials must have adequate mechanical properties to bear physiological levels of load, which is where most polymers alone, despite other advantages, fall short. According to Wolff's law, the loading on bone should be perfectly applied. Otherwise, the bone will remodel itself. So the loading on the bone should not be increased and decreased. For this matter, the mechanical modulus of the implant should be close to bone. Polymer composite material is introduced to attain lightweight implant along with similar mechanical modulus.

Two polymer composite materials are applied as two beam layers. Carbon fiber reinforced-polyethretherketone (CFR-PEEK) and hydroxyapatite-polyetheretherketone (HA-PEEK) are the composition of the hemispherical shaped acetabular cup. CFR-PEEK has been investigated for acetabular horseshoe-shape cup and HA-PEEK prepared and characterized for bone in-growth scaffolds. CFR-PEEK was carried out as the internal layer to enhance the strength and wear resistance and HA-PEEK as the external layer to enhance the deposition of HA coating on cup. This promotes the osteointegration of cup into the acetabulum.

Plastic welding process is carried out to bond these two layers. Three different welding methods was addressed [3] namely friction welding, ultrasonic welding, and hot plate welding processes [3]. Due to samples dimension, ultrasonic welding process is applied for this matter. The bonding strength of welding area was evaluated by single cantilever beam (SCB) test. The objective of this study was to prepare a basic contributed model in beam shape to examine this novel composition supposed to apply for acetabular cup. The beam specimens were prepared by injection molding process.

Material and Methods

Material. Carbon fiber reinforced - Polyetheretherketone (CFR-PEEK) with 30% chopped carbon fiber (Invibio Ltd.) was addressed to provide transfer loading to the pelvis bone from the femoral head. For any potential implant material, it is important to consider biocompatibility issues. MOTIS G was considered because its testing history is known. Extensive testing to ISO 10993 Standard, demonstrates bio-compatibility and bio-stability for use in long term implant applications; this is supported by US FDA Drug and Device Master files [4]. This composite utilizes a high strength PEEK thermoplastic as the matrix and a high strength carbon fiber as the reinforcement. Both the PEEK and the carbon fiber materials were shown to be highly biocompatible [5]. The percentage of carbon fiber and HA as filler in composite was determined to attain the nearly same mechanical strength of bone and implant. The mechanical properties of cortical bone and CFR-PEEK [4] are cited at Table 1.

Table 1 Mechanical properties of cortical bone and CFR-PEEK [4]

	Cortical Bone	CFR-PEEK
Tensile Modulus (GPa)	17.7	15
Flexural Modulus (GPa)	12.8	12.5
Tensile strength (MPa)	133	155

Hydroxyapatite-polyetheretherketone (HA-PEEK) with 20% Wt of HA is the other polymer composite material that is an alternative to apply to make implant strongly bonded to the pelvis bone. The existence of HA, results to better connection of HA-PEEK and phosphate calcium inside the pelvis bone. It is anticipated that by incorporating particulate HA into the PEEK matrix, the mechanical performance of the material, particularly the Young's modulus could be improved considerably. Furthermore, the presence of bioactive HA would subsequently enhance implant fixation with proper provision for their interactions with the host tissue.

Composition. There is other issue that some other investigations were addressed on. To better connection of Implant to enhance implant fixation with host tissues and specially bone, HA $[Ca_{10}(PO_4)_6(OH)_2]$ or other formulation of calcium phosphate is coating on surface of implant that is in contact with bone. In this investigation, the other layer is added to the main layer (CFR-PEEK) to attain better coating of HA on the substrate and connection with host tissues.

Material Processing. The single screw extrusion machine was used to compound of HA and PEEK with 20 and 30 % Wt. of HA. Due to high melt temperature of PEEK, the new machine was fabricated and applied. The HA-PEEK compound was granulized to feed the injection molding machine.

Specimen Preparation. Beam specimens prepared by Injection molding process. Due to high melt temperature of PEEK composite material, modification of machine is required. For this matter, the higher temperature range controllers and ceramic heaters were installed on machine. The dimension of specimens was determined due to the ASTM D790 Standard to apply for flexural test. In same process, CFR-PEEK granules injected to mold to get the CFR-PEEK samples. In this matter, injecting CFR-PEEK was more difficult than HA-PEEK. High flow rate of CFR-PEEK needs to increase the injection pressure and nozzle temperature to respectively 10 MPa and 410°C.

Welding Process. The latest commercially acetabular cup has a metallic or ceramic liner and an outer shell is formed of a bio-medically acceptable polymer. Any suitable molding technique, such as injection or more preferably compression molding, may be used to over-mold the polymeric material from its powder or granule form around the inner liner [1]. In this study the outer shell and the inner liner supposed to be polymer composite material with same polymeric matrix. In this regard, usual over molding process could not be proceed due to the same melt temperature of two components. From the alternative methods, Mechanical fasteners cause to pull free of the composite polymer material due to high localized stresses and adhesive is difficult to handle because of hard process of joint preparation and surface cleanliness. In addition, adhesive application can be messy, requiring extensive clean-up, and hazardous vapors may be given off during curing. Stress cracking can occur from a reaction between the polymer and particular adhesives, normally prior to or during curing [6]. Thermally welding of plastics using Ultrasonic, friction, or hot plate welding techniques has been addressed for PEEK and short or chopped fiber reinforced PEEK composites [6].

Ultrasonic Welding. Ultrasonic welding process was applied to weld the components. Among the advantages of this process; welding time, cleanness, and weld dimension are considerable in contrast to many other welding methods. Welding times are short and there is no need for elaborate ventilation systems to remove fumes or heat. It is commonly used in the healthcare industry because it does not introduce contaminants or sources of degradation to the weld that may affect the biocompatibility of the medical device [6]. Also the small dimension of the components would be suitable to apply ultrasonic welding process. Weld time, hold time, weld pressure, and amplitude of vibration could be controlled by the ultrasonic welder with 2800 watts output capability (KSONIC-Taiwan).

Energy Director. Since PEEK polymer has such a high melting point, it requires considerable amounts of energy to achieve a good bond. In this way, energy director made on the surface of HA-PEEK layer. Triangular energy director was applied to concentrate ultrasonic energy (Fig. 3) within the contact surface. Due to vibration, ultrasonic energy transmits to heat energy to melt the energy director firstly and it fills up the empty space of contact area. Triangular energy director with 0.6 mm height was machined on one side of HA-PEEK surface. CFR-PEEK melt processing is hard to flow. It was also needed to make energy director on the surface of CFR-PEEK layer at the interface.

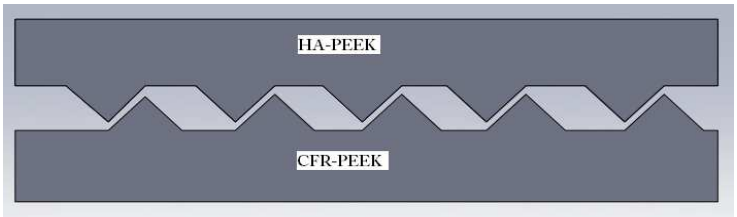


Fig. 3 Energy directors on both layers

Single Cantilever Beam Test (SCB). Strength of welding bonding examined by single cantilever beam test (SCB). In terms of measuring the strength, Fracture toughness criteria is evaluated by this test [8]. Applying load in SCB test needs to cut part of HA-PEEK specimen. Before cutting, Aluminum foil with 35×6 mm was inserted at the end of the contact surface. It means 35 mm of contact area would not be welded. This was done to make pre-crack at the interface so that the crack propagate in the interface line. The large percentage of loading should transfer to the interface. Low thickness of CFR-PEEK (3 mm) increases the possibility of fracture. If the CFR-PEEK fractures, before the crack propagated until certain length of interface, test would be failed. Woven glass fiber polymer (GFRP) carried out to make the composition more rigid for this case. The flexural strength of CFR-PEEK was increased by jointing 4 layers with different orientation (0/45/0/45) (woven glass fiber polymer component) via a strong adhesive "SICADO". In same process, 3 Layers of glass fiber in different orientation 0/45/0 stuck on the upper surface of HA-PEEK layer. Instron universal testing machine was applied to do this test. The final component was clamped as Fig. 4. Via this machine, the load - displacement was obtained. Then specimen compliance - crack length cube (C-a^3) was determined. The interfacial fracture energy G_c, was calculated using Eq. 1.

$$G_c = \frac{P^2}{2B}\frac{dC}{da} \text{ [7]} \quad (1)$$

Where P is the applied force, B is the specimen width, C is the specimen compliance and a, the crack length. The specimen compliance is determined as a function of crack length and a linear curve fit as Eq. 2.

$$C = C_0 + ka^3 \text{ [7]} \quad (2)$$

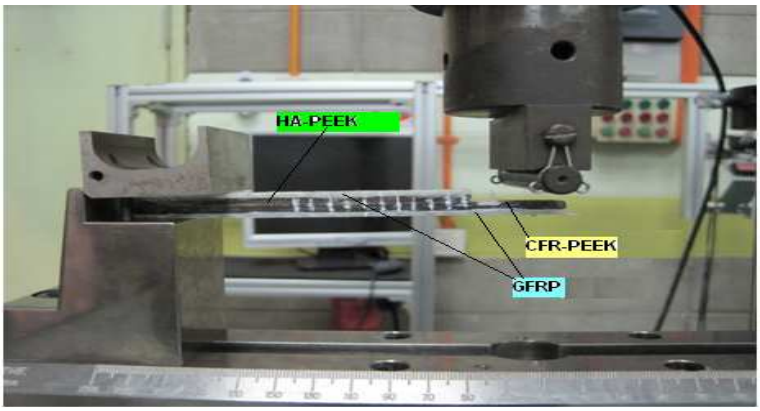


Fig. 4 SCB test by Instron universal testing machine

Results and Discussion

It was observed that high amplitude and Near field ultrasonic welding was applicable to joint PEEK composite material with optimum results. Several experiments were performed to reach to the suitable range of parameters values. With a high vibration amplitude 100 μm, a good weld strength can be obtained using a pressure of about 100 psi , 3 sec. weld time, and 2 sec hold time. Fig. 5 and 6 show the load-displacement diagram and crack propagating gained by SCB test for interface of 20% HA-PEEK and CFR-PEEK composition respectively. Fig. 7 and Fig. 8 were plotted respectively for compliance-crack length and interfacial fracture energy.

Summary

Plastic and particularly polymer composite materials processing area applying for biomedical Implant investigations, has more challenging issues than metal and ceramic based material. In this regard, thermal behavior of composite polymers is different. As it was attained in this research HA-PEEK and CFR-PEEK had a different injecting and welding processes. It is related to different characteristics of fillers inside the composite. In biomedical industry, clean and accurate processes needed to evaluate and developed. High level of care must be taken to handle biomedical research. Here the ultrasonic welding was evaluated to joint two polymer composite material layers. This kind of processes has not been investigated in hip joint implant and even similar human join implant like knee or shoulder. As SCB test results, ultrasonic welding process could be addressed to use as a good alternative bonding processes in biomedical investigation.

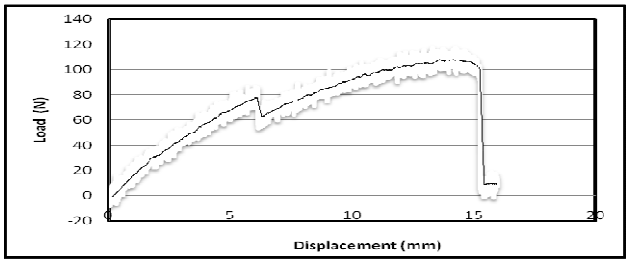


Fig. 5 Typical load - displacement response for the tested specimen

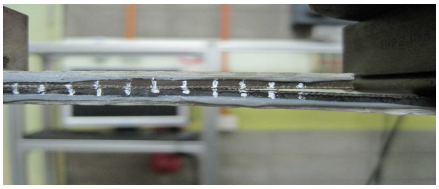


Fig. 6 Crack propagating at the interface

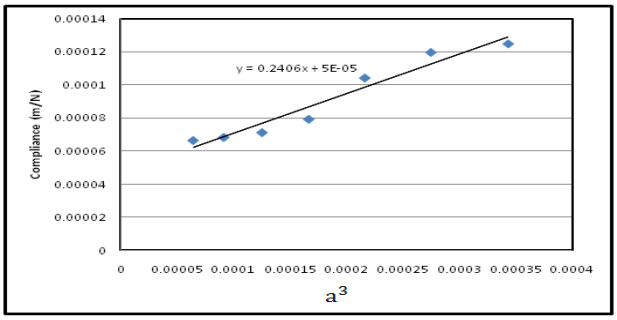


Fig. 7 Typical plot of compliance - crack length cube

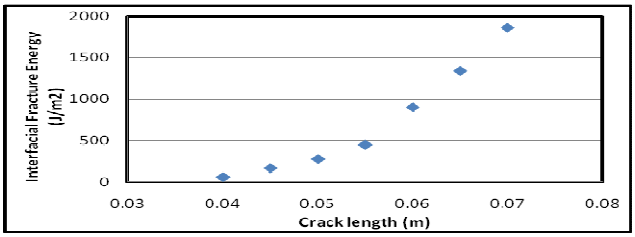


Fig. 8 Interfacial fracture energy resistance curve on specimen

References

[1] R.J. Bateman, and R. A. Scott, “Acetabular Cups and methods of their manufacturing", US Patent 5,879,404 (1999).

[2] Information on “Hip Joint (acetabulum and femur bone concern) "Mahidol University webpage http://www.mahidol.ac.th

[3] Troughton, M. J. " Handbook of Plastics Joining : a Practical Guide, 2nd ed. ", (2008) William Andrew Publishing, New York.

[4] Invibio Ltd. " MOTIS™ Polymer Typical Material Properties" Chicago, Il.

[5] R. Moore, P. Beredjiklian, R. Rhoad, S. Theiss, J. Cuckler, P. Duchyene, D.G. Baker: J. Biomed. Mater. Res. 34(2) (1997). 137–147.

[6] E.M. Petrie, *Handbook of Adhesives and Sealants,* McGraw- Hill, New York (2000).

[7] H. Kiratisaevee, University of Liverpool PhD Thesis , " Fracture properties and impact responses of novel lightweight sandwich structures", (2004)

© (2011) Trans Tech Publications, Switzerland
doi:10.4028/www.scientific.net/KEM.471-472.951

Experimental Investigation and Finite Element Analysis of Dynamic Behavior and Damage of Glass/Epoxy Tubular Structures

Mostapha Tarfaoui[1,a] and Papa Birame Gning[2,b]

[1]ENSIETA / LBMS-MSN, 2 rue Francois Verny, 29806 Brest Cedex 9, France

[2]ISAT Nevers, 49 rue Mademoiselle Bourgeois - 58027 Nevers

[a]mostapha.tarfaoui@ensieta.fr, [b]papa-birame.gning@u-bourgogne.fr

Keywords: Tubular composite structures, impact, damage, delamination, finite element analysis.

Abstract. This paper presents finite element analysis (FEA) of static and dynamic tests of thick filament wound glass/epoxy tubes. The first part involves the validation of elastic properties and identification of damage initiation and its development in dynamic tests. The results of FEA of the dynamic tests without damage appeared satisfactory. An impact model, including material property degradation, is used for damage prediction. The simulated damage is compared with that obtained experimentally. The sizes of projected and cumulated surfaces are of the same order of magnitude as in the experimental measurements.

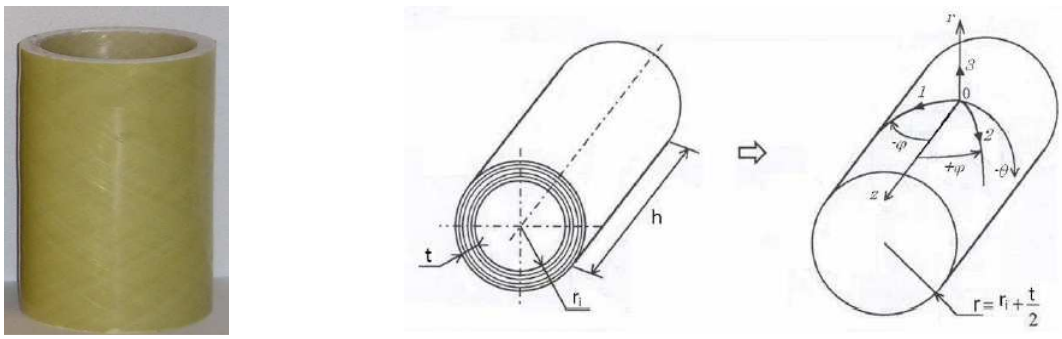
Introduction

During their use, one notes that certain impacted composite cylinders do not sustain operating pressures, which correspond to the dimensioning values. However the damage introduced by accidental impact can jeopardize the capacity to fulfill the dedicated function. Indeed, taking into account the low speed of the immersed objects, it is a question of studying the impact behavior at the time of a low-energy impact having a null incidence with the projectile. The composite structures have a higher specific rigidity than metallic materials. However, because of the stratification of their layers, with weak interfaces, they are very sensitive to impact [1-4]. This laminate damage is difficult to detect. The lack of understanding of the tolerance to the shocks for the tubes is one of the aspects, which prevent a greater use. In order to better make safe the use of the composite structures in marine environment, it is important to evaluate and predict the damage resulting from an impact with a low incidental speed and to assess the harmfulness of the damage compared to a stress in external hydrostatic pressure.

After having carried out the tests on the composite cylinders [5,6], in this paper one is interested in their modeling. Initially, certain models are used for validating the characteristics of material constitutive of the structures and predicting their elastic behavior at the time of static and dynamic loadings with a low speed and incidental energy. Then, the prediction of the damage post-impact of the composite enclosures is studied.

Materials, Geometry and Reference Mark

The materials examined in the study are all manufactured using the filament winding process. E-glass fibers were impregnated with a low viscosity epoxy resin. These cylinders are treated at 125° C for 7 hours and the measured fiber volume fraction V_f is 62 %. Porosity is about 10 %. The Dimensions of the tubes are given in Table 1. The samples used in impact and pressure testing are 110 mm long. Micrographic observations show a $[\pm 55]_{10}$ stacking sequence lay-up. Material properties are shown in Table 2. Fig. 1 shows the principal notations and coordinates adopted in this study.



(a) Sample Mat1 *(b)* Tube coordinates and notations

Fig. 1. Principal notations and coordinates

The tubes are composed of isotropic transverse plies. The implemented material takes the characteristics given in tables 1 and 2 with a fragile elastic behavior. Non-linearity of materials is not taken into account in modeling. In finite element models, we make the assumption that all the plies are alternatively directed with ±55°.

Table 1: Sample geometry

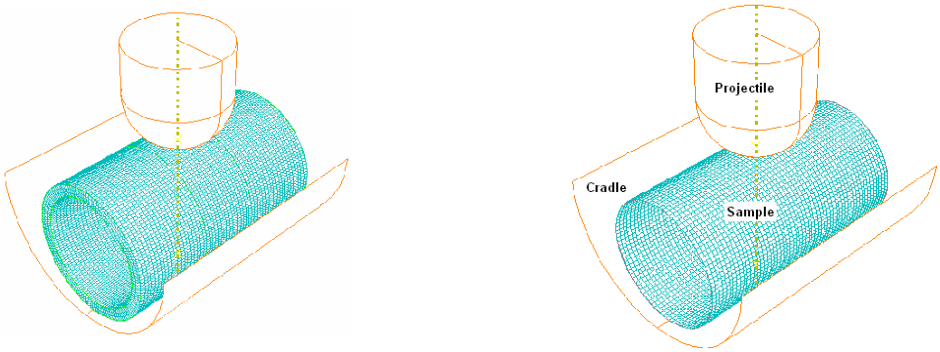
Sample	Internal diameter, d_i (mm)	Wall thickness, t (mm)	Tube length, h (mm)	Stacking sequence
Mat1	55	6	110	$[\pm 55°]_{10}$

Table 2. Material properties used for modeling

Material	E_{11} (GPa)	E_{22} (GPa)	G_{12} (GPa)	ν_{12}
Glass/epoxy ply 0°	49.5	15.9	5.6	0.255

Finite Element Analysis (FEA)

The studied cylinders are thick ($d_i/t > 10$) because of dimensioning to the buckling which confers a strong thickness to them. Furthermore, they are modeled by two types of finite elements, solid and shell elements, represented in Fig. 2.



(a) Solid model *(a) Shell model*

Fig. 2. Modeling by finite elements of the impactoring of cylinder

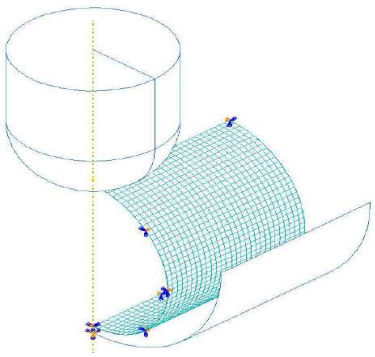
The models presented were studied using ABAQUS version 6.2 [7]. Shell elements with reduced integration S4R with MIDLIN formulation in impact cases available in the library were used with geometric nonlinearity. Based on microscopic observations, the tube thickness was modeled as a laminated cylindrical shell and solid with transversely isotropic plies. The impactor, plate and

cradle, were considered as rigid bodies and were taken as the "master surface". The potential contact area of the cylinder was taken as a "slave surface" so the individual nodes of the composite cylinder were constrained not to penetrate the surfaces of the rigid bodies whereas the contrary was permitted due to the higher stiffness of the latter. The relative motions of the contact surfaces were modeled as "small sliding", which assumes that contact surfaces do not move very much relative to each other. The contact algorithm used is based on the penalty method.

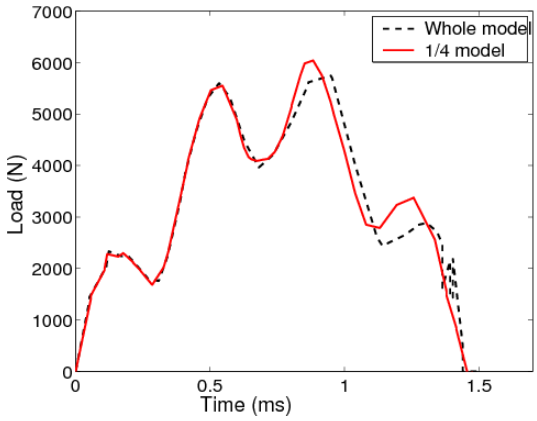
Impact without Damage.

A series of impact tests was performed on 40 cylinders. A new cylinder was impacted for each test, using a 1.6 kg, 50 mm diameter hemispherical steel impactor. Increasing drop height varied the impact energy. This study is presented by Gning and Tarfaoui in [5-6]. These papers present experimental results obtained from quasi-static and impact indentation tests on thick ±55° filament wound glass/epoxy tubes intended for underwater applications. In this part, one proposes to examine the prediction of the dynamic responses of the cylinders under impact by finite element analysis.

Symmetry Effect. In order to reduce the computing times by the reduction in the elements number of the models without harming the quality of the results of simulation, a strategy consists of exploiting symmetries which the geometries can exhibit, Fig. 3a. The identified symmetry planes are orthogonal to each other, containing one the axis of the cylinder and the other the plane, with middle height of the specimen. Knowing that there are terms of coupling membrane/twist related to the $[\pm 55]_n$ lay-up, it should be checked that their effects do not deteriorate the modeling of a quarter of cylinder instead of the complete tube while being ensured to put the good conditions of symmetry, Fig. 3b. The results are compared in Fig. 4a. The two models give the same responses for the contact load and the displacement of the projectile versus time. This satisfactory result had to work on a quarter of cylinder with shell elements.



(a) ¼ FE Model



(b) 2 J impact (1.55 m/s)

Fig. 3. Simulation with ¼ FE Model of cylinder

Elastic Responses. Results of FEA are compared with filtered experimental measurements. The comparisons in force and displacement of the model with measurements on Mat1 tubes give satisfactory correlations for impacts of up to an energy of 3J (1.94m/s), Fig. 4. Beyond that, the prediction of the FE model brings less satisfaction. The impact model with 4J (2.27m/s) reveals that simulation over-estimates the forces while the duration of contact as well as the displacement of the projectile predicted are weaker compared with experimental measurements. These results are in agreement with the tests that show that the impact with an incidental energy of 3J (1.94m/s) does not create an observable damage in specimens. The creation of damage is noted starting from 4J (2.27m/s). Thus, one can conclude that the modeling of the tube by shell elements as well as the projectile and the cradle by rigid bodies is sufficient to represent the elastic phenomena in impact.

In addition, it also arises that this modeling is limited since the damage intervenes in impacted material. This aspect is particularly developed in section 4.

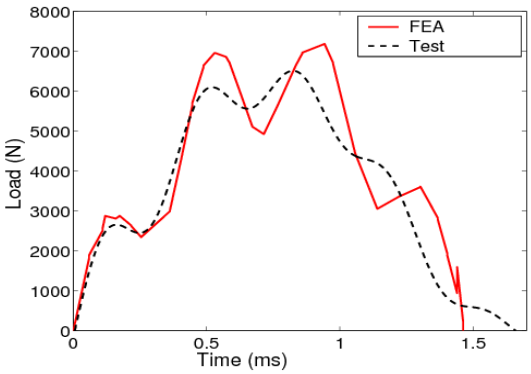


Fig. 4. Force versus time plots measured and predicted, 3J impact (1.94m/s)

Numerical Study of the Damage

All preceding simulations related to tubes behavior were compared and validated by experimental measurements. The tests showed that beyond a certain incidental energy, there is creation of the damage in the wall of the tubes tested. These damages correspond to through-the-thickness delamination, which propagate as the incident energy increases. After static punching or impact tests, the damage mechanism is the same [5-6]. Firstly, a small local indentation at the contact point is noted for low incident speeds or energies. At that level only the superficial resin coat layer of about 0.3 mm thickness is damaged. Then, after the threshold energy level is reached, delamination occurs through the thickness as noted by Alderson and Evans [9]. In the next section, we will be interested in numerical modeling of the damage in the composite tubular structures.

Damage Modeling: Material Property Degradation. To simulate the evolution of the damage, modeling must take into account the various damage occurring at the impact tests. It is not necessary that it accounts for all the physical phenomena observed if their presence does not affect in a relevant way the behavior of the tubes. Also, it was decided to restore only the damage of the matrix and fiber/matrix shearing. For that, the criteria of Hashin [11] were used.

The expressions (1) and (2) predict the matrix cracking, respectively in traction or compression, when e_m reaches unity. Relation (3) predicts fiber/matrix shearing for a value of e_f equal to 1. These criteria are calculated in all the integration points of all the layers of the cylinder. No distinction is made in the model between the initiation and the propagation of the damage.

$$\left(\frac{\sigma_2}{Y_c}\right)^2 + \left(\frac{\sigma_{12}}{S}\right)^2 = e_m^2 \qquad (1)$$

$$\left(\frac{\sigma_2}{Y_t}\right)^2 + \left(\frac{\sigma_{12}}{S}\right)^2 = e_m^2 \qquad (2)$$

$$\left(\frac{\sigma_1}{X_c}\right)^2 + \left(\frac{\sigma_{12}}{S}\right)^2 = e_f^2 \qquad (3)$$

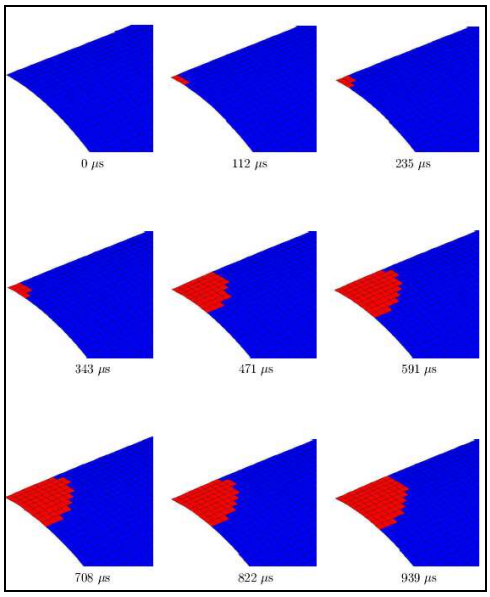
In progressive failure analysis, once failures are detected in a ply, the corresponding material properties are degraded. Since the damage initiation was observed along all the edges of specimen, a uniform mesh size was used. A standard user subroutine USDFLD in ABAQUS was written, which allows the user to define material properties as function of the field variables at a material point. The material properties of the laminated tube were defined to be dependent upon two field variables.

The states of material taken into account are the healthy case, the damage of the matrix and the decohesion fiber/matrix presented in table 3. The field variables FV1 and FV2 respectively represent the matrix cracking and fiber-matrix shearing. They are initially null and reach unity when e_m and e_f are equal to 1. When variables FV=1, they cannot vary any more and material once damaged remains in this state. The elastic initial properties, in connection with degradation, are set to 0 as one can see in table 3. The procedure described here is developed in ABAQUS/Standard with the user subroutine USDFLD [12].

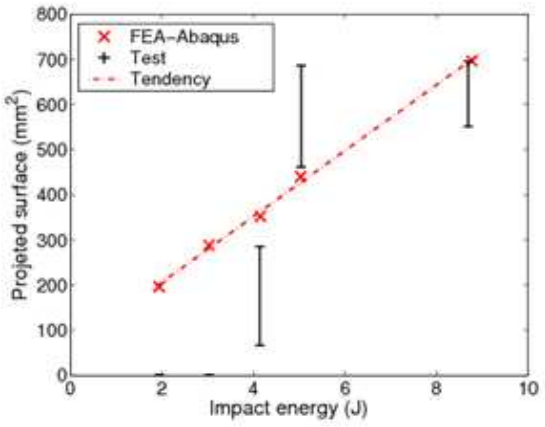
Table 3. Dependence of the elastic properties on the field's variables FV1 and FV2

State of material	Elastic properties				FV1	FV2
Undamaged	E_1	E_2	ν_{12}	G_{12}	0	0
Matrix cracks	E_1	0	0	G_{12}	1	0
Fiber-matrix shearing	E_1	E_2	0	0	0	1

Damage Evolution. The progressive failure analysis methodology uses the C^0 four-node shell element S4R of the ABAQUS element library based on first order shear deformation theory, due to its better performance in large deformation analysis. Loads and displacement versus time are coherent with experimental measurements. Fig. 5a show the evolution of the field variable FV1 corresponding to the laminate damage with various increments for 9J impact energy. The figure represents the external faces of the impacted zone, respectively. The damage is initiated and progresses as much as the tube becomes deformed and this until the maximum deformation. When the impactor rebounds, the damage does not evolve any more.



(a) External surface, 9J impact (3.30m/s)



(b) Projected surface

Fig. 5. Numerical and experimental damaged zone

To validate this modeling, we measure the evolution of the projected and cumulated delaminated area as a function of incident energy. Fig. 5b compares the evolutions of the surfaces predicted by the model with experimental measurements on Mat1. A reasonable coherence between the numerical and experimental results is noted. The model predicts a damage for impact energy of 2-3J, which is not observed on the tested samples. This can be related to the sensitivity of the experimental methods of control for such low sizes of damage.

Summary

All elastic simulations are validated by the experimental results. With the new contact law on the indentation tests, the elastic response of quasi-static impacting is well predicted. Under impact, the dynamic responses without damage are well simulated just like the loading in biaxial stress of the tubes. The taking into account of the damage in impact modeling gives a zone damaged with an aspect in the form of sand glass. This volume is conical, overall, without any healthy part in its center. The differences between the models and experimental measurements can hold several factors:

1. The choice of the failure criterion uncoupling the damages, arbitrarily carried on that of Hashin can be discussed. Indeed, the delamination as well as the crushing of the layers is not taken into account by these models. All the out-of-plane effects are neglected ;
2. The data feeding the criteria (*Xc*, *Yc*, *Yt* and *S*) are very delicate to identify in experiments in the case of tubular composite structures. There is, thus, a considerable uncertainty as regards the reliability of the failure values used in FEA.

References

[1] K. S. Krishnamuthy, P. Mahajan, and R. K. Mittal: Composites Structures, 59(2003) :15-36

[2] S. J. Kim, N. S. Goo, and T. W. Kim: Composites Science and Technology, 57(1997): 763-773

[3] A. P. Christoforou and S. R. Swanson: Journal of Applied Mechanics, (27) (1990): 376-82,

[4] H. Y. Choi and F. K. Chang: Journal of Composite Materials, 26(14) (1992). : 2134-69,

[5] P.B. Gning, M. Tarfaoui, F. Collombet and P. Davies: Composites PART B: Engineering, Volume 36, Issue 4, June 2005, Pages 306-318.

[6] P.B. Gning, M. Tarfaoui, P. Davies and F. Collombet: Journal of Composite Materials, Vol. 39, (2005) No. 10, 917-928.

[7] Hibitt, Karlsson, and Sorensen. ABAQUS 6.3 User's Manual. 2003.

[8] O. C. Zienckiewicz. La méthode des éléments finis. Traduit de la 3ème édition anglaise, Mc Graw-Hill eds, 1979.

[9] Alderson KL, Evans KE: Composites. Vol. 23, (1992). N°3, p. 167-173

[10] Abrate S. Impact on composite structures. Cambridge University Press eds, (1998).

[11] Z. Hashin: Journal of Applied Mechanics, 47 (1980): 329-334,

[12] Hibitt, Karlsson, and Sorensen. ABAQUS 6.3 Example problems Manual. (2003).

© (2011) Trans Tech Publications, Switzerland
doi:10.4028/www.scientific.net/KEM.471-472.957

Curing Characteristics, Fatigue Life and Morphological Properties of Natural Rubber Nanocomposites with Halloysite Nanotubes (HNTs)/Carbon Black (CB) Hybrid Filler

Siti Zuliana Salleh[1,a], Hanafi Ismail[1,b] and Zulkifli Ahmad[1,c]

[1]School of Materials and Mineral Resources Engineering, Engineering Campus, Universiti Sains Malaysia, 14300 Nibong Tebal, Penang, Malaysia

[a]szs88893@student.usm.my, [b]hanafi@eng.usm.my, [c]zulkifli@eng.usm.my

Keywords: Halloysite nanotubes, carbon black, natural rubber, curing characteristics, fatigue and morphological properties.

Abstract. In this research, natural rubber (NR) with halloysite nanotubes(HNTs)/carbon black (CB) hybrid filler at various filler loading was investigated where the total filler loading used in each compound were 40 phr. The curing characteristics, fatigue life and morphological properties of HNTs/CB/NR nanocomposites were studied. Laboratory two-roll mill was used for mixing process. The results revealed that vulcanizates containing more HNTs in hybrid filler exhibit longer scorch time (t_{s2}) and cure time (t_{90}) for curing characteristics and higher in fatigue life compared to vulcanizates with 40 phr of CB. The images from scanning electron microscope (SEM) confirmed that replacement of carbon black with halloysite nanotubes improved the fatigue life by showing more tearing surface on vulcanizates.

Introduction

Nowadays, necessary reinforcing fillers are added into natural rubber (NR) in most cases in order to gain the appropriate properties for specific applications [1]. For example, the addition of CB into NR matrix can increased the tensile strength, tear strength, modulus and abrasion resistant while silica provide unique combination of tear strength, abrasion resistance, aging resistance and adhesion properties [2]. Since both shows promising properties hence the combinations of both filler is expected to exhibit desirable properties of the individual constituents just like Ko et al. [3] have proven in their work.

In this work, new clay mineral from kaolin group named HNTs is chosen to be used together with CB as hybrid filler filled NR. The unique properties of HNTs such as hollow tubular structure like carbon nanotubes [4], less hydroxyl group available than montmorillonite and kaolinite [5] and shows better dispersion property than other natural silicates [6] is expected to give better comparative properties with the combination of carbon black.

The main objective of this project is to investigate the potential effect of various HNTs/CB hybrids loading on the properties of natural rubber nanocomposites.

Experimental

Materials. Halloysite nanotubes were purchased from Imerys Tableware Asia Limited, New Zealand while carbon black was purchased from Malayan Carbon (M) Ltd. Natural rubber named SMR L which was purchased from Rubber Research Institute Malaysia (RRIM) was used as matrix while the other ingredients such as N-cyclohexyl-2-benzothiazole sulfenamide (CBS), 2,2 methylene-bis-(4-methyl-6-tert-butylphenol) (BKF), sulfur, zinc oxide and stearic acid were supplied from Bayer (M) Sdn. Bh. and the amount used for these ingredients were 0.5, 1.0, 2.5, 5.0 and 3.0 parts per hundred rubber (phr).

Five compounds of HNTs/CB/NR nanocomposites with different ratio (parts per hundred rubber, phr) as listed in Table 1 were mixed by using laboratory two-roll mill model XK-160 with the size of 160 mm x 320 mm. Each compound has the same composition except the amount of HNTs and CB varied in different ratio but the total amount of hybrid filler in each compound was kept constant at 40 phr.

Table 1: The variation ratio (parts per hundred rubber, phr) of halloysite nanotubes and carbon black for HNTs/CB/NR nanocomposites.

Ingredients	Content (phr)				
	C1	**C2**	**C3**	**C4**	**C5**
HNT	0.0	10.0	20.0	30.0	40.0
CB	40.0	30.0	20.0	10.0	0.0

Measurements

Curing characteristics. Monsanto Moving Die Rheometer (MDR 2000) was used to investigate the curing characteristics for each HNTs/CB/NR nanocomposites at 150 °C. Cure time (t_{90}), scorch time (t_{s2}), and maximum torque (M_H) were obtained from this test. From these data, curing rate index (CRI) was calculated by using this formulation (1):

$$\text{Curing Rate Index (CRI)} = 100 / (t_{90}-t_{s2}) \quad (1)\ [7]$$

Fatigue properties. The sheet with 22.9 cm x 7.6 cm x 0.15 cm and beaded edges obtained from the compression moulded were cut into dumbbell shaped by using a BS type E dumbbell cutter and were cut at right angles to the grain. Monsanto Fatigue-to-Failure Tester (FTFT) was used for fatigue test where the samples were subjected to repeated cyclic strain at 100 cpm with extension ratio 2.01 ± 0.05. For each natural rubber nanocomposite, six samples were examined for the fatigue life while only the first four samples with the highest cyclic were chosen to be used in Japanese Industrial Standard (J.I.S) average. The calculated data was fatigue life in kilocycles (kc). The J.I.S average formulation was calculated by the equation (2):

$$\text{J.I.S average} = 0.5A + 0.3B + 0.1(C + D) \quad (2)\ [6]$$

Where A is the highest value of cyclic followed by B, C and D respectively.

The morphology of fatigue fracture surfaces of nanocomposites were observed under a Supra-35VP field emission scanning electron microscope (SEM). The fracture end surfaces were cut and mounted on aluminium stubs before coated with a thin layer of Pd-Au prior the test.

Results and discussion

Curing characteristics. Fig. 1 shows the effect of various ratio of HNTs/CB hybrid on scorch time (t_{s2}) and cure time (t_{90}) of NR nanocomposites. It can be clearly seen that the replacement of HNTs with CB caused decrement in t_{s2} and t_{90}. This is due the fact that each type of filler possesses different properties such as particle size, structure and aspect ratio which contribute to different effect towards curing characteristics [8]. HNTs contain silanol groups that able to absorb vulcanization ingredients especially accelerator that would retard the vulcanization as explained by Ismail et al. [9,10] while CB able to activate the vulcanizing process through the promotion of hydrogen sulfide formation and the rupture of S-N linkages when heated with sulfenamides in rubber either in the presence of other compounding ingredients.

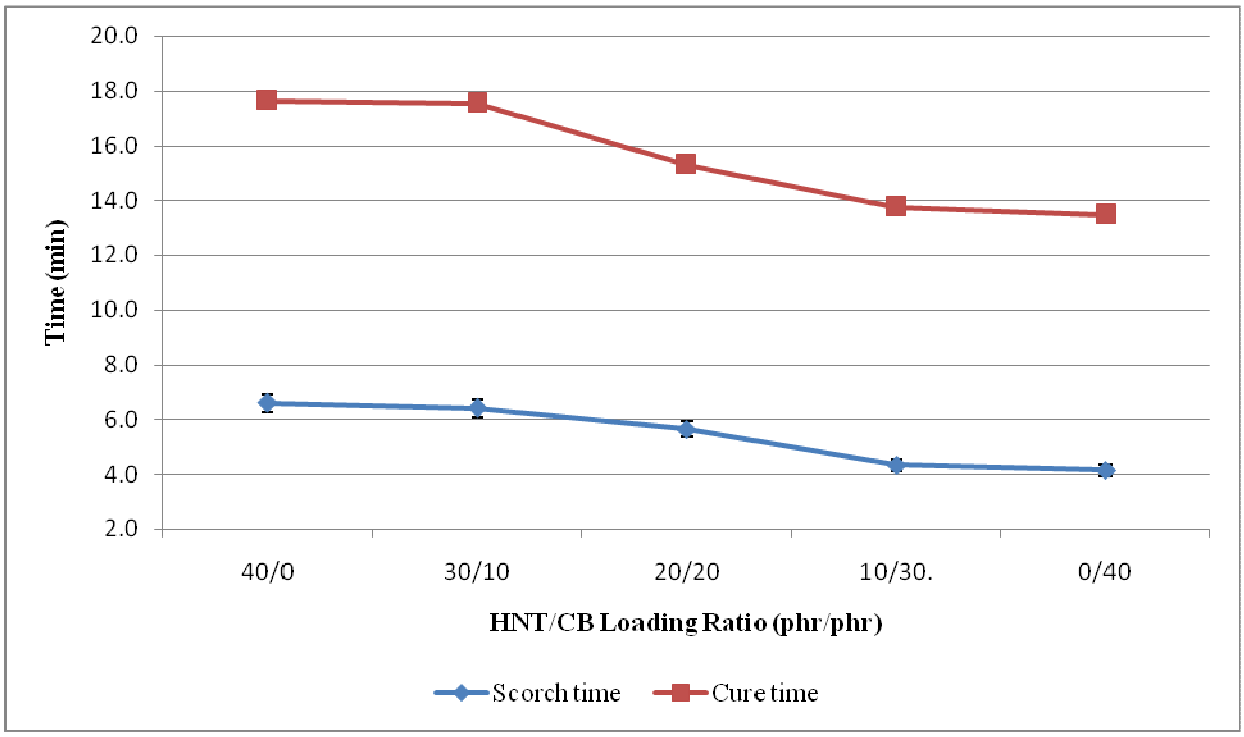


Fig. 1: Scorch time and cure time for HNTs/CB hybrid with varies filler loading ratio for NR nanocomposites.

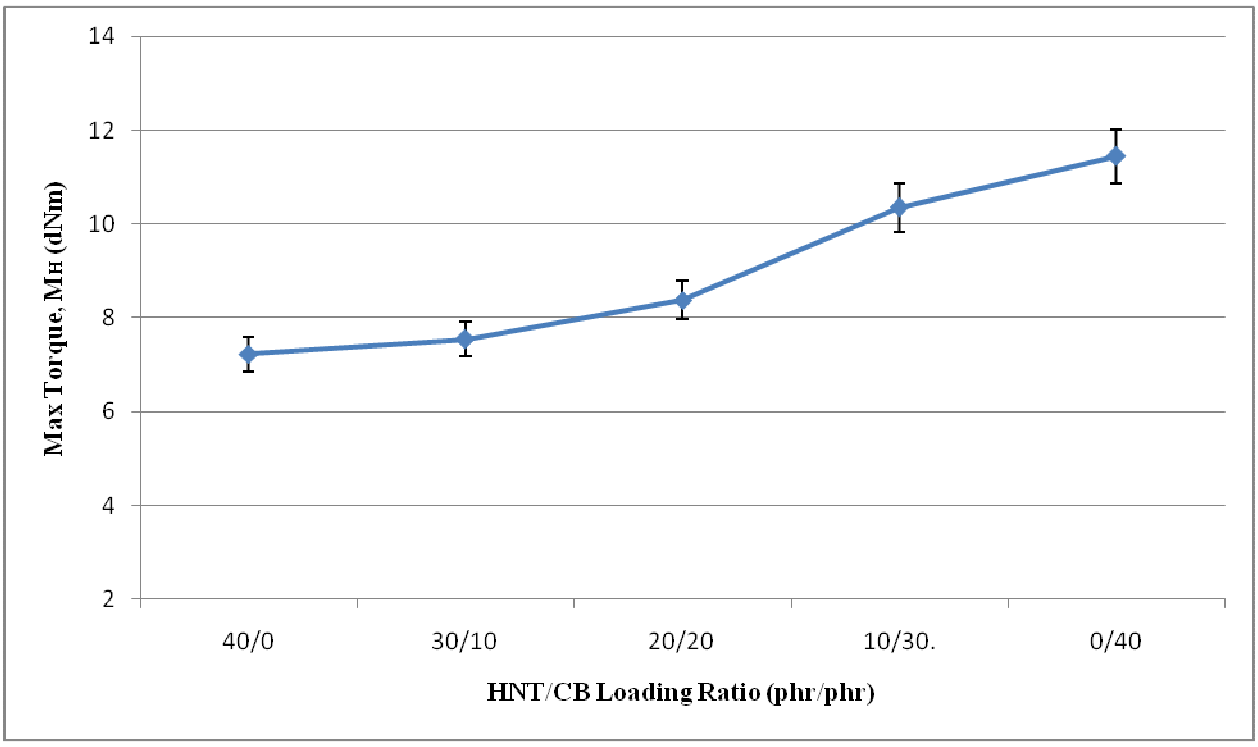


Fig. 2: Maximum torque for HNTs/CB hybrid with varies filler loading ratio for NR nanocomposites.

The addition of CB to replace the HNTs caused increment in maximum torque (M_H) as plotted in Fig. 2. Teh et al. [8] stated that the smaller size of filler should give larger surface area that can shows greater rubber-filler interaction which then tends to impose extra resistance to flow as a higher restriction to molecular motion of the macromolecules. However, the M_H obtained shows reversely even though the size of HNTs is smaller than CB but still unable to interact with NR as effectively as CB since HNTs is polar that unable to show better interaction as CB. Thus, resulted low M_H for NR filled with more HNTs than CB content.

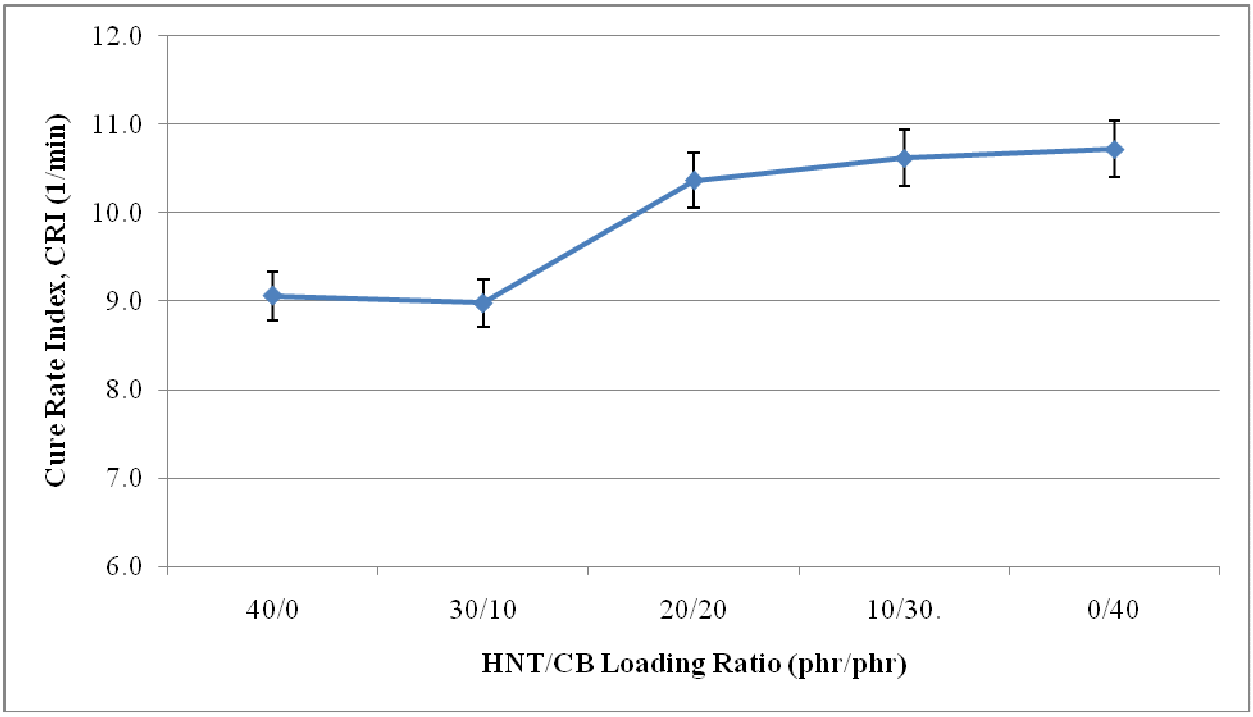


Fig. 3: Cure rate index for HNTs/CB hybrid with various filler loading ratio filled NR nanocomposites.

Fig. 3 shows the effect of various HNTs/CB hybrids loading towards the cure rate index (CRI) of NR nanocomposites where it can be observed that the reduction of HNTs caused higher CRI which indicates shorter optimum crosslink formation compared to the nanocomposites with more HNTs. This is have been explained before which is due to the properties of HNTs that able to absorb vulcanization ingredients thus delayed the vulcanization process.

Fatigue Properties. The effect of HNTs/CB loading on fatigue life of NR nanocomposites is plotted in Fig. 4. From this figure, it can be seen that the addition of more CB than HNTs caused reduction in fatigue life. This can be related to the behavior of HNTs that able to retain the elasticity of rubber matrix. Since CB able to form crosslink network effectively with natural rubber matrix that consequently increased the stiffness of nanocomposites which responsible to decrement of elasticity. El-Sabbagh et al. [11] also stated similar results. Sajjayanukul et al. [12] explained that the due to the dilution effect caused the amount of deformable rubber is diluted by the underfomable rigid particles of carbon black.

Both figures in Fig. 5 (a) and (b) show two distinct zones which represent the typical fatigue surface of natural rubber composites. The differences between those two figures are the area of zone 1 and 2. Zone 1 represent the initial stage of fatigue life where generally when zone 1 is larger than zone 2 indicates higher fatigue life. This is because more resistance towards cyclic deformation which verified from more tearing surfaces denoted as zone 1, ductile failure. While, when zone 2 is larger than zone 1 as shown in Fig. 5 (b) indicate brittle failure which occured rapidly due to less tearing surfaces that responsible to slow down the failure of fatigue life. Ismail et al. [13] stated that fast and unstable propagation is believed to occur leading to catastrophic failure.

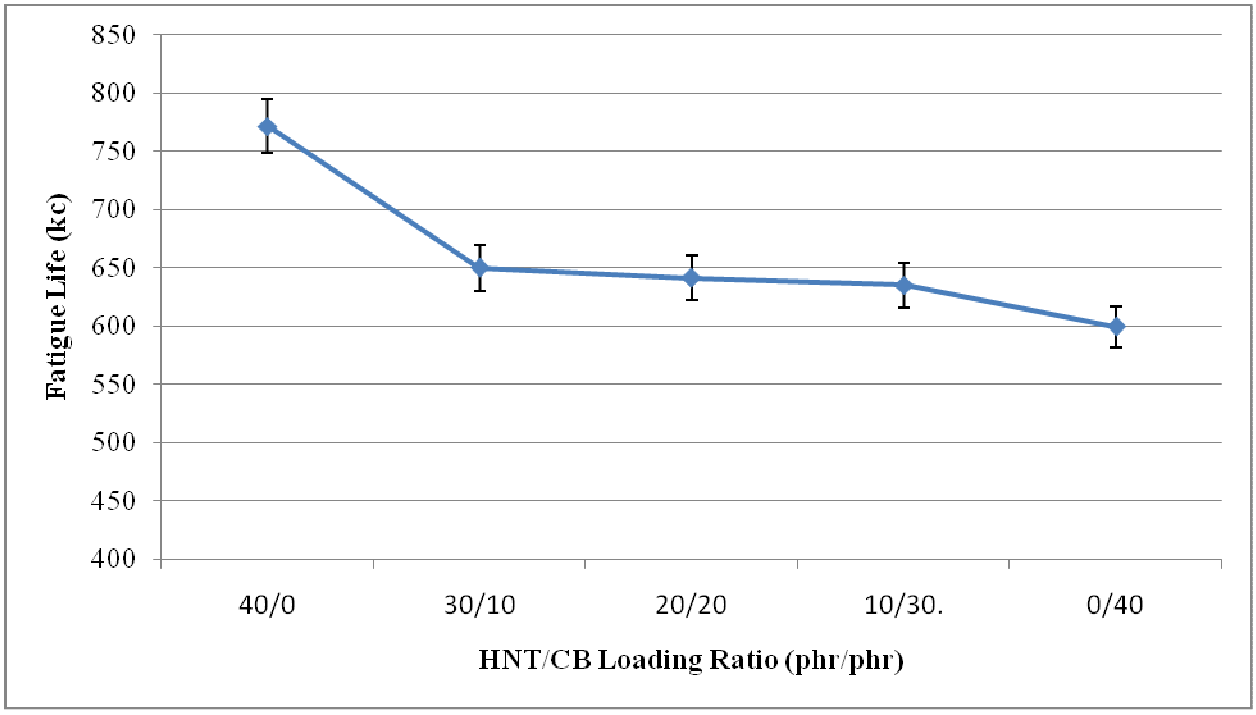


Fig. 4: Fatigue life of HNTs/CB hybrids filled NR nanocomposites with various filler ratio.

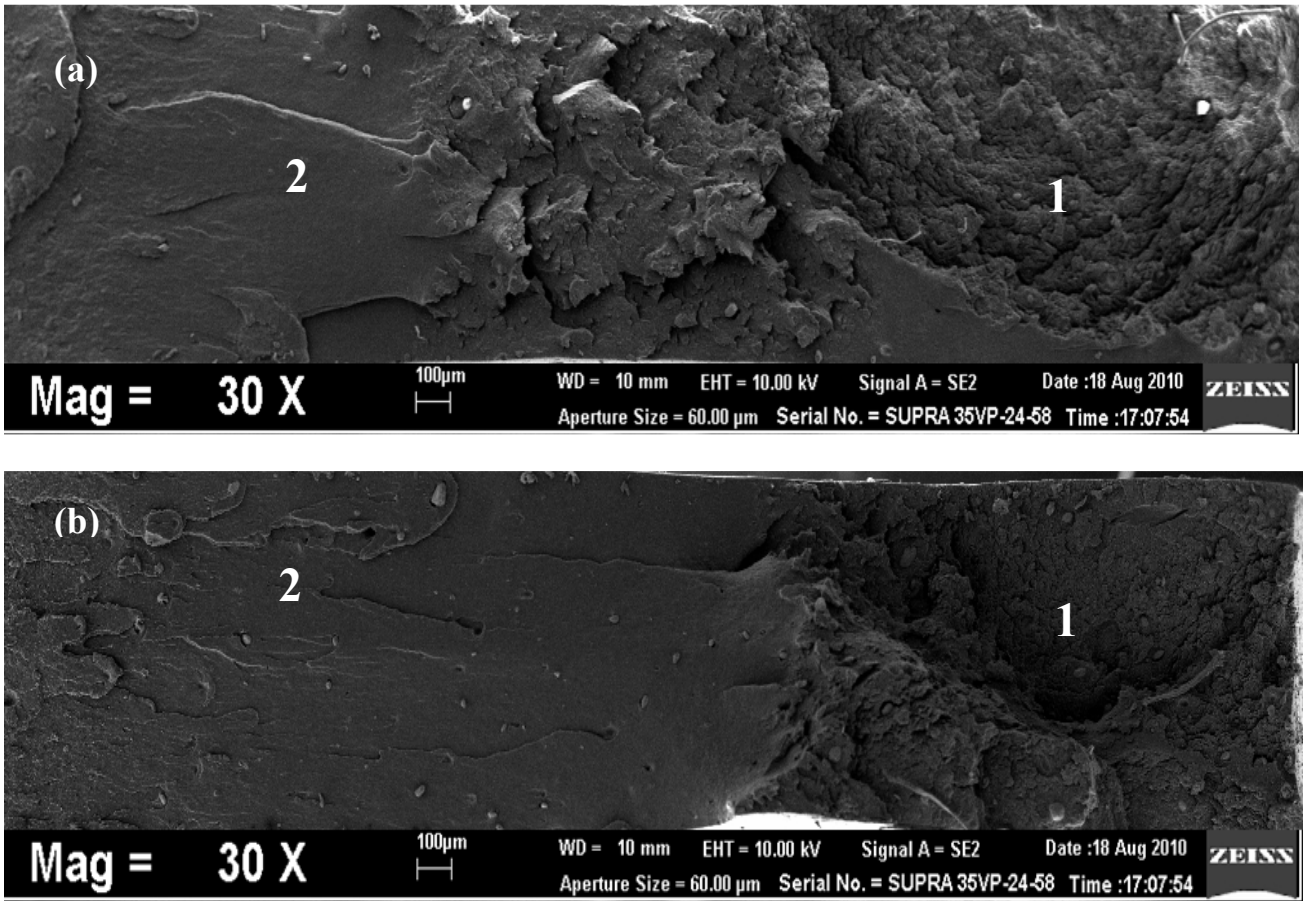


Fig. 5: Fatigue life surface for (a) C1 [40/0 phr/phr] and (b) C3 [20/20 phr/phr] of HNTs/CB/NR nanocomposites

Summary

The results revealed that vulcanizates containing HNTs in hybrid filler exhibit longer scorch time (t_{s2}) and cure time (t_{90}) for curing characteristics and higher in fatigue life compared to vulcanizates with 40 phr of CB. The images from scanning electron microscope (SEM) confirmed that replacement of CB with HNTs improved the fatigue life by showing more tearing surface on vulcanizates.

Acknowledgement

The author would like to thank the Universiti Sains Malaysia for the financial support under USM fellowship scheme for her MSc study.

References

[1] N. Rattanasom, T. Saowapark, and C. Deeprasertkul: Polym Test 26 (2007), p. 369.

[2] A.S. Hashim, B. Azahari, Y. Ikelda and S. Kohjiya: Rubber Chem Tech 71 (1998), p. 289.

[3] Y.C. Ko and G. Park: Korean J Chem Eng 24(6) (2007), p. 975.

[4] S. Deng and J. Zhang, J. Wu: Polym 49 (2008), p. 5119.

[5] M. Du, B. Guo, Y. Lei, M. Liu and D. Jia: Polym 49 (2008), p. 4871.

[6] H. Ismail, A.M. Norjulia and Z. Ahmad: Polym-Plast Tech Eng 49 (2010), p. 938.

[7] H. Ismail, P. Pasbakhsh, M.N. Ahmad Fauzi, A. Abu Bakar: Polym-Plast Tech Eng 48 (2009), p. 313.

[8] P.L. Teh, Z.A. Ishak, A.S. Hashim, J. Karger-Kocsis and U.S. Ishiaku: J App Polym Sci 94 (2004), p. 2438.

[9] H. Ismail and H. Anuar: Polym Test 19 (2000), p. 349.

[10] H. Ismail, B.T. Poh, K.S. Tan and M. Moorthy: Polym Int 52 (2003), p. 685.

[11] S.H. El-Sabbagh, M.N. Ismail and A.A. Yehia: J Elast Plast 33 (2001), p. 263.

[12] T. Sajjayanukul, P. Sae-Oui and C. Sirisinha: J App Polym Sci 97 (2005), p. 2197.

[13] H. Ismail, H. Anuar and Y. Tsukahara: Polym Int 48 (1999), p. 607.

© (2011) Trans Tech Publications, Switzerland
doi:10.4028/www.scientific.net/KEM.471-472.963

Effects of Processing Temperature and Chemical Treatment on Tensile Strength of Kenaf Fiber - Reinforced Polypropylene Waste Composites

Hermawan Judawisastra[1,a], Fella Falencia[1,a], Akbar H.D. Abdullah[2,b]

[1]Material Engineering Department, Faculty of Mechanical and Aerospace Engineering,

Bandung Institute of Technology (ITB), Ganesa 10 Bandung 40132, Indonesia

[2] Research Center for Physics, LIPI, Bandung 40135, Indonesia

[a]hermawan.judawisastra@material.itb.ac.id,[b]Akba001@fisika.lipi.go.id

Keywords: kenaf fiber, polypropylene, natural fiber, thermoplastic composites, chemical treatment.

Abstract. In this research, the influence of processing temperatures and fiber chemical treatments to mechanical properties of polypropylene (PP) waste – kenaf fiber composites was investigated. Results from experimental and theoretical calculation of composite tensile strength were compared. The composites were made of PP wastes and unidirectional kenaf fiber, and manufactured by hot press molding. The processing temperature variations were 175 ^{o}C, 185°C and 195 ^{o}C. The chemical treatment used were alkaline and permanganate treatment. Kenaf fiber – PP composites were successfully made with the void volume fraction less than 5%, maximum fiber volume fraction 48% and maximum longitudinal tensile strength 110 MPa or 238% higher than PP's strength. For non- and alkali treated fiber composites, 185°C was the optimum processing temperature. Elevated processing temperature up to 195°C could decrease composite strength due to the degradation of fiber-matrix interface. The effect of permanganate treatment did not significantly affect the composites strength. However, the improvement of interfacial properties at elevated temperature was found by the use of permanganate treatment.

Introduction

Kenaf fiber is one of prospective natural fiber for composite reinforcement [1]. The use of thermoplastic matrices, compared to thermosetting matrices, will have a shorter cycle time as well as re-processability. Polypropylene (PP) thermoplastic wastes are a lot found in sheet forms that make them easy to be produced as thermoplastic composite. The use of sheet form will ease the impregnation process of highly viscous PP matrix into the fiber bundles [2,3]. Moreover, this should also minimize the quality decreased of the recycled PP product as the recycling process will be shortened by using direct plastic sheet wastes [4]. Fiber-reinforced polymer composites made from combination of renewable natural fibers and recyclable thermoplastic polymers will provide an attractive eco-friendly quality to the resulting natural fiber reinforced polymer composites [4,5]. However, in order to achieve required mechanical properties of the composites, some points shall be highly considered: the high viscosity of liquid thermoplastics, low degradation temperature of natural fiber and matrix, and poor fiber-matrix interfacial strength [1, 3-6]. Processing temperature optimization is required for successful matrix impregnation and minimum degradation of fiber and matrix. Interfacial strength can be improved by treating the fiber with chemicals [7]. In this research, the influence of processing temperatures and fiber chemical treatments to the tensile strength of PP waste – kenaf fiber composites was investigated.

Research Methodology

Stitched unidirectional kenaf fiber preform, 1 mm thick, was used as reinforcement. Polypropylene (PP) waste was taken from plastic-file waste. The plastic waste used had the thickness 0.21 mm and areal density 0.02 gr/cm^2. Both fiber preform and plastic-file waste were cut into 14 cm x 14 cm dimensions. The fiber and matrix were characterized by means of Fourier

Transform Infrared (FTIR) spectroscopy, differential scanning calorimetry (DSC) and tensile testing. FTIR spectroscopy was performed to evaluate the PP sheet. Tensile testing was performed to obtain tensile strength of PP waste, kenaf fiber and yarn. Tensile strength of PP waste was determined by means of Instron 1195 tensile machine, according to ASTM D-638 from compression molded specimen type 1. Tensile test on kenaf fiber and yarn was carried out by means of Textechno Fafegraph and Testometric tensile machines respectively. The speed of the test was 7.5 mm and the specimen gage length was 50 mm. Twenty specimens each for fiber and yarn were used in this test. Characteristic strength of fiber and yarn were determined from Weibull data distribution.

The chemical treatment used for kenaf fiber were alkaline and permanganate treatment. For alkaline treatment, the fiber was immersed in 5% Sodium hydroxide solution (NaOH) for 4 hours [2]. For permanganate treatment, the fiber was immersed in 0.2% potassium permanganate solution ($KMnO_4$) for 2 hours [7]. After the chemical treatment, the fiber was dried at 105°C for 5 hours. PP waste – kenaf composite was manufactured by hot press molding technique. Prior to composite production, the fibers (untreated and treated) were dried in at 105°C for 30 minutes to ensure that there was no water vapor in the fiber. Three layers kenaf fiber preforms were sandwiched in between PP sheets to achieve 50% weight fractions of fiber and PP. The processing pressure was kept constant at 75 bar at the hydraulic or 3.9 bar on the composite sample. The processing temperature was varied at 175 ^{o}C, 185°C and 195 ^{o}C. The density of kenaf fibers, PP and the composites were measured according to ASTM D-792. The results were used to determine the volume fraction of material constituents and fraction of void in the composite according to ASTM D-2734 and modified ASTM D-3171 standards. Longitudinal tensile strength of the composites was tested using Instron 1195 according to ASTM D-3039 with gage length 100 mm and testing speed 2 mm/min. Three specimens were used in this test for each variable (Table 1).

Table 1. Sample code

Sample Code	Variation	
	Chemical Treatment	Processing Temperature (^{o}C)
NT175	Non-Treated (NT)	175
NT185		185
NT195		195
AT175	Alkaline Treated (AT)	175
AT185		185
AT195		195
PT185	Permanganate Treated (PT)	185
PT195		195

The longitudinal strength of composites was also analyzed by means of rule of mixture model and Rossen's statistically modified models as follows [8]:

$$\sigma_c = \sigma_f \, . \, V_f + \sigma_m \, . (1 - V_f) \quad (1)$$

$$\sigma_c = \sigma_f \, . \, V_f \, [(1 - V_f)^{½} / V_f^{½}]^{-1/2\beta} \quad (2)$$

where:

σ_c = Longitudinal composite strength (MPa)
σ_f = Longitudinal fiber strength (MPa)
σ_m = Matrix strength (MPa)
V_f = Fiber volume fraction
β = Fiber Weibull modulus

Result and Discussion

Characteristic of Constituent Materials. FTIR test result for PP waste is shown in Fig.1. It can be seen that there are significant peaks in the wavenumber of 2850/cm-3000/cm cm and 1350/cm-1480/cm which are the peaks of the C-H bonding. This result shows that the main composition of the plastic sheet is PP. Other significant peaks in the wavenumber of 750/cm-1300/cm shows the aromatic compound of additives that were added into the PP sheet.

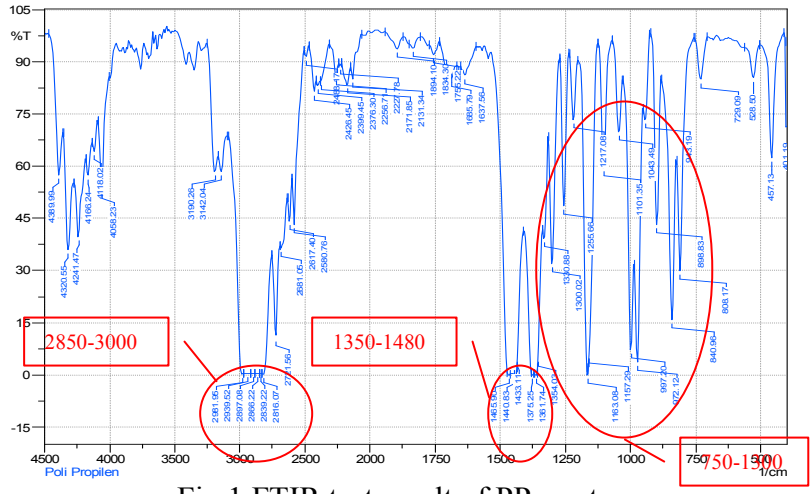


Fig.1 FTIR test result of PP waste

DSC test result for PP waste and kenaf fiber is shown in Fig. 2 and Fig. 3. From Fig.2, it can be shown that the melting point of PP waste is about 175°C. Fig.3 shows that the kenaf fiber remains stable until the temperature of 250°C.

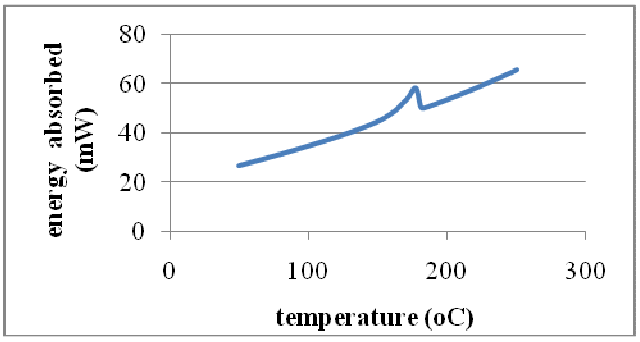


Fig.2 DSC test result of PP waste

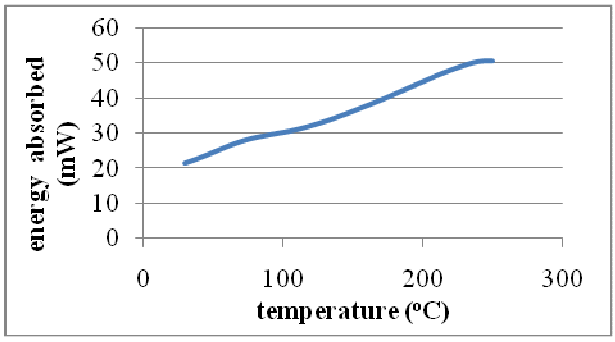


Fig.3 DSC test result of kenaf fiber

Table 2 shows the tensile strength data of the kenaf fiber and PP waste. The higher strength of the kenaf fiber compared to the PP waste shows the potential reinforcement of kenaf fiber for PP composite production. The fiber and yarn strengths were increased by alkaline treatment but the permanganate treatment decreased the tensile strength data. The increased of tensile strength by alkaline treatment was due to lignin and hemicellulose content reduction in the kenaf fiber. Consequently, the cellulose volume fraction in the kenaf fiber will be increased and resulted in higher tensile strength [2,7]. The reduction of tensile strength due to permanganate treatment is possible due to degradation of cellulose chain by excess of permanganate treatment [7].

Physical Properties of Composites. Visually, the appearance of manufactured composites was good; the surface was relatively flat and smooth without andy visible void in the surface. The composites had thickness within the range of 1.8-2.0 mm and the density was in a range of 1,0019 – 1,0416 gr/cm^3.Void volume (Vv) fractions of the composites were shown in Fig.4. The maximum void volume fraction for load bearing composites is 5 % [4]. Most of the composites shows void volume fraction less than 5% except for composites non-treated 175°C and alkaline treated 195°C. For non-treated and alkaline treated composites, the minimum void fraction was reached at 185°C processing temperature. The higher void volume fraction at 175°C processing temperature might be due to high viscosity of liquid matrix which resulted in limited impregnation of matrix into the fibers. The higher void volume fraction at 195°C processing temperature might be related to the effect of the thermal degradation on the hydrophilic fibers [6]. A high void content results in a poor fiber-matrix interface which later can decrease the load bearing capacity of the composites [4].

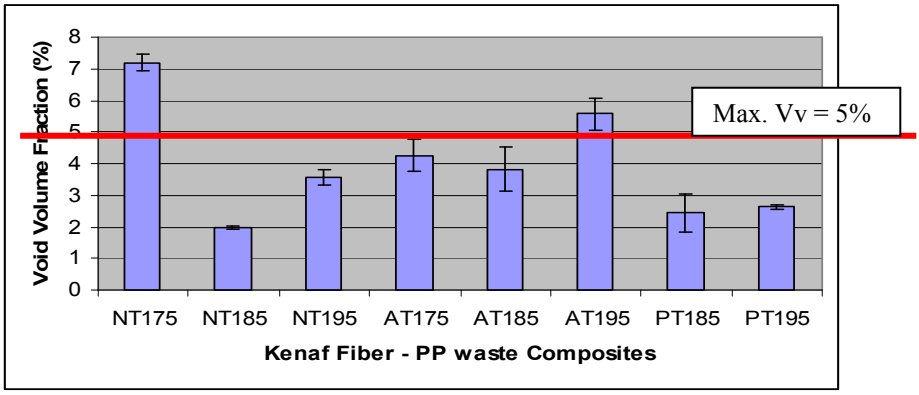


Fig.4 Void volume fraction of the composites

For permanganate treated composite, the void fraction was quite stable when the processing temperature was raised. This is due to the higher temperature stability of the hydrophobic fibers (after permanganate treatment). Thermal degradation rate of natural fiber could be accelerated by raising temperature and the presence of water [6]. This kind of natural fibers degradation may produces gases as degradation product which later, could be trapped and resulting in voids inside the composite. Hydrophobic fiber binds less water molecules than hydrophilic one. Permanganate treatment resulted in hydrophobic fiber [7] that lowering the effect of thermal degradation rate of the processing temperature because of the absence of water molecule. This made the void in permanganate treated composite was quite stable at 195°C processing temperature. Fig.5 shows fiber volume fraction of the composites which is ranging from 37% up to 48%. The effect of alkaline treatment seems to increase fiber volume fraction, especially at 185°C and 195°C processing temperatures. This was possible since the alkaline treatment might reduce the fiber diameter and resulted in more compact fibers inside the composites [2].

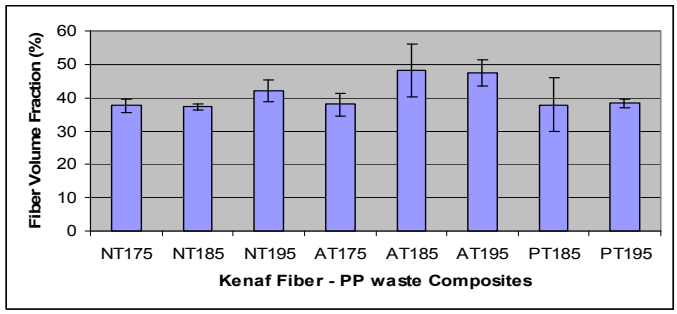


Fig.5 Fiber volume fraction data of composites

Longitudinal Tensile Strength of Composites. Table 3 shows the tensile strength data of composites. The maximum longitudinal tensile strength is 110 MPa or 238% higher than PP's strength (29.8 MPa). The highest composite strength was achieved at the highest fiber volume fraction (48%) produced by alkaline treated at 185°C processing temperature. The composite strength is proportional with the fiber volume fraction. In order to evaluate the effect of chemical treatment and processing temperature, the composite strength shall have the same fiber volume fraction. Hence, the tensile test data were normalized to 37% fiber volume fraction. The actual data and normalized strength of the composites were tabulated in Table 2. Normalized composites strength data are also depicted in Fig.6.

Table 2. Actual data and normalized longitudinal tensile strength of composites

Sample Code	Void Volume Fraction	Actual Data		Normalized Data	
		Fiber Volume Fraction	Tensile Strength (MPa)	Fiber Volume Fraction	Tensile Strength (MPa)
NT175	7.20%	37.6%	39.0 ± 3.4	37%	38.4 ± 3.3
NT185	1.98%	37.2%	77.6 ± 9.4	37%	77.6 ± 9.3
NT195	3.58%	42.0%	34.5 ± 2.6	37%	31.1 ± 2.3
AT175	4.25%	38.0%	37.4 ± 3.6	37%	36.4 ± 3.5
AT185	3.82%	48.0%	109.5 ± 12.2	37%	84.4 ± 9.4
AT195	5.58%	47.4%	77.3 ± 9.2	37%	60.9 ± 7.2
PT185	2.44%	37.8%	74.3 ± 5,1	37%	74.3 ± 5.0
PT195	2.63%	38.3%	76.5 ± 2.9	37%	76.5 ± 2.8

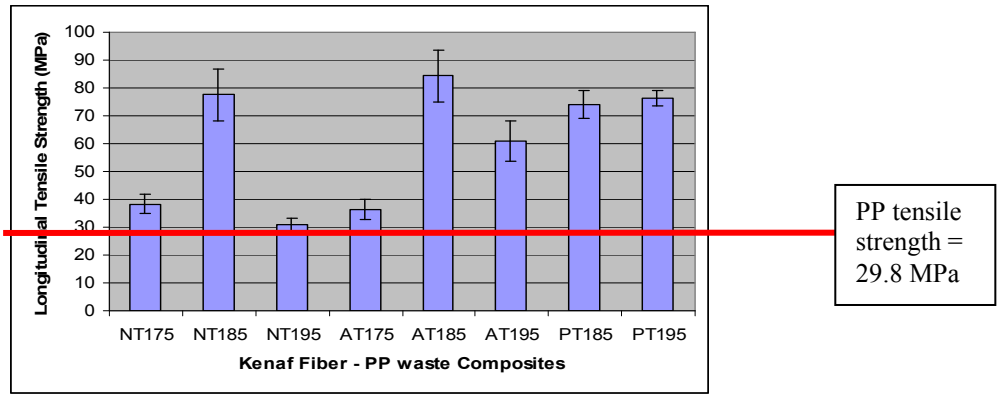


Fig.6 Normalized (V_f = 37%) longitudinal strength of composites

From Fig. 6, it can be seen that the maximum tensile strength of non-treated and alkaline treated was achieved at 185°C processing temperature. The composite strength increased significantly when the processing temperature was raised from 175°C to 185°C. This was due to the lower viscosity of PP at higher temperature 185°C which resulted in better impregnation. When the processing temperature was raised from 185°C to 195°C, the composite tensile strength was decreased by 30-60%. At 195°C, the thermal degradation might occur on the fiber and produced void in the interface which harmed the interface strength and later weakened the composites [4,6]. For permanganate treated fiber, the composite tensile strength did not change significantly when the temperature was raised from 185°C to 195°C.

Summary

PP waste - kenaf fiber composites were successfully made with the void volume fraction less than 5%, maximum fiber volume fraction 48% and maximum longitudinal tensile strength 110 MPa or 238% higher than PP's strength. For non- and alkali treated fiber composites, 185°C was the optimum processing temperature. Elevated processing temperature up to 195°C could the decrease composite strength by 30-60% due to the fiber thermal degradation which resulted in poor fiber-matrix interface. The effect of permanganate treatment did not significantly affect the composites strength. However, the improvement of interfacial properties at elevated temperature 195°C was found by the use of permanganate treatment.

References

[1] B.H. Lee, H.J. Kim and W.R. Yu: Fibers and Polymers Vol.10 (1) (2009) pp. 83-90.

[2] D. Annur, H. Judawisastra and A. H. D. Abdullah: Arena Tekstil, Vol.24 (2) (2009) (in Indonesian language).

[3] X. Liu and G. Dai: Frontiers of Chemical Engineering in China, Vol. 2 (2) (2009) pp. 145-149.

[4] B. T. Åström: Manufacturing of Polymer Composite, London : Chapman and Hall (1997) pp.263-264, 295.

[5] X. Li, S. Panigrahi and L. G. Tabil: Applied Engineering in Agriculture Vol. 25 (4) (2009) pp. 525-531.

[6] Van, S. L. Le. :1st edition, New York : Pergamon Press, (1989) pp. 271-273.

[7] X. Li, L. G. Tabil and S. Panigrahi: Journal of Polymers and the Environment Vol. 15 (1) (2007) pp. 25–33.

[8] T. W. Chou, *Microstructural design of fiber composite*, Cambridge University Press, (1992).

© (2011) Trans Tech Publications, Switzerland
doi:10.4028/www.scientific.net/KEM.471-472.969

Damage Evolution in Structural Steel at Different Loading Conditions

Reem Majeed Al-Himairee[1,a], Farid Hamid Abed[1,b], and Adil K. Al-Tamimi[1,c]

[1]Department of Civil Engineering, American University of Sharjah,

Sharjah, United Arab Emirates

[a]g00018081@aus.edu, [b]fabed@aus.edu, [c]atamimi@aus.edu

Keywords: continuum damage mechanics; ductile damage; mechanical characterization; steel; finite element analysis; strain rate

Abstract. This paper presents an experimental and numerical characterization of ductile damage evolution in steel subjected to large plastic deformations. The main objective of this research is to better understand damage initiation and evolution in structural steel throughout the deformation process at different strain rates. The proposed study relies on a continuum damage mechanics approach that involves characteristic parameters to describe the accumulation of plastic strain, the damage variable, and the strain rates. The work was divided into experimental, and simulation phases. The experimental phase involved testing under monotonic uniaxial tensile loading under varying strain rates. The obtained material parameters are then used as the basic data in the simulations that are performed afterwards. Finally, this model was implemented as a new user defined material in the finite element analysis software ABAQUS where damage was quantified. Initial results of this research showed that a simple model with substantial cost and time saving can be developed for damage assessment in steel. The rate of loading is a main sensitive parameter that affects both damage initiation and propagation, as they increased significantly with increasing loading rate. Beyond the ultimate load, the strain energy was sufficient to cause the damage to increase without any further applied load.

Introduction

Real life structural materials are exposed to different types of loadings leading to material deterioration and change in their structural/mechanical properties. This progressive physical process of degradation in the mechanical properties with complete loss of stress carrying capacity is commonly referred to as damage. Damage diminishes material strength, hardness, modulus of elasticity, density, and the yield stress. In the last two decades, the micro-structural concepts to define material failure have received wide attention as a better alternative to classical mechanics methodologies. This was based on the knowledge that the processes responsible for macroscopic failure are deeply rooted in the material microstructure. Since the early work of Kachanov in 1958, the Continuum Damage Mechanics (CDM) framework for ductile damage was later developed mainly by Lemaitre and Chaboche. [1] shows that the phenomenon of damage is characterized by the initiation, coalescence and growth of micro-defects such as micro-voids and micro-cracks at any stress concentrators, resulting in complete failure of the material as shown in Fig. 1. These micro-defects or discontinuities in solid materials were identified by [2] as micro-cracks or voids in metals, interface decohesions between cement, sand, and aggregates in concrete, and bonds breakage in polymers and composites. A damage parameter φ is introduced, which represents the damage evolution. When $\varphi=0$, the material is undamaged. On the other hand, when $\varphi=1$ the effective area is zero and material is totally damaged with a complete loss of material's structural integrity (i.e., fracture), Fig. 1. The theoretical value of φ is between $0\leq\varphi\leq1$, while in reality its critical value is usually set to be between $0.2\leq \varphi_{cr}\leq0.8$ for metals[3].

Following the same scheme, several damage models using special expressions for the damage dissipation potential have been proposed by different authors [4- 7]. However, in most cases these models were able to describe only damage evolution for particular metals; furthermore, some of the model parameters do not have a clear physical meaning and identification procedure.

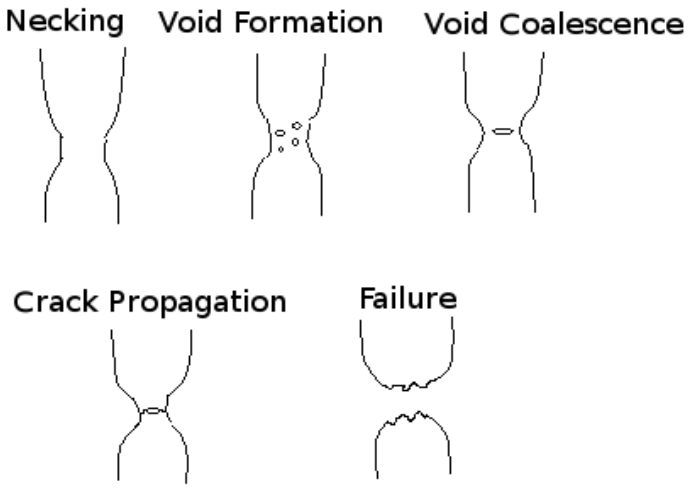


Fig. 1 Damage in terms of crack evolution, Ref [8]

Damage is anisotropic in nature as proposed by [9, 10] and others which makes identification of its parameters very difficult [11]. However, assuming isotropic damage in many cases is not too far from reality, at least in the deformation range up to the maximum engineering stress. A scalar damage variable is widely employed in the literature due to its simplicity and efficiency.

In general, damaging processes are reflected in a progressive material deterioration that can be measured through the decrease of strength, stiffness, toughness, etc. There are many ways to measure degradation in materials. [2] explained eight different experimental methods (direct and indirect) to measure damage based on the effective stress concept. The direct measurements include the observation of micrographic pictures using digital microscopes to measure the areas of cracks and the density variation measurement. The non direct destructive measurements are measurement of change in the elastic modulus, ultrasonic waves propagation and the non direct non destructive methods are the hardness variation measurement and the electric potential. However, reliable measurements of damage are still nowadays a challenging task that requires cost, time, and technology. It would be therefore of interest to have a simpler method for characterizing damage in these systems.

An experimental and numerical characterization of ductile isotropic damage evolution in steel subjected to large plastic deformations is proposed in this work. To this end, a set of tensile tests were firstly carried out on round steel specimens in order to obtain their stress-strain curves which allow, in turn, to derive their elastic, strain hardening and damage characteristic parameters. In particular, a new damage identification procedure based on the energy principles is described.
The corresponding numerical results are validated with the numerical results of the decreasing elastic modulus measurements. The reported research aims to address a key question associated with ductile design, namely: Can a simple to model parameter be developed in the future as a tool for finite element modeling (FEM), which will be able to predict when failure of an element has been reached and supplement or even replace the need to base element failure on full scale testing? The proposed technique in the next sections offers a practical solution to this question.

Energy-Based Damage Model

The adopted energy model considers the area under stress-strain curve as a measure of the materials capacity to accumulate damage. Once this capacity has been used up, the damage reaches 100% and failure will occur. The damage variable will be:

$$\varphi_p = \varphi_F \left(\frac{U_p}{U_T}\right)^n. \quad (1)$$

where φ_f is the critical damage at failure, φ_p is the damage at any point during the deformation process and U_p is the corresponding energy at this point, $U_T$is the total energy and n gives the exponent of damage in relation to displacement. The energy can be determined using the following expression, where σ and ε are true stresses and strains:

$$U = \int_0^{\varepsilon_p} \sigma \, d\varepsilon. \tag{2}$$

Finite Element Simulation

Crack propagation in the structure is often simulated with finite element (FE) analysis based on continuum mechanics. There are four common methods to simulate crack propagation in a finite element model. These are element splitting, nodes separation, decreasing elements stiffness and deleting damaged elements. In this research, the third technique has been used in order to simulate crack propagation and evaluate the damage variable. The predicted responses have been calculated by employing the ABAQUS finite element code. For each strain rate, the damage parameter for all the elements in the model was calculated once on the basis of energy principles.

During simulation, the numerical prediction depends on the correct description of the material behavior. Mechanical properties were obtained from the uniaxial tensile tests of steel, as shown in Fig. 2, and the hardening behavior was mimicked using Johnson cook model (See Eq. 3).

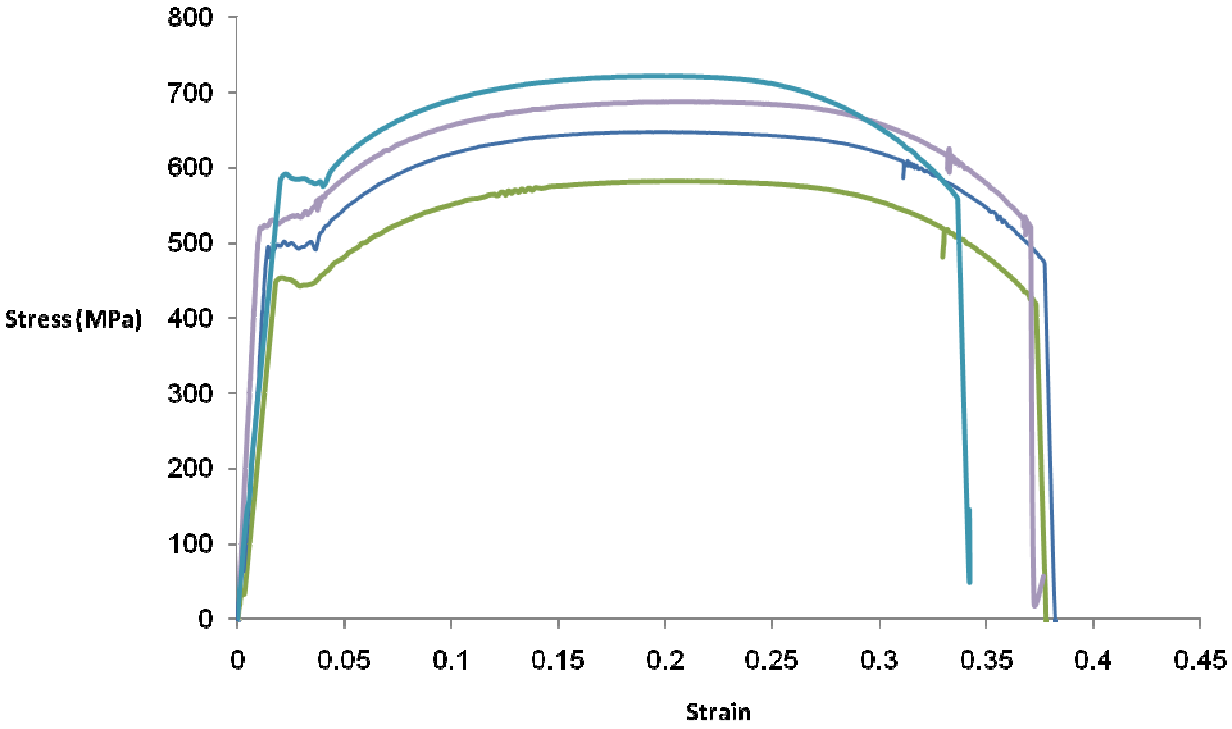


Fig. 2 Stress-strain curves from uniaxial tensile test for steel round specimens at different strain rates: 0.000333 s^{-1} (lowest curve) – 0.00333 s^{-1} - 0.01 s^{-1} – 0.1 s^{-1} (highest curve)

The initiation of a crack in the structure is assumed to occur at any point when the damage parameter reaches its critical value, φ_c, a value at which ductile failure will occur. In our numerical analysis this value at any Gauss point was chosen as 1. At this stage the damaged elements are removed and the crack will advance.

$$\bar{\sigma} = [A + B(\bar{\varepsilon}^{pl})^n]\left[1 + C\ln\left(\frac{\dot{\bar{\varepsilon}}^{pl}}{\dot{\varepsilon}_0}\right)\right]. \quad (3)$$

Where:
$\bar{\sigma}$ is the yield stress at nonzero strain rate;

A, B, C and n are material parameters measured at or below the transition temperature
$\bar{\varepsilon}^{pl}$ is the equivalent plastic strain
$\dot{\bar{\varepsilon}}^{pl}$ and $\dot{\varepsilon}_o$ is the equivalent plastic strain rate

Symmetry conditions are imposed in order to model only one quarter of the geometry. This requires that all nodes along the x=0 axis have their x-displacements constrained to zero; all nodes along the y=0 axis have zero y-displacement. The solution is obtained using axisymmetric elements with the option for geometric and material nonlinearity. A quarter numerical model consists of 1453 elements and 1602 nodes.

The finite element mesh is shown in Fig.3. Assuming axisymmetry for the cylindrical specimen, a quarter of the problem is discretized with a height of 12.5mm (half of the initial gage length) and a linear radius variation along the bar according to the geometry specifications. The mesh is built up in order to have an element dimension of about 0.3 mm in the region where failure is expected to occur, which is in the range of typical dimension of a RVE in metals [12]. More elements are placed near the center of the specimen at x=0 and fewer at the end of the bar at x=100.

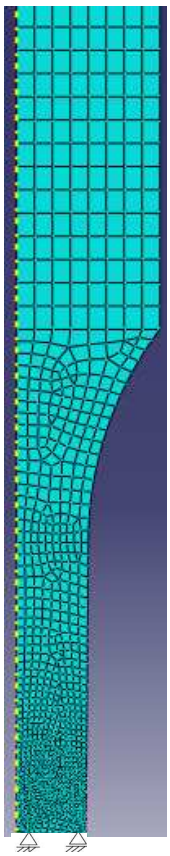


Fig. 3 One quarter of cylindrical steel specimen

Results and Discussion

The finite element implementation of the proposed constitutive law is carried out, resulting in the set of nodal displacements and nodal damage variables resulting from the adopted particular technique. Additionally the model can detect the initiation time for damage.

In order to test the implementation, the flow curve was determined first. The evaluation of the stresses and strains was done at the Gaussian points along the x=0 axis. The experimental values are represented accurately by these calculations. It can be seen in Fig. 4 that the equivalent plastic strain is uniform along the smallest cross-section and the shear stresses at the neck are equal to zero. Results are compared and discussed in terms of the effect of loading rate on the damage level

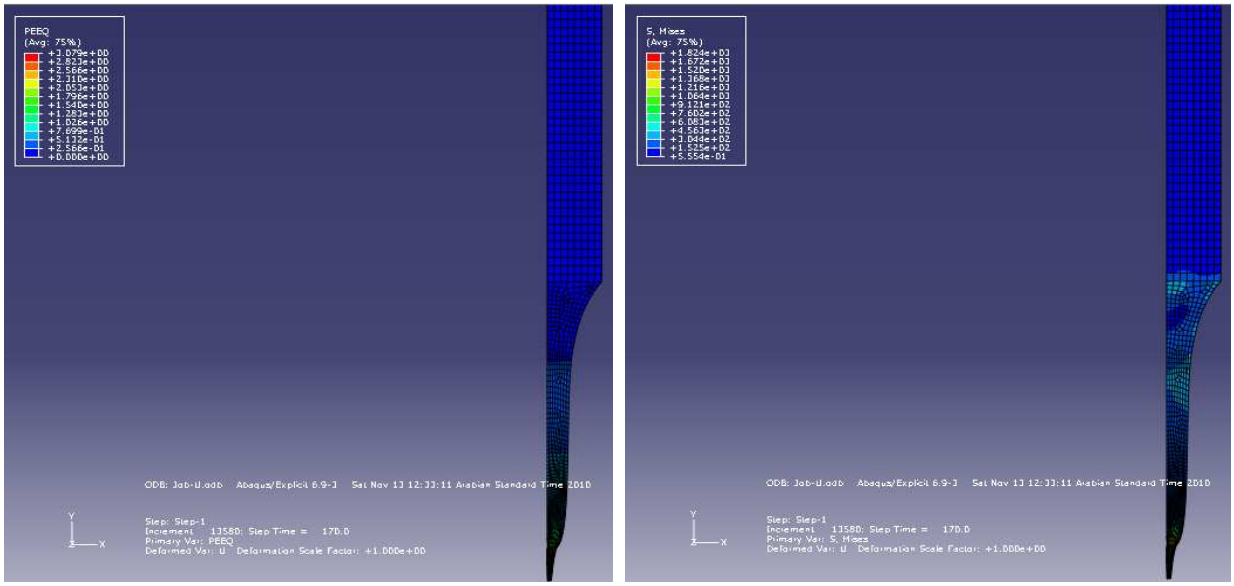


Fig. 4 Views of the neck section with contours showing equivalent plastic strain and mises stresses

Effect of Strain Rate on Damage Briefly, the deformation of materials under load depends on factors, such as atomic structure, rate of loading, and temperature. To understand the deformation characteristics of each individual material completely, an extensive knowledge of its atomic and molecular structure is required. However, in practice, the general constitutive stress-strain relation is obtained without considering the complexity of the atomic structure.

For all tests, an increase in strength was observed with increasing strain rates. Based on the results of tensile tests with various loading rates and finite element simulations, the effect of loading rate on damage is significant (Refer to Fig. 5).

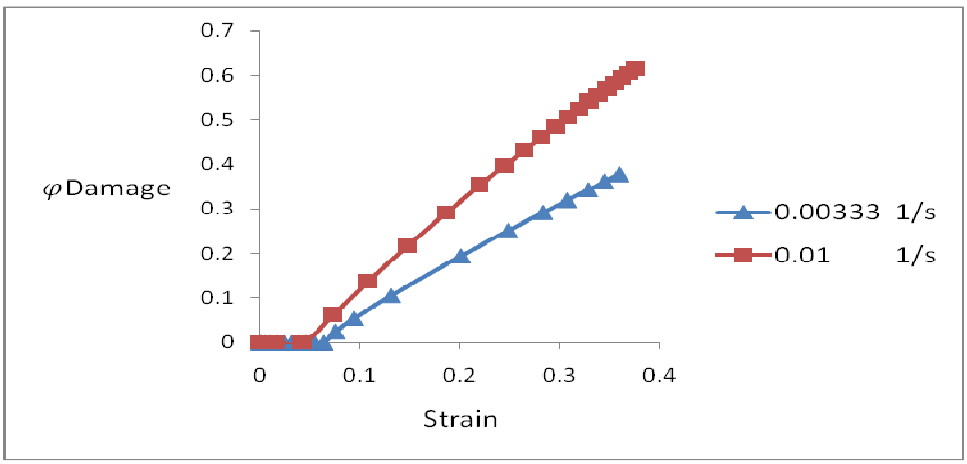


Fig. 5 Damage vs. Strain for different strain rates

Summary

In this paper, a procedure for the evaluation of parameters of the continuum damage mechanics model has been developed and applied to the case of steel. Both the numerical procedure and identification of material parameters were verified on the basis of uniaxial tension test. The fully coupled constitutive elastic–plastic-damage model has been implemented in ABAQUS to simulate the ductile damage behavior of steel bar. The comparisons indicate good agreement between the simulated and experimental results. This paper develops a simple and powerful damage parameter to predict failure. An effort was made to keep the models as simple as possible but still correctly represent the behavior of the structure in order to gain some acceptance among practitioners.

Future work might include further use of experimental techniques, e.g. variation of electrical resistance or ultrasonic test method, for the determination of the damage. The model needs to be verified for different types of loading conditions, specimen geometries, and different metals

References

[1] J.L. Chaboche: Technische Mechanik. Vol.23 (2003), p.113.

[2] J. Lemaitre and J. Dufailly: Engineering Fracture Mechanics. Vol.28 (1987), p. 643.

[3] J. Lemaitre: Nuclear engineering and design. Vol. 80 (1984), p. 233.

[4] H. W. Tai: Engineering Fracture Mechanics. Vol.36 (1990), p. 853.

[5] S.Chandrakanth and P. C. Pandey: International Journal of Fracture. Vol.60 (1993), p.73.

[6] N. Bonora, D. Gentile and A. Pirondi: J. Strain Anal. Eng. Des. Vol.39 (2004), p.639.

[7] M. Zheng, C. Hu, Z.J. Luo and X. Zheng: Engineering Fracture Mechanics. Vol. 53 (1996), p. 653.

[8] Figure on http://upload.wikimedia.org/

[9] J.L. Chaboche: Nuclear Engineering and Design. Vol.79 (1984), p309.

[10] S. Murakami: *CISM Courses and Lectures No. 295,* edited by D. Krajcinovic and J. Lemaitre, Springer (1987).

[11] R.K. Abu Al-Rub and G.Z. Voyiadjis: International Journal of Solids and Structures, Vol.40 (2003), p. 2611.

[12] J. Lemaitre: *A Course on Damage Mechanics* (Springer, Berlin 1996).

© (2011) Trans Tech Publications, Switzerland
doi:10.4028/www.scientific.net/KEM.471-472.975

Modeling of Stiffness Reduction of Vibration Conveyor Springs Subjected to Ultra High Cyclic Loading under High Humidity

Takahiko Yoshi[1,a], Kazuya Okubo[1,b], and Toru Fujii[1,c]

[1] Tatara-miyakodani, Kyotanabe, Kyoto, Japan,

[a]dtj0381@mail4.doshisha.ac.jp, [b]kokubo@mail.doshisha.ac.jp,[c]tfujii@mail.doshisha.ac.jp

Keywords; stiffness reduction, high humidity, cfrtp, cfrp, creep, fatigue

Abstract. Significant stiffness reduction of the plate spring due to delaminations around the interwoven cloths could be prevented by using CFRTP (carbon fiber cloth and Polyethylene Terephthalate (PET)) rather than that by using CFRP (carbon fiber cloth and epoxy), when ultra high cyclic loading was applied to the plate spring under high humidity condition. To explain the result, the prediction model of stiffness reduction was introduced considering time-dependent crack propagation accompanying with creep deformation around the crack tip. Stiffness reduction of CFRP under high humidity condition was not only determined by cyclic crack propagation but also by time-dependent crack propagation accompanying with creep deformation around the crack tip. It was found that CFRTP was effective material of the plate springs on vibration conveyer for the uses under high humidity condition to prevent significant stiffness reduction, where the crack propagation accompanying with creep deformation should be prevented around the crack tip.

Introduction

For vibration conveyor that transfers small parts on a flexible plate by high speed oscillation, CFRP (carbon fiber reinforced plastic) was frequently used for the material of the plate spring which produces the vibration, because not only of high specific modulus and high handling ability [1-5] but also of excellent proof property against the corrosion with rust during the commercial uses even at high humidity condition. In this case, the plate spring made of CFRP was subjected to ultra high cyclic fatigue loading with the oscillation. In the use of the vibration conveyor for long term with lots of years, the performance of the conveyor might be degraded with time due to the stiffness reduction of the plate spring made of the CFRP. To keep constant natural response which was initially set at installation of the machine, it is expected to prevent the significant stiffness reduction of the plate spring during fatigue up to ultra high cycles. For practical uses, this paper proposes a new design which prevents the significant degradation with stiffness change of the plate spring subjected to ultra high cyclic fatigue loading under high humidity condition for vibration conveyor. At first, this study investigated the stiffness reduction of the plate springs made of CFRP (Carbon cloth and epoxy) in the condition. For evaluation of the stiffness reduction, the change of frequency determined by natural response of the plate spring was investigated during the fatigue test. Internal damage state was investigated after 10^8 cyclic loading. Finally, the prediction models of the stiffness reduction were introduced to characterize mechanical behaviors of the plate springs at high humidity condition.

Experimental Procedures

Materials. The material system used, at first, in this study was CFRP (carbon fiber cloth /epoxy composite) fabricated with the prepreg (Mitsubishi Rayon TR3110MS/331GMP).The specimens (CFRP) of the plate springs with 82mm by 56mm and 1.5mm of thickness were obtained after cut from the laminated cloth ply panel pressed under 3MPa with 8 plies of prepreg at 130 °C by conventional heat pressing machine and then cured at 60 °C for 9 hours.

Instead of epoxy for the matrix of the specimen, PET film was also utilized as the material of matrix to fabricate the CFRTP as explained in later section. The PET film was commercially available (A2012) by Mitsubishi Rayon. For the fabrication of CFRTP, carbon fibre cloth

(Mitsubishi Rayon TR3110MS) was used as the reinforcement. To obtain the pre-form of the panel of CFRTP with the PET matrix, 8 and 9 plies of carbon fibre cloth and the PET film were alternately laid up, respectively, before the press under 3MPa at 275 °C for 10 minutes.

High Speed Cyclic Bending Test. Schematic view of high speed bending test is shown in Fig.1. Two specimens were set to the test machine with 15 degree of inclined angle from vertical axis at room condition and 95 percent of relative humidity (95%RH), respectively. The upper ends of the specimens were vibrated with attached magnet piece by electromagnetic induction induced by alternating current to the coil. The cyclic ratio (R) of the repeated displacement with sine wave was kept to -1 (perfect alternation) during the fatigue test. The amplitude of cyclic displacement at the upper end of plate springs was kept constant to 2.0mm during the fatigue test by constantly adjusting the frequency which produced the constant displacement to the conveyor, where the frequency was initially set to 60 hertz at the beginning of fatigue test.

During the fatigue test the stiffness reductions of specimens (CFRP and CFRTP) were evaluated by monitoring the change of frequency determined by the natural response of the plate springs. The natural response w_i of the plate spring was defined as

$$w_i = B_i^2 \sqrt{\frac{EI}{\rho A}} \quad (i = 1,2,3,...) \tag{1}$$

where B_i, EI, ρ, A are modulus defined by resonance order, bending modulus , mass by the unit volume and cross sectional area, respectively [6]. Over 1.0x10^8 cycles of loading, the fatigue test was expired where fatigue limit was defined in this study.

Water Absorption Test. The stiffness change of the plate springs was investigated after the stock for 500 hours of the specimen at room condition and 95%RH without loading. After the water absorption, the flexural stiffness was determined with the relationship between reaction force and constraint displacement by the simple bending test as shown in Fig.2.

FCP (Fatigue Crack Propagation) Test with ENF (End Notched Flexure) Specimen. Fig.3 shows schematic view of FCP (fatigue crack propagation) test with ENF specimen. The test condition on FCP was the same as that for high speed bending test in previous section. The mode II energy release rate G_{II} can be evaluated by

$$G_{\mathrm{II}} = \frac{3Eh^3}{2a^4} C^2 \tag{2}$$

where E, h, C, a are Young's modulus, thickness of plate specimen, load compliance and crack length measured with microscope, respectively [7-9].

The range of energy release rate ΔG_{II} was taken to represent the effect of cyclic loading on the FCP rate $\mathrm{d}a/\mathrm{d}N$. In this case, ΔG_{II} has been taken as

$$\Delta G_{\mathrm{II}} = G_{\mathrm{II}\max} - G_{\mathrm{II}\min} \tag{3}$$

from Eq.2.

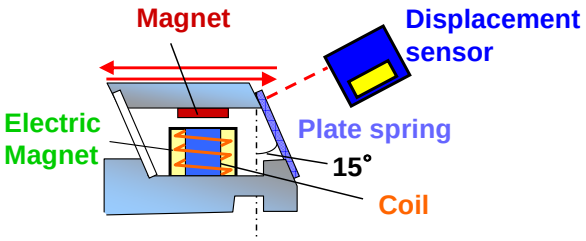


Fig. 1 Schematic view of high speed bending fatigue testing machine.

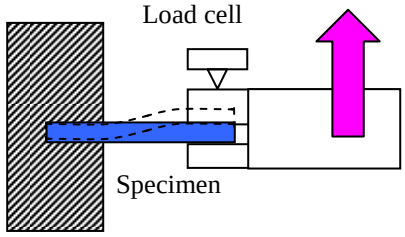


Fig. 2 Schematic View of flexural stiffness test of plate springs.

CCP (Creep Crack Propagation) Test with ENF (End Notched Flexure) Specimen. Schematic view of CCP (Creep crack propagation) test with ENF specimen is shown in Fig.4. The 2.0mm of constraint displacement was kept at the end of the ENF specimen during the creep test. The CCP of the fatigue damaged specimens was observed with optical microscope after 3x10^7 and 6x10^7 cycles of fatigue loading was applied on the FCP test.

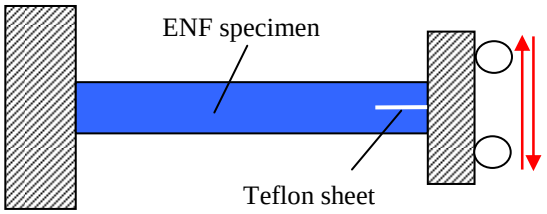


Fig. 3 Schematic view of FCP test with ENF specimen.

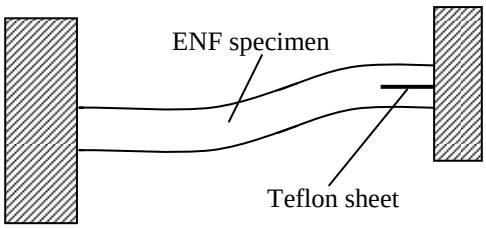


Fig. 4 Schematic view of CCP test with ENF specimen.

Results and Discussion

Stiffness Reduction of CFRP Spring under Ultra High Cyclic Fatigue. Fig.5 shows the reduction ratio of the natural frequency of the CFRP spring with respect to the number of loading cycles. The ratio of frequency was remarkably reduced after $3.0\times10\text{^}7$ cycles at each condition when the CFRP spring was subjected to ultra high cyclic fatigue loading. Significant stiffness reduction after $3.0\times10\text{^}7$ cycles was observed at 95%RH compared with that at room condition. Fig.6 shows the microscopic damage state at around top, middle and bottom cloth in the CFRP specimen, respectively, after 1.0x10^8 cycles. At 95%RH lots of delaminations in the shear direction were observed around the interwoven cloths of the CFRP. It was considered that the delaminations changed the second moment of area and these changes induced the bending stiffness reduction of the plate springs under high humidity condition.

Stiffness Reduction of CFRTP Spring without Loading. To prevent the stiffness reduction accompanying with such damages which might be induced by the hydrolysis in epoxy under high humidity condition, PET film was utilized as the material of matrix for the CFRTP spring plate, in which PET does not have hydroxyl in its molecular structure. Before cyclic fatigue test, water absorption of the CFRTP was investigated by simple absorption test. The moisture content M is calculated by

$$M\,\% = \frac{w_t - w_0}{w_0} \times 100 \tag{4}$$

where w_t is measured weight of the specimen at the time, t and w_0 is the initial dry weight. After the water absorption, the static flexural test was conducted to evaluate the stiffness change. The stiffness reduction ratio of the CFRTP at 95%RH was almost equal with that at room condition even after 500 hours for water absorption, while absorbed moisture content of CFRTP at 95%RH was high compared with that at room condition, as shown in Fig.7**.**

Stiffness Reduction of CFRTP Spring under Ultra High Cyclic Fatigue. Fig.8 shows the reduction ratio of the frequency with respect to the loading cycles of the CFRTP spring. After $6.0\times10\text{^}7$ cycles of fatigue loading, the reduction of frequency of the CFRTP spring was partly gradual compared with that of CFRP spring under high humidity condition. Final reduction at fatigue limit (10^8 cycles) was also prevented when the CFRTP was utilized for the material of plate springs. Microscopic state of interwoven cloths in CFRTP after ultra high cyclic bending test is shown in Fig.9. Few delaminations were observed around the interwoven cloths of the CFRTP spring. Significant stiffness reduction of the plate springs due to delaminations around the interwoven cloths could be prevented by using CFRTP rather than that by using CFRP, when ultra high cyclic loading was applied to the plate springs under high humidity condition.

FCP between Carbon Cloths of CFRP Spring. Fig.10 shows relations between FCP rate $\mathrm{d}a/\mathrm{d}N$ and mode II energy release rate range ΔG_{II} of each ENF specimen. These experimental data of the CFRP at room condition express a log-linear relationship between $\log \mathrm{d}a/\mathrm{d}N$ and $\log \Delta G_{\mathrm{II}}$. In general, FCP rate $\mathrm{d}a/\mathrm{d}N$ is defined by Paris's law as follow.

$$\frac{\mathrm{d}a}{\mathrm{d}N} = C_f (\Delta G_{\mathrm{II}})^{m_f} \tag{5}$$

where C_f and m_f are experimentally obtained contents. These experimentally contents C_f and m_f are associated with physical properties of the material. At room condition, the experimental result of the CFRP showed in good agreement with Paris's law. In contrast when the CFRP specimen was utilized at 95%RH, Paris's law was not applicable to explain the result of FCP.

Prediction Model of Stiffness Reduction of CFRP Spring. To explain these results in previous section, the prediction model of stiffness reduction was introduced considering time-dependent crack propagation accompanying with creep deformation around the crack tip. Fig.11 shows the change of creep crack length of the CFRP specimen with respect to the test time. Significant CCP from the initial notch of CFRP at 95%RH was observed when the CFRP specimen was subjected to the creep loading. It is considered that, with the effect of moisture-induced swelling of material of matrix, the crack propagation of CFRP at 95%RH was affected by creep deformation at the crack tip. Where CCP induced by creep deformation at the crack tip, it has been found that CCP rate $\mathrm{d}a/\mathrm{d}t$ can be described by Norton's creep power law as follow [10-12]

$$\frac{\mathrm{d}a}{\mathrm{d}t} = C_c (C^*)^{m_c} \tag{6}$$

where C_c and m_c are material constants that can be measured experimentally and C^* is creep fracture mechanics parameter. Here, the crack propagation rate $\mathrm{d}a/\mathrm{d}N$ at high humidity condition was calculated as follow.

$$\frac{\mathrm{d}a}{\mathrm{d}N} = C_f (\Delta G_{\mathrm{II}})^{m_f} + C_c \left(\frac{1}{F} - \frac{N}{F^2} \frac{\mathrm{d}F}{\mathrm{d}N} \right) (C^*)^{m_c} \tag{7}$$

where F is the frequency of cyclic loading. Fig.12 shows comparison of experimental result of crack propagation of CFRP at 95%RH and that of prediction model. The crack propagation rate of CFRP at 95%RH estimated by this model showed in agreement with the test result. The stiffness reduction of CFRP under high humidity condition was not only determined by cyclic crack propagation but also by creep crack propagation induced by creep deformation at the crack tip.

Prediction Model of Stiffness Reduction of CFRTP Spring. Fig.13 shows the change of creep crack length of the CFRTP specimen with respect to the test time. The CCP (Creep crack propagation) was not observed remarkably from the initial notch of CFRTP at 95%RH. This experimental data suggested that the material constant C_c shown in Eq.7 was almost 0. It was found that CFRTP was effective material of the plate springs on vibration conveyer for the use under high humidity condition to prevent significant stiffness reduction, where the crack propagation accompanying with creep deformation should be prevented around the crack tip.

Summary

Significant stiffness reduction of the plate springs due to delaminations around the interwoven cloths could be prevented by using CFRTP (carbon fiber cloth and Polyethylene Terephthalate (PET)) rather than that by using CFRP (carbon fiber cloth and epoxy), when ultra high cyclic loading was applied to the plate springs under high humidity condition. When the cyclic fatigue loading was applied to the plate cut from CFRP panel, delaminations around interwoven cloths in the shear direction changed the second moment of area and these changes induced the bending stiffness reduction of the plate springs under high humidity condition.

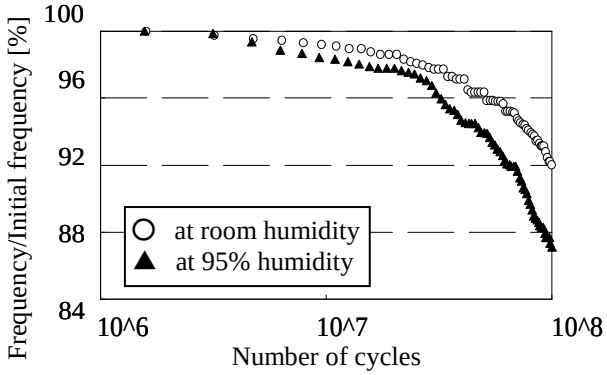


Fig. 5 Reduction ratio of frequency of CFRP spring

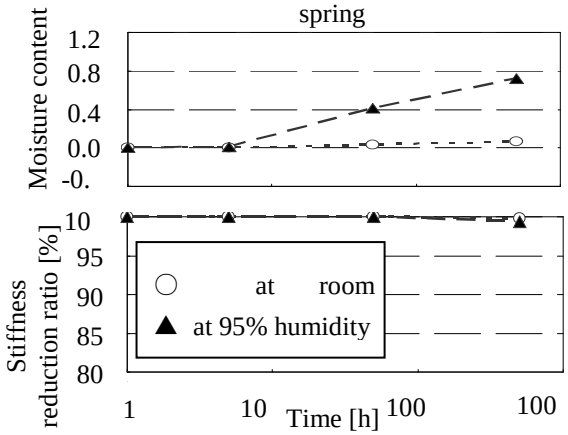


Fig. 7 Relations of water absorption between stiffness reduction of CFRTP spring.

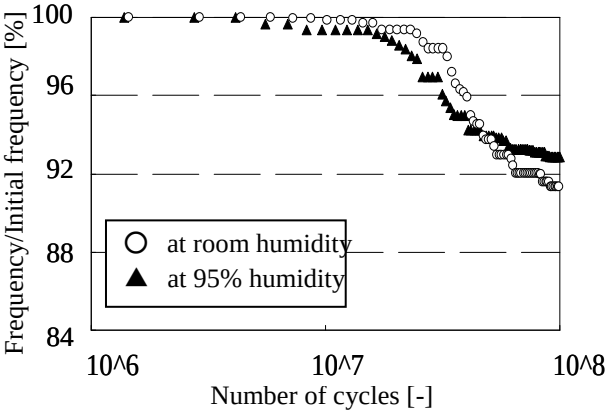


Fig. 8 Reduction ratio of frequency of CFRTP spring with respect to number of cycles.

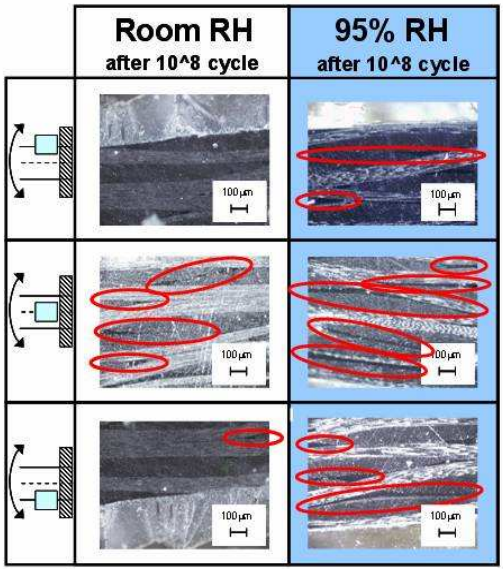


Fig. 6 Microscopic damage state around interwoven cloths in CFRP spring after 8th power 10 loading cycles.

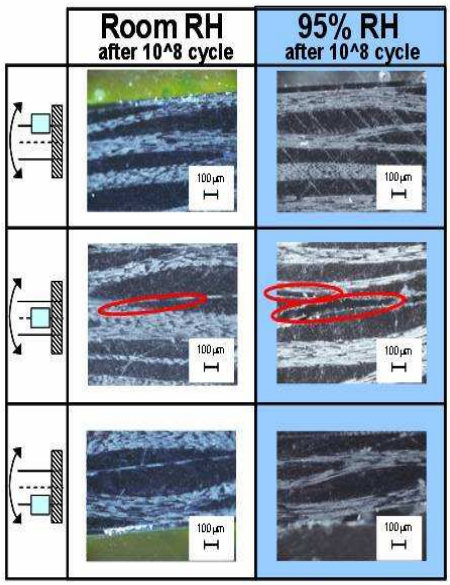


Fig. 9 Microscopic damage state around interwoven cloths in CFRTP spring after 8th power 10 loading cycles.

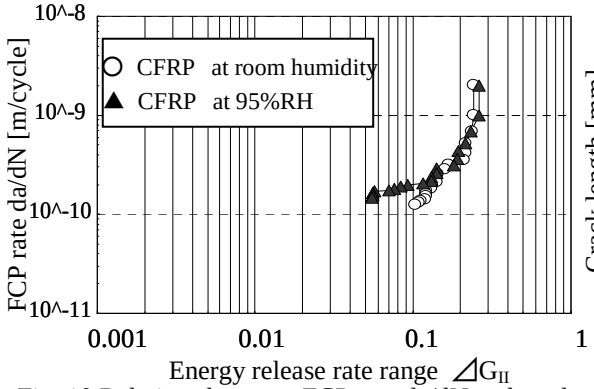


Fig. 10 Relations between FCP rate da/dN and mode II energy release rate range ΔG_{II}.

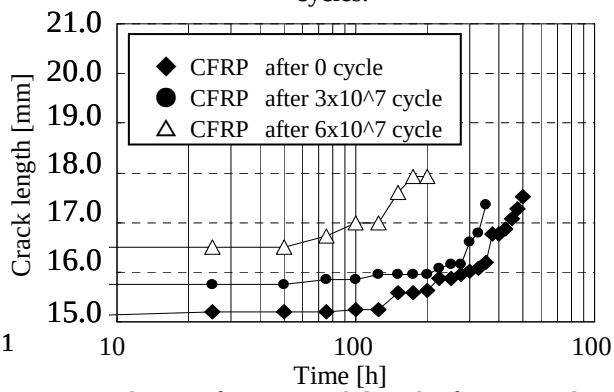


Fig. 11 Change of creep Crack length of CFRP with respect to test time h.

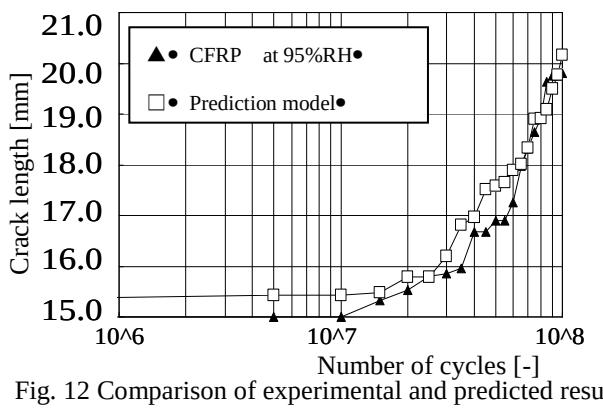


Fig. 12 Comparison of experimental and predicted results of crack length (CFRP, 95%RH).

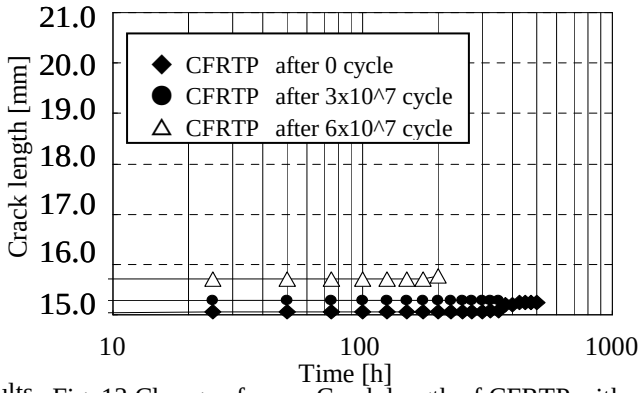


Fig. 13 Change of creep Crack length of CFRTP with respect to test time h.

References

[1] F.I.Addeessio, International Journal of Solids and Structures 34 (1997), 2003-2024

[2] M.V.Housur, M.Adbullah, Composite Structure 67 (2005), 253-262

[3] C.Breen, F.Guild, M.Pavier, Composites Part.A 36 (2005), 205-211

[4] B.L.Wardle and P.A.Lagace, J. AIAA, 35, 2 (1997), 389-396

[5] T. Gomez, R. Zaera, E. Barbero, C. Navarro, Composite Part.B 36 (2005), 41-50

[6] W.T.Thomson, MECHANICAL VIBRATION (1976), 187-197

[7] A.J. Rusell and K.N.Street, Proceedings of ICCM IV (1982), 279

[8] G.A.O.Davies, P. Robinson, J. Robson and D. Eady, Composites Part A 28 (1997), 757-765

[9] M.A.Meggilaro, J.T.P.Castro, International Journal of Fatigue 25 (2003), 843-854

[10] M.Yatomi, C.M.Davies, K.M.Nikbin, Engineering Fracture Mechanics 75 (2008), 5140-5150

[11] H.K.Kim, Materials and Design 30 (2003), 2454-2459

[12] H.Mao, S.Mahadevan, International Journal of Fatigue 22 (2000), 789-797

© (2011) Trans Tech Publications, Switzerland
doi:10.4028/www.scientific.net/KEM.471-472.981

Lay-Up Design of Low Wind Speed Composite Turbine Blade

Indra H. Nugroho[1,a], Hermawan Judawisastra[1], M. Giri Suada[1] and Mardjono Siswosuwarno[1]

[1]Faculty of Mechanical and Aerospace Engineering

Bandung Institute of Technology, Ganesha 10, Bandung 40132, Indonesia

[a]hastoadi@yahoo.com

Keywords: low wind speed wind turbine, composite design, tsai-hill criteria, unidirectional, woven

Abstract. Glass fiber reinforced polymer (GFRP) is a common composite material used for wind turbine blades because of its good strength to weight ratio. This paper describes the design process of GFRP material for a low wind speed (LWS) turbine blade. The wind turbine analyzed in this study is a 3-blades horizontal axis wind turbine (HAWT) with NACA 4415 airfoil and rotor diameter of 5 m. Parameters for the blade are thickness of skin and spar, lamination angle, and stacking sequence of the laminae. The design approach uses Carpet Plot Method based on Tsai-Hill failure criteria. Materials analyzed in this study are unidirectional E-glass fiber/epoxy composite and plain weave woven roving WR200 E-glass fiber/epoxy composite. There are 15 material configurations analyzed using a finite element software. The result shows top five of the composites configuration consisting of minimum 3 plies of 0°/90° direction fiber for the skin and ±45° direction fiber for the spar. The optimum configuration is $[(0/90)]_3$ for the skin and (±45°) for the spar both using plain weave woven roving WR200 E-glass fiber/epoxy composite. This configuration has margin of safety of 1.42 based on maximum principal stress and maximum deflection of 346 mm which is 0.14 of the total blade length. The predicted overall weight of the blade is 1.52 kg.

Introduction

Wind energy has been shown to be one of the most feasible sources of renewable energy with low carbon footprint (< 10 g CO_2/kWh) compared to solar cell (almost 60 g CO_2/kWh) [1]. This fact encourages the development of wind turbines in many areas, even in low averaged wind speed areas (< 5 m/s). In order to generate power required for low averaged wind speed area, a wind turbine must have a minimum weight and fulfil the strength and the stiffness requirements. Many small wind turbines which are operated in low wind speed area have blades made of balsa wood [2]. Later development shows blades made of Glass Fiber Reinforced Polymer (GFRP), and due to the low averaged wind speed, many blade structures only has hollow structure without support structure, such as spar or ribs [3,4].

This paper adopts the spar structure to be applied on a low wind speed (LWS) turbine blade. The use of spar will increase the stiffness of the blade in flapwise direction. This increment will reduce the power loss caused by the rotor area reduction due to blade deflection [5]. The blade will use Glass Fiber Reinforced Polymer (GFRP) as material for the skin and the spar. Glass Fiber Reinforced Polymer (GFRP) is a common composite material used for wind turbine blades because of its good strength to weight ratio [6]. The GFRP has to be designed regarding to the minimum thickness, fiber orientation and stacking sequence to obtain the optimum material configuration for wind turbine blade. This paper describes the design process of GFRP material for a low wind speed (LWS) turbine blade.

Description of the Blade

The wind turbine analyzed in this study is a 3-blades horizontal axis wind turbine (HAWT) with NACA 4415 airfoil and rotor diameter of 5 m. A 3-blades HAWT has low rotor solidity and gives high rotation [7], while the NACA 4415 airfoil has high aerodynamic efficiency [8]. The cut-in wind speed is 2.5 m/s so it can be operated in very low wind speed area. The rated wind speed is 10 m/s. The cut-off wind speed is 15 m/s. The structural layout of the blade is depicted on Fig.1. Fig. 2 shows the dimension of the maximum and minimum chord length of the blade. The spar will be positioned 20% of the chord length from the leading edge.

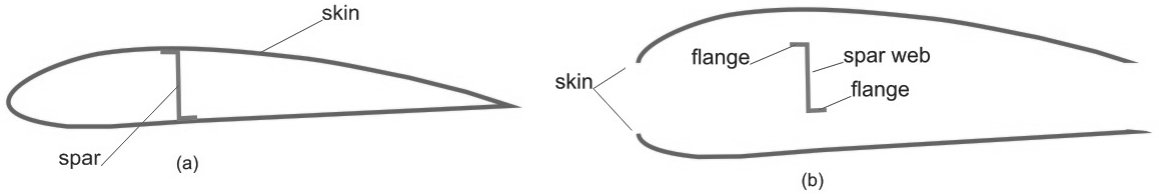


Fig.1 (a) Structural layout of the blade. (b) Parts of the blade.

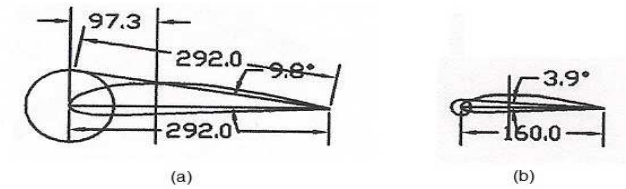


Fig. 2 Chord length of the blade (mm). (a) Maximum (b) Minimum.

Design Requirements and Objective

The criteria for the blade structure are to fulfil the strength and stiffness required to be operated in the rated wind speed with margin of safety (M.S) between 1 and 1.5 based on maximum principal stress and maximum deflection-to-blade length ratio of 0.2. The design objective is specified performance with minimum mass which also lead to minimum cost.

The maximum M.S value of 1.5 is chosen in order to limit the weight of the blade. The higher M.S implicates the higher the thickness of the blade which lead to higher mass, higher weight, and higher cost. The M.S value of 1.5 also means that the blade can be operated in maximum wind speed of 15.8 m/s which exceeds the cut-off speed. The stiffness requirement is set based on results presented by Ahlström [5] which shows the influence of wind turbine blade deflection on power production. The maximum deflection-to-blade length ratio of 0.2 limits the power-loss to 10% of rated power.

Design Strategy

In the design process loads taken into account are aerodynamic load, inertia load, and gravity load. The aerodynamic load is determined using a computational fluid dynamics (CFD) software. The simulation is done in the rated wind-speed of 10 m/s.

The structure of the blade is modeled by using a finite element modeling (FEM) software. Parameters for the blade are thickness of skin and spar, lamination angle, and stacking sequence of the laminae. The blade with quasi-isotropic material is analyzed to obtain the maximum stress resultant. The design approach uses Carpet Plot Method based on Tsai-Hill failure criteria. Materials analyzed in this study are unidirectional E-glass fiber/epoxy composite and plain weave woven roving WR200 E-glass fiber/epoxy composite. There are 16 material configuration being analyzed. The weighted-points matrix is used in the selection process. The flowchart of the design process shows on Fig. 3.

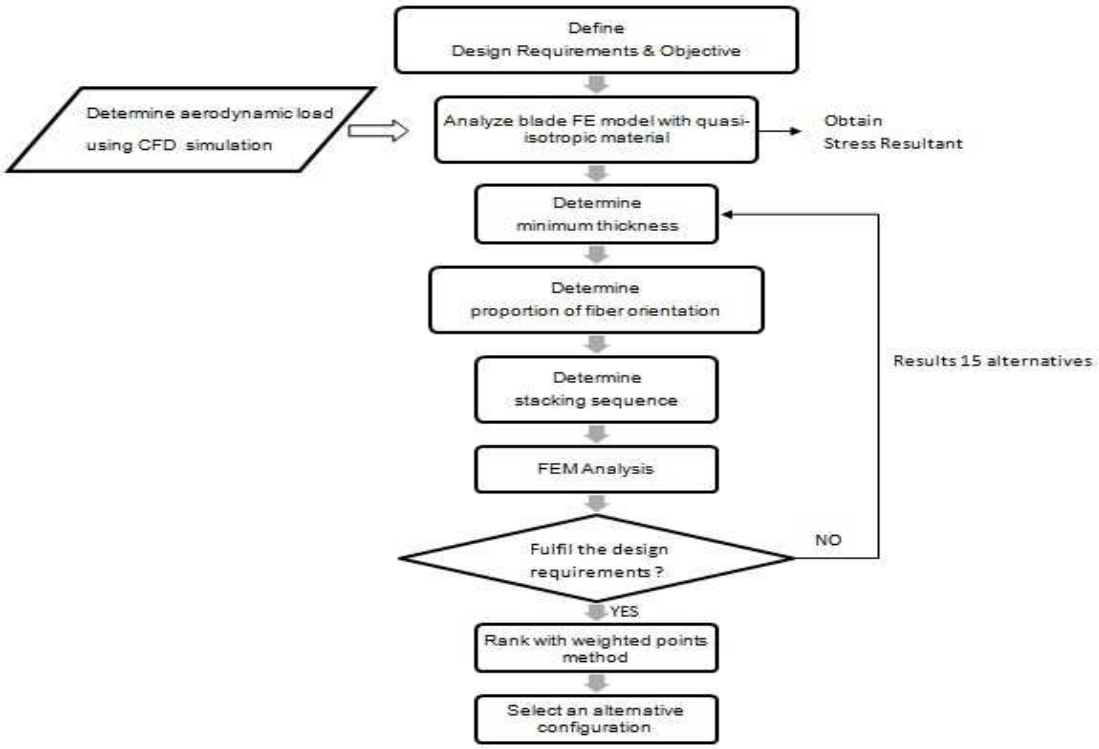


Fig. 3 Flowchart of the design process

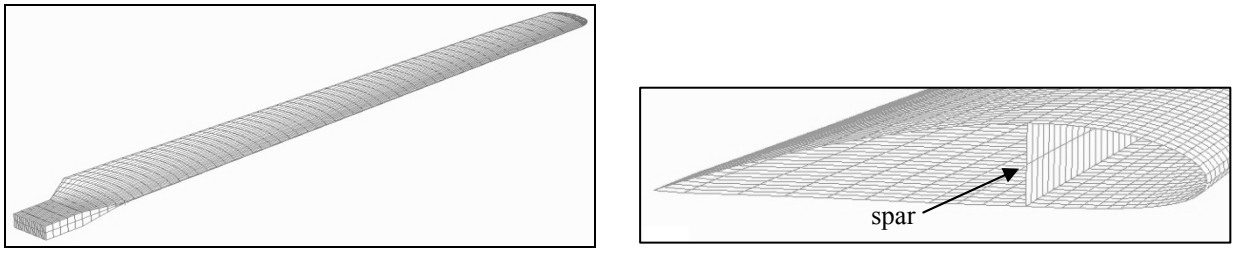
CFD Simulation of Wind Turbine Aerodynamic Loads

The simulation is done in the rated wind-speed of 10 m/s in order to obtain the aerodynamic load. The air is modeled at 25°C with density of 1.185 kg/m^3. This condition gives static pressure of 102573 Pa which is used as input for the rotor as well as the rated wind speed.

The fluid is modeled with tetrahedral element. Area around the blade is meshed with finer mesh in order to obtain more accurate result without significantly increase the element number. The element type and mesh selection is done based on computer ability. Tetrahedral element requires less complex calculation [9]. The result obtained from CFD simulation is total pressure. The simulation result also shows that the rated wind-speed of 10 m/s and static pressure of 102573 Pa yield 2485 W of power. This result only differ 0.6 % with theoritical analysis of the wind turbine, which is 2500 W.

Stress Analysis of Blade Structure Using Finite Element Model

Due to symmetric geometry of the rotor, the structural analysis is done only for one blade (Fig. 4a). Skin and spar are modeled with QUAD4 element, which is quadrilateral shell element (Fig. 4b). The hub is modeled with HEXA8 element, which is hexagonal solid 3D element, in order to modeled the polyurethane foam core material of the hub.



(a) (b)

Fig.4 FE Model of the blade (a) Overview (b) Cross section

The number of element is exactly the same number of element on blade surface modeled on CFD. This condition eases the matching process between CFD and FEM models. Loads taken into account are aerodynamic load, inertia load, and gravity load. The constraints are pin constraints on positions of the bolt connection between blade and hub.

The inertia load is calculated from :

$$F_{inertia} = \omega^2 mr \quad (1)$$

where ω is the rotational speed of the blade which is 300 rpm, m is the mass of the blade, r is the radius of the blade. The first model to be analyzed has quasi-isotropic material, which is $[0/90/45/-45]_s$ glass fiber epoxy. This material is chosen in order to obtain stress resultant to be used as ground for further step of the material design.

Composite Material Design with Carpet Plot Method

Based on Classical Lamination Theory [10,11], a laminate is subjected to loading in its plane. The stress resultans are denoted as Nx, Ny, Txy = Tyx. These are membrane stress resultants. The basic FE model with quasi-isotropic material gives results as shown on Fig. 5. Fig. 5 shows the maximum stress resultant occurs on the area near the hub. This stress concentration happens due to the shape transition from airfoil shape to the tetrahedral shape of the hub. Based on this condition, the hub area needs to be reinforced. On the skin of the blade, the maximum stress resultants are: Nx = 0.15 N/mm, Nz = 32.33 N/mm, and Txz = 16.09 N/mm. The maximum stress resultants occurs on the spar are: Ny = 8.65 x 10^{-5} N/mm, Nz = 4.35 N/mm, and Tyz = 2.18 N/mm.

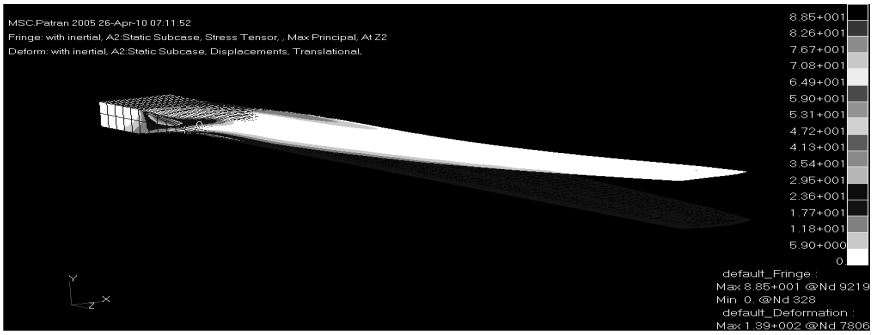


Fig. 5 Stress distribution on quasi-isotropic model

The first candidate material is unidirectional (UD) E-glass fiber/epoxy with thickness (t) 0.13 mm, fiber volume fraction (v_f) of 0.6, specific mass (ρ) of 2.08 g/cc, longitudinal tensile fracture strength (σ_l) of 1250 MPa, and longitudinal elastic modulus (E) of 45 GPa. The proportions of each ply using UD material for skin and spar are shown on Table 1.

Table 1. Proportions of each ply using UD material

	Skin	Spar
0° orientation	14 %	15 %
90° orientation	0 %	0 %
±45° orientation	86 %	85 %

Based on carpet plot method described above, the minimum thickness of the laminate for the skin is 1.12 mm which is equal to 9 plies. For the spar, the minimum thickness is 0.15 mm or 2 plies.

Iteration Process

The laminate for first iteration is unidirectional (UD) E-glass fiber/epoxy with configuration of [45°/-45°/45°/-45°/0°]s for the skin and [45°/-45°] for the spar. The result from FEM analysis gives maximum stress of 88.5 MPa, which has Margin of Safety (M.S) of 13.12 and maximum deflection of 139 mm, which has ratio to blade length of 0.06. The second iteration step is to replace the unidirectional (UD) E-glass fiber/epoxy with plain weave woven roving (WR200) E-glass fiber/epoxy which has thickness (t) 0.22 mm, fiber volume fraction (v_f) of 0.5, specific mass (ρ) of 1.9 g/cc, longitudinal tensile fracture strength (σ_l) of 400 MPa, and longitudinal elastic modulus (E) of 20 GPa. Thus, the configuration is WR$[(\pm45°)_4/(0°/90°)]_s$ for the skin and WR$(\pm45°)_2$ for the spar. The result from FEM analysis gives maximum stress of 43 MPa, which has Margin of Safety (M.S) of 8.3 and maximum deflection of 124 mm, which has ratio to blade length of 0.05.

The third iteration step is to reduce the weight of the blade by reduce the number of plies using in the first iteration step. The configuration becomes [45°/-45°/0°]s for the skin and [45°/-45°] for the spar. The fourth iteration step is to reduce the weight of the blade by reduce the number of plies using in the second iteration step. The configuration becomes WR$[(\pm45°)_2/(0°/90°)]_s$ for the skin and WR(±45°) for the spar. The fifth iteration step is to reduce the weight of the blade by reduce the number of plies using in the fourth iteration step. The configuration becomes WR$[(\pm45°)/(0°/90°)]_s$ for the skin and WR(±45°) for the spar. The results is shown on Table 2.

Table 2. Results of FEM analysis for 1st to 5th iteration

	Configuration	Stress (MPa)	M.S	Deflection (mm)	Deflection-to-blade length ratio	Mass (kg)
1	Skin : [45°/-45°/45°/-45°/0°]s	88,5	13,12	139	0,06	2,91
	Spar : [45°/-45°]					
2	Skin : WR $[(\pm45°)_4/(0°/90°)]$s	43	8,30	124	0,05	4,26
	Spar : WR $(\pm45°)_2$					
3	Skin : [45°/-45°/0°]s	198	5,32	310	0,13	1,5
	Spar : [45°/-45°]					
4	Skin : WR $[(\pm45°)_2/(0°/90°)]$s	95,6	3,18	272	0,11	2,47
	Spar : WR (±45°)					
5	Skin : WR $[(\pm45°)/(0°/90°)]$s	181	1,2	449	0,19	1,52
	Spar : WR (±45°)					

In order to vary the stacking sequence, a different approach is made. The blade is assumed as a beam with distributed load. Thus, the flexural stress distribution along the beam cross section can be assumed has maximum value at the outer side/skin of the beam. While the shear stress along beam cross section assumed has maximum value at the center part of the beam. Based on these conditions it can be concluded that for the blade skin dominant plies of 0° orientation should be used at the outer side. At the center of the blade skin, plies of ±45° orientation should be used. Based on the beam assumption, the next step of design iteration is done to vary the stacking sequence. There are 10 more configurations analyzed.

Selection Process

To single out one of the composite material configuration from the 15 alternatives already generated in the previous step, a method called weighted objectives method is used. The weighted objectives method provides a means of assesing and comparing alternative designs, using differentially weighted objectives. This method assigns numerical weights to objectives, and numerical scores to the performances of alternative designs measured against these objectives [6].

In this method, all alternatives configuration is ranked based on objectives, i.e : Margin of Safety, deflection-to-blade length ratio, mass, cost, and availability. The next step is to give scores to the ranked alternatives. First rank get 10 scores, second get 9 scores, third get 8 scores, and so on until 10th rank get 1 score. Ranked 11th to 15th alternatives get no score. Then, based on weighted objectives method, numerical weights is assigned to the criteria. In this project, a total values of 100 is assigned to the criteria which is divided to 5 criteria as shown on Table 3. These values is multiplied by the scores obtained by each alternatives design in the previous step. The shaded columns show the top 5 alternatives.

Table 3. Alternative Design with Weighted Points

	Weigh t Value	Iteration Nr.														
		1	2	3	4	5	6	7	8	9	10	11	12	13	14	15
Margin of Safety	10	0	0	0	0	50	0	70	0	0	90	100	0	70	0	90
Deflection ratio	10	90	100	20	40	0	60	0	0	70	0	10	60	0	80	40
Mass (kg)	30	0	0	240	0	150	30	150	270	240	300	150	240	150	0	0
Cost (IDR)	30	0	0	120	0	240	0	240	270	120	300	240	120	240	0	30
Availability	20	0	200	0	200	200	0	200	0	0	0	200	0	200	200	200
Total Score		90	300	380	240	640	90	660	540	430	690	700	420	660	280	360

It can be seen that the top alternatives configuration is iteration number 11 which has laminate configuration of WR $[(0°/90°)]_3$ for the skin and WR (±45°) for the spar.

Summary

The result shows top five of the composites configuration consisting of minimum 3 plies of 0°/90° direction fiber for the skin and ±45° direction fiber for the spar. The optimum configuration is $[(0/90)]_3$ for the skin and (±45°) for the spar both using plain weave woven roving WR200 E-glass fiber/epoxy composite. This configuration has margin of safety of 1.42 based on maximum principal stress and maximum deflection of 346 mm which is 0.14 of the total blade length. Due to the uniform thickness along the blade span, this configuration is not the best configuration to obtain the optimum composite structure design for the low averaged wind speed wind turbine. A sectional approach can be made along the blade span. The skin thickness then can gradually reduced within sections.

References

[1] United Kingdom Parliementary Office of Science and Technology. *Postnote on Carbon Footprint of Electricity Generation*. November 2006.
[2] Campos, T.S. et.al, *Wind Rotor Blade Construction* (Intermediate Technology Development Group, 2001).
[3] *Composites in Wind Energy: From Financing, Material Selection to Maintenance*, Wind Energy Forum Proceedings, October 2009.
[4] *2009-2013: No Slow Down in Global Wind Developments*, JEC Composites Magazine, Juni 2009.
[5] Ahlström, Anders: Wind Energ. (2006); 9:237–249.
[6] Philips, Leslie N., *Design with Advanced Composite Materials*, The Design Council, London (1989).
[7] Christensen, K., *Catalogue of Small Windmills from 5 W to 50 kW*, Nordic Folkecenter for Renewable Energy, 2006.
[8] Cagle, D.R. et al, *Evaluation of Airfoils for Small Wind Turbines*, Alternatve Energy Institute, 2006.
[9] *ANSYS CFX User's Manual* (2005).
[10] Gay, Daniel, *Composites Materials: Design and Applications*, CRC Press (2003).
[11] Cross, Nigel, *Engineering Design Methods : Strategies for Product Design*, John Wiley & Sons, London (2008).

© (2011) Trans Tech Publications, Switzerland
doi:10.4028/www.scientific.net/KEM.471-472.987

Effect of Stitching Density of Nonwoven Fiber Mat Towards Mechanical Properties of Kenaf Reinforced Epoxy Composites Produced by Resin Transfer Moulding (RTM)

Muhamad Saifuddin Salim[1,a], Zainal Arifin Mohd. Ishak[1,b] and Suhail Abdul Hamid[1,c]

[1]School of Material and Mineral Resources Engineering,

Universiti Sains Malaysia, Penang, Malaysia

[a]mss09_fr0252@student.usm.my, [b]zarifin.ishak@gmail.com, [c]simplesue86@gmail.com

Keywords: stitching density, nonwoven needle punched fiber mat, epoxy, resin transfer molding

Abstract. This study will focus on the usage of kenaf as a natural fibre in producing a composite materials consists of epoxy resin by resin transfer moulding (RTM). The variation amount of fiber loading and nonwoven fibre mat condition seems can give significant changes in properties of polymer composite in terms of mechanical aspects. Optimization of stitching density of nonwoven kenaf fibre mat manages to increase the mechanical behaviour. At higher degree of fibre loading, these enhancement properties are more apparent. Depending upon the direction of stitching process in producing nonwoven kenaf fiber mat, the composite obtained exhibit anisotropy behaviour in which the mechanical properties are vary upon the stitching direction of nonwoven mat.

Introduction

The utilization of natural fibres has move into higher level of applications and has move from their traditional markets to other potential fields such as buildings, automotive and furniture industries. The good features in producing these natural fibre-based components originates from their low cost, light weight, and less abrasive compared to synthetic fibre-based products. Realizing the promising potential of kenaf fibre, Malaysian government recently announced kenaf plant will be the third commodity plant for the nation after palm oil and rubber plant [1]. The key of this study is the utilization of nonwoven pilot plant to produce stitched kenaf fibre mat as natural fibre reinforcement. Mat with uniform fibre arrangement and even thickness can be obtained using this pilot plant. RTM was consequently selected as the manufacturing process used in this study. There have been no previous works in which kenaf fibre mat have been used as the reinforcement together with epoxy as matrix in laminates manufactured by RTM. This study is a fundamental study in order to gain information regarding the effectiveness of using nonwoven pilot plant to produce well structured kenaf fibre mat for reinforcement in thermosetting composites.

Experimental

Materials. Kenaf fiber were supplied locally by Kenaf Fiber Industries Sdn. Bhd. Epoxy Resin together with Epoxy hardener Epicote 816 obtained from HexionTM. was used as a matrix. This epoxy resins is low viscosity with 1.61 Pa.s and density of 1.13kg/cm^3

Production of Kenaf Fiber Mat. Kenaf in a bale form will undergo series of processing from opening, carding, cross lapping, and needle punching process. Each stage is crucial in order to minimize shortening the fibre length of this natural fibre. Kenaf in a bale form is first fed into fibre opening which has the ability to open long stapled fibres. Kenaf fibre bits are then been carded to obtain fluffier fibre having almost identical length of 8cm to 12cm. This process helps to breaks up locks and unorganized clumps of fibre and then aligns the individual fibres so that they are more or less parallel with each other. This process is important as uncarded kenaf tend to break during needle punching process. The speed of this ongoing process was set to 0.2m/s. This machine is

connected directly to the cross lapper. Carded kenaf fiber then was arrange by cross lapper machine to produce multiple layers of kenaf before feeding into needle punching machine through a conveyor. Thickness of kenaf fiber mat obtained are controlable parameters which can be altered during this stage by adjusting the gap beween carding machine oulet and needle punching machine conveyor. The gap has been set to maximum value with 300mm. Multilayered kenaf was then compressed and punched as it enters through needle punching machine. Stitching density value need to be set to optimum value as it will determine the strength of the mat produced. The stitching density value of this machine can be calculated using Equation 1

$$\text{Stitching Density, SD } (cm^{-2}) = \frac{\text{Needles per cm of working width x 10}}{\text{Feed per Stroke in mm}} \quad (1)$$

Stitching density can be vary by altering number of needles, changing the pass-through speed hence the feed per stroke value and modifying the draft off speed. Three values of stitching density are used in producing kenaf fibre mat having linear density as in Table 1.

Table 1 Stitching Density with respectively Linear Density Value

Stitching Density (cm^{-2})	*Linear Density (gm^{-2})*
25	910
50	1300
75	1100

Kenaf fiber mat which was ready then was cut into 30cm X 20cm according to the mould cavity size. Before being introduced into mould cavity, kenaf fiber mat was placed in the oven with temperature 60°C for 3 hours for drying purpose. Rassman et. al reported that tests were conducted and it was determined that if the fibres were removed from the oven and sealed inside the mould within 2 min, they did not absorb a significant amount of moisture [2].

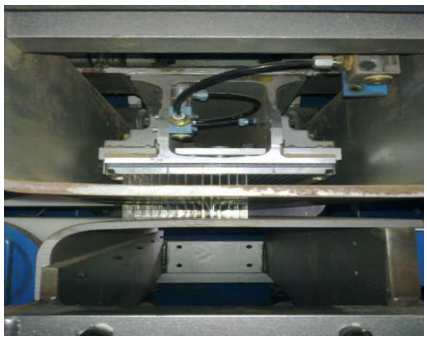
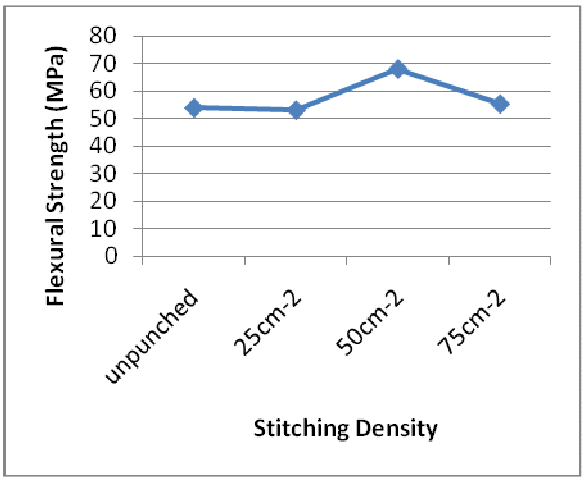


Fig. 1 Needle Punching Machine

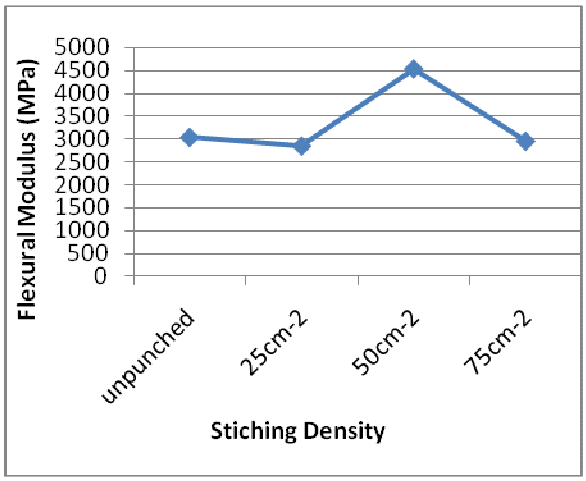
Production of Composite Laminate. An RTM machine designed and built to inject resin into the mould. through an injecting gun. In this study, epoxy resin and curing agent are mixed in a long and spiral static mixer before injecting into the mould through an injecting gun. The injecting gun is equipped with cleaning mechanism allowing for this system to be purged with air and then flushed with methylene chloride. The mould used consists of an upper mould plate and lower mould plate. The cavity of the mould is sized to produce laminates measuring 30cm X 20cm. Resin is injected into the mould through a single inlet port located at the edge of the lower mould plate and catchpot is attached at the middle of the mould to detect mould filing progress. Laminates were produced with fibre weight fractions of 15%, 25% and 35%. The maximum fibre weight fraction that could be attained without a complicated closing mechanism or excessive mould deflection was 35%.

Result and Discussion

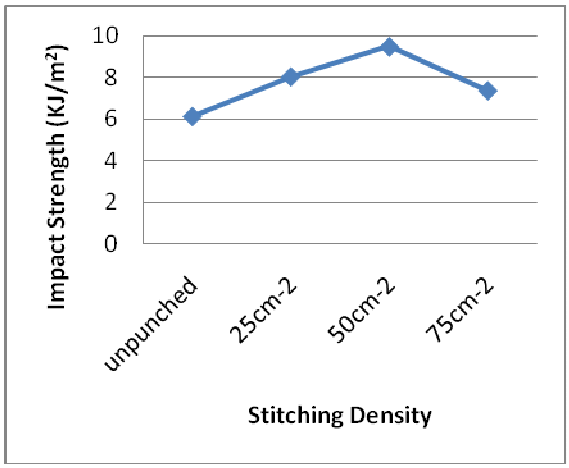
Effects of stitching density towards mechanical strength of composite



(a) Flexural Strength



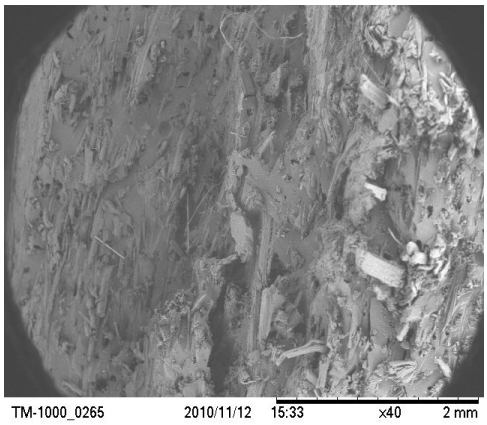
(b) Flexural Modulus



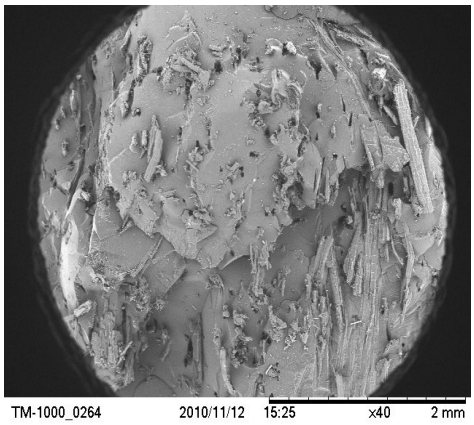
(a) Impact Strength

Fig. 2 Mechanical Properties of Composite with Respect to Stitching Density Value for 35 % Wf

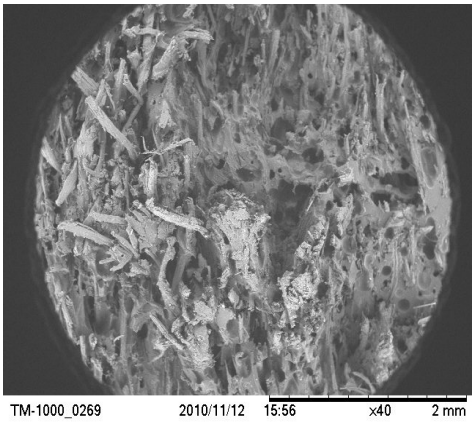
According to Sapuan et al. properties of the natural fibre composites is influenced by several factors such as stress strain behaviour of fibre and matrix phases, the phase volume fractions as well as the fibre orientation and distribution [3]. It was also pointed out that the mechanical properties of any material depend on the details of its structure [4]. By modifying the condition of the reinforcement which is the stitching density of nonwoven mat, the mechanical properties of the composite can be enhanced. Stitching or punching process of non woven fibre mat may induce formation of natural fibre network thus stress transfer distribution within fibre can easily occur. On the other hand, fibre to matrix interaction remains in a good manner since the RTM method was utilized. Base on the graphs in Fig. 2, the optimum stitching density is $50cm^{-2}$. Lower stitching density value of $25cm^{-2}$ is not sufficient enough to withstand flexural and impact load while higher value will result in shortening fiber length hence reducing the reinforcement ability.



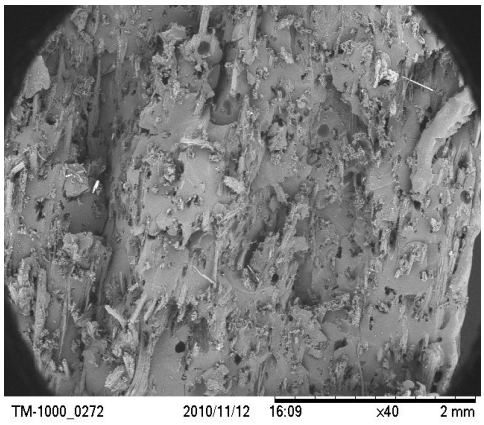
(a) Unpunched Kenaf Mat



(b) Punched with 25cm^{-2} SD



(c) Punched with 50cm^{-2} SD



(d) Punched with 75cm^{-2} SD

Fig. 3 SEM Micrographs of rupture surface for 35 % W_f composites with different value of stitching density

SEM micrographs exhibit rupture surface of the composite. Non uniform and unorganized fiber is observed for unpunched kenaf fibre mat in Fig. 3(a) while well organized fibre can be seen in Fig. 3 (c) for optimum value of stitching density. Low value of stitching density as shown in Fig. 3(b) and higher value in Fig. 3(d) are not able to enhance the reinforcing ability of kenaf fibre mat.

Fiber Loading and Anisotropy behaviour of composites

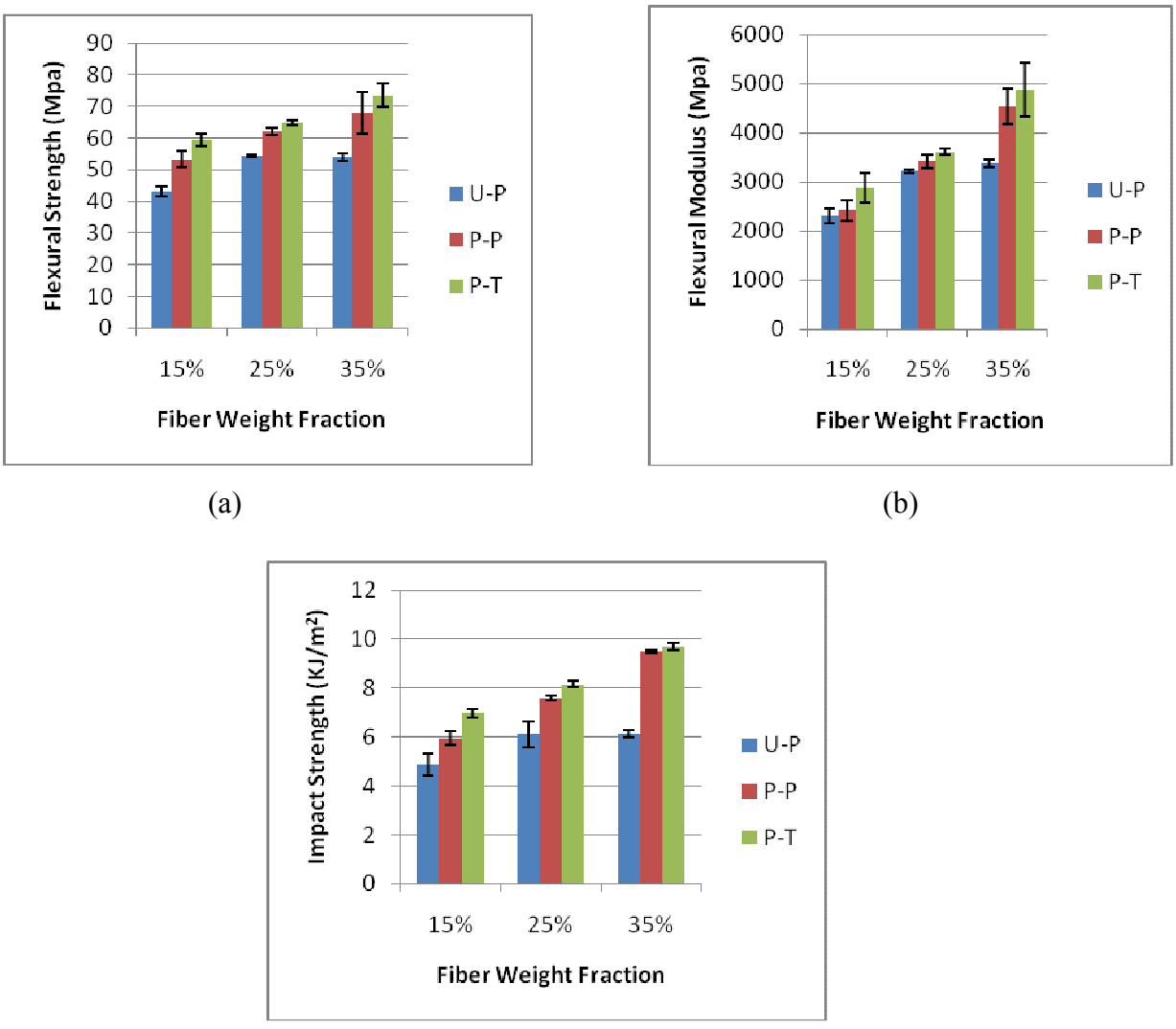


Fig. 4 Mechanical properties of composite with different condition of kenaf fibre mat

The dependence of mechanical properties of the composite upon fibre loading and effect of punching process of kenaf fiber mat is shown in Fig. 4. The flexural strength and modulus of the composite seems to be improved as higher fibre loading is incorporated into it. In addition to that, punched kenaf fibre used will tend to increase the packing density even more besides needle punched kenaf fibre mat will increase physical entanglement between individual fibre. Well structured kenaf fibre mat in this case punched mat difficult to tear apart thus can impart better modulus and strength to the composites laminates when compared to its unpunched counterpart. Anisotropy behaviour of composite was also been analyzed. Composite having unpunched kenaf fibre mat will be referred as U-P, P-P is for composite with punched kenaf fibre mat and the mechanical strength is obtained parallel with punching direction while P-T will refer to the transverse direction. Composite laminates exhibit better mechanical properties in transverse direction from the direction of punching process.

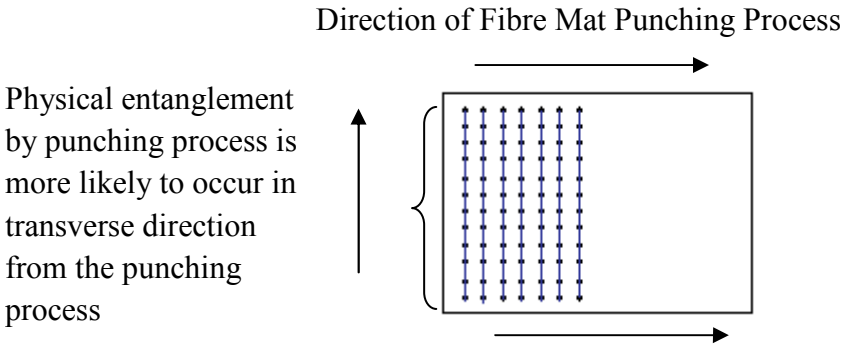


Fig. 5 Direction of physical entanglement network in kenaf fiber mat

Fibre matrix interaction may also contribute to the overall strength of the composite. Research found that maximum amount of kenaf fibre which can be fits into RTM mould is $35W_f$%. At this amount of fibres, a decreasing pattern of flexural strength, flexural modulus and impact strength for unpunched fibres are observed. At higher fibre loading, there is a strong tendency for fibre–fibre interaction. This leads to poor wetting of fibres and fibre dispersion. In such systems, the crack initiation and its propagation will be easier at higher loadings [5]. David Rouison et al. also observed the same trend in hemp fibre reinforced polyester composites [6]. Addition of unorganized fibers creates more regions of stress concentrations that require less energy to initiate a crack. Cracks are initiated at places of high stress concentration such as the fiber ends, defects, or at the interface region where the adhesion between the two phases is very poor [7]. Knowing that unpunched kenaf fibre is used, more fibre ends exist. Otherwise effect occurs for punched kenaf fibre as more fibre loading more apparent increment of impact strength is observed.

Summary

Optimum value of stitching density for kenaf fibre mat is 50 cm^{-2}. Lower value will result in producing loose fibre mat while at higher value kenaf fibre tend to break the fibre into shorter length thus the mechanical properties will be deteriorated. The mechanical strength of composite will increase in increasing amount of fibre loading for composites produced by punched kenaf fiber mat. However for unpunched fibre mat, above 35% W_f, the mechanical properties will drop. Proper wetting of fibre and matrix for punched kenaf fibre mat gives better physical and mechanical properties of the composites produced as stress distribution and stress transfer mechanism are more likely to occur even at high amount of fibre loading. Punched kenaf fibre mat can resembled the properties of continuous fibre in which the fibre orientation is arranged in such a way that amount of fibre ends is reduced thus reducing flaws and crack initiation region hence impart better impact strength of the composites obtained. The formation of physical entanglement during stitching of the mat tend to occur in transverse direction and responsible to composite laminates having anisotropy behaviour in which mechanical properties in transverse direction are better.

References

[1] Information on http://www.lktn.gov.my
[2] Rassmann, R.G. Reid, and R. Paskaramoorthy 'Effects of processing conditions on the mechanical and water absorption properties of resin transfer moulded kenaf fibre reinforced polyester composite laminate'.
[3] Sapuan, S. M, Harimi, M., and Maleque, M.A.: The Arabian Journal for Science and Engineering, 28(2003), 171-181.
[4] Rowell, J.K., J.S. Han and J.S. Rowell: Nat. Polymers Agrofibers Composites (2000).
[5] Sreekumar PA, Jospeh K, Unnikrishnan G, Thomas S.: Compos Sci Technol (2007);67:453–61.
[6] Rouison David, Sain Mohini, Couturier M.: Compos Sci Technol (2006);66:895.
[7]. *Cox,* H. L.: *Brit. .I. Appl. Phys, 3 (1952) 72.*

© (2011) Trans Tech Publications, Switzerland
doi:10.4028/www.scientific.net/KEM.471-472.993

Synthesis of Tio_2/Zno Core/Shell Type Nanocomposite via Sol-Gel Method

Mohammad Reza Golobostanfard[1,a], Reza Ebrahimifard[1] and Hossein Abdizadeh[1]

[1]School of Metallurgy & Materials Engineering,

University of Tehran, Tehran, Iran

[a]Mohammadreza.Golbostanfard@gmail.com

Keywords: TiO_2/ZnO Nanocomposite, core/shell type powder, sol-gel

Abstract. TiO_2/ZnO Nanocomposite powders with different Zn/Ti ratios were synthesized via sol-gel method. The as prepared and calcined Titania nanopowders were added to the ZnO sols. Also the as prepared and calcined ZnO nanopowders were separately added to the TiO_2 sols. However, in the latter case, the nanocomposite never formed due to the high acidity of the sols. After gelation, the powders were dried and calcined at 500°C for 1h. The phase composition, structure, morphology and optoelectrical properties of the powders were characterized by means of X-ray diffraction (XRD), field emission scanning electron microscopy (FESEM), UV-Vis photospectroscopy and photoluminescence spectroscopy (PL). The XRD patterns confirm the presence of TiO_2 and ZnO crystalline phases in the TiO_2 particles/ZnO sol samples. The FESEM micrographs show that TiO_2/ZnO nanocomposites heat treated at 500°C were formed with average diameter of about 250nm with 50nm ZnO particles on clusters of 40nm TiO_2 particles. It was found that the optoelectronic properties of the nanocomposites were improved according to the UV-Vis and photoluminescence spectroscopy.

Introduction

Among all oxide semiconductors, TiO_2 and ZnO are two most important non-stoichiometry wide band gap semiconductors, which can be used in many areas such as photocatalysis for degradation of organic pollutants, purification of air and water, solar cells, and other optoelectronic devices, due to their size tunable physicochemical properties, high surface activities, cost effectiveness, non-toxicity, and strong oxidizing power [1-3].

TiO_2 has three main phases in normal pressures including Rutile, Anatase and Brookite. Brookite phase was rarely formed at ambient temperatures. However, rutile phase has very low electron mobility and far lower photocatalytic properties than anatase phase. Bulk Anatase TiO_2 has the indirect band gap of ~3.2eV [4]. ZnO, a well known II-VI compound semiconductor, has the direct band gap of ~3.37eV and exciton binding energy of 60meV at room temperature [5, 6]. Moreover, the carrier mobility in ZnO is higher than Anatase, while its chemical stability is lower. Also, ZnO can be doped both n- and p-type [7]. The main drawbacks of these semiconductors are the fast recombination rate and narrow adsorption in the light spectrum. Mixing these semiconductors caused: 1. extending the light adsorption spectrum and improving the light efficiency utilization and 2. suppressing the recombination of photo generated electron/hole pairs [8].

TiO_2/ZnO composites have been synthesized with variety of methods including atomic layer deposition [9], electrospinning [1], sol-gel method [5] and so on. Sol-gel method has many advantages such as excellent compositional control, homogeneity on the molecular level, lower crystallization temperature, and good control on the microstructure. The core/shell type structure has been prepared by the hydrothermal and other methods synthesized cores and sol-gel coated shell [3, 7, 10]. However, in this article for the first time, the core/shell type nanocomposites have been prepared simply by incorporating the sol-gel synthesized nanoparticles in the sol of counterparts and compared with mixed oxide structure. The sols have lowest possible organic addition in order to decrease the destructive effect of these additives.

Experimental

Zinc acetate dehydrate ($Zn(CH_3COO)_2.2H_2O$ - ZnAc) and Titanium tetra-isopropoxide ($C_{12}H_{28}O_4Ti$ - TTiP), two main precursors, anyhyrous ethanol (C_2H_5OH - EtOH) for solvent, nitric acid 70% (HNO_3) for control of hydrolysis and condensation of TiO_2 sol-gel process, and triethylamine ($C_6H_{15}N$ - TeA) for dissolving, dispersing and reacting in ZnO sol-gel process were purchased from Merck Chemicals. Dionized water (DI) with resistance of 18.2 MΩ.cm was used in all experiments. All the chemicals were reagent grade and used as received.

The sol-gel method was used for synthesizing both TiO_2 and ZnO nanoparticles. For TiO_2 nanoparticles preparation, TTiP was dissolved in EtOH and stirred for 10min (solution A). Separate solution containing equal amount of EtOH with solution A, DI water, and HNO_3 were mixed and added dropwise to solution A under vigorous stirring for 15min. The molar ratios of the components were fixed at TTiP : DIW : HNO_3 = 1: 4 : 0.5. The prepared transparent sol (S(T), pH~1) was converted to transparent gel after 2 days. The gel was dried in 100˚C for about 3h and grinned (so-called P(T)). Then the obtained powders calcined at 450˚C for 1h (hereafter called C(T)). For synthesizing ZnO nanoparticles, ZnAc and TeA in 0.5 molar ratio were added to the required amount of EtOH and stirred for 15min. Tansparent sol of ZnO (S(Z), pH~7.5) converts to gel after about 1 week. The ZnO gel was dried at 150˚C for 1h and grinned (so-called P(Z)). The obtained powders were calcined at 500˚C for 1h (hereafter called C(Z)).

For preparation of core/shell type TiO_2@ZnO or mixed oxide nanocomposites, the nanoparticles of P(T) and C(T) after dispersion and sonication in EtOH were added dropwise to S(Z) in different Zn/(Zn+Ti) = 0.25, 0.5, and 0.75 molar ratios (called P(T)/S(Z) 1/3, (P(T) or C(T))/S(Z) 1/1, and P(T)/S(Z) 3/1, respectively) and stirred until all the solvents evaporated. On the other hand, for preparation of TiO_2/ZnO nanocomposites with ZnO nanoparticles in TiO_2 sols, P(Z) and C(Z) nanoparticles after dispersion and sonication in EtOH, also were added to S(T) in Zn/(Zn+Ti) = 0.5 molar ratio and stirred until all the solvent evaporated (S(T)/(P(Z) or C(Z))). All the samples were dried at 100˚C for about 3h and after grinding, calcined at different heat treatment temperatures of 500, 700, and 900˚C for 1h.

X-ray diffraction (XRD) measurements with scanning speed of 1.5˚/min were performed on a Philips PW1730 X-ray diffractometer using Cu K_α radiation (λ=1.5405 Å, 40kV, 30mA). The size and morphologies of the resultant nanocomposites were observed by Hitachi S4160 field emission scanning electron microscope (FESEM) equipped with energy dispersive X-ray analyzer (EDX). The diffuse reflectance UV-Vis absorption spectra (DRS) were measured using Avalight DH-S Avaspec 2048 TEC. The photoluminescence (PL) spectra were taken on Perkin Elmer luminescence spectrophotometer for UV emission and PL Avantes avaspec 2048 for green emission spectroscopy.

Results and Discussion

The core/shell type nanocomposites of TiO_2@ZnO were synthesized via sol-gel method, including synthesis of the core material, which will be shown that it could be possible only in P(T)/S(Z) samples heat treated at 500˚C for 1h. In the other cases, S(T)/P(Z) and S(T)/C(Z), none of expected nanocomposites were formed due to the high acidity of the TiO_2 sols. Also, in the case of C(T)/S(Z) random mixed oxide nanocomposite was formed and the core/shell type structure was never reached.

Fig. 1 (left) shows XRD patterns of the P(T)/S(Z) 1/3, P(T)/S(Z) 1/1, P(T)/S(Z) 3/1, C(T)/S(Z), S(T)/P(Z), and S(T)/C(Z) samples calcined at 500 °C for 1h. Formation of ZnO is more sensible than TiO_2 because ZnO peaks are more intense than TiO_2 naturally. It could be seen that anatase phase was formed instead of thermodynamicly stable phase Rutile due to the insufficient calcination time. Samples (P(T) or C(T)/S(Z)) demonstrated more crystallized ZnO and TiO_2 (anatase and rutile) phase compared with samples (S(T)/P(Z) or C(Z)). In P(T)/S(Z), increasing the ratio of Zn/Zn+Ti from 0.25 to 0.75, increase ZnO peaks, while in TiO_2 rich sample, anatase is the dominant phase. In the case of S(T)/P(Z), ZnO phase was not detected due to the existence of large amount of zinc acetate in uncalcined powder, which simply dissolved in S(T). Based on TiO_2-ZnO

phase diagram [11], $ZnTiO_3$ in Zn/Ti+Zn = 0.5 should be crystallized, while due to the insufficient calcination time, $ZnTiO_3$ was not formed from obtained sol. So, no indexed peaks of $ZnTiO_3$ were detected. In S(T)/C(Z) sample, due to the low chemical stability of ZnO particles in S(T) acidic sol (pH~1), a large portion of ZnO dissolved in the sol, and $ZnTiO_3$ could not formed due to the reason mentioned above.

XRD patterns of P(T)/S(Z) and C(T)/S(Z) calcined at 500, 700, and 900 °C are shown in Fig. 1 (right). Increasing calcination temperature causes promotion of peaks intensity as well as formation of new phases. $ZnTiO_3$ exists in 700 and 900°C calcination temperatures beside ZnO and TiO_2 peaks while in 500 °C there are no perovskite peaks. In this article utmost attempt has been done to eliminate formation of perovskite structure as an unfavorable phase beside ZnO and TiO_2, then calcination temperatures of 700 and 900°C were not suitable to achieve TiO_2/ZnO nanocomposite. The ratio of Zn/Zn+Ti changes in the surface of the particles dispersed in sols, means that the core of the particles was not participate in the process and then in some area Zn/Zn+Ti deviated from 0.5. As a result, in high ratios of Zn/Zn+Ti and high calcination temperatures, formation probability of Zn_2TiO_4 (spinel phase) increases.

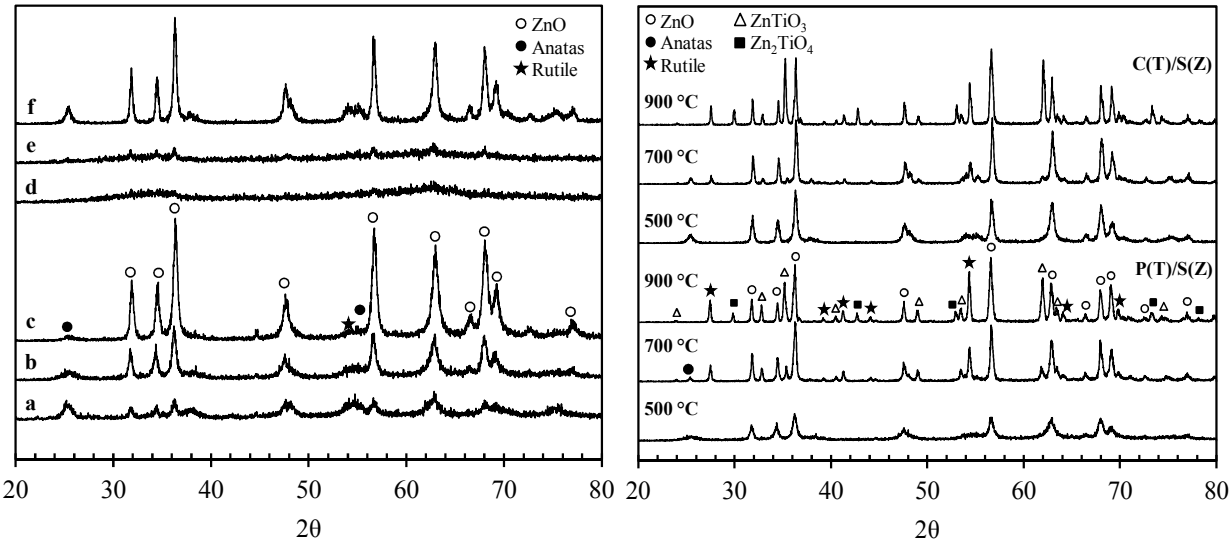
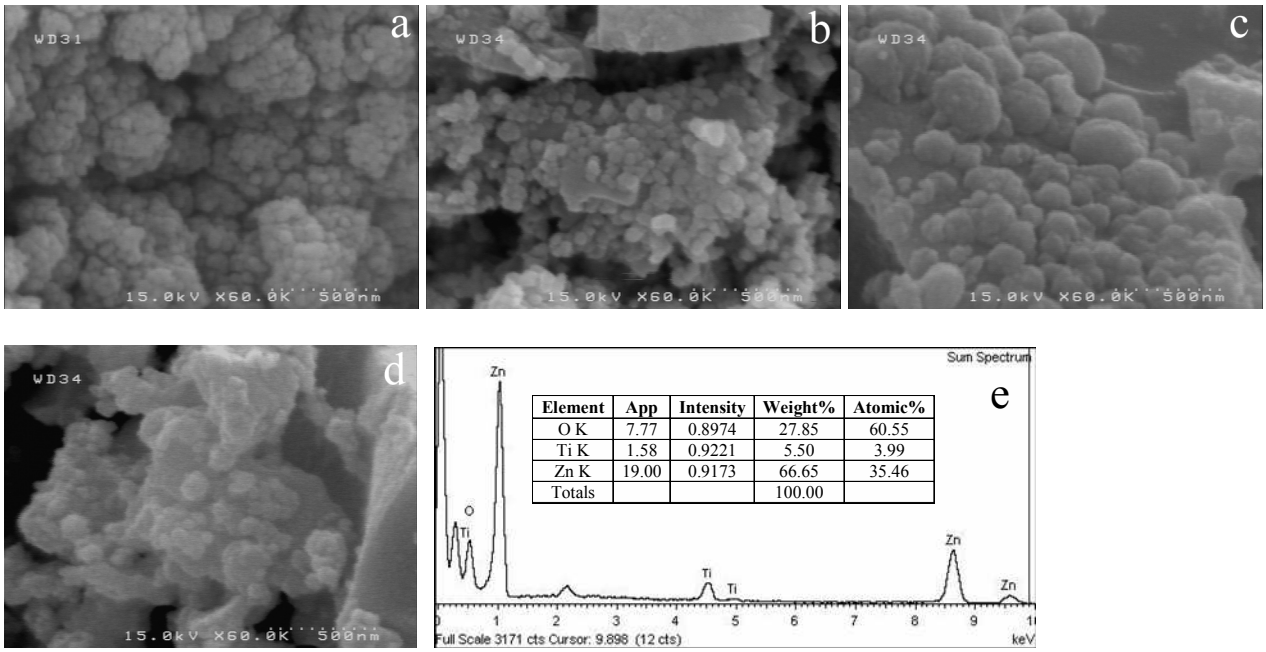


Fig. 1 XRD patterns of left: a) P(T)/S(Z) 1/3, b) P(T)/S(Z) 1/1, c) P(T)/S(Z) 3/1, d) S(T)/P(Z), e) S(T)/C(Z), and f) C(T)/S(Z) calcined at 500 °C; right: XRD patterns of P(T)/S(Z) and C(T)/S(Z) samples calcined at 500, 700, 900°C.

Figs. 2a and 2b shows the FESEM micrographs of P(T)/S(Z) and C(T)/S(Z) calcined at 500˚C for 1h, respectively. It could be seen that core/shell type nanocomposite is formed with the average diameter of about 250nm consisting of clusters of 40nm TiO_2 particles cover with 50nm ZnO particles in P(T)/S(Z) samples. However, in C(T)/S(Z) samples, random mixed oxide morphology is formed, which may be due to the instability of the relative larger and agglomerated calcined TiO_2 particles cause instability of the sols and settling down of the particles during the preparation process. This figure reveals ZnO nanoparticles with average diameter of about 50nm are formed on the agglomerated TiO_2 particles in the nearly mixed oxide configuration. FESEM micrographs of the P(T)/S(Z) 1/3 and P(T)/S(Z) 3/1 are shown in Figs. 2c and 2d, respectively. It could be seen from Fig. 2c that in some area the core/shell type structure is obtained beside the TiO_2 agglomerated nanoparticles due to the excess amount of TiO_2 molar percent. However, in higher molar ratios of ZnO the core/shell type structure nanocomposite particles are formed only in very low amount and ZnO rich nanoparticles are the major phase in this sample. In order to clarify the element composition of the core/shell type nanocomposite (especially the shell composition) in P(T)/S(Z) 1/1 sample, the EDS analysis conducted on the surface of this sample which indicates in the Fig. 2e. Elements of zinc (Zn) and Oxygen (O) as the major element and titanium (Ti) as the minor one are detected which confirms the formation of ZnO shell on TiO_2 cluster.



Element	App	Intensity	Weight%	Atomic%
O K	7.77	0.8974	27.85	60.55
Ti K	1.58	0.9221	5.50	3.99
Zn K	19.00	0.9173	66.65	35.46
Totals			100.00	

Fig. 2 FESEM micrographs of samples a) P(T)/S(Z) 1/1, b) C(T)/S(Z) 1/1, c) P(T)/S(Z) 1/3, d) P(T)/S(Z) 3/1 calcined at 500°C for 1h and e) EDX analysis of P(T)/S(Z) 1/1.

In order to obtain optoelectrical properties of TiO_2/ZnO nanocomposite, the optical absorbance of TiO_2, ZnO, P(T)/S(Z) 1/3, P(T)/S(Z) 1/1, and P(T)/S(Z) 3/1 calcined at 500°C for 1h samples was measured. Fig. 3 (left) shows the diffuse reflectance spectra of these samples. Generally, according to the samples spectra, absorption values of pure TiO_2 and ZnO enhance by making TiO_2/ZnO nanocomposite in different Zn/Zn+Ti ratios. This phenomenon is well demonstrated in P(T)/S(Z) 1/1 and P(T)/S(Z) 3/1 in UV region, especially in P(T)/S(Z) 3/1 with maximum absorbance. On the other hand, the absorbance in P(T)/S(Z) 1/3 reaches the highest value in visible region.

The optical band gap of the semiconductors has been calculated by the following equation:

$$\alpha h\nu = A\,(h\nu - E_g)^n \qquad (1)$$

where α is absorption coefficient, $h\nu$ is photon energy, E_g is optical band gap, and A is constant. Extrapolation of $(\alpha h\nu)^2$ vs. hν for direct band gap and $(\alpha h\nu)^{0.5}$ vs. hν for indirect band gap semiconductors to α = 0, get the optical band gap (E_g). By plotting $(\alpha h\nu)^2$ vs. hν and $(\alpha h\nu)^{0.5}$ vs. hν for pure TiO_2, consists of anatase and rutile phase, more realistic band gap as well as more extrapolation fitting is elicited from $(\alpha h\nu)^2$ vs. hν, which proof that TiO_2 prefers to be a direct band gap semiconductor. In fact, the quantum confinement of TiO_2 crystallites is responsible for converting band gap of TiO_2 to direct one [12], as observed in Si quantum dots [13]. Fig. 3 (right) shows Tauc plot for TiO_2, ZnO, P(T)/S(Z) 1/3, P(T)/S(Z) 1/1, and P(T)/S(Z) 3/1 calcined at 500°C for 1h samples. It reveals from Tauc plot that ZnO shows the maximum optical band gap (E_g = 3.27eV) and by increasing the ratio of TiO_2/ZnO, red shift in band gap occurrs and the band gap decreases to 3.19eV for P(T)/S(Z) 3/1, 3.13eV for P(T)/S(Z) 1/1, 3eV for P(T)/S(Z) 1/3 and 2.98eV for pure TiO_2, respectively. This calculated band gap shows slight difference with that of anatase which may be due to the existence of rutile phase.

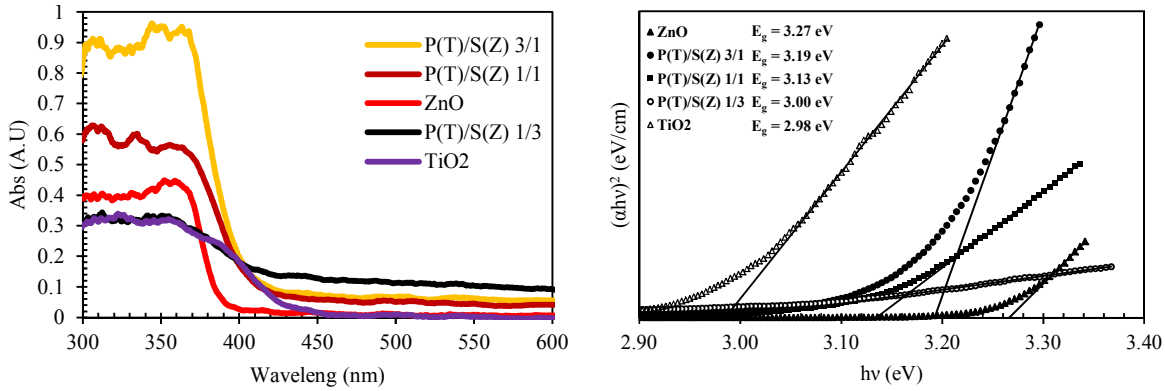


Fig. 3 left: DRS UV-Vis absorbance spectra of TiO_2, ZnO, P(T)/S(Z) 1/3, P(T)/S(Z) 1/1, and P(T)/S(Z) 3/1 calcined at 500°C; right: $(\alpha h\nu)^2$ vs. hν diagram and calculation of band gap.

Fig. 4 (left) indicates the PL spectra of TiO_2, ZnO, P(T)/S(Z) 1/3, P(T)/S(Z) 1/1, and P(T)/S(Z) 3/1 calcined at 500˚C for 1h with an excitation wave length of 330nm. For these samples there are a strong characteristic peaks at around 390nm due to a near band edge emission. Among all samples, ZnO has the highest UV emission peak due to its direct band gap. While, TiO_2 nanocrystallite with direct band gap shows the low UV emission peak compared to ZnO. UV emission peak of sample P(T)/S(Z) 1/1 shows reduction compared to ZnO and slightly blue shift. This emission for P(T)/S(Z) 3/1 demonstrates more reduction without any sensible shift and in P(T)/S(Z) 1/3 reaches the lowest measured amount. The slight blue shift of the UV emission for P(T)/S(Z) 1/1 may be due to the tuning the bang gap energy by making composite of these semiconductors. The reduction in UV emission in these samples could be ascribed to the fluorescence resonance energy transfer (FRET) between ZnO and TiO_2 which causes separation of electron-hole pairs and thus inhibition of exciton recombination. Schematic diagram of electron-hole separation process of ZnO/Anatase/Rutile illustrates in Fig. 4 (right). According to this diagram, the conduction band (CB) of ZnO is higher than that of Anatase and CB of Anatase is higher than that of Rutile. The same trend could be observed for valence band (VB) of these semiconductors. Upon light excitation, the electrons transfer from the CB of ZnO through that of Anatase to that of Rutile. Conversely, holes migrate from VB of Rutile through that of Anatase to that of ZnO. Such an efficient charge separation increases the lifetime of charge carriers and reduces the recombination of electron-hole pairs. Moreover, in addition to the reason mentioned above, three major competition processes, radiation trap recombination, non-radiative recombination, and exciton recombination, acquire after irradiation of UV light. Increasing the probabilities of the former two, lead to decreasing the UV emission [10]. Thus in all nanocomposite samples reduction in UV emission could be observed. However, it could be seen that P(T)/S(Z) 1/1 has the lower reduction in UV emission compared to P(T)/S(Z) 3/1. As discussed before, P(T)/S(Z) 1/1 has the morphology of core/shell type but P(T)/S(Z) 3/1 has the structure of mixed oxide. The shielding effect due to the thick layer of ZnO on the surface of TiO_2 affects the emission spectra of this sample. It could be said that for P(T)/S(Z) 1/3 emission, an optimal amount of TiO_2/ZnO exists (Zn/Zn+Ti < 0.5) which causes the lowest recombination rate and highest quantum efficiency which leads to lowest luminescence spectra.

Inset of Fig. 4 (right) shows PL green emissions of TiO_2, ZnO, and P(T)/S(Z) 1/1 with an excitation wave length of 380nm. There is a very weak green emission observed for TiO_2 and P(T)/S(Z) 1/1 samples around 550nm due to a deep level emission. This emission has five main reasons including: 1. ionized oxygen vacancies; 2. oxygen interstitials; 3. zinc or titanium vacancies; 4. interface/surface related defects; and 5. electronic impurity levels formed by doping between VB and CB. All of these reasons is responsible for increasing the green emission of P(T)/S(Z) 1/1 sample compare to that of TiO_2.

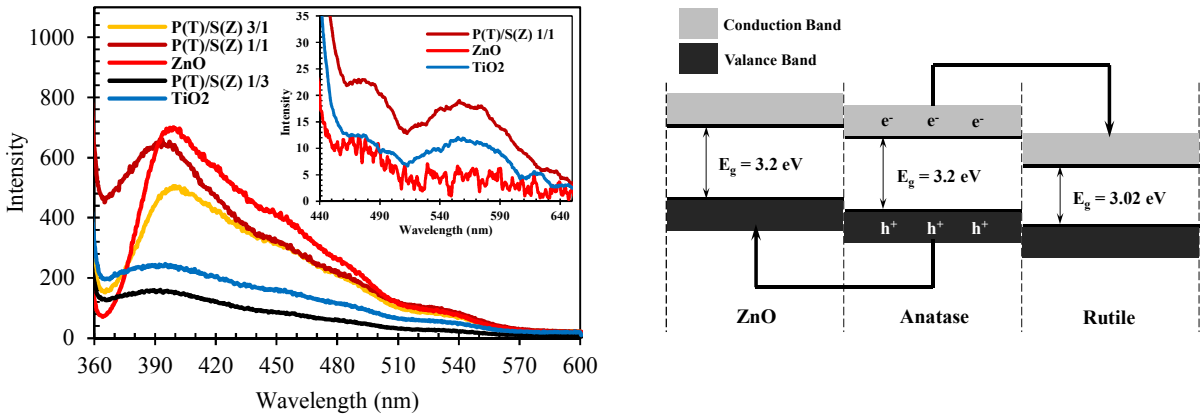


Fig. 4 left: PL spectra UV emission of TiO_2, ZnO, P(T)/S(Z) 1/3, P(T)/S(Z) 1/1, and P(T)/S(Z) 3/1 calcined at 500°C. Inset: PL green emission of TiO_2, ZnO, and P(T)/S(Z) 1/1; right: Schematic diagram of electron-hole separation process of ZnO/Anatase/Rutile.

Summary

The core/shell type nanocomposites of TiO_2@ZnO were synthesized via sol-gel method only in P(T)/S(Z) samples heat treated at 500˚C. In the case of C(T)/S(Z) random mixed oxide nanocomposite was formed. The XRD results indicated that in all samples calicined at 500˚C Anatase, Rutile and ZnO were detected and increasing the calcinations temperature caused the formation of other phases. Nanocomposites of TiO_2@ZnO with diameter of about 250nm consisting of 50nm ZnO particles on clusters of 40nm TiO_2 particles were observed and EDX result proved the formation of ZnO shell. DRS spectra showed that increase in Zn/Zn+Ti leads to band gap blue shift and improvement of absorbance in UV region. It was observed that UV emission of the samples enhanced by making composite of these oxides. UV absorption and PL emission in core/shell type nanocomposite were improved relative to the pure TiO_2 and ZnO, but the lowest PL emission in nanocomposite with mixed oxide structure was reached and highest UV absorption was observed.

References

[1] R. Liu, H. Ye, X. Xiong, H. Liu: Mater. Chem. Phys. Vol. 121 (2010), p. 432

[2] H. Wang, Z. Wu, Y. Liu, Z. Sheng: J. Mol. Catal. A: Chem. Vol. 287 (2008), p. 176

[3] M. Liao, C. Hsu, D. Chen: J. Solid State Chem. Vol. 179 (2006), p. 2020

[4] R. Asahi, W. Manstadt, A. J. Freeman: Phys. Rev. B: Condens. Matter. Vol. 61 (2000), p. 7459

[5] L. Schmidt-Mende and J. L. MacManus-Driscoll: Mater. Today Vol. 10 (2007), p.40

[6] A.B. Djurisic, A.M.C. Ng, X.Y. Chen: Prog. Quantum electron. Vol. 34 (2010), p. 191

[7] W. Wu, Y.W. Cai, J.F. Chen, A. Martin, L.X. Wen: J. Mater. Sci. Vol. 41 (2006), p. 5845

[8] J. Tian, L. Chen, J. Dai, X. Wang, Y. Yin, P. Wu: Ceram. Int. Vol. 35 (2009), p. 2261

[9] D. M. King, X. Liang, C. S. Carney, L. F. Hakim, P. Li, A. W. Weimer: Adv. Funct. Mater. Vol. 18 (2008), p. 607

[10] N. M. Bahadur, T. Furusawa, M. Sato, N. Suzuki: Mater. Res. Bull. Vol. 45 (2010), p. 1383

[11] J. Yang and J. H. Swisher: Mater. Charact. Vol. 37 (1996), p.153

[12] K. M. Reddya, S. V. Manorama, A. R. Reddy: Mater. Chem. Phys. Vol. 78 (2002), p. 239

[13] B. Delley, E. F. Steigmeier: Phys. Rev. B: Condens. Matter Vol. 47 (1993), p. 1397

© (2011) Trans Tech Publications, Switzerland
doi:10.4028/www.scientific.net/KEM.471-472.999

Life Cycle Assessment of Particulate Recycled Low Density Polyethylene and Recycled Polypropylene Reinforced with Talc and Fiberglass

Mariam AlMa'adeed[1,a], Gozde Ozerkan[1,b], Ramazan Kahraman[2,c], Saravanan Rajendran[3,d] and Alma Hodzic[3,e]

[1]Materials Technology Unit, Qatar University, Doha, Qatar

[2]Chemical Engineering Department, Qatar University, Doha, Qatar

[3]Composite Systems Innovation Centre, The University of Sheffield, UK

[a]m.alali@qu.edu.qa , [b]gozdeozerkan@qu.edu.qa, [c]ramazank@qu.edu.qa, [d]S.Rajendran@sheffield.ac.uk, [e]A.Hodzic@sheffield.ac.uk

Keywords: life cycle assessment, thermoplastics, mineral fillers, recycling

Abstract. Although recycled polymers and reinforced polymer composites have been in use for many years there is little information available on their environmental impacts. The goal of the present study is to analyze the environmental impact of new composite materials obtained from the combination of recycled thermoplastics (polypropylene [PP] and polyethylene [PE]) with mineral fillers like talc and with glass fiber. The environmental impact of these composite materials is compared to the impact of virgin PP and PE. The recycled and virgin materials were compared using life cycle assessment method according to their environmental effects. Within the scope of the study, GaBi software was used for Life Cycle Assessment (LCA) analysis. From cradle-to-grave life cycle inventory studies were performed for 1 kg of each of the thermoplastics. Landfilling was considered as reference scenario and compared with filled recycled plastics. A quantitative impact assessment was performed for four environmental impact categories, global warming (GWP) over a hundred years, human toxicity (HTP), abiotic depletion (ADP) and acidification potential (AP) were taken into consideration during LCA. In the comparison of recycled and virgin polymers, it was seen that recycling has lower environmental effect for different impact assessment methods like acidification potential, abiotic depletion, human toxicity and global warming.

Introduction

Conventional plastics have earned a dominant position in numerous fields over other materials such as wood, metals, glass, ceramics etc. because of their low manufacturing costs, low density, small weight and excellent mechanical, thermal, chemical properties. However, conventional plastics not only consume nonrenewable finite resources, but also impact heavily upon waste disposal, and over the past decades, it has been found that those disadvantages found in conventional plastics can be overcome by the development of alternative modified plastics, combining them with other substances like fillers, reinforcing fibers, stabilizers, plasticizers etc. [1, 2]. Now polymer matrix composites are very popular among those due to their low cost and simple fabrication method, and it is defined as the material consisting of a polymer (resin) matrix combined with a fibrous reinforcing dispersed phase. Polymer matrices may either be derived from renewable resources or more commonly be composed of synthetic, fossil fuel derived polymers featuring variable proportions of virgin and recycled thermoplastics. Reinforcement of polymers by string fibrous network permits fabrication of polymer matrix composites characterized by their high specific stiffness, high specific strength and controlled anisotropy, lightweight, impact resistance, fatigue strength, good abrasion resistance, good corrosion resistance and low cost which make them very attractive structural materials. On the other hand, the main disadvantages of polymer matrix composites are low thermal resistance and high coefficient of thermal expansion [1, 3, 4].

Over the past decade, the use of composites has grown considerably in the field of wood decking and in the automotive industry with countless new applications now being envisioned for the future [5]. However, in order to confirm such optimistic prospects, the environmental performance of those new materials throughout their entire life cycle, from raw material acquisition to disposal, should be properly assessed.

A few studies have looked at comparative life cycle assessment studies of composites. In 1999, Diener and Siehler deal with an underfloor panel made from fiberglass reinforced polypropylene (PP) and PP reinforced with flax used to protect the chassis while improving the aerodynamics of the Mercedes-Benz A-class car [6].

Wotzel et al., Gärtner and Reinhardt and Schmidt and Beyer performed LCA studies of automotive parts and the data on life cycle emissions for the ABS and Epoxy resins were based on APME eco-profiles. In these studies, the conventional part was manufactured by injection molding of virgin acrylonitrile-butadiene-styrene, while the bio-based component was made of a composite consisting of hemp fibers and epoxy resin plus hardener [7, 8, 9].

Corbiere-Nicollier et al. reports a comparison of LCAs of transport pallets made from glass fiber reinforced PP and china reed fiber reinforced PP. The system boundary for the LCA covers PP production, china reed cultivation, fiber extraction, compatibilizer production, intermediate transport, pallet production, pallet use and incineration for the NFR pallet. Similarly, glass fiber production, PP production, pallet production, transport, pallet use, and end of life incineration are modeled for the GFR pallet LCA [10].

This paper presents the results of the environmental impact analyses of new composites materials obtained from the combination of recycled thermoplastics (polypropylene [PP] and low density polyethylene [LDPE]) with mineral fillers like talc and glass fiber (14 μm diameter and treated for good coupling to thermoplastics). The environmental impact of these composite materials was compared to the impact of virgin PP and LDPE. Some of the samples were tested in tensile mode to determine how effective the fillers/combination of fillers are in enhancing structural properties. Furthermore, the recycled and virgin materials were compared using life cycle assessment method according to their environmental effects.

Life Cycle Assessment

Goal and Scope Definition. The goal of this study is to compare the environmental impact of virgin PP and LDPE with recycled PP and LDPE, and also to analyze the environmental impact of newly developed composite materials obtained from the combination of recycled PP and LDPE with talc and glass fiber. In the study, 1 kg of material was defined as the functional unit for calculations and comparative purposes. Plastic waste is recovered into recycled LDPE and PP in industrial facilities where waste is ground, washed, dried and granulated. The impact associated with the disposal of each material is assessed for landfilling. Within the scope of the study, GaBi software was used for LCA analysis.

Life Cycle Inventory Analysis. An LCA was carried out for each new composite material and for virgin and recycled LDPE and PP using GaBi LCA software. The input materials (proportions) of these compounds are described in Table 1. The data required for constructing the inventory regarding the manufacturing of polymers and fibers, injection molding and service life of LDPE and PP were retrieved from various supporting database as Ecoinvent and Buwal 250 found in GaBi impact assessment software with modification for Qatar. Furthermore, in each material, transportation and electricity systems were also taken into consideration. The life cycle diagrams of virgin LDPE/PP and recycled LDPE/PP are presented in Fig. 1 and 2, respectively.

Table 1 Proportions of Tested Materials

Comparison #	Composite Material Definition	Comparison Type
1	100 % Virgin LDPE – 100 % Recycled LDPE – 100 % Virgin PP – 100 % Recycled PP	Recycled LDPE - Virgin LDPE Recycled PP – Virgin PP
2	85%LDPE+15%GF - 85%LDPE+15%TALC - 85%PP+15%GF- 85% PP+%15TALC	GF – TALC Recycled LDPE – Recycled PP

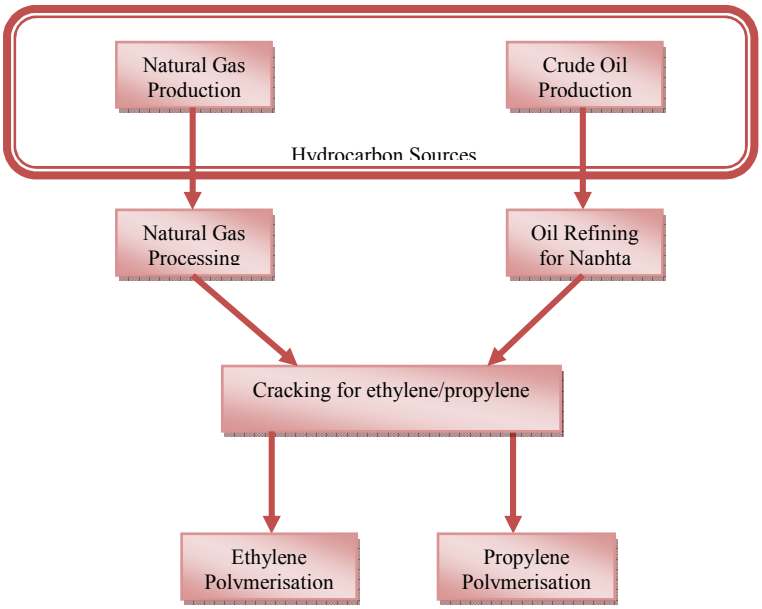


Fig. 1 Low Density Polyethylene and Polypropylene Production

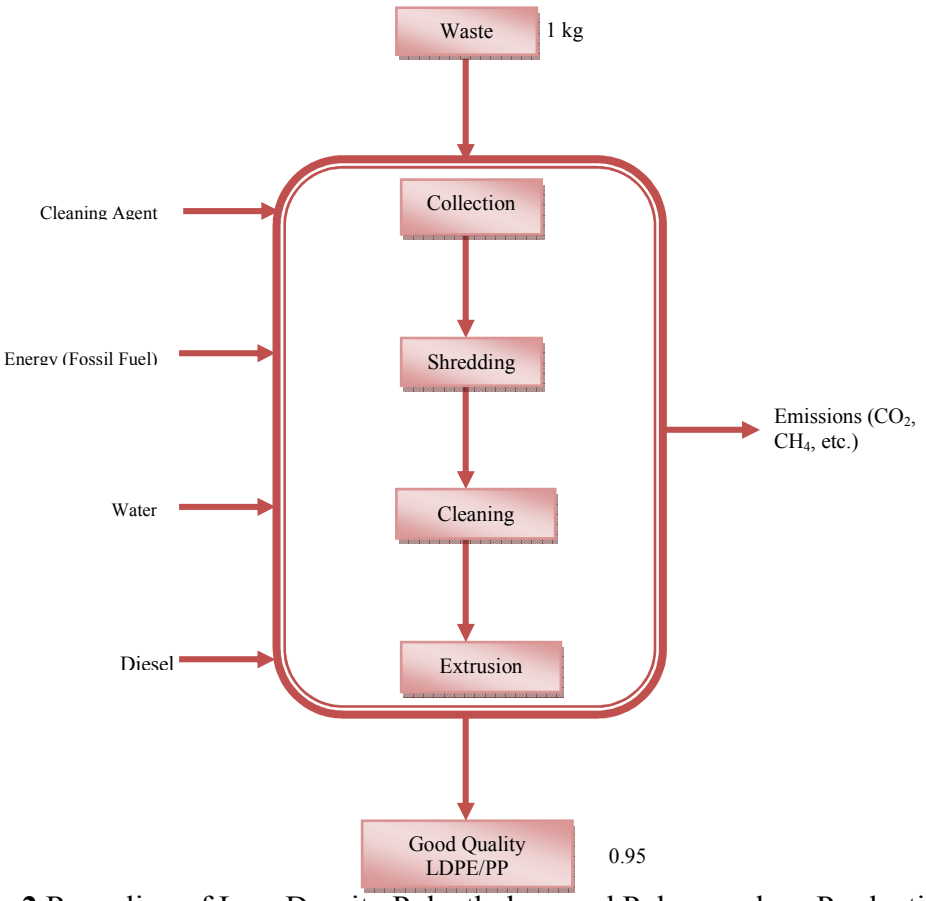
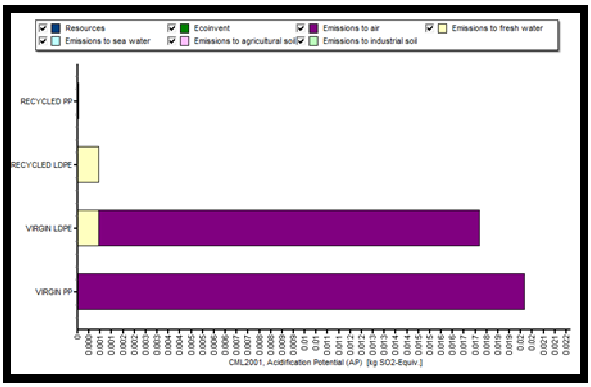


Fig. 2 Recycling of Low Density Polyethylene and Polypropylene Production

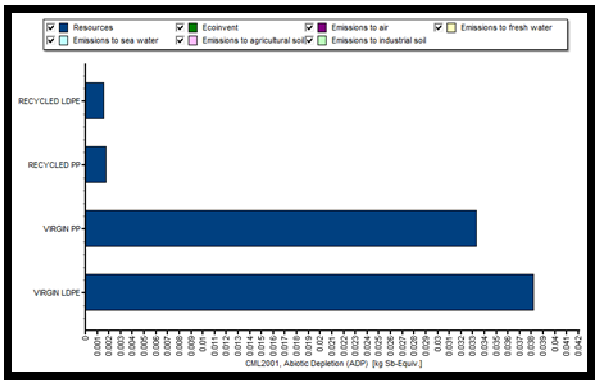
Life Cycle Impact Assessment. The method used for impact assessment was CML 2001. This method was developed by the Institute of Environmental Sciences, University of Leiden (Netherlands). The LCA focused on five selected obligatory impact categories:

- Abiotic resources depletion (MJ equivalent),
- Acidification potential (kg SO_2 equivalent),
- Global Warming potential (GWP100, kg of CO_2 equivalent),
- Human Toxicity potential (kg DCB equivalent).

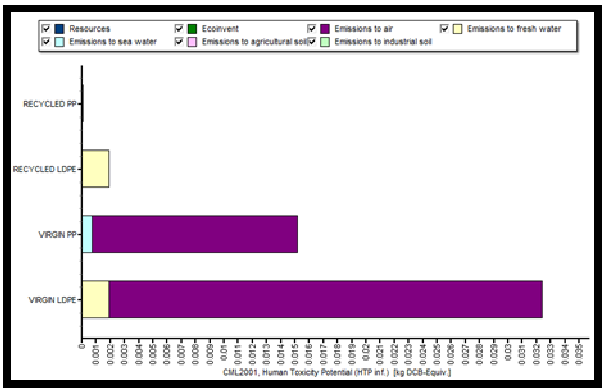
Fig. 5(a-d) presents the comparison of virgin low density polyethylene (LDPE), recycled LDPE, virgin PP and recycled PP for different environmental impacts point of views. In this analysis, for recycling, it was thought that LDPE and PP in the landfill will be recycled and used instead of producing new LDPE and PP. In both cases, landfill was thought as a disposal method after using them. All life cycle steps were compared to see their environmental effect. As seen from the figures, the life cycle of a recycled LDPE and PP has a lower environmental impact than that of virgin LDPE and PP. Furthermore, it can be seen from the Fig. 3a and 3c, recycled LDPE and virgin LDPE has approximately equal value of emissions to fresh water, however, virgin LDPE has also impact on emissions to air from the acidification potential and human toxicity point of view.



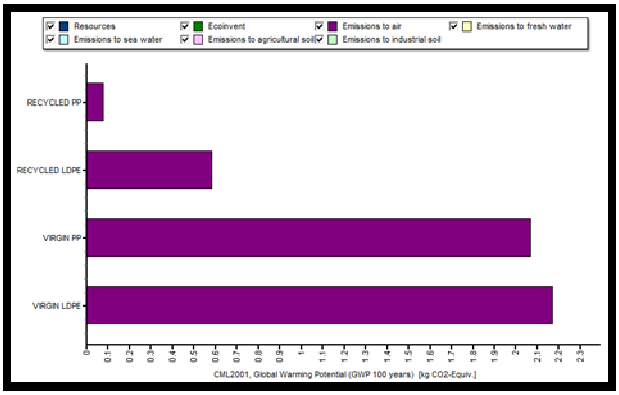
(a) Acidification Potential (AP)



(b) Abiotic Depletion Potential (ADP)



(c) Human Toxicity Potential (HTP)

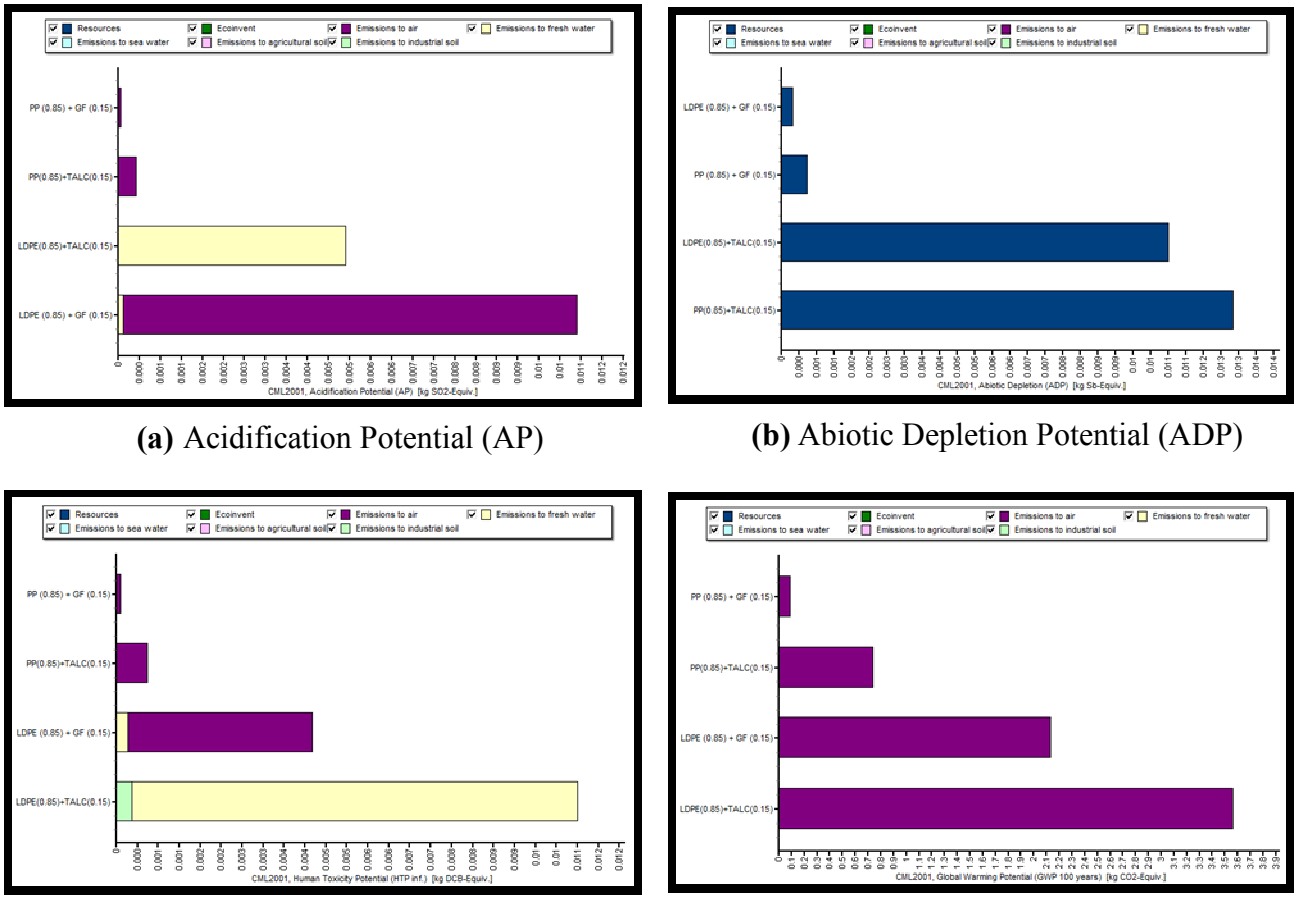


(d) Global Warming Potential (GWP)

Fig. 3 Comparison of Virgin and Recycled Low Density Polyethylene, and Virgin and Recycled Polypropylene

On the other hand, Fig. 4(a-d) present the comparison of newly developed composite materials obtained by combining recycled and virgin LDPE and PP polymer matrices with talc and glass fiber. In these comparison, in order to develop composite materials, amount of fillers were kept constant as 15% of glass fiber or talc and 85% of LDPE or PP. At the end of the comparison it can

be seen that the hazardous environmental effect of talc is higher than that of glass fiber. The impact assessment step in the Fig. 6 indicates that composite product developed from recycled matrix is much greener than the composite product developed from the virgin matrix. The environmental impact of manufacturing phase is very high for virgin resin, since monomer extraction and polymerization are highly energy intensive process. The recycling process is not highly energy intensive. The processes involved are washing, sorting, cleaning, drying and extrusion. This makes recycled matrix greener than the virgin material. The overall life cycle score indicates that both glass fiber filled and talc filled recycled composites are much friendlier to the environment than composites made of virgin resin.



(a) Acidification Potential (AP)

(b) Abiotic Depletion Potential (ADP)

(c) Human Toxicity Potential (HTP)

(d) Global Warming Potential (GWP)

Fig. 4 Comparison of Combined Recycled and Virgin Low Density Polyethylene and Polypropylene Reinforced with Talc and Glass Fiber

Summary

In this study, the environmental impact analyses of newly developed composite materials obtained from the combination of recycled thermoplastics, PP and LDPE, with mineral fillers, glass fiber and talc, were compared with environmental impact composite materials obtained by combining virgin thermoplastics PP and LDPE with glass fiber and talc. Within the scope of the environmental analysis, life cycle assessment method was performed. As a result of life cycle assessment of virgin and recycled PP and LDPE, it was concluded that the life cycle of a recycled LDPE and PP has a lower environmental impact than that of virgin LDPE and PP. From the life cycle assessment comparison of newly developed composite materials obtained by combining recycled and virgin LDPE and PP polymer matrices with talc and glass fiber it can be concluded that the hazardous environmental effect of talc is higher than that of glass fiber, and composite product developed from recycled matrix is much greener than the composite product developed from the virgin matrix.

Acknowledgments
This work has been developed with a support from by Qatar Science and Technology Park in Qatar. The support of Qatar University is also appreciated.

References

[1] R. Vidal, P. Martínez and D. Garraín, International Journal of Life Cycle Assessment, Vol. 14 (2009), p. 73-82

[2] P. Martínez,., D. Garraín and R. Vidal: 3rd International Conference on Life Cycle Management, Zurich, (2007)

[3] Y. Ivanov, V. Cheskhov and M. Natova: (Kluwer Academic Publishers, The Netherlands 2001).

[4] E. Trujillo, L. Osorio, A.W. Van Vuure, J. Ivens and I. Verpoest: 14th European Conference on Composite Materials, Budapest, Hungary (2010)

[5] P. Fowler, J. Hugues and R. Elías, Journal of Science in Food and Agriculture, Vol. 86 (2007a), p. 1781-1789.

[6] J. Diener and U. Siehler: "Ökologischer Vergleich von NMT- und GMT-Bauteilen, Angew Makromol Chem, Vol. 272 (1999), p. 1-4.

[7] K. Wötzel, R. Wirth and R. Flake, Angew Makromol Chem, Vol. 272(4763) (1999), p.121-127.

[8] S. Gärtner and G. Reinhardt: Proceedings of the 2nd World Conference on Biomass for Energy, Industry and Climate Protection, Rome, Italy (2004).

[9] W. Schmidt, and H. Beyer: Life Cycle Study on a Natural Fiber Reinforced Component, SAE Technical Paper, SAE Total Life Cycle Conference, Austria (1998).

[10] T. Corbiere-Nicollier, L.B. Gfeller, L. Lundquist, Y. Leterrier, J. Manson and O. Jolliet, Resource Conservative Recycling, Vol. 33 (2001), p. 267-287.

© (2011) Trans Tech Publications, Switzerland
doi:10.4028/www.scientific.net/KEM.471-472.1005

Differential Cubature Method for Static Solution of Laminated Shells of Revolution with Mixed Boundary Conditions

S.M. Mousavi[1,a]

[1]Department of Mechanical Engineering, Amirkabir University of Technology 424, Hafez Avenue, Tehran 158754413, Iran

[a] Mousavi.se@gmail.com

Keywords: differential cubature method; shells of revolution; bending analysis.

Abstract. The bending analysis of laminated shells of revolution, such as spherical, conical and cylindrical panels, is carried out utilizing the differential cubature method (DCM). To do so, a general software based on the DCM is developed which can tackle shells of revolution with symmetric and unsymmetric lamination sequence. Analysis of shells with general Loading and various combinations of clamped, simply supported, free and mixed boundary condition, may be carried out having acceptable accuracy. Using first order shear deformation theory, fifteen first order partial differential equations are obtained which contain fifteen unknowns in terms of displacements, rotations, moments and forces. Utilizing all of these equations results in the capability of the method to deal with any kinds of boundary conditions. Comparison of the results obtained by the DCM, shows very good agreement with the results of other numerical and analytical methods, while having less computational effort.

Introduction

Shells are the main part of many structures utilized for various applications. Among those, shells of revolution are more common. In order to achieve the best mechanical design, analysis of such structures in various Loading conditions including static and dynamic is inevitable. Since for most cases, there is too much limitation in developing analytical solution, numerical procedures have been utilized to obtain the response of structures. In this area, methods such as finite element [1,2], boundary element [3], finite difference [4], and generalized differential quadrature [5] have been quite useful. Considering the important roles of these numerical methods, there is always need to develope their ability or if possible, establish new methods which result in more accuracy with less effort.

Differential Cubature Method (DCM) was established by Ciavn in 1994 as an efficient procedure to obtain solutions for partial differential equations with a relatively small number of grid points and less computational effort .

The DCM was presented in [6] as an efficient procedure to obtain solutions for partial differential equations with a relatively small number of grid points and less computational effort. However, reported applications of the DCM in the open literature are restricted to analyses of plates, including bending [7-9] and vibration [10]. Also Static bending analysis of laminated cylindrical panels is carried out [12]. Although DCM is not a new method and has been utilized in the above mentioned problems, it seems that still its ability has not been thoroughly presented.

In the present article, DCM is utilized for the static analysis of shells of revolution. Considering the assumptions of the first shear deformaion theory, the complete form of governing partial differential equations of the problem is utilized. In order to extend the capability of the solution procedure to solving various boundaru conditions, all panel variables including displacements, rotations, moment and force resultants are maintained in the governing equations. Having applyed the DCM to the governing equations and the boundary conditions, a system of linear algebraic equations is obtained. Good agreement of the results with those of other numerical techniques depicts the ability of the DCM for structural analysis.

Formulation

Utilizing first shear deformation theory, governing equations of shells of revolution may be derived. In this section, the static equations are introduced for a general shell of revolution and simplified for the static solution of cylindrical, conical and spherical shells.

The governing equations include the equilibrium equations and the constitutive equations. Considering the assumptions of the first shear deformation theory, the equilibrium equations are as follows [13]

$$\begin{aligned}
&\frac{1}{R_\phi R_\theta \sin\phi}\left[N_\phi R_\theta \cos\phi + N_{\phi\phi} R_\theta \sin\phi + N_{\theta\phi,\theta} R_\phi - N_\theta R_\theta \cos\phi\right] + \frac{Q_\phi}{R_\phi} + q_\phi = 0\\
&\frac{1}{R_\phi R_\theta \sin\phi}\left[N_{\theta,\theta} R_\phi + N_{\theta\phi} R_\theta \cos\phi + N_{\phi\theta,\phi} R_\theta \sin\phi + N_{\phi\theta} R_\theta \cos\phi\right] + \frac{Q_\theta}{R_\theta} + q_\theta = 0\\
&\frac{1}{R_\phi R_\theta \sin\phi}\left[Q_\phi R_\phi \cos\phi + Q_{\phi,\phi} R_\theta \sin\phi + Q_{\theta,\theta} R_\phi\right] - \frac{N_\phi}{R_\phi} - \frac{N_\theta}{R_\theta} + q_n = 0\\
&\frac{1}{R_\phi R_\theta \sin\phi}\left[M_{\phi,\phi} R_\theta \sin\phi + M_\phi R_\theta \cos\phi + M_{\theta\phi,\theta} R_\phi - M_\theta R_\theta \cos\phi\right] - Q_\phi = 0\\
&\frac{1}{R_\phi R_\theta \sin\phi}\left[M_{\theta,\theta} R_\phi + M_{\phi\theta,\phi} R_\theta \sin\phi + M_{\phi\theta} R_\theta + M_{\theta\phi} R_\theta \cos\phi\right] - Q_\theta = 0
\end{aligned} \tag{1}$$

where the (ϕ,θ) and (R_ϕ, R_θ) are curvilinear co-ordinates and curvature radius of the revolution surface respectively. Q_i, N_{ij} and M_{ij} represent shear and normal forces and moments, u_ϕ, u_θ and w are displacement components and β_ϕ and β_θ are rotations of the tangents to the reference surface, q_ϕ, q_θ and q_n represent the external force vectors.

The constitutive equations may be derived for a shell of revolution as follows:

$$\begin{Bmatrix} N_\varphi \\ N_{\phi\theta} \\ Q_\phi \\ N_\theta \\ N_{\theta\phi} \\ Q_\theta \\ M_\phi \\ M_{\phi\theta} \\ M_\theta \\ M_{\theta\phi} \end{Bmatrix} = \begin{bmatrix} G_{11} & G_{16} & 0 & A_{12} & A_{16} & 0 & H_{11} & H_{16} & B_{12} & B_{16} \\ G_{61} & G_{66} & 0 & A_{62} & A_{66} & 0 & H_{61} & H_{66} & B_{62} & B_{66} \\ 0 & 0 & AA_{55} & 0 & 0 & A_{54} & 0 & 0 & 0 & 0 \\ A_{21} & A_{26} & 0 & G'_{22} & G'_{26} & 0 & B_{21} & B_{26} & H'_{22} & H'_{26} \\ A_{61} & A_{66} & 0 & G'_{62} & G'_{66} & 0 & B_{61} & B_{66} & H'_{62} & H'_{66} \\ 0 & 0 & A_{45} & 0 & 0 & BB_{44} & 0 & 0 & 0 & 0 \\ H_{11} & H_{16} & 0 & B_{12} & B_{16} & 0 & J_{11} & J_{16} & D_{12} & D_{16} \\ H_{61} & H_{66} & 0 & B_{62} & B_{66} & 0 & J_{61} & J_{66} & D_{62} & D_{66} \\ B_{21} & B_{26} & 0 & H'_{22} & H'_{26} & 0 & D_{21} & D_{26} & J'_{22} & J'_{26} \\ B_{61} & B_{66} & 0 & H'_{62} & H'_{66} & 0 & D_{61} & D_{66} & J'_{61} & J'_{66} \end{bmatrix} \begin{Bmatrix} \varepsilon_\phi^0 \\ \gamma_\phi^0 \\ \mu_\phi^0 \\ \varepsilon_\theta^0 \\ \gamma_\theta^0 \\ \mu_\theta^0 \\ \kappa_\phi \\ \tau_\phi \\ \kappa_\theta \\ \tau_\theta \end{Bmatrix} \tag{2}$$

in which extensional stiffness A_{ij}, bending-extensional coupling stiffness B_{ij}, bending stiffness D_{ij}, rigidity moduli of elasticity G_{ij} and $G'_{ij}, H_{ij}, J_{ij}, H'_{ij}$ and J'_{ij} are:

$$G_{ij} = A_{ij} + a_1 B_{ij} + a_2 D_{ij} + a_3 E_{ij}, \quad H_{ij} = B_{ij} + a_1 D_{ij} + a_2 E_{ij} + a_3 F_{ij}$$
$$G'_{ij} = A_{ij} + b_1 B_{ij} + b_2 D_{ij} + b_3 E_{ij}, \; H'_{ij} = B_{ij} + b_1 D_{ij} + b_2 E_{ij} + b_3 F_{ij}$$
$$J_{ij} = D_{ij} + a_1 E_{ij} + a_2 F_{ij} + a_3 C_{ij}, \quad J'_{ij} = D_{ij} + b_1 E_{ij} + b_2 F_{ij} + b_3 C_{ij}$$
$$a_1 = \frac{1}{R_2} - \frac{1}{R_1}, \; a_2 = \frac{1}{R_1}\left(\frac{1}{R_1} - \frac{1}{R_2}\right), \; a_3 = \frac{1}{R_1^2 R_2},$$
$$b_1 = \frac{1}{R_1} - \frac{1}{R_2}, \; b_2 = \frac{1}{R_2}\left(\frac{1}{R_2} - \frac{1}{R_1}\right), \; b_3 = \frac{1}{R_2^2 R_1} \tag{3}$$

and

$$A_{ij} = \sum_{k=1}^{N} \left(\overline{Q_{ij}}\right)_k \left(h_k - h_{k-1}\right), \; B_{ij} = \frac{1}{2}\sum_{k=1}^{N} \left(\overline{Q_{ij}}\right)_k \left(h_k^{\,2} - h_{k-1}^{\,2}\right), \; D_{ij} = \frac{1}{3}\sum_{k=1}^{N} \left(\overline{Q_{ij}}\right)_k \left(h_k^{\,3} - h_{k-1}^{\,3}\right)$$
$$E_{ij} = \frac{1}{4}\sum_{k=1}^{N} \left(\overline{Q_{ij}}\right)_k \left(h_k^{\,4} - h_{k-1}^{\,4}\right), \; F_{ij} = \frac{1}{5}\sum_{k=1}^{N} \left(\overline{Q_{ij}}\right)_k \left(h_k^{\,5} - h_{k-1}^{\,5}\right), \; C_{ij} = \frac{1}{6}\sum_{k=1}^{N} \left(\overline{Q_{ij}}\right)_k \left(h_k^{\,6} - h_{k-1}^{\,6}\right)$$
$$i, j = 1,6,2,6 \tag{4}$$

where h_k is thickness of the lamina and $\overline{Q_{ij}}$ are defined as:

$$\bar{Q}_{11} = Q_{11}m^4 + 2(Q_{12} + 2Q_{66})m^2 n^2 + Q_{22}n^4 \;, \; \bar{Q}_{12} = (Q_{11} + Q_{22} - 4Q_{66})m^2 n^2 + Q_{12}(m^4 + n^4) \;,$$
$$\bar{Q}_{22} = Q_{11}n^4 + 2(Q_{12} + 2Q_{66})m^2 n^2 + Q_{22}m^4 \;, \; \bar{Q}_{45} = (Q_{55} - Q_{44})mn \;,$$
$$\bar{Q}_{16} = (Q_{11} - Q_{12} - 2Q_{66})m^3 n + (Q_{12} - Q_{22} + 2Q_{66})mn^3 \;,$$
$$\bar{Q}_{26} = (Q_{11} - Q_{12} - 2Q_{66})mn^3 + (Q_{12} - Q_{22} + 2Q_{66})m^3 n \;\; \bar{Q}_{44} = Q_{44}m^2 + Q_{55}n^2 \;,$$
$$\bar{Q}_{55} = Q_{44}n^2 + Q_{55}m^2 \;, \; \bar{Q}_{66} = (Q_{11} + Q_{22} - 2Q_{12} - 2Q_{66})m^2 n^2 + Q_{66}(m^4 + n^4) \tag{5}$$

while $m = \cos\theta$, $n = \sin\theta$ and the orientation angle θ i.e. the angle between fiber direction and the panel coordinate system**.** θ is measured counter-clockwise. Q_{ij} denote the elastic stiffness in the material coordinates (local axes) and are defined as follows:

$$Q_{11} = E_1/\Delta; Q_{12} = E_1\nu_{21}/\Delta; Q_{22} = E_2/\Delta; Q_{44} = G_{33}; Q_{55} = G_{13}; Q_{66} = G_{12}; \Delta = 1 - \nu_{12}\nu_{21} \tag{6}$$

where E_{ij}, G_{ij} and ν_{ij} are, respectively, Young's moduli of elasticity in the principal directions, shear moduli of each lamina, and Poisson ratios characterizing the transverse contraction (expansion) under tension (compression) in the directions of the coordinate axes.

Also in eqs (2), the components of linear strain should be substituted as functions of displacement. These functions are entitled kinematic relations and are as follows.

$$\varepsilon_\phi^0=\frac{1}{R_\phi}\left(w+\frac{\partial U_\phi}{\partial\phi}\right),\ \kappa_\phi=\frac{1}{R_\phi}\frac{\partial\beta_\phi}{\partial\phi},\ \varepsilon_\theta^0=\frac{1}{R_\theta\sin\phi}\frac{\partial U_\theta}{\partial\theta}+\frac{1}{R_\phi}\cot g\phi U_\phi+\frac{W}{R_\theta},$$
$$\kappa_\theta=\frac{1}{R_\theta\sin\phi}\frac{\partial\beta_\theta}{\partial\theta}+\frac{\beta_\phi}{R_\phi}\cot g\phi,\ \gamma_\phi^0=\frac{1}{R_\phi}\frac{\partial U_\theta}{\partial\phi},\ \tau_\phi=\frac{1}{R_\phi}\frac{\partial\beta_\theta}{\partial\phi},\gamma_\theta^0=\frac{1}{R_\theta\sin\phi}\frac{\partial U_\phi}{\partial\theta}-\frac{U_\theta}{R_\phi}\cot g\phi,$$
$$\tau_\theta=\frac{1}{R_\theta\sin\phi}\frac{\partial\beta_\phi}{\partial\theta}+\frac{\beta_\theta}{R_\phi}\cot g\phi,\ \mu_\phi^0=\frac{1}{R_\phi}\frac{\partial W}{\partial\phi}-\frac{U_\phi}{R_\phi}+\beta_\phi,\ \mu_\theta^0=\frac{1}{R_\theta\sin\phi}\frac{\partial W}{\partial\theta}-\frac{U_\theta}{R_\theta}+\beta_\theta,$$

(7)

Eqs. (1) and (2) construct the fifteen governing equations for a shell of revolution. Boundary conditions for the panel can be any combination of:

Free (F):	*x=Const.:* $N_{\phi\phi}=N_{\phi\theta}=Q_\phi=M_{\phi\phi}=M_{\phi\theta}=0$	$\theta=Const.:$ $N_{\theta\phi}=N_{\theta\theta}=Q_\theta=M_{\theta\phi}=M_{\theta\theta}=0$
Simply supported (S):	*x=Const.:* $N_{\phi\phi}=u_\theta=w=M_{\phi\phi}=\beta_\theta=0$	$\theta=Const.:$ $N_{\theta\theta}=u_\phi=w=M_{\theta\theta}=\beta_\phi=0$
Clamped (C):	*x=Const.* and θ*=Const.* : $u_\phi=u_\theta=w=\beta_\phi=\beta_\theta=0$	

(8)

Utilizing the DCM

In order to use the DCM technique, the proper grid should be generated in the domain. [12] Then the DCM should be applied to the governing equations and boundary conditions to obtain a system of linear algebraic equations. This system should be solved in the domain to obtain the static solution of the shell. The detailed methodology is explained elsewhere [12]. The solution of this system of linear algebraic equations may be implemented in a computer code in and be executed for any kinds of shells of revolution.

Numerical Results and Discussion

Three shells of revolution including cylindrical, spherical and conical shells are analyzed here. Considering the following relations $\phi=x,\theta=\theta,R_\phi=\infty,R_\theta=R$, the analysis of a cylindrical shell may be done utilizing the software. Applying $R_\phi=R,R_\theta=R$ to the software the static solution of a spherical shell is obtained. Also for analyzing a conical shell we have $R_\phi=\infty,R_\theta=x\tan\alpha,\phi=\pi/2-\alpha,R_\phi d\phi=dx$ in which x is the distance from the apex and α is the half apex angle. For the sake of brevity, only one example is included. Consider a clamped *(90°/0°/90°)* conical shell panel for which the following relationships are assumed between the top radius R_t , bottom radius R_b and the thickness of the shell h.

$$R_t=0.8R_b;\ L=R_b;\ R_b/h=10 \tag{9}$$

The material properties are $G_{12}/E_2=0.5;G_{23}/E_2=0.2;\nu_{12}=0.25$. The shell is subjected to uniform lateral pressure *p*. The nondimensionalized central deflection obtained from DCM with the result of [14] is reported in Table 1.

Table 1 Central deflection $\overline{w} = 100E_2h^3w / pR_b^4$ of clamped *(90°/0°/90°)* conical shell panel

Theory	$E_1/E_2 = 2$	$E_1/E_2 = 10$	$E_1/E_2 = 20$	$E_1/E_2 = 30$
FSDT [10]	0.3646	0.1270	0.0751	0.0538
HSDT [10]	0.3323	0.1117	0.0675	0.0493
present	0.3557	0.1210	0.0721	0.0514

Comparison of the results depicts that the DCM results are between those of FSDT and HSDT [14]. This proves that for FSDT, the DCM reaches a better approximation than FEM.

Summary

Carrying out different cases in bending analysis of shells of revolution shows the ability of the DCM in the static structural analysis. On the other hand the time and effort costs of the DCM are less than those of other numerical methods such as FEM, DQ and GDQ. Further investigations of this method for dynamic analysis of the shells, might prove its capability in other fields of structural analysis.

References

[1] Qatu M. S., Algothani A., Computers and Structures Vol 52(3) (1994), p. 529-539.

[2] Reddy, J. N., 2nd edition, CRC Press; 2004.

[3] Jianqiao, Y., Applied Mathematical Modeling Vol 12(5) (1988), p 467-470.

[4] Smith, T. A., Journal of Sound and Vibration Vol 230(5) (2000), p 1119-1145.

[5] Aghdam, M. M., Farahani, M. R. N., Dashty, M., Rezaei Niya, S. M., Applied Mechanics and Materials Vol 5 (2006), p 407-414.

[6] Civan, F., Numerical Methods for Partial Differential Equations Vol 10(5) (1994), p. 545-567.

[7] Liew, K.M. and Liu, L., Computer Methods in Applied Mechanics and Engineering Vol 145(1-2) (1997), p. 1–10.

[8] Liu F.L., Liew K.M., International Journal of Solids and Structures Vol 35(28-29) (1998), p. 3655–3674.

[9] Teo, T.M. and Liew, K.M., International Journal of Mechanical Sciences Vol 44(6) (2002), p. 1179–1194.

[10] Wu, L. and Liu, J., International Journal of Mechanical Sciences Vol 47 (2005), p. 63–81.

[11] Mousavi S. M., Aghdam M. M., Seventh International Conference on Composite science and Technology ICCST/7 (2009).

[12] Mousavi S. M., Aghdam M. M., Journal of Mechanics of Materials and Structures Vol 4(3) (2009), p. 509-521.

[13] Toorani, M. H., Lakis, A. A., Journal of Sound and Vibration Vol 237(4) (2000), p. 561-615.

[14] Bhaskar, K., Varadan, T. K, Computers & Structures, 40(4) (1991), p 815-819.

© (2011) Trans Tech Publications, Switzerland
doi:10.4028/www.scientific.net/KEM.471-472.1010

Effects of Direct Current and Pulse Electrodeposition Parameters on the Properties of Nano Cobalt Coatings

S. R. Allahkaram[1,a], N. Towhid[1,b], M. Siadat Cheraghi[1,c]

[1]School of Metallurgy and Materials Engineering, University College of Engineering,

University of Tehran, Tehran, Iran

[a] akaram@ut.ac.ir, [b]ntowhidi@ut.ac.ir, [c]mohsensiadat@ut.ac.ir

Keywords: pulse plating, dc plating, duty cycle, frequency, current efficiency

Abstract. The aim of this study was to investigate the effects of direct current (DC) and pulse current (PC) parameters on the properties of cobalt (Co) coatings electrodeposited from a chloride acidic bath. The effects of peak current density, frequency and duty cycle on the surface morphology, crystal size, thickness, current efficiency, and preferred orientation of the deposits were investigated by scanning electron microscopy (SEM) and X-ray diffraction (XRD). The experimental thickness of the deposit was lower for pulse plating compared to that of DC plating. The current efficiency was comparatively higher for pulse plating. Less porosity and fine grains were formed by pulse plating. From XRD analysis, the calculated grain sizes of nano and micro Co coatings were around 65nm and 430nm, respectively. The results showed that, with an increase in duty cycle, grain sizes would increase, too. As pulse frequency was increased to 50Hz, grain sizes would also decrease. However, at higher frequencies, grain sizes would increase again.

Introduction

Nanocrystalline materials have been the subjects of intensive research both in the scientific and industrial communities, because of their ultrahigh strength, superior wear resistance, and improved super plastic extensibility compared with their conventional coarse grained counterparts. In many engineering applications, surface coatings are used to increase the lifetime of components exposed to corrosion conditions [1]. In recent years, there has been considerable interest in understanding the corrosion resistance of nanocrystalline metals produced by electrodeposition. Cobalt is a strategic metal finding use in diverse commercial, industrial, medical, and military applications. Other uses include additions in HSLA steels, cemented carbide tools, magnetic alloys, battery electrodes, preparation of Co^{60} radiation sources, body implants and in electroplating. Non metallic uses include those in ceramics, catalysts, paint pigments, steel belted radials, etc [2]. Co has a high potential for application in the micro electronics and sensor technology, especially because of its excellent magnetic properties [3]. In addition, Co has been also shown to possess good magnetic properties, i.e., high saturation magnetization [4] and good thermal stability [5, 6] as a metal, its largest use is in super alloys for critical applications in defense and industry. Pulse electrodeposition is a modern electrochemical method that improves/modifies the quality of the deposits better than that of direct current. In the case of pulse plating, as in any electrodeposition process, the microstructure of the layer is dependent on crystallization and growth, During crystallization, the population of adatoms on the surface due to the applied higher current density is higher than in the case of direct current deposition, resulting in a smaller grain size in the coating [7]. More recently, nanocrystalline Co has been identified as one of the candidate materials for replacing hexavalent chromium plating in wear resistant coating applications. In this study Pulse electroplating technique was used for coating of nano Cobalt onto copper. The coating applied by cathodic pulse electrodeposition and the variation of electrochemical parameters such as current density and pulse conditions caused a marked change in the microstructure of the deposit. Characterization of coated was investigated by XRD, and SEM techniques. Chemical properties could be adjusted by

electrochemical parameters, such as t_{on}, t_{off} and chemical composition of electrolyte. The deposited cobalt on the copper substrate in the experimental conditions achieved ultra fine crystalline structure in the range of 45 to 85 nm.

Material and Methods

Cu sheet with a plated area of 1cm×1cm and high purity Co were used as cathode and anode, respectively. Before electroplating process, the samples were polished with emery papers and thoroughly degreased in an appropriate alkaline solution for 3min at 70˚C. After a thorough rinse with distilled water, the samples were etched in 5% HCl for 30s to neutralize the remnants of alkaline solution and to activate the surface. Finally, the substrates were rinsed again with distilled water and dried by air. After surface preparations, the samples were immediately put in the electrolyte, in order to prevent formation of oxide layer on their surfaces. The chemicals used for this study were of Merck analytical grade. The electrolyte used for pulse current (PC) electrodeposition contained cobalt chloride (210 g/l) and boric acid (20 g/l). The pH of electrolyte was adjusted to 3 by adding HCl and deposition was carried out at 45 ˚C. The thickness of the coatings was fixed to approximately 12µm. The surface morphology of the coatings was investigated by using scanning electron microscope (SEM). The phase composition of coatings was also determined via X-ray diffraction (XRD) analysis.

Discussion

The influence of 10% pulse duty cycle at a frequency of 50Hz with peak current density 70mAcm^{-2} on coating properties such as thickness, grain size and current efficiency of the plating process was studied. In addition the influence of pulse duty cycle and frequency on morphology and grain size of Co coatings was also studied. Table 1 shows the optimum parameters setting for a peak current density 70mAcm^{-2} for DC and Pulse plating of Co coatings. The thickness of the deposit was estimated using the following formula:

$$T = \frac{w}{d \times A} \tag{1}$$

Where w is weight electrodeposited, A is coating area and d is the density,

$$w = \frac{I_{ave} \times t \times M}{n \times 900} \tag{2}$$

Where I_{ave} is average current density (peak current density × duty cycle), M is atomic mass, n is valency and t is the real time in seconds.

Table 1 Parameter setting for DC and pulse plating at peak current density 70mAcm^{-2}

	Theoretical weight(g)	Weight electrodeposited(g)	Theoretical thickness(µm)	Experimental thickness(µm)	Current efficiency (%)
DC plating	0.0291	0.0213	24.82	23.93	73.2
Pulse plating(10%, 50Hz)	0.0108	0.0096	11.53	10.78	88.8

The effect of current density was more significant, when considering pulse current. The current interruption allowed equilibrium of metal ion concentration. Higher peak pulse current was necessary in order to deposit a given amount of metal in a set time, than would be the case with DC,

in order to compensate for the off-time when no deposition occurred. A consequence of using the higher current in the case of pulsing was that higher deposition over potentials resulted, which promoted the nucleation process. Therefore, finer grain deposits were formed. The increase of current density had increased the amount of electrodeposition. In DC plating, the deposits were not smooth and it had coarse grained. Plate thickness from one part to the next was not uniform. Plating speed was less and current efficiency was also less. But with the pulse plating, the above said properties were improved. Pulse plating led to smoother, fine grained deposit and less porosity. Plating speed could also be increased, which led to an increasing current efficiency.

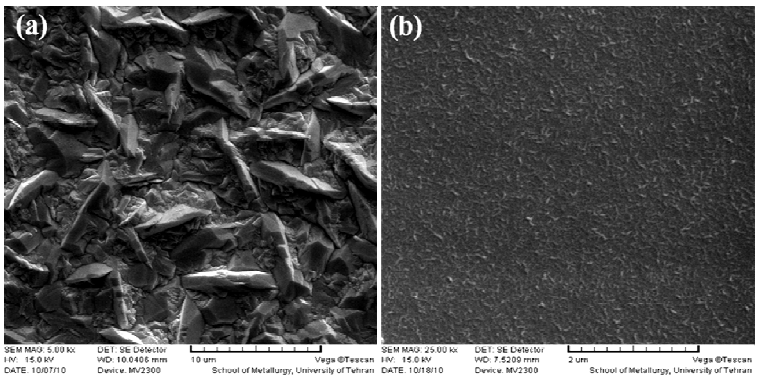


Fig. 1 Surface morphology of Co coatings (a) DC plated (b) PC plated

The surface morphology of the Co coatings formed by pulse plating were studied via SEM. The grain size was studied by XRD analysis. Figures 2 and 3 showed the SEM micrograph of Co coating obtained by pulse plating in different conditions in order to study the influence of duty cycle and frequency of pulse electrodeposition. The effects of duty cycle and pulse frequency on the surface morphologies of Co deposited under a peak current density of 70mAcm^{-2} were shown in Figs. 2 and 3, respectively. However, as shown in Fig. 2 and 3, the surface of nano Co coatings exhibited much denser structure and smoother surface, using conventional SEM observations, but the grain size of the coatings could not be resolved. It was difficult to detect surface cracks on the given pulsed Co coatings at small duty cycle. As the duty cycle pulse was increased, the adventions of flake shape nodules occurred and became larger. Although the Co surface prepared by the pulse current at higher duty cycle had slightly dissolved area, its nodule shape and size were similar to those of the Co coating prepared by direct plating. Fig. 2 illustrated the surface morphology of Co coating obtained at peak current density of 70mAcm^{-2} and 50Hz frequency with different duty cycle.

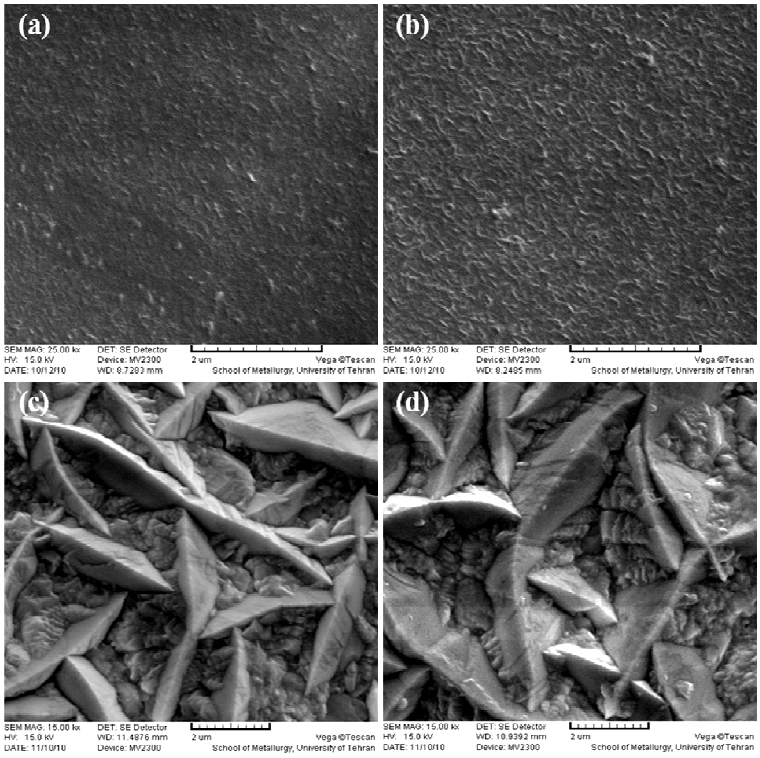


Fig. 2 Surface morphology of Co coatings PC plated at peak current pulse 70mAcm^{-2} and 50Hz frequency with different duty cycle (a) 10% (b) 20% (c) 60% (d) 80%

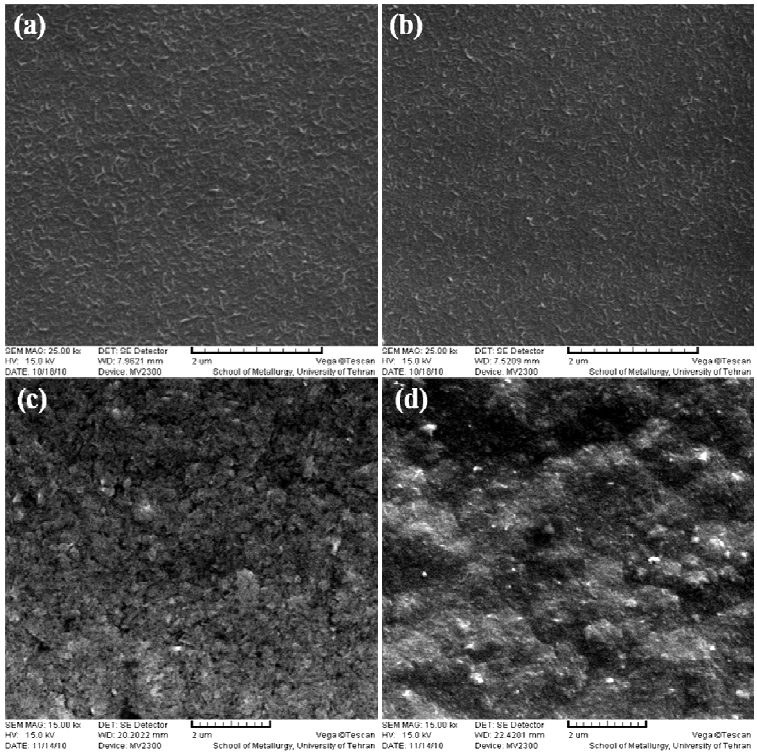


Fig. 3 Surface morphology of Co coatings PC plated at peak current pulse 70mAcm^{-2} and 10% duty cycle with different Frequency (a) 10Hz (b) 50Hz (c) 200Hz (d) 400Hz

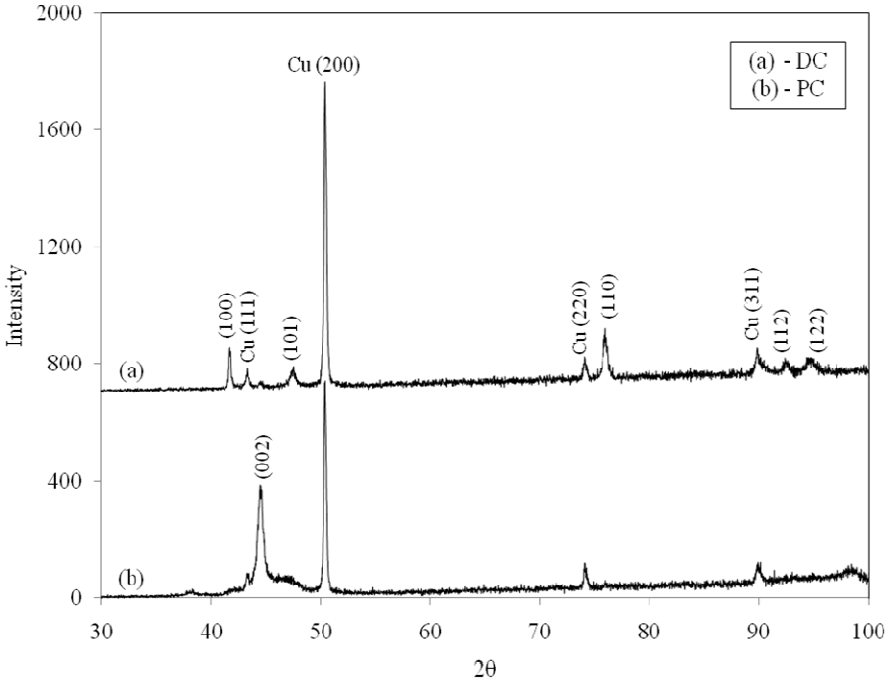


Fig. 4 XRD plots for cobalt grown on copper substrates using electrochemical deposition

It can be seen in Fig. 2 that at small duty cycle the surface was smooth and coherent and the grains had nodular shapes with low grain size. With increasing in duty cycle, it could be seen the grain size was increasing, as shown in Fig. 2 d and e, the Co coating showed a rather regularly branched structure with extended acicular 2–4 μm length crystallites. However, as the duty cycle was increased, the surface became rougher, which could be observed when mass transfer limitations were encountered. The micrograph marked (c) and (d) in Fig. 2 showed that for higher duty cycle and higher frequency, fibril shaped grains were formed. The surface was less compact with a larger duty cycle and frequency, although grain boundaries were visible in both cases. However, it affected morphology significantly and produced very fine grains at low frequency and duty cycle that became coarser as duty cycle and frequency increased [8]. At a pulse frequency of 50Hz, the grain size of the coatings became smallest and with an increase in duty cycle, and the average current density.

It can be seen in Fig. 3, increasing in pulse frequency up to 50Hz, at first led to reduction of the grain size of the Co coatings and then at higher pulse frequency 50Hz, the grain size was significantly increased. At a duty cycle of 10%, the grain size of the coatings became finer with a decrease in the pulse frequency, due to mitigation of the smoothing effects and an increase of the actual applied current density. Fig. 4 shows the XRD patterns of micro Co and nano Co. The measured peaks for all tested samples were well matched to an hcp structure. The XRD patterns of nano Co show a considerable peak broadening due to the ultra-fine grain size and a strong basal (002) texture as compared to the micro Co. The position of diffraction peaks remains constant indicating that the lattice parameters were unchanged by the nanoprocessing. The grain size of the samples has been estimated from the boarding of the X-ray diffraction peak using the Sherrer's equation as follows:

$$D = \frac{0.9 \times \lambda}{\beta \times cos\theta} \tag{3}$$

Where θ is the diffraction angle, λ is the X-ray wavelength and β is full width at half maximum of the diffraction peaks. It is calculated that the grain size around 65nm for 10% duty cycle and 50Hz frequency at peak current density 70mAcm^{-2} and 430nm for DC plating at peak current density 70mAcm^{-2}.

Summary

1. It has been observed that the plating thickness is not uniform in DC plating. The experimental results indicate that the thickness of the Co deposit is lower for pulse plating as compared to that of DC plating.

2. The current efficiency is comparatively higher for pulse plating. Less porosity and finer grains are formed by pulse plating compared to that of formed by DC plating.

3. With increasing duty cycle, the grain size of the coatings is increased in stepwise condition, however at higher duty cycles, grain size is significantly larger.

4. Increasing the pulse frequency, at first leads to a reduction of the grain size of the Co coatings and then beyond 50Hz pulse frequency grain size is dramatically increased.

References

[1] L. Wang, Y. Lin, Z. Zenga, W. Liu, Q. Xue, L. Hu and J. Zhang: Electrochemical Acta, Vol. 52 (2007), p. 4342

[2] I. G. Sharma, P. Alex, A. C. Bidaye, and A. K. Suri: Hydrometallurgy, Vol. 80 (2005), p. 132

[3] A. Sahari, A. Azizi, N. Fenineche, G. Schmerber, and A. Dinia: Materials Chemistry and Physics, Vol. 108 (2008), p. 345

[4] M. J. Aus, C. Cheung, B. Szpunar, and U. Erb: Materials Science Letters, Vol. 17 (1998), p. 1949

[5] G. D. Hibbard, K. T. Aust, and U. Erb: Acta Materialia, Vol. 54 (2006), p. 2501

[6] H. Jung, A. Alfantazi: Electrochimica Acta, Vol. 51 (2006), p. 1806

[7] B. Tury, M. L. Varsányi and S. Roy: Surface & Coatings Technology, Vol. 200 (2006), p. 6713

[8] Y. Liu and M. Pritzker: Applied Electrochemistry, Vol. 33 (2003), p. 1143

© (2011) Trans Tech Publications, Switzerland
doi:10.4028/www.scientific.net/KEM.471-472.1016

Vibration of Nonlocal Euler Beams using Chebyshev Polynomials

Seyyed Amir Mahdi Ghannadpour[1, a], Bijan Mohammadi[2,b]

[1] Aerospace Engineering Department, Faculty of New Technologies and Engineering,
Shahid Beheshti University, G.C., Tehran, Iran

[2] School of Mechanical Engineering,
Iran University of Science and Technology, Tehran, Iran

[a]a_ghannadpour@sbu.ac.ir, [b]bijan_mohammadi@iust.ac.ir

Keywords: Eringen's nonlocal elasticity, Vibration analysis, Chebyshev polynomials, Euler beam

Abstract. This paper is concerned with the free vibration problem for micro/nano beams modelled after Eringen's nonlocal elasticity theory and Euler beam theory. The small scale effect is taken into consideration in the former theory. The natural frequencies are obtained using the Hamilton's principle and Chebyshev polynomial functions. The present method, which uses Rayleigh–Ritz technique in this paper, provides an efficient and extremely accurate vibration solution of micro/nano beams where the effects of small scale are significant. Numerical results for a variety of some micro/nano beams with various boundary conditions are given and compared with the available results wherever possible. Through the comparison of the results and the appropriate discussion, the knowledge of the level of capability of the developed method is promoted.

Introduction

In recent years, nonlocal elasticity has been widely used due to small length scale in micro- and nano-applications of beam, plate and shell-type structures. Basic difference between local elasticity and nonlocal elasticity is relation of stress and strain: stress at a point is related to strain at that point in local elasticity, whereas in nonlocal elasticity stress at a point is related to strains at all points in the continuum. It should be noted that in nonlocal elasticity, the internal forces between the atoms and internal length scale are considered in definition of constitutive equations by Eringen [1,2,3].

Since his pioneering study, many researchers have applied this concept for the bending, buckling and vibration analyses of micro- and nano-structures. Wang et al. [4] have analyzed the elastic buckling behavior of micro- and nano-rods/tubes based on Eringen's nonlocal elasticity theory and the Timoshenko beam theory. The governing equations and the boundary conditions have been derived using the principle of virtual work. Explicit expressions for the critical buckling loads have been derived for axially loaded rods/tubes with various end conditions. He [5] has also analyzed free vibration of micro/nano beams based on both Eringen's nonlocal elasticity theory and Timoshenko beam theory. The small scale effect was taken into consideration in the former theory while the effects of transverse shear deformation and rotary inertia were accounted for in the latter theory. The governing equations and the boundary conditions have been derived using Hamilton's principle. These equations have been solved analytically for the vibration frequencies of beams with various end conditions. A version of nonlocal elasticity was proposed by Peddieson et al. [6] to formulate a nonlocal version of Euler-Bernoulli beam theory. They concluded that nonlocal continuum mechanics could potentially play a useful role in the analysis related to nanotechnology applications. Since the attempt on applying nonlocal continuous models was conducted, applications of nonlocal Euler–Bernoulli beam model have been employed in studying nano-beams mechanical behaviors. Pantano et al. [7] investigated the axial buckling of single and multi-walled carbon nanotubes using finite element simulations. Wang et al [8] studied the flexural and buckling behavior of single wall carbon nanotubes (SWCNT) using beam and shell models.

In the literature, the most attention has been focused on deriving the variational formulation of the governing equations and boundary conditions of nanostructures. Ghannadpour and Mohammadi were the first who investigated the behavior of nanostructures using numerical methods [9]. They have studied the buckling behavior of micro- and nano-rods/tubes based on nonlocal Timoshenko beam theory using Chebyshev polynomials. The critical buckling loads have been obtained using the theorem of minimum total potential energy and Chebyshev polynomial functions. However, no work appears related to the vibration behavior of nanostructures using numerical methods.

The aim of this paper is to present the vibration behavior of micro/nano Euler beams based on Eringen's nonlocal elasticity theory. The vibration frequencies of the beams are obtained using Hamilton's principle and Chebyshev polynomial functions. The present method, which uses Rayleigh–Ritz technique in this paper, provides an efficient and extremely accurate vibration solution.

Theoretical Developments

According to the Euler-Bernoulli beam theory, the strain-displacement relations are given by

$$\varepsilon_{xx} = -z\frac{\mathrm{d}^2 w}{\mathrm{d}x^2}. \tag{1}$$

where x is the longitudinal coordinate measured from the left end of the beam, z the coordinate measured from the midplane of the beam, w the transverse displacement and ε_{xx} the normal strain.

The strain energy U and the kinetic energy T of the beam are given respectively by the following equations

$$U = -\frac{1}{2}\int_0^L M\frac{\mathrm{d}^2 w}{\mathrm{d}x^2}\mathrm{d}x.$$

$$T = \frac{1}{2}\int_0^L \rho A\omega^2 w^2\,\mathrm{d}x. \tag{2}$$

where ω is the circular frequency of vibration, A the cross-sectional area of the beam, ρ the mass density of the beam material, L the length of the beam and $M = \int_A \sigma_{xx} z\,\mathrm{d}A$ the bending moment. In the definition of the M, σ_{xx} is the normal stress. It must be noted that the bending moment for the nonlocal beam theory is different due to the nonlocal constitutive relations as will be shown below.

For an elastic material in the one-dimensional case, the simplified nonlocal constitutive relations may be expressed as [5]

$$\sigma_{xx} - (e_0 a)^2\frac{\mathrm{d}^2\sigma_{xx}}{\mathrm{d}x^2} = E\varepsilon_{xx}. \tag{3}$$

where E is the Young's modulus, and $e_0 a$ is the scale coefficient that incorporates the small scale effect. Multiplying Eq. (3) by $z\,\mathrm{d}A$ and integrating the result over the area A yields

$$M - (e_0 a)^2\frac{\mathrm{d}^2 M}{\mathrm{d}x^2} = -EI\frac{\mathrm{d}^2 w}{\mathrm{d}x^2}. \tag{4}$$

where I is the second moment of area. The constitutive relation for the shear stress and strain, however, remains the same as in the local beam theory. By using the constitutive relation for the

shear stress and strain and two equilibrium equations governing the vibration behavior of beams [5], the bending moment for the nonlocal beam theory can be obtained as follow

$$M = -EI\frac{\mathrm{d}^2 w}{\mathrm{d}x^2} - (e_0 a)^2 \rho A \omega^2 w . \tag{5}$$

By substituting the Eq. (5) into the Eq. (2), the potential energy of the beam U can be obtained as follow

$$U = \frac{1}{2}\int_0^L \left(EI\left(\frac{\mathrm{d}^2 w}{\mathrm{d}x^2}\right)^2 + (e_0 a)^2 \rho A \omega^2 w \frac{\mathrm{d}^2 w}{\mathrm{d}x^2} \right) \mathrm{d}x . \tag{6}$$

The difference between the kinetic energy and potential energy of the beam can be expressed as

$$T - U = \frac{1}{2}\int_0^L \left(\rho A \omega^2 w^2 - EI\left(\frac{\mathrm{d}^2 w}{\mathrm{d}x^2}\right)^2 - (e_0 a)^2 \rho A \omega^2 w \frac{\mathrm{d}^2 w}{\mathrm{d}x^2} \right) \mathrm{d}x . \tag{7}$$

It is noted that the only unknown function in the above equation is the transverse displacement w. By knowing the transverse displacement field w, the Eq. (7) can be obtained. By using the Hamilton's principle, the difference between the kinetic energy and potential energy of the beam must be minimized. That is to say the partial differentiation of the Eq. (7) with respect to unknown parameters in turn leads an eigenvalue problem. The procedure that postulates the displacement field w will be shown below.

The Transverse Displacement Field W

The Rayleigh-Ritz technique requires the expansion of the unknown functions in infinite series. By assuming a sufficient number of functions, it is possible to obtain the exact solution of the problem considered. However, the displacement functions should be complete in the function space and inappropriate choices of the unknown functions cause very slow convergence rates.

It is interesting to note that this technique has not been used by researchers to study the vibration problem of micro/nano beams. In this study, after defining non-dimensional coordinate as $\zeta = x/L$ the displacement function $w(\zeta)$ is written in the form of series of Chebyshev polynomials multiplied by a boundary function, which ensures that the displacement component satisfies the essential boundary conditions of the beam, i.e.

$$w(\zeta) = F(\zeta)\sum_{i=0}^{\infty} P_i(\zeta) . \tag{8}$$

where $P_i(\zeta)(i = 0,1,2,...)$ is the one-dimensional ith Chebyshev polynomial. Note that $F(\zeta)$ is the boundary function corresponding to the displacement function $w(\zeta)$ which can be written as

$$F(\zeta) = \zeta^{\alpha}(1-\zeta)^{\beta} . \tag{9}$$

Here, α and β take values of $\alpha, \beta = 0,1,2$ corresponding to the free, pined and clamped end conditions, respectively. It should be noted that using the Chebyshev polynomial series as the admissible functions has two advantages. One is that $P_i(\zeta)(i = 0,1,2,...)$ is a set of complete and

orthogonal series. Therefore, more rapid convergence in the numerical computation can be accomplished compared with other polynomial series. The other is that the Chebyshev polynomial can be expressed in simple and uniform form, which reduces the coding effort. The first two terms of the Chebyshev polynomials are as follow

$$P_0(\zeta) = 1.$$
$$P_1(\zeta) = \zeta. \tag{10}$$

The other functions can be calculated by the following recursive relationship.

$$P_{i+1}(\zeta) = 2\zeta P_i(\zeta) - P_{i-1}(\zeta). \tag{11}$$

Results and Discussions

In presenting the results in this study, the following nondimensional terms are used.

$$\lambda^2 = \omega^2 \frac{\rho A L^4}{EI}.$$
$$\alpha = \frac{e_0 a}{L}. \tag{12}$$

where λ and α , respectively, are called frequency parameter and scaling effect parameter. In calculating the results of this paper, the length of the beams under consideration is assumed to be 6.78 nm.

The convergence studies carried out for the frequency parameter $\sqrt{\lambda}$ of a nano beam for first mode of vibration with the scaling effect parameter α of 3 are tabulated in Table 1. In this table, the two endes of the beam are of a variety of combinations, namely simply-simply (SS), clamped-clamped (CC), clamped-simply (CS) and clamped-free (CF). It is seen that the frequency parameters obtained with 4 and 5 terms are identical. However, for the sake of confidence, all of the results presented for frequency parameters have been calculated using $n = 10$. In Table 1 the frequency parameters are also compared with the results of Wang et al. [5]. As can be seen there is an excellent agreement between the results. It is noted that in Ref. [5], the frequency parameters are obtained by solving the governing equations.

Table 1. Frequency parameter $\sqrt{\lambda}$ convergence study with $\alpha = 3$

n	SS	CS	CC	CF
2	2.680382	3.285675	3.918502	1.901881
3	2.680382	3.282888	3.918502	1.901292
4	2.679996	3.282844	3.918368	1.901291
5	2.679996	3.282840	3.918368	1.901291
6	2.679996	3.282840	3.918368	1.901291
7	2.679996	3.282840	3.918368	1.901291
8	2.679996	3.282840	3.918368	1.901291
9	2.679996	3.282840	3.918368	1.901291
10	2.679996	3.282840	3.918368	1.901291
Ref. [5]	2.68	3.2828	3.9184	1.9154
% Diff	0.00	0.00	0.00	-0.74

The percentage differences, given in Table 1, between present results and results of Ref. [5] are calculated according to the following equation

$$\text{Diff.}\% = \frac{\sqrt{\lambda}_{\text{present}} - \sqrt{\lambda}_{\text{Ref.[5]}}}{\sqrt{\lambda}_{\text{Ref.[5]}}} \times 100. \tag{13}$$

In resume of generating the results, it is desired to investigate the effect of small scale on the frequency parameter. In order to investigate the effect of small scale on the frequency parameter for the SS beam, the relationship between the frequency ratio (i.e. ratio of the frequency parameter λ_{NL} of the nonlocal Euler beam to the corresponding local Euler beam λ_{L}) and the small scale coefficient $e_0 a$ for three vibration modes are shown in Fig. 1.

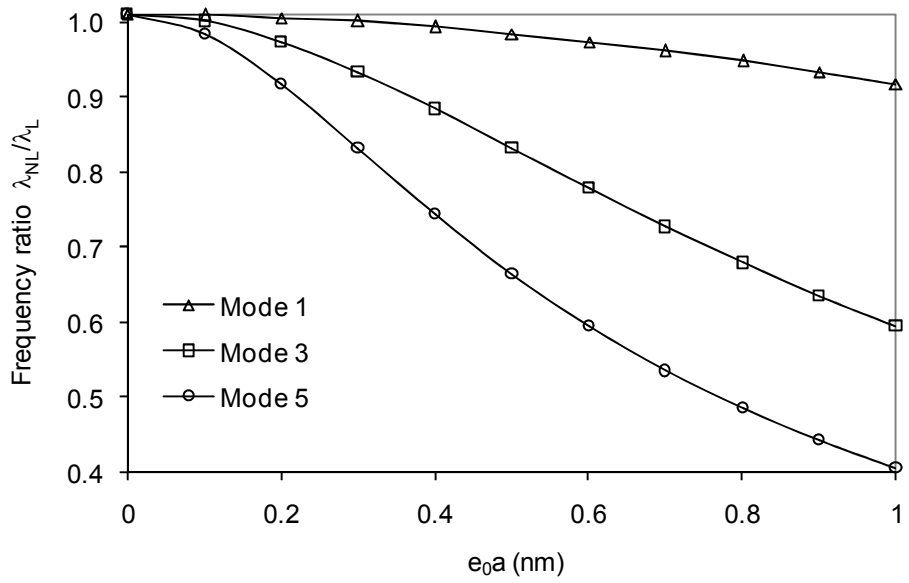


Fig. 1 Small scale effect on the frequency ratio for a simply supported (SS) beam

References

[1] A. C. Eringen: Int. J. Eng. Sci. Vol. 10, (1972), p. 1–16.

[2] A. C. Eringen and D. G. B. Edelen: Int. J. Eng. Sci. Vol. 10, (1972), p. 233–48.

[3] A. C. Eringen: J. Appl. Phys. Vol. 54, (1983), p. 4703–10.

[4] C. M. Wang, Y. Y. Zhang, Sai Sudha Ramesh and S. Kitipornchai: J. Phys. D: Appl. Phys. Vol 39, (2006), 3904–3909.

[5] C. M. Wang, Y. Y. Zhang and X. Q. He: Nanotechnolgy. Vol 18, (2007), 1-9.

[6] Peddieson J., Buchanan G.R., McNitt R.P.: Int. J. Eng. Sci. Vol. 41, (2003), 305–312.

[7] Pantano A., Boyce M.C., Parks D. M.: J. Eng. Mater. & Tech., Vol. 126, (2004), 279–284.

[8] Wang Q., Varadan V.K.: Smart Mater. & Struct., Vol. 14, (2005), 281–286.

[9] S. A. M. Ghannadpour and B. Mohammadi: Advanced Materials Research, 123-125, (2010), 619-622.

© (2011) Trans Tech Publications, Switzerland
doi:10.4028/www.scientific.net/KEM.471-472.1022

An Investigation on Relative Post-buckling Stiffness Variations of Symmetrically Cross-ply Laminates

Seyyed Amir Mahdi Ghannadpour[1, a], Hamid Reza Ovesy[2,b] and Mohammad Hajikazemi[2]

[1] Aerospace Engineering Department., Faculty of New Technologies and Engineering, Shahid Beheshti University, G.C., Tehran, Iran

[2] Department of Aerospace Engineering and Centre of Excellence in Computational Aerospace Engineering, Amirkabir University of Technology, Tehran, Iran

[a]a_ghannadpour@sbu.ac.ir, [b]ovesy@aut.ac.ir

Keywords: Finite Strip Method, Relative Post-buckling, Symmetric Cross-ply Laminates, Von-Karman Equations

Abstract. In this paper, the theoretical developments of an exact finite strip for the buckling and initial post-buckling analyses of symmetrically cross-ply laminates are presented. The so-called exact finite strip is developed based on the concept that it is effectively a plate. In the development process, the Von-Karman's equilibrium equation is solved exactly to obtain the buckling loads and the corresponding form of out-of-plane buckling deflection modes. The investigation of thin flat plate buckling behavior is then extended to an initial post-buckling study with the assumption that the deflected form immediately after the buckling is the same as that obtained for the buckling. The post-buckling study is effectively a single-term analysis, which is attempted by utilizing the so-called semi-energy method. In this method, the Von-Karman's compatibility equation governing the behavior of symmetrically laminated composite plates is used together with a consideration of the total strain energy of the plate. Through the solution of the compatibility equation, the in-plane displacement functions are developed in terms of the unknown coefficient in the assumed out-of-plane deflection function. These in-plane and out-of-plane deflected functions are then substituted in the total strain energy expressions and the theorem of minimum total potential energy is applied to solve for the unknown coefficient. The developed method is subsequently applied to investigate the relative post-buckling stiffness variations of some representative thin symmetric cross-ply laminates for which the results are also obtained through the application of a semi-analytical finite strip method.

Introduction

Composite laminated plates and plate structures are increasingly used as structural components in various branches of engineering such as aerospace and marine engineering. These structures are often employed in situations where they are subjected to in-plane compressive loading. Thus it is important to accurately predict the buckling and initial post-buckling behavior of such structures.

Ovesy et al. [1,2,3] have developed a Semi-energy post-local-buckling FSM in which the out-of-plane displacement of the finite strip is the only displacement which is postulated by a deflected form. The developed Semi-energy FSM (S-e FSM) has been applied to analyze the post-local-buckling behavior of isotropic thin flat plates [1], isotropic open channel section [2] and isotropic box section struts [3].

Recently, Ghannadpour and Ovesy [4,5,6] have developed a full-analytical post-local-buckling FSM in which the solution of the von-Karman's equilibrium equation was substituted into the von-Karman's compatibility equation. It is noted that in their analysis, only one of the calculated out-of-plane buckling deflection modes, corresponding to the lowest buckling load, i.e. the first mode is used for the initial post-buckling study.

More recently, Ghannadpour and Ovesy [7] have developed an exact finite strip for the buckling analysis of symmetrically laminated composite plates and prismatic plate structures. In their analysis, the von-Kármán's equilibrium equation governing the behavior of symmetrically laminated composite plates is solved exactly to obtain the general form of out-of-plane buckling deflection mode for the corresponding strip.

In this paper, the theoretical developments of an exact finite strip for the buckling and initial post-buckling analyses of symmetrically laminated composite plates are presented. The present method, which is designated by the name Full-analytical Finite Strip Method, provides an efficient and extremely accurate buckling and relative post-buckling stiffness solution. The developed method is subsequently applied to investigate the relative post-buckling stiffness variations of some representative thin symmetric cross-ply laminates for which the results are also obtained through the application of a semi-analytical finite strip method.

Theoretical developments of the Full-analytical Finite Strip Method (F-a FSM)

The positive directions of the edge forces and displacements are shown in Fig. 1. It is noted that the in-plane shear force, in-plane transverse force, out-of-plane shear force and bending moment per unit length of the plate/strip edge are denoted by P_x, P_y, P_z and M_y respectively.

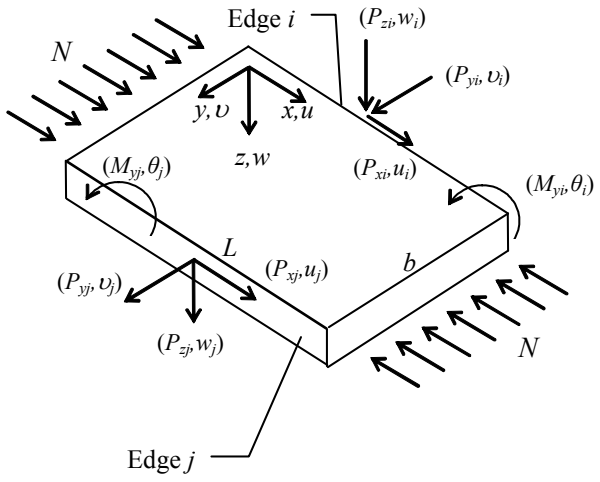


Fig. 1 A typical exact finite strip

The subscripts *i* and *j* denote the corresponding values of forces/ displacements at edges *i* and *j*, respectively. It can be seen in Fig. 1 that the nodal line forces and moments can be expressed in terms of internal in-plane forces and normal displacements on the edges as follows:

$$P_{xi} = -N_{xy}\Big|_{y=0}, \quad P_{xj} = N_{xy}\Big|_{y=b}, \quad P_{yi} = -N_y\Big|_{y=0}, \quad P_{yj} = N_y\Big|_{y=b}.$$

$$P_{zi} = \left[D_{22}^* \frac{\partial^3 w}{\partial y^3} + (D_{12}^* + 4D_{66}^*) \frac{\partial^3 w}{\partial x^2 \partial y} \right]_{y=0}, \; P_{zj} = -\left[D_{22}^* \frac{\partial^3 w}{\partial y^3} + (D_{12}^* + 4D_{66}^*) \frac{\partial^3 w}{\partial x^2 \partial y} \right]_{y=b}.$$

$$M_{yi} = -\left[D_{22}^* \frac{\partial^2 w}{\partial y^2} + D_{12}^* \frac{\partial^2 w}{\partial x^2} \right]_{y=0}, \quad M_{yj} = \left[D_{22}^* \frac{\partial^2 w}{\partial y^2} + D_{12}^* \frac{\partial^2 w}{\partial x^2} \right]_{y=b}. \tag{1}$$

The out-of-plane buckling deflection mode w_1 is obtained by trying to solve the Von-Karman's equilibrium equation. This gives:

$$D_{11}^* w_{1,xxxx} + 2(D_{12}^* + 2D_{66}^*) w_{1,xxyy} + D_{22}^* w_{1,yyyy} = \left| F_{0,yy} w_{1,xx} + F_{0,xx} w_{1,yy} - 2F_{0,xy} w_{1,xy} \right|. \tag{2}$$

It is noted that in the remaining of the paper, the subscripts $_{0,1,2}$ are used for pre-buckling, buckling and post-buckling stages, respectively. Substituting out-of-plane buckling deflection mode $w_1(x,y) = f_{w1}(y)\sin(\lambda x)$ into above equation and assuming that in the pre-buckling stage the plate/strip is subjected to the compressive axial load N rearranging leads to the following fourth-order ordinary differential equation:

$$f_{w1}'''' - 2\lambda^2 \overline{T}\, f_{w1}'' + \lambda^4(\overline{T}^2 - \overline{L}) f_{w1} = 0, \overline{L} = \frac{N}{\lambda^2 D_{22}^*} - \frac{D_{11}^*}{D_{22}^*} + \overline{T}^2,\ \overline{T} = \frac{D_{12}^* + 2D_{66}^*}{D_{22}^*}, \lambda = \pi / L. \tag{3}$$

The solution of above equation depends on whether $\overline{L} < 0$, $\overline{L} = 0$, $0 < \overline{L} < \overline{T}^2$, $\overline{L} = \overline{T}^2$ or $\overline{L} > \overline{T}^2$. Thus, the solution of fourth-order ordinary differential Eq. (3) which satisfies the displacement boundary conditions can be obtained analytically in terms of the edge displacements $\underset{\sim}{\mathbf{d}}_1$. Substituting the solution of fourth-order ordinary differential Eq. (3) into Eq. (1) yields the force boundary conditions for the moment and out-of-plane edge shear force as:

$$\underset{\sim}{\mathbf{p}}_1 = \underset{\sim}{\mathbf{k}}_1 \underset{\sim}{\mathbf{d}}_1. \tag{4}$$

where $\underset{\sim}{\mathbf{k}}_1$ denotes the strip out-of-plane stiffness matrix. By applying these expressions to obtain the stiffness matrices of individual strips, the exact overall stiffness matrix $\underset{\sim}{\mathbf{K}}_1$ for the whole structure can be assembled by using the conventional routines of finite element analysis. The corresponding buckling problem can finally be expressed as the eigenvalue problem:

$$\underset{\sim}{\mathbf{K}}_1(N)\underset{\sim}{\mathbf{D}}_1 = 0. \tag{5}$$

Having obtained an exact shape of the deflected form at buckling, the analysis of post-buckling behavior can proceed on the assumption that the deflected form in the immediate post-buckling range is identical to that at buckling, with only the deflection magnitudes varying $w_2(x,y) = \delta . w_1(x,y)$. The stresses occurring in the plate after the buckling are related to the deflection of the plate via the Von-Karman's compatibility equation. By using the semi-energy post-buckling procedure, the general form of the post-buckling in-plane displacement functions $u_2(x,y)$ and $\upsilon_2(x,y)$ corresponding to the out-of-plane buckling deflection mode and the deflection coefficient δ can eventually be derived as

$$u_2(x,y) = -\varepsilon x + \delta^2 f_{u2}(y)\sin(2\lambda x).$$
$$\upsilon_2(x,y) = -\frac{A_{12}^*}{A_{11}^*}\varepsilon y + \delta^2\left[g_{\upsilon 2}(y) + f_{\upsilon 2}(y)\cos(2\lambda x) + -g_{\upsilon 2}(0) + f_{\upsilon 2}(0)\right] + \upsilon_2(0,0). \tag{6}$$

where ε is the end-shortening strain. By calculating the membrane and shearing stress resultants per unit length N_y and N_{xy} and substituting into Eq. (1) for in-plane shear force and in-plane transverse force, amplitudes of $\underset{\sim}{\mathbf{p}}_2 = \left\{P_{2xi}, P_{2yi}, P_{2xj}, P_{2yj}\right\}^T$ in the post-buckling region, after assembly, can be expressed by the following equation:

$$\underset{\sim}{\mathbf{K}}_2 \underset{\sim}{\mathbf{D}}_2 = \underset{\sim}{\mathbf{F}}_2. \tag{7}$$

These in-plane and out-of-plane deflected functions are then substituted in the total strain energy expressions and the theorem of minimum total potential energy is applied to solve for the unknown coefficient. The total longitudinal force/load acting on a plate at a given cross section along the plate length, corresponding to a prescribed end-shortening strain, is obtained by summation of all strip forces P_s at the same cross section. The slop of the actual post-buckling curve at the buckling point is the so-called initial post-buckling stiffness S^*. Therefore, the relative post-buckling stiffness defined as the ratio of the post-buckling stiffness to the pre-buckling stiffness can be calculated.

Due to space limitations, the detailed fundamental elements of the theory for the developed conventional S-a FSM are not included in the current paper. The interested readers are referred to an earlier publication by Ovesy and Ghannadpour [8].

Results and Discussions

Figs. 2 and 3 represent the comparison of the relative stiffness obtained by the developed method (F-a FSM) as well as the results obtained by S-a FSM. The plates are simply supported on all sides. It is noted that the width to thickness ratio b/t is 100. In these figures, the plates are symmetrically laminated cross-ply $[0/90]_s$ which are constructed of plies having the properties $G_{12}/E_2 = 0.5$ and $v_{12} = 0.25$ whilst the ratio of E_1/E_2 is different for the figures.

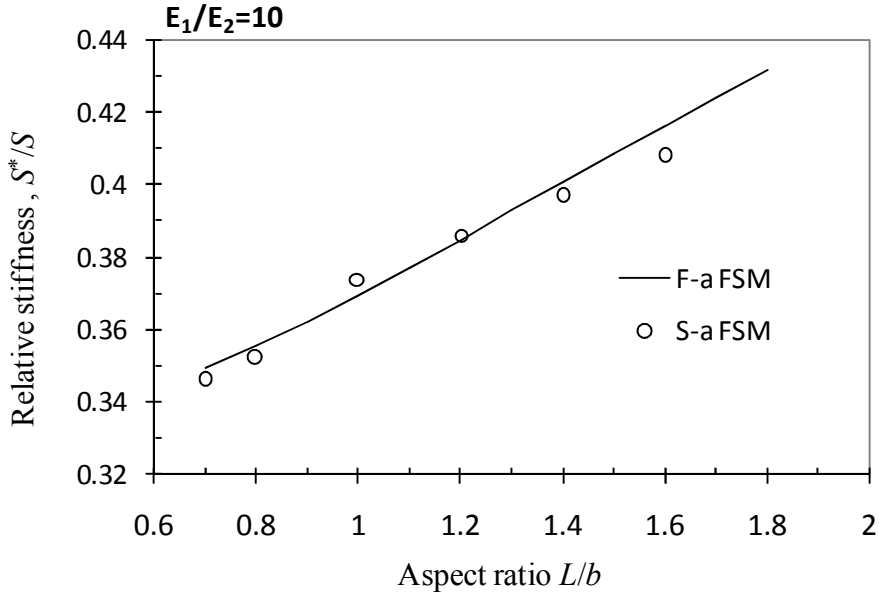


Fig. 2 Variation of the relative stiffness with the aspect ratio for plates which are constructed of plies having $E_1/E_2 = 10$

It is seen in the figures that the relative stiffness is increased by the increase in the aspect ratio. Obviously, if the number of buckle half-waves were allowed to take values more than 1, i.e. the constant value assumed in the current study, the afore-mentioned behaviour might change accordingly.

The figures also show that there is a good agreement between the results of the F-a FSM method and those obtained by S-a FSM approach. The results of F-a FSM approach are obtained by implementing significantly small number of degrees of freedom in comparison to those normally required by the S-a FSM. This can be considered as one of the major advantages of the current study. It is also worth mentioning that in the approximate methods such as Finite Element Method (FEM), S-a FSM, semi-energy FSM or Spline FSM, the calculation of the values of relative stiffness is very time consuming due to the incremental nature of the solution strategy in these methods.

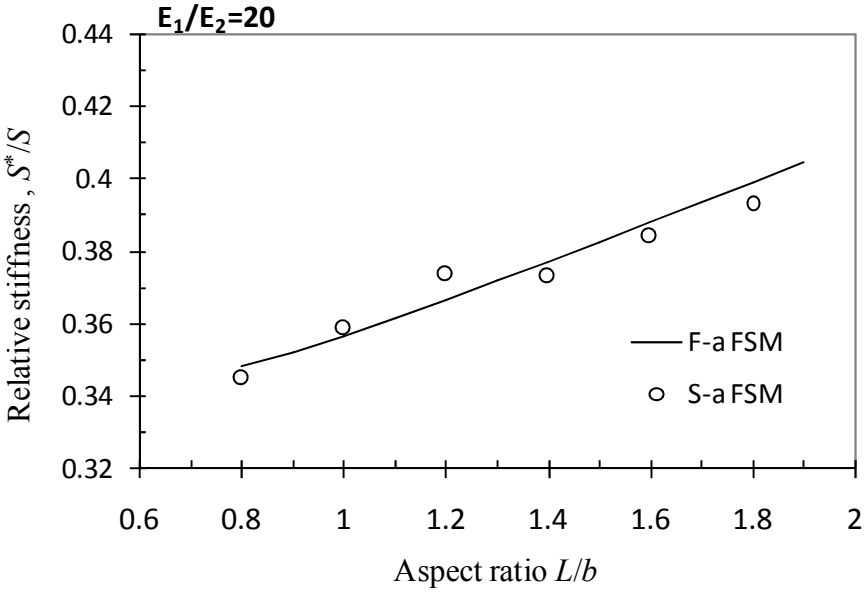


Fig. 3 Variation of the relative stiffness with the aspect ratio for plates which are constructed of plies having $E_1 / E_2 = 20$

Fig. 4 shows the variation of the relative stiffness, i.e. S^* / S at the instant of buckling, with the ratio of E_1 / E_2 . In this figure, the plates are simply supported on all sides and the aspect ratio of the plates is assumed to be 1 (i.e. $L / b = 1$). It is seen in the figure that the relative stiffness is increased by the decrease in the value of E_1 / E_2.

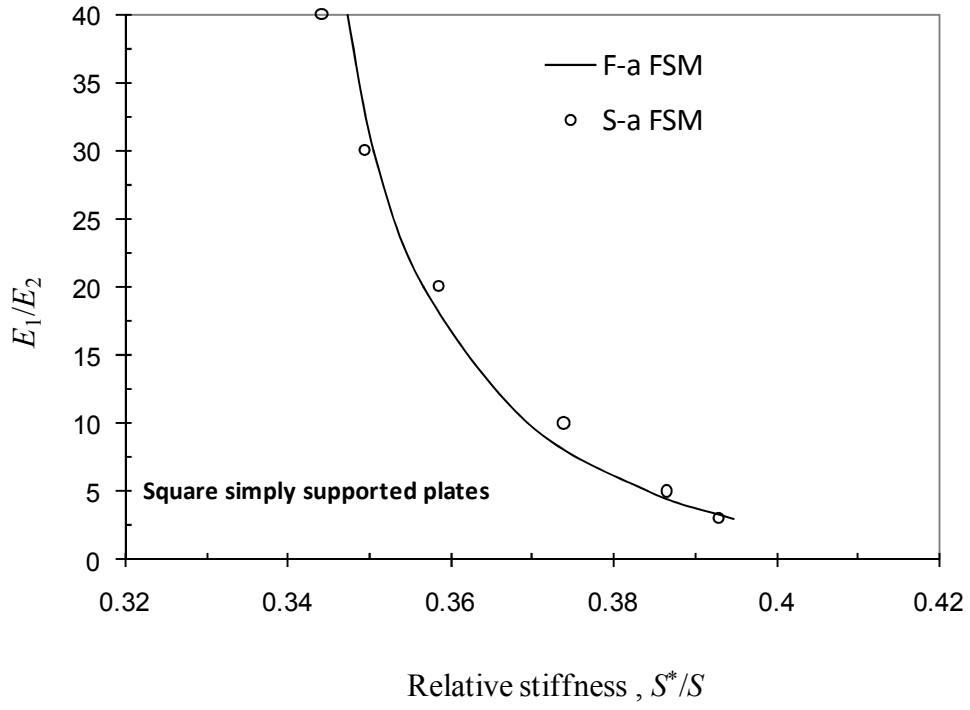


Fig. 4 Variation of the relative stiffness with the ratio of E_1 / E_2

The values of relative post-buckling stiffness obtained by the F-a FSM method are also extremely accurate at the buckling point because the exact buckling mode shape and corresponding buckling coefficient are used in the post-buckling analysis.

Summary

Theoretical developments of two finite strip methods for the initial post-buckling analyses of symmetrically cross-ply laminates have been presented. In the S-a FSM post-buckling approach, all the displacements are postulated by the appropriate shape functions whilst in the development process of the F-a FSM approach, the von-Karman's equilibrium equation is solved exactly to obtain the buckling load and the corresponding form of out-of-plane buckling deflection mode. The F-a FSM post-buckling study is then attempted with the assumption that the deflected form immediately after the buckling is the same as that obtained for the buckling, and the so-called semi-energy method is utilized. It is realized that the F-a FSM analysis is benefiting from considerably less computational effort due to the implementation of a single strip.

References

[1] H.R. Ovesy, J. Loughlan and S.A.M. Ghannadpour: Int. J. of Mech. Sci. Vol. 47 (2005), p. 1923-1948.

[2] H.R. Ovesy, J. Loughlan and S.A.M. Ghannadpour: Comput. and Struct. Vol. 84 (2006), p. 855-872.

[3] H.R. Ovesy, J. Loughlan, S.A.M. Ghannadpour and G. Morada: Thin-Walled Struct. Vol. 44 (2006), p. 623-637.

[4] H.R. Ovesy and S.A.M. Ghannadpour: Struct. Eng. and Mech. Vol. 31 (2009), p. 181-210.

[5] S.A.M. Ghannadpour and H.R. Ovesy: Int. J. of Mech. Sci. Vol. 50 (2008), p. 1354-1364.

[6] S.A.M. Ghannadpour and H.R. Ovesy: Eng. Comput.: Int. J. for Computer-Aided Eng. and Soft. Vol. 26 (2009), p. 868-893.

[7] S.A.M. Ghannadpour and H.R. Ovesy: Comp. Struct. Vol. 89 (2009), p. 151-158.

[8] H.R. Ovesy and S.A.M. Ghannadpour: Comp. Struct. Vol. 75 (2006), p. 100-105.

© (2011) Trans Tech Publications, Switzerland
doi:10.4028/www.scientific.net/KEM.471-472.1028

A Preliminary Study on Translational Kinetic Energy Absorption Using Coconut-fiber (Coir) Sheets as a Potential Impact-worthy Constituent in Advanced Aerospace Material

Nuraishah Bazilah Affandi[1, a], Azmin Shakrine Mohd. Rafie[2,b], Shahnor Basri[3,c], Fairuz Izzuddin Romli[4,d], Dayang Laila Abang Abdul Majid[5,e] and F. Mustapha[6,f]

[1, 2, 3, 4] Department of Aerospace Engineering, Faculty of Engineering, Universiti Putra Malaysia (UPM), 43400 Selangor, Malaysia.

[a]gulaley@gmail.com, [b]azmin@eng.upm.edu.my, [c]shahnor@eng.upm.edu.my, [d]firomli@eng.upm.edu.my, [e]dlaila@eng.upm.edu.my, [f]faizal@eng.upm.edu.my

Keywords: coconut, coir, fiber, energy, impact, kinetic, translational

Abstract. Known as "coir", the fibrous husk of the coconut fruit has potential for integration as a constituent in impact-resisting aerospace materials. As a preliminary study, kinetic energy absorption of this natural fiber is studied prior to further testing, for instance; a non-ballistic surface impacted at high velocity by a small mass is the equivalent mock-up to runway debris. The purpose of this study is to find the relationship between the thickness of the fiber with the kinetic energy absorption. Fabricated fiber panels measuring $10\times10\times t$ cm with various thickness are subjected to mild steel projectiles launched by a light gas gun at a constant pressure. The velocity of the projectiles is set to be consistent with the velocity range of typical transport-category aircraft. The impact response of the panels aids in predicting the required amendments where plies of coir sheets are increased to which perforation is impossible. The relationship established from the experimental results is then used to predict the amount of layers required for total translational kinetic energy absorption.

Introduction

The coconut fruit is botanically categorized as a drupe [1]. Referring to Fig. 1; the coconut husk consists of the exocarp and mesocarp [1], specifically known as *coir* [2]. The shell of the coconut is the endocarp [3] while the coconut flesh is the endosperm.

Duration for the coconut shell to decompose takes a long time [4], thus its presence in abundance is an environmental threat. Meanwhile, a much lighter substitute is necessary among ballistic reinforcing fibers [5] as glass-fiber is considered the heaviest fiber (E-glass: 2.55 g/cm^3 [6]). Since coir has the lowest density (1.25 g/cm^3 [6]) among commercially available natural fibers it has a potential to be used as ballistic reinforcing fiber, especially in aerospace application where weight is a paramount issue. During operation, the aircraft skin has to be able to withstand impacts by runway debris [7] and this condition can be simulated by a high speed ballistic test.

Experiments conducted previously [8] showed that a coconut shell powder-based composite is unfavorable over fiber due to inability to retain its previous form post impact. With this knowledge, this study focuses on the potential of using coir sheets as an impact-worthy constituent in advanced aerospace material. Furthering the former studies, terminal ballistic [9] analysis was conducted on the translational kinetic energy absorbed by the coir sheets which is given by Eq. 1:

$$E_t = \frac{1}{2}mv^2 \quad (1)$$

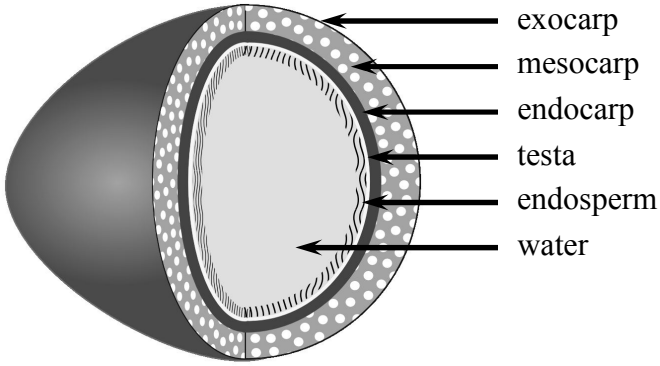


Fig. 1: Anatomy of the coconut fruit.

Methodology

The experiment divided into two basic processes: the fabrication of coir sheet specimens, and the ballistic testing.

Coir sheets. Custom-made coir sheets used for this study is approximately 100(W)×100mm(L) in dimensions and have random fiber orientation. Each sheet weighs an average of 12g. The coir sheets were left in its original packaging and stored away from direct sunlight at ambient room temperature under dry conditions. Necessary amounts of sheets were withdrawn only when required during the fabrication process.

Mold. A compression mechanism presented in Fig. 2 is applied in the fabrication process of the specimens. The apparatus comprises of two pieces of plywood, each partly wrapped with aluminum 6061-T6 sheet. Contact adhesive is necessary to adhere the aluminum sheet to the plywood.

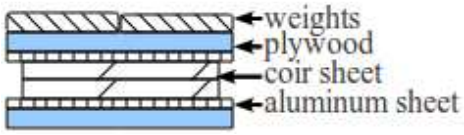


Fig. 2: Compression mechanism.

Surfaces of the aluminum sheet and plywood that come into contact with one another are cleaned from contaminants and oily residue. Then the surfaces are layered thinly with the adhering substance and left until nearly dry. Later on, both of the adhesive-layered surfaces are met, and the aluminum surface is pounded with a rubber mallet.

Duration for the adhesive to dry depends on the thickness of the spread, which can range from 5 to 10 minutes or more. To test whether the layered adhesive is about dry, another surface clear of adhesive such as a ruler is put into contact with the adhesive. The reaction from the adhesive is observed as the ruler is pried away. If the ruler comes away without the adhesive stretching yet traces of adhesiveness is present, that indicates the adhesive is nearly dry, and is ready for use. However, if the adhesive clings to the ruler, this indicates additional time is required for it to dry further.

Specimen fabrication process. The hand lay-up technique is used in the fabrication process. Surfaces possibly coming into contact with coir sheets or epoxy were layered with a release agent prior to fabrication. The ratio of epoxide resin to polyamine hardener is 2:1 by weight. The combined mixture was hand-stirred unidirectional for 3 minutes and used within 20 minutes. Initiation of the curing process starts as soon as the resin and hardener interact. Beyond the usability time, excess epoxy is discarded as the curing process has begun to take place.

Aided by Fig. 3, the following explains the epoxy application for a 2-layer specimen. Throughout the whole experiment, selected surfaces of coir sheets are applied with a 2mm-thick layer of epoxy for about 6 seconds. First, the epoxy is applied to Surface A2, followed by Surface B2. Then coir sheet Layer B is stacked on top of Layer A as configured in Fig. 3; thus Surface A2 and B1 are now bonded. Next, Surface A1 is layered with epoxy and is turned upside-down, thus

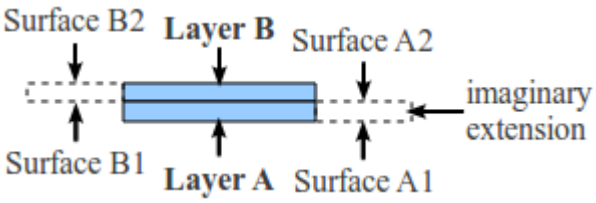


Fig. 4: Applying epoxy and stacking sheets.

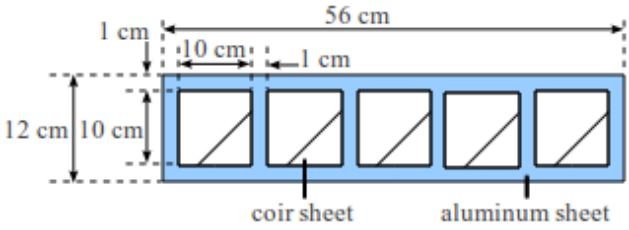


Fig. 3: Layout of the mold.

Layer A is now on top of Layer B.

As for a one-layer stack (consisting of a single coir sheet), epoxy is applied to both of its surfaces. Similar to the 2-layer specimen; the latter applied surface becomes the topmost surface.

Completed stacks are arranged in the mold as shown in Fig. 4. Weights weighing a total of 300N are arranged as shown in Fig. 2 to compress the specimens which are left to cure for 48 hours at ambient room temperature. Basically, each stack is applied a pressure of 6kPa.

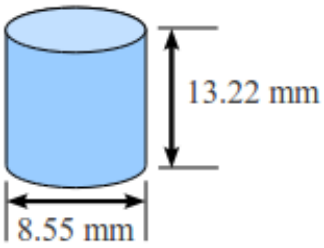


Fig. 5: Average dimensions of the blunt-faced mild steel projectile.

Projectile. Blunt-faced projectiles made of mild steel weighing an average of 5.737g is used. Further dimensions of the projectile are shown in Fig. 5.

Calibration. Calibration of the specific projectile noted in Fig. 5 is carried out ahead of the experiment. The calibrated velocity of the projectile launched at 200psi is 205m/s.

Terminal ballistic process. A light-gas gun is used to launch the blunt-faced projectiles to simulate the impact by a small mass onto a non-ballistic surface at high velocity. Helium is used as the working gas. An individual coir sheet specimen is secured to the test rig in between two metal plates with circular apertures, as shown in Fig. 6. Then the projectile is launched at a pressure of 200psi. Subsequently, an unused specimen is substituted in place of the utilized specimen for succeeding tests. Each specimen is used once.

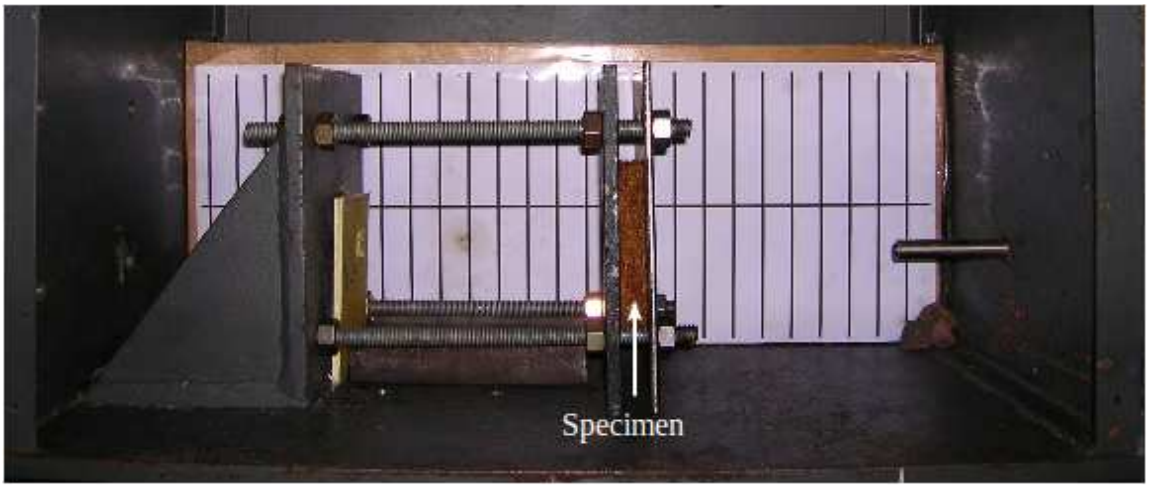


Fig. 6: Coir sheet specimen secured to the test rig.

Velocities before and after the projectile impact are calculated by means of a high-speed camera set to capture at 30,000 frames per second. Use of Eq. 1 further enables attainment of the translational kinetic energy absorbed during impact, calculated as such:

$$E_t = \frac{1}{2} m\left(v_i^{\,2} - v_f^{\,2}\right) \tag{2}$$

where m is the mass of the projectile, v_i is the initial velocity (pre-impact), and v_f is the final velocity (post-impact).

Results and Discussion

The experiment is conducted for one-layer up to six-layer coir sheet specimens. For each specimen, five samples are fabricated and tested. In total, the number of samples is 30. The test results are tabulated in Table 1.

Table 1: Experimental results of post-impact velocity.

Specimen	Post-impact velocity (m/s)					
	Sample 1	Sample 2	Sample 3	Sample 4	Sample 5	**Average**
1-layer	197.91	190.03	185.13	186.73	190.00	**189.96**
2-layer	175.97	185.90	177.76	176.91	189.13	**181.13**
3-layer	176.28	175.88	166.00	174.16	160.95	**170.66**
4-layer	150.05	160.22	140.88	144.69	156.80	**150.53**
5-layer	151.25	136.04	140.75	146.78	142.98	**143.56**
6-layer	145.83	125.67	46.04*	147.57	147.20	**141.57**

**Omitted.*

Each data point in Fig. 7 represents the average post-impact velocity for each type of specimen. The drop in post-impact velocity with increase in coir sheet layers is predicted because the increase in the number of layers for the specimen theoretically also increases its energy absorption capability.

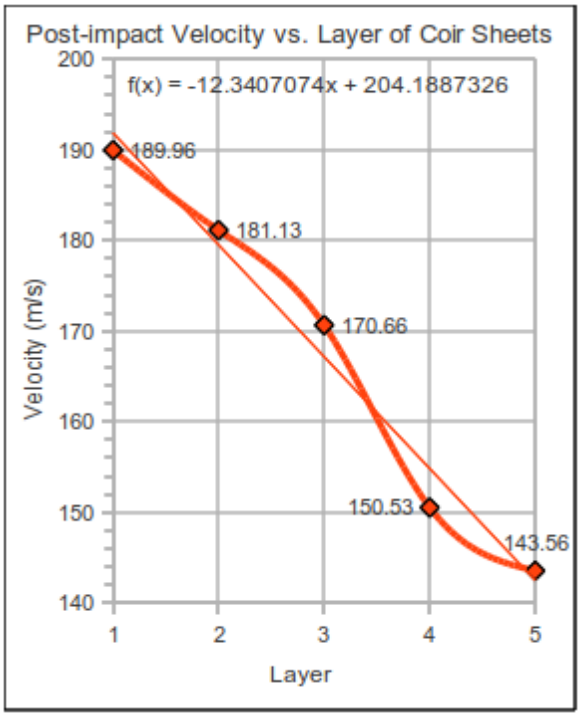


Fig. 7: Post-impact velocity

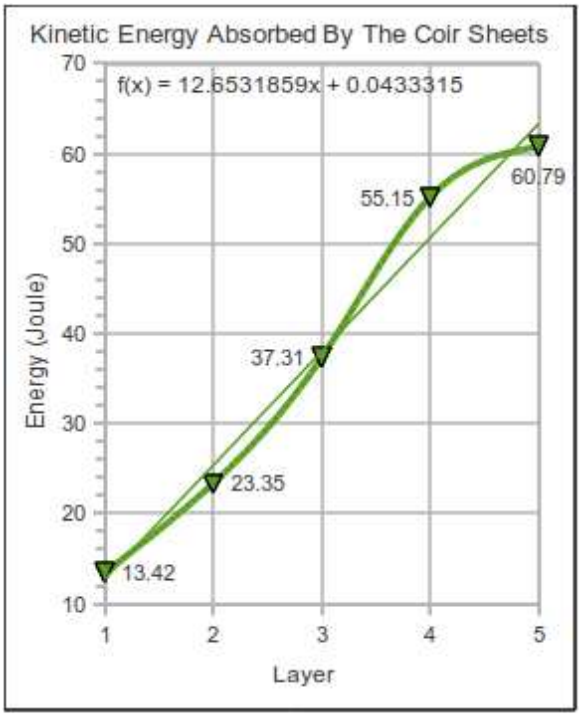


Fig. 8: Translational kinetic energy absorbed by stacks with various layers

Using the same data, Fig. 8 is constructed using Eq. 2. The translational kinetic energy absorption equation, which is obtained from the best fit line of the observed data points in Fig. 7, is as follows:

$$f(x) = 12.7x + 0.04 \quad (3)$$

This mathematical relationship enables the prediction of the required layers for non-perforation by means of extrapolation. It is should be noted that this equation is derived using experimental results for one-layer to five-layer coir sheet specimens. The results for six-layer coir sheet specimen on the other hand, are used to measure the goodness of the equation. The error is calculated and shown in Table 2.

Table 2: Validation.

Specimen	Actual Absorbed Energy (J)	Predicted Absorbed Energy (J)	Error (%)
6-layer	65.08	76.24	17.1

It can be seen that the error is just about 17.1%, which can be contributed to the precision in the testing apparatus used and specimen fabrication process. This nevertheless indicates that the equation can be appropriately applied to estimate the energy absorption of higher stacks of coir sheets.

Working under the impression that the total translational kinetic energy absorption by coir sheets is plausible, the calibrated velocity is plugged into Eq. 2 as the initial velocity while the final velocity is set to zero. The calculated energy of 120.55J is expected to be the maximum energy generated by the projectile. Plugging this calculated energy into Eq. 3, a stack of 10 layers of coir sheets is predicted to be capable of absorbing the whole translational kinetic energy developed by the projectile.

Summary
An equation that captures the relationship between thickness of the coir fiber and its kinetic energy absorption capability has been established from the experimental results. It is further validated and concluded from its low error percentage to have a good prediction for energy absorption of higher stacks of coir sheets. The observed performance of the coir sheets shows its suitability to be used as advanced aerospace material. Its ability in absorbing translational kinetic energy, coupled with its light weight and low cost characteristics, demonstrates potential for further development.

Further Works
As predicted by the equation derived through experimental results, non-perforation of the specimen is possible with a stack consisting of 10 layers of coir sheets. The experimental proof of this prediction is yet to be performed, thus it is beneficial to be the starting point in future works. In addition, the study can also be branched out by increasing the compression pressure applied during fabrication with the use of, for instance, a hydraulic compression machine.

Acknowledgement
The authors acknowledge the financial support of the Research University Grant Scheme (RUGS) Universiti Putra Malaysia, Vot. number 91310 and also Department of Aerospace for theirs equipments and staff support.

References

[1] *Handbook of Plant and Crop Physiology*, edited by M. Pessarakli, 2nd ed., Marcel Dekker Inc., NY (2002).

[2] S.K. Bhatia and J.L. Smith: *Bridging the Gap Between Engineering and the Global World: A Case Study of the Coconut (Coir) Fiber Industry in Kerala, India*. Morgan & Claypool Publishers. (2008).

[3] P.K. Thampan,: *Handbook On Coconut Palm*. Oxford & IBH Publishing Co. (1981)

[4] S.N. Monteiro, L.A.H. Terrones, J.R.M. D'Almeida: Polymer Testing Vol. 27 (2008) p. 591-5.

[5] V.P. McConnell: Reinforced Plastics Vol. 50, Issue 11 (2006) p. 20-5.

[6] W.D. Brouwer: Common Fund for Commodities - Alternative Applications for Sisal and Henequen - Technical Paper No. 14. Proceedings of a Seminar held by the Food and Agriculture Organization of the UN (FAO) and the Common Fund for Commodities (CFC), Rome, 13 December 2000.

[7] W.J. Cantwell and J. Morton: Composites Vol. 22, Issue 5 (1991) p. 347-62.

[8] N.B. Affandi, A.S.M. Rafie, and S. Basri,: Proceedings of Aerotech III 2009. Department of Aerospace Engineering, Universiti Putra Malaysia (2009) p. 61-6.

[9] K.G. Sellier and B.P. Kneubuehl: *Wound Ballistics and the Scientific Background*. Elsevier Health Sciences. (1994)

© (2011) Trans Tech Publications, Switzerland
doi:10.4028/www.scientific.net/KEM.471-472.1034

Sugar Palm Fibre-Reinforced Unsaturated Polyester Composite Interface Characterisation by Pull-out Test

Z. Leman[1,a], S.M. Sapuan[1,b] and S. Suppiah[1]

[1]Department of Mechanical and Manufacturing Engineering,

Universiti Putra Malaysia, 43400 Serdang, Selangor, Malaysia

[a]zleman@eng.upm.edu.my, [b]sapuan@eng.upm.edu.my

Keywords: natural fibre, surface modification, sugar palm, unsaturated polyester

Abstract. Polymer composites using natural fibres as the reinforcing agents have found their use in many applications. However, they do suffer from a few limitations, due to the hydrophilicity of the natural fibres which results in low compatibility with the hydrophobic polymer matrices. This paper aims to determine the best sugar palm *(Arenga pinnata)* fibre surface treatment to improve the fibre-matrix interfacial adhesion. Fibre surface modifications were carried out by water retting process where the fibres were immersed in sea water, pond water and sewage water for the period of 30 days. The test samples were fabricated by placing a single fibre in an unsaturated polyester resin. Single-fibre pull-out tests showed that freshwater-treated fibres possessed the highest interfacial shear strength, followed by untreated fibres, sewage water-treated fibres, and sea water-treated fibres. Further surface analyses of the samples were performed using a Scanning Electron Microscope (SEM) and an Energy Dispersive X-ray Spectroscopy (EDS) system.

Introduction

As a tropical country, Malaysia has abundant resources of natural fibres and one of the highly promising ones is the sugar palm *(Arenga pinnata)* fibre. Traditionally, the local people use the fibres to make brooms, brushes, and ropes especially for cordage on ships. Although the fibre is well known among the locals to have high strength and durability but very little research [1-4] has been done to study the full potential of this fibre.

It is well known that the performance of composites depends on the properties of the individual components and their interfacial compatibility. To improve the interfacial bonding, fibre surface modification must be performed by some method [5-10]. This study focused on the interfacial shear strengths of fibres that had undergone biological surface modification. The effects of the treatments on the mechanical properties of the biocomposites and the surface morphology of the fibres are presented in the following sections.

Materials and Method

Materials. The sugar palm fibres were obtained from the rural area of the State of Pahang, Malaysia. The fibres are black/brown in colour with diameters of up to 0.50 mm and are naturally found wrapped around the tree trunk at the base of the palm leaf ribs. Unlike many other natural fibres, sugar palm fibres are directly obtained from the tree which does not require a secondary process to yield the fibres. Other fibres like kenaf and jute are usually subjected to the water retting process before the fibres can actually be harvested.

The matrix used was unsaturated polyester resin (Reversol P9509) and hardener, supplied by Revertex (Malaysia) Sdn Bhd. The mixing ratio used was 98:2. The fibres were subjected to biological treatments in: i) sea water at Lumut, Perak, ii) fresh water pond at the Faculty of Engineering, UPM and iii) sewage water from a housing area water treatment pond at Taman Serdang Jaya, Seri Kembangan, Selangor. The pH values of the treatment solutions prior to and post-treatment were also recorded.

Methods

Treatment process. The fibres were immersed for 30 consecutive days in sea water, pond water, and sewage water treatments. The results from these three treatment methods would be compared to an untreated control batch of fibres. After each treatment the fibres were taken out and washed thoroughly with tap water to remove any foreign materials and then dried in a room with good ventilation for 5 days. It was important to ensure that the fibres were thoroughly dried because fibres with residual moisture content could cause micro cracking during composite fabrication.

Test Specimen Preparation. The treated fibres were then cut into strips of 50 mm in length. The fibres were then inserted into a silicone rubber mould with many cavities. Each cavity had a dimension of 20 x 15 x 5 mm. The fibres were adjusted until they protruded 3 mm into the mould.

The prepared resin was then poured into the moulds and then set aside to cure in room temperatures for 2 hours. After 2 hours, the composites were carefully removed from the mould and left to fully harden for a further 24 hours. A paper grip was then glued 10 mm away from the emergent end of the fibre. The completed test specimen is shown in Figure 1.



Fig. 1. Completed test specimen

Single-fibre pull-out tests. The test specimens were then tested using the INSTRON 3365 Dual Column Testing Machine. The top and bottom clamps were affixed 10 mm apart from each other, using the paper grip as a guide. The machine was then run at a constant pulling speed of 0.1 mm/minute. The testing took place at a room temperature of 23°C ± 2 with a controlled indoor humidity of 50% ± 5. The test sample was pulled continuously until the fibre-matrix interface completely debonded and the fibre was pulled free from the resin as shown in Figure 2. The interfacial shear strength was then calculated using the following equation:

$$\sigma = \frac{F}{\pi d \ell}$$

where,
σ : Interfacial shear strength, MPa
F : Load at yield, N
A : Original surface area of fibre within matrix, m^2
d : Fibre diameter, m
ℓ : Critical embedded length, m

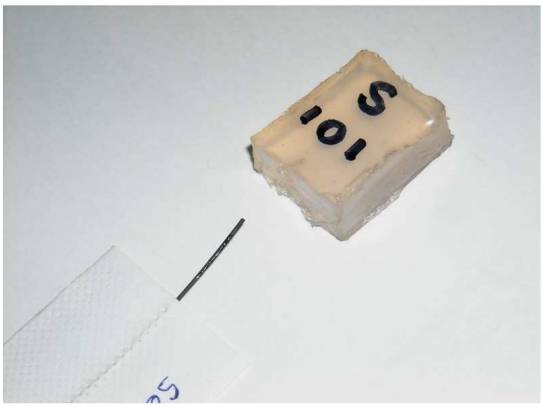


Fig. 2. Successful fibre pull-out

Microscopy and Spectroscopy Analysis. A scanning electron microscope (SEM) machine was then used to study the surface morphology of the fibre under different types of surface treatments. The images were also analysed using an Energy Dispersive X-ray Spectroscopy (EDS) system. The microscopic analysis of the surface morphology was important in characterising any structural changes that had occurred during treatment and how it affected the interfacial bonding between the fibre and the resin. The spectroscopy analysis provided vital information on the elemental composition on the surface of the fibres. The fibres were coated with a thin layer of gold using the coating machine in order to produce an image with sufficient contrast on the SEM.

Results and Discussions

pH Tests. As shown in Figure 3, all three treatment solutions became more acidic after the fibres were soaked for 30 consecutive days.

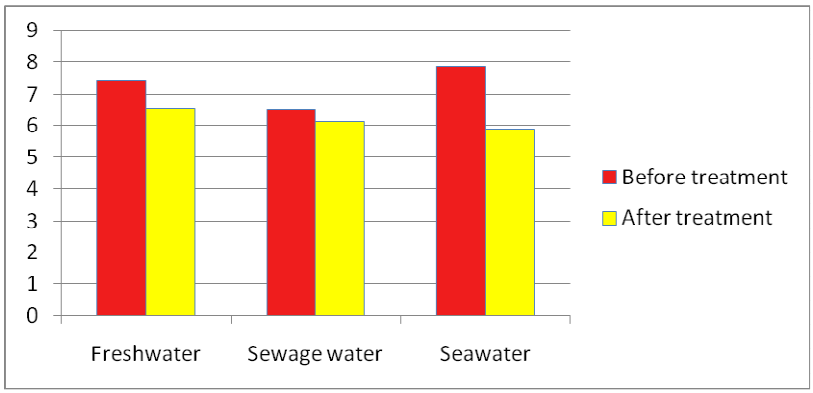


Fig. 3. pH values of treatment solutions

Single-Fibre Pull-Out Tests. 10 specimens for each treatment method were successfully subjected to the pull-out tests. The average interfacial shear strength values for each type of treatment are shown in Figure 4.

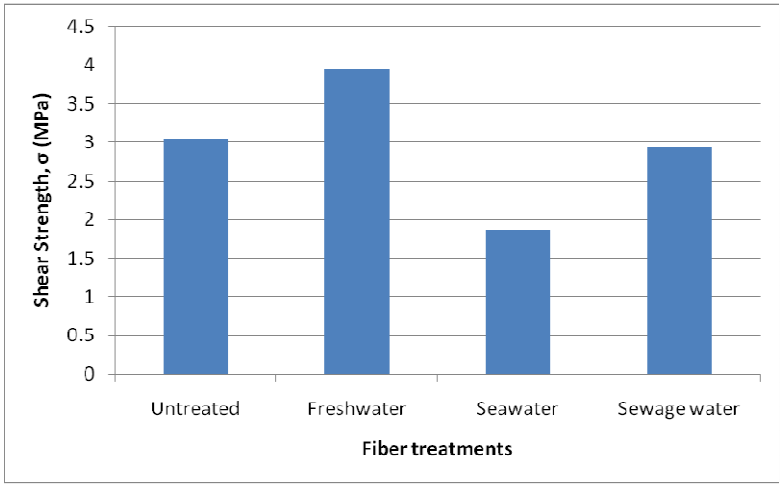
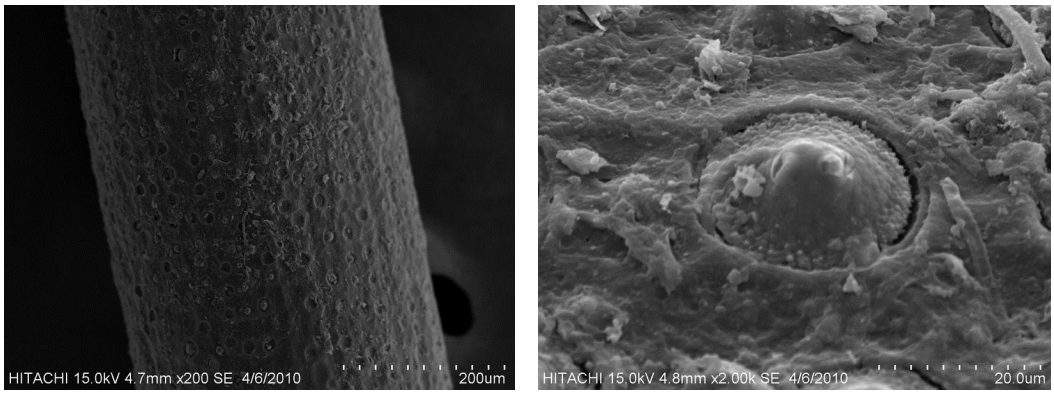


Fig. 4. Average interfacial shear strength

The control group of untreated sugar palm fibres possessed an average interfacial shear strength value of 3.040 MPa. Freshwater treatment resulted in an average value of 3.940 MPa; an increase of 22.84% over the control batch. Sea water treatment significantly worsened the performance of the fibres, causing a drop of 62.57% to 1.870 MPa. The third treatment with sewage water was remarkably similar with the untreated batch, posting a slight drop of 3.33% to 2.942 MPa.

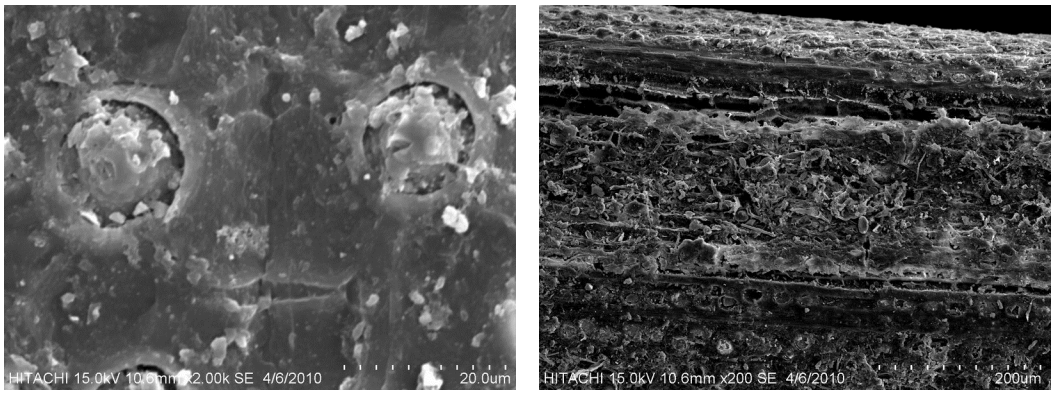
Fibre Surface Morphology. The test specimens were analysed using a Scanning Electron Microscope in order to help explain the results of the single-fibre pull-out tests. The SEM analysis revealed that the surface of the untreated sugar palm fibre was covered by a smooth and waxy layer of hemicelluloses and pectin, as shown in Figure 5(a). It is responsible for the protection of the inner layer which consists of lignin. This waxy outer layer is highly hydrophilic and results in poor interfacial bonding when used in composites.



(a) (b)

Fig. 5. SEM photomicrograph of a) untreated sugar palm fibre and b) freshwater-treated sugar palm fibre

30 days of treatment with freshwater resulted in a surface morphology that was visibly rougher than the untreated fibres. Figure 5(b) shows the degradation of the waxy layer of hemicelluloses and the emergence of circular pustules from the tiny pores on the fibre. EDS analysis revealed extremely concentrated levels of silica all along the surface of the pustule.



(a) (b)

Fig. 6. SEM photomicrograph of a) sewage water-treated sugar palm fibre and b) sea water-treated sugar palm fibre

Figure 6(a) shows the surface of the fibres treated for 30 days in sewage water. The pustules in the pores were significantly degraded and worn down. EDS analysis still resulted in elevated levels of silica, though at reduced amounts compared to previous samples. Sea water treatment resulted in the most rough fibre surface as shown in Figure 6(b). Most of the pustules were missing altogether from the fibre. EDS analysis showed that the levels of silica were vastly reduced with the remaining traces scattered in isolated sections of the fibre. The untreated sugar palm fibres posted an average interfacial shear strength value due to the fact that the fibres were still covered in the smooth waxy layer of hemicelluloses and pectin. The presence of this layer made bonding with the resin difficult. Freshwater treatment removed most of this waxy layer and exposed the silica-rich layer below. This resulted in much improved levels of bonding between resin and fibre. Sewage water and sea water treatments removed both the waxy hemicelluloses layer and the silica pustules below. As such they posted very poor values of interfacial shear strength of the composite.

Summary

Single-fibre pull-out testing of treated sugar palm fibres from an unsaturated polyester resin yielded mixed results. Although freshwater treatment improved the interfacial shear strength, sea water and sewage water treatments significantly worsened the performance of the composite. The sugar palm fibres also showed vastly different surface morphologies as seen under the Scanning Electron Microscope. Further analysis using an Energy Dispersive X-ray Spectroscopy system showed that there seemed to be a correlation between the results of the single-fibre pull-out tests and the levels of silica detected in the fibres. Freshwater treatment of sugar palm fibres seems to have the best potential to greatly improve the mechanical properties of the final composite.

Acknowledgements

The authors would like to thank the staff at the Department of Mechanical and Manufacturing Engineering, Universiti Putra Malaysia for the help with the mechanical tests. Special thanks are also due to the staff at the Department of Chemical and Environmental Engineering, Universiti Putra Malaysia for the help rendered during the SEM and EDS work.

References

[1] Sastra, H.Y., Siregar, J.P., Sapuan, S.M., Leman, Z. and Hamdan, M.M: American J. Appl. Sci., Special Issue (2005), p. 21-24.

[2] Z. Leman, S.M. Sapuan, M. Azwan, M.M. H.M. Ahmad, and M. A. Maleque: Polymer-Plastics Technology and Engineering Vol. 47 (2008), p. 606–612.

[3] Z. Leman, S.M. Sapuan, A.M. Saifol, M.A. Maleque, M.M.H.M. Ahmad: Materials and Design Vol. 29 (2008), p. 1666-1670.

[4] D. Bachtiar, S.M. Sapuan, M.M.H.M. Ahmad: J. Appl. Technol., Vol. 4 (2006), p. 1-7.

[5] Sreekala, M.S., Kumaran, M.G., Joseph, S., Jacob, M., and Thomas, S.: Appl. Composite Mater. Vol. 7 (2000), p. 295-329.

[6] Karlsson, J.O., Blachot, J.F., Peguy, A., and Gatenholm, P.: Polymer Composites, Vol. 17 (1996), p. 300-304.

[7] Bisanda, E.T.N.: Appl. Composite Mater. Vol. 7 (2000), p. 331-339.

[8] Liu, W., Mohanty, A.K., Drzal, L.T., Askel, P., and Misra, M.: J. Mater. Sci. Vol. 39 (2004), p. 1051-1054.

[9] Gomes, A., Goda, K., and Ohgi, J.: JSME Int. J. Series A Vol. 47 (2004), p. 541-546.

[10] Mwaikambo, L.Y., and Ansell, M.P.: J. Appl. Polymer Sci. Vol. 84 (2002), p. 2222-2234.

© (2011) Trans Tech Publications, Switzerland
doi:10.4028/www.scientific.net/KEM.471-472.1040

Doping Of Palladium in Silica Nanofibers via Electrospinning and Sol-Gel Synthesize as Hydrogen Storage Material

Samaneh Shahgaldi[1,2,a], Zahira Yaakob [1,2,b], Dariush Jafar Khadem [1,c], Wan Ramli Wan Daud[1,2,d], Edy Herianto Majlan[1]

[a]Fuel Cell Institute, Universiti Kebangsaan Malaysia,

43600 UKM Bangi, Selangor

[b]Faculty of Chemical Engineering, Universiti Kebangsaan Malaysia,

43600 UKM Bangi, Selangor

[a]Sami_shahgaldi@yahoo.com, [b]zahira@eng.ukm.my, [c]D.Khadem@ukm.my, [d]wramli@eng.ukm.my

Keywords: silica nanofibers, silica palladium nanofibers, electrospinning, surface area

Abstract. In recent years, one dimensional nanostructure, nanowires, nanofibers with unique properties have been a subject of intense research due to reduction of devise dimension, potential properties from the re-arrangement at the molecular level and high surface area. There are many methods for synthesize such as laser ablation, chemical vapour deposition, solution method micro pulling down method but all these method faced to the major disadvantages of being complicated with long wasting time and relatively high expense . The electrospinning recently used for producing ceramic, metal, and carbon nanofibers. In this report, we incorporate palladium into silica nanofibers for the first time, and the effect of doping of palladium into the silica nanofibers is investigated. The different ratio of palladium to silica and comparing with silica nanofibers is also reported. The composition, morphology, structure and surface area of silica, and silica palladium nanofibers were investigated by thermo gravimetric analysis (TGA), x-ray diffraction (XRD), scanning electron microscopy (SEM),Fourier transform infrared spectroscopy (FT-IR), and Micromeriics. To the best of our knowledge, investigation on characteristic on Silica palladium nanofibers has not been reported up to now. The result reveal that the silica nanofibers compare to silica doped with palladium have lower diameter, and also by increasing the temperature above 600 °C, the reduction in length of nanofibers happened. High surface area of silica palladium nanofibers can be one of the promising materials for hydrogen storage.

Introduction

Hydrogen gas with many advantages such as lightweight, abundant, regenerable energy source, non toxic and produces an environmentally friendly oxidation by-product has been focused as an ideal fuel in fuel cells. In spite of obvious advantages, an immediate incorporation of hydrogen faces some problems. The hydrogen economy can be divided of five main parts Production, Delivery, Storage, Conversion, and Application. Nowadays, production, and conversion are technologically feasible but hydrogen storage material with high capacity still need more researches [1-5]. Hydrogen compression, liquefaction, and in sorbent materials are three main method for storage. Most promising method is sorbent material with high volumetric/ gravimetric capacity, fast sorption kinetics, high surface area, and high tolerance to recycling. Carbon nanotubes and carbon nanofibers have been introduced as promising materials for hydrogen storage [6-8]. Additionally,

boron nitride nanotubes, boron nitride nanofibers, TiS_2, MoS_2, and ZnO have also been focused by researches as possible hydrogen storage materials [9-12]. More recently, silica nanostructure have attracted considerable interest because of high specific surface area and porosity, good thermal stability, and good mechanical properties and demonstrate applications in many fields such as storage, sensors, catalysts, membrane, drug delivery, electrode materials and etc [12-15]. Jin Bae and et al reported hydrogen adsorption capacity in the lithium dispersed silica nanotubes [16]. Yan Han and et al investigated hydrogen storage electrochemically in CoB–silica nanochains [17]. There are variety method for synthesize silica nanostructure (nanoparticles, nanotubes, nanofibers, nanosphere, etc) such as flame aerosol technology, chemical vapor deposition, radio-frequency and direct current plasma enhanced chemical vapor deposition and so on, By these method, the controlling the procedure for large quantities of silica nanomaterials has needed intensive and sophisticated design strategies with long wasting time and relatively high expense [18-20]. As a result, synthesize with advantages of high production, simplicity, and cost effective still remains challenging. The electrospinning recently used for producing carbon, polymer, metal nanofibers with solving all disadvantages of above methods with simplicity, minimizing the spinning process time and cost and maximize convenience, quality and diameter control method for preparing nanofibers in bulk amount [21-23]. In this method, desired precursors, prepared by sol gel are mixed with a polymer as a spinning aid. After being homogenous, ejected from capillary, to which is applied a high electric field. The jet emission starts when the surface tension of solution droplet is overcome by electric field. In best of our knowledge, for the first time in this paper we reported the synthesize of silica doped palladium nanofibers with measuring surface area and porosity in order to achieve suitable material for hydrogen storage.

Experimental

All materials were used as produced without further purification. Tetraethyl orthosilicate (TEOS) (99.9%), Polyvinylpyrrolidone (PVP, Mw: 1300000) was purchased from sigma Aldrich, ethanol (100% purity, BDH, England), deionised water, Hydrochloric acid, palladium. For the electrospinning of silica and silica doped palladium nanofibers, a typical precursor gel solution was prepared as mentioned below. First, 1.5 g TEOS was dissolved in 5ml ethanol and vigorously stirred for 1 h, then 4 ml distilled water and HCL was added drop by drop into the mixture and silica gel was formed by further 2h stirring. One of the famous silicon alkoxide for production of silica structure is TEOS,that can be shown by simple reaction. In this reaction Ethoxy groups are substitute by OH groups via hydrolysis and then dehydration has been achieved among hydroxyl groups of different molecules. Siloxane polymer chain improved by chemical condensation to form high molecular weight. However, Variety structure has been synthesized at different conditions [23].

$$Si(OC_2H_5)_4 + xH_2O \rightarrow Si(OH)_x(OR)_{n_x} + xC_2H_5OH$$

$$—Si—OH + HO—Si \rightarrow —Si—O—Si— + H2O$$

In the next step, proper amount of PVP was dropped into the primary mixture, and then the reaction proceeded in ultrasonic for another 2h. In the electrospinning process, the precursor sol-gel solution prepared above was immediately drawn into a plastic syringe equipped with a stainless needle. When the applied electric field overcomes the surface tension of the droplet, a charged jet of solution is ejected. Due to the bending instability, jet become longer and thinner until it collects on the collector. A DC voltage of 18 kv applied by a high-voltage supply. The feeding rate of precursor solution was controlled by a syringe pump (new Eva pump systems model NE=1000) at 0.5 ml/h. A piece of aluminium was placed 15 cm from the top of needle, and used to collect the nanofibers. All electrospinning processes were done in room temperature. PVP/ Silica nanofibers were collected

from collector and calcined at 600 °C to obtain silica nanofibers. For comparing silica with silica doped palladium nanofibers, 1 %wt and 1.5wt% Palladium was added to the sol-gel in constant condition respectively.

Characterisation

Electrospun nanofibers were analyzed to thermo gravimetric analysis (TGA), because of determination of the temperature of possible decomposition and phase change. This measurement was performed with a heating rate of 5 °C/min up to 1000°C. The desired structure after calcinations was characterized by XRD using Cu Kα 1 radiation with a primary monochromator 40kV and 40mA, with 2θ varying from 10^0 to 80^0 and an X'Celerator detector to characterise the crystal structure of the specimens. The morphology of the nanofibers was examined by SEM and TEM. The textural properties was analysed by Micromeritics.

Results

The shape and diameter of produced electrospun fibers can be controlled by many parameters. The most important factors are type and concentration of polymers with suitable solvent in sol gel. Moreover, others effective parameters related to electrospinning such as voltage, feeding rate, humidity, temperature and distance between nozzle and collector were indicated. In recent years, many publication is belong to investigation of the controlling the condition. Based on the researches and our works by using the optimize condition we focused on the approaching the desired structure. Silica sol-gel precursors were electrospun with or without palladium and the morphology of fibers were investigated in this part by SEM. Figure.1 (a, b) reveals the image of as spun nanofibers without any calcinations. In the top of image (a) the sol-gel was spun without polymer, in the absence of PVP no nanofibers was seen in the surface due to low viscosity of solution. In electrospinning, polymer often use as a carrier. Polyvinylpyrrolidone with special characteristic is chosen as the base polymer for electrospinning due to suitability in reaction with nitrate and also, the good solubility in alcohols and water with different molecular weight from 1×10^3 to 1.3×10^6. It is observed that, the as spun uniforms nanofibers have smooth surface because of amorphous structure and diameter around 300- 600nm. Figure.1 (c, d) shows silica nanofibers after calcinations at 600 °C, by calcinations the average diameter of fibers change to 100-400nm, this reduction in diameter could be related to the loss of polymer. In the case of fibers involving palladium with different concentration of 1% wt and 2%wt, that was shown by Figure 1. (e-h) respectively, the diameter of fibers slightly increased. This increasing is definitely related to the adding of palladium into the sol-gel and increasing the viscosity of solution. Normally, higher viscosity of sol-gel forms thicker fibers via electrospinning. The diameter of silica palladium nanofibers are up to 1 micrometer. To better understand the growth patterns of palladium particles in silica nanofibers, it characterized by TEM. Figure. 5, Shows uniform distribution of 3-7 nm palladium nano particles on silica nanofibers. TG curves in Figure. 2 (a, b) belong to spun nanofibers with and without palladium performed the mechanism of decomposition of samples. The first step below 200°C could be related to the loss of water, ethanol and moisture in the composites. The second major weight loss, was observed from 200 °C and 298 °C is due to the decomposition of side- chain of polymer. Major weight loss from 400 °C is belonging to degradation of PVP. By increasing the temperature C-H, C-C, C=O, and C-N bond were broken. Weight loss From 320°C to 500 °C could be related to the release of water which is prepared from the condensation of silanol in the silica framework. The silica palladium has more thermal stability to compare with silica. The first 13% weight loss is probably due to the loss of the surface absorbed water or residual water and ethanol in the composite fibers. The second 6% weight loss, is due to the decomposition of the side-chain. The major weight loss is related to decomposition of main chain of polymer, and the last small weight

loss was observed due to the water from condensation of silanol. Figure. 3. (a-c) shows the XRD patterns of silica with or without palladium nanofibers after calcinations. Peak (a) depicts one equatorial peak at 2θ: 23° to 27° that reveal characteristics of amorphous silica. Peak (b, c) reveals the amorphous silica with palladium. The chemical structure of silica nanofibers as spinning and after calcinations measured with Fourier transform infrared spectroscopy as depicts in Figure. 4. It is seen that the peak at 2958, 1459 cm^{-1} and 1645 cm^{-1} are for the C-H vibration of methyl, methylene and C=O vibration of the polymer respectively. Absorption peaks at 795, 965, 1142 cm^{-1} and broad peak in 3370 cm^{-1} are belong to Si–O–Si vibration and O–H vibration respectively. By calcinations of fibers, it can be seen decreasing in the of C-H, C=O, and Si-OH and also increasing in Si-O, this changing in intensity happened by pyrogenation of PVP and condensation of hydrolyzed precursor. By comparing the typical absorptions peak for methyl or methylene of ethoxy group with the silica peak, it is obvious that the ethoxy group was changed to the silanol due to the hydrolyzing of TEOS. Nitrogen absorption isotherm of silica palladium is presented in Figure. 6. As it can be seen there is a significant change above 0.1 P/P0, which indicates mesopores and macropores of the sample. Silica palladium by reaching to 500 cc/g of nitrogen adsorption at 1P/P0 has developed pore structure and also it shows specific surface area of about 943.29 m^2/g and total pore volume of 0.7856 $cm^3/$ g. Synthesized silica palladium nanofibers compare to silica nanofibers, silica nanotubes , nanochain even carbon nanotubes and carbon nanofibers has better characteristic for hydrogen storage.

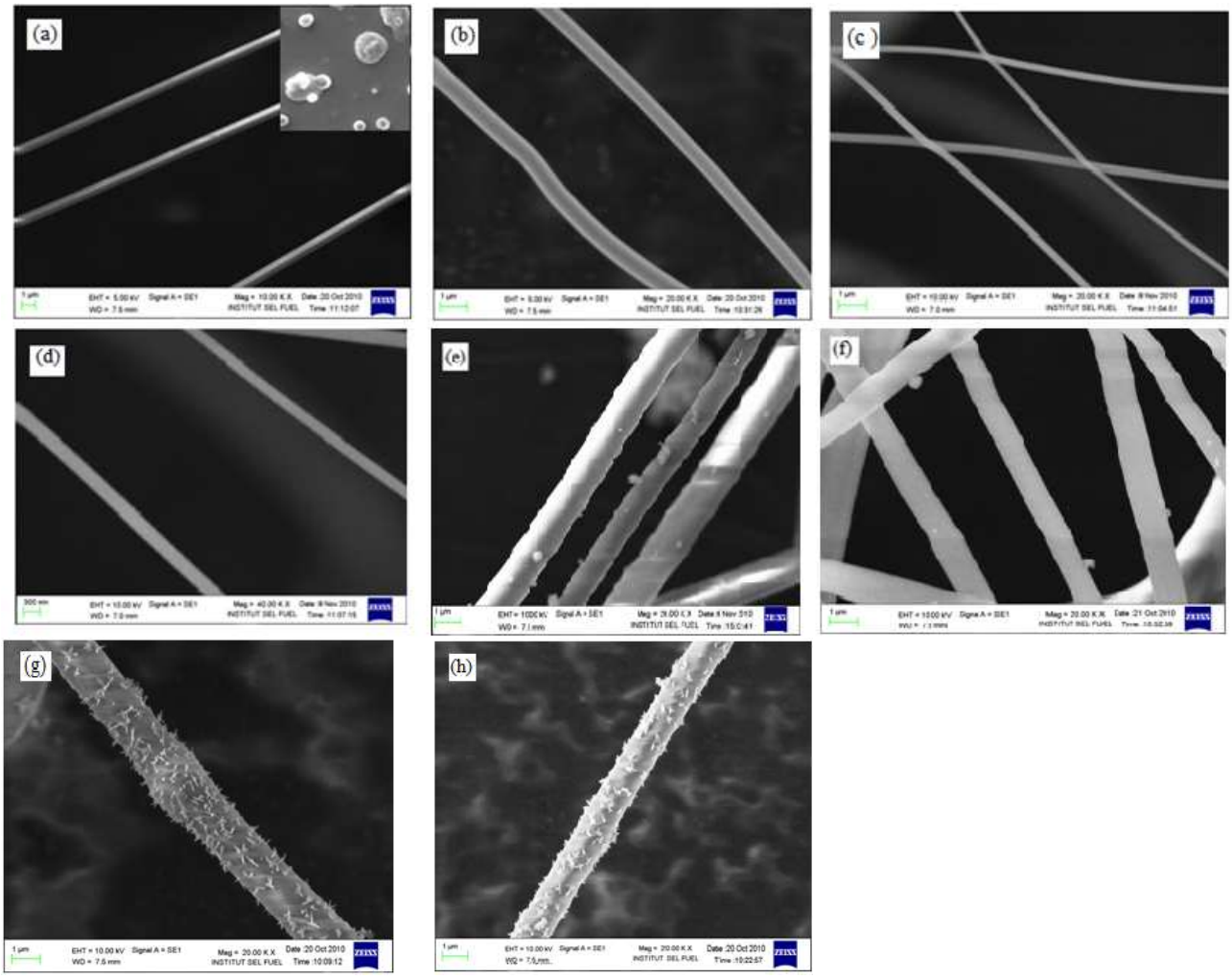


Fig. 1 SEM image of the sample: (a, b) as spun silica nanofibers, (c, d) after calcinations, (e) as spun with 1%wt Pd, (f) after calcinations, (g)spun with 2%wt pd, (h) after calcinations

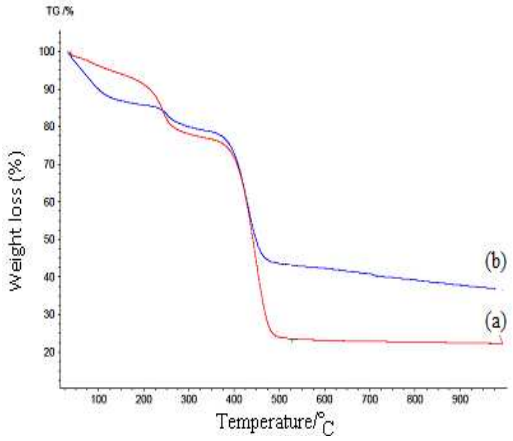


Figure.2(a, b) thermogravimetric analysis of silica and silica palladium nanofibers calcined at 600◦C

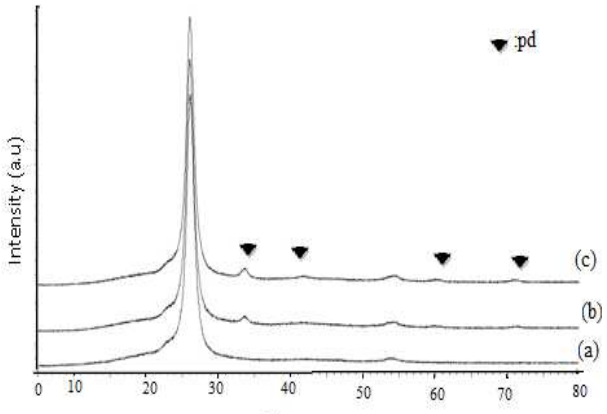


Figure. 3.XRD pattern of (a) silica nanofibers (b) silicananofibers calcineat 600 ◦C (C) Silica palladium calcined at 700◦C

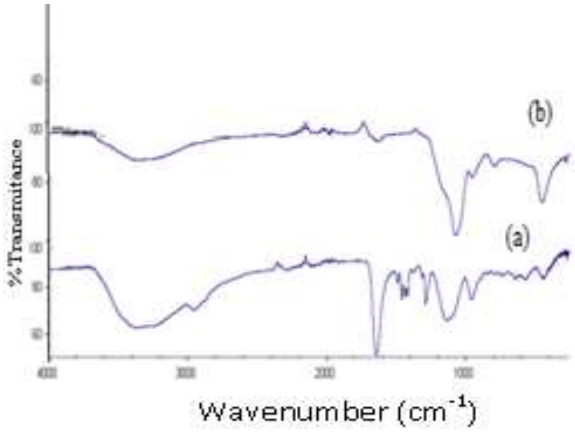


Figure.4.FT-IR spectra (a) pvp\ silica nanofibers(b)silica nanofibers calcined at 600◦C

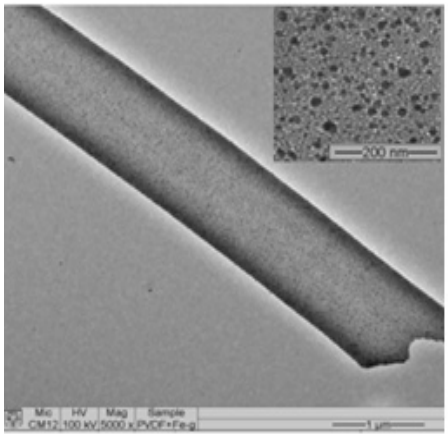


Figure.5.shows TEM image of silica palladium after calcinations at 600◦C

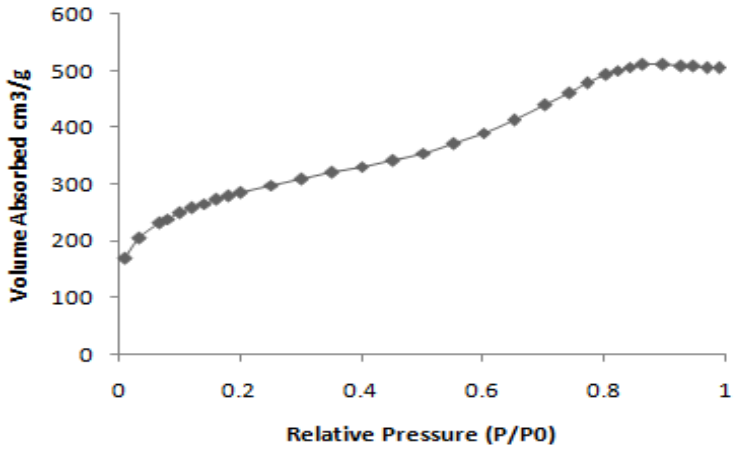


Figure.6.Nitrogen adsorption isotherm of silica palladium

Summary

In summary, silica and silica palladium nanofibers were successfully synthesized by sol-gel via electrospinning. By using this method, long and continuous nanofibers in bulk amount and cost effective way was prepared. Spun silica /polymer nanofibers with around 300- 600nm have smooth surface due to the amorphous structure, after calcinations at 600 °C the diameter decreased to 100-300 nm. Polymer has main role to producing fibers, by spinning without polymer just beads remain in the surface. By adding 1wt% and 2wt% palladium to the sol-gel, silica palladium nanofibers with increasing in fibers diameter produced. This increasing is definitely related to the adding of palladium into the sol-gel and increasing the viscosity of solution. Normally, higher viscosity of sol-gel forms thicker fibers via electrospinning. Uniform distribution of palladium was shown by TEM. Silica palladium nanofibers with specific surface area of about 943.29 m^2/g and total pore volume of 0.7856 cm^3/ g can be one of the most promising candidates for hydrogen storage.

References

[1] Yang RT. Carbon 2000;38(4):623–6.
[2] Volpe M, Cleri F. Chem Phys Letter 2003;371(3–4):476–82.
[3] J.S. Im, S.J. Park, T.J. Kim, Y.H. Kim, Y.S. Lee, Journal of Colloid and Interface Science 318 (2008) 530.
[4] NVutzenadel C, NVuttel A, Chartouni D, Schlapbach L. Electrochem Solid-State Lett 1999;2(1):30–2.
[5] N. Zhang, N. Lior, International Journal of Hydrogen Energy 33(2008) 214.
[6] L. Trevisani, M. Fabbri, F. Negrini, Cryogenics 47 (2007) 113.
[7] G. Hermosilla-Lara, G. Momen, P.H. Marty, B. Le Neindre, K. Hassouni, International Journal of Hydrogen Energy 32 (2007) 1542.
[8] H.K. Jin, Y.S. Lee, I.P. Hong, Catalysis Today 120 (2007) 399.
[9] Seung-Hoon Jhi, Young-Kyun Kwon, PhysicalL Review B **69**, 245407 (2004)
[10] Hui Pan, Jizhong Luo, Han Sun, Yuanping Feng, Cheekok Poh and Jianyi Lin, Journal Nanotechnology, vol 17,no 12
[11] X. Chen, X. P. Gao, H. Zhang, Z. Zhou, W. K. Hu, *J. Phys. Chem. B*, **2005**, *109* (23), pp 11525–11529
[12] Jun Chen, Suo-Long Li, Zhan-Liang Tao, Yu-Tian Shen, and Chun-Xiang Cui, *J. Am. Chem. Soc.*, 2003, *125* (18), pp 5284–5285
[13] Sheppard DA, Buckley CE, Maitland CF. Journal Alloys Comp 2005;404–406:405–8.
[14] Si Cheng, Dezhi Shen, Xinsheng Zhu, Xingguang Tian, Dongying Zhou, Li-Juan Fan, European Polymer Journal 45 (2009) 2767–2778
[15] Wnek GE, Carr ME, Simpson DG, Bowlin GL. Nano Lett 2003;3:213.
[16] Jin Bae Lee, Soon Chang Lee, Sang Moon Lee, and Hae Jin Kim, Journal chemical Physics letter,Vol 463, 2007, p 162-166.
[17] Yan Han[a], Yijing Wang, , Yaping Wang, Lifang Jiao, and Huatang Yuan ,j hydrogen energy, vol 35, 2010 ,issue 15, 8177-8181
[18] Kim C, Yang KS. Appl Phys Lett 2003;83:1216.
[19] Yoshimoto Y, Shin YM, Rerai H, Cacanti JP, Jin HJ. Biomaterials 2003;24:2077.
[20] Ilic B, Craighead HG, Krylov S, Senaratne W, Ober C, Neuzil P. J Appl Phys 2004;95:3694–703.
[21] Buchko CJ, Chen LC, Shen Y, Martin DC. Polymer 1999;40(26):7397–407.
[22] Deitzel JM, Kleinmeyer JD, Hirvonen JK, Tan NC. Polymer 2001;42(19):261–72
[23] Kenji Iimura, Toshiyuki Oi, Michitaka Suzuki, Mitsuaki Hirota,Journal Advanced Powder Technology 21 (2010) 64–68.

© (2011) Trans Tech Publications, Switzerland
doi:10.4028/www.scientific.net/KEM.471-472.1046

Effect of Nickel Composition and Preparation Method for Production of Hydrogen via Glycerol Steam Reforming

Lukman Hakim[1,a], Zahira Yaakob[1,2b], Manal Ismail[1,2c], Wan Ramli Wan Daud[1,2d] and Edy Herianto Majlan[1,e]

[1]Fuel Cell Institute, Universiti Kebangsaan Malaysia,

43600 Bangi, Selangor, Malaysia

[2]Chemical Engineering Department, Universiti Kebangsaan Malaysia,

43600 Bangi, Selangor, Malaysia

[a]hakim@eng.ukm.my, [b]zahira@eng.ukm.my, [c]manal@eng.ukm.my, [d]wramli@eng.ukm.my, [e]edy@ukm.my

Keywords: Glycerol, steam reforming, nickel /hydroxyapatite catalyst, impregnation, sol-gel, hydrogen production, surface area.

Abstract. The need and development of cleaner and greener alternative technologies using the heterogeneous catalytic system in the synthesis of fuel is very important. In this work hydrogen production via steam reforming of glycerol ($C_3H_8O_3$) was carried out over nickel supported on hydroxyapatite [$Ca_5(PO_4)_3(OH)$] as a biomaterial catalyst. The time reaction is carried out for 240 minutes in a fixed-bed reactor fixed at 600 ^oC and atmospheric pressure with the water-to-glycerol feed ratio of 8:1. Catalysts were prepared by mean of impregnation and sol-gel method with varied nickel loadings (3, 6, 9, 12 %) on hydroxyapatite. The catalysts were characterized by BET surface area, X-ray diffraction, and SEM-EDX techniques. It is found that 3 wt% of nickel loading prepared via sol-gel method exhibit the higher hydrogen production rates (63.62 % - 74.16 %) in comparison to the other nickel loadings.

Introduction

After the effect of climate change is immense, such as the increase in the earth's temperature and rise in sea level, considerable attention was focused on development of alternate energy resources. At present, air pollution of fossil based fuels is a serious concern; therefore, developing of environmental friendly fuels is a necessity. Besides that, due to the shortage of resources and price of the hydrocarbon fuels become more expensive, this is a strong reason to find and develop renewable fuel resources.

At present, a glut of glycerol is expected in the world marked and therefore, it is essential to find useful applications for glycerol. One possibility of using glycerol ($C_3H_8O_3$) from by-product biodiesel industry is as a promising renewable source to produce hydrogen. In comparison to another hydrogen resources like as methanol and ethanol, glycerol steam reforming (SR) can produce much more hydrogen molecules [1].

Using hydrogen as an energy resource for fuel cell powered electric vehicles seems to be the most promising way to realize environmental friendly and sustainable energy. With the use of hydrogen in fuel cell systems, there are very low (almost zero) emission of carbon substances and no emissions of other air pollutants such as nitrogen dioxide, sulphur dioxide [2].

The overall reaction of glycerol SR is as following (Eq.1).

$$C_3H_8O_{3\,(g)} + 3H_2O_{\,(g)} \longrightarrow 7H_{2\,(g)} + 3CO_{2\,(g)} \quad (\Delta H^o_{298} = +123\ kJ/mol) \qquad (1)$$

Catalysts for steam reforming of biomass such as methanol, ethanol, and glycerol are mainly based on nickel as an active component supported on various oxides with high thermal stability and porous solids [3,4,5]. Nickel is the most extensively studied catalyst because it is effective for steam

reforming and as well as cheap. The nickel based catalyst have some problems of the catalysts' deactivation caused by carbon deposition and the sintering of the catalyst particle during the preparation and operating conditions. The sintering of nickel and it support not only reduce active component, but also can obstruct reaction on the catalysts because the active area be come decrease [6].

Usage hydroxyapatite [$Ca_5(PO_4)_3(OH)$], as a substrate for the catalyst of hydrogen production from methane was first reported on 2007 [7]. However, using of this type of supported catalyst for hydrogen production from glycerol and water have not yet reported Hydroxyapatite (HAP) have a potency to be developed as catalyst support because this biomaterial has a mesoporous structure and particle size of 5 – 40 nm [8]. Mesoporous structure has particle size 2-50 nm, has a high surface area and high porosity, as a result, hydroxyapatite can use as an excellent high surface area support to make heterogeneous catalysts. HAP can be extracted from bone, tooth and mineral rock, exhibits good stability at the high temperatures. The molecule structure of $Ca_5(PO_4)_3(OH)$ consists of PO_4^{3-} tetrahedral, O-H group and calcium. Hydroxyapatite possess Ca^{2+} sites surrounded by PO_4^{3-} tetrahedral parallel to the hexagonal axis and are of considerable interest in many areas because of their ion-exchange ability, adsorption capacity, and acid base properties.

In practice, different heterogeneous catalyst preparation methods have been used to adjust the structure of supports. Consequently, physical and chemical properties of the catalyst are modified. Generally, preparation heterogeneous catalysts divided two basic preparation classes: bulk catalysts and impregnation/supported catalysts. Impregnation catalysts are commonly used in the case of precious metals or unstable compound. Here, the active metal precursor is deposited on porous bulk support such as Ni supported on alumina and silica. One of the bulk catalyst preparations which commonly used is sol-gel method because this methods have several promising advantages. In general, catalysts preparation by sol-gel methods have been recognized for their versatility, which allows better control of the texture, composition, homogeneity and structure properties of the final solids [9].

Experimental

Catalyst Preparation. Catalysts were prepared by mean of impregnation and sol-gel method using nickel nitrate hexahydrate [$Ni(NO_3)_2.6H_2O$] (Sigma-Aldrich) on hydroxyapatite [$Ca_5(PO_4)_3(OH)$] (Sigma-Aldrich) as support. Via impregnation method, the nickel precursor was dissolved in deionize water with varied in 3%, 6%, 9%, and 12 %. Nickel aqueous solutions with varied nickel were loading on hydroxyapatite (HAP) supported with continuous stirring for 3 hours. After Ni loading, the catalyst was dried at 120 ^oC over night in the oven and subsequently calcined at 500 ^oC for 5 hours in air atmosphere of an electric furnace.

Ni/HAP catalyst by sol-gel method was synthesis with suitable amount hydroxyapatite (HAP) and nitrite-acid (65%, Merk) were dissolved in poly vinyl alcohol (98%,Merk] and deonized water to form sol with molar ratio 1:100:0.07. This solution was mixed with vigorous stirring at 80 ^oC for 24 hours under the reflux conditions. The formed gel was aged in the sealed flask over night. Nickel aqueous solution with varied nickel (3,6,9,12%) were added to sol (HAP) and mixture at 80 ^oC to get a thick paste. The catalysts were dried at 120 ^oC over night and finally calcined at 500 ^oC for 5 hours in air atmosphere.

Catalyst Characterization. The surface area of the catalyst was measured in Altamira Instrument-AMI 200. The sample 0.5 gram were previously out gassed at 120 ^oC for 1 hours. N_2 adsorption-desorption isotherms were obtain at -196 ^oC and specific areas were calculated from these isotherms using the Brunaer-Emet-Teller (BET) method.

Surface morphology and component ratio of catalyst was studies by LEO 1450VP scanning electron microscope equipped with energy dispersive X-ray (EDX). Field-emission scanning electron microscope (FE SEM) images have been obtained by a SUPRA 55VP instrument.

Catalyst Performance Testing. Figure 1 shows the schematic of glycerol steam reforming process The. tubular reactor was made of stainless steel (i.e. length: 39 mm, inside diameter: 6.35 mm, wall thickness: 0.9 mm) and reactor was placed in an electric furnace equipped with K-type thermocouples located inside of the reactor at the position of the catalysts bed.

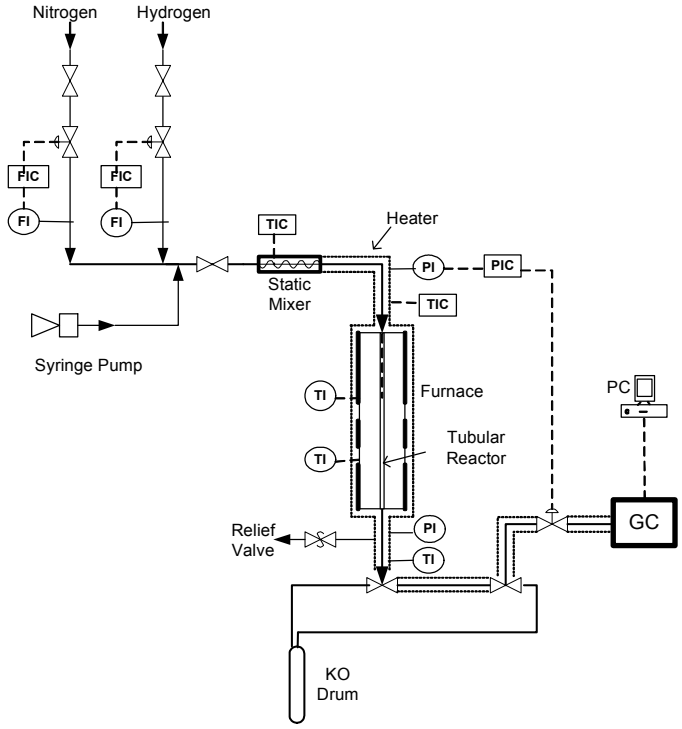


Fig.1. Schematic of glycerol steam reforming setup

To carry out the catalytically test, 0.5 gram of the catalyst powder placed in the middle of the reactor tube and fixed by quartz wool. Before activation, each catalyst was heated for 30 min on 120 ^{o}C. The catalysts activated in situ by reducing in a N_2 flow of 35 ml/min with 10% H_2 at 300 ^{o}C for 1 hours. Steam reforming experiment was carried out at 600 ^{o}C under atmospheric pressure. Water-to-Glycerol feed ratio 8:1 at constant flow rate 0.005 ml/min was introduced into the fixed bed micro reactor using PHD 440 syringe pump into a vaporizer where it was heated to 320 ^{o}C mixed with a N_2 stream coming from the mass-flow controller. The reaction time 4 hours and the gas samples were analyzed each 30 min using a gas chromatograph (GC) instrument (Clarus 500 Perkin Elmer with FID and TCD detector).

Result and Discussion

Catalyst Characterization. Table 1 shows the surface area of all Ni catalysts supported on HAP resulted from Brunauer, Emmett and Teller (BET) method. The 3% Ni/HAP by sol-gel method exhibit higher surface area among the others Ni loading. We know that the higher surface area of the catalyst (3% Ni/HAP) accelerate the rate of steam reforming reaction and maximal glycerol conversion achieved**.**

Table 1. The surface area of Ni/Hap catalyst

Catalyst	Surface Area (m^2/g)	
	(sol-gel method)	(impregnation method)
3% Ni/HAP	115.4821	92.1860
6% Ni/HAP	107.2350	88.8381
9% Ni/HAP	70.5779	87.1152
12% Ni/HAP	98.3441	83.8325

Scanning electron microscope and chemical analysis of all Ni/HAP catalysts resulted from (SEM)-EDX instrumental tests are illustrated in Figure 2. Catalysts morphology of 3, 6, 9 and 12% Ni/HAP with impregnation and sol-gel method showed different texture. It can be concluded that by increasing of the loading Ni promoter more smooth and compact morphology resulted. This can infer that Ni metal are due to affect of catalysts morphology and cause of sintering catalysts.

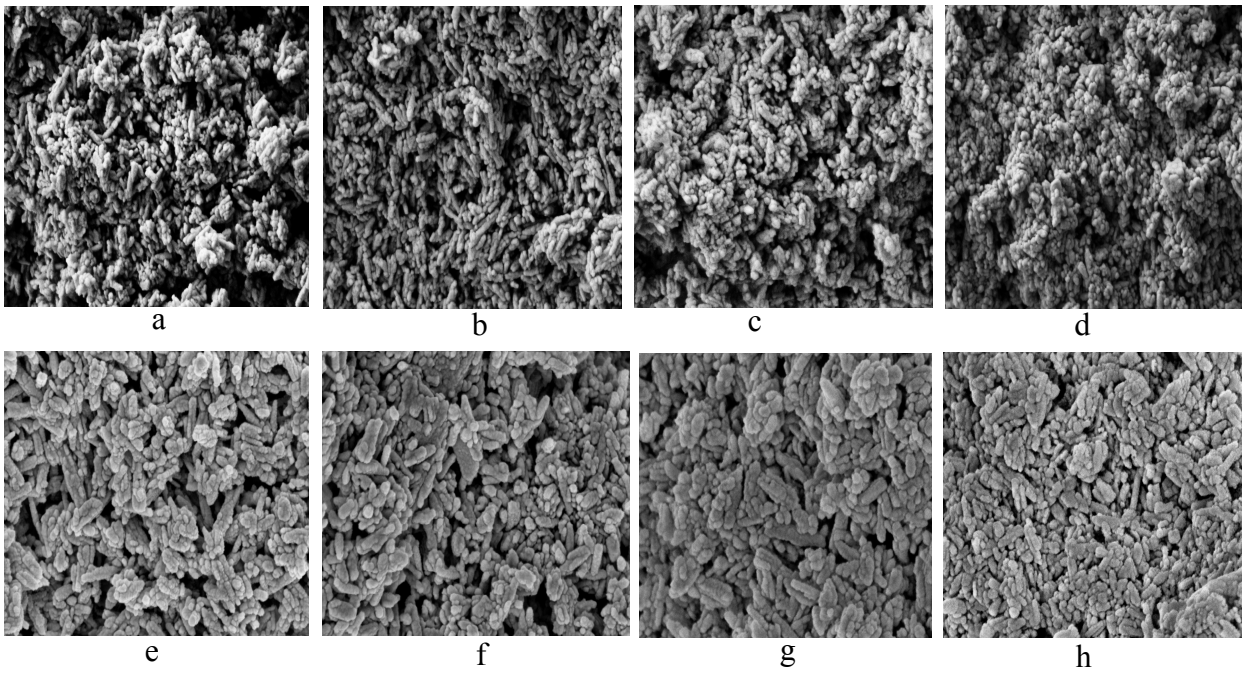


Fig.2. SEM images of catalyst Ni/HAP preparation by impregnation, (a) 3% Ni/HAP, (b) 6% Ni/HAP, (c) 9% Ni/HAP, (d) 12% Ni/HAP; by sol-gel, (e) 3% Ni/HAP, (f) 6% Ni/HAP, (g) 9% Ni/HAP, (h) 12% Ni/HAP

In this case, we know that the sintering of nickel and it support not only reduce active component, but also can obstruct reaction on the catalysts because the active area be come decrease and caused lower hydrogen yield.

Comparing catalysts morphology by impregnation and sol-gel method shows that the sol-gel method more homogeneously dispersed and homogeneity texture. Dispersability of active metal on the surface of catalysts is crucial in determining the reaction activity. Thus, the specific surface area (SA) is a very important property for catalysts. The preparation catalysts' method strongly influences the characteristic of the final heterogeneous catalysts. Sol-gel derived hydroxyapatite have high surface areas and more porous as showed in Table 1. From image resulted showed that nickel supported on hydroxyapatite by sol-gel method have more stable support structure and higher nickel dispersion than by impregnation method. Therefore, sol-gel method for preparation heterogeneous catalysts more used for to get higher surface area and homogeneity texture, but impregnation method easier and cheaper for make commercial catalysts.

Have been mentioned that SEM resulted showed that increasing Ni loading on hydroxyapatite the structure of catalysts became dense or sintering happened in catalysts. Sintering occurred happened during preparation catalysts (calcinations). For 3% Ni loading the porosity of catalysts still higher compared 6,9,12% Ni loading. One reason is that nickel has a high affinity with carbon and to form as nickel carbide.

The XRD patterns of Ni/Hap catalysts are presented in Figure 3. Analysis of XRD patterns recorded for diffractions of NiO on hydroxyapatite were observed in all the samples. The diffraction peaks around the 2θ angle of 37.2^{o}, 43.2^{o}, 63.0^{o} 75.5^{o}, and 79.5^{o} are characteristic of nickel oxide and shows relatively sharp. It indicated that nickel loading on hydroxyapatite were the major crystalline phases and the peak reflection due to NiO increased along the loading nickel on hydroxyapatite. We can see that from HAP pattern to 12% Ni loading shown the peak around 2θ angle 38.0^{o} grew by increasing content nickel on hydroxyapatite.

Investigation of the crystalline phases presents in the as calcinated catalysts was performed by X-ray diffraction analysis. The XRD patterns of Ni/HAP catalysts by sol-gel method with different Ni loading on hydroxyapatite are shown that a part of nickel (as Ni^{2+}) may incorporate into the phosphate structure by taking the position of Ca^{2+}.

This occurrence has been mentioned that HAP with possess Ca^{2+} sites surrounded by PO_4^{3-} tetrahedral parallel to the hexagonal axis, which have attracted considerable interest due to their potential usefulness as adsorbents and ion-exchangers. Therefore, hydroxyapatite excellent application of these materials as catalysts or catalyst supports.

As the nickel content increased further, the amount of NiO phases in the fresh catalyst increased. In 12%Ni/HAP having the highest nickel content among the other catalyst, the amount of NiO in the fresh sample was quite larger than other Ni loading.

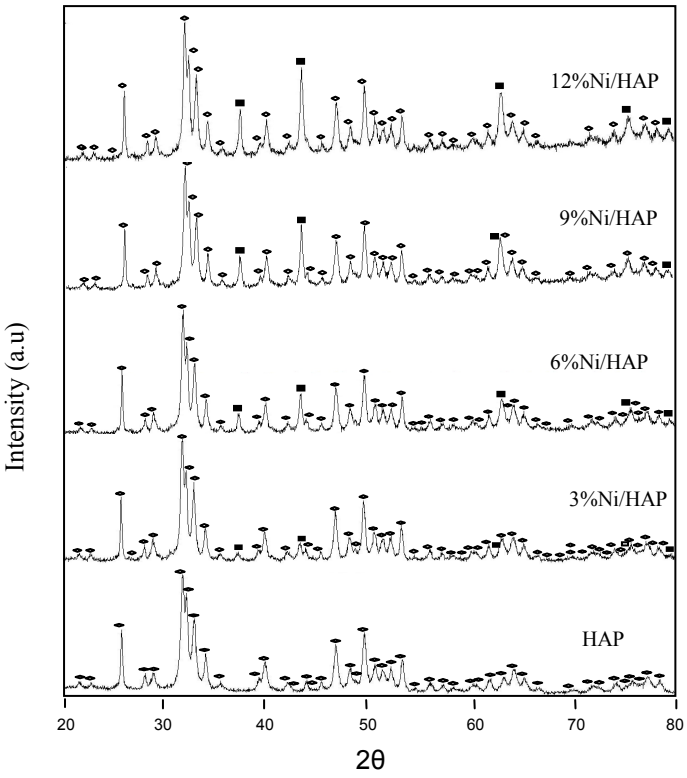


Fig.3. XRD patterns of Ni/HAP catalysts by Sol-gel method with different loading nickel on hydroxyapatite (◊ : $Ca_5(PO_4)_3(OH)$; ■ : NiO)

Catalytic Activity. Catalytic activity was evaluated in terms of glycerol conversion (mol %). Glycerol steam reforming reaction on Ni/HAP catalyst at 600 ^oC and atmospheric pressure showed that the extent of Ni loading (3, 6, 9, and 12%) on HAP could influence the hydrogen yield of SR. Figure 4 shows the effect of Ni loading on hydrogen production versus reaction time. Results as certain that the sample of 3% Ni/HAP with sol-gel and impregnation method resulted higher hydrogen selectivity compared others loading during the whole examined time period. For higher H_2 yield has shows 3% nickel loading with sol gel method (63.62 to 74.16 mol %) and impregnation method (57.63 to 67.84 mol%).

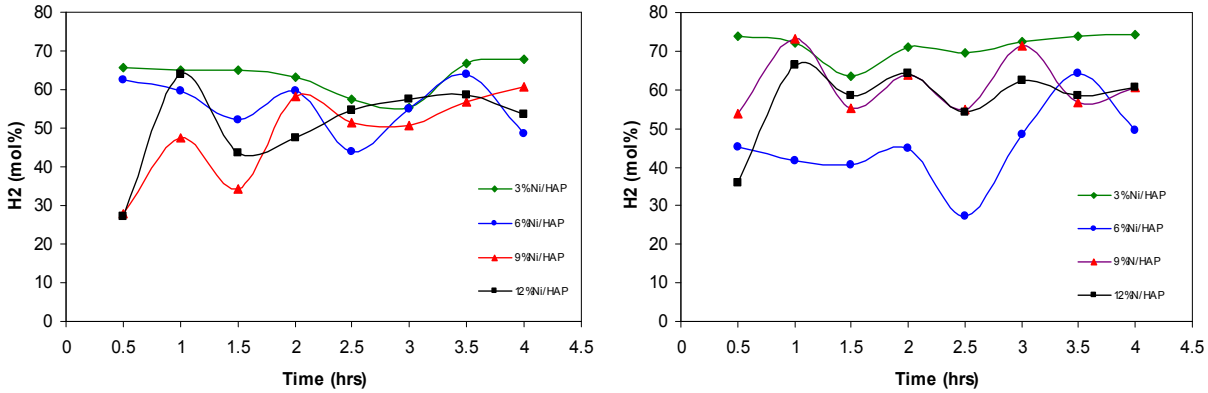


Fig.4 Hydrogen selectivity and glycerol conversion over Ni/HAP with different Ni loadings and ratio water/glycerol at 600 ^oC: a) Ni/HAP by impregnation method; b) Ni/HAP by sol-gel method

Other loading nickel loading (6, 9, 12%) shows lower hydrogen production compared 3% nickel loading. This result revealed that the conversion of glycerol could not fully occur and hydrogen yield was very lower. This case caused that Ni as active component have been sintering with hydroxyapatite and causing decreased active component and surface area of catalysts. Morphology resulted of catalysts show that porosity become smaller by increasing of the Ni loading on HAP as well as its BET results show that the surface area of this catalyst decreased remarkably, which could consider as a reason for lower reactivity of the catalyst. Concerning the catalyst durability, it is obvious that in the case of 3% Ni/HAP catalyst, the glycerol conversion (i.e. hydrogen production) in W/G feed ratio 8/1 during time reaction 240 minutes shows almost constant hydrogen production.

Summary

The study on steam reforming of glycerol for hydrogen production over Ni catalysts supported on HAP showed quite promising catalytic performance for hydrogen production. Under the reaction conditions (600 ^{o}C at atmospheric pressure) investigated, among eight catalysts with different nickel loading and different preparation method. For preparation sol-gel method have shown that 3% Nickel loading on hydroxyapatite was found to be the best performing catalyst in terms of hydrogen production. This matter caused that 3 % Ni loading on hydroxyapatite have higher surface area and more porous. In this matter showed that the Ni component as active metal not occured sintering with support. Maximum hydrogen production of 74.16 mol % achieved with 3% Ni loaded catalyst with sol-gel method. Images from SEM showed that with increasing Ni loading on hydroxyapatite can make sintering with it support during calcinations and caused porosity and surface area of catalysts smaller and steam reforming reaction become slowly.

References

[1]. A.S Esteban, A.C. Miguel: International Journal of Hydrogen Energy Vol. 35 (2010), p. 5902-5907

[2]. CRS Report for Congress, Congressional Research Service, 2004

[3]. B. Zhang, X. Tang, Y. Li, Y. Xu, W. Shen: International Journal of Hydrogen Energy, Vol. 32 (2007), p. 2367-2373

[4]. S. Adikhari, S.D. Fernando, S. Haryanto: Renewable Energy Vol. 33 (2008), p. 2097-1100

[5]. A. Iriondo, V.L. Barior, J.F. Cambra, P.L. Arias,M.B. Guemez, R.M. Navarro, Sanchez-Sanchez, J.L.G. Fierro: Top Catal Vol. 49 (2008), p. 46-58

[6]. J. Sehested: Journal of Catalysis Vol. 217 (2003), p. 417- 426

[7]. J. Ashok, A.S. Kumar, M. Subrahmanyam, A. Venugopa: Catal Lett. 121:283-290, 2008.

[8]. R. Atir, S. Mallouk, K. Bougrin, M. Soufiaoui, A. Laghzizil: Synthetic Communication Vol. 36 (2006), p. 111-120

[9]. M. Campati, G. Fornasari, Vaccari: Catalysis Today Vol. 77 (2003), p. 299-314

© (2011) Trans Tech Publications, Switzerland
doi:10.4028/www.scientific.net/KEM.471-472.1052

The Influence of Li on the Tensile Properties of Al-Mg_2Si Metal Matrix Composite

R. Khorshidi[1,a], M. Emamy[2,b] and A. Honarbakhsh Raouf[3,c]

[1] Department of Materials, Faculty of Engineering,

Semnan University, Semnan, Iran

[2] School of Metallurgy and Materials,

University of Tehran, Iran

[3] Department of Materials, Faculty of Engineering,

Semnan University, Semnan, Iran

[a]Khorshidi_re@yahoo.com, [b]emamy@ut.ac.ir, [c]abhonar@yahoo.com

Keyword: Al-Mg_2Si composite, Li, UTS, elongation value, Fracture surface.

Abstract. The present research is undertaken to study the influence of Li on the tensile properties of Al-15%Mg_2Si metal matrix composite. The tensile test results show that adding 0.15%Li to the composite raises the UTS and elongation values, insignificantly. In the point of fracture behaviour of the composite, the addition of 0.15%Li converts the fracture behaviour from brittle, with cleavage facets, to ductile, with fine ductile dimples.

Introduction

Particulate metal matrix composites (PMMCs) are one type of MMC which has attracted attention due to their inherent isotropic properties and lower costs [1,2]. Among the numerous methods for PMMCs, in-situ processes produce good particle wetting, even distribution of the reinforcing phase and thermodynamically stable systems [3,4].

As a new group of PMMCs, the in-situ Al-Mg_2Si compositesare good candidates to replace Al-Si alloys used in many industrial applications because of the presence of Mg_2Si intermetallics have a high melting temperature, low density, low thermal expansion coefficient (TEC) and high elastic modulus. But, the presence of coarse primary Mg_2Si particles in the composite matrix leads to poor tensile properties. Thus, composites with coarse primary Mg_2Si particles must be modified to obtain appropriate mechanical properties [5-7].The enhancement of mechanical properties may be attained by modifying both primary and secondary Mg_2Si particles [4].

Several investigations have been carried out for the modification of primary Mg_2Si morphologies in hypereutectic Al-Mg_2Si alloys [1]. Some researches show that the modification of Al-Mg_2Si in the microstructure can be achieved by the additions of phosphorous [3], strontium [8], K_2TiF_6 [6] to the liquid alloy. Consequently, the structural modification is one of the most attractive methods for improving the ductility and strength of these MMCs [6,9].

The present work has been carried out to evaluate the effect of different Li concentrations on the microstructure and tensile properties of an in-situ hypereutectic Al-15%Mg_2Si composite.

Experimental Procedure

Al-15%Mg_2Si composite as primary ingots were prepared in an electrical resistance furnace using a 10 kg clay-graphite crucible using Al, Mg and Si. After reaching 800 °C, Mg and Si were added into the Al melt. Table 1 shows the chemical composition of hypereutectic Al-15%Mg_2Si MMCs. The parent ingots were cut to fit a small SiC crucible (with 1kg capacity) and were melted in an electrical resistance furnace. When the temperature reached 750°C, pure Li wrapped in

aluminium foil was added in small increments, to prepare alloys with 0, 0.05, 0.1, 0.15 and 0.25wt.%Li. An addition of flux powder ensured that the melt surface remained covered.

Table 1. Chemical composition of in situ Al-15%Mg_2Si primary ingots (wt. %).

Materials	Chemical composition (wt.%)
Si	5.750
Mg	9.650
Fe	0.130
Ni	0.030
Zn	0.009
Al	Base

Previous experience indicated that it was necessary to add 20% additional Li to be certain that the target composition was reached. Degassing was conducted by using dry tablets containing C_2Cl_6 (0.3 wt.% of the molten alloy) for about 3min. After stirring and cleaning off the dross, the alloys were poured into a steel mould preheated to 200°C. The mould was made according to the ASTM B 108-03a standard (Fig. 1a). The tensile test specimens were made according to ASTM B557M-02a standard shown in Fig. 1b. Tensile tests were carried out in SANTAM-STN150 machine (2 tons LOAD CELL) with a constant cross-head speed of 1 mm/min. The fracture characteristics of the specimens were also examined by scanning electron microscopy (SEM) in a Vega©Tescan SEM with the energy dispersive X-ray analysis (EDX) accessory. The microstructural characteristics of the specimens were also examined by optical microscopy.

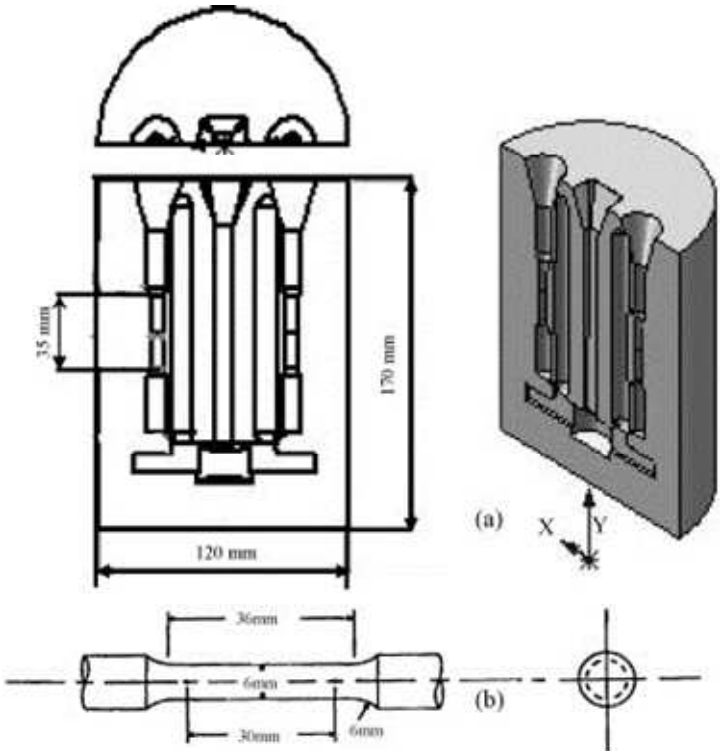


Fig.1. The schematic of: (a) Casting mould and (b) tensile test specimen.

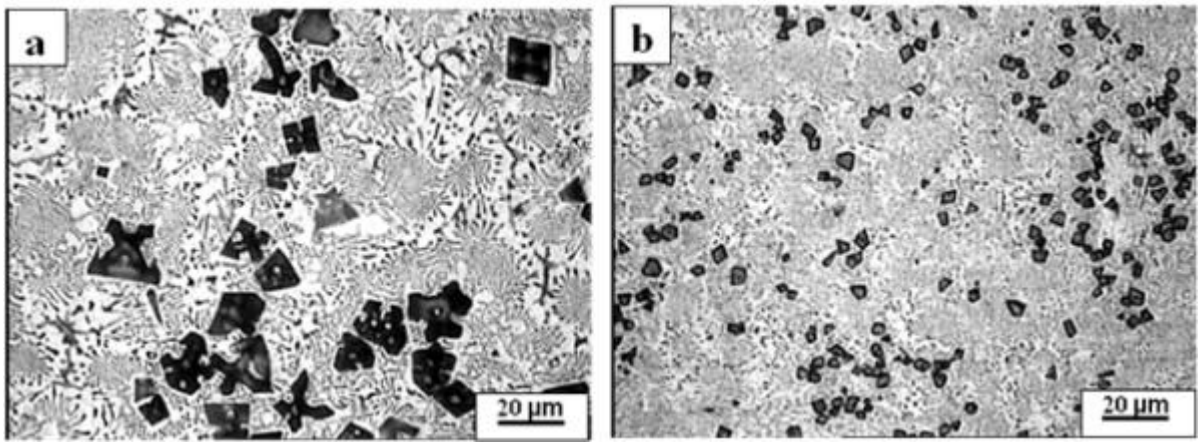


Fig. 2. Optical microscope microstructures of in-situ Al- 15wt.%Mg_2Si composites with different Li contents: (a) 0 wt.% and (b) 0.15 wt.%.

Result and Discussion

Microstructural Studies. The optical microscope microstructures of the composite without and with 0.15%Li addition are compared in Fig. 2a and b. According to the pseudobinary phase diagram of Al-Mg_2Si system (Fig.3), the composition of Al-15%Mg_2Si consists of the primary Mg_2Si and α-Al phases. The dark particles are the primary Mg_2Si and the bright phase is α-Al. From Fig. 2a, it is clearly seen that the morphology of the primary unmodified Mg_2Si particles is irregular, often dendritic, with average size 32µm. Dendritic morphology of particles is expected, since cooling rate in this work is high. Similar dendritic morphology of Mg_2Si in non-modified Al-Mg_2Si composite has been reported in literatures [5,9,10]. After 0.15% Li addition, primary Mg_2Si is seen to be fully polyhedral and its size decreases to 4µm (Fig. 2b). It is clear that the Li addition reduces the size of primary Mg_2Si particles more than 85%, although its volume fraction remains constant. Furthermore, Li addition introduces a good distribution of primary Mg_2Si particles in the matrix.

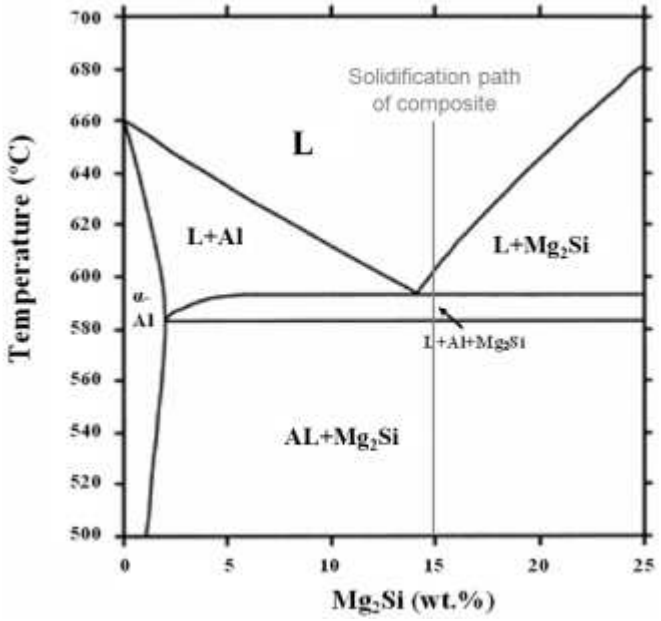


Fig. 3. Equilibrium phase diagram of Al-Mg_2Si pseudobinary section [4].

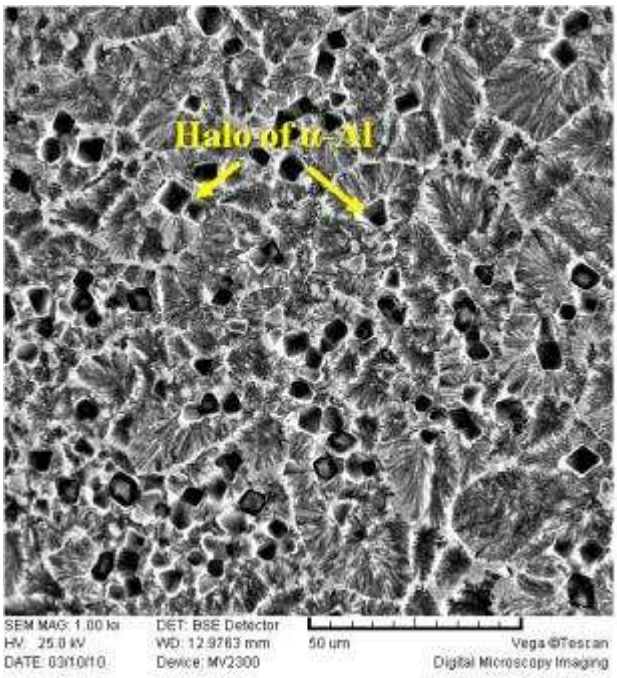


Fig. 4. SEM micrograph shows halo of α-Al around primary Mg_2Si particles in 0.15%Li modified Al-15% Mg_2Si composite.

As can be seen in Fig. 4, all the primary particles are surrounded by a layer of α-Al. In previous work, Zhang et al. proposed that Mg_2Si particles act as heterogeneous sites for the nucleation of α-Al [4] which seems curiously irrelevant. After the formation of the primary Mg_2Si particles, it is obvious from Fig. 3 that the subsequent solidification happens by nucleation and growth of a layer of α-Al around the particles. With the addition of 0.15%Li, the nucleation sites for α-Al phases are increased due to the enhanced number of the primary Mg_2Si particles and basically, the volume fraction of α-Al in the matrix increases.

Tensile Properties. Fig. 5 depicts the effect of Li modification on the UTS and elongation values of the MMC specimens as a function of added Li contents.

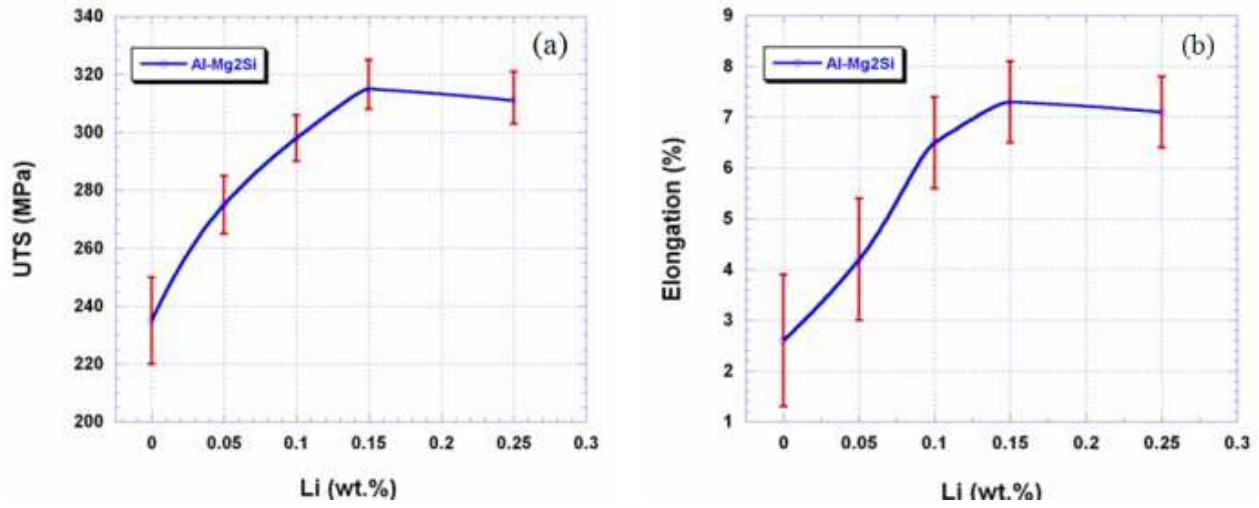


Fig. 5. Tensile properties as a function of auditioned Li contents: (a) UTS and (b) elongation (%).

It is evident from Fig. 5 that Li modification has a significant influence on tensile properties of the composite and raises the UTS and elongation values of the unmodified MMC from 235MPa and 2.6% to 313MPa and 7%, respectively.

Fractography. Damage in particulate metal matrix composite generally occurs at two types: particle fracture and particle decohesion [11]. As is expected from previous work [12] when load is applied, the matrix plastically deforms and gently stress transfers to the particles. The particle size and the strength of matrix/particle interface are commonly identified as the two important factors on fracture behaviour. The influence of particle size on tensile behaviour is investigated by several researchers [11,12]. Results indicate an increase in strength and ductility by decrease in particle size. Another effective agent on the fracture behaviour is interfacialstrength between particle and matrix. When the matrix is strong enough with high yield stress, dominant failure mechanism is normally particle fracture. However, if the matrix/particle interface bonding is weakened, the load will not transfer to particles and decohesion fracture arises. Moreover, it is sometimes seen that the two mechanisms can coexist in fracture process one sample [11].
Figures 6a and b exhibit typical fracture surfaces of Al-15wt.%Mg_2Si composite with and without Li. From Fig. 6a, both decohered and cracked particles are present simultaneously in the unmodified matrix structure. The eutectic Mg_2Si in unmodified matrix is clearly shown with arrow (1). Arrow (2) also depicts some dechohered particles in matrix structure. The 0.15%Li modified composite contains more cracked particles (arrow 3) with a large amount of fine dimples (arrow 4) which is obviously observed in wide area of face. According to the previous studies [13], with a decrease in particle size and an increase in fine dimples elongation value rises. Since the most area of fine dimples appear in face of 0.15%Li modified composite, the highest elongation value of 7% attains in this case.

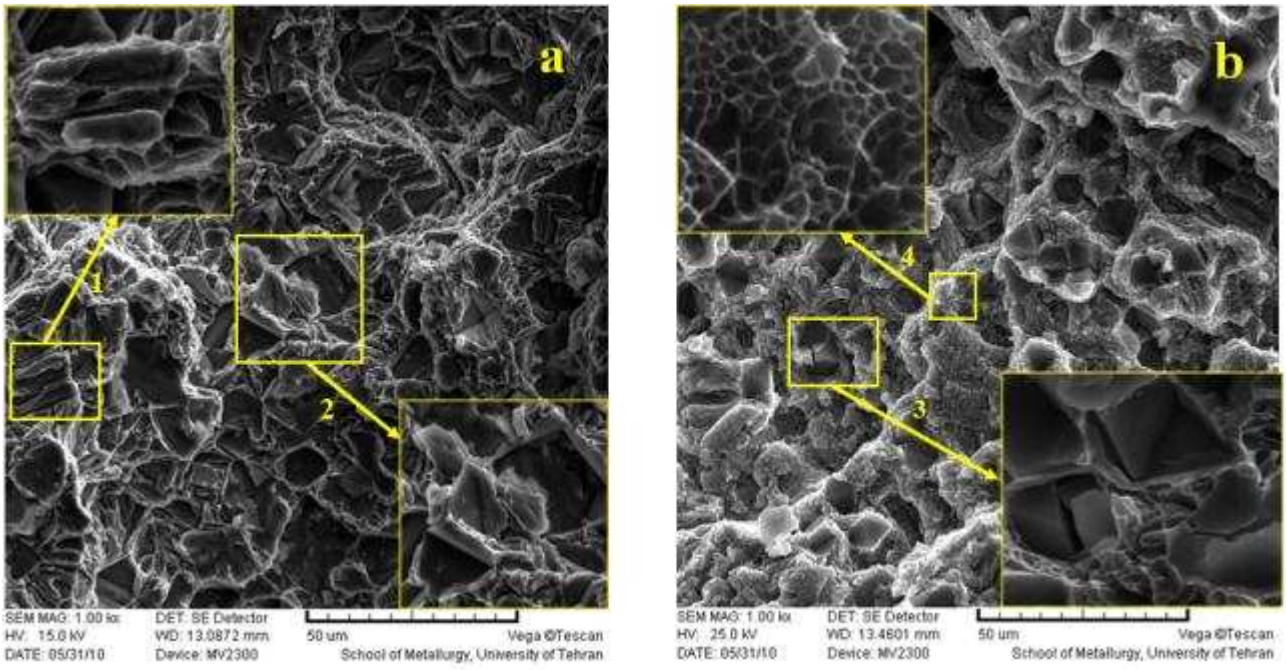


Fig. 6. Tensile fracture surfaces of the Al-15wt.%Mg_2Si hypereutectic composite without and with Li addition: (a) unmodified and (b) modified by adding 0.15%Li.

The presence of several cleavage planes on the fractured surface (Fig. 6a) indicates the brittle fracture surface of the unmodified composite. But, addition of Li up to 0.15wt.% increases fine dimples and fracture converts to mainly ductile fracture (Fig. 6b). Thereupon, the present results in Fig. 5b show a rather significant ductility after modification. The highest elongation value of 7% was obtained for the modified sample by 0.15wt.% Li addition.

Summary

The influence of different Li contents on the microstructural and tensile properties of in situ Al–15% Mg_2Si composite was studied and the following conclusions can be drawn:The addition of 0.15wt.%Li

1. Changes size of primary Mg_2Si from 32μm to 4μm and its morphology from irregular or dendritic to polyhedral.
2. Creates a good distribution of primary Mg_2Si particles in the matrix.
3. Alters the morphology of the eutectic Mg_2Si phase from flake-like to coral-like.
4. Has a significant influence on the tensile properties so that increases both UTS and elongation values, markedly.
5. Fracture micrographs specify a brittle fracture in unmodified composite but Li addition increases fine dimples and fracture process conducts to ductile fracture.

Acknowledgment

The authors would like to thank Semnan and Tehran Universities for financial support of this work.

References

[1] Y.G. Zhou, Q.D. Qin, W. Zhou, Y.H. Liang, J. Alloys Compd. 389 (2005) L1-L4.

[2] R. Hadian, M. Emamy, N. Varahram, N. Nemati, Mater. Sci. Eng. A 490 (2008) 250-257.

[3] Q.D. Qin, Y.G. Zhao, W. Zhou, P.J. Cong, Mater. Sci. Eng. A 447 (2007) 186-191.

[4] J. Zhang, Z. Fan, Y.Q. Wang, B.L. Zhou, Mater. Sci. Eng. A 281 (2000) 104-112.

[5] Y.G. Zhao, Q.D. Qin, Y.Q. Zhao, Y.H. Liang, Q.C. Jiang, Mater. Lett. 58 (2004) 2192-2194.

[6] Q.D. Qin, Y.G. Zhao, Y. H. Liang, W. Zhou,J. Alloys Compd. 399 (2005) 106-109.

[7] Q.D. Qin, Y.G. Zhao, P.J. Cong, Y.H. Liang, W. Zhou, J. Alloys Compd. 420 (2006) 121-125.

[8] C.L. Xu, H.Y. Wang, Y.F. Yang, Q.C. Jiang, Mater. Sci. Eng. A 452-453 (2007) 341-346.

[9] Q.D. Qin, Y.G. Zhao, C. Liu, P.J. Cong, W. Zhou, Y.H. Liang, J. Alloys Compd. 416 (2006) 143-147.

[10] Q.D. Qin, Y.G. Zhao, J. Alloys Compd. 462 (2008) L28-L31.

[11] C. Li, X. Liu, Y. Wu, J. Alloys Compd. 465 (2008) 145-150.

[12] L. Hengcheng, S. Yu, S. Guoxiong, Mater. Sci. Eng. A 358 (2003) 164-170.

[13] K. Darowicki, J. Orlikowski, Comput, Mater. Sci. 39 (2007) 880-886.

© (2011) Trans Tech Publications, Switzerland
doi:10.4028/www.scientific.net/KEM.471-472.1058

Effect of Fiber Loading on the Mechanical Properties of Kenaf Fiber Reinforced Thermoplastic Polyurethane Composite

Y. A. El-Shekeil[1, a], S.M. Sapuan[1, b], E.S. Zainudin[2, c] and Khalina Abdan[3, d]

[1] Department of Mechanical and Manufacturing Engineering,
Universiti Putra Malaysia, 43400 UPM, Serdang, Selangor, Malaysia
[2] Laboratory of Bio-Composite Technology, Institute of Tropical Forestry and Forest Products,
Universiti Putra Malaysia, 43400 UPM, Serdang, Selangor, Malaysia
[3] Department of Biological and Agricultural Engineering,
Universiti Putra Malaysia, 43400 UPM, Serdang, Selangor, Malaysia
[a]y_shekeil@yahoo.com, [b]sapuan@eng.upm.edu.my, [c]edisyam@eng.upm.edu.my,
[d]khalina@eng.upm.edu.my

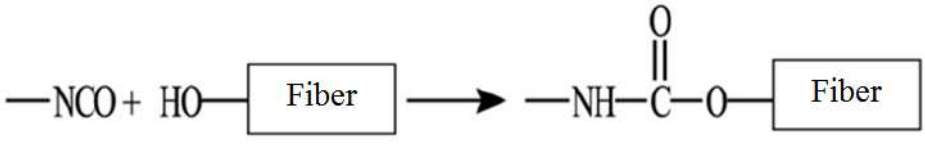
Keywords: Natural fiber composites, thermoplastic polyurethane, Kenaf fibers, mechanical properties

Abstract. In this study, composites of themoplastic polyurethane (TPU) reinforced with short fiber (*Hibiscus Cannabinus*) Kenaf (KF) were prepared via melt blending method using Haake Polydrive R600 internal mixer. The composites were prepared with different fiber loading: 10%, 20%, 30%, 40%, 50% and 60% (by weight), with the optimum blending parameters: 190 °C, 11 min, and 40 rpm for temperature, time and speed, respectively. Five samples were cut from the composite sheet. Mean value was taken for each composite according to ASTM standards. A 30% fiber loading has shown the best tensile strength. A 50% fiber loading has shown the best flexural strength, while the tensile and flexural modulus has shown an increasing trend. Impact strength has shown a decreasing trend with the increase of fiber loading.

Introduction

Eco-friendly natural fibers are novel materials for 21st century and can be of great importance to the materials world [1,2]. Increasing interest on natural fiber reinforced polymers is due to many benefits such as less abrasiveness to equipment, renewability, biodegradability and reduction in weight and cost. Incompatibility is amongst the difficulties that face natural fiber polymer composites. The reason behind incompatibility is that most polymers used in this field are hydrophobic; however the natural fibers are hydrophilic. This makes lack of adhesion and wettability, therefore coupling agents and binders in the interface are used to help make a better adhesion. In this paper the advantage of polyurethane is its hydropholicity (i. e. it is polar in nature).

Main components of polyurethane are polyols and isocyanates. The active isocyanate group can react with most materials that have active hydrogen groups [3]. In the case of natural fiber composites it will react with the hydroxyl group available in the cellulose. This reaction is shown in Scheme 1. Isocyanate has been used as coupling agent for this reason [4-6]. As stated by Özgür and Oksman: "When the polyurethane is used as a matrix, it is believed that no adhesion problem would occur and the dispersion would be much better" [7].



Scheme 1. Reaction between Isocyanate and OH group in the cellulose.

Polyurethane thermoset has been compound with different natural fibers [8-13]. Thermoset PU has been composed successfully with natural fibers by other scholars, however thermoplastic polyurethane reinforced natural fiber composites have not yet been a focus of any scholars. What

makes the difference between thermoset and thermoplastic polyurethane is the addition of diols (chain extenders) to the isocyanates and polyols that will result in a polymer that is not chemically cross-linked (i. e. a recyclable and reformable polymer). Knowing the advantages of thermoplastics (e. g. reformability, lesser processing time and energy, better toughness, and recyclability) makes this study viable. Thermoplastic polyurethane most important properties are excellent abrasion resistance, good mechanical properties with rubber-like elasticity and tear resistance.

Kenaf (Hibiscus cannabinus L., Malvaceae) has a short growing period, high biomass output and good mechanical properties. It reaches 3-4 meters in 4-5 months. It can yield two or three harvests a year in tropical climates [14,15]. It can produce 5-10 tons of dry fiber per acre. Two types of fibers can be extracted from this plant; bast fiber which is the outer layer, and core fiber which is the inner part. Morphological and chemical analysis by Ashori et. al. [16] indicated that bast and core fibers were significantly different. Bast fiber represents nearly 1/3 of the plant and core represents 2/3.

Kenaf is planted commercially in China, Myanmar, India, Bangladesh and Thailand. Malaysia has paid more attention towards planting Kenaf. Since 2000 more than RM 48 million has been spent by Malaysian government for research of kenaf plantation and utilization [17]. Objective of this work is to study the effect of fiber loading on the mechanical properties of kenaf fiber reinforced thermoplastic polyurethane composite.

Material

Polyester based thermoplastic polyurethane (TPU) was obtained from Bayer Co. (Malaysia) Sdn Bhd, Petaling Jaya, Selangor, Malaysia. Specific Gravity of TPU is 1.21. Tensile strength is 48 MPa. Melting temperature is 210 °C. Hardness is 55 D. Kenaf V36 bast fiber was supplied from KEFI (Malaysia) Sdn Bhd, Setiu, Terengganu, Malaysia.

Method

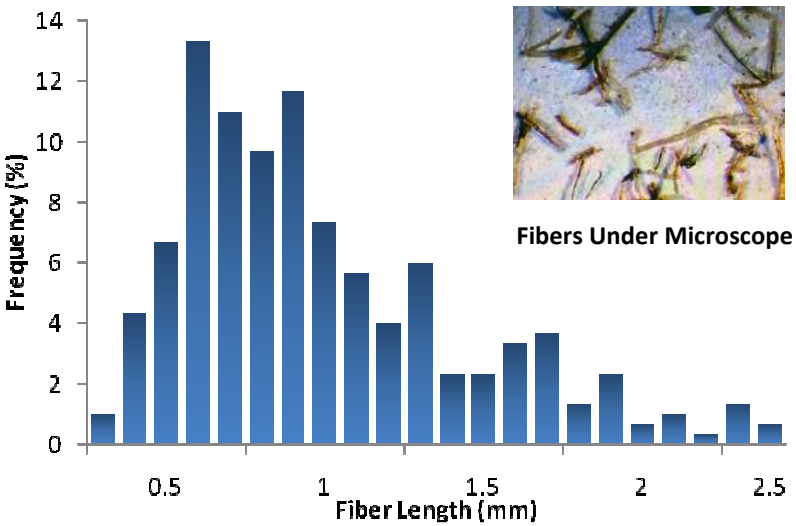
Preparation of Fiber. Bast fiber was extracted by mechanical decrotication. Pulverized fiber was sieved using auto shaker. Fibers collected between sizes 120-50 mesh were used in this study based on optimum tensile, flexural and impact strengths. Three hundred fiber lengths and diameters were measured using (Leica MS 5 microscope). Distribution of fiber length and distribution of aspect ratio (L/D) of the fibers is shown in Fig. 1.

Preparation of Composite. TPU-KF composite was compound using Haake Polydrive R600 internal mixer at the optimum processing parameters 190 °C, 11 min and 40 rpm of temperature, time and rotating speed; respectively. Matrix was charged into the mixer until torque was stabilized then fiber was added. The sample was hot pressed for 10 min at 190 °C. Prior to full-press; the sample was pre-heated for 7 min at 190 °C. The sheet was then placed between two plates of a cold press to cool at 25 °C for 5 min. The samples were prepared at different fiber loading: 10%, 20%, 30%, 40%, 50% and 60% (by weight).

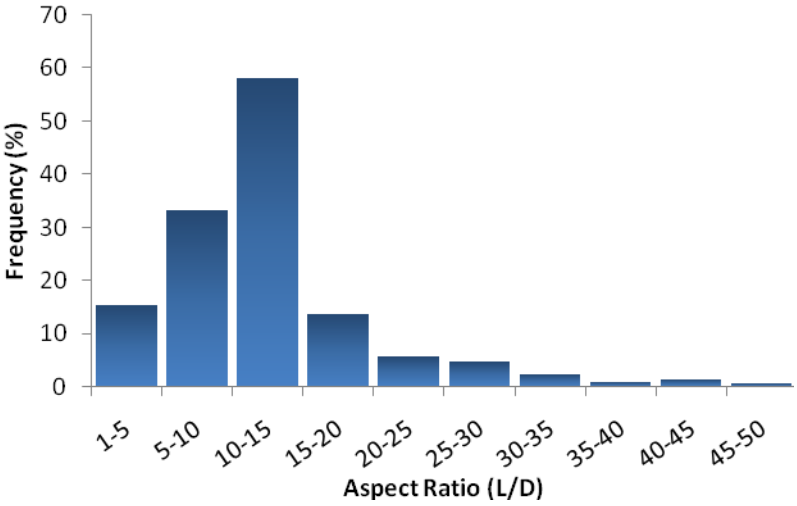
Characterization of Composite. Tensile properties were measured using Instron 3365 machine, according to ASTM D 638. The specimens were prepared by cutting them into dumbbell shapes using a hydraulic cutter machine. Five specimens were tested with crosshead speed of 5 mm/min.

Three point bending flexural test was conducted using Instron 3365 machine, according to ASTM D 790. The specimens were cut using a band saw machine with dimensions of 130 x 13 x 3 mm. Five specimens were tested with a crosshead-speed of 2 mm/min.

Notched impact strength was measured using 43-02-01 Monitor Impact Tester according to ASTM D 256. Dimensions of samples were 63 x 13 x 3 mm. At least five samples were tested. The impact strength (kJ/m^2) was calculated by dividing the recorded absorbed impact energy by the cross-section area of the samples.



(a)



(b)

Fig. 1. (a) Distribution of fiber length, (b) Distribution of fiber aspect ratio.

Results and Discussion

Effect of Fiber Loading on Tensile Properties of TPU-KF Composite. Fig. 2 shows the effect of fiber loading on tensile properties of TPU-KF composite. It can be seen from Fig. 2 that the strength of the composite is increasing up to 30% fiber loading. The 40% and 50% loading has shown lower strength by about 19% and 25%, respectively. The higher strength of 30% fiber loading is attributed to strong bonding between fiber and matrix. At low level of fiber loading the fibers are not able to transfer the load to one another leading to decrease in strength. At intermediate fiber loading the fibers effectively participate in the stress transfer. At higher levels of fiber content the fibers are not sufficiently wetted by the matrix, and the increased population of fibers leads to agglomeration, hence stress transfer gets blocked [1,18]. Increasing the fiber loading resulted in more than 1800% increment in modulus; whereas the modulus of 10% fiber loading is 46.5 MPa, and the modulus of 60% fiber loading is 906 MPa.

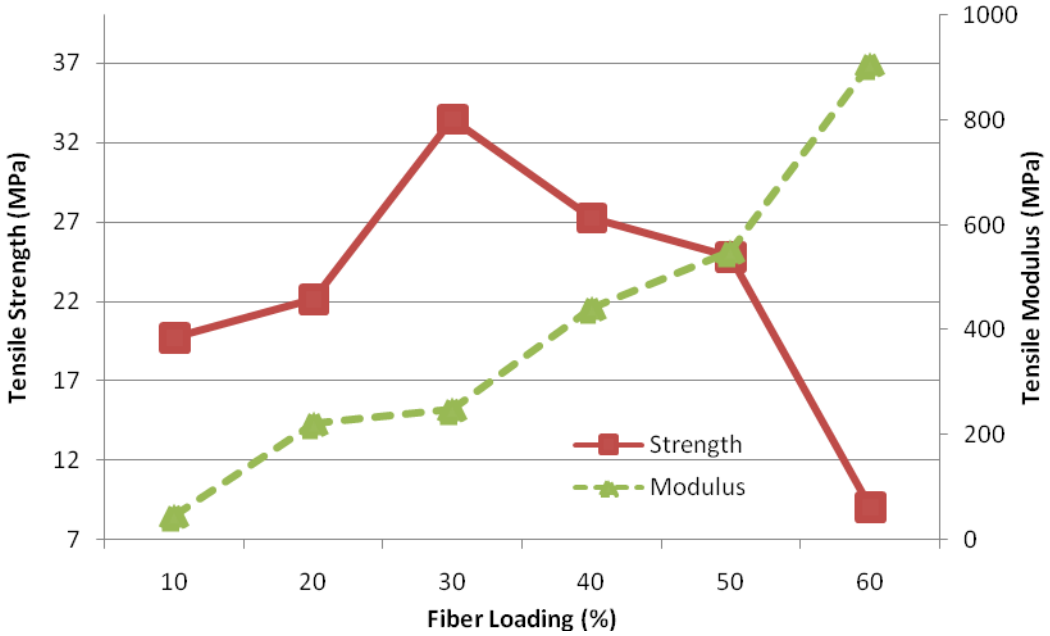


Fig. 2. Effect of fiber loading on tensile properties of TPU-KF Composite.

Effect of Fiber Loading on Flexural Properties of TPU-KF Composite. Fig. 3 shows the effect of fiber loading on flexural properties of TPU-KF composite. Flexural strength is increased more than 110% by increasing fiber loading from 10% to 50%. Then the flexural strength showed slight decrease by about 7% from 37.1 MPa to 34.5 MPa for 50% and 60% fiber loading, respectively. Flexural modulus showed an increasing trend by increasing fiber loading. It was nearly tripled (i. e. 293%) from 757 MPa to 2978 MPa for 10% to 60% fiber loading; respectively. Flexural test bending consists of two stresses that occur at the two sides of specimen simultaneously with shear stress at the axisymmetric plane. Thus, the failure takes place when the bending or shear failure occurs [1,19,20].

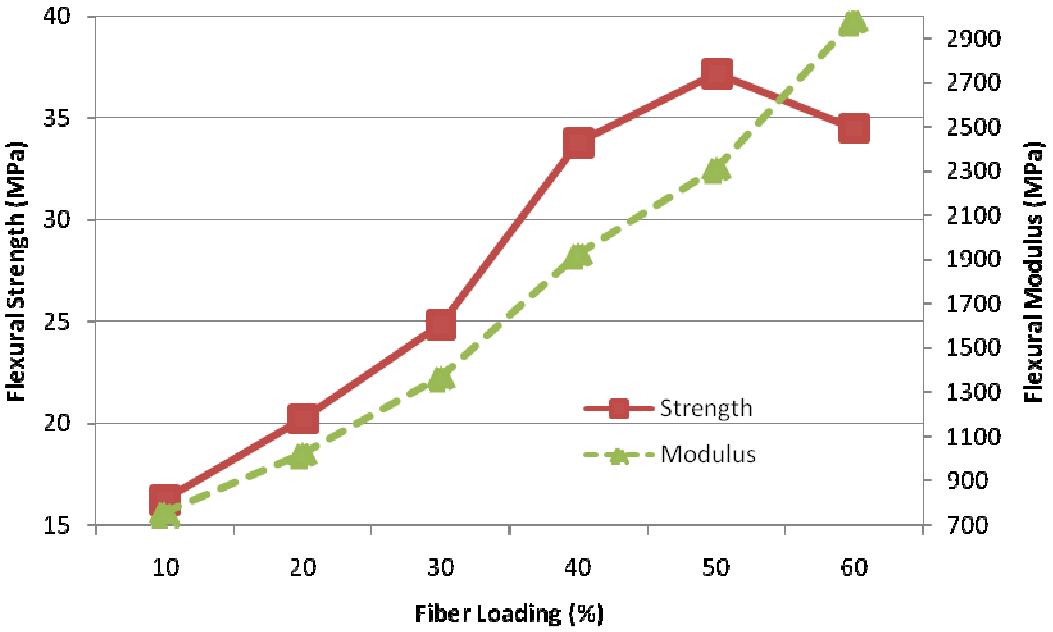


Fig. 3. Effect of fiber loading on flexural properties of TPU-KF composite.

Effect of Fiber Loading on Impact Strength of TPU-KF Composite. Fig. 4 shows the effect of fiber loading on the impact strength of TPU-KF composite. The impact showed decreasing trend accompanied with fiber loading. This is attributed to the high impact resistance of virgin TPU. Adding fibers to TPU resulted in less energy absorbed by the composite. It is stated by Joffe and co-workers. [21] that decrease of impact strength of thermoplastics with addition of reinforcement is usually observed in short fiber natural fiber composites.

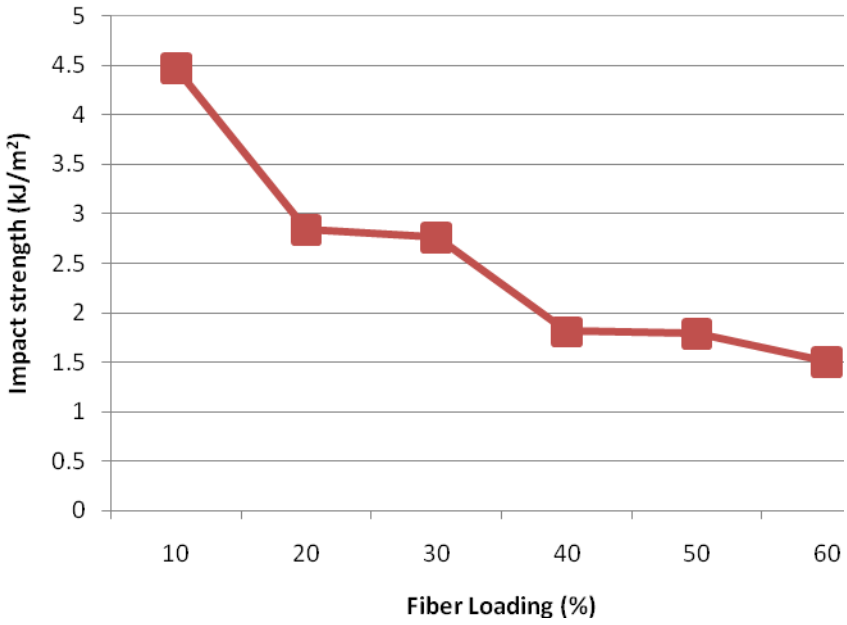


Fig. 4. Effect of fiber loading on impact strength of TPU-KF composite.

Summary

In conclusion, this study can be summarized in three points. First, the increase in fiber loading increased the tensile and flexural strength of the composite until a specific point then the strength decreased. A 30% fiber loading gave the highest tensile strength, while 50% fiber loading gave the best flexural strength. Second, the increase in fiber loading resulted in tremendous increment of tensile modulus of about 1800%. In case of flexural strength there was an increase in modulus too with fiber loading. A 60% of fiber loading gave approximately three times the flexural modulus of 10% fiber loading. Third, the impact strength decreased drastically by addition of fiber loading.

Acknowledgments

Fundamental Research Grant Scheme (FRGS), Ministry of Higher Education Malaysia grant number (01-10-10-924FR) is acknowledged for support of this study. The authors wish to thank Bayer Co. (Malaysia) Sdn Bhd, Petaling Jaya, Selangor, Malaysia for the TPU supply and information.

References

[1] Özturk, S. J. Compos. Mater. 44(19), (2010), 2265.

[2] Mohanty, A. K., Wibowo, A., Misra, M., & Drzal, L. T. Composites Part A 35(3), (2004), pp. 363–370.

[3] Gao, Z. H., Gu, J. Y., Wang, X. M., Li, Z. G., & Bai, X. D. Pigment and Resin Technology, 34(5), (2005), p. 282.

[4] Girones, J., Pimenta, M. T. B., Vilaseca, F., de Carvalho, A. J. F., Mutje, P., & Curvelo, A. A. S. Carbohydr. Polym, 68(3), (2007), pp. 537–543.

[5] Lee, S. H., & Wang, S. Composites Part A, 37(1), (2006), pp. 80–91.

[6] Rozman, H. D., Tan, K. W., Kumar, R. N., & Abubakar, A. J. Appl. Polym. Sci., 81(6), (2001), pp. 1333–1340.

[7] Özgür Seydibeyoglu, M., & Oksman, K. (2008). Novel nanocomposites based on polyurethane and micro fibrillated cellulose. Composites Science and Technology, 68(3-4), 908–914.

[8] Rozman, H. D., Ahmadhilmi, K. R., & Abubakar, A. Polym. Test., 23(5), (2004), pp. 559–565.

[9] Rozman, H. D., Yeo, Y. S., Tay, G. S., & Abubakar, A. Polym Test, 22(6), (2003), pp. 617–623.

[10] Rozman, H. D., Tay, G. S., Abubakar, A., & Kumar, R. N. Eur. Polym. J. 37(9), (2001), pp. 1759–1765.

[11] Rozman, H. D., & Tay, G. S. J. Appl. Polym. Sci. (2008). 110(6).

[12] Mat Amin, K. A., & Haji Badri, K. J. Appl. Polym. Sci. (2007), 105(5).

[13] Bledzki, A. K., Zhang, W., & Chate, A. Compos. Sci. Technol. 61(16), (2001), pp. 2405–2411.

[14] H. Hutchinson. Mech. Engr. 128(7), 2006, pp. 26-33.

[15] Holbery, J., & Houston, D. (2006). JOM, 58(11), pp. 80–86.

[16] Ashori, A., Harun, J., Raverty, W., & Yusoff, M. Polym. Plast. Technol. Eng. *45*, (2006). pp. 131-134.

[17] Jalaluddin Harun. (2009, February 8). Presented at the International Conference on Prospects of Jute & Kenaf as Natural Fibres, Dhaka, Bangladesh.

[18] Jacob, M., Thomas, S., & Varughese, K. T. Compos. Sci. Technol. 64(7-8), (2004), pp. 955–965.

[19] Joseph, S., Sreekala, M. S., Oommen, Z., Koshy, P., & Thomas, S. Compos. Sci. Technol. 62(14), (2002), 1857–1868.

[20] Mishra, S., Mohanty, A. K., Drzal, L. T., Misra, M., Parija, S., Nayak, S. K., & Tripathy, S. S. Compos. Sci. Technol. 63(10), (2003), pp. 1377–1385.

[21] Joffe R., & Andersons J. *Mechanical performance of thermoplastic matrix natural-fibre composites.* In Pickering,, K., & Kim Louise Pickering, M. (Eds.). *Properties and Performance of Natural Fibre Composites*. (pp. 443). (CRC Press. 2008).

© (2011) Trans Tech Publications, Switzerland
doi:10.4028/www.scientific.net/KEM.471-472.1064

Flexural Mechanical Characteristic of Sawdust and Chipwood Filled Epoxy Composites

S. Hisham[1,a], A.A. Faieza[1,b] N. Ismail[1], S.M. Sapuan[1] and M.S. Ibrahim [1]

[1]Department of Mechanical and Manufacturing Engineering,

Universiti Putra Malaysia, 43400 Serdang, Selangor, Malaysia

[a]hishams@iprom.unikl.edu.my

Keywords: Sawdust and chip wood, wood composites, epoxy composites

Abstract. A study was conducted with the objective of gathering the information through flexural (three-point bending) testing. This research presents the testing results concerning the mechanical properties, modulus of elasticity (MOE) and modulus of rupture (MOR) of natural fiber reinforced composite. Resin were used as a matrix and untreated wood fibres contents 14% by weight as a filler treatment parameters to obtain better compatibility involving wood fibres Sawdust (SW) and Chipwood (CW) and epoxy. The feasibility of processing the composite prepared manually from waste wood and epoxy using open molding was investigated. The tests that have been conducted are in according to ASTM (D790-97) for flexural properties test method. Statistical analysis using ANOVA one way and two way showed that the differences of results obtained from those SW and CW fiber composite samples are significant, which confirm a very firm mechanical performance of the composites through flexural tests. This shows the producing a good quality of SW and CW fibre composite which maybe can use for furniture utilities.

Introduction

Composites are used because overall properties of the composites are greater to those of the individual components. In the related literature, it has been reported that most polymer composites involve fibre reinforcement, for instance, Bamboo fiber reinforced polypropylene composites [1], oil palm empty fruit bunch (EFB)-polypropylene composites [2], Bamboo fibre filled natural rubber composites [3], and woodfibre reinforced polymer composites [4]. Potentially biomass residue formed in ash was studied as cement replacement material for cement and concrete composite [5].

The aim of this study is to determine the flexural properties of SW and CW/Epoxy composite. This study is important for thermoplastics manufacturer from furniture, and other related industries to find out the suitable materials with shown good flexural properties for making their products [6]. Susan et al, [7] studied for composites containing recycled plastics and wood fiber offer an interesting combination of properties, as well as lower cost than competitive materials. This is where the use of composite materials has directly enhance the capability of commercial and wood composite in term of weight saving, strength and maneuverability [8].

According to Ajay et al, and Lai et al, [9-10] wood fibres have gained significant as reinforcing materials for commercial thermoplastic and also as a potential alternative to inorganic fillers for various applications. The interfacial adhesion can be improved by using compatibilizers or coupling agents. From the recent work years 2007 to 2008 suggested that used of maleated polypropylene (MAPP) significantly improved the fibre matrix bonding.

According to Chawla [11] reinforcement not need necessarily be in the form of long fibers. It can be particles, flakes, whiskers, short fibers, continuous fibers, or sheets. Typically, reinforcing materials are strong with low densities while the matrix is usually a ductile, or tough material [12]. Bledzki and Gassan [13], studied about composites reinforced with cellulose based fibres, and introduce the appropriate fiber to the matrix materials and the chosen resin is an important thing to produce composite. Natural fiber-composite have considerable potential to replace conventional materials like metal, plastic and wood in structural and non-structural applications, especially in furniture industry [13-14-15].

Stark and Leslie [16-17], found that wood flour-polypropylene (PP) composites with 20 wt% wood flour reached equilibrium after 1500 hour in a water bath and absorbed only 1.4% moisture while composites with 40 wt% loading reached equilibrium after 1200 h water submersion and absorbed approximately 9.0% moisture. Drying of fibres before processing is an important factor, because water on the fibre surface acts likes a separating agent in the fibre–matrix interface [18].

Bledzki et al, [18] stated that epoxy is a matrices material better than polyester. According Chawla [19] Epoxies are most commonly used in carbon fiber composites. This is because their mechanical properties are superior. Epoxy resins are more expensive than polyesters, but they have a better moisture resistance, low shrinkage on curing (about 3%), a higher maximum use temperature, and good adhesion with glass fiber. Epoxy resins are easily and quickly cured at any temperature from 5°C to 150°C, depending on the choice of curing agent [20].

Experimental procedure

Materials and Processing. The two type of waste fiber used for specimens were sawdust (SW) and chip wood (CW), the waste wood are from all type species of timber. The sieve will be shaking manually to facilitate separation a variety of sized particle. Three size of sieve were used to segregate the chip wood (CW) and sawdust (SW) fiber. The fiber collected from each sieve was separated into three different size groups namely large fiber called “coarse”. The medium fiber called “rough” and the fine fiber called “soft fiber”. The process requires about 30 minutes for screening into three different categories. The collected fiber for each group was dried overnight to remove the moisture content and kept in the polyethylene bag to avoid from fungus growth.Type of Epoxy Resin used is ASASIN 142 A/B. The recommended usage mixing ratio is 100 parts of ASASIN 142A to 42 parts of ASASIN 142B.

Mechanical testing. The specimens and testing were according to an American Society for Testing Materials (ASTM) standard size. All material used in the test was conditioned to the flexural test method I-A (three point bending) a specimen with nominal dimensions of 6 mm x 13 mm x 130 mm, a span length of 100mm and a deflection rate of 2.8 mm/min cross-head speed were used for all test. Six flexural specimens were tested for each composite formulation and test condition. The flexural strength and modulus of elasticity were measured using equations show below as.

$$\mathrm{MOR}=3Pl/2bd^2$$

where P is the maximum load carried by the specimen ,l is the support span, b and d are the specimen breadth and depth, respectively.

$$\mathrm{MOE}=ml^3/4bd^3,$$

where l is the support span, b and d are the specimen breadth and depth, respectively, measured at the nearest undisturbed location to the region of failure, and m is the slope of the load–deflection curve during elastic deformation.

The composite sample was in the form of rectangle shape for flexural test.Flexural properties such as strength and modulus were carried out according to the ASTM D790-79. The Instron machine Model 5565 was used.

Type of analysis. The morphological properties and fractured surface of SW/Epoxy and CW/Epoxy composite were taken and examined using the scanning electron microscopy (SEM). The sample was mounted on the circular disk and its observation surface was gold coated using the SEM Coating Unit Valtec SCD 005 Coater for 3 minutes before viewing under SEM. The Environmetal Scanning Electron Microscope (ESEM), model Philips XL 30 was employed to examine the individual composites.

The Statical Package for Social Sciences (SPSS) was used for analysis. A One Way and Two Way Analysis of Varian (ANOVA) was performed to determine the significant different. The multiple comparison of Tukey's Studentized Range Honestly Significant Difference (HSD) test was used to compare SW and CW fiber composite.

Result and discussion

The flexural properties of composites were determined using a three-point bending which is the flexural strength and modulus of elasticity of these SW/Epoxy and CW/Epoxy. Figure 1.1 shows mean of flexural modulus of elasticity (MOE) composites for both SW and CW. Mean stress at MOE for coarse SW is 2414.466 MPa, course CW is 1373.762 MPa, rough SW is 1324.329 MPa, and rough CW is 2682.045 MPa, soft SW 225.595 MPa and soft CW 1923.25 MPa. The effect of different composite with SW/Epoxy and CW/Epoxy used shown the trend within the fiber size. Meanwhile, the increase trend was observe the value of SW/Epoxy composite containing soft size was found 2252.595MPa which is 6.6% lowers than the epoxy control sample, where the value of CW/Epoxy composite containing rough size was found 2682.045MPa which is 11.2% higher than the epoxy control sample. The apparent decrease in modulus of the elasticity of the SW/Epoxy composite at this content could be associated with poor distribution of the fibres within the matrix because the untreated fibre tends to form a group.

Bledzki et al, [21] found the addition of MAPP-L increase the flexural strength and but flexural modulus of composites remain unchanged, according to them the modulus of short fibre reinforced composites depend mainly of fibre loading, fibre length and modulus of matrix and fibre.On the other hand the size of particle for SW/Epoxy from soft to rough and course showed a tendency to get worse at modulus of elasticity. Figure show the relationship between the flexural MOE and the filler size for the SW/Epoxy and CW/Epoxy composite prepared without treated fibres.

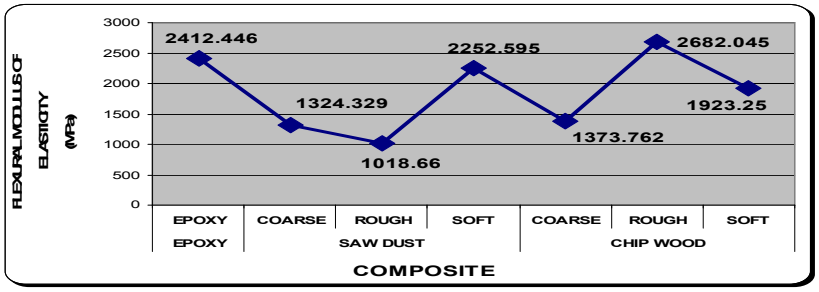


Fig.1.1: Flexural Modulus of Elasticity

When the amounts of SW and CW fibers in the Epoxy matrix increased, the flexural strength also increased. Figure 1.2 shows the flexural stress of SW/Epoxy and CW/Epoxy as prepared from different size of fibers. Those composite loaded with fiber 14% show significant different of mean against fiber sizes. The increase in flexural stress might contribute to the more stiffness properties due to increasing amount of CW fibers but against to SW fibers.

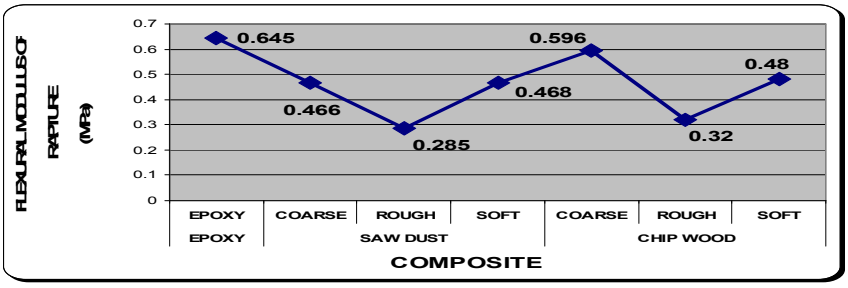


Fig. 1.2: Flexural Modulus of Rapture

It was observed that the increase trend was significant when the particle size increase especially for CW. However, for SW is disparate the trend shows the increasing from soft SW to Rough but decrease to Coarse. This is contradictory result was reported by Nakamura et al, [22] and he found that the flexural strength increased with the decreased in particle size. In this study those composite loaded with soft to rough particle size remarkable increase of flexural stress. However, those composite load with rough to coarse particle size were found vary with increase for CW and decrease for SW.

Figure 1.3 to 1.8 show SEM micrograph the cross section of the fractured surface of SW/Epoxy and CW/Epoxy composites on flexural that the interface fibre/matrix was not good enough it present a lot of cavities, where fibre supposed to be imbedded. The flexural fracture surface of the SW/Epoxy and CW/Epoxy with three different sizes are show, the cavities can bee seen between fibre and epoxy matrix polymer. The presences of these cavities clearly indicate the poor interfacial adhesion between the epoxy matrix polymers. This result contributes the poor flexural properties. The pull out traces and the particle were bigger in the large particle size CW/Epoxy (14mm - 15mm) filled fibre composite than in the smaller particle size CW/Epoxy (4mm - 5mm) filled composite. This result confirm that the flexural strength of SW/Epoxy composite of sawdust (100 mesh) filled is higher than that of SW/Epoxy composite (200 mesh and 50 mesh) and the rough particle size offer better dispersion between sawdust and the matrix polymers.

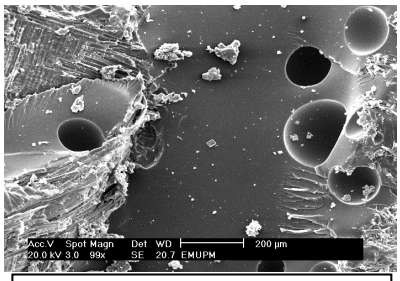


Fig.1.3: SEM micrograph of coarse flexural test CW/Epoxy composite magnification 100x. Fibre size 14-15 mm

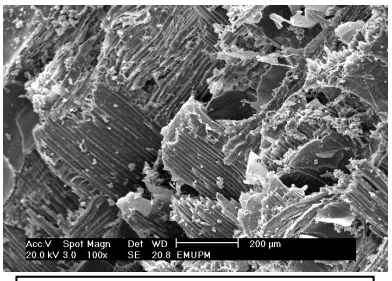


Fig.1.4: SEM micrograph of coarse flexural test CW/Epoxy composite magnification 100x. Fibre size 9-10 mm

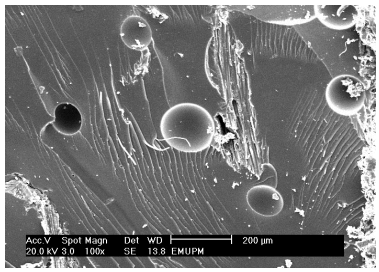


Fig.1.5: SEM micrograph of coarse flexural test CW/Epoxy composite magnification 100x. Fibre size 4-5 mm

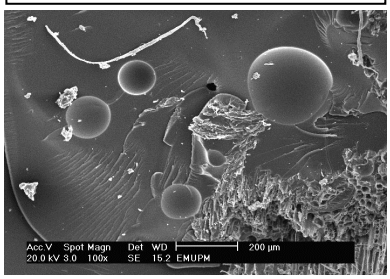


Fig.1.6: SEM micrograph of coarse flexural test SW/Epoxy composite magnification 100x. Fibre size 0.20-0.30 mm

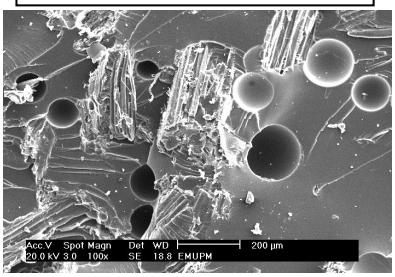


Fig.1.7: SEM micrograph of coarse flexural test SW/Epoxy composite magnification 100x.
Fibre size 0.12-0.15 mm

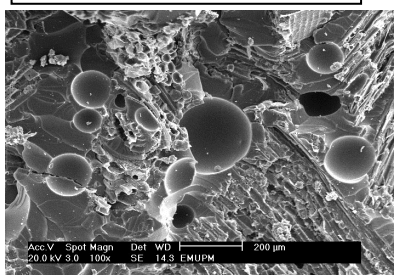


Fig.1.8: SEM micrograph of coarse flexural test SW/Epoxy composite magnification 100x.
Fibre size 0.25-0.30 mm

The possibility of using SW and CW fiber composite in the furniture industry, is higher due their MOR and MOE characteristics. Because the characteristic of furniture failures was not depending only on jointing system, to confirm the ability of withstand with strength and fulfill a requirement on physical performance.

When the amount of size increased for course 14mm-15mm of CW in the Epoxy, the Flexural strength is increased. Nevertheless, the flexural strength will be decreased for rough 100 mesh or 0.12-0.15mm when the size increased for SW. However, for CW/Epoxy showed the decreased of trend from soft particle to rough particle and increasing from rough to coarse particle. Sun et al, [23] found that the strength decreased with increasing filler loading (wt.%) of the composites. The addition of 40 wt.% wood flour resulted in a decrease in strength of about 9.2%, compared with the pure PP. A similar result was reported in a previous study, in which the addition of 20 wt.% wood flour to Polypropylene (PP) gave rise to a 9.5% strength reduction compared with pure Polypropylene (PP).

Summary
A lot of aspect has to be taking into account while are doing the preparation of composite materials. The mechanical properties of SW/Epoxy and CW/Epoxy composites shows that the experimental result demonstrated that different size of fibre could enhance the flexural strength of wood fibre composites. It also found that size of particle could closely decrease flexural strength of wood fibre composites. Generally, the impact strength of SW/Epoxy and CW/Epoxy increase with waste wood in different size and fibre fillet with 14% by weight.

Morphology of SW/Epoxy and CW/epoxy composites material was also studied using Scanning electron microscopy (SEM). Flexural fractured surface showed in the SEM studied confirmed the adhesion between wood particle and the epoxy matrix image showed that the untreated fillers (SW and CW) produced a very good fibre and epoxy interfacial interaction, since both the fibre impregnation and sticking of the fibre with the matrix were excellent. The observation indicated that there are distinct gaps between the matrix and there are voids around the wood particle which indicating poor adhesion. From the flexural interface also show that the untreated sawdust shows the poor adhesion between the sawdust and matrix surface and there are a voids around the sawdust particle. The matrix is the component that holds the filler together to form the bulk of the material. Beside that, surface structure also influenced the mechanical properties.

It can be summarized that the study has achieved its objective in developing the wood composite and to determine its mechanical properties. The gripping to hold the specimens to eliminate or minimize slippage of the specimen in the grip, also very important because it will be influence the result data printed produce by computer. In order to avoid from any circumstances, mistake to the technical data on setting up the control panel, and download all the data must follow the standard ASTM for flexural testing.

References

[1] Chen, X., Gue, Q. and. Mi, Y.: J. Appl. Polym. Sci., Vol.69, (1998) p.1891-1899

[2] Rozman, H.D., Saad, M.J. and Ishak, Z.A.M.: Polym. Test. Vol. 22, (2003), p. 335-341

[3] Hanafi Ismail,M.R. Edyham and B.Wirjosentono:Polymer Testing Vol. 21, 2, (2002) p. 139-144

[4] Krishnam Jayaraman, Battaiharyya: Mechanical performance of wood fiber –waste materials conversation & recycle, 41 (2004), p. 307-319

[5] A.U.Elinwa and Y.A.Mahmood: Cement and Concrete Composites Vol. 24,(2002), p.219–222

[6] A.K. Bledzki and J. Gassan: Prog Polym Sci. Vol.24, (1999), p. 221–274

[7] Susan E. Selke and Indrek Wichman: Applied Science & Manufacturing Vol. 35,3, (2004), p.321-326

[8] Jozsef Bodig, Benjamin A. Jayne in: Mechanics of Wood and Wood Composites, edited by Van Nostrand Reinhold Company, Library of Congress Cataloging in Publication Data (1982).

[9] Ajay Karmarkin, S.S. Chauhan, Jayant M. Modak and Manas Chanda: Applied Science and Manufacturing Vol. 38, 2, (2006), p. 227-233

[10] S.M. Lai, F.C. Yeh, Y. Wang, H.C. Chan and H.F. Shen: J Appl. Polym. Sci. Vol.87,3, (2003) p.487–496

[11] K.K. Chawla, in: Fibrous Materials First published, Cambridge. Library of Congress cataloguing in publication data, Cambridge University (1998), in press.

[12] J.P. Schaffer, A. Saxena, S.D. Antolovich, T.H. Sanders, Jr. and S. B., in: The Science and Design of Engineering Materials; edited by Warner, Chicago (2006).

[13] A.K. Bledzki and J. Gassan: Prog Polym Sci. Vol.24, (1999), p. 221–274

[14] R.M.N. Arib,S. M. Sapuan, M.M.H.M. Ahmad, M.T. Paridah, H.M.D. Khairul Zaman: Materials and Design, Vol. 27, (2004) p.391-396.

[15] S.M. Sapuan, M.A. Maleque: Material and Design Vol.26 (2005), p. 65-71

[16] Nicole M. Stark, Robert E. Rawlands: Wood and fibre science, Vol.35 (2003) p. 167-174

[17] Leslie Holliday: Composite Materials. American Elsevier Publishing Company Inc. Amsterdam Elsevier applied Science. Amsterdam /London/ New York, (1989)

[18] A.K. Bledzki and J. Gassan: Prog Polym Sci. Vol.24, (1999), p. 221–274

[19] K.K. Chawla Composite, in: Materials Science and Engineering. Second Edition Library of Congress Cataloging-in-Publication Data (1998).

[20] A.K Bledzki, M. Letman, A. Visksen and L. Rence: A comparison of compounding process and wood type for wood fiber PP composite. 36. (2004), pp 759-797

[21] Nakamura, Y.M., Yamaguchi, M. Okuba and Matsumoto T: Effect of composite and polypropylene melt flow on polypropylene - waste newspaper composite. In Proceeding Annual Technical Conference Society of Plastics Industry (1992) p. 602.

[22] Sun-Young Lee, Han-SeungYang, Hyun-Joong Kim, Chan-Seo Jeong, Byeong-Soo Lim and Jong-Nam Lee: Composite Structures Vol. 65, (2004), p. 45-46.

[23] Sun-Young Lee, Han-SeungYang, Hyun-Joong Kim, Chan-Seo Jeong, Byeong-Soo Lim and Jong-Nam Lee: Composite Structures Vol. 65, (2004), p. 45-46.

© (2011) Trans Tech Publications, Switzerland
doi:10.4028/www.scientific.net/KEM.471-472.1070

Tensile Properties and Micromorphologies of Sawdust and Chipwood Filled Epoxy Composites

S. Hisham[1,a], A.A. Faieza[1,b] N. Ismail[1], S.M. Sapuan[1] and M.S. Ibrahim [1]

[1] Department of Mechanical and Manufacturing Engineering,

Universiti Putra Malaysia, 43400 Serdang, Selangor, Malaysia

[a]hishams@iprom.unikl.edu.my

Keywords: Sawdust, chip wood, wood composites, epoxy composites

Abstract. In this study, waste wood product obtained from the timber industry originating from various type of wood has been investigated. Research work carried out on the three different sizes of fiber derived from the sawdust (SW) and chip wood (CW). The SW and CW fiber and epoxy resin were blended together respectively using hand tools machine, all specimens of fiber composite were prepared accordance to the ASTM standards. Tensile and morphological properties provide an excellent measure of the degree of reinforcement provided by the fiber to the composite. The tensile modulus increased with the filler size from coast to rough of composites both SW and CW but decreases steadily with the wood–fiber size from rough to soft content. Statistical analysis using one way and two ways analysis of variances (ANOVA) showed that the differences of results obtained from those SW and CW fiber composite samples are significant, which confirm a very firm mechanical performance of the composites through tensile tests. This shows the producing a good quality of SW and CW fibres composite which maybe used for home furniture utilities.

Introduction

The furniture manufacturing industry in Malaysia has grown significantly in the past decade. Modern furniture design, require the use of wood composites with high strength properties [1]. Sapuan et al, [2,3] describes banana fiber composite has a very stable mechanical behaviors and the use of banana woven fabric reinforcement epoxy composite for household furniture telephone stand is unique in presentation and aesthetically pleasing.

The composites containing wood fiber offer an interesting combination of properties, lower cost, weight saving, strength and maneuverability. The most polymer composites involve as fiber reinforcement, such as bamboo, oil palm empty fruit bunch, and ash from timber waste has been studied [4-7]. A composite are combinations two materials called the reinforcing phase and matrix phase [8-10]. A previous study was performed using composite polypropylene and wood flour. By modification of the filler used sodium hydroxide for treated filler and also wood flour, with two different sizes (coarse and fine) [11]. The surface of wood flour used as reinforcement in polypropylene/wood composites was successfully modified by benzylation. The failure of composite materials are depend on its sizes, fiber geometric, plane ratio, volume fraction, fiber direction and the methods of making composites [12-14].

However, such a modification usually does not solve all the problems [15]. Cellulose and wood flour is often modified with chemical in order to increase the strength of the particles, to decrease water absorption or to improve composite properties generally [17,20]. Mostly natural fiber are hydrophilic in nature and their moisture content can be 3% -13%[14].The surface of natural fiber provides a good adhesion to the matrix in a composite structure [17,18]. The porous magnitude of oil palm fiber was intensively investigated by Sreekala et al, [19]. Angelo et al, [20] found that the cause of failure for all composites was due to fiber pullout followed by matrix failure and other chemical methods involve changing the surface tension to improve impregnation of the fibers by a matrix [9]. A lot of resin can be use depending on type of usage, the suitable procedure and cost of making. Epoxies are the most common matrix better than other thermoset resins because are easily

to apply on fibers, low shrinkage percentage also have good chemicals resistance and high dimensional stability is good in stressed conditions.

The objectives of this study are to develop a new type of composite materials specimens, which are sawdust (SD) and chip wood fiber (CW) reinforcement epoxy composite and to determine the mechanical characteristic and properties using tensile testing of a new composites specimens.

Experimental

Two type of waste fiber used for specimens were sawdust(SW) and chipwood(CW), The process take about 30 minutes for screening into three different categories and each group was dried overnight to remove the moisture content. The sieve will be shaking manually to separation into three different size groups namely "coarse" ,"rough" and "soft fiber".

A hand tools machine was used consistently during compounding process. The resin used is epoxy and the amount of the mixing ratio between ASASIN 142A and ASASIN 142B is 100:40 and 14 wt% is a fiber and the specimens is 6 mm thickness according to the ASTM standard. The tensile properties were performed at room temperature according to ASTM D 638 using universal testing machine, model 6566 with load applied was specified at 10kN 2.5 mm/min cross-head speed was set up for the type IV tensile specimens. The morphological properties and fractured surface of SW/epoxy and CW/epoxy composite were examined using the scanning electron microscopy (SEM).

The Statistical Package for the Social Sciences (SPSS) was used to analysis of SW and CW fiber composite. To determine a significant difference a one way and two way analysis of varian (ANOVA) was performed. The multiple comparison of tukey's studentized range honestly significant difference (HSD) test was used to compare SW and CW fiber composite.

Result and discussion

Figure 1 shows the tensile strength of SW/epoxy was higher at rough than that of course, and lower than that of soft SW/epoxy composite. As SW/epoxy increase the size, the substantial tensile strength could be attributing to weak interfacial adhesion between fibre and matrix polymer, which promote crack formation at the interfacial area. All the size shows significantly different α=0.05. It can be seen that the tensile strength of CW/epoxy composite increase gradually with the different size of chip wood in the composite.

The increasing trend in tensile strength for the fiber may be attributing the superior mechanical interlocking among the surface of rough SW and the epoxy. The roughening of this fiber probably promoted mechanical interfacial bonding between the fiber and the matrix, but is against to the course of SW and also to the CW compare between sawdust and chip wood.

Miller et al, [21] have assessed the testing results show that plastics from the waste stream can be used to make wood fibre-reinforced composite materials with good mechanical properties. The decreasing of the tensile strength is due to the wetting of the fibre by the matrix as the ratio of filler surface area to matrix volume reached higher values [22].

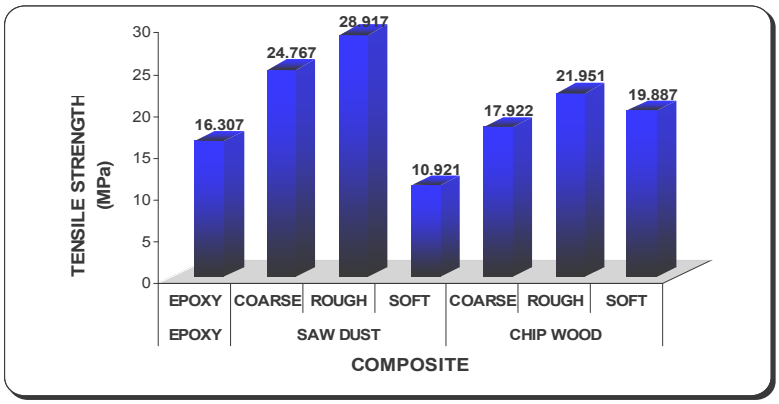


Fig. 1: Tensile strength of SW/Epoxy and CW/Epoxy with different size of filler reinforced composites

Figure 2 shows the maximum values of tensile elongation for composites

were rough SW/epoxy and course CW/epoxy. The trend on elongation at break, were probably caused of a few reason. First, a poor dispersion of fibre as the fibre content was different size in the matrix. Second the wood sawdust and chip wood is hydrophilic in nature and was chemically untreated (in this part of studied), the fibre might have picked up the moisture for the duration of storage, processing and testing. It was through in this work that the moisture might have interface with the adsorption effects by reducing the effect of physical bonding and potentially acting as a lubricant between the fibre and surface and epoxy. Third the increase of interfacial defect or debonding between epoxy and wood sawdust and chip wood fibres due to of untreated fibres.

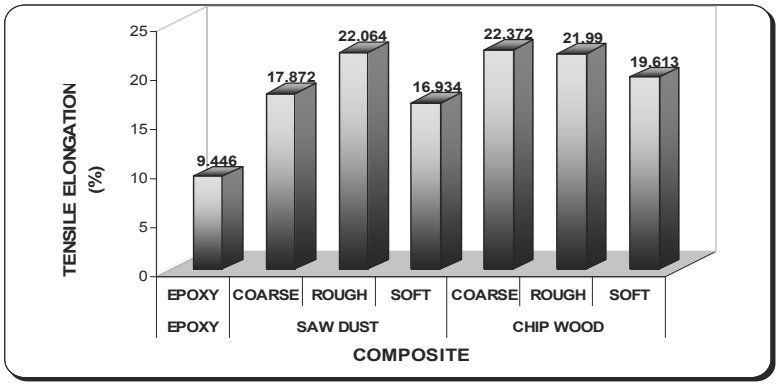


Fig.2: Tensile elongation of SW/Epoxy and CW/Epoxy with different size of filler reinforced composites

Figure 3 shows mean tensile young modulus for both SW/epoxy and CW/epoxy composites. Mean tensile modulus for coarse SW is 860.116 MPa, coarse CW is 737.815 MPa, rough SW is 889.988 MPa, rough CW is 902.331 MPa, soft SW 386.873 MPa and soft SW 386.873 MPa and soft CW 851.313 MPa. The effected of different fiber size increase with fiber size from soft to rough both SW and CW. Meanwhile the constant trend was observe for both SW and CW but dropped when both size is increase for coarse. However the fiber showed a bit higher for tensile young modulus value at coarse as compare to the CW coarse fiber size. The absent of fibers in coarse of fiber for both SW and CW was observed to reduce the young modulus and this might contribute to poor disproportion of SW and CW fiber in the matrix.

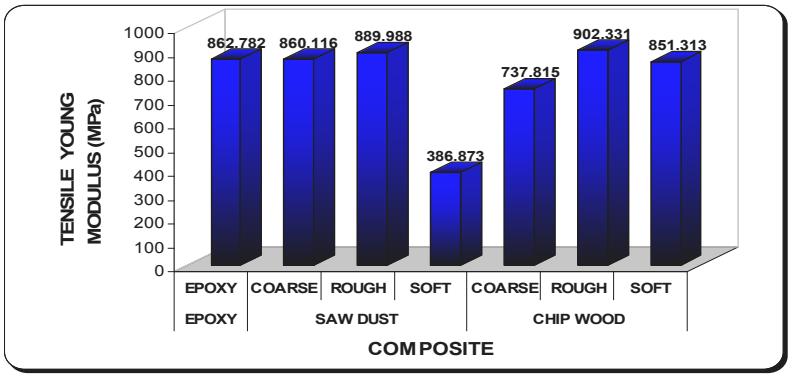


Fig.3: Tensile Young Modulus

It is not like the pervious study by Facea et al, [23] mention that the tensile modulus data for all the composites was show the linearly increase with an increase of fibre loading. Nicole et al, [24] also studied the effect of a maleated polypropylene coupling agent on composite properties. Increases in tensile strength and modulus of the wood flour composites were found to correspond with increases in aspect ratio. The higher aspect ratio of the wood fiber had little effect on impact energy. The maleated polypropylene coupling agent caused greater strength increases in wood fiber composites than in wood flour composites. The coupling agent did not significantly affect tensile modules.

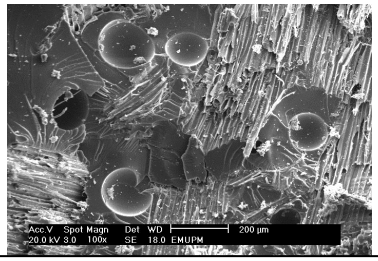


Fig. 4: SEM micrograph of course tensile test of SW/Epoxy composite magnification 100x. Fibre size 0.25-0.30mm

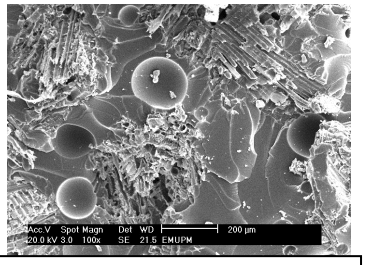


Fig. 5: SEM micrograph of course tensile test of SW/Epoxy composite magnification 100x. Fibre size 0.12-0.15mm

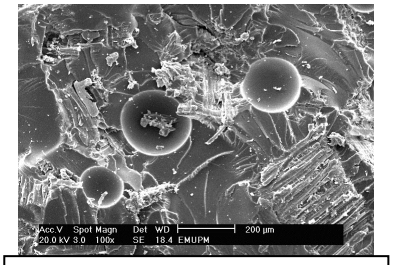


Fig. 6: SEM micrograph of course tensile test of SW/Epoxy composite magnification 100x. Fibre size 0.063-0.075mm

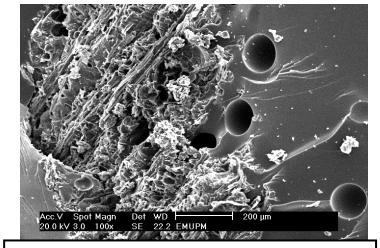


Fig. 7: SEM micrograph of course tensile test of CW/Epoxy composite magnification 100x. Fibre size 14-15 mm

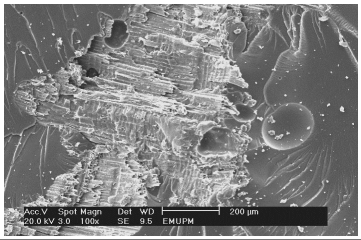


Fig. 8: SEM micrograph of course tensile test of CW/Epoxy composite magnification 100x. Fibre size 9-10 mm

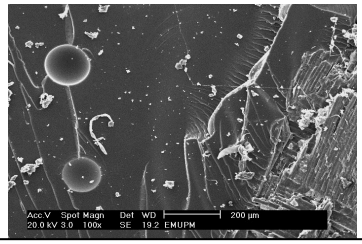


Fig. 9: SEM micrograph of course tensile test of CW/Epoxy composite magnification 100x. Fibre size 4-5 mm

Fig. 4 to 9 shows the SEM micrograph the cross section of the fractured surface of SW/epoxy and CW/epoxy composites on tensile test with difference size. Although there is a bigger contact surface between filler and matrix for coarse CW/epoxy was used, the adhesion is not good because there are crack or empty spaces at the interface. The images also show very little fibre pull out and splitting indicating a good bond and interfacial adhesion between the matrix and the fibre.

The composites with untreated fiber sawdust and chip wood for tensile shown in fig. 4 to 9 reveal that some bubbles occur at the interface between the polymer matrixes and also there are voids at fibers surroundings. As reported in [25] cell nucleation tends to take place at the interface between the polymer and the additives (i.e., the fibers) a phenomenon called heterogeneous nucleation. Since the purpose of the cellulose fibers is to enhance the material performance, these voids may offset the fiber reinforcing functions significantly. This is why in the mechanical tests microcellular injection molded composites tend to have lower strengths.

Sun et al, [26] found that the tensile strength decreased with increasing filler loading (wt.%) of the composites. The addition of 40 wt.% wood flour resulted in a decrease in strength of about 9.2%, compared with the pure polypropylene (PP). A similar result was reported in a previous study, in which the addition of 20 wt.% wood flour to PP gave rise to a 9.5% strength reduction compared with pure polypropylene [26].

Summary

From this study the amount of different size wood waste SW and CW used as fibre reinforced epoxy composite by content is 14 % by weight. The mechanical properties of SW/epoxy and CW/epoxy composites showed that the different size of fibre could enhance the tensile strength of wood fibre composites.

The micro morphological images from SEM showed that the untreated fillers (SW and CW) produced fairly good interfacial interactions, fibers attached to the resin with excellent. The observation indicated that there is distinct gaps between the matrix and the wood indicating poor adhesion composite with sawdust. It is also possible to observe patterns from wood fibres, which was so weakly bonded to the matrix that they have been released from the matrix during fracture.

This causes sawdust float on the surface might be it will not distribute separately in the epoxy matrix. On the other hand, it was observed that tensile strength and tensile young modulus increase trend when soft to rough particle but slightly decrease when rough to coarse particle fiber composite of SW and CW/epoxy composite.

References

[1] C.A. Eckelman: Forest Product Journal, Vol.16, 3, (1966) p. 21-24

[2] S.M. Sapuan, M.A. Maleque: Material and Design Vol.26, (2005) p. 65-71

[3] S.M. Sapuan, S.A. Mustasher, E.S. Zainudin, N. Harun, M, N. A. Mahmud, J. Mohamad, E.Y. Chew : Seminar On Manufacturing and Material Product (2006)

[4] X. Chen, Q. Gue, Y. Mi: Journal Appl. Polym. Sci., Vol. 69, (1998), p.1891-1899

[5] H.D. Rozman, M.J. Saad, Z.A.M. Ishak: Polym. Test., Vol. 22, (2003) p. 335-341

[6] H. Ismail, M.R. Edyham, B. Wirjosentono: Polymer Testing, Vol. 21, 2, (2002) p. 139-144

[7] A.U. Elinwa, Y.A. Mahmood: Cement & Concrete Composites, Vol. 24, 2, (2002) p.219–222

[8] K.B. Armstrong, R.T. Barret in: *Care and repair of advance composite*, Society Engineering Inc, Warrendale, PA, (1998), p.1-419

[9] A.K. Bledzki, J. Gassan: Prog Polym Sci. Vol. 24, (1999), p. 221–274

[10] M.N. Ichazo, C. Albano, J. Gonzalez, R. Perera, M.V. Candal: Comp. Struct.,Vol. 54, (2001) p. 207-214

[11] Magnus Bengtsson, Paul Gatenholm, Kristiina Oksman:Sci. & Tech., Vol. 65, 10, (2005), p. 1468-1479

[12] M.Morreale, R. Scaffaro A. Maio, F.P. La Mantia: App. Sci. & Manuf., Vol. 39, (2008), p. 503-513

[13] Krishnan Kumar Chawla: Sci. & Eng. Springer, (1998) p. 303-346

[14] Axel Nechwatal, Klaus-Peter Mieck, Thomas: Comp. Sci. & Tech., Vol. 63, (2003) p.1273-1279

[15] P. Vollenberg, D. Heikens, H.C.B. Ladan: Polym. Compos. Vol. 9(6), (1988), p. 382–388

[16] Han-Seung Yang, Hyun-Joong Kim, Hee-Jun Park: Jour. Comp. Struct., Vol.72, (2006), p. 429-437

[17] J. Gassan, AK. Bledzki: Comp. Sci. Tech. Vol.59, (1997), p. 1-7

[18] N. Jorg, R. Ulrich in: Activities in biocomposites. Material Today, London: Elsevier Science Ltd. (2003), p.44-48, in press.

[19] M.S. Sreekala, S. Thomas: Composites Sci. & Tech., Vol.63, (2003), p. 861-869

[20] G. Angelo Facea, T. Mark Kortscho, Ning Yin: Comp. Sci. & Tech., Vol. 67, (2007), p. 2454-2466

[21] N.A. Miller, M.S. Jones, C.D. Sterling: Poly. Comp., Vol. 62, (1998), p. 97–102

[22] B. English, P. Chow, and D. Bajwa in: *Paper and Composite from Agro Base Resources*. Rowell, R., Young, R., Rowell J., New Jersey, (1997), p. 269-300

[23] G. Angelo Facea, T. Mark Kortscho, Ning Yin: Comp. Sci. & Tech., Vol. 67, (2007), p. 2454-2466

[24] M.S. Nicol, E.R. Robert: wood and fibre science, Vol. 35, (2003), p. 167-174.

[25] N.S. Ramesh, D. H. Rasmussen, G.A. Campbell: Polymer Engin. & Sci., Vol.34, (1994), p.1685

[26] Sun-Young Lee, Han-Seung Yang, Hyun-Joong Kim, Chan-Seo Jeong, Byeong-Soo Lim, Jong-Nam Lee: Composite Structures, Vol.65, (2004) p. 459-460

© (2011) Trans Tech Publications, Switzerland
doi:10.4028/www.scientific.net/KEM.471-472.1075

A New Finite Fracture Mechanics Approach for Assessing the Strength of Bonded Lap Joints

Philipp Weißgraeber[1,a] and Wilfried Becker[1,b]

[1] Fachgebiet Strukturmechanik, Technische Universität Darmstadt,

Hochschulstraße 1, D-64289 Darmstadt, Germany

[a] weissgraeber@fsm.tu-darmstadt.de, [b] becker@fsm.tu-darmstadt.de

Keywords: Adhesive joint, fracture load prediction, finite fracture mechanics

Abstract. For the widespread use of adhesive joints an exact and reliable prediction of the strength is mandatory. In this work, a new approach to assess the strength of single lap joints is presented. The approach is based on the hybrid criterion as postulated by Leguillon in the framework of finite fracture mechanics. It strictly combines a consideration of an energy release balance and a fulfillment of a strength criterion. The present work is based on a simple model of the joint behavior and assumptions about crack initiation. From the stress distribution of the classical shear lag theory an incremental energy release rate is derived and is used to formulate the optimization problem of the failure load. The resulting predictions of critical failure loads are compared to experimental results of single lap joints. It is shown that the new approach is able to physically describe crack formation and the corresponding critical load within the framework and limitations of the underlying assumptions and simplifications. The work closes with a discussion of the limitations and an outlook on possible improvements of the underlying models and assumptions.

Introduction

The ability to correctly predict the strength of adhesive joints is of great importance for the widespread use of adhesive technology. In the last decades, various approaches have been suggested. The main ideas can be summarized as: assessing the strength by effective stresses, by analyses of the singular elastic field or by damage mechanics/cohesive models. A comprehensive review can be found in [1,2].

In the present work, an approach is presented that combines a stress criterion and an energy criterion in the framework of finite fracture mechanics [3] as postulated by Leguillon [4] and is used to assess the strength of a bonded lap joint. This approach can be applied to stress fields containing stress/strain singularities without restrictions in contrast to approaches based on effective strength or damage mechanics. Furthermore, no assumptions about existing cracks have to be made, which are for example needed in fracture mechanics assessments. The presented approach is of analytical nature based on approximate closed-form solutions of the stress fields. It allows for quick parameter studies without expensive numerical calculations.

The hybrid criterion has already been successfully applied to model crack initiation either based on asymptotic formulations [5,6] or by means of direct numerical formulations [7,9,10].

The classical shear lag theory by Volkersen [11], providing solely a shear stress distribution which is constant over the adhesive thickness, is used as the underlying model for the mechanical behavior of the joint. With certain assumptions about spontaneous crack initiation and a maximum stress criterion the optimization problem of the failure load is derived. A comparison of the approach with experimental results is performed and the next steps to enhance the approach are discussed.

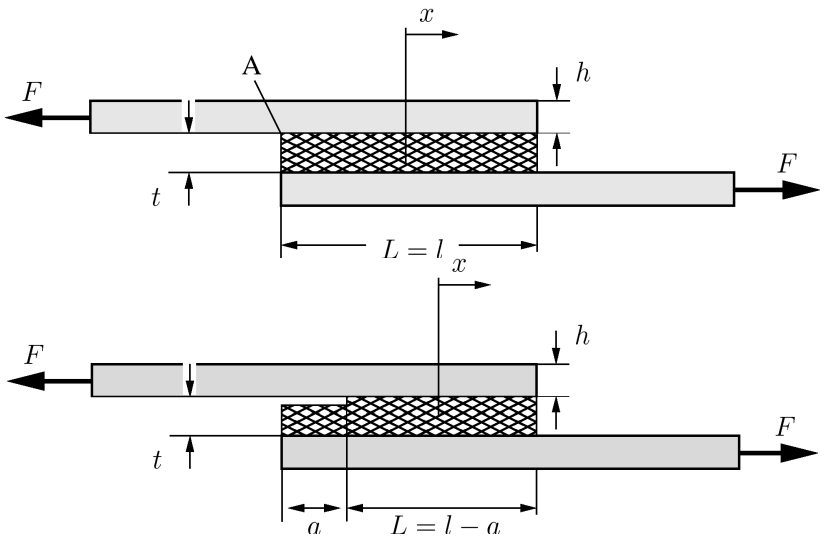


Fig. 1 Idealization of the single lap joint before and after the spontaneous formation of a crack.

Theoretical Formulation

Hybrid Criterion for Crack Initiation. In this work the hybrid crack initiation criterion by Leguillon is utilized for assessing the strength of a lap joint. The fundamental hypothesis of this criterion is the spontaneous formation of a crack with the finite area ΔA provided that a stress criterion is fulfilled on the entire area of the newly created crack and that the corresponding incremental energy release rate $\overline{G}$ is greater than or equal to the fracture resistance G_C of the material. Both conditions must hold simultaneously. In case of static, linear elasticity with mechanical energy transport the criterion can be given as:

$$f(\underline{\sigma}) \geq 1 \ \wedge \ \overline{G} = -\frac{\Delta \Pi}{\Delta A} \geq G_C \tag{1}$$

whereas f is a suitable strength criterion for the stress state $\underline{\sigma}$, such as the criterion of maximum principal stress, v. Mises yield stress or Drucker-Prager criterion. $\Delta\Pi$ is the change of potential energy of the uncracked and cracked structure. In limiting cases this criterion reduces approximately to Griffith's energy criterion (sharp crack) or to a mere stress criterion (sufficiently large body with homogeneous stress field).

Thus, the resulting failure load is the smallest load satisfying the criterion (1) for any potential crack of area ΔA.

Modeling of the Lap Joint and the Crack Initiation. A symmetric single lap joint (SLJ) is considered and modeled with the very simplifying shear lag theory developed by Volkersen [11]. In this theory the shear stress is assumed to be constant over the thickness of the adhesive layer. The adherends are modeled as membranes with constant longitudinal stresses over the thickness.

For a single lap joint (see fig. 1) with a general overlapping length L, adherend thickness h, joint width b and thickness t of the adhesive layer, the shear stress distribution and the section forces $N_{1,2}$ of the upper and lower adherends (denoted as 1 and 2) result in:

$$\tau_{xy} = \frac{F\lambda}{2b} \frac{\cosh \lambda x}{\sinh \frac{\lambda L}{2}}, \tag{2}$$

$$N_{1,2} = \frac{F}{2}\left(1 \mp \frac{\sinh \lambda x}{\sinh \frac{\lambda L}{2}}\right) \tag{3}$$

$$\text{with } \lambda = \sqrt{\frac{2G_a}{Eht}}. \tag{4}$$

Herein, E denotes the Young's modulus of the adherends and G_a the shear modulus of the adhesive. F is the outer load acting in longitudinal direction at the ends of the adherend and x is the coordinate in longitudinal direction originating in the middle of the SLJ.

The stress distribution shows maximal peak stresses at the joint ends, namely

$$\tau_{peak} = \frac{F\lambda}{2b} \coth \frac{\lambda L}{2}. \tag{5}$$

As known from experiments, cracks will appear at the re-entrant corners of the adherend and the adhesive layers, which is denoted for instance by A in fig. 1 or of course symmetrically on the other side. In the case of a spontaneous formation of a crack, it is assumed that the part of the adhesive layer and the adjoining adherend below the horizontal crack are stress free. With this assumption crack propagation corresponds to a shortening of the adhesive and an elongation of the free adherend [12,13]. These simplifications allow for the use of the previously given stress distribution for the cracked single lap joint.

The incremental energy release rate $\overline{G}$ is calculated from the change of compliance ΔC of the single lap joint in the crack initiation. The compliance consists of the elongation of the adherends and the shear deformation of the adhesive layer:

$$\overline{G} = \frac{1}{2}\frac{\Delta C}{\Delta A}F^2 = \frac{1}{2}\frac{C_{cracked} - C_{uncracked}}{ab}F^2 \tag{6}$$

$$\text{with} \quad C_{cracked} = \frac{t}{G_a}\frac{\tau_{peak}^{(L=l-a)}}{F} + \frac{l-a}{2Ehb} + \frac{a}{Ehb} \quad \text{and} \quad C_{uncracked} = \frac{t}{G_a}\frac{\tau_{peak}^{(L=l)}}{F} + \frac{l}{2Ehb} \tag{7}$$

resulting in

$$\overline{G} = \frac{F^2}{4Ehb^2}\left(1 + \frac{2}{\lambda a}\left(\coth \frac{\lambda(l-a)}{2} - \coth \frac{\lambda l}{2}\right)\right). \tag{8}$$

This incremental energy release rate describes the energy released per surface area in the spontaneous formation of a crack of length a. There is a dependence on the thickness of the adhesive layer in a way that thicker adhesive layers lead to higher energy release rates. Thus, the incremental energy release rate covers the thickness effect, which leads to lower failure loads with increasing thicknesses of the adhesive layer.

Taking the limit of the incremental energy release rate (8) with respect to the crack length a leads to the (differential) energy release rate of a lap joint in pure shear as given by Hu and François [12].

Computation of the Failure Load. The failure load of the single lap joint for a given stress criterion and fracture resistance of the adhesive bonding can be determined from an optimization problem. The smallest load for any crack length a that simultaneously fulfills the stress and the energy criterion, is

Table 1 Geometric properties of the twelve test series of the experiments of Golgio et al [14].

	Test series											
Series	#1	#2	#3	#4	#5	#6	#7	#8	#9	#10	#11	#12
b [mm]	20	20	20	20	20	20	20	20	20	20	20	20
h [mm]	2	2	2	2	2	2	4	4	4	4	4	4
t [mm]	0.1	0.1	0.1	0.25	0.25	0.25	0.1	0.1	0.1	0.25	0.25	0.25
l [mm]	5	15	25	5	15	25	5	15	25	5	15	25

the load at which the spontaneous formation of the crack appears and will be called failure load F_f. With the use of a simple stress criterion with a critical shear stress S the criterion (1) leads to

$$F_f = \min_{F,a} \left\{ F \mid \overline{G}(F,a) \geq G_C ; \tau_{peak}(F,a) \geq S \right\}. \tag{9}$$

This optimization problem is based on the explicit expressions for the energy release rate and the stress distribution. Hence, it can quickly be solved with any algorithms suitable for constrained, nonlinear problems, for example downhill-simplex or genetic algorithms. Such an optimization, implemented in a mathematical toolbox, is performed almost instantaneously on a current personal computer.

Comparison with Experimental Results

For a short survey of the capability of the present approach a comparison to results from literature is performed. The experimental results of Goglio et al. [14] were used. Tests on single lap joints with steel adherends (structural steel S355 EN 10028) bonded with an acrylic structural adhesive (Loctite 330 by Henkel used with spray activator) have been performed. In total 12 test series with different joint dimensions were examined. The dimensions are given in Table 1. Loading was imposed with a cross-head speed of about 1mm/min. The elastic properties of the steel adherends are set according to the work of Goglio et al. to $E = 206\,\text{GPa}$ and $\nu = 0.29$. The elastic properties of the adhesive layer are $E_a = 880\,\text{MPa}$ and $\nu = 0.15$ corresponding to $G_a = 383\,\text{MPa}$.
The 2%-proof load given is compared to the results predicted by the current criterion. As no appropriate material data are available the parameter set that leads to the best agreement with the experimental results is identified. In order to do so the deviation between the model and the experimental results is calculated as

$$s = \sqrt{\frac{1}{n}\sum_{i=1}^{n}\left(\frac{F_{\text{exp}}^{(i)} - F_{hyb}^{(i)}}{F_{\text{exp}}^{(i)}}\right)^2}, \tag{10}$$

wherein n is the number of tested SLJ. F_{exp} and F_{hyb} are the failure loads according to the experiments respectively the present hybrid criterion. The deviation (10) is minimized with respect to the material parameters S and G_C. A direct use of material data obtained from standard tests is not possible due to the simplifications in the underlying model.

The resulting failure loads are also compared to a peak stress criterion based on the stress distribution given in (2). Here, the critical stress parameter again has to be identified by best agreement with the respective experimental results. The results of this comparison are shown in Table 2 for all test series and in Table 3 for the specimen with equal lengths ($l = 5\text{mm}$, $l = 15\text{mm}$, $l = 25\text{mm}$).
It can be seen that, considering all 12 test series (Table 2), the predictions of the present criterion are only slightly better than the peak stress criterion. Nevertheless, in the case of SLJ with constant overlapping length (Table 3), the present criterion leads to an agreement with the results of the experiments, which is much better than the results of the peak stress criterion.

The deviation of the predicted failure loads and the experimental results originate from the simplifications of the underlying theory. The major shortcoming of the criterion in its present form is the neglect of peel stresses due to adherend bending. As these peel stresses are strongly dependent on the overlapping length, especially when considering moment factors [15,16], this can explain the inability of the present criterion to correctly predict the failure loads of SLJ with unequal overlapping length.

Furthermore the shear deflection of the adherends and the variation of the stresses over the thickness of the adhesive layer are neglected [1,2].

Table 2 Comparison of failure load predictions and the experimental results for all SLJ specimen.

	Test series											
Results [N]	#1	#2	#3	#4	#5	#6	#7	#8	#9	#10	#11	#12
experimental	2826	4709	5352	2622	4374	5227	2839	5702	6134	2664	5290	6843
present	1859	4598	5658	1856	4989	6962	1874	5141	7083	1870	5296	7965
peak stress	1855	4375	5330	1896	5097	7113	1889	4957	6711	1910	5410	8138

Table 3 Comparison of failure load predictions and the experimental results for specimen with equal overlapping length.

l=5mm				
	test series			
results [N]	#1	#4	#7	#10
experimental	2826	2622	2839	2664
present	2817	2632	2848	2652
peak stress	2681	2740	2731	2761

l=15mm				
	test series			
results [N]	#2	#5	#8	#11
experimental	4709	4374	5702	5290
present	4335	5051	4912	5361
peak stress	4935	4682	5330	4970

l=25mm				
	test series			
results [N]	#3	#6	#9	#12
experimental	5352	5227	6134	6843
present	4534	6051	5708	6922
peak stress	5092	5552	6311	6352

Potential Enhancements of the Approach

As outlined in the preceding section, the criterion is able to physically describe failure initiation in SLJ, except for the effect of the overlapping length, which is not incorporated correctly as the comparison to the experiments revealed. To improve the performance of the criterion and to correctly describe all dependencies, the approach has to be refined. Currently a simple shear-lag analysis that only considers mode-II behavior of the adhesive layer and neglects peel-stresses forms the basis of the criterion.

Improved models of the joint behavior that take into account peel-stresses due to bending of the adherends, large deflections of the adherends, shear deflection of the adherends or traction free edges of the adhesive layers [1,2] can be employed for a more realistic modeling. The effect of consideration of non-linear material laws of the adhesive and the singular stress fields at the re-entrant, multimaterial corners on the performance of the criterion have to be analyzed as well.

For a detailed analysis of arbitrarily shaped joints, for example with spew fillets or chamfers, a finite element analysis (FEA) can of course be used, too. The hybrid criterion can then be implemented in a surrounding procedure that identifies the energy release rate in a discrete manner. Such analyses have already been successfully performed to analyze interface failure [8,17] or laminate edge effects in composites [9] or to analyze crack formation in notched brittle specimens [18]. With a FEA even an analysis of cracks with arbitrary shapes or orientations is possible. The computational effort of such numerical analyses is of course significantly higher than compared to a solution based on closed-form equations.

Summary

This work has presented a new approach to assess the strength of adhesively bonded single lap joints. A finite fracture mechanics approach was applied that requires a simultaneous fulfillment of a stress criterion and an energy criterion. The resulting criterion is a physically based criterion with two material parameters and is commonly referred to as a hybrid criterion. In combination with a strongly simplified model of the joint behavior, namely the classical shear lag theory, a simple criterion for the failure load of the bonded joint was derived. The evaluation of this criterion requires an optimization to find the lowest and hence relevant load that satisfies the hybrid criterion. The resulting criterion was compared with experiments of single lap joints with steel adherends performed by Goglio et al. The comparison showed that the hybrid criterion is able to describe important dependencies of the SLJ parameters on the failure load within the framework and limitations of the underlying modeling. Possible enhancements of the approach have been addressed in the preceding section. The use of improved joint behavior models should render the performance of an optimization to identify the material parameters dispensable and material parameters from standard tests applicable.

References

[1] R. Adams, J. Comyn and W. Wake: *Structural adhesive joints in engineering* (CRC Press, 1997).

[2] *Modeling of Adhesively Bonded Joints* eds: L. F. M. da Silva and A. Öchsner (Springer, 2008).

[3] P. Cornetti, N. Pugno, A. Carpinteri and D. Taylor: Eng. Fract. Mech. Vol. 73(14) (2006) p. 2021.

[4] D. Leguillon: European Journal of Mechanics - A/Solids Vol. 21(1) (2002) p. 61.

[5] D. Leguillon, J. Laurencin and M. Dupeux: Eur. J. Mech. A. Solids Vol. 22(4) (2003) p. 509.

[6] Z. Yosibash, E. Priel and D. Leguillon: Int. J. Fract. Vol. 141(1) (2006) p. 291.

[7] E. Martin, D. Leguillon and N. Carrère: Int. J. Solids Struct. Vol. 47(9) (2010) p. 1297.

[8] A. Müller, W. Becker, D. Stolten and J. Hohe: Eng. Fract. Mech. Vol. 73(8) (2006) p. 994.

[9] J. Hebel and W. Becker: PAMM Vol. 6(1) (2006) p. 169.

[10] J. Hebel, R. Dieringer and W. Becker: Eng. Fract. Mech. Vol. In Press, (2010) accepted.

[11] O. Volkersen: Luftfahrtforschung Vol. 15 (1938) p. 41.

[12] G. K. Hu and D. François: J. Adhes. Vol. 37(4) (1992) p. 261.

[13] S. Krenk: Eng. Fract. Mech. Vol. 43(4) (1992) p. 549.

[14] L. Goglio, M. Rossetto and E. Dragoni: Int. J. Adhes. Adhes. Vol. 28(8) (2008) p. 427.

[15] M. Goland and E. Reissner: J. Appl. Mech. Vol. 66 (1944) p. A17.

[16] L. Hart-Smith: NASA CR Vol. 112236 (1973) p. 1.

[17] E. Martin and D. Leguillon: Int. J. Solids Struct. Vol. 41(24-25) (2004) p. 6937.

[18] J. Hebel and W. Becker: Mech. Adv. Mater. Struct. Vol. 15(6-7) (2008) p. 410.

© (2011) Trans Tech Publications, Switzerland
doi:10.4028/www.scientific.net/KEM.471-472.1081

Metal Matrix Composites: Solidification Parameters of Aluminium-11.8% Silicon Alloy Reinforced with Titanium Carbide Particulates

N. Fatchurrohman[1a], S. Sulaiman[1b], M.K.A. Ariffin[1c], A.A.Faieza[1d] and B.T.H.T. Baharudin[1e]

[1] Department of Mechanical and Manufacturing Engineering,
Universiti Putra Malaysia 43400 UPM Serdang, Selangor, Malaysia
[a]nanang_fat@yahoo.com, [b]suddin@eng.upm.edu.my, [c]khairol@eng.upm.edu.my,
[d]faieza@eng.upm.edu.my, [e]tuah@eng.upm.edu.my

Keywords: Metal matrix composites, Aluminium alloy, Titanium carbide particulates, Solidification parameters

Abstract. In this study, solidification analysis of metal matrix composite, aluminium-11.8% silicon alloy matrix reinforced with titanium carbide particulates is performed. Sand casting method is used as the manufacturing method to produce the specimens. Thermal measurements during the casting process are captured and solidification graphs are plotted to represent the solidification characteristic. Solidification analysis is performed by interpreting the solidification graphs. Parameters such as; the nucleation of primary alpha phase temperature, liquidus arrest temperature, liquidus undercooling, eutectic growth temperature and solidification time are presented. The results show that introduction of second phase particulates into a matrix alloy have affected the various time and temperature parameters of its solidification properties.

Nomenclature

T_{nuc} : nucleation temperature
T_{liq} : liquidus arrest temperature
ΔT_{liq} : liquidus undercooling
T_{eut} : eutectic growth temperature
T_{fin} : end of eutectic reaction temperature
t_{sol} : solidification time

Introduction

The world's marketplace for metal matrix composites (MMCs) consumed 4.4 million kg in 2008 and expected to raise to 5.9 million in 2013, comprising of an annual growth rate around 5.9% [1]. Increasing demand of MMCs utilisations are especially for high temperature, high strength and stiffness materials such as in turbine engines and other applications. MMCs are nearly always more expensive than the most conventional materials they are replacing. As a result, they are found where improved properties and performance can justify the added cost.

Metal matrix composites (MMCs), like the monolithic metals and alloys, the characteristics of the cast MMCs are largely dependent on the solidification behaviour which is dictated by the thermo-physical properties of the reinforcement, matrix materials and the mould [2].

Previous study performed by [3] showed that the solidification rate increases with the introduction of particulates reinforcement, reaches a maximum and then decreases with increasing particulates reinforcement content due to lower heat transfer rates within the solidifying melt owing to the reduced effective thermal diffusivity of the composite system. Introduction of ceramic particulates reinforcement into the metal matrix alloy reduces the liquidus temperature. Contemporary research on solidification of MMCs [4], had found that the solidification time of primary dendrites is affected because of the presence of the ceramic particulates. Further study of MMCs, indicates that various solidification parameters have an effect on the microstructure and the

mechanical properties of the cast MMCs [5]. The objective of the present study is to investigate the solidification parameters of titanium carbide particulates reinforced aluminium-11.8% silicon alloy matrix composites.

Methodology

In this research, aluminium-11.8% silicon alloy (LM6) casting specimen was produced by sand casting, this material was used as the matrix material. MMCs specimens with volume fractions of 5 and 15% of titanium carbide particulates (TiCp) were reinforced to the LM6 matrix. Reinforcing an aluminium alloy with reinforcement material yields a material that displays physical and mechanical properties of both the metal matrix and the reinforcement material. The toughness and formability of aluminium can be combined with the strength of reinforcement material [6].

A carbon dioxide processed silica sand mould was used to produce the specimens during gravity casting. The mould was cylindrically shaped and specifically designed to meet the research objective which is to study the solidification characteristics. Previous researchers [2,7-8], had used this type of shape to study the solidification of MMCs. Vortex technique was used to mix the reinforcement and matrix components of the MMCs casting. Vortex method is a straightforward mixing process used to stir the reinforcement particulates and the metal or alloy matrix in the crucible. The speed of the stirring blade used in the vortex method can be controlled with the aid of a digital controller, which enabled to pour the mixture at the required viscosity and fluidity level [9]. The melt was poured at a temperature of 720°C into the mould and immediately a cotton cloth was covered at the top as an insulation. Thermal measurements during the casting process were performed inside the mould. A K-type thermocouple of 0.45 mm size was used to measure the temperature variation of the molten slurry MMCs during the casting process. The tip of the thermocouples was located at the center, of the mould. The temperature measurements were recorded using a computer aided data acquisition system.

Result and discussion

Solidification is the phenomena of latent heat liberation during the phase change of molten metal from liquid to solid during the casting. The final microstructure composition of the product being cast and the manner in which solidification occurs have an effect on properties of the casting [10]. Solidification graphs can be interpreted by parameters, such as the nucleation of primary alpha phase temperature, liquidus arrest temperature, liquidus undercooling, eutectic growth temperature and solidification time [4]. These parameters are presented by the schematic diagram below.

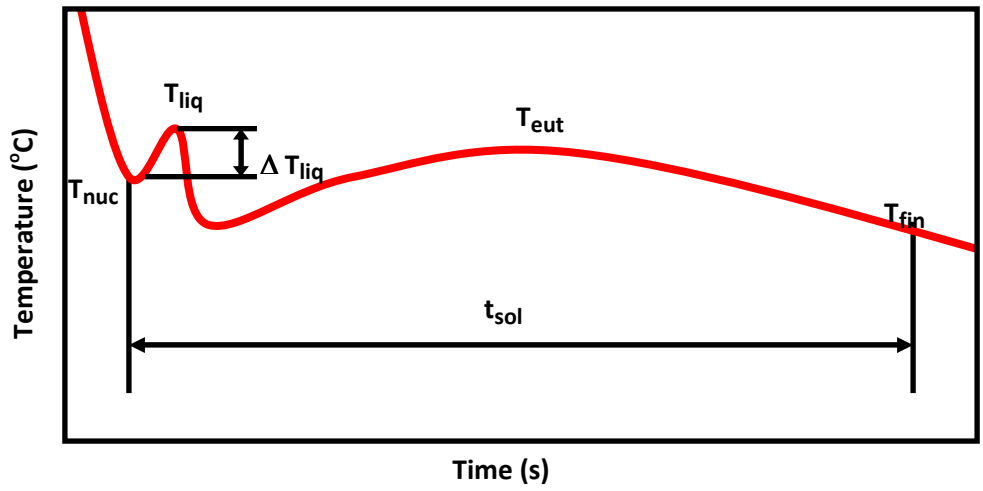


Figure 1 Representation of thermal analysis parameters on the solidification graph.

The solidification graphs were obtained by measuring the temperature of the LM6 alloy and MMCs casting during cooling and solidification throughout the casting process. The temperature measurements in the center of the casting was used as the data to plot the graphs. Graphs were plotted with the temperature as the value (Y-axis) against time as the category (X-axis). They were plotted and shown in Figure 2. In this test, solidification occurred between 582°C and 574°C.

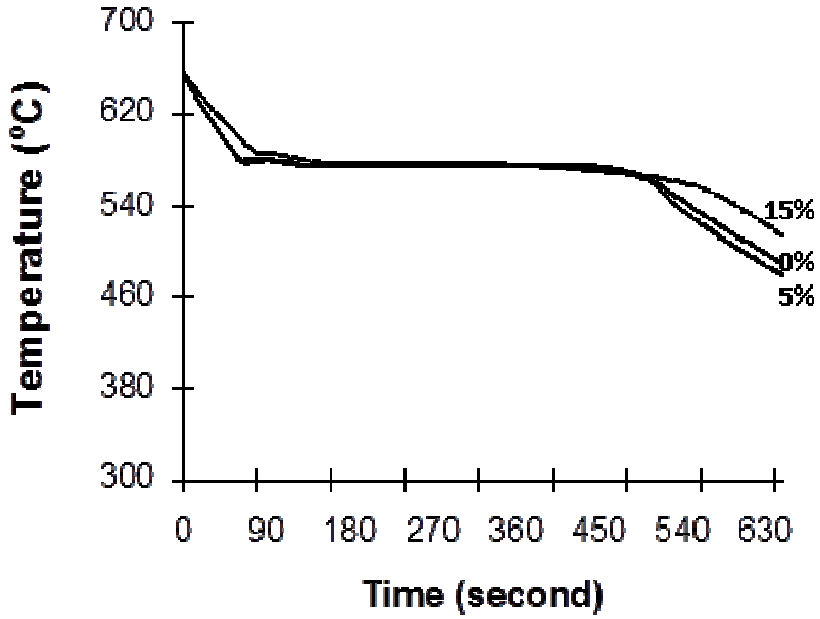


Figure 2 Solidification graphs of LM6 (0% TiCp) and MMCs (5 and 15% TiCp) specimens.

The solidification parameters, such as the nucleation of primary alpha phase temperature, liquidus arrest temperature,liquidus undercooling, eutectic growth temperature and solidification time are presented by the table below.

Table 1 Solidification parameters of LM6-TiCp MMCs casting specimens.

Solidification Parameters	Volume Fractions (%) of TiCp reinforcement addition		
	0	5	15
T_{nuc}	576.86	577.14	578.5
T_{liq}	579.61	579.63	580.21
ΔT_{liq}	2.75	2.49	1.71
T_{eut}	576.98	576.58	575.98
T_{fin}	573.94	573.97	573.94
t_{sol}	391	369	268

Nucleation temperature (T_{nuc}) is the point where the primary alpha (α) phase starts to form and the liquidus arrest temperature (T_{liq}) is the point when phase change from liquid to solid occurred during the cooling process. The increment addition of TiCp to the system raised the liquidus arrest temperature, this indicates that the addition of TiCp influence the starting formation of the primary α phase of the LM6 alloy shifting to higher temperatures. The liquidus undercooling or (ΔT_{liq}) is the difference between liquidus arrest temperature and nucleation temperature of the primary α phase. It can be seen that the liquidus undercooling of the MMCs samples produced by sand mould decreased as the addition of TiCp is increased. From this it can be drawn that faster nucleation of the primary α phase of the LM6 alloy occurred as increment addition of TiCp is introduced into the MMCs system. The eutectic growth temperature (T_{eut}) is the point where

microstructural formation of the eutectic start to take place. It can be drawn that as more TiCp is added into the system the eutectic growth temperature decreases. Total solidification time (t_{sol}) can be defined as the time taken from the beginning of solidification until the end of eutectic reaction. Samples of MMCs produced have shorter total solidification time as the addition of TiCp is increased. This can be explained as more nucleation sites exist in the solidified MMCs incoherent with increased addition of TiCp. Faster solidification rate is promoted due to the presence of thermally insulating TiCp contents which reduce the amount of heat to be removed. It is reported that high solidification rate gives rise to a much finer cast microstructure [11].

Summary

The way in which solidification occurs have an effect on properties of the casting. In this study solidification analysis is performed and interpreted by parameters such as the nucleation of primary alpha phase temperature, liquidus arrest temperature,liquidus undercooling, eutectic growth temperature and solidification time. The introduction of second phase particulates into a matrix alloy have affected the various time and temperature parameters of its solidification curve. This paper shows that addition of TiCp into LM6 matrix will produce shorter total solidification time. It is also concluded that faster nucleation of the primary α-phase of the LM6 alloy occurred as increment addition of TiCp is introduced into the aluminium alloy matrix.

References

[1] C. Swift: *Advanced Materials Metal Matrix Composites: The Global Market Report.*

Information on http://www.bccresearch.com/report/AVM012D.html. Accessed on 10/01/2011.

[2] N. Chawla and K.K Chawla: Metal Matrix Composites. Springer Science and Business Media, Inc. New York USA (2006).

[3] T.P.D. Rajan, K. Narayan Prabhu, R.M. Pillai, and B.C. Pai: Compos. Sci. Technol. Vol. 67 (2007), pp. 70–78.

[4] S. Wu, Y. You, P. An, T. Kanno, H. Nakae: J. Mater. Sci. Vol. 37 (2002), pp. 1855–1860**.**

[5] R. Asthana: J. Mater. Sci. Vol. 33 (1998) pp. 1679–1698.

[6] K.H.W. Seah, J. Hemanth and S.C Sharma:. Mater. Design Vol. 24 (2003), pp. 87–93.

[7] A. Cetin and A. Kalkanli: J. Mater. Process. Tech. Vol. 205 (2008), pp. 1–8.

[8] J.C. Baez, C. Gonzalez*,* M.R. Chavez, M. Castro and J. Juarez: J. Mater. Process. Tech.Vol. 153–154 (2004), pp. 531–536**.**

[9] T.R. Vijayaram, *Properties of Metal Matrix Composite of Aluminium-11.8% Silicon Reinforced with Different Particulates*, PhD dissertation, University Putra Malaysia, Malaysia (2006).

[10] K.B. Rundman, *Metal Casting. Reference Book*. Dept. of Materials Science and Engineering Michigan Tech. University, Michigan, USA (2004).

[11] P.A. Karnezis, G. Durrant G. and B. Cantor: Mater. Characterization Vol. 40 (1998), pp. 97–109.

© (2011) Trans Tech Publications, Switzerland
doi:10.4028/www.scientific.net/KEM.471-472.1085

Parametric Study on Cohesive Element for Composite Fuselage Model

N. W.Sim [1, a], F. Mustapha[1, b], R. Varatharajoo[1], R. Zahari [1] and D.L Majid[1]

[1]Department of Aerospace Engineering, University Putra Malaysia, Malaysia

[a]weisim1984@yahoo.com, [b] faizal@eng.upm.edu.my

Keywords: Cohesive element, C-Glass Composite. Fuselage Structure, FEA.

Abstract. In this paper, a numerical simulation on a new fabrication miniature composite fuselage structure- a woven composite laminated with an adhesively bonded butt joint under the axial compression loading is presented. A FEA via Abaqus/Explicit was utilized to capture the complete compressive responses to predict the crushing behaviour and its mechanical strength from the initial compression loading till its final failure mode. A woven C-glass fiber/epoxy 200 g/m^2 composite laminated [90_8] with the orthotropic elastic material properties is modeled as a continuum composite layup in the proposed numerical model. The adhesively bonded joint progression was modeled using the cohesive element technique. The proposed model was used to observe the crushing load and collapse modes under the axial compression impact. The finite element results showed a good agreement with the experimental results under the actual quasi-static tests. The validation code was extended to further undergo parametric studies in order to visualise the effect of angle orientations and special laminate cases as to attain the optimum design criteria for the proposed composite structure.

Introduction

The disadvantages of the filament winding composite fabrication process can be formulated in terms of expensive equipment, time consuming production process and inflexibility regarding the shape of the structure to be wound [1].Yusri (2009) has successfully developed a new fabrication technique of a miniature composite fuselage [2]. The objective of this new fabrication is to evaluate the possibility of using combining mould technique to replace the technique of filament winding by integrating woven fiber composite laminated with adhesive butt joint to sustain axial compression impact from debonding failure. The successful of the aforementioned new fabrication technique encouraged author on further investigation potential of this new fabrication technique to implement in real aerospace world.

Crushing analysis. There is reasonable amount of crushing simulation work done using Abaqus. Chiara Bisagni studied the dynamic buckling due to impulsive loading of thin-walled carbon fiber reinforced plastics shell structures under axial compression. The approach are numerically solved using a finite element code (ABAQUS/Explicit) and validated by experimental static buckling tests [3]. In recent studies by Azam Tafreshi, modelling of delaminated composite cylindrical shells under axial compression were considered and material was assumed to be linear [4-5]. An experimental investigation into crushing behaviour of filamanent-wound laminated cone-cone intersection composite shell under uniform axial load and nonlinear finite element analysis using ABAQUS/Explicit on axially crushed cotton fibre composite corrugated tubes were presented by E.Mahdi [6-7]. M. Tarfaoui investigated both experimentally and numerically dynamic response and damage modelling of filament wound glass/epoxy tubes [8]. Crush simulation and experimental validation on filament wound C-glass fiber/epoxy 200 g/m^2 miniature fuselage have been carried out by Noorfaizal [9].

There are many publications available on the buckling analysis of filament wound cylindrical shells and tube subject to axial compression. To the author's knowledge, there is no information available relevant to this research which is crushing analysis on adhesive bonded joint in a composite cylindrical shell structure under axial compression.

FEA Methodology

The fuselage structure consist of five-layer composite orthotropic, woven C-glass fiber/epoxy 200 g/m2 $[90]_8$ with total thickness of 3.0mm. This proposed model consisted of two deformable parts for two fuselage sections, two adhesive layers, and two rigid surfaces as tools (RS1 and RS2). Fuselage sections and adhesive are modeled as deformable parts that can deform under load. Fig. 1 shows the arrangement of the components. RS1 is displaced 80mm downward at Z-direction to crash toward the fuselage section bonded with adhesive joint; RS2 is fixed to hold in position during axial. The crushing responses from initial compression loading to final failure under geometrically nonlinear deformations are observed.

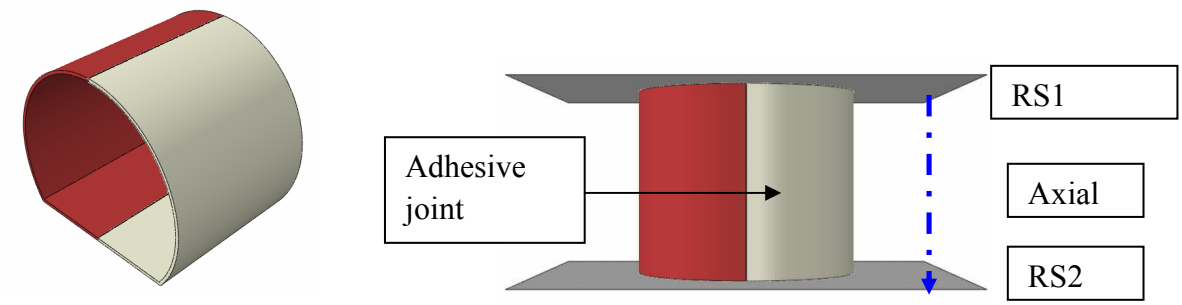


Fig. 1: Component arrangement

Result and Disscussion

Load-displacement Diagram. At the beginning of the loading process, the applied load increases linearly up to the point **2,** where the load maximum is reached, which is 78KN at 2.4mm displacement. After that, the experimental load-displacement curve and the numerical load-displacement curve drop off sharply to point **4.** At point 4, debonding was observed between the fuselage sections during compression of 5.2mm. The collapse modes at each stage are shown in Fig.2.

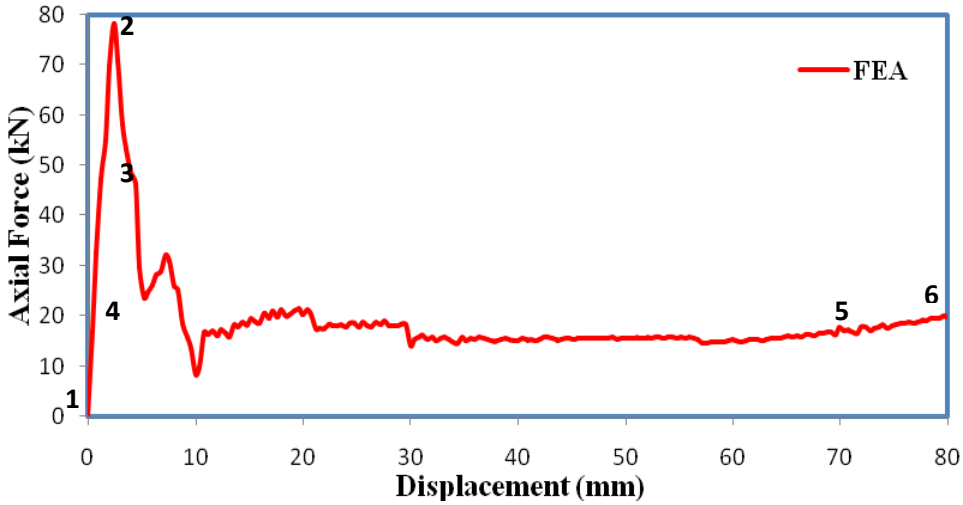


Fig. 2: Load-displacement diagram from FEA model

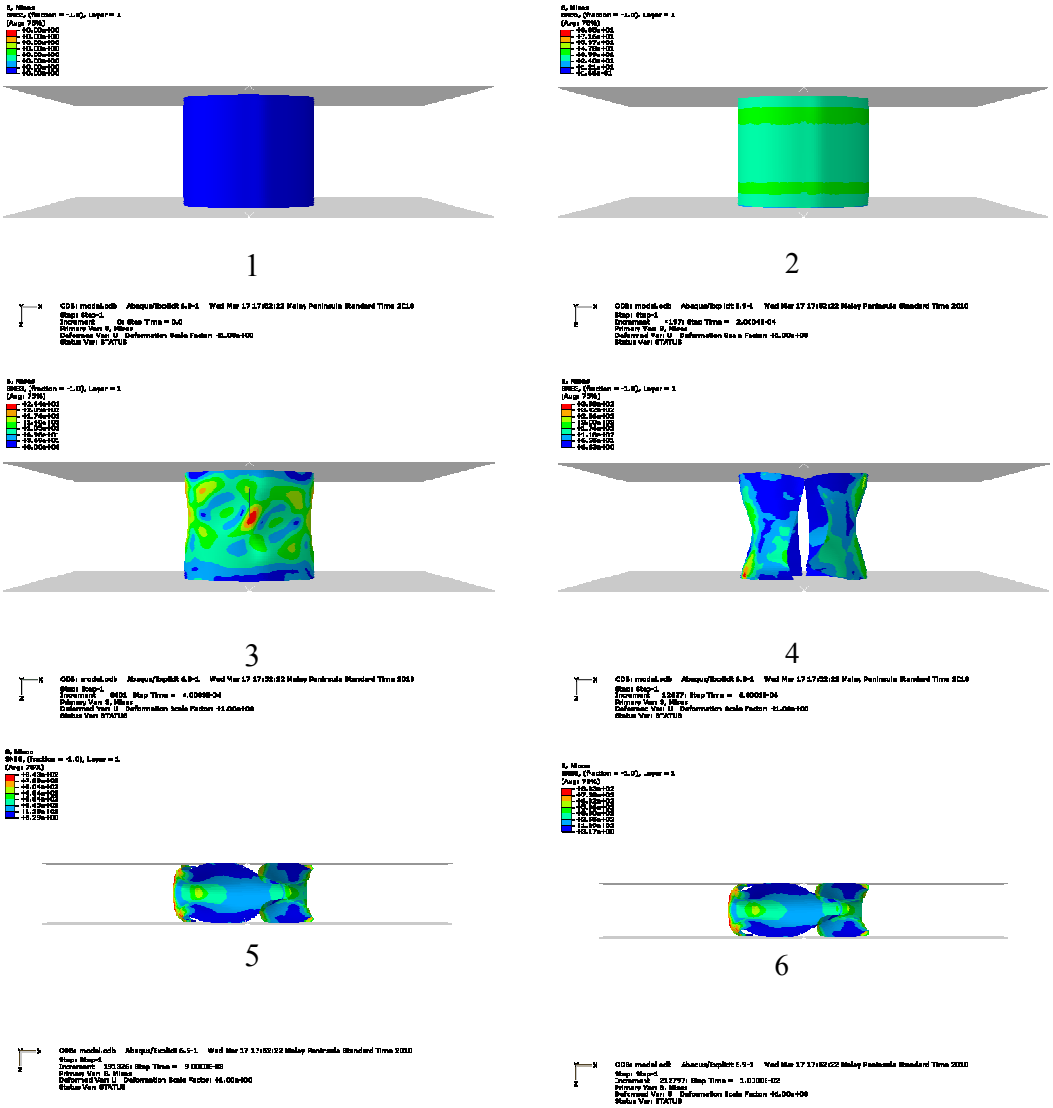


Fig.3: Collapse modes from FEA mode

FEA Validation. The agreement between the experiment and numerical results is good throughout the loading process. The trend during crushing loading for both experiment and numerical is very similar. At the beginning of the loading process, the applied load increases linearly up to the point where the load maximum is reached. After that, the experimental load-displacement curve and the numerical load-displacement curve drop off sharply at approximately the same displacement. For visual comparison of the peak load value attained by the experiment and the numerical analysis, the peak load for the experiment specimen is 77KN and 78KN for numerical results. The error in percentage of the peak load between the experiment and the failure theories used to simulate the progressive damage is found to be 1%. The collapse modes and crushing behavior for both experiment and numerical are found correlated.

[Table 1]: Discrepancy (%) between FEA and Experimental (test case 1) Peak Load

Test	Peak load (KN)	Displacement (mm)
FEA Simulation	78	2.4
Experiment test case	77	3.79
Discrepancy (%)	1	57

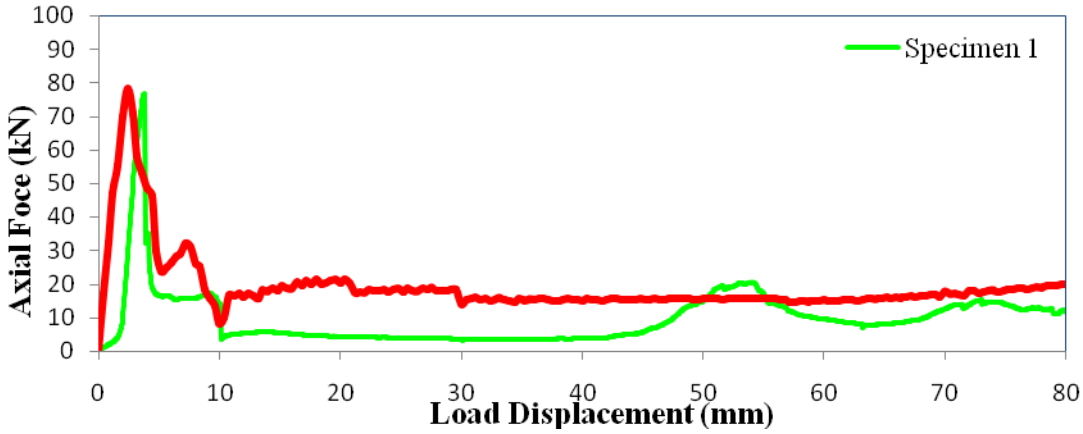
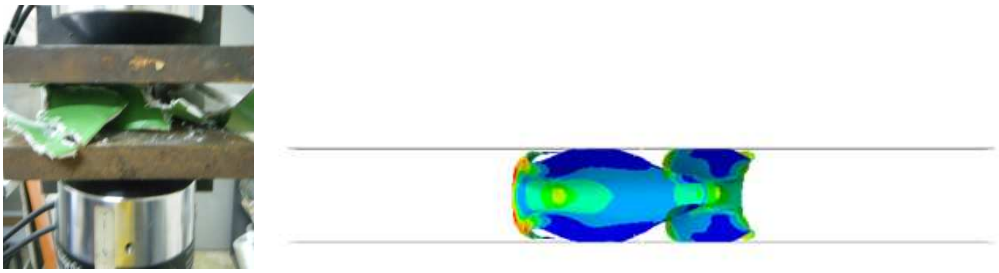


Fig.4: Load-displacement diagram experimental test vs FEA results



Experiment **FEA**

Fig.5: Collapse modes for experimental test vs FEA results

Parametric Study. Various angles of the lamina are considered in the analysis to obtain and visualize the effect of the angle of orientation. Each of the fuselage sections modeled consists of 8 plies of C-Glass/Epoxy 200 g/m^2 in the special cases of laminates [3] shown in Table 2. The cases of laminates are symmetric laminates, cross-ply laminates, angle-ply laminates, antisymmetric laminates, balanced laminates and quasi-isotropic laminates.

[Table 2]: Special cases of laminates

Laminate	Orientation	Abbreviation
Antisymmetric	$[45_4/-45_4]$	Antisym
Angle-Ply Symmetric	$[-45/45/-45/45]_s$	APLSym
Angle-Ply	[-45/45/-45/45/-45/45/-45/45]	APL
Cross-Ply Symmetric	$[0/90/0/90]_s$	CPLSym
Cross-Ply	[0/90/0/90/0/90/0/90]	CPL
Balanced	[45/-45/-45/45/-45/-45/45/45]	BalL
Quasi-Isotropic	$[45/-45/90/0]_s$	QuaIso

Fig.6 shows the results of the load-displacement response for the special cases of laminates when they are applied to the fuselage sections. It shows that there are two patterns of load-displacement curves namely pattern X (i.e. CPLSym with CPL) and pattern Y (i.e. Antisym, APLSym, APL, BalL with QuaIso). Pattern X seems to have more resistance to the applied load than pattern Y. FEA predicted the more or less the same amount of peak load for laminates Antisym, APLSym, APL and BalL namely 90 KN. CPLSym and CPL laminates seems to have approximately the same

amount of peak load, 78-80KN. QuaIso laminate peak load falls in between of the two groups that is 85 KN. Both patterns more or less maintain constant loads after attaining the lowest loads and fail at approximately 2.4 mm displacement. CPLSym and CPL were found giving similar trends to the baseline model of $[90]_8$.

[Table 3]: Comparison of baseline and special cases of laminates

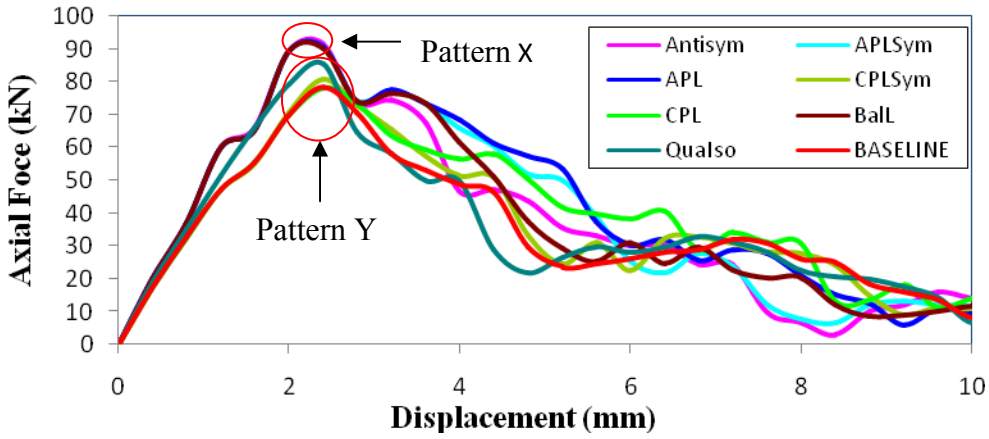


Fig. 6: FEA Load-displacement curve of special laminates (Enlarged)

Summary

Concluding the main findings and results of the previously described numerical simulation and its correlation with experimental results. FEA using ABAQUS/Explicit is able to reproduce satisfactory the load-deflection response that were observed in the series of the experimental works. FEA results pertaining to the main crushing characteristics (peak load and crush energy) are very close to the experimental results. A reliable FEA model to predict the adhesive joint fabrication miniature composite fuselage structure under compression was successfully developed. Adhesive joint was successfully modeled by using cohesive element to predict adhesive behavior and strength.The validated FEA model was extended for parametric study and giving a good insight on how ply orientation in affecting the structure strength.

Test	Peak load (KN)	Displacement (mm)
Baseline	78	2.4
Antisymmetric	91	2.4
Angle-Ply Symmetric	90	2.4
Angle-Ply	90	2.4
Cross-Ply Symmetric	80	2.4
Cross-Ply	78	2.4
Balanced	90	2.4
Quasi-Isotropic	85	2.4

Acknowledgment
The authors would like to thank to Universiti Putra Malaysia for providing the research grant (RUGS 91157) for this research work

References

[1] S. Koussios*, O.K. Bergsma, A. Beukers. Composites: Part A Vol. 35 (2004) p. 181–195.

[2] Y. Dahdi.I.Edi, F.Mustapha. R.Zahari. Proceedings of AEROTECH II. (2009)

[3] Chiara Bisagni. Thin-Walled Structures Vol. 43 (2005) p. 499–514.

[4] Tafreshi.A. Composite Structures Vol.72 (2006) p. 401–418.

[5] Azam Tafreshi. Composite Structures Vol. 64 (2004) p. 511–520.

[6] E.Mahdi, B.B.Sahari, A.M.S. Hamouda, Y.A.Khalid. Composite Structures Vol. 51 (2001) p. 211-219.

[7] E. Mahdi , A.S. Mokhtar, N.A. Asari, F. Elfaki, E.J. Abdullah. Composite Structures Vol. 75 (2006) p. 39–48.

[8] M. Tarfaoui, P.B. Gning, L. Hamitouche. Composites: Part A Vol. 39 (2008) p. 1–12.

[9] N .Haji Yidris, A.M. Mokhtar. Universiti Putra Malaysia. (2007)

© (2011) Trans Tech Publications, Switzerland
doi:10.4028/www.scientific.net/KEM.471-472.1091

Manufacturing High Performance Wood Composite Panel from Paulownia

Ali Rafighi[1, a] and Taghi Tabarsa[2, b]

[1] Faculty of Forestry and Wood Technology,
Gorgan University of Agricultural Sciences and Natural Resources,
Gorgan, Golestan, Iran.
[2] Faculty of Forestry and Wood Technology,
Gorgan University of Agricultural Sciences and Natural Resources,
Gorgan, Golestan, Iran.

Ali.rafighi@gmail.com, T.tabarsa@yahoo.com

Keywords : Manufacturing, wood composite panel, fast growing, paulownia.

Abstract. Regarding conservation policies of natural forests and environmental concerns forced wood composite panel manufacturers to consider using other lingo-cellulosic resources. Plantation fast growing species such as poplar, eucalyptus , paulownia and others is already started in many countries. Fast growing trees usually produce light wood with low strength so manufacturer has low certainty on using them for manufacturing wood composite panel. This study oriented toward examination of application of paulownia wood particle for manufacturing wood composite panel. In this study, specific press pressure at two levels (30 bar and 40 bar) , and press time at two levels (8 and 12 minutes) were used as independent variables. 12 experimental panels were made in laboratory. Mechanical properties such as MOR, MOE and IB were evaluated. Results showed that panels made at press pressure of 40 bar and press time of 12 minutes presented the highest MOR (41.28 MPa) and MOE (4128 MPa) but the highest IB (1.14 MPa) was observed in composite panels made at press pressure of 30 bar and press time of 8 minutes. Based on EN Standard MOR of Particleboard ranged from 12 to 15 MPa and MOE ranged from 2500 to 3000 MPa and IB ranged from 0.4 to 0.6 MPa . Comparing Above mentioned values with EN values it can be seen that Mechanical properties of wood composite panels made from paulownia are much higher than EN standard. These results are very good ground to focus on fast growing species such as paulownia to compensate wood raw material shortcoming in wood industry.

Introduction

Reduction in wood harvesting from Iran natural forest has caused serious impact on wood industry[3]. Capacity of production in most mills has reduced during last 5 years and some of them in uncertain situation and may shot down if wood supply problem is not solved. Utilization of wood from fast growing species plantation is one of the alternatives. Paulownia is a very fast growing species. Its density is ranged from 0.28 to 0.35 gr/cm ^{3}and its chemical components contains : cellulose 47.25%, hemicelluloses 29.71% , lignin 20.23% and extractives 2.71%. its PH is 5.38. This study has been oriented towards investigation on application paulownia for manufacturing particleboard in mixture with native species.

Methods and Materials

In this study, press pressure and press time were considered as variables. Other parameters were kept constant for all experimental boards. Regarding variables, four conditions for manufacturing experimental boards were provided and three replicates were made from each manufacturing conditions. Totally 12 experimental 3 layer-boards were manufactured .Physical and mechanical properties of experimental boards were determined following DIN68763. Data was analyzed using SPSS software.

Results and discussion

Effect of variables on modulus of rupture (MOR) is shown in Figure 1. Particleboard MOR is ranged from 5 to 20 MPa [6]. As seen, MOR of all manufactured experimental particleboard from mixture of paulownia and industrial wood particles is higher than control. Among manufactured experimental boards, those manufactured using press pressure of 40 bar and hot pressed for 12 minutes presented the highest MOR (41.28 MPa). It means that MOR has been improved 100 percent by utilization of paulownia.

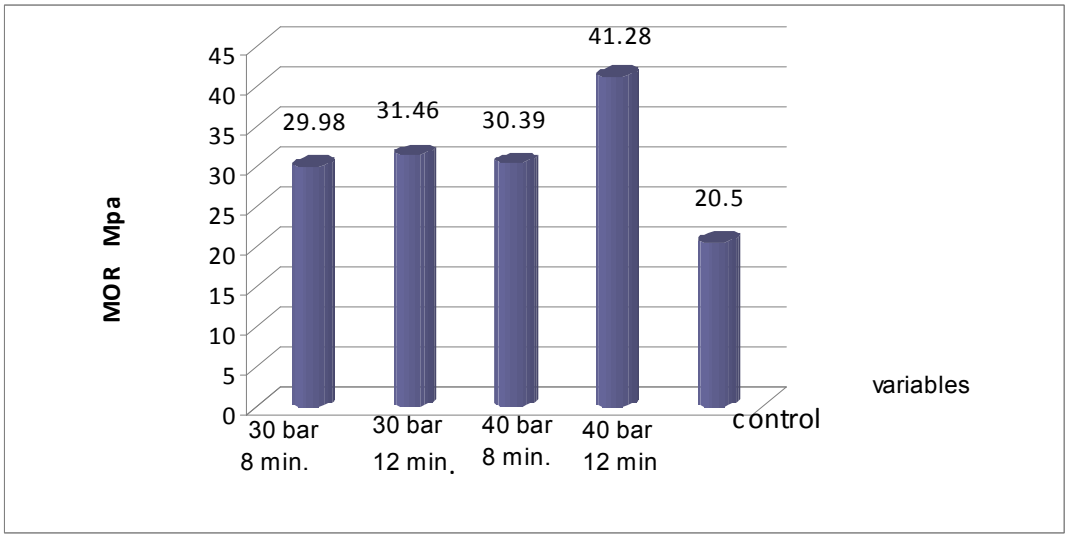


Fig. 1 Effect of variables on MOR

Effect of variables on MOE is presented in Figure 2. As it is seen, MOE of all experimental panels is higher than MOE of control panel. The highest MOE (4128 MPa) is presented by expermimental boards manufactured at press pressure of 40 bar and hot pressed for 12 minutes.

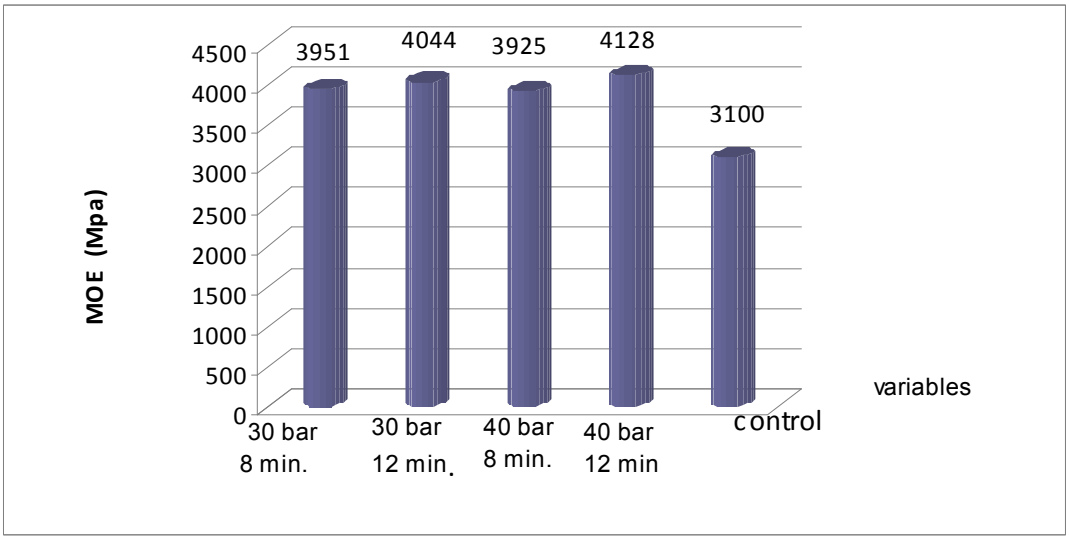


Fig. 2 Effect of variables on MOE

Effect of variables on IB of experimental boards is shown in Figure 3. As seen, the highest IB is presented by boards manufactured at press pressure of 30 bar and hot pressed for 8 minutes. IB of other experimental boards is equal with control.

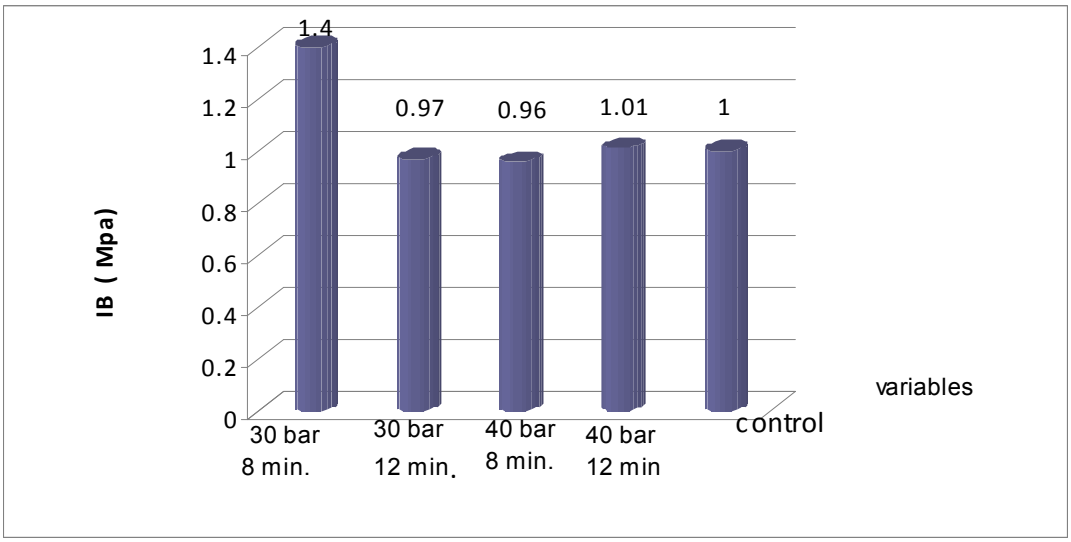


Fig. 3 Effect of variables on IB

Effect of variables on water absorption (WA) is illustrated in figure 4. As seen, WA after two hours water soaking is very low compared with absorption after 24 hours water soaking. On the other hand when press pressure and press time increased water absorption decreased. Generally water absorption of all boards is in the standard range of particle board.

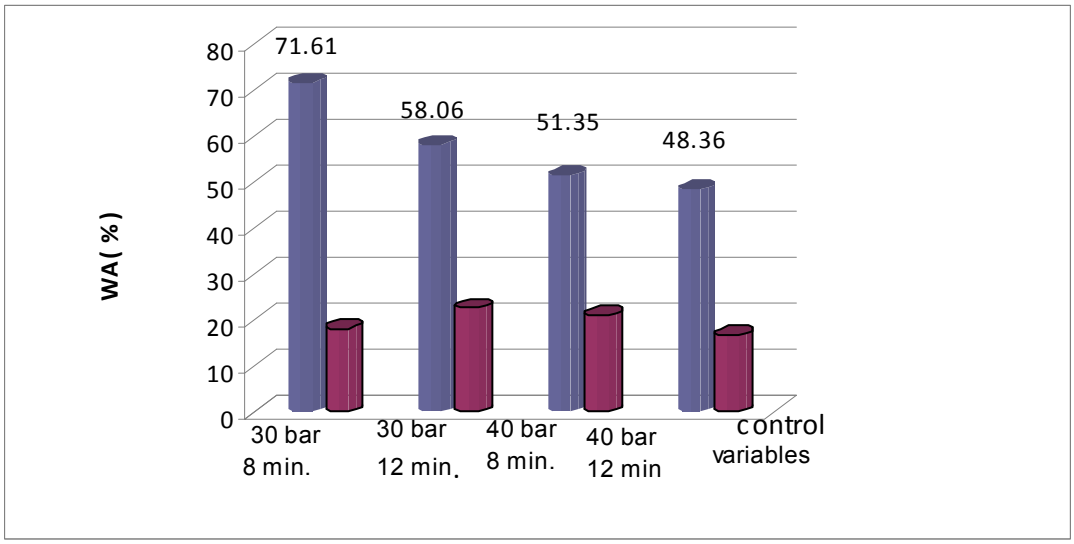


Fig. 4 Effect of variables on WA

The most important properties of paulownia is related to its low density. Low dense material allow high compression ratio [2 , 4 and 5] which improves MOR and MOE. Press pressure help mat to be compressed for this reson higher compression resulted to higher compression ratio and so higher MOR and MOE. Press time allows completion of resin curing [1]for this resean in most cases board properties improved by increasing press time.

Results of this study revealed that paulownia is a promising species in manufacturing particleboard. From practical and economical view it is suggested to utilize paulownia in mixture with other species specially heavy species because it is a very light species.

References

[1] Ashori, A. and A. Nourbakhsh. 2008. Effect of press time and resin content on physical and mechanical properties of particleboard panels made from the underutilized low quality raw materials. Journal of industerial crop products, 28: 225-230

[2] Dooshosseini, K. 2000, Technology and applications of wood composite panels, Tehran university publication. Pp648.

[3] Tabarsa, T. and L. Salimi ghahfarkhi. 2001. Investigation on utilization of avirmadis pround branches in manufacturing particleboard. Proceedings of conference of renewable raw materals utilizations. Azad university/ kharesgan/ Iran.

[4] Tabarsa, T. and M. Fasrsi. 2006. Effect of improving of paulownia in manufacturing particleboard from eucalyptus. Part 1. Extractives and modulus of rupture. Iran journal of natural resources 59(1):225-237.

[5] Tabarsa, T; K. doosthosseini and M. Fasrsi 2010. Effect of improving of paulownia in manufacturing particleboard from eucalyptus. Part 2. Modulus of elasticity and thickness swelling. Iran journal of natural resources 63(1):23-37.

[6] Wood Hand book 1999. Forest product society. Report-EPL-GRT-113

© (2011) Trans Tech Publications, Switzerland
doi:10.4028/www.scientific.net/KEM.471-472.1095

Kenaf Nanofiber/Polylactic Acid (PLA) Nanocomposite

Agnes Surai Lasat[1], Khalina Abdan[1,3,a] and Nor Azowa Ibrahim[1,2,b]

[1] Laboratory of BioComposite Technology,

Institute of Tropical Forestry and Forest Products,

Universiti Putra Malaysia, 43400 UPM Serdang, Selangor, Malaysia

[2] Department of Chemistry,

Universiti Putra Malaysia, 43400 UPM Serdang, Selangor, Malaysia

[3] Department of Biological and Agricultural Engineering,

Universiti Putra Malaysia, 43400 UPM Serdang, Selangor, Malaysia

[a]khalina@eng.upm.edu.my, [b]azowaib@science.upm.edu.my

Keywords: Kenaf, PLA, Nanocomposite

Abstract. Kenaf fiber was treated with alkaline to reduce lignin content and tested under Fourier transform infrared spectroscopy (FTIR). FTIR result showed that peak at 1146 cm^{-1} which is acetyl group of lignin was reduced in treated fiber while disappearing of carbonyl group in treated kenaf fiber at 1750cm^{-1} was significantly shown compared to untreated kenaf fiber. Treated fiber undergoes mechanical size decrement process by high pressure homogenizer with 500bar pressure and 60 passes. Transmission Electron microscopy (TEM) was used to determine size and distribution of fiber. Moreover, morphology of nanofiber was observed under scanning electron microscope (SEM). Nanofiber (3%, 5%, 8% and 10%) was mixed with PLA using internal mixer and then compressed with hot pressed to produce specimen for tensile test. Tensile strength and tensile modulus of nanocomposite with 10% of nanofiber increased by 30% and 85% respectively compared to pure PLA.

Introduction

Over the last five years, global consumption of biodegradable polymers has shown strong growth. Demand has been fuelled by growing public demand for sustainable packaging materials, growth in compositing infrastructures, the introduction of wider variety of biodegradable polymers, product improvements and a narrowing of the price differential between biopolymers and petrochemical based plastics. According to David K. Platt in his book, PLA is the most certified biodegradable plastic in Japan with most applications found in the packaging sector. During the period of 2005-2010, Asia pacific biodegradable plastics consumption is forecast to grow at compound annual growth rate of 16.7% to reach 38,500 tones in 2010. Hence, many studies on the mechanical properties of natural fiber reinforced with PLA have been developed by other researched with different types of fiber, such as: kenaf [9] [10] and Cellulose Nanofiber (CNF) [1] [7]. These fibers have many advantages including low cost, low density, no abrasion of processing equipment, similar moduli, good thermal properties and biodegradability. However, kenaf fibers which were used in these studies are incompatible with polymers due to their hydrophilic nature while polymer is hydrophobic [8]. In order to enhance the properties of PLA and kenaf fiber, kenaf fiber have been treated with sodium hydroxide and 3-aminopropyltriethoxylane (APS), coupling agent [4]. After undergo modification, kenaf fiber and polymer is more compatible and enhance their mechanical properties. Echhorn revealed that modification by alkalization improved in surface tension, wetting ability, swelling, adhesion and compatibility with polymeric materials [12].

Nano-sized reinforcement from renewable resources has caught loads attention recently. The advantages of nanofibers as compared micro-sized fibers are an enhancement of the mechanical properties with decrease in fiber size due to large surface area [13]. Ozgur et al also revealed that nanofibril reinforced polyurethane increased mechanical properties compared to micro size composite [5]. The main objectives of this study are to prepare kenaf nanofiber and to investigate the effect of kenaf nanofiber loading on mechanical properties of nanofiber/PLA composites.

Experimental Procedures

Materials. Kenaf stem (V36) is obtained from Lembaga Tembakau Malaysia (LTN), Kelantan. Biodegradable polymer which derived from corn is purchased from BASF Plastic technologies USA. The acetic acid, ethanol, Sodium Hydroxide (NAOH), 3-Aminopropyltriethoxysilane (ASP) and triacetin is purchased from MERCK (Germany).

Fiber Surface Modification. Kenaf fibers were soaked in 5% w/v of sodium hydroxide solution (alkaline treatment) for 2 hours at room temperature [4]. The fibers were washed with abundant of distilled water containing a small amount of acetic acid. Washing process was continued until the water no longer indicated any alkalinity. Next, the fibers were kept in air for 2 days. After alkaline treatment, the fibers were treated with silane (surface-treatment) where 5 wt% of ASP was mixed in 40:60 of water-ethanol solution [4]. This solution was stirred for 1 hour (pH adjusted to 4 with acetic acid) before immersed kenaf fiber for 3 hours. Fibers then washed with abundant of water and dried in open air for 3 days before oven dried for 24 hours at 60^0C.

Preparation of Nanofiber. Dried fibers were grinded with 250 μm pulverisette and crushed with cyro-crusher before proceed to homogenization process. In cyro-crusher, fiber was immersed in liquid nitrogen and crushed using a mortar and pestle. Crushed fiber was dispersed in water with a concentration of 0.2 wt% fibers for 2 days (stirred continuously) before homogenization process. The suspensions fibers were passed through the homogenizer for 60 passes and the pressure was held constant at 500 bar [6] [15].

Preparation of Kenaf /PLA Nanocomposite. Nanocomposite was prepared using melt blending technique and compression moulding. PLA pellet was dried at 80^oC for 24 hours before processing in vacuum oven in order to remove moisture and prevent void formation [4]. 5 wt% of triacetin solution was mixed with PLA to improve tensile properties of the nanocomposite [9]. Next, 3%, 5%, 8% and 10% of fiber loading in composite was melt blending under 160^0C, 30 rpm for 30 min. After blending, nanocomposite was preheated under 160^0C for 10 min without applying pressure before pressed under 1700 psi for 10 min then cooled till 90^0C.

Fiber Characterization. The functional groups of the treated and untreated fiber were determined by Fourier Transform Infrared Spectroscopy (FTIR) Perkin-Elmer spectrum 2000 instrument with the diamond total reflectance (ATR) techniques. The samples were analyzed for the wave number range of 250-4000 cm^{-1}. The morphology of kenaf fiber after and before homogenization process was compared with scanning electron microscope (SEM) under a Philips XL40 with acceleration voltage of 20 Kv at room temperature. Transmission electron microscopy (TEM) was used to observe size and distribution of nanofiber. One drop of a dilute kenaf nanofiber suspension was deposited on carbon-coated grids and allowed to dry before observed under TEM.

Mechanical Testing. Tensile test of nanocomposite is performed by Instron Universal Testing Machine (model 3365) according to ASTM D638 standard (type V) using bluehill2 software at crosshead speed of 1mm/min. Seven specimens were prepared and analyzed. Tensile strength and tensile modulus was calculated by following equations:

$$Tensile\ strength\ (MPa) = \frac{Maximum\ Load\ (N)}{Area\ of\ sample\ mm^2}$$

$$Tensile\ modulus\ (MPa) = \frac{Load(N)\ x\ L_0(mm)}{Area\ (mm^2) x\ \Delta L\ (mm)}$$

Results and Discussion

Fourier Transform Infrared Spectroscopy (FTIR). Untreated and treated (alkaline and silane treatment) kenaf fibers were studied under FTIR to determine changes in functional groups before and after fiber surface modification. Figure 1 shows that C-O stretch (1146 cm^{-1}) of acetyl group of lignin in treated fiber was reduced compared to virgin fiber. The peak at about 1750 cm^{-1} in virgin kenaf fiber was assigned to the C=O stretching of the acetyl group in hemicelluloses [16]. Figure 1 shows that this peak disappeared completely in spectra of fiber surface modification indicating removal of hemicellulose. Disappearance of hemicelluloses increased the polymerization of native cellulose in kenaf fiber hence results in higher stress development in fiber [2].

Morphology of Nanofiber Under SEM. Figure 2(b) shows the fiber decreased into very small size of fibril after homogenization process. It is clearly shown that homogenization process results in fibrillation of fibers resulting in small fibrils which reduce to nano size. Seydibeyogly et al. showed that, after 60 passes of homogenization process the number of fibrils increased [6].

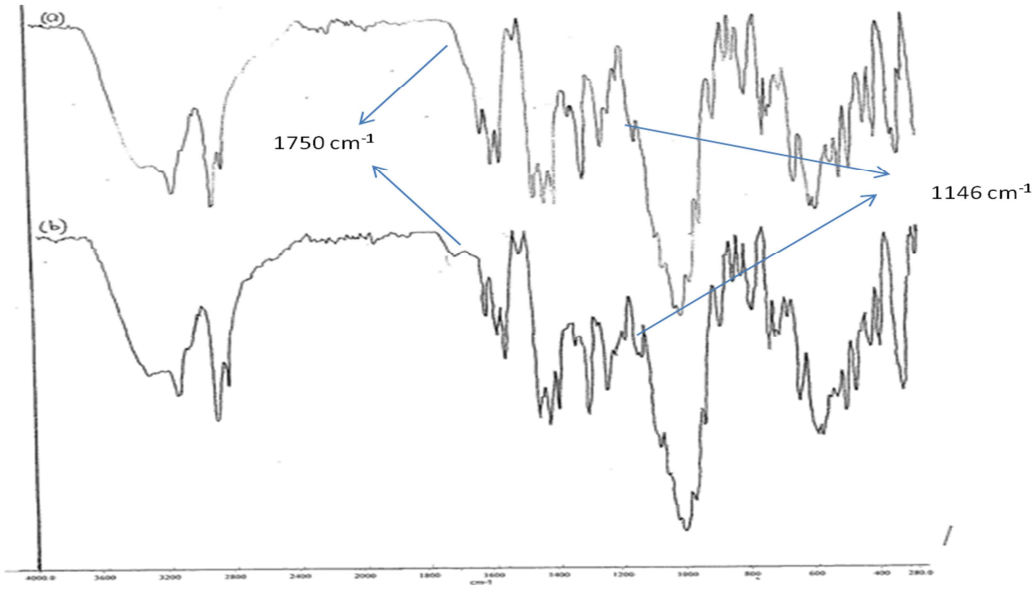


Fig. 1. (a) FTIR spectra treated kenaf fiber (b) FTIR spectra untreated kenaf fiber

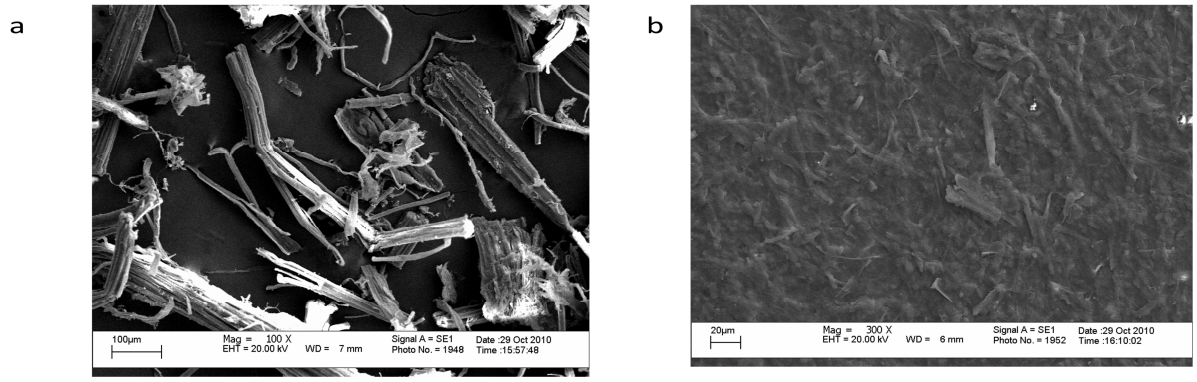


Fig. 2. Scanning electron micrograph of fiber (a) before homogenization process (b) after homogenization process

Size Distribution of Nanofiber. The nanofiber was obtained after the efficient mechanism of reduction in size of their diameters. The diameter of nanofiber are between 10 nm-100 nm as shown in Figure 3. Figure 4 showed that different measurement of nanofiber in each of micrograph of TEM. After taken about 68 of nanofiber measurement, there are 38% of the nanofibers were in 30 nm -50 nm diameter while 30% of others were in between 10 nm-30 nm. Hence, 60% of the fibers are in 10 nm-50 nm size of diameters.

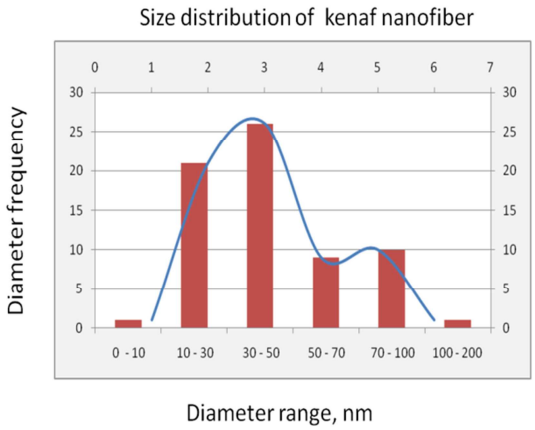


Fig. 3. Size distribution of kenaf nanofiber showing that diameter range between 10nm-100nm

Mechanical Performance of Kenaf /PLA Nanocomposite. The tensile strength of pure PLA and 3%, 5%, 8% and 10% of nanofiber loading in composites were shown in Figure 5. 3% of nanofiber loading showed that the tensile strength is slightly reduced compare to the pure PLA. Ibrahim et al [9] determined that poor dispersion and distribution of fiber will not improve the adhesion between fiber and PLA matrix. This comprehend that small amount of 3% nanofiber gave poor dispersion and distribution of fiber leads to poor adhesion between the fiber and PLA matrix. Started from 5% to 10% of nanofiber loading the tensile strength was increased gradually as the amount of nanofiber increased. The tensile strength of 10% nanofiber loading was increased by 28% compared with neat PLA which increased form 33 MPa to 42 MPa. Figure 6 shows that no significant increase in modulus tensile for neat PLA and 3% nanofiber but gradually increased from 5% to 10% of nanofiber loading. Modulus tensile was increased by 83% with 10% of nanofiber loading which increased from 482 MPa to 884 MPa.

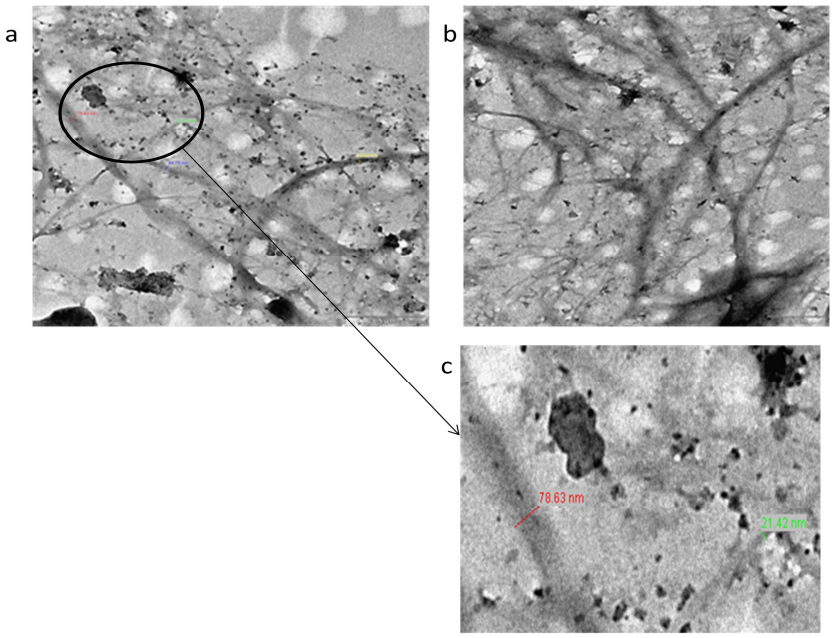


Fig. 4. TEM micrographs of different measurement of nanofiber after homogenization process.

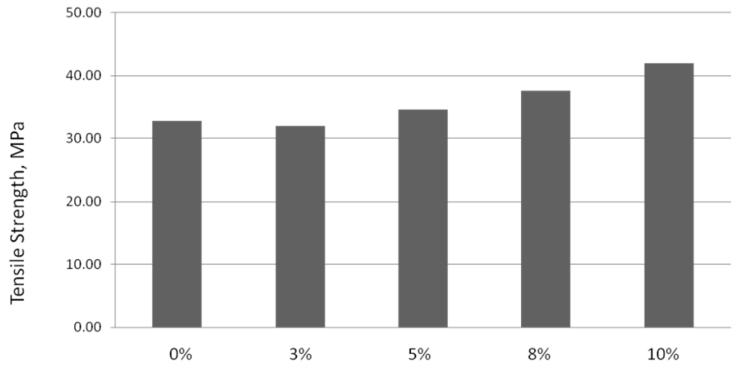


Fig. 5. Tensile strength of neat PLA (0%) and nanocomposite in 3%, 5%, 8% and 10% of nanofiber loading

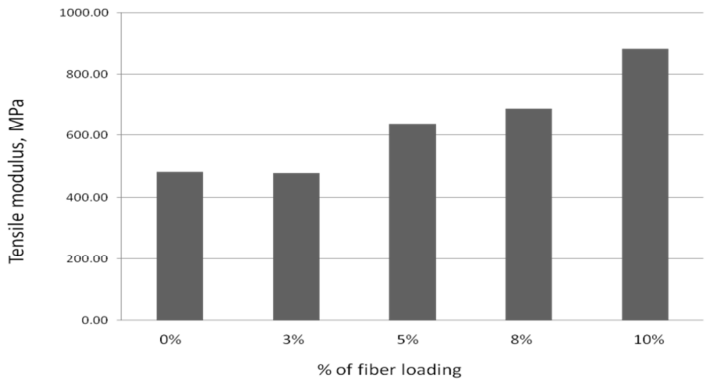


Fig. 6. Modulus tensile of neat PLA (0%) and nanocomposite in 3%, 5%, 8% and 10 % of nanofiber loading

Summary

FTIR results showed that the fiber surface modification using alkaline and silane treatments could successfully be used to remove lignin and hemicelluloses. It is worth to noticed that high shear mechanical defibrillation by homogenization process is important to achieve nanofiber sizes. Microscopy (TEM) studies revealed that the nanofiber diameters were between 10 nm and 50 nm. The most remarkable result of tensile strength is shown in nanocomposite with 10% nanofiber content. The tensile modulus is increased nearly 90% and tensile strength nearly 30% better than neat PLA. Nanofibers have great potential in high-end applications and can be utilizes in medical devices like biocompatible drug delivery system.

Acknowledgements

Million thanks to all the staffs in Introp and Biosains (Microscopy Units) especially to En Rafiuz for his assistance with the electron microscopy studies. Abundant helps from family and my friends especially, Then Yoon Yee, Kamarul Arifin Hadithon, Mehdi Jonoobi, Maizatulnisa Othman, Lukman Hakim Zaini, Jonathan Paran and Isabel Freddy.

References

[1] A. Bhatnagar and M. Sain: J. Reinforced Plastics and Composites Vol. 24(2005).

[2] A.K Bledzki: Progress in Polymer Science, Vol. 24 (1998) p. 221-274.

[3] Dennis Smith et al. Poly(lactic acid) Derived Fibers with Enhanced Performance, National textiles Center Annual Report : November 2005.

[4] Masuda S. Huda: Composites Sci. Technol. Vol. 68 (2008), p. 424-432.

[5] Ozgur Seydibeyoglu et al : Composites Sci. Technol. Vol. 68 (2008), p. 908-914.

[6] Maya Jacob John et al: Vol. 40 (2009), p. 442-448.

[7] Medhi Jonoobi: Composites Sci. Technol. Vol. 70 (2010), p. 1742-1747.

[8] Nor Azowa Ibrahim et al: J. of Reinforced Plastics and Composites Vol. 29 (2009), No. 14/2010.

[9] Nor Azowa Ibrahim et al: J. Reinforced Plastics and Composites Vol. 0 (2009), No. 00/2009.

[10] Shinji Ochi: Mech. Mater. Vol. 40 (2007), p. 446-452.

[11] Qing Shen et al: A Comparison of the Surface Properties of Lignin and Sulfonated Lignin by FTIR Spectroscopy and Wicking Technique, Colloids and Surfaces A : Physicochem. Eng. Aspects Vol.320 (2008) p. 57-60.

[12] S.J. Erichhorn et al: J. Mater. Sci. Vol. 36 (2001), p. 2107-2131.

[13] Oksman et al: ASC Symposium Series 938, Oxford Press (2006) p. 2-8.

[14] David K. Platt: Biodegradable Polymers Market Report, Smithers Rapra Limited (2006), p. 42-48.

[15] A.N. Nakagaito et al: Applied Physics Vol. A 78 (2004), p. 547-552.

[16] Sgriccia et al.: Characterization of Natural Fiber Surfaces and Natural Fiber Composites, Compos. Part A 39(10) (2008), p. 1632-1637.

© (2011) Trans Tech Publications, Switzerland
doi:10.4028/www.scientific.net/KEM.471-472.1101

Simulation of Thermoset Injection for Bulk Moulding Compounds (BMC)

M.K.A. Ariffin[a], S. Sulaiman[b], B.T.H.T Baharuddin, Tang Sai Hong and S.Sreenivasan[c]

Department of Mechanical and Manufacturing Engineering

Universiti Putra Malaysia, 43400 UPM, Serdang, Selangor, Malaysia

[a]khairol@eng.upm.edu [b]suddin@eng.upm.edu.my and [c]s_sarma82@yahoo.com

Keywords: Bulk Moulding Compounds, Thermoset, Injection Moulding and Autodesk Moldflow Plastics Insight®.

Abstract. This paper discusses about the simulation of the process of injection moulding for thermoset materials namely Bulk Moulding Compounds (BMC). BMC is a polyester resin based compound with glass fibre additives. In this paper a complex part was used to simulate and obtain the parameters for moulding BMC. Autodesk Moldflow Plastics Insight® was used to run the simulation. Two main parameters i.e. Injection time and mould temperature were considered. Six different sets of parameters were used and the settings were optimized. The obtained optimized settings are 15.08 seconds and 145°C. The obtained parameters were then applied and the actual part was tested using an injection-moulding machine. After the simulation, changes were also made to the actual mould to improve the moulding conditions. Extra air vents were added at the problematic areas to ease the flow. There was an average variance of 7% which was thought to be acceptable as the simulation considers the ideal condition, where as there may be external factors such as the machine wear and tear during the actual moulding of the part. It can be said that the simulation was run successfully and tested during actual moulding.

Introduction

Fibre reinforced polymer composites consist of a reinforcing fibre embedded in a polymeric matrix material. The resulting composite material has a high strength/weight ratio when compared to traditional metallic materials. The matrix protects the brittle reinforcing fibre and transfers the load to the fibre. Carbon fibres possessing high modulus and strength are often used. Examples of fibres that are used are like glass fibres and natural fibres. These fibre reinforcements help increase certain properties like tensile strength, heat resistance, arc resistance etc. In the electrical industry, the increase in arc resistance is highly desirable especially in the manufacture and application of circuit breakers. So highly specialized material such as bulk moulding compound or BMC is used. BMC may contain up to 50% fibre.

Finite Element Analysis. A three-dimensional model finite element program for calculating the flow behaviour of epoxy casting has also been previously developed [1]. This paper discusses the control volume based finite element method. The authors are mainly concerned about the flow of material during epoxy casting and not during reaction injection moulding. The authors are also only considering a single material, but have concluded that the same process is applicable to other thermosets. This may be highly inaccurate as there are differences between injection and casting. Further studies were done by Lo et al [2]. In their research a general three-dimensional model of the RIM process was developed. The model was used to predict not only the temperature and conversion changes with time but also the front position and shape during filling. The model was capable of describing the transient, spatially distributed

behaviour within a thick RIM mould. Using measured physical and chemical properties of the RIM system; mould-ability can be determined in advance. The paper concentrates on the model structure and its solution. From their studies Wilkinson and White [5] have looked in the residual stress generated during the thermoset injection moulding.

Furthermore, the complexity of the mould, which changes the flow, has been reviewed by Benitez-Rangel and others [6] show that the FEA models consider the shape and size of the mould. So it may not be entirely accurate to just simulate the filling of a cylindrical mould. A screw type Injection moulding machine is probably the most extensively used machine for processing short-fibre reinforced thermosets. The fibre/resin mixture, whether it is preblended or fed as a physical mixture, is fed into the hopper and transferred into the heated barrel. The material softens by the heat transfer from the barrel wall. At the same time, the screw rotates to apply high-shear process to further heat the material and fill the barrel. The softened material is collected in front of the screw by the rotation of the screw, and then injected with a high pressure into the mould cavity through the runner and the gate [3]. The mould is heated to the curing temperature of the resin in case of thermoset composites. The level of automation of this method is the highest among many processing methods. Due to the intensive mixing with high-shear and passage through a narrow gate, extensive fibre damage occurs; therefore, injection moulding for composite materials is suitable only with short fibre reinforced or particulate-filled polymers. The ram plunger is forced into the barrel by air pressure. Insufficient air pressure can result in a short shot condition in which the mould cavity is incompletely filled resulting in a rejected part [4].

Simulation

Three Dimensional Part Data Preparation. The three-dimensional part data is considered raw data even if the data has been used for other purposes such as generating the numerical codes for the Milling machine to create the mould or even to teach or set up the numerical codes for the Coordinate measurement machines. The raw data would have to be cleaned and any missing elements restored. Any out of place elements will also have to replaced or deleted. This is done using Solidworks ®. Also all extremely small dimensions such as the dimensions below 0.002 mm need to be removed and the surrounding structures needs to be joined. This is due to the fact that the researcher has chosen 0.002mm as the mesh size. Some features of the Three-dimensional geometry may not be that important for the FEA but increase the complexity of meshing drastically. The increased complexity of the mesh may provide inaccurate results.

Mesh Preparation. For this project Meshing was done using Altair Hyperworks® software. Initially the model was converted from the native format to parasolid or x_t format. Then the data was loaded into the Altair Hyperworks® Software. As explained earlier, during meshing a suitable element size should be chosen. This is to enable a smooth simulation as well as the most accurate results. For Autodesk Moldflow®, the analysis type and part type will determine the mesh type. For the simulation a three dimensional tetrahedral mesh is used. This is due to the multiple thickness of the part.

Material Selection. The actual material used is BMC RNC 870 GY69-2A made by Eternal Showa Highpolymer Co. Ltd from Thailand. This material has 25% fibre content. However as most material data is classified and the manufacturer was unwilling to reveal or share it, a representative material was chosen. The material that was chosen was Menzolit™ BMC 01 (also known as Menzolit™ BMC 2800). This is one of the materials readily available in Autodesk Moldflow®. The comparison between the two materials is show in the table below. The actual Material specifications are also given after the table. From the table it can be observed that, apart from the Fibre content, other values do not differ much. Thus the Menzolit™ BMC 2800 was chosen to represent the actual material during simulation. A comparison is shown in Table 1.

Table 1. A Comparison between the Actual Material and the Simulated Material

Property	Unit	BMC RNC GY69-2A	MENZOLIT BMC 01
Base	---	Unsaturated Polyester	Unsaturated Polyester
Fibre Content	%	25	30
Specific Gravity	----	1.86 ± 0.05	1.80
Shrinkage	%	0.02 ± 0.03	0.00
Water absorption	%	< 0.2	< 0.5
Heat Distortion	°C	> 200	> 200
Flexural Strength	MPa	> 130	> 80
Flexural Modulus	GPa	> 10	> 10
Impact Strength	KJ/m^2	> 30	25
Insulation resistance	Ω	$1 X 10^{12}$	$1 X 10^{12}$
Comparative Tracking Index	CTI	> 600	600

Actual Part Moulding. During moulding it is important to closely match the parameters obtained from the simulation. Any deviation from the parameters may render the results invalid. This is due to the reason that the physical moulded parts are being used as a benchmark for the simulation. The machine used is a Meiki model M-150CL-BMC 150 tonnage machine. The injection unit is a plunger type injection unit driven by two injection cylinders and hydraulic motor with a vertical press to compress the perform material and remove air bubbles before injection. The machine's capacity is 490 cm3 material volume and 880 grams material mass.

Simulation Results

Results obtained from the simulation were used in real world application. This will validate the simulation findings as well solve the problems that are being faced during actual moulding of the part. Before actually being able to get the optimum results, the simulation needs to be run using various parameters that have been set by the researcher. Once these parameters are applied to the simulation software a relationship between the parameters and the results would be seen. From the relationship, further fine-tuning will be done to the parameters. Certain parameters, which are found to be out of relation, are eliminated from the simulation considerations. Only the relevant parameters will be used in further calculations. The parameters of the simulation is shown in table 2.

Table 2 List of Settings Used

Set Parameters	Injection Time (Seconds)	Mould Temperature (°C)
1	5	145
2	5	160
3	10	145
4	10	160
5	15	145
6	15	160

Graphical Results

Average Velocity. The Average velocity result shows the average magnitude of velocity of the polymer inside the mould cavity over time. The Average velocity result can be used to determine areas with a high flow rate. High velocity values for a particular model section could indicate a high flow rate, meaning there could be filling problems such as over-packing or flash. This could also mean that polymer flow is unbalanced, where polymer flows fast through one section and flows slowly through another section of the part.

Another use is to determine sections or areas of the mould where the melt flow slows down. This may be due to gas trapped. In the result above it is noticeable that the flow has sped up at a certain area. This is depicted in Fig. 1. Other reasons may be that the gate is too far away. However, this result does correspond to the actual moulding result, which often shows short moulding at the particular area. So other results will be compared before any judgement is made. The average velocities for the other area are obtained as 0.527 cm/s. For this area, the average velocity is obtained as 21.145 cm/s.

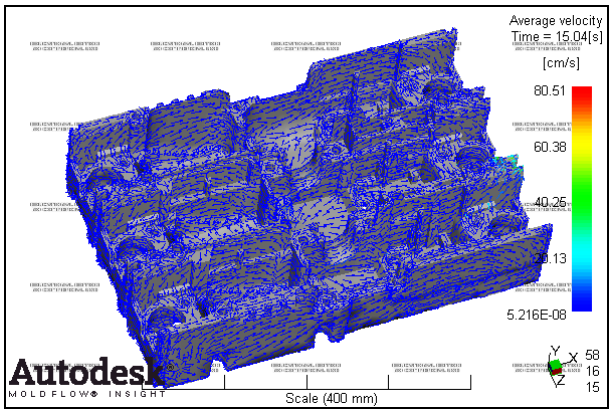


Fig. 1: Average Velocity

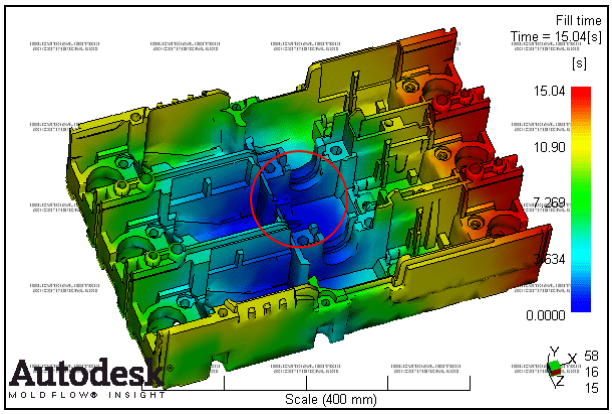


Fig. 2: Filling Time

Filling Time. The filling time depicted in Fig. 2 clearly shows that one area of the part is filled faster than the other. This may be due to the fact that the runner balancing was not done during the part design. As the runner has been built into the mould and could not be changed, other solutions should be found. If the part is allowed to run at current conditions, problems may appear. On the left of the part (where the fill time is faster), over-packing might occur. On the right of the part, under-packing may occur. There may even be short moulding at this area. As shown from the calculations, the injection time here is depicted as 15.04 seconds.

Pressure at the End of Fill. The pressure at the end of the filling time depicts the pressure gradient at the end of the filling cycle. At the beginning the pressure is set at the level of 1 atmospheric pressure (atm) or 101.325 KPa. From there, the pressure will slowly rise when the melt is filling the cavity. In the result here the maximum pressure is shown at 230.8 KPa or about 2 atm. However there is a low-pressure spot. This is shown in Fig. 3. This may be due to the fact that the high velocity results in low pressure. So there are problems in terms of pressure at this area. The part may be under-packed or there may be short moulding at this area.

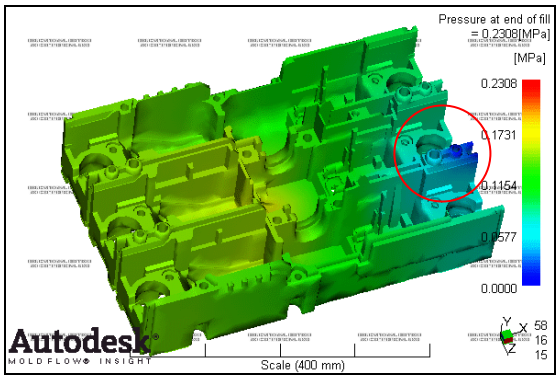


Fig. 3: Pressures at the End of Fill

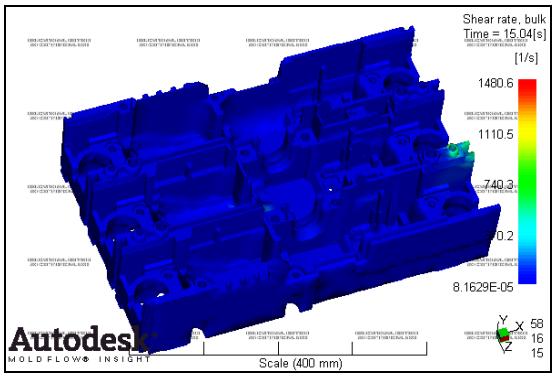


Fig. 4: Bulk Shear Rate

Comparison of Results from Simulation and Actual Moulding

The simulation results such as fill time, maximum injection pressure and clamping force, are compared with the readings obtained from the machine during moulding of the part. This is shown in Figure 4.16. From the table it can be observed that there are slight differences from the simulation and the actual machine output. In the comparison the error percentage is also calculated. The simulation results are considered the true and controlled environment due to the ideal conditions. From the comparison it can be seen that the difference in clamping force and Average Velocity is quite high 21.80% and 16.28% respectively. This may be due to a few reasons. The first one would be the slight differences between the materials.

The actual injected material only has 25 percent fibre, where as the simulated material has 30 percent fibre. Studies by Arnaud Millischer and Didier Delaunay materials with higher fibre content tend to be more viscous. Higher viscosity means resistance to flow is higher, so the injection pressure and the shear stress are lower due to the lower fibre content of the actual moulded part. The part weight is higher for the moulded part as it includes the runners. For the simulation, the runners are excluded. Another reason may be the condition of the mould, the mould may have been subjected to wear and tear. The simulations consider the mould to be in an ideal condition. Furthermore the machine itself was manufactured in 1995. There will be a substantial amount of deterioration to the machine itself. However minor the attrition is, it will definitely play a part in the difference of results. The additions of the air vents are also not considered in the simulation.

Table 3: Comparison between Machine Output and Simulation Results

Results	Fill Time (s)	Maximum Injection Pressure (KPa)	Clamping Force (t)	Average Velocity (cm/s)	Weight (g)
Simulation	15.040	23.08	0.4105	0.43	394.59
Actual	15.575	21.21	0.500	0.50	401.00
Error (%)	3.56	8.10	21.8	16.28	1.62

Summary

The simulation was done successfully. This means that the objective of studying and simulating the reaction injection moulding of BMC was successful or achieved. The lower temperature generally generates a better result; however the temperature and any setting used should be within the recommended processing guide for the material. If this is not adhered to the results may be adverse and the whole study may not be successful. It can also be said that filling time has a linear relationship with number of hot spots generated. All these deductions where proven to be true using Pearson's product-moment correlation coefficient, which was calculated for each of the above said result.

As the study has been proven to be successful, many if not all of the problems that the research set out to solve has been solved. However this doesn't mean that future studies may not be undertaken to further validate and or improve on the findings. A weakness that can be noticed in this study is that it doesn't take into considerations the percentage of fibre content in the moulding material i.e. BMC. The study assumes that the percentage of fibre content does not affect the results. This may or may not be correct.

References

[1] Mitani, T. and Hamada, H. (2005). A flow simulation for the epoxy casting process using a 3D finite-element. Polymer Engineering & Science. Volume 45. Issue 3. 364–374. .

[2] Lo, Y.W., Reible, D.D., Collier, J.R. and Chen, C.H. (1994). Three-dimensional modeling of reaction injection molding. I. Polymer Engineering and Science. Volume 34. Issue 18. 1393-1400

[3] Kamal, M.R., Liu, S.J., Isayev, A., Bogaerds, C.B. and Agassant, J.F. (2009). Injection Molding: Technology and Fundamentals. Munich. Hanser Gardner Publications.

[4] Johannaber, F. (2008). Injection molding machines; a user's guide, 4th edition. Munich. Hanser Gardner Publications.

[5] Wilkinson, S.B. and White, J.R. (1998). Residual stresses in short-glass-fibre-reinforced thermoset injection mouldings. Journal of Materials Science Volume 33. 3101-3108.

[6] Benitez-Rangel, J., Domínguez-González, A., Herrera-Ruiz, G. and Delgado-Rosas, M. (2007). Filling Process in Injection Mold: A Review. Polymer-Plastics Technology and Engineering, volume 46. issue 7. 721-727.

© (2011) Trans Tech Publications, Switzerland
doi:10.4028/www.scientific.net/KEM.471-472.1107

Flutter Analysis of a Hybrid Plate-Like Fiber-Reinforced Composite Wing

D.L.A.A. Majid[1,a], S. Basri[1,b], R. Varatharajoo[1,c] and A.H.Attaran[2,d]

[1]Department of Aerospace Engineering,
Universiti Putra Malaysia, 43400 Serdang, Selangor, Malaysia
[2]TU Bergakademie Freiberg, Institute of Mechanics and Fluid Dynamics,
Lampadiusstrasse 4, D-09596 Freiberg, Germany
[a]dlaila@eng.upm.edu.my, [b]shahnor@eng.upm.edu.my, [c]renu99@gmx.de
and [d]abdolhamid.attaran@imfd.tu-freiberg.de

Keyword: flutter, aeroelasticity, hybrid, laminated plate

Abstract. The aeroelastic flutter of a laminated hybrid composite wing was investigated. The composite wing was modelled as composite plates and the aeroelastic analysis has been carried out in the frequency-domain. Pre-determined fiber orientation of a 3-layers carbon/epoxy and glass/epoxy laminated plate has been employed with various aspect ratios. The modal approach and the Doublet-lattice Method (DLM) have been used herein to calculate the normal modes and the unsteady aerodynamics of the plate. The structural and aerodynamic models were connected using surface splines and the flutter speed has been calculated using the p-k method that provides the eigenvalues at different air densities and airstream velocities. The study showed that it is imperative that the carbon/epoxy should be employed in the outermost layers in order to improve the flutter speed and flutter frequency.

Introduction

Aeroelasticity is a study of the interactions of flexible aircraft structures and aerodynamic loads, which results in deformations that may have severe consequences on an aircraft's performance and stability. A particular aeroelastic effect, flutter, results into violent vibrations of structure leading to catastrophic failures. Due to their destructive nature, the aeroelastic phenomena need to be controlled. One obvious way is to make the aircraft structure more rigid, which introduces weight penalty in the gross weight of the aircraft. However, one of the objectives in the design of aircraft structures is to reduce weight, thus, employing this method is not the solution. Therefore, efforts had begun to include aeroelasticity into the design process. There are several ways to do this. One way is redistributing the mass of the wing through the topology optimization (spacing of ribs, spars). Another way is through an active control employing thin patches called piezoelectrics that are bonded to a structure and strains induced on the patches by applying electrical fields. The structure thus deforms due to its compatibility relations between the piezoelectric.

An alternative way is to passively control such phenomena by exploiting composite materials, which coincidently are much lighter compared to the conventional metal airframe structures. The technology to design for a desired aeroelastic response of a lifting surface using the advanced filamentary composite materials is known as aeroelastic tailoring [1]. The initial effort on aeroelastic tailoring was during the 1960's as reported by Weisshaar [2].The idea is to orientate the fibers of composite materials in such a way as to create the bending-torsion couplings that can alleviate the flutter speed. Realizing the significance of aeroelastic tailoring by incorporating the advanced composite materials, numerous research works are dedicated in developing and producing the optimum composite structures with the ply lay-up, number of plies and thickness as design variables.

In 1997, Kuttenkeuler and Ringertz [3] conducted the aeroelastic tailoring study of orthotropic woven glassfiber laminates as opposed to previous works that mostly considered unidirectional laminates. Majid et al. [4] conducted a similar research employing 3-layers laminated plate and study the effect of sweep angles and the stacking sequence. Results showed that the orientations of the outermost layers will dictate the nature of the bend-twist coupling as well as the type of the flutter mode. Attaran et al. [5] extended the work to include the effect of aspect ratios. In this paper, an aeroelastic tailoring investigation is conducted by employing the laminated plates of carbon/epoxy and glass/epoxy hybrids. The idea here is to produce laminates which are featuring both the economical advantage of glass and the high stiffness-to-weight ratio of carbon fiber.

Methodology

The plates were made up of 3 layers combination of symmetric carbon/epoxy and glass/epoxy laminates, as this was the minimum number of lay-up [4,5], which can be used to provide the effect of tailoring. Both materials are of the woven type and the laminates are fabricated using the hand lay-up process. The number of layers was maintained throughout the analysis to assure an invariant weight. There are four configurations employed with pred-determined fiber orientations; which are G-G-G[0_3], G-G-G[60/0/60],G-C-G [60/0/60] and C-G-C [60/0/60]. The 60° orientation is employed as the bend-twist coupling is at maximum. The mechanical properties were obtained experimentally via tensile test in accordance to ASTM D3039 standard and given in table 1. These values are used in the subsequent numerical analysis.

Table 1: Mechanical properties of carbon/epoxy and glass/epoxy laminates.

	Carbon/epoxy	Glass/epoxy
Longitudinal young modulus, E_{11}	29.5 GPa	12.85 GPa
Transverse young modulus, E_{22}	15.5 GPa	10.24 GPa
In-plane shear modulus, G_{12}	4.4 GPa	1.49 GPa
Density	550 kg/m^3	990.1 kg/m^3

Aeroelastic analysis of baseline and other model configurations is performed using MSC.Nastran, a general-purpose finite element analysis computer program. MSC.Patran is the pre- and post-processor for Nastran. The MSc-Nastran's aeroelastic solver presupposes a structural model, an aerodynamic model, and their interconnection by splines. The normal modes are solved in the structural modelling whereas the aerodynamics are modelled using the Doublet-Lattice method (DLM) based on the linearized aerodynamic potential theory. The governing equation of any aeroelastic system, based on Newton's law of motion can be written in matrix form as

$$[M]\{\ddot{x}(t)\}+[C]\{\dot{x}(t)\}+[K]\{x(t)\}=\{F(t)\} \tag{1}$$

where $[M]$, $[C]$ and $[K]$ are the mass, damping and stiffness matrices, $\{x(t)\}$ is the structural deformation and $\{F(t)\}$ represents the aerodynamic force applied on the structure. This is an eigenvalue problem that can be solved either in time or frequency domain. The following briefly describe the flutter solution technique that can be employed. There are 3 common flutter solution methods, the K-method, the KE-method and the PK method. The PK-method is applied and its principal advantage is that it produces results directly from given values of airstream velocities, whereas the K- and KE-methods require iteration to determine the reduced frequency of flutter. The fundamental equation for modal flutter analysis by the PK-method is [6]

$$\left[M_{hh}p^2+\left(B_{hh}-\frac{1}{4}\wp\bar{c}VQ^I_{hh}/k\right)p+\left(K_{hh}-\frac{1}{2}\wp V^2Q^R_{hh}\right)\right]\{u_h\}=0 \tag{2}$$

where M_{hh}, B_{hh}, K_{hh}, Q^I_{hh} and Q^R_{hh} each represents the modal matrix for mass, damping, stiffness, aerodynamic damping and aerodynamic stiffness. p, $\wp$, $\bar{c}$, V, k and u_h are the eigenvalue, air density, reference length ($b/2$), velocity, reduced frequency($\omega\bar{c}/2V$) and modal amplitude vector, respectively. The values of velocity V and the reduced frequency k were required in order to run the PK-method. The velocity was ranged from 10m/s to 100 m/s while the reduced frequency was ranged from 0.001 to 1.0. Flutter is defined when the damping is zero while sweeping through the airspeed. The small value of k (0.001) was used in order to compute the divergence speed if divergence occur before flutter [6]. The models are modeled with CQUAD4 elements due to its common application for modeling plates, shells and membranes. A convergence analysis was carried out to evaluate the suitable number of element in the specimens. The numerical results were also validated experimentally.

The experimental flutter test was performed in the (1.0 by 1.0) m^2 subsonic wind tunnel in Department of Aerospace Engineering, Faculty of Engineering, Universiti Putra Malaysia. The cantilevered composite plates are fixed to a wall-mount that replaces one side of the windows of the test section (Fig. 1). The test sample was instrumented with strain gages to record the bending and torsional strains. The tunnel speed was slowly raised until a speed was reached whereby the amplitudes of oscillation in bending and torsion increased rapidly and merged. At this point, the airspeed is recorded and will be known as the flutter speed. The flutter frequency is determined from the time history plot of both strains. The whole set-up is as shown in Fig. 1.

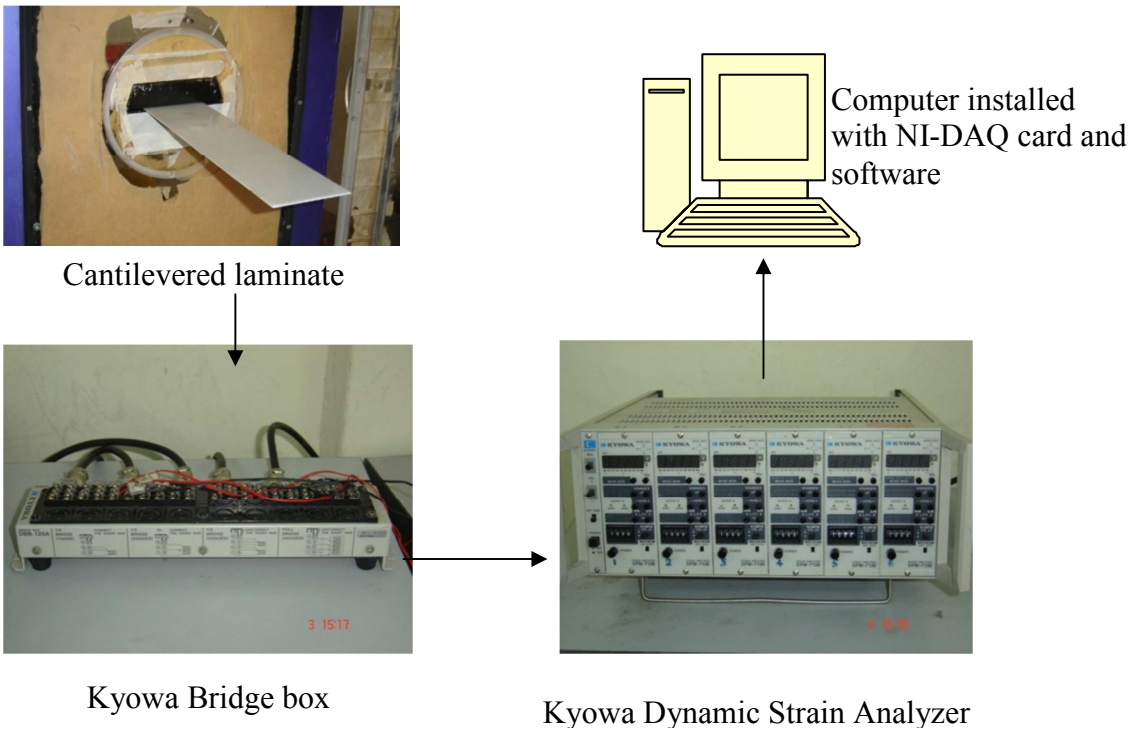


Fig. 1. Experimental setup for flutter test

Results

Experimental Validation. The experimental validation was performed on the baseline configuration (aspect ratio=5) whereby the hard-point flutter onset is defined when the amplitude of oscillations of both the bending and tosional strains rapidly increased. Zooming into that area, as shown Fig. 2, as the response amplitude increases, the stretching strain stiffness of the plate increases which limits the plate's range of motion and thereafter, the amplitude is maintained constant. This phenomenon is known as limit cycle oscillation (LCO) and the experimental techniques employed herein were reported in reference [7]. Flutter is usually typified by a diverging oscillation until the whole structural system physically fails but in the context of the cantilevered

flat plate, the limit cycle amplitude, the post-flutter response that occurred indicates the non-linearity of the system. Both numerical and experimental results are comparable whereby the predicted flutter frequency is 16.7 Hz whereas from experiment, it is measured at 16.0 Hz (from Fig. 2). The measured flutter speed is at 23.7 m/s is in agreement with the predicted value of 21.3 m/s.

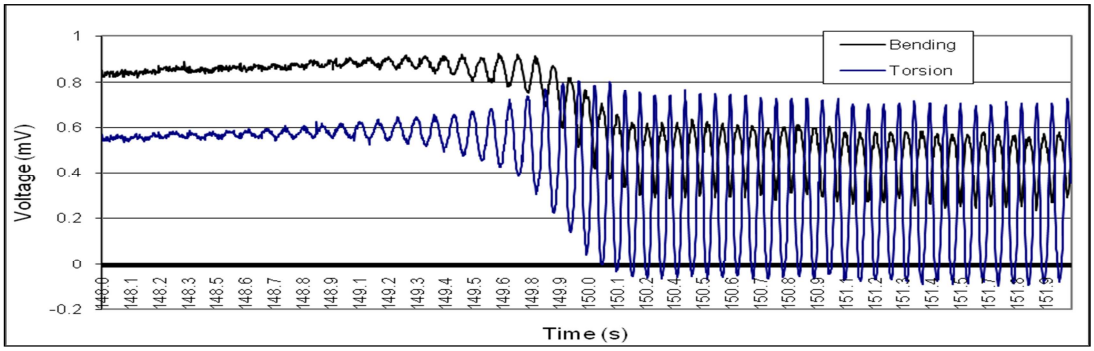
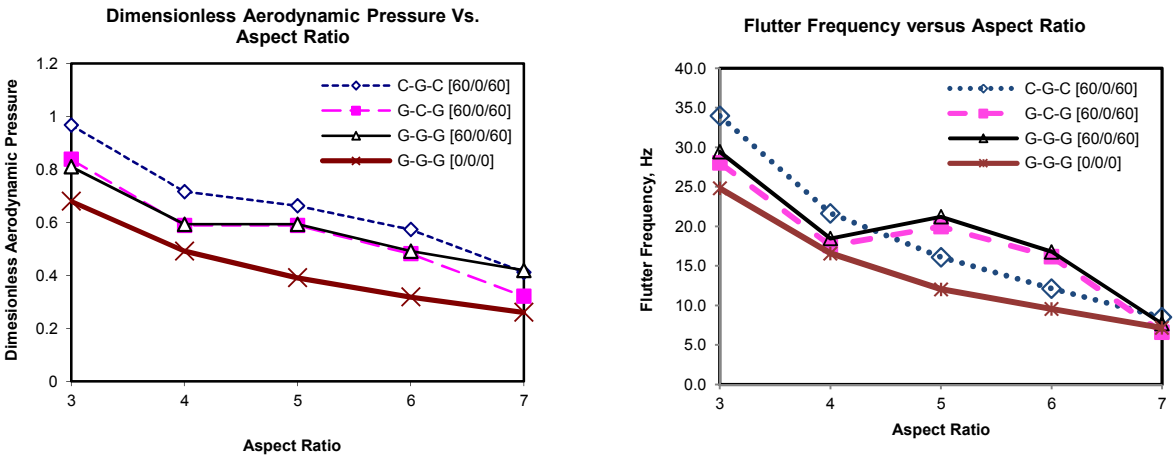


Fig. 2: Time histories at flutter onset for glass/epoxy laminated plate

Numerical Analysis. From the numerical analysis, the computed non-dimensional dynamic pressure and flutter frequency versus aspect ratio is given in Fig. 3. Non-dimensional dynamic pressure is proportional to the flutter speed. It is shown that the decrease in aspect ratio generally will result in an increase in the flutter speed as indicated in all four configurations. The flutter frequency also shows the same behaviour. As aspect ratio increases, the overall stiffness of the cantilevered plate reduces, hence lowers the normal modes of the plate which subsequently will lower the flutter frequency as well as the flutter speed.

When comparing the baseline configuration [0_3] with the rest, optimizing the orientation of the outermost layers will result in a beneficial bend-twist coupling that will make the plate harder to flutter. However, between glass/epoxy laminates [60/0/60] and hybrid G-C-G [60/0/60], there is no significant change indicating that the mid-ply contribution is somewhat not important. As expected, placing the carbon/epoxy at the outer layers increases the overall stiffness tremendously and as a result, increases the flutter speed and flutter frequency. The density of carbon/epoxy laminate is about half of the density of glass/epoxy laminate; therefore, employing carbon in the configuration of composite wing will enhance the aeroelastic properties as well as reduces the overall weight.

In terms of the flutter mode shapes, it will assume the same shape as the dominant structural mode when damping is zero. The flutter mode shapes for aspect ratio of 5 for all the configurations are given in Fig. 4. The flutter modes for all the configurations are of the bending type whereby it assumed the second normal mode of the plate. This means that when flutter occurs, the plate will oscillate in a bending mode with a constant amplitude. Looking at the deformations plot, the hybrid plates have higher amplitudes of deformation as compared to the baseline configuration indicating a more forceful vibration mode.



(a) (b)

Fig. 3: (a) Non-dimensional dynamic pressure and (b) flutter frequency versus aspect ratio

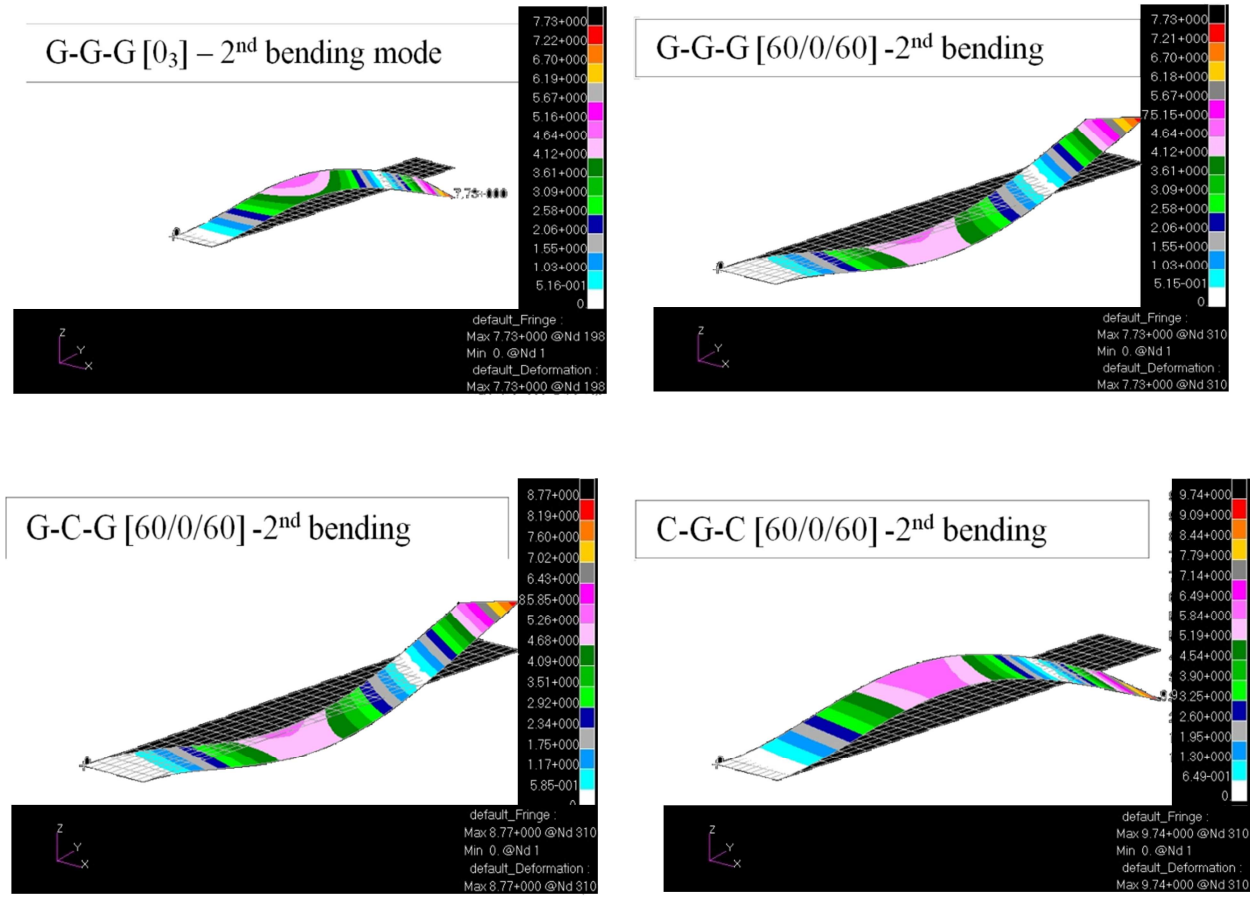


Fig. 4: Flutter mode shapes

Summary

The present paper has successfully shown that implementing hybrid configurations on an aircraft wing can improved on the aeroelastic properties through the manipulation of the bend-twist coupling. The effects of aspect ratio have been studied on the flutter speed of a cantilevered laminated composite plate. Results showed that flutter speed is increased with a lower aspect ratio. It is also found that it is beneficial to implement the a higher stiffness-to-weight carbon/epoxy laminate in the outer layers rather than in the inner layer whereby the effects induced are more significant. In conclusion, aeroelastic tailoring is achieved through hybid composite laminates in conjunction with varying the ply orientation of the outer layers of the laminates.

References

[1] V.C. Sherrer, T.J. Hertz and M.H: J. Aircraft, Vol.18, No.11, pp. 976 – 983

[2] Weisshaar, Terrence, Aeroelasticity Role in Innovative UAV Design and Optimization – the Way Things Ought to Be, http://roger.ecn.purdue.edu/~aae556/resources/Israel_paper.pdf

[3] Kuttenkeuler, J. and Ringertz, U. Aeroelastic Design Optimization with Experimental verification, Department of Aeronautics, Royal Institute of Technology, Report No. 96-33, National Program for Aeronautics Research project 254, May 7, 1997.

[4] A. Attaran, D.L. Majid, S. Basri and A.S. Mohd Rafie: Jurnal Mekanikal, Issue 22, Dec 2006.

[5] A. Attaran, D.L. Majid, S. Basri, A.S. Mohd Rafie, and E.J. Abdullah: Mechanica Acta 196, 161-173 (2008)

[6] Rodden, W. P., Johnson, E. H.: MSC.NASTRAN V68 Aeroelastic analysis user's guide, Vol. 1.

[7] DL Majid and S Basri. LCO flutter of cantilevered woven glass/epoxy laminate in subsonic flow, Acta Mechanica Sinica. 2008 24(1)

© (2011) Trans Tech Publications, Switzerland
doi:10.4028/www.scientific.net/KEM.471-472.1113

Selection of Polymeric Based Material Composite for Fibreglass Boat Components using Expert System

A.M. Fairuz[a], S.M. Sapuan[b] and E.S. Zainudin[c]

Department of Mechanical & Manufacturing,

Faculty of Engineering, Universiti Putra Malaysia, 43400 Serdang, Selangor, Malaysia

[a]mfairuzam@gmail.com, [b]sapuan@eng.upm.edu.my, [c]edisyam@eng.upm.edu.my

Keywords: material selection, weighting factor, expert system, boat structure

Abstract. In new era in marine industries especially in fibreglass boat construction, a proper material need to be consider for the product perfomance and economical. This paper ilustrate how the selection has been perform to select most suitable material for related body and structure component of fibreglass boat. Expert System has been using as a tool of selection and polymeric based material reinforced with different composition of fibreglass as candidate material. Ranking system has been implemented according to various factors to reveal the best polymeric based material composite for each fibreglass boat component.

Introduction

Even though boat structure has been developed for a thousand years ago, but the research on the material and structure still continue. Material and structure being an important element in term safety, weight reduction, stability, reliability, and cost reduction.

Now a day in the ship construction, polymeric based material such as fibre glass reinforced plastic has been widely used to replace wood and steel in boat structure. The advantage of this material is flexibility in fabrication, light weight, corrosion resistance and lower in manufacturing cost [1]. In term of physical and mechanical properties, this class of materials also comparable with other convenstional material such as steel and wood.

There have been reported that there are thousands of polymeric based material [2] which need a system to store and retrieve the data easily. In conventional way, designer may work through the tables of properties in various databases. However, the databases of the materials are limited and difficult to update bacause of lacking data from supplier or manufaturer. The encouraging growth in the information technology Jee [4] suggest to construct new database or reused existing database of material properties.

Recently, the existing program and website provide information related to new material especially polymeric based material lead the usable information to the designers and engineers. Example Cambridge Material Selector (CMS), Computer Aided Material Selector by Uniform Standard (CAMPUS) and FUNDUS is example program assist in the material selection. IDES, MATWEB, MATBASE, MEMnets and PRAGTIC are an online database for material properties.

Computer aided material selection have been replace a traditional method such as weighting properties method by Farag 1997 [5], Haan and Koppelaars using set method [6], the identification of the critical properties method [7], cost per unit property method [8]. Computer system that stored and processed the data related to the material assist designer to retrieve and make a proper decision on the material selection before design and fabricate the component.

In the past, there are many researcher have been developed computer aided for material selection. Bergamaschi [9] and Boose [10] developed computer aided system for material selection base on polymeric composite materials. In both system, all data of the material were processed and stored in the database system. Spainhour [11] describe the development of a conceptual data model for composite materials data. He illustrates basic elements of a composite materials database using

data modelling approach by filtering the information content down to the concepts of entities, attributes, and relationship among entities and attributes.

Experts system is a computer program that emulates the interaction that a person would have asking a human expert for advice or a recommendation. Jackson [12] defined that expert system is a computer program that represent and reasons with knowledge of some specialist subject with a view to solving problems or given advices. Hence, experts system becomes well-liked to solve multi criteria decision making. Expert system are finding many application in industry including the area of design, trouble shooting, failure analysis, manufacturing, materials selection and material substitution [13]

Material Selection Framework

The expert system is a major important tool in the material selection procedure. For each structure component several rule are created. These are also known as chaining [14] by using forward chaining technique. The constraint or limited values are selected from the product design specification. A chaining occur when a conclusion match to the premise of another rules [15].

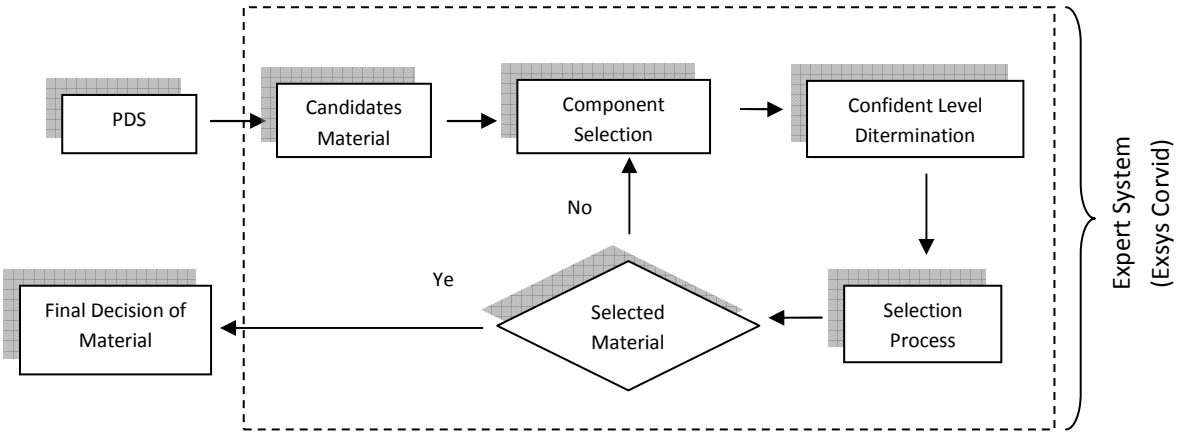


Fig. 1: Material Selection Process Flow Chart

Material selection framework for the selection of polymeric based material composite for boat components is show in Fig. 1. The aim of this selection framework is to facilitate material engineer to make decision on the best polymeric based material composite that suit design requirement of boat components. Firstly, candidate or alternative materials need to be identify that normally or suitable used in fibreglass boat component. After candidate or alternative materials have been determined, various factor that influence boat component (body, rib, stand and beam) need to be considered. Material engineer need to ditermine confident level depend on important priority of the various factors to optimize the selection. Then, the selection process to ditermine the most optimum decision is performed using expert system approach.

Polymeric Based Material Composite Selection for Fibreglass Boat Components Process

In material selection system, data properties of candidate material either quantitative value or qualitative value are stored in data spreadsheet. The data properties of material were collect from handbook [16], supplier and group discussion and then compile and stored in data spreadsheet. Quantitative data such as tensile strength, tensile modulus, flexural modulus, density and compress strength used numerical value in scoring system. Qualitative data such as material price and impact strength using ‘very low’, ‘low’, ‘medium’, ‘high’, and ‘very high’ term were used scoring system.

The system also used user interface confident that influence the scoring system. Each factor has confident level that control by material engineer to make the selection more flexible. Each factor can be priority considerations depend on the environmental or design issue and can select from 0 to 10. If 0 mean the factor will neglect and 10 is the most important.

In the logic block system, problem solving rules 'If' (premis) - 'Then' (solution) were using to constructed solution for given material selection specification. 'If' term is using for material properties constraint, 'Then' rules were constructed by mathematical formula for material score. All material properties constraint will be consider and calcualte using the mathematical formula then used in sub-scoring system (refer with: Eq. 1). If the value in the category of material properties is below the component specification, the equation will multiply with negative value of confident level. Sub-scoring in each category will be accumulated and the highest score will be rank of the material suitable to choose and display as the result.

$$Sub - score = \frac{Numerical\ value\ of\ properties}{\text{Highest value in the same category}} \times confident\ level \quad (1)$$

Results and Discussion

The expert system approach has a ability to make a optimum decision on the polymeric based material composite for fibreglass boat component and can rank the materials according to the various factor was set for each component. Table 1-4 show the important various factor and the confident level that influence the selection of material for fibreglass boat component. Table 5-8 show the result of the material selection for 4 different part of the fibreglass boat component.

Table 1: Confident level of material selection for body part

Criteria	Confident	Criteria	Confident
Tensile Strength	5	Impact Strength	0
Tensile Modulus	10	Density	10
Flexural Modulus	10	Water Absorbtion	10
Compressive Strength	0	Material Cost	10

Table 2: Confident level of material selection for rib part

Criteria	Confident	Criteria	Confident
Tensile Strength	5	Impact Strength	10
Tensile Modulus	5	Density	10
Flexural Modulus	10	Water Absorbtion	5
Compressive Strength	10	Material Cost	10

Table 3: Confident level of material selection for stand part

Criteria	Confident	Criteria	Confident
Tensile Strength	5	Impact Strength	0
Tensile Modulus	5	Density	3
Flexural Modulus	5	Water Absorbtion	3
Compressive Strength	10	Material Cost	10

Table 4: Confident level of material selection for beam part

Criteria	Confident
Tensile Strength	5
Tensile Modulus	5
Flexural Modulus	10
Compressive Strength	0

Criteria	Confident
Impact Strength	10
Density	5
Water Absorbtion	5
Material Cost	10

Table 5: Body boat material

Rank	Material	Fibre Glass Contain	Description	Score
1	Polyester	40%	High Glass	72
2	Polyester	25%	Strend Mat	56
3	Polyester	24%	Strend Mat	30
4	Polyester	50%	Woven Roving	6
5	Polyester	30%	Strend Mat	-26

Table 6: Material selection result for rib

Rank	Material	Fibre Glass Contain	Score
1	Polyethylene Terephthalate	45%	95
2	Polyethylene Terephthalate	30%	64
3	Styrene-acrylonitrile Copolymer	20%	46
4	Polyphenylene Oxide	20%	36
5	Polyethylene Terephthalate	20%	27

Table 7: Material selection result for stand

Rank	Material	Fibre Glass Contain	Score
1	Polyethylene Terephthalate	30%	80
2	Polyethylene Terephthalate	45%	57
3	Styrene-acrylonitrile Copolymer	20%	35
4	Polyethylene Terephthalate	20%	21
5	Polypropylene	20%	19

Table 8: Material selection result for beam

Rank	Material	Fibre Glass Contain	Score
1	Polyester	45%	72
2	Polyester	50%	56
3	Polyester	60%	30
4	Epoxy	40%	6
5	Polyester	70%	-26

Summary

The developed system assist on low cost and expert level decision on the polymeric based material composite by the non-expert material engineer or designer. The system also revealed the most suitable material composite for boat components; Polyester reinforced with 40% fibreglass for body, PET reinforced with 45% fibreglass for rib, PET reinforced with 30% fibreglass for stand, and Polyester reinforced with 45% fibreglass for beam. The user also can change the criteria priority level depend on the important of each criteria and the result of material selection also will change. This shows the system is smart enough to manupulate even the variation from user and database entered.

References

[1] Rudd, C.D. and K.N. Kendall: Proceeding of the Institution of Mechanical Engineers, Part B, 206(B2), p. 77, (1992).

[2] D.V. Rosato: In International Encyclopedia of Composites, Vol 3, editor: S.M. Lee. VCH, Cambridge, U.K, (1990)

[3] D.H. Jee and K.J. Kang: Mater Design;21(3) pp 199–206, (2000).

[4] M.M. Farag: Materials Selection for Engineering Design. Prentice Hall Europe, London, (1997)

[5] L. D. Hann and T. Koppelaars: Applied Mathematics for Database Professional. Apress, (2007)

[6] D.R. Askeland: The science and Engineering of Materials. PWS Publishing Company, pp. 1-19. (1994)

[7] W.D. Callister Jr.: Materials Science and Engineering. An Introduction, John Wiley & Sons Inc., pp.716-721. (1994)

[8] S. Bergamanchi, G. Bombarda, L. Piancastelli and C. Sartori: Proceeding of the IEEE Data and Knowledge Systems for Manufacturing 2nd International Conferrence, Gaitherburg, pp. 140-141, (1989).

[9] J.H. Boose: A System for Transfer Human Expertise. Editor: J.S. *Kowalik, Knowledge-based Problem Solving* (Prentice Hall) pp 68-111, (1986)

[10] L.K. Spainhour: Advanced Composite Material Property Data Modelling for Engineering Analysis and Design. 4th Vol. ASTM STP 1257, Editors: C.P. Sturrock and E.F. Begley, American Society for Testing and Materials, Philadelphia, pp. 110-126, (1995)

[11] P. Jackson: Introduction to Expert Systems, Addison-Wesley, New York. (1990)

[12] M.M. Farag: Quantitative Method of Material Selection. Handbook of Material Selection. (2002)

[13] Exsys Corvid Knowledge Automation Expert System Development Manual. Exsys Inc, U.S.A, pp 9-24 (2008)

[14] S.M. Sapuan and H.S. Abdalla: Ap. Sc. & Mfc. Vol. 29, pp 731-742, (1998)

[15] Rosato D.V. Reinforced Plastic Handbook. Elsevier Ltd, pp 880-996, (2004)

© (2011) Trans Tech Publications, Switzerland
doi:10.4028/www.scientific.net/KEM.471-472.1118

Tensile and Thermal Conductivity Properties of Epoxy Nanocomposites Thin Film by Spin Coating Technique

T. V. Voo[1,a], M. Mariatti[2,b], L. C. Sim[3,c]

[1,2] School of Material and Mineral Resources, Universiti Sains Malaysia, Pulau Pinang, Malaysia

[3]Intel Technology (M) Sdn. Bhd Penang, Malaysia

[a]richard_nalvin@hotmail.com, [b]mariatti@eng.usm.my, [C]lim.chong.sim@intel.com

Keywords*:* epoxy, nanocomposites, thermal conductivity, Thin Film

Abstract. This work aims to enhance thermal conductivity of thin film without compromising the other properties of polymer. In this study, three types of fillers in nano size with high thermal conductivity properties were studied; silicon nitride, boron nitride and synthetic diamond. The contents of fillers were varied between 0-2 vol. %. Epoxy nano-composite solution filled with high thermal conductivity fillers was spun at 1500-2000 rpm to produce thin film in the thickness of 40-60 μm. Thermal conductivity properties were measured by using hot disc technique. It was found that the thermal conductivity increases as filler loading increases. The mechanical properties of the thin film epoxy composites were determined by using tensile test (ASTM D882). As predicted, the tensile modulus was found increasing with the addition of fillers and reasonable agreements were obtained from the SEM images of the fracture surfaces.

Introduction

Polymeric materials in a bulk form are widely used in technological applications due to the extraordinary range of properties accessible in such as light weight, low cost, and ease of processing. Realizing the needs of smaller, thinner, and lighter devices, research on polymeric thin films are generating many interest from electronic industries [1]. The reduced dimensionality of multilayer leads to interesting phenomena when the film thickness is comparable or smaller than characteristics length. The properties of thin film are reported to be drastically different from that of the bulk materials [2, 3]. There exist huge variety of thin film deposition process and technologies which originate from physical or chemical processes. Previously, polymeric thin film has been produced by dip coating method. The dipping process is dependent on the required thickness, by which to produce a single layer it takes a minute or longer to complete [4]. In this method, the substrate is immersed in a colloidal solution and withdrawn vertically or with an inclination at a certain velocity. There are also other methods for fabricating thin films such as drop coating method [5], capillary immersion force [6], and electrophoretic deposition [7] which have been reported.

For a technique to be industrially applied, it must be fast, low cost, and must permit a large area of uniform thin layer to be assembled with high surface coverage. Spin coating method is one such technique that has potential for industrial application since it fulfills the industry requirement [8]. Spin coating is a well-established technology which in the past has been used in the manufacture of photoresists and oxide coatings for screens [9, 10]. There is a substantial scientific literature on the spin-coating process and useful reviews on the subject are given by Scriven [11] and Larson and Rehg [12]. Emslie et al. [9] described how a Newtonian fluid thins under the action of a centrifugal rotation on a flat disc. His model explained the importance of spin speed, liquid viscosity, and spin time on the film thickness.

In the present study, the effects of filler loading on tensile and thermal conductivity properties of thin film were investigated. Note that, in this research the maximum filler loading has been limited to 2 vol. % due to high viscosity which is a major constraint in spin coating method.

Experimental

Materials

The epoxy resin used in this study was supplied by Hexion Specialty Chemicals, Inc which acts as a matrix in the polymer composite. It is also chemically known as bisphenol-A-(epichlorohydrin) with a density of 1.16 g/cm^3 at 298 K. The curing agent used in this study was polyether amine EC 301 with a density 0.948 g/cm^3, supplied by BASF Corporation. The curing agent has low viscosity and long pot life. Silicon nitride (SN), boron nitride (BN) and synthetic diamond (SD) are supplied by Aldrich, Inc, Qinhuangdao Taiji Ring Nano-products Co.Ltd and He Yuan Zhong Lian Nanotechnology Co., Ltd., respectively were used as fillers in this research. The materials properties have been summarized and shown in Table 1. All fillers were dried at 110^{0}C for 24 hours in vacuum oven to eliminate moisture absorption before stored in desiccators.

Table 1: Material properties of fillers used [13-19].

Filler	Epoxy	SN	BN	SD
Density (g/cm^3)	1.16[a]	3.44[a]	2.29[a]	3.05[a]
Thermal conductivity (W/mK)	0.15-0.25	150	300	2000
CTE (ppm/^{0}C)	61[a]	3.2	<0.5	0.8
Modulus (GPa)	0.282[a]	257	43	967
Filler shape	-	Spherical [a,b]	Hexagonal[a]/ Non-Spherical,Irregular[b]	Spherical[a,b]
Mean particle size /d_{50}% (nm)	-	<50[a] (37.86[b])	60-100[a] (87.44[b])	3-10[a] (6.02[b])

a: Information provided by the suppliers

b: Measured from experiment

Preparation of epoxy filled nano-particles

The volume fraction of filler on composite was calculated based on the rule of mixtures:

$$V_f = \frac{W_f \rho_m}{W_f \rho_m + W_m \rho_f} \quad (1)$$

where W_f = weight of filler, W_m= weight of matrix, ρ_m= density of matrix and ρ_f= density of filler

The loading of nano particles were varied from 0 to 2 vol.% with respect to the epoxy resin. The mixing of epoxy resin and nano-particles were carried out by using ultrasonic agitation method. The mixtures of epoxy resin and filler were sonicated for 30 min to achieve uniform dispersion of filler in the epoxy resin. The sonication was performed at room temperature. The mixtures were then added with curing agent in the ratio of 100:32 by weight (epoxy: curing agent) and were further sonicated for 2 min followed by degassing under vacuum oven for 15 min to remove the entrapped air. The final mixture was ready for spin coating process.

Spin Coating Process

Spin coating technique generally involved with three-steps in order to produce uniform films: fluid deposited at the center of rotating disk; spinning process which accelerates the fluid and causes rapid thinning; and solvent evaporation rates from the film while the centrifugation continues. The mixture solutions which consist of epoxy resin, nano-fillers and curing agent were spun on Desk-Top Precision spin coater model G3P-12. Thin films of 30-50 μm in thickness were formed in 40 s at speeds ranging from 1500-2000 rpm. The films produced were subsequently pre-cured at 80^{0}C for 2 h followed by post-cured at 125^{0}C for 3 h.

Measurement

The tensile properties from all filler loading were determined according to ASTM D882-02 at a crosshead speed rate of 10.16 mm/min. The humidity and temperature were maintained at 50% and 25^0C, respectively. The testing was performed by using Instron 3366 machine. Tensile modulus was calculated from the initial linear portion of the stress-strain curve. At least five samples were tested for each filler loading to minimize the error. Samples for microstructure observation under the Scanning Electron Microscopy (SEM, model S360, Leica Cambridge Ltd) were prepared from cross sectional of the fracture surfaces of tensile specimens. Meanwhile thermal conductivity of the thin film epoxy nanocomposites was determined by using hot disk thermal constant analyzer, which is conducted in accordance to the ISO 22007-2:2008.

Results and Discussion

Tensile properties of thin film epoxy composite

Table 2 presents the tensile modulus, tensile strength and elongation at break which used to evaluate the tensile properties of pure epoxy and its nano-composites with the addition of different fillers respectively. Overall, the tensile modulus and tensile strength increase as the filler loading increases up to 2 vol. % which strengthen the reinforcement effect expected from the nano-particles except in the case of BN thin film composites. BN exhibits contrary effect to those seen in SN and SD thin film composites in which the addition of BN caused a decrease in tensile strength of the thin film.

The increase in tensile modulus and tensile strength of SN and SD thin film composites can be explained by presumably good adhesion and bonding exist between the filler and matrix which contribute to the positive reinforcement effect. In overall, the SD filled thin film showed higher elastic modulus and tensile strength properties compared to SN and BN thin film composites. This is due to the intrinsic nature of the SD which has high elastic modulus, 967 GPa compared to SN, 257 GPa and BN, 43 GPa (Table 1). It is also noted that the elastic modulus increases rapidly with the increase of nanoparticles in the range of 0-1 vol. % compared to nanoparticles in the range of 1-2 vol. %. This may be due to the fact that the dispersion of low filler loading of nanoparticles (<1 vol. %) in epoxy matrix is better than of high filler loading (>1 vol. %) and thus contributed to better homogenous stress transfer. Meanwhile the decrease in the tensile strength of BN thin film composites was due to the present of voids which visibly seen in the SEM micrograph of fracture surface (Figure 1c). This suggests that the interaction between BN nanoparticles and epoxy matrix was relatively week; hence the nanoparticles were easily peeled from the epoxy matrix which weakens the strength of the composites. Therefore significant reductions in tensile strength of BN thin film composites were observed in this research.

On the contrary, the elongation at break decreases as filler loading increases. According to Wypych [20], the elongation is usually inversely proportional to the tensile strength. As the filler loading increases, the polymer composite starting to show brittle behavior due to decrease in amount of a tough material available in the system and hence the decrease in elongation at break was expected. Leong et. al [21] reported the tendency of finer particles to agglomerate and Yong et. al [22] showed that the tendency to agglomerate increases as filler content increases which would trigger easily premature fracture of samples. The tendency to form agglomeration is contributed by the greater numbers of active surface area in finer particles compared in large particles.

The SEM images of tensile fracture surfaces with different fillers are presented in the Figure 1. The neat epoxy has a fairly smooth fracture surface, which is a typical brittle fracture as shown in the Figure 1a. In contrast with the finding in neat epoxy, it is found that the fracture surface of the nano-filled epoxy composite showed more features due to plastic deformation. The fracture surfaces of SD, BN and SN thin film composite showed rougher and ragged like waves. The fracture surface roughness signifies that the resistance to crack propagation is high in which the crack had not propagated as easily as in unfilled epoxy. The fracture surface roughness helps to create more torturous path and thus more energy are required for propagating the crack [23]. This produces higher strength to failure and improved the strength of thin film nanocomposites. In addition, nano-

scale particles which have high surface area will contribute to the connection and strong interaction matrix. Therefore, the external loads can be transferred via the resin matrix to the nano-particles filler effectively, which foil the expansion of micro-cracks due to the stress-concentration [24-26], and improve the strength of composites. Some voids (marked by circles) were clearly seen present on the fracture surface of BN thin film composites, as shown in Figure 2(c).

Table 2: Tensile properties of unfilled epoxy and epoxy filled with nanoparticles at 0.5-2 vol %.

Sample	Filler Loading (vol. %)	Elastic Modulus [MPa]	Tensile Strength [MPa]	Elongation at break (%)
Unfilled epoxy	-	1442 ± 70	35.5 ± 1.4	3.56 ± 0.17
SN	0.5	1550 ± 71	37.5 ± 6.0	3.23 ± 0.36
	1	1851 ± 112	46.2 ± 3.1	2.85 ± 0.53
	1.5	1937 ± 59	56.6 ± 3.1	2.83 ± 0.24
	2	2001 ± 92	60.9 ± 5.4	2.48 ± 0.53
BN	0.5	1488 ± 32	35.1 ± 7.2	2.35 ± 0.27
	1	1559 ± 144	30.4 ± 5.3	2.32 ± 0.36
	1.5	1647 ± 166	29.7 ± 1.9	2.04 ± 0.11
	2	1780 ± 61	27.9 ± 2.0	1.97 ± 0.23
SD	0.5	1777 ± 77	48.6 ± 3.6	3.04 ± 0.13
	1	2123 ± 66	60.1 ± 6.8	2.92 ± 0.26
	1.5	2412 ± 154	68.1 ± 4.8	2.85 ± 0.19
	2	2547± 72	71.1 ± 2.6	2.55 ± 0.29

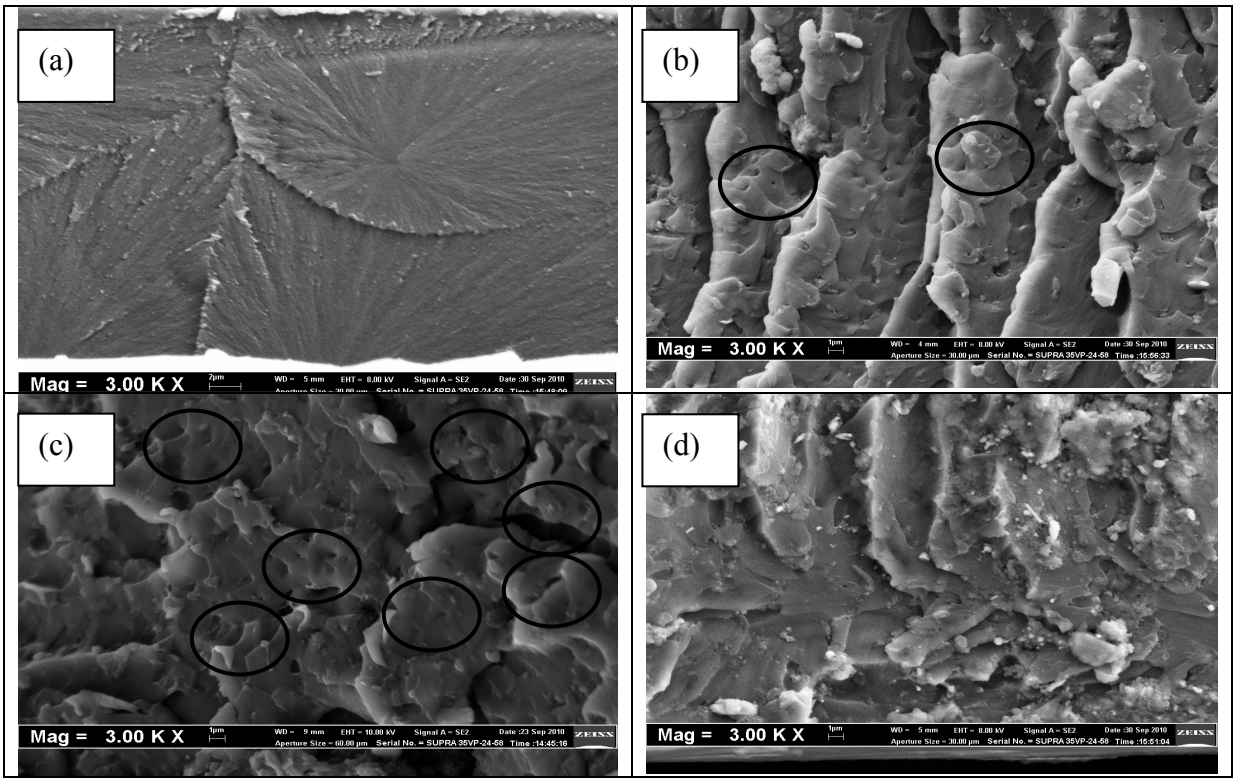


Figure 1: SEM micrographs showing the fracture surface morphology of: **a)** Unfilled epoxy **b)** 2 vol. % SN **c)** 2 vol. % BN **d)** 2 vol. %. SD, thin film composites (3000x magnification)

Thermal Conductivity

Figure 2 shows the effect of filler loadings on thermal conductivity of epoxy filled nanocomposites. As it was expected, the addition of inorganic filler increased the thermal conductivity of the polymer matrix with increasing filler content. The thermal conductivity of SD, SN and BN are much higher than that of epoxy resin, hence the incorporation of these fillers will result in an increased in the thermal conductivity of the composite. The tendency to form agglomerates increase as the as the filler content increases. Therefore, the higher heat conduction in filled composites thin film samples can be attributed to the large amount of agglomerates as can be seen in the SEM fracture micrograph.

For any given filler content, SD thin film composites samples showed a higher thermal conductivity than SN and BN thin film composites. When the loading of SD was at 2 vol. %, the thermal conductivity of the thin film composites reached 0.2026 W/mK compared to unfilled epoxy with 0.1137 W/mK, which means almost 78% increase. This can be due to a combination of few factors. The effect of intrinsic thermal conductivity is the clear factor as SD has extremely good heat conduction property (2000 W/mK). In addition, the small size effect of nanoparticles also results in better heat conduction property. The large surface area of small size fillers provides greater probability of contact between the filler particles which leads to higher thermal conductivity. Therefore, the higher thermal conductivity in SD filled thin film samples can be explained since it has smaller size filler compared to SN and BN. The effect of particle size on thermal conductivity of composites has been reported by few authors who suggested the similar behaviors [16]. It is also worth to note that that BN and SN thin film composites have almost the same conductivity in spite of having different in individual thermal conductivity (300 W/mK for BN and 150 W/mK for SN)

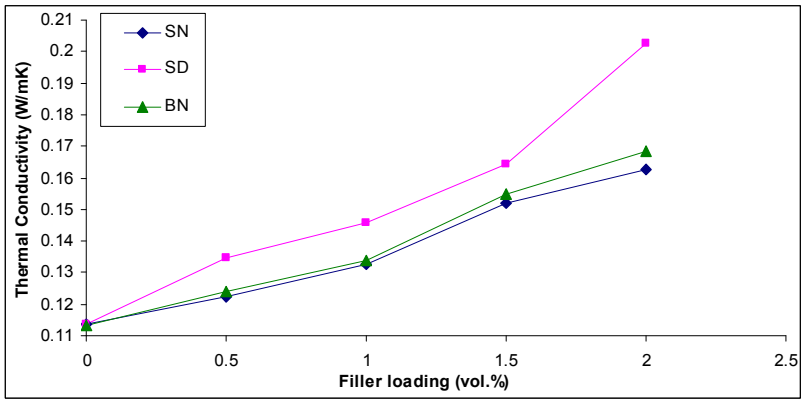


Figure 2: Thermal Conductivity of SD, SN and BN thin film epoxy nanocomposites.

Summary

Thermal conductivity of thin film composites can be improved by the addition of materials with high thermal conductivity property. The improvement is dependant on the intrinsic thermal conductivity and the size of the particles. Hence SD with extremely high intrinsic thermal conductivity (2000 W/mK) and smaller size, compared to SN and BN, showed better performance in heat conduction. The tensile properties such as elastic modulus and tensile strength of thin film were increasing with increase in filler loading. However the elongations at breaks slightly reduced as filler content increase due to brittle behavior.

Acknowledgements

The authors gratefully acknowledge Intel Technology (M) Sdn. Bhd for granting the research fund, No. 6050175 which made this research possible. The first author would also like to thank Universiti Sains Malaysia for awarding USM-RU-PRGS grant (No: 1001/PBAHAN/8033022) which facilitates the whole process of research.

References

[1] W.Menz, J. Mohr, O. Paul, Microsystem Technology, Wiley-VCH, Weinheim1, (2001).

[2] Kiyotaka Wasa, Makoto Kitabatake, Hideaki Adachi,. Thin Film Matarials Technology, Wiliam Andrew publishing, (2004).

[3] Richard P.Vince, Joost J.Vlassak, , Annu.Rev.Mater.Sci.(1996), 26:431-62

[4] James Rickman, Centrifugal Process Improves Thin Film, Los Alamos, N.M., 29, 2001.

[5] C.L. Haynes, A.D. MacFarland, M.T. Smith, J.C. Hulteen, R.P. Van Duyne, , J. Phys. Chem. B 106 (2002) 1898–1902.

[6] T. Okubo, S. Chujo, S. Maenosono, Y. Yamaguchi, J. Nanopart. Res. 5 (2003) 111–117.

[7] J.S. Ahn, P.T. Hammond, M.F. Rubner, I. Lee, , Colloid Surf. A-Physicochem. Eng. Aspects 259 (2005) 45–53.

[8] Takashi Ogi, Luis Balam Modesto-Lopez, Ferry Iskandar, Kikuo Okuyama, , Colloids and Surface A: Physicocehm. Eng. Apspects 297 (2007) 71-78

[9] Emslie, A.G., Bonner, F.T., Peck, L.G.,. Journal of Applied Physics (1958):29 (5), 858–862.

[10] Hall, D.B., Underhill, P., Torkelson, J.M.,. Polymer Engineering and Science (1998), 38 (12), 2039–2045.

[11] Scriven, L.E. Physics and applications of dip coating and spin coating. Materials Research Society Symposium Proceedings (1988) 121, 717–729.

[12] Larson, R.G., Rehg, T.J., Spin coating. In: Kistler, S.F., Schweizer, P.M.(Eds.), Liquid Film Coating: Scientific Principles and Their Technological Implications. Chapman & Hall, London (1997), pp. 673–708

[13] Hirao, K.,Watari, K., Hayashi, H.,and Kitayama, K., MRS Bull., (2001) 26(6), pp. 451-455

[14] Karl E.Spear,John P.Dismukes, Synthetic Diamond:Emerging CVD Science and Technology, John Wiley and Sons, INC. (1994) p.314

[15] Lee, H.; Neville, K. Handbook of Epoxy Resins; McGraw Hill: New York. (1982)

[16] C. P Wong and Raja S. Bollampally, International Symposium on Advanced Packaging Materials, (1999)

[17] Shenderov OA, Gruen DM, Ultrananocrystalline diamond: synthesis, properties, and applications. New York:William Andrew Publishing, (2006)

[18] Bharat Bhusnan, Springer handbook of nanotechnology, 2nd Edition, New York: Springer, (2006), pp.1699

[19] R.E. Smallman, R. J. Bishop.Physical Metallurgy and Materials Engineering:Science, Process, Applications. Elsevier Science Ltd, London, England. (1999) 6th Edition, pp.326

[20] Wypych G. Handbook of Fillers, . 2nd edi., Vol. 131. Toronto, New York; Ont.:Chem Tec..p. (2000) 241-75, 347-58

[21] Y. W. Leong. M. B. Abu Bakar, Z. A. Mohd Ishak, A. Ariffin, B. Pukanszky, J.Appl. Poly. Sci., (2004) 91, 3315.

[22] Zhao Y-Q et. al. Composites: Part B. (2010)

[23] Wu, C. L., Zhang, M. Q., Rong, M. Z. and Friedrich, K, Composites Science and Technology, (2002) 62: 1327-1340.

[24] Gojny F. H. Wichmann M H G, PKE U K, Fiedler B, Schulte K.. J. Composites Science and Technology, (2004) 15 (64): 2363-2371.

[25] Ren Yu, Li fend, Cheng H-M, et al. 2003.. J. Carbon, (2003) 41 (11) 2177- 2179.

[26] Park J M, Kim D S, Lee J R, Kim T W.. J. Mater. Sci. Eng. C, 2003, 23(6/8): 971-975.

© (2011) Trans Tech Publications, Switzerland
doi:10.4028/www.scientific.net/KEM.471-472.1124

A Structural Health Monitoring of a Pitch Catch Active Sensing of PZT Sensor on Normal, Damage and Repair Aircraft Spoiler

Mohd Aris, K .D[1,a], Mustapha F.[2,b], Sapuan S. M.[2,c] and Majid D. L[2,d]

[1]Universiti Kuala Lumpur, Malaysian Institute of Aviation Technology,

2891, Jalan Jenderam Hulu 43800 Dengkil, Selangor, MALAYSIA

[2]Department of Chemical Engineering,

Universiti Putra Malaysia, 43400 UPM Serdang, Selangor, MALAYSIA

[a]khdahri@miat.unikl.edu.my, [b]faizal@eng.upm.edu.my, [c]sapuan@eng.upm.edu.my,

[d]dlaila@eng.upm.edu.my

Keyword: Structural health monitoring system, composite repair, lead zirconate titate (PZT) sensors and outlier analysis

Abstract. At present, aircraft structural integrity is a concerned due to heavy usage of composite materials and cost saving on the operational. Structural health monitoring system is one of condition based monitoring introduced to supplement the current aircraft maintenance non destructive inspection. One approach is to embed or attach sensors such as lead zirconate titanate (PZT) to detect the anomalies either passively or actively. Due to the aircraft operational environment the defects and damage are likely to occur. Repair has to be carried out as per recommended and the requirement to replace back the sensors are important in order to monitor back the structure at post repair situation. The Lamb waves generated by using the PZT sensor can be used to monitor the surface structural integrity for damage or pristine condition. The effect of the lamb wave signals when surface condition of the aircraft component changes is concerned. One hundred data sets were recorded for the undamaged, damage and repair condition. An outlier analysis was used to analyze the situation by overlaying the isolated signal spectrum and the range of the voltage peak to peak (V_{pp}) mean values. Different signals were observed for different type of structural condition tested and more tests were required to make a conclusive solution.

Introduction

The use of composite material for primary structure has been exponentially increased from 1980 until present. The usage was initially at 7% and has increased up to 50% presently [1]. Engineered composite materials are known as the advanced composite material has superior properties compared to metallic structure. However, due to the fiber composite anisotropic characteristics and different combination of fibers and matrixes have resulted new challenges in terms of damage, defect and repair methodology. This presents a challenging task in order to establish the remaining strength and life of the structure. The most common type of damage is due to impact that can lead to significant degradation of the material properties. Low velocity impact especially on CFRP structure can lead to barely visible damage (BVD).

In order to determine the degree of damage on composite structure, various types of non destructive testing/ inspection/ evaluation (NDT/I/E) have been developed. Currently, there is limitation of a single NDT/I/E techniques to detect all type of defects existed on the composite structure. The main NDT/I/E techniques are visual inspection, eddy current, ultrasonic inspection, acoustic emission, laser shearography and thermography [2]. The limitation of current NDT/I/E procedures still can effectively detect severe voids, disbond and delaminations in the composite component but are unable to detect weak or potentially weak bond [3]. The use of the PZT sensors can monitor this irregularity either passively or actively at the initiation level.

Theoretical Background

The use of advanced composite materials has changed the aircraft structure design and maintenance philosophies. When a metallic structure is damaged, a simple removal and replacement of the area can be done by using mechanical fastener which is rivets. For composite structure they are typically four types of repair approach which are external bonded patches, flush or scarf bonded patches, bolted patches and bolted & bonded patches. However the level of recovery of operating strain possible, by repair, is dependent on the stiffness of the laminate. The actual load to be transmitted by the joint is governed by the equation [5]

$$P = e_a E_x t \quad (1)$$

Where, P, e_a, E_x, and t are actual load, ultimate design strain, modulus in the primary loading direction and the laminate thickness respectively. Whereas a simple strength of materials can be applied to scrutinized the scarf join for the maximum allowable stress[6]. The equation is given by

$$Pmax = \sigma_u t \leq \frac{\tau_y t}{sin\theta cos\theta} \quad (2)$$

Studies have shown the use of PZT sensors on experimental aircraft component such as flaps and wings are promising [7] and [8]. For this experiment, an aircraft spoiler was used as the experimental subject by mounting the sensor arbitrarily on the spoiler's surface.

Most of the structural damage diagnosis was done thru analytical or finite element modeling [8], [9] and [10]. Although the results were accepted but it requires a powerful computing hardware, labor intensive interaction and modeling errors before a solution can be converged. Statistical Pattern Recognition through Outlier Analysis is the driving mechanism in analyzing the waveform spectrum produces by the active interaction of the PZT sensors in this experiment. The principles were 1) Operational Evaluation, 2) Data Acquisition & Cleansing, 3) Feature Extraction & Data Reduction and 4) Statistical Model Development or Prognosis [11]. Only no. 1 and 2 were concerned in this paper.

Outlier detection can be considered as the detection of cluster, which deviates from other normal trend cluster. One of the most common discordance tests is based on the deviation statistic [12] given by

$$z_i = \frac{d_i - \bar{d}}{\sigma} \quad (3)$$

where z_i is the outlier index for univariate data, d_i is the potential outlier and $\bar{d}$ and σ are the mean sample and standard deviation. The multivariate discordance test was known as Mahalanobis square distance given by

$$Z_i = (x_i - \bar{x})^T \Sigma^{-1} (x_i - \bar{x}) \quad (4)$$

where Z_i is the outlier index for multivariate data, xi is the potential outlier vector and x is the sample mean vector and e is the sample co-variance matrix [12] and [13]. The result of the above equation is congregated when the distance of a data vector is higher than a preset threshold level.

The pitch catch active sensing method [14] was used in this experiment. The APC 850 PZT sensors were produced by APC International, USA with a diameter of 10mm by thickness of 0.5mm. The investigation involved with three structural conditions on spoiler's surface in which subjected to normal/ undamaged, damage and repair area. Two PZT sensors were placed at 100mm apart acting as an active system. One sensor was set to be the actuator with the signal came from the function generator and the other one as the receiver connected to the oscilloscope for data capturing.

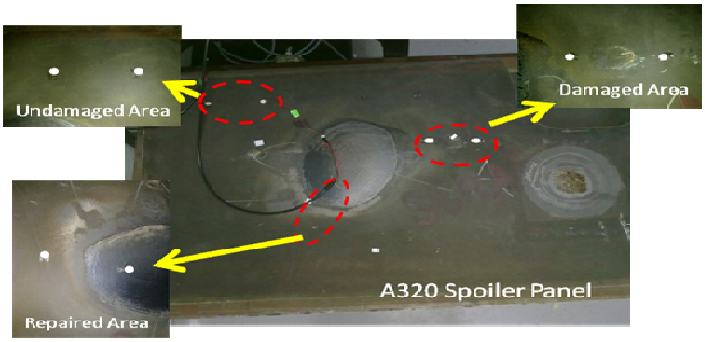
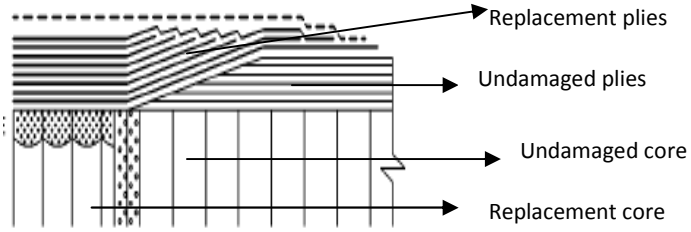


Fig. 1. Locations of the structural conditions and PZT sensor placements

The simulated damaged area was made by impacting the face plane with a blunt object. It created a partially damage crate about 20mm by 30mm with a partial depth of 10mm deep. For this experiment, the damage parameter was not a major concerned since the comparison only involved between undamaged and damaged surface. The repair area has similar initial damage as the previous condition. A flush type repair was conducted in accordance with the Airbus Structural Repair Manual (SRM). The hot bonder used was HCS9000B from Heatcon Inc.



Curing Parameters

Curing Temperature = 250^0F

Curing Time = 120 min

Soaking and Cooling Rate = 5^0F/min

Fig. 2. Typical flush patch repair applied on the spoiler and the hot bond curing parameters

Equipment set up. The scope of the research was concentrated on the use of active monitoring through PZT sensors on aircraft spoiler outer surface. Statistical pattern recognition was used to analyze the lamb wave generated by the PZT actuator. [15] The test was conducted by retrieving 100 data sets per structural conditions. By using Sigmaplot software each data sets were plotted and overlaid on each other. However, due to limitation of the processing power and the hardware, only five plots can be grouped at each time. Since there is 25000 points captured, the wave packets were investigated at 1000 points intervals. The first data set encountered a significant spike was isolated for further investigation. Once the isolated dataset has been highlighted, they were further bifurcate at 500 points for overlaid within their grouped structural conditions.

The set up of the system is shown in the figure below. The equipment used are TG1010A wave generator from TTi, GDS 2104 4 channel oscilloscope from GWs Instek, APC 850 Sensors from APC International, Sigmaplot software for replotting and analysis and Airbus A320 Spoiler donated by Spirit Aerosystem Malaysia. The setting for the wave generator was as follow, Freq = 50.000kHz, V= +10.0, V_{pp} = 50Ω, DC = +0.00mV (+0.00mV), Sym = 50.0% (50%), Source = TGEN[A], TGEN = 3ms at 333.3 Hz, Burst Count = 0005, Phase = $+000^0$ ($+000^0$). The receiver was connected to the oscilloscope and further fine turning need to be conducted in order to achieve the desired signal.

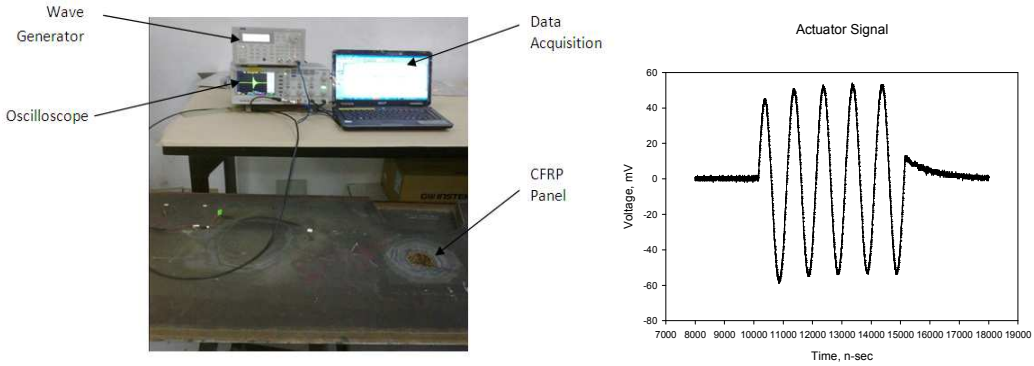


Fig. 3. a) The set up of the equipment together with the specimen and b) the burst signal.

Results and Discussion

A total of 100 wave packets were taken for each conditions stated. Each wave packets consisted of 25000 points by default from the oscilloscope. From the 25000 points, it was then grouped to 1000 intervals data set for analysis. There were two significant spike occurred each at point 12000 ~ 13000 and 18000 ~19000 as shown in Figure 4. By judgment, the first group of the spike was concerned and the data packet was zoomed again in 500 data intervals. Figure 5 shows the results of the wave packet upon synthesized by the 500 points.

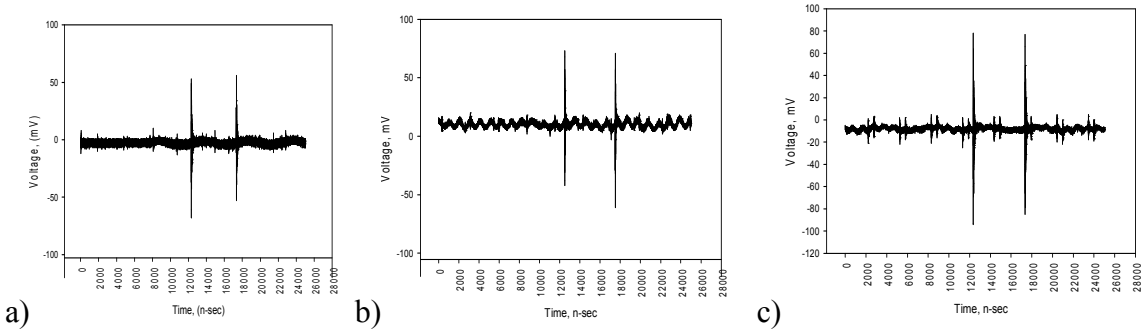


Fig. 4. Wave packet samples from a) undamaged, and b) damaged structural conditions c) repaired structural conditions.

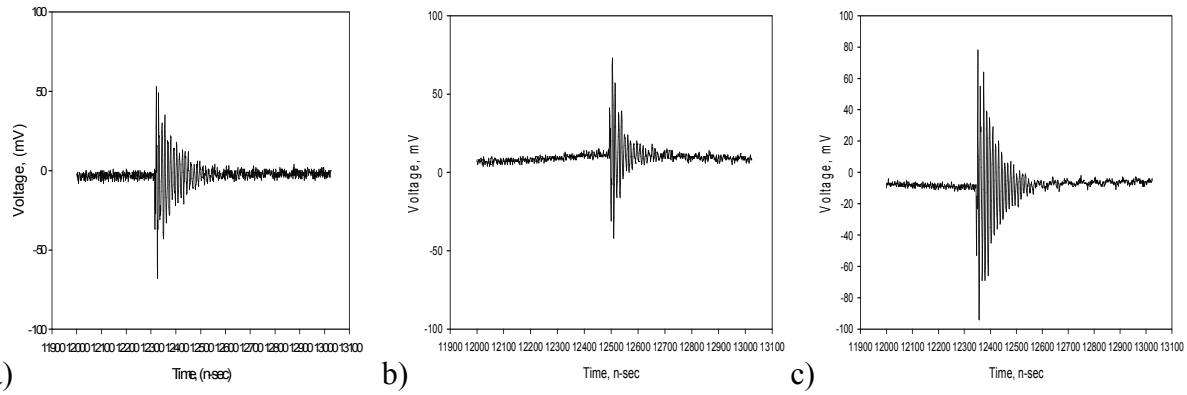


Fig. 5. Wave packet samples from a) undamaged, b) damaged and c) repaired structural conditions after synthesized.

Then, each of the structural conditions data were compared between each other to ensure the signals was homogeneous to each other. There were no references as the references were only the behavior of the waves themselves. The scattering of the V_{pp} at the concerned wave packets were also examined between the three conditions in Figure 6.

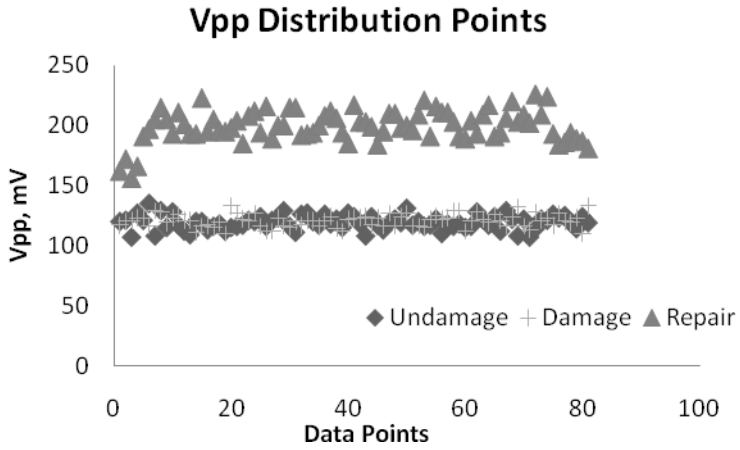


Fig. 6. V_{pp} distribution among the structural conditions

The V_{pp} showed similar values for the undamaged and damaged structure condition. It was assumed that the wave travel without discontinuity due to partial damage at that particular area. However several other types of damage need to be examined before any conclusive evidence can be finalized. A further post processing was done by overlapping the three conditions in one graph with similar time-domain comparison. The most common interest point lies within points 12250 ~ 12750. This was the first spike seen in the wave packet. In the earlier V_{pp} comparison, the distribution data between the damage and undamaged were identical. Therefore it was difficult to interpret the data for the latter machine learning process. However, when all three data was overlapped, a significant different can be seen as shown in Figure 7.

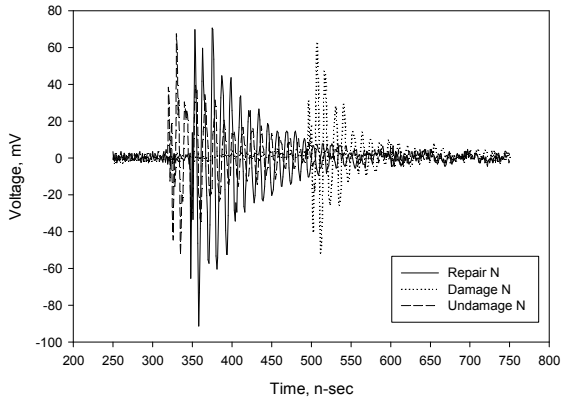


Fig. 7. Overlay Outlier Pattern for different structural condition

The undamaged signals appear at the initial time frame indicated that there was a clean surface wave travelling from the actuator to the receiver. However, once the partial damage was introduced, the spike appear later about 200nsec due to the discontinuity of the spoiler surface. The unaffected wave bifurcated to the receiver with delay. For the repair condition, since the surface integrity has been restored by the flush repair, the continuity of the surface wave was preserved again with delay about 50 nsec .

Summary

The outlier analysis can be applied to differentiate the condition of the surface integrity. However a more comprehensive data need to be considered when different types of damages are a major concerned. It was found that the PZT sensors can act well with the three conditions tested. The signal processing used is very robust due to a preliminary study on this event. The outlier comparison was proved to be applicable in showing the different wave packet generated received by the active sensing PZT sensors. However the distribution of V_{pp} was not convincing as it cannot differentiate the damage and partially damage panel. The PZT conditional configuration and at arbitrary locations are needed in order have a more confident result.

References

[1] The World Wide Composite Industry Structure, Trends and Innovation: New 2010 release, JEC Composite, 2010
[2] Soutis C. and Diamanti K.: Progress in Aerospace Sciences Vol. 46 (2010), p 342 -353.
[3] Baker A., Dutton S. and Kelly D.: Composite Materials for Aircraft Structure, AIAA Inc. (2004), p 290-295.
[4] Baker A., Dutton S. and Kelly D.: Materials for Aircraft Structure, AIAA Inc. (2004), p 290-295.
[5] Mujica L.E. et al., Impact Damage Detection in Aircraft Composites Using Knowledge-Based Reasoning, Structural Health Monitoring Vol. 7 (2008), p 215-230
[6] Kim I. and Park C.Y.: J. Int. Mater. Syst. Structures Vol. 19 (2008), p 319-324,
[7] Chang F. K and Ihn J. B.: Pitch Catch Active Sensing Methods in Strucural Health Monitoring for Aircraft Structures, Structural Health Monitoring Vol. 7 (2008), p 5-19.
[8] Kesavan A., John S and Herszberg: J. Int. Mater. Syst. Structures Vol. 19-63, p 63-72.
[9] Oyekoya O. O., Mba D. U. and El Zafrany: Composite Structures Vol. 89 (2009) p 134-142.
[10] Ostachowicz W. M.: Computers and Structures Vol. 86 (2008), p 454-462.
[11] Worden K, Manson G and Filler N. R. J.: J. Sound Vibration Vol. 229(2000), p 647-667
[12] Webb A.R, Statistical Pattern Recognition, John Wiley and Sons Ltd, (2002).
[13] Inman D.J. et al, Damage Prognosis for Aerospace, Civil and Mechanical Systems, John Wiley and Sons Ltd., 2005
[14] Ihn J and Chang F. K., Pitch Catch Active Sensing Methods in Structural Health Monitoring for Aircraft Structures, Structural Health Monitoring Vol. 7 (2008), p 1-19.
[15] Webb A.R, Statistical Pattern Recognition, John Wiley and Sons Ltd, (2002)
[16] Park et al: J. Sound and Vibration Vol. 286 (2005), p 229- 250.

© (2011) Trans Tech Publications, Switzerland
doi:10.4028/www.scientific.net/KEM.471-472.1130

Effect of Filler Loading and Coupling Agent on Tensile and Impact Properties of Polypropylene with Oil Palm Ash Composites

M.S. Ibrahim[1, a], A.A. Faieza[2], S.M. Sapuan[1, 2] and S.M. Tahir[2]

[1]Laboratory of Advanced Materials and Nanotechnology, Institute of Advanced Technology, Universiti Putra Malaysia, 43400, Serdang, Selangor, Malaysia

[2]Department of Mechanical and Manufacturing Engineering, Universiti Putra Malaysia 43400, Serdang, Selangor, Malaysia

[a]mshukriibrahim@gmail.com

Keywords: Oil Palm Ash, particulate filler, composites

Abstract. The purpose of this research is to investigate the effect of filler loading and using coupling agent on tensile and impact properties of thermoplastic polypropylene composite with oil palm ash (OPA) powder. This research is intended to discover the dependant various effect of loading percentage weight of filler OPA and coupling agent maleated anhydrate polypropilene (MAPP) on tensile and impact properties of thermoplastic composite. This materials is weighed as OPA loading percentage 0%, 1%, 3%, 5% and 7% while the loading percentage of coupling agent MAPP 0%, 3%, 6%, 10% and 12% affect the mechanical properties of thermoplastic composite. Mixture process has been carried out using double-screwed extruder machine at constant speed and temperature,while board manufacturing of PP/OPA composite are made used hot press and cold press machine. Loading OPA and MAPP effect on polypropylene composite were tested through mechanical testing , specifically for tensile and impact properties. All testing methods are predicated from ASTM's standard (American Society for Testing and Material). Results showed lower OPA content and highest MAPP in ratio giving the highest tensile and impact strength of the composite.

Introduction

Particulate-filled polymer composites have wide industrial applications to improve the stiffness and toughness of polymers, especially to enhance their barrier properties and their resistance to fire and ignition. Addition of particulate fillers sometimes results in undesired properties such as brittleness or opacity. Commonly, particulate fillers are usually quoted their prices basis in weight terms, while the majority of their composites are used in volume basis. Hence, the potential cost comparison of polymer and filler costs must therefore be made on volume basis.

Advantages of particulate filler from natural resources over man-made fibers include low density, low cost, low toxicity and biodegradibility. These advantages are good to be applied in the plastics, automobile and packaging industries to cut down on material cost [1].

Some researchers have studied the potential of filler from rice husk in thermoplastic composites [2-6]. Han et al,[2] studied on mechanical and morphological properties of PP reinforced rice husk flour; Hanafi et al,[4] studied on same properties but using rice husk ash. In this research, agro-waste from palm oil mill incinerator, oil palm ash was used as the particulate filler in thermoplastic polymer, polypropylene was used as the matrix polymer to prepare a particle-reinforced composite. Compared with common filler and other synthetic fibers, these palm oil mill resources materials could be used throughout the world and reproduced [7], decreased timeline used for their production, and are inexpensive. Furthermore, they are biodegradable [6] and do not leave residues or result in by-products that are toxic when combusted. Previously Hanafi et al, [8] studied on effects of palm-ash-filled natural rubber composites, they concluded that the tensile modulus increases with increasing palm ash loading, but the tensile strength, fatigue life, and elongation at break exhibit the opposite trend. The reduction of these properties can be attributed to the poor filler–matrix interaction. Hence, by using MAPP (maleated anhydride polypropylene) the bonding strength between the filler and the matrix polymer will improve [13-14].

Experimental

Materials and Equipments. This study used Oil Palm Ash (OPA) obtained from incinerator Palm Oil Mill at Ulu Keratong, Johor, Malaysia. Thermoplastic Polypropylene (PP) and compatibilizer, maleated anhydrate polypropylene (MAPP) produced by Titanpro Company. Equipments used for this experimental work were Grinder machine (Retsch, Germany); hot furnace; XRD (Siemens Model D500); Double Screw Extruder (HAAKE, 919905); Hot-press and cold-press machine from Wood Machining Laboratory and Image analyzer from School of Industrial Technology.

Experimental methods. Oil palm ash obtained from oil palm mill was sieved by fine size sieve (80 mesh size). Fine OPA powder is collected and was further grind to reduce the size of particulate filler. OPA sample were put into grinder gradually in practicable amount and keep in high temperature condition which is 250°C in hot furnace to 24 hours for hydration purposes.

This experiment has been carried out with different loading percentage of OPA (0%,1%,3%,5% and 7%) and MAPP (0%,3%,6%,10% and 12%). Pre-mixing has been applied to mix PP, OPA and the coupling agent as the mixtures. This thermoplastic PP/OPA was compounded using double screws extruder to become thin cylindrical shape known as pellets. Pellets of PP/OPA were put into 150x150x3 mm^3 sized mould and forming sheets of specimens under the hot press and cold press. The specimens of required dimensions were cut from the sheets and used for testing.

Tensile tests were conducted according to ASTM D638-99 [10]. Tensile testing of thermoplastic polypropylene composites specimens with different loading percentage of OPA and MAPP were carried out using Instron Universal testing machine Model 5582 with a crosshead speed of 5 mm per min and gauge length of 80mm. Rectangular specimens of size 150X10X3 mm^3 were used for testing.

Unnotched Izod impact tests were conducted according to ASTM D 256-97 [9] at room temperature using a pendulum impact testing machine. The test specimen was 80mm long and the cross sectional area, 24mm^2. For evaluation of tensile and impact properties, five specimens were tested for each different loading percentage of OPA and MAPP.

Results and Discussion

Tensile Properties. Fig. 1 shows the tensile strength for thermoplastic PP composites with various loading percentage OPA filler.

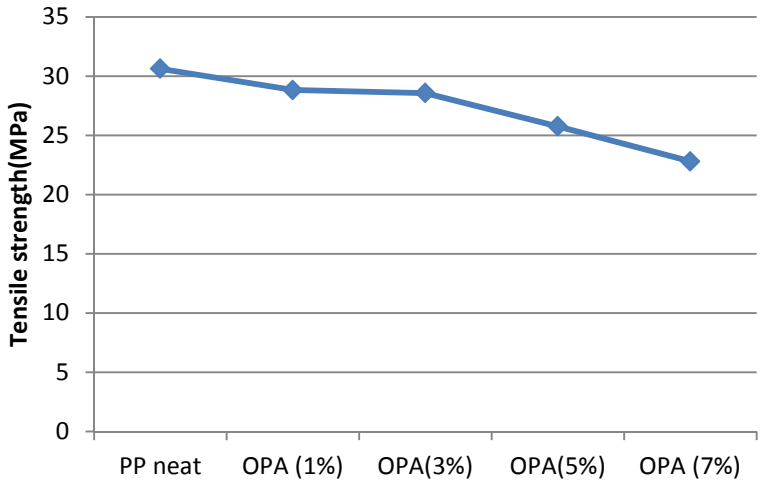


Fig.1: Effect on tensile strength for various loading OPA filler, wt.%

Tensile strength of the specimens for different loading percentage of OPA filler were decrease aligned with increasing OPA filler in ratio 1%,3%,5% and 7%. This obtained result have same trend as previous studies.

According to Han et al. [2] and Hanafi et al. [4], the tensile strengths of the composites decreased with increasing filler loading. The tensile strength decreased with increasing filler loading might be due to the poor interfacial bonding between hydrophilic filler and hydrophobic matrix polymer as shown in Fig. 1. These increments of filler loading affect weakness bonding between the hydrophilic filler and the hydrophobic matrix polymer. Other than that, unlike synthetic fibers such as glass and carbon fibers that have a uniform cross-sectional area and relatively high aspect ratio, that is, the length-to-diameter ratio, *l/d*, for irregular-shaped fillers, like OPA, their capability to support stress transmitted from the polymer matrix is rather poor. A similar observation was reported by Rozman et al. [11] and Fuad et al. [15] for RH-filled PP composites. Apart from having a similar geometrical factor to that of RH, OPA has a strong tendency to form agglomerates that result in poor adhesion of the filler to the PP matrix.

Agglomeration of OPA particulates filler are due to the moisture behavior at the surface of particles which intense tendency of OPA particles to agglomerates each other. These agglomerates are referred to as flocs and can arise due to loss of colloidal stability in polymerizing systems. Furthermore, flocs inside thermoplastic polypropylene composites might affect the bonding strength between the filler and the matrix polymer. As the hypothesis, high loading of OPA filler will decrease tensile strength of polypropylene thermoplastic composites.

Hence, coupling agent was used to improve the bonding strength between the filler and the matrix polymer Coupling agent that has been used for this research was maleated anhydride polypropylene. With the addition of the coupling agent, tensile strength of the composite significantly improved up to the same level of pure PP.

According to Han et al. [2] and Mohanty et al. [12] mechanical properties thermoplastic polypropylene with particulate-filled composites could be enhance by loading coupling agent during the compounding the filler with matrix. As shown in Fig. 2, tensile strength are decrease by increment loading percentage of OPA and MAPP but these values are higher than tensile strength of neat PP which is 31.5MPa, except for the ratio of OPA/MAPP of 7%:12%.

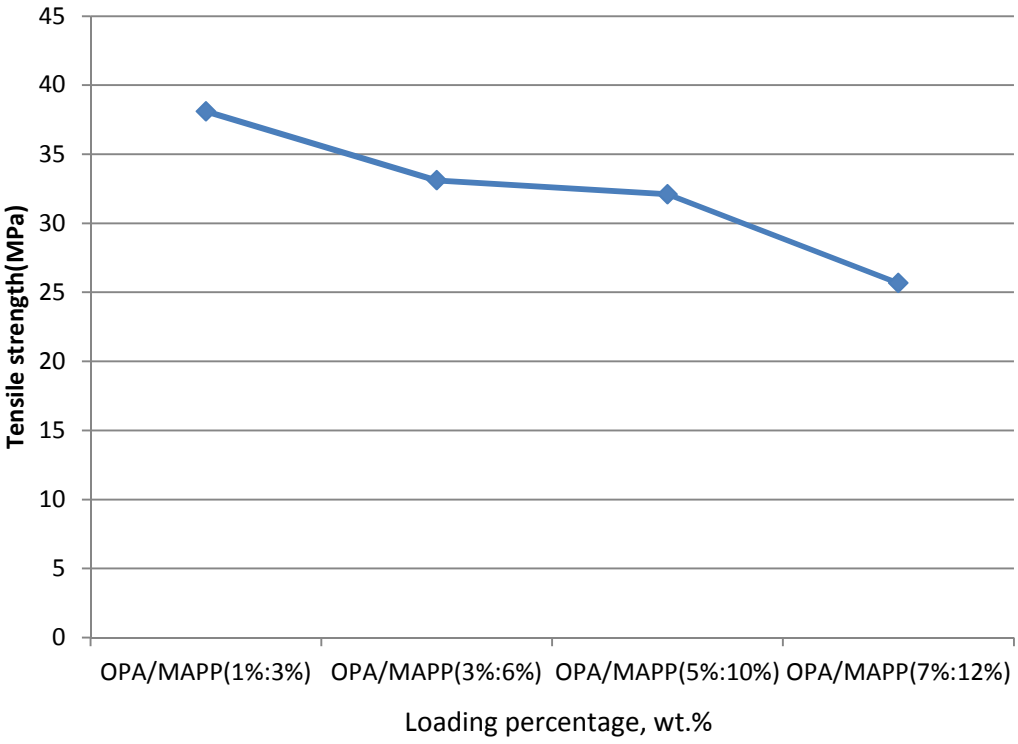


Fig.2: Effect on tensile strength for various loading coupling agent, wt.%

Results shown are about the comparison of tensile strength for different loading percentage of OPA with MAPP and without MAPP are shown in Fig. 3. Tensile strength for OPA-filled polypropylene composites with MAPP is much higher than without MAPP. Composition of OPA and MAPP were playing an important role to determine tensile properties o specimens. The effect of loading MAPP to modify the interfacial bonding between polymer matrixes with OPA filler by wetting in polymer chain is referred to previous studies [2-12].

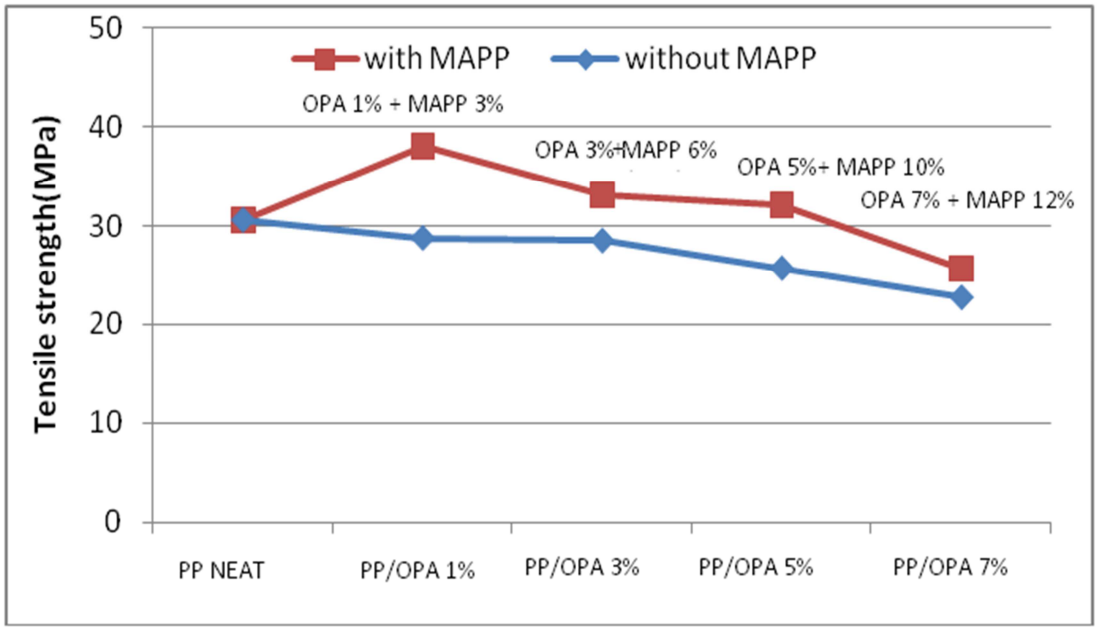


Fig.3: Effect on tensile strength for various loading OPA with coupling agent and without coupling agent, wt.%

Loading MAPP in composition of PP/OPA composites not only used to modify particle surface but also the PP matrix to achieve better interfacial bonding and mechanical properties in composites.

Impact properties. Result shown in Fig. 4 is Izod test which is reported in energy lost per unit of specimen thickness or cross-sectional area. In the graphically data shown the impact strength of the neat PP is extremely higher than PP/OPA composites.

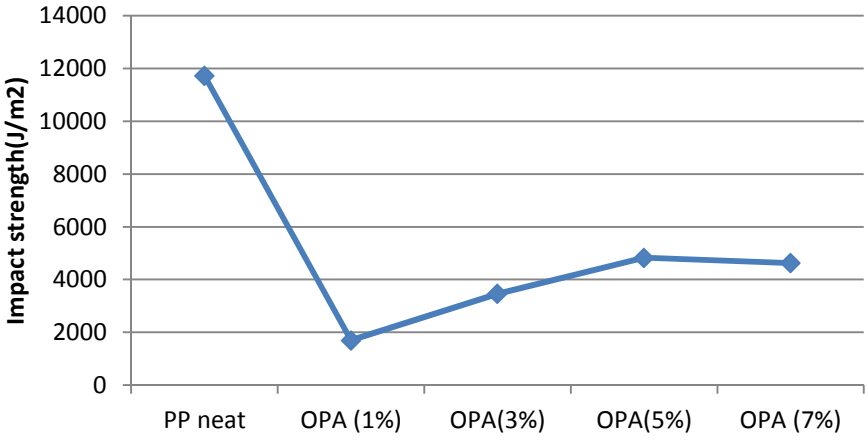


Fig.4: Effect on impact strength for various loading OPA filler, wt.%

According to [2] the Izod impact strength of the composites decreased as the filler content increased. In the case of higher filler content, the particles might be ease to form some defects in the PP matrix due to the interaction between neighboring particles being enhanced, and these defects might generate small cracks under impact load, leading to no increase or reduction of the impact fracture strength of these composite systems.

The significant result have been shown in Fig. 4, impact strength were dependently increasing affect with loading OPA from 1% loading percentage until 5% loading percentage. This result cause by filled OPA particles might generate stress concentration in matrix chain to produce shear yield and absorb plastically impact deformation energy. In addition to reduce initiation crack in the matrix chain under impact load when the filler concentration is low, these loaded particles may absorb impact deformation energy, resulting in improving considerably the impact strength of these composite systems.

Results shown in Fig. 5 are about the comparison of impact strength for difference loading percentage of OPA with MAPP and without MAPP. Impact strength for OPA-filled polypropylene composites with MAPP is much higher than without MAPP.

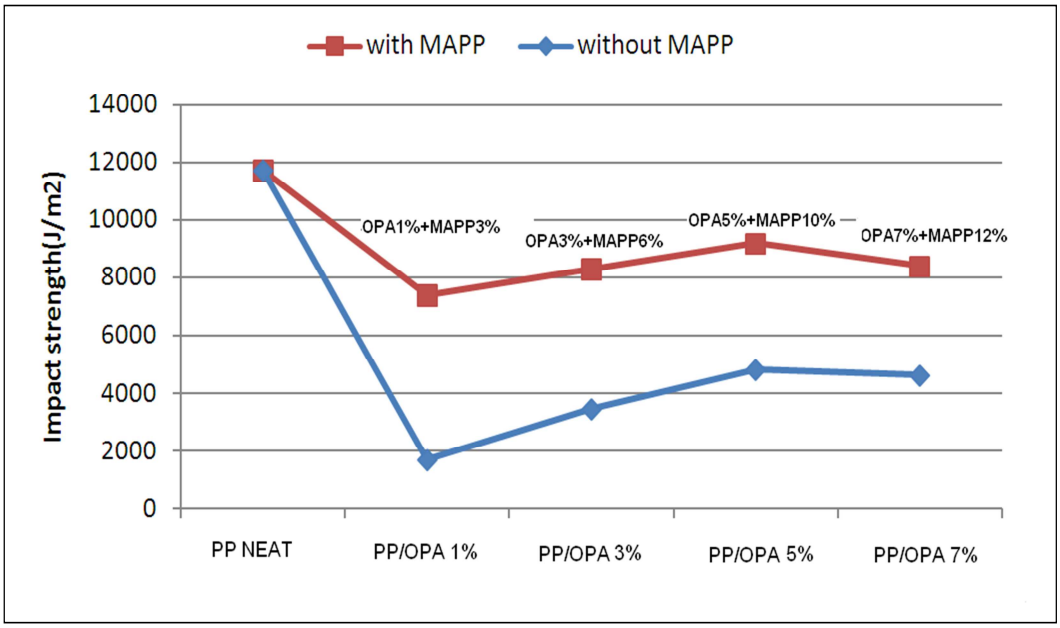


Fig.5: Effect on impact strength for various loading OPA with coupling agent and without coupling agent, wt.%

Summary

A large number of factors influence the properties of OPA filled polypropylene. The particle size and distribution of OPA, its aspect ratio and attrition during processing, the molecular weight and functionality of the MAPP all plays important roles in the determination composite properties. This literature concluded, tensile properties of polypropylene decreased with increasing loading OPA filler without coupling agent. However, when using MAPP-treated OPA, the positive significant effects have been shown to tensile strength of PP/OPA composites. This resulted by maleated anhydride polypropylene wetting particle in matrix and increase the bonding between filler and matrix. Without coupling agent, impact properties PP/OPA decrease sharply, due to agglomeration of OPA particles in matrix. However, with coupling agent, impact strength of PP/OPA is positively increased.

References

[1] R.N. Rothon: Particulate-Filled Polymer Composites Second Edition (Rapra Technology Ltd. 2003).

[2] Han.-S. Yang, H.-J. Kim, J. Son, H-J. Park, B-J. Lee and T.-S. Hwang: Composite Structure, Vol.63, (2004), p. 305-312

[3] Han.-S. Yang, H.-J. Kim, J. Son, H-J. Park, B-J. Lee and T.-S. Hwang: Composites Structure, Vol. 77, (2007),p. 45-55

[4] H. Ismail, J.M. Nizam and H.P.S. Abdul Khalil: Polymer Testing, Vol. 20, (2000), p. 125-133

[5] S. Siriwardena, H. Ismail, U.S. Ishiaku and M.C.S. Perera: Journal Of Applied Polymer Science, Vol.85, (2002), p. 438-453

[6] G.Hattotuwa , B. Premalal, H. Ismail and A. Baharin: Polymer Testing, Vol.21, (2002), p. 833-839

[7] R.E. Jacobson, M.S. Engineer, D.F. Caulfield, R.M. Rowell, A.R. Sanadi In: Proceedings of 2nd biomass conference of the Americas: Energy, Environment, Agriculture, And Industry; August 21–24, Portland, OR Golden, CO: National Renewable Energy Laboratory,(1995) p. 1171–1180.

[8] H. Ismail and F.S. Haw: Jour. Of Applied Polym. Sci., Vol. 110, Issue 5, (2008), p.2867-2876.

[9] Annual book of ASTM standards; 1997. American Society for Testing and Materials, 100 Barr Harbor Dr., West Conshohocken,PA 19428, United States.

[10] Annual book of ASTM standards; 1999. American Society for Testing and Materials, 100 Barr Harbor Dr., West Conshohocken,PA 19428, United States.

[11] Z.A. Mohd. Ishak, B.N. Yow, B.L. Ng, H.P.S.A.Khalil and H.D. Rozman: Journal of Applied Polymer Science, Vol. 81, 3, (2001), p. 742–753

[12] S. Mohanty, S.K. Nayak, S.K. Verma and S.S. Tripathy: Journal of Reinforced Plastics and Composites, Vol. 20, No. 4, (2001), p. 321-334.

[13] Roger M. Rowell, in: *Property enhanced Natural Fiber Composite Materials Based on Chemical Modification*.(Science and Technology of Polymers and Advanced Materials; Edited by P.N. Prasad et al., New York (1998), in press.

[14] K Bledzki, S Reihmane, J Gassan: J. Appl. Polym. Sci., Vol. 59, (1996), p.1329.

[15] M. Y. A. Fuad, Z. Ismail, Z. A. M. Ishak and A. K. M. Omar: Eur. Polym. J., Vol. 31, No. 9, (1995) p. 885-893.

© (2011) Trans Tech Publications, Switzerland
doi:10.4028/www.scientific.net/KEM.471-472.1136

Multisphere Ceramic Composite Concept and Its Numerical Study of The Ballistic Response

Sebastian STANISLAWEK[1, a], Andrzej MORKA[1,b] , Tadeusz NIEZGODA[1,c]

[1]2 Kaliskiego Street, 00-908 Warsaw, Poland

[a]sstanislawek@wat.edu.pl, [b]amorka@wat.edu.pl, [c]tniezgoda@wat.edu.pl

Keywords: computational mechanics, ballistic protection, composite armor, ceramics

Abstract. Numerical investigations were performed to determine the influence of the spherical convex shape ceramic - alumina composite in reference to the standard double layer panel. All versions of the target were verified in an impact test including influence upon the position of the AP (Armor Piercing) 7,62x51HHS impact. The crucial parameter which was used for this verification was change in time of the PROJECTILE kinetic energy.

The problem has been solved with the usage of the modeling and simulation methods as well as finite elements method implemented in LS-DYNA software. Space discretization for each option was built by three dimension elements guarantying satisfying accuracy of the calculations. For material behavior simulation specific models including the influence of the strain rate and temperature changes were considered. Projectile's core made of HHS and aluminum plate material were described by Johnson-Cook model and ceramic target with Johnson-Holmquist model. In the studied panels the area surrounding back edges was supported by rigid wall.

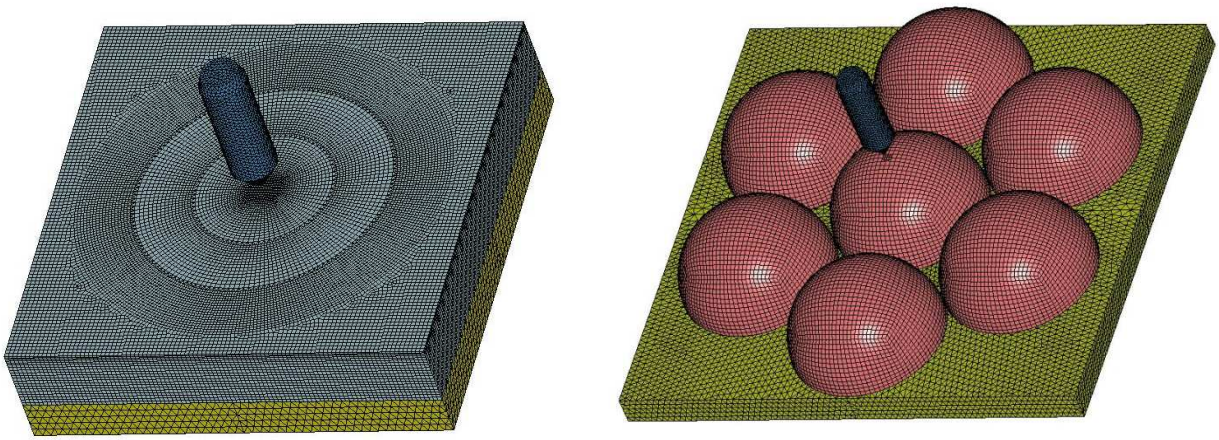
The obtained results show interesting properties of the new structures considering their ballistic resistance. However only certain places were chosen for tests, the protection ability against projectile attack is in general higher than the reference model. What is particularly interesting during the 6.6mm from the sphere center impact the sphere surface trajectory deviation effect is present. A projectile is not stopped here by material strength but the front layer shape. Moreover it can be assumed that this phenomenon will take place on majority of points on the sphere surface. Despite this fact, a ceramic multi sphere layer is less susceptible to overall destruction, depending on the impact point. The results of those numerical simulations can be used for designing of modern armor protection systems against hard kinetic projectiles.

Introduction

Military technologists seek to develop protective systems which are both effective and lightweight. Protectors made of steel have been used widely in military applications due to their good technological database and cheap production. Therefore, intensive studies has been carried out to manufacture materials not only with high density but also high bulk and shear module to prevent large deformations; high yielding stress to preserve the amour resistance to failure and high dynamic tensile stress to avoid material rupture when tensile waves appear. This expectations can met only when an amour consist of differential material layers[1]. Most experimental and numerical research indicate that a protector made of ceramic material should be placed in the front and supported by other less brittle materials. Some structures have even been successfully implemented in commercial applications and nowadays became standard military equipment in developed countries[2]. In this paper the concept of the panel ballistic protection ability is not typically based on the layers ratio but the front material shape. Ceramic protector is built with half sphere shape protectors connected with an Aluminum Alloy (AA) base layer. This may lead to projectile trajectory deviation and finally higher energy dissipation. The described panel is impacted with HHS projectile, which energy dissipation is analyzed, with the comparison to the standard flat panel with the same area density ratio.

Problem Description

A series of basic test have been held for an identical HHS projectile, moving with 854m/s speed and striking the target always perpendicularly. A reference panel was built with two rectangular prisms, the front one had 8mm width and a thinner back one 5mm which is presented in fig1.a). The examined structure consisted of backing plate and a set of half sphere shapes with a diameter 13,2mm. Such dimension guaranteed the same areal density as in a reference front layer. The implemented models simulated HHS, AA and ceramic materials, basing on real material data verified in literature [4], [5], [6]. Al203 ceramic was used in the front and was backed with AA 2024 alloy.



(a) (b)

Fig 1. a) reference model structure, b) model with half spheres

Problem Solution and Analysis of the Results

All FEM models were built using brick elements, such solution made all the calculation stable during the whole impact process. An initial speed was defined for the projectile with the same initial value for each example. A backing plate was supported in the neighborhood of its edges, the front panel is in one option simply laying and another tied to the backing plate. LS-Dyna software [3] was used to calculate each variant with explicit time integration method. Kinetic energy of the projectile is the key parameter being analyzed without including the debris energy. In the fig.2 we can see the energy value for both situations. For the reference model curves are almost identical. For the sphere panel we can see a small difference however the full observation is not possible because projectile cannot penetrate the target. However, it should be taken into consideration during the panel designing, for further research we will not discuss connection between layers.

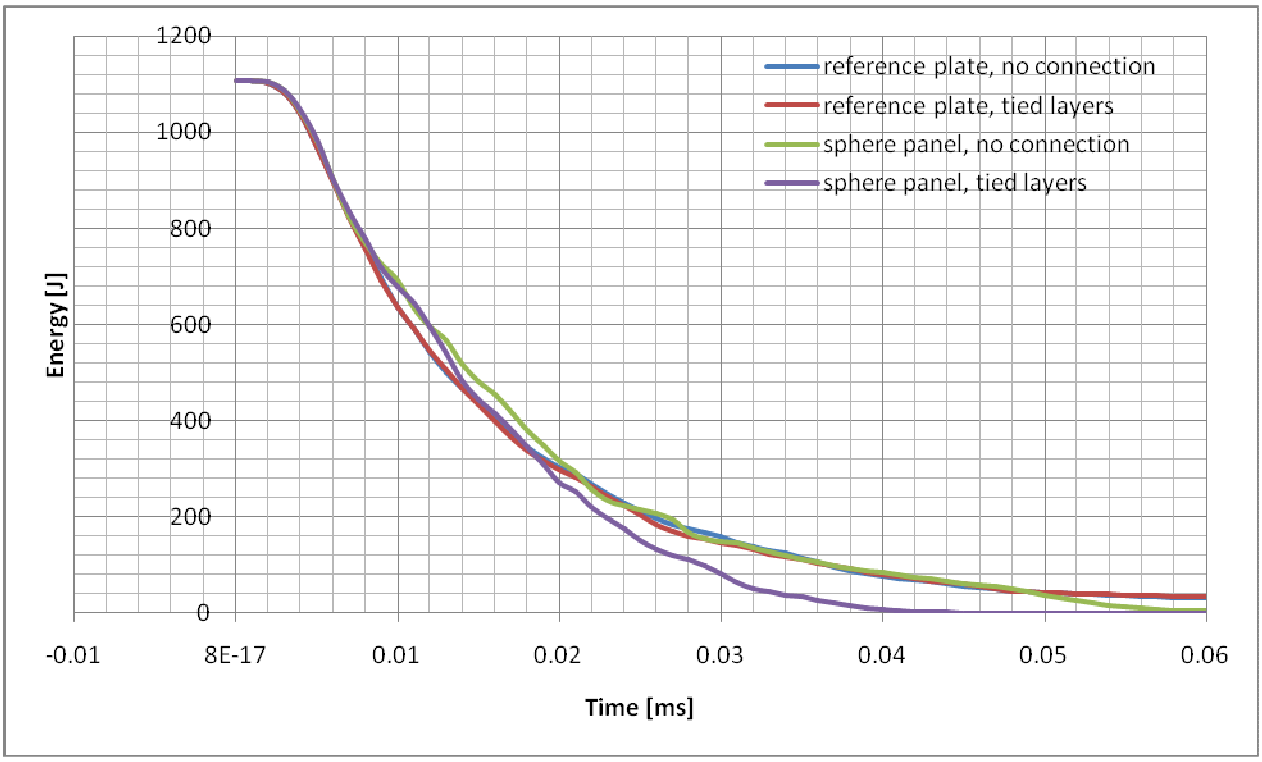


Fig.2. Kinetic energy of the projectile for reference model and sphere panel

Effectiveness of each panel was verified in a previously described numerical test where a projectile impacts the target in key places. Its result is shown in fig.3 indicate that the impact in the middle of the sphere is most effective and stops the projectile, which is caused simply by the width of the layer in this place. In reference model and impact between spheres tests we observe the penetration, energy is on similar level. A very interesting effect can be observed for the impact 6.6mm from the centre of sphere, here the bullet trajectory is deviated and the projectile is moving in a random direction. It seems to be the most effective way to stop the projectile, however, for full verification of the energy consumption a test with more massive bullet should be done.

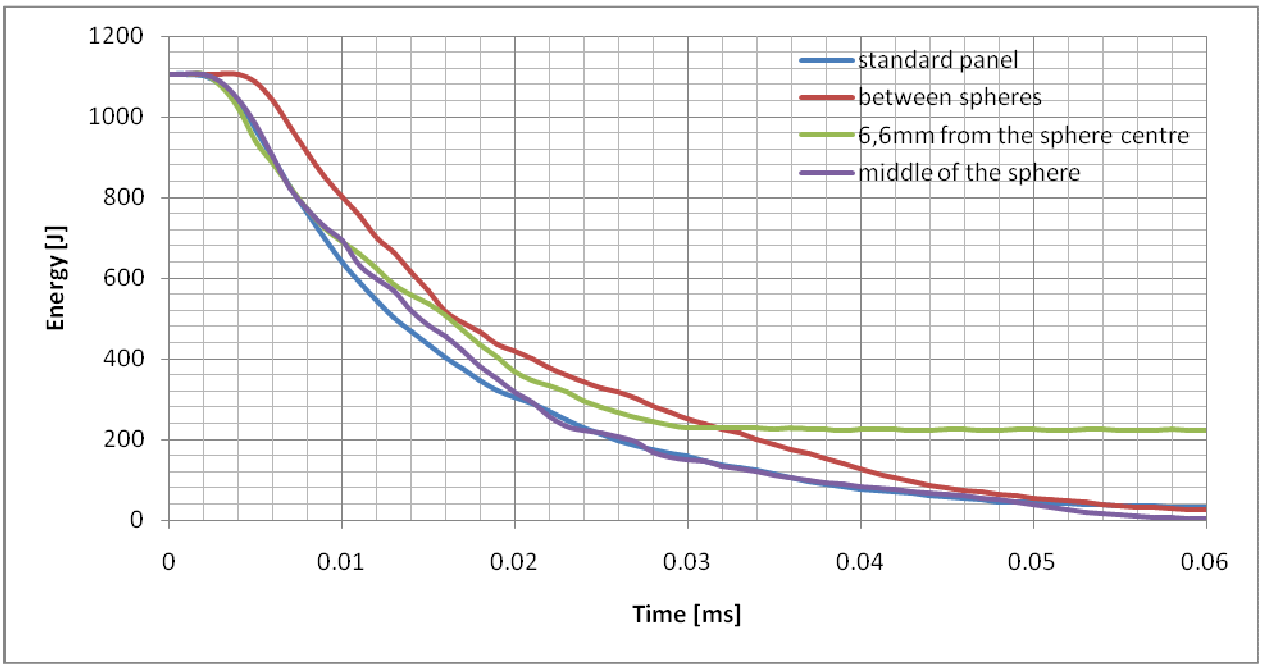


Fig.3. Kinetic energy of the projectile during impact each variant

Not only the projectile energy is important for the armor but also the plate structure after the impact. Due to ceramic tendency for cracking, a damage parameter becomes one of the most crucial. In fig.4, 5, 6 and 7 this parameter is presented for the reference plate and plate with spheres in three variants. It is clear that panel with spheres has superior properties to the continuous plate. The destruction refers only to impacted sphere and is the smallest in the impact 6.6mm from the center. The ability of the multi-sphere panel to protect from further attack is much higher.

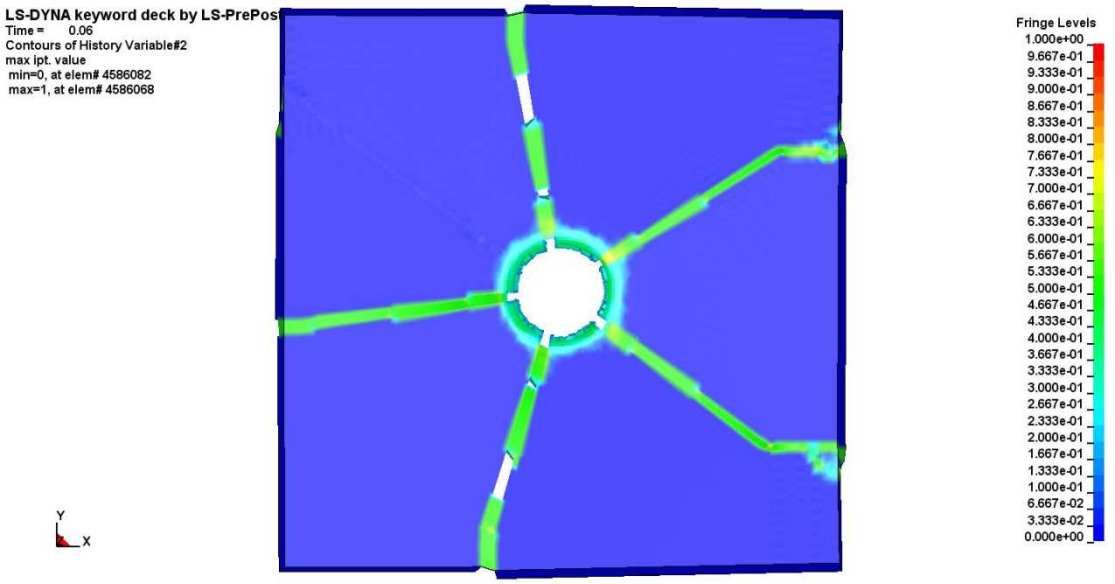


Fig.4. Damage parameter - reference panel

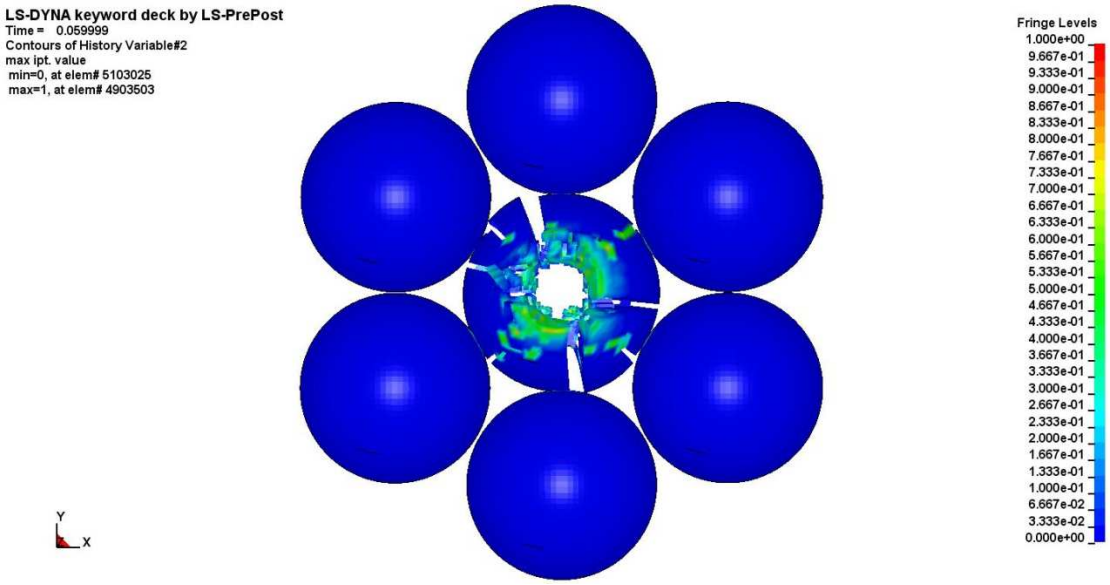


Fig.5. Damage parameter, middle impact

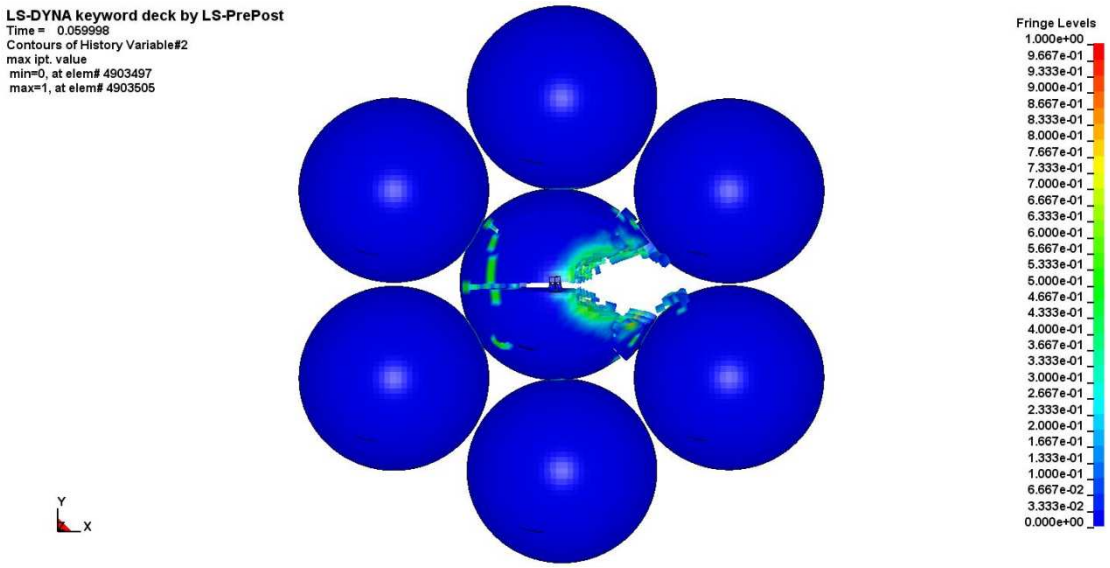


Fig.6. Damage parameter, impact 6.6mm from the center

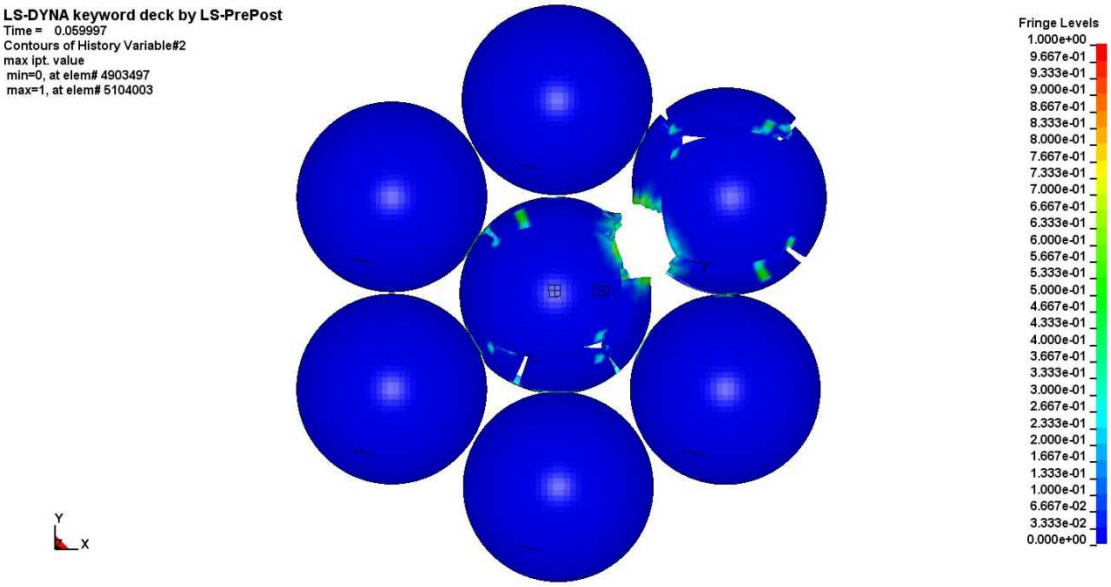


Fig.6. Damage parameter – impact between spheres

Summary

The obtained results show interesting properties of the new structures considering their ballistic resistance. However only certain places were chosen for tests, the protection ability against projectile attack is in general higher than the reference model. What is particularly interesting during the 6.6mm from the sphere center impact the sphere surface trajectory deviation effect is present. A projectile is not stopped here by material strength but the front layer shape. Moreover it can be assumed that this phenomenon will take place on majority of points on the sphere surface. Despite this fact, a ceramic multi sphere layer is less susceptible to overall destruction, depending on the impact point. The results of those numerical simulations can be used for designing of modern armor protection systems against hard kinetic projectiles.

References

[1] Mustafa U¨ beyli, R. Orhan Yıldırım, Bilgehan O¨ gel, *On the comparison of the ballistic performance of steel and laminated composite armors laminated composite armors*, Materials and Design 28 (2007) 1257–1262

[2] Professor Paul J Hogg, *Composites for Ballistic Applications*

[3] *Ls-Dyna Keyword User's Manual*, May 2010 Version 971/Rev 5

[4] Nilsson M., *Constitutive model for Armox 500T and Armox 600T at low and medium strain rates*, Swedish Defence Research Agency, TR FOI-R-1068-SE, 2003

[5] Johnson G.R., Cook W.H., *A Constitutive Model and Data for Metals Subjected to Large Strains, High Strain Rates and High Temperatures*, Proceedings of the 7th International Symposium on Ballistics, The Hague, The Netherlands, April 1983.

[6] Panov Vili, *Modelling of behaviour of metals at high strain rates*, Cranfield University, PhD Thesis, 2005

© (2011) Trans Tech Publications, Switzerland
doi:10.4028/www.scientific.net/KEM.471-472.1142

A Composite Consisting of a Set of Hexagonal Ceramic Bars - The Numerical Study of The Ballistic Resistance

Sebastian STANISLAWEK[1, a], Andrzej MORKA[1,b] , Tadeusz NIEZGODA[1,c]

[1]2 Kaliskiego Street, 00-908 Warsaw, Poland

[a]sstanislawek@wat.edu.pl, [b]amorka@wat.edu.pl, [c]tniezgoda@wat.edu.pl

Keywords: computational mechanics, ballistic protection, composite armor, ceramics

Abstract. The paper presents a numerical study of a double layer composite panels impacted by a AP (Armor Piercing) 51WC projectile. The standard panel is built with aluminum and Al2O3 ceramic continuum layers while the studied model consists of the same aluminum plate but the front one is built with a set of hexagonal ceramic bars. The bar width and the impact position influence on the ballistic resistance are analyzed and compared with the reference solution.
The problem has been solved with the usage of the modeling and simulation methods as well as finite elements method implemented in LS-DYNA software. Space discretization for each option was built by three dimension elements guarantying satisfying accuracy of the calculations. For material behavior simulation specific models including the influence of the strain rate and temperature changes were considered. Projectile Tungsten Curbide and aluminum plate material were described by Johnson-Cook model and ceramic target by Johnson-Holmquist model. In the studied panels the area surrounding back edges was supported by a rigid wall. The obtained results show interesting properties of the examined structures considering their ballistic resistance. All tests has given clear results about ballistic protection panel response under WC projectile impact. Panels consisting of sets of hexagonal ceramic bars are slightly easier to penetrate, reference model is stronger by 19% for smaller bars and by only 7% for bigger rods. Despite this fact, the ceramic layer is much less susceptible to overall destruction what makes it more applicable for the armor usage. Furthermore, little influence of the projectile impact point and consequently a part of the bar which is first destroyed is proved.

Introduction

The use of modern amour against ballistic threats is very important with respect to saving energy and increasing mobility. Steel protectors have been used widely in military applications, they have a very good technological database and can be produced cheaply. However, such materials are relatively heavy what makes them unsuitable for lightweight vehicles. Therefore, intensive studies has been carried out recently in order to design composite amour composed of material layers made of fiber laminates, ceramics, rubbers, metals [1]. Some structures have been successfully implemented in commercial applications and nowadays became standard military equipment in developed countries [2]. In this research an innovative double layer metal-ceramic composite is numerically analyzed basing on previous studies. However, the concept of the panel ballistic protection ability is not typically based on the layers ratio but the front material shape. Ceramic protector is built with tightly packed hexagon rods connected with an Aluminum Alloy (AA) base layer. The described panel is impacted with WC core projectile, which energy dissipation is analyzed, with the comparison to the standard flat panel with the same area density ratio.

Problem Description

A series of basic test have been held for an identical WC core projectile, moving with 854m/s speed and striking the target always perpendicularly. A protection panel was built with two rectangular prisms, the front one has dimension 50x50x8mm and a thinner back one is 50x50x5mm. A reference amour consisted of continuous plates what is depicted in fig.1.a while investigated

plates were built with hexagon rods of two diagonals for two variants. In the first version the size was 3mm- fig.1.b, in second one only 1mm – fig.1.c. The Implemented models simulated WC, AA and ceramic materials, basing on real modulus verified in literature [4], [5], [6]. Al203 ceramic was used in the front and was backed with AA 2024 alloy.

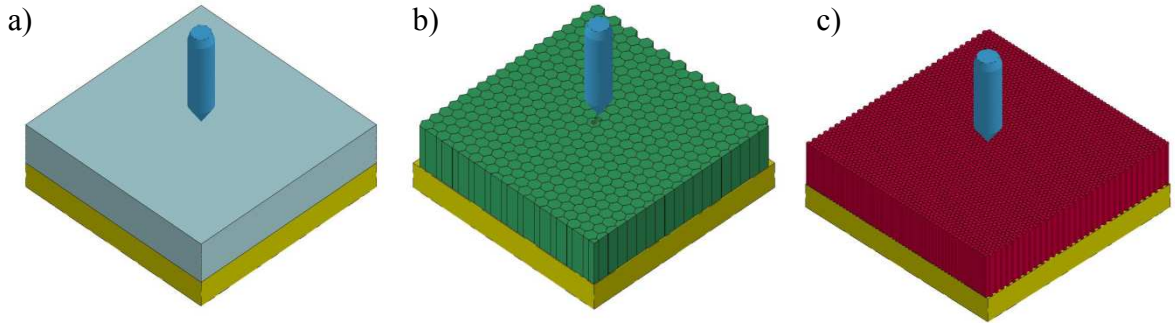


Fig1. a) reference model structure, b) model with massive rods, c) model with thin rods

Problem Solution and Analysis of the Results

All FEM models were built using brick and tetra elements. An initial speed was defined for the projectile with the same initial value for each examples. A backing plate was supported in the neighborhood of its edges, the front panel is in one option simply laying and another tied to the backing plate. LS-Dyna software [3] was used to calculate each variant with explicit time integration method. Kinetic energy of the projectile is the key parameter being analyzed without including the debris energy. In the fig.2 we can see the energy value for both situations. For the reference model curves are almost identical and for 3mm roads front panel the difference is negligible. Therefore, for further research we will not take connection between layers in consideration.

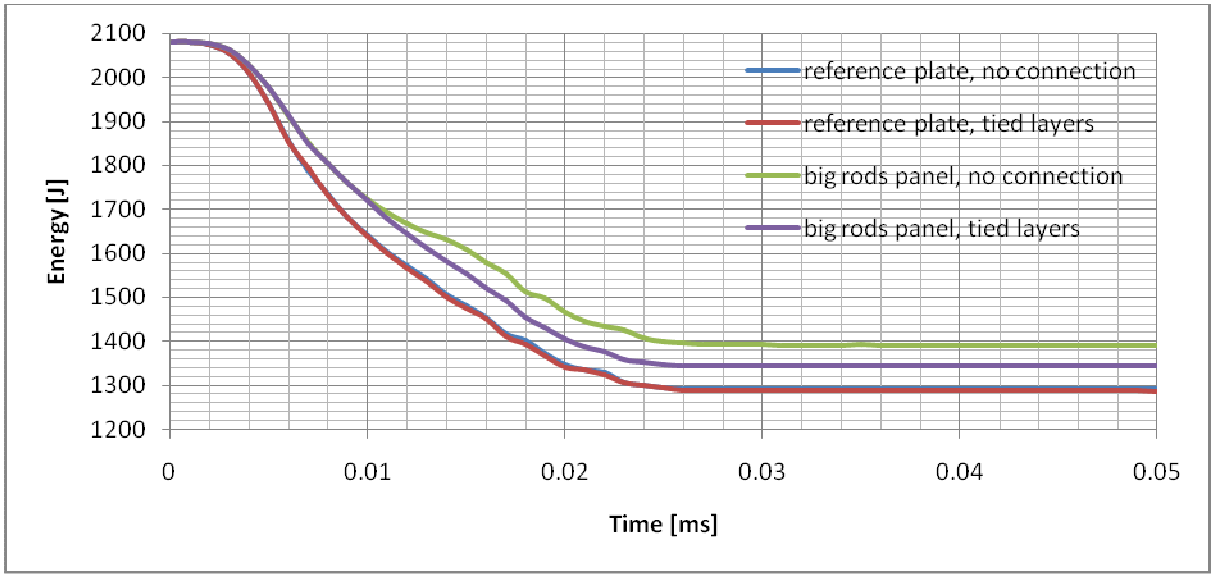


Fig.2. Kinetic energy of the projectile for reference model and big rod front panel

Effectiveness of each panel was verified in a previously described numerical test where a projectile impacts the target in the middle of the ceramic rod. Its result is shown in fig.3. Results indicate that reference model absorption is the highest, the smaller rods are the less an armor is effective. The final test considered the influence of the impact point, the point where the bullet starts penetrating a rod. Simulation was performed for a rod with 3mm diagonal as it has proven higher strength. Two additional points were chosen, one between them and another in the weakest point where three rods meet. Concluding from the graph depicted in the fig.7 frontal impact is most effective, however, results are very similar.

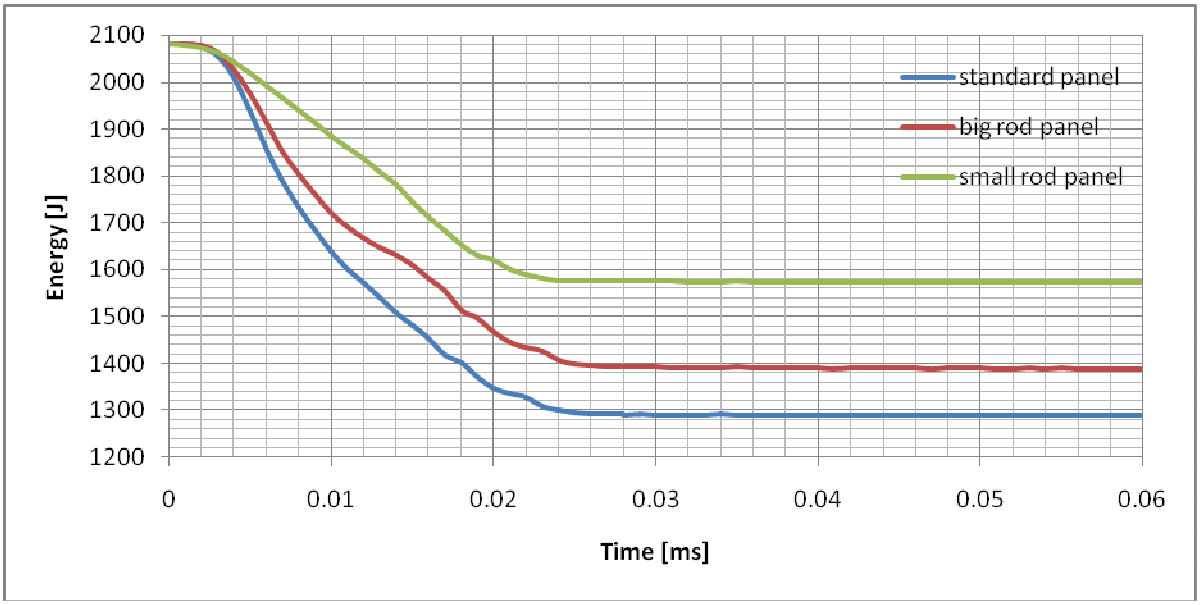


Fig.3. Kinetic energy of the projectile during impact each variant

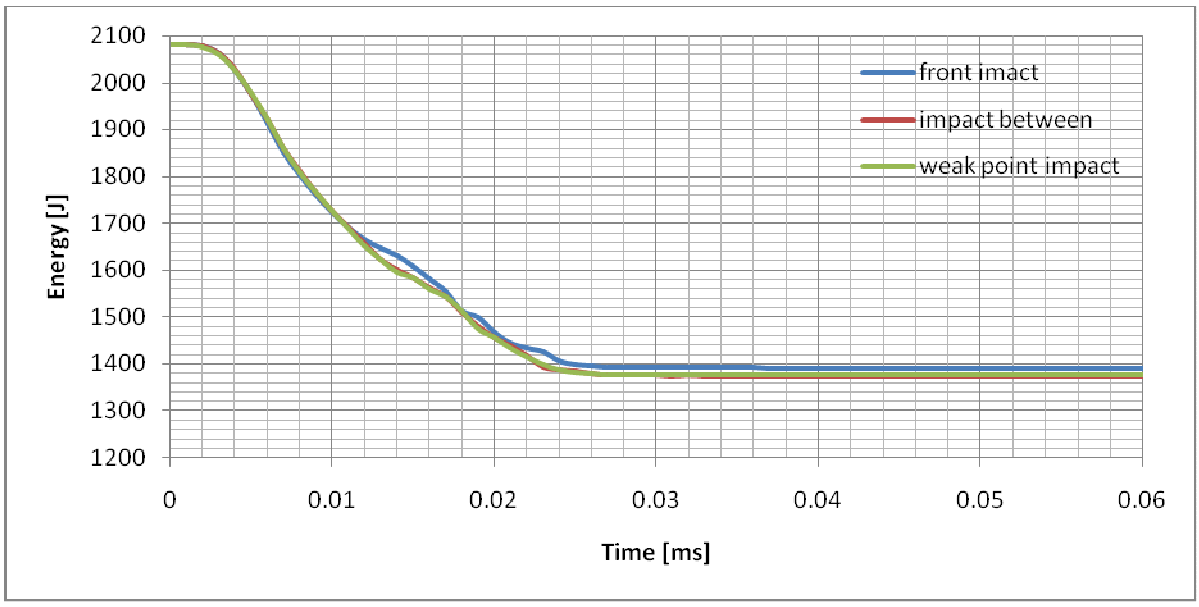


Fig.4. Influence of the projectile impact point on projectile energy

Not only the projectile energy is important for the armor but also the plate structure after the impact. Due to ceramic tendency for cracking, a damage parameter becomes one of the most crucial. On fig.5, 6 and 7 this parameter is presented for both tied and not tied plates for reference variant, small and big rods. It is clear that panels with rods have superior properties to the continuous plate, the deformation of the plate is mainly present in the surrounding of the impact whole and has little influence on the further part of the structure. The ability of the multi-rod panel to protect from further attack is much higher.

a) b)

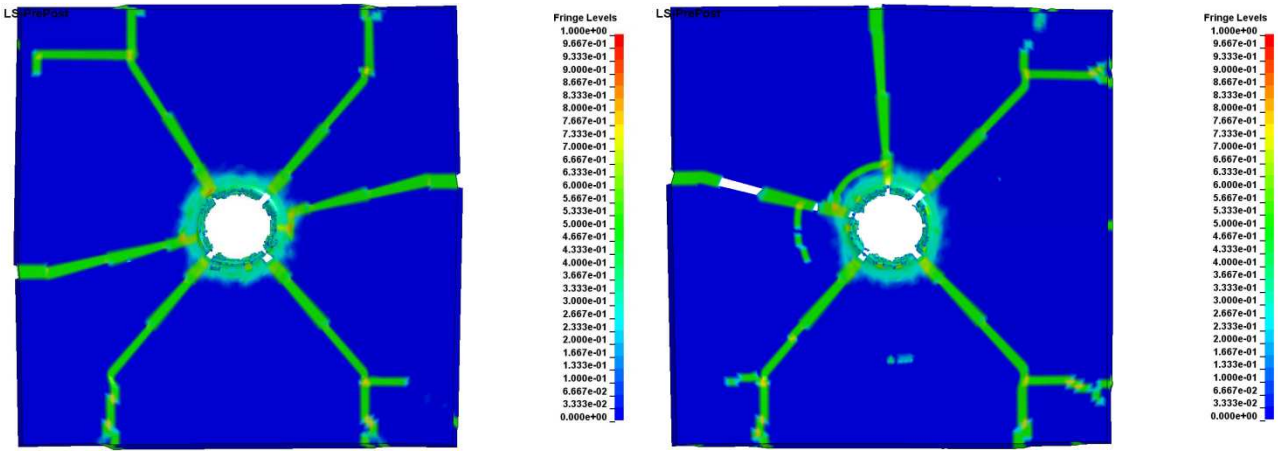


Fig.5. Damage parameter a) reference panel b) reference panel tied to backing layer

a) b)

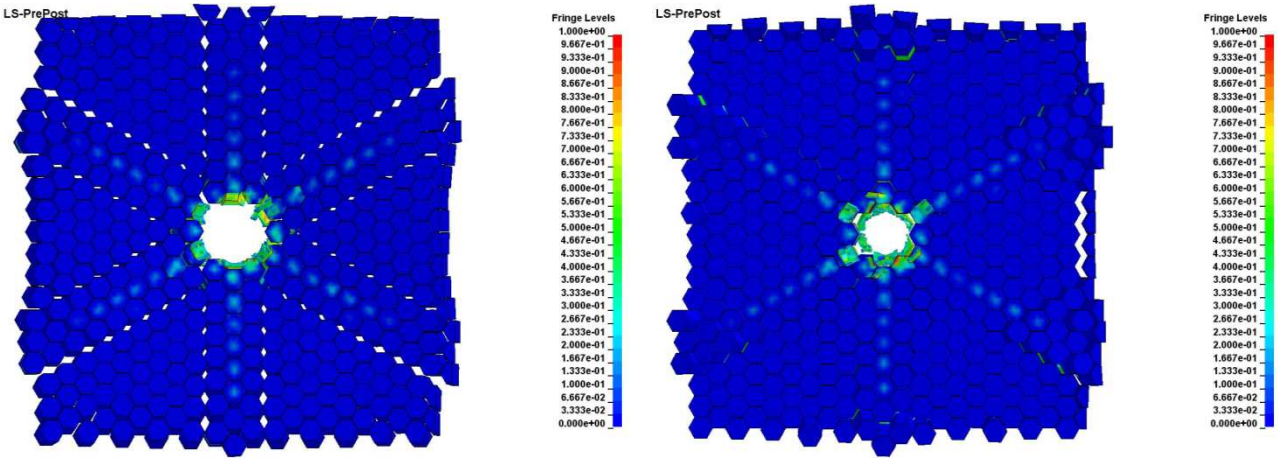


Fig.6. Damage parameter a) big rods panel b) big rod panel tied to backing plate

a) b)

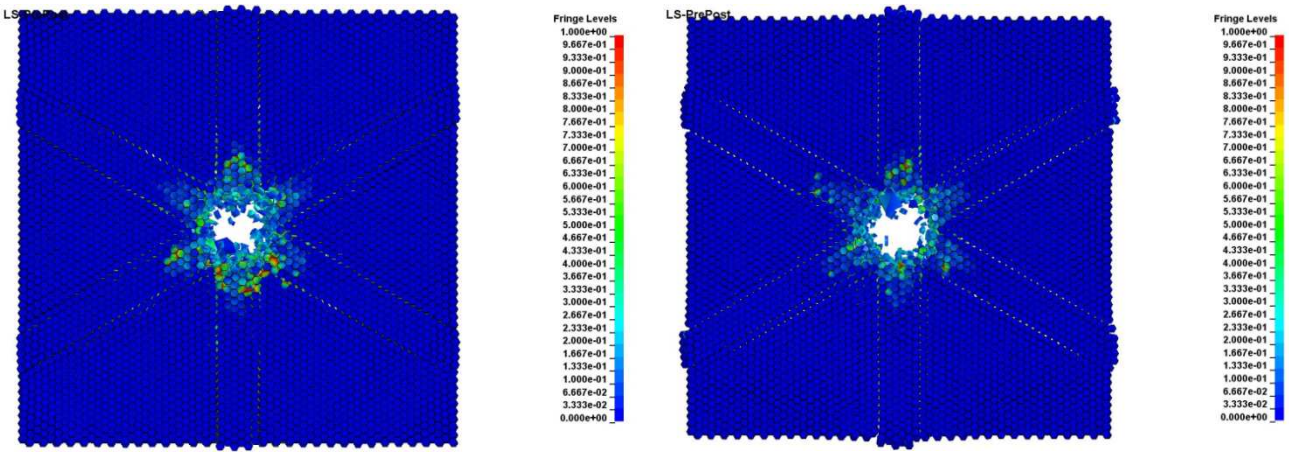


Fig.7. Damage parameter a) small rods panel b) small rod panel tied to backing plate

Summary

The obtained results show interesting properties of the new structures considering their ballistic resistance. All tests has given clear results about ballistic protection panel response under the WC projectile impact. Panels consisting of sets of hexagonal ceramic bars are slightly easier to penetrate, reference model is stronger by 19% for smaller bars and by only 7% for bigger rods. Despite this fact, a ceramic layer is much less susceptible to overall destruction which makes it more applicable for armor usage. Furthermore, little influence of the projectile impact point and consequently a part of the bar which is first destroyed is proved. The results of those numerical simulations can be used for designing of modern armor protection systems against hard kinetic projectiles.

References

[1] Mustafa U¨ beyli, R. Orhan Yıldırım, Bilgehan O¨ gel, *On the comparison of the ballistic performance of steel and laminated composite armors laminated composite armors*, Materials and Design 28 (2007) 1257–1262,

[2] Professor Paul J Hogg, *Composites for Ballistic Applications*

[3] *Ls-Dyna Keyword User's Manual*, May 2010 Version 971/Rev 5

[4] Nilsson M., *Constitutive model for Armox 500T and Armox 600T at low and medium strain rates*, Swedish Defence Research Agency, TR FOI-R-1068-SE, 2003

[5] Johnson G.R., Cook W.H., *A Constitutive Model and Data for Metals Subjected to Large Strains, High Strain Rates and High Temperatures*, Proceedings of the 7th International Symposium on Ballistics, The Hague, The Netherlands, April 1983.

[6] Panov Vili, *Modelling of behaviour of metals at high strain rates*, Cranfield University, PhD Thesis, 2005

© (2011) Trans Tech Publications, Switzerland
doi:10.4028/www.scientific.net/KEM.471-472.1147

Effects of Impregnation Time on Physical and Tensile Properties of Impregnated Sugar Palm (*Arenga pinnata*) Fibres

M.R. Ishak[1,a], Z. Leman[1,b], S.M. Sapuan[1,c], M.Z.A. Rahman[2,d], U.M.K. Anwar[3,4,e]

[1]Department of Mechanical and Manufacturing Engineering, Universiti Putra Malaysia, 43400 UPM Serdang, Selangor, Malaysia
[2]Department of Chemistry, Universiti Putra Malaysia, 43400 UPM Serdang, Selangor, Malaysia
[3]Wood Finishing Laboratory, Forest Research Institute Malaysia (FRIM), 52109 Kepong, Selangor, Malaysia
[4]Institute of Tropical Forestry and Forest Products (INTROP), Universiti Putra Malaysia, 43400 UPM Serdang, Selangor, Malaysia

[a]mridhwanishak@yahoo.com, [b]zleman@eng.upm.edu.my, [c]sapuan@eng.upm.edu.my, [d]mzaki@fsas.upm.edu.my, [e]mkanwar@frim.gov.my

Keywords: Sugar palm fibre, vacuum resin impregnation, impregnation time, *Arenga pinnata*

Abstract. The aim of this study is to investigate the effect of impregnation time on physical and tensile properties of sugar palm (*Arenga pinnata*) fibres. The fibre was impregnated with phenol formaldehyde (PF) and unsaturated polyester (UP) with various impregnation times (0, 5, 10, 15, 20, 25 min) at constant impregnation pressure of 1000 mmHg, before it was released within 30 s. Significant improvement in physical properties was observed after being impregnated for 5 min especially for fibre impregnated with PF due to its low moisture content (MC) and water absorption (WA). However, no significant changes in specific gravity for both impregnated fibres were observed. Fibre impregnated with UP for 5 min shows notable improvement in tensile strength and better fibre toughness while the fibre impregnated with PF showed lower tensile strength and elongation at break and higher tensile modulus than control specimen. Since the PF-impregnated fibre become brittle and results in lower fibre toughness as shown in the stress strain behavior, this causes for poor fibre properties. However, there was no significant difference ($p \leq 0.05$) between all impregnated fibres in physical and tensile properties after impregnation time was extended from 10 to 25 min. In general, by increasing time of impregnation did not give much effect in improving physical and tensile properties of fibres.

Introduction

There are a number of research was being carried out in development of biocomposite materials from natural fibres. Natural fibres include kenaf, jute, oil palm, pineapple leaf, banana pseudo stem, sugarcane bagasse, flax, basalt and sugar palm fibres are abundance of source, low cost, low density, high specific properties, friendlier to human health and environment and biodegradable when disposed [1]. For these reasons, they become preferred material to be used instead of glass fibre and would also serve as an alternative source of timber which now facing problem of de-forestration [2].

However, biocomposites made from natural fibre have very limited applications for outdoor. It is well understood that natural fibres are hydrophilic in nature due to the presence of hydroxyl (OH) groups throughout its structure especially at cellulose and hemicellulose portions [3]. When natural fibre is exposed to high humidity environment, these hydroxyl groups attract and hold water molecules through chemical bond that is called hydrogen bonding. The prolonged water exposure causes the fibre to degrade biologically because organisms recognize the carbohydrate polymers (mainly the hemicelluloses) in the cell wall and have very specific enzyme systems capable of hydrolyzing these polymers into digestible units. Biodegradation of the high molecular weight

cellulose weakens the fibre cell wall because crystalline cellulose is primarily responsible for the strength of the cell wall [4].

Secondly, all natural fibres are made of macrofibrils which are held together to be one single fibre. Since macrofibril naturally has an open hollow called lumen, it allows water to fill in and penetrates into fibre cell wall when the fibre is exposed to humid environment. Thus, the presence of water molecule results in fibre swelling, and shrinking when the composite is in dry condition. Frequent dimensional instability (fibre swelling in humid environment and shrinking in dry condition) would damage the composite interfacial bonding while biological attack would also damage fibre structure and decreases the composite mechanical properties [3]. Thus, the composite can no longer sustain their properties and has high tendency to break which usually happens to fibre composite products. These are the main reason why most natural fibre composites have very limited use in application or extremely impossible to be used for outdoor applications.

Thus, this study focuses on physical modification on fibre through vacuum resin impregnation process. This study was to impregnate the fibre lumen and enclose the fibre with resin in order to prevent water penetration into the fibre. This process is to be done before the fibre is used for composite reinforcement which is targeted for application of outdoor furniture. It offers a simple and low cost method which is expected to open the door for the broader use of natural fibre composite which often has inadequate properties to withstand high humid environment especially for outdoor application. The effect of impregnation times (0, 5, 10, 15, 20 and 25 min) and comparative study on different polymer used as impregnation agent; phenol formaldehyde and unsaturated polyester on physical and tensile properties of sugar palm fibres were the main objectives of this study.

Materials and Method

Sugar palm (*Arenga pinnata*) fibres were obtained from Kampung Kuala Jempol, Negeri Sembilan, Malaysia. The fibres were obtained from matured sugar palm trees, age more than 6 years and a height of 20 m. The fibres were washed and air dried for 24 h before being oven dried in an oven type MERMERT at 60 °C for 24 h. Phenol formaldehyde (PF) with molecular weight of 600 and unsaturated polyester (UP) type isophtalic with molecular weight of 2000 were used as material of impregnation resin, supplied by Pultrution Innovative Sdn. Bhd., Seremban, Negeri Sembilan, Malaysia.

Impregnation of the fibres. The sugar palm fibres were submerged in a beaker of 1000 mL which was filled with impregnation resin agent; PF and UP and placed inside a glass vessel. The glass vessel was evacuated at various impregnation times; 0, 5, 10, 15, 20, 25 min at constant pressure of 1000 mmHg (133.32 kPa) before the vacuum vessel is slowly released within 30 s. The impregnated fibres were taken out and weighed using an analytical balance which was capable of reading up to 0.0001 g for determination of resin absorption (RA) using the equation as follows;

$$\text{Resin absorption, } RA\ (\%) = (m_b - m_a) / m_a \times 100 \quad (1)$$

where m_a = mass of fibre before impregnated (g), m_b = mass of fibre after impregnated (g)

The impregnated fibres were then cured in an oven at temperature of 140 ºC for 30 min.

Determination of physical properties. The density, specific gravity, moisture content, water absorption of fibres were determined using the following equations;

$$\text{Density, } \rho\ (g/cm^3) = m_o / V_g \quad (2)$$

where m_o = mass of oven dry fibre (g), V_g = green volume of fibre (cm^3)

$$\text{Specific gravity, } SG = \rho_f / \rho_w \quad (3)$$

where ρ_f = density of fibres (g/cm^3); ρ_w = density of water (g/cm^3)

$$\text{Moisture content, } MC\ (\%) = (m_a - m_o) / m_o \times 100 \quad (4)$$

where m_a = mass of air dry fibre (g), m_o = mass of oven dry fibre (g)

Water absorption, $WA\ (\%) = (m_2 - m_1) / m_1 \times 100$ (5)

where m_1 = mass of fibre before soaking (g), m_2 = mass of fibre after soaking in distilled water for 24 h

Determination of Tensile Properties. The control and impregnated (PF and UP) fibres with various impregnation times (0, 5, 10, 15, 20, 25 min) were tested for single fibre test in according to ASTM D 3379. A total of 150 specimens were prepared and tested in room temperature of 23 °C and relative humidity of 50% using universal testing machine type Instron with load capacity of 5 kN.

Method of Result Analysis. The mean of samples were used to show any changes in physical and tensile properties of impregnated fibres. Standard error was used to show the significant difference between the variables. The results were analyzed using statistical package for the social sciences (SPSS) software. One-way analysis of variance (ANOVA) was used to determine whether increasing impregnation time gives any significant effect on physical and tensile properties of fibre at $p \leq 0.05$.

Results and Discussion

Physical Properties of Impregnated Fibre. The effect of impregnation times (5, 10, 15, 20, 25 min) on RA of sugar palm fibre is shown in Table 1. The results show that there is no significant effect on RA of impregnated fibres when impregnation time is extended from 5 to 25 min for both PF and UP. It also can be observed in Table 1 that the fibre impregnated with PF had higher than UP where in ranges of 250.74-262.33% and 228.88-243.40%, respectively. It could be explained due to low molecular weight resin of PF was used (600) while UP was 2000. Thus, it allows PF resin to be able to absorb easily onto the fibre compared to UP.

Table 1: RA of impregnated sugar palm fibre PF and UP at various impregnation times

Time, T (min)		5	10	15	20	25
RA (%)	PF	253.97 a (9.45)	262.33 a (11.79)	250.74 a (6.94)	257.34 a (8.66)	252.26 a (9.92)
	UP	235.76 a (2.35)	238.99 a (5.96)	243.40 a (8.70)	228.88 a (6.51)	237.99 a (5.44)

Note: mean followed with the same letters [a, b] in row were not significantly different ($p \leq 0.05$), values in parentheses are standard error

The effect of impregnation time on specific gravity (SG) is shown in Table 2. No significant difference ($p \leq 0.05$) was found within all impregnated fibres (PF and UP) when impregnation time was extended. In other word, it can be said that by increasing time of impregnation times; 5 to 25 min did not give significant effect to their SG.

Table 2: SG of impregnated sugar palm fibre with PF and UP at various impregnation times

Time, T (min)		Control	5	10	15	20	25
Specific gravity, SG	PF	1.23 a (0.02)	1.24 a (0.03)	1.23 a (0.04)	1.24 a (0.03)	1.23 a (0.03)	1.26 a (0.03)
	UP	1.23 a (0.02)	1.19 a (0.08)	1.22 a (0.05)	1.24 a (0.06)	1.24 a (0.06)	1.27 a (0.05)

Note: mean followed with the same letters [a, b] in row were not significantly different ($p \leq 0.05$), values in parentheses are standard error

The moisture content (MC) of control and impregnated fibres with various impregnation times are presented in Table 3. Significant improvement of physical properties is observed where MC decreased from 8.17% to the ranges of 0.7-0.73% and 0.79-0.97% when impregnated with PF and UP, respectively. The reduction of MC shows that resins were able to protect the fibres from

gaining moisture from the surrounding [5]. Since polymer is hydrophobic in nature, it encloses and protects the fibre to absorb moisture. It also can be observed in Table 3 that the fibre impregnated with PF had lower MC than UP. This is due to higher resin absorbed (as reported in RA) led the fibres to have higher resistant to moisture compared to those fibres impregnated with UP.

Table 3: MC of PF and UP-impregnated sugar palm fibre at various impregnation times

Time, T (min)		Control	5	10	15	20	25
Moisture content, MC (%)	PF	8.17 a (0.47)	0.71 b (0.19)	0.73 b (0.47)	0.73 b (0.33)	0.70 b (0.43)	0.71 b (0.30)
	UP	8.17 a (0.47)	0.83 b (0.14)	0.92 b (0.35)	0.79 b (0.48)	0.97 b (0.31)	0.89 b (0.30)

Note: mean followed with the same letters [a, b] in row were not significantly different ($p \leq 0.05$), values in parentheses are standard error

The effect of impregnation on water absorption (WA) is shown in Table 4. The lower WA is further evidence of improvement in physical properties of the impregnated fibre. The impregnated fibre showed significant reduction in MC in the ranges of 62.50-66.18% for PF and 63.35-68.37% for UP, while control specimen was 111.40%. The improvement in WA could be explained due to penetration of resin in the fibre. When the fibre was being impregnated, the applied pressure had forced resin to penetrate into all voids and filled in fibre lumen before it cured in the oven. Thus, the fibre became resistant to water since their lumens were filled with resin and fibre surface was enclosed with cured resin. Thus, it acts as an effective element inhibit or reduce WA. It can also be observed that WA of fibre impregnated with PF was lower than UP. It can be explained due to higher resin absorbed (as higher RA) than UP led the fibres to be more resistant to water. Similar trend has been reported previously, WA significantly increased after the fibres were impregnated at 5 min but no significant difference ($p \leq 0.05$) was found when impregnation time was extended for both fibres.

Table 4: WA of PF and UP-impregnated sugar palm fibre at various impregnation times

Time, T (min)		Control	5	10	15	20	25
Water absorption, WA (%)	PF	111.40 a (7.12)	62.63 b (3.48)	62.50 b (7.15)	66.18 b (5.19)	63.85 b (4.89)	64.12 b (4.00)
	UP	111.40 a (7.12)	67.02 b (2.77)	68.37 b (2.51)	64.76 b (5.38)	67.22 b (4.96)	63.35 b (5.07)

Note: mean followed with the same letters [a, b] in row were not significantly different ($p \leq 0.05$), values in parentheses are standard error

Tensile Properties of Impregnated Fibre. The impregnated fibres were tested for single fibre tensile test and their tensile stress-strain behavior is shown in Fig. 1. It showed that the fibre properties significantly changed after being impregnated with polymer resin. It can be observed that there are three different behaviors of fibres; control, PF-impregnated and UP-impregnated fibres. The highest stress is found at the fibre impregnated with UP while the lowest strain is found at the fibre impregnated with PF resin. Based on stress-strain behavior, generally it can be said that the highest toughness is found at the fibres impregnated with UP followed by control specimen while the lowest is found at fibre impregnated with PF resin. The toughness of the fibres were measured with the area underneath the stress-strain curve (Fig. 1) which indicates how much energy that material can absorb before failure. Through this point of view, the UP-impregnated fibres is said to have slightly strong and tough than control specimen while the PF-impregnated fibres were the lowest.

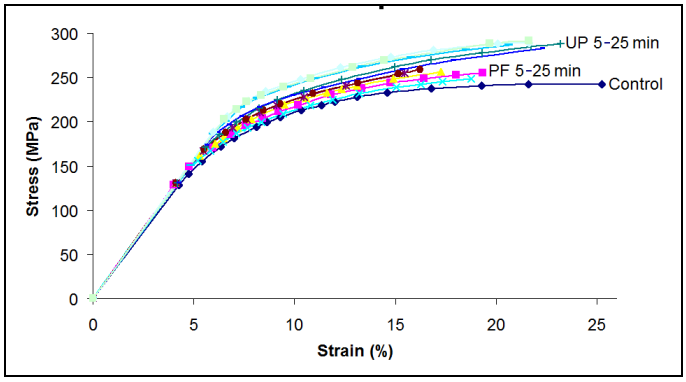


Fig. 1: Stress-strain behavior of PF and UP-impregnated sugar palm fibre at various impregnation times

Table 5 shows the mean values of tensile properties of sugar palm fibre after being impregnated with PF and UP under various impregnation times (5-25 min). Improvement in tensile strength after 5 min of impregnation was observed for both PF and UP-impregnated fibres. The improvement can be explained that the impregnated resin did not only reduce water penetration into fibre cell wall but at the same time would also act to reinforce the fibre structure. However, impregnation process has more significant effect in improvement in physical properties rather than in mechanical properties which slightly improved. As can be seen in Table 5, impregnation of fibre resulted to increase tensile modulus, indicating that the resin that was locked in the fibre lumen during impregnation process had caused the fibre become a rigid fibre and stiffer and had increased tensile modulus of the fibres. The result was expected since the impregnated fibres became hard and stiffer when it was cured. The highest tensile modulus is found significantly when the fibre impregnated with PF at 10 min while 5 min for UP and no significant increase after exceeded these impregnation times. The increase of tensile modulus particularly at PF resin can be attributed due to its higher tensile modulus of PF than UP.

Table 5: Tensile properties of PF and UP-impregnated sugar palm fibre at various impregnation times

Time, T (min)		Control	5	10	15	20	25
Tensile strength (MPa)	PF	241.93 a (2.47)	254.85 b (4.99)	256.30 b (6.50)	248.51 b (7.07)	254.67 b (6.38)	257.14 b (6.02)
	UP	241.93 a (2.47)	283.75 b (6.21)	280.98 b (5.35)	285.06 b (6.07)	288.17 b (6.61)	290.36 b (5.29)
Tensile modulus (GPa)	PF	3.07 a (0.01)	3.13 b (0.01)	3.17 c (0.01)	3.17 c (0.01)	3.18 c (0.01)	3.17 c (0.01)
	UP	3.07 a (0.01)	3.11 b (0.01)	3.12 b (0.01)	3.13 b (0.01)	3.11 b (0.01)	3.11 b (0.01)
Elongation at break (%)	PF	25.16 a (0.31)	19.37 b (4.05)	17.29 b (2.19)	18.71 b (3.35)	15.44 b (4.21)	16.25 b (3.53)
	UP	25.16 a (0.31)	23.09 b (1.62)	22.21 b (1.12)	20.62 b (3.19)	21.82 b (2.22)	21.67 b (2.37)

Note: mean followed with the same letters [a, b] in row were not significantly different ($p \leq 0.05$), values in parentheses are standard error

In term of elongation at break, it was inversely proportional to tensile modulus where it decreased after being impregnated as shown in Table 5. Since the elongation at break of PF is very low, the brittle nature of PF resin decreases elongation of fibre dominantly and followed with UP resin. This is evident that the behavior of fibre significantly changed after being impregnated where the ductility nature of sugar palm fibre has decreased. However, similar behavior as been observed in tensile strength and physical properties, no significant difference ($p \leq 0.05$) in elongation at break was observed for impregnated fibre of PF and UP after being impregnated for 5 min. This explains that impregnation with polymer resin improved physical (MC and WA) and tensile properties of fibres. However, the parameter of study; impregnation time did not give any significant contribution to further improve the physical and tensile properties of impregnated fibres. These may attributed due to low pressure used (1000 mmHg) which did not give significant effect to the fibre properties even impregnation time was extended.

Summary

Physical and tensile properties of control and impregnated sugar palm fibre with PF and UP at various impregnation times (5, 10, 15, 20 and 25 min) were studied. Significant improvement in physical properties (RA, MC and WA) were observed after the fibre being impregnated for 5 min while no significant changes in SG for all impregnation times. However, no significant difference at ($p \leq 0.05$) was observed after impregnation time was extended from 10 to 25 min. For the effect of impregnation time on mechanical properties of fibre, the fibres impregnated with UP showed better tensile properties than PF after the fibre being impregnated for 5 min. It was observed that tensile strength and elongation at break of UP-impregnated fibres were higher than PF which result to better fibre toughness as can be seen in stress strain behavior. Similar to physical properties, no significant improvement in tensile properties were observed when impregnation time exceeded than 5 min. In general, this study concluded that impregnation with polymer resin; PF and UP thermoset polymers improved physical and tensile properties when the fibres impregnated for 5 min but no improvement after impregnation time was extended from 10 to 25 min. It shows that by increasing time of impregnation does not give much significant improvement in physical and tensile properties of sugar palm fibres. Different parameter of study is proposed to be done such as by increasing impregnation pressure which might give more significant effects to fibre properties.

Acknowledgements

The authors would like to acknowledge Ministry of Agriculture and Agro-Based Industry (MOA) of Malaysia for funding the research grant (Science Fund, project number: 05-01-04-SF1114).

References

[1] Ishak, M.R., A.M.M. Edeerozey, Othman, I.S., Leman, Z., Sapuan, S.M., *IOP Conference Series: Materials Science and Engineering* Vol. 11(1) (2010) 012006.

[2] Ishak, M.R., Leman, Z., Sapuan, S.M., Salleh, M.Y., Misri, S. *International Journal of Mechanical and Material Engineering (IJMME)* Vol. 4(3) (2009) p. 316-320

[3] Ishak, M.R., Sapuan, S.M., Leman, Z., Sahari, J. and Ibrahim, M.S. 2010. In *Proceeding of the 2nd Postgraduate Seminar on Natural Fibre Composite 2010*, 18-19 February

[4] Rowell, R.M. In *Science and Technology of Polymers and Advanced Materials*, ed. P.N., Prasad, J.E., Mark, S.H., Kandil, Z.H., Kafafi, Plenum Press: New York, 1998.

[5] U.M.K. Anwar, M.T. Paridah, H. Hamdan, S.M. Sapuan, E.S. Bakar Industrial Crops and Products Vol. 29 (2009) p. 214–219

© (2011) Trans Tech Publications, Switzerland
doi:10.4028/www.scientific.net/KEM.471-472.1153

Effects of Impregnation Pressure on Physical and Tensile Properties of Impregnated Sugar Palm (*Arenga pinnata*) Fibres

M.R. Ishak[1,a], Z. Leman[1,b], S.M. Sapuan[1,c], M.Z.A. Rahman[2,d], U.M.K. Anwar[3,4,e]

[1]Department of Mechanical and Manufacturing Engineering,
Universiti Putra Malaysia, 43400 UPM Serdang, Selangor, Malaysia
[2]Department of Chemistry, Universiti Putra Malaysia,
43400 UPM Serdang, Selangor, Malaysia
[3]Wood Finishing Laboratory, Forest Research Institute Malaysia (FRIM),
52109 Kepong, Selangor, Malaysia
[4]Institute of Tropical Forestry and Forest Products (INTROP),
Universiti Putra Malaysia, 43400 UPM Serdang, Selangor, Malaysia

[a]mridhwanishak@yahoo.com, [b]zleman@eng.upm.edu.my, [c]sapuan@eng.upm.edu.my,
[d]mzaki@fsas.upm.edu.my, [e]mkanwar@frim.gov.my

Keywords: Sugar palm fibre, vacuum resin impregnation, impregnation pressure, *Arenga pinnata*

Abstract. The aim of this study is to investigate the effect of impregnation pressure on physical and tensile properties of sugar palm (*Arenga pinnata*) fibres. The fibre was impregnated with phenol formaldehyde (PF) and unsaturated polyester (UP) with different impregnation pressures (1000, 900, 800, 700, 600 and 500 mmHg) at constant impregnation time of 5 min. Significant improvement in physical properties was observed due to reduction of moisture content (MC) and water absorption (WA) after being impregnated from 1000 to 500 mmHg while PF-impregnated fibre was showing more superior. Improvement in mechanical properties was also observed after being impregnated where much better tensile properties and toughness were found at UP-impregnated fibres while PF-impregnated fibres were found to be very much lower in toughness. This study concluded that in order to improve physical and tensile properties of sugar palm fibre, the fibre is proposed be impregnated with UP resin with impregnation pressure of 600 mmHg for 5 min.

Introduction

One of the drawback of natural fibre is their hydrophilic nature due to the presence of hydroxyl (OH) groups throughout its structure especially for cellulose and hemicellulose portions [1]. When natural fibre is exposed to high humidity environment, these hydroxyl groups attract and hold water molecules by chemical bond that is called hydrogen bonding. Details about these circumstances are discussed in detail in our recent study [2]. These are the main reasons why biocomposite products have very limited in outdoor applications. Thus, this study focused on physical modification on fibre through vacuum resin impregnation process. The principle idea behind this process is to impregnate the fibre lumen and to enclose the fibre surface with thermoset resin in order to prevent water penetration into the fibre before being used for composite reinforcement. Since our recent study [2] has found that impregnation time did not give much significant improvement in physical and tensile properties of sugar palm fibres, hence, the aim of this study is to understand the effect of impregnation pressure on physical and tensile properties of sugar palm fibres, which might contribute significantly effect to the fibre properties.

Materials and Method

Since this study was a continuation from our previous study [2], hence, similar materials and method was used with different variable of impregnation pressure instead of impregnation time. The

sugar palm fibres were impregnated with different pressures of 1000, 900, 800, 700, 600 and 500 mmHg (133.32, 119.99, 106.66, 93.33, 79.99 and 66.66 kPa) at constant impregnation time of 5 min. Surface morphological of fibres were observed using optical microscope model Lieca MS 5 with constant magnification of 400.

Results and Discussion

Physical Properties of Impregnated Fibre. The resin absorption (RA) of control and impregnated palm fibres at various impregnation pressures are shown in Table 1. Significant increase in RA was observed when the fibre was impregnated with polymer resin. The increase of RA was found much higher at PF-impregnated fibre as the impregnation pressure increased where the highest RA found at 500 mmHg while 600 mmHg for UP. The higher RA of PF-impregnated fibres was due to low molecular weight of PF that has deposited extensively into fibre lumen compared to UP. Since low molecular weight of polymer has short branching in polymer unit allows the resin to be able to have deep penetration into fibre cell wall. This is an important factor in impregnation of resin because penetration of resin depends on the size of the oligomer or polymer [3].

Table 1: RA of PF and UP-impregnated sugar palm fibres at various impregnation pressures

Pressure, P (mmHg)		1000	900	800	700	600	500
Resin absorption, RA (%)	PF	240.89 a (5.59)	302.04 b (6.05)	345.21 c (11.53)	383.97 d (5.05)	409.94 e (4.42)	420.21 f (0.59)
	UP	231.67 a (8.58)	262.33 b (2.57)	305.71 c (4.58)	334.64 d (5.40)	352.68 e (2.89)	357.79 e (2.60)

Note: mean followed with the same letters [a, b] in row were not significantly different ($p \leq 0.05$), values in parentheses are standard error

The effect of impregnation pressure on specific gravity (SG) of fibre is shown in Table 2. This is further evidence that the fibre was physically impregnated due to increasing SG. The SG of fibre was slightly increasing in fibre when impregnated with PF at 600 and 500 mmHg. However, no significant changes in SG for the fibre impregnated with UP. These results was good since impregnation with UP did not increase in their weight, while only a small increase was found when impregnated with PF (600 and 500 mmHg). The significant increase in SG of PF-impregnated fibres (at 600 and 500 mmHg) was expected because it absorbed more resin as reported in RA, this can be explained through its low molecular weight resin of PF. According to Stamm and Seborg [4], the molecular size of the resin must be sufficiently small to allow the penetration of the cell wall, requiring that the resin to be unpolymerized or only slightly polymerized.

Table 2: SG of PF and UP-impregnated sugar palm fibres at various impregnation pressures

Pressure, P (mmHg)		Control	1000	900	800	700	600	500
Specific gravity, SG	PF	1.22 a (0.02)	1.22 a (0.01)	1.24 a (0.01)	1.25 a (0.01)	1.27 a (0.03)	1.29 b (0.02)	1.33 c (0.03)
	UP	1.22 a (0.02)	1.22 a (0.01)	1.23 a (0.01)	1.24 a (0.02)	1.25 a (0.02)	1.25 a (0.01)	1.26 a (0.01)

Note: mean followed with the same letters [a, b] in row were not significantly different ($p \leq 0.05$), values in parentheses are standard error

The results of moisture content (MC) of control and impregnated fibres at various impregnation pressures are shown in Table 3. Significant improvement in physical properties was observed due to reduction of MC after being impregnated with polymer resin. The MC was found to be reduced after impregnated at the pressure of 800 mmHg for both resin types (0.41-0.46 % for PF; 0.44-0.53 % for UP) while no reduction was noticed when pressure was increased (700-500 mmHg). The higher MC of control specimen (8.19 %) was caused by absorption of moisture into fibre cell wall. It was due to its natural structure of open hollow called lumen and hydrophilic nature of natural fibre. When natural fibres are exposed to high humidity environment, the first water molecules are

absorbed directly onto hydrophilic groups of the fibre material and then, the other water molecules are attracted either to other hydrophilic groups or they may form further layers on top of the water molecules already absorbed [5-6]. According to Chen [7], at high humidity levels, liquid water may be held by the forces of surface tension in capillary spaces available in the material. Thus, this study has successfully proven that the penetration of water molecules were inhibited by enclosing the fibre with hydrophobic materials such as polymer resin through fibre-resin impregnation process. When the impregnated fibre was cured in the oven, the fibre became moisture resistant since it was enclosed with cured resin and inhibited moisture absorption. It can be seen in Table 3 that MC of fibre impregnated with PF and UP resin was reduced considerably.

Table 3: MC of PF and UP-impregnated sugar palm fibres at various impregnation pressures

Pressure, P (mmHg)		Control	1000	900	800	700	600	500
Moisture content, MC (%)	PF	8.19 a (0.08)	0.75 b (0.02)	0.63 c (0.01)	0.46 d (0.09)	0.41 d (0.12)	0.42 d (0.05)	0.46 d (0.09)
	UP	8.19 a (0.08)	0.87 b (0.03)	0.79 c (0.01)	0.44 d (0.02)	0.48 d (0.04)	0.53 d (0.04)	0.49 d (0.04)

Note: mean followed with the same letters [a, b] in row were not significantly different ($p \leq 0.05$), values in parentheses are standard error

Further evidence of improvement in physical properties is shown in Table 4 where significant reduction of water absorption (WA) was observed. The WA was reduced when the resin was impregnated at pressures of 500 and 600 mmHg for PF and UP respectively. Similar to the reduction of MC, the resin acts effectively in reducing MC in humid environment, it also reduced WA during water immersion (24 h). The resin was deposited extensively into fibre cell wall and also enclosed the hydrophilic fibre which caused the fibre to become highly water resistant.

Table 4: WA of PF and UP-impregnated sugar palm fibres at various impregnation pressures

Pressure, P (mmHg)		Control	1000	900	800	700	600	500
Water absorption, WA (%)	PF	116.82 a (6.39)	61.64 b (2.12)	42.84 c (4.09)	30.49 d (0.46)	26.03 e (0.64)	24.32 f (0.02)	22.52 g (0.15)
	UP	116.82 a (6.39)	63.49 b (2.09)	46.55 c (2.30)	33.01 d (0.55)	26.61 e (0.23)	23.97 f (0.51)	23.31 f (0.03)

Note: mean followed with the same letters [a, b] in row were not significantly different ($p \leq 0.05$), values in parentheses are standard error

It can be understood by observing Fig. 1-7 where the fibres were enclosed with the resin after being impregnated. The surface of control and UP-impregnated fibres were significantly different. Fig 1 shows clearly that their natural surface of control specimen where different from Fig. 2-7 where the impregnated fibres were enclosed with UP resin. It also can be observed that the fibre impregnated with 500 mmHg (Fig. 7) of impregnation pressure was fully enclosed with resin while fibre impregnated at 1000 mmHg (Fig. 2) seemed to be partially enclosed. This might answer the reason of different physical properties of impregnated fibres where increased in RA and SG while decreased MC and WA as the impregnation pressure was increased from 1000 to 500 mmHg.



Fig. 1: Control

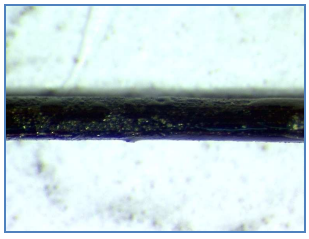


Fig. 2: 1000 mmHg

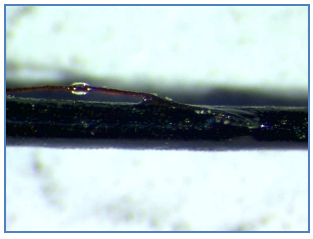


Fig. 3: 900 mmHg

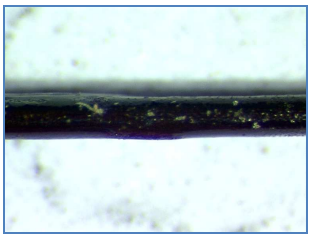


Fig. 4: 800 mmHg

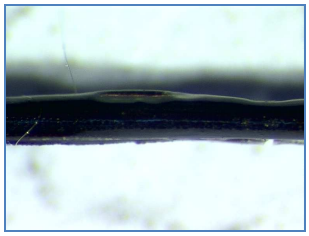


Fig. 5: 700 mmHg

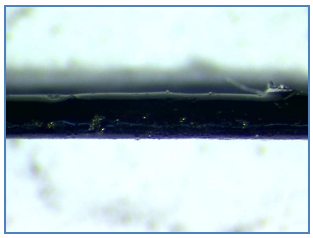


Fig. 6: 600 mmHg

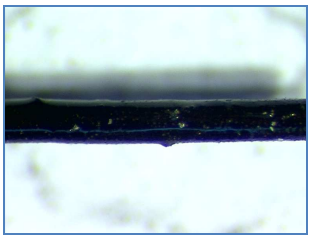


Fig. 7: 500 mmHg

Tensile Properties of Impregnated Fibre. Fig. 8 shows tensile stress strain behavior of control and impregnated fibres at various impregnation pressures. It showed that the behavior of fibre was obviously changed after impregnation pressure was increased. It was clearly observed in Fig. 8 that the tensile strength and modulus of impregnated fibres (PF and UP) increased while the elongation at break decreased.

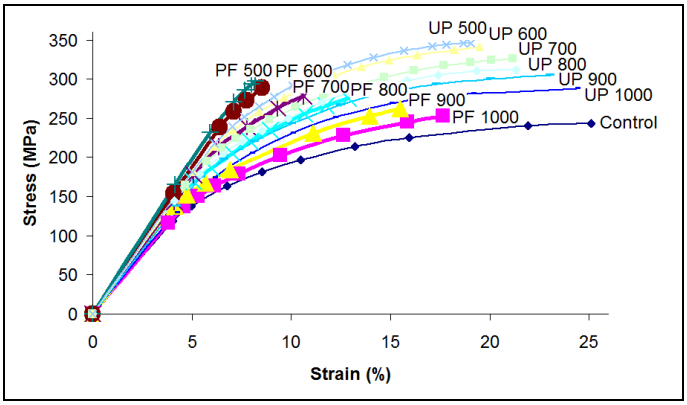


Fig. 8. Stress-strain behavior of PF and UP-impregnated sugar palm fibre at various impregnation pressures

It is shown in Table 5 that tensile strength of PF and UP-impregnated fibres significantly increased as the impregnation pressure was increased where the improvement is more pronounced in UP-impregnated fibres. The highest tensile strength of PF and UP-impregnated fibres was found at impregnation pressure of 500 mmHg and 600 mmHg, respectively. The increase of tensile strength showed that the resin that was impregnated in the fibre cell wall did not only acts to improve physical properties but at the same time had increased the strength of the fibre. Similar to tensile strength, the resin that was locked in the fibre caused the fibre became rigid and stiffer where approaching the behavior of brittle nature PF and UP resin. It is shown in Table 5 that the increase of tensile modulus showing the impregnated fibre became brittle. Different trend obtained in tensile strength, the PF-impregnated fibres had significantly higher tensile modulus than UP-impregnated fibres which both impregnated fibres had reached maximum at 600 mmHg as shown in Table 5. As been observed in Fig. 8, the elongation at break for both impregnated fibres decreases where PF was found to be much lower compared to that of UP. The maximum decrease of elongation at break of PF and UP-impregnated fibres was found at 500 and 600 mmHg, respectively. It is clearly that the more resin absorbed, the behavior of thermoset resin (PF and UP)

was more influence in the fibre which is brittle and having low elongation at break compared to control specimen (24 %) [8-9].

Table 5: Tensile properties of PF and UP-impregnated sugar palm fibre at various impregnation pressures

Pressure, P (mmHg)		Control	1000	900	800	700	600	500
Tensile strength (MPa)	PF	243.77 a (1.46)	251.39 b (3.43)	263.36 c (4.15)	271.44 d (3.59)	279.88 e (2.70)	288.41 f (4.55)	297.67 g (5.43)
	UP	243.77 a (1.46)	287.84 b (3.99)	304.59 c (2.32)	312.99 d (4.52)	326.07 e (3.35)	341.60 f (4.33)	344.71 f (3.68)
Tensile modulus (GPa)	PF	3.07 a (0.22)	3.15 b (0.16)	3.39 c (0.04)	3.55 d (0.05)	3.73 e (0.00)	3.89 f (0.03)	3.98 f (0.06)
	UP	3.07 a (0.22)	3.10 b (0.08)	3.27 c (0.03)	3.41 d (0.03)	3.51 e (0.01)	3.59 f (0.01)	3.60 f (0.01)
Elongation at break (%)	PF	25.16 a (0.34)	17.66 b (0.23)	15.50 c (0.42)	12.88 d (0.44)	10.595 e (0.40)	8.60 f (0.47)	6.26 g (0.20)
	UP	25.16 a (0.34)	24.24 b (0.16)	22.945 c (0.29)	21.455 d (0.17)	20.95 e (0.19)	19.17 f (0.21)	19.05 f (0.15)

Note: mean followed with the same letters [a, b] in row were not significantly different ($p \leq 0.05$), values in parentheses are standard error

In general, it can be said that fibre-resin impregnation with thermosetting polymer improves mechanical properties of sugar palm fibre. Similar finding was reported by many researchers where resin impregnation has improved the mechanical properties of several lignocellulosic materials [10-12]. Based on stress-strain graph theory, the area covered under stress strain curve represents as material toughness which indicates total energy that material can absorb before rupturing. A material is said to be strong and tough if it ruptures at high stress and exhibiting high strain values. While for material of low in toughness, it may be strong (has high ultimate stress) but having low strain values (usually happen at brittle materials). Thus, a high stress and strain values will result to high toughness and it is desirable properties of fibre to be produced for composite reinforcement. This is an important factor for engineers in selection, modification or designing a new type of material in order to ensure that the material is strong and tough. In other word, it is good to have materials with high modulus which can resist deformation, but in the real situation, it is a lot better for a materials to bend than to break, and if bending, stretching or deforming in some way prevents the materials from breaking [13-14]. Thus, it is an important criterion to not only produce a high modulus and strength of fibre but to consider the fibre should be strong and tough.

This is an important issue should be discussed in this study since the impregnated fibres increased stress values but indicating significant decreased elongation at break which may result to reduce the fibre toughness. Based on stress-strain graph theory, it can be observed that the PF-impregnated fibres showed significant drop in toughness especially at the fibre impregnated at high pressure (600 and 500 mmHg) as shown in Fig. 8. For the fibre impregnated with UP, it was observed that tensile strength increased where slightly decreased elongation at break. Based on the area covered under stress strain curve, the toughness of UP-impregnated fibres were still reliable and higher than control specimen while PF-impregnated fibres showed the lowest. Furthermore, by using PF resin as impregnation agent has increased tensile modulus which represent the increment in brittleness of fibre compared to UP as shown in Table 5. In fact, it is good to have a material with good toughness rather than to produce a brittle materials especially for material used in structural applications. Then, by considering their final weight which contribute to its end products (composite), the PF-impregnated fibres showed significant increase in SG where increased their weight as a result of higher RA. As it was mentioned earlier, through impregnation with UP did not increase the SG (weight). Also considering on human safety and environment, it is well known that the formaldehyde reaction of PF will cause deadly effect to human health and environment.

Statistically considering the results obtained in both physical and mechanical properties and taking into concern about human and environmental friendly; it is worth noting that in order to improve physical and tensile properties of sugar palm fibre, the fibre is proposed to be impregnated with UP resin with impregnation pressure of 600 mmHg for 5 min.

Summary
Physical and tensile properties of control and impregnated sugar palm fibre with PF and UP at various impregnation pressures (1000, 900, 800, 700, 600 and 500 mmHg) were studied. Significant improvement ($p \leq 0.05$) in physical (RA, SG, MC and WA) and tensile properties were observed after impregnation pressure was extended from 1000 to 500 mmHg. It was observed that fibre impregnated with thermoset polymer resin (PF and UP) showed notable improvement in physical properties while PF was more superior. However, for mechanical properties, the UP-impregnated fibres exhibited much better tensile performance while PF-impregnated fibres significant drop in toughness. This study concluded that in order to improve physical and tensile properties of sugar palm fibre, the fibre should be impregnated with UP resin with impregnation pressure of 600 mmHg for 5 min. In general, this study has proven that fibre-resin impregnation with thermoset polymer has great potential for properties enhancement of natural fibres.

Acknowledgements
The authors would like to acknowledge Ministry of Agriculture and Agro-Based Industry (MOA) of Malaysia for funding the research grant (Science Fund, project number: 05-01-04-SF1114).

References

[1] Ishak, M.R., Sapuan, S.M., Leman, Z., Sahari, J. and Ibrahim, M.S. 2010. In *Proceeding of the 2nd Postgraduate Seminar on Natural Fibre Composite 2010*, 18-19 February

[2] M.R. Ishak, Z. Leman, S.M. Sapuan, M.Z.A. Rahman and U.M.K. Anwar. Key Engineering Materials. 2011

[3] Ibach, R.R., Ellis, W.D. (*2005*) In *Handbook of Wood Chemistry and Wood Composites. Edited by Roger M. Rowell 2005 p.421-445. CRC Press*

[4] Stamm, A.J. and Seborg, R.M. Resin treated wood – impreg. USDA Forest Service, Forest Products Laboratory, Report No. 1380

[5] Morton, W.E. and Hearle, J.W.S. Manchester: The Textile Institute; 1993.

[6] Peirce, F.T. J. Text Inst 1929 Vol. 29 T 133-150

[7] Chen, H. Miao, M. and Ding, X. Composites: Part A Vol 40 (2009) p. 2013-2019.

[8] Ishak, M.R., Sapuan, S.M., Leman, Z., Sahari, J., Ibrahim, M.S. 2010. In *The 4th World Engineering Congress (WEC 2010), Kuching, Sarawak, Malaysia, 2-5 August.*

[9] Sahari, J., Sapuan, S.M., Zaki, M.A.R., Ishak, M.R., Ibrahim, M.S. 2010. In *The 4th World Engineering Congress (WEC 2010), Kuching, Sarawak, Malaysia, 2-5 August.*

[10] Deka, M., Saikia, C.N., 2000. *Bioresour. Technol.* Vol. 73 p. 179–181

[11] Shams, M.I., Yano, H., Endou, K., 2004. Wood Sci. Vol. 50 p. 337–342

[12] U.M.K. Anwar, M.T. Paridah, H. Hamdan, S.M. Sapuan, E.S. Bakar Industrial Crops and Products Vol. 29 (2009) p. 214–219

[13] Jang, B. Z.; *Advanced Polymer Composites: Principles and Applications*, ASM International, Materials Park, OH, 1994.

[14] Odian, George; *Principles of Polymerization, 3rd ed.*, J. Wiley, New York, 1991.

© (2011) Trans Tech Publications, Switzerland
doi:10.4028/www.scientific.net/KEM.471-472.1159

Indentation Analysis of In-Plane Prestressed Composite Sandwich Plates: An Improved Contact Law

Mehdi Hosseini[1, a], Seyyed Mohammad Reza Khalili[1, 2, b]

and Keramat Malekzadeh Fard[1, c]

[1]Centre of Excellence for Research in Advanced Materials and Structures,
Faculty of Mechanical Engineering, K.N. Toosi University of Technology, Tehran, Iran
[2]Faculty of Engineering, Kingston University, London, UK

[a]m.hosseini27@gmail.com, [b]smrkhalili2005@gmail.com, [c]k.malekzadeh@gmail.com

Keywords: composite sandwich plate; contact law; indentation

Abstract. In this article a closed form solution is derived for the deformation response of a composite sandwich plate subjected to static indentation of a flat-ended cylindrical indenter. The facesheet deflection is several times the laminate thickness so that bending moments may be neglected and only membrane forces are considered in the facesheet. In contrast to the existing analytical model for the indentation of composite sandwich plates, in the present model, the stacking sequence of the facesheets can be completely arbitrary, so that the shear-extension coupling terms, i.e. A_{16} and A_{26}, can also be included in the analysis. Furthermore, in the present model the effects of the initial in-plane normal and shear stresses on the edges of the sandwich plate are also considered. An improved contact law is derived based on the minimum total potential energy principle. The elastic strain energy, the plastic work dissipated in crushing the core and the external work are calculated using an appropriate shape function for the facesheet deflection. The relations between the indentation load and the deflection and length of deformation are obtained by minimization of the total potential energy. Analytical predictions of the load-indentation response compare well with experimental results. The effects of stacking sequence, ply thickness, number of layers and initial in-plane forces on the load-indentation response are studied and discussed.

Introduction

Sandwich structures with laminated composite facesheets and lightweight core materials are being used increasingly as primary load-carrying components in the modern technology. However, a thorough understanding of their mechanical behavior and failure is needed before they can be safely and efficiently used. The aim of this paper is to develop an analytical procedure for predicting the deformation of composite sandwich plates.

A great deal of research on the contact loading of composite sandwich panels has been experimental and/or numerical in nature. Few analytical solutions have been proposed for the problem because of the complicated interaction between the composite facesheet and core during deformation and failure. Ambur and Cruz [1] carried out a local-global analysis to determine the contact force and displacement of the panel. Olsson and McManus [2] set up an analytical model for the indentation of sandwich panels. A complete review of the subject of impact on sandwich structures was carried out by Abrate [3]. Turk and Hoo Fatt [4] derived closed form solutions for the deformation and fracture responses of a composite sandwich plate subjected to static indentation of a hemispherical-nose indenter. Gong and Lam [5] used a spring-mass model having two degrees-of-freedom in order to determine the history of contact force produced during impact. They also included structural damping in their model. Hoo Fatt and Park [6] obtained approximate solutions for the static indentation of sandwich panels using the principle of minimum potential energy. Olsson [7] also gave an engineering method for predicting the impact response and damage in sandwich panels. Zhou and Stronge [8] studied the impact response of thin, lightweight circular sandwich panels with simply supported boundaries.

In this paper, analytical solutions are derived for the indentation chracteristics of composite sandwich plates. The stacking sequence of the facesheets can be completely arbitrary, so that the shear-extension coupling terms, i.e. A_{16} and A_{26}, can be included in the analysis. Moreover, the effects of the initial in-plane normal and shear stresses on the edges of the sandwich plate are also considered. Analytical predictions of the load-indentation response are compared with experimental results and the effects of some important parameters on the load-indentation response are investigated.

Load-indentation Characteristics. A composite sandwich plate of dimensions $a \times b$, with laminated facesheets of thickness h and core thickness H is considered. The sandwich plate is rigidly supported and subjected to static indentation at the origin by a rigid, flat-ended cylinder of radius R and length L. It is assumed that the laminate deformations are several times the laminate thickness so that the laminate can be considered as a membrane, i.e., bending resistance of the facesheet is neglected.

The minimum total potential energy principle is utilized to derive the load-indentation relation. The total potential energy Π is [9]:

$$\Pi = U + D - W. \tag{1}$$

where U is the elastic strain energy of the facesheet, D the plastic work dissipated in crushing the core and W the external work done. The indented surface of the facesheet w is assumed to be in the form:

$$w(x,y) = \begin{cases} \delta \quad for\ 0 \le x^2 + y^2 \le R^2. \\ \delta\left[1 - \dfrac{(x-R)}{(\xi - R)}\right]^2 \left[1 - \dfrac{(y-R)}{(\xi - R)}\right]^2. \\ for\ R^2 \le x^2 + y^2 \le \xi^2, \quad x \ge 0, \quad y \ge 0. \end{cases} \tag{2}$$

where δ is the deflection under the indenter, ξ the length of the deformation zone and R the radius of the indenter. The above function is assumed to be symmetric with respect to both x- and y-axis. Coefficients of the above function satisfy the boundary conditions: zero slope and deflection at the boundary of the deformation zone. The elastic strain energy U in the facesheet due to membrane forces is:

$$U = \frac{1}{2}\int_R^{\xi}\int_R^{\xi} \left\{ A_{11}\left(\frac{\partial w}{\partial x}\right)^4 + A_{22}\left(\frac{\partial w}{\partial y}\right)^4 + 4A_{66}\left(\frac{\partial w}{\partial x}\right)^2\left(\frac{\partial w}{\partial y}\right)^2 + 2A_{12}\left(\frac{\partial w}{\partial x}\right)^2\left(\frac{\partial w}{\partial y}\right)^2 + 4A_{16}\left(\frac{\partial w}{\partial x}\right)^3\left(\frac{\partial w}{\partial y}\right) + 4A_{26}\left(\frac{\partial w}{\partial x}\right)\left(\frac{\partial w}{\partial y}\right)^3 \right\} dxdy. \tag{3}$$

where A_{ij} are the laminate extentional stiffnesses. Substituting derivatives of Eq. (2) into Eq. (3) gives:

$$U = \frac{\delta^4 E_1}{(R - \xi)^2}. \tag{4}$$

where

$$E_1 = \left(\frac{8}{45} A_{11} + \frac{8}{45} A_{22} + \frac{32}{49} A_{66} + \frac{16}{49} A_{12} + \frac{2}{3} A_{16} + \frac{2}{3} A_{26} \right). \quad (5)$$

The plastic work dissipated in crushing the core is:

$$D = \pi q R^2 \delta + 4 \int_R^{\xi} \int_R^{\xi} q w dx dy. \quad (6)$$

Where q is the crushing strength of the core. Using the profile given by Eq. (2), one gets:

$$D = \pi q R^2 \delta + \frac{4}{9} q \delta \left(R - \xi \right)^2. \quad (7)$$

The external work W done is:

$$W = P\delta - \frac{1}{2} \int_S \left\{ N_{xx} \left(\frac{\partial w}{\partial x} \right)^2 + N_{yy} \left(\frac{\partial w}{\partial y} \right)^2 + N_{xy} \frac{\partial w}{\partial x} \frac{\partial w}{\partial y} \right\} dS = P\delta - \frac{1}{30} \delta^2 \left(16 N_{xx} + 16 N_{yy} + 15 N_{xy} \right). \quad (8)$$

where P is the indentation force, N_{xx}, N_{yy} and N_{xy} are the initial in-plane forces acting on the edges of the sandwich plate and dS is the surface area. Therefore, the total potential energy is:

$$\Pi = \frac{\delta^4 E_1}{\left(R - \xi \right)^2} + \pi q R^2 \delta + \frac{4}{9} q \delta \left(R - \xi \right)^2 - P\delta + \frac{1}{30} \delta^2 \left(16 N_{xx} + 16 N_{yy} + 15 N_{xy} \right). \quad (9)$$

Minimizing Π with respect to δ gives:

$$P = \frac{4\delta^3 E_1}{\left(R - \xi \right)^2} + \pi q R^2 + \frac{4}{9} q \left(R - \xi \right)^2 + \frac{1}{15} \delta \left(16 N_{xx} + 16 N_{yy} + 15 N_{xy} \right). \quad (10)$$

Similarly minimizing P with respct to ξ gives:

$$\xi = \frac{0.0974 \left(10^5 \delta^3 E_1 q^3 \right)^{1/4}}{q} + R. \quad (11)$$

Substituting Eq. (11) into Eq. (10) gives the load-indentation relation (contact law) as:

$$\mathrm{P} = \frac{8\sqrt{E_1 q}\,\delta^{3/2}}{3} + \pi q R^2 + \frac{1}{15} \delta \left(16 N_{xx} + 16 N_{yy} + 15 N_{xy} \right). \quad (12)$$

Comparison with experimental results. Williamson and Lagace [10] performed a series of static indentation tests on rigidly supported composite sandwich plates made with AS4/3501-6 carbon/epoxy facesheet and Nomex honeycomb core. The indenter was hemispherical-nose cylinder made from case-hardened steel. Material and geometric properties of the sandwich plate and indenter are given in Table 1.

Table 1: Material and geometric properties of the sandwich plate and indenter

facesheet	$a \times a = 102 \times 102 [mm^2]$ (square panel) $h_k = 0.175 [mm]$ (ply thickness)	core	$H = 25.4\ [mm]$ (core thickness) $q = 1.389\ [MPa]$ (crushing resistance)
Ply stiffness	$E_{11} = 142\ [GPa]$ (longitudinal stiffness) $E_{22} = 9.8\ [GPa]$ (transverse stiffness) $G_{12} = 7.1 [GPa]$ (in-plane shear modulus) $\nu_{12} = 0.3$ (poisson's ratio)	indenter	$D = 25.4 [mm]$ (diameter)

The experimental load-indentation curve for the rigidly supported C/E composite sandwich with $[0/90]$ facesheets is shown in Fig. 1. The facesheet thickness is 0.35 mm and it can be seen that the elastic indentation is several times the facesheet thickness. With these large deflections the top facesheet can be modeled as a membrane on a rigid-plastic foundation. The load-indentation response that is predicted by Eq. (12) is also plotted in Fig. 1 for comparison. It is observed that the analytical predictions are in good agreement with the experimental results.

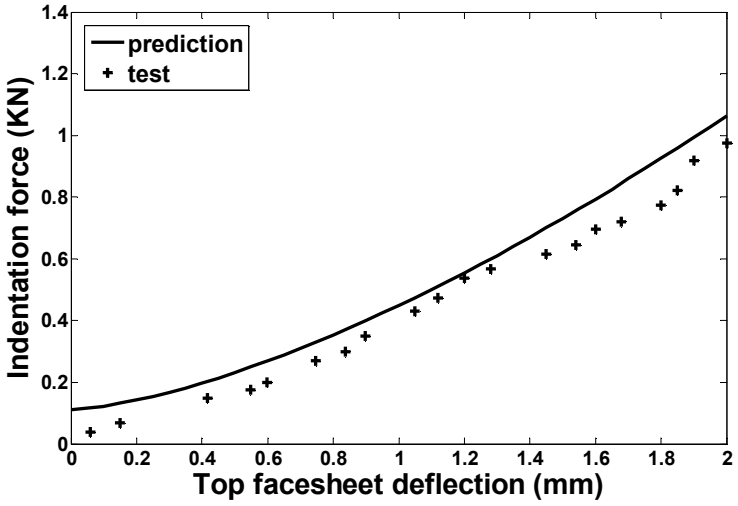


Fig. 1: Indentation force vs. top facesheet deflection for rigidly supported C/E composite sandwich plate

Effects of ply thickness, number of layers, stacking sequence and initial in-plane stresses on the load-indentation response. The effects of some important parameters on the load-indentation response of the composite sandwich plates are shown in Figs. 2-5. The material and geometric properties of the considered sandwich plates and indenters are given in Table 1. The initial in-plane forces for Figs. 2-4 are zero. As Fig. 2 shows, by increasing the ply thickness in facesheet, the indentation decreases. Increasing the number of layers of the facesheet causes the indentation to decrease, as shown in Fig. 3. Effect of stacking sequence of the facesheet on the load-indentation response is illustrated in Fig. 4. Among the stacking sequences considered the highest and the lowest indentation resistances are corresponded to $[45\ -45]_3$ and $[0\ 90]_3$ laminate configurations respectively. It is concluded that by choosing a proper stacking sequence for the facesheet, the indentation resistance of the sandwich plate can be improved. In Fig. 5, if the case with zero initial in-plane forces be considered as a reference state, it is observed that the positive initial in-plane forces decrease the indentation while the negative ones increase it.

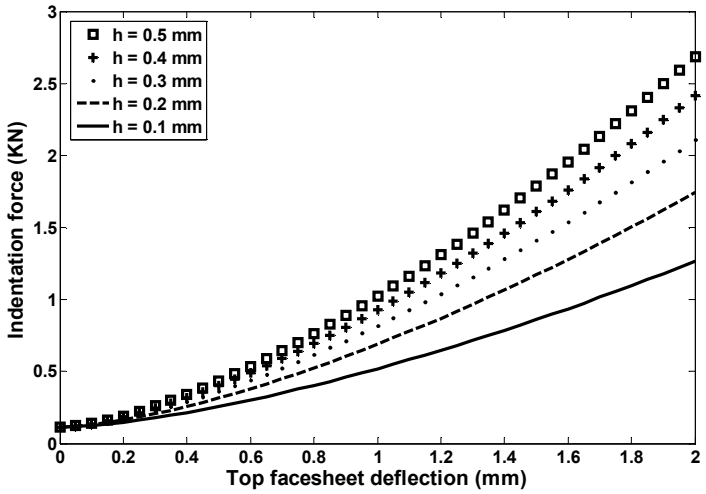


Fig. 2: Indentation force vs. top facesheet deflection for different values of the ply thickness ($[0/90/45/-45]$ facesheets)

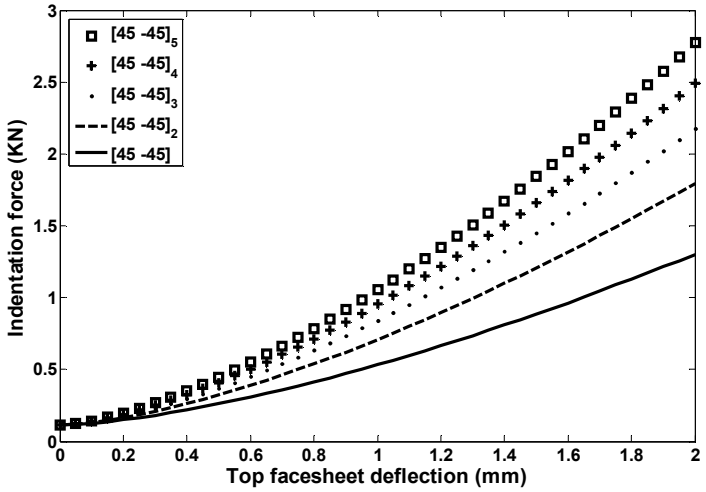


Fig. 3: Indentation force vs. top facesheet deflection for different number of layers of the facesheet

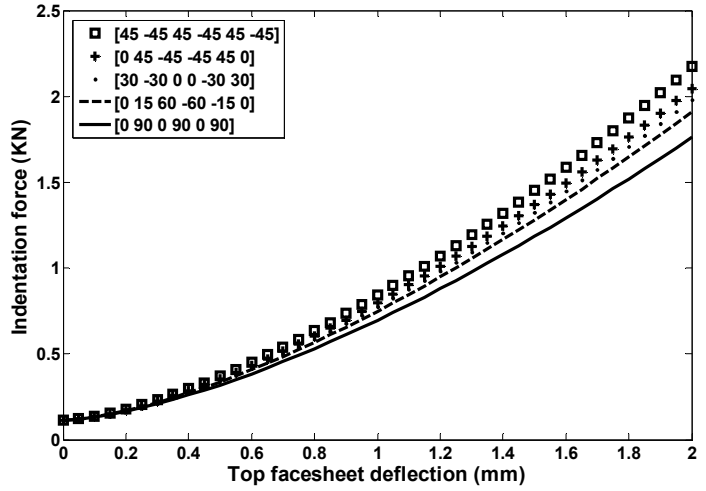


Fig. 4: Indentation force vs. top facesheet deflection for different stacking sequences of the facesheet

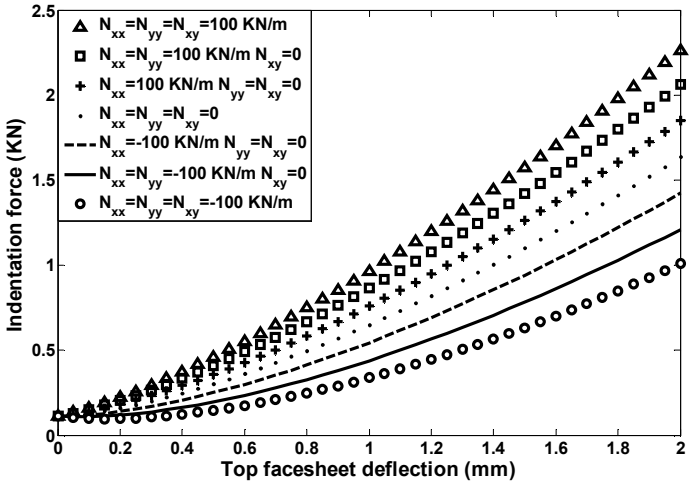


Fig. 5: Indentation force vs. top facesheet deflection for different initial in-plane forces ($[0/90/45/-45]$ facesheets)

Summary

An analytical approach was developed for the contact problem of a composite sandwich plate indented by a flat-ended cylinder. An impeoved contact law was derived by taking into consideration the effects of arbitrary stacking sequence for the facesheets as well as the initial in-plane forces acting on the edges of the sandwich plate, which were neglected in the previous works. Analytical prediction for the indentation force-top facesheet deflection response was compared well with the experimental data. The effects of different parameters such as ply thickness, number of layers, stacking sequence and initial in-plane stresses on the load-indentation response of the sandwich plate were studied.

References

[1] D.R. Ambur and J.R. Cruz: 1995: AIAA Paper code: 95-1460-CP.

[2] R. Olsson and HL. McManus: AIAA J, Vol. 34 (1996), pp. 1238–44.

[3] S. Abrate: Applied Mechanics Review, Vol. 50, issue 2 (1997), pp. 69–82.

[4] M.H. Turk and M.S. Hoo Fatt: Composites: Part B, Vol. 30, (1999), pp. 157–165.

[5] S.W. Gong and K.Y. Lam: AIAA Journal, Vol. 38, issue 9 (2000), pp. 1730–1735.

[6] M.S. Hoo Fatt and K.S. Park: Composite Structures, Vol. 52, (2001), pp. 335-351.

[7] R. Olsson: Journal of Sandwich Structures and Materials, Vol. 4, (2002), pp. 3–29.

[8] D.W. Zhou and W.J. Stronge: International Journal of Mechanical Sciences, Vol. 48, (2006), pp. 1031–1045.

[9] K. Malekzadeh, M.R. Khalili and R.K. Mittal: Journal of Sandwich Structures and Materials, Vol. 8, (2006), pp. 157-181.

[10] JE. Williamson and PA. Lagace: In Proceeding of the Eighth ASC Technical Conference, Cleveland, OH, (1993), pp. 287-97.

© (2011) Trans Tech Publications, Switzerland
doi:10.4028/www.scientific.net/KEM.471-472.1165

The Influence of Yttrium Rich Intermetallic Phases and Heat Treatment on the Microstructure, Hardness and Wear Properties of Al-15%Mg_2Si Composite

H.R Jafari Nodooshan[1,a], M.Emamy[2, b], N. Nemati[3, c], A. Bahrami[4, d]

[1]Young researcher club, Islamic Azad University South Tehran Branch, (IAU), Tehran, Iran

[2]School of Metallurgy and Materials, University of Tehran, North Kargar St., Tehran11365-4563, Iran

[3]Department of Materials Engineering, Sahand University of Technology, Tabriz, Iran.

[4]Imam Khomeini International University, Qazvin, Iran

[a]hamidj_63@yahoo.com, [b]emamy@ut.ac.ir, [c]narguess.nemati@gmail.com, [d]amin.bah@gmail.com

Keywords: Hardness measurement, Wear resistance, Composites, Intermetallics, Casting

Abstract. This study was undertaken to investigate the effect of different concentrations of Yttrium (0.1, 0.3, 0.5, 1.0 wt.%) and heat treatment on the microstructure, hardness and wear resistance of an in-situ cast composite (Al-15%Mg_2Si). The microstructural study of the composite before and after solution and ageing showed both primary and secondary Mg_2Si phases in all specimens and intermetallics containing Y (Al_2Y) were visible after Solution at 520 °C for 4 hours. Hardness measurement demonstrates that the addition of Y increases the hardness gradually but a reduction in the hardness of heat treated specimen's occurs with the addition of Y (≥ 0.5%Y).Wear tests were performed using a pin on disk apparatus. The MMCs were rubbed against a carbon steel pin under a load of 10 and 20 N at a sliding velocity of 0.1 ms^{-1}; track length of 1500 m. The degree of improvement in dry sliding wear resistance brought about by Y addition is strongly dependent on the formation of Yttrium rich intermetallic phases as well as heat treatment influence and the wear behavior determined through the precise measurement of weight loss of the samples and wear rates. Worn surfaces were analyzed by scanning electron microscopy (SEM).

Introduction

The growing demand to reduce energy consumption by developing more fuel efficient vehicles is a challenge for the automotive industry. Recently, a large number of metal matrix composites(MMCs) have been developed for high-performance applications in automotive industries. The properties of particulate metal matrix composites (PMMCs), make them ideal candidates to replace steel and iron in the automotive industry. Al-based composites reinforced with particulates of Mg_2Si have been introduced as a new group of composites that offer attractive advantages such as low density, good wear resistance and good cast ability [1]. They are considered new engineering materials, and may be viable replacement for the dense materials in automobile engine parts and airplane components which are in exposure of matting and adhesive condition. In situ preparation of Al–Mg_2Si composites is one of the most effective ways to fabricate these PMMCs since advantages like an even distribution of the reinforcing phase, good particle wetting, and low costs of production are usually achieved.

Mg_2Si is a hard intermetallic compound with a high melting point (1085 °C). Its low density and low coefficient of thermal expansion coupled with a reasonably high elastic modulus make it a good choice for use as a reinforcing agent [2]. The equilibrium phase diagram shows that Mg_2Si[3] particles are the primary phase $(Mg_2Si)_P$ during solidification. Then α-Al and secondary Mg_2Si co-solidify from the liquid alloy in the narrow ternary phase area. Several works have been focused on the modification of the eutectic and primary Si crystals and Mg_2Si in Al–Mg-Si alloys with the addition of various alloying elements such as Sr, Ti, B, Zr and Cu, modification effect of RE elements such as Ce, La, Y, Nd and mischmetal and additional quantities of silicon [3-5] have been

investigated. Recently the effects of Zr, Ti, B and Cu on these alloys were investigated and the results showed a substantial change in size and morphology of the Mg_2Si particles [3].

Addition of Y in Mg-Si alloys has been investigated before but very few studies have been done on effect of Y in Al-Mg_2Si composite. Yttrium was added into Mg±Mg_2Si composites as a refiner and the size of primary Mg_2Si particles were reduced [6].

In the present study, the modification effect of yttrium and heat treatment cycles such as solution and ageing on microstructure and mechanical properties of Al-15%Mg_2Si composites are investigated .The objective of this study is to evaluate the wear resistance and hardness of these composites by exerting heat treatment cycles accompanied with adding up to 1%Y to the alloy.

Experimental Procedure

Industrially pure Mg, Al ingot and Si were used as starting materials to prepare Al–5.5wt.% Si - 9.7wt%Mg alloy, which corresponds to a composition of Al–15wt.% Mg_2Si composite .All the materials were preheated at 200 °C and the alloy was melted in an electrical resistance furnace using a 10 kg graphite crucible. Table 1 shows the chemical composition of hypereutectic Al–15% Mg_2Si. After about 15 min, the desired amounts of Mg–20wt%.Y master alloys were added to the Al-Mg_2Si melts, respectively. Ten minutes after Y addition (0.1, 0.3, 0.5 and 1.0 wt%) the solution was hand stirred with a graphite rod for about 1 min to ensure complete mixing in the molten. During the melting period continuous addition of flux powder was used to ensure the melt surface was covered. Degassing was conducted by using dry tablets containing C_2Cl_6 (0.3 wt.% of the molten alloy) for about 5 min .After stirring and cleaning off the dross, alloys with different compositions were poured into the cast iron mould .The mould was prepared according to B108-03a ASTM standard [3].

Table 1. Chemical composition of Al-15%Mg_2Si primary ingots (wt. %).

Si	Mg	Fe	Cu	Mn	Cr	Ni	Zn	Ti	Al
5.87	9.93	0.14	0.03	0.09	0.11	0.02	0.08	0.01	Base

MMCs were studied in two different conditions: as -cast and after solution heat treatment. The conditions used for the heat treatment were solutionizing at 520 °C for 4 hrs. Microstructural studies were made on polished sample surfaces which were selected from the gauge length portion of the test bars (6 mm diameter).The cut sections were polished and then etched by HF (1%) to reveal the structure. Quantitative data on the microstructures were determined using an optical microscope equipped with an image analysis system (MIP). The microstructural characteristics of the specimens also were examined applying scanning electron microscopy performed in a Vega©Tescan SEM operated at 20 Kv equipped with the energy dispersive X-ray analysis (EDX).

The hardness of the as-cast and heat-treated specimens was measured using a Brinell hardness tester and under ASTM E10 standard, with a load of 30.0 kg and a 2.5 mm diameter ball of indenter. Each reading was an average of at least five separate measurements. In order to perform the wear tests according to ASTM standard G99, a pin on disc conventional wear testing machine was applied. The wear test conditions and applied setup were accordingly room temperature, a counter face of AISI 52100 steel which was hardened to 62 HRC. The wear specimens were machined from the as-cast and heat treated samples in the form of cylindrical pin with 5 mm diameter and 12 mm height and then grinded/polished to a 1 μm finish. The wear test was carried out at a constant sliding velocity of 0.1 m/s (200 rpm) and under two normal loads of 10 and 20 N with sliding distance of 1500 m. At least three wear samples were tested for each specimen. The pins were cleaned thoroughly and then were weighed using an electronic balance (GR200-AND) with an accuracy of 0.1 mg. The weight loss due to the test was calculated after each 250 m sliding distance and the wear rate was measured according to the formula: It should be mentioned that to

measure the volume loss (m^3) of the samples, the experimental density (Archimedes) of the specimens were first measured and then applied.

$$Wear\ rate\ (mm^3/km) = \frac{Volume\ loss\ (mm^3)}{Sliding\ distance\ (m)} \quad (1)$$

The worn surfaces were examined by SEM to recognize wear mechanisms.

Results and Discussion

Microstructural characterization. [Fig. 1a] shows a typical microstructure of the unmodified and unheat treated Al–15wt.% Mg_2Si composite that consists of dark faceted particles of primary Mg_2Si and bright α-Al grains in a matrix of Al–Mg_2Si eutectic cells. It should be mentioned that as shown in Fig. 1a the coarse dendritic crystals are primary Mg_2Si particles, while the fibrous type particles are eutectic Mg_2Si, However, an interesting microstructural feature observed in Fig. 1a is that all the primary Mg_2Si crystals are surrounded by a layer of α-Al, around which the fine eutectic structures of Mg_2Si+Al are formed. Fig. 1a and b show the SEM microstructures of Al–15wt.% Mg_2Si composite without Y and with 1.0wt.% Y addition before solution, respectively.

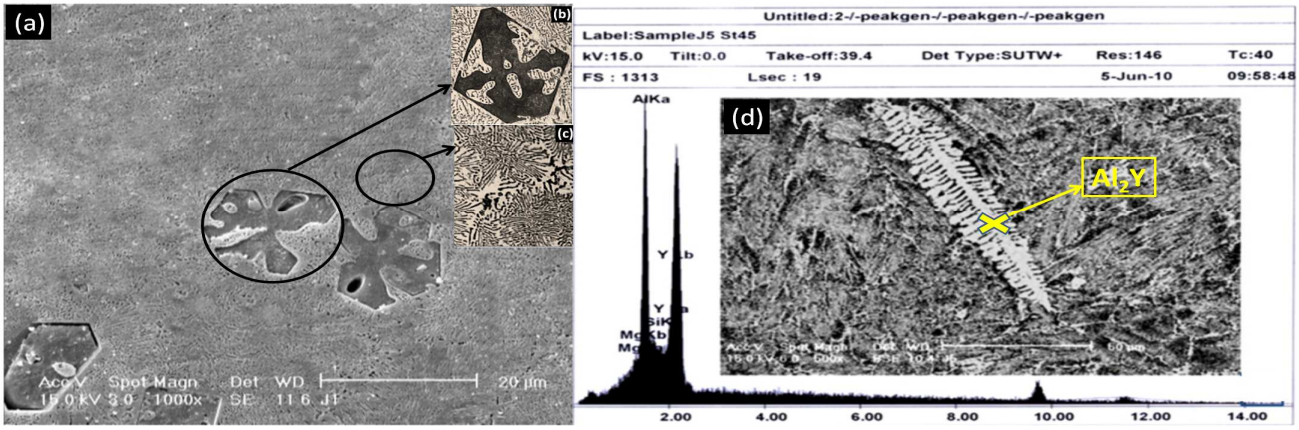


Fig. 1. (a) SEM micrograph of Al-15wt.% Mg_2Si cast in-situ composite, (b) primary Mg_2Si, (c) pseudo-eutectic Mg_2Si and (d) SEM micrograph and EDX point analysis of Al-15wt.% Mg_2Si containing 1wt.% Y.

Further microstructural observations on the heat treated and Y containing specimens revealed the formation of some Y rich intermetallic compounds in the Al–Mg_2Si composite in bright areas.

Fig. 1a and b show the high magnification SEM micrograph , EDX analysis of Al, Mg, Si and Y elements, and EDX of the Al-15%Mg_2Si composite with 1.0wt.% Y addition, after solution and ageing, respectively. It can be seen from EDX result that the white point compound is a compound containing Al and Y. Based on the EDX, it can be claimed that these compounds are Al_2Y intermetallics mainly formed as a result of solution. As it is observed in Fig. 1b, other than well distribution of Al_2Y in α-Al phase, the intermetallic compounds are also present in primary Mg_2Si dendritic crystals just after solution. As it is obvious, Y addition did not change the size of the primary Mg_2Si particles significantly, but the microstructures of the composite and monolithic alloys in heat treated condition, depict near spherical shape of eutectic silicon in aluminum matrix and eutectic network broken up of the composite. The microstructure variation of composite due to heat treatment (solution) is seemed to be similar to that observed in heat treated monolithic alloy has altered their morphology through which the feathery shape of the particles has been increased. Further addition of Y (up to 1%) in company with solution treatment decreased the feathery like morphology of the particles and causes the presence of Al_2Y intermetallics to be more clear which are observed in the form of light-colour dendrites.

Hardness measurement. [Fig. 2] shows the variations of hardnesses in Al-15wt.%Mg_2Si and Y added MMC, all in heat treated states. It is well known that the presence of intermetallics particles in soft matrix can significantly contribute to higher values of hardness due to the thermal expansion coefficient (CTE) mismatch between the matrix and intermetallics particles [7]. As can be seen in this figure, hardness improvement by the addition of Y content and solution treatment does not have a regular ascending trend. In Al–Si–Mg ternary alloys, the presence of Mg and Si together can promote to the formation of Mg_2Si precipitates causing the hardening. After solution, the hardness of the specimens containing Y >0.1 is significantly enhanced due to formation of Y containing intermetallics compounds and even distribution of the particles through the solutionized matrix the optimum level of Y for hardness improvement is shown to be 0.3wt.%.

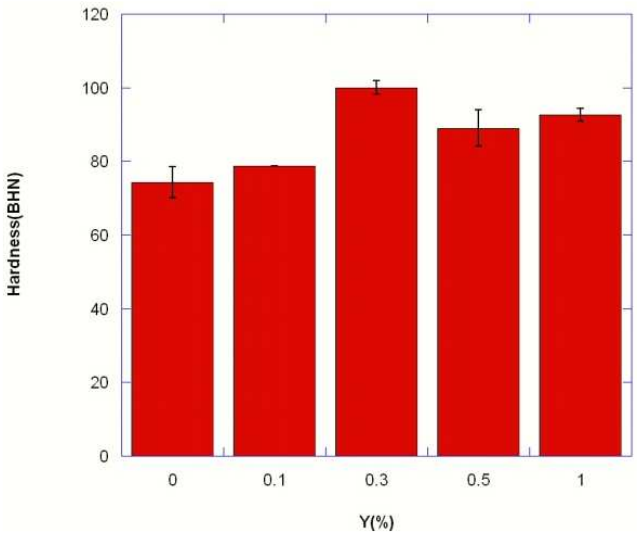


Fig. 2. Hardness variation of heat treated samples via Y content.

Wear behavior. In addition to the improvement of hardness, excessive enhancement in wear resistance of the Y added composites also observed. Heat treatment effect on the wear behavior of cast composite weight loss of Al-Mg_2Si composite and Y added cast composites as a function of sliding distance with and without heat treatment at nominal loads of 10 and 20 N are shown in Fig. 3a-d. Under an appropriate conditions (good bonding between matrix and reinforcement), the addition of refiner element (Y) to Al-15wt.%Mg_2Si matrix composite can contribute to the better wear behavior as compared to the monolithic alloy. In general, the reduction in wear rate is influenced by the efficiency of refiner and solution results. As can be seen from Fig. 3a-d, by the addition of yttrium to the Al-Mg_2Si matrix, weight loss can decrease to some extent under nominal loads of 10 N and 20 N, respectively, it is observed that adding Y up to 1wt.% can reduce the wear weight loss of the composite under both applied loads but as expected wear weight loss values at same distances are higher under 20 N applied loads for similar specimens. Heat treatment could change the wear resistance of Y added samples and brings about an increase in wear weight loss of 1wt.% Y containing and this happened due to formation of Y containing intermetallics and morphology alteration of primary Mg_2Si particles to a feathery shape (Fig. 3).

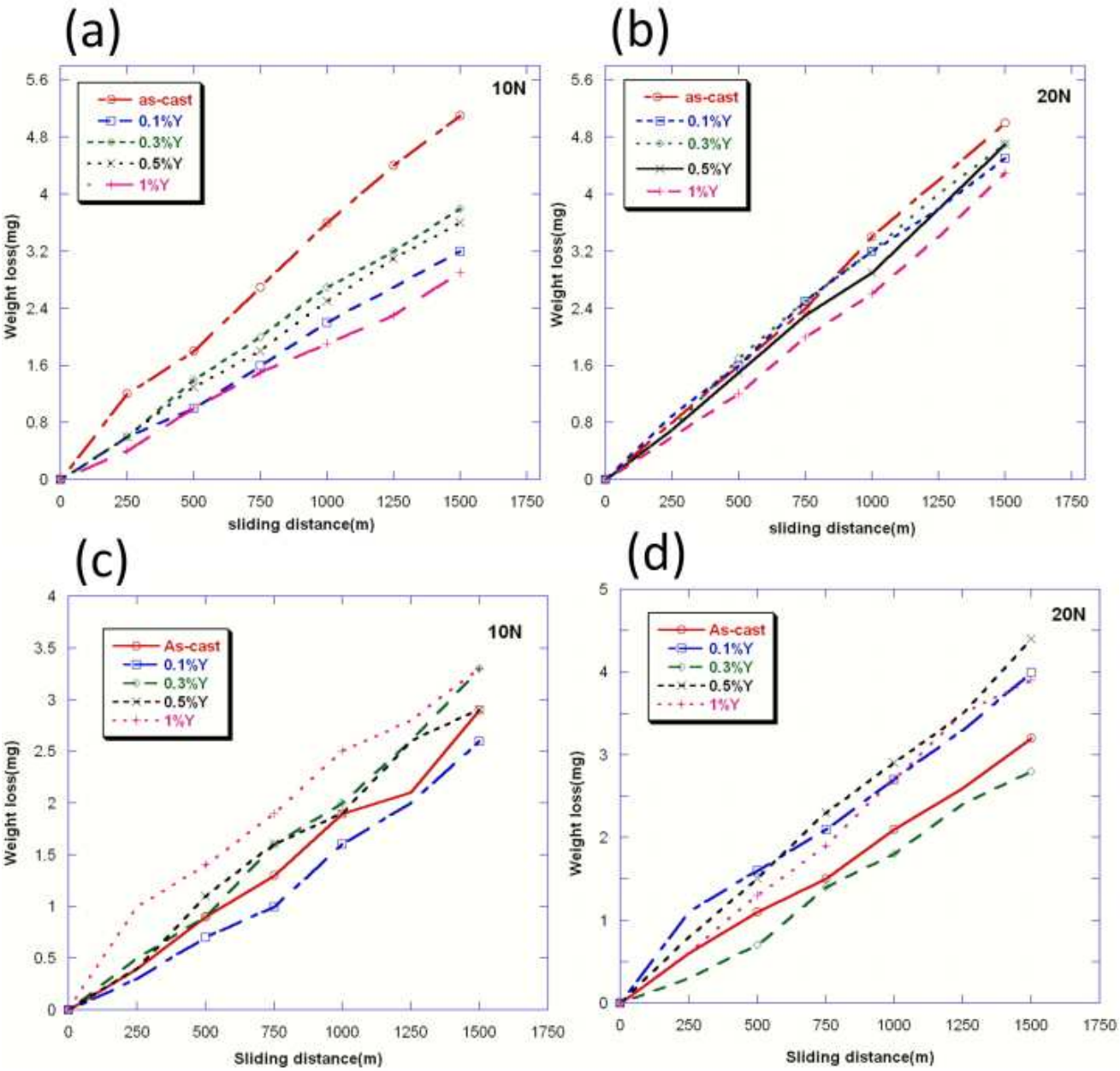


Fig. 3. Weight loss values of samples- non heat treated (a) under 10 N applied load, (b) under 20 N applied load and Weight loss values of samples-heat treated (c) under 10 N applied load, (d) under 20 N applied load.

Fig. 4 represents the variation of wear rates as a function of applied loads for unrefined and Y-added composites with and without heat treatment. The obtained results suggested that wear resistance of as-cast Al-15wt.%Mg_2Si composites significantly increased by performing heat treatment (solution treatment) at the applied loads of 10 and 20 N, as seen in Fig. 4. This improvement in wear results can be attributed to the enhancement of alloy hardness due to the particle reinforcing of Y-containing intermetallics (Al_2Y), precipitation, hardening and eutectic network broken up as a result of heat treatment. In addition, it seems that under lower applied load (10 N), regarding to stresses lower than the particle fracture threshold, Mg_2Si and Al_2Y particles acted as load bearing elements. In this state, particulate reinforced aluminum matrix composite exhibited higher wear resistance. It is interesting to note that at higher applied load (20 N), there are no substantial differences between wear resistances of heat treated and unheat treated specimens. It seems that at higher applied load (20 N), severe plastic deformation of surface and subsurface regions causes to rise of temperature during dry sliding wear test. Contact between a steel disk and the worn surfaces [7]. It is observed from studying the worn surfaces that, complex wear mechanisms are present in worn surfaces. It is observed from that the dominant wear mechanism in Y added specimens is abrasive wear.

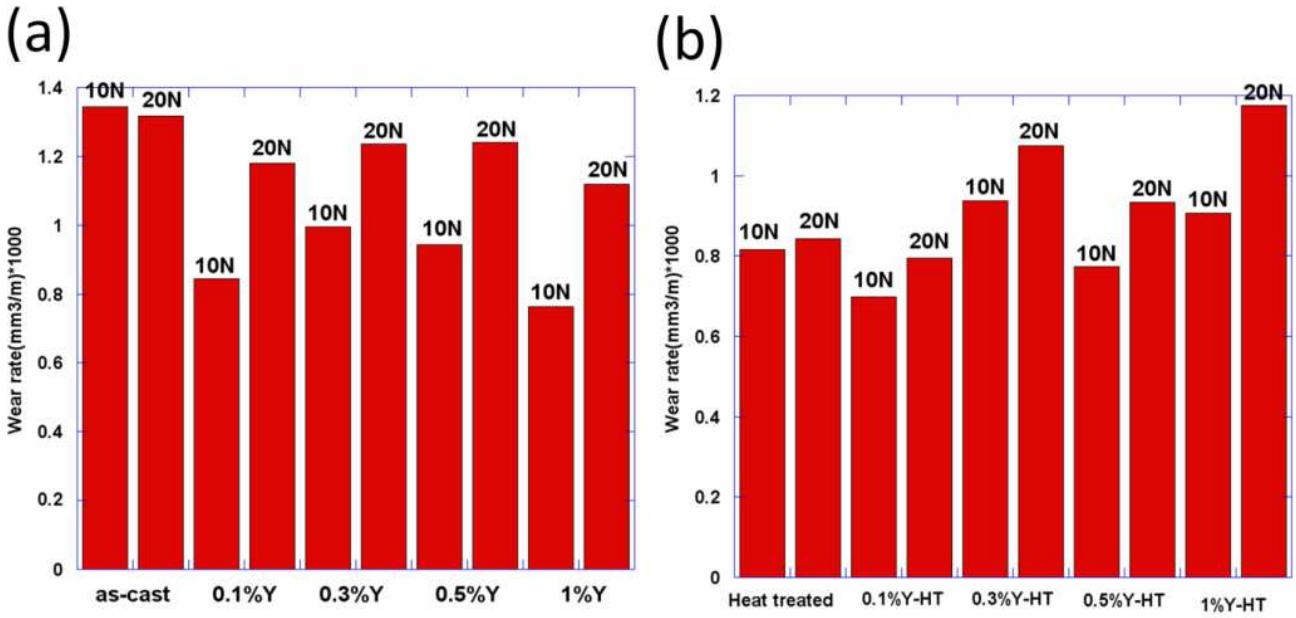


Fig. 4. Wear rate variations via Y content of composites under 10 and 20 N applied load (a)samples- non heat treated and (b)samples-heat treated

Summary

1. Addition of Y has changed the morphology of the primary Mg_2Si particles and has altered the eutectic structure significantly.
2. Solution has made Y containing intermetallics to have an even distribution through the matrix.
3. The optimum level of Y for hardness enhancement in heat treated composites is observed to be 0.3wt%.
4. The wear resistance of composites is enhanced by adding Y, and in heat treated condition the best resistance to wear belongs to 1wt.%Y added composite under both applied loads and in unheat treated samples, the best wear resistance belongs to 0.3Wt.% Y added composite which in accordance with hardness results.

References

[1] L. Lu, K.K. Thong, M. Gupta, Comp, J. Sci. & Tech. Vol. 63, 2003, 627–632.

[2] Q.D. Qin, Y.G. Zhao, W. Zhou and P.J. Cong, J. Mat. Sci. Eng. A Vol. 447, 2007, 168-191.

[3] M. Emamy, N. Nemati, A. Heidarzadeh, J. Mat. Sci. Eng. A Vol. 527, 2010, 2998–3004.

[4] J. Zhang, Z. Fan, Y. Wang, B. Zhou, J. Mat. Sci. Lett. Vol. 18, 1999, 783-784.

[5] J. Zhang, Z. Fan, Y.Q. Wang and B.L. Zhou, J. Scripta. Mater, Vol. 42, 2000, 1101–1106.

[6] Q.C. Jiang, H.Y. Wang, Y. Wang, B.X. Ma, J.G. Wang, Mater. Sci. Eng. A Vol. 392, 2005, 130–135.

[7] HR. Lashgari, A.R. Sufizadeh, M. Emamy. Mater Design Vol. 31, 2010, 2187-2195.

© (2011) Trans Tech Publications, Switzerland
doi:10.4028/www.scientific.net/KEM.471-472.1171

Microstructure and Tensile Properties of Al-15wt%Mg_2Si Composite after Hot Extrusion and Heat Treatment

A. Bahrami[1,a], A. Razaghian[1,b], M. Emamy[2,c], H.R. Jafari[3,d], G. S. Mousavi[2,e]
[1]Imam Khomeini International University, Qazvin, Iran
[2] School of Metallurgy and Materials, University of Tehran, Tehran, Iran
[3]South Tehran Branch, Islamic Azad University (IAU), Tehran, Iran
[a]amin.bah@gmail.com, [b]razaghian_ahmad@yahoo.com, [c]emamy@ut.ac.ir,
[d]hamidj_63@yahoo.com, [e]stillgym86@yahoo.com

Keywords: Al-Mg_2Si composite; hot extrusion; mechanical properties; heat treatment; microstructure.

Abstract. In this study, the relationship between microstructures and mechanical properties of the extrusion processed Al-15wt.%Mg_2Si composite was investigated after applying various extrusion ratios (6:1, 12:1 and 18:1) and solution treatment. Various techniques including metallography, tensile testing and SEM fractography were utilized to characterize the mechanical behavior of the MMC. Results demonstrated that extruded and heat treated composite possesses considerably higher strength and enhanced ductility in comparison with the as-cast samples. It was also found that heat treatment and extrusion processes do not change the primary Mg_2Si morphology considerably, but its size increases as extrusion ratio decreased. Heat treatment and extrusion ratio effects on tensile strength, elongation of extruded specimens were also studied in this work.

Introduction

With the enlargement of modern industry, the production of light materials with high strength is required. Aluminum metal matrix composites (MMCs), as a class of advanced engineering materials have been developed for high performance applications because of their recuperated properties such as excellent castability, low density and good wear resistance [1].

In situ preparation of Al–Mg_2Si composites seems to be the best way of fabricating such PMMCs since advantages like an even distribution of the reinforcing phase; good particle wetting and low costs of production are usually achieved. There have been reports of Mg–Mg_2Si composites made by mechanical alloying and hot extrusion methods in which the alloys show good tensile properties, but they are rather expensive. Therefore, over the last few years, efforts have been made to produce such composites by casting processes [2]. However, it is necessary to note that the presence of brittle and nearly no deformable reinforcements in MMCs can result in undesirable phenomena, such as fracture of reinforcement, debonding of interface, or surface cracking in the extruded product [3].

It is known that secondary processing of the discontinuously reinforced MMCs can lead to break up of particle agglomerates, reduction or elimination of porosity and improved bonding, all of which contribute to improve the mechanical properties of these materials [4].

While there have been a number of studies to tailor the properties of aluminum using different types and amount of reinforcement, there has been no attempt made to study the effect of the level of deformation such as extrusion ratio on the microstructure and tensile properties of Al-Mg_2Si composites.

Experimental

Industrially pure metals (Al, Mg) and Si were used as starting materials to prepare Al–15% Mg_2Si composite ingots. All materials were heated in an electrical resistance furnace using a 10 kg SiC crucible. The composite was remelted in another electrical resistance furnace. When the temperature reached 750 ºC and after stirring and cleaning off the dross, composite was poured into the cast iron mould (Fig. 1a). During the melting period continuous addition of flux powder was used to ensure the melt surface was covered. Degassing was conducted by using dry tablets containing C_2Cl_6 (0.3wt.% of the molten alloy) for about 5min.

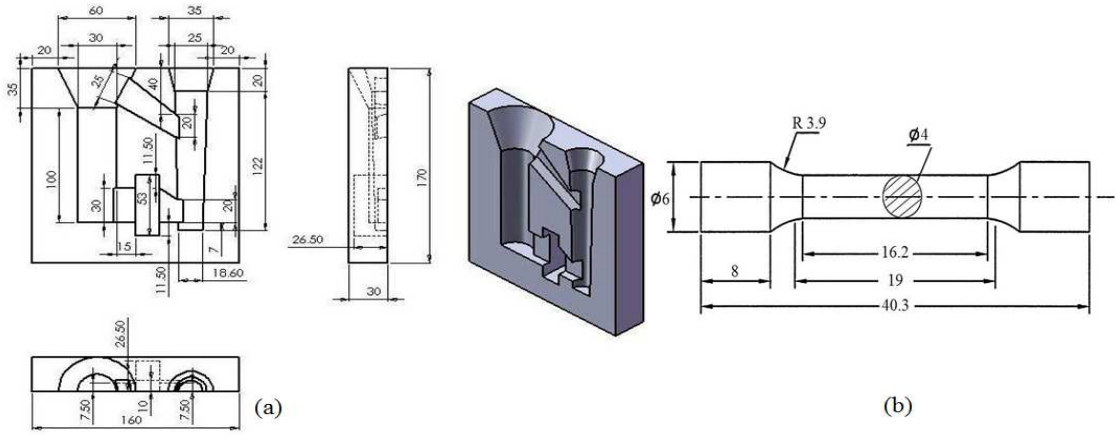


Fig. 1. (a) The schematic of cast iron mould, and (b) Sketch map of tensile samples.

After casting, composite billets were manually cut into 28 mm in length and 29 mm in diameter in order to be filled into a container. Some Al-15 wt.% Mg_2Si billets were exposed to homogenizing treatment in the furnace at 520 ºC for 4 h. Having completed the curing time, the same billets were exposed to slow cooling in furnace. Then these billets were hot extruded by using a hydraulic press at a ram speed of 1 mm/s with the extrusion ratios (which is the ratio of the initial cross-section area of the billet to the final cross-sectional area after extrusion) of 6:1, 12:1, and 18:1, and a temperature of 450ºC. Extrusion process was carried out with using graphite base oil between metal and dies. The density of the samples was measured using Archimedes' principle according to ISO 2738 standard. The measured density was compared to the value obtained using rule-of-mixtures so as to determine the volume fraction of porosity. The samples were precision weighed in an electronic balance to an accuracy of 0.1 mg. According to ASTM E8-04 small size, round tensile samples were machined along the extrusion direction and room temperature uniaxial tension tests were carried out in a fully automated SANTAM tensile testing machine at a constant cross head speed of 1 mm/s. The sketch of tensile sample is seen in Fig. 1b. Metallographic specimens were prepared through standard routines by polishing and etching in hydrofluoric acid (HF) solution (0.5%). Fracture surfaces of tensile specimens were examined in a scanning electron microscope (SEM) (VEGA-TESCAN) to determine the predominant fracture mode.

Result and discussion

Microstructure. Fig. 2a shows a typical microstructure of Al–15 wt.% Mg_2Si composite, which according to the pseudo-binary phase diagram (Fig. 2b), consists of dark faceted particles of primary Mg_2Si and bright α-Al grains in a matrix of Al–Mg_2Si eutectic cells. Consequently, primary Mg_2Si particles will act naturally as heterogeneous sites for the nucleation of α-Al in order to decrease the interfacial energy [5].

Figures 3 and 4 show the microstructures of Al–15 wt.% Mg_2Si composite at two different conditions: as-extruded and homogenized and extruded (heated at 450 ºC for 1 h before extrusion). Each figure also includes composite microstructure in different extrusion ratios. After extruding the

composite, in both of conditions, the primary bulky polygonal Mg_2Si was broken up preliminarily and the Al-Mg_2Si eutectic cells in the as-cast microstructure changed into bands due to the plastic flow of matrix along the extrusion direction which also causes the elimination of casting defects, such as porosities and shrinkages.

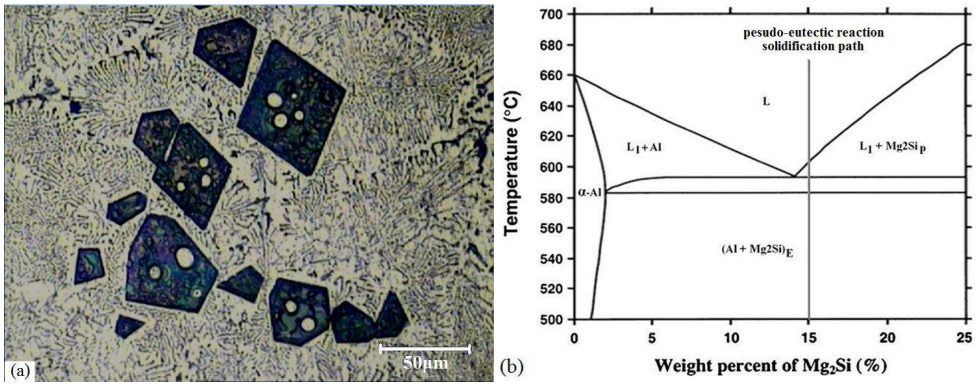


Fig. 2. (a) microstructure of as cast Al–15% Mg_2Si composite and (b) Pseudo-binary phase diagram of Al–Mg_2Si [5].

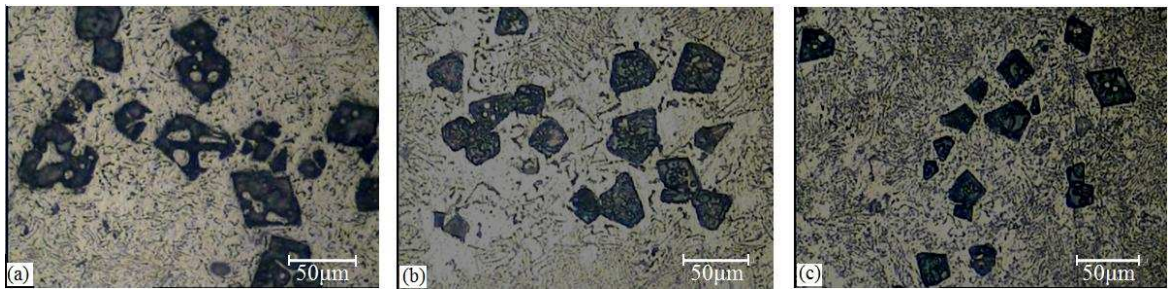


Fig. 3. Effect of extrusion ratio on the microstructures of Al-15 wt.% Mg_2Si composites at as-extruded state: (a) extruded at the ratios of 6:1; (b) 12:1; (c) 18:1.

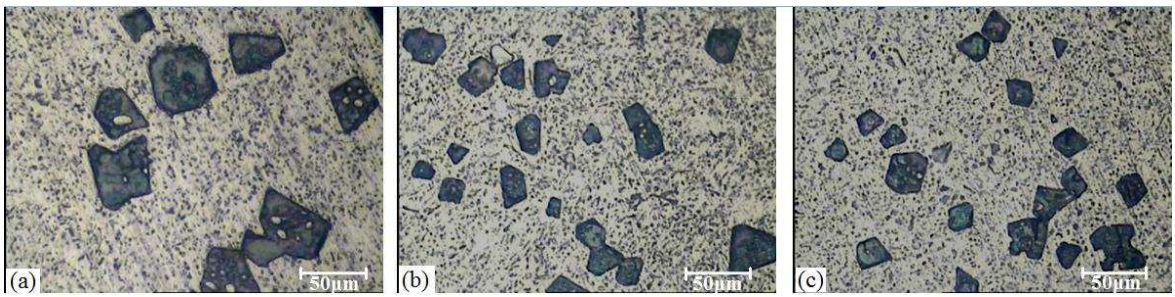


Fig. 4. Effect of extrusion ratio on the microstructures of Al-15 wt.% Mg_2Si composites at homogenized state: (a) extruded at the ratios of 6:1; (b) 12:1; (c) 18:1.

As shown in Fig. 3a, the distribution of primary Mg_2Si crystals is not uniform. Further fragmentation of Mg_2Si particle was seen after extrusion process. Figures 3 and 4 show the improved distribution of Mg_2Si in the structure and more uniform structure. The microstructure of homogenized (4h at 520 ºC) composite are presented in Fig. 4. From Fig. 4, it is clear that the morphology of Mg_2Si paticles do not change seriously but size of this particles increase and eutectic phase changes from flake like to fine dot-like.

It should be mentioned that the distribution of Mg_2Si particles is more homogeneous as extrusion ratio increases from 1:6 to 1:18. The porosity values of the composites in as-cast state and after extrusion are illustrated in Fig. 5. The decreased porosity of MMCs during extrusion is due to the compressive forces generated by the interaction of the composite billet with the extrusion container and die, resulting in the flow of the matrix alloy into the voids under the applied shear forces. In fact, application of the extrusion process to MMCs causes the pores and the separations at the matrix-reinforcement interfaces to be closed up leading to improved mechanical properties.

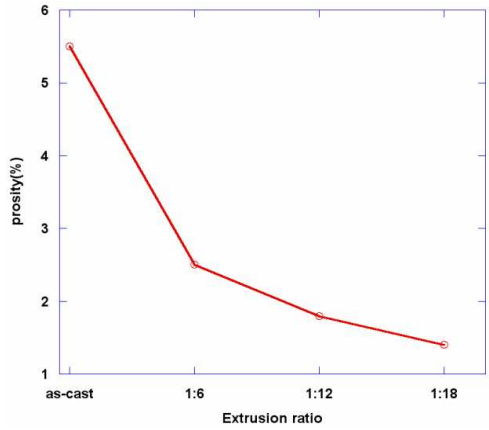


Fig. 5. Effect of extrusion ratio on porosity

Strength and elongation. The variation of ultimate tensile strength (UTS) and elongation values with extrusion ratio are illustrated in Fig. 6. It is evident that the homogenized and extruded specimens with extrusion ratio of 1:18 samples reveal great elongation values, but as-extruded with extrusion ratio of 1:18 show highest UTS values.

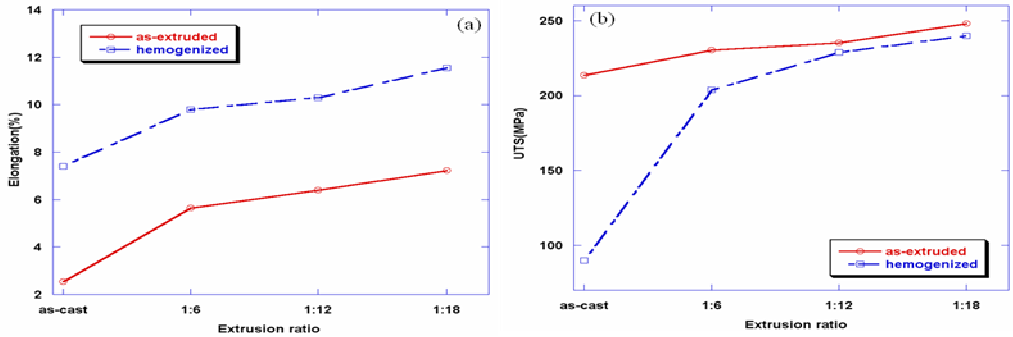


Fig. 6. Effect of extrusion ratio on the (a) elongation and (b) ultimate tensile strength of Al-15 wt.% Mg2Si after the extrusion process in different states.

These results are in agreement with literature [6–9] and can be related to reduction of the porosity content, refinement of the microstructure and obtaining a more homogeneous distribution of the particles in the matrix as compared to the as-cast microstructures.

As hard phases, the Mg_2Si crystals exist in the composite with coarse dendritic or bulky polygonal morphology and thus make the matrix discontinuous. Moreover, stress concentrations easily occur in the matrix near the sharp tips of the Mg_2Si crystals and thus the micro-crack is inclined to nucleate at the sharp tips and propagate along the interfaces between matrixes and Mg_2Si crystals. As a consequence, the mechanical properties of composite are prominently deteriorated by coarse Mg_2Si crystals [10].

In order to extrude the composite at higher ratios, further extrusion forces are required leading to higher shear stress levels. As a consequence, the more severe deviatoric stresses, generated by the larger extrusion loads, led to the increased particle breakage and formation of more fragmented tiny particles. Hence, average size of Mg_2Si crystals decreased and with increasing in extrusion ratio also sharp tips of Mg_2Si crystals decreased. In as-cast composites, a low level of ductility is unavoidable due to the high porosity content and early void formation at low strains during tensile elongation. However, it is possible to obtain higher levels of ductility by reducing the porosity content and improving the bond between the reinforcing particles and the matrix [11].

The observed low ductility in the as-cast samples can be explained by the heterogeneity in particle distribution and mainly by the high porosity content. The application of hot extrusion process to the billets of Al-15wt. %Mg_2Si composite decreased the porosity content and particle clustering; therefore, the ductility levels of the composites were improved. After the Mg_2Si/Al

composite is homogenized, its matrix is changed to fine dot-like and content of α-phase in matrix increased. Thus, it is reasonable that the elongation is increased in comparison with as-extruded samples.

Tensile Fracture Behavior. Fig. 7 exhibits a typical fracture surface of an Al–Mg_2Si composite in as-cast condition, which is composed of large facets, suggesting a brittle mode of failure. The fracture planes of almost all coarse Mg_2Si particles exhibit clear cleavage creating a rapid fracture deriving from their intrinsic brittleness and precracked structure. In the presence of such particles two major phenomena are well known: particle decohesion and particle fracture [12].

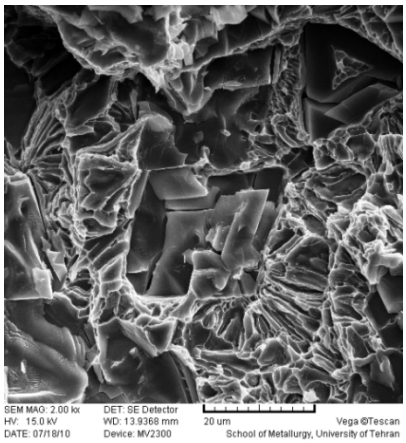


Fig. 7. SEM fractographs of the as-cast composite shows fractured Mg_2Si particles and particle decohision in the matrix.

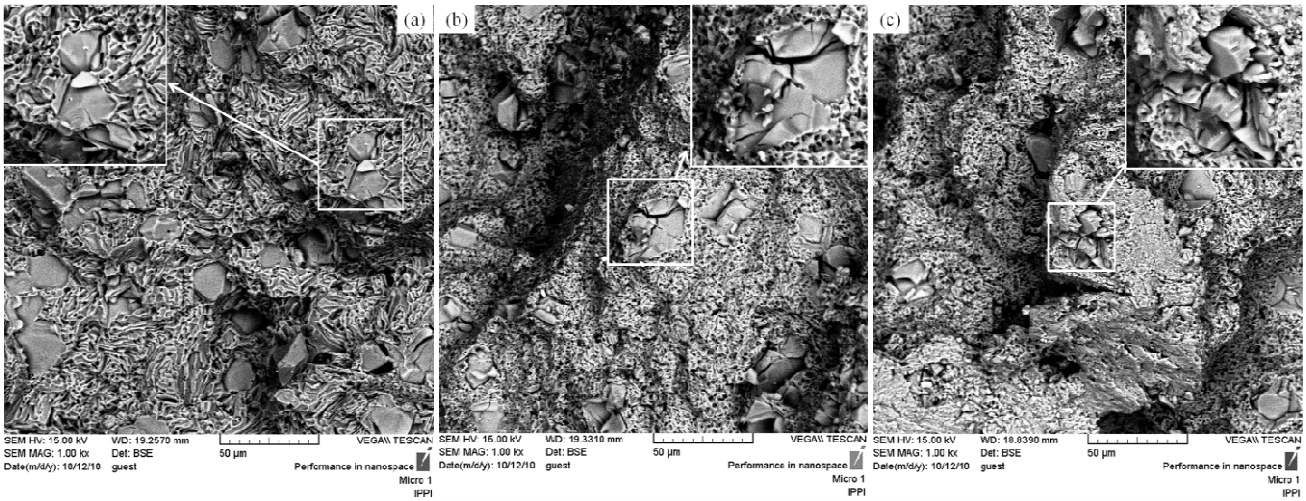


Fig. 8. SEM fractographs, showing the fracture surfaces of Al–Mg2Si composites extruded with different extrusion ratios: (a) 6:1 (b) 12:1(c) 18:1.

Figures 8 and 9 show particle decohesion ,particle cracking and dimples in fractured surface of the extruded composite before and after heat treatment. As seen, in as-cast state, sample with 6:1 extrusion ratio, dimples present the fracture surface are rather coarse and elongated. As known, dimples with honeycomb appearance are characteristics of a ductile mode of fracture.

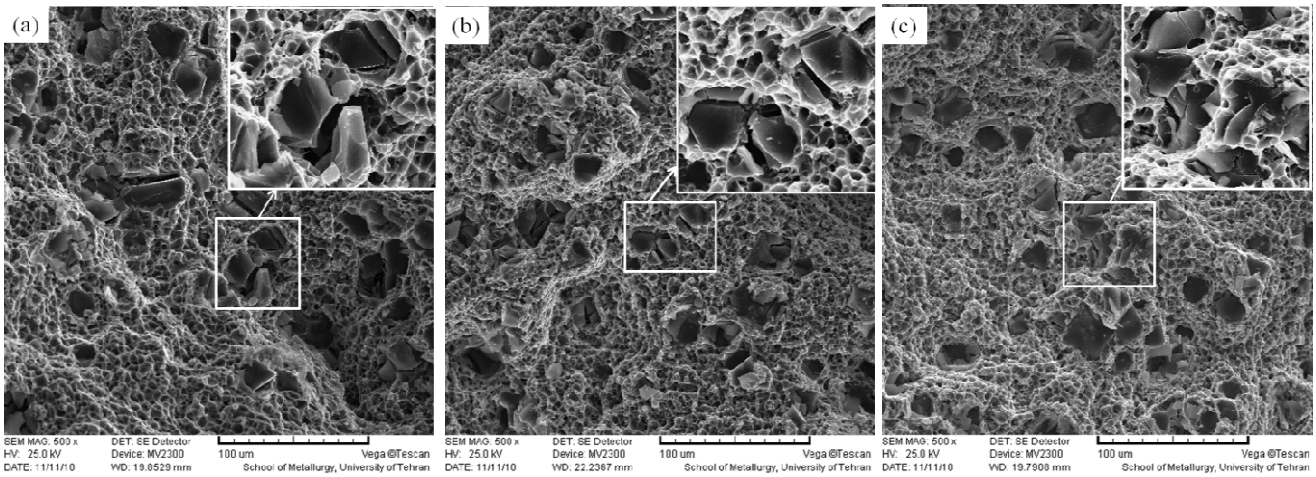


Fig. 9. SEM fractographs, showing the fracture surfaces of Al–Mg2Si composites homogenized and extruded with different extrusion ratios: (a) 6:1 (b) 12:1(c) 18:1.

Fig. 9 a-c exhibit typical fracture surfaces of Al–Mg_2Si composite at different extrusion ratios after homogenizing. As seen, in comparison with as-cast state dimples have been increased and in both of states (as-cast and homogenized) by increasing the extrusion ratio also they have become finer in size. Combination of these reasons shows that the mode of fracture has been changed from the brittle to ductile.

Summary

The hot extrusion process resulted in significant improvement in tensile ductility and considerable increase in tensile strength of Al-15 wt%. Mg_2Si composites in addition by increasing the extrusion ratio, the percentage of elongation to fracture and tensile strength properties of the composite samples increased since refinement of the microstructure and reduction of porosity content were more pronounced at higher total deformation levels.

The average size of the Mg_2Si particles was reduced during extrusion indicating particle fragmentation and last but not least when the as-cast composite was homogenized at 520 ˚C for 4 h, the primary Mg_2Si apparently did not change, while the eutectic phase changed to fine dot-like. In comparison with as-cast, also dimples have been increased.

References

[1] L. Hengcheng, S. Yu, S. Guoxiong, Mater. Sci. Eng. A, Vol. 358, 2003, 164-170.
[2] E.E. Schimid, K. Von Oldenbrug, G. Frommeyer, Z. Metallkde. Vol.81, 1990, 809.
[3] J. Hashim, L. Looney, M. S. J. Hashmi, J. Mater. Process. Tech., Vol. 123, 2002, 258–263.
[4] H. Nakae And S. Wu, Mat. Sci. Eng. A, Vol. 252, 1998, 232–238.
[5] R. Hadian, M. Emamy, N. Varahram, N. Nemati, J. Mater. Sci. Eng. A , Vol. 490, 2008, 450–457.
[6] U. Cocen And K. Onel, Compos. Sci. Technol., Vol. 62, 2002, 275–282.
[7] Y. H. Seo And C. G. Kang, Compos. Sci. Technol., Vol. 59, 1999, 643–654.
[8] S. H. Hong, K. H. Chung and C. H. Lee, Mat. Sci. Eng. A, Vol. 206, 1996, 225–232.
[9] C. H. J. Davies, W. C. Chen and J. K. Brimacombe, Scripta. Metal., Vol. 37(3),1995, 309–314.
[10] G.Y. Yuan, M.P. Liu, Q.D. Wang, Y.P. Zhu,W.J. Ding, Acta Metal.Sin.Vol.38, 2002, 1105.
[11] P. E. Mchugh, R. J. Asaro, and C. F. Shih, Acta Metall. Mater., Vol. 41(5),1993, 1477–1488.
[12] L. Babout, Acta Mater. Vol. 52, 2004, 4517–4525.

© (2011) Trans Tech Publications, Switzerland
doi:10.4028/www.scientific.net/KEM.471-472.1177

Vibration Analysis of Thick Arbitrarily Laminated Plates of Various Shapes and Edge Conditions

T. Pervez[1], F.K.S. Al-Jahwari[1,a] and A.C. Seibi[2]

[1] Mechanical and Industrial Engineering Department
College of Engineering, Sultan Qaboos University, P.O.Box # 33, Al-Khod 123, Oman
[2] Petroleum Institute, Abu Dhabi, United Arab Emirates

[a] farooq@squ.edu.om

Keywords: Composite plates, Shear deformation theories, Free vibration, Finite element analysis, Arbitrary laminate, Edge effects

Abstract. Free vibration analysis of arbitrarily laminated plates of quad, penta and hexagonal shapes, which have combinations of clamped, simply supported and free edge conditions is performed. The finite element formulation is based on first and higher order shear deformation theories to study the free vibration response of thick laminated composite plates. A finite element code is developed incorporating shear deformation theories using an 8-noded serendipity element. The effect of plate shape, arbitrary lamination and different edge conditions on natural frequencies and mode shapes are investigated. A systematic study is carried out to determine the influence of material orthotropy and aspect ratio on free vibration response. For various cases, the comparisons of results from present study showed good agreement with those published in the literature.

Introduction

Composite materials are finding increased usage in aerospace, propulsion, shipping, sports and consumer industries. The distinguishing feature of a composite material is its high specific strength and stiffness, together with directional dependency of properties. The first feature means that significant weight reduction is achievable. The directionality factor complicates structural design but, at the same time, leads to a new degree of freedom in that the strength and stiffness of the material may be tailored precisely to the quantity and in the direction required for a specific application. Therefore strength-to weight and stiffness to weight ratios are two important criteria for using composites over other conventional materials.

Plate analysis is basically a three-dimensional problem. The two-dimensional theories can be derived by making suitable assumptions about the kinematics of displacements and/or the distribution of stress through the thickness of the plate. There are many techniques available for reducing the three-dimensional equations of the theory of elasticity to two-dimensional equations. The principal aspect of this reduction problem is summarized by Gol'denveizer [1]. These techniques are grouped into five categories:

1. Hypotheses techniques.
    - Semi-inverse method,
    - Method of trigonometric functions,
    - Method of full range Fourier series expansion.
2. Expansion techniques.
    - Method of initial functions,
    - Method of symbolic integrations.

3. Asymptotic expansion technique.
4. Method of successive approximations.
5. Mixed methods.

In all the above methods, reduction is carried out using the thickness coordinate except for the asymptotic expansion method in which, generally, a nondimensional parameter such as thickness to length ratio is used.

Various theories originally developed for homogeneous isotropic thin, moderately thick and very thick plates are extended to the laminated anisotropic plates. Also new refined shear deformation theories have been developed for more accurate analyses of anisotropic laminated composites. These theories are classified into two different categories:

1. Equivalent single layer theories, and
2. Discrete layer theories or layer-wise theories.

The historical perspective for the analysis of anisotropic plates based on classical plate theory and shear deformable plate theories was summarized by Vimson and Chou [2]. The theories adopting the equivalent single-layer approach are based on expanding the displacement field through the thickness in a power series. Various researchers have reviewed the research done so far [3].

This paper presents a higher order shear deformation theory (HSDT) based on equivalent single layer approach at which an in-plane cubic polynomial displacement field with independent coefficients was adopted to study the free vibration of thick anisotropic laminated plates at different boundary conditions and geometrical shapes. A finite element code was developed based on this higher order theory using an 8-noded isoparametric element. The code results were already verified for static stress analysis against 3D elasticity solution and previous work done by other researchers in the area of refined theories.

Problem Formulation. Consider a rectangular plate of thickness ‘h’ composed of a finite number, n, of fiber reinforced orthotropic laminas with fibers oriented at angles θ_1, θ_2,.....θ_n as shown in Figure 1.

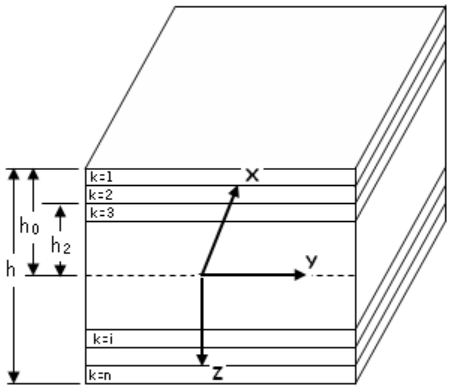


Figure 1: Geometry of orthotropic laminated plate

The coordinate system is taken such that the x–y-plane coincides with the middle plane of the plate and the z-axis is perpendicular to that middle plane. Shear deformation theories for a laminated plate can be developed using a displacement field of the following form

$$u = u_0(x,y,0) - z\,(C_1\psi_x) + z^3\left[(C_2\alpha_x) + C_3\frac{4}{3h^2}(\psi_x + \frac{\partial w}{\partial x})\right]$$
$$v = v_0(x,y,0) - z(C_1\psi_y) + z^3\left[(C_2\alpha_y + C_3\frac{4}{3h^2}(\psi_y + \frac{\partial w}{\partial y})\right] \quad (1)$$
$$w(x,y,z) = w_0(x,y,0)$$

where (u,v,w) are the displacements of a generic point (x,y,z) in a laminated plate and (u_0,v_0,w_0) are the displacements at point (x,y,0) in the reference plane of the laminated plate, ψ_x, and ψ_y are the rotations of the normals of the reference plane about y-axis and x-axis, and α_x, and α_y are warping variables in xz and yz planes, respectively. Warping variables in transverse shear planes, when included as an independent variable in the assumed displacement field eliminate the need of shear correction factor to accurately determine transverse shear stresses. Shear correction factors are used in first order shear deformation theories. Using the displacement field of equation (1), the associated strains are:

$$\boldsymbol{\varepsilon} = \{\varepsilon_x,\ \varepsilon_y, \gamma_{xy}, \gamma_{xz}, \gamma_{yz}\} = \boldsymbol{\varepsilon}_p - z\,\boldsymbol{\varepsilon}_f + z^3\boldsymbol{\varepsilon}_w + \boldsymbol{\gamma}_s + 3z^2\boldsymbol{\gamma}_{sw} \quad (2)$$

where $\boldsymbol{\varepsilon}_p$, $\boldsymbol{\varepsilon}_f$, $\boldsymbol{\varepsilon}_w$, $\boldsymbol{\gamma}_s$ and $\boldsymbol{\gamma}_{sw}$ are extensional, flexure, warp, shear and shear warp strains, defined as

$$\boldsymbol{\varepsilon}_p = \left(\frac{\partial u_0}{\partial x}\quad \frac{\partial v_0}{\partial y}\quad \frac{\partial v_0}{\partial x}+\frac{\partial u_0}{\partial y}\right)^T \qquad \boldsymbol{\varepsilon}_f = \left(\frac{\partial \psi_x}{\partial x}\quad \frac{\partial \psi_y}{\partial y}\quad \frac{\partial \psi_y}{\partial x}+\frac{\partial \psi_x}{\partial y}\right)^T$$

$$\boldsymbol{\varepsilon}_w = \left(\frac{\partial \alpha_x}{\partial x}\quad \frac{\partial \alpha_y}{\partial y}\quad \frac{\partial \alpha_y}{\partial x}+\frac{\partial \alpha_x}{\partial y}\right)^T \quad \boldsymbol{\gamma}_s = \left(\frac{\partial w_0}{\partial x}+\psi_x \quad \frac{\partial w_0}{\partial y}+\psi_y\right)^T \quad \boldsymbol{\gamma}_{sw} = \left[\alpha_x \quad \alpha_y\right]^T$$

The constitutive relations for in-plane (σ_x, σ_y, τ_{xy}) and transverse stresses (τ_{xz}, τ_{yz}), under a plane stress state, and for the the k-th orthotropic lamina of constant thickness 'h' can be written in Cartesian coordinate system as follows:

$$\begin{bmatrix}\sigma_x\\ \sigma_y\\ \tau_{xy}\\ \tau_{xz}\\ \tau_{yz}\end{bmatrix}^{(k)} = \begin{bmatrix}\overline{Q}_{11} & \overline{Q}_{12} & \overline{Q}_{16} & 0 & 0\\ \overline{Q}_{12} & \overline{Q}_{22} & \overline{Q}_{26} & 0 & 0\\ \overline{Q}_{16} & \overline{Q}_{26} & \overline{Q}_{66} & 0 & 0\\ 0 & 0 & 0 & \overline{R}_{44} & \overline{R}_{45}\\ 0 & 0 & 0 & \overline{R}_{45} & \overline{R}_{55}\end{bmatrix}^{(k)} \begin{bmatrix}\varepsilon_x\\ \varepsilon_y\\ \gamma_{xy}\\ \gamma_{xz}\\ \gamma_{yz}\end{bmatrix}^{(k)} \quad (3)$$

where the elements $\overline{Q}_{ij}$ (i,j=1,2,6) and $\overline{R}_{lm}$ (l,m=4,5) are reduced elastic constants. The calculation of these constants in terms of material parameters (E, ν) is discussed in [4]. In order to derive the constitutive equation for the laminate the force, moment and warp resultant vectors [**N, M, P**] are defined using in-plane stresses, while shear force and shear warp resultant vectors [**Q, S**] are defined using transverse stresses as given below:

$$[\mathbf{N, M, P}] = \int_{-\frac{h}{2}}^{\frac{h}{2}} \begin{bmatrix}\sigma_x\\ \sigma_y\\ \tau_{xy}\end{bmatrix}\left[1,\ z,\ z^3\right] dz \qquad [\mathbf{Q, S}] = \int_{-\frac{h}{2}}^{\frac{h}{2}} \begin{bmatrix}\tau_{xz}\\ \tau_{yz}\end{bmatrix}\left[1,\ z^2\right] dz \quad (4)$$

Substituting stresses from equation (3) in equation (4), and integrating through the thickness gives:

$$\begin{bmatrix} \mathbf{N} \\ \mathbf{M} \\ \mathbf{P} \\ \mathbf{Q} \\ \mathbf{S} \end{bmatrix} = \begin{bmatrix} \mathrm{Z} & \mathrm{I} & \mathrm{J} & 0 & 0 \\ \mathrm{I} & \Gamma & \mathrm{L} & 0 & 0 \\ \mathrm{J} & \mathrm{L} & \Lambda & 0 & 0 \\ 0 & 0 & 0 & \mathrm{H} & 3\mathrm{C} \\ 0 & 0 & 0 & 3\mathrm{C} & 9\mathrm{Y} \end{bmatrix} \begin{bmatrix} \varepsilon_p \\ \varepsilon_f \\ \varepsilon_w \\ \varepsilon_s \\ \varepsilon_{sw} \end{bmatrix} \tag{5}$$

Equation (5) represents the constitutive relation between stress resultants and corresponding strain of a laminated orthotropic plate based on higher order shear deformation theory. In equation (5), the elements [Z, I, J, Γ, *L*, Δ] are 3x3 matrices and [H, C, Y] are 2x2 matrices, which can be determined using equation (6).

$$[\mathrm{Z, I, J, \Gamma}, L, \Delta] = \sum_{(k)} \int_{z_{k-1_1}}^{z_k} [\overline{Q}]^{(k)} [1,\ z,\ z^3,\ z^2,\ z^4,\ z^6]\ dz \tag{6a}$$

$$[\mathrm{H, C, Y}] = \sum_{(k)} \int_{z_{k-1}}^{z_k} [\overline{R}]^{(k)} [1,\ z^2,\ z^4]\ dz \tag{6b}$$

where z_k and z_{k-1} are the z-coordinates of the top and bottom surfaces of the k-th lamina.

The finite element equations are obtained by discretizing the plane domain into 'N' 8-node serendipity elements. Each element 'e' has 8 nodes, where each node i (i=1,.....,8) has seven degrees of freedom i.e. $(u_0, v_0, w_0, \psi_{y0}, \psi_{x0}, \alpha_{x0}, \alpha_{y0})$. For simplicity, same interpolation functions are used for all seven variables over each element. Based on the assumption of small displacements, one can write the following for each element e:

$$\boldsymbol{\varepsilon}_p^e = [\mathbf{B}_\mathrm{p}]^\mathrm{e}\{\mathbf{d}\}^\mathrm{e} \quad \boldsymbol{\varepsilon}_f^e = [\mathbf{B}_\mathrm{f}]^\mathrm{e}\{\mathbf{d}\}^\mathrm{e} \quad \boldsymbol{\varepsilon}_w^e = [\mathbf{B}_\mathrm{w}]^\mathrm{e}\{\mathbf{d}\}^\mathrm{e} \quad \gamma_s^e = [\mathbf{B}_\mathrm{s}]^\mathrm{e}\{\mathbf{d}\}^\mathrm{e} \quad \gamma_{sw}^e = [\mathbf{B}_\mathrm{sw}]^\mathrm{e}\{\mathbf{d}\}^\mathrm{e}$$

Where B_p, B_f, B_w, B_s, and B_{sw} are the generalized strain displacement matrices.

Using the principal of virtual work for the plate [4], the assembled stiffness matrix **[K]** can be represented as:

$$\begin{aligned}\mathbf{[K]} = \sum_e \int_{A_e} \{ &[\mathbf{B}_\mathrm{p}]^\mathrm{T}[\mathrm{Z}][\mathbf{B}_\mathrm{p}] + [\mathbf{B}_\mathrm{p}]^\mathrm{T}[\mathrm{I}][\mathbf{B}_\mathrm{f}] + [\mathbf{B}_\mathrm{p}]^\mathrm{T}[\mathrm{J}][\mathbf{B}_\mathrm{w}] + [\mathbf{B}_\mathrm{f}]^\mathrm{T}[\mathrm{I}][\mathbf{B}_\mathrm{p}] + [\mathbf{B}_\mathrm{f}]^\mathrm{T}[\Gamma][\mathbf{B}_\mathrm{f}] + \\ &+ [\mathbf{B}_\mathrm{f}]^\mathrm{T}[\mathrm{L}][\mathbf{B}_\mathrm{w}] + [\mathbf{B}_\mathrm{w}]^\mathrm{T}[\mathrm{J}][\mathbf{B}_\mathrm{p}] + [\mathbf{B}_\mathrm{w}]^\mathrm{T}[\mathrm{L}][\mathbf{B}_\mathrm{f}] + [\mathbf{B}_\mathrm{w}]^\mathrm{T}[\Lambda][\mathbf{B}_\mathrm{w}] + [\mathbf{B}_\mathrm{s}]^\mathrm{T}[\mathrm{H}][\mathbf{B}_\mathrm{s}] \\ &+ [\mathbf{B}_\mathrm{s}]^\mathrm{T}\, 3[\mathrm{C}][\mathbf{B}_\mathrm{sw}] + [\mathbf{B}_\mathrm{sw}]^\mathrm{T}[\mathrm{C}][\mathbf{B}_\mathrm{s}] + [\mathbf{B}_\mathrm{sw}]^\mathrm{T}\, 9[\mathrm{Y}][\mathbf{B}_\mathrm{sw}] \}\ dA\end{aligned} \tag{7}$$

The generalized eigenproblems can be represented as;

$$\mathbf{k\Phi = \lambda M\Phi} \tag{8}$$

where **K** and **M** are, respectively, the stiffness matrix and mass matrix of the finite element assemblage. The eigenvalues **λ**, and eigenvectors **Φ**, are the free vibration frequencies (radians/second) squared, w_i^2, and corresponding mode shape vectors, respectively. The assembled stiffness matrix is as shown in (7) while the mass matrix was constructed of a diagonally lumped mass matrix using Labatto lumping at which a diagonal length equal to the total number of degrees of freedom in the system (NSVAB) is formally equivalent to a numerical integration with NSVAB points for the element kinetic energy:

$$T^e = \sum_{i=1}^{NSVAB} m_i T_i \quad where\ T_i = \frac{1}{2}\dot{u}_i^2$$

A finite element program is developed in FORTRAN using above equations to carry out the numerical calculations and the results obtained using this program is referred in this paper as 'Present HSDT'. The Jacobi iterative method was used for the solution of eigenvalues.

Results and Discussion

Three different plate geometries had been considered for the numerical results, namely, square, pentagon, and hexagon plate shapes with different boundary conditions, fibers orientation, and material properties. Completely reduced integration is employed for extension, bending, shear, warp and shear-warp terms. The results of HSDT were compared to those exists in literature for validity. However, it is known that an exact solution of the problem where complex geometries are under consideration like polygons is at least difficult to be achieved. All previous solutions from literature introduced for comparisons in this paper are approximate solutions and the accuracy of each is depending on the method used for modeling and for solution of equation (8).

Shi et. al. [5] assumes FSDT with Linear in-plane displacement field through the laminate thickness. FSDT with 16 terms of double truncated Fourier series using Galerkin solution procedure was used to obtain the natural frequencies. The need to those 16 terms was revealed from a convergence study conducted by the authors. Table 1 shows a comparison between HSDT results and those obtained in [5] for a fully clamped two-layered [$0^o/45^o$] moderately thick square plate. Both results are very close indicating the validity of present HSDT for natural frequency analysis.

Table 1. Normalized frequencies w^* for a fully clamped two-layered [$0^o/45^o$] moderately thick square plate

	w^*							
	Present HSDT HSDT using FEM with 16 8-noded Elements and 7 DOF/node.				Ref. [5] FSDT with 16 terms of double truncated Fourier series using Galerkin solution procedure.			
Modes	1	2	3	4	5	6	7	8
Present HSDT	15.935	23.856	30.719	33.207	37.446	42.371	46.963	50.829
Ref. [5]	15.484	23.367	29.965	33.120	37.692	42.908	46.907	49.205
a/h = 10; $E_1/E_2 = 25$, $G_{12} = G_{13} = 0.5E_2$, $G_{23} = 0.2E_2$, v = 0.25, $w^* = w_i\, b^2 \sqrt{\rho/(h^2 E_2)}$								

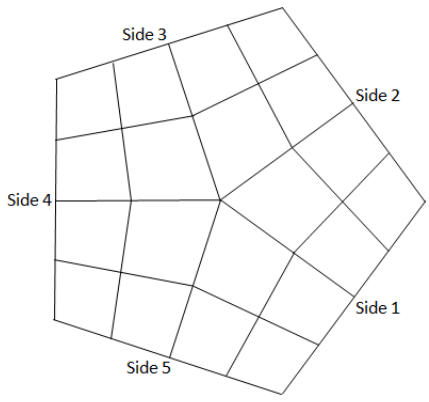


Figure 2. Mesh of the pentagon plate (20 elements with 81 nodes using 8-noded element)

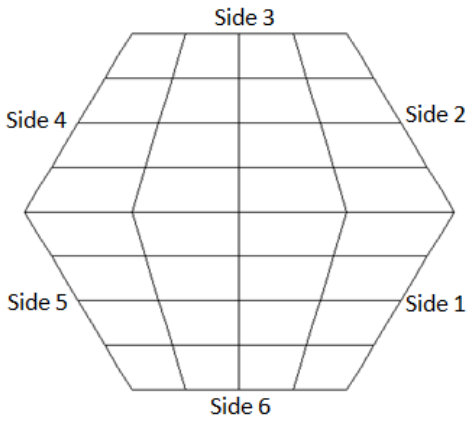


Figure 3. Mesh of the hexagon plate (32 elements with 121 nodes using 8-noded element)

The normalized frequencies of a fully clamped laminated pentagon plate are presented in table 2 for HSDT against those obtained in [6]. The accuracy and computational efficiency of HSDT is very evident hence only 20 elements (7 degrees of freedom per node) were sufficient compared to 80 elements (36 degrees of freedom per node) to converge for natural frequencies. Moreover, the assumed cubic displacement field with independent polynomial coefficients across the plate thickness was capable of reducing the emerging error of using lumped mass system compared to the consistent mass system used in [6].

Table 2. Normalized frequencies λ_i of a fully clamped laminated pentagon plate.

Present HSDT		Ref. [6]				
• HSDT using FEM. • Using 20 Elements and 7 DOF/node. • Lumped mass matrix.		• Lagrange's equations of motion coupled with FEM • Using 80 Elements and 36 DOF/node. • Consistent mass matrix.				
Lamination Sequence		λ_1	λ_2	λ_3	λ_4	λ_5
$[0/45]_s$	Present HSDT	38.7055	67.9702	94.2430	98.1402	128.8873
	Ref. [6]	41.1625	63.4076	92.1572	92.6718	125.986
$[0/60]_s$	Present HSDT	34.3205	61.4618	83.2303	89.5492	134.5692
	Ref. [6]	41.0725	64.8991	94.1414	99.5247	137.759
$E_1/E_2 = 10$, $G_{12}/E_2 = 0.25$, $v = 0.3$, $\lambda_i = w_i a^2 \sqrt{\rho h/D_{22}}$						

The results of four-layered moderately thick hexagonal plate with different lamination sequence and boundary conditions are given in table 3. An increase in the natural frequency is observed for higher modes of frequency when the inner layers fiber orientation angle changed from 0° to 45° except for CFFFFFF case. There is no obvious trend of natural frequency values dependency on fiber orientation and boundary conditions that can be concluded either in this paper neither in previous studies included in this paper. Further study with selective combinations are needed for solid conclusions about it.

Table 3. Normalized frequencies λ_i for a four-layered moderately thick hexagonal plate with different lamination sequence and boundary conditions.

Lamination Sequence	BC	λ_1	λ_2	λ_3	λ_4	λ_5
$[0/0]_s$	CCCCCC*	14.8435	25.3068	67.2737	118.7593	148.1486
	CFFSFF*	15.9448	49.1584	58.2690	87.5910	101.7305
	CFFFFF*	14.4754	39.7121	58.0364	83.2613	108.0862
$[0/45]_s$	CCCCCC*	13.2767	74.9416	103.8787	157.7674	176.1359
	CFFSFF*	6.4864	9.5408	29.7449	109.7751	128.6172
	CFFFFF*	14.8626	35.1013	52.5322	71.7870	92.7004
a/h = 10; E_1 = 175 GPa, E_2 = 7 GPa, $G_{12} = G_{13}$ = 3.5 GPa, G_{23} = 1.4 GPa, v_{12} = 0.25, $\lambda_i = w_i b^2 \sqrt{\rho/(h^2 E_2)}$						
* See figure 2 & 3 for the sequence of edges.						

References

1. Gol'denveizer, A. L., PMM, Vol. 32, No.4, pp. 684-695 (1968).
2. Vmson, J. R., and Chou, T. W., Applied Science Pub. Ltd., London (1975).
3. Reddy, J. N., and Robbins, D. H., Vol. 47, pp.147-169 (1994).
4. Pervez Tasneem, Al-Zebdeh Khalid, Farooq K. Al-Jahwari, Appl. Compos. Mater., pp 499-514 (2010).
5. Jian Wei Shi, Akihiro Nakatani, Hiroshi Kitagawa, Composite Structures, Vol. 63, pp.115-122 (2004).
6. S. S. A. Ghazi, F. A. Barki and H. M. Safwat, Computers & Structures, Vol. 62, No. 2, pp.395-407 (1997).

© (2011) Trans Tech Publications, Switzerland
doi:10.4028/www.scientific.net/KEM.471-472.1184

Influence of Iron Oxide Nano Particles on Electrospun Poly (Vinylidene fluride)-based Carbon Nanofibers on Hydrogen Storage

Samaneh Shahgaldi[a,1,2], Zahira Yaakob[b,1,2], Norazrina Mat jali[c,1,2], Dariush Jafar Khadem[d,1,2], Wan Ramli Wan Daud[e,1,2] and Edy Herianto Majlan [f,1]

[1]Fuel Cell Institute, University Kebangsaan Malaysia, 43600 UKM Bangi, Selangor.
[2]Faculty of Chemical Engineering, University Kebangsaan Malaysia, 43600 UKM Bangi, Selangor.

[a]Sami_shahgaldi@yahoo.com, [b]zahira@eng.ukm.my, [c]azrina@eng.ukm.my, [d]D.Khadem@ukm.my, [e]wramli@eng.ukm.my, [f]edy@vlsi.eng.ukm.my.

Keywords: Carbon Nanofibers, PVDF, Iron oxide, Dehydrofluorination

Abstract. Electrospun Poly (vinylidene fluoride) (PVdF) fine fiber of 100-300 nm in diameter in ribbon shape was synthesized through the electrospinning process via sol-gel. In order to synthesize infusible nanofibers all processing of dehydrofluorination and carbonization was investigated. Iron nanoparticles was doped with PVDF nanofibers in order to be effective in surface area, and porosity to increase the hydrogen storage. The composition, morphology, structure and surface area of PVDF/Iron Oxide nanofibers were investigated by thermo gravimetric analysis (TGA) to determinate the temperature of possible decomposition and crystallinity, scanning electron microscopy (SEM), transmission electron microscopy (TEM), Micromeritics (ASAP2020) used to study the textural properties of the sample, like surface area, total pore volume, and micro pore volume. The result shows that the PVDF without dehydrofluorination treatment for infusibility become melt at around 160 ◦C. By adding the iron oxide nanoparticles as a catalyst it can improve the characteristic of the carbon fiber for hydrogen storage. In best of our knowledge, PVDF doping with iron oxide investigated for first time.

Introduction

Nowadays, development of greener technology has been increasing as the demanding of alternative energy. This is a strategy to overcome two major concern of the world which is decreasing world supply of fossil fuels and global warming so do as climate change. Many types of energy have been investigated, including wind [1], biomass [2], solar [3], geothermal [4] and hydrogen energies [5]. Hydrogen is chosen because no pollutans are created when it is burned as a fuel. However, due to its explosiveness, an efficient storage method is needed for the widespread application of fuel cells and the adoption of hydrogen as an energy source. Many researchers have paid attention to hydrogen adsorption in nanostructured carbon base materials, such as activated carbons, carbon nanotubes, and carbon nanofibers [6]. More recently, Several studies have been done to polymers such as Polyacronitrile (PAN) and Poly(vinylide fluoride) (PVDF) for increasing storage. PAN have been used widely in production of carbon fibers because of relatively high carbon yield, thermally stable and extremely oriented molecular structure [7]. Ideal hydrogen storage materials should have the following characteristics: high specific surface area (SSA), well developed micropores, and many active sites on the surface, such as oxygen functional groups, fluorine groups, or rare-earth-metal nanoparticles [8]. Carbon nanofibers are believed can store hydrogen because of their porous nanostructure. It also can be used as a hydrogen storage material because it can offer a high specific surface area and high porosity, making it light [9]. Microporous carbon materials contain pores with a width not greater than a few hydrogen molecules are found to be more effective for hydrogen storage when compared to dynamic diameter of hydrogen molecule which is 0.4059 nm. PVdF and sarane polymers are polymers that can be used in obtaining meso

porous carbon [10]. PVDF was chosen as a starting polymer by taking account the processability of this polymer into various geometries [11]. Metal/metal oxides have been added to carbon as a catalyst to increase the hydrogen storage capacities.[12-14]. Nanofibers in this study were prepared by using electrospinning method. Electrospinning is a simple method for producing fibers from a rich variety of materials including polymers, composites and ceramics. It is a powerful method for producing ultrafine polymer fibers within the range of a few to a few hundreds nanometers in diameters, which can hardly be produced by traditional method [15]. Microporous carbon nanofibers were prepared through carbonization of electrospun PVdF nanofibers at high temperature. Their composition, structural, morphology and surface area were investigated and discussed in this paper. Adding metal to carbon materials increase the absorption of the hydrogen as a catalyst as a result, we synthesized PVDF/Iron oxide nanofibers by electrospinning.

Experimental

Materials. Poly (vinylidene fluoride) (PVDF, Sigma Aldrich) was used as a carbon nanofibers source, Acetone /N,N-dimethyl formamide (DMF) mixture was utilized as solvent. Iron oxide used as a catalyst. Potassium hydroxide (KOH) and tetrabutylammonium bromide was applied to nanofibers for dehydroflourination.

Methodology. Electrospun PVDF nanofibers were synthesized with a polymer solution with or without Iron oxide in aceton / dimethylformamide mixture via electrospinning. Proper solvent is one of the most important factor in electrospinning.DMF was used due to the appropriate boiling point (426 k) and excellent conductivity. The PVDF sol-gel was prepared with 15% wt PVDF and ratio of [DMF/Acetone: Iron oxide = 5 : 5 : 1] in continuous stirring at room temperature for 2h to obtain a well-dissolved solution in a baker. The final homogeneous viscous solution was immediately drawn into the hypodermic syringe. This syringe is utilized to force the polymer solution to flow through a needle. The needle was attached to a high voltage supply (electrospinze high voltage) that is able to produce DC potentials up to 30 kv. The solution feeding rate was controlled at the rate of 0.4 ml/ h using a motor syringe pump (new era pump). All nanofibers were collected in the collator in distinct distance between nozzle and collector. Electrospinning was carried out under the following conditions: Voltage: 20 Kv, Feeding rate: 0.4 ml/h, distance up to collector: 13cm. After collecting nanofibers from the aluminium foil, they were chemically dehydrofluorinated in the KOH 8M aqueous solution including 0.2 mmol tetrabutyl ammonium bromide at 50 °C for 1h as shown in Fig. 1. Subsequently, dehydrofluorinated nanofibers were carbonized at 1200 °C without any further activation process.

Characterization

PVDF nanofibers and PVDF/ Iron Oxide nanofibers analyzed by thermo gravimetric analysis (TGA) to determine the temperature of possible decomposition and phase change. This measurement was performed with a heating rate of 5 °C/min up to 1000°C. The texture and morphology of nanofibers after spin, after dehydroflurination and carbonization were examined by SEM. The nitrogen gas adsorption-desorption isotherms of the carbon nanofibers were measured by Micromeretics 2020.

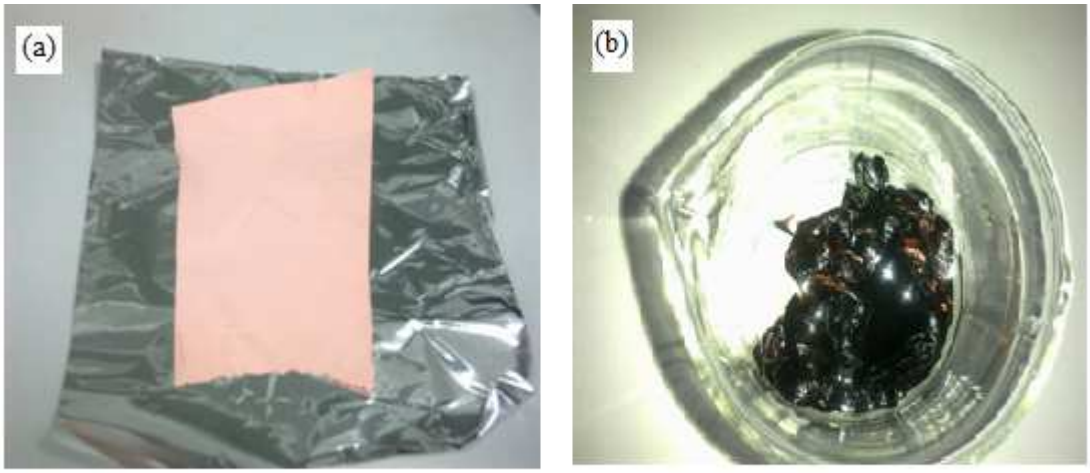


Figure.1.(a) PVDF / Iron oxide nanofibers after spinning (b) PVDF/Iron oxide after 30 min dehydrofluorination

Result and Discussion

Poly (vinylidene fluoride) is one of polymer that can form mesoporous or microporous materials without any activation. Structure of PVDF depends on dehydroflourination due to the infusibility, without dehydroflourination as spun PVDF nanofibers would be melted at 165 °C. Fig.2 shows morphology of samples. Fig. 2 (a, b, c) reveals as spun PVDF nanofibers with iron oxide nanopartricles the surface of fibers is a bit smooth and have diameter about 100-500 nm. Fig. 2(d) depict the rough surface and grainy structure of PVDF/Iron after dehydroflourination and carbonization. The morphology of carbon nanofibers synthesized from PVDF mainly depends on dehydrofluorination[16]. The slight dehydroflourination of spun PVDF nanofibers can produce inhomogeneous structure and unreacted crystalline which would be melted in high temperature of carbonization, but for highly dehydroflourination, homogenous and nonprous nanofibers synthesized during carbonization. To better understand the growth patterns of iron oxide nanoparticles in carbon nanofibers, the nanofibers characterized by TEM as was shown in Fig. 3. TEM image shows that the iron oxide nanoparticles in some part become cluster with irregular size, and also nanofibers remained after carbonization.

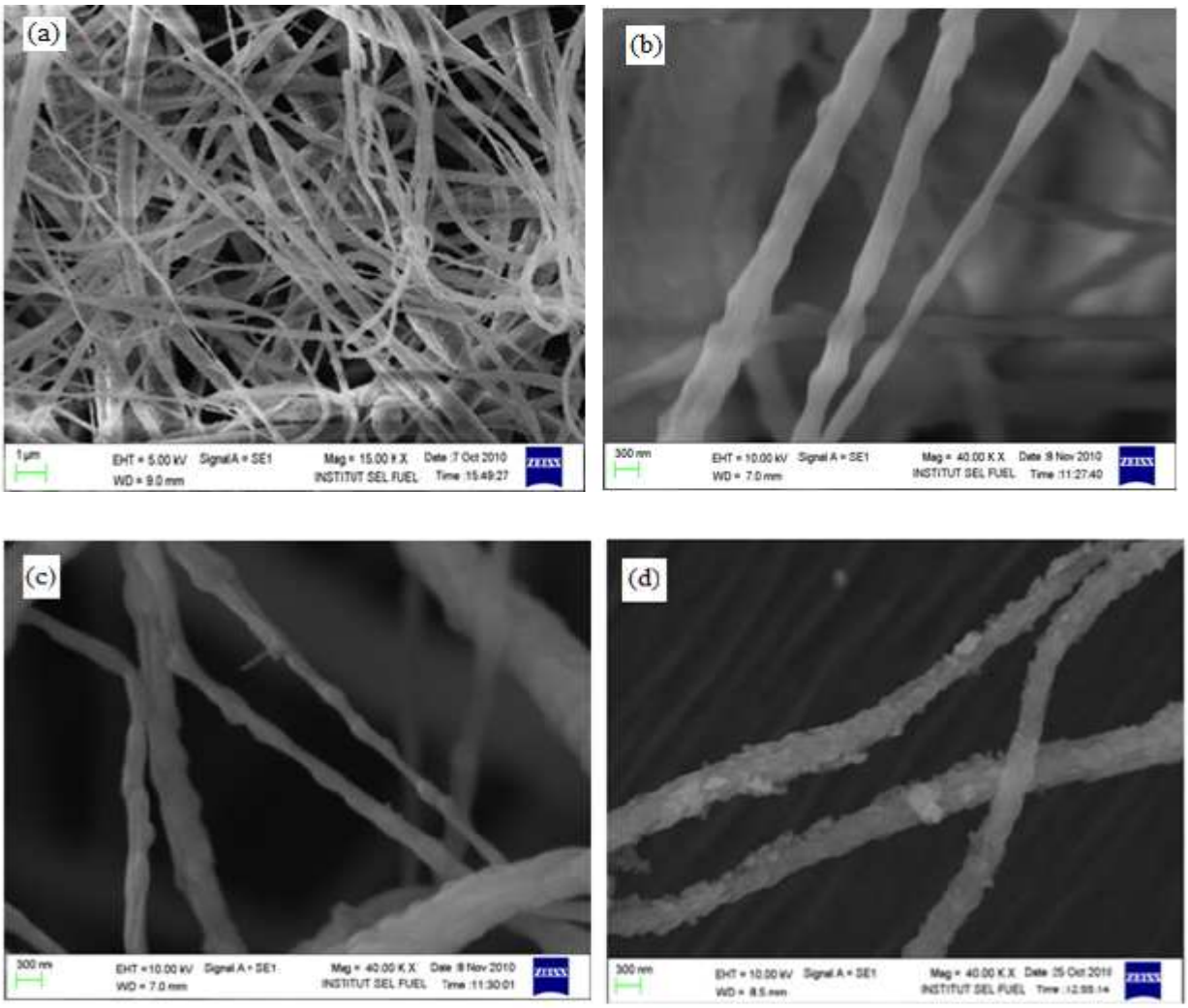


Fig.2. Shows SEM image of (a,b.c) electrospun PVDF/Iron oxide nanofibers (d) PVDF/Iron oxide nanofibers after carbonization

TGA curve for electrospun PVDF/Iron oxide nanofibers before and after dehydrofluorinatin depict in Fig. 4 (a) and (b) respectively. PVDF is very highly thermal stable polymer. In Fig. 4 (a), it is clearly shown that for PVDF, weight loss does not occur before 450 °C, but, for temperatures more than 450 °C it undergoes a strong degradation. On the other hand, after dehydrofluorination, the light weight loss below 200°C is belong to water or solvent in the surface of materials. The weight loss near 500 °C is belonging to disappearing of hydrofluoric and F fraction. Fig.5 (a and b) shows FT-IR spectra of PVDF/ Iron oxide before and after dehydroflourination respectively. Fig. (b) reveals PVDF polymer spectrum absorption peaks in 1403, 1235, 1179, and 881cm^{-1} wave number that proved by reference [18]. On the other hand, The peaks belong to $–CH_2$, and C=C in 1400 and 1607 cm^{-1} should be related to the formation of polyene in the effect of dehydroflourination as shown in Fig.5 (b). The nature of PVDF / Iron oxide nanofibers is characterized by Raman Spectroscopy. The two main peaks located at around 1390 (Dband) and 1600 cm^{-1} (G-band), should be belong to defects, carbonaceous particles and graphitized carbon lattices respectively. Ratio intensities of D band to G band can show the graphitic nature of carbon nanofibers [17]. The Raman result can show carbon nanofibers with average degree of disorder. Fig. 7 shows nitrogen adsorption of sample. The adsorption isotherm of carbon nanofibers increased with increasing the relative pressure, which indicates mesopores and macropores of the sample. By reaching to 420 cc/g of nitrogen adsorption at 1P/P0 has developed pore structure and also it shows specific surface area of about 530 m^2/g and total pore volume of 0.83 cm^3/ g.

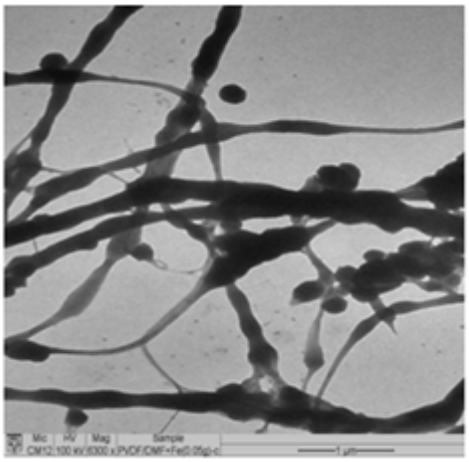


Fig.3.TEM image of electrospun PVDF/Iron oxide nanofibers after dehydrofluorination

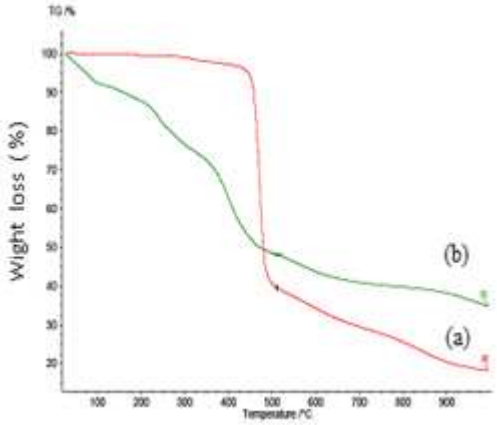


Fig.4(a, b). TGA curve of thermal decomposition, (a) as spun PVDF/Iron oxide (b) PVDF/Iron oxide nanofibers after dehydrofluorination

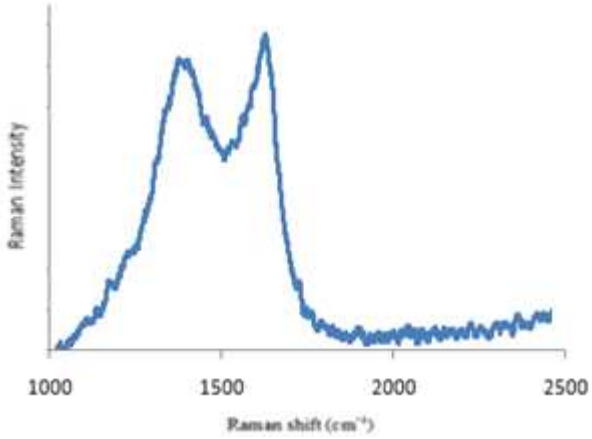


Fig.6. Raman spectra of PVDF/Iron oxide nanofibers after carbonization

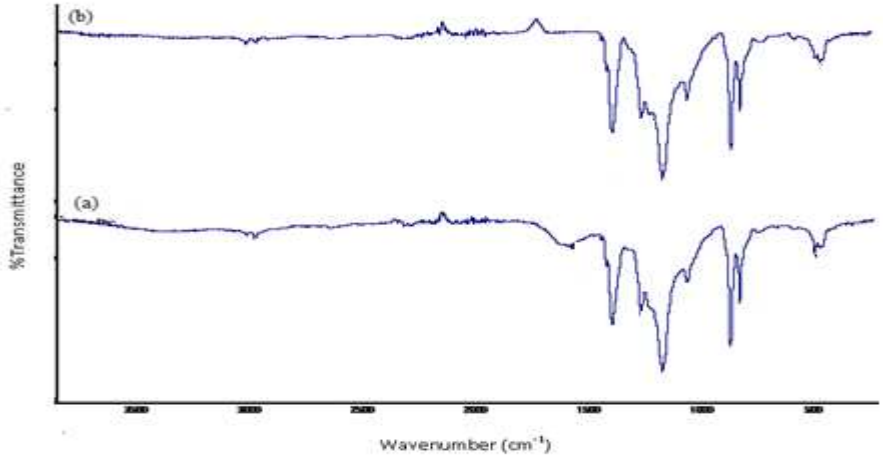


Fig.5.FT-IR spectra of (a) PVDF/Iron oxide nanofibers after dehydrofluorination, (b) as spun PVDF/Iron oxide nanofibers

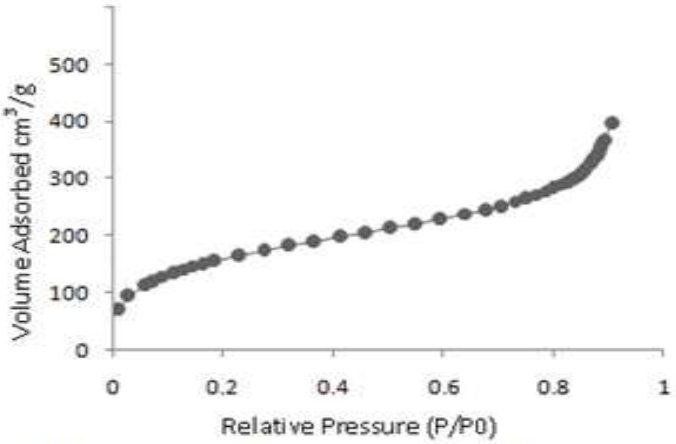


Figure.7. Nitrogen adsorption isotherm of PVDF/Iron oxide after carbonization

Summary

In conclusion, PVDF / iron oxide nanofibers were successfully synthesized via electrospinning method. Metal oxide add to carbon material in order to act as a catalyst and increase the hydrogen storage. High production, simplicity and cost effective are advantages of this method. Carbon nanofibers with high surface area formed from PVDF after dehydroflourination and carbonization. As spun nanofibers with 100-500nm in diameter have smooth surface and it has rough surface with grainy structure after carbonization. Formation of carbon nanofibers clearly were shown by raman spectroscopy. Nitrogen adsorption isotherms shows surface area about 530 m^2/g and total pore volume of 0.83 cm^3/ g.

References

[1] NR. Banapurmath, Tewari PG, Hosmath RS: Renew Energy vol 33(9),2008, 1982–8.

[2] A. Zabaniotou, O. Ioannidou, E. Antonakou, A. Lappas:.Int J Hydrogen Energy vol 33(10),2008,2433–44.

[3] G .Makaka, EL. Meyer, M. McPherson:Renew Energy vol 33(9),2008, 1959–73.

[4] M. Kanoglu, I. Dincer, MA. Rosen: Int J Hydrogen Energy vol 32(17), 2007, 4250–7.

[5] BJ. Kim, YS. Lee, SJ. Park: Int J Hydrogen Energy vol 33(9),2008, 2254–9.

[6] H.Takagi, H. Hatori, Y. Soneda, N. Yoshizawa, Y. Yamada: Mater Sci Eng B – Solid State Mater Adv Technol vol 108(1–2),2004,143–7.

[7] M.S.A.Rahaman,A.F.Ismail, A.Mustafa: Degrad. Stab., Vol. 92, 2007,1421-1432.

[8] RT .Yang.J Carbon 2000;38:623–6.

[9] SJ.Park, BJ.Kim,YS.Lee, MJ: Int J Hydrogen Energy vol 33(6),20081706–10.

[10] J. Yamashita, M. Shioya, T. Kikutani, and T. Hashimoto, Vol 39, *Carbon*, , 207 (2001).

[11] Yamashita,J, Shioya M, Kikutani T, Hashimoto T, Carbon 39 (2001) 207–214.

[12] Campesi R, Cuevas F, Gadiou R, Leroy E, Hirscher M, Vix- Guterl C, et al. Carbon 2008; 46(2):20614.

[13] Leela Mohana Reddy A, Ramaprabhu S. Int JHydrogen Energy 2008;33(3):1028–34.

[14] Im JS, Kwon O, Kim YH, Park SJ, Lee YS. Microporous Mesoporous Mater 2008; 115(3):514–21.

[15] P.W. Gibson, H. Schreuder-Gibson, D. Rivin, Colloids Surf. A 469 (1999) 187.

[16] Gauden PA, Terzyk AP, Furmaniak S, Weso1owski RP, Kowalczyk P, Garbacz JK. Impact of an adsorbed phase nonideality in the calculation of the filling pressure of carbon slit-like micropores. Carbon 2004;42(3):573–83.

[17] Zhang J, Zou H, Qing Q, Yang Y, Li Q, Liu Z, et al. J Phys Chem B 2003; 107:3712–8.

[18] A.J. Lovinger In: D.C. Basset, Editor:*J Polymers-1*, Applied Science Publishers Ltd., London and New York (1982), pp. 195–273.

Keywords Index

(3-Aminopropyl)trimethoxysilanes 898
3D Elastic 658

A

Abaca Fibre 821
ABAQUS 634, 703
Absorption 438
Acetabular Cup 945
Adhesive Joint 610, 1075
Aeroelasticity 1107
Aging 403
Agriculture Residues 55
Al-Mg_2Si Composite 1052, 1171
Al/SiC Nanocomposite Powders 420
Albumen 928
Alkali Treatment 191
Aluminum Alloy 349, 1081
Amorphous 804
Analysis 343
Analysis of Variance (ANOVA) 361
Analytical Solution 279
Angle-Ply 263
ANSYS 432
ANSYS Package 426
Anti-Symmetric Angle Ply Laminate 432
Anti-Symmetric Laminates 426
Antioxidant 151
Apparent Shear Stress 513
Apparent Viscosity 513
Arbitrary Laminate 1177
Arcan 703, 886
Arenga pinnata 1147, 1153
Artificial Ageing 349
Artificial Neural Network (ANN) 221
Asymmetrically Laminated Beams 745
Autodesk Moldflow Plastics Insight 1101

B

Bagasse 31, 167
Ballistic Protection 1136, 1142
Banana Fiber 686
Banana Pseudostem Fiber Reinforced Polymer Composite 444
Batch Formulation 933
Batch Method 62
Beam 73
Bending Analysis 1005
Bending Strength 502
Binder Separation 409
Bioactivity 325
Bioactivity Properties 303
Biocomposites 55, 563, 781
Biodegradable 397
Bismuth Oxide 97
Blend 115
Blister Test 315
Board Density 49
Boat Structure 1113
Bolted Joint 939
Buckling 530
Buckling Pressure 833
Bulk Moulding Compounds 1101
BVID 904

C

C-Glass Composite 1085
Calcination 596
Cantilever Beam 578
Carbon Black (CB) 26, 957
Carbon Fiber 652
Carbon Fiber Reinforced Polyetheretherketone 945
Carbon Fiber Reinforced Polymer (CFRP) 73, 590, 692, 697, 975
Carbon Nanotubes (CNT) 127, 157, 162
Carbon Nanowires 1184
Carbon/Epoxy Composite 484
Carbothermal Reduction 670
Cast Composite 727
Casting 1165
Casting Process 601
Catalyst 596
Cathode 179
Cellulose 145, 786, 815
Cement Bonded Particleboard 572
Ceramic 1136, 1142
CFRP Laminate 79
CFRTP 975
Channel Profile 578
Characterization 20

Chebyshev Polynomials 1016
Chemical Treatment 963
Chip Wood 1064, 1070
Chitosan (CS) 851
Classical Laminated Plate Theory 709
Clay 769
Coconut 1028
Coconut Coir 391
Coefficient of Thermal Expansion CTE 179
Cohesive Element 568, 1085
Coir 1028
Cold Isostatic Pressing (CIP) 245
Compatibilisation 472, 478
Composite 1, 20, 145, 263, 303, 325, 367, 373, 379, 403, 513, 652, 703, 715, 721, 886, 928, 1130, 1165
Composite Armor 1136, 1142
Composite Cathode 268
Composite Decking 552
Composite Design 981
Composite Laminate 568
Composite Material 103, 221
Composite Panel 59
Composite Plate 1177
Composite Repair 1124
Composite Sandwich Plate 658, 1159
Composite Skew Plate 739
Composite Structure 466
Compression 763
Compression after Impact (CAI) 646
Compression Molding 733
Compressive Strength 449
Computational Mechanics 1136, 1142
Computer Simulation 601
Concrete 343
Conditioned 674
Conducting Polymer Composite (CPC) 361
Conductivity 274, 379
Consolidation Pressure 798
Construction Waste 449
Contact Law 1159
Continuum Damage Mechanics 969
Copper Oxide Nanofibers 792
Core/Shell Type Powder 993
Correction Factor 703
Corrosion 203, 325
Cotton Fiber 291, 928
Coupling Agent 62, 507
Cp-Ti 325
Crack 892
Cracking Load 79
Cracking Mechanism 922
Creep 975
Creep Recovery 257
Crushing Force 664
Cu-TaC Composite 798
Curing 403
Curing Characteristics 845, 851, 957
Curing Temperature 415
Curing Time 415
Current Efficiency 1010
Cyclic Loading 568, 697
Cylindrical Panel 337
Cylindrical Shell 466

D

D-Spacing 490
Damage 1, 367, 461, 951
Damage Detection 809
Damage Tolerance 173
DC Plating 1010
De-Bonding 79
Defect 274
Deflection 73
Dehydrofluorination 1184
Delamination 568, 606, 874, 886, 951
Design of Experiments (DoE) 233
Diaphragm Behavior 552
Differential Cubature Method 1005
Differential Scanning Calorimetry (DSC) 415, 490
Dispersion 162
DMA 815
Dominant Process Zone 606
Dose Rate 775
Ductile Damage 969
Duty Cycle 1010
Dynamic-Instability 466

E

E-Glass Fiber (E-GF) 227
E-Glass/Epoxy Composite 484

EB Irradiation 775
Edge Effect 263
Edge Effects 1177
EDS 490
EDX 309
Elastoplastic Contact 367
Electrical Conductivity 157, 361
Electrical Properties 109, 162
Electrospinning 43, 542, 792, 1040
Elitist-Genetic Algorithm 331, 337
Elongation Value 1052
Energy 1028
Energy Absorbed 646
Energy Absorption 215, 664
Energy Release Rate 315
Energy Storage 37
Epoxidised Natural Rubber 518
Epoxidized Natural Rubber (ENR) 851
Epoxy 191, 987, 1118
Epoxy Composite 1064, 1070
Epoxy Injection 692
Equal-Channel Angular Pressing (ECAP) 127
Eringen's Nonlocal Elasticity 1016
ESEM 815
Euler Beam 1016
Exfoliation 197
Experimental Study 291
Expert System 1113
External Pressure 833
External Strengthening Systems 697
Extrusion Molding 239

F

Fabrication 20
Failure 173
Failure Analysis 646
Failure Mechanism 939
Failure Mode 590
Fast Growing 1091
Fatigue 173, 221, 975
Fatigue Life 628
Fatigue Property 957
Fe-TiC Composite 670
Fiber 674, 680, 839, 1028
Fiber Metal Laminate 524
Fiber Metal Laminated Plate 331
Fiber Reinforced Composite 227, 809, 939
Fiber Reinforced Plastic (FRP) 26
Fiber Reinforcement 552
Fibre-Resin Impregnation 1147, 1153
Filler 26
Filling 601
Finite Element (FE) 343
Finite Element Analysis (FEA) 37, 833, 951, 969, 1085, 1177
Finite Element Model (FEM) 279
Finite Fracture Mechanics 1075
Finite Strip 331, 337
Finite Strip Method 426, 432, 466, 757, 1022
Fire 343
First-Order Shear Deformation Theory 709, 757
Flame Retardancy 751
Flammability 640
Flaw Assessment 904
Flexural Strength 79, 361, 449, 697
Fluidity 420
Flutter 1107
Fly Ash (FA) 26
Fracture 1
Fracture Load Prediction 1075
Fracture Mechanic 315, 703
Fracture Surface 1052
Fracture Toughness 315, 874, 880, 886
Free Vibration 133, 1177
Free Vibration Analysis 739
Frequency 1010
Front Bumper Beam 484
FRP Ratio 73
FTIR 507
Functionalisation 162
Functionally Graded Material (FGM) 140, 709, 757
Functionally Graded Plate 133
Fuselage Structure 1085

G

Galerkin's Method 616
Gel Time 763
General Domes 833
GFRP 763
Glas Ceramics 245
Glass Fiber 686, 874

Glass Fibre Composite 343, 892
Glass Reinforced Plastic 279
Glass Transition Temperature 415
Glycerol 1046
Graphite 361
Green Compact Mechanical Strength 558
Green Compression Strength 769
Guided Wave Ultrasonics 809

H

Halloysite Nanotubes 622, 628, 957
Hardboards 572
Hardness 127, 157, 349, 496
Hardness Measurements 1165
Healing Efficiency 548
Heat Treatment 1171
Hematite 670
High-Density Polyethylene 303, 444, 827
High Humidity 975
High Impact Polystyrene (HIPS) 821
Higher-Order Shear Deformation Theory 709
Hollow Fiber 548
Honeycomb 461
Hot Extrusion 1171
Humidity Sensor 542
Hybrid 674, 1107
Hybrid Composite Structure 916
Hybrid Compound 596
Hybrid Square Tubes 664
Hybridisation 680, 686
Hydrodynamic Friction 733
Hydrogen Production 1046
Hydroxyapatite (HA) 303, 325, 827, 898
Hydroxyapatite Polyetheretherketone 945
Hydroxyapatite-Titanium 140
Hydroxyl Apatite 121

I

I-Beam 590
Impact 367, 951, 1028
Impact Analysis 634
Impact Localization 910
Impact Modifier 821
Impact Property 721
Impregnation 1046
Impregnation Pressure 1153
Impregnation Time 1147
In Situ Powder Metallurgy 420
Indentation 1159
Infrared Camera 103
Injection Molding 1101
Interdigital Electrode 542
Interface Element 606
Interfacial Adhesion 320
Interfacial Shear Strength 781
Intermetallic 1165
Internal Bending 839
Internal Energy 484
Ionic Liquid (IL) 786
Iron Oxide 1184
Irregular Composite Pipes 279

K

Kaoline 185
Kenaf 239, 438, 507, 513, 563, 1095
Kenaf Fiber 191, 227, 297, 781, 963, 1058
Kenaf-Plastic Composite 239
Kenaf/PP Composite 438
Kinetics 1028

L

$La_{0.6}Sr_{0.4}Co_{0.2}Fe_{0.8}O_3$ (LSCF) 179
Laminated Composite Plates 530, 536
Laminated Panel 616
Laminated Plate 1107
Large Deflection 709
Large Deflection Behavior 432
Lateral Torsional Buckling 578
Lay-Up 403
LDH 209
LDPE Foam 751
Lead-Free 67
Lead-Free Solder Pastes 257
Lead Zirconate Titate (PZT) 1124
Length 680
Li 1052
Life Cycle Assessment (LCA) 999
Lignocellulosic Fiber 507
LM6 721, 727
Loading 680

Low Cost 640
Low-Velocity Impact 461, 524, 646
Low Wind Speed Wind Turbine 981
LSCF6428 268
Lubricating Layer 733

M

Maelic Anhydride (MAH) 821
Manufacturing 1091
MAPP 20
Material 185
Material Selection 1113
Mathematical Model 664
MDF Boards 839
Mechanical 109, 827
Mechanical Alloying (MA) 798, 804
Mechanical Characterization 969
Mechanical Property 43, 59, 85, 91, 121, 167, 239, 303, 444, 572, 652, 715, 1171
Mechanical Vibration 721
Melt Compounding 197
Metal Injection Molding (MIM) 409, 558
Metal Matrix Composite (MMC) 721, 727, 1081
MFI 652
Micro-Analysis 309
Micro-Meso 263
Microcrystalline Cellulose 355
Micromechanical 781
Microstructure 179, 584, 751, 1171
Milling Speed 804
Mineral Fillers 999
Mixed-Mode 880
Mixing 674
Modified Arcan Specimen 880
Modulus 680
Moisture 769
Moisture Content 403
Montmorillonite 786
Morphological Property 957
Morphology 403, 472, 478
Multi Layer Rotor 37
Multi-Term Extended Kantorovich Method 739
Multilayer Fiberglass 85
Multiscale Modelling 1, 916
Muscovite 197
MWCNT-Alumina 596

N

Nano Alumina 121
Nano-Composite 7, 67, 115, 162, 209, 355, 415, 490, 496, 518, 542, 584, 751, 775, 786, 1095, 1118
Nano-Fiber 251, 542
Nano Fibres 43
Nano-SiC 203
Nano-Single Screw Extruder 898
Nanocrystalline Material 127
Nanomaterials 67
Nanotechnology 251
Natural Aging 349
Natural Fiber Composite 167, 297, 1058
Natural Fibre 191, 640, 963, 1034
Natural Frequency 658
Natural Rubber (NR) 622, 628, 845, 957
NbC Phase 804
Ni-P Coating 203
Nickel/Hydroxyapatite Catalyst 1046
Non-Destructive Evaluation (NDE) 904
Non-Destructive Testing (NDT) 103
Non-Linear Finite Element Model 530, 536
Nonlinear Analysis 745
Nonlinear Vibration 616
Nonwoven Needle Punched Fiber Mat 987

O

Oblique Loading 215
Oil Palm Ash 1130
Oil Palm Frond 55
OMMT 775
One Shot Process 391
Optimization 331, 337
Organoclay 7, 115, 584
Oscillatory Test 257
Outlier Analysis 1124
Oxygen Transmission 775

P

PA6 518

Pack 185
Palm 145
PAN Based Carbon/Epoxy Composite 880
Panel Density 59
Paper 251
Parameter 674
Parameters Process 233
Particle Size 109
Particleboard 49
Particulate Filler 1130
Paulownia 85, 715, 1091
Perturbation Method 616
Physical Properties 31, 43, 85, 91, 455, 572
Pitch Base Carbon Fiber 916
Plastic Region 763
Plywood 715
PMPPIC 507
Poly (vinylidene fluoride) (PVDF) 355
Poly(lactic acid) (PLA) 781, 815, 1095
Polyamide 6/Polypropylene Blend 7
Polyester 26
Polyetheretherketone (PEEK) 898
Polyethylene (PE) 121
Polymer 763
Polymer Composite 320, 945
Polymer Concentration 43
Polynomial Classifiers 221
Polypropilen 185
Polypropylene (PP) 20, 145, 209, 239, 472, 478, 652, 963
Polypropylene Honeycomb 524
Polypropylene Layered Silicate Nanocomposite 197
Polypropylene Thermoplastic Honeycomb 646
Polyurethane Foam 391, 584
Polyurethane Moulding 391
Porosity 179
Porous Composite Cathode 97
Post-Buckling 530
Post Buckling Analysis 426
Powder Consolidation 127
Power Law 709, 757
Pre-Crack 692
Press Condition 91
Pressure-Less Method 140, 933
Pressureless Sintering 179
Processing 145, 674
Progressive Damage 263
Protonic Electrochemical Cell 373
Pukanszky Model 320
Pulp 251
Pulse Plating 1010
Pultruded Composite Tube 215
Pultruded Fiber Reinforced Plastic 578
PVC 507
PVDF 1184

Q

Quality Control 103
Quartz-Silicon Dioxide Strength 727

R

Radiation 121
Radome 563
Rattan Fiber 845
Recycled 62
Recycled Acrylonitrile Butadiene Rubber 472, 478
Recycled Glass 245
Recycled HDPE 151
Recycled Polyethylene Terephthalate 622, 628
Recycling 999
Reduction 596
Reinforced 674
Reinforced Ceramic Shell Mould 922
Reinforced Concrete (RC) 692
Reinforced Concrete Beam 692, 697
Relative Post-Buckling 1022
Repeated Water Immersion 438
Resin Content 49, 59
Resin Transfer Molding (RTM) 987
Response Suface Methodology (RSM) 821
Retention 438
Rheological Behavior 827
Rheology 67, 257, 513
Rheology Properties 109, 409
Rice Husk 59, 922
Rice Husk Powder 472, 478
Rubber-Filler Interaction 845
Rubber-Toughened 7

S

Sago Starch 397

Sandwich Panel 85, 461
Sandwich Structure 524, 610
Sawdust 1064, 1070
Scanning Electron Microscope (SEM) 127, 309, 490, 845, 933
SDC 268
SDC-$(Li/Na)_2CO_3$ 179
SDC Carbonate 268
Second Order Shear Deformation 133
Self-Healing 548
Semi-Energy Approach 426, 432
Semi Interpenetrating Networks 309
Sensors Analysis 1124
Shape Factor 279
Shape Memory Alloy Actuator 530, 536
Shear Deformation Theory 1177
Shearography 904
Shells of Revolution 1005
Shrinkage 763
Silane 472, 478
Silica 622, 628
Silica Nanofibers 1040
Silica Palladium Nanofibers 1040
Silk Fiber 20
Simulation 634
Single Layer Particleboard 31
Sintered 274
Sintering 140, 245
Sintering Optimization 933
Slenderness 31
Slurry Painting Method 97
Smart 185
SMC 733
Soda Lime Silica Glass 933
Sodium Hydroxide (NaOH) 227
Sol-Gel 274, 379, 993, 1046
Solder Paste 67
Solidification 601
Solidification Parameters 1081
Sonication 490, 496
Space Charge Layer 274
Spacecraft Flywheel 37
Specific Energy Absorption 484
Split Hopkinson Pressure Bar (SHPB) Apparatus 385
Spurious Stress Oscillation 606
Steam Reforming 1046
Steel 590, 969
Stiffened Panel 910
Stiffness 502
Stiffness Reduction 975
Stitch Density 987
Strain Energy Release Rate (SERR) 610, 892
Strain-Rate 969
Strength Property 55
Strength Reduction 548
Strengthened Beam 79
Strengthening 590
Stress Intensity Factor (SIF) 880, 892
Stress-Strain Curve 385
Structural Health Monitoring (SHM) 809
Structural Health Monitoring System 1124
Structural Integrity 1
Structural Performance 73
Sugar Palm 1034
Sugar Palm Fibre 1147, 1153
Sugar Palm Tree 502
Sugarcane Bagasse 49
Surface Area 792, 1040, 1046
Surface Modification 1034
Surface Quality 31
Surface Roughness (SR) 233
Sustained Loading 73
Symmetric Cross-Ply Laminates 1022

T

TaC Phase 798
Taguchi Method 361, 558
Tailing Sand 769
Tannin-Phenol Formaldehyde 715
Tea Residues 572
TEM 127
Temperature 343, 733
Temperature Dependent 133
Tensile 680
Tensile Properties 472, 478, 496, 845
Testing 291
Textile 62
Thermal Buckling 536, 757
Thermal Conductivity (TC) 584, 751, 1118
Thermal Imaging 103
Thermal Post-Buckling 536
Thermal Stability 209, 815
Thermo-Mechanical Vibration 745

Thermoplastic 167
Thermoplastic Composite 173, 963
Thermoplastic Natural Rubber (TPNR) 115
Thermoplastic Polyurethane (TPU) 297, 1058
Thermoplastic Starch (TPS) 397
Thermoplastics 999
Thermoset 1101
Thermoset Based Nanocomposites 157
Thermosonics 904
Thickness Swelling 62, 455
Thin Film 1118
Three-Dimensional Composite Structure 916
Three Layer Particleboard 31
Time Reversal 910
TiO_2/ZnO Nanocomposite 993
Titanium Carbide Particulates 1081
Toughening 518
Translational 1028
Tsai-Hill Criteria 981
Tubular Composite Structures 951
Turning 233

U

Ultra High Molecular Weight Polyethylene 827
Ultrasonic Welding 945
Unidirectional 20, 981
Unidirectional Composites 291
Unsaturated Polyester 502, 686, 1034
Urea-Formaldehyde 59
UTS 1052
UV 928

V

Vibration Analysis (VA) 1016
Virtual Crack Closure Technique (VCCT) 610
Viscoelastic Core 658
Von-Karman Equations 1022
Von Karman's Compatibility Equation 426, 432

W

Walnut/Almond Shells 91
Waste Management 449
Water Absorption 455, 928
Wave Propagation 910
Wavelet Analysis 809
Wax 49
Wear Resistance 1165
Weight Ratio 227
Weighting Factor 1113
Wood-Based Composite 91
Wood Composite 1064, 1070
Wood Composite Panel 1091
Wood Industry 251
Wood Particle 31
Wood-Plastic 62
Wood Plastic Composite (WPC) 151, 640
Woven 981

X

X-Ray Diffraction (XRD) 490

Y

Yoghurt 185

Z

Zeolite 320
Zirconium 349

Authors Index

A

Ab Ghani, M.H. 151
Abbasi, S. 145
Abdalla, J.A. 692, 697
Abdan, K. 167
Abdi, B. 833
Abdizadeh, H. 993
Abdrahman, M.F. 507
Abdul Hamid, S. 987
Abdul Kadir, M.R. 303, 827, 945
Abdul Kudus, M.H. 596
Abdul Majid, D.L.A. 37, 133, 140, 928, 1028, 1107, 1124
Abdul Razak, S.N. 610
Abdullah, A. 769
Abdullah, A.H.D. 963
Abdullah, H. 268
Abdullah, H.Z. 391
Abdullah, M.F. 409, 558, 634
Abdullah, M.R. 898, 945
Abed, F.H. 969
Abu Bakar, A. 227
Abu Bakar, N.A. 59
Abu-Sharkh, B. 145
Adilen, S. 449
Adinoyi, M.J. 490, 496
Affandi, N.B. 1028
Aghdam, M.M. 739, 745
Agung, E.H. 821
Ahmad Rasyid, M.F. 197
Ahmad, M. 121, 827
Ahmad, Z. 957
Ahmed, E. 73, 79
Ahmed, M. 20
Ahsan, Q. 20
Ainun, Z.M. 251
Aji, I.S. 513, 674, 680
Akbarshahi, H. 664
Akhlaghi, F. 420
Akil, H.M. 197, 385, 461, 524, 596
Akmil, N. 121
Al-Aqeeli, N. 490, 496
Al-Himairee, R.M. 969
Al-Jahwari, F.K.S. 1177
Al-Ma'adeed, M. 999
Al-Qadhi, M. 415
Al-Tamimi, A.K. 692, 697, 969
Al Toubat, S. 552
Alavijeh, H.S. 745
Ali, A. 103
Allahkaram, S.R. 203, 1010
Almond, D.P. 904
Amir, A.F. 646
Anuar, H. 397, 775, 781, 928
Anuar, K. 233
Anwar, U.M.K. 1147, 1153
Aravinthan, T. 763
Ariffin, A.A. 215
Arifin, M.K.A. 601, 634, 721, 727, 769, 1081, 1101
Assaee, H. 432
Attaran, A.H. 1107
Awad, Z.K. 343
Ayob, A. 530, 536, 833
Ayoob, N.F. 245, 933
Azhari, C.H. 43
Azmah Hanim, M.A. 686
Azman, H. 7, 518
Azmi, M.A. 391
Azura, A.R. 622, 628

B

Badarulzaman, N.A. 922
Baharudin, B.T.H.T. 721, 727, 769, 1081, 1101
Bahrami, A. 1165, 1171
Bahrinejad, A. 91
Balakrishnan, H. 7
Barakat, S. 552
Bargh, H.G. 331, 337, 616
Basri, S. 1028, 1107
Bayat, M. 133, 140
Beaumont, P.W.R. 1
Becker, W. 1075
Bose, A.C. 325

C

Che Haron, C.H. 558

Cheraghi, M.S. 1010
Chiawea, L. 67
Choupani, N. 703, 874, 880, 886
Christoforou, A.P. 367
Chu, W.M. 67, 257
Chua Abdullah, M.I.H. 409, 558
Ciampa, F. 910

D

Dahlan, K.Z.M. 827
Dashtizadeh, Z. 103
De Angelis, G. 904
Dedikarni, 97
Doh, S.I. 449
Dönmez Çavdar, A. 572
Durairaja, R. 67, 257
Dzulkurnain, N.A. 274

E

Ebrahimifard, R. 993
Eker, A.A. 185
Eker, B. 185
El Kadi, H.A. 221
El-Shekeil, Y.A. 297, 1058
Emamy, M. 1052, 1165, 1171
Esmaeilian, G. 721
Eyvazzadeh, A. 584

F

Faieza, A.A. 1064, 1070, 1081, 1130
Fairuz, A.M. 1113
Faizal, A.R.M. 239
Falencia, F. 963
Fallah, A. 739, 745
Fard, K.M. 1159
Farrokhabadi, A. 263, 548
Fatchurrohman, N. 1081
Fauzi, F.M. 55
Fauziah, M.Y. 403, 928
Fazilati, J. 466
Fujii, T. 975

G

Ganji, M. 715
Gasem, Z.M. 490, 496
Ghannadpour, S.A.M. 757, 1016, 1022
Ghayour, M.H. 606
Gning, P.B. 951
Goharian, A. 945
Gohil, P.P. 291
Golobostanfard, M.R. 993

H

Had, J. 916
Hajikazemi, M. 426, 432, 709, 1022
Haldar, A.K. 173
Hamdan, M.M. 821
Hamid, M.R.Y. 640
Hanafi, I. 227, 472, 478, 622, 628, 845, 851, 957
Hanifawati, I.N. 686
Haniffah, W.H. 438
Haris, M.Y. 563
Harun, J. 839
Harun, Z. 922
Hasmaliza, M. 596
Hassan, N.M.I.N. 634
Hawileh, R. 692, 697
Heitzmann, M.T. 309, 315
Hesari, F.A. 542
Heydari, M.H. 703, 886
Hisham, S. 1064, 1070
Hodzic, A. 999
Hong, T.S. 1101
Hosseini-Toudeshky, H. 263, 568, 606
Hosseini, M. 1159
Hosseinmardi, A. 542
Hou, M. 309, 315, 355
Husin, M.R. 303
Hussin, K. 472, 478
Hwei, N.M. 43

I

Ibrahim, M.S. 1064, 1070, 1130
Ibrahim, N.A. 652, 1095
Ibrahim, S. 373
Idris, M.I. 391
Imran, M. 7
Ishak, M.R. 1147, 1153
Ishak, Z.A.M. 987
Islam, M.M. 20, 763

Islam, M.S. 20
Ismail, A. 868
Ismail, A.B. 349
Ismail, I.K. 279
Ismail, N. 233, 1064, 1070
Ismarrubie, Z.N. 444, 455, 502
Iswandi, 109

J

Jadee, K.J. 939
Jafari Nodooshan, H.R. 1165, 1171
Jalaluddin, H. 239
Jalalvand, M. 606
Jamal, N.A. 775
Jarot, R. 179
Jasemzadeh, A. 568
Judawisastra, H. 963, 981
Jumaat, M.Z. 590
Juoi, J.M. 245, 933

K

Kahle, R. 37
Kahraman, R. 145, 999
Kakati, K. 209
Kakyal, A. 892
Kalaycioğlu, H. 572
Kamarudin, N.H. 922
Kamarulzaman, N. 373
Kargarnovin, M.H. 739
Karim, S.S.A. 43
Kasiri, A. 751
Keyanpour-Rad, M. 542
Khadem, D.J. 792, 1040, 1184
Khalaf, A. 285
Khalili, S.M.R. 1159
Khalina, A. 103, 239, 297, 438, 513, 674, 680, 815, 839, 868, 1058, 1095
Khanjanzadeh, H. 62, 91
Khazaeian, A. 85, 91
Khoramshahi, A. 874
Khorshidi, R. 1052
Koid, C.H. 449
Kovács, J.G. 781
Kulíšek, V. 916
Kumar, P. 892
Kumaresh Babu, S.P. 127

L

Laila, D. 563
Lasat, A.S. 1095
Law, J. 191
Leman, Z. 1034, 1147, 1153
Leong, K.C. 67, 257
Liew, C.K. 809
Limouei, S.S. 658
Lukman, H. 1046
Luqman, C.A. 121

M

Mahdi, M.A. 868
Majeed, M.A. 367
Majid, D.L. 530, 536, 1085
Majlan, E.H. 179, 792, 1040, 1046, 1184
Manal, I. 1046
Manikandan, V. 26
Manisekar, K. 26
Mariatti, M. 1118
Mat Jali, N. 1184
Mat, U.W. 518, 786, 898
Meo, M. 904, 910
Merah, N. 415, 490, 496
Mezghani, K. 415
Mirzaei, M. 664
Moazami-Goudarzi, M. 420
Mohamed, N.S. 274, 373, 379
Mohammadi, B. 263, 568, 1016
Mohd Aris, K.D. 1124
Mohd Ishak, Z.A. 320
Mohieldin, S.D. 251
Morka, A. 1136, 1142
Morlin, B. 781
Mosalmani, R. 733
Mousavi, G.S. 1171
Mousavi, S.M. 1005
Mozafari, H. 833
Mozaffari, A. 548
Muchtar, A. 97, 179, 268, 361
Muda, N. 373

Muhamad, N. 97, 179, 268, 361, 409, 558
Muhammed, S. 49, 55, 59
Muniandy, K. 845
Mustapha, F. 37, 133, 140, 530, 536, 563, 1028, 1085, 1124
Mustofa, U. 821
Mutasher, S.A. 191
Muthupandi, V. 325

N

Nabil, H. 622, 628
Nademi, M. 548
Narmashiri, K. 590
Nassirnia, M. 757
Navid, N. 518, 786
Nemati, N. 1165
Ng, G.Y. 449
Niezgoda, T. 1136, 1142
Nugroho, I.H. 981
Nuraini, A.A. 484
Nursherida, J.M. 484

O

Ohadi, A. 658
Okubo, K. 975
Omar, M.F. 385
Othman, A.R. 610, 646, 939
Othman, N. 320, 845, 851
Ousman, H. 552
Ovesy, H.R. 426, 432, 466, 757, 1022
Ozerkan, G. 999

P

Paridah, M.T. 251
Pasharavesh, A. 745
Paton, R. 309, 315
Pervez, T. 285, 1177
Pickering, S.G. 904
Pirayesh, H. 62, 91
Poh, A. 191
Polimeno, U. 904
Prakash, A. 209
Pugazhenthi, G. 209

Q

Qu, X.L. 285

R

Rafie, A.S.M. 1028
Rafighi, A. 1091
Ragunathan, S. 472, 478
Rahman, A.A. 379
Rahman, H.A. 268
Rahman, M.Z.A. 455, 502, 1147, 1153
Rahman, W.A.W.A. 303
Raja, R.S. 26
Rajendran, S. 999
Rameshbabu, N. 325
Ramezani-Oliaee, M. 709
Ramli Sulong, N.H. 590
Raouf, A.H. 1052
Rasch, R. 309
Rashid, R. 115
Rashidi, A.R. 898, 945
Rasib, S.Z.M. 804
Rasid, Z.A. 530, 536
Razaghian, A. 1171
Razak, S.B.A. 775
Razavi, S. 616
Renuganth, V. 37, 530, 536, 1085, 1107
Rezaei, M. 584, 751
Rieder, K.A. 552
Romli, F.I. 1028
Rosli, N.R. 245, 933
Rosli, Z.M. 933
Royan, R.N. 157, 162
Růžička, M. 916

S

Sadighi, M. 658, 664
Sadr-Lahidjani, M.H. 331, 337, 426, 432, 616, 709
Saffian, H.A. 839
Sahari, B.B. 484
Sahari, J. 109, 157, 162, 215, 361, 455, 502
Sahrim , A.H. 115, 151, 640
Salihin Hassin, M. 670
Salim, M.S. 987

Salleh, E.M. 798
Salleh, M.A.M. 652
Salleh, S.Z. 957
Samayamutthirian, P. 670
Sapuan, S.M. 133, 140, 167, 297, 438, 455, 502, 674, 680, 686, 821, 1034, 1058, 1064, 1070, 1113, 1124, 1130, 1147, 1153
Saravanan, M.S.S. 127
Sawal, N. 461
Sayuti, M. 601, 721, 727
Seangatith, S. 578
Seibi, A. 279, 285, 1177
Selamat, M.Z. 361
Senthilvelan, S. 173
Shaaban, A. 245
Shaari, S.M. 851
Shahgaldi, S. 792, 1040, 1184
Shahidan, N.S. 49
Shahrjerdi, A. 133, 140
Shaikh, A.A. 291
Shakeri, A. 85
Shakeri, M. 664
Sharif, J.M. 197
Shaya, M. 518, 786
Shokrieh, M.M. 733
Shooshtari, A. 616
Sim, L.C. 1118
Sim, N.W. 1085
Sirimanna, C.S. 763
Siswosuwarno, M. 981
Sivaprasad, K. 127
Sobhani, M. 85
Sobuz, H.R. 73, 79
Sreenivasan, S. 1101
Stanislawek, S. 1136, 1142
Suada, M.G. 981
Suan, L.M. 67
Subramanian, S. 325
Suherman, H. 162, 215
Sulaiman, M. 379
Sulaiman, S. 233, 601, 721, 727, 769, 1081, 1101
Sulong, A.B. 43, 109, 157, 162, 215, 409, 558
Suppiah, S. 1034
Suraya, S. 601, 721, 727
Syuhada, W.N.W.N. 239

T

Tabarsa, T. 31, 62, 85, 715, 1091
Tahir, P.M. 839
Tahir, S.M. 1130
Talib, R.A. 815
Tan, C.Y. 524
Tang, X.G. 355
Tarfaoui, M. 951
Tawakkal, I.S.M.A. 815
Teo, S.H. 449
Than, A.M. 191
Thumrongvut, J. 578
Towhid, N. 1010
Truss, R. 355

U

Uher, O. 916
Umar, A.H. 239

V

Valizadeh, M. 584
Veidt, M. 309, 315, 809
Venkateswarlu, K. 325
Vijayaram, T.R. 727, 769
Voo, T.V. 1118

W

Wahab, M.S. 922
Wahit, M.U.B. 7, 303, 827, 945
Wan Daud, W.R. 97, 179, 792, 1040, 1046, 1184
Wea, L.C. 257
Wehbi, M.H. 692
Weißgraeber, P. 1075
Wirawan, R. 167

Y

Ya'acob, A.M. 227

Yaakob, Z. 792, 1040, 1046, 1184
Yahya, N.H.N. 409
Yel, H. 572
Yigit, A.S. 367
Yoshi, T. 975
Yunus, R. 167, 652
Yusaf, T.F. 343
Yusof, M.R. 43
Yusof, Y. 397, 403
Yussuf, A.A. 786
Yusuf, M. 233

Z

Zahari, N.H. 652
Zahari, R. 37, 133, 140, 530, 536, 563, 1085
Zaharri, N. 320
Zahurin, H. 403, 563, 928
Zain, S.N.Z.M. 444
Zainal, A.A. 385
Zainuddin, E.S. 513, 674, 680, 686
Zainudin, E.S. 239, 251, 297, 444, 507, 563, 1058, 1113
Zakaria, M.S. 349
Zaman, D.K.M. 121, 227, 821
Zandi, F. 751
Zarebidaki, A. 203
Zawawi, E.Z.E. 115
Zawawi, N.A. 868
Ziaee, M. 880
Zou, J. 355
Zuhailawati, H. 670, 798, 804
Zuraida, A. 397, 403, 781, 928